SELCUK UNIVERSITY
FACULTY OF TECHNOLOGY

ICENTE'17

INTERNATIONAL CONFERENCE ON ENGINEERING TECHNOLOGIES

December 07-09, 2017

Konya/TURKEY

PROCEEDINGS

Editor
Ismail SARITAS

E-ISBN: 978-605-67535-4-1





International Conference on Engineering Technologies

International Conference, ICENTE
Konya, Turkey, December 07-09, 2017

Proceedings

Editor
Ismail SARITAS

International Conference on Engineering Technologies, **ICENTE'17**
Konya, Turkey, December 07-09, 2017



International Conference on Engineering Technologies

International Conference, ICENTE
Konya, Turkey, December 07-09, 2017

Proceedings

Editor
Ismail SARITAS

Bu kitaptaki bilgilerin her türlü sorumluluğu yazarlarına aittir.

E-ISBN: 978-605-67535-4-1

Saday Mühendislik Sertifika No: 35542

www.saday.com.tr

Saday Mühendislik

Kürden Mh. Temizciler Sk. No:5 Meram / KONYA
Tel: 0.332 323 07 39

December – 2017

© Her hakkı saklıdır. Bu kitabın tamamı yada bir kısmı, yazarların izni olmaksızın, elektronik, mekanik, fotokopi yada herhangibir kayıt sistemi ile çoğaltılamaz, yayınlanamaz, depolanamaz.

EDITOR :

Ismail SARITAS
Selcuk University, Turkey
Depertmant of Electrical and Electronics Engineering, Faculty of Technology
Alaeddin Keykubat Campus 42031 Konya, Turkey
isaritas@selcuk.edu.tr

ASSISTANT EDITORS :

Ilker Ali OZKAN
Selcuk University, Turkey
Depertmant of Computer Engineering, Faculty of Technology
Alaeddin Keykubat Campus 42031 Konya, Turkey
ilkerozkan@selcuk.edu.tr

Murat KOKLU
Selcuk University, Turkey
Depertmant of Computer Engineering, Faculty of Technology
Alaeddin Keykubat Campus 42031 Konya, Turkey
mkoklu@selcuk.edu.tr

PREFACE

International Conference on Engineering Technologies (ICENTE'17) has been organized in Konya, Turkey on 07-09 December, 2017.

The main objective of ICENTE'17 is to present the latest research and results of scientists related to Electrical and Electronics, Biomedical, Computer, Mechanical, Mechatronics, Metallurgical and Materials Engineerings. This conference provides opportunities for the different areas delegates to exchange new ideas and application experiences face to face, to establish business or research relations and to find global partners for future collaboration.

All full paper submissions have been double blind and peer reviewed and evaluated based on originality, technical and/or research content/depth, correctness, relevance to conference, contributions, and readability. Selected papers presented in the conference that match with the topics of the journals will be published in the Journal of Selcuk Technic,

At this conference, there are 617 paper submissions from 10 different countries and 94 universities. Each paper proposal was evaluated by two reviewers. And finally, 363 papers will be presented at our conference.

In particular we would like to thank Prof. Dr. Mustafa SAHIN, Rector of Selcuk University; Prof.Dr. Omer Faruk BAY, Gazi University; Assist. Prof. Dr. Lilia GEORGIEVA, Heriot-Watt University; Journal of Selcuk Technic. They have made a crucial contribution towards the success of this conference. Our thanks also go to the section editors and colleagues in our conference office.

Ismail SARITAS
Editor

PROGRAMME COMMITTEES

HONORARY CHAIR :

Mustafa Sahin, Rector of Selcuk University, Turkey

CHAIR :

Ismail Saritas, Selcuk University, Turkey

CO-CHAIR :

Necmettin Tarakcioglu, Selcuk University - Turkey
Mehmet Cunkas, Selcuk University - Turkey
Fatih Basciftci, Selcuk University - Turkey
Haci Saglam, Selcuk University - Turkey
Alla Anohina Naumeca, Riga Technical University – Latvia

PUBLICATION CHAIR :

Ilker Ali Ozkan, Selcuk University, Turkey
Murat Koklu, Selcuk University, Turkey

INTERNATIONAL ADVISORY BOARD

Gabriel Luna Sandoval, Mexico
Silyan Sibinov Arsov, Bulgaria
Alexander Sudnitson, Estonia
Alla Anohina Naumeca, Latvia
Almoataz Youssef Abdelaziz, Egypt
Amar Ramdane Cherif, France
Anca Loana Andreescu, Bulgaria
Anne Villems, Estonia
Antonella Reitano, Italy
Antonio Mendes, Portugal
Artan Luma, Makedonia
Asrun Matthiasdottir, Israel
Biagio Lenzitti, Italy
Binod Kumar, India
Boris Akanaev, Kazakhstan
DimiTurkeyis Dranidis, Greece
Domenico Tegolo, Italy
Eisha Akanksha, India
Elinda Kajo Mece, Romania
Heinz DieTurkeyich Wuttke, Germany
Howard Duncan, Ireland
Huse Fatkic, Bosnia and Herzegovina
Ivan Jelinek, Czech Republic
Jan Vom Brocke, Liechtenstein
Janis Grundspenkis, Latvia
Janusz Jablonowski, Poland
Jiri Srba, Denmark
Karl Jones, United Kingdom
Laurentiu Cristian Deaconu, Romania
Luca Lombardi, Italy
Majida Ali Abed Meshari, Iraq
Mahdi Shahbakhti, United States
Marco Porta, Italy
Mirjana Ivanovic, Serbia
Muhammad Zia Ur Rehman, Pakistan
Natasa Hoic Bozic, Croatia
Thomas Engel, Luxembourg
Pantha Ghosal, Australia
Pino Caballero Gil, Spain
Stavros Christodoulakis, Greece
Stavros Nikolopoulos, Greece

Tatjana Dulinskiene, Lithuania
Virginio Cantoni, Italy
Yuri Pavlov, Bulgaria
Zarifa Jabrayilova, Azerbaijan
Adem Alpaslan Altun, Turkey
Saadetdin Herdem, Turkey
Ibrahim Uyanik, Turkey
Mehmet Turan Demirci, Turkey
Novruz Allahverdi, Turkey
Erdal Bekiroglu, Turkey
Ahmet Fenercioglu, Turkey
Ahmet Afsin Kulaksiz, Turkey
Temel Kayikcioglu, Turkey
Muciz Ozcan, Turkey
Mumtaz Mutluer, Turkey
Hakan Isik, Turkey
Hulusi Karaca, Turkey
Hayri Arabaci, Turkey
Erdinc Kocer, Turkey
Mehmet Akif Sahman, Turkey
Tugce Demirdelen, Turkey
Engin Ozdemir, Turkey
M Ugras Cuma, Turkey
Bahattin Karakaya, Turkey
Mehmet Akbaba, Turkey
Miroslav Neslusan, Slovakia
Hamza Bensouilah, Algeria
Jaharah A Ghani, Malaysia
Ulvi Seker, Turkey
Ihsan Korkut, Turkey
Hamit Saruhan, Turkey
Nihat Yildirim, Turkey
Ertugrul Durak, Turkey
Hasan Gokkaya, Turkey
Nikolaos Blasis, Greece
Mehmet Cengiz Kayacan, Turkey
Erol Turkes, Turkey
Arif Gok, Turkey
Spiridon Cretu, Romania
Kadir Gok, Turkey
Tahir Sag, Turkey
Aristomenis Antoniadis, Greece
Murat Koklu, Turkey
Humar Kahramanli, Turkey
Alina Ivan Dramogir, Romania
Sakir Tasdemir, Turkey
Ilker Ali Ozkan, Turkey
Shahabuddin Memon, Pakistan
Hakan Gokmese, Turkey

ORGANIZING COMMITTEE

Alla Anohina Naumeca, Latvia
Silyan Sibinov Arsov, Bulgaria
Angel Smrikarov, Bulgaria
Lilia Georgieva, United Kingdom
Ismail Saritas, Turkey
Necmettin Tarakcioglu, Turkey
Haci Saglam, Turkey
Fatih Basciftci, Turkey
Mehmet Cunkas, Turkey
Hayri Arabaci, Turkey
Polyxeni Arapi, Greece
Saadetdin Herdem, Turkey

TECHNICAL COMMITTEE

Ilker Ali Ozkan, Turkey
Esra Kaya, Turkey
Eyub Canli, Turkey
Harun Sepet, Turkey
Burak Tezcan, Turkey

CONTENTS

EMPIRICAL MODE DECOMPOSITION BASED FEATURE EXTRACTION FOR INTELLIGENT EMOTION RECOGNITION 1
AHMET MERT, FATIH ONAY, AYDIN AKAN

THE IMPORTANCE OF MEDICAL IMAGING AND OVERVIEW OF USING 3D PRINTER 5
HAKAN BURCIN ERDOGUS

ANALYSİS OF CALCİUM AND PHOSPHORUS İN HUMAN BONE USİNG SCANNİNG ELECTRON MİCROSCOPY WİTH ENERGY DİSPERSİVE X-RAY SPECTROSCOPY (SEM-EDX) 9
TUBA CAYIR, YUNUS AKALTUN, OZCAN GUNDOGDU

XRF CHARACTERIZATION OF DISEASED HUMAN BONE SPECIMENS 13
TUBA CAYIR, YUNUS AKALTUN, OZCAN GUNDOGDU

PREPARATION OF PATTERNED SCAFFOLD FOR TISSUE ENGINEERING APPLICATION 18
AYSE ZEHRA AROGUZ, HIDAYET SARIOGULLARI

FOR PATIENT WITH END STAGE AMYOTROPHIC LATERAL SCLEROSIS ALS PATIENTS INTELLIGENT BED CONTROL DUE TO SIMULTANEOUS PATIENT EYE MOVEMENT 21
AZIZ KAGITCI, ISMAIL SARITAS

BIOREFINERY CONCEPT CURRENT STATUS AND FUTURE PROSPECTS 27
MELIH SONER CELIKTAS, MERVE UYAN, FIKRET MUGE ALPTEKIN

WATER TREATMENT WITH THE USE OF REDUCED GRAPHENE OXIDE FILTRATION 33
OZGE BILDI CERAN, INCI SEVGILI, BARIS SIMSEK, OSMAN NURI SARA

A COPING WITH BREAST CANCER DIAGNOSIS USING A NORMALIZED TEXTURE FEATURE SET 38
IDIL ISIKLI ESENER, SEMIH ERGIN, TOLGA YUKSEL

A PRACTICAL REGION OF INTEREST ROI DETECTION APPROACH FOR SUSPICIOUS REGION IDENTIFICATION IN BREAST CANCER DIAGNOSIS 44
IDIL ISIKLI ESENER, SEMIH ERGIN, TOLGA YUKSEL

CLASSIFICATION OF TEXT FILES WITH DIFFERENT SUBJECTS USING NAIVE BAYES METHOD 48
KUBRA UYAR, ERKAN ULKER

DETECTION OF MISSING PILLS ON TABLET USING IMAGE PROCESSING METHODS 51
KUBRA UYAR, ERKAN ULKER

THE COMPUTERIZED SEMANTIC ANALYSIS STUDY WITH REALITY MODELS CREATED VIA SUMO ONTOLOGY 55
YELDA FIRAT

ACCESSING TO INFORMATION VIA BLUETOOTH LOW ENERGY BEACONS **61**
BURAK KAAN OZBEK, SERAP TEPE, A HALIM ZAIM

SPECTRUM CALCULATION OF MASSIVE STAR FORMATION REGION BY GPU PROGRAMMING **64**
YASEMIN POYRAZ KOCAK, SELCUK SEVGEN, PETER SCHILKE, THOMAS MOELLER

A NEW TRUST BASED ALGORITHM FOR A SECURE AND RESILIENT CLUSTER HEADS **67**
MOHAMED AICHE, NOUREDDINE IDBOUFKER, LAILA SAKKILA, MOHAMMED BOUSMAH, ATIKA RIVENQ, ABDELGHAFOUR BERRAISOUL

DEFINING A PROCESS TO IMPROVE CODE REVIEW EFFICIENCY IN SOFTWARE DEVELOPMENT **74**
MUSTAFA ERSAHIN

LITERATURE REVIEW AND RESEARCH MODEL PROPOSAL FOR PREDICTING WATER POLLUTION AND FLOODING IN TIGRIS AND EUPHRATES RIVERS **79**
THAER IBRAHIM, IBRAHIM AKMAN, ATILA BOSTAN

OBJECTS UNDER VARYING ILLUMINATION CONDITIONS ANALYZE HISTOGRAM STATISTICAL AND COLOR SPACES INFORMATION WITH IMAGE PROCESSING TECHNIQUES **83**
BIRKAN BUYUKARIKAN, ISMAIL SERKAN UNCU

AN APPLICATION TO INTRUSION PREVENTION IN WIRELESS NETWORKS **87**
MUNTASSER HAMZAH, CELAL OZTURK

BUSİNESS PERFORMANCE TRACKİNG SYSTEM DESİGN **92**
GIZEM YILMAZ CELIK, HUMAR KAHRAMANLI

DESIGNING A LOW COST ARM BASED MICRO COMPUTER CLUSTER FOR BIG DATA ANALYSIS **97**
TURGAY TUGAY BILGIN, RECEP ALI YILMAZ, SENOL ZAFER ERDOGAN

THE DESIGNING OF MACHINE VISION SYSTEM BASED ON IMAGE PROCESSING WHICH IS FOR GEOMETRIC SHAPED EXTRUSION PROFILES INCLUDING DIFFERENT INNER CELLS **102**
MURAT AKDOGAN, SULEYMAN YALDIZ

WORD2VEC BASED SENTIMENT ANALYSIS FOR TURKISH TEXTS **106**
METIN BILGIN, HALDUN KOKTAS

SECURITY OF WEB APPLICATIONS **109**
HAKAN BILGIN, MUSTAFA ERSAHIN

SECURITY ANALYSIS OF RPL FOR IOT **114**
OUSSAMA MOUNNAN, NOUREDDINE IDBOUFKER

THE ENHANCEMENT OF CANNY EDGE DETECTION ALGORITHM USING PREWITT ROBERT AND SOBEL KERNELS **120**
SUMEYYA ILKIN, SELIN HANGISI, MERVE TAFRALI, SUHAP SAHIN

WOUND EDGE DETECTION OPERATION USING ENHANCED CANNY EDGE DETECTION ALGORITHM ON DERMATOLOGICAL IMAGES **125**
SUMEYYA ILKIN, MERVE TAFRALI, SELIN HANGISI, SUHAP SAHIN

A NOVEL EVALUATION APPROACH FOR THE SYSTEMS TRANSFORMING SOFTWARE REQUIREMENTS TO OBJECT ORIENTED SOURCE CODE **129**
FATMA BOZYIGIT, OZLEM AKTAS, DENIZ KILINC

IMPLEMENTATION OF VIRTUAL REALITY ENHANCED CONTINUOUS PERFORMANCE TEST DESIGNED FOR ATTENTION DEFICIT HYPERACTIVITY DISORDER DIAGNOSIS **135**
MUSTAFA CEM KASAPBASI, CAN EYUPOGLU, TUNA BARAN URUT, YUSUF TURAN, ALPER OSMAN KARAAGACLI, YUSUF CAN SEZGENC

ORDER BASED EMIGRANT CREATION STRATEGY FOR PARALLEL ARTIFICIAL BEE COLONY ALGORITHM **139**
ALPEREN AKSOY, SELCUK ASLAN, DERVIS KARABOGA

RISK MANAGEMENT IN STARTUPS HOW USING LEAN PRINCIPLES HELPS STARTUPS MANAGE THEIR RISKS MORE EFFICIENTLY **146**
CEREN CUBUKCU, SEVINC GULSECEN, SEDA TOLUN TAYALI

MOTIVATIONS TO DEVELOP AN INFORMATION SYSTEM FOR PEOPLE WITH DOWN SYNDROME **151**
HAITHAM AL TAMEEMI, TURAN ERMAN ERKAN

PREDICT PUBLIC OPINION IN ONLINE REVIEWS WITH IMBALANCE DATASET AND FEATURE NUMBER **155**
MAHMOUD MURAD, MURAT EKINCI

CLASSIFICATION OF DIABETES DATASET WITH ANN TRAINED BY VORTEX SEARCH **161**
ZAINAB ABDULLAH JALIL, TAHIR SAG

ARTIFICIAL ALGAE ALGORITHM ON TRAINING ARTIFICIAL NEURAL NETWORKS **165**
BAHAEDDIN TURKOGLU, ERSIN KAYA

ANALYSIS AND SEGMENTATION OF ANNOUNCEMENTS IN THE TURKISH UNIVERSITIES **170**
GIZEM ORTAC, TURGAY TUGAY BILGIN

FACE RECOGNITION USING EIGENFACE VS FISHERFACES **176**
M AKCAY, NACIYE NUR SARIBEY

AN ANALYSIS OF MOBILE METHODS ON WEB BASED AUTHENTICATION **180**
SULTAN ZAVRAK, SEYHMUS YILMAZ, HUSEYIN BODUR, FATIH KAYAALP

SOLVE COMPLEX PROBLEMS USING ARTIFICIAL NEURAL NETWORK LEARNED BY PSO **184**
SAEED MAHMOOD, GULAY TEZEL

THE DEVELOPMENT OF PENETRATION TEST LAB FOR THE WEB APPLICATION SECURITY TRAINING **189**
AHMET GUREL, FURKAN ERTAS, ECIR UGUR KUCUKSILLE, MEHMET ALI YALCINKAYA

OSAS EVALUATION BY MEANS OF MACHINE LEARNING AND ARTIFICIAL NEURAL NETWORKS BY USING POLISOMNOGRAPHIC REPORT DATA **195**
BEYZA NUR AKILOTU, SEDA ARSLAN TUNCER

EVALUATION OF THE EFFECT OF CPAP DEVICE ON REM SLEEP IN OSAS PATIENTS USING ANN AND SVM **198**
BEYZA NUR AKILOTU, SEDA ARSLAN TUNCER

ESTIMATION OF LAKE VAN MONTHLY AVERAGE WATER LEVEL CHANGE BY USING ARTIFICIAL INTELLIGENCE METHODS **201**
CIHANGIR KOYCEGIZ, MERAL BUYUKYILDIZ

APPLICATION OF ARTIFICIAL NEURAL NETWORKS ON BUILDING ENERGY ESTIMATION **206**
MURAT ALTUN, AHMET BAHADDIN ERSOZ, TURKER TEKE, TOLGA KURT, ASLI AKCAMETE GUNGOR, ONUR PEKCAN

DEVELOPMENT OF BLOOD DONATION APPLICATION FOR MOBILE DEVICES WITH ANDROID OPERATING SYSTEM **210**
ERKAN YESIL, CEMIL SUNGUR

A FEATURE BASED COMPARISON OF SDN EMULATION AND SIMULATION TOOLS **214**
SULTAN ZAVRAK, MURAT ISKEFIYELI

HUMAN ACTIVITY RECOGNITION ON SMARTPHONES USING A MULTICLASS ARTIFICIAL NEURAL NETWORK **218**
ALI YASAR, ISMAIL SARITAS

PERFORMANCE COMPARISON OF DIFFERENT SIZED REGIONS OF INTEREST ON FISH CLASSIFICATION **222**
BILAL ISCIMEN, YAKUP KUTLU, CEMAL TURAN

A TEXT CLASSIFICATION APPLICATION POET DETECTION FROM POETRY **228**
DURMUS OZKAN SAHIN, OGUZ EMRE KURAL, ERDAL KILIC, ARMAGAN KARABINA

CLASSIFICATION OF PHISHING DETECTION DATA ON WEB SITES WITH BAYESIAN REGULARIZED ARTIFICIAL NEURAL NETWORKS **231**
ALI YASAR, ISMAIL SARITAS

THE PERFORMANCE ANALYSIS OF OPTICAL BURST SWITCHING BY RANDOM FOREST ALGORITHM **235**
SEVDANUR GENC, DUYGU BAGCI, GIZEM ORTAC, OGUZHAN DAS

A NEW APPROACH TO SWARM INTELLIGENCE SALP SWARM OPTIMIZATION ALGORITHM WITH UNCONSTRAINED PROBLEMS **238**
CEM BAYDOGAN

ESTIMATION OF UNBALANCE COST DUE TO DEMAND PREDICTION ERRORS USING ARTIFICIAL NEURAL NETWORK **242**
ABDULLAH ERDAL TUMER, CANKAT YAVUZ, SABRI KOCER

AUGMENTED REALITY APPLICATION IN LEARNING GEOMETRIC SHAPES **246**
FATIH BASCIFTCI, BETUL YILMAZ, BUSE GOK, SEMA TUFAN

APPLICATION OF OPT AINET ALGORITHM TO SPECTRAL FEATURES FOR FEATURE SELECTION **249**
SEMIYE DEMIRCAN, HUMAR KAHRAMANLI

RISK MANAGEMENT IN IT PROJECT **253**
ADEM ALPASLAN ALTUN, ANAR TAGHIYEV

CRITICAL NODE DETECTION IN WSN BASED ON ENERGY CONSUMPTION **259**
SYED MOHSIN ALI SHAH, FAHIM AZIZ UMRANI, SHANZAH MOHSIN, ABDUL WAHEED UMRANI

COMPARISON OF 3D AND 2D MAGNETOSTATIC ANALYSIS OF 6 4 POLE SRM **263**
CIHAN SAHIN, MEVLUT KARACOR

CASCADED H BRIDGES FOR HARMONIC CURRENT COMPENSATION IN ACTIVE POWER FILTER **268**
HAMED SOODI, AHMET METE VURAL

STATOR FAUT DETECTION FOR THE INPUT OUPUT CONTROL OF THE PERMANENT MAGNET SYNCHRONOUS MOTOR **277**
MAANANI YACINE, MENACER AREZKI, HARZELLI IMADEDDINE, ZOUZOU SARRA

COMPARISON OF WIND POWER INTEGRATION GRID CODES OF VARIOUS COUNTRIES **283**
KUBRA NUR AKPINAR, MUAMMER OZDEMIR

AN INTEGER PROGRAMMING MODEL FOR AN ENERGY OPTIMAL TRAIN OPERATION **288**
KEMAL KESKIN, ABDURRAHMAN KARAMANCIOGLU

COMPARISON OF DIFFERENT CLASSIFICATION METHODS USING AUTOREGRESSIVE ESTIMATION FOR CERVICAL MUSCLES BASED SEMG SIGNALS **292**
GUZIN OZMEN, AHMET HAKAN AKMEKCI, BURAK YILMAZ

COMPARATIVE PERFORMANCE ANALYSIS OF PV TECHNOLOGIES IN EASTERN PROVINCE OF ZAMBIA **296**
MABVUTO MWANZA, KIVANC BASARAN, NUMAN SABIT CETIN, KORAY ULGEN

ESTABLISHMENT OF AN FPGA BASED REAL TIME IM EXPERIMENTAL SETUP **304**
REMZI INAN, MURAT BARUT

COMPARATIVE STUDY BETWEEN SENSORLESS VECTOR CONTROL AND NONLINEAR CONTROL FOR PMSM BASED ON EXTENDED KALMAN FILTER EKF **309**
MAANANI YACINE, MENACER AREZKI, HARZELLI IMADEDDINE

DEVELOPMENT OF WEARABLE PEDOMETER BY USING 3 AXIS MEMS ACCELEROMETER **315**
OMAR MUTHANNA KHUDHUR, ERGUN ERCELEBI

MRAS SPEED OBSERVER FOR SENSORLESS ADAPTIVE INTELLIGENT BACKSTEPPING CONTROLLER OF INDUCTION MACHINES **320**
SALIM ISSAOUNI, ABDESSELEM BOULKROUNE, HACHEMI CHEKIREB

DESIGN AND IMPLEMENTATION OF INTELLIGENT LI ION BATTERY CHARGER **326**
ABDULRAHMAN MAHMOOD FAIHAN, ERGUN ERCELEBI

NEW HYBRID MOTOR DESIGN BASED ON MCSRM **331**
MEVLUT KARACOR, CIHAN SAHIN

SMARTPHONE CONTROLLED ULTRASONIC NONDESTRUCTIVE TESTING SYSTEM DESIGN **335**
SAMET GUL, AHMET TURAN OZDEMIR

MICROWAVE ABSORBER DESIGN IN LAYERED STRUCTURE USING DIFFERENTIAL EVOLUTIONARY ALGORITHM **339**
SIBEL YENIKAYA, GOKHAN YENIKAYA, AHMET COSKUN, MESUT TOZAN

ON FRACTIONAL ORDER PI CONTROLLER AN ANALYSIS ON INTEGER ORDER SYSTEMS WITH INTEGRAL PERFORMANCE CRITERIA **344**
ERDAL COKMEZ, IBRAHIM KAYA

DESIGN OF FLOATING POINT PI CURRENT CONTROLLER FOR SPEED CONTROL OF IPMSM USING FPGA **349**
ABDULHASAN ALTAEY, AHMET AFSIN KULAKSIZ

OPERATION STRATEGY FOR SINGLE PHASE TO THREE PHASE MATRIX CONVERTER **356**
SECIL GENC, GUVEN ONBILGIN

SWITCHED H2 STATE FEEDBACK CONTROL FOR POLYTOPIC SYSTEMS BASED ON DWELL TIME **361**
EMRE KEMER, EMMANUEL PREMPAIN

THE EFFECTS ON MODEL PERFORMANCE OF VALIDATION METHODS FOR WIND SPEED PREDICTION **366**
SECKIN KARASU, AYTAC ALTAN, ZEHRA SARAC, RIFAT HACIOGLU

OPTIMAL SENSING TIME FOR SENSING BASED DYNAMIC SPECTRUM SHARING SCHEME IN COGNITIVE RADIO **371**
SAVAS SAHIN, DAMLA KUNTALP

AN OVERVIEW OF ELECTROMAGNETIC METHODS FOR BREAST CANCER DETECTION AND A NOVEL ANTENNA DESIGN FOR MICROWAVE IMAGING **377**
ALI RECAI CELIK, MUHAMMED BAHADDIN KURT, SELCUK HELHEL

BANDWIDTH ENHANCEMENT OF SMALL L SHAPED UWB MONOPOLE ANTENNA WITH A MODIFIED GROUND PLANE **384**
ALI RECAI CELIK, MUHAMMED BAHADDIN KURT, SELCUK HELHEL

BEHAVIORAL MODELING OF A MEMS ACCELEROMETER USING MATLAB SIMULINK **388**
MEHMET DEMIRTAS, MEHMET AKIF ERISMIS, SALIH GUNES

CHALLENGES AND SOLUTIONS FOR IOT APPLICATIONS IN THE IRON AND STEEL INDUSTRY **391**
ARIF TUNUZ, MUSTAFA KARA, MURAT FURAT

REVIEW ON USING FPGA IN SENSORLESS SPEED CONTROL OF PMSM **397**
ABDULHASAN ALTAEY, AHMET AFSIN KULAKSIZ, HUSEYIN DOGAN

DESIGN AND PERFORMANCE ANALYSIS OF A WIRELESS SHORT PACKET PROTOCOL BASED MULTI HOP NETWORK FOR DATA COMMUNICATION IN ELEVATOR SYSTEMS **403**
MUHAMMED MAJED LAJENE, SAIT ESER KARLIK

HIGH EFFICIENCY DESIGN AND SIMULATION OF A FRONT END AC DC PFC CONVERTER FOR EV BATTERY CHARGER **408**
SEVILAY CETIN, NAZIM YILDIZ

THE EFFECT OF THE NUMBER OF BLADES ON ELECTRICAL ENERGY PRODUCTION SYSTEM BY USING A VERTICAL BARREL FROM WIND ENERGY **413**
RABIA GULER YILDIRIM, AHMED ABDALAZIZ

DISTRIBUTED LMP ALGORITHM FOR FREQUENCY ESTIMATION OVER A NETWORK **419**
HADI ZAYYANI, ALI SHADEMANFAR

HIGH GAIN OBSERVER FOR SENSORLESS INPUT OUTPUT LINEARIZING CONTROL FOR INDUCTION MOTOR WITH BROKEN ROTOR BAR FAULT **424**
HARZELLI IMADEDDINE, MENACER AREZKI, MAANANI YACINE, AMEID TAREK

A DEEP LEARNING APPLICATION HANDWRITING CLASSIFICATION **430**
KURSAD UCAR, HASAN ERDINC KOCER

SHORT TERM LOAD FORECASTING FOR MICROGRIDS BASED ON FUZZY LOGIC **434**
JISTO TAPIWA MUTSENA, MUSTAFA BAYSAL

WEARABLE SAFETY KIT **440**
ENGIN GULGOR, IBRAHIM SAMURLU, ERSIN BERBEROGLU, KALENDER DIRIK, GOKHAN SEREF TOKMAK, ABDULSAMET CAKMAK, AHMET TURAN OZDEMIR

DETERMINATION OF FAULTS IN HVDC NETWORKS **444**
FATIH UNAL, SAMI EKICI

CELLULAR ROBOTIC AUTOMATION FOR BASE CHASSIS WELDING **452**
IBRAHIM SAMURLU, AHMET TURAN OZDEMIR

DETERMINATION OF ELECTROMAGNETIC FIELD VALUES FOR BREAST TUMOR DETECTION WITH THE DESIGNED VIVALDI ANTENNA **456**
BEYZA NEYISCI, RABIA TOP, SEYFETTIN SINAN GULTEKIN, DILEK UZER

ELLIPTIC MICROSTRIP ANTENNA DESIGN ON WOOLEN FELT MATERIAL FOR DETECTION OF CARDIO-VESSEL OCCLUSION **460**
OZEN BAYRAKTAR, RABIA TOP, DILEK UZER, SEYFETTIN SINAN GULTEKIN

DETERMINATION OF ELECTROMAGNETIC FIELD VALUES BY DESIGNING CIRCULAR MICROSTRIP ANTENNA FOR DETERMINATION OF CARDIAC OCCLUSION **464**
RABIA TOP, SEYFETTIN SINAN GULTEKIN, DILEK UZER

ANALYSIS OF ENHANCED EXPONENTIAL REACHING LAW CONTROL SYSTEM PARAMETERS FOR MAGNETIC LEVITATION SYSTEM **468**
DINCER MADEN, IRFAN YAZICI

WIND POWER FORECASTING USING FUZZY MODEL **473**
HASAN HUSEYIN CEVIK, MEHMET CUNKAS

DEVELOPMENT OF DIGITAL MEDICAL WEIGHT SCALE USING 32 BIT ARM BASED MICRO CONTROLLER **477**
NOOR HUSSIEN JUMAAH, ERGUN ERCELEBI

TUMOR TYPE DETECTION USING NAIVE BAYES ALGORITHM ON GENE EXPRESSION CANCER RNA SEQ DATA SET **482**
FAHRIYE GEMCI FURAT, TURGAY IBRIKCI

PERFORMANCE EVALUATION OF DIFFERENT UPLINK RESOURCE ALLOCATION ALGORITHMS IN LTE NETWORKS **487**
HAVVA ESRA BILISIK, RADOSVETA SOKULLU

SENSORLESS ROTOR SPEED OBTAINED BY USING SPEED OF ROTOR FLUX SPACE VECTORS AND SLIP SPEED **493**
YAVUZ USER

HARDWARE IN THE LOOP SIMULATION OF A NOVEL NONLINEAR PI CONTROLLER ON FPGA **496**
SIRIN AKKAYA, HANDAN NAK, ALI FUAT ERGENC

NETWORK REDUCTION METHODS ON DG PLANNING STUDIES **501**
KADIR DOGANSAHIN, BEDRI KEKEZOGLU, ALI AJDER, RECEP YUMURTACI

DETERMINATION OF TRAFFIC INTENSITY WITH OPTIMUM DETECTION OF VEHICLE COUNT USING VIRTUAL ZONE **506**
SEYITALI ILYAS, YAVUZ USER

IMPROVING POWER FACTOR WITH IMPLEMENTATION OF PFC BOOST CIRCUIT DESIGN **510**
MUHSIN FATIH SEKER, YAVUZ USER

DESIGN AND APPLICATION OF FPGA BASED MODBUS GATEWAY MODULE **514**
SIRIN AKKAYA, ONUR AKBATI, ALI FUAT ERGENC

STOCKWELL TRANSFORM AND ITS PERFORMANCE COMPARISON ON THE STAGE OF FAULT ESTIMATION IN HIGH VOLTAGE DIRECT CURRENT TRANSMISSION LINES **520**
FATIH UNAL, SAMI EKICI

AUTOMATIC CAPACITOR SWITCHING FOR SELF EXCITED INDUCTION GENERATOR USING NON LINEAR REGRESSION FOR WIND POWER APPLICATION **526**
ERSIN SELCUK, HAYRI ARABACI

MODELING AND TECHNO ECONOMIC ANALYSIS OF BUILDING INTEGRATED PHOTOVOLTAIC BIPV SYSTEMS IN CENTRAL ANATOLIA REGION **530**
GUL NIHAL GUGUL

PHOTOVOLTAIC POWERED EXTERIOR LED LIGHTING SYSTEM WITH WIRELESS COMMUNICATION **536**
MURAT SEZER, SALIH GUNES

INCREASING THERMAL TRANSFER PRINTER HEAD VIA CONTROLLING HISTORY DATA RELATED TO SPEED AND TEMPERATURE **538**
AHMET YAGBASAN, SALIH GUNES

CLASSIFICATION FOR DIFFERENT DATABASES USING ARTIFICIAL NEURAL NETWORK WITH 10 FOLD CROSS VALIDATION **541**
ESRA KAYA, ISMAIL SARITAS

A STUDY ON THE USAGE OF TOBACCO WASTE ASH AS A MINERAL ADMIXTURE IN CONCRETE TECHNOLOGY **545**
SERHAT CELIKTEN, MEHMET CANBAZ

UTILIZATION OF CHROME ORE CONCENTRATION PLANT TAILINGS AS FINE AGGREGATE IN READY MIXED CONCRETE **549**
SERHAT CELIKTEN, MEHMET CANBAZ

INVESTIGATION OF THE SOUND ABSORPTION PROPERTIES OF WASTE COTTON LICHEN NONWOVEN MATERIALS **553**
SEYDA EYUPOGLU, NIGAR MERDAN, EMINE DILARA KOCAK, HABIP DAYIOGLU

PAVEMENTS COVERED FOR HEAT ISOLATION TO GET PEDESTRIAN THERMAL COMFORT **555**
MEHMET KEMAL GOKAY, KEMAL DOGAN, CIHAN YASAR

EFFECTS OF THE STONE POWDER ON SOME MECHANICAL PROPERTIES OF CLAYEY SOIL **560**
MAIS IBRAHIM

THE EFFECT OF BORON DOPING MOLARITY ON STRUCTURAL OPTICAL ELECTRICAL AND THERMOLUMINECCENCE PROPERTIES OF INDIUM OXIDE FILMS GROWTH BY SPRAY PROLYSIS TECHNIQUE **566**
MEHMET TEMIZ, RABIA GULER YILDIRIM, METIN BEDIR

VOLATILE ORGANIC COMPOUND REMOVAL USING POLYURETHANE BASED SELECTIVE MEMBRANE **572**
FILIZ UGUR NIGIZ, NILUFER HILMIOGLU

DEVELOPMENT OF EFFICIENT GREEN CATALYST CATALYTIC MEMBRANE FOR THE ESTERIFICATION OF ACETIC ACID WITH GLYCEROL **577**
DERYA UNLU, NILUFER HILMIOGLU

FABRICATING ORGANIC COMPOUND PELLETS IN THE FORM OF SYNTHETIC COAL **580**
MEHMET KEMAL GOKAY, ALI ARAS, KEMAL DOGAN

ACTIVATED CARBON PRODUCTION FROM PEAT **584**
HALE SUTCU

FIBER PRODUCTION FROM AGRICULTURAL OKRA WASTES AND COMPARATIVE INVESTIGATION OF SURFACE MODIFICATIONS APPLIED ON OKRA FIBERS IN DIFFERENT METHODS **587**
BUSRA ARDIC, E DILARA KOCAK, NIGAR MERDAN, ILKER MISTIK

INVESTIGATION OF MECHANICAL PROPERTIES OF PLATANUS ORIENTALIS POLYETHYLENE TEREPHTHALATE NONWOVEN COMPOSITE MATERIALS **594**
SIBEL KIZILKAYA, BURCU YILMAZ SAHINBASKAN, ILKER MISTIK, AYBEN ADALET IZGI

INVESTIGATION OF SOUND ABSORPTION PROPERTIES OF OKRA NONWOVEN MATERIALS **598**
EMINE DILARA KOCAK, ADALET AYBEN IZGI, BURCU YILMAZ SAHINBASKAN, ILKER MISTIK, BUSRA ARDIC

STUDIES ON MECHANICAL PERFORMANCE OF CYNARA SCOLYMUS PET NONWOVEN COMPOSITES **602**
ADALET AYBEN IZGI, BURCU YILMAZ SAHINBASKAN, EMINE DILARA KOCAK, NIGAR MERDAN, BUSRA ARDIC

OBSERVATION OF EFFECT OF TI ON PROPERTIES OF A356 ALLOY UNDER DIFFERENT HOLDING TIMES **606**
MUHAMMET ULUDAG, MIKDAT GURTARAN, DERYA DISPINAR

EXPERIMENTAL STUDY OF A BLAST FURNACE SLAG STABILIZED SOIL REINFORCED WITH NATURAL FIBERS **609**
MUSTAPHA HIDJEB, IHCENE LAMRI

SHEAR STRENGTH OF A CEMENTED SOIL REINFORCED WITH SYNTHETIC FIBERS **614**
IHCENE LAMRI, M HIDJEB

INVESTIGATION OF DUCTILITY OF POLYPROPLENE FIBRE REINFORCED CONCRETE BEAMS **618**
NILDEM TAYSI, AHMED N ABDALAH, AHMMAD A ABBASS

THE BURST FAILURE BEHAVIORS OF SIO2 NANOPARTICLE FILLED ELLIPTICAL SURFACE CRACKED 55 6 FILAMENT WOUND BFREPOXY COMPOSITE PIPES **622**
MEHMET TURAN DEMIRCI, NECMETTIN TARAKCIOGLU, AHMET AVCI

THE FEASIBILITY OF USING WOOD PLASTIC COMPOSITES IN COMPOSITE I JOIST MANUFACTURE **626**
SAADETTIN MURAT ONAT, FAHRETTIN YILMAZ, ABDULLAH ISTEK

THE FATIGUE FAILURES OF 55 6 FILAMENT WOUND BFR EPOXY COMPOSITE PIPES **631**
MEHMET TURAN DEMIRCI, NECMETTIN TARAKCIOGLU

INVESTIGATION OF THE EFFECT OF TIN SN ON MICROSTRUCTURE AND HARDNESS PROPERTIES OF GRAY CAST IRON **634**
RECAI KUS, BEKIR AKGUL

SMAZZLE A DEMONSTRATIVE CASE STUDY FOR MODULAR DESIGN OF MECHATRONIC PRODUCTS **638**
ZUHAL ERDEN

DESIGN AND SIMULATION OF A SINGLE SPHERICAL WHEEL ROBOT **644**
IBRAHIM SAT, HUSEYIN OKTAY ERKOL

REAL TIME REMOTE CONTROL OF ROBOTIC HAND SYSTEM **648**
MUSA SADIK UNAL, ERSIN ERTURK, MUSTAFA CEM KASAPBASI, ERDEM YAVUZ, UFUK SANVER

EFFECT OF UNDERWATER SOUND SPEED PROFILE ON TARGET PARAMETER ESTIMATION **652**
AHMET GUNES

MODELLING AND PID CONTROL OF SCARA ROBOT **658**
MUHAMMED ARIF SEN, VELI BAKIRCIOGLU, METE KALYONCU

OBTAINING DYNAMIC CHARACTERISTICS OF ELECTROHYDRAULIC SERVO SYSTEMS CASE STUDY OF PARKER D1FP PROPORTIONAL VALVE **662**
VELI BAKIRCIOGLU, MUHAMMED ARIF SEN, METE KALYONCU

DESIGN A ROBOT INSECT INSPIRED BY THE CAMOUFLAGE CHARACTERISTICS OF THE LEAF INSECT **668**
SAMET CIKLACANDIR, OZLEM KARABIBER, YALCIN KALAFAT, FATIH CEMAL CAN

NUMERICAL SIMULATION COMPUTING OF THE COLLAPSES OF HARBOURS SILOS OF WHEAT STORAGE 30000 TONS CAPACITY **672**
BOUZEROURA MANSOUR

NUMERICAL SIMULATION OF INTERNAL TURBULENT FLOWS **679**
TAHIR KARASU

ENERGY AND EXERGY ANALYSIS OF AN ORGANIC RANKINE CYCLE USING DIFFERENT WORKING FLUIDS FROM WASTE HEAT RECOVERY **689**
ESRA OZDEMIR, MUHSIN KILIC

A NOVEL APPROACH TO GRIPPING MECHANISM **696**
OSMAN ACAR, ZIYA SAKA

PROPOSING DESIGN PARAMETERS FOR AN OPTIMUM ADHESIVE JOINT STRENGTH **701**
IBRAHIM KOCABAS, PAVEL SVANDA

BIVARIATE ROBUST DESIGN UNDER GAMMA NOISE **705**
MELIS ZEYBEK, ONUR KOKSOY

PYROLYSIS AND KINETIC ANALYSES OF BANYAN TREE FICUS BENGHALENSIS PLANT BIOMASS WASTE FOR BIO ENERGY POTENTIAL **709**
TANVEER RASOOL, V C SRIVASTAVA, M N S KHAN

PERFORMANCE PREDICTION OF A DIESEL ENGINE FUELED WITH DIESEL BIODIESEL ETHANOL BLENDS USING ANN **714**
BAHAR SAYIN KUL, MURAT CINIVIZ, ALI KAHRAMAN, ILKER ORS

EFFECT OF HYDROTHERMAL AGEING ON THE MECHANICAL PROPERTIES OF FRP COMPOSITE TUBES **719**
YASIN AKIN, MEMDUH KARA

EFFECT OF FLY ASH AND SUPER PLASTICIZER ON PERMEABILITY OF SOIL CEMENT MIXING MATERIALS **723**
YAVUZ YENGINAR, MURAT OLGUN

CONCEPTUAL DESIGN OF AN ANNULAR TYPE COMBUSTION CHAMBER **728**
OSMAN KOCAASLAN, KURSAD MELIH GULEREN

NUMERICAL ANALYSIS OF BT1 WIND TUNNEL EXPERIMENT USING OPENFOAM **733**
MUHAMMED BURAK AGIR, THOMAS SCANLON, AHMET SAMANCI

ENERGY CONVERSION CHARACTERISTICS OF A VARIETY OF SOLID WASTE SAMPLES THROUGH MICROWAVE PLASMA GASIFICATION PROCESS **739**
MELDA CARPINLIOGLU, AYTAC SANLISOY

EFFECTS OF LIQUID NITROGEN ADDITION TO INTAKE AIR ON THE PERFORMANCE AND NO FORMATION OF A GASOLINE ENGINE **744**
AHMET KAYA, GUVEN GONCA

SHOCK RESPONSE ANALYSIS OF ONE AUTOMOTIVE DAY TIME RUNNING LIGHT DRL **748**
BARIS EDIZ, ERHAN AY, TANER CAL, SEVDA TELLI CETIN

RETROFITTING OF A POWER PLANT STEAM HEADERS IN A PETROCHEMICAL COMPLEX USING EXERGY ANALYSIS **752**
ZEHRA OZCELIK, GULCE KALYONCU, DILEK CELENK

NUMERICAL MODELLING OF ALUMINUM FOAM FOR COMPARING FOAM FILLED PARTIALLY FOAM FILLED AND EMPTY CRASH BOXES **757**
BETUL GULCIMEN CAKAN, CIHAT ENSARIOGLU

EFFECT OF THE FURNITURE ON THE THERMAL EFFICIENCY OF ROOM HEATING A CFD STUDY **763**
ALI KIBAR, KADRI SULEYMAN YIGIT

NUMERICAL SOLUTION OF EULER EQUATIONS BY USING HCUSP SCHEME ON MULTI BLOCK GRIDS **767**
MURAT UYGUN

PHOTOVOLTAIC THERMAL PV T POWERED MULTI GENERATION SYSTEMS A REVIEW **772**
ERMAN KADIR OZTEKIN, PINAR MERT CUCE, ERDEM CUCE

TECHNO ECONOMIC ANALYSIS OF SOLAR DOMESTIC HOT WATER SYSTEM FOR SINGLE DETACHED DWELLINGS IN KONYA **775**
GUL NIHAL GUGUL

WATER TREATMENT WITH NATURAL ZEOLITE **780**
MELDA CARPINLIOGLU, MURTAZA YILDIRIM

MATHEMATICAL MODELING OF THE DOOR CLOSER MECHANISM **786**
SEZGIN ESER, SEVDA TELLI CETIN, OSMAN KOPMAZ

INVESTIGATION OF SUSPENSION SYSTEM ANALYSIS OF N2 CATEGORY VEHICLES CONVERTED TO M2 CATEGORY VEHICLES **790**
SERKAN ILDES, KEMAL ERSAN

EFFECT OF GEARBOX STRUCTURAL DESIGN ON THE VIBRATION LEVELS **795**
RAFET CAN UMUTLU, BERKAN HIZARCI, CEM DALBICER, HASAN OZTURK, ZEKI KIRAL

EFFECT OF INLET PRESSURE AND COLD HOT WATER TREATMENT ON GYPSUM SAMPLES FROM FGD UNITE OF POWER PLANT IN TERMS OF DEHUMIDIFICATION PSD AND CHEMICAL COMPOSITION **800**
IHSAN TOROGLU, HALIL IBRAHIM GONUL, SERDAR YILMAZ, SAIT KIZGUT, DILEK CUHADAROGLU, MEHMET BILEN

EVALUATION OF HIGH SPEED TRAIN NOISE POLLUTION **805**
ALI ERDEM CERCEVIK, SUHEYLA YEREL KANDEMIR, MUSTAFA OZGUR YAYLI

EFFECTS ON THE SURFACE QUALITY IN THE MACHINING PROCESSES OF THE TOOL VIBRATIONS **809**
EROL TURKES, SULEYMAN NESELI, MUMIN SAHIN, SELCUK SELVI

INVESTIGATION OF TORREFACTION PROCESS CONDITION ACCORDING TO CHARACTERIZATION AND PROCESS YIELD FOR POULTRY LITTER **916**
OZBEN KUTLU, GUNNUR KOCAR

ASSESSMENT OF ENERGY CONSUMPTION IN TURKEY **821**
SUHEYLA YEREL KANDEMIR, ALI ERDEM CERCEVIK, HUSEYIN ANKARA

IMPROVED BIOHYDROGEN PRODUCTION FROM FRUIT AND VEGETABLE WASTES THROUGH DARK DRY ANAEROBIC FERMENTATION **825**
HARIS NALAKATH ABUBACKAR, OKYANUS YAZGIN, BENSU GUNAY, KUBRA ARSLAN, TUGBA KESKIN GUNDOGDU, DUYGU KARAALP YAVUZYILMAZ, NURI AZBAR

INVESTIGATION OF SIZING CRITERIA FOR CANTILEVER RETAINING WALL WITH TAGUCHI OPTIMIZATION **829**
OZCAN TAN, IBRAHIM HAKKI ERKAN, ESRA URAY

FATIGUE LIFE ANALYSIS USING RANDOM VIBRATION DATA **835**
KEMAL YAMAN, EMRE OKUR, ALI OZTURK

OPTIMUM DESIGN OF HORIZONTALLY LOADED SHORT PILES **840**
OZCAN TAN, IBRAHIM HAKKI ERKAN, MURAT OLGUN

COMPUTER AIDED FORCE ANALYSIS OF HIGH SPEED TURNING OF METAL MATRIX COMPOSITES **846**
ALI OSMAN ER

FUZZY INFERENCE SYSTEM APPLICATION FOR PARAMETER SETTING IN CHANGEOVERS OF PLASTIC INJECTION MOLDS **851**
MAHMUT KEMAL KARASU, LATIF SALUM

INVESTIGATING OF COMPRESSIVE AND TENSILE STRENGTHS WITH DEFORMATION ABILITIES OF SAND SOILS IMPROVED WITH WASTE RUBBERS **860**
EKREM BURAK TOKA, MURAT OLGUN

PRE FEASIBILITY STUDY OF ESKISEHIR LANDFILL GAS TO ENERGY **865**
CIHANGIR KALE, MURAT GOKCEK

ESTIMATION OF LANDFILL GAS AND ENERGY POTENTIAL IN TURKEY **868**
CIHANGIR KALE, MURAT GOKCEK

THE STRUCTURES WHICH ARE INSPIRED BY LATTICES OF METALS UNDER MOVING LOAD **872**
SERKAN GULER, MURAT YILDIZ

DYNAMIC ANALYSIS OF STRUCTURES WHICH ARE INSPIRED BY LATTICES OF METALS **876**
SERKAN GULER, MURAT YILDIZ

MODAL ANALYSIS OF STRUCTURES WHICH ARE INSPIRED BY LATTICES OF METALS **883**
SERKAN GULER, MURAT YILDIZ

COOLING PERFORMANCE COMPARISON OF PLATE PIN FIN PIN FIN AND PLATE FIN HEAT SINKS UNDER FORCED CONVECTION WITH NUMERICAL ANALYSIS **887**
AHMET KOCA, HALIL IBRAHIM YAMAC

THE EFFECT OF BLOW UP RATIO ON THE MECHANICAL PROPERTIES OF POLYTHENE FILMS **893**
IDIL TARTICI, MEHMET ALI GUVENC, SELCUK MISTIKOGLU

A REVIEW ON THE METAL COATING TECHNIQUES FOR COMPARE TRIBOLOGICAL BEHAVIOR OF SURFACES OPERATING HIGH TEMPERATURES **899**
HASAN KAHRAMAN, MEHMET ALI GUVENC, SELCUK MISTIKOGLU

MOST EFFICIENT USE OF TWO TYPES OF ELECTRIC LOCOMOTIVES FOR LOAD TRANSPORTATION **908**
MINE SERTSOZ, MEHMET FIDAN, MEHMET KURBAN

DESIGN AND ANALYSIS OF SPUR GEAR PAIRS REGARDING MACRO AND MICRO PROFILE GENERATION AND SAFETY STANDARDS **912**
BURAK SAHIN, ABDULLAH AKPOLAT, NIHAT YILDIRIM

THERMODYNAMIC COMPARISON OF VARIOUS SPRAY DRYERS FOR CERAMIC INDUSTRY **921**
HASAN CAGLAYAN, HAKAN CALISKAN

THE COMPARISON OF CLASSICAL THERMOSTAT AND CONTROLLED 3 WAY VALVE CONFIGURATION IN ENGINE COOLING SYSTEM OF SI ENGINE APPLICATION **926**
GALIP KALTAKKIRAN, ALIRIZA KALELI, HADI GHASEMI ZAVARAGH, ERDOGAN GUNER

NUMERICAL INVESTIGATION OF INLET TURBULENCE INTENSITY EFFECT ON MULTIPLE IMPINGING JETS FOR HIGH JET TO JET DISTANCE **933**
PERIHAN CULUN

THE EFFECTS OF USING A STIRRER ON THE THERMAL PERFORMANCE OF A WATER JACKETED HEAT EXCHANGER **937**
HALIL BAYRAM, GOKHAN SEVILGEN

MATRIX INDEXING APPROACH FOR A FUZZY LOGIC BASED CONTROLLER IN INDUCTION MOTOR PROTECTION **940**
OKAN UYAR, MEHMET CUNKAS

IMPLEMENTATION AND COMPARISON OF TEXT COMPRESSION ALGORITHMS IN IMAGE STEGANOGRAPHY **944**
OZCAN CATALTAS, KEMAL TUTUNCU

CORE LOSS ESTIMATION MODEL FOR AN INTEGRATED MAGNETIC CURRENT DOUBLER SOFT SWITCHED FULL-BRIDGE DC-DC CONVERTER **948**
YASEMIN ONER, SEVILAY CETIN

Empirical Mode Decomposition Based Feature Extraction for Intelligent Emotion Recognition

A. MERT[1], F. ONAY[1] and A. AKAN[2]

[1]Bursa Technical University, Bursa/Turkey, {ahmet.mert@btu.edu.tr, fatih.onay@btu.edu.tr}
[2]Izmir Katip Çelebi University, Izmir/Turkey, aydin.akan@ikcü.edu.tr

***Abstract* – In this paper, advanced decomposition capability of the multivariate empirical mode decomposition (MEMD) for emotional states recognition. MEMD is an advanced decomposition technique to analyze non-linear and non-stationary signals. Without a priori basis selection, a signal can be decomposed into a set of oscillations called intrinsic mode functions. Due to non-stationary and multichannel properties of the EEG signals, the MEMD based signal processing is proposed for feature extraction, and evaluated for emotion recognition. First, the multichannel EEG signals decomposes into IMFs, and then time-domain and frequency-domain signal processing techniques including Hjorth parameters, power spectral density, entropy, and correlation are applied to obtain feature vector for valance and arousal scale recognition. The proposed MEMD based feature extraction is performed on DEAP emotional EEG data using artificial neural network, and the correct rates are compared to the previous studies.**

***Keywords* - Multivariate empirical mode decomposition, Emotion recognition, Valence and arousal scale, Electroencephalogram.**

I. INTRODUCTION

TWo dimensional scaling namely cognitive emotional map is used for emotion recognition using EEG signals [1]. The valence scale in this 2D cognitive emotion ranges from negative to positive. So, valence score can state emotions from unpleasant feelings (e.g. sad) to pleasant level (e.g. happy). The arousal state is used to quantify activity or inactivity as low level (e.g. bored) to high level (e.g. excited). The valence and arousal scales are associated to the beta and alpha bands of the recorded EEG signals from the scalp [2]. Spectral properties in alfa band in EEG signals (8-13 Hz) are correlated with inactivity of the brain, while the beta band (14-30 Hz) is the indicator of brain activity. For this reason, the most popular and successful technique for estimation of the arousal level is the power ratio of EEG signal in alpha/beta bands. Valence level of a participant is also estimated frequency-domain methods such as power spectral density (PSD) of EEG. Activation of the right hemisphere of the brain is an indicator of valence scale. Thus, PSD differences between the left lob and right lob are used to predict valence level. Shortly, valence scale is estimated using asymmetric properties of EEG signals while arousal level is based on band spectral properties of the EEG channels [2, 3]. However, emotion recognition using EEG signals is still a challenging study due to unknown brain functions subjective affectivity.

"A database for emotion recognition analysis using physiological signals", (DEAP) [3] is a recent study and a data set on the multichannel EEG recordings. The first proposed methods by the owners of the data set are based spectral powers of 32 EEG channels in alpha, beta and gamma bands with spectral power asymmetrical properties of the bands between the 14 channels of left and right lobes for classification For this dataset, accuracy rates of 62% and 57.6% for high/low arousal and high/low valence scale recognition are obtained using spectral features, and leave-one-participant out (LOO) cross-validation with naive Bayes classifier (BC). In another study, EEG recordings of the DEAP data set are classified using deep learning network (DLN) after principal component analysis (PCA). The correct rates of $53.42\% \pm 9.4$, and $52.03\% \pm 9.4$ and for three (high, neutral and low) valence and arousal classification are reported [4]. For benchmarking purpose, the same feature extraction methods and LOO with the original study of the DEAP data set are implemented.

In this paper, MEMD based emotional parameter estimation method is proposed to recognize the emotional state as high/low valence and high/low arousal. The MEMD algorithm is deployed to decompose multichannel EEG signals into IMFs, and these oscillations are analyzed using time and frequency-domain methods to cover each EEG channel properties with their asymmetrical differences. The performance of the proposed feature extraction based on MEMD and classification using artificial neural network (ANN) are performed on EEG recordings, and the 2-D cognitive emotional scales of the DEAP data set for benchmarking.

II. MULTIVARIATE EMPIRICAL MODE DECOMPOSITON

Empirical mode decomposition (EMD) was proposed as an advanced adaptive signal processing algorithm by Huang et al. in 1998 [5]. EMD is used to decompose a multicomponent signal into a set of amplitude and frequency modulated oscillations called intrinsic mode functions (IMFs) The EMD algorithm is basically consists of Sifting process based on envelope extraction. The detailed steps of the EMD can be

summarized as [6].

(i) Determine local maxima and minima as M_i, $i = 1, 2, \ldots,$ and m_k ,$k = 1, 2, \ldots,$ in $x(n)$.

(ii) Find upper and lower envelopes by the interpolating signals $M(n) = f_M(M_i, n)$, and $m(n) = f_m(m_k, n)$ using cubic spline.

(iii) Compute the mean of the envelopes, $h(n) = [M(n) + m(n)]/2$.

(iv) If $h(n)$ satisfies IMF conditions, save it as an IMF $\phi(n) = h(n)$, and remove $h(n)$ from the signal; $x(n) = x(n) - h(n)$.

(v) If $x(n)$ is trend (DC component) or stopping criterion is existed theresidue is saved as $r(n) = h(n)$.

Finally, the original signal can be represented by the IMFs as follows;

$$x(n) = \sum_{i=1}^{L} \varphi_i(n) + r(n) \quad (1)$$

There are two criteria in order to assume $h(n)$ as an IMF. First criterion is that the number of zero crossings and the number of the extrema must be equal or must differ by one at most. Second criterion is related to being zero mean process, the mean of the upper and lower envelope should be zero [5].

The EMD algorithm is revised and extended to enhance its capability on multivariate signal decomposition. The extended versions for multivariate signals are named bivariate, trivariate and multivariate empirical mode decomposition (BEMD, TEMD, and MEMD) [7-9]. These extended versions of the EMD have similar processes in the algorithm, but multidimensional envelope extraction is deployed [10].

The multivariate versions of the EMD are more advantageous and practical than mono-component EMD for processing multichannel signals. For MEMD, the IMFs of the channels have close properties in time-frequency domains. For example, the first IMFs of the multichannel EEG have similar autocorrelation properties, frequency fluctuations or bandwidths. In case EMD is used for decomposition each EEG channel separately, the number of IMFs and their properties can change over each channel.

The filter bank of the EMD and MEMD have also investigated, and it was reported that filter bank properties are also adaptive and dependent on the statistical properties of the signal(s) [11]. Also, the dyadic filter bank structures of the EMD and MEMD have been investigated using white Gaussian noise, and shown in Figure 1.

Referring the Figure 1, MEMD splits the signal into a set of bandlimited oscillations. Spectrum of the decomposed oscillations of the EEG signals is the main principle of our proposed method for emotional state classification.

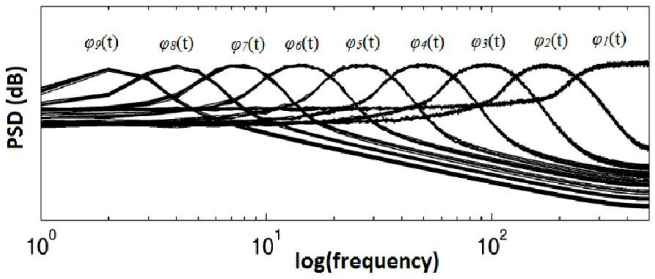


Figure 1: Multivariate empirical mode decomposition dyadic filter bank structure [9].

III. DATA SET

DEAP emotional EEG is a multimodal data set [3] to analyze human affective states. It consists of 32 channel EEG recordings of 32 participants while watching video clips as stimuli. According to 10/20 electrode placement, 32 EEG signals were acquired with 512 Hz sampling frequency. After this recording phase, they were asked to assess their levels of arousal and valence scale using self-assessment manikins (SAM) [3] given in Figure 2.

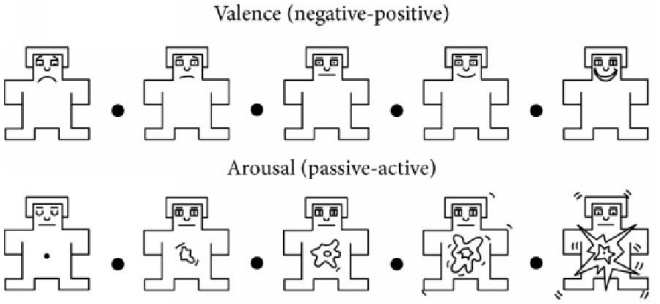


Figure 2: Self-assessment manikin.

The valence from positive to negative (e.g. from happy to sad) while the arousal scales extends from active to passive (e.g. from excited to passive). In the study of the DEAP database [3], the emotional states were mapped into 2 level of arousal and valance states. High/low valence and high/low arousal states were classified. Thus, the four quadrants of the 2D cognitive valence and arousal ranges are shown in Figure. 3 [3], and these are adopted to low/high states.

IV. MEMD BASED EMOTION RECOGNITION

Filter bank of the MEMD based feature extraction is proposed for emotion recognition. Dyadic filter bank of the MEMD yields to band-limited multicomponent IMFs, and their time and frequency-domain properties such as entropy, spectral and correlation with asymmetrical changes are implemented as feature vector extraction.

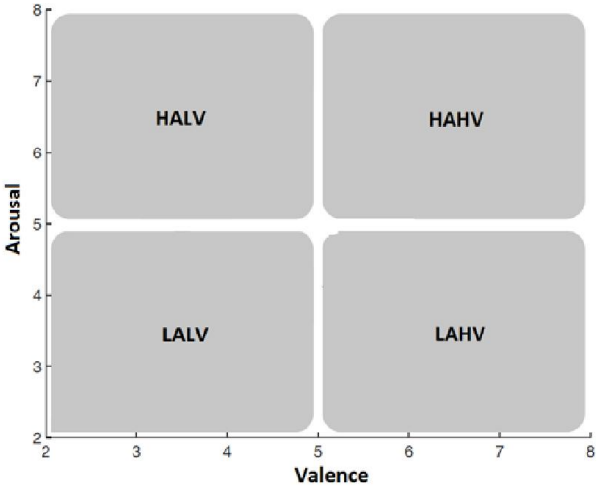


Figure 3: Valence-arousal quadrants for 2D cognitive emotional state (e.g. high arousal and low valence is denoted as HALV).

In the original DEAP study [3], 32 channel EEG signals are used, but we use recordings of only 18 EEG channels (8 left, 8 right and 2 central channels in the frontal lobs) to reduce computational burden. The motivational and emotional parts of the brain exist in these lobs [2]. So, it is assumed that the selected channels in Figure 4 can include sufficient information about the emotional state.

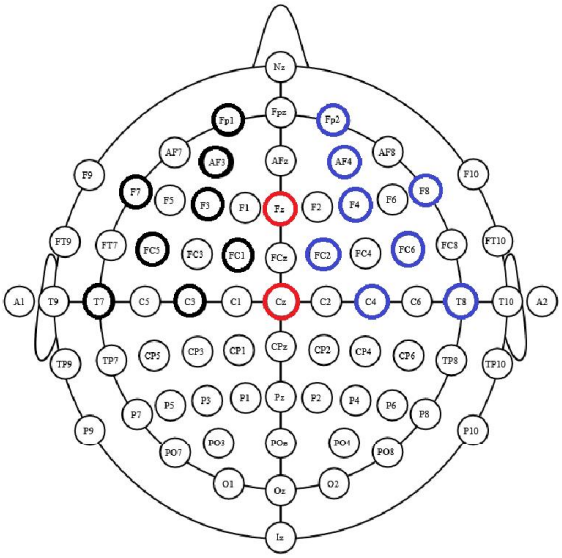


Figure 4: The selected frontal and central channels for feature extraction.

Signal analyzing method namely PSDs, power, power ratios, entropies, and Hjorth parameters of the IMFs of eighteen EEG channels are extracted for arousal state estimation. Also, asymmetrical analyses are also obtained computing correlation coefficients, power differences, coherence, relative entropies and power ratios between 8 left and right channels. Also, the eight EEG channels are existed as virtual channels subtracting left eight channels from the right ones to enhance asymmetrical analysis. Finally, the proposed MEMD based emotional state classification is given in Figure 5.

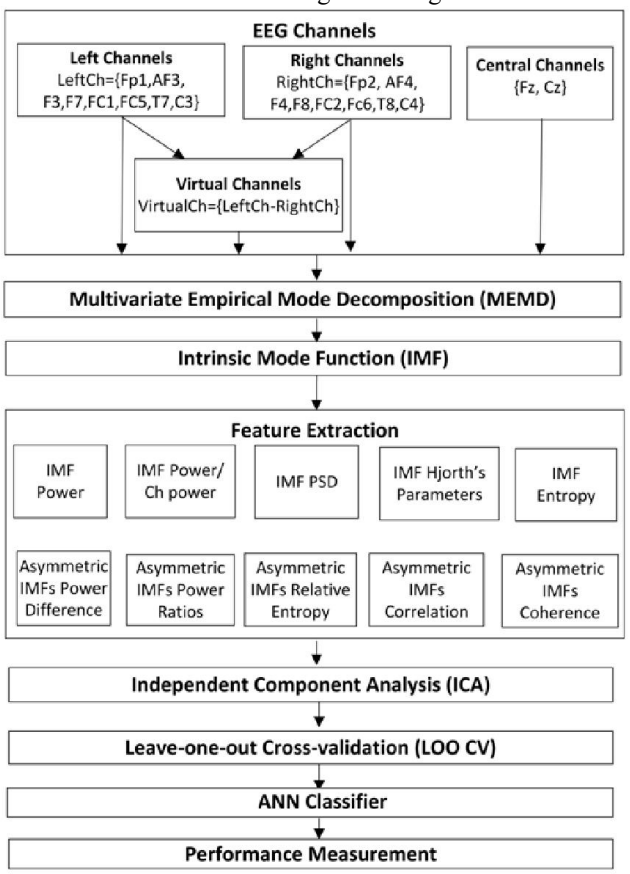


Figure 5: Proposed MEMD based emotional state classification scheme.

After the multivariate IMFs are extracted, the given methods are applied to construct feature vector for classification. Therefore, 7419 dimensional feature vector is extracted for one emotional state. Due to high dimensional feature space, Independent component analysis (ICA) [14] is used for dimension reduction of the proposed feature set. After that, 40 valence/ arousal levels belonging to a participant are used as testing data, while the others' levels are used for training. This type of validation called LOO cross-validation is performed to evaluate the accuracy of the proposed MEMD method with and ANN classifier.

V. RESULTS

The proposed MEMD based method is performed on the publicly available DEAP emotional data set. High/low valence and high/low arousal emotional states of the 20 participants are classified using the proposed MEMD based features with ANN classifier. After, extracted 7419 dimensional feature vector is using MEMD method, the huge dimensional space are reduced to 250 independent components (ICs) referring the retained 97.24% of eigenvalues shown in Figure 6. After that,

they are used as training and testing data in the rest of the study.

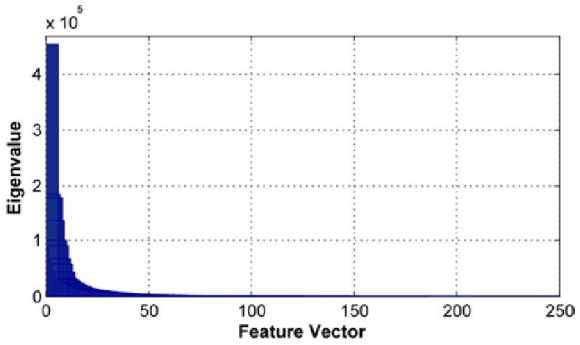


Figure 6: Corresponding eigenvalues of the extracted feature set.

40 valence and arousal emotional states of each participant are used as testing feature vector, and the other samples are used for ANN training, respectively. Thus, LOO cross-validation scheme is implemented. The proposed MEMD based features are evaluated using ANN algorithm consisting of two hidden layers with up to 20 neurons. The classification results of the proposed method are shown in Figure 7.

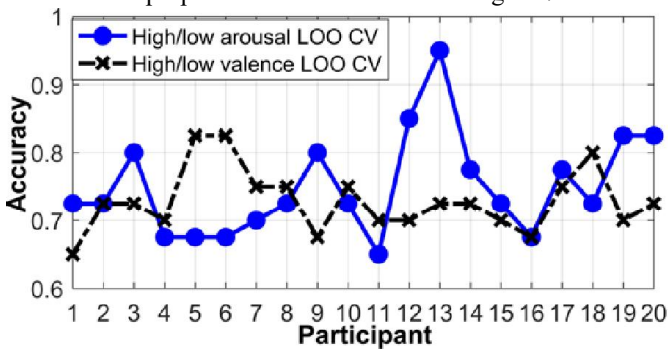


Figure 7: High/low valence and high/low arousal classification results.

The proposed method with ANN and LOO cross-validation method yields correct rates of 72.87% ± 4.68, and 75% ± 7.48, and for high/low valence, and high/low (H/L) arousal, respectively. In addition to these average rates, the lowest score is obtained as 65% for the 11th participant while the highest arousal accuracy level is of 95% for the 13th participant. The lowest and highest valence scores are 65% and 82.5% and for the 1st and 5th participants. Finally, the proposed MEMD based emotional state classification is compared to the papers which DEAP data set is used, and the results are given in Table 1.

Table 1. The comparison of the proposed method with previous studies.

Study	Recognition	Accuracy (%)
Koelstra al. [3]	H/L arousal	62.00
	H/L valence	57.60
Jirayucharoensak et al. [4]	H/L arousal	52.03±9.74
	H/L valence	53.42±9.64
This Study	H/L arousal	75.00±7.48
	H/L valence	72.87±4.68

VI. CONCLUSION

A multivariate empirical mode decomposition (MEMD) based EEG signal decomposition is proposed for emotional state classification as high/low valence and high/low arousal states. Publicly available multichannel and multimodal database called DEAP emotional EEG dataset are used for comparison and benchmarking. The accuracy rates of the emotion recognition of the proposed method are evaluated and compared with the previous studies. The decomposed multivariate intrinsic mode functions (IMFs) of the EEG signals are analyzed using power spectral density, Hjorth parameters, band power ratios, entropy, correlation spectral power asymmetry, and coherence. The accuracy rates of the proposed methods indicate that our method outperforms the previous studies which use the same EEG data set. Neural Network classification yield the accuracy of 72.87%, 75% for valence, and arousal states, respectively using the extracted features.

REFERENCES

[1] J. A. Russell, "A circumplex model of affect," *Journal of Personality and Social Psychology*, vol. 39, pp. 1161–1178, 1980.

[2] D. O. Bos, "EEG-based Emotion Recognition: The Influence of Visual and Auditory Stimuli," *Capita Selecta (MSc course)*, 2007.

[3] S. Koelstra, C. Muhl, M. Soleymani, J. S. Lee, A. Yazdani, T. Ebrahimi, T. Pun, A. Nijholt, and I. Patras, "DEAP: A database for emotion analysis; Using physiological signals," *IEEE Transactions on Affective Computing*, vol. 3, pp. 18–31, 2012.

[4] S. Jirayucharoensak, S. Pangum, and P. Israsena, "EEG-based Emotion Recognition using Deep Learning Network with Principal Component based Covariate Shift Adaptation," *The Scientific World Journal*, vol. 2014, pp. Article ID 627892, 2014

[5] N. E. Huang, Z. Shen, S. R. Long, M. C. Wu, H. H. Shih, Q. Zheng, N.-C. Yen, C. C. Tung, and H. H. Liu, "The empirical mode decomposition and the Hilbert spectrum for nonlinear and non-stationary time series analysis," *Proceedings of the Royal Society A: Mathematical, Physical and Engineering Sciences*, vol. 454, pp. 903–995, 1998.

[6] R.T. Rato, M.D. Ortigueira, and A.G. Batista, "On the HHT, its problems, and some solutions," *Mechanical Systems and Signal Processing*, vol. 22, pp. 1374–1394, 2008.

[7] G. Rilling, P. Flandrin, P. Gonçalves, and J. M Lilly, "Bivariate Empirical Mode Decomposition," *IEEE Signal Processing Letters*, vol. 14, 2007.

[8] Naveed Ur Rehman and Danilo P. Mandic, "Empirical mode decomposition for trivariate signals," *IEEE Transactions on Signal Processing*, vol. 58, pp. 1059– 1068, 2010.

[9] N. Rehman and D. P Mandic, "Multivariate empirical mode decomposition," *Proceedings of the Royal Society A: Mathematical, Physical and Engineering Sciences*, vol. 466, pp. 1291–1302, 2009.

[10] P. Flandrin and P. Goncalves, "Emprical mode decompositions as data-driven wavelet-like expansions," *International Journal of Wavelets, Multiresolution and Information Processing*, vol. 02, pp. 477– 496, 2004.

[11] A. Mert and A. Akan, "Detrended fluctuation thresholding for empirical mode decomposition based denoising," *Digital Signal Processing*, vol. 32, pp. 48– 56, 2014.

[12] N.U. Rehman and D. P. Mandic, "Filter bank property of multivariate empirical mode decomposition," *IEEE Transactions on Signal Processing*, vol. 59, pp. 2421–2426, 2011.

[13] J.D Morris, "Observations: Sam: the self-assessment manikin; an efficient cross-cultural measurement of emotional response," *Journal of advertising research*, vol. 35, no. 6, pp. 63–68, 1995.

[14] A. Hyvarinen and E. Oja, "Independent component analysis: algorithms and applications," *Neural Networks*, vol. 13, 411–430, 2000.

The Importance of Medical Imaging and Overview of Using 3D Printer

H.B.ERDOGUS[1]

[1] Kavram Vocational College of Higher Education, Istanbul/Turkey, hakan.erdogus@kavram.edu.tr

Abstract **- Additive manufacturing, in other words three dimensional printing technologies has entered our lives by the definition of "industrial revolution". Complex geometries that can't be overcomed by traditional methods can be produced easily to additive manufacturing technologies. Three dimensional printing technology, although some limitations, is evident not only in design but also in terms of production for future years. In this study, the importance of medical imaging in diagnosis and treatment has been researched and the use of models produced in three-dimensions after the processing of imaging data has been investigated in medical field. Researchers have shown that; three dimensional models are great benefit in various biomedical researchers, to training of medical students and to planning before surgery. Innovations such as the decrease of production costs in the coming years with development of three-dimensional printing technology, faster anatomical modeling and direct bioprinting of organs will further expand in field of medical used.**

Keywords **- Additive Manufacturing, 3D Printing Technologies, Medical Imaging, Bioprinting.**

I. INTRODUCTION

The technologies of manufacturing industry improves according to needs of individual and times. People's interests are differentiation of living conditions, and the economic revolutions that arise from economic needs, become the fourth industrial revolution with the Internet of Things (IOT) and Additive Manufacturing (AM) or 3D Printing (3DP) technology. The additive manufacturing technology enables design of complex internal structure and specific designed parts which are difficult to make with conventional methods can be produced easily. Additive manufacturing or 3D printing is based on principle of dividing three-dimensional imaging data into slices and solid models are built on a layer-by-layer by means of a special printer, unlike conventional methods. In order to create solid object from imaging data the object visual information must be designed in computer aided design (CAD) programs or solid model after 3D scanning. One of the most important areas where imaging data used is most prevalent are in the medical field. CT (Computer Tomography) and Magnetic Resonance Imaging (MRI) techniques, which allow the detection of many pathological indications during the diagnosis stage, are among the preferred methods for creating medical image data. In this study, the anatomical model is obtained by acquiring image data and passing through some stages has been mentioned the benefits of surgical operation planning, diagnosis and patient-specific treatment.

II. RAPID PROTOTYPING AND 3D PRINTING TECHNOLOGIES

3D printing technology has been known over time as "autofabrication" or "rapid prototyping" was developed as a rapid model or prototype in the first years. The rapid models are produced by three-dimensional printers or rapid prototyping machines which are used materials such as metal, plastic and ceramics. Generally used area of rapid prototyping technologies are automotive, aerospace, architecture, shoemaking, jewelery, education and medical applications. Rapid prototype part is designed in a computer aided design program. The design can be started from sketch, or it can be created by processing point cloud data by obtained three-dimensional scanner. The model geometry is often defined in stereolithography (STL) format and transferred to a special printer [1].

In recent years, rapid prototyping and used of three-dimensional printers have been increased in the medical field. These printers use STL data which is obtained from CT scanners and image analysis devices for direct prototype production. The greatest difficulty in surgical applications isn't visible in imaging data which is the presence of some voids in the anatomic internal structure that are caught in CT. The fact that the prototype model, which is printed in three dimensions, can be produced transparently provides a better understanding of the internal structure [2].

III. MEDICAL IMAGING FOR 3D ANATOMIC MODEL

Visualization allows people to make comparisons and interpretations using visual power by transforming data or information into pictures. Data visualization is based on the visualization of data sets such as financial, medical, industrial and commercial data. Medical field visualized data is often used; diagnosis, treatment and surgical operation. There are many ways to acquire the image of scan human body. The main visualization techniques are used in CT and MRI [3,4].

CT is one of the quality control methods used for internal and external measurements of parts with complex geometries in industrial applications. CT measurements is also applied to the complex parts produced by additive manufacturing method and have unsufficient information about internal structure, together with measurements taken from parts made with traditional production methods [5]. Visualization techniques should be used correctly to create a successful three-

dimensional anatomic model [6]. Therefore, the processing of image data has a critical role in enabling specialists to achieve accurate diagnosis [7]. It has been determined that objects must be modeled by their internal properties and surface interactions to generate three-dimensional visual images from CT and MRI data. The CT sections are taken from any organ are passed through some stages according to the volume coating method and a visualized model is created. These sections, which are obtained independently from each other, can be separated and removed by image segmentation techniques. One of brain tumor application, as seen in Figure 1, only the tumor surface area is determined and other unused regions can be deleted. The surface area and volume of the tumor separated from the brain can be calculated with special software.

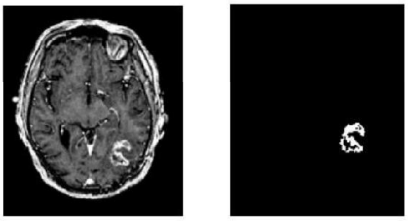


Figure 1: Axial section of brain and tumor

CT and MRI techniques are based on the classification and segmentation of image data related to the patient anatomy into specific sections in significant planes. However, radiology specialists and surgical team to be treated are having difficulty in interpreting two-dimensional images taken in cross-sections. Surgical experts find it hardly difficult to transfer this information to the surgical operation team, even if three-dimensional visual imagination is generated from the cross-sectional data of tissues or organs [8]. In order to overcome this difficulty, the two dimensional sections are assembled to create volumetric anatomical structures.

DICOM (Digital Imaging and Communications in Medicine) images from CT are converted into three-dimensional mesh geometry using cross-section contours by finishing tools (Blueprint Modeling). Anatomical geometry data can be optimized with CAD software before is transformed to STL data and sent to 3D printer. The process results in the conversion from anatomical images to physical objects (Fig 2) involves radical changes in the future of the modern surgeon, despite of factors such as high production costs and long printing times. Bioprinting has a toolpath planning that varies according to biomaterial used as difference from the 3D anatomical model production [3, 7, 9, 10].

IV. MEDICAL APPLICATIONS OF 3D PRINTING

Three-dimensional printing technologies that have many different kinds of applications in the medical field; anatomical model production, surgical device design, and personalized implant / prosthesis construction. Medical imaging techniques used for diagnosis practice are great help to radiologists in detecting and interpreting anomalies in patient anatomy.

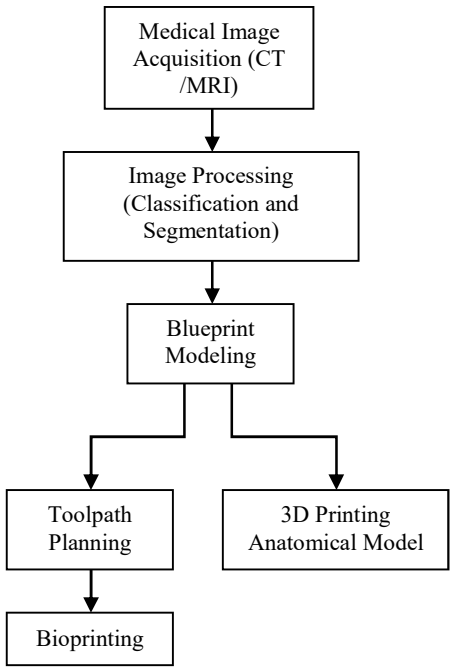


Figure 2: The process flow from medical imaging to 3D anatomic model or bioprinting.

For this reason, computer-aided diagnosis must be performed successfully for medical imaging. There are two important elements for extracting a three-dimensional model from a radiological image. The first of these is the sensitivity of the patient's anatomy and the second is that radiologist can construct a pathologic structure of three-dimensional models [11,12].

Three-dimensional "biomodels" containing anatomical structure is used diagnosis, surgical operation planning, simulation, neurosurgery and medical education [13, 14]. Before giving the most appropriate decision when performing the surgical planning; calculation of possible risks, simplification and comprehension of a complex anatomical structure is necessary for successing of surgical operation. For example, operation of osteolytic lesion in cervical spine is very difficult for surgeons. Three-dimensional printing technology is a very good application and is effective in the visualization and emergence of this tumor [15]. Similarly, anatomic model object provides theoretical and practical advantages for improving complex pathologies in cardiac surgeons. The enlargement of three-dimensional cardiac model including tumor on the right ventricle using CT data has supported to pre-operative planning. The position of main heart tumor and the amount of influence has become clearer by means of three-dimensional model. In the cardiovascular anatomy sometimes can not be predicted to certain conditions due to patient-specific anatomy. It is very difficult for surgeons to decide and plan ahead of operation. In a study for pediatric and adult cardiac surgery, abnormalities such as

congenital defects can be easily seen on a three-dimensional model (Fig 3), so that some unexpected patient-specific conditions can be analyzed [16, 17].



Figure 3: 3D printing model illustrated with sections

In another application, surgeons used a three-dimensional model was produced by rapid prototyping technique when decided on complex neck morphology aneurysm. When CT data were analyzed for a patient with a 6.6cm internal aortic aneurysm at 75 years of age, some difficulties were encountered with the way of intervention. The three-dimensional model has an important role in determining the most suitable tool to be used for repairing damaged parts in the neck area [18]. Rapid prototyping technology is also very important for neuroscience research because of its ability to produce designs with complex geometries. The low error rate and reproducibility make rapid prototyping technology attractive. This technology provides a multifunctional platform with complex modes of production that allows for neural activities [19]. In a study of structural brain abnormality in children, ventricular volumes were calculated via a three-dimensional model generated from MR data. The selected children were compared whose with normal brain morphology and abnormal brain structure. In three-dimensional visualization and volumetric measurements, morphological abnormalities have been investigated in detail. In this case, abnormal ventricular anatomy is better understood [20]. Additive manufacturing technology has given new perspectives to prosthetics and orthosis applications. The geometry of orthosis sketch is designed on paper and AFO model is custom-made with FDM and manufactured at low cost. A titanium heel bone prosthesis for removing an abnormal lesion in the right calcaneus of a 71-year-old patient has been replaced with a successful operation [21, 22]. When surgeons have planned an operation, for example, a patient is prepared for an osteotomy operation, visualization is occured from CT data, then these data is used 3D printed models that is produced three-dimensional printer. At this point, surgeons have rehearsed correction and osteonomic intervention that gives to patient the most appropriate result in terms of functional and aesthetic outcomes on the three-dimensional model. One of the most important benefits of this method is that the patient's exposure to anesthesia and blood loss is reduced, and fewer injuries have occurred [6]. A surgical intervention to a patient who has suffered a traffic accident and maxillary skeleton needs to established at correct positioning of the maxilla and mandible bones. So that, three-dimensional model is created by SLS (Selective Laser Sintering) method and the bones are placed correctly in one-to-one correspondence (Fig 4) [22].

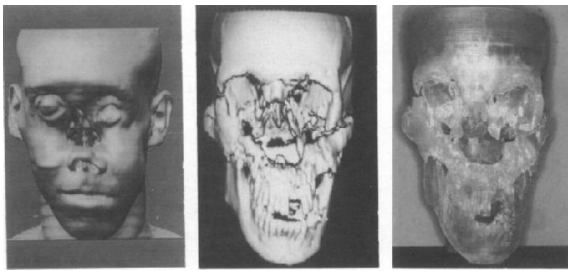


Figure 4: From left to right showing 3D soft tissue MRI image of damaged area, CT scan facial bone image and SLS 3D printing model

Some parts of bridge that is made of titanium material cause damage in and around the mandibular. More than 50% of them are caused to mechanical damage such as screw breakage, screw loss or infection on the locking bone plate. To overcome this problem, the locking bone plate which is reproduced with high dimensional accuracy and suitable symmetry made of three-dimensional printing technology has been placed successfully in the mandible [23]. Medical imaging is necessary for precise of identification that is determined specific information to the anatomy of patient. By means of medical imaging, CT and MRI data can be processed to prepare templates that are suitable for patient-specific implant construction. For example; measurements of an implant intended for damaged region of eye can be obtained by CT image data. In the next step, the implant produced with rapid prototyping technology can be successfully applied to the damaged region [24, 25]. In the case of live organ transplantation, vascular structure models also can be printed in three-dimensional by used medical images. Additive manufacturing technologies are great benefits of surgical team for proving and determining of surgical techniques. However, additional information is provided by three-dimensional model for allowing different surgical approaches. In addition, pathological and surgical risks can be presented to patients through anatomic models [23, 26].

Medical students are traditionally trained through cadavers. This experience needs to gain for achieving treatment of patients. Complex anatomic structures of two-dimensional or three-dimensional image acquisition may be inadequate from some patients prior to surgical intervention. Because of this, three-dimensional printed models of anatomic and pathologic structures are useful when a patient-specific surgical operation is planned. The enlarged three-dimensional models, which are used as a good training model for middle ear surgery, have greatly contributed to the education of medical students. Students have the opportunity to apply shaving on their actual bone on the model produced by SLS technology [7, 23, 28].

Today, the problem of organ failure is increasing due to people's long life, genetic and natural factors. One of the most common cases of tissue or organ transplants isn't to access appropriate donor. In order to overcome this problem, artificial organ production studies were carried out using cell knowledge which causes biological, mechanical and biochemical transformation of tissue. In the light of these studies, "Bio-Additive Manufacturing" as called "Bioprinting" technologies is improved in based on tissue engineering, which has been discovered through laboratory studies. By means of this breakthrough discovery is expected that the bioprinted kidney, liver, pancreas and heart will occur soon [28].

V. CONCLUSION AND ADVICES

Additive manufacturing or three-dimensional printing technology is developed by the purpose of test components produced in aerospace industry, has become increasingly used everywhere, including medical industry. The use of medical imaging and three-dimensional anatomic model has been reduced to four basic categories: 1) when planning before surgical operation by acquiring detailed information about the patient in the diagnosis, 2) in order to producing direct organs as called bioprinting, 3) while to producing patient-specific implant or prosthesis, 4) for teaching medical students with an individual pathological structure. Surgeon's works on the 3D model that is necessary to the most appropriate decision for successful operation before vital surgical intervention. Additive manufacturing technology evolves in the coming years; advanced technology three-dimensional printers are expected to be used in every hospital. As with each new production technology, there are some limiting factors in the additive manufacturing as well; the three-dimensional model is produced at high cost, special image information of patients can be safeguarded while being transferred to manufacturer, and is taken to long time of model production and post-processing. Fortunately, in futures anatomic models will be produced more precisely, quickly and lower cost.

REFERENCES

[1] H.B. Erdoğuş, "Using Reverse Engineering Applications and Design 3D Surface Modeling", Selcuk University Mechanical Engineering Project-2, Page:1-15, 2006.

[2] A. Gebhard and J.S. Hötter, "Additive Manufacturing 3D Printing for Prototyping and Manufacturing",page: 332-335, 2016.

[3] D. Üstünalan, N. Erden, "3D Medical Visualization", Final Project, İ.T.Ü. Computer Engineering, Computer Science, 2009.

[4] P.W.M Ferry, A.N.D Marco, J.K. Travis, M. Jos, J.B. Paulo and W.H. Dietmar, "Additive manufacturing of tissues and organs", *Progress in Polymer Science*,37:1079–1104, 2012.

[5] L.De.,S. Chiffr Carmignato, J.-P. Kruth, R. Schmitt and Weckenmann A., "Industrial applications of computed tomography", *CIRP Annals*, Volume 63, Issue 2, , Pages 655-677, 2014.

[6] A. Marro, T. Bandukwala , and W. Mak, "3D printing and medical imaging: A review of the methods and applications", *Current Problems in Diagnostic Radiology*, Volume 45, Issue 1, Pages 2–9, 2015.

[7] F. Rengier, A. Mehndiratta, H. von Tengg-Kobligk, C.M. Zechmann, R. Unterhinninghofen, H.U. Kauczor and F.L. Giesel, "3D printing based on imaging data: review of medical applications", *International Journal of Computer Assisted Radiology and Surgery*, 5(4):335-41, July 2010.

[8] S. Doğan and M.O. Altan "Detection of tumors by using CT, MR slices and digital images", *itüdergisi/d mühendislik,* Cilt:2, Sayı:4, 45-55, 2003.

[9] H. H Malik, A.R.J Darwood, S. Shaunak, O. Mulki and Baskaradas A. "Three-dimensional printing in surgery: a review of current surgical applications", *Journal of Surgical Research*, Volume 199, Issue 2, Pages 512-522. Dec 2015.

[10] İ.Ozbolat, H.Gudapati., "A review on design for bioprinting", Bioprinting 3,1-14. 2016.

[11] K. Doi, "Diagnostic imaging over the last 50 years: researchand development in medical imaging science and technology", *Physics in Medicine and Biology*, 51(13), R5–R27, Jun 2006.

[12] D. Mitsouras, P. Liacouras, A. Imanzadeh, A.A. Giannopoulos, T. Cai, K.K. Kumamaru, E. George, N. Wake, E.J. Caterson, B. Pomahac, V.B. Ho, G.T. Grant, F.J. Rybicki, "Medical 3D Printing for the Radiologist", *Radiographics*, 35(7):1965-88, Nov-Dec 2015.

[13] G. Wurm, B. Tomancok, P. Pogady, K. Holl and J. Trenkler "Cerebrovascular stereolithographic biomodeling for aneurysm surgery", *Journal of Neurosurgery,* 100(1):139-4, Jan 2004.

[14] W.M. Rozen, J.W Ting, M. Leung, T. Wu, D. Ying and J. Leong, "Advancing image-guided surgery in microvascular mandibular reconstruction: combining bony and vascular imaging with computed tomography-guided stereolithographic bone modeling", *Plastic and Reconstructive Surgery*, 130(1):227e-229e, Jul 2012.

[15] P.W. Silva, R. Amorim, D.A.F. Bezerra, M. Masini and A. Neuropsiquiatr, "Aplication of the stereolithography technique in complex spine surgery", *Arquivos de Neuro-Psiquiatria*, vol.65 no.2b,443-445, 2007.

[16] D. Schmauss, S. Haeberle, C. Hagl and R. Sodian, "Three-dimensional printing in cardiac surgery and inventional cardiology: a single-centre experience", *European Journal of Cardio-Thoracic Surgery*, 47(6), 1044–1052, Jun 2015.

[17] D. Schmauss, N. Gerber and R. Sodian, "Three-dimensional printing of models for surgical planning in patients with primary cardiac tumors", *The Journal of Thoracic and Cardiovascular Surgery*,145 (5), 1407-1408, May 2013.

[18] M.D. Tam, S.D. Laycock, J.R. Brown, M. Jakeways, "3D Printing of an Aortic Aneurysm to Facilitate Decision Making and Device Selection for Endovascular Aneurysm Repair in Complex Neck Anatomy", *Journal of Endovascular Therapy*, 20(6):863-7, Dec 2013.

[19] P. Tek, T.C. Chiganos, J.S. Mohammed, D.T. Eddington, C.P. Fall, P. Ifft and P.J. Rousche, "Rapid prototyping for neuroscience and neural engineering", *Journal of Neuroscience Methods*,172(2):263-9, Jul 30 2008.

[20] F.L. Giesel, A.R. Hart, H.K. Hahn, E. Wignall, F. Rengier, R. Talanow, I.D. Wilkinson, C.M. Zechmann, M.A. Weber, H.U. Kauczor , M. Essig and P.D. Griffiths, "3D Reconstructions of the Cerebral Ventricles and Volume Quantification in Children with Brain Malformations", *Academic Radiology*, 16(5):610-7, May 2009.

[21] L. Aydın and S. Küçük, "Design and Construction of Ankle Foot Orthosis By Means Of Three-Dımentional Prınters", *Tıp Teknolojileri Ulusal Kongresi*,129-132. 2014.

[22] J. Imanishi and P.F.M. Choong, "Three-dimensional printed calcaneal prosthesis following total calcanectomy", *International Journal of Surgery Case Reports*, 10: 83–87, 2015.

[23] M. McGurk, A. A. Amis, P. Potamianos and N. M. Goodger, "Rapid prototyping techniques for anatomical modeling in medicine", *Annals of the Royal College of Surgeons of England*, 79(3): 169–174. May 1997.

[24] J.J Ballyns and L. J. Bonassar, "Image-guided tissue engineering", *Journal of Cellular and Molecular Medicine*, 13(8A):1428-36. Aug 2009.

[25] M.T. Elgalal., M. Kozakiewicz, M. Olszycki, B. Walkowiak and L. Stefanczyk, "Custom implant design and surgical pre-planning using rapid prototyping and anatomical models for the repair of orbital floor fractures", *Europen Society of Radiology*, Page 1-17. 2009.

[26] N.N. Zein, I.A.Hanouneh, P.D. Bishop, M. Samaan, B. Eghtesad, C. Quintini, C. Miller, L.Yerian and Klatte R.,"3-Dimentional (3D) Print of Liver for Preoperative Planning in Live Donor Liver Transplantation", *Liver Transplantation*, 19(12):1304-10. Dec 2013.

[27] Ü. Uslu, "Tomografik Görüntü Verilerinden 3-Boyutlu CAD Modelin Oluşturulması", Yüksek Lisans Tezi,Y.T.Ü Fen Bilimleri Enstitüsü, 2006,

[28] Barnatt. C.,"3D Printing Second Edition", *Published by ExplainingTheFuture.com*, page: 175-197, 2014.

Analysis of Calcium and Phosphorus in Human Bone Using Scanning Electron Microscopy With Energy Dispersive X-Ray Spectroscopy (SEM-EDX)

T. ÇAYIR[1], Y. AKALTUN[2], Ö. GÜNDOĞDU[1]
[1] Kocaeli University, Kocaeli/Turkey, tubacyr@hotmail.com
[2]Erzincan University, Erzincan/Turkey, yakaltun@hotmail.com
[1]Kocaeli University, Kocaeli /Turkey, o.gundo@gmail.com

***Abstract* - In this study, we investigated of ten bone and cartilaginous specimens taken during surgery from the male and the female. The bone-cartilage samples with disease were investigated for their structural and elemental properties. The bone-cartilage samples with disease were characterized by scanning electron microscopy- energy dispersive X-ray spectroscopy (SEM-EDX). The changes in bone cartilage samples taken from patients in the direction of the obtained data were examined.**

***Keywords* - Bone- Cartilage, SEM, EDX.**

I. INTRODUCTION

OSTEOARTHRITIS (OA) is a major public health problem affecting half the population over 65 years old. Recently, several major publications have characterized calcifications present in damaged cartilage tissue [1–3]. In osteoarthritis (OA) all of the joint components are involved in the process of degeneration such as synovium, cartilage, calcified cartilage, Subchondral bone and trabecular bone [4]. It characterized by articular cartilage degradation which can affect many joints in the body, but is particularly common in weight-bearing joints such as the knee and hip. The loss of cartilage can lead to joint space narrowing, pain, and loss of function and finally leads to the need for total joint replacement. Factors such as previous joint injuries, obesity, the effects of aging on cartilage matrix composition, matrix structure and genetic factors are involved in the pathogenesis of OA. However the exact pathophysiology remains unclear. Recently, studies in animal models have permitted the evaluation of time dependent histomorphometric changes in articular cartilage relative to those in the subchondral bone plate at disease onset and during progression [5]. The major components in subchondral bone are inorganic component (60-70%) which is calcium and phosphorus, organic component (10%) which is collagen type I, the rest of all is water (10-20%). The inorganic component plays an important role for mechanical strength of the bone [6]. Calcium (Ca^{2+})-containing crystals, including basic Ca^{2+} phosphate crystals (BCP: $Ca_5(PO_4)_3OH$) and Ca^{2+} pyrophosphate dihydrate (CPPD: $Ca_2P_2O_7{\cdot}2H_2O$) [7] have been identified as worsening factors [8].

Ten human bone-cartilage specimens from the surgery of humans are reported in this paper. Male and female patients 65 years old and over 65 years old. While five of the samples are of a female osteoarthritic bone-cartilage the other is a male osteoarthritic bone-cartilage. Prior to the sample analysis, there were no fixations, embedding or surface processing. This work is an effort to characterize the diseased female and male bone-cartilage by using a combination of techniques such as scanning electron microscopy- energy dispersive X-ray spectroscopy (SEM-EDX). The aim of this study is to make comparison of structural, elemental properties of diseased female and male bone-cartilage samples.

II. MATERIAL AND METHODS

Human bone-cartilages from total hip replacement procedures were used, due to surgical intervention in response to a degenerative joint disease. The bone-cartilages specimens were sourced from the department of Orthopedics and Traumatology at Kocaeli University (Turkey). Using a water-cooled diamond saw (Isomet 1000 Precision) several sections at certain thicknesses were cut perpendicular to the articular surface from the superior aspect of the bone-cartilages specimens, the sections being of different diameters (~ 15–25mm) and height (~ 15–20mm),with thicknesses ranging from 200µm to 300µm. These sections were subsequently soaked in distilled water to remove any bone marrow and loose particulate matter. Morphological and elementel investigations were conducted on a scanning electron microscopy (Zeiss Supra 50 VP model SEM-EDX) with an acceleration voltage of 25 kV.

III. RESULTS AND DISCUSSIONS

The surface morphology and elemental analysis of the diseased female and male bone-cartilage specimens were characterized by scanning electron microscopy and energy dispersive X-Ray spectrometer. Figure 1 shows the SEM images of the healthy

bone-cartilage (control) sample. Result Figure 1 shows that healthy bone-cartilage have a porous structure.

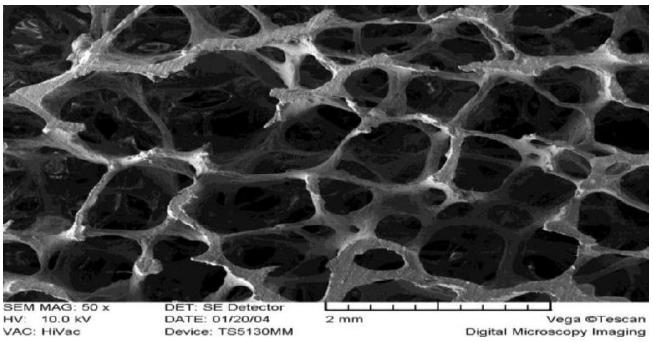


Figure 1: SEM image of healthy human bone.

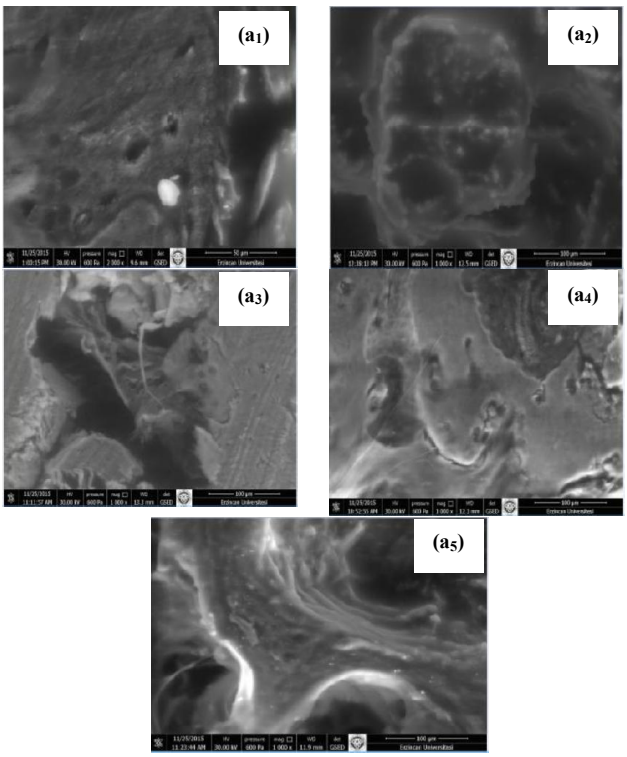


Figure 2: SEM image of bone specimens from five diseased female patients.

The cartilage surface contains the presence of lacuna, chondrocytes and the chondroblasts structures. For the osteoarthritic bone-cartilage, the level of surface deformation increased. Because of deterioration cartilage surface has occurred as the disease progresses. In bone cartilage specimens taken from female patients, it is seen that the porous structure is deteriorated due to osteoarthritis. And it causes the cellular structures in the bone to change.

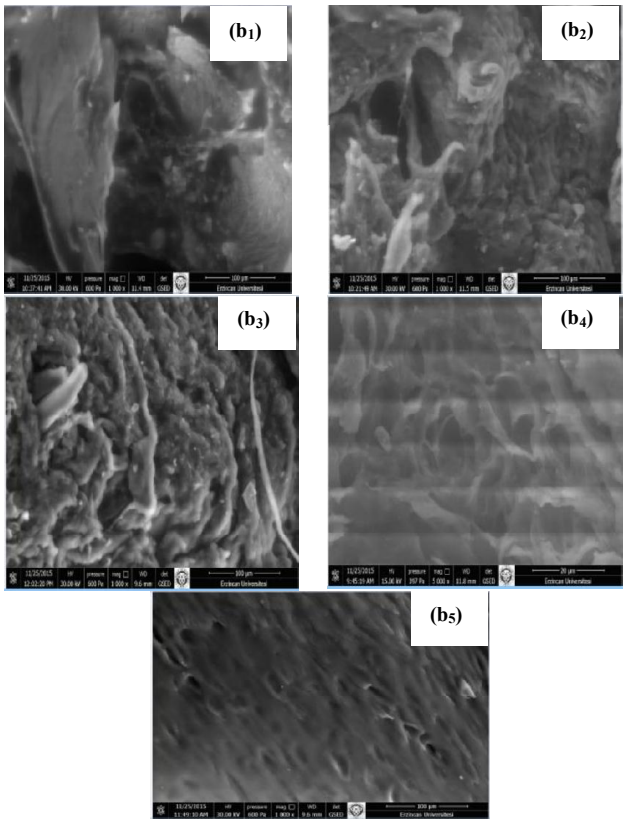


Figure 3: SEM image of bone specimens from five diseased male patients.

It is observed that the structural decay in males is less in the direction of the Fig. 3 SEM images than in the female patients, considering the relatively age function. Surface porosity and cellular structure of bone and cartilage specimens are seen to be more uniform than female.

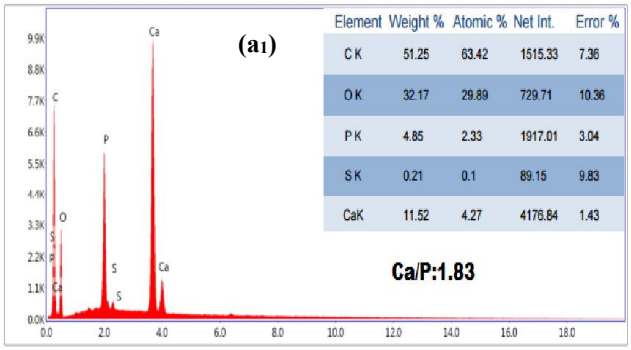
Figure 4 shows the EDX data of the osteoarthritic female and male bone-cartilage specimens. Figure 4 shows that female and male bone-cartilage samples have elements such as Ca, P, S, C, etc. It is evident that bone cartilage samples have more amounts of elements such as calcium, phosphorus, etc., than the diseased cartilage.

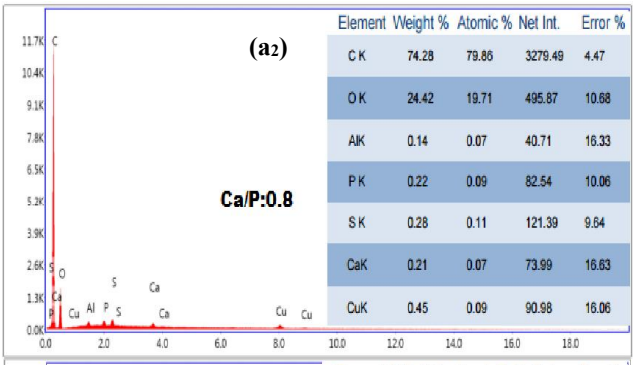
In healthy humans, the Ca / P atomic ratio in the bone structure is 1.67. This rate can vary depending on the region where the bone is located. An indication is that the specificity of the Ca/P ratio improves upon that for Ca and P concentrations and may be more reliable in the diagnosis of bone disorders [9].

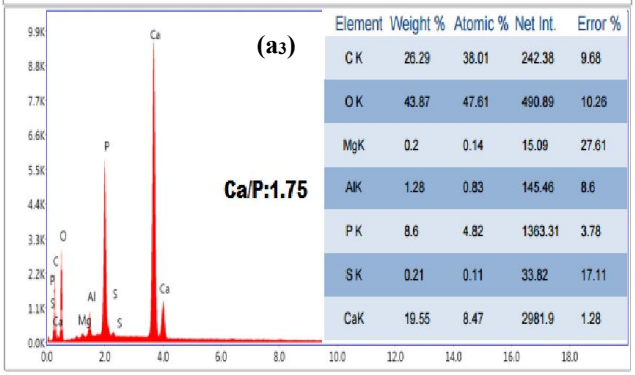
Table 1. Comparison of Ca / P ratio of male and female patients.

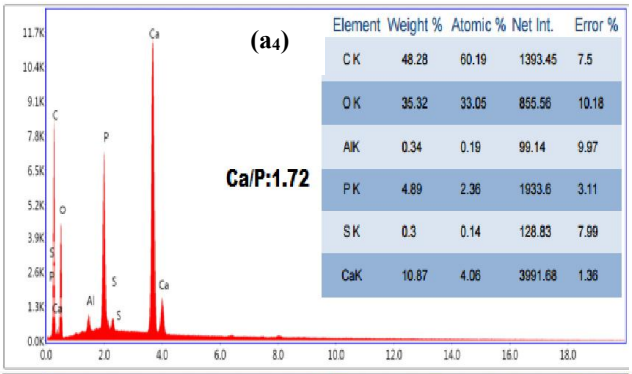
Patients	Ca/P Rate	Patients	Ca/P Rate
Female a_1	1.83	Male b_1	1.97
Female a_2	0.8	Male b_2	3.77
Female a_3	1.75	Male b_3	3.33
Female a_4	1.72	Male b_4	1.83
Female a_5	2.07	Male b_5	2.09

The skeletal Ca/P ratio has been shown to be a good index of bone quality. In addition, results presented here also confirm that there is a relationship between bone loss and a lowered Ca/P ratio. As nowadays we can measure bone Ca/P ratio in vivo for use as a clinical indicator [10.11], such measurements could also be useful for the treatment of the bone diseases in which, along with bone loss, the bone quality is affected. Bone quality, in addition to bone density, plays an important role in bone strength, and is strongly related to the Ca/P ratio.









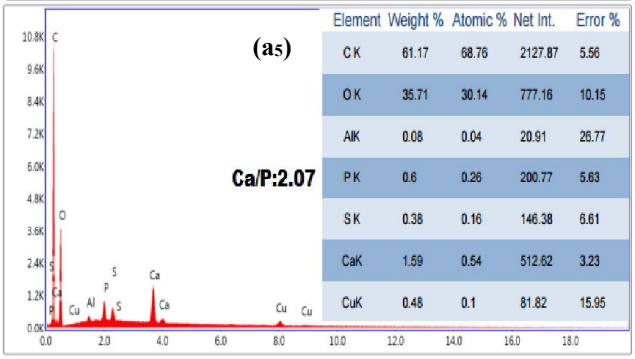
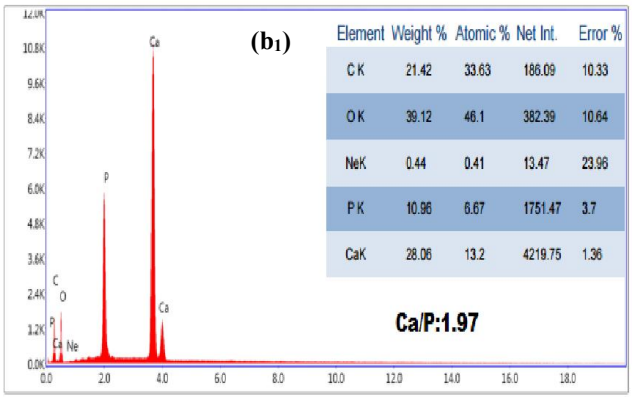
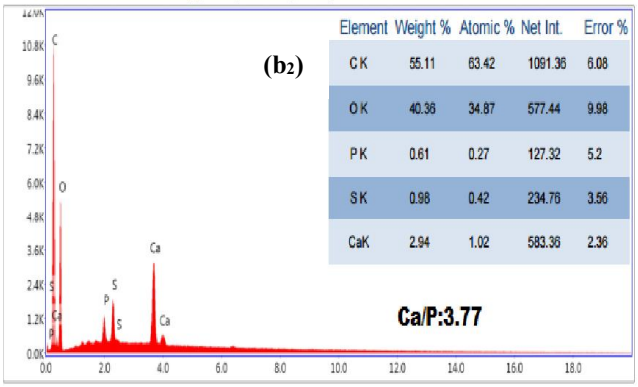


Figure 4: EDX image of bone specimens from five diseased female patients.





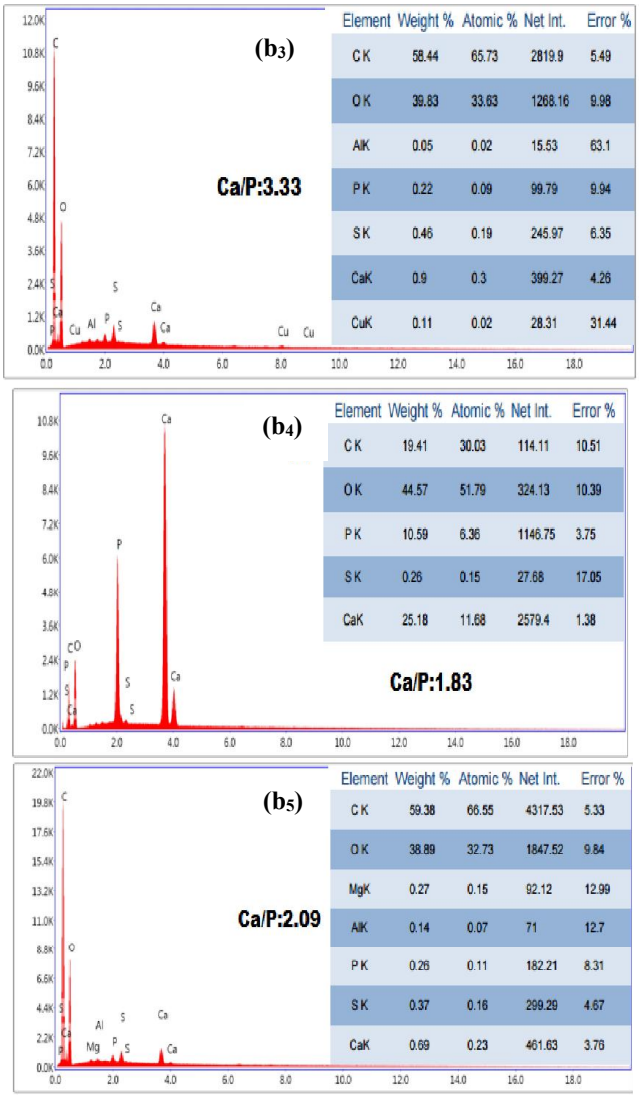


Figure 5: EDX image of bone specimens from five diseased male patients.

Therefore, it might be possible to use this biomarker for the effective diagnostic and classification criteria of osteoporosis and related diseases. Ca/P ratio is not distributed homogenously along the osteoporotic bone [12] and high Ca/P regions could form a potential criterion to enhance our perspective on osteoporosis treatment and monitoring.

IV. Conclusion

In this study, structural and elemental analysis of bone cartilage specimens taken from different regions of ten patients was performed. According to the SEM results, it is seen that the pore structure of the bone cartilage structures of the female patients is impaired and the surface is not smooth. Male patients have better structural characteristics than female patients.

EDX was used for elemental analysis. According to the results, the Ca / P ratio was out of 1.67. According to the values in the table, Ca / P ratio of female patients shows that it is closer to normal value than male. If female's disease had osteoporosis, we could look at the literature and say that this result might be very different. SEM and EDX results do not support each other. Studies on this subject will continue.

Acknowledgment

We would like to acknowledge the financial support given by the Kocaeli University Research Foundation, Project No: 2017/088.

References

[1] Lau AG, Kindig MW, Kent RW. (2011)Morphology, distribution, mineral density and volume fraction of human calcified costal cartilage. *Acta Biomater* 7*(3),*1202–1209.

[2] St-Pierre JP, Pilliar RM, Grynpas MD, Kandel RA. (2010) Calcification of cartilage formed in vitro on calcium polyphosphate bone substitutes is regulated by inorganic polyphosphate. *Acta Biomater* 6*(8),*3302–3309.

[3] Thouverey C, Bechkoff G, Pikula S, Buchet R. (2009) Inorganic pyrophosphate as a regulator of hydroxyapatite or calcium pyrophosphate dihydratemineral deposition by matrix vesicles. *Osteoarthritis Cartilage* 17*(1)*,64–72.

[4] S.R. Goldring, (2012) Alteration in periarticular bone and cross talk between Subchondral bone and articular cartilage in osteoarthritis, *Ther. Adv. Musculoskelet. Dis.* 4, 249-258.

[5] M.B. Goldring, S.R. Goldring, (2007) Osteoarthritis, *J. Cell Physiol*. 213, 626-634.

[6] J. Rhoa, L. Kuhn-Spearingb, P. Ziouposc, (1998) Mechanical properties and the hierarchical structure of bone, *Med. Eng. Phys*. 20, 92-102.

[7] Zhang W, Doherty M, Bardin T, Barskova V, Guerne PA, Jansen TL, (2011) European league against rheumatism recommendations for calcium pyrophosphate deposition. Part I: terminology and diagnosis. *Ann Rheum Dis* 70*(4),*563–70.

[8] Mandel N, Mandel G. (1988) Calcium pyrophosphate crystal deposition in model systems. *Rheum Dis Clin North Am* 14*(2),*321–40.

[9] Nikolaos Kourkoumelis, Ioannis Balatsoukas, and Margaret Tzaphlidou(2012 Mart) Ca/P concentration ratio at different sites of normal and osteoporotic rabbit bones evaluated by Auger and energy dispersive X-ray spectroscopy, *J Biol Phys*. 38*(2)*, 279–291.

[10] Fountos, G., Yasumura, S., Glaros, D. (1997).The skeletal calcium/phosphorus ratio: a new in vivo method of determination. *Med. Phys.* 24, 1303–1310.

[11] Fountos, G., Tzaphlidou, M., Kounadi, E., Glaros, D, (1999). In vivo measurement of radius calcium/phosphorus ratio by X-ray absorptiometry. *Appl. Radiat. Isotopes* 51,273–278.

[12] Tzaphlidou M, Speller R, Royle G, Griffiths J, Olivo A, Pani S, Longo R. (2005). High resolution Ca/P maps of bone architecture in 3D synchrotron radiation microtomographic images. *Appl. Radiat. Isotopes*. 62 pp.569–575.

XRF Characterization of Diseased Human Bone Specimens

T. ÇAYIR[1], Y. AKALTUN[2], Ö. GÜNDOĞDU[1]
[1] Kocaeli University, Kocaeli/Turkey, tubacyr@hotmail.com
[2]Erzincan University, Erzincan/Turkey, yakaltun@hotmail.com
[1]Kocaeli University, Kocaeli /Turkey, o.gundo@gmail.com

***Abstract* - In this study, bone-cartilage specimens taken during surgery were examined from patients. Twelve samples were used. Male and female sample numbers are the same. The bone-cartilage samples with disease were investigated for their elemental properties. The bone-cartilage samples with disease were characterized by Mikro-X-ray fluorescence (XRF). Elemental analysis was performed using this device and mapping of bone cartilage specimens. According to the male and the female, the results are compared. The results show that the percentage of the elements found in the bone depends on age and sex and the calcium ratio in female is higher than in male.**

***Keywords* - The male and the female, Bone- cartilage, XRF, Mapping.**

I. INTRODUCTION

LATELY, some public diseases have become not only a clinical problems, but public health problems as well, especially in poor and developing countries. One of these diseases is osteoporosis. It is defined as a systemic skeletal disease characterized by a decrease in bone mass and deterioration of the microarchitecture. Increase of bone fragility and a greater susceptibly to fractures [1] also occur. This is not the unique definition and there are many other definitions of this disease. In all of them, it is not possible to talk about osteoporosis without mentioning some fundamentals words such as, fracture, density, pores and calcium. In osteoporosis, bone mineral density decreases, causing bone fragility to increase.

In recent years, a consensus has been reached: bone mineral density alone does not explain or and predict bone health. It is necessary to look beyond this parameter, to take into consideration other aspects such as trabecular bone microarchitecture. In this context, mineral concentration and distribution of elements, such as calcium and phosphorous, have the same degree of importance. These two chemical elements, in the form of hydroxyapatite ($Ca_{10}(PO_4)_6(OH)_2$), are bone components and play an important role in the maintenance of skeletal strength. X-ray fluorescence is an analytical technique widely used to identify chemical elements in environmental, industrial and medical areas. Micro X-ray fluorescence investigates sample regions with a spatial resolution at the micrometer scale. It allows the determination not only the concentration of elements but also of their distribution. The use of synchrotron radiation in this type of research has some advantages over other X-ray sources, such as its high brilliance allowing a lower limit of detection [2].

Twelve human bone-cartilage specimens from the surgery of humans are reported in this paper. While six of the samples are of a female bone-cartilage the other is a male bone-cartilage. Prior to the sample analysis, there were no fixations, embedding or surface processing. This work is an effort to characterize the diseased female and male bone-cartilage by using a Mikro-X-ray fluorescence (XRF).The aim of this study is to make comparison of elemental properties of diseased female and male bone-cartilage samples. Mapping was done to see the superficial elemental distribution of bone cartilage specimens.

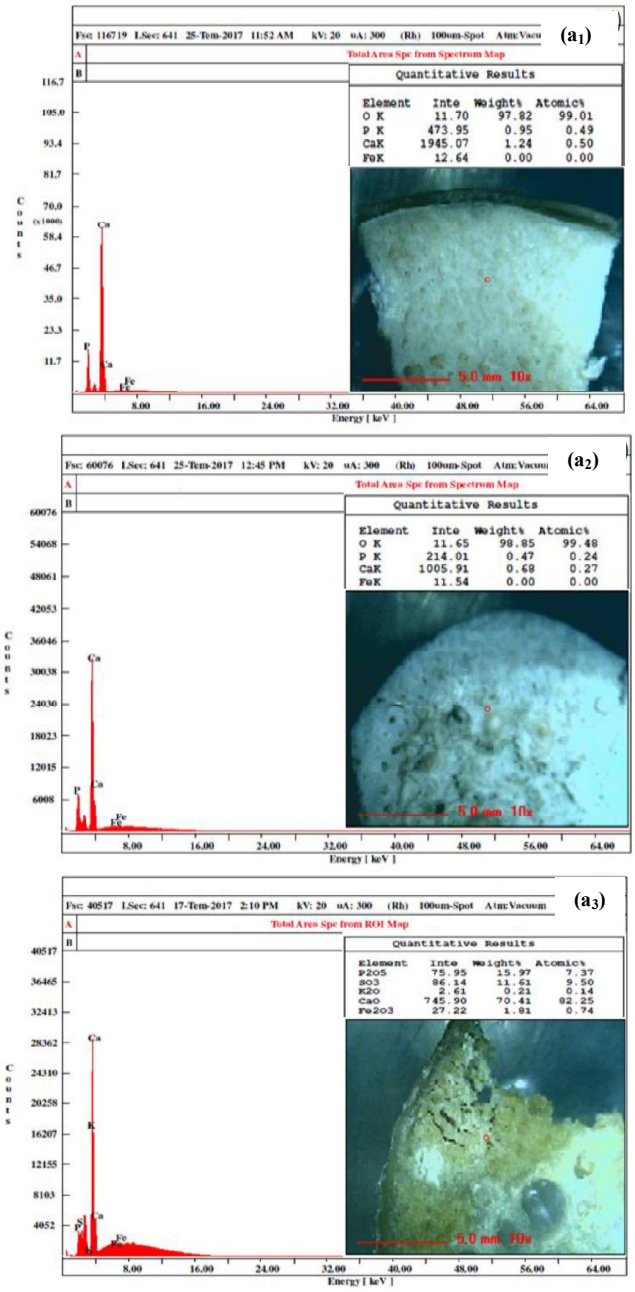
II. MATERIAL AND METHODS

Human bone-cartilages specimens from total hip replacement procedures were used, due to surgical intervention in response to a degenerative joint disease.The femoral heads were sourced from the department of Orthopedics and Traumatology at Kocaeli University(Turkey). Using a water-cooled diamond saw(Isomet 1000 Precision) several sections at certain thicknesses were cut perpendicular to the articular surface from the superior aspect of the bone-cartilages specimens, the sections being of different diameters (~ 15–25mm) and height (~ 15–20mm),with thicknesses ranging from 200µm to 300µm. These sections were subsequently soaked in distilled water to remove any bone marrow and loose particulate matter. Elementel investigations were conducted on a scanning electron microscopy (Zeiss Supra 50 VP model SEM-EDX) with an acceleration voltage of 25 kV. XRF experiments involved use of Eagle III XRF Spectrometry model at the basic science application and research center in Erzincan University (BSA-RC, Erzincan, Turkey). All the experiments were performed at 20 kV Mo K radiation with a focal spot size of 50µm × 50µm and a Si detector.

III. RESULT AND DISCUSSIONS

The elemental analysis of the diseased female and male bone-cartilage specimens were characterized by Micro X-ray fluorescence spectrometry. In healthy humans, the Ca / P atomic ratio in the bone structure is 1.67. This rate can vary depending on the region where the bone is located. An

indication is that the specificity of the Ca/P ratio improves upon that for Ca and P concentrations and may be more reliable in the diagnosis of bone disorders [3]. Twelve patients underwent XRF measurements. In Figures 1 and 2, bone-cartilage specimens taken from patients have a picture, percentage of the existing elements, and graphical representation of the existing elements with the aid of the XRF instrument.



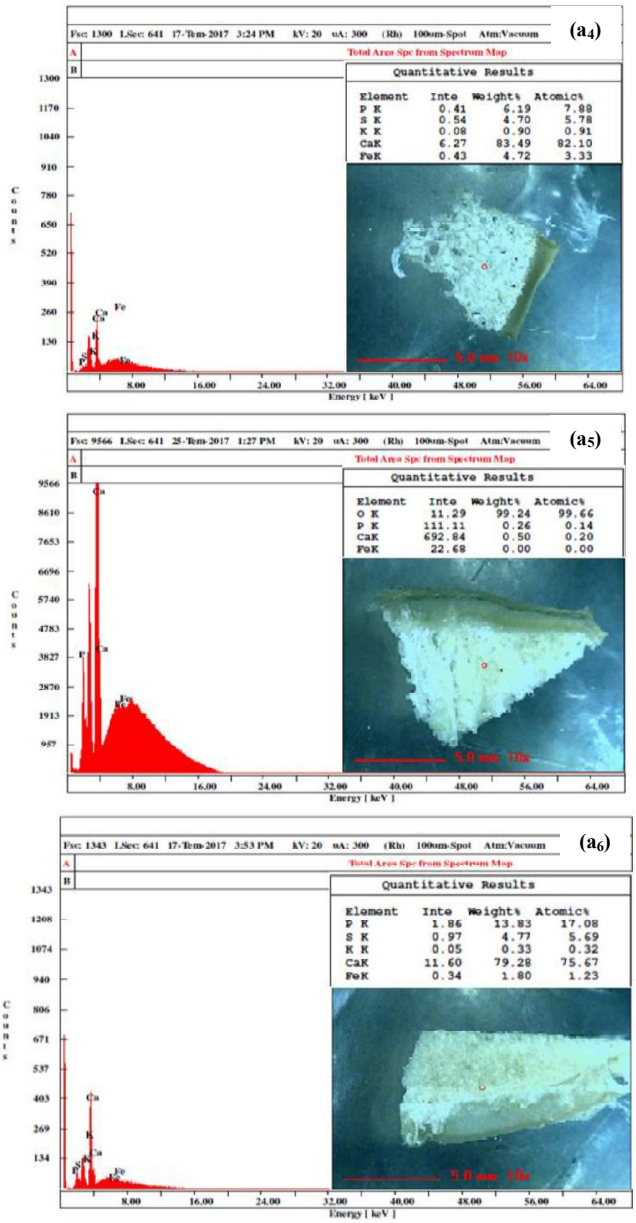
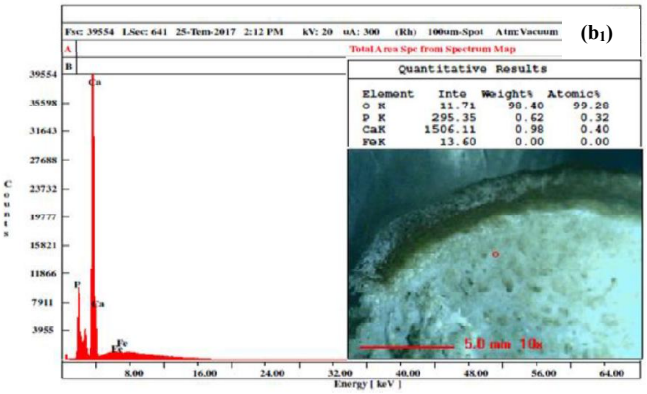
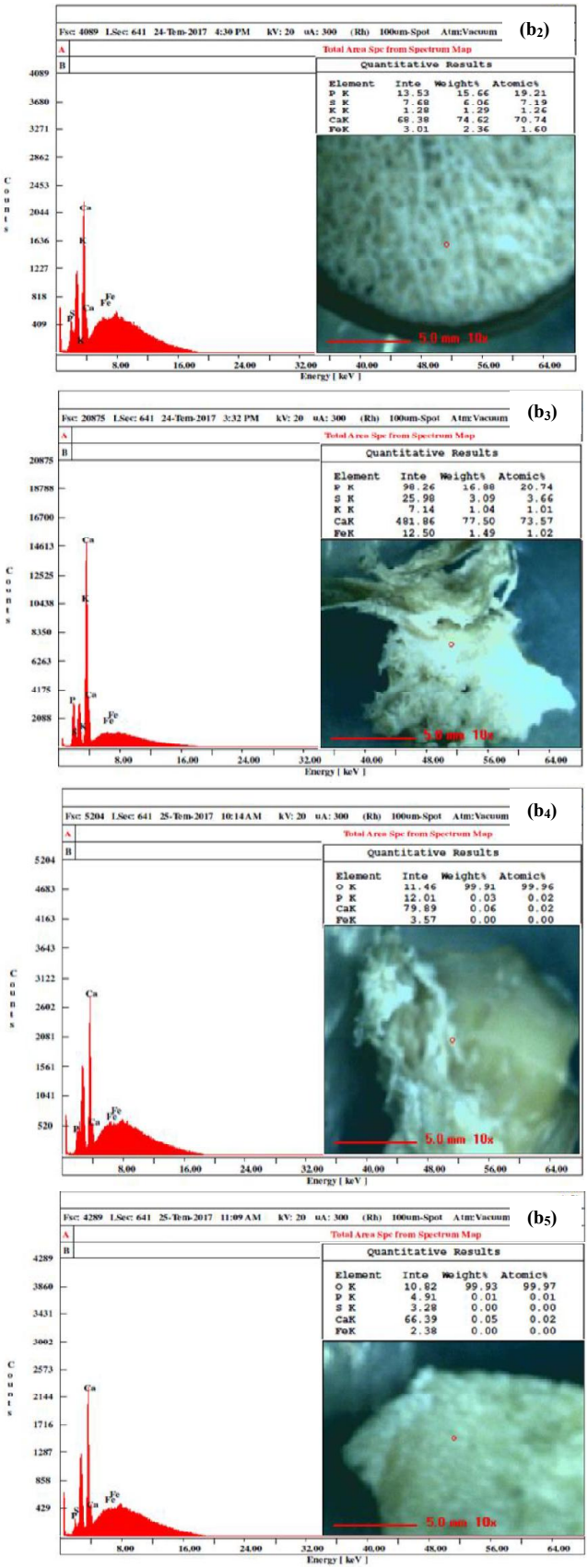


Figure 1: XRF image of bone specimens from six diseased female patients.





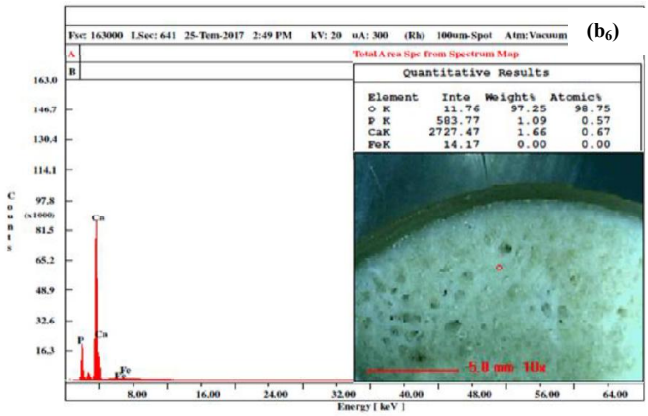
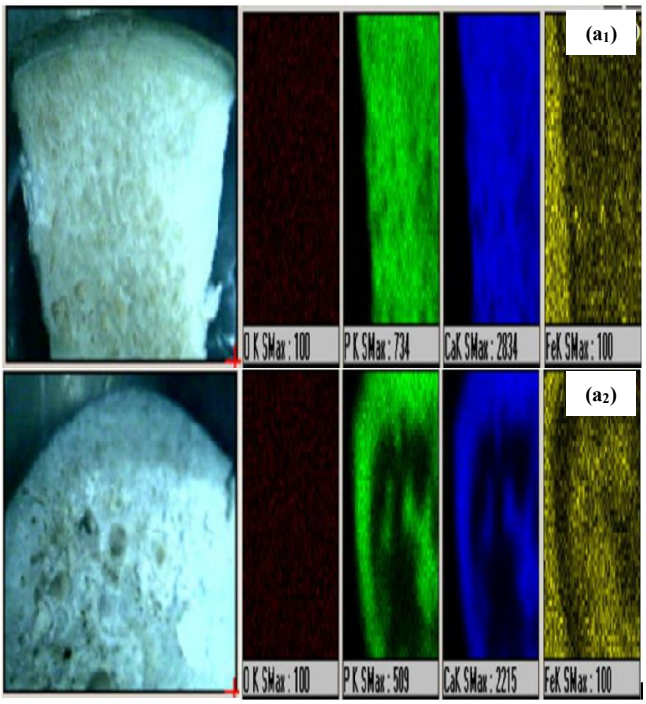


Figure 2: XRF image of bone specimens from six diseased male patients.

According to XRF results in Figures 1 and 2; the bone-cartilage samples taken from female and male patients were also found to contain Ca, P, S and K elements. The two major mineral constituents of the bone are calcium and phosphate. As the age of the patients is 65 years and over, the ratio of Ca in the male and female patients is higher than that of the P. The bone-cartilage structure is degraded depending on age. The rate of calcium phosphate in female patients is higher than that of male.



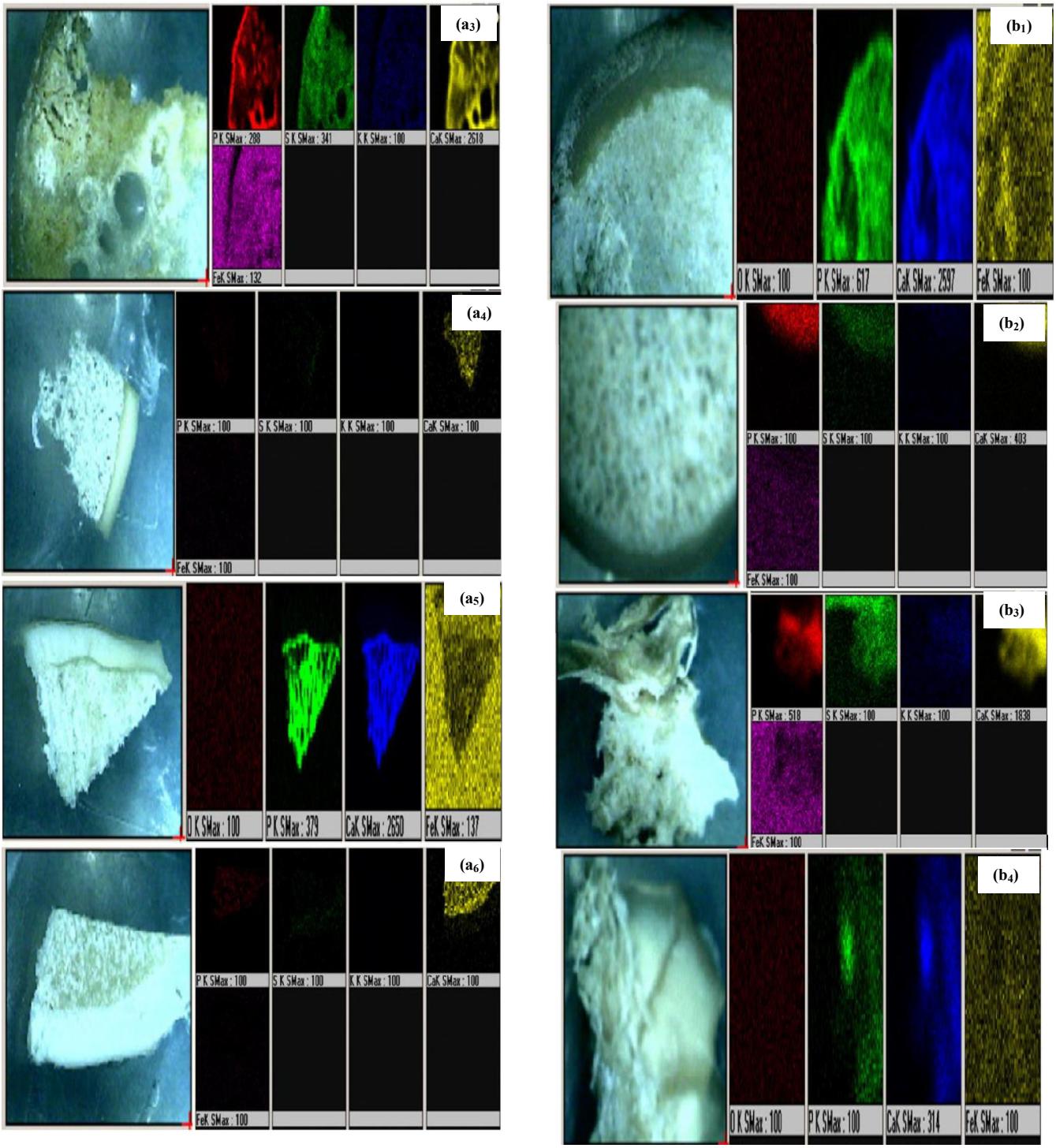


Figure 3: XRF mapping image of bone specimens from six diseased female patients.

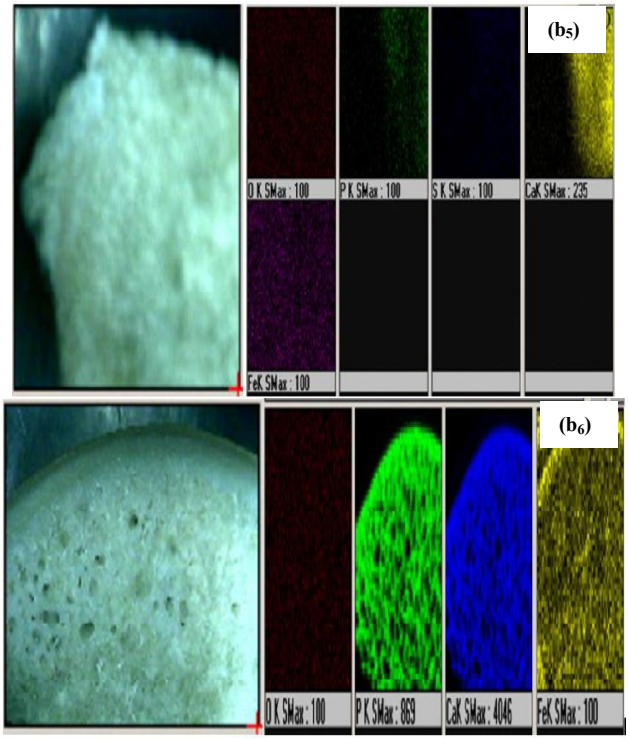


Figure 4: XRF mapping image of bone specimens from six diseased male patients.

Mapping method was used on bone-cartilage specimens using XRF instrument and the superficial distribution of the elements on each sample is shown in Figures 3 and 4. Figures 3 and 4 show areas with red, P, green, S, blue K and yellow calcium, respectively.

Table 1. Comparison of Ca / P ratio of male and female patients.

Patients	Ca/P Rate	Patients	Ca/P Rate
Female a_1	10.41	Male b_1	3.68
Female a_2	4.43	Male b_2	1.25
Female a_3	1.42	Male b_3	2.0
Female a_4	11.16	Male b_4	1.2
Female a_5	1.13	Male b_5	3.54
Female a_6	1.02	Male b_6	1.0

The skeletal Ca/P ratio has been shown to be a good index of bone quality. In addition, results presented here also confirm that there is a relationship between bone loss and a lowered Ca/P ratio. As nowadays we can measure bone Ca/P ratio in vivo for use as a clinical indicator [4, 5], such measurements could also be useful for the treatment of the bone diseases in which, along with bone loss, the bone quality is affected. Bone quality, in addition to bone density, plays an important role in bone strength, and is strongly related to the Ca/P ratio. Table 1 shows that the Ca / P ratio of female patients a, b and d were 10.41, 4.43 and 11.46, respectively. The Ca / P ratio of the patients we named as b_1 and b_5 in male patients were 3.68 and 3.54, respectively. Among the female patients, calcification was seen in patients referred to as a_1, a_2, and a_4. These patients also have a higher rate of calcium than other female patients. According to the results we have obtained, in patients with male patients the patients named b_1 and b_5 have been calcifications.

IV. Conclusion

In this study, structural and elemental analysis of bone cartilage specimens taken from different regions of twelve patients was performed. Elemental analysis was performed with XRF instrument. The results show that the calcium ratio in female is higher than in male. The percentage of the elements found in the bone depends on age and sex and the percentages are determined. This shows that the calcium phosphate ratio is also an amorphous phase in both female and male, depending on sex and age.

This suggests that the specificity of the Ca/P ratio is better than that of Ca and P concentrations and may be more reliable for the diagnosis of bone disorders.

Acknowledgment

We would like to acknowledge the financial support given by the Kocaeli University Research Foundation, Project No: 2017/088.

References

[1] NIH Consensus Panel on Osteoporosis Prevention, (2001)Diagnosis, and Therapy. *J Am Med Assoc* 285:785.

[2] I. Lima, M.J. Anjos, M.L.F. Farias, T.U. Pantaleão, V.M. Corrêa da Costa, R.T. Lopes, (2008) Evaluation of osteoporotic bone structure through synchrotron radiation X-ray microfluorescence images, *European Journal of Radiology* 68S, S95–S99.

[3] Nikolaos Kourkoumelis, Ioannis Balatsoukas, and Margaret Tzaphlidou(2012 Mart) Ca/P concentration ratio at different sites of normal and osteoporotic rabbit bones evaluated by Auger and energy dispersive X-ray spectroscopy, *J Biol Phys*. 38*(2)*, 279–291.

[4] Fountos, G., Yasumura, S., Glaros, D. (1997).The skeletal calcium/phosphorus ratio: a new in vivo method of determination. *Med. Phys.* 24, 1303–1310.

[5] Fountos, G., Tzaphlidou, M., Kounadi, E., Glaros, D, (1999). In vivo measurement of radius calcium/phosphorus ratio by X-ray absorptiometry. *Appl. Radiat. Isotopes* 51,273–278.

Preparation of Patterned Scaffold for Tissue Engineering Application.

A. AROGUZ* and H.SARIOGULLARI
Istanbul University, Faculty of Engineering, Istanbul, Turkey
aroguz@istanbul.edu.tr

Abstract
The aim of this study is to prepare patterned polimeric retainers using biopolimers and to examine their biotechnological applications. For this purpose, micro patterned polymeric materials were prepared and their morphological properties were analyzed using scanning electron microscope (SEM) and optical microscopy (OM).

For their biotechnological applications, L929 fibroblasts cells were seeded on the surface of these materials and the growth of cells present on these surfaces were spectroscopically quantified using a Neutral Red uptake assay. During the experimental work cell growth was observed on the prepared samples. More efficient results were observed on some samples. Because of their usability in the cell growth studies and researches, the biomaterials prepared in this work as scaffold will contribute to the tissue engineering investigations.

Keywords **–** Soft lithography, biomaterial, cell growth, scaffold, pattern, tissue,

I. INTRODUCTION

In recent years, an increase of scientific studies on the micro and nano-sized structures of the materials is observed. In particular, lithography method allows the investigation of the behavior of micro-scale structures economically and without requiring fully-equipped laboratories. Soft lithography, which is one of the lithography techniques, finds wide application areas to produce biosensors and prototype devices to be used in tissue engineering [1-4].
Soft lithography techniques allows to control growing of the cell. The controllability of cells grown in scaffolds constructed by micro-printing in a cellular environment can be increased by this technique. In addition, studies on biosensors and hybrid systems in tissue and cell engineering are enhancement. Soft lithography technique is one of the patterning techniques used; polydimethylsiloxane (PDMS) molds and micro channels [5,6].

Tissue scaffolds form the surface necessary for cells to adhere. Mechanical continuity with physiological and biologically relevant changes [7,8]. It also helps regenerate the extracellular matrix in its natural form. Tissue scaffolds must be formed from biodegradable materials and they must be degradable in the environment of the living system. Once the proper environment is established, the material should not produce toxic material without losing its biocompatibility. It should also be in a porous structure suitable for the passage of cells and nutrients. These biomaterials can be new composite materials formed by natural polymers (collagen, chitosan, alginate etc.), bioceramics (tricalcium phosphate, hydroxyapatite) or their mixtures. The aim of this study to prepare tissue scaffolds by processing of the biomaterials. For this purpose polydimethylsiloxane (PDMS) molds were prepared in this study. The patterned structured molds were used to transfer of the patterned onto the glass material coated with titanium dioxide. For comparison, growth and proliferation of cells on PDMS molds were investigated.

II. MATERIALS & METHODS

Materials:
Polidimetilsiloksan (PDMS); General formula of PDMS is $CH_3[Si(CH_3)_2O]_n\ Si(CH_3)_3$ and purchased from Down Crown company. It was used for pattern transfer. Its commercial name is Sylgard 184 dür. Its density is 0,980 $g.cm^{-3}$. Ethanol,Sulphuric acid, Hydrogen peroxide and acetic acid were supplied from Merck company. Polietilen glikol dimetilakrilat (PEG-DMA), $(C_4H_5O)(C_2H_4O)_n$ $(C_4H_5O_2)$, Undecanethiol and Octadecan ethiol were obtained from Sigma – Aldrich .

Experimental
The steps of the experiment are given as follow:

- Preparation of PDMS mold
- Titanium coating of microscope glass
- Design of alkanetiolated pattern on titanium coated
- microscope glass with PDMS mold
- Cell seeding on patterned surfaces

Preparing of PDMS mold

•Drawing photomasks in computer environment
•Removing the photomask
•Photoresist in coating on the microscope glass
•patterned of photoresist
•Formation of fluid PDMS polymer

•Pouring of PDMS onto photoresist

• solidified PDMS mold
Pattern Creation on Titanium Coated Microscope Cam with PDMS Molding.After produced patterned surface cell growth experiments were followed.

Figure 1 shows schematically the experimental procedure.

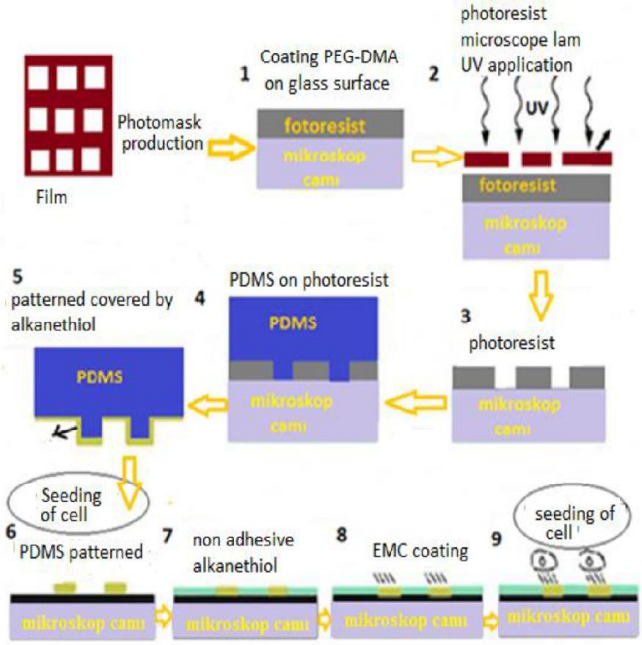


Figure 1: Schematically the experimental set procedure.

The prepared PDMS molds were used to transfer the patterns on the photomask onto the glass substrate coated with titanium dioxide.
For comparison, growth and proliferation of cells on PDMS molds were investigated. These materials have been found to be biocompatible constructs suitable for cell growth and proliferation.

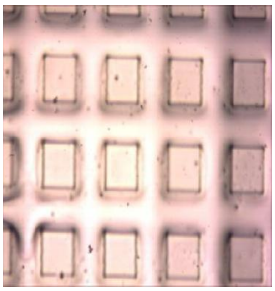


Figure 2: Patterned photoresist



Figure 3: PDMS Pattern

Seeding cell on the surface of the material:

250,000 pieces of cells were seeded on titanium coated glass to investigste the growth of cells with **Neutral Red Assay**. The alkanethiol was used in the preparation of titanium-coated glassware. The increase or decrease in the number of cells under the influence of various chemicals has been observed. L929 mouse fibroplast cells were used in the study. The concentrations of the cells on the titanium-coated glass were monitored by spectrophotometry with the concentration of the neutral red solution retained by the cells. For this purpose, absorbance values of the neutral red solution used in the study were determined separately by UV-spectrophotometric measurements.

RESULTS & DISCUSSION

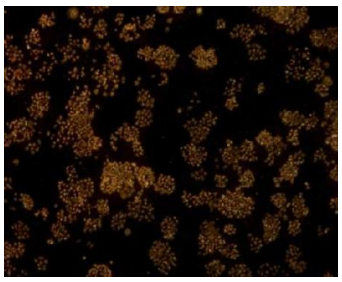


Figure 3:Cell seeded on the material surface

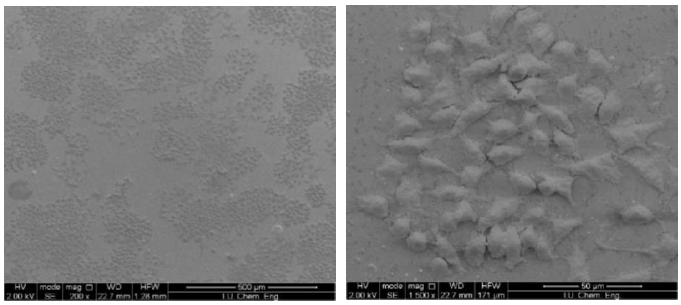


Figure 4: A) 200 x magnification B) 1500 x magnification of SEM

In this study, polymer scaffolds were prepared by lithography technique under different conditions. As a biotechnological application of prepared specimens, cell seeding and

multiplication were investigated. Cell growth was observed in all samples where cell seeding was performed. Successful results were obtained in the sample prepared using hexadecanethiol in 60% acetic acid. Similar features have been observed in Suh et al.'s study [9]. When alkanethiol effect was examined in PEG-DMA coated samples, undecanethiol was found to give better results. Scaffold structures prepared in different shapes are used for various purposes in tissue engineering. It is expected that the scaffolds prepared in this study will be used effectively in tissue engineering and biotechnological applications in cell duplication studies.

Acknowledgment
This work was supported by the Research Fund of the Istanbul University. Project number: BAP-42735. Financial support of Istanbul University is gratefully acknowledged.

REFERENCES

[1] J. Lu and R.P. Wool, "Novel thermosetting resins for SMC application (2001)

[2]. S.Yang,K.F. Leong,Z. Du,C.K. Chua, The design of scaffolds for use in tissue engineering, *Traditional factors, tissue engineering Part I*, 7, 679–689 (2001)

[3]. A.K. Vogt, G. Wrobel, W. Meyer ,W. Knoll, Offenhausser A., , Synaptic plasticity in micropatterned neuronal Networks, *Biomaterials,* 26, 2549–57 (2005)

[4]. K.E.Schmalenberg, K.E. Uhrich. Micropatterned polymer substrates control alignment of proliferating Schwann cells to direct neuronal regeneration, *Biomaterials,* 26, 1423–30 (2005)

[5]. C.A. Scotchford, M.Ball, M. Winkelmann, J.Voros, C. Csucs, D.M. Brunette, G. Danuser, M. Textor, Chemically patterned, metal-oxide-based surfaces produced by photolithographic techniques for studying protein– and cell– interactions, II: protein adsorption and early cell interactions, *Biomaterials,* 24, 1147–58 (2003)

[6]. M.E.Hasenbein M.E., T.T. Andersen, R. Bizios, Micropatterned surfaces modified with select peptides promote exclusive interactions with osteoblasts, *Biomaterials*, 23, 3937–42 (2002)

[7]. A.L.Thangawng, M.A. Swartz, M.R.Glucksberg, R.S. Ruoff, An ultra-thin PDMS membrane as a bio/micro–nano interface: fabrication and characterization, *Biomed microdevices,* 132– 138 (2007)

[8]. M.Mrksich, E.D. Laura, J. Tien, E.I. Donald, G.M. Whitesides. Using Microcontact Printing Pattern The Attachment of Mammalian Cells to Self- Assembled Monolayers of Alkanethiolates on Transparent Films of Gold and Silver, Experiment cell research 235, 305-313 (1997)

[9]. K.y. Suh, I. Seong, A. Khademhosseini, P.E. Laibinis, R. Langer, A simple soft lithographic route to fabrication of poly(ethlenehlycol) microstructures for protein and cell patterning, *Biomaterials*, 25 557-563 (2004)

For patient with end-stage Amyotrophic Lateral Sclerosis (ALS) patients, intelligent bed control due to simultaneous patient eye movement

A.KAGITCI[1] and I.SARITAS[2]

[1] Adil Karaagac Vocational and Technical Anatolian High School, Konya/Turkey, azizkgt@hotmail.com
[2]Selcuk University, Konya/Turkey, isaritas@selcuk.edu.tr

A*bstract-A*myotrophic Lateral Sclerosis (ALS), also named as motor neuron disease, is a disease originating from the loss of motor neuron cells (neurons) in spinal cord and the area named as brain stem in central nervous system. The loss of these cells causes that patient lives bedridden in end-stage by leading to weakness and myolysis (atrophy) in muscles. However, there would be no deterioration in mental functions and memory[17].

Because of weakness in motive power, patients have difficulty in getting in touch with other people and making necessary bed moves for the protection of health of the body. Development of an image processing-based real time smart bed control system, which would make possible to remove these negative cases through blinking behaviors, constitutes the main goal of this study. Therefore, an image capture and processing station has been available with the patient's side. Bed movement has been determined with respect to blinking behaviors of the patient by connecting data imported to patient bed's control card.

Keywords **–ALS, image processing, smart bed, blinking**

I. INTRODUCTION

Human health is one of the main reasons shaping this study as an important subject being the basis of majority of scientific researches. One of the important subjects in the sense is that patients with end-stage ALS can meet their some needs without needing any helper at hospital or home. The fact that in-patients can be interfered in case of emergency as soon as possible matters to patients' lives. Therefore, nurses or patient relatives should be informed of patient's situation quickly in case of emergency. At the same time, a warning module is used in the smart bed system with this aim. Wearable accessories were mostly used in the past so that body movements could be recognized by computer systems. Today, thanks to development of processor technology and software potentiality, it can be applied in the most basic manner with the help of only one camera or body movements can be perceived by computer systems by using stereo visual techniques through multiple cameras. This development is shown in the fields of human-computer interaction, robot control, virtual reality and interactive graph [1].

Reviewing eyelid's opening and closing movements creates a significant model to be able to answer the questions on such matters as people's reactions to external factors or nervous system-based eyelid movements. To make samplings, it is necessary to perceive eyelid's mechanical movement in the way it can be a processable answer and to record it [2].

A human-machine interface has been proposed by Chau and Betke for its use by severe disabled people. People with such diseases as Amyotrophic Lateral Sclerosis (ALS) cannot control or move any other parts of their bodies out of their eyes. The proposed system creates an input to end up with a mouse click on computer system by determining people's eye blink orders and measuring their periods. The system detects the place of eyes from involuntary eye blinks in the first few seconds and then monitors eye with an online template. If an instantaneous change of depth or head movement in user occurs, the system would restart. There is no need for prerecorded patterns or special lighting for operation of the system. The system works at the rate of 30 frames per second by cheap USB cameras. Such parameters as different lights and environments have led to more accuracy and to increases in detection of voluntary and involuntary eye blinks in widely experiments [1, 6].

The system developed by Ince and Yang has made technologically convenient view tracking application for decades. However, the currently used systems are expensive. One of the reasons for the study is to research the methods of reduction of these costs. To detect pupil, an accurate and quick algorithm has been suggested. The introduced algorithm has been built on differential geometry [1, 13].

In a study by Brandt & Associates, visual driver monitoring system has been introduced with the aim of observing drivers' head and eye blink sequences. The system can detect fatigue and monotony symptoms based

on these measured traits. Basic advantages of the system proposed against the existing ones are its use to ensure a good price/performance ratio of standard hardware, rapid calculation time and the potentiality to measure in darkness and to be able to care about monotony. Image analysis has been made in a rough-thin architecture. Firstly, driver's face has been detected based on developed Haar ripple train. Then, eyes on face have been looked for and eye blink with optic flow analysis of eye area has been measured. Performance of the system has successfully been tested under ideal and natural conditions [1, 16].

Helping people's special needs is a subject cared by society and continuously new applications are interested in the subject in response to technological development. In a study by Corno and his friends, a system providing choice of certain points of the screen has been introduced by using views of the user, whose most important traits are simplicity and affordability, as computer input by the method of eye monitoring [1, 14].

A study by Wei-Gang and Associates has been recommended an automatic eye blink translator system for severe disabled people. Firstly, SVM has been applied and then eye blink has been monitored. After that, eye blink behavior has been coded by being translated into binary system. Then, eye blink order has been translated into a command for human-machine interface [1,15].

In this project, the patient's face and then eyes in his image taken by a camera will be found by Haar Cascade classifier within OpenCV image library. To be able to monitor eye blink, pupil of the patient will be detected by circular Hough transformation. Those digital data analyzed by image processing algorithms will be processed with Python program. Necessary commands will be sent onto patient bed's control card and the system will be checked. In response to certain eye blink movements of the patient, the system is activated. These movements have been pre-taught to the patient before. Hence, eye-blink rule sequences of the patient have been determined. When these special sequences occur by the patient, bed used by the patient comes to the position desired by him by changing its position. At the same time, the patient will be able to enable a call system attached to bed in any negative case. The fact that the system has a usable structure will provide that it would appeal to a large mass, whose physical disability rate is high.

II.METHOD

In this study, it will be realized that motionless patient front view images captured by camera would be assessed and consequently coded messages given by the patient in the form of eye blink would be transmitted into a control card. Through this control card, the control process of patient bed position motors and authorized warning system will be executed. The system is designed as computer program, camera, computer and model and the warning system is composed of siren and beacon lamp.

Footage of the camera placed in front of patient will constantly be checked by computer program (PYTHON). When patient composes one of the recognized eye blink series, message will be transmitted to bed position motors or warning system identified in the relevant series.

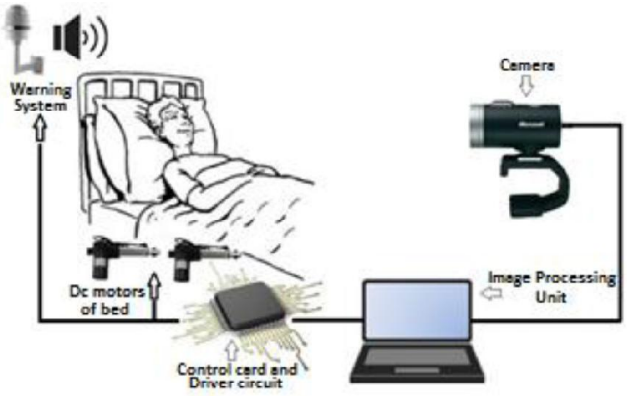


Figure-1 General structure of the system

II. I. Camera

Our goal in this study is to turn eye blink movements into commands by transmitting patient's eye blink movements onto computer. Therefore, it is to provide that patient can check the system by himself. Image sensors in the cameras used today are generally complementary metal oxide semiconductor (CMOS) and charge coupled device (CCD). CCD was found by Willard BOYLE and George SMITH at BELL laboratories in 1970[3].

Cameras with CCD and CMOS sensors have advantages and disadvantages with respect to each other. However, what is desirable here is to take the best image under every condition. Used technology, data transfer rate, resolution and FPS-frame per second are determinant attributes.

In our study, 1080p Full HD Camera of the A4 Tech firm shown in Figure 2 will be used. The camera we use comes up with results near 30 fps in all resolution values. It is crucial that FPS rate should be high enough to make real-time process. Universal Serial Bus (USB) is used as data transfer technology on the camera. The fact that the camera has a high FPS rate brings flexibility into software to be developed. If frames aren't processed quickly enough, performance of the system would decrease by exceeding real-time process limit [1].

Choice of the quickest way in the methods of image processing used and of field of interest as least as possible will considerably impress processing speed. That's why, camera, the only input device of the system, has a key role.



Figure-2 A4-Tech 1080p Full HD Kamera

II.II. Program and Flow Algorithm

Python as software and OpenCV as image processing library will be used.

Python is a high degree object-oriented, interpretive, modular and interactive programming language. There is an existing potentiality to develop software with Python in such many fields as system programming, user interface programming, network programming, application and database software programming [12].

OpenCV is a "Computer Vision" library licensed with BSD license by being developed by Intel. The fact that it is developed by aiming at real-time applications especially, free of charge including its commercial use and can be used on such different platforms as Windows, Linux, MacOS X makes it step forward from other image processing instruments. CV (Computer Vision) is one of the five basic libraries containing high degree algorithms [10].

Face detection methods were summarized in the study of Yang & Associates. In the relevant study, face detection methods were collected under four titles. They are knowledge-, constant trait-, template matching- and view-based face detection methods. Face detection is the phase to determine whether there is a face in image captured as input image and if available, where the face is. Output of face determination is input of face detection and eye situation. That's why, the fact that this phase is carried out truly and effectively would directly affect accuracy and activity of the system to design [11].

In the designed system application, Haar cascade classifier model, widely used in determination and detection of objects for face and eye determination, has been used.

To find and monitor objects in very useful and necessary videos or images for image processing, haar Cascade classifier you can find in OpenCV library were composed by Paul Viola and Micheal Jones as a solution for this problem. At the same time, it is also known as Viola and Jones object detection framework. In the most basic sense, objects to be wanted to be found according to a certain algorithm are introduced to computer at first and then objects are tried to be found by scanning images or video frames including similar shapes [1].

In the study, Haar cascade classifiers (HKS), a powerful method against dimension/orientation changes in detection of the place of human face candidate areas on real-time flown video image by using Haar attributes, have been used.

First of all, face area is determined with the help of Haar classifier. Then, eyes are determined by running Haar classifier again in determined face area. That kind of consecutive use of Haar classifier has positively affected outputs of the system under variable ambient conditions by preventing incorrect determinations.

Because eye blink movement is the main element of our study, Circular Hough transformation has been used to determine the circular form in eye's visual image.

Hough transformation is a frequently-used analysis algorithm to determine lines and other shapes (generally circular) in visual images. Basically, it has been developed to determine straight lines in black and white images. Besides, it is used in determination of non-linear and non-straight curves [4].

Eye blink movements taken will be transmitted onto Python program simultaneously. Thanks to patient interface program patient' eye blink movements are used with OpenCV view library, it will be assessed according to the algorithm given in Figure 3.

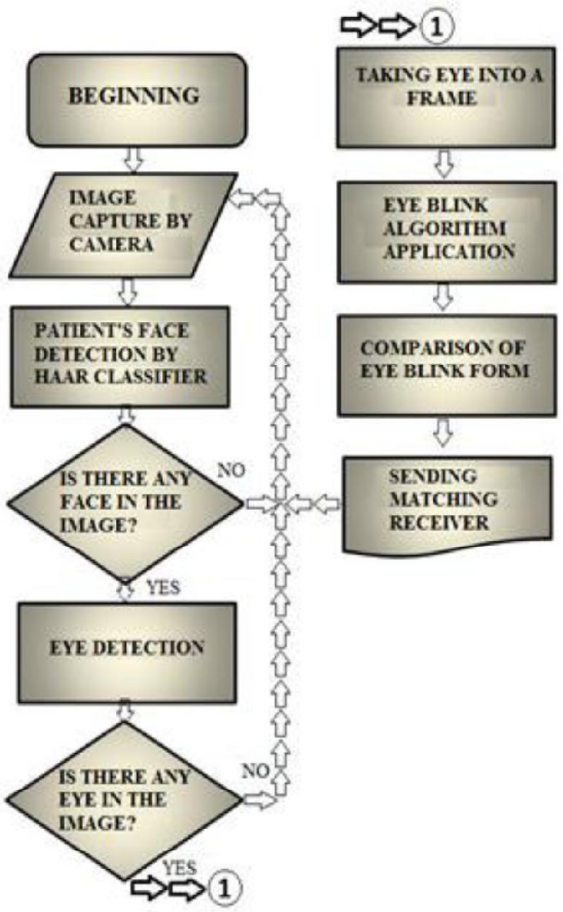


Figure -3 Software Flow Chart [1].

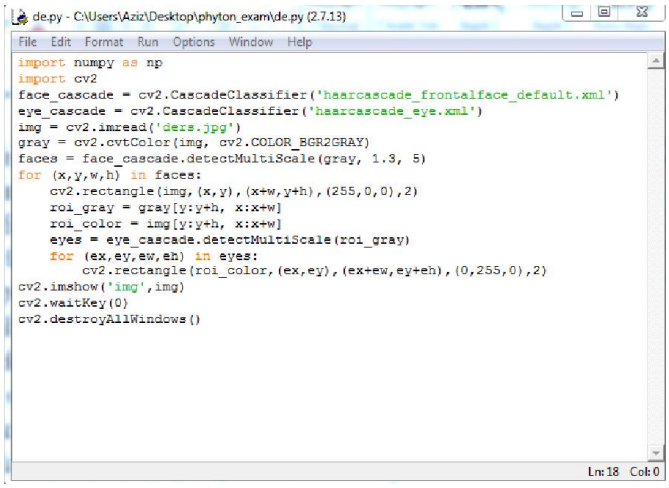


Figure-4 Haar Cascade Python software

By using Python program, the necessary software for the process of face and then of eye detection in an image will be as seen in Figure 4.

When the software given in Figure 4 is applied to an image, face area has been determined first. Then, the part of eye has been determined. In Figure 5, an image Haar Cascade classifier has been applied to is seen.

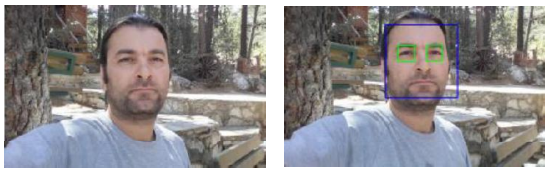


Figure-5 Face and eye detection by Haar Cascade classifier

The part constituting the main theme of our study is to detect eye blink movement. By using Python program, the necessary software for the process of face and then of eye detection through camera will be as seen in Figure 6.

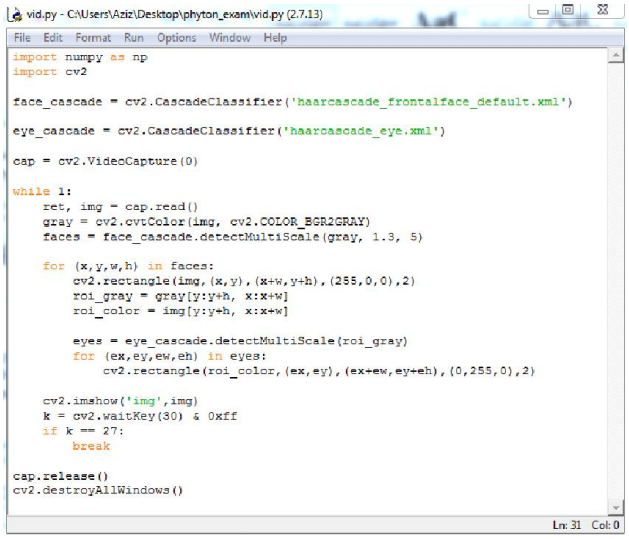


Figure-6 Haar Cascade classifier face and eye detections with the help of camera.

II. III. Control Card and Driver Circuit

Arduino is very popular in the whole world today. When we search on the Internet, we can see tens of and even hundreds of Arduino projects. In addition, Arduino cod base is very developed with the contribution of developers. There are existing libraries for a lot of hardware. Arduino has a lot of variations. These cards are still being developed.

In this study, Arduino as control card and UNO model shown in Figure 7 as model have been used. Arduino UNO is an Arduino card using ATmega328 microcontroller. Arduino UNO has 14 digital input / output pins. 6 out of them can be used as PWM output. In addition, it has 6 analog inputs, a 16 MHz crystal oscillator, USB connection, power jack (2.1 mm), ICSP header and reset button [8].

Hardware and pins on Arduino can be easily controlled by codes loaded onto Arduino. There are Atmel microprocessors on Arduino to process those codes written by programmer. Types of Arduino depend on types of those microprocessors. If a code written for a type of Arduino doesn't use hardware unique to that type, it would work on other types of Arduino with no problems. That's why, most of Arduino projects almost work on every type of Arduino [9].

Pins on Arduino can supply 50 mA current at maximum. It is impossible that DC motors we will use for smart bed design work at this current value. Motor driver circuit should be used to be able to control motor by Arduino card.

Variation of motor driver circuit generally varies by the value of current it can give. Because DC motors we will use in our study is test-purpose, motor driver given in Figure 8 will be sufficient.



Figure-7 Arduino UNO [8].



Figure-8 L298N Motor Driver Card [8].

L298 N motor driver circuit is a driver to control two motors at the same time. It can supply approximately 2 A

current per channel. Along with DC motor, it is used in driving step motor.

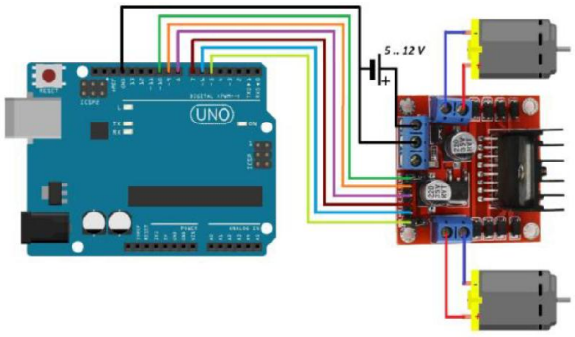


Figure-9 Arduino UNO DC motor connection [5].

II. IV. Arduino Communication with Python

We will read data on SerialPort by using Python programming language and exporting data to our Arduino UNO card over SerialPort. We will make these processes by using the module named PySerial on Python.

As an example of the communication between Arduino UNO and Python program, a connection scheme of led control is shown in Figure 10.

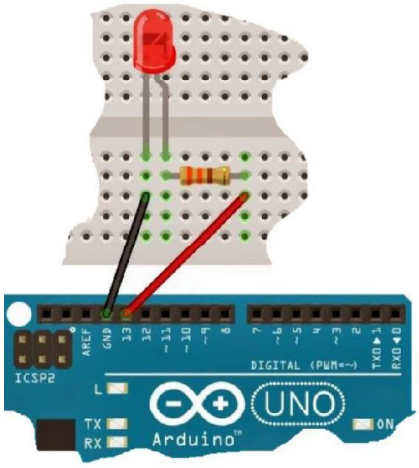


Figure-10 Arduino UNO Led connection [7].

As seen in Figure 10, we will try to turn the LED connected to 13th pin on. In the essence of our study, DC motor controlling patient bed and devices to be used for warning system will take this LED's place. It will be appropriate to connect a 330 ohm resistor before the LED we will use because it is 2,2 volt[7].

If data from serial port with Arduino code sequence given in Figure 11 is '1', it would turn LED on, if it is '0', it would turn LED off.

```
int led = 13;
void setup()
{
pinMode(led, OUTPUT);
Serial. begin(9600);
}
```

The connection diagram of Arduino UNO and L298N motor driver card is seen in Figure 9 [5].

```
void loop()
{
if(Serial. available())
{
int oku = Serial. read();
if(oku=='0')
{
digitalWrite(led, LOW);
Serial. println("Led Yandi");
}
Else if (oku=='1')
{
digitalWrite(led, HIGH);
Serial. println("Led Söndü");
}
}
}
```

Figure-11 Arduino UNO code sequence [7]

In the case given in Figure 12, we send the command of "1" in Python code sequence, therefore LED turns on. When Arduino detects the command, it will show the command of "LED turns on" to us [7].

```
deger = 1
serialport = Serial. Serial('COM3', 9600)
serialport. write(bytes(deger, 'utf-8'))
serialport. flush()
print(serialport. readline())
```

Figure-12 Python program code sequence [7]

Bed model to be used as patient bed has been designed as a patient bed with 2 motors. Position changes of bed motors are shown in Figure 13. When patient's eye blink movements has one of the predetermined values, bed motors' positions will change.

There is a warning unit connected to the control card of patient bed in the system at the same system. This unit will become active when one of the pre-taught eye blink movements. This unit to be used as vocal and visual warning pointers is shown in Figure 14.

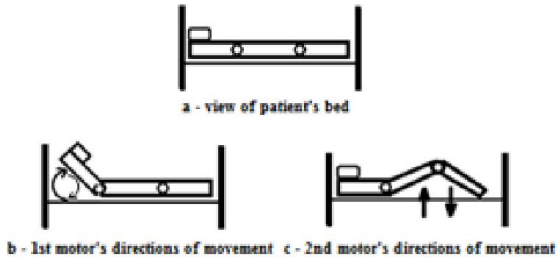


Figure-13 Patient Bed's motor positions



Figure-14 Vocal and visual warning system

III. CONCLUSION

It is aimed in this study that patients with end-stage ALS disease can meet their certain needs with eye blink movements. Smart bed system has been recommended with this aim. It is necessary to recognize a set of commands with eye blink movements for all necessary commands in the usability of beds by severe-disabled people within the scope of this system. Therefore, it is required that patient's eye blink movements are interpreted with the help of a camera. We interpret this process with code structure we write by Python program and activate control and warning systems of patient bed with conclusion data.

We use OpenCV Library for recognition of user's eye blink movements by camera. Eye blink movements from camera provide us with understanding what he wants to from his eye with the help of code structure written on Python programs and OpenCV Library Haar cascade classifier. It is ensured by the comparison of patient's pre-taught eye blink behaviors. As a result of this comparison, our control card would activate motors or warning system.

Arduino UNO has been used as control card. Because Arduino UNO gives various opportunities for the communication of a computer and another Arduino or other microcontrollers. In addition, it provides that computer software sees this card a com port.

Development of the system we recommend is that it is ensured that people with ALS and severe physical disability use certain bed movements and use of warning systems through their eye movements at homes or hospitals. Therefore, it is foreseen to rise the standard of living of that kind of patients.

The next phase is the application of commands to home, hospital or a disabled chair or process over wireless connection or Bluetooth. The fact that the system has portable dimensions provides ease of use.

REFERENCES

[1] Özyurt O., 2012, Design and application of real-time communication system for disabled patients, Postgraduate Thesis, T.C. Selçuk University, Institute of Science, Department of Electronic and Computer Systems, Konya.

[2] Fikirli M.A., Uzunoğlu C.P.,Solmaz I.A.,Uğur M.,2015,Dedectıon of eye-blink movements with Sensors ,Elektrik-Elektronik Mühendisliği Bölümü İstanbul Üniversitesi, İstanbul

[3] Taylor, S.A., 1998, CCD and CMOS Imaging Array Technologies: Technology Review, Xerox Research Centre Europe Cambridge Laboratory, EPC-1998-106.

[4] Temiz M.S., Külür S., 2011, Rectification of video image with the help of breakpoints, TMMOB Chamber of Map and Cadaster Engineers, 13. Turkish Map Scientific and Technical Congress 1822, Ankara.

[5] L298n Arduino Library,07.10.2017, http://www.instructables.com/id/L298n-Arduino-Library/

[6] Chau, M., Betke, M., 2005, Real Time Eye Tracking and Blink Detection with USB Cameras, Boston University Computer Science, No. 2005-12.

[7] Arduino Communication with Python,05.10.2017, https://www.python.tc/python-ile-arduino-haberlesmesi/

[8] What's Arduino / Genuıno Uno,06.10.2017, http://www.robotiksistem.com/arduino_uno_ozellikleri.html

[9] Açık F.,2015, Pong Game with Arduino, Department of Computer Engineering, Faculty of Engineering, Karadeniz Technical University, Design Project, Trabzon

[10] Erişti E.,2010, A New Breath in Image Processing, OPENCV, Academic Informatics'10 – XII. Academic Informatics Conference Proceedings, Muğla University, Muğla

[11] Yang G.,Thomas S.H. ,1994,Human face detection in a complex background pattern recognition, Vol.27,No. I,pp,53-63, Elsevier.Science.Ltd

[12] What's Python 01.10.2017, https://www.pythontr.com/makale/python-nedir-235,

[13] İnce, G.F., Yang, T.C., 2009, A New Low-Cost Eye Tracking and Blink Detection Approach: Extracting Eye Features with Blob Extraction, 5th International Conference on Intelligent Computing, South Korea, 526-533.

[14] Corno, F., Farinetti, L., Signorile, I., 2002, A Cost-Effective Solutıon For eye-gaze Assistive Technology, Multimedia and Expo, ICME '02, Lausanne, Switzerland 433-436.

[15] Wei-Gang, C., Huang, C.L., Hwang, W.L., 2007, An Automatic Eye Wink Interpretation System For The Disable, International Conference on Multimedia and Expo, ICME 2007,Beijing, China, 979 – 982.

[16] Brandt, T., Stemmer, R., Rakotonirainy, A., 2004, Affordable Visual Driver Monitoring System for Fatigue and Monotony, Intemational Conference on Systems, Man and Cybemetics, The Hague, Netherlands, 6451-6456.

[17] What's Amyotrofik lateral skleroz(ALS) ,24.01.2017 https://tr.wikipedia.org/wiki/Amyotrofik_lateral_skleroz

Biorefinery concept: Current status and future prospects

Melih Soner Çeliktaş, Merve Uyan, F. Müge Alptekin

Ege University, İzmir/Turkey,merveuyn@gmail.com

Ege University, İzmir/Turkey,f.mugealptekin@gmail.com

Abstract - **A brief review has been done of studies in biorefinery, in order to provide an introduction to the subject from the market potential. A biorefinery can be considered to be an integral unit that can accept various biological nonfood feedstocks and convert them into a range of useful products including chemicals, energy, and materials. Bio-based products are a great curiosity question of whether it gets to replace fossil-based products. Biomass, a renewable source of carbon, is guaranteed a place in the new energy portfolio for the foreseeable future. The use of renewable energy sources efficiently as possible with biorafinery concept. Today, the factory is going to study the conceptual stage with integrated Biorafinery system; although the future seems to be successful.**

Keywords - **Biorefinery concept, Techno-economic analysis, Bioeconomy, Biofuels, Market potential of biorefinery.**

INTRODUCTION

Biorefineries, as the name suggests, have so far been conceptualised around energy and biofuels. A biorefinery is a facility, somewhat analogous to the petroleum refinery, which integrates biomass conversion processes and technologies to produce fuels, power and chemicals. Biorefinery systems have emerged as an attractive route for energy generation, in the form of combined heat and power (CHP) and biofuels, alongside chemical production, with great promise for reduced environmental impact [1,2].

If all of the bioresources within the biorefinery structure are efficiently used, including the biological leftovers from a cascade transformation process approach, a nearly zero waste production is achieved. Nowadays global biorefinery concept mainly includes terrestrial biomass with plants and foreston top and only small part has recently been devoted to algae [3]. Since mainly first and second generation biomass is used for liquid biofuels production, it is significantly affecting the economy due to the competition for food and energy.

As bioethanol, biodiesel, biogas or biomethane in the world, the most widely produced a large part of the first generation of biofuels biofuels were classed at the beginning of the 2000s [4]. It is observed reduction in greenhouse gases as a result of the use of the first generation biofuels but food is not sustainable due to the excessive demand. This demand, the food industry waste or in this sector of the inevaluation products has emerged from the second generation biofuels [5]. The second generation biofuels are more environmentally friendly [6] and competitive [7] than the first generation biofuels. The implementation of non-food, lignocellulosic natural resources is of particular interest, in order to minimize the impacts on the food and fodder markets.

Marine macroalgae or seaweed have a high potential to partly replace terrestrial biomass. With current research going on in this field it is already declared that algae is a 3rd generation bioresource and doesn't compete with food and feed plants, nor is using resources for their growth [3].

Increasing efforts are being made to reduce the dependency of the world economy on crude oil as an exhaustible natural resource. One of the most promising approaches is to develop processes that allow the use of biomass as an alternative natural resource base [8]. In this sense, the biorefinery concept emerges as an option similar to oil refineries, where biomass is fractionated into added value products with different yields and distributions. Moreover, these distributions vary widely depending on the physical and chemical nature of the raw material as well as on the economic interest of the process [9, 10, 11, 12, 13].This estimate includes biorefinery products that could replace fossil-based products that are chemically identical (e.g. ethylene from bioethanol can replace ethylene from natural gas) and those that could substitute for products having similar functionality (e.g. polylactic acid can substitute polyethylene terephthalate used for plastic bottles) [14].

To ensure sustainable use of biomass, cascading approach has been developed which promotes that product with the highest value is made first, then the second highest is made and so on. Bioenergy and biofuels are made using leftovers from other production processes. This approach increases resource efficiency and adds even higher value to used biomass, which is a part of circular economy. Increased resource efficiency also is saving the raw material supply, because biomass can be used repeatedly. With this principle usually the problem is that leftover biomass has to be transported from one location to another to continue with the next step of production, but biorefinery concept solves this problem since the concept is meant to be implemented in one location [3].

As a result, GHG emissions reduction, fossil energy saving and economic potential of biorefinery products have become important measures that make a biorefinery a plausible alternative to crude oil refineries [15].

The Role in Industry of the Biorefinery

The biorefinery concept has been practised widely in the corn wet mill industry, the pulp and paper industry and, more recently, the biofuel industry through the expansion of their product portfolios with value added products in the search for improved process economics and environmental sustainability [16, 17].

The Communication on the Lead Market Initiative (COM(2007) 860 final) indicated six sectors as lead markets: eHealth, protective textiles, sustainable construction, recycling, bio-based products, and renewable energies [18].

In order to decide on a suitable product portfolio, the following five criteria were formulated [19] :

- High theoretical product yields from substrate.
- Market interest in the product as an end product or as an industrially important intermediate.
- High production volume (current or potential).
- Nonfood use of the product.
- Ability to be biologically synthesized from the common sugars derived from various forms of biomass.

IEA Bioenergy Task 42 recently coined a formal definition for biorefinery as "the sustainable processing of biomass into a spectrum of bio-based products (food, feed, chemicals and/or materials) and bioenergy (biofuels, power and/or heat)" (Figure 1).

This means that a biorefinery can be a concept, a facility, a process, a plant, or even a cluster of facilities that obviously requires the integration of many different areas of knowledge encompassing chemical engineering, chemistry, biology and biochemistry, biomolecular engineering, and other fields [20].

In this way, biorefining can provide a sustainable approach to valuable products that can also improve biomass processing economics as well as environmental footprint (e.g., GHG savings) if a fully integrated concept is developed [20].

The integration of bioconversion and appropriate chemical technologies is critical to the successful translation of refinery concepts to aqueous transformations.

In the case of chemical technologies and chemical production, this means the use of green chemistry methods including heterogeneous catalysis and the application of green chemistry principles [20].

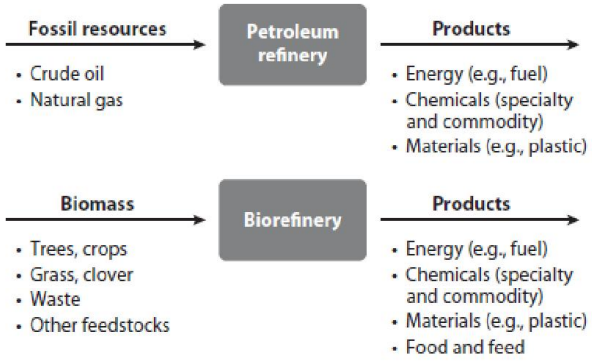


Figure 1. The biorefinery concept: from biomass to valuable products via low-environmental-impact valorization practices.

The main focus of biorefinery systems which will come into operation within the next years is on the production of transportation biofuels. The selection of the most interesting biofuels is based on the possibility that they can be mixed with gasoline, kerosene, diesel, and natural gas, reflecting the main advantage of using the already existing infrastructure in the transportation sector. The volume and prices of present and forecasted products should be **market competitive** [21].

Biorefineries show promises both for industrialized and developing countries. New competences, new job opportunities, and new markets are also expected to elaborate. The economic value of biomass is determined by the revenue from the various products on the market and the production costs (e.g., capital and operation costs) of the various products [21].

In addition, also the size of the market is relevant for the economic feasibility of biorefining. In most of the cases, products with a high market value have a relative small market (e.g., speciality chemicals) and vice versa (e.g., liquid transportation fuels). Economic values of fossil feedstocks to be possibly substituted by biomass show large differences (Table1).

Table 1. Fossil-derived product substitution options (cost price per GJ end product)

	Fossil Feed Stock (€3/GJ)	Biomass Cost (€3/GJ)
Heat	3(coal)	4
Power	6(coal)	22
Transportation fuel	8(oil)	10
Avarage bulk chemicals	30(oil)	75

The economic value of biomass feedstocks grossly exceeds the value associated with their caloric value (which is only €3/GJ). They could represent values of up to €75/GJ, provided that components could be obtained in a pure form.

Assuming a biomass yield of 10–20 tonnes of dry weight per hectare per year and that the biomass will just be used for its caloric value, this would represent a value of €450–900/ha

per year, values that are too low for farmers in Western Europe to make an acceptable standard of living. Things would be different if we could separate biomass into fractions that can be used to produce food, feed, biobased products (chemicals, materials), and/or bioenergy (fuels, power, and/or heat). As we saw above, separated biomass fractions can generate financial returns exceeding their caloric value alone. Assuming that 20% of biomass is suitable to produce chemical compounds, 40% to produce biofuels, and the remainder to produce power and heat, a biomass yield of 10–20 tonnes dry matter per hectare biomass yield potentially could generate € 2000– 4000/ha, enough for farmers to make an acceptable standard of living [21].

Even accounting for unavailability of supply LNG markets are not expected to rebalance before the mid-2020s. For now, LNG prices remain low (Figure 2), only one final investment decision (FID) for new liquefaction facilities has been taken in 2017, and demand, while growing robustly, is not keeping pace with the addition of supply [22].

The economic production of transportation biofuels is often a challenge. The coproduction of chemicals, materials, food, and feed can generate the necessary added value. Recently a paper was published highlighting all biobased chemicals with immediate potential as biorefinery "value-added products". The selected products are either demonstrating strong market growth or have significant industry investment in development and demonstration programs [21].Table 2 gives an overview of the major similarities and dissimilarities of petrochemical refineries and biorefineries.

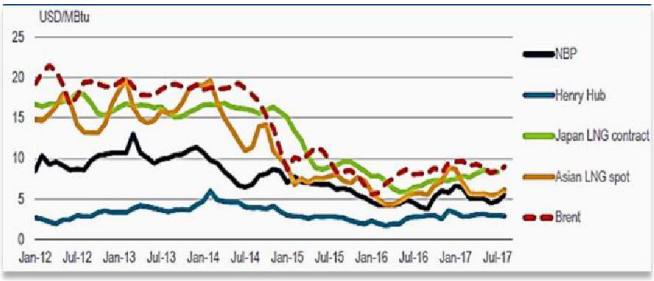


Figure 2. Gas price development, 2012-17

Note: NBP = National Balancing Point (United Kingdom).

Sources: NBP, Henry Hub, Japan LNG contract and Brent data: Bloomberg Finance LP; Asian LNG spot data: ICIS (2017a), *ICIS LNG Edge*, www.icis.com/energy/liquefied-natural-gas/lng-edge (subscription required).

Biorefining requires further innovation but offers opportunities to all economic sectors. Building a biobased economy can help to overcome present difficulties while laying the foundation of an environmentally benign industry [21].

Table 2. Comparison of refineries and biorefineries regarding to feedstocks, building block composition, processes, and chemical intermediates produced at commercial scale

	Refinery Biorefinery	**Biorefinery**
Feedstock	Feedstock relatively homogeneous	Feedstock heterogeneous regarding bulk components e.g., carbohydrates, lignin, proteins, oils
		extractives, and/or ash Most of the starting material present in polymeric form
		(cellulose, starch, proteins, lignin)
	Low in oxygen content	High in oxygen content
	The weight of the product (mole/mole) generally increases with processing	The weight of the product (mole/ mole) generally decreases with processing
		It is important to perceive the functionality in the starting material
Building block	Main building blocks: Ethylene, propylene, methane, benzene, toluene, xylene isomers.	Main building blocks: Glucose, xylose, fatty acids (e.g., oleic, stearic, sebacic)
(Bio)chemical processes	Almost exclusively chemical processes	Combination of chemical and biotechnological processes
	Introduction of heteroatoms (O, N, S)	Removal of oxygen
	Relative homogeneous processes to arrive to building blocks: Steam cracking, catalytic reforming	Relative heterogeneous processes to arrive to building blocks
	Wide range of conversion chemistries	Smaller range of conversion chemistries: Dehydration, hydrogenation, fermentation
Chemical intermediates produced	Many	Few but increasing (e.g., ethanol, furfural, biodiesel, mono-ethanolglycol, lactic acid, succinic acid, …)

Biomass-Biorefinery-Bioeconomy

Biorefineries are a promising integrated approach for the co-production of both valueadded products (bio-materials, bio-chemicals, bio-plastics, food, feed) and bioenergy (biofuels, biogas, heat and/or electricity). The bio-based economy integrates the full range of natural and renewable biological resources (land and sea resources, biodiversity and biological materials (plant, animal and microbial)—and biological processes. In this respect, a bio-based economy is nothing new in itself, as before the industrial revolution, economies were mainly bio-based. Biomass is already used as feedstock for example wood based materials, pulp and paper production, biomass-derivedfibres, and as biofuel feedstock (from oilcrops, starch and sugar crops). Nevertheless, the transition toward a modern bio-based economy implies challenges such as the sustainability of biomass raw material, efficiency in biomass use and economy of scalesin biomass mobilization [27].

Biorefinery can use various combinations of feedstock and conversion technologies to produce a variety of producs. However, most of the existing biorefinery concepts use limited feedstock and technologies, and soley produce bioetanol or biodiesel. Only a small fraction of materials are used for chemical and chemistry products that have a higher value-added [28]. Because of that the use of biomass for the production of platform chemicals has recently become an important research topic [11]. Economical and production advantages increase with the overall level of integration in the biorefinery. By missing of the existing biorefinery concepts, which are limited in the using a one feedstock and producing one product. Thanks to continuous developments in the areas of feedstock, conversion process (biochemical, chemical, and thermochemical), and their integration with powerful downstream seperations will enable more economical and environmentally sustainable options of integrated biorefinery. By integrated biorefinery concepts, it has been enabled to spreading of biorefinery implentation within a wider geographical area in all of Europe. So, the EuroBioRef project is focused on enhanced and deploying a highly integrated and varied concept with feedstock, technologies and processes that can be bundled to enable and define a new interweaved value chain with integrated flexible biorefinery facilities.

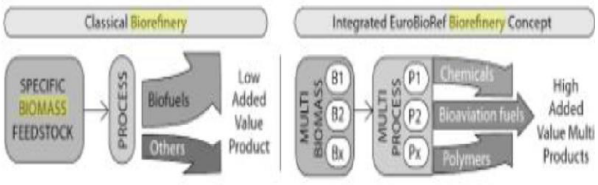


Figure 3. The EureBioRef integrated biorefinery approach

As it is understand from Figure 3 when used one specific biomass feedstock produce low-added value product, multi biomass feedstock can produce high-added value multi products by using multi-integrated process [28].

Renewable platform chemicals are often linked technologically to the biorefinery – the latter could be viewed as a key technological solution for the integrated production of food, feed, materials and products [29]. Such a step could integrate the chemical industry into the so-called bioeconomy. The main goals are to strategically reduce the dependency on crude oil and to mitigate the greenhouse gas emissions as well as the negative impacts on the environment caused by the processing and ultimately the burning of fossil carbon sources [30]. During these exciting developments it is important not to lose sight of the greenhouse gas related impacts, concern for which underpins much of the rationale behind biorefinery and bioeconomy accomplishments so far [31]. The current global market size for ethylene accounts for 127 Mt/a with a share of 0.2% (0.25 Mt/a) coming from biomass resources [30].

Future Prospects of the Biorefinery Concept

According to the Energy Information Administration (EIA, 2015), today present the annual total electricity production is 4.10 × 106 GWh. This electricity is mainly generated from fossil fuels which will cause greenhouse gases emission, particularly carbon dioxide (CO2). Electricity generation will increase our dependence on fossil fuels increases. It has been found in so many foresight studies. EIA (2015) data by looking at the energy production in 2040 will reach 21.46% increase of 5.22 × 106 GW h values. With an annual production of approximately 144 x 10 6 m 3 and a worldwide share of more than 3% based on energy content, biofuels already play a significant role in the transport fuel sector [34]. The potential biorefinery market throughout the entire biomass value chain globally has been projected as $295 billion by 2020 [35].

The mandatory targets for the use of renewable energy in transport has boosted the use of biofuels in the EU reaching 564 PJ in 2012. The NREAPs (National Renewable Energy Action Plan) forecasted a use of biofuels of about 1216 PJ Mtoe in 2020, representing more than 90% of the renewable energy expected to be used in transport (Banja et al., 2013). The NREAPs estimate that about 105 PJ lignocellulosic biofuels could be used in transport in 2020, but this depends on their commercial availability and prices.

Another study predicts; In 2011, global biofuels production stood at 1,897,000 barrels per day, up from 1,635,000 barrels per day in 2009 — a 16 percent rise in just two years. Production levels are expected to reach 2,500,000 barrels per day by 2020 [36].

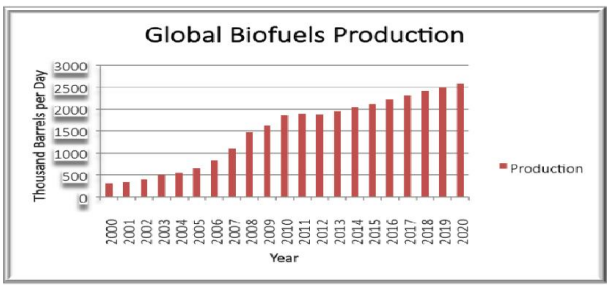


Figure 4. Global Biofuels Production

As a negative predictions; According to UNEP, 35.7 million ha were used for biofuel production in 2008 and an estimated 80 million ha are to be used by 2020.

The production of biofuels and energy is used by a majority of the resources of the forest is observed. Wood pellets of international trade, sectors constituted 7% of demand of the energy and transport in 2010. Different countries consider renewable energy targets established by taking into account the, international demand, come out on top biofuels and biomass supply is expected. For this reason, in particular the relatively limited domestic resources, such as the European Union and India's imports of biofuels and biomass is foreseen to give the speed. The imbalance in the distribution of biomass resource potential and boosting the share of bio-energy in energy production of envisioning due to political targets in 2035 biomass and biofuel is thought that she was going to 40 million TEP (in 2010 the inter-regional 6 million TEP). This increase in the scope of the United States, Canada and Russia is expected to be the largest exporters of biomass. United States and Brazil's are expected to pull head to biofuel production [38].

The best alternatives appear to be fuels of the future, especially fuels derived from microalgae. Replacing all the transport fuel consumed in the United States with biodiesel will require 0.53 billion m3 of biodiesel annually at the current rate of consumption. Oil crops, waste cooking oil and animal fat cannot realistically satisfy this demand. For example, meeting only half the existing U.S. transport fuel needs by biodiesel, would require unsustainably large cultivation areas for major oil crops. This is shown in Table 3 using the average oil yield per hectare from various crops, the cropping area needed to meet 50% of the U.S. transport fuel needs is calculated in column 3 (Table 3). In column 4 (Table 3) this area is expressed as a percentage of the total cropping area of the United States. If oil palm, a high-yielding oil crop can be grown, 24% of the total cropland will need to be devoted to its cultivation to meet only 50% of the transport fuel needs. Clearly, oil crops cannot significantly contribute to replacing petroleum derived liquid fuels in the foreseeable future. This sitituation changes when microalgeas are used instead of crops. Between 1 and 3% of the total U.S. cropping area would be sufficient for producing algal biomass that satisfies 50% of the transport fuel needs [39].

Table 3. Comparison of some sources of biodiesel

Crop	Oil yield (L/ha)	Land area needed (M ha)[a]	Percent of existing US cropping area[a]
Corn	172	1540	846
Soybean	446	594	326
Canola	1190	223	122
Jatropha	1892	140	77
Coconut	2689	99	54
Oil palm	5950	45	24
Microalgae[b]	136,900	2	1.1
Microalgae[c]	58,700	4.5	2.5

[a] For meeting 50% of all transport fuel needs of the United States.
[b] 70% oil (by wt) in biomass.
[c] 30% oil (by wt) in biomass.

Microalgea have various oil content as their spieces. Both high level oil content and less land requier they may be only sources of biodiesel that has the potential to displace crop.

Conclusions

Biorefineries are more conceptually for this moment, but the studies suggest that it may gain biorafiner with an integrated system. It should be adopted as the main material for biofuels as well as high added value byproducts is quite precious and future market share. Byproducts of biorefinery are expected to rise in the use of chemicals and materials industries. It also provides the formation of a new market for natural resources and forestry and agricultural waste. When taking into account of unsufficient land, nonfood and feedstock, the best alternative to appear of fuel is that derived from migroalgae. High level oil content and rapid growing ratio of microalgae give a future for clean fuel, chemical and energy. That apart from according to the projections made in the study exhaustible natural source the fossil fuels reducing the dependence on with using of biofuels is promising. Although the surge in oil prices are unstable, biorafineries will be the technology of 2020.

Reference

[1] Kamm, B., Kamm, M., 2005. Principles of biorefineries. Appl. Microbiol. Biotechnol. 64, 137–145 pp.

[2] Cherubini, F., Jungmeier, G., Wellisch, M., Willke, T., Skiadas, I., Van Ree, R., Jong, E., 2009. Toward a common classification approach for biorefinery systems. Biofuels Bioprod. Biorefining 3, 534–546 pp. Dalgaard, R., Schmidt, J.,

[3] Balina K.*, Romagnoli F., Blumberga D. (2017). Seaweed biorefinery concept for sustainable use of marine resources. International Scientific Conference "Environmental and Climate Technologies", Riga, Latvia. Energy Procedia, 128,504-511.

[4] Kim, S., and Dale, BE, 2005, Life cycle assessment of various cropping systems utiliized for producing biofuels: bioethanol and biodisel, Biomass Bienergy, 29: 426-439 pp.

[5] Stoeglehner, G., and Narodoslawsky, M., 2009, How sustainable are Biofuels? Answer and further questions arising from an ecological footprint perpective, Bioressource Technology, 16: 3825-38030 pp.

[6] Deurwaarsder, EP, 2005, Overview and analysis of national report of the EU biofuels directive: prospects and barriers for 2005, ECN (Energy Research Centre of the Netherlands). Available: http://www.ecn.nl/docs/library/report/2005/c05042.pdf

[7] Detchon, A., 2005, Biofuels our future: A primer. UN foundation. Available: http://www.energyfuturecoalition.org/biofuels/BioFuelsFAQ.pdf

[8] Müller-Langer, F., Majer, S., O'Keeffe, S., 2014. Benchmarking biofuels – a comparison of technical, economic and environmental indicators. Energy Sustainability Soc. 4, 20 pp.

[9] Demirbas, A., 2009. Biorefineries: current activities and future developments. Energy Conversion and Management 50, 2782–2801 pp.

[10] Lyko, H., Deerberg, G., Weidner, E., 2009. Coupled production in biorefineries—combined use of biomass as a

source of energy, fuels and materials. Journal of Biotechnology 142, 78–86 pp.

[11] Posada, J.A., Patel, A.D., Roes, A., Blok, K., Faaij, A.P.C., Patel, M.K., 2013. Potential of bioethanol as a chemical building block for biorefineries: preliminary sustainability assessment of 12 bioethanol-based products. Bioresour Technol. 135, 490–499 pp.

[12] Moncada, J., El-Halwagi, M.M., Cardona, C.A., 2013a. Techno-economic analysis for a sugarcane biorefinery: Colombian case. Bioresource Technology 135, 533–543 pp.

[13] Moncada, J., Matallana, L.G., Cardona, C.A., 2013b. Selection of process pathways for biorefinery design using optimization tools: a Colombian Case for conversion of sugarcane bagasse to ethanol, poly-3-hydroxybutyrate (PHB), and energy. Industrial & Engineering Chemistry Research 52, 4132–4145 pp.

[14] Martinez-Hernandez, E., Campbell, G.M., Sadhukhan, J., 2013, Economic value and environmental impact (EVEI) analysis of biorefinery systems, Chemical Engineering Research and Design, 9 1, 1418–1426 pp.

[15] Brehmer, B., Boom, R.M., Sanders, J., 2009. Maximum fossil fuel feedstock replacement potential of petrochemicals via biorefineries. Chem. Eng. Res. Des. 87, 1103–1119 pp.

[16] Lynd, L.R., Wyman, C., Laser, M., Johnson, D., Landucci, R., 2005. Strategic Biorefinery Analysis: Review of Existing Biorefinery Examples. NREL, Golden, CO, USA. Available: http://www.nrel.gov/docs/fy06osti/34895.pdf

[17] Janssen, M., 2012. Market potential of biorefinery products. In: Sanden, B. (Ed.), Systems Perspectives on Biorefineries. Chalmers University of Technology, Göteborg, Sweden, 26–35 pp.

[18] EC, 2007d. A Lead Market Initiative for Europe, COM(2007) 860 Final.

[19] Landucci, R., Goodman, B., Wyman, C., 1994. Methodology for evaluating the economics of biologically producing chemicals and materials from alternative feedstocks. Appl. Biochem. Biotechnol. 45, 677–696 pp.

[20] Clark J., Luque R. (2012). Green Chemistry, Biofuels and Biorefinery. Annual Review of Chemical and Biomolecular Engineering, Available: https://www.researchgate.net/publication/223981255

[21] de Jong E., Jungmeier G. (2015). Biorefinery Concepts in Comparison to Petrochemical Refineries, Industrial Biorefineries and White Biotechnology, Available: http://dx.doi.org/10.1016/B978-0-444-63453-5.00001-X

[22] OECD/IEA,2017, Global Gas Security Review, Available: http://www.iea.org/t&c/.

[23] Cherubini, F., Jungmeier, G., Mandl, M., Wellisch, M., Philips, C., Joergensen, H., Biorefineries, Adding Value to the Sustainable Utilisation of Biomass, IEA Bioenergy Publication T42:2009:01, IEA Bioenergy Task 42 on Biorefineries, 2009.

[24] Biochem, 2010. Report on the"Assessment of the Bio-based Products Market Potential for Innovation", Final Report, Grant agreement no . SI2.549080-256268, 2010.

[25] Rødsrud, G., Lersch, M., Sjöde, S., 2012. History and future of world's most advanced biorefinery in operation. Biomass Bioenergy 46, 46–59 pp.

[26] JRC, 2013. Technology Map of the European Strategic Energy Technology Plan (SET-Plan). Technology Descriptions, Joint Research Centre.

[27] Scarlat, N., Dallemand, JF, Monforti-Ferrario, F., Nita, V., 2015, The role of biomass and bioenergy in a future bioeconomy: Policies and facts, Environmental Development, 15; 3–34 pp.

[28] Aresta, M., Dibenetto, A., Dumeignil, F., Gruyter, de, W., 2012. A new concept of biorefinery comes into operation: The EuroBioRef. Biorefinery:From Biomass to Chemicals and Fuels. 2-3 pp.

[29] Kamm, B., & Kamm, M. (2007). Biorefineries – Multi-product processes.Advances in Biochemical Engineering and Biotechnolgy, 105, 175–204 pp.

[30] Taylor, R., Nattrass, L., Alberts, G., Robson, P., Chudziak, C., Bauen, A., Libelli, I.M., Lotti, G., Prussi, M., Nistri, R., Chiaramonti, D., López Contreras, A., Bos, H., Eggink, G., Springer, J., Bakker, R., van Ree, R., 2015. From the Sugar Platform to Biofuels and Biochemical. Final Report for the European Commission, E4tech Ltd, London.

[31] Kajaste, R. (2014). Chemicals from biomass – Managing greenhouse gas emissions n biorefinery production chains: A review.Journal of Cleaner Production, 75, 1–10.

[32] Naik, S. N., Goud, V. V., Rout, P. K., & Dalai, A. K. (2010). Production of first and second generation biofuels: A comprehensive review.Renewable and Sustainable Energy Reviews, 14, 578–597 pp.

[33] U.S Energy Information Administration (EIA), 2015. Annual energy outlook 2015: electric power sector, electricity supply, disposition, prices, and emissions. Available: http://www.eia.gov/oiaf/aeo/tablebrowser/#release=AEO2015&subject=6-AEO2015&table=8-AEO2015&region=0-0&cases=ref2015-d021915a [cited January 2016].

[34] Müller-Langer, F., Majer, S., O'Keeffe, S., 2014. Benchmarking biofuels – a comparison of technical, economic and environmental indicators. Energy Sustainability Soc. 4, 20 pp.

[35] King, D., 2010. The Future of Industrial Biorefineries. World Economic Forum, Switzerland. Available:

http://www3.weforum.org/docs/WEF FutureIndustrial Biorefineries Report 2010.pdf

[36] Rampalli, S., 2014, Don't Count It Out: Biofuels Industry Holds Much Promise

http://www.renewableenergyworld.com/articles/2014/06/dont-count-it-out-biofuels-industry-holds-much-promise.html

[37] UNEP, 2011, Towards a Green Economy: Pathways to Sustainable Development and Poverty Eradication, Available: http://www.unep.org/greeneconomy

[38] Deolitte, 2014, Biomass golden age. Available: http://www2.deloitte.com/tr/tr/pages/energy-and-resources/articles/golden-age-of-biomass-article.html

[39] Chisti, Y., 2007, Biodiesel from algae. Biotechnology Advanteces. 25; 294-306 pp.

Water Treatment with the Use of Reduced Graphene Oxide Filtration

Ö. BİLDİ CERAN[1], İ. SEVGİLİ[2], B. ŞİMŞEK[1] and O. N. ŞARA[3]

[1] Çankırı Karatekin University, Çankırı/Turkey, ozgebildi@karatekin.edu.tr
[1] Çankırı Karatekin University, Çankırı/Turkey, bsimsek@karatekin.edu.tr
[2] Çankırı Municipality, Water and Service Association, Çankırı/Turkey, inci_sevgili@hotmail.com
[3]Bursa Technical University, Bursa/Turkey, osman.sara@btu.edu.tr

***Abstract* - Graphene based nanomaterials are thought to be a new opportunity for the development of antibacterial materials and water purification. In this study, the physical, chemical and microbiological recovery rates of raw water were analyzed after the filtration with reduced graphene oxide. Microorganisms such as E. coli fecal, Salmonella, Enterococcus, Pseudomona aeruginosa, Staphylococcus aureus and E. coliform were successfully inhibited with using rGO in the ratio of 0.1 (v/v). In water treatment with rGO-based filtration, improvement rates of hardness, dissolved oxygen, turbidity and color properties were obtained 16.5%, 4.2%, 72.6% and 46.2% respectively.**

***Keywords* - Reduced graphene oxide, water purification, antimicrobial properties**

I. Introduction

Bacterial infection has become one of the world's largest public health issues, reported in millions of people every year [1]. Antibacterial agents are widely used in day-to-day life for the prevention of health issues due to the microorganisms [2]. The removal of bacteria from water is an important process for drinking and sanitation systems against growing outbreaks of water borne diseases [3]. Accordingly, developing material surface coatings with effective antibacterial abilities is vital for human health [4]. Due to the resistance of pathogenic bacteria against common antibacterial agents in the environment, developing novel, low cost, and environmentally friendly antibacterial agents is of current interest [1]. This purpose, several nontraditional antibacterial agents, such as carbon nanotubes [5], metal nanoparticles [6, 7] and metal oxide nanoparticles [7], have been explored in the literature. Recently, graphene based materials have been proposed as a novel effective antibacterial material, with a severe cytotoxic effect on bacteria [8, 9].

Graphene based materials are among the most promising engineering nanomaterials due to their unique electronic, thermal and mechanical properties [10-12]. These nanomaterials have been used as antibacterial agents with their physicochemical properties, such as large specific surface area, high electrophoretic mobility, high thermal conductivity, high mechanical strength and biocompatibility [1, 13, 14]. Additionally, graphene based materials have been reported to have superior antibacterial properties with minimal or no cytotoxicity to human and animal cells. As such these materials may be employed for biomedical applications [9]. Spreading microorganisms are particularly vulnerable to graphene based nanomaterials effects, since the antibacterial properties of graphene based materials have been proven by many studies [12, 15].

The extraordinary properties of graphene based materials, including antimicrobial activity, are also found in reduced graphene oxide (rGO) [11, 16]. A limited number of studies are available in the literature on the antibacterial effect of rGO. Liu at al. reported that rGO causes 75% loss of viability of Escherichia coli (E. coli) and Staphylococcus aureus (S. aureus) after 4 hour incubation [10]. In another study, bacterial concentrations of E. coli and S. aureus were inhibited by 60.4% and 67.6% with using rGO [12]. Gurunathan at al. investigated that antibacterial activity of rGO in Pseudomonas aeruginosa, which is a common Gram-negative bacterium that can cause disease in humans and animals. In addition bacterial growth was measured as turbidity. After 4 hour incubation, the loss of P. aeruginosa viability was 86% treated with rGO and turbidity measurements steadily decreased over a 6 hour period [17].

The above studies deepened our understanding of the interaction between rGO and bacteria. In this study microbiological analyzes were performed in order to evaluate antibacterial effectiveness of reduced graphene oxide on Total viable count, E-coli fecal, Enterococcus, Salmonella, Pseudomona aeruginosa (P. Aeruginosa), Staphylococcus aureus (S. Aureus) and E. coliform differently from existing literature. In addition to microbiological analyzes, alkalinity, conductivity, dissolved oxygen, turbidity, color, iron, mangan, nitrate, TIC (Total inorganic carbon), TOC (Total organic carbon), hardness, calcium and magnesium tests were performed on treated water with rGO.

II. Materials and Method

A. Materials

Graphite powder (<50µm, extra pure of 99.50 wt%), sodium nitrate (extra pure), sulfuric acid (98% for analysis), potassium permanganate (for analysis, pH 7-9), hydrogen peroxide (30%), hydrochloric acid (37%), sodium borohydride, acetone, ethanol are supplied from Merck Millipore.

B. Method

rGO synthesis

Graphene oxide was synthesized by the Hummers method. Graphite (initiation material), sodium nitrate and sulfuric acid were added into a reactor which was kept at 5°C under continuous stirring for 2h via cooled circulating water circulating. Then, potassium permanganate was slowly added into the reactor and stirred at 5°C for 2h using magnetic stirrer. Then the reaction temperature was slowly raised to 35°C. The mixture was stirred at 35°C for 30 min. Deionized water was added to the suspension and the reaction temperature was raised to 98°C as a result of the hydration heat. The oxidation process was terminated by adding 200 ml deionized water and hydrogen peroxide. Yellowish/brown color product was separated with vacuum filtration and graphene oxide powders were washed for five times with diluted hydrochloric acid solution in order to remove metal ions. Then, these powders were dried at 50°C into an oven for 12 h. GO was mechanically mixed in distilled water. It was treated thoroughly in an ultrasonic bath for three hours. Subsequently, sodium borohydride was added graphene oxide suspension. The suspension was heated in water circulator under pressurized reactor with 6 bar pressure for 24 hours and at 120°C, respectively. The precipitated reduced graphene oxides were separated by centrifugation and filtration. Reduced graphene oxides were washed with acetone, distilled water and ethanol. Then these powders were dried in the under vacuum for 24 hours.

Microbiological Analyzes

The antibacterial effect of reduced graphene oxide was studied against E. coli fecal, Enterococcus, Salmonella, P. aeruginosa, S. aureus, E-coliform and total viable count. Microbiological analyzes were carried out according to the standards of the Turkish Standards Institute (TS266). Membrane filter setup was prepared for reduced graphene oxide (dispersion was prepared to have a solid liquid ratio of 0.01% v/v). A filter system was placed on the growth medium prepared with pure water. Microbiological culture samples were taken for incubation according to the TS266 [12, 18]. Unfiltered raw water was used as a control experiment. In order to observe the effect of rGO, analyzes were made in comparison with the control experiment.

III. Characterization of rGO

rGO was characterized by FTIR, Raman, XRD and SEM-EDX. The characterization of the synthesized rGO via FTIR spectroscopy was depicted at Figure 1a. After the sodium borohydride reduction, H_2O molecules and much of the groups which contains oxide (Carbonyl C=O, hydroxyl O-H) of GO are removed according to FTIR spectra [19].

As seen in the XRD graphic, absenting of the (002) reflection peak in the diffraction pattern of the rGO demonstrates the absolute exfoliation of the GO. The formation of few layers of rGO sheets lead to broad peak around 23°. The band at 43° related to the turbostratic band of disordered rGO (Figure 1b) [20].

ID/IG values which should be maximized have been increased during the reduction process due to the formation of some new and smaller sp2 domains in Raman spectra (Figure 1c) [17, 21]. Scanning electron microscopy (SEM) employed to characterize the morphology of rGO. SEM images of rGO were shown in Figure 1d [10, 17].

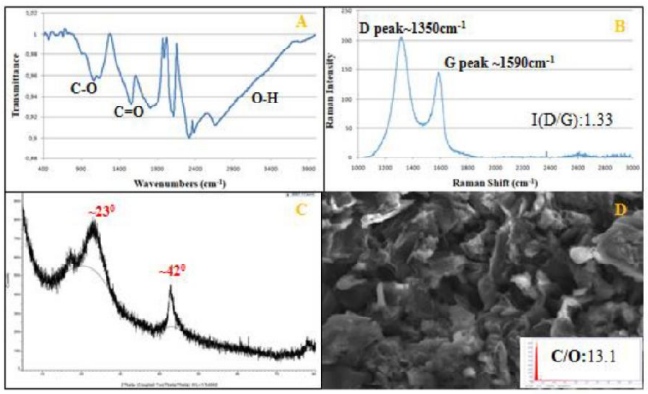


Figure 1: Characterization of rGO (a) FTIR, (b) Raman spectroscopy, (c) XRD analysis and (d) SEM-EDX (10µm)

IV. Purification Performance of rGO

A. Effect of rGO on Water Properties

HACH DR3900 Spectroscopy was used to determine water properties. Performance of raw water and treated water with rGO were analyzed physically, chemically and biologically. Alkalinity is important in the control of corrosion, which effect of drinking water pipes. High alkalinity is not harmful to human health but makes drinking water unpleasant [22]. Alkalinity amount in raw water decreased with reduced graphene oxide used in filter system. A high dissolved oxygen level in water is good because it improve the taste of drinking water. However, high dissolved oxygen levels speed up corrosion in water pipes [22]. It was observed that the conductivity and dissolved oxygen amount decreased with using rGO. The conductivity and dissolved oxygen amount of treated water with rGO is in accordance with TS266 standards.

Turbidity is a widely used parameter to evaluate the performance of water as it has close relationships with other parameters such as concentration of suspended solids and microbial population [23]. The color of the water is not necessarily dangerous and undesirable. However, some harmful microorganisms may live on foreign materials forming color [22]. So turbidity and color are important visual criteria for drinking water. Especially, when the turbidity is considered, it seems that the rGO is very successful in the treatment process. Iron and manganese help some bacteria for growing in water and cause clogging of the pipe. The presence of nitrate in drinking water causes various diseases. Calcium and magnesium are two important factors affecting hardness of water [22]. The disposal of metals, metallic elements and chemicals in raw water has been analyzed. rGO has been

successful in disposal of iron, nitrate, mangan, calcium and magnesium.

Dissolved matter in the water comes from the presence of organic and inorganic pollutants. And these pollutants affect water properties such as taste, hardness, corrosion [24]. When the disposal of organic and inorganic pollutants with rGO is analyzed, it appears that the reduced graphene oxide is successful in removing organic pollutants from water. However, the recovery of inorganic pollutants has not been achieved. The presence of minerals in drinking water (hardness) is preferred not only because of the health benefits, but also the flavor. On the other hand, soft water tastes salty and is sometimes not suitable for drinking. However, excess water hardness often causes deposits in pipes and in household appliances, which can harbor microbial communities [24]. In addition, rGO appears to be very effective for removing hardness of raw water. According to TSE266 standard, soft quality water is obtained.

B. Effect of rGO on the Microbiological Properties of Water

In this study it is aimed to prevent growing of microorganisms that reduce water quality and threaten human health with filtration of raw water with rGO. Antimicrobial activity of rGO was tested against the following microbial strains: Total viable count, E-coli fecal, Enterococcus, Salmonella, P. aeruginosa, S. aureus ve E. coliform. Reduced graphene oxide has been effective in removing of E-coli fecal, Enterococcus, Salmonella, P. aeruginosa, S. aureus and E. coliform from water. Especially rGO coated membrane filter showed strong antimicrobial activity against microorganisms such as Enterococcus, P. aeruginosa and E.coliform.

V. Results and Discussion

The units of the investigated properties of water are: $CaCO_3$ mg/l (alkalinity), µmhos/cm (conductivity), O_2 mg/l (dissolved O_2), NTU (Turbidity), Pt-Co (Color), Fe mg/l (iron), Mn mg/l (mangan), NO_3 mg/l (nitrate), Mg/l (TIC), CO_2 mg/l (TOC), Fs° (hardness), mg/l (calcium and magnesium). Experimental results of alkalinity, dissolved oxygen, conductivity, turbidity, color, iron, mangan, nitrate, TIC, TOC and hardness for raw water and treated water with rGO were shown at Figure 2.

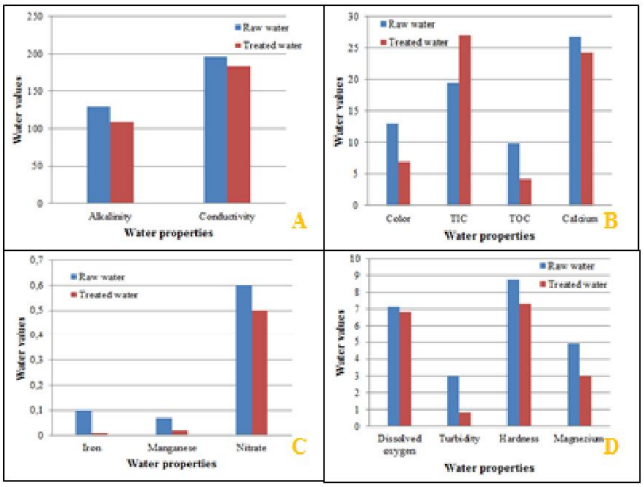


Figure 2: Characterization of rGO (a) FTIR, (b) Raman spectroscopy, (c) XRD analysis and (d) SEM-EDX (10µm)

As can be seen in the figure, rGO has decreased the alkalinity, conductivity, color, dissolved oxygen, turbidity and hardness of the water. When values of TIC and TOC are considered, TIC value did not decrease but TOC value decreased. The alkalinity of the raw water was 130 mg/l, and the alkalinity of the treated water with rGO was 109 mg/l. The results show that the water with the desired alkalinity can be obtained by reduced graphene oxide filtration.

Turbidity of water treated with rGO was measured 0.82 NTU which is under TS266 standard (1NTU). Color of the treated water with rGO measured as 7 Pt-Co whereas the color of raw water measured as 13 Pt-Co. Microbiological analyzes results of raw water and treated water with rGO were shown at Table 1.

Table 1: Microbiological characteristics of raw water and treated water with rGO

Quality criteria	Number of colonies (Raw water)	Number of colonies (Treated water)
Total viable count	500	500
E-coli fecal	500	281
Enterococcus	22	0
Salmonella	37	24
P. aeruginosa	500	2
S. aureus	500	207
E. coliform	500	99

If water is used for any purpose, it should not contain pathogenic microorganisms. Membrane filtration method, which is the most commonly used method in microbiological analyzes (Figure 3), has been used. To better understand the health and environmental impacts of rGO, microbiological tests were made on various bacteria. The results show that rGO shows significant antibacterial activities against above bacteria. The most remarkable effect of rGO filtration was on Enterococcus and P. aeruginosa. At the same timer GO induced loss of viability of E-coli fecal, Salmonella, S. Aureus and E.coliform.

rGO can be more successful in water purification. Two ways are suggested for this purpose: solid/liquid ratio can be increased and composites can be made with antibacterial nanomaterials. Thus, the microbiological, physical and chemical treatment of the water will be more successful.

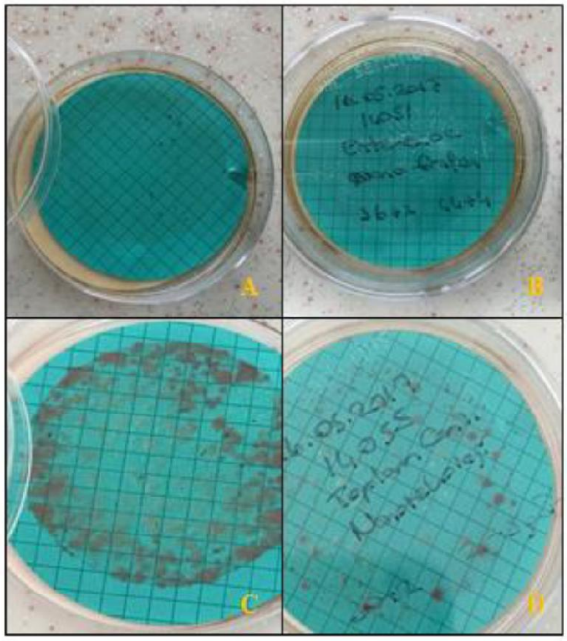


Figure 3:Microbiological analyzes, (a) Enterococcus (raw water), (b) Enterococcus (treated water), (c) Total viable count (raw water) and (d) Total viable count (treated water)

VI. Conclusion

In this study firstly rGO was synthesized and characterized, then rGO dispersion has been prepared to 0.01(v/v). After that the physical (turbidity, color), chemical (hardness, TIC, TOC) and microbiological properties have been determined as the quality criteria of raw and treated water with rGO based filtration membrane synthesis process. Microbiological analyzes were carried out according to the standards of the Turkish Standards Institute. In addition, the physical and chemical properties of water treated with rGO were also analyzed. Some of the physical and chemical quality criteria for drinking water are alkalinity, dissolved oxygen, turbidity, color, iron, manganese, nitrate, TIC, TOC, hardness, calcium and magnesium. For this reason measurements were taken for these criteria.

rGO has decreased the alkalinity of the water %16.2, dissolved oxygen of the water %4.2, conductivity of the water %6.3 compared to the raw water. Raw water filtrated with rGO proved color improvement of %46.2, whereas turbidity showed %72.6 improvement rates.

Reduced graphene oxide filtration was very effective of iron, mangan and nitrate ions elimination rates were found as %90 %68 ve %16.7 respectively.

Improvement rates on TOC and hardness were found as %58 and %16.5, whereas reduced graphene oxide filtration was not effective on TIC elimination. This method was determined to be partly effective on calcium and magnesium elimination. Elimination rates were observed as %9 for calcium and %39 for magnesium.

The antibacterial properties of rGO were tested against the Total viable count, E. coli fecal, Enterococcus, Salmonella, P. aeruginosa, S. aureus and E. Coliform. Reduced graphene oxide filter method was successful on elimination of microorganisms. rGO respectively induced 44%, 100%, 35%, 99%, 58% and 80% loss of viability of E-coli fecal, Enterococcus, Salmonella, P. Aeruginosa, S. Aureus and E.coliform. rGO has higher antimicrobial ability against Enterococcus and P. Aeruginosa (respectively causing death of 100% and 99% of the bacteria) than against other bacteria. But there was no significant improvement in the Total viable count.

The present study showed that rGO exhibited antibacterial properties. As a conclusion rGO nano materials are convenient for drinking water filtration and provides cheaper alternative to conventional methods.

ACKNOWLEDGMENT

Authors thank to Çankırı Municipality, Water and Service Association.

References

[1] Moghayedi, M., et al., Kinetics and mechanism of antibacterial activity and cytotoxicity of Ag-RGO nanocomposite. Colloids and Surfaces B: Biointerfaces, 2017. 159: p. 366-374.
[2] Krishnamoorthy, K., et al., Antibacterial efficiency of graphene nanosheets against pathogenic bacteria via lipid peroxidation. The Journal of Physical Chemistry C, 2012. 116(32): p. 17280-17287.
[3] Bao, Q., D. Zhang, and P. Qi, Synthesis and characterization of silver nanoparticle and graphene oxide nanosheet composites as a bactericidal agent for water disinfection. Journal of colloid and interface science, 2011. 360(2): p. 463-470.
[4] Hegab, H.M., et al., The controversial antibacterial activity of graphene-based materials. Carbon, 2016. 105: p. 362-376.
[5] Ali, Q., et al., Novel Multifunctional Carbon Nanotube Containing Silver and Iron Oxide Nanoparticles for Antimicrobial Applications in Water Treatment. Materials Today: Proceedings, 2017. 4(1): p. 57-64.
[6] Ahmed, S., et al., A review on plants extract mediated synthesis of silver nanoparticles for antimicrobial applications: a green expertise. Journal of advanced research, 2016. 7(1): p. 17-28.
[7] Shankar, S. and J.-W. Rhim, Facile approach for large-scale production of metal and metal oxide nanoparticles and preparation of antibacterial cotton pads. Carbohydrate Polymers, 2017. 163: p. 137-145.
[8] Ji, H., H. Sun, and X. Qu, Antibacterial applications of graphene-based nanomaterials: recent achievements and challenges. Advanced drug delivery reviews, 2016. 105: p. 176-189.
[9] Kellici, S., et al., A single rapid route for the synthesis of reduced graphene oxide with antibacterial activities. RSC Advances, 2014. 4(29): p. 14858-14861.
[10] Liu, S., et al., Antibacterial Activity of Graphite, Graphite Oxide, Graphene Oxide, and Reduced Graphene Oxide: Membrane and Oxidative Stress. ACS Nano, 2011. 5(9): p. 6971-6980.
[11] Gurunathan, S., et al., Antibacterial activity of dithiothreitol reduced graphene oxide. Journal of Industrial and Engineering Chemistry, 2013. 19(4): p. 1280-1288.
[12] Guo, Z., et al., Toxicity and transformation of graphene oxide and reduced graphene oxide in bacteria biofilm. Science of The Total Environment, 2017. 580: p. 1300-1308.
[13] Zeng, X., et al., Silver/Reduced Graphene Oxide Hydrogel as Novel Bactericidal Filter for Point-of-Use Water Disinfection. Advanced Functional Materials, 2015. 25(27): p. 4344-4351.
[14] Carmalin Sophia, A., et al., Application of graphene based materials for adsorption of pharmaceutical traces from water and wastewater-a

review. Desalination and Water Treatment, 2016. 57(57): p. 27573-27586.
[15] Hu, W., et al., Graphene-based antibacterial paper. ACS nano, 2010. 4(7): p. 4317-4323.
[16] Barua, S., et al., One step preparation of a biocompatible, antimicrobial reduced graphene oxide–silver nanohybrid as a topical antimicrobial agent. RSC Advances, 2014. 4(19): p. 9777-9783.
[17] Gurunathan, S., et al., Oxidative stress-mediated antibacterial activity of graphene oxide and reduced graphene oxide in Pseudomonas aeruginosa. International journal of nanomedicine, 2012. 7: p. 5901.
[18] Liu, H., H. Wang, and X. Zhang, Facile fabrication of freestanding ultrathin reduced graphene oxide membranes for water purification. Advanced materials, 2015. 27(2): p. 249-254.
[19] Sawangphruk, M., et al., Synthesis and antifungal activity of reduced graphene oxide nanosheets. Carbon, 2012. 50(14): p. 5156-5161.
[20] Trapalis, A., et al., TiO 2/graphene composite photocatalysts for NOx removal: A comparison of surfactant-stabilized graphene and reduced graphene oxide. Applied Catalysis B: Environmental, 2016. 180: p. 637-647.
[21] Xu, C., et al., Fabrication and characteristics of reduced graphene oxide produced with different green reductants. PloS one, 2015. 10(12): p. e0144842.
[22] WHO, G., Guidelines for drinking-water quality. World Health Organization, 2011. 216: p. 303-4.
[23] Stein, D., et al., Performance management of small water treatment plant operations: a decision support system. Water and Environment Journal, 2017.
[24] Egemen, Ö. and U. Sunlu, Su kalitesi. Ege Üniv. Su Ürünleri Fak. Yayın, 1999(14).

A Coping with Breast Cancer Diagnosis using a Normalized Texture Feature Set

İdil IŞIKLI ESENER[1], Semih ERGİN[2] and Tolga YÜKSEL[3]

[1] Bilecik Seyh Edebali University, Bilecik/Turkey, idil.isikli@bilecik.edu.tr
[2] Eskisehir Osmangazi University, Eskisehir/Turkey, sergin@ogu.edu.tr
[3] Bilecik Seyh Edebali University, Bilecik/Turkey, tolga.yuksel@bilecik.edu.tr

Abstract **- A novel mammographic feature ensemble is proposed for breast cancer diagnosis on a computer-aided diagnosis (CAD) system in this paper. The proposed feature ensemble is verified on a publicly available database constructed by the Mammographic Image Analysis Society (MIAS). The CAD system in this paper consists of four fundamental stages: pre-processing, suspicious region (region of interest – ROI) detection, mammographic feature extraction, and breast cancer diagnosis. In the pre-processing stage, digitization noise reduction, artifact suppression and background removal, and pectoral muscle removal are realized using median filtering, morphological operations, and a region growing method, respectively. Then, in the second stage, ROI detection is performed using Chan-Vese active contour modelling by manual initial contour selection. In the feature extraction stage, 11-dimensional mammographic size, density, contour, and shape features are extracted from the ROIs detected in the second stage. These features are indexed to the values between 1 and 10 to eliminate the domination of high-valued features over others. Finally, in the last stage, the indexed mammographic features are classified according to their health status into normal, benign cancer, and malignant cancer using Logistic Linear Classifier (LLC) by 5-fold cross-validation technique and 83.25% classification accuracy is achieved. The confusion matrix of the study shows that malignant cancer is successfully diagnosed.**

Keywords **- Breast cancer, digital mammography, computer-aided diagnosis, feature extraction, mammographic features.**

I. INTRODUCTION

MORTALITY rate caused by breast cancer can be reduced by early diagnosis [1]. Breast cancer screening methods include self-examination, clinical breast examination, mammography, ultrasound imaging, magnetic resonance imaging and tissue aspiration. Mammography, examined in this paper, is one of the imaging techniques used to diagnose breast cancer by obtaining the Cranio-Caudal (CC) and Mediolateral Oblique (MLO)-view graphs by compressing the breast applying low dose radiation.

The calcifications, well-defined masses, asymmetry between two breasts of a patient, architectural distortion on breast parenchyma, alterations in skin and trabeculae, and axillary lymph node pathologies are the symptoms of breast cancer analyzed by radiologists.

Microcalcifications, known as cancer precursor, seem as radiopaque (bright) masses smaller than 1 mm. Regular-shaped microcalcifications with uniform distribution are considered as benign cancer precursors while irregular-shaped microcalcifications indicate the malignant cancer risk.

Macrocalcifications, calcifications larger than 1 mm, sign the benign cancer possibility although all types of calcifications are thought as malignant cancer precursors if they place in ductal system.

Radiologists analyze masses according to their density, shape, contour, size, accompanying findings, and changes according to old films. The radiolucency (darkness) of masses show benignity while radiopaque ones are considered as malignant cancer cells. Undetermined contours or increment in the size and irregularity of the mass rise the risk of malignancy. Although how irregular-shaped or unbounded-contoured the mass is, it is said to be benign if it contains fat.

Radiologists state that the determination of these symptoms is directly related to the breast tissue type. The Breast Imaging-Reporting and Data System (BI-RADS) categorizes the breast tissue types as fatty, fatty-glandular, heterogeneously-dense, and extremely dense. The symptoms are easily determined in fatty-breast tissue types while it becomes more difficult as the breast tissue type becomes denser. In this respect, using computer-aided diagnosis (CAD) systems increase the sensitivity of cancer diagnosis by providing radiologists reconsideration of mammography images. A typical CAD system generally comprises four stages: pre-processing, region of interest (ROI) detection, feature extraction, and classification. In the pre-processing stage, contrast and structural enhancement operations are realized. The suspicious regions, namely ROIs, on mammography images for breast cancer are detected in the ROI detection stage, and features of these ROIs are extracted in the following stage. Finally, in the classification stage, breast cancer diagnosis is achieved.

There are several methods for the feature extraction stage of a CAD system for breast cancer diagnosis in the literature. These techniques mainly focus on statistical [2,3], model-based [4, 5], graph-theoretic [6], and signal processing [7] or frequency spectrum [8] techniques. Besides, mammographic features [9–11] like shape, spicule index, contour, size, density, and brightness are also used in the literature.

In this paper, a CAD system performing mammographic

feature extraction is proposed for breast cancer diagnosis. In the first stage of the proposed system, pre-processing of mammography images is realized for digitization noise reduction, artifact suppression and background removal, and pectoral muscle removal. Then, in the second stage, ROI detection is executed, and mammographic feature extraction is achieved in the third stage. Finally, breast cancer diagnosis is accomplished in the last stage.

This paper is organized as follows: The database used in this study, the pre-processing and the ROI detection stages of the proposed CAD system are briefly explained in the following section. The mammographic feature extraction is also explicitly described, and breast cancer diagnosis procedure is given in this section. The obtained results and the discussions are given in Section 3. The main conclusions are presented in the last section.

II. MATERIAL AND METHODS

A. Database

A publicly available database constructed by the Mammographic Image Analysis Society (MIAS) is used for the verification of the proposed system in this paper. The MIAS database comprises MLO-view whole-breast mammography images at a size of 1024×1024 and a resolution of 8 byte/pixel in ".pgm" format [12]. This database includes 322 images of 161 patients with three breast tissue types: 106 fatty, 104 glandular, and 112 dense where some of the images have more than one abnormality resulting in 330 diagnoses with 207 normal, 69 benign, and 54 malignant cases with more than one abnormality in some of the images [12]. The database also includes the ground truth information of the images. Sample images of each class in the MIAS database are shown in Figure 1. The rows and the columns in the figure show samples of health status and breast tissue types, respectively. The images are resized into 256×256 for ease of computation.

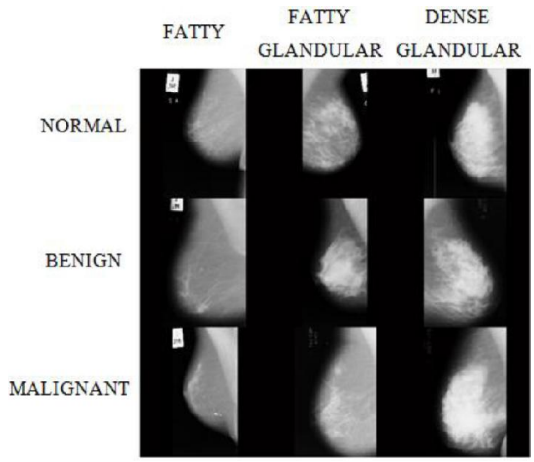


Figure 1: Sample mammography images in the MIAS database.

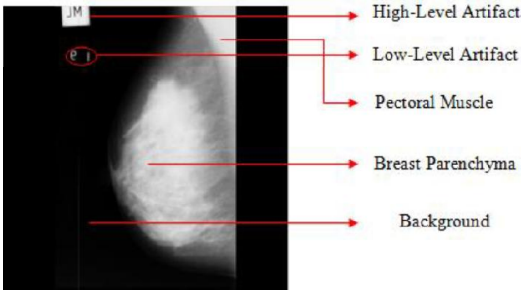


Figure 2: Sample mammography image.

B. Pre-Processing

ROI detection is an essential stage for CAD systems in terms of both reliability and complexity instead of using whole-breast mammography images. ROI detection is realized by considering the intensity differences based on the reason of ROIs having brighter intensity levels than the breast parenchyma. As it can be clearly seen in a sample mammography image in Figure 2, the presence of pectoral muscles in MLO-view mammography images, the low- and high-level artifacts caused by labeling, and speckle noise due to digitization aggravates the intensity-based ROI detection procedure. Hence, a pre-processing stage is realized in this paper to eliminate the negative effects of these factors.

The images in the database are median filtered for digitization noise reduction in this paper [13]. Then, artefact suppression and background removal operations are executed by assuming the largest area in the binary level of the mammography image as the breast parenchyma, and the images are left-aligned to have the pectoral muscles at the upper left corner of the images [13]. The algorithm proposed by Nagi et al. is applied to determine the orientation of the images [14]. After all, pectoral muscle removal is realized using a region growing algorithm by an intensity-based initial seed point selection and applying a post-processing using a gradient-based methodology [13]. The pre-processing steps are visualized on a sample mammography image in Figure 3.

C. Suspicious Region Detection

Region-based Chan-Vese active contour modelling is used for ROI detection from mammography images in this paper. Initial contour of the modelling is selected manually as a point having the suspect of containing any abnormality.

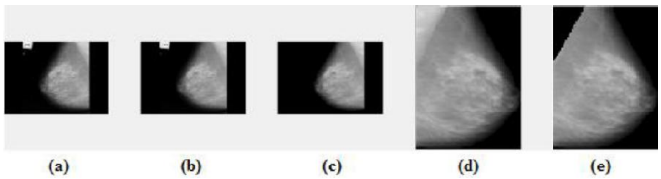


Figure 3: The pre-processing steps of the proposed system: (a) The original image, (b) The noise-reduced image, (c) The artifacts-suppressed and background-removed image, (d) The left-aligned image, (e) The pectoral muscle-removed image.

Then, connected component analysis is applied to the segmented region obtained by applying Chan-Vese active contour modelling to the selected point to remove irrelevant pixels, and filling operation is performed for enhancement. ROI detection scheme used in this paper is shown on a sample mammography image in Figure 4.

D. Mammographic Feature Extraction

Radiologists analyze the abnormalities in mammography images by examining the density, shape, contour, size of the abnormalities, accompanying findings, and changes according to old films, and plan the diagnostic process.

Although the radiolucency of masses indicates benignity as radiopacity signs malignancy, it can be deceptive to think malignancy for a dense tissue-typed breast. Hence, other mammographic symptoms also need to be analyzed. The risk of malignancy increases as the shape of the abnormality becomes irregular-shaped, unbounded-contoured, or larger-sized however, it shows benignity if it contains fat. Sample ROI images with various density, contour, and shape are illustrated in Figures 5, 6, and 7, respectively.

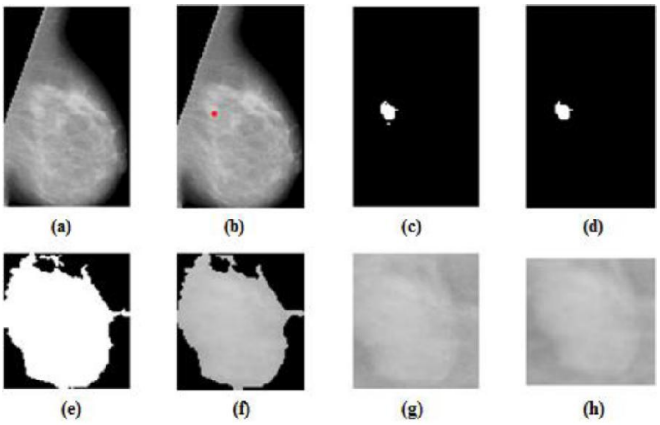


Figure 4: The phases for the proposed ROI detection system: (a)The pre-processed image, (b) The user-defined initial point for the Chan-Vese algorithm, (c) The segmented ROI in the original binary image, (d) The enhanced ROI in the original binary image, (e) The binary ROI image, (f) The gray-scale binary image, (g) The segmented ROI region, (h) The reference ROI region.



Figure 5: Sample ROI images with various types of density [15].



Figure 6: Sample ROI images with various types of contour [22].

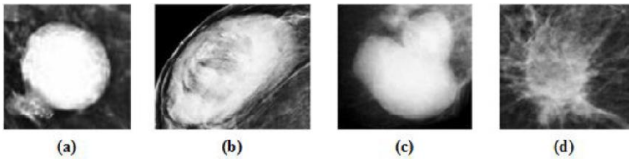


Figure 7: Sample ROI images with various types of shape [22].

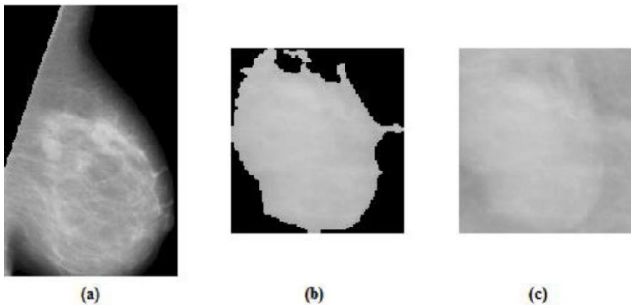


Figure 8: Images used for the mammographic feature extraction: (a) A sample breast parenchyma, (b) A sample ROI, (c) A sample ROI patch.

In the view of such information, mammographic features defining the size, density, contour, and shape of the abnormalities are extracted in this paper. As shown in Figure 8, the breast parenchyma, ROIs, and ROI patches are used for the feature extraction stage.

For defining the size feature of the abnormality, initially, the area of the ROI is calculated as the total number of pixels within it. The size feature is than defined as the ratio of the area of the ROI and the area of the whole-breast to eliminate the effect of large breasts. The area borders of the breast parenchyma and the ROI are shown on a sample mammography image in Figure 9.

The density of a ROI is defined by breast density, degree of ROI radiolucency, and degree of ROI radiopacity. The breast density is calculated by the ratio of the number of pixels with intensity level higher than a certain threshold to the area of the breast parenchyma. Three different threshold values are specified to segment the whole-breast mammography image into the background, the breast parenchyma, the pectoral muscle, and the ROI using Otsu's N-thresholding technique. By analyzing the obtained segments, the optimum threshold is selected as the average of the second and the third thresholds.

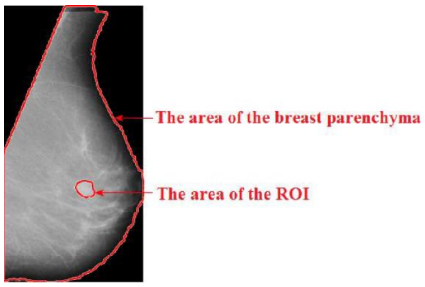


Figure 9: The area borders of the breast parenchyma and the ROI.

The degree of ROI radiolucency is calculated based on the knowledge of increased benignity possibility of the abnormality comprises fat. It is defined as the ration of number of pixels darker than a specified threshold to the number of pixels within the ROI. The optimum threshold for radiolucency is selected as 200 by trial and error in this paper.

The degree of radiopacity is computed based on the fact that brighter abnormalities increase the risk of malignancy. It is defined as the ratio of the maximum to the minimum intensity levels of the ROI.

The contour information of a ROI is defined as the prominence of the contour in the parenchyma and by calculation of boundedness of the contour. The prominence of a contour is directly related with the similarity of the ROI and the parenchyma densities as seen in Figure 6 (d). Hence, prominence of a contour is calculated as the ratio of mean intensities of ROI and the breast parenchyma.

The boundedness of a ROI is the measure of how contours are bounded (Figure 6 (a)) or not (Figure 6 (e)). Compactness, computed as given in (1), is defined for boundedness in this paper. The terms C, a, p, and r refer to the compactness, area, perimeter, and the radius of the ROI, respectively.

$$C = 1 - \frac{4\pi a}{p^2} \qquad a = \pi r^2 \tag{1}$$

Compactness is zero when the ROI is perfect bounded, and increases inversely proportional to the boundedness.

The shape of a ROI is defined according to its roundness, ovality, eccentricity, solidity, and irregularity in this paper. The roundness feature is computed as given in (2). The term A in the equation is the total number of pixels within the ROI, r and R refer to the radius and roundness of the ROI, respectively. The major, minor, and radius axes on a sample mammography image is shown in Figure 10. It is clear from the equation that the roundness is equal to one when the ROI have a perfect circle shape, and deviates from one otherwise.

$$R = \frac{A}{\pi r^2} \qquad r = \frac{\text{Major Axis Length}}{\text{Minor Axis Length}} \tag{2}$$

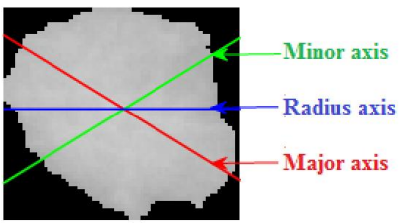


Figure 10: The major, minor, and radius axes on a sample mammography image.

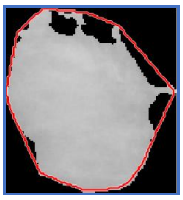


Figure 11: The smallest convex area of the ROI of a sample mammography image.

Similarly, the ovality (O) and eccentricity (E) indicate how a ROI have an oval and an ellipse shape, respectively. The ovality is calculated as given in (3), and the eccentricity is formulated as in (4).

$$O = 2 \cdot \frac{\text{Major Axis Length} - \text{Minor Axis Length}}{\text{Major Axis Length} + \text{Minor Axis Length}} \tag{3}$$

$$E = \frac{\sqrt{(\text{Major Axis Length}/2)^2 - (\text{Minor Axis Length}/2)^2}}{\text{Major Axis Length}/2} \tag{4}$$

The solidity of a ROI defines the regularity of its shape. The smallest convex area surrounding the ROI is computed. Then, the ratio of the area of the ROI to this convex area is defined as solidity. The smallest convex area of the ROI of a sample mammography image is shown as red in Figure 11.

Finally, the ROI irregularity is computed as the rate of number of changes to the number of total pixels on the ROI contours. The ROI irregularity is larger for irregular ROIs like shown in Figure 7(d), and smaller for regular ones.

E. Breast Cancer Diagnosis

In the last stage of the proposed system, breast cancer diagnosis is achieved classifying the 11-dimensional mammographic features extracted from the ROIs of 110 selected images in the MIAS database which are marked as 52 normal cases, 40 benign cancers, and 18 malignant cancers in the ground truth. Logistic Linear Classifier (LLC) is used for the classification with 5-fold cross-validation technique. It means that 95% of each class (49 normal, 38 benign cancers, and 17 malignant cancers) are used for training while the remaining 5% (3 normal, 2 benign cancers, and 1 malignant cancers) are treated as the test parts. The process is repeated for each fold in the cross-validation technique, and the average evaluation metrics are obtained.

F. Technical Computational Sources

The proposed CAD system in this paper is executed using MATLAB R2015a designed by MathWorks. The determination of thresholds by the Otsu's N-thresholding technique is realized via the Image Segmentation and Analysis while the measurements of area (a), perimeter (p), major and minor axis lengths are computed by using Image Region Analyzer, and the Chan-Vese algorithm is run using Image Segmenter applications in the Image Processing Toolbox 9.2 of MATLAB R2015a.

Table 1: Performance evaluation metrics and their mathematical representations.

Performance Evaluation Metrics	Mathematical Representations
TP: True Positive TN: True Negative	
FP: False Positive FN: False Negative	
C : Number of classes	N_i : number of data in the i. class
SNS	$\%SNS = \frac{TP}{TP+FN} \cdot 100$
SPC	$\%SPC = \frac{TN}{TN+FP} \cdot 100$
PPV	$\%PPV = \frac{TP}{TP+FP} \cdot 100$
NPV	$\%NPV = \frac{TN}{TN+FN} \cdot 100$
FPR	$\%FPR = \frac{FP}{FP+TN} \cdot 100$
FNR	$\%FNR = \frac{FN}{TP+FN} \cdot 100$
FDR	$\%FDR = \frac{FP}{TP+FP} \cdot 100$
FOR	$\%FOR = \frac{FN}{TN+FN} \cdot 100$
ACC	$\%ACC = \frac{\sum_{i=1}^{c} SNS_i \cdot N_i}{\sum_{i=1}^{c} N_i} \cdot 100$

G. *Performance Evaluation Metrics*

The metrics sensitivity (SNS), specificity (SPC), positive predictive value (PPV), negative predictive value (NPV), false-positive rate (FPR), false negative rate (FNR), false discovery rate (FDR), false omission rate (FOR), and accuracy (ACC) are used for the evaluation of the performance of the CAD system in this study. The mathematical representations of these metrics are given in Table 1.

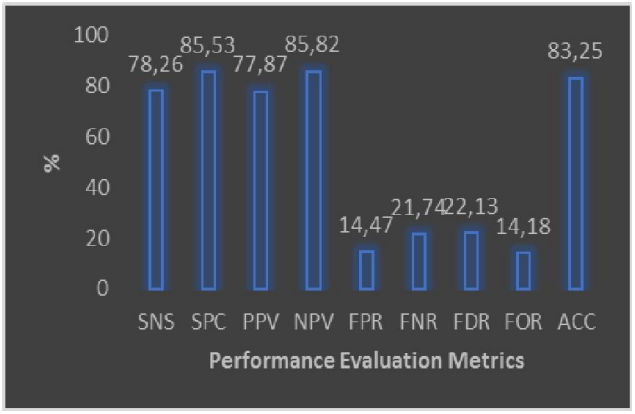


Figure 12: The achieved average performance evaluation metrics of the proposed system.

Table 2: Total confusion matrix obtained from the proposed system.

		Predicted Classes		
		Normal	Benign	Malignant
Actual Classes	Normal	46	9	0
	Benign	11	25	4
	Malignant	1	0	19

III. RESULTS AND DISCUSSION

The mammographic features are indexed to the values between 1 and 10 to eliminate the domination of high-valued features over others. Breast cancer diagnosis is accomplished by classifying the resultant 11-dimensional mammographic feature vector by LLC using 5-fold cross-validation technique according to their health status. The achieved average performance evaluation metrics are shown in Figure 12, and the obtained total confusion matrix is given in Table 2.

IV. CONCLUSION

A CAD system performing mammographic feature extraction is proposed for breast cancer diagnosis in this paper. The proposed system is verified on the selected 110 images in the MIAS database. These images consist of 52 normal cases, 40 benign, and 18 malignant cancers. Mammographic feature extraction is realized on pre-processed and ROI-detected images. These mammographic features basically define the size, density, contour, and shape of the ROIs that are stated as the preliminary symptoms of breast cancer on mammography. In this paper, breast density, degree of ROI radiolucency, and degree of ROI radiopacity is calculated for the density information of a ROI where the prominence and the compactness are computed as the ROI contour descriptors, and roundness, ovality, eccentricity, solidity, and irregularity are the ROI shape descriptors. Then, these features are indexed to the values between 1 and 10 to eliminate the domination of high-valued features over others. Finally, breast cancer diagnosis is achieved by classifying the resultant 11-dimensional mammographic feature vector by LLC using 5-fold cross-validation technique with an average accuracy of 83.25%.

It is observed that the mammography images with malignant cancer are successfully classified. This consequence explicitly shows the reliability of the proposed system. The false-positive and the false-negative results of benign cancer class belong to the normal class as seen in Table 2. This situation indicates that the mammographic features extracted in this paper only differentiates the malignancy.

In conclusion, it is thought that the success of the proposed system can be increased by improving the mammographic features as they can magnificently classify all classes in the future studies.

REFERENCES

[1] A. Jemal, F. Bray, M. M. Center, J. Ferlay, E. Ward, and D. Forman, "Global cancer statistics," *CA: A Cancer Journal for Clinicians*, vol. 61, pp. 69–90, 2011.

[2] K. Ganesan, U. R. Acharya, C. K. Chua, L. C. Min, B. Matthew, and A. K. Thomas, "Decision support system for breast cancer detection using mammograms," in *Conf. Rec. 2013 Institution of Mechanical Engineers*, pp. 721–732.

[3] B. Shradhananda, M. Banshidhar, and D. Ratnakar, "Mammogram classification using two dimensional discrete wavelet transform and gray-level co-occurrence matrix for detection of breast cancer," *Neurocomputing*, vol. 154, pp. 1–4, 2015.

[4] S. K. Biswas and D. P. Mukherjee, "Recognizing architectural distortion in mammogram: a multiscale texture modeling approach with GMM," *IEEE Transactions on Biomedical Engineering*, vol. 58, pp. 2023–2030, 2011.

[5] N. R. Pal, B. Bhowmick, S. K. Patel, S. Pal, and J. Das, "A multistage neural network aided system for detection of microcalcifications in digitized mammograms," *Neurocomputing*, vol. 71, pp. 2625–2634, 2008.

[6] Z. Chen, H. Strange, A. Oliver, E. R. E. Denton, C. Boggis, and R. Zwiggelaar, "Topological modeling and classification of mammographic microcalcification clusters," *IEEE Transactions on BioMedical Engineering*, vol. 62, pp. 1203– 1214, 2015.

[7] A. Papadopoulos, D. I. Fotiadis, and L. Costaridou, "Improvement of microcalcification cluster detection in mammography utilizing image enhancement techniques," *Computers in Biology and Medicine*, vol. 38, pp. 1045–1055, 2008.

[8] A. N. Karahaliou, I. S. Boniatis, S. G. Skiadopoulos, F. N. Sakellaropoulos, N. S. Arikidis, E. A. Likaki, G. S. Panayiotakis, and L. I. Costaridou, "Breast cancer diagnosis: analyzing texture of tissue surrounding microcalcifications," *IEEE Transactions on Information Technology in Biomedicine*, vol. 12, pp. 731–738, 2008.

[9] A. Keleş, A. Keleş, and U. Yavuz, "Expert system based on neuro-fuzzy rules for diagnosis breast cancer," *Expert Systems with Applications*, vol. 38, pp. 5719–5726, 2011.

[10] M. M. R. Krishnan, S. Banerjee, C. Chakraborty, C. Chakraborty, and A. K. Ray, "Statistical analysis of mammographic features and its classification using support vector machine," *Expert Systems with Applications*, vol. 37, pp. 470–478, 2010.

[11] B. Verma, P. McLeod, and A. Klevansky, "A novel soft cluster neural network for the classification of suspicious areas in digital mammograms," *Pattern Recognition*, vol. 42, pp. 1845–1852, 2009.

[12] J. Suckling, J. Parker, D.R. Dance, S. Astley, I. Hutt, C.R.M. Boggis, I. Ricketts, E. Stamatakis, N. Cerneaz, S. L. Kok, P. Taylor, D. Betal, and J. Savage, "The mammographic image analysis society digital mammogram database," *Exerpta Medica International Congress Series*, vol. 1069, pp. 375-378, 1994.

[13] I. Isıklı Esener, S. Ergin, and T. Yüksel, "A genuine GLCM-based feature extraction for breast tissue classification on mammograms," *International Journal of Intelligent Systems and Applications in Engineering*, vol. 4 (Special Issue), pp. 124-129, 2016.

[14] J. Nagi, S. A. Kareem, F. Nagi, S. K. Ahmed, "Automated breast profile segmentation for ROI detection using digital mammograms," in *Conf. Rec. 2010 IEEE EMBS Conference on Biomedical Engineering & Sciences*, pp. 87-92.

[15] F. Chockri, M. H. Farida, "Mammographic mass classification according to Bi-RADS lexicon," *IET Computer Vision*, vol. 11, pp. 189-198, 2016.

A Practical Region-Of-Interest (ROI) Detection Approach for Suspicious Region Identification in Breast Cancer Diagnosis

İdil IŞIKLI ESENER[1], Semih ERGİN[2] and Tolga YÜKSEL[3]

[1] Bilecik Seyh Edebali University, Bilecik/Turkey, idil.isikli@bilecik.edu.tr
[2] Eskisehir Osmangazi University, Eskisehir/Turkey, sergin@ogu.edu.tr
[3] Bilecik Seyh Edebali University, Bilecik/Turkey, tolga.yuksel@bilecik.edu.tr

***Abstract* - In this paper, an automated computer-aided detection (CADe) system for breast cancer is proposed and verified on a publicly available database constructed by the Mammographic Image Analysis Society (MIAS). This database consists of 330 diagnoses with 207 normal, 69 benign, and 54 malignant cases with more than one abnormality in some of the mediolateral-oblique (MLO)-view images. Initially, a pre-processing stage is realized to eliminate the negative effects of digitization noise, labelling artifacts, and pectoral muscles for an intensity-based ROI detection scheme. In this stage, digitization noise reduction is realized via median filtering. Then, artefact suppression and background removal operations are executed by assuming the largest area in the binary level of the mammography image as the breast parenchyma. Then, a region growing algorithm is used for pectoral muscle removal. In the second stage of the proposed CADe system, ROI detection for breast cancer is realized using Chan-Vese active contour modelling. The initial contour of the modelling is manually selected by the user in the proposed system. Chan-Vese active contour modelling is then applied to the initial-manual-selected contour by executing one and two iterations, and two different possible ROI segments are obtained. A decision criterion, which computes the percentage change in the difference of the mean value differences of the inside and outside of the segmented ROI to the mean value of the inside of the segmented ROI for both iteration results, is constituted for the selection of the resultant ROI. In this respect, the possible ROI segment with high change rate in the decision criterion is selected as the resultant ROI. Finally, connected component analysis is applied to the ROI image to remove irrelevant pixels, and filling operation is performed for enhancement. Satisfactory results are obtained by the proposed CADe system.**

***Keywords* – Breast cancer, digital mammography, computer-aided detection, Chan-Vese active contour modelling.**

I. INTRODUCTION

COMPUTER-aided detection (CADe) and computer-aided diagnosis (CAD) systems for breast cancer allow radiologists to reconsider mammography images resulting in increased sensitivity of early detection which can reduce the mortality rate.

Analysis of suspicious regions for breast cancer (Region-Of-Interest - ROI) instead of whole mammography images in CAD systems is more efficient in terms of both reliability and complexity. The abnormalities in the breast parenchyma are defined as the gray-level differences in the mammography image. Differentiating the gray-levels in the parenchyma becomes difficult when digitization noise, labelling artifacts, and pectoral muscles occur in the mediolateral oblique (MLO)-view whole-breast mammography images. Hence, a pre-processing stage becomes the initial step of a CAD/CADe system. Smoothing filters [1], histogram processing operations [2], and frequency-domain operations [3] are frequently used methods for noise reduction while morphological operations are used for artifact suppression [4]. The studies on pectoral muscle removal in the literature focus on line detection methods [5], graph-based approaches [6], and region-based approaches [7].

ROI detection can be performed by either edge-based or region-based methods. Template matching [8, 9], isocontour mapping [10], image thresholding [11, 12], fuzzy C-means clustering [13, 14], probabilistic approaches [15] are commonly used methods for ROI detection in the literature.

An automated CADe system for breast cancer diagnosis is proposed in this paper. A pre-processing of mammography images is implemented for digitization noise reduction, artifact suppression and background removal, and pectoral muscle removal in the first stage of the proposed system.

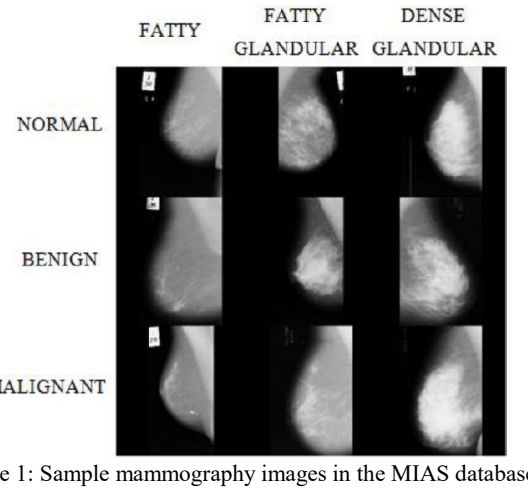


Figure 1: Sample mammography images in the MIAS database.

ROI detection is achieved by the Chan-Vese active contour modeling [16] initialized by a user-defined single point, and morphological post-processing is performed for segmentation enhancement in the second stage.

This paper is organized as follows: The database and the method used for ROI detection is explained in Section 2 while the experimental studies are defined in Section 3. Finally, the main conclusions are presented in the last section.

II. MATERIALS AND METHODS

A. Database

A publicly available database constructed by the Mammographic Image Analysis Society (MIAS) is used for the verification of the proposed CADe system in this paper. This database comprises 322 MLO-view mammography images of 161 patients having three breast tissue types of 106 fatty, 104 glandular, and 112 dense; and 330 diagnoses with 207 normal, 69 benign, and 54 malignant cases with more than one abnormality in some of the images [17]. The images are in ".pgm" imaging format at a size of at a 1024×1024 and resolution of 8 bits/pixel. The database also includes the ground truth information of the images. The images are resized into 256×256 for ease of computation in this paper. Sample images of each class in the MIAS database are shown in Figure 1. The rows and the columns in the figure show samples of health status and breast tissue types, respectively.

B. Active Contour Modelling

The original active contour modelling is stated as defining a closed elastic spline, namely snake, on the edges of the ROIs in an image [18]. A two-dimensional snake modelled by active contour algorithm is represented as given in (1). The terms x and y are the coordinates of the position of the snake defined by the parametric definition set element s dependent to time t.

$$v[\vec{s}] = (x(s,t), y(s,t)) \quad , \quad 0 \le s \le 1 \tag{1}$$

The closed spline in this algorithm is defined by the movement of the snake achieved by energy minimization where the position of the snake on an image $E(\vec{v})$ is defined as the sum of the energy of the image $E_{img}(\vec{v})$, the internal energy $E_{\text{int}}(\vec{v})$ and the external energy $E_{ext}(\vec{v})$ as given in (2).

$$E(\vec{v}) = E_{img}(\vec{v}) + E_{\text{int}}(\vec{v}) + E_{ext}(\vec{v}) \tag{2}$$

The energy of the image moves the snake to the details of the image like lines or edges while the internal energy controls the shape of the snake and the external energy encourages the snake to be close to the local minimums in the ROI according to the gradient magnitudes [19]. The active contour algorithm starts by the selection of an initial snake inside or outside of the ROI, and continues with the movement of the snake by iterations until the snake takes the shape of the ROI which means the high image gradient is reached and the energy balance is satisfied.

C. Chan-Vese Active Contour Modelling

The regional active contour modelling proposed by Chan and Vese segments the ROI of an image without using the gradient information conversely to the original active contour modelling [16]. The initial contour is selected as a mask by this algorithm, and energy minimization is satisfied by contracting and expanding the size of the mask. Chan and Vese define the energy function based on the Mumford-Shah method and level set analysis [16]. The energy function $F^{MS}(u,C)$ of the Mumford-Shah method for an image u_0, is defined as given in (3). The term C in the equation refer to the boundary of the contour that separates the image into the ROI and the background.

$$\inf\left\{F^{MS}(u,C)\right\} = \int_{\Omega} (u-u_0)^2\,dxdy + \int_{\Omega \setminus C} |\nabla u|^2\,dxdy + \nu|C| \tag{3}$$

The equation (3) is reduced to equation (4) when c_i is assumed constant for $u = \forall\Omega_i$ [].

$$\begin{aligned} E^{MS}(u,C) &= \sum_i \int_{\Omega} (u-c_i)^2\,dxdy + \nu|C| \\ c_i &= mean(u_0) \quad , \quad u_0 \subset c_i \end{aligned} \tag{4}$$

In respect of Mumford-Shah method, the reduced energy function defined by the Chan-Vese algorithm for an image u_0 that is segmented in two regions by the initial contour C is given in (5). The terms c_1 and c_2 in the equation refer to the averages of the regions inside and outside of the contour C, respectively.

$$\begin{aligned} F(c_1,c_2,C) &= \mu \cdot \text{Length}(C) \\ &\quad + \lambda_1 \int_{inside(C)} |u_0(x,y) - c_1|^2\,dxdy \\ &\quad + \lambda_2 \int_{outside(C)} |u_0(x,y) - c_2|^2\,dxdy \\ &= \mu \cdot \text{Length}(C) + F_1(C) + F_2(C) \end{aligned} \tag{5}$$

The first term, $\mu \cdot \text{Length}(C)$, in the energy function is the term of regularization that prevents the final contour to combine with a small area due to noise while $F_1(C)$ and $F_2(C)$ are the energy of the regions inside and outside of the contour C, that force the contour to contract and expand,

respectively.

The level-set function $\phi(x, y)$ is applied to compute the energies $F_1(C)$ and $F_2(C)$ by the Chan-Vese algorithm. The representation contour C by the level-set function are given in (6), and the movement of the contour is defined as given in (7).

$$C = \{(x, y) : \phi(x, y) = 0\} \quad , \quad \forall (x, y) \in u_0 \tag{6}$$

$$\frac{\partial C}{\partial t} = \frac{\partial \phi(x, y)}{\partial t} \tag{7}$$

The level-set function maybe positive, negative, or equal to zero based on the bilateral positional state of the ROI and the contour C. Positivity and negativity of the level-set function indicate that the contour is outside and inside of the ROI, respectively while the contour is said to be on the boundary of the ROI if the level-set function is equal to zero that means the energy balance is achieved. The algorithm continues until the number of maximum iterations is reached unless the energy balance is satisfied.

III. EXPERIMENTAL STUDY

An automated CADe system comprises typically two main stages, the pre-processing and the ROI detection, is proposed in this paper. The pre-processing stage of the proposed system consists of three phases. Initially digitization noise reduction is realized via median filtering [20]. In the second phase, artifact suppression and background removal operations are executed by some morphological operations. The largest area of the whole-breast mammography image is assumed to be the breast parenchyma in this phase [20]. Finally, pectoral muscle removal is performed in the last phase. A region growing algorithm is used for pectoral muscle removal where the initial seed point is selected using region-based intensity-level differences of the mammography image, and a post-processing sub-phase is realized based on image gradients [20]. The phases of the pre-processing stage are shown on a sample mammography image in Figure 2.

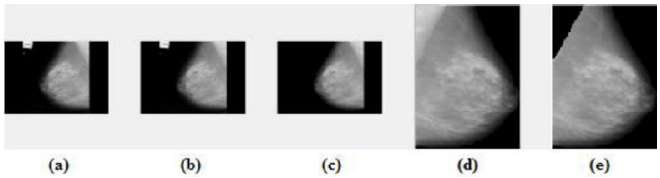


Figure 2: The phases for the pre-processing stage of the proposed system:
(a) The original image, (b) The noise-reduced image, (c) The artifacts-suppressed and background-removed image, (d) The left-aligned image, (e) The pectoral muscle-removed image.

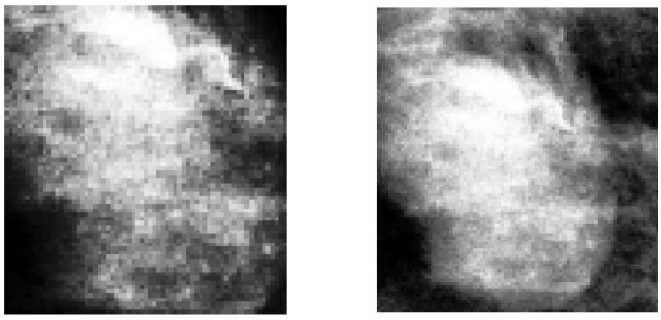


Figure 3: The possible segmented ROIs by both iterations of a sample mammography images:
(a) The segmented ROI after 1 iteration, (b) The segmented ROI after 2 iterations.

In the second stage of the proposed CADe system, ROI detection is achieved using region-based Chan-Vese active contour modeling [16]. The initial contour for the Chan-Vese algorithm is manually selected as a single point instead of a multi-dimensional mask originally proposed by Chan and Vese [16], by the user to give the chance of analyzing all suspected regions in the proposed system. It is observed that the Chan-Vese algorithm segments almost the same regions of the ROIs after two iterations. Hence, this algorithm is applied to all pre-processed images on the user-defined initial point at a maximum number of iterations of two acquiring two possible ROI segments. Then, a decision criterion, given in (8), is formulated for the selection of the resultant ROI in this paper.

$$Differentiation\ Rate = 100 \cdot \frac{\mu_{inside} - \mu_{outside}}{\mu_{inside}} \tag{8}$$

The terms μ_{inside} and $\mu_{outside}$ in the equation refer to the mean values of the regions inside and outside of the segmentation boundary, respectively. The decision criterion formulated as given in (8) compares the percentage differentiation rate of the mean values of inside and outside of the possible ROIs segmented by the Chan-Vese algorithm in one and two iterations. A low percentage rate of differentiation indicates the presence of areas outside the ROI that are similar to the segmented region in terms of intensity. It is visible to continue the iterations for a better segmentation in this case. Hence, the possible ROI with high percentage differentiation rate is selected as the resultant ROI. The possible segmented ROIs by both iterations of a sample mammography images are shown in Figure 3. The images in the figure are histogram equalized for a better visualization.

There may be irrelevant and missing pixels on the selected ROIs as seen in Figure 4(c). Therefore, a post-processing on the ROIs is performed for removing irrelevant and missing pixels by applying connected component analysis and morphological filling operation to the ROIs, respectively for enhancement. Finally, the ROIs are removed from the original binary image. The phases for the ROI detection system proposed in this paper are visualized on a sample

mammography image in Figure 4.

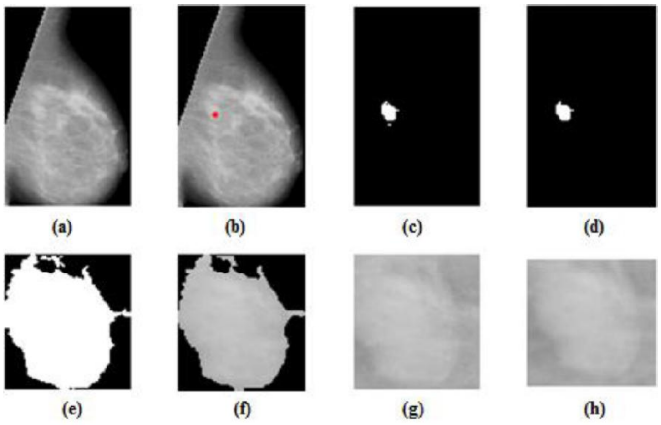


Figure 4: The phases for the proposed ROI detection system: (a)The pre-processed image, (b) The user-defined initial point for the Chan-Vese algorithm, (c) The segmented ROI in the original binary image, (d) The enhanced ROI in the original binary image, (e) The binary ROI image, (f) The gray-scale binary image, (g) The segmented ROI region, (h) The reference ROI region.

IV. CONCLUSION

A practical CADe system is proposed for breast cancer diagnosis and verified using the MIAS database in this paper. Initially, a pre-processing stage is realized, and then ROI detection is performed by the Chan-Vese active contour modeling [16]. The MIAS database has the ground-truth of a ROI any image about the center coordinates and the radius of the pad that encircle the ROI. However, there is no information about the contours of the ROI. Therefore, the reference ROIs of all the images in the database are verified, and the success of the proposed system is considered by a radiologist manually.

It is observed that the proposed system gives satisfactory results for the ROI detection. Besides, the proposed system enables the radiologists to analyze all the regions intended by the user-defined initial point selection for the segmentation algorithm. This consequence shows that the proposed CADe system is nonrestrictive.

REFERENCES

[1] B. Gupta and M. Tiwari, "A tool supported approach for brightness preserving contrast enhancement and mass segmentation of mammogram images using histogram modified grey relational analysis," *Multidimensional Systems and Signal Processing*, pp. 1–19, 2016.

[2] Z. Yang, M. Dong, Y. Guo, X. Gao, K. Wang, B. Shi, and Y. Ma, "A new method of microcalcifications detection in digitized mammograms based on improved simplified PCNN," *Neurocomputing*, vol. 218, pp. 79–90, 2016.

[3] J. Anitha and J. Dinesh Peter, "Mammogram segmentation using maximal cell strength updation in cellular automata," *Medical & Biological Engineering & Computing*, vol. 53, pp. 737–749, 2015.

[4] J. Nagi, S. A. Kareem, F. Nagi, and S. K. Ahmed, "Automated breast profile segmentation for ROI detection using digital mammograms," in *Conf. Rec. 2010 IEEE EMBS Conference on Biomedical Engineering & Sciences,* pp. 87–92.

[5] M. Mustra and M. Grgic, "Robust automatic breast and pectoral muscle segmentation from scanned mammograms," *Signal Process*, vol. 93, pp. 2817-2827, 2013.

[6] I. Domingues I, J. S. Cardoso, I. Amaral, I. Moreira, P. Passarinho, J. S. Comba, R. Correia, and M. J. Cardoso, "Pectoral muscle detection in mammograms based on the shortest path with endpoints learnt by SVMs," *Eng Med Biol*, pp. 3158-3161, 2010.

[7] J. Anitha, J. D. Peter, and S. I. A. Pandian, "A dual stage adaptive thresholding (DuSAT) for automatic mass detection in mammograms," *Comput Meth Prog Bio*, vol. 138, pp. 93-104, 2017.

[8] S. Xu and C. Pei, "Hierarchical matching for mass detection of masses in mammograms," in *Conf. Rec. 2011 Int. Conf. Electr. Control Eng*., pp. 4523-4526.

[9] S. C. Tai, Z. S. Chen, and W. T. Tsai, "An automatic mass detection system in mammograms based on complex texture features," *IEEE Journal of Biomedical and Health Informatics,* vol. 18, pp. 618-627, March 2014.

[10] B. W. Hong and B. S. Sohn, "Segmentation of regions of interests in mammograms in a topographic approach," *IEEE Transactions on Information Technology in Biomedicine*, vol. 14, pp. 129-139, January 2010.

[11] D. Cascio, F. Fauci, R. Magro, G. Raso, R. Belloti, F. De Carlo, S. Tangaro, G. De Nunzio, M. Quarta, G. Forni, A. Lauria, M. E. Fantacci, A. Retico, G. L. Masala, P. Oliva, S. Bagnasco, S. C. Cheran, and E. Lopez Torres, "Mammogram segmentation by contour searching and mass lesions classification with neural network," *IEEE Transactions on Nuclear Science*, vol. 53, pp. 2827-2833, October 2006.

[12] R. D. Ghongade and D. G. Wakde, "Detection and classification of breast cancer from digital mammograms using RF and RF-ELM algorithm," in *Conf. Rec. 2017 1st International Conference on Electronics, Materials Engineering and Nano-Technology*, pp. 1-6.

[13] K. L. Kashyap, M. K. Bajpai, and P. Khanna, "Breast cancer detection in digital mammograms," in *Conf. Rec. 2015 IEEE Int. Conf. on Imaging Systems and Techniques*, pp. 1-6.

[14] S. Gu, Y. Yi, Y. Chen, J. Wang, and J. U. Kim, "Study on breast mass segmentation in mammograms," in *Conf. Rec. 2015 3rd International Conference on Computer, Information and Application*, pp. 22-25.

[15] M. A. Al-Masni, M. A. Al-Antari, J. M. Park, G. Gi, T. Y. Kim, P. Rivera, E. Valarezo, and T. S. Kim, "Detection and classification of the breast abnormalities in digital mammograms via regional convolutional neural network," in *Conf. Rec. 2017 39th International Conference of the IEEE Engineering in Medicine and Biology Society*, pp. 1230-1233.

[16] T. F. Chan and L. A. Vese, "Active contours without edges," *IEEE Transactions on Image Processing*, vol. 10, pp. 266-277, 2001.

[17] J. Suckling, J. Parker, D. R. Dance, S. Astley, I. Hutt, C. R. M. Boggis, I. Ricketts, E. Stamatakis, N. Cerneaz, S. L. Kok, P. Taylor, D. Betal, and J. Savage, "The mammographic image analysis society digital mammogram database," *Exerpta Medica International Congress Series*, vol. 1069, pp. 375-378, 1994.

[18] M. Kass, A. Witkin, and D. Terzopoulos, "Snakes: Active Contour Models," *International Journal of Computer Vision*, pp. 321-331, 1998.

[19] E. Isıkcı and D. G. Duru, "Multipl Skleroz Manyetik Rezonans Görüntülerinde Aktif Kontur Modeli ile Lezyon Tespiti," *in Conf. Rec. 2015 Tip Teknolojileri Ulusal Kongresi*, pp. 122-125.

[20] I. Isıklı Esener, S. Ergin, and T. Yüksel, "A genuine GLCM-based feature extraction for breast tissue classification on mammograms," *International Journal of Intelligent Systems and Applications in Engineering*, vol. 4 (Special Issue), pp. 124-129, 2016.

Classification of Text Files with Different Subjects using Naive Bayes Method

Kübra UYAR[1] and Erkan ÜLKER[1]

[1] Selcuk University, Konya/Turkey, kubrauyar@selcuk.edu.tr
[1]Selcuk University, Konya/Turkey, eulker@selcuk.edu.tr

Abstract **- Text classification has become one of the key techniques for organizing information over the recent years. It can be used for organizing document databases, filtering spam emails, routing e-mails, identifying languages or sentiment analyses. In addition, the flow and storage of information and documents in the electronic environment have increased considerably. This situation has released rapid access to the requested document. Because of this need, it is aimed to increase access quality by classifying documents in the electronic environment. In this paper, Naive Bayes classification method which is based on the popular Bayes' probability theorem was used for the classification of text-containing documents. This method is generally chosen as the baseline in text classification because of its fast and easy implementation. Documents may be classified according to their subjects or other attributes such as author, document type, and printing year. In this paper, we categorize text files according to their content. Text documents with different subjects in the folder are stored separately in the "*Array List*" data structure. Each word read from the file is checked for stopword before it is added to treemap. Because these words do not have a distinctive feature in text classification, so there is no need to participate in the calculation of probability. In addition, characters without any meaning such as spaces, numbers and punctuation marks in the documents have been eliminated and the capital letters have been converted into lowercase letters. As a result, for each document read, the results of the probabilities are compared and the document at that time is categorized depending on likelihood. Consequently, we can categorize text documents effectively by spending less time than expected.**

Keywords **- Bayes theorem, document classification, machine learning, probability, stop words.**

I. INTRODUCTION

The field of text classification has taken attention lots of interest from machine learning and the industry. Text classification, also named topic classification, is a methodology to categorize pieces of text into classes. Simple Bayesian classifiers is a probabilistic approach which uses a collection of labeled training examples in order to estimate the parameters of the generative model. Therefore, classification on new examples is performed with Bayes' rule. Naive Bayes model is easy to implement and especially useful for large datasets. In addition to simplicity, Naive Bayes is known to outperform even highly sophisticated classification methods. Real-time prediction, multi-class prediction, text classification, spam filtering, sentiment analyses and recommendation systems are among Naive Bayes Algorithm applications. The main aim of the paper is to determine the category of the mentioned papers by looking at the content properties of the previously categorized paper. In literature, various classification methods have been developed in the direction of this study such as Naive Bayes, decision trees, k-nearest neighbor model, maximum entropy models, fuzzy logic theory approaches, support vector machines and artificial neural networks.In this study, Naive Bayes classification method has been used. In the literature, a large number of approaches are presented for solving the text classification problem. Wang and Sun[1] proposed maximum margin projection (MMP) used to obtain low dimensional feature space and least square support vector machines (LS-SVM). According to extracted semantic features, LS-SVM classifier was used to classify the test documents. Zhao et al.[2] worked on a novel solution to classify uncertain XML documents using two uncertain learning algorithms based on Extreme Learning Machine (ELM).Wu et al.[3] suggested a new classification approach based on Wikipedia matching which is called efficient Wikipedia semantic matching approach, represents each document as a concept vector in the Wikipedia semantic space in order to understand text semantics. Agnihotri et al.[4] proposed a novel Variable Global Feature Selection Scheme (VGFSS) select number of features from each class depending on the distribution of terms in the classes. The algorithm ensures the minimum number of terms selected from each class. Finally, Bhushan and Danti[5] addressed the problem of text classification by considering Sentence-Vector Space Model (S-VSM) and unigram representation models for the text document. In order to capture effective semantic information, a neural network based representation for text document was preferred.

This article is ordered as follows: a brief introduction of various techniques of text classification and literature review are presented in Section 1. Naive Bayes approach and its mathematical definition are presented in Section 2. This section also includes learning algorithms. The use of Naïve Bayes in text classification and the experimental results are presented in Section 3. Finally, this article will be concluded by drawing conclusions of Naive Bayes method for text classification in Section 4.

II. Related Work

Naive Bayes Algorithm and Mathematics of the Algorithm

The basis of Naive Bayes algorithm withstands Bayes' theorem or in other words, Bayes' rule or Bayes' law. It provides a method to calculate the conditional probability. For instance, we can obtain the probability of an event based on previous knowledge available on the events. The theorem calculates the posterior probability such as $P(c|x)$ and $P(x|c)$ from $P(c)$ and $P(x)$ probability values. This approach is called conditional independence assumes that the effect of the value of x on a class of c is independent of the values of other values. The probability is calculated as follows:

$$P(c|x) = \frac{P(x|c)P(c)}{P(x)}$$

where $P(x|c)$ is the conditional probability of occurrence of event x given the event c is true, $P(c)$ and $P(x)$ are the probabilities of the occurrence of event c and x respectively, and $P(c|x)$ is the probability of the occurrence of event c given the event x is true. The terminology in the Bayesian method of probability is as follows:

- c is called the proposition and x is called the evidence.
- $P(c)$ is called the prior probability of proposition and $P(x)$ is called the prior probability of evidence.
- $P(c|x)$ is called the posterior.
- $P(x|c)$ is the likelihood.

Bayes' rule is applied for a document x for class c. In a machine learning classification problem, there are multiple features $(x_1, x_2, \dots, x_n)$ and classes $(c_1, c_2, \dots, c_k)$. The main purpose of the Naive Bayes algorithm is to calculate the conditional probability of an object with a feature vector $x_1, x_2, \dots, x_n$ belongs to a particular class c_i. As a result, the equation can be shown as follows:

$$P(c_i|x_1, x_2, \dots, x_n) = \frac{P(x_1, x_2, \dots, x_n|c_i) * P(c_i)}{P(x_1, x_2, \dots, x_n)} \text{ for } 1 \le i \le k$$

Finally, the equation can be updated as follows:

$$P(x_1, x_2, \dots, x_n|c_i)P(c_i)$$

$$= P(c_i|x_1, x_2, \dots, x_n)P(x_1, x_2, \dots, x_n, c_i)$$
$$= P(x_1|x_2, \dots, x_n\ c_i) * P(x_2, \dots, x_n, c_i)$$

$$= P(x_1|x_2, \dots, x_n\ c_i) * P(x_2|x_3, \dots, x_n, c_i) * P(x_3, \dots, x_n, c_i)$$

$$= \cdots$$

$$= P(x_1|x_2, \dots, x_n\ c_i) *$$
$$P(x_2|x_3, \dots, x_n, c_i) \dots P(x_{n-1}|x_n, c_i) * P(x_n, c_i) * P(c_i)$$

The conditional probability term, $P(x_j|x_{j+1}, \dots, x_n, c_i)$ becomes$P(x_j|c_i)$ because of the assumption that features are independent. We can obtain the following easy equation:

$$P(c_i|x_1, x_2, \dots, x_n) = \left(\prod_{j=1}^{j=n} P(x_j|c_i)\right) * \frac{P(c_i)}{P(x_1, x_2, \dots, x_n)}$$

for $1 \le i \le k$. The expression $P(x_1, x_2, \dots, x_n)$ is constant for all classes. In order to obtain the result, we can use the equation below:

$$P(c_i|x_1, x_2, \dots, x_n) \propto \left(\prod_{j=1}^{j=n} P(x_j|c_i)\right) * P(c_i), \qquad 1 \le i \le k$$

Learning Algorithms

Machine learning methods are generally divided into supervised and unsupervised learning algorithms. Mathematically, supervised learning where you have input variables (X) and output variable (Y) aims to learn the mapping function from the input to the output. It can be defined as an equation as follows:

$$Y = f(X)$$

Learning from the training dataset in the process of learning an algorithm can be described as a teacher supervising the learning process. The algorithm makes predictions on the training dataset. Learning terminates when the algorithm reaches a satisfactory performance. Supervised learning problems can be grouped into regression and classification problems.

Unsupervised learning is where there are only input data and no corresponding output variable. This learning algorithm process data without labels and are trained to find patterns. In order to learn more about the data, this approach tries to model the underlying structure in the data. The cause of calling unsupervised learning is that there is no teacher and correct answer. Examples of traditional unsupervised learning algorithms are principal component analysis, association problems, and clustering methods.

III. Text Classification using naïve Bayes

Most text classification techniques use some word featurization. It turns the text into a numeric representation. This numeric representation allows easy and fast computing. One of the notable techniques is the bag of words which consists of computing the frequency of each word in the text as a histogram[6]. This model is commonly used in methods of document classification where the frequency of each word is used as a feature for training a classifier.

In the related study, training documents were collected firstly and grouping operations were performed according to the categories. According to training documents, attribute word values were created. This process has followed the steps of training and testing the system. Firstly, collected and grouped training documents are processed. During this process, words are taken from the documents and characters that do not have

any meaning such as numbers, spaces, and punctuation marks are eliminated. Stopwords which have not any important meaning extracted from the word list. The stopwords determined in the application can be listed as follows:

ama
ben
ilk
sen
ile
çok
bile
hem
her
bir
gibi
kez
pek
ise
var

Moreover, all words are converted to lowercase. Following this phase, the word and word number attribute values are created for the categories. The training text files located in each category folder are imported into the system in order. After preprocessing the text files, the words are examined sequentially. The words that can be taken into consideration are kept as the number of items in the word and document as the attribute vector value.

120 text files including sports, economy, and health issues were prepared. Each subject contains 40 text documents.

In the testing process, different approaches can be used to measure the success of the method. The main purpose of supervised learning is that the trained system can produce a logical answer to an unknown example on the same subject. With the limited training examples, the system needs to be both trained and its performance measured neutrally. In this process, cross-validation techniques can be used. It is a technique to evaluate predictive models by dividing the original sample into a training set to train the model, and a test set to evaluate it. In this study, k cross-validation was preferred. The original sample was randomly partitioned into k equal size subsamples. Of the k subsamples, a single subsample is retained as the validation data for testing the model, and the remaining k-1 subsamples are used as training data. As a result of the tests, a text document can easily be classified.

IV. CONCLUSİON

Naive Bayes algorithm is very fast and it needs low storage requirements. Proposed classification technique is very robust to irrelevant features without affecting results. It classifies the text documents with different subjects in high accuracy.

ACKNOWLEDGMENT

This study was funded by OYP with Project 2017-OYP-075.

REFERENCES

1. Wang, Z.Q. and X. Sun, *Document classification algorithm based on MMP and LS-SVM.* Ceis 2011, 2011. **15**.
2. Zhao, X.G., et al., *Uncertain XML documents classification using Extreme Learning Machine.* Neurocomputing, 2016. **174**: p. 375-382.
3. Wu, Z.D., et al., *An efficient Wikipedia semantic matching approach to text document classification.* Information Sciences, 2017. **393**: p. 15-28.
4. Agnihotri, D., K. Verma, and P. Tripathi, *Variable Global Feature Selection Scheme for automatic classification of text documents.* Expert Systems with Applications, 2017. **81**: p. 268-281.
5. Bhushan, S.N.B. and A. Danti, *Classification of text documents based on score level fusion approach.* Pattern Recognition Letters, 2017. **94**: p. 118-126.
6. Fierro, M.G., *A gentle introduction to text classification and sentiment analysis.* 2017.

Detection of Missing Pills on Tablet using Image Processing Methods

Kübra UYAR[1] and Erkan ULKER[2]

[1] Selcuk University, Konya/Turkey, kubrauyar@selcuk.edu.tr
[2]Selcuk University, Konya/Turkey, eulker@selcuk.edu.tr

Abstract - **Image processing is the processing of images in real life that have been rendered into a digital image as an input 'image', creating a new image as a result of alteration of that picture's properties. Images usually contain noise because they are transferred from analog image to digital image. Some pre-operations are performed to analyze the image such as filtering, segmentation, and edge detection. These operations enable some of the features and details of the image to the foreground. The potential for the utilization of image processing methods in engineering has been investigated along with their theoretical essences and their application in the area of engineering. In this context, a software was developed to determine the number of pills in the tablets passing through the production band, to check whether the missing packaging was made, and to determine the color of the pill in the production band. Tablet pictures in different colors were picked randomly as input picture. In order to simulate the production band, 60 recorded images were displayed randomly at intervals of 5 seconds. Due to image processing methods, many operations can be performed automatically. It was determined that image processing techniques could be used for the determination of some properties of the image. As a result, the success and scope of the methods have been evaluated and some suggestions have been made.**

Keywords - **Image processing, missing pill, noisy image, RGB image, segmentation.**

I. INTRODUCTION

Computer-aided image processing is based on the human vision system and has entered into every aspect of our daily lives. Significant results are derived from the image at the end of image processing. With such applications, transactions can become fast, easy and economical. Image processing has a wide range of applications in the industry as well as many other fields. Thanks to developing technologies, it is now possible to perform quality control automatically and a hundred percent securely. Image processing based quality control systems used in industrial applications analyze and monitor the quality of products. Many processes such as detection of industrial faults, counting, and classification of objects can easily be done with image processing methods. Image processing consists of a series of operations. The process begins with the capturing of the scene, followed by the use of different techniques for the purpose.

In the literature, there are many applications of image processing in the industrial field. Some industries use human beings' inspection to classify the quality of their products visually. This could be done automatically through digital image processing. Affonso et al. [1] investigated the classification of the quality of wood boards using the convolutional neural network. They extracted texture descriptor from wood images. Nateri et al.[2] evaluated yarn defects which deteriorate the quality of products by image processing techniques. The yarn defects were identified based on their geometric shape and surface area. Barbedo [3] presented a new approach which is based on conventional digital images for counting whiteflies in soybean leaves. Song [4] et al. worked on automatic fruit recognition and counting using multiple images. At the end of the study, image analysis automatically counted fruits which have complex shape and color. Finally, Çelik et al.[5] presented a study for detecting cloth fabric mistakes automatically. The methods which are wavelet transform, Gabor filter, and Fourier transform was evaluated according to results. Image processing techniques have been used in many areas and successful results have been achieved that make human life easier.

II. RELATED WORK

Inferences were made by performing some operations on the images taken, such as edge detection or filtering. According to our application, there are a number of pills on the tablet. In some cases, some pill points are left empty due to the reasons for production. By this study, a distinction can be made by determining the color of the pill and pills on the tablet can be counted to determine if the tablets are full.

1. Segmentation

Segmentation is the process of separating a whole constituent in a picture from the background or other objects. In order to be able to talk about the existence of an object in the image, it must have a distinguishable feature from the other parts of the image, and it must apply to all of the objects. The main difference is the brightness in the image. A segmentation operation based on the difference in brightness is performed by the thresholding operator. Adaptive thresholding algorithms can also be used for this purpose. Another difference is the differences in colors or patterns. Detection of differences in patterns is more difficult. Transforms such as Fast Fourier Transform (FFT), Wavelet (wavelet) are adopted in determining the repetitions in the patterns. In segmentation, the main purpose is to separate the parts of the image according to one or more characteristics.

Segmentation can be examined under two important headings as thresholding and edge detection.

Thresholding: It is called thresholding of binary images according to whether the image brightness value is larger or smaller than a certain value. A gray-scale image is converted to a black-and-white image by selecting the threshold value. Looking at the threshold value, each pixel value is expressed as 0 or 255. Moreover, thresholding can also be performed using the double threshold value. The graphical representation of the thresholding process and the resultant image obtained when thresholding on a sample image is given in Fig. 1.

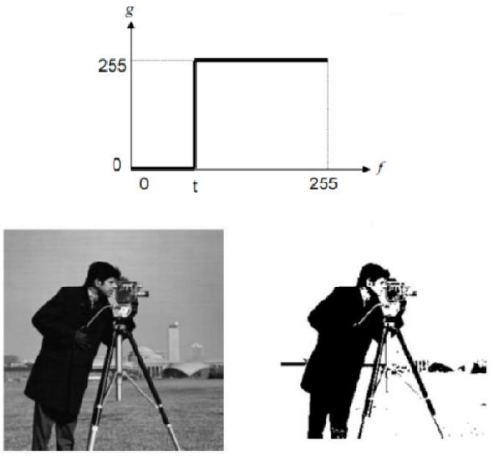


Fig 1: Graphical presentation of thresholding and thresholding on a sample image

Edge Detection: It is an approach that sharpens color transitions and makes it easier to get objects or differences in the image. Edges include some of the most useful information in an image. Edges are used to measure the size of an object in an image, to separate the object from the background, to classify and recognize the object. Edge detection can be examined in three main stages:

1. Noise reduction: Noise suppression as much as possible without affecting significant edges.
2. Edge reinforcement: Use of a filter with a higher response at the edges.
3. Edge detection: It is decided that the meaningful edges of the hatches from the filter outputs are noise.

In order to catch color transitions (changes) in edge detection methods, the difference between the neighboring pixels, that is, the derivative is evaluated. As a result of the derivation process, the color difference is close to zero because the difference is close to zero in regions with no significant color transition. Sobel, Prewitt, Laplace, Roberts, Zero-cross, and Canny are the important methods used to find the edge.

2. Filtering

Filtering is a process that is performed to increase the readability of images or to extract the necessary information from these images. Making improvements and emphasizing is an important step before analyzing the image. In this stage filters that smoothen and sharpen the image are used. Smoothing filters such as mean, median, gaussian filter reduce noise on the image and blur the image. Sharpening filters emphasize detail and improve blurred details. Sharpening filters include Sobel, Prewitt, Laplace, Canny, and Roberts.

3. Morphological Operations

The meaning of the morphological word is "the structure, shape, and form of an object", the relationship between the parts of an object. In order to perform morphological operations, it is necessary to first determine the image taking and the structural element.

Binary images sometimes may contain numerous imperfections after some simple thresholding operations. Morphological image processing aims to remove the imperfections by accounting for the form and structure of the image. Morphological image processing is a collection of nonlinear operations related to the shape or morphology of features in an image. Morphological operations are especially suited to the processing of binary images but these operations can also be applied to greyscale images.

Morphological techniques probe an image with a small shape or template called a structural element which is small binary image contains the value of zero or one. The structural element is placed at all possible locations in the image and it is compared with the corresponding neighborhood of pixels. Some operations test whether the element "fits" within the neighborhood, while others test whether it "hits" or intersects the neighborhood. The structural element can be any of the different geometric shapes. The most common ones are square, rectangular and circle. Examples of structural elements are given in Fig. 2.

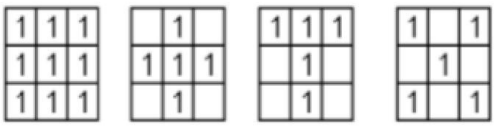


Fig 2: Examples of structural elements

The basic morphological operations used in image processing are as follows:

Erosion: It causes erosion from the edges of the image. As a result, the pixel groups and the gaps between them shrink as shown in Fig. 3. Noisy shapes are recovered with the selected structural element. Points that are fully aligned with the image of the structural element are processed. The points except for the center point of the structural element are changed.



Fig 3. Before (left) and after (right) erosion

Dilation: This process extends the edges of the binary image. As a result, the pixel groups grow and the gaps between them shrink as shown in Fig.4. If the central point of the structural element receives the same value as the image, the entire structural element is transferred to the image.



Fig 4. Before (left) and after (right) dilation

Opening: It is basically the dilation operator process following the erosion operator. The spaces between the objects and objects in the image are cleaned according to the size of the structural element. Objects on the image become slightly smaller than the original image. With the opening process, two objects close to each other will be separated without causing too much change as shown in Fig.5.



Fig 5: Opening example

Closing: It is the application of erosion process immediately after the dilation process. Two objects close to each other are connected to each other without much change. At the end of the closing, the dots in the image close each other and the main lines in the image are wider. Similar to the expansion process, the gap between adjacent dots in the closing process is filled as shown in Fig.6.



Fig 6: Closing example

III. APPLICATION

In the study, a software was developed to determine the number of pills in the tablets passing through the production band, to check if the missing packaging was made, and to determine the color of the pill in the production band. Here are some pill tablet pictures in different colors randomly selected as an input image. In order to simulate the production band, 60 recorded images shown in Fig. 7 were displayed randomly at intervals of 5 seconds. How many tablets will pass through the production band can be determined by the user.

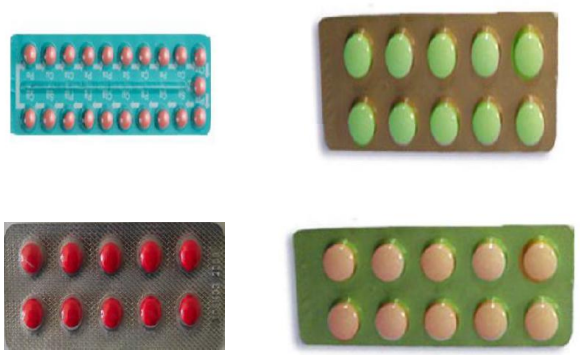


Fig 7. Pill tablet pictures in different colors

In the RGB color model, each color appears as its main red, green, and blue spectral components. The number of bits used to represent each pixel in the RGB color space is called the pixel depth. Accordingly, it can be said that each RGB color pixel has 24-bit depth. In this study, the color of the pill was determined by looking at the gray level values of the pixels in each layer (red, green, blue).

After the segmentation process, some small parts that did not belong to the pill appeared on the image. These parts are considered as noise and cause the calculation of the number of pills to be erroneous. The Gauss filter was used as a preliminary process to remove these noises. This filter is a filter created by removing the noise from the view through the details.

Then the opening process, which is morphological operations, is used to remove small anomalies such as a few pixel objects and protrusions from the image. In addition, the closing operation was performed to fill gaps in the pills found and make the pill lines more visible.

Neighbor pixel values are looked at to determine the number and find the number. The relationship of a pixel to neighboring pixels can be briefly summarized as follows: A pixel at (x, y) coordinates has four neighbors, two horizontal and two vertical, as shown below; $(x + 1, y), (x - 1, y), (x, y + 1), (x, y - 1)$. Here, each pixel (x, y) is 1 unit away. On the other hand, operations can also be performed by looking at the corner neighborhoods of the corresponding pixel. In the work we have done, analyzes have been carried out by looking at the neighborhoods at the corners.

(x-1,y-1)	(x-1,y)	(x-1,y+1)
(x,y-1)	(x,y)	(x,y+1)
(x+1,y-1)	(x+1,y)	(x+1,y+1)

Fig 8: The neighbors of the (x, y) pixel

The application interface is shown in Fig. 9. When you click on the "Start to Show Products" button, the recorded images are starting to show randomly. To simulate the production band, a 5 second wait period is added between the images to be shown.

When displayed on the left side of the image, the back panel uses the necessary image processing techniques to indicate the color of the pill and the number of the pill in the image. How many tablets will pass through the production band is determined by the user.

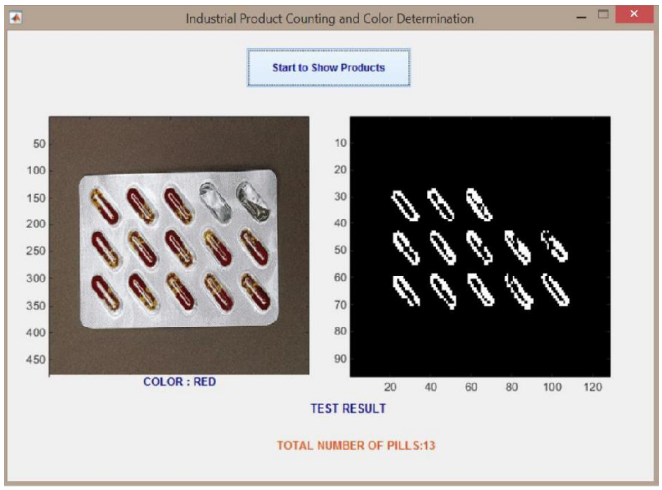


Fig 9: Application Interface

IV. RESULTS AND DISCUSSION

In this study, a data set was created with medicine boxes consisting of different color pills. Each tablet has a different number of pills. Pill tablet images were taken and color characteristics were examined and missing pill tablets were found according to certain criteria.

V. CONCLUSION

The industries are not always interested in the most accurate technique for a given problem, but most appropriate for the expected results, there must be a balance between accuracy and computational cost. Image processing methods provide many industrial conveniences to the field. It can automatically track some processes that need to be followed by humans and gives satisfactory results. At the end of the simulation, the application can indicates the color of the pills and determine the tablets with missing pills.

ACKNOWLEDGMENT

This study was funded by OYP with Project 2017-OYP-075.

REFERENCES

1. Affonso, C., et al., *Deep learning for biological image classification.* Expert Systems with Applications, 2017. **85**: p. 114-122.
2. Nateri, A.S., F. Ebrahimi, and N. Sadeghzade, *Evaluation of yarn defects by image processing technique.* Optik, 2014. **125**(20): p. 5998-6002.
3. Barbedo, J.G.A., *Using digital image processing for counting whiteflies on soybean leaves.* Journal of Asia-Pacific Entomology, 2014. **17**(4): p. 685-694.
4. Song, Y., et al., *Automatic fruit recognition and counting from multiple images.* Biosystems Engineering, 2014. **118**: p. 203-215.
5. ÇELİK, H.İ., L.C. DÜLGER, and M. TOPALBEKİROĞLU, *Görüntü İşleme Teknikleri Kullanarak Kumaş Hatalarının Belirlenmesi.* Tekstil Teknolojileri Elektronik Dergisi, 2012. **6**(1): p. 22-39.

The Computerized Semantic Analysis Study With Reality Models Created Via SUMO Ontology

Y.FIRAT[1]

[1] Çanakkale Onsekiz Mart University, Çanakkale/Turkey, yfirat@comu.edu.tr

***Abstract* - Both natural language processing and computational linguistic studies which have been realized in recent years consist of understanding the formal structure and content of the human mind. The most general models created by the human mind are ontologies. Due to their size, ontologies carry potentials in making errors and omissions. Therefore, they should be prepared in computer environment. This requires them to be formal. Attempts are made to reach the real implications of the concepts by means of these models of reality which are prepared by using a formal language together with lexical resources. Thus, the relationship between ontology which expresses the mind structure of human beings and language is also provided. Sumo is one of the ontologies created for this purpose. In this study, the reality models created by thematic role lattices in computer media via the Sumo ontology have been included. In addition, it has been aimed that these reality models which have been created should contribute to the semantic analysis of Turkish.**

***Keywords* - Formal Ontology, Sumo, Tematik Roles, Concept Latices, Formal Concept Analysis.**

I. INTRODUCTION

The human mind has a complex structure that encompasses the conscious processes of brain (thinking, perception, disposition, etc.). The language that reveals itself as a reality in the determination of thought and actions plays an important role in the shaping and interpretation of mental functions.

Both natural language processing and computational linguistic studies which have been realized in recent years consist of understanding the formal structure and content of the human mind [2].

The most general models that give the human mind structure are ontologies. For this reason, a relationship between ontologies and language needs to be established. Ontologies express the definitions of concepts and their relations to one another in a domain. Due to the fact that they are large in size, they contain mistakes and shortcomings when they are prepared by human hands. For this reason, they must be prepared in computer media. This requires them to be formal. Thus, the modeling of the expressions and the reality models created in the computer media is provided throughly [8].

The purpose of this study is to realize the relationship between lattice-based ontology type developed in computer media and language mathematically.

With the studies realized in recent years, the relation of language has been tried to be establised with some formal ontologies by using lexical resources (FrameNet, WodNet, etc.) prepared for English in electronic media. SUMO (Suggested Upper Merged Ontology) ontology is one of them.

There is only a mapping for namespaces in association with SUMO's WordNet dictionary. Synonym sets (sysnets) for noun, verb and adjective words and WordNet, which shows some semantic relations between them do not contain rich semantic details and formal definitions of concepts. Therefore, it does not give the necessary solution in relation to SUMO [14, 16].

However, because the concepts in the relation between SUMO's FrameNet lexical source are missing in terms of lexical information, it is seen that the correct matching has not been done. For this reason, using the thematic roles that serve as an interface in ensuring compatibility between meaning and form becomes a necessity. The real implications of the concepts are obtained by being used the thematic roles in multi-dimensional layers with the theory of Formal Concept Analysis. Thus, the relation of language between these reality models formed by the thematic role lattices is also provided.

Within this context, in the second part of the study, the thematic roles which show the semantic relation between the ontology and the rule have been described and the background information about the description of the formal ontology and the reality models created by thematic role lattices via the SUMO ontology has been given. In the third part, the computerized implementation of a reality model constructed by the thematic role lattices with the corpus-based annotation method has been shown. The semantic analysis of Turkish has been aimed in this computerized realization.

II. RELEATED LITERATURE

A. Thematic Roles

The thematic role is the semantic relation that a noun phrase interrelates with the action of the sentence [4].

The main thematic roles are:

THEME- the one moving or staying in a place

AGENT - the one who initiates or realizes an action

PATIENT - the one affected by an action
SOURCE - the exit point of a movement
GOAL - Where the movement is directed
LOCATION - Place where something is
PATH - The point that an entity moves
EXPERIENCER - the one feeling, perceiving or recognizing an event
INSTRUMENT - the one used to perform an action

B. Formal Ontology

From a general point of view, the reality models defined using a formal language are called formal ontology. Especially, the semantic analysis of language requires using a model of reality [4].

In this sense, Formal Concept Analysis Theory is the way to create reality models.

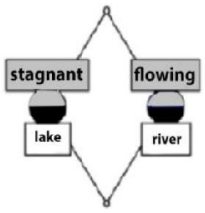
Formal Concept Analysis is a theory of data analysis that defines the conceptual structures among data sets. It is the mathematical theory of concepts. In other words, it is a concept hierarchy. It consists of concept properties given in the formal context and the objects having these properties. These objects and properties are the special conditions shared commonly in all the ontology types [1, 6].

In this hierarchy, all the concepts are organized in order by sub-concept and top- concept relation. The set ranked in this way is called the concept lattice. This concept lattice is shown as a diagram. In particular, the elements or concepts that form the language are placed in this diagram as a knot in the form of lines combined from the upper concept to sub- concept.

An ontology design that Formal Concept Analysis is used can be shown in the form of a figure known as Hasse Diagram below and a table of this diagram in Figure 1 [17].

	flowing	stagnant
Lake		X
River	X	

(a)



(b)

(a) Figure 1: The table consisting of objects and properties

(b) Figure 1: The conceptual lattice consisting of objects and properties

In Figure 1 (b), there are two concepts in the lattice. In this diagram, *the flowing* and *stagnant* refer to properties, *lake* and *river* refer to objects.

1) Sumo ontology

SUMO ontology is a kind of ontology used for various information processing systems. This type of ontology is made up of very general terms such as object, property and relationship.

As Niles and Pease expressed, SUMO is an easily accessible ontology that describes the concepts it contains in it and the relationships among them. Here, entities are ranked in a hierarchy from general concepts to specific concepts [15].

At the same time, SUMO ontology is an open source that includes the formal ontology of 20,000 words and 70,000 axioms [22].

Another important property of SUMO is the use of some various rules. These formal definitions or rules clearly state the meanings of words in ontology [18].

In this sense, a lexical source is required in Sumo ontology. The lexical resource that is compatible with Sumo comparatively is FrameNet.

FrameNet is a model based on semantic roles. These roles can not be linked directly to the language. Therefore, this model is associated with SUMO ontology, and the relationship with language is provided.

FrameNet which is based on Frame Semantics consists of F-Frames and LU-Lexical Units that associate these frames [5].

Frames, in this sense, are the schematic representations of conceptual structures [21].

While a semantic framework represents a set of concepts related to events, the roles or arguments represented for each frame are the frame elements each. At the same time, these frame elements are the arguments connected to lexical units within a sentence. English FrameNet prepared by Berkeley University has more than 780 frames, about 10,000 lexical unit frames and 135,000 marked sentences describing the frame elements [11, 3].

In order to understand and recognize the frame, lexical unit, and frame members that are the basic components of the FrameNet model better, the REVENGE frame can be reviewed through the existing FrameNet lexical source [21].

- The name of the frame is the REVENGE
- Equivalent words to the lexical unit are avenge, avenger, revenge (noun), revenge (verb), get back, get even, get even with. The set that these lexical units create is a frame, that is, connotates the REVENGE frame.
- The most obvious arguments in this frame are AVENGER, PUNISHMENT, OFFENDER, INJURY. Each of these arguments is a frame element. If it is to need to show these components by an sample sentence from the current FrameNet lexical source,

(1) [They $_{\text{AVENGER}}$] took **revenge** [for the deaths of two loyalist prisoners $_{\text{INJURY}}$]

As Tonelli and Pianta noted, FrameNet, the lexical source based on a corpus, is a conceptual model, termed a frame and that contains their prototype states. The frames here are defined as the classes that the words connotate [20].

In relation with Sumo-FrameNet, FrameNet Semantic Types (STs) and their associations are expressed in the first-order logic language of SUO-KIF (Knowledge Interchange Format) [7].

For example; The SOURCE semantic type is defined as the relation (? rel-relation) between the origin (? p-point) and source (? src-source) in SUO-KIF.

SUMO, using the FrameNet, needs the semantic types (ST) or semantic roles of frame elements (words). FrameNet defines forty semantic types and they are listed in the type hierarchy. For example, the ATTACK frame has the SENTIENT semantic type that is in the ASSAILANT frame member. These semantic types taking place in FrameNet make sense

when they are matched with SUMO classes. But SUMO is quite shallow compared to their classes. For this reason, SUMO classes are also used as semantic types.

Figure 2 shows the alignment of a part of the FrameNet semantic type (role) hierarchy with SUMO.

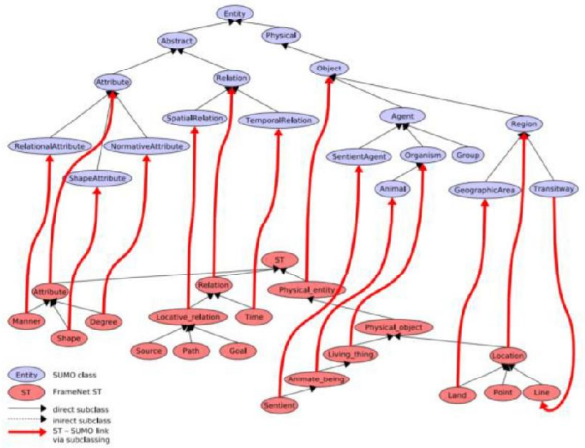


Figure 2: Bindings of a portion of the FrameNet STs to SUMO.

The SUMO class hierarchy is partially different from the semantic type (role) hierarchy of the FrameNet. As seen in Figure 2, SUMO separates abstract and physical entities from each other. It is therefore noticed that this detail distinguishes the SUMO classes from semantic types (roles). While some semantic roles in the FrameNet are mapped with SUMO classes, there is no match at some time. In such cases, meanings are redefined in SUO - KIF [19].

Despite all the development work fulfilled, the arguments in the SUMO ontology, where FrameNet is used, are missing in the sense of lexical information. For example; Some semantic types, such as SENTIENT in FrameNet, correspond to the intersection of more than one SUMO classes. It is not necessary that a SENTIENTAGENT in SUMO is to be alive when it is considered being sensitive to be vital. For example, The ORGANIZATIONS (INSTITUTIONS) in SUMO are also SENTIENTAGENT. For this reason, it is seen that the correct mappings are not realized between the class and frame elements in the SUMO-FrameNet pair.

C. *Thematic Role Lattices*

As can be seen from the information above, the relationship between ontology and language is one of the important aspects of natural language processing. Thus, the ontologies used by the arguments that make up the discourse are important sources of conceptual content of the expressions. The structures especially formed with thematic roles can be used as a reality model together with the lexicon in semantic technologies.

In the studies conducted up to today, the thematic roles have been shown in a linear hierarchy. Here, these roles have been studied as three dimensions by showing them in multi-dimensional layers, that is, in fractal lattices, with the Formal Conceptual Analysis Theory. Thus, the reality models have been created by reaching the true meanings of the words through the analyses of the various types of thematic roles defined in these layers (such as constituting the solution of different thematic roles in the same position).

It has been seen that the thematic roles shown in the lattices can contribute to the semantic analysis of Turkish, especially through a Turkish corpus.

As Kılıçaslan and Güner stated, the data given in a formal sense in the context of the Formal Concept Analysis Theory consist of two clusters and a statement that relates the two clusters. While one of the clusters contains the properties, the other includes objects that have these characteristics. The lattices obtained in this way allow the data to be modelled in a hierarchical organization [9].

If this situation is to be expressed in a sample English / Turkish sentence;

(2) a. Alice sent Melissa the parrot from Kuwait
b. Ali Meltem-e Konya-dan papağan-ı gönderdi.

Ali/Alice plays the role of AGENT, Meltem/Melissa undertakes both the PATIENT and GOAL role, whereas Konya/Kuwait takes the role of SOURCE because of its ablative case (from/-dan). The lattice graphics generated for this sentence is the same as in Figure 3.

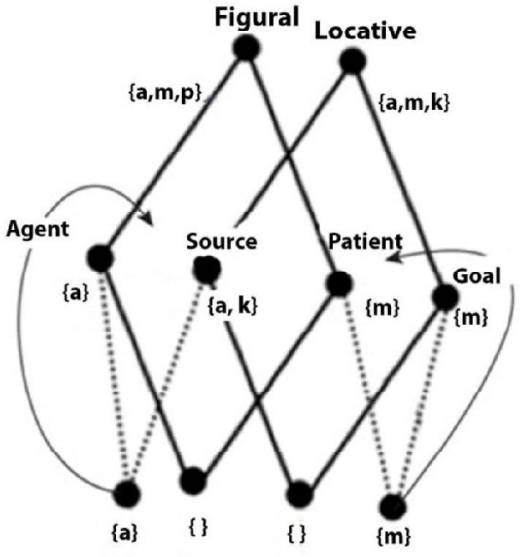


Figure 3: Sample thematic role lattice.

As shown in the lattice diagram in Figure 3, when the objects are expressed at the bottom of the nodes, the properties are placed at the top of the node. The letters that make up the set of objects are *a (Alice/Ali), m (Melissa/Meltem), p (parrot/papağan), k (Kuwait/Konya)*.

By means of the thematic role analysis of the Turkish sentence shown below, the real implications (semantic roles) of the concepts have been obtained and the semantic analysis of Turkish has been tried to be realized.

(3) a. Çocuk kalemi masaya koydu.
b. The child put the pen on the table.

The analysis of the thematic role of the sentence has been shown in Table 1 and its semantic analysis and thematic role

lattices have been shown in Figure 4.

Table 1: Thematic role analysis of the sample Turkish sentence numbered (3).

Thematic roles	Cocuk$_{AGENT/SOURCE}$ kalemi$_{THEME}$ masaya$_{GOAL}$ **koydu**.
Semantic roles	Cocuk$_{PERSON}$ kalemi$_{ITEM}$ masaya$_{PLACE}$ koydu.

In the *koymak (put)* action in Table 1, as *çocuk (the child)* intentionally and consciously performs the event, he receives the thematic role of the AGENT. It becomes *koyan* (*the person)* who plays the semantic role. The word *kalem-i (the pencil)* assumes the role of THEME from accusative case. It takes *madde* (*item)* semantic role. Since *masa-ya (on the table)* determines the position of the pencil, it takes *yer (the place)* semantic role through the GOAL thematic role.

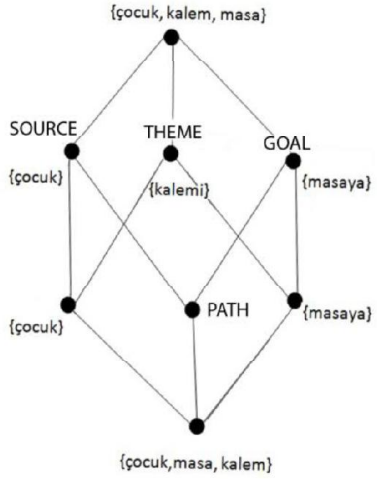


Figure 4: The semantic analysis of Turkish sentence numbered (3) with the thematic lattices.

As can be seen in Figure 4, the words belonging to the sentence are arranged relationally through the lattices along with their thematic roles. Thus, they become meaningful by being modelled by concept lattices as well as by their properties.

III. Material and Method

The aim of this section is to introduce the computerized implementation of a reality model towards the semantic analysis of Turkish. The application has been developed by corpus based annotation method within the framework of Formal Concept Analysis. The corpus used combines 1033 sentences.

The corpuses are large databases where a variety of oral or written texts in a language are brought together and usually processed through computers. Taking advantage of a corpus in a number of subfields of linguistics is to contribute to research as a scientific method [13].

In the field of natural language processing in recent years, abundant data, that is, a corpus, are needed for the successful use of statistical models which have been used predominantly [12].

The annotation is the coding of electronic texts (clauses) taking place in a corpus [10].

The annotation tool used in this study has been implemented by being used the PHP (Hypertext Preprocessor) language and the database created in MySQL (My Sequential Query Language). This tool is a page position that runs in the web media. In this application study, there is a database file named yelda_tool.sql with marked data. (yelda_tool.sql database can be accessed from http://www.yelda1367.com:2082/, and the tool can be accessed via http://www.yelda1367.com/member/login *tool username*: yelda1367@hotmail.com, *tool password*: beko1996).

In Figure 5, the interface where the morphological/ syntactic and thematic role markings of a sample Turkish sentence pertaining to this study corpus have been implemented is shown. In Figure 6, the lattice diagram which gives the real meanings and which has been issued automatically via the thematic roles of the arguments belonging to the selected sample sentence is accessed. In figure 7, the advanced lattice model can be seen [23].

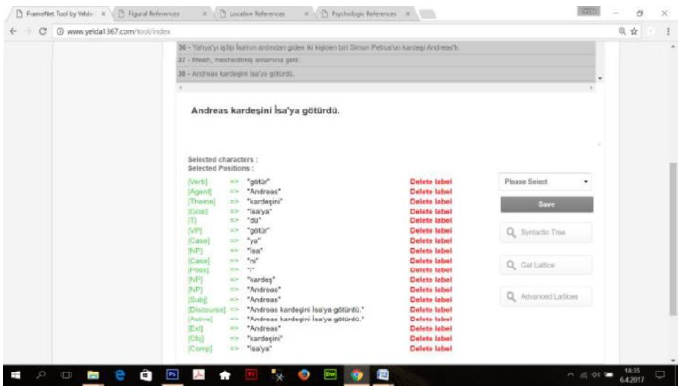


Figure 5: The annotation tool.

As shown in Figure 5, the thematic role and morphological/syntactic annotations of the arguments of the sentence have been made. The morphological / syntactic properties of this sentence are as follows:

- NP (Noun Phrase)
- VP (Verb Phrase)
- Case
- T (Tense)
- Poss (Possessive)

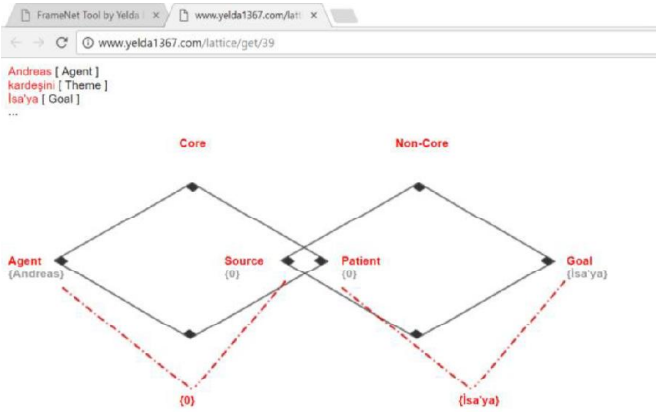


Figure 6: The lattice diagram issued automatically of the marked sample sentence.

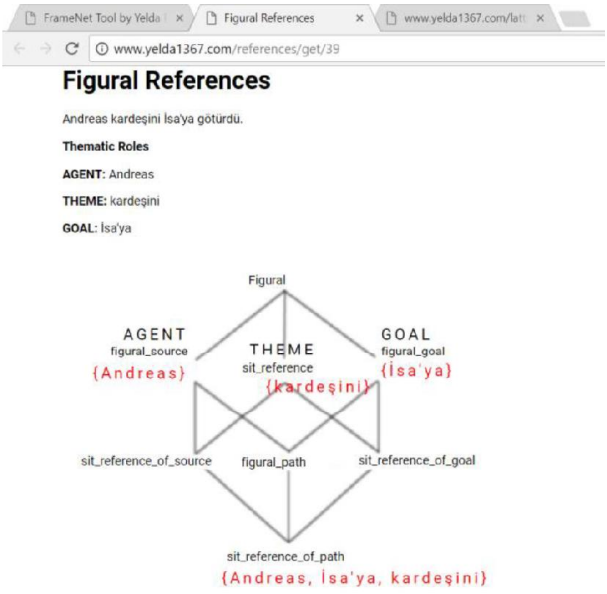


Figure 7: The advanced lattice diagram.

As shown in Figure 7, *the figural* term refers to the roles of the action. Also, *a situational reference (sit_reference)* is to an entity what an entity is to a location.

IV. CONCLUSION

In linguistics, the semantic roles are of great importance in classifying of arguments belonging to a sentence. The modelling of words or arguments with thematic role lattices gives their real implications in the sense of lexical knowledge. The information obtained from these models is integrated into many lexical sources by being kept them in databases. The semantic implications obtained in this way constitute an important source for the studies of natural language processing and computational linguistics.

REFERENCES

[1] M. Benes, and V. Snasel, "Deducing Design Class Hierarchy from Object Properties", *5th International Conference on ISM' 2002*, Rožnov pod Radhoštěm. Czech Republic, 22-24 April 2002.

[2] N. Chomsky, *Syntactic Structures*. The Hague/Paris: Mouton, 13, 1957.

[3] K. Erk, and S. Pado, S, "Shalmaneser – a toolchain for shallow semantic parsing", *In Proceedings of LREC-06*, Genova, Italy, 2006.

[4] Y. Fırat, Y. Kılıçaslan, and Ö. Uçar, "Bilgisayar Ortamında Biçimsel Ontoloji Oluşturulması" *Yükseköğretim ve Bilim Dergisi/Journal of Higher Education and Science,* vol. 3, no. 1, pp. 80-84, 2013.

[5] C. J. Fillmore, "Frame semantics and the nature of language", *Annals of the New York Academy of Sciences*, vol. 280, pp. 20-32, 1976.

[6] B. Ganter, B and R. Wille, *Formal Concept Analysis Mathematical Foundation*. Berlin: Springer, Verlag, 1999.

[7] M. Genesereth, "Knowledge interchange format", *In Proceedings of the Second International Conference on the Principles of Knowledge Representation and Reasoning*, Morgan Kaufman Publishers, pp. 238-249, 1991.

[8] T. R. Gruber, "A Translation Approach to Portable Ontology Specifications", *Knowledge Acquisition*, vol.5, no. 2, pp. 199-220, 1993.

[9] Y. Kılıçaslan, and E. S. Güner, "Filtering Machine Translation Results with Automatically Constructed Concep Lattices", *Proceedings of 8th International Conference on Concept Lattices and Their Applications (CLA 2011)*, Nancy, France, pp. 59-73, 2011.

[10] Y. Kılıçaslan, Ö. Uçar, and Y. Özkan, "FrameNet Tekniği ile İki Dilli Ontoloji Hizalaması", *NWSA-Engineering Sciences*, vol. 7, no. 2, pp. 505-520, 2012.

[11] K. Litkowski, "Senseval-3 task: Automatic labeling of semantic roles", *In Senseval-3: Third International Workshop on the Evaluation of Systems for the Semantic Analysis of Text*, Association for Computational Linguistics, pp. 9-12, 2004.

[12] C. D. Manning, and H. Schütze, *Foundations of Statistical Natural Language Processing*. Cambridge MA: MIT Press, 1999.

[13] T. Mc Enery, and A. Wilson, *Corpus Linguistics*. Edinburgh: Edinburgh University Press, 1996.

[14] G. A. Miller, R. Beckwith, C. Fellbaum, D. Gross and K. Miller, "Introduction to WordNet: An On-line Lexical Database", *Int J Lexicography*, vol. 3, no. 4, pp. 235-244, 1990.

[15] I. Niles, and A. Pease, "Towards a standard upper ontology", *In Proc. of the 2nd Int. Conf. on Formal Ontology in Information Systems (FOIS-2001)*, Ogunquit, Maine, vol. 2001, pp. 2-9, 2001.

[16] I. Niles, and A. Pease, "Linking lexicons and ontologies: Mapping wordnet to the suggested upper merged ontolog", *In Proceedings of the 2003 International Conference on Information and Knowledge Engineering*, pp. 412-416, June 23-26 2003.

[17] M. Obitko, V. Snasel, and J. Smid, "Designing Ontologies Using Formal Concept Analysis", *Proceedings of the International Conference on Communications in Computing*, *CIC'04*, Las Vegas, Nevada, USA, June 21-24 2004.

[18] A. Pease, "The sigma ontology development environment", *In working notes of the IJCAI-2003 Wkshp. on Ontologies and Distributed System*, vol. 71 of CEUR Workshop Proceeding series, Acapulco, Mexico, 2003.

[19] J. Scheffczyk, A. Pease, and M. Ellsworth, "Linking FrameNet to the Suggested Upper Merged Ontology", *Formal Ontology in Information Systems-Proceedings of the Fourth International Conference*, vol. 150, pp. 289-300, 2006.

[20] S. Tonelli, S, and E. Pianta, 'Three issues in cross-language frame information transfer', *International Conference RANLP*, Borovets, Bulgaria, pp. 441-448, 2009.

[21] F. J. Valverde, and Albacete, "Explaining the Structure of FrameNet with Concept Lattices", *Formal Concept Analysis:Third International Conference*, ICFCA 2005, Lens, Vol. 3403, pp. 79-94, France, 2005.

[22] G. de Melo, F. Suchanek, and A. Pease," Integrating YAGO into the Suggested Upper Merged Ontology", *In Proceedings of the 20th IEEE International Conference on Tools with Artificial Intelligence (ICTAI 2008)*, IEEE Computer Society, Los Alamitos, CA, USA, 2008.

[23] Y. Fırat, " Computerized Implementation of Concept Lattices Formed with Reference Parameters", *Erzincan University, Journal of Science and Technolgy*, vol. 10, no. 1, pp. 90-111, 2017.

Accessing To Information Via Bluetooth Low Energy Beacons

B.K. ÖZBEK[1], S. TEPE[2] and A.H. ZAİM[3]

[1] Istanbul Commerce University, Istanbul/Turkey, ozbekburakkan@outlook.com
[2]Uskudar University, Istanbul/Turkey, serap.tepe@uskudar.edu.tr
[1] Istanbul Commerce University, Istanbul/Turkey, azaim@ticaret.edu.tr

***Abstract* - Emergence of Bluetooth 4.0(BLE) devices have begun to make much longer connections and communications, consuming far less energy. The beacons are one of the biggest innovations that BLE brings. In this study, a system has been developed including hardware and software components. The software -web app- contains information related with people's daily activities. For example, stock market information, news, weather forecats are similar data collected by beacons. On the other hand, low-energy beacons are used to enable people to view this application. Thus, this makes it possible for people to access this information regardless of the Wi-Fi connection and the location.**

***Keywords* - BLE, beacon, physical web**

I. INTRODUCTION

There are many topics to be learned or followed in daily life. Social media sharing, stock market tracking, reading news, listening to music, keeping notes, weather control and so on, which are not common to every person on earth but are common to the majority, are examples. Although it is not difficult to access this information, it is important to be dependent on Wi-Fi, to have transitions between applications, and all this information that needs to be accessed throughout the day requires great effort and time. When considering the ways to solve these problems, the solution to be addressed was aimed at eliminating all these troubles. In addition, there was a need for an idea that could be held not only technically but also costly in terms of usability and not to be lost in the technology of the age we are in. From this point of view, a web application (containing these information) was considered. It was intended to be supported by low-energy beacons, which can be considered as an access point. (Figure 1) In this way, users who are close to the locations where the beacons bearing information of the web application are place, will be able to access the above-mentioned data groups independently of side factors such as Wi-Fi. Moreover, they could do this by consuming the least amount of power in their smart devices. Bluetooth Smart systems can deliver precise data about tagged items that improves efficiency and this ability will bring many other benefits to the business community and to consumers alike in the near future. In this study, a system has been developed including hardware and software components. The software -web app- contains information related with people's daily activities.

AUTHOR	DATE	PAPER	METHOD
Chong Shao; Shahriar Nirjon	2017	Image Storage and Broadcast via BLE	Raspberry Pi takes photo and and broadcast it from beacon
Hsi-Yuan Tsai,Guang-Heng Chen,Huang-Chen Lee	2017	Using Low-Cost,Non-Sensor-Equipped BLE Beacons to Track People's Movements	The BLE beacon broadcast BLE adver. While people are in motion. A beacon receiver can detect them.
Marek Novak, Otakar Wilfert / Tomas Simicek	2017	Visible Light Communication Beacon System for Internet of Things	The algorithm to detect transmitting LED
Fernando Alonso, Alvaro Castro, Miguel A.Salichs	2017	Identification and distance estimation of users and objects by means of electronic beacons in social robotics	Using Bluetooth Low Energy beacons in social robots for human-robot interaction
Irene Luque Ruiz, Miguel Angel Gomez-Nieto	2017	Combining of NFC, BLE and Physical Web Technologies for Objects Authentication on IoT Scenarios	Providing secure communication users and web browser using ble,nfc,physical web triangle
Manuel Castillo-Cara, Edgar Huaranga, Giovanny M.	2016	Ray: Smart indoor/outdoor route for the blind using Bluetooth 4.0 BLE	Presented prototype of a mobility assistant for visual impaired users
M.Gentili, R.Sannino, M.Petracca	2016	BlueVoice : Voice Communications over BLE in the Internet of Things Scenario	BlueVoice App Requires a Comm. Bandwith of 64.3 kbps to transmit audio
Shahid Raza, Prasant Misra, Zhitao He, Thiemo Voigt	2016	Building the IoT with Bluetooth Smart	Information about Iot and Bluetooth
Michael Wang, Jack Brassil	2015	Managing Large Scale, Ultra-Dense Beacon Deployments in Smart Campuses	Develop a prototype with beacon that time-varying advertisement
Riya Lodha, Suruchi Gupta, Harshil Jain, Harish Narula	2015	Bluetooth Smart based Attendance Management System	Solving the problem of attendance monitoring using a Bluetooth Smart

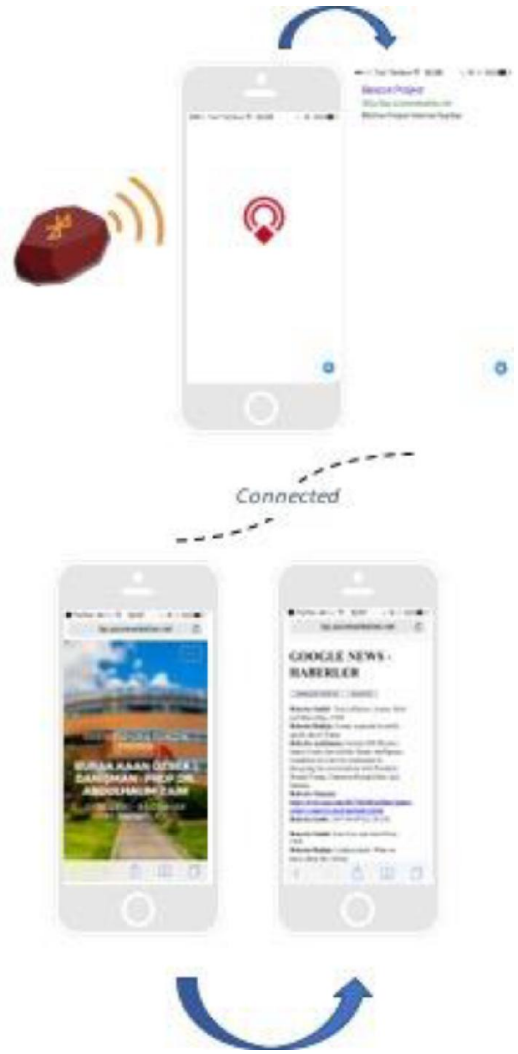


Fig. 1: An image from system

II. IMPLEMENTATION

The system has two main stages. The first step is driven by the beacon that broadcasts the web application to the user, and the second step is the web application that the user can view.

(1) Software Development: Using .NET Framework, the mentioned web application was developed (Fig.2) in accordance with the following headings:
   a. News Page
   b. Songs Page
   c. Stock Market Tracking Page
   d. Note Page
   e. Weather Information Page
   f. Social Media Links

(2) Publishing Web-App: Domain received for web-application. Here we will call xxx.com

(3) Generating URL: Using eddystone beacon url generator [1], the required format was created.

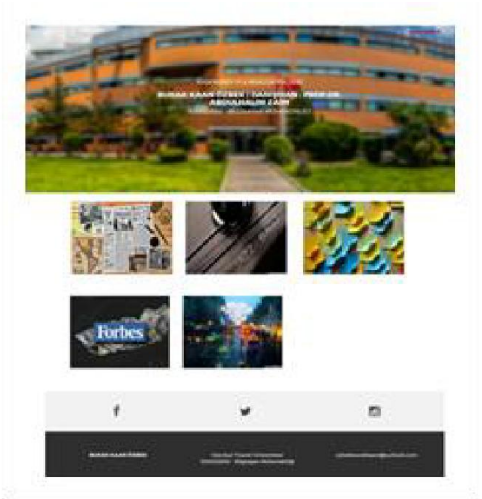


Fig. 2: Homepage of Web-App

```
/* Result: */
uint8_t advdata[] =
{
  0x03,  // Length of Service List
  0x03,  // Param: Service List
  0xAA, 0xFE,  // Eddystone ID
  0x0A,  // Length of Service Data
  0x16,  // Service Data
  0xAA, 0xFE, // Eddystone ID
  0x10,  // Frame type: URL
  0xF8, // Power
  0x01, // https://www.
  'x',
  'x',
  'x',
  0x07, // .com
};
```

Fig. 3: Beacon format for URL

(4) Broadcasting: After the beacon was installed and the software was prepared, the system became available. Apple users have been able to view the web application being signaled by beacon, using the Chrome physical web [2] feature found on their phone. The user interface and beacon are shown in Figure 1. Users who do not have a chrome browser on their phone, can use PhyWeb [3] Application in the App Store in the same way.

(5) Final: The users have captured the signal and applied it, they are able to enter the page they want and perform the operations they need, independent of Wi-Fi and extra applications.

III. Conclusion

From the very first time that Bluetooth 4.0 (BLE) entered our lives, research and development work has begun on it. We want to be a part of this technology by interest. And we have done a study on the uninterrupted access to information from the main subjects of our day. While we doing this, we used beacons from the most useful and savvy technologies that BLE offered us. In addition, we have been benefited from open source applications and platforms provided by Microsoft in the software section.

As a future research plan, we intend to focus on Fin Tech applications, which are short for financial technologies. In general, we will work to save time by reducing human and device interaction.

References

[1] Eddystone URL Generator, https://www.mkompf.com/tech/eddystoneurl.html

[2] Endüstri 4.0, (2016), "*Endüstri Tarihine Kısa Bir Yolculuk*", http://www.endustri40.com/endustri-tarihine-kisa-bir-yolculuk/

[3] R. Heydon, *Bluetooth Low Energy: The Developer's Handbook*. Indiana, 2012.

[4] Ibeaconinsider, "What is iBeacon", "How does BLE communication work?"

[5] http://www.ibeacon.com/what-is-ibeacon-a-guide-to-beacons/

[6] Microsoft, (2000), "*Shaping the Internet Age*", Gates, B https://news.microsoft.com/2000/12/01/shaping-the-internet-age/

[7] Webopedia, "beacon", "*Privacy Concerncs and Examples of Beacon Use"* http://www.webopedia.com/TERM/B/beacon.html

[8] *8 Ways Eddystone and the Physical Web can Make your Daily Life Easier*, https://blog.beaconstac.com/2016/03/8-ways-eddystone-and-the-physical-web-can-make-your-daily-life-easier/, March 3,2016

Spectrum Calculation of Massive Star Formation Region by Using GPU Programming

Y. POYRAZ KOÇAK[1] S. SEVGEN[1] P. SCHILKE[2] T. MOLLER[2]

[1] Istanbul University, Istanbul/Turkey, yasemin.poyraz@istanbul.edu.tr
[1] Istanbul University, Istanbul/Turkey, sevgens@istanbul.edu.tr
[2] Cologne University, Cologne/Germany, schilke@ph1.uni-koeln.de
[2] Cologne University, Cologne/Germany, moeller@ph1.uni-koeln.de

***Abstract* - Astronomy is one of the oldest sciences and focused on acquiring and analyzing data. Everyday, size of the acquiring data from observation instruments such as ALMA (Atamaca Large Millimeter Array) is growing. This study is part of the project called XCLASS (extended CASA Line Analysis Software Suite) which getting data from ALMA. XCLASS is a program that helps to model astronomical data. In this study, compute-intensitive parts of the myXCLASS is tool of the XCLASS program is loaded to the GPU. With GPU programming, it is achieved faster results by uploading to the GPU. This project will be a good source for future data-rich ALMA studies.**

***Keywords* – Astroinformatics, CUDA, Parallel Programming, GPU, Spectrum.**

I. INTRODUCTION

Astronomy is a scientific field that has to work with a lot of data. Now and in the future, the amount of data obtained with observations made with very broadband telescopes will reach enormous amounts. The processing of these large numbers of data consists of four steps. These are theoretical study, observation, computer simulation and data mining and machine learning respectively [1]. The first two are related to astronomers. The 3rd and 4th steps are specialization of computer scientists. The concept of astroinformatics is a combination of astronomy and informatics [2]. Data mining and machine learning have a very important role in astroinformatics. There are many studies on astroinformatics in literature.

In [3], a new multiple-classifier approach for spectral spatial classification of hyper spectral images was proposed. Several classifiers were used independently to classify an image. For every pixel, if all the classifiers had assigned this pixel to the same class, the pixel was kept as a marker. A minimum spanning forest was built. Each tree was rooted on a classification driven marker and forms a region in the spectral-spatial classification map. Experimental results were presented for two hyperspectral airborne images. The method significantly improved classification accuracies when compared with previously proposed classification techniques.

The authors of [4] described the automated spectral classification, redshift determination, and parameter measurement pipeline in use for the Baryon Oscillation Spectroscopic Survey.

In [5], authors presented spectral-spatial classification of hyperspectral images. Spatial information was extracted from set of pixels. Mathematical morphology was used to derive morphological characteristics such as size, orientation and contrast of the spatial. After, the morphological neighborhood was defined and used to derive additional features for classification. Classification process was realised by using support vector machine.

In [6], a new multifeature model which was aiming to construct a support vector machine (SVM) ensemble combining multiple spectral and spatial features were proposed at pixel and object levels. In this study, features employed include a gray-level co-occurrence matrix, differential morphological profiles, and an urban complexity index. Three algorithms were proposed to integrate the multifeature SVMs. These are certainty voting, probabilistic fusion and an object-based semantic approach, respectively. The proposed algorithms are compared with other multifeature SVM methods including the vector stacking, feature selection, and composite kernels. Hyperspectral digital imagery collection experiment DC Mall data set and two WorldView-2 data sets were used. It is found that the multifeature model with semantic-based post processing provides more accurate classification results.

This study is a part of the ALMA(Atamaca Large Millimeter Array) which is an international project in the field of astronomy. It has most powerful instrument of the world in millimeter (mm) and sub-millimeter radio bands, also provides enormous improvements in sensitivity, resolution and imaging fidelity. ALMA gives important information about galaxy evolution while getting high-resolution images of protostars, starforming regions, dust-enshrouded galaxies, and solar system objects [7].

Common Astronomy Software Applications (CASA) is a powerful software for post-processing. It includes only basic functions to model astronomical data. CASA offers data modeling using the XCLASS program, a one-dimensional radiation transfer program that uses CDMS (Cologne Database Molecular Spectroscopy)/JPL (Jet Propulsion Laboratory) molecule data. XCLASS (extended CASA Line Analysis

Software Suite) is a toolbox for the CASA. It has new functions for modeling data which are taken from Interferometric and single dish telescopes.In XCLASS there are two tools named MAGIX and myXCLASS. From these tools, myXCLASS calculates synthetic spectra using the radioactive transfer equation for isothermal objects. The XCLASS program works on Linux and Mac platforms [8].In this study, compute-intensitive parts of the myXCLASS part of the XCLASS (Extended CASA(Common Astronomy Software Applications) Line Analysis Software Suite)line identification program, which provides insight into the data obtained from the ALMA device are realised by using GPU programming.

The CUDA Fortran, the programming language of Compute Unified Device Architecture (CUDA), is formed by using the expansions of Fortran programming languages. We should point out here that the parallel pro- gramming functions in a CUDA Fortran are called kernels. A CUDA Fortran program executes serial codes on the CPU and executes parallel kernels on the GPU. The programmer organizes these threads into a hierarchy of thread blocks and grids [9, 10, 11, 12]. When compared to the central processing unit (CPU), GPU has more cores and transistors in the kernel. This makes GPU more effective than CPU parallel processing problems. Thus, faster results are obtained in this study by using GPU programming.

II. XCLASS - (EXTENDED CASA LINE ANALYSIS SOFTWARE SUITE)

With technological development, CASA (Common Astronomical Software Applications) software has been developed by the University of Cologne to reduce astronomical data which are taken from serial and single-dish telescopes. XCLASS (extended CASA Line Analysis Software Suite) is a toolbox for the CASA software. structure of the XCLASS software is shown in Fig.1 [13].

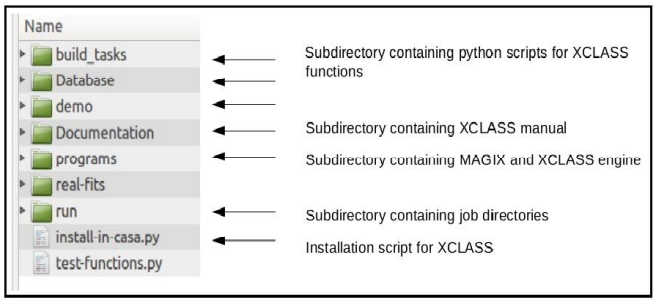


Figure 1: Structure of the XCLASS program [14].

myXCLASS calculates synthetic spectra by solving radiative transfer equation for an isotermal object. There are 4 fortran files in myXCLASS program. These are:

- Module myXCLASS Core.f90
- Module myXCLASS GPU.f90
- Module myXCLASS MPI.f90
- Module myXCLASS SMP.f90

Modifications on Module myXCLASS Core.f90 have been made. In this file contains core subroutines of myXCLASS program. Fig.2 shows subroutines in the Model myXCLASS core.f90 file. In Figure 2, yellow colored rectangles indicates that modified subroutines. DetectionEquation from yellow colored subroutines is translated to GPU version by using Cuda Fortran programming language.

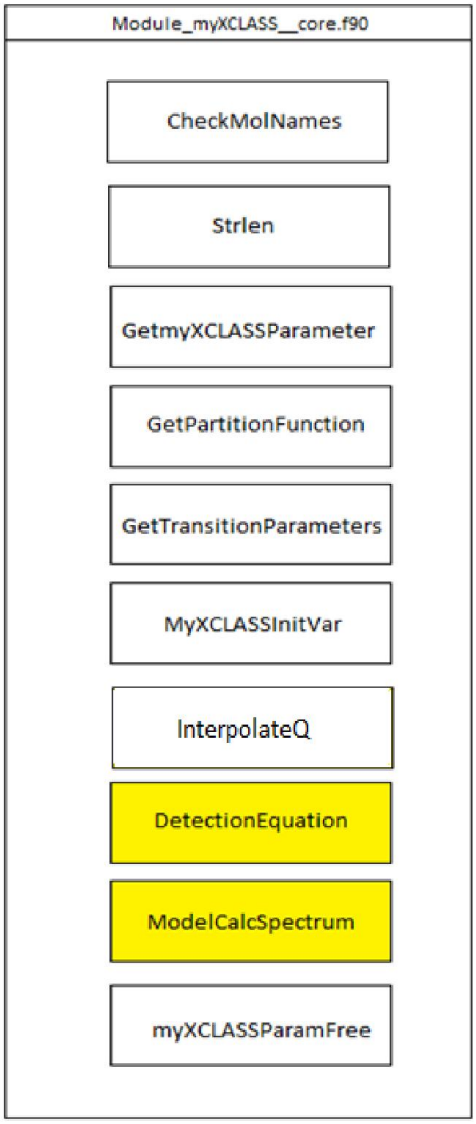


Figure 2 : Structure of Model myXCLASS core.f90 file.

III. DETECTION EQUATION

This is a kernel rewriten by using cuda fortran that calculates the detection equation for a given frequency myXCLASS calculates synthetic spectra by solving radiative transfer equation for an isotermal object. If transition is not located within given frequency range the kernel is terminated without doing anything. Rayleight-Jeans temperatures [15] value is determined. In physics, means the Rayleigh-Jeans is

an approximation to the spectral radiance of electromagnetic radiation at all wavelengths. After that determination of brightness for dust temperature and intensity for emission processes are realised.

IV. Conclusion

In this paper, we have implemented using the Graphic Processing Unit (GPU) Programming for the purpose of accelerating spectrum calculation. Our approach has proved to be a faster working system and have less total processing times in spectrum calculation. We have used two GPU graphic cards to acceslerate the performance of the spectrum calculation. Properties of the GPU graphic cards are shown in Table 1.

Table 1 : Properties of the GPU graphic cards.

Properties Name	Values
Device Name	Tesla K20m
Memory Clock Rate (KHz)	2600000
Memory Bus Width (bits)	320
Peak Memory Bandwidth (GB/s)	208.00

Table 2 : Experimental results.

Subroutine Name	Working time on CPU	Working time on GPU
DetectionEquation	0.079980 ms	0.000001 ms

These are play a key role in spectrum calculation. Experimental results are shown at Table 2. We have also observed that the data size has a great impact on the performance of XCLASS program. Another possibility to improve our presented results may be the use of more graphics cards. In future work, Purpose of the Project is to classify the data which are collected from massive star formation regions and to reduce the data size. Thus, the potential interesting formations are going to be identified. Eventually, the most distinctive molecular lines of massive star-forming regions are going to be revealed. Another purpose is that processing-intensive portions of the application are going to realised by GPU programming and results are going to gotten rapidly. This project is going to be good resource for ALMA projects that is going to work with multi-dimensional data in the future, the method and the algorithm we have proposed for spectrum calculation can be improved by new algorithms to be implemented on new GPU graphic cards.

References

[1] N. M. Ball, R. J. Brunner, ”Data Mining and Machine Learning in Astronomy”, International Journal of Modern Physics,, vol. 2, no.19, pp: 1049-1106, August, 2010.

[2] Wikipedia. (2017, January 6). Astroinformatik. Available: https://en.wikipedia.org/wiki/Astroinformatics.

[3] Y. Tarabalka, J. Chanussot, J. A. Benediktsson, ”Multiple Spectral-Spatial Classification Approach for Hyperspectral Data”, IEEE Transactions on Geoscience and Remote Sensing, Vol. 48, No.11, pp: 4122 - 4132, November, 2010.

[4] S.A. Bolton, D.J. Schlegel, E. Aubourg, S. Bailey, V. Bhardwaj, J.R. Brownstein, S. Burles, Y.-M. Chen, K. Dawson, D.J. Eisenstein, J.E. Gunn, G. R. Knapp, C.P. Loomis, R.H. Lupton, C. Maraston, D. Muna, A.D. Myers, M.D. Olmstead, N. Padmanabhan, I. Paris, W.J. Percival, P. Petitjean, C.M. Rockosi, N.P. Ross, D. P. Schneider, Y. Shu, M.A. Strauss, D. Thomas, C.A. Tremonti, D.A. Wake, B. A. Weaver, W.M. Wood-Vasey, ”Spectral Classsification and Redshift Measurement for the SDSS-III Baryon Oscillation Spectroscopic Survey”, The Astronomical Journal, vol. 144, no.5, pp: 20:40, November, 2012.

[5] M. Fauvel, Y. Tarabalka, J. A. Benediktsson, ”Advances in Spectral-Spatial Classification of Hyperspectral Images”, Proceedings of the IEEE,, vol. 101, no.3, pp: 652 - 675, March, 2013.

[6] X. Huang, L. Zhang, ”An SVM Ensemble Approach Combining Spectral, Structural, and Semantic Features for theClassification of High-Resolution Remotely Sensed Imagery”, IEEE Transactions on Geoscience and Remote Sensing,, vol. 51, no.1, pp: 257-272, January, 2013.

[7] Argelander-Institut fur Astronomie der Universitat Bonn I. Physikalisches Institut der Universitat zu Koeln. (2013, December 1). ALMA Tools-Within the German Node of the European ALMA Regional Center). Available: https://www.eso.org/sci/facilities/alma/arc.html.

[8] T. Moller, C. Endres, P. Schilke, ”eXtended CASA Line Analysis Software Suite(XCLASS)”, Instrumentation and Methods for Astrophysics,, vol. 598, pp: 20, January, 2017.

[9] NVIDIA and PGI Compiler. (2017, April 8). CUDA Fortran. Available: https://developer.nvidia.com/cuda-fortran

[10] NVIDIA and PGI Compiler. (2017, April 10). Introduction to PGI CUDA Fortran. Available: http://www.pgroup.com/lit/articles/insider/v1n3a2.htm.

[11] PGI Compilers and Tools, ”CUDA Fortran Programming Guide and Reference Version 2017”, NVIDIA Corporation, 2017.

[12] G. Ruetsch, M. Fatica, ”CUDA Fortran for Scientists and Engineers”, NVIDIA Corporation, Santa Clara, USA, 2013.

[13] T. Moeller, P. Schilke, ”Manual for XCLASS-Interface”, ALMA, Cologne, Germany, 2017.

[14] A. Sanchez-Monge, ”XCLASS: automatic line fitting of ALMA data Tutorial”, ALMA, Cologne, Germany, 2017.

[15] Wikipedia, (2017, April 30). Rayleigh-Jeans Laws. Available:

A new trust-based algorithm for a secure and resilient cluster heads

Mohamed Aiche[1], Noureddine Idboufker[2], Laila Sakkila[3], Mohammed Bousmah[1], Atika Rivenq[3] andAbdelghafourBerraisoul
[1]LTI laboratory, ENSA El jadida, ChouaibDoukkali University, El jadidaMorroco,mohamedaiche1@gmail.com
[2]TIM laboratory, ENSA Marrakech, Cadi Ayyad University, Marrakech Morroco, n_idboufker@yahoo.fr
[3]Univ. Valenciennes, CNRS, Univ. Lille, YNCREA, Centrale Lille, UMR 8520 - IEMN, DOAE, F-59313 Valenciennes, France,laila.sakkila@univ-valenciennes.fr

***Abstract* - The progressive advancement of wireless technologies has given rise to vehicle networks also called VANETs that represent communication systems based on the exchange of information between vehicles V2V (Vehicle-to-Vehicle) or from the vehicle to the infrastructure attached to roadside V2I (Vehicle-to-Infrastructure). Reliable Information exchange helps to overcome the increase of road accidents while improving users quality of experience (QoE).**

However, the amount of exchanged information has to be optimized. For this, the clustering is a real solution by regrouping vehicles in clusters according to specific proprieties like geographic localization, velocity, and others...VANETs security also increasingly an important and fundamental challenge. A VANET must be secured by avoiding attacks in order to maintain its value while improving the quality of experience of users.

In this paper, the cyber security of clustered VANET will be approached in order to increase the security and the reliability of control plan information. Our contribution is based on the election of two cluster heads in order make possible the load balancing between them. Furthermore, the head(s) election process is based on a new algorithm that takes into account the reputation score of each vehicle.

***Keywords* - VANET, Clustering, Security, Reputation, QoE**

I. Introduction:

The increase in road accidents, natural disasters and terrorist acts in transport are serious events which endanger a large number of transport users. These situations are continuously increasing and call for a rapid reaction. As part of the management of these situations, the rapid detection of road accidents and the immediate communication of information between vehicles and with the infrastructure can be vital. The exchange of information, the identification of potentially dangerous obstacles and accident alerts provide the basic services to ensure road safety. In recent years, the world of road transport has focused on the operation of wireless communication systems to meet security requirements. In fact, the majority of accidents can be avoided if drivers are warned of the danger.

It is therefore essential to share information between vehicles (V2V) on the one hand and between vehicles and infrastructures (V2I) on the other hand. The aim is to cooperate several vehicles, transmit more and more information and share it through wireless telecommunication networks

Securing these communications is fundamental so that they are not intentionally attacked or disrupted and therefore rendered inoperable at the time of crisis. In this paper, the Cyber security of connected vehicle will be approached in order to increase the security and the reliability of the systems of treatment and communication of the information in the transport, taking into account the risks of cyber-attacks.

In our work, we suggest a solution based on the reputation and the trust established between the nodes for election of Cluster Head to ensure a secured routing while optimizing network resources.

1. Reliability and accuracy

We emphasize on the reliability and accuracy of the messages in real time. An unreliable message can lead to various consequences which clearly affect the safety of road users by causing material and body damage. These messages can be received through a dysfunction of equipment that is a part of the Vanet system, which is intentionally sent or generated by malicious users sharing false information. Consequently, the evaluation of the reliability and the speed of transmission of the messages generated by a vehicle are very important in the VANETs.

In a large Vanet environment, we assume that the vehicles have a low (or not) confidence relationship between them [2]. The question raised is how do vehicles decide to rely on a message?

In [2] a message is considered reliable if 1) the integrity of the message is valid, 2) the message has been generated and announced by a legitimate vehicle, and 3) there is a means to "measure" the reliability of the message.
The evaluation of message's reliability is a role of the vehicle's reputation that generates this message and the degree of confidence that a waiter can express, allowing him to make decisions and act on messages quickly.
To consider a message as reliable, it is necessary to take into account the sufficiently high reputation of its transmitter. This can be calculated with parameters and metrics exchanged in the Vanets
We suggest a security model that takes into account the topological dynamic of clusters. This model contributes to the security in the Vanets and the improvement of resources management by the load distribution assured by secondary head-clusters.
The clusters formed as well as the selection of the head-cluster must satisfy the condition of maintaining the stability of the topology to simplify routing and security.

2. Threats and Vulnerabilities in Vanets

Connected, increasingly intelligent, the automobile is changing. But this evolution has a setback; the vehicle becomes a true computer platform and becomes more and more attractive target...

Today, vehicles rely on a multitude of embedded control units (ECUs) that govern information and entertainment systems as well as the most critical functions: injection, braking and, for an increasing number of vehicles with driving or parking assistance functions, the steering.
Devices such as USB sticks, Bluetooth, embedded GSM chips, wifi ... are now very common on board, and are as many possible gateways for a hacker wishing to access the various on board computers of the vehicle. Security would be, it is estimated, equivalent to that of the PCs at the beginning of Internet...

Remote locking system, diagnostics, communication with road infrastructures via dedicated radio stations, transmission of diagnostic information to the constructor via cellular data, and hosting of other essential functions, in particular for Safety with the deployment of airbags, traction control, anti-lock braking system (ABS)… are also possible openings which can be exploited by the attackers.

Automotive safety researchers have demonstrated the vulnerabilities of connected vehicles by performing several frightening exploits [23]: for example, a team has managed to remotely hijack an Internet-connected infotainment system used by several models of cars. With the software upgrade feature, they were able to install malicious software to control the vehicle's control systems. Another team of researchers has created malicious software that can interfere with the car's control software when the diagnostic equipment is connected to the vehicle's on-board diagnostic ports.

Ad hoc vehicular networks are exposed to a large number of vulnerabilities, especially at the routing level. Studying vulnerabilities of VANETs can help us recognize all attacks to avoid.
The main objectives of malicious behaviors are: discovery of routing information, data discovery, degradation of network performance and network topology modification.
The securing of these networks generally aims to guarantee 5 main objectives: *Confidentiality, Integrity, Availability, Non-repudiation and Authentication*
Establishing a secure environment that meets the security needs of each VANET application requires knowledge of all attacks to avoid. The main objectives of malicious behaviors are: discovery of routing information, data discovery, degradation of network performance and network topology modification.

3. Routing in the VANETs

The main challenge for Vanets is to design routing protocols that are robust (Fault Tolerant, adaptive to the mobility of nodes) and scalable. This property allows the protocol to maintain reasonable performance when the network size or the number of nodes increases.

Given the very dynamic with highly decentralized architectures, it is crucial to determine the most suitable routing protocol for this type of network, and then to secure it in order to provide an optimal and secure routing for the data. Furthermore, the rapid change of topology in VANET due to high mobility, routing with capability of ensuring security is more problematic than Ad-hoc networks. Therefore, a static hierarchy is not appropriate for such a dynamic network topology. There are two main classes of protocols in Vanets which are topology-based and position-based routing protocols. Due to this selecting a routing protocol in VANET becomes a major challenge for researchers.

Among all these protocols, there are the cluster-based protocols attempts to elect a single node, called cluster-head, which is responsible for transmitting the aggregated data to the base station.

4. Clustering

In a highly dynamic network such as VANET, the mobility of nodes disrupts the hierarchical structure and causes frequent group reorganizations [16]. This instability translates into more exchanged messages and poor performance.

The property of cluster's stability seems to be paramount for these dynamic networks. The idea is to group the vehicles according to their spatial or temporal dependencies. The spatial dependencies are represented by the position of the vehicle and its distance from another, its direction of movement or the quality of its radio link with another vehicle. The temporal dependencies are the speed of movement of the vehicle and especially the relative speed between two vehicles.
The Vanets raise many questions due to the continuous changes in the topology, particularly concerning dynamic routing. Each node must participate in the discovery phase necessary for the establishment of the path, the transfer of the exchanged packets and the maintenance of this path. In addition, due to limited resources in self-organizing networks, in terms of bandwidth and energy, roads construction and their maintenance must be done with a minimum of control traffic
The hierarchy of VANET provides interesting solutions to the problems of suffering of vehicle Ad-hoc networks with discontinuous connectivity and limited capacity. This approach is well suited to VANETs because the dynamic of traffic drive to the creation of "natural" groups or convoys on the highway.
The nodes of each cluster are supervised by their cluster-head which can coordinate the access to the channel and save the wastage of resources in the retransmission due to access collisions and interference by limiting interactions between nodes. Within a cluster, communications can take place in several jumps. In this work, we limit ourselves to problems related to security. There are other works that discuss limiting congestion within the cluster, such as maximum cluster length in km without limiting the number of vehicles in the cluster. Within the cluster, the graph representing the network must be connected and communication between vehicles will be ensured by means of an intra-cluster routing protocol [17].

We suggest a clustering technique that organizes the nodes of the network into virtual groups, geographically close according to certain rules while improving the security of the network. This improvement is mainly due to better access control combined with the most secure Cluster Head selection.

5. Trust and Reputation

Trust: Trust is defined as a particular level of subjective probability, or an entity evaluates another or a group of entities that will perform a particular action and may be carried out or compromise the system. When we say that someone is trustworthy, we implicitly imply that he will do something in our expectation so that we can cooperate with him.

Reputation: The reputation term is the opinion of one entity or set of entities on another and that can be described as a long-term collective measure of trust that can be used to decide whether a vehicle is malicious or honest.

The entity in a Vanet environment receives a message related to the routing process from other entities. Once received, the message should be checked as well as its reliability. For this purpose, we proceed to verify the sender entity in order to calculate its degree of confidence by the method based on reputation. We assume that if an entity is valid and trustworthy, the information that it sends is reliable but for optimum security reasons we propose the implementation of a second verification involving a trust third-party body which will update the overall reputation of the entity at issue.

II. Related works

To facilitate the implementation of trust and reputation management in ad hoc networks, various trust and reputation measures have been designed and integrated into various applications in the literature and many efforts have been devoted to research in this domain. Some of them are already deployed. With the difference in the pattern of their architecture, their reputation and trust establishment processes.
Some articles include the threshold method to ensure the validity of the message and the legitimacy of the sender, others rely on network modeling and models based on trust and reputation are described In [2], [5], [6], [7], [8], [11]. We will discuss those that are most closely related to our work. Other researches propose a framework that provides hardware-based security and uses symmetric / asymmetric cryptography for message exchange.
One of the first approaches in introducing a distributed reputation system was the vehicle Ad-Hoc Network (VARS) reputation system [13]. [14] Calculates the reputation of the vehicle, depending on the similarities of different recommending, deciding whether an event message is trustworthy or not. However, this work does not cover the aspects of vehicle's privacy. The authors of [15], suggested a framework for analyzing the behavior of other people in the neighborhood, based on movement-related data to detect erroneous behaviors. The works mentioned above do not deal with the coexistence of the reputation system and the pseudonyms mechanism. Moreover, theses works are based on a distributed reputation system. In models based on trust and reputation, a decentralized infrastructure is adopted. However, the problem with decentralized infrastructures is related to robustness which is not often guaranteed.

Our work is based on a hybrid reputation system that combines the two centralized and distributed approaches to encourage cooperation and dissuade selfish behavior in ad hoc mobile networks.

III. Proposed Model

Applications of Intelligent Transport Systems (ITS) are applications of new technologies that emerge new uses and new solutions to manage urban flows, passenger and merchandise mobility and information processing in normal and disrupted situation as well as payment devices. They were deployed for the first time in the Vanets by adding new functions to apprehend their environment by means of sensors, to communicate with other vehicles via wireless or 3G / LTE radio interfaces and to process this information and Make decisions about the behavior of the vehicle using an on-board computer [17].

The model we propose is based on the addition of a new function to the ITS system. This function consists of an authority (TA) which ensures the centralized management of trust within a Vanets.
Vanet environment consists of road units (RSUs) which are widely deployed and each vehicle in the network is equipped with an onboard unit (OBU) allowing communication with the other entities of the network as well as dealing with different processing.
TA : Authority of confidence and certification. Taking into account the security parameters, the authority generates and publishes its own public key, public keys of the RSUs as well as those of the vehicles. This authority also makes available the list of global reputation scores and the list of revocations. Reputation scores are a pillar of our Vanets security model.
RSU : Road Side Unit are the edge units connected via secure channels to the trust authority TA, while providing connectivity and service to vehicles. Feedback from user vehicles and updates of vehicle travel information will be transmitted by RSUs to TA. RSUs can be considered as data relays between vehicles and the TA trust authority. We assume that RSUs are largely or little deployed along roads. In areas where RSUs are present, vehicles will be able to update information in a timely manner.
Cluster: A set of vehicles bundled in a geographically accurate zone and allowing shared parameters and satisfying a defined reputation score.
Vehicle: a node on the road that wants to reach its destination more comfortably and more energy efficient and benefiting from the services offered by a cluster. This vehicle is required to give feedback on the Head cluster after its removal from the cluster.
Cluster Head: Is determined by an election algorithm based on trust. From the point of view of message's exchange, the cluster Head represents the nodes of the cluster with respect to the other clusters of the Vanets.

In our trust model, we make some assumptions and we define the trust levels of different roles in the model of the suggested system.
The vehicle's reliability is based on a collection of opinions on a particular vehicle. In a situation where reliable and unreliable vehicles are mixed, providing a service contributing to Vanet safety policy may be high risk. This makes the selection of a homogeneous vehicle group problematic.
The confidence model we propose is applicable for the following communication scenarios:
Direct: the evaluation by a vehicle V_i of the reputation (TD) of a vehicle Vj is done by analyzing the messages sent by the latter to the node i. The reputation score assigned by the vehicle is therefore the result of the interaction experiment of the vehicle Vi with the vehicle Vj. This value is communicated to the TA authority after each ??
Indirect: the evaluation by a vehicle Vi of the reputation (TI) of a vehicle Vj is done by analyzing the reputation scores received by Vi from all the vehicles V / {Vi, Vj} at destination of the node i. This implies the second-hand transitivity of trust relations provided by nodes
Based on the ITS infrastructure: the TA trust authority we offer allows the ITS to provide its reputation score (T_{TA}) for each Vanet vehicle. T_{TA} is an essential component of the calculation of the overall confidence score (TG) of a vehicle. We believe that the TTA reputation of a vehicle must take into account (1) compliance with TTP's current transport policies and (2) reputation based on TOA vehicle history.
TOA is a score that records the performance of a vehicle V_I at the end of its CH role within a cluster. TOA can be established according to two scenarios. Scenario 1 in which the score is attributed by the vehicles of the same cluster at the end of their interactions with the vehicle CH. This score is then transmitted to the trust authority TA. The second scenario adapts to the centralized architectures in which the ITS has a precise knowledge of all the security messages exchanged in the Vanets.
In addition, the trust authority is responsible for Certifying pseudonyms to ensure non-repudiation and revocation of certificates. A vehicle can prove to another vehicle the confidence of an assertion (its certified statement) with the knowledge of the secret information (its ID) without revealing it. This approach has been maintained by the central authority, which determines the signatures of each node.

1. Initialization:

The trust authority TA must always assign a private key for each RSU deployed at the roadside to avoid any potential malicious RSU problem [7].

Each vehicle also records its interactions with another vehicle, including the number of successful interactions and total interactions.
Each vehicle can use a number of short-term public-private key pairs (called pseudonyms that do not reveal the identity of the node) instead of using a single long-term public-private key pair. Each vehicle uses a pseudonym for a short period of time and then switches to another. This list is maintained by the certification authority that updates it to have the list of revocations distributed by the RSUs.
The trust authority also has an overall reputation score for each vehicle. We suggest that initially all cars have the same reputation.
During the period of communication with the RSU, the vehicles communicate with the trust authorities to obtain the updated global reputation of the other vehicles and provide the list of messages exchanged for the verification and the update of the global reputation scores.
We consider vehicles that are active in a local area; therefore, we only get the list of global reputations of all vehicles that are nearby.
Each node maintains a neighboring table that includes its neighbors of communication. A node estimates the distance of the sender-receiver using its own coordinates, the location in the message received and the driving time.
The cluster-head is determined by an election algorithm that can constitute the initialization of the cluster. The cluster formation algorithms also include node addition or removal functions [21][22].
Each cluster has at least one cluster head (CH) selected or elected by other nodes in the cluster. The size varies from one cluster to another and depends mainly on the transmission range of the communication device.
Several metrics have been proposed in the literature to elect all cluster heads. The selection algorithm assumes certain information about each node such as its mobility, the power of the received signals, the direction, the energy level or its geographical position and the road number on which it is engaged.
The model proposed by [22] ensures cluster stability defined by a long lifetime of CH, long lifetime of cluster members and low CH change rate.
A cluster head constructs a minimal overlap graph based on information about its cluster topology. Routing requests are broadcasted on the built tree reducing the overhead.
Reviews of the CH selection algorithms in terms of safety
Our model proposes a new algorithm of CH selection based on the scoring technique. This algorithm aims to overcome the limitations of the CH selection algorithms in terms of security. It reduces the risk associated with selecting a dishonest vehicle such as CH. Indeed, the algorithm proposed is based on the calculation of the reputation scores obtained from the trust authority TA and the direct and indirect testimonies of the adjacent vehicles.

2. Step 1:

A vehicle Vi which sets off on the road, begins with a state "Indeterminate US", floods the network with markup messages containing the following information (Entity ID, Route ID, Position, Speed, Transmission range, Direction)
This is sent with a Timer T, if the T expires and the condition of the vehicle is still indeterminate then the vehicle proclaims Cluster Head and can offer its Cluster services.

3. Step 2:

Cluster Head Election
In [2], we propose to calculate the global reputation in accordance with time. Nevertheless, justify the abandon of the reasoning of the temporal scale for the benefit of the calculation of the reputation based on the experience.
The ultimate goal when designing an application over a communication network is end-user satisfaction, which is now called a satisfactory level of quality of experience (QoE). For an application in the Vanets, the main component of the QoE is the perceived quality, ie the quality of the behavior observed by the authority that governs the laws in force regarding the transport policy in the country.
This perceptual quality takes into account a single factor that determines the quality of service of a vehicle (for example the number of offenses committed). This hypothesis expresses the QoE as an exponential function of the quality of service degradation $e^{-\lambda(E_{k+1}-E_k)}$
A vehicle Vi can obtain the overall reputation of a vehicle Vj ${T_{TA}}^{E_k}$at a time k based on the quality of experience.
The proposed model is based on the calculation of the reputation score of all the vehicles belonging to a cluster. This score is calculated by a vehicle i for a vehicle j using the formula below:
The reputation of a vehicle j is calculated centrally at reputation authority level. For this, the authority proceeds as follows:

1- Reception of the reputation score $T_{I(j)}$ of the vehicle j established by each vehicle i belonging to the cluster, due to its experience as customer of the vehicle j performing the function CHP / S

2- Aggregation of the scores received (phase 1) to establish the reputation score of the vehicle j

$$T_{(j)}{}^{(E_k)} = Avg(\ T_{I(i,j)})^{(E_k)}$$

3- Reception of the reputation score () related to transport policies respect of the vehicle j.

4 -Calculation and update, by the trust authority, of the overall reputation score of the vehicle j

$$TG_{(j)}^{(E_k)} = \alpha T_j^{(E_k)} + \beta T_{TP}^{(E_k)}$$

In addition, and due to a change in the cluster composition, the trust authority can transmit reputation scores to vehicle demand.

α and β are chosen to satisfy α + β = 1 so as to reflect the transport strategy objective. Indeed, some transport authorities are intransigent in terms of compliance with the Highway Code and must in this case choose the coefficient β closest to 1.

The vehicles with the two highest scores will be elected Primary Cluster Head (PCH) and Secondary Cluster (SCH) respectively.

The PCH is the node of the cluster whose responsibility is to ensure the interconnection of the cluster with the other clusters of the network. This will relieve the nodes of the cluster as well as the links that interconnect them.

Indeed, the basic algorithms simply elect a Head by cluster, we talk then about a flat algorithm at a single level.

The CH constitutes a point of failure which strongly affects the availability of the network and subsequently the services offered by the latter. For this purpose, the use of SCH will certainly serve to improve the resilience of networks through the use of PCH which will serve as a backup element in case of PCH failure. Moreover, the use of a single CH is confronted with the constraint of resistance to the scale factor insofar as the performances of the latter are affected in large scale contexts. For this purpose, the use of the SCH will contribute to the improvement of the performances through the possibility of implementing load sharing policies between the PCH and SCH. These policies can be designed according to the QoS requirements of the services offered within the cluster.

Other algorithms choose multiple cluster heads from among all cluster heads already selected at the previous level. They then introduce a cluster-head hierarchy. In this case, we are talking about multilevel hierarchical algorithms

Step 3: access to the cluster

When a vehicle in a US state receives a markup message from a Head cluster, it compares the consistency of its physical parameters, such as its position, direction, speed and transmission range related to what transmitted by the CH. For this purpose, the comparison algorithms such as (ref) can be used. In order for the vehicle to benefit from the service of the CH it must send a request to join the cluster head. The latter relies on the reputation calculation function to decide whether or not to accept this request. The accepted vehicle passes from the US state to the CM state and is defined with the cluster ID.

For the stability needs of the cluster we propose not to recalculate the reputation scores in the same cluster.

The access to cluster allows the vehicle to benefit from the services offered by the PCH and the SCH previously designated at the end of the election phase. The transition from state CM to state US depends on the consistency of the physical parameters.

At the end of his experience within the cluster, a vehicle leaving a cluster must send its feedback on the Head cluster and its neighborhood as well as the safety messages exchanged with the nearest trust authority.

IV. Conclusion

The model proposed in this paper makes it possible to choose a secured vehicle; one relies on the score of its reputation and confidence. The latter offers its services for the good behavior of a cluster to avoid disasters on the road.

The model also allows to distribute the loads between the main cluster head and the one that is secondary in the case of high demand to the main head cluster thus allowing the resilience of the network.

Acknowledgments

The present research work has been supported by European Union, the French Government and the region "Haut de France" through SECOURT project(cyber -SEcurity in COmmUnicant systems for Transport) as part ofELSAT 2020 project (Ecomobility, Logistics, Security and Adaptability in Transport to 2020).

REFERENCES

1. *REPLACE: A Reliable Trust-based Platoon Service Recommendation Scheme in VANET Hao Hu, Student Member, IEEE, Rongxing Lu, Senior Member, IEEE, Zonghua Zhang and Jun Shao*
2. *A Reputation-Based Announcement Scheme for VANETs Qin Li, Amizah Malip, Keith M. Martin, Siaw-Lynn Ng, and Jie Zhang*
3. *Vehicular Security Through Reputation and Plausibility Checks Sanjay K. Dhurandher, Mohammad S. Obaidat, Fellow, IEEE, Amrit Jaiswal, Akanksha Tiwari, and Ankur Tyagi*
4. *Trustworthy Parking Communities: Helping Your Neighbor to Find a Space Julian Timpner, Student Member, IEEE, Dominik Schurmann, Student Member, IEEE and Lars Wolf, Member, IEEE*
5. *ARS: Anonymous Reputation System for Vehicular Ad hoc Networks Luz Marina Santos Jaimes, Kifayat Ullahz and Edson dos Santos Moreira ICMC, University of Sao Paulo,*

Sao Carlos Campus, Brazil yDepartment of Systems Engineering, University of Pamplona, Pamplona, Colombia Department of Computer Science, CECOS University, Peshawar, Pakistan Email: lsantos@unipamplona.edu.co, kfytullah@gmail.com, edson@icmc.usp.br

6. *VTrust: A Robust Trust Framework for Relay Selection in Hybrid Vehicular Communications, Hao Hu, Rongxing Lu, and Zonghua Zhang School of Electrical and Electronic Engineering, Nanyang Technological University, 50 Nanyang Avenue, Singapore 639798 Institut Mines-Tel ecom/TELECOM Lille and CNRS UMR 5157 SAMOVAR, France Email: hhu002@e.ntu.edu.sg; rxlu@ntu.edu.sg; zonghua.zhang@telecom-lille.fr*
7. *RGTE: A Reputation-based Global Trust Establishment in VANETs , Xiaoqing Li The State Key Laboratory of Integrated Service Networks Xidian University Xi'an, Shaanxi 710071, P.R. China E-mail: xqli@mail.xidian.edu.cn Xuejun Li The State Key Laboratory of Integrated Service Networks Xidian University Xi'an, Shaanxi 710071, P.R. China E-mail: aluckydd @mail.xidian.edu.cn Jicheng Liu The State Key Laboratory of Integrated Service Networks Xidian University Xi'an, Shaanxi 710071, P.R. China E-mail: ljc723@126.com Weiying Sun The State Key Laboratory of Integrated Service Networks Xidian University Xi'an, Shaanxi 710071, P.R. China E-mail: s_w_y888@126.com*
8. *SURVEY: Reputation and Trust Management in VANETs, Jitendra Singh Sengar, BVM College of Technology & Management, Gwalior, MP, India jitendrasinghsengar@gmail.com*
9. *Security Threats on Vehicular Ad Hoc Networks(VANET): A Review Paper Senthil Ganesh N.I Year M.Tech., Deptt. of Telecommunication Engineering, SRM University, Chennai, India.Email: senthilganesh90@gmail.comRanjani S.Asst. Professor, Deptt. of Telecommunication Networks, SRM University Chennai, India. Email: ranjani.s@ktr.srmuniv.ac.in*
10. *P. Golle, D. H. Greene, and J. Staddon, "Detecting and correcting malicious data in VANETs," in Proc. 1st ACM Int. Workshop Veh. Ad HocNetw., 2004, pp. 29–37*
11. *"Towards expanded trust management for agents in vehicular ad hoc networks," U. Minhas, J. Zhang, T. Tran, and R. Cohen Int. J. Comput. ntell. Theory Pract., vol. 5, no. 1, pp. 3–15, Jun. 2010.*
12. *A multi-Objective Genetic Algorithm-Based Adaptive Weighted Clustering Protocol in Vanet*
13. *VARS: A Vehicle Ad-Hoc Network Reputation SystemFlorian D¨ otzer BMW Group Research and Technology Hanauerstrasse 46, 80992 Munich, Germany florian.doetzer@bmw.de Lars Fischer, Przemyslaw Magiera Technical University of Darmstadt, Dep. of Computer Science, Research Group IT-Security Hochschulstr. 10, 64289 Darmstadt, Germany {lars@sec|pmagiera@rbg}.informatik.tu-darmstadt.de*
14. *A Similarity based Trust and Reputation Management Framework for VANETs, Nianhua Yang, Department of Computer Science & Engineering, Shanghai Jiaotong UniversityShanghai 200240, China School of Business Information Management, Shanghai Institute of Foreign Trade, Shanghai 201620, China yangnh@sjtu.edu.cn*
15. *Vehicle behavior analysis to enhance security in vanets, R. K. Schmidt, T. Leinm¨ uller, E. Schoch, A. Held, and G. Sch¨ afer, in Proceedings of the 4th IEEE Vehicle-to-Vehicle Communications Workshop (V2VCOM2008), 2008.*
16. *Limiting the Impact of Mobility on Ad Hoc Clustering Rituparna Ghosh, and Stefano Basagni Dept. of Electrical and Computer Engineering, Northeastern University Boston, MA, U.S.A. rghosh@ece.neu.edu, basagni@ece.neu.edu*
17. *Hiérarchisation dans les réseaux ad hoc de véhicules Véronique Veque, Colette Johnen*
18. *Efficient Clustering based OLSR Routing Protocol for VANET Ruchi Mehra Department of computer Science and Engineering, Chandigarh University, Gharuan, Mohali, Punjab, IndiaRasmeet S. Bali Department of Computer Science and Engineering, Thapar University, Patiala, Punjab, Indi, Prabhsharan Kaur Department of Computer Science and Engineering, Chandigarh University, Gharuan, Mohali, Punjab, India*
19. *Performance Enhancement of VANETs Using Cluster Based Routing M.Hari Prasad P. Kowsalya , P.G. Student, Department of Electronics and Communication Engineering, K.L.N College of Information Technology, Manamadurai Taluk, Sivagangai , Tamilnadu, India Associate Professor, Department of Electronics and Communication Engineering, K.L.N College of Information Technology, Manamadurai Taluk, Sivagangai , Tamilnadu, India*
20. *A TRUST BASED CLUSTERING WITH ANT COLONY ROUTING IN V ANET Rashmi Ranjan Sahoo", Rameswar Panda", Dhiren Kumar Beherab, Mrinal Kanti Naskarc, ADES Lab, Department of ETCE, Jadavpur University, Kolkata-700032, India Department of mechanical Eng ineering, I GIT, Sarang, Od isha -759143 ,India*
21. *Design of Protocol For Cluster Based Routing In VANET Using Fire Fly Algorithm Akansha Sachdev Komal Mehta, Dr.Latesh Malik GHRCE Nagpur,Indi*
22. *Cluster Head Selection Algorithm in Vehicular Ad Hoc Networks, BOUCHRA MARZAK, HICHAM TOUMI, MOHAMED TALEA, ELHABIB BENLAHMAR, 18th ITC Specialist Seminar on Quality of Experience, Markus Fiedler, Fran¸cois Blouin, Patrik Arlos, Karlskrona, May 29–30, 2008 Department of Telecommunication Systems School of Engineering Blekinge Institute of Technology*
23. *Cyber Threats Facing Autonomous and Connected Vehicle s: Future Challenges, Parkinson, Simon, Ward, Paul, Wilson, Kyle M. and Mille, Jonathan, University of Huddersfield 2017*

Defining a Process to Improve Code Review Efficiency in Software Development

M. ERŞAHİN

Dokuz Eylül University, İzmir/Turkey, mustafa.ersahin@gmail.com

***Abstract* – Code review process is one of the important parts of software development. In general, a commit that may have many files should be inspected by at least two developers. After that, if there are not any syntactic or logical errors, resources are merged to repository by an approver. This process takes too much time in large development teams and effects the continuous integration's duration. A new "buddy check" process is defined to improve code review efficiency. An extra responsibility is given to "buddy checkers" to review their friends' commitments in a tight timeframe. A significant improvement was performed on "first action time" and "merge time" for a commit by the help of this process. There are other effects of this process such as; number of reviews on a commit is raised, bug rates are decreased and the effort of the quality assurance team is decreased. As a result, the process that is defined improved the efficiency of our development processes.**

***Keywords* – Software Engineering, Efficiency, Code Review, Continuous Integration**

I. INTRODUCTION

SOFTWARE Engineering is an engineering discipline associated with the development of reliable and efficient software that works on machines. There are several phases that are systematic and cost effective to software development processes. These phases are Feasibility Study, Requirement Analysis, Design, Development, Testing and Maintenance. Sequential order of these phases is also called Software development lifecycle (SDLC).

Software Engineering techniques and processes are being used more and more by many companies that provides commercial solutions for end users. Most of the techniques and processes are produced for software that have better quality. Therefore, importance of the software quality is getting higher. One of the main problems that threats the software quality are bugs. It is very important to find and fix a bug in software development lifecycle because total cost of the bugs may affect project budget. There can be a bug on any phase of the lifecycle, however, if you find the bug quicker, you can reduce these maintenance costs. In this paper, one of the development phase activities that called code review is discussed and a new process to improve this activities efficiency is proposed.

Code review is an inspection of source code of a software by developer that is different than code author(committer). Code review is a common Software Engineering practice and the first place to find coding related issues in software development. There are two main goals to achieve by code review;

- Reducing the errors during the development in order to prevent wasteful testing time and production errors.
- Standardizing the software development process such as environment architecture, coding styles etc. This provides also less future maintenance cost.

There are some code review approaches and practices that help to achieve these purposes are used in software development processes. All these processes are discussed in detailed next chapter.

II. CODE REVIEW

Code review is systematic examination of computer source code. It is intended to find mistakes overlooked in software development, improving the overall quality of software [1]. After the definition of the code review, these topics should be discussed:

- How can source code be reviewed?
- Why code review is needed?
- What are the common issues that affect the success of code reviews?

These topics are very important to have an efficient code review process. Many software companies define their own process according to development environment, project and customer priorities, development team size etc.

In this paper, a new process that called "buddy check" is discussed as a case study in our software development lifecycle.

A. Code Review Approaches

Code review is an activity that the whole development team should involve. There are common approaches on code review such as manual code review and automated core review. Both of them are useful for achieving code review goals.

At first, an automated code review was wanted to be started. This kind of code review generally deals with coding style. Development team should discuss and decide some rules that

must to obey while writing code. For example; each line length must be less than 120 character, function declaration should contain predefined keys etc. Automated code review process is executed at compile time. If there is an existing inconsistent code block, compilation fails with detail information about the problems found. There are several tools that called linter for this process and they have all predefined coding styles and rules that specialized to development language. These linters allow to define custom rules to check source code. Automated code review tools provide us a standardized source code that is written by project developers. Therefore, it is easy to read, understand and maintain the source code.

The other core review approach is manual code review. At first, manual review can be done with traditional peer programming or a code review tool. Classical pair programming is an agile software development technique in which two programmers work together at one workstation [1]. Traditionally, one programmer writes code while the other reviews each line of code as it is typed in. The two programmers switch roles frequently. Some obvious benefits can be achieved with pair programming:

- Fewer bugs
- Lower cost on production maintenance
- Knowledge transfer

[2]. Another benefit is that both developers acquire a good understanding of all the written code; they know what the design choices are and how the code works. From many aspects, this reduces the fragmentation of knowledge within a team. There are some limitations and disadvantages across to these benefits. Pair programming is suitable for centrally located teams but geographically distributed teams are increased in last few years. Pair programming costs much more than solo programming. Also, there are some creativity issues according to working conditions. Although developers should be able to convince a partner of the merits of an idea in pair programming, creativity needs independence. Therefore, it is not possible to execute pair programming in many software development company. Another manual code review approach is using a code review tool.

As it is told before, distributed teams are getting more popular in the software development industry. Using an online code review tool is very useful to inspect other developer's code. There are several code review tools available in the market to do it. Some of them are packaged with a source control tool. Gerrit, TFS Code review, Crucible is the most popular code review tools. All of these tools enable your developers to review, find and eliminate buggy resources before the code is merged to repository under the source control. This approach is more cost effective than pair programming. As a reviewer, does not have to work with the code author while he/she is developing. He/she only checks the code after author's commitment. Also, online code review allows to all developers in team to review a commitment of other developers. Therefore, more than one developer can inspect a commitment for possible bugs. Probability of finding a buggy resource is getting higher by the help of extra reviewers. In short, online core review approach is more effective than pair programming in lots of software development cases.

Code review approaches and general advantages to each other are discussed in this section. The necessity of Code Review is discussed in the next chapter.

B. Importance of Code Review

In general, code review has two main purposes that are pointed before. Achieving those purposes are very important for software development lifecycle. In addition to those purposes, every development team that execute code review process have got indirect positive effects.

Code review improves the code quality. As it is told that while discussing the automated core review approach, but this time improvement of the quality is related for different inputs. This is not about standards and code linting. It is about making code more efficient. Everyone in development team has their own background and experience, so they always a good idea to suggest smarter solution, better design, more performed code in code review. Therefore, it is highly possible to improve code quality with code review.

Code review provides two-way improvement on new developers and senior developers. When new members join the team, senior or more experienced developers should mentor them to understand both processes and development standards. Code review helps developer to get feedback on his/her work to improve coding skills. Also, newer members with fresh eyes can suggest a new perspective to current code base or existing knowledge. Therefore, code review is very useful to make everyone better in development team.

Another positive effect of code review is project familiarity. When a team works on a project a developer will heavily work on one large part for a while, while another one is working on something else entirely. Doing code reviews helps people familiarize themselves with code they haven't written but might be asked to maintain in the future. It promotes knowledge of the codebase across the team, and is likely to speed up future development.

C. Code Review Pitfalls

Until now, code review and its importance in software development processes are discussed. Across to all these positive effects, sometimes code review can cause destructive effects both developers and project lifecycle. Some experimental results show that code review fails in a few conditions although everything is fine.

At first, each member of the development team should believe the importance of the code review and why they do this activity. Some developers consider this process can be time consuming. If there is anyone who does not believe this process,

it cannot contribute any improvement, feedback etc.

The other thing that can be negative effect on author is tone of the comment. As a well-known fact that positive criticism is very important to build trust among the team members. Across to this, if the review comment has direct or indirect messages that can be evaluate as personal attack, code review can harm both the team spirit and project success.

Another common problem with code reviews can be that people do not do them. This can happen for a number of reasons according working conditions or to developer's personal thinking. For example; large development teams with multiple project that are developing simultaneously have this kind of problem. When a developer looks at review list, lots of commitments from different developers are waiting for review. Then he/she may think that someone else may review these commitments and he/she may skip. If the number of developers that have this behavior, reviews may need to wait on the list much more time. Authors might be blocked on the ongoing feature while waiting for their comments on commitments.

As a result, the cases that are discussed in this section cause ineffective and unsuccessful code review process. These cases can be more according to software development methodology, development team formation etc.

The questions about code review are discussed such as; definition of code review, common approaches of code review, importance of code review and issues that threats code review until now. A new case study and results in next section are explained in the next section.

III. CASE STUDY

In this section, the new code review process is presented with the real experiments. At first, the development team formation and code review approach is described.

We have been working on a software company that has three different locations. We have twenty developers that each of them is a part of at least one project. Some of them have to support more than one project simultaneously. Online code review is preferred than pair programming because of location and cost issues. Our version control system is combination of Git and Gerrit for integrated code review tool. Also, Jenkins is used for continuous integration processes. Jenkins's role in code review process is discussed later. At first, some information about Gerrit is given that is the focus of this paper. Many statistics from Gerrit database are provided to check and compare our processes improvement.

A. Gerrit Code Review

Gerrit Code Review tool is a modern tool that facilitates a traceable code review process for git-based software projects. [3] There are different roles in this approach. These roles are author, reviewer, verifier. Author uploads collection of proposed changes to Gerrit server. The reviewers are responsible for critiquing the changes proposed within the patch by leaving comments for the author to address to discuss. Verifiers test the related bug or feature to see whether there is an error. Everyone in development team should work synchronously to have a successful and efficient code review process.

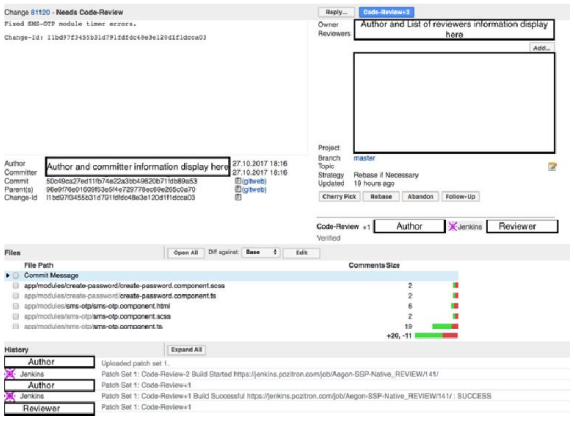


Figure 1: An example Gerrit code review.

In our process, integrated tests do not exists in this phase. Our verification process directly related with continuous integration system that exists. If a patch-set uploaded to Git server, Jenkins automatically triggers a build for related project. If build is completed and all test cases are executed successfully, Jenkins will verify the patch-set.

There is an example for our code review flow in the Figure 1. This flow starts with author's code upload action. Jenkins triggers a build immediately to verify patch set. While the build process going on, author gives a score to patch set that own. Then automated build is finished successfully and Jenkins has verified the patch by giving a score 1. After the patch being verified, the author, should invite reviewers manually in tool interface. Invitation process can be automatized according to some configurations, too. As it can be seen on the Figure 1, one of the invited reviewers has finished the review and he/she has given a positive score 1. At least two developers except author give positive score then patch set is ready for submission to repository on version control system. Any reviewer that has submit authorization can submit the patch set to the repository to finish code review flow.

An internal performance evaluation system is used that includes both individual and project specific metrics. There are also analyzed code review metrics. Moreover, there are detailed analysis from Gerrit database. Some of these statistics that are first review time, submit duration and average code review per commitment which are not satisfying. We have selected "first

review time" to compare team's attention on code. Merge duration can show author's technical qualification and ownership by the help of some other statistics. The last metric is important because more reviews for different point of views can increase finding buggy sources. Table 1 show us statistics of three different team for these topics.

Therefore, it is thought that techniques should be changed in a different way or it is needed to apply new rules.

Table 1: Code Review Statistics.

	First Review Time	Merge (Submit) Duration	Average Code Review per Commitment
TEAM 1	77.44	245.01	3.34
TEAM 2	66.88	287.03	2.67
TEAM 3	102.32	488.78	3.23

An internal phase that called "Buddy Check" is defined as a part of code review processes. It is explained this next section.

B. Buddy Check

Buddy Check is a different approach that have some rules in the code review process. The aim of the buddy check is basically to build code review awareness and responsibility between team member. If it succeeds, it is believed that each metric will be improve positively.

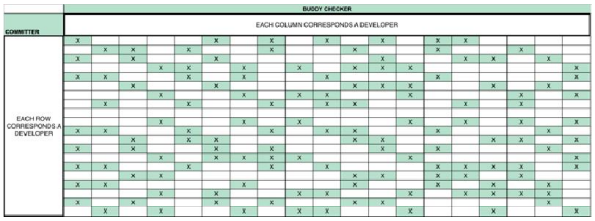


Figure 2: Buddy Checker groups.

To achieve these purposes, a matrix of developers have been created to define a buddy checker group. Figure 2 shows the large matrix. Each buddy group contains at least seven developer. These group's formation based on technical skills, project knowledges, personal experience and locations of developers. Then a checklist has been created after long discussions between development team for code review. Table 2 shows these checklist items that should be checked while review the code. These items are only common items. Actually, there are several items according to the development language and framework, but there is no need to give details of them.

Table 2: Code Review Checklist.

"Null" check should be performed where syntactically need
Check function names and variables for meaningful and readable names
Use common utility methods
Check localizations of components for Multilanguage support
Check formatting of the code. Send the well formatted code at least for the change in the code to improve code quality.
Check folder structure when a new class is added to make sure it is right place
Check unit tests

In addition to this, communication groups have been created for each buddy check group on internal communication and messaging tool. These groups can be used to inform the buddy groups and to discuss the commitments.
Then targeted time limitations for metrics have been defined such as;

- Every commitment/patch set should be reviewed in half an hour. (first review time < 30 minutes)
- A commitment should be submitted to repository in two hours. (submit duration < 120 minutes)

Buddy check process has been started to be executed in only one team firstly since September. It is seen that developers feel more responsible to each other when buddy channels are analyzed. There are more information sharing and knowledge transfer between developers in communication channels than before. After a period that approximately two months, great improvements existed on metrics what are prioritized. Table 3 shows the latest statistics from Gerrit database.

Table 3: Code Review Statistics after Buddy Check.

	First Review Time	Merge (Submit) Duration	Average Code Review per Commitment
TEAM 1 without Buddy Check	77.44	245.01	3.34
TEAM 1 with Buddy Check	38.48	162.81	3.93
Improvement	%50.3	%33.55	%17.81

Although the targeted time limitations are very tight according to current statistics, results are impressing about team's performance when compared with the previous results. Team has been successful on our goals and now executes more efficient code review process than past.

Buddy review approach provides some benefits on our software development processes such as;

- Code review awareness and responsibility
- More standardized code according to the predefined rules
- Better knowledge about projects that they do not work
- More bug free packages
- Faster code review process and reduced blocked time for authors
- Reduced overall development efforts
- More satisfied customers

A significant improvement performed on software quality according to these benefits. Any new feature or issue on current

software can go live faster than past. This velocity is very important in any projects that includes financial transactions. Generally, both of these items satisfy customers in software industry. Overall effort of development lifecycle is reduced by the help of this process.

The new approach on code review process is introduced that called buddy check and shared its effects on our development processes.

IV. Conclusion

Software development processes are very important for software companies. Every phase of software development lifecycle affect software quality and cost directly. It is known that code review is one of the major activity to find and fix some bugs and unstandardized codes. Then a study is performed about code review to improve current processes' efficiency. It is defined that a buddy check activity or process to have a review standard and build responsibility between the development team members. Then it is succeeded on our case study at the end of two months. Now, there is a more efficient code review process than before.

References

[1] Kolawa, Adam; Huizinga Dorota, *Automated Defect Prevention: Best Practices in Software Development* H. Poor, *An Introduction to Signal Detection and Estimation*. *Wiley-IEEE Computer Society Press* pp.260. 2007

[2] Shore, James, *The art of agile development, O'Reilly Media, Inc*. 2007

[3] Shane McIntosh; Yasutaka Kamei; Bram Adams; Ahmed E.Hassan, *The Impact of Code Review Coverage and Code Review Participation on Software Quality*

Literature Review and Research Model Proposal for Predicting Water Pollution and Flooding in Tigris and Euphrates Rivers

T. IBRAHIM[1], A. BOSTAN[2], and I.AKMAN[3]

Atilim University, Ankara /Turkey, [1] thairking78@gmail.com
Atilim University, Ankara /Turkey, {[2] atila.bostan, [3] ibrahim.akman}@atilim.edu.tr

Abstract - Water is the essential component of life on the earth, but it may sometimes pose a threat to lives and properties of citizens. This article explicitly focuses on two types of threats namely pollution and floods. It provides a comparative literature survey to understand the nature of the threats towards avoiding their damages. Presented article also intends to develop a prediction mechanism for the threats considering available data and algorithms, and proposes a model in this respect. Implementation of the model will be the subject of following studies.

Keywords **- Prediction model, Water flooding, Water pollution.**

I. INTRODUCTION

River water is the most important source of fresh water that used to meet the needs of humans, animals and plants. In spite of this importance, it poses a great danger to the lives of citizens if the nature of this wealth does not understood well and attention to the threats expected from it. Water bodies, especially rivers and lakes, are more susceptible to pollution than other water sources because they are in direct contact with various human activities [1]. The agricultural sector is one of the most water-consuming sectors. Thus, its wastewater (necessarily) is larger; these pollutants contain not only salts dissolved from the soil, but also the pollutants that caused by the use of fertilizers and pesticides. Wastewater for the industrial sector also leaks into the riverbeds and because of its high toxicity it causes serious diseases for humans. Water bodies also affected by emissions from large plants that use fossil fuels as one of the power generators to operate them. These pollutants contribute indirectly to pollution through their interaction with the rainwater and precipitation with acid rain that harms the physical and chemical characteristics of the water bodies, especially the lakes whose water replenishment is weak, which reduces their ability to self-purify the water [2].

Pollution rates calculated in the water bodies by calculating the values of the (Biochemical Oxygen Demand (BOD) / Chemical Oxygen Demand (COD)). If the values of the first are higher than the second values, the water of the stream is polluted and unfit for human use, it often has an unpleasant smell, color and taste.

Water is free of pollution if dissolved oxygen values range from (5-10) mg/l depending on seasons of the year (temperature and cold) [3].

Floods can be also a direct threat to the population and public property due to the high rate of precipitation, severe rainstorms, high seas and melting of snow in the upper reaches of the watercourse, which raise the water level to an extent exceeding the discharge capacity of the water stream.

In order to avoid the destructive effects of flooding, through the establishment of multi-meteorological stations along the waterway. To monitor the changes in climates and water levels in addition, to identify the seasons of floods and coordination with the countries of the basin for the purpose of the exchange of information and experiences to take the necessary precautions to reduce the potential negative effects [4].

Floods related to the various natural factors that are going on in the surface and layers of earth, such as geological and climatic factors, these factors directly affect the movement of water in the seas, oceans and riverbeds. The occurrence of an earthquake in the bottoms of one of the oceans or seas in the world leads to its water imbalance. The abrupt rise or fall in the water level causes a series of abnormal vibrations at the level of the water layers to restore the water balance, leading to concussions in the movement of the sea waves to hit the beaches. Changes in the levels of water pressure in the seabed are pushing vast amounts of water from high-pressure areas to low-pressure areas. To restore water pressure balance, leading to the occurrence of undersea currents and waves that affect total water movement in seas and oceans creating devastating floods in specific areas as opposed to low levels of water in other areas of the sea [5].

The different levels of pressure at the orbital lines on the Earth's surface cause winds from highlands to lowlands, causing storms and strong rainstorms, which cause flooding. Heavy rainfall leads to increase water levels in rivers, which is more than rivers capacity, causing flooding.

Another reason for the flooding is the rise in temperature, which leads to the melting of large amounts of snow in the main waterways, leading to a rise in water level.

Finally, the collapse of the dams by natural and structural factors led to the flow of large quantities of water from the lakes of these dams to the waterways beyond the discharge capacity of these waterways, which leads to flooding [6].

The rest of the article is arrange in the following manner. Section II is on previous studies, Section III is on problems, Section IV is the methodology, and finally, Section V is on conclusions.

II. PREVIOUS STUDIES

The authors tried to deal with water threats by understanding the nature of these threats. On the side of water pollution. Clean Water Team have detect the pollution types that effect watercolor and the cause of pollution into natural and industrial causes [7]. József Konyha has proposed indicators of rivers water pollution which are (pH, redox potential, conductivity, dissolved oxygen, ammonium and chloride ion amount), also developed a system called (The wide area measurement system (WAMS)) that contains of multi sensor device which sense six types of pollution as well as water level, this device communicate via the GPRS network. Because of limitations of WSNs such as (energy scarce, small memory footprint, and limited processing capabilities), as well as sensors are deployed in large numbers, which can be costly because of high price of these sensors [8]. Catalin Negru, et al tried to surpass the WSN limitations by proposing a cost efficient cloud-based service oriented architecture [9].

Another alternative used to detect pollution, which is image processing, in this method, a high quality pictures captured by using fixed cameras or satellites images. These images analyzed by using different image processing algorithms to obtain the useful information about pollution or flooding. Kar, et al tries to envisage the detection of metal pollutants using Hyperspectral data in river water with the spectral analysis of absorption features beyond the optical range, with the application of various image-processing techniques [10]. Ranhotra argued the detection of salinity of seawater, he depends on capturing satellite images for different seawater areas and analyze these images by using image-processing algorithms to get information, and he has detected different types of water pollution as well as salinity [11]. Also Karnawat, et al tried to detect water turbidity by using high quality camera and image processing algorithms in a combination with old data that stored in data base, at the end he conclude that the results of his method were very close to results that comes from the traditional way of normal analyses of water samples in the laboratory. However, his method saves time and money [12].

On the water flooding side. Hiroi, et al Monitor water level by capturing different images for same location during the day and at night they used Infrared cameras to monitor the same location then they analyzed these images and measure the level of water compared to a fixed point to detect the flooding [13].

Adnan, et al Suggested a prediction model for flooding for three hours this model has the ability to predict the river water level by using NNARX (Neural Network Auto-Regressive model with exogenous inputs) model with develop modelling strategy [14]. This model gives a good result for three hours' prediction. However, it still need to develop to be able to predict for more than three hours.

Keong, et al discussed a comparative study between three types of Artificial neural network algorithm which used in flooding prediction, these algorithms are (Bayesian Regularization (BR) back-propagation, Levenberg-Marquardt (LM) back-propagation and Gradient Descent (GD) back-propagation), they used two years' historical data to predict flooding. They found that Bayesian Regularization back-propagation algorithm is a multi-use algorithm and it is more convenient for flooding prediction [15].

Natural disasters such as (earthquakes, floods, volcanoes, air pollution, water pollution, soil pollution, etc.) and their impacts are consider life-threatening hazards on the Earth's surface. It is therefore essential to look for sophisticated methods and practical and rapid methods to fill many gaps in the lack of understanding of the changing nature of these disasters. These advanced methods can find the ideal solutions that provide the scientific and practical analysis of the causes and transformations of these disasters before, during and after their occurrence in order to understand their impact, their dimensions and how to better control their effects [16].

The ideal solution for monitoring and mitigating the disaster includes the formation of an effective early warning system covering the geographical area of the disaster by providing the necessary information at the maximum speed, facilitating the communication and movement process and providing accurate monitoring of changing circumstances in keeping with these disasters and controlling their transformations and impacts. In order to enable disaster management or decision makers to perform their work properly [17].

Many different technologies used to predict water flooding and pollution, like water level monitoring, water speed monitoring, chemical sensing, and use simulations. etc. [18], these technologies gives different results, but the world needs technologies with more reliability to avoid these disasters.

III. PROBLEMS

According to the literature review, which covered by authors, the following problems was identify:

- Water pollution and flooding are serious risks to the life and property of citizens. However, the traditional methods that used to detect these risks are insufficient to avoid the damage caused by these risks because they do not detect in sufficient time.
- Real time detection needs Information and Communication Technology (ICT), to deliver information to decision makers at the right time.
- The use of sensors, commonly preferred as WSNs helps in detection of many types of pollution, but these sensors have limitations as well as this method is very costly because we need many sensors to cover wide area.
- The alternative method is the use of cameras to detect pollution and flooding. This method can be implement by using either satellite image that has the ability to cover wide area but its images cannot be clear in cloudy or dusty weather, or by using fixed cameras, which are not affect by weather conditions but at the same time they cannot cover wide area.

IV. METHODOLOGY

Information is the backbone of any information system. Therefore, the authors tried to gather information that related to flooding and pollution in Tigris and Euphrates Rivers. However, each river has its own debris and turbidity characteristics. These characteristics are not fixed. They are

subject to change with time and changing environmental conditions.

This information will used as a raw material that needs many refining processes to reach the final stage, which is flooding and pollution forecasting. The methodology of this research will divided into many steps as shown in figure 1, some of these steps will be discuss in this article, the rest of the steps will be discussed in the future articles, these steps are:

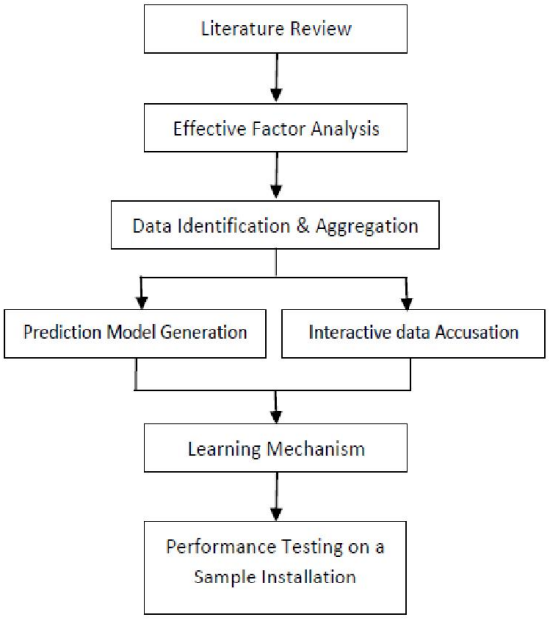


Figure 1: the research methodology steps

A. *Research Methodology*

The authors used a systematic review method to review the literatures. This method means summarizing the results obtained from previous studies; it help make sense of many kinds of data. In addition, it is a way of reviewing all the data and results from research about a particular question in a standardized systematic way.

More previous studies will be studied to get a clear vision, and to identify the effective factors in pollution and flood prediction.

B. *Data Aggregation Methodology*

The authors collected historical data related to flooding and pollution in Tigris and Euphrates Rivers. Regarding the pollution side, the data obtained for the Euphrates River were for the period from 2005 to 2015. The samples were analyzed manually; also, they were taken periodically every 15 days. The data obtained for the Tigris were from 2013 to 2015, and the samples were examined by sensors. The samples were analyzed every 15 minutes. Regarding the flooding side, the data obtained for water discharge for the Tigris and Euphrates Rivers were collected for the period from 1931 to 2015.

In addition, the author conducted personal interviews with officials of the Ministry of Water Resources and the Ministry of Environment in Iraq to get information about pollution and water levels in the Tigris and Euphrates Rivers. As well as, he discussed the ways of measuring pollution and flooding. Moreover, the types of procedures to be followed for protection from the risk of pollution and flooding.

All these data will be organize and analyze in data analysis step to obtain useful information for the prediction system.

C. *Data Analysis Methodology*

The authors will analyze all the collected data using statistical analysis methods. All this data will be analyze to obtain useful information. This information will be the input of the prediction system, in order to have a reliable prediction for flooding and pollution.

V. CONCLUSION

Flooding and pollution prediction system is refers to the use of statistic methods, artificial intelligence, and information and communication technology (ICT), in order to manage the data that related to flooding and pollution, and to obtain useful information from these data, to have a reliable prediction system.

The aim of the study is to present the literature and the research methodology for pollution and flooding prediction in Tigris and Euphrates Rivers. In addition, to determine the most flooding and pollution detection problems.

This study can be the first step to develop a new prediction system. Finally, we can say that this article explain the first step of this system, and the other steps of it will be the subject of the next study.

REFERENCES

[1] E. Al-Othman " Effect of Waste water in water Quality of Euphrates river between Ramadan & Heet cities" AL-Anbar University, 2010.

[2] S. Alrobaiee, "Water pollution - causes and treatments", http://www.watersexpert.se/ , 2014.

[3] Northeast Georgia Regional Development Center, "Watershed Protection Plan Development Guidebook", 1998, https://epd.georgia.gov/sites/epd.georgia.gov/files/related_files/site_page/devwtrplan_b.pdf.

[4] Lenka Gaňová, "Floods - their definition, causes, consequences and state of art", 2011, http://www.svf.tuke.sk/erasmusip/Ganova.pdf.G. R. Faulhaber, "Design of service systems with priority reservation," in *Conf. Rec. 1995 IEEE Int. Conf. Communications,* pp. 3–8.

[5] Arndt, et al, "Influence of snow depth and surface flooding on lighttransmission through Antarctic pack ice", Journal of Geophysical Research Oceans, 2017.

[6] Sebastiaan N. Jonkman, Ilan Kelman, "An analysis of the causes and circumstances of flood disaster deaths", © Overseas Development Institute, 2005, http://www.tbm.tudelft.nl/fileadmin/Faculteit/CiTG/Over_de_faculteit/Afdelingen/Afdeling_Waterbouwkunde/sectie_waterbouwkunde/people/personal/gelder/publications/citations/doc/citatie135.pdf.

[7] Clean Water Team, "Color of Water Fact Sheet", State Water Resources Control Board, 2004.

[8] József Konyha, "Grid-based wide area water quality measurement system for surface water", © 2016 IEEE, 2016.

[9] Catalin Negru, Mariana Mocanu, Costin Chiru, Aurelian Draghia, Radu Drobot, "Cost efficient cloud-based service oriented architecture for water pollution prediction", © 2015 IEEE, 2015.

[10] Soumyashree Kar , V.S. Rathore , P.K. Champati ray , Richa Sharma , S.K. Swain, "Classification of river water pollution using Hyperion data", © 2016 Elsevier B.V, 2016.

[11] Sarvraj Singh Ranhotra, "Detection of Salinity of Sea Water using Image Processing Techniques", © 2014 IEEE, 2014.

[12] Vaibhav Karnawat, Dr.S.L.Patil, "Turbidity detection using Image Processing", © 2016 IEEE, 2016.

[13] Kei Hiroi, Nobuo Kawaguchi,"FloodEye: Real-time Flash Flood Prediction System for Urban Complex Water Flow", © 2016 IEEE, 2016.

[14] Adnan, et al, "A 3-Hours River Water Level Flood Prediction Model Using NNARX with Improves Modelling Strategy", 2016 IEEE.
[15] Keong, et al, "Artificial Neural Network Flood Prediction for Sungai Isap Residence", © 2016 IEEE, 2016.
[16] H.A.Salih, "Design of disaster early warning systems using artificial intelligence ", Higher Commission for Scientific Research - Damascus - Syria, 2013, http://www.arsco.org/detailed/a8fbcc55-1c65-48bd-be39-67872f50decf.
[17] C. Skotner, A. Klinting, H. C. Ammentorp, F. Hansen, J. Høst-Madsen, Q. M. Lu, H. Junshan, "A Tailored GIS-based Forecasting System of Songhua River Basin, 2013, China", https://www.semanticscholar.org/paper/A-Tailored-GIS-based-Forecasting-System-of-Songhua-Skotner Ammentorp/e0a5c3f5d918f35ae5d4d596c07dafd9034338e4.
[18] Preeti Chawla, Nitasha Hasteer, Prashant Kumar, C.Ghanshyam, Manisha Singh, "Prediction of Pollution Potential of Indian Rivers using empirical equation consisting of water quality parameters", © 2015 IEEE, 2015.

Objects under Varying Illumination Conditions Analyze Histogram Statistical and Color Space Information with Image Processing Techniques

B.BÜYÜKARIKAN[1] and İ.S.ÜNCÜ[2]

[1] Selçuk University, Konya/Turkey, birkan@selcuk.edu.tr
[2]Süleyman Demirel University, Isparta/Turkey, serkanuncu@sdu.edu.tr

Abstract **- The objects in environment in machine vision application can benefit to determine color of objects and histogram information. But, under varying lighting the objects may not appear as the same objects because they can be seen in different colors. In this study, statistical results (Min, Max, Standard Deviation etc.) of histogram information of different types of objects using different LED illumination armatures were found with image processing techniques and this software created with C# programming language. In addition, some color spaces of objects under varying illumination and the nearest color information that appears the object were determined by an algorithm.**

Keywords **- LED illumination, histogram statistical, color spaces, image processing techniques.**

I. INTRODUCTION

Lighting by CIE ensures that the environment and objects can be seen as necessary using light [1]. However, one of the important problems in machine vision applications is; the view of the object changes from one view to another. For this reason, changes in the lighting conditions cause different perception of the images of the objects [2]. In recognizing objects, images derived from an object under viewing conditions provide information about that object [3]. For this reason, when illuminating objects, the color properties of the light and the surface properties of objects are important considerations. So the surfaces of the objects are visible in their true colors under daylight [4].

Colors contain lots of information for object recognition [5]. A good image should provide expected look over the correctly apprehended hue, lightness and chroma of the colors [6]. The goal is to optimize the dynamics of the illumination and the contrast of the view to be taken [7]. Thus, after the captured object is digitized by image processing techniques, histogram statistics and color information are obtained. This information can be provided to identify the object and determine the effects of the illumination on the object.

In literature, the effects of illumination on objects;

Swain and Ballard (1991) obtained color histograms using colored objects. Thus, they developed a histogram-based technique as a solution to object recognition problems [5]. Jacobs et al. (1998) provided recognition of two views taken from objects, according to Lambertian reflection under changing lighting conditions [3]. Belhumeur and Kriegman (1998) proved that according to the Lambertian reflection of an n-pixel image set of a convex object under the changing light sources of an object [2]. Allen et al. (1999) classified objects with Radial Basis Neural Networks using color data obtained from images taken under different illumination conditions [8]. Phung et al. (2005) determined color representation of skin segmentation, color quantization and classification algorithms with histogram. Technique using Bayesian classifier [9]. Akhloufi et al. (2007) were used statistical information to classify color texture. In addition, they tested their data according to the RGB, HSL and La* b* color spaces [10]. Choi et al. (2009) presented a color editing method to automatically recognize identical objects in images captured in different environments [11].

In this study, it is aimed to determine the information of objects in different color spaces under different illumination conditions by using the pixel results of the histogram information of the objects. In this case, the software was created using Visual Studio C# programming language. The image of the object has been captured and the information of the object has been determined with the image processing techniques. The objects, RGB, HLS, CIE XYZ and CIE Lab color space information are determined. The parameters as minimum, maximum, median, mean, standard deviation etc. for each color value (Red, Green, Blue and Grey) are calculated using histogram information. Also, under different lighting conditions, the color seen by the object was found.

II. HISTOGRAM STATISTICAL AND COLOR SPACES OVERVIEW

A. Histogram Statistical

The histogram is the number of pixels of each light value in the image [12]. It found a digital image histogram, as in (1). Here, r_k is the color level of k, n_k the total pixel number in that color level, and n is the total number of pixels on the image [13]. With histogram information, the minimum value is the minimum, the maximum value is the maximum, and the frequency value of the intensity value range is median.

$$P(r_k) = \frac{n_k}{n} \quad (1)$$

Skewness is asymmetry in a statistical distribution. The skewness of luminance histogram and standard deviation are found as in (2). Here; I (x, y) is a lighting value at a pixel, m is the average lighting level, N is the pixel number of the image, and σ is the standard deviation [14]. The variance is the square of the standard deviation, as in (3).

$$\text{Skewness} = \frac{\sum(\mathrm{I(x,y)-m})^3}{\mathrm{N}*(\sigma)^3}$$

$$\sigma = \sqrt{\frac{\sum(\mathrm{I(x,y)-m})^2}{N}} \quad (2)$$

$$\sigma^2 = \frac{\sum(\mathrm{X_i-\overline{X}})^2}{\mathrm{N}} \quad (3)$$

Standard error is a measure of the spread of averages of the same size samples that can be selected from the same population [15]. Standard error as in (4):

$$\mathrm{SE} = \frac{\sigma}{\mathrm{N}} \quad (4)$$

B. Color Spaces

In the machine vision system, pictures can be caught via a CCD camera which turns electromagnetic radio into electric signal. These signals are digitized and the color of each pixel is determined. The color of each pixel in the image is represented by RGB (Red, Green and Blue) components [16]. RGB values of Pixels can be transformed other color spaces.

RGB color model

Colors are determined for three colors red (R), green (G) and blue (B) [17]. This color space is commonly used to process and store digital image data [18, 19]. The RGB color cube is shown in figure 1.

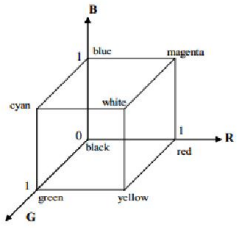


Figure 1: RGB color space

HLS color model

The HLS color model can be linearly converted from RGB. For this reason it is connected to the device and is not linear [20]. Hue, it is the color that an area dominates and saturation is the ratio of the brightness of the color [21]. In order to convert from RGB to HSL color model, firstly R, G, B values are normalized between 0-1 as in (5). From the values of R ', G', B', the smallest and largest values are found as in (6). Hue, saturation and lightness values as in (7) [22, 23].

$$R' = \frac{R}{255}$$

$$G' = \frac{G}{255} \quad (5)$$

$$B' = \frac{B}{255}$$

$$C_{max} = \max(R', G', B')$$
$$C_{min} = \min(R', G', B') \quad (6)$$
$$\Delta = \mathrm{C_{max}} - \mathrm{C_{min}}$$

$$H = \begin{cases} 60 * \frac{G'-B'}{\Delta}, & C_{max} = R' \\ 60 * \left[\frac{B'-R'}{\Delta} + 2\right] & C_{max} = G' \\ 60 * \left[\frac{R'-G'}{\Delta} + 4\right] & C_{max} = B' \end{cases}$$

$$S = \begin{cases} 0, & \Delta = 0 \\ \frac{\Delta}{1-|2L-1|}, & \Delta > 0 \end{cases} \quad (7)$$

$$L = \frac{C_{max} + C_{min}}{2}$$

CIE XYZ color model

The linear RGB values in the range [0, 1] can be converted to CIE XYZ values using the matrix transformation, corresponding to the range [0, 1]. CIE XYZ color model as in (8) [24].

$$\begin{bmatrix} \mathrm{X} \\ \mathrm{Y} \\ \mathrm{Z} \end{bmatrix} = \begin{bmatrix} 0.412453 & 0.357580 & 0.180423 \\ 0.212671 & 0.715160 & 0.072169 \\ 0.019334 & 0.119193 & 0.950227 \end{bmatrix} * \begin{bmatrix} \mathrm{R} \\ \mathrm{G} \\ \mathrm{B} \end{bmatrix} \quad (8)$$

CIE Lab color model

It is one of the two homogeneous color spaces proposed by CIE color measurements in 1976 [25]. The color space starts with the finding of the XYZ values of the color stimulus and it is computed with a specified reference color stimulus [6]. After being converted from RGB to CIE XYZ color model, the CIE Lab value is calculated as in (9) [26-28].

$$\mathrm{L} = 116\left(\frac{\mathrm{Y}}{\mathrm{Y_n}}\right)$$
$$\mathrm{a} = 500\left[\mathrm{f}\left(\frac{\mathrm{X}}{\mathrm{n}}\right) - \mathrm{f}\left(\frac{\mathrm{Y}}{\mathrm{Y_n}}\right)\right] \quad (9)$$
$$\mathrm{b} = 200\left[\mathrm{f}\left(\frac{\mathrm{Y}}{\mathrm{Y_n}}\right) - \mathrm{f}\left(\frac{\mathrm{Z}}{\mathrm{n}}\right)\right]$$
$$\mathrm{f(q)} = \begin{cases} \mathrm{q}^{\frac{1}{3}} & \mathrm{q} \geq 0.008856 \\ 7.787\mathrm{q} + 16/116 & \mathrm{q} < 0.008856 \end{cases}$$

III. THE OBJECTS UNDER VARYING ILLUMINATION CONDITIONS ANALYZE HISTOGRAM STATISTICAL AND COLOR SPACES INFORMATION

The color of the captured object affects three factors. These are spectral content of ambient illumination, spectral reflection of scene surfaces and the response of the imaging system [29]. For this reason, even when viewed with the same imaging system, the color of the object appears differently if the color temperature of the light source is changed [30].

LED illumination of the LED lighting fixtures used in machine vision systems are shown in The Dome figure 2a and Coaxial figure 2b. In order to determine the characteristics of

these objects which are going to be illumination via light resource, these systems form an interaction. In the study, a light pool was used to eliminate the effects of external conditions on the images. Images were obtained using LED armature and imaging system. When capturing images of objects, the luminous levels of the LED armature are set to maximum.



a b

Figure 2: LED armature

Two objects in the system; colored glass and textile. Images of these objects are captured on both LED armature. The flow chart of the software used to process the image values obtained in Fig. 3 is given.

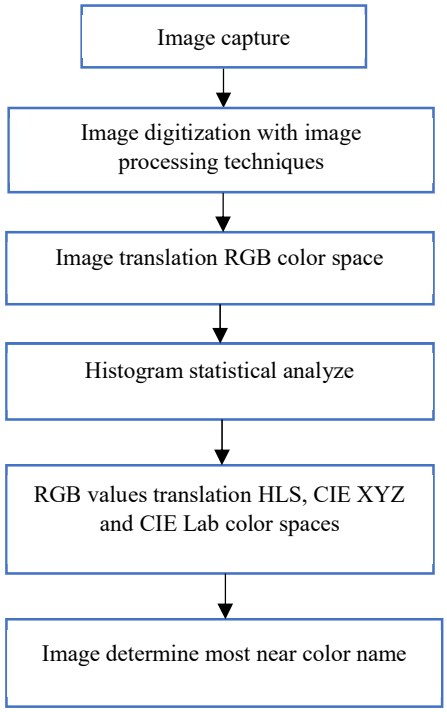


Figure 3: Software flow diagram

Gray level histogram statistics of the images taken in Table 1 are given. Digitized image values, it appear to be perceived at different pixel values with illumination and imaging system.

Table 1: Histogram statistical

	Min	Max	Mean	Median	S.D.	Count	S.E.	Skewness
Textile								
A	85	118	95.68	93	6.586	722	0.24	-1029.4
B	103	130	112.22	111	6.13	3249	0.10	-418.24
Colored glass								
A	86	254	132.17	123	31.98	20445	0.22	1.94
B	105	222	124.16	115	23.64	6804	0.28	7.38
*A is dome armature, B is coaxial armature								

In Table 2, the values of the color spaces under that illumination are determined.

Table 2: Color spaces of the object

Color space		**Textile**		**Colored Glass**	
		A	B	A	B
RGB	R	99	105	125	146
	G	98	138	138	151
	B	72	103	103	154
HLS	H	0.96	2.9	1.38	3.38
	L	85.5	110	120.5	150
	S	0.16	0.05	0.14	0.03
XYZ	X	0.11	0.15	0.20	0.29
	Y	0.12	0.16	0.23	0.31
	Z	0.08	0.18	0.16	0.35
Lab	L	40.98	47.60	55.60	62.15
	a	-8.38	-8.50	-16.29	-6.83
	b	12.60	-3.91	14.16	-6.14
*A is dome armature, B is coaxial armature					

Color of the objects appear in the under varying illumination as in Table 3.

Table 3: Color of the objects

Object		Appearing color	
	Real Color of Object	Dome	Coaxial
Textile		DarkOliveGreen	Gray
Colored glass		DimGray	LightStateGray

IV. CONCLUSION

Lighting is important in achieving the attributes of objects in machine vision applications. In Visual Studio C #, the software was created and the histogram information of the objects and the statistical results of this information were found and the color space information of the object was calculated.

As a result, the use of lighting according to the qualities of the objects is necessary for the correct identification of their attributes. Also, taking the color of surface of object as it looks by means of image processing techniques makes calculation of value of shining of object easier.

ACKNOWLEDGMENT

This research is a part of a project which was supported by TÜBİTAK in 2013-2014 (project number: 113E291).We are indebted to TÜBİTAK which provided support for the financial

support in this project. I would also like to thank SU BAP, who provided financial support with the project number 17703064 at the time of my presentation.

REFERENCES

[1] IESNA, *Lighting Handbook Hardcover*. New York: Illuminating Engineering Press, 2000.

[2] P. N. Belhumeur, D. J. Kriegman, "What Is the Set of Images of an Object Under All Possible Illumination Conditions?", *International Journal of Computer Vision*, vol. 28, pp. 245-260, 1998.

[3] D. W. Jacobs, P. N. Belhumeur, R. Basri, "Comparing Images Under Variable Illumination", in Conf. Rec. 1998. Computer Vision and Pattern Recognition, 1998 IEEE Computer Society Conference on, pp. 610-617.

[4] M. Yavuz, R. Ünver, "Yapı Yüzeylerinin Görünen Renkleri Üzerine Bir İnceleme", *in Conf. Rec. 2008 7. Ulusal Aydınlatma Kongresi*, pp. 51-59.

[5] M. J. Swain, D. H. Ballard, "Color indexing", *International. Journal of Computer Vision*, vol.7, pp. 11-32, 1991.

[6] P. Bodrogi, T. Q. Khanh, *Illumination, Color and Imaging: Evaluation and Optimization of Visual Displays*. Weinheim: Wiley-Vch, 2012.

[7] A. Erhardt-Ferron, *Theory and Applications of Digital Image Processing*. Offenburg: University of Applied Sciences, 2000.

[8] M. J. Allen, I. M. Coulson, N. E. Goung, Q. Mehdi, "Classifying Coloured Objects Under Different Lighting Conditions Using The HSV Colour Model and a Neural Network", *in Conf. Rec. 1999 European Control Conferance*, pp. 3975-3981.

[9] S. L. Phung, A. Bouzerdoum, D. Chai, "Skin Segmentation Using Color Pixel Classification: Analysis and Comparison", *IEEE Transactions On Pattern Analysis And Machine Intelligence*, vol. 27, pp. 148-154, 2005.

[10] M. A. Akhloufi, W. B. Larbi, X. Maldague, "Framework for color-texture classification in machine vision inspection of industrial products", *in Conf. Rec. 2007 International Conference on Systems, Man and Cybernetics,* pp. 1067-1071.

[11] Y-J. Choi, Y-B. Lee, W-D. Cho, "Color Correction for Object Identification from Images with Different Color Illimunation", *in Conf. Rec. 2009 International Joint Conference on INC,* pp. 1598-1603.

[12] Adobe, (2014). Camera Raw'da Renk ve Ton Ayarlamaları Yapma. [Online]. Available: http://helpx.adobe.com/tr/creative-suite/using/makecolor-tonal-adjustments-camera.html

[13] R. C. Gonzalez, R. E. Woods, *Digital Image Processing*. Massachusetts: Addison Wesley, 1992.

[14] I. Motoyoshi, S. Nishida, L. Sharan, E. H. Adelson, "Image Statistics and The Perception of Surface Qualities", *Nature News and Views*, vol. 447, pp. 206-209, May 2007.

[15] K. Sümbüloğlu, V. Sümbüloğlu, *Biyoistatistik*. Ankara: Hatiboğlu Yayınları, 2002.

[16] Y. Gong, C. H. Chuan, G. Xiaoyi, "Image Indexing and Retrieval Based on Color Histograms", *Multimedia Tools and Applications,* vol. 2, pp. 133-156, March 1996.

[17] J. D. Foley, A. v. Dam, S. K. Feiner, J. F. Hughes, *Computer Graphics: Principles and Practice*. New York: Addison Wesley, 1990.

[18] M. J. Jones, J. M. Rehg, "Statistical color models with application to skin detection", *in Conf. Rec. 1999 Computer Vision and Pattern Recognition,* pp. 274-280.

[19] J. Brand, J. S. Mason, "A comparative assessment of three approaches to pixel level human skin-detection", *in Conf. Rec. 2000 International Conference on Pattern Recognition*, pp.1056-1059.

[20] A. Ford, A. Robert, (1998, August). Colour Space Conversions. [Online]. pp.1-31. Available: http://poynton.ca/PDFs/coloureq.pdf

[21] C. Poynton, (1997, March). Frequently Asked Questions about Color 1997. [Online]. pp. 1-24. Available: http://poynton.ca/PDFs/ColorFAQ.pdf

[22] T. Acharya, A. K. Ray, *Image Processing: Principles and Applications*. Canada: Wiley & Sons, Inc., 2005.

[23] Rapidtables, (2014). RGB to HSL color conversion. [Online]. Available: http://www.rapidtables.com/convert/color/rgb-to-hsl.htm

[24] C. A. Poynton, *A Technical Introduction to Digital Video*. New York: John Wiley & Sons, Inc., 1996.

[25] *CIE*, Colorimetry, Commission Internationale de I Éclairage. 2004.

[26] G. Wyszecki, W. S. Stiles, *Color Science: Concepts and Methods, Quantitative Data and Formulae*. New York: McGraw-Hill, 1982.

[27] G. A. Agoston, *Color Theory and Its Application in Art and Design*, Berlin: Springer-Verlag, 1987.

[28] H. R. Kang, *Color Technology for Electronic Imaging Devices*, Bellingham: SPIE Optical Engineering Press, 1997.

[29] R. Jain, R. Kasturi, B. G. Schunck, *Machine Vision*. New York: McGraw Hill, 1995.

[30] R. Platt, *The Professional Guide to Photo Data*. London: Mitchell Beazley, 1995.

An Application to Intrusion Prevention in Wireless Networks

M. HAMZAH and C. OZTURK
Engineering Faculty, Erciyes University, Kayseri / Turkiye
montaser_hamza@yahoo.com, celal@erciyes.edu.tr

Abstract — The attacks to several major wireless networking like Man-In-The-Middle, Denial of Services and Session Hijacking showed that no open computer network is defended against snooping. The wireless network is particularly weak due to its features of the open medium and lack of a clear policy of defense. Numerous of the attacks detection methods developed on a fixed wired network cannot be used in the wireless network. This research first checks the vulnerabilities of a wireless networking, the reason why there is a necessary for attacks detection, and how to have attacks prevention from the first attack on the network. An application is proposed to protect the network by giving a block to all IPs ranges except for the administrator computer and closing all MACs addresses. So that no one can access to the router or to works sniffing, gathering information and scanning by the network.

Keywords- Attacks to wireless networks; ARP poisoning; Detection; Prevention.

I. Introduction

THe Communications have security challenges (either infrastructure or services) like a great challenge posed by the information technology resources. The presence of the same technical, organizational, and human barriers to meet this challenge should be noted.

The protection of information in the event of a breach is necessary, though not sufficient, where the degree of exposure increases once the stage of information processing and storage is reached. Hasty rush and unregulated security tools hinder use, harm the operations, and adversely affect the performance of IT systems. For example, protecting data encryption during the transition process is useless if it will be stored later in the non-security. Similarly, the establishment of a security system, such as "firewall" will be remembered if it is allowed for connections that exceed the value of this system. [1]

Such lack of awareness and information security were not given the importance and necessary attention due to illegal software usage to such a high level compared to other countries. Institutions cannot understand the importance of the matter before the beginning of a nuisance. However, because of the complexity and diversity of the threats it has not seen enough of this technology to be used in many different security technologies. [2]

An application is designed to develop a way for protection against attackers in wireless networks. The application is coded by using the Python programming language for kali Linux system, because it has already been pre-installed in it. Also,The application protects the network by giving a block to all IPs ranges except for the administrator computer and closing all MACs addresses. so that no one can access the router or sniffing work, gathering information and scanning by the network.

II. Related Work

The employment of static ARP entries, as expounded in [3] has been uses and still is the choice means to defend against and counteract any ARP cache poisoning attack in general. It can create a static MAC address, thereby creating entries constantly, which in turn deter attackers from applying ARP spoofing in the network. This entry is made by rapidly utilizing a Windows command such as ARP-sip_address mac_address. However, this method is not considered suitable for large networks due to potential complications for the network administrator to manage and update these tables in the network. it gives security against ARP poisoning. Each host has a public/private key pair Certificate by a local trusted performance on the LAN, which operates as a Certification Committee. The Messages are digitally signed by the sender to prevent the injection of fake or snooping information in [4]. The new modified techniques are proposed which could efficiently secure our ARP against the attacker and protect important data from any may happen sniff both internally and externally. The efficiency of these methods has been shown mathematically without any major impact on the performance of the network. With the help of various tools ARP cache is being monitored systematically and if any malicious activity is encountered, it is intimidated to the administrator immediately [5]. It focuses on comparing various techniques that are utilized to protect the users from these attacks by providing practical notes based on a network parameters time, scalability and highlighted the valid method, in the end, to fight the attacks at a superior level [6]. Network intrusion detection systems (NIDS) usually, rely on accurate string matching techniques. rely on the selection of algorithm implementation and the frequency with which it is applied, this model matching will improve performance bottleneck [7]. It has been analyzing the ways that SSL stripping can be utilized by attackers and

present a countermeasure against such attacks. It has also expoilted the browser's history to create a security profile for each visited website. Any profile containing information about the exact use of SSL on each website and every future connection to that site are verified against it. It has been demonstrated that SSL stripping attacks can be circumvented with the utilization of accepted overhead, without help from web servers or trusted third parties [9]. It has been considering three critical and unique attack models, namely dynamic pharming, deceptive captive portal and SSLStrip attacks, and it is shown that there is no single defense solution except SSLock. it has conducted employability analysis which further justifies the proposal in terms of its high unit rate. SSLock is the just method that is practical and light-weight for application trade, opt-in and zero-initialization for service providers, and privacy-preserving for generic users [10]. an attack is detectible by the protocol, should a client receive a reply from a website without a protocol header or only a HTTP header. Its principal drawback is that it is a client-side detection system which can only be utilized to detect an SSL stripping attack [11]. Anticap, the ARP reply and check it with the MAC address before stored in the ARP cache. If this MAC address is determined to be different from the already cached one, then it detects whether that address is still alive. If that MAC address is found to be active, then this new update is ignored, and it is also added to the list of banned MAC addresses. Its weakness is that it trusts that the ARP entry already cached is the allowed one which creates a critical condition of a race among the attacker and the victim. also, it can the host cache is updated with false ARP entry before the actual host could update, the legitimate user gets blocked under like circumstances [12]. The Anti Sniff application can detect promiscuous network cards. It operates by sending a series of nicely made packets in a special order to a victim system, sniffing the results and performing the timing experiments against the victim. By measuring the timing results and monitoring the victim responses on the network, it can be defined if the victim is in promiscuous mode [13]. A non-cryptographic approach is taken in MR-ARP if any new IP, MAC binding request occurs, then the authenticity of that request is verified by voting, and if more than a 50-percent response comes into the service of that binding, then only the binding is accepted. If no response is present, then it has considered this binding as genuine thereby indicating the reason for any other node not voting against the node and as a final result, the binding is accepted. This requirement can be satisfied in the Ethernet, but it may not be correcting in the wireless LAN on account of the traffic rate agreement based on the signal-to-noise ratio (SNR) [14].

III. Materials

A. The Main Concept of Project

To know the first technique that hackers utilize, it is important to know how connecting to the internet. This connection either via Ethernet cable or Wi-Fi. The connection by the Ethernet is less serious than wireless connect, the wireless is further common because Ethernet will ascertain that the attacker is one of the existing users within network. Wi-Fi is more dangerous because it is possible for a hacker to be outside the building or close to it while attacking and the hacker will be completely unknown. As such, in the world of Wi-Fi, there are a lot of technologies such as data encryption.

The first step in attacking is a reconnaissance or the gathering of information using applications to obtain such information. Most of these applications use a protocol or technical ARP. [15] Experienced hackers always use reconnaissance process mentioned earlier for information that will enable access to the router. When they get to the router, they can manipulate the entire network.

The questions remain, are there other ways? The answer is yes. There are other ways such as ICMP and others that can be isolated through the router. Certain attributes can be set in the router in case of any user attack to stop such user. In this case, the application will block IP attacker who will not be able to connect to the router again. The attacker can use the ARP but cannot access the entire router. [16]

B. Explain the algorithm

When entering the field of networking and a specific network, the most dangerous thing to face is an internal attacker as opposed to an outside the attacker because the latter will need to work set-ups to enter the network as it is downright in front of a firewall and a lot of barriers must be surpassed to for the outside attacker to be able to penetrate the network. Internal attacker already exists within the network and knows the password and many things about the network.

To protect the network from such cases, an application is designed to support the process of listening in the network. If convergence for all users is listened out, the application will reveal the process to block possible attacks. The application works through private IP as well and possibly identifier and stop the attacker.

IV. The Methodology of Application

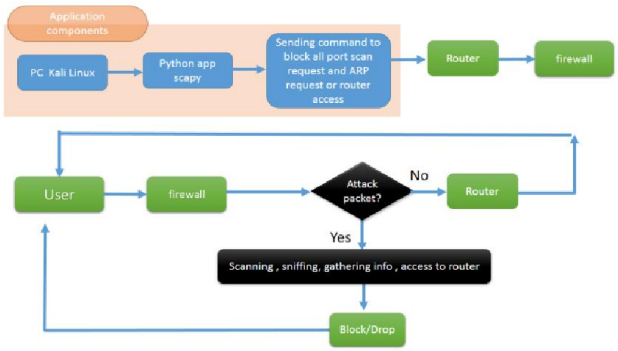


Fig 1. The Application Components

In this section, (figure 1) the flowchart of the suggested system is shown. The purpose is to protect and prevent any attack against network, using the application by the admin that the application is tied with the network, and running it,

sending command to block all port scan request and ARP request or access to router within the network.

A. The Proposed Algorithms

The steps of the algorithm are:
Output: The monitor of ARP request in the network.
Input: admin IP

Step1: Include a set of libraries that will be used in the application.
Step 2: Create function working on the implementation of GUI, GUI content on, one label for IP admin, and two buttons the first one for protect and the second one for stop and exit from application.
Step3: function working on the implementation of ssh connection.
Step4: Create function for ssh connection.
Step5: set up a dictionary and that the idea is to save the two variables or values and including the application that will store IP and Mac.
Step6: create a function that will monitor any ARP condition that occurs within the network, take the argument on the packet, and obtain information of the attacker (IP, MAC).
Step7: Create a Taste function that works inside on sniffing. This sniffing is running the Arp _monitor, and the presence of the filter to see only the ARP with all the information inside the packet.

B. Methodology

It can be noted that before the implementation and uncovering, the attacker could have entered the network and access a lot of information. This of course can be done using Nmap. It would be possible to see the penetration tools used by this program and how the attacker can access significant amount of information when using such program.
When the application is run, the interface will appear as shown in the figure below (figure 2). The interface contains a label. The administrator put its own IP to be excluded from the block. Then, the application gives a block to all the range from the IPs except for the administrator's IP.

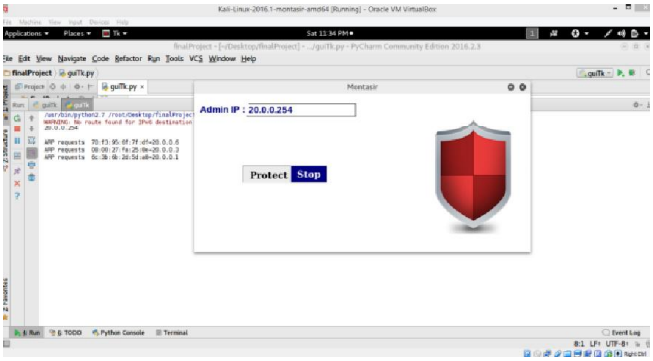


Fig 2. The Application running

So, we will ensure that no user can try using Sniffing or scanning or gathering information. And cannot access to the interface of the router through the browser, from any computer except for the administrator computer. As shown in the figures, used nmap program and the commands (Scan a single IP address Nmap 20.0.0.1, Detect OS and services Nmap –A 20.0.0.1, Nmap – sV 20.0.0.1, Nmap – sU 20.0.0.1) Before and After running the application and block all the IPs :

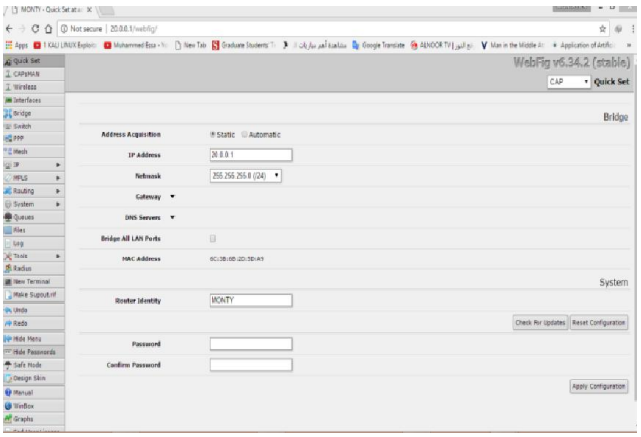


Fig 3. The router interface through the browser before

Table (1) showing the results for Nmap 20.0.0.1 before and after using the Application

Before Block	After Block
Nmap scan report foe 20.0.0.1 Host is up (0.0020s latency). Not shown: 994 closed ports Port State Service VERSION 21/tcp open ftp MikroTic router ftpd 6.34.2 22/tcp open ssh MikroTic routerOS sshd (protocol 2.0) 23/tcp open telnet Linux telneted 80/tcp open http MikroTic router config ftpd 8291/tcp open unknown MAC Address: 6C:3B:6B:2D:5D:A8 (unknown) Service Info: Host: MONTY; OSs : Linux , RouterOS; Device: router ; CEP: cpe:/o: mikrotic: routeros, cpe:/o:linux:linux_kernel	Nmap scan report foe 20.0.0.1 Host is up (0.00089s latency). All 1000 scanned ports on 20.0.0.1 are filtered. MAC Address: 6C:3B:6B:2D:5D:A8 (unknown)

Table (2) showing the results for Nmap – sV 20.0.0.1 before and after using the application

Before Block	After Block
Nmap scan report foe 20.0.0.1 Host is up (0.0020s latency). Not shown: 994 closed ports Port State Service 21/tcp open ftp 22/tcp open ssh 23/tcp open telnet 80/tcp open http 2000/tcp open cisco-sccp 8291/tcp open unknown MAC Address: 6C:3B:6B:2D:5D:A8 (unknown)	Nmap scan report foe 20.0.0.1 Host is up (0.0020s latency). All 1000 scanned ports on 20.0.0.1 are filtered. MAC Address: 6C:3B:6B:2D:5D:A8 (unknown)

Table (3) showing the results for Nmap – sU 20.0.0.1before and after using the Application

Before Block	After Block
Nmap scan report foe 20.0.0.1 Host is up (0.00077s latency). Not shown: 999 closed ports Port State Service 67/udp open | filtered dhcps MAC Address: 6C:3B:6B:2D:5D:A8 (unknown)	Nmap scan report foe 20.0.0.1 Host is up (0.035s latency). All 1000 scanned ports on 20.0.0.1 are open | filtered MAC Address: 6C:3B:6B:2D:5D:A8 (unknown)

Table (4) showing the results for Nmap –A 20.0.0.1 before and after using the Application

Before Block	After Block
Nmap scan report foe 20.0.0.1 Host is up (0.0020s latency). Not shown: 994 closed ports Port State Service VERSION 21/tcp open ftp MikroTic router ftpd 6.34.2 22/tcp open ssh MikroTic routerOS sshd (protocol 2.0) | ssh-hostkey: | 1024 b1:a6:f1:53:35:b2:8c:a0:2a:bb:5d:f4:e2:9a:2 8:48 (DSA) | 2048 8a:e6:7a:98:83:93:58:62:27:2a:ef:a9:a9:2b:e 0:28 (RSA) 23/tcp open telnet Linux telneted 80/tcp open http MikroTic router config ftpd | http-robots.txt: 1 disallowed entry | / | http.titel: routerOS router configuration page 2000/tcp open bandwidth-test MikroTic bandwidth-test server 8291/tcp open winbox MikroTic winbox MAC Address: 6C:3B:6B:2D:5D:A8 (unknown) Devise type: general purpose Running: Linux 2.6.x|3.x OS CEP: cpe:/o:linux:linux_kernel:2.6 cpe:/o:linux:linux_kernel:3 OS details: Linux 2.6.32 - 3.10 Network Disance: 1 host Service Info: Host: MONTY; OSs : Linux , RouterOS; Device: router ; CEP: cpe:/o: mikrotic: routeros, cpe:/o: linux:linux_kernel TRACEROUTE HOP RTT ADDRESS 1 1.27 ms 20.0.0.1	Nmap scan report foe 20.0.0.1 Host is up (0.0020s latency). All 1000 scanned ports on 20.0.0.1 are filtered. MAC Address: 6C:3B: 6B:2D:5D:A8 (unknown) Too many fingerprinter mach this host to give specific OS details Network Disance: 1 host TRACEROUTE HOP RTT ADDRESS 1 1.27 ms 20.0.0.1

V. DISCUSSION

In this study, it is shown that when the application is not operated and there is an attack on the network, a lot of information will be compromised, which the first step is for any attacker who wants to attack and penetrate a network. If the attacker obtains the information, the attacker will find out about the weaknesses of the network and the gaps that can be used to penetrate the network. This process is called information gathering. Of course, this all happens when the attacker is outside the network. If the attacker was inside, he will attempt to access the router and the main server and do some tampering after obtaining the information.

When running the application will be an exception to the admin IP address, and give a block to all the range of the IPs, so that no users can reach to the router, a scanning or Sniffing or gathering information of the network. As such, and after the application is operated and results are seen and discussed, it can be said that a new and successful application has been designed. The application could defend the network against any attack.

VI. CONCLUSION

Through continuing investigation, this study has shown a new application for better a detection and prevention of attacks in wireless networks. The packet analysis and anomaly detection should be done locally in each connection to the network. Moreover, attacks detection should get the place in all networking layers in an integrated cross-layer manner. Currently, we are continuing our research in the attacks issues. We are planning to design new applications to detect and prevent attacks against networks.

REFERENCES

[1] Zhang, Yongguang, and L. Wenke. "Intrusion detection in wireless ad-hoc networks." In Proceedings of the 6th annual international conference on Mobile computing and networking, pp. 275-283. ACM, 2000.

[2] Lach, J. "Sniffing local network and its detecting." Studia Informatica 24, no. 2B (2003): 289-296.

[3] Kwon, Kyohyeok, Seongjin Ahn, and Jin Chung. "Network security management using ARP spoofing." Computational Science and Its Applications–ICCSA 2004 (2004): 142-149.

[4] Whalen, Sean. "An introduction to arp spoofing." Node99 [Online Document], April (2001)..

[5] Bruschi, Danilo, Alberto Ornaghi, and Emilia Rosti. "S-ARP: a secure address resolution protocol." In Computer Security Applications Conference, 2003. Proceedings. 19th Annual, pp. 66-74. IEEE, 2003.

[6] Kaur, Inderjeet. "Detection and prevention of ARP cache poisoning." PhD diss., THAPAR UNIVERSITY PATIALA, 2013.

[7] Kaur, Goldendeep, and Jyoteesh Malhotra. "Comparative Investigation of ARP Poisoning Mitigation Techniques using Standard Testbed for Wireless Networks." International Journal of Computer Applications 121, no. 13 (2015).

[8] Coit, C. Jason, Stuart Staniford, and Joseph McAlerney. "Towards faster string matching for intrusion detection or exceeding the speed of snort." In DARPA Information Survivability Conference & Exposition II, 2001. DISCEX'01. Proceedings, vol. 1, pp. 367-373. IEEE, 2001.

[9] Tripunitara, Mahesh V., and Partha Dutta. "A middleware approach to asynchronous and backward compatible detection and prevention of ARP cache poisoning." In Computer Security Applications Conference, 1999.(ACSAC'99) Proceedings. 15th Annual, pp. 303-309. IEEE, 1999.

[10] Nikiforakis, Nick, Yves Younan, and Wouter Joosen. "HProxy: Client-side detection of SSL stripping attacks." In International Conference on Detection of Intrusions and Malware, and Vulnerability Assessment, pp. 200-218. Springer Berlin Heidelberg, 2010.

[11] Fung, Adonis PH, and K. W. Cheung. "SSLock: sustaining the trust on entities brought by SSL." In Proceedings of the 5th ACM Symposium on Information, Computer and Communications Security, pp. 204-213. ACM, 2010.

[12] Singh, Jaideep, Sandeep Dhariwal, and Rajeev Kumar. "A Detailed Survey of ARP Poisoning Detection and Mitigation Techniques."

[13] Goyal, Vipul, and Rohit Tripathy. "An efficient solution to the ARP cache poisoning problem." In Australasian Conference on Information Security and Privacy, pp. 40-51. Springer Berlin Heidelberg, 2005.

[14] Nam, Seung Yeob, Dongwon Kim, and Jeongeun Kim. "Enhanced ARP: preventing ARP poisoning-based man-in-the-middle attacks." IEEE communications letters 14, no. 2 (2010): 187-189.

[15] Ramachandran, V., & Nandi, S. (2005, December). Detecting ARP spoofing: An active technique. In International Conference on Information Systems Security (pp. 239-250). Springer Berlin Heidelberg.

[16] Tripunitara, M. V., & Dutta, P. (1999). A middleware approach to asynchronous and backward compatible detection and prevention of ARP cache poisoning. In Computer Security Applications Conference, 1999.(ACSAC'99) Proceedings. 15th Annual (pp. 303-309). IEEE.

Business Performance Tracking System Design

Gizem YILMAZ ÇELİK[1]
Yrd. Doç. Dr. Humar KAHRAMANLI[2]

[1]Selçuk University Information Technology Engineering, gizemyilmaz6@gmail.com
[2]Selçuk University Faculty Of Technology, hkahramanli@selcuk.edu.tr

Abstract

Employee performance in the business is measured by how well the business contributes to improving business results and achieving business goals. Goal; is to increase both the time and the production efficiency by reducing production losses. Measuring the production performance of the personnel in the enterprises, bringing personnel planning to a better level and providing wage and salary management.

In this study, the performance of the personnel or the machines used in production was measured by determining the time or quantity standards. According to these standards, how much time was spent in the production process, how much production was made, and percentage yields were determined.

Business Performance Monitoring System; evaluation and reporting of data on the detection of the failures that can occur in the production process and the elimination of them in the production process.

Keywords **- Personnel Performance Tracking System, Performance Performance, Performance Attendance, Performance Attendance at Operations.**

I. INTRODUCTION

The development and institutionalization of companies play an important role as well, as the quality of life and the creation of conditions of rapidly developing societies are playing a big role [1].

Businesses are required to provide feedback in order to determine whether their objectives are still valid and whether their business activities are working to achieve their objectives. They provide this feedback with performance traits and yield values.

Today's advances in technology and innovations in the management approach are driving businesses to better manage their business processes. Determination of performance criteria for more efficient management of processes, establishment of performance management systems by ensuring that these processes are related to strategy. Leading use is a powerful performance management system that distinguishes between success and failure. Because the performance management system facilitates a quantitative decision that can track how well they reach the goals and objectives they identifycreate exporting environments, can create effective induction systems that can analyze their employees more effectively, can use the time effectively and increase customer satisfaction and quality and productivity [1].

With solutions produced by businesses using Information Technologies [1];

- Reduction of costs,
- Providing support to the decision-making process,
- Effective use of time,
- More reliable and faster information flow,
- Easy access to information,
- Convenience in reporting is expected.

Measuring business performance in today's competitive environment; increasingly important in the context of preserving business and market share. Controlling and monitoring the event seems to have a more dynamic structure [1].

With the Performance Tracking System, it is aimed to report on the percentage of time that the personnel has obtained and what time period. Not only the personnel, but also the efficiency of the machines used in the production will be measured. In this regard, it is easier for you to find the width of the product.

This research aims to make the manager's manager clear and clear awareness of his or her tasks, to provide more constructive and more objective feedback to his / her employees, more effective guidance, more effective planning of personal development and training needs and more efficient relations with his / her subordinates.

Effective use of time is required to produce quality products. For this reason, it is aimed to detect and remove the factors that decrease the performance.

II. METHOD

This research was programmed using the FileMaker program.

FileMaker is among the database management systems in the personal use segment. Looking at the amount of databases that it can manage, it is capable of managing medium-sized data bursts easily [2].

It constitutes the universe of the research, the number of employees is large and the machines for production are used.

As an example, a company was used in Konya where CNC machines were used and the personnel needed to produce a certain number of jobs each day.

III. İNTERPRETATİON OF APPLİCATİONS AND FİNDİNGS

Performance management and follow-up systems involve the development and implementation of tools and approaches that will enable employees to work effectively and efficiently in the direction of organizational goals.

In order for a performance-focused human resources regime to be implemented; [4]

- The recruitment of those with high performance,
- Teaching and learning tools,
- Factors driving performance,
- Adequate employment placement, which allows staff to use their existing potential and capacity,
- To promote the leadership behaviors of managers,
- Often performance-based oversight and evaluation of assigned tasks,
- Recognition of good performance in tangible or intangible ways,
- Rewarding positive performance and ensuring career advancement.

With this application, not only the personnel, but also the productivity of the used machines are measured.

By using the necessary usage periods, how much loss during production, how much productivity is obtained for that day or for specific time periods, and the performance of the machine can be seen higher.

Performance measurement helps determine how much progress the institution has made to its pre-determined strategic goals and objectives, the strengths and weaknesses of the organization, and the future priorities of the organization.

With performance measurement;

- To what extent the institution has achieved its strategic goals and objectives.
- Best performance is rewarded.
- It is determined how much the employees perceive the work they do. If so, the education deficiencies are resolved, or else they are directed to other departments.
- Obtain valid reasons for promotions or deductions.

We have defined 2 types of users fort he program now. This can then be increased according to the desire or the staff to use the program at the firm. One of these is the calculator fort he author, the admin user fort he backplane if changes or additions are needed, and the calculations fort he authorized person or staff who will maket he entries. After users have logged in to the system, th 'Home' screen appears.



Figure 1: Home Screenshot

With this screen, they can go to the menu that they want and they can make registry entries or make changes. Other pages also have quick transitions to return to this screen or to quickly access other menus.

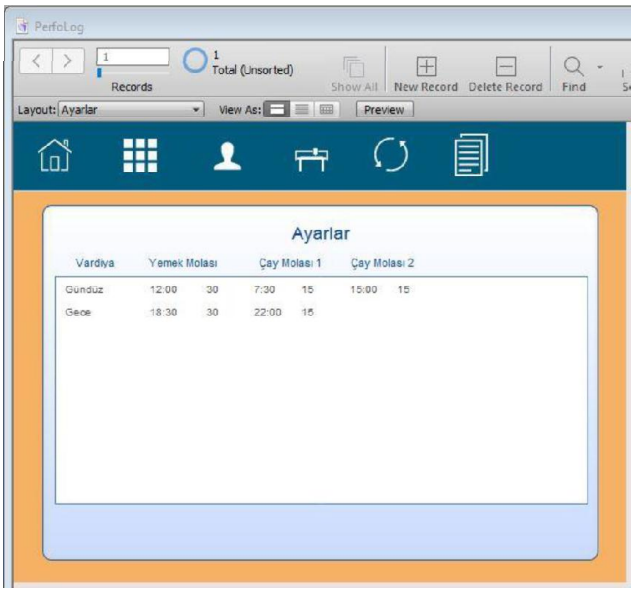


Figure 2: Settings Screenshot

They enter the time intervals and durations of the shifts with the settings screen.

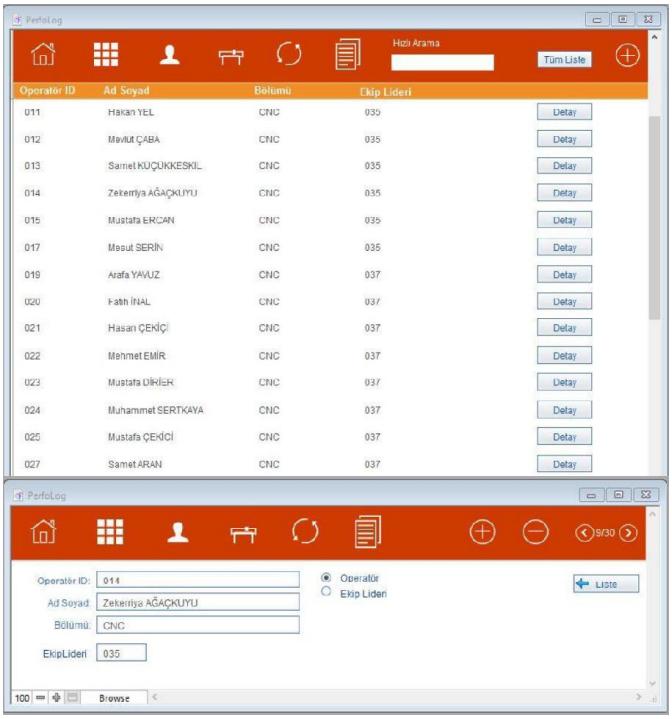


Figure 3: Staff Screenshot

Operators can go to the staff menu with the menu and by clicking on the detail button. In this way, who is working in which department, team leader or operator, and operator, who is the leader of the team is entering information in the form.

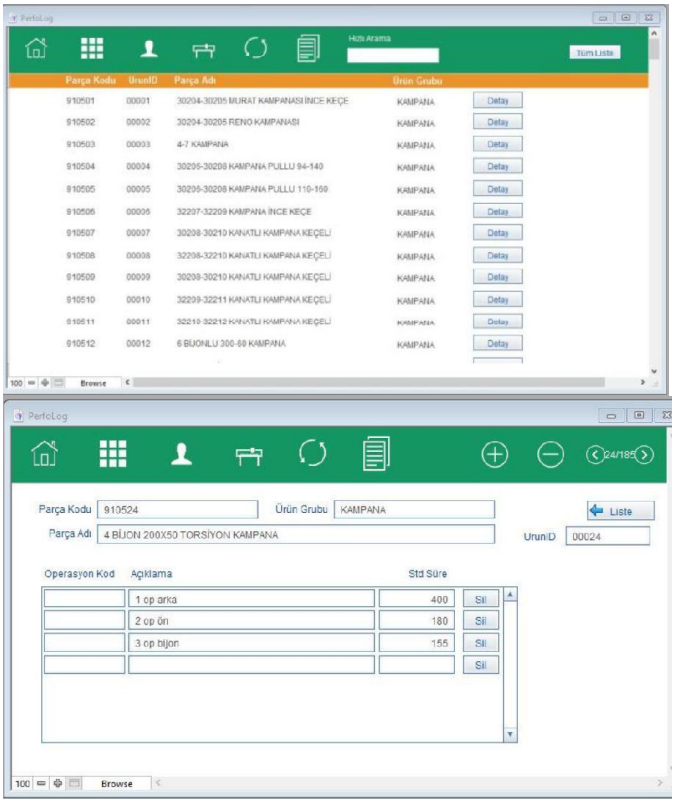


Figure 3: Parts Screenshot

You can also see a list of parts used in production with the track menu. You can access to the parts card with the detail button. This is the part where we can get problem answers such as which product group belongs, which operation steps are required for that part, and what is the standard time for them.

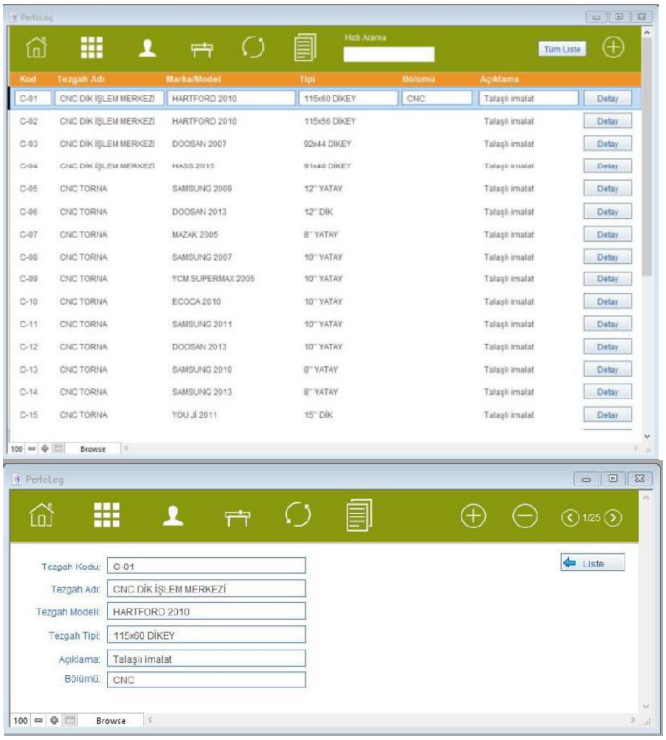


Figure 4: Machine Screenshot

We can see the main machines used in the parts production with the machine menu, we can make the arrangements and attachments in detail.

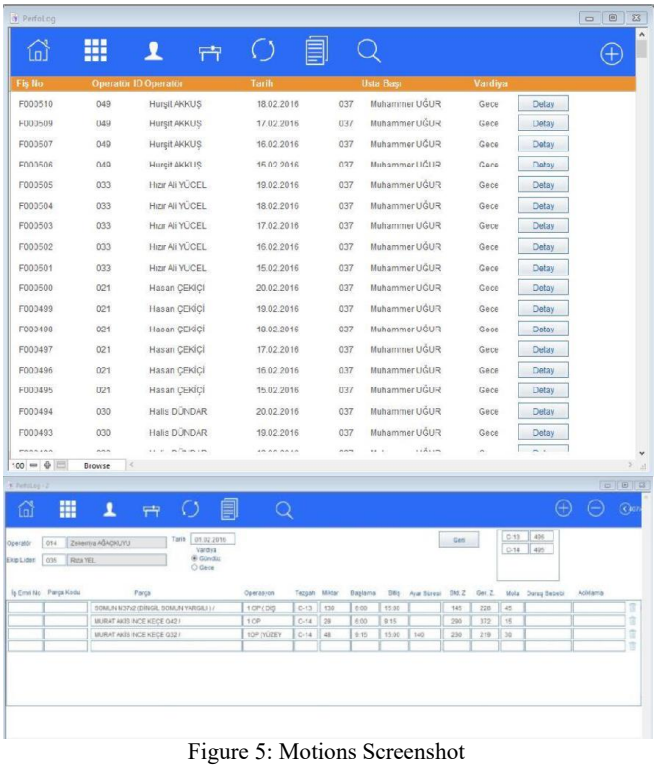


Figure 5: Motions Screenshot

With the motion menu, we are able to enter the necessary information for reporting purposes. Namely; who can figure out which information, which production, how much time it has spent, how much work has started on which bench to perform the operation step.

Our goal is to use the program;



Figure 6: Reporting Options Screenshots

By filling in these filter options, they can see the report screen they want.

Below are examples of personnel, machinery, parts, machine stop cause and failure stop reports. On this count, who can make the determination of how much production is done on what date, what machine cause, what machine cause, how long it has been stopped and how much loss to the company. If it is a company working as a premium, it will also be easier to make a calculation of how much premium will be given to which staff.

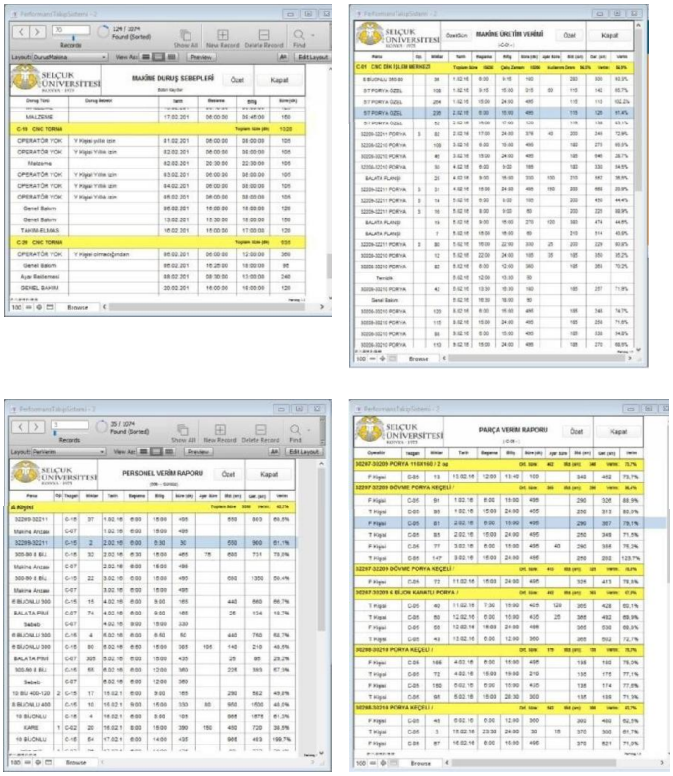


Figure 7: Report Examples Screenshots

Records of the operators working in the institution and the machines that should be used in production are entered into the application. How much time is spent as a standard for which machine they are kept. The break times within the organization are recorded and information such as how long the machine used during production, stopped, and what caused the stop is recorded. If these stops or failures become frequent during production, measures are taken to remove them.

With the performance reports, the injustices that may occur within the institution are removed. It will be prevented from wasting time. If the operators / operators who use the machines in production are lacking in terms of training, trainings are organized to remove them.

In order to create sweet competition environments within the firm, choices like moon elephant can be made. The best performing operators will be rewarded.

Reports of movements within the organization can be printed out to be evaluated when they arrive.

IV. RESULTS

Performance measurement is the way in which products, services or processes are fulfilled and their duties are measured in an impartial manner within a program.

If we look at the point of business; self-evaluation, benchmarking, quality control, cost and efficiency analysis, reporting, training etc. performance measurement.

Developments in information technologies are constantly affecting and changing business operations in terms of cost, time, quality and service. Information technologies provide significant contributions in reducing bureaucratic procedures

in management activities, increasing internal and external communication, supervising employees and maintaining the effectiveness of managerial decisions.

For the purpose of my work; By doing business performance measurements, they can monitor who is working and how successful they are in the company. They also have the opportunity to take precautions as if they were researching the cause of the situation if they stop working during working hours. By combining this monitoring with technology, they can produce fast, efficient and controlled jobs.

REFERENCES

[1] M. Zerenler, "Performans Ölçüm Sistemleri Tasarımı ve Üretim Sistemlerinin Performansının Ölçümüne Yönelik Bir Araştırma," *Ekonomik ve Sosyal Araştırmalar Dergisi*, pp. 1-36, 2005.

[2] G. Güven, (2016, November), Veritabanı Programlama: FileMaker Pro, Available: http://iibf.erciyes.edu.tr/guven/bil2/B2K03.pdf.

[3] R. J. Vidmar. (1992, August). On the use of atmospheric plasmas as electromagnetic reflectors. *IEEE Trans. Plasma Sci.* [Online]. *21(3).* pp. 876—880. Available: http://www.halcyon.com/pub/journals/21ps03-vidmar

[4] A. APAN. (2011, May). "Yeni Kamu İşletimi Ve Performans Yönetimi". *Türk İdare Dergisi, pp. 57-86.*

Designing A Low Cost Arm Based Micro Computer Cluster for Big Data Analysis

T.T.BİLGİN[1], R.A.YILMAZ[2] and Ş.Z. ERDOĞAN[3]

[1] Bursa Technical University, Bursa/Turkey, turgay.bilgin@btu.edu.tr
[2]Tanı İletişim Hizmetleri, İstanbul/Turkey, recepy@tani.com.tr
[3]Konya Gıda ve Tarım University, Konya/Turkey, senol.erdogan@gidatarim.edu.tr

***Abstract* - Big data processing requires too much computing resources and huge costs. This paper shows that the problem can be solved with cheap ARM-based microcomputers. Hadoop Distributed File System (HDFS) is de facto standard for storing and processing big data. HDFS uses MapReduce programming model for parallel processing. Hadoop is also called as an "ecosystem". In this study, Apache Hadoop and MapReduce based applications have proven to be able to run on ARM based microcomputer clusters. The proposed system was tested under normal room temperature, not in air-conditioned system rooms. No additional cooling system has been employed. Although the capacity of the micro supercomputer is limited to 5 nodes, it has been demonstrated that the system can be expanded very simply and quickly. A web based resource monitoring application called ganglia was used for resource monitoring. Total run time and Memory usages has been recorded for 1,2,3 and 4 servers and Speedup has been calculated. The results show that ARM-based micro computers can be used to build computing clusters as an alternative to midrange servers.**

***Keywords* – Big Data, Arm Based Computers, Distributed File Systems.**

I. INTRODUCTION

In recent years, the use of economical and low power consuming micro servers has increased. State of art single card computers have already attained the performance of entry level traditional servers. It is stated that micro-servers are emerging as an energy-saving alternative for data centers [1].

The constant increase in volume, variety and velocity of large data forces data centers to use scalable resources and to use energy efficiently. Traditionally, data centers use x86-64 server nodes with high power requirements ranging from tens to hundreds of watts. On the other hand, the performance of low power consumption systems developed for mobile devices has increased significantly in recent years. These developments enable the adaptation of micro servers to the data centers, as indicated by the big industry players. In this context, systematic studies are being conducted on the performance of micro servers compared to traditional large servers and it is considered to be useful for next generation data centers.

In this study, Apache Hadoop distributed file system infrastructure was implemented on low cost single card computers and a benchmark application was executed on this system. While executing the benchmark application, very low energy consumption is achieved and it has been shown that the computing clusters can be created with low costs using single card computers. In the upcoming periods, it is envisaged that system rooms can handle very large data by the help of hundreds of ARM based microcomputer systems that can fit into a single server cabinet instead of costly high powered servers. Such systems are expected to be used commercially in the near future.

II. RELATED WORK

There are studies in the literature about creating computational clusters with low cost single card computers. Some of them can be summarized as follows.

The study by Ali Anwar et al. [2] examines Hadoop performance on micro supercomputers (ARM based minicomputers). In this study, the authors examined the suitability of the computational clusters created with micro-servers to the popular Hadoop platform. A quantitative study has been carried out on five hardware configurations with six different MapReduce benchmark application. To compare different configurations, "PerfEC", a comprehensive measurement metric that includes performance, energy consumption and acquisition of applications is designed. Experiments in test clusters show that in applications such as TeraSort, RandomWriter and Grep, microservers exhibit better PerfEC values than traditional clusters.

Similarly, micro-servers running 3000-node simulations with real-world data from Facebook have shown similar performance to standard servers. On the other hand, it has been shown that the cost of owning micro servers can be reduced by 60% and energy savings of up to 31%.

The researches of Shaun Franks and Johnathan Yerby [3] on low cost Raspberry Pi devices is as follows; their paper describes the creation of a super minicomputer system using Raspberry Pi devices. A computing cluster has been created using open source software, and it has been demonstrated that parallel computation and distributed storage applications ran flawlessly on this cluster.

Dumitrel Loghin, Bogdan Marius Tudor, Hao Zhang, Beng Chin Ooi and Yong Meng Teo [4] explored performance analysis of Big Data applications on small ARM based systems. Hadoop MapReduce and MySQL applications are run on ARM based single card computers and Intel Xeon server clusters. Their time and energy usage is calculated. The total cost of

running the workloads on the ARM and Xeon nodes has been compared. This research shows that there is no single rule that fits all data types in order to decide the efficiency of the execution of large data workloads on either micro or large servers. Running I/O intensive MapReduce workloads on Xeon nodes was seen to be more successful. Conversely, database query processing is more energy-efficient and less costly on ARM servers. The authors stated that, when small software modifications are made, it is explained that the processor-intensive MapReduce workloads can be processed almost four times cheaper on ARM nodes than Xeon servers.

III. HARDWARE INFRASTRUCTURE

Five Raspberry Pi 2 Model B devices were used in this study. Additional Raspberry Pi devices can be added to the designed structure afterwards. In addition to Raspberry Pi devices, five 2A 5V power adapter, one 8 port network switch, one 9V switch adapter and a monitor with HDMI display port are used due to the necessity of operating system installation.

The technical specifications of the Raspberry Pi 2 Model B are as follows:

- Quad-Core ARM Cortex-A7 CPU (900MHz),
- 1GB SDRAM,
- Power + 5V / 2A,
- MicroUSB socket,
- Network interface 10/100 BaseT RJ45 Ethernet.

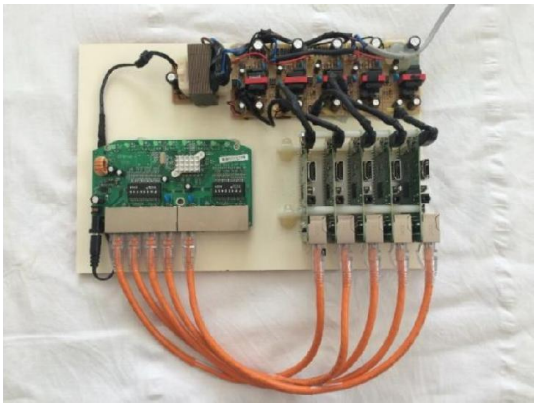


Figure 1: General view of the 5 node ARM cluster.

All parts are fixed and the electronic components have been wired on the plexiglass floor. The general appearance of the system is shown in figure 1. Each of the Raspberry Pi devices is connected to the network via network switch. Internet access is provided to the devices using the Switch's WLAN port.

IV. SOFTWARE INFRASTRUCTURE

A. *Operating system and platform*

Debian Linux based Raspbian is used as the default operating system. The Hadoop version 2.6.0 is used which was the most up-to-date version when the tests have been carried out. The Java runtime environment was also the latest 1.8.0.33 version.

B. *Ganglia Distributed Monitoring Application*

Ganglia application is a resource and performance monitoring application developed for computing clusters. It has a web-based interface. The application installed on the server side collects resource consumption information through the client package installed on the clients. On the server side only one service (gmond) runs. The web GUI application can be installed on any server. In this study, gmond package was installed in all of Raspberry Pi devices. Ganglia web application has been installed in an another virtual server. Since the web interface of Ganglia application is developed in PHP language, Apache and PHP are also installed into the virtual server. The screenshot in figure 2 shows the Ganglia home page. As information comes from the servers, information about resource usage momentarily displayed on the charts and graphs. Measurements of the same property of each server are shown with different colored lines on the same graph.

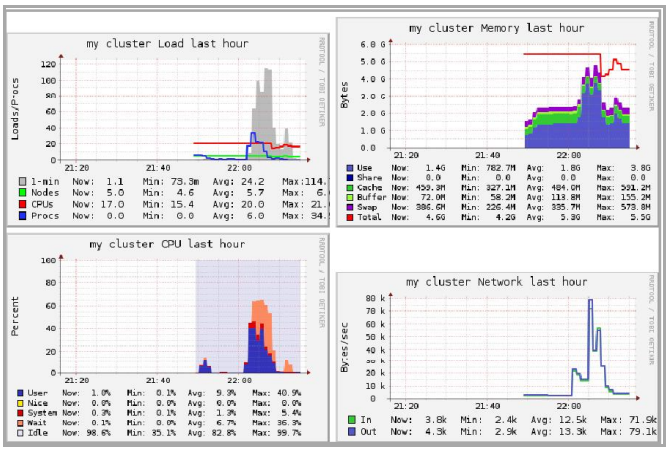


Figure 2: Ganglia web application home page.

The ganglia home page shows the total resource usage of all connected servers. As shown in figure 3, information about a single server can also be selected.

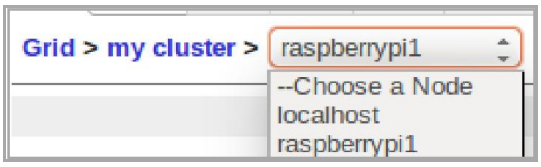


Figure 3. Server selection in Ganglia application.

The main page of Ganglia contains the cluster's load, memory, CPU usage, and graphs of network traffic. When either of the servers are selected, CPU usage or Network usage can be observed in greater detail, as shown in figure 4 and figure 5. The application records this information so that it can be used retrospectively.

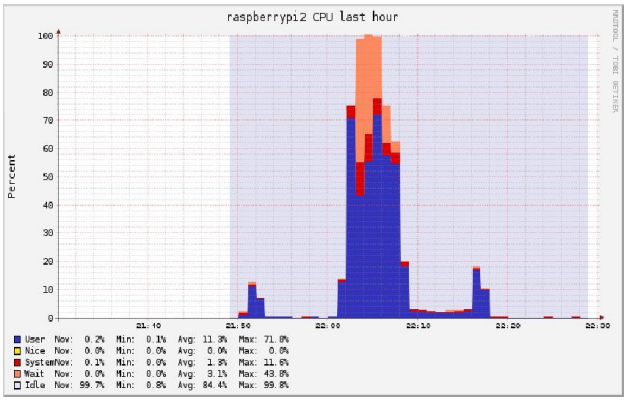


Figure 4. CPU utilization plot of the node 2. (colors indicates user, nice, system, wait and idle times)

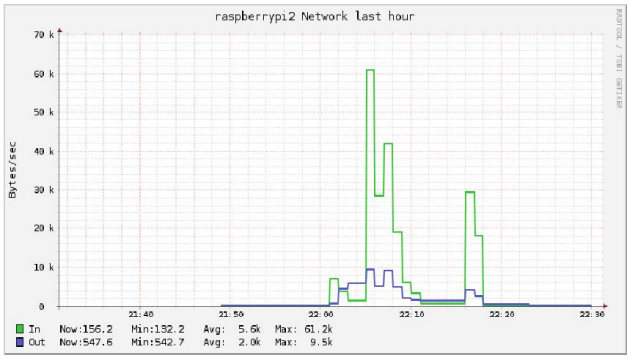


Figure 5. The network resource usage plot of the node 2. (green indicates inbound traffic, blue indicates outbound).

V. BENCHMARK RESULTS

A. Dataset

The test application is planned to consume the highest CPU power of Raspberry Pi devices. Therefore, large data sets have been created. Data sets were generated by downloading the plain text versions of the books in Gutenberg Project Web Site [5]. The goal is to count how many times the words are repeated in text files. The following preparatory procedures were carried out before the test. First, the text files need to be stored in the Hadoop HDFS file system. A large text data set was created by copying and pasting the 1.2 MB file named "file.txt" 50 times with different names. These files are copied to the "TestDir" directory created in the HDFS file system with the following command.

```
hadoop dfs -put /home/pi/hadoop/hadoop-data/dosyalar/* /TestDir/
```

The "WordCount" application selected as benchmark software which is included in the "hadoop-mapreduce-examples-2.6.0.jar" that ships with the Hadoop installation. When the application starts running, MapReduce process and resource usage information can be tracked via the web interface called Jobtracker. Figure 6 shows a screenshot of the Jobtracker application.

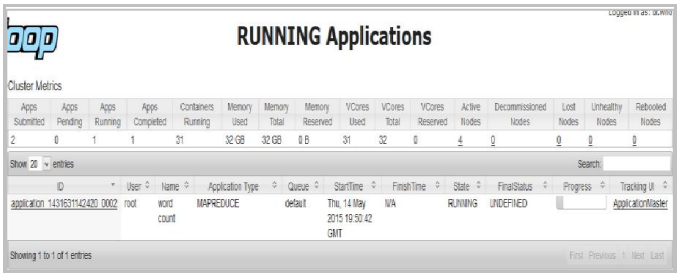


Figure 6. JobTracker web interface.

Figure 7 shows all active applications running on the system and the map and reduce statuses of MapReduce jobs and the completion percentages of the applications.

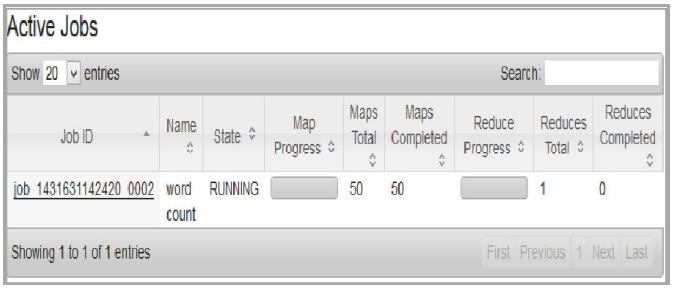


Figure 7. Active applications running on the Hadoop system

B. WordCount Example Program

Since the Hadoop ecosystem is Java-based, the MapReduce applications that runs on Hadoop are usually developed on the Java programming language. Thanks to the Hadoop system's ability to support different software languages, applications can also be developed using programming languages such as C, R and Python. It is also possible to write high-level MapReduce queries using Apache Pig and Apache Hive.

In this study, the Java based "WordCount" sample application which is available in Hadoop installation is used. Text files that are given as an input parameter to this application are processed in parallel and the total number of occurence of each words are counted. Although the "WordCount" example seems to be an easy example to write on Java or any other language, it is a fact that it can be very costly as the data set size grows. With the "WordCount" example used in experiments, it is possible to process very large text files on the Hadoop cluster using the MapReduce technique. In the example application Map and Reduce methods are inherited from Mapper and Reducer classes.

C. Benchmark Results

When the Wordcount application is run on a single server, it completes its job in a total of 1189 seconds. During the application's run time period, the resource usage data is collected by Ganglia.

When Wordcount runs on two servers, it completes its job in

a total of 719 seconds. When it runs on three servers, it completes the job in a total of 511 seconds. If the number of servers increased to four, it completes its job in a total of 387 seconds.

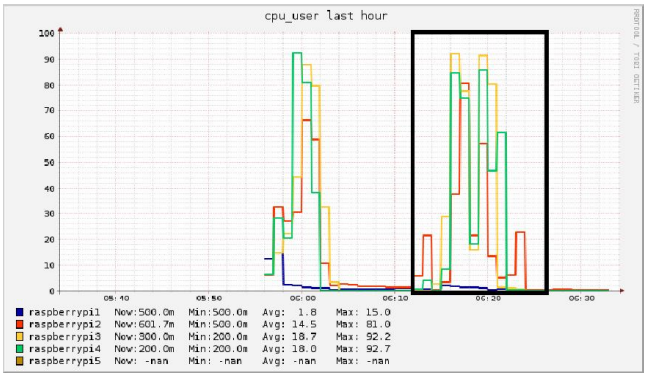


Figure 8. CPU usage vs time plot for the three servers.

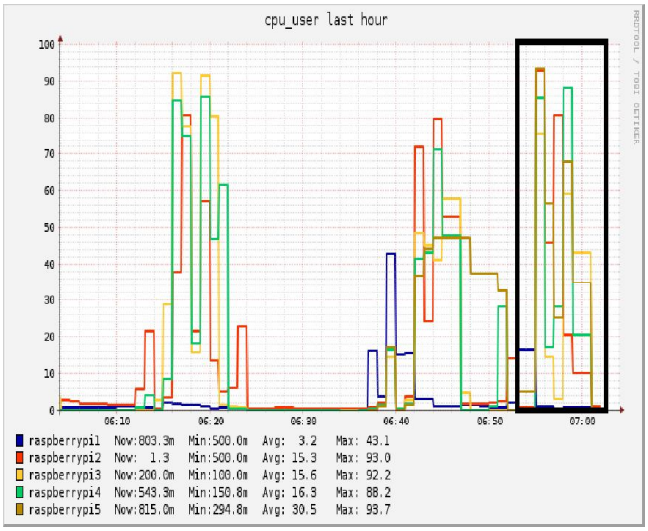


Figure 9. CPU usage vs time plot for the four servers.

Plots of CPU resource usage are shown in Figure 8 and Figure 9. The time slot of the application's run time interval is marked in a black frame on the plots. Each color represents a different server on the plots.

D. Speedup Calculations

As the number of servers increases, it appears that jobs are completed faster. The total running times of the jobs according to the number of servers are given in Table 1. Using the given data in the table, the speedup can be calculated as shown in equation 1.

$$SpeedUp = \frac{T_{serial}}{T_{parallel}} \quad (1)$$

Table 1. SpeedUp values according to the number of servers.

No Of CPU	Total Run Time (secs)	SpeedUp
1	1189	1
2	719	1,65
3	511	2,33
4	387	3,07

The calculated speedup values are also given in Table 1. The graph given in Figure 10 has been plotted using total run times and the number of servers. The following conclusion can be drawn from the graph. As the number of servers increases, the run time exponentially decreases.

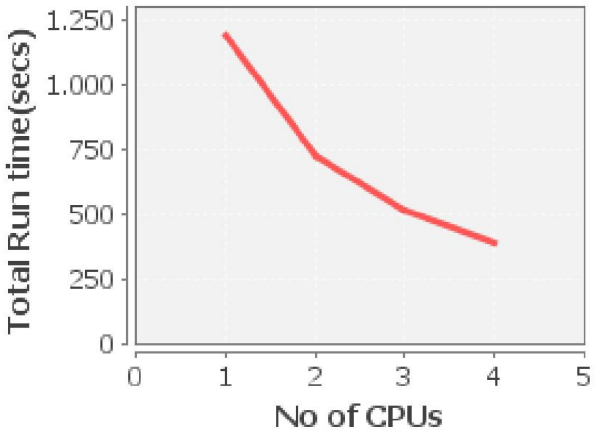


Figure 10. Graph of run times versus the number of servers.

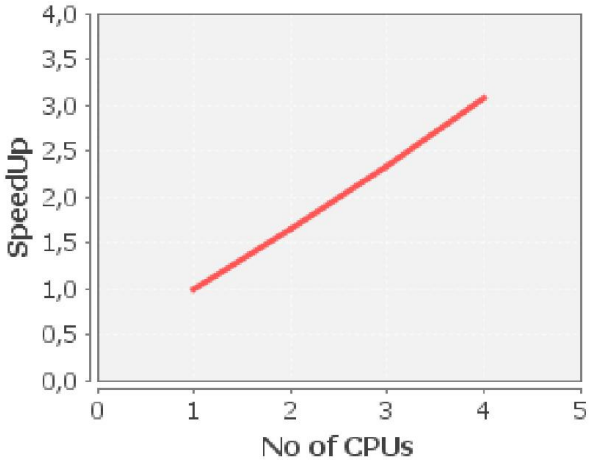


Figure 11. SpeedUp versus the number of servers plot.

The speedup versus the number of servers are given in Figure 11. As the number of servers increases, the speedup increases linearly. No overhead effect was observed in the graph because we could employ only 4 servers (1 master 4 worker). If the number of servers could be increased more, overhead effect will be probably observed.

VI. Conclusion

In this study, Apache Hadoop and MapReduce applications were run on low cost micro servers. It has been shown that Apache Hadoop and its components can run smoothly on ARM processor-based microcomputers. Tests were conducted at room temperature, not in air-conditioned system rooms. It has been shown that microcomputers can be included in system rooms together with commercially large computer systems. It has also been shown that they can be used in enterprise infrastructure for operations requiring high CPU usage, such as large data processing. Although the micro supercomputers created during the study were limited to 5 servers, it was explained that the scaling could be very simple and fast. Since the number of available servers are not large enough, the overhead situation where SpeedUp starts to decrease could not observed.

References

[1] Ou, Zhonghong, et al. "Energy-and cost-efficiency analysis of arm-based clusters." Cluster, Cloud and Grid Computing (CCGrid), 2012 12th IEEE/ACM International Symposium on. IEEE, 2012.

[2] Ali Anwar, Krish K. R., and Ali R. Butt. On the Use of Microservers in Supporting Hadoop Applications. In Proceedings of the IEEE International Conference on Cluster Computing (Cluster), Madrid, Spain, pages 66-74, September 2014.

[3] Franks, Shaun and Yerby, Johnathan, Creating a Low-cost Supercomputer with Raspberry Pi 8-9, SAIS 2014

[4] Dumitrel Loghin, Bogdan Marius Tudor, Hao Zhang, Beng Chin Ooi, Yong Meng Teo, A Performance Study of Big Data on Small Nodes, Department of Computer Science National University of Singapore, 2-9, 2015

[5] Project Gutenberg, http://www.gutenberg.org/ebooks/, (Access Date: Feb 2016)

The Designing of Machine Vision System Based on Image Processing which is for Geometric Shaped Extrusion Profiles Including Different Inner Cells

M. AKDOĞAN[1] and S. YALDIZ[2]

[1]Adil Karaagac Vocational and Technical Anatolian High School, Konya/Turkey, akdoganmurat@hotmail.com
[2]Selcuk University Technology Faculty, Mech. Eng. Department, Konya/Turkey, syaldiz@selcuk.edu.tr

***Abstract*— In order to increase quality and efficiency in production area, machine vision systems are spreading. One of main subjects which researchers study on is the designing system providing production with high speed and quality, desired tolerance and low cost. Besides, the discipline aimed at, while the quality is being kept, defective production is minimized. The purpose of this application is that the designing an autonomous online 2 dimensional measurement system. This system, which determines whether desired dimensions and precisions belonging to sensitive areas of complicated geometric shapes coming from extrusion line are appropriate or not. The images of complicated shaped profile parts, taken by digital camera, are first processed a sequential operations which are correcting defective images caused by working environment, then various image processing algorithms are applied to carry out 2 dimensional measurement. Why 2 dimensional measurement system using image processing method; Increasing The Capacity of Line, Decreasing Production of Non-Standard Materials, Improving Quality of Profiles, Minimizing consumption of raw materials, Minimizing the Cost of Labour, This is Necessary for Ensuring Trust to Business and Competing with Other Manufacturers. The most important characteristic of this operation separating other process is that online controlling of complicated extruded parts. This operation is both tested by computer as offline and applied with online extrusion line. The acquiring results are compared with the results obtained by conventional systems, then the positive and negative aspects of both systems evaluated.**

***Keywords*— Image Processing, Quality Control, Measurement.**

I. INTRODUCTION

Extruded profile part's wall thickness and gasket gaps direct impact on profile quality so need a sampling inspection to determine its thickness between tolerances or not. It is generally used Vernier callipers measurement for profile wall thickness and gasket gaps. Main shortcomings come outs from contact measurement due to fact that worker, lack precision or not good calibrated measurement device and so on. This paper introduces a kind of extruded profile thickness detection method based on image processing, and the result shows that it can well solve the wall thickness and gasket gaps dimensions. To obtain images used high resolution image sensor (CCD). Profile boundaries fundamental importance in image processing so edge detection significantly reduces the amount of data and filters out useless information. Edge detection is in the forefront of image processing for object detection. In this paper firstly getting image from CCD and then some noise remove operations performed. Afterwards image thresholding applied to achieve interested image area. And then, segmentation of image algorithm, contours finding algorithm used. Lastly, improved algorithm used finished image and measured thickness of extruded profiles.

II. PROPOSED MEASUREMENT METHOD

This study proposes a complex shaped extruded products 2 dimensional size measurement based on data mining. The method includes three steps.

- Acquiring extruded profile image and pre-process.
- Extract the contour regions of profile.
- Using contours of profile measuring profile outer size, wall thickness, gasket gaps and specific areas size via improved algorithm.

A. Acquaring extruded profile and pre-process

To find out useful information and data, this study getting image. Then, using some filters extract the noise removed images. This process is very important section before contour extracting step. Because, if wrong selected contour count of profile, next step is not success. In this step another important thing is lightening. Lightening is vital importance of well acquiring images.

1) *The automatic measurement station:* CCD camera (Elp-Usb 8MP 5-50 mm varifocal lens, Sony IMX179 sensor camera) are placed at the end of the conveyor, in such a position takes an cross-section image of profile just some seconds before their cutting. For calibration used known references of profile's horizontal and vertical outer dimensions. An illuminator (30W 5600/3200K Dimmable 396 Led video light lamp) lights up the profile sections in order to

increase image contrast. It can ensure image clearer and brighter in case of dark condition. One sensor on the side of profile detect the presence of a profile in front of the cameras thus triggering the image acquisition and processing. Figure1. shows camera, Figure 2. shows Illuminator, Figure 3. shows production line and Figure 4. shows Algorithm steps.



Figure 1: Elp Camera



Figure 2: Illuminator

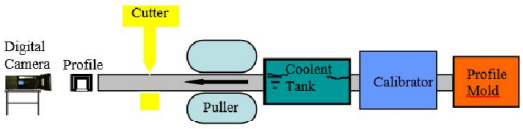


Figure 3: Profile production line

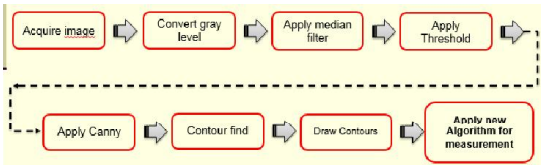


Figure 4: Algorithm steps

2) Image Thresholding: Thresholding is the simplest method of image segmentation. From a grayscale image. Thresholding can be used to create binary images [1]. Figure 5. shows a thresholding view of profile image. For this operation used equation is shown (1).

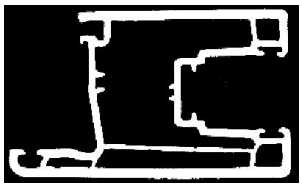
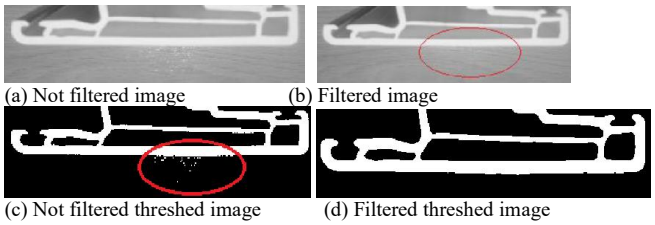


Figure 5: Threshed image of profile.

$$G_{x,y} = \begin{cases} 1, f(x,y) \geq T(x,y) \\ 0, f(x,y) < T(x,y) \end{cases}$$

(1)

3) Median Filtering Operation: In image processing most suitable filter must be selected among the many filter [2]. Median filter is used some kind of noise reduction on an image. Median filtering is very widely used in digital image processing because, under certain conditions, it preserves edges while removing noise. Figure 6. (a) shows a not filtered view of profile image. After pre-processing, (b) shows median filtered view of profile binary image, (c) shows a not filtered view of profile image after thresholding, (d) shows median filtered view of profile binary image after thresholding.



(a) Not filtered image (b) Filtered image

(c) Not filtered threshed image (d) Filtered threshed image

Figure 6: Median Filtering Operations

4) Gaussian Filtering Operation: Gaussian filtering is used to blur images and remove noise but in our image not good result so not used in our system. For this operation used equation is shown (2).
Figure 7. shows a gaussian filtered view of profile image after thresholding.



Figure 7: Gaussian filtered image

$$G_{x,y} = \frac{1}{2\pi\sigma^2} \cdot \ell^{\frac{-(x^2+y^2)}{2\sigma^2}}$$

(2)

5) *Edge Detection:* Edge detection is an image processing technique for finding the boundaries of objects within images. It works by detecting discontinuities in brightness. Edge detection is used for image segmentation and data extraction in areas. Canny edge detection algorithm is used in this study.
For this operation used equation is shown (3) and (4). Figure 8. shows a Canny edge detection profile image after thresholding.

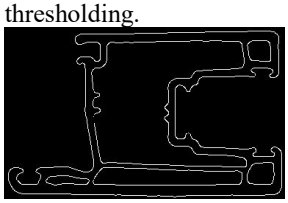


Figure 8: Canny edge detection image

$$G_x = \begin{bmatrix} -1 & 0 & 1 \\ -2 & 0 & 2 \\ -1 & 0 & 1 \end{bmatrix} G_y = \begin{bmatrix} -1 & -2 & -1 \\ 0 & 0 & 0 \\ 1 & 2 & 1 \end{bmatrix}$$

(3)

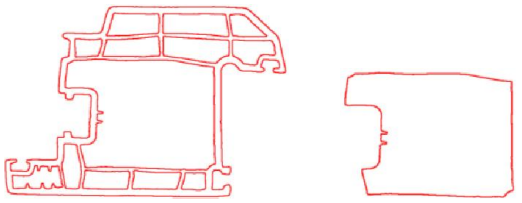
$$G = \sqrt{G_x^{\,2} + G_y^{\,2}} \theta = \arctan\left(\frac{G_y}{G_x}\right)$$

(4)

B. Two Dimensional contour detection procedure

The well-known edge-based segmentation algorithm proposed by Canny [3]. First a Gaussian low pass filtering is carried out with a 20·20 mask with sigma equal to 1.6. The algorithm then searches for those points (at the edges) where the gradient of the grey level is maximum, since these are expected to correspond to the contour points that are of interest. A binary image that contains the object of interest. OpenCV uses the Suzuki algorithm to perform contour tracing [4]. In this algorithm, firstly the upper left contour pixel is found. Then, the neighborhood of the first

pixel is checked in clockwise direction to find the next pixel of the contour. From now on, the search for the other pixels of the contour is done in anti-clockwise direction and ends when the first two pixels of the contour are found again. Polygonal representation performed and all contours described by a tree. This generates a collection of external contours. Figure 9. shows some of image contours. Opencv command;
cv2.drawContours (image, contours, x, (0,0,255),2). x is contour number.



(a) Contour -1 (ALL) (b) Contour 5



(a) Contour 6 (b) Contour 3

Figure 9: Image Contours

C. *Image Based Measurement results*

Figure 10. shows technical drawing of PVC window profile cross section view. Figure 11 is real image of product.

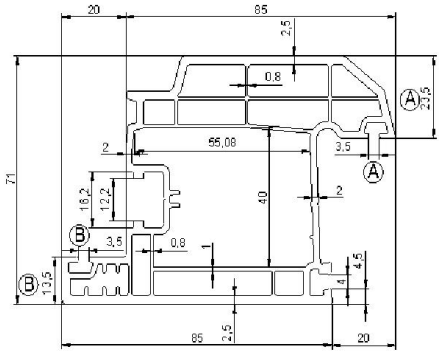


Figure 10: Technical Drawing

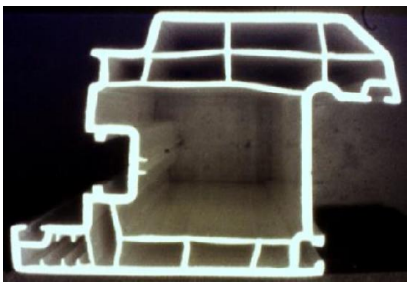


Figure 11: Real İmage

The algorithm were implemented by Python 2.7. and performed on a Windows 7 Professional operation system. To generate the rules, one of the extruded PVC window profiles used. Figure 12. presents the result of the profile image, the proposed method performed complex shaped product. Algorithm firstly find starting point of contours, and than calculate next point difference. If difference is plus, continue otherwise stop and store that point. This is first corner, same method adopted all contours including inner for gasket gaps measure. For wall thickness of profile, outer and inner contours's specific region decided and calculating the between two contours pixel sizes. All pixels scaling, according to the profile's most outer dimensions. Figure 13. Shows some parts of program written in Python and OpenCV.

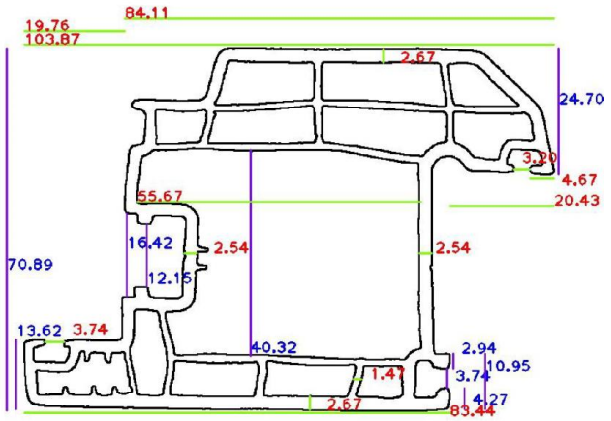
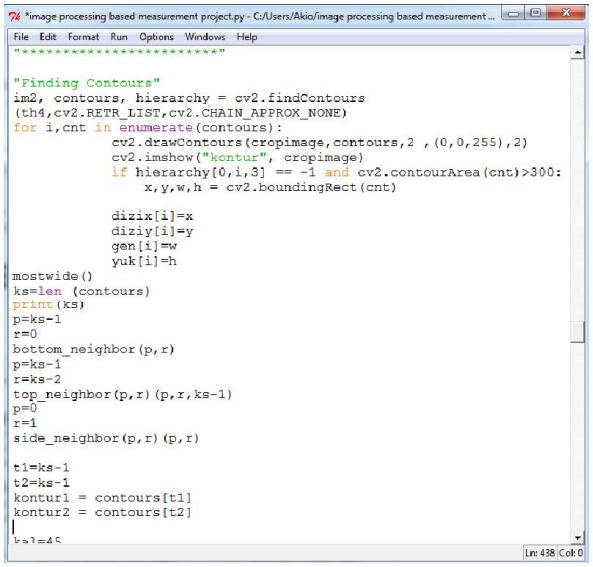


Figure 12: Measured image via image processing



```
*image processing based measurement project.py - C:/Users/Akio/image processing based measurement ...
File Edit Format Run Options Windows Help
"************************"

"Finding Contours"
im2, contours, hierarchy = cv2.findContours
(th4,cv2.RETR_LIST,cv2.CHAIN_APPROX_NONE)
for i,cnt in enumerate(contours):
            cv2.drawContours(cropimage,contours,2 ,(0,0,255),2)
            cv2.imshow("kontur", cropimage)
            if hierarchy[0,i,3] == -1 and cv2.contourArea(cnt)>300:
                x,y,w,h = cv2.boundingRect(cnt)

            dizix[i]=x
            diziy[i]=y
            gen[i]=w
            yuk[i]=h
mostwide()
ks=len (contours)
print(ks)
p=ks-1
r=0
bottom_neighbor(p,r)
p=ks-1
r=ks-2
top_neighbor(p,r)(p,r,ks-1)
p=0
r=1
side_neighbor(p,r)(p,r)

t1=ks-1
t2=ks-1
kontur1 = contours[t1]
kontur2 = contours[t2]
Ln: 438 Col: 0
```

Figure 13: Program parts of measurement system on Python

Profile dimensions is shown in Table 1. If we examine table 1, we can say image based measurement method results is nearly same as classical measurement method's. Maximum difference equal to 0.17 mm is measured, thus confirming all results is in the tolerances.

Table 1: Result of Measurements

		Std.	Min.	Max.	Real Measure	Image Based Measure	Difference
Wall Thickness	**Top**	2,50	2,50	---	2,50	2,67	0,17
	Bottom	2,50	2,50	---	2,50	2,67	0,17
	Right	2,50	2,50	---	2,50	2,54	0,04
	Left	2,50	2,50	---	2,50	2,54	0,04
Gasket Ch. Top R.		3,50	3,30	3,70	3,20	3,20	0,00
Gasket Ch. Bot. L.		3,50	3,30	3,70	3,80	3,74	-0,06
Espagnolette bed		16,20	16,00	16,40	16,45	16,42	-0,03
Espagnolette bed b.		12,20	12,00	12,40	12,15	12,15	0,00
Left width		71,00	70,70	71,30	71,00	70,89	-0,11
Inner width		55,40	54,90	56,40	55,55	55,67	0,12
Inner height		40,00	39,50	41,00	40,30	40,32	0,02
A		23,50	23,30	23,70	24,65	24,70	0,05
B		13,50	13,30	13,70	13,55	13,62	0,07

III. CONCLUSIONS

This study presents a complex shaped extruded products measurement method using image processing technics. The proposed method can measure wall thickness, inner and outer sizes, lined channels, gasket channels with a high accuracy. The experimental results show that the proposed method is better for complex shaped products comparing to usual geometrics profiles like as circle, square. On-line measurement can be used to continuously monitor the dimensional quality of any profile, and alarm the operator when any problem occurs. The experimental results show the algorithm is fast and requires minimum user interaction. This work is easily applicable for the companies that produce extrusion pvc products and decreases the risk factor to 0 that is caused by the human source.

Future research focuses are concentrated on improve the more robust algorithm for profile which is different geometric shapes.

ACKNOWLEDGMENT

We are grateful to the Selcuk University Scientific Research Projects Coordinator. This work was supported by Selcuk University Scientific Research Projects Coordination Unit with 16201037 Doctora Thesis Project.
Bu çalışma, Selcuk Üniversitesi Bilimsel Araştırma Projeleri Koordinasyon Birimi tarafından 16201037 kodlu Doktora Tez Projesi ile desteklenmiştir.

REFERENCES

[1] Shapiro, Linda G. & Stockman, George C. (2002). "Computer Vision". Prentice Hall. ISBN 0-13-030796-3

[2] Demigny D., On Optimal Linear Filtering for Edge Detection, IEEE Transactions On İmage Processing, 2002, 11, 728-737

[3] J.F. Canny, A computational approach to edge detection, IEEE Transactions on Pattern Analysis and Machine Intelligence PAMI-8 (6) (1986) 679–698.

[4] Suzuki, S. and Abe, K., Topological Structural Analysis of Digitized Binary Images by Border Following. CVGIP 30 1, pp 32-46 (1985)

[5] C. Liguori. A. Paolillo. A. Pietrosanto. "An on-line stereovision system for dimensional measurement of rubber extrusions". Measurement 35 (2004) 221-231

Word2Vec Based Sentiment Analysis for Turkish Texts

M. BİLGİN[1] and H. KÖKTAŞ[2]

[1] Bursa Technical University, Bursa/Turkey, metin.bilgin@btu.edu.tr
[2] Bursa Technical University, Bursa/Turkey, haldun.koktas@btu.edu.tr

***Abstract*— Parallel to technological developments in today's world, the development of microblog sites has also been accelerated. Millions of tweets are shared daily on Twitter, one of the most popular microblogging sites. Interpretation of interpretations made about companies and people and extraction of meaningful information is one of the most important problems in today's world. It is very important and valuable that a company can make an opinion from a millions of interpretations about a product that it sells. In this study, it was aimed to do sentiment analysis via Twitter on Turkish. A supervised learning and Word2Vec based system was designed and implemented on the training-test set to measure success on different machine learning algorithms.**

***Index Terms*—Supervised Learning, Word2vec, Sentiment Analysis, Natural Language Processing, Machine Learning**

I. INTRODUCTION

Sentiment analysis is the process of extracting the dominant sentiment in a text using natural language processing (NLP) techniques. The texts with the sentiment that they have previously contained are given as supervised learning and then the success of the system is tested again with previously labeled texts. From this point of view, sentimental analysis is basically a classification process.

Classification of machine learning problems where the labels of the samples are discrete. Each item in the training data belongs to a specific class. The learning algorithm generates a model using the data when it encounters a new data it determines which class the data belongs to. The process is called supervised if the classes are specified in the training dataset, unsupervised if not.

The commonly used method for the classification problem is the bag of words model. In this model, the document appears as a set of words for which the order of arrangement is not important. The bag of words model is actually a special case of the N-gram model. In the N-gram model, the document is sorted according to the value of variable N. For example, if N = 2 (bigram) the words (in order) are two in pairs, and if N = 3 (trigram), three in three. In this order, the first N words starting from the beginning of the sentence, then the first N words are continued from the second word, and so on. Bag of words model is N = 1 (bigram) in N-gram model.

The Word2vec model, unlike the N-gram model, also takes into account similarities between words. The details of this model are explained in the third chapter.

II. PREVIOUS STUDIES

In Zhang et al.'s work, a positive-negative-tagged sentimental analysis was conducted on 100,000 Chinese comments of a product obtained from the trial using various classification and learning methods. In the study of two separate experiments on the basis of Lexicon and part of speech, the combination of word2vec and SVMperf was accuracy of 89.95% on lexion basis and 90.30% on part speech [1].

Dickinson et al. sentiment analysis was conducted using n-gram and word2vec methods to investigate how a firm's stock price change affected the sentiment of the tweets about the product. As a result of the study, 65% success was achieved for the n-gram method and 75% success was achieved in the word2 vec method [2].

Tang et al. conducted another sentiment analysis on the tweets. Unlike the others in this study, it was tried to show how various word embedding methods changed the accuracy of the system [3].

Polpinij et al. conducted another empirical analysis of hotel reviews. In this study where Word2vec method is used, SVM is used as learning algorithm [4].

Şahin et al. performed word2 vec and SVM based classification on turkish texts. It was investigated how the processing of root or attached words affected the system performance in the study in which 22,729 Turkish documents were used [5].

Xue et al. performed sentiment analysis using word2vec on Sina Weibo, a Chinese microblogging site. The other side of the work is a model for building a sentiment dictionary using Word2VEC. Later, it was aimed to determine the sentimental tendency of documents using this dictionary. As a result of the study, success was obtained as 0.94 for positive documents, 0.96 for negative documents, and 0.85 for neutral documents [6].

In order to investigate the effect of educational methods in sentiment analysis on performance, Çetin experimented with 2 dimensions on 2 data sets. As a result, educational methods have been found to be more successful [7].

III. METHOD

A. Dataset

In the study, a data set with 3000 Turkish tweets in total, labeled as positive, negative and neutral, was used [8]. This dataset was created by a group of students who took courses in expert systems at Yıldız Technical University for text classification and sentiment analysis studies. Documents in this set are labeled as 756 positive, 1287 negative, and 957 neutral.

B. Pre-processing

In natural language processing, various pre-proccessing operations are performed before the main method is applied. Usually the first step is the tokenization process in which the document is divided into one or more word groups. After this process, the document is expressed in word list. Another important pre-processing step in NLP is to convert the entire document to lower case so that it does not adversely affect the result. The words obtained after these operations have a suffixed structure. Studies have shown that to work with root word gives more accuracy. In this study, 3000 tweets in separate files were converted into a single text file. The RegexpTokenizer method of the Natural Language Toolkit library is used for deleting punctuation marks and tokenization. [9] For the stemming process, TurkishStemmer method developed for Turkish was used [10].

C. Representing Text with Word2vec

The word2vec method, developed by Thomas Mikolov et al., is the most commonly used word embedding method today. This method, which is performed in two ways, either embeds a word or a group of words and attempts to predict the context in which this group is located (Skip-Gram). The other method is to guess the word or group of words in the given context (CBOW). These methods are illustrated in figure 1.

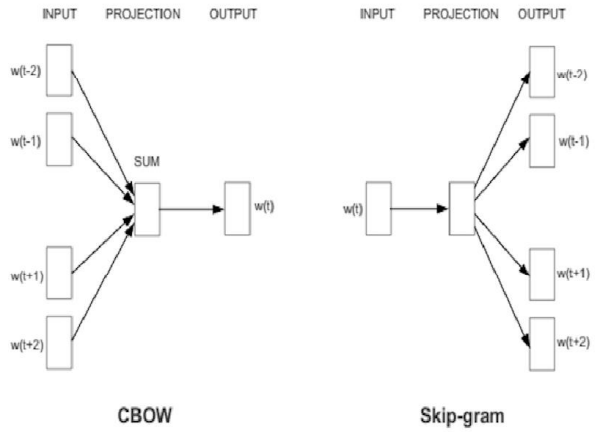


Figure 1. CBOW and skip-gram models [11]

When the results of this method are examined, it is seen that words that are close to each other which has closer meaning in vector space and vice versa. Thus, the word2vec method takes into account the semantic similarities of the words, unlike the other methods. Figure 2 shows how this state is expressed in vector space.

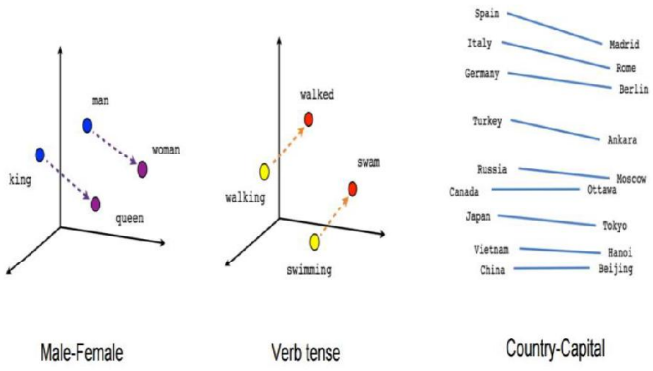


Fıgure 2. Vector-space respresentation [12]

The study was repeated for cbow and skip-gram. Then the results were compared. The parameters used in word2vec as in Table 1.

Table 1. Parameters

Parameter	Value
Debug	2
Size	500
Window	5
Negative	5
Hs	0
Min_count	5
CBOW	0-Skip gram 1-CBOW

Because the classification process is based on documents; it is necessary to find the vectors of these words from the word vectors. For this process, the vocabularies of the words contained in each document are extracted from the file that is output from Word2Vec. Then the average of these vectors was taken and document vectors were obtained.

	Attribute 1	Attribute 2	Attribute 3	..	Attribute 500
Bugün	0.324	0.0142	0.015	..	0.03
okula	0.02	0.31	0.156	..	0.221
gittim.	1.12	0.52	2.5	..	1.003
Document Vector (Average)	0.488	0.2814	0.890	..	0.418

Figure 3. Creation of Document Vector

The resulting document vectors are collected in a single csv file and given to machine learning software called Weka. In this software the cross-validation method is utlized. The performance of the system is compared using the SMO algorithm which is an application SVM and the NaiveBayes.

Cross-validation equally divides the dataset by the user-specified variable rate. After that, the experiment is repeated by changing the data which is separated for training and test. The results of this experiment are discussed in the fifth chapter. For this study, k, 10 (ten), the parameter of the cross-validation method, is chosen. The system is run in the form of dividing the data into 10 pieces and separating 1 piece each time as a test set. The performance of the system was calculated by taking the results of the 10 different test sets obtained.

IV. EXPERIMENTAL RESULTS

After the necessary pre-processing has been performed, the system has been tested separately for skip-gram and cbow using NaiveBayes and SMO methods. Confusion matrices are shown in Table 2-5.

Table 2. Skip-gram confusion matrix with NaiveBayes

Skip-Gram	Positive	Negative	Neutral
Positive	757	0	0
Negative	32	1255	0
Neutral	28	0	929

Table 3. Skip-gram confusion matrix with SMO

Skip-Gram	Positive	Negative	Neutral
Positive	754	2	1
Negative	0	1286	1
Neutral	0	0	957

Table 4. CBOW confusion matrix with NaiveBayes

CBOW	Positive	Negative	Neutral
Positive	102	0	1
Negative	74	2420	76
Neutral	21	12	923

Table 5. CBOW confusion matrix with SMO

CBOW	Positive	Negative	Neutral
Positive	101	0	2
Negative	0	2562	8
Neutral	1	18	937

The accuracy values obtained for two different Word2Vec methods (skip gram- CBOW) and two different machine learning algorithms (NB and SMO) are given in table 6.

Table 6. Results

	Skip-Gram	CBOW
Naive Bayes	0.98	0.949
SMO	0.9986	0.992

V. CONCLUSION AND FUTURE WORKS

The most successful method in our study is 99.986% with skip-gram and SMO. The NaiveBayes algorithm yields a good result for the skip-gram, but the success for the cbow is relatively low.

SMO is a newer and more advanced method than NaiveBayes. Therefore, the higher the success rate, the expected result. Looking back to Table 6, it is seen that the skip gram method gives more accurate results than the cbow method in both algorithms. If the skip-g is small and the cbow is thought to give more accurate results in larger datasets, the result will be in accordance with expectations.

In this study, it is aimed to compare the word2vec method with the addition of the stopwords preprocessing and using the bag of word (term frequency - inverse term frequency, etc.) methods. It is also planned to do the same work on this level using an English dataset with the current method.

REFERENCES

[1] Dongwen Zhang, Hua Xu, Zengcai Su, Yunfeng Xu, "*Chinese comments sentiment classification based on word2vec and SVMperf*", Expert Systems with Applications, Volume 42, Issue 4, Pages 1857-1863, March 2015

[2] Dickinson, B. and Hu, W. (2015) "*Sentiment Analysis of Investor Opinions on Twitter. Social Networking*", 4, 62-71. doi: 10.4236/sn.2015.43008.

[3] Tang, D., Wei, F., Yang, N., Zhou, M., Liu, T., & Qin, B, "*Learning Sentiment-Specific Word Embedding for Twitter Sentiment Classification*", Proceedings of the 52nd Annual Meeting of the Association for Computational Linguistics (Volume 1: Long Papers), 2014

[4] Polpinij, Jantima, et al. "*Word2Vec Approach for Sentiment Classification Relating to Hotel Reviews.*" Advances in Intelligent Systems and Computing Recent Advances in Information and Communication Technology 2017, pp. 308–316, 2017

[5] Sahin, Gurkan. "*Turkish document classification based on Word2Vec and SVM classifier.*" 2017 25th Signal Processing and Communications Applications Conference (SIU), 2017

[6] XUE, Bai; FU, Chen; SHAOBIN, Zhan. *A study on sentiment computing and classification of sina weibo with word2vec*. In: Big Data (BigData Congress), 2014 IEEE International Congress on. IEEE, p. 358-363, 2014

[7] Cetin, M., and M. F. Amasyali. "*Supervised and traditional term weighting methods for sentiment analysis.*", 21st Signal Processing and Communications Applications Conference (SIU), 2013,

[8] Çetin, M., Amasyali, M., " *Eğiticili ve Geleneksel Terim Ağırlıklandırma Yöntemleriyle Duygu Analizi",* SIU, 2013 , Available: http://www.kemik.yildiz.edu.tr/data/File/3000tweet.rar

[9] Available: http://www.nltk.org/

[10] Available: https://github.com/otuncelli/turkish-stemmer-python

[11] Mikolov, Tomas, et al. "*Efficient estimation of word representations in vector space*." arXiv preprint arXiv:1301.3781, 2013

[12] Available: https://www.tensorflow.org/tutorials/word2vec

Security of Web Applications

H.BİLGİN[1] and M.ERŞAHİN[2]

[1] Monitise MEA, İzmir/Turkey, hakan.bilgin@monitise.com
[2] Dokuz Eylül University, İzmir/Turkey, mustafa.ersahin@gmail.com

Abstract **- This study aims to show how security flaws of web applications can threat information security. Web Application Security is a branch of Information Security which focuses on web application level security flaws and their solutions. Evolution of Web continues with a big momentum. The amount of information shared over Web increases every day, various business domains continue to integrate their operations to the digital world. This brings its own risks and makes Information Security of Web Applications more important than ever.**

Most common and serious Web vulnerabilities have been analyzed along with their solutions. This study focuses on how web developers can already prevent security problems during the development life cycle. What are the best practices to follow before/during the development and post-development phases? Which security tools can be used to support developers?

Building totally secure web applications is not an easy job. Following security standards and development cycles with security concerns can already prevent most of the potential problems. A security checklist for web developers came out at the end of the study. Evolving web technologies and new security threats force us to keep this checklist up to date. We are working on a mechanism which will keep this checklist up to date.

Keywords **– Web Application, Security, Development, Checklist, Security Knowledge Framework**

I. Introduction

IT has been a long time that web applications became much more than web sites with static content. Evolution of the World Wide Web created web applications with greater abilities and still continues to provide brand new solutions to all kind of market needs.

Web applications are the most used technology for information and service delivery over Internet. Organizations from various different domains continue to move their operations to the digital world. Mobile and Web based technologies come at the top of the list. These digital services can be security critical and may contain sensitive information (e.g., financial, health). Fast growing and evolving web environment brings up its own risks. Guaranteeing security for vast amount of information is not an easy task and not totally achievable. On the other hand, security breaches may result in loss of enormous amount of information and money along with ethical and legal consequences [1].

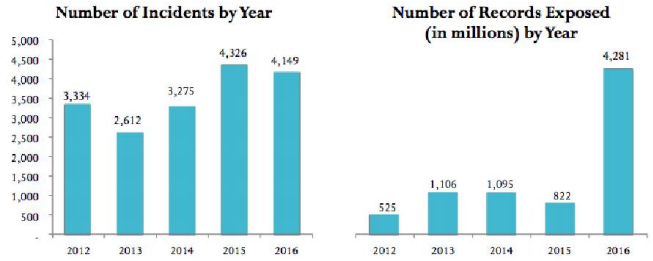


Figure 1: Security Breach Trends of 2012 – 2016 [2]

According to Data Breach Trends 2016 report of RiskBased Security, 4,281 millions of records have been exposed in 2016, while it was only 822 millions in 2015 [2]. Even though the number of reported incidents has decreased in 2016, consequences of the incidents became much worse. We see that there is not any correlation between the number of incidents and their results. This fact reminds us that one simple security breach may have serious consequences. Security standards must be followed completely without ignoring any potential threat to minimize all kind of risks.

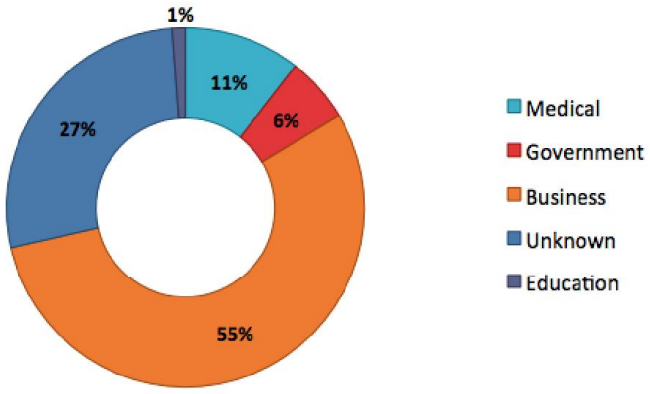


Figure 2: Security Breach Trends of 2016 by Industry [2]

Business industry was the first target of attackers, followed by medical and government establishments [2].

Sources of these incidents may vary but this study will focus only on web application threats and their precautions. Study will try to look from developers' point of view and examine their role on developing secure applications.

II. State of Web Applications

Web application attacks represent the greatest threat to an organization's security. Web app attacks represented 40% of breaches in 2015 [3]. According to analyzes of WhiteHat Security, 5 to 32 vulnerabilities have been found on thousands of web applications across different industries. The same study shows us that only 5% of web applications have exceptional application security, 40% of applications have a lot to improve about security. Detecting a vulnerability does not solve the problem automatically. Taking action to fix these vulnerabilities takes time also. Average open time of critical vulnerabilities is over 300 days. High-risk vulnerabilities stay open more than 500 days [3]. Average open time of a vulnerability is an important parameter. High age values increase the chance of attackers to profit these vulnerabilities. Unfortunately, considerable number of web applications stay always vulnerable, not only in specific time periods. Around 40% of Banking & Financial Services web applications, half of the Health and Retail web applications and more than half of the Manufacturing, Food & Beverage, and IT web applications remain always vulnerable [3]. These values show us that organizations cannot directly fix detected vulnerabilities.

Once your application goes live, fixing these vulnerabilities may cost much more than taking precautions during the development phase. Remediating vulnerable servers may create down times which will cause money loss, decrease the customer satisfaction and reputation of the product. Transforming a web application which has been developed without security concerns to a secure web application can be more painful than initial implementation. For example, changing the old and weak password policy of a web application will force all existing users to update their password. Managing this process will cost to the organization. This could be avoided by following security standards at the beginning and launching the web application with the correct password policy.

In today's world, development with security concerns is a must. Software companies must cultivate culture of security prioritized development. Security must be a priority as much as the functionality of an application.

Software developers should stay competent on security subjects. List of security threats is not static. It is evolving along with technologies. More complex technologies create more complex security problems. Developers cannot cope with this situation alone; they must be supported with standards and other helper tools.

OWASP is the main source of information about security standards, practices and supporting tools. Thanks to its big and open community, OWASP remains as an up to date, reliable and educational address for individuals and organizations. OWASP has many educational documents and projects for software developers to cope with security problems.

III. Security Threats and Preventions

The OWASP Top Ten project aims to decide what are the most critical web application security flaws. These top ten list is created by broad consensus of project community. Original goal of the Top 10 was raising awareness amongst developers but it has been a *de facto* application security standard with time. Last official release of Top 10 was in 2013 but 2017 version is on the way with its second candidate.

The OWASP Top 10 for 2017 is constructed based on more than 40 security firm reports and industry surveys. Data is collected from more than 100,000 applications and APIs.

Web technologies and architectures have been significantly changed over the last few years. Single page applications have replaced many server rendered web sites. We can now call JavaScript as assembly of web. Rise of the SPA frameworks like Angular and React moved servers' responsibility to the client side (browsers). Event based server Node.js became very popular. Mobile apps and single page applications started to share same APIs.

Microservices written in node.js and Spring Boot are replacing older enterprise service bus applications using EJBs and so on. Old code that never expected to be communicated with directly from the Internet is now sitting behind an API or RESTful web service. The assumptions that underlie this code, such as trusted callers, are simply not valid [4].

This evolution has reshaped the OWASP Top 10 list as below.

OWASP Top 10 2013	±	OWASP Top 10 2017
A1 – Injection	→	A1:2017 – Injection
A2 – Broken Authentication and Session Management	→	A2:2017 – Broken Authentication and Session Management
A3 – Cross-Site Scripting (XSS)	↘	A3:2013 – Sensitive Data Exposure
A4 – Insecure Direct Object References [Merged+A7]	U	A4:2017 – XML External Entity (XXE) [NEW]
A5 – Security Misconfiguration	↘	A5:2017 – Broken Access Control [Merged]
A6 – Sensitive Data Exposure	↗	A6:2017 – Security Misconfiguration
A7 – Missing Function Level Access Contr [Merged+A4]	U	A7:2017 – Cross-Site Scripting (XSS)
A8 – Cross-Site Request Forgery (CSRF)	☒	A8:2017 – Insecure Deserialization [NEW, Community]
A9 – Using Components with Known Vulnerabilities	→	A9:2017 – Using Components with Known Vulnerabilities
A10 – Unvalidated Redirects and Forwards	☒	A10:2017 – Insufficient Logging & Monitoring [NEW, Comm.]

Figure 3: OWASP Top Ten 2013 - 2017 Industry [4]

As we can see above XML External Entity (XXE), Insecure Deserialization and Insufficient Logging & Monitoring have entered to the list. Insecure Direct Object References and Missing Function Level Access Control merged as Broken Access Control and took 5th place. Cross-Site Request (CSRF)

and Unvalidated Redirects and Forwards take no more place in Top 10 list but they should not be forgotten.

1) Injection

SQL, OS and LDAP injections happen when untrusted data and instructions are sent as a part of command or query. Injected commands may have very serious results like dropping whole database or accessing data without authorization.

Preventions;

- Building secure APIs which avoid query or command concatenation. Using ORMs or Entity Framework with parameterized queries is the best defense mechanism.
- Applying white list input validation.
- Escaping special characters in dynamic queries.
- Using LIMIT and other SQL controls in queries will keep the damage low in case of injection.

2) Broken Authentication and Session Management

Limiting application functions by user identification is generally vulnerable. Vulnerable session management allow attackers to access passwords, keys or sessions tokens and gain all access rights of real users.

Preventions;

- Never go to live with default credentials. Specially for admin users.
- Store hashed password with modern algorithms like Argon2 or PBKDF2.
- Set strong password policy. Detect weak passwords including commonly used words. Accept pass phrases.
- Define strong registration and credential recovery procedures against account enumeration attacks.
- Implement multi-factor authentication.
- Keep and watch authentication logs to detect brute force and other attacks and alert administrator.

3) Sensitive Data Exposure

Web APIs are not threating sensitive data with extra protection. Sensitive data must be protected with encryption and special precautions must be taken during the exchange with the browser.

Preventions;

- Classify all processed, stored or transmitted data. Apply different level of security control per class.
- Apply privacy laws and regulations to sensitive data.
- Never store sensitive data if not necessary. Safe delete the data as soon as possible.
- Encrypt all sensitive data. Use TLS. Enforce it with HTTP Strict Transport Policy HSTS.
- Use up to date and strong encryption algorithms, keys, protocols and ciphers.
- Disable cache for response which contain sensitive data.
- Store hashed password with modern algorithms like Argon2 or PBKDF2. Keep delay factor as high as possible.

4) XML External Entity (XXE)

This new vulnerability entered to Top 10 list from a high position. Reason of this serious vulnerability is old and poorly configured XML processors which evaluates external entity references within XML documents. External entities can access to internal files, execute remote code and make denial of service attacks like Billion Laughs attacks.

```
<?xml version="1.0" encoding="ISO-8859-1"?>
 <!DOCTYPE foo [
 <!ELEMENT foo ANY >
 <!ENTITY xxe SYSTEM "file:///etc/passwd" >]>
 <foo>&xxe;</foo>
```

Figure 4: XXE attack for extracting data from server [4]

Preventions;

- Developer awareness is important to detect potential XXE attacks.
- Disable external entity processing in all XML parsers of the application.
- Validate all incoming XML and XSL file uploads by XSD validation.
- Use white listing input validation to check XML file content.
- Upgrade SOAP to latest version.
- Upgrade all third party and underlying XML processor libraries including OS libraries. Using dependency checker supported by CVE feeds will decrease the risk.

5) Broken Access Control

Constructing a robust authentication and session management sometimes may not be enough. Attackers can't steal session info or credentials but they can still use more privileged user rights if user roles and their restrictions have not been defined properly. Attackers may access and modify other users' data without breaking any authentication rules.

Preventions;

- Access control must be implemented in trusted server-side where attackers cannot modify access conditions.
- Implement user role and access right control mechanisms once and re-use them in all application.
- Give users only required rights, do not give unnecessary read, create, update or delete rights. Give these rights by record.
- Disable web server directory listing. Do not keep metadata files in web roots.
- Log and watch access failures and alert admins.

6) Security Misconfiguration

Bad security configurations or using default configurations without any changes is very common. Wrong configurations can expose sensitive data.

Preventions;

- Development, QA and Prod environments must be configured identically including all dependency versions.
- Deployment processes must be standardized and should be automated.
- Never install unnecessary dependencies, documentations.
- Follow CVE updates.

7) Cross-Site Scripting (XSS)

Two thirds of applications contain this vulnerability. Attacker can execute scripts in victim's browser which can steal sessions, deface web sites or redirect to malicious sites.

Preventions;

- Using some up to date frameworks like React prevents XSS attacks automatically.
- Escaping untrusted HTTP request data and applying context sensitive encoding. They are explained in detail in OWASP cheat sheet.
- Enabling Content Security Policy header.

8) Insecure Deserialization

Applications may deserialize insecure objects without any control. This leads remote code execution, user spoofing and privilege elevations.

Preventions;

- Do not accept serialized objects from untrusted sources.
- Deserialize only primitive data types if possible.
- Run deserialization in isolated, very low privileged environments.
- Enforce strict type constraints during deserialization. Accept only predefined object patterns.
- Log and observe deserialization operations.

9) Using Components with Known Vulnerabilities

Nearly all complex applications have series of dependencies which have same privileges as application itself. An application can be implemented according to high level security standards but one vulnerable dependency can make whole application vulnerable as well. Because of that dependency management and vulnerability tracking is vital.

Preventions;

- Remove unused dependencies.
- Use vulnerability detection tools like versions, DependencyCheck and retire.js.
- Follow feeds of CVE and NVD vulnerabilities of dependencies with an automated process.
- Accept dependencies only from official sources, repositories. Prefer signed packages.

10) Insufficient Logging & Monitoring

Lack of logging in your application causes delay in breach detection. Detailed logging of your application supported with log analyze tools can detect incidents much more earlier.

Preventions;

- All login, access control and input validation failures must be logged.
- Enable log monitoring which can detect suspicious log patterns and raise alerts.
- Don't forget to obfuscate sensitive data in log files.

IV. Secure Software Development

This fresh Top 10 list will update the priorities of developers and whole industry. Even though the top ten covers 80-90% of all common attacks and threats we cannot stop with that. OWASP Developer's Guide, Testing Guide, Code Review Guide and Cheat Sheet documents are essential for complete protection. Top 10 list and these supporting documents keep evolving. Even without changing a single line of code, applications may become vulnerable with time [4].

Developers must digest various documents and standards in order to create and maintain an application with OWASP Application Security Verification Standard (ASVS). Developers alone cannot achieve this. Developers should use supporting tools and focus on standards rather than focusing on specific vulnerabilities.

As discussed in previous chapters, having an application secure by design in much more better and easier than chasing vulnerabilities and patching your application after incidents occur. Developers must be educated and guided about up to date security standards. Developers must apply security principles to software development cycles in order to have secure by design applications. All these responsibilities can create too much work for developers and specialization on security can take too much time.

Security Knowledge Framework project is a perfect match for developers and security specialist requirements. This project aims to educate and guide developers for secure development. It contains knowledge base, checklists and code examples to achieve security standards on desired levels.

We have installed a SKF instance for test purposes. We saw that it has been designed to work in parallel with agile software development methods. The steps that are followed on SKF, during the software development cycle can be listed as below.

- Firstly, a project must be created in SKF which will represent a security clone of our real software project.
- ASVS level (opportunistic, standard, advanced) must be decided according the requirements of the project.
- Name, description and version of security project must be cloned from original project.
- Pre-development settings questions must be answered correctly. According to answers SKF will shape the security checklist at the end.
- We add our first sprint and answer questions about the sprint content which will shape the security checklist.
- Security project is now created and a security checklist has come out for first sprint.
- Developers can review the checklist and update the status of every item in the list like updating a functional task status on a Scrum board.
- Once the developer closes the security item, Security Specialist user can verify the item and task becomes closed before the next sprint.
- Every time a new sprint starts, a security sprint must be started in parallel. SKF produces a new security checklist for every Sprint according to the Sprint content.

Security checklists produced by SKF come with explanations and necessary directions to cheat sheets and knowledge bases.

V. Conclusion

Applying secure code practices and creating secure by design web applications is not easy to achieve. On the other hand, there are plenty of guides and standards for testers, developers, managers and organizations, provided by OWASP community. These guides show us the path towards secure web applications. However, digesting all these standards in daily development life does not seem realistic. Using Security Knowledge Framework will discipline the developers and increase the security awareness of organizations.

Tracking vulnerabilities of application dependencies is as important as secure development of application itself. Your fully secure application can become vulnerable because of its dependencies. CVE tracking tools must be absolutely used.

We believe that developers will create more secure web applications with support of SKF. SKF will provide up to date security checklists, decrease the effort of developer to follow evolving security standards.

References

[1] X. Li, Y Xue, *A Survey on web application security*. Vanderbilt Univ., Nashville, TN, 2011.

[2] *RiskBased Security Data Breach Quick Report,* Risk Based Security, Inc., Ricmond, AZ, 2017. Available: https://pages.riskbasedsecurity.com/hubfs/Reports/2016_Year_End_Data_Breach_QuickView_Report.pdf

[3] *Web Applications Security Statistics Report,* WhiteHat Security, Inc., 3970 Freedom Circle Santa Clara, CA, 2016. Available: https://info.whitehatsec.com/rs/675-YBI-674/images/WH-2016-Stats-Report-FINAL.pdf

[4] *OWASP Top Ten Project 2017 Report Release Candidate 2.* Available: https://www.owasp.org/images/b/b0/OWASP_Top_10_2017_RC2_Final.pdf

Security analysis of RPL for IoT

MOUNNAN oussama and IDBOUFKER Noureddin
University Lorraine, France, oussama.mounnan@gmail.com
TIM Laboratory, Ensa Marrakesh, Cadi Ayyad University, Morocco, n_idboufker @yahoo.fr

Abstract **- A Low and Lossy Network (LLN) is the result of Interconnecting different Internet of Things (IoT) objects. In an LLN virtual or physical connected objects communicate and interact with each other and with their environment, making possible to recover, to store, to transfer and to process exchanged data. These data will then be used to carry out actions, analyze, and create management tools. IoT is considering a new world of connected intelligent devices or objects together with human ones in which the quality of life is improved. These objects have limited electrical resources, and are often connected by low-quality radio links. Traditional routing protocols are not suitable for this context. A routing protocol called RPL was specially designed by the Internet Engineering Task Force (IETF) for Routing Over Low and Lossy Network (ROLL). RPL is used in order to respond to the specific constraints imposed by such networks in terms of limited energy, low calculation capacity, etc..**

Nevertheless, this protocol remains vulnerable to security attacks. If protection mechanisms exist, their implementation is costly, hence the value of an approach for identifying, assessing and treating the risks. As routing is a critical function in any type of network, the purpose of our paper is to focus on the RPL protocol that governs routing in LLNs for IoT, and what are the resulting security issues , especially an analysis of two specific attacks: the DAG incoherence attack and the attack on the version number and finally its security mechanisms.

Keywords **- IoT, Security, RPL, DODAG, Version Number.**

I. Introduction

The Internet of Things has become one of the challenges, and opens up perspectives of evolution in technological and scientific subjects. IoT's interest is multiple, both from the point of view of the civil users and from that of the companies are their concern. Awareness of this area is causing a rapid evolution of technologies, and an integration of a wide range of diversified media: the concept of "objects" aims to put no limit as to the possibilities of implementing technological tools in everyday elements. Wireless sensor networks are typically used to study a specific environment through data. The exchanges of these data are generally routed from a closer sensor to a collection station: this is called multi-hop communications. In order to overcome the constraints associated with sensors (limited energy, low calculation capacity, etc.), the scientific community is working to develop new, lightweight, reliable and energy-saving communication protocols. The deployment of low-power and lossy networks called LLN and IP packet routing is one of the main issues of IoT. The ROLL (Routing Over Low Power and Lossy Network [1]) of the IETF is working on this problem and has just produced its official protocol, RPL (Routing Protocol for LLNs). The ROLL group has already produced several RFCs detailing the requests of these LLNs: RFC 5867 [2], RFC 5826 [3], RFC 5673 [4] and RFC 5548 [5]. They also normalized the distribution algorithm used by RPL, Trickle (RFC 6206 [6]). The RPL is de facto a routing protocol for the Internet of Things and it's based on the Trickle algorithm of RFC 6550 [7]. Since its standardization, RPL has contributed to the improvement of communications in the world of tiny. Nevertheless, this protocol remains vulnerable to numerous security attacks. The purpose of this article is to define routing mechanisms for networks of machines with limited capacities and that are connected by short-range and often scrambled radio links, in particular the RPL protocol, the RPL routing topology and the analysis of the most known vulnerabilities of this protocol namely the analysis of two attacks and finally the security mechanisms of RPL.

II. IoT Technologies

The Internet of Things (IoT) and its protocols are the attention of the industry which makes the evolution of this one very fast. IoT technologies allow things, or devices that are not computers, to act intelligently and make collaborative decisions that are beneficial to certain applications. The underlying technologies of ubiquitous computing, Integrated sensors, communication and Internet protocols allow the IoT to provide its meaning. However, they impose many challenges and present the need for specialized protocol standards. The principle of the Internet of Things results in the deployment of networks with Low power and Lossy Networks called LLN . These networks allow many embedded devices like sensors to communicate with one another. A routing protocol called RPL has been specially designed by the IETF to meet the specific constraints imposed by this type of network (energy limit, low computing capacity, etc.). There are dozens of different technologies, each with its own particularities in terms of energy consumption, cost, output and scope.

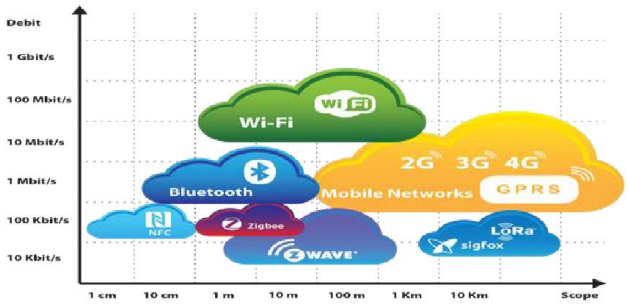


Figure 1: Comparison of the range and the rate of the main standards of wireless connectivity.

Two main networks categories exist on the market:

Long-range networks such as Sigfox, LoRa or cellular technologies (GSM, 2G, 3G, ...) are able to pass data between devices over vast distances. "They are used by companies that want to connect kilometers of infrastructure to the Internet or smart cities projects, for example.

Short-range networks such as Wi-Fi, Z-Wave, ZigBee or Bluetooth Low Energy, make it possible to transfer data over short distances. or in the consumer wearable market. A connected bracelet is never very far from the phone to which it transfers its data.

III. Routing in Sensor Networks

objective of a routing protocol is to find a route between two nodes of the network. In sensors networks, in addition to the problem related to distributed operation, networks nodes are under a high energy constraint because they operate on batteries. Therefore, multi-hop routing protocols already standardized by the IETF are not suitable because they result in high energy consumption of the nodes. Mainly, routing protocols in resource-limited networks must operate under a set of constraints that routing protocols dedicated to ad-hoc networks [8] generally do not take into account. For this reason, a new Routing Protocol for Low Power and Lossy Networks (RPL), which is much more energy-optimized, was developed by the IETF. The RPL protocol allows both point-to-point (P2P), point-to-multipoint (P2MP) and multipoint-to-point (MP2P) communication. Traditionally, routing protocols can be divided into two categories depending on how routing information is propagated: reactive protocols and proactive protocols.

A. Reactive Routing protocols

They work by building roads on demand and maintaining them only if necessary, meaning that a source is trying to communicate with a destination. The main advantage compared to a proactive approach comes from the fact that there is no need to maintain route if no traffic is generated on the network. However, since the route does not exist before its use, a delay corresponding to the creation of the route is introduced during routing of the packet [9].

B. Proactive routing protocols

For them, it is assumed that each node of the network must have a route to any destination, at any time. Therefore, a proactive routing protocol builds roads before they are needed [18]. In order to keep a routing table up to date, these protocols use periodic updates by sending routing messages at a certain frequency. These periodic updates must be fast enough to take into account changes in topologies and network conditions, but not too fast so as not to overload the network as a signaling message.

IV. RPL protocol

RPL is an IPv6 routing protocol with a distance vector that constructs a Destination Oriented Directed Acyclic Graph (DODAG) using an objective function [10] consisting of metrics and / or constraints. Procedure of construction of the DODAG. In a DODAG, the nodes can be grouped in three types based on the tasks they assume.

- The root, also known as the LBR (Low Power and Lossy Network Border Router) [11], plays a very important role in the network. The root is responsible for sending the DIO messages used to build the DODAG.
- Parent nodes or routers. A parent node has at least one child (a node of lower rank). The parent node ensures the flow of information between the root and its children.
- The leaf nodes are nodes that have no wires. They are only connected to their parent node that transmits to them the information from the root of the DODAG.

The DODAG graph formed by the RPL protocol is a logical routing topology built from a physical network using a number of criteria provided by the system administrator.

The first step is to broadcast the DIO messages by the root or LBR in the DODAG. In its neighborhood at a jump. Secondly, each node that received the DIO sent by the LBR will use the objective function contained in the DIO message and the preferred parent choice algorithm to choose its favorite parent. Once the preferred parent is chosen, the node sends a DAO [12] message to that parent to indicate its choice. These DAO messages contain information that allows the root to construct paths to the leaf nodes of the DODAG. The third step concerns of the nodes that have chosen the LBR as a parent. These will in turn broadcast DIO messages in multicast in their vicinity. The process in step 3 continues until all the nodes in the network connect to the DODAG.

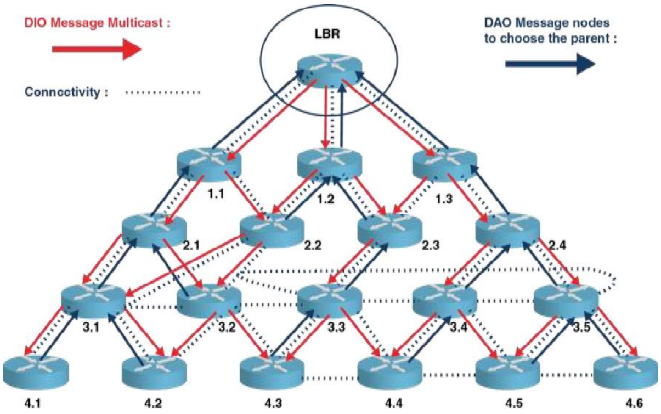


Figure 2: Final DODDAG built by the RPL

A. Format of the DODAG information Object DIO.

The DODAG information object carries information that allows a node to discover an RPL instance, learn its configuration parameters and select a set of DODAG's parents and maintain the DODAG.

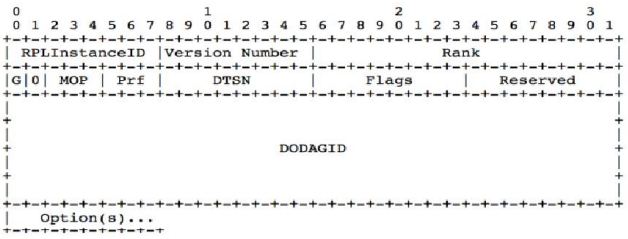


Figure 3: DIO Basic Format

B. Format of the Destination Advertisement Object DAO.

Destination Advertisement Object (DAO) is used to propagate destination information up along the DODAG. In storage mode, the DAO message is unicast by the child to the selected parent (s). In non-storage mode, the DAO message is unicast at the DODAG root. The message may eventually be DAO, upon explicit request or error, be recognized by its destination with an Acknowledgment message (DAO-ACK) to the sender of the DAO.

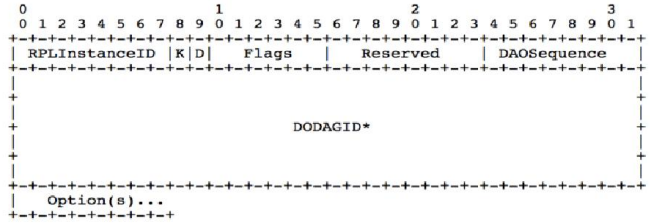


Figure 4: The DAO base object.

The '*' indicates that DODAGID is not always present, as described below.

C. The different metrics of the RPL protocol.

RPL routing metrics can be grouped into two classes:

- Node-based metrics is the metric on the hop count and the metric on the residual energy of the nodes (Node Energy).
- Link-based metrics include link quality (LQ), Latency, Throughput, and the expected number of retransmission (ETX).

The choice of the metric to be used for building the DODAG is configured at the root node. The root will disseminate the objective function containing the metric in the DIO messages through a reserved field called "OCP" (Objective Code Point).

D. The operating modes of the RPL protocol.

Depending on the capacity of the nodes in terms of memory and the possible size of the network, the RPL protocol offers two modes of operation, Storing mode and Non-Storing mode.

1) Operation "Non-Storing mode."

In non-Storing mode, only root is able to store routing information. The other nodes on the network retain only the addresses of their direct parent. All the information on the structuring of the DODAG is transmitted to the root in the DAO messages. In case of need to route data to any destination, the nodes transmit this data to the root through their parent. The root will route at the source to the correct destination. In this mode of operation, each node generates its DAO message and then sends it to the DODAG root through multi-hop communications. The DAO message sent is a response to a received DIO message, figure (b).

2) The "Storing mode" operation.

In this mode of operation, the intermediate nodes are able to keep in memory the routing information then redirect the received data to the correct destination by consulting the routing information. Unlike the "Non Storing mode", in the "Storing mode", not all DOA messages are transmitted to root. Each node transmits its message to its direct parent (parent to a jump) that maintains a routing table at its level, figure (a).

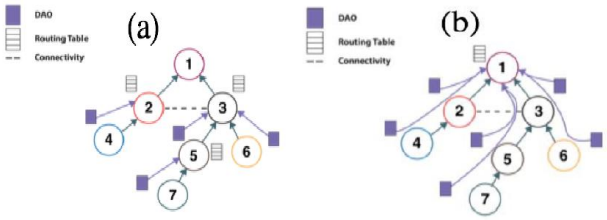


Figure 5 : Operating modes of the RPL protocol

E. RPL protocol control messages.

For RPL, messages involved in building and maintaining DODAG are:

- DODAG Information Object (DIO), initiated by the LBR and retransmitted in multicast by its neighbors.
- DODAG Destination Advertisement Object (DAO), send by the child nodes to their parent.
- DODAG Information Solicitation (DIS), can be sent by all nodes except the LBR.
- Destination Advertisement Object Acknowledgment (DAO_ACK), sent by a parent node to its child. Except for DAO and DAO_ACK messages, the other two messages have a local target and are sent in multicast to neighbors using link IPv6 addresses local.

The DAO and DAO_ACK messages are sent to them in unicast using either a global address or a single local address.

F. DODAG repair Mechanism

DODAG mechanism is initiated by the LBR. Each DODAG initiated by the root has a version number. The repair operation consists of incrementing the number of the current DODAG version in order to create a new version. The nodes in the new version of the DODAG can choose a new position whose rank is smaller compared to the rank of the old version. The root always has the rank 0. The transmission of the control messages (the DIO messages in particular) by the RPL protocol is controlled by a particular timer called "Trickle timer". The Trickle timer algorithm reduces the transmission of DIO messages when the network is stable.

V. Attacks on IoT Components.

The most traditional attacks are based on listening to traffic (passive attacks) and man in the middle (active attacks) allowing the interception of data transmitted in clear text, or encrypted if encryption is provided natively by the communication protocol or by the application. In the world of connected objects, there are several protocols for interconnecting equipment. These protocols allow communication between different short and long distance equipment, in secured or non-secure ways, and some of them even allow networks of connected objects to be established. Long-range networks designed for low-power equipment (LPWAN) are particularly sensitive to data interception or equipment spoofing. Short-distance communication protocols are not, however, more secure. The security measures set up are often rudimentary and can be either broken after interception of exchanges that are not very secure, or bypassed during the execution of interception by an attack of the "man in the middle ". Faced with the many security challenges of the Internet of objects, we will analyze two attacks that are

more responsive to the inconsistency attack DAG and that of version number.

A. Inconsistency attacks DAG.

In theory, the mechanism for validating the data path, presented above, aims to improve the general reliability of the network. However, it is possible to divert this feature to attack the network. Indeed, an attacker can make nodes believe that there are loops while the topology is stable. Two approaches can be adopted by the attacker:

- Create malicious packets directly with the flag 'R' and the wrong direction positioned,
- Modify the packets that pass through it by positioning the flags contained in the extension header .

In both cases, the immediate consequence of this attack is flooding the network with control messages, since all victim nodes that have received malicious packets and their vicinity will reset their Trickle timer. This will ultimately reduce the service life of time of the network. In the second case, the modified packets will be deleted by the attacker's parent (node 2 described in the scenario a in figure (a), which will generate a black hole deported to this parent where the data packets will be east.

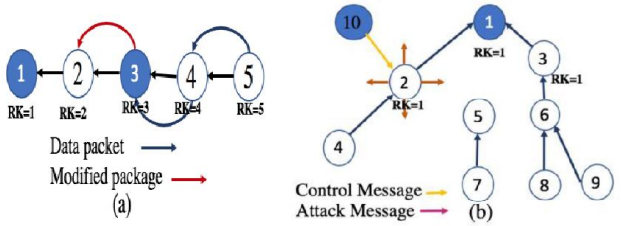


Figure 6: DAG Inconsistency Attack Scenario.

DAG incoherence attack: In order to reduce the impact of such an attack on the network, several countermeasures can be envisaged and applied. The first is proposed by the authors of RFC 6553 [13]. It is to limit the number of resets of the timer Trickle due to the detection of inconsistencies DAG at 20 per hour. The second countermeasure proposed by Anthéa Mayzaud and Anuj Sehgal and Rémi Badonnel and Isabelle Chrisment [14], is also to limit the number of resets, but they using a dynamic threshold λ (r) as defined by the formula. E pkts represents the number of packets received with flag 'R' and D pkt, the number of legitimate data packets that were transferred by the node. The variable r is computed locally by each node; α has been set in such a way that the threshold never reaches a zero value, β has been determined so that, in an unattacked state, the threshold is equal to the value of the fixed threshold proposed by the authors of RFC6553 i.e. 20, γ is used to vary the slope of the decreasing exponential in order to take into account the aggressiveness of the attacker.

$$\lambda(r) = b\ \alpha+\beta \cdot e^{1-\gamma \cdot} r\ c \text{ avec } r = E\ pkt / D\ pkt, \alpha= 5, \beta=15\ e, \gamma= 25$$

B. Attacks on version number.

The version number is an important field in DIO messages. It must be propagated without modification along the DODAG. Only the root can increment it to create a new version of the DODAG to revalidate the integrity of the network and allow a global repair. If a node announces an older version, it means that it has not migrated to the new version and should not be chosen as a parent. An attacker can change the version of the DODAG by unlawfully incrementing the corresponding field in his DIO messages before transmitting them to his neighbors. This will result in the potential generation of loops in the graph and the entire reconstruction of the DODAG involving a depletion of the battery of the nodes.

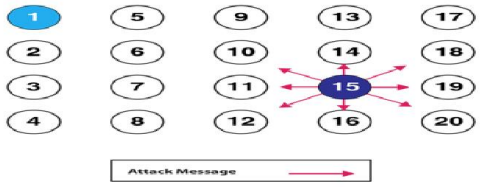


Figure 7: Scenario used for the attack on the version number

To counter this attack, Dvir et al proposed a security mechanism called VeRa 5 [15] that prevents a compromised node from usurping the root by modifying the version number. The solution uses an authentication system based on hash operations and signatures with shared keys. A node can thus verify that it is the root that is at the origin of the change of version. However, the authors of TRAIL: Topology Authentication in RPL [16] [17] showed that VeRa was not safe. They proposed TRAIL 6 by taking up the general idea of VeRa but including challenges to be signed by the root. They also showed that their solution was reliable at a relatively low cost compared to gain in the event of an attack. This countermeasure can thus be considered as a risk treatment even though it is not dynamically activatable, which could be extended for this solution.

VI. RPL Security.

RPL supports three security modes. The first one is 'Insecure mode'. In this security mode, RPL uses the basic DIS, DIO, DAO, and DAO-ACK messages, which have no security. The second one is 'Preinstalled mode' where, RPL uses secure messages to join an RPL instance, a node must have a preinstalled key. A node can use the preinstalled key to join the RPL as a host or router. In the last mode called 'Authenticated mode' where, RPL uses secure messages. To join an RPL instance, a node must have a preinstalled key. By using this preinstalled key, a node can join the network as a host only. To join the network as a router, the node must obtain a second key from a key authority. This authority key can authenticate that the requester is allowed to be a router before providing the second key.

A. Join a secure network.

RPL security assumes that " a node wishing to join a secure network was preconfigured with a shared key to communicate with neighbors and the root RPL. To join a secure RPL, a node must listen to secure DIOs or trigger secure DIOs by sending a secure DIS. In addition, secure DIO and DIS messages have rules. If the message is sent, the initial secure DIS must set the key identifier mode field to 0 (00) and set the security level field to 1 (001). The key used must be the preconfigured group key (Key Index0x00). When a node resets its Trickle timer in response to a secure DIS, the next DIO it transmits must be a secure DIO with the same security

configuration as the secure DIS. If the node receives several secure DIS messages before it transmits a DIO, the secure DIO must have the same security configuration as the last DIS it responds to. Furthermore, when a node sends a DIO in response to a secure unicast DIS, the DIO must be a secure DIO.

The above rules mean that in RPL instances where bit 'A' is set, using Key Index 0x00, a node can join the RPL instance as a host but not as a router. A node must communicate with a key authority to obtain a key that will allow it to act as a router.

B. Installing the keys.

Authenticated mode requires a router to dynamically install the new keys once they have joined a network as a host. Having joined the network as a host, the node uses standard IP messaging to communicate with an authorization server, which can provide new keys. The protocol to obtain the keys is out of reach for this specification and is to be elaborated in the future specifications. It is necessary to develop keys so that RPL operates securely in the authenticated mode.

C. Consistency checks.

RPL nodes send Consistency Check CC messages to protect against attacks and synchronize the counter. If a node receives a CC unicast message with the 'R' bit cleared, and it is a member or is about to join the associated DODAG, it must reply with a CC unicast message to the sender. This response must have the 'R' bit set, and it must have the same DC fields nonce, RPL InstanceID and DODAGID as the message it received. If a node receives a CC multicast message, it must reject the message without further processing.

Consistency check messages allow nodes to issue a response challenge to validate the current counter value of a node. Because the CC nuncio is generated by the challenger, an opponent replaying the messages is unlikely to generate a correct response. The counter of the response to the consistency check allows the challenger to validate the values he hears.

D. Counters.

In the simplest case, the counter value is an unsigned integer that the node increases once or many times on each secure RPL transmission. The counter MAY represents a timestamp which has the following properties:

- The time stamp must be at least six bytes in length.
- The timestamp must be at 1024 Hz (binary millisecond).
- The start time of the time stamp must be January 1, 1970, 12:00:00 AM UTC.
- If the counter represents a timestamp, the value of the counter must be a value calculated as follows. Let T be the timestamp, let S be the start time of the key used and E be the end time of the key. Both S and E are represented using the same three rules as the timestamp described above. If E> T <S, then the counter is invalid and a node must not generate a packet. Otherwise the value of the counter is equal to T-S.
- If the counter represents such a timestamp, a node may define the flag "T" of the security section of the RPL secure packets.
- If the Counter field does not have such a timestamp, then the node must not set the "T" flag.
- If a node does not have a local timestamp that complies with the above rules, it should ignore the "T" flag.
- If a node supports these timestamps and receives a message with the flag "T" , it can apply the time check on the received message. If a node receives a message without the 'T' flag, it should not apply this time check.

E. Transmission of outgoing packets.

The requirement for security protection and the security level applied to an outgoing RPL packet must be determined by the node security policy database. When secure RPL messages are to be transmitted, an RPL node must be configured in the security section (T, Sec, KIM, and LVL) in the outgoing RPL packet to describe the level of protection and the security settings that are applied. The security subfield bit of the RPL message code field must be configured to indicate the secure RPL message.

The counter value used in building the AES-128 CCM to secure the outgoing packet must be incremented of the last counter transmitted to the particular destination address. When a timestamp counter is applied (indicated with the 'T' flag set), the locally held timestamp counter must be included in the transmitted secure RPL message.

The cryptographic algorithm used to secure the outgoing packet must be specified in the security policy database of the node and must be specified in the value of the Sec field defined in the output field of the message. The security policy also specifies the algorithm and level of protection in the form of authentication, encryption and potential use of signatures that apply to the outgoing packet.

F. Receiving incoming packets.

The receiver uses the RPL security control fields to determine the necessary processing of the security of packages. For the message type when the sender is unknown or does not respect the local security policy, a node must reject the packets without further processing. It can raise a management alert, and must not send messages in response(as indicated by the 'T' flag). The message security level (LVL) indicates an encrypted RPL message, the node uses the key information identified through the KIM field, and the nonce CCM includes the message payload decryption processing. The CCM nonce will be derived from the message counter field and the other received and maintained locally the information. The content of the plaintext shall be obtained by invoking the inverse cryptographic operation mode specified by the Sec field of the received packet. The recipient shall use the nonce CCM and identify the key information to verify the integrity of the incoming packet.

Depending on the security policy specified, a node can apply a replay to protect a received RPL message. The replay test should be performed before the authentication of the received packet. The counter, obtained from the incoming packet, must be compared to the incoming counter maintained in the address of the original node provided.

G. *Verifying time stamp keys (timestamp).*

If the "T" flag of a message is set and a node has a local timestamp that follows the requirements of section 10.4, then a node can verify the message's time consistency. The node calculates the time of transmission of the message by adding the value of the counter to the start time of the associated key. If this transmission time exceeds the end time of the key, the node can reject the message without further delay. If the transmission time is too long in the past or in the future relatively to the local time of the receiver, the message can be rejected without further processing.

H. *Coverage of integrity and confidentiality.*

MACs (Message Authentication Code) and signatures are computed on all unsecured IPv6 packets. When calculating MACs and signatures, mutable IPv6 fields are considered to be filled with zeros in accordance with the rules in [RFC4302] [18] (IPsec standalone header). The MACs and signatures calculations are performed before any compression that can apply the reduction of the layers.
When a RPL ICMPv6 message is encrypted, encryption starts at the first byte after the security section and continues to the last byte of the packet. The IPv6 header, the ICMPv6 header, and the RPL message are not encrypted until the end of the security section because they are needed to decrypt the packet correctly. The additional authentication data begins with the start of the IPv6 header and ends with the last byte of the RPL.

İ. *Signatures.*

If the KIM indicates the use of signatures (a value of 3), then the node adds a signature to the payload of the packet data. The Security Level (LVL) field describes the length of this signature. The signature scheme in RPL for security mode 3 is an instantiation of the RSA algorithm (RSASSA-PSS) as defined in Section 8.1 of [RFC3447] [19]. As a public key, it uses the pair (n, e), where n is an RSA module of 2048 bits or 3072 bits and e = 2 ^ {16} +1. It uses CCM Mode [RFC3610] as an encryption system with M = 0 (as stream-encrypt). Note that [RFC3610] [20] refuses CCM mode with M = 0, RPL explicitly allows CCM mode with M = 0 when used in conjunction with a signature because the signature provides sufficient data authentication. The RSA signatures on this form provide sufficient protection for RPL networks. An implementation that supports RSA signature with 2048 bits or 3072 bits should support verification of both 2048-bit and 3072-bit RSA signatures. This allows for an upgrade path for an RPL deployment.

VII. Conclusion

This paper focused on the RPL protocol and the possible security mechanisms to ensure the confidentiality, integrity and authenticity of the data transmitted or received by this protocol. In addition, it was proposed to analyze two most notable attacks: Attack on the version number of the DODAG and attack on the inconsistency of the DAG, as well as its countermeasures while respecting the constraints of Low-power and Lossy networks. Technical safety is one of the first problems faced by manufacturers and industrials: Preventing malicious use of a device is essential to avoid disastrous human and economic consequences. This data can also be a source of information about a physical environment, and thus identify its weaknesses and shortcomings. The strong production of data forces us to rethink of the notion of privacy, and raises ethical questions about the storage and use of this data. Consequently, the concept of Big Data joins connected objects, which feed it consistently, through the collection of massive data on users.

References

[1] "Routing Over Low power and Lossy networks (roll) -.". Available: https://datatracker.ietf.org/wg/roll/charter/ .

[2] J. Martocci, W. Vermeylen, N. Riou, and P. D. Mil, "Building Automation Routing Requirements in Low Power and Lossy Networks.". Available: https://tools.ietf.org/html/rfc5867.

[3] A. Brandt and G. Porcu, "Home Automation Routing Requirements in Low Power and Lossy Networks." Available: https://tools.ietf.org/html/rfc5826.

[4] S. Dwars, T. Phinney, P. Thubert, and K. Pister, "Industrial Routing Requirements in Low Power and Lossy Networks." Available: https://tools.ietf.org/html/rfc5673.

[5] M. Dohler, D. Barthel, T. Watteyne, and T. Winter, "Urban WSNs Routing Requirements in Low Power and Lossy Networks." Available: https://tools.ietf.org/html/rfc5548.

[6] P. Levis and T. H. Clausen, "The Trickle Algorithm." Available: https://tools.ietf.org/html/rfc6206.

[7] "Blog Stéphane Bortzmeyer: RFC 6550: RPL: IPv6 Routing Protocol for Low power and Lossy Networks." Available: http://www.bortzmeyer.org/6550.html.

[8] "La présentation du mode Ad-Hoc." Available: http://www.pouf.org/documentation/securite/html/node27.html .

[9] "Les réseaux wifi maillés." Available: https://wapiti.telecom-lille.fr/commun/ens/peda/options/st/rio/pub/exposes/exposesrio2007/Houriez-Doumer/Proactifs.html .

[10] P. T. <pthubert@cisco.com>, "Objective Function Zero for the Routing Protocol for Low-Power and Lossy Networks (RPL)." Available: https://tools.ietf.org/html/rfc6552 .

[11] J. Vasseur, "Terms Used in Routing for Low-Power and Lossy Networks." Available: https://tools.ietf.org/html/rfc7102 .

[12] "A Service Discovery Framework in IPv6 over Low-power Wireless Personal Area Network (PDF Download Available)," ResearchGate. Available:https://www.researchgate.net/publication/304625682_A_Service_Discovery_Framework_in_IPv6_over_Lowpower_Wireless_Personal_Area_Network.

[13] J. W. H. <jhui@archrock.com>, "The Routing Protocol for Low-Power and Lossy Networks (RPL) Option for Carrying RPL Information in Data-Plane Datagrams." Available: https://tools.ietf.org/html/rfc6553.

[14] A. Mayzaud, A. Sehgal, R. Badonnel, and I. Chrisment, "Gestion de risques appliquée aux réseaux RPL," presented at the 9ème Conférence sur la Sécurité des Architectures Réseaux et des Systèmes d'Information, 2014.

[15] L. Dora, A. Dvir, L. Buttyan, and T. Holczer, "Version Number and Rank Authentication." Available: https://tools.ietf.org/html/draft-dvir-roll-security-authentication-01.

[16] "Routing Metrics Used for Path Calculation in Low-Power and Lossy Networks." Available: https://tools.ietf.org/html/rfc6551 .

[17] H. Perrey, M. Landsmann, O. Ugus, M. Wählisch, and T. C. Schmidt, "TRAIL: Topology Authentication in RPL," in *Proceedings of the 2016 International Conference on Embedded Wireless Systems and Networks*, USA, 2016, pp. 59–64.

[18] "RFC 4302 - IP Authentication Header." Available: https://tools.ietf.org/html/rfc4302 .

[19] Available: https://www.ietf.org/rfc/rfc3447.txt

[20] D. Whiting, N. Ferguson, and R. Housley, "Counter with CBC-MAC (CCM)." Available: https://tools.ietf.org/html/rfc3610.

[21] "pluws-ttar-16.pdf." Available: http://www.inf.fu-berlin.de/users/waehl/papers/pluws-ttar-16.pdf .

[22] "Format du message ICMPv6 - Livre IPv6." Available: http://livre.g6.asso.fr/index.php/Format_du_message_ICMPv6 .

The Enhancement of Canny Edge Detection Algorithm Using Prewitt, Robert and Sobel Kernels

S. İLKİN[1], F.S. HANGİŞİ[1], M. TAFRALI[1] and S. ŞAHİN[1]

[1] Kocaeli University, Kocaeli/Turkey, {sumeyya.ilkin, selin.hangisi, merve.tafrali, suhap.sahin}@kocaeli.edu.tr

***Abstract* - Different methods are used to find the edges on the images. Canny edge detection algorithm is one of the most successful methods. Although it yields successful results, the processing load is very complicated. In this study, to enhance the Canny edge detection algorithm, enhancement was performed on the Canny edge detection algorithm using kernels which used in Sobel, Robert and Prewitt methods. The enhanced Canny edge detection algorithm was compared using Canny edge detection algorithm which using 3x3 gauss kernel and Canny edge detection algorithm which using a 5x5 gauss kernel. Study was tested using a special dataset. The results obtained after the test phase were compared using Mean Square Error (MSE), Peak Signal-to-Noise Ratio (PSNR), Correlation Index (CI) and Time elapsed (TE) metrics. As a result of the comparison, it was determined that enhanced Canny edge detection algorithm which using the Sobel kernel gives the most effective result.**

***Keywords* - Image processing, Canny edge detection algorithm, Sobel operator, Robert edge detection method, Prewitt edge detection method.**

I. INTRODUCTION

ONE of the most important aspects of image processing is the algorithms used for edge detection. With these algorithms it is possible to find the edges in any image. An edge in an image is an important factor affecting the physical changes of the image. Edge detection is the process of identifying and locating sharp discontinuities which characterize boundaries of objects in an image. Edge detection is one of the most essential steps in image processing for analyzing the objects on image [1].

Edge detection is mostly used for the object detection and feature extraction. But it is not always possible to obtain ideal edges from images [1, 2]. Edge detection operator needs to be chosen to be responsive to gradual change [3]. The edge is the boundary separating the two regions with relatively large gray-tone value differences between them. Therefore, many edge detection methods are based on the calculation of local derivatives. The most commonly used edge detection algorithms are Prewitt, Robert, Sobel, Canny, Marr and Hilldreth [4]. In the literature shows that, these algorithms have been used on gray-level images for edge detection purposes [4-8].

The Canny algorithm is one of the most successful edge detection methods [9]. Although it yields successful results, the processing load is very complicated. In this study, for improve the performance of Canny edge detection algorithm, an enhancement on Canny edge detection algorithm was made. This enhancement on the Canny edge detection algorithm was performed using kernels which used in Sobel, Robert and Prewitt methods.

The rest of this paper is organized as; Section 2 presents the methods used, this is followed by experiments and results which are obtained from metrics in Section 3 and finally Section 4 concludes the paper.

II. METHODS USED

Canny edge detection algorithm is a multi-stage edge detection algorithm designed to detect sharp edges in the image. Developed by John F. Canny in 1986 [10]. Although more complex than other edge detection algorithms, Canny is one of the best edge detection algorithms. Canny's algorithm is based on the mathematical expression of the three main goals:

- Low error rate; the perceived edges are as close to the actual edges as possible.
- The edge points can be well defined; the distance between the specified points and the actual edge center is the minimum.
- Single edge point answer; the sensor has only one point for each right edge, the smallest local maximum around the right edge.

It is a very effective method for detecting the edges on the image. A softening filter is applied before the image is derived. With Canny edge detection algorithm, it generates edges with a single pixel thickness and merges broken lines. The steps of the Canny algorithm are shown below;

- Noise in the image is reduced by taking convolution with the Gaussian kernel. The Mean or Median filter can also be used outside the Gaussian filter.
- Gradient operator is applied. In this way, the size and direction of the gradient are calculated.
- The edges are thinned using Non Maxima compression.
- Binary thresholding is applied so that undesired refinement is performed.
- After the strong-weak separation, the impression is applied and the final image is given with the main edges [11].

In the following subsections, the steps of the enhanced Canny algorithm are described in detail.

A. Noise Reduction

Noise reduction must be done for edge detection in the image. In this study, for reducing the noises and sharpening the edges the Mean filtering method and the Gauss filtering method was used.

The mean filter is a low pass filter. The low-pass filter is a filter that allows processing of signals over a certain frequency. The Gaussian filter is used to blur/soften the images and reduce noise on the image [11].

The Gaussian filter is mainly used in digital image processing for image smoothing and noise reduction, which involves averaging pixel values in an image [12]. The image must be smoothed for edge detection. In (1) shows the Gaussian function.

$$G(x,y) = \frac{1}{2\pi\sigma^2} e^{-\frac{x^2+y^2}{2\sigma^2}} \quad (1)$$

The Gaussian function is an operator used for smoothing. Here, x, y give the standard deviation of the image coordinate information, σ, associated with the probability distribution.

B. Finding the Gradient Operator

In this study, we used three different kernel operators to determine the gradient used in the Canny algorithm's steps.

After the Gaussian filter step of the Canny edge detection algorithm, we applied the Sobel, Robert and Prewitt kernels on the gradient operator step separately.

1) Sobel Operator

Edges occur where there is a discontinuity in the intensity function in the image. Gradient-based detection methods are take the first-order derivative of the intensity value across the image [13]. When a numerical image is evaluated as a function, it is based on the idea that the gradient value on a point is formed as vector sums of gradient values that can be obtained in four central directions in 3 × 3 neighborhood. Vector sums of these gradient values; provides an average value over the gradient measurements. For the 3x3 neighborhood, the gradient value of the center point is found as the vector sums of the orthogonal vector pairs.

There are two convolution kernels in the sobel operator. These enable the determination of locations with sudden light intensity variations in the image. In (2) shows these kernels.

$$\begin{bmatrix} 1 & 2 & 1 \\ 0 & 0 & 0 \\ -1 & -2 & -1 \end{bmatrix} \quad \begin{bmatrix} 1 & 0 & -1 \\ 2 & 0 & -2 \\ 1 & 0 & -1 \end{bmatrix} \quad \begin{bmatrix} 2 & 1 & 0 \\ 1 & 0 & -1 \\ 0 & -1 & -1 \end{bmatrix} \quad (2)$$

Fig. 1. shows the flow chart of the Sobel enhancement of Canny edge detection algorithm.

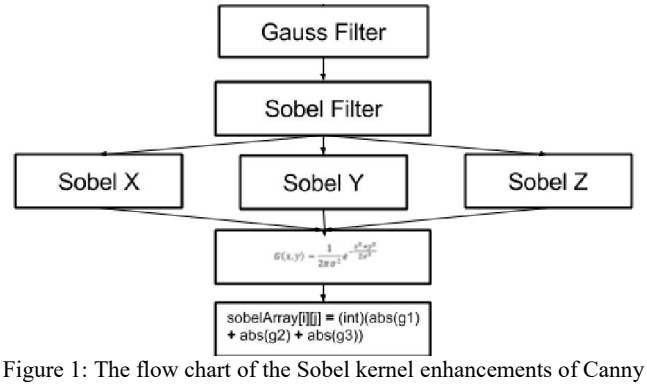


Figure 1: The flow chart of the Sobel kernel enhancements of Canny edge detection algorithm.

2) Prewitt Operator

It provides vertical and horizontal sharpness like a sobel operator. Prewitt filter is a fast method for edge detection. The difference from the Sobel filter is the spectral response. It is only suitable for noisy images with good contrast [14]. In (3) shows Prewitt kernels.

$$\begin{bmatrix} -1 & -1 & -1 \\ 0 & 0 & 0 \\ 1 & 1 & 1 \end{bmatrix} \quad \begin{bmatrix} -1 & 0 & 1 \\ -1 & 0 & 1 \\ -1 & 0 & 1 \end{bmatrix}$$
$$\begin{bmatrix} -1 & -1 & 0 \\ -1 & 0 & 1 \\ 0 & 1 & 1 \end{bmatrix} \quad \begin{bmatrix} 1 & 1 & 0 \\ 1 & 0 & -1 \\ 0 & -1 & -1 \end{bmatrix} \quad (3)$$

Fig. 2. shows the flow chart of the Prewitt enhancement of Canny edge detection algorithm.

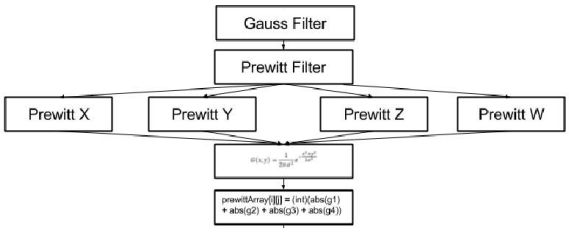


Figure 2: The flow chart of the Prewitt kernel enhancements of Canny edge detection algorithm.

3) Robert Operator

The oldest operator used for the image processing. With this operator, only the edges are obtained either horizontally or vertically. Because it has a fast and simple application, it is highly preferred in real time applications.

The Robert operator performs a 2-dimensional spatial gradient measurement, which can be simply and quickly calculated on an image. The operator consists of a pair of 2X2 convolution kernels as shown in (4). One of the kernels is simply rotated 90 ° from the other. This operator is very similar to the Sobel operator [14].

$$\begin{bmatrix} 2 & 1 & 0 \\ 1 & 0 & -1 \\ 0 & -1 & 2 \end{bmatrix} \quad \begin{bmatrix} 0 & -1 & -2 \\ 1 & 0 & -1 \\ 2 & 2 & 0 \end{bmatrix} \quad (4)$$

In Fig. 3. shows the flow chart of the Robert enhancements of Canny edge detection algorithm.

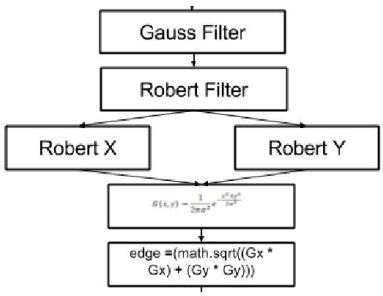


Figure 3: The flow chart of the Robert kernel enhancements of Canny edge detection algorithm.

C. Edge Thinning

The edges of obtained images after using operators are thick. For thinning the edges, the method of suppressing non-maximum pixel values is used.

In this method, the image is scanned in the direction of the gradient of the image and is set to zero if the pixel is not the local maximum. In (5) shows that calculation. In (6) calculates the size of the gradient operator, and in (7) calculates the direction of the gradient operator.

$$\frac{\partial^2}{\partial n^2} G * g = 0 \quad (5)$$

$$G = \sqrt{Gx^2 + Gy^2} \quad (6)$$

$$\theta = \arctan\left(\frac{Gy}{Gx}\right) \quad (7)$$

After the gradient direction is calculated for each pixel, it is desired that two additional neighboring pixels in the direction of the obtained angle value are selected, so that the median pixel has a high value therefrom. If this condition is not met, the median pixel is eliminated from the edge image by zeroing. In this way, only the pixels which have the maximum gradient values are left perpendicular to the edges [10].

D. Binary Thresholding and Edge Separation

In the last step of the Canny edge detection algorithm is the edge separation. Two threshold values, high and low, are used to test the pixel continuity in the edge image. The following steps are taken for the continuity test: Two threshold levels, high and low, are determined and for each point:

- If the maximum edge gradient (pixel value) perpendicular to the edge is higher than the high threshold, it is left as the edge.
- If the peak maximum gradient amplitude from the edge is lower than the low threshold, zero is set.
- If the pixel value is between the high and low thresholds, then this pixel is allowed to remain an edge if there is an adjacent neighbor that exceeds the high threshold.
- If there is no neighbor that crosses the threshold, it is eliminated from the edge image by pulling zero.

After these steps image edges are obtained.

III. Experimental Results

In this study, the developed improvements have been tested on the dataset to determine the Canny enhancement which gives the best result. The dataset which we used consists of 50 different face images.

The proposed enhancements in this study were developed by using Python language. And testing process was performed on Python environment. In the test phase, the enhanced Canny edge detection algorithms were compared using Canny edge detection algorithm which using 3x3 gauss kernel and which using a 5x5 gauss kernel from the OpenCV image library. In Fig. 4 shows the test results of each enhancement separately.

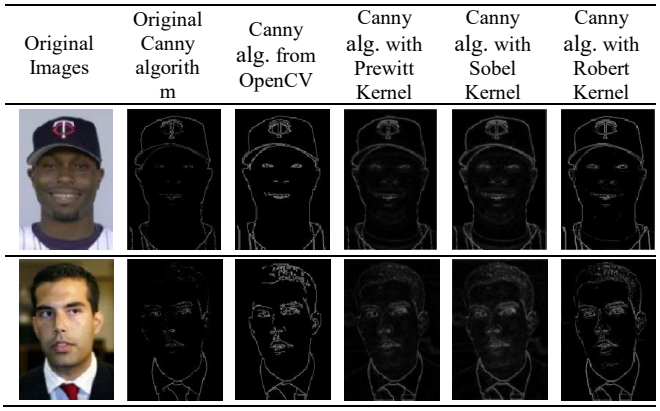


Figure 4: Some examples of test results from face dataset.

After those comparisons, we analyzed the test results by using MSE, PSNR, CI and TE metrics. In Table 1 show the average results of the metrics which we obtained from 50 images.

Table 1: Average results of the PSNR, MSE, CI and TE metrics.

	PSNR	MSE	CI	TE
Original Canny algorithm	5,7596	18261,780	0,03556	2,0669
Canny algorithm from OpenCV	5,6247	18626,372	0,04018	**0,0041**
Canny alg. with Sobel Kernel	**6,1750**	**16597,172**	0,05254	3,2337
Canny alg. with Prewitt Kernel	6,1387	16781,212	**0,05433**	4,8283
Canny alg. with Robert Kernel	5,8596	17791,860	0,05274	2,5320

And Fig. 5 (a)-(d) shows the graphical display of enhanced Canny edge detection algorithms' metrics results.

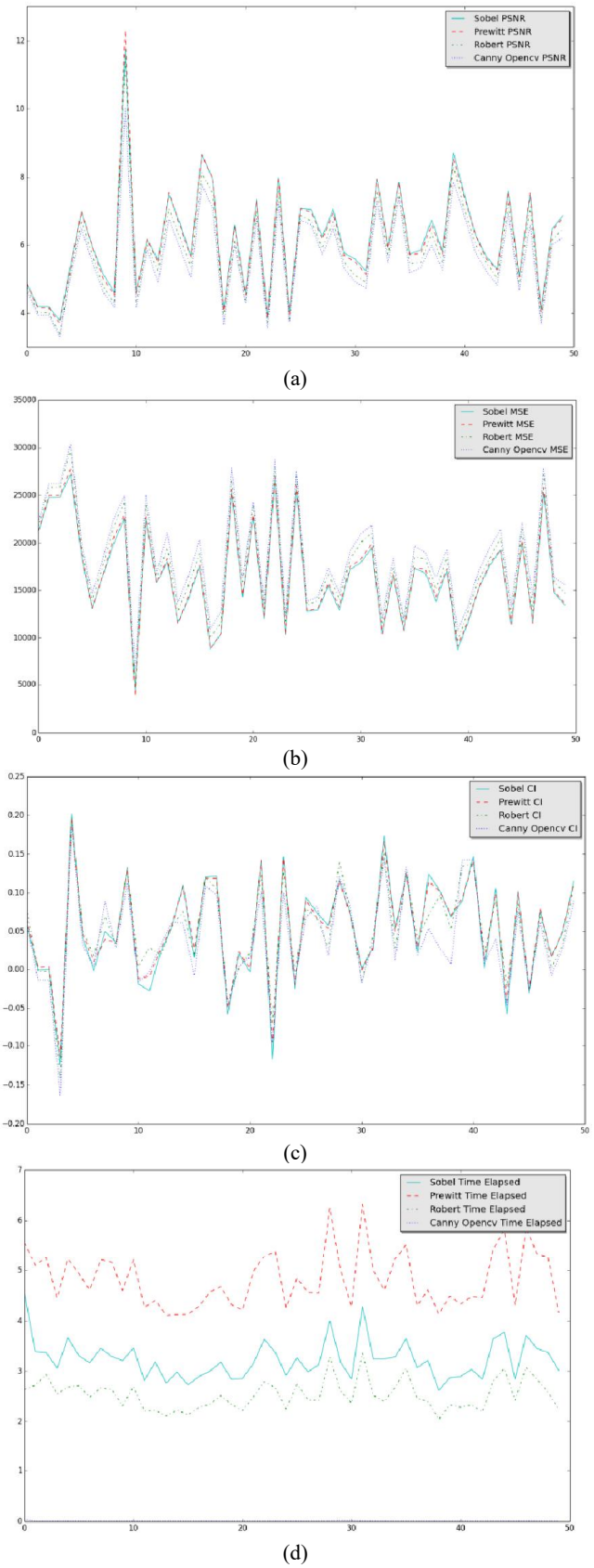


Figure 5: a) PSNR, b) MSE, c) CI, and d) TE metric graphics of the enhancements of the Canny edge detection algorithm.

As shown in Table 1, the performance of the enhancements of the Canny's algoritm varies depending on the resolution and sharpness of the images used. The Sobel kernel enhancement of the Canny's algorithm gives the most successful results in terms of the PSNR and MSE metrics used. The other hand if we consider the duration time of these enhancements, it is observed that the Canny's algorithm which uses 5x5 gauss kernel from OpenCV image library gives the most successful results. But when we consider the correctness of the edges which are found, this enhancement is failed according to the other enhancements. And in the correlational base it is observed that the Prewitt kernel enhancement of the Canny's algorithm gives the most successful result in terms of the CI metric used.

It is observed that the Sobel kernel enhancement of the Canny's algorithm gives very successful results by looking at the Table 1 in general.

IV. Conclusion

In this study, the enhancements were made on Canny edge detection algorithm's gradient operator step for improve the Canny's edge detection algorithm performance. For this, the Prewitt, Sobel and Robert operators' kernels were chosen to use. The enhanced Canny edge detection algorithm was compared using Canny edge detection algorithm which using 3x3 gauss kernel and which using a 5x5 gauss kernel from OpenCV image library. Study was tested using same face dataset which consisting of 50 different images for each enhancement. It was determined that enhanced Canny edge detection algorithm which using the Sobel kernel on the gradient operation step gives the most effective result according to the metric results.

References

[1] T. Sahoo, and S. Pine, "Design and simulation of various edge detection techniques using Matlab Simulink," in *2016 IEEE International Conference on Signal Processing, Communication, Power and Embedded System (SCOPES)*, pp. 1224–1228.

[2] S.B. Shabari, S. Surendra, and M. Siddappa, "Development and implementation of graphical user interface for image preprocessing using Matlab," *International Journal of Computer Applications,* vol. 161(9), pp. 37—41, March 2017.

[3] D. Rao, and R. Sapna, "A review on edge detection technique in image processing techniques," *IJSRSET*, vol. 2(6), pp. 345—349, 2016.

[4] G. Aravindh, and C.S. Manikandababu, "Algorithm and implementation of distributed canny edge detector on fpga," *ARPN Journal of Engineering and Applied Sciences,* vol. 10(7), pp. 3208—3216, April 2015.

[5] M. Basu, "Gaussian-based edge-detection methods – a survey," *IEEE Transactions on Systems, Man, Cybernetics, Part C: Applications and Reviews*, vol. 32(3), pp. 252—260, August 2002.

[6] G.W. Wei, and Y.Q. Jia, "Synchronization–based image edge detection," *Europhysics Letters*, vol. 59(6), pp. 814—819, 2002.

[7] G.N. Chaple, R.D. Daruwala, and M.S. Gofane, "Comparisions of Robert, Prewitt, Sobel operator based edge detection methods for real time uses on FPGA," in *2015 IEEE International Conference on Technologies for Sustainable Development (ICTSD)*, pp. 1—4.

[8] K.L. Vijaykumar, and R. Savitri, "Analysis of edge detection algorithms for content extraction from images," *IJSRSET*, vol. (2)2, pp. 628—631, 2016.

[9] N. Mahmood, A. Shah, A. Waqas, A. Abubakar, S. Kamran, and S.B. Zaidi, "Image segmentation methods and edge detection: an application

to knee joint articular cartilage edge detection," *Journal of Theoretical and Applied Information Technology*, vol. 71(1), pp. 87–96, 2015.
[10] J. Canny, "A computational approach to edge detection," *IEEE Transactions on Pattern Analysis and Machine Intelligence*, vol. PAMI-8(6), pp. 679–698, 1986.
[11] R.C. Gonzales, and R.E. Woods, *Digital Image Processing*, 3rd ed., New Jersey: Prentice Hall, 2008.
[12] D.M. Panicker, B. Radhakrishnan, T.G. Nidhin, and L.P. Suresh, "Traffic density analysis on highway using Marr-Hildreth operator," in *2016 IEEE International Conference on Emerging Technological Trends (ICETT)*, pp. 1–7.
[13] D. Tian, J. Wu, and Y. Yang, "A fractional-order edge detection operator for medical image structure feature extraction," in *the 26th IEEE Control and Decision Conference (2014 CCDC)*, pp. 5173–5176.
[14] M. Juneja, and S.S. Parvinder, "Performance evaluation of edge detection techniques for images in spatial domain," *International Journal of Computer Theory and Engineering,* vol. 1(5), pp. 614–621, 2009.

Wound Edge Detection Operation Using Enhanced Canny Edge Detection Algorithm on Dermatological Images

S. İLKİN[1], M. TAFRALI[1], F.S. HANGİŞİ[1] and S. ŞAHİN[1]

[1] Kocaeli University, Kocaeli/Turkey, {sumeyya.ilkin, merve.tafrali, selin.hangisi, suhap.sahin}@kocaeli.edu.tr

***Abstract* - Edge detection is the process of finding sharper separations or sharp transitions in the image. Various methods are used for edge detection on images. Canny, Sobel, Prewitt, Rosenfeld, Marr-Hildreth and Laplacian are some of these methods. The Canny algorithm is one of the most successful edge detection methods. In this study, the Canny edge detection algorithm which enhanced by using the Sobel kernel was used to determine the edges of the melanomas on the dermatological images. During the test phase, a special dermatological image dataset consisting of 70 images was used. The test results were analyzed using Mean Square Error (MSE), Peak Signal-to-Noise Ratio (PSNR), Correlation Index (CI) and Time Elapsed (TE) metrics. As a result of the analysis performed, it was found that the enhancement of Canny edge detection algorithm gave more effective results in melanoma edge detection operations on dermatological images.**

***Keywords* - Medical image processing, Canny edge detection, Dermatologic images, Wound detection, Melanoma detection.**

I. INTRODUCTION

BASAL-CELL cancer, squamous-cell cancer and melanoma are the three main types of skin cancer. The first two of them are known as non-melanoma skin cancer. Generally, non-melanoma skin cancer is one of the treatable skin cancer types. But Melanoma is the most aggressive skin cancer type [1]. Melanoma represents one of most malignant tumors associated with melanocytes in pigmented cells of the skin. And it is a dermatological disease which has the higher rate of death among the skin cancer types. According to the Skin Cancer Foundation, during the past decades the incidence of skin cancer has increasing rapidly. If melanoma detection is at earlier stages, it can be curable successfully. The early detection of melanoma can achieve cure ratios of over 95% [2]. And this success rate can decrease the death number of skin cancer.

Melanoma is commonly shown itself with some changes on the skin such as in color, size, contour, configuration, or new pigmented lesions. Thus, diagnosis of melanoma is hard even for experienced dermatologists. According to the record it was found that 60% claim lodged against Medical Protection Society for faulty diagnosis by doctors [3]. Therefore computer assisted diagnostic tool for melanoma detection is becoming necessary [4].

Since the diagnosis of melanoma can be made visually, the algorithms and studies developed in the digital environment have great importance in the early diagnosis stage of the disease. Developed algorithms and applications provide convenience for doctors and patients [5]. Due to this, applications and algorithms have been developed.

Sundar et al. [6] propose an algorithm for early detection of melanoma using Multiclass support vector machine. Zeljkovic et al. [4] offer the potential cutaneous melanoma automated detection algorithm equally successfully applicable to various skin colors. Choudhury et al. [7] propose a multilayer decomposition aided method based on textural and color feature for detection and classification of skin cancer images. Kumar et al. [8] propose an efficient image segmentation algorithm using radial search technique to extract true border of dermoscopy skin images containing wounds.

In this study we propose an algorithm which is an enhancement of Canny edge detection algorithm for edge detection of the melanomas on the dermatological images.

The rest of this paper is organized as, Section 2 presents the proposed algorithm for edge detection of wound on images, this is followed by experimental results which are obtained from metrics in Section 3 and finally Section 4 concludes the paper.

II. THE PROPOSED ALGORITHM

In this paper, we aim to find the edges of the melanoma area on the dermatological images. Edge detection is the process of finding sharper separations or sharp transitions in the image. Various methods are used for edge detection on images. Canny edge detection algorithm is one of the edge detection algorithms. It is a very effective method for detecting the wound edges on the dermatological images [3]. However Canny's algorithm's processing load is very complicated. For this reason we chose to use an enhancement of Canny's algoritm. This enhancement was made on the gradient step of the algorithm. We used Sobel kernel for finding the gradient value. Fig. 1 gives the algorithm flowchart.

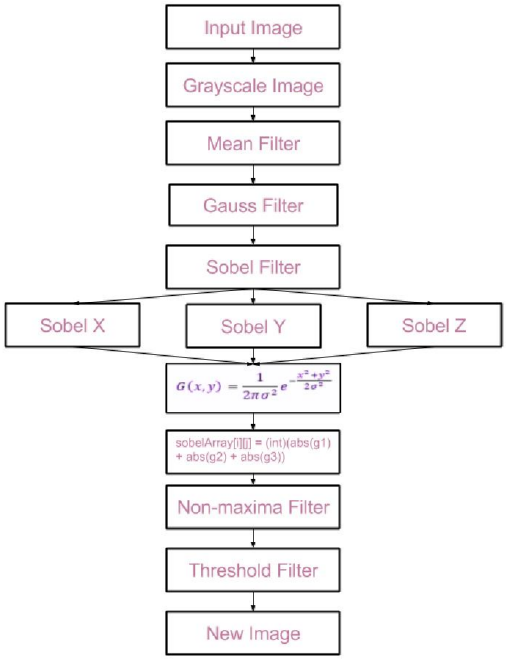


Figure 1: The flow chart of the Sobel kernel enhancements of Canny edge detection algorithm.

The first step of the algorithm, for reducing the noises and sharpening the edges the Mean filtering method and the Gauss filtering method was used. The image must be smoothed for edge detection. In (1) gives the Gauss filtering function.

$$G(x,y) = \frac{1}{2\pi\sigma^2} e^{-\frac{x^2+y^2}{2\sigma^2}} \quad (1)$$

Here, x, y give the standard deviation of the image coordinate information, σ is the probability distribution. After the Gaussian filter step, we applied the Sobel kernels on the gradient operator step for finding the gradient value. The gradient value on a point is formed as vector sums of gradient values that can be obtained in four central directions in 3 × 3 neighborhood. There are two convolution kernels in the sobel operator. Sobel kernel in (2) is applied to each pixel in the image in both direction.

$$\begin{bmatrix} 1 & 2 & 1 \\ 0 & 0 & 0 \\ -1 & -2 & -1 \end{bmatrix} \quad \begin{bmatrix} 1 & 0 & -1 \\ 2 & 0 & -2 \\ 1 & 0 & -1 \end{bmatrix} \quad \begin{bmatrix} 2 & 1 & 0 \\ 1 & 0 & -1 \\ 0 & -1 & -1 \end{bmatrix} \quad (2)$$

Strength of the edge is determined by gradient magnitude while direction of the gradient is used to determine for each pixel the direction with the largest change in intensity [9]. The image is scanned in the direction of the gradient of the image and is set to zero if the pixel is not the local maximum. In (3) calculates the size of the gradient operator, and (4) calculates the direction of the gradient operator.

$$G = \sqrt{Gx^2 + Gy^2} \quad (3)$$

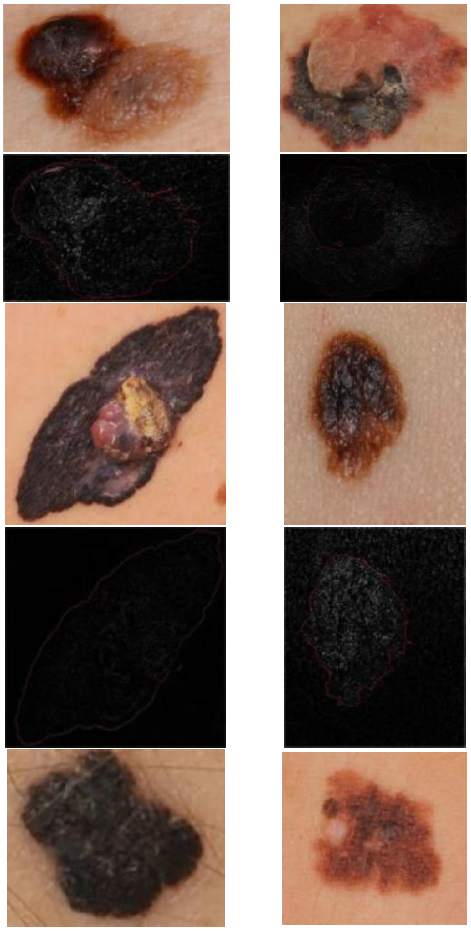
$$\theta = \arctan\left(\frac{Gy}{Gx}\right) \quad (4)$$

After the gradient direction is calculated for each pixel, it is desired that two additional neighboring pixels in the direction of the obtained angle value are selected. In this way, only the pixels which have the maximum gradient values are left perpendicular to the edges. When this step is finished the next step which is the reduction in edge numbers is performed using double threshold to separate strong, weak and suppressed edges. Weak edges are finally preserved or suppressed [9]. After these steps melanoma edges are obtained and have been drawn as a new image.

III. Experimental Results

In this study, the application developed to reach the early and accurate diagnosis of the disease by using the extraction of the diseased region was tested on 70 pictures. The dataset consists of 70 melanoma images from the digital image archive of the Department of Dermatology of the University of Groningen University Medical Center (UMCG) used for the development and testing of the MED-NODE system for skin cancer detection from macroscopic images.

The proposed algorithm was developed by using Python language. And testing process was performed on Python environment. Fig. 2 shows some of the test results which consist of different types of melanomas.



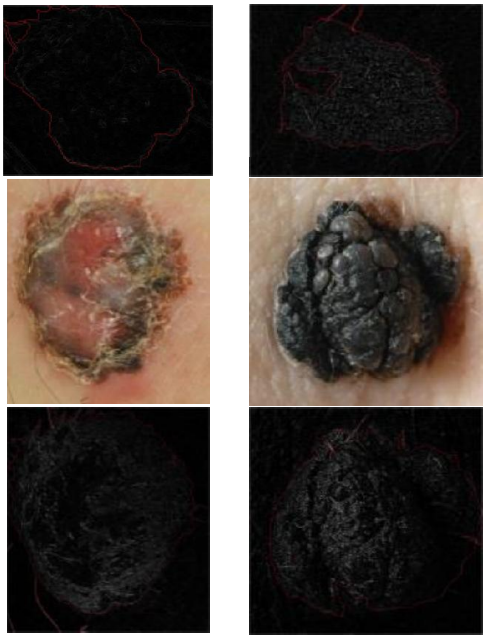


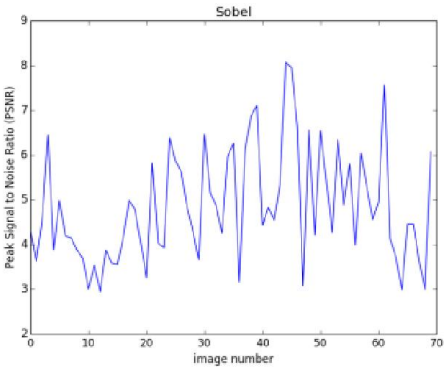
Figure 2: Examples of the test results which consist of different types of melanomas.

We analyzed the test results by using MSE, PSNR, CI and TE metrics. In Table 1 gives the average results of the metrics which we obtained from 70 melanoma images.

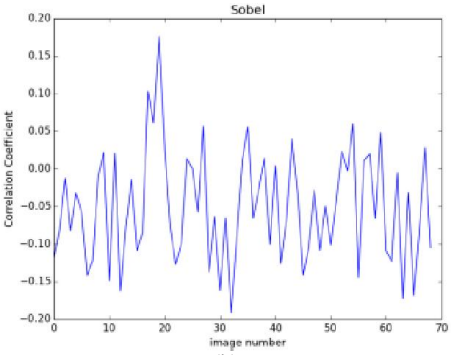
Table 1: Average results of the PSNR, MSE, CI and TE metrics.

Method / Metrics	Canny's enhancement with Sobel Kernel
PSNR	4,856520896
MSE	22118,44396
CI	-0,05057784216
TE	31,09135676

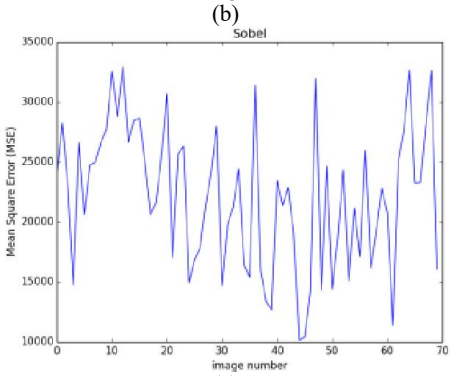
And Fig. 3 (a)-(d) gives the graphical display of Canny's enhanced algorithm metrics results.



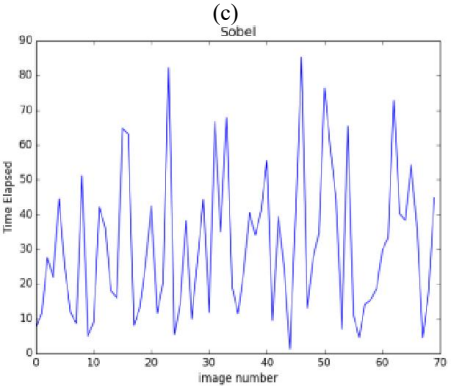
(a)



(b)



(c)



(d)

Figure 3: a) PSNR, b) CI, c) MSE, and d) TE metric graphics of the enhanced Canny edge detection algorithm with Sobel kernel.

As shown in Table 1, the performance of the enhancements of the Canny's algorithm varies depending on the resolution, sharpness and the melanoma's type of the images used. It is observed that the Sobel kernel enhancement of the Canny's algorithm gives very successful results for the melanoma area detection on the dermatological images.

IV. Conclusion

In this study, an enhanced Canny edge detection algorithm was used for melanoma area detection on dermatological images. This enhancement was made by using Sobel kernels in the gradient finding step of the Canny edge detection algorithm for improve the Canny's edge detection algorithm performance. Study was tested using a special dataset which consisting of 70 images with different types of melanoma on the skin. The test results were analyzed using MSE, PSNR, CI and TE metrics. In conclusion, the proposed enhanced Canny edge detection algorithm which using the Sobel kernel on the

gradient operation step gives effective results in melanoma edge detection operations on dermatological images. Also this study will shed light on the future studies for the estimation of the skin cancer from dermatological images.

REFERENCES

[1] F. Thompson, M.K. Jeyakumar, "Review of segmentation methods on malignant melanoma," in *IEEE 2016 International Conference on Circuit, Power and Computing Technologies (ICCPCT)*, pp. 1—6.

[2] J. Cowell, V.J.M. Cunha, "Identification of cancerous lesions in unconstrained images," in *IEEE 2009 Second International Conference in Visualisation VIZ'09*, pp. 177—181.

[3] D. Singh, D. Gautam, M. Ahmed, "Detection techniques for melanoma diagnosis: A performance evaluation," in *IEEE 2014 International Conference on Signal Propagation and Computer Technology (ICSPCT)*, pp. 567—572.

[4] V. Zeljkovic, C. Druzgalski, S. Bojic-Minic, C. Tameze, P. Mayorga, "Supplemental melanoma diagnosis for darker skin complexion gradients," in *IEEE 2015 Health Care Exchanges (PAHCE)*, pp. 1—8.

[5] H. Ozkan, R. Gurleyen, E. Usta, R.K. Kumrular, "Automatic skin lesion segmentation," in *IEEE 2017 Electric Electronics, Computer Science, Biomedical Engineerings' Meeting (EBBT)*, pp. 1—3.

[6] R.S. Sundar, M. Vadivel, "Performance analysis of melanoma early detection using skin lession classification system," in *IEEE 2016 International Conference on Circuit, Power and Computing Technologies (ICCPCT)*, pp. 1—5.

[7] D. Choudhury, A. Naug, S. Ghosh, "Texture and color feature based WLS framework aided skin cancer classification using MSVM and ELM," in *IEEE 2015 Annual India Conference (INDICON),* pp. 1—6.

[8] C.V. Kumar, V. Malathy, "Image processing based wound assessment system for patients with diabetes using six classification algorithms," in *IEEE 2016 International Conference on Electrical, Electronics, and Optimization Techniques (ICEEOT)*, pp. 744—747.

[9] M. Nikolic, E. Tuba, M. Tuba, "Edge detection in medical ultrasound images using adjusted Canny edge detection algorithm," in *IEEE 2016 24th Telecommunications Forum (TELFOR)*, pp. 1—4.

An Evaluation Method Proposal for NLP-based Automatic Requirement to Code Transformation Systems

Fatma Bozyiğit[1], Özlem Aktaş[2] and Deniz Kılınç[3]
[1]Graduate School of Natural and Applied Sciences, Dokuz Eylul University, Izmir/Turkey
[2]Computer Engineering Department, Dokuz Eylul University, Izmir/Turkey
[3]Software Engineering Department, Manisa Celal Bayar University, Manisa/Turkey

***Abstract*— Software requirements include user needs and descriptions of the necessary modules for the planned system. Therefore, analysis of the requirements provides information for the software design, and facilities coding phase. Recently, it is seen that studies automatically generating source code by analyzing requirements in Object Oriented (OO) paradigm have commonly been used in software engineering area. It is observed that these studies perform evaluation process with commonly used measures such as precision, recall, and F-measure. These measures consider that certain evaluation criteria (classes, attributes, and operations and so on) have the same priority. However, this approach may lead to misevaluation, because the priorities of the criteria can be relative according to opinions of experts who evaluate the system. Thus, we present a novel evaluation approach for the systems automatically generating OO code in this paper. Our method calculates weights of the evaluation criteria by using Analytical Hierarchy Process (AHP), after specific criteria affecting the decision problem are determined. As a result of the study, it is observed that the evaluation method with weighting the criteria conducts more accurate and realistic results on the automatic OO source code generation works.**

Keywords - software requirements; Object Oriented (OO) design; source code transformation; validation; Multi Criteria Decision Making (MCDM); Analytical Hierarchy Process (AHP)

I. INTRODUCTION

The requirement document that includes customer needs has significant effect in the success of software projects. It includes keywords related to the planned system, and it plays an active role in the smooth progress of the software projects [1]. Therefore, the information in the requirement documents created at the initial stage of the Software Development Life Cycle (SDLC) is used to the end of implementation phase.

The analysis of the requirement document provides information about the general framework of planned systems, and it facilities coding phase. For instance, the requirement document of a software designed in Object Oriented (OO) paradigm contains important keywords such as the classes, attributes, methods and relationships to be included in the model revealed.

With recent development in the technology, studies implementing automatic transformation from software requirements into OO-based source code become widespread. The common aim of automatic transformation studies is creating a model to reduce workload of a software development and expedite the preparation phase of a software [2]. When these studies are examined, it is seen that commonly used measurements such as precision, recall and F-measure are used for the evaluation process. By using these measurements, it is demonstrated whether a produced model is a reasonable representation of the actual system [3]. These measures consider evaluation factors (OO design elements) as if they have the same priority. However, it is necessary to consider that the specified criteria for the evaluation of source codes have different priorities. The priorities of these criteria vary depending on the views of decision makers who evaluate the system.

In this paper, we propose Analytical Hierarchy Process (AHP) [4] based validation of the studies, which utilize automatic OO-based source code transformation from textual requirements. According to this, OO-based source code documents are evaluated by considering weights of the criteria (classes, attributes, methods, relationship type, etc.) which can be varied depending on decision makers. The weights of evaluation criteria are determined by using AHP method, which is a well-known Multi Criteria Decision Making (MCDM) tool and widely used in various decision-making problems. The proposed approach is evaluated on a particular study, which is presented by Bozyigit et al. [5]. As a result, it has been observed that the evaluation by using AHP gives more realistic results than the accuracy rate calculated with precision, recall and F-measure in the study of Bozyigit et al. [5].

Outline: The remainder of the paper is organized as follows: Section II gives information about previous works that implement automatic transformation process from textual requirements into source code. Section III presents an existing approach automatically generating source code. Sections IV presents the proposed model for evaluation and validation process. Finally, Section V concludes the paper.

II. REVIEWED WORKS

It is observed that there are a few studies generating OO-based source code from textual requirement document in the literature. It is realized that all of the studies discussed and analysed in this paper benefit from the commonly used parameters such as precision, recall and F-measure in evaluation section. None of them use from any statistical

method and expert opinion to validate their study.

Bajwa et al. propose a study that implement automatic OO-based code generation in Java and VB.Net from the English requirement documents [6]. They used a simple matrix representing accuracy rate of generated models. Overall accuracy is calculated by average of total accuracy of all categories (class, attribute, method and relationship). It is indicated that accuracy rate of the study is between 80% and 85%.

Tripathy et al. present a study that transform incomplete and ambiguous requirement documents into XML source code [7]. They use classical performance metrics such as precision, recall, F-measure to evaluate their approach. The relevance of the classes identified in the source code is indicated by precision, the ability of the automation to generate all classes is indicated by the recall percentage. They calculate over-specification to determine number of unnecessary but correctly identified classes.

Shinde et al. propose a study, which implements OO-based code generation in Java from user modelling information by using strong semantic support [8]. To test the performance of the extracted models and generated source code, five parameters are used such that; number of objects and classes, number of attributes, number of methods, number of associations and number of actors. A simple matrix of generated models is created and so validation process is completed on this matrix.

Bozyigit et al. generate source codes in Java and C# by utilizing OO analysis on software requirement documents in their study, which is called as AutoClass [5]. ATM model [9] is used as dataset in evaluation of study. Validation of the proposed system is done with evaluation measures including recall, precision and F-Measure. It is calculated that accuracy of the system is 93 %.

III. General Methodology In Reviewed Approaches

It is observed that similar approaches are utilized in the studies, which transform textual requirements into OO-based source codes. Figure 1 shows the general framework of these studies. First, the textual requirements are formatted by pre-processing step within certain constraints. Then, the source code generation is completed by compositing the model elements revealed by the transformation process. Finally, evaluation of proposed model are performed.

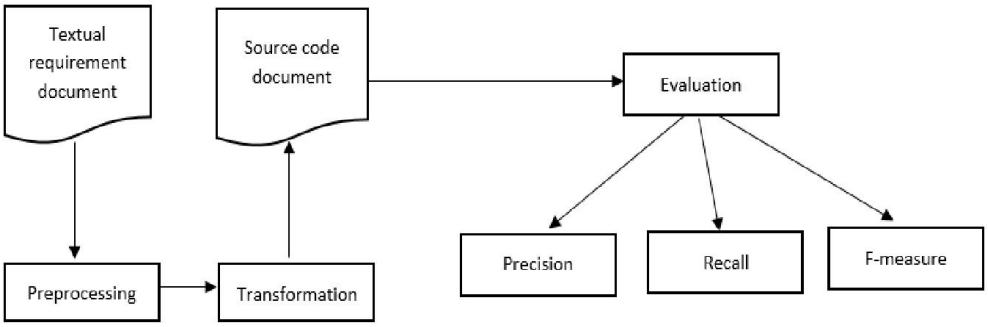


Figure 1: General architecture of reviewed approaches

A. General Transformation Method

Requirement analysis enables to determine the purpose, functionalities, actors, events, and interfaces of proposed software system. Therefore, requirement analysis forms the basis of code transformation studies. Natural Language Processing (NLP) methods can be used in the initial step of requirement analysis part of code transformation studies. Figure 2 shows the general architecture of NLP methods used in code transformation models. The first step in NLP frame is tokenization, which separates textual documents into tokens. Then, word groups obtained after tokenization process are stemmed. Finally, the NLP step is completed by applying the Part of Speech (POS) tagging to label each word according to the position in the sentence. The POS tags are set up to input for rule-based model.

After completing the NLP part, the obtained data is processed to generate OO-based source code. Rule-based systems manipulate data, which is extracted by NLP to interpret knowledge in a useful way. Rule-based models enable identification of classes, attributes, methods, relations, and other elements in OOP design by using meaningful statements in textual requirements obtained with NLP processes.

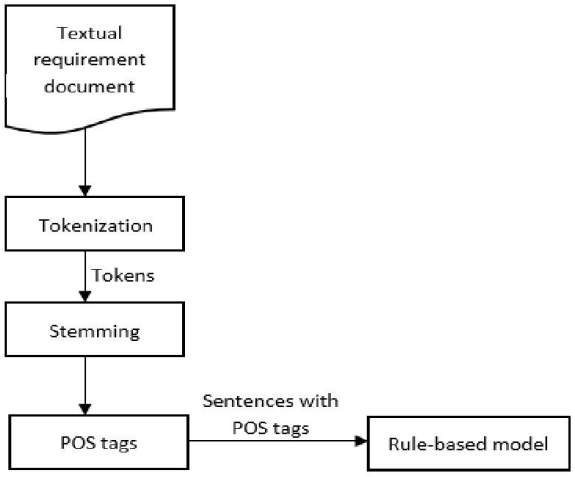


Figure 2: Basic NLP steps in reviewed studies

The following rules are commonly used to transform textual data into OO-based software code when studies implementing code generation are reviewed.

- All nouns in the requirement document are candidates to be class or attribute names.
- Nouns with the highest frequency are more likely to be

class names.

- The verbs in the sentence are candidates for the method names.
- Verbs connecting two names give information about relationships between classes.
- If a verb is in the following list {include, involve, contain, consist etc.}, then aggregation or composition relationship may be revealed between classes.

B. Evaluation Model of Reviewed Works

The validation of studies implementing OO-based source code generation checks whether the obtained code contains the keywords in the software requirement document. These keywords are classes, attributes, methods, relationships, relationship type, etc. that should be included in OO design.

It is observed that all of the studies discussed in the paper benefit from the precision, recall and F-measure parameters, which are the scoring concept of statistical science in the evaluation phase [10]. The number of the classes, attributes, methods and relationships in the generated source code are compared with a standard model and missing model elements are determined. Accuracy of proposed model is calculated by taking into consideration the elements that are required, missing or excessive.

The precision is obtained by the ratio of the correct data to the total data, and it is calculated according to the equation given in Formula 1. TP (true positive) denotes the number of objects that are correctly extracted by system. FP (false positive) refers to the number of objects that the system confirms as true when indeed it is not.

$$Precision\ (\mathrm{Pr}) = \frac{TP}{TP + FP} \tag{1}$$

The recall metric is calculated by the ratio of the correct data to the expected correct data, it is given in Formula 2. FN (false negatives) in the equation refers to the number of correct data, which could not be found.

$$Recall\ (Re) = \frac{TP}{TP + FN} \tag{2}$$

In order to calculate the accuracy of the proposed model, the harmonic mean of the precision and recall values are obtained and the F-measure is calculated according to the equation given in Formula 3.

$$F_{measure} = \frac{2(Pr \times Re)}{Pr + Re} \tag{3}$$

Table 1 shows the evaluation results of a case study (one of the reviewed studies) conducted by Bozyigit et al. [5]. The precision, recall and F-measure values, which are calculated based on the expected and obtained data as a result of the study, are shown in Table 2.

Table 1: Evaluation results of AutoClass[8]

	Class	**Relationship**	**Attribute**	**Method**
AutoClass [8]	10	11	3	8
Expected values	10	13	3	9

Table 2: F-Measures of the evaluation criteria in Autoclass[8]

	Class	**Relationship**	**Attribute**	**Method**
Precision	1	0.92	1	0.8
Recall	1	0.85	1	0.89
F-measure	1	0.88	1	0.84

The accuracy rate of AutoClass [5] is calculated as 93% regarding the F-measure value for each criterion in Table 2. All criteria are considered equally weighted and arithmetic mean of all F-measure values is calculated as shown in Equation 4.

$$\begin{aligned} F_{measure} &= \frac{Class + \mathrm{Re}\,lationship + Attribute + Method}{4} \\ F_{measure} &= \frac{1 + 0.88 + 1 + 0.84}{4} \\ F_{measure} &= 0.93 \end{aligned} \tag{4}$$

IV. Proposed Model

It is a challenging task to validate the studies, which utilize source code transformation from requirement documents, because the evaluation phase is highly dependent on personal opinions and it is subjective in nature. Therefore, firstly, decision-making problem should be defined, and then factors affecting decision points and importance values of these factors should be determined [11]. In this case, AHP method that is created under MCDM would be so befitting. Thus, a novel approach is presented in this study, and it is demonstrated in Figure 3. The evaluation part, which includes AHP, has a novelty, because none of the studies in the literature generating source code from requirements uses criteria weighting process in the evaluation phase.

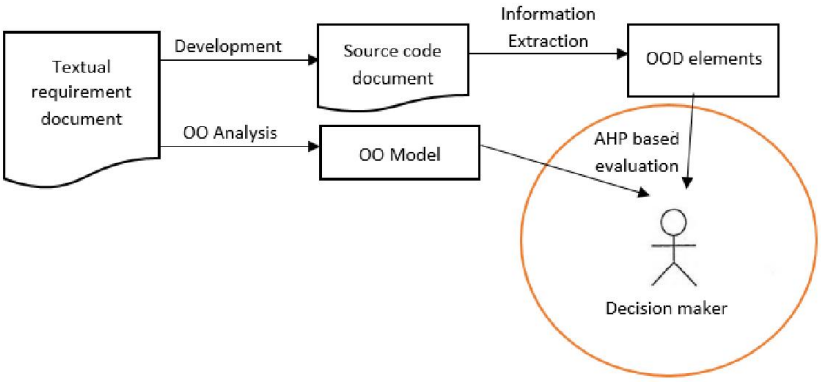


Figure 3: Proposed model

In the literature, AHP is widely used tool for dealing with various decision-making problems. It enables the decision makers to define criteria and calculate weight for each criterion to make the best decision. AHP starts with the construction of a functional hierarchy to decompose complex systems into their basic parts according to their required relationships [12]. To determine weights of criteria by using AHP, there are four main steps to be done.

Step 1: The evaluation criteria are taken into consideration and alternatives are chosen to make the best decision.

- There are multiple criteria affecting the accuracy of the OO-based source code and the importance of the criteria is relative. The criteria specified by three decision makers participating in this study are as follows.
- Classes: Finding all classes in the OO-based model completely,
- Attributes: Finding set of attributes and placing them in the related classes,
- Methods: Finding set of methods and placing them in the related classes,
- Relationships: Finding all relationships between classes and organize them correctly,
- Relationship type (composition, aggregation, inheritance, association vb.): Defining relationships type inter classes correctly.
- Many to many relationship: Showing whether there are many to many relationships between the two classes.

Step 2: Comparison matrix of factors which is N×N square matrix A, is created [13].

$$A = \begin{bmatrix} a_{11} & a_{12} & \cdots & a_{1n} \\ a_{21} & a_{22} & \cdots & a_{2n} \\ \vdots & \vdots & & \vdots \\ a_{n1} & a_{n2} & \cdots & a_{nn} \end{bmatrix}$$

In this step, decision makers are asked to compare the criteria at a given level on a pairwise basis in order to estimate their relative importance. A nine-point scale is commonly used to demonstrate the experts' preference between options as equal importance, moderate importance, strong importance, very strong importance, or extreme importance preferred. Table 3 shows the pairwise comparison of each criteria belongs to three decision makers participating in the study. It is assumed that the Criterion 1 is equally or more important than the Criterion 2.

Table 3: Importance of each criterion with respect to AHP priorities

#	Criterion 1	Criterion 2	Equal (1)	The importance value of Criterion 1 over Criterion 2							
				2	3	4	5	6	7	8	9
1	Class	Relationship				X					
2	Class	Attribute					X				
3	Class	Method					X				
4	Class	Relationship type							X		
5	Class	Many to many association									X
6	Relationship	Attribute		X							
7	Relationship	Method		X							
8	Relationship	Relationship type				X					
9	Relationship	Many to many association						X			
10	Attributes	Method	X								
11	Attributes	Relationship type		X							
12	Attributes	Many to many association				X					

13	Methods	Relationship type		X							
4	Methods	Many to Many Association				X					
15	Relationship type	Many to Many Association		X							

According the values in Table 3, $N \times N$ comparison matrix A is created. The diagonal elements of the comparison matrix are set to 1, because the relevant factor is compared with itself in this case. As seen in Table 3, the first criterion in the first row is four times important than second one according to the decision maker. Thus, the element in the first row and second column is set to 4 and the element in the second row and first column is set to ¼ the matrix A according to Equation 4.

$$a_{ji} = \frac{1}{a_{ij}} \tag{4}$$

The comparison matrix is showed in Table 4.

Table 4: Comparison Matrıx A

	1	**2**	**3**	**4**	**5**	**6**
1	1	4.00	5.00	5.00	7.00	9.00
2	0.25	1	2.00	2.00	4.00	6.00
3	0.20	0.50	1	1.00	2.00	4.00
4	0.20	0.50	1.00	1	2.00	4.00
5	0.14	0.25	0.50	0.50	1	2.00
6	0.11	0.17	0.25	0.25	0.50	1

Step 3: AHP assigns a score to each option according to the decision makers' pairwise comparison with respect to the considered criterion.

The column vectors are determined before calculating the weights of all of these criteria; a column vector is denoted as B_i where i is from 1 to n (the number of criteria). They are represented as Equation 5.

$$B_i = [b_{11}\ b_{21} \ldots\ b_{n1}]^T \tag{5}$$

Equation 6 is used for calculating values of the elements in the column vector B_i.

$$b_{ij} = \frac{a_{ij}}{\sum_{i=1}^{n} a_{ij}} \tag{6}$$

All column vectors B_i are joined in order to form C matrix as shown in (7).

$$C = \begin{bmatrix} 0.52 & 0.62 & 0.51 & 0.51 & 0.42 & 0.35 \\ 0.13 & 0.16 & 0.21 & 0.21 & 0.24 & 0.23 \\ 0.11 & 0.08 & 0.10 & 0.10 & 0.12 & 0.15 \\ 0.11 & 0.08 & 0.10 & 0.10 & 0.12 & 0.15 \\ 0.07 & 0.04 & 0.05 & 0.05 & 0.06 & 0.08 \\ 0.06 & 0.03 & 0.03 & 0.03 & 0.03 & 0.04 \end{bmatrix} \tag{7}$$

Percentage importance distribution of each criterion is obtained by using C matrix. Therefore, arithmetic average of row components, which is comprised C matrix, is taken and then column vector W that is called priority vector is calculated. Using C matrix, percentage importance distribution of criteria is calculated and W is illustrated in Formula 8.

$$W = [w_1\ w_{2\ldots} w_n]^T, w_i = \frac{\sum_{j=1}^{n} cij}{n} \tag{8}$$

Table 5 shows the elements of the priority vector obtained from the comparison matrix constructed by averaging the pairwise comparison values of the 3 decision makers.

Table 5: Weights of each criteria calculated by AHP

Category		**Priority**	**Rank**
C1	Class	50.0%	1
C2	Relationship	19.3%	2
C3	Attribute	10.8%	3
C4	Method	10.8%	3
C5	Relationship type	5.8%	5
C6	Many to many association	3.3%	6

The F-measure value obtained for each criterion in the AutoClass study [5] (in Table 2) is multiplied by the criteria weights determined according to the AHP result as in Equation 9, and a new accuracy ratio is obtained. The F-measure value of a criterion that is weighted by AHP but not evaluated in Auto Class is set to 0. As a result, new accuracy rate is determined as 86%. Remark that the accuracy rate is determined as 93% in AutoClass [5] by calculating precision, recall and F-measure.

$$\begin{aligned} Accuracy &= (w_1 \times C_1) + (w_2 \times C_2) + (w_3 \times C_3) \ldots + (w_6 \times C_6) \\ Accuracy &= (0.5 \times 1) + (0.19 \times 0.88) + \ldots\ldots + (0.03 \times 0) \\ Accuracy &= 0.86 \end{aligned} \tag{9}$$

V. CONCLUSION

Transformation of requirements into source code is a vital step in software development. Although it is mostly done manually, there are available approaches to automate this step of SDLC. Performance evaluation and validation process in the studies which automatically transform requirement documents into source codes are evaluated by commonly used measure methods such that recall, precision and F-measure. The evaluation criteria are considered to be equal in these methods. However, the priority of these criteria varies depending on views of users. Thus, we proposed a novel approach in which accuracy rate calculated by using weights of criteria. The weights of criteria are obtained by using opinion of the three experts, and then AHP method. Our novel approach evaluated on the particular study, which is presented by Bozyigit et al., AutoClass [5]. It is observed that our novel approach gives more realistic results in the evaluation of studies generating OO-based source codes from requirements. This is because; we base our approach on

expert opinions while other studies do not include them.

REFERENCES

[1] A. Van Lamsweerde, Requirements engineering. Chichester [u.a.]: Wiley, 2013.

[2] F. Budinsky, M. Finnie, J. Vlissides and P. Yu, "Automatic code generation from design patterns", IBM Systems Journal, vol. 35, no. 2, pp. 151-171, 1996.

[3] M. Zelkowitz and D. Wallace, "Experimental validation in software engineering", Information and Software Technology, vol. 39, no. 11, pp. 735-743, 1997.

[4] T. Saaty, "How to Make a Decision: The Analytic Hierarchy Process", Interfaces, vol. 24, no. 6, pp. 19-43, 1994.

[5] F. Bozyiğit, Ö. Aktaş and D. Kılınç, "AutoClass: Automatic Text to OOP Concept Identification Model", International Journal of Computer Applications, vol. 150, no. 10, pp. 29-34, 2016.

[6] S.I. Bajwa, A. Samad, and S. Mumtaz, "Object Oriented Software Modelling Using NLP Based Knowledge Extraction", European Journal of Scientific Research, vol. 35, no. 1, pp. 22-33, 2009.

[7] A. Tripathy, A. Agrawal and S. Rath, "Requirement Analysis using Natural Language Processing", in Fifth International Conference on Advances in Computer Engineering, 2014.

[8] S. K. Shinde, V. Bhojane and P. Mahajan, "NLP based Object Oriented Analysis and Design from Requirement Specification", International Journal of Computer Applications, vol. 47, no. 21, pp. 30-34, 2012.

[9] R. James, Object-oriented modeling and design. Englewood Cliffs, NJ: Prentice-hall, 1991.

[10] J. Makhoul, “Performance measures for information extraction”, in Proceedings of DARPA broadcast news workshop, 1999.

[11] E. Triantaphyllou, Multi-criteria decision making methods. Dordrecht [u.a.]: Kluwer, 2010.

[12] T. Saaty, Fundamentals of Decision Making and Priority Theory with the Analytic Hierarchy Process. RWS Publications, 2000.

[13] E. Nasiboglu, A. Bozyigit, and Y. Diker, “Analysis and evaluation methodology for route planning applications in public transportation”, in Application of Information and Communication Technologies (AICT), pp. 477-481, 2015.

Implementation of Virtual Reality Enhanced Continuous Performance Test Designed for Attention Deficit Hyperactivity Disorder Diagnosis

Mustafa Cem Kasapbasi, Can Eyupoglu, Tuna Baran Urut, Yusuf Turan, Alper Osman Karaagacli, Yusuf Can Sezgenc

Istanbul Commerce University, Department of Computer Engineering, Istanbul/Turkey
{mckasapbasi, ceyupoglu}@ticaret.edu.tr, {tunaurut, y.turan34, alperkaraagacli, yusufcansezgenc}@gmail.com

***Abstract* - The purpose of the study is to implement a virtual reality (VR) enhanced continuous performance test (CPT) specifically designed as an aid to attention deficit hyperactivity disorder (ADHD) diagnosis with the newest enabling technologies. To realize such an objective, firstly, the VR technology enabled ADHD diagnosis methodologies are investigated and required metrics are analyzed. Then, a new model is constructed in order to measure the required metrics and an assessment methodology is adopted to evaluate such metrics to cooperate with the created VR application. As the contribution, a new measurement model and procedure are presented and the effectiveness of the system is going to be examined in future studies.**

***Keywords* - virtual reality, continuous performance test, attention deficit hyperactivity disorder diagnosis**

I. Introduction

THIS study is intended to research and develop an application using virtual reality (VR) technology to provide aid and solution to people who lack attention for various reasons or who want to make their attention more intensive and specially to school-age children affected by modern technology. Attention is the power to concentrate thoughts on something. As can be seen in detail in literature, attention deficit is usually correlated with hyperactive disorder by scientists and referred to as attention deficit hyperactivity disorder (ADHD). Studies up to 15 years show that there is no evidence for attention deficit that practical drug treatment improves the long-term prognosis [1, 2].

According to these results, similar studies on this area are necessary for treating attention deficit. It is seen that there are lots of studies in various countries about ADHD. To the best of the authors' knowledge, however, there is no work in this context in Turkey. In this work, VR applications are investigated and put in practice to help in identifying problems of attention deficit using the Unity VR infrastructure. The developed applications are intended to be accessible by everyone. Therefore, the applications are developed for smartphones which are ubiquitous in everyday use.

The rest of the paper is organized as follows. In Section II, related works are given. Section III introduces the proposed methodology. Section IV investigates the results of the methods used in this study. Finally, conclusions and future works are summarized in Section V.

II. Related Works

In literature, since attention deficit is usually correlated with hyperactivity disorder, they are investigated together. Attention can be divided into 5 basic parts to describe the lack of attention. These are focus, constant, selective, alternative, and dividing attention. Focus attention: reacting to certain stimuli, constant attention: permanent condensation in the work done, selective attention: not distracting by other factors while engaging in a topic, alternative attention: changing the focus to a different subject, and dividing attention: focus on more than one subject [3].

Children diagnosed with ADHD usually have problems in the public sphere. They are easily bored and behave without thinking. This is the most common childhood time behavior disorder. The disorder directly affects children's relationships with their teachers, families, friends, and siblings. Also, it causes difficulties in their learning life [4, 5]. The number of people with ADHD who are diagnosed with attention deficit is increasing. Besides, the number of people with ADHD is 3-7% without a complete measurement [6].

Many treatment techniques have been proposed and implemented for the treatment of ADHD in the past years. The tests done on paper used in the treatment cannot be employed on every patient. Attention deficit patients cannot pay enough attention on the long-term tests. Especially in children, these tests are not brittle and interesting, reducing the success rate of the test.

Drug treatment with adverse effects may affect children's future mental and physical development. Psychoactive drug treatment is a treatment that is avoided by parents at first because there is no proven effect on long-term ADHD

symptoms. This is only recommended for severely sick children. In other cases, improvements are made using technology [7].

In literature, VR technologies have been demonstrated in various studies which they have shown promise for these patients [8]. It has been found that the patients using VR technologies provide longer duration of concentration by removing image boundaries compared to other methods (paper test, drug, rehabilitation, etc.) [3, 9]. This is not only beneficial for children with attention deficit, but also for those who are physically handicapped. It has the potential to provide equal opportunity in education and avoid obstacles. In order to support curriculum training with VR, classes have been observed to be used in a variety of studies [10, 11].

VR systems also help to reduce the symptoms of illness without having to be diagnosed with a medical diagnosis and constantly monitored by a child psychologist [11-15].

III. Proposed Methodology

A. Continuous Performance Test

In order to improve the attention deficit, it has been pointed out that it is important to develop tasks such as working memory, auditory memory, and certain visual memory [16]. These tasks should be encouraged to listen, followed by verbal instructions to scan the environment, words of hidden treasures, letters, faces and objects, so that attention and organizational skills will be increased to trigger audible processes.

Continuous performance test (CPT) was first offered by [17] which demonstrated that brain damaged child and adults had difficulty in keeping attention and distinguishing if or if not a target letter in a randomized sequence of letters had followed a cue letter.

The fundamental nature of the CPT remained the same, although tests may vary in length and type of stimulus. They were all indicated as repetitive, boring task, and attendee must keep focus over a certain time period. Tests may use numbers, symbols or even sounds.

Test of variables of attention (TOVA) is a neuropsychological evaluation and it measures a person's attention while screening for ADHD [18]. The most common metrics used in the CPT to measure the attention of the patient are listed and described below [19]:

Correct detection: this is a simple counter that counts the number of times the patient replied to the target stimulus. Better attention capacity is indicated with higher rates of correct detections.

Reaction times: this is a measurement for the amount of time between the presentation of the stimulus and the patient's response. This measure is generally calculated with standard deviation to understand the variability.

Omission errors: this is another counter that demonstrates the number of times the target was offered, but the patient did not respond/click the mouse. High omission rates show that the subject is either not paying attention to stimuli that the person may have distractibility or has a sluggish response.

Commission errors: this is a score that states the number of times the patient responded, but no target was presented. Difficulties with impulsivity are indicated with a fast reaction time and high commission error rate. A slow reaction time with high commission and omission errors generally points to inattention.

The other metrics not measured commonly are: hit reaction time (HRT), HRT standard deviation, variance, perseverance (random or anticipatory response i.e. HRT<100ms), and block measure to understand sustained attention.

B. Proposed Measuring Model and Application

In order to measure the aforementioned metrics, an infrastructure establishment is needed. Therefore, proper object classes were designed and modelled which are utilized in the developed VR attention CPT games in Unity according to UML diagrams depicted in Figure 1. Furthermore, a new framework was developed for measuring timeline of the actions and reactions of the subject those are basically outputs with timestamp associated with each interaction and stimuli.

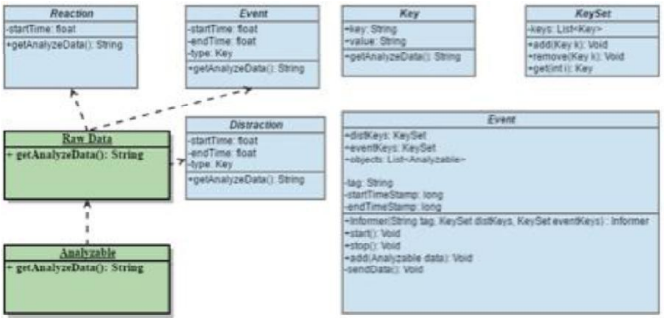


Figure 1: UML diagram of the proposed system to measure the metrics.

Since reviewed CPT tests are found as boring, our aim is to produce attention detection games that children may have fun while using. For this reason, entertainment situations of the games made within the scope of the project are taken into consideration. In this sense, the games have been gradually made more fun so that the correctness of the data can be checked. Within the scope of this process, four different games were developed. All games were designed to engage children in a school environment. Thus, they can feel as if they are at school. In this context, a virtual classroom was created with audio and visual distractions like sound of a motorcycle and a flying paper plane. These distractions are used while expecting an attention from a subject.

C. Experiment Setup

Mobile phone attachable VR glasses were utilized in the study. To get the reaction of the user, a Bluetooth joystick and a cable mouse were attached to the mobile phone. Unity was chosen as the development environment.

IV. Results and Discussion

In this work, four different games are developed as shown in Figure 2. The developed attention measuring games are designed for school age children. It is planned that the games will be experimented on the two groups which are test and control. Test group will consist of children medically diagnosed with attention deficit and control group will compose of relatively normal reacting children. This phase of the study is not completed yet, however, the first impressions of adults for experiment are very encouraging. The results of the experiments on children will be presented in the following studies.

V. Conclusion and Future Works

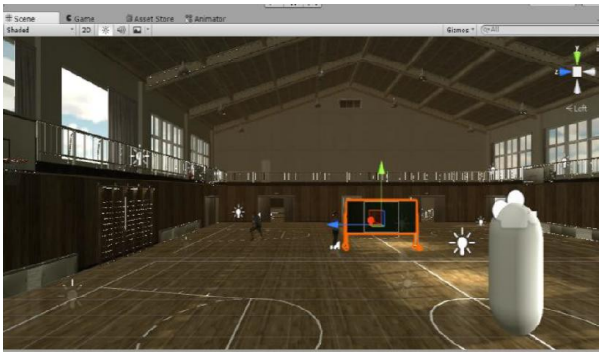
In this study, experimental applications, namely, virtual classroom, auditorium hall, gym, and pool, designed for children suffering from ADHD are presented. The aim of the study is to ease the diagnoses process and if possible improve the attention of children. A new model and measurement procedure are presented. Suitable metrics are investigated and embedded in every developed game. The effectiveness of the system will be measured with the forthcoming experiments with aforementioned control and test groups. It is expected to obtain a meaningful and distinguishable correlation between test and control groups.



(a) Virtual classroom



(b) Virtual auditorium hall



(c) Virtual gym



(d) Virtual pool

Figure 2: Plot locations of attendance game scenarios.

Acknowledgment

This work is supported by Publication, Research, and Project Coordination Council of Istanbul Commerce University under the grant on 26.12.2016 with decision number E33492.

References

[1] P. S. Jensen, S. P. Hinshaw, J. M. Swanson, L. L. Greenhill, C. K. Conners, L. E. Arnold, H. B. Abikoff, G. Elliott, L. Hechtman, B. Hoza, J. S. March, J. H. Newcorn, J. B. Severe, B. Vitiello, K. Wells, and T. Wigal, "Findings from the NIMH Multimodal Treatment Study of ADHD (MTA): implications and applications for primary care providers," *Journal of Developmental and Behavioral Pediatrics*, vol. 22, no. 1, pp. 60–73, February 2001.

[2] H. Abikoff, L. Hechtman, R. G. Klein, G. Weiss, K. Fleiss, J. Etcovitch, L. Cousins, B. Greenfield, D. Martin, and S. Pollack, "Symptomatic improvement in children with ADHD treated with long-term methylphenidate and multimodal psychosocial treatment," *Journal of the American Academy of Child & Adolescent Psychiatry*, vol. 43, no. 7, pp. 802–811, July 2004.

[3] B. H. Cho, J. M. Lee, J. H. Ku, D. P. Jang, J. S. Kim, I. Y. Kim, J. H. Lee, and S. I. Kim, "Attention Enhancement System using virtual reality and EEG biofeedback," in *Proceedings of the IEEE Virtual Reality 2002 (VR'02)*, Orlando, FL, USA, pp. 156–163, 24–28 March 2002.

[4] J. M. Lee, B. H. Cho, J. H. Ku, J. S. Kim, J. H. Lee, I. Y. Kim, and S. I. Kim, "A study on the system for treatment of ADHD using virtual reality," in *23rd Annual International Conference of the IEEE Engineering in Medicine and Biology Society*, Istanbul, Turkey, pp. 3754–3757, 25–28 Oct. 2001.

[5] S. Shiri, A. Tenenbaum, O. Sapir-Budnero, and I. D. Wexler, "Elevating hope among children with Attention deficit and hyperactivity disorder through virtual reality," *Frontiers in Human Neuroscience*, vol. 8, article 198, pp. 1–4, May 2014.

[6] *Diagnostic and statistical manual of mental disorders: DSM-IV-TR*, American Psychiatric Association Publishing, 2000.

[7] S. C. Yeh, C. F. Tsai, Y. C. Fan, and A. Rizzo, "An innovative ADHD assessment system using virtual reality," in *2012 IEEE EMBS Conference on Biomedical Engineering and Sciences (IECBES)*, Langkawi, Malaysia, pp. 78–83, 17–19 Dec. 2012.
[8] Y. Hashemian, M. Gotsis, and D. Baron, "[DEMO] Adventurous Dreaming Highflying Dragon: A full body game for children with Attention Deficit Hyperactivity Disorder (ADHD)," in *2014 IEEE International Symposium on Mixed and Augmented Reality (ISMAR)*, Munich, Germany, pp. 341–342, 10–12 Sept. 2014.
[9] G. Riva, "Virtual environments in clinical psychology," *Psychotherapy*, vol. 40, pp. 68–76, 2003.
[10] N. Alm, J. L. Arnott, I. R. Murray, and I. Buchanan, "Virtual reality for putting people with disabilities in control," in *1998 IEEE International Conference on Systems, Man, and Cybernetics*, San Diego, CA, USA, pp. 1174–1179, 14–14 Oct. 1998.
[11] S. Young and J. M. Amarasinghe, "Practitioner review: Non-pharmacological treatments for ADHD: a lifespan approach," *Journal of Child Psychology and Psychiatry*, vol. 51, no. 2, pp. 116–133, February 2010.
[12] O. G. Berwid and J. M. Halperin, "Emerging support for a role of exercise in attention-deficit/hyperactivity disorder intervention planning," *Current Psychiatry Reports*, vol. 14, no. 5, pp. 543–551, October 2012.
[13] G. A. Fabiano, W. E. Pelham Jr, E. K. Coles, E. M. Gnagy, A. Chronis-Tuscan, and B. C. O'Connor, "A meta-analysis of behavioral treatments for attention-deficit/hyperactivity disorder," *Clinical Psychology Review*, vol. 29, no. 2, pp. 129–140, March 2009.
[14] J. M. Halperin, D. J. Marks, A. C. Bedard, A. Chacko, J. T. Curchack, C. A. Yoon, and D. M. Healey, "Training executive, attention, and motor skills: a proof-of-concept study in preschool children With ADHD," *Journal of Attention Disorders*, vol. 17, no. 8, pp. 711–721, November 2013.
[15] S. M. Watson, C. Richels, A. P. Michalek, and A. Raymer, "Psychosocial treatments for ADHD: a systematic appraisal of the evidence," *Journal of Attention Disorders*, vol. 19, no. 1, pp. 3–10, January 2015.
[16] R. Rijo, P. Costa, P. Machado, D. Bastos, P. Matos, A. Silva, J. Ferrinho, N. Almeida, A. Oliveira, S. Xavier, S. Santos, C. Oliveira, S. Brites, V. Martins, A. Pereira, and S. Fernandes, "Mysterious Bones Unearthed:Development of an Online Therapeuticserious Game for Children with Attention Deficit-hyperactivity Disorder," *Procedia Computer Science*, vol. 64, pp. 1208–1216, 2015.
[17] L. H. Beck, E. D. Bransome Jr, A. F. Mirsky, H. E. Rosvold, and I. Sarason, "A continuous performance test of brain damage," *Journal of Consulting Psychology*, vol. 20, no. 5, pp. 343–350, October 1956.
[18] L. M. Greenberg, *TOVA - Continuous Performance/Attention Test*, Allied Products Neurofeedback Instrument Corp.
[19] C. K. Conners, *Conners' Continuous Performance Test II: Computer Program for Windows Technical Guide and Software Manual*, North Tonawanda, NY: Multi-Health Systems, 2000.

Order Based Emigrant Creation Strategy for Parallel Artificial Bee Colony Algorithm

A.AKSOY[1], S. ASLAN[2], D. KARABOGA[3]

[1] Alanya Alaaddin Keykubat University, Engineering Faculty, Department of Computer Engineering, Antalya/Turkey, alperen.aksoy@alanya.edu.tr
[2]Ondokuz Mayıs University, Engineering Faculty, Department of Computer Engineering, Samsun/Turkey, selcuk.aslan@omu.edu.tr
[3]Erciyes University, Engineering Faculty, Department of Computer Engineering, Kayseri/Turkey, karaboga@erciyes.edu.tr

***Abstract* - Artificial Bee Colony (ABC) algorithm inspired by the foraging behaviors of real honey bees is one of the most important swarm intelligence based optimization algorithms. When considering the robust and phase divided structure of the ABC algorithm, it is clearly seen that ABC algorithm is intrinsically suitable for parallelization. In this paper, we proposed a new emigrant creation strategy for parallel ABC algorithm. The proposed model named order based emigrant creation strategy depends on sending best food source in a subcolony after modifying it with another food source chosen sequentially from the same subcolony at each migration time. Experimental studies on a set of numerical benchmark functions showed that parallel ABC algorithm powered by the newly proposed model significantly improved quality of the final solutions and convergence performance when compared with standard serial ABC algorithm and parallel ABC algorithm for which the best food sources in the subcolonies directly used as emigrants.**

Keywords - swarm intelligence, Artificial Bee Colony algorithm, parallelization, mobile platform.

I. INTRODUCTION

In recent years, modeling complex biological behaviors of species living together has become a major technique for solving optimization problems and many nature-inspired algorithms have been proposed including Ant Colony Optimization (ACO), Particle Swarm Optimization (PSO) and Bacterial Foraging Optimization (BFO), Artificial Bee Colony (ABC) and so on [1] – [4]. Although all of these population based optimization algorithms successfully applied fundamental mechanisms that are leading to emerge swarm intelligence, ABC algorithm is in a special position due to its phase divided structure, easy implementation and also requiring less control parameters [1] – [4].

By considering the advantages of ABC algorithm, researchers used it for solving different types of problems ranging from aligning three or more biological sequences [5], [6] and guessing their three-dimensional structures [7] to training deep neural networks [8], image segmentation [9] to designing filters [10]. Although original ABC algorithm produced sufficiently good results in most cases, some studies have been made to further increase the quality of the final solutions and change the convergence characteristics of the algorithm. Zhu and Kwong proposed the gbest-guided ABC algorithm in which the parameters of the best food source is used instead of the parameters of the randomly determined food source [11]. Coelho and Alotto changed the candidate generation equation of the ABC algorithm by utilizing the coefficients extracted from the Gaussian distribution [12]. Karaboga and Gorkemli changed the search characteristics of the onlooker bees and proposed a new ABC algorithm variant called quick-ABC algorithm [13]. Gao and Liu used mutation operation of Differential Evolution (DE) algorithm and proposed a new ABC algorithm [14]. Xiang et al. combined ABC algorithm and DE and solved numerical optimization problems successfully [15]. Wu et al. propose HHSABC algorithm that is based on the combination of Harmony Search (HS) and ABC algorithms [16]. Banitalebi et al. proposed an improved ABC algorithm by combining it with the Estimation of Distribution (ED) algorithm [17].

Another important studies about the ABC algorithm were made on the parallelization of it for distributed and shared memory based architectures. Narasimhan parallelized ABC algorithm by dividing the whole bee colony into subcolonies and then assigning them to the different compute units [18]. In order to maintain population diversity, copies of each subcolony is also stored in the global memory [18]. Banharnsakun et at. parallelized ABC algorithm for distributed memory based architectures [19]. After completion of predetermined number of cycles, local best food sources of the two randomly determined subcolonies are exchanged [19]. Luo et al. introduced a new emigrant exchange schema called ripple-communication and applied it to the parallel ABC algorithm [20]. Experimental studies showed that ripple-communication schema increased the accuracy of the ABC

algorithm [20]. Subotic et al. utilized multiple bee colonies in their parallel implementation of ABC algorithm [21], [22]. Each colony is in communication by shared local best food sources among them [21], [22]. The effect of the migration period, migration topology and number of subcolonies on the parallel implementation of the ABC algorithm was investigated detailly by Basturk and Akay [23]. They first tested parallel ABC algorithm for solving high-dimensional numeric optimization problems and thenu training neural networks for classification problems [23]. Karaboga and Aslan focused on the emigrant selection and creation approaches for the parallel ABC algorithm [24]. They first proposed a new emigrant creation approach in which the local best food source is modified before it is sent to the neighbor subcolony. Secondly, they used all local best food sources to generate a global emigrant and the sent it to all subcolonies [25].

Utilizing local best food sources as an emigrant is common part for most of the parallel implementations of the ABC algorithm. However, if the local best food sources can not be improved between two consecutive migration period, it is possible to see the same solution more than once in the same subcolony. If the subpopulation diversity that has already been decreased by dividing the whole colony is also deteriorated because of the same food sources coming from the neighbor subcolonies, parallelization of the ABC algorithm does not go beyond a study only aiming at acceleration with the power of the compute units. In order to overcome these mentioned issues, we proposed a new technique called order based emigrant creation strategy. In order based emigrant creation strategy, the local best food source found at the current migration time of a subcolony is powered with the more useful parameters of another food source. However, the selection of the auxiliary food source for the local best is managed in a sequential manner for decreasing the possibility of sending the same emigrant. The rest of the paper is organized as follows: In the second section, fundamental steps of the ABC algorithm is introduced. Order based emigrant creation strategy and its working schema are summarized in the third section. Experimental studies and conclusion are given in the fourth and fifth sections, respectively.

II. ARTIFICIAL BEE COLONY ALGORITHM

ABC algorithm proposed by Karaboga at 2005 is inspired by the intelligent foraging behaviors as real honey bees. In ABC algorithm the whole colony is divided into three groups by considering special foraging characteristics of the bees [26]. The first group of bees is composed of the employed bees. Employed bees are responsible for finding food sources and carry nectar extracted from the sources. When employed bees come back to the hive, they share information about the nectar quality of the sources, distance to the hive and so on, with the second group of bees. The second group of bees consists of onlooker bees. Onlooker bees wait on the hive and select a food source to exploit it after checking the information supplied by the employed bees. The food source selection of the onlooker bees is not a randomized procedure directly. Selection probability of a food source has a relationship with its quality and if the nectar quality of a food source is high, its preference by onlookers is also high when compared other sources [26]. After an onlooker bee selects a food source, she continues the source exploration and exploitation processes as done by the employed bees. The final group of bees in the ABC algorithm consists of scout bees. Scout bees like onlooker bees wait on the hive, but food source selection behavior of them is managed by an internal motivation that leads to send scouts to unvisited food sources randomly [26]. The bee phases determined by the employed, onlooker and scout bees and their cyclical relationships continue until the end of a predetermined number of iterations-cycles is completed are given in the Algorithm 1.

A. Generating Initial Food Sources

In ABC algorithm, each food source corresponds possible solutions of the optimization problem being solved and nectar amounts of the sources are related with the fitness values of them. ABC algorithm generates these food sources randomly before employed bees are assigned to them. The *jth* parameter of the *ith* food source or solution within *SN* different solutions is determined randomly between lower bound of the parameter showed by x_j^{min} and upper bound of the parameter showed by x_j^{max} using the Eq. 1 [26].

$$X_{ij} = x_j^{\min} + rand(0,1)(x_j^{\max} - x_j^{\min}) \quad j = 1,2, \ldots D \quad (1)$$

In Eq. 1, D corresponds to the number of parameters being optimized and $rand(0,1)$ is used to define a random number of varies between 0 and 1.

Algorithm 1 Fundamental steps of the ABC algorithm

```
1: Initialization:
2:     Assign values to the control parameters.
3:     Generate SN initial food sources with D parameters.
4: Repeat
5:     //Employed bee phase
6:     for i ← 1…SN do
7:     Generate new solution around the memorized one.
8:     Apply greedy selection between new and memorized sources.
9:     end for
10:    //Onlooker bee phase
11:    sentBees ← 0, currentSource ← 1
12:    Find probability values of each food source.
13:    while sentBees ≠ SN do
14:        if p_currentSource > rand(0, 1) then
15:        sentBees ← sentBees + 1:
16:        Generate new solution around the selected one.
17:        Apply greedy selection between new and memorized sources.
18:        end if
19:         currentSource = (currentSource + 1) mod SN:
20:    end while
21:    //Scout bee phase
22:    Determine the abandoned food source.
23:    Generate a new source for this abandoned food source.
24: Until Termination criteria is met
```

B. Sending Employed and Onlooker Bees

After generating initial population of *SN* different food sources, each food source is associated with only one employed bee by the ABC algorithm. The mathematical model used by the employed bees to generate a candidate food source around the memorized one is given in the Eq. (2) [26].

$$v_{ij} = x_{ij} + \phi_{ij}(x_{ij} - x_{kj}) \tag{2}$$

In the Eq. (2), v_{ij} is the parameter value of the candidate v_i food source whose parameters are same with the parameters of the x_i food source except the *jth* parameter [26]. x_{ij} and x_{kj} are the parameter values of the *jth* parameter of the x_i and x_k food sources, respectively and Θ_{ij} corresponds to a random number between -1 and 1 [26]. If the $fit(v_i)$ fitness value of the v_i food source calculated as in the Eq. (3) for a minimization problem is bigger than the $fit(x_i)$ fitness value of the x_i food source, the employed bee applies a greedy selection procedure between x_i and v_i food sources and trial counter for x_i food source is set to zero. Otherwise, the trial counter for x_i food source is incremented by one to show that it is not improved in the current cycle.

$$fit(x_i) = \begin{cases} 1 + |obj(x_i)|; & if\ obj(x_i) > 0 \\ 1/(1 + obj(x_i)); & if\ obj(x_i) \le 0 \end{cases} \tag{3}$$

When the employed bee phase is completed, the food sources memorized by the employed bees are introduced to onlooker bees. As mentioned before selection of a food source is not a randomized operation exactly and it is directed by the qualities of the food sources [26]. In ABC algorithm, to direct the source selection procedure of the onlooker bees, each food source is identified by a selection probability. Selection probability of the x_i food source that increases with the appropriate fitness values of it is calculated as in the Eq. (4). When the selection procedure is completed, the onlooker bees associated with these sources become employed bees and generate candidate food sources by utilizing the Eq. (2) [26].

$$p(x_i) = \frac{fit(x_i)}{\sum_{j}^{SN} fit(x_j)} \tag{4}$$

C. Abandoning Consumed Food Sources

In ABC algorithm, it is easily seen that the exploitation characteristics of the employed and onlooker bee phases are more dominant than the exploration characteristics of them [26]. However, for a proper search process, exploration and exploitation operations should be balanced. This subtle balance between exploration and exploitation is maintained by the scout bee phase. In scout bee phase, a food source is abandoned if required and a scout bee for abandoned food source is sent from hive to find a food source that has been discovered yet. The decision about which food source will be abandoned is made by comparing trial counters of them with ABC algorithm specific control parameters called *limit* [26]. The food source for which its trial counter exceeds the *limit* parameters value at most is abandoned and a new food source created by the Eq. (2) is replaced with the consumed one. The value of the *limit* parameter for a numerical optimization problem is determined by the Eq. (5) given below [26].

$$\lceil a \times SN \times D \rceil and\ a \in \quad ^{+} \tag{5}$$

III. ORDER BASED EMIGRANT CREATION STRATEGY

If the parallelization approach of the ABC algorithm depends on dividing the whole colony into subcolonies and then assigning them to the different compute nodes or processor cores, it is clearly seen that the best food source found at the current migration time are chosen for sending to the neighbor subcolony or subcolonies in the vast majority of the studies. Determining a food source as an emigrant is not a single decision that should be made when parallelization of a population algorithm to decrease the execution time without deteriorating the quality of the final solutions and convergence characteristics. After deciding which sources are chosen as emigrants, they should send to the neighbor subcolonies in order to maintain the diversity and increase the quality of the existing solutions. The neighborhood relationship between subcolonies is directly determined by applying one of the commonly used migration topologies given in the Fig. (1) below.

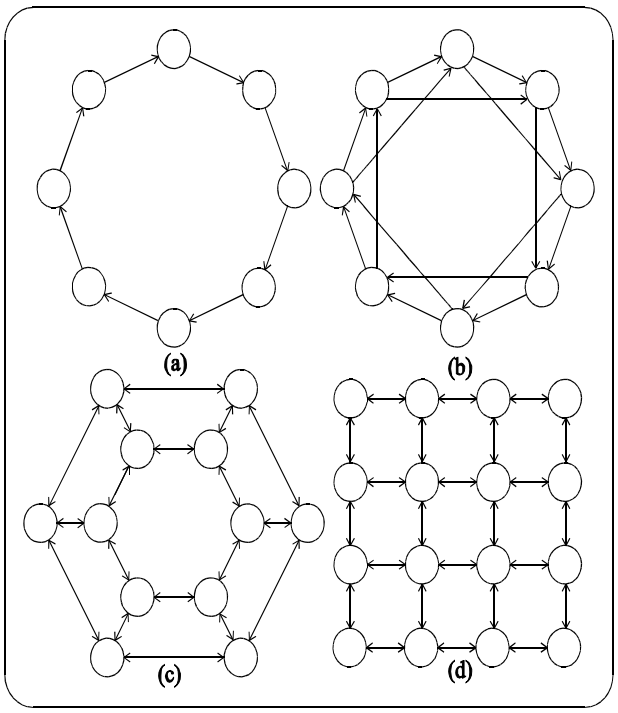


Figure 1: Ring (a), Ring 1+1 (b), Tourus (c) and Lattice (d) topologies

Although all of these topologies have some advantages, their implementations require certain number of compute nodes or processor cores and migration period or interval should be carefully chosen to decrease the total execution time on the acceptable rates. When the neighborhood topology is chosen by considering system resources and the appropriate subcolony size is determined, the required population diversity is maintained by most of the topologies at the limited rates. By considering these situations, it can be said that type of information being exchanged between subcolonies becomes more important in parallelized implementations.

Choosing the best food source in a subcolony and then sending them to the neighbor subcolony and then replacing it with the worst food source in the neighbor subcolony might be observed the most appropriate emigrant selection-creation strategy. However, mentioned emigrant strategy has some possible disadvantages. One of the main drawbacks stemmed from utilizing the best food sources as emigrants is related with the solution diversity. If the best food source used as an emigrant for the previous migration time cannot be improved until the next migration time, the same solution is sent more than once to the neighbor subcolony. Another drawback about the distribution of the best food sources is that whether the food sources are enough to reflect the properties of the other solutions. The best food source determined as emigrant does not always guarantee that all of its parameters can be useful for generating candidate solutions.

In the proposed model, each food source is utilized in the emigrant creation procedure sequentially by considering their orders or indexes. Sending food sources sequentially can be thought appropriate because of the ability of distributing diverse information. However, if the emigrant selection-creation procedure is managed without considering fitness values of the emigrants or the subcolony where emigrants are sent contains food sources whose fitness values are better than the emigrants, the computational and communication burden are not worth sending and receiving emigrants. In other words, it can be said that the food source determined to be sent to the neighbor subcolony should be enough in terms of quality and increase the population diversity. By considering all of these limitations originated from the conventional emigrant creation-selection schemas, we proposed a new emigrant creation-selection strategy in which the best food source found at the current migration period is modified with the more suitable parameters of a food source that is changed sequentially in the same population for each migration period. The pseudo code given in the Algorithm 2 summarized the newly proposed strategy called order based emigrant creation.

Algorithm 2 Order based emigrant creation strategy

1: *sizeOfSubcolony* ← number of food resources in the subcolony.
2: *migPeriod* ← the counter shows many times migration occurred.
3: b ← index of best food source in the subcolony.
4: $ord \leftarrow (migPeriod) mod (sizeOfSubColony)$
5: **if** $b == ord$ **then**
6: $ord \leftarrow (ord+1) mod (sizeOfSubcolony)$.
7: **end if**
8: $x_b \leftarrow$ food source with the index b.
9: $x_{ord} \leftarrow$ food source with the index ord.
10: **for** $j \leftarrow 1 \ldots D$ **do**
11: $temp \leftarrow x_{b,j}$
12: $x_{b,j} = x_{ord,j}$
13: $fit_{emigrant} \leftarrow calcFit(x_b)$.
14: **if** $fit_{emigrant} < fit(x_b)$ **then**
15: $x_{b,j} \leftarrow temp$.
16: **else**
17: $fit(x_b) \leftarrow fit_{emigrant}$
18: **end if**
19: **end for**

When the pseudo code given in the Algorithm 2 is investigated, it is clearly seen that the *jth* parameter of the best food source x_b is updated by the corresponding parameter of the x_{ord} food source. x_{ord} food source is determined by applying modulo operation between *currentMigIndex* and *sizeOfSubcolony* that increment *ord* index one by one for each migration period. Although x_b food source is not improved between two subsequent migration time, p and $p+1$, order based emigrant strategy guarantees that it is sent to the neighbor subcolony after modification with x_{ord} and $x_{(ord+1)}$ food sources, respectively.

IV. EXPERIMENTAL STUDIES

Standard serial implementation of the ABC algorithm, s-ABC, its parallel implementation, p-ABC in which the best food source in a subcolony is chosen as an emigrant and it is changed with the worst food source in the neighbor subcolony and finally the parallel implementation with order based emigrant creation strategy, ord-p-ABC in which the best food source prepared by the mentioned strategy for migration is chosen as an emigrant and it is changed with the worst food source in the neighbor subcolony are tested using three different numerical benchmark functions given in the Table I below. The first function, f_1 is the Sphere function. This function has a single global minimum located at the [0, 0,…,0] point in the search space and lower and upper bounds of the parameters are set to -100 and 100, respectively. The second function, f_2 is Griewank function and has many local minimums that are regularly distributed on the search space. The global minimum of the Griewank function is located at the [0, 0,…,0] point and the values that can be assigned to the parameters are limited between -600 and 600. The last function, f_3 , is Rosenbrock function. Because of the difficulty for finding global optimum that is located at the end of a long and narrow valley, this function is frequently used to check the

convergence performance of the optimization algorithms. The global minimum of the Rosenbrock function is located at the [1, 1,…,1] point in the search space and lower and upper bounds of the parameters are set to -100 and 100, respectively.

TABLE I: Benchmark functions used in comparison

Function	Formulation
f_1	$f_1(\vec{x}) = \sum_{i=1}^{D} \left(x_i^2 \right)$
f_2	$f_2(\vec{x}) = \frac{1}{4000}\left(\sum_{i=1}^{D} x_i^2, \right) - \left(\prod_{i=1}^{D} cos\left(\frac{x_i}{\sqrt{i}} \right) \right) + 1$
f_3	$f_3(\vec{x}) = \sum_{i=1}^{D-1} \left(100(x_{i+1} - x_i^2)^2 + (x_i - 1)^2 \right)$

When solving the optimization problems with s-ABC, p-ABC and ord-p-ABC algorithms, number of food sources was taken equal to 100 and number of parameters was set to 500. The maximum cycle number was set to \$2000\$ and *limit* parameter value was taken equal to the number of parameters. For p-ABC and ord-p-ABC algorithms, ring neighborhood topology was used and the whole colony was divided into four equal subcolonies and finally migration frequency was taken one percent of the maximum cycle number. All the experiments were performed on an Android® 5.1.1 operating system working on a mobile platform that is equipped with an ARM® based processor running 1.3 GHz with 1GB of RAM. s-ABC, p-ABC and ord-p-ABC algorithms were written in C programming language and parallelization and required synchronization between subcolonies were maintained by utilizing the built-in functions of the *pthreads* library. Each of the function was tested 20 different times with random seeds. Average best objective function values and standard deviations calculated over 20 different runs were recorded and given in the Tables II – IV.

When the results given in the Tables II, III and IV are investigated, it is seen that ord-p-ABC algorithm produced better average best objective function values than s-ABC and p-ABC algorithms for all of f_1, f_2, f_3 functions. While the results obtained by the p-ABC algorithm lagged slightly behind the results obtained by the s-ABC algorithm especially for the f_1 and f_3 functions, ord-p-ABC algorithm overcame the main issue to do with the decreased population diversity of the subcolonies that leads to deteriorate the performance of the p-ABC algorithm and produced at least 10^5 times better results for the function f_1, 10^4 times better results for the function f_2 and 10^6 times better results for the function f_3 that the s-ABC and p-ABC algorithms.

TABLE II: Comparison of s-ABC and p-ABC algorithms

Func.	s-ABC		p-ABC	
	Mean	Std. Dev.	Mean	Std. Dev.
f_1	6.548575e+04	1.171718e+04	1.035821e+05	1.469255e+04
f_2	6.524802e+02	8.983277e+01	9.449440e+02	1.022350e+02
f_3	2.557243e+09	3.227430e+09	2.356143e+10	5.546746e+09

TABLE III: Comparison of s-ABC and ord-p-ABC algorithms

Func.	s-ABC		ord-p-ABC	
	Mean	Std. Dev.	Mean	Std. Dev.
f_1	6.548575e+04	1.171718e+04	4.640619e-01	5.420124e-01
f_2	6.524802e+02	8.983277e+01	9.077554e-02	6.457029e-02
f_3	2.557243e+09	3.227430e+09	3.291103e+03	3.390808e+03

TABLE IV: Comparison of p-ABC and ord-p-ABC algorithms

Func.	p-ABC		ord-p-ABC	
	Mean	Std. Dev.	Mean	Std. Dev.
f_1	1.035821e+05	1.469255e+04	4.640619e-01	5.420124e-01
f_2	9.449440e+02	1.022350e+02	9.077554e-02	6.457029e-02
f_3	2.356143e+10	5.546746e+09	3.291103e+03	3.390808e+03

Another comparison between serial and parallel implementations of the ABC algorithms was made by considering average execution times obtained from the 20 different runs in terms of second, speedup and efficiency values. The speedup is a ratio between serial and parallel execution times of the algorithms and it's maximum value can be equal to number of computing nodes or cores. Efficiency is another measure that can be found by divining speedup measure to the number of computing nodes or cores. The maximum value of the efficiency measure can be equal to 1. When the results given in the Table V and VI are analyzed, it is understood that order based emigrant creation strategy brings extra burden to the total execution time of the algorithm compared with the p-ABC algorithm. Because of the execution time needed to employ order based emigrant creation strategy, the average execution time of the ord-p-ABC algorithm is 9.194% higher than the average running time of the p-ABC algorithm for function f_1, 9.743% higher than the average running time of the p-ABC algorithm for function f_2 and finally 34.242% higher than the average running time of the p-ABC algorithm for function f_3. There is another point should be noted that when the computational complexities of the benchmark problems increase, the difference between execution times between p-ABC and ord-p-ABC algorithms decrease. The relationship between complexity of the functions and execution time of the parallel ABC algorithm showed that compute intensive problems are more suitable for order based emigrant creation strategy.

TABLE V: Speedup and efficiency values of p-ABC

Func.	s-ABC (exec. time)	p-ABC (exec. time)	Speedup	Efficiency
f_1	2.995314	1.774507	1.687969	0.421992
f_2	33.764449	10.905223	3.096172	0.774043
f_3	6.527048	2.033796	3.209293	0.802323

TABLE VI: Speedup and efficiency values of ord-p-ABC

Func.	s-ABC (exec. time)	ord-p-ABC (exec. time)	Speedup	Efficiency
f_1	2.995314	1.937657	1.545844	0.386461
f_2	33.764449	11.967766	2.821283	0.705321
f_3	6.527048	2.730220	2.390668	0.597667

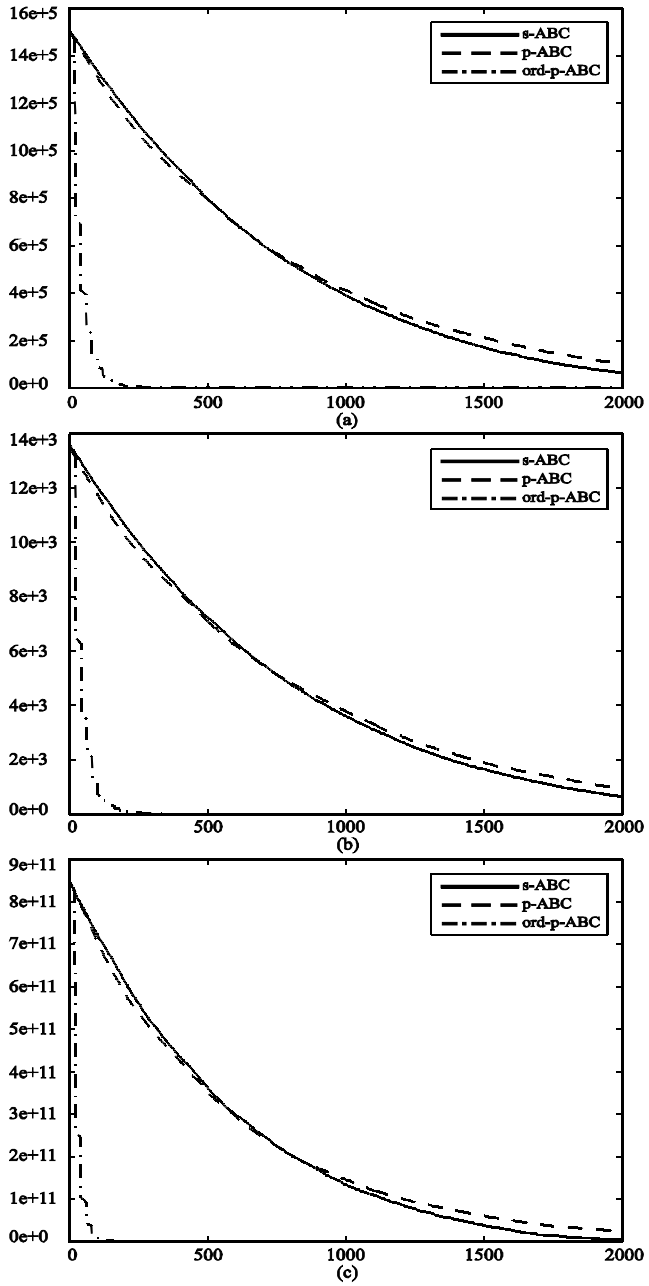


Figure 2: Convergence graphics of the ABC algorithms for f_1 (a), f_2 (b) and f_3 (c) functions

In order to analyze the effect of order based emigrant creation strategy on the convergence performance of the parallelized ABC algorithm, the graphics given in the Fig. (2) should be examined. As seen from the graphics, it is clear that the convergence performance of the ord-p-ABC algorithm is remarkably better than those of s-ABC and p-ABC algorithms. While p-ABC algorithm converges a bit faster that the s-ABC algorithm within the first quarter of the total number of cycles, s-ABC algorithm provides a sustainable convergence to the global optimum within the remaining cycles for the f_1, f_2 and f_3 functions. With the start of the distribution of the emigrant food sources, ord-p-ABC algorithm quickly diverges from the convergence curves of the s-ABC and p-ABC algorithms and maintains its superior performance until the end of the cycles.

V. CONCLUSION

In this study, we proposed a new emigrant creation strategy in which the best food source found in the current migration period is modified by the more appropriate parameters of another food source determined sequentially. Newly proposed approach that is also called order based emigration creation strategy is used with the parallel implementation of the ABC algorithm. Experimental studies showed that order based emigrant creation strategy is significantly improved the quality of the finals solutions and convergence performance of the parallel ABC algorithm compared with the conventional serial and parallel implementation of the algorithm.

REFERENCES

[1] B. Kumar, D. Kumar, "A Review on Artificial Bee Colony Algorithm", International Journal of Engineering & Technologies, vol. 2, no. 3, 2013.

[2] J.C. Bansal, H. Sharma, S.S. Jadon, "Artificial Bee Colony Algorithm: A Survey", International Journal of Advanced Intelligence Paradigm, vol. 5, pp: 123-159, 2013.

[3] A.L. Bolaji, A.T. Khader, M.A. Al-Betar, M.A. Awadallah, "Artificial Bee Colony Algorithm, its Variants and Applications: A Survey", Journal of Theoretical & Applied Information Technology, vol. 47, no. 2, pp: 434-459, 2013.

[4] D. Karaboga, B. Gorkemli, C. Ozturk, N. Karaboga, "A Comprehensive Survey: Artificial Bee Colony Algorithm and Applications", Artificial Intelligence Review, vol. 42, no. 1, pp: 21-57, 2014.

[5] P. Borovska, V. Gancheva, N. Landzhev, "Massively Parallel Algorithm for Multiple Biological Sequences Alignment", International Confe-rence on, 2013, pp: 638-642.

[6] S. Aslan, C. Öztürk, "A New Artificial Bee Colony Algorithm to Solve the Multiple Sequence Alignment Problem", International Journal of Data Mining and Bioinformatics, vol. 14, no. 4, pp: 332-353, 2016.

[7] T. Batbat, C. Ozturk, "Protein Structure Prediction with Discrete Artificial Bee Colony Algorithm", International Journal of Informatics Technologies, vol. 9, no. 3, 2016.

[8] H. Badem, A. Baştürk, A. Çalışkan, M. Yüksel, "A New Efficient Training Strategy for Deep Neural Networks by Hybridization of Artificial Bee Colony and Limited-Memory BFGS Optimization Algorithms", Neurocompuing, 2017.

[9] B. Akay, D. Karaboga, "A Survey on the Applications of Artificial Bee Colony in Signal, Image and Video Processing", Signal, Image and Video Processing, vol. 9, pp: 967-990, 2015.

[10] N. Karaboga, “A new design method based on artificial bee colony algorithm for digital IIR filters”, Journal of the Franklin Institute, vol. 346, no. 4, pp: 328-348, 2009.

[11] G. Zhu, S. Kwong, “Gbest-guided Artificial Bee Colony Algorithm for Numerical Function Optimization”, Applied mathematics and computa-tion, vol. 217, no. 7, pp: 3166-3173, 2010.

[12] L. dos Santos Coelho, P. Alotto, “Gaussian artificial bee colony algorithm approach applied to Loneys′ solenoid benchmark problem”, IEEE Transactions on Magnetics, vol. 47, no. 5, pp: 1326-1329, 2011.

[13] D. Karaboga, B. Gorkemli, “A quick artificial bee colony (qABC) algorithm and its performance on optimization problems”, Applied Soft Computing, vol. 23, pp: 227-238, 2014.

[14] W. Gao, S. Liu, “Improved artificial bee colony algorithm for global optimization”, Information Processing Letters, vol. 111, no. 17, pp: 871-882, 2011.

[15] W. Xiang, S. Ma, M. An, “Habcde: a hybrid evolutionary algorithm based on artificial bee colony algorithm and differential evolution”, Applied Mathematics and Computation, vol. 238, pp: 370-386, 2014.

[16] B. Wu, C. Qian, W. Ni, S. Fan, “Hybrid harmony search and artificial bee colony algorithm for global optimization problems”, Computers & Mathematics with Applications, vol. 64, no. 8, pp: 2621-2634, 2012.

[17] A. Banitalebi, M. I. A. Aziz, A. Bahar, Z. A. Aziz, “Enhanced compact artificial bee colony”, Information Sciences, vol. 298, pp: 491-511, 2015.

[18] H. Narasimhan, “Parallel Artificial Bee Colony (PABC) Algorithm", World Congress on Nature and Biologically Inspired Computing (Na-BIC), Coimbatore, India, 2009, pp: 306-311.

[19] A. Banharnsakun, T. Achalakul, B. Sirinaovakul, “Artificial Bee Colony Algorithm on Distributed Environments", Second World Congress on Nature and Biologically Inspired Computing (NaBIC), Fukuoka, 2010, pp: 13-18.

[20] R. Luo, T.S. Pan, P.W. Tsai, J.S. Pan, “Parallelized Artificial Bee Colony Algorithm with Ripple-Communication Strategy", Fourth International Conference on Genetic and Evolutionary Computing (ICGEC), Shen-zen, 2010, pp: 350-353.

[21] M. Subotic, M. Tuba, N. Stanarevic, “Parallelization of the Artificial Bee Colony Algorithm", Proceedings of the 11th WSEAS International Conference on Neural Networks, Evolutionary Computing and Fuzzy Systems, 2010, pp: 191-196.

[22] M. Subotic, M. Tuba, N. Stanarevic, “Different Approaches in Parallelization of the Artificial Bee Colony Algorithm", International Journal of Mathematical Models and Methods in Applied Sciences, vol. 5, pp: 755-762, 2011.

[23] A. Baştürk, R. Akay, “Performance Analysis of The Coarse-Grained Parallel Model of The Artificial Bee Colony Algorithm", Information Sciences, vol. 253, pp: 34-55, 2013.

[24] D. Karaboga, S. Aslan, “Best Supported Emigrant Creation for Parallel Implementation of Artificial Bee Colony Algorithm", IU-Journal of Electrical & Electronics Engineering, vol. 16, no. 2, pp: 2055-2064, 2016.

[25] S. Aslan, H. Badem, D. Karaboga, A. Baştürk, “A New Sychronous Parallel Artificial Bee Colony Algorithm", 1st International Conference on Engineering Technology and Applied Sciences, 2016, pp: 734-744.

[26] D. Karaboga, S. Aslan, “A Discrete Artificial Bee Colony Algorithm for Detecting Transcription Factor Binding Sites in DNA Sequences", Genetics and Molecular Research, vol. 15, no. 2, 2016.

Risk Management in Startups: How Using Lean Principles Helps Startups Manage Their Risks More Efficiently

C.ÇUBUKÇU[1] , S.GÜLSEÇEN[2], S. TOLUN TAYALI[3]

[1] Maltepe University, Istanbul/Turkey, ceren.cubukcu@gmail.com
[2] Istanbul University, Istanbul/Turkey, gulsecen@istanbul.edu.tr
[3] Istanbul University, Istanbul/Turkey, stolun@istanbul.edu.tr

***Abstract* - The goal of this paper is to analyze the startup companies which used lean principles in order to grow. Building a startup is a complex task with full of uncertainties. Therefore, when startups implement lean principles into practice, they also reduce their risks and increase their chances of survival. Although risk management for businesses is a topic that has been covered widely in literature, risk management for startup companies is a pretty recent topic which needs to be examined further. This article first highlights the growing interest to the topic of risk management in startups. Then, it explains lean principles and finally, examines the case studies of three startup companies; Dropbox, Zappos and Groupon to show how applying lean principles helped them become successful. The paper ends with conclusions of the work along with recommendations for future research topics.**

***Keywords* – Risk Management, Lean Principles, Startups, Innovation, Entrepreneurship**

I. INTRODUCTION

Innovation is a risky business and over 98% of new product ideas fail [1]. Nonetheless, risk processes do not require a strategy of risk avoidance but an early identification and management [2]. Therefore, integrating risk management principles can help innovation projects become successful. Foremost among these innovators and risk takers are startups. New startup companies are founded every day. Today's technology such as cloud systems, web development platforms, open source software and mobile technologies makes it easy to implement an internet or mobile technology project [3]. Nowadays anyone who wants to start a digital business can carry out this with the tools they use for free or for a small fee. However, not all of these businesses succeed because building a startup is very risky which is full of uncertainties. In fact, startups failure rate is 90% [4].

One of the most common reasons why startups fail is that they run out of money while trying to build their products [5]. Startups have limited resources in terms of people and tight deadlines [3]. In addition, cofounders often make the mistake of falling in love with their own ideas and neglect the customers completely. They build the product they believe is the right solution for the market but after launch, they realize that they actually built the wrong product and customers want something else. Unfortunately, understanding what the right product should be takes time and meanwhile, because these startups have wasted all of their time and money building the wrong product, many of them fail [5].

Risk management in innovation projects of corporations is a topic that has been covered before in different studies. Studies recommend stage gate approach, which is also called the waterfall approach, for new innovations [6]. This approach divides the project into many different stages allowing the project owners to make the decision of abandoning the project or moving on the next stage [6]. However, the traditional waterfall model for developing a product is not suitable for many startups due to their time and budget restraints. Thus, startups should apply agile processes to develop their products and lean principles for managing their risks. Nonetheless, literature lacks information about risk management in startups. This study aims to fill this gap by providing an overview of lean principles and how startups which use these principles can reduce their risks of failure and become successful.

In the following sections of this paper, in order to draw attention to the importance of risk management in startups and entrepreneurship, a search in Web of Science database is conducted for papers which include the keywords "risk management" and "entrepreneurship". The results of this search show us the growing interest to the topic. Then, a theoretical review of lean principles is presented using recent studies in literature in addition to case studies of several startup companies including Dropbox, Zappos and Groupon which used lean principles for better risk management. Finally, the conclusions of the study are presented.

II. RISK MANAGEMENT IN STARTUPS

Risk management is a topic that has been covered a lot in the scientific community. However, it has been studied mainly in the context of enterprises. Entrepreneurship and startup topics were also examined by researchers but the combination of risk management and entrepreneurship has been neglected most of the time. In order to emphasize the growing interest to the topic of risk management in entrepreneurship, a search has been conducted in ISI Web of Knowledge database. This study has been inspired from a previous study of Trimi and Mirabent [7]. The keywords "risk management" and "entrepreneurship" has been searched for the past 10 years, from 2007 until 2017. The search results returned 63 papers. Figure 1 below shows how these papers are distributed over time. From this figure, it can be understood that the research interest in this topic has been growing especially since 2013. When the research has been further restricted to include the keywords "risk management" and "startup", the search results only returned 6 papers.

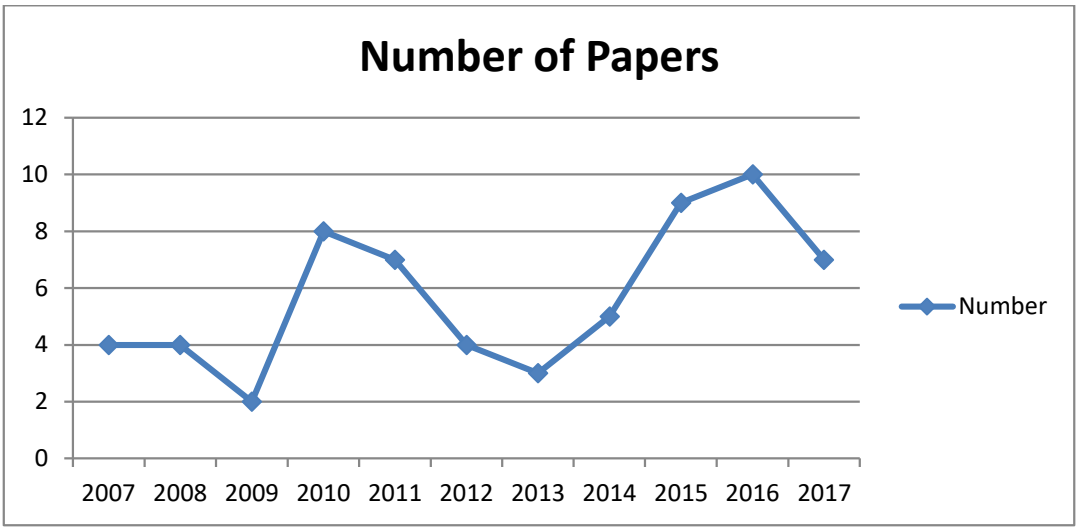


Figure 1: Distribution of papers between the years 2007-2017

A. A. Lean Principles

Lean basically has seven principles. These are; optimize the whole, eliminate waste, build quality in, learn constantly, deliver fast, engage everyone and keep getting better [8]. These principles originate from lean manufacturing. Unlike Henry Ford's style of mass production, Japanese Toyota launched a new system to produce automobiles with almost half the number of labor hours and much faster inventory turns compared to its US competitors [8]. This system enabled Toyota to do "just in time" (JIT) final assembly and shipment to dealers eliminating most of the excess inventories [8]. Later on, researchers in MIT popularized the terms JIT and lean and actually, started to associate lean with agile software development process. Nowadays, lean stands for a less bureaucratic, more iterative and flexible software development model. Moreover, due to Eric Ries's "The Lean Startup" book, it is now the must-used method of building a startup [9].

In order to increase their chances of getting successful, startups should implement lean principles into practice. Unlike the traditional waterfall method, lean principles minimize waste in terms of time and money. It simply creates more value for customers with fewer resources [10]. Most importantly, it requires constant engagement with customers and a continuous learning environment [8]. As a result of this, startups only build the minimum viable product (MVP) for their launches. MVP is a version of a new product which allows a team to collect the maximum amount of validated learning about customers with the least effort [9]. After building the MVP, startups shouldn't terminate the product development but instead, continue testing the product with new hypotheses and keep refining it again. From Figure 2, it can be seen that lean product development is a continuous loop.

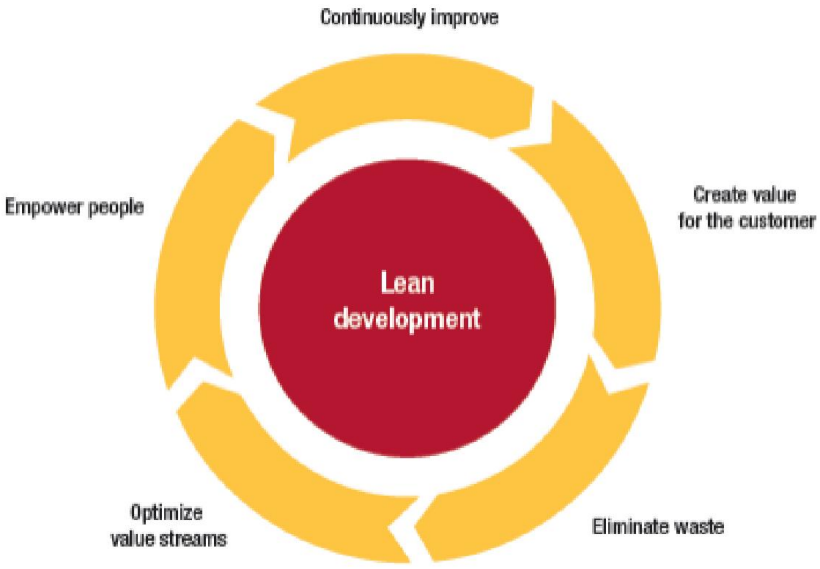


Figure 2: Lean product development cycle [11]

This continuous product development life cycle is also called Build-Measure-Learn. In this method, the build step refers to building a MVP. MVP doesn't need to be an actual product. It can be a prototype or simply a landing page, a presentation, a video or anything that allows you to measure your target segment [12]. The measure step refers to getting traction and feedback from customers. In this step, you will understand if there is enough interest in your product to keep developing it or not. Finally, the learn step refers to what you learnt from this feedback and how you are going to transform this knowledge into the product development. There are two ways forward from this step on. You will decide whether to persevere or pivot, which is another main concept within the lean startup strategy [3].

Pivoting means a change in the direction of where the company is going based on feedback from customers. Most successful startup companies often end up changing directions based on customer data and in fact, many of them shift into a completely new direction [3]. These shifts can be changes in customer targets such as aiming to market for different customer segments from the one intended at the beginning. It can be changing the product completely or changing only some of the features of the product. It can also be a change in the business model such as transforming the product to be subscription based rather than transaction based [5]. After pivoting, startups should test their new models with new hypotheses to figure out whether this change is actually what they need or they need something else. Startups often fear that pivoting means failure but pivoting is not a sign of failure in the concept of lean strategy. Thus, startups shouldn't fear from pivoting.

As it is understood from above, in the lean context the focus is always on delivering customer value while minimizing waste and learning constantly from feedbacks to keep altering the product. In this way, the risk of wasting a lot of money for building a product that no one wants is minimized. On the contrary, when the products are built according to the requirements of customers, startups can sell their products and maintain a successful business. In the next section, case studies of startups which implemented lean principles into their product developments will be discussed together with how implementing these principles helped them reduce their risks will be explained.

III. CASE STUDIES

In this section, the case studies of startup companies which successfully implemented lean principles into practice will be analyzed with examples. These companies are Dropbox, Zappos and Groupon.

A. Dropbox Case Study

Dropbox started with a simple landing page which explains what the product is. There was also a field in the landing page where interested users could leave their email addresses to get further information about the developments of the product. Figure 3 shows the first landing page of Dropbox. The company received 5,000 signups with this landing page [13]. However, the actual peak came when the company launched a 3 minute demo video in 2007 [14]. They published this video in a platform called Digg, a platform for early adopters of any new technology. The video drew people to

the Dropbox website and their signups grew from 5,000 to 75,000 in just one night [14]. Dropbox used this video to measure the interest in their products because they didn't want to waste the time and energy to build a product that no one wants. Dropbox didn't even have an actual product to release. They only had a video which looked like a demo of the product. In this case, this video was their MVP.



Figure 3: Dropbox landing page in 2006 [13]

The company decided whether to continue with the product development, to quit developing the product completely or to pivot it. Due to the growing interest in their products, founders of Dropbox decided to continue the development process. Dropbox reached to 1 million users in 7 months and in 15 months, in January 2010, it reached to 4 million registered users [13]. Dropbox reached these 4 million users with the help of its 75,000 early adopters because these adopters referred Dropbox to their friends. After understanding that referrals are driving most of the business, founders did some pivots along the way especially in online marketing strategies in order to cut their customer acquisition costs and gave importance to referrals. Now, the company is valued at $10 billion and has over 500 million users, saving a cumulative 1.2 billion files daily [14].

B. Zappos Case Study

Zappos used the Build-Measure-Learn method to test its hypothesis. When Zappos started out in 1999, founders didn't know if people were ready to buy shoes online [15]. However, building an ecommerce website with inventory management and a distribution center would cost the founders thousands of dollars and they didn't want to take this risk just to test this hypothesis of whether people would buy shoes online. Instead, they used a much simpler approach. They talked with the local shoe stores, took the pictures of their products and posted these pictures online to a much simpler website. This website was their MVP. If people bought shoes from the website, they would go to the store, buy the product from the full price and then, ship it themselves. From Figure 4, Zappos' MVP life cycle solution can be seen. First, they built a simple website, then; they run an online campaign to drive traffic to the website. Later on, they measured whether there are enough sales and finally proved their hypotheses. "Through this process, the hypothesis was validated and the full site was built – which was then sold to Amazon for a billion dollars [16]."

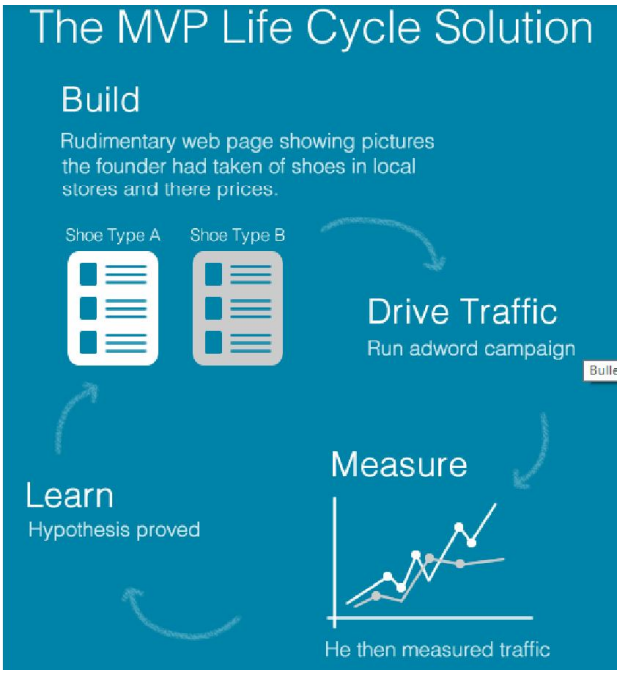


Figure 4: Zappos MVP solution [17]

C. Groupon Case Study

One of the most famous pivots of the tech history belongs to Groupon. Groupon was actually a website called "The Point" launched in 2007 [18]. The Point was a fundraising website for social good projects running on a tipping point system. It was similar to the crowdfunding logic used today which only allows campaigns to receive the donations only if the project reaches enough backers. Then, The Point's founder, Andrew Mason, decided to apply this concept to commerce and launched Groupon in 2008 as a side project [19]. The idea behind Groupon was based on getting discount for group buying. For example; if 20 people want to buy the same shirt, then, they should get a discount for it. This concept was already available for buying

concert or theater tickets so why not apply it to shopping. Groupon started giving discounts on local activities and services, all of which would only be unlocked if enough users signed up. Eventually, Groupon outweighed The Point and became Mason's main business. Groupon's format spread so quickly around the world that every country founded its own Groupon and the company acquired some of its clones around the world becoming the daily deal tycoon we know today.

IV. CONCLUSIONS

This paper uses case studies of Dropbox, Zappos and Groupon which applied the lean principles into their processes for better risk management. Based on these case studies, it can be clearly understood that when startups implement lean principles, their success rate increases dramatically. This is due to the fact that lean startups give importance to the customers rather than the product. They avoid waste in terms of time and money by getting customer feedback in every major milestone of the product development. Therefore, when the product is launched, customers finally have a solution that matches to their problems. As a result, startups can sell their products and become successful.

Different strategies of lean principles were explained in this study through examples. In Dropbox example, the importance of MVP is emphasized. In Zappos case, Build-Measure-Learn method is explained. Finally, in Groupon method, the importance of pivoting is described. As a result, all three of them reduced their risks significantly and became the successful companies we know today. In this study, startups located in the US and which are very well known by everyone have been examined. There are many other startups in different parts of the world that implement lean principles in order to reduce their risks. Future researches can include different startups from different countries. Also, another future research topic worth exploring can be the challenges startups face while implementing lean principles.

V. REFERENCES

[1] Mullins, John Walker, and Randy Komisar. *Getting to plan B: Breaking through to a better business model*. Harvard Business Press, 2009.

[2] Keizera, Jimme A., Johannes IM Halman, and Michael Song. "From experience: applying the risk diagnosing methodology." Journal of product innovation management 19, no. 3 (2002): 213-232.

[3] Bosch, Jan, Helena Holmström Olsson, Jens Björk, and Jens Ljungblad. "The early stage software startup development model: a framework for operationalizing lean principles in software startups." In *Lean Enterprise Software and Systems*, pp. 1-15. Springer, Berlin, Heidelberg, 2013.

[4] Forbes.com. (2017). *Forbes Welcome*. [online] Available at: https://www.forbes.com/sites/neilpatel/2015/01/16/90-of-startups-will-fail-heres-what-you-need-to-know-about-the-10/#234d88346679 [Accessed 15 Oct. 2017].

[5] Nobel, Carmen. "Teaching a Lean Startup Strategy." *HBS Working Knowledge* (2011): 1-2.

[6] Bowers, John, and Alireza Khorakian. "Integrating risk management in the innovation project." *European Journal of innovation management* 17, no. 1 (2014): 25-40.

[7] Trimi, Silvana, and Jasmina Berbegal-Mirabent. "Business model innovation in entrepreneurship." *International Entrepreneurship and Management Journal* 8, no. 4 (2012): 449-465.

[8] Poppendieck, Mary, and Michael A. Cusumano. "Lean software development: A tutorial." *IEEE software* 29, no. 5 (2012): 26-32.

[9] Ries, E., 2011. The lean startup: How today's entrepreneurs use continuous innovation to create radically successful businesses. 1st edition, Crown Business, ISBN: 978-030-788-789-4

[10] Bicheno, John, and Matthias Holweg. *The lean toolbox*. Vol. 4. Buckingham: PICSIE books, 2000.

[11] Ebert, Christof, Pekka Abrahamsson, and Nilay Oza. "Lean software development." IEEE Software 29, no. 5 (2012): 22-25.

[12] Mindtools.com. (2017). The Build-Measure-Learn Feedback Loop: Creating Real Value by Testing Ideas. [online] Available at: https://www.mindtools.com/pages/article/build-measure-learn.htm [Accessed 24 Oct. 2017].

[13] Kumar (2017). Dropbox: Building Business Through Lean Startup Principles. [online] Slideshare.net. Available at: https://www.slideshare.net/vishaltx/dropbox-startup-lessons-learned-16991502 [Accessed 24 Oct. 2017].

[14] Medium. (2017). How Uber, Airbnb & Dropbox Released MVPs to Achieve Rapid Growth. [online] Available at: https://medium.com/@LoganTjm/how-uber-airbnb-dropbox-released-mvps-to-achieve-rapid-growth-d823ac6eaed5 [Accessed 24 Oct. 2017].

[15] Muckersie, E. (2017). FreshMinds - 3 examples of lean startup in action. [online] Freshminds.net. Available at: http://www.freshminds.net/2016/09/3-examples-of-lean-startup/ [Accessed 24 Oct. 2017].

[16] Ford, M. and Ford, M. (2017). The Lean Startup Methodology. [online] MATTYFORD. Available at: https://mattyford.com/blog/2014/11/11/the-lean-startup-methodology [Accessed 24 Oct. 2017].

[17] Bullet Marketing. (2017). Lean Startup Zappos: How Zappo's Validated Business Model With Lean. [online] Available at: https://www.bullethq.com/lean-startup-zappos-how-zappos-validated-their-business-model-with-lean/ [Accessed 24 Oct. 2017].

[18] Bryant, M. (2017). 10 Great Tech Company Pivots - TNW Insider. [online] The Next Web. Available at: https://thenextweb.com/insider/2011/09/13/10-great-tech-company-pivots/ [Accessed 24 Oct. 2017].

[19] Washington Post. (2017). The 7 greatest pivots in tech history. [online] Available at: https://www.washingtonpost.com/news/innovations/wp/2015/07/02/the-7-greatest-pivots-in-tech-history/?utm_term=.7c23b7b5e7fa [Accessed 24 Oct. 2017].

Motivations to Develop an Information System for People with Down Syndrome

Haitham AL-TAMEEMI[1]

Turan Erman Erkan[2]

[1] Atilim University, Ankara/Turkey, hai_mah2003@yahoo.com
[2]Atilim University, Ankara/Turkey, erman.erkan@atilim.edu.tr

***Abstract* - Health Information Technology (HIT) is refers to the use of electronic methods in order to manage information system about the health status for individuals. People with Down syndrome classify as intellectual disability, and they needs to support in all scopes especially in their health status. The aim of this article is to determine the most health problems and other problems related to healthcare that face people with Down syndrome by review some literatures. These problems can be a first step to develop a new system for them to provide a proactive health service, in addition to manage, monitor, and track their health status. Finally, the proposed step for this system will listed, but the components of it will be the subject of the next study.**

***Keywords* – Down syndrome, Healthcare, Health Information System, Information System, Information Technology, system Development.**

I. Introduction

John Langdon Down is the first physician described Down syndrome (DS) as a kind of disability in 1866. He describe it as a genetic condition (not a human disease) shows in 1 of 700 babies in the world [1]. This condition appear if human cells contain an extra copy of chromosome 21 (Three copies of chromosome 21). This chromosome leads to an imbalance in the body's physiological functions. In addition, limit the ability of some functions to work normally, and emergence the health problems [2]. DS classified in three types of genetic variation [3]:

1) Trisomy 21 is the most common type and effect on 94% of cases. It found when all human cells contains three copies of chromosome 21. This type of DS leads to a defect in the external face shape, as well as dysfunction in the vital functions.
2) Translocation is rare condition and effect on 4% of cases. It found when all human cells contains two copies of chromosome 21 but one of them attached with another chromosome. This type of DS leads to appear a health problem that related with DS.
3) Mosaicism is less common type and effect on 2% of cases. It found when some human cells contains three copies of chromosome 21. Babies with this type are look like normal, but they have little bit health problems that related with DS.

Information technology contribute today's to success the business global environment through invest it in all life scopes. Health information system is one of invest information system and technology in healthcare by using a set of components and activities to manage and enhance provide health services to citizen by collect, store, retrieve, and transfer information electronically. Also, Health information technology refer to activities with technologies that working in health sector to manage and support this sector electronically. Therefore, design any system or application needs to cover problems that face customers, to identify their need of this system or technologies [4, 5]. This is what authors will focus on in the next section. Follow that, evaluate these problems and the methodology of this work and the planning of future studies.

II. Health Status of People with Down Syndrome

In this section, some articles about the most health problems for people with DS will surveyed.

In the beginning we want to say, that the non-compliance with the guidelines of medical academies contributes to lack the controlling of disease especially when we talking about people with DS. Williams made a survey about 124 children with DS, and he discovered that they do not receive recommend health care services according of 2001 American Academy of Pediatrics. He said that they lack adherence recommendations tested of some diseases like: blood test was 55%, thyroid function test was 61%, audiology test was 33%, ophthalmology test 43%, and otolaryngologist lower of others [6].

A. Cognitive Deficit

Cognitive deficit describe individual's weakness in mental processes to dealing with information in the society. Intelligence Quotient (IQ) is standardized intelligence test used to measure the cognitive deficit, and if it is less than 70 it means this person fall in low range. IQ test for person with DS can be in the best case is between 50 -70, or can be less than 50. This scope can limit a person's ability in their attention, decision-making, ability to speaking and memorizing [7, 8].

B. Hearing Loss

The good hearing contribute to develop speech and language as well as socialization. However, for people with DS it is a big problem because it occur in more than 75% of them [8-10]. in the Sie Center for DS at Children's Hospital Colorado a retrospective study for 308 child's proved that the permanent hearing loss was occur in 24.9% of them, and between 22%-30% of them had a transient hearing loss. In the German Special Olympics Summer Games 2004 and Japan Special Olympics Winter Game 2005 a Special

Olympics Healthy Hearing Program used to detect the hearing problems for Athletes, and the results shows there around 40% of them failed to pass this test. Ultimately must to note that the early diagnosis and follow up, in addition to use Hearing aids can helps people who had this condition especially for young. For this reasons the physicians recommends to make an auditory testing every two years for them. [8-14].

C. Obstructive Sleep Apnea

Obstructive sleep apnea is one of the most health problem faced people with DS, it occur in up of 50% of them, the certain characteristic physical features and structural abnormalities contribute to develop this problem such as large tongue and maxillary hypoplasia, in addition other features such as obese. This health condition can cause other health problems such as cardiovascular disease. A Polysomnography or sleep study are usually used to diagnoses this condition during sleep to collect the data related sleep such as monitoring the Oxygen levels and sleep behaviors, and the physicians recommend to make this test every two years for people with DS [9, 15-18].

D. Heart Defect

The previous studies refer the percentage of heart defect of people with DS over up 50% of them. For this reasons the American Academy of Pediatrics (AAP) recommends an echocardiogram (a sound “picture” of the heart) for all infants with DS and evaluation from a pediatric cardiologist [8].

Pediatric with DS in Saudi Arabia also have a high percentage of congenital heart defect according a retrospective study of patient from August 2001 to October 2014. This study shows the percentage of this condition is about 69.5% of the participants (230 patients). The most common type is Atrial Septal Defect (33.5%) follow that Ventricular Septal Defect (26.5%), atrioventricular septal defect (21.7%), Patent Ductus Arteriosus (21.7%), and 11.7% have other types of heart defect [19].

Mitral valve prolapse also one of the most common heart defect of DS that need to monitoring constantly over the time by make some medical tests, it occur about 57% of patients with DS [9].

There is association between congenital heart defects and other health problems, for this reasons some physicians can recommend to make an overall testing if a patient have heart defect. for example in southern Brazil, a 89 of 127 (70.1%) patients between 6 and 48 months had some type of congenital heart disease, 37.7% of them need urgent surgery, and 70% of them had associated with congenital heart disease [20]. In addition, monitoring patients especially who have a sleep apnea or snoring is necessary to control the patient's health status [21].

Mıhçı et al., also established a paper-research about the heart diseases of DS in Turkey, and they found approximately 72% of them have a different heart diseases concluded a congenital heart disease [22].

Finally, we must say that people with DS have a large health problems and conditions more than normal people. Some of these problems needs an immediate care, others need to a continue care and follow-up. Guralnick shows that the earlier intervention for people with DS will be improve their life [23, 24].

E. Gastrointestinal diseases

The earlier diagnosis help the specialists to identify the health problems. Some of this diseases caused death. Gastrointestinal diseases like High prevalence of GERD and swallowing disorders is one of common DS diseases. It occur about 12% of patients with DS. Massimo and Staiano shows the motility disorders was complicate the phenotype of primary diseases for this kind of patients. Therefore, the need to follow-up and monitor these diseases is urgent need to diagnoses and rescue of patients from a dangerous diseases [9, 25, 26].

F. Hypothyroidism

Hypothyroidism occur about 10-40%, the physicians recommend to make test for thyroid-stimulating hormone levels annually especially if the patients have some kind of heart defect. Maire and her partner make a pilot and exploratory study about the relationship between heart diseases and other diseases like Dementia Test Battery (DTB) for Alzheimer and hypothyroidism. This sample applied for 29 patients, the analysis of these information shows a high related with between heart disease and low score of DTB in people who have a treated hypothyroidism [9, 27, 28].

G. Other problems related with healthcare

In addition medical problems. People with DS face another problem that related to their health status.

Insurance is one of the important required of humane especially for people with disability [29]. For example, a survey reports in the United States from 2002 to 2003 shows that 60% of adults 19-29 with disability don't have an insurance, this prove they have lack of health care while they are most in need of this service [30].

Smith shows that the family physician's approach is a based to provide the good medical care for all people especially who have a DS [9].

At present, the diagnosis of DS could happen before child is born. For example, in United State there are 87% of parents know their child is DS after born, this leads parents afraid for the future of their child. In Spain, a survey of 467 mothers of children with DS said they do not have an optimal health services before born of DS, and they recommend providing a professional physicians to deal with them. In addition, get an optimal support from the government and society [31].

Moreover, the cost of medical services, Boulet et al. said that the child with DS still face a challenges of increase the cost of healthcare services. He presented a study about the 2004 Medstat MarketScan database to estimate the healthcare services for children. and he concluded that the child with DS have a 12 to 13 times higher cost than others without DS if they have a cardiac conditions, and about 7 times higher if they don't have a cardiac conditions [32]

Dr. Stein explained that the behavior of adults with DS can change according of several factors, these factors base

on the social life like loss of their older brothers and friends, death of lover, out of the home, transfer into work situation, etc. [33].

The responsibility to provide medical services rest to all medical service providers (public and private), especially those who have a special case such as DS. Therefore, Marshall et al. said DS and their parents need support in five scopes: during birth, accessing to medical services, manage medical services, supporting in all their life scopes. So, they made interviews for a random sample that consist of 50 persons (5 therapists, 7 nurses, 25 coordinators, 10 parents English-speakers, and 3 parents Spanish-speakers) to understand the experience of all of them to dealing with DS. This team identified some challenges related to access the information about DS to increase their knowledge and experience about dealing with them. The authors concluded that the problems related to unavailable special-clinic to treat, monitor, and track people with DS. So, the healthcare system until now don't able to provide services for DS and their families, at the time they need a high quality supports in all life scope [34].

III. Evaluate Problems of Down Syndrome

As we shown in previous section, people with DS face big challenges to life independently in the society. In this section, we try to determine these problems.

1) People with DS do not able to describe their medical case, because DS is a type of intelligent disability, and they often needs someone to supervise them.
2) People with DS need a special medical care, because they have big medical problems. In addition, there are a relationship between some diseases.
3) People with DS lack early medical intervention.
4) People with DS lack supporting in all scopes like full insurance.
5) The communication between doctors and people with DS is still weak, because they do not have family doctors to solve their medical and social problems (do not apply family doctor approach).
6) Some people with DS needs continuous periodic reviews.

IV. Methodology

Developing new system needs to gather information about the problems in general.

Therefore, the author tried to cover these problems from the previous study. In addition, he will prepare a questionnaire form to distribute among families whose have a member with DS. This questionnaire will contain set of questions about DS to confirm previous studies, such as (did DS have health problem, problem type, did they have a family doctor, how many time DS face an emergency case, did they have a health support, and so on), this questionnaire will distribute to get results, and finally statistical analysis will carry out and compare it with previous study.

A development system approach or application with all steps and components will determine later.

V. Conclusion

According the previous studies and problems that presented previously, we conclude that these problems for DS can be a motivation for us to think about dedicate new system or application to manage, protect, and control the DS life style especially in their health scope.

References

[1] Megarbane A, Ravel A, Mircher C, et al, "The 50th anniversary of the discovery of trisomy 21: the past, present, and future of research and treatment of Down syndrome", Genet Med 2009;11:611-6.

[2] Kazemi Mohammad, Mansoor Salehi, and Majid Kheirollahi. "Down Syndrome: Current Status, Challenges and Future Perspectives", International Journal of Molecular and Cellular Medicine 5.3 (2016): 125.

[3] Cliff Cunningham, "Down syndrome: an introduction for parents and carers" Souvenir Press, 2011.

[4] Lippeveld, Theo, et al. "Design and implementation of health information systems." (2000).

[5] Cliff, Barbara. "Using Technology to Enhance Patient-Centered Care." Journal Of Healthcare Management 57.5 (2012): 301-303.

[6] Williams, Katie, et al. "Disparities in Health Supervision for Children With Down Syndrome." Clinical Pediatrics (2017): 0009922816685817.

[7] Diana W Schofield. "Cognitive Deficits", PsyD Assistant Professor of Pediatrics, available web site: http://emedicine.medscape.com/article/917629-overview#a2, last update : Jan 20, 2016.

[8] Bull, Marilyn J, "Health supervision for children with Down syndrome", Pediatrics 128.2 (2011): 393-406.

[9] Smith, DAVID S. "Health care management of adults with Down syndrome." American family physician 64.6 (2001): 1031-1044.

[10] Sacks, Ben, and Amanda Wood. "Hearing disorders in children with Down syndrome." Down Syndrome News and Update 3.2 (2003): 38-41.

[11] Nightengale, Emily, et al. "Understanding Hearing and Hearing Loss in Children With Down Syndrome." American Journal of Audiology26.3 (2017): 301-308.

[12] Kumar Sinha, Ashok, et al. "Hearing screening outcomes for persons with intellectual disability: a preliminary report of findings from the 2005 Special Olympics World Winter Games." International journal of audiology 47.7 (2008): 399-403.

[13] Neumann, Katrin, et al. "Auditory status of persons with intellectual disability at the German Special Olympic Games: Status auditivo de las personas con discapacidad intelectual en los Juegos Olímpicos Especiales de Alemania." International journal of audiology 45.2 (2006): 83-90.

[14] Hildmann, A., H. Hildmann, and A. Kessler. "Hearing disorders in children with Down's syndrome." Laryngo-rhino-otologie 81.1 (2002): 3-7.

[15] Rosen, Dennis. "Obstructive sleep apnea in children with Down syndrome." Sleep Disordered Breathing in Children. Humana Press, 2012. 303-312.

[16] Skotko, Brian G., et al. "A predictive model for obstructive sleep apnea and Down syndrome." American Journal of Medical Genetics Part A 173.4 (2017): 889-896.

[17] Trois, Maria S., et al. "Obstructive sleep apnea in adults with Down syndrome." Journal of clinical sleep medicine: JCSM: official publication of the American Academy of Sleep Medicine 5.4 (2009): 317.

[18] Murto, Kimmo. "Understanding obstructive sleep apnea Syndrome in Children." Current Anesthesiology Reports 5.2 (2015): 125-139.

[19] Alsuhaibani, G., et al. "76. Profile and spectrum of congenital heart defect in pediatric patient with down syndrome." Journal of the Saudi Heart Association 28.3 (2016): 218-219.

[20] Faria, Paula F., et al. "Association between congenital heart defects and severe infections in children with Down syndrome." Revista Portuguesa de Cardiologia (English Edition) 33.1 (2014): 15-18.

[21] Dooley, Kenneth J. "Congenital Heart Disease and Down Syndrome." Health Care for People with Intellectual and Developmental Disabilities across the Lifespan. Springer International Publishing, 2016. 1301-1310.

[22] Mihci, Ercan, et al., "Evaluation of congenital heart diseases and thyroid abnormalities in children with Down syndrome/Down sendromlu çocuklarda konjenital kalp hastaliklari ve tiroid

anormalliklerinin degerlendirilmesi" Anadulu Kardiyoloji Dergisi: AKD 10.5 (2010): 440.
[23] Guralnick, Michael J. "Early intervention approaches to enhance the peer-related social competence of young children with developmental delays: A historical perspective." Infants and young children 23.2 (2010): 73.
[24] Guralnick, Michael J. "Why early intervention works: A systems perspective." Infants and young children 24.1 (2011): 6.
[25] Massimo M., and Staiano A., "Motility Problems in Developmental Disorders: Cerebral Palsy, Down Syndrome, Williams Syndrome, Autism, Turner's Syndrome, Noonan's Syndrome, Rett Syndrome, and Prader-Willi Syndrome.", Pediatric Neurogastroenterology. Springer International Publishing, 2017. 303-309.
[26] Said, S. A. M., et al., "Down syndrome associated with hypothyroidism and chronic pericardial effusion: echocardiographic follow-up", Netherlands Heart Journal 15.2 (2007): 67-70.
[27] Percy, Maire E., and Walter J. Lukiw. "Is heart disease a risk factor for low dementia test battery scores in older persons with Down syndrome? Exploratory, pilot study, and commentary." International Journal of Developmental Disabilities (2017): 1-14.
[28] Pierce, Melinda J., Stephen H. LaFranchi, and Joseph D. Pinter. "Characterization of Thyroid Abnormalities in a Large Cohort of Children with Down Syndrome." Hormone Research in Paediatrics87.3 (2017): 170-178.
[29] White Patience H., "Access to health care: health insurance considerations for young adults with special health care needs/disabilities", Pediatrics110.Supplement 3 (2002): 1328-1335.
[30] Callahan, S. Todd, and William O. Cooper, "Access to health care for young adults with disabling chronic conditions", Archives of pediatrics & adolescent medicine 160.2 (2006): 178-182.
[31] Skotko Brian, and Ricardo Canal Bedia, "Postnatal support for mothers of children with Down syndrome", Mental Retardation 43.3 (2005): 196-212.
[32] Boulet Sheree L., et al., "Health care expenditures for infants and young children with Down syndrome in a privately insured population", The Journal of pediatrics 153.2 (2008): 241-246.
[33] Stein, D. Bethesda, "Supporting Positive Behavior in Children and Teens with Down Syndrome", MD: Woodbine House. (2016).
[34] Marshall, J., et al., "Services and supports for young children with Down syndrome: parent and provider perspectives", Child: care, health and development 41.3 (2015): 365-373.

Predict Public Opinion in Online Reviews with Imbalance Dataset and Feature Number

M. MURAD[1] and M. EKINCI[2]

[1]Karadeniz Technical University, Trabzon/Turkey, mahmoudmurad@ktu.edu.tr
[2]Karadeniz Technical University, Trabzon/Turkey, ekinci@ktu.edu.tr

Abstract - **Because of the importance of online reviews, many types of research have been conducted to better understand users' opinion. One of the problems in online reviews is the imbalance in datasets and feature numbers. In this paper, user's opinion is considered to be a set of feeling, and to better understand and predict users' feeling, a combination of Natural Language Processing and Machine Learning algorithms used. However, to solve the imbalance problem, based on dynamic domain-specific dictionaries, a new technique in feature extraction has been introduced. We experimented this technique on Yelp dataset with multiple scenarios. Results showed great improvement on performance when using the proposed technique.**

Keywords – **Opinion Mining, Text Classification, Natural Language Processing, Recommendation System, Feature Extraction.**

I. INTRODUCTION

THE popularity of online reviews has been increasing rapidly in recent years and taking major responsibility in users' decision making prosses. That is why most of the business websites like Amazon, Alibaba, and Yelp provide different reviewing systems for their users, reviewing a business could benefit both the company and the customer, from the company perspective: reviews point out what customer prefer and disfavor, which helps the company to meet the customer's requirements and expectations, and eventually, lead to business profits. From the customer perspective: prior studies [1,2] have identified that online reviews and recommendations could have an impact on customer decisions when purchase a product, visit a place, or eat some kind of food. Therefore, understanding users' reviews is a hot research area [3], where researchers try to understand the hidden factors in reviews that motivate the public to interact with reviews (voting) [4,5,6], writing review and rating [7], or what influence users to participate in online communities [8].

The public opinion about a review can be measured through the provided feedback systems by online communities, such as the helpful voting system in Amazon, in which every review related with the number of people founded that review as a helpful, or the voting system of Yelp, which provide three voting options (useful, funny, or cool) for every review, where the Yelp users could choose one or more option to express their opinion about a specific review. Accordingly, public opinion could be considered as a set of feeling, differed from one online reviewing community to another, in Yelp the set of feeling would be useful, funny, or cool because of the voting system provided by the site.

Due to the importance and popularity of online reviews, prediction of good-quality reviews could be quite helpful to increase business profits and users' experience. A good-quality definition could change based on the nature of the reviews, the problem being discussed, and the perspective of the reader. For example, in Yelp for some users, a review with useful votes can be potential for a good- quality review and can affect the users' opinion.

However, one of the common problems in data mining is data imbalance, in which most of the data records belong to one class or more. Imbalance also could be in the number of feature for every record, which makes variable dimension for every feature vector. Such problems lead to insufficient classification. In this paper, we are trying to address this problem by introducing new technique in feature extraction could help in prediction public opinion. We will use a dataset obtained from the feedback voting system in Yelp community, and in addition to our technique, we will use a combination of Natural Language Process (NLP) and Machine learning (ML) algorithms.

Yelp[1] is an online reviewing site, aimed to connect people with great local businesses, founded in 2004, with millions of unique visitors every month through its different platforms, Yelpers (yelp users) have written more than 135 million reviews by the end of the second quarter of 2017.

Our contributions in this paper: First, to the best of our knowledge, we are the first to consider the feedback votes as a prediction problem in the Yelp dataset. Second: based on dynamic domain-specific dictionaries, we introduce a new technique for feature extraction.

As any prediction problem, we started with data cleaning and preprocessing, and in our baseline case, we used two methods from Natural Language Process (NLP), the Bag-Of-Words (POW) and part-of-speech tagging (POS). For prediction, we considered every feedback option as a class, thus, we have three basic classes useful, funny, or cool, and a fourth class if the review did not get any vote which we will call noVotes, then we used three machine learning algorithms, Naive Bayes, linear Support Vector Machine

[1]https://www.yelp.com/about

(SVM), and Logistic Regression for classification.

Due to imbalance in the number of instances in every class and imbalance in the number of features extracted from every review, the accuracy in the smaller classes in the baseline case was almost zero, to overcome this problem, we introduce a new technique based on dynamic domain-specific dictionaries that help improve accuracy in the smaller classes to reach more than 60%.

The remainder of this paper contains the related work to our work, description of the methodology of our work, the used dataset and the cleaning process, and then we describe our experiments on feature extraction methods and machine learning algorithms, finally, we conclude this paper with the discussion of the result and summarization of our work with possible future work.

II. RELATED WORK

Online reviews have been the subject of many studies lately, each study them from different aspects and perspectives. The work of Bakhshi et al. [5] inspired us to look deeper into online reviews' text in Yelp, while their work, by using statistical methods, focusing on exploring and understanding the hidden relationships between user, business, and review, with the feedback options (*useful*, *funny*, or *cool*) in an analytical perspective, we in the other hand, by using NLP and ML algorithms, focusing on just the reviews' text and its relationship with the feedback options in Yelp to predicted public opinion.

Our work in specific focus on two objectives, understanding the features in the review's text, and based on those features predict the public opinion. There is a considerably work in the first objective. Hu & Liu [9] in their work for summarization users review and extract user's opinion, they used a set of adjectives and could it "*opinion words*" to determine wither a sentence positive or negative, as they and earlier study [10] conclude that adjectives express opinions. Accordingly, in part of our feature extraction experimentations, we considered adjectives to be a representor of opinions. Moreover, we added adverbs to represent opinions together with adjectives.

In other related works to opinion mining, Kobayashi et al. [11] defines opinion - in term of product features - as a triple "*evaluated subject, focused attribute, value*" and for opinion extraction, they collect a list of expressions to define every element in the triple. In the Value list -which represents opinions- they found that most of which were adjectives. Due to the different in the domain of our dataset, as stated before, opinions are represented as *useful*, *funny*, and *cool* in this paper, and for those opinions, we collect a domain-specific dictionaries.

For the second objective of our work, the field of prediction or classification in online reviews is mostly addressed from two orientations: *First*, polarity classification, or in other word, sentiment classification, which is determine wither the text is positive or negative, Pang et al. [12] is an early work on the sentiment problem, they used machine learning algorithms to solve the sentiment classification problem. Kim & Hovy [13] looked at the problem from diffident side, their system first determines the polarity of every word in the sentence, then combines every word's polarity to produce the sentiment for the whole sentence. *Second*, rating-based analyzing and classification, in most of the online reviews sites such as Amazon, Alibaba, and Yelp, a numeric rating is provided to review writers. As mentioned before, that rating system can have huge impact on users' decision. Qu el al. [3] introduce a *Bag-of-Opinions* method to predict numerical rating of product reviews, they assign a numerical score for each extracted opinion, to be learned by a regression algorithm. According to [3] "*Numerical review rating prediction is harder than classifying by polarity.*" McAuley & Leskovec [14] they apply a statistical model to understand the hidden relationship between numerical rating and reviews' text, which they suggest will justify users' rating and lead to better predicting.

The work of Zhang et al. [15] addressed a similar problem to that in our work, by using the number of votes and reviews' text only, they developed a probabilistic model to predict the helpfulness of online reviews. However, in this paper, we consider four differed feedbacks i.e., useful, funny, cool and *noVote*.

III. METHODOLOGY

The methodology applied in this work is consists of two parts: NLP for feature analyzing and extraction, and ML for prediction.

A. Feature analyzing and extraction

The most important step in our work is to understand and extract features from reviews' text. The purpose of using NLP is to provide to ML algorithms the input feature vector. To do so, we used two common methods in NLP:

Bag-of-words (POW) is one of the most used methods in NLP for text analyzing [3,16,15], basically, the method takes text as input and produce a vector contains every word in the input text.

Part-of-speech (POS) is a very useful approach to classify words based on their parts of speech (nouns, verbs, adjective, etc.). We used the Stanford Log-linear Part-Of-Speech Tagger [17] for extract adjectives and adverbs as mentioned before.

The above methods gave us poor result in terms of accuracy (as will be present in the experiments section) for that we introduce a new technique to prepare our feature vectors (section 4).

B. Prediction

For the prediction part of our work, we used three common machine learning algorithms widely used for text problems [12,15].

Naive Bayes algorithm: a probabilistic classifier based on the Bayes' theorem with the assumption of independence between the features. Basically, if we have a feature vector $X = [x_1,x_2,x_3,..,x_n]$ and a set of class labels $C = [c_1,c_2,..,c_n]$, to predict the probability of that vector X being belong to class C, we can apply the Bayes' rule,

$$P(C \mid X) = P(C)\,P(X \mid C) / P(X) \quad (1)$$

Linear Support Vector Machine (linear SVM) algorithm: a widely used algorithm for classification and regression. SVM built a hyperplane/s to separate the training dataset points, for example, if we have a set of feature vectors $[x_1,x_2,..,x_n]$, we need to find the hyperplane that has the largest distance to the nearest feature vector of any class.

Logistic regression algorithm: a popular model used to solve classification problem, it can be used as binomial or multinomial model. For the binomial problems, the sigmoid function,

$$f(x) = \frac{1}{1+e^{-x}} \quad (2)$$

could be applied to predict the probability of the classes. However, for a multinomial problem (K classes), we can apply the softmax function,

$$f(x) = \frac{e^{x}}{\sum_{k=1}^{N} e^{x_k}} \quad (3)$$

We will use those three machine learning algorithms with different feature extraction methods to solve our prediction problem.

IV. PROPOSED TECHNIQUE

In this work, we propose a new technique to overcome the problem of imbalance in features number. Typically, any text review consists of words, and after using the above NLP methods, we will have a changeable number of features in the output feature vector. Consequently, every review will have different dimension number, which will lead to inconsistence in the training mechanism in our classifier. To solve this problem, we do as follows: *First,* we generate a raw feature vector for every review in the dataset by apply the NLP methods. *Second*, we build a dictionary for every class in the dataset, a feature will be included in the dictionary for class *A,* if and only if it appears in the class A samples and not in the other classes' samples. For example, if we have sample reviews for classes ***a***, ***b***, ***c***, and ***d***, then we create a set for every class, that set contains all the features appears in the class's sample and the frequency number of every feature. The members of every sets are represented as tuple *<feature, frequency number>,* thus, for every class, now we have a set of features A, B, C, and D. but the features in A could be in the other classes, so A dictionary will be = *A - B - C - D.*

Third, we determine the final feature vector size by taking the average size of all the feature vectors. Let the average size be *avgSize*. *Finally*, for every review, the feature vector size could be less than *avgSize*, more than *avgSize*, or equal to *avgSize*. To make all vectors in same size, we apply *algorithm 1*.

A. Algorithm

Our algorithm starts by initialize two variables, the *avgSize* from step three, and a *threshold*. Then we have two cases:

If the size of the current vector of feature is less than *avgSize*, then we use the getFeatureFromDictionary() method, which takes the class name (*useful, fuuny*, *cool, or noVote*) of the current feature vector as a parameter, and return the most frequent feature in the class dictionary, then move the dictionary pointer the next feature.

If the size of the current vector is bigger than *avgSize*, we then randomly check a feature from the current vector, if that feature *is not* in the class dictionary, then we remove it.

Another related case to the second case, if the current vector size is bigger than *avgSize*, and all or most of its features are indeed in its class dictionary, in this case, after a number of iterations (*threshold*) we randomly remove features from the vector until it matches the *avgSize*. This special case will be optimized and improved in the future work.

V. EXPERIMENTS

In our experiments, we implemented six different scenarios as baseline scenarios, then we applied the proposed technique to those scenarios. Finally, we compare the result of the baseline with our proposed technique.

In this section, we are going to explain the obtained dataset, the baseline scenarios, and the scenarios based on the proposed feature extraction technique. The result to be discussed in the next section.

```
initialize avgSize & threshold;
int counter;
For every feature vector i in dataset
    while(i.size()!= avgSize)
       if (i.size() < avgSize)
              i.add(getFeatureFromDictionary(i.getClass));

       else if (i.size() > instanceSize)
                int RandomNum = getRandomNumber();
                counter++;
                if( ! (i.getClassDictinory().contains(i.getFeatuer(RandomNum))) )
                   i.remove(i.getFeature(RandomNum));

       else if (counter > threshold)
              while(i.size() != avgSize)
                    i.remove(RandomNum);
```

Algorithm 1.

A. Dataset

To demonstrate the problem probably, we used the dataset provided by Yelp Challenge[1]. The dataset contains reviews for businesses from 12 diffident metropolitan areas across 4 countries, because we need as much as possible of consisted reviews, we chose to constrict our work to the Phoenix city and reviews on Restaurants. The final dataset contains 711,891 reviews for 9,754 restaurants in the Phoenix city. Based on the number of votes for each feedback option in Yelp site, we divided our dataset into four classes, *useful*, *funny*, *cool*, and *noVotes*. When divided the reviews, we suppose that a review is belongs -for example- to class *useful* if the *useful* votes are higher than other feedback votes and has at least two votes. The distribution of reviews over the four classes is presenting by *table 1*.

Table 1: Distribution of reviews.

Class	# of reviews
noVotes	570,751
Useful	111,418
Funny	15,046
Cool	14,676

We chose two to be the minimum number of votes for two reasons, because if we chose one vote, the classes will contain a lot of noise, and one vote will not indicate the review's opinion, besides, obviously we have imbalance dataset, so if we chose number more than two, the number of reviews in *funny* and *cool* classes will very small and will lead to incomplete training for those classes.

B. Baseline

One of the most popular ways to predict a class in text problem, is using the POW method for feature extracting and machine learning algorithms for predicting. However, in our baseline scenario, in addition to the POW method and the three ML algorithms mentioned in 3.3 section, we also considered POS method for feature extracting. Our final baseline model is six different scenarios:

Scenario#1 using POW with Naive Bayes algorithm.
Scenario#2 using POW with linear SVM algorithm.
Scenario#3 using POW with Logistic Regression algorithm.
Scenario#4 using POS with Naive Bayes algorithm.
Scenario#5 using POS with linear SVM algorithm.
Scenario#6 using POS with Logistic Regression algorithm.

In our implementation of baseline model and proposed method, we divided the dataset to training dataset (%70) and testing dataset (%30). The baseline results will be used for comparison with the proposed model results.

C. Proposed technique scenarios

The average number of features in our dataset after cleaning the data from stop-words and applying the POW method is 60 (avgSize=60), and after applying the POS method is 20. POS produce smaller number than POW because in POS we just select the adjectives and adverbs from text as explanted before. Then we used our technique to modify the original dataset in a way that all the feature vectors (every feature vector represents a review) will have the same size. Finally, the six different scenarios of experiments will be conducted on our modified dataset to compare it's results with the baseline model.

All our experiments are implemented in a cluster consists of one master and four workers, using Apache Spark with Java programming language. Spark[2] is a fast and general engine for large-scale data processing. Powered[3] by a big companies and organizations such as NASA, Amazon, Alibaba, eBay, IBM, Samsung, and Yahoo!.

D. Feature weighting

The ML algorithms we used in this paper uses numerical inputs, therefore, as a middle step between NLP methods and ML algorithms we needed a feature weighting method to transform the text feature vector to numerical feature vector. A common weighting method is TF–IDF.

TF-IDF[4] is short for (term frequency–inverse document frequency). Exceedingly used method in text maiming problem for feature weighting, it's basic idea to evaluate how much a feature is important in a document (review in our case) in a dataset of documents. Suppose we have feature *t* in a review *d* in dataset D, the first part of the method, Term frequency TF(t,d) is the number of times that *t* appears in *d*. The second part is DF(t,D) which is the number of reviews in dataset *D* contains feature *t*. TF(t,d) alone cannot reflect the importance of a feature, because some features may rapidly appears in all reviews in D, which means those features does not have any importance. Therefore, inverse *I* of *DF(t,D)* is being applied,

$$IDF(t, D) = \log \frac{|D|+1}{DF(t,D)+1} \quad (4)$$

where |D| is the number of reviews in D. And because the method uses log, if a feature appears in all reviews, the result of IDF(t,D) would be zero, and since TF-IDF is the product value of TF(t,d) and IDF(t,D), the final value of TF-IDF for that feature would be zero.

VI. RESULT AND DISCUSSION

The complete result of our experiments is shown in *tables 2,3,4,5,6,7.* Because of the imbalanced in our dataset (*table 1*), we did not consider *accuracy* as evaluation metric, but we considered *precision* and *recall*. To explain why we cannot use accuracy metric in our work, the best accuracy in the baseline model was in the logistic regression classifier with 79%, however, if we look at *table 4,* clearly, most of the true predictions was from one class (*noVotes*) and almost zero in other classes (*Funny, Cool*), therefore, we cannot rely on accuracy to evaluate classifiers in our problem.

[1] https://www.yelp.com/dataset/challenge

[2] https://spark.apache.org

[3] https://spark.apache.org/powered-by.html

[4] https://spark.apache.org/docs/latest/ml-features.html

Table 2: Result of Baseline with Naïve Bayes algorithm.

Class	Baseline - Naive Bayes			
	Bag-of-Words		Part-of-Speech	
	precision	recall	precision	recall
noVotes	0.8494	0.7131	0.8381	0.8119
Useful	0.2583	0.2958	0.2808	0.2817
Funny	0.3085	0.1453	0.0939	0.1447
Cool	0.0379	0.1484	0.0396	0.0647

Table 3: Result of Baseline with Linear SVM algorithm.

Class	Baseline – Linear SVM			
	Bag-of-Words		Part-of-Speech	
	precision	recall	precision	recall
noVotes	0.8212	0.9430	0.8066	0.9853
Useful	0.3220	0.1390	0.3104	0.0323
Funny	0.1342	0.1342	0.1140	0.0128
Cool	0.0570	0.0138	0.0421	0.0031

Table 4: Result of Baseline with Logistic regression algorithm.

Class	Baseline - Logistic regression			
	Bag-of-Words		Part-of-Speech	
	precision	recall	precision	recall
noVotes	0.8199	0.9641	0.8124	0.9825
Useful	0.3927	0.1409	0.4336	0.0840
Funny	0.3464	0.0174	0.2608	0.0039
Cool	0.0873	0.0024	0.0862	0.0011

Table 5: Result of proposed method with Naïve Bayes algorithm.

Class	Proposed method - Naive Bayes			
	Bag-of-Words		Part-of-Speech	
	precision	recall	precision	recall
noVotes	0.9996	0.7428	0.9974	0.7421
Useful	0.4505	0.9489	0.4185	0.9537
Funny	0.3887	0.7393	0.5280	0.6009
Cool	0.4088	0.6790	0.5172	0.5754

Table 6: Result of proposed method with Linear SVM algorithm.

Class	Proposed method – Linear SVM			
	Bag-of-Words		Part-of-Speech	
	precision	recall	precision	recall
noVotes	0.8808	0.9928	0.8716	0.9949
Useful	0.9225	0.4435	0.9468	0.4051
Funny	0.9161	0.4448	0.9339	0.4311
Cool	0.9466	0.4627	0.9411	0.4275

Table 7: Result of proposed method with Logistic regression algorithm

Class	Proposed method - Logistic regression			
	Bag-of-Words		Part-of-Speech	
	precision	recall	precision	recall
noVotes	0.8740	0.9944	0.8656	0.9970
Useful	0.9160	0.4252	0.9518	0.3746
Funny	0.9885	0.3472	0.9932	0.3326
Cool	0.9908	0.3707	0.9912	0.3344

And to better understand of the results, we can use *F-score* (average of precision and recall). The results indicate that our method outperformed the baseline model, specially, in the *funny* and *cool* classes. Because the result for *funny* and *cool* classes was the worst in baseline, we will compare it's result with the proposed method to show the improvement that our method provides.

The performance of Naive Bayes in baseline with scenario#4 was the worst with F-score equals to 0.1139 and 0.0491 for *funny* and *cool* classes. While the same scenario in our proposed method has 0.5621 and 0.5447 F-score for the same classes. Moreover, Linear SVM preform the best with scenario#2 having F-score 0.5989 and 0.6216. We noticed that the overall performance of Linear SVM and Logistic Regression was relative close to each other, while Naive Bayes in this work was one step behind.

We believe that the worse performance of baseline model was because of two reasons. *First*, the imbalance number of instances in our dataset. *Second*, the imbalance number of features in the feature vectors. Therefore, because it trained almost on just one class (*noVotes*), classifiers cannot properly understand the natural of our dataset in the training cycles. However, with our method, we overcome the imbalance problem by making all our feature vectors the same size. Even though the dataset still imbalanced and class *noVotes* has 80% of the dataset, but with the efficient way we used in feature extraction, we get promising result in our experiments for the small classes.

VII. CONCLUSION

In this paper, we addressed the problem of predication public opinion from online reviews with imbalance dataset and feature number. To solve the imbalance problem, we introduced a new technique in feature extraction, our technique is based on dictionaries collected from the dataset itself, then we used *algorithm 1* to normalize the imbalanced feature vectors.

We used a dataset provided by Yelp site, where Yelp users can vote for one or more feedback on each review, so we divided the users' opinion into four categories (useful, funny, cool, and noVotes). For Yelp dataset, our technique overcome the baseline model and provide promising performance. Even though we used Yelp dataset, but we believe that our technique can be used in any similar problem.

For future work, we can improve the special case mentioned in section 4. Also, we categorized reviews based on the number of votes (section 5.1) so that every review belongs to one class, however, reviews could be belonging to more than one class but with different percentage. Finally, we intend to use deep learning for machine learning.

REFERENCES

[1] S.-y. W. J. Y. Pei-Yu Chen, "The Impact of Online Recommendations and Consumer Feedback on Sales," in ICIS 2004 Proceedings, paper 58., 2004.

[2] R. B. QiangYe, "The impact of online user reviews on hotel room sales," International Journal of Hospitality Management, vol. 28, no. 1, pp. 180-182, 2009.
[3] G. I. G. W. Lizhen Qu, "The bag-of-opinions method for review rating prediction from sparse text patterns," in Proceedings of the 23rd International Conference on Computational Linguistics, pages 913-921. , Beijing, China, 2010.
[4] P. K. D. A. S. Saeideh Bakhshi, "If It Is Funny, It Is Mean: Understanding Social Perceptions of Yelp Online Reviews," in Proceedings of the 18th International Conference on Supporting Group Work, pages 46-52., Sanibel Island, Florida, USA, 2014.
[5] P. K. D. A. S. Saeideh Bakhshi, "Understanding Online Reviews: Funny, Cool or Useful?," in Proceedings of the 18th ACM Conference on Computer Supported Cooperative Work & Social Computing, pages 1270-1276., Vancouver, BC, Canada, 2015.
[6] G. K. J. K. L. L. Cristian Danescu-Niculescu-Mizil, "How opinions are received by online communities: a case study on amazon.com helpfulness votes," in Proceedings of the 18th international conference on World wide web, pages 141-150., Madrid, Spain, 2009.
[7] L. H. K. M. A. N. Rajesh Vasa, "A preliminary analysis of mobile app user reviews," in Proceedings of the 24th Australian Computer-Human Interaction Conference, pages 241-244., Melbourne, Australia , 2012.
[8] P. K. E. G. Saeideh Bakhshi, "Demographics, weather and online reviews: a study of restaurant recommendations," in Proceedings of the 23rd international conference on World wide web, pages 443-454., Seoul, Korea, 2014.
[9] B. L. Minqing Hu, "Mining and summarizing customer reviews," in Proceedings of the tenth ACM SIGKDD international conference on Knowledge discovery and data mining, pages 168-177., Seattle, WA, USA, 2004.
[10] J. Wiebe, "Learning Subjective Adjectives from Corpora," in Proceedings of the Seventeenth National Conference on Artificial Intelligence and Twelfth Conference on Innovative Applications of Artificial Intelligence, pages 735-740., 2000.
[11] K. I. Y. M. K. T. Nozomi Kobayashi, "Collecting evaluative expressions for opinion extraction," in Proceedings of the First international joint conference on Natural Language Processing, pages 596-605., Hainan Island, China , 2004.
[12] L. L. S. V. Bo Pang, "Thumbs up? Sentiment Classification using Machine Learning," in Proceedings of the Conference on Empirical Methods in Natural Language Processing - Volume 10, pages 79-86., Stroudsburg, PA, USA, 2002.
[13] E. H. Soo-Min Kim, "Determining the sentiment of opinions," in Proceedings of the 20th international conference on Computational Linguistics, Article No. 1367., Geneva, Switzerland , 2004.
[14] J. L. Julian McAuley, "Hidden factors and hidden topics: understanding rating dimensions with review text," in roceedings of the 7th ACM conference on Recommender systems, pages 165-172., Hong Kong, China, 2013.
[15] T. T. Y. M. Richong Zhang, "Recommender systems from "words of few mouths"," in Proceedings of the Twenty-Second international joint conference on Artificial Intelligence, pages 2379-2384., Barcelona, Catalonia, Spain, 2011.
[16] M. T. Georgios Paltoglou, "More than Bag-of-Words: Sentence-based Document Representation for Sentiment Analysis," in Proceedings of Recent Advances in Natural Language Processing, pages 546–552., Hissar, Bulgaria., 2013.
[17] D. K. C. M. Y. S. Kristina Toutanova, "Feature-Rich Part-of-Speech Tagging with a Cyclic Dependency Network," in In Proceedings of HLT-NAACL 2003, pages 173-180. , Edmonton, Canada, 2003.

Classification of Diabetes Dataset with ANN Trained by Vortex Search

ZAINAB A. JALIL[1] and Tahir SAĞ[2]

[1] Selcuk University, Konya/Turkey, zeynepcelil@yahoo.com
[2] Selcuk University, Konya/Turkey, tahirsag@selcuk.edu.tr

***Abstract* - Artificial Neural Networks (ANN) are artificial intelligence techniques in which the biological brain is attempting to simulate learning and information storage capabilities. In ANN, the connection weights storing information are combined in a parallel and sequential manner. The learning of artificial neural networks is the process of finding optimal values that are appropriate for weights of network topology. In this study, Vortex search (VS) algorithm, which has recently developed as a single-solution based optimization algorithm, is proposed for ANN training. The performance of presented training approach is analyzed by comparing with traditional and modern optimization methods. The mostly used ANN architecture is the model of multilayer feedforward perceptron (MLP). The same network topology and training strategy is applied to the Diabetes data set taken from the UCI database. VS algorithm is tested by classification performance on MLP training. VS algorithm is also compared with particle swarm optimization (PSO) and artificial bee colony optimization (ABC) algorithms. All algorithms are run under the same conditions. In comparison of the results obtained for diabetes disease, the proposed training strategy based on VS algorithm has achieved the best outcomes for ANN.**

***Keywords* - Vortex Search algorithm, ANN Training, Diabetes.**

I. INTRODUCTION

NEURAL network is a concept born due to the scientific interest about Artificial Intelligence (AI) in the middle of 1950s. The AI is the capacity of an electronic data to perform functions and reasoning typical of the human mind. It has been studied for years in order to achieve human-like intelligence in many spaces, such as speech and image recognition. Artificial neural networks are inspired by the architecture of the human central nervous system, which consists of a large number of cells *(neurons)* running in parallel to facilitate decision-making the fastest. These simple units are connected to each other by electrical stimulus called *synapse*. Similarly, in the ANN model synaptic activity was presented by a matrix of weight *(numerical values)* updated by like-human learning process. The direct advantage of this approach is that neuron-computing devices do not need programmed, but on the contrary, the random selection of initial weights induces the learn-making from the process of adjusting the weights itself by accessing the minimum error of prediction. The procedure used to make the learning process was called learning algorithm which is a function that can modify the synaptic weight of the network [1].

Until now, there are many optimization algorithms used in the literature for the training artificial neural networks. One of them is Artificial Bee Colony algorithm was proposed for ANN training. It was designed to solve XOR, 3-Bit Parity, Encoder-Decoder test problems and different classification test problems from UCI machine learning repository. In ANN training, performance of ABC algorithm was compared with performance of BP and LM backpropagation algorithms, GA, DG and PSO algorithms. ANN-ABC gave more successful results as the highest classification success and performance [2].

In order to solve medical diagnostic problems, the performance between global and local techniques applied to the training of neural network classifiers were investigated by İnce and et al [3]. Two popular neural network training methods were applied on the feed-forward, fully-connected ANNs which conventional backpropagation (BP) and particle swarm optimization were used. Performance analysis and evaluation were performed on three medical diagnostic problems (breast cancer, heart disease and diabetes) from Proben1 benchmark dataset. BP is found to be more efficient in terms of calculation than PSO.

Tarigan et al. [4] trained ANN by using Genetic Algorithms (GA) for Plate recognition which is used for automatic parking gate or automatic ticketing system. Genetic algorithm was used to find the optimal number of hidden neuron, learning rate, and momentum rate. Determined the effectiveness of GA on Backpropagation Neural Network (BPNN) that is applied to the Automatic Plate Number Recognizer (APNR). GA optimized backpropagation neural network is faster than non-optimized backpropagation neural network.

The purpose of the study is vortex search algorithm not previously proposed in the literature for the training of artificial neural networks. It is aimed to use VS optimization algorithm in the training of artificial neural networks and to research algorithm performance. It was developed as an alternative training method and its performance is compared with the performances of Artificial Bee Colony (ABC) [5] and Particle Swarm Optimization (PSO) [6] metaheuristic techniques. The data set to be used for testing was taken from the UCI database *(machine learning repository of University of California at Irvine)* [7]. Experimental studies and analyzes have been carried out on the diabetes data test classification problem from the UCI machine learning repository in order to analyze the effectiveness of the vortex search algorithm.

This paper organized as follows. In section II, materials and method used in this study are given. In the methods subsection, the concepts of vortex search algorithm are briefly explained while the contexts of the datasets are detailed in materials subsection. Then the proposed method is described in section III. Finally, the results are given in section IV.

II. Materials and Methods

A. Vortex Search Algorithm

The Vortex search algorithm (VS) is a native algorithm first developed in 2015 for solving single-objective optimization problems [8]. The algorithm is inspired by the vortex pattern generated by the vortex flow of the mixed liquids. In recent years, both the single-solution based and population-based metaheuristics have successfully implemented many actual world optimization problems. These algorithms produce solutions by discovering the search field efficiently while reducing the effective size of the search. The Vortex Search (VS) algorithm is a single-solution based metaheuristic algorithm. The success of a metaheuristic method on a specific optimization problem is defined by its ability to establish a good stabilize between the explorative and exploitative.

In a two-dimensional space, a vortex design was modeled by a series of nested circles. First, the starting center μ_0 of the outer (biggest) circle of the vortex was determined. μ_0 was calculated using the following equation. So, the circle was centered in the search space.

$$\mu_0 = \frac{upperlimit + lowerlimit}{2} \quad (1)$$

$$\sigma_0 = \frac{\max(upperlimit) - \min(lowerlimit)}{2} \quad (2)$$

Here, σ_0 can also be thought of as the first radius (r_0) of the outer circle. When small changes are needed in the first steps, r0 is chosen as a great value. Thus, in initial step a full coverage of the search field is provided by the outer circle. This process has provided a bird's-eye view.

Using the Gaussian distribution, random values are created around the first center in the d-dimensional space.

$$p(x|\mu,\Sigma) = \frac{1}{\sqrt{(2\Pi)^d|\Sigma|}} exp\left\{-\frac{1}{2}(x-\mu)^T\Sigma^{-1}(x-\mu)\right\} \quad (3)$$

In the choosing stage, the best solution s' $\in$ $C_0(s)$ was selected and stored in memory from $C_0(s)$ to change the current circle center μ_0. Prior to choosing stage, the candidate solutions must be provided to be inside the search limits. For this purpose, the solutions that exceed boundaries were shifted into limits, as in the following equation.

$$s_k^i = \begin{cases} \text{rand.}\left(\text{upperlimit}^i - \text{lowerlimit}^i\right) + \text{lowerlimit}^i, & s_k^i < \text{lowerlimit}^i \\ s_k^i & \text{lowerlimit}^i \leqslant s_k^i \leqslant \text{upperlimit}^i \\ \text{rand.}\left(\text{upperlimit}^i - \text{lowerlimit}^i\right) + \text{lowerlimit}^i, & s_k^i > \text{upperlimit}^i \end{cases} \quad (4)$$

Then, the memorized best solution s_0 was appointed to be the center of the second circle. During the production phase of the second step, the effective radius (r1) of this new circle was reduced. Next, a new set of solutions C1(s) was created around the new center. In the choosing stage of the second step, the new set of solutions C1(s) was evaluated to select a solution s'$\in$C1(s). If the selected solution is better than the best solution found so far, then this solution was assigned to be the new best solution and it was memorized. Next, the center of the third circle was assigned to be the memorized best solution found so far. This process was repeated until the termination conditions are met. It is demonstrated in Fig 1.

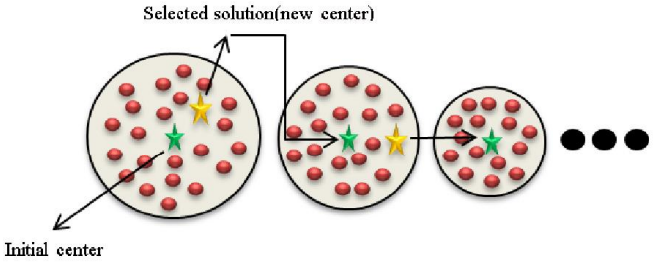


Figure 1: A sample drawing of the search process [8].

In this way, once the algorithm is over, the resulting pattern appears as a vortex-like structure, where the center of the smallest circle is the optimum point found by the algorithm. A representative pattern for a two-dimensional optimization problem for which the upper and lower limits are between the [-10, 10] interval, appears in Fig 2.

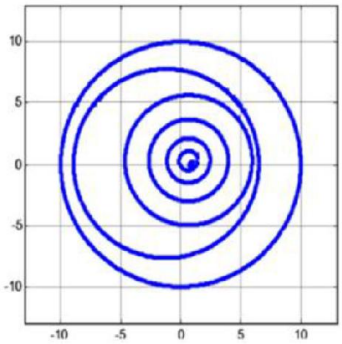


Figure 2: Vortex-like structure after a search process [8].

In VS algorithm, the inverse incomplete gamma function was used to decrease the value of the radius during each iteration pass. The incomplete gamma function given in the equations below most commonly arises in probability theory, particularly in those applications involving the chi-square distribution [9].

$\gamma(x,a) = \int_0^x e^{-t}t^{a-1}dt$ a>0

$\Gamma(x,a) = \int_x^\infty e^{-t}t^{a-1}dt$ a>0

Thus, it follows that,

$\gamma(x,a) + \Gamma(x,a) = \Gamma(a)$ (5)

Where $\Gamma(a)$ is known as the gamma function.

MATLAB also provides some tools for the calculation of functions including, gamma function (gamma), incomplete gamma function (gammainc), and inverse incomplete gamma (gammaincinv) function. The inverse incomplete gamma function (gammaincinv), calculates the inverse of the incomplete gamma function with respect to the integration limit x and represented as gammaincinv(x,a) in MATLAB [8].

In this study, the VS algorithm is applied to the diabetes data set from the UCI databases in the data warehouse in the feedforward ANN training. It has not been shown as the main goal finding the most suitable architecture for the developed artificial neural network model or finding the lowest possible error. However, the aim is to demonstrate that the VS algorithm is as competitive as other algorithms in network training and to discuss its success. PSO, ABC and other meta-heuristic algorithms are applied and run under the same conditions. The success of the obtained outcomes is discussed comparatively. The schematic diagram of the MLP model is shown in Fig 3.

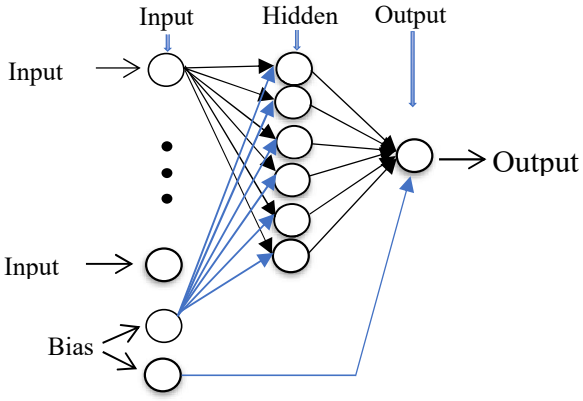


Figure 3: Feed forward MLP topology (8x6x1) for diabetes.

B. *Materials*

Pima Indians Diabetes Dataset was created in Applied Physics Laboratory of the Johns Hopkins University. All patients enrolled in this dataset are females at least 21 years old of Pima Indian heritage. Dataset contains 768 instances which have eight attributes [7].

The attributes are:

1. Number of times pregnant
2. Plasma glucose concentration 2 hours in an oral glucose tolerance test.
3. Diastolic blood pressure (mm Hg)
4. Triceps skin fold thickness (mm)
5. 2-Hour serum insulin (mu U/ml)
6. Body mass index (weight in kg/(height in m)^2)
7. Diabetes pedigree function
8. Age (years)

The class labels are tested positive for diabetes (Class 1) and tested negative for diabetes (Class 0) which have 268 and 500 instances respectively [10].

III. Experimental Results

The all algorithms were applied to dataset for 10 independent trails consisting 100 iterations. Each running was started with randomly generated populations. The logarithm sigmoid function was chosen as the transfer function in each network selected for each problem. Network training was terminated when the mean square error rate (MSE) between input and output is less than or equal to 0.01, or when the maximum number of loop is reached. The formulation of MSE is given in Eq (6).

$$MSE = \frac{1}{\mathrm{N}}\sum_{j=1}^{\mathrm{N}}\sum_{k=1}^{P}(d_k - o_k)^2 \qquad (6)$$

Here, d_k desired output value and o_k produced output value; shows the number of output neurons P and the number of samples N.

The median ($\tilde{x}$), mean for the measured values (central tendencies) of all the problems and the interquartile range (IQR), standard deviation (SD) values for the statistical distributions were calculated. The results with the best value in the test problems were highlighted by dark gray background color. If multiple algorithms can reach the same best value, the algorithm with the smaller IRQ value was considered the best.

The diabetes data set was selected from the UCI data warehouse to evaluate the performance of the vortex search algorithm. The classification performance of the VS algorithm was compared with the performance of the PSO and ABC algorithms. The first data part of 75% of the diabetes problem in the database was used as the training data set and the remaining 25% was used as the test data. Diabetes properties of the data set are shown in Table 1. These are topology of ANN, total number of weights called size, and total number of samples.

Table 1. Parameters of the MLP network used and diabetes problem.

Problem	ANN topology	Size	Example number
Diabetes	8-6-1	61	768

In this study, MLP-VS, MLP-ABC and MLP-PSO algorithms were trained using their own methods and test results were obtained using the same training data sets. Data set properties using VS, ABC and PSO algorithms are given in Table 1 and shown result in Table 2.

Table 2. Classification successes

Problem		VS	ABC	PSO
Diabetes	Median	0.221932	0.223128	0.223122
	IQR	0.00460013	0.00892751	0.00635094
	Mean	0.22166	0.224304	0.222617
	SD	0.00452353	0.00574394	0.0066864

From Table 2 it can clearly be seen that the VS algorithm obtained better training performance in all scenarios from ABC and PSO. The highest achieved test performance by VS, was run with 100 iterations, population size 30, 6 neurons in

hidden layers and the parameter range as [-20, 20]. The mean and median MSE values used as classification accuracy are 0.22166 and 0.221932, respectively. Also, the convergence of the VS-based ANN training for 100 iterations can be seen in Fig 4.

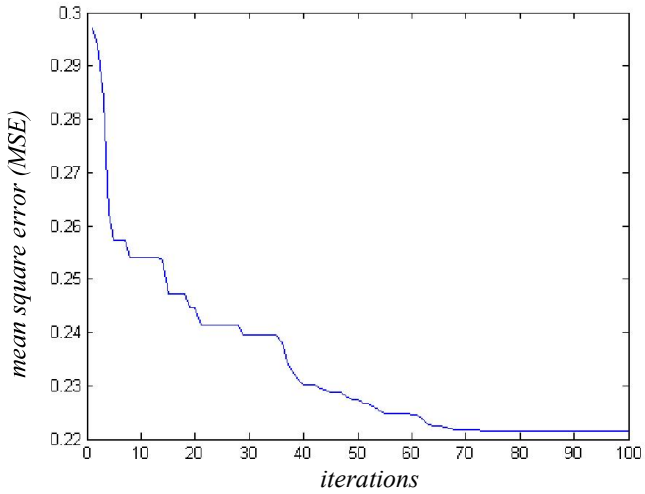


Figure 4: VS convergence characteristic for median running.

IV. Conclusion

A new ANN training approach depend on VS algorithm was presented in this study. It was applied to Pima Indian dataset which was collected from the people who have the doubt of diabetes disease. Vortex search algorithm which was previously not proposed for ANN training in the literature. VS has been used to train the network during the application of classification and test problem solving in multi-layered feedforward artificial neural networks. ANN-VS, ANN-ABC and ANN-PSO training models were separately run and the results are compared with each other. All algorithms were tested by multiple running. ANN-VS model achieved more successful results with the highest classification accuracy among the algorithms. The maximum classification accuracy with 0.221932 median and 0.22166 mean MSE values, is obtained by ANN-VS training model. Consequently, experimental results are shown that ANN model trained by vortex search is a viable approach in the classification.

Acknowledgment

This study has been made within the scope of ZAINAB A. JALIL's ongoing master thesis on computer engineering in Selcuk University.

References

[1] Salento, U., Micelli, F., Salento, U., Aiello, M. A., Salento, U., Cascardi, A. Aiello, M. A. (2017). An Artificial Neural Networks model for the prediction of the compressive strength of FRP- confined concrete compressive strength of FRP-confined concrete circular columns. *Engineering Structures*, *140*(September), 199–208. https://doi.org/10.1016/j.engstruct.2017.02.047

[2] Karaboga D., and Ozturk, C. (2011). A novel clustering approach: Artificial Bee colony (ABC) algorithm: Applied Soft Computing 11, 652-657. https://doi.org/10.1016/j.asoc.2009.12.025

[3] Ince, T., Kiranyaz, S., Pulkkinen, J., and Gabbouj, M. (2010). Evaluation of global and local training techniques over feed-forward neural network architecture spaces for computer-aided medical diagnosis. *Expert Systems With Applications*, *37*(12), 8450–8461. https://doi.org/10.1016/j.eswa.2010.05.033

[4] Tarigan, J., Diedan, R., and Suryana, Y. (2017). Plate Recognition Using Backpropagation Neural Network and Genetic Algorithm *Procedia Computer Science*, *116*, 365–372. https://doi.org/10.1016/j.procs.2017.10.068

[5] Karaboga, D., An idea based on honey bee swarm for numerical optimization. 2005, Technical report-tr06, Erciyes university, engineering faculty, computer engineering department.

[6] Kennedy J. and Eberhart R. C. (1995). Particle swarm optimization. Proceedings of IEEE International Conference on Neural Networks, Perth, Australia, Vol. IV, pp. 1942-1948.

[7] Frank, A., Asuncion, A., UCI machine learning repository, Irvine, CA: University of California, School of Information and Computer Science, volume 21, 2010.

[8] Doğan, B., and Ölmez, T. (2015). A new metaheuristic for numerical function optimization: Vortex Search algorithm. *Information Sciences*, *293*, 125–145. https://doi.org/10.1016/j.ins.2014.08.053

[9] Doğan, B. and Ölmez, T. (2015). Vortex search algorithm for the analog active filter component selection problem, International Journal of Electronics and Communications (AEÜ), *69*, 1243–1253. https://doi.org/10.1016/j.aeue.2015.05.005

[10] Cheruku, R., Edla, D. R., & Kuppili, V. (2017). SM-RuleMiner: Spider monkey based rule miner using novel fitness function for diabetes classification. *Computers in Biology and Medicine*, *81*(August 2016), 79–92. https://doi.org/10.1016/j.compbiomed.2016.12.009

Artificial Algae Algorithm (AAA) on Training Artificial Neural Network

B. TURKOGLU[1] and E. KAYA[1]

[1]Selcuk University, Konya/Turkey, bahaeddinturkoglu@gmail.com
[1]Selcuk University, Konya/Turkey, ersinkaya@selcuk.edu.tr

***Abstract* - In this study the recently proposed Artificial Algae Algorithm (AAA) for training Multi-Layer Perceptron (MLP) for the first time in the literature. Artificial algae algorithm is a nature-inspired metaheuristic optimization algorithm. Five classification dataset (Liver, Parkinson, Breast cancer, Vertebral, Diabetes) from UCI (University of California, Irvine) database is utilized to benchmark the performance of the proposed method. For verification, the results compared to six swarm based algorithm. Results (confusion matrix, local minima avoidance, average and best accuracy rate, convergence curve, execution time and standard deviation) show that artificial algae algorithm very competitive performance for training multilayer perceptron.**

***Keywords* - Training neural network, Multilayer perceptron, Optimization, Artificial Algae Algorithm**

I. INTRODUCTION

ANN are artificial nets that mimic biological neural networks in the human brain. The general working principle of artificial neural networks is to convert an input set into an output set. MLP is a feed forward neural network model that is formed by combining perceptron. It has an input layer, at least one hidden layer and one output layer. It is effective in solving nonlinear problems. The network must be trained to produce accurate output values for the input data shown [1].

Network training is based on the principle of minimizing the difference between the expected output and the output produced by the network. Training is the process of finding the most appropriate weight values. This is an optimization problem.

The training process of artificial neural networks directly affects the performance of the network. There are two main categories of network training: a) Gradient-based methods b) Stochastic methods.

The backpropagation algorithm and its variants are accepted as standard examples of gradient-based methods. Gradient-based methods have main disadvantages; high dependence on initial parameters, tendency to be trapped in local minimum and early convergence[2-4]. As an alternative to Gradient-based approaches in the literature, heuristic search algorithms have been proposed to optimize MLP networks.

Unlike gradient-based algorithms, meta-heuristic methods show high efficiency in avoiding local minimums[3, 5-7]. Stochastic based algorithms are principally involving randomness to move from local search to global search. for this reason, it is more suitable for global optimization [8].

Seiffert used Genetic Algorithms for MLP training in 2001 and argued that the genetic algorithm is better than the backpropagation algorithm when the problem is more complex and multidimensional [9].

MLP can be trained by swarm intelligence optimization algorithms. Swarm intelligence is the modeling of species that behave intelligently in the form of swarms such as birds, fish, wolves, whales. They are used to find the optimal solution in optimization problems. Every agent (individual) in the swarm represent a possible solution. Each agent by self-organized with lots of information sharing between agents in the swarm will try to move to the appropriate solution.

The most popular examples of swarm-based algorithms are the particle swarm optimization (PSO), artificial bee colony (ABC), ant colony optimization (ACO), gray wolf optimization(GWO) and whale optimization algorithm(WOA).[2, 10-13]

There are a lot of studies in the literature using MLP training swarm intelligence [2, 14-18].

There are many algorithms for MLP training in the literature, but local minimum problem still exists. According to the no-free-lunch theorem (NFL), an optimization algorithm can't achieve success in all of the optimization problems [19, 20].

Artificial Algae Algorithm for MLP training was proposed in this study for first time. In section 2, the AAA algorithm will be explained.

II. ARTIFICIAL ALGAE ALGORİTHM

Artificial algae algorithm is a meta-heuristic optimization algorithm inspired by the properties and living behavior of moving microalgae [21]. An algae colony is a group of algae living together. Every colony represents a possible solution. Algae population consists of algae colonies.

Each algae colonies shows a growth according to the environment. Initially, the greatness of all algae colonies is one. The growth kinetics of the algae colony is calculated by equation 1 and 2.

$$\mu_i = \frac{\mu_{\max} S}{K_s + S} \tag{1}$$

$$G_i = G_i \times \mu_i \tag{2}$$

where μ_{max} is the maximum specific growth rate (1/time), and K_S is the substrate saturation constant (mass/volume), G_i the size of algae colony.

AAA, there are three main section which are evolutionary process, helical movement and adaptation.

A. Evolutionary process

The algae colony that finds a good solution grows and develop. If the algae colonies don't find a good solution, they cannot develop and die. In evolutionary process, the algae colonies are sorted by their greatness. At a randomly selected size, one dimension of the smallest algae column is kill and one size of the largest algae column is copied instead (Eqs. (3) - (5)).

$$\text{biggest}^t = \max G_i^t, \qquad i = 1,2,\dots N \tag{3}$$

$$\text{smallest}^t = \min G_i^t, \qquad i = 1,2,\dots N \tag{4}$$

$$\text{smallest}_m^t = \text{biggest}_m^t, \qquad m = 1,2,\dots D \tag{5}$$

where D is the problem dimension, biggest is the biggest algae colony and smallest is the smallest one.

B. Helical movement

At the beginning of each cycle, the energy is calculated in proportion to the greatness of the algae colonies (normalizing their greatness). In each cycle of the algae colony, the helical movement is determined by how many times this energy will be displaced in the solution space. Energies are direct proportional to the food concentration. The algae colony, which finds a better solution, suffers from energy loss by half (e / 2) of the initial energy loss parameter. The algae colony, which don't find a better solution, suffers from energy loss as much as the energy loss parameter (e). The friction force is proportional to the greatness of the algae colony. As the friction surfaces of the algae cells grow, the helical movements are slower in the liquid. This increases the local search ability (exploitation). Little algae cells have more global search capabilities (exploration). When we take the algae colony as the sphere and the size as the volume (G) in the calculations, the friction surface becomes half the surface area (τ). Shown in Eqs. 4.

$$\tau(x_i) = 2\pi \left(\sqrt[3]{\frac{3G_i}{4\pi}} \right)^2 \tag{4}$$

where τ (xi) is the friction surface.

The random three dimension of an algae colony selected by the tournament method for the helical movement is determined. The friction surface of the algae colony calculates the step size of the movement (Eqs. (5) -(7)).

$$x_{im}^{t+1} = x_{im}^t + \left(x_{jm}^t - x_{im}^t\right)\left(\Delta - \tau^t(x_i)\right)p \tag{5}$$

$$x_{ik}^{t+1} = x_{ik}^t + \left(x_{jk}^t - x_{ik}^t\right)\left(\Delta - \tau^t(x_i)\right)\cos\alpha \tag{6}$$

$$x_{il}^{t+1} = x_{il}^t + \left(x_{jl}^t - x_{il}^t\right)\left(\Delta - \tau^t(x_i)\right)\sin\beta \tag{7}$$

where X^t_{ik} , X^t_{il} and X^t_{im} are x, y and z coordinates of *i*th algae cell $\alpha,\beta \in [0, 2]$; $p \in [-1, 1]$; Δ is shear force; $\tau^t(x_i)$ is the friction surface area of *i*th algae cell.

C. Adaptation

Adaptation is a process in which algae colony survive but don't grow sufficiently to try to resemble the largest algae colony.

In the initially, the starvation level of each algae colony is zero. The result of the helical movement is an increase of one in the starvation level of the algae colony which can't find a better solution. The algae colony, which has the highest starvation level, is subjected to adaptation procedure after each helical motion cycle (Eqs. 8-9).

$$\text{starving}^t = \max A_i^t, \qquad i = 1,2,\dots N \tag{8}$$

$$\text{starving}^{t+1} = \text{starving}^t + (\text{biggest}^t - \text{starving}^t) \times \text{rand} \tag{9}$$

where A^t_i is the starvation value of *i*th algae colony in time t, starving^t is the algal colony with the highest starvation value in time t. The adaptation parameter (Ap) determines whether

adaptation process would be applied in time t or not. Ap is constant on the interval [0, 1].

III. AAA Based MLP Trainer

Each algae colony (agent) is a possible solution. Each agent represents the weight and bias parameters of the MLP network. The candidate neural network is a one-dimensional vector representing the solution. The vector consists of three parts as shown in figure 1 [3]. the weights between the input and the hidden layer, the weights between the hidden layer and the output layer, and the bias of the hidden and output neurons. Biases shift the sigmoid function.

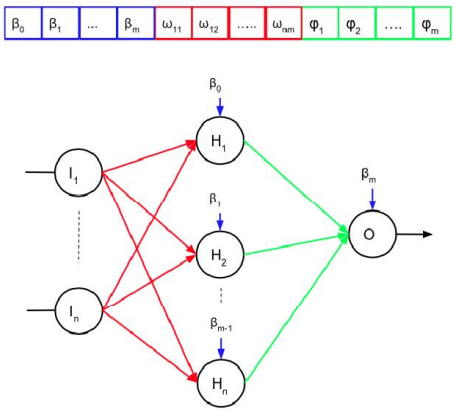


Figure 1: Assigning a AAA search agent vector to an MLP

The fitness value of the generated agents is calculated in MLP. The fitness function is the mean square error (MSE). The fitness function is the sum of the squared difference between the actual output of the network and the output calculated of the network. MSE is shown in Eqs. 10.

$$\mathrm{MSE} = \frac{1}{n}\sum_{i=1}^{n}(y - \hat{y})^2 \qquad (10)$$

where y is the actual value, yˆ is the predicted value, and n is number of instances in the training dataset.

Firstly, the agent is randomly generated as many as the number of individuals in the population. Each agent represents an MLP network. The fitness of the MLP nets produced is evaluated using the fitness function (MSE). The location of search agents is updated according to the location update formula in AAA (Eqs. (5) - (7)). The processes are repeated until the maximum iteration or the specified error amount is reached. Finally, the MLP network with the minimum MSE value is tested on the portion of the data set that is reserved for testing. the purpose of the training algorithm is to find an MLP network with a minimum MSE that models the training samples in the datasets. Shown in figure 2 [22]

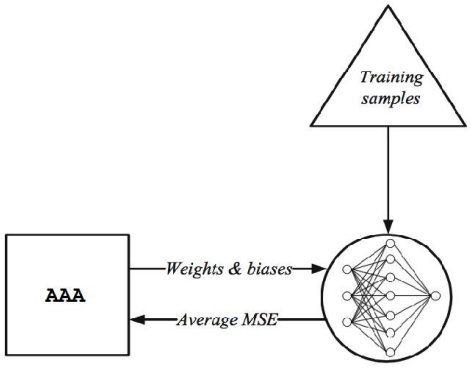


Figure 2: AAA provides MLP with weights/biases and receives average MSE for all training samples

IV. Result and Discussion

In this section the proposed method is benchmarked using five classification datasets from UCI. Parkinson dataset, liver dataset, breast cancer dataset, vertebral dataset and diabetes dataset. The number of test samples and training samples belonging to these data sets is shown in the table 1. For verification, the results compared to six swarm based algorithm. Particle swarm optimization, gray wolf optimizer, firefly algorithm, whale optimization algorithm, multi-verse optimizer, moth flame optimizer, and cuckoo search algorithm.

Table 1: MLP structure, dimension and samples for each dataset

Classification Datasets	Train/Test Samples	Number of Attributes	MLP structure	Dimension
Liver	79 / 41	6	6-13-1	105
Parkinson	128 / 67	22	22-45-1	1081
Breast cancer	461 / 238	8	8-17-1	171
Vertebral	204 / 106	6	6-13-1	105
Diabetes	506 / 262	8	8-17-1	171

A. Experimental Setup

For all experiments and all algorithms, we used EvoloPy. EvoloPy is an open source nature-inspired optimization algorithm toolbox in Python. All datasets are separated into 66% for training and 34% for testing and datasets are normalized using min–max normalization. All experiments are executed for thirty different runs. Each run contains 500 iterations. The number of individuals in the population was determined as 40. The algorithms were run on 20000 fitness calculations. The weights of the artificial neural network are real numbers in the range [-1, 1]. The number of neurons in the hidden layer is found by the formula $2 \times N + 1$, where N is number of dataset features [23, 24]. The designed MLP structure is shown in table 1.

B. *Discussion and Analysis of the Result*

The average of 30 run in result. Execution time is evaluated in seconds. The results show that the artificial algae algorithm classifies these data sets with at least 75% success. The standard deviation value of the AAA algorithm is low, indicating that there is no dependence on the initial parameters. Also proves that it is avoiding local minimums. Vertebral and liver datasets, the execution time is short because the training data sets is few. The results are shown on the table 2- 6.

Artificial algae algorithm has the highest accuracy rate, the best average accuracy rate and the best execution time in the liver dataset. In breast cancer dataset and Parkinson dataset, AAA has the highest accuracy rate and the best execution time. The AAA in the vertebral data set and the diabetes data set results is very competitive with other algorithms [3, 22].

Table 2: Result of liver dataset

Algorithm	AVG	STD	Best	Execution Time
AAA	**0.763**	0.012	**0.796**	**85.35**
CS	0.733	0.028	0.771	170.6
GWO	0.423	0.000	0.423	92.56
MFO	0.759	0.013	0.779	88.71
MVO	0.753	0.014	0.779	87.48
PSO	0.757	0.019	0.796	90.19
WOA	0.428	0.027	0.576	87.35

Table 2: Result of parkinson dataset

Algorithm	AVG	STD	Best	Execution Time
AAA	0.855	0.026	**0.895**	**57.78**
CS	0.830	0.027	0.880	121.5
GWO	0.761	0.000	0.761	138.9
MFO	0.854	0.025	0.895	96.25
MVO	**0.874**	0.021	0.910	84.85
PSO	0.814	0.043	0.895	113.5
WOA	0.759	0.007	0.761	84.41

Table 2: Result of breast cancer dataset

Algorithm	AVG	STD	Best	Execution Time
AAA	0.976	0.006	**0.991**	**173.7**
CS	0.971	0.006	0.983	349.5
GWO	0.659	0.000	0.659	185.9
MFO	**0.979**	0.006	0.987	180.8
MVO	0.979	0.003	0.983	178.5
PSO	0.970	0.008	0.983	198.2
WOA	0.665	0.032	0.836	177.2

Table 2: Result of vertebral dataset

Algorithm	AVG	STD	Best	Execution Time
AAA	0.876	0.013	0.896	**77.38**
CS	0.861	0.026	0.905	154.1
GWO	0.707	0.000	0.707	84.39
MFO	0.872	0.012	0.896	80.59
MVO	**0.878**	0.014	0.905	79.44
PSO	0.873	0.018	**0.915**	82.16
WOA	0.707	0.000	0.707	79.32

Table 2: Result of diabetes dataset

Algorithm	AVG	STD	Best	Execution Time
AAA	0.750	0.008	0.763	219.9
CS	0.748	0.009	0.770	382.8
GWO	0.366	0.000	0.366	202.5
MFO	0.754	0.012	0.770	197.4
MVO	**0.757**	0.010	0.778	**194.6**
PSO	0.751	0.010	**0.797**	199.5
WOA	0.375	0.048	0.633	205.1

V. CONCLUSION

In this work, for the first time in the literature, the performance of artificial algae algorithm on MLP training was evaluated. The AAA was implemented for the problem. The AAA was used to determine optimal weight and bias values. The proposed method was applied to the five popular classification data sets. The results were compared with six well-known algorithms in the literature.

In future studies the AAA algorithm can be used to determine the number of hidden layers and the number of neurons in the hidden layer. AAA can be applied in the optimization of conventional neural networks. To find the number of layers of the convolutional neural networks and to optimize the kernel values(weight) in this layer.

REFERENCES

[1] Basheer, I. and M. Hajmeer, *Artificial neural networks: fundamentals, computing, design, and application.* Journal of microbiological methods, 2000. **43**(1): p. 3-31.

[2] Karaboga, D., B. Akay, and C. Ozturk, *Artificial bee colony (ABC) optimization algorithm for training feed-forward neural networks.* MDAI, 2007. **7**: p. 318-319.

[3] Aljarah, I., H. Faris, and S. Mirjalili, *Optimizing connection weights in neural networks using the whale optimization algorithm.* Soft Computing, 2016: p. 1-15.

[4] Rakitianskaia, A.S. and A.P. Engelbrecht, *Training feedforward neural networks with dynamic particle swarm optimisation.* Swarm Intelligence, 2012. **6**(3): p. 233-270.

[5] Črepinšek, M., S.-H. Liu, and M. Mernik, *Exploration and exploitation in evolutionary algorithms: a survey.* ACM Computing Surveys (CSUR), 2013. **45**(3): p. 35.

[6] Xu, G., *An adaptive parameter tuning of particle swarm optimization algorithm.* Applied Mathematics and Computation, 2013. **219**(9): p. 4560-4569.

[7] Mirjalili, S., S.Z.M. Hashim, and H.M. Sardroudi, *Training feedforward neural networks using hybrid particle swarm optimization and gravitational search algorithm.* Applied Mathematics and Computation, 2012. **218**(22): p. 11125-11137.

[8] Yang, X.-S., *Nature-inspired optimization algorithms*. 2014: Elsevier.

[9] Seiffert, U. *Multiple layer perceptron training using genetic algorithms*. in *ESANN*. 2001.

[10] Kennedy, J., *Particle swarm optimization*, in *Encyclopedia of machine learning*. 2011, Springer. p. 760-766.

[11] Dorigo, M., M. Birattari, and T. Stutzle, *Ant colony optimization.* IEEE computational intelligence magazine, 2006. **1**(4): p. 28-39.

[12] Mirjalili, S., S.M. Mirjalili, and A. Lewis, *Grey wolf optimizer.* Advances in Engineering Software, 2014. **69**: p. 46-61.

[13] Mirjalili, S. and A. Lewis, *The whale optimization algorithm.* Advances in Engineering Software, 2016. **95**: p. 51-67.

[14] Yu, J., S. Wang, and L. Xi, *Evolving artificial neural networks using an improved PSO and DPSO.* Neurocomputing, 2008. **71**(4): p. 1054-1060.

[15] Mendes, R., et al. *Particle swarms for feedforward neural network training*. in *Neural Networks, 2002. IJCNN'02. Proceedings of the 2002 International Joint Conference on*. 2002. IEEE.

[16] Meissner, M., M. Schmuker, and G. Schneider, *Optimized Particle Swarm Optimization (OPSO) and its application to artificial neural network training.* BMC bioinformatics, 2006. **7**(1): p. 125.

[17] Blum, C. and K. Socha. *Training feed-forward neural networks with ant colony optimization: An application to pattern classification*. in *Hybrid Intelligent Systems, 2005. HIS'05. Fifth International Conference on*. 2005. IEEE.

[18] Socha, K. and C. Blum, *An ant colony optimization algorithm for continuous optimization: application to feed-forward neural network training.* Neural Computing and Applications, 2007. **16**(3): p. 235-247.

[19] Wolpert, D.H. and W.G. Macready, *No free lunch theorems for optimization.* IEEE transactions on evolutionary computation, 1997. **1**(1): p. 67-82.

[20] Ho, Y.-C. and D.L. Pepyne, *Simple explanation of the no-free-lunch theorem and its implications.* Journal of optimization theory and applications, 2002. **115**(3): p. 549-570.

[21] Uymaz, S.A., G. Tezel, and E. Yel, *Artificial algae algorithm (AAA) for nonlinear global optimization.* Applied Soft Computing, 2015. **31**: p. 153-171.

[22] Mirjalili, S., *How effective is the Grey Wolf optimizer in training multi-layer perceptrons.* Applied Intelligence, 2015. **43**(1): p. 150-161.

[23] Mirjalili, S., S.M. Mirjalili, and A. Lewis, *Let a biogeography-based optimizer train your multi-layer perceptron.* Information Sciences, 2014. **269**: p. 188-209.

[24] Wdaa, A.S.I. and A. Sttar, *Differential evolution for neural networks learning enhancement*. 2008, Universiti Teknologi Malaysia.

Analysis And Segmentation Of Announcements In The Turkish Universities

G.ORTAÇ[1] and T.T.BİLGİN[1]

[1] Bursa Technical University, Bursa/Turkey, gizem.ortac@btu.edu.tr, turgay.bilgin@btu.edu.tr,

Abstract - **With the increasing of large amount information in unstructured text documents, text mining technology or knowledge discovery from text (KDT) has been emerging as a new and exciting research area. Text mining is a multidisciplinary field that involves machine learning, natural language processing (NLP), information retrieval (IR) and knowledge management to deal with extraction of knowledge and patterns from unstructured text documents. Therefore, a number of techniques have been developed to discover trends and outliers in text data rather than enabling information access as a traditional focus. In this study, it is aimed to analyze of announcements of the universities in Turkey and reveal hidden relationships between them in terms of research areas, activities, programs and other facilities by using text mining. The proposed study includes three steps. The first step is pre-processing that relies on reading and parsing documents, filtering, typo error correction, keyword extraction and transformation. The second step deals with mining the data. In this step, hierarchical clustering techniques are used for clustering the text data. The last step is visualization and presentation by generating tag clouds. Our results show that, subjects of the announcements are generally similar for most of the universities. However, some universities emphasize the terms related to research, congress and internationalization on their announcements.**

Keywords **– data mining, text mining, text clustering, hierarchical clustering, KNIME**

I. INTRODUCTION

Last few decades, with the rapid technological advances in science and information fields, huge amount of data has been collected from different sources such as sensors, monitoring systems, mobile and smartphone applications. Because of this growth of internet traffic, it is difficult to manually analyze the data for decision making and extract usable information. Data mining techniques offer the most appropriate solutions to deal with these problems.

Data mining can be described as a process of extraction of useful information and analyzing it from different perspectives to produce a specific model [1]. It performs well on structured data. On the other hand, unstructured data may contain large amounts of hidden and useful information. For this reason, text mining techniques are needed to deal with such unstructured data. Text mining, also known as text data mining or knowledge discovery from textual databases, refers generally to the process of extracting interesting and non-trivial patterns or knowledge from unstructured text documents [2].

Text mining deals with unstructured and fuzzy data sets such as emails, full-text documents and HTML files, etc. It combines techniques from data mining, machine learning, natural language processing and information retrieval.

Since computers cannot handle linguistic patterns such as slang, spelling variations and contextual meaning, unstructured text has to be checked and converted into the vector-space model before any advanced text mining. Many natural language processing technologies have been developed to teach computers natural language. These technologies are used in the text mining for data extraction, summarization, categorization, clustering, concept linkage and visualization [3].

In this paper, we present a text mining workflow, which analyzes announcements sections of websites of Turkish universities to investigate relationships among them. Our purpose is to discover the correlation in various fields such as research, technological developments, social and academic activities. The information extraction and text mining have been performed by the KNIME platform with Text Processing plugin [4] which allows tagging, filtering, frequency computation, data structure transformation and other preprocessing tasks of data.

II. RELATED WORK

Text clustering has great practical importance of structuring large document collections. A. Trappey, C.V. Trappey, F.C. Hsu nd D.W. Hsiao proposed a fuzzy ontology-based document clustering technique that makes the clustering results more natural and understandable [5]. M. Mahdavi, H. Abolhassani ve Harmony developed the clustering methods based on similarity-based approaches and model-based approaches [6]. Navaneethakumar, V. M. and Chandrasekar, C. presented the web document based text clustering method and analyzed this method with the concept based mining models using a different set of datasets [7]. The proposed method aimed to improve clustering efficiency. Gupta, V. developed an application domain where text mining can be used in clustering, concept linkage, information visualization, information retrieval, topic tracking, summarization and question answering [8]. Yassine, M., and Hajj, H. worked on extracting emotional interaction in online social networks, which includes a model for data collection, database schemas, data processing and data mining steps [9].

III. DATA RETRIEVAL

The announcements published on the university websites were obtained using a software called Selenium WebDriver tool that merges Selenium tool and a web driver that can directly communicate with the browser. Selenium WebDriver provides a comprehensive programming interface for controlling web browser and it can be manually controlled by a specific command set [10]. In this study, Chrome Driver has been chosen to control the Google Chrome browser. The driver navigates the university announcements page URL's and collects text data and removes the formatting tags. The text data was collected from 102 universities in Turkey in October 2017.

IV. DATA PREPROCESSING

Pre-processing step is the process of cleaning and preparing the text for classification. The text data set has to be cleaned and transformed into a proper data structure in order to process data on the KNIME platform. The KNIME Text Processing plugin was used to process the textual data. It is a powerful tool for parsing textual documents and operating in multiple manners [4].

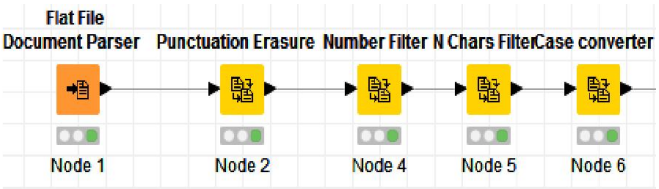


Figure 1: Pre-processing nodes of KNIME text mining plug-in.

As seen from Fig.1, the first step in preprocessing is reading and parsing the documents by using "*Flat File Document Parser*" node to represent data in document form. After reading and parsing, all punctuation marks and numbers were removed and all text was converted to lower case. The terms occur less than a threshold value were discarded by mean of a "N Char Filter" [11].

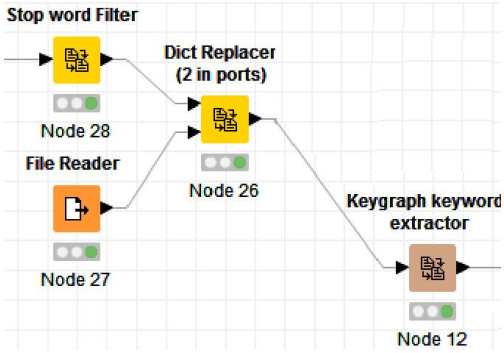


Figure 2: Stop Words filtering and keyword extractor nodes of KNIME text mining plug-in.

After basic cleaning procedures, stemming was applied to reduce the individual words into their common root-form using a stemmer for Turkish language. Stemming also includes removal of suffixes and inappropriate pluralization. Frequent words called "stopwords" were also removed to improve text mining results. This step leads to decrease the number of the dimension of data and improves accuracy [12].

In order to further reduce the number of words, "*Keygraph keyword extractor*" node used to produce a short summary of the data with a set of significant words. These operations have been performed by the nodes shown at Fig. 2. After this step, the documents are tagged with these selected keywords. The Keygraph algorithm extracts the information based on the term frequency and number of occurrences [4].

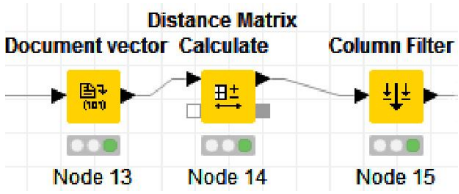


Figure 3: Transformation steps of the textual data set.

After text preprocessing had been completed, individual keywords were transformed into a vector representation by using the *"Document Vector"* node. The document vectors are a numerical representation of documents and used for hierarchical clustering. Manhattan and Euclidean based distance matrices calculated by *"Distance Matrix Calculate"* node [4]. "Column filter" node removes some unnecessary columns generated by the distance matrix calculator node. After generating the matrix as shown in Fig.3, it is possible to apply data mining methods such as clustering over these document vectors.

V. DATA MINING

In this study, we used the hierarchical clustering to perform document clustering.

The document clustering algorithms operate on the document distance matrix. In hierarchical clustering, all data objects are individual clusters at the beginning. The distances between these clusters are calculated and the clusters that are closest to each other are merged. This process continues until one cluster remains [3].

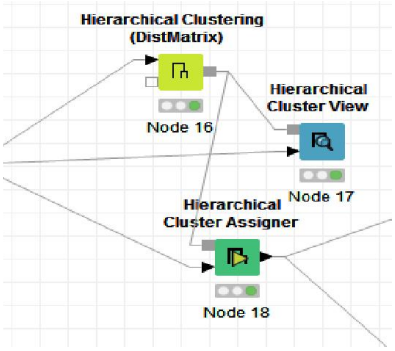


Figure 4: Hierarchical Clustering steps

Hierarchical clustering has two forms, namely agglomerative and divisive hierarchical clustering [13]. In this study, bottom-up or agglomerative form is used. The agglomerative starts with single member clusters and then merges these atomic clusters into larger clusters until reaching a single cluster [14].

In KNIME, *"Hierarchical Clustering (DistMatrix)"* node is used for hierarchically clusters the input data using the distance matrix that is obtained by "Distance Matrix Calculate" node. However, in order to determine the distance between clusters, a similarity measure or linkage [15] has to be defined. Linkage types can be described as follows:

A. *Single-linkage clustering :*

In this clustering method, the link between two clusters is defined by an element pair (one in each cluster) that are closest to each other. The similarity between two clusters is defined by nearest distance from any point of one cluster to any point of the other cluster [16].

B. *Complete-linkage clustering :*

The distance between two clusters is defined by the maximum distance from any point of one cluster to any point of the other cluster [17].

C. *Average-linkage clustering :*

The distance between two clusters is defined by an average distance from any point of one cluster to any point of the other cluster [18].

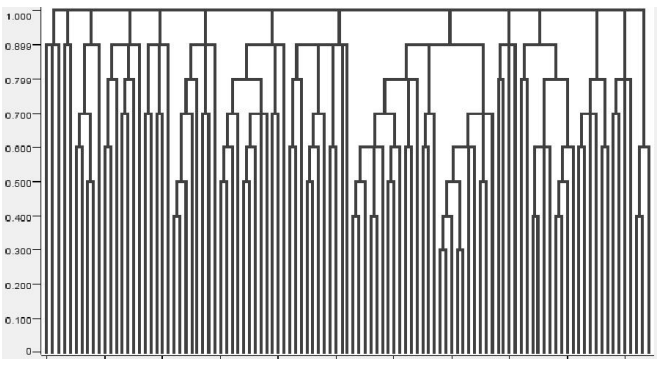


Figure 5: Dendrogram of the hierarchical clustering

In this study, average-linkage clustering method was preferred. After hierarchical clustering had been completed, *"Hierarchical Clustering Assigner"* node was used to assign cluster numbers to dataset rows. As it can be shown on Fig.4, *"Hierarchical Cluster View"* node was implemented to create a clustering tree and display the dendrogram. A dendrogram displays the result of a hierarchical clustering. At the bottom of the plot, every data point is assumed as one cluster in dendrogram. After that, the closest two data points are combined and this procedure applied to all remaining data points. Those clusters which are closest to each other are combined and finally all data points are merged into one cluster. The y coordinate shows the distance between the objects or clusters [4].

In this study, the horizontal line cut threshold of the dendrogram has been chosen as 0.95. The dendrogram has been given on the Fig. 5.

VI. DATA PRESENTATION AND RESULTS

The relative term frequency (TF) is an important parameter which is computed by dividing the absolute frequency of a term by the number of all terms of that document [4]. The TF calculation node is used to provide input for the Tag Cloud nodded.

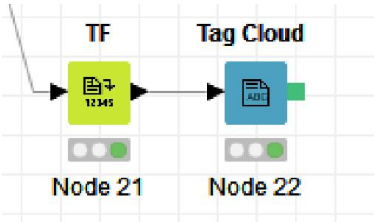


Figure 8: The relative term frequency step

As shown in Fig.8, the *"Tag Cloud"* node employed to create a typical tag cloud. Tags are single words, and the importance of each tag is shown with various font sizes or colors. Tag cloud is widely used visualization technique in text mining.

As seen in the dendrogram shown in Fig. 5, total 14 clusters were discovered in this study. The tag clouds of each cluster and the members of each cluster are given below. The clusters are numbered starting from 0.



Figure 9: Tag cloud of cluster 0.

Members of cluster 0 are Çankaya, Dicle and Karamanoğlu Mehmet Bey universities.Figure 9 shows a tag cloud of cluster 0. As seen in the tag cloud, the announcements are mostly about the term "üniversite".



Figure 10: Tag cloud of cluster 1.

Members of cluster 1 are Dokuz Eylül and Sağlık Bilimleri universities.Figure 10 shows a tag cloud of cluster 1. As seen in the tag cloud, the announcements are mostly about the terms “havacılık”, “kongre”,”kardiyoloji”,”tıbbi”,”çalıştay”.



Figure 11: Tag cloud of cluster 2.

Members of cluster 2 are Atatürk, Siirt, İstanbul Ticaret, Trakya and Uşak universities. Figure 11 shows a tag cloud of cluster 2. As seen in the tag cloud, the announcements are mostly about the terms “duyurular” and “eğitim”.



Figure 12: Tag cloud of cluster 3.

Members of cluster 3 are Lefke Avrupa, Bandırma 17 Eylül, Bayburt, Cumhuriyet, Ege, Erzincan and Mehmet Akif universities. Figure 12 shows a tag cloud of cluster 3. As seen in the tag cloud, the announcements are mostly about the terms “kayıt”,”detay” and “öğrenci”.

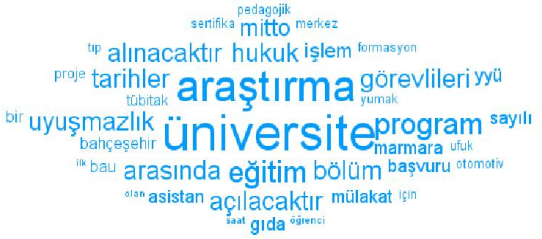


Figure 13: Tag cloud of cluster 4.

Members of cluster 4 are Bahçeşehir, KTO Karatay, Marmara, Mef and Yüzüncüyıl, Yalova and Yaşar universities. Figure 13 shows a tag cloud of cluster 4. As seen in the tag cloud, the announcements are mostly about the terms “üniversite” and “araştırma”.



Figure 14: Tag cloud of cluster 5.

Members of cluster 5 are Bitlis Eren, Abant İzzet Baysal, Kapadokya, Kırklareli, İstanbul Şehir universities.Figure 14 shows a tag cloud of cluster 5. As seen in the tag cloud, the announcements are mostly about the terms “başvuru” and “dönem”.



Figure 15: Tag cloud of cluster 6.

Members of cluster 6 are Bartın, Başkent, Bingöl, Çanakkale 18 Mart, Erciyes, Gaziantep, Hitit, İzmir Demokrasi, İzmir Ekonomi, İstanbul Teknik, Kırıkkale and İnönü universities. Figure 15 shows a tag cloud of cluster 6. As seen in the tag cloud, the announcements are mostly about the terms “üniversite” and “öğrenci”.



Figure 16: Tag cloud of cluster 7.

Members of cluster 7 are Avrasya, Batman, Bilgi, Biruni, Bursa Teknik, Çağ, Giresun, İzmir Yüksek Teknoloji, Kastamonu, Kilis and Kocaeli universities. Figure 16 shows a tag cloud of cluster 16. As seen in the tag cloud, the announcements are mostly about the terms “sınav” and “sonuç”.



Figure 17: Tag cloud of cluster 8.

Members of cluster 8 are İstanbul Ayvansaray, Bilecik Şeyh Edebali Dicle, Beykoz, Bozok, Çukurova, Doğuş,

Dumlupınar, Konya Gıda Tarım, Harran, İstanbul Bilim, İstinye, Karatekin, İstanbul Kent, Selçuk, Karadeniz Teknik, Munzur, Sinop, Şırnak, İstanbul Şişli, TED, Türk Hava Kurumu and Uludağ universities. Figure 17 shows a tag cloud of cluster 8. As seen in the tag cloud, the announcements are mostly about the terms "öğretim" and "yıl".



Figure 18: Tag cloud of cluster 9.

Members of cluster 9 are Düzce, İstanbul Medeniyet, Özyeğin and Selçuk universities. Figure 18 shows a tag cloud of cluster 9. As seen in the tag cloud, the announcements are mostly about the term "uluslararası","duyuru" and "detay".



Figure 19: Tag cloud of cluster 10.

Members of cluster 10 are Atılım, Beykent, Erzurum Teknik, Galatasaray, Maltepe, Medipol, Sanko, Türk Alman, Ufuk and Üsküdar universities. Figure 19 shows a tag cloud of cluster 10. As seen in the tag cloud, the announcements are mostly about the terms "sonuç","fakülte" and "görevlisi"



Figure 20: Tag cloud of cluster 11.

Members of cluster 11 are Bülent Ecevit, Celal Bayar, Kafkas, Karabuk, and Kavram universities. Figure 20 shows a tag cloud of cluster 11. As seen in the tag cloud, the announcements are mostly about the terms "ilan","alım" and "öğretim".



Figure 21: Tag cloud of cluster 12.

Members of cluster 12 are Bezmialem, Fırat, İstanbul Sabahattin Zaim and Yeditepe universities. Figure 21 shows a tag cloud of cluster 12. As seen in the tag cloud, the announcements are mostly about the terms "detay","üniversite" and "tarih".



Figure 22: Tag cloud of cluster 13

Members of cluster 13 are Gümüşhane and Kadir Has universities. Figure 22 shows a tag cloud of cluster 13. As seen in the tag cloud, the announcements are mostly about the term "enstitü".

VII. CONCLUSION

As a result of clustering, all universities were clustered to fourteen clusters. The term "university" has been widely used in the clusters 0, 4 and 12. In the clusters 2, 3, 5, 7, 8, 10, 11 the terms such as "registration", "application", "result", "announcement" are frequently used. The clusters numbered 1, 9 and 13 are quite different from the general tendency. Those universities fall into cluster 1 have frequently used the terms "aviation", "cardiology" and "congress". Cluster 9 emphasizes the term "international". Cluster 13 emphasizes announcements about the "institute."

VIII. REFERENCES

[1] Feldman, Ronen, and James Sanger. The text mining handbook: advanced approaches in analyzing unstructured data. Cambridge university press, 2007.

[2] Hearst, M. A. (1997). Text data mining: Issues, techniques, and the relationship to information access. In Presentation notes for UW/MS workshop on data mining (pp. 112-117).

[3] Berkhin, Pavel. "A survey of clustering data mining techniques." Grouping multidimensional data 25 (2006): 71

[4] Thiel, Kilian. "The KNIME Text Processing Plugin." (2009).

[5] A. Trappey, C.V. Trappey, F.C. Hsu, D.W. Hsiao, A fuzzy ontological knowledge document clustering methodology, IEEE Trans. Syst. Man Cybern. B: Cybern. 39 (3) (2009) 806–814.

[6] M. Mahdavi, H. Abolhassani, Harmony K-means algorithm for document clustering, Data Min. Knowl. Discov. 18 (3) (2009) 370–391.

[7] Navaneethakumar, V. M., & Chandrasekar, C. (2012). A consistent web documents based text clustering using concept based mining model.

[8] Gupta, V. (2009). A survey of text mining techniques and applications. Journal of Emerging Technologies in Web Intelligence, 1(1) (August).

[9] Yassine, M., & Hajj, H. (2010). A framework for emotion mining from text in online social networks. In IEEE international conference on data mining workshops (pp. 1136–1142). Sydney, NSW: IEEE publications.

[10] Gojare, Satish, Rahul Joshi, and Dhanashree Gaigaware. "Analysis and Design of Selenium WebDriver Automation Testing Framework." Procedia Computer Science 50 (2015): 341-346.

[11] Miner, Gary. Practical text mining and statistical analysis for non-structured text data applications. Academic Press, 2012.

[12] Sedding, Julian, and Dimitar Kazakov. "Wordnet-based text document clustering." proceedings of the 3rd workshop on robust methods in analysis of natural language data. Association for Computational Linguistics, 2004.

[13] F. Murtagh, A survey of recent advances in hierarchical clustering algorithms which use cluster centers, Comput. J. 26 (4) (1984) 354–359.
[14] Berkhin, Pavel. "A survey of clustering data mining techniques." Grouping multidimensional data 25 (2006): 71.
[15] A.K. Jain, M.N. Murty, P.J. Flynn, Data clustering: a review, ACM Comput. Surv. 31 (3) (1999) 264–323.
[16] P. Sneath, R. Sokal, Numerical Taxonomy, W.H. Freeman Co, San Francisco, CA, 1973.
[17] B. King, Step-wise clustering procedures, J. Am. Stat. Assoc. 69 (317) (1967) 86–101.
[18] J.H. Ward, Hierarchical grouping to optimize an objective function, J. Am. Stat.Assoc. 58 (301) (1963) 236–244.
[19] Alsmadi, Izzat, and Ikdam Alhami. "Clustering and classification of email contents." Journal of King Saud University-Computer and Information Sciences 27.1 (2015): 46-57.

Face Recognition using Eigenface vs. Fisherfaces

M. AKÇAY[1] and Naciye Nur SARIBEY [1]

[1] Dumlupinar University, Kutahya/Turkey, makcay26@gmail.com
[1]Dumlupinar University, Kutahya/Turkey, nnursaribey@gmail.com

Abstract **- Face recognition issue gained more interest recently due to its various applications and the high security demand. In this paper, we will have a comparative study of two methods for face recognition. Our projection method is based on Fisher's Linear Discriminant and produces well separated classes in a low-dimensional subspace, even under severe variation in lighting and facial expressions. The Eigenface technique, another method is based on linearly projecting the image space to a low dimensional subspace, has similar computational requirements. After the implementation of two methods, the advantages and disadvantages of each approach and the difficulties for the implementation will be discussed.**

Keywords **- Face recognition, Eigenface, Fisher's Linear Discriminant.**

I. INTRODUCTION

Facial recognition problem has been the subject of research for many years. This system has seen in identity verification, criminal identification, public areas such as stadium airport, smart home systems, web environment, age and sex analysis, and security locks on the phone.

Facial recognition is also one of the difficulties encountered in face position changes, lighting changes, facial changes over time, person multiplicity to identify and speed of calculation. Since each square of a picture does not represent a face, it is first necessary to identify the faces in the picture. The Viola and Jones face detection method will be used for this process [1].

Firstly, a formal method of classifying faces was proposed by Francis Galton [2, 3] in 1888. During the 1980's, work on face recognition remained largely dormant. Since the 1990's, the research interest in face recognition has grown significantly [4].

The two approaches used for facial recognition have been examined in this study. The Eigenface approach is based on PCA (Principle Component Analysis). The Fisherfaces approach uses LDA (Linear Discriminant Analysis). A system to compare Eigenface and Fisherfaces approaches will be developed and their advantages and disadvantages will be examined.

Haarcascade approach will be examined in the second part of the study, Eigenface approach will be discussed in the third part, Fisherfaces approach will be examined in the fourth part, information about the system developed in the fifth part will be given, and results and suggestions will be given in the sixth part.

II. FACE DETECTION

Some of the face detection methods are Template Matching, Haarcascade, Local Binary Pattern (LBP) and Histogram of Oriented Gradients (HOG). The method to be used in the study is Haarcascade method. The Haar Cascade classifier was introduced by Paul Viola and Michael Jones in 2001 [1].

The following steps are followed in this method:

1) Haar Features

The simple features used are reminiscent of Haar basis functions (Fig. 1.):

• Two-rectangle feature: difference between the sum of the pixels within two rectangular regions

• Three-rectangle feature: sum within two outside rectangles subtracted from the sum in a center rectangle

• Four-rectangle feature: difference between diagonal pairs of rectangles [2].

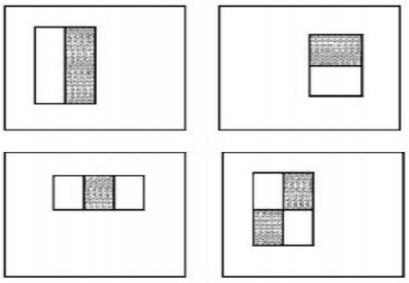


Fig. 1. Haar Features

The first two features selected by AdaBoost for the task of face detection are easily interpreted:

• First feature: the region of the eyes is often darker than the region of the nose and cheeks

• Second feature: the eyes are darker than the bridge of the nose [1].

2) Integral Image

The integral image at location (x, y) contains the sum of the pixels above and to the left of (x, y), inclusive (Fig. 2.):

$$ii(x, y) = \sum_{x' \le x, y' \le y} i(x', y'), \quad (1)$$

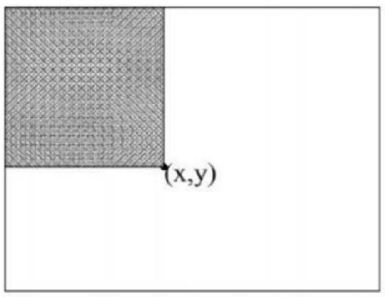


Fig. 2. Integral Image

3) Cascading Classifier

Each classifier layer in the structure scans a different region in the feature space. The simple classifiers used here are decision trees with at least two leaves. Haar attributes are given as input to these classifiers. Simpler classifiers are used to reject the majority of sub windows. Then, more complex classifiers are called upon to achieve low false positive rates. (Fig. 3.)

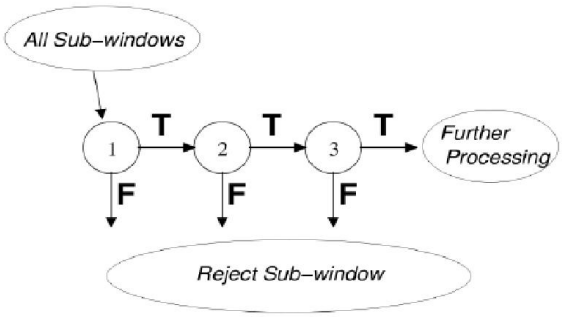


Fig. 3. Cascading Classifier

4) Adaboost Algorithm

The Adaboost algorithm from the "Adaptive Boosting" expansion was introduced by Yoav Freund and Robert Schapire. AdaBoost is used both to select the features and to train the classifier.

Let's say the plus signs in the D1 data set represent the images with the human face, and the minus signs represent the images without the face inside. If the D1 dataset is classified and the images without the blue side face show the images with the red side face, then 3 misclassifications occur. The weight of these incorrect samples is increased and the data set (D2) is updated. When it is reclassified again, 3 misclassifications arise, which are called weak classifiers. (Fig.4.)

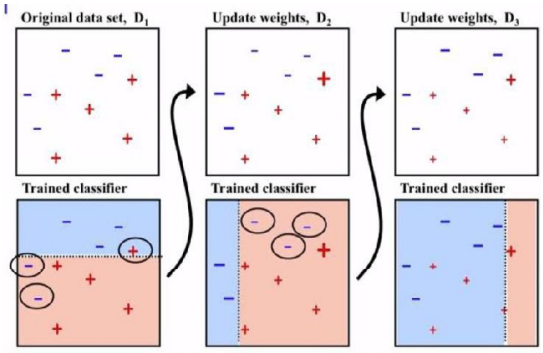


Fig. 4. Weak Classifiers

A strong classifier (Fig. 5.) is obtained by combining weak classifiers. Thus, after each weak classifier is trained, a general error calculation is performed using these weights, and a new weak classifier on the next attribute is trained in consideration of this error.

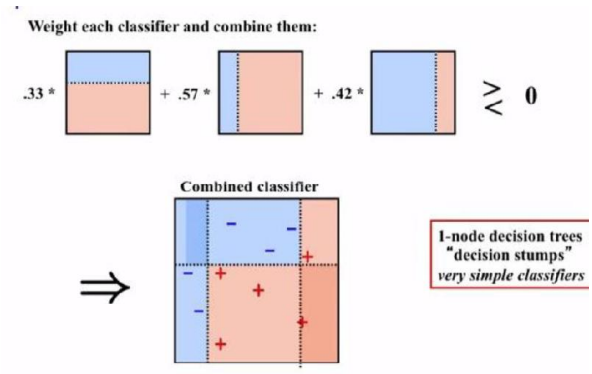


Fig. 5.Strong Classifier

III. EIGENFACE

The Eigenface approach to recognition was developed by Sirovich and Kirby [6] in 1987 and used by face classification by Matthew Turk and Alex Pentland [7]. Principal Component Analysis [8] is used in Eigenface approach. In this analysis method, an N-dimensional covariance matrix of an N-dimensional data is found. The matrix has N eigenvalues. The eigenvalue is the variance of the data of the eigenvector corresponding to the corresponding eigenvalue. The M eigenvectors corresponding to the first M eigenvalues with the largest variance are found. Eigenvector is projected and reduced from N dimension to M dimension.

The training set of face images be $\Gamma_1, \Gamma_2, \ldots, \Gamma_M$. The average face of the set is defined by

$$\Psi = \frac{1}{M}\sum_{n=1}^{M}\Gamma_n$$

Each face differs from the average by the vector

$$\Phi_j = \Gamma_j - \Psi$$

This set of very large vectors is then subject to principal component analysis, which seeks a set of M orthonormal vectors, u_n, which best describes the distribution of the data [6].

Each of these u_n vectors is selected so as to maximize the coefficients defined below.

$$\lambda_k = \frac{1}{M}\sum_{n=1}^{M}(u_k^T \Phi_n)^2 \qquad (2)$$

The u_n vectors are required to provide (3) with orthonormal condition.

$$u_l^T u_k = \delta_{lk} = \begin{cases} 1, l = k \\ 0, l \neq k \end{cases} \qquad (3)$$

u_k vectors and λ_k constants are the eigenvectors and eigenvalues, respectively, of the covariance matrix C defined below.

$$C = \frac{1}{M}\sum_{n=1}^{M}\Phi_n\Phi_n^T = AA^T \qquad (4)$$

$$A = [\Phi_1 \Phi_2 \dots \Phi_M] \qquad (5)$$

The eigenvectors of the matrix C defined above form the eigenfaces of face space that we are interested in. Note that for face images of size NxN, the matrix C is dimension N^2XN^2. It is not useful to have the eigenvalues of a matrix of this magnitude. However, for situations where the number of pictures in the training set is too small for the size of the picture space ($M << N^2$), a useful covariance is possible [10].

By using eigenfaces, the feature vector Ω^T of any face image can be found as follows.

$$w_k = u_k^T (\Gamma - \Psi) \qquad (6)$$

$$\Omega^T = [w_1 w_2 \dots w_M] \qquad (7)$$

Any face image to face space

$$\Gamma = \Psi + \sum_{i=1}^{M} w_i u_i \qquad (8)$$

can be recovered approximately by projection [7].

IV. FISHERFACE

Fisherface approach is used for classification-based recognition. Fisherface method uses Fisher's Linear Discriminant (FLD). Linear Discriminant Analysis (LDA) can be derived from an idea by R.A. Fisher in 1936. LDA examines the distribution of classes and separates the classes from one another using the differences between the mean values.

This method selects W in [5] in such a way that the ratio of the between-class scatter and the within class scatter is maximized. Again, let us consider a set of N sample images $\{x_1, x_2, \dots, x_N\}$ taking values in an n-dimensional image space, and assume that each image belongs to one of c classes $\{X_1, X_2, \dots, X_c\}$.

Let the between-class scatter matrix be defined as

$$S_B = \sum_{i=1}^{c} N_i(\mu_i - \mu)(\mu_i - \mu)^T \qquad (9)$$

and the within-class scatter matrix be defined as

$$S_W = \sum_{i=1}^{c}\sum_{\mathbf{x}_k \in X_i}(\mathbf{x}_k - \mu_i)(\mathbf{x}_k - \mu_i)^T \qquad (10)$$

where μ_i is the mean image of class X_i, N_i is the number of samples in class X_i, and μ is the mean image of all samples. If SW is nonsingular, the optimal projection Wopt is chosen as the matrix with orthonormal columns which maximizes the ratio of the determinant of the between-class scatter matrix of the projected samples to the determinant of the within-class scatter matrix of the projected samples, i.e.,

$$W_{opt} = \arg\max_W \frac{|W^T S_B W|}{|W^T S_W W|} = [\mathbf{w}_1 \mathbf{w}_2 \dots \mathbf{w}_m] \qquad (11)$$

where $\{w_i \mid i = 1, 2, \dots, m\}$ is the set of generalized eigenvectors of S_B and S_W corresponding to the m largest generalized eigenvalues $\{\lambda_i \mid i = 1, 2, \dots, m\}$, i.e.,

$$S_B \mathbf{w}_i = \lambda_i S_W \mathbf{w}_i, \quad i = 1, 2, \dots, m. \qquad (12)$$

Note that there are at most $c - 1$ nonzero generalized eigenvalues, and so an upper bound on m is $c - 1$, where c is the number of classes.

In the face recognition problem, one is confronted with the difficulty that the within-class scatter matrix $S_W \in R^{n \times n}$ is always singular [11].

V. DEVELOPED SYSTEM

Since the C sharp programming language is chosen for the face recognition system, the wrapper EmguCV of the OpenCV library will be used [12].

A. OpenCV Library

The OpenCV library is written in C and C ++ programming languages. It is an open source, BSD-licensed free library and is platform independent and can work on Linux, Windows, Android, and MacOS.

The OpenCV library contains more than 2500 algorithms for image processing and machine learning. With these algorithms face recognition, distinguishing objects, to identify human movements, object classification, plate recognition, to be able to operate on three dimensional image and image comparison operations can be done.

B. EmguCV Wrapper

EmguCV is an OpenCV wrapper. Wrapper establishes the connection between the .net application and the OpenCV library. (Fig. 6.) EmguCV makes it easy to develop image processing applications with C #, VB, VC++, Xamarin or Iron Python and Unity under the .Net framework. EmguCV Wrapper works on Windows, Linux, Mac OS X, Mac iOS, Android and MS Windows Phone platforms.



Fig. 6. EmguCV wrapper

The developed system will first detect the faces and put them into a rectangle. The faces will be brought to the same size and converted to gray mode and trained. Testing of trained faces will be done with one of Eigenface or Fisherfaces methods. (Fig. 7.)

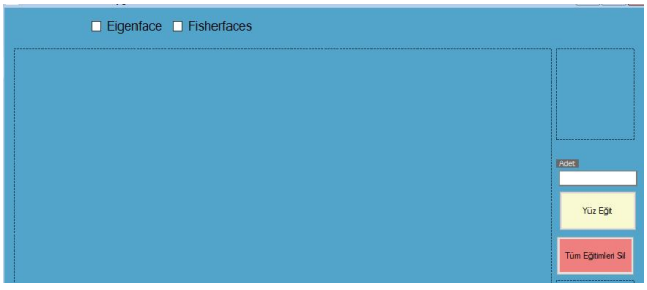


Fig.7. Developed system with C#

VI. CONCLUSION

Eigenface and Fisherfaces methods will be used in the study to compare the face recognition performance between the two methods against environment variables, face position and face expression. Thus, it will be seen in which conditions both methods work well. At the end of these studies, a facial recognition system will be developed with deep neural network, which is the subject of research today. It is expected that face recognition performance will increase with this method.

VII. REFERENCES

[1] P. Viola, M. J. Jones, "Robust Real-time Object Detection", ICCV Workshop on Statistical and Computation Theories of Vision, 2001.

[2] F. Galton, "Personal identification and description 1, 1", *Nature*, pp.173-177, 21 June1988.

[3] F. Galton, "Personal identification and description-II", *Nature*, pp. 201-203, 28 June 1988.

[4] D. Chakrborty. S. K. Saha, A. Bhuiyan, "Face Recognition using Eigenvector and Principle Component Analysis", *International Journal of Computer Applications,* (ISBN: 0975 – 8887), Volume 50 – No.10, July 2012.

[5] P. N. Belhumeur, J. P. Hespanha, D. J. Kriegman, "Eigenfaces vs Fisherfaces Recognition Using Class Specific Linear Projection", *European Conf. Computer Vision,* pp., 45–58 , 1996.

[6] Kirby and Sirovich, "Application of the Karhunen-Loeve procedure for the characterization of human faces", *IEEE Trans. PAMI*, vol. 12, pp. 103-108, 1990.

[7] M. Turk, A. Pentland, "Eigenfaces for recognition", *Journal of Cognitive Neuroscience*, Vol. 3, pp. 71- 86, 1991.

[8] A. M. Martinez, A. C. Kak, "PCA versus LDA", IEEE Trans. Pattern Analysis and Machine Intelligence, Vol. 23, 2001, pp.228-233

[9] R. Chellappa, C. Wilson, S. Sirohey, "Human and Machine Recognition of Faces: A Survey", *Proc". IEEE*, vol 83, no. 5, pp. 705–740, 1995.

[10] M. Gökmen, B., Kurt, F.,Kahraman,, F. Çapar, "Çok Amaçlı Gürbüz Yüz Tanıma", *TUBITAK*, pp.18-19, 2007.

[11] N. Seo, "Eigenfaces and Fisherfaces", University of Maryland, for pdf http://note.sonots.com/?plugin=attach&refer=SciSoftware%2FFaceRecognition&openfile=EigenFisherFace.pdf

[12] For OpenCV Library - https://opencv.org/

An Analysis of Mobile Methods on Web Based Authentication

S. ZAVRAK[1], Ş. YILMAZ[1], H. BODUR[1] and F. KAYAALP[1]

[1] Duzce University, Duzce/Turkey, sultanzavrak@duzce.edu.tr
[1] Duzce University, Duzce/Turkey, seyhmusyilmaz@duzce.edu.tr
[1] Duzce University, Duzce/Turkey, huseyinbodur@duzce.edu.tr
[1] Duzce University, Duzce/Turkey, fatihkayaalp@duzce.edu.tr

Abstract **- Today, many daily activities that require physical effort can be done over the internet with the rapid development of technology. While users perform their transactions on the internet, they should not encounter any security problems and face financial loses. For this reason, web systems used to perform these operations must be protected with high security. Security methods can be divided into many parts within themselves. One of these is the existence of an authentication mechanism in the web system. The purpose of the authentication mechanism is to determine that the person performing the transaction on the web system is the real person requesting the transaction, not an attacker. In this study, various authentication methods have been explained and compared.**

Keywords **- Web Based Authentication, Authentication Techniques, Biometric Methods.**

I. INTRODUCTION

The continuous development of the technology and the internet increases the number of operations carried out on the internet. People are able to perform transactions which they could do with physical effort aforetime through devices connected to the internet from where they are sitting. Today, many transactions such as shopping, banking transactions, e-government transactions, bill payment, etc. can be carried out over the internet and this provides simplicity for the people. But besides the advantages of simplicity, this situation also has some disadvantages. Security problems are at the source of these disadvantages. Web systems which we do electronic transactions by using our private information need to be protected with high security. Because malicious people may want to gain access to our private information through various methods of attack and to make profits by using this information. People can be subjected to pecuniary and moral damages as a result of obtaining personal or card information. In addition to this, there may be attacks on web systems that are operated by people to get services. These attacks are aimed at hijacking the web system and damaging directly the system, and the registrants who are in the system. The continuous development of technology not only allows the development of methods that will increase the security of web systems, but also causes the increase of attack methods. For this reason, systems should be protected at the highest security level as possible. One of the most important issues for web systems is that a person can safely login to the system, in other words, to provide secure authentication. Today, many methods have been developed to provide secure authentication and many studies have been done on this subject. In one of these studies, Xie et al. developed a web authentication application by using the QR code method and compared it with other authentication methods in terms of usability, security and applicability [1]. In another study Malutan and Grosan explained web authentication and identity management techniques and they aimed to protect users from attacks by developing a virtual keyboard application in which random letters are assigned to numbers [2]. In the other work, Sakib and Huang developed a password entry method named Textact. In the method, it is aimed to create correct ciphers by applying italic, bold, underlined, adding, deleting and displacement actions on the characters in a text. The advantage of the method is that password characters can be selected anywhere in the text [3]. In another study, Al-Bajjari and Yuan developed an optimized authentication method for web applications. They have made possible the transmission of secure messages that is resistant to many attacks by making use of HMAC (Hashed Message Authentication Code) hashing and AES (Advanced Encryption Standart) encryption algorithms in the method [4]. In another study, Monfared et al. examined the security problems of authentication on mobile devices, proposed a new method based on biometric authentication with a website to increase mobile authentication security and usability [5]. In another study, Kolekar and Vaidya used CAPTCHA (Completely Automated Public Turing test to tell Computers and Humans Apart) schemes on an Android-based mobile device application for registration and login operations. In the application they have developed, a user who wants to login to the system must select one of the various authentication schemes and pass the Captcha password in that scheme. The study also made comparisons of various Captcha schemes [6]. In another study, Yıldırım and Varol developed a mobile application based web authentication. They have made the generation of a one-time password by controlling the IMEI (International Mobile Equipment Identity) number of the

mobile device in addition to the user's fingerprint information and login to the web system using this password over a period of time in application [7]. Since web authentication is an indispensable part of many systems today, there are many different studies on this subject in the literature. In this study, information about authentication and web-based authentication methods are given and web based authentication methods are compared with each other.

II. Authentication Methods

Login with a Password: In this method, the authentication process is usually provided by a password that the user pre-determines. Today, this is the most common method of authentication. Many users will only log in with a character-based password that they know for authentication process. Too much use of this method for authentication has led to an increase in the types of attacks that are done to break the method. Examples of attack types are the middle man attack [8], phishing attack [9], or password guess attack [10].

Biometric methods: Biometric methods include techniques such as fingerprint recognition, voice recognition, iris recognition or face recognition. Biometric properties are different in each person. For this reason, these methods are highly reliable. But since it requires additional hardware cost, the usage rate is lower than login with a password. The most widely used biometric technique is fingerprint recognition. Fingerprint recognition is briefly compared to the patterns on the finger in the predefined database.

Voice recognition, also called Automatic Speech Recognition (ASR), examines grammars and accents during natural speech of a person. Each person's voice track is different and occurs by analyzing more than 50 unique physical qualities. Examples of these qualities are mouth shape, mouth size, nasal, behavioral factors including pronunciation, accentuation, speed of speech and accent.

Iris recognition is a biometric authentication method that includes sample recognition techniques based on high-resolution images of the subject's eye.

Face recognition involves scanning 14 to 22 faces of 80 different points on a person's face to create an 84-byte face trace. Examples of these points include the distance between the eyes, the width of the nose, the depth of the eyeholes, or the cheeks.

Smart Cards: Smart cards contain information that uniquely identifies the owner. In smart card usage, no password or any special information known by the user is sent to the remote server.

Instead, the certificate information contained in the smart card is sent and the application on the server authenticates by issuing this information. However, since mapping is done on the application side, manipulation is obvious.

III. Web Based Authentication

Two-factor authentication must be done in order for the web-based authentication process to be secure. Two different authentication schemes utilize two different components to determine the user identity. These components can be a user-independent technique, in addition to a password known to the user. Some methods that are used for two different authentication methods in Web-based systems are:

One-Time Password: A one-time password is generated by the authenticating application and transmitted to the user in different ways. This way may be through a trusted page driven by the application, or it may be an SMS (Short Message Service) message sent to the person's mobile device. One-time use has a duration of use. If it is not used within this period, it will be invalid. A generated password cannot be reused. If a payment is to be made on a web application, the disposable password message for the mobile phone, which is a second authentication step on the payment completion page, can be given as an example of this method.

QR (Quick Response) Code: Some web services use the QR code method as the secondary phase of authentication. In this method, the system generates a QR code. A mobile device connected to the Internet and the authentication server is required to read the code and send it to the server. Often, the user mobile device also needs to have an application, or an app extension associated with authentication. Yandex, WhatsApp etc. many applications use this method.

Biometric Methods: Until recently, the availability of additional hardware devices was often required for the use of biometric methods in applications. This led to increased cost in the system used. In recent years, increasing the hardware features of mobile devices and integrating modules such as cameras, fingerprint readers into mobile devices have enabled application security to be carried at high levels without additional cost.

Today, many devices and applications can be opened with fingerprint, face-to-face audio identification of the module integrated in the device. These modules can also be used within external applications. With similar modules, it is possible to obtain biometric traces to provide identification of the identity of a person to a web system on the mobile device and to provide the necessary control mechanism.

IV. Evaluation

When we examine web based authentication methods; the individual user must have an external device (typically mobile device) in order for sending the one-time password to the individual user via an application or the SMS channel, asking the individual user to read the QR code generated by the system, or obtaining a bio-signature to identify the biometric identity. This ensures the authenticity of the user logging on the system and thus, thus increases the security of web systems. However, it makes the user dependent to a device.

At this point, it is necessary to consider the possibility of

losing or being stolen the mobile device which they use to log in to the web system.

When an attacker seizes the person's mobile device and if the person's username and password information are stored on the person's mobile device or on the web system with various cookies, the attacker can easily pass the authentication mechanism of the web application by using the one-time password or QR code which are sent to the device.

One-time password and QR code mechanisms have a high security level. However, the security problem is not caused by the authentication mechanism of the web system but the device connected to this system. For this reason, it is assumed that the device is used only by the valid user and security of the device is necessary enough to the extent that it cannot be broken by foreign or unscrupulous users.

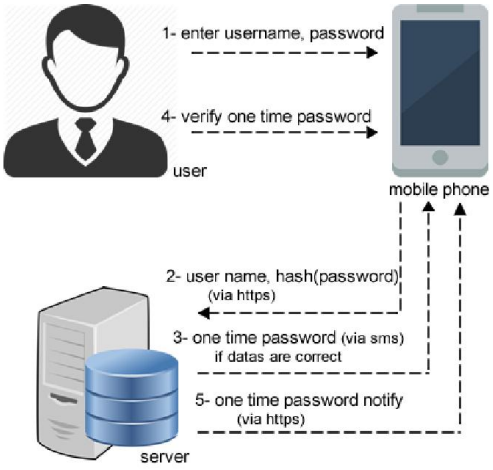


Figure 1: OTP-Based Two-Factor Authentication Procedure Steps.

In Figure 1, an authentication scheme, which the secondary factor is a one-time password, is presented. In Step 3 of the scheme, the server must first verify the hashing of the username and password in step 2 before sending the one-time password. The user transmits the one-time password to the server from the secure channel to the mobile device at step 4. Then, the process of two-factor authentication is completed.

Biometric methods only allow the use of a bio-signature that is obtainable from the user. These methods still maintain the authentication security (secondary safety) in high levels even if someone's mobile device gets stolen by an attacker.

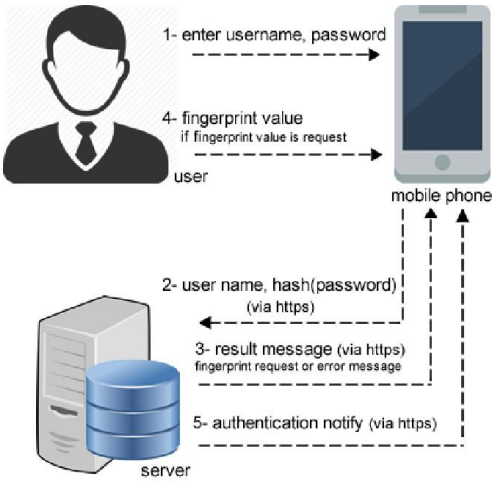


Figure 2: Fingerprint-based Two Factor Authentication Steps.

An authentication scheme which is the secondary factor is fingerprint value is given in Figure 2. When transmitting signature values obtained by using biometric methods on web systems, some encryption-based or hashing algorithms must be used. Bio-identity data which is obtained from the user should never be transmitted explicitly. Otherwise, this will lead to security vulnerability. The encryption or hashing algorithms should be chosen among the algorithms which are considered to be reliable nowadays.

Table 1: The Security Comparison of Two Factor Authentication Methods.

Authentication Method	**Verification Security**	**Verification Security in Case of Device Hijacking**	**User Device Requirement for Authentication**
One-Time Password Method	High	Low	Yes
QR Code Method	High	Low	No
Biometric Methods	High	High	No

The comparison of the security aspects of two-factor authentication methods commonly used today is given in Table 1. While authentication security is high in all three methods, the first two methods lose credibility if an attacker steals the mobile device used for authentication. Besides, in the one-time password method, if the password is transmitted to the user as an SMS message, the user must confirm the password which is sent to the cell phone registered to the system within a certain period of time.

V. CONCLUSION

In this study, we provide information about authentication methods, more specifically about the web based two factor authentication methods used today and examine into and

compare the advantages and disadvantages of web based authentication methods. The continuous development of technology not only enhances the security level of authentication mechanisms, but it also increases the attack methods used to break these mechanisms. In the study, it was stated that the two-factor authentication methods based on the biometric features of the user provide the highest reliability mechanism.

REFERENCES

[1] Xie, Mengjun, et al. "CamAuth: Securing Web Authentication with Camera." High Assurance Systems Engineering (HASE), 2015 IEEE 16th International Symposium on. IEEE, 2015.

[2] Malutan, Raul, and Cälina Grosan. "Web authentication methods using single sign on method and virtual keyboard." Grid, Cloud & High Performance Computing in Science (ROLCG), 2015 Conference. IEEE, 2015.

[3] Sakib, Muhammad N., and Chin-Tser Huang. "Textact: A text-action based web authentication scheme." Global Communications Conference (GLOBECOM), 2012 IEEE. IEEE, 2012.

[4] Al-Bajjari, Amro Louay, and Ling Yuan. "Optimized Authentication Scheme for Web Application." Service-Oriented Computing and Applications (SOCA), 2016 IEEE 9th International Conference on. IEEE, 2016.

[5] Monfared, Sharareh, et al. "BioALeg-Enabling Biometric Authentication in Legacy Web Sites." Reliable Distributed Systems Workshops (SRDSW), 2016 IEEE 35th Symposium on. IEEE, 2016.

[6] Kolekar, Vikas K., and Milindkumar B. Vaidya. "Click and session based—Captcha as graphical password authentication schemes for smart phone and web." Information Processing (ICIP), 2015 International Conference on. IEEE, 2015.

[7] Yıldırım, Nilay, and Asaf Varol. "Android based mobile application development for web login authentication using fingerprint recognition feature." Signal Processing and Communications Applications Conference (SIU), 2015 23th. IEEE, 2015.

[8] Braun, Johannes. "Ubiquitous support of multi path probing: Preventing man in the middle attacks on Internet communication." Communications and Network Security (CNS), 2014 IEEE Conference on. IEEE, 2014.

[9] Yue, Chuan, and Haining Wang. "BogusBiter: A transparent protection against phishing attacks." ACM Transactions on Internet Technology (TOIT) 10.2 (2010): 6.

[10] Bonneau, Joseph. "The science of guessing: analyzing an anonymized corpus of 70 million passwords." Security and Privacy (SP), 2012 IEEE Symposium on. IEEE, 2012.

Solve Complex Problems using Artificial Neural Network Learned by PSO

SAEED SHAKIR MAHMOOD [1] and GÜLAY.TEZEL[2]

[1] Selcuk University, Konya/Turkey, alkasmk@gmail.com
[2]Selcuk University, Konya/Turkey, gtezel@selcuk.edu.tr

Abstract - Complex data classification is a prime data mining problem being discussed about for a decade that has attracted several researchers around the world. Most classifiers are designed so as to learn from the data itself using a training process, because complete expert knowledge to determine classifier parameters is impracticable. This paper proposes a hybrid methodology based on machine learning paradigm. This paradigm integrates the successful exploration mechanism called self-regulated learning capability of the artificial neural network with the particle swarm optimization (PSO) algorithm.
As a ANN learning by pso method, is a single-hidden layer feedforward neural network (FFNN), proved to be an excellent classifier with large number of hidden layer neurons. In this research, PSO is used to determine the optimum set of parameters for the pso , thus reducing the number of hidden layer neurons, and it further improves the network generalization performance. The proposed method is experimented on three benchmarked datasets of the UCI Machine Learning Repository for handling complex dataset classification. Simulation results show that the proposed approach is able to achieve good generalization performance, compared to the results of other classifiers.

Keywords - **Artificial neural networks, Hybrid ANN_PSO ,Complex data ,Feedforward neural network , Particle Swarm Optimization**

I. INTRODUCTION

Artificial Neural Networks (ANNs) are system composed of neurons organized in input, output, and hidden layers. The neurons are connected to each other by a set of synaptic weights. An ANN is a powerful tool that has been applied in a broad range of problems such as complex data, Medical Dataset, pattern recognition, forecasting, and regression. During the learning process, the ANN continuously changes their synaptic values until the acquired knowledge is sufficient (until a specific number of iterations is reached or until a goal error value is achieved). When the learning process or the training stage has finished, it is mandatory to evaluate the generalization capabilities of the ANN using samples of the problem, different to those used during the training stage. Finally, it is expected that the ANN can classify with an acceptable accuracy the patterns from a particular problem during the training and testing stage.

Several classic algorithms to train an ANN have been proposed and developed in the last years. However, many of them can stay trapped in nondesirable solutions; that is, they will be far from the optimum or the best solution. Moreover, most of these algorithms cannot explore multimodal and noncontinuous surfaces. Therefore, other kinds of techniques, such as optimization algorithms, are necessary for training an ANN.

optimization algorithms have a good acceptance by the Artificial Intelligence community because they are powerful optimization tools and can solve very complex optimization problems. For a given problem, NNPSO can explore big multimodal and non-continuous search spaces and can find the best solution, near the optimum value. PSO are based on nature's behaviour described as swarm intelligence. This concept is defined in [1] as a property of systems composed of unintelligent agents with limited individual capabilities but with an intelligent collective behaviour.
There are several works that use evolutionary and optimization algorithms to train ANN as another fundamental form of learning [2]. Metaheuristic methods for training neural networks are based on local search, population methods, and others such as cooperative coevolutionary models [3].
An excellent work where the authors show an extensive literature review of evolutionary algorithms that are used to evolve ANN is [2]. However, most of the reported researches are focused only on the evolution of the synaptic weights, parameters [4], or involve the evolution of the neuron's numbers for hidden layers, but the number of hidden layers is established previously by the designer. Moreover, the researchers do not involve the evolution of transfer functions, which are an important element of an ANN that determines the output of each neuron.
For example, in [5], the authors proposed a method that combines Ant Colony Optimization (ACO) to find a particular architecture (the connections) for an ANN and Particle Swarm Optimization (PSO) to adjust the synaptic weights. Other researches like [6] implemented a modification of PSO mixed with Simulated Annealing (SA) to obtain a set of synaptic weights and ANN thresholds. In [7], the authors use Evolutionary Programming to get the architecture and the set of weights with the aim to solve classification and prediction problems. Another example is [8] where Genetic Programming is used to obtain graphs that represent different topologies. In [9], the Differential Evolution (DE) algorithm was applied to design an ANN to solve a weather forecasting problem. In [10], the authors use a PSO algorithm to adjust the synaptic weights to model the daily rainfall-runoff relationship in Malaysia. In [11], the authors compare the back-propagation method versus basic PSO to adjust only the synaptic weights of an ANN for solving classification problems. In [12], the set of weights are evolved using the Differential Evolution and basic PSO.

In other works like [13], the three principle elements of an ANN are evolved at the same time: architecture, transfer functions, and synaptic weights.

2. Materials and methods

2.1. Neural network learned by backpropagation

Backpropagation [14] is generally used to train multilayer ANNs. A multilayer backpropagation network includes an input layer, at least one hidden layer, and an output layer. The backpropagation algorithm is a supervised learning method and aims to optimize weights and biases between the input layer and the output layer depending on the output error of the network. The input vector is given to the input layer and reaches the final output layer after passing through hidden layers. Each neuron in the network transmits the result to all neurons of the next layer after receiving the arithmetical addition of the weighted signal from the previous layer's neurons, depending on the activation function.

The ANN's training by backpropagation operates consistently in both forward computing and backward computing, as given in Figure 1, where *X1* and *X2* are inputs and *C1, C2,* and *C3* are output vectors of the layers. *W1* and *W2* are weight matrices; *W3* is a weight vector; $\theta 1$, $\theta 2$, and $\theta 3$ are bias vectors; and E1, E2, and E3 bias inputs are chosen as 1. NET1, NET2, and NET3 are net input vectors for the related layer. Sigmoid activation function (φ) is preferred for all neurons. φ' is the derivative of the activation function. $\delta 1$,$\delta 2$, and $\delta 3$ are local gradient vectors.

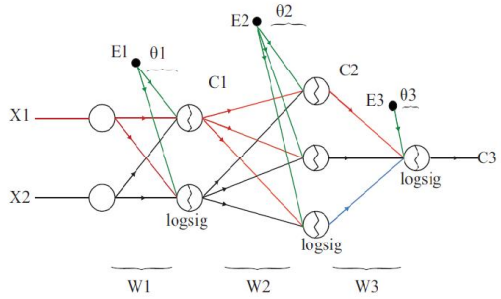


Figure 1. a) Forward computing schematic structure.

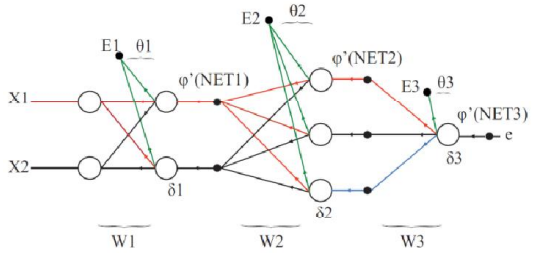


Figure 1.b) backward computing schematic structure (transpose network).

2.2. Neural network learned by PSO

PSO, one of the population-based heuristic optimization methods, was first developed by Kennedy and Eberhart in 1995 [15], inspired by social behavior in flocks of birds or schools of fish while finding food.

The PSO algorithm is initialized with a group of random particles (candidate solutions for the problem) and then searches for an optimal solution by updating its individuals. In each generation, each particle is updated based on 2 special particles: *pbest* is the personal best solution of each particle found so far, and *gbest* is the global best solution found so far by any particle in the swarm (population) [16]. Figure 2 shows the updating procedure of a particle by vectorial representation.
The algorithm's pseudocode is the following:

for *each particle* ***do***
initialize the particle with random values
end for
Do
for *each particle* ***do***
Calculate fitness value of the particle
if fi*tness value of the current particle < fitness value of the pbest particle* ***then***
update the pbest particle
end if
end for
gbest = the particle whose fitness value is equal to min(fitness values of all particles)
for *each particle* ***do***
update velocity and position of the current particle
end for
while *stop criterion (maximum generation number or target fitness value of the gbest particle) is provided*

The V_{ij}^{k} and X_{ij}^{k} variables in Figure 2 are respectively the *j* th velocity component and the *j*th (j = 1, 2,..., D) position component of the *i*th (i = 1, 2, 3, . . . , N) particle at generation *k* . N is the number of particles in the swarm. D is the dimension size of the search space.
Position figures and tables at the top and bottom of each column if possible.

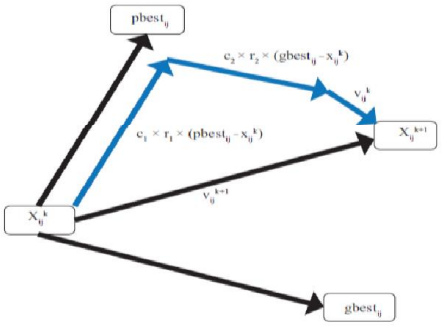


Figure 2. The velocity and position updating of a particle at *k* th generation [22,23].

For the basic PSO [15], the velocity updating and the position updating are calculated by Eqs. (1) and (2), respectively. In these equations, *r1* and *r2* are 2 uniformly distributed random numbers in the interval of (0,1). *c1* and *c2* are positive acceleration constants, usually *c1* + *c2* = 4.

$$v_{ij}^{k+1} = v_{ij}^{k} + c1 \times r1\left(pbest_{ij} - x_{ij}^{k}\right) + c1 \times r1 \times \left(gbest_{ij} - x_{ij}^{k}\right) \quad (1)$$

$$x_{ij}^{k+1} = x_{ij}^{k} + v_{ij}^{k+1} \quad (2)$$

In an improved PSO version [17], an inertia weight(w) parameter shown in Eq. (3) is added into the equation of velocity updating.

$$v_{ij}^{k+1} = w^{k} \times v_{ij}^{k} + c1 \times r1\left(pbest_{ij} - x_{ij}^{k}\right) + c1 \times r1 \times \left(gbest_{ij} - x_{ij}^{k}\right) \quad (3)$$

w is used to balance the global and local search [17] and can be updated using Eq. (4) or (5) by generations.
In Eq. (4), w*max* and w*min* are maximum and minimum values of inertia weight; n is maximum generation number. The α & β variables in Eq. (5) are the decrease factors and are used to linearly decrease inertia weight.

$$w^k = w_{max} - k \times \frac{(w_{max} - w_{min})}{n} \quad (4)$$

$$w^k = \alpha + rand \times \beta \quad (5)$$

In this study, PSO is used to train an ANN to obtain an optimum network model and to improve the performance of the ANN. During the training phase, the mean squared error (MSE) is used to calculate the fitness value of a particle (P*i*) by Eq. (6), where *e* is the error between desired and obtained outputs after presenting the *i*th datum to the network, and *S* is the number of data in the training dataset. The structure of the P*i* particle is given by Eq. (7).

$$MSE = \frac{1}{2S}\sum_{i=0}^{s} e_i^2 \quad (6)$$

$$P_i = [w1^i_{11}\, w1^i_{12} \ldots . \theta 1^i_{11} \ldots w2^i_{11}\, w2^i_{12} \ldots \theta 2^i_{11} .. w3^i_1 \ldots \theta 3^i_{11}] \quad (7)$$

The flowchart given in Figure 3 [18] shows the training and testing processes of the PSONN. The ANN's training process starts with random initialization of weights and biases, which indicates the numerical values of the connections between layers. These weights and biases are individuals to each particle, as given in Eq. (7). The number of connections between layers refers to the particle size or search space dimension. The stop criterion in Figure 3 is chosen as the maximum generation number or target fitness value of the *gbest* particle:

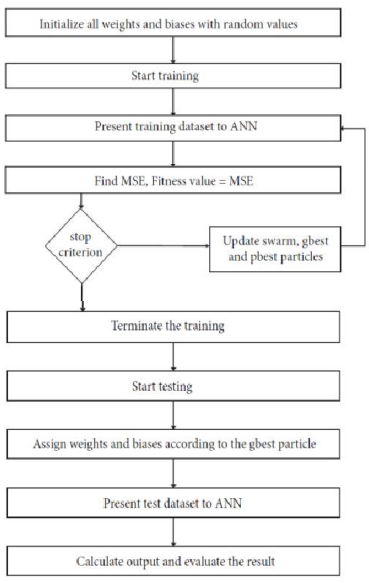


Figure 3. Flowchart for the training and testing of the PSONN.

3. Experimental Results and Discussion

The performance of the proposed ANN_PSO method is experimented on three real benchmark classification problems (UCI Machine Learning Repository).Out of the data samples, 70% is employed for training process and 30% for testing process. The specification of these problems is listed in Table 1.

Table 1: Description of datasets.

Dataset	Number of instances	Number of features	Number of classes
Pima Indians Diabetes	768	8	2
Cleveland Heart Disease	296	13	5
Hepatitis	155	19	2

The training dataset was used to train the PSONNs. Each network consists of an input layer, a hidden layer, and an output layer, as shown in Figure 4. X1, X2, X3, and X4 are inputs obtained from statistical values as depicted above; Y is the output. The desired output value is 0 for negativity and 1 for positivity in having the disease. W1 and W2 are connection weight matrices; $\theta 1$ and $\theta 2$ are bias vectors. Threshold inputs are used in the layers; their values are chosen as 1. Sigmoid activation function was preferred.

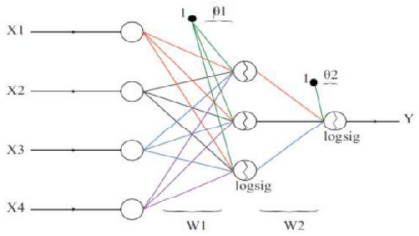


Figure 4. Schematic structure of the neural network..

On applying the proposed ANN_PSO algorithm for the considered medical datasets from the repositories, the dataset features are selected and the parameters, classification accuracy, sensitivity, and specificity, are noted and tabulated. Hence, in this case, the performance of the proposed method is evaluated in terms of sensitivity, specificity, and accuracy. In general, sensitivity and specificity are the statistical measures employed basically to carry out the performance of classification functions. A perfect classifier or a predictor will be described as 100% sensitive and 100% specific. Since the considered application is of medical dataset involving complex data, the classification should be carried out in an accurate manner. Henceforth, sensitivity and specificity are chosen to be the parametric indices for carrying out the medical dataset classification.
Sensitivity (true positive fraction) is the probability that a diagnostic test is positive, given that the person has the disease:

$$\text{Sensitivity} = \frac{TP}{TP+FN} \quad (8)$$

Specificity (true negative fraction) is the probability that a diagnostic test is negative, given that the person does not have the disease:

$$\text{Specificity} = \frac{TN}{TN+FP} \quad (9)$$

Accuracy is the probability that a diagnostic test is correctly performed:

$$\text{Accuracy} = \frac{(TP+TN)}{(TP+TN+FP+FN)} \quad (10)$$

where TP (true positives) is correctly classified positive cases.
TN (true negative) is correctly classified negative cases.
FP (false positives) is incorrectly classified negative cases.
FN (false negative) is incorrectly classified positive cases.

3.1. Pima Indians Diabetes Dataset.

The performance of the different feature selection methods for the Pima Indians Diabetes dataset is shown in Table 2. It is noted that, on applying the basic ANN approach with that of PSO, in comparison with the other methods accuracy and the other parameters are increased to a value of 88.95% for accuracy and 99.15 and 100 for sensitivity and specificity with original dataset. The proposed ANN_PSO approach achieved the accuracy rate of 86.52% with (1,2,6,7,8) selected features, accuracy rate of 89.60% with (1,2,6,8) selected features and accuracy rate of 89.32% with (2,6,8) selected features.

Table 2: Comparison of Classification results with Pima Indians Diabetes dataset

Methodology adopted	Accuracy	Sensitivity	Specificity
Optimized LVQ (10x CV) [19]	96.70	91.29	92.34
Big LVQ (10x CV) [19]	96.80	95.23	96.10
AIRS (10x CV) [19]	97.20	96.92	95.00
Supervised fuzzy clustering (10x CV) [20]	95.57	98.23	97.36
Fuzzy-AIS-knn (10x CV) [21]	99.14	99.56	100
F-score + support vector machine [22]	99.51	99.24	98.61
Association rule + neural network [23]	97.4	93.12	91.26
Artificial metaplasticity neural network [24]	99.26	100	97.89
Mean selection method [25]	95.99	93	97
Half selection method [25]	96.71	94	98
Neural network for threshold selection [25]	97.28	94	99
proposed ANN_PSO	88.95	99.15	100

3.2. Cleveland Heart Disease Dataset.

The results for the Cleveland Heart Disease dataset can be seen in Table 3. As a five-class classification problem is dealt instead of a binary class classification problem, the Region of Convergence is omitted. It is to be noted that a classification accuracy of 83.82%, sensitivity of 0.83, and a specificity of 0.85 were noted when the original features of the dataset were considered. On applying the proposed ANN_PSO approach, the best accuracy of 93.63% is achieved. This accuracy is achieved with only three features, compared with that of the 13 features of the original dataset.
The proposed ANN_PSO approach achieved the accuracy rate of 93.80% with (3,9,11,12) selected features, accuracy rate of 93.54% with (3,8,9,11,12) selected features , accuracy rate of 94.48% with(3,8,9,10,11,12) selected features and accuracy rate of 93.17% with(3,8,9,10,11,12,13) selected features

Table 3: Comparison of Classification results with Cleveland Heart Disease dataset.

Methodology adopted	Accuracy (%)	Sensitivity (%)	Specificity (%)
C4.5 [27]	81.11	77.23	76.58
Naive Bayes [27]	81.48	80.97	81.22
BNND [27]	81.11	82.13	80.42
BNNF [27]	80.96	76.93	75.81
AIRS [28]	84.50	75.34	72.96
Hybrid neural network [30]	87.40	93.00	78.50
Neural networks ensemble [29]	89.01	80.95	95.91
Mean selection method [25]	81.75	82	82
Half selection method [25]	83.44	84	83
Neural network for threshold selection [25]	84.46	82	82
Proposed ANN_PSO with original features	83.82	83	85

3.3. Hepatitis Dataset.

The results for the Hepatitis dataset are shown in Table 4. From the results, it is inferred that the proposed ANN_PSO approach yields a better accuracy of 82.46%, sensitivity 92.25%, and specificity 86.45% with that of the original features.
The proposed ANN_PSO approach achieved the accuracy rate of 77.52% with (6,11,12,13,14,17,19) selected features, accuracy rate of 66.60% with (2,5,6,10,11,12,13,14,17,19) selected features, accuracy rate of 79.32% with (5,6,11,12,13,14,17,19) selected features and accuracy rate of 79.32% with (11,12,13,14,17,19) selected features.

Table 4: Comparison of classifcation results with Hepatitis dataset.

Methodology adopted	Accuracy(%)	Sensitivity (%)	Specificity (%)
Conventional artificial neural network [26]	97.00	92.31	94.5
Mean selection method [25]	82.58	87	60
Half selection method [25]	85.16	90	66
Neural network for threshold selection [25]	85.16	90	66
Proposed ANN_PSO	82.46	92.25	86.45

4. CONCLUSION

In this research a new hybrid algorithm that integrates the proposed neural network with the particle swarm optimization (PSO) for the solution of classification problems is presented. To Optimize the input weights and hidden biases and minimum norm least-square scheme, an improved PSO is used to analytically determine the output weights. The PSO is enhanced by incorporating a mechanism which diversifies the search behavior of the particles so that the algorithm finds much better solutions. The performance of the proposed NN framework using PSO was better than the performance of the other methods reported in the literature for three benchmark datasets from the UCI Machine Learning Repository which are used for evaluation. The results also show that in the proposed framework the number of neurons in the hidden layer and the relevant input variables does need to be selected by trial-and-error, thus reducing the network size and improving the generalization capability.

REFERENCES

[1] G. Beni and J. Wang, "Swarm intelligence in cellular robotic systems," in Robots and Biological Systems: Towards a New Bionics? vol. 102 of NATO ASI Series, pp. 703–712, Springer, Berlin, Germany, 1993.

[2] X. Yao, “Evolving artificial neural networks,” Proceedings of the IEEE, vol. 87, no. 9, pp. 1423–1447, 1999.
[3] E. Alba and R. Martí, Metaheuristic Procedures for Training Neural Networks, Operations Research/Computer Science Interfaces Series, Springer, New York, NY, USA, 2006.
[4] J. Yu, L. Xi, and S. Wang, “An improved particle swarm optimization for evolving feedforward artificial neural networks,” Neural Processing Letters, vol. 26, no. 3, pp. 217–231, 2007.
[5] M. Conforth and Y. Meng, “Toward evolving neural networks using bio-inspired algorithms,” in IC-AI, H. R. Arabnia and Y. Mun, Eds., pp. 413–419, CSREA Press, 2008.
[6] Y. Da and G. Xiurun, “An improved PSO-based ANN with simulated annealing technique,” Neurocomputing, vol. 63, pp. 527–533, 2005.
[7] X. Yao and Y. Liu, “A new evolutionary system for evolving artificial neural networks,” IEEE Transactions on Neural Networks, vol. 8, no. 3, pp. 694–713, 1997.
[8] D. Rivero and D. Periscal, “Evolving graphs for ann development and simplification,” in Encyclopedia of Artificial Intelligence, J. R. Rabuñal, J. Dorado, and A. Pazos, Eds., pp. 618–624, IGI Global, 2009.
[9] H. M. Abdul-Kader, “Neural networks training based on differential evolution algorithm compared with other architectures for weather forecasting34,” International Journal of Computer Science and Network Security, vol. 9, no. 3, pp. 92–99, 2009.
[10] K. K. Kuok, S. Harun, and S. M. Shamsuddin, “Particle swarm optimization feedforward neural network for modeling runoff,” International Journal of Environmental Science and Technology, vol. 7, no. 1, pp. 67–78, 2010.
[11] B. A. Garro, H. Sossa, and R. A. Vázquez, “Back-propagation vs particle swarm optimization algorithm: which algorithm is better to adjust the synaptic weights of a feed-forward ANN?” International Journal of Artificial Intelligence, vol. 7, no. 11, pp. 208–218, 2011.
[12] B. Garro, H. Sossa, and R. Vazquez, “Evolving neural networks: a comparison between differential evolution and particle swarm optimization,” in Advances in Swarm Intelligence, Y. Tan, Y. Shi, Y. Chai, and G. Wang, Eds., vol. 6728 of Lecture Notes in Computer Science, pp. 447–454, Springer, Berlin, Germany, 2011.
[13] B. A. Garro, H. Sossa, and R. A. Vazquez, “Design of artificial neural networks using a modified particle swarm optimization algorithm,” in Proceedings of the International Joint Conference on Neural Networks (IJCNN '09), pp. 938–945, IEEE, Atlanta, Ga, USA, June 2009.
[14] J. Kennedy, R.C. Eberhart, \Particle swarm optimization", Proceedings of the IEEE International Conference on Neural Networks, Vol. 4, pp. 1942{1948, 1995.
[15] S. Bağış, \System modelling by using artificial intelligence algorithms", MSc, Erciyes University, Kayseri, Turkey,2009 (in Turkish with English abstract).
[16] L. Liu, W. Liu, D.A. Cartes, \Particle swarm optimization based parameter identi_cation applied to permanent [1] magnet synchronous motors", Engineering Applications of Arti_cial Intelligence, Vol. 21, pp. 1092{1100, 2008.
[17] Y. Shi, R.C. Eberhart, \Empirical study of particle swarm optimization", Proceedings of the IEEE Congress on Evolutionary Computation, pp. 1945{1950, 1999.
[18] Y. Shi, R.C. Eberhart, \Empirical study of particle swarm optimization", Proceedings of the IEEE Congress on Evolutionary Computation, pp. 1945{1950, 1999.
D. E.Goodman Jr., L. C. Boggess, andA. B.Watkins, “Artificial immune system classification of multiple-class problems,” in Proceedings of the Artificial Neutral Networks in Engineering Conference (ANNIE ’02), pp. 179–184, November 2002.
[19] J. Abonyi and F. Szeifert, “Supervised fuzzy clustering for the identification of fuzzy classifiers,” Pattern Recognition Letters, vol. 24, no. 14, pp. 2195–2207, 2003.
[20] S. S¸ahan, K. Polat, H. Kodaz, and S. G¨unes¸, “A new hybrid method based on fuzzy-artificial immune system and k-nn algorithm for breast cancer diagnosis,” Computers in Biology and Medicine, vol. 37, no. 3, pp. 415–423, 2007.
[21] M. F. Akay, “Support vector machines combined with feature selection for breast cancer diagnosis,” Expert Systems with Applications, vol. 36, no. 2, pp. 3240–3247, 2009.
[22] M. Karabatak and M. C. Ince, “An expert system for detection of breast cancer based on association rules and neural network,” Expert Systems with Applications, vol. 36, no. 2, pp. 3465–3469, 2009.
[23] A. Marcano-Cede˜no, J. Quintanilla-Dom´ınguez, and D. Andina, “WBCD breast cancer database classification applying artificial metaplasticity neural network,” Expert Systems with Applications, vol. 38, no. 8, pp. 9573–9579, 2011.
[24] P. Jaganathan and R. Kuppuchamy, “A threshold fuzzy entropy based feature selection for medical database classification,” *Computers in Biology and Medicine*, vol. 43, no. 12, pp. 2222–2229, 2013.
[25] G. Reibnegger, G.Weiss, G.Werner-Felmayer, G. Judmaier, and H.Wachter, “Neural networks as a tool for utilizing laboratory information: comparison with linear discriminant analysis and with classification and regression trees,” Proceedings of the National Academy of Sciences of the United States of America, vol. 88, no. 24, pp. 11426–11430, 1991.
[26] K. Polat, S. Sahan, H. Kodaz, and S. G¨unes, “A new classification method to diagnosis heart disease: supervised artificial immune system (AIRS),” in Proceedings of the Turkish Symposium on Artificial Intelligence and Neural Networks (TAINN '05), 2005.
[27] R. Das, I. Turkoglu, and A. Sengur, “Effective diagnosis of heart disease through neural networks ensembles,” Expert Systems with Applications, vol. 36, no. 4, pp. 7675–7680, 2009.
[28] H. Kahramanli and N. Allahverdi, “Design of a hybrid system for the diabetes and heart diseases,” Expert Systems with Applications, vol. 35, no. 1-2, pp. 82–89, 2008.
[29] N. Cheung, Machine learning techniques for medical analysis [M.S. thesis], University of Queensland, 2001.

The Development of Penetration Test Lab For The Web Application Security Training

Eternus Web Application Security Lab -EWASL

A.GÜREL[1], F.ERTAŞ[2], E.U.KÜÇÜKSİLLE[3], M.A.YALÇINKAYA[4]

[1] Innovera Information Technologies, İstanbul/Turkey, ahmet.gurel@innoverabt.com
[2]ID3 Software And Information Technologies, İstanbul/Turkey, furkan.ertas@id3.com.tr
[3]Süleyman Demirel University, ecirkucuksille@sdu.edu.tr
[4]Süleyman Demirel University, mehmetyalcinkaya@sdu.edu.tr

***Abstract* - In today's Informatic world, many operations such as shopping, communication, research, banking and even citizenship procedures can be carried out through web applications. The widespread usage of web applications and the handling of sensitive data have made such applications the number one target for cyber attackers. The increase in attacks against Web applications has also increased the importance of web application security. The most important factor in ensuring web application security is Web application penetration tests. The most important aid for experts who want to perform effective and successful penetration testing is the web application security labs in which they can do various attack experiments. In this study; we developed a web application security lab called EWASL that contains major web vulnerabilities and allows penetration testing experiments to be conducted on those vulnerabilities. Developed EWASL differs from the laboratories in the literature due to the fact that vulnerabilities are listed both under the headings and hidden within the pages. Another feature that distinguishes EWASL from other laboratories is that it contributes to develop secure software development by means of showing the malicious codes that cause vulnerabilities and the reliable codes that should be written in place of them.**

***Keywords* – Web application security, web application vulnerabilities, penetration test, secure software development.**

I. INTRODUCTION

Today; all the institutions and organizations taking place in different fields make use of the web applications in an efficient way for the purpose of being able to reach the masses they serve faster and providing more effective service. Users could carry out many processes such as shopping, research, file transfer and communication via social network upon the web applications. In addition; in many countries in which our country is also included, citizens conduct their various citizenship processes via the web applications belonging to their countries. Web applications have become the window of institutions, companies and even countries to the outer world; in other words, they have become their showcases. The realization of such important processes and working with critical data have caused to the increase in the importance of the concept of web application security. Any intrusion to be made towards the mentioned applications will both cause to the loss of respectability and serious financial loss.

The common use of web applications in different fields and purposes has caused to a serious increase in the number and type of the intrusions made towards the mentioned applications. Cyber intruders take advantage of various vulnerabilities taking place upon in the web applications and they carry out some activities such as penetration o the server systems, takeover of the user account data defined in the web application and prevention of access to the web applications. Due to such an increase in the intrusions made to the web applications and the damages occurring after the intrusions and reaching serious dimensions, institutions and organizations subject the web applications to penetration tests in certain periods. Experts check the existence of various vulnerabilities on the web applications in the mentioned penetration tests. The penetration tests carried out on web applications could be carried out manually or automatically via various vulnerability scanners by the security team.

Many vulnerability scanners such as Netsparker and Acunetix SQLMap could be used for the automatic detection of the vulnerabilities taking place in the web applications [1]. Web applications are scanned against possible vulnerabilities with the use of the mentioned vulnerability scanners and the detected vulnerabilities are reported to the user. Although automatic vulnerability scanners are very successful in the detection of certain vulnerabilities, they are insufficient against the new vulnerabilities or those hard to detect automatically due to its structure. It is necessary for the security experts to know the logic behind the mentioned vulnerabilities and in which areas they could occur for the purpose of being able detect themselves the possible vulnerabilities on the web applications without the automatized devices. For the reason; the mentioned experts need the environments in which they could easily carry out their penetration tests regarding the different kinds of vulnerabilities without the fear of doing any harm to the website.

In the past, many test environments were developed which were formed for the security experts to improve themselves in

the web application penetration tests and which contain different types of web application vulnerabilities. Thanks to the web applications such as OWASP WebGoat, DVWA, Mutilidae, Mutilidae II on which there are various vulnerabilities, people could make intrusions towards the main vulnerabilities such as SQL injection and cross site scripting and in this way, they could practice [2]. However; when the developed applications have been examined, differences could be observed among them. WebGoat and DVWA applications separately submit the main web application vulnerabilities under headlines and it makes people practice upon the scenarios. In Mutilidae and Mutilidae 2 applications, vulnerabilities are hidden in various pages of the application. It is necessary for the person who will conduct tests on this application firstly to detect the vulnerabilities and to exploit the vulnerability.

In this study; web application security lab called EWASL (Eternus Web Application Security Lab) has been developed for the software developers to understand the web application vulnerabilities and in this way, to develop secure code and for the cyber security expert candidates to be able to conduct tests regarding the mentioned vulnerabilities in the lab environment. Because EWASL contains different types of web application vulnerabilities within itself, it provides web penetration test opportunities for the related people in this field. In addition; it gives safe software development tips for the users and shows the harmful code blocks causing to vulnerabilities and the secure code blocks necessary to be replaced. In this way; EWASL provides secure software development opportunities for the web application developers.

In the 2nd part of the conducted study, the main vulnerabilities taking place in the web applications have been examined. In the 3rd part, the structure of the developed EWASL application, its interfaces, test environments it provides and its differences from the existent web penetration test labs. The conducted study has been completed with the sharing of the attained results.

II. Web application Vulnerabilities

Network-based intrusions towards the institutions have given their place to web-based intrusions together with the power and efficiency of various network security systems such as security wall, intrusion detection systems (IDS) and intrusion prevention systems (IPS). Cyber intruders directly target the web applications instead of eluding the mentioned network systems one by one; because, the intruders could access to the web server and database server taking place behind the mentioned network security systems with a vulnerability they could exploit on the web applications.

According to the security report published in April in 2017 by Symantec being one of the most commonly known security companies; the ratio of the web sites in which vulnerability has been detected is 76% in 2014, 78% in 2015 and again 76% in 2016 within the scans conducted on the web sites. 20% of the mentioned detected vulnerabilities in 2014, 15% in 2015 and 9% in 2016 have been determined as critical vulnerabilities [3]. When the attained data have been examined, it has been observed that approximately three out of four web applications subjected to the scanning contain various vulnerabilities.
According to the security report published in 2017 by OWASP; SQL injection, cross site scripting (XSS), file inclusion and file upload are the main most dangerous and common vulnerabilities taking place in the web applications [4].

A. SQL Injection

If the harmful SQL expressions written in the input areas taking place in the web applications are placed in the dynamic SQL query without any additional inspection and operated in the mentioned query database server, it means that there is SQL injection vulnerability [5]. Harmful SQL commands are entered by the intruders to the areas such as the browser address bar, user login areas and search areas in which data input could be made in the intrusions of SQL injection and the data for which the intruder does not have any authority to display are reached [6].

There are 4 different SQL injections in the literature as basic SQL injection, Union-based SQL injection, blind SQL injection and time-based SQL injection. In basic SQL injection, various expressions such as ' or '1'='1 are written to the input areas and the data not within the authority are tried to be displayed. In Union-based SQL injection; 'Union' (query integration) command of SQL language is benefitted. Many data are attained from the returning error messages in response to the dynamic query formed with the use of union command [7]. What is considered in the blind SQL injection is whether the response given by the targeted page to the manipulations of the intruder is true or false. In the time-based SQL injections, time-themed functions of the databases are used to evade data from the database without any permission.

B. Cross Site Scripting (XSS)

The vulnerability of cross site scripting is the process of placing the input taken from the web application inside the resource code of the page to be shown to the user without any inspection and operating the scripts (inputs) sent by the intruder by the user at the end of this action [8].

XSS vulnerabilities are the main most dangerous vulnerabilities for the web applications. It may occur in many web applications realized with the different programming languages due to the fact that it is independent of the programming language. In XSS-based intrusions, the intruders include some harmful codes to the web applications. In XSS intrusions, intruders mainly use two methods. In the first used method; the input areas taking place in the page and requiring data entrance from the user are targeted. Search box and comment areas could be shown as examples for this. In the second method used by the intruders, XSS codes are added in addition to the address taking place in the URL area.

The most common XSS vulnerability types known in literature are the reflected and stored XSS vulnerabilities. In

the intrusions realized with the use of reflected XSS vulnerability, the intruders generally target the input areas such as URL areas, search and login. The realized intrusion could be seen by the person realizing the intrusion. The visitors in the web site cannot see the mentioned attack. For this reason; in the reflected XSS intrusions realized on the URL area, the intruder tries to expand his/her URL address with various communication channels like e-mail [9].

Another XSS-based intrusion type commonly used by the intruders is the stored XSS intrusions. In this type of intrusion, the areas such as forums, comment areas and visitor books are targeted. The harmful XSS codes embedded by those intruding these areas are saved in the database. Afterwards; each user visiting the page in which harmful codes have been embedded is exposed to XSS intrusion at the moment s/he displays the page.

C. File Inclusion

The vulnerability of file inclusion provides opportunities for an intruder to access to the unauthorized or delicate files taking place in the web server or to operate harmful file in the web server by using the 'include' function. This vulnerability mainly occurs with the transmission of the user input to the file inclusion commands without any convenient verification. This vulnerability causes to the operation of harmful codes on the server or to the revelation of the data taking place in the delicate files. There are two types of file inclusion vulnerabilities in literature. These are remote file inclusion-RFI and local file inclusion-LFI [10].

Intruders could read and operate the files in the servers they target via the LFI-based intrusions. This could sometimes be very dangerous; because, the intruder could reach very important data with a LFI-based intrusion if the web server operates with a wrongly structured and high authority level. Although the RFI vulnerabilities are easier to exploit, the mentioned vulnerability is less common. In RFI-based intrusions, the intruders could implement the harmful codes they keep in their own systems instead of accessing to the local files taking place in the server they target.

D. File Upload

The vulnerability of file upload may occur in the web applications with file upload module in which the profile images, photos or other file attachments taking place in the web applications could be uploaded. In the mentioned vulnerability; critical processes such as data collection about the system and command operation could be carried out by loading harmful files (shell) out of the desired format due to the fact the secure file upload steps have not been realized during the file upload. In the event that only the extension and Content-Type information are checked while taking the files from the user, the intruder changes the mentioned data himself/herself and s/he could easily elude the security precautions.

III. Eternus Web Application Security Lab- (Ewasl)

The increase in the number and types of the intrusions made regarding the web applications has increased the importance of the penetration tests carried out on the web applications. In our country; Banking Regulation and Supervision Agency (BRSA) has made it obligatory to conduct the penetration tests at least once per year for the data systems their institutions own [11]. After this resolution, the importance of the security experts having the competence to be able to carry out the mentioned tests has increased. Web application security labs overtake a very important function for the experts with the competence to be able to carry out penetration tests on web applications to be able to be raised; because, the mentioned labs provide opportunities for the conduction of various test trials without the fear of doing any harm to the web application, web server and database server. In addition; it provides opportunities for the users to conduct different types of intrusion and test trials due to the fact that it contains different kinds of vulnerabilities within the same period of time. EWASL provides serious advantages for the users who would like to improve themselves in the issue of the web application penetration tests via this perspective it has.

EWASL has been developed by using modern web technologies of computer sciences. The interface of EWASL has been developed responsively with the use of Bootstrap CSS Framework. EWASL has been programmed with PHP language. PDO Library has been used for the conduction of database processes. MySQL database management system has been used for the storage of the data.

The existent web application security lab has been developed in two ways. Vulnerabilities have been submitted to the users under separate headlines in the labs such WebGoat and DVWA. The users enter the page of the vulnerability they desire to conduct penetration test and try to solve the related scenarios. In the second type labs such as Mutilidae and Mutilidea 2, vulnerabilities are hidden in the web application. Because EWASL lab contains both hidden vulnerabilities and main vulnerabilities given under separate headlines due to its structure, it is included in both categories. EWASL is the only lab having this property in the literature.

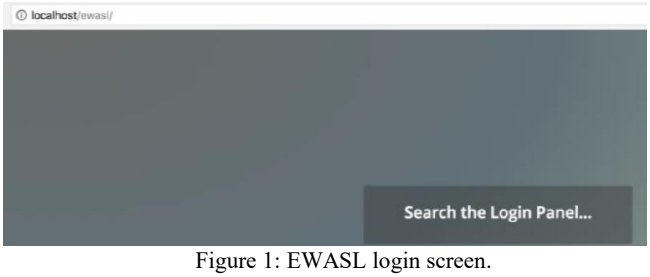


Figure 1: EWASL login screen.

The login screen of EWASL is shown in Figure 1. The login panel belonging to the application has not been given directly in the login screen, but the user is requested to successfully login the application by finding it himself/herself.

The login panel is hidden for the purpose of preventing its

targeting by the unauthorized intruders in some web applications. Panel addresses are written in robots.txt for the purpose of preventing the indexing of the mentioned login panel by the search engines and they are prevented for visits by the search engines. The expression /robots.txt has been added to the end of the application URL address for EWASL application to reach robots.txt file. The mentioned file content is shown in Figure 2.

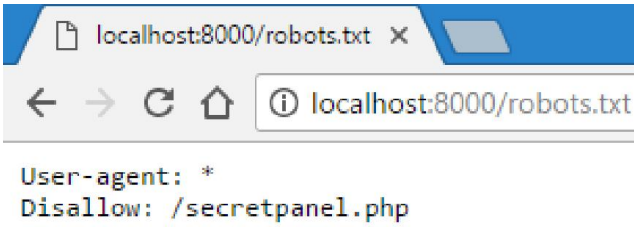


Figure 2: Content of EWASL robots.txt file

When the file content has been examined, it could be seen that the extension of EWASL login panel is /secretpanel.php. When the URL of the application is changed as localhost:8000/secretpanel.php, EWASL login screen has been reached. EWASL login screen is shown in Figure 3. After finding the login screen, the users are requested to login the application to be able to reach EWASL web vulnerability tests. However; because these data will not be owned by the users in the eye of intruders, they need to elude the mentioned step in a way.



Figure 3: EWASL login panel.

The mentioned login panel has been structured in a way that the values entered to the areas of username and password will be placed to the dynamic query without any inspection. The users need to realize SQL injection to elude this step. Login is made to EWASL with admin authority by entering the expression ‘ or ‘1’=’1 to the e-mail (username) and password parts. The screen image belonging to EWASL main screen is shown in Figure 4.

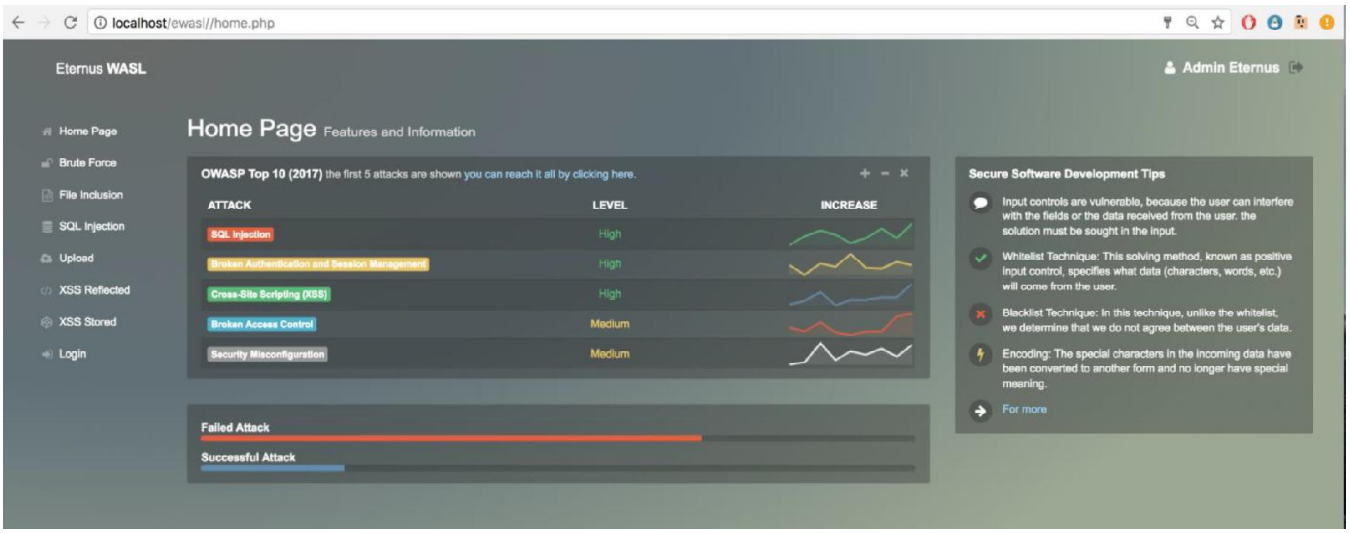


Figure 4: EWASL main screen.

EWASL provides safe software development information for the programmers desiring to develop web applications not containing the mentioned vulnerabilities by learning the most popular web vulnerabilities as well as providing a secure test environment for the users desiring to conduct penetration tests on web applications. Web application developers have been explained the main secure software development concepts such as input control, white list technique, blacklist technique and encoding. The users demanding more detailed information in the issue of secure software development are directed to OWASP site which is an open-resource security society upon the same part.

When one of the vulnerabilities taking place on the left part of EWASL main menu is selected, transition to the page in which the mentioned vulnerabilities exist is conducted. For instance; the page containing file upload vulnerability is shown in Figure 5.

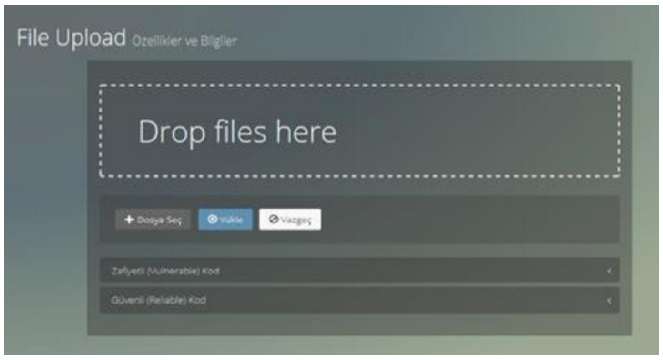


Figure 5: Test page of file upload vulnerabilities.

In the mentioned panel, the vulnerability which may occur in file upload modules owned by many web applications today could be examined. The file upload module taking place in the test scenario shown in Figure 5 only gives the opportunity of loading image file to the system. As it could be examined in the second part, harmful files could be added to the mentioned modules out of the allowed formats by the intruders. If the related example is scripted, users firstly try to load a file with different extension such as Shell.php to the system. However; because the system only allows the loading of files with .jpg extension, users need to try different techniques. When the page resource is examined in the related example; it could be seen that whether the file extensions are only jpg or not in the web application has been checked, but the files with php extension have been allowed by the server. In this situation; when the users rename the harmful software they operate as Shell.php.jpg, web application allows the loading of the mentioned file to the system. Web proxy software items such as BurpSuite and Zap could be used to rename the file as Shell.php again by correcting its extension before going to the server. In this way, the file loaded to the web application with jpg extension could be given the extension php before transmission to the server and the test could be completed successfully.

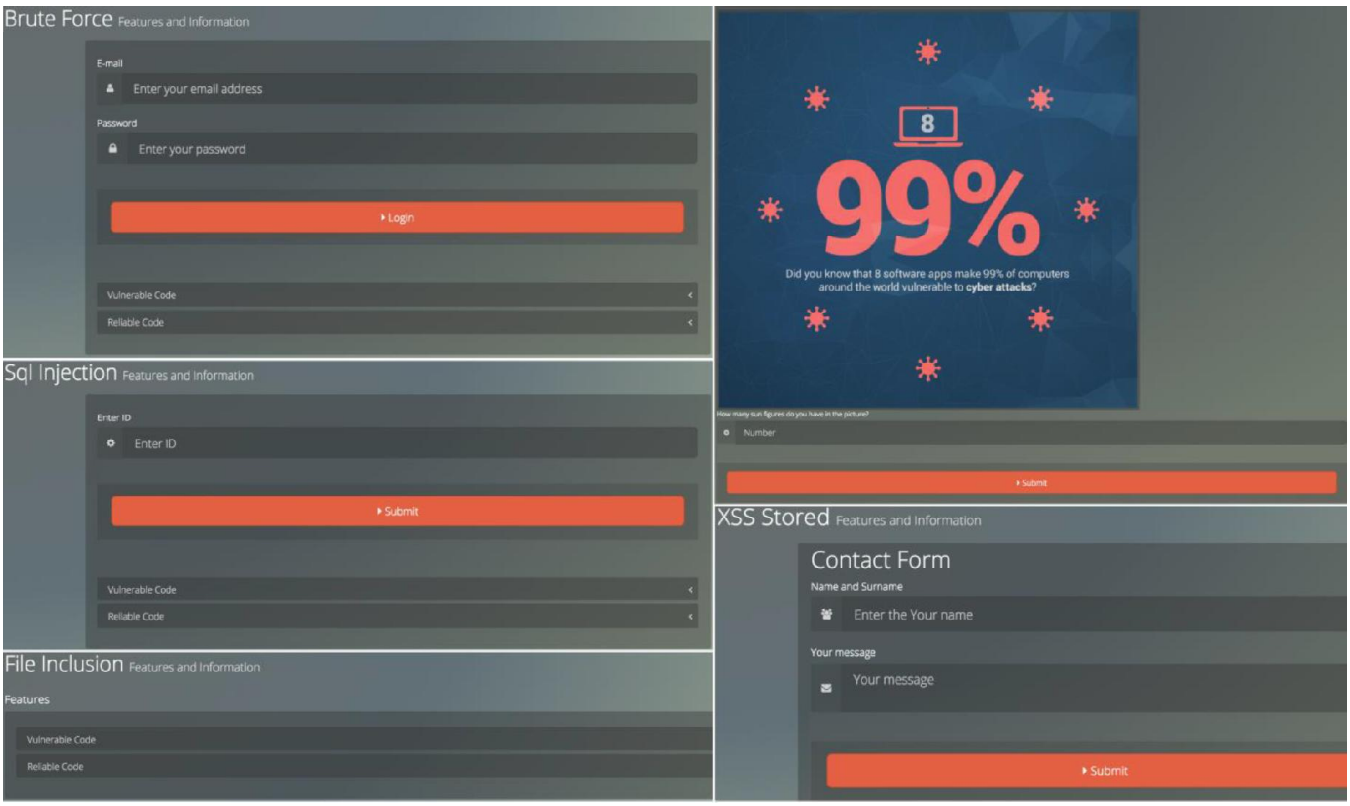


Figure 6: Test screens belonging to various vulnerabilities taking place in EWASL.

The test screens belonging to the vulnerabilities of brute force, SQL injection, reflected XSS, stored XSS and file inclusion taking place in EWASL are shown in Figure 6. The users could reach the mentioned screens according to their names from the right panel on the EWASL main menu shown in Figure 4.

When the screen images shown in Figure 5 and 6 have been examined, it could be seen that the tabs “vulnerable code” and “reliable code” are existent in each vulnerability screen. Another opportunity provided by EWASL to the users desiring to gain experience in the issue of secure software development is that it shows the secure codes necessary to be written for the error codes and vulnerabilities causing to each vulnerability not to occur. In this way; web application developers will have knowledge in the issue of what kind of coding techniques they need to use to prevent the occurrence of main vulnerabilities

during the development.

IV. Results

A web application security lab called EWASL has been developed in this study. It provides the opportunity to the users desiring to improve themselves in the issue of web application penetration tests for being able to conduct tests without the fear of doing harm to the real systems due to the fact that it contains main web vulnerabilities inside its developed lab. EWASL shows differences from the web application security labs taking place in the literature because of the fact that it submits the main web vulnerabilities both under a menu and in a categorized way and it requires the users to find them by themselves by hiding the vulnerabilities in different pages. In addition; EWASL gives tips in the issue of secure software development for the web application developers inside itself. Moreover; it also shows each vulnerability on the test screen, the harmful codes causing to vulnerability and the secure codes necessary to be written instead of those codes. In this way, web application developers could see what kind of coding techniques they need to use for the non-occurrence of the listed vulnerabilities while developing their applications.

References

[1] U. K. Singh, & C. Joshi, "Quantifying Security Risk by Critical Network Vulnerabilities Assessment". International Journal of Computer Applications. Vol. 0975–8887, pp. 156, 26-33.

[2] J. Turla. (2012, September). "Guide for Setting Up a Vulnerable Lab for Pentesting". Available: http://resources.infosecinstitute.com/hacking-lab

[3] Symantech. (2017, April). "2017 Internet Security Threat Report". Available: https://www.symantec.com/security-center/threat-report

[4] OWASP. (2017, April). "The Ten Most Critical Web Application Security Risks". Available: https://www.owasp.org/index.php/Top_10_2017-Top_10

[5] A. Kieyzun, P. J. Guo, K. Jayaraman, M. D.Ernst. "Automatic Creation Of SQL Injection And Cross-site Scripting Intrusions". 31st International Conference On Software Engineering, 16-24 May, Vancouver, Canada, pp. 199-209.

[6] D. Demirol, R. Daş, M. Baykara, "SQL Enjeksiyon Saldırı Uygulaması and Güvenlik Önerileri", 1st International Symposium on Digital Forensics and Security, 20-21 May, Elazığ, pp. 62-66.

[7] M. Taşçı. (2014, December). "SQL Injection Nedir? Türleri Nelerdir?". http://www.merttasci.com/blog/sql-injection/

[8] A. Özel, S. Eken, "Javacsript Güvenlik Açıkları and Güncel Çözüm Önerileri". 7th International Conference on Information Security & Cryptology. 17-18 October, İstanbul, pp. 252-257.

[9] E. Çelik. (2011, November). "Derinlemesine XSS (DOM, Stored, Reflected) Saldırısı". Available: http://eyupcelik.com.tr/guvenlik/403-derinlemesine-xss-dom-stored-reflected-saldirisi

[10] P. Trivedi. (2014, December). "File Inclusion Attacks". Available: http://resources.infosecinstitute.com/file-inclusion-attacks/

[11] M. A. Yalçınkaya, E. U. Küçüksille, "Uygulamalı Sızma Testleri Pentest Lab", ,Abaküs Kitap, 2015, pp. 6.

OSAS Evaluation By Means Of Machine Learning And Artificial Neural Networks By Using Polisomnographic Report Data

B.N.AKILOTU[1] and S.A.TUNCER[1]

[1] Fırat University, Elazığ/Turkey, rtbmnur@gmail.com
[1] Fırat University, Elazığ/Turkey, satuncer@gmail.com

Abstract **- Sleep apnea, breathing during sleep at least 10 sec. 20% below the level. Sleep apnea divides the disease into 3 in itself. These; central sleep apnea (CSA), obstructive sleep apnea (OSAS) and mixed sleep apnea (MSA). EKG, EEG, EMG, EOG, Respiration and PPG etc. the signals are used to diagnose sleep apnea. This study examined polysomnographic report records of humans, not OSAS patients. Evolution 1, Stage 2, Stage 3 and REM were used for sleeping time. Stage 1 is the stage of transition to sleep and sleep is superficial. In stage 2, sleep is still superficial, and the brain is beginning to prepare for deep sleep. Stage 3 is the period for deep sleep. From the time of all sleep to the time of waking, REM sleep is 20-25% in healthy people. In the study, REM compliance entries and parameters are used. REM sleep duration and change of the variable. A total of 50 polysomnographic report data were used in the study. Of these, 65% were withdrawn as training data and 35% of the data were used unlimitedly. Artificial neural networks and support vector machines were used as the classifier in the study. In the polysomnographic report, the duration of sleep stages (Stage 1, Stage 2, Stage 3) and the REM sleep history were entered in the classification methods. Classification method. Performance evaluation resulted in 81.25% with artificial neural networks, achievement of success, support vector machines achieved 72.9167% success. 81.25% have the conviction that OSAS can successfully affect REM sleep. It is expected to help OSAS estimation studies.**

Keywords **- Obstructive Sleep Apnea *(*OSAS), Artificial Neural Networks (YSA) , SVM, REM Sleep**

I. INTRODUCTION

The sleep apnea is a discomfort that resembles a simple snoring that starts with a period of respiration pausing during sleep. As a result of this discomfort, there are negative consequences such as heart attacks, irregular heartbeat, heart growth, paralysis and death. Indication of this disease mixed with simple snoring; noisy and excessive snoring, restless sleep, insomnia, high blood pressure, weight gain, lack of attention and so on. [1]. This disease, which should be treated absolutely, must first be diagnosed by examining the necessary signals with PSG. These signals are PPG signals. PPG signals are EKG, EEG, EMG, EOG signals. These signals can be used to diagnose diseases with the necessary signal processing methods. He only has to start using different methods for expensive and time consuming methods. These methods are classifying diseases such as YSA and SVM. The database was used by OSAS.

The effect of OSAS on sleep stages and the effect on REM sleep is the subject of this study. Sleep stages are divided into three. Stage 1; At this stage the person prepares for sleep. Body and brain functions shift to normal levels. Stage 2; sleep transition. One is at this stage between sleep and wakefulness. The stage 1 phase has been bypassed. Stage 3; deep sleep phase. At this stage, the person is completely fit. REM sleep is the period when the person is at maximum level of brain power.

The effect of OSAS disease on these stages and REM sleep has been examined. The review was subjected to separate performance evaluations using both YSA and SVM.

II. MATERIAL

The study benefited from the Fırat University Medical Faculty Research Hospital Sleep Room data. The data used are for both normal and OSAS patients. Patients and Stage 1, Stage 2, Stage 3 and REM sleep episodes of each person were prepared according to the polysomnographic report. We have applied the normalization rule that we have specified in this data and have brought our values to 0/1. We used min-max normalization as normalization rule.

Data of 12 nonpatient and data of 36 patients with OSAS were analyzed by YSA and SVM, and the effect of the disease on the disease and REM sleep was evaluated.

The program used in the study is the Weka program. The Weka program is a program used to analyze data in classifiers and decision trees used in data mining. In 1996 the first official version was released. It is often used for academic research and industrial applications [2]. It is used for operations based on data analysis and estimator modeling [2]. It is easier to use thanks to its graphical interface, which makes it easier to use than other data mining applications. It has a portable application because it is used with the Java programming language [2].

Pre-estimation, data analysis and data mining applications are widely used in the literature as an application platform. There is a hierarchical structure within itself. Also according to the applications used, the program makes an analysis in itself and puts the appropriate classifiers into the usable position.

Table 1: Recipients of non-ill persons

Person	Stage 1	Stage 2	Stage3	Rem sleep
K1	0.7	71,5	13,3	14,4
K2	1,3	68,6	13,6	16,5
K3	0,5	73,9	11,7	13,9
K4	0,4	64,3	24,2	11,1
K5	0	61,3	27,2	11,5
K6	0	39,6	51,1	9,3
K7	1,4	60,5	19,7	18,4
K8	6,2	49,1	28,8	15,9
K9	0,6	58,3	17,4	23,7
K10	0,7	69,3	16,7	13,3
K11	1,5	66	23	9,5
K12	1,9	47,2	23,5	27,5

Table 2: The data of 20 patients

Person	Stage 1	Stage 2	Stage3	Rem sleep
K1	0,9	62,9	23,5	12,8
K2	0,5	73,6	10,8	15,0
K3	0,3	44,4	52,1	3,2
K4	0,1	84,9	10,6	4,3
K5	1,3	53,8	30,4	14,5
K6	0	42,9	45,5	11,6
K7	0	73,7	21,5	4,8
K8	0,2	44,1	19,5	36,2
K9	0,4	62,2	19,3	18
K10	0,6	51,7	29,5	18,1
K11	0,3	43,2	35,5	21
K12	4	53,5	18	24,5
K13	0,7	34,4	39,2	25,6
K14	0,6	54,7	27,9	16,8
K15	1,9	63,1	11,4	23,5
K16	2,2	78,6	19,2	0
K17	0,3	54,2	40,1	5,4
K18	2,9	67,7	5,3	24,1
K19	1,3	55,1	26,9	16,8
K20	0	49,2	42,3	8,4

III. METHOD

By using the Weka program used in the study, it was evaluated with the applications of YSA and SVM classification. Training and test data were returned to 0/1 by normalization method. The normalization method used is the min-max normalization method (1):

$$x = \frac{x - x_{min}}{x_{max} - x_{min}} \quad (1)$$

The necessary information about the classification methods used is as follows:

A. Artificial Neural Network (YSA)

Artificial neural networks aim to make the functions that the human brain can do to machines (computer systems) [3]. To these; pre-forecasting, medical procedures, industry, military fields. The main structure of artificial neural networks consists of input, intermediate and output layers. The number of intermediate layers or intermediate layer content is designed separately for each application. This is because determining the number of intermediate layers ensures that the artificial neural network can take full education. Systems that do not fully accomplish their education either can not learn or encounter memorization. Therefore, we need to design the net structure of artificial neural networks in the most accurate way. We first need to normalize the data that will be used when constructing the structure of YSA (2).

$$x = \frac{x - x_{min}}{x_{max} - x_{min}} \quad (2)$$

The data subjected to the normalization process is added to the intermediate layer with the addition function, the addition function coming from the activation function is processed and sent to the output layer. The majority function (3) is used as the total function. Sigmoid function is also used as an activation function.

$$net = \sum_{i=1}^{N} sgn(x_i * w_i) \quad (3)$$

$$sigmoid = {}^{1}/_{1 + e^{-net}} \quad (4)$$

B. *Support Vector Machines (SVM)*

One of the methods used outside of YSA as a classification method is SVM, that is, support vector machines. The SVM, known as the educational learning method, is one of the best classification methods in the literature. As test and learning data, the data are separated and trained to include the classification of the new data (test data) to which class belongs [4]. In order for the separated classes to be distinguished from each other, it is ensured that there are high level differences between them [5]. Thus, by using training data, it is tried to calculate exactly which class of new test data belongs.

IV. PERFORMANCE EVALUATION

Our input parameters used in the study; Stage 1, Stage 2, Stage 3, REM sleep is a polysomnographic report. Table 3 shows the performance evaluation of the effect of the disease on the sleep phases and REM sleep by giving 0/1 output of OSAS patients and non-OSAS patients as an outcome. The performances of SVM and YSA classifiers are separately calculated and evaluated. The same test and training data were compared.

Table 3: Performance evaluation

Methods	Learning data %	Test data %	Performance %
YSA	66	34	81,25
SVM	66	34	72,9167

V. CONCLUSION

In the study, it was investigated whether sleep stages and REM sleep affected negatively due to OSAS disease. In this application, the patient had a negative effect on the sleep stages and REM sleep compared to the patients who were not ill. In the study, two classifiers were used separately and the performance evaluation was made to the result of the study. It is seen that YSA application performs better than SVM application. The performance evaluations were found to be the closest classifier to the correct comparable results. It was seen that only the YSA application, which showed good performances when the two classifiers were evaluated separately on the correct result percentage, proved to be more accurate in this study.

It is known that OSAS disease is a discomfort to be treated. Considering the fact that it should not be confused with simple snoring and its negative effect on the sleep stages, fatigue, carelessness and insomnia are the result of this disease. In the absence of treatment, it can be observed that these effects will continue to increase due to the negative effects on the sleep stages and the level of REM sleep that the whole mind is resting.

REFERENCES

[1]B.Uludağ, Sleep Apnea Syndrome, Avaliable: http://www.burhanettinuludag.com.tr/Herkes/uyku%20apnesi/
[2]P.Tapkan,L.Özbakır,A.Baykasoğlu, ndustrial Engineering Software and Applications Congress,2011,syf.247
[3] I. Ö. Pekel , Electronic Magazine of Odtü Computer Society
[4] N.G. Mutlu , Data Mining Support Vector Machines Prezi
[5] B.Diri, Avaliable: Yıldız Tecnic University, Machine Learning–ML-10.pdf

Evaluation of the Effect of CPAP Device on REM Sleep in OSAS Patients Using YSA and SVM

B.N.AKILOTU[1] and S.A.TUNCER[1]

[1] Fırat University, Elazığ/Turkey, rtbmnur@gmail.com
[1] Fırat University, Elazığ/Turkey, satuncer@gmail.com

Abstract **- Sleep apnea is one of the most important factors of snoring. It is also called breathing during sleep. Depending on the level of apnea it is repeated many times in the night and lasts for at least 10 seconds. During this time, the patient's tongue root or tonsils grow and the airway is blocked. The most common method used to diagnose sleep apnea is to examine polysomnographic records. EKG, EEG, EMG, EOG, Respiration and PPG signals are examined and disease diagnosis is performed. Sleep apnea is divided into 3 as central sleep apnea (CSA), obstructive sleep apnea (OSAS) and mixed sleep apnea (MSA). Data from OSAS patients were used in the study. Polysomnographic records include the percentage of REM sleep time. REM sleep is the state in which dreams are seen and the human mind's activities are at the highest level. People with sleep apnea use a device called CPAP device for comfortable sleeping, getting rid of the pussy and opening the respiratory tract. The REM sleep levels before and after the CPAP device were compared in this report. Data set entries were used as a percentage of REM sleep time before CPAP and as a percentage of REM sleep time after CPAP. The negative result of the positive result on the Rem sleeping time of the CPAP device is discussed. Artificial neural networks (YSA) and SVM were used for the study. As a result of the study, it was seen that the CPAP device increased the level of REM sleep time by 74.41%.**

Keywords **- Obstructive Sleep Apnea (OSAS), REM Sleep, Artificial Neural Networks (YSA), SVM, CPAP**

I. INTRODUCTION

Sleep apnea is an important neurological disorder caused by the airflow that occurs during respiration during sleep and particularly during the period of Stage 3 or REM sleep, lasting 10 seconds or longer and causing the sleep system and order of the individual to deteriorate [1]. It causes situations that result in death if mixed with simple snoring and the doctor can not diagnose the disease under the supervision of a doctor [2]. Polysomnography (PSG) is the most standardized method used to diagnose disease. With this method, it is determined whether patients have a simple snoring or a sleep apnea. Various signals are processed in PSG. These are the signals of heart and pulse measurements such as EKG, EEG and EMG. These signals are processed by various signal processing techniques to make estimates for apnea diagnosis [2]. In this study, data from the OSAS disease type of sleep apnea were used. This study examined whether the device called REM sleep and CPAP affects the performance of REM sleep in patients with OSAS (obstructive sleep apnea) positively or negatively.

REM sleep is the time interval when the human brain is most active. Sleep is the period of dreaming. It occurs between 5 and 30 minutes every 90 minutes during the sleeping period [3]. At the same time, metabolism and brain activity increase [3]. Healthy people have 20-25% of REM sleep periods [3].

CPAP device is one of the methods used in the treatment of sleep apnea. Positive airway pressure is also reported in the literature, which was used by Colin Sullivan in 1981 [4]. By compressing the room air by means of the CPAP device, it pumped up to create an adjustable pressure and air flow [4]. The pressure range required for each level disease is different because it is adjustable. Continuous positive pressure air flow is given to the upper respiratory tracts [4].

This study investigates whether there is an increase in performance in REM sleep as the CPAP device is mostly preventing sleep apnea. These examinations were made on the data sets available using YSA and SVM.

II. MATERIAL

The study benefited from the Fırat University Medical Faculty Research Hospital Sleep Room data. The pre-CPAP and post-CPAP REM sleep levels of 43 OSAS patients in the used data set were examined. The state of being useless is 1/0.The data in Table 1 obtained in the polysomnographic report were evaluated separately by YSA and SVM. And the performance results are given separately in two methods.

The program used in practice is the Weka program, which is used especially in academic fields in data mining research. This program was developed by Waikato University and was first published in 1996 [5]. The Weka program is an application used in data mining and machine learning applications [5]. It is used in many systems such as data analysis and preliminary estimation applications. It has graphical interface. For this reason, the user provides easier implementation than other data mining and analysis programs. This makes the Weka program preferable. Academic and industrial sense of many uses. There is a hierarchical structure

in itself [5]. At the same time, after loading this program dataset, it deactivates those applications, classifier algorithms, which applications are not suitable. That is, the program selects the most accurate algorithms by classifying it in itself.

Table 1: Status information for 43 people before and after CPAP

Persons	Pre - CPAP	Post - CPAP	State
K1	2,6	8,1	1
K2	16,2	39	1
K3	19	8,3	0
K4	18,1	1,1	0
K5	5,5	10,2	1
K6	0	13,2	1
K7	0,2	28,9	1
K8	9,1	8,7	0
K9	8,2	20	1
K10	5,7	13	1
K11	30,8	31,7	1
K12	11,7	11,5	0
K13	13,6	10,9	0
K14	16,7	23,6	1
K15	10,2	10,9	1
K16	14,1	14,6	1
K17	17,3	19,2	1
K18	11,7	14,8	1
K19	8,7	16	1
K20	3,3	22,8	1
K21	5,6	26,4	1
K22	6,3	27,1	1
K23	22,1	27,5	1
K24	6,8	38	1
K25	12,8	25,4	1
K26	0,6	0	0
K27	12,3	15,2	1
K28	3,6	9,4	1
K29	9,1	0	0
K30	20	20,5	1
K31	20,4	14,4	0
K32	5,4	14,2	1
K33	3,2	12,9	1
K34	2,3	12,6	1
K35	14,7	11,1	0
K36	15,4	26,6	1
K37	8,3	5,4	0
K38	11,9	10,2	0
K39	22,2	24,4	1
K40	11,7	16,5	1
K41	7,5	12,3	1
K42	10,1	16,5	1
K43	16	3,7	0

III. METHOD

In our practice, YSA and SVM were used as classifier. These methods were tried separately and the results were compared.The data were subjected to normalization before use. For this, max-min normalization rule is chosen (1).

$$x = \frac{\mathrm{x} - \mathrm{xmin}}{\mathrm{xmax} - \mathrm{xmin}} \qquad (1)$$

The classification methods used in the study are explained below:

A. YSA (Artificial Neural Network)

It is a model for adapting the learning, understanding and conclusion features to the machine by mimicking the working mechanism of the human brain [6]. Artificial neural networks are made up of layers. These are the input, intermediate and output layers. The number of intermediate layers depends on the system to be implemented. The data are processed by normalization (2). Then, operations are performed on the data using the addition and activation function. In our application, tansig as activation function (3) and max total function (4) as addition function.

$$x = \frac{\mathrm{x} - \mathrm{xmin}}{\mathrm{xmax} - \mathrm{xmin}} \qquad (2)$$

$$tansig = \frac{e^{net} + e^{-net}}{e^{net} - e^{-net}} \qquad (3)$$

$net = \max(xi * wi)$ // x: neuron, w: neuron weight (4)

B. SVM (Support Vector Machines)

Another method that is widely used in classification today is SVM. It is one of the simplest and most effective methods. Educational learning methods are among the best methods used in the literature in this regard. It is a method of learning a machine that tries to make the most accurate prediction on new arrivals by using learning data [7]. It allows the classes to have a hyperplane to distinguish one from another [8]. Both classes that are separated in this way find the furthest line. In this way, using the training data, it finds out which side of the border the test data is located with the line and inserts this data into the border side which is determined.

IV. PERFORMANCE EVALUATION

Our input parameters used in the study are REM sleep before CPAP and REM sleep after CPAP and output as ineffective. These data were evaluated using SVM and YSA classification methods. The effect of the CPAP device on the REM sleep level in OSAS patients was assessed. Performance evaluation is given in Table 2:

Table 2: Performance evaluation

Methods	Learning data and test data (cross validation) %	Performance %
YSA	10	74.41
SVM	10	67,00

V. CONCLUSION

Sleep is not just a rest, contrary to what you usually think. Behaviorally, all motor activity is reduced or limited, and response to stimuli is reduced by about 1/3 of our lives [3]. The sleeping event contains REM sleep, which reaches maximum levels of deep-thinking activities. REM sleep is more active than ever since the mind has never been. At the same time, the main center of relaxation occurs at this REM sleep level. The CPAP device used in the OSAS disease is trying to provide sleep at a better level. In this study, either this percentage increase in the incidence of REM sleep, or in some patients decreased detection was applied at the end of REM sleep device. For the discussion topic, the level of interaction for the OSAS patients at any level will be tried to be determined in future studies that are negative.

REFERENCES

[1] Z.Tabak, Feasibility Analysis of Sleep Apnea Detection from Heart And Respiratory Sounds, Başkent Unıversity , Bioengineering, Graduate Thesis, 2015

[2]G.Karamustafaoğlu, Automatic detection of sleep apnea by processing of polysomnography signals, Istanbul Unıversity, Bioengineering Graduate Thesis, 2014

[3] G.Güleç, Uludağ University, Avaliable: http://uykubozuklugu.uludag.edu.tr/dersnotlari001.htm

[4]D.A.Tavlı, Inönü University, Uyku Apne Sendromlu Bireylerde Cpap Tedavisinin Eeg'de Izlenen Uyku Iğcikleri Uzerine Etkisi, Master Thesis, 2013

[5] [2]P.Tapkan,L.Özbakır,A.Baykasoğlu, ndustrial Engineering Software and Applications Congress,2011,syf.247

[6] I. Ö. Pekel , Odtü Bilgisayar Topluluğu Elektronik Dergisi

[7] Nazlı Gülüm Mutlu Veri Madenciliği Destek Vektör Makineleri Prezi

[8]B.Diri, Avaliable: Yıldız Teknik University, Makine Ögrenmesi –ML-10.pdf

Estimation of Lake Van Monthly Average Water Level Change by Using Artificial Intelligence Methods

C. KOYCEGIZ[1] and M. BUYUKYILDIZ[1]

[1] Selcuk University, Konya/Turkey, cihangir@selcuk.edu.tr
[1]Selcuk University, Konya/Turkey, meralbyildiz@selcuk.edu.tr

Abstract **- In this study, it was aimed to estimate the water level change using the monthly average water level data of 1944-2005 periods, Van Lake which is Turkey's largest lake. For this purpose, Generalized Regression Neural Network (GRNN), Radial Basis Neural Network (RBNN) and Support Vector Regression (SVR) methods are used. Different input combinations, consisting of different lag time series of water level (L) data (L_{t-1}, L_{t-2}, L_{t-3}, L_{t-4}), were used in the models established for estimating monthly lake levels. The performance of the models was evaluated using square root mean squared error (RMSE), mean absolute error (MAE) and efficiency coefficient (EC). According to the results obtained, the ε-SVR-M4 model with EC = 0.712 value for testing period was the most successful model to estimate monthly average water level change of Lake Van.**

Keywords **- Lake Van, Generalized Regression Neural Network, Support Vector Machine, Radial Basis Neural Network**

I. INTRODUCTION

Lakes that are extremely open to external influences and basins containing them constitute one of the most important components of water resources. Climate changes and various human activities are affecting lake water levels. Precipitation, flow, evaporation, drinking water supply, irrigation water and waters used for energy cause change of lake water level Changes in lake water levels cause important economic losses in lake environments, and sometimes even nature changes that are not possible to recover again [1, 2].

Determination of the change in lake level is crucial for planning and construction work, ensuring the management and productivity of agricultural areas, sustaining aquatic life and operating drinking water facilities in lakes and their surrounding areas.

Changes at the lake level can be observed regularly at observation stations to be installed in certain locations, or can be estimated using mathematical methods such as the water balance model. Recently, various artificial intelligence methods such as Artificial Neural Networks (ANN) and Support Vector Machines (SVM), which are used to predict many hydrological parameters, are also widely used in predicting lake levels [3, 4, 5, 6, 7, 8, 9, 10].

Altunkaynak [8] used ANN models for water level estimation and compared the results with ARMA models. As a result, ANN models were found to be more successful than ARMA models in lake water level estimation. Yadav [11] used a hybrid wavelet-support vector machine (WA-SVM) model to estimate the daily lake water change. Daily lake water level along with other hydro-meteorological data had been used as input to estimate the lake water level up to 20 days ahead. Various combinations of input data had been used to obtain the best model structure.

Kavehkar et al. [12] used the Genetic Programming (GP) model to estimate the daily water level change of Urmia Lake in Iran and compared the results with those obtained from the ANN models. Khan and Coulibaly [13] used the SVM method in estimating the monthly mean water level of Lake Erie during the period 1918-2001 and compared the results with the multilayer perceptron (MLP) and seasonal autoregressive (SAR) models. Wei [14] studied the performance of traditional Gaussian SVM models with Wavelet SVM using two station data at Tanshui River Basin in northern Taiwan to estimate the hourly water level. Unes et al. [15] predicted daily reservoir levels for Millers Ferry Dam on the Alabama River in USA using artificial neural networks (ANN). The results of the optimal ANN models were compared with conventional auto-regressive models (AR), auto-regressive moving average (ARMA), multi-linear regression (MLR) models. The comparison results show that the ANN models perform better than the conventional models.

The aim of this study is to estimate the change of the monthly mean water level of Lake Van, the largest lake in Turkey, with various artificial intelligence methods (GRNN, RBNN and SVM).

II. METHODS

A. Generalized Regression Neural Network

The Generalized Regression Neural Network (GRNN) proposed by Spetch and developed as an alternative to forward feed backward propagation algorithms does not require an iterative training procedure between the input and output variables [16]. The GRNN method is used to estimate

continuous variables as in standard regression techniques. The network structure of GRNN is shown in Figure 1. The GRNN consists of four layers: 1) input, 2) pattern, 3) summation, and 4) output layers.

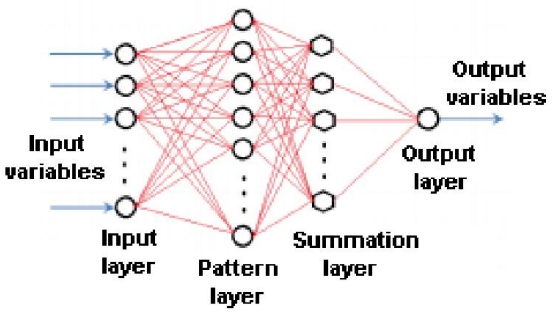


Figure 1: The network structure of GRNN

In the first layer, the total number of input variables is equal to the number of input units. The input layer is linked to the pattern layer where each neuron symbolizes a training pattern. The second layer sends processed information to the summation layer through the pattern neurons. The summation layer consists of S-summation and D-summation neurons, which are connected to the pattern layer unit [17]. The sum of the weighted responses of the pattern layer is calculated by the S-summation neurons, while the D-summation neurons compute the un-weighted outputs. Finally, in the output layer, the division of the output of each S-summation neuron by D-summation neuron gives the output value. More descriptions about the GRNN model can be found in the literature [16, 18].

B. *Support Vector Machine*

For the first time, Support Vector Machines (SVMs) has been introduced for classification and regression type problem solving by Vapnik [19]. SVMs are defined as two categories for: support vector classification (SVC) and support vector regression (SVR) in the literature. SVMs are a machine learning method. In traditional machine learning methods, there are problems of having a lot of training data, low convergence rate, local minimum attachment and over fitting / under fitting [20]. SVM is based on structural risk minimization and is based on these problems [21]. The idea of SVR is based on the computation of a linear regression function in a high dimensional feature space where the input data are mapped by a nonlinear function. The regression function with SVR is given in the following equation [22].

$$f(x)=\sum_{i=1}^{N}(\alpha_i-\alpha_i^*)K(x,z)+b_i \quad (1)$$

Here, $(\alpha^i-\alpha_i^*)$ are the Lagrange multipliers, K (x, z) are expressed as, the inner product kernel function defined according to the Mercer theorem, and b is the bias value.

In this study, ε-SVR was used as SVR model. ε-SVR was proposed to introduce an alternative ε-insensitive loss function by Vapnik [19]. In SVR, the error on any training data should be less than ε [23]. In the success of SVR, it is of great importance that the insensitive error constant (ε), the regularization constant (C) and the kernel function parameters are determined. However, there are no specific criteria for selecting the kernel function and model parameters [24]. In this study, radial based kernel function was used and expressed as follows. Here, γ is the kernel parameter that provides radius control. The SVM architecture is shown in Figure 2.

$$K(x_i,x)=\exp(-\gamma\left\|x_i-x_j\right\|^2 \quad (2)$$

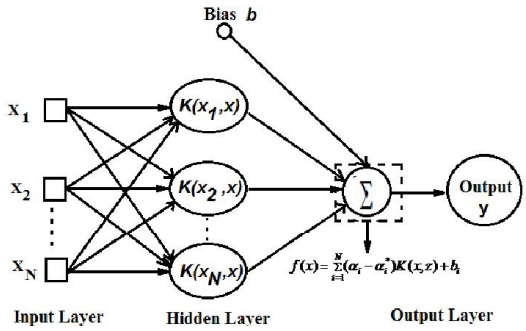


Figure 2: The SVM architecture

C. *Radial Basis Neural Network*

Radial Basis Neural Networks (RBNN) introduced by Broomhead and Lowe [25], have an input layer, hidden layer and output layer (Figure 3).

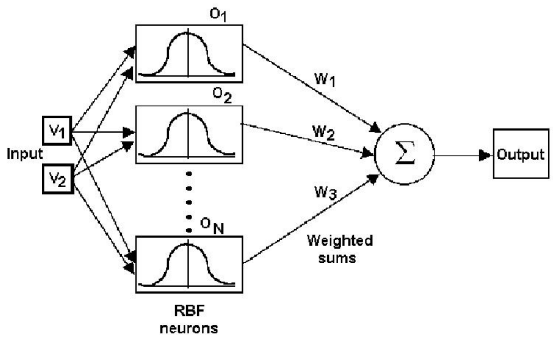


Figure 3: The network structure of RBNN

However, unlike classical ANN structures, RBNNs have a single hidden layer where radial functions are used as the activation function for the network.

The operation principle of an RBNN can be described as the process of determining the relationship between input and output by generating linear combinations of output values generated by these functions with appropriate weight values at the output layer by determining RBNNs having appropriate width and center values in the hidden layer depending on the input data [26].

The structure of RBNNs is similar to back propagation functions. The difference in RBNN, the neurons in the hidden layer comprise Gaussian transfer functions whose outputs are

inversely proportional to the distance from the center of the neuron. There is also a linear activation function in the output layer. The network training in RBNN consists of two stages. Firstly, the weights from the input to hidden layer are determined, and then the weights from the hidden to output layer. The training/learning of RBNN is very fast. The disadvantage of RBNN is that it needs more data so that it can deliver as accurate results as back propagation networks [26].

III. Case Study and Data

Lake Van is a volcanic set that formed as a consequence of the explosion of Nemrut volcanic mountain within the boundaries of Bitlis province. Lake Van is the world's largest soda lake, and is the biggest lake of Turkey in terms of surface area (Figure 4). Van Lake has a surface area of 3,713 km^2, a volume of 607 km^3 and maximum depth of 450 meters (Ahlat and Adilcevaz) [27]. The Lake Van is shown in Figure 4.



Figure 4: Lake Van and Tatvan Lake Observation Station

In this study, monthly average water level data measured by the Electricity Affairs Administration (EIE) at the Lake Van Lake-Lake Tatvan observation station (GGI) (Figure 4) were used to estimate for the change in the monthly water level (L) of Lake Van. The precipitation area of Lake Van-Tatvan GGI is 16096 km^2 and the altitude is 1648 m. The data used were 744 data between 1944-2005 period, the first 518 months data for training and the remaining 226 months data for testing were used in the study. To estimate monthly water level, different lag time series of L data (L_{t-1}, L_{t-2}, L_{t-3} and L_{t-4}) were used as input variables, while values of change in water level (L) were used as output. In this study, level values were given as elevation so the values of change in level per month were determined by taking the differences in elevation compared to the previous month.

IV. Application and Results

GRNN, RBNN and ε-SVR was used to estimate the monthly change of lake water level in Lake Van. Before applying the artificial intelligence methods, the data were made un-dimensional between 0.2 and 1 using Eq. 3.

$$X_{norm} = 0.2 + 0.8 \times \frac{X_i - X_{\min}}{X_{\max} - X_{\min}} \quad (3)$$

Where; X_{norm}, X_i, X_{min} and X_{max} represent the normalized, observed, minimum and maximum data values, respectively.

The models to estimate monthly average lake level were obtained using four different input combinations consisting of different lag time series of monthly average water level (L) (Lt-1, Lt-2, Lt-3 and Lt-4) v and the effect of each input combination on water level variation was examined. Input combinations and the outputs are given in Table 1.

Table 1: Model names and input combinations

Model Names	Inputs	Output
M1	L_{t-1}	
M2	L_{t-1}, L_{t-2}	L
M3	L_{t-1}, L_{t-2}, L_{t-3}	
M4	L_{t-1}, L_{t-2}, L_{t-3}, L_{t-4}	

Mean absolute error (MAE), root mean square error (RMSE) and efficiency coefficient (EC) criteria were used in evaluating the performance of established models. The performance criteria used in the study are described in the equations of 4, 5 and 6, respectively.

$$MAE = \frac{1}{N}\sum_{i=1}^{N}\left|Xi - Yi\right| \quad (4)$$

$$RMSE = \sqrt{\frac{1}{N}\sum_{i=1}^{N}(Xi - Yi)^2} \quad (5)$$

$$EC = 1 - \frac{\sum_{i=1}^{N}(Xi - Yi)^2}{\sum_{i=1}^{N}(Xi - \overline{X})^2} \quad (6)$$

A software package known as LIBSVM Software was used for the ε-SVR method and all model applications were performed in MATLAB 2010b.

The spread parameter (γ) for four different input combinations was tested with an increase of 0.01 in the range [0.01 5] to estimate the water level change with the GRNN technique. In the implementation of the RBNN models, the number of neurons in the hidden layer, which significantly affected the performance of the model, was determined by 1 increments between [2 20] and spread parameter (σ) by 0.01 increments between 0.01 and 5.

In ε-SVR applications, Radial Basis Kernel Function which is widely used in the literature as kernel function is used. The error term (ε), regularization factor (C) and kernel function parameter (γ) affecting the performance of the SVR models were obtained by testing the ranges of [0.01 0.5], [1 100] and

[0.1 8], respectively. In the models obtained for all three methods, the most successful models for each input combination were determined according to the highest EC values with the lowest MAE and RMSE. As a result of these evaluations, the most successful network structures obtained for test data are shown in Table 2, MAE and RMSE values are shown in Figure 5, and EC values are shown in Figure 6.

Table 2: The most successful model structures in testing period

Model Names	Inputs	Model Network Structures		
		GRNN (γ)	RBNN (σ, neuron number)	ε-SVR (C, ε, γ)
M1	L_{t-1}	0.02	0.11, 6	20, 0.03, 18.8
M2	L_{t-1}, L_{t-2}	0.02	0.34, 20	20, 0.01, 19.9
M3	L_{t-1}, L_{t-2}, L_{t-3}	0.03	0.12, 20	11, 0.03, 19.9
M4	L_{t-1}, L_{t-2}, L_{t-3}, L_{t-4}	0.03	0.14, 19	9, 0.01, 19.7

According to Table 2, the initial values of the GRNN and RBNN models are the spread parameter values, while the second value in the RBNN models is the number of neurons in the hidden layer. The values in the ε-SVR network construction represent to C, ε and γ values, respectively.

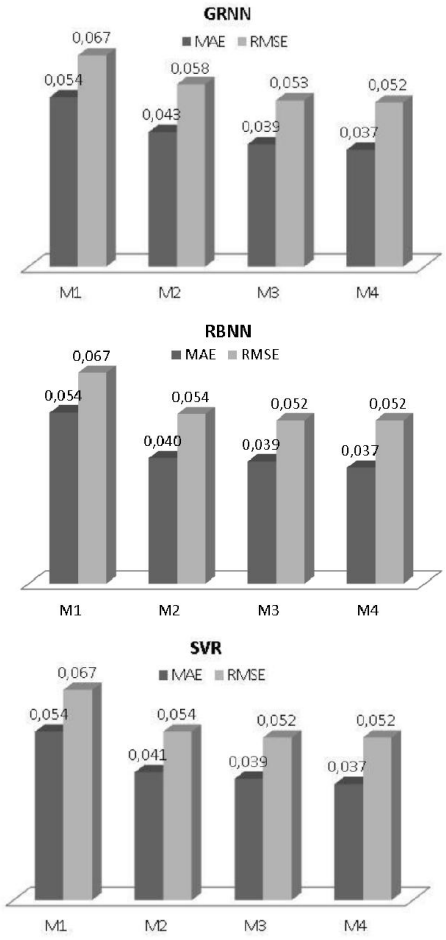


Figure 5: MAE and RMSE values of the most successful models obtained testing period

The MAE and RMSE values according to Figure 5 have values very close to each other in all the methods used for each input combination. In all of the artificial intelligence methods used, the M4 models (L_{t-1}, L_{t-2}, L_{t-3}, L_{t-4} input combinations) obtained using the lowest MAE and RMSE values were the most successful models. In all three methods, the M1 models (L_{t-1} input combination) with the highest MAE and RMSE values in the monthly average water level change prediction are the models with the lowest performance.

According to the EC values obtained for the GRNN, RBNN and ε-SVR models, the most successful input combination was obtained in M4 and the lowest input combination in M1 models (Figure 6).

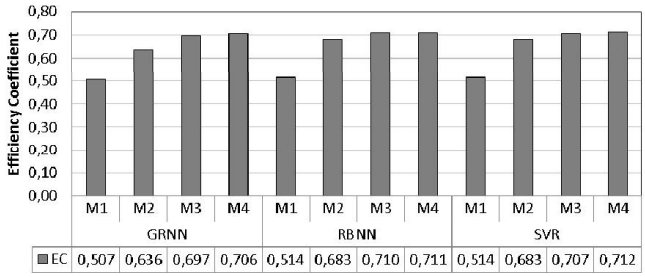


Figure 6: EC values of the most successful models obtained testing period

Among the M4 models with the most successful input combination, the ε-SVR model with the highest EC=0.712 value with the lowest MAE=0.037 and RMSE=0.052 value was more successful than the other methods. GRNN models showed the lowest performance in all combinations. RBNN models and ε-SVR models gave almost the same result in all performance criteria. As a result, ε-SVR-M4 model with the values of C = 9, ε = 0.01 and γ = 19.7 is the most successful model in estimating the monthly average water level change of Van Lake. The scatter diagram for the testing period ε-SVR-M4 is shown in Figure 7.

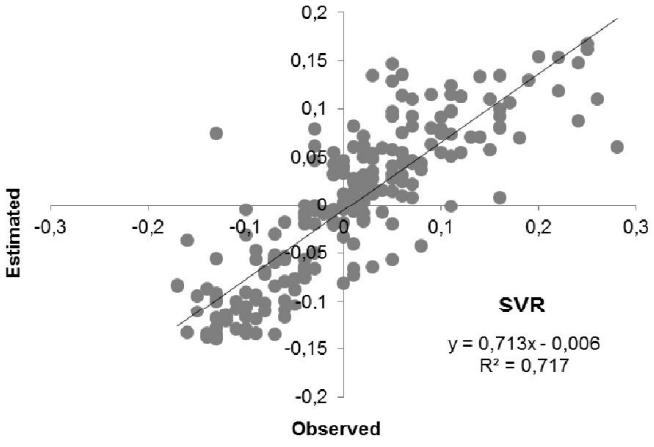


Figure 7: Scatter diagram of ε-SVR model in testing period for Lake Van

V. CONCLUSIONS

In this study, the potential use of Artificial Intelligence methods to model lake water levels has been investigated. For this purpose, monthly average water level data during 1944-2005 belonging to Lake Van in Turkey were used. The water level change values of each month were calculated by taking the level differences of the previous month and the models were obtained by ε-SVR, RBNN and GRNN methods. While the model was established, four different input combinations consisting of Lt-1, Lt-2, Lt-3, Lt-4 lag time series were used. When the performances of the installed models were examined, the most successful input combination in each method was the M4 combination, where Lt-1, Lt-2, Lt-3, Lt-4 variables were used. The most unsuccessful results in the methods used were obtained in the M1 combination where Lt-1 is used as input in the established models. The most successful method according to EC values is ε-SVR. In the RBNN method, the success achieved in the ε-SVR method is very close to success. In this study, the GRNN method is the least successful method in all input combinations.

Estimation of water level change with appropriate accuracy of such models is important for studies on the management of water resources such as flood control, water resource management, recreational activities, and ecosystem sustainability.

REFERENCES

[1] T. M. Cengiz and E. Kahya, "Türkiye göl su seviyelerinin eğilim ve harmonik analizi," *İtüdergisi /dmühendislik, vol.* 5, pp. 215–224, 2006 (in Turkish).

[2] O. Kisi, J. Shiri, and B. Nikoofar, " Forecasting daily lake levels using artificial intelligence approaches," *Comput Geosci, vol.* 41, pp. 169–180, 2012.

[3] I. Ebtehaj, and H. Bonakdari, "Performance evaluation of adaptive neural fuzzy inference system for sediment transport in sewers.," *Water Resour Manag,* vol. 28, pp. 4765–4779, 2014.H. Poor, *An Introduction to Signal Detection and Estimation*. New York: Springer-Verlag, 1985.

[4] M. Buyukyildiz G. Tezel, and V. Yilmaz, "Estimation of the change in lake water level by artificial intelligence methods," *Water Resour Manag,* vol. 28, pp. 4747–4763, 2014.

[5] M. Sulaiman, A. El-Shafie, O. Karim, and H. Basri, "Improved water level forecasting performance by using optimal steepness coefficients in an artificial neural network," Water Resour Manag, vol. 25, pp. 2525–2541, 2011.

[6] H. Kakahaji, H. D. Banadaki, A. Kakahaji, and A. Kakahaji, "Prediction of Urmia Lake water-level fluctuations by using analytical, linear statistic and intelligent methods," *Water Resour Manag*, vol. 27, pp. 4469–4492, 2013.

[7] V. Guldal and H. Tongal, "Comparison of recurrent neural network, adaptive neuro-fuzzy inference system and stochastic models in Eğirdir lake level forecasting," *Water Resour Manag*, vol. 24, pp.105–128, 2010.

[8] A. Altunkaynak, "Forecasting surface water level fluctuations of Lake Van by artificial neural networks," *Water Resour Manag*, vol. 21, pp. 399–408, 2007.

[9] Y. Seo, S. Kim, O. Kisi, and V. P. Singh, "Daily water level forecasting using wavelet decomposition and artificial intelligence techniques," *J Hydrol,* vol. 520, pp. 224–243, 2015.

[10] H. Afiq, E. Ahmed, N. Ali, A. Othman, K. Aini, and H. M. Mukhlisi, "Daily forecasting of dam water levels: comparing a support vector machine (SVM) model with adaptive neuro fuzzy inference system (ANFIS)," *Water Resour Manag*, vol. 27, pp. 3803–3823, 2013.

[11] B. Yadav, "A Hybrid Wavelet-Support Vector Machine model for Prediction of Lake water level Fluctuations Using Hydro-Meteorological Data," *Measurement,* vol. 103 , March 2017,

[12] S. Kavehkar, M. A. Ghorbani, V. Khokhlov, A. Ashrafzadeh, and S. Darbandi, "Exploiting two intelligent models to predict water level: a field study of Urmia lake," *Iran Int J Civil Environ Eng*, vol. 3, pp.162–166, 2011.

[13] M. S. Khan, and P. Coulibaly, "Application of support vector machine in lake water level prediction," *Hydr. Eng,* vol. 11, pp. 199–205, 2006.

[14] C. C. Wei, "Wavelet kernel support vector machines forecasting techniques: case study on water-level predictions during typhoons," *Expert Syst Appl,* vol. 39, pp.5189–5199, 2012.

[15] F. Unes, M. Demirci, O. Kisi, "Prediction of Millers Ferry Dam Reservoir Level in USA Using Artificial Neural Network," P*eriodica Polytechnica Civil Engineering, vol.* 59, pp. 309–318, 2015.

[16] D. F. Specht, "A general regression neural network," *IEEE Trans. Neural Networks*, vol. 2, pp. 568–576, 1991.

[17] M. Zounemat-Kermani and M. Teshnehlab, "Using adaptive neuro-fuzzy inference system for hydrological time series prediction," *Appl Soft Comput*, vol. 8, pp. 928–936, 2008.

[18] L. H. Tsoukalas and R. E. Uhrig, *Fuzzy and Neural Approaches in Engineering.* John Wiley Inc., New York, USA, 1997.

[19] V. Vapnik, *The Nature of Statistical Learning Theory.* Springer, New York, 1995.

[20] W. Lu, W. Wang, A. Leung, S. Lo, R. Yuen, Z. Xu, and H. Fan, "Air pollutant parameter forecasting using support vector machines.", *Proceedings of the 2002 International Joint Conference on Neural Networks.1, pp.* 630–635, 2002.

[21] J. Shen, Z. J. Pei, and E. S. Lee, "Support vector regression in the analysis of soft-pad grinding of wire-sawn silicon wafers. *CITSA 2004/ISAS 2004,* pp. 19–24, 2004.

[22] R. Salat, and S. Osowski, "Accurate fault location in the power transmission line using support vector machine approach, power systems," *IEEE Transactions on* , vol. 19, pp.879–886, 2004.

[23] M. Pal, and G. Arun, "Prediction of the end-depth ratio and discharge in semi-circular and circular shaped channels using support vector machines," *Flow Meas Instrum,* vol. 17, pp. 49–57, 2006.

[24] H. Lin, "Support vector machines for regression and its application for prediction of machine degradation based on vibration signal," Thesis Master of Science, University of Alberta, Edmonton, Alberta, 2006.

[25] D. Broomhead, and D. Lowe, " Multivariable functional interpolation and adaptive networks," *Complex Systems,* vol. 2, pp. 568–576, 1988.

[26] M. Verleysen, and K. Hlavackova, "An optimized RBF network for approximation of functions," *Proceedings European Symposium on Artificial Neural Networks*. Brussels, Belgium, pp 175–180, 1994.

[27] D. E. Akyuz, "Van Gölü Su Seviyesinin Veri Madenciliği Metodları ile İncelenmesi," *Van Gölü Hidrolojisi ve Kirliliği Konferansı,* , pp. 65-73, 21-22 Ağustos 2008.

Application of Artificial Neural Networks on Building Energy Estimation

M.ALTUN*[1], A.B.ERSOZ[1], T.TEKE[1], T.KURT[1], A.AKCAMETE-GUNGOR[1] and O.PEKCAN[1]

[1] Middle East Technical University, Ankara/Turkey,* mualtun@metu.edu.tr

***Abstract* -The decision makers in the building design stage need to give more importance for energy efficient solutions to improve the performance the building in its operational phase. In practice, they are expected to generate alternative designs in the early design stage and use complicated building simulation tools to estimate building energy use of these alternatives more accurately; however, this is a time-consuming procedure and it is difficult to evaluate different alternatives in the limited time of a design period. For this reason, emerging artificial intelligence (AI) algorithms are becoming popular amongst practitioners in the industry to study the energy performance evaluation. Their inherently fast nature makes AI algorithms suitable for this topic depending on the database generated. In this study, an Artificial Neural Network (ANN) is developed to estimate energy performance of the buildings efficiently based on a previously generated dataset including building properties and energy loads. The ANN is constructed based on different network topologies, activation functions and learning rates combinations to provide more accurate results on heating and cooling loads. The results of the study are presented and compared with the results in the previous studies. It shows the right parameter combination for ANN generates quite competitive results with the ones from the previous studies.**

***Keywords* - Energy efficiency, energy performance analysis, artificial intelligence, artificial neural network**

I. INTRODUCTION

There has been a considerable increase in the energy consumption thanks to the improvements in technology and increase in the world population and industrial activities. Buildings share one of biggest piece of this increased energy pie which is estimated to be nearly 40% of global energy consumption [1]. This increase in the last few decades regarding buildings stems from the increased need for heating, ventilation and air conditioning, which plays an important role in regulating the indoor climate and is responsible for the most of the energy use in these buildings. Therefore, it has become one of the trending research topics considering the increased energy waste that has raised concerns on global warming and other environmental problems.

Estimation of building performance plays a prominent role to analyze the building performance comprehensively for proposing energy-efficient solutions. Various approaches have been developed to estimate building energy performance such as (i) engineering calculations, (ii) field measurement based statistical approaches, (iii) hybrid approaches and (iv) artificial intelligence (AI) algorithms [2,3]. Engineering calculations simulate the physical behavior of the building system and its interactions with environment into thermo-dynamic equations to estimate building energy use [4]. Field measurement based statistical approaches directly use measured energy data obtained via detailed monitoring or utility bill disaggregating estimation to estimate building performance. Hybrid approaches combine both calculation and measurement based estimation. For these approaches, also called white box or forward approaches, design parameters which influence building performance are determined in advance. Then, using some mathematical operations, building energy performance is estimated as an output of the analysis. On the other hand, for the conditions where design inputs and energy performance outputs are known, AI algorithms aim developing black box best-fit models to maximize model accuracy based on these known set of inputs and outputs.

Chari and Christodoulou [5] state that selecting which estimation approach to use for the analysis depends on the conditions considering data availability, time efficiency, cost-effectiveness, designer's capabilities and design phase. All these parameters also determine the the detail level of energy model and the accuracy level of analysis. For instance, building energy simulation tools as engineering calculation simulators such as EnergyPlus, TRNSYS and Ecotect include various features and capabilities to simulate building performance in detail. Therefore, they require a high level of knowledge on the behavior of physical building system and designer's expertise on the construction of an energy model accurately based on various factors such as weather conditions, especially the dry-bulb temperature, the building construction and thermal property of the physical materials used, occupancy conditions, sub-level components such as lighting, Heating, Ventilating, and Air-Conditioning (HVAC) systems, their performance and schedules. Therefore, assumptions based on considerable amount of missing data or drawing details fluctuate the accuracy level of the energy analysis. On the other hand, AI algorithms only need design inputs and energy use outputs to construct the models. Moreover, establishment of a detailed energy monitoring system for the existing buildings is quite expensive and time-consuming compared to analyses according to the engineering calculations and AI algorithms although the measured data offer the most accurate energy performance result. However, use of similar measured data with design parameters via statistical models and AI algorithms is quite time-efficient and cheaper compared to the measured one. Furthermore, to optimize building energy

performance in the design stage or in retrofit projects, numerous analyses are required to compare efficiency of design alternatives. For the measurement based analysis, availability of all design alternatives is quite improbable or too expensive. On the other hand, analysis of detailed energy model of a complex building for all design alternatives requires a considerable amount of time. Therefore, availability of inputs (design parameters) and outputs (measurement or analyses based energy use data) makes the application of AI algorithms both easy and relatively fast compared to simulation based analyses.

AI algorithms can offer time efficient [6] and cost effective solutions depending on availability of data sets. A well-trained AI prediction model can be used to (i) estimate performance of new design alternatives or (ii) use of constructed model to evaluate various alternatives for energy-efficient building design. In the early design stage of new buildings, the designer can use AI algorithms to generate best-fit model via (i) using measured datasets of similar existing buildings to compare its results with energy simulation model results for accuracy evaluation of these two approaches or (ii) using energy simulation inputs and results to check whether accuracy level of the model is suitable (a) to estimate performance of new design alternative or (b) to use constructed model for fast optimization in the design stage due to time limitation.

Multiple linear regression models construct a mathematical relationship between several independent input variables and energy use variable(s). Thanks to its less computational time requirement and without the need of any parameter tuning, the model is applicable to long-term building energy use estimation [7]. On the other hand, nonlinear behavior of an energy model limits the performance of this statistical regression method significantly. Therefore, in this study, a Artificial Neural Network (ANN) based method was developed to estimate the energy performance of the buildings efficiently based on a dataset previously generated via building simulation tool Ecotect. The ANN was constructed using different configurations of various topologies, activation functions and learning rates. The obtained results were presented and compared with the results in the previous studies to discuss this performance of the ANN based approach on energy efficiency analysis of the buildings.

II. Artificial Neural Networks

ANNs are nonlinear learning algorithms inspired from human brain, in which complex relationships between inputs and outputs are modeled. Typical ANN consists of three layers, input, hidden and output layer, respectively. In each layer, there are interconnected artificial neurons including an activation function, which transforms input to its output activation. Different activation functions and the alternatives of hidden layer and neuron count would construct distinct ANN topologies, which can be applied to variety of problems.

Due to their effective non-linear problem solving capabilities, ANNs are one of the most common AI tools to estimate building energy consumption. According to Kumar et al. [6] ANNs generate more reliable results compared to traditional simulation models and regression techniques. Therefore, there are numerous studies which utilize ANNs to analyze various types of buildings in terms of heating and cooling costs, electricity consumption, and HVAC systems.

One of the first ANN models to estimate the required amount of heating energy is developed by Kalogirou et al. [8]. Their model is a neural network trained with the consumption data of 225 buildings using back propagation. There are several studies which use the same model to estimate heating energy requirements of various types of other buildings [8, 9]. Later, a study by Olofsson and Andersson [11] presented a model to estimate the annual heating costs of a building by using measurements in a few weeks. The accuracy of the prediction model is especially high in cases of single family buildings.

For estimating the cooling demands of buildings, Yokoyama et al. [12] provided a back propagation neural network based approach. To identify the model parameters for the neural network, they proposed a global optimization method called modal trimming. Kreider et al. [13] developed a model based on a recurrent neural network, using hourly energy consumption data to estimate future energy needs for the heating and cooling. Using this model, Ben-Nakhi and Mahmoud [14] estimated cooling load of three buildings for 2001 using data obtained throughout 1997-2000. Kalogirou [15] and Yan and Yao[16] used a neural network to estimate a building's heating and cooling load based on different climate conditions.

Martellotta et al. [17] generated alternative designs based on building features, heating/cooling set points and occupant behaviors and simulates them via EnergyPlus to obtain hourly heating energy and electricity requirement for producing data sets to construct ANN model. The model predicts heating energy efficiently; however, addition of electricity effect, its accuracy worsened although it still generates reasonable results.

In addition to the estimation of energy demand due to heating and cooling systems, there are ANN models proposed to estimate the general electricity consumption of buildings. Javeed et al. [18] developed a model to correlate electricity consumption with the weather and the occupancy of the residential buildings. González and Zamarreño [19] studied on a feedback based ANN to estimate hourly energy consumption in residential buildings. On the other hand, Azadehet al. [20] offered a model to estimate the annual electricity demand of energy intensive manufacturing buildings. There are also models tailored for office buildings in addition to industrial and residential buildings. Wong et al.[21] used an ANN model to estimate the electricity usage for cooling, heating, and lighting for office buildings with day-lighting controls in subtropical climates.

ANNs can also be used for the optimization of HVAC systems. Hou et al. [22] estimated air-conditioning load in a building, whereas Lee et al. [23] tried to detect and diagnose failures in the HVAC system. Aydinalp et al. [24] investigated the use of neural networks to estimate appliance, lighting and space cooling energy consumption in Canadian residential sector. In their follow-up work, neural network models were

developed to estimate the space and domestic hot-water heating energy consumptions in the same sector [25].

III. METHOD

In this study, among the various neural network types, a multi-layered feed forward neural network is implemented. This neural network is trained using back-propagation algorithm.

Implemented algorithm is capable of building a network according to the given configuration. Configurable topological parameters are the number of hidden layers and the number of perceptrons in each hidden layer. For instance, <4,8> represents two hidden layer network in which there are four percentrons in the first layer and eight perceptrons in the second layer. Other parameters are activation function types and learning rates.

Combinations of all four parameters were applied to the network for the same dataset to select best configuration(s) of parameters which minimize the error between estimated and expected outputs. 24 different solution sets presented in Table 1 including 4 topologies, 2 activation functions with 3 different learning rates are generated

Table 1: Configurable parameters and options

Topologies	Activation functions	Learning rates
<12> <20> <4,8> <3,5,8>	Linear: $y(x) = 0.1x$ Sigmoid: $y(x) = \frac{1}{1+e^{-x}}$	0.001 0.01 0.1

Activation functions which are available in the algorithm are linear and sigmoid functions. Feature values are all normalized to [0, 1] range to avoid divergence of weights. When using linear activation function, there is no need to normalize output values since linear functions can generate in the range of real numbers. However, when sigmoid function is chosen, the results are expected to be in the range of [0, 1]. Thus, activation function is not applied in perceptrons of the output layer. Therefore, the results generated by the network is not squeezed in between 0 and 1.

The best parameter set is determined by using Mean Absolute Error (MAE) as in (1). This metric is calculated using the average absolute differences between estimated (y_i) and expected ($\hat{y}_i$) output results.

$$MAE = \frac{1}{N}\sum_{i=1}^{N}\left|y_i - \hat{y}_i\right| \quad (1)$$

IV. DATASET

A previously generated data, which was created by Angeliki Xifara and processed by Athanasios Tsanas, was used in this study [26]. The dataset consists of 768 examples of building energy analysis results which were obtained using 12 different building shapes. The buildings differ from each other considering their glazing area, the glazing area distribution, and the orientation, amongst other parameters. The analyses were performed in in Ecotect software. In each analysis, heating and cooling load of the buildings are simulated using eight distinct features summarized in Table 2.

Table 2: Mathematical representation of the input (X) and output (Y) variables

X_1	Relative Compactness
X_2	Surface Area
X_3	Wall Area
X_4	Roof Area
X_5	Overall Height
X_6	Orientation
X_7	Glazing Area
X_8	Glazing Area Distribution
Y_1	Heating Load
Y_2	Cooling Load

V. RESULTS AND DISCUSSION

In this study, 4-fold cross-validation was applied to calculate the results of each combination to avoid fluctuations due to data order. The dataset were divided into four folds randomly and three of them were trained by ANN and tested with the remaining one. After applying this process for each fold, average accuracy of these folds result in the accuracy of the model built.

Among 24 trial solutions, the best results were obtained for the solution with <20> topology, sigmoid activation function and 0.01 learning rate parameter settings. It estimates heating and cooling loads with 0.35 and 0.8 error values. Other results considering combinations of topologies and activation functions and learning rates for best solution of these combinations are presented in Table 3.

Table 3: Configurations and their MAE results

Topology	Activation function	Learning rate	MAE Heating Load	MAE Cooling Load
<12>	Sigmoid	0.01	0.46	1.12
<20>	Sigmoid	0.01	0.35	0.80
<4,8>	Sigmoid	0.01	0.68	1.33
<3,5,8>	Sigmoid	0.001	1.52	1.07
<12>	Linear	0.01	2.18	2.36
<20>	Linear	0.01	2.18	2.36
<4,8>	Linear	0.001	2.16	2.42
<3,5,8>	Linear	0.001	2.16	2.42

The results indicate that heating and cooling load show nonlinear behavior; therefore, they can be modeled more efficiently with sigmoid activation function compared to the linear one. Moreover, topology does not directly determine the accuracy of the model. For heating load, as number of layers in the topology increases, ANN works more efficiently with linear activation functions while its performance worsens with sigmoid function. Therefore, synergy between topology and

activation function plays more prominent role in the accuracy improvement of the model. On the other hand, ANN generates more accurate solutions with smaller learning rates (0.01 and 0.001) whereas higher learning rate (0.1) decreases the convergence ability of the model for this dataset.

In previous studies, Tsanas and Xifara [26] developed a comprehensive framework to estimate heating and cooling loads using same dataset. They calculated the results using two different methods namely, Iteratively Reweighted Least Squares (IRLS) and Random Forests (RF). Performance of proposed ANN is compared with these two methods and presented in Table 4. The comparison demonstrates that, ANN generates competitive results and shows superior performance compared to both methods.

Table 4: Comparison of methods using MAE values

Objective	Proposed ANN	IRLS[26]	RF[26]
MAE Heating Load	0.35	2.14	0.51
MAE Cooling Load	0.80	2.21	1.42

VI. Conclusion

In this paper, we proposed an ANN model to provide fast and accurate building energy performance estimation by adjusting topologies, activation functions and learning rates of the model. The ANN generates comparable results to other AI algorithms. In the future studies, parameter set can be extended by implementing different activation functions and topologies to improve efficiency of the ANN. Moreover, deep learning algorithms can be applied to a more extensive dataset to see how efficiently deep learning works in building energy estimation.

References

[1] P. H. Shaikh, N. B. M. Nor, P. Nallagownden, I. Elamvazuthi, and T. Ibrahim, "A review on optimized control systems for building energy and comfort management of smart sustainable buildings," *Renew. Sustain. Energy Rev.*, vol. 34, pp. 409–429, Jun. 2014.

[2] N. Fumo, "A review on the basics of building energy estimation," *Renew. Sustain. Energy Rev.*, vol. 31, pp. 53–60, 2014.

[3] A. Foucquier, S. Robert, F. Suard, L. Stéphan, and A. Jay, "State of the art in building modelling and energy performances prediction: A review," *Renew. Sustain. Energy Rev.*, vol. 23, pp. 272–288, 2013.

[4] H. X. Zhao and F. Magoulès, "A review on the prediction of building energy consumption," *Renewable and Sustainable Energy Reviews*, vol. 16, no. 6. Pergamon, pp. 3586–3592, 01-Aug-2012.

[5] A. Chari and S. Christodoulou, "Building energy performance prediction using neural networks," *Energy Effic.*, vol. 10, no. 5, pp. 1315–1327, 2017.

[6] R. Kumar, R. K. Aggarwal, and J. D. Sharma, "Energy analysis of a building using artificial neural network: A review," *Energy Build.*, vol. 65, pp. 352–358, Oct. 2013.

[7] Z. Wang and R. S. Srinivasan, "A review of artificial intelligence based building energy use prediction: Contrasting the capabilities of single and ensemble prediction models," *Renewable and Sustainable Energy Reviews*, vol. 75. Pergamon, pp. 796–808, 01-Aug-2017.

[8] S. Kalogirou, C. Neocleous, and C. Schizas, "Building heating load estimation using artificial neural networks," in *Proceedings of Clima 2000 Conference*, 1997, pp. 1–8.

[9] T. Olofsson, S. Andersson, and R. Östin, "A method for predicting the annual building heating demand based on limited performance data," *Energy Build.*, vol. 28, no. 1, pp. 101–108, Aug. 1998.

[10] B. B. Ekici and U. T. Aksoy, "Prediction of building energy consumption by using artificial neural networks," *Adv. Eng. Softw.*, vol. 40, no. 5, pp. 356–362, May 2009.

[11] T. Olofsson and S. Andersson, "Long-term energy demand predictions based on short-term measured data," *Energy Build.*, vol. 33, no. 2, pp. 85–91, Jan. 2001.

[12] R. Yokoyama, T. Wakui, and R. Satake, "Prediction of energy demands using neural network with model identification by global optimization," *Energy Convers. Manag.*, vol. 50, no. 2, pp. 319–327, Feb. 2009.

[13] J. F. Kreider, D. E. Claridge, P. Curtiss, R. Dodier, J. S. Haberl, and M. Krarti, "Building Energy Use Prediction and System Identification Using Recurrent Neural Networks," *J. Sol. Energy Eng.*, vol. 117, no. 3, pp. 161–166, Aug. 1995.

[14] A. E. Ben-Nakhi and M. A. Mahmoud, "Cooling load prediction for buildings using general regression neural networks," *Energy Convers. Manag.*, vol. 45, no. 13–14, pp. 2127–2141, Aug. 2004.

[15] S. Kalogirou, "Artificial neural networks for the prediction of the energy consumption of a passive solar building," *Energy*, vol. 25, no. 5, pp. 479–491, May 2000.

[16] C. Yan and J. Yao, "Application of ANN for the prediction of building energy consumption at different climate zones with HDD and CDD," in *2nd International Conference on Future Computer and Communication*, 2010, pp. 286–289.

[17] F. Martellotta, U. Ayr, P. Stefanizzi, A. Sacchetti, and G. Riganti, "On the use of artificial neural networks to model household energy consumptions," *Energy Procedia*, vol. 126, pp. 250–257, Sep. 2017.

[18] S. Javeed Nizami and A. Z. Al-Garni, "Forecasting electric energy consumption using neural networks," *Energy Policy*, vol. 23, no. 12, pp. 1097–1104, Dec. 1995.

[19] P. A. González and J. M. Zamarreño, "Prediction of hourly energy consumption in buildings based on a feedback artificial neural network," *Energy Build.*, vol. 37, no. 6, pp. 595–601, Jun. 2005.

[20] A. Azadeh, S. F. Ghaderi, and S. Sohrabkhani, "Annual electricity consumption forecasting by neural network in high energy consuming industrial sectors," *Energy Convers. Manag.*, vol. 49, no. 8, pp. 2272–2278, Aug. 2008.

[21] S. L. Wong, K. K. W. Wan, and T. N. T. Lam, "Artificial neural networks for energy analysis of office buildings with daylighting," *Appl. Energy*, vol. 87, no. 2, pp. 551–557, Feb. 2010.

[22] Z. Hou, Z. Lian, Y. Yao, and X. Yuan, "Cooling-load prediction by the combination of rough set theory and an artificial neural-network based on data-fusion technique," *Appl. Energy*, vol. 83, no. 9, pp. 1033–1046, Sep. 2006.

[23] W. Y. Lee, J. M. House, and N. H. Kyong, "Subsystem level fault diagnosis of a building's air-handling unit using general regression neural networks," *Appl. Energy*, vol. 77, no. 2, pp. 153–170, Feb. 2004.

[24] M. Aydinalp, V. Ismet Ugursal, and A. S. Fung, "Modeling of the appliance, lighting, and space-cooling energy consumptions in the residential sector using neural networks," *Appl. Energy*, vol. 71, no. 2, pp. 87–110, Feb. 2002.

[25] M. Aydinalp, V. I. Ugursal, and A. S. Fung, "Modeling of the space and domestic hot-water heating energy-consumption in the residential sector using neural networks," *Appl. Energy*, vol. 79, no. 2, pp. 159–178, Oct. 2004.

[26] A. Tsanas and A. Xifara, "Accurate quantitative estimation of energy performance of residential buildings using statistical machine learning tools," *Energy Build.*, vol. 49, pp. 560–567, Jun. 2012.

Development of Blood Donation Application for Mobile Devices with Android Operating System

E.YESIL[1] and C. SUNGUR[2]

[1] Pamukkale University, Denizli/Turkey, eyesil@pau.edu.tr
[2]Selcuk University, Konya/Turkey, csungur@selcuk.edu.tr

***Abstract* - Blood can be considered to be one of the most basic elements of life, which can only be sourced by a human being whenever needed. Therefore, it is a sign of sacrifice to donate blood with the intention of meeting the needs of other individuals. When there is an urgent need for blood donation so that a person can maintain a healthy life, it is necessary to reach at donors as quickly as possible. In this study, it was aimed to bring together the individuals who want to donate blood in emergency situations and the individuals who are looking for blood. A blood donation application that can run in Android environments, which is one of the most common mobile operating systems today, has been developed. The application aims to bring together the volunteers wishing to donate blood with the individuals who are in need of blood, based on the province and district they are located in Turkey.**

***Keywords* - Android, Blood Donation, Application Development**

I. INTRODUCTION

Blood can be considered to be one of the most basic elements of life, which is produced and used by the body. Despite all the innovations both in the field of medicine and in the field of technology, an element of metabolism that is equivalent to human blood, has not been presented as an alternative, yet. Therefore, the need for blood can emerge in the event of an accident, during a major surgery, in a variety of blood diseases and in many other cases. In such a case, the blood is taken from a healthy person and transfused to the person in need of blood, which is defined as "Blood Donation" [1].

It is a sign of sacrifice to donate blood with the intention of meeting another individual's need for blood. This sacrifice is a result of the instinct to do favor to others. Blood donation is a voluntary act for which one expects no return [2]. It is necessary to increase the number of individuals who can voluntarily donate blood on a regular basis to meet the needs. The planning required to meet the current need at the fastest rate is a social obligation, indeed. The efforts to provide the blood and blood products needed are defined as the "national blood program" [3].

Within the frame of the national blood program, Turkey started operating the first blood donation centers under the body of the Turkish Red Crescent in 1957 in Istanbul and Ankara. While the percentage of the satisfaction of the need for blood was around 20% in the early years, this rate has reached 80% today. In cases where the need is not met, hospitals find alternative solutions such as blood exchange and compulsory blood donation as required by the need for flood. While the proportion of individuals making voluntary blood donations in developed countries is 5% of the total population, it is 3.6% in Turkey [4]. As the proportion of the number of blood donors is low compared to the total population, there is the increased risk of not being able to meet the needs for blood.

In the first stage of this study, the researches where mobile applications were developed to bring together the benevolent blood donors and the persons in need of blood, were reviewed. In the second part of the study, the applications reviewed in the literature were evaluated to develop a mobile application that can run on Android platforms. In the last part, the further developmental stages of the application were discussed.

II. EXAMPLES OF BLOOD DONATION APPLICATION

In this part of the study, examples of mobile applications in the literature on blood donation and blood need will be examined.

Turhan (2012) offers a location-based blood donor query in the blood donation application, which he named as 'RhPP' [5]. The user login screen of the application is shown in Figure 1.

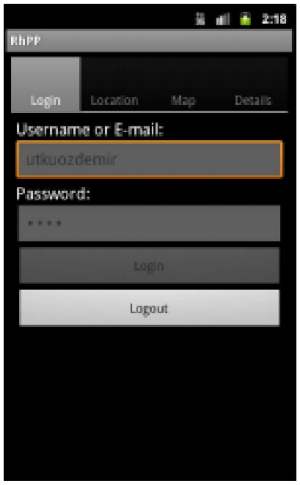


Figure 1: RhPP Login Screen [5]

As soon as the application is entered, it automatically updates location information at specific intervals. The application screen, where the update frequency is defined, is as shown in Figure 2.

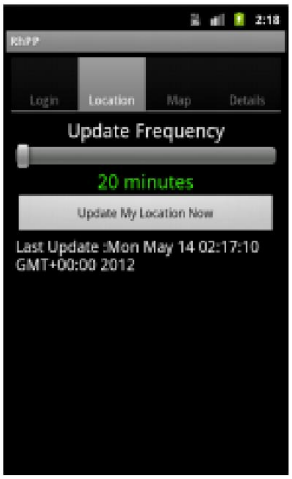


Figure 2: RhPP location update screen [5]

When the individual in need of blood is matched with the individual by the application, the location information of both users is shared with each other. The screen image showing the distance between them can be seen in Figure 3.

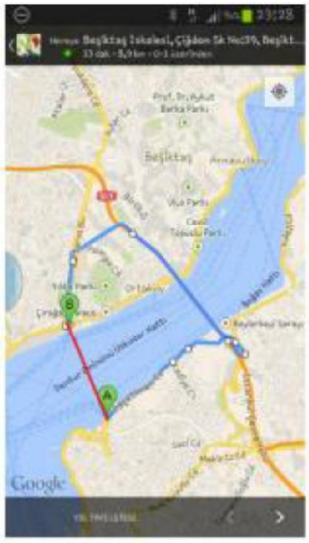


Figure 3: RhPP user matching screen [5]

In the application they developed, Kurlekar et al. (2017) created a registration screen for the user who wants to donate blood [6]. This screen is as shown in Figure 4.



Figure 4: Blood donation volunteer registration screen [6]

The registration screen of the application for the user who is looking for blood is shown in Figure 5.



Figure 5: The registration screen for the user who is looking for blood [6]

The application has a database of blood donors and the users looking for blood. The screen for data query is as shown in Figure 6. If the users are matched, the application sends a text message.



Figure 6: Data query screen [6]

In the application they developed, Sundarde et al. (2015) aimed to form blood donation teams [7]. An example from blood donation teams is shown in Figure 7.

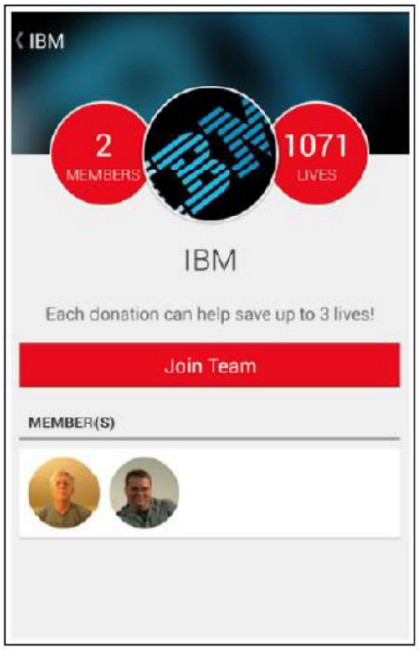


Figure 7: Blood donation team joining screen [7]

Blood donors in the team will score points for their team with each donation. The score chart of the application is shown in Figure 8.

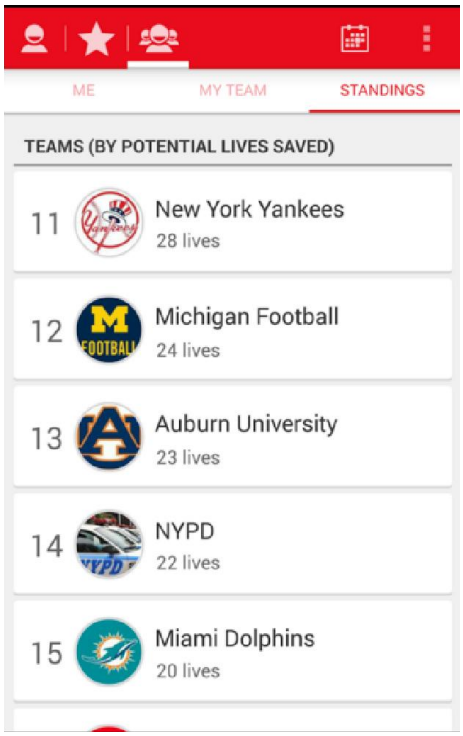


Figure 8: Blood donation team score chart [7]

The application offers small rewards to blood donation teams that rate high. The rewards screen is as shown in Figure 9.

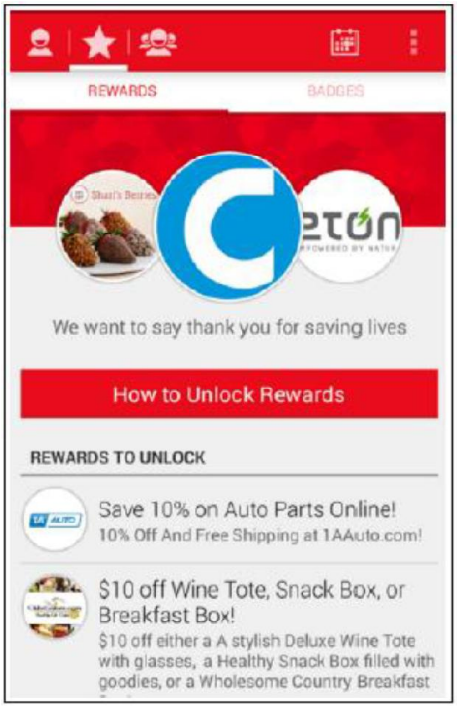


Figure 9: The Rewards Screen [7]

III. APPLICATION DEVELOPMENT

Following the review of the applications in the literature, the application development stage came. The user registration screen of the application is as shown in Figure 10.

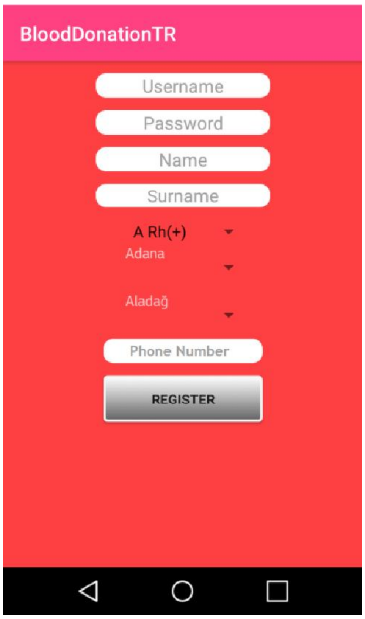


Figure 10: User registration screen

The login screen of the application is shown in Figure 11.

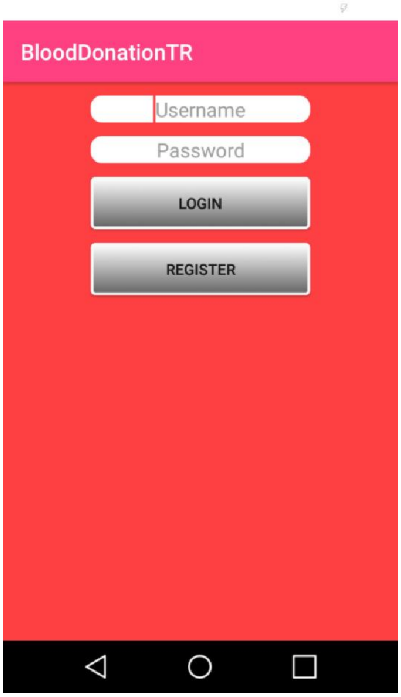


Figure 11: User login screen

Users who sign into the application can make province, district and blood group-based query. If a matching blood donor is found as a result of the query, his/her name, surname and phone number information are displayed on the screen. The query screen is as shown in Figure 12.

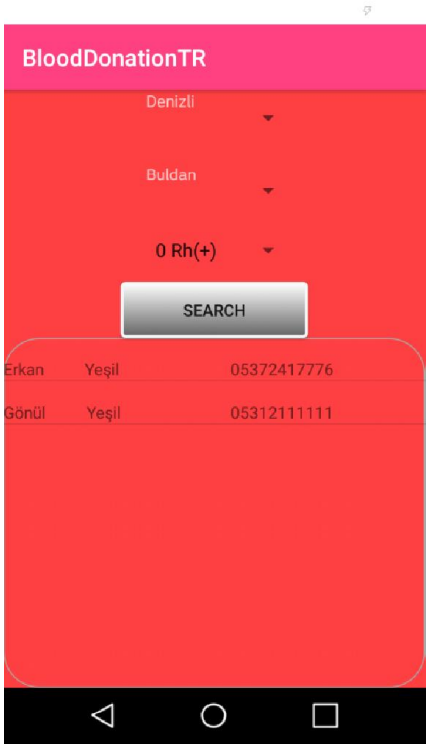


Figure 12: Query screen

IV. CONCLUSION AND RECOMMENDATIONS

In this study, three applications that bring together the blood donors and the ones looking for blood, were examined and a relevant application was developed.

The following updates are envisaged for the future versions of the developed application.

- Enabling communication via the application instead of providing the phone number information of the blood donor.
- Enabling query by using the location service
- Updating registration information

Encouragement of the use of mobile applications is recommended since it will be possible to reach a greater number of individuals through these applications in cases where the need for blood cannot be met.

REFERENCES

[1] Yıldız, Ç., Emekdaş, G., Kanık, A., Tiftik, N., Solaz, N., Aslan, G., Tezcan, S., Serin, M.S., Erden, S., Helvacı, İ., Otağ, F., Neden Kan Bağışlamıyoruz? Mersin İlinde Yaşayanlarda Kan Bağışına Genel Bakış: Anket Çalışması. *İnfeksiyon Dergisi* 20(1):41-55, 2006.

[2] Hablemitoğlu, Ş., Özkan, Y., & Yıldırım, U. F. (2010). Bir Fedakârlık Örneği Olarak "Kan Bağışı". *Sosyal Politika Çalışmaları Dergisi*, 20(20).

[3] Kaya, E., Sezek, F., & Doğan, S. (2007). Üniversite öğrencilerinin kan bağışına karşı tutumları ve kan bağışında alan bilgilerinin etkisinin incelenmesi. *Cankaya University Journal of Arts and Sciences*, 1(7).

[4] http://www.kanver.org/sayfa/e-kutuphane/dunyada-ve-turkiye-de-kan-bankaciligi/43 - Erişim Tarihi 26.10.2017

[5] Turhan, S., "An Android Application for volunteer Blood Donors" Department of Computer Engineering, Galatasaray University, Istanbul, TURKEY, 2012.

[6] Kurlekar, S. P., Pranali, K., Komal, R., Shrutika, M., & Aishwarya, M. (2017). Andriod APP for Quick Access of Blood Bank. *Journal of Embedded Systems and Processing*, 2(1).

[7] Sundarde, C., Jain, S., Shaikh E., (2015), Advancement of Blood Donation Application, online: http://www.academia.edu/download/40610251/AdvancementofBloodDonationApplications.pdf

A Feature-Based Comparison of SDN Emulation and Simulation Tools

S. ZAVRAK[1,2] and M. ISKEFIYELI[2]

[1] Duzce University, Duzce/Turkey, sultanzavrak@duzce.edu.tr
[2] Sakarya University, Sakarya/Turkey, miskef@sakarya.edu.tr

***Abstract* - Software-Defined Networking (SDN) is a network paradigm that facilitates network management by combining control functions on a centralized controller and enables network innovation with network programmability. Network testing environments are needed for developing novel solutions that are developed by utilizing the opportunities provided by SDN which contributes significantly to the future internet. There are many simulation and emulation software tools available in the literature that provide the necessary testing environment. In this study, a feature-based comparison of these tools is done features in terms of testbed mode, emulation approach, scalability, real controller support, etc.**

***Keywords* – Software-Defined Networking, emulation tools, simulation tools, OpenFlow.**

I. Introduction

Software Defined Networking (SDN) [1], is a new network paradigm that enables network devices to be managed by a centralized software controller. The purpose of SDN is to simplify network management and contribute to network innovation by enabling the capability of network programming [2]. The SDN architecture separates the control and data planes, which are the vertical integrations in the traditional networking devices, and moves the control functions to a central controller [3]. In the SDN architecture, it is important to provide communication between the central software controller and the data plane devices. OpenFlow [1, 4] is the protocol that emerged as a solution to this need by defining the messages between the controller and switches, and the internal structure of the switches. In SDN environments, because the control logic is managed entirely by the SDN controller, new controller implementations must be thoroughly tested and flawed before they are used in the targeted production networks [5].

There are several different approaches to testing the correctness and performance of a newly developed protocols in networks [7]. The first one is the necessity of performing tests on an experimental testbed, where the experimental environment created using real devices which are very expensive and thus, they cannot be used by most users. A second approach is the simulation which models the real devices and functions in a software environment. It is accepted by many users for reasons such as the use of simulation is scalable, low cost and fast compared to real time. An important disadvantage of using simulation is that results may differ significantly from experimental results if real devices and functions are not realistically simulated [6]. The third and final approach is emulation, which allows real devices and applications to be used and interaction between simulated devices.

Various simulation and emulation software have been developed to test applications developed for OpenFlow-enabled networks since the SDN architecture has come to the fore. These software tools have different characteristics as well as similar aspects. In this study, a feature-based comparison of certain simulation and emulation tools is made and a short review is presented depending on their problems or limitations.

The paper organized as follows. The SDN architecture is explained in Section2. In Section 3, the feature-based comparison of the simulation and emulation tools on SDN-based networks is done. In the last section, concluding remarks are stated.

II. Software-Defined Networking Architecture

The definition of SDN according to Open Networking Foundation (ONF) [7] is a new architecture that separates network control and forwarding functions from each other by making available the network control to be directly programmable and the infrastructure to be abstracted for network services and applications. In such an architecture, infrastructure devices act as simple forwarding engines that handle packets arriving according to several rules produced instantaneously by a controller in the control layer in accordance with pre-described program logic. The controller usually operates on a distant server and communicates over a secured connection through the forwarding elements employing a number of standardized instructions. ONF offers a top-level architecture that divides SDN vertically into three main functional layers [8].

- Infrastructure Layer: This layer, called as the data plane as well, is composed of Forwarding Elements that comprise physical and virtual switches which can be accessed by an open interface.
- Control Layer: This layer, also called as the control plane, is composed of a certain number of software-based SDN controllers that provide united control functionality over open APIs to manage network forwarding behavior over an open interface. Three different communication interfaces permit controllers to cooperate with each other: Southbound, Northbound, East/Westbound.

- Application Layer: This layer is composed mainly of end-user applications which use SDN communication and network services.

In Figure 1, some key parts of this architecture such as the infrastructure layer, the control layer and the application layer, and the communication interfaces between these three layers is illustrated in detail.

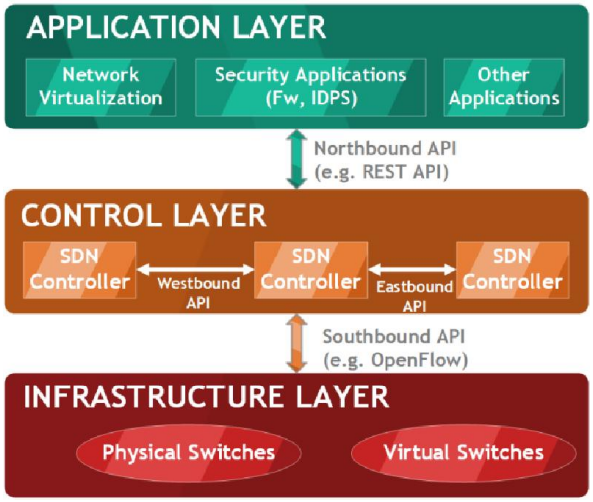


Figure 1: SDN Architecture

The forwarding elements (usually switches) must support a southbound API (usually OpenFlow) in order to be useful in the SDN architecture. The OpenFlow-enabled switch can be divided into three fundamental elements [1]. These elements are hardware layer (or data path), software layer (or control path), and OpenFlow protocol:

- The data path consists of one or more flow tables and a group table that perform packet search and forwarding. A flow table consists of flow entries associated with actions which tell how to handle the flow. The flow tables are usually filled in by the controller and allow to describe supplementary techniques of flow control.
- The control path is a channel that links the control to the switch for programming and signaling goals. Commands and packets are interchanged via this channel by employing the OpenFlow protocol.
- The OpenFlow protocol allows communication between switches and controllers. Modified messages can contain information such as received packets, sent packages, statistics gathering data and the actions to be performed in certain flows ... etc.

III. SDN-SUPPORTED SIMULATION AND EMULATION TOOLS

A. Emulation Tools

The aim of using simulation and emulation software is to build prototype of the network and test it at minimum cost without the need for physical devices. Many simulation and emulation tools were developed to simulate and emulate the switches which support OpenFlow protocol and SDN protocols.

The first study is Mininet [9] which focus on emulation of the SDN. Its main purpose is to afford a fast and simplicity for prototyping and evaluating SDN protocols and other controller applications. Mininet uses software-based OpenFlow switches in virtualized containers and in this way, provides the precise equivalent semantics of hardware-based OpenFlow switches. In other words, the controller or its applications implemented and tested in Mininet can be deployed in a real OpenFlow-enabled network without the need of any modification.

Mininet-HiFi [10] is developed on top of Mininet by improving the Container-Based (lightweight) Emulation which is an environment of switches, links, and virtual hosts runs on a modern multi-core server, using real application and kernel code with software-emulated network components. Mininet-HiFi includes mechanisms to impose resource provisioning, performance isolation, and precise monitoring for performance fidelity by using lightweight, OS-level virtualization methods. The improvement of the reproducibility of networking research is among the main purposes of Mininet-HiFi.

Mininet-WiFi [5] is a solution to emulate wireless SDN networks supporting high-fidelity experiments that imitate real networking environments. It is developed by extending the well-known emulator Mininet by adding the virtual wireless stations and access points built on the very popular Linux wireless device driver to the emulation platform in a way that will not compromise that the lightweight virtualization software architecture and the unique SDN abilities.

Mininet CE [11] and SDN Cloud DC [12] are implemented by extending Mininet to support large-scale network simulations. Because the natural restriction of Mininet consisting up to 2000 nodes in the emulated network makes an original form of Mininet barely applicable in the Global network, Mininet-CE tries to solve this limitation by placing upper level software over Mininet that could combine several separate instances of Mininet into one Cluster, which is virtual or physical machine with Linux Operating System.

SDN Cloud DC [12] is a novel framework permitting to implement and evaluate new OpenFlow–supported controllers for Cloud Datacenters. The framework is developed by enhancing both Mininet and POX controller with all the software modules required to emulate novel management and control network resources (SDN-based intra-DC network) policies of IT such as network traffic generation, DC topology discovery, etc.

Recently, the emulation platforms based on distributed approach were proposed in order to enable large-scale experiments. One of these is MaxiNet [13] which is developed by improving Mininet to extend over an emulated network over numerous physical machines. In this way, several thousand nodes can be emulated and this allows large scale network (e.g. data center networks) experiments.

Another emulation platform based on distributed approach is Distributed OpenFlow Testbed (DOT) [14], which allows provisioning the emulated network through a cluster of physical or virtual machines. The platform of DOT offers promised network and computing resources for the emulated elements (i.e., switches, links, and hosts) different from Mininet and thus

Table 1: The feature-based comparison of emulation and simulation tools

Name	Testbed mode	Emulation Approach	Programming Language	OpenFlow version	Scalability (Targeted Networks)	Real Controller Support	GUI Support	Price
Mininet [9]	Emulation	Centralized	Python	1.3	Middle (up to 2000 nodes)	Yes	Yes	Free
Mininet-HiFi [10]	Emulation	Centralized	Python	1.3	Large	Yes	Yes	Free
Mininet-Wifi [5]	Emulation	Centralized	Python	1.3	Middle (Wireless Networks)	Yes	Yes	Free
Mininet-CE [11]	Emulation	Centralized (Multiple Mininet instances)	Python	1.3	Large	Yes	Yes	Free
SDN Cloud DC [12]	Emulation	Centralized	Python	1.3	Large (e.g. DC networks)	Yes (POX)	Yes	Free
MaxiNet [13]	Emulation	Distributed (Multiple virtual machines)	Python	1.3	Large (e.g. DC networks)	Yes	Yes	Free
DOT [14]	Emulation	Distributed (Multiple virtual machines)	C++	1.3	Large (e.g. DC networks, wide-area networks)	Yes	Yes	Free
ns-3 [15]	Simulation	-	C++	0.8.9	Large	No	Yes	Free
fs-sdn [16]	Simulation	-	Python	1.3	Large	Yes	Yes	Free
Estinet [17]	Emulation & Simulation	Centralized	C/C++	1.3	Large (also Wireless networks)	Yes	Yes	Commercial

can simply scale with network traffic volume and network size to emulate such as large data centers and wide-area networks.

B. Simulation Tools

Because the OpenFlow-enabled switches are incorporated to ns-3 simulation platform [15], which is recent version of ns-2, it can be used to simulate OpenFlow-enabled networks. It allows the configuration of switches via OpenFlow API. It currently supports OpenFlow 0.8.

Another simulation tool is fs-sdn [16], which is developed by extending the fs simulation engine [18] by integrating OpenFlow-enabled controller and switching elements. The main purpose of this simulator is to concentrate the problem of prototyping and evaluating newly developed SDN-supported controller applications precisely, quickly, at large scale, thus allowing simple transition to real-world controller software like POX [19] and NOX [20].

The last one is EstiNet [17], which is commercial network simulation program. It has the characteristics of both simulator and emulator tools all together, and is used to test the functions and evaluate the performances of OpenFlow-enabled networks and controller applications. The main idea of EstiNet is to use a unique kernel reentering simulation methodology to enable unchanged real applications to function on nodes in its simulated network [21]. Therefore, real controllers such as NOX/POX [19, 20] or Floodlight [22], can smoothly operate on a host in an EstiNet simulated network to command hundreds of simulated OpenFlow-enabled elements. Because EstiNet uses real-world OpenFlow controllers, network applications, and TCP/IP protocol stack, it produces accurate, and reproducible SDN-based controller application performance results.

IV. Conclusion

Several emulation and simulation tools are developed to test and evaluate SDN-based networks. We concisely review them by comparing the features in terms of testbed mode, emulation approach, scalability, real controller support, etc. According to feature-based comparison, Mininet is most appropriate solution to middle scale networks. On the other hand, the tools such as Mininet-CE, SDN Cloud DC, MaxiNet, and DOT are mostly suitable for large scale networks. Because the limitations of ns-3 such as only supporting outdated OpenFlow version, and not supporting external controller, it is not suitable to model updated SDN environments. Estinet is most suitable tool, because it can be used to model both wired and wireless networks beside the disadvantage of being commercial.

As a future work, we plan to make performance-based comparison of these tools under specific scenarios.

Acknowledgment

S. Zavrak is supported by The Scientific and Technological Research Council of Turkey (TUBITAK) under 2211/C PhD

Scholarship Programme for Priority Areas.

REFERENCES

[1] N. McKeown *et al.*, "OpenFlow: enabling innovation in campus networks," *SIGCOMM Comput. Commun. Rev.,* vol. 38, no. 2, pp. 69-74, 2008.

[2] D. Kreutz, F. M. V. Ramos, P. E. Verissimo, C. E. Rothenberg, S. Azodolmolky, and S. Uhlig, "Software-Defined Networking: A Comprehensive Survey," *Proceedings of the IEEE,* vol. 103, no. 1, pp. 14-76, 2015.

[3] B. A. A. Nunes, M. Mendonca, X.-N. Nguyen, K. Obraczka, and T. Turletti, "A Survey of Software-Defined Networking: Past, Present, and Future of Programmable Networks," *IEEE Communications Surveys & Tutorials,* vol. 16, no. 3, pp. 1617-1634, 2014.

[4] *The OpenFlow Switch Specification*. [Online]. Available: http://OpenFlowSwitch.org. [Accessed: 30 November 2017].

[5] R. R. Fontes, S. Afzal, S. H. Brito, M. A. Santos, and C. E. Rothenberg, "Mininet-WiFi: Emulating software-defined wireless networks," in *Network and Service Management (CNSM), 2015 11th International Conference on*, 2015, pp. 384-389: IEEE.

[6] S.-Y. Wang, C.-L. Chou, and C.-M. Yang, "EstiNet openflow network simulator and emulator," *IEEE Communications Magazine,* vol. 51, no. 9, pp. 110-117, 2013.

[7] *Open Networking Foundation*. [Online]. Available: https://www.opennetworking.org/. [Accessed].

[8] ONF, "Software-Defined Networking: The New Norm for Networks," 2012, Available: http://www.opennetworking.org/images/stories/downloads/sdn-resources/white-papers/wp-sdn-newnorm.pdf.

[9] Mininet Team. *Mininet: An Instant Virtual Network on your Laptop (or other PC) - Mininet*. [Online]. Available: http://mininet.org/. [Accessed: 30 November 2017].

[10] N. Handigol, B. Heller, V. Jeyakumar, B. Lantz, and N. McKeown, "Reproducible network experiments using container-based emulation," in *Proceedings of the 8th international conference on Emerging networking experiments and technologies*, 2012, pp. 253-264: ACM.

[11] V. Antonenko and R. Smelyanskiy, "Global network modelling based on mininet approach," presented at the Proceedings of the second ACM SIGCOMM workshop on Hot topics in software defined networking, Hong Kong, China, 2013.

[12] J. Teixeira, G. Antichi, D. Adami, A. Del Chiaro, S. Giordano, and A. Santos, "Datacenter in a box: Test your sdn cloud-datacenter controller at home," in *Software Defined Networks (EWSDN), 2013 Second European Workshop on*, 2013, pp. 99-104: IEEE.

[13] P. Wette, M. Draxler, A. Schwabe, F. Wallaschek, M. H. Zahraee, and H. Karl, "Maxinet: Distributed emulation of software-defined networks," in *Networking Conference, 2014 IFIP*, 2014, pp. 1-9: IEEE.

[14] A. R. Roy, M. F. Bari, M. F. Zhani, R. Ahmed, and R. Boutaba, "Design and management of DOT: A Distributed OpenFlow Testbed," in *Network Operations and Management Symposium (NOMS), 2014 IEEE*, 2014, pp. 1-9.

[15] ns3. *OpenFlow switch support — ns-3 vns-3-dev documentation*. 2017, [Online]. Available: https://www.nsnam.org/docs/release/3.13/models/html/openflow-switch.html. [Accessed: 29 November 2017].

[16] M. Gupta, J. Sommers, and P. Barford, "Fast, accurate simulation for SDN prototyping," presented at the Proceedings of the second ACM SIGCOMM workshop on Hot topics in software defined networking, Hong Kong, China, 2013.

[17] EstiNet. *EstiNet 9.0 Simulator*. [Online]. Available: http://www.estinet.com/ns/?page_id=21140. [Accessed: 30 November 2017].

[18] J. Sommers, R. Bowden, B. Eriksson, P. Barford, M. Roughan, and N. Duffield, "Efficient network-wide flow record generation," in *INFOCOM, 2011 Proceedings IEEE*, 2011, pp. 2363-2371: IEEE.

[19] *The POX Controller* 2017, [Online]. Available: https://github.com/noxrepo/pox. [Accessed: 30 Novemver 2017].

[20] *NOX SDN Controller*. 2017, [Online]. Available: http://www.noxrepo.org/. [Accessed: 30 November 2017].

[21] W. Shie-Yuan, C. Chih-Liang, and Y. Chun-Ming, "EstiNet openflow network simulator and emulator," *Communications Magazine, IEEE,* vol. 51, no. 9, pp. 110-117, 2013.

[22] Floodlight. *Floodlight OpenFlow Controller*. [Online]. Available: http://www.projectfloodlight.org/floodlight/. [Accessed: 30 November 2017].

Human Activity Recognition on Smartphones using a Multiclass Artificial Neural Network

Ali YASAR[1], Ismail SARITAS[2]

[1] ComputerProgramming, Guneysinir Vocational School of Higher Education Selcuk University Guneysinir, Konya, 42190, aliyasar@selcuk.edu.tr,+905055204696

[2]Faculty of Technology, Electrical and Electronics Engineering Selcuk University, Konya, 42031

***Abstract* - Ten years ago, it was not foreseen that there would be such a huge increase in the use of mobile phones and that there would be a wide variety of competitions that can compete with today's applications. We can understand that the increase in the interest of most adults in mobile applications should not lower their mobile phones from their hands; which clearly demonstrates how mobile phones penetrate people's lives and how today's society has become an inseparable part. Ever since the development of smartphones, people are more and more interested in getting new applications and games every day. In our work, a classification study has been conducted to determine what activities people have through smartphones. In our study, the Human Activity Recognition database was built from the recordings of 30 study participants performing activities of daily living (ADL) while carrying a waist-mounted smartphone with embedded inertial sensors. The objective is to classify activities into one of the six activities performed. Artificial neural network (ANN) was used for classification and R = 99,942%. This is a high success for classification.**

***Keywords* - Smartphone, Human Activity, ANN**

I. INTRODUCTION

Mobile communication is now widely recognized as a technology leader and solution provider in urban areas and remote locations all over the world. As of the end of 2011, universal mobile connections reached a value of 6 billion, which is comparable to 87% of the world population. On the other hand, these values, which were 5.4 in 2010 and 4.7 billion in 2009, show a considerable increase in mobile subscription [1].

Activity Based Computation [2] seeks to capture the situation of the user and its environment by using heterogeneous sensors to adapt to outsourced computing resources. When these sensors are connected to the body of cismin, they allow continuous monitoring of a large number of physiological signals. This has an attractive use in health care applications; Use of Ambient Intelligence (AMI) in daily activities for older people. In this article, we present a system for human Physical Activity Recognition (AR) using smartphone inertial sensors.

Our work has been classified with ANN using the Human Activity Recognition with Smartphones data at https://www.kaggle.com/uciml/human-activity-recognition-with-smartphones

1. Material and Methodolgy

The experiments have been carried out with a group of 30 volunteers within an age bracket of 19-48 years. Each person performed six activities (WALKING, WALKING_UPSTAIRS, WALKING_DOWNSTAIRS, SITTING, STANDING, LAYING) wearing a smartphone (Samsung Galaxy S II) on the waist. Using its embedded accelerometer and gyroscope, we captured 3-axial linear acceleration and 3-axial angular velocity at a constant rate of 50Hz. The experiments have been video-recorded to label the data manually. In the process, 2947 samples were classified.

The sensor signals (accelerometer and gyroscope) were pre-processed by applying noise filters and then sampled in fixed-width sliding windows of 2.56 sec and 50% overlap (128 readings/window). The sensor acceleration signal, which has gravitational and body motion components, was separated using a Butterworth low-pass filter into body acceleration and gravity. The gravitational force is assumed to have only low frequency components, therefore a filter with 0.3 Hz cutoff frequency was used. From each window, a vector of features was obtained by calculating variables from the time and frequency domain[3].

For each record in the dataset, the following are provided:

• Triaxial acceleration (total acceleration) from the acceleration and estimated body acceleration.

• Triaxial angular velocity from gyroscope.

• A 561-specific vector with time and frequency domain variables.

• Activity tag.

• An identifier of the person performing the experiment.

Recognition of Human Activity is an active research area in which methods of understanding human behavior are developed by interpreting characteristics derived from movement, location, physiological signals and environmental information. This field is the first component of the index to access Intelligent Interaction (cognition) in conjunction with Cognitive Environments, data analysis, decision making and action [4,5] and our research topic[6].

2.1. Artificial Neural Network

Today we live in computer age and systematically we are on the way to creating artificial intelligence. In addition, one of the possible ways in which AI can take place is to find ways to generalize the patterns. Solving this problem will not only help us to create a program that generates thought, but also to understand how we think.

20. Beginning in the middle of the century, scientists have developed a set of mathematical models and algorithms that are widely used in pattern recognition and classification of objects. These models are now called artificial neural networks. Now there are many different architectures of good neural networks in certain tasks. For example, the basic tasks that can be solved using this technology are:

1. Clustering

2. Forecast

3. Model recognition

4. Decision-making and management

5. Data compression

6. Approach

Artificial neural networks are one of the most popular aspects of research now. Our programs based on this technology may no longer speak, recognize the model of different objects, but do not understand the meaning of these things. Now there are various AI-related experiments in the artificial intelligence world that encourage the submersion of humanity. When it comes to thinking, your future in IT will depend on research in this area, which will help to develop the highest technology of all time[7].

The artificial neural network model that constitutes our system is shown in Fig. 1. [8].

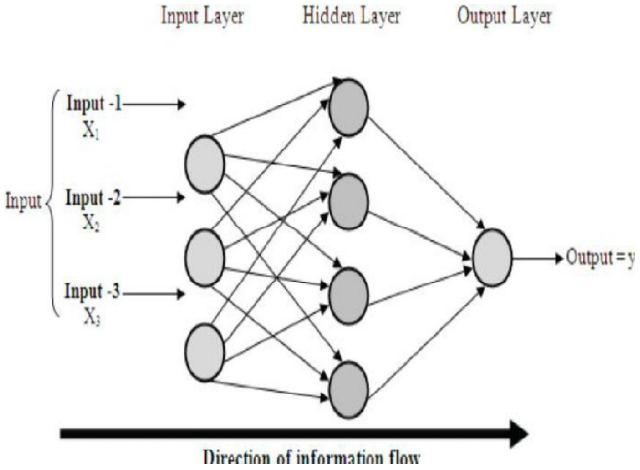


Fig. 1. The structure of ANN

2.2. Artificial Neural Network Application For A Data Set

In this study, the following transactions are performed for determining if the Human Activity Recognition Using Smartphones Data Set are human activity the data set of 1,372 units of Human Activity Recognition Using Smartphones Data Set.

- As testing data, 206 units (15%) of data have been chosen randomly.
- As validation data, 206 units (15%) of data have been chosen randomly.
- As training data, the remaining 960 units (70%) of data have been chosen.

In this study, a feed forward network structure that contains an input layer, a hidden layer and an output layer (Fig. 1) was used. The Back Propagation algorithm was used in the training procedure.

The regression graph of the training data set is shown in Fig. 2.

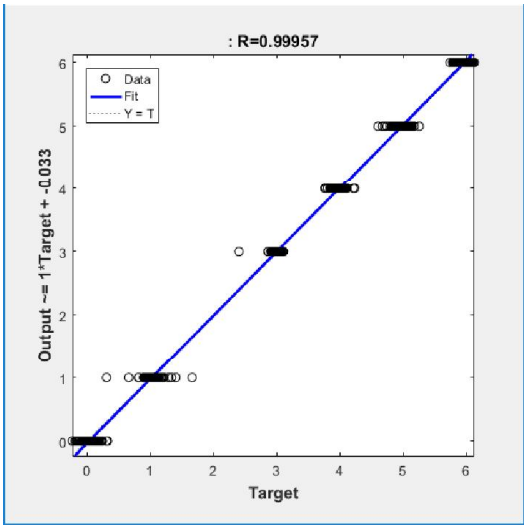


Fig. 2 Regression of Training Data Set

The regression graph of the testing data set is shown in Fig. 3.

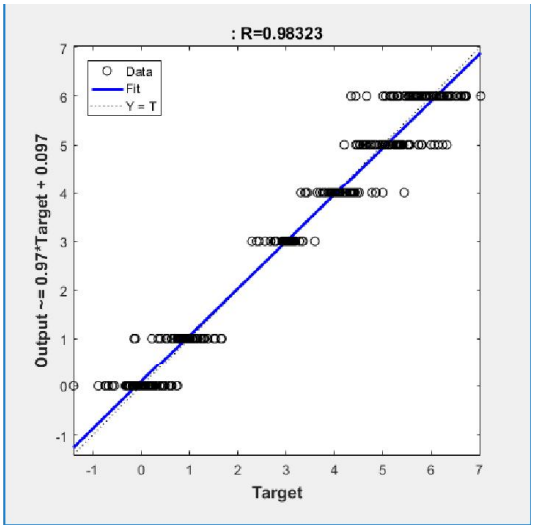


Fig. 3 Regression of Testing Data Set

The regression graph of the validation data set is shown in Fig. 4.

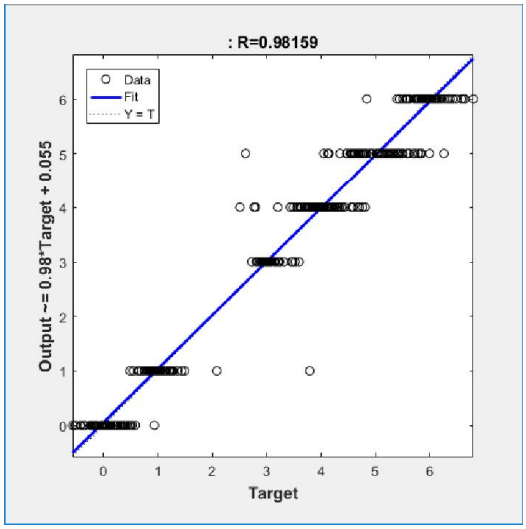


Fig. 4 Regression of Training Data Set

The regression graph of the output is shown in Fig. 5.

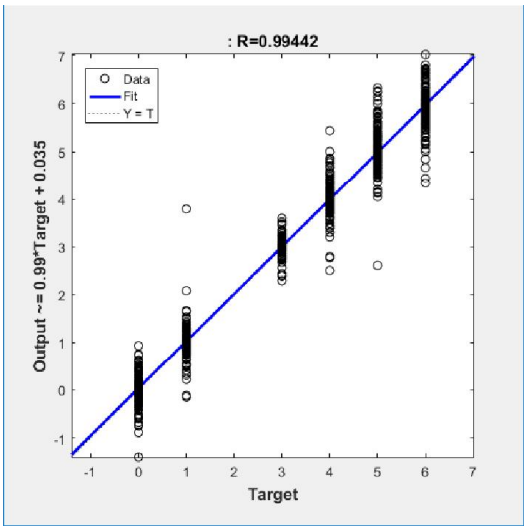


Fig. 5 Regression of Output Set

2. Result and Discussion

The comparison of experimental measurement values for Human Activity Recognition Using Smartphones test data set and ANN estimation values are shown in Fig. 6. All the randomly selected data used for test is different than the data used for training process.

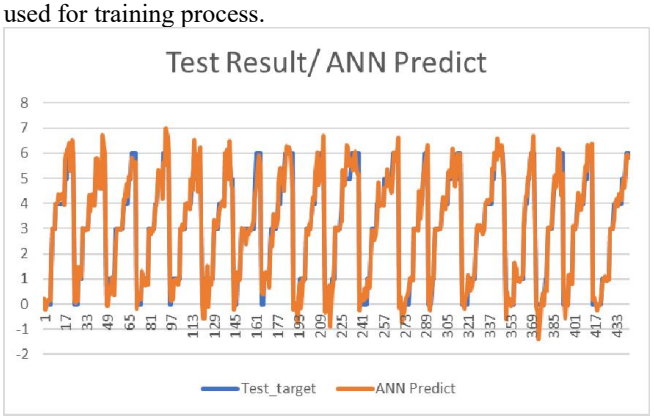


Fig. 6 Test Result / ANN Predict

The comparison of experimental measurement values for Human Activity Recognition Using Smartphones validation data set and ANN estimation values are shown in Fig. 7. All the randomly selected data used for validation is different than the data used for training process

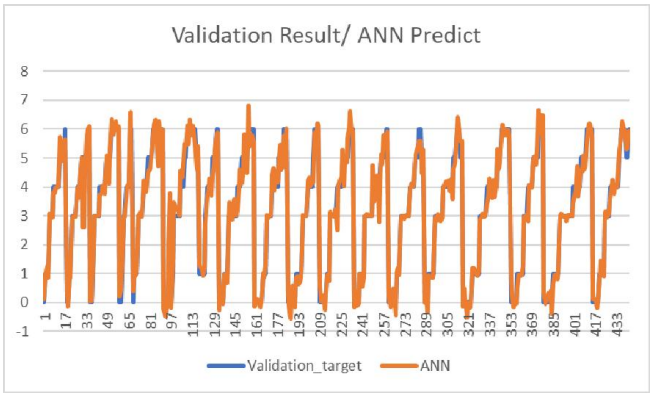


Fig. 7 Validation Result / ANN Predict

Finally, the graph of the values obtained from the remaining data which is the estimation of ANN is shown in Fig. 8.

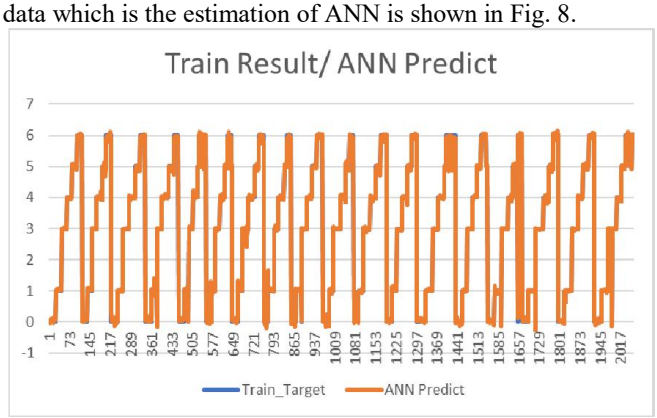


Fig. 8 Train Result / ANN Predict

As seen in the figures, the estimation results and dataset results are almost overlapping. The deviation between experimental and estimated results is very small and negligible for any Human Activity Recognition Using Smartphones performance.

3. CONCLUSIONS

In this study, it has been concluded that ANN can be used in the clustering procedure and better results can be achieved. According to the results, it has been observed that 99% and above classification accuracy can be achieved

(1) ACKNOWLEDGEMENTS

This study has been supported by Selcuk University's Scientific Research Unit (BAP). Contributors gratefully acknowledge support of their work by the Institute of Agrophysics of the Polish Academy of Sciences in Lublin and http://archive.ics.uci.edu/ml/index.html and https://www.kaggle.com/uciml/human-activity-recognition-with-smartphones

REFERENCES

[1] Çınar, S., 2014, Mobil Android Ortamında Parmak İzi Tanıma ve Kimlik Doğrulama Sisteminin Geliştirilmesi. Yüksek Lisans Tezi.

[2] Davies, N., Siewiorek, D.P., Sukthankar, R.: Activity-based computing. IEEE Pervasive Computing 7(2), 20–21 (2008)

[3] https://www.kaggle.com/uciml/human-activity-recognition-with-smartphones [Last Access: 15 Ekim 2017]

[4] R. Parasuraman, T.B. Sheridan, and C.D. Wickens. A model for types and levels of human interaction with automation. IEEE Transactions on Systems, Man and Cybernetics,30(3):286 –297, may 2000.

[5] M Gandetto, L Marchesooti, S Sciutto, D Negroni, and CS Regazzoni. From multi-sensor surveillance towards smart interactive spaces. In IEEE International Conference on Multimedia and Expo, volume 1, pages I–641, 2003.

[6] Reyes-Ortiz, J. L., Ghio, A., Parra, X., Anguita, D., Cabestany, J., & Catala, A. (2013, April). Human Activity and Motion Disorder Recognition: towards smarter Interactive Cognitive Environments. In ESANN.

[7] Teslenko, S., Korotenko, L. M., & Nechai, N. M. (2017). Artificial neural networks.

[8] Kabir, G., & Hasin, M. A. A. (2013). Comparative analysis of artificial neural networks and neuro-fuzzy models for multicriteria demand forecasting. International Journal of Fuzzy System Applications (IJFSA), 3(1), 1-24.A.K. Geim, I. V. Grigorieva, van Waals Heterostructure. Nature 499 (July(7459)) (2013) 419–425.

Performance Comparison of Different Sized Regions of Interest on Fish Classification

BİLAL İŞÇİMEN[1*], YAKUP KUTLU[2], CEMAL TURAN[3]

[1] Kirikhan Vocational School, Mustafa Kemal University, Hatay/Turkey, biscimen@mku.edu.tr
[2] Faculty of Engineering and Natural Sciences, Iskenderun Technical University, Hatay/Turkey, yakup.kutlu@iste.edu.tr
[3] Faculty of Marine Sciences and Technology, Iskenderun Technical University, Hatay/Turkey, cemal.turan@iste.edu.tr

Abstract - **In this study, different sized regions of interest were obtained from fish images and these were used for fish species classification. A previously proposed region of interest obtaining method was upgraded in order to acquire wider regions of interest. Depending on general accuracies of classification performances, comparison between these regions of interest was made. According to comparison results the effects of the different sized regions of interest were discussed for classification purposes of fish species. This study was performed by using a database which consists of 1321 fish images. These fish images include fish samples from 16 fish families and 35 fish species. All images were colored in RGB color space. But two different feature sets were extracted for fishes by examining images both in RGB and HSV color spaces. Feature extraction was performed by using a color based method. For each color space, seven statistical features were extracted from each component of the color space. Two feature sets were acquired for each fish sample by combining the extracted statistical features according to color spaces. The obtained feature sets from RGB and HSV color spaces were used separately for classification purposes. Classification was performed according to families and species by using Nearest Neighbor algorithm as classifier. According to classification results, the best performances on general accuracies were achieved as 93.5% and 91% for fish families and species classification respectively.**

Keywords – **Fish classification, fish species, ROI, color based classification**

I. INTRODUCTION

Automatic fish classification systems' development is getting an important task. The requirement of fish classification systems is rising from the reason that they can be used by researchers for the purposes of fish counting, stock assessments, evaluating ecological impacts, monitoring fish behavior, and ext. [1]. Additionally, the scientists believe that there are more than 1200 venomous fish species in over 24600 different fish species in the world. Avoiding from harms of the venomous species can be possible by making use of fish classification systems. In spite of the necessity for fish classification, it is a difficult task to be performed manually. The developments in computer technologies offer an insight into computer vision and image processing methods to be getting commonly used for the purposes of fish classification.

There are some studies using various features in order to classify fishes. Kutlu et al. proposed a multistage system that can separate fishes taxonomically in three stages by using morphological shape properties within Nearest Neighbor algorithm [2]. Kutlu et al. performed a fish species classification system utilizing Deep Belief Networks by using morphometric measurements [3]. Maasz et al. identified fish species with a high accuracy by applying MALDI-TOF MS method in order to extract features [4]. Hasija et al. performed the classification of fish species by using a novel method which is based on an improved image-set matching approach, which makes use of Graph-Embedding Discriminant Analysis [5]. Siddiqui et al. presented a computer vision method which is based on deep learning techniques. A cross-layer pooling algorithm using a pre-trained Convolutional Neural Network as a generalized feature detector is proposed in this work. Classification was performed by a SVM classifier for fish species from underwater video imagery [6]. Bothmann et al. used under water sonar videos to extract features which are based on shape and movement of the fishes in order to present a real time fish classification system [7]. Shafait et al. presented an image set based approach for fish species identification by utilizing from Principal Component Analysis [8]. Chuang et al. presented an unsupervised feature learning and object recognition system by using geometric attributes of the fish body within a hierarchical partial classifier [9]. Mizuno et al. performed the classification purpose by using normalized cross correlation obtained from a new method using high resolution acoustic video camera [10]. Ogunlana et al. presented a Support Vector Machine based method for fish classification by extracting the body and five fin lengths of the fishes as features [11]. Iscimen et al. presented a method which is based on centroid-contour distances of fish images in order to classify fish species with two dorsal fins [12]. Iscimen et al. presented a Naive Bayesian classifier based system for fish families and species classification by using biometric measurement techniques [13]. D'Elia et al. used frequency response, morphometric, bathymetric or other energetic parameters as features within a multi-frequency acoustics approach to detect and classify fish species [14]. Fabic et al. described a method by using blob counting and Zernike moment-based shape analysis for fish detection, counting, and

species classification from underwater video sequences [15]. Alsmadi et al. presented a fish recognition system based on features extraction from size and shape measurements using neural network [16]. Cabreira et al. applied methods on digital echo recordings of schools which involving artificial neural networks (ANNs) for the automatic recognition and classification. Energetic, morphometric, and bathymetric school descriptors were extracted from the echo-recordings as the input for the ANNs [17].

Also, there are some studies taking advantage of color and texture features for fish classification purposes. Iscimen et al. proposed a color based method for fish species classification which is using statistical features extracted from different color space's components [18, 19]. Daramola et al. proposed a method by using Singular Value Decomposition in order to extract features of fish body pattern [20]. Huang et al. presented a balance-enforced optimized tree with reject option for the purpose of live fish recognition. The proposed system is using features which are a combination of color, shape and texture properties [21]. Hernández-Serna et al. obtained a combination of geometrical, morphological, and texture features which are extracted by using image processing methods. Fish identification was performed by using the obtained feature set within an Artificial Neural Networks classifier [22]. Chuang et al. presented an underwater fish species recognition system by using a systematic hierarchical partial classification algorithm. The extracted features are consist of size, shape and texture attributes of fish body parts [23]. Hu et al. presented a method for classifying fish species based on color and texture features by using a multi-class support vector machine [24]. Alsmadi et al. presented a fish recognition system based on features extraction from color texture measurements by using back-propagation classifier [25].

The aim of this study is obtaining wider regions of interest on fish images by upgrading a previously proposed method [18] and making comparison between classification performances of the fishes according to these regions of interest. The obtained regions of interest were used within a color based statistical feature extraction method. The features were extracted by examining images both in RGB and HSV color spaces and the acquired feature sets were used in classification separately. Classifications were performed according to families and species. The proposed system is performing various image processing methods for mentioned purposes and these are explained in detail in remaining of the paper.

II. MATERIALS AND METHODS

The structure of the proposed system is consists of data acquiring, preprocessing, feature extraction, classification and performance measurement phases. Details of the processes are described in the following subsections.

A. Acquiring the Database

A fish database which consists of 1321 fish images was used in this study. In each image, a fish was located on a white background floor with the same position and the images were taken from different distances. Figure 1 shows a sample of taken images. The database totally consists of 35 fish species from 16 fish families. Each species include different numbers of samples. Table 1 shows variance of the collected database. The definition of species and systematic discrimination were performed according to [26].

Table 1: Variance of the collected database

Families Name	**Species Name**	**Number of Fish Samples**
Apogonidae	*Apogon queketti*	18
Apogonidae	*Apogon smithi*	29
Carangidae	*Caranx rhoncus*	8
Dactyloperidae	*Dactylopterus volitans*	26
Haemulidae	*Pomadasys stridens*	116
Moronidae	*Dicentrarchus labrax*	30
Moronidae	*Dicentrarchus punctatus*	18
Mullidae	*Mullus barbatus*	15
Mullidae	*Mullus surmuletus*	44
Mullidae	*Upeneus mollucensis*	19
Nemipteridae	*Nemipterus randalli*	18
Sciaenidae	*Argyrosomus regius*	21
Sciaenidae	*Sciaena umbra*	9
Sciaenidae	*Umbrina cirrosa*	5
Scombridae	*Sarda sarda*	128
Serranidae	*Epinephelus aeneus*	38
Serranidae	*Epinephelus caninus*	15
Serranidae	*Epinephelus costae*	108
Serranidae	*Epinephelus marginatus*	124
Serranidae	*Hyporthodus haifensis*	17
Serranidae	*Mycteroperca rubra*	33
Sparidae	*Diplodus annularis*	5
Sparidae	*Lithognathus mormyrus*	7
Sparidae	*Oblada melanura*	15
Sparidae	*Pagellus erythrinus*	9
Sparidae	*Pagrus caeruleostictus*	5
Sparidae	*Sparus aurata*	50
Sphyraenidae	*Sphyraena sphyraena*	26
Synodontidae	*Saurida undosquamis*	22
Teraponidae	*Pelates quadrilineaetus*	18
Tetraodontidae	*Lagocephalus suezensis*	5
Triglidae	*Aspitrigla cuculus*	22
Triglidae	*Chelidonichthys lastoviza*	98
Triglidae	*Chelidonichthys lucernus*	141
Triglidae	*Trigla lyra*	59
Total Number of Samples		**1321**



Figure 1: A sample of taken images from database

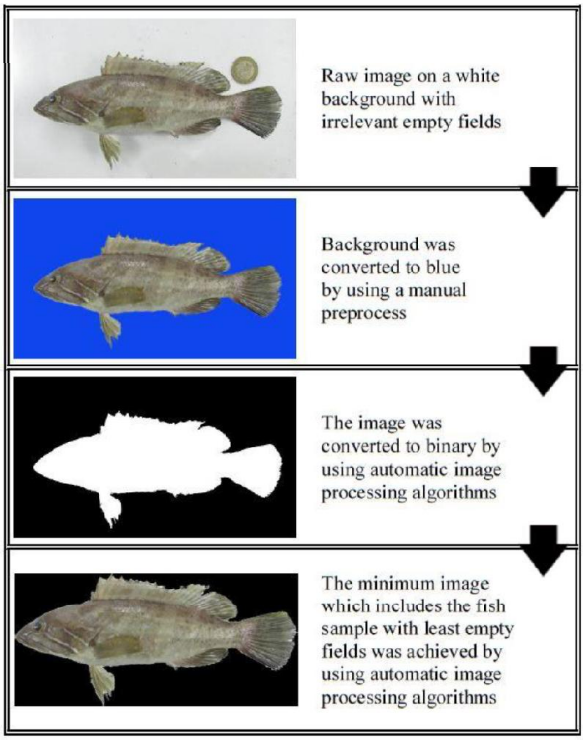


Figure 2: Image processing phases from raw image to gained minimum image which includes the fish sample

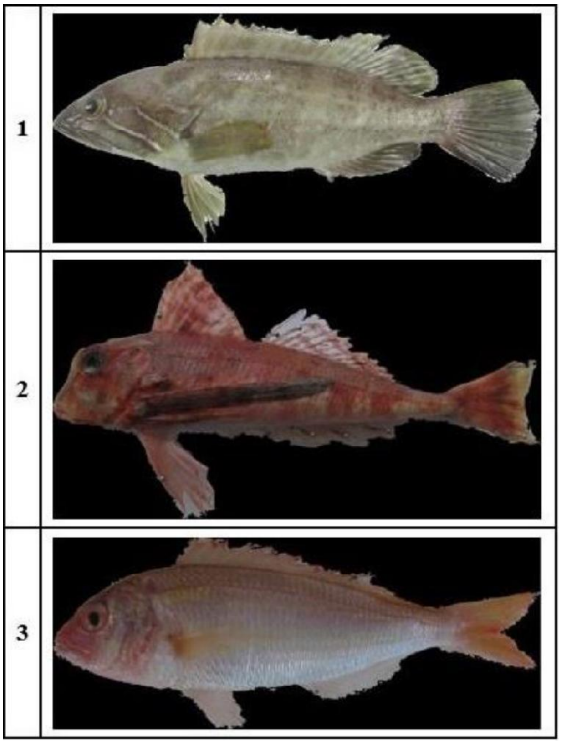


Figure 3: Fish samples from different species take different sized areas in image. The species of the fish samples: 1) *Epinephelus aeneus*, 2) *Chelidonichthys lastoviza*, 3) *Nemipterus randalli*

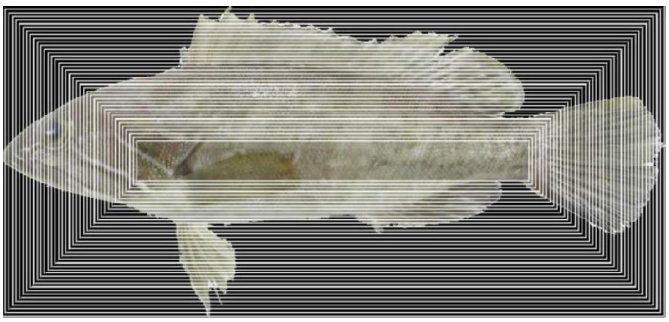


Figure 4: Actual subtracting process. One frame is subtracting in per time.

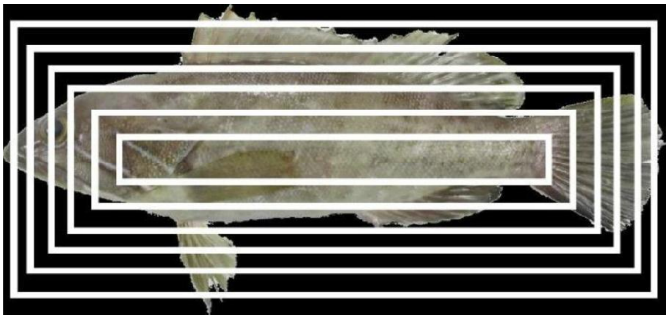


Figure 5: Representative illustration of the subtracting process with wider frames.

B. Preprocessing

It is aforementioned that all images were taken on a white background. In spite of that, some image noises might be arise from background or environmental conditions. In an attempt to reduce the negative environmental conditions, all images' backgrounds were manually converted to blue before image processing. The images include irrelevant empty fields apart from the fish sample. Therefore, after converting the background to blue a series of automatic image processing algorithms were applied on each image to gain the minimum image including the fish sample with least empty fields. Figure 2 shows the image processing phases from raw image to gained minimum image which includes fish sample. The following steps are performed for this task:

- The colored input image was in RGB color space. This image was converted to grayscale image.
- The grayscale image was converted to binary image. Canny Filter was applied for edge detection.
- Edge disorders were fixed by filtering the binary image with a morphometric structure element which is shaped in a 3-by-3 matrix. The fish sample's edges became more apparent by this process.
- Missing or overflowing pixel issues were fixed by applying erosion and dilation processes.
- The whole apparent area of the fish sample was detected by filling the inner sides of edges.
- The minimum image was gained which includes the fish sample with least empty fields. The image was in RGB color space. The fish sample was colored and the background was black.

Each of the fish samples takes different sized areas in images (Figure 3). This case is rising an issue about selecting

region of interest. It is necessary to interest on a solid fish texture and avoid considering black background due to using a color based feature extraction method. For this purpose, each four sides of the image (left border, right border, top border, bottom border) were assumed as a frame. Each frame of the minimum image was subtracted consecutively from outside to inside until a solid fish texture remains. Figure 4 shows the actual subtraction process which is performed by subtracting one frame in per time. Figure 5 shows a representative illustration which explains the subtracting process with wider frames.

Frame subtracting process can provide wider region of interest in the event of having quadratic shaped objects on image. Fish objects' shapes are distant from quadratic shape due to having various fins on their body and cauda. The general shape of the fishes is getting wider from mouth toward body and is getting thinner again from body toward cauda. Also same issue exists in direction from dorsal fins toward lower fins. In order to overcome this issue and obtain a more quadratic object in image, the image was cropped from its four sides. Hence, the fish object lost some of its body parts and came in a more quadratic shape. After the cropping, frame subtracting process was applied on cropped image and a wider region of interest was obtained (Figure 6). Cropping process was performed with cropping rates as 5%, 10%, 15%, 20% and 25% separately. Due to the variance on cropping rates, regions of interest with different sizes were obtained. Table 2 shows sample region of interest dimension values of some fish sample according to cropping rates. These values may vary for each different fish sample because of the size variance between fishes.

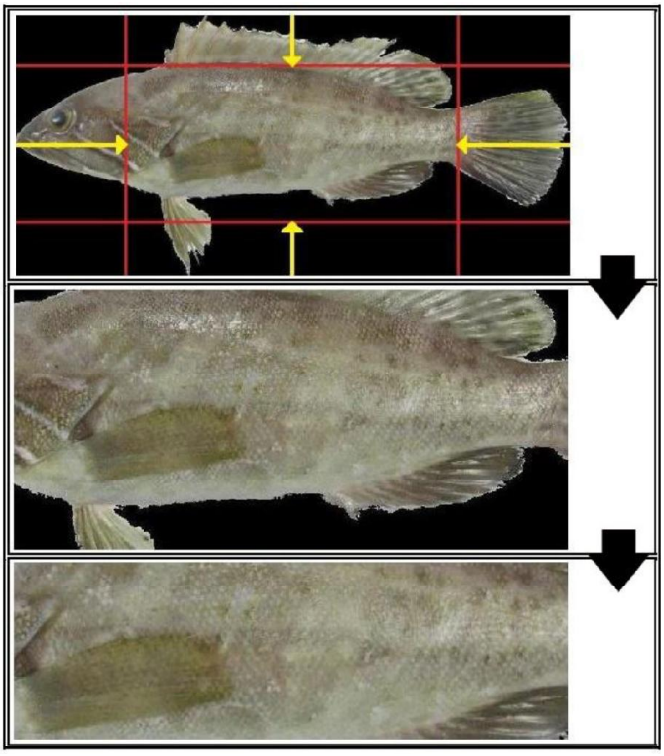


Figure 6: Applying subtracting process after cropping the image from its four sides

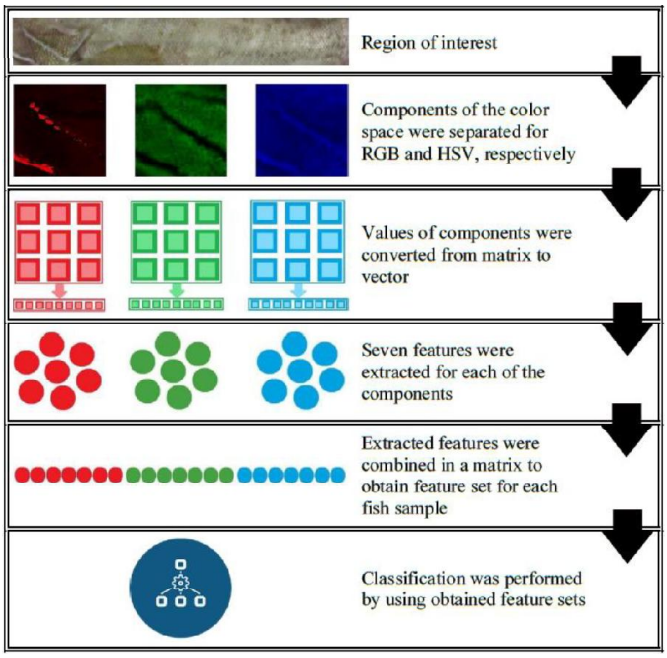


Figure 7: Phases of feature extraction

Table 2. An example of size comparison between regions of interest according to cropping rates. The given values may vary for each different fish sample

Cropping Rate	Region of Interest Height	Region of Interest Width	Total Area of the Region of Interest
Non-Cropped	64 pixel	605 pixel	38720 pixels
Cropped 5%	65 pixel	552 pixel	35880 pixels
Cropped 10%	85 pixel	518 pixel	44030 pixels
Cropped 15%	131 pixel	510 pixel	66810 pixels
Cropped 20%	151 pixel	476 pixel	71876 pixels
Cropped 25 %	167 pixel	438 pixel	73146 pixels

Table 3. Comparison of classification performances

	HSV Color Space		RGB Color Space	
Cropping Rate	**Families Classification**	**Species Classification**	**Families Classification**	**Species Classification**
Non-Cropped	90.9%	86.0%	81.1%	75.9%
Cropped 5%	91.9%	87.7%	83.3%	76.5%
Cropped 10%	91.6%	88.8%	81.4%	78.3%
Cropped 15%	91.9%	88.8%	84.9%	80.0%
Cropped 20%	92.3%	89.8%	85.5%	82.2%
Cropped 25%	93.5%	91.0%	85.0%	81.8%

C. Feature Extraction

The obtained regions of interest were handled both in RGB and HSV color spaces. Feature sets for both color spaces obtained and used separately for classification purposes. Feature extraction performed by using the red, green, blue components of the RGB color space and hue, saturation, value

components of the HSV color space separate from each other. Values of the color spaces' components were in a matrix that having same dimension with the region of interest image which they belong to. Since each obtained region of interest image has different dimensions, the number of extracted features may vary according to row and column sizes of the images. In order to fix this issue, values of the color spaces' components were converted from matrix to a vector before feature extraction. Afterwards, seven statistical features were extracted from these vectors for each of these components respectively. The extracted features from three components of the color space were combined in a new vector in order to obtain the feature set of the fish samples. Hence, there were totally 21 features in each feature set. The extracted features are minimum value, maximum value, mean value, variance, standard deviation, kurtosis, skewness. Figure 7 shows the phases of feature extraction from region of interest to classification.

D. Classification and Performance Measurement

Classification purposes were performed by using Nearest Neighbor algorithm [27]. In this method, an unclassified sample of data is compared with all classified samples applying the Euclidian Distance method on their features. The class of the unclassified sample is selected as the class of its nearest neighbor which has the nearest distance to unclassified sample.

Performance measurement was performed by using five-fold cross validation schema. The 5-fold cross validation process is performed by dividing randomly the dataset in 5 disjoint sets. The four of divided sets are used for the purposes of training and the remaining one is used for testing. This procedure is repeated along a period of time in a process of using each set for testing. Performance of classifications was measured in terms of general accuracies.

III. CONCLUSION

This study purposed an approach to obtain different sized regions of interest and make comparison between their classification performances by using them within a color based statistical feature extraction method. All images were preprocessed to obtain a minimum image including a colored fish sample with a black background. The obtained images were cropped from their four sides with cropping rates from 5% to 25% increasing by fives. Hence, regions of interest with different sizes were obtained according to each cropping size. These regions of interest examined in RGB and HSV color spaces separately. The acquired feature sets from RGB and HSV color spaces were used separately for classification. Classification purposes were performed according to families and species by using the Nearest Neighbor algorithm as classifier. Table 3 shows a comparison of classification results between non-cropped images' and cropped images' features in terms of general accuracy achievement.

The compared results show that cropping the images is raising the classification performances according to non-cropped images. All cropped images' performances better than non-cropped images. Also the increment of the classification performance is getting higher on cropped images as long as increasing the cropping rate. This fact has an inaccuracy for just 4 classification results in total of 20 classification results of cropped images. Additionally, this study shows that the proposed color based feature extraction method provides much better performance by using HSV color space than using RGB color space for both families and species classification. Also, families classification has greater results according to species classification for both of the color spaces in all cropping rates. As a result, 1321 fish samples from 16 families and 35 species were classified with best general accuracies of 93.5% and 91% for families and species classification respectively.

Table 2 shows that increasing the cropping size increases the row sizes and decreases the column sizes of the regions of interest. This fact might be arise from cropping the images with the same rate along the X axis (left border and right border) and the Y axis (top border and bottom border). Using different cropping rates for the X and Y axises might cause to have more field that can be used as region of interest.

REFERENCES

[1] Benson, B., Cho, J., Goshorn, D., Kastner, R. (2009). Field programmable gate array (FPGA) based fish detection using Haar classifiers. American Academy of Underwater Sciences.

[2] Kutlu, Y., Iscimen, B., & Turan, C. (2017). Multi-Stage Fish Classification System Using Morphometry. Fresenius Environmental Bulletin, 26(3), 1911-1917.

[3] Kutlu, Y., Altan, G., İşçimen, B., Doğdu, S. A., & Turan, C. (2017). Recognition of species of Triglidae Family using Deep Learning. Journal of the Black Sea/Mediterranean Environment, 23(1).

[4] Maasz, G., Takács, P., Boda, P., Varbiro, G., & Pirger, Z. (2017). Mayfly and fish species identification and sex determination in bleak (Alburnus alburnus) by MALDI-TOF mass spectrometry. Science of The Total Environment, 601, 317-325.

[5] Hasija, S., Buragohain, M. J., & Indu, S. (2017, February). Fish Species Classification Using Graph Embedding Discriminant Analysis. In Machine Vision and Information Technology (CMVIT), International Conference on (pp. 81-86). IEEE.

[6] Siddiqui, S. A., Salman, A., Malik, M. I., Shafait, F., Mian, A., Shortis, M. R., & Harvey, E. S. (2017). Automatic fish species classification in underwater videos: exploiting pre-trained deep neural network models to compensate for limited labelled data. ICES Journal of Marine Science, fsx109.

[7] Bothmann, L., Windmann, M., Kauermann, G. (2016). Realtime classification of fish in underwater sonar videos. Journal of the Royal Statistical Society: Series C (Applied Statistics).

[8] Shafait, F., Mian, A., Shortis, M., Ghanem, B., Culverhouse, P. F., Edgington, D., Cline, D., Ravanbakhsh, M., Seager, J., Harvey, E. S. (2016). Fish identification from videos captured in uncontrolled underwater environments. ICES Journal of Marine Science: Journal du Conseil, 73 (10): 2737-2746.

[9] Chuang, M. C., Hwang, J. N., Williams, K. (2016). A Feature Learning and Object Recognition Framework for Underwater Fish Images. IEEE Transactions on Image Processing, 25(4): 1862-1872.

[10] Mizuno, K., Liu, X., Asada, A., Ashizawa, J., Fujimoto, Y., Shimada, T. (2015). Application of a high-resolution acoustic video camera to fish classification: An experimental study. Underwater Technology (UT), IEEE, pp. 1-4.

[11] Ogunlana, S.O., Olabode, O., Oluwadare, S.A.A., Iwasokun, G.B. (2015). Fish Classification Using Support Vector Machine. African Journal of Computing & ICT, 8(2): 75-82.

[12] Iscimen, B., Kutlu, Y., Uyan, A., Turan, C. (2015). Classification of fish species with two dorsal fins using centroid-contour distance. 23nd Signal Processing and Communications Applications Conference (SIU), pp. 1981-1984.

[13] Iscimen, B., Kutlu, Y., Reyhaniye, A. N., Turan, C. (2014). Image analysis methods on fish recognition. 22nd Signal Processing and Communications Applications Conference (SIU), pp. 1411-1414.

[14] D'Elia, M., Patti, B., Bonanno, A., Fontana, I., Giacalone, G., Basilone, G., Fernandes, P.G. (2014). Analysis of backscatter properties and application of classification procedures for the identification of small pelagic fish species in the Central Mediterranean. Fisheries Research, 149, 33-42.

[15] Fabic, J. N., Turla, I. E., Capacillo, J.A., David, L.T., Naval, P.C. (2013). Fish population estimation and species classification from underwater video sequences using blob counting and shape analysis. Underwater Technology Symposium (UT), IEEE International, pp. 1-6.

[16] Alsmadi, M. K., Omar, K. B., Noah, S.A., Almarashdeh, I. (2010). Fish recognition based on robust features extraction from size and shape measurements using neural network. Journal of Computer Science, 6 (10): 1088.

[17] Cabreira, A.G., Tripode, M., Madirolas, A. (2009). Artificial neural networks for fish-species identification. ICES Journal of Marine Science: Journal du Conseil.

[18] Iscimen, B., Kutlu, Y., Turan, C. (2017). Classification of Serranidae Species Using Color Based Statistical Features. Natural and Engineering Sciences, 2(1), 25-34.

[19] Iscimen, B., Kutlu, Y., Turan, C. (2017). Classification of Fish Families Using Texture Analysis. The 3rd International Symposium on EuroAsian Biodiversity (SEAB), pp. 23.

[20] Daramola, S.A., Omololu, O. (2016). Fish Classification Algorithm using Single Value Decomposition. International Journal of Innovative Research in Science, Engineering and Technology, 5 (2): 1621-1626.

[21] Huang, P.X., Boom, B.J., Fisher, R.B. (2015). Hierarchical classification with reject option for live fish recognition. Machine Vision and Applications, 26 (1): 89-102.

[22] Hernández-Serna, A., & Jiménez-Segura, L. F. (2014). Automatic identification of species with neural networks. PeerJ, 2, e563.

[23] Chuang, M.C., Hwang, J.N., Kuo, F.F., Shan, M.K., Williams, K. (2014). Recognizing live fish species by hierarchical partial classification based on the exponential benefit. IEEE International Conference on Image Processing (ICIP), pp. 5232-5236.

[24] Hu, J., Li, D., Duan, Q., Han, Y., Chen, G., Si, X. (2012). Fish species classification by color, texture and multi-class support vector machine using computer vision. Computers and Electronics in Agriculture, 88, 133-140.

[25] Alsmadi, M. K., Omar, K.B., Noah, S.A., Almarashdeh, I. (2010). Fish recognition based on robust features extraction from color texture measurements using back-propagation classifier. Journal of Theoritical and Applied Information Technology.

[26] Turan, C., Erguden, D., Gürlek, M., Yaglioglu, D., Keskin, Ç. (2007). Atlas and systematics of marine Bony fishes of Turkey. Nobel, Adana, Turkey.

[27] Cunningham, P., Delany, S.J. (2007). k-Nearest neighbour classifiers.Multiple Classifier Systems, 1-17.

A Text Classification Application: Poet Detection from Poetry

DURMUŞ ÖZKAN ŞAHİN[1], OĞUZ EMRE KURAL[1], ERDAL KILIÇ[1] and ARMAĞAN KARABİNA[1]

[1] Ondokuz Mayıs University, Samsun/Turkey,
{durmus.sahin, oguz.kural, erdal.kilic, armagan.karabina}@bil.omu.edu.tr

***Abstract* – With the widespread use of the internet, the size of the text data increases day by day. Poems can be given as an example of the growing text. In this study, we aim to classify poetry according to poet. Firstly, data set consisting of three different poets' poetry written in English have been constructed. Then, text categorization techniques are implemented on it. Chi-Square (CHI) technique are used for feature selection. In addition, five different classification algorithms are tried. These algorithms are Sequential minimal optimization (SMO), Naïve Bayes (NB), C4.5 decision tree, Random Forest (RF) and k-nearest neighbors (KNN). Although each classifier showed very different results, over the 70% classification success rate was taken by SMO technique.**

***Keywords* – poet detection, poetry data, text classification, text mining**

I. INTRODUCTION

WITH the widespread use of the internet, text data have augmented day by day. Therefore, produced and recorded in the type of text data have to be operated by computers. For that reason obtaining and using meaningful information from these data will facilitate the work of people. Text mining is multi discipline; it makes use of such as data mining, artificial intelligent, natural language processing and information retrieval. Text classification is one of the most widely studied areas in text mining. It is a supervised learning problem. To solve this problem, firstly, data separated into two parts called train and test data. In the next step, classification algorithms applied training data. In the last step classifier models predict label of text by means of learning model. There are many text-mining studies in the literature.

Spam mail detection: Email is the simplest and cheapest communication tools in daily life. Most of the received emails are the text. These mails are two parts, named spam and non-spam. Some advertisement companies or bad people prefer to send spam mails to users. Spam mails give rise to waste of time and slow down daily work. Therefore, spam mails have to be found and not delivered to the users. Spam mail detection is binary text classification application [1, 2].

Web page classification: Web pages occur in HyperText Markup Language (HTML) files. There are some information based on text in these files. If text-mining techniques apply to these files, web pages may classify by the computers [3].

Author detection: Text-mining methods apply to the books or column so that author of texts can be recognized [4, 5].

There are very different studies apart from the above popular topics. These studies are gender of text's authors [6], automatic text summarization [7], automatic question answering systems [8], sentiment analysis on text [9, 10], music genre classification on lyrics [11, 12], television-rating prediction with social media [13] and automatic news article classification [14 – 16].

In this study, we aim to classify poetry according to poet. The first part of the study is to generate corpus. Thus, poetry of three different poets are taken from web page [17]. Poets are Adryan Rotica, Lamar Cole and Richard Allen Beevor. Generating data set is balanced. After corpus have generated, text classification techniques were applied to the corpus.

II. MATERIAL AND METHOD

Although computers can read text files, classifiers cannot understand them. In addition, texts are named unstructured data. For this reason, text files have to convert into the numerical data so that they can be structured data anymore. In Figure-1 flowchart shows general text classification applications' steps.

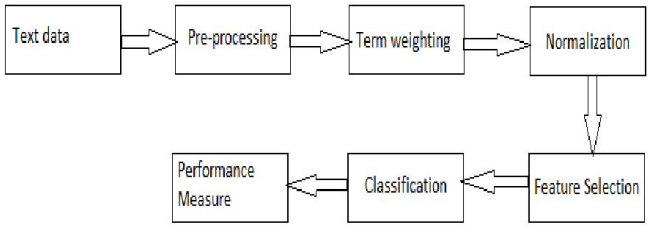


Figure 1: Text classification steps

Text files transform into structured data via pre-processing and term weighting steps. Each of steps are detailed sub sections.

A. Pre-processing

The words in the documents are not always in the same form. These words should be converted to the same style because they have the same importance. If words is not transformed into same style, the numbers of words are different so that may lead to misleading results. In pre-processing step, all the words converted uppercase into lowercase, punctuation marks and digits deleted, tokenization done according to white space

character, found stemming type all the words and stop words deleted. We prefer Porter Stemmer to find stem of words [18].

B. Term weighting

Any term is very few in some documents but it can be seen very much in some documents. Therefore, the term weighting must reveal this distinction. Term Frequency – Inverse Document Frequency (TF.IDF) was used as term weighting method that is frequently used in text classification. TF is the number of occurrences in a document. IDF is

$$IDF = \log\left(\frac{N}{a+c}\right) \quad (1)$$

given Equation 1. In Equation 1, N is the number of documents in the whole collection, a is the number of documents in the positive category that contain this term, c is the number of documents in the negative category that contain this term. The weight of the term is calculated by multiplying TF by IDF.

C. Feature selection

The operation of classification algorithms takes a long time. At the same time, the operation of these algorithms is directly related to the size of the data. Bag of words model is preferred in traditional text categorization applications. Document vectors are created using all the words in the training set. For this reason, documents are represented in terms of tens of thousands. Majority of these terms are not considered to affect important information because they do not affect the classification success positively. Instead of using all the terms in the bag of words, little word vector is preferred. Little vector is the best subset of bag of words. By means of feature selection, memory wastage can be prevented by reducing vector size. Runtime of the text classification process reduce.

Feature selection methods are generally divided into three main groups [19, 20]. These are filtering, wrapper and embedded methods. In feature selection step, one of the filtering method CHI is used. CHI is

$$CHI(t_j, c_i) = N\frac{(ad-bc)^2}{(a+c)(b+d)(a+b)(c+d)} \quad (2)$$

given Equation 2. In Equation 2, the CHI score of the t_j term in class c_i is calculated. N, a and c is emphasized in Equation 1. b is the number of documents in the positive category that do not contain this term and d is the number of documents in the negative category that do not contain this term. The CHI scores of all terms are calculated. Subsequently these values of CHI sort big to small. The greatest value is the most relevant with related category. If CHI value of any term is 0, it is not relevant with related category.

D. Classification

WEKA is data mining tool that is used in the classification stage [21]. There are a lot of data mining and machine learning algorithms in WEKA tools. SMO based Support Vector Machine (SVM), NB based probability model, C4.5 and RF based decision tree and KNN are used in this study.

E. Data set

Table-1 shows poems and their poetry distribution. Data set divided approximately 60% train and 40% test. Because of the number of poetry is close this data set is balanced.

Table 1: Poems-poetry distribution

Poems	Train	Test
Adryan Rotica	284	189
Lamar Cole	241	162
Richard Allen Beevor	227	152

F. Performance Measure

With the performance measurement, the accuracy of belonging to the relevant class is evaluated. A sample that is actually labeled positively in the dataset, if it is classified as positive in the classification result, it is named True-Positive (TP). A sample that is actually labeled negative in the dataset, if it is classified as negative in the classification result, it is named True-Negative (TN). A sample that is actually labeled negative in the dataset, if it is classified as positive in the classification result, it is named False-Positive (FP). A sample that is actually labeled positive in the dataset, if it is classified as negative in the classification result, it is named False-Negative (FP). These states are shown on the Table-2 as confusion matrix.

Table 2: Confusion matrix

Real / Predict	C1	C2
C1	TP	FP
C2	FN	TN

The most used performance measure in text classification is F-score. F-score is the harmonic mean of precision and recall values. Precision (π) and recall (ρ) are given Equation 3 and Equation 4 respectively.

$$\pi = \frac{TP}{TP+FP} \quad (3)$$

$$\rho = \frac{TP}{TP+FN} \quad (4)$$

If harmonic mean of π and ρ values are calculated,

$$F = \frac{2\pi\rho}{\pi+\rho} \quad (5)$$

F-score is taken place as Equation 5. To evaluate classification success F-score is preferred.

III. RESULTS

The performance results of 5 different classifiers with different working models are given in Figure 2.

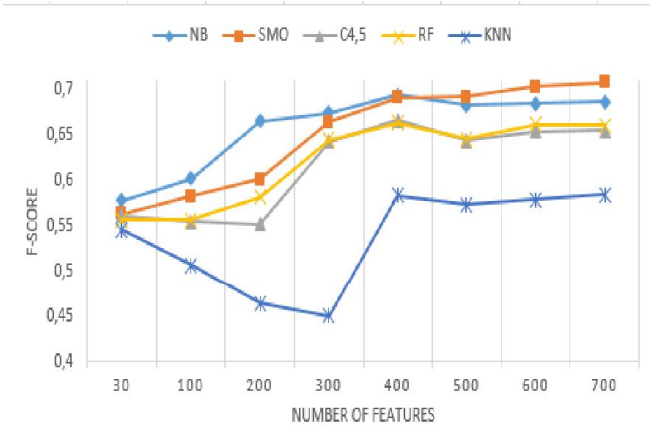


Figure 2: Success of classification algorithms

When 30 features used, the best classifier is NB. However, the worst classifier is KNN. As long as number of features increase, the success rate of all classifiers excluding KNN go up. The best classification rate is 0,7067 F-score that occurs with SMO in 700 features. Success of RF and C4.5 is similar but they don't exceed KNN and SMO.

As a result, English poetry were classified according to poets. If we use larger data set, more effective text classification results can be obtained. Instead of traditional text classification methods, semantic text classification method may be preferred. Because, poets use very special sentences while writing poetry. As a future work, we aim to generate different poetry data set to classify genre of poetry with text classification.

REFERENCES

[1] A M. K. Chae, A. Alsadoon, P. W. C. Prasad and S. Sreedharan, "Spam filtering email classification (SFECM) using gain and graph mining algorithm" 2017 2nd International Conference on Anti-Cyber Crimes (ICACC), Abha, pp. 217-222, 2017.

[2] T. Vyas, P. Prajapati and S. Gadhwal, "A survey and evaluation of supervised machine learning techniques for spam e-mail filtering" 2015 IEEE International Conference on Electrical, Computer and Communication Technologies (ICECCT), Coimbatore, pp. 1-7, 2015.

[3] S. A. Özel, "A Web page classification system based on a genetic algorithm using tagged-terms as features", Expert Systems with Applications, 38(4), pp. 3407-3415, 2011.

[4] M. Yasdi and B. Diri, "Author recognition by Abstract Feature Extraction" 2012 20th Signal Processing and Communications Applications Conference (SIU), Mugla, pp. 1-4, 2012.
doi: 10.1109/SIU.2012.6204690

[5] P. Tüfekci and E. Uzun, "Author detection by using different term weighting schemes" 2013 21st Signal Processing and Communications Applications Conference (SIU), Haspolat, pp. 1-4, 2013.
doi: 10.1109/SIU.2013.6531190

[6] S. Doğan, B. Diri, "Türkçe Dokümanlar için N-gram Tabanlı Yeni Bir Sınıflandırma: Yazar, Tür ve Cinsiyet" Türkiye Bilişim Vakfı Bilgisayar Bilimleri ve Mühendisliği Dergisi, 4(4), pp. 83-92, 2010.

[7] A. Güran, S. N. Arslan, E. Kılıç and B. Diri, "Sentence selection methods for text summarization" 2014 22nd Signal Processing and Communications Applications Conference (SIU), Trabzon, pp. 192-195, 2014.
doi: 10.1109/SIU.2014.6830198

[8] M. Amasyalı, B. Diri, "Bir Soru Cevaplama Sistemi: BayBilmiş", Türkiye Bilişim Vakfı Bilgisayar Bilimleri ve Mühendisliği Dergisi, 1, pp. 37-51, 2005.

[9] C. Parlak, B. Diri, "Farklı Veri Setleri Arasında Duygu Tanıma Çalışması" Dokuz Eylül Üniversitesi Mühendislik Fakültesi, Mühendislik Bilimleri Dergisi, 16(48), pp. 21-29, 2014.

[10] M. Meral and B. Diri, "Sentiment analysis on Twitter," 2014 22nd Signal Processing and Communications Applications Conference (SIU), Trabzon, pp. 690-693, 2014.
doi: 10.1109/SIU.2014.6830323

[11] Ö. Çoban and I. Karabey, "Music genre classification with word and document vectors" 2017 25th Signal Processing and Communications Applications Conference (SIU), Antalya, pp. 1-4, 2017.
doi: 10.1109/SIU.2017.7960145

[12] Ö. Çoban and G. T. Özyer, "Music genre classification from Turkish lyrics" 2016 24th Signal Processing and Communication Application Conference (SIU), Zonguldak, pp. 101-104, 2016.
doi: 10.1109/SIU.2016.7495686

[13] C. Akarsu and B. Diri, "Turkish TV rating prediction with Twitter" 2016 24th Signal Processing and Communication Application Conference (SIU), Zonguldak, Turkey, pp. 345-348, 2016.
doi: 10.1109/SIU.2016.7495748

[14] M. F. Amasyali and T. Yildirim, "Automatic text categorization of news articles" Proceedings of the IEEE 12th Signal Processing and Communications Applications Conference, pp. 224-226, 2004.
doi: 10.1109/SIU.2004.1338299

[15] P. Tüfekci, E. Uzun and B. Sevinç, "Text classification of web based news articles by using Turkish grammatical features" 2012 20th Signal Processing and Communications Applications Conference (SIU), Mugla, pp. 1-4, 2012.
doi: 10.1109/SIU.2012.6204565

[16] E. Kiliç, M. R. Tavus and Z. Karhan, "Classification of breaking news taken from the online news sites" 2015 23nd Signal Processing and Communications Applications Conference (SIU), Malatya, pp. 363-366, 2015.
doi: 10.1109/SIU.2015.7129834

[17] https://www.poemhunter.com/ebooks/ Last access: October 2017

[18] https://tartarus.org/martin/PorterStemmer/ Last access: October 2017

[19] Gunal, S.; "*Hybrid feature selection for text classification*", Turkish Journal of Electrical Engineering and Computer Sciences, vol. 20, pp. 1296-1311, 2012.

[20] Uysal, A. K.; Gunal, S., "*Text classification using genetic algorithm oriented latent semantic features*", Expert Systems with Applications, vol. 41, pp. 5938-5947, 2014.

[21] https://www.cs.waikato.ac.nz/ml/weka/ Last access: October 2017.

Classification of Phishing Detection Data on Web Sites with Bayesian Regularized Artificial Neural Networks

Ali YASAR[1] and Ismail SARITAS[2]

[1]ComputerProgramming, Guneysinir Vocational School of Higher Education Selcuk University

Guneysinir, Konya, 42190, aliyasar@selcuk.edu.tr,+905055204696

[2]Faculty of Technology, Electrical and Electronics Engineering Selcuk University, Konya

Abstract - **Website phishing is among the important security challenges for the online community because there are a large numbers of online users. Website phishing occurs through a secure website from which such sensitive information as usernames and passwords is obtained from online users. The methods to be used as solutions are black lists, white lists and the use of search methods in order to minimize the risk. The phishing problem is a vital issue particularly in industry, notably in e-banking and e-commerce as regards payments. Neda Abdelhamid et al. have studied different legitimate and phishy websites and collected 1353 different websites from difference sources. Phishing websites were taken from Phishtank data archive (www.phishtank.com), which is a free community site at which users can submit, verify, track and share phishing data. The legitimate websites were obtained from Yahoo and from starting point directories through a web script developed in PHP. The PHP script was embedded into a browser and 548 legitimate websites were collected out of 1353 websites. There are 702 phishing URLs, and 103 suspicious URLs. When a website is labelled SUSPICIOUS, that website can be either phishy or legitimate, which implies that the website had both legit and phishy features. We used Bayesian regularized artificial neural networks (BRANN) to classify the data. In our study, we also calculated R as 91,839%. This is a successful result.**

Keywords - **BRANN, Pushing, UCI, Database, Classification**

I. INTRODUCTION

Today, phishing is a actual threat on the Internet. According to a report by an American security firm, RSA, there have been approximately 33,000 phishing attacks globally every month in 2012, causing a loss of $687 million. For this reason, fighting against phishing attacks is highly important. One popular and widely-deployed solution with browsers is to integrate a blacklist-site list into them. Yet, this solution, which is unable to detect new attacks if the database is outdated, seems not to be effective if the number of phishing attacks should increase every day[1].

Today, phishing attacks pose one of the biggest threats to the Internet in network security [2]. Phishers are attempting to hide confidential information such as user name, password and credit card details in disguise of a trusted entity in an online communication. To achieve this, attackers often employ a series of web site spoofing techniques to trick them into revealing confidential information which has an economic value. In an ordinary attack [2], a large number of fake e-mails are randomly sent to Internet users. These emails are often disguised as if they were from a legal commercial corporation, like a bank. Recipients of the mail will be urged to update their personal information with the warning that their online bank accounts may be suspended if the requested form is not fulfilled out. Such an attack is very common and effective in persuading users.

Our work has been classified with ANN using Website Phishing Data Set at [3]

II. MATERIAL AND METHODOLOGY

The internet is important not only for individual users but also for organizations which do their business online. Nowadays, many organizations offer online trading and online sales of services and goods [4]. However, internet-users may fall prey to different types of online threats that might cause financial damages, identity theft, and loss of private information. Therefore, the internet comes as a channel for commercial exchanges [5]. In this study, the PHP script was plugged with a browser and 548 legitimate websites were collected out of 1353 websites. There were 702 phishing URLs, and 103 suspicious URLs. There were 9 different data we would use. These were typed into the system as input and the results were estimated. The information about our input set is given below[5].

1. Server Form Handler (SFH): Once the user submits his information, the webpage will transfer the information to a server which can process it. Typically, the information would be processed from the same domain where the webpage is being loaded. Either phishers resort to making the server form handler empty or the information is transferred to somewhere different from the legitimate domain.

Rule : SFH If 'about : blank' or empty → Phishy

SHD redirects to a different domain → Suspicious
else → Legit

2. Using a Pop-up window: Usually, authenticated sites do not request the users to submit their credentials via a popup window.

Rule : rightClick disabled → Phishy
rightClick showing alert → Suspicious
else → Legit

3. Fake HTTPs protocol/SSL final: The fact that HTTPs protocol shows up whenever sensitive information is being transferred reflects that the user is certainly connected to an honest website. However, phishers may use a fake HTTPs protocol to deceive users. Therefore, it is definitely recommended to check whether the HTTPs protocol is offered by a trusted issuer such as GeoTrust, GoDaddy, VeriSign, etc.

Rule : use of https & trusted issuer & age >= 2 years Legit
using https & issuer is not trusted → Suspicious
else → Phishy

4. Request URL: A webpage is usually composed of a text and certain objects such as images and videos. Typically, these objects are loaded into the webpage from the same server of the webpage. If the objects are loaded from a domain other than the one typed in the URL address bar, the webpage is potentially suspicious.

Rule : request URL < 22% →Legit
request URL %>=22% and <= 61% → Suspicious
else →Phishy

5. URL of anchor: It looks like the URL feature, but here the links within the webpage may point to a domain different from the domain typed in the URL address bar.

Rule : URL anchor % < 31% →Legit
URL anchor % >= and <= 67% →Suspicious
else →Phishy

6. Website traffic: Legitimate websites usually have high traffic since they are visited regularly. As phishing websites normally have a relatively short life-span, they have no web traffic or they have low ranking. It is recommended that a legitimate webpage have a rank more than or equal to 150,000 in the Alexadatabase (Alexa the Web Information Company, 2011). N. Abdelhamid et al. / Expert Systems with Applications 41 (2014) 5948–5959 5955

Rule : webTraffic < 150; 000 →Legit
webTraffic > 150; 000 →Suspicious
else → Phishy

7. URL Length: Phishers hide the suspicious part of the URL to redirect the information submitted by users or redirect the uploaded page to a suspicious domain. Scientifically, there is no reliable standard length that differentiates between phishing URLs and legitimate ones [6]. It is therefore suggested that, when the URL length is greater than 54 characters, the URL should be considered phishy.

Rule : If URL length < 54 → Legit
URL length >= 54 and <=75 → Suspicious
Else →Phishy

8. Age of domain: Websites that have an online presence of less than 1 year may be considered risky.

Rule : age <= 6 months → Legit
else → Phishy

9. IP address: Using an IP address in the domain name of the URL is an indicator that someone is trying to access the personal information. This trick involves links that may begin with an IP address most companies no longer use. In the frequency analysis conducted earlier, 20% of the data contain ''IP'' address and all of them are associated with phishy websites.

Rule : If IP address exists in URL →Phishy
Else →Legit

10. Result features hold categorical values such as ''Legitimate'', ''Suspicious'' and ''Phishy''. These values are represented by the numerical values 1, 0 and -1, respectively.

2.1. Bayesian regulated artificial neural networks (BRANN)

Bayesian regulated artificial neural networks (BRANNs) are more robust than standard back propagation nets and can reduce or eliminate long cross-validation requirements. Bayesian regularization is a mathematical operation that transforms a nonlinear stress into a "well-posed" statistical problem in the form of back stress. The advantage of BRANNs is that the models are robust and verification process scaled as O (N2) is unnecessary in normal regression methods such as back propagation. These networks offer solutions to a number of problems that emerge in the QSAR model, such as model selection, model robustness, validation set selection, validation effort size, and network architecture optimization. Evidence procedures force an over transport, providing an objective Bayesian criterion for stopping training. Also, overloading is difficult because BRANN calculates and trains effective network parameters or weights, effectively turning off irrelevant networks. This effective number is much smaller than the standard fully connected back-propagation neural network weights. Automatic Rearrange Detection (ARD) of input variables can be used with BRANNs, which permits the network to "guess" the importance of each entry. The ARD method assures that irrelevant or high-order correlation indices used in the model are ignored and that they are the most important variable to model the efficacy data [7]. The BRANN model that forms the basis of our system is shown in Fig. 1

variable to model the efficacy data [7]. The BRANN model that constitutes our system is shown in Fig. 1.

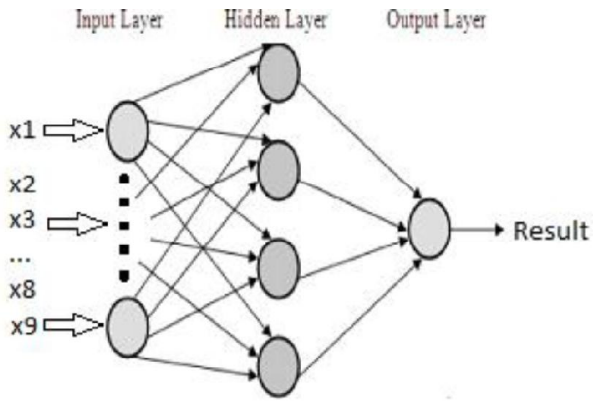


Fig. 1. The Structure of BRANN

2.2. Artificial Neural Network Application For A Data Set

In this study, the following transactions are performed for determining if the Human Activity Recognition Using Smartphones Data Set are human activity the data set of 1,353 units of Human Activity Recognition Using Smartphones Data Set.

- As testing data, 135 units (10%) of data have been chosen randomly.
- As training data, the remaining 1218 units (90%) of data have been chosen.

In this study, a feed forward network structure that contains an input layer, a hidden layer and an output layer (Fig. 1) was used. This algorithm typically requires more time, but can result in good generalization for difficult, small or noisy datasets. Training stops according to adaptive weight minimization (regularization).

The regression graph of the training data set is shown in Fig. 2.

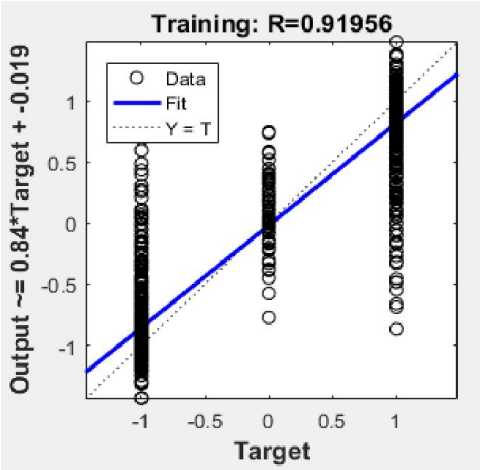


Fig. 2. Regression of Training Data Set

The regression graph of the testing data set is shown in Fig. 3.

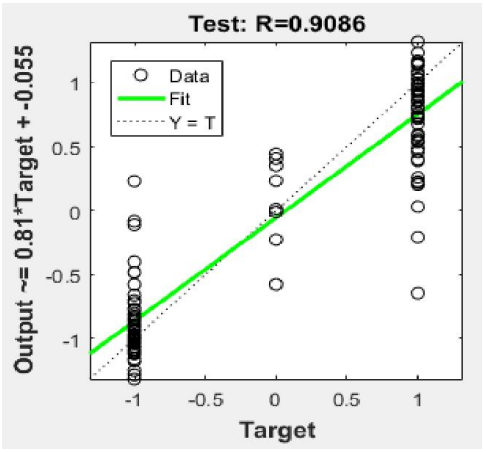


Fig. 3. Regression of Testing Data Set

The regression graph of the output is shown in Fig. 4.

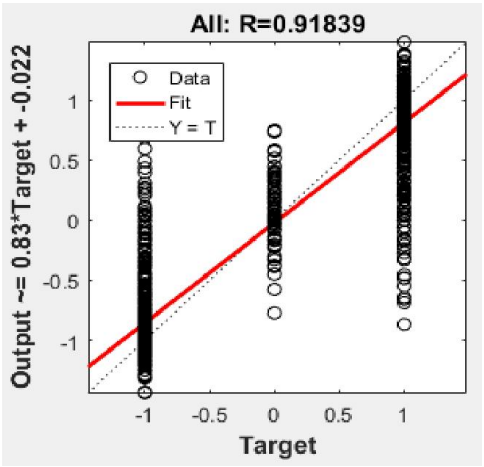


Fig. 4. Regression of Output Set

Graphic of Neural Network training performance is given in figure 5.

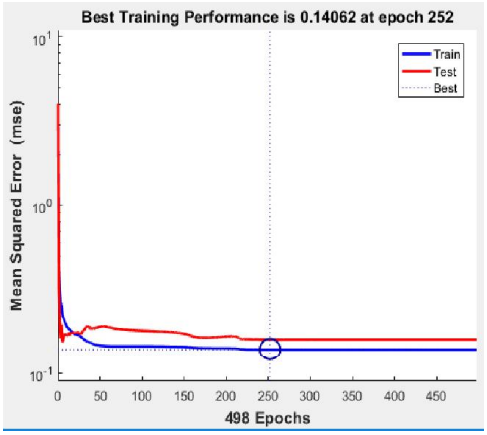


Fig. 5. Best Training Performances

The error analysis graph of my work is given in Fig.6

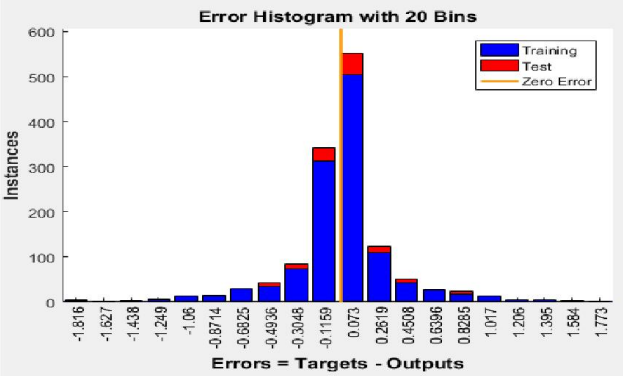


Fig. 6. Error Histogram

III. RESULT AND DISCUSSION

The comparison of experimental measurement values for Website Phishing Data Set and BRANN estimation values are shown in Fig. 7. All the randomly selected data used for test is different than the data used for training process.

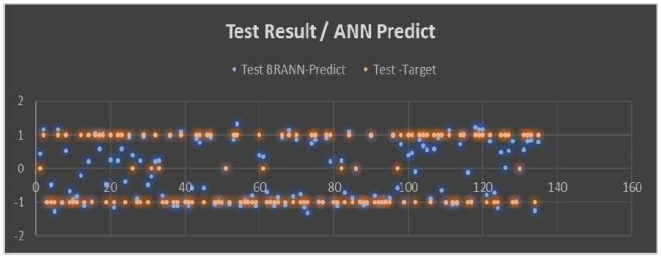


Fig. 7. Test Result / ANN Predict

Finally, the graph of the values obtained from the remaining data which is the estimation of BRANN is shown in Fig. 8.

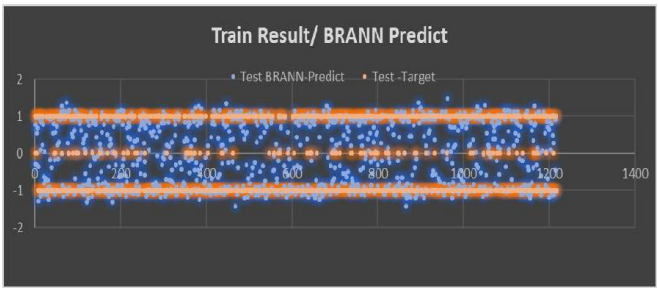


Fig. 8. Train Result / ANN Predict

As seen in the figures, the estimation results and dataset results are almost overlapping. The deviation between experimental and estimated results is very small and negligible for any Human Activity Recognition Using Smartphones performance.

IV. CONCLUSIONS

In this study, it has been concluded that BRANN can be used in the clustering procedure and better results can be achieved. According to the results, it has been observed that 90% and above classification accuracy can be achieved.

ACKNOWLEDGEMENTS

This study has been supported by Selcuk University's Scientific Research Unit (BAP). Contributors gratefully acknowledge support of their work by the Institute of Agrophysics of the Polish Academy of Sciences in Lublin and http://archive.ics.uci.edu/ml/datasets/Website+Phishing.

REFERENCES

[1] Pham, T. A., Nguyen, Q. U., & Nguyen, X. H. (2014). Phishing attacks detection using genetic programming. In Knowledge and Systems Engineering (pp. 185-195). Springer, Cham.

[2] Ludl, C., McAllister, S., Kirda, E., Kruegel, C.: On the effectiveness of techniques to detect phishing sites. In: H¨ammerli, B.M., Sommer, R. (eds.) DIMVA 2007. LNCS, vol. 4579, pp. 20–39. Springer, Heidelberg (2007)

[3] http://archive.ics.uci.edu/ml/datasets/Website+Phishing.

[4] Liu, J., & Ye, Y. (2001). In E-commerce agents, marketplace solutions, security issues, and supply and demand; 2001 (pp. 1–6). London, UK.

[5] Abdelhamid, N., Ayesh, A., & Thabtah, F. (2014). Phishing detection based associative classification data mining. Expert Systems with Applications, 41(13), 5948-5959.

[6] Mohammad, R., Thabtah, F., & McCluskey, L. (2012). An assessment of features related to phishing websites using an automated technique. In The 7th international conference for internet technology and secured transactions (ICITST-2012). London: ICITST

[7] Burden, F., & Winkler, D. (2009). Bayesian regularization of neural networks. Artificial Neural Networks: Methods and Application

The Performance Analysis of Optical Burst Switching by Random Forest Algorithm

S. GENÇ[1], D. BAĞCI[2], G. ORTAÇ[3], O. DAŞ[4]

[1] Kastamonu University, Kastamonu/Turkey, sgenc@kastamonu.edu.tr
[2] Dokuz Eylul University, Izmir/Turkey, duygu.bagci@deu.edu.tr
[3] Bursa Teknik University, Bursa/Turkey, gizem.ortac@btu.edu.tr
[4] Dokuz Eylul University, Izmir/Turkey, oguzhan.das@deu.edu.tr

Abstract – Optical networks are suggested as the most suitable platform for services and applications that require bandwidth and cope with continuously increasing internet users. Especially, to achieve communication in multiple connections; applications that require high bandwidth and based on multicast are necessary. Thus, it is estimated that in near future, Optical Burst Switching (OBS) will be constitute the chief background of all optical network. In this study, analyses have been performed to deal with a random attack. Ada Boost, NaiveBayes, BayesNet, Sequential Minimal Optimization (SMO), Multilayer Perceptron, K-Means, Decision Tree (J48) and Random Forest classification algorithms, which are machine learning techniques that present in weka library, have been used on dataset which are composed of computer test simulation data. Successes of those algorithms have been investigated. It has been concluded from experimental results that Random Forest has shown the best performance with 100% accuracy-success ratio. Consequently, it has proven that suggested classification algorithm can be successful against attacks on network.

Keywords – Optical Burst Switching Network, OBS, Optical Networks, Machine Learning, Random Forest Algorithm.

I. INTRODUCTION

Optical networks enable to solve many problems that occur in present computer networks (Bandwidth etc.) and in addition to provide a huge capacity, they also ensure a common network background that supported by several services [1,2]. Besides, in optical network, band width can be adjusted for any needs flexibly [3,4]. Optical network can be defined as a modern network technology which enables to transmit information by sending light via optical fibers from one point to another [5]. Due to the preciptious growth of users of internet, a new period in optical technology have been demanded for internet traffic since the last decade, ultimately. Three divisions have been arranged as Optical Circuit Switching (OCS), Optical Packet Switching (OPS) and Optical Burst Switching(OBS) [6].

It is called OBS that packages, which want to reach to the same node are transmitted in larger optical packages, that is, in bursts. In OBS configuration, incoming IP packages gather in virtual queues (one in each destination point) to constitute optical bursts. Then, a control package is produced and transmitted via control channel in optical network to reserve appropriate sources in path before an offset time (latency time) that has determined from data and to reserve an time slot [7].

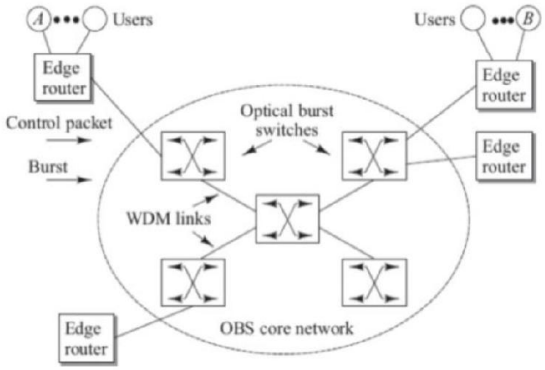


Figure 1 : Generic structure of an optinal burst switching (OBS) network [8].

It takes time to process control package in every node of OBS. Control package always leads data burst. Control package and data send in different times and different channels. Lastly, bursts are separated at the exit node of network. Thus, OBS can simplify network control and hardware design without loss in performance, significantly. In OBS configuration, a data channel is only reserved from incoming to outgoing of burst. This situation provides to OBS to reach the highest efficiency. In OBS, control package carries information of offset time in addition to routing information [9,10]. OBS is shown on figure 1.

II. LITERATURE

Kaur and Singh have used genetic algorithm to prevent DDoS attacks ,which make the outgoing wavelength from core node busy by intruder, in OBS [11].

Rajab et al., have studied on securing OBS network from BHP flooding attack. The have proposed a security classification that enables core switches to detect BHP attack and measure the performance of incoming nodes. With this method, in all traffic load cases under BHP attack, the overall packet dropping rate is measured as 5% [12].

III. EXPERIMENTS

A. Dataset

In this study, it is benefitted from the test data which have been applied in the method that Rajab et al. have been used

against attacks to OBS network. Data set have been downloaded from UCI website [13].

Table 1: This caption is centered [13].

Attribute	Description
Node	This is the number of the sending node (numeric).
Utilized Bandwidth Rate	This is the normalization of Used Bandwidth (numeric).
Packet Drop Rate	This is the normalization of Percentage Of Lost Pcaket Rate(numeric).
Reserved Bandwidth	Initial reserved Bandwidth assigned (given) to each node, the user (usr) in the experiments assign these values. (numeric).
Average Delay Time Per Sec	Average Delay Time (per second) for each node. This is (End-to End Delay). (numeric).
Percentage Of Lost Pcaket Rate	Percentage of Packets Drop Rate for each node (numeric).
Percentage Of Lost Byte Rate	Percentage of Lost Byte Rate for each node (numeric).
Packet Received Rate	Total received packets (per second) for each node based on Reserved Bandwidth (numeric).
Used Bandwidth	This is what each node could reserve from the Reserved Bandwidth (numeric).
Lost Bandwidth	The amount of lost Bandwidth by each node from Reserved Bandwidth (numeric).
Packet Size Byte	Packets size in Byte assigned specifically for each node to transmit. Note: 60 Byte will be added to the 1440 for the IP Header and the UDP Header ((Data size 1440 Byte) + (IP Header 40 Byte) + (UDP Header 20 Byte)) =1500 Byte (numeric).
Packet Transmitted	Total transmitted packets (per second) for each node based on the Reserved Bandwidth (numeric).
Packet Received	Total received packets (per second) for each node based on the Reserved Bandwidth (numeric).
Packet lost:	Total lost packets (per second) for each node, which based on the Lost Bandwidth (numeric).
Transmitted Byte	Total transmitted Byte (per second) for each node (numeric).
Received Byte	Total received Byte (per second) for each node based on the Reserved Bandwidth (numeric).
10 Run AVG Drop Rate	Average packet drop rate for 10 consecutive (run) iterations (numeric).
10 Run AVG Bandwidth Use	Average Bandwidth utilized for 10 consecutive (run) iterations (numeric).
10 Run Delay	Average delay time for 10 consecutive (run) iterations (numeric).
Node Status' {B, NB, P NB}	initial classification of nodes based on Packet Drop Rate, Used Bandwidth and Average Delay Time Per Sec. B = Behaving, NB = Not Behaving and P NB = Potentially Not Behaving. (Categorical)
Flood Status	Percentage of flood per node based on Packet Drop Rate Medium and high level of BHP flood attack in case B (numeric).
Class ' {NB-No Block, Block, No Block, NB-Wait}	The final classification of nodes based on Packet Drop Rate, Reserved Bandwidth, Iteration, Used Bandwidth, Packet Drop Rate. This is for case B (Categorical).

B. *Data Properties*

Dataset comprises 22 attributes and 1075 numbers of instance. These properties are: node, utilized bandwidth rate, packet drop rate, reserved bandwidth, Average Delay Time Per Sec, Percentage Of Lost Pcaket Rate, Percentage Of Lost Byte Rate, Packet Received Rate, Used Bandwidth, Lost Bandwidth, Packet Size Byte, Packet Transmitted, Packet Received, Packet lost, Transmitted Byte, Received Byte, 10-Run AVG Drop Rate, 10-Run AVG Bandwidth Use, 10-Run Delay and node status and class.

C. *Classification Algorithms*

All experiments have been performed by Weka software (version 3.8) using 10-fold cross validation strategy [14]. Ada Boost, Naive Bayes, Bayes Net, Sequential Minimal Optimization (SMO), Multilayer Perceptron, K-Means, Decision Tree (J48) and Random Forest classification algorithms have been applied on data sets.

D. *Criteria on comparing classification algorithms*

1) *Model Success Criteria*

a) *Accuracy – Error Rate*

The most popular and simply method to measure the success of model is the accuracy ratio of model. It is the ratio of accurately classified sample number (TP + TN) to total sample number (TP + TN + FP + FN). Error ratio, on the other hand, is the completer to 1 of accuracy ratio (1-accuracy ratio).

$$Accuracy = \frac{(TP + TN)}{(TP + FP + FN + TN)} \quad (1)$$

$$ErrorRate = \frac{(FP + FN)}{(TP + FP + FN + TN)} \quad (2)$$

b) *Precision*

Precision, is the ratio of true positive sample number that its class has estimated as 1 to all sample number that their class has also estimated as 1.

$$\mathrm{Pr}ecision = \frac{TP}{(TP + FP)} \quad (3)$$

c) *Recall*

It is the ratio of accurately classified positive sample number and total positive sample number.

$$\mathrm{Re}call = \frac{TP}{(TP + FN)} \quad (4)$$

d) *F-Measure*

Precision and recall is not enough to obtain a meaningful result. Evaluating both criteria give more accurate results. F-measure, which is the harmonic average of precision and recall, enables to utilize these criteria together.

$$FMeasure = \frac{2DK}{(D+K)} \quad (5)$$

2) Kappa Statistic

Variation between spectators can be measured in every situation when two or more spectator evaluate the same thing [15]. Kappa number changes between -1 and +1. If complete harmony is present, K will be equal to 1. If spectating harmony is equal to chance depended harmony or bigger than that value, $K \geq 0$ whereas if it is smaller than that value, $K < 0$. Interpreting range of kappa number is 0 and 1, Negative values are not reliable. On the other hand, values that are bigger than 0.4 is acceptable [16]. Kappa number has calculated as:

$$KappaStatic = \frac{(P_0 - P_C)}{(1 - P_C)} \quad (6)$$

P_0 Accepted rate, P_c Expected rate of acceptance.

IV. Experimental Results

By using machine learning approach and classification algorithms like Ada Boost, Naive Bayes, Bayes Net, Sequential Minimal Optimization (SMO), Multilayer Perceptron, K-Means, Decision Tree (J48) and Random Forest, which are present in Weka library, model have been created using data from dataset. Algorithms success have been measured and shown in table 2 according to model success criteria and kappa statistic that have been used in these classification algorithms.

Table 2. Accuracy results of classification algorithms

Classifier	Accuracy %	Precision	Recall	F-Measure	Kappa Statistic
Ada Boost	60.9302	0.397	0.609	0.472	0.3277
Navie Bayes	71.814	0.738	0.718	0.719	0.5972
SMO	78.9767	0.787	0.790	0.786	0.6827
BayesNet	87.814	0.892	0.878	0.880	0.824
Multilayer Perceptron	96.5581	0.966	0.966	0.966	0.9488
K - Means	99.0698	0.991	0.991	0.991	0.9862
J48	99.6279	0.996	0.996	0.996	0.9945
Random Forest	100	1.0	1.0	1.0	1.0

By considering accuracy, precision and recall criterion, the best result has been obtained from Random Forest algorithm. According to those criteria again, J48, K-Means, MP, Bayes Net, Naive Bayes and Ada Boost has followed Random Forest algorithm, respectively.

When evaluating both precision and recall by other means when considering the F-measure, again Random Forest algorithm gives the best result. Additionally, it has seen that when kappa number approximates to 1, the results have not been obtained by chance.

Generally, when interpreting results, the best performance has been shown by Random Forest algorithm by 100%.

V. Conclusion

In this study, machine learning techniques and methods on dataset which is about of test data performance of conducted simulation studies of OBS have been investigated. Performance comparison of classification algorithms of dataset have been performed by considering model success criteria and kappa statistic value. Ada Boost, Naive Bayes, Bayes Net, Sequential Minimal Optimization (SMO), Multilayer Perceptron, K-Means, Decision Tree (J48) and Random Forest classification algorithms that are present in Weka library have been used.

It has been concluded that the accuracy have been affected by data distribution in dataset classes when model success criteria and kappa statistic results have been taken into consideration. The best performance has shown by Random Forest classification with 100% overall accuracy.

It is necessary that in burst composition, the most ideal burst dimensions on algorithm should be specified by taken time and burst threshold value into account. Considering burst composition methods and parameters on OBS, the most ideal classification will be performed by Random Forest algorithm in terms of accuracy. Thus, during DDoS attacks and core node based wavelength attacks, Random Forest algorithm can make those attacks busy by its high performance and it can prevent nodes of attacked network by isolating they completely.

References

[1] Rouskas, G.N., and Perros, H.G., "A Tutorial on Optical Networks", Networking Tutorials 2002, Springer-Verlag, LNCS 2497, 155-194, 2002.

[2] Yoo, S.J.B., "Optical Packet and Burst Switching Technologies for the Future Photonic Internet", Journal of Lightwave Technology, 24(12), 4468-4492, 2006.].

[3] Battestilli T. and Perros H., "An Introduction to Optical Burst Switching", IEEE Communications Optical Magazine, Vol.41, pp.10-15, 2003.

[4] Ramaswami, R. and Sivarajan, K.N., "Optical Networks". Morgan Kaufmann, United States of America, 1-55860-655-6, 2002.].

[5] Chatterjee, S., Pawlowski, S. : All-Optical Network. Commun. Acm 42, 74- 83 (1999)).

[6] Wen B, Bhide NM, Shenai RK, Sivalingam KM. Optical wavelength division multiplexing network simulator: Architecture and performance studies. SPIE Optical Networks Magazine. 2001 Sep-Oct; 2(5):16–26.

[7] Kantarci, B., Oktug, S.F., 2008. Loss RateBased Burst Assembly to Resolve Contention in Optical Burst Switching Networks, IET Commun., 2, 1, 137-143p.

[8] Available : https://www.slideshare.net/kritika91jawa/optical-networks-50518454

[9] Qiao, C., Chen, Y., Staley, J., 2003. The Potentials of Optical Burst Switching (OBS), Optical Fiber Communication Conference, OFC, Atlanta,Georgia.

[10] Kantarci, B., Oktug, S.F., Atmaca, T., 2007. Performance of OBS Techniques Under SelfSimilar Traffic Based on Various Burst Assembly Techniques, Sciencedirect, Computer Communications 30, 315-327

[11] Kaur, Harmanpreet, and Shamandeep Singh. "Prevention of DDOS in Optical Burst Switching using Genetic Algorithm." Indian Journal of Science and Technology 9.36 (2016).

[12] A. Rajab, C. T. Huang, M. Alshargabi, and J. Cobb, Countering Burst Header Packet Flooding Attack in Optical Burst Switching Network, In: International Conference on Information Security Practice and Experience, Springer International Publishing, pp. 315 - 329, Nov 16 2016.]

[13] Available: http://archive.ics.uci.edu/ml/machine-learning-databases/00404/

[14] Available : https://www.cs.waikato.ac.nz/ml/weka/downloading.html

[15] Anthony J. Viera, MD; Joanne M. Garrett, PhD (2005),Understanding Interobserver Agreement:The Kappa Statistic.

[16] Landis, J. Richard, and Gary G. Koch. "The measurement of observer agreement for categorical data." biometrics 33.1 (1977): 159-174.

A New Approach to Swarm Intelligence: Salp Swarm Optimization Algorithm with Unconstrained Problems

C.BAYDOGAN[1] and B. ALATAS[2]

[1]Firat University, Elazig/Turkey, cembaydogan@gmail.com
[2]Firat University, Elazig/Turkey, balatas@gmail.com

***Abstract* – In this paper a new heuristic algorithm based on herd intelligence which is called salp swarm optimization algorithm (SSA) was applied. Salp swarm optimization algorithm simulates salp swarms behavior to solve optimization problems. Firstly the biological structure of salp swarm optimization algorithm was examined and then mathematically expressed by evolutionary operators. Artificial intelligence optimization algorithms based on different intelligence that still maintain the update in the literature have been selected and compared with salp swarm optimization algorithm under equal conditions within unconstrained optimization problems. The properties of the optimization test problems are also included in the study. These optimization problems are chosen as unimodal (UM) and multimodal (MM). In the face of UM and MM optimization problems, the salp swarm optimization algorithm is explained with the tables and graphs of the superior and missing aspects of the other algorithms.**

***Keywords* – Optimization, Swarm Intelligence, Salp Swarm Optimization Algorithm.**

I. INTRODUCTION

IT is acknowledged that the most important human activities are decision making. Whether it is social, economic, business, technological, decisions have a lot to impact our lives. Optimization techniques play a crucial role in finding the best ways to maximize a problem or a decision maker's maximum benefit from available resources. Optimization techniques can be divided into two categories as traditional optimization techniques and modern optimization techniques. Traditional optimization techniques are used to solve the general linear optimization problem [1]. Many optimization problems such as unconstrained optimization problems, large scale unconstrained optimization problems, linear constrained optimization problems, nonlinear constrained optimization problems have been sought [2-3]. Many engineering problems to be resolved with the traditional method is very complex and difficult [4-5].

With the development of modern computer technologies, it has become more difficult to solve various problems with traditional optimization algorithms [6-7]. Researchers have begun to look for and suggest optimization methods that are called modern optimization algorithms which are smarter and more efficient. Over the past few years, the number of optimization algorithms inspired by nature has become increasingly important. Nature serves as an efficient resource for designing the artificial computing system to solve complex problems. These include many artificial intelligence optimization algorithms such as genetic algorithm (GA) [8], whale optimization algorithm (WOA) [9], particle swarm optimization algorithm (PSO) [10], cat swarm algorithm (CSA) [11], social spider optimization algorithm (SSO) [12], artificial bee colony algorithm (ABC) [13], ant colony optimization algorithm (ACO) [14], differential evolution algorithm (DE) [15], bacterial foraging optimization algorithm (BFO) [16], firefly optimization algorithm (FF) [17], cuckoo optimization algorithm (COA) [18].

In this study, the performance of salp swarm optimization algorithm (SSA) against unimodal and multimodal optimization problems is investigated. The performance evaluation between the social spider algorithm (SSO) and moth flame optimization algorithm (MFO), which are among the heuristic optimization algorithms existing in the literature, and the salp swarm optimization algorithm is performed [21-22]. The performance results are given in detail with the tables and graphs in the experiments and results section.

II. SALP SWARM OPTIMIZATION ALGORITHM (SSA)

A. The Biologic Structure of SSA

Salp is called transparent fish. The all organs of this fish are transparent expect for orange tongue. There is like a jelly structure that feels it is covered with fish scales when touched. The salps is a living species that pumping water into the body and moving it shrinks by stretching. Although it is invertebrate, it is known as a pre-primitive and primitive living species that gives an idea of how vertebrate creatures develop in the evolutionary process [19].

These tiny fish in the form of barrels, in the ocean, feed the waters through the feeding filters and planktons at this point will be eaten. The life cycle of the salps lives in the form of an individual or a swarm community. Salps can live alone or swarm. Living in a large group, the shrapnel ties together their bodies in chains and they feed and grow together. This

movement of the salps is shown in Figure 1. The salps reproduce in two ways as sexual and asexual. The salps come together to form a colony in sexual reproduction. In asexual reproduction salps are alone [20].

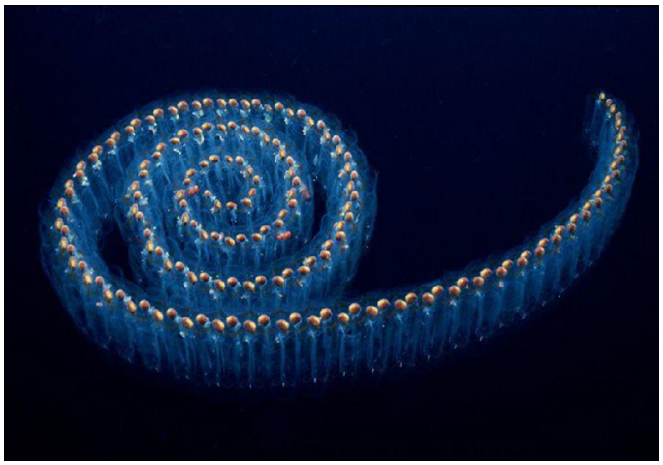


Figure 1: The movement of salp swarm in the ocean

B. Mathematical Model and SSA

In order to mathematically model the salp swarm, two teams are separated as the leaders and followers. The leader in the front of the swarm is considered a leader. All the parts behind the leader in the swarm are considered followers. The location of the salp is defined in an *n* dimensional search field; where *n* is the variable number of a particular problem. A two-dimensional matrix called *x* stores the entire salps position. There is an evolutionary operator called *F*, which is the target of the swarm in search space. This *F* also represents the source of food. Equation 1 is used to update the leader's position [23].

$$x_j^1 = \begin{cases} F_j + c_1\left((ub_j - lb_j)c_2 + lb_j\right), & c_3 \geq 0 \\ F_j - c_1\left((ub_j - lb_j)c_2 + lb_j\right), & c_3 < 0 \end{cases} \quad (1)$$

where x_j^1 represents the first salp (leader) position in the *j*th dimension. The most important parameter of the SSA is c_1. Exploration and exploitation are balanced as in Equation 2:

$$c_1 = 2^{e^{-\left(\frac{4l}{L}\right)}} \quad (2)$$

where *l* and *L*, respectively, indicate current iteration and the maximum number of iterations. Equation 3 is used to update the position of follower salps.

$$x_j^i = \frac{1}{2}(x_j^i + x_j^{i-1}) \quad (3)$$

All the steps of the SSA algorithm are as shown in Figure 2.

```
Initialize the salp population xi(i = 1, 2, ..., n) considering ub and lb
while(end condition is not satisfied)
Calculate the fitness of each search agent(salp)
F=the best search agent Update c1 by Eq. (2)
   for each salp (xi)
      if(i==1)
         Update the position of the leading salp by Eq. (1)
      else
         Update the position of the follower salp by Eq. (3)
      end
   end
   Amend the salps based on the upper and lower bounds of
variables
end
return F
```

Figure 2: Pseudo code of the salp swarm algorithm [23]

.

III. Experiments And Results

There are many optimization problems in engineering and literature to measure the success of artificial intelligence optimization algorithms. The problems and characteristics to be used in this study are summarized in Table 1 in detail. The problems were selected as UM and MM.

Table 1: Benchmark Functions

Functions	Lower and Upper Limits	Min	D	Type	Equation
f1–Sphere	[-5.12, 5.12]	0	30	UM	$\sum_{i=1}^{n} x_i^2$
f2–Rosenbrock	[-30, 30]	0	30	UM	$\sum_{i=1}^{n-1}\left[100(x_{i+1}-x_i)+(x_i-1)^2\right]$
f3–Powell	[-4, 5]	0	24	UM	$\sum_{i=1}^{n/4}\left[\begin{matrix}(x_{4i-3}+10x_{4i-2})^2+5(x_{4i-1}-x_{4i})^2 \\ +(x_{4i-2}-2x_{4i-1})^4+10(x_{4i-3}-x_{4i})^4\end{matrix}\right]$
f4–Rastrigin	[-5.12, 5.12]	0	30	MM	$\sum_{i=1}^{n}\left[x_i-10\cos(2\pi x_i)+10\right]$
f5–Ackley	[-32, 32]	0	30	MM	$-20\exp\left(-0.2\sqrt{\frac{1}{n}\sum_{i=1}^{n}x_i}\right)-\exp\left(\frac{1}{n}\sum_{i=1}^{n}\cos(2\pi x_i)\right)+20+e$
f6–Griewank	[-600, 600]	0	30	MM	$\frac{1}{4000}\sum_{i=1}^{n}x_i^2-\prod_{i=1}^{n}\cos\left(\frac{x_i}{\sqrt{i}}\right)+1$

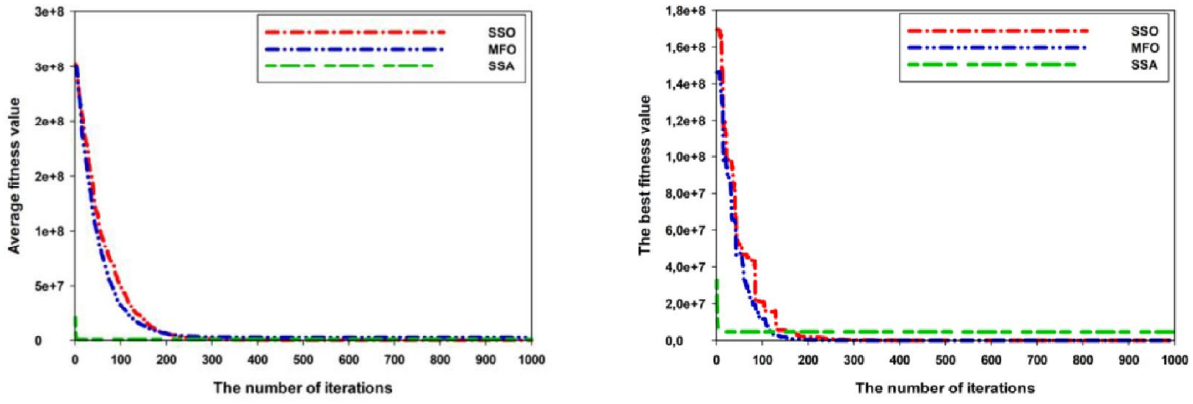
In order to investigate the ability to solve the selected optimization problems of the salp swarm optimization algorithm, comparative experiments were carried out under equal conditions with the moth flame optimization algorithm (MFO) and the social spider optimization algorithm (SSO). Each experiment is run 30 times and the performances of all algorithms are presented in Table 2.

Table 2: Comparison of Algorithm

Functions	Algorithms	The Best Value	The Worst Value	Mean	Median	Standard Deviation
	SSO	1.41E-003	1.06E-002	5.51E-003	5.26E-003	2.08E-003
f_1	MFO	2.66E-008	5.24E+001	6.99E+000	5.54E-007	1.52E+001
	SSA	**1.08E+001**	**2.87E+001**	**1.97E+001**	**1.97E-001**	**4.44E-000**
	SSO	2.95E+002	9.63E+002	5.09E+002	4.75E+002	1.49E+002
f_2	MFO	1.02E+000	8.00E+007	2.68E+006	2.02E+002	1.46E+007
	SSA	**6.35E+005**	**8.53E+006**	**4.37E+006**	**4.47E+006**	**1.63E+006**
	SSO	1.43E+000	8.47E+000	4.03E+000	3.81E+000	1.85E+000
f_3	MFO	8.75E-003	3.74E+003	6.40E+002	1.47E+002	1.01E+003
	SSA	**2.62E+002**	**1.31E+003**	**7.71E+002**	**7.61E+002**	**2.49E+002**
	SSO	3.52E+001	5.78E+001	4.66E+001	4.89E+001	6.30E+000
f_4	MFO	7.86E+001	2.46E+002	1.54E+002	1.55E+002	4.29E+001
	SSA	**1.93E+002**	**2.63E+002**	**2.30E+002**	**2.33E+002**	**1.72E+001**
	SSO	3.11E-001	1.15E+000	7.43E-001	7.17E-001	2.03E-001
f_5	MFO	1.09E-002	1.99E+001	1.44E+001	1.90E+001	7.86E+000
	SSA	**1.30E+001**	**1.59E+001**	**1.47E+001**	**1.48E+001**	**6.92E-001**
	SSO	7.41E-001	1.03E+000	9.73E-001	1.00E+000	7.27E-002
f_6	MFO	1.01E-004	1.80E+002	2.11E+001	2.34E-002	4.56E+001
	SSA	**4.80E+001**	**1.17E+002**	**7.45E+001**	**7.11E+001**	**1.77E+001**

Table 2 was formed by calculating the best value, the worst value, mean, median, standard deviation values for SSO, MFO, SSA algorithms.

The convergence graphs of the algorithms for the obtained results are shown in Figure 3.



(a) (b)

Figure 3: (a) Average fitness graph for Rosenbrock Function
(b) The best fitness graph for Rosenbrock Function

IV. Conclusion

In this study, general information about artificial intelligence optimization algorithms is given and inferences about the successes of these algorithms against solving engineering problems and against optimization problems have been made. The salp swarm optimization algorithm (SSA), which is at the focus of the study, avoids early convergence

and is ambitious to reach a global minimum or maximum, has been investigated, primarily in terms of its biological structure, its mathematical expression, and the steps of the algorithm.

It can be safely concluded that the SSA algorithm is an appropriate algorithm for solving optimization problems and engineering problems, as evidenced by the average and best fit values of 30 experiments on the problem solving struggle that has been introduced with various algorithms.

The most important conclusion to be drawn from this study is that the problem for all algorithms and the more exciting results can be obtained if the initial parameter values of the algorithm are set very well.

REFERENCES

[1] Dantzig, G.B.: On the need for a systems optimization laboratory, in optimization methods for resource allocation. In: Cottle, R.W., Karup, J. (eds.) Proceedings of a 1971 NATO Conference. English Universities Press, London, 1974.

[2] Albers, D.J., Reid, C.: An interview with George B. Dantzig: the father of linear programming. The College Mathematics Journal 17(4), 292–314, 1986.

[3] Gleick, J.: Breakthrough in problem solving, New York Times, November 18, 1984.

[4] Rao, V.R., Iyengar, N.G.R., Rao, S.S.: Optimization of wing structures to satisfy strength and frequency requirement. Computers and Structures 10(4), 669–674, 1979.

[5] Nanakorn, P., Konlakarn, M.: An adaptive penalty function in genetic algorithms for structural design optimization. Computers and Structures 79(29-30), 2527–2539, 2001.

[6] Fogel, D.B.: The advantage of evolutionary computation. In: Proceeding of Biocomputing Emergent Computation, pp. 1–11. World Scientific Press, Singapore, 1997.

[7] Coello Coello, C.A.: Theoretical and numerical constraint-handling techniques used with evolutionary algorithms: A survey of the state of the art. Computer Methods in Applied Mechanics and Engineering 191(11-12), 1245–1287, 2002.

[8] Goldberg, D. E.. Genetic Algorithms in Search, Optimization and Machine Learning, Addison-Wesley, Reading, MA, 1989.

[9] Mirjalili, S., Lewis, A. The whale optimization algorithm. Advances in Engineering Software 95:51–67, 2016.

[10] Kennedy, J., & Eberhart, R. Particle swarm optimization. In Proceedings of the 1995 IEEE international conference on neural networks (Vol. 4, pp. 1942–1948), 1995.

[11] S.-C. Chu, P.-W. Tsai Computational intelligence based on the behavior of cats International Journal of Innovative Computing, Information and Control, Vol. 3 pp. 163-173, 2007.

[12] James J.Q. "A Social Spider Algorithm for Global Optimization" Technical Report No. TR-2003-004, Dept. of Electrical & Electronic Engineering, The University of Hong Kong, 2013.

[13] Karaboga, D. An idea based on honey bee swarm for numerical optimization. Technical report-TR06. Engineering Faculty, Computer Engineering Department, Erciyes University, 2005.

[14] M. Dorigo and G. Di Caro, "The ant colony optimization meta-heuristic," in New Ideas in Optimization, D. Corne, M. Dorigo, and F. Glover, Eds. New York: McGraw-Hill, pp. 11–32, 1999.

[15] R. Storn and K. V. Price, "Differential evolution-A simple and efficient heuristic for global optimization over continuous Spaces," J. Global Optim., vol. 11, pp. 341–359, 1997.

[16] Passino, K. M. Biomimicry of bacterial foraging for distributed optimization and control. IEEE Control Systems Magazine, 22(3), 52–67, 2002.

[17] X-S. Yang Firefly algorithm, Lévy flights and global optimization M. Bramer, *et al.* (Eds.), Research and development in intelligent systems XXVI, Springer-Verlag, London pp. 209-218, 2010.

[18] Rajabioun, R. Cuckoo optimization algorithm. Applied Soft Computing, 11, 5508–5518, 2011.

[19] P. A. Anderson and Q. Bone, "Communication between individuals in salp chains II. Physiology," Proceedings of the Royal Society of London B: Biological Sciences, vol. 210, pp. 559-574, 1980.

[20] V. Andersen and P. Nival, "A model of the population dynamics of salps in coastal waters of the Ligurian Sea," Journal of plankton research, vol. 8, pp. 1091-1110, 1986.

[21] E. Cuevas, M. Cienfuegos, D. Zald´ıvar, and M. P´erez-Cisnero, "A swarm optimization Algorithm inspired in the behavior of the social-spider," *Expert Systems with Applications*, vol. 40, no. 16, pp. 6374–6384, 2013.

[22] Mirjalili, S: Moth-flame optimization algorithm: A novel nature-inspired heuristic paradigm, Knowledge-Based Systems 89, page 228–249 (2015).

[23] Mirjalili S, Saremi S: Salp Swarm Algorithm: A bio-inspired optimizer for engineering design problems, Advances in Engineering Software (2017).

Estimation of Unbalance Cost due to Demand Prediction Errors Using Artificial Neural Network

Abdullah Erdal TÜMER[1], Cankat YAVUZ[1] and Sabri KOÇER[1*]

[1] Necmettin Erbakan University, Konya/Turkey, tumer@konya.edu.tr
[1]Necmettine Erbakan University, Konya/Turkey, cankat.yavuz@gmail.com
[1] Necmettin Erbakan University, Konya/Turkey, skocer@konya.edu.tr *corresponding author

***Abstract* - Estimation of energy demand is used as an important tool for decision makers determining company strategies and policies. Apart from this, the fact that the actual consumption differs from the forecast is harmful for the economy of the company and even for the economy of the big scale. In this study, it is aimed to estimate the imbalance aberration caused by demand forecast deviation with Artificial Neural Networks and to evaluate its results.**

***Keywords* – Artificial Neural Network, Demand Prediction, Unbalance cost, prediction, Energy Demand**

I. INTRODUCTION

ACCURATE estimation of the amount of energy needed by countries is important for decision makers that determine energy strategies and policies. Particularly, in energy-driven outsourcing countries and in developing countries where demand for electricity is rising relatively fast, the demand forecasts become even more important. On the basis of this precept lies both economic and political reasons. It is economically important; energy consumption has affected many economic parameters such as current account deficit, inflation and growth. Furthermore, the liberalization of energy markets, which are becoming increasingly widespread throughout the world, has led to the energy prices being determined by supply and demand to a large extent. For this reason, imbalances are generally punished in other examples of energy markets in the world and in Turkey.

Electricity is an energy that must be consumed when it is produced because it cannot be stored, or rather it is very costly to store. Therefore, demand forecasts in electricity markets are indispensable. In order to meet the electricity need, TETAŞ (Türkiye Elektrik Ticaret ve Taahhüt A.Ş.- Turkey Electricity Trade and Contracting Co.) receives energy with bilateral agreement depending on the estimations that it has sent from 1 year ago. However, estimates made a year ago do not adequately reflect the needs of the present day, and companies are aiming to get the energy they need by estimating demand in the Day Ahead Market (DAM). However, if the amount of energy received by TETAŞ cannot meet the amount of energy in the day, or if it is in excess of the amount of energy, companies have to provide the supply demand balance by selling the excess electricity on
their hands or by purchasing the missing part from this market. This situation causes the imbalance costs. This loss must be able to be controlled / predicted.

Recently, studies have been carried out on electricity energy consumption and load forecasting, distribution and planning analysis in electricity generation. In the paper entitled "Grey prediction with rolling mechanism for electricity demand forecasting of Turkey" are proposed in the estimation of electricity demand. The study shows that the GPRM approach can be used as a useful tool for short-term load estimation for Turkey [1].

For Niğde in Turkey, load estimation was performed by two different methods. These methods are artificial neural network backpropagation algorithm and nonlinear trend analysis moving average methods. It has been shown that the most appropriate method is artificial neural network. The estimates obtained by both methods of 2001 were compared with the actual values and it was found that the estimation results are very close to the real values [2].

Turkey's electricity consumption is modeled using the Support Vector Regression. According to the model result, Turkey's electricity consumption in the next 20 years will reach 284.9 TWh, which is estimated to be about twice the 2006 value. They stated that the relevant institutions should plan a significant increase in the future power plant capacity [3].

In order to estimate China's energy demand from the countries with the highest energy consumption and to examine the dynamic nature of electricity consumption, a statistical power consumption model from 1980 to 2012 was developed. It was developed using the model Intelligent Swarm Firefly algorithm [4].

Many other similar works have been proposed either in the past [5–9] or more recently [10–14].

In this study, models were developed to predict demand for electricity in the DAM using artificial neural networks (ANN). Different architectures have been tried to achieve the most optimal prediction in the developed models.

II. MATERIALS AND METHODS

A. Artificial Neural Networks

Artificial neural networks can collect information about samples, make generalizations, and then decide on those samples using information they have learned in comparison with samples they have never seen before. The goal of an ANN is to compute between output and input values with some internal calculations [15]. The first computational model of artificial neural networks was based on 1943 by W.S. McCulloch ve W.A. Pitts [16]. ANN is widely used in various fields such as prediction [17], control systems [18], classification [19], optimization [20] and decision making [21]. ANNs are a parallel distribution processing method in which neurons and weights linked to neurons are put together. The relationship between the input and output can be learned, simply based on the basic principle of operation. A multilayer sensor (MLP) is one of the best-known types of ANNs consisting of an input layer, an output layer, and one or more hidden layers [22].

There are activation functions defined between layers. The most common ones are given in Table 1.

Table 1: Transfer functions common used in algorithms

Transfer function	Algorithm
Tansig	tansig(n) = 2(1 + exp (-2n)) – 1
Purelin	purelin(n) = n, for all n
Logsig	logsig(n) = 1(1 + exp (-n))

Also there are many different types of training algorithms. One of the most common training algorithms is Feed Forward Back Propagation algorithm (FFBP) [23].

B. Data Collection

The data were obtained from TETAS web page [24]. TETAŞ, which was established as the first and only public wholesale company of Turkey with the split of Turkish Electricity Generation and Transmission Company (TEAS) in 2001 as part of the liberalization activities in the energy sector, is an Economic State Entity limited to the responsibility of the State and is in compliance with the general energy and economy policy of the State electricity trading and contracting activities. 120 data were taken from the TETAŞ web page.

DAM (Day Ahead Market), MCP (Market Clearing Price), DBA (Distribution Bilateral Agreement) and RBA (Retail Bilateral Agreement) were used as input data. The owning cost is considered as output data for each model. The statistics belong the data are given table 2.

Table 2. The ranges of data set and their statistic

Parameters	Data Statistic		
	Ranges	Mean ± S.D.	Unit
Input Layer			
MCP	10,1 - 227,2	149,6 ± 52,53	Lira
DAM	302,8 - 647,8	450,6 ± 77,01	
DBA	4,0 - 248,0	116,5 ± 41,13	MWh
RBA	150,0 – 386,0	271,3 ± 54,20	MWh
Output Layer			
O. Cost	-12636,9-52258,2	13051,7 ± 14421,7	Lira

This data was used as 100 training data and the remaining 20 pieces were used for testing purposes. RBA. the amount of energy received from the TETAŞ for the retail company, DBA, the amount of energy received from the TETAŞ is estimated, and the estimate of the DAM is the estimate for the day. Depending on the structure of the energy market, companies can buy from the market in several different ways. As stated earlier, the prices in the liberalizing market and the electricity market are determined by hourly supply and demand amounts. The MCP shown in our data set shows the actual hourly prices, which are based on the supply and demand balance.

And in order to obtain convergence within a reasonable number of cycles, the input and output data should be usually normalized. Normalization method as follows:

$$x^{'} = 0{,}8 * \frac{x_i - x_{min}}{x_{max} - x_{min}} + 0{,}1 \quad [1]$$

where $x^{'}$ is the normalized value, x is the original data, xmax and xmin, respectively, is the maximum and minimum values, thus the scaled data ranging between 0,1 and 0,9.

C. Network Properties

Neural network based modeling were performed using MATLAB. 24 different models were developed to find the architect who made the most optimal prediction. The network properties used in these models are as follows:

- Network type: Feed-Forward Back-Propagation.
- Training function: TRAINLM.
- Adaption learning function: LEARNGDM.
- Performance function: MSE.
- Number of hidden layers: 1,2.
- Number of Neurons: 1-14
- Input Layer Transfer function: logsig, purelin and tansig
- Output Layer Transfer function: purelin
- Iterations numbers : 1000

The mean square error (MSE) was applied as the error function calculated from the following equation [25]:

$$\text{RMSE} = \sqrt{\frac{1}{n}\sum_1^n (X_s - X_p)^2} \quad [2]$$

$$R^2 = 1 - \frac{\sum_1^n (x_p - x_e)^2 \sum_1^n (x_p - x_e)\,2}{\sum_1^n (x_e - \bar{x})^2} \quad [3]$$

$$\text{MAE} = \frac{1}{n}\sum_{j=1}^{n} |y_j - \hat{y}_j| \quad [4]$$

where n is the number of data points, $q_{i,pre}$ is the network prediction,

$q_{i,exp}$ is the experimental response and i is an index of the data.

y_i is the measurement,

$\hat{y}_i$ is the true value.

III. Result and Discussion

In this study, ANN models were developed to estimate the imbalance loss caused by the electricity demand forecast deviation of energy market suppliers. Levenberg-Marquardt (TrainLM) backpropagation algorithm, Hyperbolic tangent sigmoid (TansiG), Log sigmoid (sigmoid) and Linear (Purelin) functions are used as transfer functions in hidden layer and output layer in ANN models. In addition, 1 or 2 hidden layers were used in each model and the training process of the model was performed using 1000 iterations. The number of neurons in the hidden layer was varied from 1-14, and the predictive value of each model was measured by MSE. The most optimal number of neurons is 14, the number of hidden layers is 1, and the learning function is trainlm. The regression values for the most optimal ANN model are shown in Fig 1.

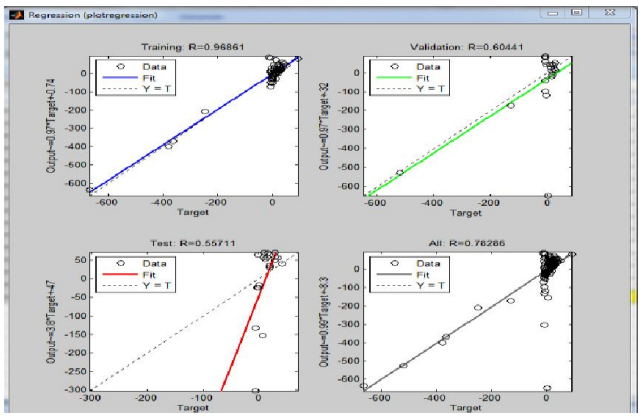


Figure 1. Optimum Network Regression

Statistical information showing the performance of the developed ANN model is summarized in Table 2. The correlation coefficient values obtained from the ANN model for the training and test data set were found to be 0.96 and 0.78, respectively.

Table 2: This caption is centered.

Optimum Structure	Statictic Value					
	Train			Test		
4-1(14)-1	RMSE	MAE	R	RMSE	MAE	R
	0,080	0,032	0,976	0,105	0,079	0,952

The accuracy of the improved ANN model is proved by the low low RMSE and high correlation coefficient values for the test data set.

The results show that the ANN algorithm identifies the relation between input and output variables in a meaningful way and that the output variable can be estimated with high accuracy.

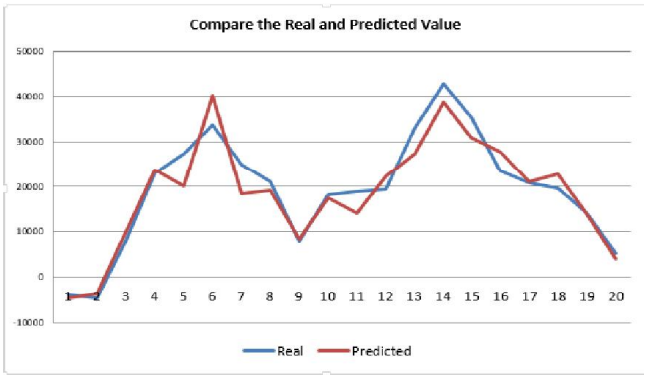


Figure 2. Compare the real and predicted value

IV. Conclusion

Artificial Neural Networks (ANN) are used successfully in modeling the problem by learning the complex relationship between input and output data in the best way. In this study, ANN models were developed to estimate the imbalance loss caused by the electricity demand forecast deviation of energy market suppliers. For this purpose, 120 different data sets obtained from the TETAŞ web page were used in the development of the ANN model. Levenberg-Marquardt backpropagation algorithm is used as a learning algorithm in the ANN models developed to estimate the imbalance loss caused by demand forecast deviation, and tansig, sigmoid, purelin function is used as an activation function in the hidden layer and output layer.

In addition, it was determined that the statistical comparison of the estimated values obtained from the established ANN models with the measurement results is the structure of the network architecture (4-1(14)-1) that best predicts the resultant R%, RMSE and MAE both traing and test study.

In the results obtained from the developed model, it was seen that the best ANN model defined the relationship between the input and output variables in the data set very well and predicted the output variables at high accuracy. This has shown that ANN can be used as a successful tool in predicting the imbalance loss caused by energy market suppliers'

deviation of electricity demand forecasts.

REFERENCES

[1] D. Akay and M. Atak, "Grey prediction with rolling mechanism for electricity demand forecasting of Turkey," *Energy*, vol. 32(9), pp. 1670-1675, 2007.

[2] T. Yalçinöz S. Herdem, and U. Eminoğlu, "Yapay sinir ağlari ile niğde bölgesinin elektrik yük tahmini," *ELECO 2002,*pp. 25-29.

[3] K. Kavaklioglu, "Modeling and prediction of Turkey's electricity consumption using Support Vector Regression," *Applied Energy*, vol. 88(1), pp. 368-375, 2011.

[4] G. Zhang, Y. Chen, Y. Yu, and S. Wu, "Intelligent Swarm Firefly Algorithm for the Prediction of China's National Electricity Consumption," *International Journal of Bio-Inspired Computing*, (In Press), 2017.

[5] W.W. Chan, and J.C. Lam, "Prediction of pollutant emission through electricity consumption by the hotel industry in Hong Kong," *International Journal of Hospitality Management*, vol. 21(4), pp. 381-391, 2002.

[6] O. Landsiedel, K. Wehrle, and S. Gotz, "Accurate prediction of power consumption in sensor networks," *In Embedded Networked Sensors, 2005, EmNetS-II. The Second IEEE Workshop,* pp. 37-44, May 2005.

[7] G. Altinay, and E. Karagol, "Electricity consumption and economic growth: evidence from Turkey," *Energy Economics*, vol. 27(6), pp. 849-856, 2005.

[8] A. Lendasse, J. Lee, V. Wertz, and M. Verleysen, "Forecasting electricity consumption using nonlinear projection and self-organizing maps," *Neurocomputing*, vol. 48(1), pp. 299-311, 2002.

[9] Y. Xu, and W. C. Lee, "On localized prediction for power efficient object tracking in sensor networks," In Distributed Computing Systems Workshops, 2003, *Proceedings. 23rd International Conference*, pp. 434-439), IEEE, May, 2003.

[10] H. Kaur, and S.Ahuja, "Time Series Analysis and Prediction of Electricity Consumption of Health Care Institution Using ARIMA Model," *In Proceedings of Sixth International Conference on Soft Computing for Problem Solving*, pp. 347-358, Springer, Singapore, 2017.

[11] R. R Rathod, and R.D.Garg, "Regional electricity consumption analysis for consumers using data mining techniques and consumer meter reading data," *International Journal of Electrical Power & Energy Systems*, vol. 78, 368-374, 2016.

[12] K. Chen, and K. Chen, "Modeling the Annual Growth Rate of Electricity Consumption of China in the 21st Century: Trends and Prediction," arXiv preprint arXiv:1710.07763, 2017.

[13] B. Dong, Z. Li, S.M. Rahman, and R. Vega, "A hybrid model approach for forecasting future residential electricity consumption," *Energy and Buildings*, vol. 117, pp. 341-351, 2016.

[14] S. Fong, M. Yuen, R.K. Wong, W. Song, and K. Cho, "Real-Time Stream Mining Electric Power Consumption Data Using Hoeffding Tree with Shadow Features," *In Advanced Data Mining and Applications: 12th International Conference, ADMA 2016, Gold Coast, QLD, Australia,* Proceedings vol. 12,(pp. 775-787, Springer International Publishing, December, 2016.

[15] V.N. Delgrange, N. Cabassud, M. Cabassud, L. Durand-Bourlier, and J.M. Laine, "Neural networks for prediction of ultrafiltration transmembrane pressure: application to drinking water production," Journal of Membrane Science vol. 150, pp. 111–123, 1998.

[16] W S McCulloch and W A Pitts, "A logical calculus of the ideas immanent in nervous Activity", Bulletin of Mathematics & Biophysics, Vol.943, Issue.5, 115-133, 1943.

[17] D.T. Bui, T.A. Tuan, H. Klempe, B. Pradhan, and I. Revhaug, "Spatial prediction models for shallow landslide hazards: a comparative assessment of the efficacy of support vector machines, artificial neural networks, kernel logistic regression, and logistic model tree," *Landslides*, vol. 13(2), pp. 361-378, 2016.

[18] J. Ahn, S. Cho, and D.H. Chung, "Analysis of energy and control efficiencies of fuzzy logic and artificial neural network technologies in the heating energy supply system responding to the changes of user demands," *Applied Energy*, vol. 190, pp. 222-231, 2017.

[19] S. Raith, E.P. Vogel, N. Anees, C. Keul, J.F. Güth, D. Edelhoff, and H. Fischer, "Artificial Neural Networks as a powerful numerical tool to classify specific features of a tooth based on 3D scan data," *Computers in biology and medicine*, vol. 80, pp. 65-76, 2017.

[20] A.H. Sebayang, H.H. Masjuki, H. C. Ong, S. Dharma, A.S. Silitonga, F. Kusumo, and J. Milano, "Optimization of bioethanol production from sorghum grains using artificial neural networks integrated with ant colony," *Industrial Crops and Products*," vol. 97, pp. 146-155, 2017.

[21] E. B. Beşikçi, O. Arslan, O. Turan, and A.I. Ölçer, "An artificial neural network based decision support system for energy efficient ship operations," *Computers & Operations Research*," vol. 66, pp. 393-401, 2016.

[22] A. M. Ghaedi, And A.Vafaei, "Applications of artificial neural networks for adsorption removal of dyes from aqueous solution: A review," *Advances in Colloid and Interface Science*, vol. 245, pp.20-39, 2017.

[23] H. Demuth, M. Beale, and M. Hagan, "Neural Network Toolbox 5: Users Guide" Natick, MA, The MathWorks Inc., 2007.

[24] www.tetas.gov.tr

[25] M. Khajeh, and K. Dastafkan, "Removal of molybdenum using silver nanoparticles from water samples: Particle swarm optimization–artificial neural network," *Journal of Industrial and Engineering Chemistry*, vol. 20(5), pp. 3014-3018, 2014.

[26] A. Witek-Krowiak, K. Chojnacka, D. Podstawczyk, A. Dawiec, and K. Pokomeda, "Application of response surface methodology and artificial neural network methods in modelling and optimization of biosorption process," *Bioresource Technology*, vol. 160, pp. 150-160, 2014.

Augmented Reality Application in Learning Geometric Shapes

B. YILMAZ, B. GÖK, S. TUFAN and F. BAŞÇİFTÇİ

Selçuk University, Konya/Turkey,
yilmazbetul@outlook.com.tr, gokbuse@outlook.com, sema_tufan@hotmail.com, basciftci@selcuk.edu.tr

***Abstract* - Augmented reality is created in the computer environment without leaving the actual environment, and interacts with software through the virtual environment. Display of objects created in the virtual environment at the specified points in the real environment. Augmented reality is used in a wide variety of ways such as e-commerce, manufacturing, shopping, journalism, sports, entertainment, health, architecture. In this study, geometric shapes were taught and the application was developed with Unity 3D, Vuforia SDK.**

***Keywords* - Augmented reality, geometrical shapes, virtual environment in education.**

I. INTRODUCTION

EMERGING technology, is used in all areas of today. While the sectors such as health, textile and transportation are influenced by technology, they have a share in being affected by technology in education. If we look at the developments in the educational environment, the blackboard and the chalk have left their place smart and the progress of the technology in education has been accelerated. In education, virtual reality and augmented reality issues have become effective in the field of technology. In the area of virtual reality and augmented reality, the application area has been increased to provide an easier and more understandable educational environment for the students. In this study, an application was prepared to help students at primary level as a target on these branches. In practice, it is aimed to teach 3 dimensional geometric shapes to students in virtual environment.

II. AUGMENTED REALITY

Augmented reality is that people are related to 3D objects in a virtual environment created in a computer environment without being abstracted from the real environment. In today's society as well as in the field, there is a growing use of reality technology. The augmented reality is that the user is intertwined with the virtual objects without breaking the connection from the real environment. That is, a real environment and a virtual environment can be combined. Augmented reality applications allow users to be interactively managed in computer-generated virtual environments.

Augmented reality is used as much as possibilities in the field of education, although it is a new technology. That is to say, the increase in the usage rate in the field of education in the future is doubtless expected. Augmented reality is also used effectively in the simulation field. That is, modeling work in car companies is carried out in the context of augmented reality, which gives the competent people the advantage both in terms of freedom and cost. In addition, when this system is used in the field of education in the schools, the motivation and interest in the learning of the students are observed to increase and the learning is facilitated. The effect of the materials reinforced with augmented reality in the field of education on vocabulary learning and reasonableness was made by Özgür Doğan as a graduate study. The effect of augmented reality, simulation and real object use on learning achievements, motivations and psychomotor performance was presented by Aslıhan Barbur as a doctoral thesis.

III. APPLICATION OF AUGMENTED REALITY IN EDUCATION

One of the areas where augmented reality is used is education. For primary school students, visuality and different perspectives in education have always been important. In this study, a model which teachers can help students to describe mathematical forms in three dimensions is presented. Model representation was performed in Unity 3D environment. It can be thought of as a Unity 3D game engine. Manipulation and simulation processes are performed by using the desired programming languages. In this study, three dimensional objects are placed on the shape when the technological device that the user uses is holding the desired one dimensional geometric shape to the camera. With augmented reality, we can actually feel like we're holding on to the three-dimensional geometric shapes that we do not have on paper.

After the installation of the Unity 3D program, in which the project is being developed, both the data base and the camera operations can be used in applications, so you have to go to https://developer.vuforia.com/ to join. To integrate the Vuforia environment into the Unity 3D program, the plugin must be included at https://developer.vuforia.com/downloads/sdk by downloading the plugin. After the downloaded file is added to Unity 3D, you should go to "License Manager" and "Target Manager" sections in "Devolop" tab on Vuforia page. In order to use the Vuforia camera plugin in the application, a project is created from the "License Manager" section to obtain the license key. Transferring photos to the database and exporting the database is done in the "Target Manager" section. The

"Add Database" button in the "Target Manager" section is clicked to create a new database and the type of media to be used for the created database is selected. In order to use the created database in the application, click the "Download Dataset" button and the file to be included in Unity 3D program is downloaded. Downloaded files are included in the project. The Unity 3D environment in which the work is performed is shown in Figure 1.

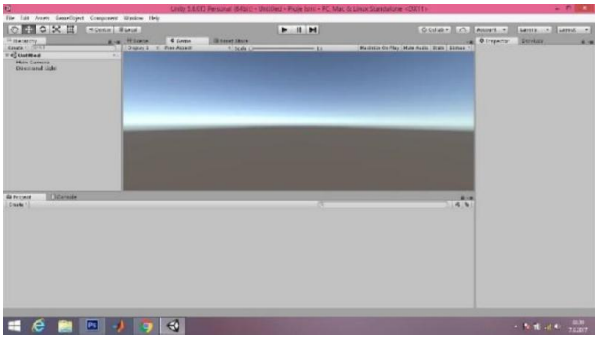


Figure 1: Unity program interface

The logical process step of the application to be performed in the field of education is shown in Figure 2.

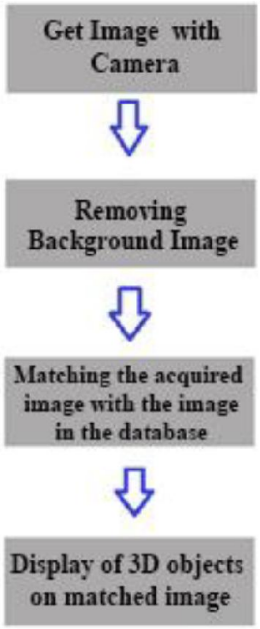


Figure 2: Logical sequence

The main screen display is set using the materials on the Unity 3D toolbar. In addition, the desired geometric shapes can be downloaded from the Asset Store within the Unity. In addition, the desired geometric shapes can be downloaded from the Asset Store within the Unity. The program has been integrated into the desired background database. Figure 3 shows the operation of the application on a fixed floor, where the drawings are completed and the necessary tools are loaded.

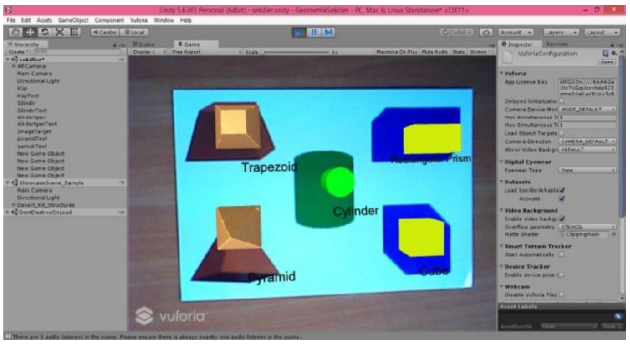


Figure 3: Application of the application on a fixed surface

In Figure 4, the user is shown in the hands of the user, independent of the floor of the application.

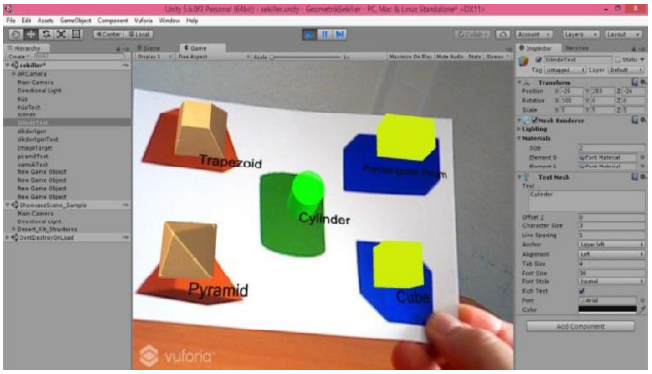


Figure 4: Application of the user in the hands of the user

In Figure 5, there is a side view of the user in his hand, independent of the floor of the application, to better illustrate the lateral areas of the geometric shapes.

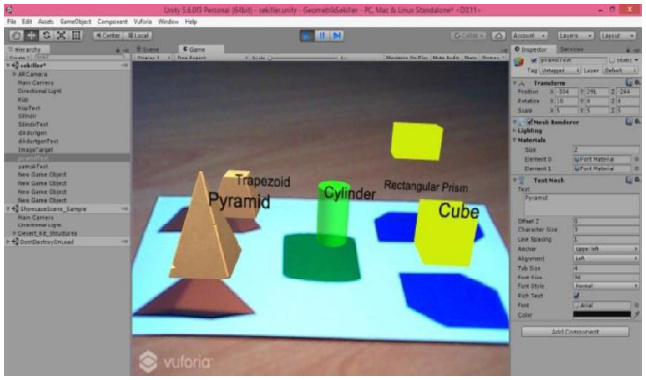


Figure 5: Lateral areas of geometric shapes used in practice

In this study, an additional camera was connected to the computer and calibration was provided to facilitate shape detection. After the coordinates of the shapes are also adjusted, the screen image is taken when the virtual environment is started. Thus, technology has entered into the field of education and visual persistence has been provided in the field of education.

IV. CONCLUSION

Augmented reality in learning of geometric shapes has been used in the field of education. This study was conducted in 27 students aged 6-8 years. 15 of these students are girls and 12 are male. 27 students were first described by drawing geometric shapes on the board and after 3 days from the students, the names of these figures were requested to be repeated and the success rate calculated. Then the geometric shapes are explained with the application made in Unity 3D program. After 3 days again the figure names are requested to be repeated and the success rate is calculated. Since the first narrative was far from visual and it was not memorable, the success rate was low and the success rate was 62.9%. The success rate of expression in this way is shown in Table 1.

Table 1: The results of the virtual environmentless expressio

Number of Right-Knowing Students	Number of Students Who Know Wrongly	Success Rate (%)
17	10	%62,9

With the application made in Unity 3D environment, the success rate was calculated as 88.8% because it increased the motivation and reminiscence by drawing attention of the students. The success rate of this narrative is shown in Table 2.

Table 2: Results of virtual media expression

Number of Right-Knowing Students	Number of Students Who Know Wrongly	Success Rate (%)
24	3	%88,8

As a result; Virtual applications have achieved serious success in the educational field. The success of these applications is based on visibility and attracting the attention of the user. Based on these results, it is thought that the number of such applications will increase in the field of education in the future.

REFERENCES

[1] Çavaş, B, Huyugüzel P ve Can B. 2004, Eğitim de Sanal Gerçeklik Uygulamaları.
[2] Kayabaşı Y. 2005, Sanal Gerçeklik ve Eğitim Amaçlı Kullanılması.
[3] Kaleci D, Demirel T, Akkuş İ, Örnek Bir Artırılmış Gerçeklik Uygulaması Örneği, 2016
[4] Erbaş Ç, Demirer V. 2014, Eğitimde Artırılmış Gerçeklik Uygulamaları: Google Glass Örneği1.
[5] Atabek. Ü. (1998) "İnternet ve Sanal Eğitim" 1.Eğitim Günleri Sempozyumu. İzmir.
[6] Erdem,H.,2013, Sanal gerçeklik ortamının-etkileşimli görsel eğitim aracı olarak-ilkokul eğitiminde kullanılması, Yüksek Lisans Tezi, Dokuz Eylül Üniversitesi Fen Bilimleri Enstitüsü, İzmir,106.
[7] Bayraktar E, Kaleli F. 2007, Sanal Gerçeklik ve Uygulama Alanları.
[8] 2013, Artırılmış Gerçeklik (Augmented Reality) Nedir? [online], http://www.regisapp.com/augmented-reality-nedir, [Ziyaret Tarihi: 11 Haziran 2017].

Application of Opt-aiNET algorithm to spectral features for feature selection

S. DEMİRCAN [1] and H. KAHRAMANLI[1]

[1] Selcuk University, Konya/Turkey, semiye@gmail.com
[1]Selcuk University, Konya/Turkey, hkahramanli@gmail.com

***Abstract* – Automatic analysis of emotion recognition has many applications and it is a developing area nowadays. Feature selection is also important step in emotion recognition. In this study automatic emotion recognition is presented with selecting features using Opt-aiNET algorithm. Firstly spectral features are extracted using Berlin Emotional Database (EMO-DB). Opt-aiNET optimization algorithm is applied for selecting the features. According to the results of the classification, it is shown that feature selection with Opt-aiNET optimization algorithm is an acceptable method.**

***Keywords* - Emotion Recognition, Spectral features, ANN, Opt-aiNET**

I. INTRODUCTION

SPEECH is most important way to denote the emotions to the other persons. Also emotion recognition is now gained great importance. In this paper we represent a feature selection method with Opt-aiNET algorithm which is an optimization algorithm.

Sentiment analysis was firstly dealt with by Nasukawa and his friends [1] in 2003. It has evolved over time to find a lot of application areas.

Emotion recognition is also important in the diagnosis of some diseases and psychological conditions. For example, when examining the acoustical characteristics of people who evidence of depression and suicide is found diagnosis-related cues. [2]. The design of advertising and marketing, and call-center applications are also mostly used application areas of emotion recognition. [3]. Emotion detection is also of great importance especially when the selecting of the significant number of incoming calls to emergency call-centers. [4]

The most important steps in emotion recognition are feature extraction and selection. The feature selection methods can be investigated in two ways as spectral and prosodic features. Mel-Frequency Cepstrum Coefficients (MFCC), Linear Predictive Coefficients (LPC) and Wavelet Transform can be considered as spectral features. Basic frequency (F0) value is one of the main prosodic features.

One of the vector features is Linear Predictive Coefficients (LPC) which have importance in characterizing spectral features of a speech sign in time environment [5, 6]. MFCC can be calculated without the necessity of LPC because while linear predictive analysis is modelling speech path, MFCC features models human ear [6]. As a result of this, MFCC method produces quite successful results in ER applications [6, 7].

The features extracted with Wavelet Transform is also used in recognition in many applications [8]. Continuous wavelet transform has been developed as an alternative to the Short Time Fourier Transform to optimize the frequency-dependent transient solutions. Even though the majority of applications are made with Discrete Wavelet (DWT)[9, 10], there are also applications uses continuous wavelet transform[11].

In this application Berlin Emotional Database (EmoDB) [5] is used. Firstly features extracted with DWT. Before the obtained features are given classifiers, some statistical features are extracted from these features and new attributes are obtained. Opt-aiNET algorithm is used for selecting the features. Selected features are given classifier. Artificial Neural Network (ANN) was used as classifier. As a result of the selection process, it is concluded that the classification success is increased so that the feature selection with opt-aiNET is an effective method.

The paper is divided four sections. In section 2, It is explained the methods used in the application. An overview of the database is given in section 3. Finally, proposed method and experimental results are dedicated in section 4.

II. METHOD

A. Opt-aiNET Algorithm

aiNET algorithm is developed for clustering which is a discrete immune network algorithm. Opt-aiNET algorithm is a little more developed state of aiNET and its adaptation for optimization of problems [12].

The Opt-aiNET algorithm shown as below [12].

Network cell: individual of the population.
Fitness: fitness of a cell in relation to an objective function to be optimized.
Affinity: Euclidean distance between two cells. (Eq. 2)

$$(XY) = \sqrt{(x_1 - x_2)^2 + (y_1 - y_2)^2} \quad \textbf{(2)}$$

Clone: offspring cells that are identical copies of their parent cell.

1. Randomly initialize a population of cells (the initial number of cells is not relevant)
2. Whereas stopping criterion
2.1. Determine the fitness of each network cell and normalize the vector of fitness.
2.2 Generate a number *Nc* of clones for each network cell.
2.3 Mutate each clone proportionally to the fitness of its parent cell, but keep the parent cell. The mutation follows Eq. 3.

$$c' = c + \alpha N(0,1) \;\; \alpha = \left(\frac{1}{\beta}\right) exp(-f^*) \quad \textbf{(3)}$$

Where c' is mutated cell c, $N(0,l)$ is a Gaussian random variable of zero mean and standard deviation $\sigma = 1$, is a parameter that controls the decay of the inverse exponential function, and f^* is the fitness of an individual normalized in the interval [0,1]. A mutation is only accepted if the mutated cell c' is within its range of domain.

2.4 Determine the fitness of all individuals of the population.

2.5 For each clone, select the cell with highest fitness and calculate the average fitness of the selected population.

2.6 If the average error of the population is not significantly different from the previous iteration, then continue. Else, return to step 2.1

2.7 Determine the affinity of all cells in the network. Suppress all but the highest fitness of those cells whose affinities are less than the suppression threshold σ and determine the number of network cells, named memory cells, after suppression.

2.8 Introduce a percentage d% of randomly generated cells and return to step 2.3. End While

B. Discrete Wavelet Transform (DWT)

The Wavelet Transform is suitable for multiresolution analysis, where the signal can be analyzed at different frequency and time scales [8].

There are several types of wavelet transforms and depending on the applications. For a continuous input signal, the time and scale parameters can be continuous, leading the Continuous Wavelet Transform (CWT). They may as well be discrete leading to Wavelet Serious expansion. Secondly the wavelet transform can be defined for discrete time signals leading to Discrete Wavelet Transform (DWT). [9]

The wavelets are shifted and expanded around discrete numerical values depending on the distance in DWT. The 2 factor is usually used for amplitude change and the mathematical expression is as follows:[13]

$$\psi(2^k t + l)$$

l: Shift factor
k: Scaling factor

Wavelet transform is a tool that separates functions, operators, or data into different frequency components and allows you to work on each component separately. In CWT, the wavelet coefficients for all scale values are calculated over the whole time axis. As a result large amount of data and processing load are occurring. DWT is developed to eliminate these disadvantages. In DWT the wavelet coefficients are calculated only at certain points by selecting the powers of the scale values two so that the number of operations is reduced.[14]

An efficient way for implementing DWT scheme by passing the signal through a series of low-pass (LP) and high-pass (HP) filter pairs developed by Mallat [15].

C. Artificial Neural Network (ANN)

ANN (Artificial Neural Network) is a parallel and distributed processing of information that is inspired by the human brain, composed of processing elements, each of which has its own memory, connected by weighted connections. [16-18]

ANN can be considered as an electronic model of neural network structure [13]. Neurons that are cells of real neural network in ANN are modelled as a knot. Networks are obtained with binding more than one knot. Multilayer structures consist with binding of two or more neural layers. In real-life problems, multilayer ANN (multi-layer perceptron) is commonly used. ANN is used widely and efficiently in many pattern recognition problems, speech recognition, and learning robot control strategies [14]. In this paper we have used ANN (Artificial Neural Network) for classification.

III. MATERIAL

In this paper we used Berlin Emotional Database (EmoDB) [10]. In Berlin Database, there are seven emotional conditions. These emotions are Anger, Boredom, Disgust, Anxiety (Fear), Joy, Sadness, Normal.

Ten actors (5 female and 5 male) simulated the emotions, producing 10 German utterances (5 short and 5 longer sentences) which could be used in everyday communication and are interpretable in all applied emotions. The frequency sample is 16 kHz.

IV. PROPOSED METHOD AND RESULTS

In this application ER is carried out with EmoDB [5]. Features are extracted from the data using DWT and some statistical features are extracted from these features. Opt-aiNET algorithm is used for selecting the features. Selected features are classified with ANN. (Fig. 1)

Firstly DWT is applied to database. The outputs of High-pass filters provide detail, D1; and the low-pass filters provide approximation, A1 [19]. The implementation of DWT is shown in Fig. 2. The wavelet coefficients were computed using the Daubechies-2 wavelet function. According to schema in Fig. 2 DWT is performed for seven levels.

In advance, the features obtained with DWT are different lengths for each data. In the first step, data reduction was made by taking statistics of each coefficient. Used statistical methods are indicated in Table 1. As shown Table 1 not only statistical values of coefficients of A (CA) values also statistical values of frequency values are used in the application.

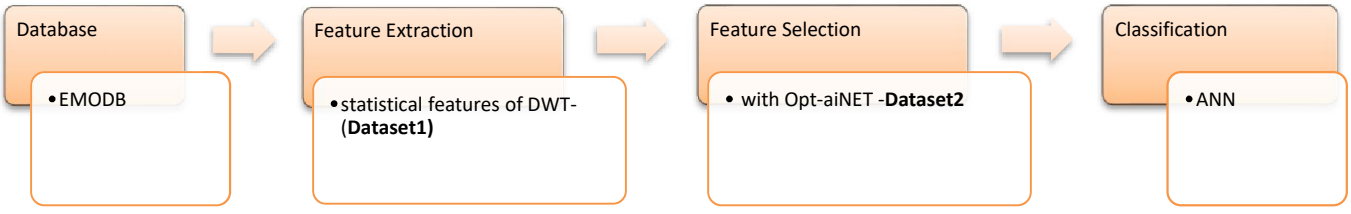


Figure 1: The steps of process for *Dataset1* and *Dataset2*

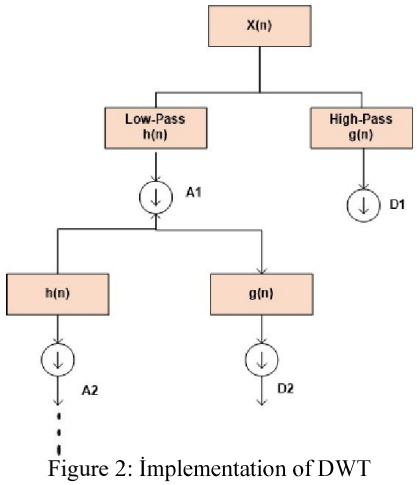


Figure 2: İmplementation of DWT

The feature group consisting of statistical values extracted from DWT was defined as *Dataset1*.

Table 1: Statistical Methods used for DWT features

DWT Features	Maximum value of CA
	Maximum value of Frequency
	Minimum value of CA
	Minimum value of Frequency
	Mean Value of CA
	Standard deviation of CA
	Skewness value of CA
	Kurtosis value of CA

Each statistical value group of CA is thought an agent in this study. Seven agents are used in the application. A brief algorithm is below:

- *Select features using with DWT*
- *Named Agents for each level of DWT as Agent1, Agent2, etc.*
- *Assigned "0" or "1" values for each agents*
- *If the Agent assigned "1", give this feature group to classification, otherwise don't use for classification.*
- *Repeat it until finding the best classification accuracy.*

In the optimization step, the population is created first with agents because the individual in the population represents the group of agents. Therefore the length of the individual in this study is seven. Individuals consist of 0s and 1s. If the value of the agent is 1, the feature group represented by this agent will be included in the classification, 0 will not be included.

For example, let the individual is (1,1,0,1,0,0,0). This vector means that the 1nd, 2th, and 4th agents are used. Classification success is used as fitness function. Opt-aiNET optimization algorithm was employed up to choose agent (or agents) that will make the classification accuracy maximum. The individual who has achieved the highest classification success as the result of the optimization has been selected for use in the future stages.

Agent groups chosen as a result of trials are modelled as feature groups with *Agent1, Agent2, Agent3* and *Agent7*. Selected features are called Dataset2.

Table 2: The result of the classification

	ANN
Dataset1	48.82%
Dataset2	71.56%

After obtaining Dataset1and Dataset2, classification is applied using ANN. As shown in Table 2, the classification result of Dataset1 is 48.82 and the classification accuracy of Datasest2 is 71.56.

V. CONCLUSION

In this study, ER from emotion data including speech signal was performed. Statistical values were extracted from feature obtained with DWT. The acquired features were selected with opt-aiNET optimization which provides better classification accuracy. The changes in classification success after optimization process using ABM were analysed. It was observed that the success of 48.82% increased to 71.56%. According to the results of the classification, feature selection with Opt-aiNET optimization algorithm is an acceptable method.

REFERENCES

[1] T. Nasukawa and J. Yi, "Sentiment analysis: capturing favorability using natural language processing," presented at the Proceedings of the 2nd international conference on Knowledge capture, Sanibel Island, FL, USA, 2003.

[2] D. J. France, R. G. Shiavi, S. Silverman, M. Silverman, and D. M. Wilkes, "Acoustical properties of speech as indicators of depression and suicidal risk," *Ieee Transactions on Biomedical Engineering,* vol. 47, pp. 829-837, Jul 2000.

[3] F. Burkhardt, T. Polzehl, J. Stegmann, F. Metze, and R. Huber, "Detecting Real Life Anger," *2009 Ieee International Conference on Acoustics, Speech, and Signal Processing, Vols 1- 8, Proceedings,* pp. 4761-4764, 2009.

[4] L. M. R. Lulia Lefter, DAvid A. van Leeuwen,Pascal Wiggers, "Automatic Stress Detection in Emergency (telephone) calls," *International J. Intelligent Defence Support Systems* vol. 4, pp. 148-168, 2011.

[5] A. Milton and S. Tamil Selvi, "Class-specific multiple classifiers scheme to recognize emotions from speech signals," *Computer Speech & Language,* vol. 28, pp. 727-742, 2014.

[6] T. L. Nwe, S. W. Foo, and L. C. De Silva, "Speech emotion recognition using hidden Markov models," *Speech Communication,* vol. 41, pp. 603-623, 2003.

[7] E. M. Albornoz, D. H. Milone, and H. L. Rufiner, "Spoken emotion recognition using hierarchical classifiers," *Computer Speech and Language,* vol. 25, pp. 556-570, Jul 2011.

[8] G. K. Verma and U. S. Tiwary, "Multimodal fusion framework: A multiresolution approach for emotion classification and recognition from physiological signals," *Neuroimage,* vol. 102, pp. 162-172, Nov 15 2014.

[9] O. Rioul and M. Vetterli, "Wavelets and signal processing," *Ieee Signal Processing Magazine,* vol. 8, pp. 14-38, Oct 1991.

[10] H. J. Go, K. C. Kwak, D. J. Lee, and M. G. Chun, "Emotion recognition from the facial image and speech signal," *Sice 2003 Annual Conference, Vols 1-3,* pp. 2890-2895, 2003.

[11] S. Ray and A. Chan, "Automatic feature extraction from wavelet coefficients using genetic algorithms," *Neural Networks for Signal Processing Xi,* pp. 233-241, 2001.

[12] L. N. de Castro and J. Timmis, "An artificial immune network for multimodal function optimization," *Cec'02: Proceedings of the 2002 Congress on Evolutionary Computation, Vols 1 and 2,* pp. 699-704, 2002.
[13] N. Arı, Ş. Özen, and Ö. H. Çolak, *DALGACIK TEORİSİ (WAVELET)*. Ankara: Palme Yayıncılık, 2008.
[14] G. Tezel, "Classification of Biomedical Signals via a New Artificial Neural Network with Adaptive Activation Function," PHD, Natural and Applied Sciences Department of Electrical and Electronics Engineering, Selcuk University Konya, 2007.
[15] S. Mallat, *A wavelet tour of signal processing*: Academic press, 1999.
[16] Ç. Elmas, *Yapay Sinir Ağları (Kuram, Mimari, Eğitim, Uygulama)* vol. 1. Ankara: Seçkin Yayıncılık, 2003.
[17] T. Kohonen, "An Introduction to Neural Computing," *Neural Networks,* vol. 1, pp. 3-16, 1988.
[18] Z. Şen, *Yapay Sinir Ağları İlkeleri*. İstanbul: Bilge Kültür Sanat, 2004.
[19] İ. Güler and E. D. Übeylı, "ECG beat classifier designed by combined neural network model," *Pattern recognition,* vol. 38, pp. 199-208, 2005.

Risk Management in IT Project

ADEM ALPASLAN ALTUN[1] and Anar TAGHIYEV[2]

[1] Selcuk University, Konya/Turkey, altun@selcuk.edu.tr
[2]Selcuk University, Konya/Turkey, anart@selcuk.edu.tr

Abstract *- IT projects commonly confront the unknown, including new technology challenges. The new and unknown bring unique risks. The benefits of risk management in projects are huge. The article describes the main aspects of implementing risk management in IT projects according to the developed organizational and methodological support. It eliminates the contradiction that arises between the requirements for risk management. The essence of the contradiction lies in the following: risk management should ensure maximum compliance of actual and planned results, with an allowable deviation of not more than 5%. At the same time, risk management should not change the existing management in IT projects (processes Waterfall, Agile, etc.). The article describes adapted methods and approaches that take into account the specifics of the IT sphere, as well as presents the results of pilot implementation of risk management in the IT project. The deviation of the fact from the plan following the completion of the IT project was 4.5%. This article gives the golden rules to apply risk management successfully in IT projects. They are based on personal experiences of the authors who has been involved in IT projects for over ten years. Also, the big pile of literature available on the subject has been condensed in this article.*

Keywords **- Risk, risk management, IT project, organizational and methodological support, risk analysis.**

I. INTRODUCTION

All projects have risks. If a potential risk of the project is not identified early, then the project will be at a high risk to complete as per schedule, within budget and to meet the expected quality. One of the current difficulties faced by a new Project Manager today is not having a sample or general risk list to refer to when identifying the project risk.

II. RISK MANAGEMENT APPROACH AND PLAN

Projects implemented in the field of information technology (hereinafter - IT projects) represent a complex set of scientific, engineering and technological disciplines that require long-term training, large investment costs, high technology, experienced specialists [1]. The complexity of implementing IT projects creates a risk zone, which leads to a reduction in the number of successful IT projects, where actual results should be equal to the planned ones. Analysis of the statistical data presented in Table 1 revealed an actual problem that is related to the occurrence of events that can have a significant negative impact on the objectives of IT projects (duration, cost, quality) [2].

Table 1: The results of implemented IT projects in the US (60%), in European (25%) and in other countries (15%) from 2004 to 2014.

	2004	2006	2008	2010	2012	2013	2014
Successful projects	29%	35%	32%	37%	39%	25%	16.2%
Incomplete projects	18%	19%	24%	21%	18%	25%	31.1%
Projects in which problems entailed a change planned goals	53%	46%	44%	42%	43%	50%	52.7%

The IT organization is exposed to a variety of factors generated by both the external and internal environment. Thus, in their work, O. Lee and D. Baby confirm this with the results of the studies carried out. Scientists come to the conclusion that external factors (natural factors, business environment) and internal (people, technologies) of the environment are the main sources of uncertainty, increasing the likelihood of financial and other losses. It means that potential threats can simultaneously come from both endogenous and exogenous environments. For example, negative risks of an exogenous environment can be threats associated with improperly planned budgets, lack of professional staff, and so on. Negative risks of the endogenous environment can be attributed to the dangers associated with fluctuations in foreign exchange markets, changes in tax legislation, and political and economic relations between countries.

In this article, "risk" will be understood as a probable event that can have both a negative and a positive impact on the successful completion of the IT project [3].

As a result of the analysis of scientific papers published on the topic of risk management, it was found that scientists are more concerned with general risks that do not reflect the specifics and specificity of the field of information technology. And the risk in most of the works is treated only from a negative point of view. In this regard, many practitioners, managers of IT organizations and IT project managers refuse to use risk management, as existing methods of risk management and their implementation significantly complicate the process of managing IT projects.

In this regard, **the purpose of the article** is to resolve the contradiction that arises between the requirements for risk management in IT projects, namely:

* Implementation of risk management should not change the existing and established management in the IT project, that is, the management in the project must remain unchanged regardless of the methodology for implementing the IT project and regardless of the used lifecycle model (Waterfall, Agile, etc.);
* Implementation of risk management in the IT project should contribute to a minimum deviation of actual results from the planned (no more than 5%).

According to statistics provided in the reports of The Standish Group International in 2014, the average deviation from the planned budgets, deadlines and quality in IT projects, developed mainly in the US and European countries, was 89%.

This contradiction was eliminated by solving the following **problems**:

1) Analysis of methods used to perform fundamental steps of risk management (Figure 1);
2) Development of organizational and methodological support for the implementation of risk management in IT projects;
3) Experimental approbation of the developed organizational and methodological support for the implementation of risk management in IT projects. The results showed that the deviation of the actual results from the planned results was 4.5%, that is, the over-expenditure of resources compared to the average deviation of 89% was reduced by 19 times.

Let us consider the solution of each problem in more detail. The development of organizational and methodical support for the process of implementation risk management in IT projects requires the creation of an integrated approach and the creation of effective risk management, through which the IT project manager can operatively identify, analyze, monitor risk events and respond to them.

Thus, the solution of the tasks posed requires the analysis and adaptation of heuristic methods (methods to find the ideal solution) for each risk management procedure.

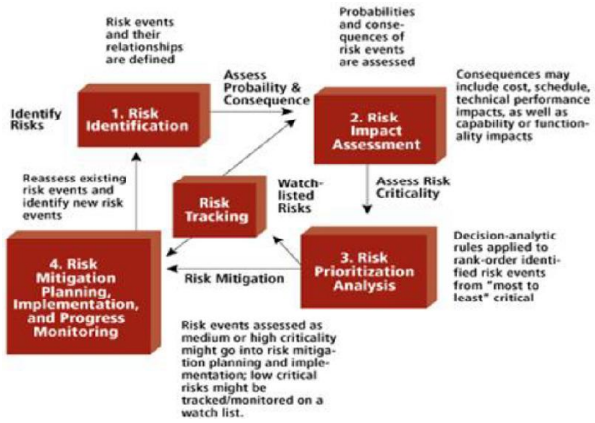


Figure 1. Fundamental Steps of Risk Management.

III. RISK IDENTIFICATION FOR AN IT PROJECT

To identify risks in IT projects, are proposed to consistently perform the following actions:

1) Analyze the project documentation, which will identify the risks associated with the planned results, the timing, the budget, the requirements, etc., and identify the risks that were previously realized in other IT projects [4];

2) Apply the "Process Decision Program Chart (PDPC)" method;

3) Use questionnaires [5];

4) Apply the method of "brainstorming", reinforcing it with the innovative game Speed Boat [6]. As participants in the "brainstorming", it is recommended that the full team of the project team be involved, including the IT project manager and invited experts [7];

5) Use the SWOT (Strengths, Weaknesses, Opportunities, Threats) analysis method. Using this method makes it possible to simultaneously identify both negative and positive risk events;

6) Conduct interviews with experts who have experience in implementing similar IT projects.

IV. ANALYSIS OF IT PROJECT RISKS

The analysis procedure is proposed to be carried out using qualitative (expert) methods for assessing the likelihood of occurrence and the impact of risk events due to the following factors:

* Limited time allocated to the planning stage in real production conditions, whereas the use of quantitative methods is a process that requires considerable labor, time resources, as well as relevant knowledge, skills and skills of the IT project manager [8];

* The use of KISS (Keep it Short and Simple) - the way of designing and developing IT projects, in which simplicity of statements is declared as the main value of the project implementation (methods of quantitative risk evaluation require significant formalization of processes);

* Use of the main approaches of flexible development, listed in the manifest of software development *Agile Manifesto* [9]. *Agile* sets priorities, according to which people and their interaction are more important than processes and tools. Therefore, the use of qualitative methods in all risk management procedures promotes the growth of interaction, trust and communication between the participants of the project team;

* Each implemented IT project is unique, according to the definition of the project, which limits the possibility of using information from previous IT projects;

* The complexity and laboriousness of using quantitative methods for small projects (duration of development not more than two months) is not expedient;

* Iterative implementation of the IT project requires a fast and flexible implementation process for all major risk management procedures.

In this connection, the following heuristic methods are suggested to use the following heuristic methods to assess the damage from the appearance of negative risks or a possible positive effect from the manifestation of positive risks:

*The first stage is "Bow-Tie" [10]. Note that the "Bow-Tie" method consolidates the features of the "Event Tree Analysis" (ETA) and "Fault Tree Analysis (FTA)" methods [11];

* Cause and effect diagram of Ishikawa (Fishbone Diagram) [12];

* Interview.

Consider the process of adapting each of the above methods, taking into account the specifics of implementing IT projects.

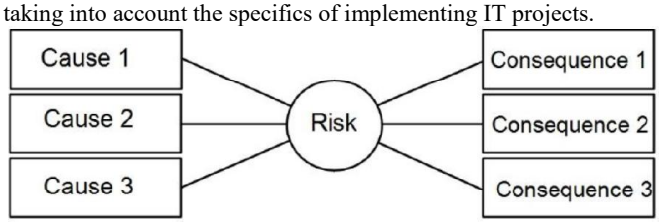


Figure 2. The method of "Bow-Tie" - the first stage.

In the algorithm of the "Bow-Tie" method, two main stages are distinguished. At the first stage, a risk analysis is performed by identifying the main sources of the risk event and determining the consequences if it occurs (Figure 2). Such actions allow the IT project manager and the project team to identify the main root causes that generate a risk event, as well as to forecast various scenarios for the development of the IT project. To identify the causes and sources of negative risks, it is proposed to use the Ishikawa cause-and-effect diagram method (Figure 3). The classical algorithm for applying the Ishikawa diagram involves a comprehensive analysis of the problem using the following main groups:

* personnel - the cause of the problem is the "human factor";

* equipment - the cause of the problem is the equipment used, machines, software, etc .;

* materials - the reason for the problem is the raw materials used;

* external environment - the cause of the problem is an exogenous environment;

* control - the cause of the problem is a poor control system that provides control;

* technology - the cause of the problem is the technological process.

The classical algorithm for using the Ishikawa cause-and-effect diagram does not fully meet the requirements for the procedure for risk analysis in IT projects [14]. For instance, in the process of implementing IT projects there is no group "production raw materials". However, a comprehensive study of risk events requires the inclusion of the group responsible for the information, since information data are the main material used in the development of IT products. Thus, the adapted Ishikawa diagram method will include the following groups:

* personnel - the participants of the project team are the cause of the risk. The sources of risky events may be lack of necessary professional skills or experience, low level of communication and trust between participants, conflicts, etc.;

* equipment - the cause of the risk is, for example, the software used, server failure, lack of Internet, etc .;

* information - the cause of the risk is, in particular, the lack of project documentation necessary for the development of an IT product, etc.;

* the external environment - the cause of the risk is the external environment of the IT project, which includes the organization where the project is being implemented, as well as subcontractors, etc .;

* control - the cause of the risk is the management style of the IT project manager (democratic, authoritarian, liberal);

* technology - the risk model is the life cycle model used in the IT project implementation: a cascade model, a V-shaped model, an incremental model, a spiral model, a rapid development model for RAD applications, and Agile.

An example of the graphical representation of the adapted Ishikawa diagram is shown in Figure 3.

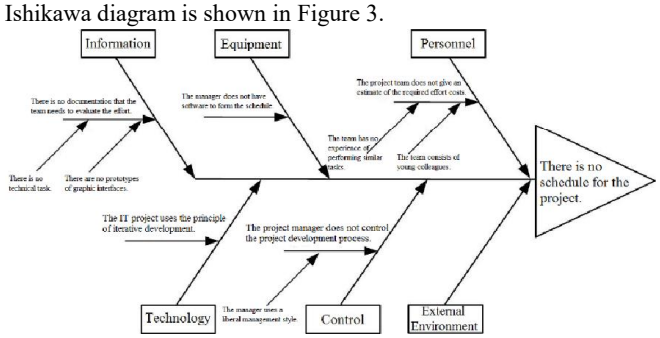


Figure 3. Adapted Ishikawa diagram for IT projects [13].

While using the methods of "Bow-Tie" and "Ishikawa diagram", new risks can be identified.

To increase the quality of the expert evaluation, was recommended to use the weight of the project team members (Table2), Formula 1 (as in below) and the verbal-numerical scale of Harrington (Table 3, Table 4).

$$x = \frac{\sum_{i=1}^{n} x_i k_i}{\mathrm{n}} \qquad (1)$$

Here, x_i - is the probability (impact) estimate given by the project participant; n - is the number of project participants; k_i - is the weight of the participant in the project.

Table 2: The weight of participants in the IT project.

Role in the project	Experience of the employee in this role over a year	Competences (education, professional development)	Total, *k*
Project manager	0,5	0,5	1
Expert	0,5	0,4	0,9
Developer	0,5	0,4	0,9
Analyst	0,5	0,4	0,9
Imposer	0,5	0,2	0,7
Designer	0,5	0,4	0,9
Tester	0,5	0,3	0,8
Customer	0,4	0,1	0,5

Table 3: The verbal-numerical Harrington scale for a qualitative evaluation of the degree of impact.

The degree of risk impact on the project	The Harrington factor (according to PMBoK)	The Harrington factor	Loss
Strong (Maximum)	0,8-1,0	5	Works in the project are stopped.
Significant	0,64-0,8	4	Works in the project are preformed with big delay.
Average	0,37-0,64	3	There is a time delay in performance of work.
Weak	0,2-0,37	2	Works in the project are performed with small delay.
Minimal	0,0-0,2	1	There are insignificant lags from the draw-up plans.
Influence is not	0,0	0	Works in the project are completely performed with the drawn-up plan.

Table 4: The verbal-numerical Harrington scale for a qualitative evaluation of the degree of impact.

The degree of risk impact on the project	The Harrington factor (according to PMBoK)	The Harrington factor	Loss
Strong (Maximum)	0,8-1,0	5	The risk is inevitable. Guaranteed risk.
Significant	0,64-0,8	4	The risk is probable.
Average	0,37-0,64	3	There is no guarantee that the risk will come, but nevertheless there is such opportunity.
Weak	0,2-0,37	2	There is the possibility of a risk.
Minimal	0,0-0,2	1	There is the potential possibility for risk.
Influence is not	0,0	0	Risk is not possible.

The received results are suggested to be visualized using the probability of occurrence and influence matrix for the negative and positive risks shown in Figures 4 and 5.

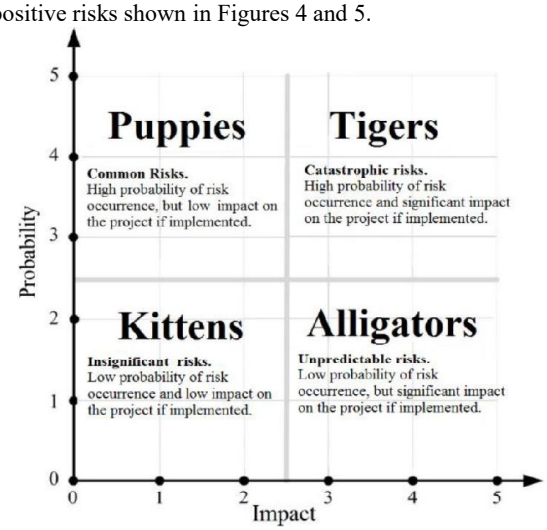


Figure 4. A matrix of probability of development and T. Mirna and F. Tkhani's influence for negative risks.

According to the classification of Merna T. and Thani F. [15], negative risks can be divided into the following categories:

* Catastrophic risks ("tigers") are risks that have a high probability of occurrence and the ability to have a significant negative impact on the IT project. The onset of one catastrophic risk leads to the suspension of the entire project;

* Unpredictable risks ("alligators") are risks that have a low probability of occurrence, but have the ability to have a significant negative impact on the IT project;

* Frequent (common) risks ("puppies") are risks that are highly likely to occur, but they are not able to have a significant impact on the IT project;

* Insignificant risks ("kittens") are risks that have a low probability of occurrence and do not have the ability to exert significant influence on the IT project. The project manager can neglect similar risks and not develop response measures.

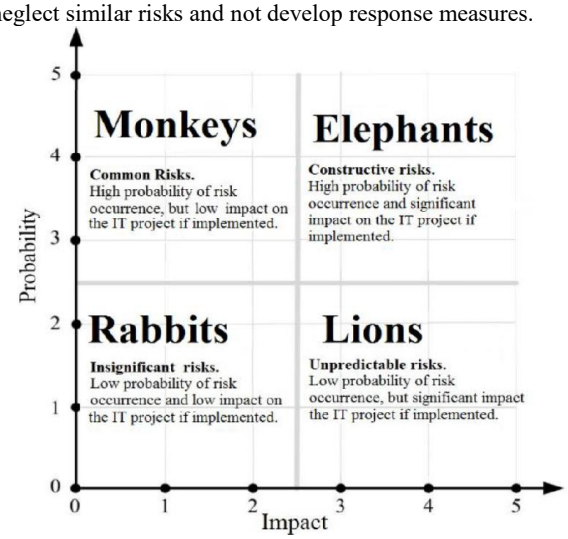


Figure 5. A matrix of probability of development and influence for positive risks.

To identify the most catastrophic negative risks in IT projects, the ranking proposed by T. Mernoy and F. Thani is optimal, because it allows you to prioritize all negative risks. So, first of all it is necessary to work with risks, which belong to the category "tigers", then with "alligators" and "puppies". The risks that fall into the category of "kittens", the manager of the IT project can be neglected.

Despite the convenience of using this classification, Merna and Thani do not offer a ranking for positive risks. In this regard, is proposed to classify positive risks using the following categories (Figure 5):

* Constructive risks ("elephants") are risks that are highly likely to occur and the ability to have a significant positive impact on the IT project;

* Unpredictable risks ("lions") are risks that have a low probability of occurrence, but have the ability to have a significant positive impact on the IT project;

* Commonly encountered risks ("monkeys") are risks that are highly likely to occur, but are not able to have a significant positive impact on the IT project

* Insignificant risks ("rabbits") are risks that have a low probability of occurrence and do not have the ability to have a significant positive impact on the IT project. Insignificant risks the IT project manager can neglect and not develop measures to respond to them.

Using the probability of occurrence and influence matrix for positive risks makes it possible to establish priority positive risk events. First of all, it is necessary to work with risks that are classified as "lions", as they can have a significant positive effect on the IT project. Then you need to work with the risks that fall into the category of "monkeys". Risks like "elephants" and "rabbits" IT project manager can be neglected, because creative (constructive) risks are guaranteed to come in the process of project implementation, and insignificant risks will not have a significant positive impact.

The development of creative (constructive) measures to respond to risks is proposed to be carried out with the help of:

* The method of "Bow-tie" - the second stage;
* Walt Disney's method;
* The method of "Six Thinking Hats";
* The method of "brainstorming";
* The Delphi method.

And for different categories of negative and positive risks, it is suggested to use various heuristic methods. For instance, for risks that have been classified as catastrophic, it is proposed to use methods that identify the causes of the risk, possible consequences and links to other risks. Such a detailed analysis of catastrophic risks enables experts to evaluate them in a comprehensive manner and more accurately determine the possible level of probability of manifestation and influence.

In real production conditions, the IT project manager does not have sufficient resources to ensure the quality management of all identified negative and positive risks. Thus, setting priorities among different risk categories enables the IT project manager and the project team to concentrate limited resources on managing the most significant risks [16]. First of all, it is necessary to develop measures of "Plan A", triggers and "Plan B" measures for negative risks that have been identified as catastrophic ("tigers"). Next, we investigate risks that fall into the category of unpredictable ("alligators") and often occur ("puppies"). The lowest priority for negative risks, defined as insignificant ("kittens").

In this connection, it is proposed to develop for risk management with high priority ("tigers" and "lions"):

* "risk response plan", or "plan A", - a plan of preventive measures for leveling, weakening, transferring, accepting for negative risks, as well as using, strengthening, dividing and accepting - for positive ones;

* triggers - indicators of the onset of risk, that is, the signs by which the person in charge of risk can understand that the preventive measures of "plan A" did not bring the expected effect;

* "retreat plan", or "plan B", - a plan of measures, which provides for actions in the event of occurrence of a risk event.

For risks that are classified as "alligators", "puppies", "monkeys", it will be sufficient to develop creative measures of "plan A" and triggers. Risks of the same category "kittens", "elephants" and "rabbits" can be neglected.

Next, we will consider the adaptation of heuristic methods for developing creative measures for responding to risks for each category in more detail.

Catastrophic risks ("tigers"). Since the catastrophic risks have a significant impact on the successful completion of the IT project, the implementation of a single risk of the "tigers" type leads to a halt in the project, therefore the development of creative activities of the "Plan A", "Plan B" and triggers is proposed to be carried out using:

* The method of "Bow-tie" - the second stage (Figure 6);
* Walt Disney's method;
* Six Thinking Hats;
* Delphi's method, enhanced interview.

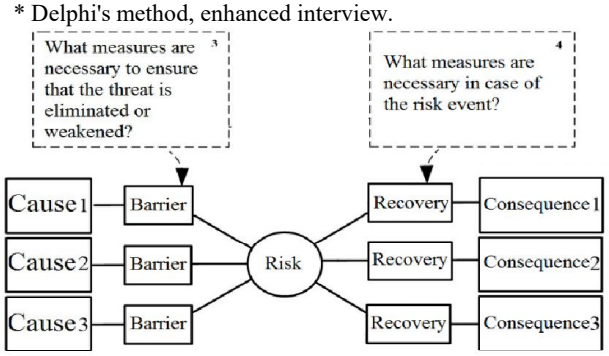


Figure 6. "Bow-tie" method - the second stage.

At the second stage of the "bow-tie" method, the IT project manager and the project team develop "barriers" ("Plan A" activities) and "restoration measures" (Plan B events). According to the rules of using the method, the identified sources of risk at the first stage give the opportunity to quickly develop "barriers" that will allow to level, weaken or transfer the risk. Formalized consequences in case of risk allow the IT project manager and the project team to develop effective measures to eliminate negative effects [17]. The "bow tie" method also makes it possible to create triggers that will signal in advance the imminent occurrence of a risky event and that the "plan A" measures did not bring the expected positive effect.

If the developed activities of "Plan A" and "Plan B" exceeded the established marginal cost of risk management measures, then the Walt Disney method or the method of separating the de Bono thinking can be used.

The essence of Walt Disney's method is a rigid division of the thinking directions of the project team members. So, at the stage of "Fantaser" the project team members offer various ideas, including fantastic ones, which can level the catastrophic risk. The Disney method will be more productive if outside experts are involved, which are not part of the IT project team. The ideas they expressed can be the basis for developing more creative activities. At the stage of "Critic", each of the proposed activities of the project team members is subjected to a critical evaluation and provides arguments that justify the ineffectiveness of these measures. The "Realist" stage includes the evaluation of the proposed activities, and the "Executor" stage - the adoption of a management decision about which activities need to prepare resources.

The Walt Disney method is recommended to be used with limited time resources, since the four main stages allow the rapid development of creative activities of "Plan A" and "Plan B". If the IT project manager and the project team have a large temporary resource, then instead of the Disney method, the method of dividing De Bono's thinking can be used.

The essence of the method "Separation of de Bono thinking", as well as the method of Walt Disney, is connected with the division of the direction of thinking, however in the de Bono method the following stages are distinguished:

* Stage II ("Red Hat") - a stage in which the project team members can express their emotional attitude to the proposed creative event without resorting to logic or reasoned answers. This stage can be used as a filter, due to which the project team members will work only with those solutions that they liked;

* Stage III ("Yellow Hat") - the stage at which the project team members express only positive arguments in favor of the proposed activities;

* Stage V ("White Hat") - the stage at which the participants of the project team use only figures and facts as arguments. Also at this stage, a final managerial decision is made as to which activities should be included in the risk response plan;

* "The Blue Hat". Edward de Bono empirically established that the method of separation of thinking works more effectively if there

is a specialist in the project team who independently performs the following functions independently of the method steps: fixes the results proposed by the team; stimulates the creative potential of the team; is responsible for strict adherence to the algorithm of the method.

Using the Delphi method can also help in the search for creative activities of "Plan A" and "Plan B". This method can be used both in the classical version, that is, through communications with experts via e-mail, and being strengthened by the "interview" method, that is, by conducting interviews with invited experts.

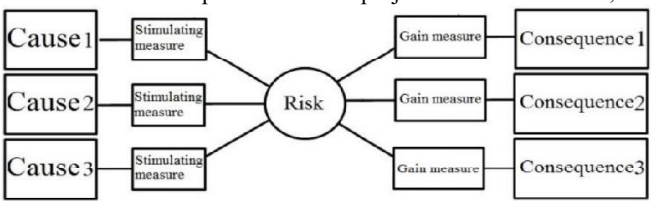
For **unpredictable risks ("alligators")** in this article was suggested to use the method of "bow tie" - the second stage and the method of Walt Disney.

Development of measures to respond to common risks ("puppies"), which do not have a significant negative impact on the successful completion of the IT project, can be carried out by the method of "bow tie" - the second stage.

Insignificant risks ("kittens") the IT project manager can be neglected. However, for the development of preventive measures (in the event that the activities of Plan A and Plan B did not exceed the marginal cost of risk management response activities), it is suggested to use the brainstorming method, in which respondents can be managers of other IT projects, senior developers , senior testing specialists, senior analysts, and so on.

Constructive risks ("elephants"). The manager of the IT project and the project team can neglect these positive risks. However, for the guaranteed approach of a positive risk event of the category "elephants", project team members can still develop preventive measures using the "brainstorming" method.

The development of measures for **unpredictable risks ("lions")** can be carried out using the method of "bow tie" - the second stage, the Walt Disney method and the Delphi method. According to the rules of use, the "bow tie" method is focused on the elaboration of "Plan A" and "Plan B" activities for negative risks that pose a threat to the successful completion of the IT project. In this connection, the



author of the article proposes to adapt the second stage of the method of developing response measures for positive risks by changing the meanings of the key concepts of the method, that is, the notion of "barrier" should be replaced by the notion of "incentive measure" and "restoration measure" (Figure 7).

Figure 7. The scheme of the "bow tie" method for positive risks.

For **common risks ("monkeys")** it is suggested to use only the method of "bow tie" - the second stage. The manager of the IT project and the project team can be neglected by developing activities for positive **insignificant risks ("rabbits").**

V. MONITORING AND CONTROL OF IT PROJECT RISKS

The optimal measure that ensures the control of triggers of identified risk events is the distribution of responsibility between the participants in the project team of the IT project, that is, the formation of personal risk responsibility. Such delegation of the control procedure can be explained by the fact that triggers of risk events are not universal and can be seen only by certain specialists. So, the trigger "during the testing there was a bug in the program code (bug)" for the risk "the functionality scheduled for iteration will not be completed in time" should be monitored by the developer of the program code, which before the IT project manager will notice the signs of the onset of the risk event.

In addition, the monitoring and control procedure can be conditioned by the chosen model of the life cycle of the IT project development [18]. For instance: if an iterative life cycle model is chosen, then the following questions are proposed for discussion by the project team:

* Are all the functionality and tasks planned for the iteration completed? If not, what are the reasons?

* Have new risk events been identified that could affect the successful completion of the IT project? If yes, then:

- assessing the likelihood of occurrence and impact for the identified risk;

- if the risk has been determined as insignificant, then it can be neglected;

- if the risk has been defined as catastrophic, unpredictable or often occurring, then it is necessary to develop response measures.

* Were there any triggers of the identified risk events? If so, then the "Plan B" measures are taken.

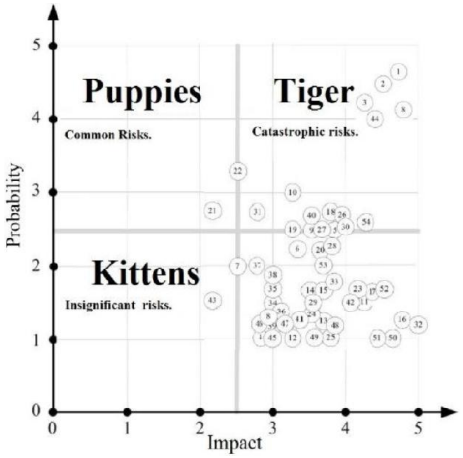


Figure 8. Identified negative project risks.

According to the developed organizational and methodological support, an experimental approbation was conducted to introduce risk management into a small IT project (the duration of development is not more than two months).

At the identification stage, the accompanying project documentation was studied and interviews were conducted with each participant of the project team. As a result, a section of the risk events register "Risk Identification" was created, which describes 54 negative and 14 positive risk events.

Using the methods of risk analysis, as well as the verbal-digital scale of Harrington, the project team members conducted an expert assessment of negative and positive risks [19].

As a result of expert assessments of the likelihood of occurrence and the impact of risk events, it was found that out of 54 (100%) negative risks: 17 (31.4%) are catastrophic, 35 (64.8%) unpredictable; 1 (1.9%) – frequently (common) occurring and 1 (1.9%) - insignificant (Figure 8). Among 14 (100%) positive risk events 10 (71.4%) are creative (constructive), 4 (28.6%) are unpredictable.

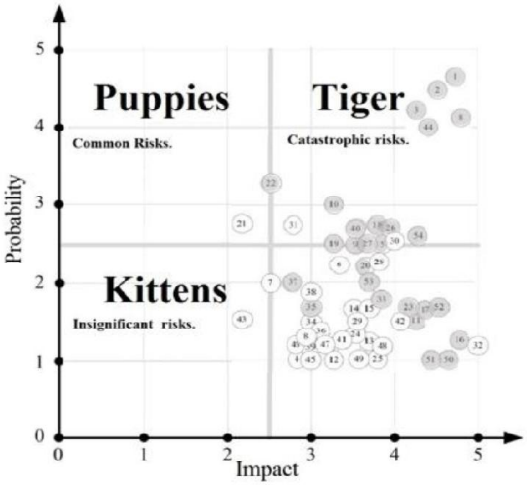


Figure 9. Negative risks for which the "plan A" measures were developed.

Since more than 70% of positive risks were identified as "elephants", that is risks that may occur in the project, regardless of the efforts of project team members, the project manager decided not to develop measures that increase the likelihood of occurrence for four risks such as "lions". Thus, the concentration of resources

was focused on managing catastrophic ("tigers") and unpredictable ("alligators") negative risks.

Prior to the implementation of the IT project, the project team members developed "Plan A" activities, triggers and "Plan B" activities for 27 identified negative risks (Figure 9).

First of all, the project team members focused their attention on the risks of the category "tigers". However, not for all risks, creative responses have been developed. For example, the risks "Project participants can get sick" and "Project participants may have force majeure" were identified as risky events that can not be managed. In this regard, out of 17 risks of the "tigers" type, preventive measures were developed and carried out only for 15.

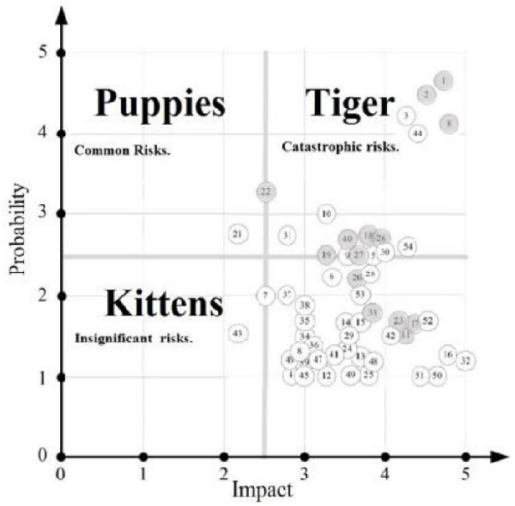


Figure 10. Negative risks for which the triggers of the "Plan B" event were developed.

For 11 out of 35 risks of the "alligators" type, we have developed creative response measures. The development of "plan A" and "plan B" for risks of the "alligators" type was conducted until the maximum cost of resources allocated to risk management was reached (Figure 10).

Upon completion of the project, the actual duration of the project implementation phase was 69 working days, which is 3 days longer than the approved baseline plan. This deviation can be explained by two unidentified risks: "Development results were not considered by the customer in due time" and "As a result of the rebranding of the customer organization, the site design has changed." These risks were transferred to the customer, because of his fault, there was a temporary delay, which affected the duration of the project.

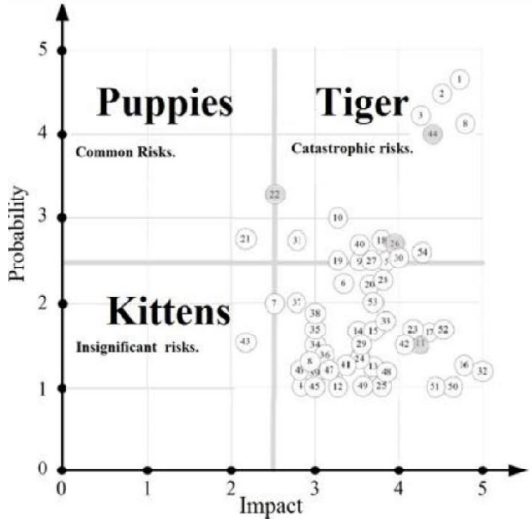


Figure 11. Negative risks that occurred during the implementation of the IT project.

According to the schedule, the duration of the IT project was 66 working days. The actual duration of the IT project was 69 working days. Thus, the deviation from the planned plans is 4.5%. Compared to the statistical data provided by The Standish Group International for 2014, the deviation for the IT project was reduced 19 times (from 89% to 4.5%) [20].

VI.CONCLUSION

Based on the conducted research and experimental approbation, the solution of the actual scientific and practical problem related to the introduction of risk management into IT projects is given. Thus, the contradiction between the requirements for risk management in IT projects, namely:

* The introduction of risk management did not change the existing management in the IT project (Waterfall);

* As a result of introduction of risk management, according to organizational and methodological support, deviation from the plan amounted to 4.5%.

REFERENCES

[1] Cooper D. F. , Grey S. , Raymond G. & Walker P. 2004. “Project Risk Management Guidelines: Managing risk in large projects and complex procurements”. Chichester, UK: J Wiley. ISBN 0-470-02281-7

[2] Barry, T. R. (2012, May). Top 10 leadership qualities of a project manager. Project Times.http://www.projecttimes.com/articles/top-10-leadership-qualities-of-a-project-manageler.html

[3] Hillson D. A. 2004. “Effective Opportunity Management for Projects: Exploiting positive risk.” Boca Raton, USA: Taylor & Francis.

[4] Hillson D. A. 2009. “Managing Risk in Projects” (part of Fundamentals of Project Management series, ed Dalcher D.). Farnham, UK: Gower.

[5] CHAOS Manifesto 2013 / The Standish Group International, 2013.

[6] CHAOS Manifesto 2014 / The Standish Group International, 2014.

[7] De Bakker K., Boonstra A., Wortmann H. Does Risk Management Contribute to IT Project Success? A Meta-Analysis of Empirical Evidence // International Journal of Project Management. 2010. No 28. P. 1–23.

[8] Vose D. 2008. “Risk Analysis – A quantitative guide” (third edition). Chichester, UK: J Wiley. ISBN 978-0-470-51284-5

[9] De Bono E. Six Thinking Hats. New York: Little, Brown Book Group Limited, 1985.

[10] Ishikawa K. Guide to Quality Control. Tokyo: Asian Productivity Organization, 1986.

[11] ISO/IEC 31010:2009. Risk management — Risk assessment techniques.

[12] Lee O.-K. D., Baby D.V. Managing Dynamic Risks in Global IT Projects: Agile Risk-management Using the Principles of Service-oriented Architecture // International Journal of Information Technology & Decision Making. 2013. Vol. 12. No 6. P. 1121–1150.

[13] Lewis S., Smith K. Lessons Learned from Real World Application of the Bow-tie Method / Prepared for Presentation at American Institute of Chemical Engineers 2010 Spring Meeting 6th Global Congress on Process Safety San Antonio, Texas, March 22–24, 2010. Unpublished.

[14] Lopez C., Salmeron J.L. Monitoring Software Maintenance Project Risks // Procedia Technology. 2012. No 5. P. 363–368.

[15] Merna T., Al-Thani F. Corporate Risk Management. 2nd ed. Chichester, UK; Hoboken, N.J.: John Wiley & Sons, Ltd., 2008.

[16] Chapman R. J. 2006. “Simple Tools And Techniques for Enterprise Risk Management”. Chichester, UK: J Wiley. ISBN 0-470-01466-0

[17] Cayman Business Systems Rev Q. (2004, January). Potential failure mode and effects analysis. History of the FMEA (slide 11). Retrieved from http://www.fmeainfocentre.com/handbooks/FMEA-N2.pdf

[18] Youssef Z., Mohamed O. Applying Ishikawa Approach for Modeling ERP Risk-effects // Journal of Theoretical and Applied Information Technology. 2015. Vol. 1. No 1. P. 51–60

[19] Cox, L.A., Jr. 2002. Risk Analysis: Foundations, Models and Methods. Boston: Kluwer Academic Publishers.

[20] Adler, R.J., R.E. Feldman, and M.S. Taggu. 1998. A Practical Guide to Heavy Tails: Statistical Techniques and Applications. Boston, Mass.: Birkhäuser.

Critical Node Detection in WSN based on Energy Consumption

S. M. A. SHAH[1], F. A. UMRANI[1], SHANZAH MOHSIN[1], and A. W. UMRANI[1]

[1] Department of Telecommunication Engineering, Mehran University, Jamshoro/Pakistan,
faheemaziz.umrani@faculty.muet.edu.pk

***Abstract* - Critical node (CN) detection is very crucial task in order to save the resources from spam or any other attack. Most of the algorithms which attempt to determine CN are based on geometrical centrality or number of links. In this paper we demonstrate using ns2 based simulations that these are not the optimal strategies. Therefore we introduced a new metric i.e. Energy consumption, of any node to precisely determine a CN or set of CNs.**

***Keywords* - AODV, Critical nodes, Energy based detection, Random and Structured topology, WSN.**

I. Introduction

In modern generation of networks, security and reliability are some of the crucial concerns. A network execution is disrupted in different situations such as a catastrophe, unexpected failure of elements or even by hostile attack. An attacker would first try to hit the network weakness or centrality. It is therefore very essential to determine the centrality of a network and shield it against most dangerous situations. The growth of network continues and interacts with other regions so it is very important to work on how the network can manage with new network nodes and connections [1].

A critical node is one whose failure or improper behavior disconnects or significantly degrades the performance of the network. Researchers have studied and gave theoretical approaches to determine the critical node. A method proposed in [1] is based on integer linear programming to anti-terrorist protection. A critical node compensation algorithm to prevent the network from partitioning is suggested in [2] along with simulation design and analysis of the proposed algorithm using NS-2.33. However there is lack of full proof in theory and practice. For a dynamic network environment, the problem to detect and update links and nodes based on metric of total pairwise connectivity is developed in [3] with two adaptive algorithms i.e., critical link algorithm and critical node algorithm. With undirected graph, authors in [4] proposes centrality measure called delay flow that comprises commuter flow and travel time.

In this paper a new approach to determine the critical node is suggested based on energy consumption. The idea is based on the argument that in a normal environment where every node transmits fixed amount of power a node consuming more active energy is a critical node, and hence, measuring the energy consumption of each node will help to determine its importance, i.e., more the energy consumption, more critical the node. The aim of this paper is to determine the criticalness (centrality) of a network based on its energy consumption.

The outlines of this paper are as follows; section II deals with the system model and the parameters set for the simulation. Section III shows the simulation results for the scenarios presented in this paper. Finally section IV gives conclusions.

Table 1: Simulation Parameters.

S.#	Parameter	Value
1	Simulation time	30 sec
2	Routing	AODV
3	Number of Mobile Nodes	100
4	Initial Power	3.4 Jules
5	Minimum Transmit Power	0.33 Watts
6	Minimum Receive Power	0.1 Watts
7	Idle Power	0.05 Watts
8	Sleep Power	0.03 Watts

II. System Model

A 100 node wireless sensor network is set up under four scenarios, three grid-wise (or structured) and one as random. The first scenario has one transmitter and one receiver, the second and third scenarios have two and four transmitter-receiver pairs, respectively. The fourth scenario uses random topology with four transmit-receive pairs. In the grid-wise topology, each node is in the close vicinity of all other nodes at equal distance. The nodes have links with all nodes in their surroundings. However, in the random topology, the nodes are scattered randomly and so were the node links. The transmitting and receiving nodes are placed on the opposite corner of the topology. In all scenarios the routing protocol used is Ad hoc On-Demand Vector (AODV) protocol. Table I shows the simulation parameters.

In the grid-wise scenarios, the number of links of the border nodes are five nodes each while the corner nodes have three links each. All other nodes (inside the outer set of nodes) have eight links each with their neighboring nodes. The links can be determined easily in figure 1.

In the random scenario, the number of links varies greatly from a minimum of twelve nodes at the corners of the topology to a

maximum of forty one nodes towards the center of the topology. The purpose of including the number of links is to bring to light the situation that whether or not the number of links can help us identify the critical nodes. In simple, the nodes with the maximum number of links should also be able to provide hints towards the detection of critical nodes. The links are shown in figure 2. We will now proceed to discuss each case separately.

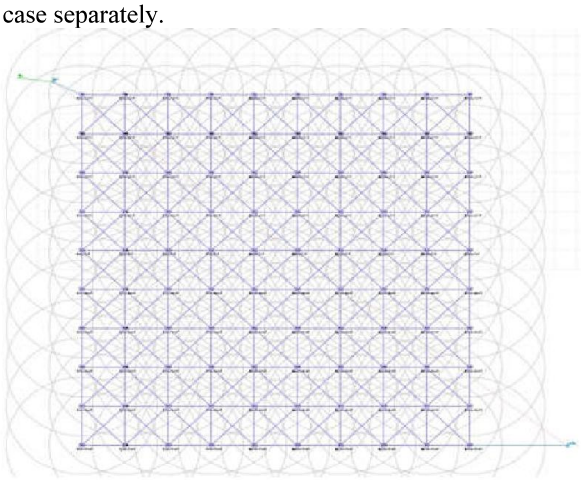


Figure 1: Node links in grid topology.

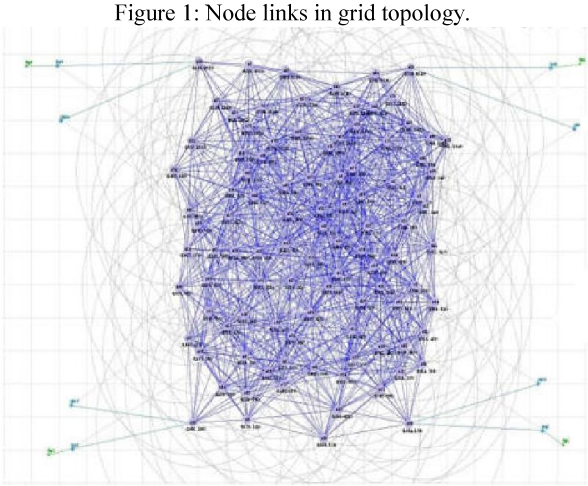


Figure 2: Node links in random topology.

A. Case 1 Scenario 1

In this scenario, node 0 acts as the transmitting node and node 99 acts as the receiving node. Node 0 has been set as having an FTP link with the node 99. The network is shown in figure 3(a). It can be seen that the corner nodes have three links each. The border and interior nodes have five and eight links each respectively.

B. Case 1 Scenario 2

In this scenario, node 0 and node 9 act as the transmitting nodes and node 90 and 99 act as the receiving nodes. Node 0 has been set as having an FTP link with the node 99 while node 9 has an FTP link with node 90. This network is shown in figure 3(b) above. As this is a grid topology, the number of links of the nodes is the same as in scenario 1.

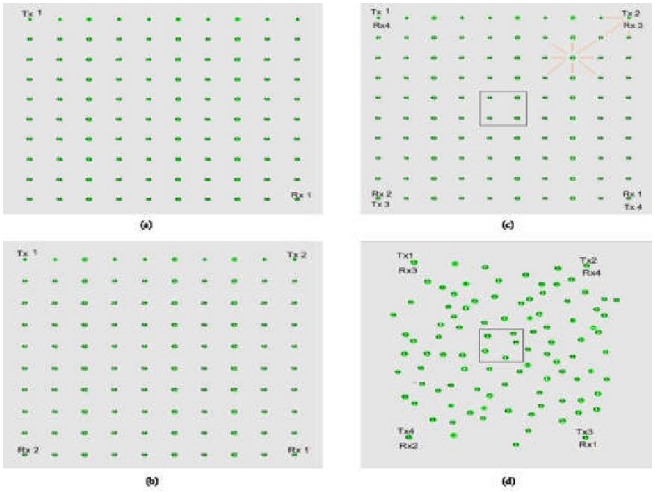


Figure 3: (a) case 1 scenario 1 (b) case 1 scenario 2 (c) case 1 scenario 3(d) case 2 scenario 1.

C. Case 1 Scenario 3

In this scenario, nodes 0, 9, 90 and 99 act as the transmitting and receiving nodes. However, Node 0 has been set as having an FTP link with the node 99, node 9 has an FTP link with node 90, node 90 has FTP link with node 9, and node 99 has FTP link with node 0. This topology is shown in figure 3(c).The nodes shown in the square box are the geometrically central nodes. A sample of nodes links are also shown in the top right corner of the figure. The node-links status is the same as in the previous two scenarios.

D. Case 2 Scenario 1

In this scenario nodes are placed randomly with nodes 50, 59, 86 and 98 act as the transmitting and receiving nodes. However, node 50 has been set as having an FTP link with the node 98, node 59 has an FTP link with node 86 and vice versa, while node 98 has FTP link with node 50. This topology is shown in figure 3(d). The box in the center highlights the nodes in the center of the topology. In the figure 3(d), the nodes towards the center are the ones that have the maximum number of links as can be easily seen in figure 2.

III. Simulation Results

A. Case 1 Scenario 1

The graph shows that there are several nodes that have used up energy during their working. The nodes numbered 0, 10, 42, 43, 53 and 73 used more energy than the other nodes. Node 0 was the source node and had the most consumption obviously. The nodes in the first tier, i.e. nodes 1, 10 and 11, were not included in the Critical node criteria as they were the closest nodes to either the source or destination. From this point of view, nodes 88, 89 and 98 were not included in the Critical node criteria as they were the nodes of the first tier of the destination node i.e., Node 99.

Hence, for our calculations, node 10 has been excluded from analysis as CN. The remaining nodes are 42, 43, 53 and 73. From figure 1, we can identify that according to topology

geometry, the nodes numbered as 44, 45, 54 and 55 should be the critical nodes. However from the figure 3(b), we can see that they are clearly not the critical nodes. The energy consuming nodes (nodes 22, 31, 41, 43, 53, 62, 73, 82 and 83) are nowhere near the center of the topology. Thus, the critical nodes, according to our energy consumption criteria, are the nodes numbered 41, 43, 53 and 73.

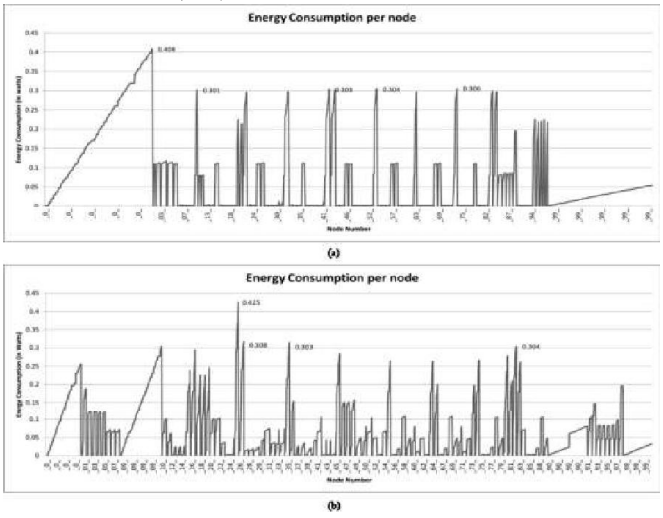


Figure 4: Energy consumption per node for scenario 1 & 2.

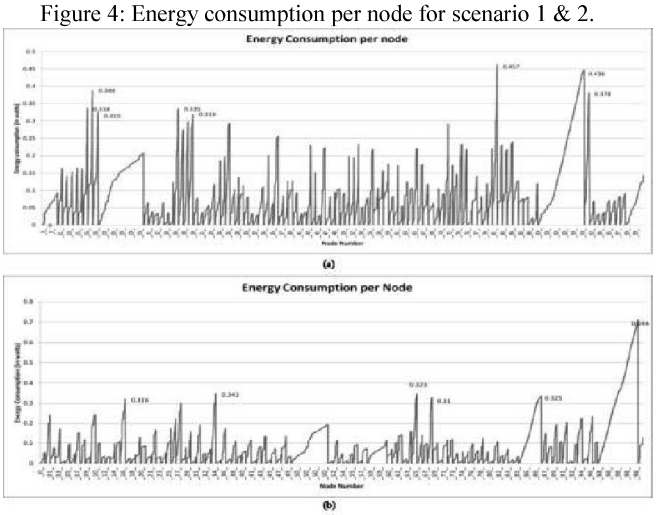


Figure 5: Energy consumption per node for scenario 3 & 4.

B. Case 1 Scenario 2

The graph for energy consumption per node for the second scenario shown in figure 3(b) is given in figure 4(b).

In the scenario 2, the nodes 0 and 9 are the transmitting or source nodes. Node 99 is the receiver for node 0 and node 90 is the receiver for node 9. Node 9 is the source node for the receiver node 90. Nodes numbered 1, 10 and 11 are the first tier of node 0. Similarly, nodes 8, 18 and 19 are the first tier for node 9, nodes 80, 89 and 91 are for node 90 and finally, nodes 88, 89 and 98 are for node 99. These twelve first tier nodes are excluded from the critical node criteria as they are the direct links to the source and destination nodes.

As in the previous topology, the nodes numbered 44, 45, 54 and 55 should be the critical nodes. However based on the graph in figure 4(b), the nodes 25, 26, 35 and 82 are the most used nodes as indicated by their energy consumption. Hence in this scenario these nodes are the Critical Nodes and they do not lie in the center of the topology nor do they provide a direct link from source to destination.

Table 2: Nodes with greatest number of links.

S.#	Node ID Number	Number of Links
1	20, 43	41
2	21	40
3	9, 83	39
4	0, 67	38
5	58, 79, 84	37
6	56, 73, 85	36
7	47, 87, 88	35

C. Case 1 Scenario 3

The energy consumption graph for third scenario shown in figure 3(c) is shown below in figure 5(a).

In this scenario 3, the nodes 0, 9, 90 and 99 are the transmitting or source nodes. Node 99 is the receiver for node 0 and node 90 is the receiver for node 9. Similarly, Node 0 is the receiver for node 99 and node 9 is the receiver for node 90. The same logic is applied between nodes 9 and 90. As in the previous scenario, Nodes numbered 1, 10 and 11 are the 1st tier of node 0. Similarly, nodes 8,18 and 19 are 1st tier for node 9, nodes 80, 89 and 91 are for node 90 and finally, nodes 88, 89 and 98 are for node 99. These twelve 1st tier nodes are excluded from the critical node criteria as they are the direct links to the source and destination nodes.

As in both the previous scenarios, the nodes numbered 44, 45, 54 and 55 should be the critical nodes. But, in the graph in figure 5(a), the nodes 06, 07, 08, 16, 19, 81, 90 and 91 are the most used nodes as indicated by their energy consumption. But, the nodes 08, 19, 81, 90, and 91 are excluded from the criteria of energy consuming critical nodes. The remaining nodes, 06, 07 and 16 are the Critical Nodes. In figure 3(c), it is clear that these three nodes are not in the center of the topology nor do they provide a direct link from source to destination. It is easily concluded that in the fixed topology scenarios, having maximum number of links does not determine the criticality of the node as all nodes had the same number of links and were able to communicate with all other surrounding nodes.

D. Case 2 Scenario 1

In this scenario, the nodes 50, 59, 86 and 98 are the transmitting or source nodes. Node 98 is the receiver for node 50 and node 86 is the receiver for node 59. Similarly, Node 50 is the receiver for node 98 and node 59 is the receiver for node 86 where in nodes 98 and 86 are the source nodes. The nodes with numbers 57 and 3 are the first tier of node 50. Similarly, nodes 39 and 54 are 1st tier for node 59, nodes 94 and 8 are for node 86 and finally, a single node 27 is the first tier node for node 98. These seven first tier nodes are excluded from the critical node criteria as they are the direct links to the source or

destination nodes.

In figure 3(d), the nodes with numbers 20, 21, 43, 45 and 84 occupy the central position of the topology and should act as the critical nodes of this network. However, the graph in figure 5(b) shows otherwise.

The nodes 16, 34, 65 and 68, 86 and 98 are the most used nodes as indicated by their energy consumption. Nodes 86 and 98 are excluded from the criteria of energy consuming critical nodes while the remaining nodes, 16, 34, 65 and 68 filter out to be the Critical Nodes. In figure 3(d), it is clear that these four nodes are not in the center of the topology nor do they provide a direct link from source to destination.

From the node-link point of view, the nodes with the greatest number of links and the exact node number and number of their links are shown in table II. From the final selected critical nodes (i.e. nodes 16, 34, 65 and 68), none of them are seen in the Table 2, which indicates that the node with greatest number of links do not necessarily qualify to be selected as critical nodes. Thus, the greatest number of links does not make a suitable criterion for the criticality of a node.

Finally, the Table III summarizes the critical nodes detected on the three metrics i.e., energy consumption, geometric centrality and number of links. The results show that geometric centrality and number of links do not make the node or set of nodes critical.

Table 3: Comparison of CND Detection based on centrality and energy detection.

Scenario	Number of Links	Centrality	Energy Detection
1	Min. 3, Max 5 to 8	44, 45, 54, 55	41, 43, 53, 73
2	Min. 3, Max 5 to 8	44, 45, 54, 55	25, 26, 35, 82
3	Min. 3, Max 5 to 8	44, 45, 54, 55	06, 07, 16
1	See table 2	20, 21, 43, 45, 84	16, 34, 65, 68

IV. CONCLUSIONS

In this paper, a new energy based approach is presented to effectively determine the Critical Node. We have proved and determined that nodes that have the most consumption of energy are the most important nodes, or Critical Nodes, of the network and that they may not lie at the center of the topology as proposed by most of the algorithms based on geometrical centrality. Also, it has been shown that the nodes with the greatest number of links do not necessarily indicate the criticalness of such nodes. Thus, the introduction of a new metric i.e. Energy consumption, of any node can precisely determine a CN or set of CNs.

REFERENCES

[1] Rinaldi, S.M., "Modeling and simulating critical infrastructures and their interdependencies," System Sciences, 2004. Proceedings of the 37th Annual Hawaii International Conference on, vol., no., pp.8 pp.,, 5-8 Jan. 2004.

[2] Arulselvan, Ashwin, Clayton W. Commander, Lily Elefteriadou, and Panos M. Pardalos. "Detecting critical nodes in sparse graphs." *Computers & Operations Research* 36, no. 7 (2009): 2193-2200.

[3] B. Sivakumar and G. Varaprasad. "Identification of Critical Node for the Efficient Performance in Manet." *International Journal of Advanced Computer Science and Applications (IJACSA)* 3.1 (2012).

[4] Y. Shen; T. N. Dinh, M. T. Thai, "Adaptive algorithms for detecting critical links and nodes in dynamic networks," MILITARY COMMUNICATIONS CONFERENCE, 2012 - MILCOM 2012 , vol., no., pp.1,6, Oct. 29 2012-Nov. 1 2012.

[5] Y. Cheng, R. K. Lee, E. P. Lim, & Z. Feida ." *DelayFlow Centrality for Identifying Critical Nodes in Transportation Networks"*. Paper presented at The international conference on Advances in Social Network Analysis and Mining (ASONAM 2013), Niagara Falls, Canada.

Comparison of 3D and 2D Magnetostatic Analysis of 6/4 Pole SRM

C.ŞAHİN[1] and M. KARAÇOR[2]

[1] Bilecik Şeyh Edebali University, Bilecik/Turkey, cihan.sahin@bilecik.edu.tr
[2]Manisa Celal Bayar University, Manisa/Turkey, mevlut.karacor@gmail.com

***Abstract* - In this study, 3D and 2D dimensional Magnetostatic analyzes of 6/4 Polar SRM(Switched Reluctance Motor) are compared. The use of SRMs is also becoming widespread with developing control techniques. It is preferred to use a wide area from the aviation industry to home appliances (vacuum clenear etc.). In addition to the development of SRM control techniques, various studies have been carried out on geometric structures. 3D and 2D Magnetostatic analyzes of geometrically designed SRMs are performed. In this study, 3D and 2D Magnetostatic analyzes of 6/4 pole SRM were performed at 10 amperes. The Torque, Inductance, Torque ripple ratios obtained from the analysis are compared. In the analysis using 3D, the torque ripple was found to be 37.20%, and in the 2D analysis, the torque ripple was obtained as 36.25%. The difference between the two analyzes was calculated as 0.95%. This has been shown to be valid for both analyzes in different studies.**

***Keywords* - SRM, Magnetostatic, Torque Ripple**

I. INTRODUCTION

Although the first Switched Reluctance Machine (SRM) was made in 1838, it did not become widespread until the late 1970s due to the difficulty of control. Since the 1960s, the development of power electronics and semiconductor switches has facilitated the control of SRM and led to an increased interest in ARM drivers. The features of the Switched Reluctance Motor (SRM) make it a strong candidate for a variety of general purpose adjustable speed applications, structural simplicity at high speeds and high temperatures, robustness, fault tolerance, high torque to inertia ratio and possible working pattern [1]. The simple structure of the SRMs, fault tolerance capability, high torque and high speed operating characteristics make it universally applicable [1-2]. SRMs are double protruding, no windings or magnets in rotor [3]. Compared to SRMs Induction motors, they have high torque and low magnetic density. Compared to permanent magnet motors, they can reach higher speeds due to the absence of windings or magnets in the rotor [4]. The main disadvantage of the SRMs is their high nonlinearity and high Torque ripple due to vibration and acoustic noise [5]. The most important reason why many studies on SRMs have been done in recent years is that the structure is simple and the cost is low [6-7]. SRMs are widely used in automotive industry, aerospace industry, railway and light rail system vehicle excavation, home appliances (brooms, white goods ...), general purpose industrial drives, servo systems, robot applications, Such as centrifugal drives [6-7]. The biggest disadvantage of SRM is; can't be directly fed from AA and DA sources and electronically switched [6-7].

II. SWITCHED RELUCTANCE MOTOR (SRM)

The SRMs are made up of rotors and stators as they are on all conventional electric machines. The number of stator and rotor dislocation poles is expressed as stator pole number / rotor pole number. For the SRM to be able to rotate, the stator and rotor pole numbers must be different. Generally, the number of stator poles is more than the number of rotor poles; 6/4, 8/6 and so on. They are manufactured. The reason for this is the desire to achieve high torque rather than high speed [7]. The stator pole number Ns and the rotor pole number Nr are expressed. In SRM, the windings on the poles on the stator are connected in series to form a phase of the machine [8]. When the appropriate phase in the SRM is excited by the correct voltage, the moving rotor begins to rotate to reduce the reluctance of the magnetic circuit. Movement of the phases in and out of the sequence results in continuity of motion. Figure 1 shows the 3-phase, 6/4 pole stator-rotor structure of the SRM.

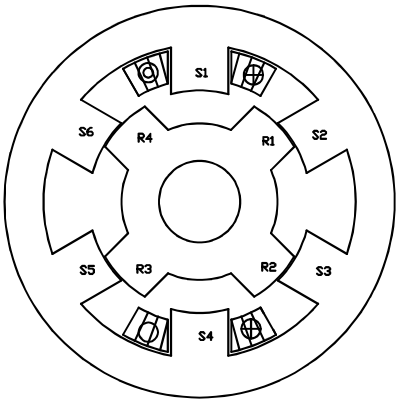


Figure 1: Classical Switched Reluctance Machine.

Reluctance can be thought of as the resistance to the magnetic circuit in the electric circuit. The difficulty with resistance flow in the electric circuit is reluctance; Is a

challenge to the circulation of the flux in the magnetic circuit. If the SRM is modeled as a magnetic circuit, the air gap between the stator and rotor as well as stator and rotor in this model is called "reluctance". Although the stator and rotor reluctances are constant, the reluctance of the air gap is varied [7,9]. In SRMs, as the air gap between the stator and rotor pole heads increases, the reluctance of the magnetic circuit also grows. The machine structure tends to reduce this high reluctance and produces torque for it. The general torque expression for classical SRMs is expressed in Equation (1). In classical Reluctance machines, the opposite inductance between phases is neglected.

$$T = \frac{1}{2} i_a^2 \frac{\partial L_a}{\partial \theta} + \frac{1}{2} i_b^2 \frac{\partial L_b}{\partial \theta} + \frac{1}{2} i_c^2 \frac{\partial L_c}{\partial \theta} \quad (1)$$

With the torque produced, the stator and rotor poles approach each other, resulting in a reduced reluctance of the magnetic circuit [7]. The desire to reduce this reluctance provides the continuity of the machine's torque. The magnetic circuit reluctance is expressed by Equation (2) [7,9].

$$\Re = \frac{F}{\phi} = \frac{Hl}{BS} = \frac{l}{\mu S} \quad (2)$$

In Equation (2) expresses reluctance, (F) magneto motor force (mmk), (ϕ) flux, (l) magnetic path length, magnetic (B) flux density, (H) magnetic field strength, (S) magnetic path cross section and (μ) magnetic permeability. The parameters l, μ and S together with the angular change of the rotor cause the change of the circuit reluctance. In SRMs, instead of reluctance, more inductance value is used as a criterion. The relation between inductance (L) and reluctance is expressed in equation (3). In Equation (3), i phase current and N is the number of turns of phase [7,9].

$$L = \frac{\Psi}{i} = \frac{N\phi}{i} = \frac{N^2}{\Re} \quad (3)$$

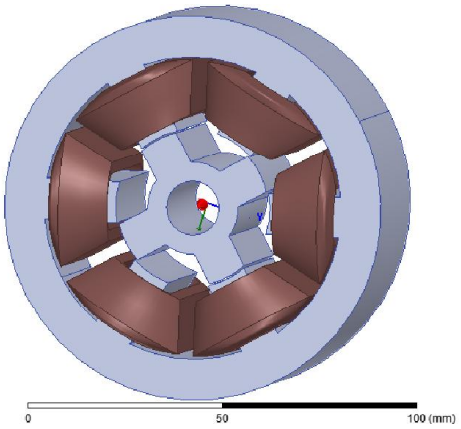
III. DESIGNED SRM GEOMETRIC MEASUREMENTS

Table 1 shows the geometric measurements of the SRM.

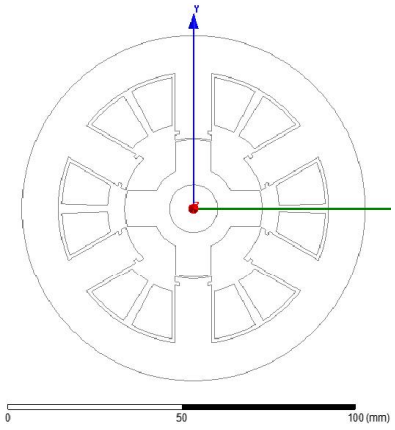
Table 1: Geometric Dimensions Of The Proposed SRM

Symbol	Value	Symbol	Value
r_0	12 mm	y_s (Rotor pole width)	10.6 mm
r_1	20 mm	y_r rotor yoke thickness	5 mm
r_2	39.4 mm	d_s stator pole height	19 mm
r_3	50 mm	Motor Depth	40 mm
t_s (Stator pole width)	10.5mm	β_r	30^0
t_r (Rotor pole width)	10.5 mm	β_s	30^0
g (air–gap length)	0.5 mm		

Figure 2 shows 2D and 3D geometric shapes of the 6/4 pole SRM. Both models have the geometric measurement given in Table 1. Because of winding structure, it is modeled differently in 3D and 2D in analysis environment. Figure 3 shows the geometric variables.



a)



b)

Figure 2: a) 3D SRM model b) 2D SRM model.

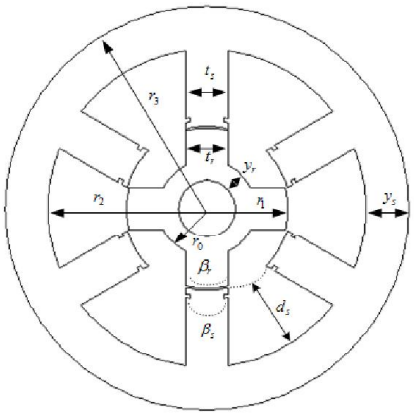
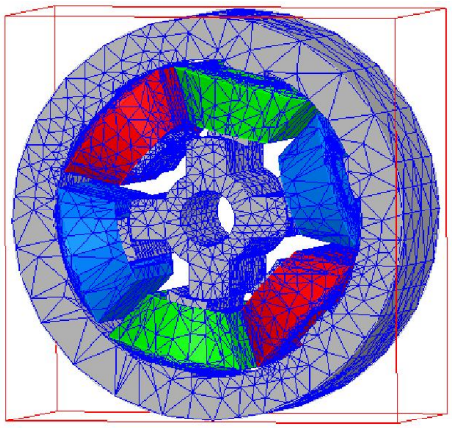


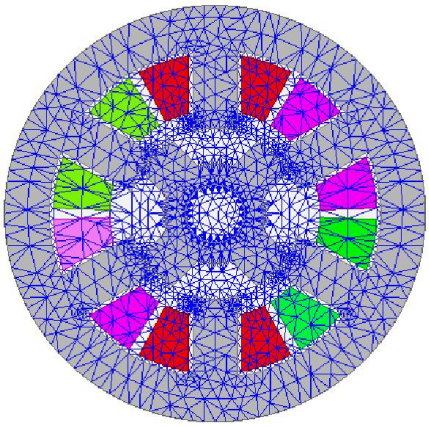
Figure 3: Geometric structure of the proposed SRM.

IV. Realization of SRM 2D / 3D Analyzes Using Finite Elements Method

As is known, different numerical methods are used in solving magnetic field problems. In the literature; There are different methods such as Finite Element Method, Finite Difference Method, Monte Carlo Method, Boundary Element Method, Load Simulation Method [10]. It is observed that the Finite Element Method (FEM) is the most used and preferred method. Because; It is possible to analyze on models created by using real engine parameters with FEM. With these analyzes, information about the behavior of the motor and its characteristics can be obtained [11]. The 2D and 3D mesh structure of the SRM is shown in Figure 4.



a)

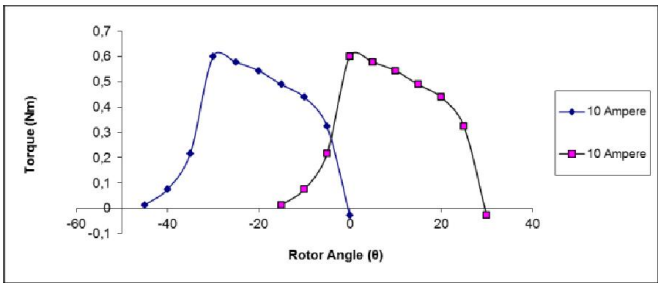


b)

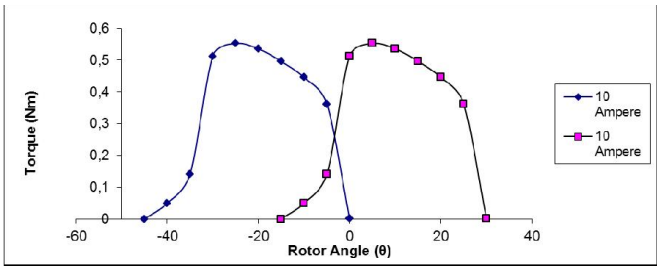
Figure 4: 6/4 pole SRM mesh structure a) 3D b) 2D.

Figure 5 shows the torque curves obtained from the results of the magnetostatic analysis of 2D and 3D models. Table 2 shows torque values. Motor step angle is 30 degrees. Therefore, the table is given 0-30 degrees. The values taken at the same angle are very close to each other. The very small differences between the values are due to the winding volume differences during design.

Figure 6 shows the inductance curves obtained from the results of the magnetostatic analysis of 2D and 3D models. Table 3 shows the inductance values. Motor step angle is 30 degrees. Therefore, the table is given 0-30 degrees.



a)

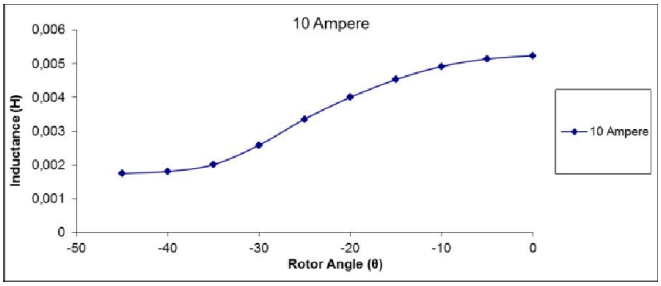


b)

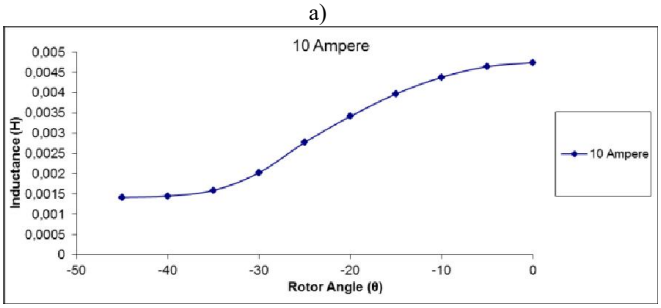
Figure 5: a) Torque curve from 3D analysis b) Torque curve from 2D analysis.

Table 2: SRM Torque Values.

Angle (θ)	2D Torque (Nm)	3D Torque (Nm)
-30	0,5127417	0,6008554
-25	0,5525741	0,5771555
-20	0,5356707	*0,5433241*
-15	0,4962279	0,488479
-10	0,4454278	0,438902
-5	0,3624125	0,3235364
0	0,0021208	-0,0275072



a)



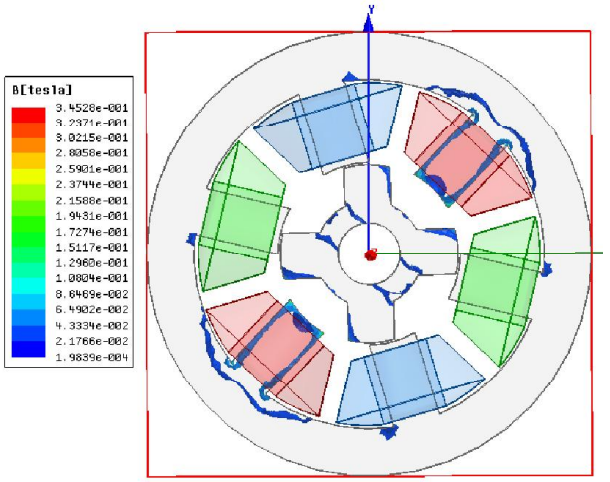
b)

Figure 6: a) the inductance curve from 3D analysis b) the inductance curve from 2D analysis

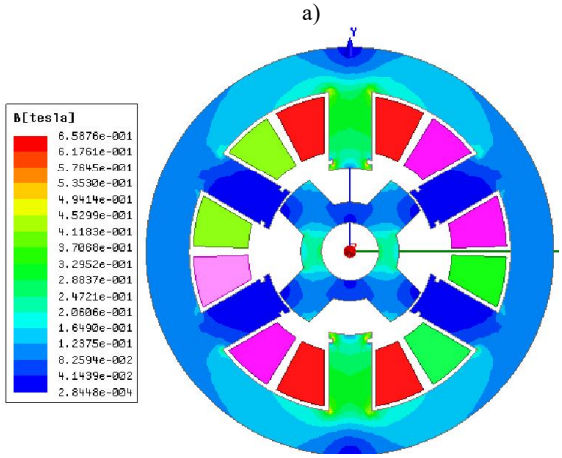
Table 3: Inductance values obtained from 3D / 2D analysis.

Angle (θ)	2D Inductance (H)	3D Inductance (H)
-30	0,002020	0,002581
-25	0,002767	0,003356
-20	0,003411	0,0040003
-15	0,003966	0,004528
-10	0,004377	0,004917
-5	0,004641	0,005139
0	0,004738	0,005235

The flux density at 10 A of the designed machine is examined in 2D in Fig. 7-a in Fig. 7-b.



a)



b)

Figure 7: Magnetic flux density SRM Model a) 3D b) 2D

Torque Ripple of the designed models is calculated at 10 Amperes. The torque ripple Td ratio is the average value of the difference between the maximum and minimum values of the moment value [12-13]. The Torque ripple fluctuation equation is given in Eq. (4). The average torque value in Equation (5) is also provided.

$$T_r = \frac{T_{\max} - T_{\min}}{T_{avg}} 100\% \quad (4)$$

$$T_{ort} = \frac{1}{T}\int_0^T T(t).dt$$

Torque ripple ratios are given in Table 4.

Table 4: Torque ripple ratios.

	2D	3D
Torque Ripple (10 A)	%36,25	% 37,20

V. CONCLUSION

In the globalizing world, energy demand is constantly increasing. This requires limited energy resources to be used as efficiently as possible. Especially in recent years, each area has been conducting research on high energy, high efficiency systems. One of these areas is the automotive sector. Today, hybrid vehicles that can use both electric energy and petroleum derivatives as fuel require high-powered electric machines. Much research has been done to meet this need and it has been revealed that the Switched Reluctance Machine (SRM) is one of the electromechanicals that can be preferred on hybrid vehicles. SRMs with a wide range of field use are preferred in every sector with developing technologies. Undoubtedly, the contribution of developing control techniques to this situation is great. Besides the control techniques of SRMs, studies on geometric structure are quite common. Different numerical methods are used to solve the magnetic field problems of electric machines. In these studies, the machines are designed in 2D and 3D and used in solution. In this study, the mangnetostatic analysis of 2D and 3D SRM models with the same measurements was made and the obtained values were compared. The desired main target for motors used in electric vehicles is a good moment characteristic. In SRMs, The torque is produced by inductance. Therefore, these two values are basically compared in the study. There are very small differences in the values obtained. This is due to small changes in the winding volume of the machine during design. In the analyzed 2D and 3D analysis results, there was a very small difference of 0.95% in terms of torque ripple. 0.95% change is due to winding end effect in 3d analysis. According to this result, the validity of the results obtained by 2D and 3D analysis is the same. As a result, the validity of 2D analysis in the rapid prototyping phase is emphasized in this study.

REFERENCES

[1] Shahabi, A. , Rashidi, A.,Afshoon, M., and Nejad, S. M. S., "Commutation angles adjustment in SRM drives to reduce torque ripple below the motor base speed," *Turkish Journal of Electrical Engineering&Computer Sciences,* 2015, doi: 10.3906/elk-1309-47

[2] W. Ding, Z. Yin, L. Liu, J. Lou, Y. Hu, and Y. Liu, "Magnetic circuit model and finite element analysis of a modular switched reluctance machine with E-core stators and multi-layer common rotors," *IET Electric Power Applications*, vol. 8, (8), pp. 296-309, 2014.
[3] Xu, Y.Z, Zhong, R.,Chen, L., and Lu, S. L., "Analytical method to optimize turn-on angle and turn off angle for switched reluctance motor drives", *IET Electric Power Applications*, , vol. 6, (9), pp. 593–603,2012.
[4] Cheng, H.,Chen, H., and Yang, Z., "Design indicators and structure optimisation of switched reluctance machine fo relectric vehicles", *IET Electric Power Applications*,vol. 9, (4), pp. 319–331, 2015.
[5] Ma, C.,Qu, L., andTang, Z., "Torque ripple reduction for mutually coupled switched reluctance motor by bipolar excitations". Proc. 2013 *IEEE International Electric Machines&Drives Conference* Chicago, USA, May, 2013.
[6] Şahin C., "Design, analysis and drive applicaton with zero current transition of mutually coupled switched reluctance machine", Phd. Thesis, University of Kocaeli, Kocaeli, Turkey, 2014.
[7] Karaçor M., "Torque ripple ruduction of mutually coupled reluctance motor", Phd. Thesis, University of Kocaeli, Kocaeli, Turkey, 2010.
[8] Duran F., "Intelligent control of industrial washing machine uses switched reluctance motor", Phd. Thesis, Gazi University ,Ankara, Turkey, 2008.
[9] Geçit İ., "Inverted switched reluctance motor and its planning", Master Thesis, University, Kayseri, Turkey, 2007.
[10] Gürdal O., Elektrik Makinalarının Tasarımı, Nobel Yayın Dağıtım Ltd. Şti., Ankara, 2000.
[11] Garip M., "The Contribution of fully pitched winding to the improvement of torque ripple in the switched reluctance motor with shaped pole tips", Phd. Thesis, Yıldız Teknik University, İstanbul, Turkey, 2002.
[12] Sheikhi A., Oraee H., Kaboli S., Dorkhah, M., "A new configuration of switched reluctance motor for reducing the torque ripple", *EPECS'09* , Sharjah, UAE, 10-12 Kasım 2009.".
[13] Desai P. C., Krishnamurthy M., Schofield N., Emadi, A., "Novel switched reluctance machine configuration with higher number of rotor poles than stator poles: Concept to implementation", *IEEE Transactions on Industrial Electronics*, vol.57, p.p.649-659, 2010.

CASCADED H-BRIDGES FOR HARMONIC CURRENT COMPENSATION IN ACTIVE POWER FILTER

Hamed Atyia Soodi (Author)
Electrical and Electronics Engineering Department
University of Gaziantep
27310 Şahinbey, Gaziantep, Turkey
E-mail: hs45149@ mail2.gantep.edu.tr

Ahmet Mete Vural (Author)
Electrical and Electronics Engineering Department
University of Gaziantep
27310 Şahinbey, Gaziantep, Turkey
E-mail: mete.vural@gaziantep.edu.tr

Abstract- In order to enhance the performance of power system, the Cascade shunt active power filters(CSAPF) an essential role is played by reducing harmonics in addition to by reactive power compensation into power systems by the help of a large concentration of non-linear loads, The (CSAPF) efficiency depends on three design criteria:(i) types of current controllers;(ii) methods used to obtain the reference current;(iii) DC link voltage control methods, Cascade H bridge converter based shunt active filter is examined with different levels and resulted a THD in range of (7.2%-2.5%) , a Phase-Shifted Carrier PWM (PSCPWM) then uses the reference current for producing the switching signals for the Cascade multilevel inverter (CMI) , In this paper, p-q theory strategies for extracting the three-phase reference currents for shunt active power filters are using, This paper concentrates on harmonic reduction in their level, five-level, seven-level, nine-level using cascaded H-bridge, To verify the effectiveness, simulation will be done using Simulink program.

Keywords— Shunt Active Power Filter: STATCOM; PI controller; Cascade multilevel inverter (CMI),; Sinusoidal Pulse Width Modulation; H-bridge Multilevel Inverter ;

I. INTRODUCTION

The reason for the proliferation of power electronic element and also non-linear loads inside the power distribution systems, there will be a problem of treatment and harmonic contamination taking on huge significance. There is in electrical equipment harmonics interpose sensitive electronic equipment and bring about undesired power losses [1-8]. The way of solving and regulating the permanent power quality problem presented by these Current harmonics given by non-linear loads, for Instance, HVDC system, converter to variable speed AC motor drive and switching power factor correction converter as result, the passive filters is used so much which were so simple and in reduced cost. Anyway, using of passive filter contains many disadvantages, such as tuning, large size as well as risk of resonance problems.

In recent times, acknowledging to the rapid development in the power semiconductor device technology which prepared high-speed as well as power switching devices as examples, MCTs, power MOSFETs, IGCTS, IGBTs etc. utilizable for the compatible compensation modern power electronics, a factor of the most known active filters is clearly "Shunt Active Power Filter" which stands for (SAPF) [2-7, 9]. SAPF has been looked for as well as developed gradually and it has been realized as a workable solution to many problems found by non-linear loads. By extracting the harmonic component of the load current to produce a reference current and sensing the load currents are the function of shunt active filter. That reference current includes harmonic components of it which the active filter must provide, feeding through a controller and as well as by generating the switching signal to switch the power switching devices of the active filter, as a result, the active filter would really give the harmonics required by the load. Finally, the AC supply will need to be provided the fundamental component for that load, producing a low harmonic sinusoidal supply.

Commonly, depending the effectiveness of SAPF has three design criteria: (1) the designing of power inverter; (2) using of current controller's types ;(3) methods used to obtain the reference current. The presented work was oriented mostly on the latter criterion. To make sure that harmonic and reactive component of load current, you should keep in mind that reference source current generation is very important. For this reason, it can be got a reference filter current when it is subtracted from total load current. For getting better filter performance, it should properly do the generation of reference source current. Because of those several methods such as multiplication and DQ transformation with sine function in addition to Fourier transform have presented in literature [9- 14], there are methods based on not real intelligence have been work on, the reason is to improve processing detecting time of harmonic current.

In power electronics, basically, the most controllable device is the two-level converters. But, this basic device injects unwanted harmonics into the power system [2]. So, there is a problem it can be overcome by the term multi-level which is come out in 1981[3]. By reducing the Total Harmonic Distortion (THD) and creating more output steps, they play an essential role.

II. ANYLATICAL DISCUSSION

a) MODELLING OF CASCADED H-BRIDGE

The N-level CMI output voltage requires M = (N-1)/2 units of identical H-bridge inverter modules along with a DC capacitor to produce N=2M+1 line-to-neutral output voltage levels.

The basic construction of nine level (2M+1=9) cascaded H-bridge inverter consisting of two (M=4) full-bridges is shown in Figure 1. Since there are four capacitors, there usually happens a voltage imbalance between capacitor voltages that should be minimized or practically eliminated with a number of techniques. Furthermore, capacitor voltage ripples can be reduced by active power control for each bridge [5]. Various methods are discussed in [6] to remove the ripples in DC voltages. This topology involving cascaded H-bridge multilevel inverters are used in many applications for reactive power compensation. The low-frequency modulation scheme is used in [6] due to the switching losses of IGBTs. According to [7] and [8], the frequency of line and commutation are almost similar

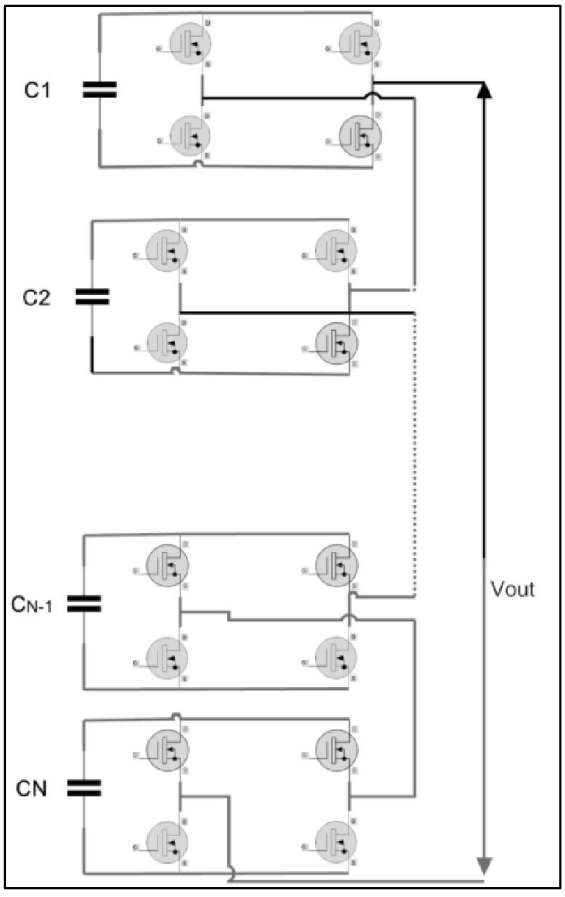


Figure 1: A basic construction of H-bridge cascaded

Each h-bridge consists of four switches and four diodes connected in parallel with switches. These diodes which are connected in anti-parallel fashion act as a full-bridge rectifier and together they are used for charging the DC capacitor. The charging energy comes from the coupling inductor. The output of h-bridge contains three levels namely positive, negative and zero level. These voltage levels when summed up to form a sinusoidal waveform. The AC output of h-bridge is given as:

$$V_{ca} = V_{ca1} + V_{ca2} + V_{ca3} + \cdots \ldots . + V_{caM} \qquad (1)$$

Where: M represents the number of inverters per phase.

The proposed topology of the cascaded multilevel inverter is modular meaning the output AC waveform can be improved by simply adding more h-bridges in the circuit. The conduction time for each h-bridge varies for example, for the first level the DC capacitor will charge less and discharge more and for the last level the DC capacitor charges more and discharges less. To solve this problem, we select suitable switch pattern swapping method which will swap the angles of switching for every half cycle as mentioned in [9] and [10]. The rectified energy accumulated in the inductor is stored in a capacitor that is linked on the DC side of the h-bridge multilevel inverter. The circulation of current and non-stop charging and discharging of an inductor can cause voltage ripples. To remove these ripples and smoothing the voltage DC capacitor is used. Figure 2 further demonstrates the process. The DC Capacitors are separate, not fed by diode rectifiers. As a result, their voltages may not be exactly balanced during operation. Simulation results have showed the fact that timing error of trigger pulses, dispersion of DC capacitor parameters and differences of power switch characteristics all contribute to voltage unbalance.

b) CASCAD SHUNT A CTIVE POWER FILTER (CSAPF)

In addition to a self-controlled dc bus and the shunt active power filter, they have a topology which are almost the same to which of a static compensator (STATCOM) and that is utilized for reactive power compensation within the power transmission systems. Shunt active power filters make up the load current harmonics by putting equal, however, opposite harmonic compensating current. It can be said that shunt active power filter, in this case, works properly as a current source putting the harmonic components which are produced by the load but phase is shifted by 180º.

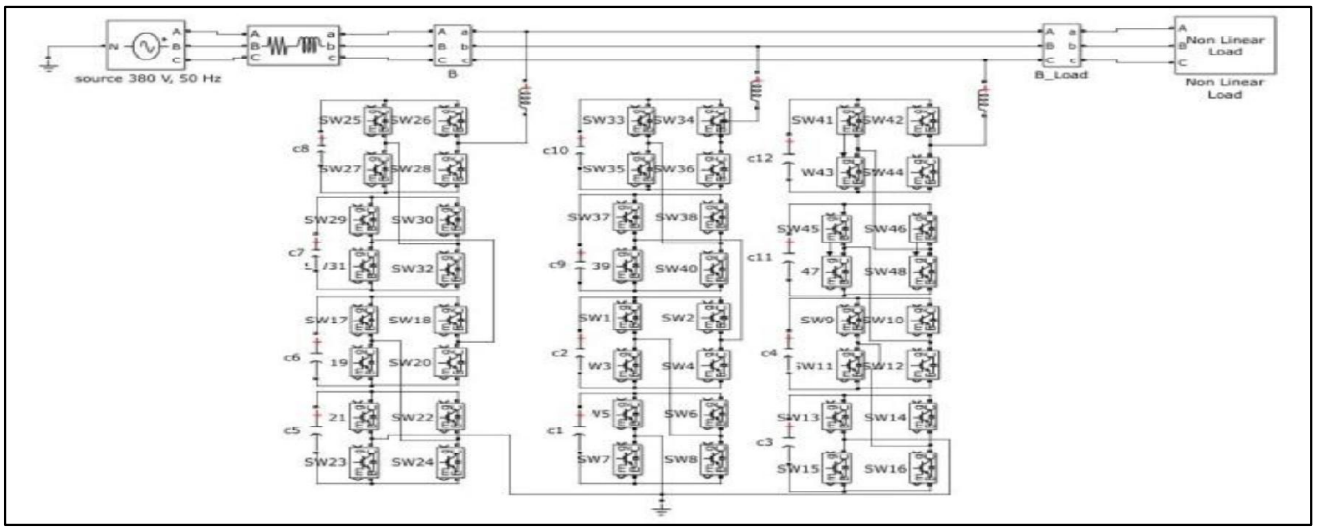


Figure 2: *Shunt power filter topology*

In this stage, there is a relation of some of the shunt active power filter that is clearly shown in its Figure 2. The use a voltage source inverter (VSI) is used as if the shunt active power filter has appeared [10]. This is dominated so that to draw a compensating current Ic from or to the utility, it calls off the harmonics on the AC side, namely, this active power filter (APF) gives the non-linearity's opposite towards the load nonlinearities. Both of them the load current, in addition to the compensating current are put by the shunt active power filter which has all the harmonics as a result, to prepare purely the source current sinusoidal. The essential item of shunt active power filter is done by compensating the reactive power and eliminating the current harmonics.

c) Power Flow for Ideal Compensation

Figure 3 depicts the single line diagram of the shunt active power filter showing power flow for ideal compensation

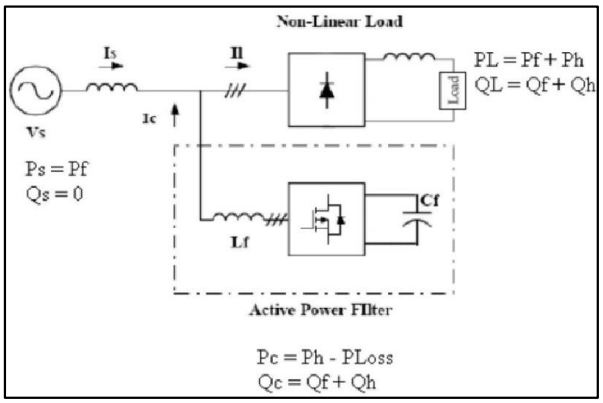


Figure 3: Shunt active filter power flow for ideal compensation

Total instantaneous power drawn by the nonlinear load can be represented as:-

$$P_{L(t)} = P_{f(t)} + P_{r(t)} + P_{h(t)} \quad (2)$$

Where;

$P_{f(t)}$ – Instantaneous fundamental (real) power absorbed by the load,

$P_r(t)$ – Instantaneous reactive power drawn by the load, and

$P_h(t)$ – Instantaneous harmonic power drawn by the load.

By achieving a unity power operation and drawing sinusoidal currents of the utility, active power filter is necessary supplying all the harmonics power demand of that the load. Active filter, at the same time, will shape a right component of power (P_Loss) of the utility, to provide switching losses and maintaining the DC link voltage which is steady .Therefore ,the ideal compensation following conditions should be fulfilled - Real power supplied by its source.

$$P_s = P_f + P_{loss} \quad (3)$$

Reactive power supplied by the source $Q_s = 0$

Real power drawn by the load $P_L = P_f + P_h$

Reactive power drawn by the load $Q_L = Q_f + Q_h$ Real power supplied by the active filter $P_c = P_h - P_{loss}$

Reactive power supplied by the active power filter

$$Q_c = Q_f + Q_h \quad (4)$$

Where,

P_L, P_f, P_h - are the total real power, fundamental real power and harmonic real power demand of the load.

Q_L, Q_f, Q_h – are the total reactive power, fundamental reactive power and harmonic reactive power demand of the load,

P_c, P_{Loss} – are the total power supplied and loss component of the active power.

d) Estimation of Reference Source Current

From the single line diagram shown in Figure 4

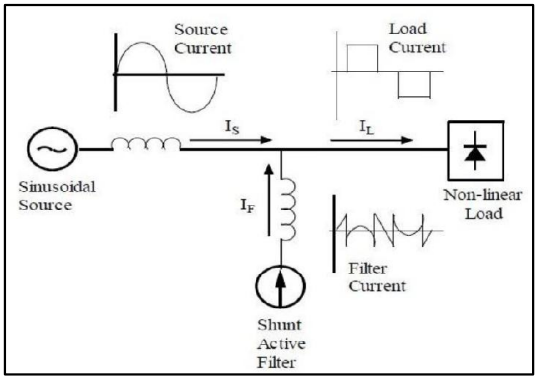


Figure 4: Filter current IF generated to compensate load current harmonics

$$is(t) = i_L(t) + ic(t) \quad (5)$$

Where,$i_s(t), i_L(t), i_c(t)$ - are the instantaneous value of source current, load current and the filter current.

The utility voltage is given by

$$Vs(t) = V_m \sin(wt) \quad (6)$$

Where, $V_s(t)$– is the instantaneous value of the source voltage.

V_m - is the peak value of the source voltage.

If non-linear load is connected then the load current will have a fundamental component and the harmonic components which can be represented as –

$$i_L(t) = \sum_{n=1}^{\infty} I_n \sin(nwt + \emptyset n) \quad (7)$$

$$i_L(t) = \sum_{n=2}^{\infty} I_n \sin(nwt + \emptyset n) + I_1 \sin(1wt + \emptyset 1) \quad (8)$$

Where: $I_1 and\ \emptyset_1$ are the amplitude of the fundamental current and its angle with respect to the fundamental voltage.

$I_n and\ \emptyset_n$ In are the amplitude of the nth harmonic current and its angle.

The instantaneous load power pL(t) can be expressed as

$$P_L(t) = V_s(t) i_L(t) \quad (9)$$

$$P_L(t) = V_m \sin wt \ \ (I_1 sinwt\ cos\emptyset_1 + \ I_1 coswt sin\emptyset_1) + V_m sinwt \sum_{n=2}^{\infty} I_n\ sin(nwt + \emptyset n) \quad (10)$$

$$P_L(t) = V_m I_1 \sin 2wt\ cos\emptyset + V_m I_1\ sinwt\ coswt\ sin\emptyset_1 + V_m sinwt \sum_{n=2}^{\infty} I_n\ sin(nwt + \emptyset n) \quad (11)$$

$$P_L(t) = P_f(t) + P_r(t) + P_h(t) \quad (12)$$

$$P_L(t) = P_f(t) + P_c(t) \quad (13)$$

In the equation (12) the term $P_f(t)$ is the real power (fundamental), the term $P_r(t)$ represents the reactive power and the term $P_h(t)$ represents the harmonic power drawn by the load. For ideal compensation only the real power (fundamental) should by supplied by the source while all other power components (reactive and the harmonic)

$$P_c(t) = P_r(t) + P_h(t) \quad (14)$$

Current supplied by the source is determined from the following equations:

$$P_r(t) = V_m I_1 sin2wt\ cos\emptyset \quad (15)$$

$$P_r(t) = V_s(t) i_s(t) \quad (16)$$

$$i_s(t) = \frac{P_r(t)}{V_s(t)} \quad (17)$$

$$i_s(t) = I_1 cos\emptyset_1 sinwt \quad (18)$$

$$i_s(t) = I_{sm} sinwt \quad (19)$$

Where

$$I_{sm} = I_1 cos\emptyset_1 \quad (20)$$

Also, there are some switching losses in the inverter. Therefore, the utility must supply a small overhead for the capacitor leaking and inverter switching losses in addition to the real power of the load.

Hence, total peak current supplied by the source

$$I_{ma} = I_{sm} + I_{sL} \quad (21)$$

Where:

I_{sL} is the loss component of current drawn from the source.

If active power filter provide the total reactive and harmonic power, then $i_s(t)$ will be in phase with the utility and pure sinusoidal. At this time, the active filter must provide the following compensation current:

$$I_c(t) = I_L(t) - i_s(t) \quad (22)$$

Hence, for the accurate and instantaneous compensation of reactive and harmonic power it is very necessary to calculate the accurate value of the instantaneous current supplied by the source,

$$I_s(t) = I_{ma}\ sinwt \quad (23)$$

The peak value of the reference current I_{ma} can be estimated by controlling the DC link voltage. The ideal compensation requires the mains current to be sinusoidal and in phase with the source voltage irrespective of load current nature. The desired source currents after compensation can be given as

$$I_{sa}^{*} = I_{ma}\ sinwt \quad (24)$$

$$I_{sb}^{*} = I_{ma}\sin(wt + 120) \quad (25)$$

$$I_{sc}^{*} = I_{ma}\sin(wt - 120) \quad (26)$$

It is clearly that peak value "I_{ma}" is approximately appraised by organizing the DC connection voltage of the inverter. DC link voltage is similar to a reference value and its fault can be carried on in a PI controller. The output of the PI controller has a major rule as the amplitude of the need source currents and the reference currents are calculated by changing that peak value in addition to the unit sine vectors in this level with the source voltages

e) Role of DC Link Capacitor

It is mainly that DC connection capacitor uses two goals the first which it keeps almost a constant DC voltage ,secondly it helps as an energy storage element to supply various actual power in the middle of the load and source during transients.

In stable state the actual power provided by the source which should be in the same amount to the actual power need of the load plus little power to make up the losses in the active filter. Thus the DC link voltage can be saved at a reference value.

Anyway, the idea is when the load condition turns to the actual power balance in the middle of the mains here; the load will be not continuous. This various actual power is made up of the DC link capacitor. This can change the DC connection voltage very far from the reference voltage. By keeping the satisfactory operation of the efficient filter, the peak value of the reference current is modified to proportionally alter the actual power drawn from the origin.

This real power charged/discharged by the capacitor compensates the real power consumed by the load. If the dc link voltage is recovered and attains the reference voltage the real power supplied by the source is supposed to be equal to that consumed by the load and also the losses.

Thus the peak value of the reference source current can be obtained by regulating the average voltage of the DC link capacitor. A smaller DC link voltage than the reference voltage means that the real power supplied by the source is not enough to supply load demand. Therefore the source current (i.e. the real power drawn from the source) needs to be increased. While a larger DC link voltage than the reference voltage tries to decrease the reference source current. There is a change can take place in capacitor voltage which is confirmed from the simulation results that clearly later in this paper.

The actual power injection might give ripples in the DC connection voltage. A little or low pass filter is commonly utilized to filter ripples, which give a finite late to go away from using this low pass filter the capacitor voltage and it is stood for at the zero crossing of the source voltages. A non-stopping changing reference current can be the compensation non-instantaneous within transient. Doing the compensation instantaneous like this, it is introduced to sample this voltage at the zero degrees and crossing (positive going) of one of the phase voltage. It does the compensation instantaneous in one phase systems, not in 3 phase systems. Additionally, just sampling once in a cycle as alike to 5/6 times in a cycle which contains a little higher DC capacitor voltage rise/dip during transients. The reason is capacitor voltage sampling at zero crossing degree of the voltage will be (six times in a cycle) and it is preferred in this stage.

III. Control Strategy of SAPF

For gathering the reference compensation currents, it needs to inject into the network at the point of connecting of the nonlinear load, this is because of the instantaneous active, reactive power method. Most popular SAPF control schemes remain. The theory, since then, has attracted a lot of functions that work in active power filter compensation strategies. The strange method of a shunt APF can be made without active energy source units. Any average power supplied by source Figure 5 depicts the block diagram for the instantaneous active and reactive power.

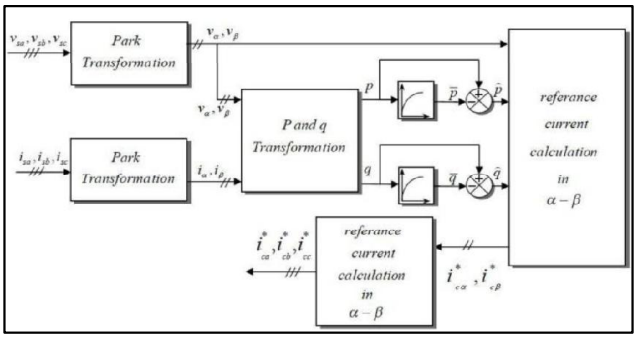


Figure 5: Block diagram of the proposed control system

Here in (p-q theory) which is the concept of instantaneous reactive power theory method which is basically compromised of a different transformation taken the (a, b, c) reference aspect of the immediate power, current signals to the α- β reference aspect [13, 14]. The instantaneous values of voltages and currents in the α-β coordinates may be taken from the following equation.

$$\begin{bmatrix} V_{\propto} \\ V_{\beta} \end{bmatrix} = \begin{bmatrix} 1 & -\frac{1}{2} & -\frac{1}{2} \\ 0 & \frac{\sqrt{3}}{2} & -\frac{\sqrt{3}}{2} \end{bmatrix} \begin{bmatrix} V_a \\ V_b \\ V_c \end{bmatrix} \quad (27)$$

$$\begin{bmatrix} I_{\propto} \\ I_{\beta} \end{bmatrix} = \begin{bmatrix} 1 & -\frac{1}{2} & -\frac{1}{2} \\ 0 & \frac{\sqrt{3}}{2} & -\frac{\sqrt{3}}{2} \end{bmatrix} \begin{bmatrix} I_a \\ I_b \\ I_c \end{bmatrix} \quad (28)$$

This transformation is valid if and only if

$$V_a(t) + V_b(t) + V_c(t) = 0 \quad (29)$$

And also if the voltages are balanced and sinusoidal. The instantaneous active and reactive powers in the $\alpha - \beta$ coordinates are calculated with the following expressions:

$$P(t) = V_{\propto}(t)I_{\propto}(t) + V_{\beta}(t)I_{\beta}(t) \quad (30)$$

$$q(t) = V_{\propto}(t)I_{\beta}(t) - V_{\beta}(t)I_{\alpha}(t) \quad (31)$$

The values of p and q can be expressed From Equation (3) and Equation (4) in terms of the dc components plus the ac components, that is:

$$P = \bar{P} + \tilde{P} \quad (32)$$

$$q = \bar{q} + \tilde{q} \quad (33)$$

Where

P: is the instantaneous power

$\bar{P}$: is the dc component of the instantaneous power

$\tilde{p}$: is the ac component of the instantaneous power, it does not have average value, and is related to the harmonic currents caused by the ac component of the instantaneous real power

q: imaginary instantaneous power

$\bar{q}$: stands for dc element of the imaginary instantaneous power, and it has a relation to the reactive power made by the basic components of currents in addition to voltages

$\tilde{q}$: stands for ac component of the immediate imaginary power and has a relation to the harmonic currents which is caused by ac component of immediate reactive power.

To make up current harmonics and reactive power which are generated by nonlinear loads, it is clear that the reference signal of the shunt active power filter has to be included in the values of $\tilde{p}$ and $\tilde{q}$. The reference currents, in this case, gotten by the SAPF which are gathered with the explanation below

$$\begin{bmatrix} I*c\alpha \\ I*_{c\beta} \end{bmatrix} = \frac{1}{V_\propto^2 + V_\beta^2}\begin{bmatrix} V_\alpha & V_\beta \\ V_\beta & -V_\alpha \end{bmatrix}\begin{bmatrix} P_L^{\sim} \\ \tilde{q}_L \end{bmatrix} \quad (34)$$

SAPF control strategy includes both of them, the first one is to compensate reactive power or the production of currents whether to leave out the undesired harmonics, however, to recharge the capacitor value requested by VDC voltage so that ensuring suitable transit of powers by supplying the inverter [9,13]. The average voltage across the capacitor terminals must be kept at a constant value. The Regulation of this voltage is made by absorbing or providing active power on the electrical network. The compensation of the reactive power brings about the storage capacity "C" which absorbs the power fluctuations, when harmonics is showed, in addition to active power control and by the losses of the converter. It must be made by adding namely , the average voltage across the capacitor terminals must be kept at a constant value. The Regulation of this voltage is made by absorbing or providing active power on the electrical network, the final compensating currents components in a, b, c reference frame are the following:

$$\begin{bmatrix} I*_{ca} \\ I*_{cb} \\ I*_{cc} \end{bmatrix} = \begin{bmatrix} 1 & 0 \\ -\frac{1}{2} & \frac{\sqrt{3}}{2} \\ -\frac{1}{2} & -\frac{\sqrt{3}}{2} \end{bmatrix}\begin{bmatrix} I*_{c\alpha} \\ I*_{c\beta} \end{bmatrix} \quad (35)$$

IV. Results and Discussion

The performance of the aimed immediate Active Power Theory (p-q Theory) method was tested inside the simulations. It was implanted in Simulink program environment namely, the system model. The SAPF was made to make up harmonics which is caused by nonlinear loads. It is, he system model parameters, shown in Table 1.A three-phase diode rectifier with a four type load was used as a harmonic producing.

- R Load (R= 30 Ω)

-RL load (R= 60 Ω and the L= 20 mH)

-RC load (R= 60 Ω and the C= 25 μF)

-Electrical motor (DC motor 5 HP 240V field 300V)

Table: Detail of system parameters

Parameters	
Supply phase voltage	**U 220 V**
Supply frequency Fs	**50 Hz**
Filter inductor Lf	**7.5 mH**
Dc link capacitor Cf	**250 μF**
Vdc	**310 V**

The filtering result can be seen in Figure 6 and Figure 7. It has shown the supply and load current, without using *CSAPF* the THD=22.7%, the deformations have now been reduced and the harmonic distortion calculated up to 2.5% Although the filtering performance especially with the low order harmonics has been improved, Cascade H bridge converter based shunt active filter is examined with different levels and resulted a THD in range of (7.2%-2.5%) this can be seen in Table 2.

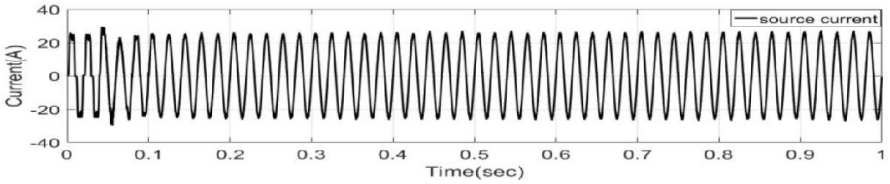


Figure 6: phase (a) supply current waveforms

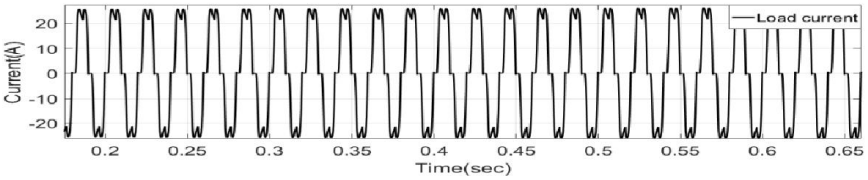


Figure 7: phase (a) load current waveforms

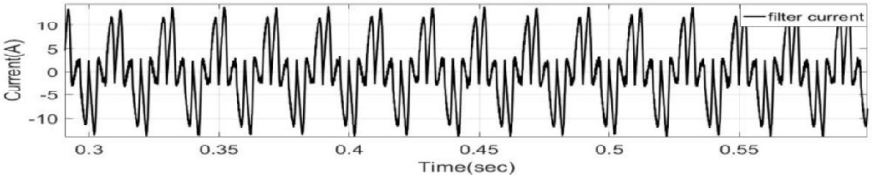


Figure 8: phase (a) filter current waveforms

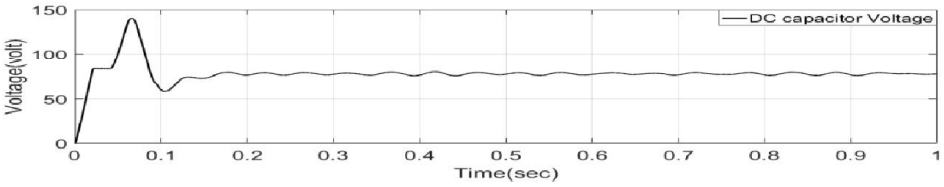


Figure 9: Average DC link voltage

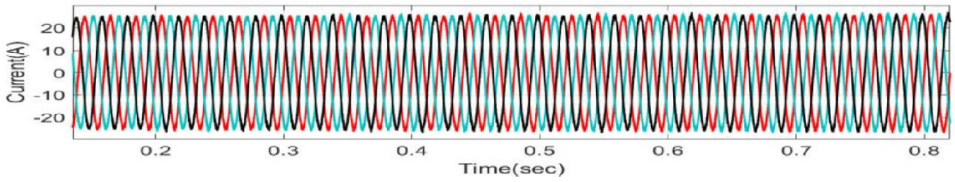


Figure 10: Three phase supply current waveforms

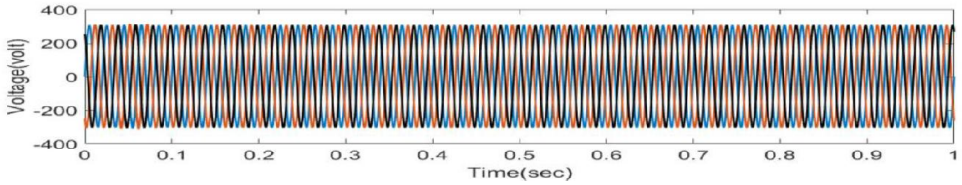


Figure 11: Three phase supply voltage waveforms

Table2: Result for each simulation

No of H-bridge	NO level	THD current Value
1	3	7.2%
2	5	5.3%
3	7	2.9%
4	9	2.5%

V. CONCLUSION

The work presented in this paper makes a significant contribution to the identification and control strategies in order to improve the CSAPF performance. (p-q theory) was verified through simulation studies, the (p-q theory) contains integrated (PI) controller, added to regulate the capacitor dc voltage of the CSAPF. The complete CSAPF structure has been implanted to compensate harmonics caused by nonlinear loads. At this level, comparative studies between the 3 level, 5 level,7 level and 9 level the most conventional techniques used to extract the harmonic component of the load current to produce reference currents, H-bridge is controlled by phase shifted pulse width modulation which produced rectangular waveform to trigger the gate in each arm of inverter. GSAPF is proposed to reduce the total harmonic distortion from 22.7% to 2.5%.

References

[1] Youssef ,K., "Industrial power quality problems Electricity Distribution," IEE Conf. Pub1 No. 482, vo1.2. June 2001, 18-

21.

[2] Dehini Rachid*, Chellali .B, 'improving the active power filters performance by robust self-tuning face to sudden change of load' Journal of Electrical Engineering V. 10/ N. 1 (JEE) 2010, pp. 65-73.

[3] M. Hagiwara, R. Maeda and H. Akagi, "Negative-Sequence Reactive-Power Control by a PWM STATCOM Based on a Modular Multilevel Cascade Converter (MMCC-SDBC)," *IEEE Transactions on Industry Applications,* vol. 48, no. 2, pp. 720 - 729, Aril, 102.

[4] C. Benachaiba, S. Dib and O. Abdelkhlek, 'Genetic Algorithm-Based Self-Learning Fuzzy PI Controller for Shunt Active filter', International Journal of Applied Engineering Research V. 1/ N. 2 (IJAER) 2006, pp. 203-216.

[5] O. Abdelkhalek, C. Benachaiba, M.Haidas, T. Benslimane, 'A new technique applied to a fuzzy regulator to control the shunt active filter DC bus voltage', journal "Information Technology and Control (ITC) 2008" , September 2008 Vol.37 No.3 (ISSN 1392-124X).

[6] Hugo.A, Ramos.C., Aurelio.M., Gary W. C., 'Real-Time Shunt Active Power Filter Compensation', IEEE TRANSACTIONS ON POWER DELIVERY, VOL. 23, NO. 4, OCTOBER 2008

[7] M. Rafiei, Verification of global optimality of the OFC active power filters by means of genetic algorithms, Proc. WSEAS Int. Conf. on Systems, Vouliagmeni, Athens, Greece, Jul. 10-12, 2006, pp. 559-564

[8] H. Akagi, S. Srianthumrong and Y. Tamai, "Comparisons in circuit configuration and filtering performance between hybrid and pure shunt active fitters", IEEE 38th Conf on Industry Applications, Vol. 2, pp. 1195-1202, October 2003..

[9] S.Rahmani, K. Al-Haddad, . F.Fnaiech. "A Three-Phase Shunt Active Power Filter for Damping of Harmonic Propagation in Power Distribution Systems " IEEE ISIE 2006, July 9-12, 2006, Montreal, Quebec, Canada, pp. 1760-1764

[10] *Hui.L, Guohai.L and Yue. S., 'A Novel harmonics Detection Method Based on Wavelet Algorithm for Active Power Filter',Proceedings of the 6th World Congress on Intelligent Control and Automation, June 21 - 23, 2006, Dalian, China.*

[11] *Y. Liu and F.L. Luo, "Trinary Hybrid Multilevel Inverter Used in STATCOM with Unbalanced Voltages", IEE Proc.-Electr. Power Appl., Vol. 152, No. 5, September 2005, pp.1203-1222.*

[12] *Jon A. Barrena, Luis Marroyo Miguel Á. Rodríguez, "Individual Voltage Balancing Strategy for PWM Cascaded H-Bridge onverter-Based STATCOM"; IEEE Transactions on Industrial Electronics,Vol. 55, No. 1, January 2008,pp. 21-29.*

[13] *Hirofumi Akagi, Shigenori Inoue, "Control and Performance of a Transformerless Cascade PWM STATCOM with Star nfiguration", IEEE Transaction on Industry Aplications, Vol 43, No. 4, ly/August 2007, pp. 1716-1723.*

[14] *Siriroj Sirisukprasert, Alex Qin Huang, "Modeling, Analysis and Control of Cascade-Multilevel Converter-Based STATCOM", IEEE Power Engineering Society General Meeting, Toronto, ON, anada, Jul. 2003, pp. 2561-2568.*

[15] *Yu Liu, Zhong Du, Alex Q Huang, "And Optimal Combination Modulation Strategy for a Seven-level Cascade Multilevel converter Based STATCOM"; Industry Applications Conference, 2006. 41st IAS Annual Meeting. Conference Record of the 2006 IEEE, pp. 1732-1737.*

[16] *Chong Han, Alex Q. Huang, "A Generalized Control Strategy of Per- Phase DC Voltage Balancing For Cascade Multilevel Converter-based STATCOM", PESC 2007. June 2007 Page(s):1746 – 1752.*

[17] *Micah E. Ortúzar, Rodrigo E. Carmi, Juan W. Dixon, Luis Morán, "Voltage-Source Active Power Filter Based on Multilevel Converter and Ultracapacitor DC Link", IEEE Transactions On Industrial Electronics, Vol. 53, No. 2, April 2006.*

[18] *Lopez, M.G.; Moran, L.T.; Espinoza, J.C.; Dixon, J.R., Performance analysis of a hybrid asymmetric multilevel inverter for high voltage active power filter applications", Industrial Electronics Society, 2003.IECON '03. The 29th Annual Conference of the IEEE; Volume 2, 2-6Nov. 2003 Page(s):1050 – 1055.*

[19] *Pérez-Ramírez J.; Cárdenas V., Miranda H. and Espinosa-Pérez G.;"Generalized DC Voltage Regulation Strategy for n:1 Relation Cascade H-Bridge Converter-Based STATCOM"; Firts Energy Convertion Congress & Expo (ECCE) Sep. 2009; pp. 2985-2990.*

[20] *K. Matsui, H. Kojima, I. Yamamoto, M. Hasegawa, and K. Ando;*

"PWM-STATCOM System Additionally having Active Filter Function"; Energy and Power Systems (EPS 2006); Chiang Mai, Thailand; March 29 – 31, 2006

Stator Faut Detection For The Input Ouput Control Of The Permanent Magnet Synchronous Motor

Y. MAANANI[1], A. MENACER[1], I. HARZELLI[1] and S. ZOUZOU[1]
[1] Biskra University, Biskra/Algeria, yacine.maanani@gmail.com
[1] Biskra University, Biskra/Algeria, menacer_arezki@hotmail.com
[1] Biskra University, Biskra/Algeria, imadeddineharzelli@yahoo.fr
[1] Biskra University, Biskra/Algeria, sara_2888@live.fr

***Abstract* - In this paper, a simple dynamic model for a PMSM with inter-turn winding fault in closed loop. The control of the PMSM is assured by the input-output control. The objective of this paper is the detection and location of the stator winding fault severity of PMSM. To achieve this objective, a mathematical model that can describe both healthy and fault conditions is developed. Simulation results match the observations of this type of fault in the literature**.

Keywords - permanent magnets synchronous machine, inter turn, fault detection, input-output control,

I. INTRODUCTION

PERMANENT magnet synchronous motor PMSM has received widespread acceptance, mainly in high performance of it's applications for renewable energy generator or industrial servo applications of accurate speed and position control. This is due to some of its excellent features such as super power density, high torque to current ratio, fast response and low noise [1].

Nonlinear control has the advantage of separately current and torque. With this control technology, engine model is broken down into two independent systems mono variable linear. Each subsystem is an independent control loop of a given variable (speed, torque, current etc.). The dynamics of the linearized system is chosen through optimal taxation of poles [2].

The PMSM are generally robust, their frequent exposure to severe circumstances inclines them to certain fault conditions after continuous operation. The possible fault modes in PMSM include electrical and mechanical sources [3]. Statistics show that the most electric motor failures are due to electrical faults, among which the stator winding faults constitute the largest portion [4]. Stator winding faults usually are caused by insulation breakdown between coils in the same phase or different phases. While the winding ″short″ usually emerges locally as an incipient fault, it can propagate rapidly, culminating in the failure of the entire phase. This is due to the increased ohmic heating associated with the high current in the shorted portion of the winding, which eventually leads to a significant rapid temperature increase and causes faster deterioration of the insulation system [5]. Therefore, an effective diagnostic system for these faults in motors is necessary to improve the reliability of such motors.

The mathematical analysis and computer simulation are more versatile and cost effective methods for gaining insight into the system dynamics under fault operating conditions. Recently, several studies on faulty electric machine dynamic modeling have been published. These studies use various methods for different purposes [6]. Fault modeling is becoming an important part of the fault diagnosis design process. In this paper, a new model for the stator winding fault of PMSM is proposed based upon the coupled magnetic circuit principle. The model is compatible with both healthy operation and operation under asymmetrical stator winding fault (turn-to-turn short) conditions. Simulation results of the fault model match the observations of this kind of fault in the literature. In the developed fault model, two parameters are used, one to represent fault location and one for fault severity. If these two parameters can be identified and are beyond a certain range, then the occurrence of a stator winding fault can be concluded.

In general, monitoring and diagnosis require the detection and analysis of signals containing specific information (symptoms or signatures) that characterizes the degradation of the machine [8].

FFT analysis of one of the stator currents has become a standard procedure for diagnosing the state of a permanent magnet synchronous motor. However [7], Even though the method gives successful results for stationary signals, it is not successful for non-stationary signals due to the inadequacy of the FFT method. Since PMSMs are operated according to the determined acceleration and deceleration reference speeds, both the amplitude and the frequency of the current drawn in these regions are dynamic [9].

II. DYNAMIC MODEL OF THE PMSM WITH INTER TURN FAULT

An inter-turn fault denotes an insulation failure between two windings in the same phase of the stator. The insulation failure is modeled by a resistance, where its value depends on the fault severity. The stator winding of a PMSM machine with inter-turn fault is represented in Fig. 1, where the fault is occurred in the phase a_s and (r_f) represents the fault insulation resistance. The sub-windings (a_{s1}) and (a_{s2}) represent the healthy and faulty part of the phase winding a respectively.

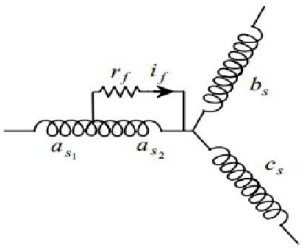


Figure 1: Three-phase winding with inter-turn fault in the phases.

When the fault resistance (r_f) decreases toward zero, the insulation fault evaluates toward an inter-turn full short-circuit. The evolution of fault insulation resistance between $r_f = \infty$ and $r_f = 0$ is very fast in most insulation materials. It is important to predict the inter-turn fault when it is not high developed and the fault resistance is still not very near to zero. Therefore, in our fault model, the fault insulation resistance is included and the machine behavior with various fault resistances is studied [10].

II 1. *FAULT MODEL IN ABC COORDINATES*

Setting up the mesh equations for the circuit in Figure 1 will express the voltage equations as:

$$V_s = [R_s][I_s] + [L_{ss}]\frac{d}{dt}[I_s] + [E_s] \quad (1)$$

where $[V_s]$, $[I_s]$ and $[E_s]$ are the stator voltage, current and back-EMF vectors:

$$V_s = [v_{as}\ v_{bs}\ v_{cs}]^T\ ,\ I_s = [I_{as}\ I_{bs}\ I_{cs}]^T\ ,\ E_s = [e_{as}\ e_{bs}\ e_{cs}]^T$$

R_s: is the phase resistance and $[L_{ss}]$ is the inductance matrix of the healthy PMSM respectively:

$$[R_s] = \begin{bmatrix} R_s & 0 & 0 \\ 0 & R_s & 0 \\ 0 & 0 & R_s \end{bmatrix} \quad ,[L_{ss}] = \begin{bmatrix} L_s & M & M \\ M & L_s & M \\ M & M & L_s \end{bmatrix}$$

Where the inductance L_s is the phase self inductance and M is the mutual inductance between phase windings of the healthy PMSM.

R_{a2} and L_{a2} represent the resistance and inductance of the faulty sub coil (a_{s2}). The parameters M_{a1a2}, M_{a2b} and M_{a2} represent respectively the mutual inductances between the sub-coil a_{s2} and the coils a_{s1}, b_s and c_s. The fault current through the insulation fault resistance r_f is also called i_f . For the machine having one slot per pole and per phase, M_{a2b} can be considered equal to M_{a2c}.

The voltage equation of the faulty loop (a_{s2}) is:

$$0 = -R_{a2}I_{as} - (L_{a2} + M_{a1a2})\frac{dI_{as}}{dt} - M_{a2b}\frac{dI_{bs}}{dt} - M_{a2c}\frac{dI_{cs}}{dt} - e_{a2} + (R_{a2} + r_f)I_f + L_{a2}\frac{dI_f}{dt} \quad (2)$$

The equations of the voltages of the three phases are thus put in the form:

$$\begin{cases} V_{as} = (R_{a1} + R_{a1})I_{as} + (L_{a1} + L_{a2} + 2M_{a1a2})\frac{d}{dt}I_{as} + (M_{a1b} + M_{a2b})\frac{d}{dt}I_{bs} + \\ (M_{a1c} + M_{a2c})\frac{d}{dt}I_{cs} + (e_{a1} + e_{a2}) - R_{a2}I_f - (L_{a2} + M_{a1a2})\frac{d}{dt}I_f \\ V_{bs} = R_s I_{bs} + L\frac{d}{dt}I_{bs} + (M_{a1b} + M_{a2b})\frac{d}{dt}I_{as} + e_{cs} + M\frac{d}{dt}I_{cs} - M_{a2b}\frac{d}{dt}I_f \\ V_{cs} = R_s I_{cs} + L\frac{d}{dt}I_{cs} + (M_{a1c} + M_{a2c})\frac{d}{dt}I_{as} + e_{cs} + M\frac{d}{dt}I_{bs} - M_{a2c}\frac{d}{dt}I_f \end{cases} \quad (3)$$

The following relations are normally allowed:

$$\begin{aligned} R_s &= R_a = R_{a1} + R_{a2} \\ L &= L_{a1} + L_{a2} + 2M_{a1a2} \\ M &= M_{a1b} + M_{a2b} \\ M &= M_{a1c} + M_{a2c} \\ e_a &= e_{a1} + e_{a2} = e_{a1} + e_f \end{aligned} \quad (4)$$

By replacing the above relations (4) in the electrical equations (3), we obtain the following matrix writing:

$$\begin{bmatrix} V_{as} \\ V_{bs} \\ V_{cs} \end{bmatrix} = R_s \begin{bmatrix} I_{as} \\ I_{bs} \\ I_{cs} \end{bmatrix} + \begin{bmatrix} L_s & 0 & 0 \\ 0 & L_s & 0 \\ 0 & 0 & L_s \end{bmatrix} \frac{d}{dt}\begin{bmatrix} I_{as} \\ I_{bs} \\ I_{cs} \end{bmatrix} + \begin{bmatrix} R_{a2} \\ 0 \\ 0 \end{bmatrix} I_f - \begin{bmatrix} L_{a2} + M_{a1a2} \\ M_{a2b} \\ M_{a2c} \end{bmatrix} \frac{dI_f}{dt} \quad (5)$$

II 2. *FAULT MODEL IN AB-COORDINATES*

For the star connected winding, the zero sequence component of the stator current is zero. Thus, the stator stationary reference frame transformation is applied:

$$\begin{bmatrix} x_\alpha \\ x_\beta \end{bmatrix} = \sqrt{\frac{2}{3}} \begin{bmatrix} 1 & -\frac{1}{2} & -\frac{1}{2} \\ 0 & \frac{\sqrt{3}}{2} & -\frac{\sqrt{3}}{2} \end{bmatrix} \begin{bmatrix} x_a \\ x_b \\ x_c \end{bmatrix} \quad (6)$$

By representing the machine stator vectors by their components in the αβ coordination, the PMSM machine equations with inter-turn fault (1) are simplified as follows:

$$[V_{\alpha\beta}] = R_s[I_{\alpha\beta}] + [L_{\alpha\beta}]\frac{d}{dt}[I_{\alpha\beta}] + [e_{\alpha\beta}] - [L'_0]\frac{d}{dt}[I_f] - [R'_0]I_f \quad (7)$$

For the faulty loop (a_{s2}), the voltage equation n the αβ coordination becomes:

$$0 = -\sqrt{\frac{2}{3}}R_{a2}I_{as} - \sqrt{\frac{2}{3}}\left(L_{a2} + M_{a1a2} - \frac{M_{a2b} + M_{a2c}}{2}\right)\frac{dI_{as}}{dt} - \frac{1}{\sqrt{2}}(M_{a2b} - M_{a2c})\frac{dI_{bs}}{dt} - M_{a2c}\frac{dI_{cs}}{dt} - e_{a2} + (R_{a2} + r_f)I_f + L_{a2}\frac{dI_f}{dt} \quad (8)$$

Finally, the machine equations with inter-turn fault (7) in αβ reference frame are written as follows:

$$\begin{bmatrix} V_\alpha \\ V_\beta \end{bmatrix} = R_s \begin{bmatrix} V_\alpha \\ V_\beta \end{bmatrix} + L_s \frac{d}{dt}\begin{bmatrix} I_\alpha \\ I_\beta \end{bmatrix} + \begin{bmatrix} e_\alpha \\ e_\beta \end{bmatrix} - \sqrt{\frac{2}{3}}\begin{bmatrix} R_{a2} \\ 0 \end{bmatrix} I_f - \begin{bmatrix} \sqrt{\frac{2}{3}}\left(L_{a2} + M_{a1a2} - \frac{M_{a2b} + M_{a2c}}{2} \right) \\ \frac{1}{\sqrt{2}}\left(M_{a2b} - M_{a2c} \right) \end{bmatrix} \frac{dI_f}{dt} \quad (9)$$

$$\begin{bmatrix} V_\alpha \\ V_\beta \\ 0 \end{bmatrix} = \begin{bmatrix} R_s & 0 & -R'_{a2} \\ 0 & R_s & 0 \\ -R'_{a2} & 0 & R'_f \end{bmatrix} \begin{bmatrix} I_\alpha \\ I_\beta \\ I_f \end{bmatrix} + \begin{bmatrix} L_s & 0 & M_{fa} \\ 0 & L_s & M_{f\beta} \\ M_{fa} & 0 & L_{a2} \end{bmatrix} \frac{d}{dt} \begin{bmatrix} I_\alpha \\ I_\beta \\ I_f \end{bmatrix} + \begin{bmatrix} e_\alpha \\ e_\beta \\ -e_f \end{bmatrix} \quad (10)$$

With:

$$R'_{a2} = \sqrt{\frac{2}{3}} R_{a2}, \quad R_f = R_{a2} + r_f, \quad e_\alpha = e_f$$

$$M_{fa} = -\sqrt{\frac{2}{3}}\left(L_{a2} + M_{a1a2} - \frac{M_{a2b} + M_{a2c}}{2} \right)$$

$$M_{f\beta} = \frac{1}{\sqrt{2}}\left(M_{a2b} - M_{a2c} \right)$$

As the zero sequence component of the current is zero, the electromagnetic torque expression (2) is:

$$T_e = \frac{e_\alpha I_\alpha + e_\beta I_\beta - e_{\alpha 2} I_f}{\Omega} \quad (11)$$

II 3. State Space Form of Fault Model

For digital simulation of the electrical machine with inter turn fault, it is more convenient to express the dynamic equations in the state space form. The (10) can be written as:

$$\frac{d}{dt}\begin{bmatrix} I_\alpha \\ I_\beta \\ I_f \end{bmatrix} = \begin{bmatrix} L_s & 0 & M_{fa} \\ 0 & L_s & M_{f\beta} \\ M_{fa} & 0 & L_{a2} \end{bmatrix}^{-1} \left(\begin{bmatrix} R_s & 0 & -R'_{a2} \\ 0 & R_s & 0 \\ -R'_{a2} & 0 & R'_f \end{bmatrix} \begin{bmatrix} I_\alpha \\ I_\beta \\ I_f \end{bmatrix} \right) + \begin{bmatrix} v_\alpha - e_\alpha \\ v_\beta - e_\beta \\ e_f \end{bmatrix} \quad (12)$$

The state vector (x) and input vector (u) are supposed as:

$$x = \begin{bmatrix} I_\alpha \\ I_\beta \\ I_f \end{bmatrix}; \quad u = \begin{bmatrix} v_\alpha - e_\alpha \\ v_\beta - e_\beta \\ e_f \end{bmatrix} \quad (13)$$

Thus, the machine fault model (10) in the state space form can be expressed as:

$$\dot{x} = Ax + Bu \quad (14)$$

With:

$$A = -\begin{bmatrix} L_s & 0 & M_{fa} \\ 0 & L_s & M_{f\beta} \\ M_{fa} & 0 & L_{a2} \end{bmatrix}^{-1} \begin{bmatrix} R_s & 0 & -R'_{a2} \\ 0 & R_s & 0 \\ -R'_{a2} & 0 & R'_f \end{bmatrix}$$

$$B = \begin{bmatrix} L_s & 0 & M_{fa} \\ 0 & L_s & M_{f\beta} \\ M_{fa} & 0 & L_{a2} \end{bmatrix}^{-1}$$

The state space equation (14) can be used for digital simulation. The simulation block diagram for PMSM with inter-turn fault is shown in Figure 2.

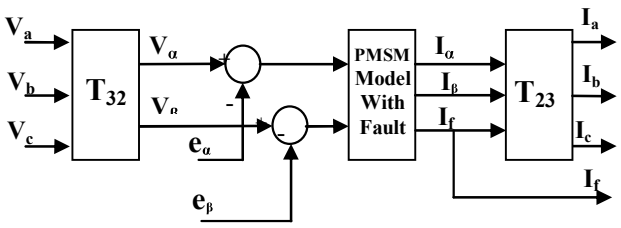


Figure 2: Block diagram of inter-turn fault model for PMSM.

III. Simulation Results for pmsm With Inter-Turn Faults

The proposed fault dynamic model (10) to (11) or (14) is used to modeling and study the PMSM with stator winding inter-turn fault. For this purpose, a four pair-pole PMSM. Using MATLAB-Simulink software, the fault model for PMSM is simulated under various inter-turn fault conditions.

Winding a_s in the external circuit is divided to two sub-winding a_{s1} and a_{s2} in series. With such a procedure, the current of the shorted part and flux linked with this branch is accessible.

First, it is considered that fault is occurred 2% of winding turns in the phase a_s and the other phases are healthy. The dynamic fault model is simulated for different values of fault insulation resistances r_f = 10Ω, 1Ω and 0.1Ω. The simulation results, concerning the phase currents (I_{abc}) and the fault current (i_f) and the torque electromagnetic are presented in Figure 3.

It can be seen that when the resistance to faults decreases and follows to a complete short circuit, the amplitude of the fault current increase and the phase currents become more and more unbalanced, the phase which fault is occurred (a_s), will be non-sinusoidal. Furthermore, the phases current will have not the same amplitude and will be unbalanced. The phase current witch the turn fault is occurred in (a_s) is much higher than other phase currents (b_s, c_s) where these phases are also affected by the fault. The torque electromagnetic present increase the fluctuation from the nominal value. This fault may also produce a small torque ripples.

Secondly, it is considered that fault insulation resistances 0.1Ω. The dynamic fault model is simulated for different values of the severity of the fault (a): μ = 1%, (b): μ = 2%, (c): μ= 3%. The simulation results, concerning the phase currents (I_{abc}) and the fault current (I_f) and the torque electromagnetic are presented in Figure 4.

Before the fault the current i_f is zero. The phase currents are unbalanced with, in addition to increasing the amplitude of the current of the defective phase compared to the other phases when the number of turns in short-circuit increases, the system of phase currents is unbalanced, although these currents retain the periodic properties.

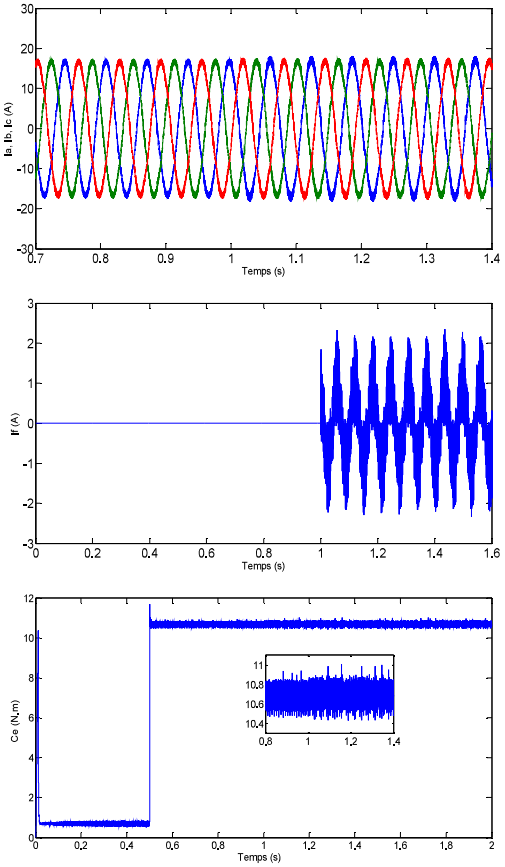
In stationary state (a_s it is the aim of this work), FFT analysis method is used to characterize signatures of different kind and strong of the short-circuit faults.

Measurements of stator currents in healthy mode and faulty mode obtained by applying with different values of the severity the fault μ, and different values of fault insulation resistances r_f.

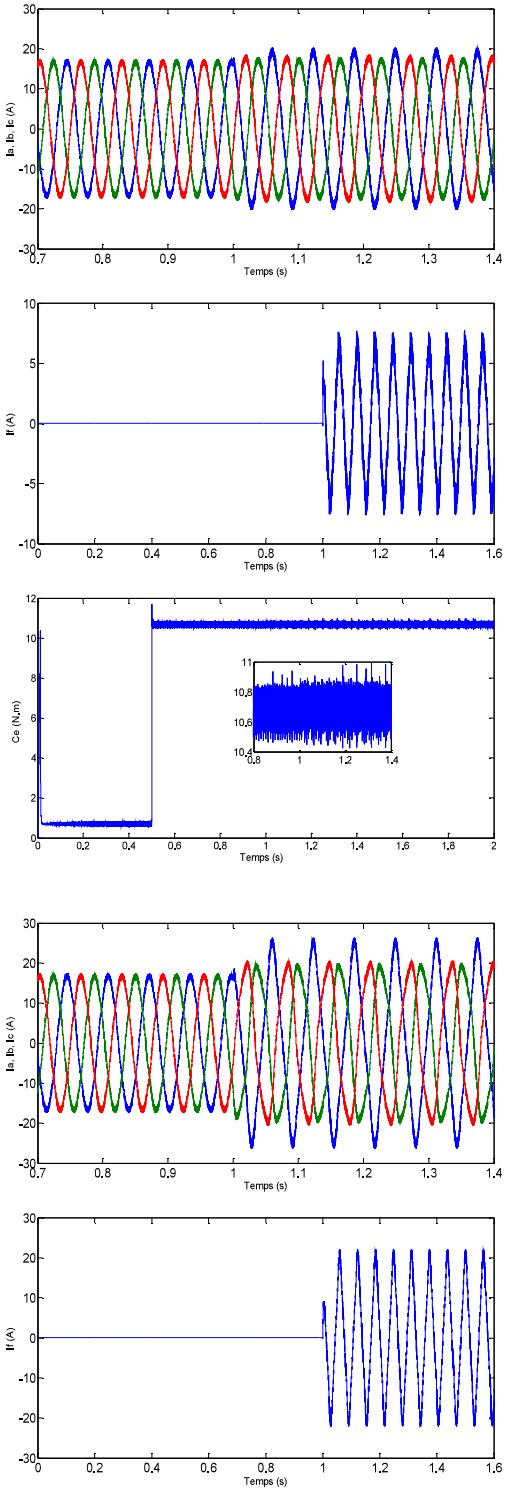
The Figure 5-6, shows the stator current FFT analysis in phase 'a' in healthy mode and faulty mode obtained by applying a 02% of the severity of the fault and insulation resistances 0.1Ω.

The table I shows the stator currents FFT analysis in the case of a single phase inter-turn fault in phase 'a' with different values of the severity of the fault (a): μ = 1%, (b): μ = 2%, (c): μ= 3% turns short circuited and insulation resistances 0.1Ω at a speed of 3000rpm. It is clear that third harmonic components are stronger than the healthy operating mode and there is an increase in this component with growth of the severity of the fault.

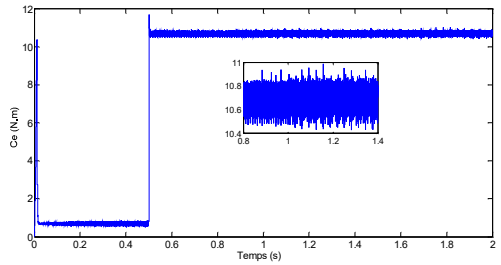
The above study shows in the table. II, FFT analysis of stator current in the case of a single phase inter-turn fault in phase 'a' for 02% of winding turns with different values of fault insulation resistances rf = 10Ω, 1Ω and 0.1Ω at a speed of 3000rpm, It can be seen that the phase currents harmonics components will increase, as the fault resistance decrease rf.



(a)

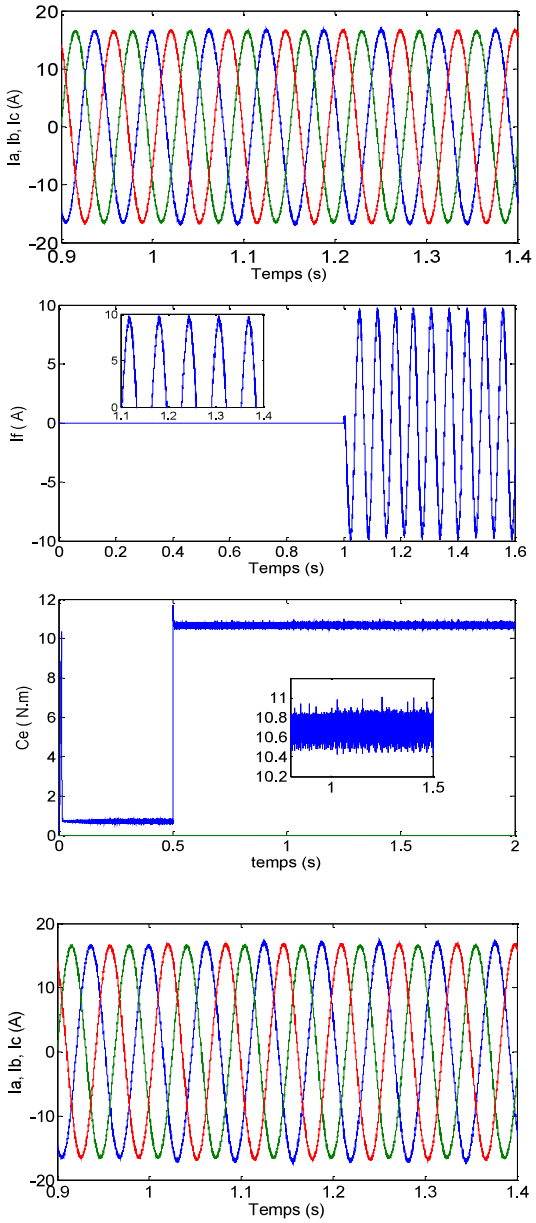


(b)

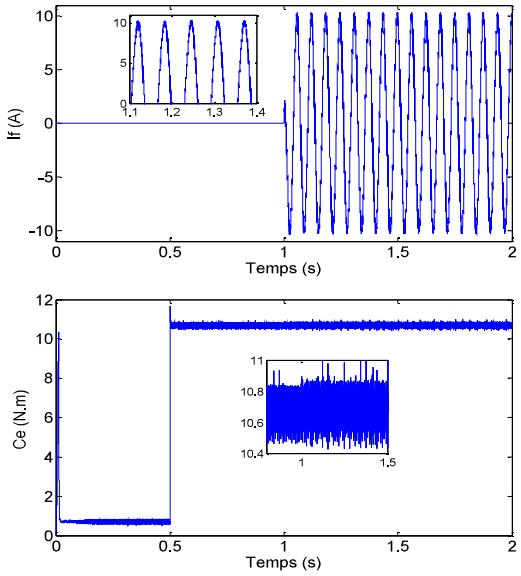


(c)

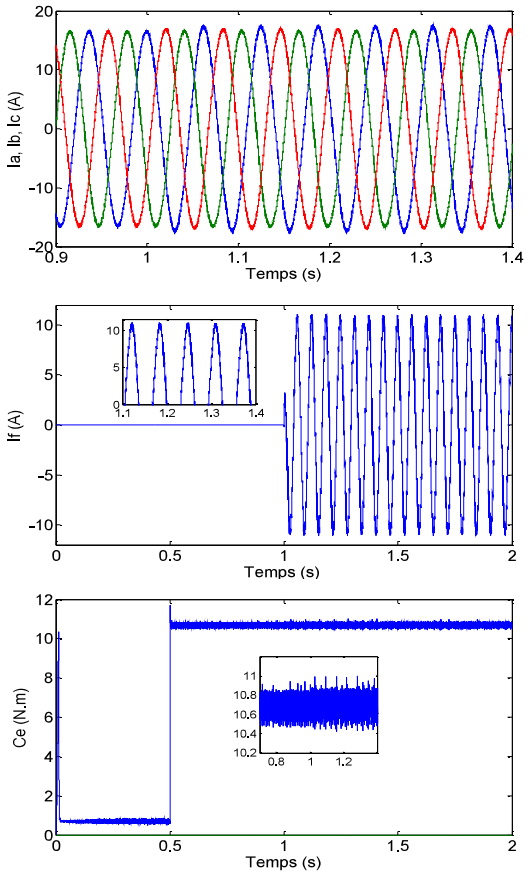
Figure 3: Phases currents, fault current and electromagnetic torque with severity of the fault (a): μ = 2%, (a) fault resistance = 10 Ω; (b) fault resistance = 1 Ω; and (c) fault resistance = 0.1 Ω.



(a)



(b)



(c)

Figure 4: Phases currents and fault currents simulates and electromagnetic torque with fault resistance r_f = 0.1 Ω and the severity of the fault (a): μ = 1%, (b): μ = 2%, (c): μ = 3%.

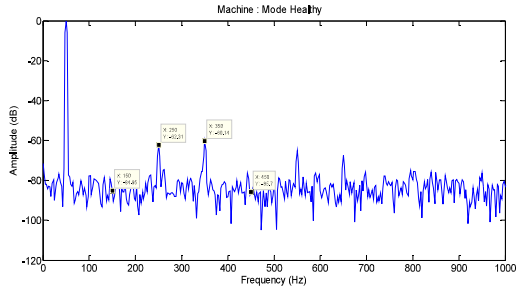


Figure 5: Spectral content of a healthy mode for PMSM, operating under rated load at 3000 r/min

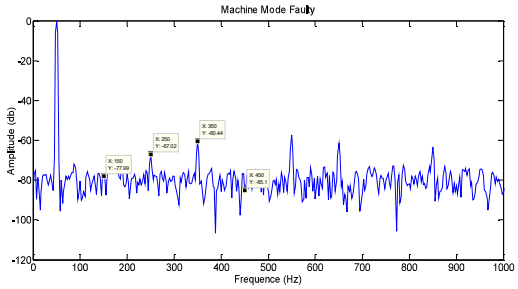


Figure 6: Spectral content of faulty mode for PMSM, operating under rated load at 3000 r/min.

TABLE I: FFT analysis of currents for different values of the severity.

State of PMSM Amplitude (dB)	50 HZ	150 HZ	250 HZ	350 HZ	450 HZ
Heath mode	0	0	-85.25	-61.63	-60.14
1% turns short circuited	0	-55.61	-71.88	-59. 74	-72.53
2% turns short circuited	0	-48.58	-68.17	-59.44	-70.14
3% turns short circuited	0	-44.72	-70.50	-62.00	-71.53

TABLE II: FFT analysis of currents for different values of fault insulation resistances.

State of PMSM Amplitude (dB)	50 HZ	150 HZ	250 HZ	350 HZ	450 HZ
Healthy mode	0	-85.25	-61.63	-60.14	-85.70
fault resistances $r_f = 10\ \Omega$	0	-55.61	-71.88	-61. 37	-56.76
fault resistances $r_f = 1\ \Omega$	0	-43.63	-68.02	-58.94	-58.81
fault resistances $r_f = 0.1\ \Omega$	0	-32.91	-67.51	-57.34	-57.69

VIII. Conclusion

To identify the stator winding fault for PMSM, this paper proposed a model that can describe both normal and fault conditions. The model has been verified by comparing the simulation results with observations in related literature. However, because there is no quantified comparison, it is difficult to evaluate the accuracy of the developed model.

The fault detection problem can be approached by identifying the two parameters associated with fault location and fault severity. Because of the complex distribution of these two parameters in the fault model, it is very difficult to design a nonlinear identification algorithm. The FFT analysis algorithm is proposed to solve the detection/identification problem indirectly. Simulation studies on the developed model under both healthy and fault conditions demonstrate the performance of the proposed algorithm.

The proposed inter-turn fault model seems to be well adapted for PMSM health monitoring and inter-turn fault diagnosis.

Appendix

$L_s = 2.82$ mH, $\phi_f = 0.108$ Wb, $R_s = 0.88\Omega$, $p = 4$,
$J = 0.0006$ kg.m2, $f = 0.007$ N.m.s/rad, In = 19A,
$L_{bob} = 0.00085$ H, $M_{bob} = -0.00005$ H.

References

[1] S.Lachtar, T.Bahi, "SVPWM performance of PMSM variable speed and impact of diagnosis sensors faults", International Conference on Technologies and Materials for Renewable Energy, Environment and Sustainability, TMREES15.

[2] Jinpeng Yu, Peng Shi, Dong Wenjie, "neural network-based adaptive dynamic area control for permanent magnet synchronous motors", IEEE Trans Neural Networks and is learning system, 2014.

[3] O. Ojo, O. Osaloni, P. Kshirsagar, "Models for the control and simulation of synchronous type machine drives under various fault conditions", in: 2002 Conference Record Ind. Appl. Conference, 37th IAS Annual Meeting, vol. 3, pp. 1533–1540.

[4] P.F. Allbrecht, J.C. Appiarius, R.M. McCoy, et al, "Assessment of the reliability of motors in utility applications – updated", IEEE Trans. Energy Convers. 1(1) (1986) 39–46

[5] J.A. Haylock, B.C. Mecrow, A. G Jack, D.J. Atkinson, "Operation of fault tolerant machines with winding failures", IEEE Trans. Energy Convers. 14 (4) (1999)1490–1495

[6] L. Harnefors and M. Hinkkanen, "Stabilization methods for sensorless induction motor drives - A survey", IEEE Journal of Emerging and Selected Topics in Power Electronics, vol. 2, no. 2, pp. 132-142, June 2014.

[7] J. Rusek , "induction machine diagnostics based on FFT analysis of current space vector", AGH University of Science and Technology, Chair of Electrical Machines. Zeszyty Problemowe – Maszyny Elektryczne Nr 93/2011.

[8] S. Saeid M. Anchehpoli, "Analysis and diagnosis of faults in the PMSM drivetrains for series hybrid electrical vehicles (SHEVs) ", Electric power. Universite de Technologie de Belfort-Montbeliard, 2013. English. Submitted on 4 Apr 2017.

[9] Y. Shi, K. Sun, L. Huang, and Y. Li, "Online identification of ermanent magnet flux based on extended kalman filter for IPMSM rive with position sensorless control", IEEE Trans. Industrial Electronics, vol.59,no.11pp.4169-4178,Nov.2012.

[10] B. Vaseghi, , N. Takorabet, "Modelling and study of PM machines with inter-turn fault dynamic model–FEM model", Electric Power Systems Research 81 (2011) 1715–1722

Comparison of Wind Power Integration Grid Codes of Various Countries

K.N.AKPINAR[1] and M. OZDEMİR[1]

[1] Ondokuz Mayıs University, Samsun/Turkey, kubranur.birlik@omu.edu.tr
[1] Ondokuz Mayıs University, Samsun /Turkey, ozdemirm@ omu.edu.tr

Abstract **- In recent years, inclination towards renewable energy has increased due to its energy supply security, green energy use, and environmental friendliness compared to traditional power plants. Especially, wind energy is preferred because its source is free and it has the advantage of energy diversity for the country. According to the capacities provided by the national transmission and distribution system, the wind power plant installation is increasing day by day. The structure of wind energy is fluctuating, meaning that it is not stable and the voltage drops that might come to the fore can damage the electricity grid. The wind turbine must remain connected to the grid and contribute to the system within certain limits during or after faults, such as voltage drops. The operating ranges and operating conditions determined by the system operators during and after the fault are called the grid code. The grid code provides reliability, safety and stability in the power plant and transmission and distribution system. In this study, the grid codes for the wind power plants of various countries were examined, and the grid codes recently published by the countries were compared with the current grid codes in Turkey.**

Keywords **- Grid Code, Grid Integration, Wind Power Plants, Connection Requirements**

I. INTRODUCTION

As the demands of the countries for wind energy increase day by day, their installed power is increasing rapidly according to the grid infrastructures. If we look at the global renewable energy capacity, the slice in the distribution pie chart of wind energy onshore and offshore is considerably big. Fig. 1 shows the cumulative installed wind capacity globally on a yearly basis. The installed wind capacity which has risen about 10 times in the last 10 years shows the increase in investments.

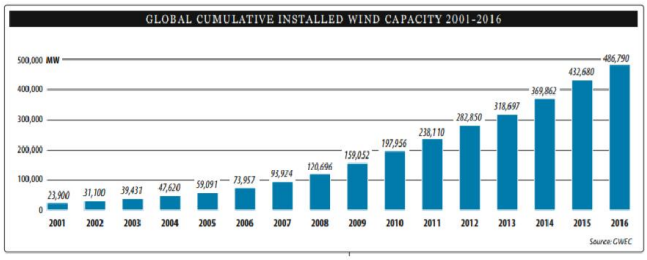
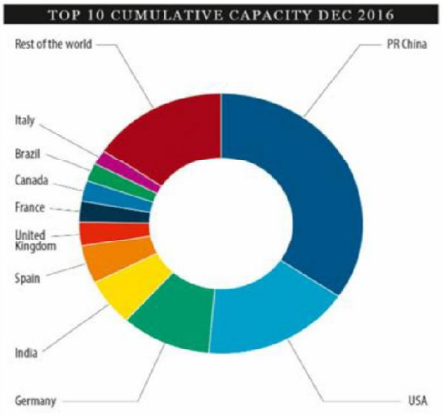


Figure 1: Global Cumulative Installed Wind Capacity [1]

Fig. 2 shows the top 10 countries in the distribution of wind energy capacity in the world. According to this, China is in the 1st place with a distribution of 34.7%, followed by USA with 16.9% and Germany with 10.3%. China and the US constitute 50% of the world's installed wind energy capacity.



Country	MW	% Share
PR China	168,732	34.7
USA	82,184	16.9
Germany	50,018	10.3
India	28,700	5.9
Spain	23,074	4.7
United Kingdom	14,543	3.0
France	12,066	2.5
Canada	11,900	2.4
Brazil*	10,740	2.2
Italy	9,257	1.9
Rest of the world	75,576	15.5
Total TOP 10	**411,214**	**84**
World Total	**486,790**	**100**

Source: GWEC

Figure 2: Wind Energy Capacity Distribution by Country [1]

There are some factors to consider if wind turbines are connected to the grid. In order to ensure that the grid to which it is connected is not damaged and its safety is ensured, the transmission and distribution system operator (TSO-DSO) has to set some rules in order to ensure uninterrupted and continuous transmission of energy to the demanding side. These rules are called grid code which is specific to every energy type. In addition, it differs from country to country

depending on grid structures. Power system manufacturers are designing and manufacturing by considering these published grid codes. They are updating the production technology according to the renewed grid codes.

Even though the grid code is widely used today, with the increasing capacity and wind farms being built, 18 years ago it was still used as a technical guide for grid integration in traditional power plants, before renewable energies became widespread [2].

In this study, the grid codes used in the integration of wind energy into the grids in different countries were examined. The criteria and graphical conditions in each country's grid regulation are explained.

II. The Grid Integration Criteria of Wind Energy Power Plants

For safe system operation, the grid operators set limit values for changes in the system. The grid codes that limit the harmful effects of the wind turbines on the network should contain some elements for system safety and reliability in case of faults. These general requirements are; frequency control, FRT (Fault Ride Through), active-reactive power limitations and voltage control.

A. Frequency Control

The cut-in and cut-out of wind turbines cause frequency fluctuations in the power system. Under normal conditions, the system frequency can include very small variations. But the big changes in the frequency cause warming and then loss of insulation. System operators have specified the appropriate forms of these frequency change intervals in the grid codes and have defined the turbine grid connection requirements.

B. Fault Ride Through Rules

Fault ride through capacity refers to the steady state of the wind turbine during a symmetrical or asymmetrical fault, ensuring continuity in the network. Some turbines do not have this capacity feature and some are supported by UPS.

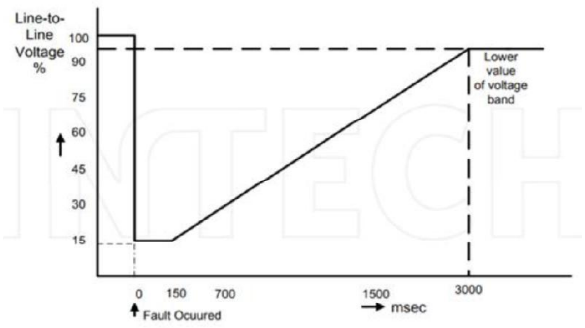


Figure 3: Voltage ride through (LVRT) capability [3]

C. Active Reactive Power Limits

Active power control under normal conditions is to set the active power output according to frequency deviations. Reactive power control is reactive power regulation against voltage changes at the common connection point. The reactive power requirement can be provided by power factor control, voltage control or reactive power set point control. The grid code supports voltage improvements with reactive power injection or active power restoration; even if voltage drops are 0 pu.

D. Voltage Control

It includes the operation of wind turbines in the working range of nominal voltage. It is one of the limits that the system operators specify in the grid code for the turbine to remain connected in the system during voltage changes. Modern turbines can provide this control.

III. Various Countries' Wind Energy Network Code Regulations

The German power grid is operated by different transmission system operators such as E.ON, EnBW, Vattenfall, RWE in different regions. The renewable energy investments of the German government are supported by the Renewable Energy Law (Erneuerbare Energien Gesetz - EEG). In 2008, the German Energy and Water Industry Association (BDEW) published grid criteria for integrating renewable energy plants to the medium voltage level of grid [4].

The principles of grid connection in England have been published by the National Grid in various numbers and versions under the title "The Grid Code". In these versions, according to Number 5 Revision 21, the grid code specified for the wind turbines [5].

The Spanish government, like other European countries, has accelerated the passage to renewable energy and has published various laws and regulations. With the publication of the law of RD 436/2004 in 2004, which focuses on renewable energy sources, the system operator was allowed to set power limits and setpoints on wind farms. The Spanish Grid System Operator (Red Electrica- REE) has published "Requirements for the voltage drop response of generation plants in special regimes" (P.O.12.3) [6].

In recent years, Italy has issued two different standards for connection to the transmission and distribution line; CEI 0-16 and CEI 0-21 standards. The CEI 0-16 standard includes requirements for connection to high and medium voltage lines. The CEI 0-21 standard has the requirements for connecting to the low voltage line, and the graphs that the active users must comply with are standard with detailed rules [7].

The necessary grid rules to comply with the wind power plants to be connected to the Turkish Electricity System have been determined by the Republic of Turkey Energy Market Regulatory Authority (EMRA) by Annex-18 'Grid Connection Criteria for Wind and Solar Energy Based Photovoltaic Production Facilities'. These criteria include wind generation facilities connected to the transmission system and licensed production facilities based on wind energy connected to the

distribution system with an installed capacity of 10 MW or more [8].

IV. Fault Ride Through Profile Comparison

Fault Ride through capacity is the condition that the voltage at the connection point of the transmission or distribution system is connected or disconnected from the system. Percentage of voltage drop and duration of failure are limiting factors. To provide system support, the active power of the production facility must be increased in nominal active power. Voltage fluctuations (0,9pu - 1,1pu) up to ± 10% at the mains connection point are normal operating conditions and Reactive Power Support should be provided according to the related regulation.

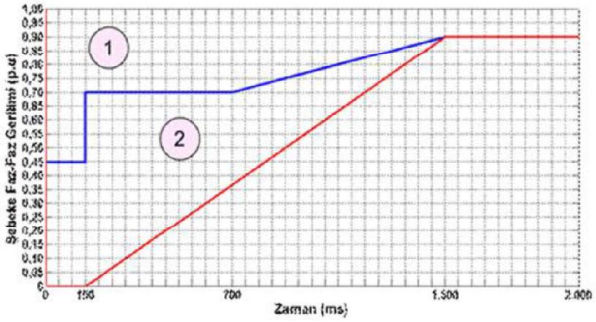


Figure 4: Turkey Transmission or Distribution System Connection Point Phase-To-Phase Voltage [8]

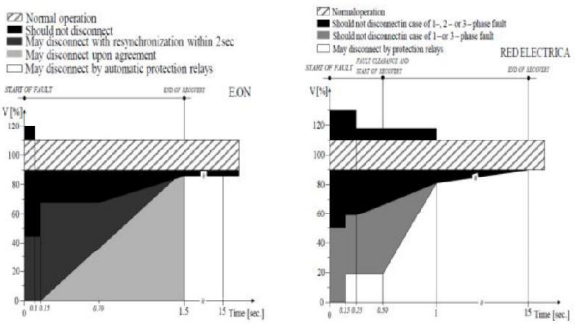


Figure 5: FRT requirements in German and Spain grid code [9]

V. Frequency Comparison

The operating frequency of the electricity grid system of each country differs according to the grid structure. Turkish grid uses 50 Hz, America uses 60 Hz and Japan uses both 50 Hz and 60 Hz locally. Deviations in the specified grid frequency are limited to the intervals specified in the country's grid codes.

According to Annex-18 of Turkish Electricity Grid Regulation, the working frequency for production facilities based on wind energy is 49 Hz - 50.5 Hz range. In the range of 48 Hz - 51.5 Hz, there is a minimum specified working time. In wind plants, if the grid frequency is above 50.3 Hz, the load should be off, if it is above 51.5 Hz, the system must be completely off [8].

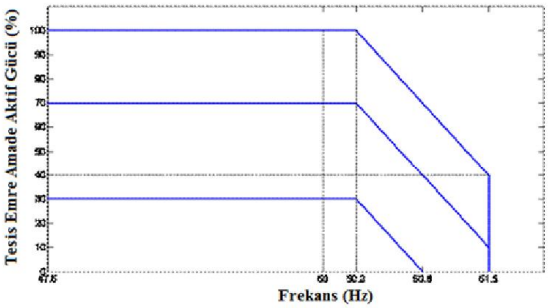
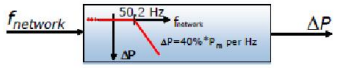


Figure 6: Power-Frequency Curve in Turkish Grid Code [8]

According to Germany Grid Code, all production units must reduce the output power over a system frequency of 50.2 Hz. Power can be reduced instantaneously by reducing the available power (Pm) by 40% / Hz. The output power is allowed to rise again as soon as the frequency drops below 50.05 Hz. The plant above 51.5 Hz and below 47.5 Hz should be disconnected from the grid [10].



$$\Delta P = 20\, P_m \frac{50.2\,Hz - f_{network}}{50\,Hz} \quad \text{at } 50.2\ Hz < f_{network} < 51.5\ Hz$$

P_m instantaneously available power

ΔP power reduction

$f_{network}$ network frequency

within the range of: $47.5\ Hz < f_{network} \leq 50.2\ Hz$ no limitation

at: $f_{network} \leq 47.5\ Hz$ and $f_{network} \geq 51.5\ Hz$ disconnection from the grid

Figure 7: Active power reduction of generating units in the case of over-frequency in Germany [9]

In the UK, the frequency of the National Electricity Transmission System is nominally 50Hz and is controlled within the limits of 49.5 - 50.5Hz unless exceptional conditions apply. In exceptional cases, the system frequency may increase to 52Hz or decrease to 47Hz [11].

VI. Active And Reactive Power Comparison

The active power output of the production facility must be automatically controllable by signals sent by the TSO. Depending on the installed power capacity, load input and load drop speed ratios are specified in the grid codes. Production plants based on wind energy must be able to operate continuously at all points for reactive power values within the limits indicated by the dark lines [12].



Figure 8: Turkey Grid Code Wind Power Plant Reactive Power Capacity Curve [8]

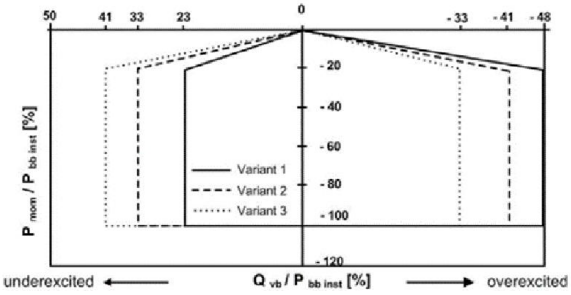


Figure 9: Three Variants of P-Q Dependencies Defined In Germany Grid Code[10]

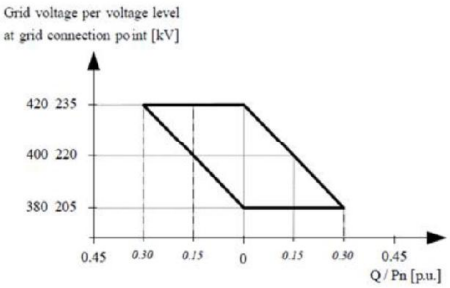


Figure 10: V-Q Dependence in Spain Grid Code[6]

In Spanish Grid Code, active power and transmission voltages minimum range is 0.15 inductive - 0.15 capacitive for all technical active power range and nominal voltage and 0.30 inductive - 0.30 capacitive as a function of the voltage [6].

Production facilities connected to the transmission system should respond to the equilibrium state changes of the connection point voltage under normal operating conditions defined between 0,9pu and 1,1pu of the connection point voltage.

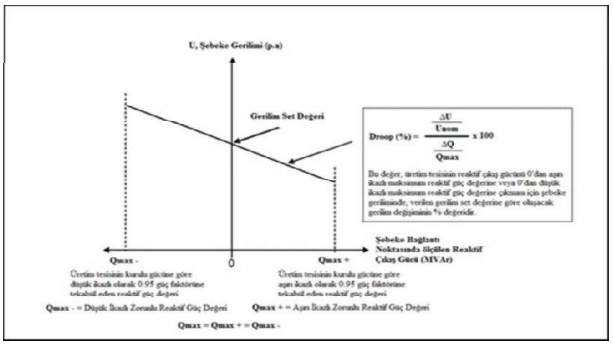


Figure 11: Reactive Power Support Curve in Turkish Grid Code [8]

VII. CONCLUSION

In this paper, basic information used in grid applications of wind energy systems is given. The grid codes required for safe, reliable and stable operation of power grid in voltage and frequency fluctuations of different countries are examined.

Many transmission and distribution company operators have published their grid codes under renewable energy grid connections. The wind system manufacturers are designing their designs according to the network code being issued. Numerous updated grid codes must be published for network integrations of growing wind farms.

In this study, the grid codes for the wind power plants of various countries which published from transmission and distribution system operators were examined, and the grid codes recently published by the different countries were compared with the current grid codes in Turkey.

This study aims to contribute to the research and comparison among the existing codes by introducing the network codes of the different countries for the researcher and users in the sector.

REFERENCES

[1] *GWEC*, Global Wind Report Annual Market Update 2016. [Online]. Available: http://gwec.net/publications/global-wind-report-2/global-wind-report-2016/

[2] T.-N. Preda, K. Uhlen and D. E. Nordgård. "An overview http://gwec.net/publications/global-wind-report-2/global-wind-report-2016/of the present grid codes for integration of distributed generation.'' *CIRED Workshop*. IEEE. Paper0020. pp. 1-4.

[3] Sharad W. Mohod and Mohan V. Aware (2013). Power Quality and Grid Code Issues in Wind Energy Conversion System, An Update on Power Quality, Dr. Dylan Lu (Ed.), *InTech,* [Online]. Available: https://www.intechopen.com/books/an-update-on-power-quality/power-quality-and-grid-code-issues-in-wind-energy-conversion-system

[4] E. Troester, ''New German Grid Codes for Connecting PV Systems to the Medium Voltage Power Grid'', *2nd International Workshop on Concentrating Photovoltaic Power Plants: Optical Design, Production, Grid Connection*, Darmstadt, Germany, 9-10 March 2009.

[5] M. Demirol, E. Akalan, T. Demirol, ''Rüzgar Elektrik Santrallerinin Şebeke Bağlantı Analizleri İçin Simülasyon Modelinin Oluşturulması. '' *Gazi Journal of Engineering Sciences*, Vol.1 Issue 3 pp. 351-368, 2015.

[6] ‘‘Red Electrica, Technical requirements for wind power and photovoltaic installations and any generating facilities whose technology does not consist on a synchronous generator directly connected to the grid O.P. 12.2’’, 2008. (www.aeolica.es).

[7] F. Adinolfi, F. Baccino, M. Marinelli, S. Massucco and F. Silvestro, ‘‘Model of a Real Medium Voltage Distribution Network for Analysis of Distributed Generation Penetration in a Smart Grid Scenario’’, *3rd IEEE PES Innovative Smart Grid Technologies Europe (ISGT Europe)*, Berlin, October 2012.

[8] *EPDK*, Elektrik Piyasası Düzenleme Kurumu, Elektrik Şebeke Yönetmeliği Ek18, ‘‘Rüzgar Ve Güneş Enerjisine Dayali Fotovoltaik Üretim Tesislerinin Şebeke Bağlanti Kriterleri’’,Resmi Gazete, 2014

[9] M. Altın, O. Goksu, R. Teodorescu, P. Rodriguez, B.B. Jensen, L. Helle, “Overview of Recent Grid Codes for Wind Power Integration’’ ,*12th International Conference on Optimization of Electrical and Electronic Equipment, OPTIM 2010,* 2010.

[10] Transmission Code 2007 – Network and System Rules of the German Transmission System Operators, Verband der Netzbetreiber VDN e.V. beim VDEW, August 2007.

[11] THE GRID CODE ISSUE 5 REVISION 14 26 August 2015 © Copyright owned by National Grid Electricity Transmission plc, all rights reserved. 2015.

[12] C. Sourkounis and P. Tourou, “Grid Code Requirements for Wind Power Integration in Europe’’, *Hindawi Publishing Corporation Conference Papers in Energy,* Volume 2013.

An Integer Programming Model for an Energy Optimal Train Operation

Kemal Keskin[1] and Abdurrahman Karamancioglu[2]

Electrical Engineering Department, Eskisehir Osmangazi University, Eskişehir, Turkey
kkeskin@ogu.edu.tr[1], akaraman@ogu.edu.tr[2]

Abstract

A well-known formulation of minimum energy train operation subject to usual time and speed constraints is a nonlinear programming problem. In this problem the decision variables to be found are the switching times where train's motion phases change within a set having a finite number of motion phases. In the literature, metaheuristic algorithms are widely used for solving this optimization problem. In this manuscript we present an integer programming model for the same optimization problem which makes it possible to use alternative solution tools. Decision variables in the proposed model are in the binary form, therefore, each of them equals either zero or one. Having such decision variables can be shown to be advantageous in certain computational platforms.

I. Introduction

Railway transportation has become more feasible in recent years thanks to advances in technology. Considering the size of railway transportation operations throughout the world, any savings in its energy consumption will accumulate to a huge total.

Due to its importance many researchers have been studying energy efficiency in railway operations for many decades. In 1975, one of the research reports came out that aimed to decrease energy consumption of Montreal Metro system by using optimal control and optimization techniques. In the report the authors considered problem as a trajectory optimization problem with various constraints. Then an heuristic direct search method was used to solve this trajectory optimization problem [4]. At the beginning of 1990's, researches focused on detailed train model and energy-optimal train operations. As an analytical optimization tool, Pontrayagin's maximum principle, was popular among energy efficient train operation studies in these years [5, 6, 7, 8, 9]. In this respect, Howlett proposed an optimal train operation strategy which has acceleration, cruising, coasting and braking phases respectively [5]. In following studies authors demonstrated expository examples of train operation strategies considering different speed levels and track slopes [6, 7].

Computational problems became easier to solve with the help of developing computer technology. As a result of that numerical methods were applied to energy efficient train operation problem onwards 2000's. Genetic algorithm [11, 12], Simulated Annealing [13], Ant colony optimization [14], Swarm optimization [15] and other heuristic algorithms were applied to energy optimal train operation problem.

This manuscript is organized as follows: In Section 2, a train motion dynamics and a typical set of operational constraints are presented. Also in the same section, a discretized version of motion dynamics together with the constraints are used to form the nonlinear programming problem. In the third section integer programming formulation of the energy optimization problem is presented. Concluding remarks take place in the last section

II. The motion dynamics and the nonlinear programming formulation

A single mass-point model of a train motion is as follows [2]:

$$\begin{aligned} \frac{dx}{dt} &= v \\ \frac{dv}{dt} &= \frac{F_t - F_b}{m} - R - R_g - R_c \end{aligned} \tag{1}$$

where x and v are vehicle's position and velocity respectively. They are constrained by $0 \leq x \leq X$ and $0 \leq v \leq v_{max}$ with X denoting the distance between the two stations where journey takes place from one to the other. The terms m, F, F_b, R, R_g and R_c are used for mass of the train, traction effort, brake effort, and resistances against the train motion respectively. Davis equation is used for the resistance of train [2]:

$$R = A + Bv + Cv^2 \tag{2}$$

The coefficients A and B are due to to mass and mechanical resistance and C is due to to air resistance. These coefficients depend on train characteristics and external forces. The gradient resistance is calculated as

$$R_g = m \cdot g \cdot sin\alpha \tag{3}$$

where g is gravitational constant and α is the gradient. The term R_c is the resistance of curves and depends on train characteristics and radius of the curve. Traction effort F provides force to move train along the rail line. Traction is calculated by

$$F = 2650 \cdot \frac{\eta \cdot P}{v} \tag{4}$$

where η is the efficiency in converting motor power to traction force, P is locomotive's horse power, v is the velocity of train and

2650 is for unit conversion [2]. The power consumption P is defined by

$$P = \frac{F \cdot v}{2650 \cdot \eta} \tag{5}$$

The total energy consumption is obtained by integrating the power throughout the operation time:

$$E = \int_0^T P dt \tag{6}$$

The upper limit T of the integral above denotes the specified journey time. It is desired to save energy through an optimal driving strategy. Throughout the journey at any given time we use one of the following elementary motions: maximum acceleration, cruising, coasting, and braking. Note that energy is consumed in the maximum acceleration and cruising phases, and no energy is consumed during the coasting and braking phases.

State variables v and x in the discrete of motion dynamics (1) in the time interval $[0, T]$ for N steps satisfy the following iterations:

$$\begin{aligned} v_{k+1} &= v_k + a_k \cdot \Delta t \\ x_{k+1} &= x_k + \Big(\frac{v_k + v_{k+1}}{2}\Big) \cdot \Delta t \\ &\forall k \in \{0, \cdots, N\} \end{aligned} \tag{7}$$

where v_k, a_k, x_k represent velocity, acceleration, position of train at step k respectively. Δt denotes step size and equals T/N. For any $k \in 0, 1, \cdots, N$, discretized dynamics are used for calculating the consumed energy, and total energy consumed throughout the trip is the sum of energy consumption at each step:

$$E = \sum_{k=0}^{N} \frac{F_k \cdot v_k}{2650 \cdot \eta} \cdot \Delta t \qquad k = 0, 1, \cdots, N \tag{8}$$

The total energy is calculated by considering the maximum acceleration and cruising phases of the above summation. In the costing and braking phases no energy is consumed due to zero traction force.

In the *maximum acceleration* phase, the traction effort is fixed at its attainable maximum value, this monotonically increases the speed. This phase starts at $k = 0$ and ends at $k = k_1$, where optimal value of k_1 is to be determined in the optimization process. In the cruising phase, the speed is fixed to a value, v_{k1}. In this phase F_k are chosen to maintain this speed, so that its values equal the resistance values occurring at the step under consideration. This phase extends between k_1 and k_2, where optimal k_2 is to be determined by solving the optimization problem. In the coasting phase, there is no traction so no energy is consumed. This phase ends with arriving at safe stopping distance. It is a function of remaining distance and actual velocity of train. The safe stooping distance is:

$$x_{ss} = \frac{v_{br}^2}{2a} \tag{9}$$

where x_{ss} is safe stopping distance, v_{br} is actual velocity of train, a is deceleration. We can write the objective function and the constraints of the optimization problem as follows:

$$\min_{k_1,k_2} \sum_{k=0}^{k_1} \frac{F_{max} \cdot v_k}{2650 \cdot \eta} \cdot \Delta t + \sum_{k=k1}^{k_2} \frac{F_k \cdot v_{k1}}{2650 \cdot \eta} \cdot \Delta t \tag{10}$$

subject to:

$$0 \le F_k \le F_{max} \tag{11}$$

$$0 \le v_k \le v_{max}; \qquad v(0) = 0; \qquad v(N) = 0 \tag{12}$$

$$(N - k_2)\Delta t \le x_{ss} \tag{13}$$

$$k_1 \le k_2 \le N \tag{14}$$

$$v_{k+1} = v_k + a_k \cdot \Delta t \tag{15}$$

$$x_{k+1} = x_k + \Big(\frac{v_k + v_{k+1}}{2}\Big) \cdot \Delta t \tag{16}$$

III. Integer Programming Formulation

Integer programming is an optimization process where the decision variables are all integers. In integer programming, therefore, feasible set of solutions are all integer-valued. Since the integers are countable subset of real numbers, searching the solutions in it obviously reduces the domain of search. However, some features of functions defined over the continuous domains, such as differentiability, do not exist for the functions defined on the integers. This limits use of some of the fast converging search tools in the optimization process.

In a special case of the integer programming, the integers of interest are either ones or zeros. This further narrows the search domain. This special case integer programming is called binary (integer) programming. The decision variables employed in our formulation are all binary integers.

The nonlinear programming formulation (10) can be written in terms of integer decision variables as

$$\begin{aligned} \min_{\phi_i,\gamma_i} & \phi_0 v_0 \frac{F_{max}\Delta t}{2650\eta} + \phi_1 v_1 \frac{F_{max}\Delta t}{2650\eta} + \cdots + \phi_N v_N \frac{F_{max}\Delta t}{2650\eta} + \\ & \gamma_0 v_0 \frac{(F_0 + F_1 + \cdots + F_N)\Delta t}{2650\eta} + \\ & \gamma_1 v_1 \frac{(F_1 + F_2 + \cdots + F_N)\Delta t}{2650\eta} + \\ & \gamma_2 v_2 \frac{(F_2 + F_3 + \cdots + F_N)\Delta t}{2650\eta} + \cdots + \gamma_N v_N \frac{(F_N)\Delta t}{2650\eta} \end{aligned} \tag{17}$$

Table 1. A comparison of the conventional and proposed models

Model	Number of decision variables	Decision space
Conventional model (10)	2	$\{0, 1, 2, \cdots, N\}$
Proposed model (17)	$2N + 2$	$\{0, 1\}$

subject to:

$$\phi_i \in \{0, 1\}, \qquad \gamma_i \in \{0, 1\} \tag{18}$$
$$\phi_i - \phi_{i+1} \geq 0, \tag{19}$$
$$\gamma_0 + \gamma_1 + \cdots + \gamma_N = 1 \tag{20}$$
$$0 \leq F_k \leq F_{max} \tag{21}$$
$$0 \leq v_k \leq v_{max} \tag{22}$$
$$v_0 = 0, \qquad v_N = 0 \tag{23}$$
$$(N - k_2)\Delta t \leq x_{ss} \tag{24}$$
$$k_1 \leq k_2 \leq N \tag{25}$$
$$v_{k+1} = v_k + a_k \cdot \Delta t \tag{26}$$
$$x_{k+1} = x_k + \left(\frac{v_k + v_{k+1}}{2}\right) \cdot \Delta t \tag{27}$$

In the above equations, terms having ϕ_i factor are related to the energy consumed in the maximum traction phase,while the γ_i terms are related to the energy consumed in the cruising phase. One may immediately notice that the formula above has $2N+2$ decision variables, namely, $\phi_i, \gamma_i, i = 0, 1, \cdots N$. However, due to the constraints, these variables are highly correlated. For instance, according to constraints (18), the ϕ_i variables are either 0 or 1, and according to constraint (19) the ϕ_i sequence is non-increasing. Therefore, the ϕ_i sequence is a concetanation of two subsequences in which the first k_1 terms are successive 1's, and the remaining k_2 terms are successive 0's as follows:

$$\underbrace{1, 1, 1, \cdots, 1, 1}_{k_1 \text{ terms}}, \underbrace{0, 0, 0, \cdots, 0, 0}_{k_2 \text{ terms}}$$

Likewise, γ_i sequence members are either 0 or 1. The constraint (20) indicates that their sum is 1. Together with the other constraints only the k_2th element is 1, other are all zeros as shown below:

$$0, 0, \cdots, 0, 0, \underbrace{1}_{k_2 \text{th term}}, 0, 0, \cdots, 0, 0$$

It is possible to introduce more correlation terms in the constraints. For instance, the minimum length of k_1 may be set to some specific value due to the minimum meaningful duration of the maximum traction phase.

In the minimization problem (17) the number of decision variables is higher than the ones in the conventional model (10). Noting that each of the decision variables takes one of the binary values, and also noting that these variables are highly correlated, the proposed method deserves a consideration. Table 1 compares the conventional and the proposed models.

Table 1 shows that in the proposed model even though the number of decision variables increases, the associated decision space becomes smaller. Computational platforms with the ability of working with small decision spaces the proposed model (17) fits better than the conventional model (10).

IV. Conclusions

For energy optimal train driving strategies, various optimization models with evolutionary solution methods exist in the literature. In this manuscript an optimization model whose decision variables are integers is presented. It has been argued that the proposed integer programming model may be advantageous in certain computational platforms.

V. References

[1] M.J. Arsahd, Attiq-ur-Rehman, A. I. Durrani, and H. Ahmad, "Mathematical modelling of train dynamics: A step towards pc train simulator.", *Journal of Faculty of Engineering & Technology*, vol. 20, no. 1, pp: 38-53, 2013

[2] K. Keskin and A. Karamancioglu, "Energy-Efficient Train Operation Using Nature-Inspired Algorithms," *Journal of Advanced Transportation*, vol. 2017, Article ID 6173795, 12 pages, 2017. doi:10.1155/2017/6173795

[3] V. K. Garg and R. V. Dukkipati, "Dynamics of railway vehicle systems", *Academic Press*, 1984

[4] H. H. Hoang, M. P. Polis, A. Haurie, "Reducing Energy Consumption through Trajectory Optimization for a Metro Network," *IEEE Transactions on Automatic Control*, vol. 20, no. 5, pp. 590-595, Oct. 1975.

[5] P. Howlett, "An Optimal Strategy for the Control of a Train," *J. Austral. Math. Soc. Ser. B*, vol. 31, pp. 454-471, 1990.

[6] C. Jiaxin, P. Howlett, "Application of Critical Velocities to the Minimisation of Fuel Consumption in the Control of Trains," *Automatica*, vol. 28, no. 1, pp. 165-169, Jan. 1992.

[7] P. Howlett, "Optimal Strategies for the Control of a Train", *Automatica*, vol. 32, no. 4, pp. 519-532, 1996

[8] P. Howlett, "The optimal Control of a Train," *Annals of Operations Research*, vol. 98, pp. 65-87, 2000.

[9] E. Khmelnitsky, "On an Optimal Control Problem of Train Operation," *IEEE Transaction on Automatic Control*, vol. 45, no. 7, Jul. 2000.

[10] R. Liu, I. M. Golovitcher, "Energy-efficient Operation of Rail Vehicles," *Transportation Research Part A*, vol. 37, pp. 917-932, 2003

[11] K. K. Wong, T. K. Ho, "Dynamic Coast Control of Train Movement with Genetic Algorithm," *International Journal of Systems Science*, vol. 35, no. 13-14, pp. 835-846, Feb. 2007.

[12] S. Acikbas, M. T. Soylemez, "Coasting Point Optimisation for Mass Rail Transit Lines using Artificial Neural Networks and Genetic Algorithms," *IET Electr. Power Appl.*, vol. 2, no. 3, pp. 172-182, 2008

[13] K. Kim, S. I. Chien, "Simulation-Based Analysis of Train Controls under Various Track Alignments," *J. Transp. Eng.*, vol. 136, pp. 937-948, 2010.

[14] S. Lu, S. Hillmansen, T. K. Ho, C. Roberts, "Single-Train Trajectory Optimization," *IEEE Trans. Intell. Transp. Syst.*, vol. 14, no. 2, Jun. 2013.

[15] M. Dominguez, A. Fernandez-Cardador, A. P. Cucala, T. Gonsalves, A Fernandez, "Multi Objective Particle Swarm Optimization Algorithm for The Design of Efficient ATO Speed Profiles in Metro Lines," *Engineering Applications of Artificial Intelligence*, vol. 29, pp. 43-53, Jan. 2014.

Comparison of different classification methods using Autoregressive estimation for cervical muscles based sEMG signals

G.ÖZMEN*[1], A.H.EKMEKCI[2], B.YILMAZ[3]

[1] Selcuk University, Faculty of Technology, Electrical and Electronics Engineering, Konya/Turkey, gozmen@selcuk.edu.tr

[2] Selcuk University, Faculty of Medicine, Department of Neurology, Konya/Turkey, hekmekci@yahoo.com

[3] Konya Food and Agriculture University, Faculty of Engineering and Architecture, Electrical and Electronics Engineering department burak.yilmaz@gidatarim.edu.tr

Abstract **Surface electromyography is a non-invasive method used to determine the electrical activity of muscles. Classification of electromyogram (EMG) signals provides information that helps in the preliminary diagnosis of many diseases. One of these diseases is the cervical disc herniation. In this study, Autoregressive (AR) estimation based feature extraction method was used for surface EMG signals obtained from cervical muscles and the success of this method on classification accuracy was investigated with various classifiers. This study consists of filtering, feature extraction, and classification steps of surface EMG signals which were obtained from Trapezius and Sternocleidomastoid (SCM) muscles of 10 healthy and 10 patients. Yule walker, Burg, and Covariant methods were used to estimate AR parameters from filtered EMG signals. The feature parameters were used as input vectors of Artificial Neural Network (ANN), k- Nearest Neighbourhood (k-NN), Naive Bayes (NB) and Support Vector Machines (SVM) classifiers. According to the classification results; Covariant and Burg feature extraction methods provide accuracy of over 90% in all classifiers. The best performance of these values was obtained by k-NN with 100% classification accuracy. The lowest classification results were obtained with Yule Walker for SCM muscle except for the k-NN classifier. The results show that; the AR method, which is used to extract features from surface EMG signals, generally provides high classification results for cervical muscles with many classifiers.**

Keywords **- surface EMG, Autoregressive Estimation, Classification**

I. INTRODUCTION

Surface electromyography (EMG) is a non-invasive technique that perceives signals with time-related characteristics, and it is useful for understanding the stimulus-response of muscles. Surface electrodes are placed on the skin and used to measure the combined activity from several motor units [1] Since the electrodes placed on the muscle perceive the sum of many action potentials, multi-channel EMG recordings allow for individual measurement of the muscle's electrical activity [2]. EMG signals are complex, non-stationary, noisy signals. The amplitude of the EMG signal is random and can usually be expressed by the Gaussian distribution. The available energy of the EMG signal is in the frequency range of 0-500 Hz, whereas the dominant energy is the range of 50-150 Hz [3]. Surface EMG is widely used for muscle strength estimation, muscle fatigue calculation and ergonomics, sports physiology, and diagnostic tools in rehabilitation medicine [4]. In addition, EMG often helps doctors to diagnose the muscle-nerve diseases. Surface EMG is used to detect pain and muscle fatigue in the cervical region so that it provides important information on the surface muscular disorders [5], [6], [7].

EMG signals are random signals which are difficult to process and are divided into two groups which are stationary and non-stationary signals. Because the processing methods for non-stationary signals are not very effective, the non-stationary signal is divided into segments which are considered stationary [8].

One of the difficulties with working with EMG is that the signal has lots of noise components, and the other is the large size of the recorded data. To overcome these problems, it is necessary to filter the EMG signals in the suitable frequency band. Besides, it is suggested to reduce the size of EMG data by using feature extraction methods.

Many methods are used for feature extraction and classification from EMG signals. In the literature, wavelet transform [9],[10],[11],[12] and Autoregressive estimation [13],[14], [15] based methods are frequently used as feature extraction methods from EMG signals. In addition, many methods are used for classifying EMG signals [16], [17] , [18],[19] .

In this study, Autoregressive feature extraction method was used for surface EMG signals obtained from cervical muscles and the success of this method on classification results was investigated with various classifiers. For this purpose, ANN, k-NN, SVM and NB classifiers were used to classify cervical disc herniation patients.

II. MATERIAL AND METHOD

In this study, filtered real EMG signals were used. The sEMG data were recorded from 10 healthy subjects and 10 patients. Patients participated this study were diagnosed with a cervical disc herniation by neurologist. Healthy subjects were selected from those who did not have any complaints from the neck region. sEMG data were recorded by a doctor and a technician in the neurology clinic with the approval of Selcuk University Medical Faculty ethics committee. The recording process was performed from Trapezius and SCM muscles simultaneously using two channels of the multi-channel EMG device. Two Ag-AgCl surface electrodes were used for each muscle. In addition, the reference electrode was placed on the other fixed stationary arm to reduce the noise problem. In this study, the surface electrode was chosen instead of the needle electrode, so the recording process was carried out non-invasively [20]. The EMG data used in this study were obtained from trapezius and SCM muscles fatigued by working for 1 min. the right arm parallel to the floor.

After recording process, filtering was performed to prepare the EMG data for classification. For this purpose surface EMG signals are filtered with a Butterworth bandpass filter of 3-1000 Hz. The filtered EMG signals were converted into an EMG segment containing 512x395 discrete samples for the feature extraction step. Three different AR methods which are Yule-Walker, Covariant and Burg were applied to the EMG signals in order to extract the features.

The Autoregressive (AR) model defines each samples of the surface EMG signal as a linear combination of previous samples and a white noise error term. The model is basically expressed in the equation (1);

$$x_n = -\sum_{i=1}^{p} a_i x_n - i + w_n \qquad (1)$$

where x_n is a sample of the model signal, α_i is AR coefficients, w_n is white noise or error sequence, and p is the order of AR model. Fourth degree AR is recommended for the calculation of the coefficients[14].

In this study, AR parameters were obtained at the 4th order which constitute the input vector of the classifiers. Whereas AR parameters were calculated at 4th order, five different coefficients were obtained for each EMG data. In Table 1, a section from the coefficients calculated for Yule walker is seen as an example. According to Table 1, the value of one of the coefficients obtained when calculating AR parameters from the 4th order is calculated as '1' for all segments. This coefficient, calculated as '1', was not used as input vector of classifiers.

TABLE1: YULE-WALKER COEFFICIENTS FOR EMG SIGNALS

	Segment Number								
YULE-WALKER coefficients	1	2	3	4	5	--	--	511	512
a1	-1,8332	-1,5886	-1,4955	-1,5081	-1,6370	---	---	-1,4458	-1,5484
a2	0,93396	0,51893	0,41493	0,45606	0,64758	---	---	0,59286	0,76667
a3	0,14732	0,26885	0,24482	0,22885	0,2276	---	---	0,04663	-0,0953
a4	-0,2393	-0,1856	-0,1480	-0,1608	-0,2262	---	---	-0,1882	-0,1148
a5	1	1	1	1	1			1	1

The AR coefficients given in Table 1 were normalized to the 0-1 range before presented to the classifier. As a result of the calculations, 4*395 input data was obtained by three AR estimator for each subject. So that, 4*3950 input data were generated for 10 healthy subjects. The same values are also valid for fatigue step obtained from patients.

III. RESULTS

In this study, ANN k-NN, SVM and NB classifiers results were compared to investigate the success of AR feature extraction method on EMG signals recorded simultaneously from Trapezius and SCM muscles.

For classification, a forward feed multilayered backpropagation algorithm, which is widely used for estimation purposes in engineering applications, was selected first. Multi-Layer feed-forward neural networks were composed of three layers: input layer, hidden layer and output layer. Hidden layer activation function and output layer activation function have been selected as 'logarithmic sigmoid' network structure. This network structure was trained with momentum and adaptive learning rate back-propagation algorithm. k neighboor value is selected '5' for k-NN algorithm. Besides, Radial Basis Function (RBF) is used for the kernel functions used in SVM algorithm.

To evaluate the classification performances cross-validation method was used. In the cross-validation method, the data set was randomly divided into "k" groups. One of these groups was left out and the remaining part was modeled. The classification performance of the generated model was tested on the excluded data. This process is alternately repeated for the other "k" group. In all algorithms, the number of cross validation is set to 5.

In this study, the confusion matrix was used to determine the classification accuracy, selectivity, and specificity. Classification accuracy was calculated by dividing the total number of the true positives obtained in the classification of control and patient subjects by the total number of data used for the test. Specificity was calculated by dividing the true positives by the total number of the true positives and false negatives. Selectivity was calculated by dividing the true negatives by the total number of the false positives and true negatives [21].

Table 2 presents the classification results for EMG signals obtained from Trapezius muscle using AR-Yule, AR-Burg and Ar-Covariant feature extraction methods.

TABLE2. COMPARISION OF CLASSIFIERS FOR TRAPEZIUS MUSCLE

Feature extraction method		Specificity(%)	Selectivity(%)	Classification Accurasy(%)
Yule-Walker	ANN	95.56	97.33	95.56
	k-NN	99	99	99.8
	NB	75.1	74.4	81.8
	SVM	79.8	79.3	79.3
Covariant	ANN	99.9	98.15	99.05
	k-NN	99.8	99.8	99.9
	NB	94.6	94.6	98.2
	SVM	97.2	97.2	97.2
Burg	ANN	100	97.5	98.71
	k-NN	99.7	99.7	99.9
	NB	95.9	95.9	98.7
	SVM	92.5	92.2	92.2

According to the Table 2, k-NN gives the best classification results with %99.9 classification accuracy for trapezius muscle using AR coefficients. ANN is the second classifier with the highest accuracy Generally NB and SVM provided over %90 accuracy for Covariant and Burg method, but they did not show the same performance for the Yule-Walker. Table 3 presents the classification results for EMG signals obtained from SCM muscle using Yule-Walker, Burg and Covariant feature extraction methods.

TABLE 3 COMPARISION OF CLASSIFIERS FOR SCM MUSCLE

Feature extraction		Specificity(%)	Selectivity(%)	Classification Accurasy(%)
AR-Yule	ANN	71.07	81.94	76.51
	k-NN	97.5	94.6	94.6
	NB	81.5	72.2	72.2
	SVM	87.1	88.3	87.1
AR-Cov	ANN	99.69	98.61	99.1
	k-NN	99.9	99.9	100
	NB	90.8	90.8	97.8
	SVM	95	95	95
AR-burg	ANN	100	99.94	99.97
	k-NN	99	99	100
	NB	99	99	99.8
	SVM	96	96	96

According to the Table 3, k-NN gives the best classification results with %100 classification accuracy for SCM muscle using Burg and Covariant coefficients. ANN is the second classifier with the highest accuracy for Burg and Covariant, but it did not provide sufficient classification accuracy for Yule-Walker method. NB and SVM provided over %90 accuracy for Covariant and Burg method, but they did not show the same performance for the Yule-Walker method.

IV. CONCLUSION

In this study, feature extraction method using Autoregressive estimation was used for surface EMG signals obtained from cervical muscles and the success of this method on classification results was investigated with various classifiers. For this purpose, ANN, k-NN, SVM and NB classifiers were used to classify cervical disc herniation patients. According to the classification results, k-NN algorithm provided the best classification accuracy for all AR estimation methods. In this study, classification of cervical disc herniation patients was performed by using AR estimation based feature extraction methods from simultaneously recorded surface EMG signals from two neck muscles.

REFERENCES

[1] J. Kimura, *Electrodiagnosis in diseases of nerve and muscle: principles and practice*. Oxford university press, 2001.

[2] M.-F. Lucas, A. Gaufriau, S. Pascual, C. Doncarli, and D. Farina, "Multi-channel surface EMG classification using support vector machines and signal-based wavelet optimization," *Biomedical Signal Processing and Control,* vol. 3, no. 2, pp. 169-174, 2008.

[3] C. J. De Luca, "The use of surface electromyography in biomechanics," *Journal of applied biomechanics,* vol. 13, no. 2, pp. 135-163, 1997.

[4] K. Masuda, T. Masuda, T. Sadoyama, M. Inaki, and S. Katsuta, "Changes in surface EMG parameters during static and dynamic fatiguing contractions," *Journal of electromyography and kinesiology,* vol. 9, no. 1, pp. 39-46, 1999.

[5] Z. Moussavi, J. Cooper, and E. Shwedyk, "Fatigue pattern of trapezius muscle in relation to its functional role," in *Engineering in Medicine and Biology Society, 1996. Bridging Disciplines for Biomedicine. Proceedings of the 18th Annual International Conference of the IEEE*, 1997, vol. 4, pp. 1451-1453: IEEE.

[6] S. Y. Kwon, C. Y. Park, J. W. Koo, H. W. Yim, and K. S. Lee, "Usefulness of Power Spectral Analysis for Measurement of Local Muscle Fatigue during Keyboard Task," *Korean Journal of Occupational and Environmental Medicine,* vol. 11, no. 4, pp. 449-459, 1999.

[7] J. Zhang, H. Song, Q. Xue, T. Liu, and F. Wang, "Study on Muscle Fatigue of Human Body Based on Surface Electromyography," in *Biomedical Engineering and Informatics, 2009. BMEI'09. 2nd International Conference on*, 2009, pp. 1-3: IEEE.

[8] B. Karlık, Y. Koçyiğit, and C. B. Fidan, "EMG İşaretlerini Sınıflamada Kullanılan İşaret İşleme Tekniklerinin Karşılaştırılması Comparison of Signal Processing Methods used for Classification of EMG Signals."

[9] A. Phinyomark, C. Limsakul, and P. Phukpattaranont, "Application of wavelet analysis in EMG feature extraction for pattern classification," *Measurement Science Review,* vol. 11, no. 2, pp. 45-52, 2011.

[10] K. Mahaphonchaikul, D. Sueaseenak, C. Pintavirooj, M. Sangworasil, and S. Tungjitkusolmun, "EMG signal feature extraction based on wavelet transform," in *Electrical Engineering/Electronics Computer Telecommunications and Information Technology (ECTI-CON), 2010 International Conference on*, 2010, pp. 327-331: IEEE.

[11] G. Wang, Z. Wang, W. Chen, and J. Zhuang, "Classification of surface EMG signals using optimal wavelet packet method based on Davies-Bouldin criterion," *Medical and Biological Engineering and Computing,* vol. 44, no. 10, pp. 865-872, 2006.

[12] J. Rafiee, M. Rafiee, F. Yavari, and M. Schoen, "Feature extraction of forearm EMG signals for prosthetics," *Expert Systems with Applications,* vol. 38, no. 4, pp. 4058-4067, 2011.

[13] O. Paiss and G. F. Inbar, "Autoregressive modeling of surface EMG and its spectrum with application to fatigue," *IEEE transactions on biomedical engineering,* no. 10, pp. 761-770, 1987.

[14] A. Phinyomark, C. Limsakul, and P. Phukpattaranont, "A novel feature extraction for robust EMG pattern recognition," *arXiv preprint arXiv:0912.3973,* 2009.

[15] J. Zhao, Z. Xie, L. Jiang, H. Cai, H. Liu, and G. Hirzinger, "EMG control for a five-fingered prosthetic hand based on wavelet transform and autoregressive model," in *Mechatronics and Automation, Proceedings of the 2006 IEEE International Conference on*, 2006, pp. 1097-1102: IEEE.

[16] K. S. Kim, H. H. Choi, C. S. Moon, and C. W. Mun, "Comparison of k-nearest neighbor, quadratic discriminant and linear discriminant analysis in classification of electromyogram signals based on the wrist-motion directions," *Current applied physics,* vol. 11, no. 3, pp. 740-745, 2011.

[17] A. Hiraiwa, K. Shimohara, and Y. Tokunaga, "EMG pattern analysis and classification by neural network," in *Systems, Man and Cybernetics, 1989. Conference Proceedings., IEEE International Conference on*, 1989, pp. 1113-1115: IEEE.

[18] A. Subasi, "Classification of EMG signals using PSO optimized SVM for diagnosis of neuromuscular disorders," *Computers in biology and medicine,* vol. 43, no. 5, pp. 576-586, 2013.

[19] F. H. Chan, Y.-S. Yang, F. Lam, Y.-T. Zhang, and P. A. Parker, "Fuzzy EMG classification for prosthesis control," *IEEE transactions on rehabilitation engineering,* vol. 8, no. 3, pp. 305-311, 2000.

[20] G. Özmen, "Servikal bölgede oluşan kas yorgunluğunun yüzey elektromiyogram bilgileri ile değerlendirilmesi," Selçuk Üniversitesi Fen Bilimleri Enstitüsü, 2013.

[21] K. Polat, S. Kara, F. Latifoğlu, and S. Güneş, "Pattern detection of atherosclerosis from carotid artery Doppler signals using fuzzy weighted pre-processing and least square support vector machine (LSSVM)," *Annals of biomedical engineering,* vol. 35, no. 5, pp. 724-732, 2007.

Comparative Performance Analysis of PV Technologies in Eastern Province of Zambia

M.MWANZA[1], K. BASARAN[2], N.S. CETIN[3] and K. ULGEN[4]

[1] Ege University, Izmir/Turkey, mabvuto_mwanza@yahoo.com
[2]Manisa Celal Bayar University, Manisa/Turkey, kivanc.basaran@cbu.edu.tr
[3] Ege University, Izmir/Turkey, ncetin@rocketmail.com
[4] Ege University, Izmir/Turkey, koray.ulgen@ege.edu.tr

Abstract **- Zambia has an average solar irradiation of 5.5 kWh/m^2/day and average 2000-3000 hours of sunshine per year. In order to diversify energy mix and achieve the sustainable development goals of energy access for all, the government of Zambia through build-own-operate mode intends to develop a total of 10MW PV power plants in Eastern provinces. This paper is therefore aimed at analyzing the performance of three types of PV technologies (CIS, C-Si, CdTe) using Photovoltaic Geographical Information System (PVGIS) in order to compare their performance for grid connected PV systems in Eastern province of Zambia. Furthermore, the effect of using tracking systems on the performance of the PV systems was also investigated. The analyzed results indicate that CdTe PV technology shows highest performance ratio of 80.17%, CIS of 73.97% and C-Si of 72.24% for fixed horizontal PV system. In short, thin film PV technologies show better performance than crystalline silicon PV technologies under the weather condition of Eastern Province of Zambia. This study is important as it present an overview performance of the three PV technologies under weather condition of Eastern Province which is vital for decision making, sustainable solar energy system development and selecting of appropriate PV technologies suitable for the weather condition in the country.**

Keywords **– Capacity factor, performance ratio, PV technology, free-standing photovoltaic (PV) plants, sustainable energy development**

I. Introduction

ENERGY is one of the basic necessities for the survival of human race. It is also important for the progress of the nation and essential factor for economic development. In other words, the absence of access to energy has a negative impact on human race and any country's economic development. The use of solar energy technologies nowadays is increasing in the world and most of the countries are trying to follow the move [1]. This has resulted in studies in order to assess the energy potentials and also show the need to use renewable energies in order to protect our planet and the environment around us [1, 2]. Sustainable deployment, selecting and development of any solar energy projects, assessing the performance of various PV technologies on the market in order to predict their performance and identifying the one suitable for that country's weather condition is very important[3,4]. Therefore, three types of PV Technologies i.e. CIS, C-Si and CdTe are commonly used on the PV market and also, this technologies are widely investigated [5,6]. Performance analysis for PV technologies under local condition is vital for identifying performance uncertainties in PV technologies and selecting appropriate type of PV technology [7], as a result various studies related to PV system performance have been carried out in different countries[3, 7-10]. The International Energy Agency has setup a number of tasks (15) for monitoring, operation and performance of solar PV systems under photovoltaic power systems programme (IEA-PVSP) [11]. As such, PV systems performance studies are carried out according to IEC 61724 standard and guidelines [7-10,12]. However, in Zambia the studies on the performance of various PV technologies in PV systems as per IEC 61724 standards are not readily available. Thus, as the country is embarking on energy diversification and targeting to reach sustainable development goals with the target of increasing access to energy for rural and urban areas in Zambia [13], the study of various PV technology performances in local weather is very important for selecting PV technology appropriate for local weather condition [7].

The aim of the paper is to study and analyze the performance of three types of PV technologies for grid connected PV systems application under the weather condition of Eastern Provinces of Zambia. Thus, the paper focuses on comparative study on the performance of three types of PV technologies and the effect of using solar tracking systems in PV systems. In order to study

the performance of these three types of PV technologies (CIS,C-Si, and CdTe) in grid connected PV system, PVGIS programme were used and a 20 kW_P free-standing PV system has been used in the analysis as a sample array in the larger PV systems. The inclination angle of PV systems was also varied to study the change in PV system total losses and compare the energy production with the system fixed on horizontal. The study show that total PV system losses for CIS and C-Si PV technologies increases with increase in inclination angle while for CdTe PV technology decrease with increasing inclination angle. In addition, fixing the PV system on horizontal resulted in more energy produced as compared to fixing it at optimal angle. For the fixed horizontal PV systems the performance ratio of CIS, C-Si and CdTe were found to be 73.97, 72.24 and 80.17%, while the total PV technology losses were 11, 12.5 and 3% respectively.

II. The Study Area

Eastern province is located in the eastern part of Zambia at the latitude of 10 to 15 degrees and longitude 30 to 34 degree east of prime meridian with an area of 69,208 square kilometers as shown in figure 1[14, 15]. In 2010 the province had a population of approximately 1,707,731 people (2010 Census) with average annual population growth rate of 2.7% [16]. The population distribution shows that 64% of the population lives in rural area and 36% lives in urban areas [13, 16, 17]. According to International Renewable Energy Agency (IRENA), Africa-EU Energy Partnership [13, 18], only about 3% of the rural population are electrified leaving the majority of the population to depend on wood fuel and other traditional energy sources for their household energy needs.

In order to achieve the sustainable development goals of access to energy for all, the government of Zambia through build-own-operate model is intending to build a total of 10MW PV system in Eastern provinces [13]. Therefore, for decision making and appropriate selection of the PV technology capable of withstanding the weather condition in Zambia for optimal utilization of solar energy, performance analysis of PV technologies in Grid Connected PV system is a must. Thus, this study is a must and very important.

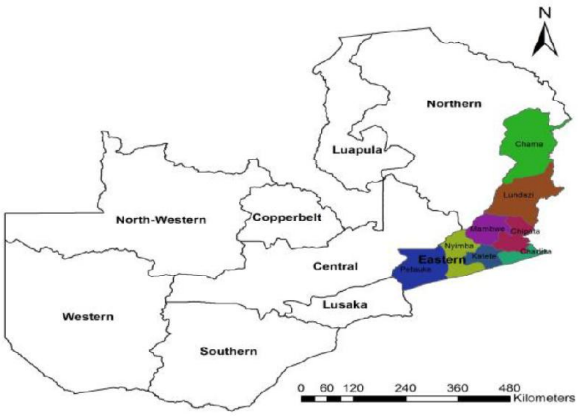


Figure 1: Location of Eastern Province in Zambia [15-ArcGIS]

A. Solar Energy Potential in Zambia

According to the previous studies and data undertaken by Meteorological Department of Zambia, the country has a significant potential of solar energy for both power production and thermal from solar energy technologies. The country has average peak sunshine of about 6-8hours per day and monthly average solar radiation of 5.5kWh/m^2-day throughout the year [19, 20]. According to (IRENA) [13], the country has the highest total yearly solar radiation of 2,750kWh/m^2-year with the highest average temperature of 30^0C.

III. PERFORMANCE EVALUATION OF PV SYSTEM

In order to evaluate the performance of grid connected PV power plants the following performance indices are normally used [7-10, 12]; yields, Normalized losses, and System efficiencies, Performance ratio and capacity factor [4]. However, in this study final yield, Normalized losses i.e Performance ratio and capacity factor has been adopted for analyzing the performance of the three types of PV technologies in PV systems considering the Eastern province of Zambia weather condition were the government is intending to build PV power plants. The Photovoltaic GIS programme has been used to study the effect of using tracking systems on the PV system performances (fixed position, vertical axis tracking and 2-axis tracking) using three types of PV technologies (CIS, C-Si, and CdTe). A 20kW_P PV system has been used in the study as a sample of the array in larger PV systems.

A. Energy Model of PV Aray

PV panels are affected by the weather conditions and efflorescence. So the energy production of the PV arrays calculation takes into consideration the efficiency of the PV technology and some other factors such as losses due to weather condition i.e temperature and dirt covering the module and the losses due to power conditioning. Equation 1 shows the energy produced by the PV arrays [21].

$$E_{A,d} = A_{PV} \cdot H_R \cdot \eta_p (1-\lambda_p)(1-\lambda_C) \quad (1)$$

Where E_A is energy output of PV array (kWh/day), A_{PV} is a array area (m^2), H_R is solar radiation on the module (kWh/m^2-day), η_p is module efficiency, λ_p is a miscellaneous module losses (i.e due to dirt covering), λ_C is a power conditioning losses

Array efficiency is a function of its nominal efficiency, η_r which is measured at a reference temperature T_r=25^{0}C [21, 22]. It is calculated as:

$$\eta_p = \eta_r \cdot [1-\beta(T_c - T_r)] \quad (2)$$

Where βa temperature coefficient for module efficiency, Tc is is a module temperature, and Tr is a reference temperature. Module (Cell) temperature is related to the ambient air temperature T_a [21, 23] as given below:

$$T_C; = T_a + \frac{G}{G_{NOCT}}(T_{NOCT} - T_{aNOCT}) \quad (3)$$

Where G is in-plane solar irradiance (W/m^2), G_{NOCT} is a solar irradiance (1000W/m^2), T_a is an ambient Temperature (^{0}C), T_{NOCT} is nominal cell operating temperature (46^{0}C), and $T_{a,NOCT}$ is reference ambient temperature (25^{0}C).

B. PV Systems Potential Electricity Generation Model

The total AC electricity generated by the PV system is the sum of the electricity produced by all array in the PV power plant measured at the point where the system fed to utility grid [3,4]. The total daily $E_{AC,DP}$ and monthly $E_{AC,mP}$ AC energy generated by plant is expressed as [3,4,7]

$$E_{AC,DP} = \sum_{t-1}^{24} E_{AC,t} \quad (5)$$

$$E_{AC,mP} = \sum_{d-1}^{N} E_{AC,DP} \quad (6)$$

Where N is a number of days in the month, $E_{AC,t}$ is a energy produced by PV power plant per hour (kWh)

C. Daily Means Yield Model

Daily mean yields are defined as the energy produced by PV array over a given period per rated installed PV capacity P_{PV}, with units of kWhd^{-1}kW^{-1} or hd^{-1}[12]. Yields shows the time period the array or PV plant would have to operate at its rated power to produce particular energy quantity [3,4, 7]. There are three types of yield namely: array yield Y_A, final PV power plant yield Y_f and reference yield Y_R [12]. Equation 7, 8 and 9 express daily array yield $Y_{A,d}$, daily final PV system yield Y_f,d and daily reference yield $Y_{R,d}$ [4, 7, 12]

$$Y_{A,d} = \frac{E_{A,.d}}{P_{PV}} \quad (7)$$

$$Y_{f,d} = \frac{E_{AC,DP}}{P_{PV}} \quad (8)$$

$$Y_{R,d} = \frac{H_R}{G_{I,ref}} \quad (9)$$

Where $G_{I,ref}$ is the module's reference in-plane irradiance (1kW/m^2), H_R is the solar Irradiation (kWh/m^2-day), and P_{PV} is the PV array rated power (W_p)

D. Normalized Losses Model

Normalized losses shows the time period during which the PV power plant have to work at its rated power in order to provide for the losses [12]. Under normalized losses three indices are considered during the evaluation namely; array capture losses L_C which shows losses in array, system losses L_S representing losses in the PV system, and performance ratio PR [12]. Thus, the L_C and L_S are given by eqs 10 and 11 [3,4,12] respectively.

$$L_C = Y_{R,d} - \cdot Y_{A,d} \cdot \quad (10)$$

$$L_S = Y_{A,d} - Y_{f,d} \cdot \quad (11)$$

Performance ratio is denoted by PR, this factor is important as it shows the overall effect of losses on the PV array's rated output power due to the PV array temperature, PV array incomplete use of the solar irradiation, and PV system component inefficiencies or failures. It is calculated as [12]

$$PR_{.} = \frac{Y_F}{Y_R} = \frac{E_{AC}}{G\eta_{STC}} \quad (12)$$

Where G-standard test condition solar radiance (1kW/m^2) and η_{STC}-array efficiency at standard test condition given as

$$\eta_{STC} = \frac{P_{PV}}{GA_{PV,A}} \quad (13)$$

Where $A_{PV,A}$-Active array area (m^2) and $P_{PV,A}$- array rated power (kW_P)

E. Capacity Factor Model

The capacity factor is a model used to show the amount of energy delivered by an electric power generation system [4]. It is defined as the ratio of the output actual annual energy generated by PV system to the amount of energy the PV system would generate if it is operated continuously at full rated power for 8760 hours in a year and it is expressed as[4,24]

$$CF_{.} = \frac{E_{AC}}{8760 \times P_{PV}} = \frac{PR \times H_t}{8760 \times P_{PV}} \quad (14)$$

Where CF is capacity factor (%), E_{AC} is Actual annual energy output [kWh/year] and P_{PV} is Full rated PV power [kW_P]

IV. RESULTS AND DISCUSSION

In this study, performance analysis of three types of PV technologies (CIS,C-Si, and CdTe) in grid connected PV system has been carried out using PVGIS programme and a 20 kW_P free-standing PV system has been used in the analysis as a sample array in the larger PV systems. During the simulation, the inclination angle of PV systems was also varied to study the change in PV system total losses and compare the energy production with the system fixed at horizontal. Furthermore, two tracking systems have been also considered in order to study the effect of these systems on PV technologies performance. The study show that total PV system

losses for CIS and C-Si PV technologies increases with increase in inclination angle while for CdTe PV technology decrease with increasing inclination angle. In addition, fixing the PV system on horizontal resulted in more energy produced as compared to fixing it at optimal angle.

Monitoring the solar radiation captured due to use of different solar tracking systems and the PV technology losses due to weather condition is very vital. Since these parameters have impacts on the energy that can be generated by the PV system. Figure 2 shows that, the use of solar tracking system in PV systems result in more solar radiation being captured, which results in more electricity production by the PV system as shown in figure 3. The annual average daily solar radiation captured varies from the lowest of 5.26kWh/m^2-day (Fixed Optimal at 16degrees) to highest of 7.84kWh/m^2-day (2-axis). The site optimal inclination angle for the panel was determined by the software which depended on a number of factors such as location(south or north, near or far from equator, etc) and the landscape (flat, hilly, slope, etc), for the location under consideration 16degrees facing North was determined as the optimal angle for installation of panels. This larger inclination angle for location near the equator could be due to the site considered is hilly.

The PV technology losses which depends on the weather condition such as temperature, dirty, low radiation etc and also on the angular reflectance for PV technologies CIS, C-Si and CdTe is found to be 11, 12.5 and 3% respectively. The PV technology losses and angular reflectance losses are shown in figure 4-6. Figure 4 and 5 shows the effect of change on PV system inclination angle on the PV technology losses, the figure 4 shows that as the inclination angle is increasing the PV technology losses due to angular reflectance increases while the losses due to temperature and low radiation decreases. However, the overall PV technology losses for CIS and C-Si increases with increase in inclination angle while for CdTe the total losses decreases with increase in inclination angle as shown in figure 5. Figure 6 shows the PV technology losses due to temperature and low radiation. The CdTe shows lowest losses due to weather condition of 3% while C-Si has the highest losses of 12.5% and CIS has 11%. Thus, it can be noticed that using CdTe PV technologies in Eastern province will result in less losses due to weather condition as compared to using CIS and C-Si.

The electricity generated by the PV system varies according to the tracking system and the PV technology used in the system. The annual average electricity generated by the 20kW$_P$ PV system fixed at horizontal (CIS, C-Si, CdTe) is 31.300, 30,600 and 33,900kWh/year. While system fixed at optimal angle (CIS, C-Si, CdTe) is 28,800, 27,700 and 31,000kWh/year. However, using the vertical Axis tracking systems in the PV system (CIS, C-Si, CdTe) resulted in energy generated of 40,900, 39,7000 and 43,400kWh/year. Yet, more energy is generated when a 2-axis tracking system is used (CIS, C-Si, CdTe) 44,300, 42,900 and 46,800kWh/year as shown in figure 3. The CdTe PV system shows highest energy generated followed by CIS while C-Si has the lowest, this is due to low weather losses experienced by CdTe PV technology as compared to CIS and C-Si. Increasing inclination angle resulte in increase in cooling effect from the wind as more wind is allowed to under the panels, thus CdTe cools faster than other two panels due to the thickness of cells. Thus, despite increase in PV angular reflectance losses with increase in inclination angle for all the panels under consideration, CdTe total losses shows reduction due to cooling effect whereas the other panels shows an increase in the losses. In addition, CdTe is affected less by temperature as compared to the other two panels under consideration.

Therefore, CdTe is much appropriate PV technology for use in PV systems in Eastern province of Zambia. In short, thin film PV technologies show better performance than crystalline silicon PV technologies in PV systems under the weather conditions of Eastern Province, this is due to the fact that thin film PV technologies experience lower temperature effect than crystalline silicon PV technologies. Thus, it is concluded that the electricity generated by PV systems is mainly influenced by PV technology characteristic, weather condition and tracking system used in the PV system.

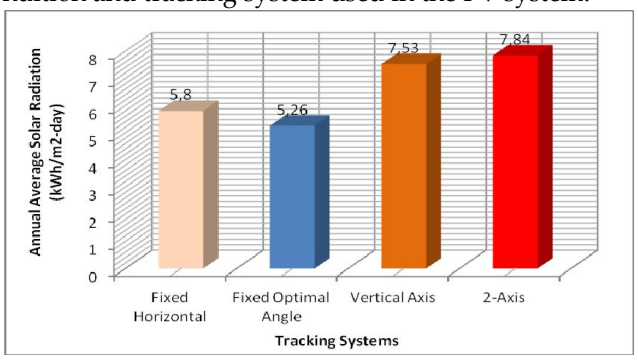


Figure 2: Annual Average Solar Radiation Captured

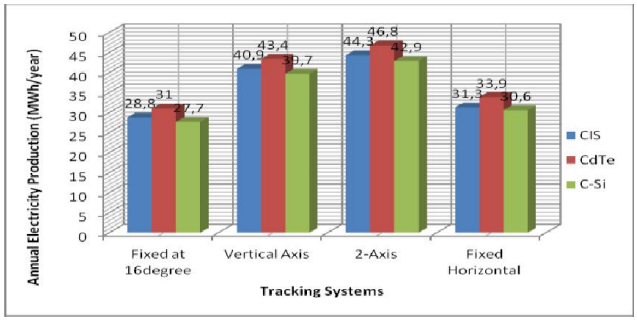


Figure 3: PV Technologies Yearly Electricity Production

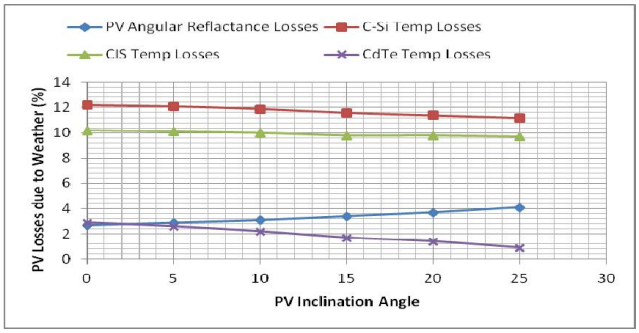


Figure 4: PV Losses Due To weather and Angular Reflectance

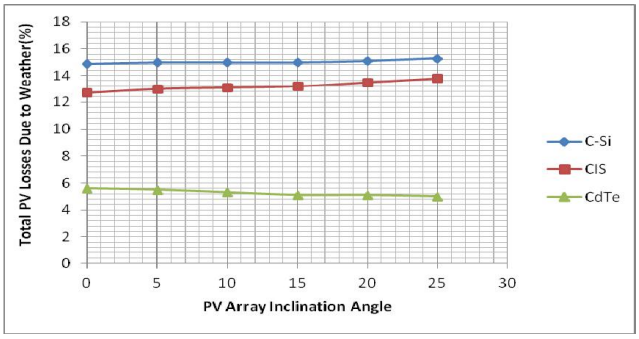


Figure 5: Total PV Technology Losses

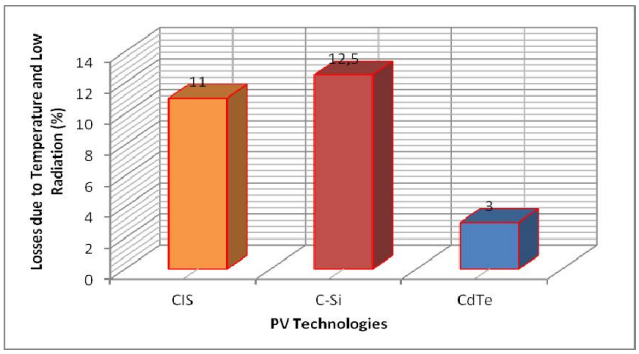


Figure 6: PV System Losses due temperature and low radiation

It can be observed from figure 7 and 8 that the yearly average capacity factor and yearly final yield for the three PV technologies shows some similarity in the way they vary with tracking system.

The capacity factor of fixed horizontal (CIS, C-Si, CdTe) power systems is found to be 17.87, 17.47 and 19.35% and for fixed optimal (CIS, C-Si, CdTe) PV systems is 16.44, 15.81 and 17.69%. While using the tracking sysems in PV system, the vertical axis tracking system (CIS, C-Si, CdTe) the capacity factor is found to be 23.34, 22.66 and 24.77% and using 2-axis tracking system in PV systems (CIS, C-Si, CdTe) resulted in capacity factor of 25.29, 24.49 and 26.71%. In all the systems it is found that the capacity factor increases with use of tracking system than in fixed systems and CdTe has the highest CF while C-Si has the lowest.

Furthermore, final yield of the PV technologies CIS, C-Si and CdTe in systems fixed at horizontal, fixed at optimal angle and using tracking systems, the CdTe PV technology is found to have the highest, followed by CIS and C-Si have the lowest as shown in figure 8 and table 3. In addition, CdTe PV technology shows highest PR (above 78%) compared to CIS (above 73%) and C-Si (above 72%) PV technologies for both fixed installed and also with tracking systems as shown in figure 9 and table 3. Thus, it is concluded that CdTe technology can perform better than CIS and C-Si technologies in the Eastern province of Zambia. However, it is important to also consider the investment costs of this systems against the payback period and the investment benefits in order to reach the optimal decision.

Generally according to literature it is expected that a titled solar panel fixed at an optimal angle to produces more energy over a year, than a horizontal fixed solar panel. However, this theory is more true for countries far from the equator than countries that lies at or near to the equator. The area under consideration is close to equator at latitude 10^0South of the equator.

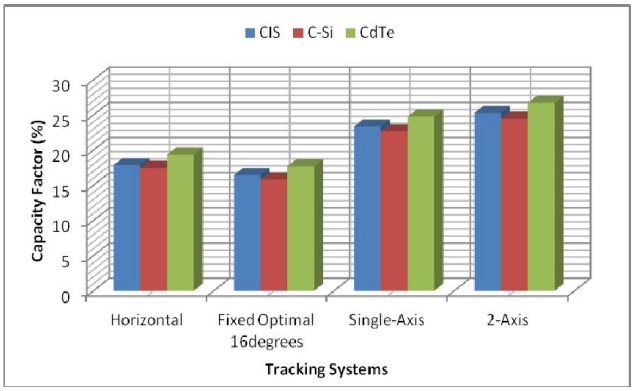


Figure 7 : Yearly Average Capacity factor

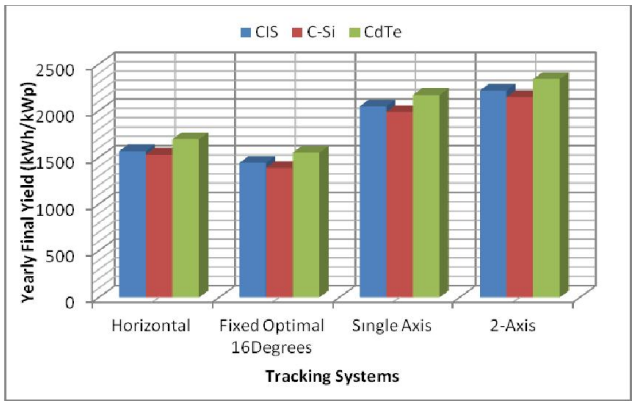


Figure 8: PV Technologies Yearly Average Final Yield

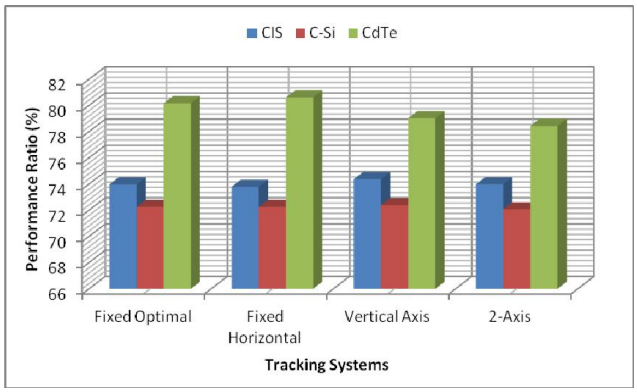


Figure 9: PV Technologies Yearly Average Performance Ratio

The study of monthly variability of solar radiation and monthly average electricity production in the province while using different solar tracking systems and PV technologies is very important for planning of the energy management, monthly electricity production and selecting the better installation of the system and appropriate PV technology. Figure 10 shows the variability of monthly solar radiation for both fixed systems and system with tracking systems. It is worth noting the effect of installing the PV system at fixed optimal angle in Eastern Province, that less solar radiation is captured between the months of March to October as compared to installing the system at Horizontal. Thus, for larger system that do not use tracking systems, installing at fixed horizontal is found to result in the optimal utilization of solar energy than installing at optimal angle. Furthermore, it is important when considering the area required for installation of the utility-scale PV systems in the Province. Installing PV systems at horizontal would reduce the required area and results in more energy generation than installing at optimal angle as it can be observed in figure 10 the captured monthly average solar radiation at fixed horizontal and finxed optimal angle

The monthly average electricity production for CdTe, CIS and C-Si PV technologies in Fixed horizontal system is shown in figure 11. Fig.11 shows the energy generation with temperature changes during the year, it is worth noting that highest energy generation and maximum cell temperatures for all the PV systems using different PV technologies is expected in the months of october, despite of higher temperatures in this month. In this month more energy is generated despite of higher temperature which is due higher solar radiation being received in this month, thus complementing the losses that may occur due to higher temperature.

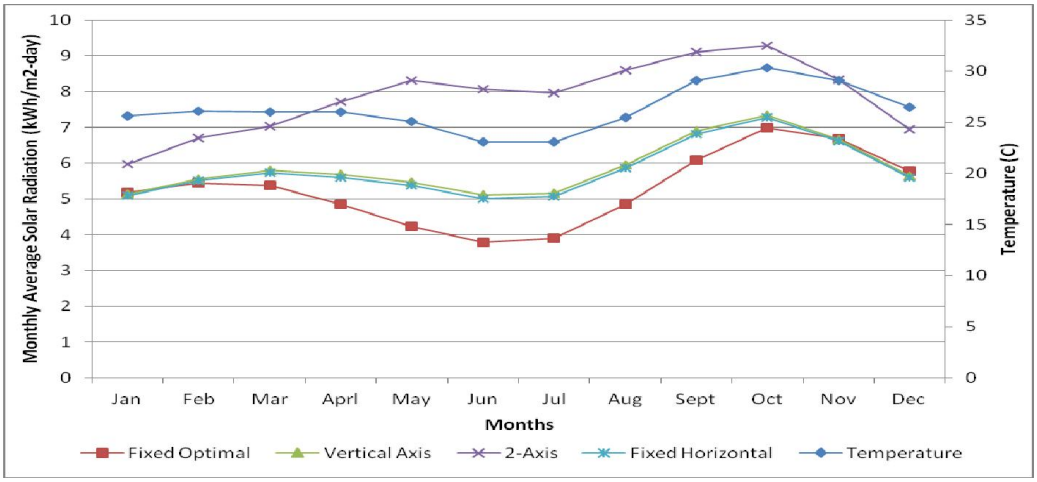


Figure 10: Comparison of Variability of Monthly average Daily Solar Radiation and Temperature

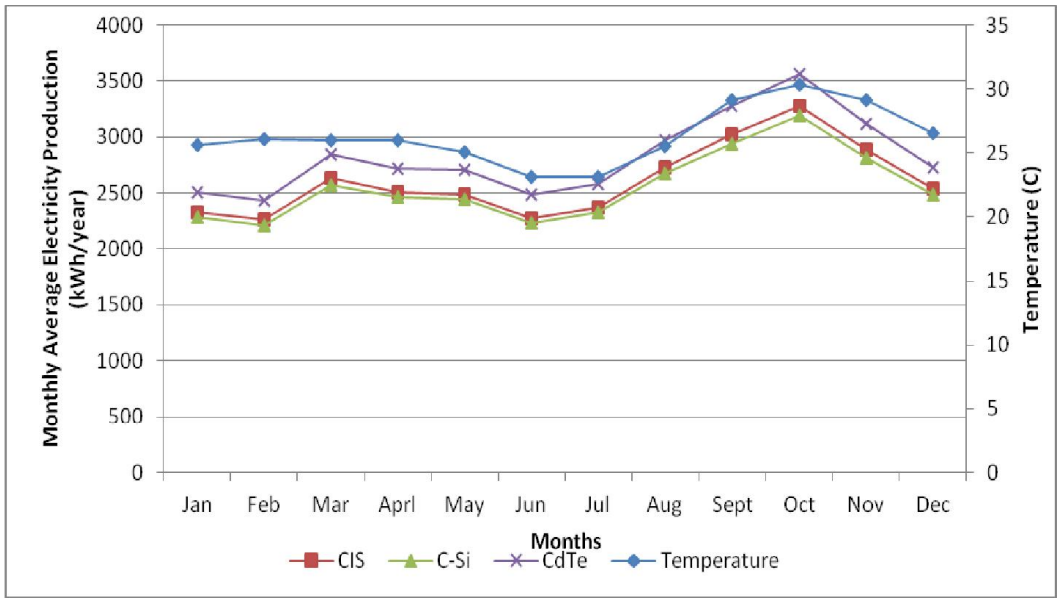


Figure 11: Comparison of Monthly Average Electricity Production and Temperature

Table 3: Comparison of Performance Parameters for Three PV Technologies

Tracking System	H	Es	PV Technology											
			CIS				C-Si				CdTe			
			$E_{AC,yr}$	$Y_{F,yr}$	CF	PR	$E_{AC,yr}$	$Y_{F,yr}$	CF	PR	$E_{AC,yr}$	$Y_{F,yr}$	CF	PR
Fixed Hozirotnal	5.80	2120	31300	1565	17.87	73.97	30600	1530	17.47	72.24	33900	1695	19.35	80.17
Fixed Optimal	5.26	1920	28800	1440	16.44	73.76	27700	1385	15.81	72.24	31000	1550	17.69	80.61
Vertical Axis	7.53	2750	40900	2045	23.34	74.37	39700	1985	22.66	72.38	43400	2170	24.77	79.02
2-Axis	7.84	2860	44300	2215	25.29	73.98	42900	2145	24.49	72.07	46800	2340	26.71	78.44

H-Annual Average Solar Radiation (kWh/m²-day)
Es-total yearly average solar energy (kWh/m²-year)
CIS-Copper Indium Selenium
C-Si-Crystalline Silicon
CdTe- Cadmium Tellur

V.CONCLUSION

The study has presented the overview of the performance of the three types of PV technologies in Eastern Province of Zambia using PVGIS. The study show that, the CdTe PV technology have better performance for PV electricity generation in Eastern Province, followed by CIS then C-Si. It has also presented the effect of using tracking system in the performance of PV systems. From the results presented, it shows that use of tracking system in PV system results in more energy production, however it has some negative effect on the overall performance ratio of the system, as it can be noticed that CdTe has better performance ratio when fixed at optimal angle than using tracking system. The performance of the PV systems in Eastern province of Zambia will vary depending on PV technology that will be used in the system, the tracking system, PV array inclination (fixed horizontal or at optimal angle), and weather/season. The analyzed results show that CdTe PV technology standout to be the best PV technology for use in PV systems in Eastern province of Zambia. For a 20kW$_P$ PV system using CdTe PV technology at fixed horizontal would produce electricity of 33,900kWh/year, with annual final yield of 1695kWh/kW$_P$ and capacity factor of 19.35% and Performance Ratio of 80.17%. . Thus, use of CdTe PV technology in PV systems appears to be one of the best effective solutions for production of sustainable and clean energy in energy generation mix in Eastern Province of Zambia.

ACKNOWLEDGMENT

The authors are grateful to University of Zambia and Turkish Government for financial support.

REFERENCES

1. H. Poor, *An Introduction to Signal Detection and Estimation*. New York: Springer-Verlag, 1985.
2. S. Chen, B. Mulgrew, and P. M. Grant, "A clustering technique for digital communications channel equalization using radial basis function networks," *IEEE Trans. Neural Networks*, vol. 4, pp. 570–578, July 1993.
3. G. R. Faulhaber, "Design of service systems with priority reservation," in *Conf. Rec. 1995 IEEE Int. Conf. Communications,* pp. 3–8.
4. J. Williams, "Narrow-band analyzer (Thesis or Dissertation style)," Ph.D. dissertation, Dept. Elect. Eng., Harvard Univ., Cambridge, MA, 1993.
5. *Motorola Semiconductor Data Manual,* Motorola Semiconductor Products Inc., Phoenix, AZ, 1989.
6. R. J. Vidmar. (1992, August). On the use of atmospheric plasmas as electromagnetic reflectors. *IEEE Trans. Plasma Sci.* [Online]. *21(3).* pp. 876—880. Available: http://www.halcyon.com/pub/journals/21ps03-vidmar

ESTABLISHMENT OF AN FPGA-BASED REAL-TIME IM EXPERIMENTAL SETUP

R. INAN[1] and M. BARUT[1]

[1] Niğde Ömer Halisdemir University, Niğde/Turkey, rinan@ohu.edu.tr
[1] Niğde Ömer Halisdemir University, Niğde/Turkey, mbarut@ohu.edu.tr

Abstract – **In this study, Serial Peripheral Interface (SPI) communication between the ADS 8568 EVM-PDK (Evolution Performance Development Kit) Analog to Digital Converter (ADC) developed by Texas Instrument and Xilinx XC5VLX110T FPGA board is implemented in order to verify Induction Motor (IM) model in real-time. Analog datas obtained from the voltage, current and torque transducers are converted to digital datas by ADC and read with FPGA simultaneously in real-time. Thus, the $\alpha\beta$- stator stationary axis components of the stator voltage ($v_{s\alpha}$ and $v_{s\beta}$) and $\alpha\beta$- axis components of the stator current ($i_{s\alpha}$ and $i_{s\beta}$) are calculated by Clarke transformation. The load torque t_L is obtained by passing the measured signals from the torque transducer through the low-pass filter which is implemented on the FPGA using 64-bit double floating number format. In addition, the signals obtained from the incremental encoder are read by the FPGA after the voltage level shifting with 74LS245P Integrated Circuit (IC), so that mechanical speed n_m (or ω_m) of the rotor can be measured. All measurement algorithms except for the lowpass filter constructed for load torque measurement are implemented with VHDL by using 32-bit single floating numbers. The real-time verification of the rotor flux-based IM model is performed offline before it is implemented on FPGA by using the stator voltages, currents and load torque measured from the IM by using the simultaneous measurement unit in real-time. Thus, an FPGA-based real-time open-loop experimental setup of IM is established for the future works about the estimator/observer based speed-sensorless control of IMs.**

Keywords **– FPGA, induction motor, parallel programming, estimated-based speed-sensorless control, VHDL.**

I. INTRODUCTION

IN the process of developing engineering designs, the verification and testing of motor controllers used for electric vehicles is a time consuming operation with high cost. Also, testing the high-power controllers can lead to safety problems [1]. As it is well-known, modelling is a mathematical expression of a physical system in all areas and simulation is a hardware or software calculation based platform where these models can be tested numerically. High accuracy and high speed modeling and analysis equipment are needed for design optimization, dynamic characteristic analysis, controller design, and transient stability analysis of electrical machines [2]. Lately, the performances of the IM control methods proposed in the literature are extensively tested on hardware in the loop (HIL) system which is basis for the real-time simulation platforms [1]. The HIL methodologies that form real-time emulator systems have a widespread acceptance since they provide a fast and safety test environment in the design of automotive, energy and aerospace, especially in the creation of measurement systems, electronic circuit design and industrial control applications [3].

On the other hand, sampling time is important in HIL simulator or in real-time emulators, if not as much as in real-time experimental environments [4]. It is known that a system must be able to be rapidly calculated in a simulation platform so that it can be realized with low sampling time. That is why FPGAs with fast processing capacity are finding applications today in real-time emulator [5]. FPGAs have low I/O latency and the ability to process in nanoseconds makes them suitable for real-time simulation of high frequency signals [2]. FPGAs offer a parallel architectural structure that can fully match the required mathematical and logical expressions of the algorithms to be implemented. The parallel simultaneously processing ability allows FPGAs to reduce sampling time [5].

There are some studies in the literature about the simulation of electrical motor control and driver algorithm with motor model and driver model or verification of the electrical motor model in FPGA-based HIL system or real-time emulator [1, 3-12]. In [3], it is demonstrated that a novel real-time emulator of a permanent magnet synchronous motor (PMSM) drive suitable for HIL testing of both healthy and faulty conditions, considering in particular stator short-circuit. This emulator is implemented on FPGA with 32-bit fixed point numbers. Ref. [6] presents a test setup for the analytical modelling of a three-phase low voltage IM drive model in closed-loop. The model is developed in MATLAB Simulink by using C language based S-functions compatible with the real-time workshop (RTW) platform which is constructed on FPGA. In [1], a nonlinear approach of a real-time IM model and control system are implemented in a National Instruments real-time platform and then, the HIL simulation results are compared with real values of IM states obtained by measurements. In [4], the IM model is verified offline on FPGA in HIL and real rotor speed obtained from the experimental setup is compared with simulation result. However, in this study, any FPGA board is not included to the real-time IM experimental setup. In [7], FPGA is programmed

by using real-time interface of Opal-RT-based platforms which utilizes a Xilinx Virtex 6 FPGA in order to model the system; The codes of FPGA are constructed by blocks. An external DSP-based controller is used to generate the signal of the converter model implemented on FPGA with IM model in HIL. The outputs obtained from the models are saved in real-time by using digital to analogue converter (DAC) and ADC connected to terminals of FPGA board for applying the gate signals obtained from DSP to the converter model. So the HIL control performance of the electrical vehicle system is tested. In [8], voltage source inverter (VSI) model, PWM technique, and IM model are implemented on FPGA with VHDL. Also, DSP–based IM experimental setup is operated under the same conditions and real-time results are compared with the simulation results obtained from the FPGA-based HIL system. Ref. [9] introduces an FPGA-based implementation of offline HIL emulator of nonlinear dynamic model of IM; A digital three-phase power source generates the required line to line voltages for emulating the manner of an ADC. In [5], a real-time HIL emulator of a synchronous motor (SM) includes SM delta-operator model, VSI model, and model of a mechanical load. However, the emulator is run on ModelSim which is the software-based simulator of the FPGA; Thus, it is not possible to say that the proposed system is tested on a hardware platform. Also Refs. [10] and [11] demonstrate offline HIL verification of the IM model on FPGA. In [12], the actual stator voltages and load torque are measured from DSP-based open-loop IM experimental setup and registered to memories of the FPGA. Then actual voltages and load torque are applied to the IM model which is implemented on FPGA. Thus, the IM model is verified offline in HIL system.

There is no clear statement in the literature about how a real-time HIL system is established in an IM experimental setup. Also it is seen from the literature that some studies are implemented offline on HIL system, but the authors affirm that the studies are about the real-time emulator of IM or a control method of IM. In addition, the results are given in a short time interval in the existing literature.

The HIL systems are classified as two types: The first type of HIL system is called as controller HIL (CHIL). In CHIL system, there is no power transfer to or from the hardware-based controller and the power system is implemented on controller as a virtual system. The other type of HIL is named as power HIL (PHIL). The PHIL system involves power transfer to or from the hardware under test [13]. Thus, in this study, a PHIL system is implemented on an FPGA-based real-time IM experimental setup to verify the rotor flux-based IM model by using the measured actual values of stator voltages and load torque of the IM and the established experimental setup is introduced in detail. The IM model and SPI communication which is used for the data transfer between the FPGA and ADC board are implemented with VHDL on FPGA. The measured real values of the states (stator voltages, stator currents, load torque and rotor speed) and results of the IM model are sent to PC via Ethernet communication which constructed on FPGA with Ethernet Wrapper core of the FPGA. Then the row Ethernet packages are grabbed by Wireshark and converted to meaningful values by PERL software language. The meaningful values about the measured states and simulation results obtained from the IM model are graphically evaluated on MATLAB.

This paper is organized as follows: After the introduction in Section I; the FPGA-based real-time IM experimental setup are defined in Section II. implementation of the SPI communication between ADC and FPGA is given in Section III while Section IV describes the discretized rotor flux-based IM model and real-time verification results. Finally, conclusions and the suggestions for the future studies are explained in Section 6

II. FPGA-Based Real-Time IM Experimental Setup

The FPGA-based open-loop IM experimental setup established with the aim of real-time online verification of the IM model is shown in Fig. 1. The components used in the experimental setup which is shown in Fig. 1 are given as follows:

- ADS 8568 EVM-PDK ADC is manufactured by Texas Instruments.
- DRBK-50 series torque transducer is produced by ETH and has 50 $[N.m]$ torque capacity to load IM.
- ERN120 series 5000 lines incremental encoder is utilized to measure the rotor mechanical speed of the IM and 74LS245P integrated circuit (IC) is used for voltage level shifting between the encoder output signal and FPGA digital I/O ports.
- LV100-400 voltage transducers and LA55-P/SP1 current transducers manufactured by LEM is utilized to measure three-phase voltages and currents of IM, respectively.
- Xilinx Virtex 5 XC5VLX110T FPGA is used for constructing the VHDL commands of IM model and evaluation commands of ADC module by using the parallel architecture of FPGA inherently.
- 2.2 $[kW]$ IM is manufactured by TEE Electric Motors.

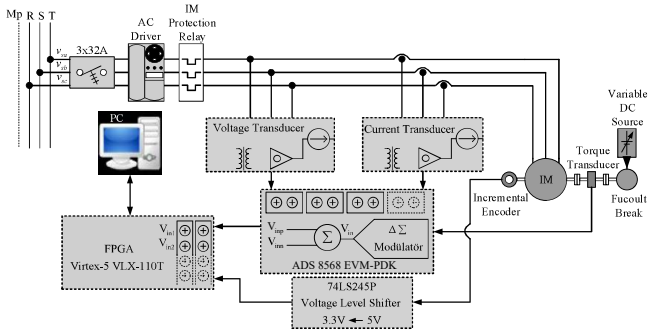


Figure l: Schematic representation of FPGA-based real-time IM experimental setup.

The ADS 8568 EVM-PDK ADC which is capable of 16-bit dual-polarity measurement is used between sensors and FPGA in order to evaluate the information obtained from the voltage, current and torque transducers in the FPGA-based real-time IM experimental setup. In addition, the 74LS245P voltage level shifter IC reducing 5 [V] to 3.3 [V] is convert the voltage level of the incremental encoder terminals to the appropriate voltage

levels of the FPGA terminals. In order to determine the exact value of the load-torque obtained from the moment transducer, the fourth-order low-pass filter is implemented in the FPGA. The coefficients of the low-pass filter implemented on the FPGA are determined by MATLAB. The discrete-time mathematical expressions of the low-pass filter are implemented using 64-bit floating point numbers to improve the accuracy of the low-pass filter.

III. Implementation of The SPI Communication Between ADC And FPGA

The ADS 8568 EVM-PDK ADC which is used to obtain real values of the three phase stator voltages, stator currents and load torque of IM from the voltage, current, and torque transducers have the following electrical features:

- 16-bit resolution.
- 8 simultanous bipolar analog input channels.
- 400 Ksps sampling rate.
- Data transfromation by SPI or Frame Synchronous (FSYN) parallel communication.
- $\mp 10\ [V]$ and $\mp 5\ [V]$ selectable analog input voltage range.
- $3.3\ [V]$ and $5\ [V]$ selectable digital output voltage level.

In case of using only EVM layer of ADS8568 EVM-PDK ADC, it is suggested that the converter data should be transferred by SPI protocol [14-15]. The SPI communication between ADC and FPGA is performed by using the timing diagram which is shown in Fig. 2. This timing diagram is offered in [14] and all time requirements are arrenged in FPGA by using a state machine loop implemented with VHDL.

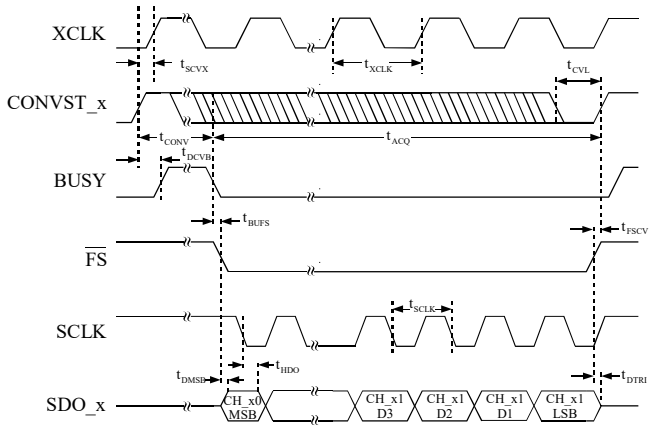


Figure 2: Timing diagram of SPI protocol [14].

The meanings and functions of the signals given in Fig. 2 are described as follows:

- XCLK indicates the internal clock frequency of ADS 8568 EVM-PDK ADC.
- CONVST_x is sent to ADC from an external microcontroller and indicates that the ADC starts analogue to digital conversion.
- BUSY is an output digital signal of the ADC and shows that whether the conversion has finished.
- ($\overline{FS}$) is an output digital signal of the ADC and describes that digital data can be read from ADC.
- SCLK is clock frequency of SPI communication sent to ADC from the external microcontroller.
- SDO_x illustrates the digital outputs of ADC (There are four digital output channels in ADC and every output channel carries 32-bit data string which is formed by putting in order two 16-bit output channels in one string)

Furthermore, the timings mentioned in Fig. 2 are given in Table 1. The SPI communication between ADC and FPGA is implemented on FPGA with VHDL by regarding the time requirements given in Table 1. Thus the three-phase stator voltages, stator currents and load torque can be measured in real-time by FPGA.

Table 1: Timing requirements for implementing the SPI communication on FPGA

Timing requirements	Time
t_{SCVX}	min 6 [ns]
t_{XCLK}	min 85.11 [ns]
t_{CONV}	max 1.7 [µs]
t_{ACQ}	min 280 [ns]
t_{CVL}	min 20 [ns]
t_{DCVB}	max 25 [ns]
t_{BUFS}	min 86 [ns]
t_{FSCV}	min 40 [ns]
t_{SCLK}	min 0.022 [µs]/max 10 [µs]
t_{DMSB}	max 12 [ns]
t_{HDO}	min 5 [ns]
t_{DTRI}	max 10 [ns]

The digital 16-bit binary data obtained from the ADC are converted to decimal values in FPGA with VHDL by using 32-bit single floating point number multiplier and divider. The quantization function given in (1) is used to obtain the decimal values of the measured quantities from the 16-bit binary values.

$$Analog\ Value\ (Decimal) = \frac{Binary\ Value\ X\ 10}{32767} \quad (1)$$

The voltage levels of outputs of the voltage, current and torque transducers are ∓ 5 [V]. However, the voltage levels of analogue input channels of the ADC are setted to ∓ 10 [V] to prevent damage caused by voltage fluctuations that can occur at the outputs of the transducers.

IV. Discretized Rotor Flux-Based IM Model and Real-Time Verification Results

In order to verify the IM model in real-time, the rotor flux based IM model is used in this study. The discretized IM model fixed with the $\alpha\beta$-stator stationary reference frame is given as below:

$$\underline{x}_e(k+1) = \underline{f}_e\left(\underline{x}_e(k), \underline{u}_e(k)\right) + \underline{w}_1$$

$$= \underline{A}_e\left(\underline{x}_e(k)\right)\underline{x}_e(k) + \underline{B}_e\underline{u}_e(k) + \underline{w}_L + \underline{w}_1 \quad (2)$$

$$\underline{Z}(k) = \underline{h}_e\left(\underline{x}_e(k)\right) + \underline{w}_2 \text{ (Measurement Equation)}$$
$$= \underline{H}_e\underline{x}_e(k) + \underline{w}_2 \quad (3)$$

The matrices given in (2) and (3) are described as follows:

$$\underline{x}_e(k) = [i_{s\alpha}(k) \quad i_{s\beta}(k) \quad \varphi_{r\alpha}(k) \quad \varphi_{r\beta}(k) \quad \omega_m(k)]^T$$

$$\underline{A}_e = \begin{bmatrix} a_1 & 0 & a_2 & a_3\omega_m(k) & 0 \\ 0 & a_1 & -a_3\omega_m(k) & a_2 & 0 \\ a_4 & 0 & a_5 & -a_6\omega_m(k) & 0 \\ 0 & a_4 & a_6\omega_m(k) & a_5 & 0 \\ -a_7\psi_{r\beta}(k) & a_7\psi_{r\alpha}(k) & 0 & 0 & a_8 \end{bmatrix}$$

$$\underline{B}_e = \begin{bmatrix} a_9 & 0 \\ 0 & a_9 \\ 0 & 0 \\ 0 & 0 \\ 0 & 0 \end{bmatrix}, \underline{w}_L = \begin{bmatrix} 0 \\ 0 \\ 0 \\ 0 \\ -a_{10} \end{bmatrix}, \underline{H}_e = \begin{bmatrix} 1 & 0 & 0 & 0 & 0 \\ 0 & 1 & 0 & 0 & 0 \end{bmatrix}$$

$$\underline{Z}(k) = [i_{s\alpha}(k) \quad i_{s\beta}(k)]^T, \underline{u}_e(k) = [v_{s\alpha}(k) \quad v_{s\beta}(k)]^T$$
$$a_1 = 1 - \left(\frac{R_s}{L_\sigma} + \frac{L_m^2 R_r'}{L_\sigma L_r'^2}\right)T, \quad a_2 = \frac{L_m R_r'}{L_\sigma L_r'^2}T, \quad a_3 = \frac{L_m p_p}{L_\sigma L_r'}T, \quad a_4 = \frac{R_r' L_m}{L_r'}T, \; a_5 = 1 - \frac{R_r'}{L_r'}T, \; a_6 = p_p T, \; a_7 = \frac{3}{2}p_p\frac{L_m}{L_r' J_T}T, \; a_8 = 1 - \frac{\beta_T}{J_T}T, \; a_9 = \frac{T}{L_\sigma}, \; a_{10} = \frac{t_L}{J_T}T$$

Here, $\underline{x}_e$ is extended state space vector. $\underline{f}_e$ is nonlinear function of states and inputs. $\underline{A}_e$,is system matrice. $\underline{u}_e$ is control input vector. $\underline{B}_e$ is input matrice. $\underline{w}_1$ is system noise. $\underline{w}_L$ is load torque effect matrice. $\underline{h}_e$ is function of outputs. $\underline{H}_e$ is measurement matrice. $\underline{w}_2$ is measurement noise. p_p is pole pair. R_s and R_r' are stator and rotor resistance, respectively. $L_\sigma = \sigma L_s$ is stator transient inductance. $\sigma = 1 - \frac{L_m^2}{L_s L_r'}$, leakage or coupling factor. L_s and L_r' are stator and rotor inductance, respectively. L_{ls} and L_{lr} are stator and rotor leakage inductance, respectively. L_m is magnetizing inductance. J_T and β_T are total inertia and viscous friction, respectively. T is sampling time.

The rated parameters of the IM used in the real-time verification of IM model are given in Table 2, the same motor parameters are also used in [16].

Table 2: IM parameters used for the verification of IM model.

P [kW]	f [Hz]	J_T[kg.m^2]	β_T [Nm/(rad/sn)]	P_p
2.2	50	0.055	0.0019	3
V [V]	I[A]	R_s[Ω]	R_r'[Ω]	L_s[H]
380	5.5	3.03	2.53	0.1466
L_r'[H]	L_m[H]	n_m[rpm]	t_L[N.m]	
0.1524	0.135	1000	20	

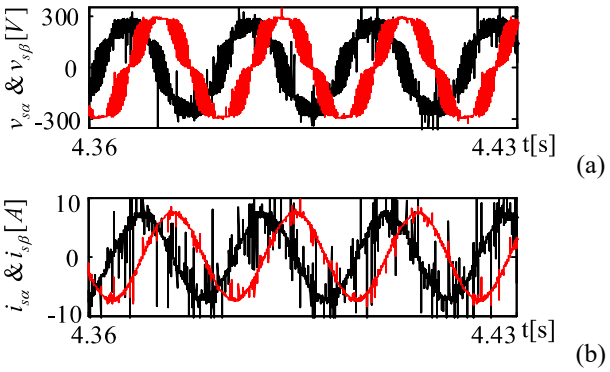
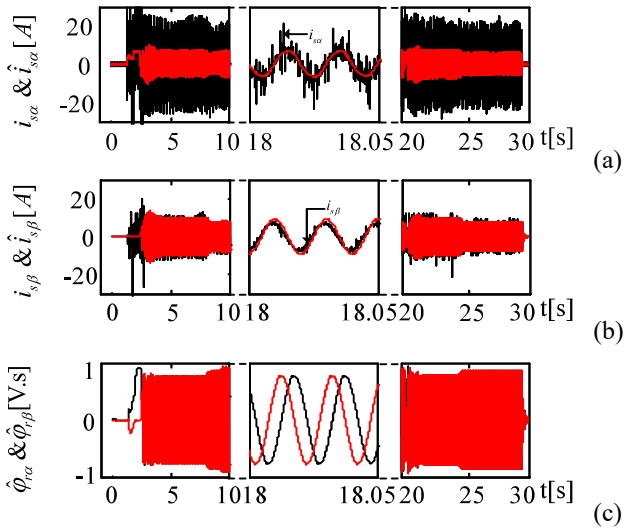


Figure 3: The real values of (a) $v_{s\alpha}$ and $v_{s\beta}$ variations, (b) $i_{s\alpha}$ and $i_{s\beta}$ variations measured from FPGA-based IM experimental setup.

The real values of $v_{s\alpha}$, $v_{s\beta}$, $i_{s\alpha}$, and $i_{s\beta}$ measured from FPGA-based IM experimental setup are shown in Fig. 3. The results of the real-time verification of the IM model on the FPGA are given in Fig. 4. As shown in Fig. 4, IM is accelerated from zero speed to rated speed under $t_L = 19\ [Nm]$ load torque and is operated at $n_m = 952\ [rpm]$ in the range of $3 \le t \le 8\ [s]$. The load torque is decreased to zero at $9.5.\ [s]$ and IM is operated at rated rotor speed ($n_m = 1000\ [rpm]$) for about $1.5\ [s]$ under no-load. The direction of rotation of IM is reversed at $9.5.\ [s]$ and operated at rated speed ($n_m = -1000\ [rpm]$) in reverse direction between at $11.5 \le t \le 15.5\ [s]$ time interval. The load torque is increased to $t_L = -18.5\ [Nm]$ at $15.5.\ [s]$ and the rotor mechanical speed is decreased to $n_m = -953\ [rpm]$ by operating the IM via an ac driver in open-loop without speed feedback. Then direction of IM is reversed and accelerated to its rated speed. The IM is operated at $n_m = 952\ [d/dk]$ in forward direction in the range of $21.5 \le t \le 25\ [s]$ under $t_L = 18.5\ [Nm]$ load torque. After that, the load torque is decreased to zero and IM is operated at rated speed $n_m = 1000\ [rpm]$ until the end of the test scenario.



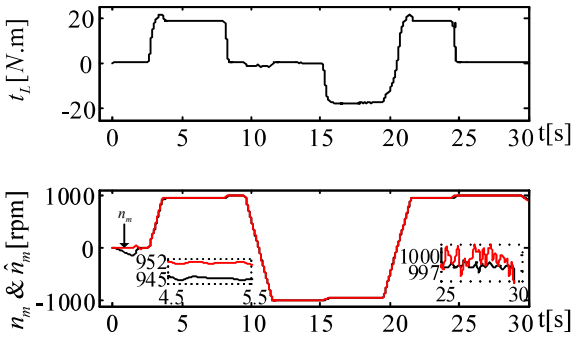


Figure 4: The actual values of the IM states measured from the real-time experimental setup and the results obtained from FPGA-based IM model; (a) $i_{s\alpha}$ vs. $\hat{\imath}_{s\alpha}$ variations, (b) $i_{s\beta}$ vs. $\hat{\imath}_{s\beta}$ variations, (c) $\hat{\varphi}_{r\alpha}$ vs. $\hat{\varphi}_{r\beta}$ variations, (d) t_L variations,(e) n_m vs. $\hat{n}_m$ variations.

It is shown that, under all speed and load torque variations, the speed and current information obtained from the IM model implemented on the FPGA overlaps with their actual values obtained from the real-time experimental setup. Thus, the accuracy of the FPGA-based IM emulator is experimentally verified.

Table 3:, The computation times of the algorithms implemented on the FPGA for the real-time verification of the IM model

Algorithm	Time (μs)
IM Model	0.69
ADC (SPI)	3.28
Total	3.97
T (Sampling Time)	15

The duration of data read from the ADC with SPI communication and the implementation time of IM model on FPGA are given in Table 3. The sampling time of the HIL system is defined as $T = 15\ [\mu s]$, despite the overall system can be implemented in $3.97\ [\mu s]$, in order to prevent the data loss while the Ethernet communication is provided between the FPGA and PC. Also, the numbers and ratios of the logical units used on the FPGA are given in Table 4.

Table 4: The numbers and ratios of the logical units used for the implementation of FPGA-based real-time emulator of the IM .

Source	Used Number	Available on FPGA	Ratio
Slice Register	21771	69120	%31
Slice LUTs	36956	69120	%53
Occupied Slices	11862	17280	%68
DSP48Es	25	64	%39

V. Conclusion

In this study, the IM rotor flux-based model is verified by using the FPGA-based real-time IM experimental setup and also the detailed description of how the experimental setup is established is presented. Here, the ADC which is used for the data acquisition from the IM is communicated with the FPGA via SPI. Thus, it is demonstrated that the IM control methods and state/parameter observers/estimators can be realized in real-time with low sampling time by using the parallel processing capability of the FPGAs. Moreover, this study confirms that FPGAs, which have gained importance in today's industry can be a good alternative with lower cost for industrial control applications.

References

[1] J. Shen, G. Xu, Y. Xu, L. Qiu, and G. Li, "National instrument-based experimental validation of a nonlinear real-time induction motor model in an EV simulation system", *2017 IEEE Int. Conf. on Industrial Technology (ICIT)*, pp. 959-964.

[2] S. Mojlish, N. Erdogan, D. Levine, and A. Davoudi, "Review of Hardware Platforms for Real-Time Simulation of Electric Machines", *IEEE Transactions on Transportation Electrification*, vol. 3 (1), pp. 130-146, March 2017.

[3] F. Alvarez-Gonzalez, A. Griffo, B. Sen, and J. Wang,"Real-Time Hardware-in-the-Loop Simulation of Permanent-Magnet Synchronous Motor Drives Under Stator Faults", *IEEE Transactions on Industrial Electronics*, vol. 64 (9), pp. 6960-6969, September 2017.

[4] N. R. Tavana and V. Dinavahi, "A General Framework for FPGA-Based Real-Time Emulation of Electrical Machines for HIL Applications", *IEEE Transactions on Industrial Electronics*, vol. 62 (4), pp. 2041-2053, April 2015.

[5] M. Dagbagi, L. Idkhajine, E. Monmasson, L. Charaabi, I. Slama-Belkhodja, "FPGA implementation of a synchronous motor real-time emulator based on delta operator", *2011 IEEE Int. Symp. on Industrial Electronics*, pp. 1581-1586.

[6] A. Ingalalli and J. V. V. N. Bapiraju, "Analytical model for real time simulation of low voltage induction motor drive", *2017 IEEE Int. Electric Machines and Drives Conf. (IEMDC)*, pp. 1-8.

[7] L. Herrera, C. Li, X. Yao, and J. Wang, "FPGA-Based Detailed Real-Time Simulation of Power Converters and Electric Machines for EV HIL Applications", *IEEE Transactions on Industry Application*, vol. 51 (2), pp. 1702-1712, March 2015.

[8] R. Gregor, G. Valenzano, J. Rodríguez-Piñeiro, and J. Rodas, "FPGA-based real-time simulation of a Dual Three-Phase Induction Machine", *2014 16th European Conf. on Power Electronics and Applications*, pp. 1-8.

[9] M. A. Esparza, R. Alvarez-Salas, H. Miranda, E. Cabal-Yepez, A. Garcia-Perez, R. J. Romero-Troncoso, and R. A. Osornio-Rios, "Real-time emulator of an induction motor: FPGA-based implementation", *2012 9th Int. Conf. on Electrical Engineering, Computing Science and Automatic Control (CCE)*, pp. 1-6.

[10] M. Dagbagi, L. Charaabi, L. Idkhajine, E. Monmasson, and I. Slama-Belkhodja, "Digital implementation using delta operator for FPGA-based induction motor emulator", *Eighth Int. Multi-Conf. on Systems, Signals Devices*, pp. 1-6.

[11] L. Charaabi, E. Monmasson, and I. Slama-Belkhodja, "FPGA-based real-time emulation of induction motor using fixed point representation", *2008 34th Annual Conf. of IEEE Industrial Electronics*, pp. 2393-2398.

[12] R. Inan, M. Barut, and F. Karakaya, "Asenkron motor modeli kullanılarak MATLAB yazılımı ile FPGA donanım ortamındaki hesaplamaların karşılaştırılması", 2012 *Otomatik Kontrol Türk Milli Komitesi Otomatik Kontrol Ulusal Toplantısı-TOK 2012*, pp. 835-839.

[13] X. Guillaud, M. O. Faruque, A. Teninge, A. H. Hariri, L. Vanfretti, M. Paolone, V. Dinavahi, P. Mitra, G. Lauss, C. Dufour, P. Forsyth, A. K. Srivastava, K. Strunz, T. Strasser, and A. Davoudi, "Applications of Real-Time Simulation Technologies in Power and Energy Systems", *IEEE Power and Energy Technology Systems Journal*, vol. 2 (3), pp. 103-115, September 2015.

[14] *ADS 8528, 8548, 8568 Data Manual*, Texas Instruments, 2016.

[15] *ADS 8568 EVM-PDK User Manual*, Texas Instruments, 2016.

[16] M. Barut, R. Demir, E. Zerdali, and R. Inan, "Real-time implementation of bi input-extended Kalman filter-based estimator for speed-sensorless control of induction motors", *IEEE Trans. on Industrial Electronics*, vol. 59 (11), pp. 4197-4206, November 2012.

Comparative Study Between Sensorless Vector Control and Nonlinear Control for PMSM Based on Extended Kalman Filter (EKF)

Y. MAANANI[1], A. MENACER[1] and I. HARZELLI[1]
[1] Biskra University, Biskra/Algeria, yacine.maanani@gmail.com
[1] Biskra University, Biskra/Algeria, menacer_arezki@hotmail.com
[1] Biskra University, Biskra/Algeria, imadeddineharzelli@yahoo.fr

***Abstract* - This paper presents the performance of sensorless nonlinear control compared with vector control of permanent magnets synchronous machine using Extended Kalman Filter (EKF) is used for estimating the speed. The robustness of the control is tested for the parameter variation and for the machine operating at low speed. The simulation results show the robustness of the filter and the overall drive system.**

***Keywords* - permanent magnets synchronous machine, vector control, input/output control, estimation, EKF.**

I. INTRODUCTION

PERMANENT magnets synchronous machines are spreading more and more as actuators in automated industries where they replace the DC motors. They have about them the advantage of having better performance (in terms of mass torque, for example) and not having mechanical commutator (collector that pose maintenance problems and behavior in difficult environments) [1], [2].

Vector control, results in electric drives with a dynamic very similar to using the DC machines. This structure, which is generally decoupled control of torque and flux. However, this control structure requires that the machine settings are accurate. This requires proper identification of parameters. Accordingly, the use of robust control algorithms, to maintain a level of decoupling and acceptable performance is necessary.

Nonlinear control has the advantage of separately current and torque. With this control technology, engine model is broken down into two independent systems mono variable linear. Each subsystem is an independent control loop of a given variable (speed, torque, current etc.). The dynamics of the linearized system is chosen through optimal taxation of poles [3].

The sensorless control strategy for permanent magnet synchronous machine (PMSM) has become a center of intensive research and development. Researchers want to avoid the problems encountered in regulatory systems, caused by the inherent imperfections of rotational motion sensors used. The incorporation of these systems may increase in complexity and size. It can also degrade the performance of the control. For these reasons, the elimination of these sensors is essential [4].

II. MATHEMATICAL MODEL OF PMSM

The electrical equation of the PMSM in the rotor reference (d-q) frame is as follows:

$$\frac{d}{dt}\begin{bmatrix} i_d \\ i_q \end{bmatrix} = \begin{bmatrix} -\frac{R_s}{L_d} & \frac{\omega_r . L_q}{L_d} \\ -\frac{\omega_r . L_d}{L_q} & -\frac{R_s}{L_q} \end{bmatrix} \begin{bmatrix} i_d \\ i_q \end{bmatrix} + \begin{bmatrix} \frac{V_d}{L_d} \\ \frac{V_q - \omega_r . \varphi_f}{L_q} \end{bmatrix} \quad (1)$$

The general mechanics equation is given by:

$$J . \frac{d\Omega}{dt} + f.\Omega = C_e - C_r \quad (2)$$

The electromagnetic torque is given by the following expression:

$$C_e = \frac{3}{2} P \left[(L_d - L_q) i_d i_q + \varphi_f i_q \right] \quad (3)$$

Where:

V_d, V_q : Direct and quadrature voltages.
I_d, I_q : Direct and quadrature current.
R_s : stator resistances.
L_d, L_q : Direct and quadrature inductances.
C_e : electromagnetic torque.
Ω : mechanical rotation velocity.
p : number pairs of poles.
J : rotor inertia.
f : viscous friction coefficient.
φ_f : flux established by rotor permanent magnets.

III. DIRECT VECTOR CONTROL OF PMSM

Direct vector control of PMSM is based on a conventional method of compensation, it is to regulate two currents i_d and i_q neglecting the coupling terms, the latter being added to the output of the correction currents to obtain tensions of V_{dref} and V_{qref} order.

To ensure the decoupled structure, the f.e.m ($\mathbf{e_d}$, $\mathbf{e_q}$) of compensation are added to the output regulators, such as [5]:

$$\begin{cases} V_q = V'_q + e_q \\ V_d = V'_d + e_q \end{cases} \quad (4)$$

With:

$$\begin{cases} e_q = -\omega_r . L_d . I_d + \omega_r . P . \varphi_f \\ e_d = -\omega_r . L_q . I_q \end{cases} \quad (5)$$

For currents I_d and I_q, and speed the PI regulators are selected.

IV. Linearization of Input-Output of the PMSM

Linearization condition for checking whether a nonlinear system admits an input output linearization is relative degree of the system [6].

The degree relative with respect to the output $y_1(x)$ is:

$$\begin{aligned} \dot{y}_1(x) &= \dot{h}_1(x) = L_{fd} h_1(x) + L_g h_1(x) U \\ &= f_1 + g_1 V_d \end{aligned} \quad (6)$$

Or x is state vector, the functions f, g and h are analytic.

The relative degree is $r_1 = 1$ gives:

$$\dot{y}_2(x) = \dot{h}_2(x) = L_f h_2(x) + L_g h_2(x) U = f_3 \quad (7)$$

Or: $L_g h_2(x) = 0$

$$\dot{y}_2(x) = L_f h_2(x) = f_3$$

The derivative of the second output does not involve input U; you must derive a second time this output:

The derivative of $h_2(x)$ dregs on g is zero, the (7) can be written as:

$$\ddot{y}_2(x) = \ddot{h}_2(x) = L^2_f h_2(x) + L_f L_g h_2(x) . U$$

With:

$$L^2_f h_2(x) = f_1 p \frac{(L_d - L_q)}{j} x_2 + f_2 \left(p \frac{(L_d - L_q)}{j} x_1 + \frac{p \varphi_f}{j} \right) - f_3 \frac{f}{j}$$

$$L_f L_g h_2(x) = \left[\frac{1}{L_d} p \frac{(L_d - L_q)}{j} x_2 + \frac{1}{L_d} p \frac{(L_d - L_q)}{j} x_1 + \frac{p \varphi_f}{j} \right]$$

The relative degree relative to y_2 and $r_2 = 2$.

The relative degree of the system is $r = r_1 + r_2 = 3$.

The system is exactly linearizable $r = n = 3$, and n is the order of 1 system.

Finally, the input-output relationship model is given by:

$$\begin{bmatrix} \dot{y}_1(x) \\ \ddot{y}_2(x) \end{bmatrix} = \begin{bmatrix} \frac{d}{dt} I_d \\ \frac{d^2}{dt^2} \Omega \end{bmatrix} = A(x) + D(x) \begin{bmatrix} Vd \\ Vq \end{bmatrix} \quad (8)$$

Or:

$$A(x) = \begin{bmatrix} f_1 \\ f_1 \, p \frac{(L_d - L_q)}{j} x_2 + f_2 \left(p \frac{(L_d - L_q)}{j} x_1 + \frac{p \varphi_f}{j} \right) - f_3 \frac{f}{j} \end{bmatrix}$$

$$D(x) = \begin{bmatrix} g_1 & 0 \\ g_1 \, p \frac{(L_d - L_q)}{j} x_2 & g_2 \, p \frac{(L_d - L_q)}{j} x_1 + \frac{p \varphi_f}{j} \end{bmatrix}$$

If the determinant of the decoupling matrix is not zero, the control condition (NL) is defined by a relationship that connects the new internal inputs (V_1, V_2) to physical input (V_d, V_q).

$$\begin{bmatrix} V_d \\ V_q \end{bmatrix} = D^{-1}(x) \left[-A(x) + \begin{pmatrix} V_1 \\ V_2 \end{pmatrix} \right] \quad (9)$$

D: is the decoupling matrix.

By replacing the term (3) in (9), we obtain a linearized and decoupled system:

$$\begin{bmatrix} \dot{y}_1(x) \\ \ddot{y}_2(x) \end{bmatrix} = \begin{bmatrix} \frac{d}{dt} I_d \\ \frac{d^2}{dt^2} \Omega \end{bmatrix} = \begin{bmatrix} V_1 \\ V_2 \end{bmatrix} \quad (10)$$

V. Non-Linear Control for the PMSM

Linearization condition for checking whether a nonlinear system admits an input output linearization is one degree of the system. [6]

$$V_1 = K_{11} (I_{dref} - I_d) + \frac{d}{dt} I_{dref} \quad (11)$$

$$V_1 = K_{22} (\Omega_{dref} - \Omega_d) + K_{21} \left(\frac{d\Omega_{dref}}{dt} - \frac{d\Omega}{dt} \right) . \frac{d^2 \Omega_{dref}}{dt^2} \quad (12)$$

Closed loop tracking, error is:

$$\begin{cases} \frac{d}{dt} e_1 + K_{11} = 0 \\ \frac{d^2}{dt^2} e_2 + K_{21} \frac{d}{dt} e_2 + K_{22} e_2 = 0 \end{cases} \quad (13)$$

With:

$$\begin{cases} e_1 = I_{dref} - I_d \\ e_2 = \Omega_{ref} - \Omega_d \end{cases}$$

The coefficients k_{11}, k_{21}, k_{22} are chosen such that:

$$\begin{cases} P + k_{11} = 0 \\ P^2 + k_{21} P + k_{22} = 0 \end{cases}$$

VI. Extended Kalman Filter (EKF)

The EKF linearised the state and measurement equations about the predicted state as an operating point [7].

This filter is based on a number of assumptions, including noise. Indeed, it assumes that the noise affecting the model are centered and white and that they are uncorrelated estimated states, in addition, the state must be uncorrelated noise measurement noise.

A. Algorithm

Given the non-linear stochastic model follows:

$$\begin{cases} X(k+1) = f(X(k),u(k)) + w(k) \\ Y(k) = h(X(k)) + v(k) \end{cases} \quad (14)$$

With:

$w(k)$: State noise vector.

$v(k)$: Measurement noise vector.

This nonlinear system is brought back into a linear system and infers the set of equations of the EKF. The estimation procedure consists of two steps:

- *Step 1: Phase prediction*

• Estimate form of prediction:

$$x(k+1)/k = f(x(k/k),u(k)) \quad (15)$$

This step will build a first estimate of the state vector at time k + 1. It then seeks to determine its variance.

• Calculation of the prediction error covariance matrix:

$$P(k+1/k) = F(k)\,P(k)\,F(k)^T + Q \quad (16)$$

With:

$$F(k) = \left.\frac{\partial f\,x(k),u(k))}{\partial x^T(k)}\right|_{x(k)=x(k/k)}$$

- *Step 2: Correction phase*

In fact, the prediction phase allows a difference between the measured output y_{k+1} and the predicted output $y_{k+1/k}$. To improve the state, we must take account of this difference and correct it through the filter gain K_{k+1}. By minimizing the variance of the error, the following expressions are obtained:

- *Calcul of the Kalman gain*:

$$K(k+1) = P(k+1/k).H(k)^T\,(H(k).P(k+1/k).H(k)^T + R)^{-1}$$

With:

$$H(k) = \left.\frac{\partial h\,(x(k))}{\partial x(k)}\right|_{x(k)=x(k)}$$

- Calcul of the covariance matrix of the error of the filter:

$$P(k+1/k+1) = P(k+1/k) - K(k+1)\,H(k)\,P(k+1/k) \quad (17)$$

- Estimation of the state vector at time k +1:

$$\hat{x}(k+1/k+1) = \hat{x}(k+1/k) + K(k+1)(y(k+1) - H\hat{x}(k+1/k)) \quad (18)$$

Figure 1: shows the block diagram of EKF [7].

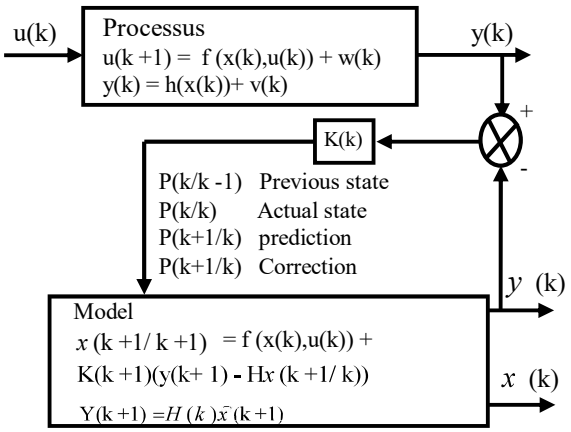


Figure 1: Principle of a Kalman Filter.

VII. Sensorless Control of PMSM Based on EKF

The choice of reference for the implementation of the EKF is essential. The ideal case would be to use the repository Park to the rotor.

In our case, we chose a model with reference to the rotor and the EKF is used to estimate the state vector x_k consists of (currents I_d and I_q, the shaft velocity Ω, values of angular position θ and the electromagnetic torque C_e). This non-linear model assumes that the mechanical speed is a state and not a setting. The model of the PMSM can be in the form:

$$\begin{cases} X(k) = f(X(k),u(k)).w(k) \\ Y(k) = h(X(k)).v(k) \end{cases} \quad (19)$$

With:

$$f(x(k),u(k)) = \left[I_d\ I_q\ \Omega\ \theta\ C_e \right] =$$

$$\begin{bmatrix} (1-T_s\frac{R_s}{L_d})I_d & p\Omega T_s\frac{L_q}{L_d}I_q & T_s\frac{1}{L_d}V_d & 0 & 0 \\ -p\Omega T_s\frac{L_d}{L_q}I_d & (1-T_s\frac{R_s}{L_q})I_d & T_s\frac{\varphi_f}{L_q}p\Omega & T_s\frac{1}{L_q}V_q & 0 \\ pT_s\frac{Ld-Lq}{J}I_dI_q & pT_s\frac{\varphi_f}{J}I_q & (1-T_s\frac{f}{J})\Omega & -T_s\frac{1}{J}C_r & 0 \\ 0 & 0 & \Omega & 0 & 0 \\ 0 & 0 & 0 & 0 & 0 \end{bmatrix}$$

And:

$$h = \left[I_d\ I_q \right]^T$$

*A. Determination of matrices **F** and **H***

The linearization matrices F and H allow us to linearize the system every minute of operation. They are given as follows:

$$F = \begin{bmatrix} 1-T_s\frac{R_s}{L_d} & p\Omega T_s\frac{L_q}{L_d} & T_s\frac{L_q}{L_d}I_q & 0 & 0 \\ -p\Omega T_s\frac{L_d}{L_q} & 1-T_s\frac{R_s}{L_q} & (-T_s\frac{\varphi_f}{L_q}+T_s\frac{L_d}{L_q}I_d) & 0 & 0 \\ pT_s\frac{L_d-L_q}{J}I_q & pT_s(\frac{L_d-L_q}{J}I_d+\frac{\varphi_f}{J}) & (1-T_s\frac{f}{J}) & 0 & -\frac{T_s}{J} \\ 0 & 0 & T_s & 1 & 0 \\ 0 & 0 & 0 & 0 & 1 \end{bmatrix}$$

And:

$$H(k)=\begin{bmatrix} 1 & 0 & 0 & 0 & 0 \\ 0 & 1 & 0 & 0 & 0 \end{bmatrix}$$

Figures 2-3 show the overall patterns of simulated vector control and the nonlinear control of PMSM, The resulting model is then estimated using the Extended Kalman Filter (EKF).

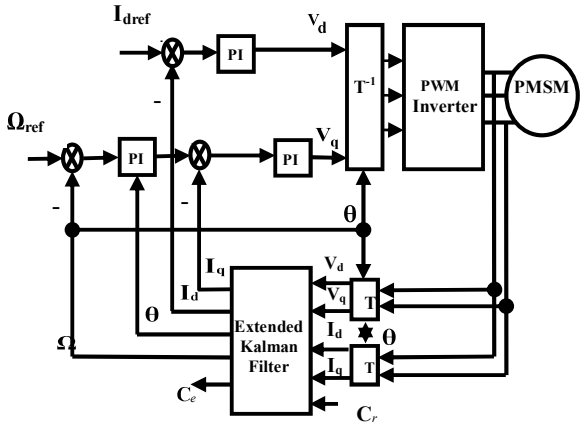


Figure 2: Sensorless direct vector control of the PMSM.

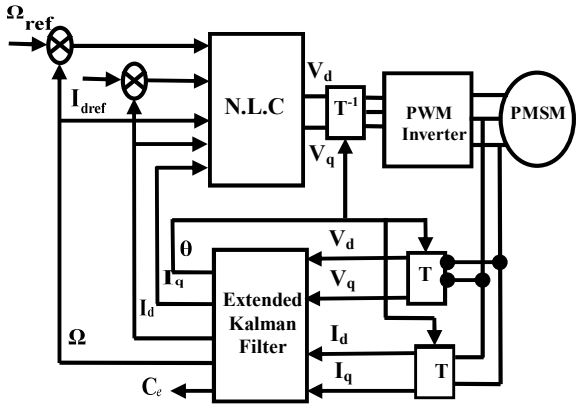


Figure 3: Sensorless nonlinear control of the PMSM.

*B. Selection of covariance matrices **Q** and **R***

It is via these matrices that pass different states measured, estimated or predicted. Their goal is to minimize errors associated with an approximate modeling and the presence of noise on the measurements. This setting requires special attention and only online control to validate the operation of the filter. However, some guidelines for understanding the influence of the adjustment of these values in relation to the dynamics and stability of the filter.

The Q matrix related to noise marring the state, sets the estimated quality of our model and its discretization. A high Q value provides a high value of gain K minimizing the importance of modeling and dynamics of the filter. The measure then has a greater relative weight. Too high a value of Q may also cause instability of the observer.

R rule matrix, in turn, measures the weight. A high value indicates an uncertainty of measurement. By cons, a low value can give significant weight to the measure. However, beware the risk of instability at low values of R.

VIII. Simulation Results

In order to understand cooperation of the EKF and the PMSM drive, a system is simulated for various tests for either vector control or the non-linear control speed.

Figure 4 shows the step response of mechanical speed, direct currents and stator and the electromagnetic torque of PMSM with a sensorless control using EKF. First, a test with no load at nominal speed setpoint 100 rad/s, is effected, then a load torque 5 N.m is applied at time t = 0.5 s. It's noted that

The non-linear control is more robust during load variation, for the vector control the speed reaches 98.496 rad /sec and 99.79 rad/sec for the non-linear control, the speed non-linear control faster than the vector control reaches the nominal value at time 0.04s, against FOC by 0.1s.

Regarding the electromagnetic torque follows much the load torque for both commands when load torque application , it's noted that the torque obtained by vector control reaches the value 7.87Nm, by the torque against the non-linear control has a max value of 5.1Nm, but the chattering is more important for vector control for both currents streams and quadratic.

The stator currents are close to the sine wave for the non-linear control. The harmonic distortion THD=2.04% for vector control and THD=0.67%, to control input-output linearization.

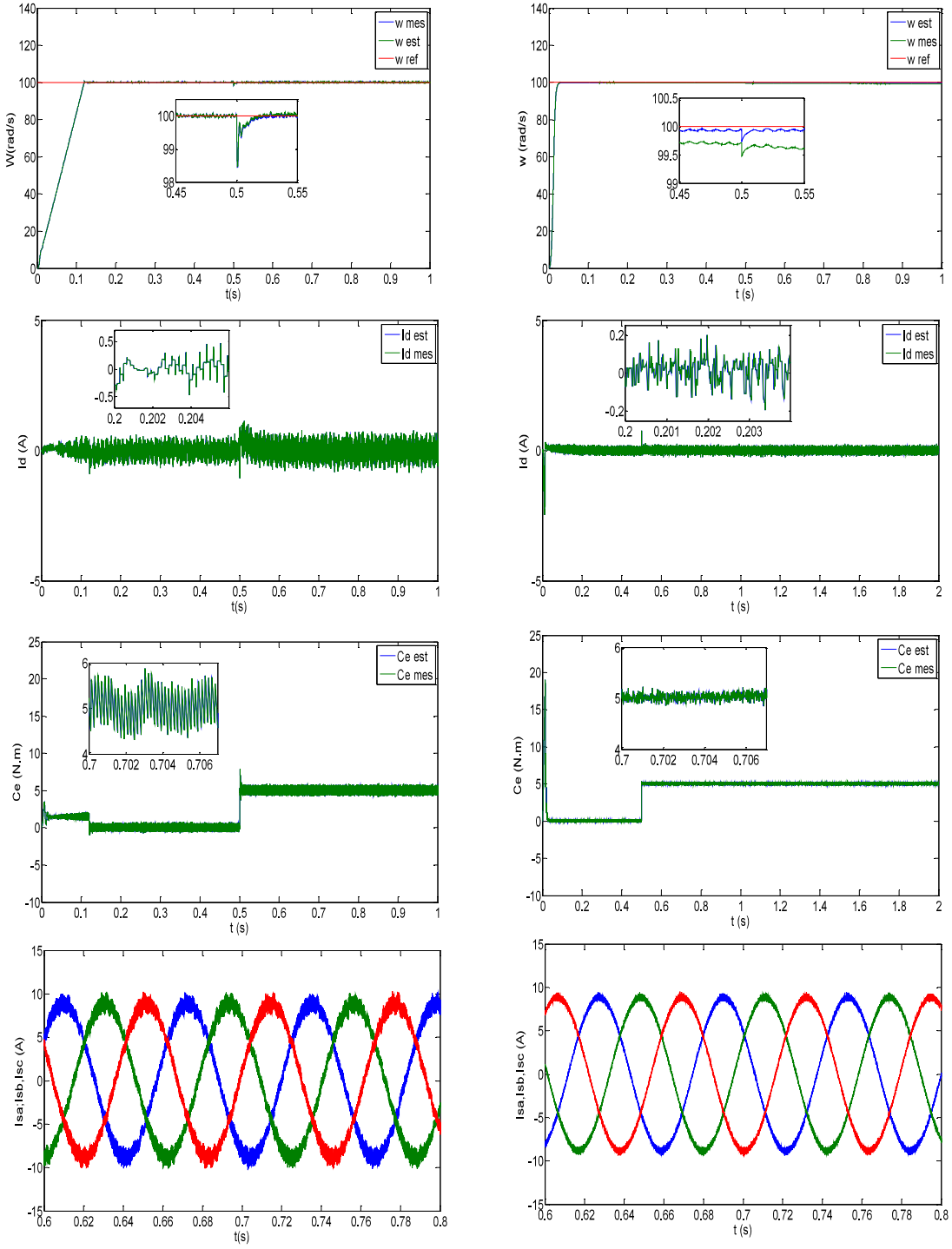


Figure 4: Simulation results of sensorless vector control and nonlinear control using EKF for PMSM.

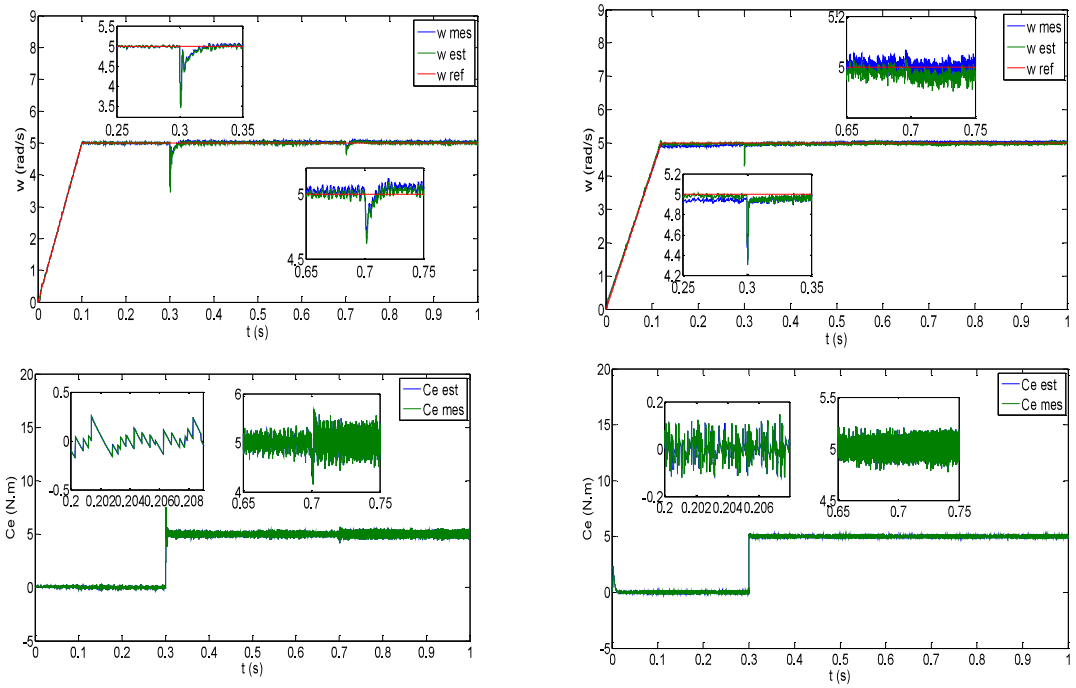


Figure 5: Simulation results of sensorless vector control and nonlinear control using EKF for PMSM at low speed and with stator resistance variation.

Figure 5 shows the robustness of the control for the stator resistance variation at time t= 0.7sec when the machine operate at low speed. For the vector control the speed and torque are affected by the variation in contrary for the input output control the variation not affect the speed and electromagnetic torque.

IX. Conclusion

In this paper, a comparative study of the sensorless vector control and nonlinear control for the permanent magnets synchronous machine PMSM is considered. The shaft velocity, currents I_d and I_q, values of angular position and the electromagnetic torque is then estimated using the EKF.

The results obtained show the effectiveness of the EKF for the stator resistance variation test as well as insensitivity to variations of the load.

The nonlinear control has the advantages namely robustness, high accuracy, stability and simplicity, very low response time, compared to the sensorless vector control using the EKF.

Appendix

$L_d = 5.8mH$, $L_q = 5.8$ mH, $\phi_f = 0.1546$ Wb, $R_s = 1.4\Omega$, p=3, J = 0.00176 kg.m2, f = 0.000388 N.m.s/rad.

References

[1] Hu Jian, Yang Qiu, Lu Hui, " robust nonlinear feedback control of chaos in PMSM system with modeling uncertainty", Applied Mathematical Modelling, 2016.

[2] Mark A. P., R. Vairamani, G.C.R. Irudayaraj, Mathematical modeling and analysis of different vector controlled CSI Fed 3 phase induction motor", J. Appl. Math., 623982-1-623982-13, 2014.

[3] Jinpeng Yu, Peng Shi, Dong Wenjie, "neural network-based adaptive dynamic area control for permanent magnet synchronous motors", IEEE Trans Neural Networks and is learning system, 2014.

[4] S. Yang and R. Lorenz, "Surface permanent-magnet machine self-sensing at zero and low speeds using improved observer for position, velocity, and disturbance torque estimation," IEEE Trans. Industry Applications, vol. 48, no. 1, pp. 151-160, Jan./Feb.2012.

[5] Y. Zhao, W. Qiao, and L. Wu, "An adaptive quasi sliding-mode rotor position observerbased sensorless control for interior permanent magnet synchronous machines," IEEE Trans. Power Electronics, vol. 28, no. 12, pp. 5618-5629, Dec. 2013.

[6] L. Harnefors and M. Hinkkanen, "Stabilization methods for sensorless induction motor drives - A survey," IEEE Journal of Emerging and Selected Topics in Power Electronics, vol. 2, no. 2, pp. 132-142, June 2014.

[7] Y. Shi, K. Sun, L. Huang, and Y. Li, "Online identification of permanent magnet flux based on extended kalman filter for IPMSM rive with position sensorless control," IEEE Trans. Industrial Electronics, vol.59,no.11pp.4169-4178,Nov.2012.

Development of Wearable Pedometer by Using 3-Axis Mems Accelerometer

Omar Muthana[1] and Ergun Erçelebi[1]

[1] University of Gaziantep, Gaziantep/Turkey, omar.m.khudhur@gmail.com
[1] University of Gaziantep, Gaziantep/Turkey, ercelebi@gantep.edu.tr

Abstract **- The digital pedometer is a wearable body device that calculates the number of steps by using the mean of the accelerometer motion detection, which is used to record the distance reached by the person and the calories burned by walking, running or jogging. This paper presents an algorithm that estimates a foot motion by detecting an arm motion. The movement of the arm has been detected by the accelerometer, its reading position and the dynamic change. This study illustrates the realization of a three-axis MEMS digital accelerometer ADXL345 in terms of a cost-benefit and an effective 8-bit low-power microchip microcontroller pic18F4550 analog device. Then, the algorithm calculates the steps taken by the operator and follows it by showing the total distance traveled by a person. The car HC-05 Bluetooth module allows a user activity tracking with a smartphone or a tablet communication pedometer.**

Keywords **– pedometer, accelerometer, adxl345, pic18f4550, MEMS sensor, I2C.**

I. INTRODUCTION

Lacking of physical activity has become an increasingly serious concern in today's society, specifically among children. For this deficiency stem , a variety of health issues and questions of how to prevent or eliminate these concerns. These issues range from obesity to osteoporosis. Activity monitors would be an integral part of any effort to learn more about these health issues. About Empirical information of physical activity would be better to be obtained through the use of an unobtrusive, but precise activity monitor. These devices should also be sufficiently versatile and adaptable so that they can be easily modified or expanded to address a variety of physical activity by extracting the physical desired measurements [1].

The digital pedometer is a type of an activity monitor device which is a portable device that counts each step a person taking by detecting the motion of the person's body through an accelerometer. The basic design of the pedometer is shown in Figure 1. It consists of a sensor feeding into an amplifier circuit that outputs a signal to the analog-to-digital converter in the microcontroller. Once the data is converted by the microcontroller, it can be processed and stored locally in the memory of the microcontroller or output to a remote location using a wireless transmission [2].

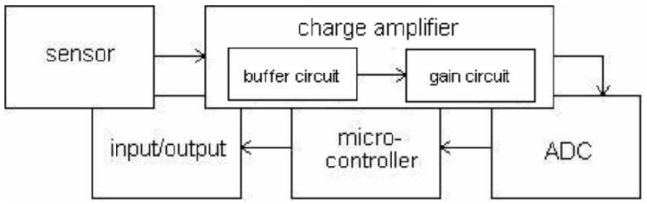


Figure 1: The basic design of the pedometer [2]

This paper will be studied in terms of how a modern technology can help professionals to enhance common and regular people upon how to maintain an acceptable level of physical activity. In the medical field, experts have accepted and acknowledged the importance of how the maintenance of health and weight loss can improve their health. The design of this device is popularly known as a pedometer that may help to encourage opportunistic activities.

II. PREVIOUS WORK

In the earlier production of a pedometer, the measurement staff was as steps of a separate wearing device, distance and speed. The monitor is only the device's internal LCD screen, so when the body walking or running, people can not know the steps, distance, or even the speed, Since the display, storage, and accelerator MEMS sensors are on the same board. Tsai et al (2004), proposed the "dynamometer" to monitor a physical activity that impacts on the emerging issue of childhood obesity. The dynamometer consists of a piezoelectric sensor that is embedded into a shoe insole and is connected to a microcontroller for data acquisition and analysis. The analysis of the signal results in information about the magnitude, frequency, and duration of a child's actions such as running and jumping. An amplifier circuit amplifies the signal produced by the sensor. '

Zhao (2010) [3], studies the characteristics of each step and a person takes or describes a reference designed by using the 3-axis ADXL345 accelerometer in a full-featured pedometer that can recognize and count steps, as well as measure distance, speed, and—to an extent—calories burned. The ADXL345's proprietary (patent pending), on-chip, 32-level first-in, first-out (FIFO) buffer can store data and operate on it

for pedometer applications to minimize a host processor intervention thus , saving system power is a big concern for portable devices. Its 13-bit resolution (4 mg/LSB) allows pedometers even to measure low-speed walking (where each step represents about 55 mg of acceleration change) with reasonable accuracy.

III. SYSTEM OVERVIEW

This simplified a digital pedometer demonstrating it by an 8-bit hardware core microcontroller with a PIC18F4550, 32 KB flash and 2048 KB data RAM and a 256 byte EEPROM, a 16-bit timer, and an 8-bit timer. A digital communication peripheral I2C from the adxl345 accelerometer and UART peripheral sampling data, the number of steps, speed and calorie data relay to the HC05 Bluetooth radio module. MCU core clock is 8MHZ internal frequency with no host clear configuration. The; 16x2 LCD independent pedometer step number displays the user interface application which will host and display the collected data on an Android phone with BT functionality [3]. Figure 2 illustrated the Digital pedometer block diagram.

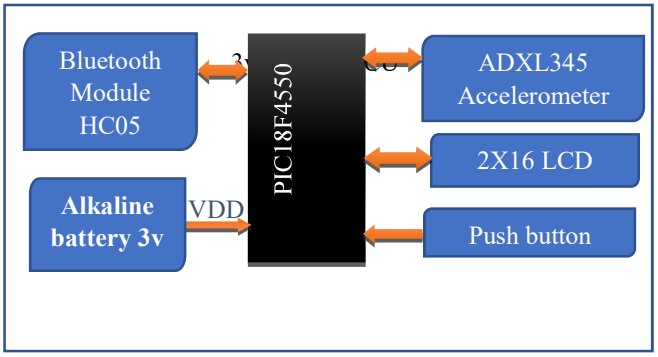


Figure 2: Digital pedometer block diagram.

The main Features of Wearable pedometer can be described in the following:

1. The LCD display is deployed to display the stand-alone pedometer.
2. User step count wears are easy to measure.
3. HC05 realizes the Bluetooth module and realizes the smartphone/tablet computer wear connection.
4. 2 megabits of EEROM storage.
5. A single layer printed circuit board PCB.
6. ICSP online serial programming.
7. Low power and accurate MEMS adxl345 acceleration sensor.
8. low-cost system.
9. Low power operation with low power PIC18F4550 MCUs.
10. Sleep Mode is activated when no motion is being detected, wakes up upon motion detection.
11. Low Power mode is activated for the ADXl345 accelerometer when no motion is being detected, wakes up upon motion detection.
12. Powered by a 3V lithium battery.
13. Lightweight as wearable.

IV. DESIGN & IMPLEMENTATION

The proposed pedometer needs to be designed in three main parts (Hardware, Interrupt on change button and software) that is illustrated in the following :

A. Hardware Design

8-Bit Low-Cost, Low-Power (Nano-W) Microchip Microcontrollers (PIC18F4550) act as a fundamental , principal platform for controlling the performance , structural, the functionality of the pedometer and operating it. (3-Axis) MEMS Accelerometer The ADXL345 is an ultra-low power, 3-axis accelerometer with up to ± 16 g) high-resolution (13-bit) measurements. The output data is digitally formatted as 16-bit twos complement, accessible via SPI (3 or 4 lines) or (I2C) digital interface, and the ADXL345 is ideal for wearable applications. The HC-(05) Bluetooth module is used as a radio wireless communication unit with a TTL serial protocol interface to send a step data from the pic18f4550 platform to a smartphone device. Figure (1) shows the overall hardware configuration.

B. The Interrupt on change button (IOC) (ON/OFF)

The quick function control is provided by the button of the pedometer via the Change Interrupt (IOC) interface. To turn the pedometer on / off, press and release quickly within a second. To reset the number of steps, press and hold the button for more than 3 seconds and releases it.

C. Software Design

The (CCS C) Compiler IDE is a C compiler for the development of embedded software for Microchip microcontrollers that supports standard (C ++) constructs of input/output streams to minimize development time. The pedometer software includes the ADXL345 driver (adxl345.h), the 2x16 LCD driver (LCD.h), and the main program (main.c), as illustrated in Figure 3.

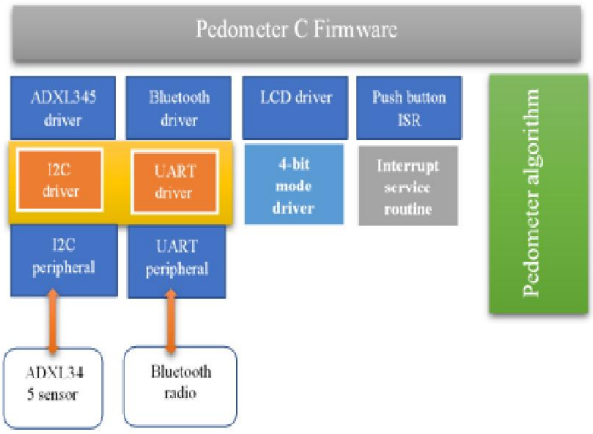


Figure 3: Software Design.

V. THEORY OF OPERATION

Our pedometer uses the Analog Devices (16-bit) triaxial digital accelerometer (ADXL345) to detect the user's motion. Every 20 ms, the sampling is generated by the accelerometer. (PIC18F4550) The pedometer firmware running in MC maintenance contains algorithms for step detection. When the start/stop button is pressed, the MCU wakes up from the low power mode and enables the accelerometer. The data in the pedometer algorithm is read by the MCU together with the read accelerometer. When the counting step is in progress, the updated step counter is sent to the radio module with the UART interface, the LCD is displayed, and the MEM button is saved in the EEPROM. Once the motion is detected, the pedometer algorithm is started, and the step counter is calculated after ten steps which have been detected. The algorithm tracks the motion and keeps the counting step until the motion stops and counts when the next ten steps are detected.The main firmware of the pedometer in the PIC18F4550 MCU has a step detection algorithm, which is often referred to as MCU motion detection. First, the MCU initializes the ADXL345 acceleration sensor. If the output data format is (16- bits), the output data rate is 50HZ, 25 milliseconds per a second (20 milliseconds) and the filter window size, when the ADXL345 data is read from the Y-axis, Push it to the (16-bit) register, the average of each reading when it is; (4) and then detecting the maximum and minimum values of the acceleration, the algorithm will now use this value as the next threshold reference, the two values (maximum and The minimum) are compared with the threshold then the algorithm determines when the step is detected. Step time from the average acceleration change very low method to zero which is the initial step time to the maximum or minimum acceleration change the value of the cycle which is the last step between the time interval to give us the step time, then in the (0.2-2 second). Figure 4 shows the pedometer algorithm procedure.

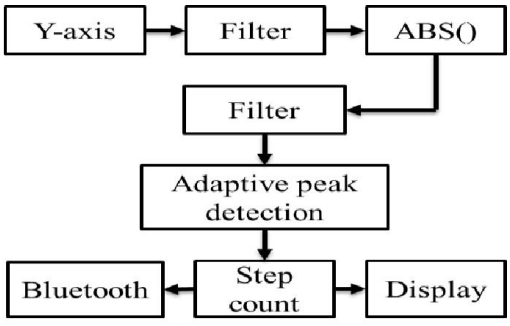


Figure 4: pedometer algorithm procedure.

The steps of the algorithm are pass throw following steps:

1) *Pedometer FIRMW Digital Filter:* First, a digital filter is needed to smooth the signals Four registers and a summing unit can be used, Of course, more registers could be used to make the acceleration data smoother, but the response time would be slower. Figure 5 shows the Digital Filter scheme.

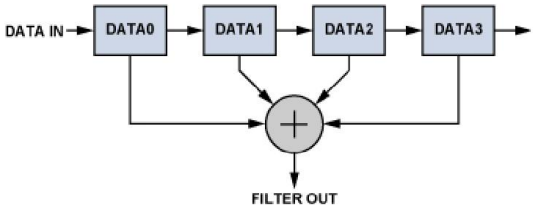


Figure 4: Digital filter.

2) Dynamic Threshold and Dynamic Precision: The system continuously updates the maximum and minimum values of the 3-axis acceleration each 50 samples. The average value, (Max + Min)/2, is called the dynamic threshold level. For the following 50 samples, this threshold level is used to determine which steps have been taken. As it is updated every 50 samples, the threshold is dynamic. This choice is adaptive and faster enough. In addition to a dynamic threshold, dynamic precision is also used for further filtering.

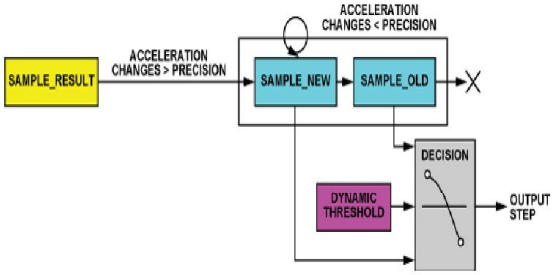


Figure 3: Dynamic threshold and dynamic precision.

A linear-shift-register and the dynamic threshold are used to determine whether an effective step has been taken. The linear-shift-register contains two registers, a sample_new register, and a sample_old register. The data in these are called *sample_new* and *sample_old*, respectively. When a new data sample comes, *sample_new* is shifted to the sample_old register unconditionally. However, whether the *sample_result* will be shifted into the sample_new register depends on a condition: If the changes in acceleration are greater than a predefined precision, the newest sample result, *sample_result*, is shifted to the sample_new register; otherwise, the sample_new register will remain unchanged. The shift register group can remove the high-frequency noise and make the decision more precise.A step is defined as happening if there is a negative slope of the acceleration plot (sample_new < sample_old) when the acceleration curve crosses below the dynamic threshold.

3) *Peak Detection:* The step counter calculates the steps from the x-axis, y-axis, or z-axis, depending on which axis's acceleration change is the largest one. If the

changes in acceleration are too small, the step counter will discard them.

The step counter can work well by using this algorithm, but sometimes it seems too sensitive. When the pedometer vibrates very rapidly or slowly from a another cause than walking or running, the step counter will also take it as a step. Such invalid vibrations must be discarded in order to find the true rhythmic steps. *Time window* and *count regulation* are used to solve this problem.

4) *Time window*: is used to discard the invalid vibrations. We assume that people can run as rapid as five steps per second and walk as slow as one step each two seconds. Thus, the interval between two valid steps is defined as being in the time window [0.2 s to 2.0 s]; all steps with intervals outside the time window should be discarded.

This algorithm uses a 50-Hz data rate (20 ms). A register named *interval* records of how many times the data have been updated during the two steps. If the value of interval is between 10 and 100, it means that the time between two steps is in the valid window; otherwise, the interval is outside the time window and the step is invalid.

5) *Count regulation* determines whether steps are part of a rhythmic pattern. The step counter has two working states: searching regulation and founding out regulation. When the step counter starts working, it starts working in searching regulation mode. Suppose that *in regulation* exists after four continuous valid steps ,then the result is refreshed and displayed,the step counter will work in founding out the regulation mode. Working in this mode, the step count will be refreshed after each valid step. But if even one invalid step is found, the step counter will return for searching the regulation mode and searching for four continuous valid steps.

VI. FUNCTIONS AND SUBROUTINE

- lcd_init () This function and subroutine initialize the 2x16 LCD display, which should be called first.
- Enable_sample () This function returns the Y-axis acceleration sensor data samples.
- Enable_step_detect () This function is the detection step and the number of updates.
- Pedo_bluetooth () This function pushes the number of steps, speed, distance to the Bluetooth module port.
- ADXl345_init () This function and subroutine initialize the ADXL345 acceleration sensor, which should be called before the step calculation.
- ISR_RB () This function and subroutine execute the statement when the interrupt is changed.

VII. RESULT

As illustrated in Figure 4, the pedometer board with 13-bit MEMS acceleration sensors ADXL345 and HC-05. Bluetooth modules and (2x16) liquid crystal displays, it also shows us the final results of the speed, distance, steps, and calories. As shown and the similarity of the values found in the application and LCD.

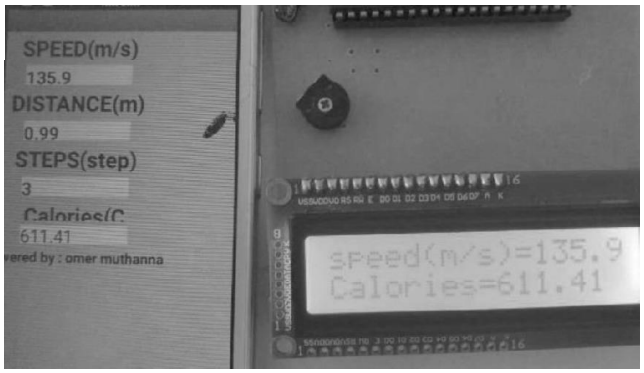


Figure 4: The final result displayed on the LCD and application.

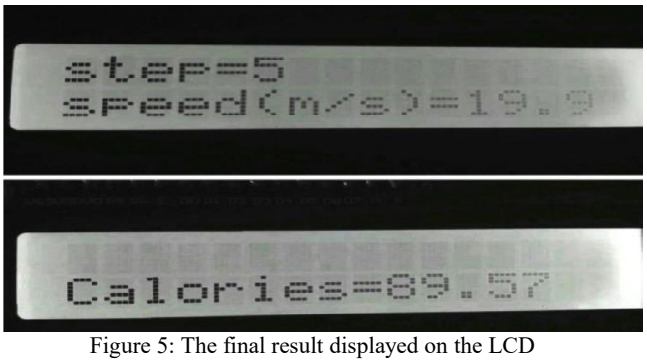


Figure 5: The final result displayed on the LCD

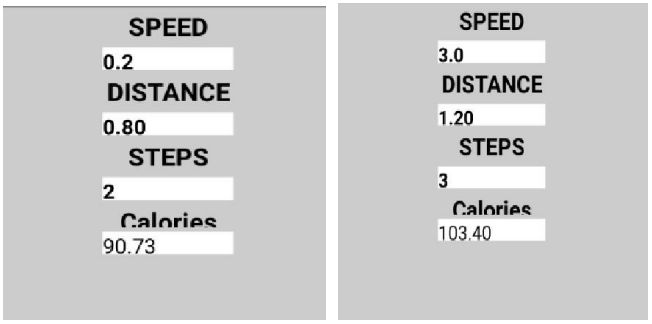


Figure 6: The final result displayed on the LCD and application.

The system has been tested in terms of distance parameter, Speed Parameter, and Calories Parameter, and the experimental results that got are in the following:

A. Distance Parameter

After computing the steps parameter according to the algorithm above, we can use Equation 1 to get the distance parameter.

$$Distance = number\ of\ steps \times distance\ per\ step \quad (1)$$

Distance per step depends on the speed and the height of the user. The step length will be longer if the user is taller or running at higher speed. The reference design updates the distance, speed, and calories parameter every two seconds. So, we use the steps counted in every two seconds to judge the current stride length.

B. Speed Parameter

Speed = *distance/time*, so Equation 2 can be used to get the speed of parameter, as steps per 2 s and stride have been calculated according to the algorithm above.

Speed = *steps per 2* s × *stride/2* s (2)

C. Calories Parameter

There are no accurate means for calculating the rate of expending calories. Some factors that determine it, including body weight, the intensity of the workout, conditioning level, and metabolism. We can estimate it by using a conventional approximation, however. Table 1 shows a typical relationship between calorie expenditure and running speed.

Table 1: Calories Expended vs. Running Speed

Running Speed (km/h)	Calories Expended (C/kg/h)
8	10
12	15
16	20
20	25

Calories (C/kg/h) = 1.25 × *running speed* (km/h) (3)

The unit of the speed parameter used above is m/s; converting km/h to m/s gives Equation 4.

Calories (C/kg/h) = 1.25 × *speed* (m/s) × 3600/1000 = 4.5 × *speed* (m/s) (4)

The calories parameter would be updated every 2 s with the distance and speed parameters. So, to account for a given athlete's weight, we can convert Equation 4 to Equation 5 as indicated. Weight (kg) is a user input, and one hour is equal to 1800 2-second intervals.

Calories (C/2 s) 4.5 × *speed* × *weight*/1800 = *speed* × *weight*/400 (5)

If the user takes a break in place after walking or running, there would be no change in steps and distance and the speed should be zero, then the calories expended can use Equation 6 since the caloric expenditure is around 1 C/kg/hour while resting.

Calories (C/2 s) = 1 × *weight*/1800 (6)

Finally, we can add calories for all 2-second intervals together to get the total calories expended.

VIII. CONCLUSION

In this paper, the 8-bit midrange (18F) series microcontrollers (PIC18F4550) were used to implement a precision, low-cost, low-cost pedometer with 8MHZ internal oscillator speed and low power, high-precision MEMS acceleration sensor. The (ADXL345) uses the HC-05 Bluetooth radio monitor the steps, speed, and distance of the smartphone. The main application of the system in the field of fitness.

REFERENCES

[1] Feng Z. 2015. Bluetooth® Low Energy Digital Pedometer Demo Design, Microchip Technology Inc., AN1906, pp.1-8.

[2] Tsai O. 2004. Dynamometer the New Activity Monitor. UNFEST Technical Report TR-CST01NOV04, Center for Sensor Technologies, Univ. of Pennsylvania, Philadelphia, pp.199-221.

[3] Zhao N. 2010. Full-Featured Pedometer Design Realized with 3-Axis Digital Accelerometer.

[4] Ayabe M., Junichiro A., Ishii K., Kohsaku T. and Tanaka H. 2008. Pedometer Accuracy During Stair Climbing and Bench Stepping Exercises. Journal of Sports Science & Medicine (J Sports Sci Me).

MRAS speed observer for sensorless adaptive intelligent backstepping controller of induction machines

S. Issaouni[1], A. Boulkroune[2] and H. Chekireb[3]

[1]LIMPAF, University of Bouira , Bouira/Algeria, autosalim@gmail.com
[2]LAJ, University of Jijel, Jijel/Algeria, boulkroune2002@yahoo.fr
[3]LCP, National Polytechnic School, Alger/Algeria, chekireb@yahoo.fr

***Abstract* - In this paper, a sensorless adaptive neuro-fuzzy backstepping control scheme is developed for induction machines with unknown model, uncertain load-torque and nonlinear friction where the speed is obtained using the Model Reference Adaptive System (MRAS). Neuro-fuzzy systems are used to online approximate the uncertain nonlinearities and an adaptive backstepping technique is employed to systematically construct the control law.**

The MRAS observer is based on two different models, one that is speed independent (reference model) and another that is speed dependent (adjustable model). The speed is estimated via the outputs of the two models.

The proposed sensorless controller guarantees the tracking errors converge to a small neighborhood of the origin and the boundedness of all closed-loop signals what demonstrate the effectiveness of the proposed approach.

***Keywords* - Induction motors; backstepping control; fuzzy adaptive control. MRAS observer, speed estimation, sensorless control.**

I. INTRODUCTION

Because the Induction machines is simple in operation, rugged and generally less expensive than either DC and synchronous motors, they are widely used in industry especially in variable speed applications.

On the other hand, the control of induction motors is a difficult task. The system is non-linear, coupled and multivariable having two control inputs (stator voltages) and two output variables (rotor speed and flux modulus), that are required to track the desired reference trajectories.

Some advanced control methods have been also used to the problems of speed and position control, such as sliding mode control [1,2], feedback linearization control [3,4], adaptive backstepping control [5,6], and neural adaptive control [7], ect. However, these control approaches have some drawbacks, namely: (1) the friction model is assumed to be linear. (2) The unmatched uncertainties have not been considered.

Adaptive fuzzy controllers for inductions motors (IM) have been developed in [8-13]. Fuzzy logic systems are used to approximate unknown nonlinearities and provide human reasoning capabilities to capture uncertainties. It has been proven that fuzzy logic can approximate any nonlinear function to any desired accuracy because of the universal approximation theorem. However, conventional fuzzy controllers (i.e. the non-adaptive fuzzy controllers) cannot adapt themselves to changes in their environment or in operating conditions. Then, it is necessary to add some form of adaptation that allows updating the controller parameters in order to maintain and improve the control performance in wide range of changing conditions.

The backstepping concept is a newly developed technique to control the nonlinear systems with a triangular structure and parameter uncertainty. In the literature, many control schemes combine the backstepping technique with adaptive neural networks or fuzzy logic systems, e.g. [7, 14]. These adaptive backstepping schemes offer a choice of design tools to accommodate uncertainties and nonlinearities.

In a sensorless induction-machine drive, the speed can be estimated by various techniques [15]. The extended Kalman filter method and the Luenberger observer construct full-order estimators based on the machine model. Sliding mode (SM) observers have been reported for the estimation of the variables of interest of the induction machine. Another viable solution for speed estimation is the model reference adaptive system (MRAS) method [15].

In this paper, first the adaptive fuzzy backstepping control for induction machines is developed, later the MRAS speed-estimation methods that are based on the adjustable model is proposed.

MRAS observers based on rotor flux, back emf and reactive power are some of the MRAS observers that have been introduced in literature [16-19].

In MRAS, some state variables with or without physical meaning are estimated in a reference model and are then compared with the estimated values coming from an adaptive model. The difference between them is then used in an adaption mechanism, which outputs the estimated value of the rotor speed and adjust the adaptive model until satisfactory performance is obtained [20].

This controller guarantees a flux regulation and an accurate speed tracking in the presence of both structured and unstructured uncertainties. Compared with the existing control

methods [8-13], the main contributions of this paper are:

- Unlike [8-13], the frictions are assumed to be modeled by a nonlinear unknown unified model. Adopting such a model can provide a more accurate representation of the induction motor dynamics, but it brings hard nonlinearities to the system model.
- The resulting controller is not only robust to structured uncertainties (stator resistance, rotor resistance, etc) and external disturbances (load torque), but also the system robustness can be achieved against the unstructured uncertainties (as unmodeled dynamics, nonlinear frictions,...).
- The controller design does not strongly depend on the model of induction motors.
- Unlike [8-10], the stability analysis and control design are rigorously derived with mild assumptions.
- The development of sensorless control of induction machines with MRAS speed observer.

Table 1: Nomenclature

R_s	Stator resistance	ω_e	Electric pulsation
R_r	Rotor resistance	ω	Angular mechanic velocity
L_s	Stator inductance	φ_{rd}	Rotor flux along d-axis
L_r	Rotor inductance	φ_{rq}	Rotor flux along q-axis
L_m	Mutual inductance	φ_r	Total rotor flux
p	Number of pole pairs	i_{sd}	Stator current along d-axis
J	Inertia	i_{sq}	Stator current along q-axis
T_l	Load torque	v_{sd}	Stator voltage along d-axis
σ	Blondel coefficient	v_{sq}	Stator voltage along q-axis
T_r	Rotor time constant	τ_F	Friction torque

II. MACHINE MODELING

In this section, the nonlinear dynamical model of an induction motor will be present. For the convenience of referencing, the meaning of the variables, parameters and coefficients is listed in Table.1 (in the Nomenclature).

The induction motor model is a highly nonlinear but under the assumptions of equal mutual inductance and a linear magnetic circuit and via the field oriented transformation, the equations for the dynamics of motor in the arbitrary rotating reference (d-q) frame are given by [3]:

$$\begin{cases} \frac{d\omega}{dt} = \frac{pL_m}{JL_r}\varphi_r i_{sq} - \frac{\tau_F}{J} - \frac{T_l}{J} \\ \frac{d\varphi_r}{dt} = \frac{L_m}{T_r} i_{sd} - \frac{1}{T_r}\varphi_r \\ \frac{di_{sq}}{dt} = -\left(\frac{R_s}{\sigma L_s} + \frac{1-\sigma}{\sigma T_r}\right) i_{sq} - \omega_e i_{sd} - \frac{pL_m\omega}{\sigma L_s L_r}\varphi_r + \frac{1}{\sigma L_s} v_{sq} \\ \frac{di_{sd}}{dt} = -\left(\frac{R_s}{\sigma L_s} + \frac{1-\sigma}{\sigma T_r}\right) i_{sd} + \omega_e i_{sq} + \frac{L_m}{\sigma L_s L_r T_r}\varphi_r + \frac{1}{\sigma L_s} v_{sd} \end{cases} \quad (1)$$

where $\sigma = 1 - \frac{L_m^2}{L_s L_r}$; $T_r = \frac{L_r}{R_r}$; $\omega_e = \omega_d + p\omega$; $\omega_d = \frac{L_m}{T_r \varphi_r} i_{sq}$

The friction term τ_F have the following nonlinear parameterizable and continuous form [21]:

$$\tau_F = F_c tanh\left(\frac{\omega}{\varepsilon}\right) + F_v\omega + F_s tanh\left(\frac{\omega}{\varepsilon}\right) e^{-\left(\omega/\eta_s\right)^2} \quad (2)$$

where F_c, F_v et F_s are the Coulomb, viscous and static friction positive coefficient respectively, and $e^{-\left(\omega/\eta_s\right)^2}$ is the rate of decay of the static friction. ε is a small positive constant.

The model of the induction motor with external disturbances can be written as follows:

$$\begin{cases} \dot{x_1} = f_1(x_1) + b_1(x_1)x_2 + d_1(x_1, x_2, t) \\ \dot{x_2} = f_2(x_1, x_2) + b_2(x_1, x_2)u + d_2(x_1, x_2, u, t) \\ y = x_1 \end{cases} \quad (3)$$

with

$$f_1(x_1) = \begin{bmatrix} -\frac{\tau_F}{J} \\ -\frac{1}{T_r}\varphi_r \end{bmatrix}, \; b_1(x_1) = \begin{bmatrix} \frac{pL_m}{JL_r}\varphi_r & 0 \\ 0 & \frac{L_m}{T_r} \end{bmatrix},$$

$$d_1(x_1, x_2, t) = \begin{bmatrix} -\frac{T_l}{J} + d_{11}(x_1, x_2, t) \\ d_{12}(x_1, x_2, t) \end{bmatrix},$$

$$f_2(x_1, x_2) = \begin{bmatrix} -\left(\frac{R_s}{\sigma L_s} + \frac{1-\sigma}{\sigma T_r}\right) i_{sq} - \omega_e i_{sd} - \frac{pL_m\omega}{\sigma L_s L_r}\varphi_r \\ -\left(\frac{R_s}{\sigma L_s} + \frac{1-\sigma}{\sigma T_r}\right) i_{sd} + \omega_e i_{sq} + \frac{L_m}{\sigma L_s L_r T_r}\varphi_r \end{bmatrix},$$

$$b_2(x_1, x_2) = \begin{bmatrix} \frac{1}{\sigma L_s} & 0 \\ 0 & \frac{1}{\sigma L_s} \end{bmatrix} \text{ and } d_2(x_1, x_2, u, t) = \begin{bmatrix} d_{21}(x_1, x_2, u, t) \\ d_{22}(x_1, x_2, u, t) \end{bmatrix}.$$

where $u = [v_{sq} \quad v_{sd}]^T$ is the control input of the system, $y = x_1 = [\omega \quad \varphi_r]^T$ is the controlled output, $x_2 = [i_{sq} \quad i_{sd}]^T$ is the vector of the stator currents, $x = [\omega \quad \varphi_r \; i_{sq} \; i_{sd}]^T$ represents the state vector. $f_i(.)$ and $b_i(.)$ are unknown smooth nonlinear functions, $d_i(.)$ is the term of unknown disturbances due to the parametric variations, non-modeled dynamics and external disturbances.

To facilitate the controller design, the state model (3) is rewritten in the following equivalent form:

$$\begin{cases} \dot{x_1} = f_1(x_1) + g_1 x_2 + \delta_1(x_1, x_2, t) \\ \dot{x_2} = f_2(x_1, x_2) + g_2 u + \delta_2(x_1, x_2, u, t) \\ y = x_1 \end{cases} \quad (4)$$

where $g_1 = \begin{bmatrix} \frac{pL_m}{JL_r} & 0 \\ 0 & \frac{L_m}{T_r} \end{bmatrix}$, $g_2 = b_2(x_1, x_2)$,

$\delta_1(x_1, x_2, t) = d_1(x_1, x_2, t) + (b_1(x_1) - g_1)x_2$,

and $\delta_2(x_1, x_2, u, t) = d_2(x_1, x_2, u, t)$.

Note that g_1 and g_2 are unknown, constant and diagonal positive define matrices. Thereafter, for a better understanding. The following notations will be used throughout this paper: $f_1 = f_1(x_1)$; $f_2 = f_2(x_1, x_2)$; $\delta_1 = \delta_1(x_1, x_2, t)$; and $\delta_2 = \delta_2(x_1, x_2, u, t)$.

The following realistic assumptions are made:

Assumption 1. *The reference speed profile* ω_{ref} *and* the flux reference φ_{ref} are bounded and derivable.

Assumption 2. *All motor parameters are assumed to be unknown.*

Assumption 3. *The load torque T_l is unknown but bounded.*

Assumption 4. *The nonlinear functions f_i and δ_i involved in the state-space model (4) are continuous and unknown.*

III. DESIGN OF FUZZY ADAPTIVE CONTROLLER

The design of the fuzzy adaptive control by backstepping is developed in [22].

The design can be proceed in two stages.

Step 1: Noting by $y_{ref} = [\omega_{ref} \quad \varphi_{ref}]^T$ the reference signal. In this case, the tracking error is given by:

$$e_1 = y_{ref} - y \tag{5}$$

The virtual control α can be constructed as

$$\alpha = \xi_1^T(x_1)\theta_1 + C_1 e_1 + v_{r1} \tag{6}$$

where $C_1 = Diag[c_{11}, c_{12}]$ is a positive-define design matrix, $v_{r1} = [v_{r11}, v_{r12}]^T$ is a robust dynamic control term that will be designed later, and θ_1 is the estimate of the unknown constant θ_1^*.

Define a new state variable α_d. Let α pass through a first-order filter with a time constant ϵ to obtain α_d as:

$$\epsilon\dot{\alpha}_d + \alpha_d = \alpha, \quad \text{where } \alpha_d(0) = \alpha(0) \tag{7}$$

By defining $e_2 = \alpha_d - x_2$;

$$g_1^{-1}\dot{e}_1 = -\xi_1^T(x_1)\tilde{\theta}_1 + e_2 - C_1 e_1 - v_{r1} + \Delta\alpha + \varepsilon_1(x_1) - g_1^{-1}\delta_1 \tag{8}$$

where $\tilde{\theta}_1 = \theta_1 - \theta_1^*$, and $\Delta\alpha = \alpha - \alpha_d$.

Assumption 5: *assuming that:*

$$|\Delta\alpha + \varepsilon_1(x_1) - g_1^{-1}\delta_1| \le (1 + \|x_1\| + \|\Delta\alpha\|)\kappa_1^* \tag{9}$$

where $\kappa_1^* = [\kappa_{11}^*, \kappa_{12}^*]^T$ is an unknown constant vector.

The associated adaptive laws can be designed as

$$\dot{\theta}_1 = -\gamma_{\theta 1}\sigma_{\theta 1}\theta_1 + \gamma_{\theta 1}\xi_1(x_1)e_1 \tag{10}$$

$$\dot{v}_{r1} = -\gamma_{r1}v_{r1} + \gamma_{r1}\left[e_1 - \frac{Sign(v_{r1})}{v_{r1}^T Sign(v_{r1}) + \delta_1^2}(1 + \|x_1\| + \|\Delta\alpha\|)\kappa_1^* |e_1|\right] \tag{11}$$

$$\dot{\delta}_1 = -\gamma_{\delta 1}\sigma_{\delta 1}\delta_1 - \gamma_{\delta 1}\frac{\delta_1}{v_{r1}^T Sign(v_{r1}) + \delta_1^2}(1 + \|x_1\| + \|\Delta\alpha\|)\kappa_1^* |e_1| \tag{12}$$

$$\dot{\kappa}_1 = -\gamma_{\kappa 1}\sigma_{\kappa 1}\kappa_1 - \gamma_{\kappa 1}(1 + \|x_1\| + \|\Delta\alpha\|)|e_1| \tag{13}$$

where $\gamma_{\theta 1}, \gamma_{r1}, \gamma_{\kappa 1}$ and $\gamma_{\delta 1}$ are strictly positive design constants, and $\sigma_{\theta 1}$, $\sigma_{\kappa 1}$ and $\sigma_{\delta 1}$ are small positive design constants.

Consider the Lyapunov candidate function as follows:

$$V_1 = \frac{1}{2}e_1^T g_1^{-1} e_1 + \frac{1}{2\gamma_{\theta 1}}\tilde{\theta}_1^T\tilde{\theta}_1 + \frac{1}{2\gamma_{\kappa 1}}\tilde{\kappa}_1^T\tilde{\kappa}_1 + \frac{1}{2\gamma_{\delta 1}}\delta_1^2 + \frac{1}{2\gamma_{r1}}v_{r1}^T v_{r1} \tag{14}$$

Its time derivative is

$$\dot{V}_1 = e_1^T g_1^{-1}\dot{e}_1 + \frac{1}{\gamma_{\theta 1}}\tilde{\theta}_1^T\dot{\theta}_1 + \frac{1}{\gamma_{\kappa 1}}\tilde{\kappa}_1^T\dot{\kappa}_1 + \frac{1}{\gamma_{\delta 1}}\delta_1\,\dot{\delta}_1 + \frac{1}{\gamma_{r1}}v_{r1}^T\dot{v}_{r1} \tag{15}$$

By considering (10)–(13), $\dot{V}_1$ can be bounded as

$$\dot{V}_1 \le -e_1^T C_1 e_1 + e_1^T e_2 - \sigma_{\theta 1}\tilde{\theta}_1^T\theta_1 - \sigma_{\kappa 1}\tilde{\kappa}_1^T\kappa_1 - \sigma_{\delta 1}\delta_1^2 - v_{r1}^T v_{r1} \tag{16}$$

In the next step, the tracking error e_2 will be stabilized.

Step 2: At this step, we will construct the control law *u*. The dynamics of e_2 are given by

$$\dot{e}_2 = \dot{\alpha}_d - \dot{x}_2 = \dot{\alpha}_d - f_2 - g_2 u - \delta_2 \tag{17}$$

To stabilize the dynamics (17), the following fuzzy adaptive controller is proposed

$$u = \xi_2^T(x)\theta_2 + C_2 e_2 + v_{r2} \tag{18}$$

where $C_2 = Diag[c_{21}, c_{22}]$ is a positive-define design matrix, $v_{r2} = [v_{r21}, v_{r22}]^T$ is a robust dynamic control term that will be designed later, and θ_2 is the estimate of the unknown constant θ_2^*.

Using (18), we can have:

$$g_2^{-1}\dot{e}_2 = -e_1 - \xi_2^T(x)\tilde{\theta}_2 - C_2 e_2 - v_{r2} + \varepsilon_2(x) - g_2^{-1}\delta_2 \tag{19}$$

where $\tilde{\theta}_2 = \theta_2 - \theta_2^*$.

Assumption 6: *assuming that:*

$$|\varepsilon_2(x) - g_2^{-1}\delta_2| \le (1 + \|x\| + \|u\|)\kappa_2^* \tag{20}$$

where $\kappa_2^* = [\kappa_{21}^*, \kappa_{22}^*]^T$ is an unknown constant vector.

The associated adaptive laws can be designed as

$$\dot{\theta}_2 = -\gamma_{\theta 2}\sigma_{\theta 2}\theta_2 + \gamma_{\theta 2}\xi_2(x)e_2 \tag{21}$$

$$\dot{v}_{r2} = -\gamma_{r2}v_{r2} + \gamma_{r2}\left[e_2 - \frac{Sign(v_{r2})}{v_{r2}^T Sign(v_{r2}) + \delta_2^2}(1 + \|x\| + \|u\|)\kappa_2^* |e_2|\right] \tag{22}$$

$$\dot{\delta}_2 = -\gamma_{\delta 2}\sigma_{\delta 2}\delta_2 - \gamma_{\delta 2}\frac{\delta_2}{v_{r2}^T Sign(v_{r2}) + \delta_2^2}(1 + \|x\| + \|u\|)\kappa_2^* |e_2| \tag{23}$$

$$\dot{\kappa}_2 = -\gamma_{\kappa 2}\sigma_{\kappa 2}\kappa_2 - \gamma_{\kappa 2}(1 + \|x\| + \|u\|)|e_2| \tag{24}$$

where $\gamma_{\theta 2}, \gamma_{r2}, \gamma_{\kappa 2}$ and $\gamma_{\delta 2}$ are strictly positive design constants and $\sigma_{\theta 2}$, $\sigma_{\kappa 2}$ and $\sigma_{\delta 2}$ are small positive design constants.

Define the Lyapunov function candidate as follows:

$$V_2 = V_1 + \frac{1}{2}e_2^T g_2^{-1} e_2 + \frac{1}{2\gamma_{\theta 2}}\tilde{\theta}_2^T\tilde{\theta}_2 + \frac{1}{2\gamma_{\kappa 2}}\tilde{\kappa}_2^T\tilde{\kappa}_2 + \frac{1}{2\gamma_{\delta 2}}\delta_2^2 + \frac{1}{2\gamma_{r2}}v_{r2}^T v_{r2} \tag{25}$$

Its time derivative is

$$\dot{V}_2 = \dot{V}_1 + e_2^T g_2^{-1}\dot{e}_2 + \frac{1}{\gamma_{\theta 2}}\tilde{\theta}_2^T\dot{\theta}_2 + \frac{1}{\gamma_{\kappa 2}}\tilde{\kappa}_2^T\dot{\kappa}_2 + \frac{1}{\gamma_{\delta 2}}\delta_2\,\dot{\delta}_2 + \frac{1}{\gamma_{r2}}v_{r2}^T\dot{v}_{r2} \tag{26}$$

By considering (21)–(24), $\dot{V}_2$ can be bounded as

$$\begin{aligned}\dot{V}_2 \le\ & -e_2^T C_2 e_2 - e_1^T C_1 e_1 - \sigma_{\theta 1}\tilde{\theta}_1^T\theta_1 - \sigma_{\kappa 1}\tilde{\kappa}_1^T\kappa_1 \\ & -\sigma_{\delta 1}\delta_1^2 - v_{r1}^T v_{r1} - \sigma_{\theta 2}\tilde{\theta}_2^T\theta_2 - \sigma_{\kappa 2}\tilde{\kappa}_2^T\kappa_2 \\ & -\sigma_{\delta 2}\delta_2^2 - v_{r2}^T v_{r2}\end{aligned} \tag{27}$$

Show that:

$$\begin{aligned} -\sigma_{\theta i}\tilde{\theta}_i^T\theta_i &\le -\frac{\sigma_{\theta i}}{2}\left\|\tilde{\theta}_i\right\|^2 + \frac{\sigma_{\theta i}}{2}\|\theta_i^*\|^2 \\ -\sigma_{\kappa i}\tilde{\kappa}_i^T\kappa_i &\le -\frac{\sigma_{\kappa i}}{2}\|\tilde{\kappa}_i\|^2 + \frac{\sigma_{\kappa i}}{2}\|\kappa_i^*\|^2 \end{aligned} \quad (28)$$

Using (28), $\dot{V}_2$ becomes:

$$\begin{aligned} \dot{V}_2 \le & -c_{1m}\|e_1\|^2 - c_{2m}\|e_2\|^2 - \frac{\sigma_{\theta 1}}{2}\left\|\tilde{\theta}_1\right\|^2 - \frac{\sigma_{\theta 2}}{2}\left\|\tilde{\theta}_2\right\|^2 \\ & - \frac{\sigma_{\kappa 1}}{2}\|\tilde{\kappa}_1\|^2 - \frac{\sigma_{\kappa 2}}{2}\|\tilde{\kappa}_2\|^2 - \sigma_{\delta 1}\delta_1^2 - v_{r1}^T v_{r1} - \sigma_{\delta 2}\delta_2^2 \\ & - v_{r2}^T v_{r2} + \pi \end{aligned} \quad (29)$$

where $\pi = \frac{\sigma_{\theta 1}}{2}\|\theta_1^*\|^2 + \frac{\sigma_{\theta 2}}{2}\|\theta_2^*\|^2 + \frac{\sigma_{\kappa 1}}{2}\|\kappa_1^*\|^2 + \frac{\sigma_{\kappa 2}}{2}\|\kappa_2^*\|^2$, $c_{1m} = min\{c_{11}, c_{12}\}$ and $c_{2m} = min\{c_{21}, c_{22}\}$.

From (25) and (29), we get:

$$\dot{V}_2 \le -\mu V_2 + \pi \quad (30)$$

where $\mu = min\{2c_{1m}/\mu_{max}(g_1^{-1}), 2c_{2m}/\mu_{max}(g_2^{-1}), \gamma_{\theta 1}\sigma_{\theta 1}, \gamma_{\theta 2}\sigma_{\theta 2}, \gamma_{\kappa 1}\sigma_{\kappa 1}, \gamma_{\kappa 2}\sigma_{\kappa 2}, 2\gamma_{\delta 1}\sigma_{\delta 1}, 2\gamma_{\delta 2}\sigma_{\delta 2}, 2\gamma_{r1}, 2\gamma_{r2}\}$

Integrating (30) over [0, t] yields

$$0 \le V_2(t) \le \frac{\pi}{\mu} + \left[V_2(0) - \frac{\pi}{\mu}\right]e^{-\mu t} \quad (31)$$

From (31), it is clear that the tracking errors and the parametric estimation errors exponentially converge to a bounded adjustable domain.

IV. MRAS SPEED OBSERVER DESIGN

The model reference adaptive system approach (MRAS) estimate the rotor speed. This method consists of using two models. The first one is the reference model and the second is an adjustable one in which two components of the rotor flux, obtained from the measurement of the currents and stator voltages are estimated.

The error between the output of the reference and the adjustable models is fed into an adaptation mechanism which is designed to estimate the speed and assure the stability of the MRAS.

A. *Reference Model*

The reference model is usually expressed by the voltage model representing the stator equations. The reference model gives the following equations for reference rotor flux components [16, 17]:

$$\begin{cases} \frac{d\varphi_{rq}}{dt} = -\frac{L_r}{L_m}\left(R_s i_{sq} + \sigma L_s \frac{di_{sq}}{dt} - v_{sq}\right) \\ \frac{d\varphi_{rd}}{dt} = -\frac{L_r}{L_m}\left(R_s i_{sd} + \sigma L_s \frac{di_{sd}}{dt} - v_{sd}\right) \end{cases} \quad (32)$$

where $\sigma = 1 - \frac{L_m^2}{L_s L_r}$

B. *Adjustable Model*

The adjustable model usually describes the rotor flux components which are expressed in terms of rotor speed and stator current and hence this model is sometimes also refereed as current model. The reference model gives the following equations:

$$\begin{cases} \frac{d\hat{\varphi}_{rq}}{dt} = \frac{L_m}{T_r} i_{sq} - \frac{1}{T_r}\hat{\varphi}_{rq} + \hat{\omega}_d\hat{\varphi}_{rd} \\ \frac{d\hat{\varphi}_{rd}}{dt} = \frac{L_m}{T_r} i_{sd} - \frac{1}{T_r}\hat{\varphi}_{rd} - \hat{\omega}_d\hat{\varphi}_{rd} \end{cases} \quad (33)$$

where $T_r = \frac{L_r}{R_r}$; $\hat{\omega}_d = \omega_e - p\hat{\omega}$

The following figure represents the observation technique structure.

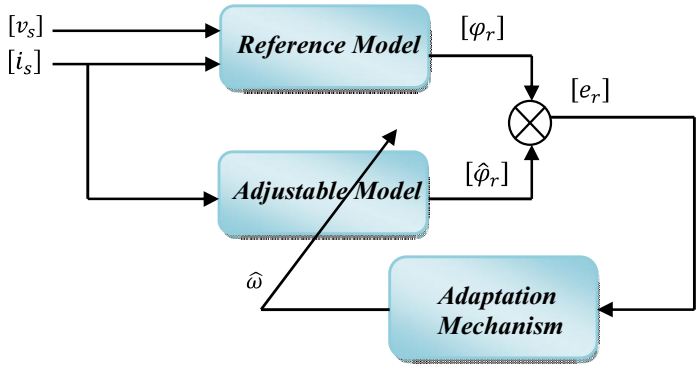


Figure 1: MRAS observer structure

Define the error between the states of the two models as follow:

$$\begin{cases} e_q = \varphi_{rd} - \hat{\varphi}_{rd} \\ e_d = \varphi_{rq} - \hat{\varphi}_{rq} \end{cases} \quad (34)$$

After deriving the errors and uses the equation (34), the error dynamic is given by:

$$\begin{cases} \dot{e}_q = -\frac{1}{T_r}e_q + \tilde{\omega}_d\varphi_{rd} + \hat{\omega}_d e_d \\ \dot{e}_d = -\frac{1}{T_r}e_d - \tilde{\omega}_d\varphi_{rq} - \hat{\omega}_d e_q \end{cases} \quad (35)$$

where $\tilde{\omega}_d = \omega_e - p\tilde{\omega}$; $\tilde{\omega} = \omega - \hat{\omega}$

The adaptive mechanism that gives the speed estimation by using the observer stability condition can be determined.

Consider the Lyapunov candidate function as follows:

$$V = \frac{1}{2}\left(e_d{}^2 + e_q{}^2 + \lambda\,\tilde{\omega}_d{}^2\right) \quad (36)$$

where λ is a positive constant.

Its time derivative is

$$\begin{aligned} \dot{V} &= e_d\dot{e}_d + e_q\dot{e}_q + \lambda\,\tilde{\omega}_d\dot{\tilde{\omega}}_d \\ &= -\frac{1}{T_r}\left(e_d{}^2 + e_q{}^2\right) + \tilde{\omega}_d\left(\lambda\,\dot{\tilde{\omega}}_d + \varphi_{rd}e_q - \varphi_{rq}e_d\right) \end{aligned} \quad (37)$$

In order to make $\dot{V}$ to be negative definite; (38) can be proposed:

$$\lambda\,\dot{\tilde{\omega}}_d + \varphi_{rd}e_q - \varphi_{rq}e_d = 0 \quad (38)$$

Note that : $\dot{\tilde{\omega}}_d = -p\dot{\tilde{\omega}}$

Moreover, if the speed is supposed as vary slowly between two moments of sampling, which means: $\dot{\omega} = 0$
Thus;

$$\dot{\tilde{\omega}}_d = -p\dot{\tilde{\omega}} \quad (39)$$

$$\Rightarrow \dot{\hat{\omega}} = \frac{1}{p\lambda}\left(\varphi_{rd}e_q - \varphi_{rq}e_d\right) \quad (40)$$

The adaptive law, that ensures the stability of the MRAS observer, is given by:

$$\hat{\omega} = K_I \int \left(\varphi_{rd}e_q - \varphi_{rq}e_d\right) dt \quad (41)$$

where $K_I = \frac{1}{p\lambda}$

In ordre to decrease the response temp of estimation and the estimation error, we can use the proportional integral mechanism as follow:

$$\hat{\omega} = K_P\left(\varphi_{rd}e_q - \varphi_{rq}e_d\right) + K_I \int \left(\varphi_{rd}e_q - \varphi_{rq}e_d\right) dt \quad (42)$$

where K_P and K_I are the proportional and integral positive coefficients.

V. SIMULATION RESULTS

The parameter values of the induction machine are given in the Table.2. The references of speed and flux are selected respectively as follows:
$\omega_{ref} = 60 + 60\ sin(\pi t)\ [rd/s]$ and $\varphi_{ref} = 1\ Wb$
It is supposed that the induction machine is subjected to a load of 5 N.m at 0.6s.
The parameters of the friction model are selected as: $F_c = 5.25$, $F_c = 9 \times 10^{-2}$, $F_c = 3.4$, $\eta_s = 5 \times 10^{-2}$.
The fuzzy system $\xi_1^T(x_1)\theta_1$ has the vector $x_1 = [x_{11}, x_{12}]^T$ as input, while the fuzzy system $\xi_2^T(x_1, x_2)\theta_2$ has the state vector $x_1 = [x_1^T, x_2^T]^T = [x_{11}, x_{12}, x_{21}, x_{22}]^T$as input. For each variable of the entries of these fuzzy systems, as in [18], we define three (one triangular and two trapezoidal) membership functions uniformly distributed on the following intervals: $[0\ 130]$ for x_{11}, $[0\ 1.3]$ for x_{12} and $[-8\ 8]$ for x_{21} and x_{22}.

Table 2: The parameters of the induction motor

parameter	**Value**	**parameter**	**Value**
Nominal power	**1.5 KW**	Nominal Frequency	**50HZ**
Nominal speed	**1420tr/mn**	pair of poles (p)	**2**
Nominal current	**3.8/6.5 A**	Blondel coefficient (σ)	**0.113**
Stator resistance (R_s)	**4.85 Ω**	Nominal voltage	**220V/380V**
Rotor resistance (R_r)	**3.805Ω**	Rotor time constant (T_r)	**0.072 s**
Stator inductance (L_s)	**0.274H**	Mutual inductance (L_m)	**0.258 H**
Rotor inductance (L_r)	**0.274H**	Inertia (J)	**0.031 Kg.m²**

The design parameters are chosen as follows: $\gamma_{\theta 1} = 20$, $\gamma_{\theta 2} = 30$, $\sigma_{\theta 1} = 20$, $\sigma_{\theta 2} = 30$, $C_1 = diag[40, 900]$, $C_2 = diag[40, 40]$, $\epsilon = 0.02$, $\gamma_{r1} = 25$, $\gamma_{\delta 1} = 10^{-6}$, $\sigma_{\delta 1} = 10^{-7}$, $\gamma_{\kappa 1} = 10^{-5}$, $\sigma_{\kappa 1} = 3$, $\gamma_{r2} = 25$, $\gamma_{\delta 2} = 10^{-6}$ $\sigma_{\delta 2} = 10^{-7}$, $\gamma_{\kappa 2} = 10^{-5}$, $\sigma_{\kappa 2} = 3$.

The initial conditions of adaptation laws are: $v_{r1}(0) = v_{r2}(0) = [2, 2]^T$, $\delta_1(0) = \delta_1(0) = 2$, $\kappa_1(0) = \kappa_2(0) = [10, 10]^T$ *and* $\theta_{1_j}(0) = \theta_{2_j}(0) = 0.01$, for $j=1,\ldots,m$, where m is the number of the fuzzy rules.
The proportional and integral coefficients are chosen as follows: $K_P = 60$ and $K_I = 100$.

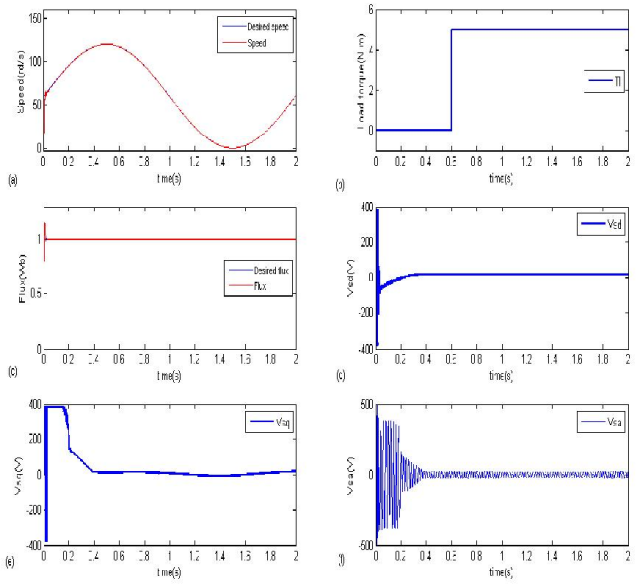


Figure 2: Response of IM for sensorless adaptive fuzzy backstepping control with nonlinear frictions and with nominal parameters: (a)The speed and its reference signal; (b)Load torque; (c)The flux and its reference signal; (d)Stator voltage along d-axis; (e)Stator voltage along q-axis; (f) First component of the 3ph stator voltage(Vsa).

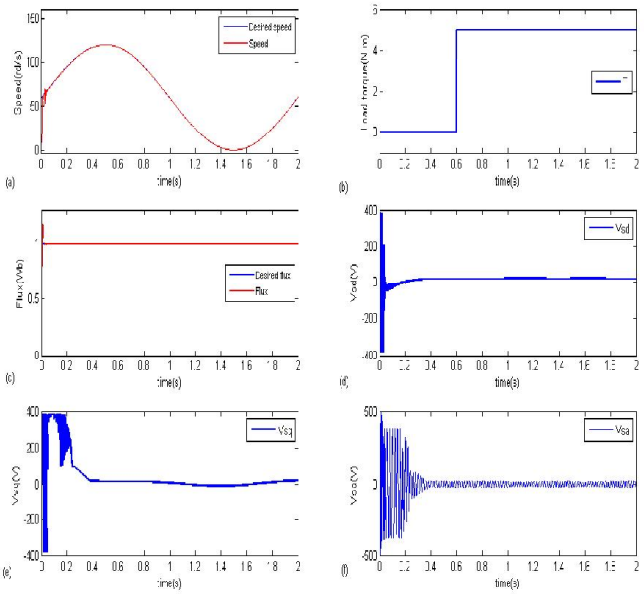


Figure 3: Response of IM for sensorless adaptive fuzzy backstepping control with nonlinear frictions and parameter variations (i.e. R_s amplified to 1%): (a)The speed and its reference signal; (b)Load torque; (c)The flux and its reference signal; (d)Stator voltage along d-axis; (e)Stator voltage along q-axis; (f) First component of the 3ph stator voltage(Vsa).

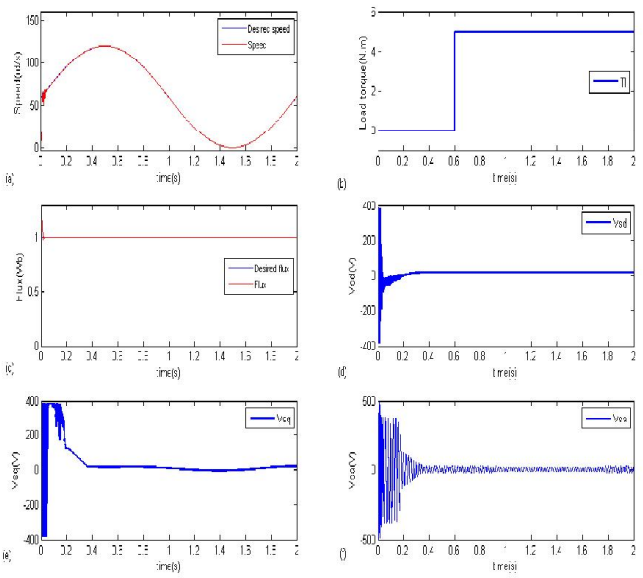


Figure 4: Response of IM for sensorless adaptive fuzzy backstepping control with nonlinear frictions and parameter variations (i.e. *Ls* and *Lr* decreased by 3%): (a)The speed and its reference signal; (b)Load torque; (c)The flux and its reference signal; (d)Stator voltage along d-axis; (e)Stator voltage along q-axis; (f) First component of the 3ph stator voltage(Vsa).

The simulation results of the proposed sensorless adaptive fuzzy backstepping controller with nonlinear frictions and with nominal parameters using the MRAS observer are shown in figure (2). According to these results, the rotor flux respects the constraints of orientation and the speed follows perfectly its imposed reference, so the MRAS observers work correctly.
The figures (3) and (4) show the performance of the sensorless adaptive fuzzy backstepping controller performance with friction model and parametric variations (i.e. the stator resistance R_s is amplified to 1% and L_s and L_r decreased by 3%). From these figures, the sensorless control using the MRAS observer is note robust in spite of the presence of parametric variations.
At time t=0s, the amplitude of some variables are important due to the motor starting because usually the starting torque is 2.5 times full-load torque and starting current is 6 to 7 times full-load current.

VI. CONCLUSION

In this article, the sensorless speed control of the induction machine using the technique of adaptive fuzzy backstepping, associated to a Speed Observer based on MRAS approach is developed.

The MRAS observer is preferred due to its simplicity which is based on two different models, one that is speed independent (reference model) and another that is speed dependent (adjustable model). The speed is estimated via the outputs of the two models.

The simulation results clearly illustrate the tracking error converge to a small neighborhood around the origin but the proposed sensorless controller is not very robust with the presence of the parameter variations.

In our future work, we will address to combine the MRAS observer with Sliding-Mode Observer.

REFERENCES

[1] R. J. Wai, K. M. Lin, and C. Y. Lin, "Total sliding-mode speed control of field oriented induction motor servo drive", In proceedings of the 5th Asian control conference, Australia, 2004.
[2] J. K. Liu and F. C. Sun, Research and development on theory and algorithms of sliding mode control. Control Theory and Applications, vol.24, no.3, 407–418, 2007.
[3] R. Marino, S. Peresada, and P.Valigi, "Adaptive input-output linearizing control of induction motors, IEEE Transactions on Automatic Control, vol.38, no.2, 208–221, 1993.
[4] J. Chiasson, "A new approach to dynamic feedback linearization control of an induction motor, IEEE Transactions on Automatic Control, vol.43, 391–397, 1998.
[5] Y. Tan, J. Chang and H. Tan, "adaptative backstepping control and friction compensation for AC servo with inertia and load uncertainties,IEEE Trans. on industrial electronics, Vo1.50, No. 5, pp. 944-952,October 2003.
[6] E. Arbin and M. Gregory, "Adaptive Backstepping Control of a Speed-Sensorless Induction Motor Under Time-Varying Load Torque and Rotor Resistance Uncertainty". Proceedings of the 38th Southeastern Symposium on System Theory, Tennessee Technological University Cookeville, TN, USA, pp 512-518, March 5-7,2006.
[7] C. M. Kwan and F. L. Lewis, "Robust backstepping control of induction motors using neural networks", IEEE Transactions on Neural Networks, vol. 11, no. 5, 1178-1187, 2000.
[8] N. Ezziani, N. Essounbouli and A. Hamzaoui, "An AFB Controller of Induction Machine under Amplitude and Rate Saturation Constraints", IEEE Industrial Electronics Society, Portugal, pp.1026-1032, 2009.
[9] N. Ezziani, N. Essounbouli and A. Hamzaoui, Backstepping Fuzzy Adaptive Controller of Induction Machine, 16th Mediterranean Conference on Control and Automation. Ajaccio, France, pp. 1622-1627, 2008.
[10] N. Ezziani, A. Hussain, N. Essounbouli and A. Hamzaoui, "Backstepping Adaptive Type-2 Fuzzy Controller for Induction Machine", IEEE International Symposium on Indus. Electronics, Cambridge (UK), pp.443-448, 2008.
[11] H.A. Youcef and M. A. Wahba, "Adaptive fuzzy MIMO control of induction motors", Expert Systems with Applications, Vol.36, No. 1, pp. 4171-4175, 2009.
[12] M. Agamy, H.A. Youcef, O. A. Sebakhy, Adaptive fuzzy variable structure control of induction motors", In Proc. of the Canadian Conference of Computer and Electrical Engineering, pp. 89-94, Niagara Falls, Canada, 2004.
[13] F. J. Lin, P. H. Shen and S. P. Hsu, "Adaptive sliding mode control for linear induction motor drive, IEE Proc.-Power Appl., Vol. 149, N.3, pp.184-194, 2002.
[14] Y. Zhang, P.Y. Peng and Z. P. Jiang, "Stable Neural Controller design for Unknown Nonlinear Systems using Backstepping", IEEE Trans. Neural Networks, 1347–1359, 2000.
[15] B. K. Bose, "Modern Power Electronics and AC Drives". Upper Saddle River, NJ: Prentice-Hall, 2002.
[16] C. Schauder. "Adaptive speed identification for vector control of induction motors without rotational transducers", IEEE Transactions on Industry Applications, 1992, 28: 1054–1061.
[17] P. Vas. "Sensorless Vector and Direct torque control", Oxford University Press, New York, 1998.
[18] F. Peng and T. Fukao. "Robust speed identification for speed-sensorless vector control of induction motors", IEEE Transactions on Industry Applications, 1994, 30: 1234–1240.
[19] S. Tamai, H. Sugimoto and M. Yano, "Speed-sensorless vector control of induction motor with model reference adaptive system", in: Conference Record of the 1985 IEEE-IAS Annual Meeting, 1985, 613–620.
[20] S. Yang, X. Li, D. Ding, X. Zhang, and Z. Xie, "Speed Sensorless Control of Induction Motor Based on Sliding-Mode Observer and MRAS", 8th International Power Electronics and Motion Control Conference, IPEMC-ECCE Asia, 2016.
[21] H. Chaoui and P. Sicard, "Adaptive Friction Compensation of Flexible-Joint Manipulators with Parametric Uncertainties, IEEE International Conference on Automation Science, 2013.
[22] S. ISSAOUNI, A. Boulkroune and H. CHEKIREB, "Adaptive Intelligent Backstepping Controller of Induction Machine", 8th International Conference on Modelling, Identification and Control (ICMIC-2016), Alger, Algeria, 15-17 November 2016.

Design And Implementation Of Intelligent Li-ion Battery Charger

Abdulrahman Mahmood Faihan, Ergun Erçelebi
Electrical and Electronics Engineering Department, University of Gaziantep
27310 Şahinbey, Gaziantep, Turkey
E-mail: abdmf2015@gmail.com, ercelebi@gantep.edu.tr

Abstract - **nowadays, Li-ion batteries are considered the best type of rechargeable batteries due to their high energy density, but it needs a specific mode of charging to avoid their exploitation. In this article, we will design an intelligent battery charger that charges the Li-ion batteries by a constant current-constant voltage mode based on pic16f876 microcontroller. The mode of charge will be shown to the user by using two LEDs, one refers to the CC mode and another one for CV mode. The voltage and current detection are implemented in our design in order to make the necessary judgment on charging state of the batteries and also to present it to the user in the LCD. Pulse Width Modulation signal was adjusted to obtain high-precision charging control. The user could adjust the cutoff voltage according to the number of series batteries that would be charged by the user. The value of cut off voltage would be also presented to the user. The value of input DC voltage which supplies the circuit will be also presented.**

***Keywords*–Li-ion Batteries, PIC16F876, Intelligent Charger, PWM Controlling.**

I. INTRODUCTION

NOwadays the peripheral electronic devices need batteries with a large capacity to work for a long time. In addition to capacity, the size of batteries is another important factor. The Li-ion batteries satisfy these two conditions with more extra advantages such as no memory effect, high operating voltage, and low self-discharge. If it were not used for a long time. It would not lose its charge quickly. Also, Li-ion cells are suitable for applications which need a large number of charge-discharge cycles because it has a long cycle life (3,000 cycles at 80% depth of discharge). But on the other side, Lithium-ion batteries, due to their high density, are vulnerable according to short-circuiting and overcharging. It may explode and occur fire hazard if it could not charge safely unlike Lead acid, Ni-Cd and Ni-MH batteries which work safely even at short-circuiting and overcharging situations because they use inflammable electrolyte and they have a low energy capacity. For this reason, we designed an intelligent lithium-ion battery charging system to control the charging current and the voltage. The charger that we will design has several advantages, it is safer towards batteries damages and low-cost. The circuit is simple and all the components are available, it presents the voltage and current values on the LCD. In addition, it presents charging mode for the user and the best feature in our design that can charge a variable number of batteries in series from 3.7 V or from 4.2 types. But on the other hand, the feature of charging a variable number of batteries in series requires a balancing circuit to make equilibrium between the batteries. This is impossible in our design it is because in balancing circuit, we need to know the accurate number of batteries which connected in series and this is not available in our design. Briefly, in this article, section II will discuss the Li-Ion charging mode and its requirements, section III will explain the hardware design, section IV will explain the details of a program design, followed by experimental results in section V. Finally, conclusions are reported in section VI.

II. BACKGROUND

Generally, there are several methods to charge various types of batteries, but for Li-ion batteries, not all the methods are suitable for the charging process. The constant current-constant voltage technique is the best method for Li-ion batteries. In this technique, the charging process is accomplished by two steps. The first one, we apply a regulating current (constant current) for the batteries, the battery current will be kept constant while the battery voltage increases during charging until it reaches the maximum allowable value (predetermined value V_{const}). The second one, the charger starts the voltage regulation phase, the applied charging voltage remains constant while the battery current decreasing and ultimately becoming very low until it reaches the end-of-charge current I_{end} as shown in fig(1). To perform this technique, we need a current feedback loop and a voltage feedback loop to adjust the duty cycle of the PWM wave to get the smooth and proper transition between the current and voltage mode.

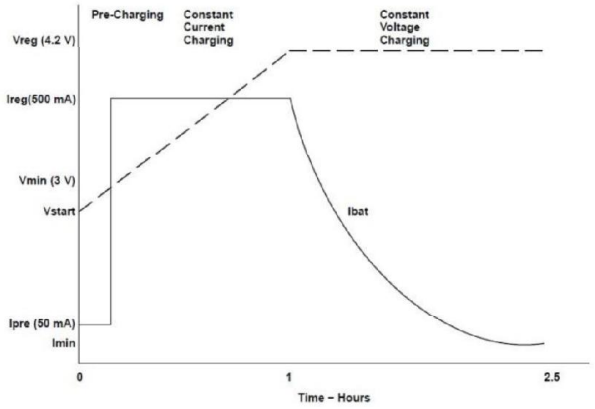


Fig 1: charging Mechanism of Li-ion batteries

III. HARDWARE DESIGN

A. Overall Design

The microcontroller (MCU) used in the charger is the PIC16F876 from microchip. It is an 8-bit microcontroller, it has 5 channels with 10-bit resolution Dedicated for the analog to digital converter(A\D converter) and it has 2 capture/compare/PWM functions. We fed the overall circuit by a 12V AC\DC converter and we fed the microcontroller and the LCD by a linear dropout LDO circuit. We used p2 as an input for the battery current feedback sensor, p4 for the battery voltage feedback sensor and p3 as an i/p for the AC/DC converter voltage measurement sensor. This MCU provides 16-bit timer used to get a high precision PWM wave. The output accuracy can achieve 1/65535 when outputs PWM. Two LEDs are connected to p5 and p6 respectively, the first one will show the constant current mode and the second one will indicate the constant voltage mode. To enable the user charging a variable number of batteries in series, we connected a variable resistor to p7. By changing the value of the resistor, we will shift the full charge voltage limit taking into consideration the value of the AC\DC converter. In our design, we used 12-volt AC\DC converter so that the maximum number of charged batteries will be 3. The 16x2 LCD is connected to port B, the first value will be presented the i/p voltage which comes from the AC\DC converter. This value gives an indication to the user about the maximum acceptable number of charged batteries in series The second value is the cutoff voltage which determined by the user according to the number of batteries, the third value is the instantaneous charge voltage while the fourth value is the charging current. Fig (2) shows the block diagram of the hardware connection.

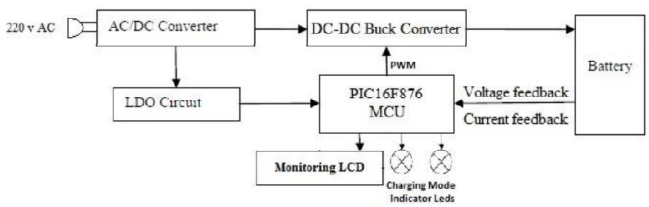


Fig 2: the block diagram of the hardware connection.

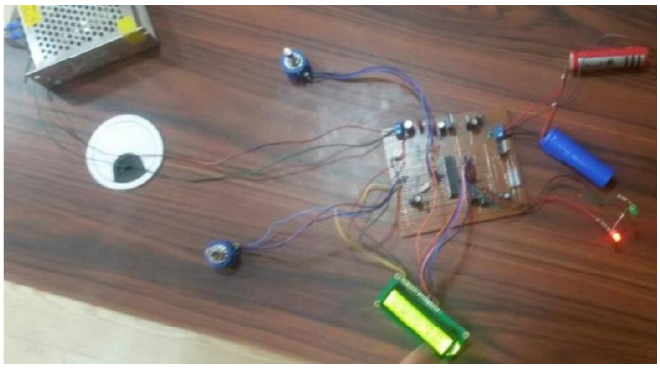


Fig 3: Initial Hardware Connection

B. Voltage, Current Sensing Circuit Design

A voltage divider is a simple circuit which turns a large voltage into a smaller one. Using just two series resistors and an input voltage, we can create an output voltage that is a fraction of the input. C1 is a filter capacitor used to remove high frequency 'noise' in the signal. High precision resistance has been employed in the charging loop to sample current values. Current values can be measured in MCU by sampling voltage values. An amplifier was added to the current sensing circuit to amplify the measuring voltage because the charging current value and the precision resistor's voltage both of them are low. Figure (4) shows the voltage and current Sensing Circuit Design.

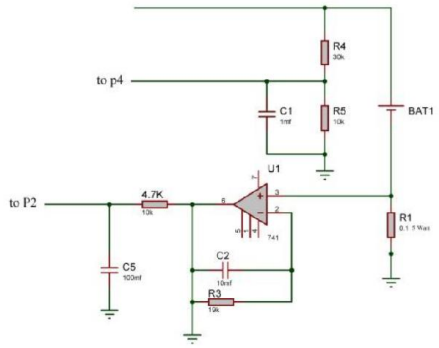


Figure 4: voltage and current Sensing Circuit

C. DC-DC Buck Converter and PWM Circuits

Since the input voltage of the AC\DC converter is 12V and the charge input voltage of the lithium battery is lower than the input voltage which is supplied by the source, it is necessary to set the step-down circuit. DC-DC Buck converter is used to convert a higher DC voltage to the required voltage value. We used the IRFZ44N power MOSFET for switching operation. It is low on-resistance, a fast switching device and passes up to 35A Continuous Drain Current at 100°C, with a freewheeling diode and LC network, acts as a low-pass filter. When the PWM wave at the high level, the switch is ON. BUCK circuit

charges the battery through the inductor and capacitor. When the capacitor is charging, the inductor's current and stored energy are gradually increasing. At this time, the diode is in reverse blocking state. The transistor switches are off when the PWM wave at the low level. Inductor's energy and current start by decreasing. The induced electromotive force, which is produced by the inductor, it makes a current flow through the diode. Current passes energy to the battery through the inductor and diode. When battery's voltage is lower than capacitor's voltage, the capacitor starts by releasing the energy to the battery. The values of the capacitor and inductor are chosen to make the cutoff frequency lower than the PWM frequency in all the time. This can help the capacitor to effectively reduce the output voltage ripple and maintaining a DC voltage level. The capacitor value is 220 µF and the inductor is 75 mH, the cutoff frequency is 1.2 kHz. DC-DC BUCK circuit is shown in Fig (5).

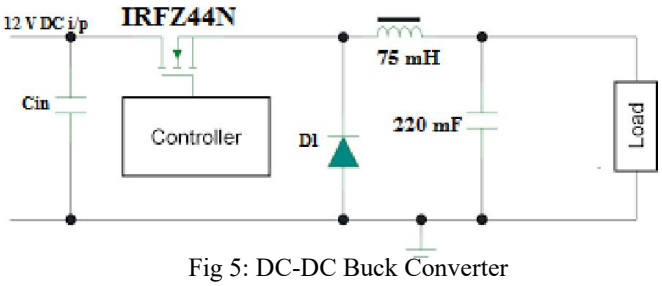


Fig 5: DC-DC Buck Converter

IV. SOFTWARE

C language was used to write the code of the charger using MicroC compiler. The following flow charts show the sequence of processes. The first flowchart shows the necessary initializations that will be done at the start of the program, the second flowchart explains the code of the constant current mode and the third flowchart shows the constant voltage mode.

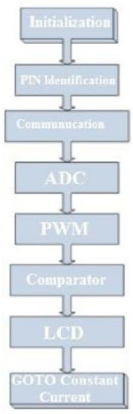


Fig 6: Program startup

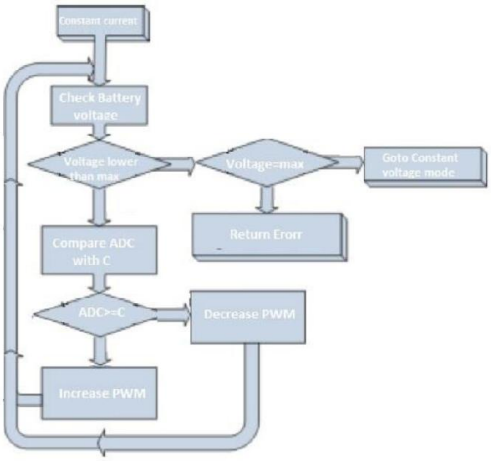


Fig 7: constant current mode flowchart

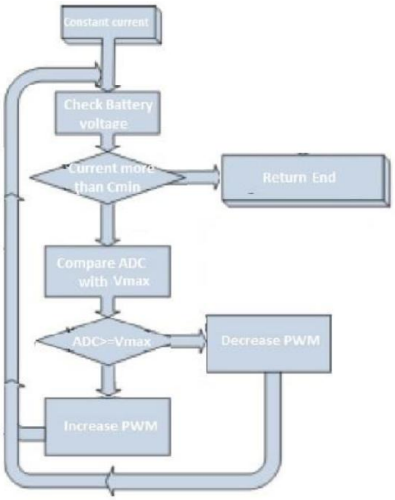


Fig 8: constant voltage mode flowchart

V. RESULTS

In order to test the charger performance, we used three groups of Li-ion batteries connected in series. Fig (9) shows an experimental board operation, the voltmeter used to measure the charging voltage and also to show the accuracy of measurement. Fig(9) shows the result of charging 3 Li-ion batteries. The first voltage reading is the input DC voltage from the AC\DC converter, it was 13.88V. The second voltage reading (Vb) is the cutoff voltage which is determined by the user using the variable resistor, we adjust it on 11.1V because we have three batteries with 3.7V for each one. The third voltage reading is the instantaneous charging voltage and the fourth reading is the charging current. When the red LED is ON, it indicates that the charging in CC mode. Fig (10) shows that the instantaneous voltage of the batteries became 11.1V. When the green LED is ON, it indicates the constant voltage mode and the drawn current is 0.84 A. In Fig(11) we noticed that the drawn current becomes 0.44A, that means the charger still in constant voltage mode and the current will decrease

until it reaches to the end-of-charge current I_{end}. Fig(12) Shows the charge of 1 Li-ion battery. We set the voltage at 3.7V and noticed that the reading of the voltmeter is the same of our design and the red LED of CC mode is ON.



Fig 9: The Experimental Results

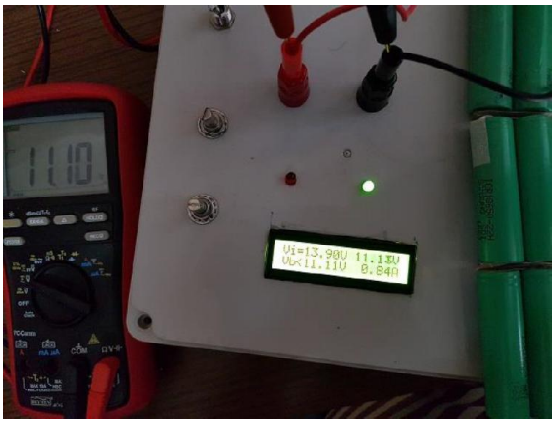


Fig 10:The Experimental Results

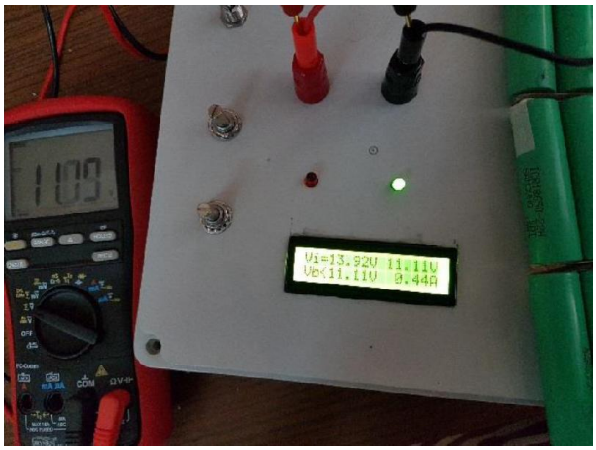


Fig 11: The Experimental Results



Fig 12: The Experimental Results

Finally, we recharged three groups of Li-ion batteries connected in series and we connect an oscilloscope to show the charging curve. Fig (13) &(14) shows the voltage charging curve. The battery voltage before the charging process was 6.5 V, so the charging curve will start from this point Then the voltages are gradually increased until it reaches the setpoint voltage which is 11.2 V in this case, then it will settle at this level while the battery current is decreasing. Fig (15) shows the charging voltage when the charger in constant voltage mode.

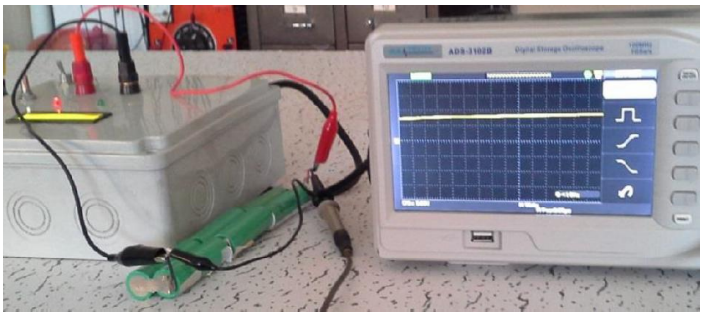


Fig 13:Voltage charging curve
Voltage scale=5V & time scale=50 Sec

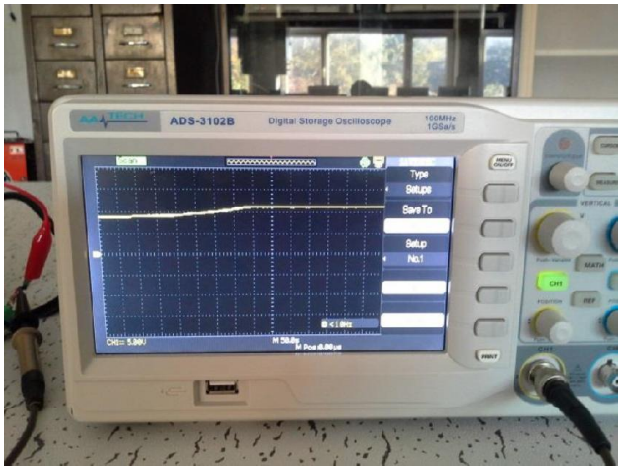


Fig 14:Voltage charging curve
Voltage scale=5V & time scale=50 Sec

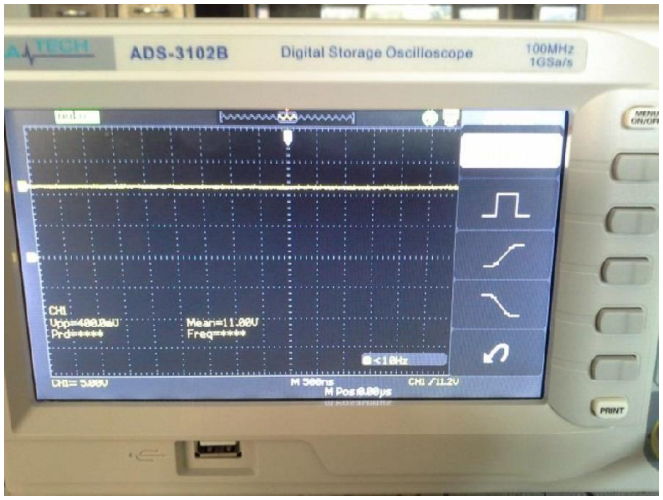


Fig 15: the charging voltage when the charger in CV mode.

VI. Conclusion

In this paper, an accurate small size, low-cost intelligent battery charger had been designed based on a PIC16f876 microcontroller to implement a safe and a quick charge operation for a variable number of serially connected Li-ion batteries. The charged topology is a constant current-constant voltage and the used technique is DC-DC buck converter. The values of voltage and current measured are presented to the user on the LCD .

References

[1] Elias, M. F. M., K. M. Nor, and A. K. Arof. "Design of smart charger for series lithium-ion batteries." *Power Electronics and Drives Systems, 2005. PEDS 2005. International Conference on*. Vol. 2. IEEE, 2005

[2] Rashid, Muhammad H. *Power electronics handbook: devices, circuits, and applications*. Academic Press, 2010

[3] Zhao, Ying, En Zhen Hou, and Xu Fang. "The Research and Design of Intelligent Battery Charger for Electric Vehicle." *Applied Mechanics and Materials*. Vol. 454. Trans Tech Publications, 2014.

[4] Wang, Wen Juan, Guang Xi Zheng, and Wei Dong Lu. "A Design of Charger with Intelligent Charging and Capacity Detection." *Applied Mechanics and Materials*. Vol. 263. Trans Tech Publications, 2013.

[5] Wang, Wen Cheng. "Intelligent Charger Design of Electric Bicycle Based on SCM." *Applied Mechanics and Materials*. Vol. 44. Trans Tech Publications, 2011.

[6] Julien, Christian, et al. "Lithium batteries." *Lithium Batteries*. Springer International Publishing, 2016. 29-68.

[7] Mazidi, Muhammad A., et al. *Pic microcontroller and embedded systems*. Prentice-Hall, Inc., 2005.

[8] Xiao-dong, MA Ai-hua ZHANG, and Wei ZHANG. "Design and Realization of Intelligent Charger for Lithium Battery Based on AVR MCU [J]." *Microcomputer Information* 5 (2009): 034.

[9] Rajendran, Parvathy, Nurul Musfirah Mazlan, and Howard Smith. "Single Cell Li-Ion Polymer Battery Charge and Discharge Characterizations for Application of Solar-Powered Unmanned Aerial Vehicle." *Key Engineering Materials*. Vol. 728. Trans Tech Publications, 2017.

New Hybrid Motor Design Based on MCSRM

M. KARAÇOR[1] and C. ŞAHİN[2]

[1] Manisa Celal Bayar University, Manisa/Turkey, mevlut.karacor@cbu.edu.tr
[2]Bilecik Seyh Edebali University, Bilecik/Turkey, cihan.sahin@bilecik.edu.tr

***Abstract* - Among the most important topics of our day are the use of energy and energy. In terms of the countries that generally import energy, energy saving and more efficient use, especially in the use of energy, is very important. Among the areas where energy use is most prevalent is the transportation sector. With the recent studies, it is aimed to reduce the dependence of the transportation sector on oil and its derivatives. In these studies, concentrated on hybrid motor technologies. In this study, that can be fully assembled in the stator and rotor electric double MCSRM (Mutually coupled switched reluctance machine) and wheels have been developed. As is known, the moment fluctuations present in MCSRMs cause high noise and associated mechanical failure. There are two motors in the design of the hybrid motor designed with the operation carried out. In the positions where the main motor's moment fluctuations are starting to increase, the auxiliary motor is activated to reduce the torque ripple. As auxiliary motors placed in the center of the wheels was assessed to be counted place of the dead. Magneto static analysis was performed to calculate the Torque ripple of MCSRM used as main motor and MCSRM used as auxiliary motor. The torque ripple of the main motor is calculated as% 59,6 when the auxiliary motor is not in operation. When the auxiliary motor is in operation, the temp. Torque ripple is calculated as% 44,5.**

***Keywords* - SRM, MCSRM, Hybrid Motor.**

I. INTRODUCTION

In order to increase the performance of the Switched Reluctance Machine, various changes have been made to the geometrical structure, if necessary. Particularly, geometry changes have been tried to find the most suitable design geometry and more torque has been tried to be produced by using the electric circuit of the SRM. In order to change the inductance profile of the SRM, working on changing the pole shapes has resulted in the modification of the generated torque profile [1].

During these studies different winding configurations have been tried to increase the torque produced by the SRM. Mecrow first proposed the MCSRM winding structure. MCSRMs have all the advantages of classical SRMs and additionally have the ability to generate 20-30% more torque. As shown in Equation 1, torque production in MCSRM produces based on opposite inductance, which is caused by the mutual effects of active phases. In the conventional SRM, the torque is produced only on the basis of the active phase inductance (Equation 2) and is less utilized than the machine's electrical circuit. For a 3-phase classical SRM, each phase contributes 1/3 of the generated torque, while this ratio is 2/3 for MCSRM. In other words, the electrical circuit is twice as effective as the conventional SRM.

$$T = \frac{1}{2} i_a i_b \frac{\partial M_{ab}}{\partial \theta} + \frac{1}{2} i_b i_c \frac{\partial M_{bc}}{\partial \theta} + \frac{1}{2} i_c i_a \frac{\partial M_{ca}}{\partial \theta} \quad (1)$$

$$T = \frac{1}{2} i_a^2 \frac{\partial L_a}{\partial \theta} + \frac{1}{2} i_b^2 \frac{\partial L_b}{\partial \theta} + \frac{1}{2} i_c^2 \frac{\partial L_c}{\partial \theta} \quad (2)$$

The torque produced by the machine is directly proportional to the flux, and Figure 1 shows the comparison of the two machine-generated fluxes. As seen in Figure 1, four times the flow produced by the active phase (one phase) in classical SRM is produced by MCSRM.

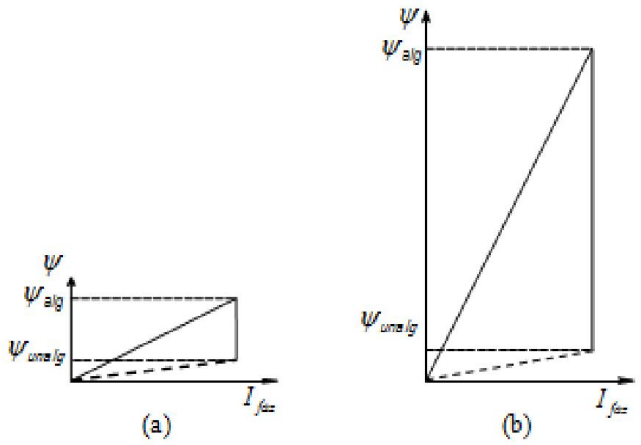


Figure 1: flux production at a- SRM, b- flux production at MCSRM.

The wisdom produced for aligned and unaligned positions of both machines is shown by the symbols ψ_{alg} and ψ_{unalg} respectively. While the two machines are operating in equal currents, the increase in flux is four times higher, but in order to be able to compare equally, MCSRM produces twice as much flux as SRM, with equal copper losses. However, due to the produced excess flux and magnetic saturation, the increase in torque production is in the range of 20% -30% [2].

Figure 2 shows the structure of MCSRM and its three-dimensional shape. As can be seen, phase windings in MCSRM do not directly wrap around the pole legs. The phase windings are deposited in a way that will take a full step into the polar spaces [3].

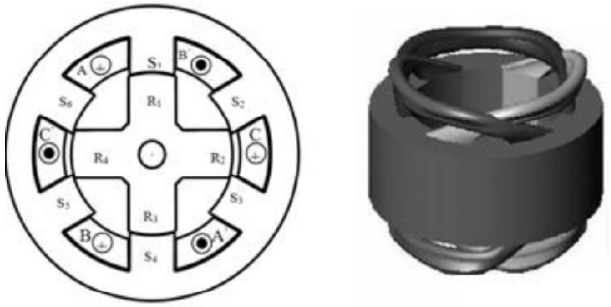


Figure 2: The structure of MCSRM and its three-dimensional appearance.

There are three different excitation types in KKARM, and the torque and mean torque produced by the excitation modes vary. The unidirectional excitation structure, the counter inductance and the current profile are shown in Figure 3.

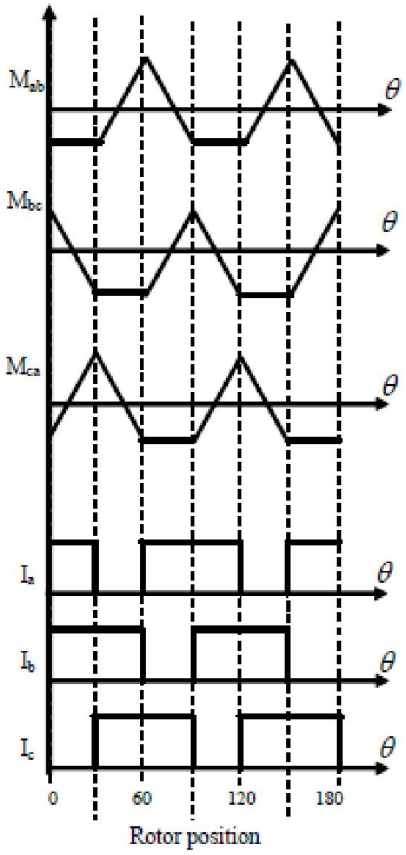


Figure 3: Mutual inductance and current characteristics of unidirectional excited MCSRM.

The machine with the opposite inductance profile is 6/4 pole and the step angle is 30º. It can easily be said that the step angle is 30º and the period is 90º due to the machine being three-phase. The opposite inductance profile shown in Figure 3 is idealized and therefore the curve exhibits a linear structure. The contrary inductance profile is divided into three sections, which are characterized by a rise in the first 30º, a landing in the second 30º and a fixed structure in the third 30º. In the unidirectional excitation phase, the phases remain at 2/3 of the transmission and at 6/4 three-phase MCSRM at 60º [5].

II. STATIC ANALYSIS OF MCSRM

Equation (3) gives the general torque expression in a 3-phase classical SRM.

$$T = \frac{1}{2} i_a^{\,2} \frac{\partial L_a}{\partial \theta} + \frac{1}{2} i_b^{\,2} \frac{\partial L_b}{\partial \theta} + \frac{1}{2} i_c^{\,2} \frac{\partial L_c}{\partial \theta} + \frac{1}{2} i_a i_b \frac{\partial M_{ab}}{\partial \theta} + \frac{1}{2} i_b i_c \frac{\partial M_{bc}}{\partial \theta} + \frac{1}{2} i_c i_a \frac{\partial M_{ca}}{\partial \theta} \quad (3)$$

Where T is the total torque; i_a, i_b, i_c, are the phase currents; La, Lb, Lc are the phase inductances; and M_{ab}, M_{bc}, M_{ac}, are the mutual inductances between the phases. The last three terms are neglected since they are usually considered negligible in classical SRMs. Eventually, torque in classical SRMs is produced by the self inductance of their active phase according to (4):

$$T = \frac{1}{2} i_a^{\,2} \frac{\partial L_a}{\partial \theta} + \frac{1}{2} i_b^{\,2} \frac{\partial L_b}{\partial \theta} + \frac{1}{2} i_c^{\,2} \frac{\partial L_c}{\partial \theta} \quad (4)$$

If it is assumed that only phase 'a' is active, simplifies as for classical SRMs:

$$T = \frac{1}{2} i_a^{\,2} \frac{\partial L_a}{\partial \theta} \quad (5)$$

The torque in MCSRM is produced based on mutual inductance, which is obtained by the effect of active phases on each other, as can be seen in (5):

$$T = \frac{1}{2} i_a i_b \frac{\partial M_{ab}}{\partial \theta} + \frac{1}{2} i_b i_c \frac{\partial M_{bc}}{\partial \theta} + \frac{1}{2} i_c i_a \frac{\partial M_{ca}}{\partial \theta} \quad (6)$$

Since two phases are active in MCSRM (assume phase 'a' and phase 'b' are active, and phase 'c' is passive), (6) turns into (7):

$$T = \frac{1}{2} i_a i_b \frac{\partial M_{ab}}{\partial \theta} \quad (7)$$

When Eqs. 5 and 7 are examined, it can be seen in Figure 4 that the torque production in the conventional SRM changes depending on the position of the inductance in the constant current and in MCSRM the opposite inductance in the constant current changes depending on the rotor position.

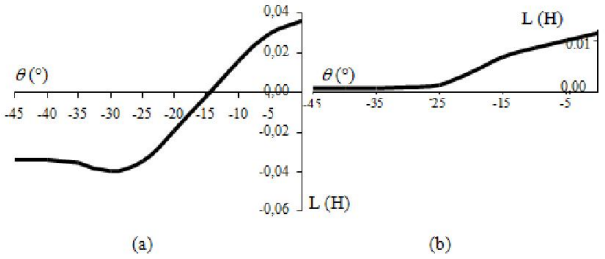


Figure 4: a-Mutual inductance and b-self inductance change curves.

III. HYBRID MOTOR STRUCTURE

As mentioned above, a hybrid motor system has been developed to reduce torque fluctuation, which is the most important problem of both SRM and MCSRM. For the analysis of the developed hybrid motor, analysis was carried out by using Finite Element Method. With this analysis, a single magneto static analysis of the internal and external motor pairs used in the proposed motor structure was carried out. Figure 5-8 shows the state of the flux lines after the analysis of the motor's mesh structure, the internal and external motors, and the moment values produced by both motors.

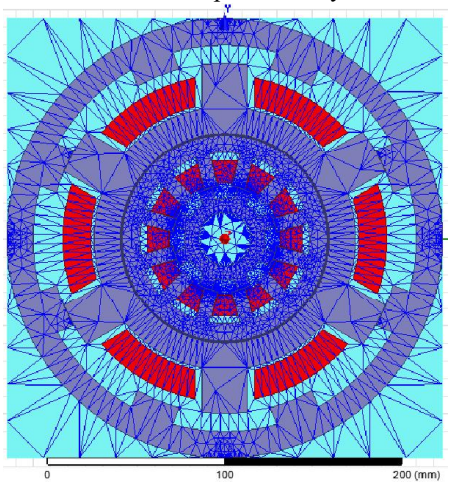


Figure 5: Hybrid motor Mesh structure.

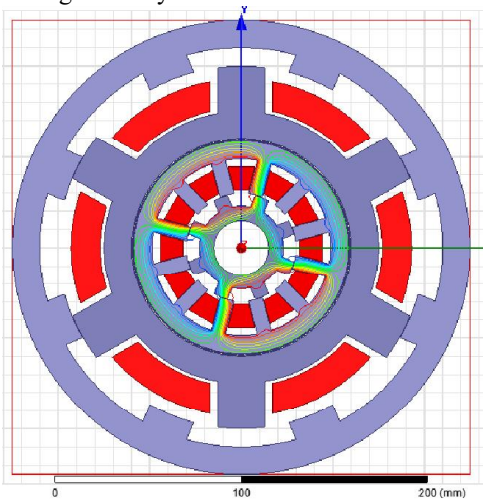


Figure 6: Internal motor flux distribution.

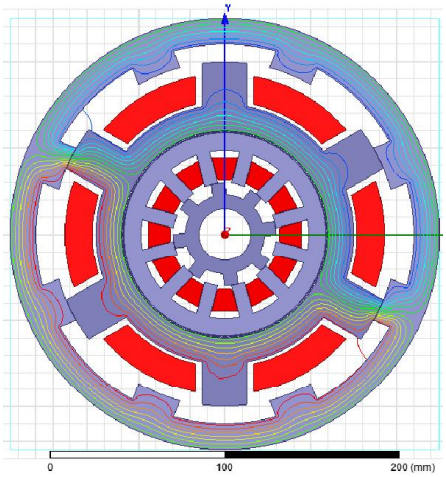


Figure 7: Internal motor flux distribution.

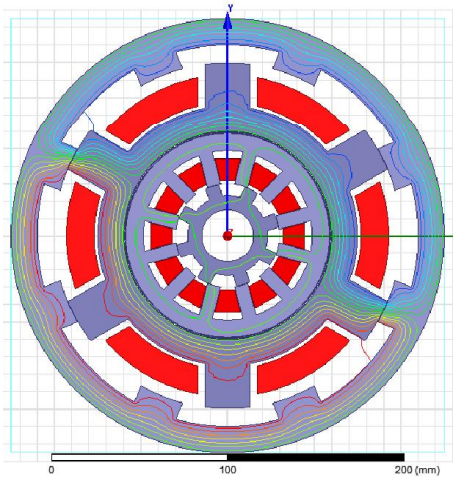


Figure 8: Internal and external motor flux distribution.

Torque Ripple calculation Md = (Mmax-Mmin) / (Mmax + Mmin) expression is used. According to this calculation method, it is seen that the maximum torque ripple in the structure where only the external motor is in operation has reached to the maximum value of 59.6%. The internal motor used in Figure 6 is only in circuit, so the motor produces an average torque of 0,4 Nm. The external motor shown in Fig. 7 only produces a torque of 1.5 Nm on average. As a result of simultaneous operation of both motors, the total minimum torque increases by 0.9 Nm and the net torque ripple decreases to 44.5%.

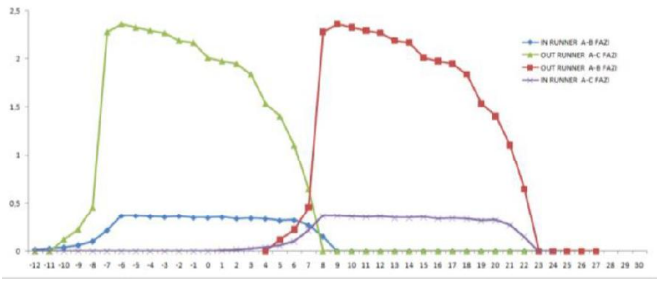


Figure 7: Torque generated by internal and external motor.

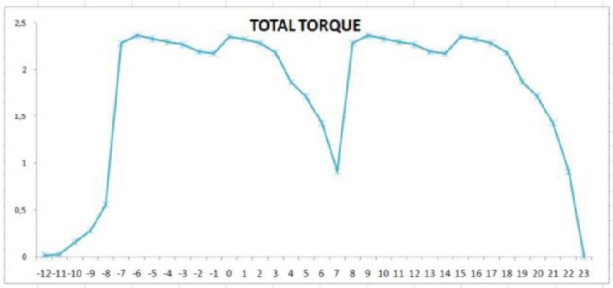


Figure 7: Total torque

IV. CONCLUSION

Although the maximum torque fluctuation in the MCSRM motor structure reached 59.6%, the proposed MCSRM structure reduced the torque ripple to 44.5%. The engine produces an average torque of 0,4 Nm when the internal motor is only in operation. The average torque of 1.5Nm is produced when the external motor is only in circuit. As a result of simultaneous operation of both motors, the total minimum torque is increased by 0.9 Nm and the result is found to be a 25% improvement in torque ripple.

REFERENCES

[1] Özoğlu, Y., "Torque ripple minimization of the switched reluctance motor by giving shape to pole tips of stator and rotor", Phd. Thesis, İstanbul Technical University, İstanbul, Turkey 1999.

[2] Yuanto, X.i, "Utility Interface Design and Mutual Coupled Switched Reluctance Machine Study for a Wind Generation System", Phd. Thesis, Rensselaer Polytechnic Institute, Troy, New York,USA, 2001.

[3] Yılmaz, K., "Anahtarlı Relüktans Motorunun Sargı Yapısı Değiştirilerek Moment Performansının İyileştirilmesi", Phd. Thesis, University of Kocaeli, Kocaeli, Turkey, 2004.

[4] Mecrow, B.C., "New Winding Configurations for Doubly Salient Reluctance Machines", *Industry Applications Society Annual Meeting, IEEE*, Houston TX USA, 1992.

[5] Emire A., "Design of 2 x 6/4 disc type switched reluctance motors with torque ripple minimization" Master Thesis. ERCİYES University, Kayseri, Turkey, 2010.

[6] Şahin C., Amac A., E., Karacor M., Emadi A., A Comparative Analysis of the Effects of Rotor Molding Clinches on Torque Ripple os Mutually Coupled SRMs, *International Review of Electrical Engineering (I.R.E.E.),* 6, pp: 1627-1635, 2011.

[7] Xu, Y., Torrey, D.A., "Study of the Mutually Coupled Switched Reluctance Machine Using the Finite Element Circuit Coupled Method", *IEE Proceedings Electric Power Applications*, vol.149, pp. 81-86, 2002.

[8] Garip, M., Ozoglu, Y., Mese, E., "An Approach to Torque Ripple Reduction in Fully Pitched Switched Reluctance Motors by Pole Tip Shaping", *11th Mediterranean Electrotechnical Conference MELECON, IEEE*, Cairo, Egypte, 2002.

[9] Ozoglu, Y., Garip, M., Mese, E., "New Pole Tip Shapes Mitigating Torque Ripple in Short Pitched and Fully Pitched Switched Reluctance Motors", *37th IAS Annual Meeting Industry Applications Conference, IEEE*, Pittsburgh PA USA, 2002.

[10] Chao Zhang, Kun Wang, Shuhui Zhang, Xiaoyong Zhu, and Li Quan, "Analysis of Variable Voltage Gain Power Converter for Switched Reluctance Motor", *IEEE Transactions On Applied Superconductivity*, vol. 26 (7), 2016.

Smartphone controlled ultrasonic nondestructive testing system design

S. GÜL[1] and A.T. ÖZDEMİR[2, 3]

[1] Bursa Technical University, Bursa/Turkey, samet.gul@btu.edu.tr
[2] Erciyes University, Kayseri/Turkey, aturan@erciyes.edu.tr
[3] Ultrasonar Defense and Aviation Technologies AS, Kayseri/Turkey, aturan@ultrasonar.com.tr

***Abstract* - The aim of this work is to design an ultrasonic non-destructive testing (NDT) system that utilizes the advanced features of smartphones and tablets. These superior features of smart devices can be listed as wide and sensitive touch screen, mobile internet connection, satisfactory CPU performance, application development environment and more. Integrating these features into a conventional NDT system increases the capabilities of the system while decreasing hardware costs. Therefore, an ultrasonic development card was designed in order to obtain these advantages. This development card is capable to measure thickness and detect internal flaws. Designed NDT system was also supported with encoder reading and ultrasonic data acquisition functions which are needed in computer controlled ultrasonic scanning systems. An android application was developed to send configuration data to the ultrasonic development board and visualize received signals captured from ultrasonic transducers. Smart devices are paired to the development card over Bluetooth communication channels. Ultrasonic signals visualized by the smart device can be saved for future investigations or shared via internet with different experts. Access to saved ultrasonic data provides the results can be evaluated in a variety of environments or monitor the inspection of a test material remotely.**

***Keywords* – Ultrasonic nondestructive testing, Smart systems, Android, Smartphone, Tablet, Hardware design.**

I. INTRODUCTION

NON destructive inspection (NDI) is a measurement and evaluation technique that gives information about inner structure of materials without harming or damaging them. There are many NDI methods and ultrasonic testing (UT) is one of them. However, it is apparent that ultrasonic method is more versatile than the other methods. In most cases, UT is used as a main or a complementary inspection method [1]. Some important advantages of UT technique can be listed such as easy to use, harmless to human and environmental health and has high accuracy [2]. Despite the fact that UT is a popular method, device prices are very expensive.

Smartphones have many advanced features and its powerful data processing capability makes them rapidly evolving technology. Nowadays, this technology has become an irreplaceable part of our lives [3].

Integrating smart devices into UT application has included many useful advantages. In this application we have designed our UT system extremely cheaper compared to the market.

The main function of the ultrasonic card developed in this study is to generate high voltage and high frequency electric pulses, digitize the incoming ultrasonic echoes and communicate with smartphone over Bluetooth. The application that we developed for smart devices can interpret and evaluate the ultrasonic data captured by the UT board.

II. SYSTEM DESIGN

The method that producing and capturing ultrasonic waves with the same single ultrasonic transducer is called pulse-echo (PE) and it is one of the most commonly used methods in ultrasonic NDI [2]. In this study, PE method was also used in our application. Figure 1 illustrates the basic idea of ultrasonic inspection process with our system.

The process of our inspection application is as follow. First, the desired configuration values for the ultrasonic test are sent from the Smartphone to the ultrasonic card via Bluetooth. When the ultrasonic card received the configuration data, the configuration of the card is accomplished such as amplification rate, desired high voltage amplitude value and other parameters. For example, "Number of Pulses" parameter is written in the corresponding address in FPGA because ultrasonic pulses are generated by MOSFET bridge controlled by an FPGA. When the configuration process is finished then the initialization process is performed by microcontroller unit (MCU). Ultrasonic waves are started to be generated by ultrasonic transducer after the initialization process completed. Reflected ultrasonic signals from the material are captured by the same ultrasonic transducer and amplified by amplifier units in ultrasonic card. Amplified signals are transferred to the digitizer unit and converted to 10 bit binary values with Analog to Digital Converter (ADC) unit. ADC outputs are connected to the FIFO memory built in the FPGA. When FIFO memory becomes full an external interrupt is created to activate MCU. FIFO memory content is transferred to External Bus Interface (EBI) of the MCU via Direct Memory Access (DMA) and MCU sends this data to the smart device over Bluetooth communication channel. The program developed for the smart phone is used to evaluate and interpret the digitized signal received.

Inspection results are displayed on smartphone screen as A-Scan graphic representation, see Figure 1. In this graph, the horizontal axis defines time and the vertical axis defines the signal strength.

A. Hardware Design

This ultrasonic development card was previously implemented on a TMSC6416 DSP development kit with several auxiliary kits [4]. We designed our custom ultrasonic card with the knowledge that we experienced our previous implementation on a commercial development kit. The general block diagram of our custom ultrasonic card is given in Figure 2. The block diagram of the system consists of four main units, Ultrasonic Analog Front End (UAFE), voltage regulation, FPGA and MCU units.

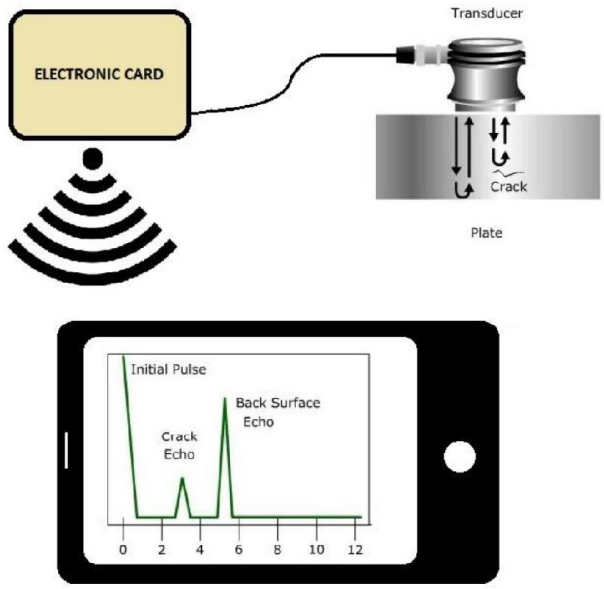


Figure 1: General overview of ultrasonic inspection process of the developed system

This card is able to produce adjustable high amplitude voltage between +40 V and +250 V. Our ultrasonic card has a programmable high-frequency ultrasonic pulse generator, 0.5 MHz to 10 MHz, in ±250 V range. Parameters of ultrasonic pulses such as amplitude, frequency, repetition frequency and number of pulses can be set by user. This ultrasonic card has also an adjustable 72 dB amplifier and a fast 100 MHz digitizer (ADC). FPGA unit is employed for data acquisition and signal processing. The MCU unit has a high-speed (200 MHz) DSP microcontroller that manages peripherals by controlling LCD screen, keypad, buzzer, buttons and set parameters of regulators, amplifiers and ADC. MCU unit also communicates with internal memories and USB port.

The ultrasonic card developed in this study supports both PE and Through Transmission (TT) ultrasonic inspection methods. Ultrasonic data acquisition system consists of two channels, A and B Channels. This means two different frequencies can be used at the same time in a single inspection. It can be operated with up to four single-element (two TT channels) and two dual-elements (two PE channels) ultrasonic piezoelectric transducers.

This development card provides ultrasonic inspection with a smartphone over Bluetooth and with a PC over USB communication channels.

Analog to digital conversion, data acquisition and data processing operations were made at very high frequencies by a 100 MHz ADC, a 50 MHz Cyclone FPGA and a 200 MHz PIC32MZ family microcontroller respectively.

B. Software Design

In this study, LG G5 H850 smartphone is used as android software development platform for ultrasonic inspection applications. This smart device has a Qualcomm MSM8996 Quad-core CPU chipset which is powerful enough to deliver satisfactory computing performance. There are two of 2.15 GHz Kryo and two of 1.6 GHz Kryo embedded CPUs in this chipset [5]. The android application that developed in this study also has the ability to save the inspection data to a SQLite database. This database can be transferred from smartphone to PC. This function gives user an opportunity to work with saved inspection data on MATLAB environment.

Structure of the data received via Bluetooth in the Android application is described in Table 1. Each package starts with hexadecimal '0xFF' value means open a new transfer. Then the package length is transmitted with two bytes, the first bit of these two byte is the most significant. The forth byte defines the package topic, and the next bytes are the data of the topic.

Table 1: The structure of the data package used in communication between the smart phone and the card

Data No	Byte0	Byte1	Byte2	Byte3	Byte4	…
Data	0xFF	0x00	0x03	0x01	0x01	…
Meaning	Start the Transfer	Package length		Package Topic	Topic Data	

The program of the Android interface consists of two main parts, which are configuration and analysis. Some features in the configuration settings menu are given as follows. "Buffer size" is the parameter that specifies the memory size of captured ultrasonic signals. This feature can be set between 200 and 16.000 samples (each sample is represented with eight bits). It limits the amount of data to be acquired after an ultrasonic wave package is sent to material. The acquisition duration of ultrasonic echoes varies depending on the ADC sampling frequency. For example, when the sampling frequency is set to 100 MHz, then sampling process will be performed by 10 ns steps. In this test if the buffer size is set to 16.000 then ultrasonic data acquisition will be performed in 160 µs (10 ns × 16.000 samples). When the sampling frequency decreased to 50 MHz, sampling will be made with 20 ns steps, and the data acquisition will be completed within 320 µs. "Pulse frequency" is used to change the frequency of high amplitude pulses depending on ultrasonic transducers. “High voltage” digitally adjusts the pulser voltage with 0.5 V steps. Depending on different types of ultrasonic tests, the number of pulses applied to the material may vary and this parameter can be changed with “The number of pulses” submenu. "Sampling frequency" is an important system parameter and defines the resolution of the acquired ultrasonic signal. The system capacity is maximum 100 MHz however 50, 25 and 12.5 MHz options are available. Mode of UT method can be switched between TT and PE by "Ultrasonic method" parameter. In TT mode channels can be set as pulser or receiver by labeling them as “Select Read Channel" or "Select Pulse Channel" options.

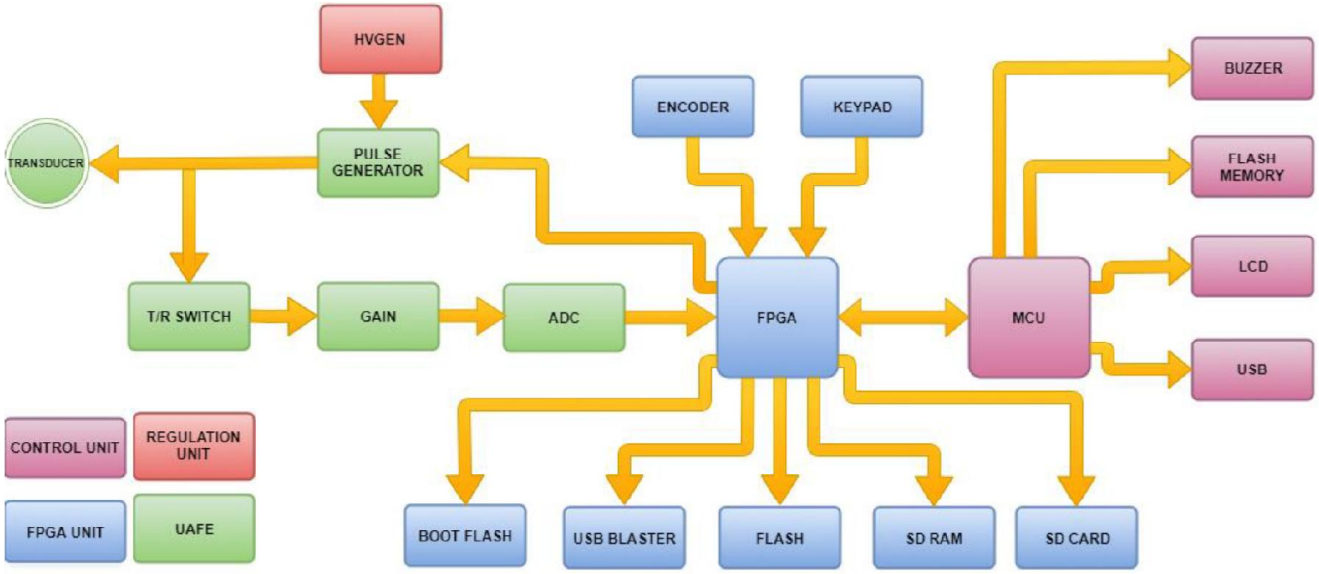


Figure 2: General block diagram of the developed card

Analysis menu has different tools and features as summarized follow. The most important analysis tool is the "graph" section and it visualizes the captured ultrasonic echoes on smartphone screen. Horizontal axis gives the number of samples (up to 16.000) and vertical axis gives signal strength (between 0-255 steps). Recorded UT data can also be recalled for visualization on the graph screen. Figure 3 shows menus on the screen. The sampling speed can be set with ADC FREQ menu. Amplification of the card can be managed with GAIN menu. A gate for measuring the thickness can be defined with GATE CONFIG menu. Different gates are shown in Figure 3 (a, b, c) as red lines. Thickness of a material can be displayed on graph screen in mm or inch. Thickness gives distance of back wall of a material or possible flaws as it shown in Figure 1. UT devices are tested with calibration blocks. CALIBRE menu is also used to test our ultrasonic card with known materials in terms of composition and thickness. We able define velocity of ultrasonic signal according to certain thickness of a calibration block.

III. Experimental Results

An ultrasonic evaluation was applied to a 63 mm tick aluminum reference block, shown in Figure 4. There are two artificially created defects on this aluminum test block at different depths. The aim of this evaluation is to demonstrate how successfully our system detects flaws in the reference block. The sampling frequency was set to 100 MHz. This means time interval between two successive samples is 10 ns. When evaluation screens (Figure 3) are examined, there are three meaningful sections in returning echoes. These include initial pulse between 800 and 1000 samples, flaw echoes returning from a defect in material between 1700 and 2000, and the back wall echo reflected from the bottom of the material between 2600 and 3000 samples. Some ultrasonic waves generated from transducers penetrate into the material while some are reflected back from the surface of the material. Signals reflected back from the surface create initial pulse. When penetrating waves encounter with a discontinuity some of them are reflected back from that point and the remaining waves continues to their path. Reflected signals from the discontinuity regions cause flaw echoes. Back wall echo refers to the ultrasonic waves that are reflected back from the bottom of the material.



Figure 3: (a) Measurement of the thickness of the material, (b) Position of the first defect in the material, (c) Position of the second defect in the material

All these three kinds of reflections are caused of acoustic impedance mismatches. When ultrasonic waves transferring from one material to another, some of them are reflected back and remaining continue to penetrate the materials. The reflection and penetration rates of ultrasonic waves vary according to materials' acoustic impedances. Reflection rate increases while penetration rate decreases with increased difference between materials' acoustic impedances.

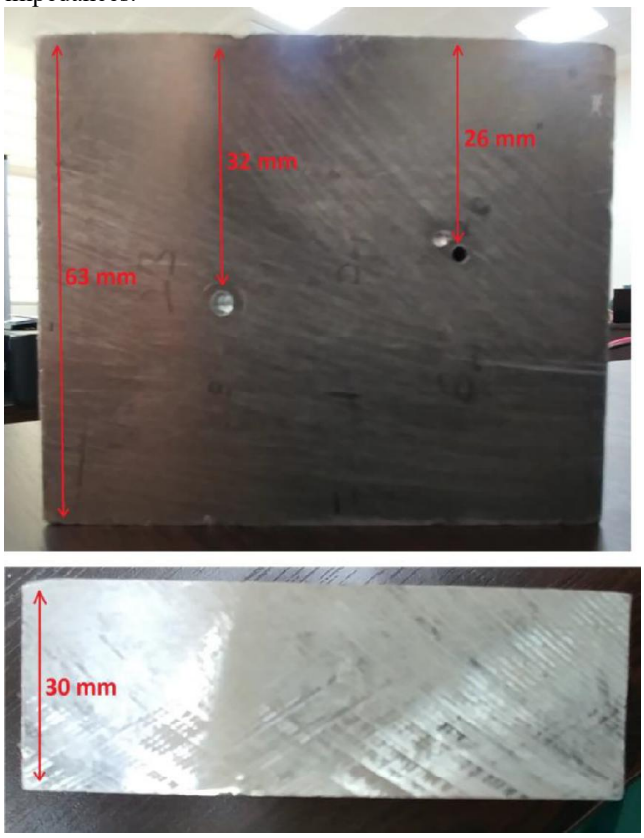


Figure 4: Aluminum reference block

The distance of a reflected echo is calculated as Equation (1). Here d is the distance between the surface of the material and the discontinuity region in an inspected material, v is the speed of sound in the material and t is the time of flight that sound needs to travel the particular distance. The reason of dividing t into two is that the ultrasonic evaluation is performed with pulse-echo method in this study. In PE method only one ultrasonic transducer is used to generate pulses and capture back echoes, therefore obtained time is composed of arrival and departure times. Since arrival and departure times are equal t is divided into two [6].

$$d = v \cdot (t/2) \quad (1)$$

Speed of sound through different materials is different [7]. Thickness of a material and the depth of the defect in it can easily be calculated by Eq. 1. Since the speed of sound in aluminum and the duration are known the depth of defect can easily be calculated. In figure 3 (a), the back wall echo of the aluminum block was evaluated. In order to find the duration of the back wall echo the number of samples between the highest peak of the initial pulse and the highest peak in the back wall echo are multiplied by 10 ns. The speed of sound in aluminum is constant and available at sources. The thickness of the material was found to be approximately 63 mm. In figure 3 (b), the location of the first defect in the aluminum block was detected at a depth of about 32 mm. In figure 3 (c), second defect was detected at a depth of about 26 mm in the aluminum block. As a result, an accurate inspection was performed using smartphone.

IV. Conclusion

A different point of view has been achieved by integrating smartphones with conventional ultrasonic NDT devices. The designed system can receive the inspection data from custom designed ultrasonic card wirelessly. Smart device can evaluate the data and control the ultrasonic card. An android program developed for smart devices that can record and evaluate the received ultrasonic signals. Smartphone can share the saved inspection data thanks to the mobile communication features. Integrating the advanced features of the smartphone brings innovative features to conventional ultrasonic NDT. For example, user can save the coordinates of the location where the inspection is made or take photos of the inspected materials. Smartphone CPUs are powerful enough to perform DSP calculations. With the development of mobile technology, the numbers of academic study is increasing [8]. For example, if DSP operations are needed and there is no enough processor power to do this on the hardware, it can be handled by a smartphone. Android NDK platform gives ability to programmer use C/C++ coding skills in android applications. For example, the grain structure of materials is scattering the ultrasonic waves and this causes noise in the received signal [9]. Removing these noises from the signal is possible and this filter can be built on smartphone instead of a DSP chip. These advantages provide a development environment for different applications for enhancing the features of the conventional NDT application.

References

[1] M. V. Brook, *Ultrasonic Inspection Technology Development and Search Unit Design: Examples of Practical Applications*. IEEE press, 2012.

[2] A.T. Özdemir, "A low-cost and highly reliable amplitude modulator design for PC-based PCI plug ultrasonic pulser receiver boards", *Electronics World*, 120 (1937), pp.30-33, 2014.

[3] A.T. Özdemir, A. Orman, "Developing an iPhone smartphone based fall detection algorithm", *Proc. 23rd Signal Processing and Communications Applications Conference (SIU),* pp. 2456-9, Malatya, Turkey, 16-19 May, 2015.

[4] A.T. Özdemir, A. Atcı, "A TMS320C6416 DSP-based high-speed data acquisition system", *Proc. 23rd Signal Processing and Communications Applications Conference (SIU),* pp. 1315-8, Malatya, Turkey, 16-19 May, 2015

[5] GSMArena. (2016, February). LG G5 H850. [Online]. Available: https://www.gsmarena.com/lg_g5-7815.php

[6] NDT Resource Center. (2012) Normal Beam Inspection. [Online]. Available: https://www.nde-ed.org/EducationResources/CommunityCollege/Ultrasonics/MeasurementTech/beaminspection.htm

[7] Olympus. Material Sound Velocities. [Online]. Available: https://www.olympus-ims.com/en/ndt-tutorials/thickness-gage/appendices-velocities/

[8] W.J. Yi, S. Gilliland, J. Saniie, "Mobile ultrasonic signal processing system using android smartphone" *IEEE 56th International Midwest Symposium on Circuits and Systems (MWSCAS),* pp. 1271-1274, 2013.

[9] J. Saniie, D.T. Nagle, K.D. Donohue, "Analysis of order statistic filters applied to ultrasonic flaw detection using split-spectrum processing," *IEEE Transactions on Ultrasonics, Ferroelectrics and Frequency Control*, vol. 38, no. 2, pp. 133-140, Mar. 1991.

Microwave Absorber Design in Layered Structure Using Differential Evolutionary Algorithm

Ahmet COŞKUN, Sibel YENİKAYA, Gökhan YENİKAYA, Mesut TOZAN

Departmant of Electrical-Electronic Engineering, University of Uludağ, Bursa, 16059, Turkey
coskun.ahmet@msn.com,sguler@uludag.edu.tr,yenikaya@uludag.edu.tr, tznmesut@gmail.com

Abstract **- In this paper, the microwave absorber which consists of several layers was designed. The aim of the designing these structures was to decrease target's radar detectability within the range of 0.5-8 GHz frequency bands by minimizing its reflection coefficient. Several materials with thicknesses ranging between 0.01 and 2 mm were considered for the design of microwave absorber. And as such they were used a with total thickness less than 5 mm. The reflection coefficient of microwave absorbers was obtained using a recursive procedure. The optimization algorithm based on differential evolution (DE) was used to obtain the fine structures that have low reflection coefficient. The obtained results were compared by literature. For this idea, the software which computes the reflection coefficient of the microwave absorber was developed in MATLAB.**

Keywords **- Electromagnetic absorbing structures, Reflection coefficient, Multilayered microwave absorber, Differential evolution.**

I.INTRODUCTION

Microwave absorbers with multilayer are very important components which are designed for specifically on civil and military applications. In recent years many studies demonstrated that minimizing reflection of radar signals on target objects by reducing radar cross section is significant [1],[2]. In order to achieve this, many researchers studied on microwave absorbers. There are a lot of publications about this subject [3]. In design of multilayer microwave absorbers it is important that the reflection coefficient should be reduced and structure should be thin. In our paper we focused on the design of the microwave absorbers. In view of the application of these absorbers in the area of low observability, the coatings need to exhibit a low reflection coefficient over a wide frequency range. The primary goal of the research reported in this paper is the development of a simple technique for designing such an absorber and for investigating the tradeoff between an absorber thickness and reflectivity. Many parameters of the absorber can be varied in order to obtain its optimal characteristics by using an optimization technique. These parameters are the number of layer, thickness of layer, frequency, and wave polarization [4].

Various techniques are proposed for designing absorbers. These techniques are genetic algorithm (GA), optimal control approach, particle swarm optimization (PSO), differential evolution (DE), central force optimization, etc. Pesque et al. [5] proposed a technique for designing absorbing coating which is based on an optimal control approach. In this method, thin absorbing coatings are designed by cascading layers of different materials which are chosen from a predefined set of available materials, such that the absorption properties of the coating are maximized over a specified frequency range, while its thickness or surface mass is minimized. Although this optimal control based algorithm was shown to be very powerful, the authors acknowledge its major drawback of convergence to only a local minimum of the cost function which was defined as the maximum reflection coefficient over the frequency band of interest. As a global optimization tool, PSO which is used for the swarms to easily reach the goal is in most effective methods recently and developed by J.Kennedy and R.C. Eberhart in 1995 [6]. PSO [7]-[9] is based on the swarming behavior of birds, fish and other creatures. This technique is similar to the GA. Recently PSO has been applied to the problem of multilayer microwave absorber design [10], [11].

GA is a search technique used in computing, to find true or approximate solutions to optimization and search problems. The basic principles of GA was developed by John Holland. Different from traditional optimization techniques, rather than using parameter sets, GA solutions are represented in binary as strings of 0s and 1s, but other encodings are also possible. Being probability rule-based, GA requires only an objective function. Rather than whole solution space, GA scans the particular parts. Therefore, GA reaches the solution faster with its effective search [12]. In [13] design of multilayer absorbers using GA is represented.

DE was introduced by Kenneth Price and Rainer Storn in 1995 [14]. It is a simple metaheuristic and stochastic population-based evolutionary algorithm (EA) for global optimization problems. DE algorithm has gradually become more popular and has been used in many practical cases because it has good convergence properties. A new version of the DE algorithm is used in this paper; namely, the self-adaptive DE. In this algorithm, the setting of the control parameters is made adaptive through the implementation of a competition into the DE algorithm [15]-[17].

In this paper, DE optimization technique is presented for designing microwave absorbers. This algorithm offers several advantages over the existing techniques. This procedure systematically determines both the thickness and the material parameters of the layers that minimize the reflection coefficient over a specified range of frequencies and the total thickness. In our study we used materials with thickness varying between 0.01 and 2 mm. The thickness and material type of multilayer microwave absorber structures with varying number of layers were determined by a MATLAB Software with DE optimization. The layer

parameters like thickness, dielectric constant and conductivity to reduce the reflectivity were determined by optimization algorithm, therefore an optimization was achieved for microwave absorber. In our study, the materials in Table 1 were used and 0 degree was selected as the angle.

II.FORMULATION OF THE PROBLEM

In this paper the reflection coefficients of the design is computed by transmission line matrix approach that used wave equations. A multi-layer microwave absorber structure is shown in Figure 1. Here, multi-layer microwave absorber which composed of the different materials with N layer is covered by the perfect conductor layer.

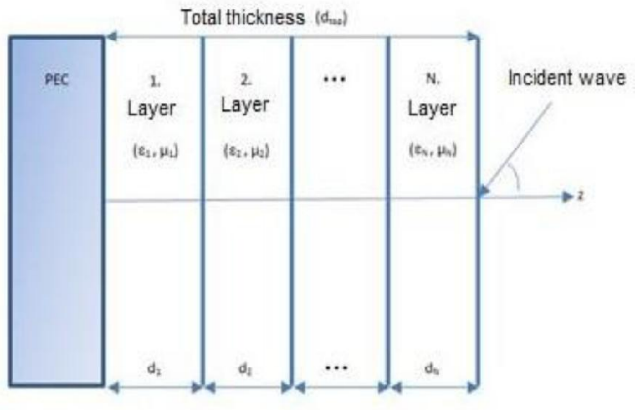


Figure 1: Multilayer microwave absorber structure [13].

Generally, the aim is to designed the multi-layer system which minimize the reflection coefficient at the specially frequency band and at the specially the angle of incidence. The reflection coefficient for the multilayered structure are calculated using a recursive procedure [18] as

$$\widetilde{R}_{i,i+1} = \frac{R_{i,i+1} + \widetilde{R}_{i+1,i+2} e^{-j2k_{i+1,z}d_{i+1}}}{1 + R_{i,i+1}\widetilde{R}_{i+1,i+2} e^{-j2k_{i+1,z}d_{i+1}}} \quad (1)$$

To TE polarization:

$$R_{i,i+1} = \frac{\mu_{i+1}k_{i,z} - \mu_i k_{i+1,z}}{\mu_{i+1}k_{i,z} + \mu_i k_{i+1,z}} \quad (2)$$

To TM polarization:

$$R_{i,i+1} = \frac{\varepsilon_{i+1}k_{i,z} - \varepsilon_i k_{i+1,z}}{\varepsilon_{i+1}k_{i,z} + \varepsilon_i k_{i+1,z}} \quad (3)$$

Where, ε_i and μ_i are the permittivity and permeability of the i.th layer, respectively. $k_{i,z} = k_i \cos\theta_i$. Where, θ_i is the incident angle of the i.th layer. The above equations are recursive relations that express $\widetilde{R}_{i,i+1}$ in terms of $\widetilde{R}_{i+1,i+2}$. The multilayer structure is shown in Figure 1.

III.THE DIFFERANTIAL EVOLUTION OPTIMIZATION

In this paper, the DE algorithm which is one of the most popular optimization methods was used. DE algorithm is an algorithm based on population and was used crossover, mutation and selection operators as used GA. The basic idea of the DE consists in alternating two populations, P and Q, of the same size, NP. A new trial point, y, is composed of the current point, x_i, of the old population and point ~u obtained by using mutation. If $f(y) < f(x_i)$, point y is inserted into the new population, Q, instead of x_i. After completion of the new population, Q, the old population, P, is replaced by Q and the search continues until the stopping condition is fulfilled [15].

The thickness of layers is obtained by using the DE algorithm that given the flow chart in Figure 2. The thickness of each layer is chosen as maximum 2 mm and the total thickness of the designed structure is chosen as maximum 5mm. Iteration number (N) is taken as 100 at the optimization process.

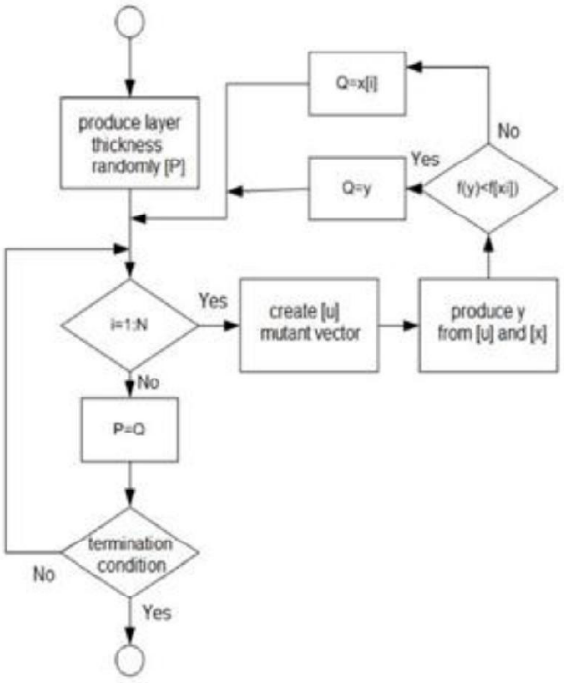


Figure 2: Flow chart of optimization.

IV.NUMERICAL RESULTS

In this paper, multilayer microwave absorbers were designed by the materials that given in Table 1. In the microwave absorber design, the optimum design was obtained by the using the different materials. The first layer where the electromagnetic waves come on the surface was taken as free space. The last layer was considered as the perfect conductor surface. The inner-layers were chosen from the materials of which the properties are given at Table 1. The thickness and materials properties of each layer were considered constant throughout the layer. And also the surface of the layers was considered infinite for the purpose of the easy calculation.

Table 1: The lists of relaxtion-type magnetic materials that used in design [13].

Lossless dielectric materials ($\mu'=1$, $\mu''=0$)				
No	ε'			
1	10			
2	15			
Lossy magnetic materials ($\varepsilon'=15$, $\varepsilon''=0$) $\mu=\mu'-j\mu''$ $\mu'(f)=\frac{\mu'(1\,GHz)}{f^a}$ $\mu''(f)=\frac{\mu''(1\,GHz)}{f^b}$				
No	μ'(1GHz)	a	μ''(1GHz)	b
3	5	0.974	10	0.961
4	3	1.000	15	0.957
5	7	1.000	12	1.000
Lossy Dielectric materials ($\mu'=1$, $\mu''=0$) $\varepsilon=\varepsilon'-j\varepsilon''$ $\varepsilon'(f)=\frac{\varepsilon'(1\,GHz)}{f^a}$ $\varepsilon''(f)=\frac{\varepsilon''(1\,GHz)}{f^b}$				
No	ε' (1GHz)	a	ε''(1GHz)	b
6	5	0.861	8	0.569
7	8	0.778	10	0.682
8	10	0.778	6	0.861
Magnetic materials ($\varepsilon'=15$, $\varepsilon''=0$) $\mu=\mu'-j\mu''$ $\mu'(f)=\frac{\mu_m {f_m}^2}{f^2+{f_m}^2}$ $\mu''(f)=\frac{\mu_m f_m f}{f^2+{f_m}^2}$				
No	μ_m	f_m(1GHz)		
9	35	0.8		
10	35	0.5		
11	30	1.0		
12	18	0.5		
13	20	1.5		
14	30	2.5		
15	30	2.5		
16	25	3.5		

The absorber with seven layers is optimized to minimize the reflection coefficient at the 0.5-8 GHz frequency range. The optimization parameters that used in this situation are given at Table 2. The design values, which are obtained when comparing with [16] reference, are shown at Table 3 and Table 4.

Table 2: Parameter values that used in the optimization.

Parameter	Value
Frequency	0.5-8 GHZ
Iteration number	100
Population number	100
CR and F coefficient	0.8

The microwave absorber structure is consisted of seven layers at the first design. First layer is considered as free space and last layer is considered as the perfect conductor layer. The properties of the inter-layers are given at Table 1. The lengths of the inter-layers are obtained by the DE algorithms for the optimization and shown in Table 3. The total thickness of the absorber is chosen as maximum 5 mm and each layer's thickness is chosen as maximum 2 mm. As seen from Figure 3, the better results than in the literature were obtained by the presented design at the desired frequency range. Especially, it can be seen that the maximum reflection coefficient is lower at the desired frequency band. Also, the total thickness which is used at this design is designed to be 12.67% thinner than the presented value at reference.

Table 3: Parameters of the microwave absorber that used in the first design.

	D11		Data from [16]	
Layer num.	Material num.	Thickness(mm)	Material num.	Thickness(mm)
Layer 1	16	0.4617	14	0.459
Layer 2	6	1.6808	6	1.817
Layer 3	6	0.6834	6	1.028
Layer 4	5	0.5320	5	0.885
Layer 5	15	0.9963	15	0.809
Total thickness (mm)		4.3542		4.998

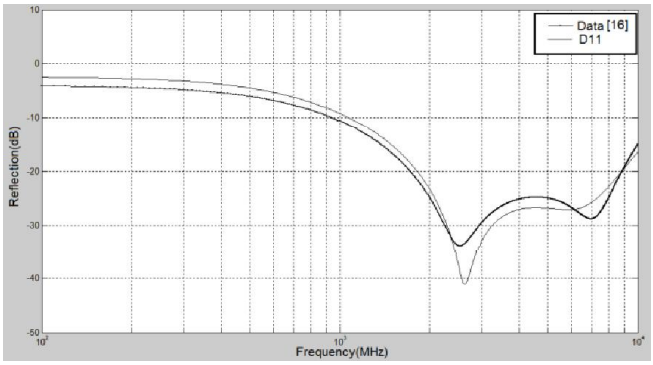


Figure 3: Reflection coefficient for design D11 described in Table 3.

In the second design an absorber with seven layers is designed to minimize reflection coefficient at the 0.5-5GHz frequency bands. The total thickness of the absorber is chosen as maximum 5 mm. The comparison values are given in Table 4. Figure 4 shows that the frequency response that is obtained by the second design. Better results are obtained by the presented design at the desired frequency band as shown in the figure. Especially, it can be seen that the maximum reflection coefficient is lower at the desired frequency band. Also, the total thickness, which is used at this design, is designed to be 13.3% thinner than the presented value at reference.

Table 4: Parameters of the microwave absorber that used in the second design.

	D22		D21		Data from [16]	
Layer num.	Material num.	Thickness(mm)	Material num.	Thickness(mm)	Material num.	Thickness(mm)
Layer 1	16	0.4648	14	0.4982	14	0.431
Layer 2	6	0.6466	6	1.0803	15	1.438
Layer 3	5	0.8946	5	1.4417	5	1.143
Layer 4	5	0.6514	4	0.7838	4	0.507
Layer 5	4	1.6641	4	1.0681	4	1.479
Total thickness (mm)		4.3215		4.8722		4.998

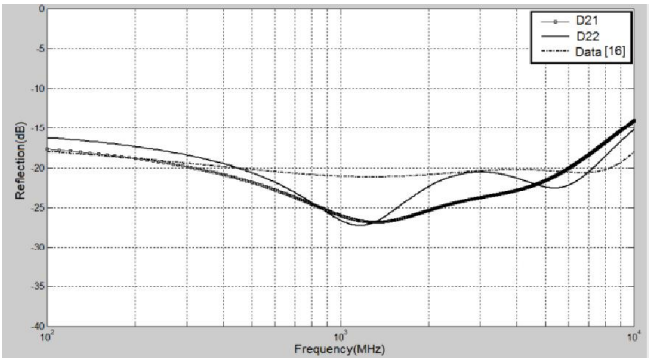


Figure 4: Reflection coefficient for designs D21 and D22 described in Table 4.

In the third design an absorber with seven layers is designed to minimize reflection coefficient at the 2-5GHz frequency bands. The total thickness of the absorber is chosen as maximum 5 mm. The comparison values are given in Table 5. Figure 5 shows that the frequency response that is obtained by the third design. As shown from figure, the better results were obtained by the presented design in the desired frequency range. Especially, it can be seen that the maximum reflection coefficient is lower at the desired frequency band. Also, the total thickness which is used at this design is designed to be 27% thinner than the presented value at reference.

Table 5: Parameters of the microwave absorber that used in the third design.

	D31		Data from [13]	
Layer num.	Material num.	Thickness(mm)	Material num.	Thickness(mm)
Layer 1	16	0.4523	16	0.486
Layer 2	6	0.9948	6	1.446
Layer 3	5	1.2263	5	1.272
Layer 4	11	0.8861	11	0.885
Layer 5	2	0.2469	2	1.155
Total thickness (mm)		3.8064		5.244

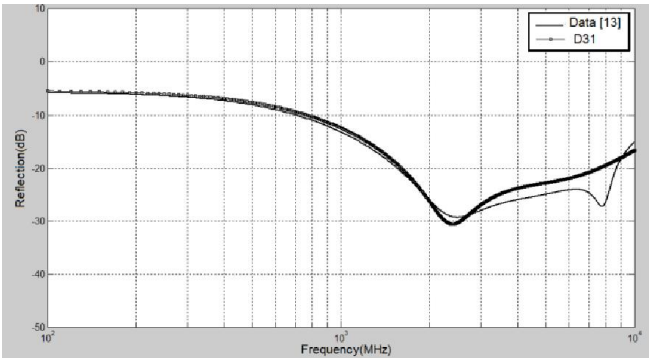


Figure 5: Reflection coefficient for design D31 described in Table 5.

In the fourth design is designed an absorber with seven layers to minimized reflection coefficient at the 2-5GHz frequency bands. The total thickness of the absorber is chosen as maximum 5 mm. The comparison values are given in Table 6. Figure 6 is shown that the frequency response that obtained by the three different designs. It is obtained the better results by the presented design at the desired frequency band as shown figure.

Table 6: Parameters of the microwave absorber that used in the fourth design.

	TT1		TT2		TT3	
Layer num.	Material num.	Thickness(mm)	Material num.	Thickness(mm)	Material num.	Thickness(mm)
Layer 1	14	0.4591	15	0.5486	14	0.4982
Layer 2	6	1.0416	5	0.1892	6	1.0803
Layer 3	5	1.5205	2	0.1966	5	1.4417
Layer 4	4	0.9277	4	1.6392	4	0.7838
Layer 5	5	0.6930	4	0.5391	4	1.0681
Total thickness (mm)		4.6418		3.1127		4.8722

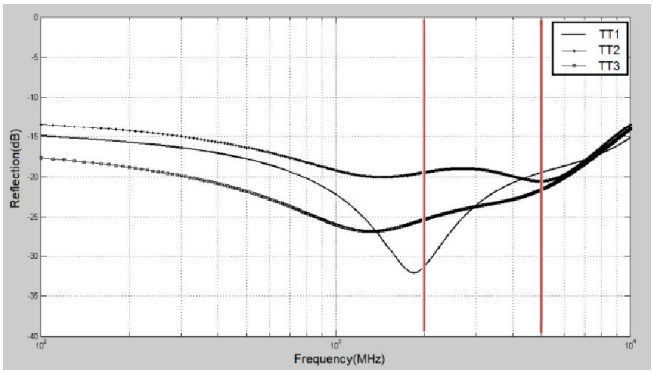


Figure 6: Reflection coefficient for designs TT1, TT2 and TT3 described in Table 6.

V.CONCLUSION

In this paper, multilayer electromagnetic absorbers are designed by the materials that are given in Table II. The thickness of materials and its placements are determined by DE algorithm that uses the values given in the Table I. The aim of these designs is to obtain the best results in the certain frequency range. Different designs have been presented which provided very good frequency response. The obtained designs are generally better than the others in the literature.

VI.REFERENCES

[1] Knott EF, Shaeffer JF,Tuley MT. *Radar Cross Section*. 2nd ed. Boston, USA, Artech House, 1993.

[2] Ruck GT, Barrick DE, Stewart WD, Krichbaum CK, *Radar Cross Section Handbook*, New York, USA, Plenum Press, 1970.

[3] Saville P, "Review of radar absorbing materials". Defence Research and Development Canada, Atlantic, Canada, TM 2005-003, 2005.

[4] Da Silva Macedo JA, De Sousa MJ, Dmitriev V. "Optimization of wide band multilayer microwave absorbers for any angle of incidence and arbitrary polarization". *SBMO/MTT-S International Microwave and Optoelectronic Conference,* Brasilia, Brazil, 25-28 Jul 2005.

[5] Pesque JJ, Bouche DP, Mittra R. "Optimization of multilayer antireflection coatings using an optimal

control method". *The Institute of Electrical and Electronics Engineers Transaction on Microwave Theory and Techniques,* 40(9), 1789-1796, 1992.

[6] Eberhart RC, Shi Y. "Particle Swarm optimization: Developments, Applications and Resources". *Congress on Evolutionary Computation,* Seoul, South Korea, 27-30 May 2001

[7] Eberhart RC, Shi Y, Kennedy J. *Swarm Intelligence*. San Fracisco, USA, Morgan Kaufmann, 2001.

[8] Eberhart RC, Shi Y. "Guest Editorial Special Issue on Particle Swarm Optimization". *The Institute of Electrical and Electronics Engineers Transaction on Evolutionary Computation,* 8(3), 201-228, 2004.

[9] Clerc M. *Particle Swarm Optimization.* Amsterdam, Netherlands, ISTE Publishing, 2006

[10] Chamaani S, Mirtaheri SA, Teshnehlab M, Shoorehdeli MA, Seydi V. "Modified Multi-Objective Particle Swarm Optimization for Electromagnetic Absorber Design". *Progress In Electromagnetics Research,* 79, 353-366, 2008.

[11] Jiang L, Cui J, Shi L, Li X. "Pareto optimal design of multilayer microwave absorbers for wide-angle incidence using genetic algorithms". *The Institution of Engineering and Technology Microwaves, Antennas & Propagation,* 3(4), 572-579, 2009.

[12] Goldberg DE. *Genetic Algorithms in Search, Optimization and Machine Learning*. 1st ed. Boston, USA, Addison-Wesley Longman Publishing, 1989.

[13] Michielssen E, Sajer J, Ranjithan S, Mittra R. "Design of lightweight, broad-band microwave absorbers using genetic algorithms". *The Institute of Electrical and Electronics Engineers Transaction on Microwave Theory and Techniques,* 41(6), 1024-1031, 1993.

[14] Feoktistov V. *Differantial Evoluation: In Search of Solutions.* 1st ed. New York, USA, Springer Science, 2006.

[15] TVRDIK J. "Differential Evolution with Competitive Setting of Control Parameters". *TASK Quarterly,* 11(1-2), 169-179, 2007.

[16] Goudos S. "Design of microwave broadband absorbers using a self-adaptive differential evolution algorithm". *International Journal of Radio Frequency and Microwave Computer-Aided Engineering,* 19(3), 364-372, 2009.

[17] Dib NI, Asi M, Sabbah A. "On the optimal design of multilayer microwave absorbers". *Progress In Electromagnetics Research C,* 13, 171-185, 2010.

[18] Chew WC. *Waves and Fields in Inhomogeneous Media*. New York, USA, Van Nostrand Reinhold, 1990.

On Fractional Order PI Controllers: An Analysis on Integer Order Systems using Integral Performance Criteria

E. ÇÖKMEZ and İ. KAYA

Dicle University, Diyarbakır/Turkey, erdal.cokmez@dicle.edu.tr
Dicle University, Diyarbakır/Turkey, ikaya@dicle.edu.tr

***Abstract* – In this study, an analysis of fractional order PI controller will be given. The analysis aims to show when the fractional order PI controller will result in better closed-loop performance: should one use it to control integer order systems? Tuning parameters of fractional order PI controller, namely K_p and K_i are determined by using integral performance criteria. To identify tuning parameters based on integral performance criteria, initial values are required. Ziegler-Nichols tuning method was used to find initial values of K_p (Proportional Gain) and K_i (Integral Gain) while fractional integrator order λ was varied in a range between 0.9 and 1.1. Finally, closed-loop system step responses have been plotted to compare performances. It has been observed that for open loop stable and unstable integer order systems integer order PI controllers result in better solutions. On the other hand, for integrating integer order systems it is possible to achieve better closed-loop responses with integer order PI controllers.**

***Keywords* – PI Controller, Fractional Order PI Controller, ISTE Optimization, Stable Processes, Integrating Processes**

I. INTRODUCTION

PID (Proportional Integral Derivative) controllers, in other words, three-term controllers are still the most popular controllers used in industry because of the advantages like simplicity, performance robustness, and the availability of many effective tuning methods based on minimum plant knowledge . In some studies, it has been shown that 90% of control loops are PI or PID controllers. On the other hand, the absence of derivative makes the controller less sensitive to noise so that PI controllers are more preferable than PID controllers [1]. This increases the importance of PI controllers.

The fractional calculus, known as a generalized form of integer calculus, has a history of more than 300 years. Its history started with a letter from Leibniz to L'Hospital on September 30, 1695 [2]. Development of technology increased studies on fractional orders systems and as a result of these studies, scientists started to use differential equations for system modeling. After that, the idea of fractional order PID controller was proposed by Podlubny in 1980 [3]. Different from classical PID controller, fractional order PID controller has two more parameters, integrator order λ, and derivative order μ. These parameters can be any real number and they make the controller more flexible. With tuning fractional orders λ and μ better responses can be observed in control systems. But, fractional PI controllers do not involve derivative. So, the fractional derivative order μ is not used for PI controllers. On the other hand, using fractional orders is not a solution that can always be used for control systems. Although there have been lots of studies on fractional PID controllers, it is not still certain that using fractional order PID controllers always give better results. So, scientists are still not sure about when to use fractional or integer order controllers.

In control theory, another problem that scientists deal with is time delay. Almost every physical system has time delay in response time and as a result of this problem computation of time response for these systems is more complicated. Generally, Pade approximation is used to approximate the time delay.

In this paper, an analysis, which is hoped to guide researchers about when to use integer or fractional order PI controllers, will be given. Integral performance criteria [4] is used to determine PI controller. During the calculation of tuning parameters of fractional order PI controller, different fractional integrator order of λ varying between 0.9 to 1.1 was assumed and the other tuning parameters of PI controller, namely K_p and K_i, were identified based on integral performance criteria. As the design method requires initial guesses, Ziegler-Nichols [5] tuning method was used to find initial tuning parameters for Proportional Gain (K_p), and Integrator Gain (K_i). For different integrator order, different controller parameters were obtained, and closed loop performances for designed fractional order PI controllers were compared.

The rest of paper is organized as follows. In Section II, Ziegler-Nichols tuning method, which is used for calculating initial parameters, is explained. Then Integral Performance Criteria is given in Section III. Simulation results and discussions are in Section IV. The paper finishes with the conclusion in Section V.

II. ZIEGLER-NICHOLS METHOD

This section gives a very brief review of Ziegler-Nichols [5] tuning method as it is used to find initial guesses for determining PI controller parameters. Although there are two Ziegler-Nichols tuning methods, only the closed loop oscillations based one is given. In this Ziegler-Nichols tuning method firstly a low/zero gain of K_p is used. Then, the value of K_p is increased until a steady-state oscillation occurs. At this point, critical K_p value is noted as K_{cr}. Period of oscillation P_{cr} is measured from the obtained oscillation. Based on these critical gain and period of oscillation, controller parameters can be found from Table I.

Table I: Ziegler-Nichols controller parameters for the second method

Controller Type	K_p	K_i	K_d
P	0.50* K_{cr}	∞	0
PI	0.45* K_{cr}	P_{cr} /1.2	0
PID	0.60* K_{cr}	0.50* P_{cr}	0.125* P_{cr}

III. INTEGRAL PERFORMANCE CRITERIA

In literature, different methods are proposed and studied to determine PID controller parameters. These methods need different system information like step response of open loop system as in Ziegler-Nichols method or some of them use the Nyquist curve of the system while the others use frequency response of the system to obtain the parameters with simple tuning laws. However, these methods may not yield the best solution to get a good closed loop response of the system. For example, Ziegler-Nichols based tuning often gives oscillatory responses. Integral performance criteria is a good alternative that can be used to get more satisfying responses [4]. This approach can only be applied to systems that its plant transfer function is known. The minimization function of integral performance criteria is given by the following equation:

$$J = \int_0^\infty \varphi[e(t), t]dt \tag{2}$$

As seen in (2), it is desired that the closed-loop system minimizes the error as a function of time. An optimum response of a system is obtained when the response that makes the value of J minimum is achieved. Integral performance criterion has different forms and optimum controller parameters depend on which form of criteria is used. The most commonly used forms of this criteria are Integral of Square Error (ISE) and Integral of Absolute Error (IAE). Performance functions of ISE and IAE are respectively given by the following equations:

$$J_{ISE} = \int_0^\infty e^2(t)dt \tag{3}$$

$$J_{IAE} = \int_0^\infty |e(t)|dt \tag{4}$$

General forms of ISE and IAE are respectively given by:

$$J_i(\delta) = \int_0^\infty \left[t^i e(\delta, t)\right]^2 dt \tag{5}$$

$$J_i(\delta) = \int_0^\infty t^i |e(\delta, t)|dt \tag{6}$$

In equations (5) and (6), δ represent parameters for the optimum response of the system. Varying value of *i* from 0 to 3 in equation (5), ISE, ISTE, IST^{2}E and IST^{3}E forms of performance criteria are obtained. In this paper, IST^{3}E criterion is used to determine tuning parameters of fractional order PI controllers.

IV. ANALYSIS OF INTEGER ORDER SYSTEMS WITH FRACTIONAL ORDER PI CONTROLLER

In this paper, (5) different integer order systems are selected to analyze closed loop performances with fractional and integer order PI controllers [5]. First, Ziegler-Nichols tuning method is used to find initial guesses for fractional PI controller parameters to use with integral performance criteria. IST^{3}E criterion is accomplished to determine optimum fractional PI controller parameters. During optimization procedure, integrator order, λ was kept constant at different values changing from 0.9 to 1.1 and remaining controller parameters, namely K_p and K_i, were calculated. Selected plants transfer functions are as listed below:

$$G_{P1} = \frac{1}{s+1}e^{-0.5s} \tag{7}$$

$$G_{P2} = \frac{1}{(s+1)^5} \tag{8}$$

$$G_{P3} = \frac{1}{s(s+1)}e^{-s} \tag{9}$$

$$G_{P4} = \frac{1}{s(s+1)^5}e^{-s} \tag{10}$$

$$G_{P5} = \frac{1}{(s-1)}e^{-0.2s} \tag{11}$$

Especially, stable, unstable and integrating processes with time delay having lower and/or higher order plants transfer functions were selected to examine the effect of the fractional PI controller on these integer order systems.

A. Example 1

Here, plant transfer function given by equation (7) is considered. Obtained controller parameters using IST^{3}E criterion are summarized in Table II.

Step responses for designed controllers are illustrated in Fig. 1. From the figure, it is clearly seen that integer integrator order results in a better system performance than fractional

integrator order. With integer PI controller, the system has a very low overshoot. But, when integrator order becomes fractional, the system yields much larger overshoots of about 80%.

Another important observation is that integer order PI controller has no steady-state error but, especially when integrator order is below 1, closed-loop systems have steady-state errors under fractional PI control, although they are negligible. Finally, it is seen that closed-loop system response of integer order PI controller has a much shorter settling time than a fractional order PI controller.

Table II: Controller parameters for example 1

Controller parameters		
λ	K_p	K_i
0.9	1.4944	2.9754
0.92	1.5538	2.9655
0.94	1.6096	2.9534
0.96	1.6606	2.9374
0.98	1.7079	2.9168
1	0.9612	0.9376
1.02	1.8582	3.0705
1.04	1.9364	3.2742
1.06	2.0023	3.4194
1.08	2.0615	3.5338
1.1	2.1163	3.6345

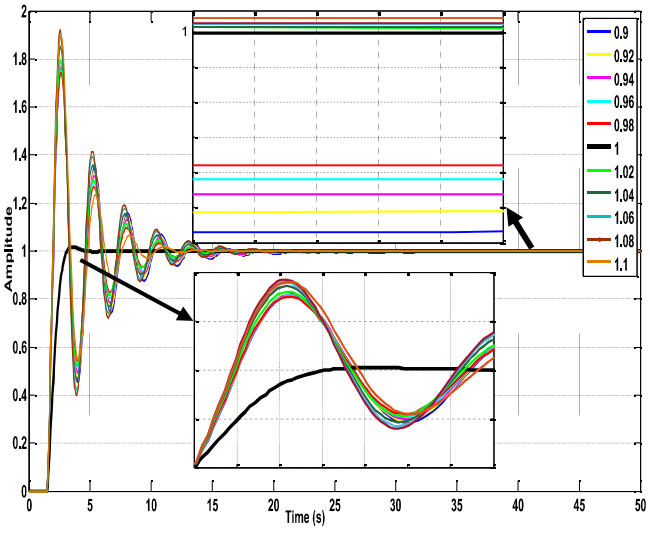


Figure 1: Step responses for plant transfer function of $e^{-0.5s}/(s+1)$ with integral performance criteria

B. Example 2

In this example, plant transfer function given by equation (8) is considered. Using IST^{3}E criterion given section III, obtained controller parameters are given in Table III.

Closed loop responses for this example are shown in Figure 2. Conclusions derived for example 1 are valid for this example as well. However, it must be noted that steady-state error related to fractional PI controllers is now more evident for integrator order of lower than 1.

Table III: Controller parameters for example 2

Controller parameters		
λ	K_p	K_i
0.9	0.5684	0.3436
0.92	0.5991	0.3284
0.94	0.6267	0.3131
0.96	0.6507	0.2976
0.98	0.6710	0.2815
1	0.4171	0.1670
1.02	0.7621	0.2790
1.04	0.835	0.3006
1.06	0.8898	0.3113
1.08	0.9337	0.3155
1.1	0.9714	0.3166

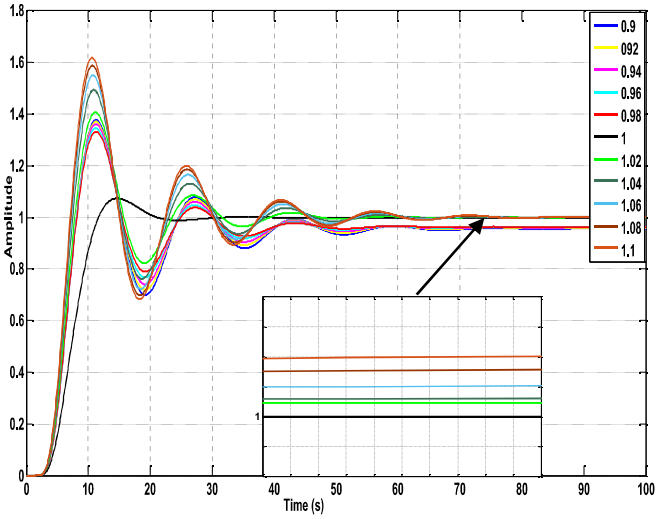


Figure 2: Step responses for plant transfer function of $1/(s+1)^5$ with integral performance criteria

C. Example 3

In contrast to the first two examples, in this example a plant transfer function with an integrator will be analyzed. The plant transfer function given in equation (9) is considered here. Obtained tuning parameters for integer and fractional order PI controllers are summarized in Table IV. As in first two examples, IST^{3}E integral performance criterion was used to calculate required controller tuning parameters, namely K_p and K_i.

Table IV: Controller parameters for example 3

Controller parameters		
λ	K_p	K_i
0.9	0.3496	0.0501
0.92	0.3488	0.0471
0.94	0.3478	0.0443
0.96	0.3475	0.0417
0.98	0.3493	0.0396
1	0.3545	0.0405
1.02	0.3705	0.0414
1.04	0.3904	0.0440
1.06	0.4067	0.0466
1.08	0.4183	0.0482
1.1	0.4273	0.0491

Step responses of controllers designed with IST^{3}E are illustrated in Figure 3. From the figure, it is seen that on the contrary of G_{p1} and G_{p2}, all systems have overshoots including a system with integer order controller. In the first two systems, when integer order PI was used, systems had very low overshoots. But when there is an integrator in the plant transfer function, as in G_{p3}, systems with integer order PI controller also have overshot. The least overshoot occurs when fractional order λ is determined to be 0.98, and when λ is 1.1 the most overshoot occurs.

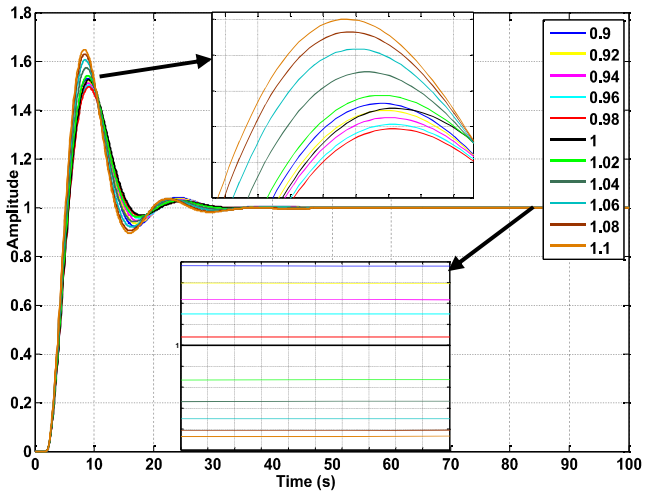


Figure 3: Step responses for plant transfer function of $e^{-s}/s(s+1)$ with integral performance criteria

D. Example 4

In this example, a high order integrating system with time delay is considered. Controller parameters obtained from Integral Performance Criteria are given in Table V.

Similar to example 3, which considers a lower order integrating process transfer function, considerably high overshoots are obtained for both integer and fractional order PI controllers. The least overshoot occurs when the integrator order λ is 0.92 and the most overshoot occurs when λ is selected as 1.1.

Table V: Controller parameters for example 4

Controller parameters		
λ	K_p	K_i
0.9	0.1063	0.0046
0.92	0.1072	0.0043
0.94	0.1082	0.0041
0.96	0.1093	0.0039
0.98	0.1105	0.0038
1	0.1123	0.0043
1.02	0.1152	0.0042
1.04	0.1185	0.0041
1.06	0.1221	0.0041
1.08	0.1253	0.0041
1.1	0.1281	0.0040

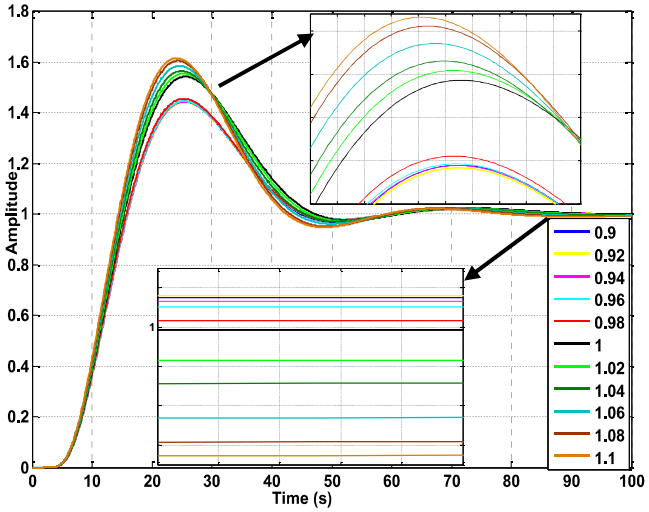


Figure 4: Step responses for plant transfer function of $e^{-s}/s(s+1)^5$ with integral performance criteria.

E. Example 5

In previous examples, open loop stable and integrating systems were considered. In this example, an unstable system with time delay is considered to be controlled by integer and fractional PI controllers. The transfer function of the unstable system is given in equation (11). Fractional and integer order PI controller parameters obtained by integral performance criteria are given in Table VI.

Step responses of designed controllers for different fractional order λ values are illustrated in Fig.5. It is seen from the figure that performance of integer order controller is better than fractional-order controllers. Fractional order controllers result in more oscillatory responses. Also, it is clearly seen that system with integer order controller has much shorter settling time.

Table VI: Controller parameters for example 5

Controller parameters		
λ	K_p	K_i
0.9	4.0079	6.1906
0.92	4.0675	6.2583
0.94	4.1210	6.3193
0.96	4.1714	6.3709
0.98	4.2146	6.4087
1	3.4284	2.6922
1.02	4.4151	6.9176
1.04	4.5129	7.4425
1.06	4.5934	7.8521
1.08	4.6649	8.2063
1.1	4.7322	8.5367

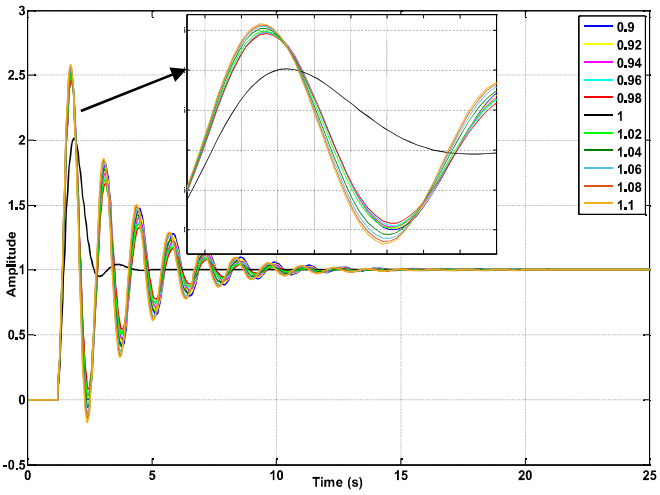


Figure 5: Step responses for plant transfer function of $e^{-0.2s}/(s-1)$ with integral performance criteria

V. CONCLUSIONS

The paper has given an analysis of the closed loop performances of integer and fractional PI controllers to control a class of integer order processes. It has been observed that for integer order open loop stable and unstable processes integer order PI controller gives much better closed-loop responses than fractional PI controllers. However, for integer order integrating processes, it is not always possible to achieve better closed-loop responses with the integer order PI controller, and with some fractional order λ value slightly better closed-loop responses have been gained.

REFERENCES

[1] C. A. Monje, Y. Chen, B. M. Vinagre, D. Xue, and V. Feliu, *Fractional-Order Systems And Control Fundamentals And Applications*. London: Springer, 2010.

[2] S. Das, *Functional Fractional Calculus for System Identification And Control*. Berlin: Springer-Verlag, 2008.

[3] I. Podlubny, "Fractional Order Systems And PID Controllers," *IEEE Trans. Automat. Contr.*, pp. 208–214, 1999.

[4] M. Zhuang and D. P. Atherton, "Tuning PID controllers with integral performance criteria," *Control 1991. Control. Int. Conf.*, no. 4, pp. 481–486, 1991.

[5] Z. G. Ziegler and N. B. Nichols, "Optimum settings for automatic controllers," *Trans ASME*, vol. 64, pp. 759–768, 1942.

Design of Floating Point PI Current Controller for Speed Control of IPMSM using FPGA

Abdulhasan Altaey[1] and Ahmet Afsin Kulaksiz[2]
[1] Ph.D. Student in Selcuk University, Konya/Turkey, Instructor in the University of Mustansiriyah, Baghdad, Iraq aaltaey13@gmail.com
[2] Associate professor in Selcuk University, Konya/Turkey, afsin@selcuk.edu.tr

***Abstract* – The PI Controller can be considered as the essential part for efficient Speed Control of the Interior Permanent Magnet Synchronous Motor. In digital control, two platforms exist to implement this controller, namely DSP and FPGA. The FPGA is more preferred than the DSP due to the concurrent facility. To obtain the full facilities of the digital control and for high accuracy speed control of motors, floating point PI Controller should be used instead of the fixed point. The problem of the FPGA is that it is programmed using VHDL or Verilog which deals only with fixed-point representation. This paper shows a full design of floating-point PI Controller using Altera DE2i-150 platform and Altera Megafunctions. The results are proven using two simulation platforms ModelSim-Altera Starter Edition 15.0 and Matlab Simulink.**

***Keywords* – FPGA, IPMSM, PI Controller, SVPWM.**

I. INTRODUCTION

The advanced features of the Interior Permanent Magnet Synchronous Motors (IPMSMs) such as high efficiency, high torque to inertia have been made them used in a lot of applications. To achieve these features, it is necessary to use high performance controller. The previous works [1-4] proved the reliability and stability of systems, which used PI Controllers. The implementation of these controllers is either analog or digital. For more accurate results, the digital approach is more preferable. In general, to implement these controllers, microprocessor, microcontroller or DSP as well as software have been used [5-8]. The disadvantage of these methods is the long time required to compile and execute the software instructions.

The other possible platform for control strategy is the FPGA. The current trend in literature shows that FPGA is more preferable than DSP because the FPGA is clock-based which means faster processing capability compared to instruction based (DSP). Also, the FPGA has the facility of concurrent operation which will reduce the processing time a lot.

The FPGA can be programmed using the VHDL or the Verilog. Both of these hardware languages deal only with fixed-point representation while precise speed control of motors requires PI Controller with floating-point processing. To alleviate this problem ALTERA has provided IP Cores dealing with this floating-point representation. Some of these IP Cores are free and some require a license. Building the PI Controller using FPGA requires mix using of VHDL or Verilog and the IP Cores.

All the IP Cores Megafunctions are clock-based. Each IP require some number of clock cycles to obtain the result.

Hence the processes that work in parallel will have different execution times. As an example, if the sampling time is 100us, clock cycle period is 20 ns and as the floating point adder, IP Core requires 7 cycles that means the adding process will be repeated by (100000)/(7*20) in each sampling time.

To solve this problem each process should have a synchronizing process using VHDL or Verilog to ensure the processes are not repeated during one sampling time.

The previous problems and for other problems such as the limited availability of the hardware sources of the FPGA platform make the researchers prefer to use fixed-point PI Controller rather than floating-point at the expense of losing the accuracy.

This paper uses a mixed design of VHDL and ALTERA IP Core Megafunctions to design a floating-point PI Controller for Speed Control of the IPMSMs. Firstly discrete time equations are derived, then the PI parameters are designed using the Root-Locus method.

A simulation package of the Electronic Design Automation (EDA) can be used to verify the algorithms that have been built using FPGA. This EDA simulator provides a verification interface between MATLAB Simulink and FPGA board. This paper uses the ModelSim-ALTERA Starter Edition 15.0 and MATLAB SIMULINK to prove the results. The results of both simulations are exactly the same which proves the design.

II. DISCRETE TIME DESIGN

Figure *1* shows a general description of the whole system of speed control of the IPMSM. According to the difference between the reference and measured speed, the Speed PI Controller Commands the proposed current values to the Current PI Controller. The Current PI controller receives these proposed values as well as it receives the measured current values. According to the error between the commanded and measured values, the Current PI Controller will command the required voltage values to the motor. According to the commanded voltage values (vd_proposed, vq_proposed), Space Vector Pulse Width Modulation Signals (SVPWM) will be constructed to drive the motor (not shown in Figure *1*). The PI Controller process time should be finished within the dead time width of the SVPWM signals.

As it is clear from Figure *1* that the motor is decoupled to two axes, namely d-axis and q-axis. The following derivations are for the q-axis and in the same way it can be done for the d-axis.

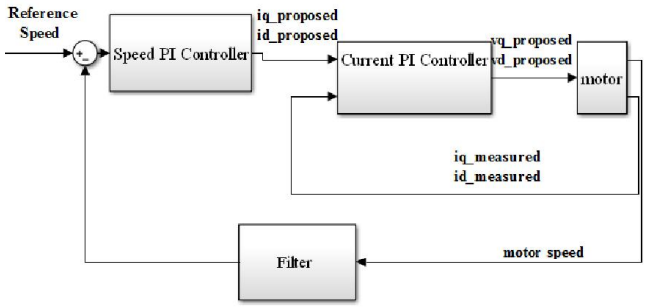


Figure 1 Speed Control Loop.

The PI controller for the q-axis current is shown in Figure *2*. Using Root Locus Method, the controller should be designed to give:

1. Zero steady-state error.
2. Fast transient response (as example for step change signal).
3. Small settling time.
4. Minimum overshoot.

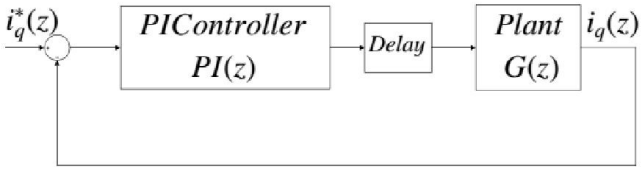


Figure 2 Current PI Controller.

$$PI_{(Z)} = (k_{pq} + k_{iq})\frac{\left(Z - \frac{k_{pq}}{k_{pq}+k_{iq}}\right)}{Z-1} \quad (1)$$

$$G_{(Z)} = \frac{k_1}{Z - k_2} \quad (2)$$

Where $k_1 = \frac{1-e^{-\frac{R_s}{L_q}T_s}}{R_s}$, $k_2 = e^{\frac{R_s}{L_q}T_s}$

R_s= Stator resistance, L_q= quadrature axis motor inductance, T_s= Sampling time

Where

$$\frac{i_{q(Z)}}{i^*_{q(Z)}} = \frac{Z^{-1}\, PI_{(Z)}G_{(Z)}}{1 + Z^{-1}\, PI_{(Z)}G_{(Z)}} = \frac{K\, PI^-_{(Z)}\, G^-_{(Z)}}{1 + K\, PI^-_{(Z)}\, G^-_{(Z)}} \quad (3)$$

The closed loop poles are determined from the characteristics equation:

$$1 + K\, PI^-_{(Z)}\, G^-_{(Z)} = 0 \quad (4)$$

Where K is the closed loop gain and equals:

$$D^-_{(Z)} = \frac{\left(Z - \frac{k_{pq}}{k_{pq}+k_{iq}}\right)}{Z(Z-1)} \quad (5)$$

$$G^-_{(Z)} = \frac{1}{Z - k_2} \quad (6)$$

$$K = (k_{pq} + k_{iq})\, k_1 \quad (7)$$

The value of the gain K is obtained from the root locus, and ω_c is the crossover frequency of the open loop transfer function G_{OL}^-.
The root locus starts from the open loop (G_{OL}^-):

$$G_{OL} = K\, PI^-_{(Z)}\, G^-_{(Z)} = K\, G^-_{OL} \quad (8)$$

$$G^-_{OL} = \frac{\left(Z - \frac{k_{pq}}{k_{pq}+k_{iq}}\right)}{Z(Z-1)(Z-k_2)} \quad (9)$$

The technical data of the motor used in this paper is shown in Table 1. The motor electric pole at $Z=k_2$ has a time constant of (L_q/R_s=14.2 ms). This long time constant can degrade the system response. To solve this problem, the zero at $\frac{k_{pq}}{k_{pq}+k_{iq}}$ is chosen to cancel this pole, hence (9) resolves to:

$$G^-_{OL} = \frac{1}{Z(Z-1)} \quad (10)$$

The root locus is shown in

Figure 3. The closed loop pole is chosen to give damping ratio of 0.947, overshoot = %0.0093 and the natural frequency is 7050Hz. The total gain is 0.263. The proportional and integral constants of the q-axis PI Controller solved as follows:

1. $\frac{k_{pq}}{k_{pq}+k_{iq}} = k_2 = e^{\frac{R_s}{L_1}T_s} = 0.993.$
2. $The\ gain\ (K) = 0.263 = (k_{pq} + k_{iq})\ (k_1).$
3. $k_1 = \frac{1-e^{\frac{R_s}{L_q}T_s}}{R_s} = 0.00195.$
4. Hence: $(k_{pq} + k_{iq}) = \frac{0.263}{0.00195} = 134.87.$
5. $k_{pq} = (k_{pq} + k_{iq})(0.993) = 133.9.$

6. $k_{iq} = 0.97$.

Table 1 IPMSM Technical Data.

Motor Type	ABB M2BJ 100L 6 B3
Nominal torque	14 Nm
Number of pole pairs	3
Stator resistance	3.59 Ω
Stator quadrature-axis inductance	0.051 H
Stator direct-axis inductance	0.036 H
Rotor permanent magnet flux	0.545 V s
Moment of Inertia	0.015 Kg m^2

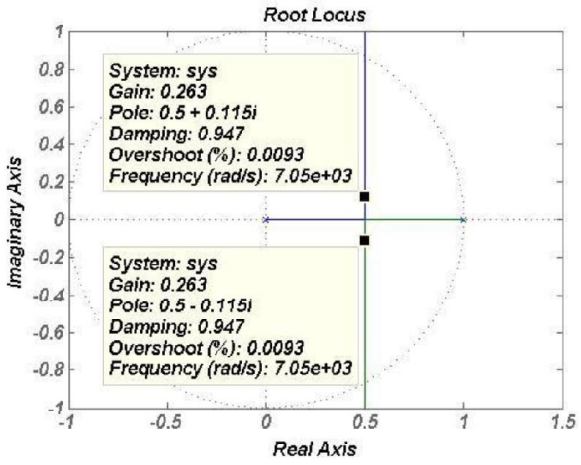


Figure 3 q-axis Current Controller Root Locus.

Applying these values in (3):

$$\frac{i_{q(Z)}}{i^*_{q(Z)}} = \frac{0.263}{Z^2 - Z + 0.263} \quad (11)$$

The step response of (11) shown in Figure 4 demonstrates that the settling time is 0.797 ms, which proves the controller stability.
The same procedure can be used for the d-axis PI Current controller.

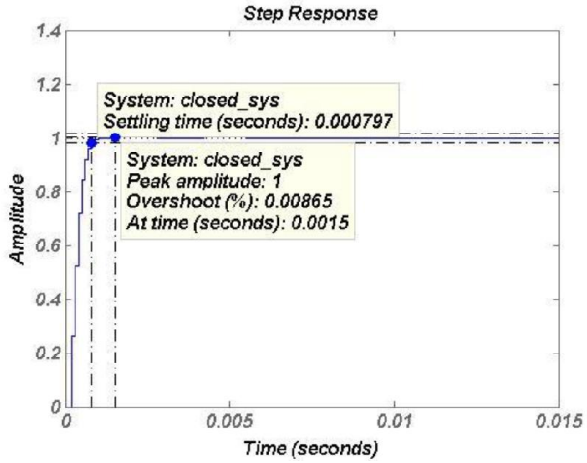


Figure 4 q-axis Step Response.

III. FPGA Design

Field Programmable Gate Array (FPGA) is low cost device with the capability of concurrent processes which is very important in applications that require parallel processing.
In most cases, the development of high performance control of the IPMSM needs FPGA with embedded processor IP (Intellectual Property) and an application IP [9][13-16]. The former is implemented by using software due to the complicated control algorithms, and the latter is implemented by hardware due to simple computation which may contain parallel computation. SVPWM is an essential part of speed control process. For an efficient system, the control process should be finalized in the dead time of the SVPWM. These SVPWM signals have been implemented using VHDL on ALTERA FPGA DE2i-150 as shown in

Figure 5. This dead time requirement is achieved by PI controller as hardware. One of the essential parts of the discrete PI Controller is the integrator shown in Figure 6 where:

$$y(n) = \frac{k_i T_s Z}{Z-1}\,\mathrm{u(n)} \quad (12)$$

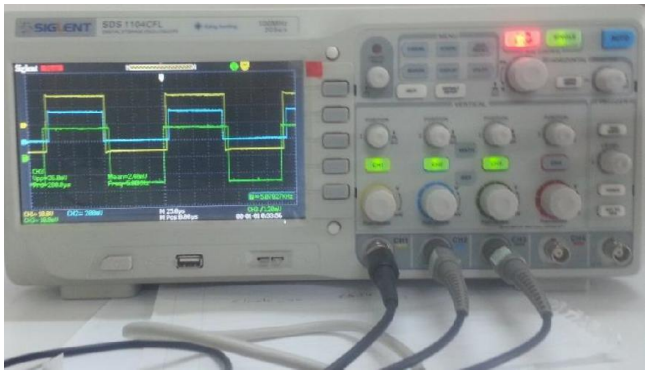


Figure 5 SVPWM Signals Using ALTERA DE2i-150.

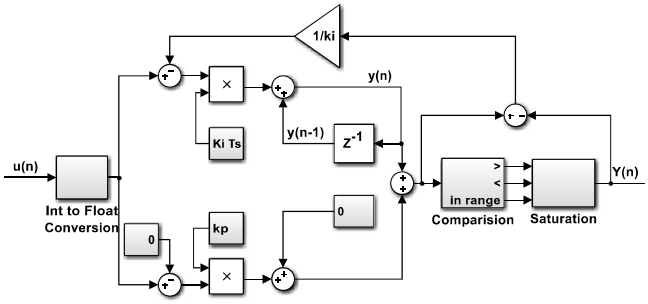


Figure 7 Balanced Path Floating Point Discrete PI Controller with Anti-Windup.

After some simplifications, Equation (12) can be written as (13).

$$y(n) = y(n-1) + k_i T_s\, u(n) \qquad (13)$$

According to these equations, the discrete PI Controller can be constructed. The current PI Controller output value is the commanded voltage of the IPMSM motor. The commanded value should not exceed the rating values. Hence anti-winding circuit [10-12] should be added to ensure that the rating values are not exceeded. To keep the precision, floating point representation is used for this PI Controller. All the mathematical operations (addition, subtraction, multiplication etc.) are done using the floating point ALTERA IP Cores. These IP Cores require different number of clock cycles to process its job. One important issue in the FPGA design is to make the signals (which is added or multiplied…) arrives at the same time. Otherwise wrong results will be obtained. To balance these paths, some part should be added as shown in

Figure 7. Instead of adding parts, a better solution exists that is by adding some algorithms similar to sample and hold. These algorithms can be written using VHDL only. According to the last discussion, the PI controller has been built using ALTERA DE2i-150 as shown in the next section.

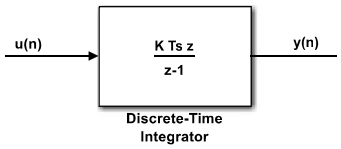


Figure 6 Back Euler Integrator.

IV. Simulation (Quartus & Matlab) Comparative Study

The response to two types of input signals: constant-input (Figure 8) and variable-input (Figure *9*) are studied. Two types of simulations have been done. The first simulation has been done to the floating-point PI Controller shown in Figure *10* using Model-Sim ALTERA STARTER EDITION 15.0. The response to the constant-input signals is shown in Figure *11* and the response to the variable-input signals is shown in Figure *12*. The second simulation has been done using MATLAB SIMULINK. The response to the constant-input signals is shown in Figure *13* and the response to the variable-input signals is shown in Figure *14*. Before doing comparison between these two simulations, it should be known that FPGA needs reset pulse and some delays to keep the synchronizing. Hence, the FPGA needs one sampling time delay before giving the response. Taking this note into consideration, a comparison between these simulation results is shown in Table *2*. The two simulation results are coincident 100% which prove the validity of the design method. This paper is a part of Ph. D. thesis, and a plan exists to apply this design experimentally.

V. Conclusion

This paper proposes a full design for floating point Discrete PI Controller for Speed Control of IPMSM using FPGA. The paper proposed to use a hybrid algorithm of VHDL which only fixed point and floating point ALTERA megafunctions (IP) Cores. The design of the Discrete PI Controller parameters has been carried out using Root Locus Method. Two Simulations have been done, one using Model-Sim ALTERA STARTER EDITION 15 and the other using MATLAB SIMULINK. The two simulation results are coincident 100% which validates the design.

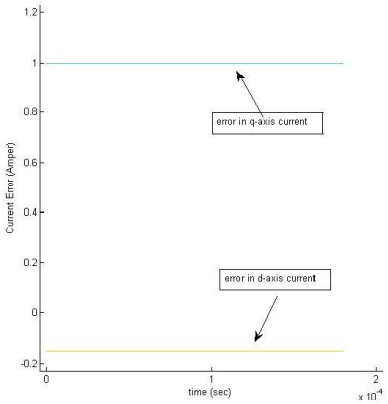


Figure 8 Constant Error Signals iq and id.

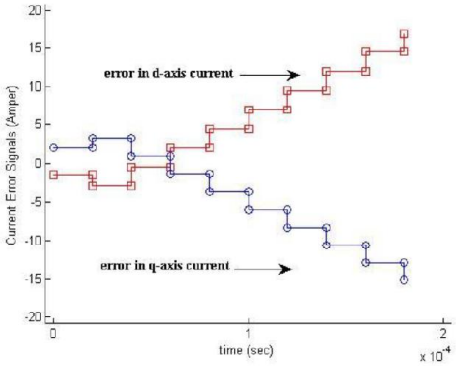


Figure 9 Variable Error Signals iq and id.

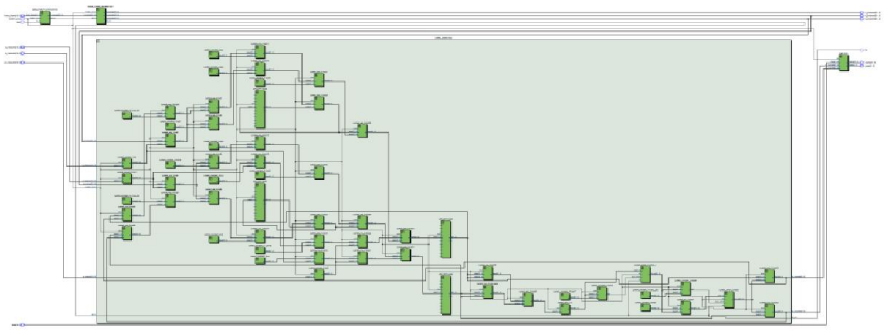


Figure 10 Final Floating Point Current PI Controller constructed using ALTERA Megafunctions and VHDL.

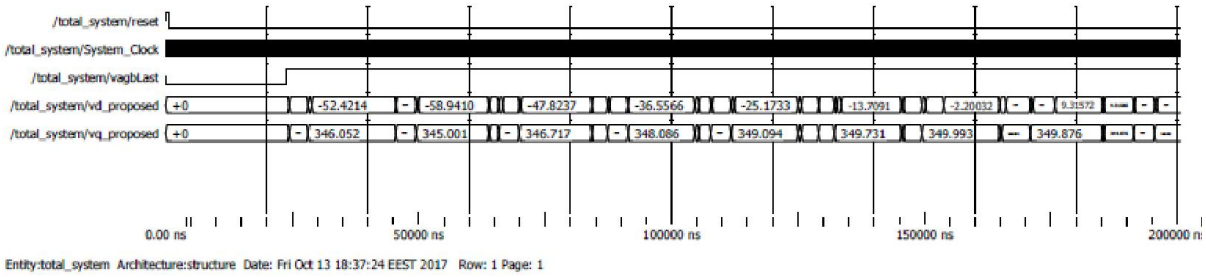


Figure 11 Simulation Results to constant-input signals Using ModelSim-ALTERA EDITION 15.0.

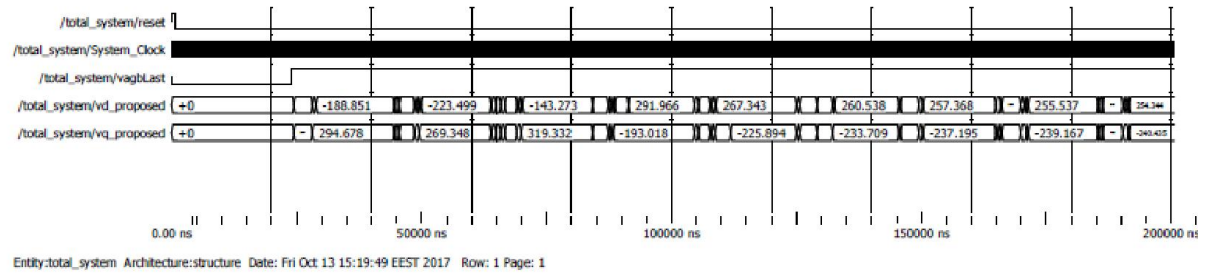


Figure 12 Simulation Results to variable-input signals Using ModelSim-ALTERA EDITION 15.0.

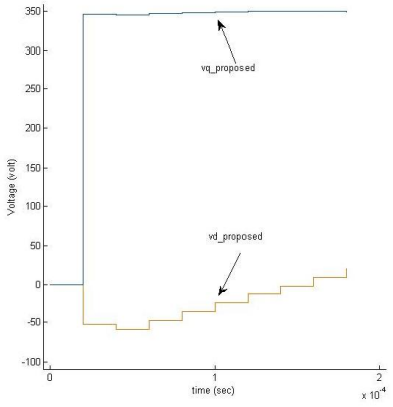


Figure 13 Simulation Results to constant-input signals Using MATLAB.

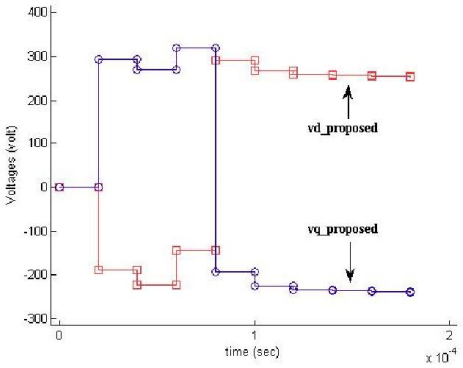


Figure 14 Simulation Results to variable-input signals Using MATLAB.

Table 2 Comparison between PI Controller Responses using Quartus and MATLAB

Sample Time (us)	PI Response using Quartus (vd , vq)	Response using MATLAB (vd , vq)
40	-188.851 , 294.678	-188.8533 , 294.6768
60	-223.499 , 269.348	-223.5000 , 269.3457
80	-143.273 , 319.332	-143.2693 , 319.3335
100	291.966 , -193,018	292.0000 , -193.0166
120	267.343 , -225.894	267.3444 , -225.8915
140	260.538 , -233.709	260.5200 , -233.7068
160	257.368 , -237.195	257.3707 , -237.1925
180	255.537, -239.167	255.5392 , -239.1646
200	254.344, -240.435	245.3463 , -240.4328

REFERENCES

[1]. R. Kannan, N. Gayathri, M. Natarajan, R. S. Sankarkumar, L. V. Iyer and N. C. Kar, "Selection of PI controller tuning parameters for speed control of PMSM using Biogeography Based Optimization algorithm," *2016 IEEE International Conference on Power Electronics, Drives and Energy Systems (PEDES)*, Trivandrum, 2016, pp. 1-6.
doi: 10.1109/PEDES.2016.7914260

URL: http://ieeexplore.ieee.org/stamp/stamp.jsp?tp=&arnumber=7914260&isnumber=7914213/

[2]. C. Li, M. Chen and S. Gao, "Fractional order PI speed control for permanent magnet synchronous motor drives," *Proceeding of the 11th World Congress on Intelligent Control and Automation*, Shenyang, 2014, pp. 4681-4685.
doi: 10.1109/WCICA.2014.7053504
URL: http://ieeexplore.ieee.org/stamp/stamp.jsp?tp=&arnumber=7053504&isnumber=7052676.

[3]. F. Khater, A. Shaltout, E. Hendawi and M. Abu El-sebah, "PI controller based on genetic algorithm for PMSM drive system," *2009 IEEE International Symposium on Industrial Electronics*, Seoul, 2009, pp. 250-255.
doi: 10.1109/ISIE.2009.5217925
URL: http://ieeexplore.ieee.org/stamp/stamp.jsp?tp=&arnumber=5217925&isnumber=5213059.

[4]. G. Ranjith Kumar, M. Arun Noyal Doss, K. N. V. Prasad and K. C. Jayasankar, "Modeling and speed control of permanent magnet synchronous Motor at constant load torque using PSIM," *International Conference on Sustainable Energy and Intelligent Systems (SEISCON 2011)*, Chennai, 2011, pp. 485-489.
doi: 10.1049/cp.2011.0411.
URL: http://ieeexplore.ieee.org/stamp/stamp.jsp?tp=&arnumber=6143359&isnumber=6143272.

[5]. Y. S. Kung et al., "Design and Implementation of a Microprocessor-Based PI Controller for PMSM Drives", Applied Mechanics and Materials, Vols. 764-765, pp. 496-500, 2015.

[6]. Yang, Ming, Li Niu, and DIAN-GUO XU. "Antiwindup design for the speed loop PI controller of a PMSM servo system." *Turkish Journal of Electrical Engineering & Computer Sciences* 21.5 (2013): 1318-1327.

[7]. L. Li, "DSP based digital control system implementation of permanent magnet synchronous motor," *The 26th Chinese Control and Decision Conference (2014 CCDC)*, Changsha, 2014, pp. 3527-3531.
doi: 10.1109/CCDC.2014.6852790
URL: http://ieeexplore.ieee.org/stamp/stamp.jsp?tp=&arnumber=6852790&isnumber=6852105.

[8]. Tariq, Mohd, et al. "Fast response Antiwindup PI speed controller of Brushless DC motor drive: Modeling, simulation and implementation on DSP." *Journal of Electrical Systems and Information Technology* 3.1 (2016): 1-13.

[9]. Ying-Shieh Kung, Chia-Sheng Chen, Kiing-Ing Wong and Ming-Hung Tsai, "Development of a FPGA-based control IC for PMSM drive with adaptive fuzzy control," *31st Annual Conference of IEEE Industrial Electronics Society, 2005. IECON 2005.*, 2005, pp. 6 pp.-.
doi: 10.1109/IECON.2005.1569134
URL: http://ieeexplore.ieee.org/stamp/stamp.jsp?tp=&arnumber=1569134&isnumber=33243.

[10]. PD Chandana Perera. Sensorless control of permanent-magnet synchronous motor drives. PhD thesis, AALBORG UNIVERSITY AALBORG, 2002.

[11]. J. Espina, A. Arias, J. Balcells and C. Ortega, "Speed Anti-Windup PI strategies review for Field Oriented Control of Permanent Magnet Synchronous Machines," 2009 Compatibility and Power Electronics, Badajoz, 2009, pp. 279-285. doi: 10.1109/CPE.2009.5156047 URL: http://ieeexplore.ieee.org/stamp/stamp.jsp?tp=&arnumber=5156047&isnumber=5155997.

[12]. K. Klinlaor and N. Chuladaycha, "Improved speed control using Anti-Windup PI controller for Direct Torque Control based on permanent magnet synchronous motor," 2012 12th International Conference on Control, Automation and Systems, JeJu Island, 2012, pp. 779-783. URL: http://ieeexplore.ieee.org/stamp/stamp.jsp?tp=&arnumber=6393288&isnumber=6393028.

[13]. M. Marufuzzaman, M. B. I. Reaz and M. A. M. Ali, "FPGA implementation of an intelligent current dq PI controller for FOC PMSM drive," 2010 International Conference on Computer Applications and Industrial Electronics, Kuala Lumpur, 2010, pp. 602-605. doi: 10.1109/ICCAIE.2010.5735005. URL: http://ieeexplore.ieee.org/stamp/stamp.jsp?tp=&arnumber=5735005&isnumber=5735003.

[14]. G. Maragliano, M. Marchesoni and L. Vaccaro, "FPGA implementation of a sensorless PMSM drive control algorithm based on algebraic method," 2010 IEEE International Symposium on Industrial Electronics, Bari, 2010, pp. 3083-3088. doi: 10.1109/ISIE.2010.5637857. URL: http://ieeexplore.ieee.org/stamp/stamp.jsp?tp=&arnumber=5637857&isnumber=5635477.

[15]. Q. Nguyen Khanh, N. D. That, Q. Nguyen Hong and Q. P. Ha, "FPGA-based fuzzy sliding mode control for sensorless PMSM drive," 2012 IEEE International Conference on Automation Science and Engineering (CASE), Seoul, 2012, pp. 172-177. doi: 10.1109/CoASE.2012.6386449. URL: http://ieeexplore.ieee.org/stamp/stamp.jsp?tp=&arnumber=6386449&isnumber=6386304.

[16]. Amornwongpeeti, Sarayut, et al. "A single chip FPGA-based solution for controlling of multi-unit PMSM motor with time-division multiplexing scheme." Microprocessors and Microsystems 39.8 (2015): 621-633.

Operation Strategy for Single Phase to Three Phase Matrix Converter

S.YILMAZ[*1] and G. ONBILGIN [1]

[1] Ondokuz Mayis University, Samsun/Turkey, secil.yilmaz@omu.edu.tr
[1] Ondokuz Mayis University, Samsun/Turkey, gonbilgi@omu.edu.tr

Abstract **- The term "phase transducer" in industrial and electrical applications is generally defined as obtaining three phase voltages from a single phase. Phase converters are used in remote areas where installation of the three-phase system is expensive. Because installing such a system requires additional transformers, transmission lines, measuring equipment, and so on. In terms of machine efficiency, power factor, and power oscillations, industrial three-phase asynchronous motors are preferred over single-phase asynchronous motors. Because of this, three-phase asynchronous motor drives are used more than single-phase asynchronous drives. However, for a three-phase asynchronous motor supply, a single-phase three-phase power converter system is required.In this study, the approach of single-phase alternating voltage on three-phase alternating voltage transformation using matrix converter was investigated. The operation of the phase converter has been described in detail and simulated with the PSIM software model. In addition, the hormonics that cause the problems such as overheating, loss, dropping of the capacitor to be used at full load were calculated and at the same time positive, negative and zero sequence components were determined with the help of symmetrical component anlaysis and the results were evaluated.**

Keywords **– Matrix converter, single phase three phase converters, symmetrical component anlaysis, hormonics.**

I. INTRODUCTION

Use of balanced three phase AC mains allows for the most efficient and economical use of electrical power. In many instances the cost of providing three phase service to remote rural areas is prohibitive due to the higher installation cost of three phase extension. Therefore SPTPC (single phase to three phase converter) is an excellent choice for situations where three phase power is not available. Proposed converter has a wide range of applications in which a three phase load is to be fed from available single phase source. Such applications include variety of forming equipments, fans, pumps, air conditioners etc. Another important application for SPTPC is in electric traction where three phase drive can be operated from single phase mains feeder. Consequently for feeding three phase loads from single phase source, single phase to three phase converter can be used and SPTPC's cost can be made a fraction of cost of providing three phase service. For this reason several phase conversion systems [1-4] have been developed and are widely in use.

In this work, matrix converter which is one of the three phase transformers is investigated and detailed study of matrix converter is given and output voltages are interpreted. To understand the operation of the matrix converter more easily, one voltage source can be divided into two voltage source in one period. One is negative and the other one is positive voltage source. This approach is named seperation and link to analyze the basic single to three phase matrix converter [6].

II. THREE PHASE MATRIX CONVERTER METHOD

Figure 1 shows the form of a matrix converter consisting solely of semiconductor switches. In the period of a single voltage source, the voltage source can be divided into two voltages. One is negative and the other is positive. In contrast to Figure 2, the matrix converter can be regarded as two equal converters.

A. Seperation

When the voltage source is in positive period, the matrix converter which converts single phase three phases is simplified as shown in the upper part of Fig. 2. To avoid a short circuit, switches Sa1 and Sa3 must not be transmitting at the same time. At least one of the switches Sa1 or Sa3 must be in transmission for an open circuit.

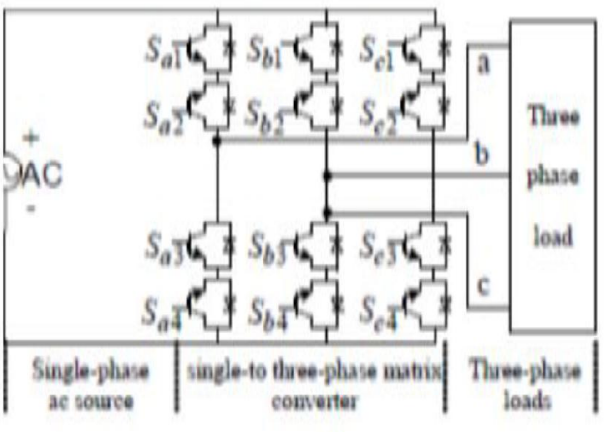


Figure 1: Matrix converter type

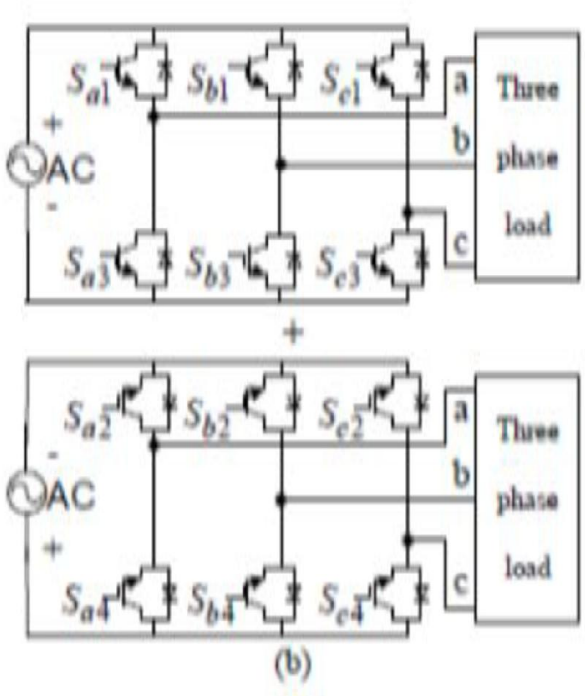


Figure 2: Seperation of matrix converter type

Sa1 switch is open and the Sa3 switch is must be off. The Sa2 switch must be on to provide current to the load source. When Sa3 is open ,Sa1 must be off and Sa4 must be on. All analyzes were carried out for phases B and C in the same way. In the positive period, the switches Sa1, Sa3, Sb1, Sb3, Sc1, Sc3 must be controlled for the energy flowing from the AC source to the load, at the same Sa2, Sa4, Sb2, Sb4, Sc2, Sc4 must be controlled to provide current path from load to source.

When the source voltage is during negative period, switches Sa2, Sa4, Sb2, Sb4, Sc2, Sc4 must be controlled for power flow from the AC source to the load. Similarly Sa1, Sa3, Sb1, Sb3, Sc1, Sc3 switches must be controlled to provide path from load to source.

B. Lİnk

In the positive source period Sa1 and Sa3 are controlled by the pulse width signal and Sa2 and Sa4 continue to stay on, while in negative source period Sa2 and Sa4 are controlled by the pulse width signal and switches Sa1 and Sa3 are kept on. The same situations occur in phases B and C, but the pulse width signal is applied at intervals of 120. table 1 shows the switching states of the switches. And figure 3 shows the operation states of the single phase to three phase matrix converter with three phase balanced resistance load when the source is during positive period.

Table 1: SWITCHING STATES OF THE SWITCHES IN MATRIX CONVERTER

States	Vab	Vbc	Vca	Switching Operation
+(100)	Vs	0	- Vs	Sa1,Sa2d,Sb3,Sb4d,Sc3,Sc4d
+(101)	Vs	- Vs	0	Sa1,Sa2d,Sb3,Sb4d,Sc1,Sc2d
+(001)	0	-Vs	Vs	Sa3,Sa4d,Sb3,Sb4d,Sc1,Sc2d
+(011)	-Vs	0	Vs	Sa3,Sa4d,Sb1,Sb2d,Sc1,Sc2d
+(010)	-Vs	Vs	0	Sb1,Sb2d,Sa3,Sa4d,Sc3,Sc4d
+(110)	0	Vs	- Vs	Sa1,Sa2d,Sb1,Sb2d,Sc3,Sc4d
+(000)	0	0	0	Sa3,Sa4d,Sb3,Sb4d,Sc3,Sc4d
+(111)	0	0	0	Sa1,Sa2d,Sb1,Sb2d,Sc1,Sc2d
-(100)	Vs	0	- Vs	Sb4,Sb3d,Sc4,Sc3d,Sa2,Sa1d
-(101)	Vs	- Vs	0	Sb4,Sb3d,Sa2,Sa1d,Sc2,Sc1d
-(001)	0	-Vs	Vs	Sa4,Sa3d,Sb4,Sb3d,Sc2,Sc1d
-(011)	-Vs	0	Vs	Sa4,Sa3d,Sb2,Sb1d,Sc2,Sc1d
-(010)	-Vs	Vs	0	Sa4,Sa3d,Sc4,Sc3d,Sb2,Sb1d
-(110)	0	Vs	- Vs	Sc4,Sc3d,Sa2,Sa1d,Sb2,Sb1d
-(000)	0	0	0	Sa4,Sa3d,Sb4,Sb3d,Sc4,Sc3d
-(111)	0	0	0	Sa2,Sa1d,Sb2,Sb1d,Sc2,Sc1d

''1'' upper arm swtich on, ''0'' lower arm switch on
''+'' period source voltage, '-'' period source voltage,
Subscript 'd' denotes diode to that switch.

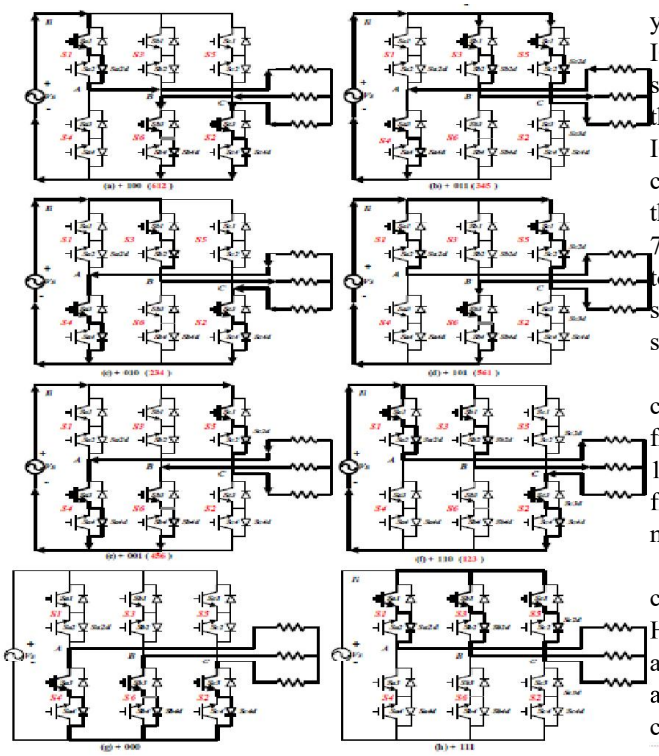


Figure 3: The operation states of the single phase to three phase matrix converter with three phase balanced resistance load when the source is during positive period

III. Material and Method

With a three phase balanced resistance load ,the validity and feasibility of the operation strategy for single phase to three phase matrix converter is confirmed by simulation in PSIM software model.

Figure 4 shows the PSIM software model and the matrix converter that converts single phase to three phase.

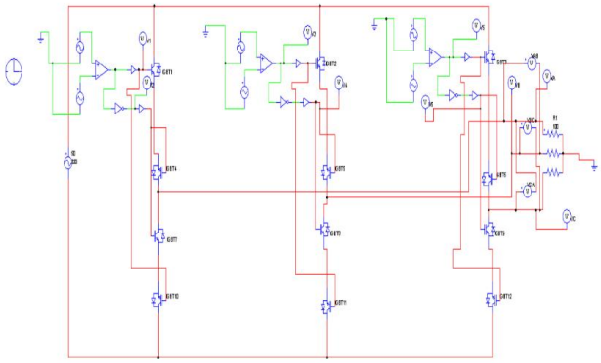


Figure 4: The operation states of the single phase to three phase matrix converter with three phase balanced resistance load when the source is during positive

IGBT switches are used in this circuit. In order to obtain the pulse width modulation (PWM) used when the switches are triggered, it is aimed to find the most suitable switching signal by changing the frequency of carrier and control signals.When you look at the Matrix converter in positive source period; IGBT1, IGBT 2, IGBT3, IGBT7, IGBT8, IGBT9 switches should be controlled for the flow of energy to the load from the source, but also in the negative source period IGBT4, IGBT5, IGBT6, IGBT10, IGBT11, IGBT12 should be controlled to provide current path from the load to source. For the matrix converter not to be short-circuited IGBT and IGBT 7 switches must not be transmission at the same time and not to be open-circuited at least one of the IGBT 1 or IGBT 7 switches must be transmission. The same condition is valid for switches connected to other phases.

In figüre 5 switching signals shows are obtained by comparing control signal which are 3 sine waves with a frequency of 500 Hz , amplitude of 1 volt , phase difference of 120 ° and carrier signal which is saw signal with 20 kHz frequency. In figüre 6 shows output voltage is obtained from matrix converter.

Similarly switching signals are obtained by comparing control signal which are 3 sine waves with a frequency of 50 Hz and amplitude of 1 volt and a phase difference of 120 ° and carrier signal which is saw signal with 20 kHz frequency and in figüre 7 shows output voltage is obtained from matrix converter.



Figure 5: Matrix converter switching signals

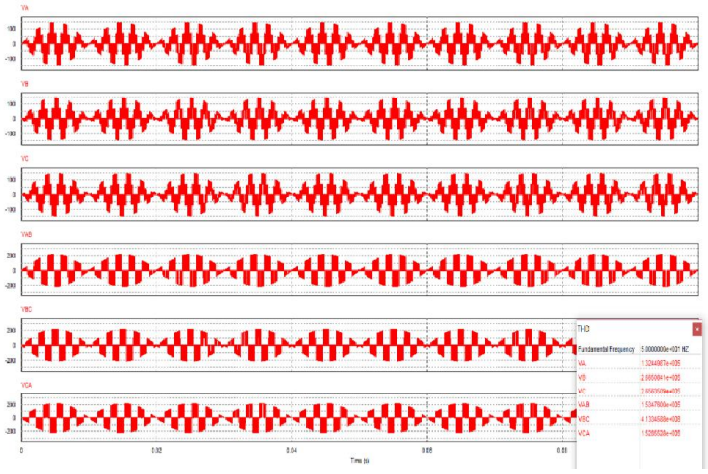


Figure 6: The voltages at the output of the matrix converter

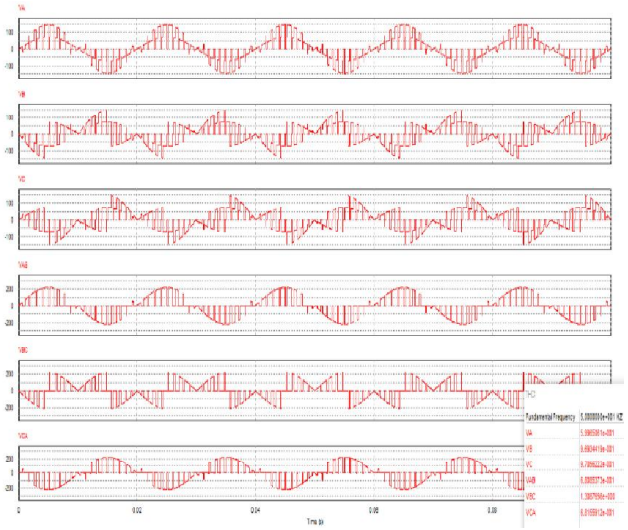


Figure 7: The voltages at the output of the matrix converter

Vab=220^{0} ,Vbc=200^{-120}, Vca=210^{120}
Va=146.66^{-30}, Vb=146.66^{-150}, Vc=146.66^{90}

IV. Simulation Results

A. Anlaysis Imbalance of Output Voltage

If the phase angle between the effective values of the phase voltages or the phase angles between successive phases is not equal, then a 3-phase system is unbalanced. The level of the imbalance is defined using the Fortescue component, with the base negative component (U1i) (or zero component (U1o) compared to the base positive component) which is given in equation 1.

$$\Delta U_i = \frac{|\overline{U_{1i}}|}{|\overline{U_{1d}}|} \text{ve} \Delta e_o = \frac{|\overline{U_{1o}}|}{|\overline{U_{1d}}|} \quad (1)$$

The Fortescue component of the output voltages of the phase converters is calculated by obtaining the positive (Vp), negative (Vn) and zero (Vo) series component voltages respectively given in equations 2, 3 and 4.

$$Vp=Va+ a^2Vb+aVc \quad (2)$$

$$Vn=Va+a\ Vb+a^2Vc \quad (3)$$

$$V0=Va+Vb+Vc \quad (4)$$

Vp = 0, Vn = 439.98∟-30, Vo= 0 nd the imbalance effect Vp/Vn was found to be zero from the equations 1, 2, 3 and 4.

B. Anlaysis Hormonic of Output Voltage

The hormonic distortion values accepted in the standards according to the international IEC 519-1992 are set at 3% for the voltage. There are problems at the hormonic ratios above the limit values, which can create dangerous and major material damage for the electrical systems. The deterioration rate of the electric energy quality can be determinated by using equation 5 defined with standards.

Total hormonic distortion (for voltage);

$$[THD]_V = \frac{\sqrt{\sum_{h=2}^{\infty} V_h^2}}{V_1} \quad (5)$$

When the total hormonic distortion is calculated in Figure 4 where the voltage obtained from the output of the matrix converter is seen Va=% 5.99, Vb = 9.68%, Vc = 9.7% Vab = 6.8%, Vbc = 13% Vca = 6.8% were obtained. Since hormonic distortion must be 3% according to accepted standards, a filter must be used at the input to reduce the total hormonic distortion at the output.

V. Conclusion

The single phase of the matrix converter is described in detail by the three-phase transformation separation and link method. The output of the matrix converter is simulated in the PSIM software model by connecting a balanced three-phase ohmic load. When the positive, negative, and zero sequence components of voltages obtained from the output are analyzed by symmetric components anlaysis, it appears that they are suitable for practical applications. The Fortescue component, known as the level of voltage imbalance that causes such effects as reverse engine torque (vibration) and overheating of asynchronous machines, has been calculated and found to be ideal. However, when the hormonic distortion of the output voltage is examined, an input filter is required to reduce the total hormonic distortion to the standard values.

Because matrix converters do not need energy-storing intermediate elements and performing AC-AC conversion in a single step, it avoids the use of large capacitors, which occupy about 1/3 of the total size in inverters, and provides a simpler AC drive. This will ensure that the matrix transformer can be used more frequently in the future.

References

[1] C. M. Hertz, "Current techniques in phase conversion systems ", IEEE Rural Electric Power Conference, 1978.
[2] T. C. Jongsma, "The application of phase converter ", *Electrical/Electronic Showcase'79*, 1979.
[3] S. B. Dewan, M. Showleh , "Steady-state of static single-phase to three-phase converters", *EEE IAS Conf. Rec*., City of Conf., 1981.
[4] S. K. Biswas, "A new static converter for the operation of three-phase motors on single-phase supply ", *Conf. Rec, IEEE-IAS Annu* , 1986.

[5] B. Baskaran, S.P. Natarajan, S. Sivagamasundari, D. Thamilarasi, "A novel matrix converter based single phase to three phase converter," *IJ-STA s*, vol. 3, no. 2, 2009, pp. 1092-107.
[6] [6] P. G. Scholar, " A novel matrix converter based single phase to three phase converter ."
[7] [7] J. Xiao, W. Zhang , H. Omori, K. Matsui, "A novel operation strategy for single to three-phase matrix converter ", *Electrical Machines and Systems, ICEMS 2009. International Conference on. IEEE*, pp. 1-6, 2009.
[8] [8] Z. Yan, R. Li, S. Xu, J. Li, " Modeling and control of high frequency link three-phase four-leg matrix converter ", *Industrial Electronics Society, IECON 2013-39th Annual Conference of the IEEE*, pp. 4886-4891, 2013.
[9] [9] M. Saito, N. Matsui, " A single-to three-phase matrix converter for a vector-controlled induction motor ", *Industry Applications Society Annual Meeting*, 2008.
[10] [10] Huber, H. George, " Phase Converters, Their Application and Current Demand ", *IEEE Transactions on Industry and General Applications*, vol. 2, pp. 280-284, 1965.
[11] Holmes, P.G., " Single-to 3-Phase Transient Phase Conversion in Induction Motor Drives ", *IEE Proceedings B-Electric Power Applications*, vol. 132, no. 5, pp. 289-296, 1985.
[12] M.H. El-Maghraby, R.H. Thejel, M.M. Ibrahim, " New approach for the anlaysis of a three-phase induction motor of different ratings connected to a single-phase supply ", *IEE Proceedings B (Electric Power Applications)*, vol.139, no. 3, pp. 145-154, 1992.
[13] D.C. Lee, Y.S. Kim, "Control of single-phase-to-three-phase AC/DC/AC PWM converters for induction motor drives ", *IEEE Transactions on Industrial Electronics*, vol.54, no.2, pp. 797-804, 2007.

Switched H_2 State-feedback Control for Polytopic Systems Based on Dwell Time

E. KEMER[1] and E. PREMPAIN[2]

[1] Usak University, Usak/Turkey, emre.kemer@usak.edu.tr
[2] University of Leicester, Leicester/UK, ep26@leicester.ac.uk

Abstract **- This paper introduces a H_2 sub-optimal approach to design state feedback controllers for switched system with parameter uncertainty. Minimum dwell time stability analysis techniques are revisited and combined with the H_2-optimal control to obtain a robust state feedback controller for switched systems. Two kinds of Lyapunov functions have been used to find a switched controller, the time varying and constant controller gains have been given for the switched system. The proposed approaches have been illustrated by means of examples.**

Keywords **- H_2-optimal control, Switched Systems, Lyapunov function, Minimum Dwell time.**

I. INTRODUCTION

Switched systems appear in many applications such as auto pilot design, heating systems, automatic transmissions, communication networks, DC-DC converters automotive engine control, and so on. Such switched control systems may consist of locally designed controllers switched according to a logic rule designed to meet the desired control objectives [1].

In the last years, the analysis and synthesis of switched systems have got more attention because of their importance in both theory and applications. For the stability analysis and control design of switched systems, many important methods have been investigated by several researchers so far (see [2–14] and references therein). For the stability analysis issue, various techniques have been mentioned such as common quadratic Lyapunov function method, multiple Lyapunov functions method, average and minimum dwell-time methods [9–17]. In most cases, common quadratic Lyapunov method does not provide a solution for given switched systems due to its conservativity. Multiple Lyapunov function method provides the asymptotic stability of the switched system for any switching signal, if the all subsystems are stable and the time interval between two consecutive switching instants is sufficiently large. From this, minimum dwell time switching theories have been developed in recent works to guarantee stability of switched linear system and obtain minimum dwell time between two consecutive switching [7–10].

Optimal control methods, which are part of the modern control theory, play an important role in many feedback control design. Optimal control focuses on the minimization of a performance index (PI) that depends on the system matrices. The PI might contain, for example, information of control effort, information of operating error, or any other features which are necessary to the user of control system. The main purpose of optimal control theory is to determine a control signal that satisfies the terminal state constraints and also minimize the PI [18].

In the current work, we address the H_2-optimal control problem, and state feedback controller synthesis for switched systems with dwell time. In this case, the switched system parameters have polytopic uncertainty. In [5], conservatism of the robust H_∞ design is reduced by using a piecewise linear quadratic Lyapunov function in time. In [6], stability and stabilization problem of switched linear systems with dwell time are solved by using the same function. In [8], this function is also used to find and minimize the L_2-gain of uncertain switched linear systems with dwell time. Using the same function, robust filter is designed in [19]. We apply here the same Lyapunov function to H_2-optimal control in order to minimize sensitivity of the system output to a zero mean white noise input.

This paper is as follows: A minimum dwell time stability analysis is presented in Section 2. The new approach to compute the robust state feedback switched controller is given in Section 3. There illustrative examples about the proposed approaches are given in Section 4. Finally, Section 5 gives conclusions.

Notation: $Tr(.)$ denotes the trace function for square matrices. The hermitian operator $He\{.\}$ is defined as $He\{\mathrm{A}\} = \mathrm{A} + \mathrm{A}^{\mathrm{T}}$. For symmetric matrices, $P > 0 (\geq 0)$ indicates that P is positive definite (semi-definite). A symmetric matrix $\begin{bmatrix} P & Q \\ Q^T & R \end{bmatrix}$ is denoted by $\begin{bmatrix} P & Q \\ * & R \end{bmatrix}$. $\Re^n$ stands for the n dimensional Euclidean space. $\Re^{p\times q}$ is the set of all $p \times q$ real matrices. N is set of natural numbers.

II. PRELIMINARIES

A switched system with polytopic uncertainty is defined as

$$\dot{x}(t) = A_{\sigma(t)}x(t) + B_{u,\sigma(t)}u(t) + B_{w,\sigma(t)}w(t),\ \forall t \geq 0 \text{ and } x(0) = x_0. \quad (1)$$

Where $x(t) \in \Re^n$ is the state, x_0 is initial condition, $u(t) \in \Re^p$, $w(t) \in \Re^r$ is the exogenous input and $\sigma(t)$ represents the switching rule between system matrices $A_i \in \Re^{n \times n}$ $i = 1, \ldots, M$. The uncertain system matrices are assumed to reside within the following polytope:

$$A_i = \sum_{j=1}^{N} \eta_j A_i^{(j)}, \qquad B_{u,i} = \sum_{j=1}^{N} \eta_j B_{u,i}^{(j)},$$
$$B_{w,i} = \sum_{j=1}^{N} \eta_j B_{w,i}^{(j)}, \qquad \sum_{j=1}^{N} \eta_j = 1, \eta_j \geq 0, \tag{2}$$

where j is the index of the polytope vertices and N denotes number of polytope vertices.

Definition 1: Dwell time is a time-interval between two switching instants $(t_1, t_2, \ldots)$. It is assumed to be equal or greater than a minimum dwell time $T_d, (t_{l+1} - t_l \geq T_d$ for $\forall l \geq 1)$.

Definition 2: Consider the index of the initial subsystem, $i_0 = \sigma(0)$ and the commutation instants $t_1, t_2, \ldots,$ where $t_{l+1} - t_l \geq T_d, \forall l \geq 1$ and $l \in \mathrm{N}$. If the minimum dwell time between two switching instants is divided into H equal sampling time intervals, then $t_{l,h}$ is defined as $t_{l,h} = t_l + hT_d / H$ for $h = 0, \ldots, H$, and $t_l = t_{l,0}$. The time-varying Lyapunov function is defined as

$$V(t) = x^T(t) P_{\sigma(t)}(t) x(t), \tag{3}$$

where $P_{\sigma(t)}(t)$ which is in $\{P_1(\mathrm{t}), \ldots P_M(\mathrm{t})\}$ according to $\sigma(\mathrm{t})$, defined as:

$$P_i(t) = \begin{cases} P_{i,h} + \left(P_{i,h+1} - P_{i,h}\right) \dfrac{\left(t - t_{l,h}\right)}{T_d / H} & t \in \left[t_{l,h}, t_{l,h+1}\right), \\ P_{i,H} & t \in \left[t_{l,H}, t_{l+1,0}\right), \\ P_{i_0,H} & t \in \left[0, t_1\right). \end{cases} \tag{4}$$

where $h = 0, \ldots, H-1$, the number of the switching is defined as $l \in \mathrm{N}$ and where H is given a positive integer. This definition shows that the matrices $P_i(t)$ are constant and equal to $P_{i_0,H}$ before the first switching instant. During the minimum dwell time, the matrices $P_i(t)$ change linearly. After the minimum dwell time, and before the following switching instant, the matrices $P_i(t)$ are constant and equal to $P_{i,H}$.

Based on the time-varying Lyapunov function, the following lemma deals with the stability of a switched system with polytopic uncertainty.

Lemma 1 ([6])**:** For a given $T_d > 0$, if there exist a set of positive definite matrices $P_{i,h} > 0$, $i = 1, \ldots, M$, $h = 0, \ldots, H$ that satisfy the following LMI's for all $i = 1, \ldots, M$ and $j = 1, \ldots, N$:

$$\frac{\left(P_{i,h+1} - P_{i,h}\right)}{T_d / H} + He\left\{P_{i,h} A_i^{(j)}\right\} < 0, \tag{5a}$$

$$\frac{\left(P_{i,h+1} - P_{i,h}\right)}{T_d / H} + He\left\{P_{i,h+1} A_i^{(j)}\right\} < 0, \tag{5b}$$

where $h = 0, \ldots, H-1$ and

$$He\left\{P_{i,H} A_i^{(j)}\right\} < 0, \tag{5c}$$

$$P_{i,H} - P_{s,0} \geq 0, \forall s \in \{1, \ldots, M\} \text{ and } s \neq i \tag{5d}$$

then the system (1) with the uncertainty (2) is globally asymptotically stable for any switching rule with dwell time that is greater than the minimum dwell time, T_d (see [6], for detailed proof).

Note that, before the first switching, the decreasing of the Lyapunov function is proved by the condition (5c). During the minimum dwell time, the conditions in (5a-b) prove that the Lyapunov function is decreasing. Then, the condition in (5c) proves that $V(t)$ is decreasing, after the minimum dwell time and before the next switching. During the switching instants, the Lyapunov function is proved to be non-increasing by the condition in (5d) [6].

The Lyapunov function (3) uses the same Lyapunov matrix (12) for all vertices of the subsystems. Hence, it is more conservative with regards to the stability conditions. This conservatism issue is reduced by using the *time-varying and parameter (vertex) dependent Lyapunov function* [6].

Definition 3: Time-varying and parameter dependent Lyapunov function is

$$V(t) = x^T(t) P_{\sigma(t)}(t) x(t), \quad P_{\sigma(t)}(t) = \sum_{j=1}^{N} \eta_j P_{\sigma(t)}^{(j)}(t),$$
$$\sum_{j=1}^{N} \eta_j = 1, \eta_j \geq 0, \tag{6}$$

where $P_{\sigma(t)}^{(j)}$ which is in $\{P_1^{(j)}(\mathrm{t}), \ldots P_M^{(j)}(\mathrm{t})\}$ according to $\sigma(\mathrm{t})$, defined as:

$$P_i^{(j)}(t) = \begin{cases} P_{i,h}^{(j)} + \left(P_{i,h+1}^{(j)} - P_{i,h}^{(j)}\right) \dfrac{\left(t - t_{l,h}\right)}{T_d / H} & t \in \left[t_{l,h}, t_{l,h+1}\right), \\ P_{i,H}^{(j)} & t \in \left[t_{l,H}, t_{l+1,0}\right), \\ P_{i_0,H}^{(j)} & t \in \left[0, t_1\right). \end{cases} \tag{7}$$

where $h = 0, \ldots, H-1$, $j = 1, \ldots, N$, the number of the switching is defined as $l \in \mathrm{N}$ and H is given a positive integer. Note that, the difference between (3) and (6) is that Lyapunov matrices in (6) depend on the sub-polytopes vertices [6].

Based on the time-varying and parameter dependent Lyapunov function, the following lemma deals with the stability of a switched system with polytopic uncertainty.

Lemma 2 ([6])**:** For a given $T_d > 0$, if there exist a set of matrices $S_{i,h}, G_{i,h}$ and positive definite matrices $P_{i,h}^{(j)} > 0$, $i = 1, \ldots, M$, $h = 0, \ldots, H$, $j = 1, \ldots, N$, such that, for all $i = 1, \ldots, M$, and $j = 1, \ldots, N$ the following conditions hold

$$\begin{bmatrix} \dfrac{\left(P_{i,h+1}^{(j)} - P_{i,h}^{(j)}\right)}{T_d / H} + He\left\{S_{i,h} A_i^{(j)}\right\} & P_{i,h}^{(j)} - S_{i,h} + A_i^{(j)T} G_{i,h}^T \\ * & -G_{i,h}^T - G_{i,h} \end{bmatrix} < 0, \tag{8a}$$

$$\begin{bmatrix} \dfrac{\left(P_{i,h+1}^{(j)}-P_{i,h}^{(j)}\right)}{T_d/H}+He\left\{S_{i,h+1}A_i^{(j)}\right\} & P_{i,h+1}^{(j)}-S_{i,h+1}+A_i^{(j)^T}G_{i,h+1}^T \\ * & -G_{i,h+1}^T-G_{i,h+1} \end{bmatrix}<0, \quad (8b)$$

where $h=0,\ldots,H-1$ and

$$\begin{bmatrix} He\left\{S_{i,H}A_i^{(j)}\right\} & P_{i,H}^{(j)}-S_{i,H}+A_i^{(j)^T}G_{i,H}^T \\ * & -G_{i,H}^T-G_{i,H} \end{bmatrix}<0, \quad (8c)$$

$$P_{i,H}^{(j)}-P_{s,0}^{(j)}\geq 0, \forall s\in\{1,\ldots,M\}, \text{and } s\neq i \quad (8d)$$

then the system (1) with an uncertainty (2) is globally asymptotically stable for any switching rule with dwell time that is greater than minimum dwell time, T_d (see [6], for detailed proof).

In this work, Lemmas 1 and 2 are used to find a stabilizing switched state feedback controller as in following section.

III. Robust Controller Design

In this section, we combine the standard H_2-optimal control and the minimum dwell time methods mentioned in the previous section. In addition, it allows us to design the state feedback H_2-optimal controller for the switched system with polytopic parameter uncertainties. Here, the sensitivity of the system output to a zero mean white noise input w is minimized by using H_2 optimization technique.

Lemma 3 (H_2-gain [21]**):** Consider a linear time-varying system,

$$\dot{x}(t)=A(t)x+B_w(t)w, \quad (9)$$

$$z(t)=C(t)x \quad (10)$$

where w is the exogenous input and z is the system output. If there exist symmetric matrices, $Q(t)>0$ and Z, then H_2-gain of the system given in (9)-(10) is less than γ, if the following conditions hold:

$$\begin{aligned} &Tr(Z)<\gamma^2,\ \begin{bmatrix} Z & B_w^T(t) \\ * & Q(t) \end{bmatrix}>0, \\ &\begin{bmatrix} -\dot{Q}(t)+He\{A(t)Q(t)\} & Q(t)C^T(t) \\ * & -I \end{bmatrix}<0, \forall t \end{aligned} \quad (11)$$

For a switched system, Q is defined as: $Q_{\sigma(t)}(t)$ with $\sigma(t)\in\{1,2,\ldots M\}$ and where $Q_i(t)$ is defined as:

$$Q_i(t)=\begin{cases} Q_{i,h}+\left(Q_{i,h+1}-Q_{i,h}\right)\dfrac{\left(t-t_{l,h}\right)}{T_d/H} & t\in[t_{l,h},t_{l,h+1}), \\ Q_{i,H} & t\in[t_{l,H},t_{l+1,0}), \\ Q_{i_0,H} & t\in[0,t_1). \end{cases} \quad (12)$$

where $h=0,\ldots,H-1$, the switching index is defined as $l\in\mathbb{N}$ and H is given a positive integer. Using Lemmas 1 and 3, the following Theorem is given for the state feedback controller gain.

Theorem 1: For a given $T_d>0$, if the set of matrices $L_{i,h}$ of compatible size and the collection of symmetric matrices, Z and $Q_{i,h}>0$, $i=1,\ldots,M$, $h=0,\ldots,H$ satisfy the following LMI's for all $i=1,\ldots,M$, and $j=1,\ldots,N$:

$$\begin{bmatrix} Z & B_{w,i}^{(j)^T} \\ * & Q_{i,h} \end{bmatrix}>0,\ \forall h\in\{0,\ldots,H\},$$

$$\begin{bmatrix} \dfrac{\left(Q_{i,h}^{(j)}-Q_{i,h+1}^{(j)}\right)}{T_d/H}+He\left\{A_i^{(j)}Q_{i,h}+B_{u,i}^{(j)}L_{i,h}\right\} & Q_{i,h}C_i^{(i)^T}+L_{i,h}{}^TD_{u,i}^{(j)^T} \\ * & -I \end{bmatrix}<0,$$

$$\begin{bmatrix} \dfrac{\left(Q_{i,h}^{(j)}-Q_{i,h+1}^{(j)}\right)}{T_d/H}+He\left\{A_i^{(j)}Q_{i,h+1}+B_{u,i}^{(j)}L_{i,h+1}\right\} & Q_{i,h+1}C_i^{(i)^T}+L_{i,h+1}{}^TD_{u,i}^{(j)^T} \\ * & -I \end{bmatrix}<0,$$

where $h=0,\ldots,H-1$ and

$$\begin{bmatrix} He\left\{A_i^{(j)}Q_{i,H}+B_{u,i}^{(j)}L_{i,H}\right\} & Q_{i,H}C_i^{(i)^T}+L_{i,H}{}^TD_{u,i}^{(j)^T} \\ * & -I \end{bmatrix}<0,$$

$Q_{i,H}-Q_{s,0}\leq 0,\ \forall s\in\{0,\ldots,M\}$ and $s\neq i$

then there exists a state-feedback regulator $K_{\sigma(t)}(t)$ which is in $\{K_1(t),\ldots K_M(t)\}$ according to $\sigma(t)$, defined as:

$$K_i(t)=\begin{cases} \overline{L}_{i,h}\overline{Q}_{i,h}^{-1} & t\in[t_{l,h},t_{l,h+1}), \\ L_{i,H}Q_{i,H}^{-1} & t\in[t_{l,H},t_{l+1,0}), \\ L_{i_0,H}Q_{i_0,H}^{-1} & t\in[0,t_1). \end{cases} \quad (13)$$

where $\overline{\mathrm{L}}_{i,h}=L_{i,h}+\left(L_{i,h+1}-L_{i,h}\right)\left(t-t_{l,h}\right)H/T_d$ and $\overline{\mathrm{Q}}_{i,h}=Q_{i,h}+\left(Q_{i,h+1}-Q_{i,h}\right)\left(t-t_{l,h}\right)H/T_d$, such that the closed-loop system (system (1) with (13) and uncertainty (2)) is quadratically stable for any switching rule with a dwell time that is greater than the minimum dwell time, T_d and such that the H_2-gain from w to z is less than or equal to $\gamma=\sqrt{Tr(Z)}$. To get the best upper bound, we need to minimize $Tr(Z)$. Note that this theorem provides a state feedback gain which is time varying during the dwell time.

In most cases, a time varying controller may not be desirable for the switched systems, so a time invariant state feedback controller can be designed using the following lemma. The parameter (vertex) dependent Lyapunov function (6) is used to reduce the conservatism in Lemma 2. Hence, we combine with this lemma and H_2-optimal control approach in Lemma 3, and then design a time invariant state feedback controller for the switched system with polytopic parameter uncertainty.

The time-varying and parameter dependent positive definite matrix, $Q_{\sigma(t)}^{(j)}$ which is in $\{Q_1^{(j)}(t),\ldots Q_M^{(j)}(t)\}$ according to $\sigma(t)$, defined as:

$$Q_i^{(j)}(t)=\begin{cases} Q_{i,h}^{(j)}+\left(Q_{i,h+1}^{(j)}-Q_{i,h}^{(j)}\right)\dfrac{\left(t-t_{l,h}\right)}{T_d/H} & t\in[t_{l,h},t_{l,h+1}), \\ Q_{i,H}^{(j)} & t\in[t_{l,H},t_{l+1,0}), \\ Q_{i_0,H}^{(j)} & t\in[0,t_1). \end{cases} \quad (14)$$

where $h=0,\ldots,H-1$, $j=1,\ldots,N$, the number of the

switching is defined as $l \in \mathrm{N}$ and H is given a positive integer. Using Lemmas 2 and 3, the following Theorem is given for a time invariant state feedback controller gain.

Theorem 2: For given scalars $\beta > 0$ and $T_d > 0$, if the set of matrices, S_i and L_i are of compatible size and the collection of symmetric matrices, Z and $Q_{i,h}^{(j)} > 0$ $i = 1,\ldots,M,\quad h = 0,\ldots,H$, $j = 1,\ldots,N$ satisfy the following LMI's for all $i = 1,\ldots,M$, and $j = 1,\ldots,N$:

$$\begin{bmatrix} Z & B_{w,i}^{(j)T} \\ * & Q_{i,h}^{(j)} \end{bmatrix} > 0,\ \forall h \in \{0,\ldots,H\},$$

$$\begin{bmatrix} \dfrac{\left(Q_{i,h}^{(j)} - Q_{i,h+1}^{(j)}\right)}{T_d / H} + \psi & \Gamma & Q_{i,h}^{(j)} - \Theta \\ * & -I & \beta(C_i^{(j)} S_i + D_{u,i}^{(j)} L_i) \\ * & * & -\beta(S_i{}^T + S_i) \end{bmatrix} < 0,$$

$$\begin{bmatrix} \dfrac{\left(Q_{i,h}^{(j)} - Q_{i,h+1}^{(j)}\right)}{T_d / H} + \psi & \Gamma & Q_{i,h+1}^{(j)} - \Theta \\ * & -I & \beta(C_i^{(j)} S_i + D_{u,i}^{(j)} L_i) \\ * & * & -\beta(S_i{}^T + S_i) \end{bmatrix} < 0,$$

where $h = 0,\ldots,H-1$ and

$$\begin{bmatrix} \psi & \Gamma & Q_{i,H}^{(j)} - \Theta \\ * & -I & \beta(C_i^{(j)} S_i + D_{u,i}^{(j)} L_i) \\ * & * & -\beta(S_i{}^T + S_i) \end{bmatrix} < 0$$

$Q_{i,H}^{(j)} - Q_{s,0}^{(j)} \le 0,\ \forall s \in \{0,\ldots,M\}$ and $s \neq i$

Here:

$\psi = He\{A_i^{(j)} S_i + B_{u,i}^{(j)} L_i\}$,

$\Gamma = S_i{}^T C_i^{(i)T} + L_i{}^T D_{u,i}^{(j)T}$,

$\Theta = S_i{}^T + \beta(A_i^{(j)} S_i + B_{u,i}^{(j)} L_i)$,

then there exists a state-feedback regulator defined as: $K_i = L_i S_i^{-1}$ such that the closed-loop system (system (1) with K_i and uncertainty (2)) is quadratically stable for any switching rule with a dwell time that is greater than the minimum dwell time, T_d and such that the H_2-gain from w to z is less than or equal to $\gamma = \sqrt{Tr(Z)}$. To get the best upper bound, we need to minimize $Tr(Z)$.

IV. Examples

Example 1 (Uncertainty)**:** Consider the system taken from [20] where the uncertainty is added to the subsystems

$$A_1 = \begin{bmatrix} \lambda & 1 \\ -2 & -1 \end{bmatrix},\quad A_2 = \begin{bmatrix} \lambda & 1 \\ -9 & -1 \end{bmatrix},\quad |\lambda| \le \overline{\lambda} \qquad (15)$$

The stability of the system is proven by using Lemma 1 and Lemma 2. The minimum dwell time results for different uncertainty values are given in Table 1 and 2.

Table 1: Minimum dwell time, T_d results of Lemma 1

$H \setminus \lambda$	0	0.2	0.4	0.6	0.8
1	0.8538	1.2443	1.9696	3.8055	21.4936
2	0.7460	1.1324	1.7168	3.1325	14.8181
5	0.6727	1.0537	1.5607	2.7588	11.7833
10	0.6503	1.0049	1.4918	2.5549	10.8656
100	0.6267	0.8644	1.3594	2.0091	9.39750

Table 2: Minimum dwell time, T_d results of Lemma 2.

$H \setminus \lambda$	0	0.2	0.4	0.6	0.8
1	0.8538	1.2333	1.8882	3.2652	7.6227
2	0.7460	1.1248	1.6536	2.7175	6.0128
5	0.6727	1.0504	1.5150	2.4186	5.2460
10	0.6503	1.0039	1.4649	2.2631	5.0168
100	0.6267	0.8643	1.3450	1.9564	4.7364

Tables 1 and 2 show that a less conservative result is found when H is increased. In addition, Lemma 2 always finds the smallest T_d. This proves that Lemma 2 gives less conservative results than Lemma 1 due to using parameter dependent Lyapunov function (6). These results encourage us to use Lemma 2 in the controller design approach.

Example 2 (Controller Design)**:** We consider the system (1) with A_1 and A_2 same as in Example 1 and

$$B_1 = \begin{bmatrix} -1 \\ 0.5 \end{bmatrix}, B_2 = \begin{bmatrix} -0.2 \\ 0.1 \end{bmatrix}, B_{w,1} = \begin{bmatrix} 0.1 \\ -2 \end{bmatrix}, B_{w,2} = \begin{bmatrix} -0.5 \\ 0.2 \end{bmatrix}, \qquad (16)$$

where the uncertainty is assumed to be $|\lambda| \le 0.8$. We seek the uncertain system (15) that satisfies the same dwell time as in the nominal system (when the uncertainty, $\overline{\lambda} = 0$). Therefore, this can be achieved using the state feedback controller design Theorems 1 and 2.

To apply the robust controller design theorems in Section 3, the system is defined as:

$$C_1 = \begin{bmatrix} 0.3 & 0 \\ 0 & 0.1 \\ 0 & 0 \end{bmatrix}, C_2 = \begin{bmatrix} 0.2 & 0 \\ 0 & 0.1 \\ 0 & 0 \end{bmatrix}, D_{u,1} = \begin{bmatrix} 0 \\ 0 \\ 0.12 \end{bmatrix}, D_{u,2} = \begin{bmatrix} 0 \\ 0 \\ 0.1 \end{bmatrix}, \qquad (17)$$

with $H = 1$ and $T_d = 0.63s$, Theorem 1 gives

$$L_{1,1} = \begin{bmatrix} 61.7532 & -27.0538 \end{bmatrix},\ Q_{1,1} = \begin{bmatrix} 11.11 & -8.5247 \\ * & 56.4358 \end{bmatrix},$$

$$L_{1,2} = \begin{bmatrix} 70.1748 & -35.5474 \end{bmatrix},\ Q_{1,2} = \begin{bmatrix} 6.006 & -3.0581 \\ * & 50.6008 \end{bmatrix},$$

$$L_{2,1} = \begin{bmatrix} 20 & -9.9994 \end{bmatrix},\quad Q_{2,1} = \begin{bmatrix} 6.1761 & -4.0448 \\ * & 56.323 \end{bmatrix},$$

$$L_{2,2} = \begin{bmatrix} 19.9998 & -10 \end{bmatrix},\quad Q_{2,2} = \begin{bmatrix} 5.8495 & -3.8761 \\ * & 52.328 \end{bmatrix}.$$

The upper bound on the closed-loop H_2-gain is $\gamma = 0.2813$ and the time varying switched state feedback controller is computed with (13).

Using Theorem 2, with $H = 1$, $\beta = 0.04$ and $T_d = 0.63s$, we get $K_1 = \begin{bmatrix} 4.3634 & 0.373 \end{bmatrix}, K_2 = \begin{bmatrix} 0.9495 & 0.0337 \end{bmatrix}$, for

which the upper bound on the closed-loop H_2-gain is $\gamma = 0.2743$.

The system is simulated with a periodic switching sequence $(t,i) = \{(0,2),(T_d,1),(2T_d,2),\ldots\}$. Here, the parameter uncertainty is chosen as $\lambda = 0.8$. The responses of the open loop switched system are given in Figure 1 which shows that the system is unstable. Here, x1 and x2 represent the states of the system. Figure 2 presents the trajectory responses of the closed-loop (controlled) switched systems with respectively a time varying and constant controller gains that are asymptotically stable.

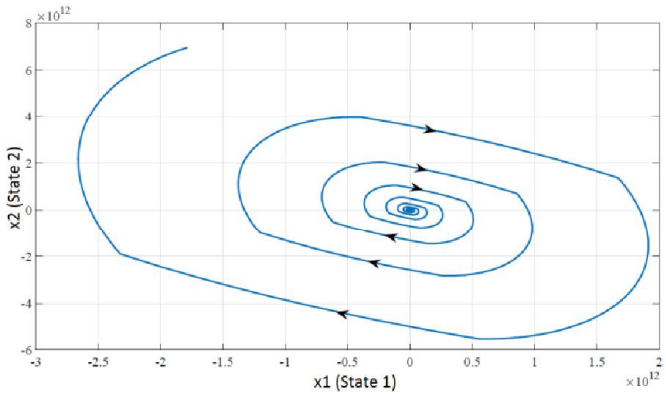


Figure 1: Open-loop responses.

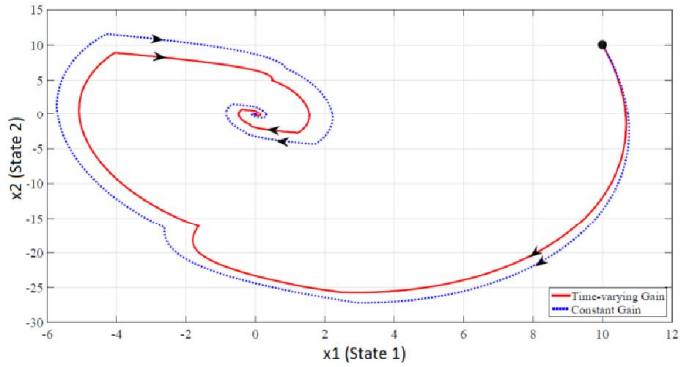


Figure 2: Closed-loop responses.

As it can be seen, the proposed control strategies can stabilize an uncertain switched system with a given dwell time. The constant controller is slower but has a smaller H_2-gain bound than the time varying controller.

V. Conclusion

In this paper, an H_2 sub-optimal state feedback controller synthesis method for switched linear systems with dwell time is presented. A time varying Lyapunov function and a parameter dependent Lyapunov function have been used to design a switched state feedback controller with H_2 bound guarantees. These approaches have been applied to illustrative examples.

In our future research, we intend to apply the proposed controller design strategies to more complex systems.

References

[1] D. Liberzon and A.S. Morse, "Basic problems in stability and design of switched systems," *Control Systems, IEEE*, vol. 19, no. 5, pp. 59-70, 1999.

[2] J. Daafouz, P. Riedinger, and C. Iung, "Stability analysis and control synthesis for switched systems: A switched Lyapunov function approach," *IEEE Transactions on Automatic Control*, vol. 47, no. 11, pp. 1883-1887, November 2002.

[3] M. Goncalves, A. Megretski, and A. Dahleh, "Global analysis of piecewise linear systems using impact maps and surface Lyapunov functions," *IEEE Transactions on Automatic* Control, vol. 48, no. 12, pp. 2089-2106, December 2003.

[4] P. Dayawansa and F. Martin, "A converse Lyapunov theorem for a class of dynamical systems which undergo switching," *IEEE Transactions on Automatic Control*, vol. 44, no. 4, pp. 751-760, April 2004.

[5] S. Boyarski and U. Shaked, "Time-convexity and time-gain-scheduling in finite-horizon robust H_∞-control," *Proceedings of the 48th IEEE Conference on Decision and Control, 2009 held jointly with the 28th Chinese Control Conference*. CDC/CCC, pp. 2765-2770, 2009.

[6] L. I. Allerhand and U. Shaked, "Robust stability and stabilization of linear switched systems with dwell time," *IEEE Transactions on Automatic Control*, vol. 56, no. 2, pp. 381-386, 2011.

[7] L. I. Allerhand and U. Shaked, "Robust state-dependent switching of linear systems with dwell time," *IEEE Transactions on Automatic Control,* vol. 58, no. 4, pp. 994-1001, 2013.

[8] L. I. Allerhand and U. Shaked,"Robust Control of Linear Systems via Switching," *IEEE Transactions on Automatic Control*, vol. 58, no. 2, pp. 506-512, 2013.

[9] J. C. Geromel, and P. Colaneri, "Stability and Stabilization of Continuous-time Switched Linear Systems," *SIAM Journal on Control and Optimization*, vol. 145, no. 5, pp. 1915-1930, 2006.

[10] L. I. Allerhand and U. Shaked, "Robust control of switched linear systems with dwell time," *Electrical and Electronics Engineers in Israel (IEEEI), 2010 IEEE 26th Convention of*, pp. 198-201, 2010.

[11] R. A. DeCarlo, M. S. Branicky, S. Pettersson and B. Lennartson, "Perspectives and results on the stability and stabilizability of hybrid systems," *Proceedings of the IEEE*, vol. 88, no. 7, pp. 1069-1082, 2000.

[12] Z. Sun and S. S. Ge, "*Stability theory of switched dynamical systems*," Springer Science & Business Media, 2011.

[13] H. Lin and P.J. Antsaklis, "Stability and Stabilizability of Switched Linear Systems: A Survey of Recent Results," *IEEE Transactions on Automatic control*, vol. 54, no. 2, pp. 308-322, 2009.

[14] D. Liberzon, *Switching in Systems and Control, ser. Systems & Control: Foundations & Applications*, Boston: Birkhäuser,2003.

[15] X. Zhao, L. Zhang, P. Shi, and M. Liu, "Stability of switched positive linear systems with average dwell time switching," *Automatica*, vol. 48, no. 6, pp. 1132-1137, June 2012.

[16] J. Hespanha and A. Morse, "Stability of switched systems with average dwell time," *Proceeding of the 38th Conference on Decision and Control*, vol. 14, no. 3, pp. 2655-2660, 1999.

[17] G. Zhai, B. Hu, K. Yasuda, and A. Michel, "Stability analysis of switched systems with stable and unstable subsystems: an average dwell time approach," *Proceeding of the American Control Conference*, pp. 200-204, 2000.

[18] W. S. Levine, *Control System Advanced Methods*, USA: Taylor and Francis Group, 2011.

[19] L. I. Allerhand and U. Shaked, "Robust estimation of linear switched systems with dwell time," *International Journal of Control Taylor & Francis*,vol. 86, no. 11, pp. 2067-2074, 2013.

[20] G. Chesi, P. Colaneri, J.C. Geromel, R. Middleton and R. Shorten, "Computing upper-bounds of the minimum dwell time of linear switched systems via homogeneous polynomial Lyapunov functions," *American Control Conference (ACC), 2010, IEEE*, pp. 2487-2492, 2010.

[21] C. Scherer, S. Weiland, "*Linear matrix inequalities in control*," Lecture Notes, Dutch Institute for Systems and Control, Delft, The Netherlands, vol. 3, 2000.

The Effects on Model Performance of Validation Methods for Wind Speed Prediction

Seçkin Karasu[1], Aytaç Altan[1], Zehra Saraç[2] and Rıfat Hacıoğlu[1]

[1] *Department of Electrical and Electronics Engineering, Bülent Ecevit University, 67100, Zonguldak, Turkey*
{seckin.karasu, aytacaltan, hacirif}@beun.edu.tr

[2] *Department of Electrical and Electronics Engineering, Bülent Ecevit University, 67100, Zonguldak, Turkey*
saraczehra@yahoo.com

***Abstract* - Increasing use of renewable energy sources every day increases the importance of studies to ensure that these resources can respond to needs in an uninterrupted and predictable manner. In this study, a wind speed predictor which gives the lowest error for different delay step numbers with different k-fold cross-validation values is obtained by using regression learning from machine learning methods. The next step wind speed is predicted using the past temperature, pressure, humidity, solar radiation values applied to the model's input. Model performances are presented in different forms such as Mean Absolute Error (MAE), Mean Squared Error (MSE) and Root Mean Squared Error (RMSE), and the model performances obtained for the different parameters are compared with MAE, MSE and RMSE from the statistical error criteria. The predicted wind speed and actual wind speed are plotted together. In addition, the regression curve for the best model is plotted. It is seen from the obtained results that the different valued k-fold cross-validation method affects the model performance. Also, the effect of the number of steps of delay in this study with different k-fold cross-validation method is examined.**

***Keywords* - Wind Speed, Prediction, Cross Validation, Regression, Machine Learning.**

I. INTRODUCTION

IN many countries, the number of network integrations of renewable energy sources, especially wind energy, is increased day by day because these resources must be clean and efficient [1, 2]. Due to the intermittent structure, studies on the elimination of adverse effects of high power plants based on wind energy on the network are carried out importance [2, 3]. In order to solve the operating problems of wind power plants, the wind speed is need to accurately predict [2, 4]. In addition, the wind speed time series is a non-linear structure with no normal distribution [2]. Therefore, it is expected that the created model for estimating the wind speed will give accurate and reliable results [4, 5]. In the literature, created models for wind speed prediction are contained different approaches based on numerical, statistical or machine learning. The validation step is applied to increase the generalization ability of the developed forecasting model and focus on the pattern in data instead of data of the model, and to avoid over-fitting [2, 8]. In this study, a 10-minute wind speed prediction is performed using Gaussian SVM (G-SVM) and Regression Trees methods, which take multiple independent variables as input such as humidity, temperature, pressure and solar radiation. Models are generated by k-fold cross validation method which has different k values in the training phase of the study and the model giving the least errors for different delay step numbers is obtained.

For the integration of wind, prediction models such as Multiple Linear Regression, K-Nearest Neighbors, Regression Trees and Random Forests are developed by using geographic position variables such as latitude and longitude with technical features such as rated power, commission year, hub height and rotor diameter. In the estimation study, different dependent variables are selected and the training phase is performed by repeating 5 times with 4-fold cross validation [1]. The short-term wind speed estimation is done by using Empirical Mode Decomposition (EMD) method and its derivatives with the models generated by combining Artificial Neural Network (ANN) and Support Vector Regression (SVR) methods. 5-fold cross validation is used during the training phase and the model performances are given as Root Mean Squared Error (RMSE) and Mean Absolute Error (MAE) [2]. The 1-hour average wind speed estimation is made for the selected attribute with correlation and attribute selection and (Multi-Layer Perceptron) MLP-based wrapper method. The proposed method is tested for five different station data. 10-fold cross validation is used during model training phase and the performance of the model is measured by MAE, the Mean Absolute Percentage Error (MAPE) and the index of agreement (IoA) [3]. The wind speed estimation for a time slot from 1 hour up to 24 hours is done by using the SVR method which optimized parameters with the Genetic Algorithm (GA). The proposed method is compared against the persistence model, and autoregressive models such as AutoRegressive (AR), AutoRegressive Moving Average (ARMA), and Auto-Regressive Integrated Moving Average (ARIMA) tuned by Akaike's Information Criterion and Ordinary Least Squares method. For model training, 10-fold cross-validation method is applied and model performance is measured by MAE, RMSE [4]. Using the one-minute time series, the prediction of the next wind speed is performed with the Nonlinear AutoRegressive (NAR) neural network model for different network parameters. The predicted values of wind speed obtained are compared with predicted values of wind speed obtained with filter methods. A 10-fold cross-validation method is applied in the training phase of the model [5]. First and second order curve fitting coefficients are obtained on independent variables such as humidity, temperature, pressure,

solar radiation. Before these coefficients are applied directly to the Nonlinear AutoRegressive eXogenous (NARX) network structure, the most suitable features are selected with ReliefF method to minimize the Mean Squared Error (MSE) value. Then, a short-time wind speed estimation is carried out with the NARX neural network. The developed models for different parameters are trained by 10-fold cross-validation method. The performance of the obtained model is measured by MAE, MSE and RMSE [6]. Wavelet Decomposition and ANN based wind speed prediction model are developed. Half of the annual data set used for training phase and other part is used for the test phase. The model performance is measured by MAPE and MAE [7]. One-day-ahead mean hourly wind speed estimation is done NARX model. With the help of AutoRegressive Integrated Moving Average (ARIMA) identification results, cross validation errors are minimized by the Fibonacci search method to select the best lag structure and the only adjustable parameter [8].

In this study, short-term wind speed prediction is made by using 1-month wind speed, temperature, pressure, humidity and solar radiation data consisting of 10-minute bars. In the preprocessing step, a moving average area filter with a filter length of 10 is used on the data. Then, models are developed for predicting wind speed with SVM based on Gaussian kernel and Regression Trees methods. The k-fold cross validation method is used during the training phase. The performance of the prediction model is investigated by changing the number of k to 2, 3, 5, 10, 15, 20, 25, 30, 35, 40, 45 and 50. Statistical indicators such as MAE, MSE and RMSE are used to express model performance. Also, the predicted wind speed versus real wind speed for the best model is plotted. It is observed that the performance of the created models varied for the selected k-fold number during the training phase. By taking this situation into consideration, the best model is determined and presented in the "Simulation and Experimental Results" section. This article is organized as follows: models and methods are presented in Section II. Simulation and experimental results are given in Section III. Conclusions are finally discussed in Section IV.

II. Models And Methods

In this study, the prediction of the next step wind speed is done by using one-month meteorological variables such as wind speed, temperature, pressure, humidity and solar radiation which are consisted from 10-minute time series. Statistical values for the used meteorological data is given in Table 1.

Table 1: Statistical values of meteorological parameters.

Parameters	Max.	Min.	Mean	Std. Dev.
Wind Speed (m/s)	11.03	0.08	2.35	2.21
Temperature (℃)	28.22	2.37	12.38	6.11
Humidity (gr/m^3)	99.00	18.50	69.75	19.28
Pressure (mbar)	1032.7	1000.5	1021.4	6.54
Solar radiation (W/m^2)	395.80	0.00	43.60	89.25

In the preprocessing step, a moving average filter with a filter length of 10 is applied to all data. Meteorological variables are taken as an input for predicting the wind speed. The prediction models are constructed with Regression Trees method and Gaussian kernel based SVM method, respectively. The k-fold cross validation method is applied to the prediction models during the training of models. The number of delay steps is tested for values 3, 4, and 5. The k-fold number is also applied to the models by changing the number of k to 2, 3, 5, 10, 15, 20, 25, 30, 35, 40, 45 and 50. Model performances are compared with each other and the best model is determined.

A. *Regression Trees*

Regression trees is a decision tree made up of leaf nodes and branches, which can predict continuous numerical values [9]. In this method, a tree structure is firstly created. The parts of the sub-brunches that are not associated with the dependent variable are pruned. The process continues until the absolute error between the real and the predicted value is at the minimum value. As a result of this stage, the most suitable tree structure is obtained [9]. In this study, split and prune criterions are taken as MSE. Minimum number of parent and minimum number of leaf are selected as 10 and 4, respectively.

B. *Support Vector Machines*

SVM method is an effective data mining tool used in multi-class classification problem and in regression problems where there is a nonlinear relationship between dependent and independent variables [10]. A support vector machine generates an n - dimensional hyperplane that optimally divides the data into two categories. The selection of the kernel function of the DVM affects the classification / regression performance [10]. In this study, the Gaussian kernel is used because the relationship between input and output in the data set is nonlinear. In this study, the Gaussian kernel function is used in SVM model because the relationship between input and output variables is non-linear.

C. *Training Stage of Models*

In the k-fold cross-validation method, the X data set is randomly divided into k pieces of equal size, and each fold is used for test purposes and others for training purposes. The overall performance of the model is calculated by taking the averages of the classification / prediction performances for all folds [10]. 10-fold cross-validation process is given in Figure 1. E notation refers to the success of the k-fold operation. Overall performance of the model is calculated by E_{ort} notation.

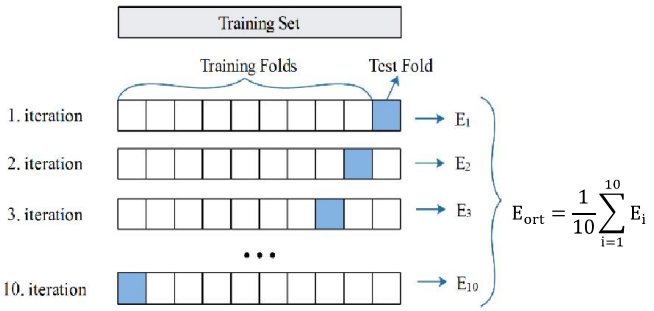


Figure 1: 10-fold cross-validation process.

D. Statistical Error Indicators

After prediction stage, the error criteria can be used to represent numerically model performance as shown in Table 2. The difference between the real time series and the predicted time series arises as an error, e_t. It is given in (1).

$$e_t = y_{real} - y_{predicted} \quad (1)$$

E. Statistical Error Indicators

The linear relationship between the actual value and the predict value is shown by the regression curve and the prediction graph is plotted for the best model.

Table 2: Statistical error criteria.

Error Criterion	**Equation**
Mean Absolute Error (MAE)	$MAE = \frac{1}{n}\sum_{i=1}^{n}\lvert e_t \rvert$
Mean Squared Error (MSE)	$MSE = \frac{1}{n}\sum_{i=1}^{n} e_t^2$
Root Mean Squared Error (RMSE)	$RMSE = \sqrt{\frac{1}{n}\sum_{i=1}^{n} e_t^2}$

F. Box and Whisker Graph

Box and Whisker Graph is a tool, developed by John W. Tukey in 1977, that explains the data array with six different properties in descriptive statistic [11, 12]. These properties are defined as first quartile (Q1), second quartile (Q2), third quartile (Q3), lower whisker, upper whisker and outliers. A sample Box and Whisker Graph is shown in Figure 2.

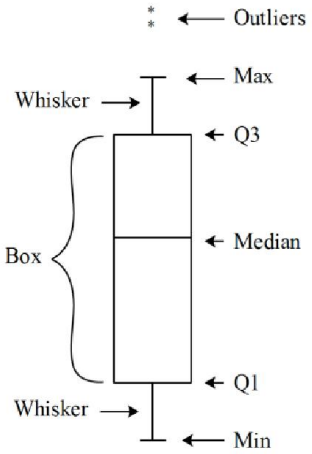


Figure 2: A sample Box and Whisker graph.

To draw Box and Whisker Graph, firstly the data array is sorted from smallest to largest one to find median value. The median value separates the data sequence into two separate clusters and is called the second quartile (Q2). After the median is removed, median values of the two clusters are obtained in the rest of data array. The median value of the first data cluster is called the first quarter (Q1) and the median value of the second data cluster is called the third quarter (Q3). The box is drawn with values Q1, Q2 and Q3. The whiskers indicate the spread of the data array. The minimum and maximum values of the data array form the whiskers, and the difference between these two values expresses the spread. After the lower limit and the upper limit are calculated according to the formulas Q1-1.5 (Q3-Q1) and Q3 + 1.5 (Q3-Q1), respectively, values of out of these limit values are defined as outliers in the data array. After this step, the lower and upper whiskers are redrawn taking into account the outlier values in the data array. In the study, the k-fold cross validation is repeated 30 times and the MAE, MSE, RMSE model errors are shown in the box-whisker graph.

III. Simulation And Experimental Results

The next step wind speed prediction is done by using one-month meteorological data taken from wind power plant in Zonguldak. The data consists of variables such as wind speed, temperature, pressure, humidity and solar radiation. Moving average filter with filter length of 10 is used for the variables on the time series. Wind speed prediction is performed on the data obtained by min max normalization process. The prediction models are constructed with Regression Trees method and Gaussian kernel based SVM method, respectively. The k-fold cross validation method is used in the training phase of the models. The success of the prediction model is examined by changing the number of k to 2, 3, 5, 10, 15, 20, 25, 30, 35, 40, 45 and 50. The effect on the performance is also investigated by changing the number of delay steps 3, 4, 5 on the dependent variables. It is also investigated the effect on the performance by changing the number of delay steps 3, 4 and 5 on the dependent variables. Box-Whisker graphs are examined for all cases. The real vs predicted graph and regression graph are drawn for the best prediction model.

Simulations are run out in MATLAB environment. MAE, MSE, RMSE change graphs are given in Figures 3-8, depending on the number of k-folds and the number of delay steps. When MAE, MSE and RMSE graphs are examined for both models, reducing the number of delay steps appears to have a positive effect on performance. When MAE graphs are examined for both models, MAE values decrease as the number of k increases. When MAE values in box-whisker graphs are examined for Regression Trees and G-SVM in different k-fold value, it is seen that the spread of the boxes, it is seen that the spread of the boxes in the regression trees method is higher than those in G-SVM method. It can be said that the G-SVM method gives a more generalized wind speed prediction model than the regression trees method. When the change of the MSE values for the number of delay steps and each k fold is examined, it is seen that the G-SVM method is superior to the Regression Trees method. For k = 40 and lag = 3, the G-SVM model is the most successful model with the lowest MSE value for wind speed prediction. For this model, the real vs. predicted plot is shown in Figure 9 and the regression plot is shown in Figure 10. Graphs also show that the model is successful and the error level is low.

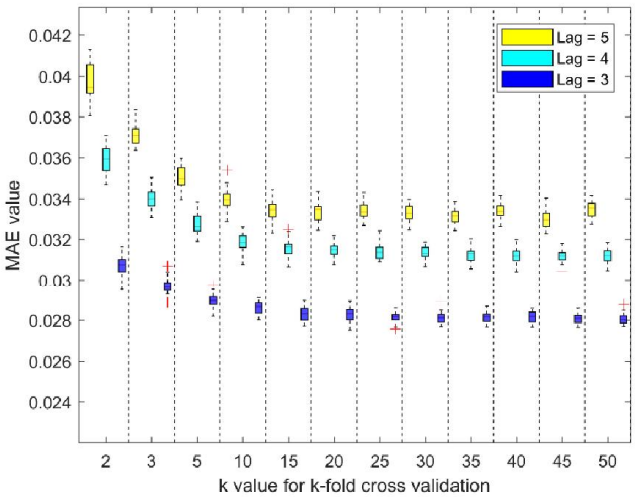


Figure 3: MAE change due to the number of delay steps and k-fold cross validation values for Regression Trees method.

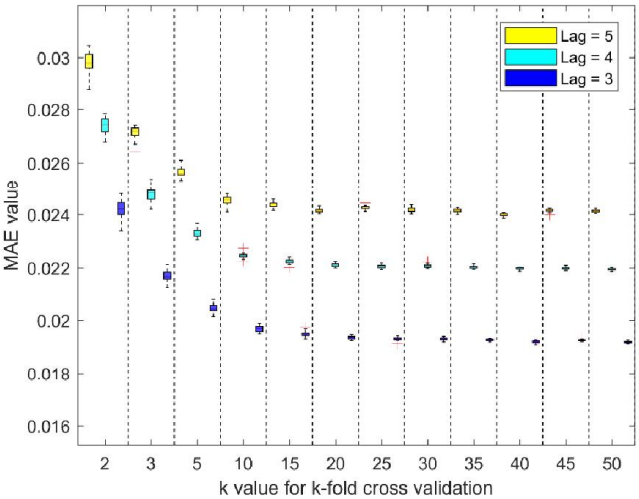


Figure 4: MAE change due to the number of delay steps and k-fold cross validation values for G-SVM.

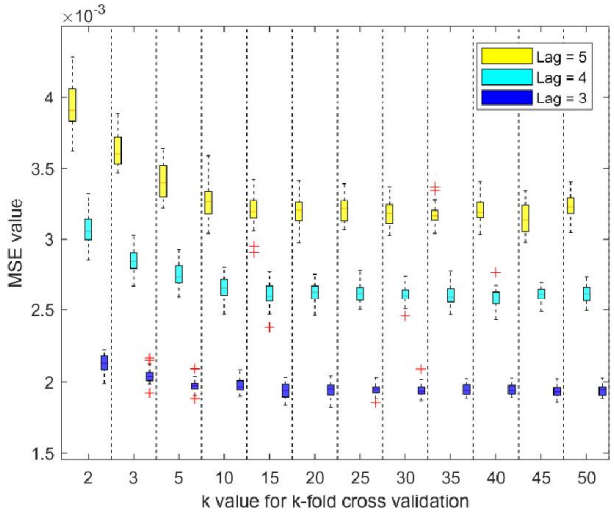


Figure 5: MSE change due to the number of delay steps and k-fold cross validation values for Regression Trees method.

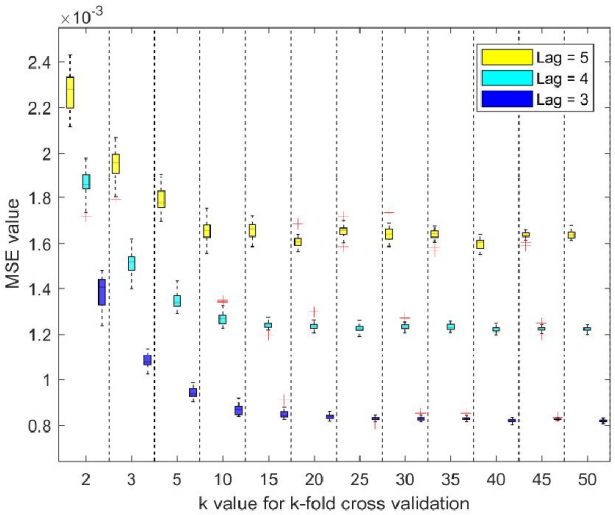


Figure 6: MSE change due to the number of delay steps and k-fold cross validation values for G-SVM.

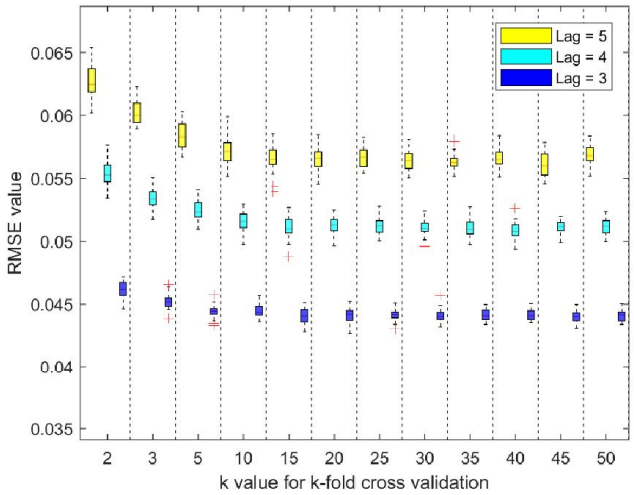


Figure 7: RMSE change due to the number of delay steps and k-fold cross validation values for Regression Trees method.

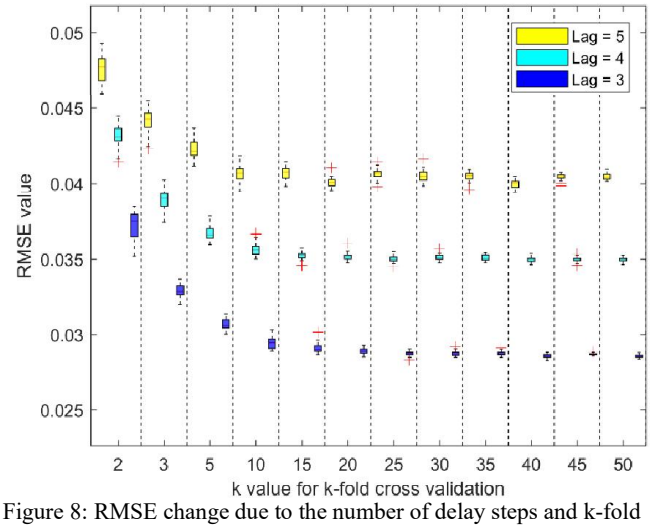


Figure 8: RMSE change due to the number of delay steps and k-fold cross validation values for G-SVM.

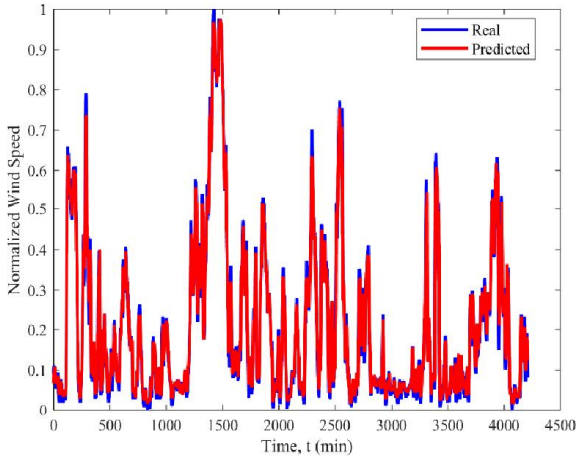


Figure 9: Wind speed prediction by G-SVM method (for 40-fold cross validation and delay step = 3).

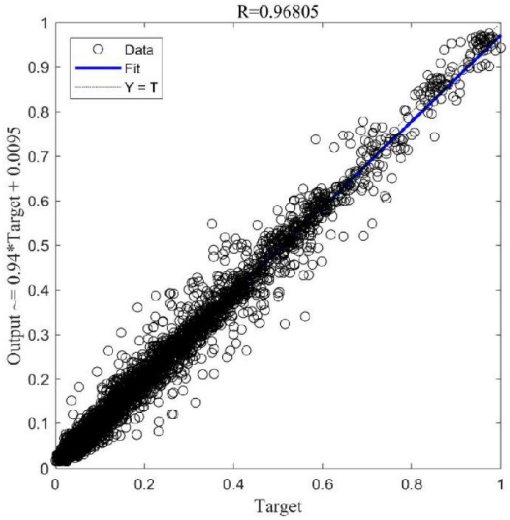


Figure 10: Regression plot for G-SVM method (for 40-fold cross validation and delay step = 3).

IV. Conclusion

In this study, wind speed prediction is made with Regression Trees and G-SVM methods by using 10-minute meteorological data obtained from the wind power plant in Zonguldak province. Variables such as temperature, pressure, humidity and solar radiation are applied to the models developed to predict the wind speed. The model training phase is performed by k-fold cross validation method for different k values. It is seen that model performance decreases with increasing number of delay steps. It is seen with the help of Box-Whisker graph which the model performance increases with increasing k-fold number. It is seen that the model obtained by G-SVM method is the model which gives the lowest wind speed prediction error for the model delay number 3 and 40-fold cross-validation method. In addition, it is shown that the performance of the wind speed prediction model is high via visual and numerical values such as the regression curve and the Pearson correlation coefficient.

Acknowledgment

This study was supported by Bülent Ecevit University (BAP Project No: 2012-17-15-01). The authors would like to thank Bülent Ecevit University for their support.

References

[1] R. Becker, and D. Thrän, "Completion of wind turbine data sets for wind integration studies applying random forests and k-nearest neighbors," *Applied Energy*, [in Press], October 2017.

[2] Y. Ren, P. N. Suganthan, and N. Srikanth, "A comparative study of empirical mode decomposition-based short-term wind speed forecasting methods," *IEEE Trans. on Sustainable Energy*, vol. 6(1), pp. 236-244, January 2015.

[3] J. A. Carta, P. Cabrera, J. M. Matías, and F. Castellano, "Comparison of feature selection methods using ANNs in MCP-wind speed methods. A case study," *Applied Energy*, vol. 158, pp. 490-507, November 2015.

[4] G. Santamaría-Bonfil, A. Reyes-Ballesteros, and C. Gershenson, "Wind speed forecasting for wind farms: A method based on support vector regression," *Renewable Energy*, vol. 85, pp. 790-809, January 2016.

[5] S. Karasu, A. Altan, Z. Saraç, and R. Hacıoğlu, "Prediction of wind speed with non-linear autoregressive (NAR) neural networks," *IEEE 25th Signal Processing and Communications Applications Conference*, 2017, pp.1-4.

[6] S. Karasu, A. Altan, Z. Saraç, and R. Hacıoğlu, "Estimation of fast varied wind speed based on NARX neural network by using curve fitting," *International Journal of Energy Applications and Technologies*, vol. 4(3), pp. 137-146, October 2017.

[7] B. Doucoure, K. Agbossou, and A. Cardenas, "Time series prediction using artificial wavelet neural network and multi-resolution analysis: Application to wind speed data," *Renewable Energy*, vol. 92, pp. 202-211, July 2016.

[8] W. Zhao, Y. M. Wei, and Z. Su, "One day ahead wind speed forecasting: A resampling-based approach," *Applied Energy*, vol. 178, pp. 886-901, September 2016.

[9] A. Troncoso, S. Salcedo-Sanz, C. Casanova-Mateo, J. C. Riquelme, and L. Prieto, "Local models-based regression trees for very short-term wind speed prediction," *Renewable Energy*, vol. 81, pp. 589-598, September 2015.

[10] P. N. Tan, V. Kumar, and M. Steinbach, *Introduction to Data Mining*. Pearson, 2005.

[11] D. C. Hoaglin, "John W. Tukey and data analysis," *Statistical Science*, vol. 18(3), pp. 311-318, August 2003.

[12] J. E. Seem, "Pattern recognition algorithm for determining days of the week with similar energy consumption profiles," *Energy and Buildings*, vol. 37(2), pp. 127-139, February 2005.

Optimal Sensing Time for Sensing Based Dynamic Spectrum Sharing Scheme in Cognitive Radio

S. SAHIN[1] and D. GURKAN KUNTALP[2]

[1]Dokuz Eylul University, Izmir/Turkey, savas.sahin@i-marinesystems.com
[2]Dokuz Eylul University, Izmir /Turkey, damla.kuntalp@deu.edu.tr

***Abstract* - Cognitive Radio (CR) concept mentioned and developed in 2000s with the aim of using spectrum more efficiently by allowing unlicensed users to access licensed bands without harmful interference that affects licensed users' quality of service (QoS). Total achievable throughput maximization of the CR system is the next step for efficiency. In this paper, we will investigate the optimal sensing time that maximizes the total achievable throughput under sensing-based spectrum sharing (SSS) dynamic access scheme which has high and low power settings according to licensed user's activity in the channel. An average interference constraint which protects licensed user from harmful interference caused by unlicensed user because of imperfect sensing and average total transmit power constraint which helps CR devices establish reasonable long term power budgets are introduced. We will discuss the effects of these constraints on optimal sensing time. We also consider a penalty condition which effects optimization of sensing time. We compare the optimal sensing time with and without penalty condition. Finally, we give simulation results to validate our analysis.**

***Keywords* – Optimal sensing time, cognitive radio, dynamic spectrum access, throughput maximization**

I. INTRODUCTION

INCREASING number of wireless applications require the efficient utilization of limited radio spectrum and therefore create the need for unconventional spectrum sharing schemes. The concept of cognitive radio (CR), which provides efficient utilization of the limited electromagnetic spectrum, was first proposed by Joseph Mitola III in a seminar at the Royal Institute of Technology in Stockholm (KTH), in 1998. CR systems increase the efficiency of spectrum utilization by allowing unlicensed users to access the licensed bands by detecting the unused spectrum assigned to licensed users. CR first detects the channel's availability. If the channel is idle, CR can use that channel and helps efficient spectrum usage; if the channel is busy, CR can either use the channel with a relatively low power setting or shutdowns some operations to save power which is a crucial operation for battery powered devices. In both cases, resources are used efficiently.

The basic tasks of cognitive systems can be classified as spectrum sensing, spectrum analysis, and spectrum access decision. It is known that spectrum sensing is a crucial task in cognitive networks, which must be performed before the cognitive user's access to the licensed spectrum in order to limit the harmful interference that effect primary users' (PUs) activity. Dynamic spectrum access can be explained as finding spectrum holes by sensing one or more channels and using these holes with associated channel parameters. Three different access schemes evaluated so far. One is opportunistic spectrum access (OSA) in which secondary user (SU) only transmits in the idle channels. The second one is called as spectrum sharing in which multiple users share the same channel . The last one, sensing-based spectrum sharing (SSS) is the hybrid version of the previous two schemes.

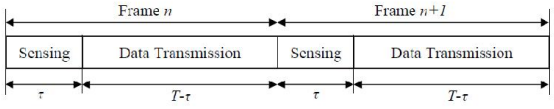


Figure 1: Frame structure of cognitive radio

Every CR network has a frame structure consists of sensing and data transmission portions as shown in Figure 1. In sensing portion of the frame, CR listens to its environment, and determines the channel state. In data transmission portion CR accesses the channel and starts the communication. For the channel's status only two possible situations exist: busy or idle; therefore spectrum sensing for spectrum access is a binary hyphotesis case. SSS scheme uses a high power configuration ($P_{s,j}^{(0)}$), when the channel is detected as idle whose probability for j^{th} channel represented with $(H_{0,j})$, and uses a relatively low power configuration ($P_{s,j}^{(1)}$), when the channel is detected as busy whose probability for j^{th} channel represented with $(H_{1,j})$; where subscript 's' denotes secondary user. Since the second situation cause interference to primary user, primary users' quality of service (QoS) can be protected by introducing average interference constraint.

It is clear that tradeoff between sensing time and total achievable throughput is a critical issue. This problem is investigated in [5] under energy detection for spectrum sensing strategy for single channel. In [6] optimal sensing time is investigated where OSA scheme used as spectrum access strategy for wideband operations which only uses idle slots for transmission. [7] studied OSA and SSS for wideband operations under average interference and average total transmit power constraints and compared results. Authors of [8] examined instantaneous constraints and average

constraints for long term achievable throughput and proved that an average power constraint leads to higher total achievable throughput.

In this paper, we will investigate optimal sensing time that maximizes total achievable throughput for SSS scheme under average interference constraints and average total transmit power constraint using energy detector technique which is easy to implement and also has low cost. We also consider that sensing is not always perfect and miss detections or false alarms occur. Different from [7], we also consider a penalty condition for the optimization problem and compare the results.

The rest of the paper is organized as follows: in Section 2 we explain the channel model and possible scenarios. Formulation of the problem and a simulation algorithm will be given in Section 3. Results of the simulations are evaluated in Section 4 and Section 5 is where we give conclusions.

II. SYSTEM MODEL

CR network consists of PU transmitter (Tx), receiver (Rx) and SU Tx and Rx which are in the same geographical area as seen in Figure 2.

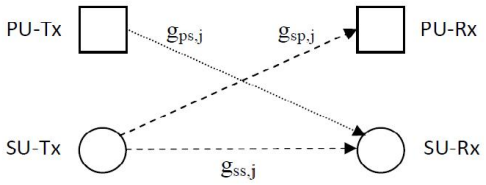


Figure 2: Cognitive radio network with channel power gains

Figure 2 also shows us the instantaneous channel power gains between PU-Tx and SU-Rx, SU-Tx and PU-Rx , SU-Tx and SU-Rx for the j^{th} channel respectively, $g_{ps,j}$, $g_{sp,j}$, $g_{ss,j}$. The channels are assumed to be flat fading and channel gains are assumed to be ergodic stationary and known at the secondary users.

Energy detector gets measurements according to sampling rate and compares the measured value with a predefined threshold to determine channel state. When the spectrum sensing is not perfect, as shown in Figure 3, interferences are inevitable. When the channel's actual status is busy, it can be detected as idle, which means miss detection, transmission is

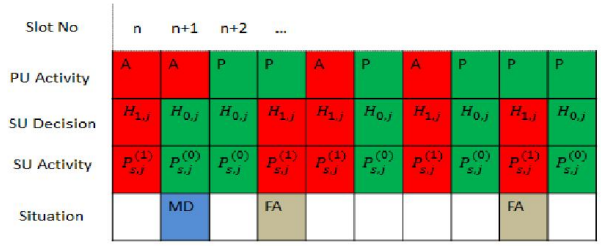


Figure 3: Imperfect sensing, A: active, P: Passive, MD: Miss Detection and FA: False Alarm

carried out by SU with high power configuration and that causes harmful interference on PU.

Probability of detection and probability of false alarm for a certain threshold can be formulated as;

$$P_{d,j}(\tau,\epsilon_j) = \mathcal{Q}\left(\left(\frac{\epsilon_j}{N_0} - \gamma_j - 1\right)\sqrt{\frac{\tau f_s}{2\gamma_j+1}}\right) \quad (1)$$

$$P_{fa,j}(\tau,\epsilon_j) = \mathcal{Q}\left(\left(\frac{\epsilon_j}{N_0} - 1\right)\sqrt{\tau f_s}\right) \quad (2)$$

where ϵ_j is the detection threshold of the detector for j^{th} channel, N_0 is the noise variance, γ_j is the received SNR from PU at the SU detector, f_s is the sampling frequency, and $\mathcal{Q}$ is the standard normal (Gaussian) cumulative distribution function, respectively [5].

III. PROBLEM FORMULATION

We are trying to find optimal sensing time that maximize the SU's ergodic capacity. CR network's ergodic capacity maximization depends on the optimization of the sensing time. Instantaneous transmission rates for possible scenarios are given below in Table 1.

Table 1: Instantaneous transmission rates according to primary user activity and secondary user decision

PU Activity	SU Decision	Insta. Trans. Rate
passive	Idle	$r_{00,j}$
passive	Busy	$r_{01,j}$
active	Idle	$r_{10,j}$
active	Busy	$r_{11,j}$

According to the given definitions, instantaneous transmission rates are given below.

$$r_{00,j} = log_2\left(1 + \frac{g_{ss,j}P_{s,j}^{(0)}}{N_0}\right) \quad (3)$$

$$r_{01,j} = log_2\left(1 + \frac{g_{ss,j}P_{s,j}^{(1)}}{N_0}\right) \quad (4)$$

$$r_{10,j} = log_2\left(1 + \frac{g_{ss,j}P_{s,j}^{(0)}}{g_{ps,j}P_{p,j}+N_0}\right) \quad (5)$$

$$r_{11,j} = log_2\left(1 + \frac{g_{ss,j}P_{s,j}^{(1)}}{g_{ps,j}P_{p,j}+N_0}\right) \quad (6)$$

Thus, the average throughput of the j^{th} channel for SU under SSS can be formulated as follow.

$$\begin{aligned} C_j = {} & P(H_{0,j})\left(1 - P_{fa,j}(\bar{\tau},\epsilon_j)\right) r_{00,j} \\ & + P(H_{0,j})P_{fa,j}(\bar{\tau},\epsilon_j) r_{01,j} \\ & + P(H_{1,j})\left(1 - P_{d,j}(\bar{\tau},\epsilon_j)\right) r_{10,j} \\ & + P(H_{1,j})P_{d,j}(\bar{\tau},\epsilon_j) r_{11,j} \end{aligned} \quad (7)$$

In Equation 7, sensing time is ignored for time being. $P(H_{0,j})$ and $P(H_{1,j})$ are probabilities that j^{th} channel is idle and busy respectively. Average interference constraint that limits the harmful interference that effects PUs' QoS and average total transmit power constraint that helps long term power budget are given in (8) and (9) respectively.

$$\frac{T-\epsilon}{T}\mathbb{E}\begin{Bmatrix} g_{sp,j}P_{s,j}^{(0)}P(H_{1,j})\left(1-P_{d,j}(\tau,\epsilon_j)\right) \\ +g_{sp,j}P_{s,j}^{(1)}P(H_{1,j})P_{d,j}(\tau,\epsilon_j) \end{Bmatrix} \leq \Gamma \tag{8}$$

$$\frac{T-\tau}{T}\mathbb{E}\begin{Bmatrix} P(H_{0,j})P_{s,j}^{(0)}\left(1-P_{fa,j}(\tau,\epsilon_j)\right) \\ +P(H_{0,j})P_{s,j}^{(1)}P_{fa,j}(\tau,\epsilon_j) \\ +P(H_{1,j})P_{s,j}^{(0)}\left(1-P_{d,j}(\tau,\epsilon_j)\right) \\ +P(H_{1,j})P_{s,j}^{(1)}P_{d,j}(\tau,\epsilon_j) \end{Bmatrix} \leq P_{av} \tag{9}$$

where P_{av} represents the average power constraint, Γ is average interference constraint and $\mathbb{E}$ is the expectation operator. Now the problem is maximization of achievable throughput under these constraints.

$$maximize_{\left\{\tau,P_{s,j}^{(0)},P_{s,j}^{(1)}\right\}}\ \mathbb{E}\left\{\frac{T-\tau}{T}C_j\left(\tau,P_{s,j}^{(0)},P_{s,j}^{(1)}\right)\right\} \tag{10}$$

Subj. to (8), (9), $P_{s,j}^{(0)}>0$, $P_{s,j}^{(1)}>0$, $T>\tau>0, j=1,..,M$

Above optimization problem is convex with respect to the transmit powers $P_s^{(0)}, P_s^{(1)}$ but not with respect to sensing time τ. According to sensing time probability of false alarm changes which directly affects the overall throughput. However, knowing that sensing time τ relies on the frame duration T makes it easy to find it by using an exhaustive search. In this manner above optimization problem can be maximized with respect to transmit powers and then optimal sensing time can be evaluated by using an exhaustive search algorithm. Optimal power allocation strategy of the CR system that maximizes ergodic capacity can be solved by using Lagrangian form given in (11).

$$\begin{aligned} &L\left(P_s^{(0)},P_s^{(1)},\lambda,\mu\right) \\ &\quad=\mathbb{E}\left\{\sum_{j=1}^{M}\frac{T-\tau}{T}\begin{pmatrix} a_{0,j}r_{00,j}+\beta_{0,j}r_{10,j} \\ +a_{1,j}r_{11,j}+\beta_{1,j}r_{01,j}\end{pmatrix}\right\} \\ &\qquad-\lambda\left[\frac{T-\tau}{T}\mathbb{E}\left\{\sum_{j=1}^{M}\begin{bmatrix}(a_{0,j}+\beta_{0,j}).P_{s,j}^{(0)} \\ +(a_{1,j}+\beta_{1,j})\end{bmatrix}\right\}-P_{av}\right] \\ &\qquad-\sum_{j=1}^{M}\mu_j\left[\frac{T-\tau}{T}.\mathbb{E}\begin{Bmatrix} g_{sp,j}\beta_{0,j}P_{s,j}^{(0)} \\ +g_{sp,j}\beta_{1,j}P_{s,j}^{(1)}\end{Bmatrix}-\Gamma\right] \end{aligned} \tag{11}$$

Solution for (11) can be countered by solving dual function of the Lagrangian and optimization can be evaluated by taking supremum of (12) with respect to transmit powers $P_s^{(0)}$, $P_s^{(1)}$.

$$g(\lambda,\mu)=\sup_{P_s^{(0)}P_s^{(1)}}L\left(P_s^{(0)},P_s^{(1)},\lambda,\mu\right) \tag{12}$$

Since Slather's conditions hold [11], duality gap between primal function and dual function is zero which means solution for the dual function is also solution for the primal optimization function.

As given in [7], dual problem (12) can be solved in two subproblems. By finding supremum of Lagrangian with respect to $P_s^{(0)}$, $P_s^{(1)}$, subproblems are given as follow.

Subproblem 1 (SP1):

$$\begin{aligned} \underset{P_s^{(0)}\geq 0}{maximize}\ &\mathbb{E}\left\{\sum_{j=1}^{M}\frac{T-\tau}{T}\left(a_{0,j}r_{00,j}+\beta_{0,j}r_{10,j}\right)\right\} \\ &-\lambda\mathbb{E}\left\{\sum_{j=1}^{M}\frac{T-\tau}{T}\left(a_{0,j}+\beta_{0,j}\right)P_{s,j}^{(0)}\right\} \\ &-\sum_{j=1}^{M}\mu_j\frac{T-\tau}{T}\mathbb{E}\left\{g_{sp,j}\beta_{0,j}P_{s,j}^{(0)}\right\} \end{aligned} \tag{13}$$

Subproblem 2 (SP2):

$$\begin{aligned} \underset{P_s^{(1)}\geq 0}{maximize}\ &\mathbb{E}\left\{\sum_{j=1}^{M}\frac{T-\tau}{T}\left(a_{1,j}r_{11,j}+\beta_{1,j}r_{01,j}\right)\right\} \\ &-\lambda\mathbb{E}\left\{\sum_{j=1}^{M}\frac{T-\tau}{T}\left(a_{1,j}+\beta_{1,j}\right)P_{s,j}^{(1)}\right\} \\ &-\sum_{j=1}^{M}\mu_j\frac{T-\tau}{T}\mathbb{E}\left\{g_{sp,j}\beta_{1,j}P_{s,j}^{(1)}\right\} \end{aligned} \tag{14}$$

Above subproblems SP1 and SP2 are convex optimization problems. If we write Lagrangians and apply Karush-Kuhn-Tucker conditions, we find the optimal power strategy as:

$$P_{s,j}^{(0)}=\left[\frac{A_{0,j}+\sqrt{\Delta_{0,j}}}{2}\right]^{+} \tag{15}$$

$$P_{s,j}^{(1)}=\left[\frac{A_{1,j}+\sqrt{\Delta_{1,j}}}{2}\right]^{+} \tag{16}$$

where;

$$A_{0,j}=\frac{log_2(e)(a_{0,j}+\beta_{0,j})}{\lambda(a_{0,j}+\beta_{0,j})+\mu_j\beta_{0,j}h}-\frac{2N_0+S_j}{g_{ss,j}} \tag{17}$$

$$\Delta_{0,j}=A_{0,j}^2-\frac{4}{g_{ss,j}}\left\{\frac{N_0^2+S_jN_0}{g_{ss,j}}-\frac{log_2(e)[a_{0,j}(N_0+S_j)+\beta_{0,j}N_0]}{\lambda(a_{0,j}+\beta_{0,j})+\mu_j\beta_{0,j}h}\right\} \tag{18}$$

$$A_{1,j}=\frac{log_2(e)(a_{1,j}+\beta_{1,j})}{\lambda(a_{1,j}+\beta_{1,j})+\mu_j\beta_{1,j}h}-\frac{2N_0+S_j}{g_{ss,j}} \tag{19}$$

$$\Delta_{1,j}=A_{1,j}^2-\frac{4}{g_{ss,j}}\left\{\frac{N_0^2+S_jN_0}{g_{ss,j}}-\frac{log_2(e)[a_{1,j}(N_0+S_j)+\beta_{1,j}N_0]}{\lambda(a_{1,j}+\beta_{1,j})+\mu_j\beta_{1,j}h}\right\} \tag{20}$$

where $S_j=g_{ps,j}P_{p,j}$, $h=g_{ps,j}$.

Optimal power strategy is defined with respect to interference and total average power constraints while maximizing the ergodic capacity. As seen from the formula optimal values of λ and μ should be evaluated. According to

the problem formulation section a small algorithm routine is shown below.

Algorithm 1:

1. Initialize channel parameters
2. Find upper bound for λ and μ matrices with Δ steps until $P_s^{(0)}$ *or* $P_s^{(1)} < 0$
3. For $\overline{\tau} = 0 : T$
   - Calculate $P_s^{(0)}$, $P_s^{(1)}$ matrix
   - Find C_j matrix
   - Take maximum of total achievable throughput matrix

   End
4. Optimal sensing time and power allocation evaluation.

$$\overline{\tau}_{opt} = argmax\ R\ (\overline{\tau}, P_s^{(0)}, P_s^{(1)})$$
$$\left[P_{s,opt}^{(0)},\ P_{s,opt}^{(1)}\right] = \left[P_s^{(0)},\ P_s^{(1)}\right]_{\overline{\tau}=\overline{\tau}_{opt}}$$

As seen from (10), if sensing time increases, total achievable throughput decreases. Knowing this dependency helps us consider a penalty term in (10) which is:

$$K\frac{(T-\tau)^2}{2} \qquad (21)$$

where K is the weight constant, T and τ in seconds, respectively [11]. Optimization problem with penalty term now expressed as:

$$maximize_{\left\{\tau, P_{s,j}^{(0)}, P_{s,j}^{(1)}\right\}} \mathbb{E}\left\{\frac{T-\tau}{T} C_j\left(\tau, P_{s,j}^{(0)}, P_{s,j}^{(1)}\right) + K\frac{(T-\tau)^2}{2}\right\} \quad (22)$$

Subj. to (8), (9), $P_{s,j}^{(0)} > 0$, $P_{s,j}^{(1)} > 0$, $T > \tau > 0, j = 1,..,M$

When we repeat the previous optimization steps in (11), (12), (13), and (14), we will find exactly the same power strategy as in (15) and (16) with parameters in (17), (18), (19), and (20). Another algorithm for the simulation of the optimization problem (22) is given below.

Algorithm 2:

1. Initialize channel parameters
2. Find upper bound for λ and μ matrices with Δ steps until $P_s^{(0)}$ *or* $P_s^{(1)} < 0$
3. For $\overline{\tau} = 0 : T$
   - Calculate $P_s^{(0)}$, $P_s^{(1)}$ matrix
   - Find C_j matrix
   - Take maximum of total achievable throughput with penalty matrix

   End
4. Optimal sensing time and power allocation evaluation.

$$\overline{\tau}_{opt} = argmax\ R\ (\overline{\tau}, P_s^{(0)}, P_s^{(1)})$$
$$\left[P_{s,opt}^{(0)},\ P_{s,opt}^{(1)}\right] = \left[P_s^{(0)},\ P_s^{(1)}\right]_{\overline{\tau}=\overline{\tau}_{opt}}$$

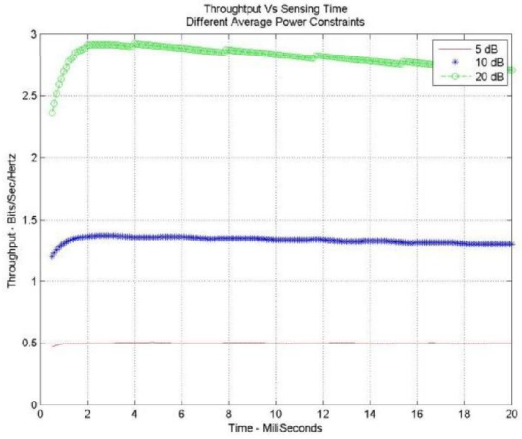


Figure 4: Throughput vs sensing time, $\Gamma = -10\ dB$, $g_{ps,j} = 0.01$, $g_{sp,j} = 0.01$, $g_{ss,j} = 0.09$, $SNR = -15\ dB$

IV. RESULTS

We made simulation studies for one narrowband channel; however it is easy to generalize the simulations for multiple channel case. Frame duration is 100 ms, primary user transmission power $P_{p,j} = 10\ dB$, target detection probability is 0.9 and channel power gains are ergodic, stationary and known at secondary user's detector for the following simulations.

Figure 4 shows the maximum achievable throughput versus sensing time with $P_{av} = 5\ dB$, $P_{av} = 10\ dB$, $P_{av} = 20\ dB$. It is seen that for almost three configurations, optimal sensing time $\overline{\tau}_{opt}$ is around 2.45 ms which is identical to findings in [5]. Another conclusion can be made for average transmit power constraint and throughput tradeoff. It is seen from Figure 4 that if constraint limit is high, which means SU can transmit with higher power settings, SU's total achievable throughput increases as expected.

As we optimize sensing time under average interference and transmit power constraints simultaneously, Figure 5 shows us that in different values they can be dominant one over other. It is seen that for $\Gamma = -5\ dB$ and $\Gamma = -10\ dB$ SU's total throughput is the same for optimal values of sensing time which means average power constraint is dominant over interference constraint which should be defined by the CR network designer. Designer can define importance of the constraints by taking into consideration of PU's QoS. When interference constraint become $\Gamma = -20\ dB$, it is seen that the roles are changed and interference constraint becomes more dominant over average transmit power constraint. Total achievable throughput of SU decreases, however protection of PU's QoS is increased. It is seen that optimal sensing time $\overline{\tau}_{opt}$ is still around 2.45 ms.

As seen from Figure 6; if SNR decreases, optimal sensing time increases which is expected. Secondary user's detector should detect signals with very low power values which might cause possible miss detections and false alarms. To be able overcome false alarms and miss detections, sensing time increases up to 12 milliseconds for $SNR = -20\ dB$ case.

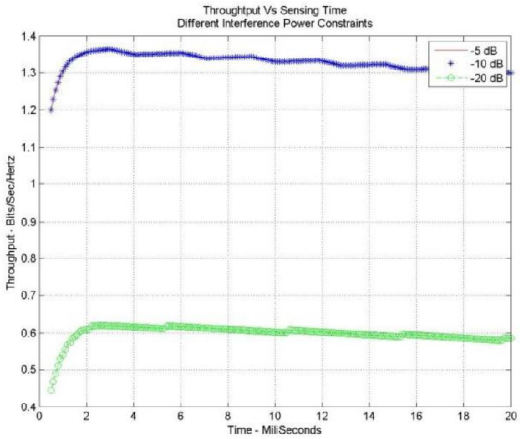


Figure 5: Throughput vs sensing time, $P_{av} = 10\ dB$, $g_{ps,j} = 0.01$, $g_{sp,j} = 0.01$, $g_{ss,j} = 0.09$, $SNR = -15\ dB$

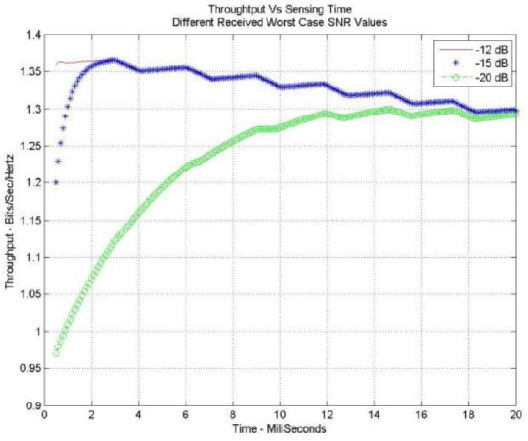


Figure 6: Throughput vs sensing time, $P_{av} = 10\ dB$, $\Gamma = -10\ dB$, $g_{ps,j} = 0.01$, $g_{sp,j} = 0.01$, $g_{ss,j} = 0.09$

In Figure 7 and Figure 8, optimal sensing time that maximizes achievable throughput is investigated with given parameters for normal optimization problem and modified optimization problem with the penalty condition. It is seen that optimal sensing time is almost the same and around $2.45\ ms$. However impact of penalty condition can easily be seen around optimal area. Using this penalty condition in a convex optimization method helps us reach the optimal solution easier with less computational effort.

V. CONCLUSION

We examine CR networks' basic components and dynamic spectrum access schemes. Understanding basic components and dynamic spectrum access strategies helps us to analyze design steps. We choose sensing-based spectrum access scheme, which is a hybrid version of opportunistic access scheme and spectrum sharing scheme, for investigation. It is seen that a tradeoff exists between sensing time and throughput of the network. Since SSS scheme is keeping transmission even PU is detected, to be able to establish tolerable interference by PU, average interference constraint introduced. For battery powered devices, long term power

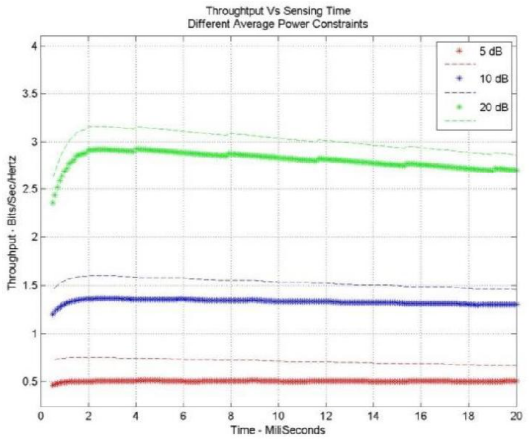


Figure 7: Throughput vs sensing time, stars without penalty term and dashed lines with penalty term calculations, $\Gamma = -10\ dB$, $g_{ps,j} = 0.01$, $g_{sp,j} = 0.01$, $g_{ss,j} = 0.09$, $SNR = -15\ dB$, $K = 50$

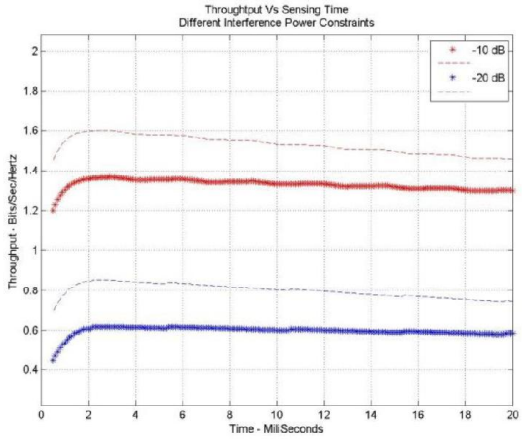


Figure 8: Throughput vs sensing time, stars without penalty term and dashed lines with penalty term calculations, $P_{av} = 10\ dB$, $g_{ps,j} = 0.01$, $g_{sp,j} = 0.01$, $g_{ss,j} = 0.09$, $SNR = -15\ dB$, $K = 50$

budget and possible interference among secondary users also are taken into consideration and average transmission power constraint introduced.

Instead of perfect detection, we consider real world scenarios where detection is not perfect and some detector faults occur. We investigate false alarm and miss detection probabilities for a given detection probability and sensing time. If sensing time decreases, false alarms and miss detections increase; if sensing time increases, total achievable throughput decreases. Under these circumstances we try to find optimal sensing time for the maximization of total ergodic throughput of the network.

SSS access scheme investigated by simulations. According to the results, optimal sensing time evaluated for one channel scenario is around $\overline{\tau}_{opt} = 2.45\ ms$ and compared to the previous investigations which is almost the same. Interference constraints and average transmit power constraints significantly effecting total achievable throughput however have very little effect on optimal sensing time. Most significant criteria on optimal sensing time is detector

performance which is related to detection probability and primary user signal's worst case received signal strength at the detector. If primary signal is not strong enough, to be able to overcome possible false alarms and miss detections, optimal sensing time increases for the evaluation of target detection probability. Penalty condition used in optimization problem helps finding the optimal value with fewer computations. Therefore, fast calculation can be possible and optimal sensing time can be adaptively changed in real time scenarios.

REFERENCES

[1] J. Mitola and G. Q. Maguire, "Cognitive radio: making software radios more personal," *IEEE Pers. Commun.*, vol.*6*, no.*6*, pp.*13-18*, Aug., 1999.

[2] Federal Communications Commission, "Notice of proposed rule making and order: Facilitating opportunities for flexible, efficient, and reliable spectrum use employing cognitive radio technologies," ET Docket No. *03-108*, Feb. 2005.

[3] S. Haykin, "Cognitive radio: brain-empowered wireless communications," *IEEE J. Select. Areas Commun.*, vol.*23*, no.*2*, pp.*201-220*, Feb., 2005

[4] Q. Zhao & B. M. Sadler, "A Survey of Dynamic Spectrum Access", *IEEE Signal Processing Magazine*, vol.*24*, no.*3*, pp.*79-89*, May, 2007

[5] Y.-C. Liang, Y. Zeng, E. C. Y. Peh, and A. T. Hoang, "Sensing-throughput tradeoff for cognitive radio networks," *IEEE Trans. Wireless Commun.*, vol.7, no.4, pp.1326-1337, Apr., 2008.

[6] Y. Pei, Y.-C. Liang, K. C. Teh, and K. H. Li, "How much time is needed for wideband spectrum sensing?" *IEEE Trans. Wireless Commun.,* vol.*8,* no.*11,* pp.*5466-5471, Nov., 2009.*

[7] S. Stotas & A. Nallatahan, "Optimal sensing time and power allocation in multiband cognitive radio networks?" *IEEE Trans. On Commun.,* vol.*59,* no.*1,* pp.*226-235, Nov., 2010.*

[8] R. Zhang, Y.-C. Liang & X. Kang, "Protecting primary users in cognitive radio networks: peak or average interference power constraint?" *in Proc. IEEE International Conf. Commun. (ICC),* Dresden, Germany, June, 2009.

[9] R. Tandra and A. Sahai, "SNR walls for signal detection" *IEEE J. Sel. Topics Signal Process.,* vol.*2*, no.*1*, pp.*4-17*, Feb., 2008.

[10] K. Hamdi and K. B. Letaief, "Power, sensing time, and throughput tradeoffs in cognitive radio systems: a cross-layer approach" in *Proc. IEEE Wireless Commun. Netw. Conf. (WCNC),* Budapest, Hungary, Apr., 2009.

[11] S. Boyd and L. Vandenberghe, *Convex Optimization.* Cambridge University Press, 2004.

An Overview of Electromagnetic Methods for Breast Cancer Detection and A Novel Antenna Design for Microwave Imaging

A.R. CELIK[1] , M.B. KURT[1] and S. HELHEL[2]

[1] Dicle University, Diyarbakir/Turkey, ali.celik@dicle.edu.tr
[1]Dicle University, Diyarbakir/Turkey, bkurt@dicle.edu.tr
[2] Akdeniz University, Antalya/Turkey, selcukhelhel@akdeniz.edu.tr

***Abstract* - There are several techniques that are used for early stages detection of breast cancer which is important to decrease the higher percentages of death cases. This paper focuses on summarizing the electromagnetic techniques for disease detection such as X-ray mammography, ultrasonography, tomosynthesis, magnetic resonance and the other emerging electromagnetic techniques. Using microwave techniques in the imaging system have recently attracted considerable attention. In this study, categories of the microwave imaging system is examined, especially radar-based ultrawideband microwave imaging technique is explained in detail. A key component of this imaging system is the antenna that is used to radiate and receive the UWB pulses. In this paper, a compact-size, UWB and directional planar antenna is developed for this aim. Analysis and the performance optimization of the proposed antenna is performed by High Frequency Structural Simulator (HFSS) software. Simulation results show that the designed antenna is suitable for using in radar-based microwave imaging systems.**

***Keywords* – Breast cancer detection, electromagnetic imaging methods, microwave imaging, ultra-wideband, directional antenna.**

I. INTRODUCTION

ACCORDING to the World Health Organization, breast cancer is the most common cancer among women worldwide [1]. Statistics clearly demonstrate the importance of this disease and its impact on the health. The early diagnosis of the disease could help to decrease the higher percentages of death cases. Malignant cells can multiply uncontrolled and spread to other tissues. Hence, detecting the cancer tumor at the early stage plays a crucial role in the treatment of disease.
An ideal breast cancer detection technique should have the following properties:

- has low health hazard,
- is sensitive to malignant tumor issue,
- determine breast cancer at a medicable stage,
- screening as fast as possible,
- is affordable, widely available, non-destructive and simple to perform,
- involve minimal discomfort, so the procedure is acceptable to women [2-4].

There are various techniques that are used for early stages detection of breast cancer such as; X-ray mammography, ultrasound technique, digital tomosynthesis and magnetic resonance imaging (MRI). However, even with the combined use of these techniques, the current method of screening for breast cancer does not meet the ideal requirements. Therefore, researchers are actively searching for alternative methods of breast imaging [5]. Some of the emerging electromagnetic techniques are electrical impedance tomography (EIT), diffuse optical tomography (DOT), biomagnetic and microwave imaging (MI). Among these techniques, MI methods have recently attracted considerable attention because it uses nonionizing radiation which is safer than ionizing radiation, i.e. X-rays used in mammography. It is noninvasive so there is no compression in MI and making the exams more comfortable than the other techniques [6].The low illumination power levels used in MI also make regular screening possible. Another advantage is that the system is low cost.
The present study aims to find out the type of techniques for tumor detection and mention about the merits and drawbacks of them clearly. The informations about the number of methods will be summarized and detailed informations about the MI methods will be provided in the paper.

II. BREAST CANCER SCREENING TECHNIQUES

Since the early diagnosis and treatment are the hot keys to survive from the breast cancer, there are many techniques that are used for detection of early stages of the breast cancer such as; mammography, ultrasound, tomosynthesis, MRI and other emerging electromagnetic techniques under development [7].

A. Mammography

Currently, the standard and frequently used technique for breast cancer screening and detection is X-ray mammography where is it being quite sensitive to the lesions in the breast by compressing the breast on X-ray image. Mammography is not sensitivity for early-stage tumor detection but only for the best and effective medical treatment. Although the X-ray mammography provides high resolution images, it's not highly reliable [8,9].

The most widely used X-ray mammography also requires painful and uncomfortable breast compression and exposes the patient to ionizing radiation. X-radiation is a form of electromagnetic radiation. Most X-rays have a wavelength ranging from 0.01 to 10 nanometers, corresponding to frequencies in the range 30 to 30.000 petahertz and energies in the range 100 eV to 100 keV, so they are in ionizing radiation class and they may be harmful for body. X-ray mammography has another limitation, especially when dealing with younger women who have dense breast tissues, because there is a few percent contrast between healthy and diseased breast tissues at X-ray frequencies [5]. One of the other drawbacks is the high miss detection which can reach 30 per cent [10] due to high false positive and negative detection.

Consequently, X-ray mammography, currently the most common imaging method for early breast cancer detection, is not highly reliable, requires painful breast compression, and exposes the patient to low levels of ionizing radiation. All of these limitations and their potential for harm, provide plenty motivation for the development of alternative methods of breast imaging.

B. Ultrasound Technique

Ultrasound technique is harmless but it is less effective than mammography and it is used as a supporting imaging method for mammography. Ultrasound imaging is based on high frequency sound waves which reflect with changing intensity from different tissues. In the breast, ultrasound is able to differentiate skin, fat, glandular tissue, and muscle. Unfortunately, it has a limitation that fat issue and tumor issue have similar acoustic features and for this reason detecting many tumors is impossible with ultrasound. Ultrasound has also been utilized in breast cancer detection with a false negative rate of 17% [11]. The other drawback of ultrasound is its disability to provide high resolution for deep and condensed tissue structure such as fatty tissues. Also ultrasound imaging requires high skill and longer time, and that is why the technique is not used commonly [12].

C. Digital Tomosynthesis

Breast tomosynthesis is based on the acquisition of three-dimensional digital image data, could help solve the problem of interpreting mammographic features produced by tissue overlap. Breast tomosynthesis has the potential to help reduce recall rates, improve the selection of patients for biopsy, and increase cancer detection rates, especially in patients with dense breasts [13]. Advantages and disadvantages of the tomosynthesis can be listed as below:

- 3-D imaging is available,
- It is able to detect the tumor which is hidden behind the dense breast tissue,
- It has less X-ray radiation according to mammography,
- It decreases the biopsy rates and increases the ratio of true diagnosis,
- It is not required more compression and provide less pain,
- It has long application and evaluation time,
- It uses big detectors and has difficulty in giving positions.

D. Magnetic Resonance Imaging (MRI)

MRI for breast cancer has been proposed since the late 1970s but until the 1980s it did not show sufficient benefit. However, the use of gadolinium as a contrast agent in MRI significantly enhanced breast cancer detection. In almost all studies, MRI has exhibited high sensitivity and it often detected small tumors missed by mammography and ultrasound [14]. MRI showed particular advantage in dense breasts where mammography typically fails to detect tumors. However, the elevated sensitivity of MRI came at the expense of modest specificity [15].

MRI has several advantages such as a high sensitivity, no ionizing radiation, and the ability to image radio graphically dense breast. However, the prime limitation of MRI is the high cost of imaging [7]. Also, MRI suffered from a higher false positive rate than any of the other screening methods. In one study [16], MRI had a specificity of only 95.4 percent, compared to 96, 99.3, and 99.8 percent for ultrasound, clinical breast exam, and mammography, respectively. This low specificity, along with the high costs associated with MRI, severely limits MRI's usefulness as an alternative or complement to mammography as a widespread screening method [5]. Some advantages and disadvantages of the different imaging techniques mentioned up to this point can be summarized as in Table 1.

Table 1: This caption is centered

Imaging Technique	Advantages	Disadvantages
X-Ray Mammography	Cheap. Availability of copying and archiving the images. Provide high resolution images.	Not convenient for women with dense breasts. Ionizing radiation, dangerous. Compressed breast, pain.
Ultrasonography	Used as scanning for women with dense breasts. Cheaper than mammography. No danger, no ionizing radiation.	More negative false rate than mammography. Cannot image the whole breast at the same time and deep locations in the breast. Cannot diagnosis malign tumors.
Tomosynthesis	3-D Image reconstruction by getting data from different angles. Increased imaging feature of lesions.	Less compression than mammography but still painful.
Magnetic Resonance Imaging	High sensitivity. No ionizing radiation	High negative false rate, high cost. Increased biopsy rates.

E. Emerging Electromagnetic Techniques

Even with the combined use of the current methods for breast cancer, screening does not meet the ideal requirements. Researchers are actively searching for alternative modalities of diagnostic breast imaging. Electrical impedance tomography, diffuse optical tomography, biomagnetic and microwave imaging techniques are some alternative techniques. EIT, a 2-D or 3-D reconstruction of the impedance of the breast, is turned out through the frequency between 100 Hz and 1 MHz [17]. EIT is achieved by placing sensors on the surface of the breast with each sensor performing a current and then voltage differences between the sensors are measured. DOT of breast cancer can be defined as the use of light to screen the optical features in the chest. DOT uses significantly higher frequencies in the near infrared range from about 650 to 950 nm in wavelength with respect to the other breast cancer detection modalities [18]. Biomagnetic technique is based on the elevated magnetic fields were detected from malignant breast tumors in comparison to benign tumors [19]

III. Microwave Imaging System

One of the leading alternative methods for breast cancer detection is to use microwave techniques in imaging. MI methods are non-invasive imaging methods. The quantities imaged in MI are the dielectric properties. The main principle of this technique is based on the significant difference in dielectric properties of malignant breast tumors and normal breast tissue in the microwave frequencies [6]. Microwave signals are the non-ionizing form of the electromagnetic waves and there is no risk to health hazard when used at low levels. Microwave detection is less expensive and safer than other modalities of detection. MI is done mainly in three category as passive, hybrid and active systems [20]. The passive method involves microwave radiometry uses radiometers to obtain the temperature differences in the breast as temperature rises in the presence of tumor than with normal breast tissue [21]. The hybrid methods use microwave energy to heat tumors and they expand and generate pressure waves which are detected by ultrasound transducers [22]. The active methods involve illuminating the breast with microwaves and then measuring transmitted or backscattered signals. Active MI can be classified as microwave tomography, microwave microscopy and ultra-wideband (UWB) radar technique.

A. Microwave Radiometry

Passive MI is usually termed as microwave radiometry and is based on the measurement of the electromagnetic field emitted by warm bodies. Temperature is the main parameter that is used here to estimate the presence of malignancy [23]. There are various causative factors to the temperature elevation related to the tumor presence: the malignant cells are more metabolically active and produce more heat, they have a reduced thermoregulatory capacity, and it is recognized that localized increases in blood volume can be associated with early tumor growth [24].

B. Microwave-Induced Thermal Acoustic Imaging

Microwave-induced thermal acoustic imaging provides two properties that high contrast in the conductivity of malignant tissues at microwave frequencies and the high spatial resolution of ultrasound imaging. The generated acoustic waves carry the information about the microwave energy absorption properties of the tissues under irradiation. The microwave energy absorbed by tumor and normal breast tissues will be significantly different and a stronger acoustic wave will be produced by the tumor. The majority of challenges are referred to inhomogeneity of the breast tissue. This leads to a nonuniform microwave energy distribution, strong interference from the skin and chest wall, and consequently, to complicated image reconstruction algorithms [24]. The biological tissues should be heated by the microwave source in a uniform manner, otherwise thermal acoustic signals will be induced by a nonuniform microwave energy distribution, resulting in images difficult to interpret.

C. Microwave Microscopy

The working principle of the microwave microscope is based on the changing in the resonant frequency of an open-ended microwave cavity resonator, which results from the interaction of the electromagnetic field of the resonator and objects positioned under the skin. This technique provides a high spatial resolution since it is based on the near-field wave tissue interaction, which is not limited by the diffraction limit [25]. Microwave microscopy for the breast cancer detection offers a number of important advantages: it avoids special processing of skin tissues and implementation of complex inverse scattering algorithms; it operates in a very narrow frequency range, thus there is no need of complex dispersive dielectric models of the breast tissues; a priori knowledge of the dielectric properties of the tumor is not critical to the success of the detection; the method can be used for detecting breast cancer in men.

D. Microwave Tomography

In tomography, image is reconstructed using a forward and inverse scattering to enhance the spatial distribution of the complete dielectric properties in the breast. The reconstruction of the electrical properties of the breast at each pixel is calculated in this system [26]. In this method, a coupling medium between the antennas and the body is used in order to refuse high reflections from the air and skin interface. Therefore, the patient orientation for these systems is different from one in microwave radiometry with the patient lying in a prone position with her breast suspended down into the tomography. The electrical properties of the medium are chosen to be close to the properties of the body to achieve the coupling of electromagnetic energy into the breast [27]. In practice however, the electrical properties of the medium depends on temperature, and any temperature drifts and unpredictable local temperature gradients affect the measurement accuracy of the system.

E. Ultrasound-Guided Microwave Imaging

Ultrasound-guided MI is such a combination of two modalities, where microwave image reconstruction is guided by ultrasonography. The ultrasound imaging is used to assemble a priory data about the breast structure and presence and shape of embedded objects. This helps to generate an optimal mesh with well refined target region for effective numerical analysis of the electromagnetic problem [28]. Consequently, the spatial resolution of ultrasound-guided microwave imaging can be enhanced resulting in more accurate imaging of tumors.

F. Ultra-wideband Radar Technique

The principle of the radar-based MI of breast is illuminating the breast with an UWB pulse and detect the reflections. The reflected signals are the data for processing to obtain images that indicate the size and location of the tumor(s) in the breast. A key component of the system is the antenna that is used to radiate and receive the ultra-wideband pulses. This method has been increasingly recommended as a regular examination and detection tool for early breast cancer detection but it is under research and investigation stage till today [7]. The detailed information will be given in the next Section.

IV. Ultrawideband Radar-Based Microwave Imaging For Breast Cancer Detection

Since the authorization of the unlicensed using of the UWB technology in the range of 3.1 GHz to 10.6 GHz by the Federal Communication Commission (FCC) in the USA [29], UWB technology has become very popular in different areas. One of these applications of this technology is UWB microwave imaging technique for breast cancer detection. In UWB applications, it is desirable for impedance bandwidth to be at least 50% to cover the lower UWB band of 3.1–5 GHz or the upper band of 6–10.6 GHz or 110% to cover the entire UWB band of 3.1–10.6 GHz [30].

UWB radar imaging, as proposed by Hagness et al. [31,32] uses an UWB pulse which involves low to high frequencies. The lower frequency band provides sufficient depth of penetration while the higher frequency band ensures the adequate resolution of the creating images. Hence, both the deeply buried and small size tumor can be detected based on the lower and higher frequency of the UWB bands [33]. From this point of view, this system is very important and candidate to become popular. The system is a similar imaging procedure to that used in surface-penetrating radar rather than using the tomographic approach of reconstructing the entire dielectric profile of the breast. In this system, there are three main system configurations: monostatic, bistatic and multistatic. The same antenna performs the task of both sending microwave signals and receiving the reflected signals in monostatic system. Bi-static system has two antennas and the target material is positioned between the receiving and transmitting antennas. Finally, in multi-static system, antenna arrays are used.

For example, experimental study of monostatic MI system for making measurement on breast phantom which has been used in [7] is shown in Figure 1.

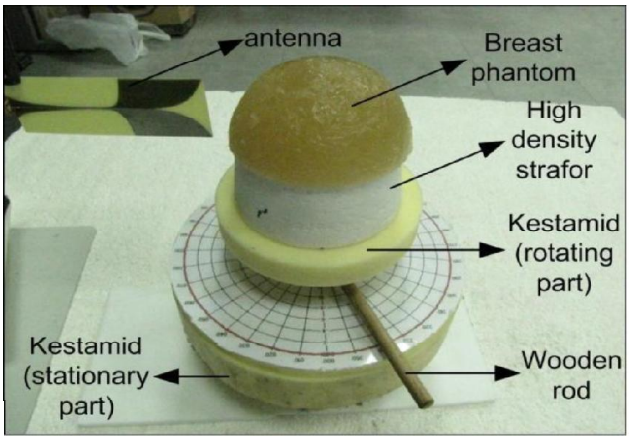


Figure 1: Experimental setup of the monostatic MI system.

There are a lot of MI systems under development for breast cancer detection. An UWB microwave imaging system was developed by Klemm et al. at the University of Bristol [34]. This system operated at higher frequencies (3-10, 4-8, 4.5-9.5 GHz) which were achieved by employing different very small UWB antennas in a hemi-sphere array encircling the breast, instead of using monopole antennas. Consequently, some attention has been directed towards the microwave tomography and UWB radar imaging for breast cancer detection because these techniques are still under development. In addition, most of the histological methods applied UWB radar imaging.

Classification of the microwave imaging systems for breast cancer diagnosis mentioned up to this point can be seen clearly in the Figure 2.

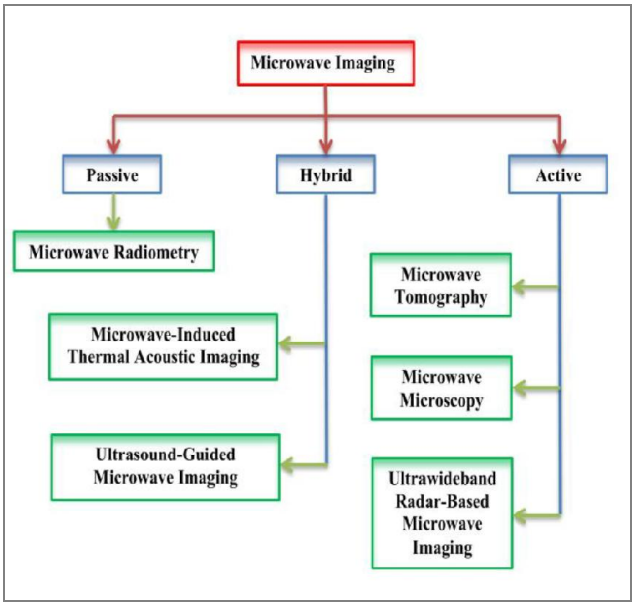


Figure 2: Microwave imaging methods

V. Antenna Design For Ultrawideband Radar-Based Microwave Imaging System

Microstrip antennas are compact and have low-profile but they have narrow bandwidth. However, microwave broadband systems, for example MI system, need UWB signal to transmit short pulses for obtain sufficient range resolution. The modified microstrip antennas which has partial ground plane is called monopole planar antenna and they are the most choosen antennas in the UWB applications because of their wide bandwidth. They are named according to their radiation patch shapes such as elliptical, square circular, rectangular or any session of these shapes. In this study, firstly a L-shaped monopole antenna with gap and T-shaped slot is examined. The geometry of the antenna and the detailed design parameters are given in Figure 3 and Table 2, respectively. Design and analysis of the antenna has been performed by HFSS software.

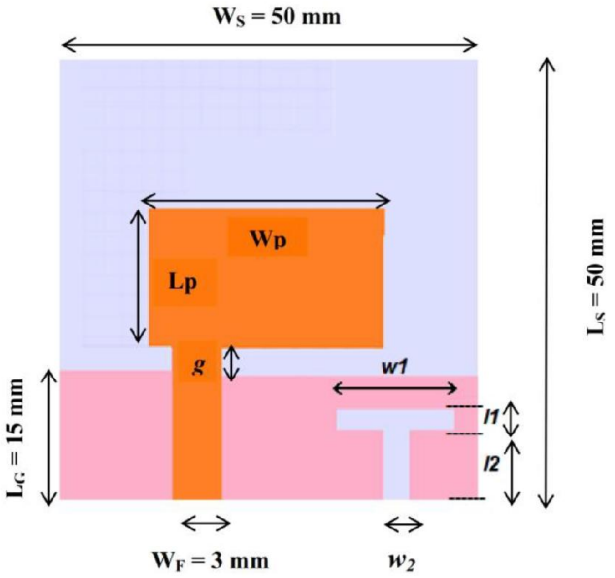


Figure 3: L-shaped monopole antenna with gap and T-shaped slot

Table 2: Design values of the L-shaped monopole antenna.

Antenna Design Parameters	Values (mm)
Length (Ls) and width (Ws) of the substrate	50 x 50
Length (Lp) and width (Wp) of the patch	15 x 22
Length (Lf) and width (Wf) of the feedline	15 x 3
Length (Lg) and width (Ws) of the ground plane	15 x 50
Gap (g) between the ground and patch	1
Length (l_1) and width (w_1) of the horizontal part of the slot	1 x 4
Length (l_2) and width (w_2) of the vertical part of the slot	4 x 1

The return loss graph of the L-shaped planar monopole antenna with T-shaped ground slot is given in Figure 4.

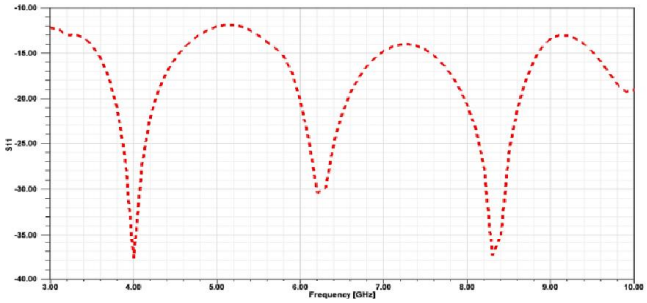


Figure 4: Return loss result of the L-shaped monopole antenna.

The return loss result shows that the antenna shown in Fig. 1 can be used for the UWB MI system from the points of bandwidth and impedance matching. However, for the radar-based UWB MI system, the antenna not only needs large bandwidth but also it should have directional radiation pattern. As it is seen from the Figure 5, this antenna has nearly omnidirectional pattern.

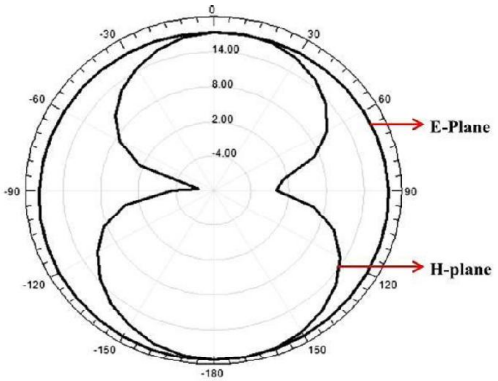


Figure 5: Radiation pattern of the antenna shown in Fig. 1 for 6 GHz frequency

After this point, we force the antenna to be directional in the desired frequency band. For this aim, a three-quarter circle conductor is added to top right-hand corner of the patch. Also a parasitic element is added to left side of the substrate. The radius (*r*) of the circle is 3 mm, the length (*l3*) and width (*w3*) of the rectangular parasitic element are the 10 mm and 3 mm, respectively. The new geometry of the antenna is shown in Figure 6.

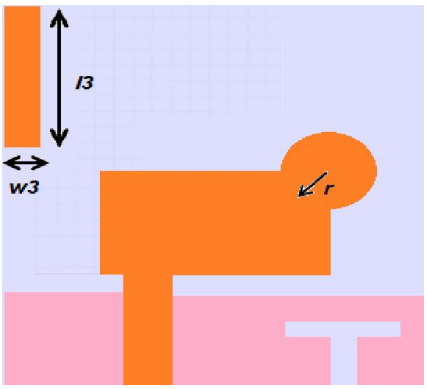


Figure 6: Proposed antenna with new geometry

VI. Results

Indeed, modification of the patch and adding parasitic element improved the directionality. Radiation patterns at the three different frequency points are shown in Figure 7. It is important to maintain the large bandwidth when making some modifications to obtain directional radiation pattern. The return loss result of the proposed antenna is also given in Figure 8.

It is clearly seen that, it still has broad frequency band and good impedance matching. The aim of the UWB and directional antenna design, which is valid for the radar-based UWB microwave imaging application, is accomplished according to these results.

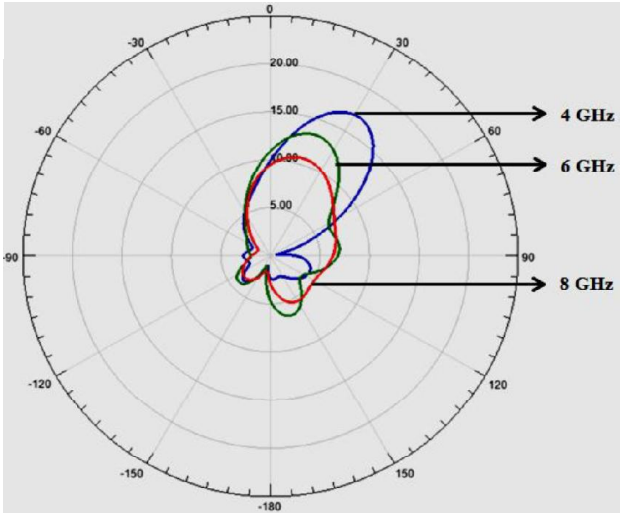


Figure 7: Radiation patterns of the proposed antenna for 4, 6 and 8 GHz.

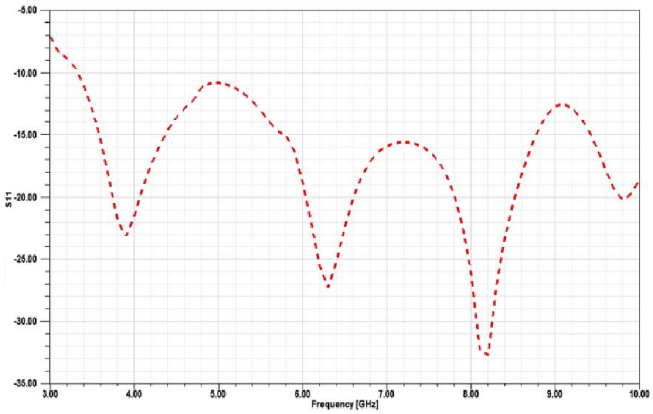


Figure 8: Return loss result of the proposed antenna.

VII. Conclusion

There are various techniques that are used for early stages detection of breast cancer such as; X-ray mammography, ultrasound technique, digital tomosynthesis and MRI. However, even with the combined use of these techniques, the current method of screening for breast cancer does not meet the ideal requirements.

One of the emerging electromagnetic methods is microwave imaging technique. This technique has recently attracted considerable attention because it uses nonionizing radiation which is safer than ionizing radiation, it is comfortable and low cost. The most important element of the system is antenna to transmit and receive the microwaves. The antenna should be UWB, compact, stable and directive. In this study, a planar monopole antenna is designed and analysis by using HFSS software. Simulation results show that the proposed can be used for the radar-based microwave imaging system.

References

[1] World Health Organization, *Breast Cancer Awareness*. Availablefrom: http://www.who.int/cancer/breast_cancer_awareness/en

[2] B. Guo, "Microwave techniques for breast cancer detection and treatment", Ph.D. thesis, Dissertation, University of Florida, 2007.

[3] A.M. Hassan and M. El-Shenawee, "Review of electromagnetic techniques for breast cancer detection", *IEEE Reviews in Biomedical Engineering,* vol. 4, pp. 103-118, 2011.

[4] S. Nass, I. Henderson and J. Lashof, "Developing technologies for the early detection of breast cancer", *Mammography and Beyond,* National Academy Press, USA, 2001.

[5] J. P. Stang, "A 3D active microwave imaging system for breast cancer screening", Ph.D thesis, Department of Electrical and Computer Engineering, Duke University, 2008.

[6] E. C. Fear, X. Li, S. C. Hagness, M. A. Stuchly, "Confocal microwave imaging for breast cancer detection: localization of tumors in three dimensions", *IEEE Transactions on Biomedical Engineering,* vol. 49, pp. 812-822, 2002.

[7] I. Unal, "A New ultrawide-band microwave imaging system with minimized mutual coupling effects for breast tumor detection", Ph.D thesis, Yeditepe University, 2013.

[8] P. Huynh, A. Jarolimek and S. Daye, "The false negative mammogram", *Radiographics,* Vol.18, pp.1137-1154, 1998.

[9] B. J. Mohammed, A. M. Abbosh and M.E. Bialkowski, "Design of tapered slot antenna operating in coupling liquid for ultrawideband microwave imaging systems", *in Proceesing of APSURSI,* Washington, USA, pp.145-148, 2011.

[10] P. T. Huynh, A. M. Jarolimek and S. Daye, "The false-negative mammogram", *Radiograph*, Vol.18, pp.1137-1154, 1998.

[11] W. Berg, L.Gutierrez, M. NessAiver, M. Bhargavan, R. Lewis and O. Ioffe, "Diagnostic accuracy of mammography, clinical examination, and MR imaging in preoperative assessment of breast cancer", *Radiology*, vol. 233, pp.830–849, 2004.

[12] D. B. Kopans, "Breast Cancer Screening with Ultrasonography", *Lancet*, Vol.354, pp.2096-2097, 1999.

[13] J. M. Park, E. A. Franken, M. Garg, L. L. Fajardo and L.T. Niklason, "Breast tomosynthesis: present considerations and future applications", *RadioGraphics*, Vol.27, pp. 231-240, 2007.

[14] S. Harms, "MRI in breast cancer diagnosis and treatment", *Current Problems in Diagnostic Radiology,* vol.25, pp.193-215.

[15] D. Ikeda, D.Baker and B. Daniel, "Magnetic resonance imaging of breast cancer: Clinical indications and breast MRI reporting system", *Journal of Magnetic Resonance Imaging*, vol.12, pp.975-983, 2000.

[16] D.B. Kopans, *Breast Imaging*, Lippincott Williams & Wilkins, USA, 2007.

[17] T. Kerner, K. Paulsen, A. Hartov, S. Soho and S. Poplack, "Electrical impedance spectroscopy of the breast: clinical imaging results", *IEEE Transactions on Medical Imaging*, vol.21, pp. 638-645, 2002.
[18] S. Konecky, "Non-Invasive Imaging of Breast Cancer with Diffusing Near-Infrared Light", Ph.D. thesis, University Pennsylvania, Philadelphia, 2007.
[19] P. Anninos, A. Kotini, N. Koutlaki, A. Adamopouos, G. Galazios and P. Anastasiadis, "Differential diagnosis of breast lesions by use of biomagnetic activity and non-linear analysis", *European Journal of Gynaecological Oncology*, vol. 21, pp. 591-595, 2000.
[20] M. D. Daud, M. A. Othman, M.F.I. Othman, "Methods of tumor detection using microwave technology: A review", *Journal of Engineering and Applied Sciences,* vol.9, pp.1450-1454, 2014.
[21] K. L. Carr, "Microwave radiometry: its importance to the detection of cancer", *IEEE Trans. Microwave Theory and Technology*, vol. 37, pp.1862-1869, 1989.
[22] L.V. Wang, X. Zhao, H. Sun and G. Ku, "Microwave-induced acoustic imaging for biological tissues", *Review of Scientific Instruments*, vol.70, pp. 3744-3748, 1999.
[23] K.L. Carr, P. Cevasco, P. Dunlea and J. Shaeffer, "Radiometric sensing: an adjuvant to mammography to determine breast biopsy" *IEEE MTT-S Int. Microwave Symp. Dig*. vol. 2, pp. 929–932, 2007.
[24] Z. Vitaliy, "Challenges in the design of microwave imaging systems for breast cancer detection", *Advances in Electrical and Computer Engineering,* vol. 1, pp. 91-96, 2011.
[25] X. Wu and O. M. Romahi, "Near-field scanning microwave microscopy for detection of subsurface biological anomalies", *Antennas and Propagation Soc. Int. Symp.*, vol. 3, pp. 2444-2447, 2004.
[26] A. Abubakar, P. Berg, and J. Mallorqui, "Imaging of biological data using a multiplicative regularized contrast source inversion method", *IEEE Transactions on Microwave Theory and Techniques,* vol. 50, pp.1761–1771, 2002.
[27] Z. Zhang and Q. Liu, "Three-dimensional nonlinear image reconstruction for microwave biomedical imaging", *IEEE Transactions on Biomedical Engineering,* vol. 51, pp. 544–548, 2004.
[28] H. Jiang, C. Li, D. Pearlstone and L. L. Fajardo, "Ultrasound-guided microwave imaging of breast cancer: tissue phantom and pilot clinical experiments", *Medical Physic*, vol. 32, pp. 2528-2535, 2005.
[29] Federal Communications Commission (2002): First order and report, *Revision of Part 15 of the Commission's Rules Regarding UltraWideband Transmission Systems*. Available: https://www.fcc.gov/document/revision-part-15-commissions-rules-regarding-ultra-wideband
[30] R. Azim, M. T. Islam and N. Misran, "Microstrip line-fed printed planar monopole antenna for uwb", *Arabian Journal for Science and Engineering*. vol. 38 pp. 2415–2422, 2013.
[31] S.C. Hagness, A. Taflove and J. E. Bridges, "Two-dimensional FDTD analysis of pulsed microwave confocal system for breast cancer detection: fixed-focus and antenna-array sensors", *IEEE Transactions on Biomedical Engineering* vol.45, pp. 1470-1479, 1998.
[32] S. C. Hagness, A. Taflove and J. E. Bridges, "Three-dimensional FDTD analysis of pulsed microwave confocal system for breast cancer detection: design of an antenna-array element", *IEEE Transactions Antennas and Propagation*, vol. 47, pp.783-791, 1999.
[33] X. Xiao and T. Kikkawa, "Influence of the organism interface on the breast cancer detection by UWB", *Applied Surface Science*. vol.255, pp.597–599, 2008.

Bandwidth Enhancement of Small L-shaped UWB Monopole Antenna with a Modified Ground Plane

A.R.CELIK[1], M.B. KURT[1] and S.HELHEL[2]

[1] Dicle University, Diyarbakir/Turkey, ali.celik@dicle.edu.tr
[1]Dicle University, Diyarbakir/Turkey, bkurt@dicle.edu.tr
[2]Akdeniz University, Antalya/Turkey, selcukhelhel@akdeniz.edu.tr

Abstract **- Broadband monopole antennas have received considerable attention owing to their attractive merits, such as ultra-wide frequency band, good radiation properties, simple structure and ease of fabrication. Since the Federal Communications Committee (FCC) permitted the unlicensed use of the ultra-wide band (UWB) frequency band in 2002, large interests in both academic and industrial fields have been attracted to research various UWB devices. Small UWB antennas have found a wide range of applications including ground penetrating radars, high data rate short range wireless local area networks, communication systems for military, UWB short pulse radars for automotive and robotics applications, C and X band applications, and UWB microwave imaging systems. In this paper, a novel compact planar UWB monopole antenna with enhanced bandwidth by use of slots and Defected Ground Structure (DGS) is presented. The size of the antenna is 50 mm x 50 mm and it has microstrip feedline. Design and analysis of the antenna has been performed by HFSS software. Simulation results show that the designed antenna has broad frequency band which covers the band between 3.1 GHz and 10.6 GHz. According the return loss results, this antenna can be used for especially radar-based UWB systems applications which require low to high frequencies.**

Keywords **– Planar monopole antenna, UWB antenna, bandwidth enhancement, defected ground structure.**

I. INTRODUCTION

Since the Federal Communications Committee (FCC) permitted the unlicensed use of the ultra-wide band (UWB) frequency band in 2002 [1], large interests in both academic and industrial fields have been attracted to research various UWB devices. The UWB covers a frequency band ranges from 3.1 to 10.6 GHz that can be used in the field of Wireless Local Area Networks (WLAN), Wireless Body Area Networks (WBAN), Wireless Personal Area Networks (WPAN), Ground Penetrating Radar (GPR) technology, communication systems for military and microwave imaging (MI) systems which wide bandwidth is required [2,3]. Broadband antennas have received considerable attention owing to their attractive merits, such as ultra-wide frequency band, good radiation properties, simple structure and ease of fabrication.

Recent UWB antenna designs focus on small printed antennas for many applications because of their ease of fabrication and their ability to be integrated with other components on the same PCBs [4-6]. A dual band UWB slotted antenna [7] and antenna with elliptical slotted ground plane [8] are designed for C and X band applications. A number of UWB antennas have been designed for GPR applications [9-11]. The study based on the lower frequency band is conducted mainly to improve the penetration depth while the designing in the higher frequency band is performed to achieve better resolution imaging for GPR systems. This operation mechanism is notable for the UWB MI system which is radar-based. There are various antenna design for the MI systems such as horn, vivaldi, elliptical and circular monopole etc [12-15]. Some of the works focus on the entire UWB frequency range to further enhance the bandwidth while others focused on gain enhancement.

Printed monopole antenna, which has little differences in comparison with microstrip antenna, is one of the among various forms of the wide-band antenna which has simple structure and easy to fabricated and integrated with printed circuit board.

Microstrip antennas are compact and have low-profile but they have narrow bandwidth. However, microwave broadband systems, for example MI systems, need UWB signal to transmit short pulses for obtain sufficient range resolution. The modified microstrip antennas which has partial ground plane is called monopole planar antenna and they are the most choosen antennas in the UWB applications because of their wide bandwidth. They are named according to their radiation patch shapes such as elliptical, square circular, rectangular or any session of these shapes.

In this study, firstly a L-shaped planar monopole antenna is showed with its return loss results. Then some modifications are done on the ground plane to improve the bandwidth and impedance matching of the antenna. Also, parametric study is demonstrated to understand the effect of probe length and results are discussed for the different cases. At the end of the design process, the aim is to say that the proposed antenna is valid for the several UWB applications.

II. L-SHAPED PLANAR MONOPOLE ANTENNA

Planar monopole antennas are named according to their radiation patch shapes. In this study, rectangular patch with shifted feedline which printed on a FR4-Epoxy substrate is used and examined. It can be developed many different combination of patch and microstrip feed line. Here we select a rectangular patch with the length (L) and width (W) of 15 mm and 22 mm, respectively. The length and width of the feedline are taken as 15 mm and 3 mm, respectively to achieve the 50Ω impedance matching. The geometry of the antenna is showed in Figure 1.

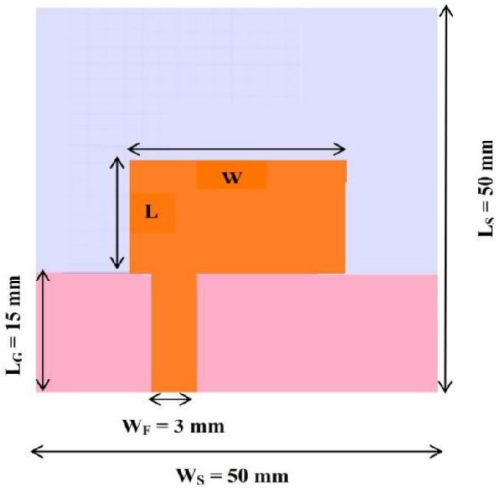


Figure 1: Printed L-shaped monopole antenna

To calculate the lower band-edge frequency of planar monopole antennas, the standard formulation is given in [16] as below:

$$f_L = \frac{7.2}{L + r}\ GHz$$

where L is the length of the rectangular patch, r is equal to W/2π and they are in centimeters.

According to the patch dimensions which we determined before, it is expected to see the lower frequency will be about 4 GHz for L=1.5 cm and W=2.2 cm. Indeed, this value is obtained in the return loss graphic of the antenna as it is seen from the Figure 2.

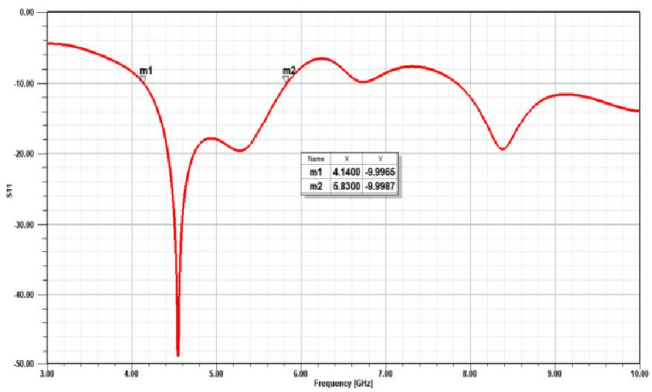


Figure 2: Return loss result of the L-shaped antenna

III. BANDWIDTH ENHANCEMENT TECHNIQUES

As mentioned above, the UWB covers a frequency band ranges from 3.1 to 10.6 GHz that can be used in the various implementations and different areas. However, according to return loss result given in Figure 2, the bandwidth is not at the desired range. Therefore, it is required to force antenna to be UWB that covers 3-10 GHz range. There are a lot of modification methods to provide bandwidth enhancement. One of these methods is using defected ground structure (DGS) to improve impedance matching and increase bandwidth of a compact UWB planar monopole [17-19]. Before starting to make some modifications on the ground plane, effect of the gap length between the ground plane and feedline is examined. After this stage, required development will be showed.

A. Effect of the Distance Between the Ground and Feedline

In the Figure 2, the return loss result has been given for the equal lengths of the ground plane and feedline. The length is equal to 15 mm which can be seen in the Figure 1. In this stage, effect of the different lengths will be investigated. In Figure 3, there is a distance ***g*** between the ground and feedline. Return loss results for g = 0 mm, g = 0.5 mm and g = 1 mm is given in Figure 4.

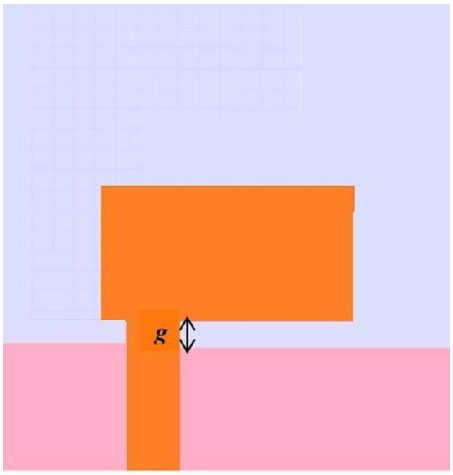


Figure 3: L-shaped monopole antenna with gap between ground plane and feedline

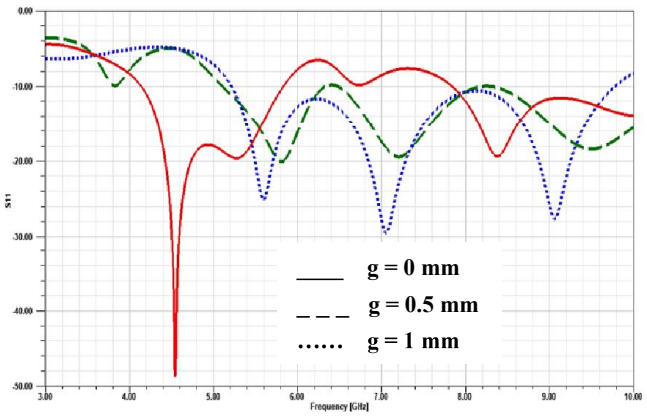


Figure 4: Return loss results for the different values of gap

B. *Slots on the Ground Plane for Bandwidth Improvement*

In the Figure 4, it is clearly seen that using gap between the ground and feedline affects the return loss well, but it still need to be improved for exactly covering the entire UWB range. For this aim there are many techniques such as etching notch or slot, adding parasitic element, changing dimension etc. In this study, we intend to use defected ground structure and it will provide by etching T-shaped slot on the ground plane. The new geometry of the antenna is shown in Figure 5. The detailed design parameters of the developed antenna are given in Table 1.

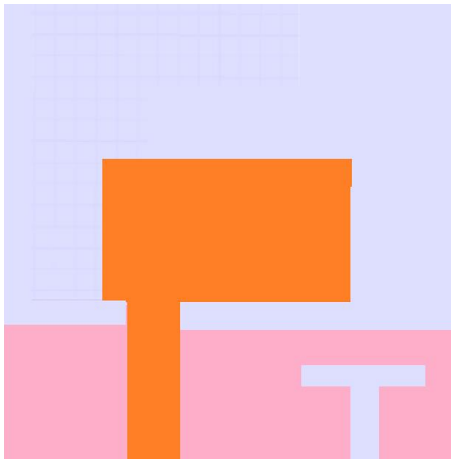


Figure 5: L-shaped monopole antenna with gap and T-shaped slot

Table 1: Design values of the proposed antenna.

Parameters	Values (mm)
Length and width of the substrate	50 x 50
Length and width of the patch	15 x 22
Length and width of the feedline	15 x 3
Length and width of the ground plane	15 x 50
Gap between the ground and patch	1
Length and width of the horizontal part of the slot	1 x 4
Length and width of the vertical part of the slot	4 x 1

IV. Results and Discussions

Performance analysis of the developed antenna has been performed by HFSS software which based on full-wave finite elements method and widely used in the design of electromagnetic structures [20]. The rate of convergence maximum delta S was taken as 0.005. Radiation boundary was located at 25mm (λ/4 for 3 GHz) away from the edges of the antenna in all directions.

The return loss graph of the L-shaped planar monopole antenna with T-shaped ground slot is given in Figure 6. It is clearly seen that the bandwidth has been increased and impedance matching has been improved by using DGS approach. The aim of the UWB antenna design, which is valid for the several UWB applications, is accomplished according to these results.

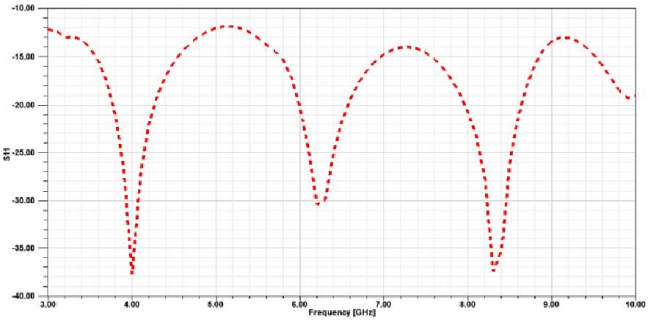


Figure 6: Return loss result of the proposed antenna

In addition to return loss result, radiation pattern of the antenna for 6 GHz is given in the Figure 7. The results confirm that the antenna has an omnidirectional radiation pattern.

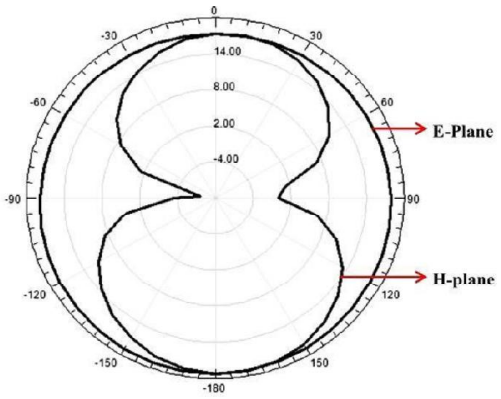


Figure 7: Radiation pattern of the antenna for 6 GHz

V. Conclusion

The modified microstrip antennas which has partial ground plane is called monopole planar antenna and they are the most preferable antennas in the UWB applications because of their broad bandwidth, compact and easy assembled structure. They are named according to their radiation patch geometry. In this study a L-shaped patch is choosen and lower frequency of the bandwidth is determined by the size of this shape. According to the antenna return loss result, it is seen that the bandwidth need to be improved. Effect of the length difference between the feedline and ground plane is investigated and optimum value has found as 1 mm. After that, DGS approach is implemented to design. T-shaped slot is used to improve both bandwidth and impedance matching. Good return loss result is obtained at the end of the design process. Bandwidth covers the entire UWB frequency range, which has permitted by the FCC in the USA for the unlicensed use of the ultra-wide band as 3.1-10.6 GHz.

This return loss result shows that the proposed can be used for the several UWB applications such as WLAN, WBAN, WPAN, GPR technology, communication systems for military and MI systems, C and X band applications etc. But some of these applications need the directional radiation patterns. In future, radiation characteristic of this antenna can be changed to obtain different patterns for desired application.

REFERENCES

[1] Federal Communications Commission (2002): First order and report, *Revision of Part 15 of the Commission's Rules Regarding UltraWideband Transmission Systems*. Available: https://www.fcc.gov/document/revision-part-15-commissions-rules-regarding-ultra-wideband

[2] X. Xiao and T. Kikkawa, "Influence of the organism interface on the breast cancer detection by UWB," *Applied Surface Science*, vol. 255, pp. 597–599, 2008.

[3] Y. Zhang, "Microwave imaging for ultra-wideband antenna based cancer detection," Ph.D. thesis, The University of Edinburgh, South Bridge, Edinburgh, Scotland, 2014.

[4] W. Zeng and J. Zhao, "Band-Notched UWB printed monopole antenna fed by tapered coplanar waveguide", in *Proceeding of 2010 IEEE International Conference on Ultra-Wideband (ICUWB 2010)*.

[5] R. A. Moody and S. K. Sharma, "Investigation on co-planar waveguide fed pentagon shape planar monopole ultra-wide bandwidth (UWB) antenna on form substrate providing invariant radiation patterns" *in Proceeding of IEEE Antennas and Propagation Society International Symposium (APSURSI),* 2010.

[6] O. Ahmed and A. R. Sebak, "A Printed monopole antenna with two steps and a circular slot for UWB applications" *IEEE Antennas Wireless Propag. Lett.* vol. 7, pp. 41- 413.

[7] M. Meloui and M. Essaaidi, "A dual ultra wide band slotted antenna for C and X bands application," *Progress In Electromagnetics Research Letters*. vol. 47, pp. 91-96, 2014.

[8] M. L. Meena, M. Kumar, G. Parmar and R. S. Meena, "Design analysis and modeling of directional UWB antenna with elliptical slotted ground structure for applications in C- & X-bands," *Progress In Electromagnetics Research C*. vol. 63, pp. 193-207, 2016.

[9] I. Hertl and M. Strycek, "UWB antennas for ground penetrating radar application," *in Proceeding of 19th International Conference on Applied Electromagnetics and Communications (ICECOM),* 2007.

[10] R. Kr, S. Gurjar and M. Sharma, "Design of stair and slotted UWB antenna using stepped-feed with modified slotted ground plane," *in Proceeding of the IJCA Proceedings on National Seminar on Recent Advances in Wireless Networks and Communication,* pp. 22–25, 2014.

[11] Y. Ranga, A. K. Verma, K. P. Esselle, and S. G. Hay, "An ultrawideband quasi-planar antenna with enhanced gain," *Progress In Electromagnetics Research C,* vol. 49, pp. 59-65, 2014.

[12] R. Chandra, A.N. Gaikwad, D. Singh and M. J. Nigam. "An approach to remove the clutter and detect the target for ultra-wideband through-wall imaging," *Journal of Geophysics and Engineering*, vol. 5, pp. 412-419, 2008.

[13] Y. Yang, C. Zhang and A. E. Fathy, "Development and implementation of ultra-wideband see-through-wall imaging system based on sampling oscilloscope." *IEEE Antennas and Wireless Propagation Letters*, vol 7, pp. 465–468, 2008.

[14] M. Dehmollaian, M. Thiel and K. Sarabandi, "Through-the-wall imaging using differential SAR," *IEEE Transactions on Geoscience and Remote Sensing,* vol. 47, pp. 1289–1296, 2009.

[15] H. Zhang, U. Zhou, Z. Wu, H. Xin and R.W. Ziolkowski, "Designs of ultra wideband (UWB) printed elliptical monopole," *Microwave and Optical Technology Letter,* vol. 52, pp. 466–471, 2009.

[16] G. Kumar G and K. P. Ray, *Broadband Microstrip Antennas, 1st ed.* Artech House: Norwood MA, USA, 2003.

[17] S. Shi, W. W. Choi, W. Che, K. W. Tam, and Q. Xue, "Ultra-wideband differential bandpass filter with narrow notched band and improved common-mode suppression by DGS," *IEEE Microwave and Wireless Component Letters,* vol. 22, pp. 185–187, 2012.

[18] J. Zhang, S. W. Cheung, L. Liu, and T. I. Yuk, "Simple notches design for ultra-wideband monopole antennas with coplanar-waveguidecoupled-fed," *Microwave and Optical Technology Letters*, vol. 55, pp. 1017–1027, 2013.

[19] M. H. Bah, J. Hong, D. A. Jamro, "Ground slotted monopole antenna design for microwave breast cancer detection based on time reversal MUSIC," *Progress In Electromagnetics Research C*, vol. 59, pp. 117–126, 2015.

[20] *Ansys HFSS,* Ansys Corporation, Canonsburg, USA, 2014.

Behavioral Modeling of a MEMS Accelerometer using MATLAB/SIMULINK

M.DEMİRTAŞ[1], M.A.ERİŞMİŞ[1] and S.GÜNEŞ[2]

[1] Necmettin Erbakan University, Konya/Turkey, mdemirtas@konya.edu.tr
[1] Necmettin Erbakan University, Konya/Turkey, maerismis@konya.edu.tr
[2] Selçuk University, Konya/Turkey, sgunes@selcuk.edu.tr

***Abstract* – In this study, a MEMS Accelerometer was modeled at behavioral level using MATLAB/SIMULINK. The acceleration sensing mechanism was modeled according to the conventional spring-mass-dashpot system. Capacitive MEMS accelerometers are widely used because of their efficiency and stability. Therefore, differential capacitors were used to simulate detection of the displacement which is a result of the applied acceleration. Finally, synchronous demodulation was used to extract the acceleration information at the output. The whole sensing and AM demodulation parts were analyzed and simulated in the same environment.**

***Keywords* – Accelerometer, MEMS, Capacitive Sensor, Behavioral Modeling**

I. INTRODUCTION

Accelerometers are used to measure acceleration and widely utilized in many areas such as engineering, medical applications, navigation, transportation, consumer electronics [1-2]. MEMS accelerometers have been developed since 1990s as an alternative to their macro scale counterparts due to their small size, low power consumption and robust sensing [3]. Generic accelerometers could be modeled as a second order spring-mass-dashpot system at behavioral level. This model can be considered as follows: a mass suspended by a spring and damping effect occurs due to the air friction. Sensing acceleration is accomplished via detection of the displacement of the proof mass in this model. Generally, capacitive methods are preferred as sensing mechanism since they offer high sensitivity, good DC response and low temperature sensitivity [4]. Capacitive sensing is performed with the measurement of capacitance change which occurs as a result of change in gap between two parallel plates, change in overlapping area of plates or change in dielectric properties [5]. Moreover, differential capacitive sensing is often used because it improves the sensitivity. Differential sensing measures the difference between two capacitances which is actually proportional to the actual applied acceleration. However, further signal process is required to detect this differential capacitive change. This is performed by interface electronics and demodulation-based circuits. Interface electronics circuits convert capacitance change into a voltage, frequency, pulse-width or current while demodulation-based circuits are used to obtain acceleration information from modulated signals [6].

II. CAPACITIVE ACCELEROMETER MODELING

The model for an accelerometer which consists of mass, spring and dashpot is given in Figure 1.

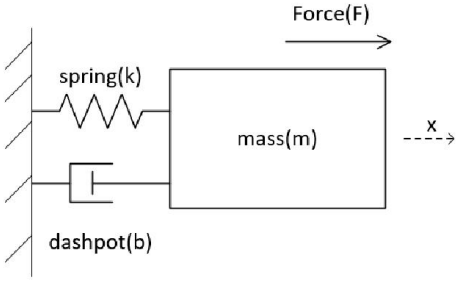


Figure 1: Accelerometer Model

When an external acceleration (a_{ext}) is experienced by the mass (m), mass is displaced by *x* relative to the initial position along the force direction. In the model, spring constant is k and it is proportional to the displacement while the damping coefficient is b which is proportional to the velocity. Considering those three forces acting on the mass, following second order differential equation (1) could be written to describe this system:

$$m\frac{d^2x}{dt^2}+b\frac{dx}{dt}+k\,x=ma_{ext} \quad (1)$$

The displacement *x* must be known in order to obtain external applied acceleration. Therefore, it must be sensed before further procession and the most widely used sensing technique is capacitive sensing [7]. A schematic structure of a capacitive accelerometer is given Figure 2. In this figure, shaded beams are shown as fixed fingers and the beams on the mass are called as movable fingers. If an external acceleration is experienced by the mass, the mass and movable fingers are displaced in the x direction while the fixed fingers remain in the same position. The fixed and movable fingers form an initial capacitance and this capacitance changes when a change in the gap between the fingers occurs.

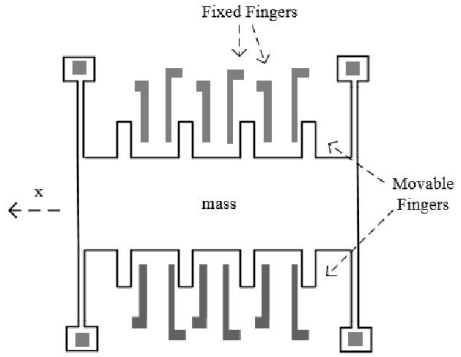


Figure 2: Schematic of a Capacitive Accelerometer

In Figure 3, x direction motion of a mass is shown. Initially, no acceleration is experienced by the mass and C_1 and C_2 are equal to each other. Therefore, the differential capacitance equals to zero. However, when mass moves in the x direction, the gap between the plates of the capacitors change which results an increase in C_1 and a decrease in C_2. Differential capacitance C_1-C_2 will be used to measure the applied acceleration because of their proportionality with each other. V_S and -V_S are actuation voltages with high frequency which are used to actuate the movable fingers.

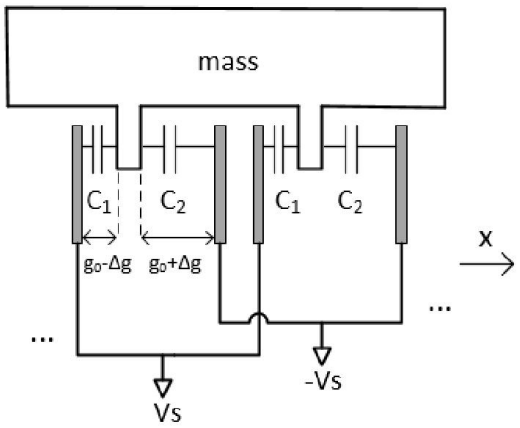


Figure 3: X-Direction Motion in Capacitive Accelerometer

Variable capacitors C_1 and C_2 form a voltage divider accepting actuation voltages as input. The output of this divider varies with this differential capacitance and it is modulated with V_S and -V_S. Consequently, a synchronous demodulation can be applied to demodulate this signal such that the output signal is multiplied with the actuation voltage and the resultant signal is low pass filtered. The final voltage is proportional with the applied acceleration. A simplified block diagram of the entire system is given Figure 4.

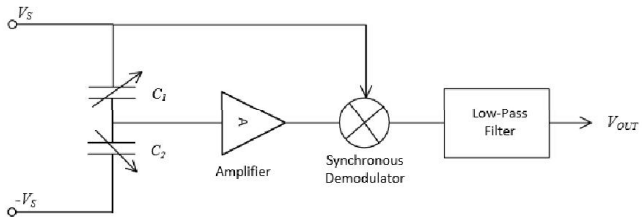


Figure 4: Overall View of the Capacitive Accelerometer

III. MATLAB/SIMULINK MODEL

The accelerometer part is simulated using the second-order mass-spring-dashpot system. The applied acceleration is converted into displacement by this model. This model is simulated using the following values: weight of the mass M=145x10^{-6} kg, spring constant k=300 N/m, damping constant b=0.1.

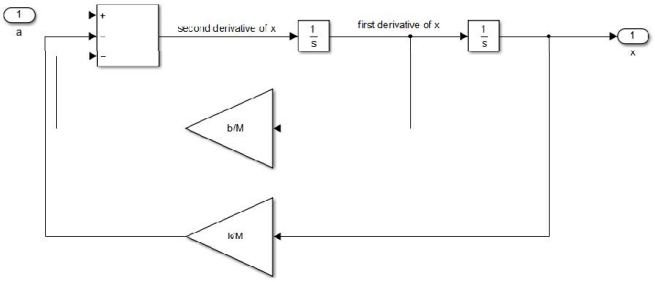


Figure 5: Accelerometer Simulink Model

A sinusoidal 10 Hz with 0.1g amplitude acceleration is applied to this system and the resultant displacement graph is shown in Figure 6.

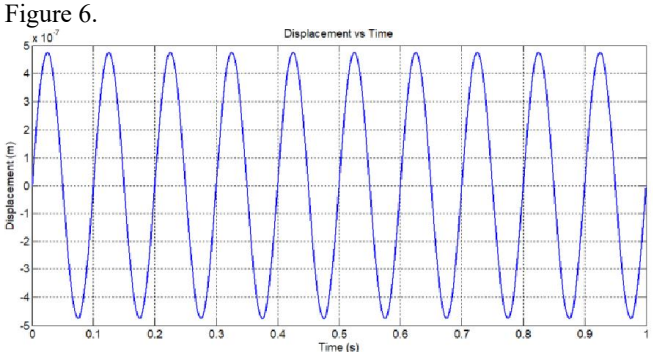


Figure 6: Displacement(x) vs Time

This displacement results in capacitance change because of the change in gap between the plates of the capacitors. In order to simulate this capacitance change, 48 capacitors with the following parameters are used: permittivity of the vacuum ε_0 = 8.85x10^{-12} F/m, area of the plates A = 3.75x10^{-8} m^2 and the initial gap g_0=3.5x10^{-6} m. Capacitance change graph for the sensed displacement and for the above parameters is given in Figure 7.

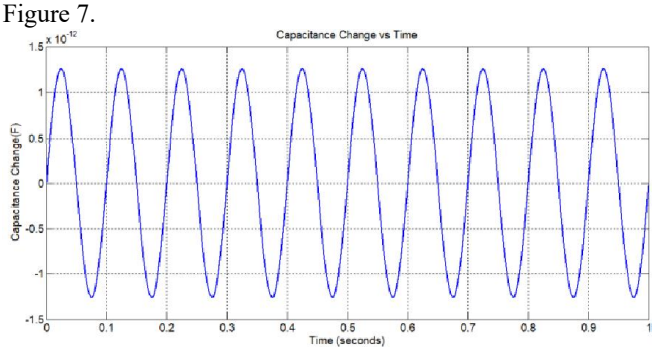


Figure 7: Capacitance Change vs Time

Now, the capacitance change is converted to voltage using a charge amplifier with a feedback capacitance of C_F=4.7 nF. This output is given by the following formula (2):

$$Vo = -\frac{\Delta C}{C_F} V_S \quad (2)$$

where V_S is the actuation or excitation voltage with high frequency. In this simulation, Vs is a sinusoidal with 159 kHz with amplitude of 1V. This signal is actually a modulated signal. The resultant voltage's graph is given Figure 8.

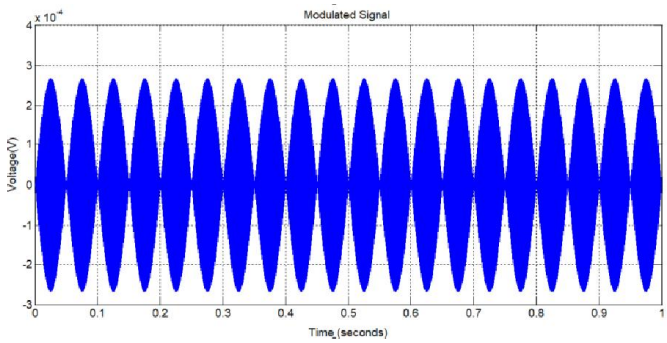


Figure 8: Modulated Signal

Then, this modulated signal is demodulated using synchronous demodulator such that it is multiplied with the actuation signal. The resultant demodulated signal is given in Figure 9.

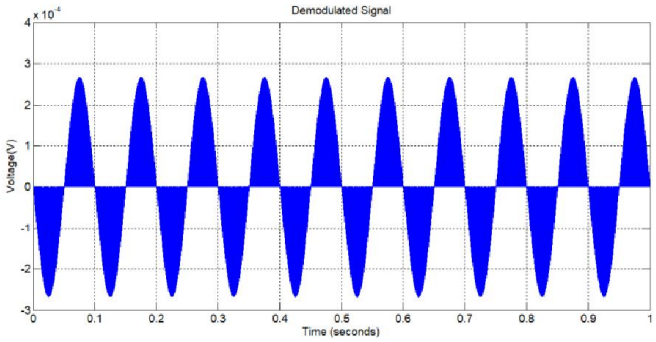


Figure 9: Demodulated Signal

The demodulated signal contains both high frequency and low frequency components. High frequency component is a result of actuation voltage while the low frequency component includes the acceleration information. Therefore, the high frequency component must be filtered out. In the simulation, a Butterworth low-pass filter with a 32 Hz pass-band edge frequency is used. The remaining low frequency component now contains the applied acceleration which is multiplied with a constant value. The final output voltage graph is given in Figure 10. It can be clearly observed that the final output signal is also a sinusoidal with a phase shift. This output signal actually contains the applied acceleration but it is shifted in time and multiplied with a constant. This output signal can be used to obtain intended acceleration value.

IV. Conclusion

In this paper, behavioral modeling of a MEMS capacitive accelerometer is given. The sensing mechanism, capacitive transduction mechanism, synchronous demodulation and low pass filtering constitutes the entire model. This model is first introduced and described. Then, the whole model is simulated in SIMULINK based on this model and using certain specifications. It is clearly seen that the model works correctly and the applied acceleration could be obtained with this model. Additionally, some non-idealities like noise can be added to this to make more accurate simulations for the future work.

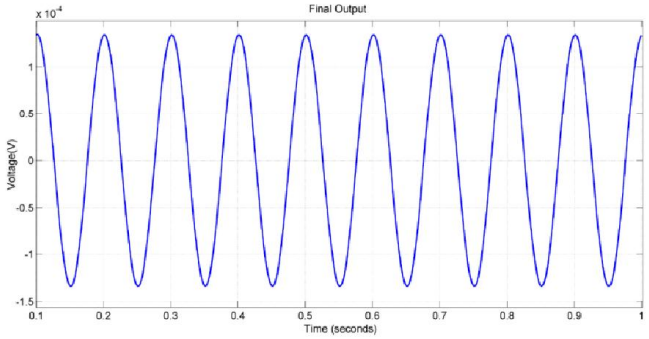


Figure 10: The Final Output Signal

References

[1] Robert B. "*MEMS sensors: past, present and future.*" Sensor Review 27.1 (2007): 7-13.

[2] Gang Z. "*Design and Simulation of a CMOS-MEMS Accelerometer*." project report, Carnegie Mellon University, Pittsburgh, PA, May (1998).

[3] M. Andrejašic, *MEMS ACCELEROMETERS,* Seminar, University of Ljubljana, 2008.

[4] Pharyansh K. and Komaragiri R. "*Performance Optimization of MEMS Capacitive Accelerometer.*" Devices, Circuits and Communications (ICDCCom), 2014 International Conference on. IEEE, 2014.

[5] Li, Hong, Han Zhiming, and Li Yanan. *"A design of differential capacitance detection circuit.*" Electronic Measurement & Instruments (ICEMI), 2015 12th IEEE International Conference on. Vol. 1. IEEE, 2015.

[6] F. Aezinia. *Design of interface circuits for capacitive sensing applications.* Diss. Applied Sciences: School of Mechatronic Systems Engineering, 2014.

[7] T. Grigorie, *The Matlab/Simulink modeling and numerical simulation of an analogue capacitive micro-accelerometer. Part 1: Open loop.* MEMSTECH 2008. International Conference on (pp. 105-114). IEEE, 2008

Challenges and Solutions for IoT Applications in the Iron and Steel Industry

A. TUNUZ[1], M. KARA[2], M. FURAT[3]

[1]Mega Recycling & Metallurgy, Hatay/Turkey, ariftunuz@gmail.com
[2]Mustafa Kemal University, Hatay/Turkey, mustafakara@mku.edu.tr
[3]Iskenderun Technical University, Hatay/Turkey, murat.furat@iste.edu.tr

***Abstract* - Connecting of devices that is usable for reaching them via a network, globally internet, is a new concept for the iron and steel industry. The concept, named as Internet of Things (IoT), brings many benefits with some critical challenges. Since iron and steel industry (ISI) plants are built large areas, communication between plants are main problem. In addition, magnetic field produced by the melting furnaces is another problem. IP capability and cyber security are the common problems for all IoT applications. Primary aim of the present study is to exhibit these challenges of IoT applications in ISI and also to suggest some solutions.**

***Keywords* - IoT, iron and steel industry, ISI, challenges and solutions.**

I. INTRODUCTION

INTERNET of Things is a concept represented by devices that communicate with each other through various communication protocols and connect to each other to form an intelligent network by sharing information. 'Things' mean communication from the machine to the machine, from the machine to the computer, from the computer to the person. In short, it refers to all the physical items that speak with each other. [1].

With the developing technology, communication via internet has been preferred frequently in daily life. This choice has accelerated connecting of communication devices, especially to the internet, i.e. laptops, mobile phones and tablets for different reasons [2]. Also, refrigerators, cars, washing machines, heaters, garage doors can be connected the Internet but it is not, currently [3].

IoT concept has been found place not only daily life of people but also manufacturing industry significantly. With IoT, the devices, machines, sensors and computers will be able to share information with themselves and with the staff. In this sense, it is great important for the industrial applications when considering the benefits of IoT. IoT is actively used in manufacturing, transportation, utilities, healthcare, etc [4].

However, some critical problems have been reported when adopting IoT to an industrial area. In the present study, application of IoT to iron and steel industry (ISI) is taken into account. It is obvious that, although most of problems are common with the other industrial applications, there are also specific problems depending on the manufacturing features of iron and steel industry. In the present study, some of common problems and specific problems are taken into account and solutions to the corresponding problems are proposed.

II. IOT IN THE IRON AND STEEL INDUSTRY

Iron and steel factories consist of integrated facilities. These facilities have been completely working with human power until 1980's. In system based on human power, labor force needs, work accidents and breakdowns were seen with high rate. At present, the ISI is faced with low productivity, difficulties in projects, steel losses and other issues that seriously hamper work efficiency. [5].

With the development of technology, these systems have left their place to automation systems. The revolution in the industry is given in Fig. 1. The benefits of using IoT can be summarized as follows [6]:

- Automation of the processes more efficiently,
- Achievement great time management
- Increment of the production rate keeping the quality of the final product,
- Connection of different types of sensors at one place,
- Better solution and analysis with all the gathered data,
- Reduction in human depended production errors and work accidents.

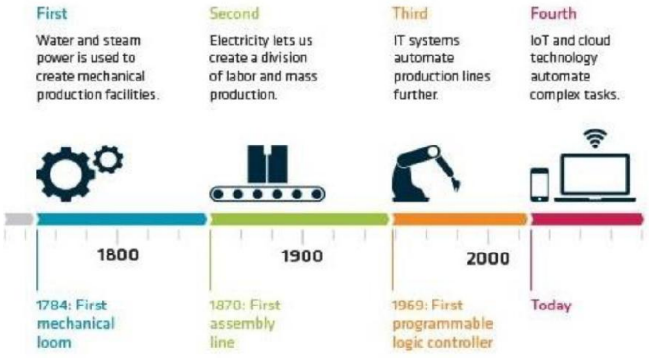


Figure 1: Industrial revolution timeline [7,8].

Automation means programmable logic control (PLC) in the ISI. The digital and analog information from the machines and field is transferred to the CPU (Central Processing Unit) by

cable. CPU communicate with SCADA by data cable (i.e. cat6). All information can be tracked with the SCADA screen as seen in Fig. 2. The SCADA is important for a system follow up in a plant. Authorized persons can check the production flow, fault conditions of motors and operation of the plant by means of SCADA. Especially, the condition of the motors is very important for a plant. Because, hundreds of motors are used even in a medium size plant. Therefore, their efficiency, reliability and power consumption need to be taken care of. Field Programmable Gate Array Integrated Circuits (FPGA ICs) exhibit long-term reliability and long lifecycles, supporting the working of motors for long hours. The production losses can be reduced to the minimum level.

When we arrived in 2000, we could reach PLCs via internet. We could control the machines, steel plants, offices indirectly via the internet as illustrated in Fig. 3. We can connect all of these information to the internet by collecting it in a center via cables. With the discovery of the IoT concept, no cable or any other interface was needed. Because we can control each device by connecting them in a network. In this respect, problems such as cable consumption, workmanship, overhead costs don't appear.

Reference to the automation system, a system that is used to indirectly connect the machines to the internet. One of the sectors that use this system most is the ISI. Operation diagram of motor control application with PLC over internet as see in Fig. 4 [9]. It can be predicted that when applying IoT to ISI, some problems will be appeared at the same time that should be overcomed.

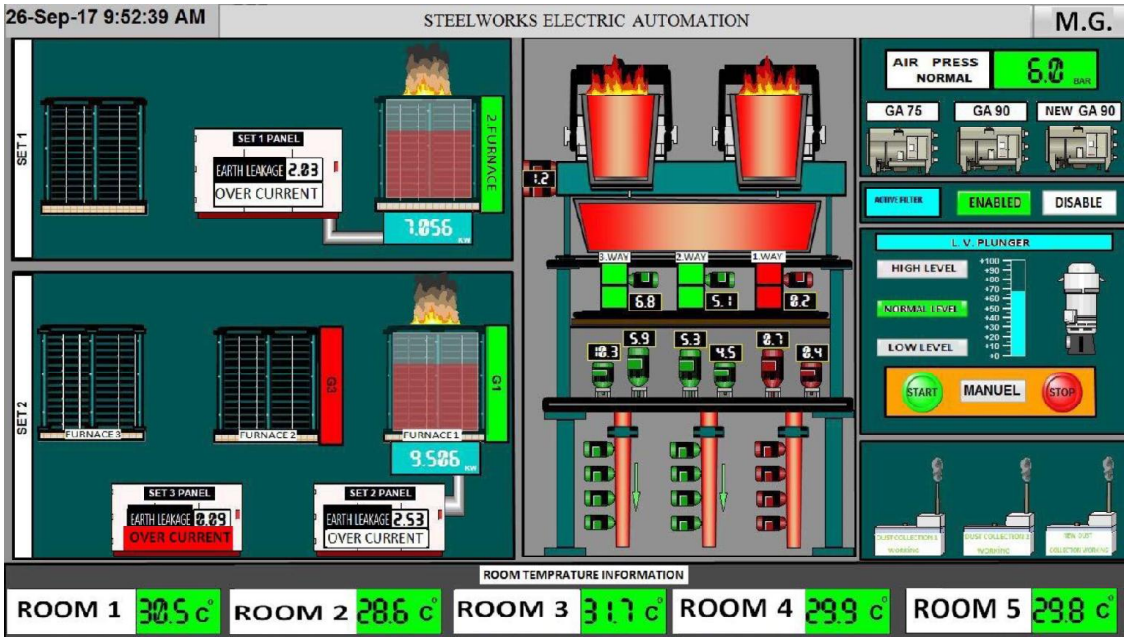


Figure 2: A SCADA screen capture used in the ISI (from Mega Metallurgy automation system).

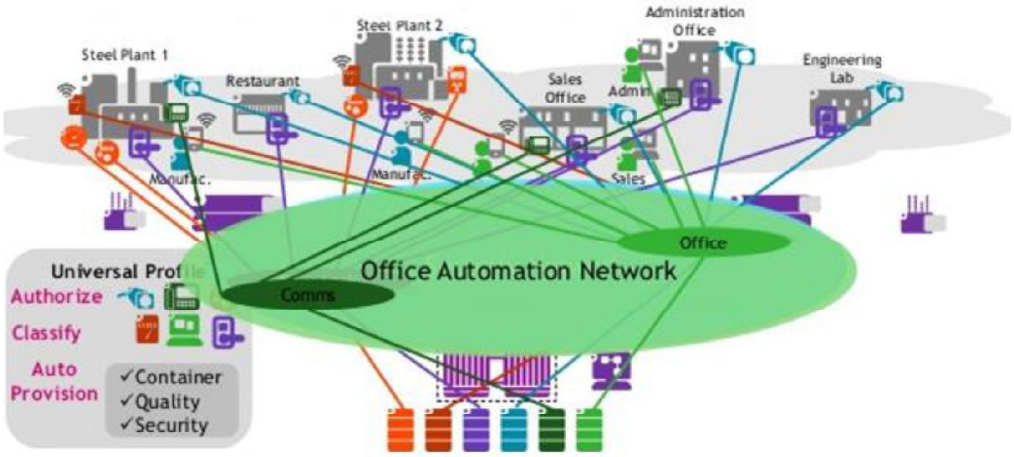


Figure 3: Automation network in ISI [6].

III. Challenges of IoT Applications in ISI

IoT is coming into in daily life day by day. Some challenges in adopting IoT to systems will come into conflict. In fact, these challenges will cause problems in ISI more often than daily life. In the present study, some of them are taken into account with some solution proposals.

A. IP Address Capability

In 2008, the number of internet connected objects was around 8 billion and it is estimated that by 2020 this number will reach 50 billion as see in Fig 5 [10]. This means there will not be enough IP addresses. In the long term, lack of IP address creates a serious problem [11] in large-scale systems.

On the industrial fields, online servers, computer systems supported by various software, and hardware system that connects over the internet to each other can be known by their IP addresses. For this reason, the transition process to IPv6 technology should be accelerated. Besides, your hardware and software must be compatible with IPv6 technology. Together with the evolving IoT technology [12], measures must be taken before IPv4 becomes unavailable.

For IPv6 technology, 3 main items are very important:

- IPv6-Compatible Operating Systems
- Suitable Router and Switch with IPv6 Support
- An ISP that enables IPv6

It is obvious that, there are many types of devices used in daily life of people, it seems impossible to connect all of them to the internet network. In addition, connection, control and protection of such amount of the devices is difficult to ensure together.

B. Magnetic Field Barrier

Melting furnaces in ISI work at high power and high frequency. Consequently, the produced magnetic field has large amplitude which brings serious problems with the wired and wireless communication systems used in the plant. Due to such amplitude of magnetic field, the system may not work well or may not work never.

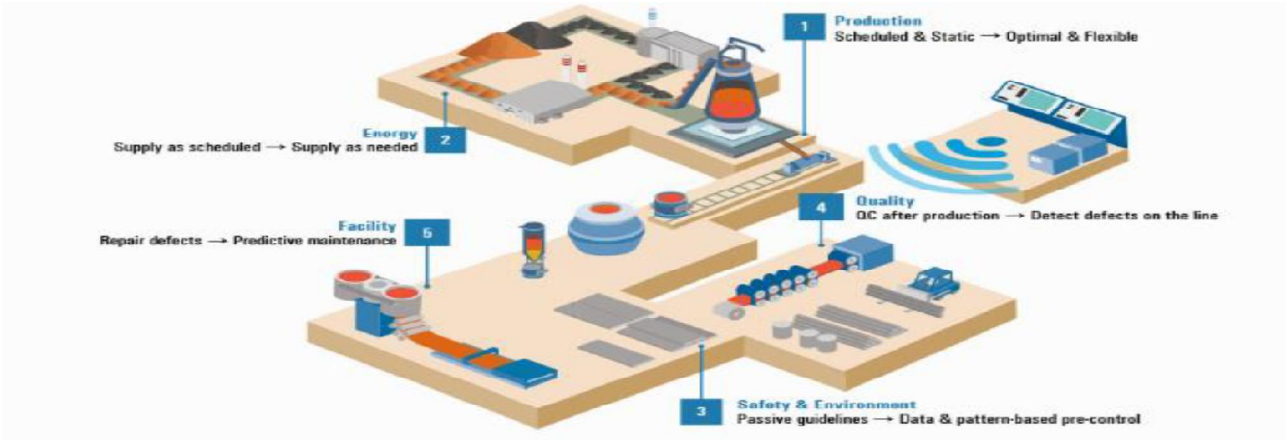


Figure 4: IoT application in ISI.

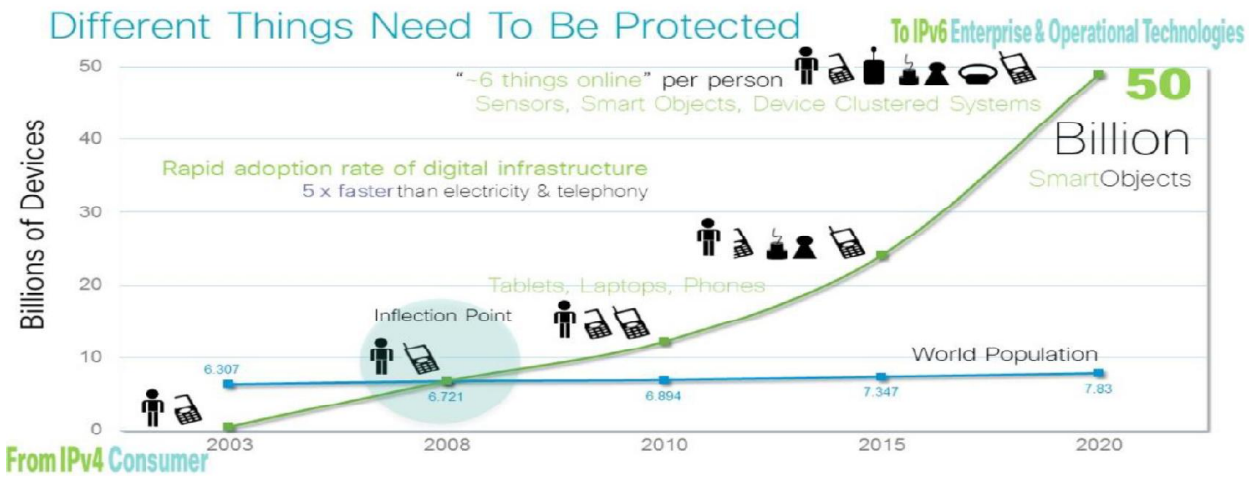


Figure 5: IP address demand rate [7].

E-ISBN: 978-605-67535-4-1

C. Distance

Due to the establishment of ISI's factories, it is necessary to build on wide areas. This situation causes the plants to be far from each other so that there can be even 1 km between two plants. It may be impossible for a data cable to carry digital data at these distances.

D. Cyber Security Issue

In recent years, cyber-attacks have significantly increased. Ensuring sustainability of the industrial system is vital importance to avoid great security problems [13]. Cyber-attacks targeting online transmission could occur larger major damages. Iron and steel industry is in charge of continuity for some critical services. It is important that these systems have security range from communication devices, computers, all of the sensors and other devices.

The human factor, automation communication risks, remote access dangers, application layer risks and system vulnerabilities are some of this security issues. Basic infrastructures, intelligent networks and various industrial areas provide strategic services. Strategic services generate valuable information and these systems have a constantly growing structure. The systems growing day by day, and the expansion of our network can bring security problems as well [14]. Industrial devices that are continuously interacting with each other in an industrial architecture are usable as long as the network topology is secure. Information collected from sensors, PLCs and similar devices is transmitted over internet network and collected from server systems. The information obtained from every point reaches the information system from transportation and operational system. At this point, internet connection is used and the internet is a world which is full of attackers. This mechanism makes our system a target for intruders. Access to the internet and the internal network is physically protected by the firewall technology. However, there are some vulnerabilities of the firewall [15]. It is possible for attackers to overcome this defense with certain methods.

IV. Suggestions

It is vital to solve problems instantly in the ISI. This industry has encountered so many applications and difficulties until now, but a solution has definitely been found. Therefore, ISI technologically has made great progress in the past few decades. The solution of today's technology, IoT, is also necessary for this industry to move forward.

A. Solution to IP Addressing of Devices

It is expected that the internet will reach more IP addresses by passing to the IPv6 system. With this development, applications of IoT technology to daily life and industry has been growing at an impressive rate. A number of some devices connected to the internet is expected to reach great numbers in a soon time. At this point, the NAT [16] (Network Address Translation) device can be the ideal solution. A router or other device can solve this problem by performing NAT between the Internet and the Intranet. The solution offered in the transition to IPv6 is provided through a developed NAT device. The end user is connected to IPv6 using a device such as a router, modem, or network key. As a result, enhanced NAT allows IPv6 clients to access IPv4 servers. The proposed solution is illustrated in Fig. 6. NAT provides security and management as well. A computer on the local network cannot reach the IP address of a computer on your network without first establishing a connection or forwarding it to your network. With the NAT device, the network can be managed and external threats can be blocked.



Figure 6: IPv6 solution with NAT device.

B. Solution to Magnetic Field Barrier for IoT Communication

The most important of the problems in connection to the ISI is the magnetic field. Operation of the furnaces with high frequency creates big problems in the connections. This problem should be avoided first in IoT applications.

Firstly, if the cable is used in the system, the cable routes must be selected in the remote areas from the magnetic field. Hereby the data is transmitted without interruption. But cable costs will increase for the cable route space. In addition, increasing the length of cable may cause data loss.

Secondly, Faraday cage can be used for magnetic field problem. Faraday cage was discovered in 1836 by the British physicist Michael Faraday. When a Faraday cage distributes that charge or radiation around the cage's exterior, it cancels out electric charges or radiation within the cage's interior. In short, a Faraday cage is a hollow conductor, in which the charge remains on the external surface of the cage [17]. If faraday cage can build to over network, Network area is preserved and protected. This will minimize and control the magnetic field problem in that region as see in Fig. 7.

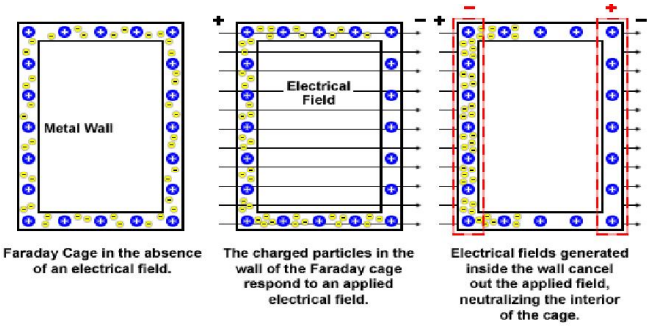


Figure 7: Faraday cage.

GSM is an effective solution to data transmission errors caused by magnetic field in the iron and steel industry. This application requires the use of a GPRS modem. GPRS modems are used to communicate with a remote PLC. It processes both analog or digital information (flow, volume,

level, temperature, humidity, weight) collected from the process area according to the PLC application and transmits this information via SMS and the connected GPRS modem. It is enough for a PLC to send a SMS that a GSM SIM card is inserted in the GPRS modem.

A computer (PC) collects and registers the PLC data that is connected to it. PLC also sends SMS to the main SCADA computer located in management department or building far from the furnaces where the magnetic field is not active as see in Fig. 8.

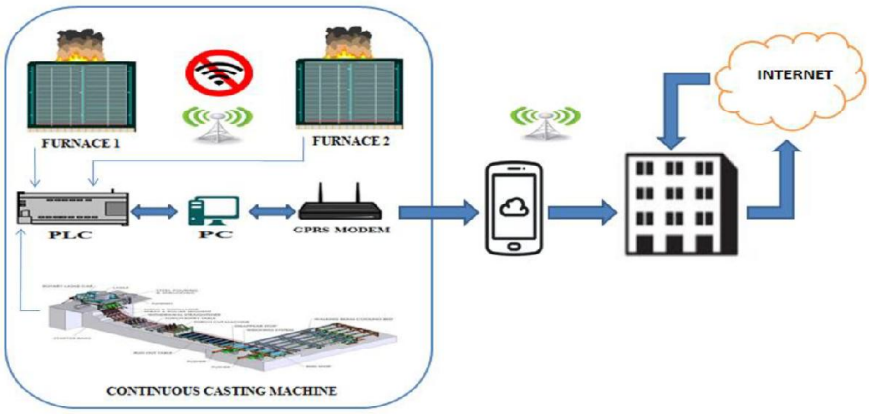


Figure 8: Data transfer with GSM.

C. *Solution to Distance*

The distance problem should be controlled by the use of cat6 cable to get information from the IP address provided to the machine. But it is suitable for the distances up to 150 meters. Longer cat6 cable may cause the data loss when transmitting. In order to transmit the data without loss, switches or repeaters are required on every 100m distance.

A roadmap, shown in Fig. 9, can be used to describe the problems of IoT in the ISI. The proposed roadmap can be used to overcome the problems which are encountered in the transmission of information obtained from IoT devices to Process Unit. The solution can easily be followed when the problem is encountered. Wireless transmission or transmission via GSM is used to overcome main distance problem. In addition, due to characteristics of ISI, magnetic field barrier may be main drawback. Faraday cage is a good candidate to overcome effect of magnetic field.

Detection and solution of a distance problem can be performed with the following steps as given in Fig. 9:

Step 1: If the data is not transmitted from IoT device to Process Unit check the distance between them.
Step 2: If the distance is under the maximum limits then use wireless.
Step 3: Otherwise, check for the magnetic field barrier and use Faraday Cage to protect wireless system from magnetic field barrier.
Step 4: If the data transmitted by the wireless system to Process Unit is not received, then use GSM for the data transmission.
Step 5: Check for the data received by the Process Unit if there is no loss when transmitting.

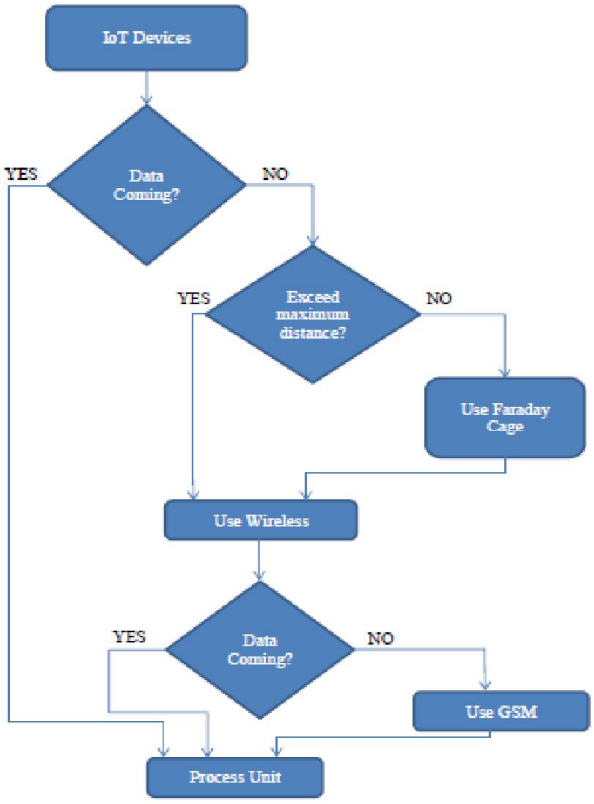


Figure 9: A roadmap to overcome transmission problems in ISI.

D. *Solution to Cyber Attacks*

Connecting most devices to the internet means that we are vulnerable to any cyber attack. Except for negatively affecting people's personal lives, a cyber attack in the industry sector will lead to enormous danger. These attacks can threaten the safety of the machines and equipment. Cyberattacks on IoT systems are very critical since they may cause physical damage and even threaten human lives in ISI [18].

The most effective way to prevent cyber attacks is to create a firewall. Firewall is designed to protect network systems from many negative content such as bad codes, viruses and hackers coming from internet as see in Fig. 10 [19]. Besides, using Firewall and Snort technology together will increase our security against intruders. All switches in our network are connected to a snort device and the switches in the network are directly connected to the Firewall. The packets passing through the firewall are connected to the internet via the router. This creates a secure network. At this point, well-designed network design creates an intensive protective shield for the industry. Identification of policy violations and abnormalities on systems should be considered against cyber-attacks. Additionally, the central monitoring system is necessary for instant intervention to the attack attempt. 7x24 automated monitoring, error detection and warning and tracing the packets for keeping logs should be provided by network manager.

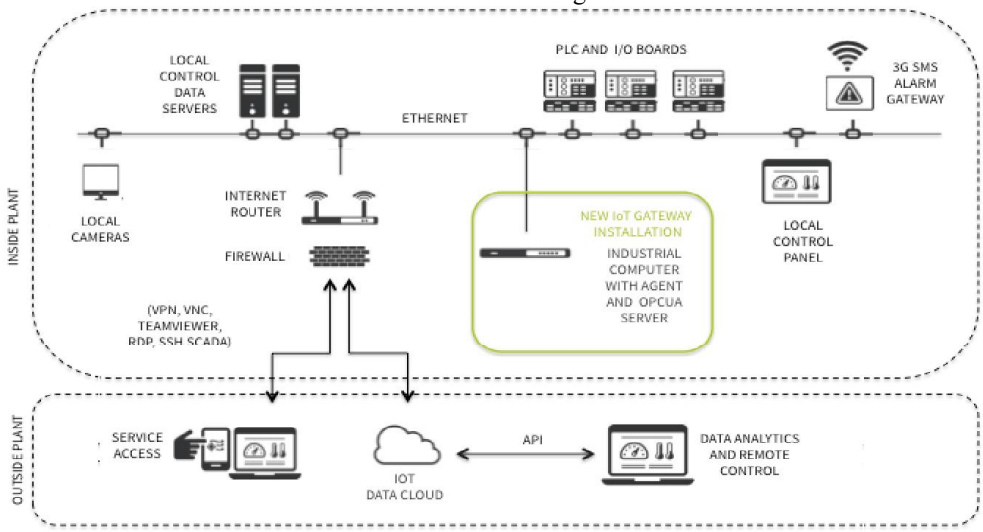


Figure 10: A sample network topology between industrial plant and Internet [16]

V. CONCLUSION

In this paper, IoT's important application in the implementation of the ISI is mentioned and some solutions are proposed for the problems. In today's technology, problems are encountered in the application of IoT in ISI such as magnetic field barrier, distance and cyber attacks and some solution methods are suggested for the corresponding problems in this paper. However, different solutions can be chosen in practice. Besides, IoT will always provide significant impact to the ISI. These suggested solutions will further improve the efficiency in ISI and will open the way for the implementation of new technologies.

REFERENCES

[1] S. C. Mukhopadhyay, Internet of Things: Challenges and Opportunities, Springer International Publishing, Switzerland, 2014.

[2] L.D. Xu, W. He and S. Li, "Internet of Things in Industries: A Survey", *IEEE Transactions on Industrial Informatics*, Vol.10(4), Nov. 2014, pp. 2223-2243.

[3] R. Jain, Introduction to Internet of Things, Lecture Notes, [Online]. Available: http://www.cse.wustl.edu/~jain/cse570-15/ftp/m_11iot.pdf

[4] The Internet of Things (IoT) – essential IoT business guide, [Online]. Available: https://www.i-scoop.eu/internet-of-things-guide/

[5] K. Yang, Tss Column: Study Application Internet Things Steel Structure Industry, [Online]. Available: https://www.linkedin.com/pulse/tss-column-study-application-internet-things-steel-structure-yang

[6] N. Thakkar, J. Sobotie, Exploring The Use of Internet of Things within the Steel Industry. [Online]. Available: http://www.etcs.ipfw.edu/~lin/CPET575_MangOfTech/575-CaseStudies/2015-Fall/1-JudithNirali-FinalReport/Judith-Nirali-Final(Presentation).pdf

[7] https://i.pinimg.com/736x/ca/09/d2/ca09d28b4a97e2b23a279203d4eaf5c6--industrial-development-industrial-revolution.jpg. [Online]

[8] Jensen, M. C. (1993). The Modern Industrial Revolution, Exit and Failure of Internal Control Systems, The Journal of Finance Vol. XLVIII, No:3, pp. 831-880.

[9] The Fourth Industrial Revolution: The Winds of Change Are Blowing in the Steel Industry. [Online]. http://globalblog.posco.com/fourth-industrial-revolution-winds-change-blowing-steel-industry.

[10] Securing the Internet of Things: A Proposed Framework. [Online]. https://www.cisco.com/c/en/us/about/security-center/secure-iot-proposed-framework.html

[11] H. Jadidoleslamy, "Weaknesses, Vulnerabilities and Elusion Strategies Against Intrusion Detection Systems", *Int. Journal of Computer Science and Engineering Survey*, Vol.4, Aug 2012, pp. 15-25.

[12] I. Lee, K. Lee, "The Internet of Things (IoT): Applications, investments, and challenges for enterprises", *Business Horizons*, Vol.58, 2015, pp. 431-440.

[13] M. Kara, M. Furat, "Security threats for industrial control systems and a solution with DMZ", *1st International Mediterranean Science and Engineering Congress,* 26-28 October 2016, Adana, Turkey.

[14] J. Jang-Jaccard, S. Nepal, "A survey of emerging threats in cybersecurity". *Journal of Computer and System Sciences*, Vol.80, 2014, pp. 973-993.

[15] S. R. Borhade, S. A. Kahate, "Intrusion Detection System based on Hashing Technique". *Global Journal of Engineering Science and Researches*, Vol. 3, 2016.

[16] L. E. Li, A. Chen, T. Bu, S. Miller, "Detecting subscribers using NAT devices in wireless data networks". *Bell Labs Technical Journal*, Vol. 14, 2009, pp. 223-233.

[17] N. Chandler, How Faraday Cages Work. [Online]. https://science.howstuffworks.com/faraday-cage.htm.

[18] A. Sadeghi, C. Wacshmann, M. Waidner, Security and Privacy Challenges in Industrial Internet of Things, *Design Automation Conference (DAC)*, 2015, San Francisco, USA.

[19] P. Scully, Understanding IoT Security – Part 3 of 3: IoT Security lessons from recent IoT projects. [Online]. https://iot-analytics.com/iot-security-lessons-from-recent-iot-projects.

Review on Using FPGA in Sensorless Speed Control of PMSM

Abdulhasan Altaey[1] and Ahmet Afsin Kulaksiz[2] and Huseyin Dogan[3]
[1] Ph.D. Student in Selcuk University, Konya/Turkey, Instructor in the University of Mustansiriyah, Baghdad, Iraq aaltaey13@gmail.com
[2] Associate professor in Selcuk University, Konya/Turkey, afsin@selcuk.edu.tr
[3] Assistant professor in Selcuk University, Konya/Turkey, huseyindogan@selcuk.edu.tr

Abstract **– The use of Permanent Magnet Synchronous Motor (PMSM) in the industry has recently increased strongly because of its advantages such as high efficiency and torque intensity. The ordinary speed control of these motors use encoders which has an effect of increasing the noise, complexity, and price of the system. To alleviate these problems, sensorless speed control is advised as an alternative which commonly used in the industry. There are a lot of available sensorless algorithms but the most efficient methods are Modal Reference Adaptive System (MRAS), Slide Mode Observer (SMO) and Extended Kalman Filter (EKF). The implementation of these methods is frequently accomplished using, either DSP or FPGA. The DSP implementation is preferred if the number of channels is less than two. For instance, in sensorless speed control of PMSM especially in the electrical vehicle applications, the number of channels is more than 10. In such cases, due to limited resources, DSP implementation is not feasible, while FPGA can provide tremendous resources and parallel programming capabilities. As the speed of the complex algorithms is a crucial parameter in sensorless control of PMSM, FPGA seems to be an alternative to the common DSP implementation of these algorithms. This paper gives a review on using FPGA in the controller that can be used for sensorless control of PMSM and propose to use simple algorithms which will reduce the number of components in FPGA-based control IC and will enable the control process to be finished in the dead time of the inverter or even decrease the required dead time.**

Keywords **– FPGA, IPMSM, PI Controller, SVPWM.**

I. Introduction

The Interior Permanent Magnet Synchronous Motors (IPMSMs) have become more and more valuable in many industrial applications because of many features such as high-power density, high torque to inertia ratio, and high efficiency. In space vector diagram, the addition of the three phase motor stator currents will create a current vector with certain magnitude and angle. By orienting this stator current vector MMF to be at 90° with respect to rotor flux, a maximum amount of torque for a given amount of stator current can be obtained. Hence it is necessary to know the rotor position information to be able to control the speed and torque of these motors. Measurement devices such as resolvers or encoders can be used to obtain rotor angle information but these devices have high prices, increase the wiring complexity and add noise to the system. To solve this problem sensorless algorithms can be applied. There are a lot of sensorless algorithms, the most famous are SMO, MRAS, Fuzzy Sliding Mode, EKF…etc. To implement these sensorless algorithms, two platforms either DSP or FPGA are mostly utilized. If the sampling rate has a moderate value and is a single-channel the DSP can be used but if sampling rates increases more than a couple of megahertz, or if the system have more than one channel, FPGAs is preferred. For instance, in sensorless speed control, if the sampling rate is 10 kHz and there are a lot of channels, FPGAs becomes more suitable option. Another criteria is that the DSPs are instruction based while FPGAs are clock based so to implement any simple mathematic process in DSP three or four initiating instruction have to be processed, as a result an additional time will be lost because of these initiating instructions

In the following section the current trend in control of PMSM will be covered and the examples in the literature where FPGA is preferred will be highlighted

II. FPGA in PMSM Control

The general block diagram for the speed control of the PMSM is shown in Figure *1*. Two controller loops exist: outer loop for the speed and inner loop for the current. The outer loop commands the reference current values, while the inner loop use these reference current values and commands the reference voltage values. These reference voltages used to generate SVPWM signals for the inverter. For successful speed control process, two conditions should be justified:

1. All the calculations should be finished within the deadtime limit of the SVPWM signals.
2. The Current controller should command the voltage values to the SVPWM signal generator block before a new value of currents come to the controller from the outer loop speed controller.

In [1], two types of controller namely Speed PI Controller and deadbeat current Controller [6-8], have been designed on FPGA platform for speed control of IPMSM. The timing chart of this FPGA design is shown in Figure *2*. Inspecting Figure *3* shows that the I_q requires about 100 μs to follow I_{qref}. This means this deadbeat current controller can track the commanded values that comes from the speed controller in 100 us. In normal current PI Controller used for PMSM the response is limited to some milliseconds. Hence using FPGA makes this design can be used in very precise speed control of the IPMSM.

An interesting FPGA module is proposed in [2], this module consists of a fuzzy controller, a reference model for the PMSM and an adjusting mechanism (to minimize the error between the rotor speed and the output of the reference model). The adaptive fuzzy control in speed

control loop is realized by software method under the NIOS embedded processor and a current vector control is implemented using PLD. The dead time for the inverter is 1 µs. Figure *4* shows that the system tracks the real speed.

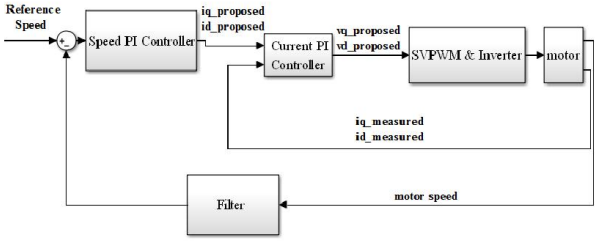


Figure 1: General Speed Control of PMSM.

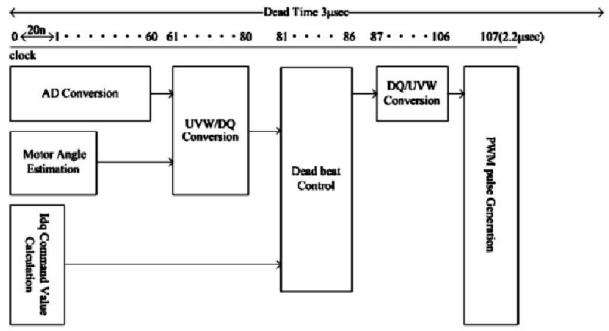


Figure 2: Timing chart of FPGA based Hardware Controller [1].

In PMSM Speed Control, one of the basic mathematical task is to find the inverse Clarke i.e. converting α-β voltages and currents to a-b-c voltages and currents as shown in (1-3):

$$i_a = i_\alpha \tag{1}$$

$$i_b = -\frac{1}{2} i_\alpha + \frac{\sqrt{3}}{2} i_\beta \tag{2}$$

$$i_c = -\frac{1}{2} i_\alpha - \frac{\sqrt{3}}{2} i_\beta \tag{3}$$

In [2] the authors are proposed the following implementation to find the value of $\frac{\sqrt{3}}{2}$:

$$\frac{\sqrt{3}}{2} = \frac{1}{2} + \frac{1}{4} + \frac{1}{16} + \frac{1}{32} + \frac{1}{64} + \frac{1}{256} + \frac{1}{512} + \frac{1}{2048} \tag{4}$$

Equation (4) is representing in FPGA as shown in Figure *5*. When applying this equation in VHDL the number of logic elements will be 125:

But it is easier to represent $\frac{\sqrt{3}}{2}$ by equation (5):

$$\frac{\sqrt{3}}{2} = \left(\frac{1}{1} - \frac{1}{8} - \frac{1}{128} - \frac{1}{1024}\right) \tag{5}$$

Equation (5) can be represented in VHDL code as shown below. The compilation report is shown in Figure *6*, where the number on logic elements have been decreased from 125 to only 54.

```
library IEEE;use IEEE.STD_LOGIC_1164.ALL;
use IEEE.STD_LOGIC_ARITH.ALL;
use IEEE.STD_LOGIC_UNSIGNED.ALL;
entity root is
port( clk    : in std_logic;
      a      : in std_logic_vector(17 downto 0);
      c      : out std_logic_vector(17 downto 0) );
end root;
architecture Behavioral of root is
signal a1,a2,a3,a4,a5: std_logic_vector(17 downto 0);
begin
process (clk) begin
if (clk'event and clk='1')  then
a1 <=a;
end if;
a1 <=a;
a2<= "000" & a1(17 downto 3);--divding by 8
a3<= "0000000" & a1(17 downto 7);--dividing by 128
a4<= "0000000000" & a1(17 downto 10);--dividing by 1024
a5<=a1-a2-a3-a4;--(sqrt(3) divided by 2 )= 1-1/8-1/128-
1/1024
c<=a5;
end process;
end Behavioral;
```

The work in [3] have designed a novel FPGA based algorithm aimed for the low speed range by injecting a high frequency signal in stator winding [9-11] and shows a good result as shown in Figure *7*Figure 8. It can be seen that the estimated speed tracks the measured speed in spite of that the reference speed is square wave which subject the system to hard transitions.

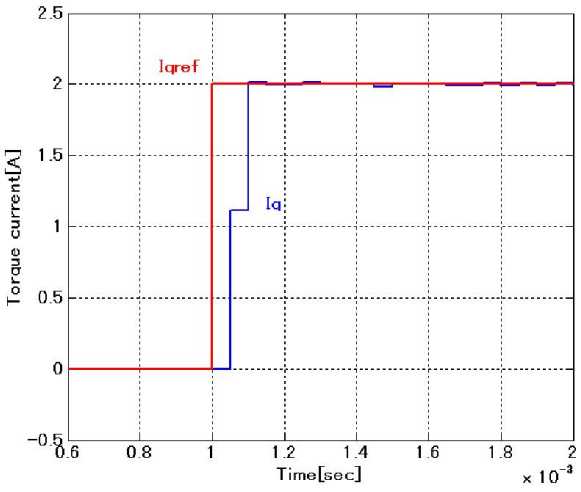


Figure 3: Simulation result for step response [1].

The work in [4] propose use two reduced order EKF work in parallel on FPGA platform as shown in
Figure 9 and shows good tracking result as shown in Figure 10. In this study, PI controller for speed and current control is used, where PI parameters are calculated only one time

during the design process which is a compromise between short rise time and minimum overshoot.

The PI controller will eventually make the control process less accurate. To alleviate the problem the model predictive control might be a possible solution.

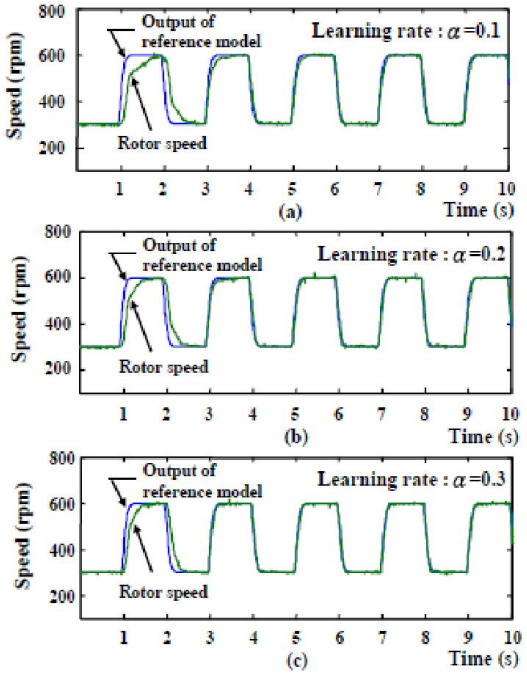


Figure 4: Tracking results between the output of reference model and the actual rotor speed under 1.0 Nm load torque but different learning rate (a) α=0.1 (b) α=0.2 (c) α=0.3 [2].

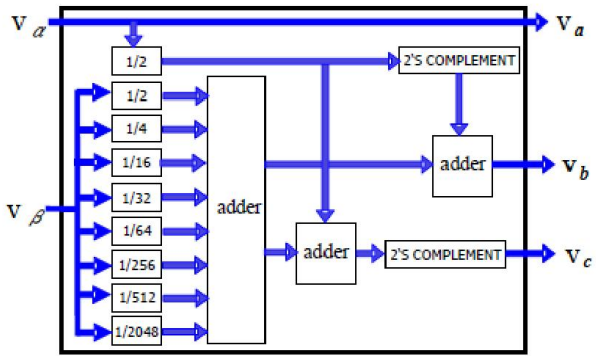


Figure 5: Inverse Clarke formulation [2].

Flow Status	Successful - Mon Aug 17 12:50:40 2015
Quartus II 64-Bit Version	15.0.0 Build 145
04/22/2015 SJ Web Edition	
Revision Name	paper2
Top-level Entity Name	root
Family	Cyclone IV GX
Device	EP4CGX150DF31C7
Timing Models	Final
Total logic elements	54 / 149,760 (< 1 %)
Total combinational functions	54 / 149,760 (< 1 %)
Dedicated logic registers	0 / 149,760 (0 %)
Total registers	0
Total pins	37 / 508 (7 %)
Total virtual pins	0
Total memory bits	0 / 6,635,520 (0 %)
Embedded Multiplier 9-bit elements	0 / 720 (0 %)
Total GXB Receiver Channel PCS	0 / 8 (0 %)
Total GXB Receiver Channel PMA	0 / 8 (0 %)
Total GXB Transmitter Channel PCS	0 / 8 (0 %)
Total GXB Transmitter Channel PMA	0 / 8 (0 %)
Total PLLs	0 / 8 (0 %)

Figure 6: Compilation Report of the VHDL code in page 2.

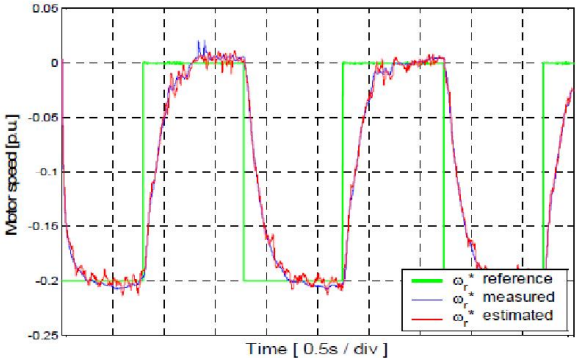


Figure 7: The reference, measured and estimated speed [3].

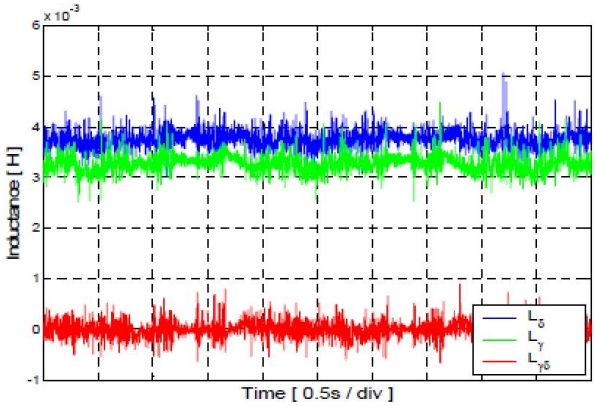


Figure 8: Estimated inductances [3].

Two types of direct torque controller (DTC) [15-17] for PMSM shown in Figure *11* have been controlled in [5]. In the controllers, single chip FPGA are used. One of the controllers was constructed by programming a soft-core CPU and hardware logic circuits written in VHDL, while the other was constructed of only hardware. This work proved that the controller which implemented solely on hardware logic circuits was able to shorten the control period and it was able to suppress the low torque ripple. So constructing all control

function completely on hardware will decrease the processing time, but at the expense on increasing of logic elements which are not a problem in large scale IC. So in this work processing time is decreased from 50µs to 20.34µs. On the other hand, the rate of total logic elements increased from 35% to 53%.

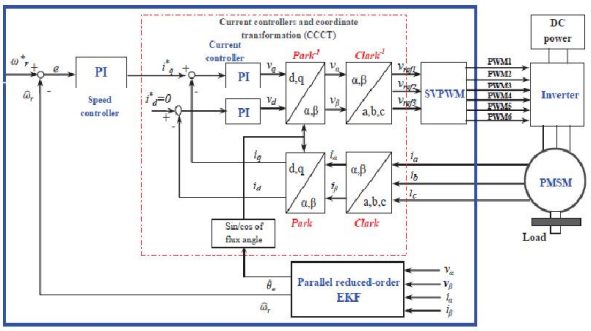


Figure 9: The proposed speed control system in [4].

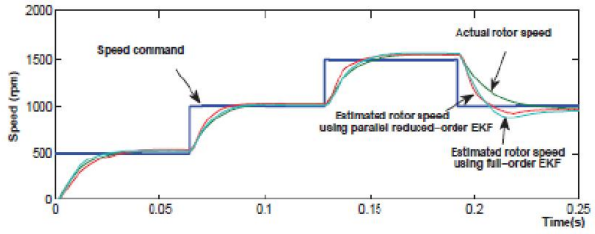


Figure 10: Speed response by using the full-order EKF and parallel reduced order EKF under speed varying from 0→500→1000→1500→1000 rpm [4].

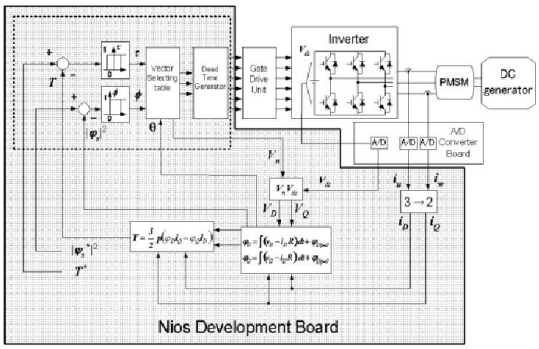


Figure 11: Block diagram of DTC for PMSM [5].

III. MODEL PREDICTIVE CONTROL

Conventional control for IPMSM are based on PI controller algorithm as shown in Figure 12, where PI parameters are calculated only one time during the design process which is a compromise between short rise time and minimum overshoot, which would decrease the accuracy of the system. Nowadays FPGAs are cheap in price and conventional PI speed and current controller have been replaced by Model Predicting Control (MCP) [18-20] using parallel computing on FPGA. This process will give more accurate results and better control system. MPC can be explained as follows: In any three-phase voltage source inverter as shown in Figure 13, six gate signals are needed. In SVPWM there are 8 states for these gate signals as shown in Table 1, where state zero and state seven are equivalent because in these two states no current flow in the inverter, hence the active states reduced to 7 states.

The scheme for MPC current control is shown in Figure 14. The errors between the commanded and estimated currents are entered to a cost function (6). This function will be implemented on FPGA platform and consists of seven internal equations. The result of these seven equations will determine which switching mode in Table 1 will be applied to the gates of the inverter.

$$cost = (i_{dcommanded} - i_d)^2 + (i_{qcommanded} - i_q)^2 \quad (6)$$

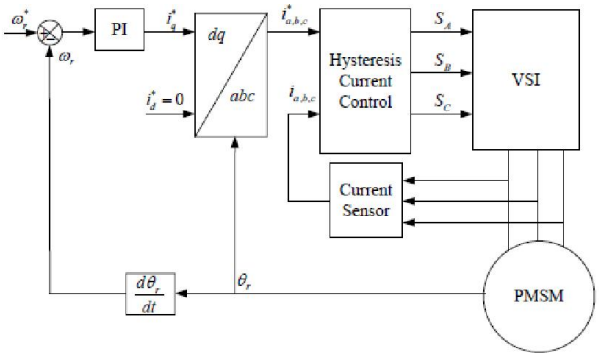


Figure 12: PI Current Controller.

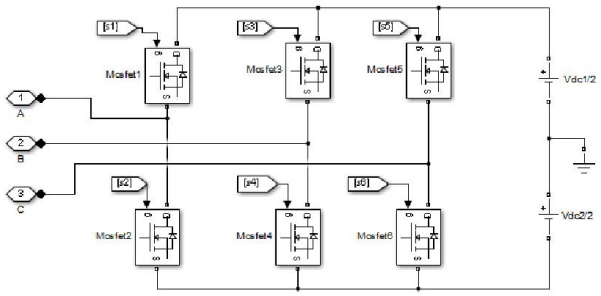


Figure 13: Three-phase bridge transistor.

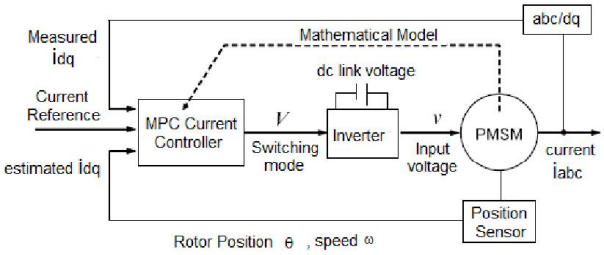


Figure 14: Model Predictive Current Control.

IV. Conclusion

The current trend in literature shows that FPGA is more preferable compared to DSP in PMSM control because of complexity of the proposed algorithm which requires a lot of channels in the speed and current control. Also, FPGA is capable of running parallel as FPGA is clock-based which means faster processing capability compared to instruction based DSP. In order to achieve an efficient system, the control process should be finalized in the dead time of the space vector pulse width modulation. In the implementation of FPGA based controller, the speed-up might be achieved by introducing hardware solutions such as the one proposed in [2], but we propose to use equation (5) instead of equation (4) because as we shown previously it will reduce the number of logic elements from 125 to 54 which means decreasing the size of components for the algorithm by 56.8 %. Sometimes to speed up the control process some challenging steps like using modal predicting current and speed control instead of PI controller should be done.

Table 1: Eight Possible Switching States.

Switching Mode	Voltage Vector	Switching Gates		
		Phase a	Phase b	Phase c
0	V0	-	-	-
1	V1	+	-	-
2	V2	+	+	-
3	V3	-	+	-
4	V4	-	+	+
5	V5	-	-	+
6	V6	+	-	+
7	V7	+	+	+

References

[1]. Tomoki Yokoyama, Asahi Kitada, “Precise Torque Control for Interior Permanent Magnet Synchronous Motor using FPGA based Hardware Controller”, IEEE GCC Conference and exhibition, November 17-20, Doha, Qatar, 2013, pp. 617 – 621.

[2]. Ying-Shieh Kung, Chia-Sheng Chen, Kiing-Ing Wong, Ming-Hung Tsai, “Development of a FPGA-based Control IC for PMSM Drive with Adaptive Fuzzy Control”, Industrial Electronics Society, 2005. IECON 2005. 31st Annual Conference of IEEE, pp. 1544-1549.

[3]. G. Maragliano, M. Marchesoni, and L. Vaccaro, “FPGA Implementation of a Sensorless PMSM Drive Control Algorithm Based on Algebraic Method”, industrial Electronics (ISIE), 2010 IEEE International Symposium on, Bari, pp. 3083 – 3088.

[4]. Nguyen Khanh Quang, Nguyen Trung Hieu, G. P. Hunter and Q. P. Ha, “FPGA-based Sensorless PMSM Drive Using Parallel Reduced-Order Extended Kalman Filter”, Control, Automation and Information Sciences (ICCAIS), 2012 International.

[5]. Yoshiharu Utsumi, Nobukazu Hoshi and Kuniomi Oguchi, “Comparison of FPGA-based Direct Torque Controllers for Permanent Magnet Synchronous Motors”, Journal of Power Electronics, Vol. 6, No. 2, pp. 114-120, April 2006.

[6]. Taka0 Kawabata, Memberı,E Ee, Takeshı Mıyashıta, And Yushın Yamamoto,” Dead Beat Control of Three Phase PWM Inverter”, lEEE Transactions On Power Electronics, Vol. 5. No. I , pp. 21-28, January 1990.

[7]. Alireza Abbaszadeh, Davood Arab Khaburi, Mohammad Ali Miremadi, Mojtaba esmaeili, “Permanent Synchronous Motor Predictive Deadbeat Current Control-Robustness Investigation”, The 6th International Power Electronics Drive Systems and Technologies Conference (PEDSTC2015) 3-4 February 2015, Shahid Beheshti University, Tehran, Iran, pp. 406-411.

[8]. NIU Li ,YANG Ming, XU Dian-guo, “Deadbeat Predictive Current Control for PMSM”, 15th International Power

Electronics and Motion Control Conference, EPE-PEMC 2012 ECCE Europe, Novi Sad, Serbia, pp. LS6b.1-1-LS6b.1-6.

[9]. R. S. Miranda, E. M. Fernandes, C. B. Jacobina, A. M. N. Lima, A. C. Oliveira, M. B. R. Correa, "Sensorless Control of a PMSM Synchronous Motor at Low Speed", IEEE Industrial Electronics, IECON 2006 - 32nd Annual Conference on, Paris, 2006, pp. 5069 – 5074.

[10]. Konrad Urbanski, "Sensorless control of PMSM high dynamic drive at low speed range", Industrial Electronics (ISIE), 2011 IEEE International Symposium on, Gdansk, pp. 728 – 732.

[11]. Yituo Li, Haifeng Lu, Wenlong Qu, Shuang Sheng, Zhengyu Wang, "Sensorless Control of PMSM Based on Low Frequency Voltage Injection at Low Speeds and Standstill", ECCE Asia Downunder (ECCE Asia), 2013 IEEE , Melbourne, VIC, pp. 781 – 787.

[12]. Albert Qiu and Bin Wu, Hassan Kojori, "Sensorless Control Of Permanent Magnet Synchronous Motor Usıng Extended Kalman Fılter",Electrical and Computer Engineering, 2004. Canadian Conference on,Vol. 3 , pp. 1557 - 1562 Vol.3.

[13]. Dariusz Janiszewski, "Extended Kalman Filter Based Speed Sensorless PMSM Control with Load Reconstruction", IEEE Industrial Electronics, IECON 2006 - 32nd Annual Conference on , Paris, pp. 1465 – 1468.

[14]. Anbang Wang, Qunjing Wang, Cungang Hu, Zhe Qian, Lufeng Ju, Jun Liu, "An EKF for PMSM Sensorless Control Based on Noise Model Identification Using Ant Colony Algorithm",Electrical Machines and Systems, 2009. ICEMS 2009. International Conference on , Tokyo, pp. 1-4.

[15]. Zordan, M., Vas, P. ; Rashed, M. ; Bolognani, S.,"Field-weakening in vector controlled and DTC PMSM drives, a comparative analysis ",Power Electronics and Variable Speed Drives, 2000. Eighth International Conference on (IEE Conf. Publ. No. 475), London, 2000, pp 493-499.

[16]. Chen Teng-fei, Han Chong-wei ; Xie Yi-na ; Zhao Yu-he, "Research on SVM-based direct torque control for PMSM of artillery speed servo system", Control and Decision Conference (CCDC), 2013 25th Chinese , Guiyang, 25-27 May 2013, pp 3727 – 3730.

[17]. Mino-Aguilar, G, Dominguez, A.M. ; Maya, R. ; Alvarez, R.,"A Direct Torque Control For A PMSM", Electronics, Communications and Computer (CONIELECOMP), 2010 20th International Conference on , Cholula, 2010, pp 260 – 264.

[18]. Zhixun Ma, Saeid Saeidi, "FPGA Implementation of Model Predictive Control With Constant Switching Frequency for PMSM Drives", IEEE Transactions On Industrial Informatics, Vol. 10, No. 4, pp 2055-2063 November 2014.

[19]. S. Bolognani, R. Kennely, S. Kuehly, G. Paccagnella, "Speed and Current Model Predictive Control of an IPM Synchronous Motor Drive", Electric Machines & Drives Conference (IEMDC), 2011 IEEE International, Niagara Falls, ON, 15-18 May 2011, pp. 1597 – 1602.

[20]. H. Kobayashi, H. Kitagawa, S. Doki, S. Okuma, "Realization of a Fast Current Control System of PMSM based on Model Predictive Control", Industrial Electronics, 2008. IECON 2008. 34th Annual Conference of IEEE, Orlando, FL., 10-13 Nov. 2008, pp. 1343 – 1348.

Design and Performance Analysis of a Wireless Short Packet Protocol Based Multi-Hop Network for Data Communication in Elevator Systems

M. M. LAJENE[1] and S. E. KARLIK[2]

[1] Uludağ University, Bursa/Turkey, majid.lajin@hotmail.com
[2] Uludağ University, Bursa/Turkey, ekarlik@uludag.edu.tr

***Abstract* - Multi-hop wireless network architectures can be used in communicating floor fixtures with the control panel of elevator systems. A novel Wireless Short Packet (WSP) protocol based non-acknowledged multi-hop wireless network design utilizing energy harvesting technology is proposed in this paper for the data communication in elevator systems. Experimental results obtained for average hop time show that the proposed network can operate in elevator systems of low-rise and medium-rise buildings. Experimental results about telegram average power emphasize that the network design can be developed to operate even in high-rise buildings. Usage of wireless technology together with energy harvesting technology provides high flexibility and enables integration of the elevator system with home automation and building management systems.**

***Keywords* – Wireless short packet protocol, multi-hop wireless network, data communication, elevator**

I. INTRODUCTION

In elevator systems, shortening the installation, maintenance and troubleshooting periods is crucial and therefore there are various solutions proposed in the literature covering those subjects [1-3]. At the same time, maintaining a high-quality, high-speed, flexible and reliable communication system for floor fixtures is very essential in application [4, 5]. Considering those points, a non-acknowledged multi-hop wireless network design using the Wireless Short Packet (WSP) protocol to control floor fixtures of elevator is proposed in this paper with the aim of benefiting from low power consumption and reliability of WSP protocol-based devices and taking the advantage of using wireless batteryless hallway call buttons. In the second section, the WSP protocol is introduced. The third section is about multi-hop wireless network architectures that can be used in *N*-floor elevator systems. The network topology and the routing technique proposed are given in the fourth section. Section five describes the experiments performed for the proposed method and displays the experimental results. The advantages and important points of using the proposed method in elevator systems are discussed in the sixth section.

II. WSP PROTOCOL

WSP protocol specifies the first three layers in OSI model. The main idea behind this protocol is keeping the communication as short as possible using Sub-1 GHz frequencies with ASK or FSK modulation to provide good range, and keeping power consumption as low as possible to be able to use energy harvesting technology in designing switches and sensors. Messages in this protocol are called telegrams and each telegram consists of at least three subtelegrams. According to the type of WSP device, there are two mechanisms used to increase the reliability of the connection. The first one is sending the same message three times (three subtelegrams) in as short a time as possible with randomized time in-between. Thus, if one or two messages witnessed a distortion, the possibility of the third message to be received would be much higher. The second mechanism is Listen Before Talk (LBT) technique, where a transceiver does not send any message before ensuring that the channel used is not crowded with same-frequency signals [6].

III. MULTI-HOP WIRELESS NETWORKS

The type of multi-hop wireless networks used to control floor fixtures is the linear one where each point can send a message to the control panel while the points in-between repeat the message sequentially till the message arrives to the control panel. The structure of a linear multi-hop wireless network is given in Figure *1*.

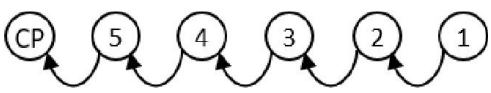


Figure 1: Example for linear multi-hop wireless network structure

In Figure *1*, the time *t* required for one hop between two adjacent nodes is called the hop time that can be determined with

$$t = t_1 + t_2 \quad (1)$$

where t_1 is the processing time and t_2 is the propagation time. Assuming that all hop times are equal, the total hop time, i.e. t_{total}, of a message sent from the first floor to the control panel (CP) is $N * t$ for an *N*-floor elevator.

t_{total} for a message sent from a source point S to CP can be computed with

$$t_{total} = (N - S + 1) * t \quad (2)$$



Figure 2: Example for linear double-jump multi-hop network structure

The linear double-jump multi-hop network displayed in Figure 2 can be another choice where telegrams travel with double jumps to reach the destination instead of making one jump at a time.

In this network, t_{total} can be calculated with

$$t_{total} = \begin{cases} \frac{(N-S+2)*t_1}{2} + \frac{(N-S+1)*t_2}{2}, & (N-S)\ is\ even \\ \frac{(N-S+3)*t_1}{2} + \frac{(N-S+1)*t_2}{2}, & (N-S)\ is\ odd \end{cases} \quad (3)$$

IV. PROPOSED NETWORK TOPOLOGY AND ROUTING TECHNIQUE

The proposed network is a non-acknowledged linear double-jump multi-hop network. The advantages of WSP protocol, i.e. providing transmission of the same message at least three times in a short period of time (approximately from 0.7 ms [7] to 1.2 ms [8] for each subtelegram) and using LBT technique, were the biggest motivation behind adopting the WSP protocol and integrating it to the proposed network. The telegram type used is VLD telegram [9], whose structure is given in Table *1*. VLD telegrams contain a variable payload up to 14 bytes in which different types of designed message can be located. RORG determines the type of telegram, and it is 0xD2 for VLD telegrams. Sender ID contains a 4-byte ID of the sender. Status field is not used in the proposed network, and CRC8 is used to detect transmission errors.

Table 1: VLD telegram structure

RORG	**Payload**	**Sender ID**				**Status**	**CRC8**
0xD2	1..14 bytes	ID_3	ID_2	ID_1	ID_0	1 byte	1 byte

There are four types of messages designed for this network and all of them have the same structure shown in Table 2. Essentially, there are three bytes responsible for the routing information; sender address, hop point address and destination address. Sender address and destination address are fixed for the message while hop point address is changed at every hop point.

Table 2: Message structure

1 byte	1 byte	1 byte	1 byte	x bytes
Sender address	Hop point address	Destination address	Message type	Data

Table 3: Message types

No.	**Message type**
1	MULTIHOP_ROUTING_TABLE_MSG
2	ROUTING_SCREEN_REFRESH_MSG
3	ROUTING_BUTTON_MSG
4	FLOOR_CALL_LAMP_MSG

Four types of messages designed for the proposed network are given in Table 3. The first message type transmits the routing tables for each individual point. The second one, which is a broadcasting message, refreshes the LCDs at each floor. The third one carries a “button is pressed” message to the control panel while the fourth one activates the floor call lamp in case the call button is pressed or deactivates it in case the cabin has reached its destination.

Each point has its individual routing table whose structure is given in Table 4. It includes all the addresses from which messages can be received considering whether the messages are in the upstream direction or in the downstream direction. Downstream route enable field is used to enable some points to re-route messages in the downstream direction which helps decreasing the number of potential telegram collisions as well as the channel traffic.

Table 4: Routing table structure

1 byte	1 byte	1 byte	1 byte	1 byte
Upstream address 1	Upstream address 2	Downstream address 1	Downstream address 2	Downstream route enable

To demonstrate the network on a 5-floor elevator, routes of messages between the control panel and floor units are shown in Figures Figure *3* and Figure *4*. The network has been designed particularly to make the last floor unit participate in each transmission to increase the signal strength between the control panel and the linear multi-hop network, especially if the control panel has been installed far from the embodiment, or in case that flooring between the machine room and the last floor has been made of special materials which may cause attenuation in radio signals. Table 5 shows the static routing tables for each floor unit that must be distributed by the control panel before the network is able to transmit messages. Double jumps help decreasing the number of transmissions, especially for the “refresh screen” type message since it occupies the biggest portion of the network traffic. “Refresh screen” messages are broadcasted by CP and forwarded using just two floor units, i.e. unit 5 and unit 3, as shown in Figure *5*.

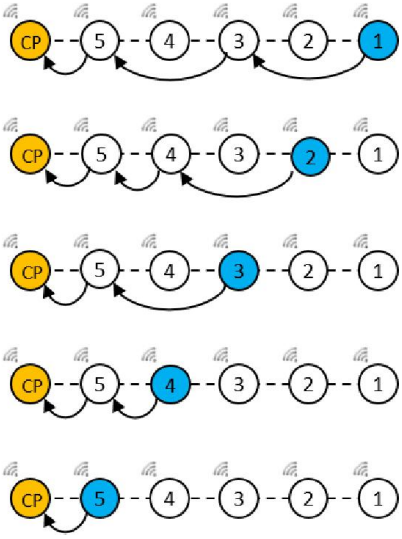


Figure 3: Routes of different messages transmitted from each individual floor unit to control panel

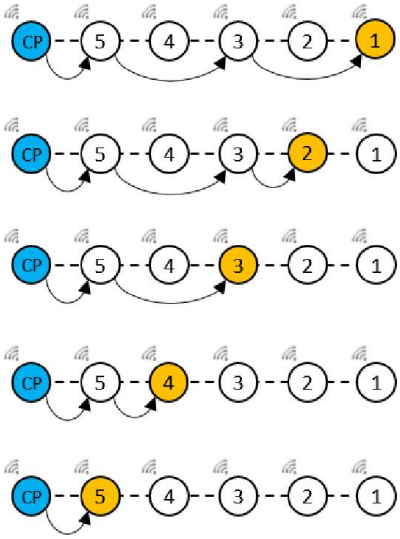


Figure 4: Routes of different messages transmitted from control panel to each individual floor unit

Table 5: Routing tables for each floor unit

Unit No.	Upstream address 1	Upstream address 2	Downstream address 1	Downstream address 2	Downstream route enable
5	3	4	254*	0	1
4	2	0	5	0	0
3	1	0	5	0	1
2	0	0	3	0	0
1	0	0	3	0	0

* Control panel's address

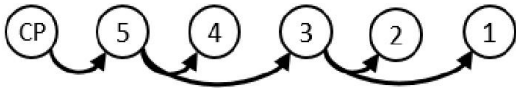


Figure 5: The route of the broadcasting telegram

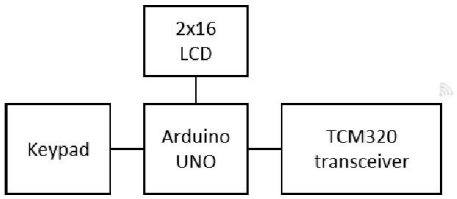


Figure 6: Floor unit

V. EXPERIMENTS

A. *Hardware and Software Integration*

The floor unit consists of four components, i.e. Arduino UNO, TCM320 transceiver, keypad and 2x16 LCD, as shown in Figure 6. TCM320 transceiver is compliant with WSP protocol specifications. Some of its technical data [8] is shown in Table 6. TCM320 module, loaded with Gateway Controller firmware, is driven by Arduino UNO through UART using ESP3 protocol [10]. Two devices have been used to receive the telegrams over a laptop computer. The first one is the USB300 gateway [11], while the second one is the EOP350 development board accompanied with a TCM320 module loaded with DolphinSniffer firmware. Telegrams have been shown and analyzed using DolphinView software [12]. The laptop computer used in experiments has an Intel(R) Core(TM) i5-6200U CPU @2.30 GHz 2.40 GHz microprocessor and the operating system is 64-bit Windows 10.

Table 6: Technical data TCM320

Antenna	8.6 cm whip
Frequency	868 MHz
Modulation	ASK
Receiver Sensitivity	-96 dBm
Data rate	125 kbps
Conducted Output Power at 50 Ω	3 dBm

B. *Hop Time Measurement*

This experiment has been conducted to find the hop time of the network. The experimental setup shown in Figure 7 has been established in the laboratory. Ten

13-byte long telegrams have been sent from unit 1 to CP with a rate of 1 telegram/s. In this case, there are two hops at units 3 and 5. USB300 gateway and DolphinView software have been used to read and analyze all telegrams sent from each individual unit in the network.

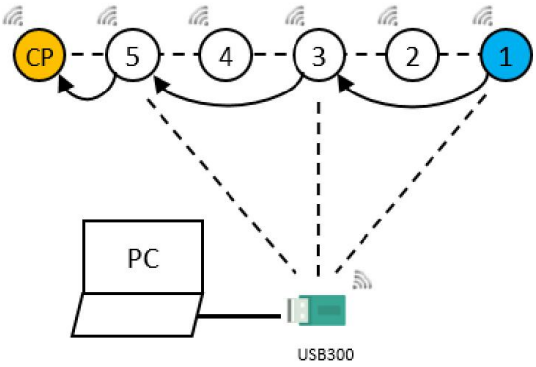


Figure 7: Hop time measurement setup

Taking into consideration that DolphinView software can show the timestamp of each received telegram, first hop time, i.e. the hop time at unit 3, has been computed by subtracting the timestamps of telegrams sent by units 1 and 3. Second hop time, i.e. the hop time at unit 5, has

been computed by subtracting the timestamps of telegrams sent by units 3 and 5. Ten telegrams have been sent to get the average hop time, thus, getting more precise values. The first average hop time and the second average hop time have been determined as 16.1 ms and 17.5 ms, respectively. Measured values are shown in Figures Figure *8* and Figure *9*. The reason behind getting a higher value for the second average hop time with respect to that of the first one is the latency occurred in receiving the second telegram, which is possibly the result of not being able to receive the first subtelegram or busyness of the radio channel causing a delay in sending the subtelegram.

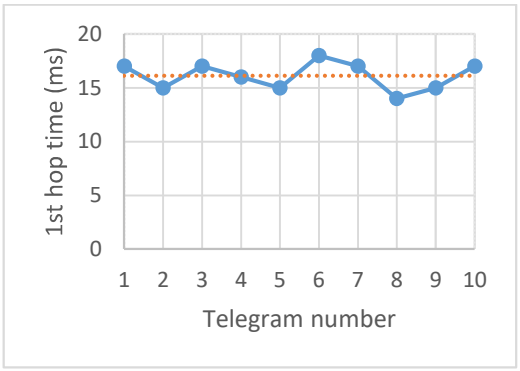


Figure 8: First hop time

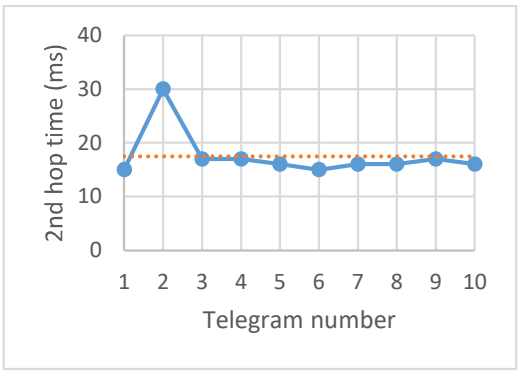


Figure 9: Second hop time

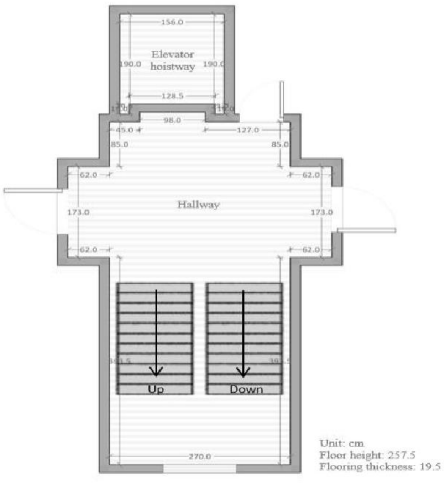


Figure 10: The floor plan of the building where the signal power experiment has been performed

C. *Signal Power Experiment*

This experiment has been conducted in a building having a floor height of 257.5 cm and a flooring thickness of 19.5 cm. The floor plan of the building where the experiment has been performed is shown in Figure 10. At the beginning, a floor unit has been fixed next to the elevator hallway door in the ground floor, and the antenna has been located in a horizontal position. The power of telegrams sent by this unit has been measured at each floor using an EOP350 development board, which is integrated with a TCM320 module loaded with DolphinSniffer firmware. The antenna of TCM320 has been located in a horizontal position and in parallel with that of the fixed floor unit as shown in Figure 11. All telegrams have been received by the laptop computer and analyzed using DolphinView software. To get more precise values, the telegram power at each floor has been measured 5 times and average value has been computed.

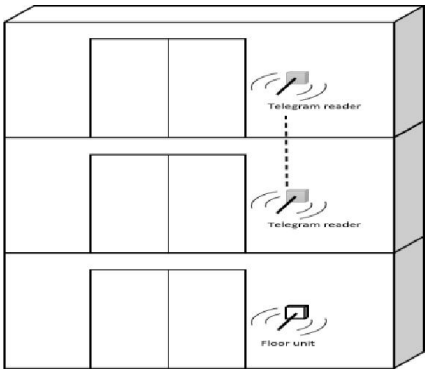


Figure 11: Signal power experimental setup

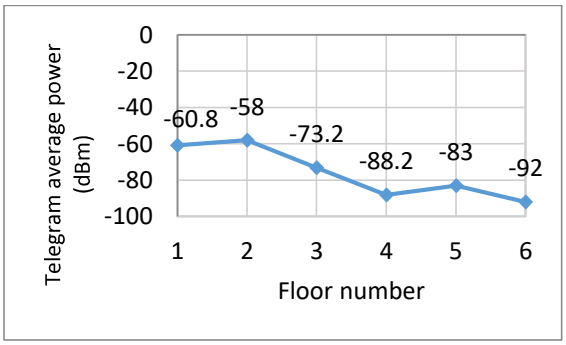


Figure 12: Telegram average power measured at each floor

As given in Figure 12, experimental results show that telegram average power at the second floor is -58 dBm, which is a 38 dBm higher value than the receiver sensitivity of TCM320 module, i.e. -96 dBm. Furthermore, experimental results obtained at each floor up to the sixth one are above the receiver sensitivity limit. This shows the ability of the network to operate not only as a double-jump network but also as a multi-jump network which helps to decrease both telegram collisions and channel traffic. Continuously decreasing telegram power is normally expected as getting far from the ground floor however two exceptional increasing experimental values have been obtained at floors 2 and 5. This is possibly due to the non-homogeneity of flooring and slightly different structural effects.

VI. INSTALLATION AND EVALUATION

Usage of wireless technology and energy harvesting switches has a considerable impact on installation, maintenance and troubleshooting periods of elevator systems. In the proposed method, there is no need to allocate separate cables for data transmission between the control panel and floor fixtures, since data is transferred wirelessly. Thus, the amount of cabling decreases resulting in a subsequent decrease in system complexity and installation costs. Furthermore, usage of energy harvesting switches requiring neither batteries nor power supply cables allows elevator call buttons to be mounted without drilling holes in walls. This has a big importance, especially when walls are coated with ceramic or porcelain avoiding splintering while drilling through tiles. Energy harvesting switches provide a high flexibility by enabling floor call buttons to be mounted on the preferred location, e.g. not only beside elevator hallway doors but also at the building entrance and beside apartment doors. Special buttons can be allocated for workers or VIP people enabling them to call elevator from a distance as shown in Figure 13.

The two mechanisms of WSP protocol, i.e. sending the same message three times in as short a time as possible with randomized time in-between and the LBT technique, help to increase and maintain the reliability of the connection. This gives floor units immunity against the adjacent devices that use the same radio frequency. However, using ASK or FSK modulation demands further caution against the interference resulted from the adjacent surveillances. Mounting floor units outside the elevator shaft helps to prevent the effects of interference occurring due to various reflections caused by elevator rails, cabin and elevator doors. At the same time, it helps to lower the multipath fading and signal cancellation. Furthermore, some additional precautions may be considered like avoiding usage of multiple other devices that use the same radio frequency to enhance the safety conditions. While distributing floor units, spectrum analyzer should be used to analyze the channel and to position floor units in a way that will help lowering the multipath fading and preventing RF signal cancellation and thus getting high quality radio signals.

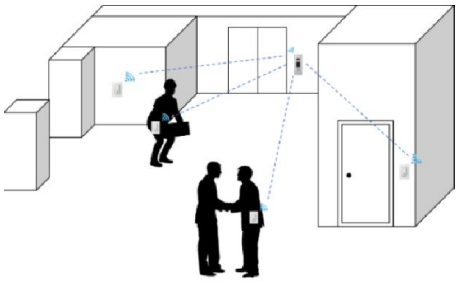


Figure 13: Different possible locations for elevator call buttons using energy harvesting technology

VII. CONCLUSION

WSP protocol has been used to design a non-acknowledged double-jump wireless network to provide data communication between floor fixtures and control panel of an elevator system. The reliability of WSP protocol is provided by iterating each message at least three times within a short period of time, in addition to the usage of LBT technique, which helps to decrease telegram collisions and channel traffic. Experimental average hop time results, i.e. 16.1 ms at the third floor and 17.5 ms at the fifth floor, show that the proposed network is able to operate in low-rise and medium-rise buildings.

Experimental results obtained for telegram average power emphasize that the network can be designed to perform multi jumps instead of double jumps providing a possibility to operate even in high-rise buildings. The results showed that the designed network can be utilized to control the floor fixtures of elevator with high reliability. Since the designed network is dedicated for gathering call button commands and processing data that does not affect the elevator control system, the elevator system is considered completely safe. Should the network have more sensitive data to process, more investigations focusing on attenuation should be performed.

Usage of wireless technology and energy harvesting technology provides the elevator system with high flexibility. Furthermore, it enables integration of the elevator system with home automation and building management systems.

REFERENCES

[1] J. Oh, N. A. M. Hootsmans, "Elevator system with wireless hall call buttons". USA Patent US 20090295550 A1, 3 Dec 2009.

[2] J. Lumme, A. Juntunen, M. Kujala, "Remote controller linkage to an elevator system". USA Patent US 5736692 A, 7 Apr 1998.

[3] Y. Jian and X. Guanghazi, "Wireless processing and design of hall-call communication system of elevator", *Journal of Shenzhen University (Science&Engineering)*, pp. 517-524, 2016.

[4] D. Crenella, M. P. Gozzo, R. R. Grzybowski, J. M. Izard, R. G. Morgan, C. J. Slabinski, "Two-part wireless communications system for elevator hallway fixtures". USA Patent US 6601679 B2, 5 Aug 2003.

[5] N. Motoyama, H. Inaba, A. Kawabata, Y. Ohkura, K. Yamashita, "Elevator system having wireless transmitting/receiving units". USA Patent US6446761 B1, 10 Sep 2002.

[6] *14543-3-10, ISO/IEC DIS, Part 3-10: Wireless Short-Packet (WSP) protocol optimized for energy harvesting — Architecture and lower layer protocols,* 2011.

[7] A. Anders, *Pushbutton Transmitter Device PTM 200 User Manual V1.1,* Germany: © EnOcean GmbH, 2005.

[8] *TCM 300/ TCM 320 (868 MHz), TCM 300U / TCM 320U (902 MHz) Transceiver Module USER MANUAL,* Germany: © EnOcean GmbH, 2016.

[9] *EnOcean Equipment Profiles (EEP) Version: 2.6.3,* USA: © EnOcean Alliance, 2015.

[10] *EnOcean Serial Protocol 3 (ESP3) V1.30,* Germany: © EnOcean GmbH, 2016.

[11] *USB 300 / USB 300C / USB 300U (OEM) USB Gateway for EnOcean Radio V1.5,* Germany: © EnOcean GmbH, 2013.

[12] *EDK 350 (868 MHz) EDK 350U (902 MHz) EnOcean Developer Kit V2.3,* Germany: ©EnOcean GmbH, 2015.

High Efficiency Design and Simulation of a Front End AC-DC PFC Converter for EV Battery Charger

S.CETIN[1] and N. YILDIZ[2]

[1] Pamukkale University, Denizli/Turkey, scetin@pau.edu.tr
[2] Enko Electronics, İzmir/Turkey, nazimyildiz90@gmail.com

***Abstract* – In this study, high efficiency design consideration of a front-end AC-DC Power Factor Correction (PFC) converter that utilizes silicon carbide power devices for Electrical Vehicle (EV) Battery Charger is presented. In order to obtain high efficiency, critical design parameters are extracted taking into consideration the loss distribution of the converter at universal line voltage range, 85-265 V_{RMS}. Then, a simulation study is presented to validate operation of the converter with extracted design parameters. Simulation study is performed with 2.5 kW output power and 400 V output voltage at 85-265 V_{RMSs}. Finally, loss and efficiency values obtained by simulation and analytically are compared and a good match is obtained.**

***Keywords* – Front-end boost converter, high efficiency design, EV battery charger.**

I. INTRODUCTION

THE use of electrical vehicle (EV) rises rapidly because of global warming, benefits in the economic area and depletion of fossil fuels. Therefore, performance improvements of EV are required to increase demands over internal combustion engines. On-board EV battery chargers allow flexibility to end user to charge EV's battery from any available power outlet. However, they bring extra volume and weight to total volume of EV. Thus, the cost of EV can be increased and its performance can be reduced. Therefore, studies on on-board EV battery chargers are focused on increasing power density and reducing weight [1].

The on-board battery charger composed of two paper stages. Front end AC-DC converter with Power Factor Correction (PFC) function is usually used at the first stage of an EV battery charger [1]-[9]. This architecture eliminates the high and low frequency ripple charging the battery without using a bulk filter capacitor [6]. The front end AC-DC converter used in this work is a conventional boost topology [10]-[11]. To keep conduction loss low at high power level continuous conduction mode (CCM) operation of boost converter is preferred. The second stage of battery charger is a dc-dc converter regulating the battery charge voltage [6]-[9]. This work is focused on the first stage of an on-board battery charger.

Silicon Carbide (SiC) power devices have many advantages over Si technology. The high breakdown electric field of SiC allows low tur-on resistance compared to Si devices [12]. The active area that current is flowing is reduced in SiC technology, this results in decreased device capacitance and operation at high switching frequencies [13]. Besides, SiC technology allows operation at high temperatures and they are more reliable at a wide range of temperatures [14]. The high switching operation capability of SiC device at high power level is presented in [15] and their high temperature operation capability is given in [16]. These advantages of SiC technology improves the converter's power density and efficiency at high power levels compared to Si technology [1], [17].

In this paper, high efficiency design procedure of a front end AC-DC converter utilizing SiC power devices is presented for the first stage of an on-board EV battery charger. The operation of the converter is tested by simulation at universal input, 85-265 V_{RMS}, and with 2.5 kW output power and 400 V output voltage. The calculated efficiency values are obtained as 90.88% and 91.03% as theoretical while the line voltage is 85 V_{RMSs} and 265 V_{RMS}.

II. LOSS ANALYSIS OF A FRONT-END AC-DC PFC CONVERTER

A front end AC-DC converter topology is shown in Figure 1. Here, L_B is the boost inductor, S_B is the boost MOSFET, D_B is the boost diode, D_{SB} is the antiparallel diode of S_B, C_o is the output filter capacitor, v_o is the output voltage, v_i is the rectified input voltage, R_o is the load resistor, v_{ac} is the line voltage, i_{ac} is the line current, i_o is the output current and i_i represents the current of boost inductor.

The converter follows the rectified input voltage to produce the output voltage. The duty cycle of S_B is varied to produce sine wave input current that is matching the line voltage, v_{ac}.

The total loss of the converter composed of diode bridge losses, boost inductor losses, boost diode losses, boost MOSFET's losses and the dielectric loss of the filter capacitor.

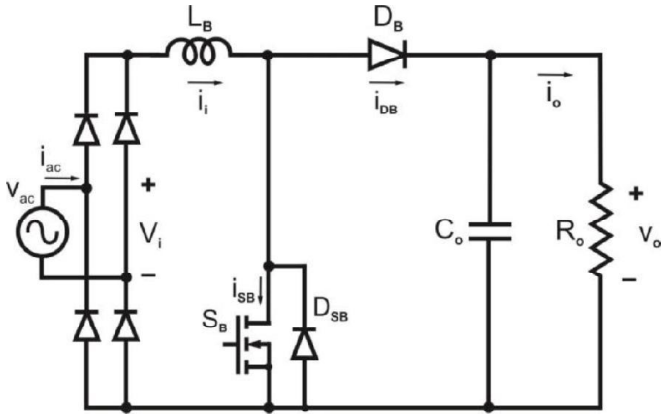


Figure 1. The circuit schematic of front-end AC-DC PFC converter.

A. Diode Bridge Losses:

Diode bridge from Crydom M5060 is used for the rectifier stage. Thus, the conduction losses of the diode bridge can be calculated as follows:

$$P_{Bridge} = 2 \times I_{LB-Avg} \times V_F \,. \quad (1)$$

Above, $I_{LB\text{-}Avg}$ is the average current of L_B inductor in one half of line period, V_F is the drop voltage of a diode in diode bridge package.

B. Boost Inductor Losses:

Boost inductor is determined as homemade. Boost inductor losses include conduction loss and core loss due to inductor current variation. The conduction loss can be calculated by

$$P_{Cond.-LB} = I_{LB-RMS}{}^2 \times R_{LB} \,. \quad (2)$$

Above, $I_{LB\text{-}RMS}$ is the root mean square (RMS) value of the inductor current, R_{LB} is the resistance of the boost inductor. The core losses can be extracted with help of datasheet of core material.

C. Boost Diode Losses:

Boost diode is selected as schottky Silicon Carbide (SiC) diode from Cree as C5D50065D. Boost diode losses are composed of conduction loss and reverse recovery loss. The conduction losses can be written as

$$P_{Cond.-DB} = I_{DB-AVG} \times V_{F-DB} + I_{DB-RMS}{}^2 \times R_t \,. \quad (3)$$

Where, $I_{DB\text{-}AVG}$ is the average value of the boost diode, $V_{F\text{-}DB}$ is the drop voltage of the boost diode, $I_{DB\text{-}RMS}$ is the RMS value of the boost diode current and R_t is the internal resistance of the boost diode.

The reverse recovery loss can be calculated as follows:

$$P_{SW-DB} = 0.5 \times V_o \times Q_C \times f_{SW} \,. \quad (4)$$

Where, f_{SW} is the switching frequency, Qc is the stored charge in junction layers of the boost diode.

D. Boost MOSFET's Losses:

The boost MOSFET is selected as SiC form Cree as C2M0040120D. MOSFET losses are composed of the conduction loss, switching loss and the gate drive loss. The conduction loss can be written as

$$P_{Cond.-SB} = i_{SB-RMS}{}^2 \times R_{DS-on} \,. \quad (5)$$

Above, $i_{SB\text{-}RMS}$ is the RMS value of MOSFET current and $R_{DS\text{-}on}$ is the turn-on resistance of the S_B MOSFET.
The switching losses can be calculated by

$$P_{SW-SB} = 0.5 \times V_o \times I_{LB-AVG} \times (t_{on} + t_{off}) f_{SW} \,. \quad (6)$$

Above, t_{on} is the turn-on transition time of S_B and the t_{off} is the turn-off transition time of S_B. The gate drive loss can be written as

$$P_{Drive-SB} = V_g \times Q_g \times f_{SW} \,. \quad (7)$$

Where V_g is the gate drive voltage, Qg is the gate charge.

E. Dielectric Losses of Filter Capacitor:

The dielectric losses of the filter capacitor can be calculated as follows:

$$P_{Co} = I_{Co-RMS}{}^2 \times ESR \quad (8)$$

Where, $I_{Co\text{-}RMS}$ is the RMS value of the capacitor current and ESR is the equivalent series resistor of the capacitor.

III. Design Procedure

The design of the circuit includes power stage design and control circuit design.

In the power stage, L_B boost inductor is designed to operate in CCM and to provide PFC according to following equation. Where D is the maximum operated duty at low line voltage $V_{ac(min)}$ and ΔI is the inductor ripple current.

$$L_B = \frac{V_{ac(min)}.D}{f_s.\Delta I} \quad (9)$$

The peak line current is obtained at low line and it can be written as

$$I_{ac(pk)} = \frac{2.P_o}{\sqrt{2}.V_{ac(min)}} \,. \quad (10)$$

The acceptable ripple current can be selected as 20%. The filter capacitor C_o can be calculated based on output voltage ripple, output power and hold-up time requirement.

The peak voltage of the boost MOSFET and boost diode is limited by the output voltage. The peak current of the boost MOSFET equal to $I_{ac(pk)}$.

For the controller design, the average current mode control method is selected. The switching control signals are produced with required control block diagrams in simulation.

Based on determined design parameters given in Table 1, efficiency values are obtained as given in Table 2 for universal

line voltage range. The calculated efficiency and simulated efficiency values are good match with each other.

Table 1: Determined Design parameters of front end AC-DC converter

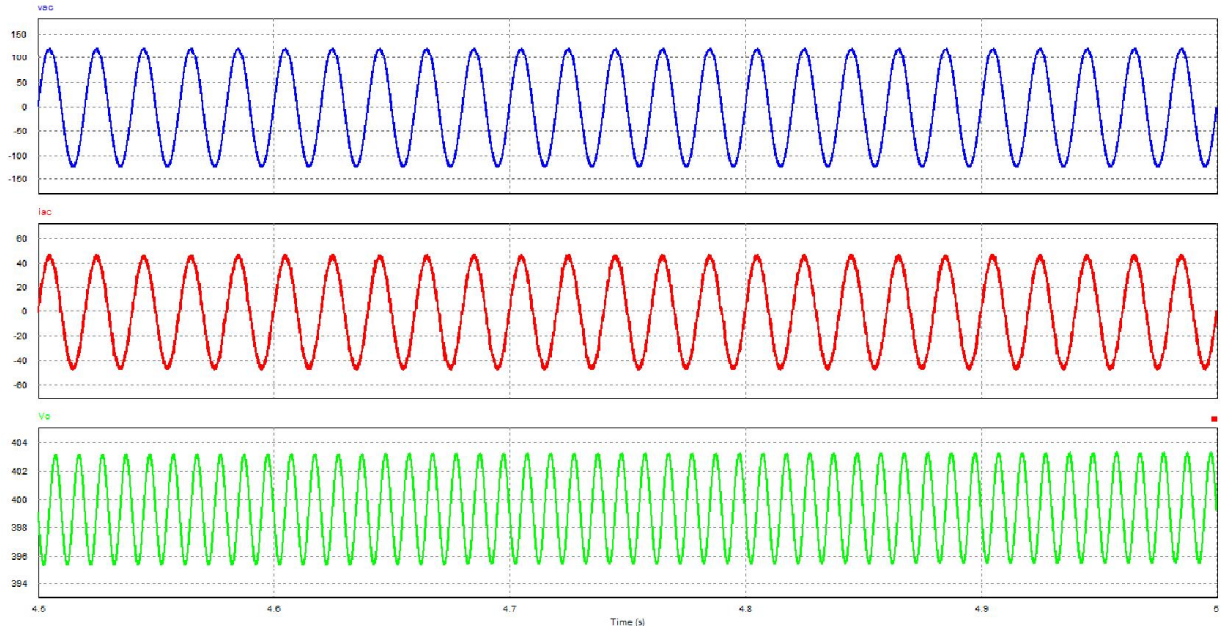
Po=2.5 kW, V_o=400V, V_{in}=85-265 V_{RMS}	
L_B	54 µH
C_o	820 µF
R_o	64 Ω
S_B	SiC C2M0040120D
D_B	SiC C5D50065D

Table 2: The obtained efficiency values for universal line range

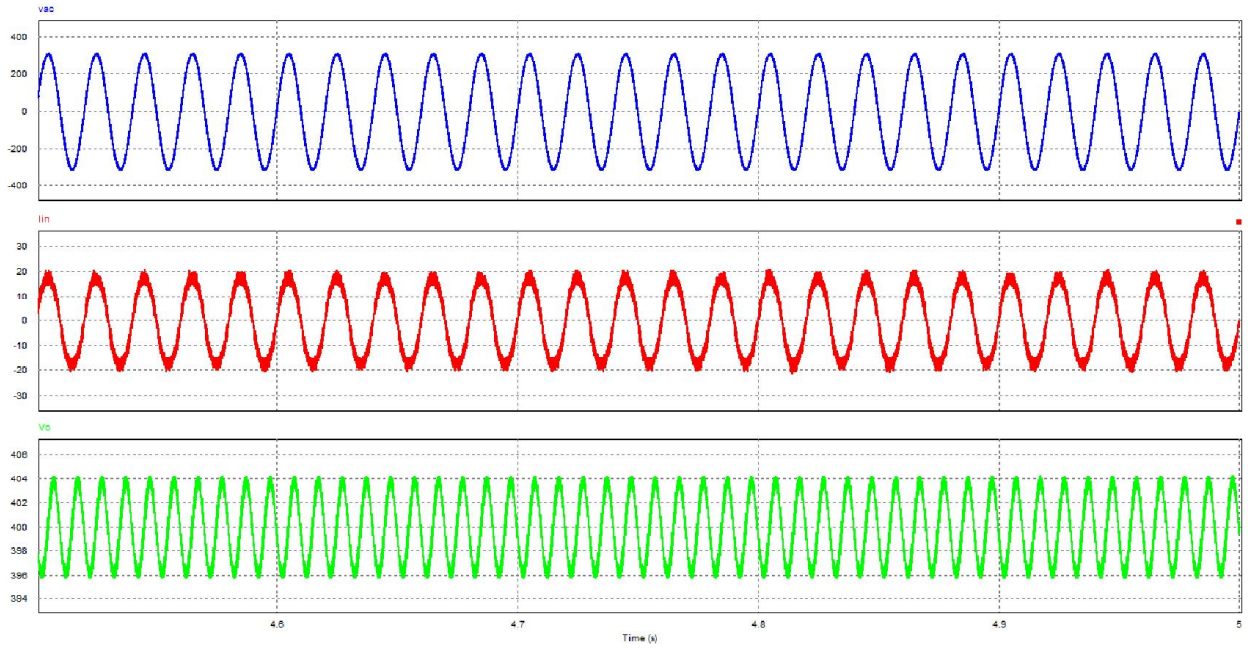
The input voltage (RMS)	Calculated Efficiency (%)	Simulated Efficiency (%)
85	90.88	91.03
220	96.57	96.76
265	97.03	97.45

IV. Simulation Study

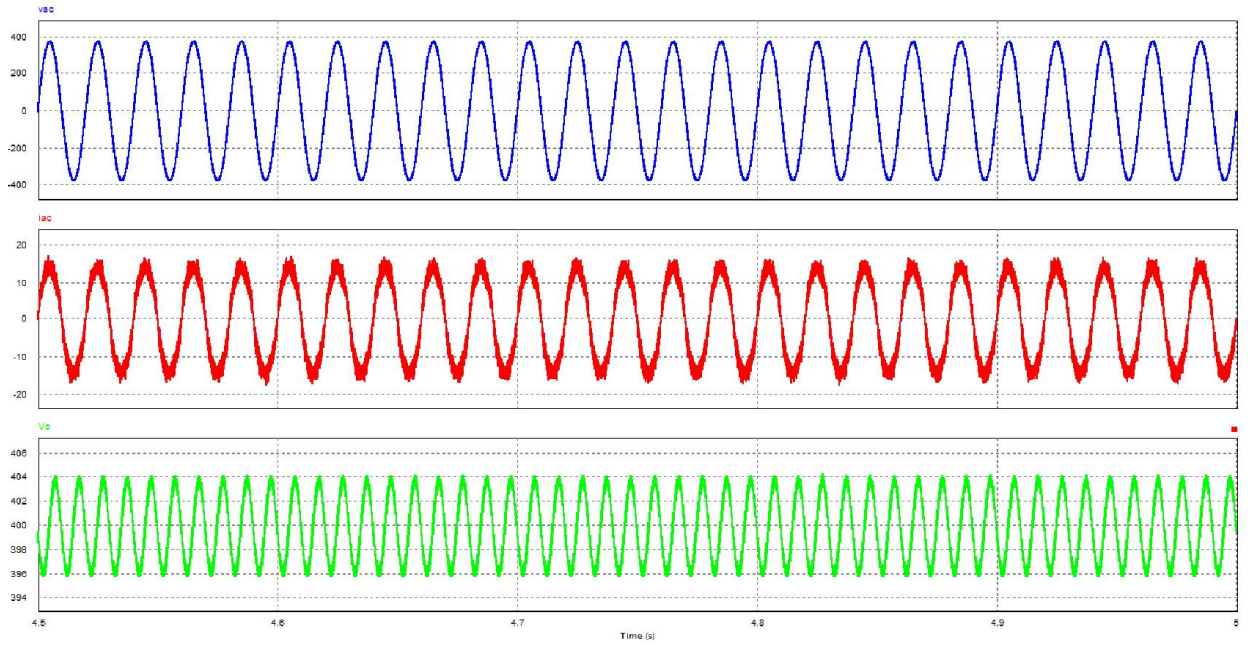
The simulation of front-end AC-DC converter is performed with 2.5 kW output power, 400 V output voltage for 85-265 V_{RMS} line voltage. The obtained waveforms for 85-265 V_{RMS} is given in Figure 2. Figure 2 (a) shows line voltage, v_{ac}, line current, i_{ac}, and the output voltage, v_o for 85 V_{RMS}. Figure 2 (b) shows line voltage, v_{ac}, line current, i_{ac}, and the output voltage, v_o for 220 V_{RMS}. Figure 2 (c) shows line voltage, v_{ac}, line current, i_{ac}, and the output voltage, v_o for 265 V_{RMS}.



(a)



(b)



(c)

Figure 2. Simulated waveforms: v_{ac} (blue), i_{ac} (red), v_o (green).

I. Conclusion

This paper presents a front end AC-DC PFC converter for the first stage of an on-board EV battery charger. The loss analysis and the design parameters of the converter is evaluated based on high efficiency. A simulation study is performed for 2.5 kW output power and 400 V output voltage when the input voltage varied between 85 V_{RMS} and 265 V_{RMS}. According to obtained design parameters, an efficiency comparison between calculation and simulation is done and obtained results are found in good match. The maximum efficiency is calculated as 97.03% at 265 V_{RMS} line voltage.

Acknowledgment

This work is supported by TUBITAK under grant number of 116E125.

References

[1] B. Whitaker, A. Barkley, Z. Cole, B. Passmore, D. Martin, T.R. McNutt, A.B. Lostetter, J.S. Lee, K. Shiozaki, "A high-density, high-efficiency, isolated on-board vehicle battery charger utilizing silicon carbide power devices," IEEE Transactions on Power Electronics, vol. 29, pp. 2606-2617, January 2014.

[2] M. Yilmaz, P.T. Krein, "Review of battery charger topologies, charging power levels, and infrastructure for plug-in electric and hybrid vehicles," IEEE Transactions on Power Electronics, vol. 28, pp. 2151-2169, May 2013.
[3] M. Grenier, M.H. Aghdam, T. Thiringer, "Design of on-board charger for plug-in hybrid electric vehicle," In Proc. Power Electronics, Machine and Drives, Brighton, England, 19-21 April 2010.
[4] S. Haghbin, K. Khan, S. Lundmark, M. Alakula, O. Carlson, M. Leksell, O. Wallmark, "Integrated chargers for EV's and PHEV's: examples and new solutions," In Proc. Int. Conf. Electrical Machines, Rome, Italy, 6-8 September 2010.
[5] A. Emadi, Y.J. Lee, K. Rajashekara, "Power electronics and motor drives in electric, hybrid electric, and plug-in hybrid electric vehicles," IEEE Trans. Ind. Appl., vol. 55, pp. 2237–2245, June 2008.
[6] F. Musavi, M. Craciun, D.S. Gautam, W. Eberle, W.A. Dunford, "An LLC resonant DC–DC converter for wide output voltage range battery charging applications," IEEE Trans. on Power Electronics, vol. 28, pp. 5437-5445, March 2013.
[7] J. Deng, S. Li, S. Hu, C.C Mi, R. Ma, "Design methodology of LLC resonant converters for electric vehicle battery chargers," IEEE Trans. On Vehicular Technology, vol. 63, pp. 1581-1592, May 2014.
[8] Z. Fang, T. Cai, S. Duan, C. Chen, "Optimal design methodology for LLC resonant converter in battery charging applications based on time-weighted average efficiency," IEEE Trans. On Power Electronics, vol. 30, pp.5469-5483, May 2015.
[9] Y. S. Dow, H. H. Kim, Y. I. Kwon, B. Y. Kim, J. C. Kim, "A study of 6.6kW on board charger for electric vehicle,", In Proc International Electric Vehicle Symposium and Exhibition, Kintex, South Korea, 3-6 May 2015.
[10] B. Lu, W. Dong, S. Wang, and F. C. Lee, "High frequency investigation of single-switch CCM power factor correction converter," in Proc. IEEE Appl. Power Electron. Conf. Expo., 2004, vol. 3, pp. 1481–1487.
[11] L. Yang, B. Lu, W. Dong, Z. Lu, M. Xu, F. C. Lee, and W. G. Odendaal, "Modeling and characterization of a 1KW CCM PFC converter for conductedEMIprediction,"inProc.IEEEAppl.PowerElectron.Conf.Expo., 2004, vol. 2, pp. 763–769.
[12] A. R. Hefner, R. Singh, J. S. Lai, D. W. Berning, S. Bouche, and C. Chapuy, "SiC power diodes provide breakthrough performance for a wide range of applications," IEEE Trans. Power Electron., vol. 16, no. 2, pp. 273–280, Mar. 2001.
[13] A. M. Abou-Alfotouh, A. V. Radun, H. Chang, and C. Winterhalter, "A 1-MHz hard-switched silicon carbide DC–DC converter," IEEE Trans. Power. Electron., vol. 21, no. 4, pp. 880–889, Jul. 2006.
[14] J. L. Hudgins, G. S. Simin, E. Santi, and M. A. Khan, "An assessment of wide bandgap semiconductors for power devices," IEEE Trans. Power Electron, vol. 18, no. 3, pp. 907–914, May 2003.
[15] H.Sheng,Z. Chen,F. Wang,andA. Millner, "Investigationof1.2 kVSiC MOSFET for high frequency high power applications," in Proc. Appl. Power Electron. Conf. Expo. (APEC), 2010, pp. 1572–1577.
[16] T. Funaki, J. C. Balda, J. Junghans, A. S. Kashyap, H. A. Mantooth, F.Barlow,T.Kimoto,andT.Hikihara,"PowerconversionwithSiCdevices at extremely high ambient temperatures," IEEE Trans. Power Electron., vol. 22, no. 4, pp. 1321–1329, Jul. 2007.
[17] H. Zhang, L. M. Tolbert, and B. Ozpineci, "Impact of SiC devices on hybrid electric and plug-in hybrid electric vehicles," IEEE Trans. Ind. Appl., vol. 47, no. 2, pp. 912–921, Mar./Apr. 2011.

The Effect of the Number of Blades on Electrical Energy Production System by Using a Vertical Barrel from Wind Energy

R. G. YILDIRIM[1] and Ahmed A. AL-HASHMAWI[2]

[1]Gaziantep University Gaziantep/Turkey, ozkan@gantep.edu.tr
[2]Gaziantep University Gaziantep/Turkey, ahmadabdlazez@gmail.com

***Abstract* - Worldwide interest in renewable energy systems has increased dramatically, due to environmental concerns like climate change and other factors. Wind power is a major source of sustainable energy, and can be harvested using both horizontal and vertical axis wind turbines. This work presents studies of a vertical axis wind turbine performance for applications in urban areas. In this project, experimental comparison and investigations were carried out to study the performance and to make a comparison between two and five blade rotor wind turbine. For this purpose, two models of two and five blades from traditional barrel were designed and manufactured. These two models were tested and investigated under the normal climate conditions of the Turkish city of Gaziantep. Both models have a self-start at low wind speeds of 20 RPM at 2 m/s wind velocity. It was observed from the measured and calculated results that the two blade rotor wind turbines is more efficient, it has a higher power coefficient under the same test condition than that of five blade rotor wind turbine. The reason is that increasing the number of blades will increase the drag surfaces against the wind air flow and causes to increase the reverse torque and leads to decrease the net torque working on the blades of a rotor wind turbine.**

***Key Words*: Vertical axis wind turbine, savonius, electric power, voltage.**

I. INTRODUCTION

TRADITIONAL energy has become expensive and an environmental hazard, therefore; it is necessary to find an alternative energy source from renewable energy sources to reduce the high usage of fossil fuels and also to reduce the damage caused by CO2 emissions. A lot of countries have gone to find new energy sources to escape the escalating disadvantages of fossil fuels and to improve alternative clean energy sources more than ever before. Wind energy is a good source of renewable energy, because of its availability throughout the year; it is also considered pollution free to the environment.

Turkey is one of the countries that tries hard to develop renewable energy sources, especially after the expansion of the Turkish economy in recent years, which led to increasing in the consumption of primary energy. Over the last 10 years a rise in the share of energy production has been seen from renewable sources [1].

Despite of the rapid increase in the use of wind as a source of electricity in the world, it is still limited to meet the needs of energy, whereas only a few regions is using it. In more than 80 countries, commercial wind turbines activities have seen widespread at the end of 2015. There are also 26 countries with more than 1 GW output, according to one of the reports. Wind energy has generated electrical power more than any other technology in 2015. Turkey is expected to add more than 4.7 GW by the end of 2015. China has added new capabilities, which alone represent nearly half of the world's additions. By the end of 2015, Denmark, Sweden, Germany, Ireland and Spain are among the leading countries of total wind power per capita [2].

At 2011, the capacity of wind power plants reached 1.729 GW in Turkey and it will reach 20 GW in 2023 according to the general wind energy policy of Turkey [3].

Wind energy was used in the distant past to provide mechanical energy such as pumping water and grinding grain. After the oil price shock in 1970, the world's population need to consume more electricity and the lack of possibility to generate in some places because of the scarcity of resources such as fossil fuels, wind power has returned to the surface again to generate electricity rather than mechanical energy [4].

In some places, especially the urban cities, there's a small wind turbine that meets the limited needs. This made everyone have the ability to make such turbines and access renewable sources easily. Where there is a classification based on the capacity produced and different sizes such as utility-scale, it is a large turbine with a capacity of 900 kW to 3 MW, industrial-scale, ranging from 50 kW to 250 kW with a medium size and residential-scale, its capacity ranges from 400 watts to approximately 50 kW with a small size turbines [5].

The basic principle of wind turbine work is to convert wind energy into mechanical energy and then convert mechanical energy to electricity [6].

There is a good efficiency of both horizontal (HAWT) and vertical (VAWT) axis wind turbines. But the (HAWT)

efficiency is better than the (VAWT) and therefore it's the most widespread in the world [7].

The main objective of this research is to study the aerodynamics characteristics for two Savonius wind turbine models and to study the two models efficiency in the electrical power generating to contribute in enhancing the performance of these two models. To achieve these goals the following arrangement must be done:

1. Designing and manufacturing two and five blades Savonius wind turbine models.
2. Calculating the speed of wind blowing on the blade, also measuring rotational speed of the turbine.
3. Calculating both voltage and electrical current that generated from the generator for obtaining value electrical power
4. Calculating both power coefficient and tip speed ratio by mathematical equations to compare them with experimental results.

A statement of the problem is the increase in negative effect of fossil fuels on the environment has forced many countries including Turkey to use renewable energy sources. Today clean domestic and renewable energy is commonly accepted as the key for future life, not for Turkey just but also for the world. As wind energy is an alternative clean energy source compared to the fossil fuels that pollute the atmosphere, systems that convert wind energy to electricity have developed rapidly.

A variable rotor with two or three or four blades was studied, with single steps and double steps, with end plates and without end plates, and overlapping ratios from 0 to 0.35 with side ratios of 0.5, 1, 2, 4 and 5. All of these elements are experimentally tested to find the optimal designs of the Savonius turbines. The results showed that the two-blade rotor is more efficient than the three-and-four blades, as well as double steps have better performance than single steps. The rotors with the end plate gave better efficiency than the rotor with no end plates. The rotors without the overlay ratio are better than rotors that have an overlay. The power factor also increases with at the highest aspect ratio (α) [8].

Experiments have been conducted by varying the number of blades from two to three in single-, two- and three-stage rotor systems. Both semicircular and twisted-bladed rotors have been tested, It is observed that the power coefficient of the rotor decreases when the number of blades got increased from two to three. Hence, with an increase of the number of blades, the rotor performance decreases. It can be concluded from the experimental evidence that a two-bladed system gives optimum performance [9]

By taking a Savonius turbine for two and three blades it was concluded that the power coefficient for both two and three blades savonius wind turbine, it appears that the power coefficient for two blades has a noticeable increasing value than the three blades. It appears that the two blade savonius wind turbines has its highest value of (0.21) at the tip speed ratio of (0.8), the three blades have a value of (0.17) at the tip speed ratio of (0.8) [10].

II. EXPERIMENTAL WORK

Vertical wind turbines do not depend on the direction of the wind, furthermore, it is known for its easy design, cheap cost and without the need of elevated places because it's operating well at low grounds, even in low winds, therefore; it's suitable for urban areas, on the other hand it is considered a low energy producing comparing with their eternal traditional competitor horizontal axis wind turbine type (HAWT). The turbine Savonius used in this experimental work is made using a barrel for two models:

- **Model one**: An empty oil barrel of 58 cm diameter was used in this study, five openings were made on the sides of the barrel working as blades, the blades were bent with an equal angles of (72º), the length of the turbine is 77.5 cm, the radius is 42 cm, the overall diameter 84 cm and the thickness is 1.33 mm, as shown in Figure 1.
- **Model two**: Take the barrel again and cut it into two halves to get two blades at equal angles 180º, the radius of the turbine is 51 cm, height 77.5 cm, the overall diameter rotor 102 cm and the thickness is 1.33 mm, as shown in Figure 2.



Figure 1: The model one of turbine Savonius.



Figure 2: The model two of turbine Savonius.

Mechanical system: is consisting of several parts, their main function is to convert wind energy to mechanical energy, the mechanical parts will be discussed in details as follows below:

- To both it a pulley of 58 cm diameter was placed at the bottom of the barrel to be in a straight line with the pulley attached at the alternator, also a (V-shaped) belt was used to connect between the two mentioned pulleys, this belt shall be the link between the mechanical and the electrical systems
- A steel shaft of 7 cm diameter was used to support the turbine, the shaft length is 290 cm with also considered as the turbine height. The turbine's barrel was placed on the upper part and the lower end of the shaft was fixed to a cylindrical base. A circular steel base of a diameter of 100 cm was used to support the turbine, the heavy weight of the steel base helped to maintain the turbine balance, also it gave the turbine more safety against the axial movement. Also additional weight was placed on the circular base to give more stability

Electrical system: is consisting of several parts, their main function is to convert the mechanical energy to electrical energy, the electrical parts will be discussed in details as follows below:

- Generator: In order to convert the mechanical energy that generates from the wind turbine rotation to electrical energy, a generator connected to the rotor shaft. The generator used in this study can generate DC and AC electricity. It's better to use the DC machines with small applications and an AC machine with large applications. The important thing for wind turbine applications is the right choice for an electric generator that suitable for needs. Factors to consider in choosing the generator are the source and type of load and the speed of the wind turbine. A washing machine motor with a (1500 RPM/min, 50 Hz), modifications were made to convert it to a permanent magnetic generator consisting of 2 and 4 Neodymium magnet, and also a pulley of 5 cm diameter was attached to the generator. Such generators don't need a gear-box which is blamable for noise and maintenance, so permanent generators are more efficient and reliable than induction generators. That's the most important reason why they are used in small applications.

Test Set-up

After searching for a suitable place inside the Gaziantep university perimeters, the suggestion was set on placing the turbine on the roof of Seyirtepe Restaurant, which located on the higher position in the university territories. The roof of the restaurant was well known of the obstacles emptiness in four directions which helped in obtaining wind current perfectly from all directions.

After choosing the suitable place, the turbine was moved from the physics laboratory- Gaziantep University to the restaurant roof as shown in Figure 3.



Figure 3 Turbine location.

Mathematical Expressions

Through the calculation of the data for the two models in this work it is necessary to perform the analysis to compare the performance of the models with the other studies. Non-dimensional coefficients are used for comparison to other similar study and authentication of the experiment. Two of these universally used non-dimensional objects are considered for this study. The power coefficient represents the energy conversion efficiency of the turbines as well as

the tip speed ratio represents the ratio of the blade tip speed to the free stream wind speed [11].
Through the equations to be listed below, we can calculate the power coefficient and find the value of the tip speed ratio across a set of different wind speed for each rotary design with two blades and five blades
The swept area of a wind turbine can get it from the dimensions of the rotor, as shown in Figure 4.

$$A = H.D \quad (1)$$

Where A The swept area, H is rotor height (m) and D the rotor diameter (m).

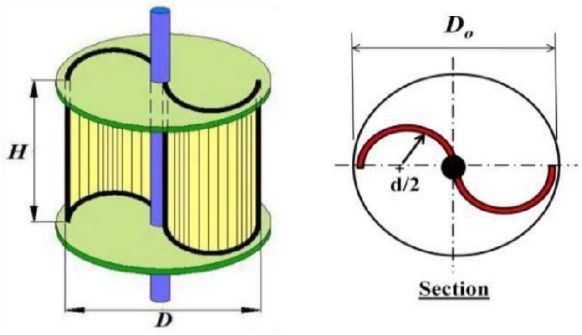


Figure 4 Schematic diagram of rotor wind turbine. [10]

The actual available power from the wind is:

$$P_a=1/2\ \rho A v^3 \quad (2)$$

Where ρ air density (kg/m^3) And v wind speeds (m/s).
The electrical power produced from the generator is:

$$P_e=I.V \quad (3)$$

Where I electric current and V voltage.

The power coefficient (Cp) is assumed by

$$C_p=P_e/P_a \quad (4)$$

The angular velocity of the rotor is:

$$\omega=2\pi N/60 \quad (5)$$

Where ω angular velocity (rad⁄sec), N rotational speed (RPM).
The tip speed ratio (λ) given by:

$$\lambda=\omega d/v \quad (6)$$

Where d is the diameter of the blade (m).

III. RESULTS AND DISCUSSION

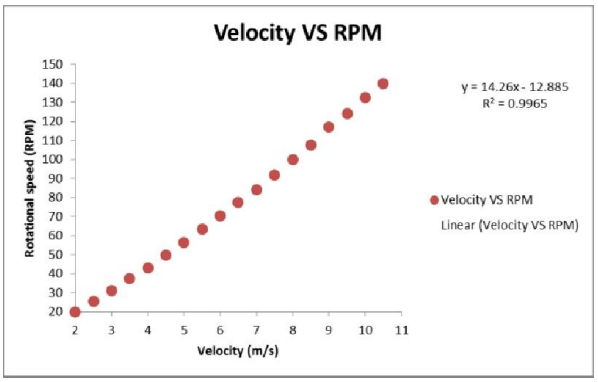


Figure 5: Relation between velocity and rotation speed of five blade rotor.

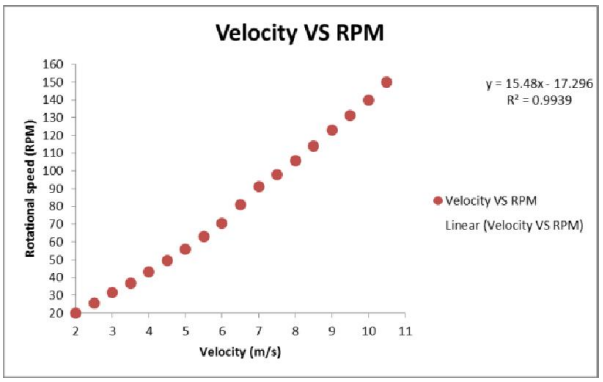


Figure 6: Relation between velocity and rotation speed of two blade rotor.

From the graph as shown in figures 5 and 6 display the relationship between the speed of rotation and wind speed ranging from(0 to 10.5) m/s for both models. Note that both models have the same the best self-starting 20 RPM at 2 m/s wind velocity, but the graph shows that the two-blade model has the highest rotational value of 150 RPM while the five blades up to 140 RPM. This is due to the increase in the number of blades leads to an increase in the number of convex surfaces that negatively affect the strength of clouds, which leads to the disruption of the speed of circulation and this affects the actual performance of the turbine.

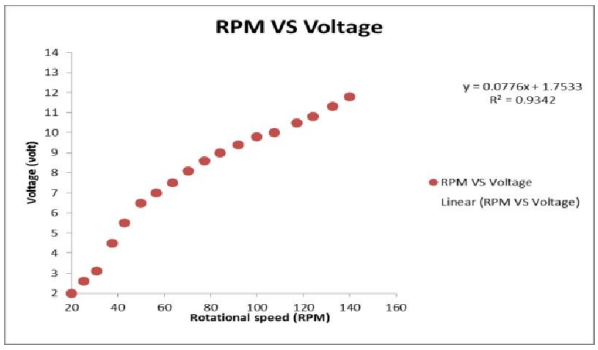


Figure 7: Relation between rotational speed and voltage of five blade rotor

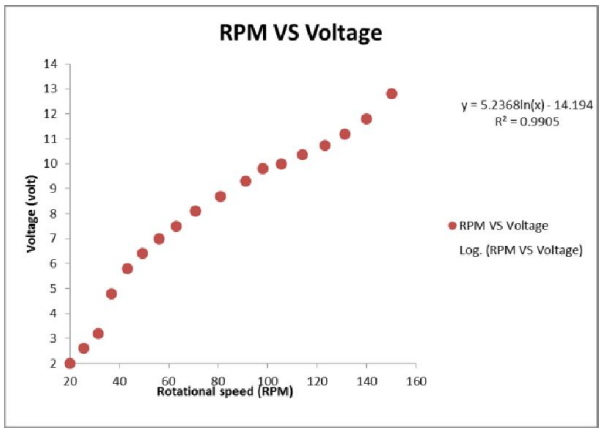


Figure 8: Relation between rotational speed and voltage of two blade rotor.

Through the graph showing the relationship between the speed of rotation and the voltage to both models as shown in figures 7 and 8. Note that the highest value of the rotational speed of 150 RPM for the two-blade model generated (12.8 volts), while the five-blade model at the highest speed of rotation 140 RPM generates (11.8 volts), at the same wind speed 10.5 m/s. This is because the ability of the two-blade model to rotate more than five blades leading to an increase in the number of generator cycles responsible for generating this voltage.

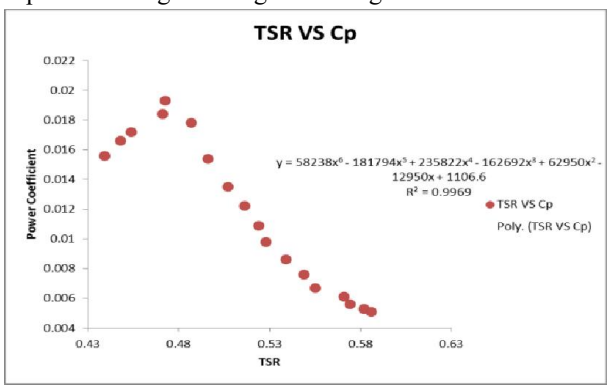


Figure 9: Relation between TSR and power coefficient of five blade rotor.

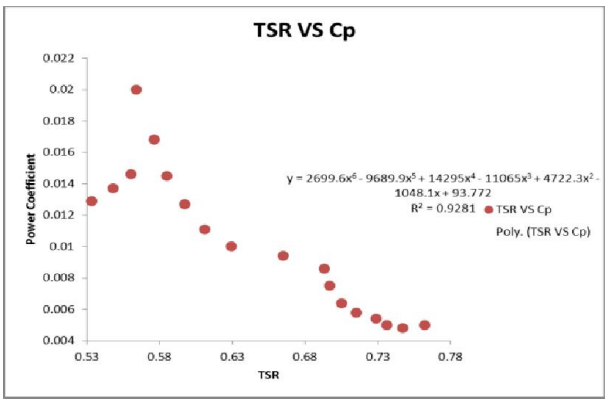


Figure 10: Relation between TSR and power coefficient of two blade rotor.

Figures 9 and 10 appear the relationship between the power coefficient, which done calculated by using equation (4) and the tip speed ratio that production from the equation (6) of the rotor made from the conventional barrel by changing the number of blades between two blades and five blades to investigating performance of each model by using the same material of hardness, thickness, alternator and load. The two-blade rotor showed the maximum power coefficient (0.02) at the tip speed ratio of (0.564) while the five-blade rotor reaches the maximum power coefficient (0.0193) at the tip speed ratio (0.472) (see Table1 and Table2). Indicating that the two-blade rotor has better efficiency than the corresponding model in this work.

I. CONCLUSION

This research investigates the performance of vertical axis wind turbine models based on the drag force under normal climatic conditions from wind speed, temperature and pressure. Two models with different number blade were used to determine the effect of changing the number of blades on performance it. It has the same material, hardness, thickness, turbine height, end plates, electric generator and load. The first model is made of a traditional barrel containing five blades of the amount of angle between it 70° while the second model contains two blades the amount of angle between it 180°. Performance coefficients for both models were determined under variable wind speed for every 5 minutes at 12 hours per day.

1) Rotor with two blades up to 150 RPM at 10.5 m/s while the five blades up to 140 RPM for the same wind speed.
2) The two blade rotor has power coefficient highest value of (0.02) at the tip speed ratio of (0.564), the five blades have a value of (0.0193) at the tip speed ratio of (0.472), this means that the two-blade rotor has better performance than the five-blade rotor.
3) The two-blade rotor generated (12.8) volts, while the five-blade rotor generates (11.8) volts, at the same wind speed 10.5 m/s. This is because the ability of the two-blade model to rotate more than five blades leading to an increase in the number of generators rotate responsible for generating this voltage.

REFERENCES

[1] Nalan, Ç. B., Murat, Ö., and Nuri, Ö., "Renewable energy market conditions and barriers in Turkey.," Renewable and Sustainable Energy Reviews, vol. 16, no. 3, pp. 1428-1436, 2009.

[2] Turkish Wind Energy Association (TWEA). (2017, march) The Wind Power, wind energy market intelligence. [Online]. http://www.thewindpower.net/

[3] Yaniktepe, B., Savrun, M. M., and Koroglu, T., "Current status of wind energy and wind energy policy in Turkey," Energy Conversion and Management, vol. 72, pp. 103-110, 2013.
[4] T. (Ed.) Ackermann, Wind power in power systems. Stockholm, Sweden: John Wiley & Sons., 2005.
[5] V. Petitfils, Setup and performance test of a small-scale vertical axis wind turbine.: Lund University, 2011.
[6] Kishore, Ravi Anant, Thibaud Coudron, and Shashank, "Small-scale wind energy portable turbine (SWEPT)," Journal of Wind Engineering and Industrial Aerodynamics, vol. 116, pp. 21-31, 2013.
[7] I Paraschivoiu, Wind turbine design: with emphasis on Darrieus concept. montreal/canada: Presses inter Polytechnique, 2002.
[8] Mahmoud, N. H., El-Haroun, A. A., Wahba, E., and N, "An experimental study on improvement of Savonius rotor performance," Alexandria Engineering Journal, vol. 51, no. 1, pp. 19-25, 2012.
[9] U. K., Thotla, S., and Maity, D Saha, "Optimum design configuration of Savonius rotor through wind tunnel experiments," Journal of Wind Engineering and Industrial Aerodynamics, vol. 96, no. 8, pp. 1359-1375, 2008.
[10] Mohammed Hadi Ali, "Experimental comparison study for Savonius wind turbine of two & three blades at low wind speed," International Journal of Modern Engineering Research (IJMER) , vol. 3, no. 5, pp. 2978-2986, 2013.
[11] MacPhee, D., and Beyene, A, "Recent advances in rotor design of vertical axis wind turbines," Wind Engineering, vol. 36, no. 6, pp. 647-665, 2012.

Distributed LMP Algorithm for Frequency Estimation over a Network

H. ZAYYANI[1] and A. SHADEMANFAR[2]

[1] Qom University of Technology (QUT), Qom/Iran, zayyani@qut.ac.ir
[2] Pooyesh University of Qom, Qom/Iran, en.alishademan@gmail.com

***Abstract* - This paper investigates the frequency estimation problem in a wireless sensor network. Frequency estimation is an important problem in signal processing where numerous algorithms are devised to estimate the frequency using a single sensor. In this paper, we want to estimate the common frequency of a distributed signal over a network. We suggest using a distributed Least Mean P-norm (LMP) algorithm for distributed frequency estimation in a network. The benefit of the proposed algorithm is that in addition to frequency, it can estimate the amplitude and phase of a sinusoidal signal as well. Simulation results show the effectiveness of the proposed algorithm in comparison to the non-distributed and one distributed notch filter-based algorithm in the literature.**

***Keywords* - Frequency estimation, distributed algorithm, wireless sensor network, Least mean p-norm, signal processing.**

I. INTRODUCTION

THIS paper investigates the frequency estimation problem in a distributed network. Frequency estimation is an important signal processing task which has applications in Doppler frequency estimation in radar, frequency monitoring of a power system, and frequency analysis in speech processing. Many algorithms are developed for frequency estimation via a single sensor which some of them are Discrete Fourier Transform (DFT) method [1], Least Mean Squares (LMS) [2], Weighted LS (WLS) [3], modified LMS [4], wavelet transform [5], Phase Lock Loop (PLL) [6], zero-crossing [7], and Kalman filter [8].

Wireless sensor network is widely used in monitoring applications [9]. Frequency estimation can be employed in a network of agents. Several agents of a network may observe a sinusoidal signal with a common frequency. They can cooperatively estimate the frequency of the system. There are three strategies for distributed estimation in a network which are incremental, consensus and diffusion [10]. Incremental strategy is sensitive to sensor failure. Moreover, it is reported that diffusion strategy outperforms consensus in adaptive networks [11]. Therefore, we focus on diffusion strategy in this paper. There are some diffusion algorithms in the literature which [12-15] are a few of them.

Distributed frequency estimation over a network is done in some recent papers [16-17]. In [16], a distributed notch filter-based algorithm is used for frequency estimation. Moreover, a distributed widely Kalman filtering approach is used for solving the problem in [17].

In this paper, a distributed LMP is suggested for distributed frequency estimation. The benefit of the proposed method is that it enables us to estimate the amplitude and the phase of the sinusoidal signal as well as frequency parameter. In this proposed algorithm, based on defining suitable local and global cost functions, a distributed diffusion algorithm is employed to estimate the common frequency of several sinusoidal signals over a network of sensors. Simulation results show the efficiency of the proposed algorithm for frequency estimation especially in low Signal to Noise Ratio (SNR). It also has less complexity than the distributed notch filter-based algorithm which uses extra notch filter to eliminate the center frequency of the sinusoid.

The outline of the paper is as follows. Section 2 is the problem formulation section. In section 3, a review of distributed estimation with the emphasis of frequency estimation is presented. Then, section 4 introduces the proposed distributed LMP algorithm. Simulation results are given in section 5. Finally, section 6 concludes the paper.

II. PROBLEM FORMULATION

Consider a sensor network of N sensors. Each node observes a sinusoidal signal which is:

$$X_k[i] = A_k \cos(\omega_0 iT + \varphi_k) + v_k[i] \quad (1)$$

where k is the index of the node, ω_0 is the common angular frequency, T is the sampling interval, A_k is the amplitude and φ_k is the initial phase of the signal. The problem is to estimate the common frequency ω_0 from all the observed signals from all the sensors of the network in a distributed manner. As we will see, in the proposed method of this paper, we will estimate the amplitude and initial phase as well as the frequency.

III. REVIEW OF DISTRIBUTED FREQUENCY ESTIMATION

A. Distributed estimation

Distributed estimation is an important topic in signal processing in the last decade [10-15]. In this field, an unknown vector is to be estimated from linear measurements of several sensors over a network. The ultimate goal is that all the

sensors in the network cooperatively and distributedly estimate the unknown vector.

There are different strategies for cooperation of nodes in a network. The first one is an incremental strategy in which the sensors in a cycle, hand in estimates serially to the adjacent sensor. After coming back the estimate to the first node in a cycle, the estimate is regarded as final estimation of this approach for the first data received in the network. This would continue at other time instants. This strategy is sensitive to sensor failure and often is not used in the practice. The second strategy is the consensus strategy in which the sensors simultaneously update the estimate based on minimizing a cost function and combine the estimates from neighborhood sensors. In the third strategy which is diffusion, the estimates are firstly updated based on minimizing a cost function. This step is called adaptation. Then, in the combination step, the estimates are combined from neighborhood of a sensor to form an improved estimate. This version of diffusion is called Adapt-Then-Combine (ATC) approach. There is another version of diffusion which is Combine-Then-Adapt (CTA). It is reported that the diffusion strategy outperforms consensus strategy in adaptive networks [18]. Therefore, in this paper, we focus on the diffusion strategy of course for the distributed frequency estimation.

Among the various diffusion algorithms [12-15], the diffusion LMS algorithm is the most widely used algorithm [12-14]. It uses a least mean square cost function to update the estimates. In [15], a least mean p-power is suggested for defining the cost function.

B. Distributed frequency estimation

In [16], a distributed notch filter-based algorithm is used for frequency estimation. Since, we compare our results to this approach; we discuss this approach in some detail. In this mentioned paper, a notch filter is used. The relation between the input and output of the notch filter is:

$$\begin{aligned} Y_k[i] &= -\rho a Y_k[i-1] - \rho^2 Y_k[i-2] \\ &\quad + X_k[i] + a X_k[i-1] + X_k[i-2] \end{aligned} \tag{1}$$

where $X_k[i]$, $Y_k[i]$ are input signal and output signal at k'th node, $a = -2\cos(\omega_0 T)$ and $\rho < 1$ are two parameters of the notch filter in which ω_0 is the center angular frequency of the notch filter and T is the sampling interval. The main idea of distributed notch filter-based algorithm is that the parameters of the notch filter are learned so that the output signal of the notch filter would be near zero. In that case, the center frequency of the filter is equal to the frequency of the signal. For being near zero, the algorithm uses the Mean Square Error (MSE) of the output signal. Then, using this cost function, the parameter a is estimated distributedly via a diffusion method. Hence, the final ATC diffusion algorithm is a two step algorithm as follows:

$$\varphi_{k,i+1} = a_{k,i} - 2\mu Y_k[i](-\rho Y_k[i-1] + X_k[i-1]) \tag{2}$$

$$a_{k,i+1} = \sum_{l \in N_k} c_{lk} \varphi_{l,i+1} \tag{3}$$

where μ is the step-size of the algorithm, c_{lk} is the combination coefficients of the network [10], and $\varphi_{k,i+1}$ is the intermediate estimation of parameter a. Then, the frequency of the input signal is estimate with the following formula:

$$\hat{\omega}_{k,i+1} = \frac{1}{T}\arccos\left(-\frac{\varphi_{k,i+1}}{2}\right) \tag{4}$$

The other method for distributed frequency estimation is the distributed widely linear Kalman filtering approach [17]. To best of our knowledge, there is no other distributed frequency estimation algorithm in the literature.

IV. The Proposed Distributed LMP Algorithm

In the proposed method, to estimate the parameters of the sinusoidal signal, we use the mean p-power or mean p-norm of the error signal as the cost function. Therefore, the local cost function at node k is defined as:

$$J_k^{loc}(\omega) = \sum_{l \in N_k} c_{lk} E\{|e_l[i]|^p\} \tag{5}$$

where we have:

$$e_l[i] = X_l[i] - \hat{A}_{l,i}\cos(\hat{\omega}_{l,i} iT + \hat{\varphi}_{l,i}) \tag{6}$$

where $X_l[i] = A_l \cos(\omega_0 iT + \varphi_l) + v_l[i]$, and $\hat{A}_{l,i}$, $\hat{\omega}_{l,i}$, $\hat{\varphi}_{l,i}$ are amplitude, frequency and phase estimates at l'th sensor at time index i. To update the parameter estimates, an steepest-descent can be used. The steepest-descent recursions are:

$$\hat{A}_{k,i+1} = \hat{A}_{k,i} - \mu_A \nabla_{\hat{A}_{k,i}}(J_k^{loc}(\omega)) \tag{7}$$

$$\hat{\varphi}_{k,i+1} = \hat{\varphi}_{k,i} - \mu_\varphi \nabla_{\hat{\varphi}_{k,i}}(J_k^{loc}(\omega)) \tag{8}$$

$$\hat{\omega}_{k,i+1} = \hat{\omega}_{k,i} - \mu_\omega \nabla_{\hat{\omega}_{k,i}}(J_k^{loc}(\omega)) \tag{9}$$

where μ_A, μ_φ and μ_ω are step-size of amplitude, phase and frequency, respectively. Smaller of the step size means the less final error and lower convergence rate. The gradients of the p norm of the error with respect to parameters are as follows:

$$\nabla_{\hat{A}_{l,i}}(|e_l[i]|^p) = p.sign(e_l[i])\,|e_l[i]|^{p-1}\,\nabla_{\hat{A}_{l,i}}(e_l[i]) \tag{10}$$

$$\nabla_{\hat{\varphi}_{l,i}}(|e_l[i]|^p) = p.sign(e_l[i])\,|e_l[i]|^{p-1}\,\nabla_{\hat{\varphi}_{l,i}}(e_l[i]) \tag{11}$$

$$\nabla_{\hat{\omega}_{l,i}}(|e_l[i]|^p) = p.sign(e_l[i])\,|e_l[i]|^{p-1}\,\nabla_{\hat{\omega}_{l,i}}(e_l[i]) \tag{12}$$

Where the gradients of the error signal with respect to the parameters are:

$$\nabla_{\hat{A}_{l,i}}(e_l[i]) = \cos(\hat{\omega}_{l,i} iT + \hat{\varphi}_{l,i}) \tag{13}$$

$$\nabla_{\hat{\varphi}_{l,i}}(e_l[i]) = \hat{A}_{l,i}\sin(\hat{\omega}_{l,i} iT + \hat{\varphi}_{l,i}) \tag{14}$$

$$\nabla_{\hat{\omega}_{l,i}}(e_l[i]) = \hat{A}_{l,i} iT \sin(\hat{\omega}_{l,i} iT + \hat{\varphi}_{l,i}) \tag{15}$$

Based on the update formulas in (7)-(9), the estimates are updated at each sensor in the adaptation step. For the combination step, the estimate of the common frequency is

combined with the following formula:

$$\hat{\omega}_{k,i+1} = \sum_{l \in N_k} c_{lk} \hat{\omega}_{l,i} \quad (16)$$

Hence, the overall algorithm is a two step ATC diffusion algorithm. The steps are:

1) Adaptation step: Adapt the parameters from (7), (8) and (9) using the relations in (10)-(15).

2) Combination step: Combine the frequency estimates from (16) to obtain a better estimate of frequency.

V. Simulation Results

This section presents the simulation results. Two experiments are performed to evaluate the performance of the proposed algorithm. The proposed algorithm is simulated with $p = 2$ and $p = 4$. The first is usually known as LMS while the second is Least Mean Fourth (LMF). In the simulations, the proposed algorithms which are nominated as distributed LMS and distributed LMP, are compared with some single sensor methods like Maximum likelihood (ML), DFT, and single sensor LMP, and distributed notch filter-based algorithm. All simulations are done with MATLAB and the sampling frequency is chosen as 500 Hz. In all simulations, we use a fully connected network with five sensors which is depicted in Figure 1. The number of Monte Carlo runs of the simulations is 100 and the results are averaged over 100 independent runs. For the performance metric, the Mean Square Error (MSE) of the frequency is used which is defined as:

$$MSE = \frac{1}{K} \sum_{k=1}^{K} (f_0 - \hat{f}_0)^2 \quad (17)$$

where $K = 100$ is the number of Monte Carlo simulations. The frequency of the sinusoids is selected as $f_0 = 50$ Hz and the initial estimate of the frequency is set to be 49Hz. In all experiments, the step sizes are selected in such a way that the algorithms are converged in 700 iterations.

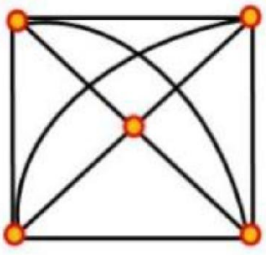


Figure 1: The fully connected network used in the simulations.

A. Experiment 1:

In this experiment, The Gaussian noise is considered. The variance of the zero mean Gaussian noise is assumed to be $\sigma^2 = 0.1$. To have different Signal to Noise Ratio (SNR), we use different amplitudes. The SNR are defined as:

$$SNR = 10 \log_{10}\left(\frac{A^2}{2\sigma^2}\right) \quad (18)$$

The figures (2) and (3) show the results of the first experiment. Figure (2) shows the transient convergence of the frequency estimates to the final value which is $f_0 = 50Hz$. In figure (2), the MSE of various algorithms is shown with respect to SNR. The proposed algorithms which are distributed LMS (with label dLMS) and distributed LMP (with label dLMP) are compared with the distributed notch filter-based algorithm (with label dNF), single sensor LMS (with label LMS), single sensor LMP (with label LMP) and DFT. Figure (3) illustrates that in the low SNRs (below 17dB), the best algorithm is the distributed LMS (distributed LMP with $p = 2$).

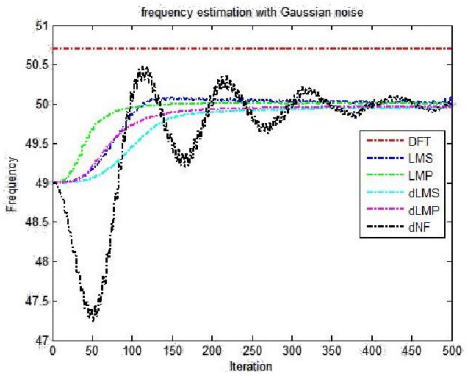


Figure 2: The fully connected network used in the simulations.

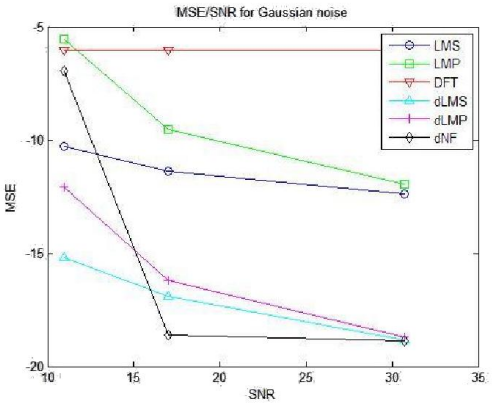


Figure 3: The fully connected network used in the simulations.

B. Experiment 2:

In this experiment, impulse noise is considered. The impulse noise assumed to be Bernoulli-Gaussian (BG) $v_k[i] = a_k[i]s_k[i]$, where $s_k[i] = 0,1$ is a Bernoulli random variable with probability $p(s_k[i] = 1) = p$ and $p(s_k[i] = 0) = 1 - p$, and the amplitude $a_k[i]$ is Gaussian with zero mean and variance σ^2. It is assumed that 10 percent of coefficients are active (non zero). So, we have $p = 0.1$ and active coefficients are Gaussian with zero mean and unit

variance ($\sigma^2 = 1$). Figure (4) and (5) show the results of the second experiment. In Figure (3), the transient response of the frequency estimate is shown. Figure (5) shows the MSE versus SNR for various algorithms. It shows that the best algorithm in low SNRs(less than 27dB) is the LMS algorithm.

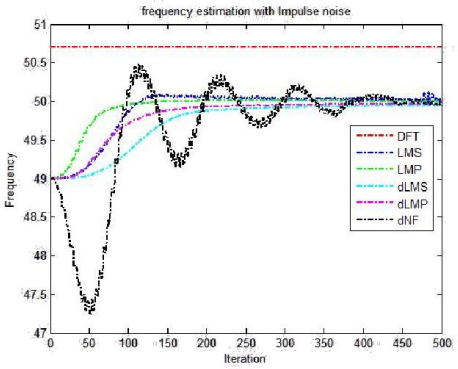


Figure 4: The fully connected network used in the simulations.

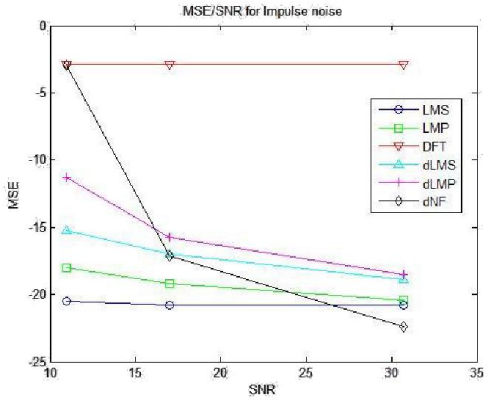


Figure 5: The fully connected network used in the simulations.

At last, we emphasize that the proposed method can estimate all the parameters of the sinusoidal signal while for example distributed notch filter-based algorithm can only estimate the frequency. Moreover, the proposed algorithm needs not an extra notch filter for filtering the sinusoidal signal.

VI. Conclusion

A distributed LMP approach is presented for estimating all the parameters of a sinusoidal signal over a network. Simulation results show the better performance of the proposed distributed LMP algorithm for $p = 2$, which is actually distributed LMS and here for the first time is used for distributed frequency estimation, especially in low SNRs and in the Gaussian noise case. Especially, simulation results show that distributed LMS ($p = 2$) is better than distributed LMF ($p = 4$) for distributed frequency estimation. In addition, the complexity of the proposed method is less than distributed notch filter-based algorithm which has an extra notch filter.

References

[1] C. Candan, "A Method For Fine Resolution Frequency Estimation From Three DFT Samples," IEEE signal processing letters, Vol. 18, No. 6, pp.351-354, June 2011.

[2] A. K. Pradhan, A. Routray, A. Basak, "Power System Frequency Estimation Using Least Mean Square Technique," IEEE Transactions On Power Delivery, Vol.20, No.3, pp.1812-1816, July 2005.

[3] M. D. Kušljevic, J. J. Tomi´c, L. D. Jovanovic, "Frequency Estimation of Three-Phase Power System Using Weighted-Least-Square Algorithm and Adaptive FIR Filtering, " IEEE Transactions on Instrumentation and Measurement, Vol. 59, No. 2, pp.322-329, February 2010.

[4] H. Zayyani, S. M. Dehghan, "frequency estimation of unbalanced three-phase power system using a new LMS algorithm," Iranian Journal Of Electrical & Electronic Engineering, Vol.11, No.1, pp.71-78, March2015.

[5] J. Ren, M. Kezunovic, "Real-Time Power System Frequency and Phasors Estimation Using Recursive Wavelet Transform, " IEEE Transactions On Power Delivery, Vol. 26, No. 3, pp.1392-1402, July 2011.

[6] P. Rodríguez, J. Pou, J. Bergas, "Decoupled Double Synchronous Reference Frame PLL for Power Converters Control," IEEE Transactions On Power Electronics, Vol. 22, No. 2, pp.584-592, March 2007.

[7] B. Milenko, R. Zeljko, "Frequency measurement of distorted signals using fourier and zero crossing techniqyes," Elsevier Electric Power Systems Research, pp.1407-1415, 2008.

[8] P. K. Dash, R. K. Jena, G. Panda, "An Extended Complex Kalman Filter for Frequency Measurement of Distorted Signals," IEEE Transactions On Instrumentation And Measurement, Vol. 49, No. 4, pp.746-753, August 2000.

[9] M. Melemary, M. Ibrahim, S. Ramakrishnan, "Wireless sensor network from theory to application," November 16, 2016 by CRC Press Taylor & Francis Group.

[10] A. H. Sayed, "Adaptive networks," Proceedings Of The IEEE, Vol.102, No.4, pp.460–497, April 2014.

[11] S. Y. Tu, A. H. Sayed, "Diffusion strategies outperforms Consensus strategies for distributed estimation," IEEE Tran. Signal Process., Vol.60, No.12, pp.6217-6234, Dec 2012.

[12] F. S. Cativelli, A. H. Sayed, "Diffusion LMS strategies for distributed estimation," IEEE Tran. Signal Process., Vol.58, No.3, pp.6217-6234, March 2010.

[13] Y. Liu, C. Li, Z. Zhang., "Diffusion sparse least mean squares over networks," IEEE Tran. Signal Process., Vol. 60, No.8, pp.4480-4485, August 2012.

[14] R. Arablouei, S. Werner, Y. F. Huang., K. Dogancay., "Distributed least mean square estimation with partial diffusion," IEEE Tran. Signal Process., Vol. 62, No.2, pp.472-484, Jan 2014.

[15] F. Wen, "Diffusion least mean p-power algorithms for distributed estimation in alpha-stable noise environments," Electronics Letters, Vol. 125, No.1, pp.122-123, July 2013.

[16] C. Li, H. Wang, "Distributed Frequency Estimation Over Sensor Network," IEEE Sensors Journal, Vol.15, No.7, pp.3973-3983, July 2015.

[17] S. Kanna, D. Dini, H. Dahir, Y. Xia, S. Y. Hui, D. P. Mandic, "Distributed Widely Linear Kalman Filtering for Frequency Estimation in Power Networks," IEEE Transactions On Signal And Information Processing Over Networks, Vol.1, No.1, pp.45-57, March2015.

High Gain Observer for Sensorless Input Output Linearizing Control for Induction Motor with Broken Rotor Bar Fault

I. HARZELLI[1], A. MENACER[1], Y. MAANANI[1] and T. AMEID[1]

[1] Biskra University, Biskra/Algeria, imadeddineharzelli@yahoo.fr
[1] Biskra University, Biskra/Algeria, menacer_arezki@hotmail.com
[1] Biskra University, Biskra/Algeria, yacine.maanani@gmail.com
[1] Biskra University, Biskra/Algeria, tarek-gnr@hotmail.fr

***Abstract* - This paper presents a modelling and a fault diagnosis of broken rotor bars in induction motor (IM) at closed loop for a sensorless nonlinear control (NLC). The strategy of control is based on the input output linearization control, using nonlinear high gain observer (HGO) in order to preserve the speed regulation and compensate the fault effect and to ensure the service continuity of the machine. The effect of the broken rotor bar is evaluated through the analysis of the direct stator current components I_{ds}. This information can be used as an indication for the fault diagnosis.**

***Keywords* - Induction motor, fault diagnosis, broken rotor bars, nonlinear control, input output linearization control, high gain observer.**

I. Introduction

The induction motor (IM) is known for its robustness, simplicity of operation and low costs and maintenance free. In a hand, like any motor exposed to mechanical or electrodynamic forces, it is lead to failures [1], and may be caused by manufacturing fault, designing fault of the engineer, environment and poor technical knowledge of the job about in handling the motor [2].

On the other hand, vector control provides good performance during transient and permanent phases. However, it requires knowledge of mechanical speed and rotor flux [3]. The difficulties of using field oriented control (FOC) arise from the modeling uncertainties due to parameter variation, magnetic saturation and load disturbances. To ensure good dynamic performance various robust control strategies for induction motor drives have been cited in the literature [4, 5]. However, the input output linearization control has focused attention owing to simple design, the perfect decoupling between the rotor speed and the flux, fast dynamic response, easy implementation and robustness to parameter variations, and also for load disturbances [6, 7].

Fault detection in electrical machines has been the subject of researches for many years [8]. Vibration is used for the detection of mechanical problems, broken rotor bars and stator short circuits in induction motor. Vibration analysis are usually installed on costly and sensitive machines, where the cost of such system can be justified [9]. That is why some researchers are looking to analyze other quantities in order to solve this problem. In [10, 11] d (direct) current axis components have been looked in closed loop. The rotor speed and the rotor flux are estimated by high gain observer (HGO) [12, 13]. The controller is based on the theory of feedback linearization. Where the reduced model of IM in healthy and faulty states is used.

This paper is organized as follows. In section 2, the dynamic of the reduced model of IM is described. The input output linearization control is designed for speed and flux magnitude controls of an IM are showed in section 3. The HGO required for rotor flux and rotor speed estimation are presented in section 4. Section 5, provides numerical simulation results of the proposed control technique in healthy and faulty states of the IM, followed by the conclusion.

II. Mathematical Induction Motors Model With Broken Rotor Bars Fault

The dynamic equations of IM can be expressed as follows [14]:

$$[L]\frac{d[I]}{dt} = [V] - [R][I] \quad (1)$$

With

$$[L] = \begin{bmatrix} L_{sc} & 0 & -\frac{N_r}{2}M_{sr} & 0 & 0 \\ 0 & L_{sc} & 0 & -\frac{N_r}{2}M_{sr} & 0 \\ -\frac{3}{2}M_{sr} & 0 & L_{rc} & 0 & 0 \\ 0 & -\frac{3}{2}M_{sr} & 0 & L_{rc} & 0 \\ 0 & 0 & 0 & 0 & L_e \end{bmatrix}$$

And

$$[R] = \begin{bmatrix} R_s & -\omega_r L_{sc} & 0 & \frac{N_r}{2}\omega_r M_{sr} & 0 \\ \omega_r L_{sc} & R_s & -\frac{N_r}{2}\omega_r M_{sr} & 0 & 0 \\ 0 & 0 & \left[R_{rdd} \quad R_{rdq}\right] & & 0 \\ 0 & 0 & \left[R_{rqd} \quad R_{rqq}\right] & & 0 \\ 0 & 0 & 0 & 0 & R_e \end{bmatrix}$$

Where

$$L_{rc} = L_{rp} - M_{rr} + 2\frac{L_e}{N_r} + 2L_e(1 - \cos\alpha)$$

$$R_r = \frac{2R_e}{N_r} + 2R_b(1 - \cos\alpha)$$

$\alpha = p\frac{2\pi}{N_r}$: Electrical angle of two rotor adjacent meshes.

The four terms are:

$$\begin{cases} R_{rdd,rqq} = R_r + \frac{2}{N_r}(1-\cos\alpha)\sum_k R_{bfk}\left(1 \pm \cos(2k-1)\alpha\right) \\ R_{rdq,rqd} = -\frac{2}{N_r}(1-\cos\alpha)\sum_k R_{bfk}\sin(2k-1)\alpha \end{cases} \quad (2)$$

In this expression (2), the summation is applied to all bars with fault. R_{bfk} is the increased resistance of the bar index **k** from its initial value before the fault.

The electromagnetic torque developed by the motor is expressed in terms of rotor currents and stator currents as:

$$C_e = \frac{3}{2}PN_r.M_{sr}(I_{ds}I_{qr} - I_{qs}I_{dr}) \quad (3)$$

The model considered allows studying the behavior at the healthy and faulty states of the IM in different operation cases.

III. Design of a Nonlinear Input Output Linearizing Controller for Induction Motors

The input output control problem is to find a state feedback such that the transformed system is input output decoupled that is, one input influence one output only [15]. The technique requires measurements of the state vector x in order to transform a multi-input nonlinear control system:

$$\begin{cases} \dot{x}=f(x)+\sum_{i\in m} g_i(x)u_i \\ y=h(x) \end{cases} \quad (z \in \Re^n, \upsilon \in \Re^m) \quad (4)$$

Into a linear and controllable one

$$\dot{z}= Az + B\upsilon \quad (z \in \Re^n, \upsilon \in \Re^m) \quad (5)$$

The control system is depicted in Figure 1 [16].

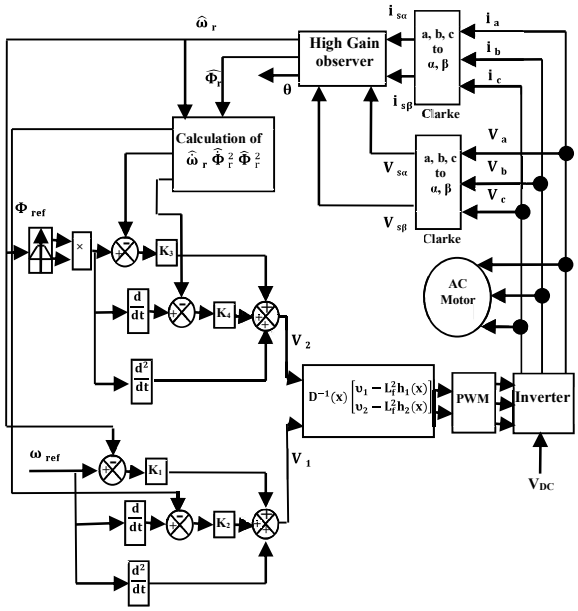


Figure 1: Block diagram of input output linearization control.

The state space model of induction motor in the (α, β) frame coordinate is given by:

$$\begin{cases} \dot{x}=f(x)+g(x).u(t) \\ y=h(x) \end{cases} \quad (6)$$

Where the state and commands vectors:

$$\begin{cases} x = \begin{bmatrix} i_{s\alpha} & i_{s\beta} & \Phi_{r\alpha} & \Phi_{r\beta} & \Omega_r \end{bmatrix}^T = \begin{bmatrix} x_1 & x_2 & x_3 & x_4 & x_5 \end{bmatrix}^T \\ u = \begin{bmatrix} V_{s\alpha} & V_{s\beta} \end{bmatrix}^T \end{cases}$$

With

$$\begin{bmatrix} \dot{x}_1 \\ \dot{x}_2 \\ \dot{x}_3 \\ \dot{x}_4 \\ \dot{x}_5 \end{bmatrix} = \begin{bmatrix} a_{r11}x_1 + a_{r12}x_3 + a_{i12}x_4x_5 + b_1V_{s\alpha} \\ a_{r11}x_2 + a_{r12}x_4 - a_{i12}x_3x_5 + b_1V_{s\beta} \\ \frac{M}{Tr}x_1 - \frac{1}{Tr}x_3 - px_4x_5 \\ \frac{M}{Tr}x_2 - \frac{1}{Tr}x_4 + px_3x_5 \\ \eta(x_2x_3 - x_1x_4) - \frac{C_r}{J} - \frac{f}{J}\Omega \end{bmatrix} \quad (7)$$

Let

$$y = \begin{bmatrix} y_1 \\ y_2 \end{bmatrix} = \begin{bmatrix} h_1(x) \\ h_2(x) \end{bmatrix} = \begin{bmatrix} \Omega \\ \Phi_r^2 = \Phi_{r\alpha}^2 + \Phi_{r\beta}^2 \end{bmatrix} \quad (8)$$

Where

$$M=-\frac{3}{2}M_{sr}\ ,\ \sigma=1-\frac{3N_rM_{sr}^2}{4L_{sc}L_{rc}}\ ,\ T_r=\frac{L_{rc}}{R_{rdd}}$$

$$\begin{cases} a_{r11}=\frac{1}{T_r}\left(\frac{\sigma-1}{\sigma}\right)-\frac{R_s}{\sigma L_{sc}}\ ,\ a_{r12}=\left(\frac{1}{T_r}\right)\left(\frac{\sigma-1}{\sigma}.\frac{2}{3M_{sr}}\right) \\ a_{r11}=\frac{1}{T_r}\left(\frac{\sigma-1}{\sigma}\right)-\frac{R_s}{\sigma L_{sc}}\ ,\ a_{r12}=\left(\frac{1}{T_r}\right)\left(\frac{\sigma-1}{\sigma}.\frac{2}{3M_{sr}}\right) \end{cases}$$

Define the change of coordinates:

$$\begin{cases} z_1=h_1(x)=x_5 \\ z_2=L_fh_1(x)=\eta(x_2x_3-x_1x_4)-\frac{C_r}{J}-\frac{f}{J}x_5 \\ z_3=h_2(x)=x_3^2+x_4^2 \\ z_4=L_fh_2(x)=-\frac{2}{T_r}\left(x_3^2+x_4^2\right)+2\frac{M}{T_r}\left(x_3x_1-x_4x_2\right) \end{cases} \quad (9)$$

This system can be written as:

$$\begin{bmatrix} \dot{z}_1 \\ \dot{z}_2 \\ \dot{z}_3 \\ \dot{z}_4 \end{bmatrix}=\begin{bmatrix} z_2 \\ L_f^2h_1(x) \\ z_4 \\ L_f^2h_2(x) \end{bmatrix}+D(x)\begin{bmatrix} V_{s\alpha} \\ V_{s\beta} \end{bmatrix} \quad (10)$$

The decoupling matrix $D(x)$ is defined as:

$$D(x)=\begin{bmatrix} L_{g_1}L_fh_1(x) & L_{g_2}L_fh_1(x) \\ L_{g_1}L_fh_2(x) & L_{g_2}L_fh_2(x) \end{bmatrix} \quad (11)$$

The decoupling matrix $D(x)$ is singular if and only if Φ_r^2 is zero which only occurs at the start up of the motor. That is, to fulfill this condition one can use in a practical setting, an open loop controller at the start up of the motor, and then switch to the nonlinear controller as soon as the flux goes up to zero. If the decoupling matrix is not singular, the nonlinear state feedback control is given by:

$$\begin{bmatrix} V_{s\alpha} \\ V_{s\beta} \end{bmatrix}=D^{-1}(x)\begin{bmatrix} V_1-L_f^2h_1(x) \\ V_2-L_f^2h_2(x) \end{bmatrix} \quad (12)$$

This controller linearizes and decouples the system, resulting in:

$$\begin{cases} h_1=V_1 \\ h_2=V_2 \end{cases} \quad (13)$$

The closed loop system (13) is input output decoupled and linear. To ensure perfect tracking of speed and flux references, V_1 and V_2 are chosen as follows:

$$\begin{cases} V_1=-k_1(\Omega-\Omega_{ref})-k_2(\Omega-\Omega_{ref})+\Omega_{ref} \\ V_2=-k_3(\Phi_r-\Phi_{ref})-k_4(\Phi_r-\Phi_{ref})+\Phi_{ref} \end{cases} \quad (14)$$

Where k_1, k_2, k_3 and k_4 are positive non-zero constants to be determined in order to make the closed loop system (13) stable and to have fast response in variable tracking.

IV. Nonlinear High Gain Observer Design For Induction Motor

The dynamic behavior in general of the induction motor belongs to a class of relatively fast systems. For computational issue, the high gain observer which admits an explicit correction gain can be considered as one of the most viable candidate in the problem of state estimation [12, 17]. To study the observation and control of the induction motor, we adopt this method in our model (6), given by:

$$\begin{cases} \dot{i}_s=\Gamma F(\Omega)\Phi_r-\lambda i_s+\frac{1}{\sigma L_{sc}}V_s \\ \dot{\Phi}_r=-F(\Omega)\Phi_r-\frac{3M_{sr}}{2T_r}i_s \end{cases} \quad (15)$$

Where

$$\Gamma=-\left(\frac{1-\sigma}{\sigma}.\frac{2}{3M_{sr}}\right),\ \lambda=\frac{R_s}{\sigma.L_{sc}}+\frac{1}{T_r}.\left(\frac{1-\sigma}{\sigma}\right),\ F(\Omega)=\frac{1}{T_r}I_2-p\,\Omega J_2$$

I_2 is the identity matrix 2x2 and $J_2=\begin{pmatrix} 0 & -1 \\ 1 & 0 \end{pmatrix}$

The equations of this observer are:

$$\begin{cases} \dot{\hat{i}}_s=\Gamma F(\Omega)\hat{\Phi}_r-\lambda\hat{i}_s+\frac{1}{\sigma L_{sc}}V_s-2\theta_1\left(\hat{i}_s-i_s\right) \\ \dot{\hat{\Phi}}_r=-F(\Omega)\hat{\Phi}_r-\frac{3M_{sr}}{2T_r}i_s-\frac{\theta_1^2}{\Gamma}F^{-1}(\Omega)\left(\hat{i}_s-i_s\right) \end{cases} \quad (16)$$

Where $\hat{i}_s$ and $\hat{\Phi}_r$ are respectively the estimates of i_s and Φ_r. Which θ_1 is a positive real. Therefore, the adaptive scheme for speed estimation is given by:

$$\hat{\Omega}=k_p\left(e_{is\alpha}.\Phi_{r\beta}-e_{is\beta}.\Phi_{r\alpha}\right)+k_i\int\left(e_{is\alpha}.\Phi_{r\beta}-e_{is\beta}.\Phi_{r\alpha}\right) \quad (17)$$

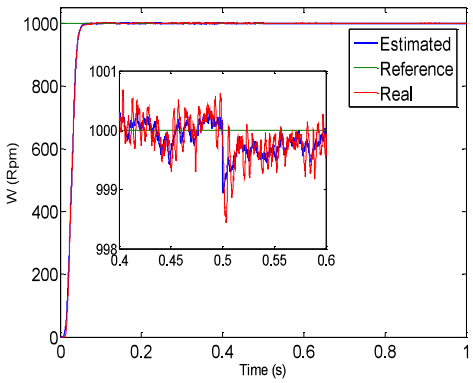
Where $e=x-\hat{x}$, k_p and k_i are respectively the proportional and integral constants.

V. Simulation Results

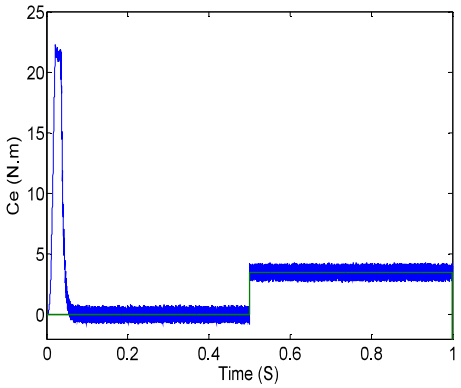
The sensorless input output linearization control of induction motor used in healthy and faulty states: 1.1 kW, 220V, 50Hz, 2-pole, a rotor with 16 bars were carried out using the Matlab/Simulink simulation package. The system parameters of the induction motor tested in this study are given in Appendix.

A. Results for healthy machine

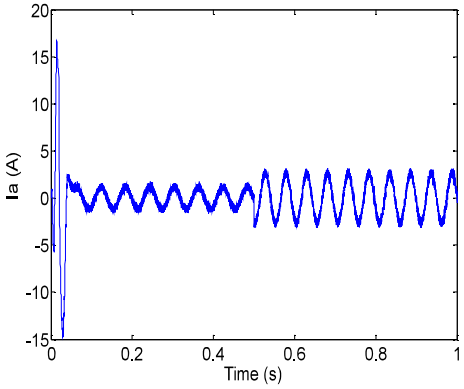
To illustrate the performances of the controller in healthy state of the machine, a simulation with a reference speed equal to 1000 rpm is realized in Figure 2, a nominal load torque equal to 3.5 Nm is applied at t=0.5s.



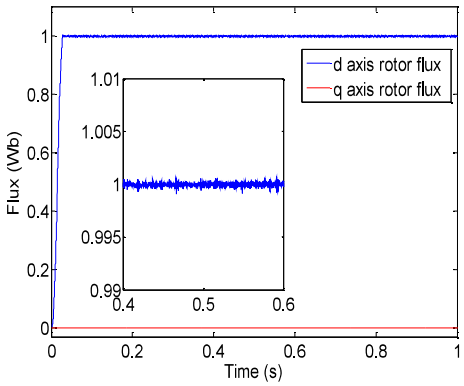
(a)



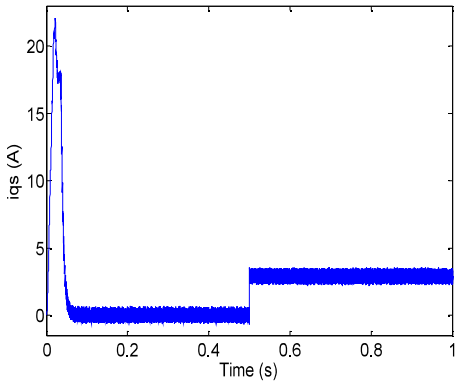
(b)



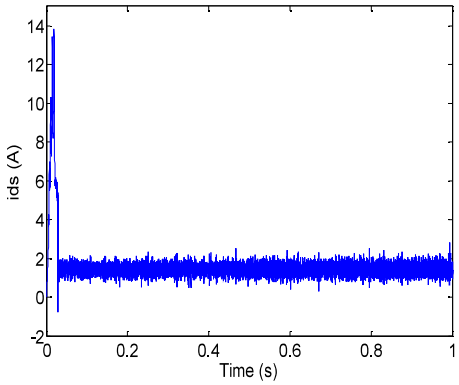
(c)



(d)



(e)

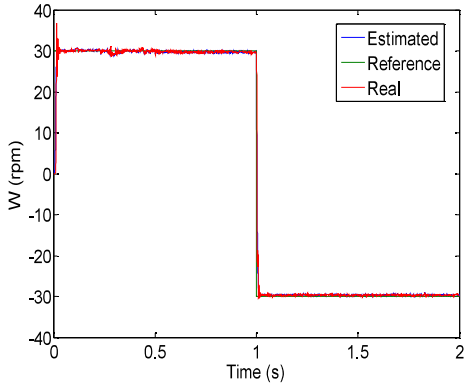


(f)

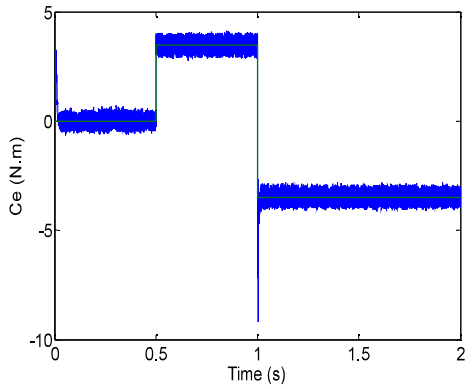
Figure 2: Input output linearization control of induction motor in healthy state: (a) speed, (b) torque, (c) stator current, (d) flux magnitude, (e) quadratic current components and (f) direct current components with the application of a load torque.

The electromagnetic torque follows the load torque and the stator phase current have a very good dynamic. Quadratic rotor flux Φ_{qr} is maintained to almost zero, direct rotor flux Φ_{dr} tracks the reference values adequately well.

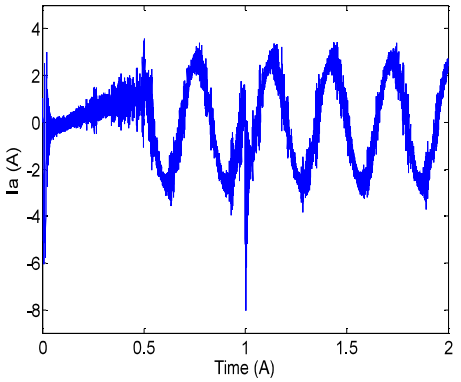
The speed reverse test is realized by changing the speed reference from 30 rpm to -30 rpm at t=1s with a nominal load torque 3.5 Nm is applied at t=0.5s in Figure 3.



(a)



(b)

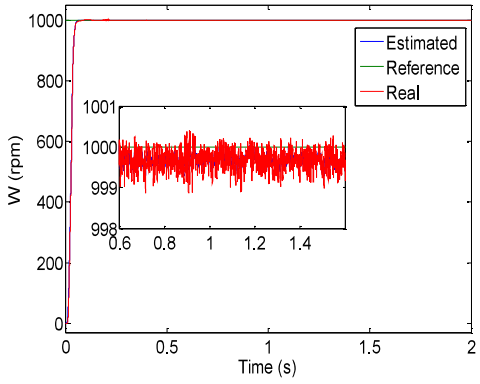


(c)

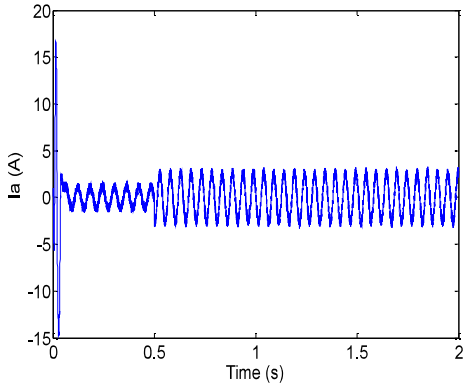
Figure 3: Reverse low speed test: (a) speed, (b) torque and (c) stator current of input output linearization control with the application of a load torque

The good performance such as robustness and convergence of the sensorless input output linearization control is revealed when the induction motor operates in low reference speed. It shows that estimate rotor speed observer and the real rotor speed converge to the reference speed with very less errors.

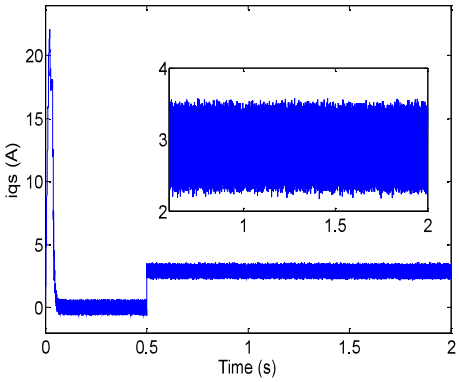
B. Results for healthy Machine with adjacent two broken rotor bars fault



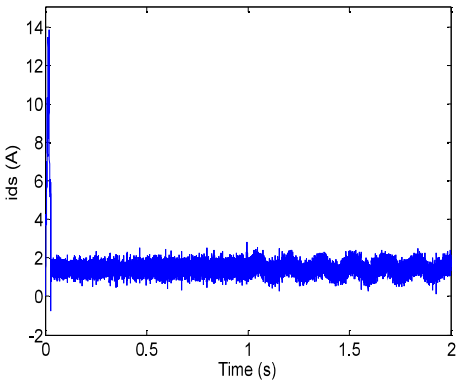
(a)



(b)



(c)



(d)

Figure 4: Input output linearization control of induction motor with two rotor broken bar: (a) speed, (b) stator current, (c) quadratic current components and (d) direct current components.

In this case the sensorless input output linearization control of the induction motor with fault is considered. Two adjacent broken rotor bars fault are applied at t=1s and the machine operate at 1000 rpm with a nominal load torque 3.5 Nm applied at t=0.5s.

The simulation results of sensorless input output linearization control using high gain observer of the induction motor with adjacent two broken rotor bars fault are shown in Figure 4. The rotor speed and torque give no information about the presence of fault due to the closed loop of input

output linearization control which mask and compensate the effect of the fault. However, the direct current I_{ds} is affected by the fault through the fluctuations. This information can be exploited for the online diagnosis of the machine in closed loop.

VI. Conclusion

In this paper, a sensorless input output linearizing control for the induction motor is considered with broken rotor bars fault. The controller shows a good performance of the induction machine in healthy and faulty states. Therefore reveals a powerful sensorless input output linearizing control using high gain observer for estimate the rotor speed and Flux where the effect of loop control by using the speed regulator that ensures the rejection of ripples. For that, the correlation with the fault severity is lost. The fault effect didn't affect the rotor speed; unlike the direct current components I_{ds} which offer a good indication about the detection of the rotor fault in closed loop.

Appendix

For the simulated induction motor

P_n: Output power	1.1kW
V_s: Stator voltage	220 V
f_s: Stator frequency	50 Hz
p: Pole number	1
R_s: Stator resistance	7.58 Ω
R_r: Rotor resistance	6.3 Ω
R_b: Rotor bar resistance	0.15 mΩ
R_e: Resistance of end ring segment	0.15 mΩ
L_b: Rotor bar inductance	0.1 µH
L_e: inductance of end ring	0.1 µH
L_{sf}: Leakage inductance of stator	26.5 mH
M_{sr}: Mutual inductance	46.42 mH
N_s: Number of turns per stator phase	160
N_r: Number of rotor bars	16
L: Length of the rotor	65 mm
g_0: Air-gap mean diameter	2.5mm
J: Inertia moment	0.0054 kgm2
F : Coefficient of damping	0.0029 Nm/rad/s

C_e , C_r,: electromagnetic torque, load torque

References

[1] P. J. Shaija and A. E. Daniel, "An Intelligent Speed Controller Design for Indirect Vector Controlled Induction Motor Drive System," *Procedia Technol.*, vol. 25, no. Raerest, pp. 801–807, 2016.

[2] V. P. Mini and S. Ushakumari, "Rotor fault analysis of an induction motor using FEM," in *2012 2nd International Conference on Power, Control and Embedded Systems*, 2012, pp. 1–7.

[3] N. Chuang, "Kalman filtering speed estimation of vector control for induction motor drive," in *2016 IEEE International Conference on Power System Technology (POWERCON)*, 2016, pp. 1–5.

[4] Y. Ben Salem and L. Sbita, "A Nonlinear State Feedback Control for Induction Motors," in *2006 IEEE International Conference on Industrial Technology*, 2006, vol. 5008, no. April, pp. 2067–2072.

[5] F. Alonge, M. Cirrincione, M. Pucci, and A. Sferlazza, "Input-output feedback linearization control of linear induction motors including the dynamic end-effects," *2014 IEEE Energy Convers. Congr. Expo. ECCE 2014*, pp. 3562–3569, 2014.

[6] A. Ammar, A. Bourek, and A. Benakcha, "Nonlinear SVM-DTC for induction motor drive using input-output feedback linearization and high order sliding mode control," *ISA Trans.*, vol. 67, pp. 428–442, Mar. 2017.

[7] C. Xia and H. Guo, "Feedback linearization control approach for Brushless Doubly-Fed Machine," *Int. J. Precis. Eng. Manuf.*, vol. 16, no. 8, pp. 1699–1709, Jul. 2015.

[8] M. O. Mustafa, G. Nikolakopoulos, T. Gustafsson, and D. Kominiak, "A fault detection scheme based on minimum identified uncertainty bounds violation for broken rotor bars in induction motors," *Control Eng. Pract.*, vol. 48, pp. 63–77, Mar. 2016.

[9] N. Bessous, S. E. Zouzou, S. Sbaa, and W. Bentrah, "A comparative study between the MCSA, DWT and the vibration analysis methods to diagnose the dynamic eccentricity fault in induction motors," in *2017 6th International Conference on Systems and Control (ICSC)*, 2017, vol. 23, no. 3, pp. 414–421.

[10] T. Ameid, A. Menacer, H. Talhaoui, and I. Harzelli, "Rotor resistance estimation using Extended Kalman filter and spectral analysis for rotor bar fault diagnosis of sensorless vector control induction motor," *Measurement*, vol. 111, pp. 243–259, Dec. 2017.

[11] T. Ameid, A. Menacer, H. Talhaoui, and I. Harzelli, "Broken rotor bar fault diagnosis using fast Fourier transform applied to field-oriented control induction machine: simulation and experimental study," *Int. J. Adv. Manuf. Technol.*, vol. 92, no. 1–4, pp. 917–928, Sep. 2017.

[12] A. Maouche, M. M'Saad, B. Bensaker, and M. Farza, "High gain adaptive observer design for sensorless state and parameter estimation of induction motors," *Int. J. Control. Autom. Syst.*, vol. 13, no. 5, pp. 1106–1117, Oct. 2015.

[13] Y. Shen, "Fault diagnosis based on high-gain observer with an update law for a class of nonlinear systems," *J. Control Theory Appl.*, vol. 8, no. 4, pp. 447–452, Nov. 2010.

[14] H. Talhaoui, A. Menacer, A. Kessal, and R. Kechida, "Fast Fourier and discrete wavelet transforms applied to sensorless vector control induction motor for rotor bar faults diagnosis," *ISA Trans.*, vol. 53, no. 5, pp. 1639–1649, Sep. 2014.

[15] W. Ai, Z. Lu, B. Li, and S. Fei, "Output feedback control for a class of nonlinear systems with actuator degradation and sensor noise," *ISA Trans.*, vol. 65, no. ii, pp. 44–50, Nov. 2016.

[16] A. Accetta, F. Alonge, M. Cirrincione, M. Pucci, and A. Sferlazza, "Feedback Linearizing Control of Induction Motor Considering Magnetic Saturation Effects," *IEEE Trans. Ind. Appl.*, vol. 52, no. 6, pp. 4843–4854, Nov. 2016.

[17] A. Dib, M. Farza, M. M'Saad, P. Dorléans, and J. F. Massieu, "High gain observer for sensorless induction motor," *IFAC Proc. Vol.*, vol. 44, no. 1, pp. 674–679, Jan. 2011.

A Deep Learning Application: Handwriting Classification

K.UÇAR[1] and H. E. KOÇER [2]

[1] Selcuk University, Konya/Turkey, kucar@selcuk.edu.tr
[2]Selcuk University, Konya/Turkey, ekocer@ selcuk.edu.tr

***Abstract* - With the rapid development of data retrieval and storage devices, it has become necessary to process large-scale data. Along with this, machine learning and artificial neural network methods have started to be used in many areas. The method developed for artificial neural networks with large computational power is deeply learned. The input of this artificial neural network is a very different feature of the images that are passed through the filters, which are various learning features. However, the importance of recognizing and classifying characters written in handwriting is increasing day by day. In this study, deep learning was applied for the classification of 36 letters and 10 numbers written in the handwriting. Each letter image was filtered through different filters and its properties were extracted and classified with a convolutional artificial neural network. The letters were analyzed using 78200 samples. With this study, 13800 letters which are not used in training are classified more correctly than 95%.**

***Keywords* – Handwriting, Deep Learning, Convolutional Neural Networks.**

I. INTRODUCTION

HANDWRITING recognition and classification are a classic problem in artificial intelligence [1]. The recent works on handwritten letter classification are often feature-based methods. These methods learn the letters by extracting different distinguishing features of the handwriting letters. In this learning technique, similarities and differences are tried to be determined by using the extracted features of the letters. As the similarity of the images increases, more distinctive features are needed. To get these features, images must be filtered. Filters find features that can be searched through the image. The size and value of the filters vary according to the features searched in the image. Figure 1 shows an example of a 3x3 edge detection filter.

$$\begin{bmatrix} -1 & 0 & 1 \\ -2 & 0 & 2 \\ -1 & 0 & 1 \end{bmatrix}$$

Figure 1: Sobel edge detection filter

A standard neural network (NN) consists of neurons that are connected one to another by weights and pass through an activation function to produce a result [2]. The neurons are located at the input layer, the output layer and the hidden layers. The input neurons are consisted of information from sensors that perceive the environment, while other neurons are created by predominantly connected neurons. Learning relates to finding the weight of the NN that exhibits the desired behavior. Depending on the problem to be solved and how the neurons are connected, this process may require chains of long causal computational steps where each step changes the total activation of the network. Deep learning is about doing the right learning in many stages. Deep Neural Networks are made up of a large number of non-linear hidden layers, so the number of connections and the trainable parameters are very large [3]. Such networks require a large number of examples because of difficulty of training and to avoid over fitting. Convolutional Neural Networks (CNNs) is a network type that has a smaller set of parameters and is easier to train than the deep neural network [4]. The ability to accurately model the input data set can be improved by changing the number of hidden layers and the trainable parameters in each layer [5]. CNNs can model the complex nonlinear relationship between input and output, although it has less trained parameters from a fully connected classic forward feed network at the same depth. CNNs usually consist of several layers of convolution and subsampling between the input and output layers. After these layers, fully connected layers come in, thus creating the layer in which the discriminative properties of the input data are located. CNN are based on the several past years [6]. However, it has suddenly become a popular feature with the success in image classification [7]. In the study performed by Cireşan and others [8], they tried to classify the handwritten number, Latin and Chinese letters, traffic signs into deep learning and classification close to the human level. Acharya and others [3] used different structures of CNNs to recognize the handwriting Devanagari characters in their deep learning application. After making the images ready for CNN, they changed the convolution layer and the fully connected layer numbers for best learning. As it is known, the videos are formed by sequencing the pictures in rapid succession. Working with videos is more difficult than working with images because of the variability and number of images in the video. Thus, in the study [9], the videos were classified by clips that consisting of several images and classified by using CNNs. It is possible to use CNNs not only in the image recognition but also in voice recognition applications [10]. In fact, it is possible to classify even the sentences that are highly variable in structure and meaning. The words in the sentence were transformed into a vector and the classification of the

sentences was made in [11]. The improvement in device technology with parallel processing capability like GPU also makes CNNs more effective [12]. CNNs require high computation with large data. But CNNs have a smaller structure than classical feed forward neural networks.

In this study, deep learning applications were performed with the features detected by different filters on the images. By motivating this fact, a convolutional neural network is considered with the determined features. 32x32 images are passed through different filters to form the convolution layer. After the convolution layer, the filter outputs are subjected to size reduction. These two steps can be repeated. After subsampling phase, a full connected layer is created. After the fully connected layer, the output layer which the classification is made comes.

II. Dataset

As the dataset an alphabet used in this study which is used to write Nepali, Hindi, Marathi and other similar languages of South and East Asia. In general there are 36 letters in voice, consonant and special letters. There are also 10 digits in the data set. The images are in case the letters are written separately. So each image has a letter. Each character has 2000 handwriting sample images. A total of 92000 samples were used in this study. The dataset was used for 85% network training and 15% for testing. Each image is constructed of 32x32 matrixes. The pixel values of the images are 0 and 1. In other words, the images consist of black and white images. The colors of the letters are white, and the background is black. Figure 2 shows a sample of all 46 characters scattered randomly. There is no extra preprocessing for CNN on these images.

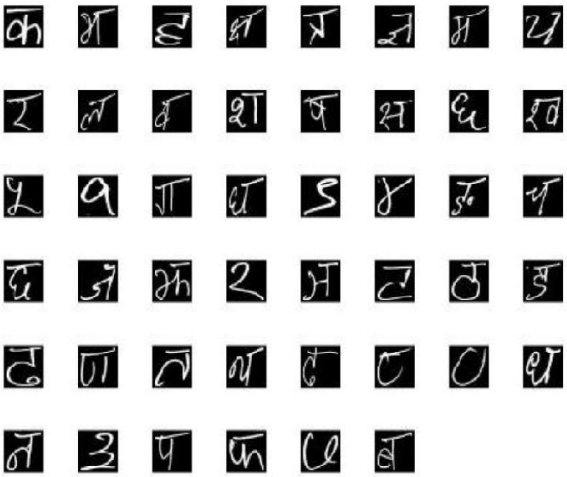


Figure 2: An example of all characters.

III. Convolutional Neural Networks For Handwriting Classification

The multilayer networks trained with gradient descent have the ability to learn, complex, high-dimensional, non-linear mappings from large datasets. Therefore, multilayer neural networks are becoming attractive for image recognition. In the conventional pattern recognition model, it is necessary to extract the related features. For this, a manually designed feature extractor ensures that relevant information is obtained from the input data. Then a trainable classifier classifies the extracted feature vectors. Fully connected multilayer networks can be used as classifiers. In addition to this, it is possible to train the feature extractor according to the output of the network [3]. In such a case a network can be fed even with raw inputs. However, a few problems arise in such a situation.

First of all, in general, the dimensions of the images are large, often consisting of hundreds of pixels. The number of trainable weights in a fully connected layer is several hundred times greater than the number of units in the layer. Thus, the capacity of the system increases and therefore a larger training set is needed. This large-scale parameter set and system requires both high storage space and slows down system training and testing. Before being sent to the input layer of a NN, the images must be normalized and placed in the center of the input field. However, such preprocess cannot be perfect for handwritings. Even for the same letters of the handwriting letter, there may be differences of character size, skew and position of handwriting letters. Due to differences in writing style, there will be changes in the distinctive features of the letters. However, a fully connected network that is as large as it can be successfully trained despite these variables. This would require multiple units with similar weight models positioned at various locations on the input. Learning these weight differences requires a large number of training examples to cover the larger area. In convolutional networks, shift invariance is obtained automatically by repeating the weight forms along the field.

A second problem is that totally dependent architects ignore the topology of the input. It is possible to present input variables in any order without affecting the result of the training. However, images have a strong 2D local structure with close pixel values. Configurations of neighboring variables can be categorized in a small number of categories. Hence the reasons for the known advantages of extracting and combining local features are local relativities. Convolutional networks impose the extract of local features by restricting the localization of the receiving areas of the hidden units.

IV. Character Recognition

The CCN handwriting recognition system used in this study is shown in Figure 3 and Figure 4. In general, CNN consists of five layers these are input, convolution, pooling full connected and output classification layer. Connections between input, convolution and pooling layers are provided with kernels.

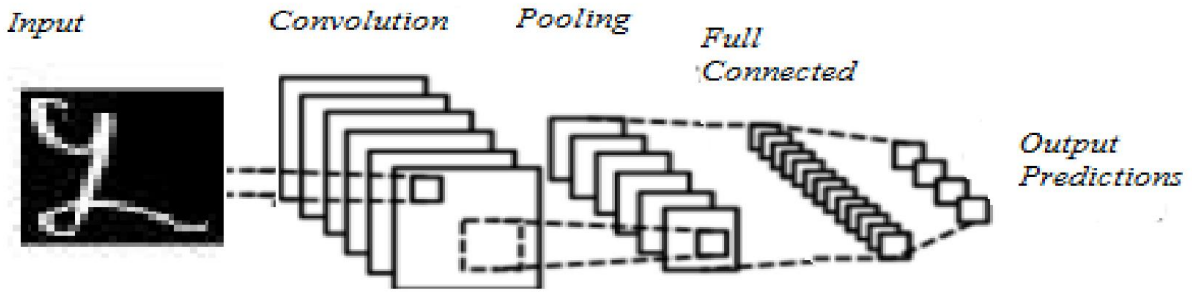


Figure 3: The structure of Convolutional Neural Network.

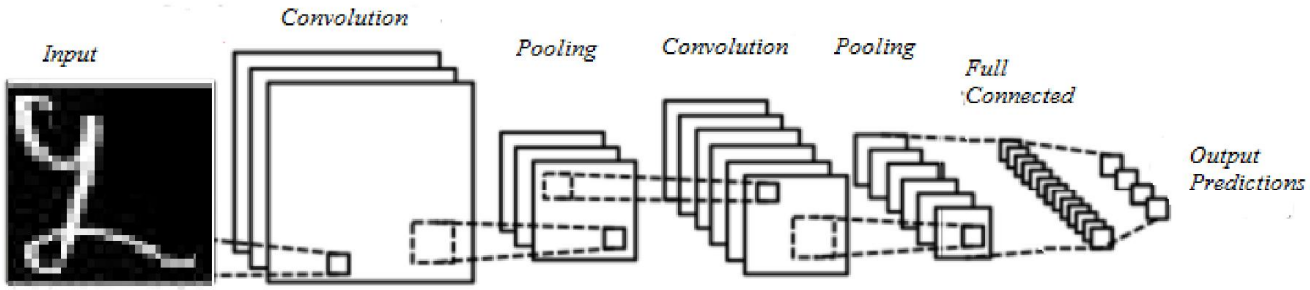


Figure 4: The structure of two convolutional and pooling layers CNN.

Kernels are traversed throughout these layers and create value for the next layer. The images in the 32x32 matrix form the input layer without any changes. The input layer does not have any learning parameters. The convolution layer, which is the first layer after the input layer, has several feature maps. The number of feature maps may vary depending on the application. The feature maps of the convolution layer were created with 5x5 kernels. Therefore, each feature map is a set of 784 point values consisting of 28x28 matrices. Each feature map in the figures is shown as 2D planes. All units in a feature map have the same weight. For this reason, they show the same features in different locations. This weight sharing also reduces the actual number of trainable parameters in each layer. The input of each unit in the layer is created with the small neighborhoods in the same position of the previous layer. The selected size of the neighbors of the previous layer changes the number of trainable weights that can be associated with each unit in a convolutional layer. Because local neighborhoods are used, only local properties can be determined. As mentioned before, 5x5 kernels are used, so the number of trainable weight is 25 for each unit. Each unit also has a trainable bias value. As the kernel size decreases and the size of the previous layer grows, the number of units increases.

After the convolution layer comes the subsampling (pooling) layer. In this layer, the size of the previous layer is reduced. At the same time, the resolution of the previous layer is reduced. Methods such as taking the average of neighboring pixels or taking the maximum value can be used for this process. However, the position of the outputs of this layer may not be sufficient by itself. The position of each feature relative to each other is more important than the absolute position, because the place of the properties of the same letters can change according to the style, size and position of writing. However, it is expected that the properties of the same letters will not change less in relation to each other. The subsampling layer contributes to the learning of the positions of properties relative to each other. It also makes the classifier stronger against shifting and distortion. The input information is converted into a small local group with the neighbors and output is produced. Therefore, the dimensions of the output of this layer depend on the size of the previous layer and the size of the group created. By taking different inputs from the previous layer each time and using the 2x2 kernel, the size of the convolution layer is reduced by half. The maximum pooling method multiplies the maximum value in the local neighbors' area by a trainable coefficient, adds a trainable bias value, and produces output.

Convolution and pooling layers are repeated in one of the two different structures used. In these layers of the network that these two layers repeat, the operations performed in the previous layers are repeated exactly. The only difference in these layers is the number of feature maps in the convolution layer.

After the subsampling layer in two different structures, the fully connected layer is located. After this step, CNN works with 1D vector. That is, size of feature maps on the layer is reduced to one size. The fully connected layers are applying non-linearity to model the input as it is in a classic forward feed network. Rectified Linear Unit is used as type of nonlinearity. The Rectified Linear Unit processes nonlinearity as $f(x) = \max(0, x)$. Since the training with is faster with gradient descent, this function is used instead of general

nonlinear functions like classical artificial neural networks.

The final stage is classification in the CNN. Each letter and number is represented by one output node. In other words, the network has a total of 46 output nodes for 36 letters and 10 digits. It is desirable that the error of the output layer is reached to the minimum during the network training phase. At the same time, according to the output error, the trainable parameters are set to reach the optimum value to reduce the network error. In the test phase at the end of the training phase, the output layer tests which handwriting character belongs to the input images. The results are presented as the rate of the correct classifications in this layer.

The depth of the neural network to be created and the size and number of the different layers to be used are directly related to the data set and the problem to be solved. Moreover, the success of the network varies with the number and size of feature maps in a layer, the size of the kernel in each layer, and the choice of non-overlapping or overlapping kernels. Therefore, in this study, different architectures were tested by changing these parameters and the results of the architecture which produced the highest accuracy in the test data set are presented.

V. Results And Discussion

In this work, dataset is trained and tested by changing iteration number and network structure. The number of convolution and pooling layers was chosen as 1 or 2. In addition, the number of feature maps included in the convolution layers was also changed to examine the effects to results. In all cases convolution was applied with an overlapped kernels of size 5x5. Pooling is performed with a filter size 2x2 that does not overlapped. The results obtained according to the work done are shown in Table 1. Accordingly, the best results were obtained from networks with a single convolution and pooling layer. It has been the case that %100 accuracy is reached in the test phase. This means that the network parameters have reached the optimum value for the data used in the train phase. It has been observed that in the same structure experiments, accuracy increases as the number of epoch increases. Accordingly, the best result is obtained from a network with 20 single-layer feature maps made with 75 epochs. The best training result is 95.62%.

The best test result achieved in the deep learning application [3] with the same dataset is presented as 98.47%. In the mentioned study, the convolution layer and the pooling layer were repeated at least twice. At the same time, the images were pre-processed before CNN was taken. However, in our study, the best test result was obtained without preprocessing of images and with a single convolution and pooling layer structure. This means training and testing phases are faster than the mentioned study when the same hardware were using.

Table 1: The results of train and test of CNN.

Number of Layers	Number of Feature Maps	Max Epoch	Train Error	Train Accuracy (%)	Test Accuracy (%)
1	10	15	0.0389	98.44	94.38
1	10	16	0.0344	99.22	94.39
1	10	20	0.0249	100	94.51
1	20	50	0.0005	100	95.49
1	20	75	0.0003	100	95.62
2	20- 2	15	0.8438	90.63	84.38
2	5- 5	15	0.2170	92.19	91.11
2	5- 5	50	0.1783	92.97	92.37
2	10- 4	50	0.3254	89.06	92.32
2	20- 5	15	0.1965	93.75	92.21
2	20- 5	50	0.1290	95.31	93.57
1	40	15	0.0198	100	93.70
1	40	50	0.0003	100	95.50

In our study, after the number of epochs is 15, the accuracy rate increases very slowly when the epoch number increases. Therefore, more epochs is needed to achieve higher accuracy.

References

[1] S. A. K. Al-Omari, P. Sumari, S. A. Al-Taweel and A. J. A. Husain, "Digital Recognition using Neural Network", Journal of Computer Science 5, pp. 427-434, 2009.

[2] Y. LeCun, L. D. Jackel, L. Bottou, C. Cortes, J. S. Denker, H. Drucker, I. Guyon, U. A. Müller, E. Sackinger, P. Simard and V. Vapnik, "Learning Algorithms for Classification: A Comparison on Hnadwrittern Digit Recognition".

[3] S. Acharya, A. K. Pant and P. K. Gyawali, "Deep Learning Based Large Scale Handwritten Devanagari Character Recognition", 9th nternational Conference on Software, Knowledge, Information Management and Applications, 2015.

[4] Y. LeCun, L. Bottou, Y. Bengio and P. Haffner, "Gradient-Based Learning Applied to Document Recognition," Proceeding of the IEEE, vol. 86, pp. 2278 - 2324 November 1998.

[5] A. Krizebsky, I. Sutskever and G. E. Hinton, "ImageNet Classification with Deep Convolutional Neural Networks,"Advances in Neural Information Processing Systems 25 (NIPS 2012).

[6] Y. LeCun, B. Boser, J. S. Denker, D. Henderson, R. E. Howard, W. Hubbard, L. D. Jackel, "Backpropagation applied to handwritten zip code recognition", Neural Computation, pp. 541–551, 1989.

[7] A. Krizhevsky, I. Sutskever, G. Hinton, "ImageNet classification with deep convolutional neural networks" NIPS, pp. 1097–1105, 2012.

[8] D. Ciresan, U. Meier and J. Schmidhuber, "Multi-column Deep Neural Networks for Image Classification", Arxiv preprint arXiv:1202.2745, 2012.

[9] A. Karpathy, G. Toderici, S. Shetty, T. Leung, R. Sukthankar and L. Fei-Fei, "Large-scale Video Classification with Convolutional Neural Networks", In IEEE conference on computer vision and pattern recognition, 2014.

[10] T.N. Sainath, A. R. Mohamed, B. Kingsbury and B. Ramabhadran, "Deep convolutional Neural Networks for LVCSR," IEEE International Conference on Acoustics, Speech and Signal Processing, pp. 8614-8618, 2013.

[11] Y. Kim, "Convolutional Neural Networks for Sentence Classification", arXivpreprint arXiv:1408.5882 .

[12] C. Dong, C. C. Loy, K. He, and X Tang, "Learning a Deep Convolutional Network for Image Super-Resolution", Springer, ECCV 2014, Part IV, LNCS 8692, pp. 184–199, 2014.

Short-term Load Forecasting for Microgrids based on Fuzzy Logic

J.T. MUTSENA[1] and M. BAYSAL[1]

[1]Yildiz Technical University, Istanbul/Turkey, jtmutsena@gmail.com
[1]Yildiz Technical University, Istanbul/Turkey, baysal@yildiz.edu.tr

Abstract **–There has been increasing interest in microgrids due to several advantages they present. Short-term load forecasting (STLF) is an essential task which must be done to ensure that microgrids are operated smoothly on a daily basis; operational costs are reduced, and the reliability of the microgrid increases. Pronounced load demand fluctuations occur in a microgrid due to its small size. Hence, designing an accurate forecast for a microgrid is an arduous process. This paper presents a STLF model which predicts load demand one hour in advance, and is based on fuzzy rules. The rules are based on temperature, time of the day, season of the year, and day type (weekend/weekday) parameters. The resulting rule base is used to simulate the model in Matlab using the Fuzzy logic toolbox. Traditional forecasting techniques which are statistical in nature require a large amount of historical data, and cannot easily be updated. The fuzzy rule-based STLF model does not require a substantial amount of data, can easily be updated, and involves no mathematical computations. The performance of the designed fuzzy rule-based STLF model is evaluated by comparing the load demand forecast values to the real-life data (actual load demand) of an 11 kilo-volt (kV) power substation in Providence, Rhodes Island.**

Keywords **– Short-term load forecasting, microgrid, fuzzy rules, load demand**

I. INTRODUCTION

A microgrid is a power system that includes multiple loads, and distributed resources that can operate connected to the main utility (grid mode) or as a single entity (island mode) [1]. Load forecasting is useful for forecasting the amount of power needed to supply the demand [1]. Forecasting refers to the prediction of the load behavior for the future. Load forecasting can be short-term, medium-term or long-term. Short-term load forecasting (STLF) involves predicting load demand from one hour to a week in advance [5]. Medium-term load forecasting (MTLF) predicts load demand from a week to a year ahead [5]. Long-term load forecasting (LTLF) predicts power consumption more than a year in advance [5]. In this paper, STLF is given precedence over MTLF, and LTLF. STLF is primarily based on the "similar day" method approach; the method solely involves finding a day in history that is similar to the forecasted day. The similarity is more often than not based on day of the week, season of the year, and weather patterns. The load of the similar day is considered as the forecast. Other STLF techniques are Linear Regression Method (LRM), Time Series Analysis (TSA), Artificial Neural Networks (ANNs), Expert Systems (ES), Fuzzy Logic (FL), Genetic Algorithms (GA), and Support Vector Machines (SVM). LRM is the most widely used statistical technique for STLF [1]. In TSA models, previous load is extrapolated to obtain future loads [8]. ANNs map the relationship between input, and output vectors in a given sample [4]. A drawback to this approach is that as conditions change the ANNs are not easily updatable to accommodate the changes. In ES, the forecast model is designed with the help of an expert [2]. However, experts may have difficulties in expressing their knowledge qualitatively [5]. As for FL, data is processed, and represented in linguistic terms. This makes fuzzy logic models readable, and comprehendible [2]. A fuzzy logic model is made up of IF-THEN statements (also known as fuzzy rules) which are derived from expert knowledge and/or from a set of historical observations or data [3]. SVM is an algorithm which provides solution for both classification, and regression problems [6]. GA are based on the process of evolution by natural selection [7]. Factors crucial for STLF are time (i.e., time of the year, day of the week, and time of the day), consumers' classes (i.e., residential, commercial, industrial etc.), and weather data. Weather data comprise of temperature, and humidity values. These two weather components greatly influence the daily load demand in a microgrid. For the purpose of this paper, a fuzzy approach to STLF is adopted. The fuzzy rule-based STLF model has a leading time of one hour. 2016 historical data provided by both the National Grid, and National Oceanic and Atmospheric Administration (NOAA) are used for modeling the forecast. IF-THEN statements are generated by drawing inferences from the observations made on the aforementioned historical data which belongs to Providence, Rhodes Island (USA). For system performance evaluation 2017 historical data for the said place are used. Figure 1 shows a typical 24 hours load demand profile for a normal, summer day in Providence. The load demand curve mirrors the life cycle of the consumers. Accordingly, the demand for power is low at midnight as most people are sleeping, and there is no need of lighting or heating the house. Peak demand occurs around 6 pm as at that time almost everybody is sitting at home with eyes glued to the television (TV), and the air conditioner on.

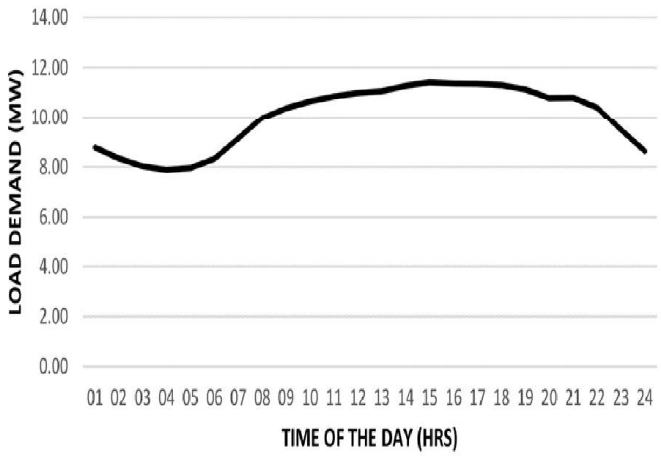


Figure 1: Typical 24 hours load curve

II. System Block Diagram

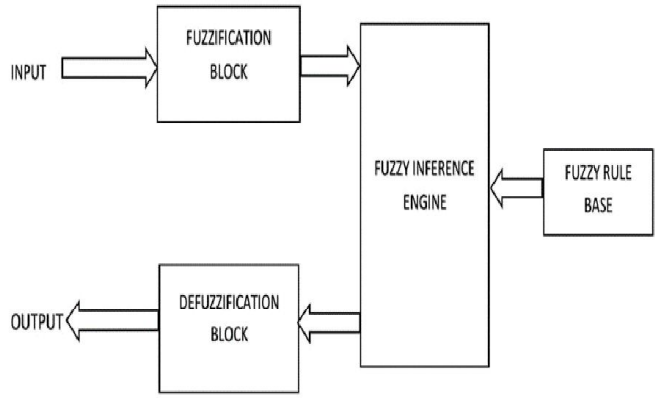


Figure 2: Fuzzy logic based load forecaster block diagram

The proposed system which is based on fuzzy logic is shown in Figure 2. The inputs to the system are hourly maximum temperature, time of the day in hours, season of the year, and day type. These crisp inputs are transformed into fuzzy by the fuzzification block. The rule base is formed after fuzzification of the input data. The rule base is just fuzzy rules based on the historical data (weather, and load demand values). The fuzzy inference engine performs inference operations on the rule base to produce the forecast load. The forecast load which is fuzzy in nature is then defuzzified by the defuzzification block to produce a crisp output. The output is compared to the actual load demand values to assess the accuracy of the forecast model system.

III. Methodology

The flow chart shown in Figure 3 summarizes the methodology used to design the fuzzy logic based load forecaster.

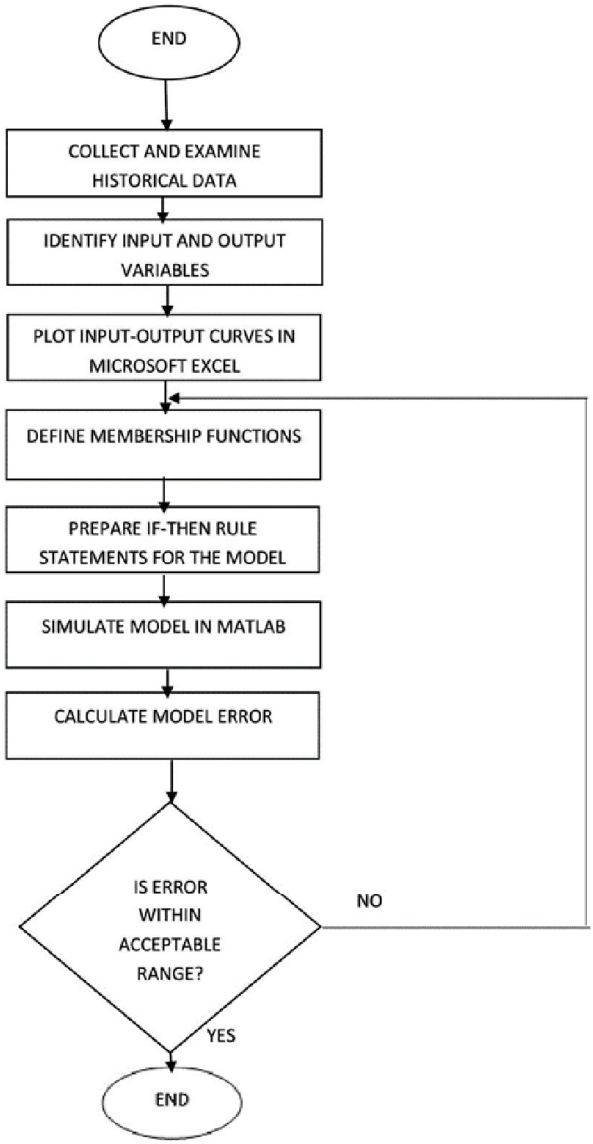


Figure 3: Flow chart

The steps taken in the design of the model are:

a. Data collection, and examination

Data belonging to Providence substation in Rhodes Island are collected from National Grid, which is the power utility company for that area. Real time and day ahead load demand, daily peak demand, and peak hour values for the year 2016, and 2017 are collected in the form of excel files. Archival weather parameters' values corresponding to the area, and period in question are provided by NOAA. The parameters are humidity, hourly and daily maximum temperature, wind speed, and pressure.

b. Input, and output variables identification

After examining the data collected the next stage involves identifying the output, and the input data. The output is load forecast. The input to the system are, season of the year, temperature, time of the day, and day type.

c. Plot input-output curves

To observe the effect of the various inputs (i.e., temperature, day type etc.) on the output (load demand) various curves are plotted. The correlation between the different inputs, and output is graphically presented in the form of curves plotted with the aid of 2013 Microsoft excel software.

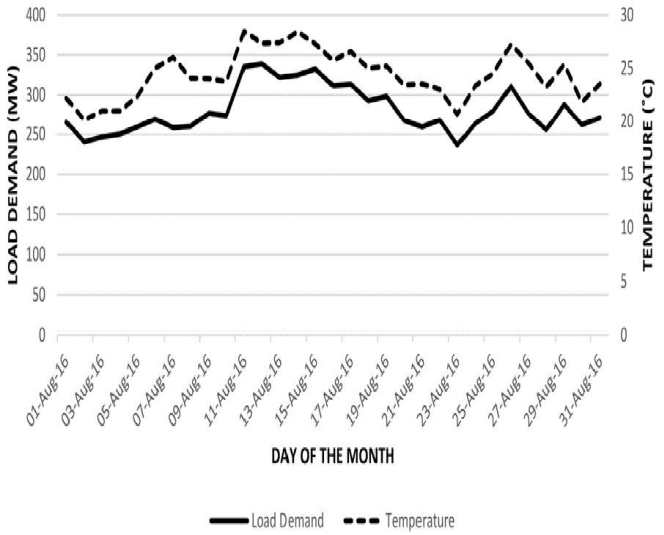


Figure 4: Input-output curves for August 2016

Figure 4 shows that as temperature increases the daily load demand increases. The month of August which falls under the summer season shows a high positive correlation between temperature, and *daily load demand*. More AC fans are used as the temperature increases, and hence the increase in power consumption. According to Providence's weather data, and *daily load demand* data there is no significant correlation between humidity, and daily load demand. Hence, humidity is not used as an input to the system.

There is a high negative correlation between temperature, and *daily load demand* in winter as shown in Figure 5. On a cold winter day more heating appliances are switched on, and subsequently the power consumption increases. As the temperature increases a decrease in use of the said appliances is noted, and the result is a decrease in power consumption.

The *daily load demand* for both spring, and fall seasons is almost constant. This can be attributed to the fact that there are no dramatic changes in temperatures throughout these seasons; the daily maximum temperature are more or less constant as show in Figure 6.

Furthermore, the *daily load demand* is low because there is minimum use of air conditioners, and heating appliances. Therefore load forecasting for spring, and fall season is based on the correlation which exists among day type, time of the day, and *peak hourly load demand*. The experience, and knowledge of the system operator are also valuable assets for forecasting power consumption in spring, and fall.

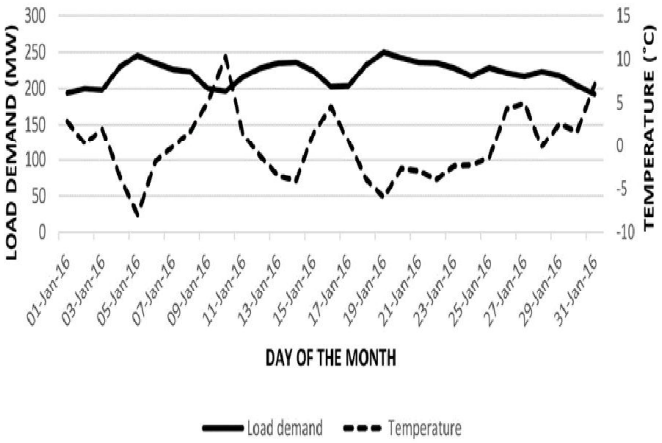


Figure 5: Input-output curves for January 2016

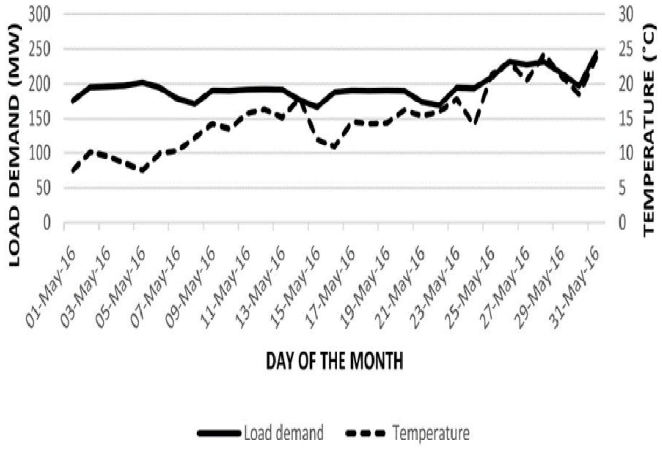


Figure 6: Input-output curves for May 2016

Another plot which is not shown here shows that *daily load demand* during the weekdays is higher than that during the weekends. During the weekend there is not much activity as people will be resting, and hence less power consumption.

d. Membership functions defining

Fuzzy logic is basically the computation of words [9]. The process whereby crisp quantities are transformed into fuzzy is known as fuzzification [9]. A fuzzy set allows elements to belong to the set partially, and each element is assigned a degree of membership in the set [9].

A membership function for a given fuzzy set has a responsibility of mapping an input value of the said set to its appropriate membership value which lies between 0, and 1. The membership function (MF) which is a curve assumes different shapes viz. triangle (Triangular MF (trimf)), trapezium (Trapezoidal MF (trapmf)) etc.

Crisp inputs viz. hourly maximum temperature, season of the year, time of the day, and day type are transformed to fuzzy.

The hourly temperature is divided into fuzzy subsets viz.

- Very very low (VVL)
- Very low (VL)
- Low (L)
- Average (A)
- High (H)
- Very high (VH)
- Very very high (VVH)

The corresponding seven triangular MFs are shown in Figure 7.

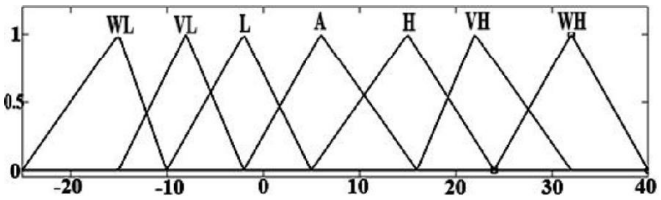


Figure 7: Input variable "temperature" MFs

For day type, the two fuzzy subsets are:

- Weekday (WD)
- Weekend (WKND)

A choice of two trapezoidal MFs is made for "day of the week" input as shown below in Figure 8.

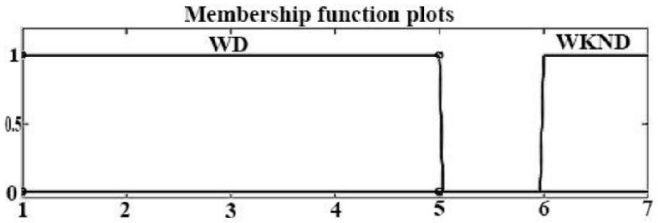


Figure 8: Input variable "day type" MFs

"Season of the year" input is transformed to four fuzzy subsets:

- Summer (S)
- Winter (W)
- Spring (SP)
- Fall (F)

The four fuzzy subsets correspond to four trapezoidal MFs as shown in Figure 9.

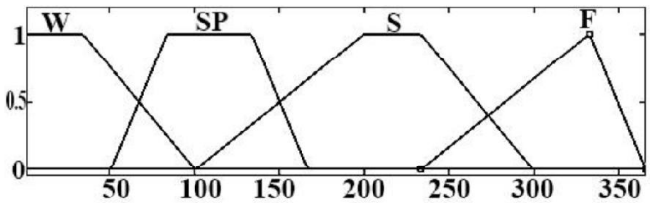


Figure 9: Input variable "season of the year" MFs

Time of the day is fuzzified to:

- Early Morning (EM)
- Mid-Morning (MM)
- Late Morning (LM)
- Noon (N)
- Late Noon (LN)
- Evening (E)
- Night (NT)

The corresponding seven triangular MFs are shown in Figure 10.

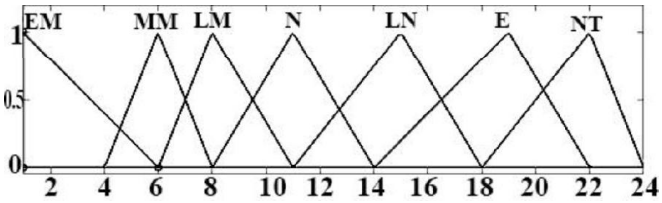


Figure 10: Input variable "time of the day" MFs

The forecast load (load demand) which is the output is divided into eighteen fuzzy subsets, and the corresponding eighteen trapezoidal MFs are shown in Figure 11.

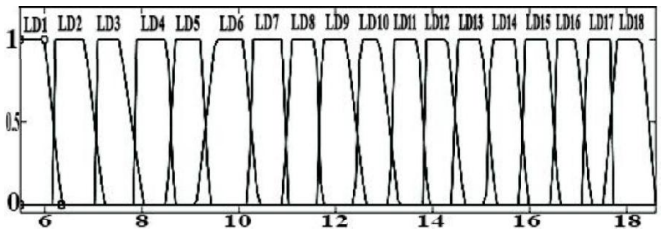


Figure 11: Output variable "load demand" MFs

For simplicity triangular, and trapezoidal MFs are chosen. Other MFs which can be used are generalized bell membership function (gbellmf), Gaussian membership function (gaussmf), sigmoidal membership function (sigmf) etc.

e. Fuzzy rules preparation

The accuracy of the model largely depends on the number of fuzzy rules, and the fuzzy rules per se. Hence, care must be taken when preparing the fuzzy rules. 224 rules based on the input, and output data are prepared for the model, and some of them are shown below:

- If (day_type is WD) and (season_of_the_year is W) and (time_of_the_day is EM) then (load_demand is LD4)(1)
- If (day_type is WD) and (season_of_the_year is W) and (time_of_the_day is MM) then (load_demand is LD5)(1)

.
.
.

- If (day_type is WKND) and (season_of_the_year is SP) and (time_of_the_day is NT) and (temperature is H) then (load_demand is LD4)(1)
- If (day_type is WKND) and (season_of_the_year is SP) and (time_of_the_day is NT) and (temperature is VH) then (load demand is LD3)(1)

The fuzzy rules assume the general form ‘‘If X is A then Y is B’’, where A and B are fuzzy sets or subsets.

f. Model simulation

Figure 12 shows the rule viewer for 224 rules prepared for the model in Matlab using the Fuzzy logic toolbox. It is used to simulate the model since it accepts input values, and gives the corresponding output value (load demand forecast value).

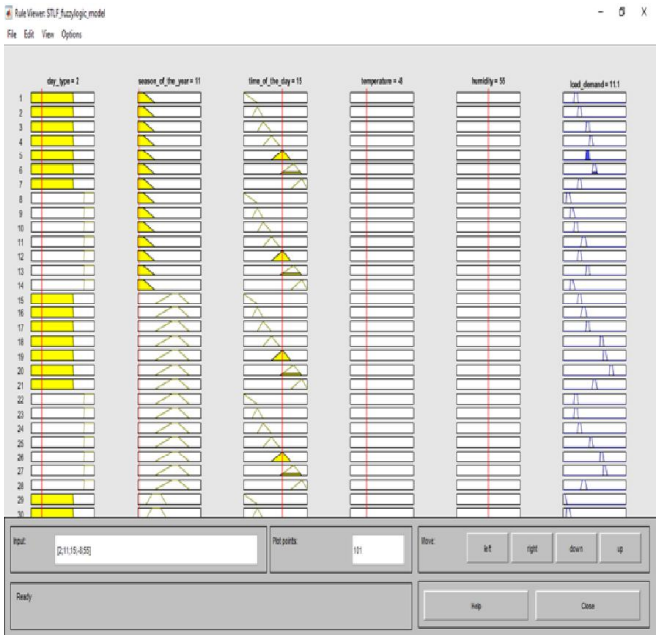


Figure 12: STLF_fuzzylogic_model rule viewer

g. Model error calculation

To evaluate the performance of the designed fuzzy rule-based STLF model its absolute error (AE) is calculated for each forecasted load demand value using equation (1) shown below.

$$AE = \frac{|Actual\ load\ demand - Load\ demand\ forecast|}{Actual\ load\ demand} \quad (1)$$

The AE value is multiplied by 100 to express it as a percentage (Absolute Percentage Error (APE)). The average of the APEs is known as the Mean Absolute Percentage Error (MAPE), which is a standard measurement for system perfomance.

IV. CASE STUDY

The methodology described above is applied to an 11 kilo-volt (kV) substation in Providence which is considered as the microgrid due to its small size. 2016 historical data is used for training the model, and the 2017 data is used for the model’s performance evaluation [10]. *The data which is used for training the model is for a period of 12 months (1 Jan 2016 to 31 Dec 2016) while that for the test data is 8 months (1 Jan 2017 to 31 Aug 2017).*

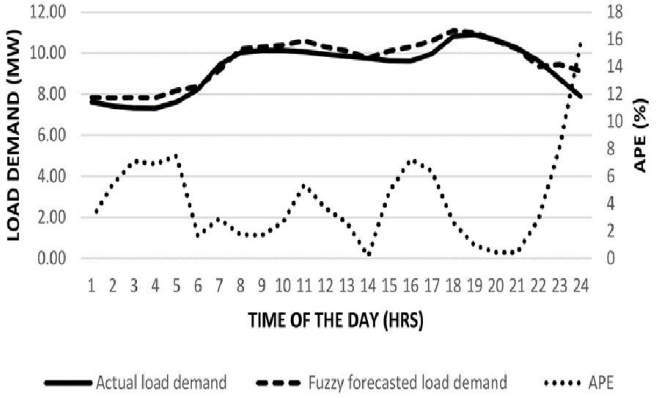


Figure 13: 24 hour load profile (28 Jan 2017)

The highest APE is 15.84% as shown in Figure 13, and the MAPE is 4.25%.

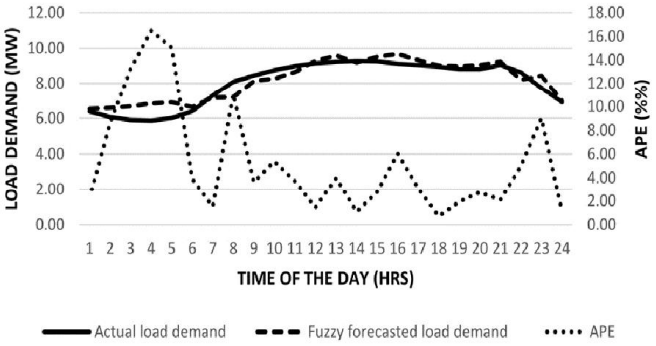


Figure 14: 24 hour load profile (12 May 2017)

The highest APE is 16.5% as shown in Figure 14, and the MAPE is 5.25%.

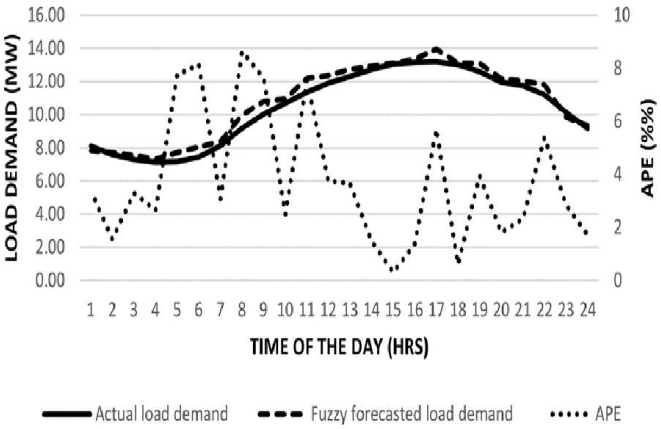


Figure 15: 24 hour load profile (4 Aug 2017)

The highest APE is 8.63% as shown in Figure 15, and the MAPE is 3.80%. The results of the forecasting study done on the said small scale power system are presented graphically as shown above.

V. Discussion

The MAPEs for winter (28 Jan 2017), and summer (4 Aug 2017) are lower than the MAPE for spring season (12 May 2017) as highlighted in section IV (Case study). This can be attributed to the fact that in winter, and summer there is a highly significant correlation between temperature, and the load demand. Hence, it is fairly easy to model, and predict load demand for winter, and summer seasons. However, the daily peak demand in summer (4 Aug 2017) is higher (13.2 MW as shown in Figure 15) than the daily peak demand in winter, which is 10.9 MW on the 28th of January, 2017. In summer more electricity is consumed since the air conditioning units for cooling only run on alternating current (ac) whereas in winter less electricity is consumed since the heating appliances are powered by both electricity, and natural gas. As for the spring season (12 May 2017) the electricity consumed is the lowest (daily peak demand is 9.29 MW as shown in Figure 14) when compared to the above said seasons; the temperatures experienced in spring season are moderately high or low, and hence depending on the temperature of the day less heating or cooling appliances are used. The use of heating or cooling appliances in accordance with the temperature, and the habits of the consumers in accordance with the day type, time of the day, and season dictate the daily power consumption pattern for a microgrid whose class of consumers is mainly residential and/ or commercial.

VI. Conclusion

The performance of the model which is evaluated on the basis of MAPE (3.8% for summer season) is quite good. The model accuracy can be improved by taking into consideration the daylight savings time of the area in which the microgrid is established (Providence, Rhodes Island). The daylight saving is responsible for decreasing the average daily load, and shifting the daily peak demand from one time of the day to another. Weather factors such as humidity, precipitation which affect power consumption can also be adopted to better the accuracy of the model. Gaussmf, and sigmf are complex types of membership functions (MFs) which can be used to improve the accuracy of the model in lieu of the simpler triangular, and trapezoidal MFs used to model the system. Nonetheless, the latter MFs can still be used, but to achieve a greater degree of accuracy an increased number of the said MFs is required. For example, to fuzzify the input variable ‘‘time of the day’’ seven triangular MFs (trimf) are used. If the number of the just said MFs is increased to eight or nine the accuracy of the model increases. Last but not least, incorporating special days, and public holidays into the model also increases the accuracy of the model.

References

[1] X. Hu, E. Ferrera, R. Tomasi, C. Pastrone, “Evaluation of Short-Term Load Forecasting Techniques Applied for Smart Micro Grids”, International Journal of Computer, Electrical, Automation, Control and Information Engineering Vol:8, No:11, 2014.

[2] Engr. B. UI Islam, “Comparison of Conventional and Modern Load Forecasting Techniques Based on Artificial Intelligence and Expert Systems”, International Journal of Computer Science Issues, Vol.8, Issue 5, No 3, September 2011.

[3] D.K Ranaweera, N.F Hubele, and G.G Karady, “Fuzzy Logic For Short-Term Load Forecasting”, Electrical Power and Energy Systems, Vol:18, No.4, pp.215-222, 1996.

[4] Short-Term Load Forecasting Using Artificial Neural Networks by Francisco Sandoval.

[5] A. Kumar Singh, Md. Muazzam, “An Overview of Electricity Demand Forecasting Techniques”, National Conference on Emerging Trends in Electrical, Instrumentation and Communication Engineering, Vol: 3, No: 3, 2013.

[6] M. Mohandes, “Support vector machines for short-term electrical load forecasting”, International Journal of Energy Research 2002, 26:335-345

[7] F. Li, X. Zhao, “The Application of Genetic Algorithm in Short-term Load Forecasting”, International Conference on Image, Vision and Computing (ICIVC 2012).

[8] V. Venkatesh, G.N Shilpa, C. Nataraja, “Development of Short-term Load Forecasting Models Using Stochastic Time Series Analysis”, International Journal Of Engineering Research and Development, Volume 9, Issue II (February 2014), PP. 31-36.

[9] Introduction to Fuzzy Logic Using MATLAB by S.N Sivanandam, S. Sumathi, and S.N. Deepa.

[10] Energy, Load, and Demand Reports for New England. Available: https://www.iso-ne.com/isoexpress/web/reports/load-and-demand/-/tree/zone-info

Wearable Safety Kit

İ.SAMURLU[1], E.GÜLGÖR[1], E.BERBEROGLU[1], K.DİRİK[1], Ş.TOKMAK[2], A.ÇAKMAK[2], A.T.ÖZDEMİR[2]

[1]Merkez Çelik AŞ, Kayseri/Turkey, ibrahim.samurlu@istikbal.com.tr, engin.gulgor@istikbal.com.tr, ersin.berberoglu@istikbal.com.tr, kalender.dirik@istikbal.com.tr
[2] Erciyes Üniversitesi, Kayseri/Turkey, tokmakha_gokhan@hotmail.com, cakmakabdulsamet@gmail.com, aturan@erciyes.edu.tr

***Abstract* - In this study, it is aimed to develop a wearable device, mounted on wrist or arm, that collects information of service staff (operator or maintenance personnel) related to vital health conditions. This device is able to stop the machine urgently according to health parameters in order to prevent work accidents. The system consists of two parts; one part is wearable unit and the other part is control unit that is integrated with the machine. These two units are paired each other over XBee communication channel. Wearable device monitors the user vital health parameters such as hearth rate, oxygen saturation, body-heat and motion data such as acceleration and rate of turn. Abnormalities in these data can be detected by the wearable unit simultaneously and if user's health condition is not stable the machine is stopped urgently by the control unit. This application is an important personal safety system and can reduce work accidents/hazards which occurs during maintenance operation. This study can be considered a good model for work safety in Industry 4.0 concept.**

***Keywords* - Wearable, Work Safety, Safety Equipment, IoT, Industry 4.0.**

I. INTRODUCTION

Today, industrial facilities are becoming more complex with the increase in machinery parks and growth of working spaces. Various methods have been proposed in the literature to prevent work accidents or to take proper security measures for minimal damage [1].

Production and maintenance activities contains intensive workloads therefore it is not surprise to see that the industry suffers from high rates of injuries and fatalities. According to TUIK (Turkish Statistical Institute), production industry's rate of non-fatal injuries is 48% greater than the average rate in Turkey as shown in Figure 1 [2].

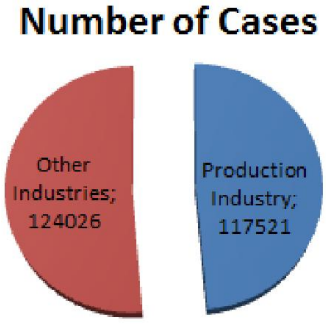


Figure-1 Number of Injury Case [2]

Number of fatal injuries arising from work accidents were gradually increased between 2012 and 2014 in Turkey according to Turkish Social Security Institution (SGK) and Turkish Occupational Health and Safety Council (ISIG) reports, as it given in Figure 2 [3]. This situation forces authorities and researchers to take proper measures in order to prevent work accidents.

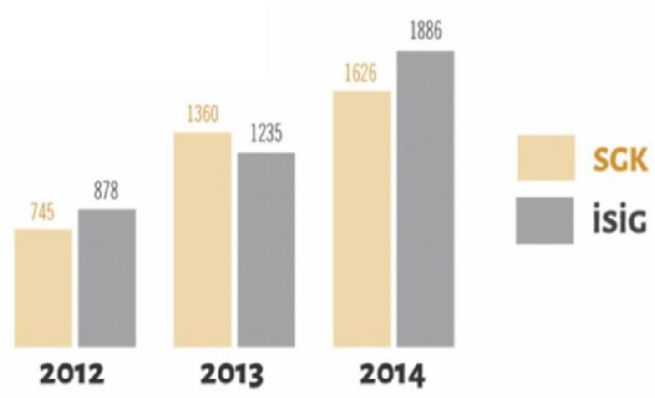


Figure 2- Number of fatal injuries [3]

Wearable devices such as smart bracelet, smart watch, smart glasses, smart clothes have been widely used in many areas [1,4]. Within the scope of this study, an industrial wearable security kit was designed and used in order to prevent work accidents. This security kit let employers, who work to operate or maintain machinery, to control the machine wirelessly. Staff who performs maintenance on a machine will be able to stop machine instantly in case of a dangerous case. This security kit collects vital body parameters like hearth rate, body temperature and oxygen saturation. These vital health parameters are associated with presenteeism, which cause loss of concentration.

Our wearable security kit uses personal health data to generate automatic responses such as stop the machine completely or disable some functions of it in order to prevent any damage that may occur. Wearable security kit that developed in this study can be considered as a good example for industry 4.0 in concept of machine to machine interactions. Thanks to cloud computing and IoT (Internet of Things) technologies this wearable security kit can interact with different devices and platforms for further applications [5].

II. CASE STUDY

The wearable security kit was tested in Merkez Çelik AŞ, very well-known furniture producer in the World, facilities located in Melikgazi/Kayseri/Turkey. A series of meetings have been made with company's OHS (Occupational Health and Safety) department, maintenance staffs and competent engineers before start to the system design. These interviews help us to understand needs, challenges and optimization opportunities about the issue in detail. In this way, a basic knowledge and understanding is achieved about the accidents that happened in industry. All work accidents happen in Merkez Çelik AŞ were investigated and some similarities were discovered in these cases.

Operational principles of machines employed in the company machinery park were analyzed one by one. Operational vulnerabilities and safety frailties occurred during maintenance activities were discussed.

Functionality of the wearable safety kit as an accessory such as eyeglasses, vest or wristwatch and advantages and disadvantages of these options were also discussed. Basic properties of our wearable security kit were determined according to these preliminary studies' results.

III. ALGORITHM

Data obtained from internal sensors (Temperature, Pulse Oximeter, Gyroscope, Accelerometer, Ultrasonic, Humidity) of the wearable safety kit is being analyzed in real time by the wearable unit and results sent to the control unit. These sensors' data are also saved to a computer for future calculations. Unusual situations can automatically be detected with these sensors' data and when it is necessary then emerging situations can be forwarded to relevant authorities via e-mail, SMS or push notifications. Data transmission between the wearable unit and the control unit is wireless.

The control unit found on machine side can wirelessly receive sensors data with vital health information of the staff who wear the wearable security kit and machine's emergency will be activated automatically when dangerous situations are detected. In normal conditions proper working scenarios are applied based on transmitted sensor data. The control algorithm of the wearable safety kit is given in Figure 3 as a block diagram.

IV. SYSTEM OVERVIEW

The system consists of two parts. The first part is the wearable unit that is worn by a staff and it contains a processor, sensors and variety of electrical components; the second part is the control unit placed on the machine side. The control unit handles machine-control by creating suitable conditions (enabling power or control) in accordance with the received sensor data from the wearable unit. These units can communicate to each other and monitor emerging situation's by analyzing sensors' data.

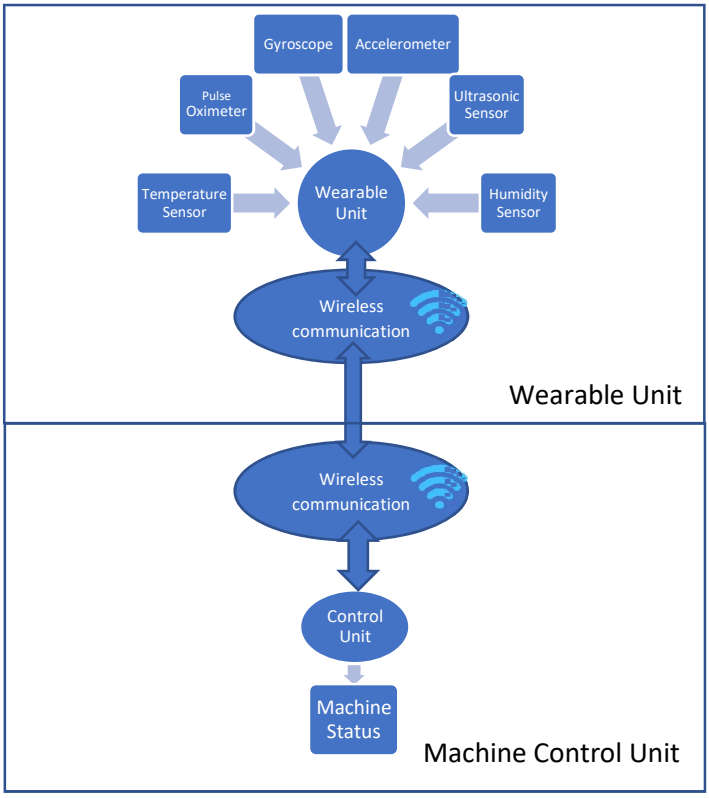


Figure-3: Operation Algorithm

A control unit of a machine can communicate with other control units and exchange information through the established network structure. A wearable unit worn by a staff is also able to pair with multiple machines at separate times however it cannot control multiple machines at the same time. In other words, one controller is able to pair and control only one machine simultaneously.

The wearable unit contains a controller, wireless communication device (XBee), OLED screen module, internal sensors and rechargeable battery pack. The control unit, it can be found on machine side, consists of a controller, wireless communication device (XBee) and relays [6,7].

A. Controller Unit

Teensy 3.2 was chosen as controller in the wearable safety kit. Thanks to its 32-bit ARM Cortex-M4 72MHz central processing unit (CPU) operations can be completed quickly [8]. This controller has 34 digital input/output pins, therefore sensors, screen and other peripherals easily connected and controlled.

B. Wireless Communication Device

XBee Pro, radio frequency is 2.4GHz and power consumption is 60mW, was used as a wireless communication device. This device supports two different communication methods that are wireless and serial. In wireless communication mode, modules are tuned to 2.4 GHz frequency band, 802.15.4 low power consumption standard is employed and long range RF communication protocol is used. Communication between the wearable and the control units is provided wirelessly but

communication between controllers is established over serial communication channel with I2C protocol [7].

Personal area network (PAN) structure is used to establish a network structure and connect all activated devices to each other. In this structure there are a single coordinator, routers and end-devices [6]. This network structure establishes an efficient communication infrastructure between machines located in a crowded machinery park. PAN network structure can be considered as a good network model for Industry 4.0. PAN network structure is shown in Figure 4.

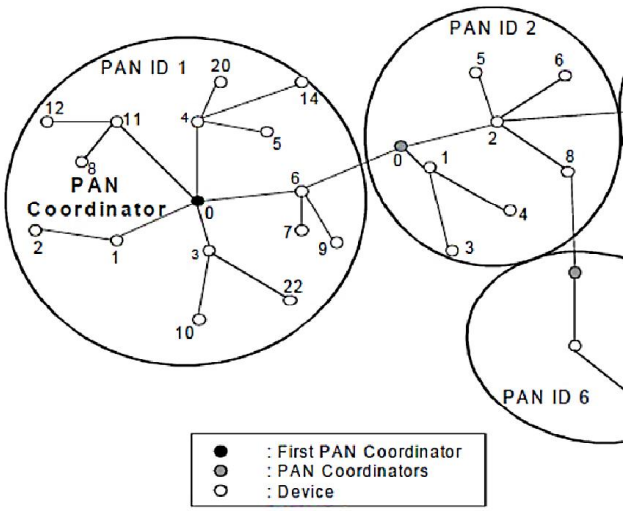


Figure-4: Sample of Established Network Structure [9]

C. Screen Module

Information screen found on the wearable unit is selected as Black-White, 0.96-inch and 128x64 pixel screen module providing low energy consumption. In this way, energy consumption in devices are tried to be minimized [10].

D. Internal Sensors

The raw data instantly obtained from gyroscope and pulse oximeter sensors are applied to software filters. Filtered data is more smooth because it is eliminated from noise. Acquiring reliable pulse and body temperature values are strongly depended on infrared measurement unit located in the sensor. Location and personal activity information can be obtained from three-axis gyroscope with dead reckoning and machine learning techniques. Therefore, when a staff experiences a fall during operation or maintenance detected by gyroscope data [4,11] and the machine can be switched off in order to prevent possible accident.

Gyroscope and pulse data are noisy and not stable. This problem causes the wearable security kit to give wrong decisions. Complementary filter method was used to cope with stabilization problem in gyroscope sensors [12]. Errors in gyroscope values were reduced and sensor response was transformed into smooth transitions by employing this filter.

E. Rechargeable Battery Block

The wearable unit contains a rechargeable battery block. The rechargeable battery energizes the wearable unit and makes the system active. Rechargeable battery is chosen as Lithium Polymer (Li-Po) type. The control unit of the wearable security kit is directly plugged in an electrical outlet therefore there is no battery block in the control unit side.

V. SAFETY LEVEL

In accordance with industrial safety standards, the safety category level of a safety equipment must be determined in terms of Safety control integrity level (SIL) degree. SIL is used to categorize potential danger of a machine. Danger risk of a machine defined by IEC 61508 (Functional Safety of Electrical/Electronic/Programmable Electronic Safety-Related Systems) and IEC 61511 (Safety Instrumented Systems for the Process Industry Sector) standards. There are four SIL degrees for safety equipments and can be calculated as Table 1 [13]. Defining SIL degree of the wearable safety kit designed in this study is mandatory part of our Application. SIL degree of the kit is found three according to risk analysis given in the table below. This analysis comprises frequency and severity of accident risks. Since the wearable safety kit uses wireless communication it can be categorized with SIL3 degree at maximum.

Table 1: SIL Degree Calculation Table [13]

SFF – HFT – SIL – Type A, Type B

Safe failure fraction (SFF)	Hardware fault tolerance (Type A – simple equipment)			Hardware fault tolerance (Type B – complex equipment)		
	0	1	2	0	1 (0*)	2 (1*)
< 60 %	SIL 1	SIL 2	SIL 3	Not permitted	SIL 1	SIL 2
60% to < 90%	SIL 2	SIL 3	SIL 4	SIL 1	SIL 2	SIL 3
90% to < 99%	SIL 3	SIL 4	SIL 4	SIL 2	SIL 3	SIL 4
≥ 99%	SIL 3	SIL 4	SIL 4	SIL 3	SIL 4	SIL 4

Suitable hardware combination that establishes security conditions was searched according to IEC 61508 and IEC 61511 standards. The system architecture aimed to be designed is given in Figure 5. SIL degree of the peripherals are determined by the lowest SIL degree of subpart of whole system. For this reason, all devices that wanted to be used with the wearable safety kit are expected to be SIL3 degree at minimum.

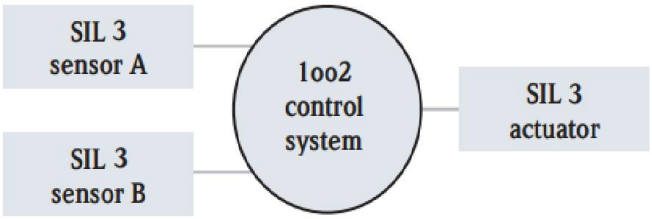


Figure 5: 2-Channel System Architecture

VI. DATABASE SYSTEM

All information that is generated from whole the system is saved to a database therefore these big amount of data can be reached anytime. Saved data contains the wearable safety kit sensors data, machine operation and maintenance durations, staff information and control history with time stamps.

VII. CONCLUSIONS

As a result of this study, two devices are designed as Master and Slave unit. Slave unit (the wearable unit) worn by staff and the master unit (control unit) placed on machine. In this way, staff's health condition is being transmit to machine control over XBee in order to reduce occupational accidents, increase work safety and facilitate machine maintenance activities.

A primitive prototype was created using Teensy development board and sensors. Control algorithm was created for transferring and processing data. Since gyroscope and pulse oximeter are nonstable and noisy complementary filter with gyroscope and average values of pulse sensor were used. Connections were tested by establishing wireless connection points between master and slave units in Merkez Çelik AŞ. Different antenna types were tried to increase range of wireless devices.

Created prototype was tested on a machine. The wearable unit was located on left wrist of the first author and a relay controlled by the control unit was serially connected to the machine emergency line. This relay was manipulated with the commands transferred by the wearable unit and fall of author automatically detected by the control unit and machine was stopped automatically. Fall decision is given by control unit in order to increase battery life on the wearable unit.

Created prototype was tried by eleven maintenance staffs and their user experience was reported. According to this report prototype must be redesigned for meet the new demands.

VIII. FUTURE WORKS

The wearable security kit may be designed as different types of accessory (hard hat, goggles, vests) to improve its ergonomic and supported with a camera. User experiences with different models of safety equipment would be compared to each other in order to find the most convenient model.

A supervisory control and data acquisition (SCADA) system would be developed. It will be possible to modify parameters or monitor machinery online with this SCADA system.

Application for SIL3 certification will be made for our safety kit.,

IX. ACKNOWLEDGEMENTS

This work was supported by Merkez Çelik A.Ş. - R&D Center

REFERENCES

[1] M. Aleksy, M. Lehtola and A. Puchakayala, "Design and Implementation of a Wearable Safety Suit", IT Convergence Practice, vol. 1, no. 1, pp. 28–36, 2013

[2] Turkish Statistic Institute, TUIK (December 2013), "Research report about work accident and health problems related to work", Available: http://www.tuik.gov.tr/PreHaberBultenleri.do?id=16118

[3] Turkish Social Security Institution, SGK (October 2017), "Work accidents and occupational diseases in Turkey for 2012-2013-2014", Available: http://www.sgk.gov.tr/wps/portal/sgk/tr/kurumsal/istatistik/sgk_istatistik_yilliklari

[4] A. T. Özdemir, B. Barshan, "Detecting falls with wearable sensors using machine learning techniques", *Sensors*, vol.14, pp.10691-10708, 2014

[5] A. T. Özdemir, C. Tunc and S. Hariri, "Autonomic fall detection", *IEEE International Conference on Cloud and Autonomic Computing*, pp. 166-170, 18-22 September 2017, Tucson, AZ, USA

[6] Digi International Inc. (October, 2017), "Wireless connectivity kit getting started guide", Available: https://www.digi.com/resources/documentation/digidocs/pdfs/90001456-13.pdf

[7] J. Albrecht, and L. Udpa, "Creating a simple Zigbee communication network using XBee", Michigan State Universtiy, Technical Presentation 2013, Available: http://www.egr.msu.edu/classes/ece480/capstone/spring13/group02/documents/Technical%20Presentation.pdf

[8] PJRC (October, 2017), "Teensy USB development board, Available: https://www.pjrc.com/store/teensy32.html

[9] Standard 802.15.4, "IEEE standard for low-rate wireless networks (WPANs)", IEEE Computers Society and IEEE Standards Association, 2015.

[10] Adafruit (October, 2017), "Monochrome OLED graphic display", Available: https://www.adafruit.com/product/326

[11] A. T. Özdemir and A. Orman, "Developing An iPhone smartphone based fall detection algorithm", *Proc. 23rd Signal Processing and Communications Applications Conference* (SIU), pp. 2456-9, 16-19 May, 2015, Malatya, Turkey

[12] J. P. How, "Inertial sensors, complementary filtering, simple Kalman filtering", Massachusetts Institute of Technology, Lecture Notes Fall 2004, Available: https://ocw.mit.edu/courses/aeronautics-and-astronautics/16-333-aircraft-stability-and-control-fall-2004/lecture-notes/lecture_15.pdf

[13] Magnetrol International (March, 2015), "Understanding safety integrity level", Available: http://us.magnetrol.com/Literature/1/41-299.5_SIL.pdf

Determination of Faults in HVDC Networks

F. ÜNAL[1] and S. EKİCİ[1]

[1] Fırat University, Elazığ/Turkey, funal@firat.edu.tr
[1]Fırat University, Elazığ/Turkey, sekici@firat.edu.tr

Abstract - **Although there are a lot of studies in the literature for determining faults on High-Voltage Alternative Current (HVAC) lines, there are only a few studies performed for automatic detection of fault location on High-Voltage Direct Current (HVDC) transmission lines. This study is devoted to determining single phase to ground faults on HVDC transmission lines by using machine learning and signal processing methods. Fault simulations were performed by using Matlab software. The recorded fault current and voltage signals are decomposed by using Discrete Wavelet Transform (DWT) for the feature extraction stage of the proposed method. 12-level decomposition with Daubechies (db4) wavelet family is preferred for time-frequency analysis. Artificial Neural Networks (ANN) and Support Vector Machines (SVM) methods are used to estimate the distance of fault locations. The results obtained show us that SVM method has a lower error rate (1.79) than ANN (3.26) in fault location estimation. This study will be an excellent example of digital distance protection of HVDC transmission which is the growing trend in the new electrical energy transmission networks.**

Keywords - **Artificial Neural Networks, Discrete Wavelet Transform, HVDC transmission lines, Support Vector Machines.**

I. INTRODUCTION

IN modern World, energy requirement that has become an indispensable part of our lives are fulfilled by increasing power plants day by days, electric grids, electronic control systems. Established those systems without regard to any human power or manual control can be thought of as the first steps towards to a single enormous system involving power systems too. HVDC transmission systems are emerging technologies that appeared in our lives soon like the concept of energy efficiency. In the use of HVDC systems for transporting high power levels to far distances, rapidly evolving high voltage converters and other high-voltage devices have a significant concern. Currently, HVDC systems are known as an efficient and robust way transmitting high power levels to far distances [1], [2]. There are many advantages to carrying with DC compared to Alternative Current (AC). Some of these are different tasks, such as small net losses for long distances, more power transmission per conductor and underground transmission as a return path. Another advantage of underground transmission is that each conductor can be considered as an independent circuit. Because of not exposed to external influences such as load current and surface effect, there are no reactive power requirements [3]. It can also perform many different tasks such that removing system synchronisation and stability problems, simpler transmission towers and connecting AC systems at a different frequency.

HVDC systems are used quite often especially for underwater and underground connection applications. To have more expensive station equipment than its counterpart is considered as the most prominent disadvantages of HVDC systems [4]. Other obstacles encountered within power transmission are mainly in the event of permanent failure, power transmission capacity is reduced to half of its value, supply of switching components to faults in multi-terminal structures, reactive power requirement of rectifier-transformer stations, costly switching and station equipment, development of fault detection and location algorithms, the operating difficulty of multiple terminal stations and challenges encountered in changing the direction of power etc. While the protection equipment and fault detection methods are similar to the AC systems, the line current and voltage characteristics are utterly different in HVDC systems. In general, fault detection methods in HVDC transmission lines are based on; impedance measurement, current and voltage signal analysis techniques, intelligent network applications and classical travelling wave protection method.

HVDC protection methods are divided into two groups. The first one is the primary protection and the second is the background protection. While HVDC systems use travelling wave protection as the primary protection algorithm, differential protection, derivative protection, over current and over voltage protection are used as background protection. Although these methods provide a low level of protection in the background protection, they prevent damage to the system components in case of failure of the primary protection components [5].

Considering the literature studies made in recent years, fault detection methods in HVDC transmission lines are being carried out intensively in different areas such as travelling wave method, signal decomposition methods, smart grid applications. In [6]–[9], the authors benefited from different approaches to the travelling wave protection during fault detection. Traveling wave method determines the location of the faults using time difference between the arrival time of travelling and reflected waves in both directions from the fault point to terminals. In the case of both terminal signals are used, the arrival time to fault point of forward and backward reflected

waves and the arrival times to the travelling wave detectors are also utilised by GPS data. In the case of using a single terminal, even though GPS data is not needed it is crucial to determine the arrival time of the reflected second wave correctly. Wavelet Transform (WT) method, which is frequently used among signal decomposition methods, is preferred for determination of high-frequency components by utilizing different decomposition packets and feature extraction. In [10], authors have proposed an approach that overcomes to problems such as boundary region distortions and noise reduction in travelling wave method by taking advantages of the modulus maxima of the wavelet transform of DC signals obtained from the rectifier side. In [11], authors discussed the fault location algorithm and test results which combining both Continuous Wavelet Transform (CWT) and travelling wave method during fault analysis on hybrid HVDC transmission lines and underground cables. In [12], authors used generalised regression neural networks (GRNN) for fault estimation and used singular value decomposition (SVD) at feature extraction stage by using travelling fault waves on HVDC transmission line. The feature vectors obtained from current and voltage signals are employed in the modelling stage to show the relationship between fault location and the travelling wave after training of neural network. In [13], authors have benefited from the simulation model on Matlab software in their work. They also benefited from the neural network that uses backpropagation algorithm during the classification of different fault conditions (L-L, L-L-G, L-G) by recorded signals on the AC side of HVDC model using voltage source converter. In [14], authors benefited from an approach to detection and location of faults using both SVM and travelling wave method in HVDC transmission lines which consist of overhead and underground lines.

In this study, virtual faults are generated in each km of the transmission line of 300 km of HVDC simulation work. DWT has used in signal decomposition stage to obtain feature vectors from fault current and voltage signals. The wavelet energy and Shannon entropy values are determined to reduce the size of feature vectors after normalisation to express each fault state using fewer data. In the fault location estimations process, a multi-layer feed forward back propagation neural network and least-squares support vector machines (LS-SVM) are employed. In this study, where only single phase-ground faults examined, it is understood from obtained graphs and regression values that the WT-LS-SVM combination has a relatively high performance in the fault location estimation process. Another result obtained from the simulations is that the performance of the proposed method is independent of the variation of fault resistance.

II. DİSCRETE WAVELET TRANSFORM

Fourier transformation is an excellent approach to the analysis of frequency-independent signals. However, it cannot give the desired results in the transient analysis. The wavelet transform is very efficient in the analysis of non-stationary signals. The resolution of the time-frequency signal can be obtained optimally [15], [16]. In the WT, which can be displaced during expressed with specific functional forms can be realised. While short-time Fourier transform (STFT) uses a fixed window function, in the WT analysis a wavelet function (x) is used. Another consideration in wavelet transform is that to define the process is continuous or discrete. In this way, a discrete or continuous sampling of the main wavelet function with shifting and scaling process can be achieved. In the DWT method, shifting and scaling operations are performed by applying discrete steps. This process is shifted or scaled around the discrete numerical values depending on the distance. The main wavelet function used in DWT is given in as in [17] and [18].

$$\psi_{j,k}(t) = \frac{1}{\sqrt{s_0^j}}\,\psi\left(\frac{t-k\tau_0\, s_0^j}{s_0^j}\right) \tag{1}$$

Where j and k are integers, $s_0 > 0$ is the scaling coefficient and τ_0 represents shifting coefficient which depends on the scaling coefficient. Another parameter that should be mentioned in DWT is the scaling function. This function provides in the determination of detail and approximate coefficients. The smaller the scaling, the more detail coefficients can be obtained from [18] and [19]. The scaling function is given in (2)

$$\varphi(t) = \sum_{j,k} \gamma(j,k)\psi_{j,k}(t) \tag{2}$$

The general expression in (3) is used to mention about shifting and scaling of the analysed f (t) signal up to j − 1 scale.

$$f(t) = \sum_k \lambda_{j-1}(k)\varphi(2^{j-1}t-k) + \sum_k \gamma_{j-1}\,\psi(2^{j-1}t-k) \tag{3}$$

In this equation, $\varphi_{j,k}(t)$ is a scaling function, $\psi_{j,k}(t)$ is the selected wavelet function and $\lambda_{j-1}(k)$ and $\gamma_{j-1}(k)$ are orthonormal coefficients. $\lambda_j(k)$ is the low pass band of the decomposed signal spectrum and $\gamma_j(k)$ is the high pass band.

A. Wavelet Entropy

Wavelet entropy is a combination of wavelet theory and entropy theory, and it is an expression of the distribution of

frequency components in different levels of the signal. Wavelet entropy theory and its applications can be used at different stages such as fault detection phase and system state identification [18], [20], [21]. When the signal $x(n)$, in which the discrete wavelet transform is performed, the detailed coefficients obtained from the high-pass filters $d_j(k)$, approximate coefficients obtained from low-pass filters $a_j(k)$ components containing the information of the frequency band at k time and the j scale is presented as $D_j(k)$ and $A_j(k)$. The mathematical representation of $D_j(k)$ and $A_j(k)$ signal components are shown in (4) and (5).

$$D_j(k): \left[2^{-(j+1)}F_s, 2^{-j}F_s\right] \quad (j = 1,2,3,\dots,m) \tag{4}$$

$$A_j(k): \left[0, 2^{-(j+1)}F_s\right] \tag{5}$$

In the above equation, f_s is sampling frequency. The original signal sequence $x(n)$ can be thought of as the sum of all components. The wavelet spectra (E_j) and wavelet energy spectra (E_{jk}) of the wavelet entropies at j scale are shown in (6) and (7) respectively.

$$E_j = \sum_k E_{jk} \tag{6}$$

$$E_{jk} = \left\|D_j(k)\right\|^2 \tag{7}$$

When using orthonormal wavelet transform, the total signal energy E and the sum of the energies of each component at j scale E_j, mathematical expression of the Wavelet Energy Entropy (WEE) value is shown in (8) as,

$$WEE = -\sum_j p_j \log p_j \tag{8}$$

where $p_j = E_j/E$ and $\sum_j p_j = 1$. There are many commonly used entropy calculation methods and some of those; Shannon, Threshold, Norm, Logarithmic Energy and Sure criteria. In this study, Shannon entropy values are calculated to represent each fault location by using fault current and voltage signals.

III. SUPPORT VECTOR MACHINES

SVM is a classification method based on statistical learning theory, optimisation theory and Vapnik-Chervonenkis dimension theory [22]. The SVM method can be thought of as transferring the original input space data to the multidimensional feature space, which can be linearized by an optimally formed separating plane. Although the SVM method is mainly developed for binary classification, there are also multi-class methods in which more than one binary SVM is used. In this way, it is possible to classify the sample space data which cannot be linearly classified into multiple classes using parabolic or exponential functions [23]. In SVM method, consisting of N observation in n-dimensional space, each data vector of a single data pair $x_i \in R^n \; and \; i = 1,2,3,\dots,N$ is defined by the class label $y_i \in \{-1,+1\}$ corresponding to this data vector. The input data of positive class $y_i = +1$ and input data belonging to the negative class $y_i = -1$ is grouped by using any $f(x)$ hyperplane selected for the classification process [29]. The definition of $y_i = +1$ and $y_i = -1$ mentioned here can be thought of as belonging first group or second group. The mathematical representation of $f(x)$ hyperplane defined for classification process is given in (9) and (10).

$$f(x) = w^T.x + b = \sum_{j=1}^{N} w_j x_j + b \tag{9}$$

$$y_i(w^T.x + b) \geq 1, \; i = 1,2,3,\dots,N \tag{10}$$

There; w is an n-dimensional vector and b is a threshold value. The main purpose of SVM method is to define the widest separating surface thanks to the support vectors. SVM's generalization ability is achieved by maximizing this splitter plane [25]. In order to maximize the range of m must be obtained minimum value of $\|\overline{w}\|$. $\|\overline{w}\|$ can be rewritten mathematically as shown in (11).

$$min\|\overline{w}\| = min\left[\frac{1}{2}w^T w\right] \tag{11}$$

SVM places the original input space data in the feature space with though kernel function and support vectors specified around the hyperplane. The linear decision function in binary form, which transfers x to L dimension and F feature space using a nonlinear vector function $\left(\phi(x) = \phi_1(x), \dots, \phi_L(x)\right)$ is given in (12). Fig.1 represents of basic classification principle of SVM.

$$f(x) = sign\left(\sum_{i=1}^{N} \alpha_i^* y_i \phi^T(x_i)\phi(x) + b^*\right) \tag{12}$$

Assuming that α^* are the optimal solution for binary problems of α and the values in this equation $(\alpha_1, \alpha_2, \alpha_3, \dots \dots \alpha_i)$ represent Lagrange multipliers [26]. This equation can be solved using a nonlinear kernel function as shown in (13) to determine which class of training sample belongs as a result of this equations.

$$x \in \begin{cases} f(x) = +1 & I.Class \\ f(x) = -1 & II.Class \end{cases} \quad (13)$$

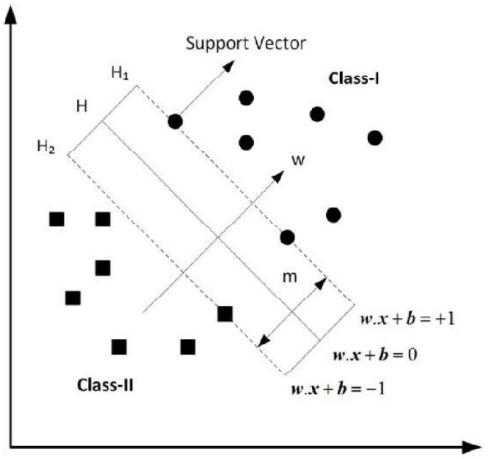


Figure 1: The optimal hyperplane and support vectors

The kernel function can be in different forms, depending on variety and complexity of the classification process. Polynomial, Radial basis or sigmoid kernel functions are some of the preferred in SVM.

A. Least-Squares Support Vector Machines

Least Squares Support Vector Machines (LS-SVM) regression method is a rearrangement of standard SVM, and it is created by combining different approaches such as regularisation networks, Gaussian process, Fisher discriminant analysis, reproducing kernel function in Hilbert Space (RKHS) [27]. Also, LS-SVM method helps in classification and determination of the optimal hyperplane through primal-dual representation for difficult optimisations [27]. LS-SVM models used in classification and non-linear regression process are derived from linear Karush-Kuhn-Tucker (KKT) systems. In LS-SVM, Vapnik's formulation rearranged from two points [27]. Firstly, the expression of inequality in SVM has taken the place of equality. Thus, the 1 value on the right side of the equation considering as a threshold becomes the target value.

This target value allows misclassifications until error value e_k is determined which result from the spread of intersection regions of projection function. In the second arrangement, this error variable used as a square expression (e_k^2) in LS-SVM. Mathematical expressions of these regularizations proposed by Suykens [27] are given in (14).

$$\underbrace{min}_{w,b,e} J_P(w,e) = \frac{1}{2} w^T w + \gamma \frac{1}{2} \sum_{k=1}^{N} e_k^2 \quad (14)$$

In this equation, e_k represents the error value, γ is regularization constant, w is n-dimensional vector of the output layer and, b is the threshold value. Primal representation can be used in linear classification problems but generally w can be an infinite dimension, so to solve this issue dual representation preferred for nonlinear classification in LS-SVM. The primal-dual representation of LS-SVM method given in (15).

$$\begin{aligned} &Primal:\ y_k[w^T \varphi(x_k) + b] = 1 - e_k \\ &Dual: sign[\textstyle\sum_{k=1}^{N} \alpha_k y_k\, K(x, x_k) + b] \end{aligned} \quad (15)$$

IV. Simulation Study

In the simulation study, a 1000 MW (500 kV, 2 kA) DC interconnection is used to transmit power from 500 kA, 5000 MVA 60 Hz network to a 345 kV, 10000 MVA, 50 Hz network. The rectifier and inverter are constructed using 12 pulse converters. The rectifier and inverter interconnected through a 300 km distributed line and two 0.5 H reactors. The control system for inverter and rectifier is created using the 12 pulse HVDC Control Block elements from the Matlab library. Two breakers are used to apply faults on the inverter AC side and rectifier DC side. AC transmission line sections are built using embedded L-R equivalent circuit and third harmonic components with an 80◦ angle to the fundamental frequency component. The converter-transformers (Wg, Wye, 0,) modelled with Three-Phase Transformer (Three-Windings) blocks. AC filters are used to prevent the odd harmonic currents spreading out on the line. Also, these filters can be thought as large capacitors at the fundamental frequency, thus providing reactive power compensation for the rectifier consumption due to the firing angle (α). DC currents (IdR and IdI) and DC voltages (Vd LR and Vd LI) defined in control blocks scaled to pu (1 pu current=2 kA, 1 pu voltage=500 kV). In normal operation, the current value of the rectifier (Id ref) and the voltage value of the inverter (Vd ref) pursue a predefined reference value in the system. They are set at 0.1 and 0.05 pu, respectively. In the simulation, control systems for both inverter and rectifier use the same Discrete HVDC Controller Block from the Simulink/SimPowerSystems library. This control block can operate in both rectifier and inverter mode. The Master Control system generates the current references for both converters and initiates the starting and stopping of the DC power transmission. In inverter control system, gamma measurement block observes the extinction angle (γ) for each 6 pulse thyristor bridge. The alpha (α) value in control system is the firing delay angle ordered by the regulator.

Fault current and voltage signals obtained from the simulation recorded at each km of 300 km between the 15th and 285th. Fault duration is kept constant for each km and appeared between [0.7-0.8] seconds after the simulation start. The monopolar HVDC transmission system benefited in this study is shown in Fig. 2. Table I gives the characteristics of the DC transmission line used in the simulation.

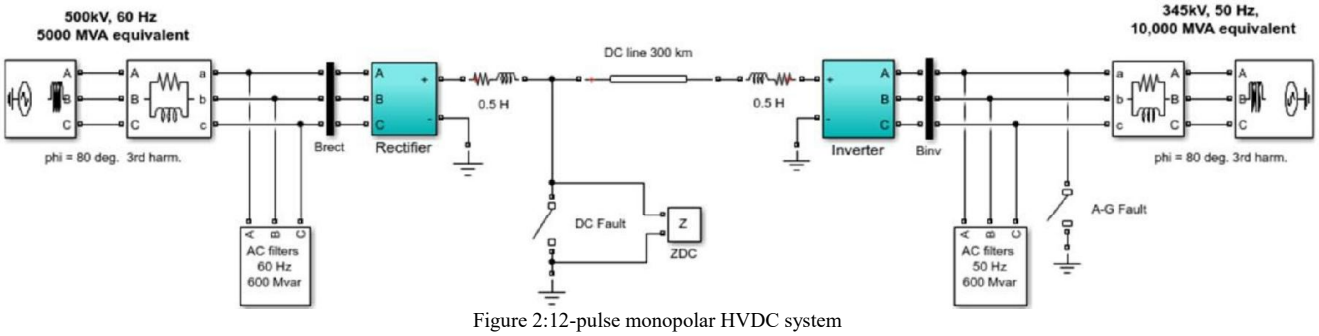


Figure 2:12-pulse monopolar HVDC system

Table I. Properties of DC transmission line in the simulation

Transmission Line	Characteristic
Length	300 km
Class	Distributed parameter
Circuit Structure	Serial RLC
Smoothing Reactors	0.5 H (2 units)
Primary voltage	0.90 (rectifier side) 0.96 (inverter side)
Sampling Time (s)	50×10-6 s
DC line voltage (kV)	500 kV
DC line current (kA)	2 kA
Fault resistance Rd	Ron (1 ohm)
Grid frequency	50 / 60 Hz
Resistance	0.015 ohm/km
Inductance	0.792.10-3 H/km
Capacitance	14.4.10-9 F/km

The current and voltage values of the rectifier side in the simulation operation under steady state and fault condition are given in Fig. 3 and Fig. 4 respectively.

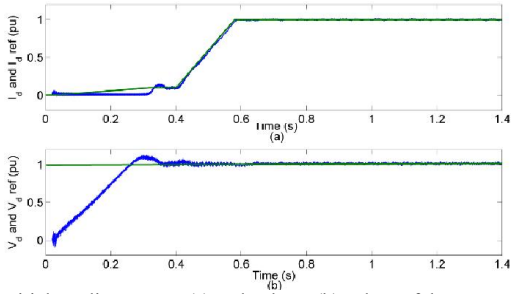


Figure 3: Initial DC line current (a) and voltage (b) values of the HVDC system

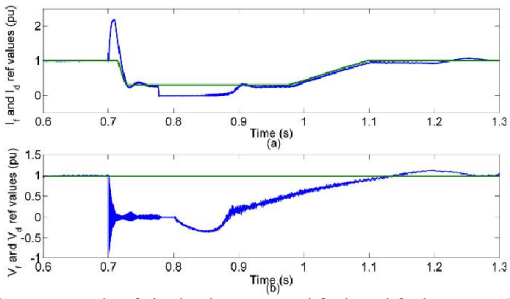


Figure 4: An example of single phase-ground fault and fault current (a) and voltage (b) occurring at 50th km of DC transmission line (rectifier side)

The alternation of DC fault current and voltage values according to nearest and farthest points selected in the simulation study are given in Fig. 5.

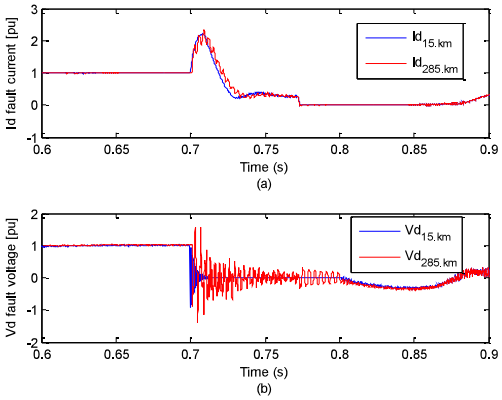


Figure 5: Alternation of DC line fault current (a) and voltage (b) values according to km

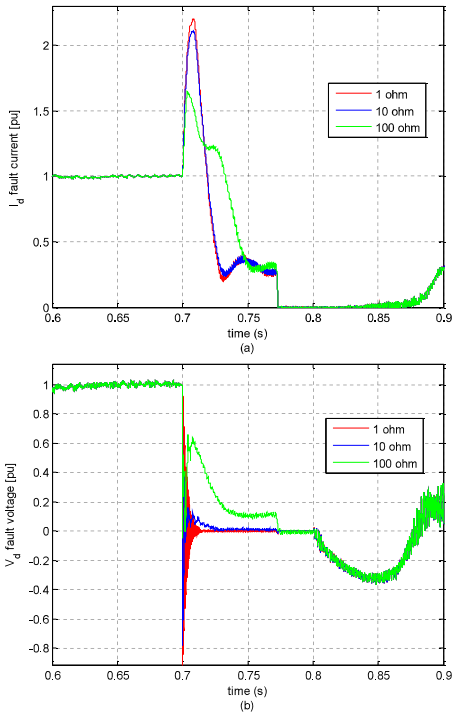


Figure 6: An example of single phase-ground fault and fault current (a) and voltage (b) occurring at 15th km of DC transmission line (rectifier side)

A. Feature Extraction

DWT method can detect the high-frequency components using of a wavelet that is shifted and scaled by discrete coefficients through the signal. In analysing the process of DWT, the original signal first passed through high and low pass filter, and the output data is decomposed to obtain approximation and detail coefficients. Subsequently, these approximation coefficients are sent to the second level to repeat the operations applied to the previous level. These process steps are continued to likewise until to desired decomposition level. Fig. 6 shows the first five levels of the DWT of the fault signal occurred at 15th km of DC line.

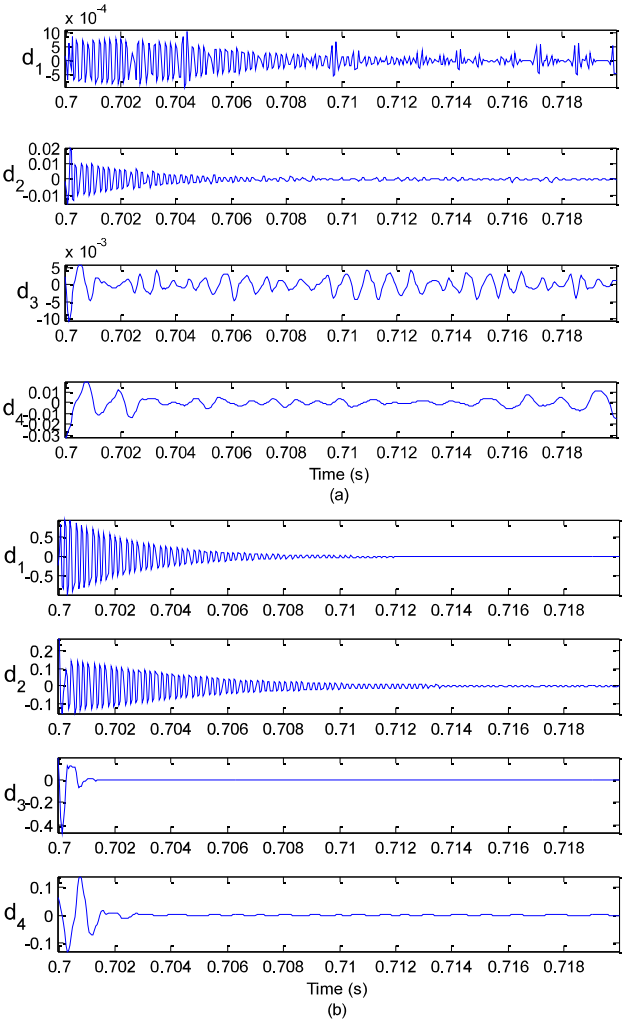


Figure 7: The first five level of DWT of the fault current (a) and voltage (b) signals at 15. km of DC line

In this study, after applying DWT to the fault current and voltage signals, 13 feature vectors in total, including 12 details and 1 approximate coefficient are obtained. Since the approximate coefficients in the 12th level contain low-frequency components, they are not considered as a distinctive feature and removed from the dataset. Thus, in total 22 feature vectors are obtained from the current and voltage signals for each km of fault point. The decomposition process of the fault current and voltage signals contains only the part of first 20 ms after the fault started. Therefore, the data set include the samples of the signals between [14000-14400] samples. As it is well known, the fault inception angle which is very important in AC fault analysis does not affect the DC fault analysis. So,

all faults simulated at the same time interval in this study. Daubechies (db4) wavelet family, which frequently preferred in fault detection, estimation and classification in power systems is selected as a mother wavelet. The sampling frequency is 20 kHz. Fig. 6 shows the first five levels of the DWT of the fault signal occurred at 15th km of DC line. Since the feature datasets obtained from DWT are very large, the datasets are reduced to smaller sizes so that there are no changes in features. For this purpose, the wavelet energy and Shannon entropy values of the DWT coefficients calculated.

B. Fault Estimation by using ANN

The feature vectors obtained after applying DWT to fault signals evaluated as the input values in training and test process of the ANN to used in the fault location prediction. The ANN used in this study is a single layer neural network which uses feed forward back propagation learning algorithm. In the training stage, the Levenberg-Marquardt training algorithm is preferred. The mean squared error (mse) is specified as the error function. Tangent sigmoid and linear activation functions are selected for input and output layer respectively. When the number of hidden layer neurons of the trained ANN specified as 20, the best performance is obtained considering the feature vectors. Other parameters that are set to find the most appropriate coefficients in hidden layer determined as iteration number =1000, maximum error value =100, minimum gradient=10−7. Training of ANN carried out considering these limitations. If ANN iteration steps reach any of the specified limit values, training has ended. In the ANN application, The input datasets distributed as 60% for training, 20% for testing and 20% for validation. Therefore, the sizes of data matrices are [22x163] for training and [22x54] for testing and validation of ANN respectively.

C. Fault Location Estimation by LS-SVM

In this study LS-SVM method preferred over the fault prediction stage for reasons such as using $\gamma\ (gamma)$ and $\sigma^2\ (sigma)$ parameters that reduce training error and regulate the sensitivity of the hyperplane. The regularization parameters monitor the relevance between training error reduction and separation surface sensitivity. In other words, ıt is a previously defined error tolerance function for curve fitting in kernel space. Another important parameter that should mention in LS-SVM is the specified kernel function. In the study, a radial basis kernel function uses to improve accuracy. The mathematical expression of radial basis kernel function is given in (16) as,

$$K(x_i, x_j) = e^{\frac{\|x_i - x_j\|^2}{2\sigma^2}} \tag{16}$$

Where, (x_i, x_j) represents training sample pairs and $\sigma^2\ (sigma)$ represents the variance of the Gaussian kernel function. Trained datasets of LS-SVM verified using 'leave-one-out' cross-validation method. By this approach, the model populated with the remaining data sets by a certain set of data excluded from each validation cycle. The performance of the model is estimated from the remaining data sets. This process repeats for each set of data and then calculates the average of different performance values to achieve a result about the fulfillment of the entire model. In the LS-SVM application, the input datasets similarly distributed as 60% for training, 20% for testing and 20% for validation. In the last case, input data matrices are for training of ANN $[22 \times 163]$, for testing and validation $[22 \times 54]$. Figure 8 represents the actual and estimated km's of ANN and LS-SVM simulations.

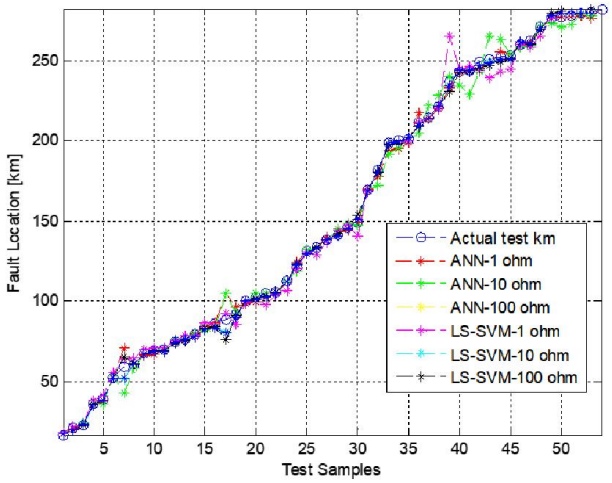


Figure 8: Fault location results of ANN and LS-SVM

Table II gives the regression parameters; root means square errors (rmse) and performance comparisons of ANN and LS- SVM simulations. Also, the inherent characteristics of LS- SVM offer it more compatible options when considering the generalisation and clustering tasks of data sets.

Table II Obtained results from ANN and LS-SVM applications under different fault resistances

Comparison parameters	ANN			LS-SVM		
	Ron=1 ohm	Ron=10 ohm	R=100 ohm	Ron=1 ohm	Ron=10 ohm	R=100 ohm

Rmse value	3.657	3.2676	3.324	1.814	1.8016	1.796
Regression value (R^2)	0.998	0.9992	0.999	0.999	0.9997	0.999
Performance (%)	97.58	96.42	98.4	98.26	98.30	98.30

V. CONCLUSION

In this study, single phase-ground faults occurred in HVDC transmission lines are examined using DWT, ANN and LS-SVM. The fault current and voltage signals obtained from simulation are recorded only on DC side of the line. These signals are decomposed using DWT for signal processing and feature extraction steps. After the calculation of energy and Shannon entropy of the fault signals, the feature vectors for ANN and LS-SVM have been obtained. LS-SVM method achieved better results than ANN method under different fault locations and fault resistances with the performance ratios above 98% for different fault resistances. Also, there is no need to determine the optimal hidden layer neurons or other parameters; more effective results can be obtained from LS-SVM. Although there are many studies performed in the literature for AC transmission line fault analysis, this study shows that the signal processing and machine learning techniques can be used for HVDC line fault analysis. In the further studies, these methods will be used for bipolar HVDC lines and multi-terminal DC interconnection systems which are preferred commonly in HVDC applications.

REFERENCES

[1] M. H. Okba, M. H. Saied, M. Mostafa, and T. Abdel-Moneim, "High voltage direct current transmission-a review, part i," Energytech 2012, IEEE, 2012.

[2] J. Setreus and L. Bertling, "Introduction to hvdc technology for reliable electrical power systems", Proceedings of the 10th International Conference on Probabilistic Methods Applied to Power Systems PMAPS'08, IEEE, 2008.

[3] D. Jovcic and K. Ahmed, High voltage direct current transmission: converters, systems and DC grids. John Wiley & Sons, 2015.

[4] J. Arrillaga, High voltage direct current transmission. Iet, 1998, no. 29.

[5] C.-K. Kim, V. K. Sood, G.-S. Jang, S.-J. Lim, and S.-J. Lee, HVDC transmission: power conversion applications in power systems. John Wiley & Sons, 2009.

[6] E. O. Schweitzer, A. Guzma´n, M. V. Mynam, V. Skendzic, B. Kasztenny, and S. Marx, "Locating faults by the travelling waves they launch,", 67th Annual Conference for Protective Relay Engineers, IEEE, 2014.

[7] Z. Yi-ning, L. Yong-hao, X. Min, and C. Ze-xiang, "A novel algorithm for hvdc line fault location based on variant travelling wave speed", 4th International Conference on Electric Utility Deregulation and Restructuring and Power Technologies. IEEE, 2011.

[8] X. Liu, A. Osman, and O. Malik, "Hybrid travelling wave/boundary protection for monopolar hvdc line," IEEE Transactions on Power Delivery, vol. 24, no. 2, pp. 569–578, 2009.

[9] G. Song, X. Cai, S. Gao, J. Suonan, and G. Li, "Natural frequency based protection and fault location for vsc-hvdc transmission lines", International Conference on Advanced Power System Automation and Protection (APAP), IEEE, 2011.

[10] X. Liu, A. Osman, and O. Malik, "Stationary wavelet transform based hvdc line protection" , 39th North American Power Symposium NAPS'07. IEEE, 2007.

[11] O. K. Nanayakkara, A. D. Rajapakse, and R. Wachal, "Location of dc line faults in conventional hvdc systems with segments of cables and overhead lines using terminal measurements," IEEE transactions on power delivery, vol. 27, no. 1, pp. 279–288, 2012.

[12] H. Cui and N. Tu, "Generalized regression neural networks based hvdc transmission line fault localization", 7th International Conference on Intelligent Human-Machine Systems and Cybernetics (IHMSC), vol. 1. IEEE, 2015.

[13] J. Nandana, P. Murthy, and S. Durga, "Vsc-hvdc transmission system analysis using neural networks," International Journal of Engineering Science and Innovative Technology (IJESIT), vol. 2, 2013.

[14] H. Livani and C. Y. Evrenosoglu, "A single-ended fault location method for segmented HVDC transmission line," Electric Power Systems Research, vol. 107, pp. 190–198, 2014.

[15] M. Abdel-Salam, A. Ahmed, and W. Ahmed, "Wavelet-based analysis for transmission line fault location," Innovative Systems Design and Engineering, vol. 4, no. 14, pp. 145–156, 2013.

[16] P. K. Murthy, J. Amarnath, S. Kamakshiah, and B. Singh, "Wavelet transform approach for detection and location of faults in hvdc system" IEEE Region 10 and the Third International Conference on Industrial and Information Systems (ICIIS). IEEE, 2008.

[17] I. Daubechies, "Ten lectures on wavelets. society for industrial and applied mathematics, 1992," Rulgers University and AT&T Bell Laboratories, vol. 1, pp. 1–36, 2009.

[18] H. Zheng-You, C. Xiaoqing, and L. Guoming, "Wavelet entropy measure definition and its application for transmission line fault detection and identification;(part i: Definition and methodology)", International Conference on Power System Technology (PowerCon 2006). IEEE, 2006.

[19] M. Vetterli and C. Herley, "Wavelets and filter banks: Theory and design," IEEE transactions on signal processing, vol. 40, no. 9, pp. 2207–2232, 1992.

[20] X. Cai, D. Parkun et al., "Determination of pumped storage capacity combining the entropy weighting method and principal component analysis," Journal of Power Technologies, vol. 94, no. 3, p. 165, 2014.

[21] L. Shang, G. Herold, J. Jaeger, R. Krebs, and A. Kumar, "High-speed fault identification and protection for hvdc line using wavelet technique," in Power Tech Proceedings, IEEE Porto, 2001.

[22] V. N. Vapnik, "An overview of statistical learning theory," IEEE transactions on neural networks, vol. 10, no. 5, pp. 988–999, 1999.

[23] V. Vapnik, The Nature of Statistical Learning Theory. Springer, 1999.

[24] C. J. Burges, "A tutorial on support vector machines for pattern recognition," Data mining and knowledge discovery, vol. 2, no. 2, pp. 121–167,1998.

[25] S. Ekici, "Support vector machines for classification and locating faults on transmission lines," Applied Soft Computing, vol. 12, no. 6, pp. 1650–1658, 2012.

[26] A. J. Smola and B. Scho¨lkopf, "A tutorial on support vector regression," Statistics and computing, vol. 14, no. 3, pp. 199–222, 2004.

[27] J. A. K. Suykens, Ed., Least Squares support vector machines. Singapore, World Scientific, 2002.

Cellular Robotic Automation for Base-Chassis Welding

İ.SAMURLU[1] and A.T.ÖZDEMİR[2]

[1] Merkez Çelik A.Ş., Kayseri/Turkey, isamurlu@gmail.com
[2]Erciyes University, Kayseri/Turkey, aturan@erciyes.edu.tr

***Abstract* - Production automation is one of the necessity of modern era industry. In this work a welding robot automation project, used to speed-up production of metal chassis of bases that are widely used in furniture market, is presented. Base chassises are constructed by welding different length of 20x20 mm sized metal rectangular-profiles. Two welding robots were used to weld these 0.91 mm thick metal profiles. Two fixtures which are used to hold these profiles in proper positions were designed too. In rotary axis servo drivers were used in order to make the welding robots to reach the welding points more easily. Program of the welding robots were developed and the parameters of the welding characteristics (ramp, speed, dynamic etc.) were defined and transferred to welding inverters. A PLC (Programmable Logic Controller) unit was used to communicate with two robots, control servo motors and pneumatic valves of the fixtures which is controlled by safety equipment used around the automation. Thanks to this automation, machine's operator can feed another fixture manually while welding robots are performing a welding operations. This automation was ensured that workers were not affected by toxic gases that emitted from welding operations. Moreover, the same amount of work was finished with fewer operators and possible work accidents were prevented.**

***Keywords* – Welding, robot, industry 4.0, PLC, automation, motion control**

I. INTRODUCTION

REVULATION of the industry 4.0 which involved to our lives in recent years and will be more important for everyone and create the intelligent production economy of the future. Companies that want to be ahead of global competition in the world of the future, need to develop intelligent robots that will work in production, distribution and R&D processes. At the same time, artificial intelligence systems to be used in these robots, internet of things, and the development of the hardware and software systems that will enable all these intelligent world to work together in harmony are among the indispensable of the revolution of the industry 4.0. Our project carried out to automate the production of metal frames bases, to improving health and safety conditions of work, increasing production quality and reducing production time. In the later parts of the article, mechanical, electronic hardware and software design of the system were explained respectively.

The rest of the paper is organized as follows: in section 2, mechanical design is described briefly. In section 3, electronic hardware design is summarized. In section 4, configuration and connection of Programmable Logic Controller (PLC) are given. In section 5, robot programming is explained. In section 6, adjusting welding parameters is described. Results are discussed in section 7.

II. MECHANICAL DESIGN

Structure in the base chassis shown in Figure 1 basically contains two long edges, two short edges and four foots plates which used to attach base feet. The final product looks like a rectangular prism.

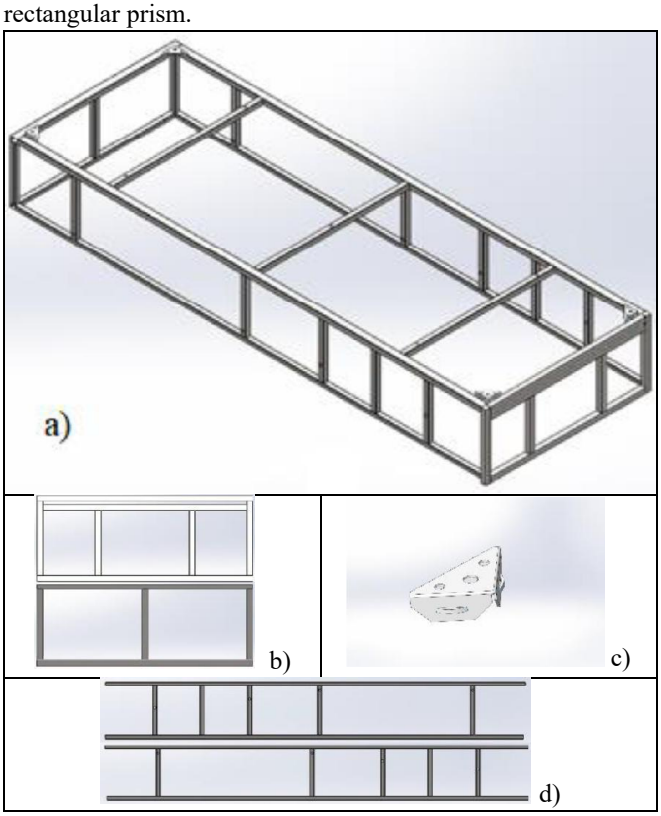


Figure 1: (a) Base chassis, (b) two short edge pieces of chassis, (c) four foot plates, (d) two long edges pieces of the chassis

We aimed to standardize and improve the quality of welding operations then decided to use six axis welding robots and welding inverters. As it is shown in Figure 2, a single-axis movable fixture which is driven by a servo motor has been implemented. Operator can easily align pieces to the fixture. This fixture simplifies robot movements to reach welding points of semi-finished product.

Operator puts pieces of base chassis parts on the fixture and these pieces are pressed with the help of the torque limiting capability of the servo motor. Robot performs the welding operation on compressed the semi-finished product.

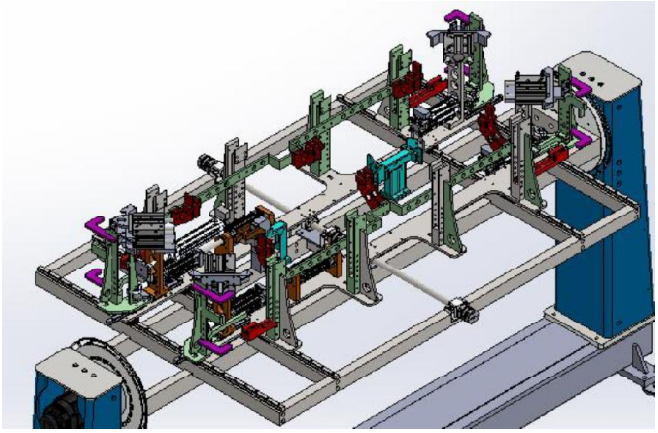


Figure 2: Empty fixture with rotary axis

In order to increase the production speed of the automation, two fixtures were produced. While welding operation is performed on a fixture by robot, operator is able to feed second fixture.

Because of distance and the number of points to be welded, number of robots are increased to two in order to decrease welding process. An external axis is added to fixture with a servo motor in order to gain turning ability. Two Yaskawa MA1440 robots with a 10kg weight carrying capacity and 1440 mm access range are selected. These parameters are defined by considering welding torches and hose packages. As seen in Figure 3, Yaskawa TrackMotion gantry unit for robots' linear mobility, Yaskawa positioners for the rotary motions of the fixtures, Fronius TPS4000 welding inverters and Siemens 1FK series servo motors were employed in automation system. With this configuration, fixture can be opened more comfortably and semi-products can be positioned more conveniently for robot welding.

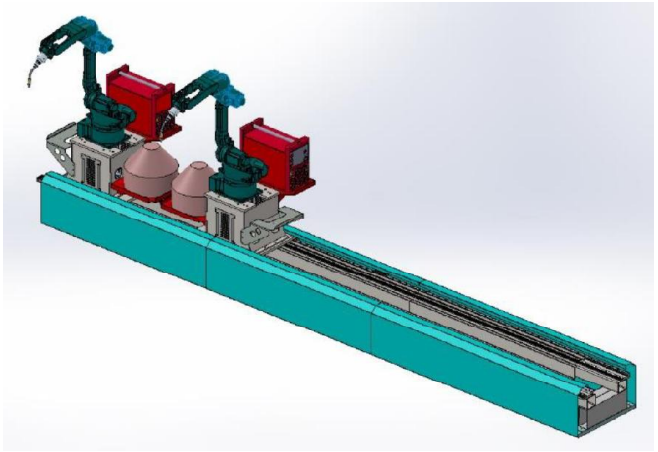


Figure 3: Track Motion linear axis for robots

Final mechanical design was completed as seen in Figure 4. Two of Yaskawa TrackMotion gantry unit and Yaskawa positioners unit are used, one for welding and another one for operator. In this way preparation of semi products by operator and welding of the semi product by robot can performed at the same time. This multitasking job is designed and operated perfectly.

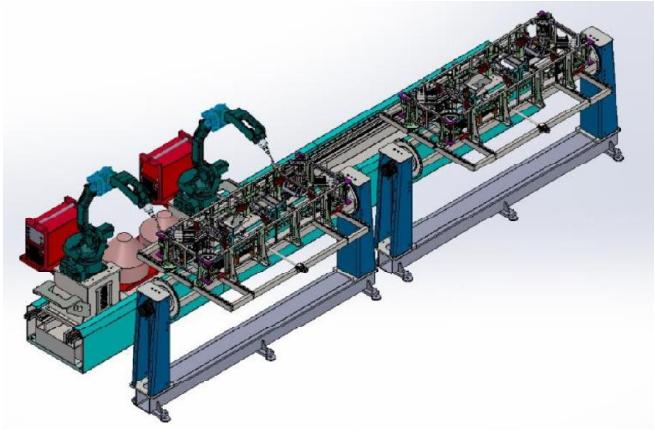


Figure 4: Completed mechanical design

III. ELECTRONIC HARDWARE DESIGN

When mechanical design was completed first then required electronic parts were determined. Siemens Safety S7-1513F PLC was selected for communicate with robot controllers, welding inverters, safety components, peripheral remote IOs and external servo motors. Master-slave communication model which is popular in Industrial applications was preferred. To establish a master slave relationship between Yaskawa MA1440 robots and the PLC, HMS Profinet Slave PCI Express Card was added to the the DX200 controller of Yaskawa MA1440 Robots. The external axis cards were installed to the DX200 controllers to increase the mobility of the robot. This makes robots to respond more flexibly of their interpolation movements. Communication between the Yaskawa MA1440 DX200 welding robots and the Fronius TPS4000 welding inverters was established with ModBus (as known "WeldCOM" in product market) communication network locally., ModBus has been as a standard on the inverters [1]. Remote IO (Input/Output) units were preferred as profinet slave, so that compatibility with the PLC is ensured.

In order to provide safe working conditions around the automation field a risk analysis was made. According to the risk analysis, safety sensors, safety switches, inductive sensors with safety outputs which can be installed in the profinet slave units were used. Then a panel was designed for mounting rail-type electronic components.

IV. PLC PROGRAMMING

TIA (Totally Integrated Automation) Portal was used for program Siemens S7-1500 PLCs. Safety Integrated Option package has been added to provide safety requirements and control of safety units. TIA Portal interface allows programmer to choose programming language such as LAD (Ladder), FBD (Function Block Diagram) or STL (Statement List). Servo motor control scenarios can also be performed with this platform. Both the software of the servo motor of fixtures and welding start conditions of the robots were implemented with TIA Portal, and uploaded to the robot controllers via Profinet. Status information of the robot motion, welding process and fault conditions were monitored by Profinet and the proper program that meet requirements were created with Tia Portal interface. Finally, Human Machine Interface (HMI) touch

panel program that allows the operator to control automation was designed. The hardware structure was created in Tia Portal with tree form is given in Figure 5.

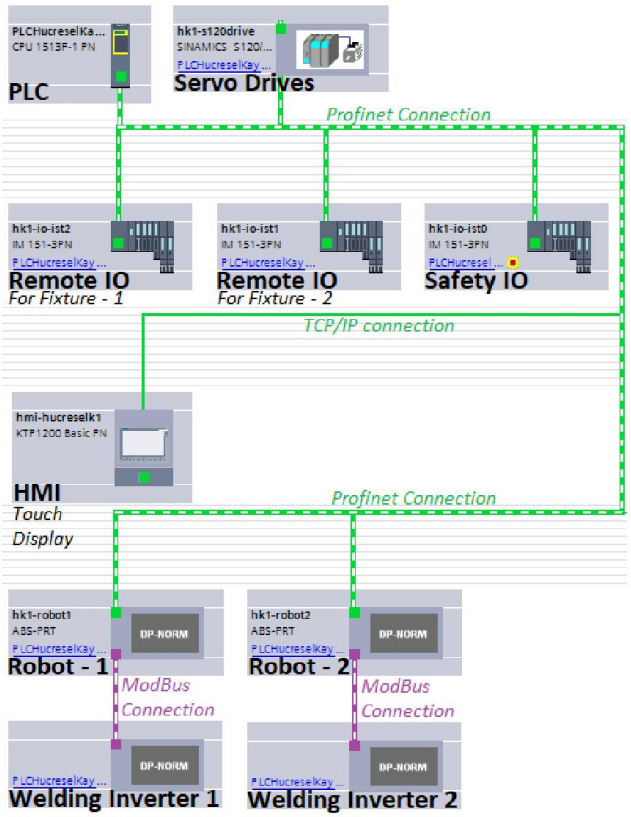


Figure 5: Electronic component tree

V. PROGRAMMING OF THE ROBOTS

Industrial robots can travel from one point to another point linearly however each axis of industrial robots can also move independently. Those movements are planned using kinematic equations, coordinate system helps to increase the ability of robot movement. The welding of the base chasses consists of several two cm long line welding processes. Since welding lines are straight, movements were planned linearly. The origin of movement starting point is referenced to the end of the torch, called the Tool Center Point (TCP) [2].

The Yaskawa DX200 controllers support different programming languages. One of them is called LAD (Ladder) and it is used to write basic control. Another one is "Inform Language" and it is used to teach the desired position of the robots to the system then makes robot move these positions independently. Basically, operator teaches welding points to the robot by taking away it to the welding points with using the robot's teach pendant. Then, when the robot is in automatic mode, it goes through the taught points and starts to make the welding process. Welding software was written as a subprogram in the main automation program by Inform language. Yaskawa Inform language has a multithread program coding platform that allows programmer to run different programs, such as control and safety programs, simultaneously.

VI. ADJUSTMENT OF WELDING PARAMETERS

The arc welding is preferred. Arc welding is a kind of welding method that makes welding by melting of the metals by excessive heat that is generated by electricity [3]. Since it is cost effective solution for additive manufacturing, arc welding has been widely employed for producing of large metal components more than three decades [4]. A welding torch connected to the robot's TCP makes welding by transferring gas and wire with a hose package mounted on the robot. In welding process CO_2 (Carbondioxide) gas, 0.6 mm diameter welding wire are used with pulse method. An inverter capable of meeting all these specifications, the Fronius TPS4000, was preferred in this project.

Fronius TPS4000 and Yaskawa DX200 controllers were paired with Modbus communication network. This network is used to transfer required parameters such as start and finish ampere values, ramp values for the ampere, gas durations, wire speeds and burn back ratio for arc welding. These parameters were used in inform language with the sample pseudo code given below.

```
0000 NOP
0001 MOVJ VJ=25.00
//Moves manipulator to position 1. (Step 1)
0002 MOVJ VJ=25.00
//Moves manipulator to position 2. (Step 2)
0003 MOVJ VJ=12.50
//Moves manipulator to welding start position. (Step 3)
0004 ARCON ASF# (1)
//Specifies manipulator arc start with job number 1.
0005 MOVL V=50
//Moves manipulator to welding end position. (Step 4)
0006 ARCOF AEF# (1)
//Specifies manipulator arc end with job number 1.
0007 MOVJ VJ=25.00
//Moves manipulator to position 3. (Step 5)
0008 MOVJ VJ=25.00
//Moves manipulator to position 4. (Step 6)
0009 END
```

VII. CONCLUSIONS

In the manner of work health and safety, the toxic gas which emitted during the welding operation has been disposed by aspiration system as well as minimizing the risk of work accidents with safety equipments placed around of this system. The whole system was surrounded by a fence, the doors of fence was controlled with safety switches with a safety PLC, were added in the automation. Dangerous work zone was blocked by laser safety scanners lest the operator causes a work accident. The rotating fixture was controlled by safety inductive sensors and safety laser sensors so that it doesn't turn when operator is in blocked zone. As a result of the risk analysis, all of these selected safety equipments (see Figure 7) have safety certificates.



Figure 7: Safety Laser Field Sensor, safety magnetic door sensor, safety laser scanner and field of application.

In this project we present a cellular robotic automation for base-chassis welding project, please see Figure 8. As it is summarized in Table 1, a considerable work force has been gained with reduced process time. Production quality has also been increased while potential work accidents have been prevented. Our automation project perfectly meets industry 4.0 features such as monitoring of production times, quantities, productivity analysis and communication of objects.



Figure 8: Completed Project

Table 1: Table of system and operator welding durations and errors for certain sizes of bases chases.

Base Chases (cm x cm)	Robotic Automation		Hand Welding	
	Duration (s)	Fault Ratio (%)	Duration (s)	Fault Ratio (%)
120x200	192	2	366	7
160x200	215	2	348	7

REFERENCES

[1] A.W. Blackett, B.J. Gilbert, M.A. Hancock, U.S. Patent No. 6.792.337. Washington, DC, 2004

[2] T.J. Tarn, S.B. Chen, "Robotic welding, intelligence and automation", C. Zhou (Ed.), Berlin: Springer. pp. 145-147, 2007

[3] E.W. Reutzel, "Hybrid laser-arc welding", Olsen, F. O. (Ed.), FL: CRC Press. pp. 3-15, 2009

[4] D. Ding, C. Shen, Z. Pan, D. Cuiuri, H. Li, N. Larkin, S. Duin, "Towards an automated robotic arc-welding-based additive manufacturing system from CAD to finished part", *Computer-Aided Design*, vol. 73, pp. 66-75, 2016

Determination of Electromagnetic Field Values for Breast Tumor Detection with the Designed VIVALDI Antenna

*Beyza NEYİŞCİ, **Rabia TOP, **S. Sinan GÜLTEKİN, **Dilek UZER
*MEDAS, Konya, ** Selcuk University Faculty of Engineering Elk. - Elt. Eng. Department
beyzaneyisci@gmail.com, rabiacaliskan@selcuk.edu.tr, sgultekin@selcuk.edu.tr, dilek_uzer@selcuk.edu.tr

Abstract - Breast cancer can cause fatal outcomes if not properly treated for many women. Early diagnosis is very important to detect and prevent cancer. There are methods such as X-ray mammography, magnetic resonance imaging and ultrasonography. But these methods are not always accurate. For example; 4% to 34% of all breast cancers are bad and benign cancerous tissue may not be detected due to the contrast problem. On the other hand, microwave imaging applications, which have been intensively studied in recent years, are seen as a promising method. With this study, a microwave application was carried out in recognition of the fact that all materials have different permittivity and conductivity properties for breast tumorous diagnosis. For the application, the Vivaldi antenna design, which is ultra-wideband (UWB), was implemented using the high frequency electromagnetic field simulation (HFSS) program. The designed antenna has FR4 base material, dielectric constant (εr) of 4.4 F/m, tangent loss of 0.0009 and base thickness of 1.575 mm. The maximum values of the electric field, magnetic field and current density parameters on the antenna which resonates in more than one region in the range of 4.4 GHz to 7.5 GHz have been obtained for non-tumorous and tumorous breast cells. This process was repeated in close and distant locations of the tumorous breast cell and the resulting differences showed the presence of the tumorous breast cell. From obtained results, it has been shown that the tumor tissue can be effectively detected with UWB Vivaldi antenna.

Keywords **- Breast Cancer, Microwave Imaging, HFSS, Vivaldi Antenna**

I. INTRODUCTION

Breast cancer is one of the most widespread types of cancer in the world. The key factor in treatment is to reliably diagnose the cancer in the early stages. Moreover, currently used clinical diagnostic methods, such as X-ray, ultra-sound and MRI, are limited by cost and reliability issues. These limitations have motivated researchers to develop a more effective, low-cost diagnostic method and involving lower ionization for cancer detection [1].

Recently, the interest of promising techniques such as confocal microwave imaging for breast tumor detection at an early stage [2, 3] has grown. The working principle of microwave imaging techniques is based on the dielectric contrast between the malignant-tumor tissues and the healthy ones [4]. In these techniques the tumor is identified from the processing of the scattered signals collected at the antennas.

Regardless of the imaging method adopted, the antenna properties play a fundamental role in the design of an RF breast cancer imaging system. The radiating elements must fulfill specific requirements in terms of operating band and field penetration into the tissues in order to combine good image resolution with mechanical feasibility and cost moderation. For instance, the bottom edge frequency plays a very critical role as the RF signal can penetrate more efficiently at low frequencies. However, this requirement must be compromised with the overall size of the antenna. On the other hand, the top edge frequency affects the achievable resolution. This cannot be too high as the contribution coming from frequencies higher than 10 GHz would be reflected by the skin layer [5].

Ultra-wideband (UWB) antennas are suitable candidates for this application as they can offer very large operating band, stable radiation properties and compact dimensions [5].

In this paper, UWB Vivaldi antenna is proposed as a method for early breast cancer detection. Proposed antenna is used for the purpose of microwave imaging over detecting cancerous tissue into breast structure and so, a simple 3D breast structure is modelled to define cancerous tissue. This antenna has advantages such as low cost, compact and easy to use with minimum size its thus good potential for early cancer detection.

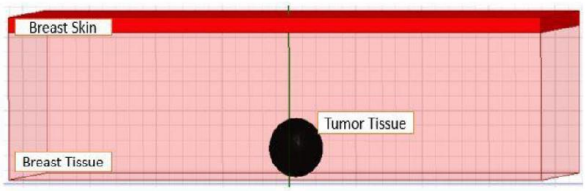
In this work, better simulation results are obtained by as the tumor approaches the antenna. The antenna structure operating at 4 GHz and 9 GHz is placed in front of breast skin and differences between electromagnetic field values according to simulations results are evaluated via graphics.

The paper is organized as follows. Sections II, III, IV and V, are respectively devoted to the introduction of the breast phantom, the antenna design, simulation & results. Conclusion is discussed in Section VI.

II. Breast Structure

The cancer detection problem is addressed by considering the simplified breast phantom displayed in Fig. 1. It consists of a rectangular prism structure with a 20x80x40 mm which simulates breast tissue layer. It consists of a rectangular prism structure with a 2x80x40 mm which simulates breast skin layer and breast skin is placed in front of the breast tissue. The tumor is a spherical of 4-mm diameter that is inserted inside the breast tissue.

Fig. 1. Breast Structure



The dielectric and conductivity constants of the used tissues are shown in Table 1 [6].

Table 1: Dielectric and conductivity constants of tissues

Tissue Type	Dielectric Constant	Conductivity Constant
Breast Tissue	9	0.4
Breast Skin	36	4
Tumor Tissue	50	4

III. Antenna Design

The proposed Vivaldi antenna model is shown in Fig 2, which also illustrates its parameters. This antenna has FR4 substrate material, dielectric constant (εr) of 4.4 F/m, tangent loss of 0.0009 and substrate thickness of 1.575 mm. Substrate dimension x is 75 mm, y is 95.5 mm. Feed length is 5 mm and feed width is 0.7207 mm. Taper length is 75 mm and width is 37.5 mm.

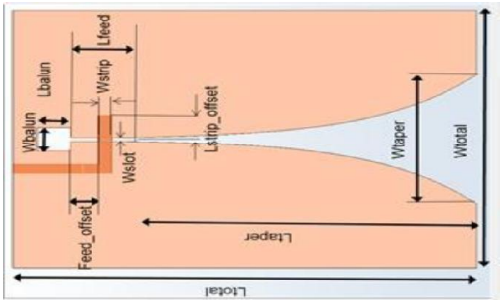


Fig. 2. Proposed Antenna Structure

The proposed antenna is placed in front of the breast structure, which is shown in Fig. 3. According to design in Fig. 3., simulations are implemented.

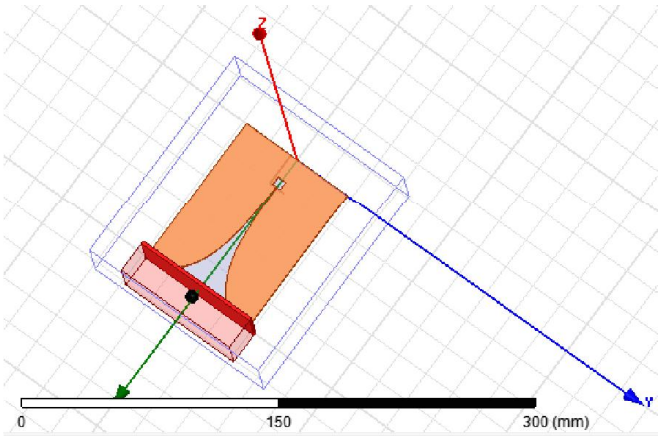


Fig. 3. Proposed Antenna Design

IV. Simulation & Results

In the study, the breast tissue is placed in front of the proposed antenna and examined for three conditions. These cases are shown in Fig. 4, Fig. 5, Fig. 6.

Fig. 4. Non-tumorous breast tissue

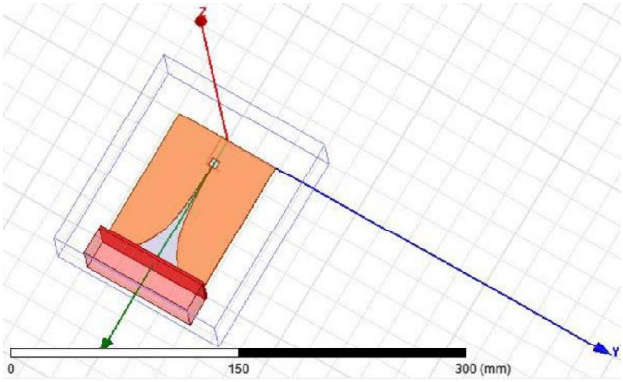
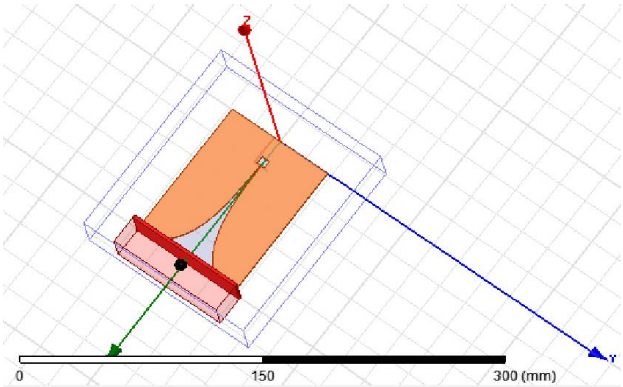


Fig. 5. The tumor is close to the antenna



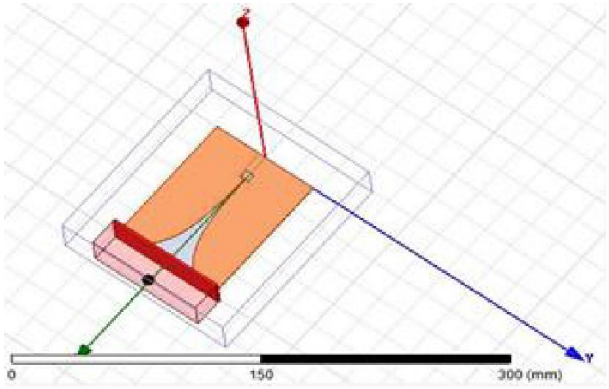


Fig. 6. The tumor is away from the antenna

The aim is to detect the tumor tissue with the proposed antenna. In addition, the antenna was examined in proximity to the tumor. Simulation of the proposed antenna for the three cases was carried out in the HFSS simulation program.

As a result of the simulations, the values of electric field, magnetic field and flux density of the proposed antenna have been obtained. The results are shown in Table 2.

Table 2: The values of electric field, magnetic field and flux density of the proposed antenna

Antenna Structure Name	Max E Field (V/m)	Max H Field (A/m)	Max J (A/m^2)
Without Breast Tumor	1814.1	10.197	15.089
The tumor is close to the antenna	2714.9	11.922	15.415
The tumor is away from the antenna	2108.1	9.1619	12.672

This table shows in the without tumor, the tumor is close to the antenna and the tumor is away from the antenna values obtained are different. The return loss curves of the proposed antenna in these three cases are shown in Fig. 7, Fig. 8, Fig. 9.

Fig. 7. When the return loss of non-tumorous breast tissue

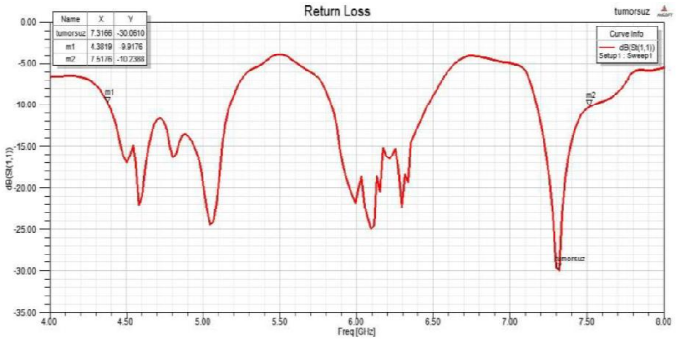


Fig. 8. When the return loss of breast tumor is close to the antenna

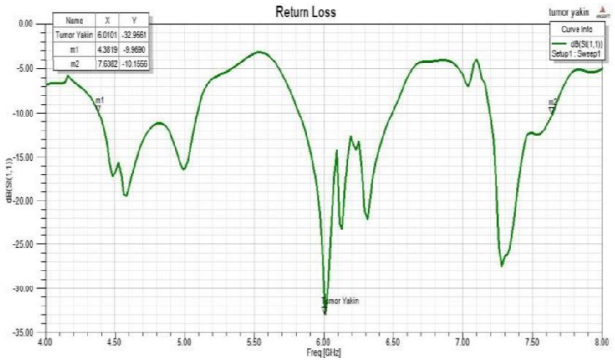
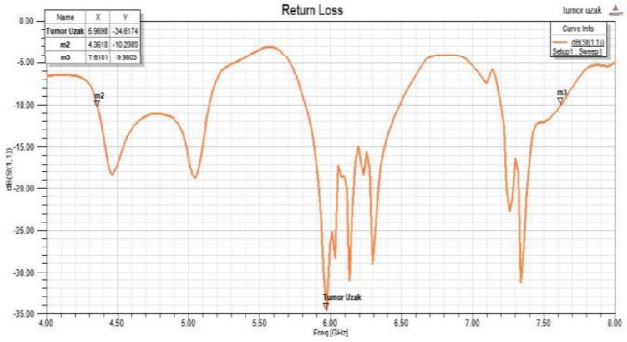


Fig. 9. When the return loss of breast tumor is away from the antenna



In Fig. 7, the proposed antenna can operate in the frequency range of 4.37 GHz - 7.51 GHz without tumor. The most efficient frequency of operation is 7.31 GHz and the return loss is -30.06 dB.

In Fig. 8, the proposed antenna can operate in the frequency range of 4.38 GHz to 7.63 GHz, close to the tumor antenna. The most efficient frequency of operation is 6.01 GHz and the return loss is -32.95 dB.

In Fig. 9, the proposed antenna can operate in the frequency range of 4.36 GHz to 7.62 GHz, extending to the tumor antenna. The most efficient frequency of operation is 5.97 GHz and the return loss is -34.61 dB.

As a result, these differences show that the antenna successfully detects the chest tumor and the tumor is better detected when the tumor approaches the antenna.

V. Conclusion

In this study, a UWB Vivaldi antenna was proposed for use in early diagnosis of breast tumor. The designed antenna was modeled and simulated with tumorous and non-tumorous breast tissue. And the obtained electromagnetic field data are evaluated.

As a result, the maximum electric field value of the non-tumorous breast tissue was 1814.1 mV/m, while it was 2714.9 mV/m in the near position and 2108.1 mV/m in the far position of the tumorous breast tissue. These results show that Vivaldi antenna application for detecting the tumorous breast tissue is very successful.

REFERENCES

[1] H. Zhang, Microwave Imaging for Ultra-Wideband Antenna Based Cancer Detection, A thesis submitted for the Degree of Doctor of Philosophy The University of Edinburgh (2014).

[2] J.M. Sill and E.C. Fear, Tissue sensing adaptive radar for breast cancer detection—Experimental investigation of simple tumor models, IEEE Trans Microwave Theory Tech 53 (2005).

[3] M. Klemm, et al., Radar-based breast cancer detection using a hemispherical antenna array—Experimental results, IEEE Trans Antennas Propag 57 (2009).

[4] M. Lazebnik, et al., A large-scale study of the ultrawideband microwave dielectric properties of normal, benign and malignant breast tissues obtained from cancer surgeries, Phys Med Biol 52 (2007).

[5] G. Ruvio, R. Solimene, A. D'Alterio, M. Ammann, R. Pierri, RF Breast Cancer Detection Employing a Noncharacterized Vivaldi Antenna and a MUSIC Inspired Algorithm (2013) .

[6] R. Calıskan, S. S. Gültekin, D. Uzer, Ö. Dündar, A Microstrip Patch Antenna Design for Breast Cancer Detection, World Conference on Technology, Innovation and Entrepreneurship (2015).

Elliptic Microstrip Antenna Design on Woolen Felt Material for Detection of Cardio-Vessel Occlusion

Özen BAYRAKTAR, Rabia TOP, Dilek UZER, S. Sinan GÜLTEKİN

Selcuk University, Konya/Turkey, ozen_bayraktar@yahoo.com.tr, rabiacaliskan@selcuk.edu.tr, dilek_uzer@selcuk.edu.tr, sgultekin@selcuk.edu.tr

Abstract **- The integration of technology and medical applications is extremely important when it comes to human life. According to the Turkish Statistical Institute's death causes study conducted in 2015, 40.3% of the causes of circulatory system and 40.2% of the causes were related to heart diseases. According to research, the most uncommon causes of death are the ones related to the heart. One of the main causes of heart problems is cardiovascular obstruction. A variety of solutions have been developed to detect these conditions. In the proposed study, vein occlusion of the heart disease was modelled on the elliptically shaped wearable microstrip antenna with a Woolen felt substrate, and the electromagnetic signals in the states where the heart was not obstructed, and the case was tried to be determined. The dielectric constant of the felt material was determined by the T-resonator method. Dielectric values of cardiovascular and adipose tissues were used for the vascular occlusion model and FR-4 was selected as the substrate material. Three elliptical pins and a central cylindrical slot were inserted into the middle of the elliptic patch area and the high frequency electromagnetic field simulation (HFSS) program was used to demonstrate that the cardiac vessel occlusion can detect electromagnetic waves. According to the results obtained, the electric field value was 1323.3 mV/m when there was no obstruction and 2268.2 mV/m when there was obstruction. This difference of 945 mV/m suggests that an elliptical microstrip antenna with substrate material selected as the seal can be selected to determine a blockage in the heart.**

Keywords **– Woolen felt, Elliptical Microstrip Antennas, T Resonator, Cardiac Cavity Closure, HFSS**

I. INTRODUCTION

The application of continuous and rapidly advancing technology to the medical field is of most importance when it comes to human life. Cardiovascular diseases and cardiovascular blockages, which are high causes of death, are the leading cause of these disorders. From the year 2016 statistics, it is known that 40.3% of the causes of death originate from the circulatory system, with the largest share being heart failure with 40.2%. However, congestion in the heart is an essential parameter of heart disease. To avoid such disturbances and to be able to make correct diagnostics, it must be to be determined the inconvenience in advance. There are applications for early diagnosis such as echocardiography (EKO) and electrocardiography (EKG). In addition to these applications, biomedical microwave imaging applications, which have been intensively studied in recent years, give promising results [1, 2]. Biomedical microwave imaging applications have increased antenna structure over the last two decades [3]. When considered the size, cost, easy design and so on. microstrip patch antennas are generally preferred [4-6]. These antenna types are used in the literature for in-body, on-body and off-body applications [7-9]. Sometimes a micro-banding strip emerging as a biosensor can appear as a wearable antenna structure [8-12].

In this proposed study, as biomedical monitoring application and biosensor application, an elliptically microstrip antenna design is proposed on Woolen felt substrate that can take place in a wearable technology product. The practice is a study where continuous follow-up can be performed without the patient going to any health centre and the obstruction of the heart's vein at low or high levels can be detected. For this purpose, a design of an elliptically shaped microstrip antenna with a felt substrate was simulated and the reflected electromagnetic signals were taken and examined, and the results evaluated. On the elliptic patch of the radiation, a slot and three shorting pins were added to reduce the antenna size and increase the bandwidth. To be able to reflect the electromagnetic signals, a heart and heart-vessel model was simulated to observe the changes. In the model, the dielectric values of cardiac vein and fat tissue were used. The dielectric constant of the substrate material is determined by the T-resonator method and the resonator dimensions are calculated. Simulations were performed using a high frequency electromagnetic field simulation (HFSS) program and it was shown that cardiac vascular occlusion can be detected by electromagnetic stimulation.

II. WOOLEN FELT TEXTILE MATERIAL USED FOR WEARABLE ANTENNA DESIGN

Fabrics are planar fibre materials and their basic properties depend on fibre and yarn construction. These properties are pore density, air volume and size, air permeability and thermal insulation. Accordingly, fabrics are flexible and compressible materials that can vary in thickness and density at low pressures. It should be noted that the felt antenna application has a rough and irregular surface which is not suitable for screen printing. The relative permeability of the seal is very close to 1 (air) because it has porosity (~ 40% by volume). The polyester felt has a dielectric loss of 5.8 dB / m and is better than FR4 (6.7 dB / m). Polyester felt has a lower distribution than woven polyester due to the high air ratio. Therefore,

polyester felt is the least loss fabric. A high nominal thickness (1.65 mm) is an additional advantage, such as efficiency and bandwidth, to improve antenna performance. However, due to its porosity, the felt is susceptible to compaction to separate the RF circuit or antenna. Since polyester felt is not suitable for silver screen printing, the use of conductive fabric is preferred for conductive parts of the antenna [19].

III. Modelled Heart Vein

The electrical properties of biological materials are different from each other, as the electrical properties of each material are different from each other. Electrical properties of the fat tissue and heart tissue are used in the study; electrical conductivity (ε), conductivity (σ) and tangential loss (tanδ). The values of these electrical properties are taken from the literature [1]. These values are also introduced in the HFSS program to perform simulations. For heart tissue, permittivity is 42.9 and for fat tissue, permittivity is 5.28 F/m.

The heart vessels and congestion are modelled as a cylindrical structure. The radius of the vein is 25 mm and the length are 70 mm. The radius and length of the obstruction are 35 mm and 10 mm, respectively. The modelled heart vein is located exactly in the patch area. Figure 1 shows the positions of the heart vein and occlusion.

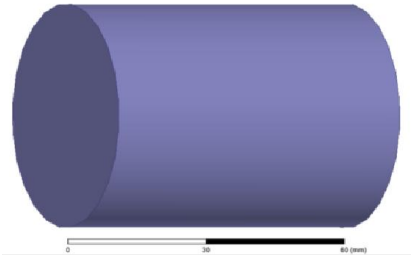


Figure 1: Modelled heart vein in HFSS

IV. Antenna Design

To determine the vessel occlusion, a microstrip antenna design has been made due to its advantages such as wearable properties, cost and patch type. The substrate material of the antenna is selected as felt, and the patch surface is designed as ellipse. On the elliptic patch of the radiation, one cylindrical slot in the center of patch and three shorting pins were added to reduce the antenna size and increase the bandwidth. Fig.2 shows the proposed antenna structure [21]. Substrate dimensions for two-axis are 32 mm. Patch dimensions, for x-axis is 30 mm and for y-axis is 28 mm. And in the center of patch there is a cylindrical slot, its diameter is 5 mm.

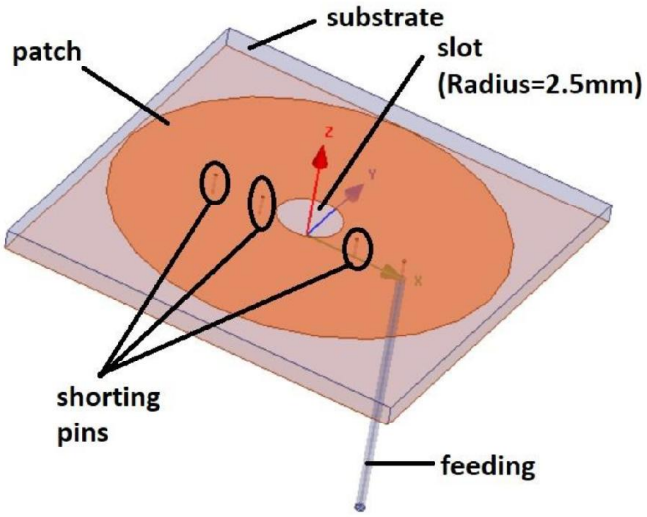


Figure 2: Proposed antenna structure

The dielectric constant of the substrate material is determined by the T-resonator method and the resonator dimensions are calculated.

4.1 T- Resonator Method

The microstrip T-resonator method is developed to provide numerous data points over a broad frequency range with a simple configuration and ease of fabrication and is used in defining the properties of different materials in the large frequency range from 1 to 20 GHz. In initial design from the literature and in this paper, the effects of external loading of the resonator due to the measurement system are not considered, and the equations used for discontinuities and loss components are not introduced. The T-resonator is composed of a simple T-pattern, which includes an open-end transmission stub and two feed lines. The T-resonator resonates at odd integer multiplies of its quarter wavelength frequency. The basic idea behind determining the values of the dielectric constant with the T-resonator is to design a resonator structure for a specific main resonant frequency. The design is based on an estimated value of the dielectric constant. From the length of open end of the resonator can be calculated [15-18].

$$L_{stb} = \frac{nc}{4f_r\sqrt{\varepsilon_{eff}}}$$

where; L_{stb}: The length of the open end of the resonator (mm),
n: The resonant coefficient of odd modes in the line,
c: The speed of light in free space (mm/s)
f_r: Resonant frequency (MHz)
ε_{eff}: Effective dielectric constant.

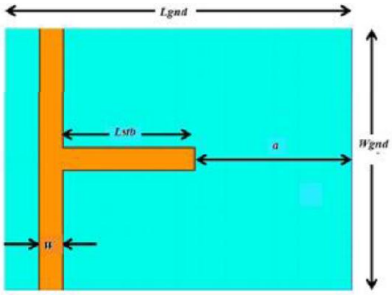


Figure 3: T resonator design

From Figure 3, T resonator parameters are explained as following:

L_{gnd}: The ground plane length,
W_{gnd}: The ground plane width,
W: The width of the feed line and open end of the resonator,
a: The distance between the ground plane edge and the resonator.

4.2 Antenna Simulation Results

The return loss S_{11} is shown in Fig.4. As you can see, there is resonance in five frequency band regions. These are 3.2, 4.9, 9.05, 11 and 12.85 GHz respectively. S_{11} values are showed in Fig. 4. The input impedance is 50Ω and the voltage standing wave ratio (VSWR) is 1.12.

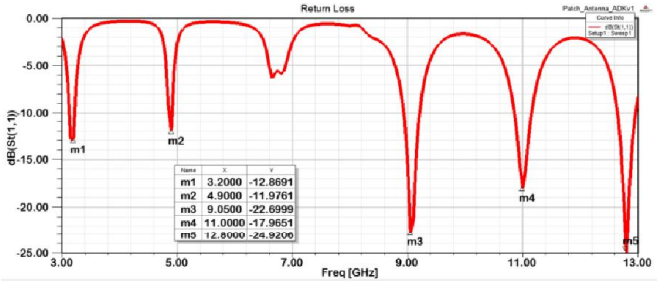


Figure 4: Return loss value of the proposed antenna

V. SIMULATION AND EVALUATION

The position of the antenna was placed exactly in correspondence to the heart, and then simulations were made. Simulations were performed when the heart and cardiac occlusion model was unblocked (model structure empty) and occluded (model structure filled with oil). In both cases, the electromagnetic field values obtained were examined and their differences were determined. Figures 5, 6, 7 and 8 show the electromagnetic field values obtained that the model structure is empty, and the model structure is filled with oil.

Table 1 gives the maximum values of the electric field, magnetic field and surface currents obtained when there is no obstruction and when there is obstruction.

Table 1 also shows the difference values of the obtained electromagnetic field values. These differences are very important for determining vascular occlusion. Figure 9 shows that the electric field values obtained depend on the state of the obstruction and the obstruction in terms of theta according to FR-4 material. When heart blockage occurs, the electric field graph will also change.

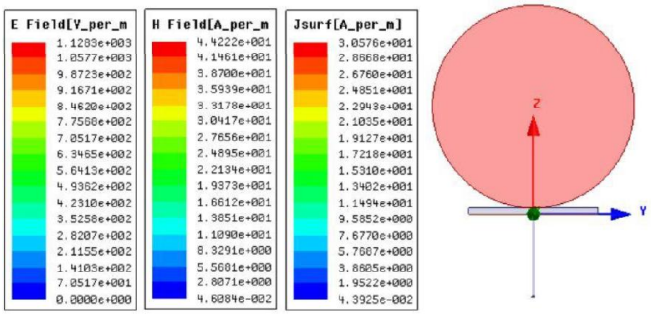


Figure 5: Obtained electromagnetic field values without occlusion (by FR-4)

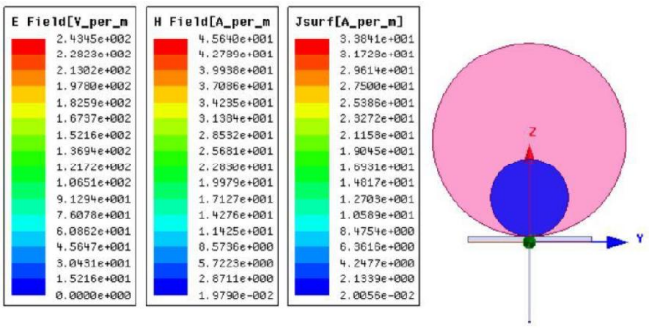


Figure 6: Obtained electromagnetic field values with occlusion (by FR-4)

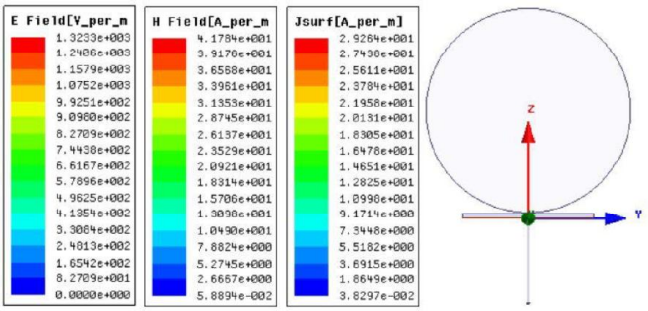


Figure 7: Obtained electromagnetic field values without occlusion (by felt)

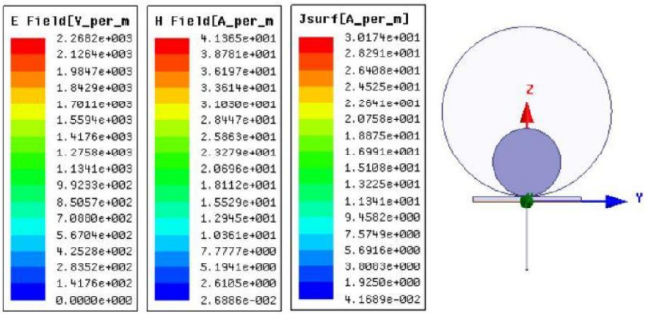


Figure 8: Obtained electromagnetic field values with occlusion (by felt)

Table 1: Obtained electromagnetic field values with and without occlusion according to substrate materials

Substrate material	Field name	E-field (mV/m)	H-field (mA/m)	J (mA/mm²)
FR-4	Without occlusion	1128.3	44.22	30.57
	With occlusion	243.45	45.64	33.8
	Difference	**884.85**	**1.42**	**3.23**
WOOLEN FELT	Without occlusion	1323.3	41.8	29.26
	With occlusion	2268.2	41.37	30.17
	Difference	**944.90**	**0.43**	**0.91**

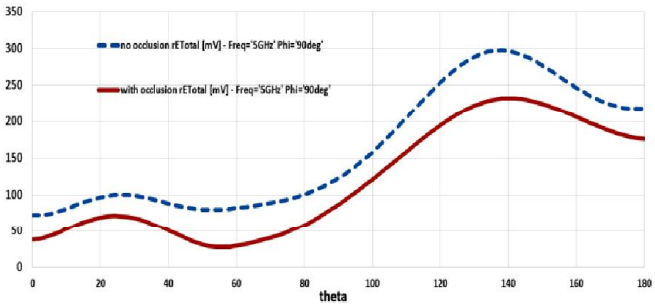


Figure 9: Results of obtained electric field values depending on theta angle by FR-4.

VI. Conclusion

An elliptical microstrip patch antenna designed to detect vessel occlusion and having three short-circuit pins and a slot was evaluated in HFSS. After the simulations, different electromagnetic field values were obtained in the presence of obstruction and in the absence of obstruction. When obstructed, the electric field value is 2268.2 mV/m, the magnetic field value is 41.37 mA/m and the surface current density is 30.17 mA/mm^2. In the absence of obstruction, the electric field value is 1323.3 mV/m, the magnetic field value is 41.8 mA/m, and the surface current density is 29.26 mA /mm^2. For this reason, there are obvious differences in field values. It is thought that these differences can be used to predict cardiovascular occlusion before vascular occlusion occurs. As a result, significant differences in the electromagnetic and surface currents obtained indicate that the antenna design with felt substrate, ellipse patch shape, slit on the patch, and pin-tied antenna is a successful antenna design.

References

[1] T. İ. Kurumu, "Ölüm nedeni istatistikleri, 2016," in *Türkiye İstatistik Kurumu Haber Bülteni* vol. 24572, ed, 2017.

[2] A. Civelek. *Koroner Arter Hastalığı*. Available: http://www.alicivelek.com/koroner-arter-hastaligi-ve-koroner-baypas-cerrahisi

[3] P. S. Hall and Y. Hao, "Antennas and propagation for body centric communications," in *Antennas and Propagation, 2006. EuCAP 2006. First European Conference on*, 2006, pp. 1-7: IEEE.

[4] R. Çalışkan, S. S. Gültekin, D. Uzer, and Ö. Dündar, "A microstrip patch antenna design for breast cancer detection," *Procedia-Social and Behavioral Sciences,* vol. 195, pp. 2905-2911, 2015.

[5] M. Nalam, N. Rani, and A. Moha, "Biomedical application of microstrip patch antenna," *Int J Innov Sci Mod Eng,* vol. 2, no. 6, pp. 319-327, 2014. S.

[6] Samal, S. Dwari, A. Dutta, and S. P. Reddy, "A Microstrip Patch antenna for biomedical applications at 2.45 GHz," in *Computers and Devices for Communication (CODEC), 2012 5th International Conference on*, 2012, pp. 1-4: IEEE.

[7] A. Alomainy, Y. Hao, C. Parini, and P. Hall, "Comparison between two different antennas for UWB on-body propagation measurements," *IEEE Antennas and Wireless Propagation Letters,* vol. 4, no. 1, pp. 31-34, 2005.

[8] T. Karacolak, A. Z. Hood, and E. Topsakal, "Design of a dual-band implantable antenna and development of skin mimicking gels for continuous glucose monitoring," *IEEE Transactions on Microwave Theory and Techniques,* vol. 56, no. 4, pp. 1001-1008, 2008.

[9] P. Soontornpipit, C. M. Furse, and Y. C. Chung, "Design of implantable microstrip antenna for communication with medical implants," *IEEE Transactions on Microwave theory and techniques,* vol. 52, no. 8, pp. 1944-1951, 2004.

[10] S. A. Kumar and T. Shanmuganantham, "Design of implantable CPW fed monopole H-slot antenna for 2.45 GHz ISM band applications," *AEU-International Journal of Electronics and Communications,* vol. 68, no. 7, pp. 661-666, 2014.

[11] S. Vaddiraju, M. Kastellorizios, A. Legassey, D. Burgess, F. Jain, and F. Papadimitrakopoulos, "Needle-implantable, wireless biosensor for continuous glucose monitoring," in *Wearable and Implantable Body Sensor Networks (BSN), 2015 IEEE 12th International Conference on*, 2015, pp. 1-5: IEEE.

[12] R. Top, S. S. Gültekin, and D. Uzer, "Modeling congestion of vessel on rectangular microstrip antenna and evaluating electromagnetic signals," in *Signal Processing and Communications Applications Conference (SIU), 2017 25th*, 2017, pp. 1-4: IEEE.

[13] R. Top, "A Transmitter Microstrip Antenna Design and Application Towards the Detection of Heart Disease Parameters," Master Thesis, the Degree of Master Of Science In Electrical-Electronics Engineering, Selcuk University, Konya, 2017.

[14] C. Gabriel, "Compilation of the Dielectric Properties of Body Tissues at RF and Microwave Frequencies," King's Coll London (United Kingdom) Dept Of Physics1996.

[15] T. Rovensky, A. Pietrikova, K. Ruman, O. Kovac, Microstrip methods for measurement of dielectric properties in High Frequency area, Electronics Technology (ISSE), 2015 38th International Spring Seminar on, vol., no., pp.188-191, 6-10 May 2015 doi: 10.1109/ ISSE. 2015.7247987.

[16] http://www.mwrf.com/test-measurement/anritsu-lecroy-promote-partnership-edi-con-2017.

[17] K.P. Lätti, M. Kettunen, J.P. Ström, and P. Silventoinen, A Review of Microstrip T-resonator Method in Determination of Dielectric Properties of Printed Circuit Board Materials, Proceedings of IEEE Instrumentation and Measurement Technology Conference, 16-19 May, Ottawa, Canada, 2005, pp. 62- 66. ISBN 0-7803-8880-1.

[18] Özen Bayraktar, Dilek Uzer, S.Sinan Gültekin "Usage of T-Resonator Method at Determination of Dielectric Constant of Fabric Materials for Wearable Antenna Designs" ICSMD-2017

[19] Salah-Eddine Adami, Plamen Proynov, Geoffrey S. Hilton, Guang Yang, Chunhong Zhang, Dibin Zhu, Yi Li, Steve P. Beeby, Ian J. Craddock "A Flexible 2.45-GHz Power Harvesting Wristband With Net System Output From −24.3 dBm of RF Power", IEEE Transactions on Microwave Theory And Techniques, DOI: 10.1109/TMTT.2017.2700299

[20] Method in Determination of Dielectric Properties of Printed Circuit Board Materials, Proceedings of IEEE Instrumentation and Measurement Technology Conference, 16-19 May, Ottawa, Canada, 2005, pp. 62- 66. ISBN 0-7803-8880-1.

[21] R. Top, "A Transmitter Microstrip Antenna Design and Application Towards the Detection of Heart Disease Parameters," Master Thesis, the Degree of Master Of Science In Electrical-Electronics Engineering, Selcuk University, Konya, 2017.

Determination of Electromagnetic Field Values by Designing Circular Microstrip Antenna for Determination of Cardiac Occlusion

Rabia TOP, Seyfettin Sinan GÜLTEKİN and Dilek UZER

Selcuk University, Konya/Turkey, rabiacaliskan@selcuk.edu.tr, sgultekin@selcuk.edu.tr, dilek_uzer@selcuk.edu.tr

Abstract **- Circulatory system diseases are the major cause of death. The biggest ratio in these causes is the heart diseases. Particularly importance in cardiac disorders are the consequences of cardiovascular occlusion. It is also extremely important that these results be determined without inconvenience. Here, the electromagnetic field values obtained with the modeling of cardiac artery occlusion using a microstrip patch antenna are evaluated. As a microstrip antenna, the substrate material of the circular microstrip antenna radiating in 3 different frequency zones (6, 7.95 and 12.95 GHz) was selected as FR-4. There are 3 short circuit pins added to reduce the size. The diameter of the designed patch equals the size of the substrate material and is 25 mm. Design and simulation use High Frequency Structural Simulator (HFSS) program. Cardiovascular modeling has been carried out according to the fact that each tissue has different electrical values as well as each material. Simulations have been done with and without fat tissue in the heart vein. The changes in the electromagnetic field values obtained as a result of the simulations made are to predict that cardiovascular obstruction can be detected in advance. For example, according to the simulation results, the electric field value obtained is 936.2 mV/m when there is no obstruction and 726.47 mV/m when congestion is concerned. Looking at these values, it is predicted that the designed antenna can be used for the detection of cardiac occlusion.**

Keywords **- Modelled Heart, Antenna, Microstrip Antenna, HFSS**

I. INTRODUCTION

In Turkey and in the world, the most death causes are related to the circulatory system and the biggest rate of these causes is heart failures. In 2016, in the study of death causes that have done by Turkey Statistical Institution 39.6 % of death causes is from the circulatory system and the greatest rate in this percentage is showed to be originated in heart failures [1]. The occlusion in heart vein is a basic parameter of heart diseases. If there is a cardiac occlusion, emergency intervention may be required to rescue patient's life. The detection of cardiovascular obstruction without surgery and without tomography has important developments in the name of humanity. Especially when considering human life, the importance of early diagnosis of cardiovascular occlusion increases [2].

Biomedical applications use antenna structure increase in the last twenty years [3]. Especially, when considering dimension, cost, easy design etc., microstrip patch antenna structures are usually preferred [4-6]. These antenna types are used in-body, on-body and off-body applications in the literature [7-9]. Sometimes the microstrip antenna, which comes out as a biosensor, can sometimes come up as a wearable antenna structure. But especially in the implantable antenna applications, microstrip patch antennas are mostly preferred [8-12].

In this study, a microstrip patch antenna is implemented to detect cardiac occlusion Because cardiac occlusion detection is targeted in advance without high-frequency medical tomography or surgical intervention. Different biological tissues have different electrical properties. Heart and its occlusion is modelled with fat have different permittivity and conductivity etc. parameters according to operating frequencies. Antenna structure is selected from [13]. There are three different frequency bands which operate. Also in the future, it is envisaged that high frequency bands will be used to detect and prevent some diseases. Here there is a modelled heart vessel structure. As cardiac occlusion, fat is used to model the heart vein. While with and without cardiac occlusion, simulations have done, and electromagnetic field values are obtained from them. Different field values are found for both cases. These differences say us that the proposed antenna can be used to detect cardiac occlusion before urgent intervention is needed.

II. ANTENNA DESIGN

A circular and probe fed microstrip patch antenna is designed because of some advantages of microstrip patch antennas such as easy design, cost, patch types etc. Substrate dimensions of the antenna is equal to diameter of patch and each of them is 25 mm. As substrate, FR-4 is selected and its permittivity is 4.4 and thickness is 1.575 mm. There are three short circuit pins inside antenna to increase operating frequencies of the proposed antenna and miniature antenna dimensions. Fig. 1 shows the proposed antenna structure.

Return loss of the antenna is showed in Fig. 2. There are three frequency bands. They are 6, 7.95 and 12.95 GHz, respectively and S_{11} values of them are -13.99, -15.64 and -23.34 dB, respectively. Antenna gain is 2.63 dB. Input impedance is 50 Ω and Voltage Standing Wave Ratio (VSWR) is 1.14. So, the proposed antenna is selected due to these antenna parameters to detect whether there is an occlusion in

heart vein or not.

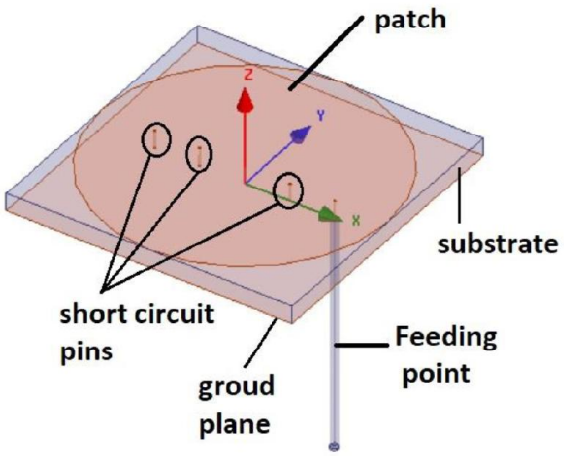


Figure 1: Proposed antenna structure

III. Modelled Heart Vein

Every material has different electrical properties than others. Biological tissues have different permittivity, conductivity and permeability than each other's, too. In this study, we have worked heart and its occlusion. So, permittivity, conductivity and loss tangent of heart are 43.97 F/m, 10.4 S/m and 0.46, respectively. Permittivity, conductivity and loss tangent of fat is described as occlusion are 4.69 F/m, 0.51 S/m and 0.193, respectively. These values are obtained from Table 1. There are three data of each tissue. And all values were collected and averaged. Then heart and fat tissues are introduced inside HFSS program to simulate.

GHz	type	F/m	S/m	tangent
6	Heart	48.62	6.12	0.37
	Fat	4.94	0.3	0.18
7.95	Heart	45.374	8.88	0.44
	Fat	4.76	0.44	0.20
12.95	Heart	37.94	16.22	0.593
	Fat	4.39	0.79	0.25

Each of heart vein and its occlusion are modelled as cyclindric structure (Fig. 3). Radius of heart vein is 25 mm and its lenght is 70 mm. The lenght of occlusion is 35 mm and its radius is 10 mm. Modelled heart structure exactly is placed on patch area of the antenna. Fig. 3 shows the position of heart vein and its occlusion.

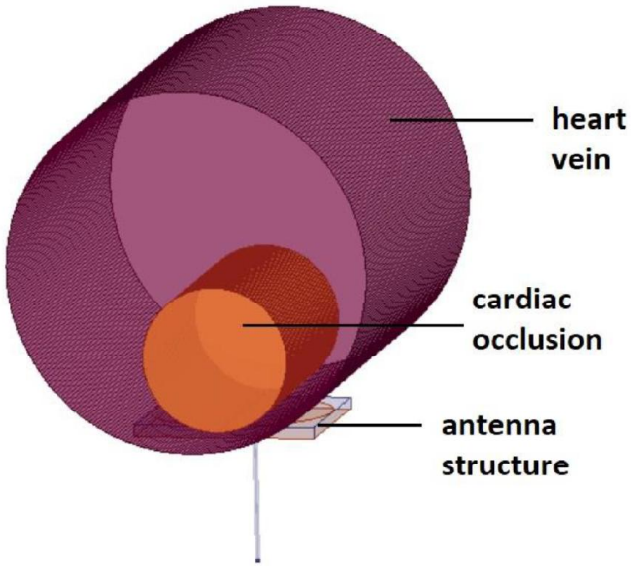


Figure 3: Modelled heart vein

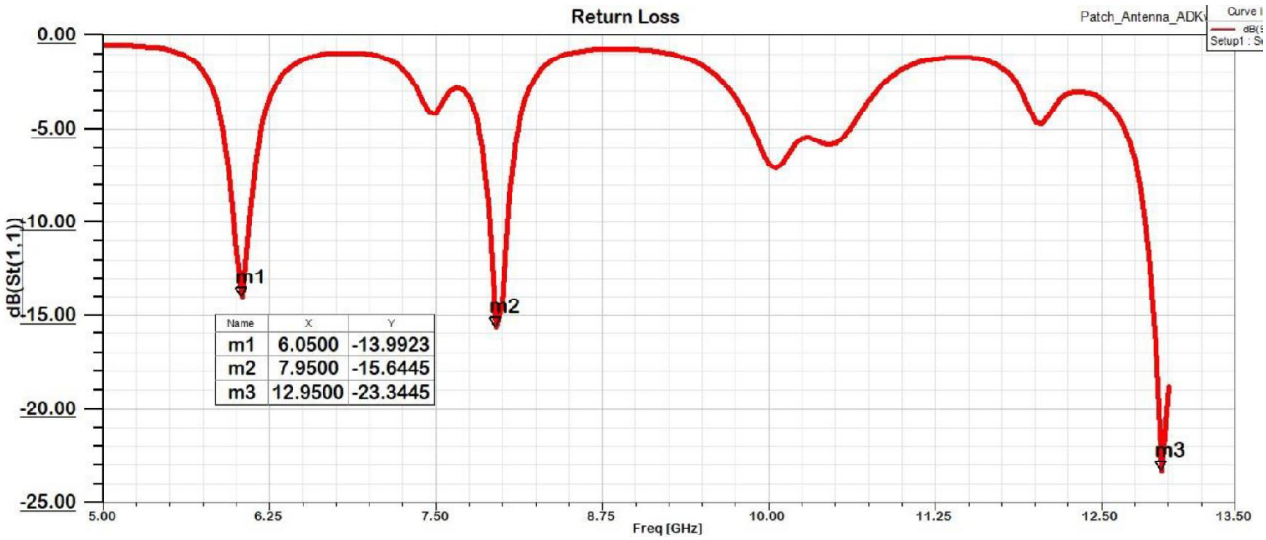


Figure 2: Return loss value of the proposed antenna

Table 1: Electrical properties of heart and fat tissue [14].

Frequency	Tissue	Permittivity	Conductivity	Loss

IV. Simulation and Evaluation

Simulations have done in HFSS program. Heart vein is exactly placed on the antenna structure. Firstly, simulation has done without cardiac occlusion and electromagnetic field values are obtained. Then simulation has done with occlusion in heart vein and different electromagnetic field values are obtained from it.

Electromagnetic field values obtained from simulations without cardiac occlusion are showed in Fig. 4. Maximum values of electric and magnetic field and surface current values are showed in Table 2.

Electromagnetic field values obtained from simulations with cardiac occlusion are showed in Fig. 5. Maximum values of electric and magnetic field and surface current values are showed in Table 2.

Figure 4: Obtained electric and magnetic field and surface current values without cardiac occlusion

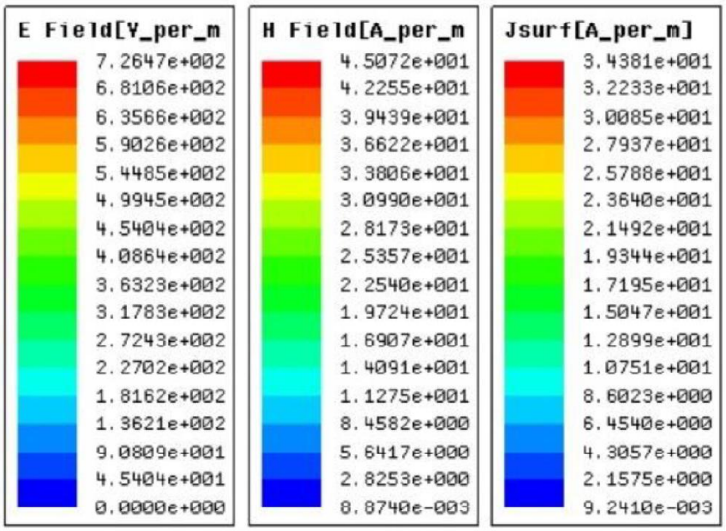
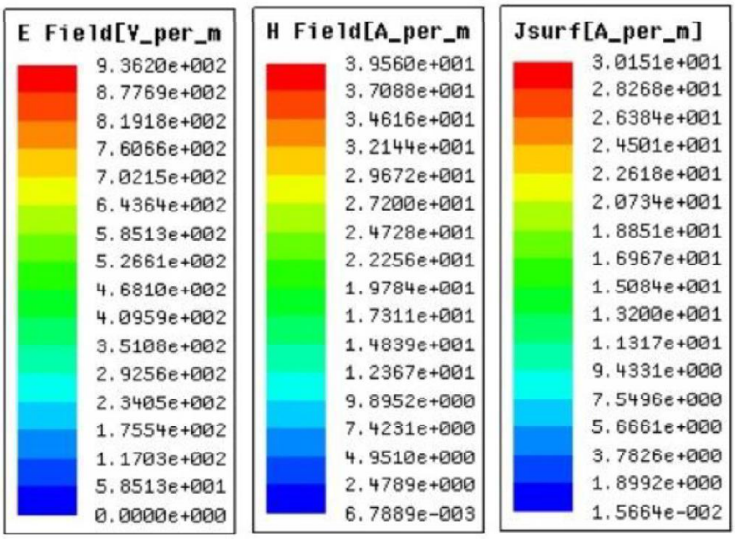


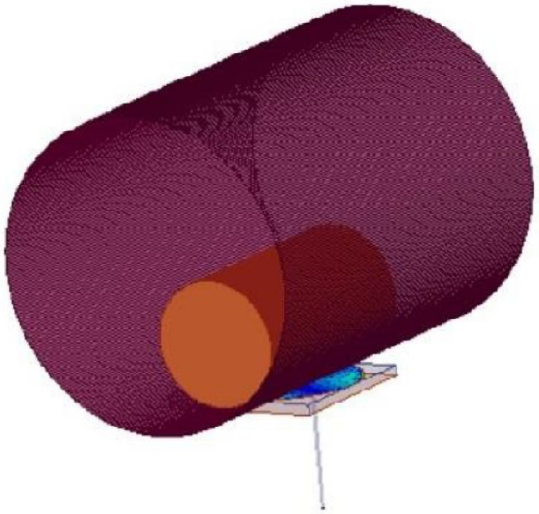
Figure 5: Obtained electric and magnetic field and surface current values with cardiac occlusion

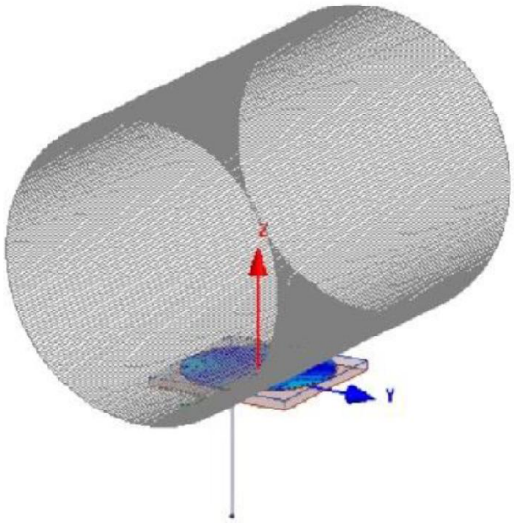
Table 2 also shows difference values of obtained electromagnetic field values. These differences are important to detect cardiac occlusion. Fig. 6 shows valuations of obtained electric field values depend on theta angle in the situation of with and without cardiac occlusion. While there is cardiac occlusion, electric field graphic also changes.

Table 2: Obtained electromagnetic field values with and without occlusion

Field name	E-field (mV/m)	H-field (mA/m)	J (mA/mm^2)
Without occlusion	**936.2**	**39.5**	**30.1**
With occlusion	**726.47**	**45.07**	**34.38**
Difference	**209.73**	**5.57**	**4.28**







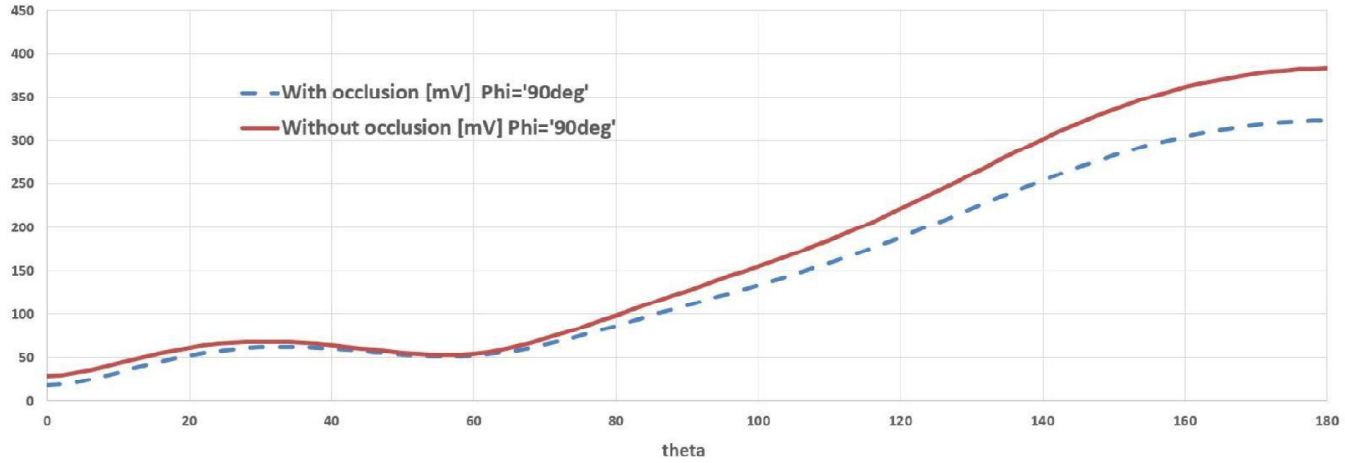


Figure 6: Valuations of obtained electric field values depending on theta angle.

V. CONCLUSION

Circular microstrip patch antenna designed to detect cardiac occlusion and has three short circuit pins is evaluated in HFSS. After simulations, while there is occlusion and there is no occlusion, different electromagnetic field values are obtained. With occlusion, electric field value is 726.47 mV/m, magnetic field value is 45.07 mA/m and surface current density is 34.38 mA/mm^2. Without occlusion electric field value is 936 mV/m, magnetic field value is 39.5 mA/m and surface current density is 30.15 mA/mm^2. Therefore, obvious differences about field values are put forth. It is thought that these differences can be used to predict cardiovascular occlusion before cardiac occlusion occurs. Finally, once selected antenna structure is considered, distinctiveness of obtained differences is possible to say a successful design.

REFERENCES

[1] T. İ. Kurumu, "Ölüm nedeni istatistikleri, 2016," in *Türkiye İstatistik Kurumu Haber Bülteni* vol. 24572, ed, 2017.

[2] A. Civelek. *Koroner Arter Hastalığı*. Available: http://www.alicivelek.com/koroner-arter-hastaligi-ve-koroner-baypas-cerrahisi

[3] P. S. Hall and Y. Hao, "Antennas and propagation for body centric communications," in *Antennas and Propagation, 2006. EuCAP 2006. First European Conference on*, 2006, pp. 1-7: IEEE.

[4] R. Çalışkan, S. S. Gültekin, D. Uzer, and Ö. Dündar, "A microstrip patch antenna design for breast cancer detection," *Procedia-Social and Behavioral Sciences,* vol. 195, pp. 2905-2911, 2015.

[5] M. Nalam, N. Rani, and A. Moha, "Biomedical application of microstrip patch antenna," *Int J Innov Sci Mod Eng,* vol. 2, no. 6, pp. 319-327, 2014.

[6] S. Samal, S. Dwari, A. Dutta, and S. P. Reddy, "A Microstrip Patch antenna for biomedical applications at 2.45 GHz," in *Computers and Devices for Communication (CODEC), 2012 5th International Conference on*, 2012, pp. 1-4: IEEE.

[7] A. Alomainy, Y. Hao, C. Parini, and P. Hall, "Comparison between two different antennas for UWB on-body propagation measurements," *IEEE Antennas and Wireless Propagation Letters,* vol. 4, no. 1, pp. 31-34, 2005.

[8] T. Karacolak, A. Z. Hood, and E. Topsakal, "Design of a dual-band implantable antenna and development of skin mimicking gels for continuous glucose monitoring," *IEEE Transactions on Microwave Theory and Techniques,* vol. 56, no. 4, pp. 1001-1008, 2008.

[9] P. Soontornpipit, C. M. Furse, and Y. C. Chung, "Design of implantable microstrip antenna for communication with medical implants," *IEEE Transactions on Microwave theory and techniques,* vol. 52, no. 8, pp. 1944-1951, 2004.

[10] S. A. Kumar and T. Shanmuganantham, "Design of implantable CPW fed monopole H-slot antenna for 2.45 GHz ISM band applications," *AEU-International Journal of Electronics and Communications,* vol. 68, no. 7, pp. 661-666, 2014.

[11] S. Vaddiraju, M. Kastellorizios, A. Legassey, D. Burgess, F. Jain, and F. Papadimitrakopoulos, "Needle-implantable, wireless biosensor for continuous glucose monitoring," in *Wearable and Implantable Body Sensor Networks (BSN), 2015 IEEE 12th International Conference on*, 2015, pp. 1-5: IEEE.

[12] R. Top, S. S. Gültekin, and D. Uzer, "Modeling congestion of vessel on rectangular microstrip antenna and evaluating electromagnetic signals," in *Signal Processing and Communications Applications Conference (SIU), 2017 25th*, 2017, pp. 1-4: IEEE.

[13] R. Top, "A Transmitter Microstrip Antenna Design and Application Towards the Detection of Heart Disease Parameters," Master Thesis, the Degree of Master Of Science In Electrical-Electronics Engineering, Selcuk University, Konya, 2017.

[14] C. Gabriel, "Compilation of the Dielectric Properties of Body Tissues at RF and Microwave Frequencies," King's Coll London (United Kingdom) Dept Of Physics1996.

Analysis of Enhanced Exponential Reaching Law Control System Parameters for Magnetic Levitation System

DİNÇER MADEN[1], *İRFAN YAZICI*[2]

[1]Duzce University, Department of Electrical&Electronics Engineering, 81620
Konuralp Campus, dincermaden@duzce.edu.tr
[2]Sakarya University, Departement of Electrical&Electronics Engineering, 54050
Esentepe Campus, iyazici@sakarya.edu.tr

Abstract **- Magnetic levitation systems provide straightforward way to overcome the problem of friction, and isolation of heath and noises. Because open loop magnetic levitation system is highly nonlinear and unstable, it is necessary to design simple, efficient and robust controller. Many new control methods are proposed to overcome this issue. One of these methods, which is Enhanced Exponential Reaching Law (EERL), provide better control performance compared to previous works. However, EERL is applied in continuous-time form. In this study, the system and the controller are modelled in discrete-time where the derivation of the input signal is provided accordingly. Furthermore, it is analyzed the control parameters (proportional rate and exponential coefficient) of the EERL structure and the effect of these parameters on the performance of the system. According to results, while the increase of proportional rate improves the reference point tracking performance and robustness of the system, the increase of exponential coefficient weakens the robustness.**

Keywords **- Magnetic levitation system, variable structure control, discrete time sliding mode control, EERL.**

I. INTRODUCTION

IN many engineering applications, friction and friction depended effects, such as heat, noise and vibration, affect the performance of the systems negatively. Magnetic levitation systems provide straightforward way to overcome the problem of friction and also for isolation of heath and noises. This technology has been widely used in many industrial areas like high precision engineering, frictionless bearings, levitation of vertical axis wind turbines, high speed maglev train in Sendai, levitation of molten iron in induction furnace and many more [1]. However, the open loop magnetic levitation system is highly nonlinear and highly unstable because of their electromechanical system dynamics. Both the sensitivity requirements of the systems which is depended on their application area and the its unstable structure, required a designing of simple, efficient and robust controller. In order to remedy this problem, many new control algorithms which are applied in magnetic levitation systems are proposed in literature. Rubio et al. investigated the modeling and control with neural networks for a magnetic levitation system. Their method has shown good tracking performance and stability is guaranteed by utilizing the Lyapunov method [2]. In [3], Iterative Feedback Tuning (IFT) algorithm is for tune a type of fractional order Proportional-Integral-Derivative (PIα D) controller. Aforementioned control strategy is tested on a hardware and reliability of this method verified. In another study, fuzzy sliding mode controller and with evolutionary programming based on a magnetic suspension system was proposed and compared with other sliding-mode control techniques then better results have been revealed [4]. The stability of this system with controller could be guaranteed when the control methods such as PID, 2-DOF PID, LQR etc. are employed. However, the control performance of these systems is limited because of their parameters are fixed [5]. In order to overcome this problem, variable structure control systems are good candidate as a solution for better performance. The sliding mode control (SMC), a type of variable structure control technique, was first revealed in the Soviet Union in the late 1950's, and the first work was carried out by Emel'yanov in early 1960' s [6]. SMC is a well-known robust control technique that can provide the desired dynamic behavior despite the uncertainties in the system, parameter changes and disturbance effects [7]. In today's modern control systems, SMC is utilized in satellite altitude control, robot manipulator control, power system control etc. SMC is a discontinuous control structure where continuous subsystems are used. In particular, the error vector of the system is forced into a desired point by switching two continuous functions. Hence SMC is subject to discontinuity on a particular surface of the state space model [8]. Besides the advantages mentioned, SMC provides the transformation of any nth order control problem into a first order one [9]. SMC strategy is realized in three modes where the first mode is the reaching mode that defines reaching the state variable to sliding surface. The remaining modes are defined as sliding mode and steady-state mode. When the state variables reach the sliding surface, the controller becomes independent of system models [10].

In the literature, several reaching laws are proposed in the context of SMC. In [11], constant proportional rate reaching law (CPRL) is used for robotic arm control. In [11], power rate

reaching law is considered. While these methods provide a limited performance, enhanced exponential reaching law (EERL) is proposed for better control performance. In [12], EERL control technique is used for permanent magnet synchronous generator (PMSG) in continuous-time form is considered. In this study, the system and the controller are modeled in discrete-time where the derivation of the input signal is provided accordingly. Furthermore, we analyze the control parameters of the EERL structure where proportional rate and exponential coefficients are taken into consideration. Then the effect of these parameters on the performance of the system is investigated.

II. Magnetic Levitation System

The general scheme of a magnetic levitation system is shown in Fig. 1. Main principle of this system is a ferromagnetic ball is levitated against the gravity by an electromagnetic force generated by a coil which is mounted at the top. An optoelectronic sensor, placed laterally, sensing the vertical position of the ferromagnetic ball x_v, by using the reflection of the ball surface. The x is distance between the center of ball and electromagnetic coil, which is controlled by coil current source. Therefore, the main goal is determining the height of the ball according to control input signal in spite of external disturbance effect.

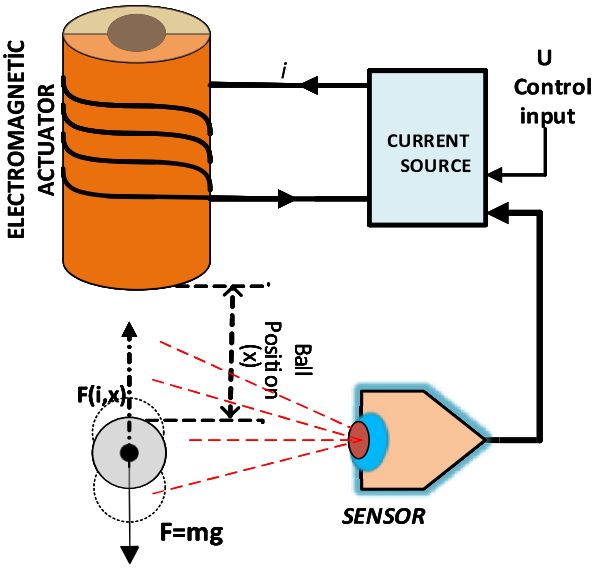


Fig. 1. Structure of magnetic levitation system

In this study, a series of simulations was carried out based on the magnetic levitation system produced by Googol Company. The realizable parameters of the system are given in Table 1. Only the forces in the vertical direction have been take into consideration in system model. That is, neglecting effect of external interference factors, steel ball is attracted electromagnetic force $F(i,x)$, against its own gravity mg. By analyzing the physical structure of magnetic levitation system, the following mathematical equations could be obtained.

$$mx = mg - k\frac{i^2}{x^2} \tag{1}$$

In above equation, g is the gravitational acceleration and k is the general gain coefficient for the coil parameters. Electromagnetic mechanical equation is represented in (2).

$$f(x,i) = k\frac{i^2}{mx^2} \tag{2}$$

Table 1. Physical parameters of magnetic levitation system

Parameters	Values
m - Mass of Ball	22 gr
g - Gravitational Acceleration	9.81 m/s2
i_0 - Equilibrium Point of Coil Current	1.2441 A
x_0 - Equilibrium Point of Ball Position	35 mm
K_x - The Gain Coefficient of Coil Current	5.8829 A/V
K_a- The Gain Coefficient of Sensor Current	458.715 V/m

Due to the system model given in (1) is in nonlinear form, it is required to linearize the system in near the equilibrium point to designing a convenient control system. When it is desired to obtain the transfer function by taking the points represented by x_0 and i_0 as equilibrium points, the equation x is obtained as follows.

$$x = g - f(x,i) \tag{3}$$

By equating the derivative as $x = 0$,

$$g = f(\mathrm{x},\mathrm{i}) \rightarrow \mathrm{i}_0, x_0 \tag{4}$$

where i_0, x_0 values can be obtained. Then k coefficient is could be expressed as below.

$$k = \frac{mgx_0^2}{i_0^2} \tag{5}$$

In order to express the system model in the form of transfer function, the $f(i,x)$ in the (1) and (2) is implemented by the Tylor series expansion and high order terms are ignored then Laplace transform is used as follow.

$$\frac{X(\mathrm{s})}{I(\mathrm{s})} = \frac{-1}{(i_0/2g)s^2 - i_0/x_0} \tag{6}$$

In the essential transfer function, the correlation between the controlled voltage value of the input signal u and value of the position sensor output xv, could be expressed as follow.

$$G(\mathrm{s}) = \frac{X_V(\mathrm{s})}{U(\mathrm{s})} = -\frac{2\mathrm{K}_x\mathrm{g}/\mathrm{K}_a i_0}{\mathrm{s}^2 - 2g/x_0} \tag{7}$$

Since, one of the poles of $G(s)$ is positive, it can be seen that the magnetic levitation system is a second order unstable system. For that reason, a suitable controller is required to make controlled ball reach the stable levitation state.

III. Design of Discrete Time Sliding Mode Controller with EERL

The main goal of the sliding mode control method is to direct the system dynamics to be controlled to a surface called the sliding surface and keep the dynamics on this surface and move towards the equilibrium point. In the phase portrait of the system, the segment from the starting point to the sliding surface is called the reaching phase. After reaching the sliding surface of the system, the movement up to the equilibrium point is defined as the sliding motion. In this regard, there are two basic steps in the implementation of the sliding mode control method [13], i.e. Expression of a sliding surface defined by $\sigma(\mathrm{x}) = 0$ to reach the equilibrium point of the system.

Design the controller which is governed the dynamics of the system to sliding surface and ensure that it remains on this surface.

Since the magnetic levitation system is a second-order, the sliding surface can be expressed by the proportional-derivational (PD) control approach based on the error dynamics as follows. The coefficient c expresses the slope of the sliding surface. The error term e, represents the difference between the required position and the current position of the steel ball.

$$\sigma(\mathrm{x}) = e + ce, c > 0 \tag{8}$$

The total control input signal must be obtained in order for both phases mentioned above to take place. This signal UT is designated as the sum of two signals, the continuous and discontinuous part.

$$U_T = U_{cont.} + U_{discont} \tag{9}$$

The continuous part which is responsible for the sliding phase is also known as the equivalent control signal in the literature and many methods have been investigated. In this study, root location method is considered about the defining of equivalent control signal. There are two approaches for achieving reaching condition. First of this is Lyapunov candidate function choosing approach which is guaranteed reachability and stability. This formulation is given as follows

$$V(\sigma) = \frac{1}{2}\sigma^2 \le -\eta|\sigma| \tag{10}$$

Where η is a strictly positive coefficient. If the condition of (10) is satisfied, the state variables of the system are reaches the sliding surface and stay there. Lyapunov based reaching condition could be defined as below.

$$\sigma\sigma \le 0 \tag{11}$$

Lyapunov candidate function approach is used for stability analysis of the system as well as control signal derivation. This technique ensures that the initial values of the variables in the state space arrive at the sliding surface in a finite time. However, it doesn't have any limitations in terms of reaching time and trajectories of state variables. In this respect, reaching law methods have been proposed. This method is a newer approach and has the ability to directly determine the dynamic of the switching function. Additional advantages of this approach include a simplification of the analyzing of sliding mode control and it has a scale of chattering level. Both the Lyapunov approach and reaching law technique give control input signal which is contain a relay function (signum). In Eq. (9), $U_{discont}$ is expressed as a discontinuous control signal since it has a term of signum function [14].

Since, the application of modern control systems via computers, microprocessors and digital signal processors is increasing day by day, the study of discrete time sliding mode control methods have been an important topic in the non-linear control literature [15]. In addition, the direct application of the continuous-time SMC to discrete-time systems takes some problems place, such as large chattering amplitude, sample and hold effects, discretization errors and instability [16]. In this respect, the controlled system and the controller need to be well expressed in discrete time. On the other hand, Lyapunov stability condition must be considered in discrete time domain. There are many stability analysis methods investigated and proposed. Sarpturk, et al. considered the following condition [17]. In this study, this reaching and stability condition is used.

$$|\sigma(k+1)| < |\sigma(k)| \tag{12}$$

In their study of discrete time sliding mode controller condition has the form as below.

$$\begin{aligned} &[\sigma(k+1) - \sigma(k)].sign(\sigma(k)) < 0 \\ &[\sigma(k+1) + \sigma(k)].sign(\sigma(k)) > 0 \end{aligned} \tag{13}$$

The state equations of the system are obtained as follows using the physical parameters in Table 1 [5].

$$\begin{aligned} x_1(t) &= x_2(t) \\ x_2(t) &= 560x_1(t) + 122u(t) \end{aligned} \tag{14}$$

The discrete-time state space form of the system must be obtained to be used in discrete time sliding mode control. In this study, the ZOH (Zero Order Hold) method has used to obtain the G and Γ matrices in $T_s = 1$ ms sampling period, as shown below

$$x(\mathrm{k}+1) = \mathrm{Gx(k)} + \Gamma u(\mathrm{k}) + d(k) \tag{15}$$

Where, $G = \begin{bmatrix} 1.003 & 0.001 \\ 0.5606 & 1.003 \end{bmatrix}$, $\Gamma = \begin{bmatrix} 0.0006 \\ 1.2298 \end{bmatrix}$ and $d(\mathrm{k})$ is

represents the disturbance input signal.

It is known that many researches have been carried out for the reaching law. In this paper, CRL and ERL were joined to take advantage of the qualifications of both. This reaching law, called EERL, allows the manipulation of both the reaching phase and the sliding phase when designing the controller. There are some key features of the EERL method which is newer than other reaching strategies, such as flexible structure, smaller reaching time, lower chattering amplitude [12]. In this study, the EERL method is redefined in discrete time form for the requirements of the discrete time modelling and. The standard formulization with sampling period for the sliding surface of discrete time EERL could be given as follows.

$$\sigma(\mathrm{k}+1) = (1-\lambda \mathrm{T}_s)\sigma(\mathrm{k}) - \frac{KT_s}{D(\sigma(\mathrm{k}))}\left|\sigma\right|^{\gamma} sign(\sigma(\mathrm{k})) \tag{16}$$

$$D(\sigma(\mathrm{k})) = \alpha + (1-\alpha)\,\mathrm{e}^{-\beta|\sigma(\mathrm{k})|} \tag{17}$$

To verifying the Lyapunov condition in (12) and (13), the result is obtained as below

$$\lambda T_s \sigma(\mathrm{k})^2 + \frac{KT_s}{D(\sigma(\mathrm{k}))}\left|\sigma(\mathrm{k})\right|^{\gamma+1} > 0 \tag{18}$$

This condition has been verified as above. The following equation can be given by considering the error dynamics and assuming that the sliding surface is linear.

$$\sigma(k) = C.\mathrm{e}(k), \qquad C = [c \quad 1] \tag{19}$$

The following equation can be written if the state variables of the system reach the switching manifold.

$$\sigma(\mathrm{k}+1) = \sigma(\mathrm{k}) = 0 \tag{20}$$

From the Eq. (16), (17) and (19) following equation is obtained.

$$Cx(k+1) = (1-\lambda T_s)\sigma(k) - \frac{KT_s}{D(\sigma(k))}\left|\sigma(k)\right| sign(\sigma(k)) \tag{21}$$

Control input signal can be defined by the following equation using discrete time EERL approach.

$$U(\mathrm{k}) = (\mathrm{CH})^{-1}\left[-CGx(\mathrm{k}) + (1-\lambda \mathrm{T}_s)\sigma(\mathrm{k}) - \frac{KT_s}{D(\sigma(\mathrm{k}))}\left|\sigma(\mathrm{k})\right|^{\gamma} sign(\sigma(\mathrm{k}))\right] \tag{22}$$

IV. Simulation Study

In this study, discrete time EERL sliding mode controller have been designed with the magnetic levitation system in Matlab/SIMULINK package program. For the modeling of the system, the physical parameters given in table 1 are used and the system is discretized by ZOH (zero order hold) method with same sampling period in all simulations. At the beginning of the simulation, a square wave with a magnitude of 0.2 units and a period of 3 seconds was selected as the reference input signal. The proportional gain coefficient and exponential rate coefficient to be discussed about how to affect the performance of the system was chosen as K=5, and $\gamma = 0.1$ respectively. The other parameters used are, C=15 $\alpha = 0.1$ and $\beta = 0.9$. First, reference tracking performance for different K values is examined and the results are given in Fig. 2.

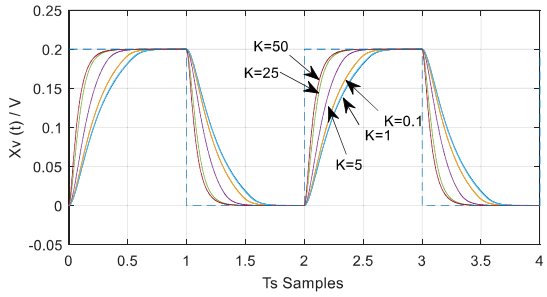


Fig 2. Position tracking curves with different K

As shown in Fig. 2, the designed controller has been successful in references point tracking. It was observed that the tracking performance changed when the γ value was kept constant and the K value was increased or decreased. It is seen that the controller performance does not change much if the K value is less than 1 or greater than 25. However, when the value of K is increased from 1 to 25, reference point tracking performance is improved. In this interval, if the change of the sliding surface amplitude is examined for 3 different K values, the results are obtained in Fig. 3.

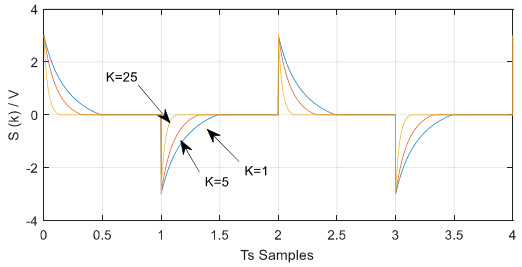


Fig. 3. Sliding surface of discrete time EERL according to different K

For K = 1, K = 5 and K = 25, the areas below the curves of sliding surface gradually narrow. If it is desired to test the robustness of the system for different values of K, the ball position is disturbed at certain moments, and this effect is better minimized at high values of K as can be seen in Fig.4.

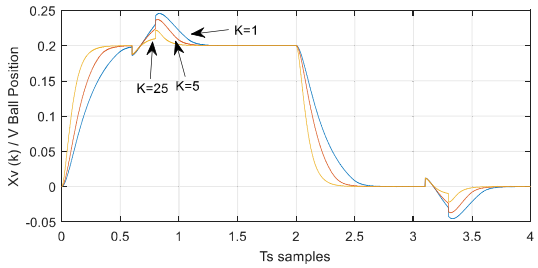


Fig. 4. Disturbance rejection behavior of system with different K

Similarly, by fixing the value of K at 5, the same examinations were performed for γ which is exponential gain coefficient and the following graphs were obtained. If the γ value is smaller than 0.1 and higher than 4.9, it does not affect the controller performance much more.

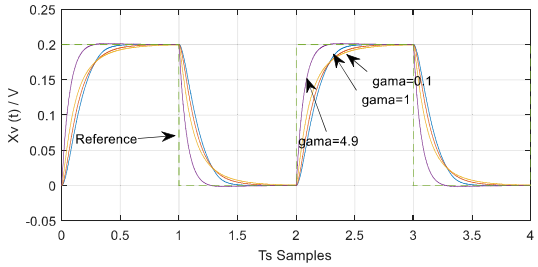


Fig. 5. Position tracking curves with different γ

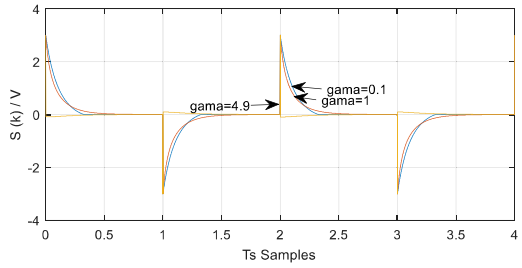


Fig. 6. Sliding surface of discrete time EERL according to different γ

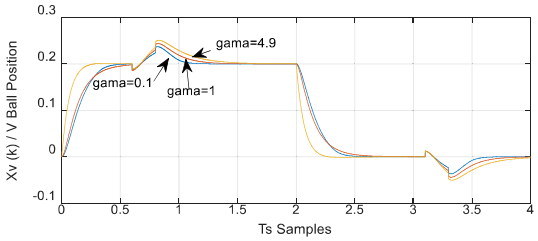


Fig. 7. Disturbance rejection behavior of system with different γ

However, contrary to the effect of the K coefficient, the increase in the γ coefficient weakens the robustness of the system. It could be observed in Fig. 7.

V. Conclusion

In this paper, a discrete time sliding mode controller is designed for the magnetic levitation system, which is the subject of many control engineering applications. The EERL technique, an efficient combination of different reaching laws, has been proposed and expressed in discrete time domain. It has been observed that the controller is working efficiently and giving good results. The operating range for the proportional and exponential coefficients in the EERL method is specified. Although the increase of both coefficients improves the reference point tracking performance of the system, exponential coefficient weakens the robustness.

References

[1] S. Pandey, P. Dwivedi, and A. S. Junghare, "A novel 2-DOF fractional-order PI-_ Dl controller with inherent anti-windup capability for a magnetic levitation system," AEU - Int. J. Electron. Commun., vol. 79, pp. 158–171, 2017.

[2] N. Effect, N. Dma, C. Fang, Y. Jing, Y. Zong, and Z. Lin, "Modeling and control with neural networks for a magnetic levitation system," Int. J. Adhes. Adhes., vol. 227, no. February 2016, pp. 113–121, 2016.

[3] M. Rezaei Estakhrouiyeh, A. Gharaveisi, and M. Vali, "Fractional order Proportional-Integral-Derivative Controller parameter selection based on iterative feedback tuning. Case study: Ball Levitation system," Trans. Inst. Meas. Control, p. 14233121769133, 2017.

[4] T. H. S. Li, C. L. Kuo, and N. R. Guo, "Design of an EP-based fuzzy sliding-mode control for a magnetic ball suspension system," Chaos, Solitons and Fractals, vol. 33, no. 5, pp. 1523–1531, 2007.

[5] X. Shao, F. Meng, Z. Chen, and Q. He, "The Exponential Reaching Law Sliding Mode Control of Magnetic Levitation System," no. 20132050, pp. 3500–3503, 2016.

[6] V. Utkin, "Variable structure systems with sliding modes," IEEE Trans. Automat. Contr., vol. 22, no. 2, pp. 212–222, 1977.

[7] P. Roy, S. Sarkar, B. K. Roy, and N. Singh, "A Comparative Study between Fractional Order SMC and SMC Applied to Magnetic Levitation System," IEEE Indian Control Conf., vol. 15, no. 33, 2017.

[8] V. I. Utkin and H.-C. Chang, "Sliding mode control on electro-mechanical systems," Mathematical Problems in Engineering, vol. 8, no. 4–5. pp. 451–473, 2002.

[9] M. F. Uslu, "SLIDING MODE SPEED CONTROL OF INDUCTION MOTORS," Kırıkkale Univercity,Institue of Science, 2005.

[10] W. Gao, Y. Wang, and A. Homaifa, "Discrete-time variable structure control systems," Ind. Electron. IEEE Trans., vol. 42, no. 2, pp. 117–122, 1995.

[11] W. Gao and J. C. Hung, "Variable Structure Control of Nonlinear Systems: A New Approach," IEEE Trans. Ind. Electron., vol. 40, no. 1, pp. 45–55, 1993.

[12] S. M. Mozayan, M. Saad, H. Vahedi, H. Fortin-Blanchette, and M. Soltani, "Sliding Mode Control of PMSG Wind Turbine Based on Enhanced Exponential Reaching Law," IEEE Trans. Ind. Electron., vol. 63, no. 10, pp. 6148–6159, 2016.

[13] W. L. Slotine, Jean Jacques, Applied nonlinear control. NEW JERSEY,USA: NJ: Prantice-Hall, Englewood Cliffs, 1991.

[14] S. Chakrabarty and A. Bartoszewicz, "Improved robustness and performance of discrete time sliding mode control systems," ISA Trans., vol. 65, pp. 143–149, 2016.

[15] X. Yu, B. Wang, and X. Li, "Computer-controlled variable structure systems: The state-of-the-art," IEEE Trans. Ind. Informatics, vol. 8, no. 2, pp. 197–205, 2012.

[16] Y. P. Chen, J. L. Chang, and S. R. Chu, "PC-based sliding-mode control applied to parallel-type double inverted pendulum system," Mechatronics, vol. 9, no. 5, pp. 553–564, 1999.

[17] S. Sarpturk, Y. Istefanopulos, and O. Kaynak, "On the stability of discrete-time sliding mode control systems," IEEE Trans. Automat. Contr., vol. 32, no. 10, pp. 930–932, 1987.

Wind Power Forecasting Using Fuzzy Model

Hasan Hüseyin Çevik, Mehmet Çunkaş

Selçuk University, Dept. of Electrical & Electronics Eng. Konya, Turkey

hasanhcevik@selcuk.edu.tr, mcunkas@selcuk.edu.tr

***Abstract*— Power generation and power demand must be balanced at all times in electric system to keep the frequency and voltage values with in the desired limits. Day ahead market is run by electric utilities to keep the balance and all market participants must join this market to buy or sell power energy. The power generated from the wind is a function of the wind speed which has uncertainty because of its nature. Wind power plant companies forecast their hourly production of next day and this process is done every day. In this study, a short-term wind power forecast is carried out. The fuzzy expert system is selected as forecast method. A wind power plant's hourly generating data of 2016 and the meteorological wind data of wind power plant's location are used to construct the forecast. While the wind speed, wind direction and six-hour wind speed average are selected as inputs for the forecast system, hourly generated wind power is determined as output. The normalized mean absolute error is found as 12.7%.**

***Keywords*— energy management, fuzzy model, wind power forecasting.**

I. INTRODUCTION

The wind is simply defined as the movement of the air and it is basically formed by two reasons. The first is that warming the atmosphere differently due to the irregular surface of the earth by the sun and second one is the world's rotation around its axis. Since early recorded history, people have used the energy of the wind for sailing, grain grinding and water pumping. With the development of electric power system, wind had a new application area and was used for generating the electric in lighting buildings remotely from centrally generated power in the early 1900s. Availability of cheap oil and low energy prices caused the wind energy to be less preferred in electricity generation until the oil shortages of the 1970s. After the oil crisis in 1973, the world had interest in alternative energy sources and started to design major wind turbine for utility electricity [1]. Especially, for last two decades, this interest has increased much more for some reasons. These are environmental concerns which are air pollution and global warming, economic uncertainties which are worldwide reductions of fossil fuel reserves and fluctuations in fossil fuel prices, and cost stability with the increasing wind turbine technology and decreasing the costs [2].

Power generation and power demand must be balanced at all times in electric system to keep the frequency and voltage values with in the desired limits. This balance is vital for electricity supply security, because industrial process and digital technologies depend on reliable electricity systems. In Turkey, Turkish Electricity Transmission Company (TEIAS) and Energy Markets Business Administration Company (EPIAS) manages the electricity system by running the energy markets and some balance mechanisms. These are day ahead market, intraday market, balancing power market, bilateral contracts, imbalance and retroactive adjustment. In day ahead market, market participants submit their next day hourly forecast values which are price and power values of generated/consumed electricity until 12:30 am every day. So reference price of electricity is determined and most of part of generation/consumption balance is secured. Intraday market is a bridge between day ahead market and balancing market. The purpose of this market is minimize or balance positive/negative imbalances because of power plant failures, fast changes in renewable generation power and power demand. Balancing power market is run to control real timely the frequency and demand of electricity [3].

There are two major uncertain values in this system and these are load demand, renewable generation. When distribution companies and high energy consumption factories such as steel factories forecast their consumption, renewable power plants forecast their generation values to submit their bids. Except bilateral contracts, all participants on demand side and generation side must join the day ahead system to buy or sell power energy. In short, forecast is not an option, it is an obligation for electric market participants.

Since generated wind power depend on atmospheric conditions, it has been called as a non-dispatchable sources [4]. Wind power forecasts are very important to reduce the uncertainty and schedule the electricity generation especially in power systems have a high rate wind power.

Wind power forecasts are classified according to the two different criteria which are time span and structure. Forecasts are divided in four group as long term, medium term, short term and very short term in term of time span. Long term forecasts are from weeks to months or years and used for wind power and power system planning. Medium term forecasts are from days to weeks and used unit commitment and maintenance scheduling. Short term forecasts are from hours to days and used for economic dispatch, reserve requirement, intraday market and day ahead market. Lastly, very short term forecast are seconds to minutes and used for wind turbine control and power system frequency control [5]. The forecasts are also divided in three group as physical, statistical and hybrid in terms of structure. In physical model, physical structure of wind power plants and numerical weather prediction data are considered. In statistical models, historical meteorological data and wind power data are used. Hybrid model is a combine of physical model and statistical model [6]. While physical mo-

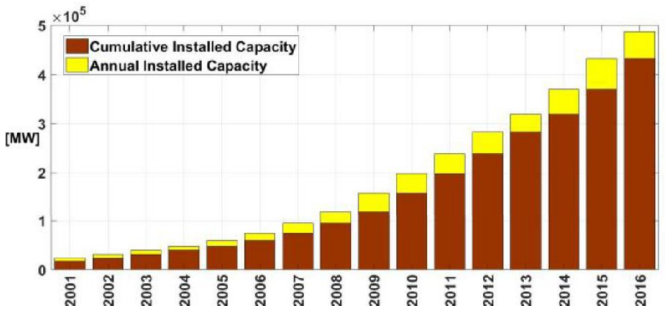


Fig. 1 Global cumulative installed wind capacity 2001-2016 [12]

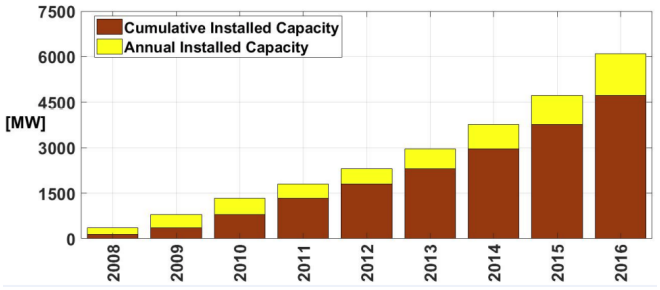


Fig. 2 Cumulative installed wind capacity in Turkey [13]

dels are generally preferred for long term forecasts, statistical models are used for short term forecast [4]. As looking the previous studies of short term wind power forecast, various methods are preferred such as support vector machines [6], artificial neural network [7,8], fuzzy logic [9], artificial neuro fuzzy inference system [10] and wavelet [11].

In this study, a short-term wind power forecast which have been done every day by wind power plants is carried out. The fuzzy expert system is selected as forecast method. A wind power plant's hourly generating data of 2016 and the meteorological wind data of wind power plant's location are used to construct the forecast model. Hourly wind speed forecasts, average of six hours wind forecast average speed and wind direction are selected as inputs and hourly generated wind power is determined as output.

The rest of paper is organized as follows. Section II gives information about status of wind power and data. While Section III presents fuzzy method, the results are given in Section IV. Section V concludes the study.

II. Data and Wind Power Status

According to the Global Wind Report 2016 published by Global Wind Energy Council, the installed wind power capacity in 2016 increased by 12.6 percent and reached about 486.6 GW. In the first three China with 34.7%, USA with 16.9 % and Germany with 10.3% [12]. Global cumulative installed wind capacity 2001-2016 can be seen in Figure 1. Although Turkey has only 1.25% of global installed capacity, especially in last years installed capacity rates increase above 25%. With the new installed capacity in 2016, Turkey is the third place after Germany and France. Cumulative installed wind capacity in Turkey is shown in Figure 2. In the end of 2016, Total capacity of Turkey reached 6106 MW and this is the 7.3% of Turkey electricity demand. There are 2658 turbines and 149 wind farms. Turkey has very rich wind resources and it is estimated 48GW from areas with >7m/s wind speed at 50 meters. One of the fastest growing power markets is Turkey in the world. Turkey wants to get of 30% of their electricity from renewable energy sources by the 2023 [12, 13].

It is difficult to find wind power production data for researcher who want to study on short term wind power forecast. Wind power plant companies think that these data are commercial secret and they are reluctant to share these data. If they share their data, they do not want to be known the wind power plant's name and location. They want that their production are normalized between 0-1 in publications. In this study, hourly power data of a wind power plant in Turkey are used to forecast. The data taken from the plant are normalized between 0-1 to mask the plant characteristic. Distribution of the produced power data is given in Figure 3. Wind data is taken from Meteorological Service of Turkish State.

There are various factors that affect the produced power of a wind turbine. The most important of these is the wind that is occurred by the atmospheric pressure difference. In fact, the power produced from a wind turbine can be calculated from rotational kinetic energy formulas. This formula is given as following:

$$P(t)=\frac{1}{2}\rho A V^3 C_p \qquad (1)$$

P is the produced power, t is time variable, ρ air density, C_p power coefficient (Betz limit-0.59), A is area swept by wings, V is the wind speed [14]. This formula is generally used in physical power forecast studies. The wind direction varies by terrain effects which plant is located. In power plant's terrain some winds have a boosting effect and some have a decreasing effect. This effect depends on the geography of power plant's terrain. Produced power from wind also depends on temperature, air pressure, terrain, topology and wind turbine

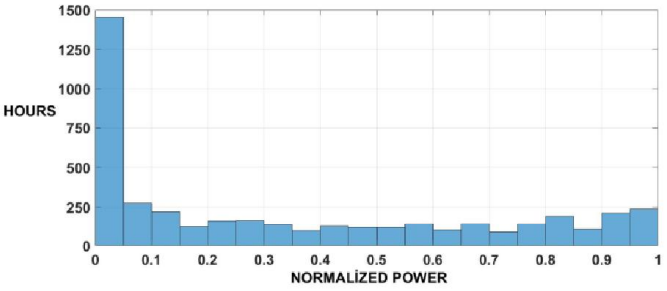


Fig. 3 Distribution of produced wind power

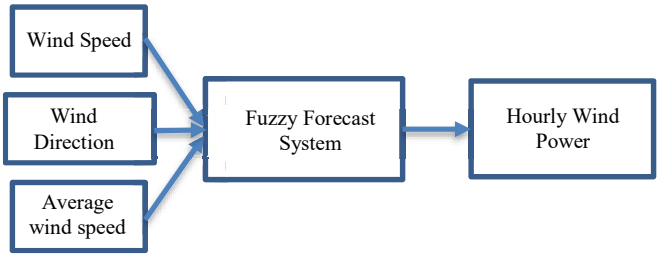


Fig. 4 Forecast system diagram

design [4]. Wind speed forecast and wind direction forecasts are usually used in short term wind power forecast studies.

In the first stage, data cleaning is made to eliminate the distorted data. As a result of this process, 12 months data have been decreased to nine months. While eight months data are selected as train data, one month data are selected as test data. The wind speed, wind direction and 6-hour wind speed average are selected as inputs to the forecast system. While wind speed and wind direction are usually selected as inputs in literature studies, unlike the other studies we have added an extra input which is named six-hour wind speed average. For this input averages of the wind speeds in the time intervals are taken respectively, 0-6, 6-12, 12-18 and 18-24. The inputs and the outputs of the system is illustrated in Figure 4.

III. Proposed Fuzzy Model

The fuzzy logic is introduced by Lotfi Zadeh and is a mathematical tool uses linguistic variables for dealing with uncertainty. It offers to a concept of computing with words' [15]. It consists of three phases which are fuzzification, interfence-rules and defuzzification. A fuzzy set is created in fuzzification phase by using linguistic variables and membership functions. When generally linguistic variables are defined as many, low, medium, few, membership functions are selected triangular, trapezoidal, sigmoid, Gaussian and generalized bell-shaped. In the second phase, an inference is made according to the rules. Rules consist of if-then conditions and a conclusion. Lastly, the resulting fuzzy output is mapped to a crisp output using the membership functions in the defuzzification step [16].

Fuzzy logic is a well-known method with successive results. Fuzzy logic has been preferred in many studies because it gives successful results in many electric power problems.

The forecast system has three inputs and one output. The wind speed input is divided into six subsets. These are named as SP1, SP2, SP3, SP4, SP5 and SP6. The membership functions of wind speed input can be seen Figure 5. The wind direction input is divided into four subsets and these are named as DR1, DR2, DR3 and DR4. The membership functions of wind direction are given in Figure 6. The average wind speed input is divided into four subsets and these are named as MEAN1, MEAN2, MEAN3 and MEAN4. The membership functions of average wind speed input are illustrated in Figure 7. Lastly, the wind power output is divided into six subsets and these are named as WP1, WP2, WP3, WP4, WP5 and WP6. The membership functions of wind power output can be seen in Figure 8. While triangular membership function is used in wind speed input and wind power output, trapezoidal membership function is preferred in wind direction input and average wind speed input.

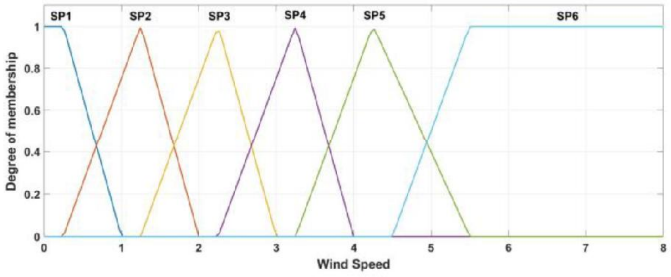


Fig. 5 Membership functions of Wind Speed

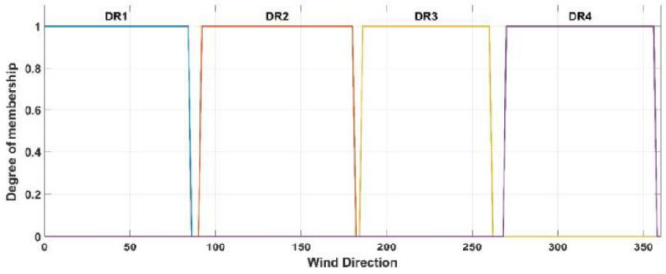


Fig. 6 Membership functions of Wind Direction Input

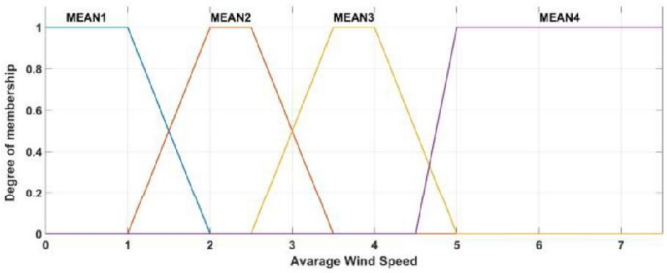


Fig. 7 Membership functions of Average Wind Speed Input

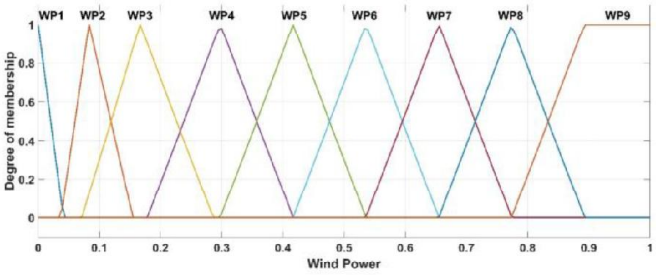


Fig. 8 Membership functions of Wind Power Output

IV. Forecast Results

There are some forecast error criteria to show the accuracy in literature. We have selected Normalized Mean Absolute Percentage Error (NMAE) to measure the forecasts. NMAE is defined as follows:

$$NMAE = \frac{\frac{1}{n}\sum_{i=1}^{n}|r_i - f_i|}{C} \; x \; 100 \qquad (2)$$

Where r is the real wind power, f is the forecasted wind power, i is the hour, n is number of samples and C is the installed wind power capacity. The normalized values calculated by dividing MAE to installed wind power capacity.

TABLE I Test time ranges and forecast errors

Test Time	NMAE (%)
24.02.2016-01.03.2016	8.9
20.06.2016-26.06.2016	13.4
20.08.2016-26.08.2016	14.8
01.11.2016-07.11.2016	13.8
Average of four weeks	12.7

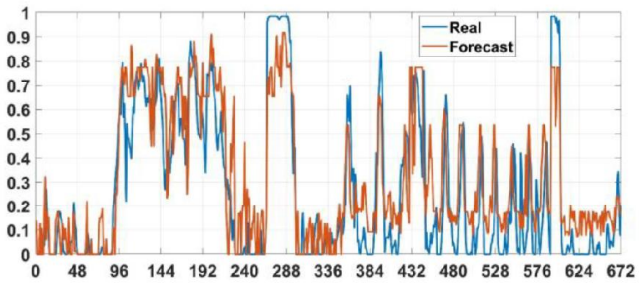


Fig. 9 Real and forecasted wind power for 4 weeks

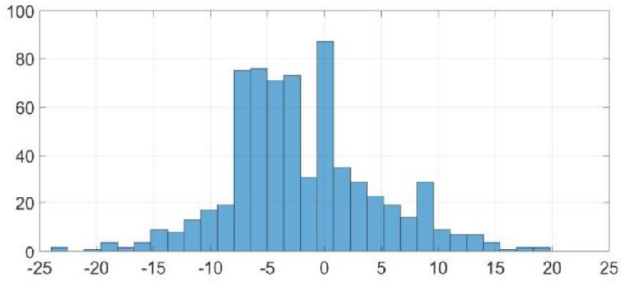


Fig. 10 Distribution of absolute errors

The normalized values calculated by dividing MAE to installed wind power capacity. Therefore, the error values of the wind power forecasts studies are easily comparable independently of the capacity of the wind power plant. In this study C is considered as 1, because wind power is normalized as between 0-1.

In Table I, test time ranges and NMAE values are given. Test data is especially selected one week from each seasons to show that the forecast works independently of the season. As looking the Table 1, while the best week is in time range between 24.02.2016-01.03.2016 as 8.9%, the worst week is in time range between 20.08.2016-26.08.2016 as 14.8%. As a result, NMAE is found as 12.7% for four weeks. The Figure 9 shows the real and forecasted wind power and Figure 10 shows distributions of the absolute errors.

V. Conclusion

This paper presents a fuzzy model for short term wind power forecast. A wind power plant's hourly generating data of 2016 and the meteorological wind data of wind power plant's location are used to construct the forecast. In the first stage, data cleaning is made to eliminate the distorted data. As a result of this process, 12 months data has been decreased to nine months. While eight months data are selected as train data, one month data are selected as test data. The wind speed, wind direction and six-hour wind speed average are selected as inputs to the forecast system. While wind speed and wind direction are usually selected as inputs in literature studies, unlike the other studies it is added an extra input which is named six-hour wind speed average. Fuzzy inference system is selected for forecast method. As a forecast result, NAME is found 12.7% for test data.

References

[1] www.windenergyfoundation.org/about-wind-energy/history/
[2] F. Fazelpour, N. Tarashkar and M. A. Rosen, "Short-term wind speed forecasting using artificial neural networks for Tehran, Iran", International Journal of Energy and Environmental Engineering, vol. 7(4), pp. 377-390, 2016.
[3] www.epias.com.tr
[4] N. Bigdeli, K. Afshar, A.S. Gazafroudi and M.Y. Ramandi, "A comparative study of optimal hybrid methods for wind power prediction in wind farm of Alberta, Canada", Renewable and sustainable energy reviews, vol. 27, pp. 20-29, 2013.
[5] Y. Zhang, J. Wang, and X. Wang, "Review on probabilistic forecasting of wind power generation", Renewable and Sustainable Energy Reviews, vol. 32, pp. 255-270, 2014.
[6] S. Buhan and I. Çadırcı, "Multistage wind-electric power forecast by using a combination of advanced statistical methods", IEEE Transactions on Industrial Informatics, vol. 11(5), pp. 1231-1242, 2015.
[7] Q. Xu, D. He, N. Zhang, C. Kang, Q. Xia, J. Bai and J. Huang, "A short-term wind power forecasting approach with adjustment of numerical weather prediction input by data mining", IEEE Transactions on Sustainable Energy, vol. 6(4), pp. 1283-1291, 2015.
[8] A. Aghajani, R. Kazemzadeh and A. Ebrahimi, "A novel hybrid approach for predicting wind farm power production based on wavelet transform, hybrid neural networks and imperialist competitive algorithm", Energy Conversion and Management, vol.121, pp. 232-240, 2016.
[9] B. Zhu, M.Y. Chen, N. Wade and L. Ran, "A prediction model for wind farm power generation based on fuzzy modeling", Procedia Environmental Sciences, vol. 12, pp. 122-129, 2012.
[10] Çevik H.H. and Çunkaş M. "Short-term wind power forecasting using ANFIS and regression methods", 6th International Conference on Advanced Technology & Sciences (ICAT), 2017, 12-15 Sep, Riga/Latvia.
[11] R. Azimi, M. Ghofrani and M. Ghayekhloo, "A hybrid wind power forecasting model based on data mining and wavelets analysis", Energy Conversion and Management, vol. 127, pp. 208-225, 2016.
[12] Global wind report 2016, Global Wind Energy Council, [Online]. Available: http://gwec.net/publications/global-wind-report-2/.
[13] Turkish Wind Energy Statistics Report, Turkey Wind Energy Association
[14] Wind Turbine Power Calculations, RWE npower renewables. Mechanical and Electrical Engineering Power Industry, The Royal Academy of Engineering,.
[15] S.N. Sivanandam, S. Sumathi and S.N. Deepa, Introduction to fuzzy logic using MATLAB, Vol. 1, Berlin: Springer, 2007.
[16] M. A. BulBul, "A Short Fuzzy Logic Tutorial. Department of Computer Engineering", Bilkent University, 2008.

Development of Digital Medical Weight Scale Using 32-Bit Arm Based Micro Controller

NOOR H. JUMAAH[1] AND ERGUN ERÇELEBI

[1] University of Gaziantep, Gaziantep/Turkey, noorjumaah6@gmail.com
University of Gaziantep, Gaziantep/Turkey, ercelebi@gantep.edu.tr

***Abstract* - This research includes the design and implementation of a modern digital weighing medical scale with an interactive connection feature for a smartphone, to be used as a daily body fitness and patient weight monitoring system. The weighing scale is of small size, strong, with low power consumption and built to be suitable for a professional medical environment. An electric transducer is used to convert the weight features into an electronic signal which is then processed using advanced digital technology.**

A medium density performance line, ARM-based, 32-bit, 72MHZ microcontroller unit (MCU) and an on-chip low noise programmable gain amplifier (PGA) with a gain of 128 dB is used for the weighing scale application. A standalone liquid crystal diode (LCD) display is used to display the weight value and a Bluetooth radio is applied to send weight data online to the smartphones for continuous monitoring of the data by medical staff. The signal processing of the system is controlled by software which is designed for this purpose.

***Keywords* - *Keywords* - Medical scale, Strain gauge, Bluetooth Weight scale, Software, Microcontroller, Transducer.**

I. INTRODUCTION

When designing the digital weight scale that read and showed the body mass index (BMI) for the fitness or `weight to digital electronic data. This data was then read by a microcontroller which translated it into visual data so it could be displayed on an LCD screen or sent to a smartphone. The transducer used to convert patient weight to a physical electrical signal is called a load cell or strain gauge.

A strain gauge [1] is a device that measures electrical resistance changes, in response to, and proportional to the strain applied to the device.

There are many types of strain gauges, including resistive and capacitive sensing devices. A capacitive load cell works on the principle of change of capacitance, which for common parallel plate capacitors, is the ability of the device to sense a certain amount of change when a voltage is applied to it.

The capacitance is directly proportional to the amount of overlap of the plates and the dielectric between the plates, and inversely proportional to the gap between the plates.

The most common strain gauge [2] is made up of very fine wire or foil, set up in a grid pattern in such a way that there is a linear change in electrical resistance when strain is applied in one specific direction, most commonly found with a base resistance of 120, 350 and 1000 ohms.

Each strain gauge has a different sensitivity to strain, which is expressed quantitatively as the gauge factor (GF). The gauge factor is defined as the ratio of fractional change in electrical resistance to the fractional change in length (strain).

Millis trains are used as very small ($e \cdot 10^{-3}$) fancy units for the strain. Strain measurements rarely involve quantities larger than a few mill strains.

So as an example: suppose you put on a strain of 500 mill strains.

A strain gauge with gauge factor of 2 will have a change in electrical resistance of only:

$2 * (500 \chi 10 - 6) = 0.1$

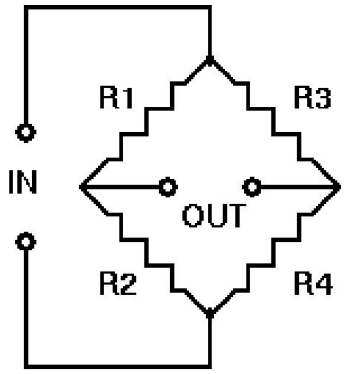


Figure 1: Circuit configuration

The best way of sending the small changes in resistance, converting them into changes of resistance and then further converting into a measurable quantity is by using a Wheatstone Bridge. This bridge has a circuit configuration of four arms with resistors and load cells applied, as shown in figure 1. The output voltage of the bridge is given in (1).

$$V_{out} = [(R_3 / (R_3 + R_4)) - (R_2 / (R_1 + R_2))] * V_{in} \quad (1)$$

The next stage of the system is a conditioning unit [3] which is designed to filter and amplify the bridge output signal or

voltage and convert the signal to digital data or a value. This is required so that the MCU can read it in serial data (0/1) sequences, or parallel data bits which will send bits as a burst at one time. For this design, an on-chip 24-bit precision ADC with a low noise 128 gain amplifier using Avia Semiconductor's patented HX711 technology has been used. This system, by using Delta-Sigma ADC technology, allows high resolution measurements with maximum accuracy. The HX711 Delta-Sigma ADC noise shaping and filtering [4] then converts the bridge signal to a 24-bit synchronous serial signal. The STM 32f103c8t6 MCU translates this signal and calibrates it to weight data. The weight data is then displayed on the LCD and the Bluetooth module sends it to the smartphone for monitoring by medical staff.

II. Literature Review

In this section, the related work in the area of digital weight scale systems development is presented. Digital weight scale systems have been used in different fields including medical, industrial and food samples.

[5] Developed a digital weighing scale for finding adulteration and cost standardization. In this work, it has been proposed a system with unique a feature that vision camera with color sensor technology to find out adulteration identification in a food sample. From the results obtained, the customer will pay the money only of pure sample that was weighed by load cell without adulterant. [6] Introduced general idea about choosing load cell for load measurements and shows the new implementation of a weight measurement system based on Amplifier/ADC/Digitizer board. This research work has the advantage of simple design and errorless, high accuracy measuring systems. The main theme of this paper is the implementation of a simple method for measurement of the load with the help of load cell and advanced instrumentation. [7] Discussed the development of a load cell based the static weighing system. In particular, the focus is on using digital filtering techniques to remove measurement noises from the extremely low frequency noise of the static weighing system. The designed system has good accuracy with high precision output. [8] Designed a microcontroller based electronic weighing and bagging machine that works fast and makes accurate measurement and also packs consecutive weights. It was suitable for granular materials. This system could take the tare weight of the weight hopper automatically; its software system was written in such a way that, some difficult conditions of the sugar factories were taken into account and it was easy to understand. The system was user-friendly and gives the required alarms.

The current system includes design and implementation of a modern digital weighing medical scale with an interactive connection feature for a smartphone, to be used as a daily body fitness and patient weight monitoring system.

III. Design & Implementation of the System

A. System configuration

The block diagram of the electronic weighing system is shown in figure 2.

The system consists of the following parts:

1) A Wheatstone Bridge, including the load cell (transducer) which converts the changes of the weight into an electronic signal.
2) An amplifier and ADC, which receives the output of the bridge, amplifies it and converts the analog to a 24-bit digital signal.
3) An STM32F03C8T6 MCU, which uses software programmed to control the operation of the system.
   1) A Bluetooth radio module.
4) A power supply, which supplies the required energy to the system to the system.
5) A display unit, to display the output of the electronic weighing system.

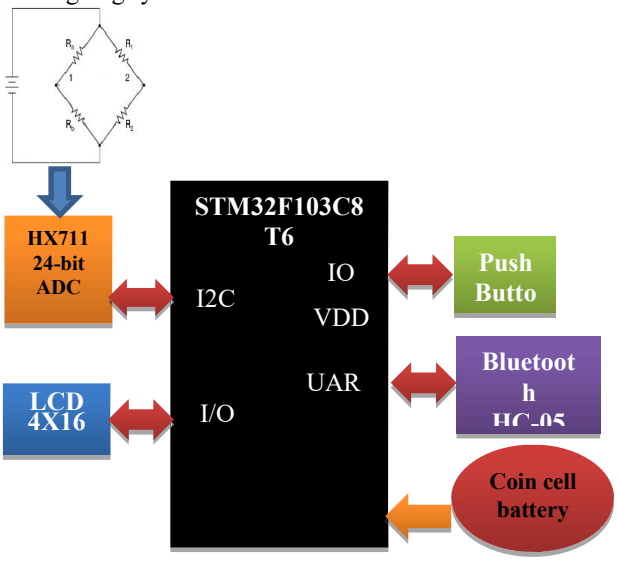


Figure 2: The block diagram of the electronic weighing system.

B. Hardware Design

1) The MCU used in the proposed design has a CPU core, a 72MHZ crystal oscillator, a 64KB flash memory, a UART debugging interface and various peripherals. These are provided on a "Blue Pill" printed circuit board.

The MCU [9] as shown in figure 3 is used to both manage and control communication as well as providing the interface to the 24-bit ADC which uses REST operations for translating the weight serial data and displaying the data on the LCD screen and Bluetooth module, through the use of binary firmware code.

The "Blue Pill" board [10] is a hardware Development Board utilizing an STM32 MCU with Arduino software IDE compiler compatibility.

2) The 24-bit ADC [11]

This is a high precision HX711 A/D converter chip. It has a specially designed high precision electronic scale design, with two analog input channels. The gain of the amplifier is programmable up to 128dB and its high precision, low current consumption makes it easy to use.

Figure 3 shows the schematic diagram of the high precision A/D converter.

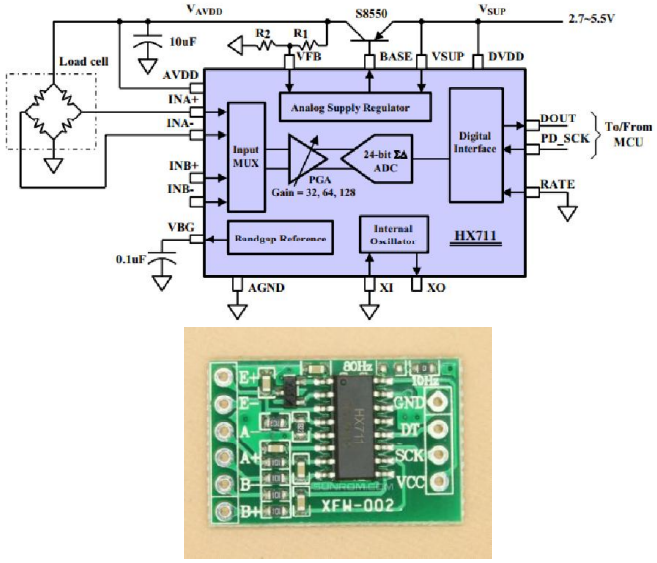


Figure 3: The schematic diagram of HX711 24-bit ADC

3) Bluetooth radio module (HC-05)

The HC-05 module [12] is easy to use Bluetooth SPP (Serial Port Protocol) module, designed for transparent wireless serial connection setup. The serial port Bluetooth module has fully qualified Bluetooth V2.0+EDR (Enhanced Data Rate) 3Mbps Modulation with a complete 2.4GHz radio transceiver and baseband. It uses a CSR Blue core 04- External single chip Bluetooth system with CMOS technology and with an Adaptive Frequency Hopping Feature (AFH). This feature gives a very highly immune and secured transmission system to protect against noise and jamming signals.

The Bluetooth module is used to transport weight data from the medical scale to the smartphone.

Figure 4 shows the HC-05 Bluetooth radio module.

Figure 5 shows the UART interface between the Bluetooth module and STM32 MCU.



Figure 4: HC-05 Bluetooth radio module

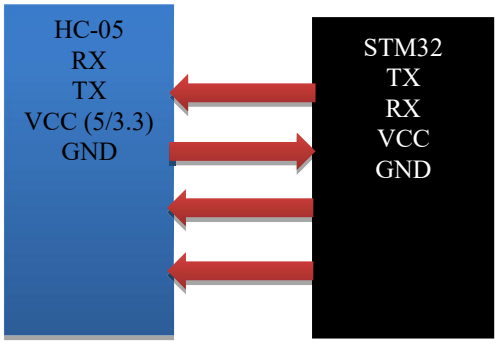


Figure 5: UART interface between Bluetooth module and STM32 MCU.

C. Software Design

The open-source Arduino Software IDE [13] makes it easy to code an algorithm and upload it to the board. The software runs on Windows, Mac OS X, and Linux.

The sentence structure, or the words and structure of the code, is like Java, C or C++ [14].

The Arduino software (both versions 1.6.12 and 1.6.13) includes a driver for the STM32 board.

Figure 6 shows the STM32 firmware block diagram of the algorithm used to design the software system.

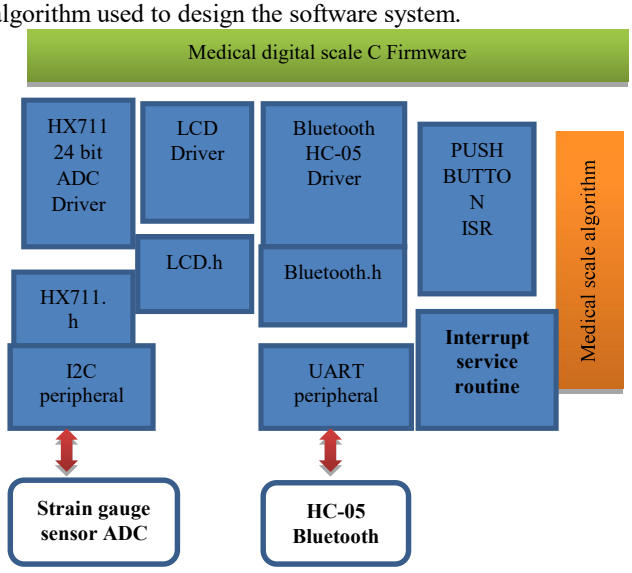


Figure 6: STM32 firmware block diagram

VI. Test, Results, and Discussion

The medical weight scale can work as standalone with internal LCD screen to display the person's weight in two standard units as kilogram and pound with the assistance of Android operating system. The output 0f the scale can be sent remotely to smartphones by Bluetooth wireless communication link.

The first step in operating the system is testing the basic connections of the HX711 to the power supply, the load cell, Bluetooth, LCD screen and the microcontroller.

The next step is testing the hx711 24-bit ADC result data line state so the HX711 serial communications protocol results in the data line (DT pin on the HX711 breakout board), which is normally in the "high" state, being pulled low by the HX711. This provides a simple test if the HX711 is connected and responding correctly (this is also the signal from the HX711 that data is ready for retrieval). The bool is_ready () routine check if hx711 is ready or not.

When output data is not ready for retrieval, digital output pin DOUT is high. The PD_SCK pin should be low. When DOUT goes to low, it indicates that the data is ready for retrieval.

The get units () routine returns the average of 10 times readings from the ADC minus tare weight divided by the scale factor after calibration.

Zero balance is the difference from the load cell (the signal between the A- and A+ pins of the HX711 breakout board) when no load is applied. This is typically stated in terms of percentage of full scale. Therefore, zero balance is the "offset" that needs to be applied when measuring and calibrating weights and represents inherent differences between the strain gauges (and strain gauge connections) that form the load cell. Full scale is simply the output from the HX711 when the load cell is fully loaded.

In order to produce data for the zero-balance load cell test, the load cell was simply connected to the HX711 without applied load and data from the HX711 collected in 30-second intervals via the RS232 connection to PC. Each data point at each successive 30-second interval was in turn the average of 20 readings taken as quickly as possible with the HX711. The results are 227193 as raw data from hx711 ADC after converting the serial 24 bit to human-readable format with no load (zero balance) and the differential input signal of the load cell (the signal between the A- and A+ pins of the HX711 breakout board) is 0.4 mv mill volt at this reading.

The weight scale results that appear on the LCD and android application come from 10 times average operation and each 5-second update the load cell readings.

Figure 7a and figure 7b show the testing of the prototype digital medical weight scale with modern load cell sensors. The weight scale can measure up to 200KG weight. It can store up to 10 weight values in the stm32 MCU EEPROM through the SET/MEM pushbuttons with an accuracy of 0.1KG. So, the system can support the weight of children and adults. The weight data can be monitored and controlled remotely through smartphone applications.



Figure 7a: The testing prototype digital medical weight scale with no load or zero balance.

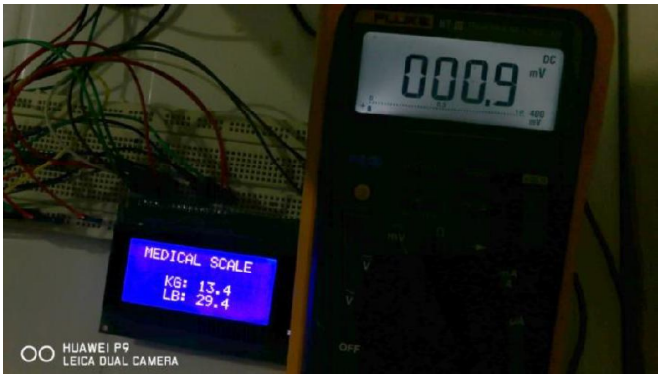


Figure 7b: The testing prototype digital medical weight scale with load scale at 13.4 kg load.

After completing the testing and calibrating of the scale different loads with known weight values are applied to the scale and output of the scale is measured.

Table 1 shows the results of the measurement: it is clear from the results the accuracy of the scale is ± grams. This accuracy is regarded very high and supports other applications which require very high accuracy in addition to medical applications.

Table 1: The output results of the electronic scale.

The real weight value in gram	The output of the scale in gram
1000	1003.2
	1002.9
	999.9
	1001.6
	1002.1
1500	1504.0
	1499.1
	1503.6
	1498.3
	1501.7
2000	2003.5
	1997.1
	2002.9
	1997.2
2500	2503.1
	1498.4
7000	7003.8
	7003.3
	6995.5
20000	20003.4
	20002.9
	20003.5
	19996.4
	20004.1

V. Conclusion

In this paper, the digital weight scale is implemented using the ARM32 CPU and high precision 24-bit analog to digital converter technology with a high sensitivity strain gauge sensor bridge. In this work an easy to use, low-cost digital weight scale with a high resolution of 0.1KG has been produced. The system has the future of displaying the weight data and also has the ability to send this data remotely through Bluetooth radio module to smartphones for continuous data monitoring. The weight scale system has been designed and implemented using advanced digital electronic technology with the Arduino software. It can be used in most environments, including home, hospital fitness centers or pharmacies. The system offers a modern, easy means of monitoring fitness and health data. The system has been tested in a real-world situation and has been found to fulfill all the requirements of a medical scale.

References

[1] SparkFun Electronics, ‘‘Getting Started with Load Cells, ’’ 2003. [Online]. Available: https://learn.sparkfun.com/tutorials/getting-started-with-load-cells. [Accessed 15 August 2017].

[2] MICROCHIP, “PIC14000,” 1996. [Online]. Available: http://ww1.microchip.com/downloads/en/DeviceDoc/40122b.pdf. [Accessed 10 August 2017].

[3] SparkFun Electronics, ‘‘SparkFun Product Page Gets a Redesign.’’ 2003. [online]. Available: https://www.sparkfun.com/. [Accessed 16 August 2017].

[4] M. Thoren, ‘‘Delta Sigma ADC Bridge Measurement Techniques, ’’Linear Technology Corporation, 2005.

[5] k. D. Gaikwad, and P. B. Dahkar, ‘‘Development of Digital Weighing Scale for Finding Adulteration & Cost Standardization,’’ International Journal of Scientific & Engineering Research, vol. 5, pp. 22-30, 2014.

[6] K. D. Gaikwad, and P.B. Dahikar, “Design and Development of Novel Weighing Scale System”, IJERT, vol. 2 pp. 1668-1671, 2013.

[7] P. B. Dahikar, and K. S. Patle, ‘‘Design of an Embedded Platform for Digital Weighing System to Enhance Measuring Capabilities’’, International Journal of Innovative Research in Computer and Communication Engineering, vol. 1, pp. 1881-1887, 2013.

[8] E. Koruk, ‘‘Design and Implementation of microcontroller based electronic weighing and bagging machine,’’ Ms.C. dissertation, Dep. Elect. and Electro. Eng., METU, Ankara, 1994.

[9] Life augmented, ‘‘STM32F103C8,’’ 2017. [online]. Available: http://www.st.com/en/microcontrollers/stm32f103c8.html. [Accessed 17 August 2017].

[10]Arduino for STM32, ‘‘Board Index.’’ 2017. [online]. Available: http://www.stm32duino.com/. [Accessed 20 August 2017].

[11] AVIASEMECONDECTOR (XIMEN) CO., LTD, ‘‘Products,’’ 2012. [online]. Available: http://www.aviaic.com/ENProducts.aspx?sort_id=43&FID=1&FID2=43. [Accessed 22 August 2017].

[12] I Tead Studio, ‘‘HC-05 -Bluetooth to Serial Port Module, ’’ 2010. [online].. Available: http://www.electronicaestudio.com/docs/istd016A.pdf. [Accessed 24 August 2017].

[13] ARDUINO, ‘‘Access the Online IDE,’’ 2017. [online]. Available: https://www.arduino.cc/en/Main/Software. [Accessed 25 August 2017].

[14] Life augmented, ‘‘STM32 forum,’’ 2016. [online]. Available: https://community.st.com/community/stm32-community/stm32-forum/content. [Accessed 27 August 2017].

Tumor Type Detection Using Naïve Bayes Algorithm on Gene Expression Cancer RNA-Seq Data Set

F. GEMCİ FURAT[1] and T. İBRİKÇİ[1]

[1] Çukurova University, Konya/Turkey, ffurat@student.cu.edu.tr
[1]Çukurova University, Konya/Turkey, ibrikci@cu.edu.tr

Abstract **- Transferring the medical data to the computer environment and carrying out the analysis is of vital importance. In the study, five different types of tumor: BRCA, KIRC, COAD, LUAD and PRAD in Gene Expression Cancer RNA-Seq Data Set are taken into accounted. The five tumor types of Gene Expression Cancer RNA-Seq Data Set on WEKA tool classified using Naive Bayes algorithm with 98.7516% accuracy, 98.5% accuracy, 98.7526% accuracy and 98.5294% accuracy by 10-fold cross validation, 50–50% train-test, 40-60% train-test, 66-34% train-test data partition, respectively.**

Keywords **–Naive Bayes, Tumor Classification, Confusion Matrix, UCI Repository, WEKA.**

I. INTRODUCTION

Along with today's developing technology, it has been possible to convert medical data into large data sets which are needed for imaging and transferring to the computer environment and analyzing. With access to big data sets, a variety of analysis algorithms have begun to be developed by scientists to analyze the data.

It is first observed that data mining algorithms give effective results on large data sets after starting with statistical studies. However, some features are needed to analyze medical data with data mining algorithms [1]. The qualities are:

- Preprocessing can be dealt with missing values and noisy in data.
- An effective algorithm can be produced that gives as high performance as possible.
- Clarity of the algorithm can be ensured for the end user.
- The results of the algorithm can be interpreted or explained.
- Number of the test data to be used in the algorithm can be reduced to the minimum number without its performance ignoring.
- The data privacy must be protected.

Data mining algorithms in medical data analysis have been applied for many years to achieve successful results [2-9].

Thanks to independent assumption of Naive Bayes algorithm was used successfully to analyze medical data such as diagnosing disease in many studies as explained in the following. In addition, the naive bayes algorithm was used to make meaningful and analyzes in so many different fields such as soil science, diagnosis of claim fraud and spam detection [10-13].

Lung Cancer Disease Detection and Diagnosis is analyzed using five different classification algorithms such as Multilayer Perceptron, Naive Bayesian, RBF Neural Network, Decision Tree and C4.5 algorithms. The most successful classification to detect Lung Cancer Disease within the five algorithms was the Naive Bayes algorithm [2].

In [5], the classification of breast cancer data was made to estimate whether it is a recurrent event Instead of breast cancer diagnosis. The classification was performed using Naive Bayes algorithm as successful as the best classifiers in the literature with low computation at high speed [5].

It is necessary to arrange the diagnosis of the disease in a shorter time in order to prevent the patient from waiting for long time results. For this reason, it is of vital important that the analysis process to take is as short as possible. For the reason, the study aimed to gain time by reducing the number of features to reduce the duration. The work was predicted whether patient is breast cancer with accuracy of 96.6% using less features of data set with Gaussian Naive Bayes algorithm [6].

Diagnosing heart disease was performed with 86.419% of accuracy using Naive Bayes algorithm on data set having 500 patients [7].

Probability of having a wild-type genotype or KRAS of 457 colon adenocarcinoma patients are calculated using Naive Bayes algorithm in [8].

RNA-Seq data of 18 clinical cancer patients were classified with 94.4% accurancy using TOD-Bayes algorithm in [9].

Waikato Environment for Knowledge Analysis is represented with WEKA is a data mining software used in the study. The WEKA tool that is open source contains many classification algorithms like Naïve Bayes, neural network and C4.5 [3].

In section 2, Gene Expression Cancer RNA-Seq Data Set, Naïve Bayes algorithm and algorithm performance evaluation

measures are introduced. The experimental results of the study such as classification accuracy and RMSE are given in section 3. The results are concluded and future work is given in section 4.

II. METHOD

A. Gene Expression Cancer RNA-Seq Data Set

Gene Expression Cancer RNA-Seq data set is obtained from UCI Repository [14,15]. The data set is part of the RNA-Seq PANCAN data set. The data set is composed of gene expressions of patients with five different types of tumor: BRCA, KIRC, COAD, LUAD and PRAD.

The data set is a 801 patient samples' collection where 136 samples are patients with PRAD tumor, 141 samples are patients with LUAD tumor, 300 samples are patient with BRCA tumor, 146 samples are patients with KIRC tumor and the remaining 78 samples are patients with COAD tumor. So all samples are divided into 5 classes as 5 tumor types as given in Table 1.

The data set contains 20531 features of each sample. The features of each sample are RNA-Seq gene expression levels that are measured with Illumina HiSeq platform.

Table 1. Distribution of patients to tumors classes in Gene Expression Cancer RNA-Seq Data Set

Tumor Classes	Samples per class
PRAD	136
LUAD	141
BRCA	300
KIRC	146
COAD	78

B. Naive Bayes Algorithm

Naïve Bayes Classifier that is also called Simple Bayes, Idiot's Bayes, and Independence Bayes is an efficient supervised learning method for both binary and multiclass classification. As well as it, it is the statistical method based on Bayes' Theorem [16,17]. Bayes theorem calculates the P(c|x), posterior probability using P(x|c), P(c) and P(x), and as given in (1).

$$P(c/x)=\frac{P(x/c)P(c)}{P(x)} \quad (1)$$

P(c|x) is the class posterior probability.
P(c) is the class prior probability.

P(x|c) is the likelihood that is the predictor given class probability.
P(x) is the predictor prior probability.

"Naive" adjective in term of Naive Bayes method comes from class conditional independence assumption. Conditional independence in Naive Bayes classifier is assumption which a predictor(x) value effect on a given class (c) is independent with other predictors values.

When there are n features in the data set to be classified, an 'n' dimensional feature vector is X : (x1,x2,x3,…. xn).

Supposed that there are 'm' classes : C1,C2,C3…Cm.

Naïve Bayes algorithm calculates the probality of belonging to each class ci of each sample X in (2,3).

$$P\ (\mathrm{x}\ /.\mathrm{c}_i)=\prod_{k=1}^{n} P(x_k / c_i) \quad (2)$$

$$P(x/c_i) = P(x_1/c_i) * P(x_2/c_i) *\ldots* P(x_i/c_i) \quad (3)$$

C. Measures for Performance Evaluation

1) Classification accuracy:

A true positive is that if the class that is found in the result of classification of a sample is correct class. The true positive is symbolized as TP [18].

False positive is that if the class that is found in the result of classification of a sample is not correct class. The false positive is symbolized as FP [18].

A confusion matrix gives numerical information about the accuracy of a predicted classification result. When all values outside the diagonal of the confusion matrix are zero, a hundred percent correct classification.

A confusion matrix is a n x n matrix for classification with n classes. The following matrix is a confusion matrix for 3-class 100% successful classification. As TP rises from 0 to 1, the success rate of the algorithm increases [18].

Confusion Matrix

a	b	c	classified as
50	0	0	| a class
0	50	0	| b class
0	0	50	| c class

TP rate for a class= 50/ (50+0+0) = 1
FP rate for a class= 0

2) Kappa Statistic (KS): Kappa statistic is calculated to evaluate measurement accuracy. The closer the K value is from 0 to 1, the more reliable the classification. When K equals 1, the correctness of classification is the safest. On the other hand, when K equals 0, the chance of classification is right and unreliable [19]. Calculation of Kappa value is given in (4).

$$K = \frac{P(A) - P(E)}{1 - P(E)} \tag{4}$$

3) Mean Absolute Error (MAE): MAE is useful measurement to use for performance evaulation of algorithm. As given in (5), it is calculated by taking the average of all absolute errors [20].

$$MAE = \frac{1}{n}\sum_{1}^{N}\left|Q_{\exp} - Q_{cal}\right| \tag{5}$$

4) Root Mean Squared Error (RMSE) [7]: RMSE is popular measurement for performance evaluation. Thanks to square root, the measurement calculates the error without canceling the positive and negative error [18].

$$RMSE = \sqrt{\frac{1}{n}\left[\sum_{1}^{N}\left(Q_{\exp} - Q_{cal}\right)^2\right]} \tag{6}$$

III. EXPERIMENTAL RESULTS

In the present study, Gene Expression Cancer RNA-Seq Data Set are obtained from UCI data repository. The data set consists of 801 samples with 20531 features.

WEKA 3.9 is used to perform experimental study. The multi-class classification process was performed with the Naive Bayes algorithm between the classification algorithms in WEKA 3.9.

Naive Bayes method is chosen to classify into 5 tumor classes. More than one different trial for preferring test and train data percentage is applied. One of them is 10-fold cross validation, one of them is that data set is split in 60% as the test and the r 40% as train data, one of them is that data set is split in 34% as the test and the r 66% as train data. is and the other is that data set is split in half as the test and the remaining half as train data. Classification performance results of the data set using Naive Bayes method with 10-fold cross validation,40-60% train-test, 66-34% train-test, and 50–50% train-test data partition is given in Table II.

As seen in the Table 2, the classification performance is very reliable because Kappa values are very close to the value 1.

As seen in Table 2, when test and train data are separated at different rates, there are significant differences in experimental results.

The following confusion matrixes for five tumor classes are produced with Naïve Bayes algorithm on Weka 3.9.

1) Confusion Matrix for classification with 10-fold cross validation

a	b	c	d	e	classified as
133	1	2	0	0	a = PRAD
0	139	2	0	0	b = LUAD
0	1	299	0	0	c = BRCA
0	2	0	144	0	d = KIRC
0	2	0	0	76	e = COAD

TP rate for PRAD class= 133/ (133+1+2+0+0) = 0.97794
FP rate for PRAD class= 0

2) Confusion Matrix for classification with 50–50% train-test data partition

a	b	c	d	e	classified as
79	1	0	0	0	a = PRAD
0	63	0	0	0	b = LUAD
0	0	149	0	0	c = BRCA
0	3	0	66	0	d = KIRC
0	2	0	0	37	e = COAD

TP rate for PRAD class=79/ (79+1+0+0+0) = 0.9875
FP rate for PRAD class= 0

3) Confusion Matrix for classification with 40-60% train-test data partition

a	b	c	d	e	classified as
86	2	0	0	0	a = PRAD
0	75	0	0	0	b = LUAD
0	0	186	0	0	c = BRCA
0	2	0	85	0	d = KIRC
0	2	0	0	43	e = COAD

TP rate for PRAD class= 86/ (86+2+0+0+0) = 0.97727
FP rate for PRAD class= 0

4) Confusion Matrix for classification with 66-34% train-test data partition

a	b	c	d	e	classified as
53	1	0	0	0	a = PRAD
0	47	0	0	0	b = LUAD
0	0	99	0	0	c = BRCA

0 1 0 46 0 | d = KIRC
0 2 0 0 23 | e = COAD

TP rate for PRAD class= 53/ (53+1+0+0+0) = 0.98148
FP rate for PRAD class= 0

TABLE 2. Classification Results of Gene Expression data set using Naïve Bayes

The performance measures of Naïve Bayes	10-fold cross validation	50–50% train-test data partition	40-60% train-test data partition	66-34% train-test data partition
The classification accuracy (%)	98.7516	98.5	98.7526	98.5294
Time Taken (seconds)	2.69	2.47	2.63	2.65
Kappa Value	0.9835	0.9802	0.9834	0.9806
MAE	0.005	0.006	0.005	0.0059
RMSE	0.0707	0.0775	0.0706	0.0767
Relative Absolute Error (%)	1.6481	1.9761	1.6408	1.9374
Root Relative Squared (%)	18.1587	19.8355	18.166	19.6421

IV. Conclusion and Future Work

In the literature, the tumor types in Gene Expression Cancer RNA-Seq Data Set has not been classified using Naive Bayes. In this study, Naive Bayes method on WEKA tool is used to classify the tumor types with 98.7516% accuracy on 2.69 seconds, 98.5% accuracy on 2.47 seconds, 98.7526% accuracy on 2.63 seconds and 98.5294% accuracy on 2.65 seonds by 10-fold cross validation, 50–50% train-test, 40-60% train-test, 66-34% train-test data partition, respectively.

As the number of data in the training set increases, the success of the algorithm is expected to increase, but this is not always the case as seen in the study. Whereas the data rate in the training set went from 40% to 66% in this study, the success of algorithm was declined on the contrary expectation in the study. In fact, it is important that the amount of data in the training set is not just the quantity, but the amount of data in the different features. The quality of data in the training set is important for classification success.

In the future works, classification of tumor types will be proposed to perform with other classification algorithms outside Naive Bayes and with feature selection methods of Naive Bayes method also.

References

[1] Al-Aidaroos, K. M., A. A. Bakar, and Z. Othman. "Medical Data Classification with Naive Bayes Approach." *Information Technology Journal* 11.9 (2012): 1166-1174.

[2] N.V. Ramana Murty and M.S. Prasad Babu, "A Critical Study of Classification Algorithms for Lung Cancer Disease Detection and Diagnosis", *International Journal of Computational Intelligence Research*, Vol.13, No. 5, pp. 1041-1048,2017.

[3] "WEKA – Data Mining Machine Learning Software", Available http://www.cs.waikato.ac.nz/ml/

[4] Kononenko, Igor, Ivan Bratko, and Matjaž Kukar. "Application of machine learning to medical diagnosis." *Machine Learning and Data Mining: Methods and Applications* 389 (1997): 408.

[5] Dumitru, Diana. "Prediction of recurrent events in breast cancer using the Naive Bayesian classification." *Annals of the University of Craiova-Mathematics and Computer Science Series* 36.2 (2009): 92-96.

[6] Gayathri, B. M., and C. P. Sumathi. "An Automated Technique using Gaussian Naïve Bayes Classifier to Classify Breast Cancer." *International Journal of Computer Applications* 148.6 (2016).

[7] Vembandasamy, K., R. Sasipriya, and E. Deepa. "Heart Diseases Detection Using Naive Bayes Algorithm." *IJISET-International Journal of Innovative Science, Engineering & Technology* 2 (2015): 441-444.

[8] Pershad, Y., Govindan, S., Hara, A. K., Borad, M. J., Bekaii-Saab, T., Wallace, A., and Oklu, R. "Using Naïve Bayesian Analysis to Determine Imaging Characteristics of KRAS Mutations in Metastatic Colon Cancer." *Diagnostics* 7.3 (2017): 50.

[9] Jiang, W., Shen, Y., Ding, Y., Ye, C., Zheng, Y., Zhao, P., and Zhang, X "A naive Bayes algorithm for tissue origin diagnosis (TOD-Bayes) of synchronous multifocal tumors in the hepatobiliary and pancreatic system," *International Journal of Cancer* (2017).

[10] Bhargavi, P., and Jyothi, S. "Applying naive bayes data mining technique for classification of agricultural land soils." *International journal of computer science and network security*. (2009). 9(8), 117-122.

[11] Viaene, S., Derrig, R. A., and Dedene, G. A "Case study of applying boosting Naive Bayes to claim fraud diagnosis." *IEEE Transactions on Knowledge and Data Engineering,* (2004). 16(5), 612-620.

[12] Arifin, D. D., and Bijaksana, M. A. "Enhancing spam detection on mobile phone Short Message Service (SMS) performance using FP-growth and Naive Bayes Classifier." In Wireless and Mobile (APWiMob), *2016 IEEE Asia Pacific Conference* on (pp. 80-84). IEEE, (2016, September)..

[13] Ma, Y., Liang, S., Chen, X., and Jia "The Approach to Detect Abnormal Access Behavior Based on Naive Bayes Algorithm. In Innovative Mobile and Internet Services in Ubiquitous Computing (IMIS), *10th International Conference* on IEEE, July 2016. p. 313-315.

[14] Blake, C. and Merz, C. UCI repository of machine learning databases. *University of California, Irvine, Dept. of Inf. and Computer Science.* (1998).

[15] Weinstein, J. N., Collisson, E. A., Mills, G. B., Shaw, K. R. M., Ozenberger, B. A., Ellrott, K.. "The cancer genome atlas pan-cancer analysis project.' *Nature genetics* 45.10 (2013): 1113-1120.

[16] J. Han and M. Kamber, Data Mining Concepts and Techniques, Elevier, 2011.

[17] Hetal Bhavsar and Amit Ganatra, "A Comparative Study of Training Algorithms for Supervised Machine Learning", *International Journal of Soft Computing and Engineering (IJSCE)* ISSN: 2231- 2307, Volume-2, Issue-4, September 2012.

[18] Margaret H. Danham, and S. Sridhar, " Data mining, Introductory and Advanced Topics", *Person education* , 1st ed., 2006.

[19] Carletta, J. "Assessing agreement on classification tasks: the kappa statistic." *Computational linguistics*, 22(2) (1996), 249-254.

[20] Chai, T. and Draxler, R. R.. "Root mean square error (RMSE) or mean absolute error (MAE)? – arguments against avoiding RMSE in the

literature." *Geoscientific Model Development* 7 (3), (2014): 1247–1250, 2014. Available http://www.geosci-model-dev.net/7/1247/2014/

Performance Evaluation of Different Uplink Resource Allocation Algorithms in LTE Networks

Havva Esra Bilisik[1] and Radosveta Sokullu[1]

[1] Ege University, Izmir/Turkey, bilisik.h@gmail.com
[1]Ege University, Izmir/Turkey, radosveta.sokullu@ege.edu.tr

***Abstract* – For many years the resource allocation in the downlink of the LTE systems was a preferred topic of interest as compared to uplink allocation. However, in recent years, the increased numbers of users and applications has caused researchers to focus attention to the uplink allocation in an attempt to ensure higher QoS while for the same available system resources. Thus, resource allocation (RA) algorithms for the uplink have become a hot topic. They tend to be more complicated because of the additional constraints paused by uplink admission control – singularity, contiguity and strict power control. Several different resource allocations schemes are gaining momentum, however there is no uniform and thorough comparison between them. Different authors compare their suggested schemes with a single popular one, trying to point out their advantages. That is why, in this paper we aim to investigate together several of the most common RA algorithms for the uplink and compare them under the same conditions. The evaluation of the algorithms is done in terms of three major performance metrics: throughput, fairness and bit error rate. Furthermore, different channel models, representing different environments and application scenarios are covered.**

***Keywords* – LTE networks, resource allocation algorithms, LTE uplink, throughput, fairness.**

I. INTRODUCTION

OVER the last two decades with the development of mobile communications the demand for better QoS and performance in communications has increased. In order to provide these demands to users the Third Generation Partnership Project (3GPP), proposed the all-IP packet based technology known as the Long Term Evolution (LTE). This new technology aims to provide better spectral flexibility, low latency, higher capacity, and better battery lifetime than previous technologies [1]. A key factor in achieving low latency is the possibility of LTE to provide a flexible deployment of the bandwidth standardized in chucks of bandwidth assignments of 1.4, 3, 5, 10, 15 and 20 MHz). LTE supports up to 100 Mbps in downlink and 50 Mbps in the uplink while the latest enhanced version of LTE known as LTE-A supports up to 1 Gbps (downlink) and 500 Mbps in the uplink [2].

The LTE uses OFDMA as an access method for the downlink (DL). In the uplink (UL) the modified form of the orthogonal frequency-division multiple access (OFDMA) known as single-carrier frequency division multiple access (SC-FDMA) is adopted to avoid high level cell interference and to reduce the Peak to Average Power Ratio (PAPR) [3]. However, despite its obvious advantages, there are some constraints due to SC-FDMA which make it more difficult to allocate resources in the uplink than in the downlink. These constraints include above all singularity, contiguity, and transmit power limitations. Singularity constraint indicates that any resource block (RB) can be allocated only to a single user. Contiguity constraint means that RBs allocated to a given user must be contiguous, and transmit power constraint states that the maximum transmit power for any user should be less or equal to 23 dBm [4].

LTE uses both time (TDD) and frequency division duplex (FDD) modes. Transmissions are segmented into time domain frames, where each frame is 10 ms and is divided into 10 consecutive subframes of 1 ms known as the Transmission Time Interval (TTI). A subframe contains two slots of 0.5 ms duration each and every slot contains 7 OFDM symbols. In the frequency domain, each subcarrier has a 15 kHz band. A RB is defined in both time and frequency domain. Each RB consists of 12 subcarriers, with a total bandwidth of 180 kHz and 0.5 ms of duration. The number RBs can changes according to the required system bandwidth. With the scalable bandwidth assignments the number of RBs per user can vary as 6, 15, 25, 50, 75 and 100 respectively.

LTE is an all-IP packet based technology as mentioned above. The network architecture consists of the Evolved Node B (eNodeB), the Evolved Packet System (EPS) and the UE. The eNodeB is the only node between the UE and the network; hence it is responsible for allocating resources to the UEs. The Packet Scheduler (PS) is the controlling entity of the eNodeB's Medium Access Control (MAC) layer, and its task is to allocate RBs to the UEs for every TTI with duration of 1 ms. Every TTI, each UE sends a sounding reference signal (SRS) to its serving eNodeB. Then based on the received SRS the eNodeB assigns a metric, called Channel Quality Metric (CQI), with values ranging 1 to 15 for each UE. . Using this metric the eNodeB knows each UEs channel quality value and generates a matrix called the "channel gain matrix" where the rows represent the UEs and the columns the available RBs. eNodeB schedules the UEs to maximize the overall spectral

efficiency by using this channel gain matrix. [5]

In this paper, some of the most popular scheduling algorithms are discussed, evaluated and compared: Round Robin (RR), Best-CQI (B-CQI) and Approximate Maximum Throughput (AMT). Different channel models and application scenarios are considered where throughput and bit error rate (BER) are used as parameters for the performance evaluation of the scheduling algorithms.

The rest of the paper is organized as follows. In section II, details and related works for the scheduling algorithms mentioned above are presented. The evaluating parameters and the performance metrics are defined in section III. The results of the evaluation and the comparison of the RR, B-CQI and AMT scheduling algorithms are given in section IV. Finally, section V concludes the paper.

II. RELATED WORKS

Resource allocation scheduling algorithms for LTE UL have been discussed by many scientists [6-12]. Because of the singularity, contiguity, and transmit power constraints, it is more difficult to allocate resources to users in the uplink as compared to the downlink. The two most popular scheduler algorithms so far are Round Robin (RR) and Best CQI (B-CQI).

RR is the simplest resource allocation algorithm compared to other scheduling algorithms. This algorithm is channel-unaware and aims to achieve high fairness. The algorithm works based on the assumption that the channel conditions do not change during the transmission time, and therefore the channel conditions are not taken into account while allocating resources among the users. RBs are assigned to users one by one, equally and fairly among all users [7]. The achieved overall fairness is high but the overall throughput is generally low compared to other algorithms. In some studies authors define and use RR algorithm as a time based algorithm. RR scheduling algorithm allocates RBs sequentially usually in circular manner [8].

Unlike RR, the B-CQI scheduling algorithm is an example of a channel-aware scheduling algorithm. It takes into account the current state of the channel while allocating resources to UEs [9]. B-CQI scheduling algorithm allocates RBs depending on how good the channel quality of a given user is. Any UE that has data to send, first has to send its CQI value to its serving eNodeB. The high CQI value indicates that the UE has good channel conditions. Therefore, the UE that has higher CQI values can be allocated more RBs as compared to UEs that lower CQI values. Because the RB allocation is done only based on the CQI value of an UE, the resources might not be fairly distributed among the UEs. B-CQI scheduling algorithm increases the throughput of some users however, reduces the fairness among UEs and especially the UEs located at the cell edge starve. In [8], the authors proposed a new scheduling algorithm which is a combination of RR and B-CQI algorithms. The new proposed algorithm uses RR algorithm in the first time slot to allocate RBs to UEs, and in the second time slot allocates RBs to UEs with higher CQI value and lowest RB allocation in the previous slot. The proposed algorithm is compared to the two commonly used schedulers RR and B-CQI in terms of fairness, throughput and average queuing delay. Results show that the proposed algorithm performs better in terms of throughput than RR algorithm and better in terms of fairness and the average delay as compared to B-CQI. The authors in [10], proposed a new Mobility Aware scheduling algorithm that takes the advantage of the simplicity of RR and B-CQI algorithms and aims to reduce their disadvantages application scenarios including mobility. The performance of the new proposed algorithm is compared to RR and B-CQI algorithm in terms of fairness, throughput and block error rate (BLER). Results show that it performs similar to RR and B-CQI in terms of fairness and throughput respectively. The authors used BLER parameter for comparison because the simulations were conducted with non-real time traffic. Therefore, it is essential to know the rate of successfully received resources. Results show that BLER parameter performs similar to B-CQI. In [11], the authors studied the throughput-fairness tradeoff investigating three different scheduling algorithms: RR, Maximum Throughput (MT) and First Maximum Expansion (FME). The results show that considering fairness among users RR gives better performance than other two algorithms; however when considering the best efforts flows RR algorithm shows the worst performance. As a conclusion, with VoIP and Video flows RR is the best scheduler.

The Approximate Maximum Throughput (AMT) algorithm was proposed by the authors in [12], aiming to solve the resource allocation problem more efficiently than a previously proposed Optimal Maximum Throughput (OMT). The AMT algorithm tries to maximize the throughput by using a heuristic approach. AMT algorithm allocates RBs to UEs with good SNR and the UEs with low SNR value are not served at all. The authors compare the algorithm in terms of throughput and BLER with B-CQI and Kwan Maximum Throughput (KMT) algorithms. Results show that the proposed AMT algorithm performs similar to B-CQI and better than KMT algorithm in terms of throughput. Considering the BLER parameter the results show that AMT and B-CQI algorithms show similar values while KMT algorithm achieves much lower BLER values.

III. EVALUATION SETUP

In this paper we present the evaluation and comparison of three major scheduling algorithms for the uplink – the RR, the B-CQI and the AMT. Our major contribution is to discuss these algorithms side by side and evaluate them under the same setup considering not only throughput and fairness but also bit error rate (BER). These methods have been established as the most suitable ones so far for scheduling resources in the uplink, however in literature there is no objective comparison of the three under the same simulation conditions. Furthermore we examine the performance of the algorithms using different channel models, namely Pedestrian B (PedB), Typical Urban (TU) and Rural Area (RA).

A. Configuration Parameters

The performance evaluations of the scheduling algorithms were conducted in single-cell environment. A single eNodeB simultaneously communicates with a different number of UEs in the cell. The simulation parameters chosen for the performance evaluation are summarized below in Table 1.

Table 1: Simulation Parameters

Parameters	Value
Simulation Time	500 TTI
Number of base station	1
Channel Model	PedB, TU, RA
Transmission model	SISO
Number of UEs	10, 30
Bandwidth	10 MHz, 15 MHz, 20 MHz
Scheduling Algorithms	RR, B-CQI, Approx. Max. Throughput

B. Channel Models

In our comparison we consider three different channel models: Pedestrian B, Typical Urban and Rural Area. The 3GPP proposes the Pedestrian channel model (PedB) for mobile users with low-mobility, with speed 30 km/h. The Typical Urban channel model (TU) represents densely populated areas with highest path loss, and the Rural Area (RA) channel model is suggested for less populated areas, having the least path loss [13].

C. Evaluation Criteria

The scheduling algorithms studied in this paper are evaluated based on three major performance metrics: aggregated throughput, fairness and bit error rate (BER).

Throughput is an important performance measure which defines the amount of data transferred successfully in a given system. Despite general clarity of the term, definitions given by different authors can vary slightly. It our work we have defined throughput as total number of useful data received successfully by the eNodeB and divided by the total simulation time. The aggregated throughput is the average of the throughput of all users in the system [14].

Fairness is a parameter that shows how fairly the available RBs are allocated among UEs. According to [4] this metric is calculated using the formula given below:

$$J \equiv \frac{\left(\sum_{i=1}^{N} T_i\right)^2}{N\sum_{i=1}^{N} T_i^2}, \quad \text{where } 0 \le J \le 1. \tag{1}$$

where we considering a LTE system consisting of one eNodeB serving N users. If T_i is the throughput (in Mbit/s) of user n, then the fairness index varies from 0 to 1.

Bit error rate (BER) is defined as the rate of errors occurring in a transmission and is calculated as a cell average using the formula given below:

$$\text{BER} = \frac{\text{Number of error bits}}{\text{Total number of bits sent}} \tag{2}$$

IV. RESULTS

The performance evaluation in this study is done using the MATLAB based Vienna LTE-A Uplink Link Level simulator developed by the Institute of Telecommunications, Vienna University of Technology [15]. It allows us to simulate different application scenarios considering varying number of UEs (from 10 to 40) and varying system bandwidth as given in LTE standards (1.4, 3, 5, 10, 15 and 20 MHz). Due to limited space only some of these results are included in the paper.

In this section we present the results of the simulations for the three algorithms. First we consider the throughput under varying user numbers and system bandwidths. Fig.1 – Fig.2 give the throughput for the different channel models as a function of the channel quality (SNR) for system bandwidth of 10 MHz/10 users per cell and 20MHz/30 users per cell respectively. From the 3 discussed algorithms B-CQI and AMT show very close performance under TU and PedB channels, while RR performs worst. However for the RA channel and SNR below 20 dB the best performing is the AMT algorithm. For 15 dB it achieves app 23% higher throughput than B-CQI and nearly 60% more than RR (see Fig.1a – Fig.1c). For higher number of users and higher system bandwidths (20 MHz/30 users per cell, Fig 2a – Fig2c) this relationship is even more strongly expressed. In case of the TU channel the 3 algorithms perform nearly equally but for the RA channel the AMT outperforms the B-CQI and RR with 36% and 62% respectively.

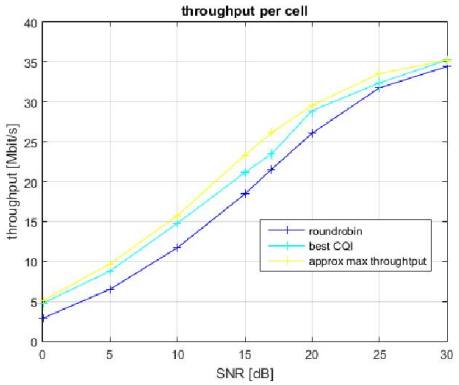


Figure 1a: Throughput/cell in TU channel, 10 MHz/10 UEs

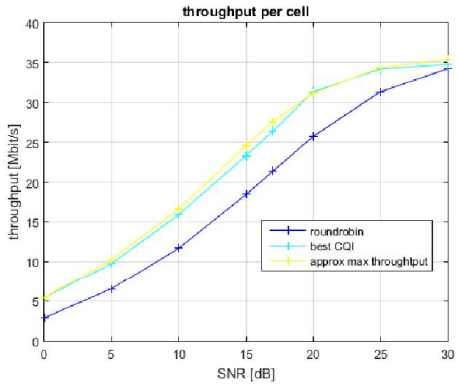


Figure 1b: Throughput/cell in PedB channel, 10 MHz/10 UEs

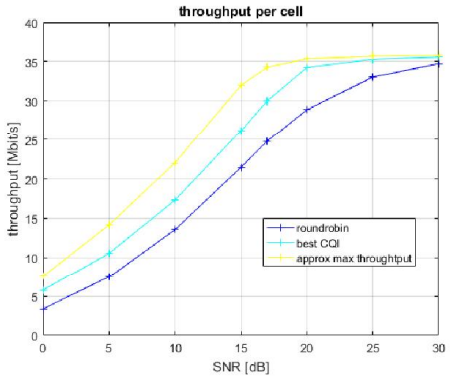


Figure 1c: Throughput/cell in RA channel, 10 MHz/10 UEs

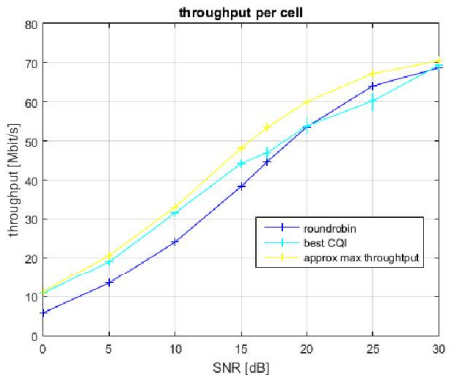


Figure 2a: Throughput/cell in TU channel, 20 MHz/30 UEs

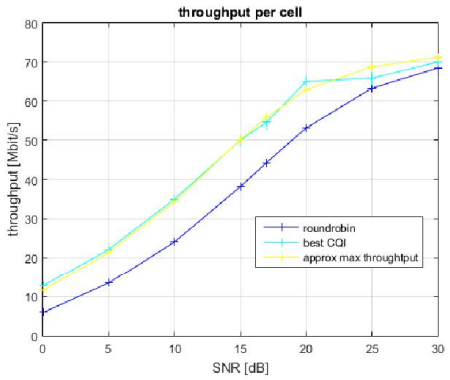


Figure 2b: Throughput/cell in PedB channel, 20 MHz/30 UEs

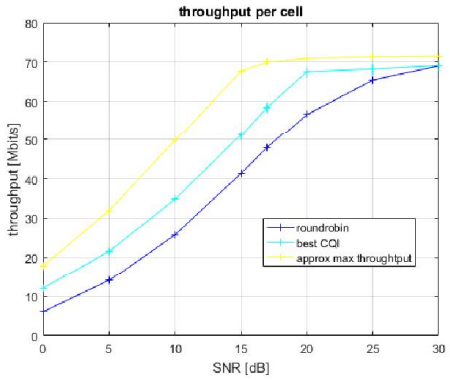


Figure 2c: Throughput/cell in RA channel, 20 MHz/30 UEs

The second performance metric we consider is fairness. Results for the fairness index for the PedB, TU and RA channels for with 10 and 30 users and varying bandwidth are presented in Table 2 below.

As expected, RR achieves the highest fairness under all channel models. However, it is interesting to notice that under the same conditions AMT performs better than the B-CQI algorithms for all channel models. Another important observation is that the variations in fairness values observed under different channel models for AMT are minimal as opposed to the B-CQI. This means that AMT can be expected to achieve very high fairness in resource allocation independent of the specific environment. The fairness of allocation provided by B-CQI is also reduced when the number of users in a cell increases i.e. its performance is sensitive to high traffic loads.

Table 2: Fairness Index Comparison

Bandwidth/ Number of UEs	Fairness Values		
	RR	**B-CQI**	**AMT**
10MHz/10UEs (PedB)	0.99	0.86	0.99
20MHz/30 UEs(PedB)	0.99	0.74	0.97
10MHz/10UEs (TU)	0.99	0.82	0.99
20MHz/30 UEs(TU)	0.99	0.69	0.99
10MHz/10UEs (RA)	0.99	0.79	0.96
20MHz/30 UEs(RA)	0.99	0.69	0.95

The last metric we discuss is the BER. The results are presented in Fig.3 – Fig.4. It can be easily noticed that the highest BER is observed for the PedB channel and the RR algorithm. Also it is interesting to notice that under poor SNR the RR performs much worse than any other algorithm. Another important point is that the BER performance of the B-CQI and AMT is nearly constant with the SNR, i.e those two algorithms are both well adapting to poor signal values irrelevant of the channel model considered. Larger variations in the BER are observed for smaller number of users, while for systems with many users the variations in the average BER are minimal.

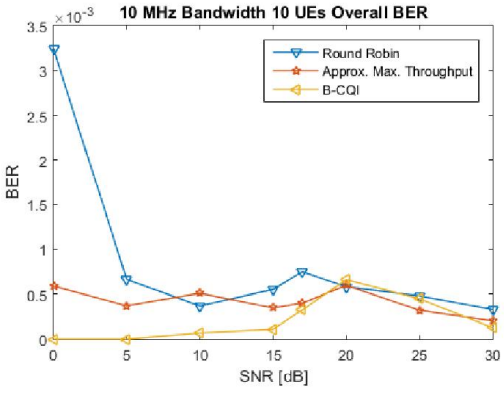


Figure 3a: BER in TU channel, 10 MHz/10 UEs

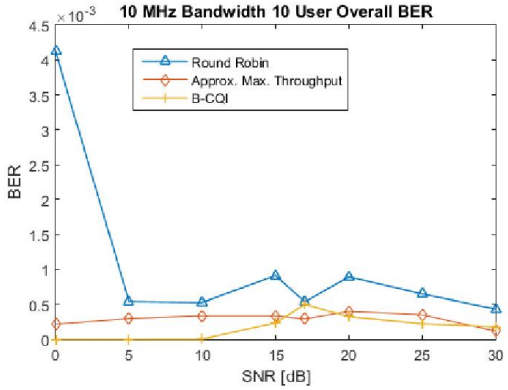


Figure 3b: BER in PedB channel, 10 MHz/10 UEs

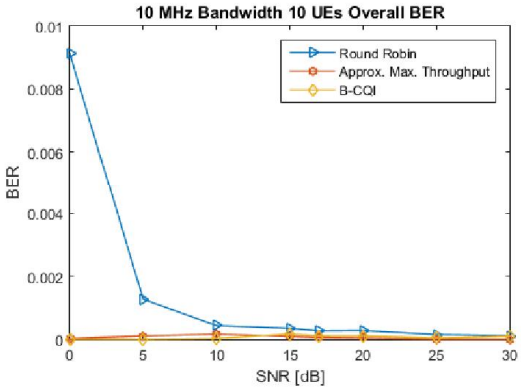


Figure 3c: BER in RA channel, 10 MHz/10 UEs

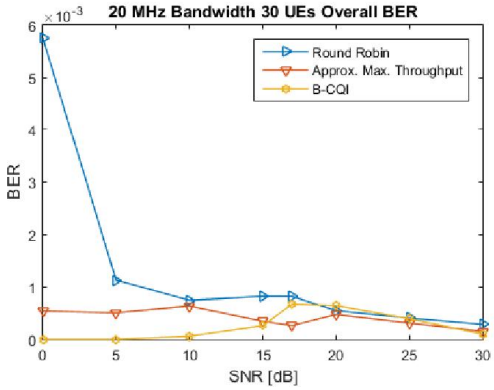


Figure 4a: BER in TU channel, 20 MHz/30 UEs

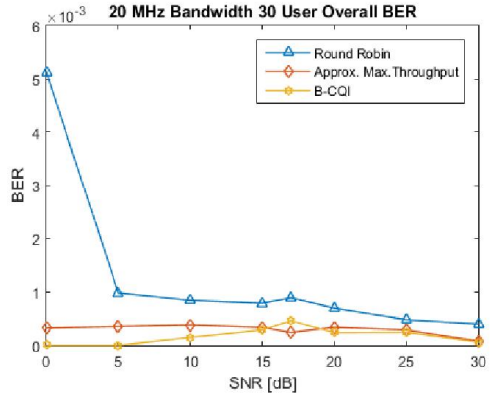


Figure 4b: BER in PedB channel, 20 MHz/30 UEs

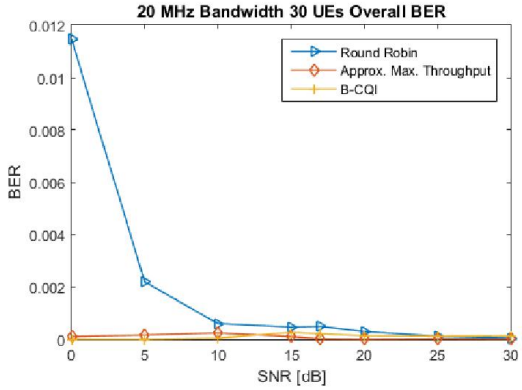


Figure 4c: BER in RA channel, 20 MHz/30 UEs

V. CONCLUSION

In this paper we investigated the performance of three major RA algorithms for the uplink in LTE systems. The main point was to compare their performance under equal conditions and study their behavior under changing numbers of users and system bandwidths. Three different channel models were considered: pedestrian with speed of around 30 km/h (PedB), typical urban (TU), and rural area (RA) channel model. The performance of the three algorithms was evaluated in terms of fairness, throughput and BER. It was observed that AMT and B-CQI performance is quite similar for lightly loaded systems (10 users with system bandwidth of 10 MHz). However when the system load is increased (30 users for 20 MHz) the AMT algorithm noticeably outperforms the others in terms of throughput. For all algorithms the best throughput performance is observed under the RA channel model. As far as the BER is considered the RR is the worst while B-CQI and AMT's performance is nearly equal. An interesting observation is that both B-CQI and AMT adapt well to the varying SNR and do not degrade their performance under low SNR values. However, in terms of fairness B-CQI not only has the worst values, but they are also highly influenced by the environment. This study can serve researchers who are interested in adopting specific RA algorithms or developing new ones for LTE systems.

REFERENCES

[1] M. Kalil, J. Samarabandu, A. Shami, and A.Al-Dweik, "Performance Evaluation of Genetic Algorithms for Resource Scheduling in LTE Uplink", in *Conf. Rec. 2014 IEEE Int. Wireless Communications and Mobile Computing Conf.* , pp. 948-952.

[2] I. F. Akyildiz, D. M. Gutierrez-Estevez, R. Balakrishnan, and E. Chavarria-Reyes, "LTE-Advanced and the Evolution to Beyond 4G (B4G) Systems ", *Physical Communication Journal*, vol. 10, pp. 31-60, March 2014.

[3] H. Safa, W. El-Hajj, and K. Tohme, "A QoS-Aware Uplink Scheduling Paradigm for LTE Networks", in *Conf. Rec. 2013 IEEE Int. Conf. on Advanced Information Networking and Applications*, pp. 1097-1104.

[4] A. Kanagasabai and A. Nayak, "Opportunistic Dual Metric Scheduling for LTE Uplink", *2015 IEEE ICC Workshop on Smart Communication Protocols and Algorithms*, pp. 1446-1451.

[5] A. Mukhopadhyay, G. Das, V. Reddy, "A Fair Uplink Scheduling Algorithm to Achieve Higher MAC Layer Throughput in LTE", in *Conf. Rec. 2015 IEEE Int. Conf. on Communications*, pp. 3119-3124.

[6] R. Khdhir, K. Mnis, L. Kamoun and L. Nuaymi, "New Scheduling Algorithm for Uplink LTE System", in *Int. Symposium on Networks, Computers and Communications*, pp. 1-5.

[7] R. D. Trivedi, and M. C. Patel, "Comparison of Different Scheduling Algorithm for LTE", *IJETAE Int. Journal of Emerging Technology and Advanced Engineering*, vol. 4, pp. 334-339, May 2014.
[8] M. Asvial, G. Dewandaru, and A. N. Rachman, "Modification of Round Robin and Best CQI Scheduling Method for 3GPP LTE Downlink", *IJTech Int. Journal of Technology,* vol. 2, pp. 130-138, April 2015.
[9] A. Marincic, and D. Simunic, "Performance Evaluation of Different Scheduling Algorithms in LTE Systems", *in Conf. Rec. 2016 IEEE Int. Convention on Information and Communication Technology, Electronics and Microelectronics*, pp.595-600.
[10] Ö. Yıldız and R. Sokullu, "A Novel Mobility Aware Downlink Scheduling Algorithm for LTE-A Networks", in *Conf. Rec. 2017 IEEE Int. Conf. on Ubiquitous and Future Networks*, pp. 300-305.
[11] R. E. Ahmed, and H. M. AlMuhallabi, "Throughput-Fairness Tradeoff in LTE Uplink Scheduling Algorithms", in *Conf. Rec. 2016 IEEE Int. Conf. on Industrial Informatics and Computer Systems*, pp. 1-4.
[12] S. Schwarz, C. Mehlführer and M. Rupp, "Low Complexity Approximate Maximum Throughput Scheduling for LTE", in *Conf. Rec. 2010 IEEE Conf. Record of the Forty Fourth Asilomar Conf. on Signals, Systems and Computers*, pp. 1563-1569.
[13] K. Elgazzar, M. Salah, A. M. Taha, and H. Hassanein, "Comparing Uplink Schedulers for LTE", in *Conf. Rec. 2010 The Int. Wireless Communications and Mobile Computing Conf.,* pp. 189-193.
[14] N. Shabbir, M. T. Sadiq, H. Kashif, and R. Ullah, "Comparison of Radio Propagation Models for Long Term Evolution (LTE) Network", *Int. Journal of Next-Generation Networks*, vol. 3, pp. 27-41, September 2011.
[15] [Online]. Available: http://nt.tuwien.ac.at/ltesimulator.

Sensorless Rotor Speed Obtained By Using Speed of Rotor Flux Space Vectors and Slip Speed

YAVUZ USER[1]

[1] Akdeniz University, Electrical &Electronics Engineering, Antalya, Tukey, yuser@akdeniz.edu.tr

Abstract **- Nowadays, no mechanical sensor is used when drivers control asynchronous motor from vectorial aspect. Various sensorless speed sensing techniques have been developed for this reason. It is significant to estimate speed with minimum error in sensorless speed sensing process. In this study, open-loop sensorless speed sensing has been performed by using motor equations' rotor flux-oriented x-y reference axis. Even if the system is open-loop, it shows high performance. Considering Matlab/Simulink outputs of this study, it is acknowledged that this estimator presents sufficient results.**

Keywords **- Sensorless open-loop speed estimation, x-y reference axis, open loop control, rotor speed, IM.**

I. INTRODUCTION

THE The fact that motor is directly dependent on constant parameters in vector control management, the machine changes when it gets heated, and that the speed needs sensors such as encoder or tachogenerator resulted in the development of sensorless vector control. In many applications, such as crane, freight elevator, printing machines and electric cars, the required momentum should be achieved up to zero speed. Achieving the required momentum at low speeds enables driver to be convenient [1,2,3,4].

Numerous studies have been conducted to measure speed data without using mechanical sensor under the control of asynchronous machine. Satisfactory and stable ones among the results obtained may be used in the areas that do not require high performance and accuracy. If no speed control is conducted, the ideal margin of error should be below 0.5%. Estimators need to take into consideration the parameter changes in asynchronous motor to carry out this kind of driver [1].

In this study, a high-performance open-loop speed estimator will be used which adopts stator flux, voltage and current. As the speed estimator is open-loop, there is no need for extra feedback equipment. It is understood that designed speed estimator asynchronous motor gives sufficient results when integrated into a system in which it is controlled vectorially.

II. OBTAINING ROTOR SPEED BY USING THE SPEED OF ROTOR FLUX SPACE VECTOR AND SLIP SPEED

This method is a high performance open-loop speed estimation control method that is currently in commercial use.

Rotor speed is not equal to the speed of stator flux in asynchronous motor. Angular velocity of rotor flux should be subtracted from rotor slip speed. For this, motor equations should be on rotor flux-oriented reference axis. Figure 1 defines x-y reference axis set.

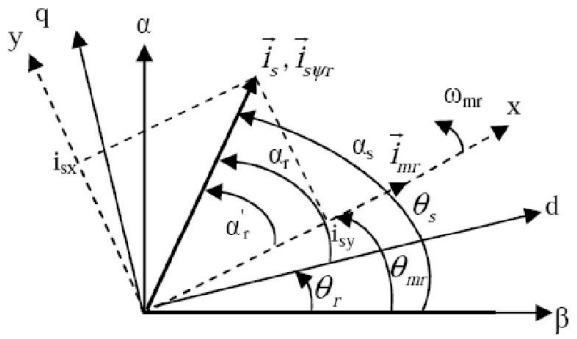


Figure 1: x-y reference axis set.

The x-y coordinate reference axis set is overlapping with the rotating rotor flux vector at ω_{mr} frequency. In x-y coordinate system, momentum is controlled with both stator x axis current isx and rotor flux and stator y axis current isy. These vectors are shown in rotor flux-oriented x-y axis set in Figure 1. Here, as rotor flux-oriented reference set and x,y general reference axis set are overlapping with rotor current space vector, the rotor current space vector on this axis can be defined as follows:

$$\vec{i}_{r\psi r} = i_{rx} + j i_{ry} = \vec{i}_r^{'} e^{-j\theta_{mr}} \quad (1)$$

In the 2nd phase rotor, on constantly rotating axis, rotor current and flux are formulated as

$$\vec{i}_r^{'} = i_{rd} + j i_{rq} \text{ ve } \psi_r^{'} = \psi_r e^{j\theta_r} = \psi_{rd} + j\psi_{rq} \quad (2)$$

And, on x-y general reference axis, rotor flux space vector is

$$\vec{\psi}_{r\psi r} = \vec{\psi}_r^{'} e^{-j\theta_{mr}} = |\vec{\psi}_r| \quad (3)$$

Here, positional angle of rotor is found via following formulae:

$$\theta_{mr} = \int \omega_{mr} dt \tag{4}$$

x-y general axis set and the components of this set rotate with this angle. Rotor magnetization flux on this axis is defined as

$$\left|\vec{\psi}_r\right| = L_m \left|\vec{i}_{mr}\right| = L_m \vec{\psi}_{r\psi r} \tag{5}$$

And, it is defined only on x axis. Stator current's x-y general reference axis components are founded in terms of the 2nd phase fixed axis set components as

$$\vec{i}_{s\psi r} = i_{sx} + j i_{sy} = \vec{i}_s e^{-j\theta_{rm}} = i_{s\alpha} e^{-j\theta_{rm}} + j i_{s\beta} e^{-j\theta_{rm}} \tag{6}$$

In terms of stator and rotor currents, rotor flux is

$$\vec{\psi}_{r\psi r} = L_r \vec{i}_{r\psi r} + L_m \vec{i}_{s\psi r} \tag{7}$$

Rotor magnetization flux on x-y reference axis is found as

$$\left|\vec{i}_{mr}\right| = \left|\vec{i}_{mr}\right| = \frac{\vec{\psi}_{r\psi r}}{L_m} = \vec{i}_{s\psi r} + (1+\theta_{mr})\vec{i}_{r\psi r} \tag{8}$$

In this axis set, rotor voltage for squirrel-cage asynchronous motor is written as

$$0 = R_r \vec{i}_{r\psi r} + \frac{d\vec{\psi}_{r\psi r}}{dt} + j(\omega_{mr} - \omega_r)\vec{\psi}_{r\psi r} \tag{9}$$

If Lm is considered as

$$\text{constant, } 0 = R_r \vec{i}_{r\psi r} + \frac{d\left|\vec{i}_{mr}\right|}{dt} + j(\omega_{mr} - \omega_r)\left|\vec{i}_{mr}\right| \tag{10}$$

is obtained by using (5). (8) equation is put in place of (10) and if both sides of the equation are divided by rotor resistance Rr and if Tr=Lr/Rr, the result is as follows:

$$T_r \frac{d\left|\vec{i}_{mr}\right|}{dt} + \left|\vec{i}_{mr}\right| = \vec{i}_{s\psi r} - j(\omega_{mr} - \omega_r) T_r \left|\vec{i}_{mr}\right| \tag{11}$$

In this formulae, the real and virtual parts of the equation can be written as follows.

$$T_r \frac{d\left|\vec{i}_{mr}\right|}{dt} + \left|\vec{i}_{mr}\right| = i_{sx} \tag{12}$$

$$\omega_{mr} = \omega_r + \frac{i_{sy}}{T_r \left|\vec{i}_{mr}\right|} \tag{13}$$

Slip frequency of rotor flux is

$$\omega_{sl} = \frac{i_{sy}}{T_r \left|\vec{i}_{mr}\right|} \tag{14}$$

In this statement, if the following representations are used with the equation (6),

$$\left|\vec{i}_{mr}\right| = \frac{\left|\vec{\psi}_r\right|}{L_m} \quad , \quad \sin\theta_{mr} = \frac{\psi_{rq}}{\left|\vec{\psi}_r\right|}, \quad \cos\theta_{mr} = \frac{\psi_{rd}}{\left|\vec{\psi}_r\right|} \tag{15}$$

Rotor sleep speed ω_{sl},

$$\omega_{sl} = \frac{-i_{s\alpha}\sin\theta_{mr} + i_{s\beta}\cos\theta_{mr}}{T_r\left|\vec{i}_{mr}\right|} = \frac{L_m(\psi_{rd} i_{s\beta} - \psi_{rq} i_{s\alpha})}{T_r\left|\vec{\psi}_r\right|^2} = \frac{2t_e R_r}{3P\left|\vec{\psi}_r\right|^2} \tag{16}$$

Rotating speed of x-y axis in respect to the 2nd phase fixed axis ωmr,

$$\omega_{mr} = \frac{d\theta_{mr}}{dt} = \frac{d}{dt}\left[\tan^{-1}\left(\frac{\psi_{rd}}{\psi_{rq}}\right)\right] = \frac{\psi_{rd}\frac{d\psi_{rq}}{dt} - \psi_{rq}\frac{d\psi_{rd}}{dt}}{\psi^2_{rd} + \psi^2_{rq}} \tag{17}$$

If we add rotor speed to rotor flux's slip speed, we get the angular speed of rotor flux. Therefore, rotor speed ωr, is found as[1];

$$\omega_r = \omega_{mr} - \omega_{sl} = \frac{\psi_{rd}\frac{d\psi_{rq}}{dt} - \psi_{rq}\frac{d\psi_{rd}}{dt}}{\left|\vec{\psi}_r\right|^2} - \frac{2t_e R_r}{3P\left|\vec{\psi}_r\right|^2} \tag{18}$$

Speed estimation carried out with the equation here is based on the motor parameters in the equation, which means it is based on L_r, L_m, L_s, R_s that are used to find flux and momentum values, and Rr values in the equation.

III. VECTORIAL CONTROL MODEL WHICH USES ASYNCHRONOUS MOTOR PARAMETERS

Figure 2 shows a motor control system which directly uses momentum control algorithm. The information needed for the equation no. 18 is obtained from this model. Vectorial control method in Figure 2 is a direct momentum control method.

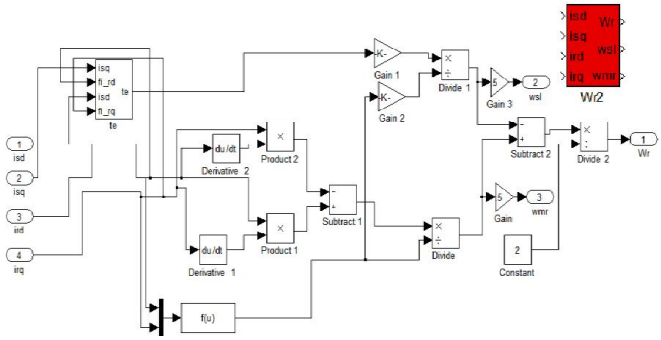


Figure 2. Obtaining of rotor speed Matlab/Simulink Model

IV. SIMULATION RESULTS

Figure 3 and 4 show open-loop speed estimation results obtained by using rotor flux in the equation no. 18. Figure 5 shows motor momentum.

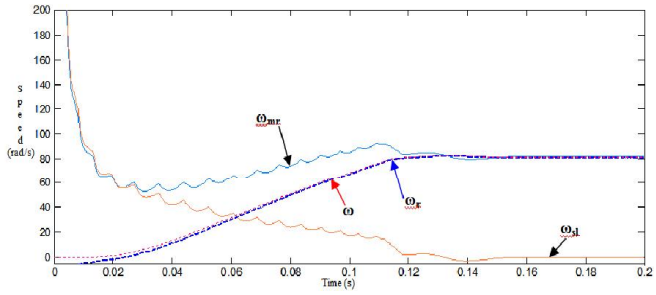


Figure 3. For the above-mentioned speed estimation method, speed components for ω_{ref}=80 rad/secs

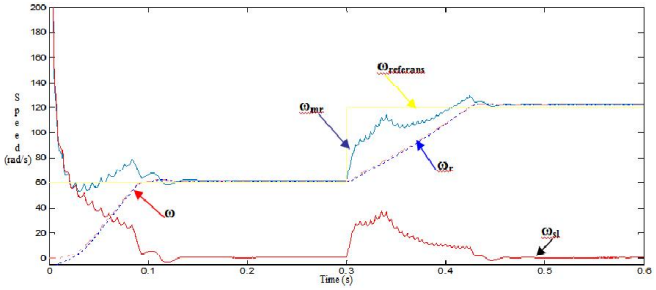


Figure 4. For the above-mentioned speed estimation method, speed components for ω_{ref}= 60 rad/secs and 120 rad/secs

Rotor flux vectorial angular speed (ωmr), rotor flux slip speed (ωsl), reference speed (ωreferans), estimated motor speed (ωr= ωmr- ωsl) are shown in Figure 3 and 4, and momentum change is shown in Figure 5. Speed estimation is carried out in about 0,13 seconds and during this time, values are seen in transition regime. Also, momentum fluctuates in transition regime and becomes stable after 0.12 seconds. In graph a, the speed is fixed to 60 rad/secs. In graph b, the speed is fixed to 60 rad/secs at first, and then raised to 120 rad/secs at 0.5 seconds. However, speed estimation result is not sufficiently accurate as the flux decreases as well at low speed. Estimations at speeds above 60 rad/secs are satisfactory.

V. RESULT

Considering graphs in detail, the accuracy level of speed estimation result decreases as the flux diminishes at low speeds. However, the speed estimator provides sufficient and satisfactory results at speeds above 60 rad/secs.

ACKNOWLEDGMENT

The research has been supported by the Research Project Department of Akdeniz University, Antalya, Turkey. (Project No: 2017.05.0102.126)

REFERENCES

[1] Vas, P., Sensorless Vector and Direct Torque Control, Oxford University Pres,1998.
[2] Lascu, C., Boldea, I. Ve Blaabjerg, F., (1998), " A Modified Direct Torque Control for Induction Motor Sensorless Drive",Industry Applications Conference, 1:415-422.
[3] Lascu, C., Boldea, I. Ve Blaabjerg, F., " A Modified Direct Torque Control for Induction Motor Sensorless Drive", IEEE Trans. On Industry Applications, 36(1):122-130, Jan.-Feb. 2000.
[4] Monti, A., Pironi, F., Sartogo, F. ve Vas, P., (1998), "New State Observer for Sensorless DTC Control", Proceedings of the 1998 7th International Conference onPower Electronics and Variable Speed Drivers, 311-317, Sept. 21-23 1998.
[5] Sarıoglu M.K., Gokasan M., Bogosyan S.,Asynchronous Machines and it's Control, Birsen Publishing, ISBN 975-511-343-6, 2003.
[6] Schauder, C., Adaptive Speed identification for vector control of induction motors without rotational transducers. IEEE. Tran.Ind.Applic.,5(IA-22): 965-970,1992.
[7] Cirrincione, M. and M. Pucci, Sensorless direct torque control of an induction motor by a TLS-based MRAS observer with adaptive integration. Automatica, 11 (41): 1843-1854, 2005.
[8] Matlab, The Langauge of Technical Computing, Using Matlab, ©Copyright 1990-2017 by The MathWorks, Inc.
[9] Simulink, Model-Based and System-Based Desing, Using Simulink, ©Copyright 1990-2017 by The MathWorks, Inc.

Hardware-in-the-loop Simulation of a Novel Nonlinear PI Controller on FPGA

Ş. AKKAYA[1], H. NAK[2] and A. F. ERGENÇ[3]

[1] Istanbul Technical University, Istanbul/Turkey, sakkaya@itu.com.tr
[2]Istanbul Technical University, Istanbul/Turkey, handan.nak@itu.edu.tr
[3]Istanbul Technical University, Istanbul/Turkey, ali.ergenc@itu.edu.tr

***Abstract* – In this paper, the implementation of a novel nonlinear PI controller on field programmable gate array (FPGA) is designed using Very High Speed Integrated Circuit Hardware Description Language. The controller structure consists of a sector bounded nonlinear function of the relative error value in cascade with a linear PI controller. Since these kind of nonlinear mathematical equations need small time period, FPGA provides a good solution because of its parallel architecture. Considering that the accurate controller output means varying scales, 32-bit single precision binary floating-point number format is used. For implementation of mathematical operations Altera Floating-Point IP Cores are used. The designed controller is tested with a second order mass-damper-spring system by help of hardware-in-the-loop simulation via Matlab/Simulink environment.**

***Keywords* – Nonlinear pi controller, FPGA, HIL simulation.**

I. Introduction

In industrial systems, linear fixed-PI controllers (if suitably tuned) provide acceptable solutions to many various applications without requiring any information about the system dynamics [1]. However, a well-known trade-off of these controllers is achieving fast responses causes overshoot, and decreasing overshoot causes slow smooth response. Moreover, in the case of parameter uncertainties and disturbance, their performance deteriorates and controller coefficients are needed to re-tune. Another notable fact is that utilizing an integral term can suppress disturbances, but it causes undesired increase of the system overshoot [2, 3]. This trade-off can be balanced by employing nonlinear coefficients in the PI (PID) control scheme. In the literature, there are many studies on modulating the linear controller gains via a nonlinear structure to improve the controller performance [4-9]. The objective of these controllers is to diminish steady state error due to disturbances while providing acceptable transient performance with small overshoot and quick response.

In this study, authors present real time implementation of their own nonlinear PI controller structure [10-11] on system-on-a-chip (SoC) architecture. In the controller structure, the nonlinear gain is function of not only the error but also the reference signal. This novel gain structure provides two essential advantages; strong control action to decrease the rise time of the system response and exponential decrease of integral action to prevent overshoot of the system response [10]. The combination of these two enhanced actions represents the innovation in PI controllers.

A field-programmable gate array (FPGA) is chosen as the SoC architecture in this study. FPGA-based implementation of controllers can efficiently meet the requirements of real time applications because of its very high parallelism capability and data transfer bandwidth, fast speed, rich I/O resources, re-configurability and shorter design cycle [12, 13]. The FPGA is currently used in many applications, including drive and power systems [12, 14-16], different control algorithms [17-19], real time electromagnetic transient emulation [13, 20-21].

In this study, Altera DE2-115 FPGA Development and Education Board is used because it provides Ethernet support via two Marvell 88E1111 Ethernet PHY chips to Matlab/Simulink environment. The real time simulation configured with Matlab and FPGA is known as FPGA-in-the-loop (FIL) simulation. FIL simulation provides the capability to use Matlab software for testing designs in real hardware for hardware description language (HDL) codes [21]. HDL code is written manually with Very High Speed Integrated Circuit Hardware Description Language (VHDL) by the help of *Quartus II 15.1 Lite Edition*.

This paper is organized as follows: in Section II, the proposed controller structure is described. In Section III, the controller implementation in FPGA is given and the implementation results are presented in Section VI. Finally, in Section V the study is reviewed and future work is discussed.

II. Controller Structure

The mathematical description of a fixed-gain PI controller is generally expressed as follows

$$u(t) = k_p e(t) + k_i \int_0^t e(t)dt \qquad (1)$$

where *u(t)* is control signal, *r(t)* is system reference, *y(t)* is system output, *e(t)* is error signal, and k_p and k_i are constant proportional and integral gains, respectively.

The proposed control structure is comprised of a sector-bounded nonlinear gain *k(e,r)* in cascade with a fixed-gain PI controller, as in (2). The block diagram of the proposed structure is illustrated in Fig. 1.

$$u(t) = \left[k_p e(t) + k_i \int_0^t e(t)dt \right] k(e,r) \qquad (2)$$

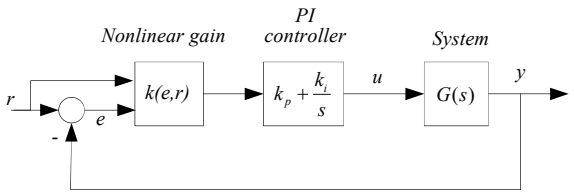


Figure 1. Nonlinear PI control system block diagram.

In this study, the nonlinear gain function *k(e,r)* is defined as

$$k(e,r) = \gamma - \alpha e^{-\beta\delta} \qquad (3)$$

where $\delta = |e(t)/r(t)|$ and, α, β and γ are positive-valued controller design parameters. Note that, the *k(e,r)* function is bounded in [γ - α, γ] with this definition.

The motivation behind using this nonlinear gain *k(e,r)* is overcoming the inevitable trade-off of fixed-gain controller between fast response with overshoot and oscillation, and slow response with no overshoot. The proposed structure is capable of accomplishing these two conflictive requirements.

In the structure, the error signal is amplified with a term, which is defined by the ratio of error to the reference and fed into fixed gain controller. When the relative error value is large, the nonlinear gain *k(e,r)* exponentially increases and the system output reaches the reference value fast. As time proceeds and the error tends to diminish, the nonlinear gain *k(e,r)* decreases and when the error vanishes, *k(e,r)* converges to its lowest value *(γ-α)*. This dynamic structure shortens the rise time and allows the system output behavior being smoother in the process of settling when compared to the fixed-gain PI controller. This structure also reduces the winding of the integral term, which is another cause of overshoot [10-11].

Considering that the other nonlinear controller structures in the literature use only error term in their nonlinear gains, this structure has an advantage because of involving relative error. In case of small reference values small error values will become more important. Similarly when the reference value is large, small errors will become less important. And this structure takes these particular cases into account via its relative error dependence.

III. Controller Implementation with VHDL

The controller interfaces are designed as a component by the help of Altera Floating-Point IP Cores using VHDL. The Altera Floating-Point IP cores enable to perform floating-point arithmetic in FPGAs through optimized parameterizable functions for Altera device architecture [24]. For the adder/subtractor function ALTFP_ADD_SUB, divider function ALTFP_DIV, multiplier function ALT_MULT, exponential function ALTFP_EXP, absolute value function ALTFP_ABS and converter function ALTFP_CONVERT are used.

The controller structure are implemented in FPGA with 32-bit single precision binary-floating-point numbers. The main advantage of using floating-point numbers instead of fixed-point and integer is that it can support a much wider range of values. Floating-point numbers are defined in the IEEE 754 Standard (32 bit and 64 bit) [23]. The standard binary floating point data is encoded on three different fields: a one bit sign field, followed by exponent bits encoding the exponent offset by a numeric bias specific to each format, and bits encoding the fractions (or mantissa). A single precision floating point format is shown in Fig. 2. Here, the most significant bit (MSB) holds the sign bit, the next 8 bits hold the exponent bits, the rest 23 least significant bits (LSBs) hold the mantissa. The total width of a binary floating-point number in the single-precision format is 32-bits with the bias of 127 [24].

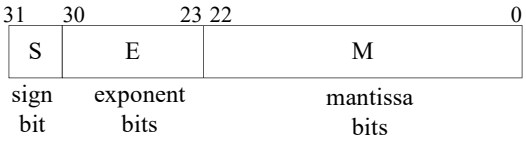


Figure 2. 32-bit single precision binary floating-point format.

The binary floating-point representation of a data, the *'0'* sign bit is used for positive and *'1'* sign bit is used for negative numbers. The exponent bits encode the exponent in base 2, and the fraction bits encode the significand without the MSB non-zero bits. For instance, the value -160.5 equals to $(-1)^1 x 2^7 x 1.25390625$, and can be represented with a negative sign, an exponent of *'7'*, and a fractional part *'.25390625'*. The exponents are biased by *127*, so the exponent 7 is represented by bit strings with values *134*. Hence, the 32 bit single precision binary floating-point format of -160.5 is obtain as below;

1	10000110	01000001000000000000000

Figure 3. 32-bit binary floating-point format of -160.5

The nonlinear and the linear parts of the controller are implemented via Altera Floating-Point IPs. The implementation of these parts are explained in detail in the following sections.

A. Nonlinear Part of the Controller

The controller inputs (error value, reference value and the constants) are defined as 32-bits *std_logic_vector* data type as described in standard logic *1164* package of the IEEE library. These values are sent to the FPGA as 32 bits binary fixed-point numbers via Matlab/Simulink environment. Then all the input values are converted into 32-bit binary floating-point number format.

The schematic diagram of the VHDL code that written for nonlinear part of the controller, *k(e,r),* are given Fig. 4. As seen from the figure, for each step of the nonlinear equation, an IP component is used.

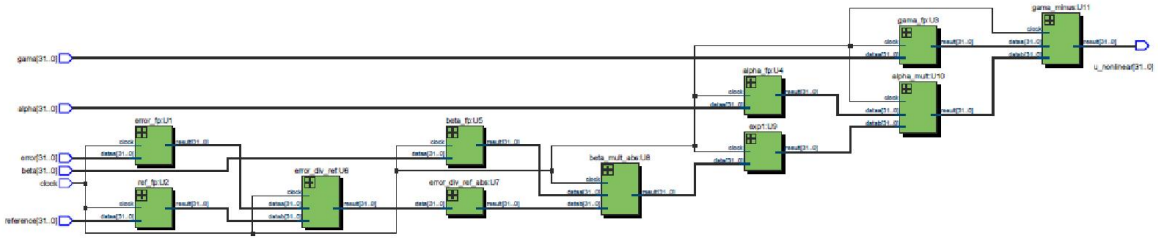


Figure 4. Implementation of nonlinear part of the controller in FPGA.

In Fig. 4, while the components U1, U2, U3, U4 and U5 convert the value of error, reference, α, β and γ into 32-bit floating-point values, the other components execute the math operations.

As an example, for values $r(t) = 1$, $e(t) = 0.368$, $\alpha = 0.4$, $\beta = 0.4$ and $\gamma = 2$, the ModelSim result is obtained as in Fig. 5. Here, the fixed-point representation of the values are given to the simulation program as an input. These values are converted into floating point representation, then the nonlinear output is obtained as the 32-bit floating representation of *1.7231531*.



Figure 5. ModelSim simulation result of nonlinear part of the controller.

B. *Linear Part of the Controller*

The linear part of the controller represents a conventional PI controller given in (1). For the implementation of this structure the discrete form of the controller is used. In (4), for a small sample time T_s, the linear part of the controller are turned into a difference equation with approximation of integral mode by backward integration rule.

$$u_{lin}[k] = K_p e[k] + u_i[k-1] + K_i e[k] \qquad (4)$$

The schematic diagram of the VHDL code is given Fig. 6.

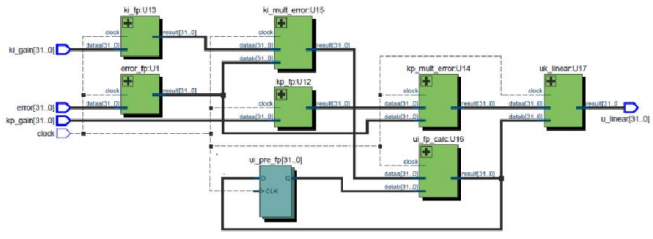


Figure 6. Implementation of linear part of the controller in FPGA.

After the linear and nonlinear part of the controller are multiplied, the controller output is obtained as a floating point number.

IV. Implementation Studies

A. *System Description*

In this section we desire to control a second order mass-spring-damper system given in Fig. 7. The transfer function between the force applied, F(s), and position, X(s), of the system is presented in (5).

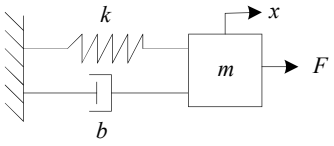


Figure 7. The schematic of second-order mass-spring-damper system.

$$\frac{X(s)}{F(s)} = \frac{1}{m\,s^2 + bs + k} \qquad (5)$$

The parameters of the system are given in Table 1. It is worth noting that with these system parameters and controller parameters including α and γ are in stable region. For stability analysis of this controller, see [10].

Table 1. Simulation parameters.

Parameter	Value
Mass, m	2.45 kg
Damping coefficient, b	9 Nsec/m
Spring constant, k	200 N/m
Proportional gain, k_p	10
Integral gain k_i	2
Controller parameter, α	0.4
Controller parameter, β	1
Controller parameter, γ	2

B. *Implementation Results*

The hardware-in-the-loop simulation diagram that connects Matlab/Simulink environment to FPGA is shown in Fig. 8. Here, the FIL block is built after the VHDL files of the controller are compiled via Matlab/Simulink. For simulations fixed-point Bogacki-Shampine (ode3) solver is used and sampling time is chosen as T_s=*0.002* sec.

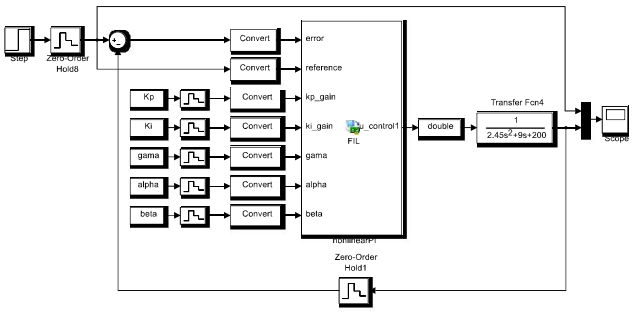


Figure 8. Simulink diagram of the HIL environment.

In the first simulation to investigate controller performance a unit step function is applied as reference signal. Also, at *t=25* a step disturbance input with the amplitude of 0.5 is applied as output disturbance. The results for system output and control signal are given in Fig. 9 and 10, respectively. It can be said that in case of nonlinear PI controller, system output approaches reference value fast and rejects the disturbance more effectively.

The variation of nonlinear gain *k(e,r)* for this case is given in Fig. 11. At *t=0*, the error value is high, nonlinear gain *k(e,r)* reaches its maximum value, 2. When the system output approaches the reference, the error decreases and nonlinear gain *k(e,r)* decreases as expected.

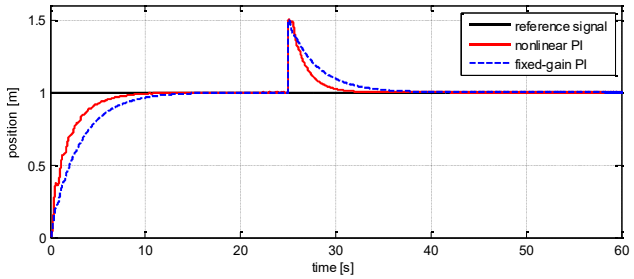


Figure 9. System responses for the nonlinear PI and fixed-gain PI controller.

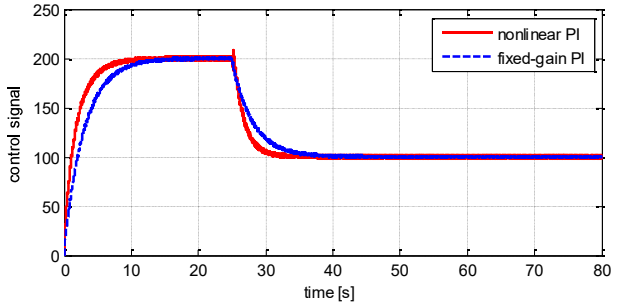


Figure 10. Control signals for the nonlinear PI and fixed-gain PI controller.

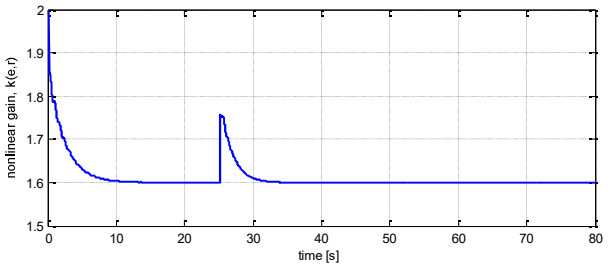


Figure 11. Variation of nonlinear gain *k(e,r)* with respect to time.

In the second simulation scenario, a sinusoidal reference signal with a frequency of 0.01 Hz and amplitude 1 is applied. The results show that nonlinear PI controller performs better at reference tracking as well (Fig. 12).

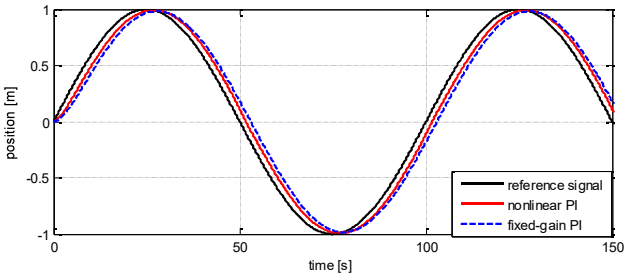


Figure 12. System responses for sinusoidal input.

V. Conclusion

In this study, a novel type of nonlinear PI controller are implemented using FPGA. All the code for the controller are written manually via VHDL using 32-bit single precision binary floating-point format. For the nonlinear arithmetic operations Altera Floating-Point IP Cores are used. For the case study, a second order mass-damper-spring system is practiced. HIL simulations are conducted to verify the control algorithm implementation on FPGA and performance of the designed structure. It is found that FPGA-based controller run properly and the transient and steady state responses of the controller are satisfactory. As future work, it is planned to use the FPGA-based controller in a real second order system.

References

[1] R. Ortega, A. Astolfi, and N. E. Barabarov, "Nonlinear PI control of uncertain systems: An alternative to parameter adaptation," *Syst. Control Lett.*, vol. 47, pp. 259–278, 2002.

[2] K. Lau, R. Middleton, "Switched integrator control schemes for integrating plants," *in Proc. Eur. Control Conf.*, 2003.

[3] K. Ang, G. Chong, Y. Li, PID control system analysis, design, and technology, *IEEE Trans. Control Syst. Technol*., vol. 13, no. 4, pp. 559–576, Jul. 2005.

[4] B.G.B. Hunnekens, M.F. Heertjes M, N. van de Wouw and H. Nijmeijer, "Performance optimization of piecewise affine variable-gain controllers for linear motion systems," *Mechatronics*, vol. 24, no. 6, pp. 648–660, Sep. 2014.

[5] B.G.B. Hunnekens, M. Heertjes, N. van de Wouw N, H. Nijmeijer, "Synthesis of variable gain integral controllers for linear motion systems," *IEEE Trans. on Contr. Syst. Technology*, 23(1), pp. 139-149, 2015.

[6] H. Seraji, "A new class of nonlinear PID controllers with robotic applications," *J. Robot. Syst.,* vol. 15, no. 3, pp. 161–173, 1998.

[7] B. Armstrong, D. Neevel, and T. Kusik, "New results in NPID control: Tracking, integral control, friction compensation and experimental results," *IEEE Trans. Control Syst. Technol.,* vol. 9, no. 2, pp. 399–406, Mar. 2001.
[8] M. Heertjes, X. Schuurbiers, and H. Nijmeijer, "Performance-improved design of N-PID controlled motion systems with application to wafer stages," *IEEE Trans. Ind. Electron.,* vol. 56, no. 5, pp. 1347–1355, May 2009.
[9] W. Lan, B. Chen, and Y. He, "On improvement of transient performance in tracking control for a class of nonlinear systems with input saturation," *Syst. Control Lett.,* vol. 55, no. 2, pp. 132–138, 2006.
[10] Ş. Akkaya, H. Nak and A. F. Ergenc, "Design, Analysis And Experimental Verification of a Novel Nonlinear Pi Controller*," Anadolu Üniversitesi Bilim Ve Teknoloji Dergisi A - Uygulamalı Bilimler ve Mühendislik,* vol. 18, no. 4, 2017.
[11] Ş. Akkaya, H. Nak and A. F. Ergenc, "Design, Stability Analysis and Simulation Studies of a New Type of PI Controller*," the 19th Turkish National Conference on Automatic Control,* 2016.
[12] E. Monmasson and M. N. Cirstea, "FPGA design methodology for industrial control systems—A review," *IEEE Trans. Ind. Electron.,* vol. 54, no. 4, pp. 1824–1842, Aug. 2007.
[13] Z. Shen and V. Dinavahi, "Dynamic variable time-stepping schemes for real-time FPGA-based nonlinear electromagnetic transient emulation," *IEEE Trans. Ind. Electron.,* vol. 64, no. 5, pp. 4006–4016, May 2017.
[14] O. Gulbudak and E. Santi, "FPGA-based model predictive controller for direct matrix converter," *IEEE Trans. Ind. Electron.,* vol. 63, no. 7, pp. 4560–4570, Jul. 2016.
[15] M. N. Cirstea and A. Dinu, "A VHDL holistic modeling approach and FPGA implementation of a digital sensorless induction motor control scheme," *IEEE Trans. Ind. Electron*., vol. 54, no. 4, pp. 1853–1864, Aug. 2007.
[16] O Jimenez, O Lucia, I. Urriza, L. A. Barragan, and D. Navarro, "Analysis and implementation of FPGA-based online parametric identification algorithms for resonant power converters*," IEEE Trans. Ind. Informat.,* vol. 10, no. 2, pp. 1144–1153, May 2014.
[17] F. Xu, H. Chen, X. Gong, and Q. Mei, "Fast nonlinear model predictive control on FPGA using particle swarm optimization," *IEEE Trans. Ind. Electron.*, vol. 63, no. 1, pp. 310–321, Jan. 2016.
[18] A. Dinu, M. N. Cirstea, and S. E. Cirstea, "Direct neural-network hardware-implementation algorithm," *IEEE Trans. Ind. Electron.,* vol. 57, no. 5, pp. 1845–1848, May 2010.
[19] Ş. Akkaya, H. D. Üzgün, O. Akbati. "Fuzzy Logic Controller Implementation with FPGA in the Loop Simulation." *Proceedings of the 2017 International Conference on Mechatronics Systems and Control Engineering*, 2017.
[20] Z. Shen and V. Dinavahi, "Real-time device-level transient electrothermal model for modular multilevel converter on FPGA," *IEEE Trans. Power Electron.,* vol. 31, no. 9, pp. 6155–6168, Sep. 2016.
[21] J. Liu and V. Dinavahi, "Detailed magnetic equivalent circuit based realtime nonlinear power transformer model on FPGA for electromagnetic transient studies," *IEEE Trans. Ind. Electron.,* vol. 63, no. 2, pp. 1191-1202, Feb. 2016.
[22] Matlab Help Documents, "*FPGA-in-the-Loop Simulation*," 2017. https://www.mathworks.com/help/hdlverifier/ug/fpga-in-the-loop-fil-simulation.html
[23]] IEEE Standards Committee, "IEEE Standard for Floating-Point Arithmetic." http://754r.ucbtest.org/drafts/754r.pdf, February 2003.
[24] Altera Corporation, "Floating-Point IP Cores User Guide," 2016. https://www.altera.com/content/dam/altera-www/global/en_US/pdfs/literature/ug/ug_altfp_mfug.pdf

Network Reduction Methods on DG Planning Studies

K. DOGANSAHIN[1], B. KEKEZOGLU[2], A. AJDER[3] and R. YUMURTACI[4]

[1] Yıldız Technical University, İstanbul/Turkey, kadird@yildiz.edu.tr
[2] Yıldız Technical University, İstanbul/Turkey, bkekez@yildiz.edu.tr
[3]Yıldız Technical University, İstanbul/Turkey, aliajder@yildiz.edu.tr
[4]Yıldız Technical University, İstanbul/Turkey, ryumur@yildiz.edu.tr

***Abstract* – Nowadays, distributed generation is a popular generation technique and its penetration in power systems is increasing each passing day. In the integration of DG into power systems, planning is of great importance. In the planning of these systems connected to the distribution networks, according to the size of the network, the computational effort to be done can be quite heavy. Various reduction methods have been proposed in the literature in order to reduce this computational load. These methods have been investigated in this paper and it has been concluded that the most suitable method for DG planning studies is the WARD method. The consistency of the WARD method in such studies was examined by a case study on the IEEE 30 bus test system.**

***Keywords* – DG planning, Network reduction methods, Ward equivalent, IEEE 30 Bus**

I. INTRODUCTION

DISTRIBUTED generation (DG) is, by its most general expression, a technique for generating electrical energy by connecting from distribution levels to power systems [1]. Distributed generation facilities are the investments that can be realized in shorter period, with lower costs and fewer risks than large power systems. Besides payback period for DG investments is shorter than that of large power plants. Thus, it provides effective solutions on supplying increasing electricity energy demand. Since the generation is performed in where the consumption takes place, DG technique helps to reduce power losses in systems. Opening up new energy fields, enabling to be used different energy sources in generation, allowing customers to meet their own energy need and to sell the surplus energy to the grid are the other benefits of DG. Nowadays, the popularity of DG, which offers such benefits in terms of both the systems and the consumers, is quite high, and hence its penetration on power systems is increasing day by day [2].

However, this DG is contrary to traditional power systems with centralized generation infrastructure [3]. In centralized structure, power flow is unidirectional from large power plants towards consumption area via transmission lines. Therefore, all subsystems in power systems are designed based on this power flow. Especially, protection scheme, which is designed based on the way of power flow, and voltage regulation which is designed as assuming that voltage drops towards end of feeders, are the most affected systems[2,4]. In order to avoid this kind of disruptive effects of DG in power systems, a well-planned integration is required [5].

As it is stated before, DG systems are integrated into power systems from distribution levels. Distribution networks are within power systems, with the highest complexity and lowest observability. Numerous system components in different structures and tasks, and a great number of consumers in different structures and characteristics takes place in that part of power systems. However, there are fewer and more limited monitoring mechanisms than other parts of power systems in distribution systems [6]. Thus, DG planning study for a distribution network corresponds to heavy computational works.

In such studies, network reduction techniques have been proposed in order to reduce the computational effort and required time, and such methods have been used in many studies in the literature . A detailed review study regarding with these methods and studies are given in [7] and a detailed expression for application of these methods are given in [8] These methods are generally grouped under two main titles, depending on their suitability of using in dynamic or steady system states [7]. In this paper, DG planning studies based on steady state conditions of power systems are taken as basis. There are many reduction methods recommended in the literature for steady-states of power systems [9]. However, the most well-known examples of these methods are Ward [10], Kron [11], Dimo's [12] and Zhukov's [13]. Among these methods, the Ward reduction method, which is considered to be most suitable for DG planning studies, comes to the forefront in terms of ease of operation and feasibility. Since the Kron method is based on modeling the loads on the system as impedance, it may intensify and singularize the impedance matrix [11]. On the other hand, Dimo's and Zhukov's methods are known as Radial Equivalent Independent (REI) reduction methods based on aggregating the busses to be reduced at a single point, so the feasibility may be low in such systems that may have different buses like distribution networks.

In this study, the IEEE 30 bus test system has been reduced to an equivalent system by using Ward reduction method. The real and the reduced system are analyzed by power flow analysis and the consistency between the systems has been examined. Finally, the same examinations were repeated on the systems by connecting a DG unit to a selected bus and the results obtained have been evaluated.

II. Network Reduction methods

In the planning of the DG connection to a distribution system, it is emphasized in the previous section that studying with the reduced system by using the reduction methods provide benefits to the user like reducing the computational efforts and time. Choosing the most appropriate reduction method among the reduction methods recommended in the literature is of great importance in terms of ease of operation and consistency of the results to be obtained.

In the Kron reduction method, which is one of the most known reduction methods in the literature, the nodal equations of the system are created with the results obtained from the solution of the real system. The equations, which belongs to the points that desired to be removed from the original system, are eliminated by the help a gauss elimination method based approach and the equivalent circuit is obtained. However, in the Kron reduction method, loads in the system are modeled as impedance and evaluated in the impedance matrix. Modeling loads as an impedance is not an appropriate approach for DG planning studies. Besides, it is inconvenient because of the possibility that it may cause singularity in the matrix operations performed during the reduction[9].

In Dimo's and Zhukov's methods, all the busses to be eliminated are aggregated in a fictitious equipotential point. The connection between this point and the original system is formed by branches with impedances defined on the loads and the voltages connected to the buses to be eliminated. In Dimo's method, an impedance value determined by the sum of all the loads connected to eliminated buses and the sum of all the currents flowing to this created fictitious point, is connected to the fictitious point as a shunt impedance. In Zhukov's method, it is assumed that a current is injected as much as the value of the total load at the eliminated busses and the voltage of the fictitious point [7].

In a study given at [9], all of these methods have been tested on IEEE 118 bus and 14 bus test systems. In the study conducted, Dimo's method showed lower consistency at higher R/X ratio, while the consistency of Zhukov's method was influenced by changes in system loads. Dimo's method may not be suitable for DG planning studies when it is considered that these studies are carried out in distribution networks which has high R / X ratios. In addition, a DG unit capacity, which is planned to be connected to the reduced system obtained by Zhukov's method, may reduce the consistency of the results.

In the study, the results obtained from the equivalent system which is reduced by using WARD reduction method has been showed the highest coherence with original system. For this reason, it has been considered that WARD reduction method may be more appropriate to be used in this study for DG planning studies.

A. WARD reduction method

The Ward reduction method is applied on the nodal equations generated by using the system admittance matrix and the current and voltage values of the points in the system obtained by using any power flow analysis [10].

The main structure of the nodal equation system is;

$$I = YV \tag{1}$$

where Y is the admittance matrix, V and I are the voltage and current vectors, respectively. The rows in the equation system are reorganized as the rows above for retained busses and the rows below removed busses

$$\begin{bmatrix} I_{RET} \\ I_{\mathrm{Re}m} \end{bmatrix} = \begin{bmatrix} Y_{RETRET} & Y_{RETREM} \\ Y_{REMRET} & Y_{REMREM} \end{bmatrix} \begin{bmatrix} V_{RET} \\ V_{REM} \end{bmatrix} \tag{2}$$

where the index RET has been used for the retained busses, and the index REM has been used for the removed bars. The following expression is obtained when the lower-row is removed by gaussian elimination approach.

$$[I_{RED}] = [Y_{RED}] \times [V_{RET}] \tag{3}$$

$$[Y_{RED}] = [Y_{RETRET} - (Y_{RETREM} \times Y^{-1}{}_{REMREM}) \times Y_{REMRET}] \tag{4}$$

$$[I_{RED}] = [I_{RET} - (Y_{RETREM} \times Y^{-1}{}_{REMREM}) \times I_{REM}] \tag{5}$$

where RED index is used for noted the values belongs to reduced system.

III. Methods of the study

In this study, the power system is reduced to an equivalent with fewer busses by the WARD method, and the use of this equivalent system in DG planning has been investigated. A MATLAB code has been developed to obtain the reduced equivalent of the system to be investigated. In the generated MATLAB code, some points have been considered as different than original WARD reduction methodology. These points and their reasons to be considered are given below.

- Normally, the system loads are assumed to be constant current values [10]. However, since extreme voltage variations are not expected in distribution systems, the loads may be modelled as constant power values. Thus, without the need to analyze the power flow of the system, reductions can be made using power quantities connected to the busses instead of currents.
- Synchronous condenser, static capacitors, line charging capacitances in the system should be considered as separate reactive power sources according to original WARD methodology [10]. In this study, only the synchronous condensers have been taken into account as it has been remarked but the static capacitors and the line load capacitances are not included in the calculations with the consideration that the effects of static capacitors on the system may not be excessive and all lines are overhead lines.

- The turn ratios of the transformers in the system are taken into account over the ratios of their nominal voltages. Step settings are not included in the calculations.

The algorithm of the MATLAB code which is based on the above principles is given in Fig. 1.

In the generated algorithm, after reading the data of the original system, the user is asked which buses to be kept in the system. At this step, in order to ensure that a consistent reduced equivalent can be obtained, attention should be paid to the following points in determining the retained buses.

- All of the voltage controlled buses (swing bus, PV busses) in the system must be kept.
- Branches with transformers and bars connected to these branches
- Buses of interest (the buses considered to be connected DG units)

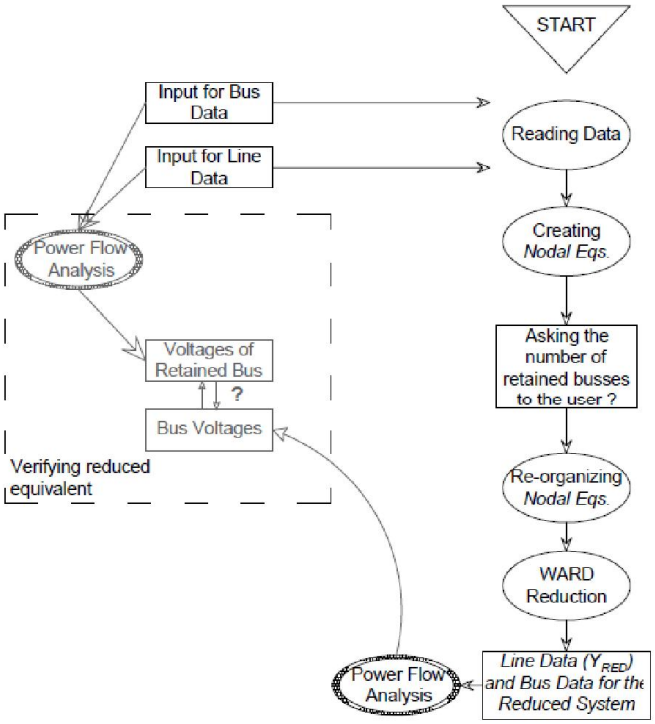


Figure 1 Flow chart of algorithm for WARD reduction

The node equations of the system are created for use in the WARD method, after the user specified the nodes selected according to the above-mentioned considerations. Instead of the currents in the node equations, load values connected to the buses are used. Thus, the loads in the eliminated buses are appropriately distributed over the remaining buses in the process of the WARD reduction method. Since all the buses containing the power sources are in the retained buses, after the reduction, the resources can be returned back to the buses they belong to.

Once the reduced equivalent system is obtained, the following algorithm is examined to ensure that this system is suitable for DG planning studies. DG unit is connected at the same bus of the both original and reduced system. The power flow analysis of both systems, for the cases with the DG unit, is performed. In practice, DG units are not allowed to be voltage controlled in power systems, so DG connected buses are considered as PQ bus in the power flow analysis. The results obtained for both systems are compared and the consistency of the reduced system for that study is examined. The flow chart of the following algorithm is given in Fig. 2.

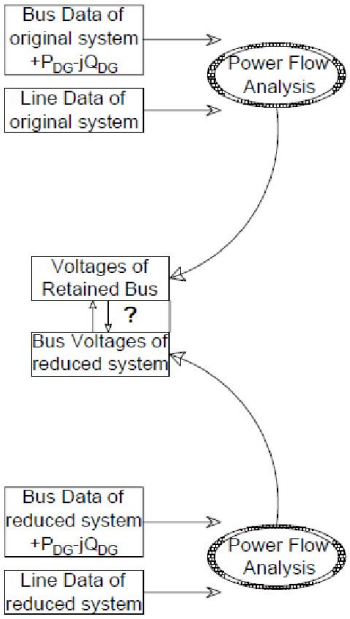


Figure 2 Flow chart of algorithm for verifying reduced system in DG planning

IV. Case Study

In this paper, a case study has been conducted with the IEEE 30 bus test system. The single line diagram of the original system is given in Fig. 3 and the data are provided by [14].

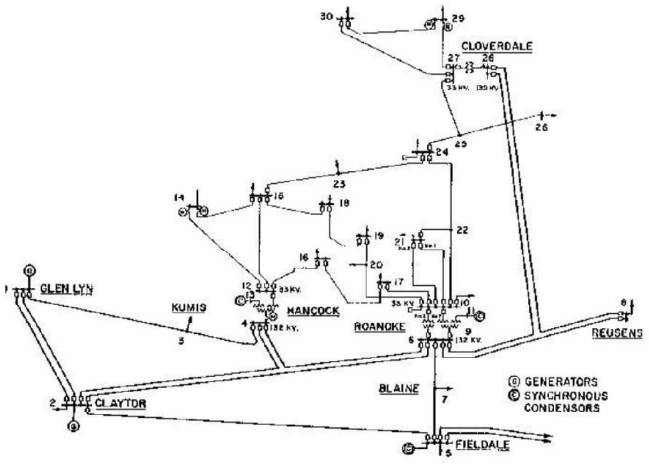


Figure 3 Single line diagram of 30 Bus test system

In the case study, it is assumed that a DG unit is connected to the test system from Bus 30. Under the guidance of the points mentioned in the previous section, the retained buses are identified and the test system has been reduced to 16-bus equivalent. The retained buses are given in the

Table 1: Numbers of the retained buses.

THE RETAINED BUSES
1, 2, 4, 5, 6, 8, 9, 10, 11, 12, 13, 14, 24, 27, 28, 30

The reduced system obtained by the developed MATLAB code is illustrated in ETAP environment as shown in Fig. 4.

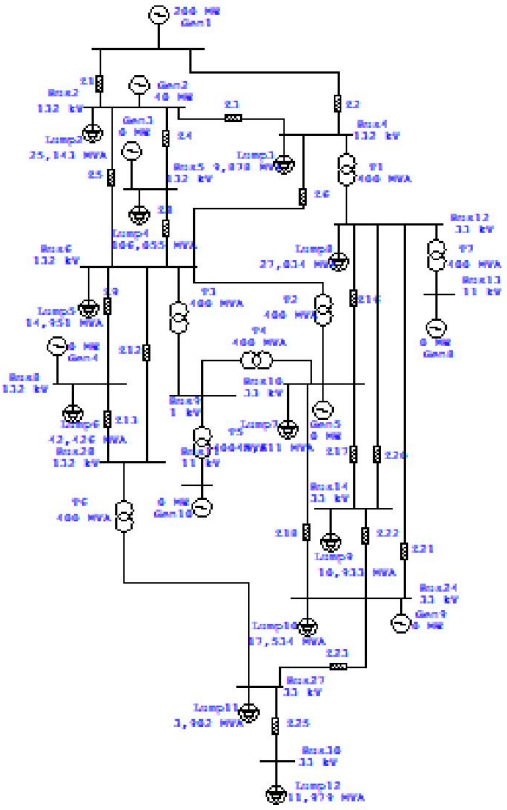


Figure 4 Single line diagram of the reduced equivalent

Power flow analysis for the original system and the obtained reduced system have been studied. The variation of the voltages obtained for the selected buses is given in Fig. 5.

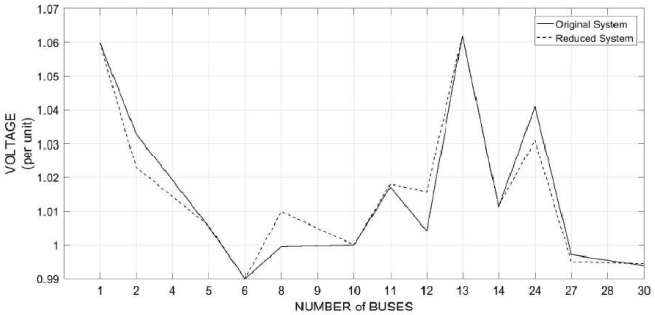


Figure 5 The voltages of the retained buses in the original system and the reduced system

After the verification of the reduced system, a 15 MVA DG unit is connected to Bus-30 with unit power factor. In both systems, power flow analyzes have been performed for the new situation and the obtained results for bus voltage have been compared in Fig. 6. As can be understood from the figure, the voltages in all the buses have increased and the results belongs to the reduced equivalent is closer to the results obtained from the original system, as in the previous case.

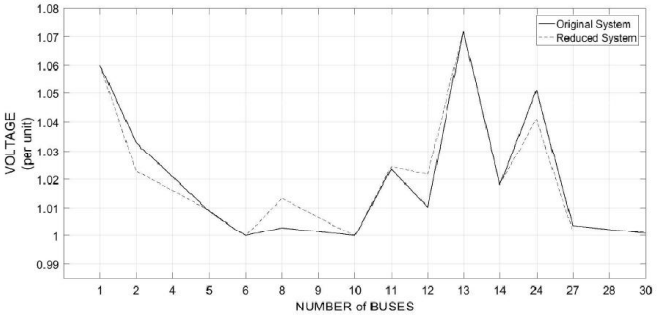


Figure 6 The voltages of the retained buses in the original system and the reduced system for DG integration case

V. CONCLUSION

In this study, the suitability of network reduction methods for DG planning studies have been investigated. The reduction methods in the literature have been evaluated in terms of their suitability for the study and the WARD method has been considered as the most suitable method among the alternatives. The WARD method has been modified by interpreting for DG planning studies. The modified method has been applied to the IEEE 30 bus test system over an algorithm developed in the MATLAB environment and the results have been compared.

The outcomes shows that the results obtained from the analyzes made with the reduced system are quite close to those of the original system. It has been proved by the study that by using these methods in DG planning studies, heavy and time-consuming computational processes can be eased, without a serious error in the results to be achieved.

REFERENCES

[1] T. Ackermann, G. Andersson, L. Söder, Distributed generation a definition, Electr. Power Syst. Res. 57 (2001) 195–204.

[2] R.C. Dugan, T.E. McDermott, Distributed Generation, IEEE Ind. Appl. Mag. (2002) 19–25.

[3] R. Rajaram, K. Sathish Kumar, N. Rajasekar, Power system reconfiguration in a radial distribution network for reducing losses and to improve voltage profile using modified plant growth simulation algorithm with Distributed Generation (DG), Energy Reports. 1 (2015) 116–122. doi:10.1016/j.egyr.2015.03.002.

[4] G. Pepermans, J. Driesen, D. Haeseldonckx, R. Belmans, W. D'haeseleer, Distributed generation: definition, benefits and issues, Energy Policy. 33 (2005) 787–798. doi:10.1016/j.enpol.2003.10.004.

[5] R.C. Dugan, T.E. McDermott, G.J. Ball, Planning for distributed generation, IEEE Ind. Appl. Mag. 7 (2001) 80–88. doi:10.1109/2943.911193.

[6] T. Gonen, Electrical Power Distribution Engineering, CRC Press, 2014.

[7] J. Machowski, J.W. Bialek, J.R. Bumby, Power System Dynamics: Stability and Control, 2008. doi:6.

[8] B. Stott, O. Alsaç, A. Monticelli, Studies on power system load flow equivalencing, IEEE Trans. Power Appar. Syst. PAS-99 (1980) 2301–2310. doi:10.1109/TPAS.1980.319798.

[9] S.M. Ashraf, B. Rathore, S. Chakrabarti, Performance analysis of static network reduction methods commonly used in power systems, 2014 Eighteenth Natl. POwer Syst. Conf. (2014) 1–6.

doi:10.1109/NPSC.2014.7103837.
[10] J.B. Ward, Equivalent Circuits for Power-Flow Studies, AIEE Trans. 68 (1949) 373–382. doi:10.1109/T-AIEE.1949.5059947.
[11] F. Dörfler, F. Bullo, Kron reduction of graphs with applications to electrical networks, IEEE Trans. Circuits Syst. I Regul. Pap. 60 (2013) 150–163. doi:10.1109/TCSI.2012.2215780.
[12] P. Dimo, Nodal analysis of power systems, International Scholarly Book Services, Inc.,Forest Grove, OR, 1975.
[13] L.A. Zhukov, Construction of Power System Electromechanical equivalents, Energy Transp. 2 (1965).
[14] Rich Christie, No Title, (n.d.). https://www2.ee.washington.edu/research/pstca/pf30/pg_tca30bus.htm (accessed October 20, 2017).

Determination of Traffic Intensity with Optimum Detection of Vehicle Count Using Virtual Zone

SEYITALI ILYAS[1] AND YAVUZ USER[2]

[1] Direct. of Trans.Plan. and Railway Sys., Antalya Metropolitan Municipality,Turkey, seyitaliant@gmail.com
[2]Akdeniz University, Electrical &Electronics Engineering, Antalya, Turkey, yuser@akdeniz.edu.tr

Abstract **- With the population increasing and population density becoming more increasing especially in cities, traffic density problems have begun to emerge. The traffic intensity causes environmental pollution due to increase of transportation time, excess consumption of fuel, together with emission of exhaust gas. Different methods are used to reduce the traffic intensity. In order to apply these methods, firstly traffic density must be determined. It is necessary to know how many vehicles pass through the requested zone. In other words, there should be done the counting of vehicle. In this study, a morphological image processing method was used for counting vehicles at the intersection. New type of virtual region has been created in the method of morphological image processing to count vehicles at the intersection without missing any of them. By this study, the contribution of the new type virtual region to the vehicle count will be determined. With the help of new type of virtual zone to be created will be shown whether or not the vehicles are counted with minimum distance from the intersection and the validity of this method will be shown in comparison with the latest methods in the literature.**

Keywords **- Intersection, Traffic intensity, Virtual zone, Morphological image processing.**

I. INTRODUCTION

THE traffic volume is the number of vehicles passing by a certain segment of the road. Traffic volume data is the data that is needed at determination of bus routes, traffic simulation programs, optimization signal durations of signalized intersections, geometric regulations of roads and intersections and several similar studies relating the subject of transportation[1].

There are manual and automated methods for measuring traffic volume. Manual methods are used for short term counts. The classification, counting and rotation is recorded by writing on paper or with the help of an electronic machinery[2].

Magnetic loop systems, video camera systems, air hose systems often used by highways are some of the automatic counting methods. In this study through a camera system, the number of vehicles passing through the designated new type of virtual area will be determined using morphological operations by using the program Matlab[3].

II. LITERATURE STUDIES

The studies executed in this system are based on image processing techniques. The image processing name (in German Bildbearbeitung) is a computer study that is oriented on changing the measured or recorded electronic (digital) image data in electronic environment (with the help of computers and software) in accordance with the purpose[4].

Yiyan WANG, Yuexian ZOU et al. have made a vehicle detection by using a camera at the intersectionon which they had examined. In image processing applications, cameras are usually focused on areas where there are traffic lights or on areas where it is approached to the intersection. In this study, a panoramic image was obtained using a single camera, and the focused area is the center of the intersection[5].

Najmeh Eghbal and Hossein Nurbakhsh proposed a new method based on image processing techniques for traffic volume measurement during signaling. In this new method (virtual loops method), the vehicles passing through the virtual area in front of the intersection are counted. The method is similar to the induction loop logic. Vehicle counting on the image was done with blob analysis[6].

In the study perfomed by Andrew H. S. Lai, George S. K. Fung et al. Has been modeled the template as a simple deformity instead of removing the vehicles from the traffic image. These templates are tool masks. Through this template, vehicle width, length, height are used as classification data. Vehicle classification was done using Maximum Likelihood classification algorithm. The biggest advantage is that it does not have infrastructure (construction) work as it is in induction loop detectors[7].

Peyman Babaei has made traffic management with video surveillance. For this management, the traffic flow must be determined. For this reason, vehicle counting, classification and tracking methods are used. In this study, a hybrid background model was used to learn the background model faster. Hybrid zones are selected from the vehicle routes. Mixture of Gaussian is used for background subtraction because it is the best result in complex situations. Vehicle classification was done with K-means clustering[8].

Ryan P. Avery, Yinhai Wang et al. have made studies based on length classification of vehicles using image processing algorithms based tools with images taken from the camera. The algorithm is implemented in C ++. The vehicle recognition process is based on the comparison of the RGB values of each pixel, and it is understood that the vehicle has arrived at a certain value (threshold 20), where the RGB values are the same but the vehicle does not pass.

It has been observed that at least 5 consecutive pixels in this system must be different from background values in order to prevent perception of unwanted distortions or hums as vehicles. In this classification, images such as human and bicycle are not calculated. Vehicle classification has begun processing immediately after vehicle recognition has started. The vehicles passing through the virtual lines placed on the strips are measured in length when they exceed the recording end limit[9].

III. CREATION OF VIRTUAL REGION

In Figure 1, the camera calibration is shown by making numerical measurements. The area of the image taken from Google Earth is plotted in AutoCAD program, proportional to the actual measurement, and is shown in figure 1. The area defined in Figure 1 shows the region in which we will process. The camera is oriented on the vehicles in this area.

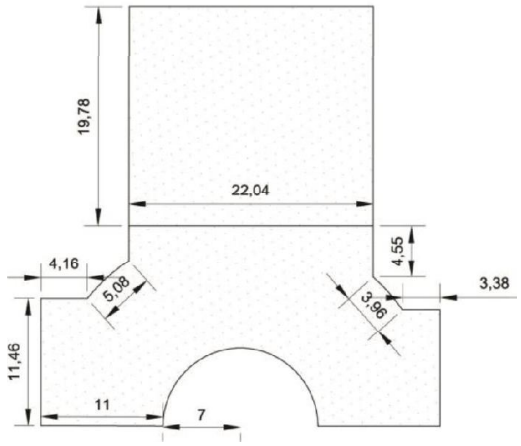


Figure 1: Image Processing Zone Component Measurements and Combinations

In Figure 2, the image processing areas are combined to show the general image and numerical measurements of the region to be processed of the image processing.

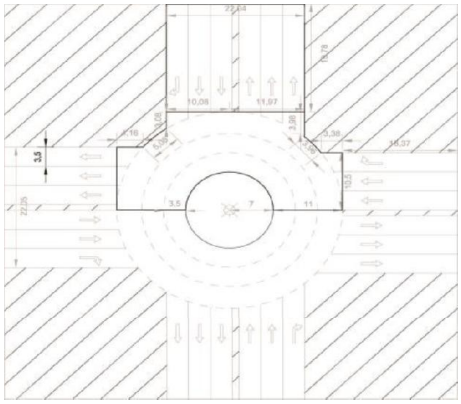


Figure 3. Region of Image Processing

IV. COUNTING STEPS IN PROGRAM MATLAB

The counting operations performed on images with the MATLAB program are described below step by step. After these transactions, it will be converted to the binary image file and the number of vehicles be calculate by using MATLAB program. Vehicle counting data will be obtained with image processing techniques.

An image is a matrix of numerically consisting of m * n pixels. Here m indicates the column number and n number indicates the row number. On figure 4 below, we will use this display as a matrix for this study, and Figure 3 shows an RGB format image.

The integers at the intersections of the rows and columns correspond to the gray level resolution of the pixel at that point. In figure 4 in matrix the values are m = 662, n = 1611.

$$f(m,n) = f(662,1611) = \begin{bmatrix} f(0,0) & f(0,1) & f(0,2) & f(0,3) & \cdots & f(0,1611) \\ f(1,0) & f(1,1) & f(1,2) & f(1,3) & \cdots & f(1,1611) \\ f(2,0) & f(2,1) & f(2,2) & f(2,3) & \cdots & f(2,1611) \\ f(3,0) & f(3,1) & f(3,2) & f(3,4) & \cdots & f(3,1611) \\ \vdots & \vdots & \vdots & \vdots & \ddots & \vdots \\ f(662,0) & f(662,1) & f(662,2) & f(662,3) & \cdots & f(662,1611) \end{bmatrix}$$

Figure 4: Representation as a matrix of digitized images



Figure 5. Image in RGB Format

a. Gray Level Resolution

The total number of pixels in an image can be defined as the resolution. The resolution increases and the sharpness in the image increases. The color variety in an image depends on the color depth or bite per pixel. Mathematically gray level resolution and bit per pixel equations are as follows.

$$L = 2^k \quad (1)$$

L shows the gray level number here. k is the bit per pixel.

In the Figure 5, k = 24, L = 2 ^ 24, L = 16777216. This value means that the gray level resolution is 16777216, which means there are 16777216 different color tones[10].

b. Conversion to gray level

The image in Figure 5 will be converted to binary (binary) image. For this, RGB image will be converted to gray level first.



Figure 6: Gray Level Image

The colors are in different wave lengths, and a 'Gray Level' is set for each pixel with the following formula, taking averages at different ratios to obtain a more apparent image[11].

$$Gray\ Level = (P(m,n).\mathrm{Re}d * 0{,}299 + p(m,n).Green * 0{,}587 + P(m,n).Blue * 0{,}114)/3 \quad (2)$$

c. Convertion to Binary Mode

The image is transformed into binary mode by rotating it according to the threshold value determined using the Otsu method. The colors below the threshold value are converted to black and white colors at the top. The images have different threshold values depending on the color distributions. If the threshold value is set too large, the image will be white, if the threshold value is set too small, the majority of the pixels will be black. Threshold values can be assigned by trial, but changes in the image occur and the automatic threshold value must be available. The average of the squares of the average value distance of the pixels in the image is calculated by the following formula and is called the variance.

$$\sigma^2 = \sum_{i=0}^{t-1} (x-\mu)^2 P\{x\} \quad (3)$$

X is the grey level value, P (x) is the ratio of the gray level value to the number of pixels in the image. μ is gray level average.

$$\sigma^2 = \sigma^2 w(t) + \sigma^2 b(t) \quad (4)$$

$\sigma^2 w(t)$ is the variance in pixels, $\sigma^2 b(t)$ is the variance between the pixels.

$$\sigma^2 b(t) = \frac{[\mu(t)\mu w(t)]^2}{w(t)[1-w(t)]} \quad (5)$$

$$w(t) = \sum_{i=0}^{t-1} P\{x\} \quad (6)$$

$$\mu(t) = \sum_{i=0}^{t-1} xP\{x\} \quad (7)$$

Each gray level value is selected as the threshold value t is calculated by the formulas below $w(t)$ and $\mu(t)$ and indicating instead of 4th equation the $\sigma^2 b(t)$ value is obtained. In case if the $\sigma^2 b(t)$ is calculated less than the value that has been calculated previously, the threshold value t making the $\sigma^2 b(t)$ the highst will be obtained[12,13].

Obtained image will have unwanted distortions or hums. In order to get rid of them, etching and expansion processes will be applied sequentially from MIKGY (morphological operations). With the etching process, the filter is routed on the image and the pixel value of the image under the center pixel is checked. If the pixel value is 1, those pixels under the filter are examined. If any of these pixels are 0, all the pixels under the filter are 0 thereby this operation is applied to the whole image. The unwanted distortions will disappear with the etching process, but the space between the vehicles will increase and the vehicles will shrink in size. By this way will be different from their actual dimensions[14]. For this reason we do the expansion process. The filter will be routed on the image as if it were in the process of etching in the expansion process and will be subject to 'logical or' operation when the pixel below it is 1. Thus, the vehicles will become close to each other and their shape will swell. Vehicles such as motorcycles and bicycles will disappear from this view, and the counting process will be more accurate[15].



Figure 7: Binary Mode Image

It is calculated that the number of vehicles leaving the intersection at Burhanettin Onat Street in the direction of Burhanettin Onat Caddesi is 1,843 vehicles / hour in the morning peak hour of the number of vehicles arriving from the roundabout on the Burhanettin Onat Street branch road of the hourly counting image processing area.

V. CONCLUSION

In this study, on one of the important intersections of Antalya- at the Sampi intersection was implemented the new type virtual region vehicle counting obtained by image processing techniques. The images taken from the camera are first converted to binary mode according to the gray level of the RGB format and the threshold value determined by the Otsu method. By applying etching and expansion using

morphological processes, the images were purified from distortions and counting was performed.

The new image processing area determined in this study counts the vehicles passing through the intersection store and calculates the incoming and outgoing vehicles at the intersection. This counting data can be used in traffic simulation programs and informs us of the number of vehicles that pass from the relevant car to the next intersection, thus providing the vehicle information to be used in green wave applications between the two intersections. Due to the camera angle, vehicles located beside large vehicles such as buses may cause lack of calculation in operation. The images taken with a more vertical camera from the center of the intersection can reduce the error margin. According to studies done in the literature, the image processing region can be processed more quickly because it is taken more regionally in this study.

ACKNOWLEDGMENT

The research has been supported by the Research Project Department of Akdeniz University, Antalya, Turkey.

REFERENCES

[1] Park, Byungkyu, Carroll Messer, and Thomas Urbanik II. "Short-term freeway traffic volume forecasting using radial basis function neural network." Transportation Research Record: Journal of the Transportation Research Board 1651 (1998): 39-47.

[2] Guıde, Instructıon. "Manual Classıfied Traffıc Counts." (2001).

[3] Müdürlüğü, Karayolları Genel, Trafik Güvenliği Dairesi Başkanlığı ve Ulaşım Etütleri Şubesi Müdürlüğü. "Trafik ve Ulaşım Bilgileri: Otoyollar ve Devlet Yollarının Trafik Dilimlerine Göre Yıllık Ortalama Günlük Trafik Değerleri ve Ulaşım Bilgileri." Strateji Geliştirme Daire Başkanlığı Ulaşım Maliyetleri ve Verimlilik Şubesi Müdürlüğü Mayıs (2011).

[4] https://tr.wikipedia.org/wiki/G%C3%B6r%C3%BCnt%C3%BC_i%C5%9Fleme

[5] Wang, Yiyan, et al. "Video image vehicle detection system for signaled traffic intersection." Hybrid Intelligent Systems, 2009. HIS'09. Ninth International Conference on. Vol. 1. IEEE, 2009.

[6] Eghbal, Najmeh, and Hossein Nurbakhsh. "Measurement of some traffic signal parameters via un-calibrated video camera." Electrical Engineering (ICEE), 2011 19th Iranian Conference on. IEEE, 2011.

[7] Lai, Andrew HS, George SK Fung, and Nelson HC Yung. "Vehicle type classification from visual-based dimension estimation." Intelligent Transportation Systems, 2001. Proceedings. 2001 IEEE. IEEE, 2001.

[8] Babaei, Peyman. "Vehicles tracking and classification using traffic zones in a hybrid scheme for intersection traffic management by smart cameras." Signal and Image Processing (ICSIP), 2010 International Conference on. IEEE, 2010.

[9] Avery, Ryan P., Yinhai Wang, and G. Scott Rutherford. "Length-based vehicle classification using images from uncalibrated video cameras." Intelligent Transportation Systems, 2004. Proceedings. The 7th International IEEE Conference on. IEEE, 2004.

[10] Gonzalez, R.C. and Woods, R.E. Digital Image Processing., Prentice Hall. (1992).

[11] Boztoprak, H., Çağlar, M.F., Merdan, M., Alternatif Morfolojik Bir Yöntemle Plaka Yerini Saptama., Biyomedikal Mühendisliği Ulusal Kongresi, Eskişehir. (2007)

[12] Kızılkaya, Aydın, 'Sayısal Görüntü İşleme.'(2006)

[13] Otsu, Nobuyuki. "A threshold selection method from gray-level histograms." IEEE transactions on systems, man, and cybernetics9.1 (1979): 62-66.

[14] Çevik, Kerim Kürşat, and Abdülkadir Çakı. "Görüntü İşleme Yöntemleriyle Araç Plakalarının Tanınarak Kapı Kontrolünün Gerçekleştirilmesi." Afyon Kocatepe Üniversitesi Fen Ve Mühendislik Bilimleri Dergisi 10.1 (2010): 31-38.

Improving Power Factor with Implementation of PFC-Boost Circuit Design

MUHSIN FATIH SEKER[1] and YAVUZ USER[2]

[1]Akdeniz University, Electrical &Electronics Engineering , Antalya, Turkey, *muhsinfatihseker@gmail.com*
[2]Akdeniz University, Electrical &Electronics Engineering, Antalya, Turkey, yuser@akdeniz.edu.tr

Abstract **- Nowadays, In spite of limited production of electrical resources is increasing excessively the consumption amount of electrical energy. For this reason ,we should take more advantage of electrical energy and we should use more productive . Especially power factor will be negatively affected at network when the number of devices are using DC -inverter Technology and using semiconductors will increase. In this study, PFC -Boost circuit has been designed which is controlled by microcontrollers and power factor is obtained by digital PI loop. PFC -Boost circuit and digital PI design ,output current and voltage of the circuit and FFT analysis graphics are presented comparatively and the change in harmonic level is shown .**

Keywords **- PFC-Boost circuit, PI control, Harmonic, Inverter.**

I. INTRODUCTION

THE Power factor is an indication of effiency of using electricity. Low power factor devices causes harmonic formation in power line. Highest power factor value is one for every device powered by AC source but practically it's not possible. That is why every device powered by AC source causes harmonics. Mainly formation harmonics by transformers, engines and generators, arc furcaces, semiconductors, switching power supplies, electric ballasts, welding machines, electric transport system, computers etc. Harmonics in the power lines causes corruption of waveforms, overheating in the synchronous and asynchronous engines because of oscillation, low efficiency in UPS's, vibration in the lighting elements and monitors, extremely high current and voltage because of resonance, interferences in video calls and voice calls, overload in basic frequency designed comparation systems because of capasitor's low capacitive reactance in harmonics frequency, overcurrent in the power lines, perforation in dielectric materials malfunction.
For electricity energy and efficiency harmonic limits allowed for AC network withdrawal are determined by national and international standards. Some of these standards;

- EN 50 006 "Limitation of disruptive effects of electrical appliances equipped with domestic appliances and the like in the power supply circuit" European standard prepared by Comit Europen de Normalisation Electrotechnique.
- IEC Norm 555-3.
- VDE 0838 western standard for electrical household appliances, Standard for VDE converters and VDE 0712 Fluorescent lamp ballastsIEEE519.
- IEC61000-3

These are energy quality standartds. EN 61000-3-2 specfied by the International Electrotechnical Commision (IEC). In Turkey these standards apply as TS EN 61000-3-2. According to this standards devices classified as A,B,C,D. It is as given Table 1.

Table 1. Harmonic Limits According to TS EN 61000-3-2 Standard

Harmonics	A class (A)	B class (A)	C class (I(n)/I1)*100	D class (mA/W)
Single Harmonics				
3	2.30	3.45	30	3.4
5	1.13	1.71	10	1.9
7	0.77	1.155	7	1.0
9	0.40	0.60	5	0.5
11	0.33	0.495	3	0.35
13	0.21	0.315	3	3.85/n
15<=n<=39	0.15*15/n	0.225*15/n	3	3.85/n
Double Harmonics				
2	1.08	1.62	2	-
4	0.43	0.645	-	-
6	0.30	0.45	-	-
8<=n<=40	0.23*8/n	0.345*8/n	-	-
*** The "n" expression indicates the ninth harmonic.**				

II. CLASSIC FULL WAVE RECTIFIERS CIRCUIT

In the figure-1 dc network connected load fully rectified by classical full wave rectification circuit. If we model as 311DC voltage and 285 ohm equivalent resistance, our load is about 340 watts[3].

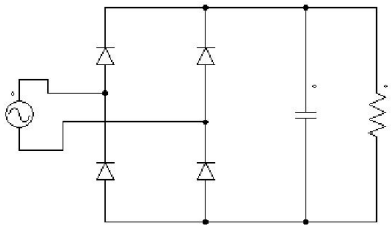


Figure 1: Classic full-wave rectifier circuit

In classical full wave rectification, current graphic from the network is shown in figure-2 and figure-3.

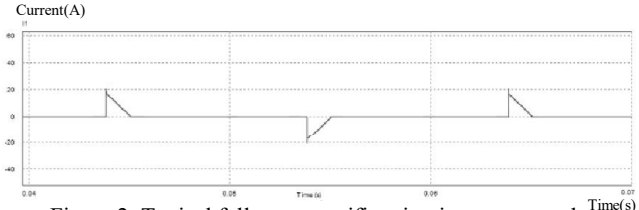


Figure 2: Typical full-wave rectifier circuit current graph

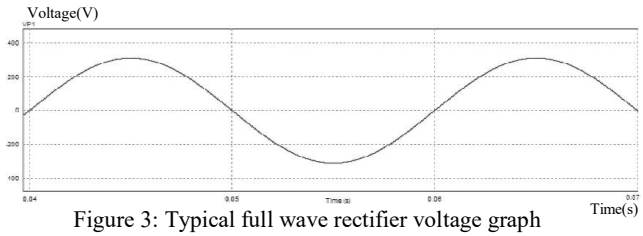


Figure 3: Typical full wave rectifier voltage graph

If FFT analysis performed on the classical full wave rectification is output, result is shown in figure 4.

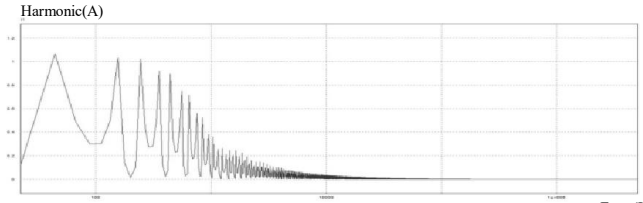


Figure 4: Typical full-wave rectifier circuit input current FFT

In figure 4 power factor calculated as 37%. This percentage cause harmonic formation in network and some problems due to harmonic formation. This is unfavorable situation for us. In this Project, attaching PFC-Boost circuit between network and present system has foreseen.

III. PFC-BOOST CIRCUIT DESIGN AND POWER FACTOR BOOST

In classic PFC-Boost main schematics show in figure 5. This figure shows our target network current.

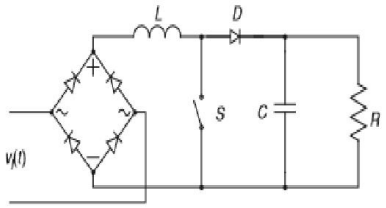


Figure 5: PFC-Boost circuit diagram

Several control paths can be followed to get same sinusoidal phase in current drawn from the network. Some of those;

- If coil current reach to requested current S switch goes into cut. With stable frequented counter S switch reactivates.
- Predetermined coil current's ripple value determines and by setting switch's position we make sure current's between (requested coil current) + 0.5*(ripple value) and (requested coil current) - 0.5*(ripple value)
- Until coil current reaches twice the requested coil current switch continues to transmission then it cuts when coil current is zero switch reactivates.

In this study an example will be taken from the output voltage with the voltage divides for the feedback control flow and this example will be compared with the reference voltage. In this way error rate will be found in PI regulator. An example will be taken from fully rectified sinusoidal by voltage divider. This example and error rate will be multiplicated. Result will show requested coil current. If current trough coil is less than requested current key will be active, if it is more switch will cut-off and control will be provided by microcontroller. Necessary way for control has shown in figure 6.

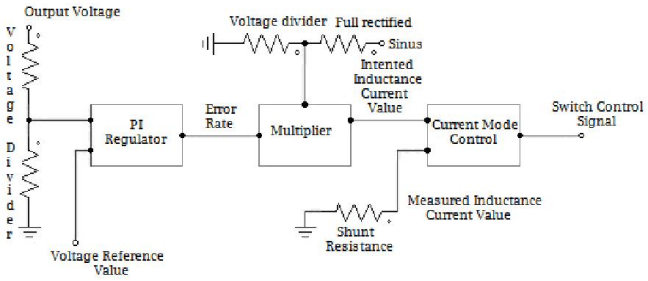


Figure 6: Schematic Representation of Control Performed

When PI regulators is writing with microcontroller for integral control

$$\int_0^t e(t)dt = T_s \sum_0^n e(n) \tag{1}$$

Microcontroller's measuring frequency "n" is measurement sequene. Code for microcontroller;

$$Error = Measured\ value - reference\ value; p = error * K_p \tag{2}$$

$$i = i + error * K_p; p_i = p + i \tag{3}$$

Coefficients must be considered. The PSIM circuit of the study is expressed by the combination of the DC/DC amplifier converter between the fully rectified state of the sinusoidal wave guide and the load as shown in figure 7.

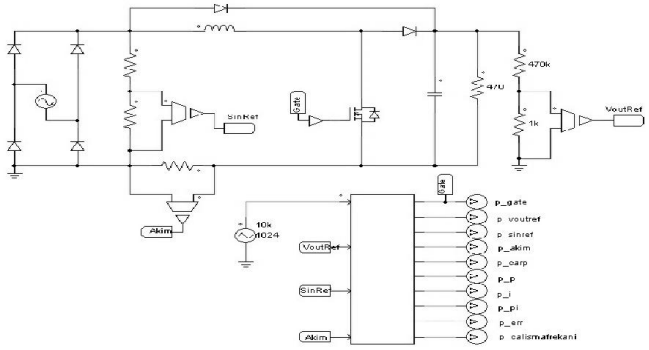


Figure 7: PFC-Boost circuit PSIM circuit diagram

Feedback was with the microcontroller studies are done on PSIM, the microcontroller was given a triangle wave to serve as a timer. Output values fort he controlled variable values of the microcontroller are read.

The fluctuation in the output voltage was found with the following equations;

$$P_{input}(t) = V_{input,\max}|\sin wt| * I_{input,\max}|\sin wt| = V_{input,rms}I_{input,rms} - V_{input,rms}I_{input,rms}\cos 2wt \quad (4)$$

expressed by this equation.If the output voltage is assumed as constant DC;

$$P_{output} = V_{output} * I_{output} \quad (5)$$

Diode's current value in figure 5,

$$I_d = I_{output} * I_C \quad (6)$$

If topology considered ideal can be considered as P_{input}=P_{output} in this situation,

$$I_d = I_{output} + I_C = \frac{V_{input,rms}I_{input,rms}}{V_{output}} - \frac{V_{input,rms}I_{input,rms}\cos 2wt}{V_{output}} \quad (7)$$

and from this equation. Id average value;

$$I_{d,average} = I_{output} = \frac{V_{input,rms}I_{input,rms}}{V_{output}} \quad (8)$$

Capacitor current has been found as;

$$I_C = -\frac{V_{input,rms}I_{input,rms}\cos 2wt}{V_{output}} = -I_d\cos 2wt \quad (9)$$

Output voltage oscillation value. it has been found as;

$$V_{output,ripple} = \frac{1}{C}\int I_C dt = -\frac{I_d}{C*2*w}\sin 2wt \quad (10)$$

As understand from here output voltage will fluctuate twice as much as the input frequency.

If the input and output voltage is assumed to be constant to easily analyze the circuit from;

$$V_L = L * \frac{di}{dt} = V_{input} \quad (11)$$

$$dt = \frac{L * di}{dt} \quad (12)$$

Here "dt" is equal to the duty cycle which is the rate at which the switch is active, multiplied by the duration of the period. That gives us "ton" rate that the switch is the transmission. If we make circuit analysis for the duration of "toff " when switch is off If we make circuit analysis for the duration of " " when switch is off.

$$V_L = L * \frac{di}{dt} = V_{input} - V_{output} \quad (13)$$

$$Duty\ cycle * (1-T) = t_{off} = \frac{L * di}{V_{input} - V_{output}} \quad (14)$$

In this equations "di" can be as the current chang in coil. Switching frequeny calculated as;

$$Switching\ frequency = f_{sw} = \frac{1}{t_{on} + t_{off}} = \frac{(V_{input} - V_{output}) * V_{input}}{di * L * V_{output}} \quad (15)$$

When the 11 no. equation reconsider from

$$L = V_{input} * \frac{dt}{di} = V_{input} * \frac{Duty\,cycle}{currentchancing * frequency} \quad (16)$$

Equation appropriate coil value can be found. If we apply the PFC-Boost circuit, the 340Watt output power, which we evaluated in the first case with respect to the conventional full-wave rectifier circuit, will be as shown in Figure 8 with the output voltage increased by 400DC with DC/DC amplifier conversion and the output load with the equivalent resistance of 470 ohms.

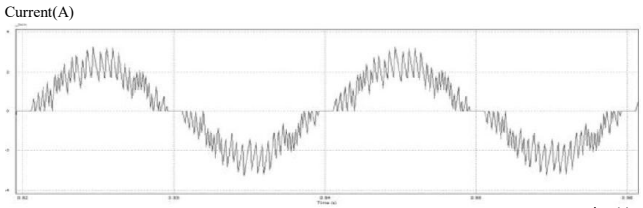


Figure 8: PFC-Boost Input Current

The FFT analysis of the current in Figure 8 will be as in Figure 9.

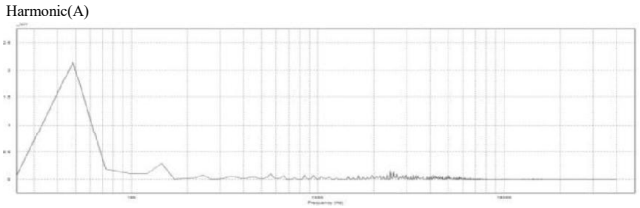


Figure 9: PFC-Boost Input Current FFT Analysis

As shown in Figure 9, the new power factor is calculated as 95% and high harmonic formation will be avoided.

The output voltage of the power factor booster circuit is 1.75% voltage fluctuation between 403V and 396V as shown in Figure 10.

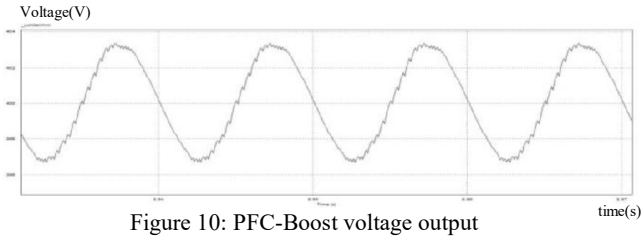


Figure 10: PFC-Boost voltage output

The switching frequency is shown in Figure 11. The switching frequency drops when the input maximum value is taken and decreases the switching losses.

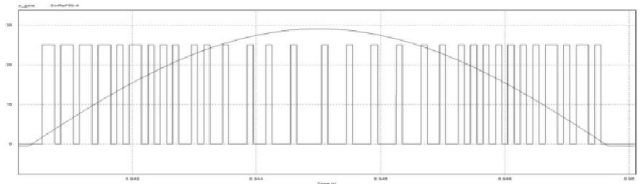


Figure 11 - Comparison of PFC-Boost gate signal and input voltage

IV. RESULTS

A low-power factor harmonic system is adapted to high power factor and harmonic limits through a microcontroller. Power factor is scaled up from %37 to 95% and high harmonic signals are eliminated. Output voltage fluctuations are reduced to %1.75.

REFERENCES

[1] [1] C. P. Basso, Switch-Mode Power Supplies Spice Simulations and Practical Designs (1st Edition), 2008
[2] [2] N. Mohan, T.M.Udeland, W.P.Robbins, Power Electronics: Converters, Applications, and Design (3rd Edition)
[3] [3] M.H. Rashid, Power Electronics: Circuits, Devices & Applications (4th Edition).
[4] [4] H. Bodur, Güç Elektroniğinde Güç Faktörü Düzeltme Yöntemleri (Yüksek lisans Ders Notları)
[5] [5] D.W.Hart, Power Electronics
[6] [6] C. BASSO, "Write your own generic SPICE Power Supplies controller models, part I and II", PCIM April/May 97
[7] [7] PFC Boost Converter Desing Guide Application Note. İnfeneon, www.infineon.com
[8] [8] CCM PFC Booost Converter Desing, İnfineon Desing Note DN 2013-01 V1.0 January/2013, www.infineon.com
[9] [9] 100-W Universal Line Input PFC Boost Converter Using the UCC28051, Texas Instruments 2004

Design and Application of FPGA Based Modbus Gateway Module

Ş. AKKAYA[1], O. AKBATI[2] and A. F. ERGENÇ[3]

[1] Istanbul Technical University, Istanbul/Turkey, sakkaya@itu.edu.tr
[2] Yildiz Technical University, Istanbul/Turkey, oakbati@yildiz.edu.tr
[3] Istanbul Technical University, Istanbul/Turkey, ali.ergenc@itu.edu.tr

***Abstract* - Industrial communication protocols are standard languages that allow data exchange among industrial devices and systems. Nowadays, the most used industrial protocols are listed as Fieldbus, Profibus, Modbus, Canbus, Devicenet and Controlnet. But, electronic devices still widely use Modbus protocols. The Modbus protocol is divided into sub-protocols that allow communication via the serial line (Modbus RTU and Modbus ASCII) and Ethernet (Modbus TCP). Despite the diversity of industrial protocols, devices need to use a gateway to communicate with the same industrial protocol or perform protocol conversion in order to be able to exchange data between each other. In this study, FPGA based Modbus gateway device which performs communication between Modbus TCP and RTU is designed. The gateway device is also configurable through Modbus TCP. The designed device is tested with the application platform and the results are given.**

***Keywords* – FPGA, Modbus TCP, Modbus RTU, Gateway**

I. INTRODUCTION

MODBUS, which is one of the most widely used industrial communication protocols today, was developed in the 1970's and new versions were created over time. Some of the biggest reasons for its widespread use are that it is easy, fast and open-source. Modbus was originally designed as a serial communication protocol. The Modbus serial communication protocol is divided into two basic sub-protocols, Modbus RTU and Modbus ASCII [1, 2]. With the development and widespread use of Ethernet technology, it became necessary to adapt the Modbus protocol to the Ethernet network and the Modbus TCP protocol was developed [3]. This means that devices on the serial line using the Modbus RTU protocol have to use a number of protocol converting devices to communicate with the devices on the Ethernet network using the Modbus TCP protocol. These converting devices are generally referred to gateways. A gateway is an interface that performs protocol conversion between networks that use different industrial communication protocols.

In the literature, it is observed that different designs were implemented on different micro controllers for the protocol conversion process. In order to ensure communication between Modbus and FlexRay protocols, an application specific controller is designed using the XGATE processors with 16-bit RISC architecture [4]. In another study, a gateway was designed using the ARM7-based LPC2290 microcontroller and the Micro C/OS real-time operating system to control data exchange between Modbus TCP and Ethernet for Plant Automation (EPA) industrial Ethernet protocols. It provides bidirectional data flow between gateway EPA and Modbus protocols. [5]. A gateway was designed using the ARM Cortex M3 and the LM3S8962 microcontroller with an integrated Ethernet controller to transmit and link different RS485 networks via Ethernet without changing the network structure and configuration [6]. Another gateway, designed using the Free-Modbus library created for the PIC32 microcontroller and embedded systems, aims to perform data exchange between different Modbus networks [7]. The gateway is designed using the STM32F007ZGT6 micro controller and various interfaces, which support Profibus, Devicenet, Ethernet / IP and Modbus RTU protocols commonly used in industrial systems. Modbus RTU is connected to UART interface while COMX interfaces is used for other protocols [8]. In another study, a gateway was designed for data exchange between Profibus-DP and Modbus RTU protocols for an industrial system. 32-bit ARM based STM32F103V microcontroller and peripheral modules are used for gateway design [9].

In this study, unlike microprocessor based gateway designs in the literature, FPGAs are used to perform protocol conversion between Modbus RTU and Modbus TCP protocols. Using hardware design features of FPGA, various hardware structures were created and at the same time an embedded processor and necessary peripheral units were created in it. The designed gateway can query both RTU and TCP protocols, thus it reduces the connection load of the master device. In addition, the gateway acts as a separate Modbus node, and all settings that related to the gateway are permanently stored in this node recorder. The master device can configure the gateway device. This configuration includes the IP addresses of the TCP nodes, the address and the baud rate of the RTU nodes to which the gateway is connected.

This paper is organized as follows: in Section II, the Modbus protocol structure is described. In Section III, the system components are given. The software and application are presented in Section IV. Finally, in Section V results are illustrated.

II. MODBUS PROTOCOL STRUCTURE

OSI (Open system Interconnection) is a seven-layer reference model that defines network communication used by

the devices. Modbus protocol is an application layer messaging protocol that is positioned at level 7 of the OSI model that provides client/server communication between devices connected on different types of buses or networks [1].

Todays, the most used Modbus protocols are Modbus RTU that uses serial communication and Modbus TCP that uses the Ethernet line. Both Modbus protocols define a simple Protocol Data Unit (PDU) independent of the underlying communication layers. The mapping of Modbus protocol on specific buses or networks can introduce some additional fields on the Application Data Unit (ADU) [3]. The additional fields are different in each Modbus protocols. The general Modbus data structure is shown in Fig. 1.

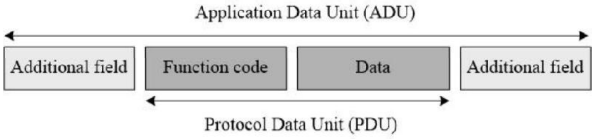


Figure 1: Modbus data structure format.

Here, the protocol data unit that is common both Modbus protocols that contain two parts. The function code indicates to the server what kind of action to perform and the data field contains request and response parameters.

A. *Modbus RTU*

Modbus RTU is an open, serial type protocol supported from master/slave architecture. A master/slave type system has one master node that issues explicit commands to one of the slave nodes and processes responses. Slave nodes do not transmit data without a request from the master node, and do not communicates with the other slaves. Modbus protocol request format is established by the master node that contains device address, function code, all data and error detection part, respectively. And, also the slave node establishes the Modbus protocol response format that includes confirm action part, any data to be returned and error detection part. If an error occurs during communication, the slave node will establish an error message and sent it as a response. According to OSI reference network model, Modbus RTU protocol defines physical layer, data link layer and application layer. At the physical layer, the protocol can be used EIA/TIA-485 (RS485) or EIA/TIA-232 (RS232) communication standards. These standards were established when Modbus was first developed. RS232 is for point to point, while RS485 is multi-drop applications. In Fig. 2, the protocol structure and in Fig. 3 the layers of Modbus RTU protocols in OSI reference model are given.

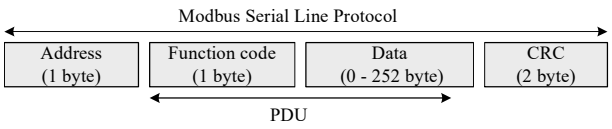


Figure 2: Modbus RTU protocol structure

Layer	ISO/OSI Model		
7	Application Layer	Modbus Application Protocol	Modbus Application Layer Client / Server
6	Presentation Layer	Empty	
5	Session Layer	Empty	
4	Transport Layer	Empty	
3	Network Layer	Empty	
2	Data Link Layer	Modbus Serial Line Protocol	Modbus Master/Slave
1	Physical Layer	EIA/TIA-485 (EIA/TIA-232)	EIA/TIA-485

Figure 3: Modbus RTU protocol OSI layers [2]

On Modbus RTU protocol, the address field contains slave address. The individual slave nodes are assigned address in the range of 1 to 247. A master addresses a slave by placing the slave address in the address field of the message. When the slave returns its response, it places its own address field to let the master know which slave is responding. The error-checking field is based on Cyclical Redundancy Checking (CRC) method that performed on the message contents. It contains a 16-bit value implemented as two 8-bit bytes.

B. *Modbus TCP*

The Modbus TCP protocol is basically the implementation of the Modbus RTU protocol via the TCP interface over Ethernet. The protocol provides a client/server communication between nodes that connected on an Ethernet TCP/IP network. Here, TCP and IP refer to Transmission Control Protocol and Internet Protocol, respectively. The primarily function of TCP is to ensure that all the packets of data are received correctly, while IP makes sure that messages are correctly addressed and routed. The TCP/IP combination is merely a transport protocol, and does not define what the data means or how the data is to be interpreted. In general, Modbus TCP protocol uses TCP/IP and Ethernet to carry of Modbus message between the devices connected to the network. That is, Modbus TCP/IP combines an Ethernet physical network with networking standard TCP/IP and a standard Modbus protocol data unit [12].

When the OSI model is considered for Modbus TCP, the physical layer and the data link layer operate together and named as network transport layer. The network transport layer is the bottom layer of the four-layer Modbus TCP-OCI model and describe how to data send to the physical network by the help of Ethernet physical layer. The data bits are transmitted by converting electrical or optic signals via RJ-45 connection socket and the CAT5 or CAT6 Ethernet cable. The network layer and the transport layer are used IP, ARP and TCP, respectively. Finally, at the top three layers (session layer, transportation layer and application layer) define the Modbus application layer. Fig. 4, shows us the Modbus TCP protocols in terms of the reference OSI model and Figure 5 shows the protocol structure.

Layer	ISO/OSI Model	
7	Application Layer	Modbus Application Protocol
6	Presentation Layer	
5	Session Layer	
4	Transport Layer	TCP
3	Network Layer	IP, ARP
2	Data Link Layer	Ethernet, MAC
1	Physical Layer	Ehternet Physical Layer

Figure 4: Modbus TCP protocol OSI layers

Ethernet Header (14 byte)	IP Header (20 byte)	TCP Header (20 byte)	Embedded message	FCS

Figure 5: Modbus TCP protocol structure

Since TCP is a connection-oriented protocol, it must establish a connection before transferring data. For the communication between devices, Modbus TCP connection require source address, destination address and connection ID. The master (client) device establishes a connection with the slave (server) devices. The server waits for an incoming connection from the client. Once a connection is established, the server then respond to the queries from the client until the client closes the connection [13]. The client and servers listen and receive Modbus data via port 502. In practice, Modbus TCP embeds a standard Modbus data frame into a TCP frame, without the Modbus checksum, as shown in the diagram given Fig. 6.

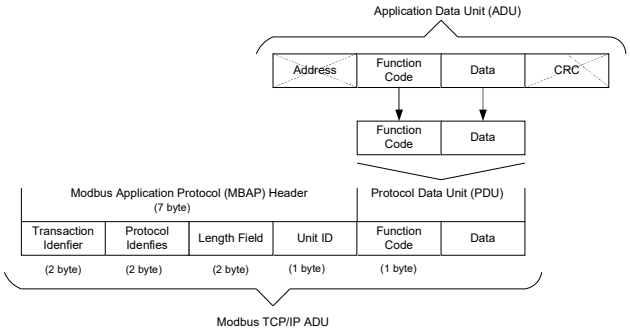


Figure 6: Modbus TCP protocol Application Data Unit [12]

Modbus TCP application data unit contains a MBAP header beside the traditional protocol data unit. MBAP header consist of 2-byte transaction identifier, 2-byte protocol identifier, 2-byte length and 1-byte unit identifier. The transaction identifier field is used for transaction pairing when multiple messages are sent along the same TCP connection by a client without waiting for a prior response. The protocol identifier field is always zero for Modbus communication. The length field is a byte count of the remaining fields and includes the unit identifier byte, function code byte and the data fields. The unit identifier is used to identify a remote server located on a non TCP/IP network [14].

III. System Components

In this section, the hardware of the designed gateway and the modules on the experimental setup are introduced. The basic elements of the system are FPGA, Wiznet TCP connection module, PLC, Modbus RTU and TCP input/output modules, network switch and RS-485 converter circuit.

A. FPGA

Field Programmable Gate Array (FPGA) is an integrated circuit that contains a brunch of logic gates and input/output circuitry. It has some important characteristics; highly integrated, fast computer speed, could be parallel and online programmed. In this study, a protocol gateway is designed to convert the Modbus RTU and TCP protocols to each other on FPGA. The components of the board are shown in Fig. 7.

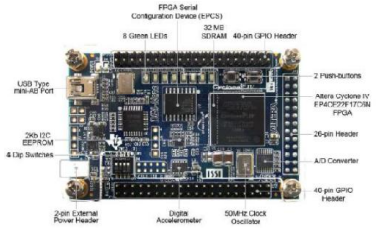


Figure 7: DE0-Nano FPGA Board [10]

As a program development tool, Altera's Quartus II programming software has been preferred. To design the gateway, the FPGA is used both the hardware design feature as well as the processor embedding feature. The VHDL language is used for the hardware design. A 32-bit SPI module is designed to communicate with the Wiznet module on the DE0 Nano and also I2C module is designed to communicate with the DE0 Nano and EEPROM module that is on it. The software processor is designed by using Qsys System Integration Tool. The C language was used for the program embedded in the processor and the Nios II Software Build Tool for Eclipse was used for Eclipse in the Quartus II platform.

B. Wiznet TCP connection Module

WizNet module is a kind of hardware TCP/IP Ethernet controller that provides internet connection to embedded systems. It contains a TCP/IP stack, MAC Ethernet and physical layer within a single chip, and allows the user to use an internet connection to their system. Fig. 8 shows the general form of the WizNet module.

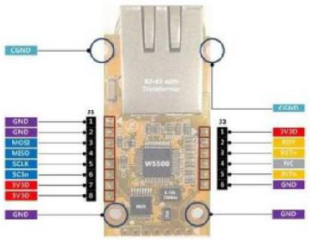


Figure 8: WizNet TCP Connection Modul [11]

The WizNet module uses a Serial Peripheral Interface (SPI) connection to communicate with embedded systems. SPI is a synchronous data link standard running in full-duplex mode. The SPI interface was designed using the VHDL programming language within the FPGA to communicate with this unit using the structure designed by Qsys.

C. PLC and Modbus I/O Modules and Network Switch

For the experimental test system., ILC150ETH PLC of Phoenix Contact is used. ILC150ETH is a device that can communicate with TCP/IP compatible devices and supports the

Modbus TCP protocol. The PLC-based application program using the PC-Worx software is used to communicate with the FPGA-based Modbus gateway and other devices on the network.

And also, ADAM Modbus RTU and TCP modules of Advantech and IL ETH BK DI8 DO4 Modbus TCP modules of Phoenix are used as Modbus RTU and TCP units for the test system.

D. RS-485 Converter Circuit

When communicating with Modbus RTU, it is needed an additional circuit between the FPGA and Modbus RTU. Generally, MAX 485 integrated circuit is used to for this adaption. The schematic of designed the RS-485 converter circuit is shown in Fig.9.

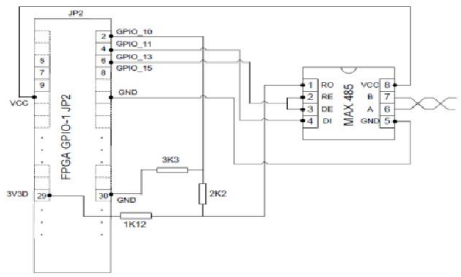


Figure 9: MAX 485 and FPGA connection circuit

IV. Software and Application

The most important component of the network is the FPGA. The FPGA's software can be examined in two parts. Among these, Qsys is the software of the peripheral devices which are created with the system integration tool. In ordinary microcontroller systems, the number and possibilities of peripheral equipment provided by the manufacturer are limited, often not changeable (number of timers and bits, number of serial communication ports, etc.). With the Qsys software, desired number of hardware with desired properties can be set by being limited with the number of elements of the FPGA type. These adjustments are then translated into VHDL or Verilog code by Qsys. Fig. 11 shows the system structure created on Qsys. The second part of the software is again the program of the selected processor in Qsys system integration tool. Eclipse programming tool is used to create the software that is going to be operated by the created CPU. In this tool the program is prepared in C language, compiled and sent to FPGA. In order for this transmission to take place, the VHDL program created with Qsys software must first be compiled and loaded into the FPGA. There is no flash memory that can be programmed in the FPGA. For this reason, the memory on DE0-Nano set contains two programs which is automatically transferred to the FPGA whenever the system is energized.

It is possible to add and modify the system structure created in the first phase of the software after converted into VHDL code. The peripheral equipment that is often required to be created cannot be created with the structures presented in the Qsys library. For example, the VHDL software for the 32-bit SPI communications equipment required by the Wiznet TCP/IP module is created by modifying an existing library. In addition, the software of RS-485 serial communication equipment with 256-byte buffer that communicates with Modbus RTU modules is created with external library components which are obtained from external sources and are still in development stage. When the gateway system is started, it first reads the configuration information from the external EEPROM. This data can also be set using the Modbus protocol. After this point, the gateway establishes the socket connection with its connected Modbus TCP devices (this is not necessary for RTU devices). It then goes on standby for requests from the main device.

The master device selects the desired device by changing the unit identifier on the protocol. Depending on the gateway configuration, the incoming request is forwarded to the related device. If the request comes for a Modbus TCP device, only the unit identifier is replaced with zero and the unit identifier is restored and sent to the master device in response from the slave device. If the request comes for the Modbus RTU device, the data is sent to the serial interface by adding the CRC and the unit identifier then the response data is received from the slave device (CRC of the incoming data is also checked), and the unit identifier is restored and sent again to the master device.

The responses to the buffer used for serial communication through the hardware waits until the operation sequence. A 256-byte buffer is created considering the limits of the Modbus RTU protocol. In Fig. 12, the entire data stream in the system is shown. The system uses four Modbus TCP and two Modbus RTU devices. In addition, Phoenix Contact ILC150ETH PLC has been added to the system as the master unit. Also, a network switch with port mirroring capability is used in the system, so that the system can be monitored. A picture of the application platform of the system is given in Fig. 10

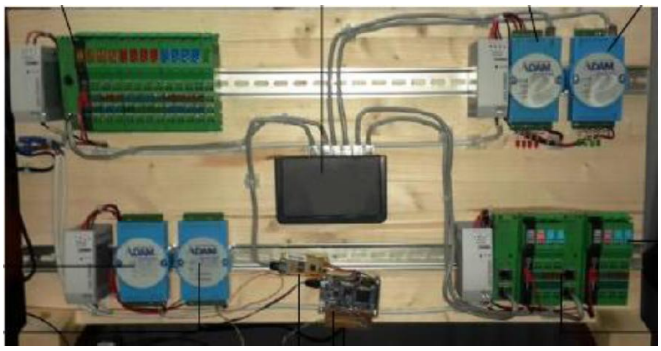


Figure 10: The experimental setup

The IP configuration of the devices used in the system is shown in Table 1.

Device	IP Adress
Gateway	192.168.1.1
PLC	192.168.1.100
ADAM 6066 (1)	192.168.1.33
ADAM 6066 (2)	192.168.1.34
IL ETH BK DI8 DO4 (1)	192.168.1.35
IL ETH BK DI8 DO4 (2)	192.168.1.36

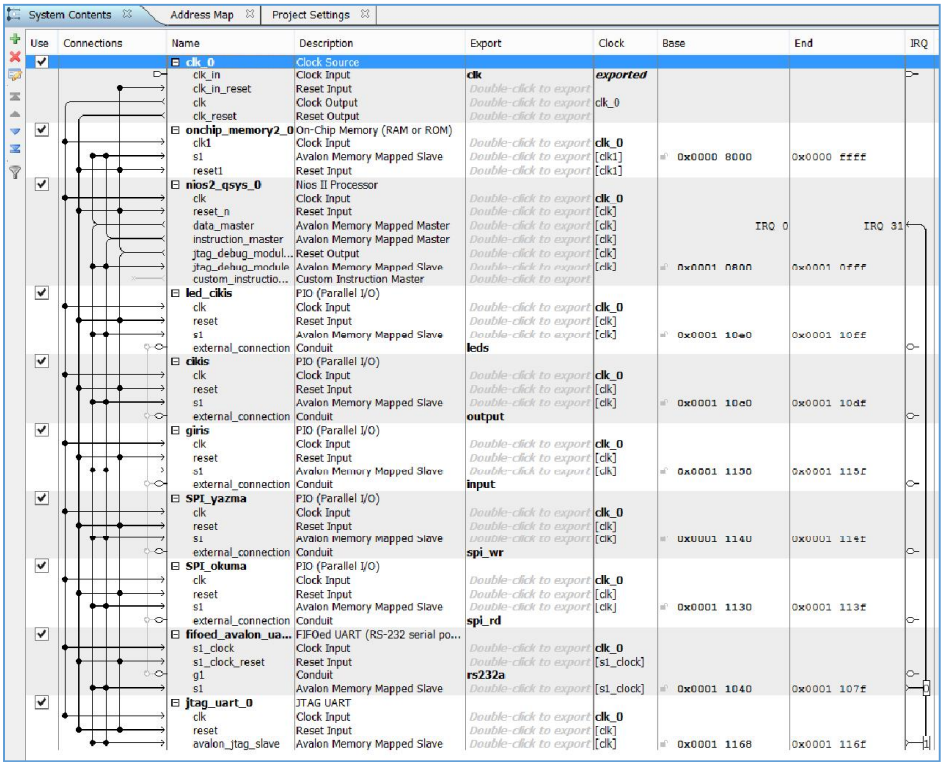


Figure 11: The system structure designed via Qsys environment

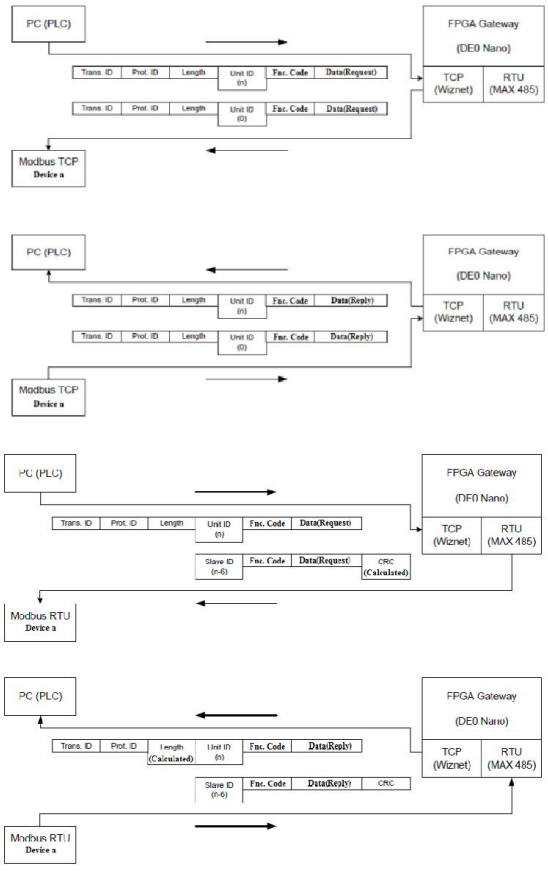


Figure 12: System data flow

The operation of the network was followed by Wireshark software. In this way, the communication of the network with both the PLC and the dependent devices can be monitored. Although all devices are on the same network, the entire data stream is passed through the gateway. Since observed packets are received over the Ethernet network, only TCP protocol flows can be observed (RTU flows are not displayed). Fig.13 shows packet flows.

V. Conclusion

In this study, a gateway was created using FPGA. The gateway has reduced the communication load of the master device by connecting both Modbus RTU and Modbus TCP devices. Since the majority of industrial devices use embedded systems, the number of connection sockets that can be created is very small. For example, this limit is eight for the PLC used in the application. Thanks to the gateway, the PLC only creates one socket connection and the remaining communication sockets can be used for other purposes.

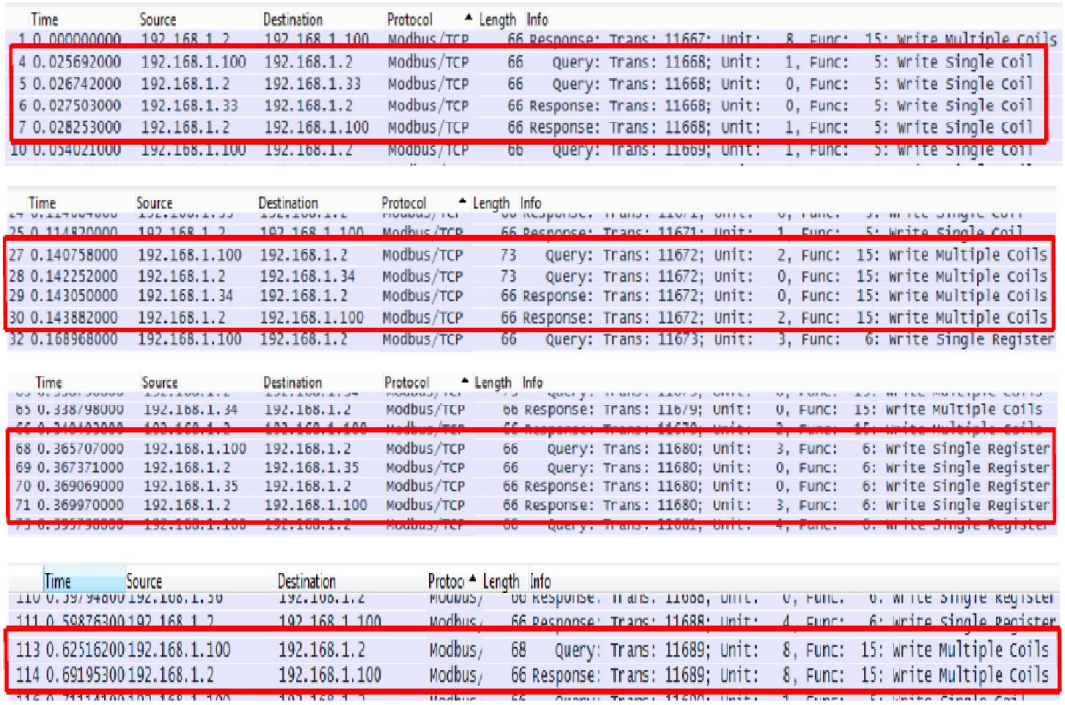


Figure 13: The packet flows of the system

REFERENCES

[1] Modbus.org, "Modbus Application Protocol Specification V1.1b3.", http://modbus.org/specs.php

[2] Modbus.org., "Modbus over Serial Line Specificaiton and Implementation guide V1.02,". http://modbus.org/specs.php

[3] Modbus.org., "Modbus Mesaging on TCP/IP Implementation Guide V1.0a." http://modbus.org/specs.php

[4] Hui, L., Hao, Z., Fei, X., & Wen, H., "Research on Communication Controller Between FlexRay and Modbus," *Proc. of the Conference on Signal Acquisition and Processing*, s: 73-76, 2009.

[5] Li, H., Zhang, H., & Peng, D., "Research and Design of Industrial Ethernet Communication Gateway on Power Station," *Proc. of the Conference on Transportation, Mechanical, and Electrical Engineering,* s: 986- 989, 2011.

[6] Chen, S., Zheng, D., & Yang, R., "Design of Preverifying Serial-Ethernet Communication Gateway Based on LM3S8962," *Proc. of the Conference on Mechatronics and Automation,* s: 1620-1624, 2013.

[7] Chiculita, C., Liviu, E., & Cristea, M. L., "Towards Multi-port Modbus Gateway," *Proc. of 4th International Symposium on In Electrical and Electronics Engineering*, s:1-4, 2013.

[8] Zhang, K. L., Li, D. H., Shi, S. C., Yang, X. S., Xiao, Z., & Gao, Q., "Design and Implementation of Multi- Protocol Self-Adaptatio Gateway," *Applied Mechanics and Materials*, 687, s: 2108-2111, 2011.

[9] Lin, Y. J., & Zhong, G. W., "The Development of Profibus/Modbus Gateway in Aluminum Roasting Draught System. *Advanced Materials Research,*898, s: 956-960, 2014.

[10] Altera Corporation, "DE0 Nano User Manual v1.9", http://www.altera.com

[11] Wiznet Corporation "Wiznet W5500 Datasheed v1.0.4." http://www.wiznet.co.kr

[12] ABB Corporation, "Industrial Manual: ANR-LAN Communication Protocol MODBUS-TCP Quick Overview" http://www.abb.com/abblibrary/DownloadCenter

[13] Simple Modbus Data Communication and Software, http://www.simplymodbus.ca/

[14] Agromag, "Introduction to Modbus TCP/IP", Prosoft Technology, https://www.prosoft-technology.com/kb/assets/intro_modbustcp.pdf

Stockwell Transform and Its Performance Comparison on the Stage of Fault Estimation in High Voltage Direct Current Transmission Lines

F. ÜNAL[1] and S. EKİCİ[2]

[1] Fırat University, Elazığ/Turkey, funal@firat.edu.tr
[2]Fırat University, Elazığ/Turkey, sekici@firat.edu.tr

Abstract **- In this study, Stockwell transform and ıts application on direct current transmission discussed. The virtual fault current and voltage signals analyzed by using Stockwell transform employed to determine the locations of single phase-ground faults. While the traditional methods like Short Time Fourier Transform (STFT) give us the time-frequency resolution information about the signal, the constant window width, and ınability to reveal the dynamics of nonstationary signals lead us to find new approaches. So, both to reveal system dynamics and to keep time-frequency-magnitude and phase information properly is important to locate fault km on high voltage direct current transmission systems. Also, support vector machines are employed to estimate the locations of single-phase ground faults.**

Keywords **- Stockwell Transform, HVDC transmission lines, Support Vector Machines, fault location estimation.**

I. INTRODUCTION

High Voltage Direct Current (HVDC) transmission has a crucial role both long distance transmission and interconnection of different frequency systems. Also, the classical applications of HVDC systems like bulk power transmission over long distances and integration of renewable energy sources to the mainland emerge its advantages against the AC transmission systems. In practical applications, converting of AC transmission lines to HVDC lines possess some superiorities as follows: upgrading capacity levels, fever corona effects, higher operating voltage characteristics, better active and reactive control, lower transmission losses and better stability levels of grids. Another motivation that needs to be mentioned is here the fast-developing switching components and the applications of power electronics in power transmission systems. By the emerging of conversion switches like thyristors and transistors accelerated the capacity of power transmission systems to withstand high voltages levels. Even if considerable progress in power transmission ratings and improvements on the reliability of thyristors enabled the competitiveness of HVDC systems, the cost of converter stations and the need of active-reactive power on the stage of conversion are some important issues to deal with in HVDC transmission. Thus traditionally, the DC transmission option has been considered economically feasible only when the transmission distances are higher than 450 km for overhead transmission. DC transmission is also an appropriate solution for the sea interconnections with the distances over 50 km. Besides the transmission capacity and other technical considerations, converter stations and the conversion process of AC to DC using high switching elements has got started more attention through voltage source converter (VSC) technologies. A detailed information can be found in references [1], [2], [3]. HVDC converter station and DC transmission line control strategies basically consist of different protection levels, but this paper will be focus only the dc transmission lines fault techniques [4] and discuss new protection strategies for this purpose. In HVDC systems, the most commonly used fault detection and protection algorithms are differential protection, traveling wave protection [5], over current and under voltage derivatives protection.However, traditional traveling wave protection of HVDC systems has some disadvantaged under high impedances faults and also need data synchronization when considering two end terminal measurement. Also, impedance measurement, Fourier based signal processing methods and wavelet transform are some of the most preferred techniques in the literature for fault analysis in DC transmission systems.

In reference [6], the authors propose an S-transform based pilot protection which uses the polarities of fault current and voltage signals to identify the fault direction. Another study of S-transform based fault identification is introduced in [7], the authors used both the time intervals of faults to predict the disturbances and represent the fault current waveforms using contour lines in the sample-frequency domain. Also, S-transform is applied in many areas to fulfill task such as; detection of voltage sag/swell and harmonics in transmission lines in [8],[9], power quality analysis in [10], high impedance faults and

transient phenomenon like(load switching, capacitor switching) in [11], diagnosing broken strands in transmission lines in [12] and power systems disturbances recognition in [13].

In this study, we will use a monopolar HVDC transmission system which is simplified equivalent circuit of CİGRE HVDC system in Matlab/Simulink. The obtained current and voltage signals are used for feature extraction stage to represent the fault signals and the actual fault distance. In the feature extraction process, S-Transform technique has been used and the performance evaluations are tested at the stage of fault estimation on DC transmission line.

II. STOCKWELL TRANSFORM

The S-transform is a method for using time-frequency representation of signals and firstly is proposed by Stockwell and colleagues in 1996 [14]. S-Transform represents frequency dependent resolution for time-frequency domain and refers to local phase information. In another point of view, S-Transform can be derived both from Continuous Wavelet Transform (CWT) by using 'phase correction' and STFT using scalable Gaussian window. In this study, we will also derive S-Transform using phase correction of CWT [14]. The CWT $W(\tau,d)$ of a function $h(t)$ is given in eq.(1)

$$W(\tau,d)=\int_{-\infty}^{+\infty}h(t)w(t-\tau,d)dt \quad (1)$$

where $w(t,d)$ is scaled copy of fundemental mother wavelet, $h(t)$ represents a function of time, τ denotes spectral domain coordinates and d represents the width of mother wavelet for controlling resolution of the time-frequency domain. The S-Transform of a function $h(t)$ is calculated with specific mother wavelet multiplied by the phase factor. The S-transform of a function $h(t)$ is given in eq.(2) [15],[14].

$$S(\tau,f)=\mathrm{e}^{i2\pi f\tau}W(\tau,d) \quad (2)$$

where the mother wavelet is preferred as the Gaussian window, and its mathematical equation is given in eq.(3)

$$w(t,f)=\frac{|f|}{\sqrt{2\pi}}e^{-\frac{t^2f^2}{2}}e^{-i2\pi ft} \quad (3)$$

Finally, both the equations (2) and (3) rearranged in eq.(4)

$$S(\tau,f)=\int_{-\infty}^{+\infty}h(t)\frac{|f|}{\sqrt{2\pi}}e^{-\frac{t^2f^2}{2}}e^{-i2\pi ft}dt \quad (4)$$

The relation between Fourier transform and S transform the respectively given in eq.(5) and eq.(6).

$$H(f)=\int_{-\infty}^{+\infty}S(\tau,f)\,d\tau \quad (5)$$

$$h(t)=\int_{-\infty}^{+\infty}\left\{\int_{-\infty}^{+\infty}S(\tau,f)d\tau\right\}e^{i2\pi ft}df \quad (6)$$

The S transform of a signal by taking the advantages of Fourier spectrum can be written as in eq.(7).

$$S(\tau,f)=\int_{-\infty}^{+\infty}H(\alpha+f)e^{-\frac{2\pi^2\alpha^2}{f^2}}e^{i2\pi\alpha\tau}d\alpha\ \ (f\neq 0) \quad (7)$$

The discrete analog values of eq.(9) can be calculated by taking advantages of Fast Fourier Transform(FFT) and convolution theorem. So, the spectrum of the signals can be decomposed into both real and imaginary components independently by not necessary to translate of the signal into the cosinusoid basis functions and thus S transform can be localize both the phase and the amplitude spectrum [8]. S transform analysis results can be considered a complex valued matrix and each row of the matrix gives us the frequency resolution of different time intervals while each column of the matrix also contains the magnitude and phase information.

There are two important issues must be mentioned in S transform analysis. The first one is the normalization factor which is represented as mathematically $\left(\sqrt{f/2\pi}\right)$ normalizes the Gaussian window to have a unit area and thus the amplitude response is not dependant on frequency. Secondly, is phase factor and represented mathematically as $\left(\mathrm{e}^{-\frac{t^2f^2}{2}}\mathrm{e}^{-\mathrm{i}2\pi\mathrm{ft}}\right)$ which are employed to generate the real and imaginary parts of the amplitude spectrum [16]. The S transform also gives us an extension of the instantaneous frequency of one dimensional signals which is called voice. The parameters of one dimentional signal τ and f_1 are used to represent a particular frequency level and mathematical expression is given in eq.(8).

$$S(\tau,f_1)=A(\tau,f_1)e^{i\phi(\tau,f_1)} \quad (8)$$

where A and ϕ represent the amplitude and phase information respectively. The ınstantaneous frequency also can be determined by using the phase information (ϕ) which is obtained from Bracewell equations [Bracewell, 1978] in some case the voice isolates a particular frequency (f_1). The 'voise' term means that it is a function of time with a constant frequency $(\mathrm{f}=\mathrm{f}_0)$ [17]. This mathematical expression is given in eq. (9).

$$IF(\tau,f_1)=\frac{1}{2\pi}\frac{\partial}{\partial\tau}\{2\pi f_1+\phi(\tau,f_1)\} \quad (9)$$

III. SIMULATION STUDY AND S- TRANSFORM ANALYSIS

A. Steady-State and Fault Conditions of HVDC Transmission Line

In this study, we will use a monopolar HVDC transmission system to obtain steady-state and fault analysis in Matlab/Simulink. DC line is 300 km length and both rectifier and inverter station uses 12 pulse converter. There are two breakers, 0.5 H reactors, and AC filters at both sides of rectifier and inverter.The DC line is a 1000 MW (500 kV, 2 kA) interconnections of two different grid. Rectifier side has a 500 kA, 5000 MVA 60 Hz AC network and inverter side has a 345 kV, 10000 MVA, 50 Hz AC network. In simulation, DC currents (IdR ve IdI) and DC voltages (Vd_LR ve Vd_LI) defined in control blocks are scaled to p.u (1 p.u. current=2 kA, 1 p.u. voltage=500 kV). There is also another control system which is called 'Master Control' and generates the current references for both converters and initiates the starting and stopping of the DC power transmission The DC transmission line properties are given in Table I.

Table 1.Properties of DC transmission line in the simulation

Transmission Line	Properties
Length	300 km
Class	Distributed parameter
Circuit Structure	Serial RLC
Connection Style	single phase-ground
Smoothing Reactors	0.5 H (2 units)
Primary voltage	0.90 (rectifier side) 0.96 (inverter side)
Sampling Time (s)	50×10^{-6} s
DC line voltage (kV)	500 kV
DC line current (kA)	2 kA
Fault resistance Rd	Ron (1 ohm)
Grid frequency	50 / 60 Hz
Multiplication factor	1:100
Per km; Resistance Inductance Capacitance	 0.015 ohm/km $0.792.10^{-3}$ H/km $14.4.10^{-9}$ F/km

The screenshot of the simulation is demonstrated in Fig .1

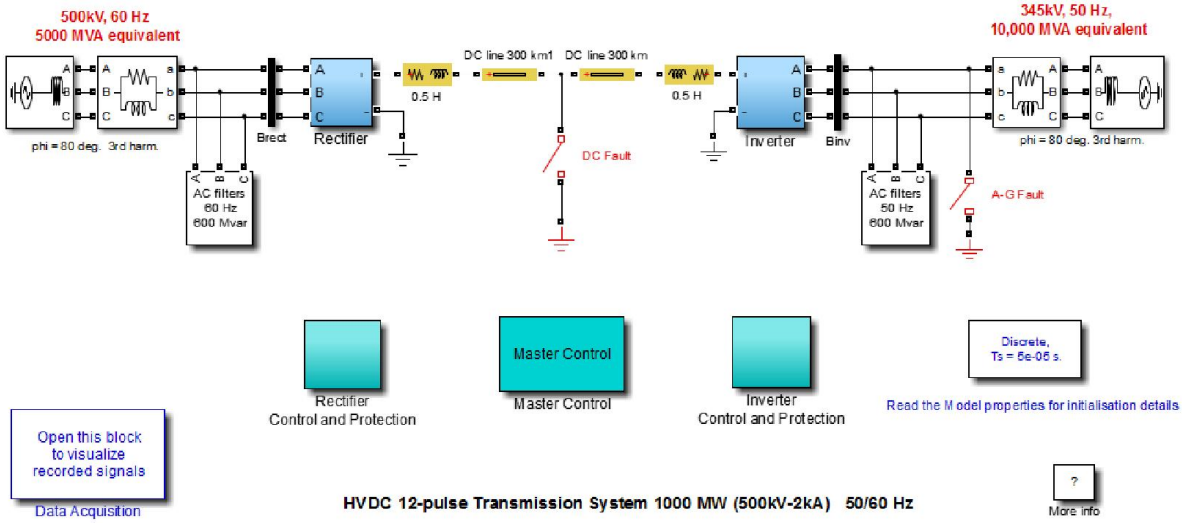


Figure 1.12 pulses monopolar HVDC system and equipment in the simulation study

In this simulation study, the fault current and voltage signals are recorded between 15.km and 285.km of DC line while the single phase-ground fault time interval kept constant for each case and defined between [0.7-0.8] seconds.

At the beginning of fault application, current increases to approximately 2.2 pu and DC voltage falls to zero at the rectifier. The Voltage-Dependent Order Limiter (VDOL) and DC protection detect the variation of both current and voltage signals and when the voltage falls into the negative region, the protection algorithm is on mode and firing angle is forced to 166 degrees. Then, rectifier operates in inverter mode until the recovery of DC voltage and current is made.

S-transformation has been applied to the first 20 ms part of current and voltage signals after the fault beginning and different notations such as time-frequency, time-maximum amplitude, time-frequency contour curves are obtained. Different fault kms and different fault resistances (Ron=1 ohm, 10 ohm, 100 ohm) also tested for ensuring the feasibility of the proposed method in praticial applications.

In order for the dynamic characteristics of the signals to be represented accurately, some useful properties such as the standard deviation of signals, energy and Shannon entropy values and maximum average amplitude values have determined. The alternation in both current and voltage signals for normal and faulted conditions has given in Fig.2

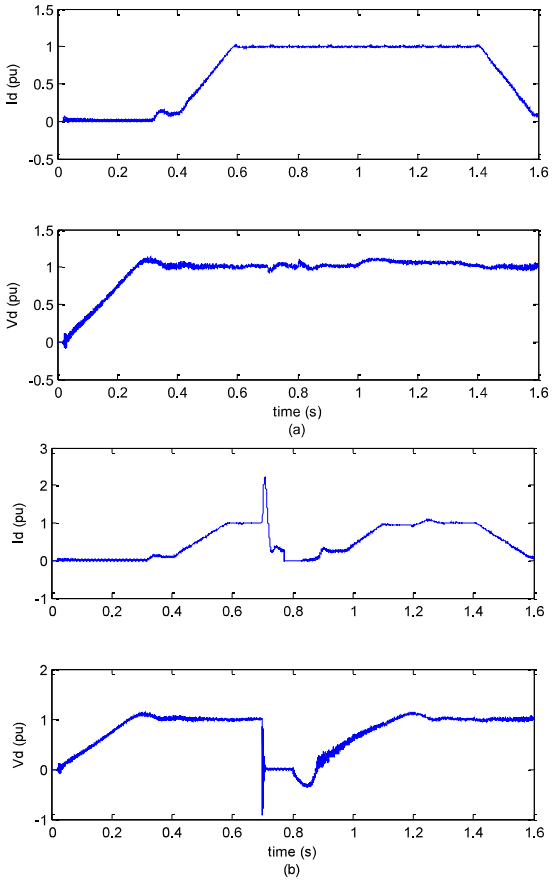


Figure 2. Current and voltage signals of dc line at 15.km (rectifier side); (a) steady state operation, (b) fault signals at 0.7 s.

As mentioned before, the fault signals and predetermined other suitable features represent the input variables for Least Squares Support Vector Machines (LS-SVM) at the stage of fault estimation. The size of those input vectors, which consist of 8 features of both voltage and current signals is [8x270] and also the sampling time of S transform has determined as 5×10^{-5} s. In contrast to STFT analysis, S transform gives more accurate time-frequency resolutions at different frequency levels because of taking advantages of variable Gaussian window and also some disadvantages encountered in CWT such as the elimination of high-frequency components are no longer issue for S transform. Different representations of the S transform of the fault voltage and current signals at the 15th km of the dc line are given in Fig.3 and Fig. 4 respectively.

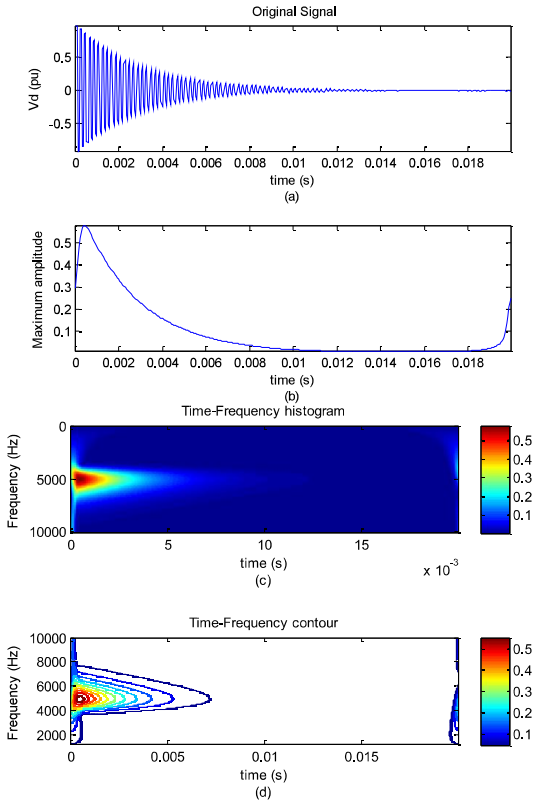


Figure 3: The S transform of the first 20 ms part after the beginning of the fault voltage signal

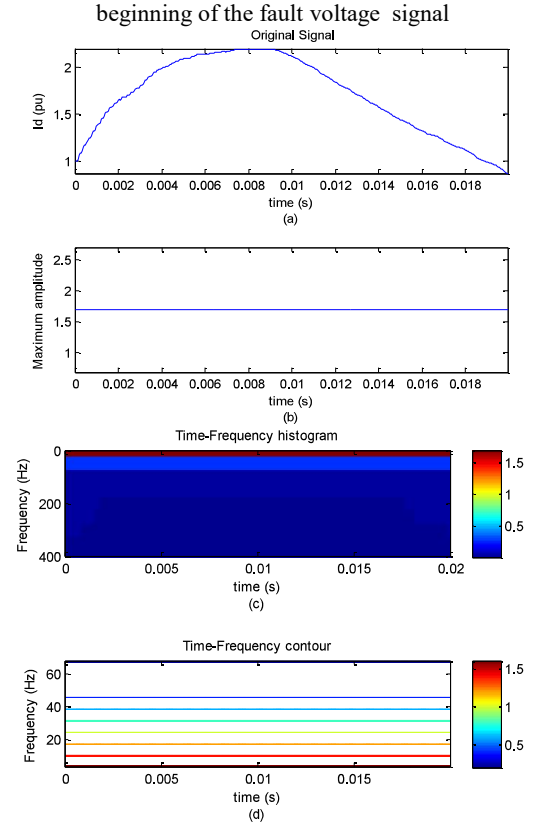


Figure 4: The S transform of the first 20 ms part after the beginning of the fault current signal.

IV. Evaluation of Performance of LS-SVM at Fault Distance Estimation Process

SVM is a classification method based on statistical learning theory, optimization theory and Vapnik-Chervonenkis dimension theory [18], [19]. The SVM method can be thought of as transferring the original input space data to the multi-dimensional feature space, which can be linearized by an optimally formed separating plane. In SVM method, consisting of N observation in n-dimensional space, each data vector of a single data pair $x_i \in R^n$ and $i \in N$ and $y_i \in \{-1, +1\}$ is defined by the class label corresponding to this data vector. The input data of first class ($y_i = +1$) and input data belonging to the second class ($y_i = -1$) is grouped by using any f(x) hyperplane selected for the classification process [20]. The mathematical representation of f(x) hyperplane defined for classification process is given in Eq. (10) and (11).

$$f(x) = w^T.x + b = \sum_{j=1}^{N} w_j x_j + b \quad (10)$$

$$y_i(w^T.x + b) \geq 1, \ (i = 1,2,3,\dots.,N) \quad (11)$$

where w is an n-dimensional vector and b is a threshold value. SVM places the original input space data in the feature space with though kernel function and support vectors specified around the hyperplane. The linear decision function in binary form, which transfers x to L dimension and F feature space using a nonlinear vector function $(\phi(x) = \phi_1(x), \dots, \phi_L(x))$ is given in Eq. (12).

$$f(x) = \text{sign}\left(\sum_{i=1}^{N} \alpha_i^* y_i \phi^T(x_i)\phi(x) + b^*\right) \quad (12)$$

where α^* are the optimal solution for binary problems of α and the values in this equation $(\alpha_1, \alpha_2, \alpha_3, \dots \dots \alpha_i)$ represent Lagrange multipliers. LS-SVM regression method is a rearrangement of standard SVM and it is created by combining different approaches such as regularization networks, Gaussian process, Fisher discriminant analysis, reproducing kernel function in Hilbert Space (RKHS) [21]. LS-SVM models used in classification and non-linear regression process are derived from linear Karush-Kuhn-Tucker (KKT) systems. In LS-SVM, Vapnik's formulation are rearranged from two points [21]. Firstly, the expression of inequality in SVM has taken the place of equality. Thus, the 1 value on the right side of the equation considering as a threshold becomes the target value. This target value allows misclassifications until error value e_k is determined which result from the spread of intersection regions of projection function. In the second arrangement, this error variable is used as a square expression (e_k^2) in LS-SVM. Mathematical expressions of these regularizations proposed by Suykens are given Eq. (13).

$$\min_{w,b,e} J_P(w, e) = \frac{1}{2} w^T w + \gamma \frac{1}{2} \sum_{k=1}^{N} e_k^2 \quad (13)$$

where e_k represents the error value, γ is regularization constant, w is n-dimensional vector of the output layer and b is the threshold value. In this study LS-SVM method preferred over the fault prediction stage for reasons such as using γ (gamma) and σ^2 (sigma) parameters that reduce training error and regulate the sensitivity of the hyperplane. The estimation of LS SVM and regression values are given in Fig.5.

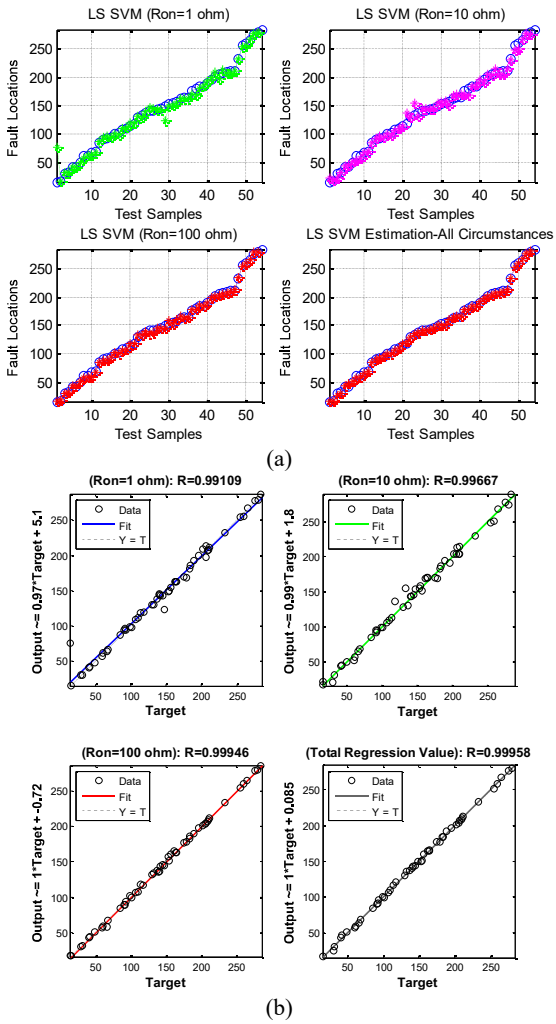


Figure 5. Estimation Results of S Transform-LS SVM application at testing stage (a) fault locations (b) regression values

The regularization parameters monitor the relevance between training error reduction and separation surface sensitivity. In the study, a radial basis kernel function has used to improve the results accuracy and also the input datasets have distributed as 60% for training, 20% for testing and 20% for validation.

V. CONCLUSION

In this study, S transform and ıts performance are examined under different fault locations and fault resistances in monopolar DC transmission lines. After the virtual fault signals has recorded in Matlab/Simulink environment, some distinguishing features such as signals energy, Shannon entropy, standard deviation of signals and maximum average amplitude has assigned for accurately represent signal dynamics. At the stage of fault location-estimation, LS SVM method has utilized and the results have compared under different scenarios. As ıt can be seen in both signal analyzing and fault estimation process, S transform possess superiorities such as stability at high-frequency levels, scalable Gaussian window and determining sudden changes. In the future applications, S transform analysis can implement on bipolar and multi-terminal HVDC transmission systems and the performances of the proposed algorithms can investigate under different scenarios.

REFERENCES

[1] J. Arrillaga, "High Voltage Direct Current Transmission Lines," in IET Power and Enegy Series, 2. Edition., vol. 29, London: The Institution of Engineering and Technology, 2011.

[2] Kim, Chan-Ki, V. K. Sood, G.-S. Jang, S.-J. Lim, and S.-J. Lee, HVDC Transmission: Power Conversion Applications in Power Systems. Singapore: Wiley-IEEE Press, 2009.

[3] A. Kalair, N. Abas, and N. Khan, "Comparative study of HVAC and HVDC transmission systems," Renew. Sustain. Energy Rev., vol. 59, pp. 1653–1675, 2016.

[4] H. Livani and C. Y. Evrenosoglu, "A single-ended fault location method for segmented HVDC transmission line," Electr. Power Syst. Res., vol. 107, pp. 190–198, 2014.

[5] Chuanxin Xi, Qing Chen, and Lei Wang, "A single-terminal traveling wave fault location method for VSC-HVDC transmission lines based on S-transform," in 2016 IEEE PES Asia-Pacific Power and Energy Engineering Conference (APPEEC), 2016, pp. 1008–1012.

[6] W. Li, Zhao, Zou, Guibin, Du, Tao, Yang, "S-transform based pilot protection method for HVDC transmission lines," in 2015 5th International Conference on Electric Utility Deregulation and Restructuring and Power Technologies (DRPT), 2015, pp. 1667–1672.

[7] P. Srikanth, A. K. Chandel, and K. A. Naik, "HVDC system fault identification using S-transform approach," in ICPCES 2010 - International Conference on Power, Control and Embedded Systems, 2010, no. 2, pp. 2–7.

[8] C. Venkatesh, S. Member, D. V. S. S. S. Sarma, S. Member, and M. Sydulu, "Detection of Voltage Sag / Swell and Harmonics Using Discrete S-Transform," no. 1, pp. 1–6.

[9] A. Amirou, Z. Zidelmal, and D. Ould-Abdeslam, "Stockwell-transform for electrical defaults localization," in 2015 3rd International Renewable and Sustainable Energy Conference (IRSEC), 2015, pp. 1–6.

[10] Z. Shi, L. Ruirui, W. Qun, J. Teargun, and H. Yang, "The Research of Power Quality Analysis Based on Improved S-Transform," no. 4, pp. 477–481, 2009.

[11] P. K. Routray, P, Mishra, M, Rout, "High Impedance Fault Detection in Radial Distribution System Using S-Transform And Neural Network," in 2015 IEEE Power, Communication and Information Technology Conference (PCITC), 2015, pp. 545–551.

[12] X. Jiang, Y. Xia, J. Hu, Z. Zhang, L. Shu, and C. Sun, "An S-Transform and Support Vector Machine (SVM)-Based Online Method for Diagnosing Broken Strands in Transmission Lines," pp. 1278–1300, 2011.

[13] J. B. Reddy, "Power System Disturbance Recognition Using Wavelet and S-Transform Techniques Power System Disturbance Recognition Using Wavelet and S-Transform Techniques," vol. 1, no. 2, 2004.

[14] R. G. Stockwell, L. Mansinha, and R. P. Lowe, "Localization of the complex spectrum: The S transform," IEEE Trans. Signal Process., vol. 44, no. 4, pp. 998–1001, 1996.

[15] Y. Wang, "The Tutorial: S Transform," Graduate Institute of Communication Engineering, National Taiwan University, Taipei (2010)., 2010. [Online]. Available: http://citeseerx.ist.psu.edu/viewdoc/download?doi=10.1.1.694.8727&rep=rep1&type=pdf.

[16] S. Azadi and A. A. Safavi, "S-Transform Based P-Wave and S-Wave Arrival Times Measurements Toward Earthquake Locating," pp. 241–246, 2011.

[17] R. G. Stockwell, "A basis for efficient representation of the S-transform," vol. 1, pp. 1–23, 2006.

[18] V. N. Vapnik, "An overview of statistical learning theory.," IEEE Trans. Neural Netw., vol. 10, no. 5, pp. 988–99, 1999.

[19] V. N. Vapnik, The Nature of Statistical Learning Theory, 2. Edition. New York, NY: Springer New York, 2000.

[20] C. J. Burges, "A Tutorial on Support Vector Machines for Pattern Recognition," Data Min. Knowl. Discov., vol. 2, no. 2, pp. 121–167, 1998.

[21] J. A. K. Brabanter,K De, Karsmakers, P. Ojeda, F. Alzate,C.,Brabanter, J. De, Pelckmans, K., Moor, B. De, Vandewalle, J., Suykens, "LS-SVMlab Toolbox User ' s Guide," Leuven-Heverlee, Belgium, 2011.

E-ISBN: 978-605-67535-4-1 Konya, Turkey, December 7-9, 2017

Automatic Capacitor Switching for Self Excited Induction Generator Using Non-Linear Regression for Wind Power Application

E. SELÇUK[1] and H. ARABACI[2]

[1] Selcuk University, Konya/Turkey, ersin.selcuk@hotmail.com
[2]Selcuk University, Konya/Turkey, hayriarabaci@selcuk.edu.tr

Abstract **- Generators for wind power plants has much importance to obtain long life and durability because of the hard environmental conditions. Especially, overseas application has extreme conditions such as wide range temperatures and humidity. In order to obtain high durability, low maintenance or no maintenance generators may have good option to install long life wind power plant. Asynchronous generator has no maintenance and only three capacitors are adequate to produce energy. On the contrary voltage regulation is not easy. Three parameters, revaluation per minute, connected capacitors and load characteristic affect the voltage regulation. Especially in order to obtain constant frequency and regulated voltage is not easy. Only one parameter is capacitor to regulate the voltage. In this study, an offline application targeted and voltage regulation is addressed for inconstant load. This study offer a mathematical approach to prediction capacitor value using non-linear regression based on experimental results.**

Keywords **- Wind power, Asynchronous generator, Non-linear Regression, Capacitor switching.**

I. INTRODUCTION

Wind power is a renewable energy power that it has increasing popularity in application. Unlike sun based power plants, wind power has extreme conditions to produce energy [1-2]. Especially overseas application has extreme conditions such as wide temperature alteration and wind force [3-4]. Maintenance is one of the biggest problems of the wind power application. Asynchronous generator is same structure with induction motor structure and has a squirrel cage as it. Thus Asynchronous generator has no maintenance through the life. Moreover Asynchronous generator has no excitation input to regulate the power [5-7]. Revaluation per minute (RPM) and capacitor are simple way to obtain voltage regulation for inconstant load. In this study, an offline generator application is designed to obtain experimental results. In order to regulate the generated voltage is used capacitors group related load. Generally capacitors are switched by dry contact structure regarding capacitor current and voltage [8-9]. Capacitors values are divided according to binary counting method to obtain maximum resolution. Thus maximum voltage regulation quality may obtain. Regulation by capacitors is not expensive and cost effective method to obtain adequate regulation. Following section is devoted to material method and experimental results to evaluate.

II. MATERIALS AND METHOD

Asynchronous generator is robust generator to produce wind power energy. Moreover asynchronous generator has no maintenance compared to other generator models and its maintenance time related to ball-bearing and roller quality. On the contrary, Asynchronous generator has no excitation voltage input to regulate the output voltage. Output voltage is can be obtained easily just connecting a capacitor at adequate rpm. Obtained voltage regulation depends on load and rpm constant characteristics. An experimental system was installed to test asynchronous generator for different loads. Obtained capacitor and RPM were noted to evaluate and create a regression. Fig. 1 shows a SEIG application for offline application.

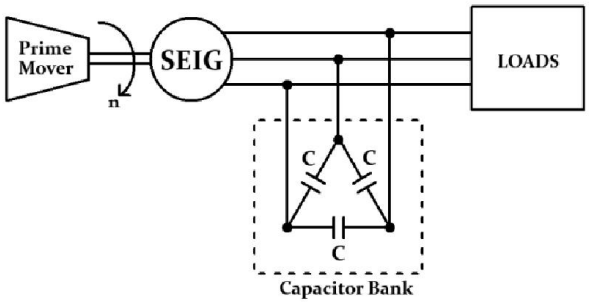


Figure 1: SEIG connection for offline in a wind power application

Capacitor is one of the most important parameter to obtain voltage regulation because of its cost effective and easy solution. Capacitor must be chosen regarding current and voltage consideration to install robust structure. In order to obtain maximum resolution, generally capacitors divided in groups regarding binary counting system [10-11].

Load characteristic is determined by adjustable resistive load. In order to obtain different loads three pieces 15 Watts (W) and three pieces 28W bulbs used. Total load can be arranged to 120W.

In order to regulate the output voltage, 0.22uF, 0.47uF, 1uF, 2uF and 4uF capacitors are used. Maximum capacitor is

handled as 3.69uF to regulate output voltage. Fig. 2 shows motor, generator and coupling.



Figure 2: SEIG and PMSM motor is coupled to each others

Experimental system includes measuring circuits to obtain voltage and current. Capacitors are connected each others as delta connection and Load is connected as star. Fig. 3 shows experiment setup, capacitors, loads and etc.

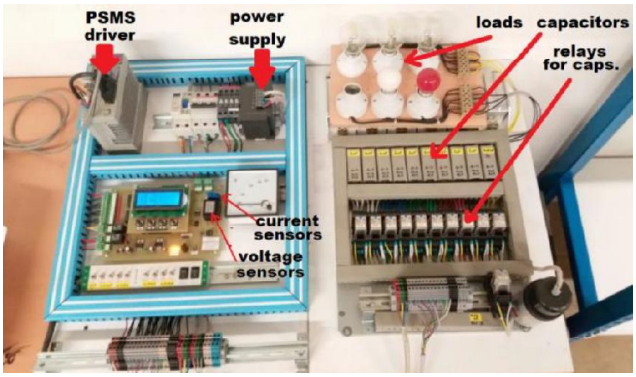


Figure 3: Used experimental setup for testing of SEIG

PMSM driver can be controlled by manually and computer to obtain high resolution rpm. Especially PMSM was chosen as higher than SEIG to reduce rpm collapsing by load characteristics. This is lead to obtain high accuracy for target equation. PMSM motor simulates wind power, SEIG generates energy and capacitor regulates to generated voltages related to load characteristics.

PMSM motor is 3000 RPM and 750W. Number of capacitors is 10.

SEIG is 250W and 1390 RPM induction motor. In order to simulate the wind flow power, computer controlled synchronous motor (750W) and synchronous motor driver unit were used. Basic connection of experiment setup block diagram was shown Fig. 4.

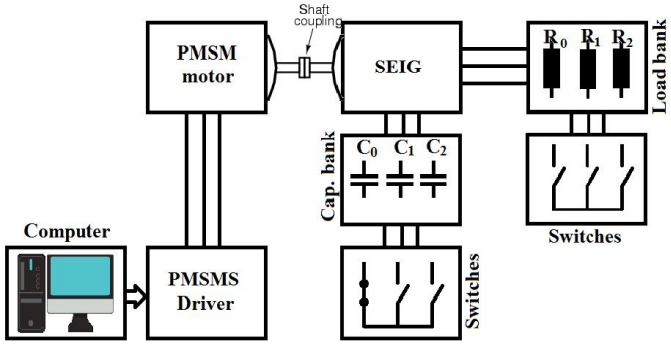


Figure 4: Block diagram of proposed system

In order to test the system, wind power simulated by computer controlled PMSM driver and PMSM motor. PSMS motor is 300W and has higher RPM than the SEIG to test over RPM behavior of SEIG output. C_0 capacitor was arranged as start-up capacitors obtain firs starting. There is no need to switch start-up capacitor. The rest ones includes on it to increase the capacitor value.

Computer can control the PMSM motor from zero to 1500 RPM with 0.1 Hz resolution. We aim to obtain constant speed to obtain certain capacitor value to regulate the output voltage.

Capacitors are connected as delta connection among the SEIG windings as Fig. 5. Computer collects the current and voltage values as real time from the experimental system to storage. Analogue digital converter has 12 bit resolution and evaluates the current 0.1Ampere resolution.

Collected current and voltage values are used to evaluate in non-linear regression to obtain capacitor characteristics.

Non-linear regression is a way to find out a solution between inputs and output [12-14]. A non-linear model is based on least squared method (LSM) to find solution between capacitor value and inputs. LSM is widely used to find a solution between input and output. Moreover system is not be linear and gives fast solution [15-17].

$$y = a + bx_1 + cx_2 + dx_3 \quad (1)$$

LSM finds a polynomial approaching between capacitor value and inputs. Here is solution is not linear to reduce prediction error.

$$\begin{pmatrix} \sum_{n=1}^{N} f(x_n)^2 & \sum_{n=1}^{N} f(x_n)g(x_n) \\ \sum_{n=1}^{N} f(x_n)g(x_n) & \sum_{n=1}^{N} g(x_n)^2 \end{pmatrix} \begin{pmatrix} a \\ b \end{pmatrix} = \begin{pmatrix} \sum_{n=1}^{N} f(x_n)y_n \\ \sum_{n=1}^{N} g(x_n)y_n \end{pmatrix} \quad (2)$$

LSM is a method to find a solution between inputs and outputs regarding minimum total error.

III. Test And Results

Proposed off line SEIG application was designed and tested with 250W SEIG. A higher motor is coupled to SEIG to simulate the wind. PMSM motor especially was chosen higher

power than the SEIG to evaluate SEIG characteristic at over speed wind power. Fig. 5 shows Computer connection of ADC to obtain current and voltage values. In this study, current was obtained from 0 to 2A and voltage was obtained 0 to 440Volts phase to phase.

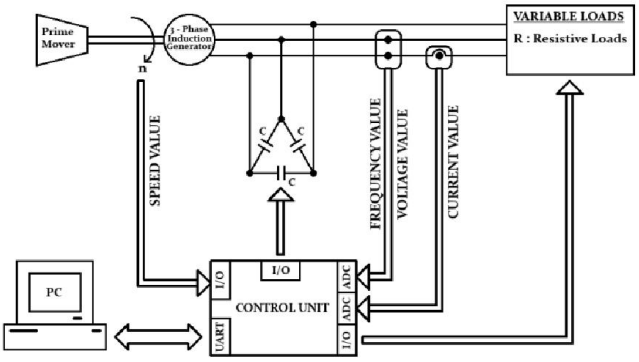


Figure 5: Designed electronics card to read generator current and voltage

Wind power simulates by PMSM motor. PMSM motor is driven by PMSM driver and speed of PMSM motor is changeable manually. As first, SEIG generator was excited by PMSM motor at determined speed to find out. Fig. 6 shows created graphic using experimental real application data.

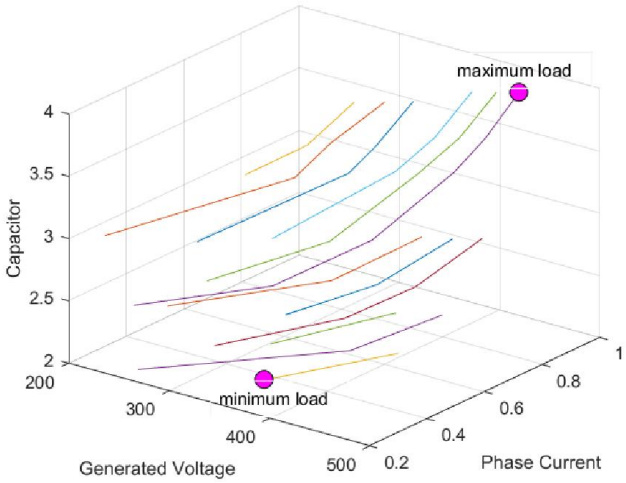


Figure 6: Relationship among load, and inputs (current, voltage and capacitor)

According to experimental results, curve fitting software is used to calculate and to obtain a function to describe the targeted capacitor related to load capacity. Curve fitting software uses the least squared model to obtain the function and shown Equ. 3

$$y = 9.22508 - 0.005452\,x_1 + 0.005489\,x_2 + 0.003758\,x_3 \qquad (3)$$

Where, x_1 is rpm, x_2 is generated voltage by generator and x_3 is current.

y curve shows capacitor value. Electronics control unit related to current instant capacitor values and combined one or more capacitor each other to obtain target capacitor. Capacitor are sequenced 1x, 2x, 4x and etc as inspired from binary counting system.

Table 1 shows used and calculated capacitor values for same target voltage. In the application, 6 capacitors are combined as 2, 0.47, 0.22, 3uF.

Table 1: Capacitors Values.

Capacitor Values			
	Max	**Average**	***Min***
Experimented	4uF	3uF	*2uF*
Calculated	3.91uF	2.71uF	*1.51uF*

From Table 1, calculated capacitor by Equ.4 is close to real experimented value. Table 2 shows maximum and minimum error point's situation in real applications. For example maximum error is obtained at 1500 RPM and there is no load during the max error. On the contrary, minimum error is obtained at 1400 RPM with 45W load characteristic.

Table 2: Capacitor Errors Situations.

Capacitor Error Situations					
	Speed	**Current**	**Voltage**	**Load**	***Max***
Max. Err	@1500	@0.88	@454	@0	*0.46*
Min. Err.	@1400	@0.58	@352	@45	*0*
Average					*-0.29*

From the Table 3, maximum error value situation is measured at no load running at 1500 RPM with 4uF capacitor using Equ.4. Voltage can be calculated as reverse for calculated capacitor.

Table 3: Voltage regulation at max, min and average error points.

Line Regulation (%)			
	Target voltage	**Obtain. Voltage**	*%*
No load	454	537	*15.4*
45W	352	352	*0*
84W	424	480.37	*11.73*

From the Table 2, maximum error value situation is measured at no load running at 1500. Capacitor could be calculated using Equ.3 according to load characteristics instantly.

Function is obtained using Curve Expert 1.3 which is free on its own website and downloadable [18]. Curve Expert finds curves between inputs values and output.

IV. Evaluation Of The Results

In this study, a SEIG application was applied and obtained real values related to load and SEIG characteristics. Although a SEIG application looks easier. It is not easy to obtain good line regulation related to redundant parameters redundancy. In this study, in order to control the line regulation real voltage current and speed are used and using these three parameters Equ.3 was created via curve expert 1.3. Obtained curve based on least squared method to find best approximation between

inputs and outputs. Curve expert calculated the Equ.3 with 0.92% success evaluated with R^2 as 0.915248. R2 is a way to measure of the success in literature and shows similarities of two variables [19-20]. During real application after experimental testing, average line regulation success obtained lower than 11.7%.

V. Conclusion

In this study, induction motor was used as generator to reduce maintenance and run under hard conditions such as cold weather conditions. This kind of application just needs capacitors to run and control the generated voltage. Because of this simplicity, induction generator has importance advance in hard running condition especially north countries which have strong winter seasons. This study uses capacitors groups to switch related to load characteristics to obtain line voltage regulation. Although SEIG characteristics depend on more than one parameter, load current, capacitors, speed, studied approximated function finds optimum line regulation with measuring only current, speed and voltage as closed system. The obtained function can be reached the experimental real results lower than 11.3%. Moreover, success can be improved by increasing the binary combination length of capacitor. In addition the small error percentage, through the load increasing regulation characteristic gets better than no load running. These results encourage us to use SEIG in wind power generation.

References

[1] Z. Hameed, Y. S. Hong, Y. M. Cho, S. H. Ahn, C. K. Song, "Condition monitoring and fault detection of wind turbines and related algorithms: A review", *Renewable and Sustainable Energy Reviews*, vol. 13, pp. 1-39, January 2009.

[2] W. Yang, P. J. Tavner, C. J. Crabtree, Y. Feng, Y. Qiu, "Wind turbine condition monitoring: technical and commercial challenges", *Wind energy*, vol. 17, pp. 673-693, May 2014.

[3] S. Heier, *Grid Integration of Wind Energy: Onshore and Offshore Conversion Systems*. John Wiley & Sons, 2014.

[4] E. Hau, *Wind Turbines: Fundamentals, Technologies, Application, Economics*. Springer Science & Business Media, 2013.

[5] J. A. Baroudi, V. Dinavahi, A. M. Knight, "A review of power converter topologies for wind generators", *Renewable Energy*, vol. 32, pp. 2369-2385, November 2007.

[6] O. Ojo, I. E. Davidson "PWM-VSI inverter-assisted stand-alone dual stator winding induction generator", *IEEE Trans. Ind. Appl.*, vol. 36, pp. 1604-1611, November 2000.

[7] S. S. Murthy, O. P. Malik, A. K. Tandon, "Analysis of self-excited induction generators", *IEE Proceedings C (Generation, Transmission and Distribution)*, vol. 129, pp. 260-265, November 1982.

[8] A. A. Girgis, C. M. Fallon, J. C. P. Rubino, R. C. Catoe, "Harmonics and transient overvoltages due to capacitor switching", *IEEE Transactions on Industry Applications,* vol. 29, November 1993.

[9] R. C. Van Sickle, J. Zaborszky, "Capacitor Switching Phenomena", Transactions of the American Institute of Electrical Engineers, *Transactions of the American Institute of Electrical Engineers*, vol. 70, July 1951.

[10] J. Dixon, Y. del Valle, M. Orchard, M. Ortuzar, L. Moran, C. Maffrand, "A full compensating system for general loads, based on a combination of thyristor binary compensator, and a PWM-IGBT active power filter", *IEEE Transactions on Industrial Electronics*, vol. 50, October 2003.

[11] J. Dixon, L. Moran, J. Rodriguez, R. Domke, "Reactive Power Compensation Technologies: State-of-the-Art Review", *Proceedings of the IEEE*, vol. 93, December 2005.

[12] G. Grégoire, "Multiple Linear Regression", *European Astronomical Society Publications Series*, vol. 66, pp. 45-72, January 2015.

[13] Y. Su, X. Gao , X. Li, D. Tao, "Multivariate Multilinear Regression", *IEEE Transactions on Systems, Man, and Cybernetics, Part B (Cybernetics)*, vol. 42, December 2012.

[14] J. Cohen, P. Cohen, S. G. West, L. S. Aiken, *Applied Multiple Regression/Correlation Analysis for the Behavioral Sciences*, Routledge, 2013.

[15] D. W. Marquardt, "An Algorithm for Least-Squares Estimation of Nonlinear Parameters", *Journal of the Society for Industrial and Applied Mathematics*, vol. 11, pp. 431–441, June 1962.

[16] P. Geladi, B. R. Kowalski, "Partial least-squares regression: a tutorial", *Analytica Chimica Acta*, vol. 185, pp. 1-17, 1986.

[17] R. J. Sanford, "Application of the least-squares method to photoelastic analysis", *Experimental Mechanics*, vol. 20, pp. 192-197, June 1980.

[18] https://www.curveexpert.net/download/ last access: 28.10.2017

[19] C. J. Willmott, "Some Comments on the Evaluation of Model Performance", *Bulletin of the American Meteorological Society*, vol. 63, pp. 1309-1313, November 1982.

[20] B. Akdemir, S. Doğan, M. H. Aksoy, E. Canli, M. Özgören, "Artificial frame filling using adaptive neural fuzzy inference system for particle image velocimetry dataset", *Sixth International Conference on Graphic and Image Processing*, vol. 9443, pp. 94431R, March 2015.

Modeling and Techno-Economic Analysis of Building-Integrated Photovoltaic (BIPV) Systems in Central Anatolia Region

G. N. Güğül[1]

[1] Selcuk University, Faculty of Technology, Computer Engineering Department, Konya/Turkey, gul.gugul@selcuk.edu.tr

Abstract - **Abstract**

The use of BIPV as on-site renewable energy source is becoming popular in energy efficient high rise buildings due to its limited roof areas and wide façade areas. Central Anatolia climate is cold but absorb high solar radiation all year round. With the increase in the number of houses in Turkey, the amount of energy consumed in the housing sector and the associated CO_2 emissions are increasing. In this study, electricity production of a building integrated photovoltaic panel system (BIPV) on the two façade of an apartment building in Konya is theoretically investigated by simulations conducted in ESP-r building energy simulation tool. Electricity production model of BIPV system is created in ESP-r. Electricity consumption of the apartment in the building is obtained by using electricity bills and survey data. Techno-economic analyzes of BIPV system, energy savings achieved and reductions in greenhouse gas emissions have been calculated. Hourly climate data, technical data of solar energy system and economic analysis data are used in the calculations.

Keywords - **Building-Integrated Photovoltaic, BIPV, zero energy building, economic analysis, ESP-r**

I. INTRODUCTION

THE amount of energy consumed in the residential sector in Turkey is increasing parallel to the increase in the number of residential units. 190.314 new residential buildings were built in Turkey in 2015 and 2016 and 3% of these buildings are located in Konya. 76% of the buildings built in Konya are high rise buildings [1]. Use of renewable energy sources in residential buildings; reduces the energy consumed by the fossil fuels while reducing the energy cost and increasing the financial value of the resident. The most suitable renewable energy source that can be applied in Turkey is solar energy due to its geographical position.

In Turkey, the second largest part of the energy consumed in residential sector is electricity with a share of 25 %. In Turkey half of the electricity production is provided by imported coal and natural gas. Due to this reason, reducing electricity consumption in the residential sector is of great importance.

There are many studies conducted to model electricity production of PV panels in residential buildings by using building energy simulation software. Some of these studies investigated the effect of PV panel on electricity generation ([2], [3], [4], [5]) and in some cases the environmental and technologic effects of PV are investigated ([6], [7])

Factors affecting the performance of the system have been investigated by researchers ([2], [8] [3], [9], [10], [11], [12]) and the energy savings provided by the system are calculated ([13], [14], [15] [16]) .

Solar panels are generally divided into three categories, monocrystalline, polycrystalline and thin film technology [17]. In this study, polycrystalline PV module model was used due to its low price compared to monocrystalline s and less influenced by external effects such as snow [18]. The electricity consumption of the house was calculated by using one year electricity bill and survey data. Finally, the energy savings achieved by using photovoltaic panels and the associated reductions in CO_2 emissions have been calculated and techno-economic analyzes have been conducted.

II. METHODOLOGY

Within the scope of the study, firstly an apartment house to be modeled is selected. Then meteorological data of Konya where the dwelling is located, architectural drawings of the dwelling and survey information are provided in order to develop geometric model. After the development of geometric data the panels were modeled by placing BIPVs on outer shell of the apartment. Then simulations are conducted for each façade of the outer shell in ESP-r. Then electricity consumption of the house was determined by using the bills and the survey data. The amount of energy savings and the amount of reduction in CO_2 emissions that can be achieved by calculating the amount of electricity generated by the generated model are calculated. This section provides information about the methodology followed during calculations and simulations.

A. Model House

Construction of the model house was completed in 2010 in Konya, Turkey. The residence has a total of 160 m^2 heated area including four bedrooms, one living room, two bathrooms, one toilet. Four people reside in the residence.

B. Collection of Data

To develop model of the house and electricity production of BIPV system in ESP-r, survey data (architecture of the

residence, power value and duration lamps, electrical appliances etc.) and meteorological data is obtained. Then to calculate electricity consumption of the apartment of the building electricity bills have been provided. Technical data of the photovoltaic panel to be modeled has been obtained from a local company.

1) Survey Data

Information about electric appliance and lamp usage of the house, electricity bills and architectural drawing of the house is obtained as a result of survey conducted with the owner. Total electricity consumption of electrical appliances and lighting are given in Table 1.

Table 1 Total electricity consumption of electrical appliances and lighting, kWh / month

Equipment		Duration, h/day	Power, W	Energy cons., kWh/ month
Boiler		1	80	2,4
Refrigerator		24	60	43,2
Stove		24	5	3,6
Oven	Under stove	0,1	700	2,1
	Microwave	0,1	700	2,1
Aspirator		0,2	100	0,6
TV	LCD.	7	80	16,8
	Plasma	2	80	4,8
	LCD	1	60	1,8
Computer	Laptop	6	40	7,2
	Laptop	6	40	7,2
Washing machine		1	500	15
Dishwasher		1	500	15
Vacuum cleaner		0,5	700	10,5
Iron		0,2	1.000	6
Coffee machine		0,1	500	1,5
Toast machine		0,1	700	2,1
Electric Stove		0,05	1.400	2,1
Food processor		0,1	700	2,1
Lighting (CFL)		3	100	9
Total				155

Monthly electricity bill information for the house was provided for 12 months from the home owner. Monthly electricity consumption of the housing is shown in Figure 1.

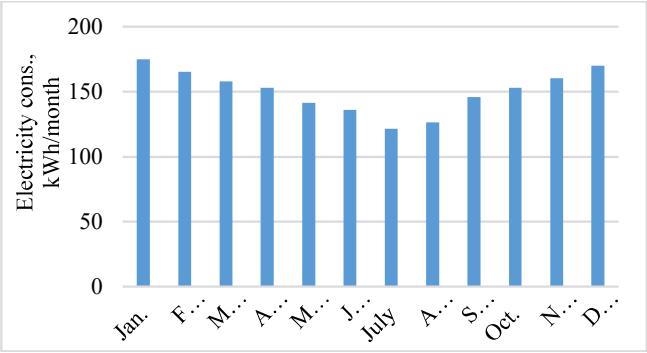


Figure 1 Monthly electricity consumption of the housing, kWh/month

According to the information obtained from the monthly bill, electricity is consumed at an average of 150 kWh/month in the residence and this value is compatible with the questionnaire data.

The residence has a total area of 160 m^2.The window area is 14 m^2, the balcony area is 12 m^2 and the outer wall area is 81 m^2 in the residence. BIPV system modelled in ESP-r is planned to have area of 20 m^2 on the east facade and 20 m^2 on the west facade. The architectural drawing of the resident is shown in Figure 2.

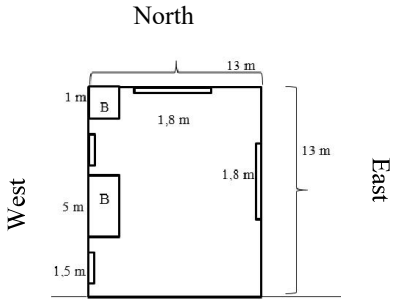


Figure 2 Architectural drawing of the residence

2) Photovoltaic Panel Data

It is decided to model the BP 380, 80-WattPolycrystalline PV module on the outer shell of the residence in ESP-r.

3) Climate data

The hourly meteorological data of Konya is obtained from hourly climate data of Ankara downloaded from the United States Department of Energy's web site [19].

Calculations are conducted by using normal climate data of Ankara, average daily solar radiation time distribution of Turkey [20] and annual solar radiation distribution (kWh/m^2) of Turkey [21]. According to this data daily average radiation time of Konya is one hour more than Ankara. According to the total annual solar radiation distribution (kWh/m^2) of Turkey total annual solar radiation per meter square of Konya is [21] 168 kWh/m^2-year more than Ankara. As a results of the calculations daily radiation data of Konya is obtained. This calculations show that, direct solar radiation of Ankara is 1.100 kW/m^2-year whereas of Konya is 1259 kW/m^2-year.

4) Greenhouse Gas Emissions Data

The greenhouse gas (GHG) emission factor resulting from electricity generation is shown in Table 2.

Table 2 Electric emission factor, kgCO_2/GWh [22]

Gas type	Emission factor
CO_2	519.732
CH_4	7,22
N_2O	4,94

5) Economic Analysis Data

During the economic analysis, the cost of the BIPV system, is obtained from a local firm. The firm has priced 40,000 TL for 40 m^2 panel application. Then, electricity price data [23] obtained for the last nine years to analyze the estimation of electricity price for the coming years. Line equation is

constructed using electricity data and the electricity prices for the following years are estimated using this equation.

C. Model development

The model is generated in ESP-r building energy simulation software. First, a geometric model is developed by using architectural drawing data of the dwelling. While the geometric model is being constructed, only one zone is formed because the photovoltaic panel is mounted on the outer shell of the residence. Later, the normal climate data for model Konya is inserted to the program.

Then BIPV system in mounted on outer shells on geometric model and electricity production of the system is estimated separately for each façade. A screenshot of the ESP-r program in which the model is created is given in Figure 3.

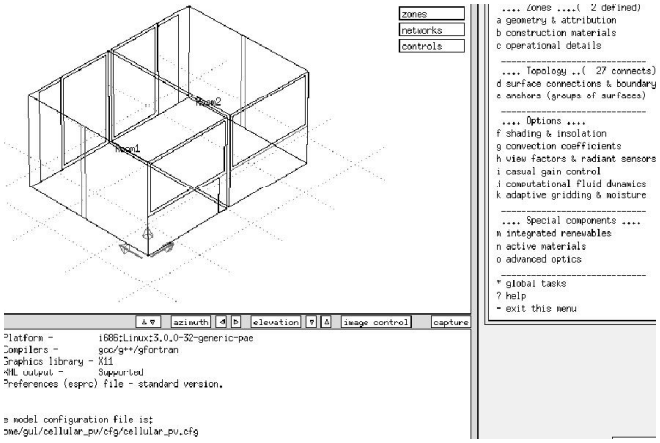


Figure 3 Screenshot of the ESP-r program for each façade

D. Reduction in Greenhouse Gas Emission

Reduction of greenhouse gas emission (kg/year) is calculated by using the emission factor for electricity generation (EEF). The amount of reduction in greenhouse gas emissions is calculated using Equation (1).

$$\mathrm{RGE} = \mathrm{ES} \times \mathrm{EEF} \tag{1}$$

Where;

$\mathrm{RGE_i}$: Reduction in GHG Emission, kg/year
ES : Energy saving, kWh/year
EEF : Electricity Emission Factor, kg-CO_2/kWh

E. Economic Analysis

During the economic analysis of the system, investment cost, electricity bill and interest rate data are used. For the calculation of the system's payback period (PBP), cost of the BIPV system is obtained from a local company. The annual Net Cash Flow (NCF) is calculated for the determination of the PBP. The NCF is calculated by equation (6)

$$\mathrm{NCF_j^{fv}} = \mathrm{CI_j^{fv}} - \mathrm{CO_j^{fv}} = (\mathrm{EP_{e,j}}(\mathrm{E_{fv}} - \mathrm{E_{fv_con}})) \tag{2}$$

Where;

$\mathrm{NCF_j^{BIPV}}$: Annual Net Cash Flow, TL/year
$\mathrm{CI_j^{BIPV}}$: Annual Cash Input, TL/year
$\mathrm{CO_j^{BIPV}}$: Annual Cash Output, TL/year
j : Year
EP : Electricity Price, TL/kWh
$\mathrm{E_{fv}}$: Electricity produced by PV, kWh/year
$\mathrm{E_{fv_con}}$: Electricity consumed for PV, kWh/year

If the interest rate remains constant for several years [24] NPV can be calculated by equation (3).

$$\mathrm{NPV} = \frac{\mathrm{NCF_1}}{(1+\mathrm{ni})} + \frac{\mathrm{NCF_2}}{(1+\mathrm{ni})^2} \cdots + \frac{\mathrm{NCF_N}}{(1+\mathrm{ni})^N} = \sum_{j=1}^{N} \frac{\mathrm{NCF}_j}{(1+\mathrm{ni})^j} \tag{3}$$

NPV : Net Present Value, TL
$\mathrm{NCF_j}$: Net Cash Flow, TL/year
ni : Nominal Interest Rate
j : Year
N : Operation time of the system, year

The minimum j value that allows the NPV to take a positive value is defined as the PBP [24].

III. Results

This section provides detailed information on the results obtained. The photovoltaic panel mounted on the outer shell of the residence is estimated to produce 5910 kWh/year. Electricity demand of the house is 1800 kWh/year. In this case, about 4110 kWh of electricity can be sold to the government per year.

A. Modeling Results

Electricity demand of the resident is provided from the grid. Electricity consumption for one year in the house was determined from the surway data and bills. The annual electricity generation with the mounth of BIPV to the east and west exterior walls of the house was modeled in the ESP-r building energy simulation program. It is estimated that the BIPV system will produce electricity of 2770 and 3140 kWh/year on the eastern and western facades, respectively. The amount of daily electricity produced according to the simulation results is given in Figure 4.

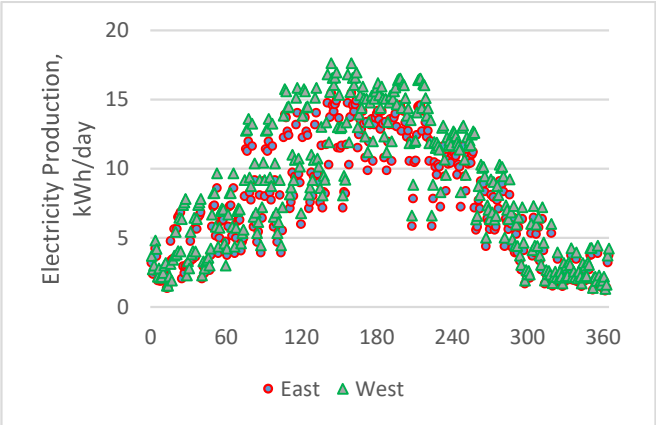


Figure 4 The amount of estimated electricity production by ESP-r, kWh/day

In the simulated model, the area and technical features of the panels placed in every facade of the house are exactly the same. Comparison of electricity production of the panels is show that, the west-facing panel produced 13% more electricity than the east-facing panel.

B. Economic Analysis Results

Electricity generation of BIPV is estimated by ESP-r as 5910 kWh/year. Annual electricity demand of the house is about 1800 kWh/year. In this case, about 4110 kWh of electricity can be sold to the government [25] per year providing the NCF increase. In this case, the change in NPV over the years is given in Figure 5.

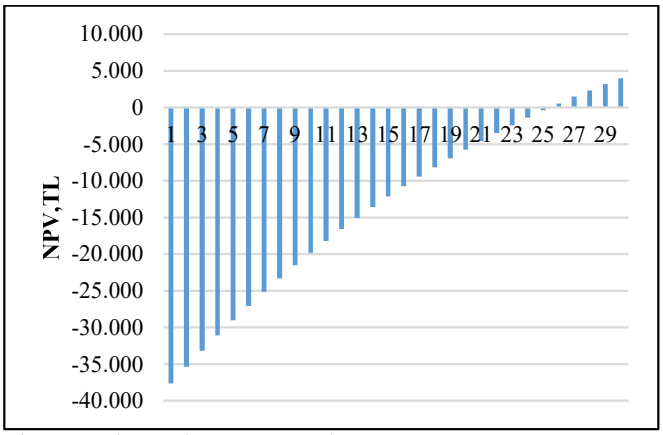


Figure 5 Change in NPV over the years

If the nominal interest rate is 0,05, PBP is calculated as 26 years.

C. Greenhouse Gas Emission Reduction

The photovoltaic panel mounted on the outer wall of the house has estimated to produce 5910 kWh/year electricity. The reduction in greenhouse gas emissions from electricity generation is shown in the Table 3.

Table 3 Reduction in GHG Emission, kg/year

	CO_2	**CH_4**	**N_2O**
Emission factor, kg CO_2/GWh [22]	519.732	7,22	4,94
Reduction in GHG Emission, kg/year	3072	0,043	0,029

IV. Conclusion and Discussion

In this study, the electricity production of BIPV system installed on the outer shell of a western and eastern facade of an apartment in a high rise building in Konya is simulated with ESP-r program. Economic analysis of the system is carried out and reductions in associated greenhouse gas emissions to be achieved are calculated. As a result of the simulations made, annual electricity generation of BIPV system is estimated as 5910 kWh/year. Electricity bills, show that the annual electricity demand of the house is 1800 kWh/year. In this case, about 4110 kWh/year of electricity can be sold to the government. It is estimated that the generated model will produce electricity of 2770 and 3139 kWh/year on the eastern and western facades respectively. The west-facing panel produced 13% more electricity than the east-facing panel. Considering the fact that the surplus electricity of the house is sold and the nominal interest rate is 0,05, PBP is calculated as 26 years. With the photovoltaic panel mounted on the outer wall of the house, it is observed that there would be 3072 kg/year reduction in CO_2 emission, 0,043 kg/year reduction in CH_4 emission and 0.029 kg/year reduction in N_2O emission.

References

[1] TUIK Bölgesel Istatistikler (2017). [Online]. Available: https://biruni.tuik.gov.tr/bolgeselistatistik/tabloYilSutunGetir.do?durum=acKapa&menuNo=221&altMenuGoster=1.

[2] T. Chow and A. Chan (2004), Numerical study of desirable solar-collector orientations for the coastal region of South China, *Applied Energy,* vol.79, no. 3, pp. 249-260.

[3] J.-H. Yoon, J. Song and S.-J. Lee (2011), Practical application of building integrated photovoltaic (BIPV) system using transparent amorphous silicon thin-film PV module, *Solar Energy,* vol. 85, no. 5, pp. 723–733.

[4] R. Eke and A. Senturk (2013), Monitoring the performance of single and triple junction amorphous silicon modules in two building integrated photovoltaic (BIPV) installations, *Applied Energy,* vol. 109, pp. 154–162, 2013.

[5] P. K. Ng and N. Mithraratne (2014), *Renewable and Sustainable Energy Reviews,* vol. 31, pp. 736–745.

[6] F. Cucchiella, I. D'Adamo and S. L. K. (2015), Environmental and economic analysis of building integrated photovoltaic systems in Italian regions, *Journal of Cleaner Production,* vol. 98, pp. 241-252.

[7] W. Wang, Y. Liu, Y. X. Xinfang Wu, W. Yu, C. Zhaoa and Y. Zhong (2016), Environmental assessments and economic performance of BAPV, *Energy and Buildings,* vol. 130, pp. 98–106.

[8] T. Chow, J. Hand and P. Strachan (2003), Building-integrated photovoltaic and thermal applications in a subtropical hotel building, *Applied Thermal Engineering,* vol. 23, no. 16, pp. 2035–2049.

[9] D. Thevenard (2005), Review And Recommendations For Improving The Modelling Of Building Integrated Photovoltaic Systems, *Ninth International IBPSA Conference*, Montreal.

[10] E. L. Didoné and A. Wagner (2013), Semi-transparent PV windows: A study for office buildings in Brazil, *Energy and Buildings,* vol. 67, p. 136–142.

[11] J. W. Lee, J. Park and H.-J. Jung (2014), A feasibility study on a building's window system based on dye-sensitized solar cells, *Energy and Buildings,* vol. 81, pp. 38–47.

[12] A. Virtuani and D. Strepparava (2017), affecting the performance of the system have been investigated silicon in different typologies of building-integrated photovoltaic (BIPV) conditions, *Solar Energy,* vol. 146, pp. 113-118.

[13] C. Maurer and T. E. Kuhn (2012), Variable g value of transparent facade collectors, *Energy and Buildings,* vol. 51, pp. 177–184.

[14] B. K. Koyunbaba, Z. Yilmaz and K. Ulgen (2013), An approach for energy modeling of a building integrated photovoltaic (BIPV) Trombe wall system, *Energy and Buildings,* vol. 67, pp. 680–688.

[15] A. Karkare, A. Dhariwal, S. Puradbhat and M. Jain (2014), Evaluating Retrofit Strategies for Greening Existing Buildings by Energy Modelling & Data Analytics, *Intelligent Green Building and Smart Grid (IGBSG)*, Taipei, Taiwan.

[16] G.Evola and G.Margani (2016), Renovation of apartment blocks with BIPV: Energy and economic evaluation in temperate climate, *Energy and Buildings,* vol. 130, pp. 794-810.

[17] Solar-Academy (2014), Güneş ve Rüzgardan Elektrik. [Online]. Available: http://www.solar-academy.com/menu_detay.asp?id=321.

[18] Solar Dukkan (2015), Mono ve Poly Fotovoltaik Güneş Paneli Farkı Nedir?, 18 4 2015. [Online]. Available: http://monovepolyfotovoltaik.blogspot.com.tr/.

[19] EnergyPlus Energy Simulation Software-Weather Data Sources, (2015). [Online]. Available: http://apps1.eere.energy.gov/buildings/energyplus/weatherdata_sources.cfm#IWEC.

[20] Türkiye Günlük Güneşlenme Süreleri (2017). [Online]. Available: https://www.mgm.gov.tr/FILES/resmi-istatistikler/Turkiye-Gunluk-Guneslenme-Suresi.pdf.

[21] Türkiye Yıllık Global Güneş Radyasyonu (2017). [Online]. Available: https://www.mgm.gov.tr/FILES/resmi-istatistikler/Turkiye-Yillik-Günes-Radyasyonu.pdf.

[22] DHMI (2016), Sera Gazı Beyanı Doğrulama Raporu, Konya: TSE.

[23] Elektrik Tarifeleri (2017). [Online]. Available: http://www.tedas.gov.tr/BilgiBankasi/Sayfalar/ElektrikTarifeleri.aspx.

[24] J. L. Bernal-Agustín and R. Dufo-López (2006), Economical and environmental analysis of grid connected photovoltaic systems in Spain, *Renewable Energy,* pp. 1107–1128.

[25] EPDK, Elektrik Satış (2017). [Online]. Available: http://webcache.googleusercontent.com/search?q=cache:www.epdk.org.tr/TR/Dokuman/5219+&cd=1&hl=tr&ct=clnk&gl=tr.

Photovoltaic Powered Exterior Led Lighting System with Wireless Communication

M. SEZER[1] and S.GÜNEŞ[2]

[1] LOGIBA, Konya/Turkey, muratsezer0@gmail.com
[2]Selcuk University, Konya/Turkey, sgunes@selcuk.edu.tr

Abstract **- Nowadays the biggest problems at lighting applications made with photovoltaic module are position change of photovoltaic panel, unawareness of end of life or stolen batteries and unawareness of the problems at lighting equipment. This situation shows that there should be a control and information system for photovoltaic powered lighting applications. This paper represents the solution of the problems of solar lighting systems. Basically, the aim of the Project is to design power electronics of photovoltaic powered lighting, to design wireless controller for photovoltaic powered lighting and to control them remotely.**

Keywords **- LED, Solar Lighting, Wireless Control Systems**

I. INTRODUCTION

The electricity consumption for lighting represents 19% of the world's total electricity consumption [1]. Lighting of street and buildings accounts for up to 75% in electricity demand of lighting [2]. Smart outdoor lighting control systems allow operative from a central panel to manage the whole lighting system and each luminaire separately.

The increasing demand of energy, the depletion of fossil fuel reserves, the unexpected events taking place on the international scene (local armed conflicts, natural disasters like earthquakes, tsunamis, floods, hurricanes, etc.) that have the potential to partially cripple the energetic systems, proves that the energy security and diversity is a serious aspect that the mankind should seriously consider when deciding the short and middle term energy policy. The general opinion shared by the most part of the specialists supports the idea that the exclusive dependence on the energy produced from fossil fuels (coal, oil, nuclear, etc.) is hazardous, unsustainable and harmful for the environment [3]. The main consideration in the present field technologies are automation, power consumption and cost effectiveness [4].

After 1999 Light Emitting Diode (LED) technology improved very fast and still improving. LEDs started to be a competitor to existing lighting sources with rapid improvement of their luminous flux, color specifications, lifetime and efficacy. Many big companies made investments about LEDs. LEDs are used very often at decorative lighting and started to be a competitor to fluorescent lamps at indoor lighting applications. About usage of outdoor lighting searches and studies are being made.

Solar cells convert light energy to electrical energy according to the conservation of energy law and are the basics of the solar systems. Photovoltaic energy is applicable almost all fields and it is started to use with lighting components during recent years. Photovoltaic panels are used for powering the off grid systems at many light based fields like signalization, local lighting, road lighting, marking etc. LED are mostly preferred these kind of lighting applications because of working with direct current and high efficiency.

Wireless networks consist of devices which communicate each other without any physical connection having wireless receivers and transmitters with wireless transmission platforms like infrared, microwave and radio frequency (RF). Nowadays most of the wireless network technology use RF for communication. Wireless communication presents to users many advantages like portability, flexibility, increasing efficiency and less installation costs. It can be used streets, parks, gardens and many outdoor applications.

Solar energy as one of the important and major renewable source of energy also proves itself useful in functioning of constructions like street-lights. In order to achieve safety and to increase the capacity of battery, charge controller is necessary module. To harness as maximum as possible energy from sun, solar tracker becomes important component. [5]

For the target products at this project, theoretical calculations, circuit schematics, simulations for the necessary parts, printed circuit boards were prepared and function tests were done.

II. PROPOSED APPROACH

The paper illustrates two major approaches.

- First approach is related to design of electronic parts of solar lighting system like dimmable LED driver, MPPT charge controller.
- Second approach is related to design of lighting control system which solves the main problems of solar lighting systems and controls the solar lights.

To be more energy efficient than classical solar lighting systems below functions are added.

- Dimming of LED module: The designed LED driver is dimmable. By this function the lighting level can be reduced and can be increased when necessary. Thus we can save energy.
- Light Dependent Resistor (LDR): It is a type of sensor which actually does this work and senses the

light as our eyes does. With LDR the lights can be turned on when it is dark.

- An accelerometer: at solar lighting systems the position of solar panel is very important to use the panel more efficient. With the accelerometer and control system the position changes can be noticed immediately.

III. Designed System

The designed system consists of LED, LED driver, solar panel, battery, MPPT charge controller, lighting control interface and software.

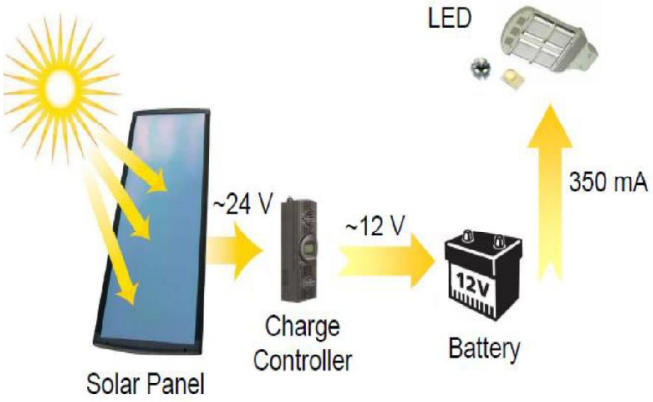


Figure 1: General structure of solar lighting system [6]

Photovoltaic powered luminaires are generally used in the parks. Thus at luminaire power selection the tenders published by public procurement authority and the luminaires used in the parks has been reviewed. Table 1 was used at calculation of solar panel and battery capacities according to selected luminaire power.

Table 1: Calculation of solar panel and battery capacities

City	Konya	
Minimum Sunrise Time	3,95 hour	December
Maximum Sunrise Time	12,16 hour	July
Average Sunrise Time	8,04 hour	

LUMINAIRE SELECTION	
	VALUE
POWER OF THE LUMINAIRE (LED)	40 W
DAILY WORKING TIME	12 hour
DAILY CONSUMED POWER	**480 Wh**

BATTERY SELECTION	
	VALUE
WORKING VOLTAGE	12 V
REQUIRED CURRENT (DAILY)	40 A
TIME THAT ENERGY PROVIDED BY BATTERY	1 day
DISCHARGE DEPTH	50%
BATTERY TEMPERATURE COEFFICIENT	1
BATTERY CAPACITY	**80 Ah**

SOLAR PANEL SELECTION	
	VALUE
PANEL UTILIZATION	75%
SOLAR PANEL CAPACITY	**162,03 W**

SELECTIONS	
	VALUE
LUMINAIRE (LED MODULE)	**40 W**
BATTERY	**100 Ah**
SOLAR PANEL	**150 Wp**

LED driver is one the electronic component that used in solar powered luminaires. The function of LED drivers are increasing/decreasing of battery voltage to LED voltage and driving LED at constant current. Application specific integrated circuits have been reviewed and a LED driver has been designed with LM3424. The LED driver can be dimmed by the lighting control interface.

An MPPT, or maximum power point tracker is an electronic DC to DC converter that optimizes the match between the solar array (PV panels), and the battery bank or utility grid. A MPPT solar charge controller is the charge controller embedded with MPPT algorithm to maximize the amount of current going into the battery from PV module. Application specific integrated circuits have been reviewed and a MPPT solar charge controller has been designed with BQ24650. The designed charge controller accommodates Li-Ion/Polymer, LiFePO4, Lead Acid Chemistries and its specifications are:

- 5-V to 28-V Input Solar Panel
- ±0.5% Charge Voltage Regulation
- ±3% Charge Current Regulation
- ±0.6% Input Voltage Regulation
- Input Overvoltage Protection
- Battery Temperature-Sensing

- Battery Absent Detection
- Thermal Shutdown

A lighting control interface has been designed to control LED driver, to get information from MPPT charger and to send the necessary data to software. With sensor inputs the interface can provide solar panel position and luminous intensity. It sends the data package to the gateway by radio frequency (RF) communication at a free ISM band (2.4 GHz). At this design PIC32MX170F256B from Microchip Company were chosen as microcontroller. It has a 32-bit RISC CPU, 256KB Flash memory and 64K SRAM memory. For RF communication MRF24J40MD from Microchip Company was chosen. MRF24J40MD is a 2.4 GHz IEEE 802.15.4 radio transceiver module intended for longer range applications. The MRF24J40MD has an integrated PCB antenna, matching circuitry, and supports the ZigBee®, MiWi™ and MiWi P2P protocols. The gateway is connected to PC software by serial communication. With the software a user can see the data package comes from the interface. The data package includes below information.

- Failure of charge controller
- Failure of LED driver
- Failure or stolen of battery
- Solar panel's position change

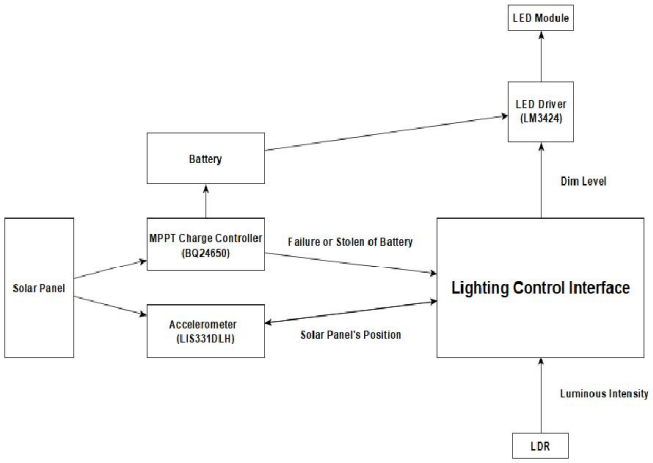


Figure 2: Photovoltaic powered exterior led lighting system with wireless communication

By the designed system a user can control the solar lighting and get information about the system. With dimming function of LED driver the user can dim the light at any time. By this way energy saving also can be done with the system.

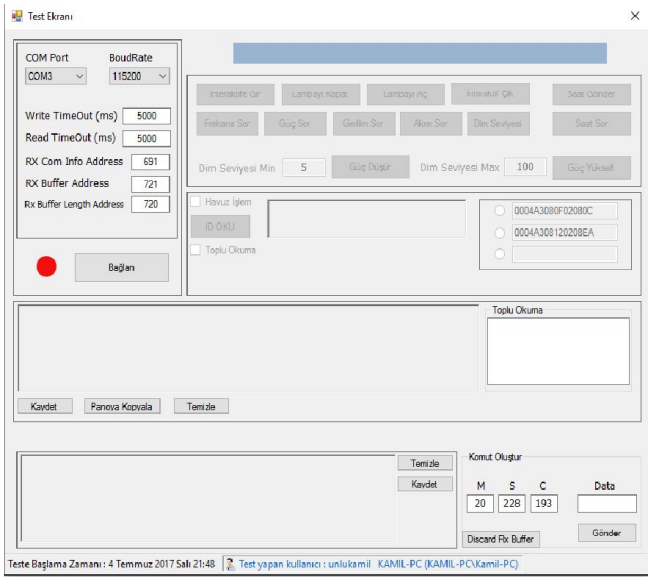


Figure 3: Screenshot of the software

IV. Conclusion

In this paper a proposed photovoltaic powered exterior led lighting system with wireless communication is described that solves the main problems of solar lighting systems and integrates new technologies, offering ease of maintenance and energy savings. This is obtained by using LED module, dimmable LED driver, LDR, accelerometer and MPPT charge controller supplied by renewable energy provided by the solar panels and by using the intelligent lighting control interface.

REFERENCES

[1] International Energy Agency. Light's Labour's Lost. Policies for Energy-efficient Lighting. In support of the G8 Plan of Action. Paris: OECD/IEA; 2006.

[2] Kazarinov LS, Shnaider DA, Barbasova TA. Automatic control systems of efficient lighting. Chelyabinsk: Publisher SUSU; 2011.

[3] Tiberiu TUDORACHE1, Constantin Daniel OANCEA2, Liviu KREINDLER3 published paper on "Performance Evaluation of a Solar Tracking PV Panel" in U.P.B. Sci. Bull., Series C, Vol. 74, Iss. 1, 2012.

[4] Sudhakar, K.S., Anil, A.A., Ashok, K.C., Bhaskar, S.S., 2013, Automatic Street Light Control System, International Journal of Emerging Technology and Advanced Engineering, 188-189.

[5] ON Semiconductor, Solar Powered LED Street Lighting, Available: http://www.onsemi.com/pub_link/Collateral/TND346-D.PDF

[6] Panchal, P., Parmar, A.P., Atodaria, V.H., Desai, P.P., 2013, Solar Led Street-Light Using Motion Sensor And Single Axis Control, International Journal of Advancements in Research & Technology, 480-483.

Increasing Thermal Transfer Printer Head via Controlling History Data Related to Speed and Temperature

A.YAĞBASAN[1] and S. GÜNEŞ[2]

[1] SAVEMA, Konya/Turkey, ahmet_ygb@hotmail.com
[2]Selcuk University, Konya/Turkey, sgunes@selcuk.edu.tr

***Abstract* - Thermal printers print quality is low in high speed applications and lower operational life in low speed applications. Main objectives of this article are to extend the operational life of the thermal print head cells and increase the print quality. This has been done by determining the status of the thermal cells previously heated or not and neighboring cells are previously heated or not. Thermal transfer printers have a shorter head lifetime at low speeds. Because the cells of the head running at low speed have to remain open for a longer time. Head life is shortened because it remains open. Print quality reduces at high speeds. Temperatures of the cells of the head should be increase rapidly in a short time. Print quality would be low because head cannot be heated rapidly in such a short time. Residual heating of thermal print head cells will be prevented. These changes increase the usage areas of thermal transfer printers and reduce production costs.**

Thermal print head life increased at low, high and normal conditional speeds. While increasing head life, prints quality also increased. Head life and print quality balanced during real life applications. Print head can run lower speed, normal speed and higher speed with acceptable quality and life span.

***Keywords* - Thermal Printer, TPH, TTOP, Print out Quality, Print Head Life**

I. INTRODUCTION

THIS study is explain thermal transfer printers print head life and print quality. Thermal Transfer Printer has been widely used in the areas like medical, food, industrial, etc. which marking and coding needed. This kind of printers installed on packaging machines in mass production factories and can get marking and coding on each product. Thermal transfer printer consists of a thermal print head and ribbon. Ribbon is ink pet film. Thermal print head is transfers ribbon ink to the media by heating ribbon depends on printing data. Each data line is printed by print head through heater cells. There is operational life of thermal cells of the thermal print head. If thermal heads cannot be capture head control signal, it causes low quality printing. Generally these printers print on media production date, expiration date, 1D barcode, 2D barcode, logo, etc. Thermal transfer printer installs on packaging machine or labeler applicator. During packaging process printers prints online on media. These are industrial printers. These printers use thermal print head and ribbon. Thermal print head has heater cell line. Heater cell line is heated ribbon according to each line of printing image sequentially. Pet film coated with ink. When thermal print head heat ribbon ink, it melts, and transferred to the media. Media must be flexible. Thermal print head is flat and while printing must touch on ribbon and media. Under pressure heated ribbon is pasted on media by print head. In figure 1, Thermal transfer printer is shown.

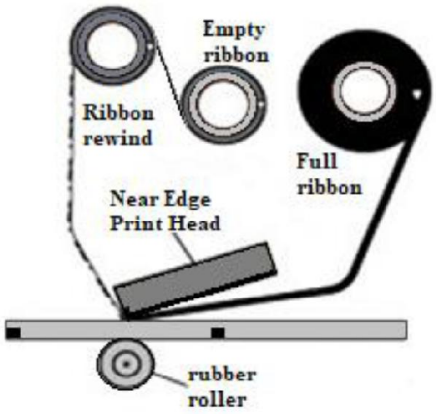


Figure 1: Thermal Transfer System

Thermal print head cells are heater of print head. Each cell is arranged on a single line. Each resistor behaves like heater. Each bit of data to be written corresponds to a resistance. These resistances corresponding to the data according to the state of the bit is turned on or off. Each data row is sent in thermal print head one by one. Each cell turned on time determines cell temperature.

Long turn on time of cells cause high temperature of print head cells. High temperature decrease operational cell life. If previously warned cells and not warned cells are powered on same period of time, always previously warned cells would be more heated. This different temperature causes low print quality and low print head life. Mass production line may be high speed, low speed and normal speed or all of may be in

same mass production line. Thermal printer print quality and life decrease when increase and decrease speed. In this article, a new approach will increase the life of thermal printer and print quality at slow speeds and high speeds. Thermal head cells temperature will be increased in short time. This short time increased temperature will increase the print quality at high speed. Large print time need to long turn on time of head cells. When turn on cells long time, cell temperature exceed maximum temperature. High temperature damages head cells. If turn on time is short, written dot of actual size does not print. Short turn on time causes low print quality. Head cells turn on time will be decreased in large print time with this article. Print head control signals will be improved to improve print quality and head life by using history approach. J. H. Jou. [1]. Worked on print head stresses temperature and deposition head cell temperature. They found stresses temperature about 400℃. They suggested deposition temperature as 220℃. Drees et al. [3]. Using history control schemes changing the strobe pattern and print quality is improved compared to approaches without history control. A design of the strobe signal obsolete value regulates head cells temperature see Shibata [6] and Fukushima [7]. A model is used in a mathematical program to compute the optimal input signals for the print head for different media with different ribbon see Nolde [2].

II. MATERIAL AND METHOD

For less than 150 mm/s speed printing, multi switching signal is applied instead of a single switching signal. This method controlled temperature of cells. Temperature exceeds maximum value to print dot in normal method. Single turn on method initiated thermal stress. Temperature increases more than requirement temperature and fall down under requirement temperature. This temperature ups and downs affect print quality and print head life. This method keeps cell temperature constant and printer prints more than one time with higher speed in a one line. This approach explained with Figure 2.

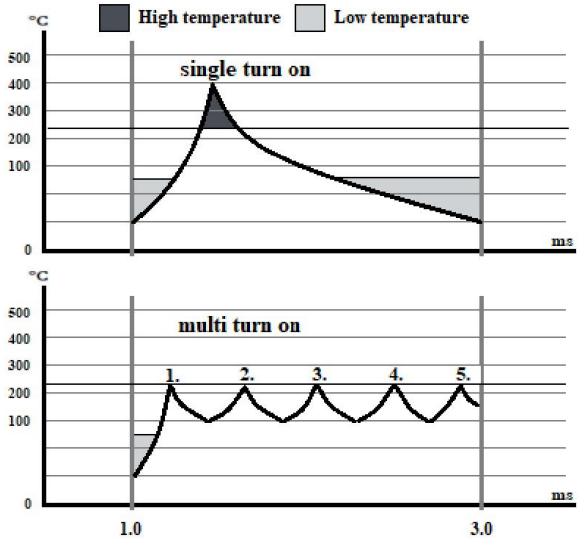


Figure 2: Low speed temperature of head cells

For more than 150 mm/s speeds, history control signals were improved. While improving control signals microscope was used. High temperature was detected areas on print with microscope. This detection is transferred ribbon shape. If ribbon spread above print direction, print head cells temperature more than required temperature. If ribbon not transferred on media, missing ribbon areas less than required temperature. In Figure 3, printed images are shown in different speed with single switching signal.

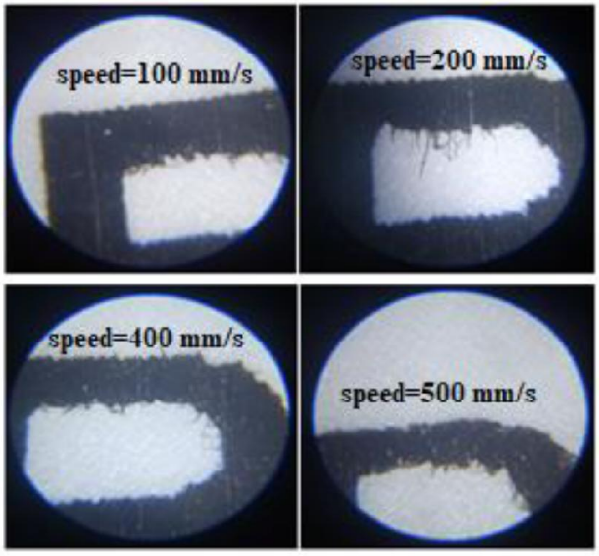


Figure 3: Printed images

History control parameters occurs in 5 stages.(Figure 4) Previously status of print head determines future print head control signal. These control signals improved according to observation of print.

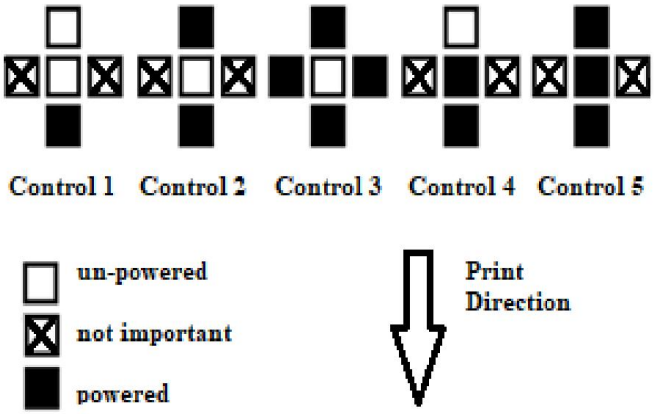


Figure 4 : History control signals

For more than 400 mm/s speed printing required low turn on time. Low turn on time cause low print head cells temperature. For high quality printing print head cell temperature must increased in short time. This method is solved this problem by external heater. External heater increases thermal printer head

temperature thus thermal printer head cells don't need large heating time. Thermal print head cells temperatures reach required temperature in short time.

III. IMPLEMENTATION

In low speed printing detected speed value. If speed value is less than 150 mm/s, speed is accepted as 150 mm/s and printed one line more than one. While printing more than one printing speed 150 mm/s. For an example if speed is 50 mm/s. Multi print value(a) must print as equation (1) as shown Figure 5.

$$a = min.print\ speed/print\ speed \quad (1)$$

$$a = 150/50 = 3\ times$$

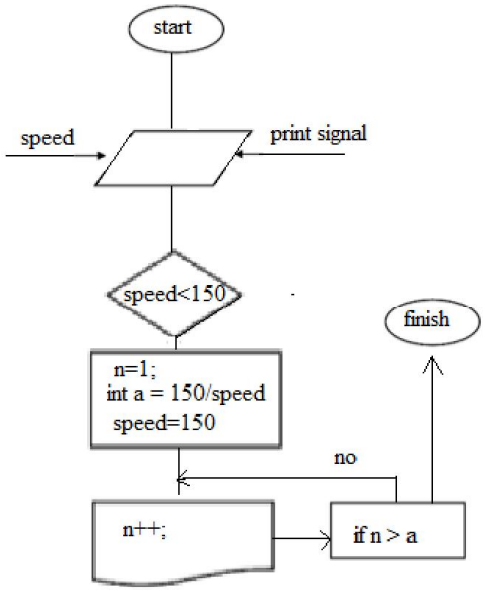


Figure 5: Multi signal print

For more than 150 mm/s condition speeds, microscope was used for detection of high and low temperature areas. If printing first line quality is low, control 1 value was increased. If first line has too much melting ribbon and spread ribbon available, control 1 value was decreased. If previous line printed and future line printed area has not transferred ribbon area, control 5 value was increased. If previously line printed and future line printed area have too much melting ribbon and spread ribbon available, control 5 value was decreased.

In high speed printing an external heater was added on print head cells. This heater increase temperature externally. Externally heated cells needed short time to reach required temperature.

IV. IMPLEMENTATION RESULT

Print outs was observed with microscope at low speed 50 mm/s and high speed 500 mm/s. Normal condition speeds history control signals used in all speeds. Print out first line transferred on media from ribbon. And middle lines transferred on ribbon without any untransffered places. Multi print signal protect head cells from high temperature and temperature stresses. Less temperature increase print head cells life. External heater decrease print head cells power time to reach requested temperature in high speed. In figure 6 shown implementation result at 50 mm/s and 500 mm/s.

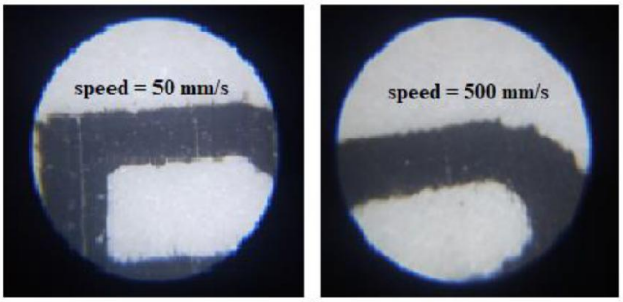


Figure 6 : Print result

V. CONCLUSION

1. Thermal Print Head is made operable at lower speeds. From 150mm/sec to 10mm/sec multiple printing methods are applied successfully. By achieving this, the working life of the thermal head is extended at low speed applications; also better printing quality.
2. The quality of the printing is increased by applying the cells to the desired heat more quickly through the external heater which is used at high speed. Due to lower period of heating time and longer times for cooling on cells, it is prevented residual warming, life of thermal print head is increased.
3. At normal speed, history control values are improved and this lead us better printing quality and also longer life on thermal print heads.

REFERENCES

[1] Jou, J. H.; Hsu, L.; Chang, L. S. "*An analysis of thermal stresses in a multilayer thin film print head. Thin Solid Films*", 1991, 201.2: 253-265.

[2] Nolde, Kristian; Morari, "Manfred. Modeling and control of thermal printing." *IEEE Transactions on Control Systems Technology*, 2010, 18.2: 405-413.

[3] Drees, F., et al. "Performances of thermal transfer printing and their improvement by model calculations." *In: CompEuro'89.'VLSI and Computer Peripherals. VLSI and Microelectronic Applications in Intelligent Peripherals and their Interconnection Networks', Proceedings. IEEE,* 1989. p. 2/40-2/42.

[4] Rohm, Print head Division, "Thermal Print head Application Manual-Basic Edition Verl," 2017. [Online]. Available: http://www.rohm.com/products/module/print head

[5] Kyocera, Manual and Technical Specifications, "Thermal Print head Products—Application Notes," 2017. [Online]. Available: http://global.kyocera.com/prdct/ios/tph/index_tech.html

[6] S. Shibata, "Thin-film thermal head with heating resistors having self controlled temperature," *in Proc. IEEE Ind. Appl. Conf. 13th IAS Ann. Meet. (IAS'95), Conf. Rec.,* 1995, vol. 3, pp. 1976–1981.

[7] I. Fukushima, "New intelligent thermal printing technology," *in Proc. Int. Conf. Digit. Printing Technol. (IS&T's NIP22),* 2006, pp. 268–271.

Classification for Different Databases Using Artificial Neural Network with 10-Fold Cross-Validation

Esra KAYA*, İsmail SARITAŞ

* *Electrical and Electronics Engineering, Faculty of Technology*
Selcuk University, Alaeddin Keykubat Yerleskesi Selcuklu, Konya, 42075 Turkey
esrakaya@selcuk.edu.tr
isaritas@selcuk.edu.tr

***Abstract*—Machine learning is now used in many areas with its fast detection and decision making features. In this study, the success of artificial neural network, one of the methods of machine learning, was measured using UCI iris, BUPA liver disease, Pima indians diabetes and Wisconsin breast cancer databases and the results were compared with other studies on the same databases. For UCI iris, Wisconsin breast cancer, BUPA liver disease and Pima indians diabetes databases, accuracy rates of 0,9866, 0,9876, 0,9072 and 0,8450 were obtained, respectively.**

***Keywords*— ANN, Classification, Cross Validation, Machine Learning, UCI Database**

I. INTRODUCTION

Pattern classification is one of the components in intelligent systems that predict and label unknown samples using a learned classifier [1]. Some of the popular classifiers are Support Vector Machines (SVM), Artificial Neural Networks (ANN), Decision Trees (DT), k Nearest Neighbor (kNN), and Linear Discriminant Analysis (LDA) [1]. The artificial neural networks method which was used in this study is based on human brain model which is a complex, nonlinear and paralel computing system [2]. Thanks to brain neurons, pattern recognition, detection and motor control, and many other operations are realized faster than the fastest digital computer in the world. As a result of this features, artificial neural network has emerged as an information processing method inspired by neurons [2].

In an artificial neural network consisting of three layers, there is an input layer, hidden layer and output layer [3]. Connections between these layers are provided with adjustable weight values [3]. The input layer is multiplied by these weight values and transmitted to the hidden layer, where it is processed by a transfer function. The processed data in the hidden layer is again multiplied by the weight values and transmitted to the output layer and so that an output is generated. This network is called a feedforward network [3]. The difference between the obtained result and the desired result is the failure of the network, and this error is returned to the network as a feedback so that the weight values of the connections between the layers are adjusted accordingly. This process is called back propagation [3].

II. RELATED WORKS

When we look at machine learning studies on different UCI databases, in 2017 Zheng et al. have developed a new Supervised Adaptive Incremental Clustering (SAIC) algorithm that aggregates data flows to accommodate dynamic databases and has observed the performance of the algorithm on fourteen UCI datasets [4]. In another study conducted in 2017, Gonzalez-Abril et al. have developed a processing technique for SVM algorithms to obtain sufficient accuracy in priority class binary system classification problems labeled as positive class and the studies were applied to eleven UCI data sets [5]. In another study conducted in 2017 over twenty UCI databases, Kassani et al. have came up with a method which is called multi-objective genetic-algorithm-modified fuzzy neural network (MOGA-FNN) by evolving kNN and fuzzy neural network (FNN) [1]. In the same year, Eghbali et al. tried to improve multi-class classification by using neighborhood search feature in error correcting output codes and applied the method to sixteen UCI databases [6]. For 65 UCI dataset, Katuwal et al. used both single and multivariate decision trees together with random vector functional link network (RVFL) [7]. In a study presented by Chang et al. in 2011, UCI iris dataset was categorized by using a Gaussian distribution based classifier [8]. In 2017, Nilashi et al. used expectation maximization (EM) method for clustering similar data in the UCI Wisconsin breast cancer dataset and classification and regression trees (CART) to create fuzzy rules for making a diagnosis [9]. In another study carried out on the same dataset, Abdel-Zaher et al. have realized data classification using unsupervised deep belief network and supervised back propagation in 2016 [10]. In 2017 for the diagnosis of breast cancer, Dora et al. have proposed an algorithm based on Gauss-Newton representation. In this study, sparse representation has been used in the selection of the training samples and the Gauss-Newton approach determines the optimal weights for the classification of the training data [11]. In 2016, a new decision tree algorithm developed by Abdar et al. was applied to the UCI liver disease dataset [12]. Also in 2016, Hayashi et al. used a recursive rule extraction algorithm combined with a sampling selection technique for the diagnosis of liver disease [13]. In 2010, Lekkas et al. worked on a method that allows on-line processing of the data by repeatedly changing the fuzzy rule base for each sample obtained from the data streams, thereby

improving the fuzzy classification and have realized the testing process of the method on the UCI Pima Indians diabetes data set [14]. Mansourypoor et al. worked on the development of an evolutionary fuzzy rule-based system based on reinforced learning and made experiments on the same dataset in 2017 [15]. The same year, Maniruzzaman et al. performed diagnostic classification of the UCI Pima Indians diabetes data set using a method based on Gaussian distribution with linear, polynomial and radial-based nuclei. The results were then compared with LDA, Quadratic Discriminant Analysis (QDA) and Naive Bayes (NB) [16].

In this study, an artificial neural network with 10-fold cross validation was applied to UCI Iris, Wisconsin breast cancer, BUPA liver disease and Pima Indians diabetes datasets. Accuracy, sensitivity and specificity values were calculated for the classifications and the accuracy rates were compared with other studies.

III. Material and Method

When we look at the properties of the datasets used for the study, there are 150 samples in the UCI iris dataset, 4 feature parameters and 3 classes; setosa, versicolor and virginica. The UCI Wisconsin breast cancer dataset contains 569 samples with 30 feature parameters and 2 classes of benign and malignant. In the UCI liver disease dataset, there are 345 samples, 6 feature parameters, and 2 classes with positive and negative disease diagnosis. Lastly, there are 768 samples in the UCI Pima Indians diabetes dataset, 8 feature parameters, and 2 classes, positive and negative for diabetes.

A resilient backpropagation algorithm has been used for the artificial neural network with 10-fold cross validation. ANNs, each of which is defined as a pattern recognition network, consists of 3 layers; input layer, hidden layer and output layer. The hidden layers used in the classification consist of 20 layers for iris, breast cancer and liver disease and 30 layers for Pima indians diabetes. For all data sets the error is calculated with the mean square error function and training continues until the desired smallest error value is reached. The maximum failure rate in the training process was 100 for iris and breast cancer, 200 for liver disease and 300 for Pima indians. The tansfer function used in network training is hyperbolic tangent sigmoid for both the connections between input and hidden layers and between hidden and output layers for iris, breast cancer and Pima Indians diabetes datasets, while it is logarithmic sigmoid between input and hidden layers and hyperbolic tangent sigmoid between hidden and output layers for liver disease dataset. In the case of cross-validated ANNs, data is divided into training and test sets. At each cross-validation fold, samples are divided according to cross-validation indices such that the samples used for test previously are used for training and some of the previously training samples are used for testing based on the indices. In ths study, 10 indexes have been allocated for cross-validation and for each fold the samples are divided accordingly using interleaved indices; 70% for training, 15% for testing and the remaining 15% for validation. Here, the total of training and validation data constitute the training data.

IV. Results and Discussions

In the confusion matrices obtained after the training of the artificial neural networks, concepts such as true positive (TP), true negative (TN), false positive (FP) and false negative (FN) provide information about the correct or incorrect classification of the data. True positive indicates that the positive data is classifed correctly. True negative means that the negative data is classified correctly. On the other hand, false positive indicates that the negative data is classified as positive and false negative indicates that the positive data is classified as negative.

According to these values, the accuracy (Acc) rate is given by the following formula [1].

$$Accuracy\ (Acc) = (TP + TN)/(TP + TN + FP + FN) \quad (1)$$

Sensitivity or true positive rate (TPR) is given by the following formula [1].

$$Sensitivity\ (TPR) = TP/(TP + FN) \quad (2)$$

Specificity or true negative ratio (TNR) is given by the following formula [1].

$$Specificity\ (TNR) = TN/(TN + FP) \quad (3)$$

Sensitivity here is the accuracy rate of positive samples. Specificity is the accuracy rate of negative samples.

Figures 1, 2, 3 and 4 show the confusion matrices of the results from the training of 10-fold cross-validated artificial neural networks applied to UCI Iris, Wisconsin breast cancer, BUPA liver disease and Pima indians diabetes datasets, respectively.



Figure 1. The Confusion Matrix of UCI Iris Dataset



Figure 2. The Confusion Matrix of UCI Wisconsin Breast Cancer Dataset



Figure 3. The Confusion Matrix of UCI BUPA Liver Disease Dataset

In Table 1, the accuracy, sensitivity and specificity results obtained for this study is shown. In Table 2, achine learning studies on the same UCI datasets in the literature are compared with the accuracy results of this study.

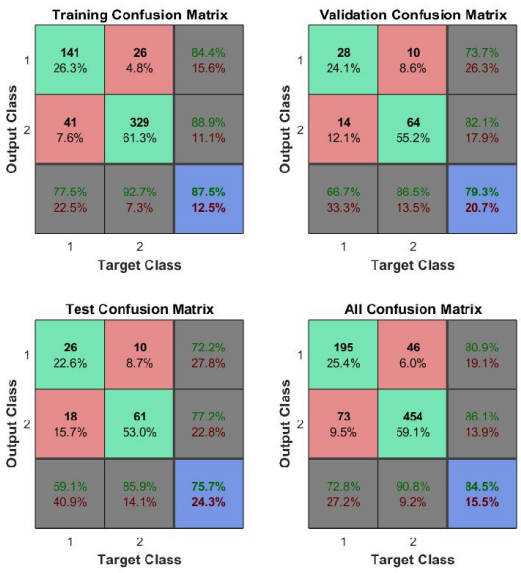


Figure 4. The Confusion Matrix of UCI Pima Indians Diabetes Dataset

Table 1. Accuracy, sensitivity and specificity results of 10-fold cross validated ANN over UCI datasets

UCI Datasets	Iris	Wisconsin Breast Cancer	BUPA Liver Disease	Pima Indians Diabetes
Accuracy	0,9866	0,9876	0,9072	0,8450
Sensitivity	1,0000	0,9971	0,8413	0,7276
	0,9600			
	1,0000			
Specificity	1,0000	0,9716	0,9550	0,9080
	1,0000			
	0,9800			

Table 2. Accuracy comparison of the 10-fold cross-validated ANN with literature studies for the same UCI datasets

	Iris	Wisconsin Breast Cancer	BUPA Liver Disease	Pima Indians Diabetes
[1] - *2017*	**98,88**		73,38	77,22
[4] - *2017*	96,30			72,50
[5] - *2017*	96,27		71,17	74,45
[6] - *2017*	92,66			
[7] - *2017*	98,65			
[8] - *2011*	96,67			
[9] - *2017*		93,20		
[10] - *2016*		**99,68**		
[11] - *2017*		99,23		
[12] - *2017*			**93,75**	
[13] - *2016*			73,48	
[14] - *2010*				79,37
[15] - *2017*				84,00
[16] - *2017*				81,97
This study	98,66	98,76	90,72	**84,50**

V. Conclusion

As shown in Table 1, the accuracy rate is quite good for iris and breast cancer data and also because the sensitivity and specificity values are also high, the true positive and the true negative values are very close to reality. The accuracy rate is acceptable for liver disease data because Table 2 clearly shows that the highest score of %93.7 obtained from another study is a little bit higher from the score of %90.72 we have achieved. The sensitivity rate for the liver is slightly lower but can be accepted depending on the accuracy achieved. The best accuracy rate for Pima Indians diabetes has been achieved by this study and when we look at the other studies, it can be seen that generally low accuracy rates were obtained up until now.

When we look at the studies [1], [4], [5] in litearture, a very good success was achieved for one dataset while low accuracies were obtained for other datasets. This is not the case for our study and we have achieved a generally stable success for all the datasets. In future studies, we will try to improve the accuracy rates obtained by using different machine learning methods which will be tested on more datasets.

References

[1] P. H. Kassani, A. B. J. Teoh, and E. Kim, "Evolutionary-modified fuzzy nearest-neighbor rule for pattern classification," *Expert Systems with Applications,* vol. 88, pp. 258-269, 2017.

[2] S. S. Haykin, S. S. Haykin, S. S. Haykin, and S. S. Haykin, *Neural networks and learning machines*. Pearson Upper Saddle River, NJ, USA:, 2009.

[3] R. O. Duda, P. E. Hart, and D. G. Stork, *Pattern classification*. John Wiley & Sons, 2012.

[4] L. Zheng, H. Huo, Y. Guo, and T. Fang, "Supervised Adaptive Incremental Clustering for data stream of chunks," *Neurocomputing,* vol. 219, pp. 502-517, 2017.

[5] L. Gonzalez-Abril, C. Angulo, H. Nuñez, and Y. Leal, "Handling binary classification problems with a priority class by using Support Vector Machines," *Applied Soft Computing,* vol. 61, pp. 661-669, 2017.

[6] N. Eghbali and G. A. Montazer, "Improving Multiclass Classification Using Neighborhood Search in Error Correcting Output Codes," *Pattern Recognition Letters,* 2017.

[7] R. Katuwal, P. Suganthan, and L. Zhang, "An ensemble of decision trees with random vector functional link networks for multi-class classification," *Applied Soft Computing,* 2017.

[8] H. Chang and A. Astolfi, "Gaussian Based Classification with Application to the Iris Data Set," *IFAC Proceedings Volumes,* vol. 44, no. 1, pp. 14271-14276, 2011.

[9] M. Nilashi, O. Ibrahim, H. Ahmadi, and L. Shahmoradi, "A knowledge-based system for breast cancer classification using fuzzy logic method," *Telematics and Informatics,* vol. 34, no. 4, pp. 133-144, 2017.

[10] A. M. Abdel-Zaher and A. M. Eldeib, "Breast cancer classification using deep belief networks," *Expert Systems with Applications,* vol. 46, pp. 139-144, 2016.

[11] L. Dora, S. Agrawal, R. Panda, and A. Abraham, "Optimal breast cancer classification using GaussNewton representation based algorithm," *Expert Systems with Applications: An International Journal,* vol. 85, no. C, pp. 134-145, 2017.

[12] M. Abdar, M. Zomorodi-Moghadam, R. Das, and I.-H. Ting, "Performance analysis of classification algorithms on early detection of liver disease," *Expert Systems with Applications,* vol. 67, pp. 239-251, 2017.

[13] Y. Hayashi and K. Fukunaga, "Accuracy of rule extraction using a recursive-rule extraction algorithm with continuous attributes combined with a sampling selection technique for the diagnosis of liver disease," *Informatics in Medicine Unlocked,* vol. 5, pp. 26-38, 2016.

[14] S. Lekkas and L. Mikhailov, "Evolving fuzzy medical diagnosis of Pima Indians diabetes and of dermatological diseases," *Artificial Intelligence in Medicine,* vol. 50, no. 2, pp. 117-126, 2010.

[15] F. Mansourypoor and S. Asadi, "Development of a Reinforcement Learning-based Evolutionary Fuzzy Rule-Based System for diabetes diagnosis," *Computers in Biology and Medicine,* 2017.

[16] M. Maniruzzaman *et al.*, "Comparative approaches for classification of diabetes mellitus data: Machine learning paradigm," *Computer Methods and Programs in Biomedicine,* vol. 152, pp. 23-34, 2017.

A Study on the Usage of Tobacco Waste Ash as a Mineral Admixture in Concrete Technology

S.CELIKTEN [1] and M. CANBAZ [2]

[1] Anadolu University, Eskisehir/Turkey, serhat51celikten@gmail.com
[2]Eskisehir Osmangazi University, Eskisehir/Turkey, canbaz2008@gmail.com

Abstract - **In Turkey, approximately 10000 tons waste occurs during the production of tobacco annually. This high amount waste has a great potential for concrete technology. Tobacco waste ash is a material that needs to be investigated with its potential to show puzzolanic activity due to its properties such as fineness, amorphous form and high silica content. So it can be said that tobacco waste ash may be used in concrete as a mineral admixture. In this conducted study, two type of tobacco waste ashes supplied from Adıyaman and Bitlis regions in Turkey were partially replaced with cement by weight at 0, 10, 20 and 30% proportions. 4 x 4 x 16 cm prism specimens prepared with mortars produced by using the binary blends of cement and ashes were cured 28 days in a water-curing tank with controlled temperature 24 ± 1 °C. Compressive and flexural strength, unit weight and ultrasonic tests were performed on the specimens at 28 days. By using the results of tests compressive and flexural strength, unit weight, ultrasonic pulse velocity, dynamic modulus of elasticity values of the mortar specimens were calculated. The experimental results reveal that the compressive and flexural strength, unit weight, ultrasonic pulse velocity, dynamic modulus of elasticity values of the mortar specimens decrease as the increasing of the tobacco waste ash content. While no improvements were observed on the monitored properties of mortar specimens containing tobacco waste ash compared to control mortar, it can be suggested that the usage of the Adıyaman tobacco waste ash at %10 by cement as a mineral admixture providing ecological and economic benefits by consumption of this non-renewable waste.**

Keywords – **Tobbaco ash, mineral admixture, mortar, physical and mechanical properties,**

I. INTRODUCTION

CEMENT is a significant material that used for civil engineering applications all over the world. Though, the consumption of cement brings about some important ecologic problems. One of these problems is the large amount of CO_2 emission resultant from the manufacturing process of the cement [1-2]. In addition to reducing cement consumption of the mineral admixture content also improves some important properties of the concrete in two ways. First way is the reaction occur between calcium hydroxide and mineral admixture resulting with the generation of the extra Calcium Silicate Hydrate gel. Second way is the filler effect of the mineral admixture due to its fineness [3]. Mineral admixtures can also reduce material costs by providing less cement consumption [4].

Many natural and artificial mineral admixtures are used in the field of construction and concrete production for various purposes. The utilization of the industrial wastes and by-products in concrete industry as mineral admixture provides the industry to be eco-friendlier and sustainable. Industrial by-products and wastes, such as, recycled plastics, silica fume, fly ash and ground granulated blast furnace slag have been successfully used as mineral admixture in concrete technology for decades [5,6]. The behaviour of these additives in concrete is physico-chemical. The physical part of this behaviour is originated from the shrinking of the size of the void in the interface between the cement and the aggregate. The main compounds SiO_2, Al_2O_3 and Fe_2O_3 should constitute great rate of the total chemical composition of the mineral admixtures in order to be used in cement and concrete. The activity of these additives is dependent on the presence of oxides and minerals in amorphous or weakly crystalline states [7].

In Turkey, about 5000-6000 tons of tobacco fabrication waste is being destroyed as dust and crumbs during the processing of the tobacco in cigarette factories, annually. In addition, tobacco waste, disposed by cigarette markets purchased the tobacco, occurs varying amounts of between 1500 and 6000 tons per year. As a result, it is necessary to evaluate this high amount of waste occurs about 10000 tons per year, in Turkey [8].

The aim of this study was to determine the possibilities of utilization of tobacco waste ash as a mineral admixture in concrete technology.

II. MATERIAL AND METHODS

A. Materials

CEM I 42.5 cement was used by production of Cimsa Eskişehir cement mill. The properties of cement are given in Table 1.

Table 1: Properties of cement

Final Setting, min.	Density, g/cm^3	Blaine, cm^2/g	Strength, MPa	Expansion, mm
260	3.17	3750	49.5	1.3

Tobacco waste ashes obtained from Adıyaman (A) and Bitlis (B) regions were used as puzzolan by cement at particular displacement ratios. The chemical properties of the ashes were given in Table 2.

Table 2: Properties of ashes

	SiO_2	Al_2O_3	Fe_2O_3	CaO	MgO	K_2O	Na_2O	SO_3	Cl^-	LOI
A	26,37	0,11	0,27	26,34	4,2	18,96	0,29	6,84	0,57	43,1
B	27,47	0,5	0,42	25,76	4,16	18,42	0,31	6,25	0,55	42,7

Eskisehir tap water was used in the mortar mixtures. The chemical analysis of the drinkable water is given in Table 3.

Table 3: Chemical analysis of the water

pH	NTU	Cl mg/l	Ca^{++} mg/l	SO_4 mg/l	Organic Material	CO^{-3} mg/l	FS0 mg/l	Mg^{++} mg/l	Total Salinity
7.7	<5	245.8	187	135	49	23	92	107,4	1540

The standard sand named RILEM Cembureau prepared by Trakya Cement Set Cement Industry and Trade Inc. suitable for TSE EN 196-1 was used.

B. Methods

Firstly, the Adıyaman and Bitlis tobaccos were burned. Than the ash-slag mixture occurred after the burning process was sieved through a 90-micron sieve and the undersize grain was utilized as puzzolan.

The mixture proportions of the mortars were determined 1, 0.5, 3 for cement, water and aggregate respectively. The tobacco waste ashes were replaced with cement by weight at 0, 10, 20, 30% ratios in mortar production. The first series made with Adıyaman ash and the second series produced with Bitlis ash. Three 4*4*16 cm prism specimens were taken from each mortar mixture. The unit weight, ultrasonic, compressive strength tests were performed on the specimens after 28-day curing period to determine the effects of the ashes on the properties of the mortars.

III. RESULTS AND DISCUSSION

A. Unit Weight

Unit weight values of hardened mortars were measured on the water-saturated dry surface specimens after pulling out from the curing pool. The results of the measurements are shown in Figure 1. As seen in Figure 1, the unit weight values of the mortars decreased up to 8% with increasing of the Adıyaman tobacco waste ash content for the first series. The probably reason of decreasing is that the specific gravity of Adıyaman tobacco waste ash is lower than that of cement. In second series, the unit weight values of the mortar specimens made with %10 and %30 Bitlis tobacco waste ash by cement decrease %1 and %3 respectively. In contrast, mortars made with % 20 Bitlis tobacco waste ash have slightly higher unit weight than the control mortar of the second series.

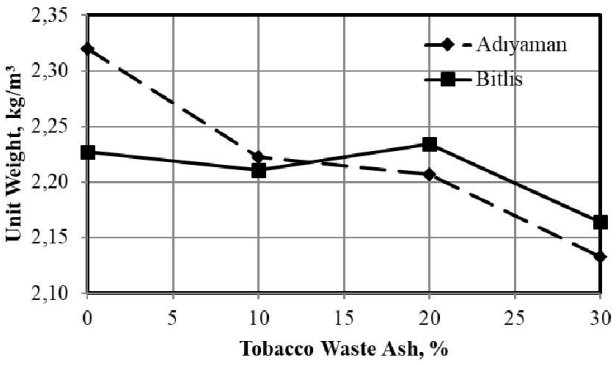


Figure 1: Unit weight values of the mortars

B. Compressive Strength

The compressive strength values of mortars in two series at the age of 28 days are illustrated in Figure 2. In the first series, the compressive strength values of the mortars including 10%, 20% and 30% Adıyaman tobacco waste ash were 6%, 16% and 31% lower than that of control mortar, respectively. In the second series, the values decreased sharply that 21%, 34% and 47% fall was observed according to the control mortar for same ash proportions. While chemical composition of the two types of ash was similar with each other, the compressive strength values of the mortars made with Adıyaman tobacco waste ash was higher than Bitlis ash. This discrepancy may be originated from their particle size, chemical reactivity and storage conditions. While mortars made with %10 Adıyaman tobacco waste ash had 6% lower compressive strength than control mortar in series one, it can be suggested that the usage of Adıyaman tobacco waste ash as mineral admixture for ecologic and economic benefits.

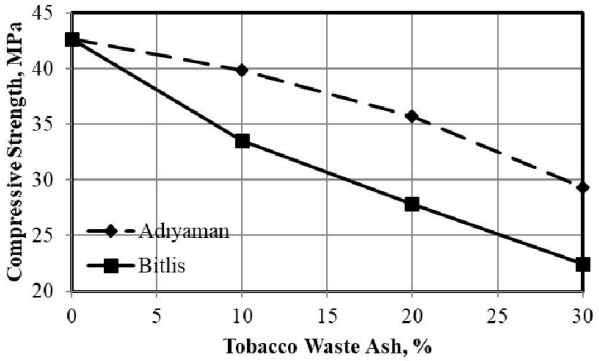


Figure 2: Compressive strength values of the mortars

C. Flexural Strength

The flexural strength values of mortar specimens in two series at the age of 28 days are shown in Figure 3. As shown in the figure, mortars made with Adıyaman and Bitlis ash had lower flexural strength with increasing of the ash content.

While, Adıyaman ash showed better compressive strength performance than Bitlis ash, it was completely adverse for the flexural strength. In the first series, the flexural strength values of the mortars including 10%, 20% and 30% Adıyaman tobacco waste ash were 13%, 15% and 19% lower than that of control mortar, respectively. In the second series, the values 1%, 2% and 11% decreased according to the control mortar for same ash proportions, respectively. However, the usage of the Adıyaman ash as mineral admixture for concrete technology was suggested according to little loss in compressive strength when compared to control mortar, flexural strength loss must be considered before the usage.

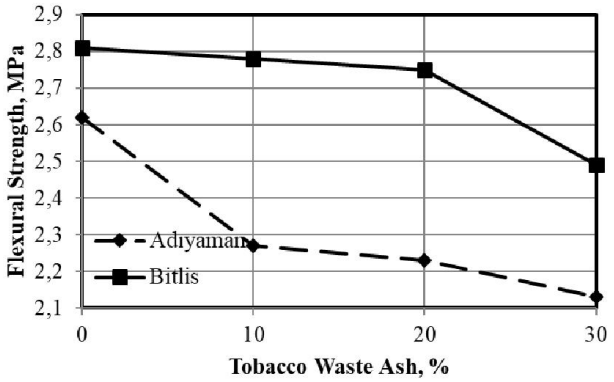


Figure 3: Flexural strength values of the mortars

D. Dynamic Modulus of Elasticity

The calculated dynamic modulus of elasticity values of the mortars according to the unit weight and ultrasonic pulse velocity values were given in the Figure 4. The dynamic elasticity values of the mortars decreased sharply with Adıyaman and Bitlis tobacco ashes content up to 29 and 65% according to control mortars, respectively. The dynamic modulus of elasticity properties of the mortars was similar with the compressive strength.

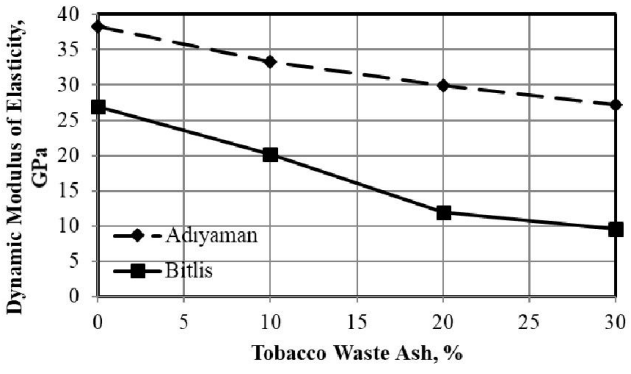


Figure 4: Dynamic modulus of elasticity of the mortars.

E. Ultrasonic Pulse Velocity

Ultrasonic pulse velocity in a material associates with the porousness, density and elastic properties of the material. The influences of Adıyaman and Bitlis tobacco waste ashes on the ultrasonic pulse velocity values of the mortar specimens were evaluated by ultrasonic measurements performed in this work. The results procured from the ultrasonic measurements of the mortar specimens at the ages of 28 days were given in Figure 5. Each ultrasonic pulse velocity result represented the average of three measurements. As seen in Figure 5, the ultrasonic pulse velocity values of the mortar specimens decreased with the tobacco waste ash content. While the ultrasonic pulse velocity values of the mortar specimens decreased slightly with Adıyaman tobacco waste ash content, the values decreased with Bitlis ash content substantially. The average value of the ultrasonic pulse velocity values of the control mortar specimens in the first series was 4.06 km/s. In the first series, as shown in Figure 5 that the mortar specimens made with 10%, 20% and 30% Adıyaman tobacco waste ash had 5%, 9% and 12% lower ultrasonic pulse velocity values than control mortar respectively. The average ultrasonic pulse velocity value of the control mortar specimens in the second series was 3.48 km/s. In the second series, it was observed that the mortar specimens made with 10%, 20% and 30% Bitlis tobacco waste ash had 13%, 33% and 40% lower ultrasonic pulse velocity values than control mortar respectively.

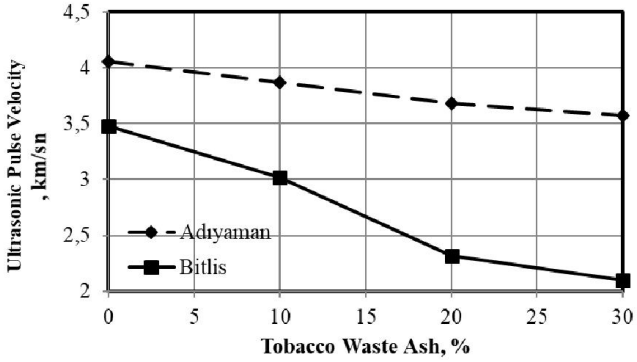


Figure 5: Ultrasonic pulse velocity values of the mortars

IV. CONCLUSIONS

From the results obtained, the following conclusions can be drawn.

- Unit weights of the mortars made with Adıyaman tobacco waste ash decreased with the ash addition. Mortars produced with Bitlis ash show similar unit weight with control mortar.
- The compressive strength of the mortars decreased with the increasing of the Adıyaman and Bitlis tobacco ashes content up to 31 and 47%, respectively.
- The ultrasonic pulse velocity values of the mortars decrease with Adıyaman ash addition slightly.

However, the values decreased with Bitlis ash addition sharply.

- A negative effect of the tobacco waste ashes was observed on the dynamic modulus of elasticity of the mortars.

From this study, utilization of the Adıyaman tobacco waste ash as a mineral admixture by cement in the concrete technology at %10 proportion can be suggested despite the negligible effects on the mechanical properties for waste management and economic purposes. However, the use of Bitlis tobacco waste ash and Adıyaman ash more than 10% was not recommended because of the adverse effects on the mortar properties. Furthermore, the study of the effect of tobacco waste ashes on the durability of mortar or concrete may be recommended for further studies.

REFERENCES

[1] G. van Oss Hendrik, C. Padovani Amy, *Cement manufacture and the environment Part II: Environmental challenges and opportunities,* J Ind Ecol;7(1):93–126, 2003.

[2] B. Uzal, L. Turanli, P.K. Mehta, "High-volume natural pozzolan concrete for structural applications", *ACI Materials Journal* 104(5):535-538, 2007.

[3] M. Limbachiya, M.S. Meddah, Y. Ouchagour, "Use of recycled concrete aggregate in fly-ash concrete", *Construction and Building Materials* 27, 439–449, 2012.

[4] D.D. Bui, J. Hu, P. Stroeven "Particle size effect on the strength of rice husk ash blended gap-graded Portland cement concrete", *Cement and Concrete Composites* 27(3), 357-366., 2005.

[5] C. Meyer, "The greening of the concrete industry", *Cement and Concrete Composites* 31:601–605, 2009.

[6] L.M. Federico, S.E. Chidiac, "Waste glass as a supplementary cementitious material in concrete – critical review of treatment methods", *Cement and Concrete Composites* 31, 606–610, 2009.

[7] D.D. Vu, *Strength properties of metakaolin-blended paste, mortarand concrete*, Delft University Press, Netherlands, 2002.

[8] E.E. Kara, "Tütün Fabrikasyon Atıklarının Toprağın Biyolojik Aktivitesi ve Azot Kazancına Etkisi", *Anadolu, J. of AARI* 6 (2), 100–111, 1996.

Utilization of Chrome Ore Concentration Plant Tailings as Fine Aggregate in Ready-mixed Concrete

S. CELIKTEN [1] and M. CANBAZ [2]

[1] Anadolu University, Eskisehir/Turkey, serhat51celikten@gmail.com
[2]Eskisehir Osmangazi University, Eskisehir/Turkey, canbaz2008@gmail.com

Abstract - **Large amount of the chrome ore concentration plant tailings was discarded during chrome ore mining process. The accumulation of the tailings takes large areas of land for the storage and causes environmental and safety problems. When the annual consumption of the ready mixed concrete per person (approximately 1.5 m^3/person) in Turkey is considered, employment of the tailings in the ready-mixed concrete may be a solution for the recovery of the tailings. In addition, using chrome tailings as a substitution for sand to produce ready-mixed concrete is a possible way to solve the resource problem of sand deficiency. The aim of this study is to investigate the utilization of the tailings taken from a chrome ore concentration plant in Eskisehir, Turkey as fine aggregate in ready-mixed concrete production. For this purpose, the tailings were partially replaced with the fine aggregate by the weight at 0, 10, 20 and 30% proportions by weight in the ready-mixed concrete mixtures. Standard curing is applied until the time of test to the 15x15x15 cm cube specimens taken from the mixtures. The unit weight, compressive strength and ultrasonic pulse velocity values of the cubic specimens were investigated in this study. Performed tests showed that replacing sand to chrome ore tailings has a potential for further investigations.**

Keywords - **Chrome ore tailings, fine aggregate, ready-mixed concrete, hardened concrete properties**

I. INTRODUCTION

WORLD chromite production was at 3.65 million tons in 1953, it reached 19 million tons in 2009. In the last decade, demand for chromium alloys has increased by about 5% per year and annual chromium ore production increased an average of 4.6% followed the demand, annually [1]. In Turkey, many chrome ore concentration plants have been established since 2000. But efficiency and capacity utilization of the plants are low [2]. If the high production quantity of the chromite to be considered, an important waste and tailings problem originated from the plants occurs in Turkey and all over the world.

Chromite is the only mineral that chromium metal one of the natural components of the earth's crust can be produced economically. The chromite is a mineral of the spinel group and crystallizes in the cubic system. The theoretical formula of chromite is $FeCr_2O_4$ but chromite minerals found in nature is symbolized by a formula of $(Mg,Fe)(Cr,Al,Fe)_2O_4$ [3]. The main industrial branches in which chromium is used are metallurgy, refractory and chemical industry. However, the chromium ores extracted from the mines often do not provide the desired product characteristics of these industries. Therefore, it is necessary rendering the chromite ores extracted from the mines to the properties desired by the industries with effective enrichment processes [4]. Chrome ore can be enriched with combing out with hand, sieving and washing to remove the silicate minerals from the ore structure. At later stages, enrichment of the chromite mineral is ensured with shaky tables, magnetic separator, flotation or heavy liquid methods and so, the residual silicate is cleared. All these processes are performed in the chrome ore concentration plants [3]. After the enrichment process is performed, a considerable amount of tailings is released from the plant. These tailings disturb the natural view and cause physical pollution and storage problems. The environmental and storage problems caused by the tailings need to be solved and economic feasibility of the tailings is worth to search for its high amount. For this purpose, an investigation was performed on the possibilities of the recovery of tailings exposed from a chrome ore concentration plant. It is revealed that the tailings can be used after sieving and washing as a lightweight construction material and a part of the tailings can be recovered [5]. An experimental study was performed on the utilization of the serpentine based chromite waste as a ceramic pigment in the colouring agent in wall tile glaze recipes and as a modifier in the floor and porcelain tile glaze recipes. According to the results of the study, the chromite waste can be used for the purposes with any problem [6]. Another study was carried out for re-beneficiation of chrome ore concentration plant tailings. After the washing and sieving processes, the wastes bigger than 0.1 mm size can be used for the production of lightweight construction material as sand. It was emphasised that there are alternative solutions for residual chromium recovery and one of them is the repeating of the concentration process on the tailings [5]. There are a lot of benefits of recycling the wastes for any purpose. As for chrome tailings, usage of the tailings in the concrete can minimize the storage and land problems around the concentration plants. And another advantage is the reduction of the sand consumption and protection of resources. The aim of this study was to recycle the tailings as fine aggregate in ready mixed concrete.

II. MATERIAL AND METHODS

A. Materials

CEM I 42,5 N type cement correspond to TS EN 197-1 and appropriate with ASTM type I was employed in this study. Crushed aggregates used to be in two sizes of 4-11mm and 11-22 mm and sand with a size of 0-4 mm were supplied from Selka ready–mixed concrete plant in Eskisehir. The aggregates used in the mixtures were in concordance with the requirements of TS 706 EN 12620+A1. The top water used as mix water in the mixtures. Chrome tailings were taken from a chrome ore concentration plant in Eskisehir. The concentrated chromium particles from the plant were shown in Figure 1. During the concentration process, there are a lot of tailings occur and disposed of from the plant. The tailings used in this study were the rest of the process.



Figure 1: Concentrated chromium particles.

As seen in Figure 2, the tailings occurred as waste from the chromium production transported to landfill area together with water.



Figure 2: Tailings occurred during the chromium production.

The concentration process was inefficient because the tailings composed of the large amount of ore. So, the tailings accumulated around the concentration plant very rapidly. Dried and stored state of the chrome tailings is shown in Figure 3. Chrome tailings hill causes storage and landfill problems with the environmental and economic disadvantages.

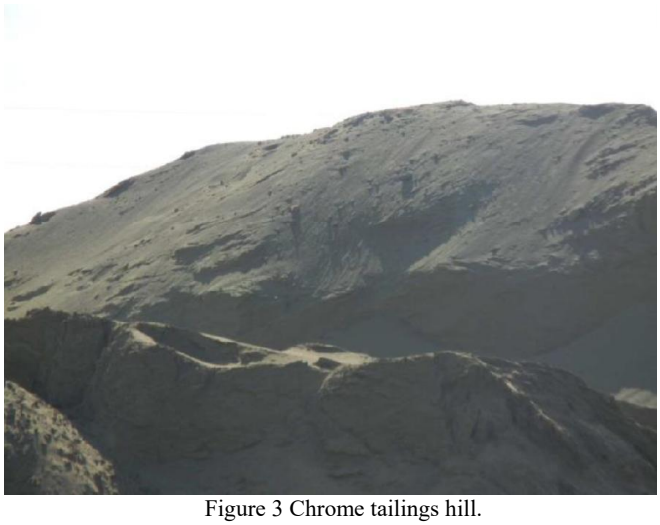


Figure 3 Chrome tailings hill.

Physical and chemical properties of the chrome tailings used in this study were given in Table 1. According to the properties, there was any drawback to use the tailings by sand in the ready mixed concrete.

Table 1: Properties of the chrome tailings

Density, kg/dm^3	Water absorption, %	Fine particulate, % (<0,063 mm)
2,72	1,6	3,6
Organic contaminant	Organic matter	ASR expansion, % (accel. Met.)
<% 0,001	Light yellow	0.01
SO_3, %	Cl, %	S, %
0,02	<0,0005	0,025

B. Methods

There are 4 series of concrete mixtures were prepared in this work. The series were determined according to the chrome tailings content. The mixture proportions of the concrete mixtures were given in Table 2. As seen in the table, the dosage of the cement was determined as 340 kg/m3. Chrome tailings were used in substitution for sand at 0, 10, 20 and 30% proportions. Water-cement ratio was 0,55 in the concrete mixtures. The slump is fixed approximately as 10 cm for all the mixtures. A modified polycarboxylic ether polymers based high range water reducing admixture with specific gravity of 1.09, was used to obtain slump value as 10 cm in concrete mixtures. The amount of admixture employed in the concrete mixtures was adjusted at the time of mixing to obtain the determined slump value.

The concrete mixtures mixed in a pan type mixer and the specimens were moulded and compressed by a vibrating table. Three 15*15*15 cm cube specimens were taken from each mixture for each test.

Table 2: Mixture proportions

Material, kg	Chrome tailings content, %			
	0	10	20	30
Cement	340	340	340	340
Water	187	187	187	187
0-4 mm sand	1100	990	880	770
4-11 mm aggregate	330	330	330	330
11-22 mm aggregate	572	572	572	572
Chrome tailings employed for sand	0	110	220	330

The unit weight, compressive strength, ultrasonic tests were performed on the specimens held in standard curing conditions for 28 days. The unit weight, ultrasonic pulse velocity, compressive strength and dynamic modulus of elasticity values were calculated and the effect of chrome tailings on these values was examined with graphs drawn.

After the pulling out of the concrete specimens from the moulds at 28 days of curing, unit weight values of the specimens were calculated in water-saturated dry surface condition. Each concrete specimen was weighed separately. Then the means of weight values of three specimens were estimated to determine a weight value of each mixture. Finally, the unit weight value of each concrete mixture was calculated by dividing the mean weight by the specimen volume.

Ultrasonic pulse velocity of any material relates to the elastic properties, compactness and porousness of the material. The ultrasonic pulse velocity values are determined on the specimens at the age of 28 days according to the equation 1.

$$Upv = (S/t)x10 \quad (1)$$

Upv is the ultrasonic pulse velocity (km/s), S is the length of the smooth wave path through the sample (cm) (i.e., 15 cm in this work), and t is the passing time of the ultrasonic pulse through S (μs) measured by ultrasonic pulse velocity test machine.

The compressive strength values of the specimens were determined by using the test methods according to TS EN 12390-3 (2010) and ASTM C39/C39M-14a (2012). The compressive strength tests are performed on the concrete specimens at a constant load with a rate of 0.10 MPa/s by using a 3000 kN capacity compression testing machine.

III. RESULTS AND DISCUSSION

The changes in the unit weight values of the concretes depending on the chrome tailings content were given in the Figure 5. When the Figure 5 examined, there was a decrease in the range of % 1-2 on the unit weight values of the concretes according to chrome content. The reason for this is that the chrome tailings has largest rain size of 2 mm which was small than the sand (4mm) and the fineness of the tailings was higher than the sand.

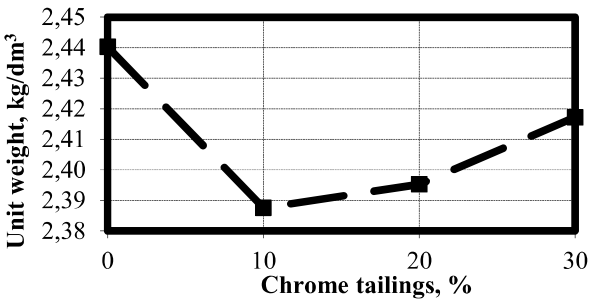


Figure 5: Variation of unit weight according to chrome tailings.

The variation of the compressive strength of the concretes with chrome tailings content was given in Figure 6. As seen in Figure 6, while the compressive strength of the concretes decreased up to 2% with the chrome tailings content until 20% proportion, the compressive strength values increased up to 5% when the proportion of the chrome tailings reached to 30%. Better workability provided by the filler effect of the chrome tailings caused better placing and compacting and so, the compressive strength of the concretes increased.

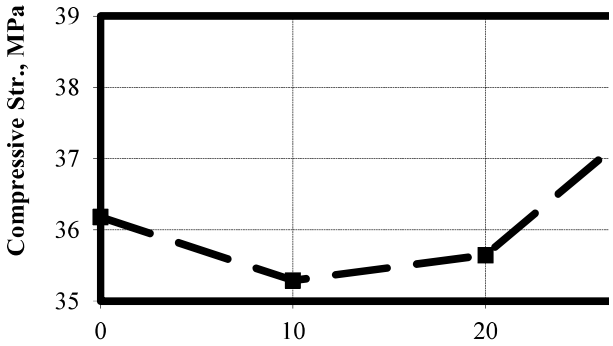


Figure 6: Variation of compressive strength of the specimens.

Ultrasonic pulse velocity values of the concrete specimes made with chrome tailings were given in Figure 7. When the Figure 7 examined, the ultrasonic pulse velocity values of the concretes contain 10% tailings decreased at 4% proportion according to control concrete sharply. In contrast, when the proportion of the chrome tailings reached 30%, the ultrasonic pulse velocity values of the concretes increased up to 6%. The ultrasonic pulse velocity values increased because of increased the occupancy rate of granulometry caused by the fine grain structure of chrome tailings.

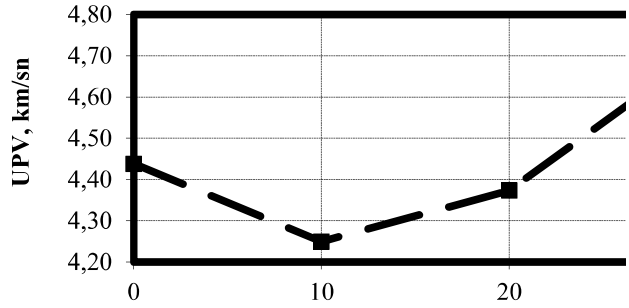


Figure 7: Ultrasonic pulse velocity variation of specimens.

The estimated dynamic modulus of elasticity values of the concretes depending on the unit weight and ultrasonic pulse velocity values were given in Figure 8. As seen in Figure 8, while the dynamic modulus of elasticity values decreased with chrome tailings content up to %10 initially, the values increased up to 11% at higher proportions according to control concrete. The results showed that the dynamic modulus of elasticity behaviour of the concretes was similar with the compressive strength. Filler effect of the chrome tailings and adaptation of the tailings with sand at higher proportions caused this behaviour to occur.

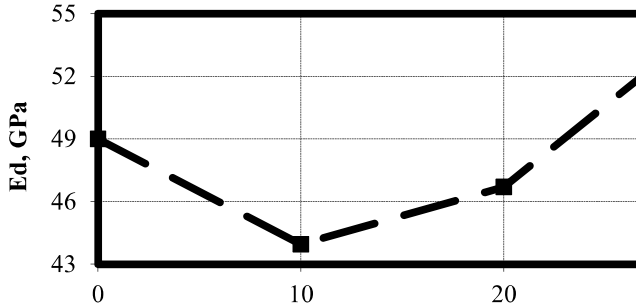


Figure 8: Dynamic elasticity values of the specimens.

IV. Conclusion

The following results were obtained in the experimental work:

- Unit weights of concretes decreased with the chrome tailings addition at low rates of 2%.
- The compressive strength of the concretes increased up to 5% with the use of chrome tailings by sand at high proportions as 30%.
- The concretes made with chrome tailings at high proportions have higher ultrasonic pulse velocity up to 6%.
- While the low chrome tailing content decreased the dynamic modulus elasticity of the concretes, high chrome content increased this property.

According to the experimental work done, the usage of the chrome ore concentration plant tailings by fine aggregate in the ready mixed concrete at %30 proportion was recommended with regards to ecological and economic benefits. However, the use of chrome tailings should not be used in low ratios because of the negative effects on the concrete properties. Furthermore, the investigation of the effect of chrome tailings on the durability of concrete may be proposed for further studies.

References

[1] S. Karahan, Y.Z. Ozkan "Türkiye Krom Madenciliğinin Geleceği, "*Madencilik ve Yer Bilimleri Dergisi*", Yıl 2, Sayı 16, 15 Temmuz 2011.

[2] S. Karahan, Y.Z. Ozkan, "Türkiye Krom Madenciliğinde Güncel Eğilimler ve Yeni Arayışlar", *Türkiye 22. Uluslararası Madencilik Kongresi ve Sergisi*, Ankara, 11-13 Mayıs 2011.

[3] DPT, Madencilik Özel İhtisas Komisyonu Raporu Endüstriyel Hammaddeleri II (Refrakter Killer ve Şiferton- Manyezit- Dolomit- Olivin- Zirkondisten,Silimanit, Andaluzit) Çalışma grubu Raporu., DPT: 2612, ÖİK: 623, s. 69-84, Ankara, 2001.

[4] B. Er., "Investigation of effects of multi gravity devices on the chrome ore benefication", *Dokuz Eylül University,, Institute of Natural and Applied Sciences*, Mining Engineering, İzmir., 2011.

[5] Yüce A. E., Güney A., Onal G., Üçköprü Krom Artıklarından Geri Kazanım ve Atık Alanının Rehabilitasyonu, *Madencilik ve Çevre Sempozyumu*, , Ankara, 5-6 Mayıs 2005.

[6] N. Kilinç Mirdali, "Usage possibility of chrome enrichment foundation Wastes in ceramic industry",University of Çukurova,,Institute of Natural and Applied Sciences, Department of Geology Engineering.

Investigation of the Sound Absorption Properties of Waste Cotton/Lichen Nonwoven Materials

Seyda Eyupoglu[1], Nigar Merdan[1], E. Dilara Kocak[2], Habip Dayioglu[1]

[1]Istanbul Commerce University, Department of Fashion and Textile Design, Istanbul/Turkey
[2]Marmara University, Department of Textile Engineering, Istanbul/Turkey
{scanbolat, nmerdan, hdayioglu}@ticaret.edu.tr, dkocak@marmara.edu.tr

***Abstract* - Over the past decade, noise pollution has become very significant global issue in the world due r to cause health and social problems. For these reasons, researchers seek for solution to noise pollution. In this context, researchers have investigated natural and synthetic based materials. Compared with synthetic materials, natural materials have been the focus researches because of being ecological, sustainable and economic. In this study, nonwoven fabrics were produced with using wastes of cotton fibers and lichens which are different ratios. After, the sound absorption properties of samples were analyzed with impedance tube. According to the results, sound absorption coefficient of samples produced with cotton wastes and lichen are promising.**

***Keywords* - waste cotton, lichen, nonwoven fabrics, sound absorption properties**

I. INTRODUCTION

TODAYS, sound insulation is a major problem of modern engineering with the technology development, modern machines were produced and started to use in every field. By the use of such high speed machines, the sound pollution is also increased. Sound insulation became compulsory in automotive, factories, various devices, and various vehicles. Sound insulation applications are based on economics and mostly the use of textile materials is investigated. Today for sound insulation purposes, glass fiber, foam, mineral fibers and various fiber reinforced composites materials have been used. In addition to these textile materials, ramie fiber, coir fiber, polyester fiber, bamboo fiber, poly(lactic acid), polypropylene, hemp, flax, and jute fiber also used. In sound insulation applications, the composite materials are widely used. Since composite materials have a porous structure, their insulation properties are considerably higher. Parallel to fiber reinforcement, the mechanical and insulation properties improve [1].

There are various studies investigated the sound absorption properties of textile materials. Young et al. produced composites using polypropylene and polyester. It was found that the composite sound absorption coefficient increased as a result of reinforcement of the composite with fibers. The sound absorption coefficient of composite was determined as 0.15-0.95 at the sound frequency between 500-2000 Hz [2].

Markiewicz et al. aimed to improve the acoustic and dielectric properties of the composite construction polypropylene-lignocellulose. Lignocellulose obtained from hemp flax, beech, pine and rape seeds with polypropylene were used as a composite. The results show that lignocellulose is suitable for use in the automotive and construction industries became of its good sound absorption properties [3].

Watanabe et al. have developed two different polyester fabrics as a sound absorbent. One of these polyesters is a flat cross-section modified polyester fiber while the other is a recycled polyester fiber. By using 2-3 denier polyester fibers, a nonwoven surface with 20-40 mm was obtained and the effect of the sound absorption coefficient was investigated. The result show that the cross-sectional structure of the fiber used on the nonwoven surface causes an increase in the surface area of the fiber resulting in improved acoustic properties of the fabric. The increased fabric thickness increased the sound absorption coefficient [4].

Parikh et al. examined the fabric properties of kenaf, polypropylene, jute, flax, cotton and polyester fibers by obtaining nonwoven surfaces with needle punch technique of 700 g/m^2 weight at different fiber ratios. These results show that the sound absorption property of the jute/polypropylene mixture was better [5].

The nonwoven surfaces are very cheap materials because of produced from fiber without yarn production. Among Textile materials, especially nonwoven fabrics are widely used in many fields of technical textiles due to their complicated constructions and suitable thicknesses. The nonwoven surfaces have the most important advantages on the construction industry as they are light weight, functional, low cost and requiring less reinforcement. They also have porous structure which makes them air permeable [6].

In this study, nonwoven fabrics were produced with using wastes of cotton fibers and lichens which are different ratios. After, the sound absorption properties of samples were analyzed with impedance tube. The results show that the sound absorption coefficient of samples improved with the decreased in the amount of lichen.

II. Materials and Methods

A. Materials

In this study, nonwoven fabrics were produced with using wastes of cotton fibers and lichens which are different ratios. The samples are produced with 100% cotton wastes, 25% lichen/75% cotton waste, and 75% lichen/25% cotton waste. The nonwoven fabric samples were produced with needle punch method.

B. Measurement of Sound Absorption Coefficient

Sound absorption coefficient of samples were analyzed according to ISO 10534-2 standard. In sound absorption measurements of samples, Brüel & Kjaer Impedance Tube based on two microphone transfer function method was used (Figure 1). Brüel & Kjaer Impedance Tube contains two tubes having different diameter. The diameter of one tube is 2.9 cm and the diameter of another tube is 10 cm. The measurement of the material in the frequency range of 0–1600 Hz was conducted with the bigger tube, whereas the smaller tube was used for the measurement of the material in the frequency range of 600–6300 Hz.

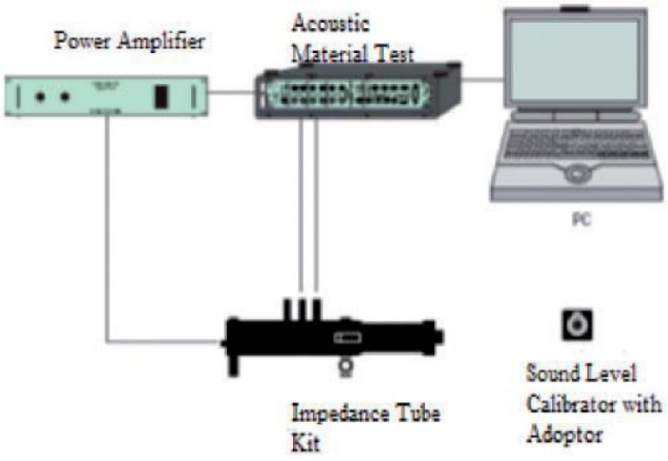


Figure 1: Impedance tube measuring instrument.

III. Results and Discussion

The sound absorption coefficients of samples were given in Figure 2 in the frequency range of 600–6300 Hz.

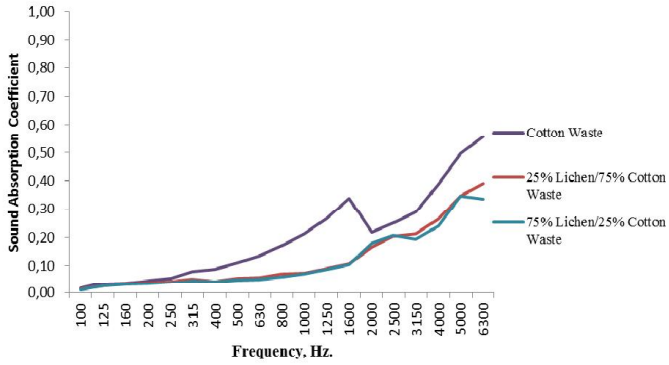


Figure 2: Sound absorption coefficients of samples.

According to the results, sound absorption coefficient of samples produced with cotton wastes and lichen are promising. The sound absorption coefficients of samples were decreased with the increased in the amount of lichen. The results show that the addition of lichen in the nonwoven causes to decrease the sound absorption coefficient of samples. The increase in the amount of cotton waste causes to increase the density of samples. As a results, the frictions which are sound waves and surface increase and the amount of sound energy converted lost heat energy rise. Sound absorption coefficient of materials not only depends on density but also depends on the material atomic, macro molecular and chain structure as well as arrangement of molecular chain of fiber.

IV. Conclusion and Future Works

In this study, in order to put good use cotton wastes and lichen, the sound insulation properties of cotton wastes and lichen was investigated. In this context, nonwoven samples were produced from cotton wastes and lichen at different ratios. According to the results, lichen causes to decrease the sound insulation capacity of nonwovens.

References

[1] S.Ersoy and H. Kucuk, "Investigation of industrial tea-leaf-fibre waste material for its sound absorption properties,"*Applied Acoustics*, vol. 70, no. 1, pp. 215-220, 2009.

[2] T.L. Yang, D.M. Chiang, and R. Chen, "Development of a novel porous laminated composite material for high sound absorption, " *Textile Research Journal*, vol. 7, pp. 675-698, 2001.

[3] E. Markiewicz, D. Paukszta, and S. Borysiak, "Acoustic and dielectric properties of polypropylene-lignocellulosic materials composites," 2012, http://cdn.intechopen.com/pdfs/37240/InTech-Acoustic_and_dielectric_properties_of_polypropylene_lignocellulosic_materials_composites.pdf.

[4] K.Watanabe, Y.Minemura, K. Nemoto, and H. Sugawara, "Development of high-performance all-polyester sound-absorbing materials," *JSAE Review*, vol. 20, pp. 357-362, 1999.

[5] D.V. Parıkh, T.A. Calamarı, A.P.S. Sawhney, E.J. Blanchard, and F.J. Screen, "Thermoformable automotive composites containing kenaf and other cellulosic fibers," *Textile Research Journal*, vol. 72, no. 8, pp. 668-672, 2002.

[6] H.K. Kaynak, and Z. Değirmenci, "Teknik tekstil uygulamalarında kullanılan nonwoven filtreler," *Tekstil Teknolojileri Elektronik Dergisi,* vol. 4, no. 2, pp. 78-84.

Pavements covered for heat isolation to get pedestrian thermal comfort

M.K. GOKAY[1], K. DOGAN[2] and C.YASAR[3]

[1] Selcuk University, Konya/Turkey, mgokay@selcuk.edu.tr
[2]Selcuk University, Konya/Turkey, kdogan@selcuk.edu.tr
[3]Selcuk University, Konya/Turkey, cyasar@gmail.com

***Abstract* – Civilization has been analyzed mostly with urbanization which coincides with the usage of stone and later concrete and steel in constructions. Nowadays we have been realized that construction materials used for houses, apartments, roads and pavements surrounding us create local microclimate which influences our living comfort. Local temperature increases due to asphalt roads and concrete pavements have recently been determined and they are remarkably effective in our everyday life. Usage of different types of aggregates in concrete mixtures to cast concrete pavement blocks might effective to decrease air temperature on the pavements. Therefore heat-resistant rocks were used to produce different sized aggregates where different plasters were produced from them to coat standard concrete pavement blocks. Pavement blocks plastered were then put under sun to test their surface temperatures. It was observed that heat-resistive materials used in plaster concretes influence heat distribution in the blocks and surface temperature of the concrete pavement blocks.**

***Keywords* – Pedestrian comfort, heat-resistive materials, concrete pavement blocks.**

I. INTRODUCTION

It is common that outside temperatures in urban areas are mostly higher than countryside. This may have certain advantages in wintertime but disadvantages in summertime due to their uncomforting influences. Concrete have been used nowadays to build apartment blocks, houses and roads. Most of the pavement blocks in urban areas are also molded by using concrete mixtures. It is common that concrete and natural stone slabs on urban roads and pavements are the main reasons of high temperature island occurrences in cities. Heat arrived from sun by radiation in summertime, heats up earth surface and cause temperature differences due to shading and surface materials' properties. Temperatures on earth surface layers which stayed whole day under the sun reach very high levels which might create local microlevel climate effects. Heated up areas are then formed "heat-islands" around them (Fig.1). Even though, these areas can continue to supply their deposited heat after sunsets, until their body temperature will reach the same level with their environmental air temperature. In hot sunny days, heating of the concrete structures, roads, walls, pavement blocks can reach a certain level which disturbs humans.

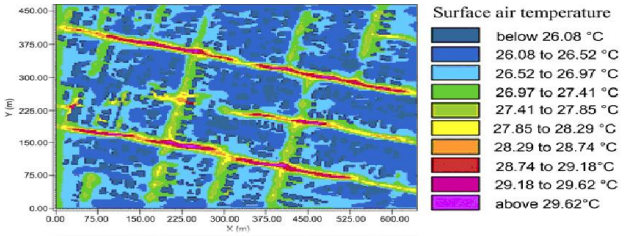


Figure 1: Temperature measured in a research performed in Los Angeles (US) on a sunny summer day, (at 02:00 pm, at a height of 1.5 meter from the ground surface), [1].

II. PROCEDURE TO GET PEDESTRIAN COMFORT

"Heat-island" has been researched for a while and therefore any decreasing actions on their temperatures are welcomed by societies. One simple way is watering sun heated roads, pavements and any other locations in summer. This action decreases their surface temperatures and gives certain degree of relaxation for people living nearby. But watering is costly due to water usage and their supply. Shadowing of the roads and especially pavements are also one of the methods used by municipalities. Trees near pavement areas, curtaining over the sunny narrow streets, bazaars, are mostly applied methods. In researches, it has been already presented that cool pavements cause significant reduction in surface air temperature. In Los Angeles city (US), there are official applications about the heat islands [2] to decrease air temperature just above the roads and pavements. In this municipality works; workers coated selected city streets and pavements by predefined gray colored cool materials [3]. Eventually, summer temperature on the tested local area had been surveyed and certain declines in air



Figure 2: Painting project for selected Los Angeles (US) streets to decrease heat island influences of local roads and pavements [3].

air temperatures (local) were reported for these projected Los Angles heat-island applications. It was reported [3] that two modified albedo (whiteness) scenarios were studied in Los Angeles application: a moderate and an extreme increase in albedo scenario. It was found that for the first case, the temperature decrease at 2.0 meters height (from the ground surface) was as high as 1.5 °C, (Celcius), and for the second case as high as 2.2 °C. The typical temperature change pattern is a decrease during daytime and little or no decrease during the night [3].

The impact of temperature depression at heat-islands would have been even greater if the albedo of all roads and pavements was increased. It is obvous that connection roads, streets, pavements, pedestrian areas, buildings roof & walls and all similar constructed surfaces increase urban areas temperatures. In this subject, Akbari analyzed the situation in cities and reported heat island mitigation solutions [5]. Besides this research, reflective pavements were applied to an urban park in Athens (Greece) by Santamouris etal. to reduce heat radiation [6]. They wrote that usage of cool (white materials which were presenting high reflectivity in infrared radiation and high emissivity) paving materials reduced peak ambient temperature during a summer day up to 1.9 ºK, (Kelvin). They reported also that temperature of the park itself decreased up to 12 ºK. In another study researchers were concentrated on cool material properties and their usage as asphalt road and concrete block coatings. They reported that [7] usage of cool materials "contribute to the mitigation of heat island effect". Santamouris etal. [7] presented also work of Synnefa etal. [8] which showed visible and infrared photograph of thin concrete plates (Fig. 3). These photographs (Fig. 3), especially the infrared images differentiate surface temperature of the thin concrete plate clearly. Infrared images demonstrated that plate numbered 1 and 4 (they had white color coatings) had lower surface temperatures (7.5 ºK lower than reference plate-3) and plate-2 (it had black colored coating) on the other hand had higher surface temperature (15.0 ºK higher than reference plate-3) [7]. Synnefa etal. tested 16 concrete plate samples in their research and 15 of them were coated with different cool materials (plate 3 was extra reference plate, it has no coatings).

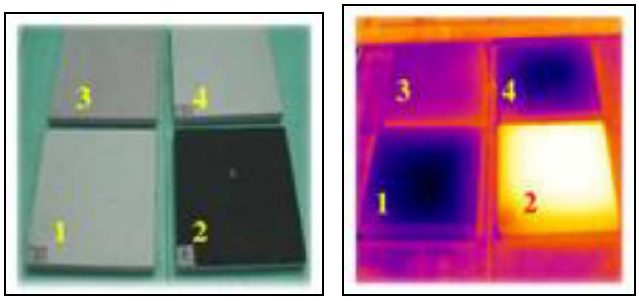


Figure 3: Visible (left) and infrared (right) images of the concrete plates which were coated with different cool materials. Concrete plates were put under sun for a while and photographs were then taken. Cool materials, coatings, used on the numbered concrete plates are; Acryl-polymer emulsion paint (white color) for plate-1; Emulsion paint (black color) for plate-2; Uncoated tile (reference) (white color) was plate-3; Alkyd, chlorine rubber coating (white color) for plate-4, [7].

Table 1: Daily (08:00-19:00) mean and mean maximum surface temperatures measured from concrete plates coated with different cool materials, [8].

Test Samples	August		September	
	Mean daily surface temp. (ºC)	Mean max daily surface temp. (ºC)	Mean daily surface temp. (ºC)	Mean max daily surface temp. (ºC)
S1	46.19	58.67	36.49	48.82
S2	33.15	40.79	27.78	35.07
S3	36.68	44.89	30.58	39.10
S4	34.68	43.17	29.06	37.30
S5	33.18	40.67	**27.74**	**34.77**
S6	44.85	56.85	36.39	47.77
S7	**52.09**	**67.92**	**40.44**	**54.63**
S8	32.82	40.73	27.90	35.52
S9	33.89	41.24	29.03	36.00
S10	44.25	54.83	36.78	47.08
S11	37.34	46.49	31.79	40.59
S12	41.72	50.68	34.79	43.50
S13	37.81	46.95	32.08	40.74
S14	33.25	39.63	28.91	35.12
S15	37.13	45.79	30.92	38.78
S16	**32.13**	**38.28**	28.63	36.07

Synnefa etal. reported that cool coating materials used in their research were available in international markets. These materials are general coating materials used in construction and civil works [8]. Description and colors of these coatings are as follows;

S1 Aluminum pigmented acrylic coating, (Silver gray color),
S2 Acrylic, ceramic coating, (White color),
S3 Acrylic, elastomeric coating, (White color),
S4 Acrylic, elastomeric coating, (White color),
S5 Alkyd, chlorine rubber coating, (White color),
S6 Aluminum pigmented, alkyd coating, (Silver gray color),
S7 Emulsion paint, (Black color),
S8 Acryl-polymer emulsion paint, (White color),
S9 Acrylic latex, (White color),
S10 Aluminum pigmented coating, (Silver color),
S11 Acrylic insulating paint, (White color),
S12 Aluminum pigmented acrylic coating, (Silver color),
S13 Epoxy polyamide coating, (White color),
S14 Acrylic paint, (White color),
S15 Uncoated tile (reference concrete plate), (White color),
S16 Acrylic elastomeric coating, (White color).

Synnefa etal. pointed that mean maximum daily surface temperature measured from coated plate surfaces during day time of August and September increased up to 67.92 ºC on the test plate-7, (S7), which had emulsion black paint as a surface coating. Minimum mean daily surface temperature measured was 32.13 ºC on the test plate-16, (S16). Mean surface temperature levels in this study demonstrate the importance of the surface coating effects.

Different approach in "heat island effect" was supplied by Yang etal. [9] and they reported that performance of heat island prevention works (pavement coatings etc.) in the canyon type locations was influenced mainly by the canyon geometry. They wrote that, in a high-density residential area, modifying pavements might change their surface temperature slightly but this action had insignificant effect on the wall temperature (Fig.4) and building energy consumptions.

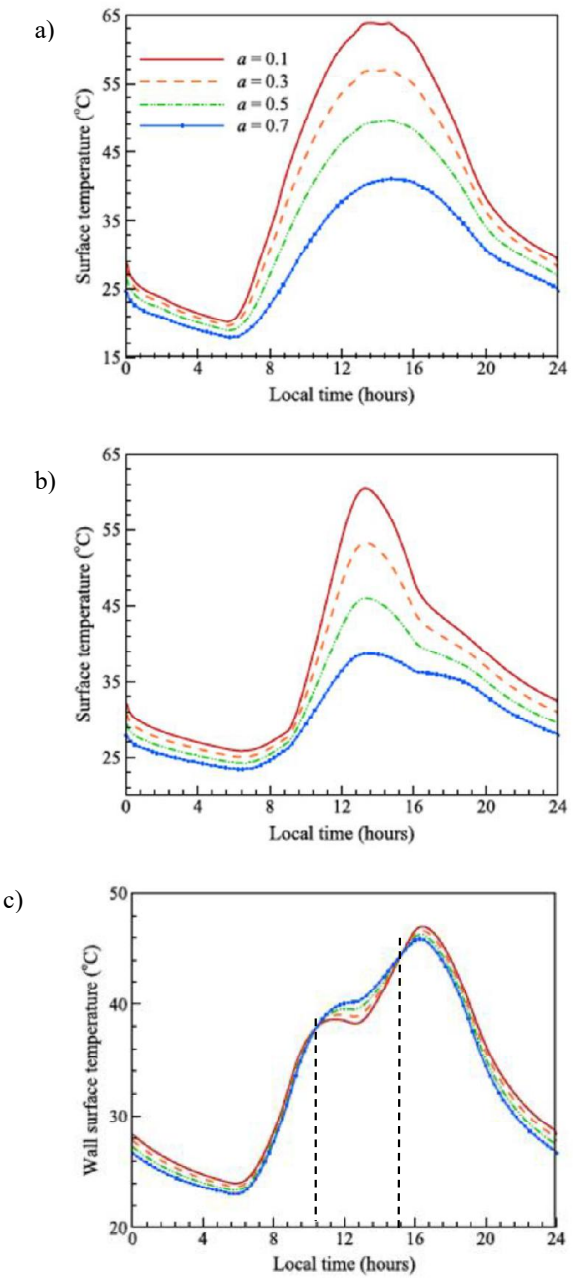


Figure 4: Average diurnal profiles of predicted temperatures with different albedo a) Temp. of pavement surfaces without canopy, b) Temp. of pavements located in a high-density residential area, with canopy; c) Simulated temperature of building wall surfaces in Phoenix (US) during 12-17 June 2012, [9].

Figure 4 illustrates some results of Yang etal. which were predicted and simulated temperature fluctuations for summer daytime of Phoenix (US). Figure 4a showed that increasing pavement albedo decreased the pavement surface temperatures considerably. Comparing Fig. 4a and Fig. 4b illustrates the influences of canopy. Shading effects in residential areas cause gradual decrease of pavement surface temperatures. The resultant test curves like given in Fig. 4b have then step downward inclinations in afternoons. Yang etal. stated [9] also that "with reduced road surface temperatures, the reflective pavement emitted less longwave radiation to the canyon environment. Nevertheless, more shortwave radiation was reflected that the combined effect of the reflective pavement was complicated". Figure 4c presents surface temperatures measured on the building walls. During diurnal cycle, increasing pavement albedo resulted in a warming effect on building walls (in between 10:30 – 15:00 local time). These researchers then wrote that; "increased wall temperature indicated that reflected shortwave radiation outweighed reduced longwave radiation from the reflective pavement" during this time period. In other time, reflective pavement led to cooling of wall surface temperatures.

III. Materials and Methods

To obtain similar local temperature decreases at heat island formed during summer daytime in Elazig, Turkey, heat-resistive materials (heat insulation minerals) which have been used in constructions industry are facilitated in this study here to produce heat sensitive floor coating materials, concrete plasters. Pavements in most of the city centers are covered usually by precast small sized, concrete blocks in Turkey. These small, 8 cm thick, concrete blocks are produced in different surface forms and shapes. Summer daytimes are very hot in Elazig. Weather temperature can reach up to 40 ºC. People have their hot weather experiences in this city like all the other hot cities. They have obstructed themselves to go outside in between 11:00 – 16:00 o'clock. Uncomfortable conditions are disturbing people in heat islands in cities due to hot building walls, hot roads and hot pavements etc. They prefer to go soil and grass covered open areas which have lower outside temperatures. However, even those places are very hot during days of August in Elazig. High temperature conditions over the asphalt roads, concrete pavements, stone slap covered city squares are common in Elazig in these hot daytimes. Therefore as a first stage of this research here; concrete heat-resistive plasters which were prepared from different heat resistive rock aggregates had been applied over standard concrete pavement blocks. In the second stage, white colored cool coating materials were used additionally to cover some of the samples used in the first stage.

Pavements in Konya and Elazig city are mostly covered by means of small precast concrete pavement blocks (one of the pavement models is give in Fig. 5). They are 8 cm thick and sometimes colored in reddish and yellowish other than the concrete's natural grayish color. Their standard aggregate sizes, Portland cement and water mixture ratios are kept stable in factories where they are pre-shapely casted together with vertically applied pressure. Similar standard mixture ratios were used in this work to produce heat-resistive plaster concrete and different plaster samples were put on the standard pavement block surfaces as thick as 1.50 cm. This sample preparation work was like thick plastering application in construction works. Plastering mixtures which were prepared for covering the ordinary concrete pavements blocks were arranged in different aggregate types. Thus, standard concrete pavement blocks handled in this study had been coated with

these especially prepared concrete plastering mixtures. The resultant heat-resistive concrete pavement blocks were then totally 9.50 cm in thickness (standard concrete thickness: 8 cm + heat resistive plaster thickness: 1.50 cm), (Fig.5).

In order to compare effectiveness of heat-resistivity, 6 different types of rock aggregates were used separately to prepare 6 different heat-resistive plasters. These aggregate types were; Aksaray pumice, Nevsehir pumice, tuffs, perlites, white marble powders, Karapinar basic pumice (black in color). For each type of heat-resistive aggregate, 3 standard concrete pavement blocks were plastered in mining engineering laboratory of Selcuk University, (Konya, Turkey). That means, each plaster type, (made up from each aggregate type), was tested through 3 pavement blocks (Fig. 5). After application of plasters, samples had been regularly wetted until the plasters and standard concrete blocks were combined together totally.

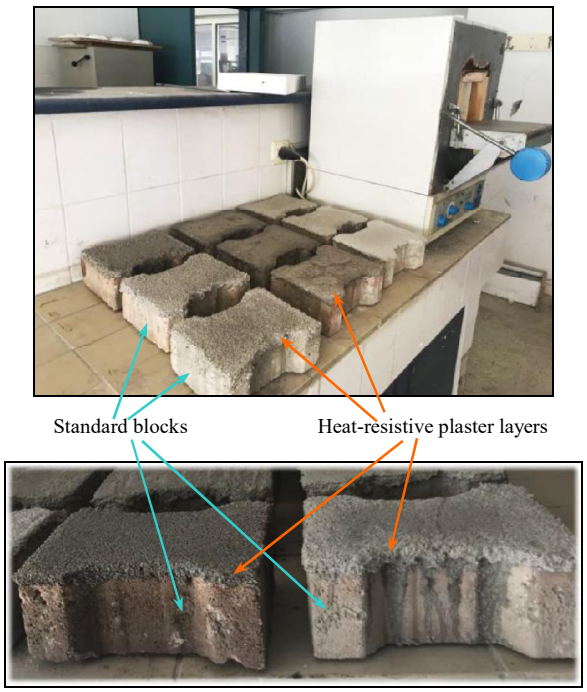
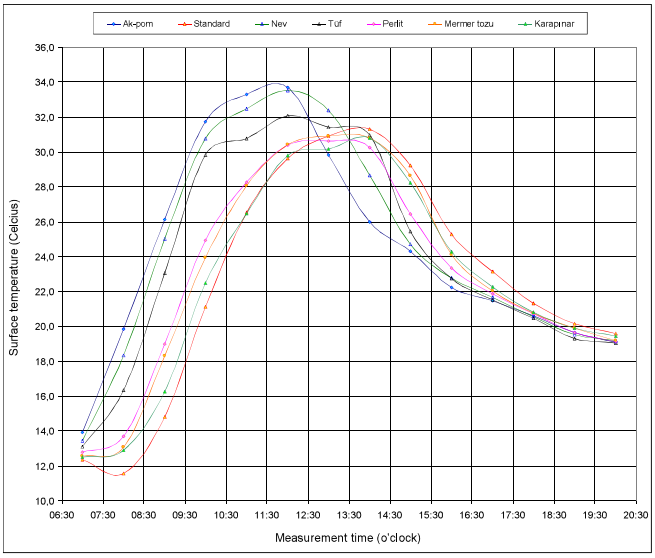


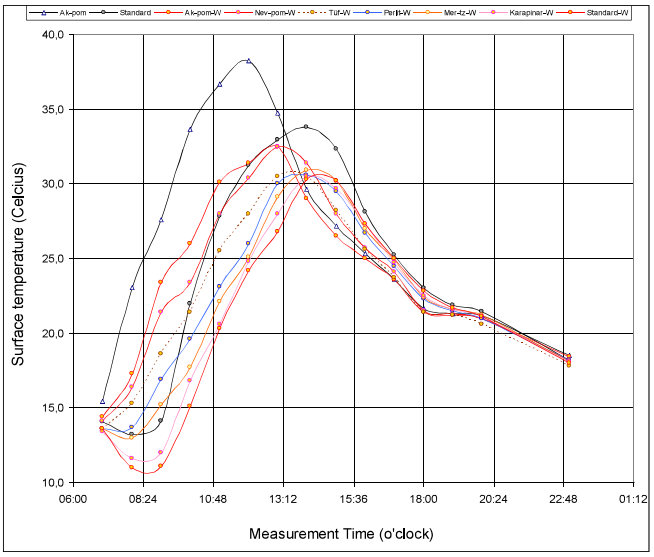
Figure 5: Heat resistive concrete pavement block samples, prepared for surface temperature tests by coating their top surfaces with especially prepared heat resistive concrete plaster.

IV. Test Results

In this study 7 different concrete pavement blocks (each has 3 samples, then 7x3= 21 test blocks totally) were taken into tests. Surface temperature measurement tests were performed in Elazig city centre, that means selected test location was an urban area which includes canopy effects. All the test samples were put on a flat floor under the sun in Fall season of 2017. First stage tests include all the heat-resistive concrete pavement blocks including the standard ones which were not plastered for reference data. After collecting surface temperature data for the first test stage, second test stage was started after applying cool coating materials (white colored) on one member of each 7 different concrete pavement block group. White coating materials used here was polyester putty (filling) and coating material. This material has common usage in automotive maintenance activities in Turkey. In order to increase the coating material effectiveness, top surface of the heat-resistance concrete pavement blocks were painted with white colored oily synthetic paint. This paint has been commonly used in buildings in Turkey. Second test stage in this research included the surface temperature data which were taken from these coated and painted pavement block surfaces. These two test stages produced enough data which are plotted separately in Fig. 6.



a)



b)

Figure 6: Mean surface temperature obtained from especially prepared heat-resistive concrete pavement blocks; a) First test stage results, (mean surface temperature fluctuation on plastered pavement blocks); b) Second test stage results (mean surface temperature fluctuation on plastered and then white cool material coated & white painted concrete pavement blocks.

V. Conclusion

This study summarized the differences in surface temperatures obtained from different pavement blocks which were plastered by different insulation materials. Heat-resistive concrete plaster layers were applied to standard pavement blocks. In order to obtain heat-resistive plaster, 6 different heat-resistive rock aggregates were used. Main consideration was to determine which heat-resistive aggregates were suitable to obtain cool pavement surfaces. Graphics obtained in this study present that effectiveness of heat-resistive pavement blocks on heat–island effects depends on albedo characteristics and heat insulation capacity of the prepared plastering concrete layers. It was determined that heat-resistive materials which can be used as plastering materials for concrete pavement blocks prevent heat transferring in concrete pavement blocks. Therefore their surface temperatures were higher than the standard block's values. Test samples which were coated with Aksaray-pumice aggregate plasters had highest mean surface temperature, (38.25 ºC at 12:00 o'clock). In this stage of the tests, highest mean surface temperature of standard concrete pavement blocks was 33.80 ºC. This was the value reached on the other hand at 14:00 o'clock. Differences in day time interval and mean surface temperature values can be explained by the thickness of heat-resistive plasters on pavement blocks and their heat resistance properties. It is important to point that, surface temperature of heat-resistive block decreased more rapidly when it was compared with the standard reference pavement block. This recognized point can be explained by heat storage capacity of the blocks. Heat-resistive plasters had obstructed heat radiating from sun and had declined the heat stored in concrete pavement blocks. Better results were obtained for pavement blocks' surface temperature effectiveness when the white polyester putty and white paint were used to coat surface of them. Pavement block's surface temperatures in this test group were plotted and highest value was determined for Aksaray pumice aggregate plaster. The surface temperature for this test sample was 32.50 ºC at 13:00 o'clock. Standard test sample in this test group had highest surface temperature value around 30.60 ºC at a time of 14:30. Surface temperature difference was 5.75 ºC for this two pavement blocks for common Autumn days of Elazig city. This result shows the effectiveness of albedo characteristic of pavement blocks. It was concluded that, heat transfer resistant materials which are used in common construction sites can be used to prepare plastering layers for concrete pavement blocks. It was evaluated that heat-resistivity of pavement block surface materials and surface albedo properties are two main influencing parameters on heat-island in urban areas.

References

[1] M. Taleghani, D. Sailor, and G.A. Ban-Weiss, "Micrometeorological simulations to predict the impacts of heat mitigation strategies on pedestrian thermal comfort in a Los Angeles neighborhood", *Environmental Research Letters*, vol. 11, n2, , IOP Publishing Ltd., Feb. 2cd 2016.

[2] N. Sauceda, "*Cool pavements, Save our streets, LA (C.F. 13-1300-S1) Public Works Cmte Item (J)"* , City of Los Angles, Sept. 2013.

[3] Inspir'action, "Los Angeles is painting its streets white to guard against climate change", *Inspiraction.news web side*, Sept, 29th 2017.

[4] A. Synnefa, A. Dandou, M. Santamouris, M. Tombrou, And N. Soulakellis, "On the Use of Cool Materials as a Heat Island Mitigation Strategy", *Journal of Applied Meteorology and Climatology*, vol. 47, pp2846-2856, Nov. 2008.

[5] H. Akbari, "Potentials of urban heat island mitigation", *Inter. Conf. of passive and low energy cooling for the built environment*, Santorini, Greece, May 2005.

[6] M. Santamouris, N. Gaitani, A. Spanoua, M. Saliaria, K. Giannopoulou, K. Vasilakopoulou, and T. Kardomateas, "Using cool paving materials to improve microclimate of urban areas – Design realization and results of the flisvos project", *Building and Environment*, vol. 53, pp128-136, July 2012.

[7] M. Santamouris, A. Synnefa and T. Karlessi, "Using advanced cool materials in the urban built environment to mitigate heat islands and improve thermal comfort conditions", *Solar Energy,* vol. 85, n12, pp3085-3102, Dec. 2011.

[8] A. Synnefa, M. Santamouris and I. Livada, "A study of the thermal performance of reflective coatings for the urban environment", *Solar Energy*, vol. 80, pp968–981, 2006.

[9] J. Yang, Z.H. Wang, K.E. Kaloush and H. Dylla, "Effect of pavement thermal properties on mitigating urban heat islands: A multi-scale modeling case study in Phoenix", *Building and Environment*, vol.108, pp110-121, 2016.

Effects of the Stone Powder on Some Mechanical Properties of the Clayey Soil

A.F.CABALAR[1] and M.IBRAHIM[1]

[1]Gaziantep University, Gaziantep/Turkey, alifiratcabalar@gmail.com
[1] Gaziantep University, Gaziantep/Turkey, meysibrahim@gmail.com

***Abstract* - The use of stone powder (SP) as a stabilizer to the clayey soil has been studied. Tests of Atterberg limits, compaction, fall cone (FCT), Laboratory vane shear (LVT), and expansion index (EI) had been carried out on soil-stone powder mixtures with fixed ratios of stone powder (0%, 5%, 10%, 15%, and 20%) by the dry weight. Results indicated that the undrained shear strength obtained from FCT and LVT has been increased at all the admixture ratios, the expansion index reduced with the increasing of the stone powder.**

***Keywords* - clayey soil, stone powder (SP), undrained shear strength.**

I. INTRODUCTION

Disposal of stone powder have been developing positively through many applications, attempts have been made in order to turn these wastes into useful construction materials. Results obtained by Nabil al-joulani [1] whose investigates the effects of using the stone powder and lime on some geotechnical properties of fine grained soil. They used 0_30% of stone powder and lime by weight then evaluated the strength, direct shear, and CBR properties. They found that the addition of 30% stone powder has increased the angle of friction (φ) by about 50% and reduce the cohesion by about 64%. Also at the same amount of stone powder addition the CBR values increased from 5.2 to 16.

Demirel [2] studied the effects of the marble stone dust on the compressive strength of concrete by adding the dust at particular proportions; the strength displayed an enhancing effect with the additive of marble stone dust. Also the sewage sludge entered in manufacturing the artificial aggregate. Also, H. M. A. Mahzuz [3] studied the use of stone powder as an alternative of sand in concrete mix and mortar. In that study, the stone powder concrete gained a compressive strength 15% higher than that of concrete with normal sand, the highest strength of mortar with stone powder reached to 33.02 MPa.

Ali and Hashmi [4] tested the 28-days compressive strength of concrete cubes that its cement partially replaced with marble dust and its sand with stone dust. The result of the cube that contains 10% marble stone and 20% stone dust recorded an increase of about 15.23% in compressive strength.

Valeria et al. [5] investigated the 28-days compressive strength of the concrete that substituted of sand by waste marble stone. The concrete provided compressive strength higher that of the control concrete mixture.

Sakalkale et al. [6] studied the effect of marble dust stone by replacing with sand for about 50% by the dry weight on the compressive strength of concrete. The result shows that there is about 10.72% increase in compressive strength.

Birinci et al [7] tested the compressive strength of the concrete after replacing 50% of sand with marble dust and limestone dust. The compressive strength of the marble sand concrete was better than that of limestone concrete.

In this study, laboratory tests were carried out to establish whether the stone powder can be effectively used as a stabilizer for the clayey soil. We aspire that this study can be useful to provide further valid uses of stone powder.

II. TEST METHOD

The soil collected from Gaziantep university campus and has been grounded into fine particles to pass through a #200 sieve. Then the fine soil and the stone powder had been dried in an electric oven for 24 hr. before being used as an additive to the clayey soil. Hence the admixtures were manufactured with SP at five ratios (0%, 5%, 10%, 15%, and 20%) by weight.

Tests like Atterberg limits, compaction, unconfined compressive strength, fall cone, laboratory vane shear, and

swelling were carried out to study the performance of the additives on the geotechnical properties of the soil.

Other tests like EDS analysis and SEM pictures were performed to the SP.

Atterberg limits tests were applied according to ASTM D4318 standard [8] to obtain liquid limit (LL), plastic limit (PL), and plasticity index (PI). Variations of PI of the soil after and before the addition of the SSA and SP were then studied. Compaction tests can obtain the maximum dry unit weight (γ_{dmax}) and optimum moisture content (OMC) of the soil and the mixtures of soil with SSA and SP specimens at various water contents. Furthermore, the obtained OMC from compaction tests was used to control the water amounts for the samples that approved to be tested for unconfined compressive strength and swelling potential tests, which were performed to find the stress; immediately without curing time; and the volumetric swell of soil specimens, respectively. The fall cone test was performed to evaluate the liquid limit (LL) and the undrained shear stress for the soil and the soil with the admixtures. Also the laboratory vane shear test was carried out to obtain the undrained shear strength.

III. RESULTS AND DISCUSSION

A. Characteristics of materials

i. Untreated soil

Table 1 shows the properties of the untreated soil. The soil in this study was categorized as SC soil according to USCS classifications. In accordance to AASHTO the soil grouped into the category of A-1-a.

ii. Stone powder

The same procedures were carried out to test the chemical components of the SP. The EDS/SEM results shown in table 2, it's seen that the SP lacks of the oxides that control-

Table 1: Properties of untreated soil

Liquid limit (LL)	34.5
Classification (USCS)	ML
Classification (AASHTO)	A-1-a
Maximum unit weight (KN/m3)	1.65
Optimum moisture content (%)	17.58
Unconfined compressive strength (KPa)	400
Plasticity index (PI)	6.55

Table 2 Results of EDS analysis for stone powder (in wt%)

Elements	Fe	Al	Si	Mg	Ca	O	C	Na	K
SP	0.172	0.513	0.634	0.243	29.34	54.648	13.403	0.15	0.02

-or accelerate the pozzolanic reaction. Furthermore, it is rich in calcium which is about 20% more than the calcium in SSA. This improves the ability of SP in enhancing the mechanical properties of soil. Also, it has regular and semi-spherical grains shape as it's seen in fig. 1.

B. Atterberg limits

In order to study the changes on the physical properties of the soil after and before adding the SP, tests of liquid limit and plastic limit were performed according to ASTM D4318 standards.

In general, the smaller PI means the better workability of soil. From the results, it can be seen that the PI of the SP admixtures increased with the amount of SP added as shown in fig. 2 and 3.

C. compaction test

The compaction is carrying out in order to re-arrange the soil particles by the process of mixing the soil with water and applying external energy to the soil. Hence, with the aid of watering and re-arranging of particles by compaction energy, the soil can reach its densest condition. The test performed according to ASTM D 1557-98, 2000) [9]. Fig.4 shows the effects of the additives on the compaction properties of the soil.

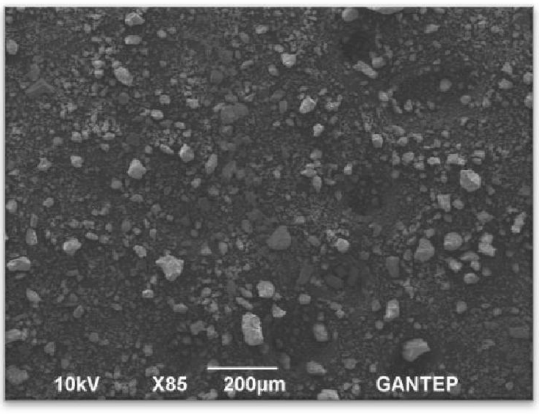


Figure 1: SEM picture of SP used during the study work.

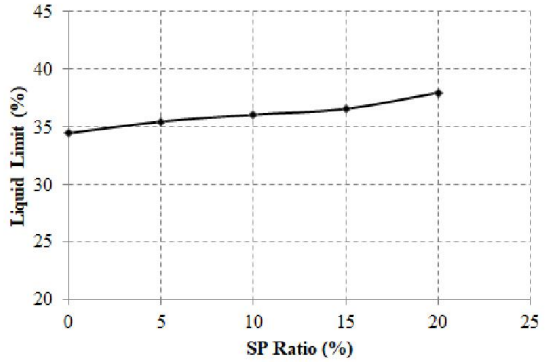


Figure 2: Variation of liquid limit with addition of stone powder.

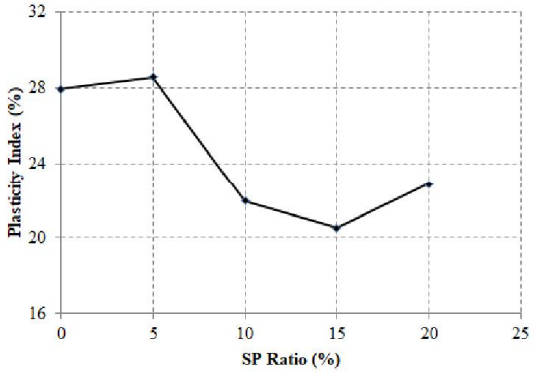


Figure 3: Effect of addition of stone powder on the plasticity index.

The results indicated that each stabilizer showed its own compaction behavior with different optimum moisture content and maximum dry density (γ_{dmax}). Although it's seen that the addition of the SSA and SP had very small impact on the compaction behavior. It is believed that the adding of the SP resulted in change of the untreated soil properties. The SP admixture improves the interlocking force between the soil particles as the optimum moisture content lowered with the amount of SP and the total stresses are conserved among the soil particles, the soil stress rises with the decrease of water generated stress. The adding of SP does not have much effect on the optimum moisture content and the dry density, the results were very close to that of the untreated soil.

D. unconfined compressive strength

Fig. 5, showing the unconfined compressive strength at different amounts of SP added to the soil and according to ASTM D 2166-98 (2000) [10]. All the specimens were tested immediately after mixing.

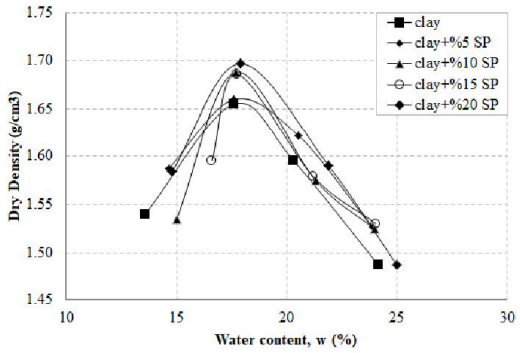


Figure 4: Effect of addition of stone powder on density-moisture content relationship.

when the treatment started with SP admixture, the UCS decreased at all stages but it is clearly noticeable that the soil tended to behave more ductile, fig 5, shows that the area under curve which is equal to the absorbed energy by the soil mixture. Ductility is the ability of the materials to deform under tensile stress or the ability of material to resist plastic deformation without rupture, it can be evaluated by the engineering strain at which the material fractures during the uniaxial tensile test. The lack in ductility is termed brittleness. In general, the differences in ductility and brittleness do not affect the strength of the material, but the material with high ductility is often more desirable. The more ductility improved at the mixture of 10% SP, as well as, the more strength was at 20% SP.

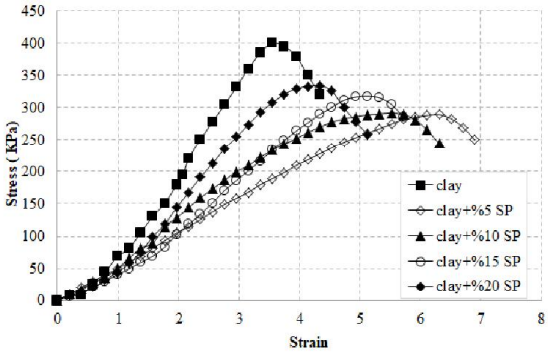


Figure 5: Effect of stone powder on the unconfined compressive strength.

E. Fall cone test

The FCT was carried out following the BS 1733 standards [11], using the British fall cone apparatus with 30º cone and 80 gm. weight. The FCT was performed to evaluate the undrained shear strength as well as to find the liquid limits for the raw soil and after the admixtures added. The soil samples had been placed in a stainless steel cup in dimensions of 55 mm diameter and 40 mm height, so the

cone tip just touches the sample surface. The cone then released into the sample for 5 s. then the penetration depth was recorded by a dial gage and the Su was calculated by the following equation:

$$s_u = k\frac{mg}{d^2} \quad (1)$$

Where, k is the factor of the cone depending on the cone angle. K = 0.0255 (Wood 1985) [12] according to the cone angle, which is 30º in this study, m is the cone mass = 80 gm, g is the earth acceleration, and d is the cone penetration depth. The liquid limits according to (BS 1377 1975) is the water content at the cone penetration of 20 mm. in fig. 6, it can be seen that the cone penetration decreases with decreasing water content, the results indicates that there is approximately linear relationship between the cone penetration and the water content for all the clay-SP mixtures

It can be seen from fig 7 that the undrained shear strength increased as the amounts of additives increased, in the same time, the strength decreases as the water content increase.

The main influential factors affecting the undrained shear strength are the cohesion and internal friction angle of the soil particles which are directly related with the soil water content. In this test, it can be seen that the SP particles reduced the clay fractions due to the flocculation and agglomeration effect. The SP particles caused a formation by increase the friction strength of the soil particles.

F. Laboratory vane shear test

The laboratory vane shear test was performed to the same samples tested in fall cone test and according to ASTM D 4648-49 standards [13]. The device consists of four blades connected at right angles to each other; the height of vane according to the standards should be twice the diameter of each blade. The test procedures are to insert the vane into the sample in a metal cup and rotating it in a constant rate until the sample fails. At the failing moment, the torque is then recorded by the dial gage to be used; with the analysis of the vane size and geometry; in the calculation of the undrained shear strength. Following equations are using in the shear strength calculations,

$$s_u = \frac{T}{K} \quad (2)$$

Where:

T =the maximum torque to shear the samples, which is the angle of rotation and the spring constant,

K = constant depend on the dimension and the shape of vane, it's measured by the Eq,

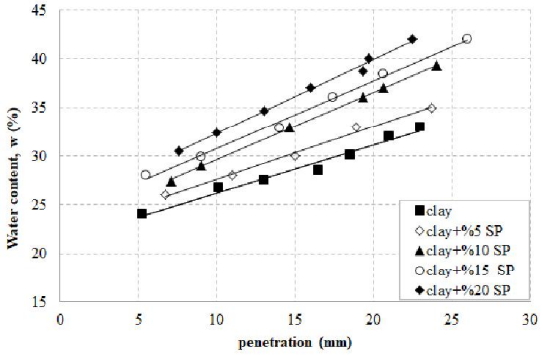


Figure 6: Relation ship between cone penetration depth and water content at different ratios of stone powder.

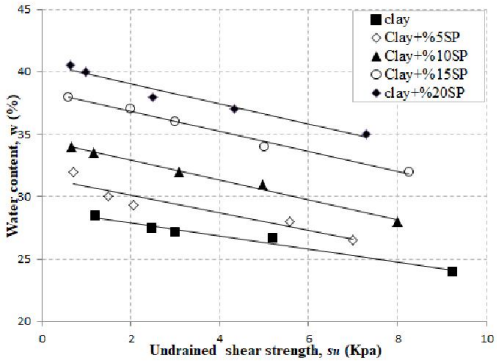


Figure 7: Variation of undrained shear strength from FCT with addition of stone powder.

$$K = \frac{\pi D^2}{2} * \left(1 + \frac{D}{3H}\right) \quad (3)$$

Where,

D is the diameter of the vane, and

H is the height of vane.

The undrained shear strength influences principally by the cohesion and internal friction angle, which are already influenced by sample water content. The relationship between the vane shear strength and the water content for the untreated and treated soil for all the additive ratios is showed in fig. 8. It seen that the undrained shear strength determined by the vane test decreases with the increase in water content for all the proportions of SP, the undrained shear strength of the treated soil at the same water content is greater than that of untreated soil. From these results, it can be realized that the addition SP leads to reducing or disappearing of clay fractions due to the flocculation and agglomeration effect, considering the particle size distribution.

G. Expansion index (Primary swell) test

This test has been carried out to determine the expansion potential of a soil in accordance with ASTM D 4829-95, 2000 test specification [14]. The expansion potential was the used to classify the soil according to table 3, (Day, Robert W., soil testing manual), as it has very low, low, medium, high, or very high expansion potential.

Test procedures were first the preparation of the soil specimens of untreated and the treated sample with the fixed ratios of additives. Each sample was mixed at it maximum dry density and optimum moisture content conditions. The soil sample was then compacted in a ring of 50 mm in diameter and 10 mm in height. The ring mould included the soil sample was then placed in a surrounding container with dry and clean porous plates above and under the ring sample. This container with the sample was then placed in the center of the consolidometer device; Initial dial reading was recording within the first 10 minutes of applying the pressure.

The container was then filled with water and allowed to swell for 24 h. The primary swell is the considered to be 10% of the expansion index which is calculated by equation (4)

Table 3: Typical soil properties based on expansion potential.

Expansion potential	Very low	low	medium	high	Very high
Expansion index (%)	0_20	21_50	51_90	91_130	>130

$$EI = \frac{1000(h_f - h_i)}{h_i} = 10(\%\ primary\ swell) \quad (4)$$

Where;

EI = the expansion index;

h_f = final reading (height) of the specimen at the end of 24 h of swelling; and

h_i = initial reading (height) of the specimen.

In general, the more fine particles soil, the more expansive soil. The soil used in the study is classified as fine soil size that is passed sieve #200. This is the cause of the high expansion potential property as well as it's prove why the SP has not been significantly affected the expansion potential because it is finer than the clay particles of the soil used.

IV. CONCLUSION

This study is dedicated to the purpose of reducing the damage of sewage sludge ash and stone powder in the form in which they are converted into effective materials. SP was applied to cohesive soil. Results from the experimental work can be concluded as follow:

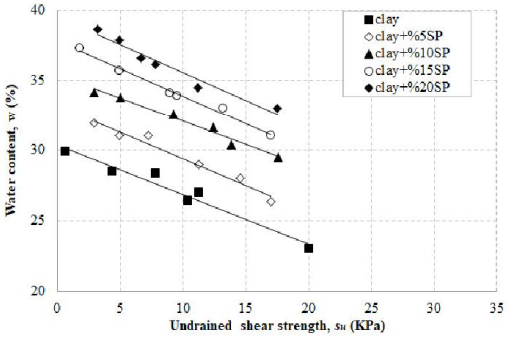


Figure 8: Variation of undrained shear strength from LVT with addition of stone powder.

1. There is an increase in liquid limit with increasing the amount of SP. The plasticity index decrease which indicate that the soil properties improved.

2. The unconfined compressive strength of SP soil samples decrease with admixture amount. The best increasing of unconfined compressive strength and increase the ductility behavior of the soil.

3. whether by the fall cone test or by the vane shear test, the undrained shear strength obtained from both fall cone and vane shear tests recorded un increase with the increasing the amount of SP.

4. The swelling potential is clearly improved for SP admixtures. This waste can be classified as helpful additives in the volumetric stabilization of soil.

REFERANCES

[1] Al-Joulani, N. (2012). Effect of Stone Powder and Lime on Strength Compaction and CBR Properties of Fine Soils. *Jordan Journal of Civil Engineering*, **6**(1), 1-16.

[2] Demirel, B. (2010). The effect of the using waste marble dust as fine sand on the mechanical properties of the concrete. *International journal of physical sciences*, **5**(9), 1372-1380.

[3] Mahzuz, H. M. A., Ahmed, A. A. M., & Yusuf, M. A. (2011). Use of stone powder in concrete and mortar as an alternative of sand. *African Journal of Environmental Science and Technology*, **5**(5), 381-388.

[4] Ahmed, A., Ugai, K., & Kamei, T. (2011). Investigation of recycled gypsum in conjunction with waste plastic trays for ground improvement. *Construction and Building Materials*, **25**(1), 208-217.

[5] Corinaldesi, V., Moriconi, G., & Naik, T. R. (2010). Characterization of marble powder for its use in mortar and concrete. *Construction and building materials*, *24*(1), 113-117.

[6] Sakalkale, A. D., & Dhawale, G. D. (2014). Experimental study on use of waste marble dust in concrete. *International Journal of Engineering Research and Applications*, **4**(10), 44-50.

[7] Binici, H., Kaplan, H., & Yilmaz, S. (2007). Influence of marble and limestone dusts as additives on some mechanical properties of concrete. *Scientific Research and Essays*, **2**(9), 372-379.

[8] ASTM. American Society for Testing and Materials. (2000). Standard test methods for liquid limit, plastic limit, and plasticity index of soils. D4318-00. West Conshohocken, PA.

[9] ASTM. American Society for Testing and Materials. (2012). Standard test methods for laboratory compaction characteristics of soil utilizing modified effort (56,000 ft-lbf/ft³ (2,700 kN-m/m3)). D1557-14. West Conshohocken, PA.

[10] ASTM. American Society for Testing and Materials. (2013). Standard test methods for unconfined compressive strength of cohesive soil. D2166/D2166M-13. West Conshohocken, PA.

[11] BS1377 (1990) "Methods of Testing of Soils for Civil Engineering

[12] Wood D.M. (1985) "Some Fall Cone Tests", Geotechnique 35, No.1, pp.64-

[13] ASTM, Standard Society for Testing and Materials, (2000), Standard test methods for Laboratory Miniature Vane Shear test for standard fine-grained clayey soil.

[14] ASTM, Standard Society for Testing and Materials, (2000), standard test method for expansion index, D4829-95, West Conshohochen, PA.

THE EFFECT OF BORON DOPING MOLARITY ON STRUCTURAL OPTICAL ELECTRICAL AND THERMOLUMINECCENCE PROPERTIES OF INDIUM OXIDE FILMS GROWTH BY SPRAY PROLYSIS TECHNIQUE

M.TEMİZ[1], R.G. YILDIRIM[2] and M. BEDİR[2]

[1] Selcuk University, Konya/Turkey, mehmettemiz@selcuk.edu.tr
[2]Gaziantep University, Gaziantep/Turkey, ozkan@gantep.edu.tr
[2]Gaziantep University, Gaziantep/Turkey, bedir@gantep.edu.tr

***Abstract* - In this report, we have succeeded in using chemical spray prolysis technique to grow high transparent and low resisteve boron doped indium oxide films. The films were deposited on glass substrates at 380 0C. The molarity of the boron were setted as 0.02, 0.03, 0.05, 0.07, 0.09 and 0,1 mol. The structural properties of boron doped films were studied using X-ray diffractometer and thermolüminescence properties were studied using Harshav TLD system 3500 manual TL reader.**

***Keywords* - In2O3 films; Spray prolysis; physical properties**

I. INTRODUCTİON

It is known that thin films of the metal oxides In2O3, are important semiconductor materials with wide band baps, good chemical stability, and transparency to visible light. With suitable doping, they represent very low resistence, giving rise to the nomenclature of transparent conducting oxide (TCO) films, and can be applied in many fields, such as transparent electrodes used on electroluminecence (EL) devices, photodetectors (PDs), solar cells, optoelectronic (OE) devices and functional materials for gas sensors, thermal reflector coatings, and surface heaters. Today, polycrystalline In2O3 films have a wide variety of applications in the manufacturing of devices such as gas sensors, flat panel displays, transparent electrode materials, solar cells, electroluminescent diodes, etc.

During the last few decades, thin films of oxide material have been developed from binary and turnery compounds using various techniques. Numerous and conventional preparation methods include vacuum and e-beam evaporation, RF and vacuum arc plasma evaporation and spray prolysis method.

The spray prolysis method is a simple, non-vacuum deposition process that offer several advantages over vacuum deposition techniques, such as cost effectiveness, large area coating capability, and ease of compositional modification. Our approch will be to obtain transparent, conductive, and intentionally doped and undoped indium oxide films by using spray prolysis method on high clean glass substrate. We used the spray prolysis technique to explore the effect of B dopants into indium oxide matrix. It is a versatile technique enabling deposition of small area uniform films. In the spray prolysis method the direct drolplet deposition at the hot substrate takes place.

Thermoluminescence (TL) technique is widely accepted as a useful and reliable technique to study defects in semiconductor materials, but the more widely spread and sucessful application of the TL is in the field of radiation dosimetry. Many phosphor material, synthetic as well as natural, have been charecterised to evaluate their feasibilty as thermoluminescence dosimeters (TLD). Boron doped and undoped indium oxide exhibits TL under irradiation with different sources and striking radiation hardness. Morover, indium oxide is inert to environmental conditions, nontoxic and insoluble in water.

II. MATERİAL AND METHOD

Spray Prolysis Method and Experimental Setup

The spray pyrolysis method is simply based on spraying a finely atomized solution onto a suitable substrate. The chemicals contained in the spray solution are expected to fulfill the following conditions.

1) On thermal decomposition the chemicals in solution form must provide species/complexes that will undergo a thermally activated chemical reaction to yield the desired thin film material.

2) The remainder of the substituents including the carrier liquid should be vaporisable the subslide temperature. The substrste has a great influence on the deposition process and substrate heating and temperature control in the process the spraying rate, the size of the sprayed particles and the spray patterns are strongly influenced by the geometry of the spray nozzle used.

After atomisation, gas stream carriers fine droplets onto a heated substrate and as the droplets approach it, in ideal conditions, the solvent is expected to vaporise entirely leading to the deposition of the non-volatile constituents. However, a variation in a droplet size will give rise to a number of different deposition processes, depending on thermal behaviour of differently sized droplets.

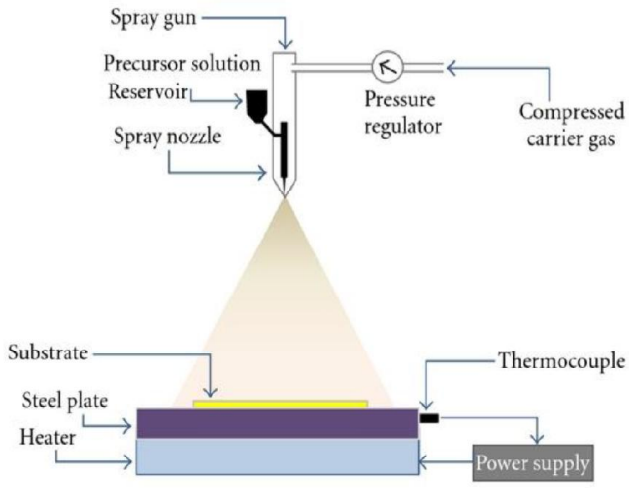


Figure 1: Schematic diagram of spray pyrolysis system

III. EXPERİMENTAL STUDIES

Substrat Cleaning

The substrate cleaning process is carried out in steps as seen in Fig.2

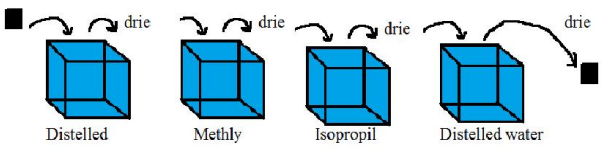


Figure 2: The cleaning process of glass substrate.

All substrates used in this study have been prepared and cleaned as follows

First: The glass substrate is immersed into the distilled water to clean the dust on its surface,15 minutes. Then it is taken out from the distilled water and dried.

Second: The substrate taken from the first cup and dried is immersed into the methyl alcohol and left there for 15 minute to clean the oily substances on the surface of the substrate, and then it is taken out from this liquid and dried in air.

Third: The dried substrate is immersed into the third cup filled with isopropil alcohol and it is treated again for 15 minutes to obtain a smooth surface.

Finally: The substrate is treated with the distilled water as in first step to clean all residues remaining on the surface of the substrate during the other processes.

Preparatıon of The Sprayıng Solutıon and Productıon of Indium Oxide Films

Indium oxide films were deposited on highly clean glass substrates (about 0.5 cm2 of geometric area) at a constant substrate temperature of 380◦C by using spray pyrolysis technique. The starting materials were used InCl3. 100 mlt spraying solution was prepared at the 0.05M, the spray flow rate was adjusted to about 0.3 mlt per minute and the distance between the nozzle (head of the sprayed source) and the substrate was kept at 20 cm in all cases.

Irradiation Part

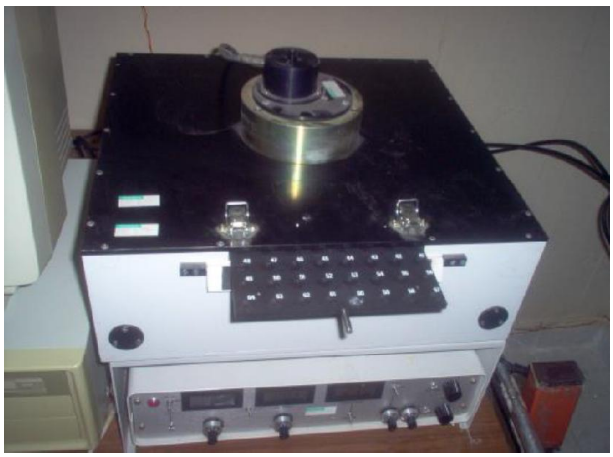


Figure3: Radiation 90Sr-90 Y b- source used in our experiment

TLD Reader

The glow curve measurements were made using a Harshaw TLD System 3500 Manual TL Reader.



Figure 4: Harshav TLD system 3500 manual TL reader

IV. MEASUREMNTS AND RESULTS

Dose Respounse Characteristics

The InO films prepared by spray depositing on to a high cleaned glass substrate. Sample is polycrystalline with cubic type structure. In this study, we have firstly investigated the dose response characteristics of In2O3 thin film from linear heating rate of 1 oC/s.

Amount of chemical used in this study,

Sample A: 0,1 mol H3BO3, 50 ml H2O

Sample B: 0,05 mol H3BO3, 50 ml H2O

Sample C: 0,03 mol H3BO3, 50 ml H2O

Sample D: 0,02 mol H3BO3, 50 ml H2O

Sample E: 0,07 mol H3BO3, 50 ml H2O

Sample F: 0,09 mol H3BO3, 50 ml H2O

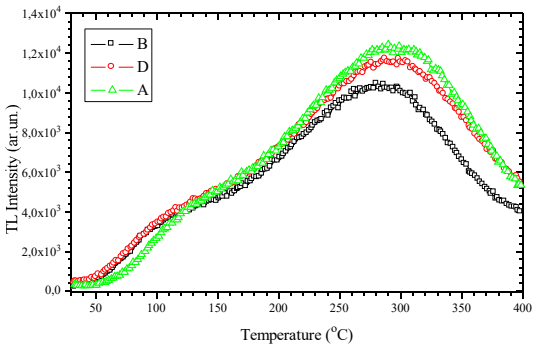


Figure 5: The glow curves of all sample A, B and D after 15 minutes β irradiaiton at a linear heating rate of 1 oC/s.

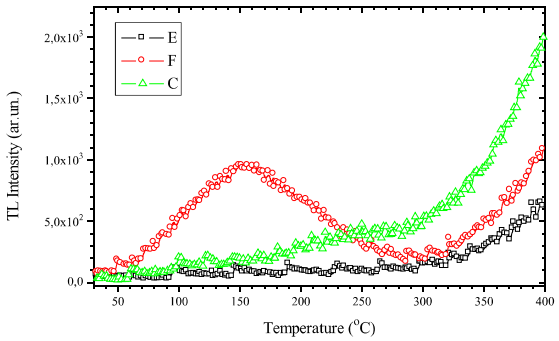


Figure 6: The glow curves of Al sample E, F and C after 15 minutes β irradiaiton at a linear heating rate of 1 oC/s.

Thermoluminescence glow curves (TL) of In2O3 thin films were obtained using a Harshaw QS 3500 Manual type TL reader, having S-11 response photomultiplier tube. TL curves were obtained using a platinum planchet at a linear heating rate of 1 oC/s up to 400 oC, except for the heating rate experiments. The samples were weighted as fifteen milligrams and were irradiated for 15 minutes at room temperature with a 90Sr–90Y beta (β) source delivering about 0.9 Gy/min.

The dosimetric characteristics of any TL material mainly depend on the sensitivity, energy response and the kinetic parameters quantitatively describing the trapping–emitting centers responsible for the TL emission.

TL glow curves showed that the H3BO3 concentration changes the glow curve structure and the maximum TL intensity of In2O3 thin film was obtained at H3BO3concentration of 0.1 mol (Fig. 4.1). TL intensities decreased with increasing H3BO3concentration.

XRD Analysis of Boron Doped $InCI_3$ Samples

All of the samples were grown on glass substrate at 3800C by using spraying pyrolysis method. Boron doped films were deposited by adding boric acid (H3BO3) as a dopant source to the solution. Boric acid presumably exists in the form of borate, BO-3 . Table 1 presents the chemical content of the spraying solution.

Table 1: The chemical content in spraying solution

$InCl_3$(M)	H_3BO_3(M)
0.1	0.02
0.1	0.03
0.1	0.05
0.1	0.07
0.1	0.09

Figures 1 from (a) to (e) represented here are showing X-ray diffraction patterns of boron doped indium choride films prepared at different boric acid molarity. X-ray diffraction measurements were carried out for films deposited by varying the molarity of H3BO3 while keeping all other parameters constant as given in Table 1.

All peaks in the diffraction pattern correspond to the hexagonal structure of mainly In(BO3)(Indium Borate) and InOCI (Indium Oxide Chloride) indexing on the basic of JCPDS card. Polycrystalline hexagonal and cubic InO of random orientation are known to show many strong X-ray diffraction peaks. All diffractograms of the prepared films clearly indicate the polycrystalline nature of the In(BO3) and InOCI films. The preferential orientations are along (102), (006), (202), (204) and (211) crystal planes. It is also indicated that the intensity of existed peaks are explicitly dependent on the variable boric acid molar concentration during crystal formation.

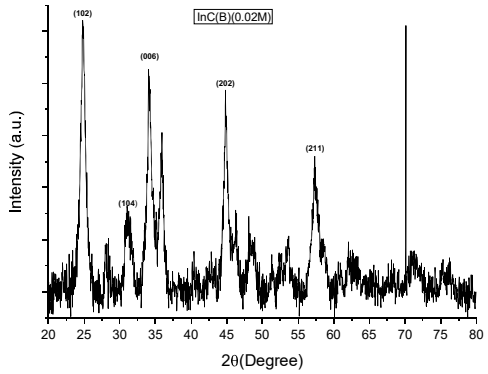


Figure 6 (a): XRD pattern of 0.02 M boric acid doped $InCl_3$

According to Table 2 and figures [from fig.1 (a)to (e)] there are two main components of crystallization of In(BO3) (indium borate and InOCl (indium oxide chloride). The crystallization of In(BO3) along (102), (104), (006) and (202) planes requires more energy than that of others lying along the planes.

With the H3BO3 molar ratio increased up to 0.09, the growth orientations of (102), (104), (006) and (202) are dominant. Further increase of the H3BO3 molar ratio results in the disappearance of (011), (201) and (105) peak. Finally, the In(BO3) film presents a (102), (006) and (202) preferential orientations at all molar ratio of H3BO3. From the above results, we can conclude that boron-doping plays an important role in the crystal orientations of In(BO3) films and effectively modifies the microstructure of the films. The preferred orientation of In(BO3) films is due to the controlled nucleation process associated with the low formation rate of In(BO3). Regardless of boron doping concentration no change of the crystal structure by boron doping ratio is observed. This gives strong support to the formation of boron doped InO films by spray pyrolysis technique.

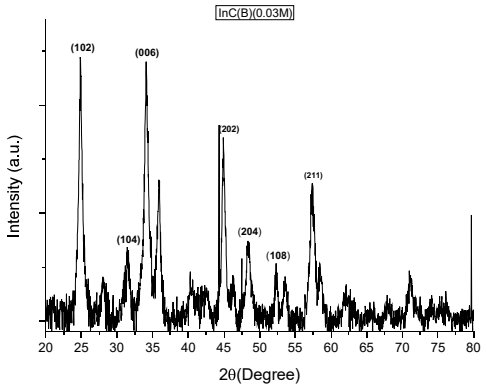


Figure 6 (b): XRD pattern of 0.03 M boric acid doped InCl3.

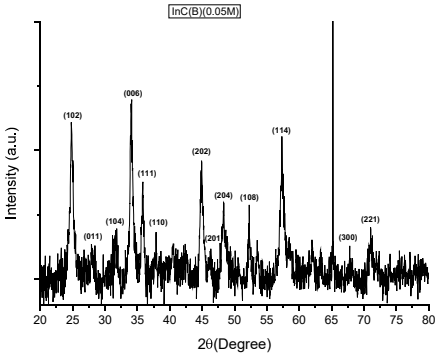


Figure 6 (c): XRD pattern of 0.05 M boric acid doped InCl3

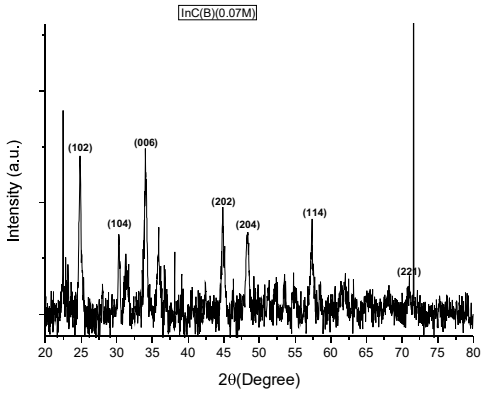


Figure 6 (d): XRD pattern of 0.07 M boric acid doped $InCl_3$

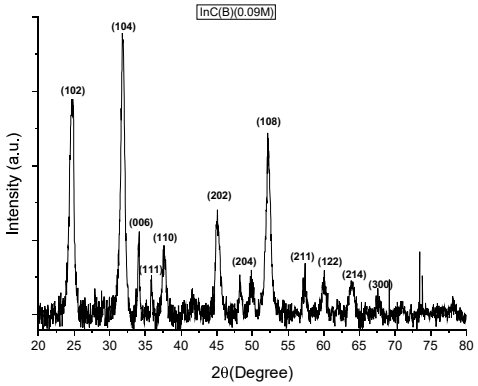


Figure 6 (e): XRD pattern of 0.09 M boric acid doped $InCl_3$

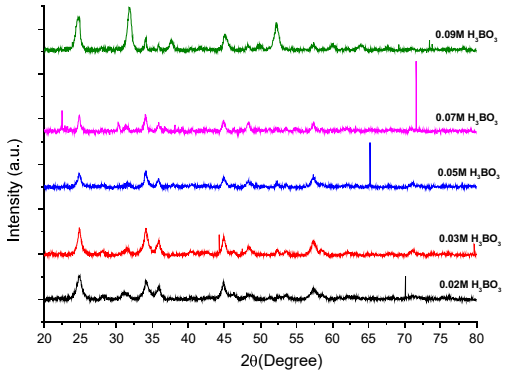


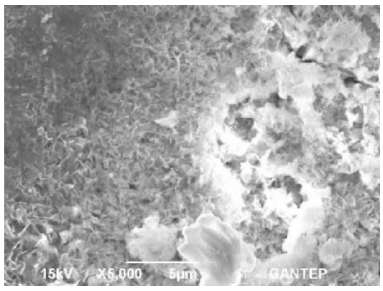
Figure 7: All XRD patterns of boric acid doped InCl3 together.

A trend is observed that intensity of the patterns of the films is to decrease with increasing of the boron doping ratio from 0.02 M to 0.05M and the FWHM value of the samples is to increase with increasing of the boron doping ratio from 0.02 M to 0.05M. And also, intensity of the patterns of the films is to increase with increasing of the boron doping ratio from 0.07 M to 0.09M and the FWHM value of the samples is to decrease with increasing of the boron doping ratio from 0.07 M to 0.09M. The sharp diffraction peaks of the narrow FWHM indicate good crystallinity with an average grain size.

The X-ray reflection peaks at different planes indicate that the films are polycrystalline over the whole studied range of boron doping concentration. The intensity of peaks and crystal orientations are influenced by the boron doping concentration.

The registered X-ray spectra fit to a In(BO3) hexagonal structure without any new reflections. There is an additional peak of InOCI phase. The traces of either CI or In have been observed. This indicates that the O-2 are substituted at In+2 sites without changing the InOCI structure.

Fig. 3 shows SEM micrographs of boron doped samples consisting of a dense layer with small crystallites. In addition, some large particles of approximately 5 m in size are embedded on the surface. Those particles are In(BO3), not those of an impurity phase, as no impurity phase is observed in the XRD pattern. Those particles are quite likely colloidal particles formed in solution and adsorbed on the substrate during the growth of the films. The formation of In(BO3) can take place heterogeneously on the substrate surface, depositing process, or homogeneously in solution, producing In(BO3) precipitates. For the deposition parameters chosen in this study, it was expected that the deposition would occur via an ion-by-ion process, but the SEM results suggest that the homogeneous process was also operative.



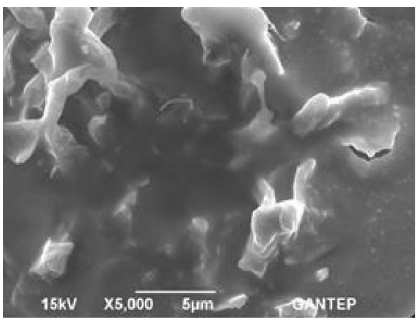


Figure 4.5 SEM micrographs of boron doped samples.

REFERENCES

1. N.G. Pramod, S.N. Pandey, Effect of Li doping on the structural, optical and formaldehyde sensing properties of In2O3 thin films,Ceramics International 41 (2015) 527-532.

2. D. Manno, M. Di Siciliano, E. Filippo, A. Serra, structural and electrical properties of In2O3/SeO2 thin films for gas-sensing applications, J. phys. D: Appl. Phys. 34 (2001) 2097.

3. Shiqi Wang, Yukai An, Lingshen Duan, Huarui Liu, Jiwen Liu,

Zhonghua Wu, Effect of Mn doping on the structural, optical, and magnetic

properties of In2O3 films, J. Vac. Sci. Technol. A 31 (2013) 061515.

4. B. Radha Krishna, T.K. Subramanyam, B. Srinivasulu Naidu, S. Uthanna,

Effect of substrate temperature on the electrical and optical properties of dc

reactive magnetron sputtered indium oxide films, Opt. Mater. 15 (2000) 217.

5. Chunyu Wang, Volker Cimalla, Genady Cherkashinin, Henry Romanus,

Majdeddin Ali, Oliver Ambacher, Transparent conducting indium oxide

thin films grown by low-temperature metal organic chemical vapor

deposition, Thin Solid Films 515 (2007) 2921.

6. F.O. Adurodija, H. Izumi, T. Ishihara, H. Yoshioka, M. Motoyama,

K. Murai, Influence of substrate temperature on the properties of indium

oxide thin films, J. Vac. Sci. Technol. A 18 (2000) 814.

7. V. Golovanov, Matti A. Maki-Jaskari, Tapio T. Rantala, G. Korotcenkov,

V. Brinzari, A. Cornet, J. Morante, Experimental and theoretical studies

of indium oxide gas sensors fabricated by spray pyrolysis, Sens.

Actuators, B 106 (2008) 563.

8. Jun Tamaki, Chizuko Naruo, Yoshifumi Yamamoto, Masao Matsuoka,

Sensing properties to dilute chlorine gas of indium oxide based thin film

sensors prepared by electron beam evaporation, Sens. Actuators, B 83 (2002)

190.

9. Wan-Young Chung, Go Sakai, Kengo Shimanoe, Norio Miura, DukDong Lee, Noboru Yamazoe, Preparation of indium oxide thin film by

spin-coating method and its gas-sensing properties, Sens. Actuators, B 46

(1998) 139.

10.https://www.researchgate.net/figure/260410518_fig4_Figure-1-XRD-patterns-of-the-In2O3-sample

Volatile organic compound removal using polyurethane based selective membrane

F. UGUR NİGİZ[1] and N. DURMAZ HİLMİOGLU[1]

[1] Kocaeli University, KocaeliTurkey, filiz.ugurr@gmail.com
[1] Kocaeli University, KocaeliTurkey, niluferhilmioglu3@gmail.com

Abstract **- In this study pervaporative separation capability of silica incorporated thermoplastic polyurethane (TPU) membrane was investigated at different case studies. Representative waste disposal for different industry was prepared synthetically. Toluene-water, chloroform-water, formic acid-water, isopropyl alcohol-water mixture were prepared in concentration of 3 wt. % and the pervaporation experiments were performed at 40 °C. Membrane morphology was analyzed using scanning electron microscopy and polarized optical microscopy. Effect of membrane preparation technique on membrane affinity to the organic mixture was also investigated and the results were evaluated as a function of degree of swelling. Better flux of 0.73 kg/m2.h and a separation factor of 14.9 were obtained at chloroform-water pervaporation. Pervaporation was also effective in toluene-water mixture separation. The quantitative results of the flux was chloroform>toluene>formic acid>isopropyl alcohol.**

Keywords **- Thermoplastic polyurethane membrane, organic-water separation, hydrophobic pervaporation, mixed matrix membrane**

I. INTRODUCTION

Industrial waste disposal includes hundreds of contaminants such as ions, radioactive elements, bacteria, volatile organic compounds (VOCs) and these impurities have potential to show toxic effect on the living cell within water ecosystem. It is a legal obligation to treat waste water before discharging to the lake, oceans or seawater [1, 2].

The concentration of each contaminant changes according to the industrialization of the region. Based on these variables, there are several purification methods for VOC purification which are used in large scale [3-6]. Distillation, carbon adsorption, air stripping, biological oxidation, coagulation, chemical treatment, and membrane separation methods are used for water treatment. Either these units are employed in-place or the waste disposal is drained to a general purification plant. In both cases, it is hard to remove small amount of dissolved chemicals from water. Most of chemicals present in waste at very low concentration (<1000 pmm), therefore, it is needed to separate them selectively using selective purification technique such as the membrane process [7-11].

Membrane separation methods (eg. nanofiltration, reverse osmosis, pervaporation) are known as cost-effective and environmentally friendly solution for water treatment. For deep purification of dissolved or very dilute disposal waste, nano-porous or non-porous membranes are preferred. Separation system via membrane is defined in several ways based on the structural nature of the membrane and the driving force between the upstream and downstream of the membrane. For example, pervaporation is a chemical potential driven process in which non-porous polymeric, inorganic or mixed matrix membranes ar[12-16]. It is an appropriate method for deep water purification when the organic contaminants are very low scale (<1000ppm). In the case of the pervaporative separation, selected ions or solvent is adsorbed to the surface of the membrane and pass through it in vapor phase.

Hydrophobic materials such as polyether-block-amid, poly(dimethyl siloxane), polyurethane, natural rubber are used for organic removal. Uragami (2014) studied for chloroform-water pervaporation using PDMS-PMMA membrane and obtained a flux of 1.9*10-5 kgm/m2.h with a separation factor of 4850 [17]. Khayet and Matsura (2004) also studied for chloroform-water mixture by using PVDF membrane [18]. Satyanarayana et al. (2004) used two different commercial membrane for toluene-water pervaporation [19]. In a study by Simone et al. (2012) Ethylene–Chlorotrifluoroethylene copolymer membrane was fabricated and used for toluene separation from water. They reported a total flux of 0.193 kg/m2.h with a separation factor of 849 at the room temperature [20]. Isopropyl alcohol-water pervaporation is a most recent study in pervaporative study. However, a big part of these studies have been performed for isopropyl alcohol dehydration by using a hydrophilic membrane [21, 22].

In this study pervaporative separation capability of silica incorporated thermoplastic polyurethane (TPU) membrane was investigated at different case studies. Thermoplastic polyurethane has very unique feature. TPU consists of both the soft polyether/polyester segment and hard aromatic urethane segment that change the adjustable segmental properties of the TPU. When TPU is used as non-porous membrane, as its soft region allows to passage of organic molecules, the hard segment gives mechanical durability over the long term separation process under forcible conditions. Additionally amine bond of urethane enhances the hydrophobicity of TPU and it contributes increasing the organic selectivity. According to the membrane preparation method, period, and solvent type, phase separation can be occurred within TPU and the crystalline structure of TPU is directly affected [23]. Therefore, in this study it was aimed to obtain high organic separation factor due to the selective nature of TPU. Representative waste disposal for different industry was prepared synthetically. Toluene-water mixture

was selected for paint and resin industry, chloroform-water mixture was selected for pulp-paper and polymer industry, formic acid-water mixture was selected for textile, and isopropyl alcohol-water mixture was selected for pharmaceutical and semiconductor industry. Effect of crystalline structure on the degree of swelling was investigated at a given temperature and feed composition of organic-water mixture. The pervaporation performance of crystalline silica loaded TPU membrane was also investigated as a function of total flux and organic separation factor. In conclusion, the silica loaded TPU membrane showed high affinity to chloroform and toluene than that of isopropyl alcohol and formic acid.

II. EXPERIMENTAL

A. Membrane Preparation

In this study silica-TPU membranes were prepared by using solution-casting method. 10 wt % TPU was dissolved in N,N-dimethylformamide and stirred for four hours at 65 °C. Then 5 wt. % silica (Ultrasil) (respect to the polymer's weight) was homogeneously dispersed into the polymer solution and stirred in ultrasonic bath. In order to determine the effect of crystalline structure on separation performance, membranes were dried in two different ways. In the first way, pre-membrane solution (TPU-DMF and silica) was dried slowly at the ambient temperature. In the second way, pre-membrane solution was dried in oven at 140 °C for four hours. The membranes dried rapidly in vacuum oven were entitled as PC-TPU for plain-crystalline TPU, SC-TPU for silica loaded crystalline TPU, and the membranes dried slowly at room temperature were entitled as PA-TPU for plain amorphous TPU, SA-TPU for silica loaded crystalline TPU.

B. Membrane Characterization

The surface morphologies of the silica loaded membrane which was dried in oven were determined by polarized microscope (POM)(Nikon Elipse) scanning electron microscopy (SEM) (JEOL JSM-6000).

C. Swelling experiment

The degree of swelling (DS)(%) test was done to evaluate the affinity of the membrane to the target component. For determination of the swelling degree, membranes were immersed in toluene-water, chloroform-water, isopropyl alcohol-water and formic acid-water solution with an organic concentration of 3 wt. %. Swelling degrees were calculated from the weight difference of the swollen (Ws) and dry (Wd) membrane as seen in Equation 1.

$$DS = ((Ws - Wd)/(Wd)) * 100 \quad (1)$$

D. Swelling experiment

Pervaporation experiments were performed in a laboratory scale pervaporation unit with a volume capacity of 250 ml. The system was also defined elsewhere [24]. The upper side of the membrane was kept in atmospheric pressure and a pressure difference was occurred between the sides of the membrane with a vacuum pressure of 1mbar on the downstream side to maintain the chemical potential gradient. To create a chemical potential gradient between the sides of the membrane play a critical role on the performance of pervaporation. According to the solution-diffusion phenomenon which defines the pervaporative separation accurately, the target component dissolved on the membrane surface, diffuses through the membrane and desorbs to downstream side resulting the chemical potential created by pressure difference.

After the better membrane type had been selected with the results of swelling experiments pervaporation were carried out at 40 °C. Experiments were performed with binary water–organic mixtures of chloroform/water, toluene/water, formic acid/water, and isopropyl alcohol/water solutions when the organic concentration in water was 3 wt. %. Permeate solution was collected in cold traps with an hourly interval and weighted to determine the flux (J)(kg/m2.h) as seen in Equation 2.

$$J = (Wp)/(A.t) \quad (2)$$

where Wp (kg) is the weight of the permeate solution, t is pervaporation time (h), A is effective membrane area (m^2).

E. Analysis

The organic separation factor (β) was calculated for four types of organic component separately using Equation 3.

$$\beta = (y_i/y_j)/(x_i/x_j) \quad (3)$$

y_i and x_i represent the organic concentration in the permeate and feed respectively. y_j and x_j show the water concentration in the permeate and feed respectively.

For this purpose, the concentrations of the organic compounds were determined in different methods. Formic acid concentration in water was determined using titration method. Isopropyl alcohol concentration in water was analyzed using gas chromatography equipped with a thermal conductive detector. Chloroform and toluene concentration in water were determined using Hach 500 UV-Vis spectroscopy.

III. RESULTS AND DISCUSSION

A. Characterization Results

Figure 1 indicates the surface morphologies of pristine (unfilled) and 10 wt. % silica filled TPU membranes. While the light phase represents the silica particle, the dark region indicates the TPU matrix. Figure 1a shows the smooth and dense structure of the unfilled TPU surface. Figure 1b indicates the homogeneous dispersing of the silica particle within the polymeric matrix. The interface regions between the silica and TPU clearly appear in Figure 1c and Figure 1d. As seen in the figure, the filled membrane was fabricated successfully without any fractures or defects between the two different structures (organic polymer-inorganic silica). This observation is very important for non-porous selective

membrane fabrication. Undesired defect-free region or voids between the polymer and inorganic particle would allow unselected passage of the other molecules with the target ones. Therefore, the mixed matrix, hybrid, and inorganic particle filled polymeric pervaporation membrane should be well fabricated without any adhesion-free region to achieve a selective separation.

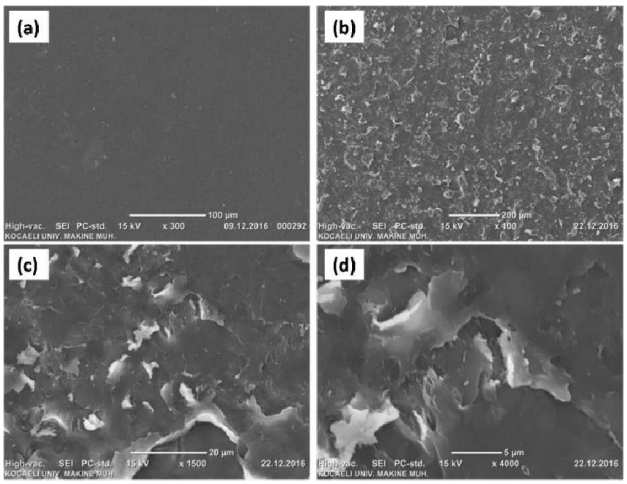


Figure 1: SEM micrographs of pristine (a) and silica filled TPU (b,c,d) membranes

The homogeneous silica distribution is also confirmed by the polarized microscope micrographs as it is indicated in Figure 2. Silica particles were well distributed within the TPU and this case would be expected to affect positively pervaporation performance of the organic-water solution.

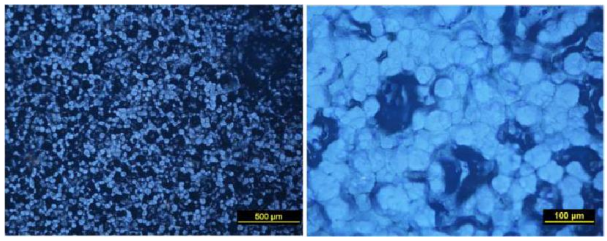


Figure 2: POM micrographs of silica filled TPU membrane

B. *Swelling Experiment*

As seen in Figure 3, thermoplastic polyurethane shows high affinity to chloroform compared to other organics. Hence it could be predicted that the separation capability of crystalline TPU would be chloroform>toluene>formic acid>isopropyl alcohol. When the membranes were dried at ambient conditions, amorphous structure of membrane showed higher swelling tendency to the solvent. Therefore, PA-TPU and SA-TPU exhibited higher swelling compared to PC-TPU and SC-TPU. Additionally, affinity of the amorphous membrane to isopropyl alcohol increased compared to crystalline.

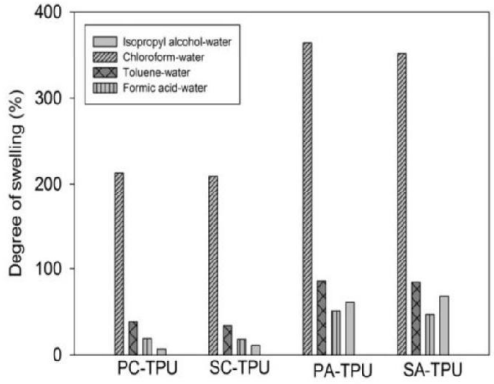


Figure 3: Swelling degree of membranes

However, the swelling degree results between the 300-400 % are very high for selective separation. Therefore, SC-TPU membrane was selected to be used for pervaporative separation of organic-water mixtures.

C. *Pervaporation experiments of organic-water solutions*

According to the swelling experiment, membrane separation studies were performed using SC-TPU membrane. Separation performances of the SC-TPU membrane in the pervaporative separation of isopropyl alcohol-water, formic acid-water, toluene-water and chloroform-water binary mixtures are presented in Figure 4 and Figure 5.

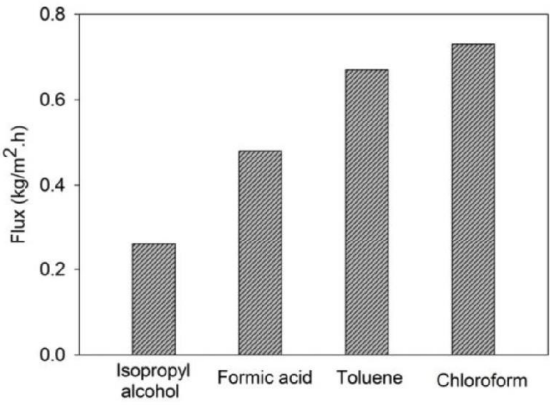


Figure 4: Total flux results of SC-TPU membrane for binary mixtures

Figure 4 indicates the flux result comparison of the different binary solutions. The flux results confirmed the swelling results. The better flux result was obtained in chloroform-water solution as 0.73 kg/m2.h. The quantitative results of the flux was chloroform>toluene>formic acid>isopropyl alcohol. This result was due to the interaction forces between the solvent and polymer. For better understanding this interaction Hensen solubility parameters were given in Table 1.

Table 1: Hensen Solubility Parameters [25]

Components	δd	δp	δH	δ
Water	15.5	16	42.3	**48.8**
Isopropyl alcohol	15.8	6.1	16.4	**23.6**
Formic acid	14.3	11.9	16.6	**37.8**
Toluene	18	14	2	**18.2**
Chloroform	17.8	3.1	5.7	**18.9**
TPU	10	8.2	9.8	**18.8**

Where (δp) represents the polar component dipole–dipole interactions, (δH) represents hydrogen bonding forces, (δd) represents the dispersive force component, and the (δ) represents Hansen solubility parameter [26]. As can be clearly seen in the Table 1, Hensen solubility of the chloroform was almost the same with the TPU, therefore, the flux value of chloroform-water solution was the highest one resulting the higher affinity of the polymer to the chloroform. The quantitative order of the Hensen parameters were chloroform>toluene>isopropyl alcohol>formic acid>water. These results were almost the same with both the swelling results and flux results.

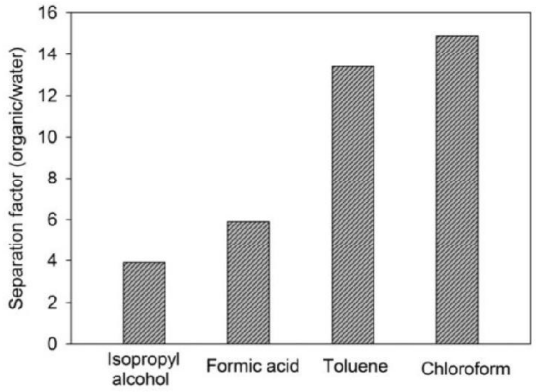


Figure 5: Separation factor results of SC-TPU membrane for binary mixtures

Better flux and separation factor was achieved in the case of chloroform-water and toluene-water solution. While the organic separation factor of 14.9 and 13.4 were achieved for chloroform-water and toluene-water binary mixtures, 5.8 and 3.7 separation factor were obtained for formic-acid and isopropyl alcohol-water binary mixtures respectively. This result attributed to affinity of the membrane to the chloroform and toluene as indicated before related to Hensen Parameters.

IV. CONCLUSIONS

In this study, an amorphous and crystalline pristine and zeolite distributed membranes were synthesized. Firstly, four different membranes were immersed in chloroform-water, toluene-water, isopropanol-water, formic acid-water binary mixtures to determine the sorption capability of the membranes to the target component. Following the swelling measurements, pervaporation experiments of the binary mixtures were performed at 40 °C temperatures with constant organic composition of 3 wt. % by using crystalline silica loaded TPU membrane. Better flux of 0.73 kg/m2.h and a separation factor of 14.9 were obtained at chloroform-water pervaporation. Pervaporation was also effective in toluene-water mixture separation. In conclusion, it can be concluded that the silica loaded TPU membrane which was dried in oven was very effective for chloroform-water and toluene-water separation.

ABBREVIATIONS

DMF : N,N-dimethylformamide
PA-TPU : Pristine-amorphous thermoplastic polyurethane
PC-TPU : Pristine-crystalline thermoplastic polyurethane
PDMS : Poly(dimethyl siloxane)
PMMA : Poly(methyl metacrylate)
POM : Polarized optical microscope
PVDF : Polyvinylidene fluoride
SA-TPU : Silica loaded-amorphous thermoplastic polyurethane
SC-TPU : Silica loaded-crystalline thermoplastic polyurethane
SEM : Scanning electron microscope
TPU : Thermoplastic polyurethane
VOCs : Volatile organic components

ACKNOWLEDGMENT

The study was financially funded by the Scientific Research Centre of Kocaeli University (2016/040).

REFERENCES

[1] S. Das, A.K. Banthia, B. Adhikari, "Removal of chlorinated volatile organic contaminants fromwater by pervaporation using a novel polyurethane urea–poly (methyl methacrylate) interpenetrating network membrane," *Chemical Engineering Science*, vol. 61, pp. 6454 – 6467 , 2006.

[2] R. Mukherjee, S. De, "Novel carbon-nanoparticle polysulfone hollow fiber mixed matrix ultrafiltration membrane: Adsorptive removal of benzene, phenol and toluene from aqueous solution," *Separation and Purification Technology*, vol. 157, pp. 229–240, 2016.

[3] S. Mohammadi, A. Kargari, H. Sanaeepur, K. Abbassian, A. Najafi, E. Mofarrah, "Phenol removal from industrial wastewaters: a short review," *Desalination and Water Treatment*, vol. 53, pp. 2215-2234, 2015.

[4] M. T. Amin, A. A. Alazba, U. Manzoor, "A Review of Removal of Pollutants from Water/Wastewater Using Different Types of Nanomaterials," *Advances in Materials Science and Engineering*, vol. 1, pp. 1-24, 2014.

[5] C. Gadipelly, A. Pérez-González, G. D. Yadav, I. Ortiz, R. Ibáñez, V. K. Rathod, KV. Marathe, "Pharmaceutical Industry Wastewater: Review of the Technologies for Water Treatment and Reuse," *Ind. Eng. Chem. Res*. vol. 53, pp. 11571−11592, 2016

[6] A. Subramania, J.G. Jacangelo, "Emerging desalination technologies for water treatment: A critical review," *Water Research,* vol. **75,** pp. 164-187, 2016.

[7] H.N. Altalyan, B. Jones, J. Bradd, L. D. Nghiem, Y. M. Alyazichi, "Removal of volatile organic compounds (VOCs) from groundwater by reverse osmosis and nanofiltration,". *Journal of Water Process Engineering*, vol. 3, pp. 9-21, 2016.

[8] M. Drobek, A. Figoli, S. Santoro, N. Navascués, J. Motuzas, S. Simone, C. Algieri, N. Gaeta, L. Querze, A. Trotta, G. Barbieri, R. Mallada, A. Julbe, E. Drioli, "PVDF-MFI mixed matrix membranes as VOCs

adsorbers," *Microporous and Mesoporous Materials*, vol. **207**, pp. 126-133, 2015

[9] T. Uragami, Y. Matsuoka, T. Miyata, "Removal of Dilute Benzene in Water through Ionic Liquid/Poly(Vinyl Chloride) Membranes by Pervaporation," *Journal of Membrane Science and Research*, vol. **2**, pp. 20-25, 2016.

[10] O. T. Mahlangu, R. Nackaerts, B. B. Mamba, A. R. D. Verliefde, "Development of hydrophilic GO-ZnO/PES membranes for treatment of pharmaceutical wastewater," *Water Science and Technology,* Article in Press, DOI: 10.2166/wst.2017.194, 2017.

[11] A. Yamada, A. Matsui, H. Tsuji, "Removal of phenol from saline water by polyamine chelating resin," *Water Science and Technology*, vol. 68 (8), pp. 1819-1824, 2013.

[12] J. H. Lv, G. M. Xiao, "Dehydration of water/pyridine mixtures by pervaporation using cellulose acetate/ polyacrylonitrile blend membrane," *Water Science and Technology, vol.* **63**, pp.1695-1700, 2011.

[13] K. Vanhercka, G. Koeckelberghs, I. F. J. Vankelecom, "Crosslinking polyimides for membrane applications: A review," *Progress in Polymer Science*, vol. 38, pp. 874–896, 2013.

[14] V. K. Thakura, S. I. Voicu, "Recent advances in cellulose and chitosan based membranes for water purification: A concise review," *Carbohydrate Polymers*, vol. 146, pp. 148–165, 2016.

[15] S.P, Nunes, KV. Peinemann, "Membrane Technology in the Chemical Industry,". Wiley: Germany, 2006.

[16] A. Basile, A. Figoli, M. Khayet, "Pervaporation, Vapour Permeation and Membrane Distillation Principles and Applications, "Woodhead Publishing, Kidlington, UK, 2016.

[17] T. Uragami, Pervaporation for Chloroform, E. Droli, L. Giorno (eds.), Encyclopedia of Me Separation Springer-Verlag Berlin Heidelberg 2014.

[18] M. Khayet, T. Matsuura, "Pervaporation and vacuum membrane distillation processes: modeling and experiments," *AIChE* vol. 50, pp.1697-1710, 2004.

[19] S.V. Satyanarayana, A. Sharma, P.K. Bhattacharya, "Composite membranes for hydrophobic pervaporation: study with the toluene–water system," *Chemical Engineering Journal*, vol. 102, pp. 171-184, 2004.

[20] S. Simone, A. Figoli, S. Santoro, F. Galiano, S.M. Alfadul, Al-Harbic, Omar A. E. Drioli, "Preparation and characterization of ECTFE solvent resistant membranes and their application in pervaporation of toluene/water mixtures," *Separation and Purification Technology*, vol. **90**, pp. 147-161, 2012.

[21] M. Amirilargani, B. Sadatni, "Poly(vinyl alcohol)/zeolitic imidazolate frameworks (ZIF-8) mixed matrix membranes for pervaporation dehydration of isopropanol," *Journal of Membrane Science*, vol. **469**, pp. 1-10, 2014.

[22] S. K. Choudhari, H. G. Premakshi, M. Y. Kariduraganavar, "Development of novel alginate–silica hybrid membranes for pervaporation dehydration of isopropanol," *Polymer Bulletin*, vol.73, pp. 743–762, 2016.

[23] G., Zhu, T. Li, "Properties of polyurethane–polystyrene graft copolymer membranes used for separating water–ethanol mixtures," *European Polymer Journal*, vol. 41, pp. 1090–1096, 2005.

[24] F. U. Nigiz, N. D. Hilmioglu, "Green solvent synthesis from biomass based source by biocatalytic membrane reactor," *Int. J. Energy Res*. vol. 40, pp. 71–80, 2016.

[25] C. M. Hansen, "Hansen Solubility Parameters, A User's Handbook" Second Edition, Taylor & Francis Group, 2007.

[26] S. R. Panda, S. De, "Preparation, characterization and antifouling properties of polyacrylonitrile /polyurethane blend membranes for water purification," RSC Adv., vol. **5**, pp. 23599–23612, 2015.

Development of efficient green catalyst "Catalytic Membrane" for the esterification of acetic acid with glycerol

D.UNLU[1] andN. HILMIOGLU[1]

[1]Kocaeli University, Kocaeli/Turkey, derya.unlu@kocaeli.edu.tr
[1]KocaeliUniversity, Kocaeli/Turkey, niluferh@kocaeli.edu.tr

Abstract **- As heterogeneous catalysts, catalytic membranes have received growing attention in recent years due to the economical and environmental concern. Generally, homogeneous catalysts are used in industry because of the high yield, but these catalysts are also associated with some major disadvantages such as recovery, reusability, equipment corrosion. Therefore, heterogeneous catalysts are preferred in reactions. Running a reaction under heterogeneous catalytic conditions has several advantages: easy to handle, safe to store, long life time, easy removal from reaction mixture by filtration and safe disposal. Especially, recovery and reuse of catalytic membrane is not need to additional neutralization, washing stages and so catalytic membrane can be used several times. In present study, catalytic composite membranes were synthesized by using polymer and heterogeneous catalyst in the laboratory.**

Polyvinyl alcohol as polymer and phosphomolybdic acid as catalyst were chosen for making catalytic membrane. Catalytic membrane was prepared by solution casting technique. Catalytic activity of the membrane was determined by esterification reaction of acetic acid and glycerol in the batch reactor. Effects of temperature, catalyst concentration and initial molar ratio on conversion values were investigated. The obtained results show that catalytic membrane can be used as an efficient catalyst.

Keywords **- Catalytic membrane, esterification reaction, green catalyst.**

I. INTRODUCTION

Renewable fuel biodiesel is usually produced by transesterification of vegetable oils with methanol. Biodiesel production will generate about 10% (w/w) glycerol as the main byproduct. This increment of biodiesel production results in the accumulation of waste glycerol. Therefore the usage of excess glycerol in the alternative processes is investigated.

Esterification of acetic acid with glycerol is a good alternative method for the production of valuable chemical from byproduct glycerol. The products of this reaction are monoacetin (MAG), diacetin (DAG) and triacetin (TAG). The usage areas of these products are freezing industry, the production of biodegradable polymers, cosmetic sector and fuel additives. In particular, DAG and TAG are used as additives for fuels such as biodiesel and gasoline. Biodiesel has weak oxidation resistance and high boiling point. These properties can be improved by using different additives. One of these fuel additives is TAG. The usage of TAG as a fuel additive improves the overall yield of biodiesel as well as improving cold flow resistance and knock properties [1,2].

The esterification reaction of glycerol with acetic acid is generally carried out in the presence of homogeneous catalysts. These homogeneous catalysts are toxic, corrosive, harmful to the environment and unrecyclable. Therefore it is important to replace homogeneous catalysts with environmentally friendly catalysts.It is possible to overcome these disadvantages by using heterogeneous acid catalysts. The acidity of the catalyst has significant effect on glycerol esterification. Due to strong Bronsted acidities, Keggin type heteropolyacids (HPA) can be used instead of homogeneous acid catalysts. Heteropolyacids are strong Bronsted acids. The main disadvantages are low thermal strengths, low surface areas, high solubility in the polar environment and separation problems of the reaction mixture. For this reason, HPAs are impregnated with support layers such as activated carbon, silica, zeolite and polymeric matrix to obtain large surface and accessible active areas [3, 4]. Thus, the heterogeneous catalysts embedded in polymeric matrix which is called as catalytic membrane can be used repeatedly as a heterogeneous catalyst in the reaction mixture.

In this study, phosphomolybdic acid was embedded in polymeric matrix for the preparation of a catalytic membrane. Catalytic membrane prepared was used as catalyst for the esterification with glycerol acetic acid in the batch reactor. Phosphomolybdic acid has low thermal resistance and surface area due to Keggin structure [1]. By the usage of the catalytic membrane in the reaction, the catalysts could be separated from the reaction mixtures easily, dissolution of the membrane in the reaction mixture could be prevented, and reused for repeated runs. It was also aimed to increase the catalytic activity by increasing the surface area of the catalyst in the membrane [3].

II. EXPERIMENTAL

A. Catalytic membrane preparation

Aqueous 10 wt% PVA (Aldrich, ≥99% hydrolyzed) was prepared at 90°C, during 3 h for the separation layer. The solutions were poured in a petri dish and allowed to dry at room temperature. In order to obtain catalytic membranes, the appropriated amounts of catalyst phosphomolybdic acid were added in aqueous 5 wt % PVA solution. Glutaraldeyhde as crosslinking agent was also added to membrane solution.

Catalytic layer of the membrane was poured onto the separation layer. The membrane was dried at room temperature.

B. Application of catalytic membrane for the esterification reaction

The reaction was carried out in batch reactor system. Schemes of membrane reactor is given in Figure 1.

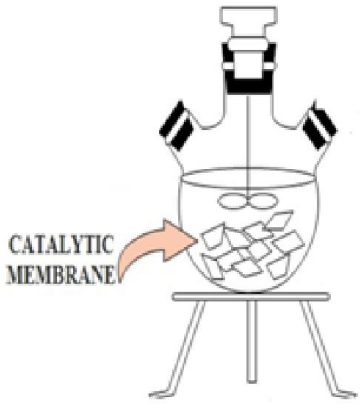


Figure 1: Batch reactor scheme [5]

The esterification reaction of acetic acid (AcAc) and glycerol (GOH) was carried out by using catalytic membrane pieces as catalyst in the batch reactor. Reaction was carried out at various temperatures, molar feed ratios (AcAc to GOH), and catalyst amounts. The reaction solution was mixed under constant stirring at 400 rpm for 7 h. Samples from the reaction mixture were taken hourly and analyzed by NaOH titration. Conversion values were calculated by Eq. (1):

$$x = \frac{N_{A0} - N_A}{N_{A0}}$$

$N_{A0}$is the mole of acetic acid in the initial solution, and N_A is the mole of acetic acid at any time.

III. Results and Discussion

A. Effect of Temperature

The acetic acid conversion as a function of reaction time at different temperatures is shown in Figure 2.

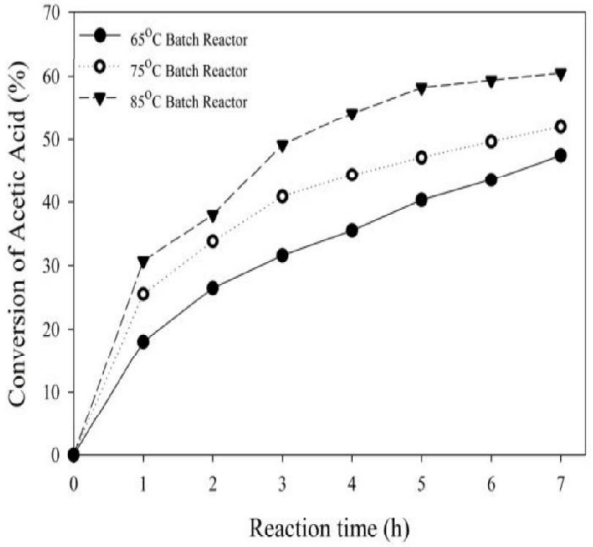


Figure 2:. Effect of the reaction temperature on conversion of acetic acid (5% catalyst loaded membrane, M=3)

With increasing the reaction time, the conversion behaviors of acetic acid in all conditions started to stabilize after the seventh hour. The acetic acid conversion increased with increasing the reaction temperature due to the endothermic properties of reaction [6]. The reaction equilibrium shifted towards the products and conversion value increased.As shown in Fig. 2, the conversion of acetic acid increased from 47.46% to 60.53% as the temperature was raised from 65◦C to 85◦C at 7 h.

B. Effect of Catalyst Loading

Figure 3 shows acetic acid conversion as a function of reaction time under different catalyst loading.

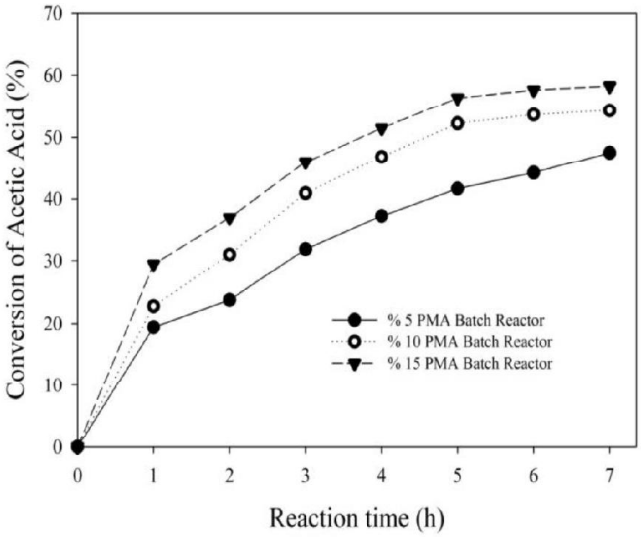


Figure 3: Effect of the catalyst concentration of the membrane on conversion of acetic acid (75ºC, M=3).

The catalyst concentration is defined as percentage by weight of PVA weight in the polymeric solution.The number of acid site was increased with increasing the catalyst loading in the

membrane. Higher catalyst loading on membrane facilitated the accessibility of the active sites and rate of reaction increased [7]. The acetic acid conversion increased with increasing the catalyst amount from 5% to 15%. The conversion values in a batch reactor and in a membrane reactor obtain as 47.54% and 58.25%, respectively.

C. Effect of Initial Molar Ratio

Figure 4 presents the acetic acid conversion as a function of reaction time under different initial molar ratios.

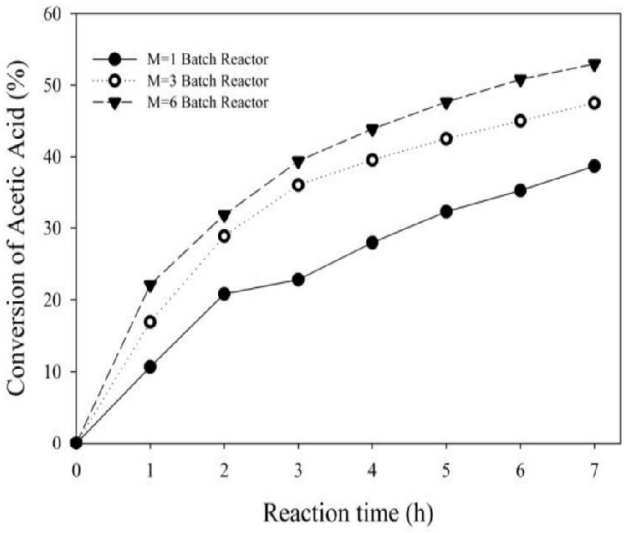


Figure 4: Effect of the initial molar ratio on conversion of acetic acid (5% catalyst loaded membrane, 75ºC)

The usage of excess reactant is an option to increase the conversion for reversible reactions. According to the Le Chatelier principle, when a change is applied to a system in dynamic equilibrium, the reaction equilibrium will shift to the products [8]. As can be seen from Figure 4, the conversion of acetic acid increased with an increase in the initial molar ratio of AcAc to GOH. When the initial molar ratio increased from 1:1 to 6:1, aceticacid conversion increased from 38.69% to 52.94% in the batch reactor.

IV. Conclusion

In this study, phosphomolybdic acid loaded PVA catalytic membrane was prepared by solution casting and was used as green catalyst for the esterification reaction of acetic acid and glycerol in the batch reactor. Phosphomolybdic acid loaded PVA catalytic membrane was found as very active in the esterification of acetic acid with glycerol.The effect of reaction parameters, such as temperature, molar feed ratioand catalyst concentration were investigated on the conversion of acetic acid. The highest acetic acid conversion of 60.53% was obtained when the reaction was performed in the conditions of 3:1 molar ratio of acetic acid to glycerol, the reaction temperature of 85◦C and catalyst loading of 5%.

The results of experiments show that environmental-friendly catalyst embedded catalytic membranes are efficient for the membrane reactor applications in the esterification reaction.

Acknowledgment

This study was financially supported by the Kocaeli University Scientific Research Projects Unit (Project number 2017/067).

References

[1] M. S.Khayoon, B. H.Hameed, "Synthesis of hybrid SBA-15 functionalized with molybdophosphoric acid as efficient catalyst for glycerol esterification to fuel additives,"*Appl Catal A Gen,* vol. 433–434,pp. 152–161, 2012.

[2] X.Liao, Y.Zhu, S.H.Wang, Y.Li, "Producing triacetylglycerol with glycerol by two steps: Esterification and acetylation,"*Fuel Process Technol*,vol. 90,pp. 988–993, 2009.

[3] P. Ferreira, I. M. Fonseca, A. M. Ramos, J. Vital, J. E. Castanheiro, "Glycerol acetylation over dodecatungstophosphoric acid immobilized into a silica matrix as catalyst,"*Appl CatalB: Environ*, vol. 91, pp. 416–422, 2009a.

[4] P.Ferreira, I.M.Fonseca, A.M.Ramos, J.Vital, J.E.Castanheiro, "Esterification of glycerol with acetic acid over dodecamolybdophosphoric acid encaged in USY zeolite,"*Catal Commun*, vol. 10, pp. 481–484, 2009b.

[5] D.Unlu, O.Ilgen, N.Durmaz Hilmioglu, "Biodiesel Additive Ethyl Levulinate Synthesis by Catalytic Membrane: SO_4^{-2}/ZrO_2 Loaded Hydroxyethyl Cellulose," *Chem Eng J*, vol. 302, pp.260-268, 2016.

[6] S.Zhu, Y.Zhu, X.Gao, T.Mo, Y.Zhu, Y.Lia, "Production of bioadditives from glycerol esterification over zirconia supported heteropolyacids,"*Bioresource Technol*, vol. 130,pp. 45-51, 2013.

[7] J.Ma, M.Zhang, L.Lu, X.Yin, J.Chen, Z. Jiang, "Intensifying esterification reaction between lactic acid and ethanol by pervaporation dehydration using chitosan TEOS hybrid membranes," Chem Eng J, vol. 155, pp. 800-809, 2009.

[8] K. Y. Nandiwale, S. K. Sonar, P. S.Niphadkar, P. N.Joshi, S. S.Deshpande, V. S.Patil, V. S.Bokade, "Catalytic Upgrading of Renewable Levulinic Acid to Ethyl Levulinate Biodiesel Using Dodecatungstophosphoric Acid Supported on Desilicated H-ZSM-5 as Catalyst," *Appl. Catal., A*, vol. 460–461, pp.90–98, 2013.

Fabricating Organic Compound Pellets in the form of Synthetic Coal

M.K GOKAY[1], A. ARAS[1] and K. DOGAN[1]

[1] Selcuk University, Konya/Turkey, mgokay@selcuk.edu.tr
[1]Selcuk University, Konya/Turkey, aliaras@selcuk.edu.tr
[1] Selcuk University, Konya/Turkey, kdogan@selcuk.edu.tr

***Abstract* - Organic materials which have been thrown away as waste are huge in volumetric amount. Agricultural products cover huge amount of organic unused plant parts which can also be source of energy. Study performed here, includes pellet preparation works of organic waste materials. These materials were then turned into synthetic coal products under high pressure (max. 200 bar) and temperature (200 ºC). Laboratory works showed that, synthetic coal products have higher calorific (max. 4636.40 Kcal/kg) values with respect to organic raw material used (min. 3767.50 Kcal/kg) in these tests.**

***Keywords* – Organic energy pellets, organic raw material, biofuels, synthetic coal**

I. INTRODUCTION

Organic compounds are widespread all over the world. Especially plants cover important part of world organic environment. Climatic seasons are directing plants life and cold weather cause them to loose their leaves. Leaves of the trees, plants bodies and unused parts of agriculturally grown products form huge amount of organic materials. Most of them stay on agriculture fields, countryside lands and forest grounds. They have turned into organic humus compounds naturally as the time pass away. Organic materials have been originated not only from tree leaves but, they can also be originated from humans, animals and agricultural by products. For example, Ozturk & Bascetincelik [1] reported that percentage of waste materials originated from corn, wheat and cotton fields were around; 31.72 %, 27.01 % and 16.12 % of total usable organic compounds originated from agricultural fields respectively. These researchers wrote also that total organic compounds originated from agricultural fields are about 13 million metric tones per year. They calculated these wastes' heating capacity around 228 PJ level. Organic materials in urban areas on the other hand have been collected by municipalities and they mostly burned out in small energy plants to obtain electricity. The circulation pattern is like this way at least in Konya, Turkey. However, collecting, hauling and storage stages of this operation need considerable handling capacity, time and operation money. In order to decrease the storage capacity of these discarded organic compounds and produce commercial products which can be sold even for individual consumers, this study was decided to concentrate on production of pellet-form bioenergy products. The final aim was producing commercial synthetic pellet type synthetic coal products from organic raw materials accumulated in countryside and urban areas.

II. BIOMASSES AND PELLETS

Heating equipments which are manufactured to burn coals and woods can also be suitable to burn organic energy pellets as well. Pellets can be shipped in bulk form and they are much more proper materials to load, haul and dump with respect to whole organic resources like wood, leaves, grasses etc. Organic discarded materials are mostly decomposed in nature and disappeared. Collecting them and making biofuel-pellets after mixing other organic merging materials have been common applications in energy business. Doring [2] reported that, organic and inorganic compounds in common organic biomass agents had been listed by Kaltschmitt & Hartmann [3] as shown in Table 1. Main compounds given in this table were cellulose, hemicellulose, lignin, resins (fats), protein and ash (inorganic content). Pellet making from organic compounds is worldwide business in countries which have considerable forests to look after.

Heinimo & Junginger [4] reported that organic pellet markets which use biomass for energy purposes are rapidly developing area. Karkania et al. [5] wrote also importance of planned action to revalue agricultural wastes. They mentioned about economic lost due to inefficient usage of agricultural discarded materials. According to them, volume of organic raw materials and their handling problems are the main factors which energy customers do not desire to use for their energy requirements.

Table 1: Organic and inorganic compounds in various biomasses [3].

Fuel	Cellulose	Hemicellulose	Lignin	Resins/Fats	Protein	Ash
Wood fuels (in % b.w.)						
Fir	42.3	22.5	28.6	2.3	–	1.2
Pine	41.9	21.5	29.5	3.2	–	1.3
Spruce	41.0	24.3	30.0	k.A.		k.A.
Ash tree	40.2	25.0	26.0	2.2	–	1.3
Beech	45.4	22.2	22.7	0.7	–	1.6
Birch	40.9	27.1	27.3	2.2	–	1.8
Poplar	48.4	18.2	21.6	2.4	–	1..3
Willow	42.9	21.9	24.7	2.0	–	1.2
Stalk-type fuels (in % dry matter)						
Wheat straw	38	29	15	–	4	6
Prairie grass	37	29	19	–	3	6
Miscanthus	43	24	19	–	3	2
Sorghum bicolor	23	14	11	–	k.A.	5
Tall fescue	25	25	14	–	13	11
Corn straw	38	26	19	–	5	6

They pointed that when organic energy materials are compacted as bio-energy pellets, they can be more easily accessible. That means these pellets have economic values in energy business. Stelte et al. [6] worked on bio-pellet production procedures and they determined the importance of pressure which should be applied on organic compounds to form bio-pellets. They also showed that in automatic pellet production; pellet-machine efficiency depends mostly organic compound properties which should be prepared in required compositions. Mckechnie et al. [7] wrote about forest-based bioenergy business which can reduce greenhouse gas emissions by displacing commonly used fossil-based energy sources. They stated that bio-pellets can be produced by using organic materials harvested in suitable seasons of forests. Biomass usage for alternative energy source in everyday life brings other considerations which engineers should handle. Alfonso et al. [8] pointed this fact and they described methodology to assess optimal management of energy use of distributed biomass resources. They concentrated the factors; logistics, biomass resources, properties (quantity, quality, seasonality and availability), plant size effect, available technologies for power, heat and solid biofuels generation, CO_2 emissions balance and quantification of potential biofuel consumers. Researcher have recently been concentrated organic materials' composition, biomass energy types, biomass energy production efficiency, pellet technologies, organic matters in pellet products, organization in organic waste managements, etc. Therefore organic materials which have been diminished without any useful influences on soil humus content are then advised to be collected and they should be used to produce biomass energy pellets. Organic materials which decompose on lands and turn into suitable humus additives in soils ought not to be used as biomass energy sources. To facilitate biomass energy sources and understand synthetic coal preparation progresses, this research were concentrated on dense organic pellet production. It was also aimed to obtain synthetic coal products by facilitating carbonic compounds of organic materials in prepared dense pellets.

III. MATERIALS AND METHODS

This study was started by collecting certain type of discarded organic compounds like; sycamore leaves and walnut shells. These samples were selected for their high level energy capacity observed in everyday life. Bio-energy capacity of organic compounds in these materials were planned to be kept and reformed as synthetic coal products. To achieve this, test samples were grinded and screened by laboratory-size vibrating screen-deck into fine sized (µm) fractions. Calorie values of these organic materials (Fig.1) were then determined to know bio-energy levels of raw organic materials (Table 2). After grinding required amount of sycamore leaves and walnut shells during the early stage of this study, they were pressurized in cylindrical mold to form small bio-energy pellets. Carbonic based additives which have cohesion properties might also be used in some cases to increase unification of pellets. Grinded sycamore leaves and walnut shells were then pressurized in hydraulic press (Fig. 2) to form disk shaped bio-energy pellets in this work.



Figure 1: Grinded and screened organic test samples; a) walnut shell powders and b) powder of sycamore leaves. They were classified in different size groups.

Table 2: Calorie levels of grinded and screened organic test samples.

Samples	Size fraction (µm)	Moisture content (%)	Calorie level (kcal/kg)
Sycamore leaves	-1180 +850	8.090	3838.90
	-425 +300	7.880	3767.50
	-150 +106	7.570	4040.60
Walnut shells	-1180 +850	3.795	4562.70
	-425 +300	5.045	4400.50
	-150 +106	5.145	4436.70

Synthetic coal or bioenergy pellet preparation was performed in especially developed pressure tool which supply

regulated heat also. Pellet preparation tests were performed at Selcuk University, Mining Engineering Department laboratory (Konya, Turkey) together with 4th years' Mining Eng. students in Spring-2017. Figure 2 illustrates pellet making equipment and hydraulic press used in this study. Heating the organic test materials during pellet making progress forms pressurized high temperature chemical reaction chamber where synthetic coal is supposed to be produced.

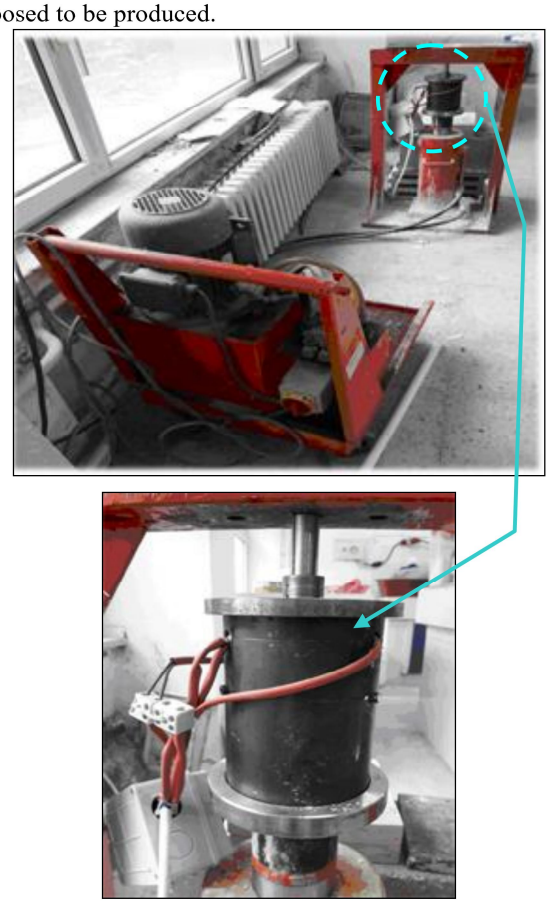


Figure 2: Organic material pellets and synthetic coal pellets were prepared by using especially developed equipment illustrated here.

Modifications in chemical compositions of organic compounds, (sycamore leaves and walnut shell), were expected to be realized. These especial chemical reactions were determined that they increase resultant bioenergy pellets' (Fig. 3) calorific values. Heating the test samples during pellet making processes and vertical pressure applied through hydraulic press require electrical energy.



Synthetic coal sample,	**Synthetic coal sample,**
. pellet from sycamore leaves, . size fraction -1180+850 µm, . pressure applied 100 bar, . pressure and heat applied 90 minutes, . temperature during pelleting 200 °C, . Organic matter feed before pelleting 4 g, . pellet weight 3.68 g	. pellet from sycamore leaves, . size fraction-1180+850 µm, . pressure applied 150 bar, . pressure and heat applied 90 minutes, . temperature during pelleting 200 °C, . Organic matter feed before pelleting 4 g, . pellet weight 3.39 g

Figure 3: Synthetic coal pellets prepared by using sycamore leaves.

Table 3a: Synthetic coal pellets' calorific values (prepared from sycamore leaves).

Samp. size (µm)	Temp. °C	Pressure (bar)	Duration (dk)	Pellet weight (g)	Caloric level (kcal/kg)
-1180 +850	200 200 200	150 100 200	90 90 90	3.39 3.68 3.61	4022.40 4034.00 4334.20
-425 +300	200 200 200	200 150 100	90 90 90	3.11 3.44 3.65	4405.60 4121.10 3975.50

Table 3b: Synthetic coal pellets' calorific values (prepared from walnut shells).

Samp. size (µm)	Temp. °C	Pressure (bar)	Duration (dk)	Pellet weight (g)	Calorie level (kcal/kg)
-1180 +850	200 200 200	150 100 200	90 90 90	3.67 3.63 3.87	4570.10 4636.40 4503.30
-425 +300	200 200 200	200 150 100	90 90 90	3.75 3.64 3.71	4562.70 4537.80 4327.30

At the end of the dense pellet making activities, economic gain balances should be performed for each bioenergy pellet products. Since this balance has been in favorable side in some countries for certain pellet products, organic bio-pellet productions are one of the energy resources there. Table 3 presents resultant calorie values of synthetic coal disks prepared during this study. Calorie values obtained here show slight increase after temperature treatment of selected organic pellets. That means; pellet making pressure values and process temperature values are two main parameters which influence the results, (pellets calorific values).

IV. Conclusions

Synthetic coal preparation works in this study produced coal like pellets which are black or dark brown in color. Their calorie values are mostly higher than 4000 kcal/kg. This calorific value level is higher than some lignite reserves sites in Turkey. Therefore, bioenergy pellets have future in economical consideration in energy business. Beside, volume

required to store organic raw materials decreased dramatically by applying synthetic coal preparation procedures. Pellets are also easy to burn in furnaces due to their solid shapes which supply enough apertures for intake air to get good burning conditions in furnaces. Biomass as an energy source should be organized systematically to obtain renewable energy. Synthetic coal product procedures use discarded organic compounds which could be positive impact on environment.

REFERENCES

[1] H.H. Ozturk and A. Bascetincelik, "Energy exploitation of agricultural biomass potential in Turkey", *Energy Exploration and Exploitation*, vol. 24, n4-5, pp313-330, 2006.

[2] S. Doring *Power from pellets technology and applications*, ISBN 978-3-642-19961-5, Springer-Verlag Publication, p223, Berlin, Heidelberg, Germany, 2013.

[3] M. Kaltschmitt and H. Hartmann, *Energy from biomass - principles, techniques and methods*, Springer-Verlag Publication, Berlin, Heidelberg, Germany, 2009.

[4] J. Heinimo and M. Junginger, "Production and trading of biomass for energy – An overview of the global status", *Biomass and Bioenergy,* vol. 33, n9, pp1310-1320, 2009.

[5] V. Karkania, E. Fanara and A. Zabaniotou, *"Review of sustainable biomass pellets production – A study for agricultural residues pellets' market in Greece", Renewable and Sustainable Energy Reviews*, vol. 16, n3, pp1426-1436, 2012.

[6] W. Stelte, J.K. Holm, A.N. Sanadic, S. Barsberg, J. Ahrenfeldt and U.B. Henriksena, "Fuel pellets from biomass: The importance of the pelletizing pressure and its dependency on the processing conditions", *Fuel*, vol. 90, n11, pp3285-3290, 2011.

[7] J. Mckechnie, S. Colombo, J. Chen and W. Mabe, "Forest Bioenergy or Forest carbon? Assessing trade-offs in greenhouse gas mitigation with wood-based fuels", *Environmental Science & Technology*, vol. 45, pp789–795, 2011.

[8] D. Alfonso, C. Perpiñá, A. Pérez-Navarro, E. Peñalvo, C.Vargas and R. Cárdenas, "Methodology for optimization of distributed biomass resources evaluation, management and final energy use", *Biomass and Bioenergy*, vol. 33, n8, pp1070-1079, 2009.

Activated Carbon Production from Peat

H. SÜTCÜ

Bülent Ecevit University, Zonguldak/Turkey, halesutcu@hotmail.com, hale.sutcu@beun.edu.tr

***Abstract* - In this study, activated carbon production from peat was investigated in two different ways: direct activated carbon production from peat and activated carbon production from char produced peat. Activated carbon production from peat was carried out by chemical activation using KOH at carbonization temperatures of 500ºC, 600ºC and 700ºC. In order to produce activated carbon from char, firstly char is produced by carbonizing peat at 300°C and 600°C. Activated carbon was also produced from char at the activation temperature of 600°C by chemical activation method using KOH. The pore structure of activated carbons was investigated using N_2 adsorption and SEM.**

***Keywords* – peat, char, activated carbon, chemical activation.**

I. INTRODUCTION

Activated carbon is an adsorbent with a specific pore structure, no structural formula, high carbon content [1]. Raw materials to be used in the production of activated carbon should be added to the area intended for the use of activated carbon, to the nature of the process, are selected according to the cost.

The most important physical property of activated carbon is the surface area. Another important parameter for the application of activated carbon is pore size. According to the definition of IUPAC (Union of Pure and Applied Chemistry), porous materials are classified in three groups: microporous materials with a pore diameter of less than 20Å and mesoporous materials with a pore diameter of 20-500Å and macroporous materials with a pore diameter of 500Å.

The number of studies on activated carbon production from peat is limited in the literature. In a study by Veksha et al., high calcium content peat was used to prepare activated carbons with CO_2 activation and the effect of the temperature on the porous characteristics of activated carbons was investigated [2]. Uraki and colleagues performed activated carbon production from peat by steam activation in an electric furnace [3]. Khadiran et al. investigated the production of activated carbon using $ZnCl_2$ and H_3PO_4 from peat soil [4].

In this study, activated carbon production from peat by chemical activation method was examined and the pore characterization of the produced activated carbons was investigated.

II. MATERIAL AND METHOD

In this study, peat was used for activated carbon production. Peat was obtained from Yeniçağa, Mengen, Bolu region. The dried peat was ground to a size of 250µm and subjected to proximate analysis according to ASTM. The results are given in Table 1.

Table 1: Proximate analyses results of peat (on dry basis, %).

Ash	Volatile matter	Fixed carbon
10,42	72,15	17,43

KOH was used for activated carbon production by chemical activation method. Carbonization in the production of activated carbon was carried out in a tubular furnace at 500°C, 600°C and 700°C for 1 hour. Peat/KOH ratio is taken as 1/1.

In addition, activated carbon production from char was also carried out. For this reason, carbonization was carried out at temperatures of 300°C and 600°C. In these experiments, the char/KOH ratio is 1/1. Activated carbon production from char was carried out at a carbonization temperature of 600°C.

The pore structure properties of activated carbons were determined using N_2 adsorption and scanning electron microscopy (SEM). Nitrogen adsorption was carried out at 77K using Quantachrome Autosorb Automated Gas Sorption system. Nitrogen adsorption isotherms were measured at a relative pressure (P/Po) range of about 10^{-5} to 1.0. Surface area data of activated carbons were determined using Brunauer-Emmett-Teller (BET) and t-plot software. The pore distribution of the carbons was determined using Dubinin-Astakhov (DA) software.

III. RESULTS AND DISCUSSION

Nitrogen adsorption isotherms of activated carbons produced from peat are shown in Fig 1.

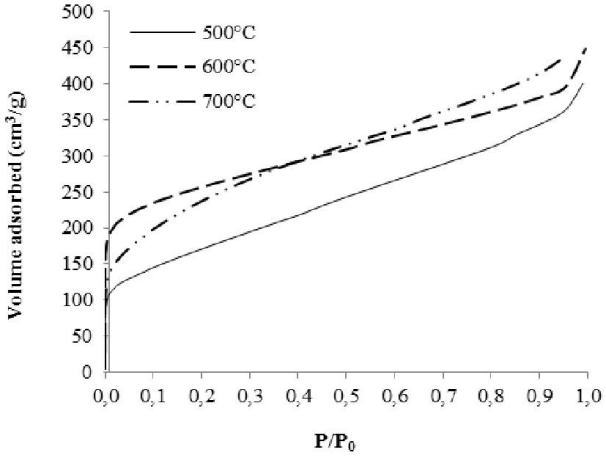


Figure 1: Adsorption isotherms of activated carbons obtained from peat.

The isotherm of the activated carbon obtained at a carbonization temperature of 500°C meets the IUPAC type II classification. This means that the activated carbon is nonporous or has a larger pore structure than the micropore. The isoterms of activated carbons obtained at carbonization temperatures of 600°C and 700°C clearly indicate the predominantly microporous nature. According to the IUPAC classification these isotherms are of type I classification and can be associated with microporous structure.

Figure 2 also shows the isotherms of activated carbons produced from char. The activated carbon obtained from char is associated with the type I microporous structure according to IUPAC classification at isotherms at both carbonization temperatures of 300°C and 600°C.

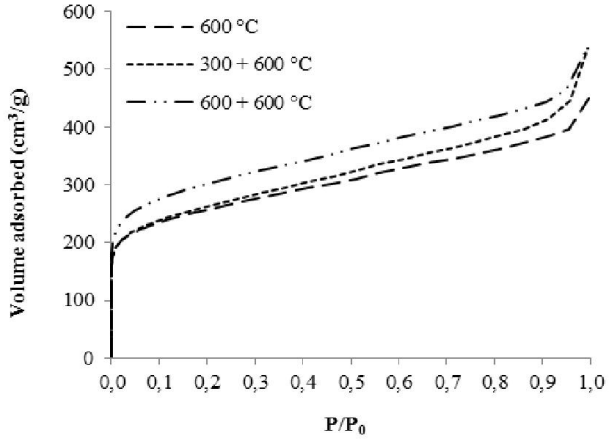


Figure 2: Adsorption isotherms of activated carbons obtained from char.

Figure 3 shows BET and micropore surface areas of activated carbons obtained from peat. Activated carbon at carbonization temperature of 600°C has the highest BET (931m^2/g) and micropore surface (543m^2/g) area compared to others.

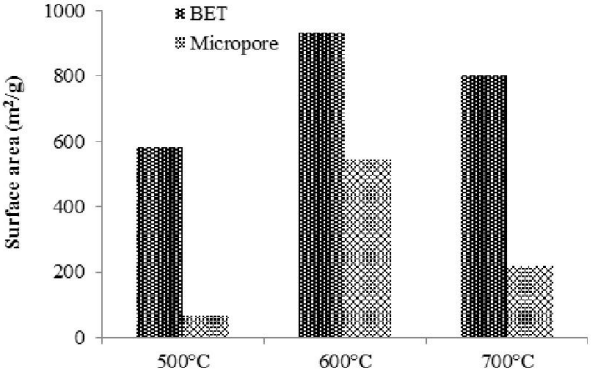


Figure 3: Surface area values of activated carbons obtained from peat.

The BET and micropore surface area values of the activated carbons from char are shown in Fig. 4. As the carbonization temperature increases, there is an increase in BET and micropore surface area. The highest BET (1095m^2/g) and micropore surface area (654m^2/g) values were obtained with char obtained at a carbonization temperature of 600°C.

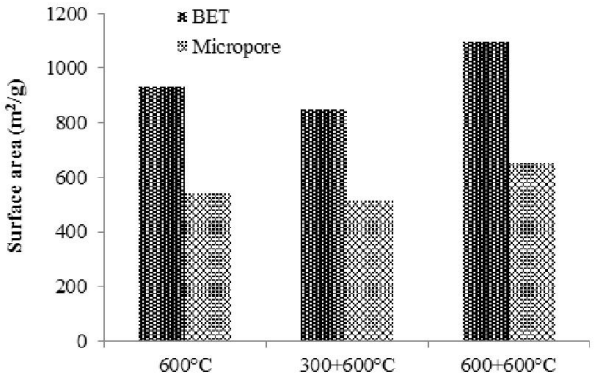


Figure 4: Surface area values of activated carbons obtained from char.

Figure 5 shows micropore and total pore volume changes of activated carbons produced from peat. Total pore volumes are close to each other. The highest micropore volume (0.2273cm^3/g) belongs to activated carbon produced from peat at a carbonization temperature of 600°C.

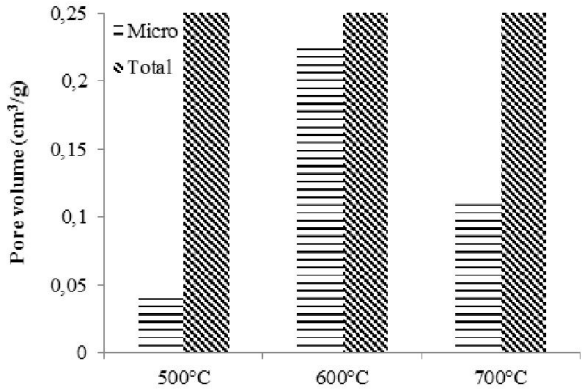


Figure 5: Pore volume of activated carbons obtained from peat.

Figure 6 shows micropore and total pore volume changes of activated carbons produced from char. Activaed carbon produced from char at the carbonization temperature of 600+600°C has the highest micropore volume (0,2731cm^3/g).

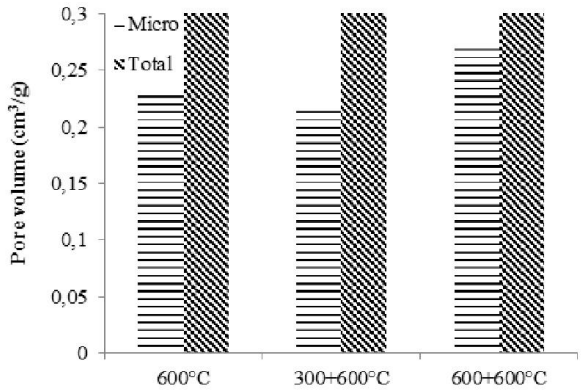


Figure 6: Pore volume of activated carbons obtained from char.

Figure 7 shows the pore size distribution of activated carbons obtained from peat. As the carbonization temperature increases, the density of micropores increases.

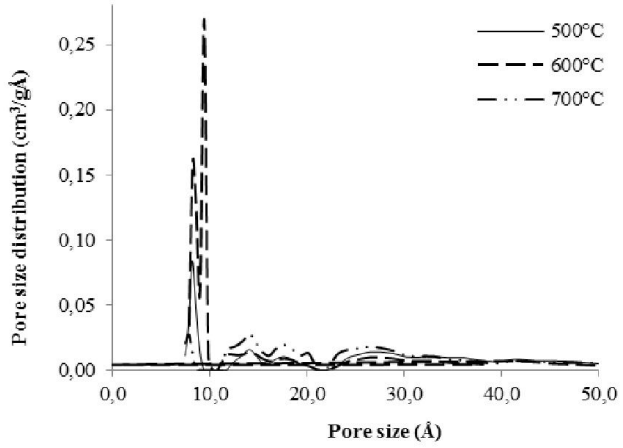


Figure 7: Pore size distribution of activated carbons obtained from peat.

Figure 8 shows the variation of pore size distribution of activated carbons obtained from char. The density of micropores is related to the carbonization temperature of char.

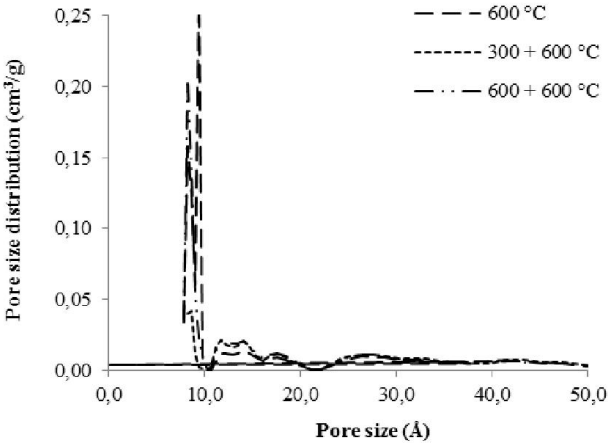
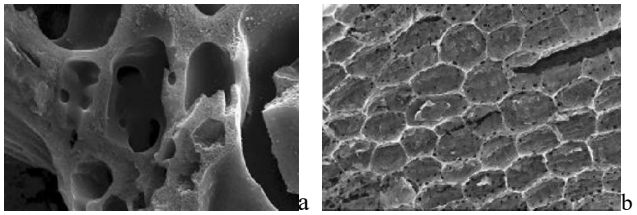


Figure 8: Pore size distribution of activated carbons obtained from char.

Figure 9 shows SEM images of activated carbons. The SEM images show that the activated carbons are dense with micropores.



a b

Figure 9: SEM images of activated carbons obtained at carbonization temperature of
a. 600°C from peat, b. 600+600°C from char.

IV. Conclusion

Peat is a suitable material for activated carbon production.

BET and micropore surface area of activated carbon obtained from peat at the carbonization temperature of 600°C, 931m^2/g and 543 m^2/g respectively.

The BET and micropore surface area of the activated carbon obtained from char at the carbonization temperature of 600+600°C was determined to be 1095 m^2/g and 654 m^2/g, respectively.

Experiments have shown that temperature affects surface characterization of activated carbons.

In further studies, surface characterization of activated carbons produced using different chemical activation agent can be examined. The adsorption ability of the produced activated carbons can be investigated.

References

[1] H. Marsh, Porosity in carbons, in Foundation Course Lectures, pp.1-20, United Kingdom, 2002.

[2] A. Veksha, E. Sasaoka and Md. A. Uddin, "The effects of temperature on the activation of peat char in the presence of high calcium content", Journal of Analytical and Applied Pyrolysis, vol. 83, pp. 131-136, 2008.

[3] Y. Uraki, Y. Tamai, M. Ogawa, S. Gaman and S. Tokura, "Preparation activated carbon from peat", bioresources.com, vol 4(1), pp. 205-2013, 2009.

[4] T. Khadiran, M.Z. Hussein, Z. Zainal and R. Rusli, "Textural and chemical properties of activated carbon prepared from tropical peat soil by chemical activation method", bioresources.com, vol. 10(1), pp. 986-1007, 2015.

Fiber Production From Agricultural Okra Wastes and Comparative Investigation of Surface Modification Applied on Okra Fibers in Different Methods

B. ARDIÇ[1], E.D. KOÇAK[2], N.MERDAN[3] and İ.MISTIK[4]

[1,2,4] Marmara University, Istanbul/Turkey, busra.ardic@marun.edu.tr, dkocak@marmara.edu.tr, imistik@marmara.edu.tr

[3] Istanbul Commerce University, Istanbul/Turkey, nmerdan@iticu.edu.tr

***Abstract* – All over the world 40 million tons of natural cellulose can be produced from the agricultural wastes, in comparison with the 70 million tons fibers that have been already produced per year in total. In industrial manufacturing, demands for bio-based lightweight materials have been increased dramatically. Okra is a popular vegetable crop but its stem is lignocellulosic biomass not yet utilized for value-added textile and composite production. Okra production is 36.171 tons/year with plantation over 6.750 ha, and okra waste is approximately 2.11 tons/da left on the field after harvest every year in Turkey. The bast fiber from okra would be similar to traditional bast fibers (kenaf, flax, hemp) possessing a good processability ready for industrial adoption.**

In this study, okra fibers have been extracted from okra stem wastes with specially designed machine. Surface modification processes have been applied to okra fibers with two different methods (Conventional and Ultrasonic Energy) by using sodium bisulphate and cellulase enzyme to improve their properties. Ultrasonic energy method is ecological and alternative method of the conventional surface process with fewer chemical, water, and energy consumptions. Mechanical properties and weight loss of the treated and untreated fibers were investigated. Ultrasonic assisted enzymatic treatment is improved the mechanical properties of the okra fiber.

***Keywords* - Okra fibers, surface modification, ultrasonic energy method**

I. INTRODUCTION

HARMS of the synthetic based polymers are discussed in recent years. Using of the natural materials instead of the synthetic based polymers are grooving rapidly [1, 2]. Properties of the natural fibers such as biodegradability, sustainability, good mechanical and thermal insulation properties, low density and price are increasing the usage of them [3-5]. Waste agricultural cellulose fibers are available resources; however, collection is the barrier to utilization. Crop fibers, particularly bast fibers, are fast growing with ready separation of fibers and high mechanical properties [6].

Okra (*Abelmoschus esculentus* L.) is the only vegetable crop of significance in the Malvaceae family and is very popular in the Indo-Pak subcontinent. In India, it ranks number one in its consumption but its original home is Ethiopia and Sudan, the north-eastern African countries. It is one of the oldest cultivated crops and presently grown in many countries and is widely distributed from Africa to Asia, southern Europe and America. It is a tropical to subtropical crop and is sensitive to frost; low temperature, water logging and drought conditions, and the cultivation from different countries have certain adapted distinguishing characteristics specific to the country to which they belong [3]. The production of okra is 8,400 tons / year [2] and most are cultivated in 1,200 ha in Texas, California, Georgia and Florida. Okra production is 36.171 tons/year with plantation over 6.750 ha, and okra waste is approximately 2.11 tons/da left on the field after harvest every year in Turkey [1].



Figure 1: Okra fiber.

This fiber is quite common in the Turkey. It grows well in the areas of the Mediterranean climate (Figure 1). When the chemical characteristics of Okra fibers are considered, it can be seen that just in the case of such fibers as kenaf, manila, sisal, jute, hemp, they consist of cellulosic polymer that are composed of various non-cellulosic impurities that do not affect the hydrophilic characteristic of okra fibers negatively (Table 1) [7-11]. Physical properties of the okra fibers are shown in Table 2 [12-16].

Table 1: Chemical constituents of okra fiber.

Chemical constituents	**%**
Cellulose	60-70
Hemicellulose	15-20
Lignin	5-10
Pectin	3.4
Oil and wax	3.9

Physical properties of the okra fibers are shown in Table 2 [12-16].

Table 2: Physical properties of okra fiber.

Fiber diameter (µm)	**Tensile strength (MPa)**	**Young modulus (GPa)**	**Elongation (%)**
40-180	234-380	5-13	2

Chemical surface treatments are required to increase the usage of the okra fibers in the industry. But conventional surface treatments consume too much water, chemicals and energy. Environmental friendly methods are existed alternative to conventional method. Surface treatments performed by using sound waves (ultrasonic) and microwave energy is alternatives environmental friendly methods [17-22]. The biological and chemical effects of ultrasonic energy were discovered firstly by Loomis in 1927. Ultrasonic energy frequency refers to sound energy ranging from 18 kHz to 10 MHz. Ultrasonic energy used in practice is divided into three categories; 20-100 kHz low frequency ultrasonic energy, 300-1000 kHz medium frequency ultrasonic energy and 2-10 MHz high frequency ultrasonic energy. Ultrasonic energy is occurred by rising microscopic bubbles known as cavitation Cavitation has chemical and mechanical effects. For example decomposing of high molecular mass by dispersion effect, and carries the chemicals to the capillaries of the fibers by degasing effect, these processes are performed by consuming low energy, low substances and in short time [23-24].

Sodium bisulphate is one of the substances used to remove substances such as lignin, oil and wax on the surface in lignocellulosic fibers. Sodium bisulphite is treated with the aromatic rings of the lignin substance in the cellulosic structures and is treated with the free hydroxyl groups of cellulose. As a result of this process, the fibers are fibrillated and the polarity of the fiber surface is increased. [25].

In recent years, enzymes have progressed rapidly in their effect on textile fibers. [29]. Cellulase is one of the most successful enzymes used in textile applications. Cellulase inhibits fiber fibrillation. The cellulase enzyme acts cellulose to hydrolyse the β (1-4) bonds along the cellulose chain, to hydrolyse the molecules on the side of the cellulose polymer and to break down short chain cellulose oligomers such as cellobiose into glucose. [26].

In this study, surface modification processes were applied to okra fiber with sodium bisulphate and cellulose enzyme by using conventional and ultrasonic methods. Mechanical properties (tensile strength, elongation, young's modulus), weight loss and morphological properties of treated and untreated okra fibers before and after the different treatment were examined.

II. EXPERIMENTAL

A. Material

Okra fibres were collected from Balıkesir region. Their overall lengths were 120 cm. These fibers were separated and cut according to their diameter and length. Okra body waste fibers were obtained by separating from plant extracts with the aid of a special machine designed to obtain fiber from lignocellulosic plants. As shown Figure 2, it was waited in the water-filled container to remove residue and adhering dirt (20 days). The fibers were shaken under running water until cleaned and they were dried in an oven at 100 °C for 2 hours (Figure 3). After dried, fiber were conditioned for 24 hours prior to testing under 20 ±2 °C and 65 ±2 %RH conditions.



Figure 2: Removal of fiber from okra body waste and appearance of extracted fibers.

The fibers were shaken under running water until cleaned and they were dried in an oven at 100 °C for 2 hours (Figure 3). After dried, fiber were conditioned for 24 hours prior to testing under 20 ±2 °C and 65 ±2 %RH conditions.



Figure 3: The oven used in drying, the final state of dried fibers and dried fibers.

B. Fiber Treatments

Okra fibres were exposed to two processes: Table 3 shows the properties of the conventional and ultrasonic processes respectively. Conventional process and ultrasonic energy process was applied in laboratory condition at different time, concentration and temperature. Kerman' Laboratory sample heater (220 Volt and 3000 Watt) was used for conventional method. Alex (220 Volt 660 Watt) ultrasonic bath was used for the ultrasonic method with 40 kHz frequencies.

In conventional process; the fibers were weighed on a precision scale and samples of 2 g weight were prepared. 400 mL distilled water at 20:1 ratio was heated to 60 °C (55 °C for enzyme) in a Kerman' Laboratory sample heater 220 Volt and 3000 Watt). According to the determined concentrations (w/v %), the prepared substance/enzyme was added. 2 g fiber sample was added and kept in the solution for the determined times (Figure 4). At the end of the time, the fibers were removed and washed 4-5 times with distilled water. The samples treated with sodium bisulphate (Merck) were neutralized by standing for 5 minutes in a 5% (/v) 100 mL pure water mixture. At the end of the time, the fibers were removed and washed 4-5 times with distilled water. The fiber samples were dried at 100 °C for 2 hours. For enzymatic treatments, the samples were treated with 1 g/L cellulase enzymes, Cellusoft L (Novozymes), at 55 °C, at pH 4.5-5.5. The samples were rinsed at 80 °C for 10 minutes and dried at room temperature.

Alex (220 Volt 660 Watt) ultrasonic bath was used in the ultrasonic method with 40 kHz frequencies (Figure 5). Surface treated okra waste fibers were rinsed in 24 °C pH 7 distilled warm water for 2 minutes and dried at 100 °C for 2 hours.

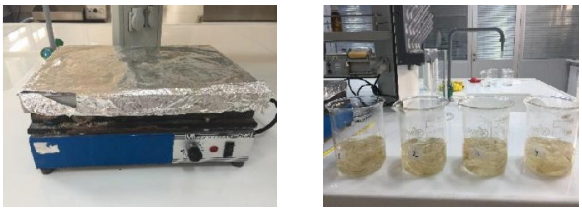


Figure 4: The heater used in the conventional method and holding in heated solution.



Figure 5: Device used in ultrasonic energy method and image of fibers treated in the device.

Table 3: Process conditions.

Method	Time (min)	Temperature (°C)	Concentration (%)	Chemicals
Conventional	10,20,30,40	60	3,5,7,10	Sodium bisulphate
		55	1	Cellulase
Ultrasonic	5,10,15,20	60	3,5,7,10	Sodium bisulphate
		55	1	Cellulase

C. Analytical Methods

The weight loss percentage (Wi) was calculated from the differences in weight using the following equation;

$$W_{i=} \frac{W_{pre}-W_{after}}{W_{pre}} \text{ x } 100\ (\%) \qquad (1)$$

D. Testing and Characterization of Okra Fibers After Chemical Treatments

Mechanical properties (elongation (%), tensile strength (N) and young's modulus (MPa)) of the untreated/treated okra fibres were determined according to ASTM D 3822 test method by using Instron 4411 (50 N Load, 10 mm/min speed) tensile test instrument.



Figure 6: Tensile strength test of okra fibers.

III. RESULTS AND DISCUSSION

The samples were weighed on a precision scale before surface modification. Each sample is surface treated, dried and conditioned after being conditioned in the laboratory. The weight measurements after the process and the weight loss values according to the process is given (Table 4). In both methods, weight loss is close to each other and in each method the chemical or enzyme gives the best result when looked for their averages.

Table 4: Weight loss results of samples.

Chemical	Method	Process time (min)	Concentration (%)	Weight loss (%)
Sodium bisulphate	Conventional	10	3	16.00
			5	4.00
			7	6.50
			10	4.15
		20	3	5.00
			5	2.00
			7	4.50
			10	5.25
		30	3	20.05
			5	18.50
			7	20.00
			10	21.00
		40	3	16.50
			5	17.00
			7	19.00
			10	15.50
	Ultrasonic	5	3	28.75
			5	27.15
			7	21.35
			10	25.75
		10	3	22.25
			5	19.55
			7	20.10
			10	22.10
		15	3	21.25
			5	21.40
			7	24.85
			10	21.25
		20	3	24.50
			5	20.05
			7	22.15
			10	24.00
Cellulase enzyme	Conventional	10	1	35.00
		20		32.95
		30		38.95
		40		41.65
	Ultrasonic	5		35.60
		10		44.80
		15		43.15
		20		41.50

The highest strength value was obtained according to the raw life in the surface modification of the okra fibers by using sodium bisulphate with conventional method at 10% concentration and 30 minutes of operation (Figure 7). As shown in Figure 8, the increase in the tensile strength of the okra fibers with respect to the untreated fiber in the surface modification by using sodium bisulphate according to the ultrasonic method was determined. The tensile strength of samples were decreased over 15 minutes.

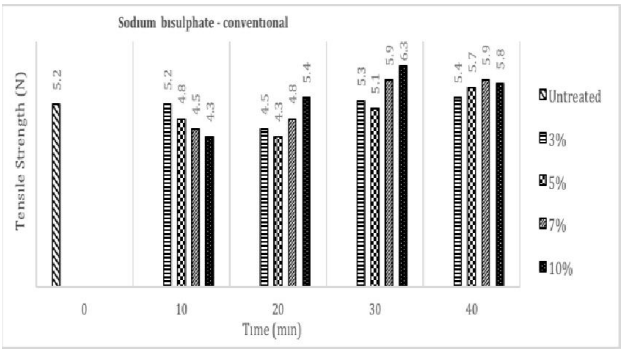


Figure 7: Tensile strength values of chemical treated (sodium bisulphate) samples with conventional method.

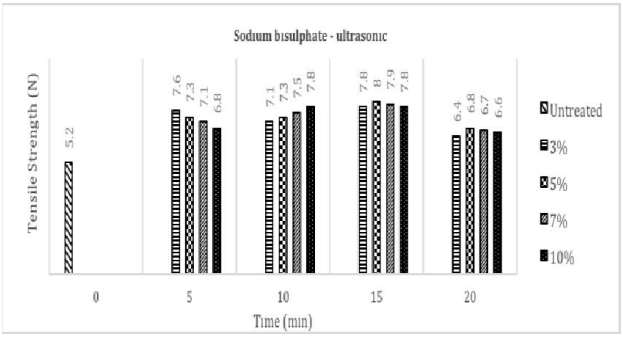


Figure 8: Tensile strength values of chemical treated (sodium bisulphate) samples with ultrasonic method.

As shown in Figure 9, the increase in the elongation (%) of the okra fibers was determined at a concentration of 10 % sodium bisulphate during 20-30 minutes of operation and at a concentration of 7 % during 40 minutes operation in conventional method. The highest elongation (%) was obtained at a concentration of 7 % sodium bisulphate during 15 minutes of operation in ultrasonic method (Figure 10).

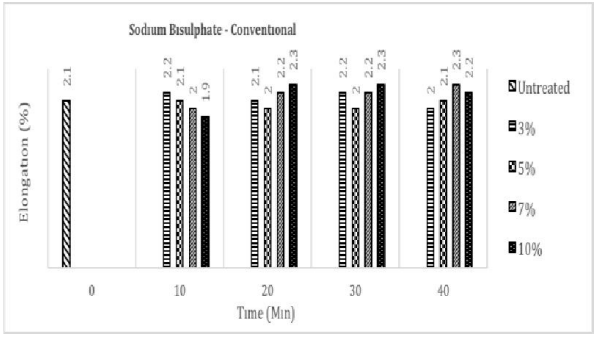


Figure 9: Elongation values of chemical treated (sodium bisulphate) samples with conventional method.

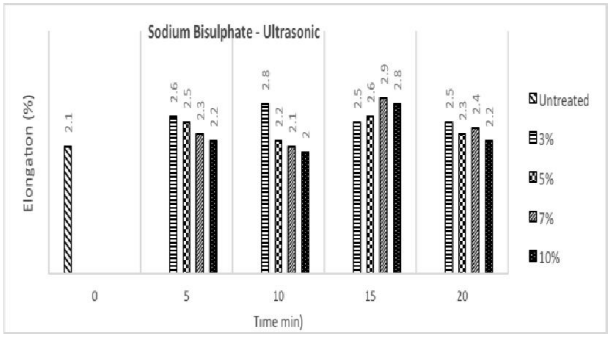


Figure 10: Elongation values of chemical treated (sodium bisulphate) samples with ultrasonic method.

The highest young's modulus value was obtained at a concentration of 10% sodium bisulfate during 30 minutes of operation in conventional method (Figure 11). As shown Figure 12, the highest young's modulus value of okra fibers was obtained at a concentration of 3% sodium bisulfate during 5 minutes of operation in ultrasonic method.

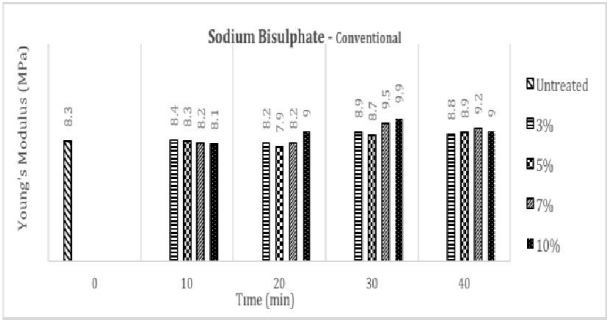


Figure 11: Young's modulus values of chemical treated (sodium bisulphate) samples with conventional method.

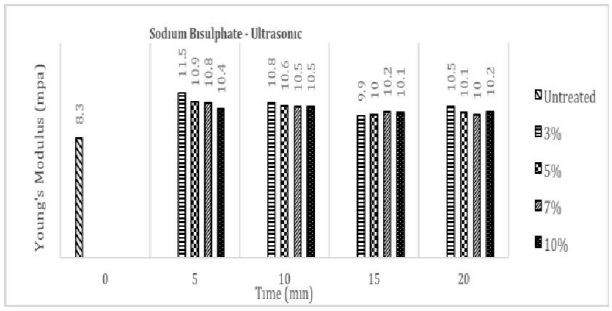


Figure 12: Young's modulus values of chemical treated (sodium bisulphate) samples with ultrasonic method.

In the surface modification of the okra fibers with the cellulase enzyme, the increase in strength was observed in each methods compared to the untreated fiber. The highest strength value was obtained with ultrasonic method at 10 minutes (Figure 13).

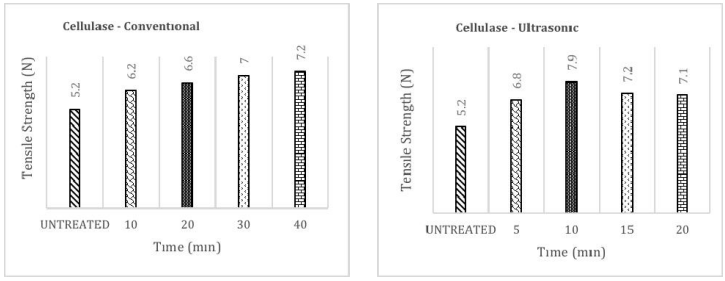


Figure 13: Tensile strength values of enzymatic treated samples with conventional and ultrasonic methods.

The enzymatic treated samples in a short time with ultrasonic method have the highest elongation /%) value (Figure 14).

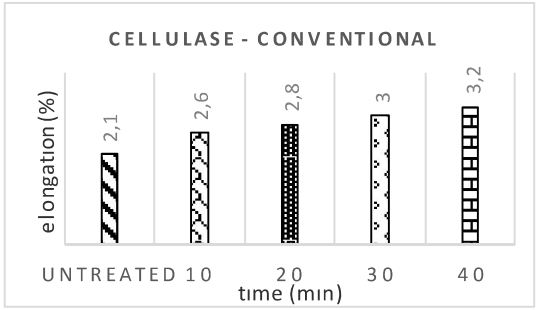


Figure 14: Elongation values of enzymatic treated samples with conventional method.

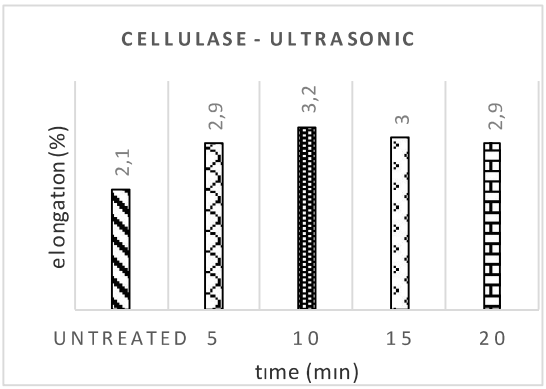


Figure 15: Elongation values of enzymatic treated samples with ultrasonic method.

The highest young's module was obtained with ultrasonic method at 10 minutes of operation, but decrease at young's modulus over 15 minutes was observed (Figure 16).

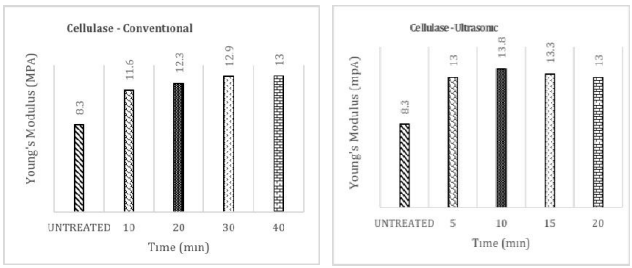


Figure 16: Young's modules values of enzymatic treated samples with conventional and ultrasonic methods.

IV. CONCLUSION

According to the tensile strength and elongation properties of the untreated and treated okra fibers higher tensile strength and elongation properties were obtained with conventional and ultrasonic processes by using sodium bisulphate and cellulase enzyme. Ultrasonic assisted enzymatic treatment process was more effective than the conventional. The reason for the ultrasonic processes to be successful is the strength achieved by sonication energy. Ultrasonic energy provide both energy time saving. Considering all these results; Sodium bisulphate and cellulase methods were found to adequately modify the fibers surfaces. In this study, mechanical properties of okra fiber improved and % weight loss increase is outstanding with the success of ridding the impurities. Weight loss results can be correlated with mechanical test results, which can be treated as a proof for enhanced interfacial interactions with conventional and ultrasonic energy treatments. According to the ultrasonic energy method results with cellulase enzyme is more effective than conventional method.

Conclusion section is not required. Although a conclusion may review the main points of the paper, do not replicate the abstract as the conclusion. A conclusion might elaborate on the importance of the work or suggest applications and extensions. A conclusion section is not required. Although a conclusion may review the main points of the paper, do not replicate the abstract as the conclusion. A conclusion might elaborate on the importance of the work or suggest applications and extensions.

ACKNOWLEDGMENT

THIS WORK WAS SUPPORTED BY TÜBITAK 1001 UNDER GRANT 215M984.

REFERENCES

[1]. Franklin W. Martin, , "Okra, Potential Multiple-Purpose Crop for the Temperate Zones and Tropics," *Economic Bottany*, V: 36(3), pp.340–345, 1982

[2] Alam, M., and Khan, G., "Chemical Analysis of Okra Bast Fiber (Abelmoschus Esculentus) and Its Physico-Chemical Properties," J. *Textile Apparel Technology management,* V:5, I:4 2007

[3] Kumar, Ds., Tony, De., Praveen Kumar, A., Kumar, Ka., Srinivasa Rao, Db., Nadendla, R., and Author, C. "A Review On: Abelmoschus Esculentus (Okra*)," Int. Res J Pharm. App Sci. Int. Res. J. Pharm. Appl. Sci*. V: 3(34), 2013

[4] Mwaikambo, L. Y., and Ansell, M. P., "Chemical Modification of Hemp, Sisal, Jute, and Kapok Fibers by Alkalization*," J. Appl. Polym. Sci.,* 84(12), pp. 2222–2234, 2002.

[5] Khan, G., and Alam, M., "Surface Chemical Treatments of Jute Fiber for High Value Composite Uses*," Res. Rev. J. Mater. Science*, V:1(2), pp. 39–44, 2013.

[6] Robert A. Shanks, "Processing Cellulose for Cellulose Fiber and Matrix Composites," *Green Composites from Natural Resources*., V: (3),pp.48, 2014.

[7] Arifuzzaman Khan, G., Ahsanul Haque, M., and Shamsul Alam, M., "Studies on Okra Bast Fibre-Reinforced Phenol Formaldehyde Resin Composites," *Biomass and Bioenergy*, Springer International Publishing, pp. 157–174, 2014.

[8] "Türkiye İstatistik Kurumu 09-May-2017 " [Online]. Available: http://www.tuik.gov.tr/PreTabloArama.do .

[9] Bledzki, A. K., and Gassan, J., "Composites Reinforced with Cellulose Based Fibres," *Prog. Polym. Sci*., V: 24(2), pp. 221–274, 1999

[10] Islam, M. S., and Pickering, K. L., "An Empirical Equation for Predicting Mechanical Property of Chemically Treated Natural Fibre Using a Statistically Designed Experiment," *Fibers Polymer*, V: 15(2), pp. 355–363, 2014.

[11] Hamideh Hajiha, Mohini Sain, and Lucia H. Mei, "Modification and Characterization of Hemp and Sisal Fibers," *J. Nat. Fibers*, V: 11(2), pp. 144–168, 2014.

[12] Pickering, K., Li, Y., Farrell, R., and Lay, M., "Interfacial Modification of Hemp Fiber Reinforced Composites Using Fungal and Alkali Treatment," *J. Biobased Mater. Bioenergy*, V: 1(1), pp. 109–117, 2007.

[13] Lipp-Symonowicz, B., Tańska, B., Wołukanis, A., and Wrzosek, H., "Influence of Enzymatic Treatment on the Flax Fibre Morphological Structure, Physico-Chemical Properties and Metrological Parameters of Yarn," *Fibres Text. East. Eur.,* V: 1(45), pp. 61–65, 2004.

[14] Rencoret, J., Aracri, E., Gutiérrez, A., José, C., Torres, A., Vidal, T., and Martinez, A., , "Structural Insights on Laccase Biografting of Ferulic Acid onto Lignocellulosic Fibers," *Biochem. Eng. J.,* V: 86, pp. 16–23, 2014.

[15] Liu, N., Shi, S., Gao, Y., and Qin, M., "Fiber Modification of Kraft Pulp with Laccase in Presence of Methyl Syringate," *Enzyme Microb. Technol*., V: 44(2), pp. 89–95, 2009,

[16] Peng, X., Zhong, L., Ren, J., and Sun, R., "Laccase and Alkali Treatments of Cellulose Fibre: Surface Lignin and Its Influences on Fibre Surface Properties and Interfacial Behaviour of Sisal Fibre/phenolic Resin," *Compos. Part A Appl. Sci. Manuf*., V: 41(12), pp. 1848–1856, 2010.

[17] Mistik, S.İ.," Effect of Ultrasonic Energy on Reductive Cleaning of Dyed Polyester Fabrics" *Asian Journal of Chemistry* V: 24-8, 3724, 2012.

[18]. Akalin, M., Merdan, N., Kocak, D., Usta, I." Effects of ultrasonic energy on the wash fastness of reactive dyes" *Ultrasonic V*: 42, pp. 161, 2004.

[19] Akalin, M., Merdan, N., Kocak, D., Usta, I." Effects of **ultrasonic** energy on dyeing of polyamide (microfibre)/Lycra blends"*Ultrasonic*s V: 42, pp.165 , 2004.

[20] Mistik, S. I., Yukseloglu, S. M." Hydrogen peroxide bleaching of cotton in ultrasonic energy." Ultrasonics, V: 43,pp. 811, 2005.

[21] Kocak, E.D.," The Influence of Ultrasonic Energy on Chemical Treatment of Surface Properties and the Properties of Composites Made of Luffa Cylindrical Fiber –Polyester Resin", Journal of Engineering Materials and Technology, Vol. 130/4, pp. 1-7, 2008.

[22]. Kocak, D.," Study of the Effects Different Chemical Compound Applied on Luffa Cylindrical Fibres with the Help of Ultrasonic Energy", *Journal of Polymer Engineering,* V: 28/8, pp. 501-515, 2008

[23] Paul A, Joseph K, Thomas S , Paul, A., Joseph, K., Thomas, S., "Effect of surface treatments on the electrical properties of low-density polyethylene composites reinforced with short sisal fibers‖," *Science direct, Compos. Sci. Technol*.,V: 57, pp. 67-79, 1997.

[24]. Rong MZ, Zhang MQ, Liu Y, Yang GC, Zeng HM "The effect of fiber treatment on the mechanical properties of unidirectional sisal-reinforced epoxy composites". Compos Sci Technol V: 61 pp. 1437 , 13-May-2017

[25]. Sreekala MS, Thomas Effect of fibre surface modification on water-sorption characteristics of oil palm fibres"*Compos Sci Technology* V: 63(6):861, (2003).

[26]. Castilho, L.R.; Medronho, R.A.; Alves, L.M.: _Production and Extraction of Pectinases Obtained by Solid State Fermentation of Agroindustrial Residues with Aspergillus Niger, *Bioresource Technology*, V: 71, pp. 45-50, 2000.

Investigation of Mechanical Properties of *Platanus orientalis* L./ Polyethylene Terephthalate Nonwoven Composite Materials

S. KIZILKAYA[1], B. YILMAZ ŞAHİNBAŞKAN[2], İ. MISTIK[3] and A.A. İZGİ [4]

[1-4] Marmara University, Istanbul/Turkey, sibelkizilkayaaaa@gmail.com, burcuyilmaz@marmara.edu.tr, imistik@marmara.edu.tr, aybenizgi@marun.edu.tr

***Abstract* - In general, manmade fibers are used commonly in forming the web-based fabrics; but nowadays environmentally friendly natural based fibers are preferred in the name of evaluation of wastes, because of their low costs and high mechanical properties as reinforcement fibers. *Platanus orientalis* (the eastern plane) grows to 25-30 m in length and 5-6 m in diameter under the name of the plane tree (Platanaceae) family in Turkey. It is found naturally in the forests in Turkey, in the creeks. In this study, wasted *Platanus orientalis* have been blended with polyethylene terephthalate fibers (PET). 100 % PET, 75/25 % *Platanus orientalis*/PET and 75/25 % PET/ *Platanus orientalis* blended fibers are carded and needle punched to fabricate lightweight nonwoven web surface. Mechanical properties of the *Platanus orientalis*/polyethylene terephthalate nonwoven composite materials have been investigated. Finally, using a blend of these *Platanus orientalis* fibers enhanced the strength properties and good young modules test results were achieved.**

***Keywords* - *Platanus orientalis* L., nonwoven, mechanical properties.**

I. Introduction

Natural resources have a dominant role in economic activity around the world [1]. Critical studies on the conservation and recycling of natural resources in recent years have led to increased interest in renewable raw material-based natural materials [2]. Natural fibers, which obtained from renewable sources, have some advantages such as high specific strength and hardness [3], low cost, low density [4], renewable [5], degradable, non toxic and low CO_2 emission. In addition, natural fibers can be biodegradable, that is, after they complete their life cycle as a product they can be degraded without damaging the natural resources [6]. Properties of the natural fibers such as biodegradability, sustainability, good mechanical and thermal insulation properties, low density and price are increasing the usage of them [7-9]. Cellulosic fibers are preferred because they are obtainable from natural sources, they are partly or completely renewable, their biodegradability, the lack of chemical additives in their production, their low density and low cost, and their contribution to the protection of ecological balance. Particularly in the composite material industry, studies on the use of cellulosic based natural fibers as reinforcing elements in composite materials are accelerating [1].

Bio-degradability is a significant contributor to natural fiber orientation. While some of the studies with natural fibers focus on such issues as strength, cost, and density by holding this topic further backwards, in fact, biodegradable composites are confronted as an important and comprehensive field at a value that can be collected under a separate heading. The interest in environmentally friendly composites, also called "green composites", increases in parallel with the increase in environmental sensitivity[10].

The use of nonwoven production techniques for the production of composite structures is advantageous in many respects due to the characteristics of production technologies. The production speed of nonwoven fabrics is faster than conventional processes. As a result of the final researches, the main application areas of untreated fabrics are technical textiles [11-12].Over the past decade, a number of studies have been conducted on the use of fibers obtained from natural and renewable sources [13-14].

The common goal of the work is to develop new composite materials that will not cause environmental problems after use by using high-biodegradability fibers instead of artificial fibers with low biodegradability and to use renewable resources. [15-16]. Composite structures obtained from these fibers provide lightness, abrasion resistance, low energy and high specific strength [17-18].

Bledzki et al. [19] says that linen and jute based fabric composites are effective in impact strength and shear modulus properties.Bakare et al. investigated the thermal and mechanical properties of sisal fibers / polyurethane composites to have good performance [20].

Wood flour and polyurethane composite based structures have been found to have an effect on the thermal conductivity as well as the enhancement of modulus and storage modulus

properties due to the increase in wood flour concentrations [21-22].

Platanus orientalis (the eastern plane) grows to 25-30 m in length and 5-6 m in diameter under the name of the plane tree (Platanaceae) family in Turkey. It is found naturally in the forests in Turkey, in the creeks [23-24].

In this study, wasted *Platanus orientalis* L. have been blended with polyethylene terephthalate fibers (PET). 100 % PET, 75/25 % *Platanus orientalis*/PET and 75/25 % PET/ Platanus orientalis blended fibers are carded and needle punched to fabricate lightweight nonwoven web surface. Mechanical properties of the *Platanus orientalis*/ polyethylene terephthalate nonwoven composite materials have been investigated. Finally, using a blend of these *Platanus orientalis* fibers enhanced the strength properties and good young modules test results were achieved.

II. EXPERIMENTAL

A. Material

Platanus orientalis L. fibers were obtained from the Bolu Abant area of Turkey. *Platanus orientalis* seeds in the hard shell are then removed. These fibers, which are the fruit of Platanus orientalis tree, were overall lengths between 2mm and 5mm. The properties of the PET fiber used in the experimental work are as follows: Tensile strength 4.5 g/den and elongation 32%.



Figure 1: Fruit of *Platanus orientalis* L.



Figure 2: *Platanus orientalis* L. fibers

B. Methods

Wasted *Platanus orientalis* L. have been blended with polyethylene terephthalate fibers (PET). 100 % PET, 75/25 % Platanus orientalis/PET and 75/25 % PET/ *Platanus orientalis* L. blended fibers are carded and needle punched to fabricate lightweight nonwoven web surface. Nonwoven production methods were preferred to produce nonwoven fabric from Wasted *Platanus orientalis* L. / PET fibers. The nonwoven fabric production was carried out at two steps as a web forming. A wool-type carding machine for forming webs from Wasted Platanus orientalis fibers and PET fiber a needle-punching machine for bonding of the webs were used. The needle-punching operations were carried out using low capacity machines instead of laboratory machines (CFS1/ 1000 mm, 650m/min) to bond staple fibers better. Firstly, Wasted Platanus orientalis / PET fibers were opened and mixed manually. The webs from Wasted Platanus orientalis / PET fibers using a wool-type carding machine were formed. Parallel-laid webs were obtained. The circular drum was used to collect the web from the carding machine instead of the cross lapper. Then, the webs were fed into the needling machines. After needling, the nonwoven fabric production was completed. The needle-punching machine parameters of all needle-punched fabrics barbed needles were used for all needle-punching machines. The punch densities of the needling machine was held constant at 75 punches per cm^2. For needled fabric, 75 punches per cm^2 were applied. The needle penetration depths were 0.50 cm at the needling machine. The weights per unit area of the produced needle-punched nonwoven fabrics were approximately $50g/m^2$ (Table 1).

Table 1: Working parameters of the needle-punching machines.

Needle penetration depth (mm)	0.50
Feeding speed of needle-punching machines (m/min	2.1
Delivery speed of needle-punching machines (m/min)	3
Needle-punching speed (rpm)	360
Needle punch density per cm^2 (punches/cm^2)	75

Table 2: Nonwoven production features.

Mixing ratios *Platanus orientalis* L. /PET (%)	Weight (g/m^2)	Thickness (cm)	Needle Density (Needle/cm^2)
100 % PET, 75/25 % and 75/25 %	50	0.50	75 (1x75)

C. Testing and Characterization

The tensile strength and elongation properties of composites were assessed on an Instron 4410 instrument, according to the ASTM D 5035 standard, (Machine direction) (Figure 3).



Figure 3: Instron 4410

III. RESULTS

The highest tensile strength was observed for 100% PET and the lowest tensile strength for 25/75 *Platanus orientalis* L. /PET. The tensile properties samples are different in the different directions of the sample due to structural anisotropy resulting from the process of sample formation. The idealized randomness of fiber orientation can lead to a reasonably isotropic behavior. The high proportion of *Platanus orientalis* L. in nonwoven composite can be improved the tensile strenght of samples. Amoung the composite it can be observed that tensile strenght of composites containing *Platanus orientalis* L. is the highest. This can be attributed to the fact that composites contain 75% *Platanus orientalis* L. fibers and are the one of the strongest samples.

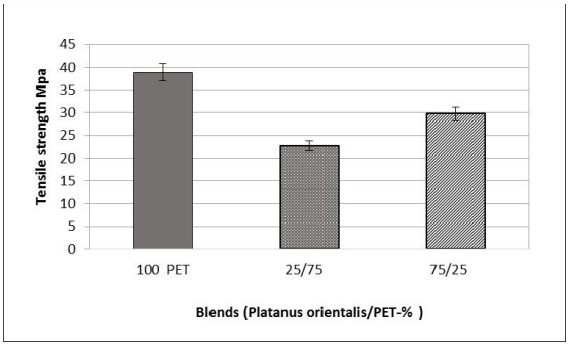


Figure 4: Tensile strength values of *Platanus orientalis* L. / PET blends.

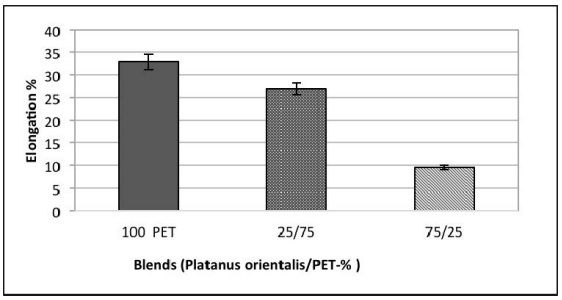


Figure 5: Elongation values of *Platanus orientalis* L. / PET blends.

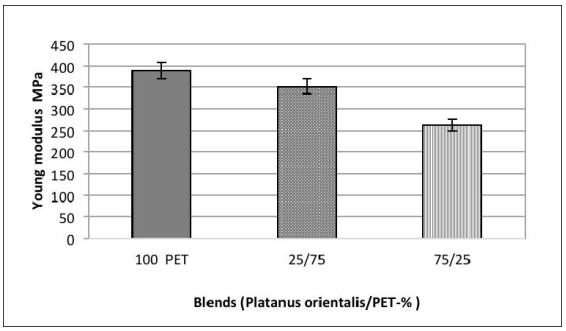


Figure 6: Young modulus values of *Platanus orientalis* L. / PET blends.

As shown in Figure 4-6, 75/25 % *Platanus orientalis* L. / PET of elongation(%) value are decreased. It can be observed that elongation % decreases the amount of *Platanus orientalis* L. The decrease in elongation value of composite may be attributed to poor interfacial bonding between PET and *Platanus orientalis* L. composites. The young modulus of 25/75 % *Platanus orientalis* L. / PET is higher than 75/25 % *Platanus orientalis* L. / PET samples. The addition of fibres allows effective stress transfer at the interface which consequently decreases the young modules.

IV. CONCLUSION

The study focused on the use of *Platanus orientalis* L. fiber blends as reinforcements in PET composites. In terms of mechanical properties, the incorporation of *Platanus orientalis* L. nonwovens improved the tensile strength. The young modules of the composites was found to be maximum for 25/75 % *Platanus orientalis* L. / PET. This was provided to lowering of elongation in reinforced composites. The results in this study showed overall improvement of tensile strength characteristics due to the increasing proportion of *Platanus orientalis* L.

REFERENCES

[1]. Koçak Emine Dilara,Merdan Nigar Evren O.Burcak " Research into the specifications of woven composites obtained from raffia fibers pretreated using the ecological method." *Textile Research Journal*. Vol: 85, Issue: 3 pp: 302-315, Feb 2015.

[2]. Kocak Dilara, Merdan Nigar, Mıstık İlker, Akalın Mehmet, Kayar Mahmut"Effect Of Different Surface Treatment Methods On Physical Properties Of Banana Fibers" *18th International Conference on Composite Structures,* Lisboa, Portugal 15-18 June 2015

[3]. Edeerozey A.M.M, at al. "Chemical modification of Kenaf fibers*". Mater Letters* V: 6 :pp. 2023–5. 2007

[4]. Zampaloni M. at al "Kenaf natural fiber reinforced polypropylene composites: a discussion on manufacturing problems and solutions". *Compos Part Appl Sci Manufacture* V: 5.38 pp. 1569–80, .2007

[5]. Mohanty AK, Misra M, Drzal LT. "Sustainable bio-composites from renewable resources: opportunities and challenges in the green materials world." *J Polymer Enviromental* V: 10(1–2) pp. 19–26. 2002

[6]. Mistik Süleyman İlker,Koçak Emine Dilara,Merdan Nigar " Effect of the Ecological Methods on the Surface Modification of the Kenaf Fibers." *Materials Science*. V: 22. pp. 409-414 2016

[7]. Li, Y., Mai Y.W., Ye, L. "Sisal Fiber And Its Composites:Review Of Recent Developments"*Composites Science Technology* V: 60, pp. 2037-2055 , 2000

[8]. Weyenberg, I. V., Ivens, J., Coster, A. D., Kino, B., Baetens, E., Verpoest, I. "Influence of processing and chemical treatment of flax fibres on their composites." *Composites* Science *and Technology*, V: 63(9), pp. 1241–1246 2003.

[9]. Alireza Ashori " Wood–plastic composites as promising green-composites for automotive industries" *Bioresource Technology* V: 99 pp. 4661–4667, 2008

[10] . Lukic´, S., Jovanic´, P., "Structural analysis of abrasive composite materials with nonwoven textile matrix", *Materials Letters*. V:58, pp. 439-440, 2004.

[11]. Rupp, J.," Techtextil: North America closes the circle", *Nonwovens Industrial Textiles* V: 2 , pp. 40– 46. 2000 .

[12]. Alemdar, A., Sain, M "Biocomposites from wheat straw nanofibers: Morphology, thermal and mechanical properties" *Composites Science and Technology* V: 68, I:2 , pp. 557–56 February 2008.

[13]. .K.G. Satyanarayana., J.L. Guimara˜es, F. Wypych .," Studies on lignocellulosic fibers of Brazil. Part I: Source, production, morphology, properties and applications" *Composites: Part A* V: 38 pp.1694–1709, 2007.

[14]. Lundquist, L., Marque, B., Hagstrand, P.O., Leterrier, Y., Ma˚nson, J.-A.E., "Novel pulp fibre reinforced thermoplastic composites. " *Composites Science and Technology* V: 63 (1), pp. 137–152. 2003.

[15]. Fa´bio Tomczak, Thais Helena Deme´trio Sydenstricker, Kestur Gundappa Satyanarayana" Studies on lignocellulosic fibers of Brazil. Part II: Morphology and properties of Brazilian coconut fibers" *Composites: Part A* v: 38 pp. 1710–1721, 2007.

[16]. Faruk O, Bledzki AK, Fink HP, Sain M". Biocomposites reinforced with natural fibers:". *Prog Polym Sci*; V: 37(11), pp.1552–96, 2012

[17]. .Bledzki AK, Gassan J. "Composites reinforced with cellulose based fibres." *Prog Polym Sci*; V: 24(2) pp. 221–74, 1999

[18]. Bakare IO, Okiemen FE, Pavithran C, Abdul Khalil HPS, Brehmakumar M."Mechanical and thermal properties of sisal fiber-reinforced rubber seed oilbased polyurethane composites." *Material Design* V: 31 pp. 4274–80, 2010.

[19]. Aranguren MI, Racz I, Marcovich NE. "Microfoams based on castor oil polyurethanes and vegetable fibers." J Applied Polymer Science V: 105, pp. 2791–800, 2007.

[20]. Casado U, Marcovich NE, Aranguren MI, Mosiewicki MA. "High-strength composites based on tung oil polyurethane and wood flour: effect of thefiller concentration on the mechanical properties." *Polymer Engineering Science* V: 49, pp. 713–21, 2009.

[21]. Racz I, Andersen E, Aranguren MI, Marcovich N. Wood flour – recycled polyolbased polyurethane lightweight composites. *J Composite Materials* V: 43 pp. 2871–84, 2009

[22]. Mohammad Peydayesh, Ahmad Rahbar-Kelishami" Adsorption of methylene blue onto Platanus orientalis leaf powder:Kinetic, equilibrium and thermodynamic studies" *Journal of Industrial and Engineering Chemistry*, V: 21 pp. 1014–1019, 2015.

[23]. Violeta Velikova, Tsonko Tsonev, Csengele Barta, Mauro Centritto, Dimitrina Koleva, Miroslava Stefanova Mira Busheva, Francesco Loreto "BVOC emissions, photosynthetic characteristics and changes in chloroplast ultrastructure of Platanus orientalis L. Exposed to elevated CO2 and high temperature" Environmental Pollution V: 157, pp. 2629–2637, 2009

[24]. Kalebek, N. Anda Babaarslan O " Fiber Selection For The Production Of Nonwovens" *In Tech Open, Published* , V: 1 , pp. 1-32, 2016.

Investigation of Sound Absorption Properties of Okra Nonwoven Materials

A.A. İZGİ[1], E.D. KOÇAK[2], İ. MISTIK[3], B.ARDIÇ [4] and B. YILMAZ ŞAHİNBAŞKAN[5]

[1-5] Marmara University, Istanbul/Turkey, aybenizgi@marun.edu.tr, dkocak@marmara.edu.tr, imistik@marmara.edu.tr, busra.ardic@marun.edu.tr, burcuyilmaz@marmara.edu.tr

Abstract **- The demand for bio-based products is recently increasing due to rapid consuming of natural sources in the world and environmental problems of synthetic production globally. The organizations and some industrialized countries are taking strict regulations for cleaning and leaving a healthy environment for future generations. They also identify the use of agricultural waste awareness and legislations lead to the use of natural materials in this direction. With 36.000 tons/year (2014) okra grown in Turkey, utilization of the okra stem wastes is becoming important for industrial use in order to contribute to the environmental cycle of the biomass by removing the wastes in their source, it will be also contributed to the recycle of the agricultural wastes by producing environmental, value added, new fiber/product.**

The agricultural plant waste fibers can be used for sound absorption and isolation while they are biodegradable, cost effective and recyclable.

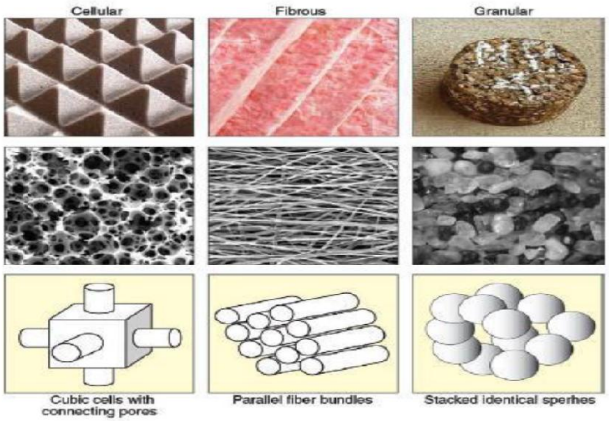
In this study, fibers have been produced from okra stem wastes by the specially designed machine separating the plant nectar from the plant stem. In order to clean and fibrillate the surface of the fiber, surface modification processes have been applied by using two different methods as conventional and microwave energy with 7 % sodium hydroxide. Then fibers with and without surface treatments have been combed and needle punched for the production of lightweight nonwoven surfaces. Sound absorption properties of okra fibers and nonwoven surfaces in different weights have been investigated.

Keywords **- Okra fibers, nonwoven, sound absorption**

I. Introduction

MODERN city life presents living condition for limited areas on daily and private lives to habitant. One of the most important disadvantages of coexistence is also sound pollution. Research on this issue has improved development of acoustic insolation on living area. Many scholars investigated the using of lignocellulosic materials in the application of sound absorbing. The primary advantages of using resin reinforced lignocellulosic materials are high stiffness and tensile strength, easily recyclability, biodegradability, abundance in the entire world, and low cost [1].

The absorbent materials in the porous structure are the best known sound absorbing materials. These are fleece materials, fibrous materials or soft rubber materials. These materials, which have sound absorbing properties, are used extensively in industries such as airplanes, automobiles ect. In an effective sound absorbing material, the sound energy that impacts the material needs to be converted to energy in another form (usually thermal energy)(Figure 1) [2].



Origin	Fibrous Material	Fiber diameter, µm
Synthetic	Ceramic	2-6
	Mineral wool (rock wool, slag wool)	3-10
	Fiber glass (continuous filament)	6-13
	Glass wool	3-7
	Graphite	5-10
	Basalt	7-13
	Bamboo	14
	Polypropylene	5-25
	Polyester	3-15
	Kevlar	12
Natural	Cotton	8-33
	Kenaf	21
	Hemp	22
	Wood	16-38
	Flax	19
	Bagasse	20
	Jute	20

Figure 1: Sound absorbing materials and their properties [2].

Moreover, many studies focused in developing natural fibers as raw material have been done and reported, such as palm, kenaf, coconut coir, and many others that have potential to be used as raw material of acoustical panel. Paddy straw was reported suitable for acoustic panel because of its high elasticity and hollow space. A single layer acoustic panel made of paddy husk reinforced sodium silicate showed the optimum sound absorption coefficient at higher silicate content in high range frequencies. Similarly, coconut and jute fiber have high potential to be used as a sound absorber material. Coconut coir fiber has good sound absorption at higher frequencies but less for the lower frequencies, so did the oil palm fiber. Higher noise absorption of oil palm is due to its higher density. Then, industrial tea-leaf-fiber waste material also has sound absorption properties at high frequencies. Besides, kenaf can be properly seen as an alternative, especially for thermo-acoustic applications and sound barriers. These show that natural fibers have high potential to be applied as raw material of sound absorbing materials [3].

In the literature, okra body plant was used for improve the sound absorption properties of nonwoven composites.

Okra fibres are extracted from the bark of okra bahmia, a plant of Malyaceae family (botanical name *Abelmoschus esculentus*)[4]. After collecting the fruits of the okra plant, the remaining amount of agricultural waste is 2.11 tons/da. The okra remaining as agricultural wastes are left in the soil as organic matter. In parallel with the increase in the population in Turkey, the demand for vegetables and fruits that humans need increasing. However, with the increasing demand, the amount of agricultural wastes also increases. For the environment, there is a need to effectively recycle and reduce environmental pollution. The evaluation of agricultural wastes that cause environmental problems and the production of new materials are thought to be important for bringing them to the industry as a new alternative raw material source [5]. Okra plants and okra fibers are shown Figure 2.



Figure 2: Okra plants and Okra fibers [6].

Surface modification processes have been applied by using two different methods as conventional and microwave energy. Microwaves are high-frequency radio waves in the infrared spectrum between 30MHz and 300 GHz. Utilization of the microwave energy power enables the use of drying, dyeing and printing in many fields of the textile sector due to its ability of fast and cost saving heating in a short time. In order to apply microwaves to a product, the product will have dielectric loss and dipolar electric loads will occur within the material when an inconstant electromagnetic field is applied. Therefore, as water molecules can easily compose dipolar electric loads, structures covering water or structures within aqueous ambient conditions are suitable for heating with microwaves. The microwave energy method is defined as an eco-friendly method as it accelerates chemical processes; it saves energy especially in reactions and has a short processing time. It seems that this method is eco-friendly, surface treatment of cellulosic and protein-based fibers[6-13]. In this study, okra fibers were treated with 7% sodium hydroxide by using conventional and microwave energy methods. Then fibers with and without surface treatments have been carding and needle punched for the production of nonwoven surfaces. Sound absorption properties of Okra nonwoven materials were investigated.

II. EXPERIMENTAL

A. Fibers

Okra fibers were obtained from the Mediterranean Region of Turkey. Their overall lengths were between 300 mm and 1200 mm. Okra body waste fibers were obtained by separating from plant extracts with the aid of a special machine designed to obtain fiber from lignocellulosic plants. Okra fibers are cut into lengths of 50mm with guillotine. It was waited in the water-filled container to remove residue and adhering dirt. (20 days). The fibers were shaken under running water until cleaned and they were dried in an oven at 100 °C for 2 hours. Drying process was carried out under laboratory conditions (20±2°C and 65±2%Relative humidity).

B. Surface Treatment

Okra fibers have been treated into two methods in which are given as conventional method and microwave method in Table 1 and 2, respectively. Conventional process was applied in laboratory condition. Microwave method was carried out with a Kenwood Mw440 at a frequency of 2.45 GHz. The microwave oven was set to Medium-Low (M-L) power of 350 W. The samples were placed in a sealed glass vessel and treated by the microwave energy according to the experimental design.

Table 1: Conventional method.

Chemical	Sodium hydroxide
Procedure	Merck
Concentration (%)	7
Temperature (°C)	60
Time (min)	20
Rinsing Process	25 °C, 10 min, pH 7 with distilled
Drying Condition	at room temperature

Table 2: Microwave method.

Chemical	Sodium hydroxide
Procedure	Merck
Concentration (%)	7
Temperature (°C)	60

Time (min)	5
Rinsing Process	25 °C, 10 min, pH 7 with distilled
Drying Condition	at room temperature

C. Production of Okra Nonwoven Surfaces

Sodium-hydroxide-treated okra fibers with conventional and microwave methods are carded and needle punched to fabricate lightweight nonwoven web surface. Nonwoven production methods were preferred to produce nonwoven fabric from okra fibers. The nonwoven fabric production was carried out at two steps as a web forming. A wool-type carding machine for forming webs from okra fibers a needle-punching machine for bonding of the webs were used. The needle-punching operations were carried out using low capacity machines instead of laboratory machines (CFS1/ 1000 mm, 650m/min) to bond staple fibers better. Firstly, okra fibers fibers were opened and mixed manually. The webs from okra fibers fibers using a wool-type carding machine were formed. Parallel-laid webs were obtained. The circular drum was used to collect the web from the carding machine instead of the cross lapper. Then, the webs were fed into the needling machines. After needling, the nonwoven fabric production was completed. The needle-punching machine parameters of all needle-punched fabrics barbed needles were used for all needle-punching machines. The punch densities of the needling machine were held constant at 75 punches per cm^2. For needled fabric, 75 punches per cm^2 were applied. The needle penetration depths were 0.50 cm at the needling machine. The weights per unit area of the produced needle-punched nonwoven fabrics were approximately 50g/m^2 (Table 3).

Table 3: Parameters for the needle-punching machines.

Needle penetration depth (cm)	0.50
Feeding speed of needle-punching machines (m/min)	2.1
Delivery speed of needle-punching machines (m/min)	3
Needle-punching speed (rpm)	360
Needle punch density per cm^2 (punches/cm^2)	75
Weight (g/m^2)	50

D. Sound Absorption Method

The material measurements are based on the two-microphone transfer-function method according to ISO 10534–2 and ASTM E1050–98 international standards which is for horizontal mounting of orientation-sensitive materials; simulation of the measurements on hanging ceilings, wall mountable. The testing apparatus is a part of a complete acoustic material testing system, featuring Brüel& Kjær PULSE™ system (Figure 4).

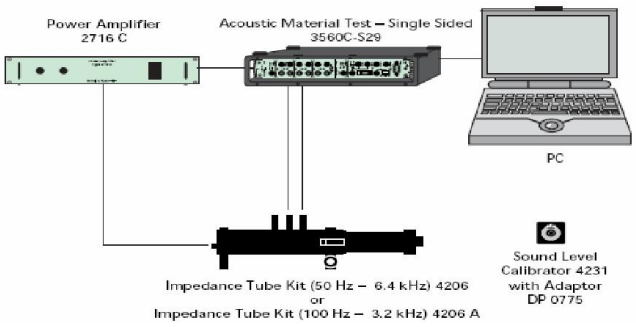


Figure 4: Measurement tester of acoustic properties [9]

III. RESULTS & DISCUSSIONS

The microwave method sodium-hydroxide-treated okra nonwoven materials have better sound absorption properties than the sodium hydroxide treated okra nonwoven materials by using conventional methods.

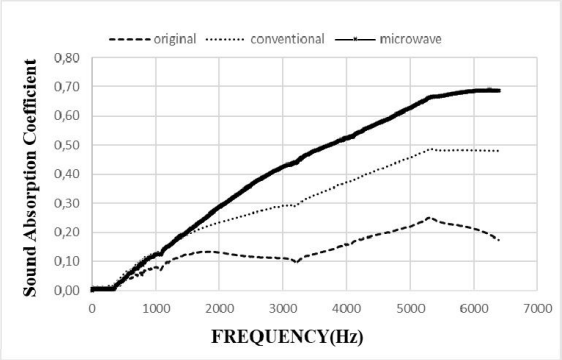


Figure 5: Sound absorption coefficient effect of different methods for surfaces treatment of okra nonwoven materials.

Microwave method increases the sound absorption properties of the okra nonwoven materials better than conventional method. Both okra fibers, which treated by using conventional and microwave methods have increasing sound absorption properties in low frequencies. The sound absorption coefficient of the nonwoven surface formed from untreated okra nonwoven materials' is the lowest among them.

ACKNOWLEDGMENT

This work was supported by Tubitak 1001 under grant 215M984.

REFERENCES

[1]. Koçak Emine Dilara,Merdan Nigar Evren O.Burcak " Research into the specifications of woven composites obtained from raffia fibers pretreated using the ecological method." *Textile Research Journal*. Vol: 85, Issue: 3 pp: 302-315, Feb 2015.

[2]. Kocak Dilara, Merdan Nigar, Mıstık İlker, Akalın Mehmet, Kayar Mahmut"Effect Of Different Surface Treatment Methods On Physical Properties Of Banana Fibers" *18th International Conference on Composite Structures,* Lisboa, Portugal 15-18 June 2015

[3]. .Edeerozey A.M.M, at al. " Chemical modification of kenaf fibers".MaterLetters V: 61, pp. 2023–5, 2007.

[4]. Zampaloni M. at al "Kenaf natural fiber reinforced polypropylene composites: a discussion on manufacturing problems and solutions". *Composite Part Applied Science Manufacture* V: 5/38 pp.1569–80, 2007.

[5]. Mohanty AK, Misra M, Drzal LT." Sustainable bio-composites from renewable resources: opportunities and challenges in the green materials world". *J Polymer Environmental* , V: 10, pp.19–26, 2002.

[6]. Canbolat, S., Dayıoğlu, H., Kocak, D., Merdan, N., 'The Investigation of the Sound Absorption Properties OF RICE HUSK/Polyurethane Composite Materials', *6th Texteh International Conference* Bucharest, Romania, October 17-18, 2013.

[7]. Arenas, J.P. and Crocker, M.J. 'Recent Trends in Porous Sound-Absorbing Materials'. *Sound & Vibration,* V: 44, pp.12-17, 2010.

[8] Ismail, Lindawati; Ghazali, Mohd. Imran; Mahzan, Shahruddin; Zaidi, Ahmad Mujahid Ahmad, 'Sound Absorption of Arenga Pinnata Natural Fiber' World Academy of Science, Engineering & Technology;Jul2010, Issue 43, p804

[9] Igor Maria De Rosa, José M. Kenny, Mohd.Maniruzzaman, Md. Moniruzzaman, Marco Monti, Debora Puglia, Carlo Santulli, and Fabrizio Sarasini, "Effect of Chemical Treatments on the Mechanical and Thermal Behaviour of Okra (Abelmoschus Esculentus*) Fibres," Composite Science Technology*.,V: **71**, pp. 246–254,2011.

[10] De Rosa IM, Kenny JM, Puglia D, Santulli C, Sarasini F. Morphological, thermal and mechanical characterization of okra (Abelmoschus esculentus) fibres as potential reinforcement in polymer composites. Compos Sci Technol 2010; 70: 116–122.

[11].Rakesh.Potluri, James Paul .K, Sd. Abdul kalam, P.Prasanthi, 'Mechanical Properties Characterization of Okra Fiber Based Green Composites& Hybrid Laminates', 5th International Conference of Materials Processing and Characterization (ICMPC 2016)

[12] Merve Yumşak 'Farklı Fiziksel Özelliklere Sahip Dokusuz Kumaşların Ses Yutum Kabiliyetlerinin İncelenmesi' , *Kahramanmaraş Sütçü İmam Üniversitesi Fen Bilimleri Enstitüsü Tekstil Mühendisliği Anabilim Dalı Yüksek Lisans Tezi* , 2010.

[13] Ekıcı, B., Kentlı, A., Kucuk, H., 'Improving Sound Absorption Property of Polyurethane Foams by Adding Tea-Leaf Fibers', *Archives of Acoustics,* V: 37**,** 4, pp. 515–520, 2012

Studies on Mechanical Performance of Cynara Scolymus/ Polyethylene terephthalate Nonwoven Composites

A.A. İZGİ[1], E.D. KOÇAK[2], B. YILMAZ ŞAHİNBAŞKAN[3], N. MERDAN[4] and B. ARDIÇ[5]

[1-3,5] Marmara Unversity, Istanbul/Turkey, aybenizgi@marun.edu.tr, dkocak@marmara.edu.tr, burcuyilmaz@marmara.edu.tr, busra.ardic@marun.edu.tr

[4] Istanbul Commerce University, Istanbul/Turkey, nmerdan@iticu.edu.tr

***Abstract* - Environmental concerns such as global warming, energy consumption and the desire to obtain products from renewable sources have led to a resurgence of interest in plant-derived products. Plant fibers with some interesting inherent properties like cost, effectiveness, renewable, available in high quality, have low fossil-fuel energy requirements, and can offer good mechanical properties has attracted it use for composite materials. Hemp, jute, flax, bagasse, coconut fiber, and bamboo are among the natural fibers which has attracted attention because of their low cost compared to synthetic fibers such as glass, carbon etc . Natural fiber reinforced composites are finding successful application in the automotive, electronics, and engineering sectors. Shortcomings with respect to moisture stability and poor strength are yet to be resolved satisfactorily.**

In this study Artichoke (*Cynara scolymus)* is obtained from the West Mediterranean Region of Turkey. Firstly the stem of plant was removed than the fibers were gained. Nonwoven surfaces were obtained at different percentages by to the mix Cynara scolymus / polyethylene terephthalate (PET) fibers.

The mechanical properties (elongation, strength, modulus of elasticity) of composite materials were investigated. The mechanical properties of non-woven surface composites of *Cynara scolymus* / PET fibers were observed with increases in elongation value, strength value (N) and elasticity modulus values compared to a 100% PET based nonwoven surface. In addition, the contact angle values of nonwoven surface composites based on *Cynara scolymus*/PET fibers were also increased.

***Keywords* - *Cynara scolymus* fibers, mechanical properties, nonwoven**

I. Introduction

NATURAL fibres will take a major role in the emerging "green" economy based on energy efficiency, the use of renewable materials in polymer products, industrial processes that reduce carbon emissions and recyclable materials that minimize waste. Natural fibres are a kind of renewable resources, which have been renewed by nature and human ingenuity for thousands of years. They are also carbon neutral; they absorb the equal amount of carbon dioxide they produce. These fibers are completely renewable, environmental friendly, high specific strength, non-abrasive, low cost, and bio-degradability. Due to these characteristics, natural fibers have recently become attractive to researchers and scientists as an alternative method for fibers reinforced composites and nonwoven materials [1].

Nowadays, natural fibers such as sisal and jute fiber composite materials are replacing the glass and carbon fibers owing to their easy availability and cost. The use of natural fibers is improved remarkably due to the fact that the field of application is improved day by day especially in automotive industries. Nowadays, natural fiber composites have gained increasing interest due to their eco-friendly properties. Many researches have been studied on these natural fibers. Natural fibers such as jute, sisal, silk and coir are inexpensive, abundant and renewable, lightweight, with low density, high toughness, and biodegradable [1]. Table 1 shows the mechanical properties of different types of potential natural fibres for composite applications [2].

Table 1: Mechanical properties of different types of natural fibers for composite application [2].

Natural Fibers	Tensile strength (MPa)	Elongation at break (%)	Young modulus (GPa)
Flax	300-1500	1.3-10	24-80
Jute	200-800	1.16-8	10-55
Sisal	80-840	2-25	9-38
Kenaf	295-1191	3.5	2.86
Pineapple	170-1627	2.4	60-82
Banana	529-914	3	27-32
Coir	106-175	14.21-49	4-6
Oil palm (empty fruit)	130-248	9.7-14	3.58
Oil palm (fruit)	80	17	-
Ramie	348-938	1.2-8	44-128
Hemp	310-900	1.6-6	30-70
Wool	120-174	25-35	2.3-3.4
Spider silk	875-972	17-18	11-13
Cotton	264-800	3-8	5-12.6

The increase in the prices of synthetic fibers due to petroleum as well as the activities aimed to protect the environment have increased the use of vegetable fibers in fabric-based fabric industry. Waste-plant based fibers are used

in many countries as reinforcements, especially in the automotive sector due to their volume, strength, porosity, resistance to abrasion and flammability, heat and sound absorption characteristics [3].

M. Ramesh *et al.* investigated the mechanical properties of sisal, jute and glass fiber reinforced polyester composites. They observed that the addition of glass fiber into jute fiber composite resulted in maximum tensile strength. In the same way they have observed that jute and sisal mixture composites sample is capable having maximum flexural strength and maximum impact strength was obtained for the sisal fiber composite [4].

PET fiber is one of the most important fibers used to form a nonwoven surface and composite. For example, the lengths of cut are adapted to the respective manufacturing procedure. Fibers are also available in different of luster and cross-sectional forms. They are inexpensive, easily produced from petrochemical sources, and have a desirable range of physical properties. They are strong, lightweight, easily dyeable and wrinkle resistant, and have very good wash wear properties. Therefore, it is mostly used in nonwoven surface and composite production [5].

Cynara scolymus L. (CS), usually known, as globe *cynara scolymus* is a wintery plant with lignocellulosic content and a perennial, strong root structure, growing longitudinally, with a hard and grooved body, and growing in a temperate and humid climate. Spain, France, Italy, Greece, Turkey, Israel, USA, Argentina and Egypt are the most artichoke-producing countries. During the industrial processing of artichokes, 80-85% of the plant is not used and is separated as solid waste. A total of 36,368 tonnes / year [6] *cynara scolymus* production is being made in Turkey, especially in the Aegean, Marmara and Mediterranean regions with a total area of about 2600 cultivation area. After collection, 2.7 ton / da waste is left on the field [7]. World countries *cynara scolymus* production and planting, according to FAO data as of 2013 are given in Table 2 as tons / year and (ha).

Table 2: *Cynara Scolymus* production in the world countries [7].

Country	Area (ha)	Production (tons)
Egypt	17 895	387 704
Italy	35 593	364 871
Spain	16 000	199 100
Peru	7 841	141 496
Argentina	4 000	106 000
China	12 000	77 000
Morocco	3 819	63 889
Algeria	4 168	53 657
USA	3 160	51 300
France	7 721	42 465
Turkey	2 600	32 173
Greece	2000	31 600

In Table 3, where the physical properties of *cynara scolymus* body waste fibers are given in comparison with other lignocellulosic fibers, it is stated that their mechanical behavior is similar to sisal, kenaf and hemp fibers. It is therefore possible to conclude that these fibers can be used as alternative reinforcing elements in polymer-based composite structures such as other lignocellulosic fibers [8].

Table 3: Mechanical properties of lignocellulosic fibers [9-10].

Fiber	Fiber diameter (µm)	Tensile strenght (MPa)	Young Modulus (GPa)	Elongation (%)
Sisal	50-200	80-640	1.46-15.8	2.5
Cotton	17	400	5.5-12.6	7-8
Flax	30-110	450-600	27.5-38	1.5-1.8
Hemp	53.7	690-873	9.93	1.6
Jute	25-200	393-773	2.5-26.5	1.5-1.8
Kenaf	43.3-140	223-624	11-14.5	1.6
Artichoke	300	100-300	6-18	2
Okra	40-180	234-380	5-13	2
Ramie	34	400-698	24.5-128	1.2-3.8

In this study nonwoven composites were produced at different percentages by to the mix *Cynara scolymus* / polyethylene terephthalate fibers. The mechanical properties (elongation (%), strength (N), modulus of elasticity (MPa)) of composite materials were investigated.

II. EXPERIMENTAL

A. Materials

Artichoke plants are obtained from the West Mediterranean Region of Turkey. A specially designed machine mechanically separated the fibers of the cynara scolymus plants. *Cynara scolymus* fibers are cut into lengths of 50mm with guillotine. The *cynara scolymus* fibres were washed with water to remove the adhering dirt. (20°C distilled water for 5 min). After treatments they were conditioned for 48 hours prior to testing under 20 ±2 °C and 65 ±2 %RH conditions. *Cynara scolymus* fibers are shown in Figure 1.



Figure

B. Cynara scolymus fiber/PET Composite Production

Cynara scolymus used in composite construction was combined with PET fibers (75/25%, 25/75%) in two different percentages. *Cynara scolymus* fibers and PET fibers have been combed and needle punched for the production of nonwoven surfaces. Nonwoven production methods were preferred to

produce nonwoven fabric from wasted *cynara scolymus*/PET fibers. The nonwoven fabric production was carried out at two steps as a web forming. A wool-type carding machine for forming webs from wasted *cynara scolymus* fibers and PET fiber a needle-punching machine for bonding of the webs were used. The needle-punching operations were carried out using low capacity machines instead of laboratory machines (CFS1/ 1000 mm, 650m/min) to bond staple fibers better. Firstly, wasted *cynara scolymus*/PET fibers were opened and mixed manually. The webs from wasted *cynara scolymus*/PET fibers a wool-type carding machine were formed. Parallel-laid webs were obtained. The circular drum was used to collect the web from the carding machine instead of the cross lapper. Then, the webs were fed into the needling machines. After needling, the nonwoven fabric production was completed. The needle-punching machine parameters of all needle-punched fabrics barbed needles were used for all needle-punching machines. The punch densities of the needling machine were held constant at 75 punches per cm^2. For needled fabric, 75 punches per cm^2 were applied. The needle penetration depths were 0.50 cm at the needling machine. The weights per unit area of the produced needle-punched nonwoven fabrics were approximately $50g/m^2$ (Table 4).

Table 4: Working parameters of the needle-punching machines.

Needle penetration depth (mm)	0.50
Feeding speed of needle-punching machines (m/min)	2.1
Delivery speed of needle-punching machines (m/min)	3
Needle-punching speed (rpm)	360
Needle punch density per cm^2 (punches/cm^2)	75

C. Contact Angle Measurement

The dynamic contact angle values of the fabric samples were measured by using PG-X Measuring Head Pocket Goniometer test device as specified in ASTM D5725-99 (2008) method. The static contact angle method is consisted in putting down a liquid drop on the solid plate. When a drop of liquid (water) is putted down on a solid (textile material) surface, three phases systems occurs: solid, liquid and gas (Figure 2).

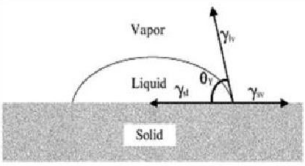


Figure 2: Static contact angle measurement with sessile drop method [12].

The physico-chemical of the solid surface, new interface solid/liquid adhesion forces and cohesion forces of the liquid are changed the drop's profile. Therefore, revealing the surface state will be affected the contact angle value according to Young's equation (1):

$$\gamma_{lv} \cos \theta = \gamma_{sv} - \gamma_{sl} \quad (1)$$

Where γ_{sv}, γ_{sl} and γ_{lv} represent the "surface tensions" of the interface solid/gas, solid/liquid and liquid/gas, respectively. 'θ' represents the contact angle [12].

The contact angle will be less than 90° on a hydrophilic surface. If the surface is hydrophobic the contact angle will be greater than 90°.

D. Testing and Characterization

Using Instron 4411 according to ASTM D638-91 tested mechanical properties of the composite structures. Testing of the composites on Instron 4411 are shown in Figure 3.



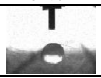
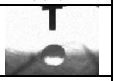
Figure 3: Testing of *Cynara scolymus* / PET nonwoven composite.

III. RESULTS AND DISCUSSION

A. Contact Angle Measurement Results

The contact angle of water droplets on fabrics can be seen in Table 4. When the contact angle values were examined, it was determined that 100% PET nonwoven surface was hydrophobic, *Cynara scolymus* mixed PET nonwoven surface was hydrophilic.

Table 4: The contact angle water droplets on *Cynara Scolymus*/PET nonwoven composite.

Samples	Time (s)				
	0	0.1	0.2	0.3	0.4
%100 PET Nonwoven Surface					
	143.8°	143.6°	144.3°	142.9°	143.4°
75/25 % *Cynara Scolymus*/PET					
	76.2°	81.8°	81.6°	79.2°	80.0°
25/75 % *Cynara Scolymus*/PET					
	71.7°	69.7°	67.6°	65.1°	65.4°

B. Results of Mechanical Testing

The tensile strength (N) of the mixed (75/25 and 25/75%) *Cynara Scolymus*/PET composites and %100 PET nonwoven surface are shown in Figure 3. The incorporation of *Cynara*

Scolymus/PET nonwovens in virgin PET nonwovens results in a general increment of mechanical properties.

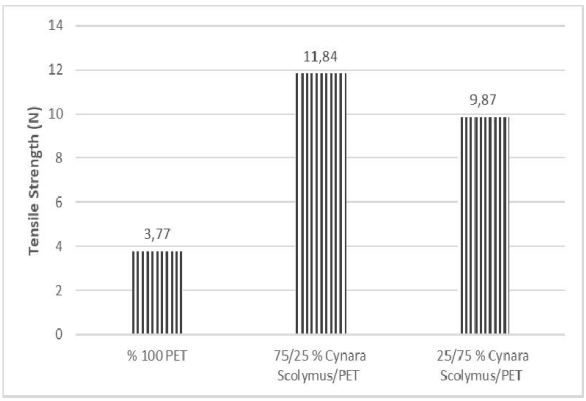
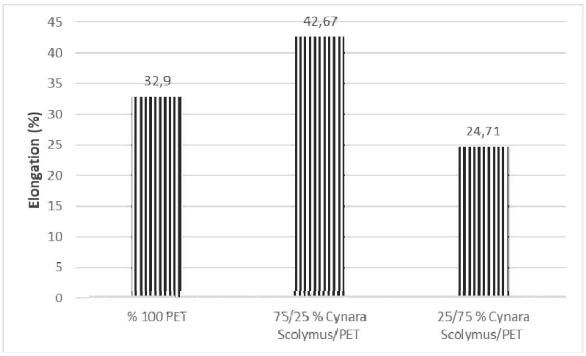


Figure 4: Tensile strength of nonwoven composites.



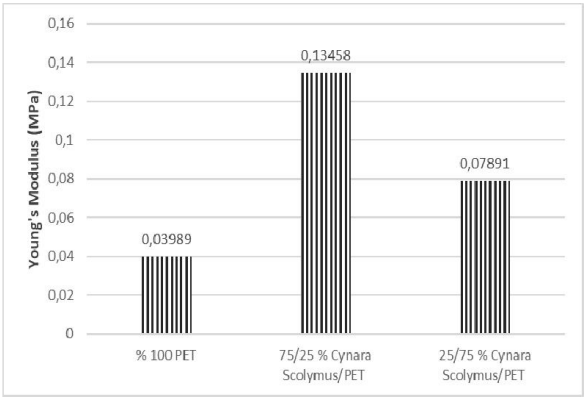


Figure 6. Young's Modulus of nonwoven composites.

Among the composites, it can be observed that tensile strength, elongation and young modulus of composites containing *Cynara Scolymus* fibres is the highest. This can be attributed to the fact that nonwoven surfaces contained Cynara Scolymus fibres are one of the strongest fibres.

IV. CONCLUSION

The effects of fiber content and fiber orientation on mechanical and contact angle properties for *Cynara Scolymus* were studied in this research work. The study revealed that the fiber content strongly influences the mechanical and water absorption property of nonwoven composites. Amount of the *Cynara scolymus* fiber influence the mechanical properties, but it strongly influences the water absorption property of composites.

The 75/25 % *Cynara Scolymus*/PET composite has shown better mechanical and lower water contact angle properties. This composite structure is the more hydrophilic sample than the other samples.

REFERENCES

[1] K. P. Ashik and R. S. Sharma, "A Review on Mechanical Properties of Natural Fiber Reinforced Hybrid Polymer Composites", Journal of Minerals and Materials Characterization and Engineering, vol 3, pp.420-426, 2015.

[2] H. Cheung, M. Ho, K. Lau, F. Cardona and D. Hui, "Natural Fibre-Reinforced Composites For Bioengineering And Environmental Engineering Applications", *Composites Part B: Engineering,* vol. 40 (7), pp. 655-663, 2009.

[3] *Changing landscape - notable developments in the automotive sector*. Nonwovens Report Internationa. World Textile Publication Ltd, pp.34, 1999.

[4] M. Ramesh, K. Palanikumar and K.H. Reddy, "Mechanical Property Evaluation of Sisal-Jute-Glass Fiber Reinforced Polyester Composites", *Composites*: *Part B,* vol. 48, pp. 1-9, 2013.

[5] N. Kelebek and O. Babaaslan, Fiber Selection for The Production of Nonwovens *'Non-woven Fabrics'. H. Jeon,* ISBN 978-953-51-2271-5.

[6] http://www.tarim.gov.tr/sgb/Belgeler/SagMenuVeriler/BUGEM.pdf, reached by 28 Oct. 2017.

[7] http://faostat.fao.org/site/567/DesktopDefault.aspx?PageID=567#ancor , FAO 2013, reached by 28 Oct. 2017.

[8] A. Bledzki, S. Reihmane and J. Gassan J. "Properties and modifi cation methods for vegetable fibers for natural fiber composites", *J Appl Polym Sci,* vol. 59, pp. 1329–1336, 1996.

[9] N. Srinivasababu, K.M.M Rao and J.S. Kumar JS, "Experimental determination of tensile properties of okra, sisal and banana fiber reinforced polyester composites", *Indian J Sci Technol,* vol.2, pp.35–38, 2009.

[10] R. Malkapuram, V. Kumar and Y.S. Negi, "Recent development in natural fiber reinforced polypropylene composites", *J Reinforced Plast Compos,* vol.28, pp. 1169–1189, 2009.

[11] V.K. Midha and A. Mukhopadyay, (2005) "Bulk and Physical Properties of Needle-Punched Nonwoven Fabrics", *Indian Journal of Fibre & Textile Research*, Vol. 30, pp. 218-229, 2005.

[12] R.J. Good, Robert J, "Contact Angle, Wetting, And Adhesion: A Critical Review", *Journal of Adhesion Science and Technology,* vol. 6 (12), pp. 1269-1302 1992.

Observation of Effect of Ti on Properties of A356 Alloy under Different Holding Times

Muhammet ULUDAĞ[1], Mikdat GURTARAN[1], Derya DIŞPINAR[2]

[1] Bursa Technical University, Bursa/Turkey, dr.uludagm@gmail.com, mikdat24@hotmail.com
[1]Istanbul University, Istanbul/Turkey, deryad@istanbul.edu.tr

***Abstract* – Aluminum is one of the most commonly found elements in nature and today it is the most used metal in engineering after steel. Aluminum and its alloys, which have features such as low density, high corrosion resistance, castability and workability, are used in important industries such as automotive and aircraft industry. Aluminum offers much better properties if it is produced with its alloy elements. These features are; mechanical strength, chemical stability, workability, thermal expansion, thermal conductivity and heat resistance.**

In this study, effect of Ti (AlTi5B1) on mechanical properties of A356 alloy was investigated under various holding duration conditions. After adding Ti into the melt, samples were collected at three different times: 0, 20 and 40 min. It was found that Ti has important effect on casting quality and mechanical properties. As holding time was increased, efficiency of Ti was decreased.

***Keywords* – A356 alloy, Grain refinement, Mechanical properties, Casting quality, Bifilm**

I. INTRODUCTION

BIFILMS are casting defects that occurs in the frame of various factors such as formation of surface oxides in aluminum casting alloys and entrainment of these oxides into the melt. As a result, mechanical properties are affected negatively. However, hydrogen has always been considered as the main cause of porosity formation in aluminum alloys. It has been proposed that the removal of hydrogen from the structure by processes such as degassing will reduce the porosity and thus improve the mechanical properties [1, 2]. On the other hand, Campbell and Dışpınar [3, 4] has been carried out an extensive work and it has been shown that dissolved hydrogen is not the main factor but only a trigger for pore formation. Bifilms are formed by the incorporation of oxide films formed by poor runner systems and turbulence during filling [5]. Once these defects are introduced into the melt, they have an effect on mechanical properties. In this frame, it is crucial that the reduction of bifilm formation or cleaning of the melt play an important role. Degassing and optimized runner and sprue design can prevent or eliminate of bifilms [6]. The humidity of the environment is also directly influential on oxide.

As the casting speed increases, the formation of porosity and bifilm also increases. In order to modify the microstructure of aluminum and its alloys, various master alloys are used [7-11]. Ti-containing (AlTixBy) or Ti-free (AlxB) master alloys are preferred for the grain refinement of aluminum alloys. Based on his experience from recent work, Campbell [6] has suggested that Ti-containing master alloys may be active in the cleaning of bifilms as well as in time-dependent grain refinement in liquid metal.

In this study, effect of Ti (AlTi5B1) on mechanical properties of A356 alloy under various holding durations was investigated.

II. EXPERIMENTAL PROCEDURE

The alloy used in the study was obtained A356 alloy was provided as cast ingots from ETI ALUMINYUM, Turkey. Chemical composition of the alloy is given in Table 1. A356 alloy ingots were cut to be charged into the crucible. A resistance furnace that has 22 kg capacity was used to melt the alloy. Grain refinement additions were made once the melt temperature had reached 740 °C.

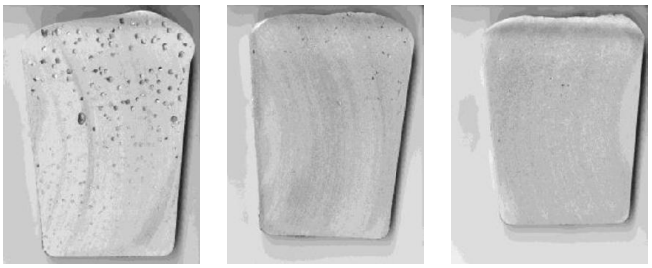
Table 1. Chemical composition (in wt. %) of the A356 alloy used in the study

Alloy	Si	Fe	Cu	Mn	Mg	Zn	Ti	Al
A356	6.80	0.19	0.003	0.001	0.30	0.011	0.108	Rem.

AlTi5B1 master was added into the melt as a grain refiner. First sample was collected once AlTi5B1 was added. Second samples and third samples were collected after 20 and 40 minutes later. Reduced Pressure Test (RPT) samples were collected each time a tensile test sample was produced. Bifilm index was used to determine casting quality and the results were compared with mechanical tests.

III. RESULT AND DISCUSSION

Representative images from analysis of RPT samples are given in Figure 1. On the images, it can be seen that bifilms tend to reduce and get smaller with increased holding time.



a b c

Figure 1. Representative images from RPT samples a) 0 min b) 20 min c) 40 min

Bifilm index and bifilm number are given in Figure 2 and 3 respectively. Changes in bifilm index and bifilm number can be seen on these charts. Bifilms affect casting quality and mechanical properties directly. As bifilm index is increased, casting quality and mechanical properties are reduced [12-14]. In this study, AlTi5B1 was added in to the melt and effect of Ti on mechanical properties depending on holding time was investigated. It can be said that effect of Ti increase in time and bifilms are reduced with Ti. This effect might be explained by the higher density of Ti with regard to density of liquid aluminum. Once Ti particles sink from top to bottom in the liquid, they take bifilms together to sink them to the bottom of the crucible. Thus, casting quality can be improved by Ti addition.

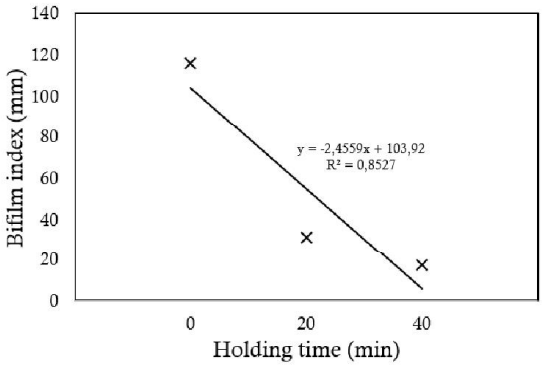


Figure 2. Changes of bifilm index by holding time

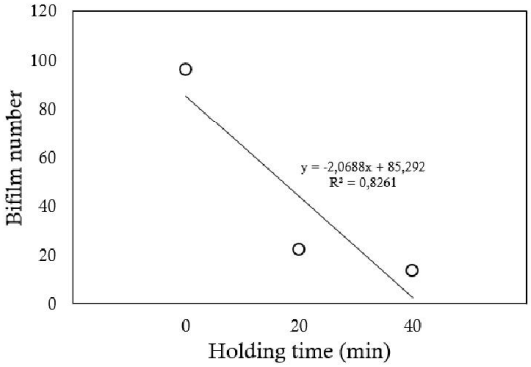


Figure 3. Changes of bifilm number by holding time

Changes of mechanical properties by holding time after adding Ti are given in Figure 4. I was mentioned that Ti affect casting qualtity by reducing bifilms. Another factor is holding time of liquid metal to reduce bifilms. It can be understood that mechanical properties such as tensile strength, yield strength and elongation can be increased by Ti (Figure 4).

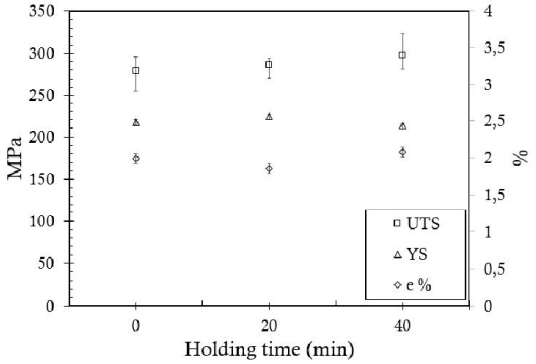


Figure 4. Changes of mechanical properties by holding time

IV. CONCLUSION

The conclusions of this study where the effect of Ti with regard to holding time on casting quality and mechanical properties can be summarized as follow:

1- A356 alloy melt quality is affected by Ti addition
2- High casting quality can be obtained by using Ti with holding time of 40 minutes.
3- There is a good relationship between casting quality (bifilm index) and mechanical properties.
4- As bifilm index is decreased, mechanical properties are increased.

REFERENCES

1. Haghayeghi, R., H. Bahai, and P. Kapranos, Effect of ultrasonic argon degassing on dissolved hydrogen in aluminium alloy. *Materials Letters*, 2012. 82(0): p. 230-232.
2. Shabestari, S.G., S.M. Miresmaeili, and S.M.A. Boutorabi, Effects of Sr-modification and melt cleanliness on melt hydrogen absorption of 319 aluminium alloy. *Journal of materials science*, 2003. 38(9): p. 1901-1907.
3. Dispinar, D. and J. Campbell, Critical assessment of reduced pressure test. Part 1: Porosity phenomena. *International Journal of Cast Metals Research*, 2004. 17(5): p. 280-286.
4. Dispinar, D. and J. Campbell, Critical assessment of reduced pressure test. Part 2: Quantification. *International Journal of Cast Metals Research*, 2004. 17(5): p. 287-294.
5. Dispinar, D. and J. Campbell, Use of bifilm index as an assessment of liquid metal quality. *International Journal of Cast Metals Research*, 2006. 19(1): p. 5-17.
6. Campbell, J., Complete casting handbook: metal casting processes, metallurgy, techniques and design. 2015: *Butterworth-Heinemann*.
7. Apelian, D., G.K. Sigworth, and K.R. Whaler, Assessment of Grain Refinement and Modification of Al-Si Foundry Alloys by Thermal Analysis. *American Foundrymen's Society Inc.*, 1984: p. 99297-99307.
8. Benny Karunakar, D., et al., Effects of grain refinement and residual elements on hot tearing in aluminum castings. *The*

International Journal of Advanced Manufacturing Technology, 2009. 45(9-10): p. 851-858.
9. Easton, M., et al. The effect of grain refinement and cooling rate on the hot tearing of wrought aluminium alloys. in *Materials science forum*. 2006. *Trans Tech Publ*.
10. Haro-Rodríguez, S., et al., On influence of Ti and Sr on microstructure, mechanical properties and quality index of cast eutectic Al–Si–Mg alloy. *Materials & Design*, 2011. 32(4): p. 1865-1871.
11. Mohanty, P.S. and J.E. Gruzleski, Mechanism of grain refinement in aluminium. *Acta Metallurgica et Materialia*, 1995. 43(5): p. 2001-2012.
12. Bozchaloei, G.E., et al., Effect of oxide bifilms on the mechanical properties of cast Al–7Si–0.3 Mg alloy and the roll of runner height after filter on their formation. *Materials Science and Engineering: A*, 2012. 548: p. 99-105.
13. Campbell, J. and M. Tiryakioğlu, Bifilm defects in Ni-based alloy castings. *Metallurgical and Materials Transactions B*, 2012. 43(4): p. 902-914.
14. Dispinar, D. and J. Campbell, Effect of casting conditions on aluminium metal quality. *Journal of Materials Processing Technology*, 2007. 182(1–3): p. 405-410.

Experimental study of a blast furnace slag stabilized, soil reinforced with natural fibers.

M.HIDJEB[1] and I.LAMRI[1]

[1] Université 20 août, Skikda/LMGHU laboratory, Algeria, mustapha_hidjeb@yahoo.fr
[1]Université 20 août, Skikda/LMGHU laboratory, Algeria, ihcene2000@yahoo.fr

Abstract - **The purpose of this work is to study the mechanical and physical properties of a chemically stabilized granular soil reinforced with natural fibers (palm fibers).**

All the direct shear tests (Casagrande) were carried out on sand samples prepared under optimal water content conditions. The shear tests were performed on samples of sand stabilized either with cement, or with blast furnace slag and finally on samples stabilized with cement or slag and reinforced with natural fibers.

In this work, it has been shown, that the shear strength parameters of the stabilized soil had significantly improved and that the reinforcement of sand with natural fibers had an important effect on the strength parameters (cohesion and internal friction angle) of the soil.

Keywords - **Shear strength, palm fiber, polypropylene fiber, cement, blast furnace slag, cohesion, friction angle.**

I. Introduction

THE very large infrastructures growth, in mainly urban areas, has been the source of land speculations which of course resulted in dramatic rise in land prices . This situation forced the building industry to think about an eventual use of lands, which were, in very close past ,classified as unsuitable for construction.

Chemical stabilization is one of the a techniques used to improve the characteristics of local soils . Lime stabilization together with cement stabilization are the most used techniques in civil engineering.

In order to improve the properties of the stabilized soil, natural fibers were added to soil-cement mixtures. In this work palm fibers were used.

It has been shown Vidal [1], that the introduction of reinforcing elements enhance shear strength of the soil cement mixture [2], [3], [4], [5].

The effects of reinforcement, design parameters including length, stiffness and number of layers (i.e. vertical spacing between layers) on the response of reinforced soil retaining walls under static gravity loading , have been investigated using numerical simulation approach[6].

The main reasons for their popularity are strength, weight, durability and of course low cost. The natural fibers sisal (agave), palm fibers are abundantly available and are cheap. It is proven that vegetal fibers used with cement mortar can produce high performance fibreboards.

Simple compression tests and CBR tests were carried out on a silty sand reinforced with palm fibers of various lengths showed an improvement of studied sand properties [3].

In order to study the shear strength simple, compressions tests were carried out on samples of cemented sand. These samples were reinforced with synthetic fibers that are distributed in an orderly fashion (3 layers and 5 layers). The results obtained showed that the samples reinforced with 5 layers are more rigid than those of three layers [4].

The purpose of using cement as a stabilizer in clay or granular soils is to improve the mechanical properties such as cohesion and internal friction angle. Cemented sand that shows brittle behaviour can be reinforced with natural or synthetic fibers to increase its strength.

A number of triaxial tests, unconfined compression tests and CBR tests, direct shear tests have been carried out by several researches over the last decades on reinforced and stabilized soils [7], [8], [9], [10].

II. Materials and Experimental Details

A. Materials

- Soil characteristic: The dune sand comes from t FIL-FILA, a region located 13 Km north-east of Skikda in Algeria. These characteristics, including particle size analysis, sand equivalent, methylene blue test, normal Proctor were determined. The results were as follows. Depending on its characteristics, the soil has been classified under Class B1: Silty Sand (According to the GTR classification). According to the physical identification tests, the soil has a maximum dry density of ρd = 1.74 g / cm3 with an optimum wop = 11.6%. According to the methylene blue test, the soil has a VBS = 0.15, indicating that this soil was a silty sand and sensitive to water. The equivalent test, ES = 80% (very clean soil).

- Cement: Chemical stabilization technique with cement is a proven technique for soil stabilization. Cement CPJ-CEM II-42.5 (Portland cement manufactured at Hadjar Essoud-Skikda) was used with different percentages to stabilize the soil used in this research. The chemical characteristics of cement were as follows. Insoluble residues = 2.28; PAF 975 =

2.41, Cao = 57.22, SiO_2 = 27.83, AL_2O_3 = 6.21, Fe_3O_3 = 3.12, MgO = 0.94, SO_3 = 2.02, CaO = 0.88, Chloride = 0.00.
Blast furnace slag**:** It is a granulated blast furnace slag with an inert particle content equal to 0.29% fresh production. In order to stabilize our soil, different percentages have been used.
The mineralogical study of blast furnace slag was carried out with X-rays and it gave the following results: CaO = 40.13, SO_3 = 0.33, SiO_2 = 37.62, AL_2O_3 = 5.98, Fe_3O_3 = 6.21, MgO = 5.10, $N_{a2}O$ = 0.30, K_2O= 1.09.

- Polypropylene fiber **:** The use of fibers is the most widely used technique in laboratory soil strengthening tests [11] , [12], [13].

Synthetic fibers, produced for use in concrete and hydraulic mortars, and today used for reinforcement of soils, are made of high density polypropylene. They have high dimensional stability. They are waterproof, resistant to abrasions, atmospheric and chemical agents, alkalis, molds, micro-organisms and high temperatures.
Polypropylene fibers were used in this study to reinforce the soil after stabilization with different percentages cement and blast furnace slag,.
Synthetic fibers, produced for use in concrete and hydraulic mortars, is today largely used for reinforcement of soils. The most used fibers in the soils are made from high density polypropylene. The characteristics of polypropylene fibers were: dimensional stability, waterproof, resistant to abrasions, atmospheric and chemical agents, alkalis, molds, microorganisms and high temperatures.
Bulk density= 0.92 g/cm^3, length = 12 mm, tensile strength= 600 MPa , Young modulus=3 kN/mm^2, melting point= 150°c.

- Palm fibers : Vegetal fibers (figure 1) are biological structures composed of cellulose, hemicelluloses and lignin [14]. In a much smaller proportion, they also contain extractible, proteins and some inorganic compounds [a]. Unlike other fiber components that have amorphous structures, celluloses have a largely crystalline structure. Crystalline cellulose is one of the polymers with the highest modulus of elasticity, about 136 GPa compared to 75 GPa of fiberglass. This rigidity comes from the crystalline structure that follows a highly ordered helical supra-molecular arrangement. It is important to note that this particular molecular structure causes during a fiber elongation, a torsion / traction coupling which can have consequences on the interface on the deformation or on the mechanisms of failure of the composite. Inside the fiber, the cellulosic chains are united in micro fibrils which by agglomerating form fibrils on several layers.

Vegetable fibers, can become a better alternative to different fibers, such as glass fibers, used until today, because of the benefits of natural fibers. Natural fibers are very inexpensive, biodegradable, renewable resource to wish, significant mechanical resistance and allow a valuation of many natural wastes.
To strengthen the soil after its stabilization using cement and granulated slag blast furnace(figure 2), palm fibers were used with different percentage and length i.e. 1.5 cm in this case.
The mechanical characteristics of palm fibers were as follows: Bulk density = 0.51 – 1.08 g/cm, elongation at failure = 7.5 – 17.4 (%), tensile strength = 170 – 290 MPa, Young modulus=2.1 – 5.25 GPa.



Figure 1: Palm fiber .



Figure 2: Blast furnace slag.

B. Experimental program

Direct shear tests under undrained unconsolidated conditions were performed on several samples at optimum water content obtained from Proctor tests. The samples were compacted in three layers (normal Proctor)..

In the first place, shear tests were carried out on untreated samples, then cement, blast furnace slag, polypropylene fiber and palm fiber were added with pre-defined percentages. The aim of the tests was to determine the effect of the fiber content on the cohesion and the angle of internal friction, as well as the effect of the addition of cement, blast furnace slag and the different types of fibers (natural and synthetic) on the mechanical behavior of the soil used in this work.

The samples were prepared under optimal conditions (maximum dry density.
(ρd max = 1.74 g / cm3, Wop = 11.6%) which are deduced from the Proctor test, is placed in the shear box whose dimensions are: L = D = 6 cm and thickness = 2 cm.

The mass of the sample was = 98.4 g and the mass of water, mw = 11.4 g.

After the introduction of the sample in shear box , a vertical load was applied, thus generating a normal stress σ = 5000, 1000, 1500 Pa kept constant throughout the test. The speed of movement is given at 0.9mm / min. Readings were taken every 15 s.

III. Results and Discussions

A. Effect of palm fibers on the cohesion and friction angle of a cemented soil

A decrease in the cohesion which is equal to 0.05 bar to 0.25% of fibers (figure 3), then it increases to reach 0.07 bar at 0.50% of fibers then it continues to increase and then reach 0.09 bar at 0.

$$y = -8000x^2 + 14000x + 3000 \quad (1)$$

$$R^2 = 1$$

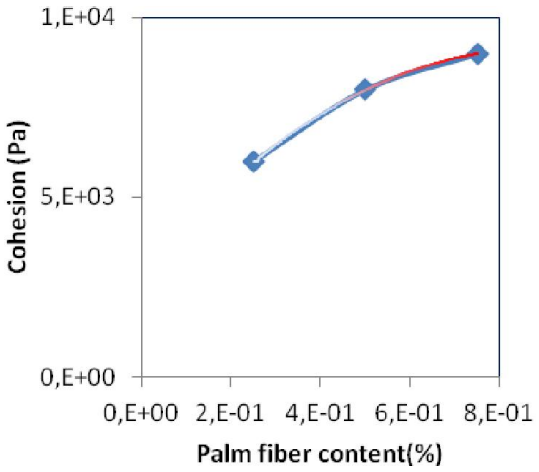


Figure 3: Cohesion vs. palm fiber content of sand stabilized with 4 % cement.

It is noted that an increase in the angle of friction to reach a value of 48.27 ° at 0.75% of palm fibers at 4% cement (figure 4). This is possibly due to the increase of the internal friction between the grains after the addition of the cement.

$$y = 14.32x^2 - 3.7x + 44.28 \quad (2)$$

$$R^2 = 1$$

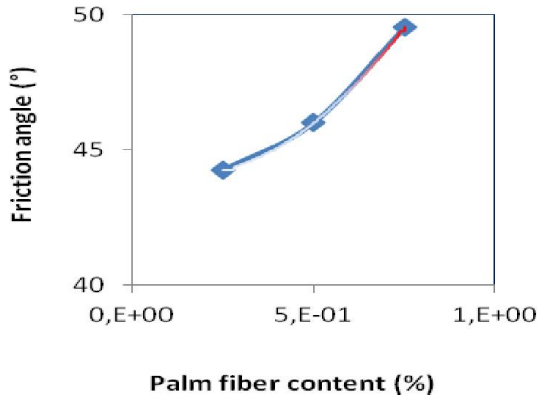


Figure 4: Internal friction angle vs. palm fiber content of sand stabilized with 4% cement.

B. Effect of polypropylene fibers on cohesion and internal friction angle on sand stabilized with slag

An increase in cohesion is observed to reach a value of 0.17 bar to 0.75% of polypropylene fibers (figure 5).

$$y = 72000x^2 - 42000x + 10000 \quad (3)$$

$$R^2 = 1$$

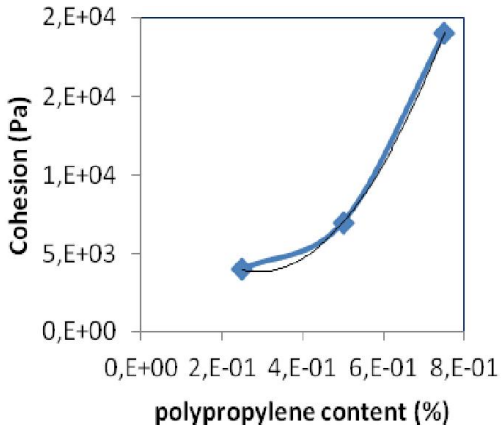


Figure 5: Cohesion vs. polypropylene fiber content of sand stabilized with 4 % slag.

It can be noticed that the angle of friction increases till it reached an optimal value varying from 35.96° at 0.50% of polypropylene fiber content , then it decreases from 35.18° at 0.75 % of polypropylene fiber content (figure 6).

$$y = -33.12x^2 + 39.04x + 25.55$$

$$R^2 = 1$$

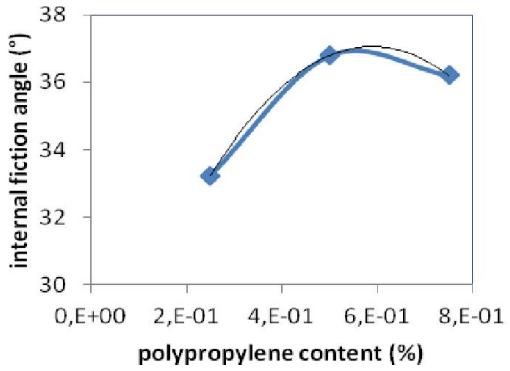


Figure 6: Internal friction angle vs. polypropylene fiber content of sand stabilized with 4% slag.

A. Effect of palm fibers on cohesion and internal friction angle on sand stabilized with slag:

II. An increase in cohesion is observed to reach a value of 0.14 bar to 0.75% of palm fibers (figure 7).

$$y = 48000x^2 - 20000x + 4000$$
$$R^2 = 1$$

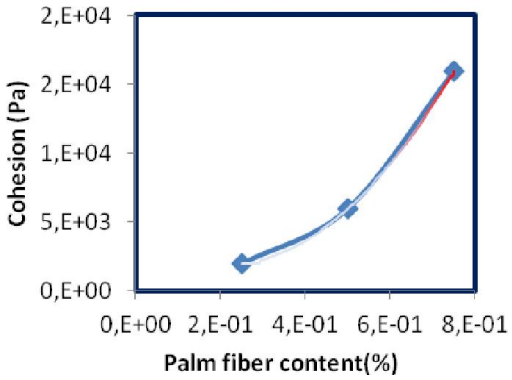


Figure 7: Cohesion vs. palm fiber content of sand stabilized with 4% slag.

It can be noticed that the angle of friction increases till it reached an optimal value varying from 42.9° at 0.50% of palm fiber content , then it decreases from 42.4° at 0.75 % of palm fiber content (figure 8).

$$y = -11.76x^2 + 12.86x + 39.51 \quad (6)$$
$$R^2 = 1$$

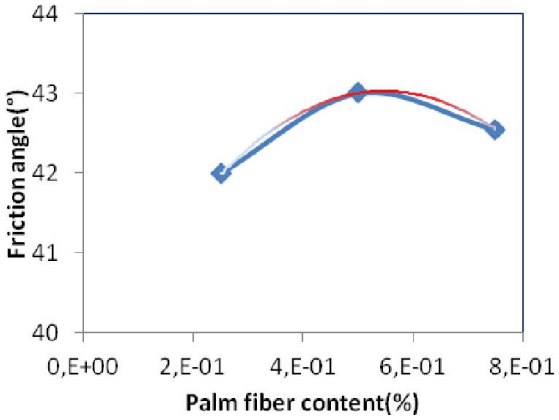


Figure 8: Internal friction angle vs. palm fiber content of sand stabilized with 4% slag.

IV. Conclusion

In this work, a dune sand from a small town of Skikda in Algeria.

Inclusions of randomly distributed polypropylene fibers and palm fibers were used as reinforcement materials while cement and palm fiber were used stabilizing materials.

The inclusion of the randomly distributed reinforcements can appreciably improve the shear strength parameters of the local soil. Fiber reinforcement significantly reduced the extent of cracks.

The effects of the fibers suggests potential applications in the reinforcement of embankments, shallow foundations, and other earthworks.

There is a linear variation of the friction angle with the percentage of fiber.

In order to verify the results of the present work the author suggests that further investigations on the behavior of cemented soils stabilized by natural and artificial fibers should be carried out.

References

[1] Vidal.H, Highway research record. 282. p. 1– 16, The principle of reinforced earth.1969.

[2] M. Ismail, H. Joer, W. Sim et M. Randolph, *Effect of cement type on shear behavior of cemented calcareous soil,* Journal of geotechnical and geo-environmental engineering .128 (6), 520 – 529, 2002.

[3] I Y. Kim, H. Kim et G. Lee, *Mechanical behaviour of lightweight soil reinforced with waste fishing net,* Geotextiles and Geomembranes 216 (6), 512-518, 2008.

[4] H. Liu, A. Deng et J. Chu, *Effect of different mixing ratios of polystyrene prepuff beads and cement on the mechanical behaviour of lightweight fill,* Geotextiles and Geomembranes. 24(6). 331-338, 2006.

[5] N. c. consoli, M. Antônio, A. Bassani et L. Festugato, *Effect of fiber-reinforcement on the strength of cemented soils,* Geotextiles and Geomembranes. (28), 344-351, 2010.

[6] M. e. al, *Influence of reinforcement parameters on the seismic response of reduced-scale reinforced soil retaining walls,* Geotextiles and geomembranes (25), 23-49, 2007.

[7] S. Ho et R. Rowe, *Effect of wall geometry on the behavior of reinforced soil walls,* Geotextiles and Geomembranes 14 (10), 521-541, 1996.

[8] K. Hatami et R. Bathurst. ASCE Journal of Geotechnical nd Geoenvironmental Engineering 132 (6), 673-684, A numerical model for reinforced soil segmental walls under surcharge loading..2006.

[9] K. Hatami, R. Bathurst et M. El-Emam, *Accelerationamplification in the backfill of reinforced soil walls of differentheights.,* Balkema, London: In Abousleiman, Y.N, Cheng, A.H.D, Ulm, F, J. Proceeding of Third biot Conference on Promechanics Norman, Oklahoma,USA pp.725-731, 2005.

[10] K. Hatami, R. Bathurst et P. Di Pietro, *static response of reinforcedsoil retaining walls with non-uniform reinforcement.,* International Journal of Geomechanics 1 (4), 477-506, 2001.

[11] T. Park et S. Tan, *Enhanced performance of reinforced soil walls by the inclusion of short fiber,* Geotextiles and Geomembranes. 23, 348-361., 2005.

[12] R. H. H. M. e. A. M. E. Basha, *Stabilization of residual soil with rice husk ash and cement,* Construction and Building Materials 19 (6), 448-453., 2005.

[13] V. K. –. e. A. K. S. Kolias, *Stabilization of clayey soils with high calcium fly ash and cement,* Cement and Concrete Composites 27 (2) 301-313., 2005.

[14] J. D. J. L. e. S. L. H. Tremblay, *Influence of the nature of organic compounds on fine soil stabilization with cement,* Canadian Geotechnical Jornal 39,535-546, 2002.

[15] M. Kattak et M. Alrashidi, *Durability and mechanistic characteristics of fiber reinforced soil-cement mixtures,* International Journal of Pavement Engineering 7(1),53-62., 2006.

[16] C. T, S. Bin, W. G, F. C et Y. C, *Strength and mechanical behaviour of short polypropylene fiber reinforced and cement stabilized clayey soil,* Geotextiles and Geomembranes (25), 194 – 202., 2007.

[17] B. Viswanadham, B. Phanikumar et R. Mukherjee, *Swelling behaviour of a geofiber-reinforced expansive soil,* Geotextiles and Geomembranes 27(1), 73-76., 2009.

[18] R. D. T. F. B. N. e. P. B. K. Ghavami, *Behaviour of composite soil reinforced with natural fibres,* Geotextiles and Geomembranes. 21, 39-48, 1999. , 1999.

Shear strength of a cemented soil reinforced with synthetic fibers.

I.LAMRI[1] and M. HIDJEB[1]

[1] Université 20 août, Skikda/ LMGHU laboratory/Algeria, ihcene2000@yahoo.fr
[1]Université 20 août, Skikda/LMGHU laboratory/Algeria, mustapha_hidjeb@yahoo.fr

Abstract - **The aim of this research work, is to understand and quantify the influence of a synthetic fiber such as polypropylene on physical and mechanical properties of a granular soil chemically stabilized with cement.**
In this work , the effectiveness of fiber reinforcement is studied from the point of view of strength.
Firstly a series of laboratory tests were carried out. Physical soil characterization tests, including particle size analysis, sand equivalent test, mythylene blue test and compaction to determine optimal conditions were carried out.
Secondly, direct shear tests (Casagrande box) were carried out on cemented sand samples prepared under optimum conditions with different percentages of polypropylene fibers.
It was clearly concluded that the influence of polypropylene fiber on the cohesion (C) and the internal friction angle (Φ) was important.
It was also demonstrated that the material used, namely polypropylene fibers, played an important role in the granular soil stabilization mechanism.

Keywords **- Stabilization, reinforcement, cement, polypropylene, shear strength.**

I. Introduction

In virtually all developing countries, Algeria is often confronted with the lack of supply of cheap local materials for the purpose of building highway, railway and other networks.

Because of high costs and environmental issues, geotechnical engineers, over the world, try to avoid the use of traditional techniques.

Soil improvement techniques are one of the tools available to the engineer to solve the problems of stability or deformation that he encounters during the development of a project.

This concept and principle was developed by Vidal [1], where he demonstrated that the introduction of reinforcing elements in a soil increases its shear strength.

Chemical stabilization and fiber reinforcement techniques are used to improve the physical and mechanical properties of soils [2].

In this framework also tests of unconfined simple compressions were carried out on samples of cemented sand in order to study the shear strength. These samples are reinforced with synthetic fibers thatt are distributed in an orderly fashion (3 layers and 5 layers). The results obtained showed that the reinforced samples with 5 layers are more rigid than three layers [3].

The use of cement as a stabilizer in clay or granular soils is intended to improve mechanical properties such as cohesion and internal friction angle [4] [5] [6] [7].

The cemented sand which exhibits a fragile behaviour can be reinforced with natural or synthetic fibers to increase its strength [8] [9] [10].

A number of triaxial tests, unconfined compression tests and CBR tests, direct shear tests have been carried out by several researches over the last decades on reinforced and stabilized soils [11] [12] [13] [14].

II. Materials and Experimental Details

A. Materials

- Soil characteristic: The sand used in this study comes from the dunes of FIL-FILA located at approximately 13 Km; north-east of Skikda- Algeria.

The soil characterization including, particle size analysis, sand equivalent, methylene Blue test, Proctor normal were carried out the LMGHU Laboratory of the university of Skikda According to the obtained results, the soil was classified as Class B1: silty sand. (According to the GTR classification). From the physical identification tests the soil has a maximum dry density ρd = 1.74 g / cm3 with an optimum Proctor wop = 11.6%.

According to the methylene blue test, the soil has a VBS = 0.15, indicating that this soil is silty sand. Sensitive to water.

Another test that was carried out is the sand equivalent test, and the results give an ES = 80% (very clean soil).

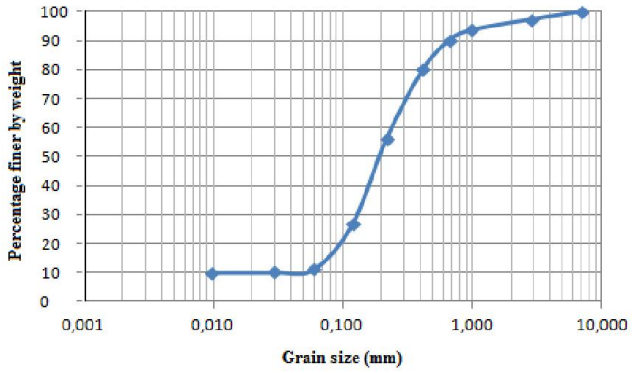


Figure 1: Grain size distribution

▪ Cement: Chemical stabilization by cement is a proven technique to improve soil strength [4] [15] [16] [17] [18].
CPJ-CEM II cement 42.5 (Portland cement manufactured at Hadjar Essoud- Skikda) was used with different percentages to stabilize the soil in question. These chemical characteristics are given below:
Insoluble residues = 2.28, PAF 975 = 2.41, Cao = 57.22, SiO_2 = 27.83, AL_2O_3 = 6.21, Fe_3O_3 = 3.12, MgO = 0.94, SO_3 = 2.02 CaO = 0.88, Chloride = 0.00.

▪ Polypropylene fiber **:** The use of fibers is the most widely used technique in laboratory soil strengthening tests [19] [8] [20]. Polypropylene fibers were used in this study to strengthen the soil after stabilization with cement.
Physical and mechanical characteristics of polypropylene fibers : Density = 0.92 g / cm3, diameter = 1.0 mm, length = 12 mm, tensile strength = 600 MPa, Young's modulus = 3 GPa, melting point = 150 ° c.



Figure 2: Polypropylene fiber.

B. Experimental program

Unconsolidated undrained (UU) straight shear tests were performed on several samples with the optimum water content obtained from the Proctor tests. The samples were compacted in three layers (normal Proctor).

In the first place, shear tests were carried out on untreated samples and then cement and polypropylene fibers were added with pre-defined percentages whose. The purpose of the tests was to determine the variation in cohesion and the angle of internal friction, according to these percentage and also the to determine the influence of the addition of cement and the synthetic fibers on the mechanical behavior of the granular soil.

The soil samples were prepared in the optimum conditions (maximum dry density (ρd max = 1.74 g / cm3, Wop = 11.6%) which are deduced from the Proctor test, is placed in the shear box whose dimensions are: L = D = 6 cm and, thickness = 2 cm.

The mass of the sample is ms = 98.4 g and the mass of water, mw = 11.4 g.

After insertion of the sample into the shearing machine, a vertical force is applied, thus generating a normal stress of σ = 5000 Pa , 1000, 1500 Pa which was maintained constant throughout the test.

The travel speed is given at 0.9 mm / min. Readings were taken every 15.

III. Results and Discussions

A. Effect of cement on the cohesion and friction angle.

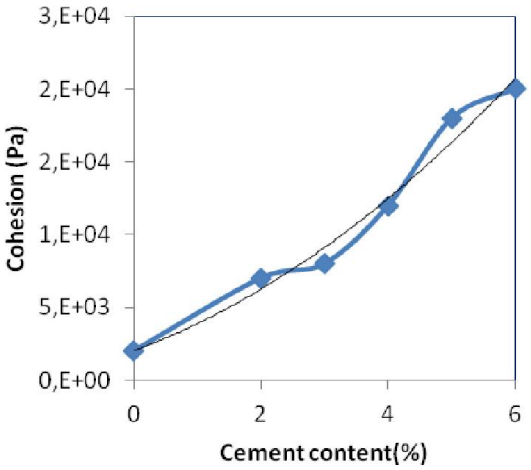


Figure 3: Cohesion vs. cement.

Figure 3 shows an appreciable increase in cohesion with the increase of cement, this is probably due to the presence of fines in the cement. The correlation equation for the variation of cohesion vs. cement content shown below.

$$y = 250x^2 + 1614.3\,x + 20357 \quad (1)$$

$$R^2 = 0.9777\ ,$$

was obtained using the least square method.
The above equation shows a a good correlation between the two curves.

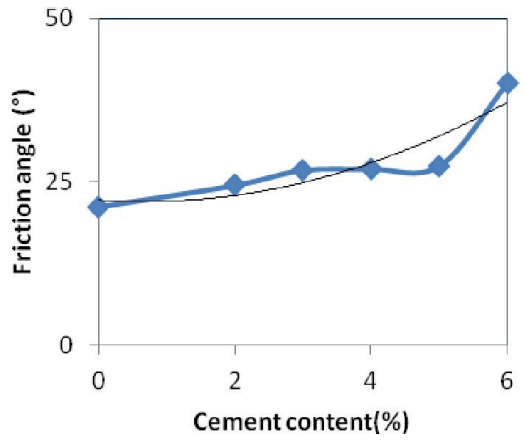


Figure 4: Friction angle vs. cement.

As far as the angle of internal friction is concerned, figure 4 shows an increase in cement added, this increase can be explained by internal friction between the grains of the soil and cement.

$$y = 0.5339x^2 + 0.7016x + 22.165 \quad (2)$$

$$R^2 = 0.8201$$

The above equation shows a good correlation between the two curves.

B. Effect of polypropylene fibers on cohesion and friction angle on cemented sand:

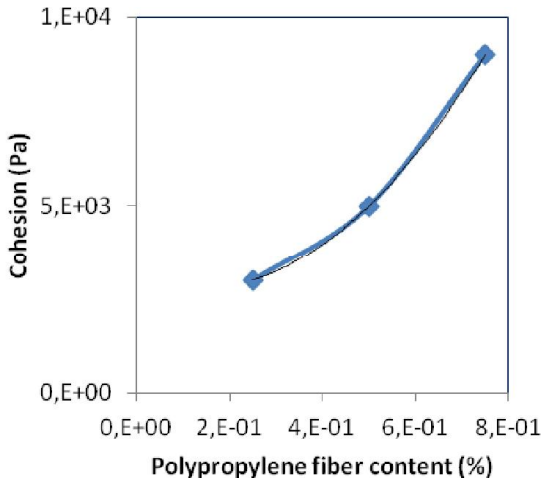


Figure 5: Cohesion vs polypropylene fiber content of sand stabilized with 4 % cement.

After the addition of the polypropylene fibers, an increase in cohesion is observed (figure 6). This is due to the pozzolanic reaction which cements the grains between them.

$$y = 16000x^2 - 4000x + 3000 \quad (3)$$

$$R^2 = 1.$$

A very good correlation between the two curves was observed.

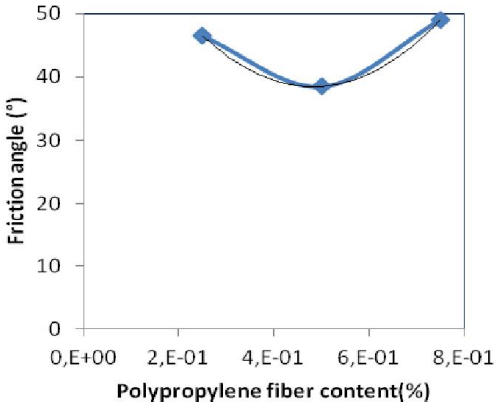


Figure 6 : Internal friction angle vs. polypropylene fiber content of sand stabilized with 4% cement.

The internal friction angle decreases to 0.5% of the added fibers and then increases to a value of 49.02 ° to 0.75% of fibers (figure 6).

$$y = 147.92x^2 - 142.9x + 72.99 \quad (4)$$

$$R^2 = 1$$

A very good correlation was observed between the two curves.

IV. Conclusion

On the basis of the results obtained from the present experimental research work, the following results may be drawn.

The addition of cement to the granular soil has an important effect on the cohesion of the soil.

- Inclusions of polypropylene fibers within the specimen as reinforcement improves the shear strength of the composite.

References

[1] Vidal.H, Highway research record. 282. p. 1– 16, The principle of reinforced earth.1969.

[2] K. Ghavami, R. D., T. Filho., B. Normando. et P. Barbosac, 1999. Behaviour of composite soil reinforced with natural fibres., *Geotextiles and Geomembranes*. 21, 39-48.

[3] S. –. S. Park, 2009. Effect of fiber reinforcement and distribution on unconfined compressive strength of fiber – reinforced cemented sand, *Geotextiles and Geomembranes*.27, 162- 166.

[4] M. Ismail, H. Joer, W. Sim et M. Randolph, *Effect of cement type on shear behavior of cemented calcareous soil,* Journal of geotechnical and geo-environmental engineering .128 (6), 520 – 529, 2002.

[5] I Y. Kim, H. Kim et G. Lee, *Mechanical behaviour of lightweight soil reinforced with waste fishing net,* Geotextiles and Geomembranes 216 (6), 512-518, 2008.

[6] H. Liu, A. Deng et J. Chu, *Effect of different mixing ratios of polystyrene prepuff beads and cement on the mechanical behaviour of lightweight fill,* Geotextiles and Geomembranes. 24(6). 331-338, 2006.

[7] N. c. consoli, M. Antônio, A. Bassani et L. Festugato, *Effect of fiber-reinforcement on the strength of cemented soils,* Geotextiles and Geomembranes. (28), 344-351, 2010.

[8] C. T, S. Bin, W. G, F. C et Y. C. Strength and mechanical behaviour of short polypropylene fiber reinforced and cement stabilized clayey soil*, Geotextiles and Geomembranes* (25), 194 – 202.2007.

[9] G. Babu, A. Vasudevan et S. Haldar. Numerical simulation of fiber-reinforcedsilty sand behaviour*, Geotextiles and Geomembranes* 26 (2), 181-188.2008.

[10] M. Ghauhan, S. Mittal et B. Moohanty. Performance evaluation of silty sand subgrade reinforced with fly ash and fibre, *Geotextiles and Geomembranes* 26 (5), 429 – 435.2008.

[11] T. Yetimoglu et O. Salbas. A study on shear strength of sands reinfrced with randomly distribted discrete fibers, *Geotextiles and Geomembranes.* 21, 103-110.2003.

[12] T. Yetimoglu, M. Inanir et O. Inanir. A study on bearing capacity of randomly distribted fiber –reinforced sand fills overlying soft clay, *Geotextiles and Geomembranes*. 23(2), 174-183.2005.

[13] S. Kaniraj et V. Gayathri. Geotechnical behaviour of fly ash mixed with randomly oriented fiber inclusions, *Geotextiles and Geomembranes*. 21, 123-149.2003.

[14] T. Park et S. Tan, *Enhanced performance of reinforced soil walls by the inclusion of short fiber,* Geotextiles and Geomembranes. 23, 348-361., 2005.

[15] E. Basha, R. Hashim, H. Mahmus et A. Muntobar. Stabilization of residual soil with rice husk ash and cement, *Construction and Building Materials* 19 (6), 448-453.2005.

[16] S. Kolias, V. Kasselouri –Rigopoulou et A. Karahalios. Stabilization of clayey soils with high calcium fly ash and cement, *Cement and Concrete Composites* 27 (2) 301-313.2005.

[17] H. Tremblay, J. Duchesne, J. Locat et S. Leroueil. Influence of the nature of organic compounds on fine soil stabilization with cement, *Canadian Geotechnical Jornal* 39,535-546.2002.

[18] A. A. Al-Rawas. Microfabric and mineralogical studies on the stabilization of an expansive soil using cemenr by-pass dust and some types of stags, *Canadian Geotechnical Jornal* 39, 1150-1167.2002.

[19] M. Kattak et M. Alrashid. Durability and mechanistic characteristics of fiber reinforced soil-cement mixtures, *International Journal of Pavement Engineering* 7(1),53-62.2006.

[20] B. Viswanadham, B. Phanikumar et R. Mukherjee. Swelling behaviour of a geofiber-reinforced expansive soil, *Geotextiles and Geomembranes* 27(1), 73-76.2009.

Investigation Of Ductility Of Polyproplene Fibre Reinforced Concrete Beams

Nildem TAYŞİ[1], Ahmed N. ABDALAH[2] and Ahmmad A. ABBASS[3]

[1] Gaziantep University, Gaziantep/Turkey, nildemtaysi@gmail.com
[2]Gaziantep University, Gaziantep/Turkey, ahmednaeem89eng@gmail.com
[3]Gaziantep University, Gaziantep/Turkey, ahmadabdlazez@gmail.com

Abstract **- The current work aims to investigate the behaviour of polypropylene PP fibres reinforced beams under four-point flexural test in which the judgment is based on the peak load resistance and the ductility. To achieve this aim, four beams, which are reinforced with PP fibers and conventional reinforcement bars are tested. The clear dimensions of the beams used in this investigation are 150 X 150 X 850 mm. Three fiber percentages (0.5, 1.0, and 1.5 %) are used, the behaviour of these beams are compared with the control beam of ordinary concrete. The results showed that beams inclusion of 0.5, 1.0, 1.5 % of fibre increases the compressive strength by 26, 26, 40 % respectively, and the first cracking load by 45, 62, 75 % respectively. In addition to that the ultimate resistance was increased by proximately 18 % when 1.5 % PP was used when it was compared with the control beams, also the ductility factor was increased by 53 % at the same PP percentage.**

Keywords **- Polypropylene, Fiber-reinforced beams, Ductile, Load deflection behavior, Ultimate load.**

I. INTRODUCTION

THE interaction between the shear strength and flexural strength is a main property that applied a preferable behavior of structural members. The brittleness of the shear behavior of the beams was attracted great attention, through enhancing the tensile strength of beams. The use of various kinds of fiber in the construction dates back to ancient times. Adding fibers randomly to concrete is one of the ways that the low cost and which lead to reinforced concrete, in addition to that fiber is enhancing the post peak behavior [1]. PP is a polymer derived from the monomeric C3H6 and is a pure hydrocarbon like paraffin wax. Polymeric fibers were not tried as concrete and cement composite reinforcement until 1965. Large scale use of polypropylene fibers in concrete did not happen until the late 1970 [2]. Conforti [3] studied the influence of adding polypropylene fiber on the shear behavior and found that the addition of PP fiber has a significant effect on improving the shear behavior of the beams when it was compared with the beam without fiber. Adulhamid Aryan [4] Experimental and analytical study of PP fiber reinforced concrete beams concluded that beams with polypropylene fibers were more ductility than concrete beams that did not contain these fibers by studying the behavior of those symptoms with and without fibers. Their energy absorption capacity and ductility parameter were calculated by using the formed load – displacement curves on the beam samples with dimensions of (30 x 20) mm and a length of 200 mm, added two V_f of PP fiber 0.6 and 0.8, also produced two beams without fibers for comparison, it was conducted concrete analytical modeling beams armed with Abaqus program [4]
According to ACI Terminology [5], the ductility can be defined as the ability of the beams to hold the deformation before failing, this ability has to be in the inelastic range without decreasing in beam strength, mathematically, ductility factor can be evaluated by dividing the ultimate deformation by yield deformation.
Park [6] states four definitions for each deformation. Figure 1 depicted these definitions.

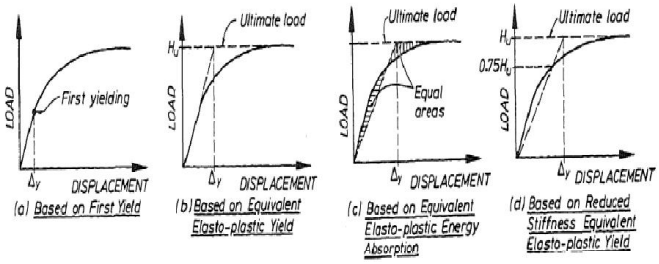


Figure 1: Yield displacement definition according to Park [6].

II. EXPERMINTAL WORK

In this study, concrete beams were reinforced with PP fiber in addition to conventional reinforcing steel bars. Three V_f PP fiber were added to the concrete beams by 0.5, 1.0 &1.5 % respectively, Table 1 shows some characteristics of fiber used in experimental work.

Table 1: PP fibers characteristics.

Density (gr/cm3)	Length (mm)	Diameter (mm)	Elongation at break (%)	Tensile strength (psi)
0.91	12	0.015	37	4,800

Fine aggregates were used at a high rate compared to coarse aggregates in order to improve the flow of stress through the beam section and to enhance the bonding between the mixture and fiber. In addition, to investigate the effect of adding fiber to the concrete mixture. The cement was used CEM II/ A-LL 42.5 R of Portland cement that agrees with EN 197-1 provisions.
Moreover, silica fume has been added by 7 % of the total weight of binder (silica fume + cement) to increase the surface

area of the binder and thus increase the surface area from 40 to 100 times.

A. Mixing and curing

The mix is designed to achieve 28 days compressive strength of 30 MPa of normal concrete, and it is expected to be increased due to the inclusion of the PP fibers.
The total percentages of the fine aggregate is 63 %, on the other hand the percentage of coarse aggregate is 37 % of the total amount of aggregate, the mix design is shown in Table 2.

Table 2: Concrete mixture design per cubic meter

Mix code	PP fiber (%)	C (Kg)	G (Kg)	S (Kg)	S.fm (kg)	HWR (kg)	W (Lt)
Control beam	0	465	680	1170	35	6.6	216
PP 0.5	0.5						
PP 1.0	1.0						
PP 1.5	1.5						

C; Cement, **G**; Gravel, **S**; Sand, **S.fm**; Silica fume, **HWR**; High water reducer, **W**; Water
The concrete mix for each beam was produced separately using the same mixing procedure, firstly the fine and coarse materials was mixed for almost 10 min, then the cementitious to get a homogeneous mix, after mixing the materials, water is added and reduce it by a calculated percentage. For final step PP fiber was added manually to the mix for the beams containing fiber. The fibrous concrete was poured in wooden beam molds and six standard cylinders of 100 mm diameter and 200 mm height, to override the errors, three cylinders are used for compressive standard test & other three cylinders for indirect tensile stander test. After 24 hours, both beam and cylinders were removed from the molds and cured in water tanks of 22 ºC for 28 days.

B. Geometry and test setup

To check the beam ductility and ultimate load, four beams were cast and tested; all beams have the same dimensions (150 mm × 150 mm × 850 mm), same conventional reinforcement is used in all beams, 2Ø8 mm conventional reinforcement bars are placed in compression and tension zone, as shown in Figure 2, the difference was in polypropylene fiber percentages used as a reinforcement. Also for all specimens stirrups are used consisting of 10Ø6.3 mm with clear cover of 15 mm, the yielding strength of Ø8 mm and the Ø6.3 mm bars were 503 and 558 MPa respectively.

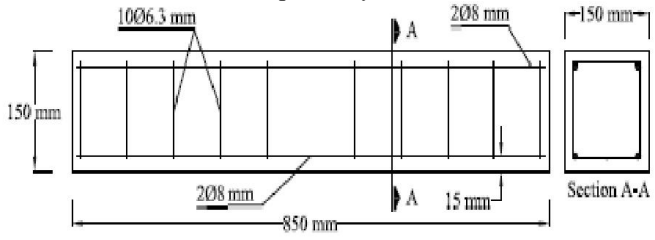


Figure 2: Geometry and reinforcement details

The four casted beams were placed on the test machine, Figure 3 shows the beams test configuration, in order to prevent the friction induce from axial forces and freely rotation, two stiff rollers represent the load and supports. The distance between the loading point and the support (a) is 250 mm, so that the shear arm (a/d) is 1.85. The load applied until the failure, in displacement control rate of 0.4 mm/min. In addition to the cross head displacement measurement, one more LVDT is attached to the beam at mid-span from bottom side. Two dial gages were measure the edge lifting and the deflection at the quarter distance of the beam (125 mm from the support).

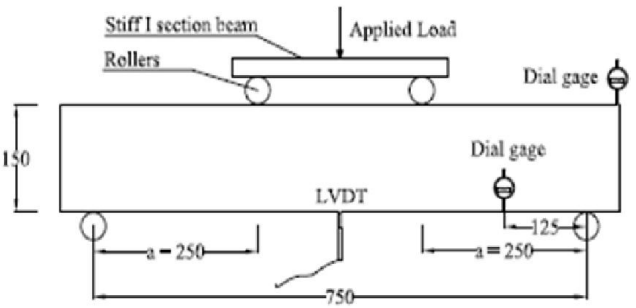


Figure 3: Beams test setup and location of the LVDT and the dial gages

III. RESULTS AND DISCUSSION

A. Mechanical properties

Table 3 presents the mechanical properties of the standard cylinders that was calculated the compressive strength f'_c according to ASTM C39 [7] and the splitting tensile strength f_{sp} according to ASTM C469 [8]. In order to reduce the error ratio, three cylinders were tested and taken the result rate for these, the results shows that the polypropylene fiber has a great impact on improving the mechanical properties, it shows that for the three percentages (V_f) of polypropylene 0.5, 1.0 & 1.5 % was improved by 26, 26 & 40 % respectively for the compressive strength and for the tensile strength the percentages of PP 0.5 &1.0 % was improved by 13 &25 % respectively but the (V_f) 1.5 % was not affected in the tensile strength.

Table 3: Concrete mechanical properties

Spec. No.	PP V_f (%)	f'_c (MPa)	$\frac{f'_c\ fiber}{f'_c\ normal}$	f_{sp} (MPa)	$\frac{f_{sp}\ fiber}{f_{sp}\ normal}$
Control beam	0.0	27	1	6.7	1.0
PP 0.5	0.5	34	1.26	7.6	1.13
PP 1.0	1.0	34	1.26	8.4	1.25
PP 1.5	1.5	38	1.40	6.9	1.02

Figure 4 shows the effective compressive and tensile strength (in term of splitting) by PP as a unity for plain concrete.

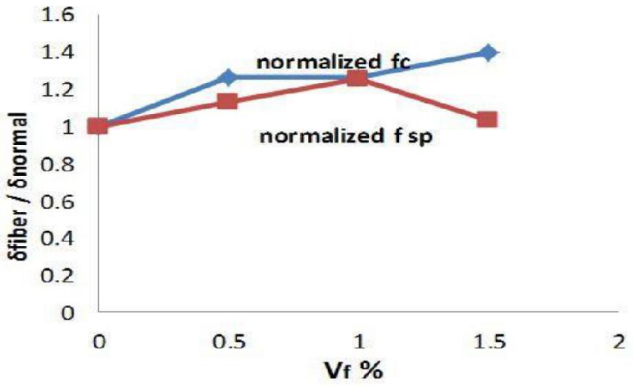


Figure 4: Effect of PP on concrete strength effective PP-FRC compressive and splitting tensile strength as a unity of plain concrete.

B. Ultimate loading resistance

Table 4 and Figure 5 shows the results of the ultimate beam strength and their corresponding displacement, in general it is clearly that the PP fiber has a great impact on improving the beams strength and the first crack load (P_{cr}) when it is compared with the beam without fiber, it shows that for the three percentages (V_f) of PP the ultimate beam strength was improved by 4, 13 & 18 % respectively and the first crack resistance loads are increased by 45, 62 & 75 % respectively. But the yielding loads are not affected because they are depending on the reinforcement bars.

Table 4: Experimental results of beams

Spec.	First crack		Yield		Ultimate		Ratio		
	P_{cr} (kN)	δ_{cr} (mm)	P_y (kN)	δ_y (mm)	P_u (kN)	δ_u (mm)	$\frac{P_{cr}}{P_u}$	μ	$\frac{\mu\ fiber}{\mu\ normal}$ (%)
Control beam	13.43	2.23	51.48	6.83	70.54	13.55	0.19	1.98	0
PP0.5	19.28	2.03	52.99	3.85	73.95	9.16	0.26	2.38	20
PP1	21.74	1.90	60.34	4.03	80.10	10.15	0.27	2.52	27
PP1.5	23.56	1.79	56.30	3.81	83.37	11.52	0.28	3.02	53

C. Load-deflection behavior

According to the deflection results shown in Table 4 where δ refers to the deflection at midpoint each beam ultimate load, it is shown that the PP fiber has a significant effect on improving the deflection behavior, for all beams the deflection values was decreased for specimens with fiber percentages (V_f) of PP by 67, 75 & 85% respectively, as shown in Figure 5.

For the specimens containing PP fiber the curve starts similar till it reach approximately 50 kN the it diverge taking different paths, on the other hand the specimen without PP fiber took a different path giving the highest deflection value.

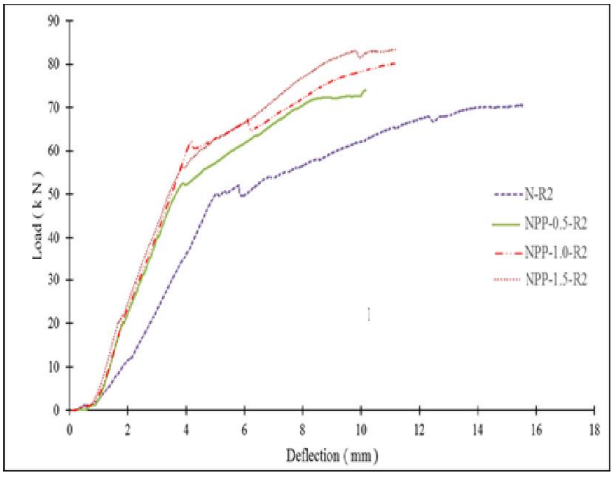


Figure 5: Load deflection curve.

D. Ductility of PP-FRC Beams

Figure 6 shows the load-deflection curves for the tested beams. The data is collected from LVDT attached to the beam at mid-span from bottom side. From Figure 5, there were nonlinear extraneous displacements, which is not a surprising thing, because it is often associated to such a test. Up to the first initiation crack, the displacement is proportional to the applied load linearly; the first cracks are hardly and carefully located on the curve. After the first crack take place, the slope of the curve was slightly changed, but still looks to be in linear increasing rate, the increasing rate continues up to yield point. After yielding of the reinforcement, the curves are increasing in nonlinear manner up to the maximum resistance load, the test is continuing until the beam is collapsed.

The ductility factor (μ) defined herein, as the ratio of the ultimate deformation (δ_u) to the yield deformation (δ_y), where the ultimate deformation is that the deformation corresponding to the maximum resistance load, and the yield deformation is that the displacement corresponding to the yield load. Figure 7 demonstrates the evolution of ductility factor (μ) considered in current work. Table 4 summarized the values of the μ and the ductility of the fibrous beams as unity for plain concrete. The comparison showed that the including of PP in the concrete increases the ductility of the tested beams. Where 0.5 % of PP increases the ductility by 20 %, duplicating the volume of PP is not significantly altered of ductility 27 % compared to 0.5 %V_f. While the addition of 1.5% improved the ductility significantly 53% compared to 1.0 %V_f.

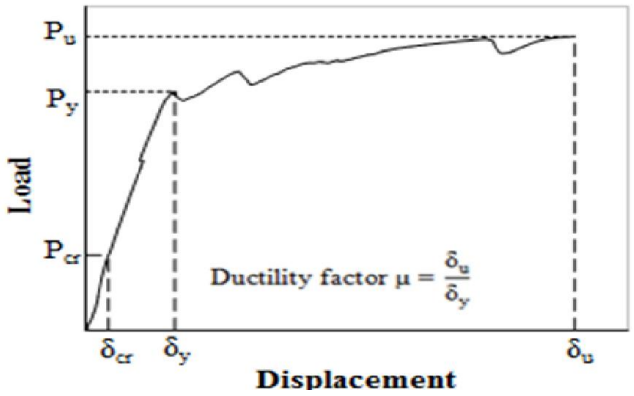


Figure 7: Definition of the ductility factor (μ) of the beams

IV. Conclusion

1) PP fiber has a great influence on improving the mechanical properties of concrete and using of PP fibers in concrete made from high fine aggregate percentages are increasing the load required to initiate the first crack.
2) For the three percentages (V_f) of PP 0.5, 1.0 & 1.5 %, the ultimate beam strength was improved by 4.0 ,13.0 & 18.0 % respectively when its compared to the beam without fiber addition.
3) Adding PP fiber has a great influence on reducing the deflection values for all beams when it is compared with the beam without polypropylene fiber. For all beams the deflection values was decreased for specimens with fiber percentages (V_f) of PP 0.5, 1.0 & 1.5 % by 67, 75 & 85 % respectively.
4) By increasing the post-cracking, the ductility of the beams is increased significantly where inclusion of 1.0 to 1.5 % of PP, the ductility is increased 27 to 53 %.
5) Fibers transferred the brittle type failure to the flexural failure by discontinuing the shear cracks.

References

[1] A. Bentur and S. Mindess, Fibre Reinforced Cementitous Composites, Second ed. Abingdon, England: Taylor & Francis, 2007.
[2] Balaguru, P.N. and Shah, S.P., Fiber-Reinforced Cement Composites, McGraw- Hill Inc., New York, 1992. Aktürk in 2006
[3] A. e. a. Conforti, "Influence of polypropylene fibre reinforcement and width-to-effective depth ratio in wide-shallow beams," Engineering Structures, vol. 88, pp. 12-21, 2015.]
[4] (ABDULHAMİD ARYAN ,2014) Experimental and Analytical Study of Polypropylene Fiber Reinforced Concrete Beams
[5] ACICT-13, ACI Concrete Terminology. Farmington Hills: American Concrete Institute, 2013.]
[6] R. Park, "Ductility Evaluation from Laboratory and Analytical Testing," in the 9th World Conference on Earthquake Engineering, Tokyo-Kyoto, Japan, 1988, pp. 605-616.
[7] C. ASTM, "Standard test method for compressive strength of cylindrical concrete specimens," Annual book of ASTM standards, vol. 4, pp. 20-24, 1997.
[8] C. ASTM C496 ,Standard Test Method for Splitting Tensile Strength of Cylindrical Concrete Specimens.

The Burst Failure Behaviors of SiO_2 Nanoparticle Filled Elliptical Surface Cracked $\pm[55]_6$ Filament Wound BFR/Epoxy Composite Pipes

Mehmet Turan DEMİRCİ[1*], Necmettin TARAKÇIOĞLU[1], Ahmet AVCI[2]

[1*] Selcuk University, Konya/Turkey, turandemirci@selcuk.edu.tr
[1,2]Selcuk University, Konya/Turkey,ntarakcioglu@selcuk.edu.tr, aavci@selcuk.edu.tr

Abstract **- In this study, in order to investigate the tangential stresses and burst failures of the semi elliptical surface cracked and un-cracked SiO_2 nanoparticle filled and unfilled $\pm[55]6$ filament wound composite pipes for determining the burst behaviors, static internal pressure burst tests were performed in terms of ASTM D 1599-99 standard at open ended condition. As a reinforcement material, a polymer matrix material and a filling nanomaterial, Basalt Fiber, A Bisphenol A (DGEBA) epoxy and 4%wt SiO_2 nanoparticles were used in filament wound composite pipes. At the end of tests, it was seen that SiO_2 nanoparticle addition increased the tangential stresses and decrease the debonding and delamination failures especially for un-cracked $\pm[55]_6$ filament wound composite pipes. Burst failures have been clearly seen all of the semi elliptical surface cracked and un-cracked SiO_2 nanoparticle filled and unfilled $\pm[55]_6$ filament wound composite pipes except un-cracked SiO_2 nanoparticle filled $\pm[55]_6$ filament wound composite pipes.**

Keywords **- Basalt Fibers, Filament Wound Composites, SiO_2 nanoparticle, Static Internal Pressure Burst Test.**

I. INTRODUCTION

Basalt Fiber Reinforced (BFR) epoxy composites have been performed in last decades. Basalt fibers have higher the mechanical properties, thermal insulation, chemical resistance, fatigue life than E-Glass Fiber. In addition, Although, Basalt Fiber shows lower the mechanical behaviors than Carbon Fiber, it's cost lower than Carbon Fiber. Therefore, Basalt Fiber has started to be preferable reinforcement materials for polymer matrix materials. Especially Basalt Fiber Reinforcement applications have been chosen at military, aerospace, the pressurized liquid and gas containers and pipe lines by using filament winding process[1-10].

In this study, the semi elliptical surface cracked and un-cracked SiO_2 nanoparticle filled and unfilled $\pm[55]_6$ filament wound composite pipes have been studied to determine the mechanical properties and burst failure behaviors .

II. EXPERIMENTAL PROCEDURE

The semi elliptical surface cracked and un-cracked SiO_2 nanoparticle filled and unfilled $\pm[55]_6$ filament wound composite pipes for determining the burst behaviors, static internal pressure burst tests were carried out according to ASTM D 1599-99 standard at open ended condition. For the manufacturing of nanoparticle filled BFR/Epoxy composites, SiO_2 nanoparticles having the features of a specific surface area of 650 m^2/g and an average primary particle diameter of 15 nm have been used as filling materials. A Bisphenol A (DGEBA) epoxy resin as a matrix material and 12KV 400 tex basalt fibers as a reinforcement material have been used in filament wound BFR/Epoxy composite pipes. At the Epoxy matrix modification, SiO_2 nanoparticle 4%wt were filled into epoxy resin and then the mixture was stirred by mechanical stirrer and ultrasonic probe stirrer during 10 min and 15 min respectively[1,18]. The SiO_2 filled and unfilled basalt fiber reinforced epoxy composite pipes were manufactured in respect of parameters of ± 55 directed winding angle, 6 layers, 72 mm internal diameter, about 2.63 mm thickness and 300 mm length(Fig 1)[1].



Figure: 1 a) The passing of fiber through into SiO_2 nanoparticle filled epoxy resin b) The manufacturing of BFR/Epoxy composite pipes[1,18].

The manufactured SiO_2 nanoparticle filled and unfilled $\pm[55]_6$ filament wound composite pipes in terms of a/c=0.2 and a/t =0.5 of the shape geometry of semi elliptical surface cracks were cut by using thin milling blade via universal milling machine. After that, the static internal pressure burst tests were applied to the semi elliptical surface cracked and un-cracked SiO_2 nanoparticle filled and unfilled $\pm[55]_6$ filament wound composite pipes by repeating three times. The internal pressure test apparatus are given in Fig.2[1].



Figure 2: Static internal pressure burst test apparatus.

The fiber fraction of all BFR/Epoxy composite pipes were determined to be about 0.61±1.5 [1,18].

III. RESULTS AND DISCUSSION

In this study, it was investigated the tangential stresses and failures of the un-cracked and 0.5 a/t semi elliptical surface cracked SiO_2 nanoparticle filled and unfilled ±[55]$_6$ filament wound composite pipes ±[55] filament wound basalt fiber reinforced epoxy according to ASTM D 1599-99 standard at open ended condition. When the fluid oil was pressurized into all of un-cracked and semi elliptical surface cracked SiO_2 nanoparticle filled and unfilled ±[55]$_6$ filament wound composite pipes, composite pipes swollen out the structure and begun to shorten the length of pipes(300mm). The rising internal pressure in composite structure imposed to open the bands of basalt fiber oriented ±[55] lay-up angles through tangential direction like shape pf scissors movement. This tangential forces as results of the increasing internal pressure of fluid have caused the shear stress at direction of perpendicular and parallel [1-6, 10]. At the end of the scissors movement of basalt fiber bands forced the opening by swelling out of structure took bigger angles than 55° winding angle given in Fig. 3. [3,6]. The opening basalt fiber band by increasing internal pressure have occurred the micro matrix crack along the fiber. And this matrix cracks have affected the interfaces of epoxy and basalt fibers. And so, the debonding failures along the basalt fibers have formed between basalt fibers and epoxy matrix material. Debonding faiures have triggered the delamination failures especially bottom of semi elliptical surface cracked of unfilled and SiO_2 nanoparticle filled ±[55]$_6$ BFR/Epoxy filament wound composite pipes. [1-2, 4-7]. By rather increasing fluid pressure fiber breakage catastrophic failures have occurred with burst. [1, 3, 6]. The tangential stressed of un-cracked and 0.5 a/t semi elliptical surface cracked SiO_2 nanoparticle filled and unfilled ±[55]$_6$ BFR/Epoxy filament wound composite pipes are presented in Fig 4.[1].

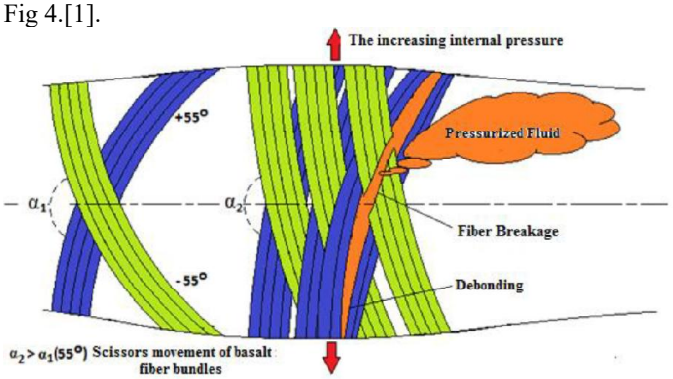


Figure: 3 Scheme of failures of ±[55]$_6$ BFR/Epoxy filament wound composite pipes under the increasing pressure of fluid[1].

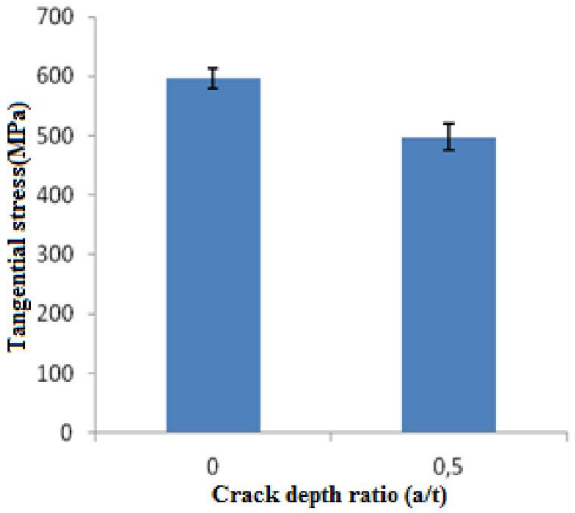


Figure: 4a The tangential stresses of the un-cracked and 0.5 a/t semi elliptical surface cracked unfilled ±[55]$_6$ filament wound composite pipes[1].

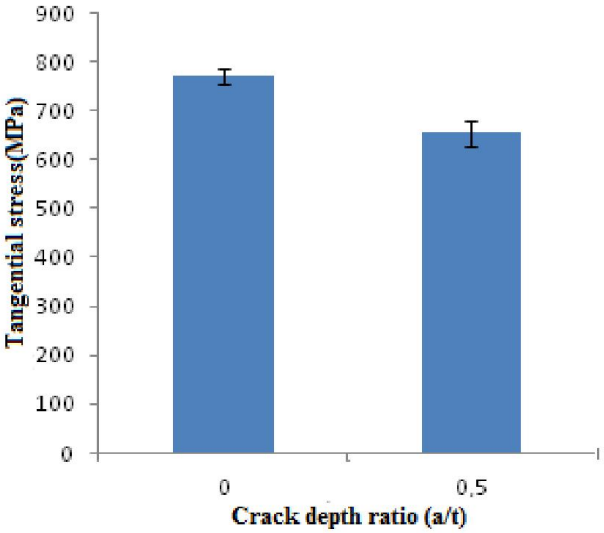


Figure 4b: The tangential stresses un-cracked and 0.5 a/t semi elliptical surface cracked SiO_2 nanoparticle filled ±[55]$_6$ filament wound composite pipes[1].

When Fig. 4 was observed, SiO_2 nanoparticle addition into epoxy matrix increased the tangential stress of un-cracked and 0.5 a/t semi elliptical surface cracked $\pm[55]_6$ filament wound composite pipes. It was commented as reason of these increases of tangential stresses that SiO_2 nanoparticle addition into epoxy that SiO_2 nanoparticles caused to improve fracture toughness and adhesion between fiber and epoxy resin by ensuring fracture mechanisms: crack propagation retarding effect by bowing and blunting of the front of cracks, occurring secondary cracks, branching of cracks, increasing elongation of epoxy matrix, plastic deformation and energy dissipation over fracture surfaces[1-11-18].

As failures of SiO_2 nanoparticle filled and unfilled un-cracked and semi elliptical surface cracked $\pm[55]_6$ filament wound composite pipes were investigated, the fiber breakage failures with burst have not been seen un-cracked and SiO_2 nanoparticle filled $\pm[55]_6$ filament wound composite pipes due to the mentioned fracture mechanisms provided by SiO_2 nanoparticles. The failure of fluid jets has been observed as result of debonding and delamination[1]. The failures of unfilled and SiO_2 nanoparticle filled un-cracked and semi elliptical surface cracked $\pm[55]_6$ filament wound composite pipes are shown in Fig. 5 and Fig. 6.

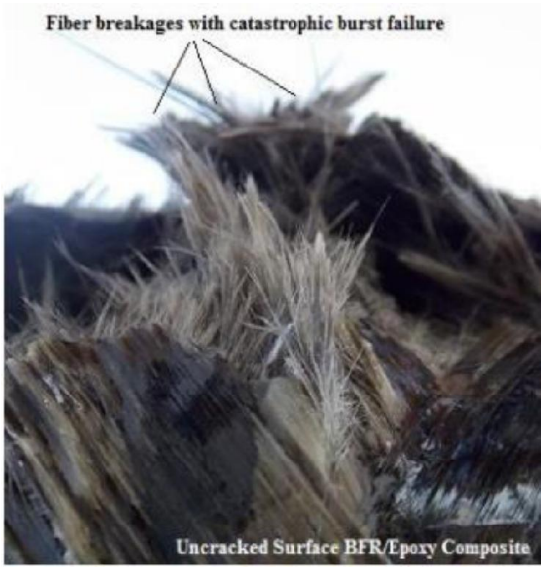


Figure 5a: The failures of unfilled and un-cracked $\pm[55]_6$ filament wound composite pipes[1,6].

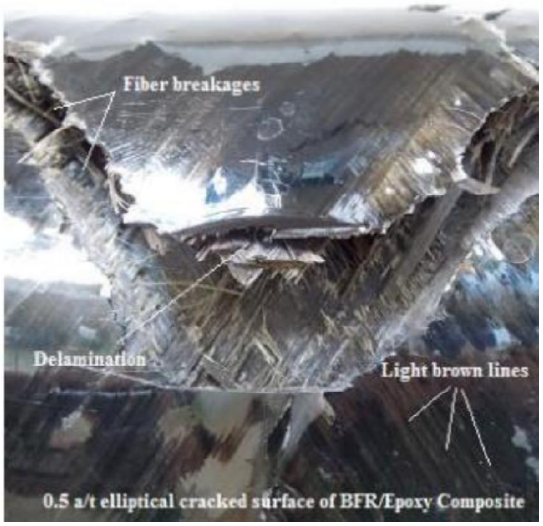


Figure 5b: The failures of unfilled and 0.5 a/t semi elliptical surface cracked $\pm[55]_6$ filament wound composite pipes[1,6].

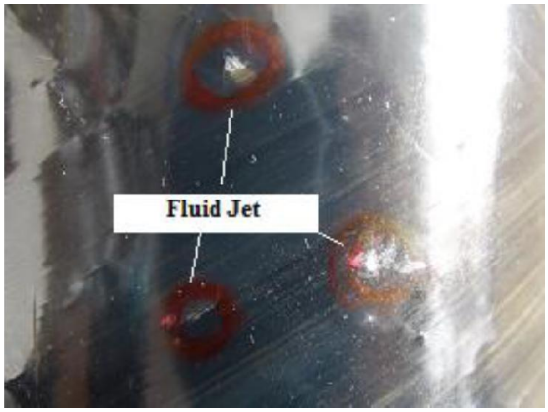


Figure 6a: The fluid jet failures of un-cracked SiO_2 nanoparticle filled $\pm[55]_6$ filament wound composite pipes[1].

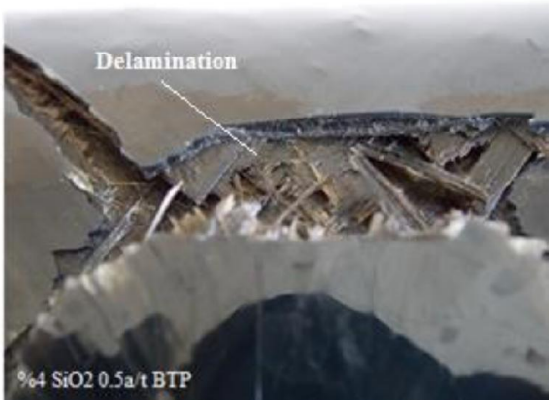


Figure 6b: The failures of 0.5a/t semi elliptical surface cracked SiO_2 nanoparticle filled $\pm[55]_6$ filament wound composite pipes[1].

IV. CONCLUSION

The results of static internal pressure tests of the un-cracked and 0.5 a/t semi elliptical surface cracked SiO_2 nanoparticle filled and unfilled $\pm[55]_6$ filament wound BFR/Epoxy

composite according to ASTM D 1599-99 standard at open ended condition have been listed in below.

- SiO_2 nanoparticle addition increased the tangential stress of $\pm[55]_6$ filament wound BFR/Epoxy composite pipes.
- It was assumed that SiO_2 nanoparticle provided the fracture mechanisms. In addition, SiO_2 nanoparticle performed to retard the fast crack propagation.
- It was seen that the fiber breakages with bust failure have been occurred at all of unfilled and semi elliptical surface cracked $\pm[55]_6$ filament wound BFR/Epoxy composite pipes. However, fluid jet failures as results of debonding and delamination have been observed at SiO_2 nanoparticle filled and un-cracked $\pm[55]_6$ filament wound BFR/Epoxy composite pipes. Matrix cracking, debonding, delamination and fiber breakages for SiO_2 nanoparticle filled semi elliptical surface cracked $\pm[55]_6$ filament wound BFR/Epoxy composite pipes have been seen at the end of static internal pressure burst tests.

ACKNOWLEDGMENT

This study was done by utilizing the Ph.D. thesis of Mehmet Turan Demirci supported by the Selcuk University Scientific Research Projects (B.A.P) under grant number 11101030.

REFERENCES

[1] Demirci M T., "The effects of SiO_2 nanoparticle addition on the fatigue behaviors of surface cracked and uncracked basalt fiber reinforced composite pipes", Ph. D. Thesis, The Graduate School of Natural and Applied Science of Selcuk University the Degree of Doctor of Philosophy in Metallurgical and Materials Engineering, Konya, Turkey, 1-179, 2015.

[2] Tarakcioglu N, Gemi L and Yapıcı A., "Fatigue failure behavior of glass/epoxy filament wound pipes under internal pressure", Composite Science and Technology, 65, 703-708, 2005.

[3] Samanci A, Avci A, Tarakcioglu N and Şahin Ö. S., "Fatigue crack growth of filament wound GRP pipes with surface crack under cyclic internal pressure", J. Mater Sci.,43, 5569-5573, 2008.

[4] Avci A, Şahin ÖS and Tarakcioglu N., "Fatigue behavior of surface cracked filament wound pipes with high tangential strength in corrosive environment", Composite Part A, 38, 1192-1199, 2007.

[5] Demirci MT, Tarakçıoğlu N, Avcı A, Yakut R, "Burst failure of basalt fiber reinforced filament wound pipe", 14th International materials symposium (IMSP'2012), Pamukkale University-Denizli-Turkey, 10-12 October, 2012.

[6] Demirci MT, Tarakçıoğlu N., Avcı A., "The burst failures of the elliptical surface cracked BFR/Epoxy Composite Pipes", 4th International Conference on Advanced Technology&Sciences (ICAT' Rome), Rome, Italy, 23-25 November, 2016.

[7] Meijer, G., and Ellyin F., "A failure envelope for ±60º filament wound glass fibre reinforced epoxy tubulars", Composite Part:A, 39, 555-564, 2008.

[8] Tarakcıoğlu, N., Samancı, A., Arıkan H., Akdemir, A., "The fatigue behavior of (±55)3 filament wound GRP pipes with a surface crack under internal pressure", Composite Structure 80, 207-211, 2007.

[9] Mertiny P., "Leakage failure in fibre-reinforced polymer composite tubular vessels at elevated temperature", Polymer Testing, 31, 25-30, 2012.

[10] Zu, L.,"Design and optimization of filament wound composite pressure vessels, Master of Science in Engineering Mechanics", Xi!an University of Technology, Xi'an, China, 2012.

[11] Deng S., Ye L., Friedrich K. Fracture behaviours of epoxy nanocomposites with nano-silica at low and evelated temperatures, Journal of Material Science, 2007; 42, 2766 – 2774.

[12] Brunnner A.J., Necala, A., Rees M., Gasser P.H. Karnmann X., Thomann R., Barbezat M. The influence of silicate-based nano-filler on the fracture toughness of epoxy resin, Engineering Fracture Mechanics, 2006; 73, 2336-2345.

[13] Han J.T. and Cho K. Nanoparticle-induced enhancement in fracture toughness of highly loaded epoxy composites over a wide temperature range, Journal of Material Science, 2006; 41, 4239-4245.

[14] Arabli V. and Aghili A. Effect of silica nanocomposites on the curing kinetics of epoxy vinyl ester resin, Proceeding of the international conference nanomaterials: Applications and Properties, 2013; 2(3), 1-4.

[15] Tzetzis D., Mansour G., Tsiafis I., Pavlidou E. Nanoidentation measurements of fumed silica epoxy reinforced nanocomposites, Journal of Reinforced Plastics and Composites, 2012; 0-14.

[16] Phonthammacha N., Chia H., He C. One-Step synthesis of oval shaped silica/epoxy nanocomposite: Process, formation mechanism and properties, The Delivery of Nanocomposites, 2012; 23, 497-508.

[17]Sadej-Bajerlain M., Gajzewski H., Andrejewska E. Monomer/modified nanosilica systems: Photopolymerization kinetics and composite characterization, Polymer, 2011; 52, 1495-1503.

[18]Demirci MT., Tarakçıoğlu N., Avcı A., Akdemir A., Demirci İ.,"Fracture Toughness (Mode I) characterization of SiO_2 nanoparticle filled basalt/epoxy filament wound composite ring with split-disk test method, Composite Part B, 2017; 119, 114-124.

The Feasibility of Using Wood Plastic Composites in Composite I-Joist Manufacture

S.M. ONAT[1], F.YILMAZ[1] and A.İSTEK[1]

[1] Bartın University, Bartın/Turkey, smuratonat@bartin.edu.tr,
[1]Bartın University f.y.67@hotmail.com
[1]Bartın University, Bartin/Turkey, aistek@bartin.edu.tr

***Abstract* - In this study, different types of composite wood I-joists are designed. The physical and mechanical properties of the I-joist specimens designed from materials such as, wood plastic composite (WPC), plywood and oriented strand board (OSB) have been determined and compared. Three different I joists, designed from WPC, plywood and OSB, were investigated as the web element combined with polyurethane (PU) glue according to the four point bending resistance test results for the designed I joists. As a result of the investigations, the average bending resistance values of I beams designed from plywood, OSB and WPC are found as 7,030 N/mm^2, 8,770 N/mm^2 and 6,886 N/mm^2 respectively. The bending resistance values are close to each other in the beams designed with the WPC. It was determined that the beam designed from OSB is higher in bending resistance than the others. In order to investigate the effect of the type of glue used in the beams on the bending resistance, the beams designed using PU glue and standard polyvinyl acetate (PVA) glue were compared. WPC material was used as the web element in the design of these beams. According to the bending resistance test results, the bending resistance value of the beams designed using PU glue was 7,030 N / mm2 while the bending resistance value of the beams designed using normal glue was found to be 3,957 N / mm2. According to the results, PU glued joists were found superior in bending by 78%. It is concluded that WPC has a potential and can be used as a web material for I joist production.**

***Keywords* – Wood Pastic Composites, Wood, I-joists, Bending Resistance, Scots Pine, Polyurethane Glue.**

I. INTRODUCTION

Composite I beams were used in airframe and wing skeletons in aircraft industry in North America in the 1920s. The highest quality coating, plywood and wood materials were used for effective performance. In the 1930's, composite I-beams started to be used in buildings in Europe [1]. Since the late 1960's, wooden I-beams or joists have been produced for special applications. It is called as an I-Joist because of the I-shaped cross-section and they are used in roof systems and flooring [2]. I joist is a material with high carrying strength due to its cross-section. Wood I-joists are built by gluing web elements i.e. plywood or oriented strandboard (OSB) panels to flanges usually made from solid wood. Wood I joists are widely used because of their increased performance, their ability to be produced in desired sizes, their light weight, their renewability and their low cost [3]. They are produced in various sizes and used for residential and commercial buildings (Figure 1).



Figure.1 Wood I-joists

The production of wood I-Beams starts by measuring and cutting the webs and flanges. The channels on the edges of the flanges are formed. After shaping the flanges, they are glued. Glued flanges are placed on web boards and pressed together. Pressed I-beams are cut to desired length. Get into the kilns for full drying of the glue. Quality checks are carried out to determine the bond quality and the smoothness of the joining of web boards. After the quality control, storage and transport operations are carried out [4].

One of the advantages of the design of the I-beams is that it allows us to utilize the best part of properties of the materials used. Structural efficiency has been increased by combining timber, plywood or OSB in the form of "I". In I-joists, the flange elements carry the moments (Figure 2), while the web elements carry the shear forces (Figure 3). Using the bending theory, the cross-sectional measurements of the headers are determined. The capacities of the body elements are determined experimentally. Bending and shear deformations are important criteria in the design of crushing and buckling capacities.

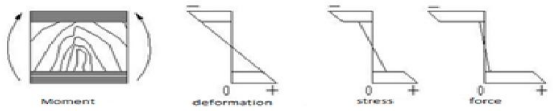


Figure 2. I joist mechanics. Moment application, shape change in determination of moment capacity, stress distributions and force distributions.

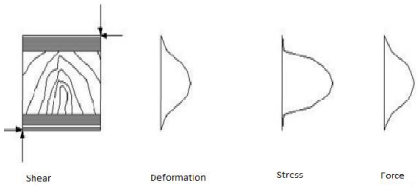


Figure 3. I-beam mechanics; Application of shear force, shear deformations, strain distributions and force distributions in determining shear capacity.

Resistance and deformation performance in I-joists are influenced by many factors such as material properties and geometry, loading condition. In I-joists, the flange elements carry bending stresses, while the web elements carry most of the shear stresses. It provides the transfer of the stresses between the elements in the glue used between the flanges and the web. The material properties of the flange elements are important. Because tensile and compressive stresses are concentrated in the flange elements due to the less elastic modulus of the web elements [2].

Wood composite panels such as plywood and OSB are generally used as web element due to the high cutting shear modulus and shear strength. If panels with low shear modulus are used for web members, beam deformation increases [5].

For electrical, heating or ventilation installations, it may be necessary to open the space in the web members of the I-joists. It has been found that the bending resistance does not affect the I-beam, even if the circular spaces in the webs reaches 70% of the web height [2]. Cavities with squared cross-sectional spaces cause stress concentration. Increased voids also reduces shear capacity and elasticity.

In this study, different composite wood I-joists types are designed. In addition, the physical and mechanical properties of the I-joists specimens designed from materials such as Scots pine, wood plastic composites (WPC), plywood and OSB have been compared.

II. MATERIAL

2.1. Wood Plastic Composites

Wood-plastic composite (WPC) is a generic name given to composites formed because of mixing plastics with lingo-cellulosic material. The word "wood" in this context does not have a narrow meaning like the piece of wood, but includes all agricultural wastes and woody material with a fibrous structure. Cellulosic filling materials can be classified in two main groups as granules and fiber materials. If the interphase binding is high, the dust particles are used as fillers or emulsifiers. Fibers can be used as reinforcing materials. Because the fibrous materials faces the applied load, they are much larger in length [6][7]. Plastics are organic polymeric materials that are usually solid at normal temperature and can be shaped or molded by mechanical methods using pressure and heat [8].

The technical characteristics of the WPC material used in the main beam design of I-joists are given in Table 1.

Table 1: Composition of the material used in making WPCs

POLYMER POLYESTER	FILLING AND SUPPLEMENTS Wood Flour, Calcite, Glass Fiber Dust	CONTRIBUTIONS Pigment and other additives
%30-40	%40-60	%0.1-2

2.2 Plywood

Plywood according to TS 2128; the veneer layers are adhered to be perpendicular to each other and the inner and outer layers on both sides of the core are generally defined as a board symmetrical to each other [9]. The plywood can be produced from softwoods and hardwoods. The veneers are obtained by peeling, cutting and slicing from the wood material and they constitute the raw material of the plywood.

The plywood is produced in such a way that the fiber directions of the layers are perpendicular to each other. Thus, dimensional stability is ensured throughout the width of the plywood, and rigidity and axial resistance in the direction perpendicular to the plane of the board are increased. Stratified structure dissipates defects, reducing possible delamination and increasing resistance when fasteners are used.

2.3. Oriented Strandboard (OSB)

Oriented strandboard (OSB) is based on the principle of gluing and waxing the chips obtained from small diameter round woods and they are placed in layers, and each layer is placed perpendicular to each other, and they were hot-pressed under certain pressure and temperature [10]. Raw materials used in the production of OSB; are wood raw materials, glues, hydrophobic materials, hardeners and preservatives.

2.4. Scots pine

Scots pine (*Pinus sylvestris* L.), which is the widest geographical spread among the existing pine species, has a very wide distribution area in Europe and Asia with a width of about 3700 km and length of 14700 km. Scots Pine is a species of the Pinaceae family, from the Gymnospermae class. It grows under different climatic and edaphic conditions. It is a very complex species with many subspecies, varieties and forms [11].

2.5. Polyurethane glue (PU)

Polyurethane glue is produced from double bonded alcohol and suitable isocyanate. It is a typical glue that resists to acids, oils, boiling water and microorganisms. The curing time at room temperature (20 ºC) is 60 minutes. When the glue completes the reaction, it expands by about twenty times the volume and there is no shrinkage on the glue layer. The increase in temperature shortens the period of curing. Pressing at temperatures above 60 ºC is not recommended [12].

2.6. Polyvinyl Acetate (PVA) glue

It is one component D3-type water based, polyvinyl acetate based, odorless emulsion adhesive. It is used for gluing wooden materials. Before applying PVA glue, we must ensure that the surface to be applied is clean and dry. The surfaces to be bonded are joined after the glue is applied and left to dry by compression method. A damp cloth should be used to clean the overflow areas. It is easily cleaned with warm water and soap. It should be stored at 5-35 ° C in sealed packages that do not receive direct sunlight. If not used, the package should be kept closed. It must be protected from getting frozen.

III. METHOD

In this study, wooden composite I-beam samples were prepared by using solid yellow pine, WPC, plywood and OSB materials. Solid wood was used in the lower and upper heads (flanges), and three kinds of I beams were designed using WPC, plywood or OSB at the body (Web) (Figure 4). These materials are bonded with PU glue, pressed under hydraulic press at room temperature for one day, and kept in controlled environment with 65% relative humidity and 20 degrees Celsius. 10 replicates for each group were prepared and tested. Also, PU glue and PVA glue were used as the adhesive in the beams during the manufacturing of I-joists with WPC . These designs made a comparison between PU glue and PVA glue in terms of mechanical performance. The dimensions of the designed beams are given in Figure 5. The density and bending resistances of the specimens were investigated. Also physical measurements were carried out.



Figure 4. Designed I-joists

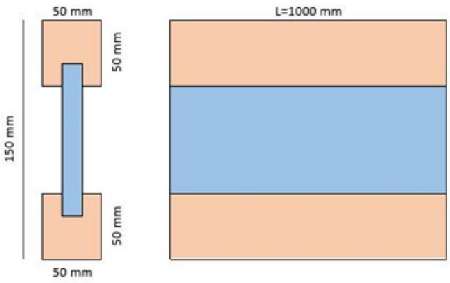
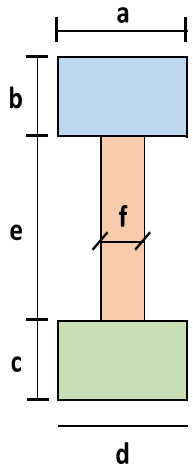


Figure 5. I-joist dimensions

3.1 Bending resistance

When mechanical testing of large quantities of wood as used in construction, knots, fiber curling, etc. are extremely important defects in terms of effects on the mechanical properties. The resistance values detected in this way had better reflect the performance of the material in use. For this reason, in this study, the bending resistance of the joists in the structural dimension was tested. The TS 2474 standard was chosen as a base for the experiments [13]. According to this standard four-point bending resistance is determined. For four-point bending resistance determination, the span between the supports is 66 cm. Two loading heads with a distance of 22 cm exerted the load placed on the supports. While the joists are placed on the supports, care has been taken to ensure that the knots remain on the tension side (top). The loading speed is set so that the movement speed of the loading heads is at most 6 mm/minute. The bending resistance values were obtained by means of the values obtained from the load applied to samples until breaking. Experiments were carried out using the "UTEST" company's "LS100 Plus" model universal testing machine. The test setup is shown in Figure 6 and 7.



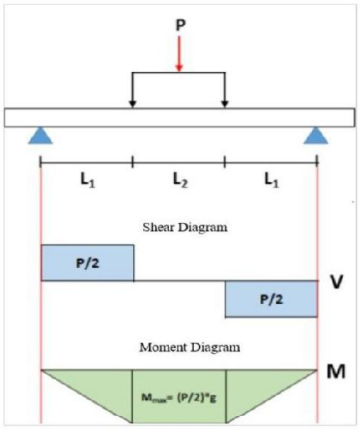


Figure 6. Four point bending test.

$$\sigma = \frac{M \cdot C}{I}$$

$$Mmax = \frac{Pmax \cdot L}{2}$$

$$C = (\frac{e}{2} * b)$$

$$I = (\frac{1}{12} * a * b^3 + a * b * (\frac{e}{2} + \frac{b}{2})^2) + (\frac{1}{12} * f * e^3) + (\frac{1}{12} * d * c^3 + d * c * (\frac{e}{2} + \frac{c}{2})^2)$$

In these equations;

σ: Bending resistance (Newton / mm2)

Mmax: Maximum bending moment (Newton * mm2)

Pmax: Maximum load (Newton)

I: Modulus of ınertia mm^4

L: Distance between supports (mm)

C: Distance between the neutral axis of I section and the top of the flange.



Figure 7. Bending test of I joists

IV. RESULTS

The average physical measurement values of I joists were presented in Table 2.

Table 2. The average physical measurement values of 3 type I joists

I Joist parts	Sample type	Cross Section Area (cm^2)	Density (gr/cm^3)	Weight(g)	1 meter I-joist weight (kg)
Upper flange	Scots pine	23.8	0.514	12.233	3.757
Web	WPC	8.4	1.560	13.104	
Lower flange	Scots pine	23.8	0.514	12.233	
Upper flange	Scots pine	23.8	0.514	12.233	3.004
Web	Plywood	8.4	0.663	5.569	
Lower flange	Scots pine	23.8	0.514	12.233	
Upper flange	Scots pine	23.8	0,514	12.233	2.939
Web	OSB	8.4	0.586	4.922	
Lower flange	Scots pine	23.8	0.514	12.233	

According to the measurements, I-joists with WPC had the highest weight compared to others because of high-density properties.

Bending resistance tests were carried out to determine the mechanical properties of the designed I joists. In the designed I beams, the bending resistance is calculated from 4 points bending test results and presented in the following Tables 3 and 4.

Table 3. Average values and Duncan test results of bending resistance based on sample type.

Sample type	Average bending strength (N/mm^2)	Standard Deviation (±)	Coefficient of Variation (%)	Duncan Test Groups
WPC (PU Glue)	6.89	1.17	0.37	b
OSB (PU Glue)	8.77	2.00	0.63	b
WPC (PVA Glue)	3.96	0.72	0.23	a
Plywood(PU Glue)	7.66	1.77	0.56	b

Table 4.ANOVA results of bending tests.

Variance	Sum of	Degrees of	Average of	F	Sig.

source	Squares	freedom(df)	Squares		
Between groups	119,47	3	39,82	17,58	0,000
Within groups	81,53	36	2,26		
Total	201,00	39	* p < 0,05		

According to the statistical analysis, the difference between groups are found significant and PVA bonded I joists was determined significantly lower than the other groups in terms of bending resistance. I joist with OSB was determined as the strongest type and it can be said that OSB is the most suitable material for I-joist manufacturing.

V. Conclusion

Three different I-joists were designed by using WPC, plywood and OSB, as the web element bonded with PU glue to Scots pine solid wood flanges. According to the results of four point bending resistance tests on the designed I joists, the average bending resistance of I-joists with WPC, OSB and plywood are found 6.89 N/mm2, 8.77 N/mm2 and 7.66 N/mm^2 respectively. The bending resistance values are close to each other in the beams designed by WPC. It is determined that the joist that is designed with OSB web material is found higher in bending resistance than the others. However, PU bonded WPC used I joists presented satisfactory results. In order to investigate the effect of the type of glue used in the beams on the bending resistance, the joists were produced by using PU glue and PVA glue and they were compared. WPC material was used as the web element in the design of these beams. According to the bending resistance test results, the bending resistance value of the joists produced with PU glue was 7.03 N/mm^2 while the bending resistance value of the joists with PVA glue was found to be 3.96 N/mm^2. According to these values, bending resistance of PU glued joists increased by 78%.

References

[1] McNatt, J.D. “Hardboard-webbed beams: Research and application”. *Forest Products Journal*, 30(10): 57-64. October, 1990.

[2] Leichti, R., Falk, R. Laufenberg, T. “Prefabricated wood l-joists: an industry overview”. *Forest Products Journal*, 40(3), 15-20. March, 1990

[3] Gagne, S. “Fiber reinforced plastic joist for the construction industry, A feasibility study”. Thesis Master of Science, Civil and Environmental Engineering, University of Wisconsin, Madison, 2000.

[4] *OSB Performance by design, oriented strand board in wood frame construction*. Structural Board Association, 2005.

[5] Leichti, R. J. 1986. “Assessing the reliability of wood composite I-beams”. PhD. Dissertation, Auburn University, Alabama,1986.

[6] Manson, J.A. ve Sperling L.H. *Polymer Blends and Composites*, Plenum Pres, New York, NY, 1976

[7] Matthews, F.L. ve Rawlings, R.D. *Composite Materials: Engineering and Science*, Chapman and Hall, New York, NY, 1994.

[8] Hüner, Ü.” Plastik Esaslı Kompozit Malzemelerin Sıcak Birleştirme İşlemlerinin İncelenmesi”. Master tezi. Trakya Üniversitesi, 2008.

[9] TS 2128 EN 313-2 Kontrplak - Sınıflandırma ve Terimler - Bölüm 2: Terimler, 2005.

[10] Kalaycıoğlu, H. Neden OSB*, Laminart Dergisi*, Sayı:12, Şubat- Mart, 2001.

[11] Tosun, S. “Sarıçamın Botanik Özellikleri”*, Ormancılık Araştırma Enstitüsü Yayınları El Kitabı Dizisi*:7, s.19, 2001.

[12] Öktem, E. “Bazı Ağaç Türlerimiz Odunlarının Yapışma Özellikleri Üzerine Araştırmalar”*, Orman Araştırma Enstitüsü Yayını, Teknik Bülten*, No: 81, Ankara, s. 23-25, 1976

[13] TS 2472. Odunda fiziksel ve mekaniksel deneyler için birim hacim ağırlığın tayini TSE Ankara. s. 1-5, 1976.

The Fatigue Failures of ±[55]$_6$ Filament Wound BFR/Epoxy Composite Pipes

Mehmet Turan DEMİRCİ[1*], Necmettin TARAKÇIOĞLU[2]

[1*] Selcuk University, Konya/Turkey, turandemirci@selcuk.edu.tr
[2]Selcuk University, Konya/Turkey,ntarakcioglu@selcuk.edu.tr

Abstract **- In this study, in order to investigate the fatigue life of ±[55]$_6$ BFR/Epoxy filament wound composite pipes, internal pressure fatigue tests were carried out in terms of ASTM D 2992-12 standard at open ended condition for different stress levels (30%, 40%, 50%, 60% and 70%). As a reinforcement and matrix materials, Basalt Fiber, A Bisphenol A (DGEBA) epoxy were used in filament wound composite pipes respectively. At the end of fatigue tests, it was seen that the increasing stress level decreased the fatigue life (cycle). In addition, by rising stress level, the fiber breakage as catastrophic failure was predominant with burst damages**

Keywords **- Basalt Fibers, Filament Wound Composites, Internal Pressure Fatigue Life.**

I. INTRODUCTION

There are many studies about the fatigue life of Glass Fiber Carbon Fiber Reinforced composites. In addition, the fatigue life of the filament wound Glass and Carbon Fiber Reinforced polymer based matrix composite have been investigated by many researchers. However, Basalt Fiber Reinforced (BFR) composites as an alternative fiber instead of them have been performed in last decades due to higher the mechanical properties, thermal insulation, chemical resistance, fatigue life than E-Glass Fiber lower cost than Carbon Fiber. The studies about the fatigue life of basalt fiber reinforced composites are insufficient in literature[1-9].

In this study, the fatigue life of ±[55]$_6$ filament wound composite pipes have been investigated to determine it as well as failure behaviors .

II. EXPERIMENTAL PROCEDURE

±[55]$_6$ filament wound composite pipes have been produced in commercial firms via CNC filament winding machine. The geometry of BFR/Epoxy composite pipe is given in Figure 1.[1].

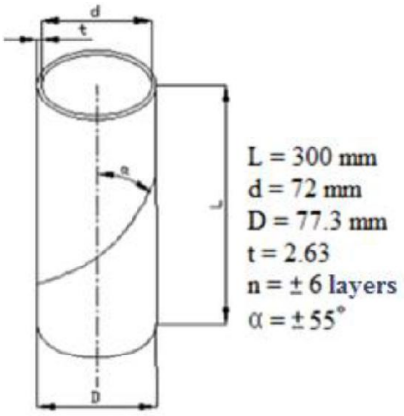


Figure 1: Geometry of BFR/Epoxy Composite Pipe[1,5].

As a reinforcement material, 12K 400 tex ±[55]$_6$ filament wound composite pipes basalt fiber was used and as a polymer matrix Bisphenol A (DGEBA) was used for ±[55]$_6$ BFR/Epoxy filament wound composite pipes[1].

The internal pressure fatigue tests were applied to ±[55]$_6$ BFR/Epoxy filament wound composite pipes at open ended condition by repeating 3 times in terms of 30, 40, 50, 60 and 70% stress of burst tangential stress of ±[55]$_6$ BFR/Epoxy filament wound composite pipe, 25 cycle/min, R=0.05 according to ASTM D 2992-12 standard. The internal pressure fatigue test equipment is given in Figure 2[1].



Figure 2: The internal pressure fatigue test equipment [1].

III. RESULTS AND DISCUSSION

The internal pressure fatigue tests of ±[55]$_6$ filament wound BFR/Epoxy composite pipes were carried out according to 30, 40, 50, 60 and 70% stress of burst tangential stress of ±[55]$_6$ BFR/Epoxy filament wound composite pipes. The burst tangential stress of ±[55]$_6$ BFR/Epoxy filament wound composite pipe was found as an average of 595 MPa. As results of internal pressure tests, the fiber breakages final failure as burst failure was observed at 40, 50, 60 and 70% stress of burst tangential stress of ±[55]$_6$ BFR/Epoxy filament wound composite pipes. When the fatigue life of BFR/Epoxy composites as S-N diagram given in Figure 3. It was found 223969N (Cycle) for 30%, 38631N for 40%, 7228N for 50%, 1569N for 60% and 589N for %70 of tangential stress. S-N curve of fatigue life of ±[55]$_6$ BFR/Epoxy filament wound composite pipes is shown in Figure 3 with standard deviation[1].

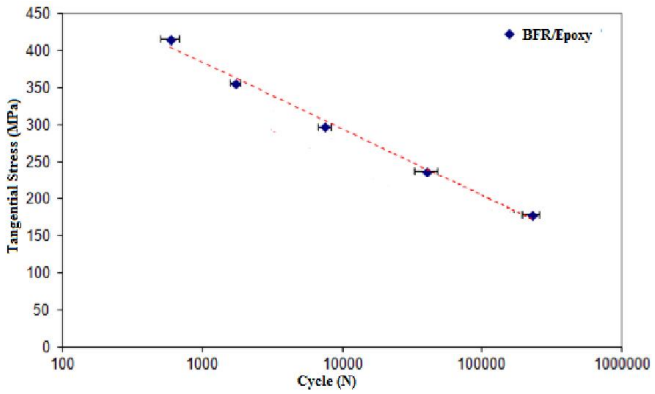


Figure 3: S-N curve of ±[55]$_6$ BFR/Epoxy filament wound composite pipes[1].

Besides with increasing internal pressure for stress levels, the structural changing has been introduced in Figure 4.

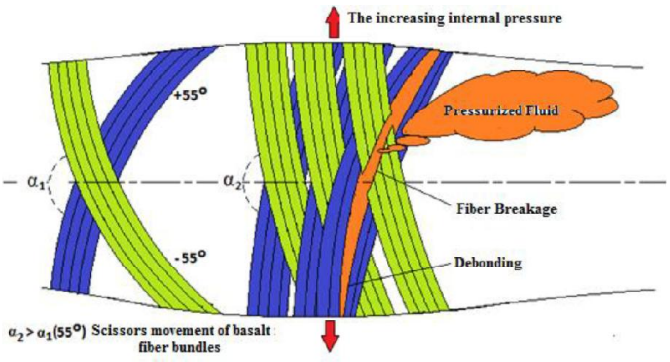


Figure: 4 Scheme of failures of ±[55]$_6$ BFR/Epoxy filament wound composite pipes under the increasing pressure of fluid[1].

While the increasing the stress levels of ±[55]$_6$ BFR/Epoxy filament wound composite pipes, the fatigue life of them decreased. It was commented that the increasing repeated loading and unloading fluid pressure caused to accelerate the forming of matrix cracking, debonding, delamination and of fiber breakage of catastrophic failures. According to stress levels of BFR/Epoxy composite pipes, firstly matrix cracking have occurred in rich epoxy resin. With increasing cycle separating of fiber and epoxy each other has formed as called "debonding failure" and then delamination failures have begun between interlaminates. The fiber breakage failure has come in existence as a catastrophic failure at weakness layers[1-9].

According to stress levels, the failures of ±[55]$_6$ BFR/Epoxy filament wound composite pipes are given in Figure 5, 6, 7, 8and 9.

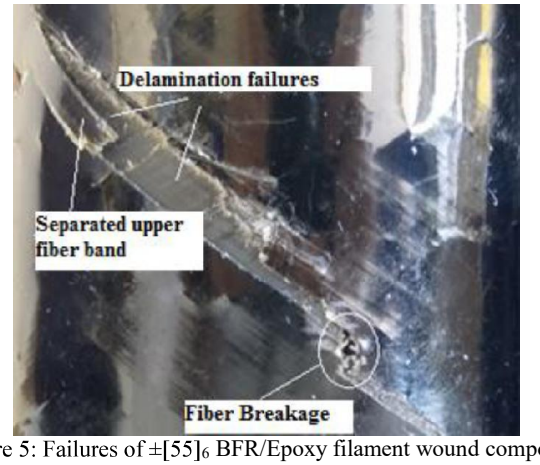


Figure 5: Failures of ±[55]$_6$ BFR/Epoxy filament wound composite pipes for %30 of tangential stress[1].



Figure 6: Failures of ±[55]$_6$ BFR/Epoxy filament wound composite pipes for %40 of tangential stress[1].

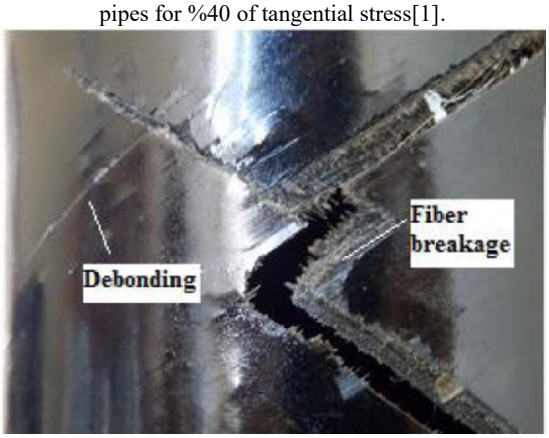


Figure 7: Failures of ±[55]$_6$ BFR/Epoxy filament wound composite pipes for %50 of tangential stress[1].

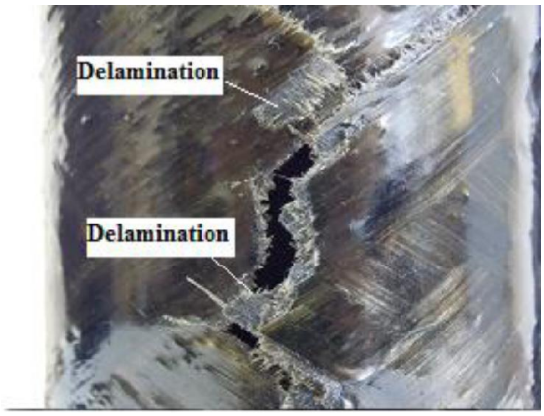


Figure 8: Failures of ±[55]$_6$ BFR/Epoxy filament wound composite pipes for %60 of tangential stress[1].

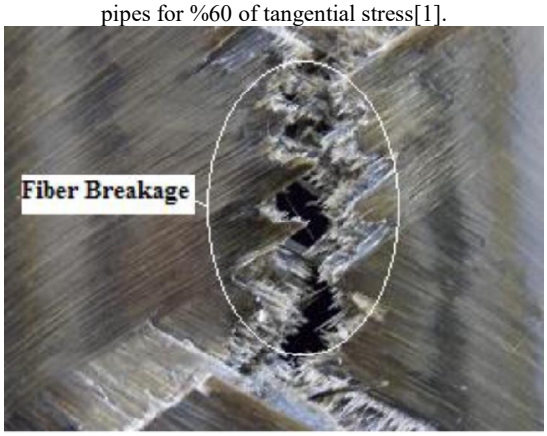


Figure 9: Failures of ±[55]$_6$ BFR/Epoxy filament wound composite pipes for %70 of tangential stress[1].

IV. CONCLUSION

The results of the internal pressure fatigue tests of ±[55]$_6$ BFR/Epoxy filament wound composite pipes at open ended condition according to 30, 40, 50, 60 and 70% stress of burst tangential stress of ±[55]$_6$ BFR/Epoxy filament wound composite pipe have been listed in below.

- The increasing tangential stress level of BFR/Epoxy composites, cycle of them decreased. And so, the fatigue life has been decreased.
- For all stress levels, BFR/Epoxy composite pipes have burst with catastrophic failure with fiber breakages. The fluid jet failure have been not seen during internal pressure fatigue tests
- Failures of debonding delamination and fiber breakage have been observed for all stress of levels of composites
- It was seen that the fiber breakage was predominant failure by increasing stress levels.

ACKNOWLEDGMENT

This study was prepared by utilizing the Ph.D. thesis of Mehmet Turan Demirci supported by the Selcuk University Scientific Research Projects (B.A.P) under grant number 11101030.

REFERENCES

[1] Demirci M T., "The effects of SiO_2 nanoparticle addition on the fatigue behaviors of surface cracked and uncracked basalt fiber reinforced composite pipes", Ph. D. Thesis, The Graduate School of Natural and Applied Science of Selcuk University the Degree of Doctor of Philosophy in Metallurgical and Materials Engineering, Konya, Turkey, 1-179, 2015.

[2] Tarakcioglu N, Gemi L and Yapıcı A., "Fatigue failure behavior of glass/epoxy filament wound pipes under internal pressure", Composite Science and Technology, 65, 703-708, 2005.

[3] Samanci A, Avci A, Tarakcioglu N and Şahin Ö. S., "Fatigue crack growth of filament wound GRP pipes with surface crack under cyclic internal pressure", J. Mater Sci.,43, 5569-5573, 2008.

[4] Avci A, Şahin ÖS and Tarakcioglu N., "Fatigue behavior of surface cracked filament wound pipes with high tangential strength in corrosive environment", Composite Part A, 38, 1192-1199, 2007.

[5] Demirci MT, Tarakçıoğlu N, Avcı A, Yakut R, "Burst failure of basalt fiber reinforced filament wound pipe", 14th International materials symposium (IMSP'2012), Pamukkale University-Denizli-Turkey, 10-12 October, 2012.

[6] Demirci MT, Tarakçıoğlu N., Avcı A., "The burst failures of the elliptical surface cracked BFR/Epoxy Composite Pipes", 4th International Conference on Advanced Technology&Sciences (ICAT' Rome), Rome, Italy, 23-25 November, 2016.

[7] Meijer, G., and Ellyin F., "A failure envelope for ±60º filament wound glass fibre reinforced epoxy tubulars", Composite Part:A, 39, 555-564, 2008.

[8] Tarakcıoğlu, N., Samancı, A., Arıkan H., Akdemir, A., "The fatigue behavior of (±55)3 filament wound GRP pipes with a surface crack under internal pressure", Composite Structure 80, 207-211, 2007.

[9] Mertiny P., "Leakage failure in fibre-reinforced polymer composite tubular vessels at elevated temperature", Polymer Testing, 31, 25-30, 2012.

Investigation of the Effect of Tin (Sn) on Microstructure and Hardness Properties of Gray Cast Iron

R.KUS[1] and B.AKGUL[2]

[1]Selcuk University, Konya/Turkey, recaikus@gmail.com
[2]Selcuk University, Konya/Turkey, bekir.akgul.13@gmail.com

Abstract - **In recent years, various alloying procession gray cast iron has been performed to prevent some of its disadvantages. In gray cast iron, alloying elements such as copper, chromium and titanium are used to increase mechanical properties. Copper is widely preferred in the industry to increase mechanical properties in gray cast iron such as tensile strength and hardness.**

In this study, tin (Sn) was added to gray cast iron material in 4 different ratios (0,03-0,06-0,09-0,12-0,15) and the effect of tin on microstructure and mechanical properties was investigated experimentally.

Hardness and microstructures were compared with two reference samples, one containing 0.4% copper and the other without any copper or tin addition. According to Brinell hardness test results, the highest hardness value was 177 HB in 0.12% tin (Sn) addition.

In the microstructure results, the highest perlitic rate was found in the sample containing 0.09% Sn. Samples with a tin content of up to 0.12% had a type A lamellar structure.

Keywords – **Gray cast iron, tin, microstructure, hardness properties.**

I. INTRODUCTION

The commercial use of cast iron is thought to be a major driver of the Industrial Revolution. The foundations of modern industrial society have been shaped by cast iron [1, 2].

Many researchers have investigated the contribution of various elements to the properties of gray cast iron. Nickel addition refines the perlite and graphite structure of gray cast iron and it has been found that it increases the toughness and hardness differences between the section thicknesses [3].

The fact that the hardness values of the developed cast iron increases as the weight % of added copper increases can be attributed to the formation of thinner ledeburite. In addition, it has been observed that as the weight % of added copper increases, the impact energy increases [4].

Sulfur is a surface active element that can exhibit many adverse effects including the promotion of degenerated graphite forms, intercellular carbides, increased cooling tendency and high hardness perlite [5].

When manganese is not present in sufficient concentrations, sulfur reacts with iron to produce a short-lived melting phase (FeS), which can cause a short-term shock [5].

Sulfur coexists with manganese in iron to form MnS, and manganese must be present in order to bind sulfur and avoid the undesirable consequences of high sulfur concentrations. As a result, the industry has always added manganese to control the sulfur in the alloy [5].

Chromium appears as carbide in iron, and if the carbon value is kept high, it increases the tendency to form white cast iron and thus improves the wear resistance of the iron [6, 7].

Shaban et al. showed that tin (Sn) increased the compact graphite and graphite aspect ratio. The effect of tin on sphero cast iron has been studied in the literature, and investigated in some industrial organizations. Its effect on gray cast iron has been investigated in this study [8].

Excessive addition of tin (Sn) in vermicular cast iron expanded the tendency of supercooling, and some in the melting system solidified based on metastability while some solidified as free cementite [9].

Increasing the content of tin (Sn) pushes the eutectic point of the melting system to the right, thereby promoting primary austenite production during solidification [10].

When the content of tin (Sn) is increased by 0.03 to 0.057 wt%, the graphite size visibly reduces, and an increase in tensile strength and impact toughness is obtained.

In addition, the increase in the amount of perlite and the decrease in the distance between the perlite layers also contribute to the strengthening of vermicular cast iron [10].

Addition of Sn shrinks vermicular graphite and homogeneously dissolves in the matrix. Sn stabilizes and refines perlite, that is, it increases the perlite content and reduces the average layer gaps of perlite. Addition of 0.057 wt% tin results in troostite with a perlite amount of over 95% in vermicular cast iron, and a stratified field separation of <83 nm [10].

More than 0.112 wt% of Sn causes the formation of undesirable free cementite, which damages mechanical properties [10].

The morphology and size of the soft graphite lamellae have a significant effect on the hardness of gray cast iron and hence the wear resistance. There is an inverse relationship between hardness and impact resistance of gray cast iron [11].

In this study, the effects of tin (Sn) addition on microstructure and mechanical properties were experimentally investigated by the addition of tin (Sn) in gray cast iron material in 5 different ratios (0.03-0.06-0.09-0.12-0.15%).

II. MATERIAL AND METHOD

The method chosen for this study is the production of hardness and microstructure samples cast in sand molds with different tin (Sn) and copper (Cu) additions under foundry conditions. Experiments were carried out on the produced samples with appropriate devices, the values obtained were examined and the results were evaluated.

For the study, two reference samples with different compositions and five research samples with different chemical compositions containing tin (Sn) were produced. The first reference sample does not contain copper and tin. The second reference sample contains copper and not tin. The other five research samples contain only tin alloy elements in different proportions.

Within the context of this study, the samples were cast in accordance with the pre-prepared conventional sand molds at suitable casting conditions and temperatures.

Casting temperature was determined as (+/-10) 1320 C^0.

During the casting of the samples, the amount of inoculation was determined as 0.04 wt% for all samples, which is the standard amount. The inoculation process was carried out in the pot. Ferrosilicon alloys containing small amounts of Ca were used as the inoculant.

The chemical composition results of the samples prepared are given in Table 1. The amount of P element was 0.039%. The amount of S element was 0.072%.

Table 1: Chemical composition of research sample.

	C (%)	Si (%) (Ladle)	Mn (%)	Cu (%)	Sn (%)
1 Unalloyed	3,471	1,812	0,463	0,067	0,001
2 (0,4 Cu)	3,471	1,812	0,463	0,435	0,001
3 (0,03 Sn)	3,471	1,812	0,463	0,067	0,030
4 (0,06 Sn)	3,471	1,812	0,463	0,067	0,060
5 (0,09 Sn)	3,471	1,812	0,463	0,067	0,090
6 (0,12 Sn)	3,471	1,812	0,463	0,067	0,120
7 (0,15 Sn)	3,471	1,812	0,463	0,067	0,150

For the casting of the samples, small pots of 30 kg were used. The alloying elements and the graining material were prepared precisely for 30 kg and placed in the pot before the molten metal was taken to the pot.

The casting process of the samples was carried out by taking the liquid metal into the pot, taking into account the casting temperature stated above.

Before being taken to cleaning and processing, the samples were numbered to prevent mixing.

Once casting was completed, the samples were left to cool down, and the cooled parts were subjected to sandblasting process to clean the sand on the surface.

The cleaned specimens were grinded to remove excess materials such as runner and burrs etc.

Finally, all samples were processed on CNC machines and brought to the appropriate forms for testing.

Tests were carried out with appropriate test devices under the same conditions for the samples brought to a standard size, and the obtained results were analyzed.

A. Investigation of Hardness Property

Within the scope of the study, sand mold casting process for hardness samples was performed initially. After casting the liquid metal into the mold cavity, the samples were allowed to cool normally in the mold.

Cooled samples were subjected to sandblasting for cleaning the sand on the surface, followed by a 5 mm chip removal process on a CNC machine to get rid of the roughness of the surface.

After the chip removal process, the surfaces of the samples for hardness evaluation were sanded with a 600-mesh sandpaper. Hardness tests of the samples were performed with the Brinell hardness measurement method.

B. Investigation of Microstructure

The specimens taken by fine cutting process from the cast samples were first subjected to sanding, followed by polishing, to make the surface ready for looking at microstructure. The graphite structure of the material was examined before the etching process, and the perlite and ferrite structure was examined after the etching process.

In order to see the ferrite and perlite structures in the microstructure of the samples, etching was carried out in a 2% nital solution for 8-10 sec. It was found that the burns occurring in the ferritic region when the waiting time was extended was misleading for the determination of perlite ratio.

Metal microscope was used to examine microstructural results.

III. DISCUSSION AND RESULTS

1) Hardness Test

As is known, the mechanical properties of cast iron depend on graphite morphology (shape, distribution, quantity and size) and matrix structures (ferrite, perlite). Literature research shows that the increase of the perlite ratio in the matrix structure and the regular distribution in the graphite morphology increase the hardness value [3, 10, 11].

Brinell hardness test was carried out at three different points on the research samples. One of the hardness values is at the midpoint and the other two are the edge hardnesses. The results of the hardness tests are shown in Table 2 with their averages. The lowest hardness value was obtained from reference sample 1, to which no alloying element was added. The closest value to this was observed in sample 3 with a tin (Sn) content of 0.03%.

Only copper (0.043% Cu) was added to sample 2. The hardness results in Table 2 demonstrate the positive effect of copper on gray cast iron hardness.

The hardness values of samples with different tin (Sn) contents of 0.03-0.06-0.09-0.12-0.15% are shown in Table 2. The highest hardness value was obtained from the sample with 0.12% tin. It was seen that the hardness value of gray cast iron containing 0.43% copper (Cu) was between the hardness values of the samples containing 0.06-0.09% tin (Sn).

Table2: Hardness Results

	0,4 Cu	**0,00 Sn**	**0,03 Sn**	**0,06 Sn**	**0,09 Sn**	**0,12 Sn**	**0,15 Sn**
Hardness (HB)	157	144	146	150	163	177	161

2) Microstructure Results

The following figures illustrate the graphite morphology and the amount of perlitic texture of the samples with different tin (Sn) content and the reference samples.

As can be seen in the microstructure results below, reference samples demonstrate an A type graphite structure (Figure 1, Figure 2). In the sample containing 0.15% tin, graphite morphology was more dispersed and rosetting was observed certain places (Figure 7). This result is in agreement with the results of Y. Lyuet al [10].

In Figure 1, the perlite ratio in the microstructure of the sample without any alloy elements is approximately 50%. In Figure 2, it is about 75% for the sample with added copper (Cu) element.

Based on the microstructure results, it was found that the increase in the amount of tin (Sn) results in an increase in perlitic structure. About 40% perlite was observed in the sample containing 0.03% tin, while this ratio increased up to 95% as the amount of tin increased. It was found that perlite amount was at the maximum level when tin amount was 0.12%.



Figure 1: Etched microstructure of the sample without Cu and Sn addition at 10X magnification.



Figure 2: Etched microstructure of the sample containing 0.4% Cu at 10X magnification.



Figure 3: Etched microstructure of the sample containing 0.03% Sn at 10X magnification.

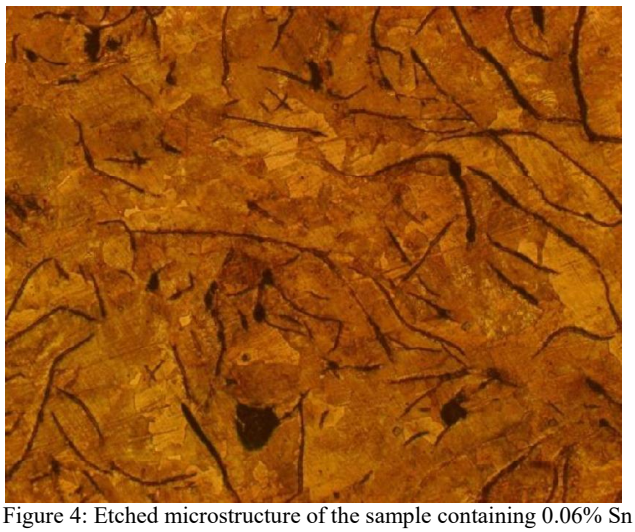


Figure 4: Etched microstructure of the sample containing 0.06% Sn at 10X magnification.



Figure 5: Etched microstructure of the sample containing 0.09% Sn at 10X magnification.



Figure 6: Etched microstructure of the sample containing 0.12% Sn at 10X magnification.



Figure 7: Etched microstructure of the sample containing 0.15% Sn at 10X magnification.

IV. CONCLUSIONS

In this study, the effects of tin (Sn) on the microstructure and mechanical properties of gray cast iron were investigated by metal microscopy and Brinell hardness tests. A few conclusions and recommendations are listed below.

Sn addition resulted in a homogeneous graphite morphology up to a ratio of 0.12% Sn, and tin was homogeneously dissolved in the composition.

The addition of Sn continuously increased the perlitic ratio. In parallel with the increase in the perlitic ratio, the hardness value also increased up to 0.12% Sn.

In this study, the highest hardness value was obtained as 177 HB in the sample containing 0.12% tin (Sn).

It is recommended to use tin with a ratio of up to 0.12%. Beyond this point, tin affects the hardness of cast iron negatively.

While the addition of 0.4% copper raised perlite ratio to a level of 75%, addition of 0.09% tin resulted in a 80% perlitic ratio.

It is recommended to use tin in order to obtain a high perlitic texture in gray cast iron microstructure.

ACKNOWLEDGMENT

The data in this paper were benefited from MSc. thesis studies of Bekir AKGUL. The authors acknowledge the support provided by the Scientific Research Projects Coordinatorship of Selcuk University Contract No:17201061.

REFERENCES

[1] Campbell, J., Complete Casting Handbook (First Edition) – Chapter 6: Casting Alloys, Elsevier Inc, 255-390, 2011.

[2] Ashby, M. F., Materials and the Environment (Second Edition) – Chapter 15: Material Profiles, Elsevier Inc, 459-595, 2013.

[3] O. Aponbiede and N. M. Okelekwe "The Effect of Chlo-ride Salts on the Mechanical Properties of Gray Cast Iron," Journal of Emerging Trends in Engineering and Applied Sciences, Vol. 2, 2011, pp. 256-259.

[4] J. O. Agunsoye, S. A. Bello, S. B. Hassan, R. G. Adeyemo, J. M. Odii, "The Effect of Copper Addition on the Mechanical and Wear Properties of Grey Cast Iron", Journal of Minerals and Materials Characterization and Engineering, 2014, 2, 470-483

[5] Richard Gundlach, Matthew Meyer, Leonard Winardi, "Influence of Mn and S on The Properties of Cast Iron Part III- Testing and Analysis" American Foundry Society, International Journal of Metalcasting/Volume 9, Issue 2, 2015

[6] Velde C (1999), The Solidification of Gray Cast Iron.

[7] Baicchi P., Nicoletto G., Konecná R. (2005), Mechanical behavior of EN-GJL30 Cast iron from three foundries, Procs. SEMDOK, Sulov.

[8] M. Shaban, A. Motallebzadeh, A. Halvaee and J. Rassizadehghani: Int. J. Mater. Sci. Innov, 2013, 1, (2), 87–100.

[9] Y. C. Peng, H. J. Jin, J. H. Liu and G. L. Li: Mater. Charact., 2012, 72, 53–58.

[10] Y. Lyu, Y. Sun, S. Liu and J. Zhao, Effect of tin on microstructure and mechanical properties of compacted graphite iron, Article in International Journal of Cast Metals Research, July 2015.

[11] Johnson O. Agunsoye, Talabi S. Isaac, Olumuyiwa I. Awe, Afemefuna T. Onwuegbuzie, Effect of Silicon Additions on the Wear Properties of Grey Cast Iron, Journal of Minerals and Materials Characterization and Engineering, Vol. 1 No. 2 (2013)

Smazzle: A Demonstrative Case Study for Modular Design of Mechatronic Products

Z.ERDEN,

Atılım University, Ankara/Turkey, zuhal.erden@atilim.edu.tr

Abstract - **Design and manufacturing of modular, platform-based products are important solutions for companies to meet ever increasing customer requirements in today's global and competitive market. Modular design methods provide companies to be able to produce a wide range of products at the lowest cost and shortest time. There is considerable amount of research on modularity for mechanical products. On the other hand, research on the conceptual structuring of mechatronic product families is quite limited. The aim of this study is to apply an existing modular design methodology for the development of a demonstrative mechatronic product family called "Smazzle", which is a smart and interactive, puzzle type mechatronic product family model for transportation tasks. The paper presents the modular design methodology for "Smazzle" as well as its physical realization.**

Keywords – **Modular mechatronics, Modularity, Mechatronic product family, Platform-based product.**

I. INTRODUCTION

THE concept of mass customization in today's global economy forces companies to offer a variety of products, satisfying individual desires and requirements of customers. Product variety in mass customization is provided by platform-based products which form product families. A product family refers to a set of similar products that are derived from a common platform and yet possesses specific features/functionality to meet particular customer requirements [1]. Platform-based product development needs modular design methodologies and therefore, development of systematic methods for assuring modularity has been a significant research topic in design science. However, most of these efforts are devoted towards mechanical products and they are generally component-dependent methods. Today, mechatronic products have become important for sustaining high living standards of people, as well as for increasing nations' competitiveness in the global marketplace. Mechatronic products are based on integrated knowledge from various engineering disciplines. Therefore, development of modularization methods for such products is an important research area that needs much contribution.

This paper presents a case study towards such a contribution to implement existing modularization methods on a smart and interactive, puzzle type mechatronic product family, called Smazzle. We have designed a system which has mainly three module types. By combining modules in these groups, different products can be designed. One of these module groups, namely the main module, is the common module in all products of the family and it has the computer and energy source. The other two module groups are the top and bottom modules. Bottom modules is for motion, and top modules are for the different operational functions. Both of these module groups have several options for different tasks. By combining a main module, a top and a bottom module, a product with a specified task can be produced.

The remaining part of this paper is organized as follows; Section 2 provides a brief literature review on modular design. In Section 3, modular design and production of Smazzle is explained. Finally, Section 4 concludes this work and describes future research directions.

II. LITERATURE SURVEY

Mass customization is an important issue that should be considered from design, production, marketing and sales perspective [2]. Companies today are changing their design and production strategies towards development of platform-based modular products (product families) to allow mass customization. Modularity has been defined as the degree to which a product's architecture is composed of modules with minimal interactions [3]. Modularity is described as a relative property of a product structure as opposed to an integral structure. In a modular structure, a module implements only one or a few main functions in its entirety, whereas in an integral structure, the functionality is spread all over the product. Even though the understanding of modularity has become more abstract and more related to functionality than geometry, a module is still fundamentally defined as a physical unit. Many research in modular product design has been devoted to the identification and development of modules.

One of the important initial studies is the heuristic method for identifying modules from functional models [4]. This method has been extended with functional modeling of the products [5] and a systematic methodology for architecting a product portfolio has been suggested [6].

Since the development of modular products requires the identification of highly interactive groups of elements and arranging (i.e., clustering) them into modules, research has also been directed towards clustering techniques [7]. An adaptable design is proposed [8] aiming at creating designs

and products that can be easily adapted for different requirements, as a generalization of modular design, product platform design, product family design and mass customization design. A modular product design methodology is developed as an integrated approach by combining several methods to allow designers to generate design solutions using modular concepts in a systematic manner. This new methodology contains four significant methods that form the integrated methodology; Generalisation, Modularisation, CUstomisation and REconfiguration (GeMoCURE) [9].

In designing product families, flexible product platforms are required. An integrated product modularization scheme is proposed for the modular identification of a flexible platform based on flow analysis, design structure matrix (DSM) and fuzzy clustering [10]. Recently, systematic methods for developing modularity of mechatronic products have been investigated by researchers. For example a modularization scheme has been developed for the modular design of mechatronics systems by integrating the DSM based modularization with the FBS (Function-behaviour-state) modeling [11].

As mechatronic products become important for sustaining high living standards of people, as well as for increasing nations' competitiveness in the global marketplace, mass customization and development of platform-based products are important for mechatronic product companies in order to be agile, so that they can develop new products in a very short period of time without changing the overall design of existing products. Therefore, companies need experience in applying systematic methods for the development of modular, platform-based mechatronic products. The above-mentioned requirements for mass customization in mechatronic product development need modular design methodologies for such products. Mechatronic products require integration of knowledge from various engineering disciplines starting from early design phases; particularly from the conceptual design stage. Thus, use of a top-down design methodology in mechatronic product development is necessary. This design methodology is based on generalization of the required overall function of the product, and then, dividing the overall function into simpler sub-functions by means of functional decomposition. Such a design methodology is a basis for the implementation of modular design methods that exist in the literature. Thus, mechatronic product design is considered to be useful for the implementation of existing modular design methods. In the following section, a case study is presented as a demonstrative example for the implementation of modular mechatronic product development.

III. MODULAR DESIGN OF SMAZZLE

In this study, a demonstrative mechatronic product family model (namely Smazzle) has been developed, as a multi-functional transportation system that could be used in emergency cases such as eartquakes or mining accidents with minimum human intervention. The system is composed of various modules with mechanical, electronic and software components. Smazzle has three different module types and alternative transportation systems with different tasks can be obtained by changing some of these modules. Figure 1 represents the overall structure for the Smazzle product family and Figure 2 depicts the material, energy and information flow in the system.

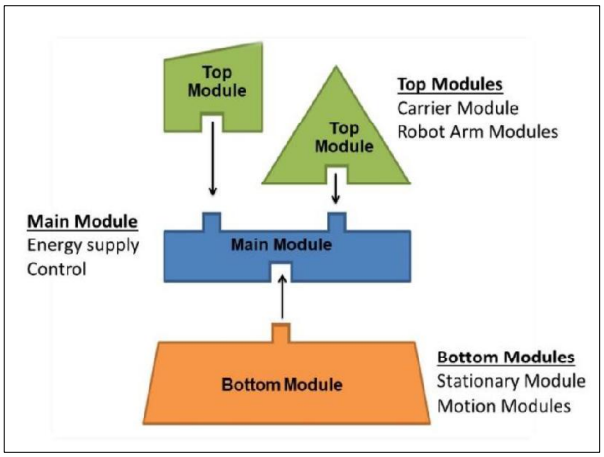


Figure 1: Modular structure of the system.

The three module types in the Smazzle product family are explained below:

A. Main Module

The main module is considered as a product platform, which is common for all products in the Smazzle product family. Main module is used to supply energy to the system and control the task execution and operation. Therefore, main module is composed of a microprocessor and a control unit with module controllers. There is server-client relationship between the modules.

B. Bottom Modules

Motion of the products in the Smazzle family is performed by using bottom modules. There are several different types of bottom modules using different components for different types of mobility such as palette, 2x4 wheels, boat, 4x4 wheels. Bottom modules are also responsible for assuring stability of motion on the ground. Two sub types exist for the bottom modules as "station module" and "motion module".

Station Module: This module is intended to be a stationary bottom module to be used as an allocated to four mobile systems. This module is able to check for availability of stations. The main task of this module is to transmits information from its sensors with electronic systems, to the other modules.

Motion Modules: These are the mobile bottom modules and the operation of these modules are as follows; Module activation is provided by two wheels and motion modules can find the way to their destination. Motion modules avoid obstacles on their way, by the help of their distance sensors.

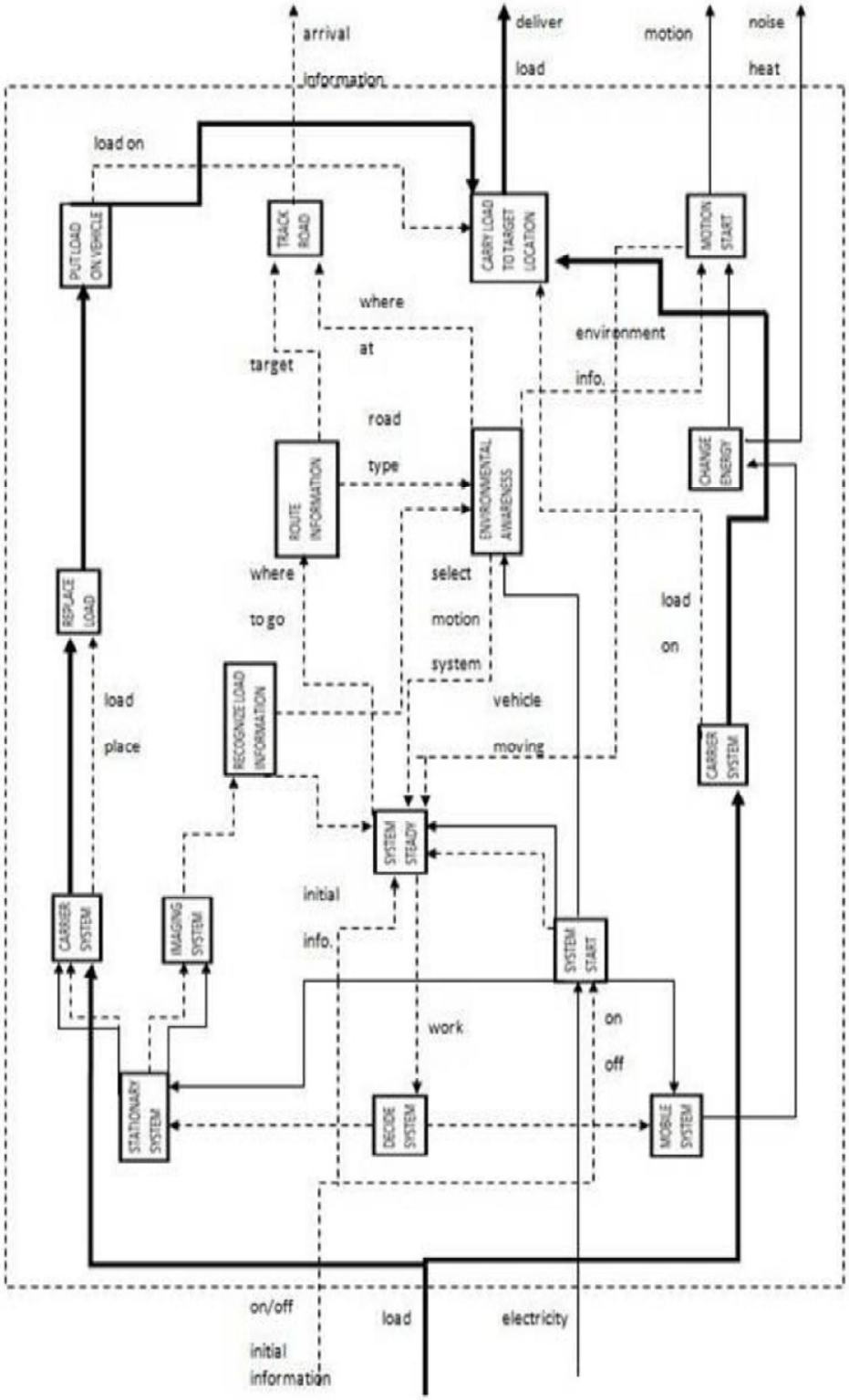


Figure 2: Energy, material and signal flows in the Smazzle system.



Figure 3: Electronic circuits in the Smazzle system.

The following bottom modules are considered in the design, although only the first one is physically produced due to budget limitations:

- Asphalt Path Module (for motion on an asphalt road)
- Soil Path Module (for motion on soil road)
- Terrain Module (for motion on a terrain surface)
- Iron Path Module (for motion on rails)
- Marine Transportation Module (for motion on rails)

C. *Top Modules*

Top modules determine the operational skills of the products in the Smazzle family. These modules are used for performing various tasks such as carrying load, gripping via a robotic arm, serving as an ambulance or fire truck.

There are two main sub-types for the top modules as;

- Carrier Modules
- Robot Arm Module

Carrier Modules: Carrier modules have been developed for handling loads. These modules are able to sense the loads via their sensors and by means of information transfer through electronic circuits (Figure 3) of the main module.

Robot Arm Module: This module provides access to various objects around the system by means of mobility gained by servo motors. Thus, a robot arm module can perform the desired movement. In addition, sub modules are attached to the upper side of the robot arm module to perform a variety of tasks via actuators. Sub-modules for the robot arm module are as follows;

- Robot Arm - Clamp Module (Gripper Module)
- Robot Arm - Hook Module
- Robot Arm - Bucket Module
- Robot Arm - Colour Recognition Module
- Robot Arm - Height Finder Module

In this study some of the above-mentioned modules are designed and produced as shown in Figure 4.a. Physical models for 4 different products in the Smazzle family are illustrated in Figure 4.b. These product models are operationally tested and the system successfully executed its tasks. Figure 5 illustrates a view of the physical test environment.

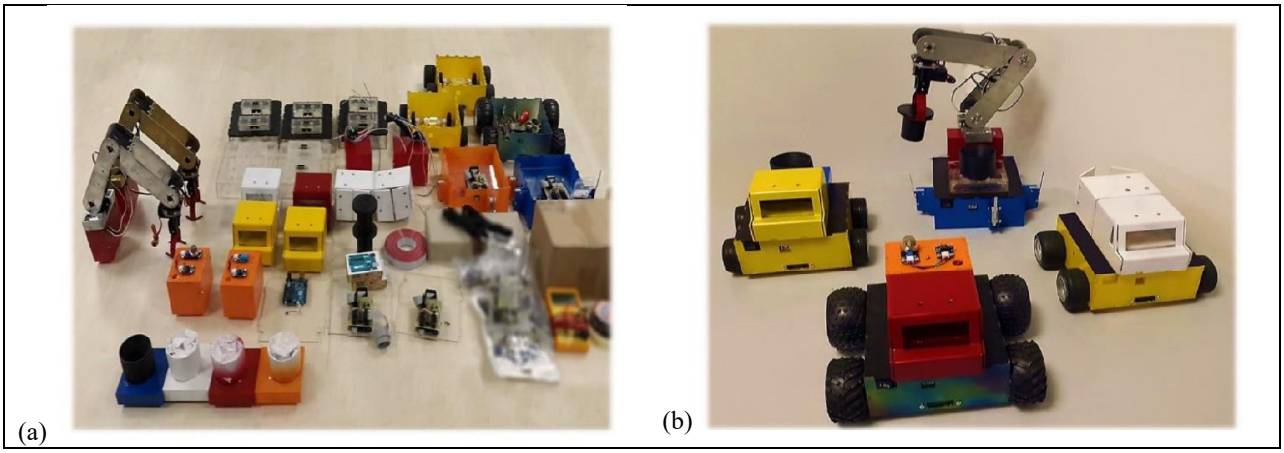


Figure 4: (a) All modules of the system. (b) Products in the family.

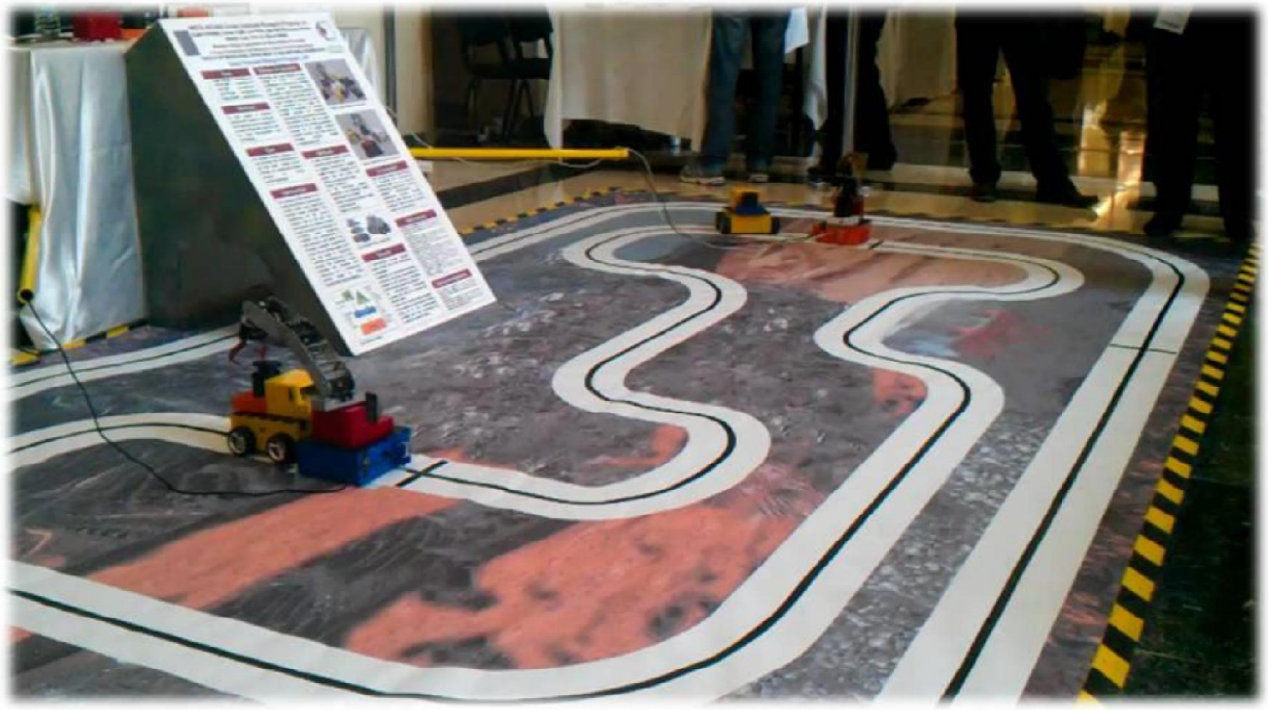


Figure 5: Operational view of the system.

IV. Conclusion

Modular design philosophy and modular products have an increasing prevalence in recent years due to changing market requirements. It is indisputable that producers need to produce modular products in order to meet today's diverse customer needs. The case study summarized in this paper is an initial study conducted at the laboratory to test the modular design methodology for mechatronic systems. In this study, the design, production and assembly of a mechatronic product family, called Smazzle has been developed. The system is composed of various modules and several products with different functionalities are developed using these modules. The system is operationally tested and all products of the family executes their tasks successfully. The work presented in this paper is one of the initial case studies for modular mechatronic design. Future research will be directed towards the development of systematic methods for modular mechatronic design to develop mechatronic product families.

Acknowledgment

This study has been conducted during 2013-2014 Academic Year as part of MECE 407-MECE 408 Undergraduate Research Projects I-II senior level courses at the Mechatronics Engineering Department and supported by Atılım University (Project No: ATÜ-LAP-A-1314-01). The author would like to appreciate her undergraduate students Çağlar Akbaba, Serkan Ilgın, Lemi İğde, Uğur Sezgin and Kerem Uyanık for their hard work and valuable efforts during this project. The author would also like to thank to Revar Otomotiv San. Tic. A.Ş. for manufacturing support.

References

[1] Jiao, J., Simpson, T. W. and Siddique, Z., (2007), "Product Family Design and Platform-Based Product Development: A State-of-the-Art Review", *Journal of Intelligent Manufacturing*, Vol.18, No.5, pp.5-29.

[2] Jørgensen, K., (2010), "Customisation and Modelling Applied to Electronic and Mechatronic Products", *NordDesign 2010*, 24-27 August 2010, Gothenburg.

[3] Gerherson, J.K., Prasad, G.J. and Zhang, Y., (2003), "Product Modularity: Definitions and Benefits", *Journal of Engineering Design*, Vol.14, No.3, pp.295-313.

[4] Stone, R.B., Wood, K.L. and Crawford, R.H., (2000), "A Heuristic Method for Identifying Modules for Product Architectures", *Design Studies*, Vol.21, No.1, pp.5-31.
[5] Pahl, G. and Beitz, W., (1996), *Engineering Design-A Systematic Approach*, London: The Design Council.
[6] Dahmus, J.B., Gonzales-Zugasti, J.P. and Otto, K.N., (2001), "Modular Product Architecture", *Design Studies*, Vol.22, No.5, pp.409-424.
[7] Yu, T., Yassine, A.A. and Goldberg, D.E., (2007), "An Information Theoretic Method for Developing Modular Architectures Using Genetic Algorithms", *Research in Engineering Design*, Vol.18, pp.91-109.
[8] Gu, P., Xue, D. and Nee, A.Y.C., (2009), "Adaptable Design: Concepts, Methods, and Applications", *Proceedings of the IMechE, Part B: Journal of Engineering Manufacture*, Vol. 223, No.11., pp. 1367-1387.
[9] Yan, X. and Stewart, B., (2010), "Developing Modular Product Family Using GeMoCURE within an SME", *International Journal of Manufacturing Research*, Vol.5 No.4, pp. 449-463.
[10] Li, Z., Cheng, Z., Feng, Y. and Yang, J., (2013), "An Integrated Method for Flexible Platform Modular Architecture Design", *Journal of Engineering Design,* Vol.24, No.1, pp.25-44.
[11] van Beek, T.J., Erden, M.S. and Tomiyama, T., (2010), "Modular Design of Mechatronic Systemswith Function Modeling", *Mechatronics*, Vol.20, No.8, pp. 850-863.

Design and Simulation of a Single Spherical Wheel Robot

İbrahim SAT[1] and Hüseyin Oktay ERKOL[2]

[1] Karabuk University, Karabuk /Turkey, satogluibrahim@gmail.com
[2] Karabuk University, Karabuk/Turkey, oktayerkol@karabuk.edu.tr

Abstract **- In this study, a robot with single spherical wheel is designed and produced. It can move to all directions on a spherical wheel like a ball and use three omnidirectional wheels placed on the ball to realize the movements. This robot has naturally unstable structure and balancing problem like a two dimensional inverted pendulum but has more complex structure and needs more complex controller than the inverted pendulum. The mathematical model of the robot is obtained using Euler-Lagrange method and simulated by the Matlab program. A PID controller is designed to balance the robot on the ball in the Z-direction. The mechanics of the robot consists of three omnidirectional wheels; three servo motors connected the wheels, a big ball as a main wheel between the robot and the ground, the body and electronic components. The designed robot body is produced by aluminum profiles and plastic parts printed by a 3D Printer. All simulations and robot production is made successfully.**

Keywords **- Single wheel robot, spherical wheel, balance control, PID.**

I. INTRODUCTION

Mobil robots are very popular and there are many studies about their design and control. One of the popular robots is the single spherical wheeled robot called Ballbot. These robots have generally three or four actuator with special wheels and can move on a ball to all directions. This structure has two basic problems. The first one is balancing on the ball and the second one is position control of the ball. The first robot with single spherical wheel was developed by Lauwers et.al at Carnegie Mellon University in 2006 [1]. However, the two or single wheel robots are older then it. Son et.al designed a two wheel, self-balancing robot called eScooter [2]. The robot controlled by adaptive back stepping controller and experimental studies was made succesfully. Another example is the robot developed by Kadis at.al. The robot has only one wheel and it can balance on the wheel when moving to any direction with a load. Proportional-Derivativ controller was used to balance control of the robot [3].

Ching-Wen Liao et.al developed a robot using a mouse-ball driving system actuated by two brushless motors. The balance control and path tracking processes are controlled by a sliding mod controller [4]. In another study, Tsai et.al developed a self-balancing and position controller for a Ballbot [5]. They made successfully simulations and experimental studies. Satici et.al developed a mathematical model and designed a PID controller for linear and non-linear models using simulations [6].

Yang et.al designed a micro ball-balancing robot with a smartphone interface and its height is only 25cm [7]. Navabi et.al developed a novel fuzzy sliding mode controller for a Ballbot and tested by simulations [8].

In this study a single spherical wheeled self-balancing robot is designed mechanically and a controller is developed to balance it in the Z-axis. The robot is modeled and simulated by Matlab program. The controller is also modeled and tested by simulations. The simulations show that the self-balancing control is successful. Position control and experimental studies are planned as a feature work.

II. MATERIAL AND METHODS

A. Mathematical Model of the Robot

A simplified, two dimensional drawing of the robot structure is given in figure 1. The body of the robot is placed on a spherical wheel. This structure is unstable and similar to inverse pendulum. All system parameters are given in Table 1. "Φ" is the angle between the Z-axis and the body. "Θ" is the angle between the body and the ball. "r" is the radius of the ball, "m_b" is the ball weight, "m_B" is the body weight, "l" is the distance between the ball center and the center of the gravity of the body, "I_b" is the inertia of the ball, "I_B" is the inertia of the body, "g" is the gravitational constant, "D_c" is coulomb friction constant and "D_v" is the viscos friction constant. All parameters used in the study are given in the Table 1 [9].

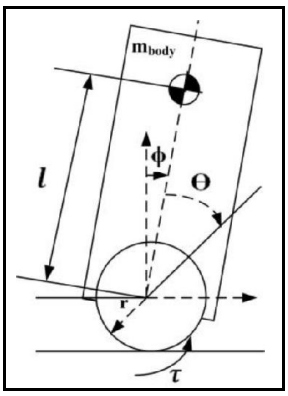


Figure 1: Drawing of the robot structure.

Table 1: System parameters.

Symbol	Parameter	Value
ϕ	Angle between the body and the Z-axis	-
Θ	Angle between the ball and the body	-
r	Radius of the ball	*0.12m*
m_b	Mass of the ball	*0.6kg*
m_B	Mass of the body	*7.227kg*
l	Distance between the ball center and the gravity center of the body	*0.37m*
I_b	Ball inertia	*0.0057kgm²*
I_B	Body inertia	*1.829kgm²*
g	Gravity constant	*9.8N/kg*
D_c	Coulomb friction	*0.00137Nm*
D_v	Viscous friction	*0.00137Nm*

The energy equations given in equation 1 and equation 2 are used to obtain the mathematical model of the robot [9]. The kinetic energy and the potential energy for the body are also given in equation 3 and 4.

$$K_b = \frac{I_b \dot{\phi}^2}{2} + \frac{m_b (r\dot{\phi}^2)^2}{2} \tag{1}$$

$$U_b = 0 \tag{2}$$

$$K_B = \frac{m_B}{2}(r^2\dot{\phi}^2 + 2rl(\dot{\phi}^2 + \dot{\phi}\dot{\theta})\cos(\phi+\theta) + l^2(\dot{\phi}+\dot{\theta})^2) + \frac{I_B}{2}(\dot{\phi}+\dot{\theta})^2 \tag{3}$$

$$U_B = m_B g l \cos(\phi+\theta) \tag{4}$$

The non-conservative forces (F_{NC}), defined using the coulomb friction and the viscos friction, is given in the equation 5. The differential equations can be obtained by Euler- Lagrangian method given in equation 6. The linearized steady-space model of the robot is given in the equation 7-17. Detailed information can be found in [9].

$$F_{NC} = D_c \operatorname{sgn}(\dot{\theta}) + D_v \dot{\theta} \tag{5}$$

$$\frac{d}{dt}\left(\frac{\partial L}{\partial \dot{q}}\right) - \frac{\partial L}{\partial q} = \begin{bmatrix}\tau \\ 0\end{bmatrix} - \begin{bmatrix} D_c \operatorname{sgn}(\dot{\theta}) + D_v\dot{\theta} \\ 0\end{bmatrix} \tag{6}$$

$$\dot{x} = Ax + Bu \tag{7}$$

$$A = \begin{bmatrix} 0 & 1 & 0 & 0 \\ \frac{A_{2,1}}{K} & 0 & 0 & \frac{A_{2,4}}{K} \\ 0 & 0 & 0 & 1 \\ \frac{A_{4,1}}{K} & 0 & 0 & \frac{A_{4,4}}{K} \end{bmatrix} \tag{8}$$

$$B = \begin{bmatrix} 0 \\ B_2 \\ 0 \\ B_4 \end{bmatrix} \tag{9}$$

$$C = \begin{bmatrix} 1 & 0 & 0 & 0 \end{bmatrix};\ D=0 \tag{10}$$

$$K = m_B m_b l^2 + I_B(m_B + m_b)r^2 + I_b(m_B l^2 + I_B) \tag{11}$$

$$A_{2,1} = \frac{g l m_B((m_b+m_B)r^2 + I_b)}{K} \tag{12}$$

$$A_{2,4} = \frac{D_v((m_B+m_B)r^2 + I_b) + D_v l m_B r}{K} \tag{13}$$

$$A_{4,1} = \frac{-l m_B(I_b g + r(g m_B r + g m_b r)) + g l^2 m_B^2 r}{K} \tag{14}$$

$$A_{4,4} = \frac{D_v + (I_B + I_b + m_b r^2 + m_B(l^2 + r^2)) + 2D_v l m_B r}{K} \tag{15}$$

$$B_2 = \frac{I_b + r^2(m_B + m_b) + l m_B r}{K} \tag{16}$$

$$B_4 = \frac{I_B + I_b + m_b r^2 + m_B(l^2 + r^2) + 2 l m_B r}{K} \tag{17}$$

B. Mechanical Design

The mechanical structure of the robot, given in figure 2, consists of three omnidirectional wheels; servo motors connected the omnidirectional wheels, the body and the ball. The omnidirectional wheels are shown in figure 3. These wheels connected to servo motors and placed on the ball. The angle that is between each wheel is 120° on the horizontal plane. The angle between the Z-axis and the wheels is 45° for each wheel. The drawings of the wheel placement on the ball are given in figure 4.

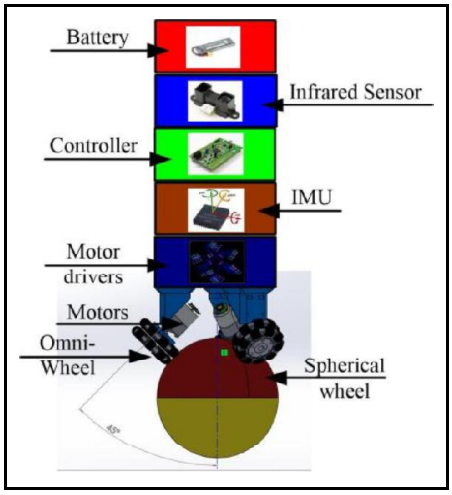


Figure 2: Mechanical structure of the robot.



Figure 3: The omnidirectional wheel.

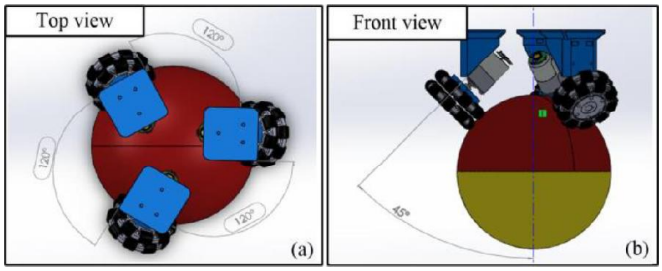


Figure 4: The placements of the wheels. a) Horizontal placement of the wheels. b) Vertical placement of the wheels.

The connection between the wheels and the body is made by the parts produced by a 3D printer. The completed connections are shown in figure *5* and the robot shown in figure 6. Aluminum profiles and plates are used to complete the robot body. The radius of the robot is 17cm and length is 133cm. total weight of the robot is *8* kg with the ball. The radius of the ball is 12 cm and its weight is 600gr.

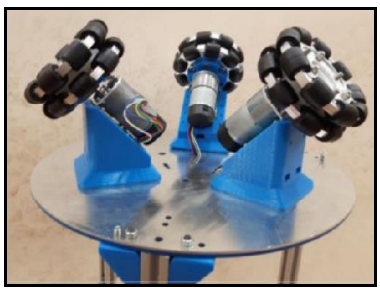


Figure 5: The placements of the wheels.



Figure 6: The front view of the robot.

C. *Controller Design*

Proportional-integral-derivative (PID) controller is used as a balance controller for the robot. A general structure of a PID controller is given in equation 18. PID controller is widely used in many applications and it has enough performance for this application. The tuning process of the PID is made by trial and error method.

$$PID = K_p e(t) + K_i \int_0^t e(t)dt + K_d \frac{de(t)}{dt} \quad (18)$$

D. SIMULATIONS

The designed robot and the controller are simulated using the Matlab program. The robot model is created using the differential equations and made the balancing control. All control study is made by simulations using the Matlab program. The general block diagram of the designed simulation is given in figure 7.

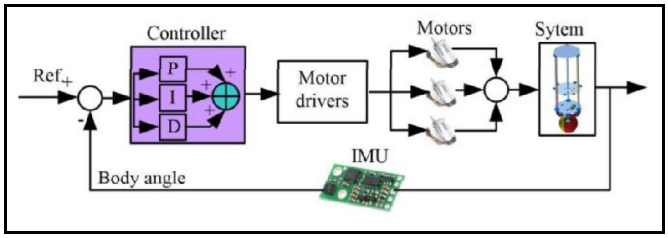


Figure 7: General block diagram of the simulation.

The PID tuning process is made by trial and error method. The used PID coefficients for the simulation are K_P=150, K_I=50 and K_D=2.

The body angle and the body position graphs are given in figure 8. The reference angle for the body is 1°. It reaches the reference angular position in 1.42s and the steady-state error is %0.03. The robot moves continuously to balance the body with desired angular position.

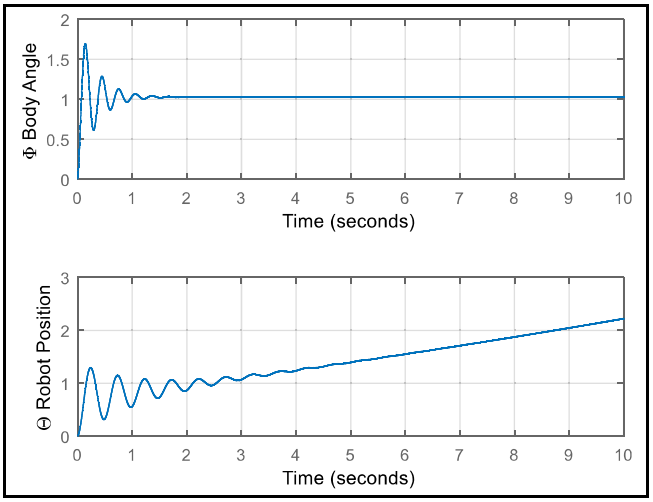


Figure 8: Simulation results.

III. CONCLUSIONS

In this study, a robot with a single spherical wheel was designed and simulated successfully. The mathematical model of the robot was obtained and a mechanical design was made using a ball, a body with aluminum and 3D printed parts, three omnidirectional wheels and motors. A simulation study was also made to see the robot balancing performance. The designed PID controller was tuned successfully and the simulation results show that the robot can balance on the desired angle in the Z-direction.

A real-world application of the balance control of the robot and position control are feature plans for this study. Some optimization applications for the controller are also part of the plans.

IV. ACKNOWLEDGMENT

This study is supported by the Department of Scientific Research Projects at Karabuk University, No: KBÜBAP-17-YL-194.

REFERENCES

[1] T. B. Lauwers, G. A. Kantor, and R. L. Hollis, "A dynamically stable single-wheeled mobile robot with inverse mouse-ball drive," *Proc. - IEEE Int. Conf. Robot. Autom.*, vol. 2006, no. 3, pp. 2884–2889, 2006.

[2] N. N. Son and H. P. H. Anh, "Adaptive backstepping self-balancing control of a two-wheel electric scooter," *Int. J. Adv. Robot. Syst.*, vol. 11, pp. 1–11, 2014.

[3] A. Kadis, D. Caldecott, A. Edwards, M. Jerbic, R. Madigan, M. Haynes, B. Cazzolato, and Z. Prime, "Modelling , simulation and control of an electric unicycle," 2010.

[4] C. W. Liao, C. C. Tsai, Y. Y. Li, and C. K. Chan, "Dynamic modeling and sliding-mode control of a Ball Robot with inverse mouse-ball drive," *Proc. SICE Annu. Conf.*, pp. 2951–2955, 2008.

[5] C. C. Tsai, M. H. Juang, C. K. Chan, C. W. Liao, and S. J. Chan, "Self-balancing and position control using multiloop approach for ball robots," *2010 Int. Conf. Syst. Sci. Eng. ICSSE 2010*, pp. 251–256, 2010.

[6] A. C. Satici, F. Ruggiero, V. Lippiello, and B. Siciliano, "Intrinsic Euler-Lagrange dynamics and control analysis of the ballbot," *Proc. Am. Control Conf.*, vol. 2016–July, pp. 5685–5690, 2016.

[7] D. Yang, E. Sihite, J. M. Friesen, and T. Bewley, "Design and control of a micro ball-balancing robot (MBBR) with orthogonal midlatitude omniwheel placement," *IEEE Int. Conf. Intell. Robot. Syst.*, vol. 2015–Decem, pp. 4098–4104, 2015.

[8] H. Navabi, S. Sadeghnejad, S. Ramezani, and J. Baltes, "Position control of the single spherical wheel mobile robot by using the fuzzy sliding mode controller," *Adv. Fuzzy Syst.*, vol. 2017, 2017.

[9] R. P. Ramírez, "Control and implementation of a single wheel holonomic vehicle," Javeriana, 2013.

Real-time Remote Control of Robotic Hand System - TeleTouch

Musa Sadık Ünal[1], Ersin Ertürk[1], Mustafa Cem Kasapbaşı[2], Erdem Yavuz[2], Ufuk Şanver[2]

[1] Kartal Anadolu Imam Hatip High School, Istanbul /Turkey, {ahmet, unalmusasadik}@gmail.com
[2]Istanbul Commerce University, Istanbul/Turkey, {mckasapbasi, eyavuz, usanver}@ticaret.edu.tr

Abstract - **Robots offer an efficient way as assistive devices to perform many errands. In this study, it is aimed to present a proof-of-concept robotic system that is called TeleTouch. TeleTouch allows mimicking user's fingers motions/gestures to be transferred in a desired remote location within an acceptable delay. In the implementation, Leap motion sensor, RaspberryPi, and Arduino kits are used. Hand model that is manufactured by 3D printers is actuated by Arduino system which drives the servo motors connected to the hand model. RaspberryPi is used not only for transferring camera view of the hand model to the controlling remote system but also for transferring fingers attributes to the Arduino system. A special software is developed in .Net platform to gather the user's attributes of the fingers from leap motion sensor. Delay times of the local and remote system are investigated and it is understood that proposed system successfully transfer motion in almost real time.**

Keywords – **robotic hand, real-time control, leap motion**

I. INTRODUCTION

THE efforts of mankind to facilitate lifesytle are based on their first years of existence. These struggles, which are anticipated as the design of new hunting tools in the Stone Age; continued as mechanization and nowadays it has reached such a dimension to produce with robots and computer-aided automation. So, machines are being designed that can either replace humans for some works or help alleviate their burden ensuring a quality and fast production. The next step in robotics in production industry is the design and usage of humanoid robots widely. Recent studies [2-8] in literature clearly show a rapid developments in the field today. Of course, these developments will also be reflected in the exploration of humanoid robot development in the near future, as well as in all areas [1].

In this study, it is aimed to develop a system that could be used in different application fields in order to contribute to the technological developments. In the proposed study, an integrated structure has been developed that uses image processing to interpret human movement. In this system, image processing technique is used without the need for any gloves or sensors unlike the reviewed studies in literature. The developed system stands out with its potential to be widely used in remote control systems as well as providing innovation in different areas of technology.

The rest of the paper is organized as follows. In Section II, details and scope of the project is given. Section III introduces the proposed methodology. Section IV investigates the results of the study. Finally, conclusions are summarized in Section V.

II. SCOPE OF THE STUDY

In the proposed study, it is aimed to develop software and the mechanical system which enables real hand movements to be imitated simultaneously by the robotic hand. In the system, hand movements are read from Leap Motion, and the collected data is transmitted to robotic hand via TCP / IP protocol. The robotic hand is connected to the processor and assessed for live hand images. The movements of hand is captured and imitated to perform the same movements. Thus, a robotic hand control system has been developed to apply remote controlled hand movements on an individual basis. The user panel has the ability to send the environment images, temperature and humidity data, and the degree of cushion stiffness it touches. Use of this kind of systems open up new possibilities such as bomb disposal, unmanned exploration, surgical operations and so on.

III. METHODOLOGY

The design of the system consists of three basic stages. The first stage includes the user interface software, which is developed in C#. The second stage is the one where the finger and hand gestures are sensed and converted to values. The image data are transferred via the TCP / IP protocol Internet. Finally, the Arduino platform is used to read sensor values and control of the servo motors. First of all, the user plugs Leap Motion to the computer. Then it starts the application. Whenever the user moves his/her hands and fingers, hand information is read and interpreted by the application. Later, the user specifies the IP address of the device he/she wants to connect to and then connects to the remote device (to a server). The remote device is actually a small computer, an embedded-system card, called RaspberryPi. Alternatively, other cards such as BeagleBone may be used. The most important feature of these cards is to have an operating system (Linux) embedded in them. With this operating system, it is possible to run complex programs that microcontrollers can not run. In this context, the Python code in RaspberryPi responds to requests to connect over IP (clients). After the

connection, the Arduino card virtually connected to Raspberry Pi reads the sensor values via the serial port and the environmental information is sent to the interface. These values are plotted in real time on the interface. Hand and fingers data from the interface are also sent to Arduino in the same way. These are converted to PWM waves for robot hand control and are provided for hand movement. In addition, the user interface from the camera on the robot hand goes to the camera image and the media data read from the sensor. Flowchart of the program looks as shown in Figure 1

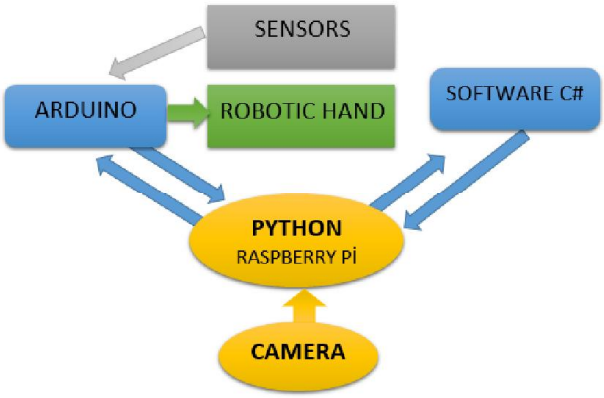


Figure 1: Flowchart of the program.

A. Leap Motion

Leap Motion is used to transfer live hand movements to the computer. Leap Motion is an electronic device marketed by Leap Motion company in 2012 to detect movements of the hand and fingers, seen in Figure 2. The working principle of Leap Motion is based on infrared lights, cameras and optical lenses. The light scattered at an angle of 150 degrees on the Y axis is returned to the camera and processed. It can measure between about 25 cm and 60 cm.



Figure 2: Leap Motion

Leap Motion uses a 3-dimensonal axes. The X and Z axes operate in the horizontal plane while the Y axis is in the vertical axis. Y axis tells the height of the hand from Leap Motion. X axis is the right and left information, and Z axis is the distance from the hand to Leap Motion. There are four main factors in the operation of Leap Motion device. These factors are listed below.

- Distance: millimeters
- Duration: microseconds
- Speed: millimeters / second
- Angle: radian

The coordinate information must be transferred to the computer by a mapping method. It is necessary to know and adjust the angles of field in Leap Motion. The image to be captured in this area will take on the shape of an inverted pyramid [9].

Developed software can detect hand movements instantly by courtesy of the introduced hand patterns. The generic functions available for hand movements are found in the Hand library. Leap Motion gives us the information of the fingers and hand. The system can also detect partially available information.

B. Developed Software in Python

In this study, the Python language is preferred for the program that will run on a Linux computer, RaspberryPi. Python is a popular programming language in the world because it is easy to use with RaspberryPi.

C. Developed Software in C#

The C # programming language is preferred to develop a user-friendly interface to run Leap Motion. Main reason for the preference of this programming Language is due to its useful SDK. Figure 3 show the user interface of the software.

.

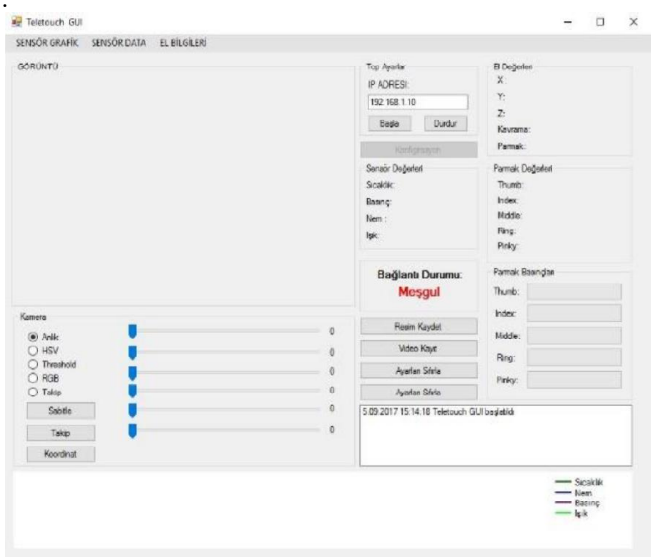


Figure 3: User interface of the software.

In order to move the finger of the robot hand, it is first necessary to detect and take movement data of the user's fingers. Leap Motion enables to use the vectors of bones on the fingers. According to anatomical research related to bones, when the hand is twisted, the twist angle can be measured between the proximal and intermediate bones. The vectors of these two bells and the angle between them are given in Figure 4.



Figure 4: Angles between bones of the user's finger.

The angle is calculated using formula given below.

$$\alpha = arccos\left((\vec{u} \cdot \vec{v})/(\|\vec{u}\|\|\vec{v}\|)\right) \quad (1)$$

D. Arduino Hardware

Arduino Hardware Platform is preferred for electronic circuit installation in the study. Because Arduino Hardware Platform is very useful for rapid prototyping and it is an open source platform. Also printed circuit (PCB) design of the electronic circuit is realized for comfortable using. This design is shown in Figure 5.



Figure 5: PCB schematic design of the hardware.

IV. Results and Discussion

One of the most important factors in system operation is how long it takes to send the hand movement commands. In the experimentation, the Arduino kit receives the data and echoes it after turning the servo motor. Then, the program in .Net platform sends command, and start a timer and measure the time elapsed. Later, the measurement is divided by 2, and certainly there exists a delay on virtual transmission line. Results of time delay at different experimentations are shown in Figure 6.

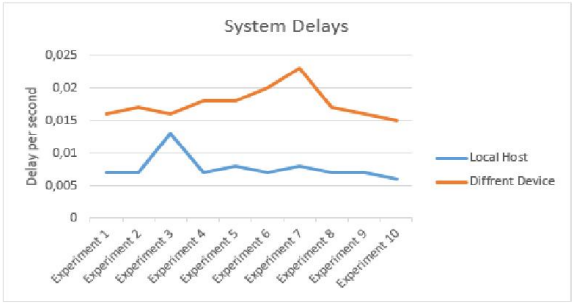


Figure 6: Time delay at different experimentations.

As a result of several experimentations, it has been observed that the average latency in the local host was 7.7 miliseconds. The delay in the RaspberryPi has been measured as 17.6 miliseconds. It has been determined that the delay in the system is mostly caused by the servo motors.

The implemented system has the possibility to take the data in three dimensions. With Leap Motion, hand depth and movement information of hand can be taken.

V. Conclusion

On the running system, the user can control the robotic hand system via TCP / IP without any glove or sensor from the C # interface. Sensor values such as humidity, temperature, pressure from the robotic system, and camera images are also displayed at the interface. The targeted live imitation has also been successful. This will enable the system to be used in many areas such as bomb disposal, unmanned exploration, surgical operations and so on and also it will open up new future developments.

Acknowledgment

This project got prize in six different competition as follows:

- TÜBİTAK - 48th Secondary Students Research Projects Competition Coding Category - Istanbul Asia Region- First Prize
- Marmara University Mechatronics and Innovation Days Freelance Category- Second Prize
- Okan University Engineering Competition Mechatronics Field- First Prize
- TÜBITAK - 48th Secondary Education Students Research Project Competition Coding Category – Turkey- Second Prize
- Çekmeköy Municipality ALIYA IZETBEGOVIC International Science Olympics Technology Category- First Prize
- International Informatics Science and Applications Project Competition- First Prize

References

[1] M. Demircioğlu, "Bilgisayar destekli robot el tasarımı ve gerçekleşmesi," Fen Bilimleri Enstitüsü, Sakarya Üniversitesi, Sakarya, 2006.

[2] P. Khanna, K. Singh, K. M. Bhurchandi, and S Chiddarwar, "Design analysis and development of low cost underactuated Robotic hand," in *2016 IEEE Int.Conference Robotics and Biomimetics (ROBIO),* pp. 2002-2007.

[3] V. P. da Fonseca, , D. J. Kucherhande, T. E. A. Oliveira, D. Zhi, and E. M. Petriu, "Fuzzy controlled object manipulation using a three-fingered robotic hand," in *2017 Annual IEEE Int. Systems Conference (SysCon),* pp. 1-6.

[4] A.Campeau-Lecours, P. L. Belzile, T. Laliberté, S. Foucault, B. Mayer-St-Onge, D. Gao, and C. Gosselin, "An articulated assistive robot for intuitive hands-on-payload manipulation," *Robotics and Computer-Integrated Manufacturing,* vol. 48, pp.182-187, 2017.

[5] P. Dhepekar and Y. G. Adhav, "Wireless robotic hand for remote operations using flex sensor," in *2016 IEEE Int.Conf. Automatic*

Control and Dynamic Optimization Techniques (ICACDOT), pp. 114-118.

[6] A. Khamis, C. H. Chen, and D. S. Naidu, "Tracking of a robotic hand via SD-DRE and SD-DVE strategies," in 2016 IEEE 11th Int. Conf. on *Control (CONTROL)*, pp. 1-6.

[7] A. Saudabayev and H. A. Varol, "Sensors for robotic hands: A survey of state of the art," *IEEE Access*, vol. 3, pp.1765-1782, 2015.

[8] R. Yazıcı and H. Karal, "An Implementation of a Robotic Vision System with Neural Networks," 2th Int. Mechatronic Design and Modeling Workshop, 1995.

[9] Avilable: https://developer.leapmotion.com/documentation/csharp/index.html.

[10] Ö. Pektaş, "Mobil bomba imha robotlarının incelenmesi ve prototip robot tasarımı," Fen Bilimleri Enstitüsü, İstanbul Üniversitesi, İstanbul, 2010.

[11] C. Sürmeli and A. Mutlu, "Mikrodenetleyiciler ile Seri İletişim," KODLAB Yayıncılık, İstanbul, 2014.

Effect of Underwater Sound Speed Profile on Target Parameter Estimation

A. GÜNEŞ[1]

[1]Atılım University, Ankara/Turkey, ahmet.gunes@atilim.edu.tr

Abstract **– Underwater acoustic simulations is an important part of the underwater acoustic research. Due to the high costs of underwater tests and difficult environment, reliable simulation methods are required. Ray tracing is one of the alternatives to use for underwater high frequency applications. In this work, we have simulated the effect of different sound speed profiles (SSPs) on underwater localization using the ray tracing method. First, the time-of-arrivals (ToAs), i.e. channel taps, are analyzed for a single sensor. The results show the fluctuations may differ considerably, per SSP. Second, the channel taps are used for the calculation of the target position by ToA measurements. The results indicate that the estimates become biased according to the SSP and a correction in the algorithm is required.**

Keywords **– Underwater acoustics, sound speed profile, ray tracing, time-of-arrival.**

I. INTRODUCTION

Since the underwater environment is not homogeneous as the atmosphere and the experiments are costly, numerical solvers are invaluable for analyzing and simulating the underwater sound propagation. In this way, the errors in the system become foreseeable. However, the propagation of sound under the water is much complex, since it is affected by many environmental parameters such as the bathymetry, sound speed profile (SSP) and so on. There is no single numerical method which can handle all of these factors perfectly. In fact, the numerical solvers focus on some of the parameters and usually make simplifications on the others. Thus, there are several numerical methods, each having their own set of advantages and drawbacks. For example, in shallow waters and at low frequencies normal mode models provide consistent results with the measurements [1]. However, when the wavelength of the received signals are much lower than the depth of the sea, the ray tracing method is a better alternative [1][2].

Underwater localization is an important problem in underwater applications. Since electromagnetic waves propagate with very high attenuation, acoustic systems are widely utilized for underwater localization systems. Based on the various measurement types like direction-of-arrival (DoA), time-of-arrival (ToA), received signal strength (RSS), time-difference-of-arrival (TDoA), the location of vehicles can be estimated [6][7][8][9][10]. One of the most commonly used systems is ToA. It uses multilateration to estimate position and requires synchronization of transmitter and receivers. Thus, the system is somewhat complex with respect to other approaches. But it also provides more accurate results.

Acoustic underwater localization systems generally use high frequencies which provide better resolution for target detection and parameter estimation. Thus, the selected numerical method must be able to handle high frequencies. Additionally, multipath effect is an important phenomenon in underwater acoustics. One must be able to obtain and incorporate the channel taps in the analysis to design a functioning system. Unlike the aerial applications, the speed of sound cannot be assumed homogeneous under the water. Sound speed is affected by the properties of sea water such as the salinity, temperature and pressure. These different properties usually differ with depth, causing several horizontal layers of different sound speeds to form. Together they are called sound speed profile (SSP) [3]. SSP causes the path of the sound to bend along the way from the target to the receiver and time-of-travel of the signal can deviate dramatically. To analyze time-of-travel, ray tracing method is chosen for simulations in this study. Ray tracing method also provides the major channel taps between the transmitter and the receiver, giving the opportunity to incorporate the effects of multipath.

In this paper, the effect of multipath and SSP are simulated using ray tracing. Moreover, these effects are evaluated for the performances of systems based on ToA measurements are compared for underwater applications. Different channel taps are considered for detection and localization purposes.

II. SIMULATIONS

Due to SSP, the signal paths distort and become curvilinear instead of linear. This results in reflections from the water surface and bottom. These reflections are the reason of multipath. When the SSP is also linear, the path of the sound become partial circles. This effect is due to the inhomogeneous nature of the sound speed. The sound speed under the water tends to be separated as horizontal layers [4]. Because of layers having different sound speeds, the sound waves behave as if they move through different materials and deviate. Different SSPs result in different deviation behaviors. Seven different SSP's are considered and they are shown in Fig.1. The scenarios are isovelocity, negative and positive gradient between 1450-1500 m/s, positive and negative gradient between 1500-1550 m/s, and negative and positive gradients with a sharper layer at the upper portion.

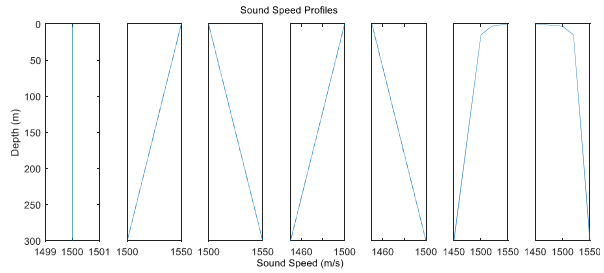


Figure 1: Sound speed profiles of different scenarios. The SSP's are referred from left to right as SSP-1, SSP-2, SSP-3 and so on, in the text.

The propagation and the paths for SSP-2 at 2000 m is shown in Figure 2. The rays bent downwards. The same simulation for SSP-3 is shown in Figure 3. The rays bent upwards in this case. Thus, all of the signal energy will not be transferred through a single channel but through multiple paths. The number and the energy of paths arriving at the receiver end depend on the SSP.

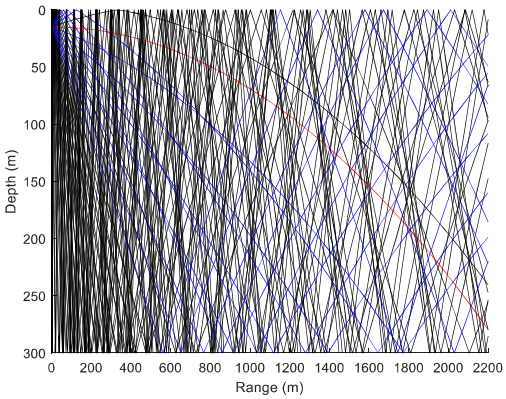


Figure 2: Rays at 2000 m distance when positive gradient, SSP-2 in Fig.1, is used. The red lines indicate the rays which reach at the receiver end without a reflection, blue rays indicate the rays with one reflection and the rest of rays are indicated with black curves.

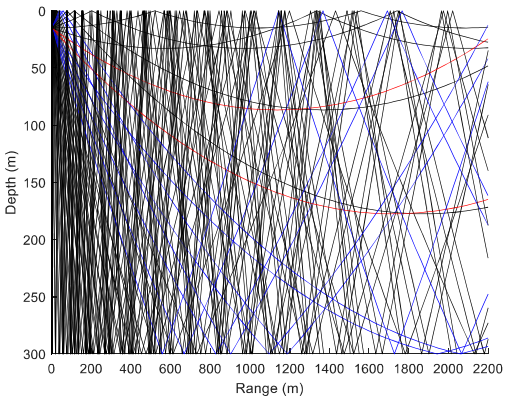


Figure 3: Rays at 2000 m distance when positive gradient, SSP-3 in Fig.1, is used.

III. Localization Technique

The maximum likelihood (ML) estimation using ToA measurements use only one detection. On the other hand, several detections are acquired at the sensor side as arrival time and amplitude pairs, per simulation step. A selection procedure must be set in order to distinguish between the detections. Selections can possibly be based on

- Maximum signal strength, i.e. highest amplitude tap
- Earliest arrival, i.e. the 1st tap
- Average time
- Median time

Using one of the above methods the number of utilized detections can be reduced to one. In this work, we use the first two detection methods: Channel tap with the highest energy and channel tap with the shortest arrival time. An example of the arrival time, amplitude pairs and 1st tap, maximum tap selection is shown in Figure 4 below. At each simulation step these taps are calculated using ray tracing and results are calculated accordingly.

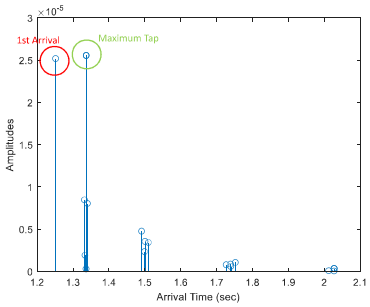


Figure 4: The arrival times and the amplitudes of the channel taps. The 1st arrival, having the least arrival time, is shown with a red circle. The maximum tap is shown with a green circle. It has the maximum amplitude among the channel taps.

There are various algorithms for ToA based localization problem [5]. Since the localization algorithm is not the focus of this paper, we use an unconstrained, simple approach. The time-of-arrival at the sensors is a function of both the position of the target and the sensors. Thus, the measurement model is

$$t_i = \frac{\|p_t - p_i\|}{c}, \quad (1)$$

where t_i and p_i are the arrival time and the position vector of the signal at the i th sensor, respectively. p_t is the position of the targets and c is the speed of sound in the medium. The ranges from each sensor are calculated from t_i as

$$r_i = c \cdot t_i \quad (2)$$

In ToA method, the position of the sensor can be estimated by the following least squares calculation [5]. Since the depths

of the target and sensors are assumed equal and 15 m, a two dimensional approach is sufficient.

$$r_i^2 = \left(x_t - x_i\right)^2 + \left(y_t - y_i\right)^2 \tag{3}$$

Reorganizing terms yield

$$r_i^2 = x_t^2 + y_t^2 - 2x_t x_i + 2y_t y_i + x_i^2 + y_i^2 \tag{4}$$

If the first sensor is assumed as the origin of the system, then $r_1^2 = x_t^2 + y_t^2$ and $p_i^2 = x_i^2 + y_i^2$. And (4) can be simplified as

$$r_i^2 = r_1^2 + p_i^2 - 2x_t x_i - 2y_t y_i \ . \tag{5}$$

and finally for each sensor we obtain

$$r_i^2 - r_1^2 - p_i^2 = -2x_t x_i - 2y_t y_i \ . \tag{6}$$

In simulations, four sensors are used. When (6) is written in matrix form for all the sensors it becomes

$$\begin{bmatrix} r_1^2 - r_1^2 - p_1^2 \\ r_2^2 - r_2^2 - p_2^2 \\ r_3^2 - r_3^2 - p_3^2 \\ r_4^2 - r_4^2 - p_4^2 \end{bmatrix} = \begin{bmatrix} -2x_1 & -2y_1 \\ -2x_2 & -2y_2 \\ -2x_3 & -2y_3 \\ -2x_4 & -2y_4 \end{bmatrix} \begin{bmatrix} x_t \\ y_t \end{bmatrix} \tag{7}$$

Defining the coefficient matrix as

$$A = \begin{bmatrix} -2x_1 & -2y_1 \\ -2x_2 & -2y_2 \\ -2x_3 & -2y_3 \\ -2x_4 & -2y_4 \end{bmatrix} \tag{8}$$

and multiplying both sides of (7) with the pseudo (Moore-Penrose) inverse of A which is equal to

$$A^+ = \left(A^T A\right)^{-1} A^T \tag{9}$$

yields the least squares estimates of the position of the target.

IV. SIMULATIONS

Two different simulations are executed in this work. In all simulations the transmitter and the receiver are positioned at 15 m depth. Scenario I is the calculation of range by the channel taps. The taps are calculated between 50-1950 m with 50 m steps, and the distribution of expected ranges are drawn in figures. Scenario II is based on the estimation of position of the target by four sensors. In all scenarios 50 rays are used in ray tracing simulations.

Scenario I:

The results of Scenario I are shown in Figure 5-9. The ranges are distributed along the black dashed lines. The red line is the mean value of the estimated ranges. The arrival times and the ranges are related simply by the sound speed as in (2). Naturally, the ranges tend to decrease as the target approaches to the sensor. For SSP's from 1 to 5, the earliest arrival, i.e. the 1st channel tap, gives very close results to the real range as seen in Figure 5-9. The difference between the measured and the real ranges are usually less than 50 m. However, except for the results of SSP-1, the ranges tend to deviate significantly from the actual ranges. There are also fluctuations at certain ranges. This is considered to be the result of bending of the paths. If the speed of sound was different these fluctuations would occur similarly but at a different distance. Although the first arrivals yield similar ranges for SSP-1 to SSP-5, the distribution of ranges extracted from channel taps depend heavily on the SSP. SSP-6 is expected to provide the worst results as the 1st taps have a flat change and sudden drops with range, as seen in Figure 10.

SSP-6 and SSP-7 have a total change of 100 m/s in sound speed with a sharp gradient at the top. Thus, these are more challenging environments. In Figure 11, the rays for SSP-6 are plotted. According to the simulations, when the targets are below 150 m depth, they cannot be detected at 2000 m distance. Figure 12 indicates that when SSP-7 is in effect, no rays can reach the sensor from the target when target is more than 300 m away. Hence, ToA localization is not applied on SSP-7 version of the scenario II.

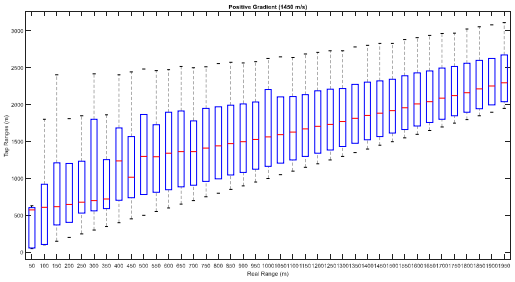


Figure 5: The real ranges vs ranges calculated using the channel taps for SSP-1.

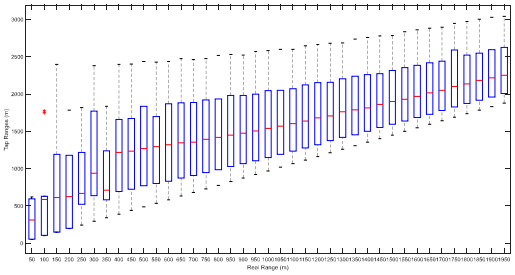


Figure 6: The real ranges vs ranges calculated using the channel

taps for SSP-2.

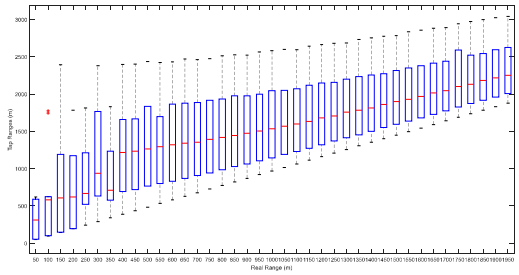


Figure 7: The real ranges vs ranges calculated using the channel taps for SSP-3.

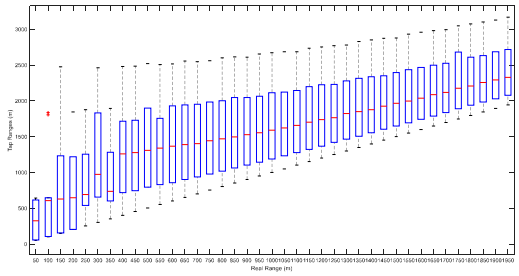


Figure 8: The real ranges vs ranges calculated using the channel taps for SSP-4.

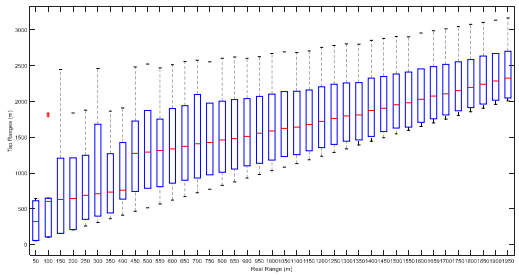


Figure 9: The real ranges vs ranges calculated using the channel taps for SSP-5.

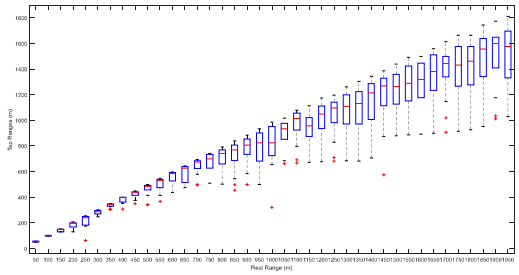


Figure 10: The real ranges vs ranges calculated using the channel taps for SSP-6.

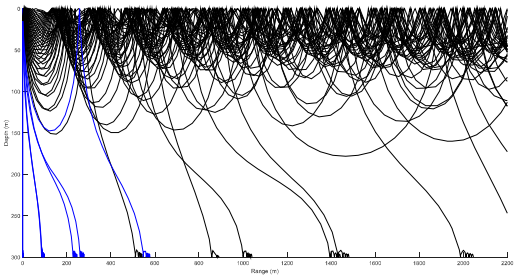


Figure 11: The rays for SSP-6.

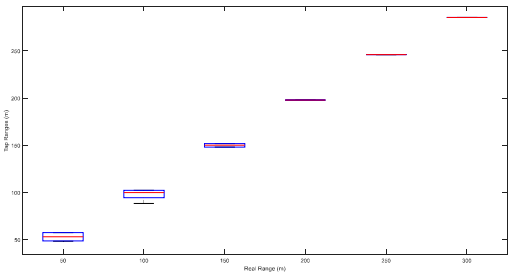


Figure 12: The real ranges vs ranges calculated using the channel taps for SSP-7.

Scenario II:

In Scenario II, there are four sensors, each at the corners of a square of 2000 m × 2000 m. The target starts the movement at coordinates $(1000\,m \times 1000\,m)$, in the middle of the area. Then it moves at a random direction with a speed of 24 kts and measurements are received from each sensor every 1 sec. 10 Monte Carlo runs are executed for each SSP. The setup of the scenario is shown in Figure 13. Except SSP-7, all of the SSP's in Figure 1 are used in this scenario.

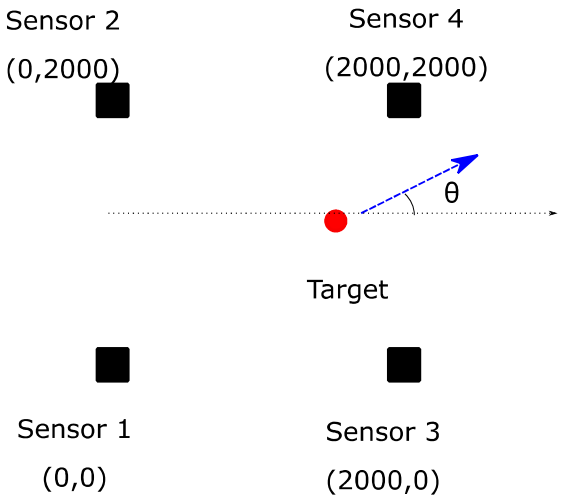


Figure 13: Localization scenario using four range-only sensors.

From the channel taps, the ranges are calculated according to (2). Then the target position is calculated using (7). The ranges of the target from different sensors according to the selected channel taps and the estimated target position for a single simulation step are presented in Figure 14.

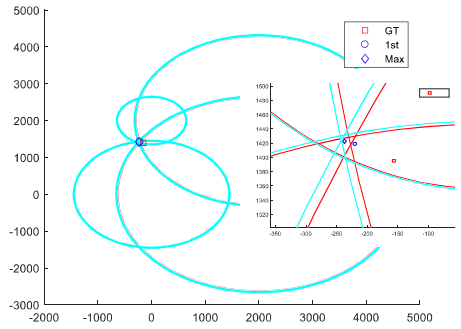


Figure 14: The ranges from different sensors and the estimated position of the target. Red and green curves indicate the ranges from sensors when the 1st taps and the maximum taps are used, respectively.

The RMS position estimation errors of the results for SSP-1 to SSP-6 are shown in Figure 15. Since SSP-6 causes very high errors, its results are plotted in Figure 16. The results indicate a change of error pattern at the 80th step. That is approximately the time when the target moves out of the square region between the sensors. The change is more significant in 1st taps. Outside the square region, both kind of detections yield similar results.

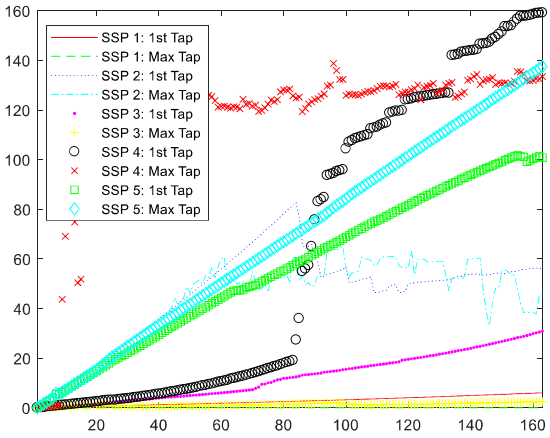


Figure 15: RMS errors for position estimates for different SSP's.

As expected, SSP-6 simulation results are worse than the others. They are presented in Figure 16, below. A different behavior under SSP-6 is the accuracy of the maximum taps. They provide twice more accuracy than the 1st taps. Thus, as a rule of thumb, in a real system design the maximum taps can be a better way to exploit.

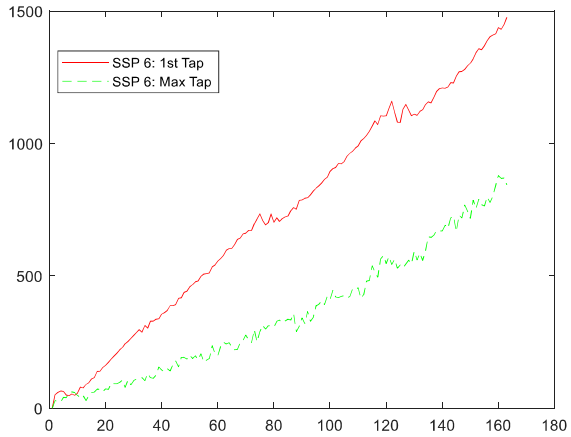


Figure 16: RMS errors for position estimates for SSP-6.

The estimation errors in all simulations deviate much and they do not approach to zero at any time instant. There seems to be a systematic error. Therefore, it can be said that ToA algorithm yields biased estimates. To overcome this problem, a different localization algorithm must be utilized.

V. Conclusion

In this paper, we analyzed the effect of SSP on underwater localization problem. Using the ray tracing method, the channel taps are obtained. Channel taps represent the energy carried by each underwater path. These taps are used as ToA measurements to estimate the x and y coordinates of a target. The acquired multipath effects and the results are consistent. Therefore, this simulation infrastructure can be considered as fit for testing the underwater localization algorithms. However, simulations with different bathymetry and sea states can be analyzed.

ToA seems to make biased estimates for localization. In the future, we will focus our effort on designing an unbiased estimator for target position.

References

[1] P. C. Etter, *Underwater Acoustic Modeling: Principles, Techniques and Applications*, CRC Express, 1995.

[2] J. M. Hovem, *Ray Trace Modeling of Underwater Sound Propagation, Modeling and Measurement Methods for Acoustic Waves for Acoustic Microdevices,* InTech, 2013.

[3] R. J. Urick, *Sound Propagation in the Sea*, U.S. Government Printing Office, 1979.

[4] A. N. Barkhatov, *Modeling of Sound Propagation in the Sea*, Consultants Bureau, 1971.

[5] K. W. Cheung, H. C. So, W.-K. Ma, Y. T. Chan, "Least squares algorithms for time-of-arrival-based mobile location," *IEEE Transactions on Signal Processing*, Vol. 52, No. 4, pp.1121-1128, 2004.

[6] T. Xu, Y. Hu, B. Zhang, G. Leus, "*RSS-based sensor localization in underwater acoustic sensor networks*," IEEE International Conference on Acoustics, Speech and Signal Processing (ICASSP), Shanghai, 2016.

[7] S. Poursheikhali, H. Zamiri-Jafarian, "*TDOA based target localization in inhomogeneous underwater wireless sensor network*," IEEE 5th International Conference on Computer and Knowledge Engineering (ICCKE), 2015.

[8] Q. Liang, B. Zhang, C. Zhao, Y. Pi, "*TDoA for passive localization: Underwater versus Terrestrial Environment*," IEEE Transactions on Parallel and Distributed Systems, Vol.24, No.10, pp.2100-2106, 2013.

[9] W. A. P. van Kleunen, K. C. H. Blom, N. Meratnia, A. B. J. Kakkeler, P. J. M. Havinga, G. J. M. Smit, "*Underwater localization by combining time-of-flight and direction-of-arrival*," IEEE/MTS OCEANS'14, Taipei, 2014.

[10] M. I. Al Hajri, A. Goian, M. Darweesh, R. Al Memari, R. M. Shubair, L. Weruaga, A. R. Kulaib, "*Hybrid RSS-DOA technique for enhanced WSN localization in a correlated environment*," International Conference on Information and Communication Technology Research (ICTRC), pp.238-241, 2015.

Modelling and PID Control of Scara Robot

M.A. ŞEN[1], V.BAKIRCIOĞLU[2] and M. KALYONCU[3]

[1] Selçuk University, Konya/Turkey, marifsen@selcuk.edu.tr
[2]Aksaray University, Aksaray/Turkey, vbakircioglu@aksaray.edu.tr
[3] Selçuk University, Konya/Turkey, mkalyoncu@selcuk.edu.tr

***Abstract* – Designing and control a robot manipulator with great performance is one of the fields of interest in the industry. In this paper, a scara robot is dynamically modeled and position control with PID controllers is realized. The main aim of this study, perform a scara robot position control in MATLAB/SimMechanics. Firstly, the computer aided design (CAD) model of the system which is built SolidWorks exported to MATLAB/SimMechanics environment. Then, applied PID controller to the system to ensure position control of joints in desired references in MATLAB/Simulink. The simulation performed and the results given graphical form to define performance of PID controllers.**

***Keywords* – Scara Robot, Modelling, MATLAB/SimMechanics, MATLAB/Simulink, PID control.**

I. INTRODUCTION

Scara robot is one of the challenging fields in industrial automation systems. Scara robots are generally used in positioning and handling devices in industrial applications. New technology studies improved the performance of control strategy of scara robot which can be used to replace human in hazardous, complex and boring tasks. Many researchers focus to study the improvement of the robot controller. Because of the nonlinearities and complex physical structure, modelling and control is a main problem for scara robots. Generally, different types of robot controller give different output performance of robot movement. Most controllers applied the scara robot such as PID, Fuzzy Logic Controller (FLC) and also the combination of the three controllers.[1]

In literature review, different studies are realized about scara robots. But the most important and similar studies are considered and given in this paper. Dynamic modeling and control of Scara type robotic systems is investigated by researcher. Şahin [2], present trajectory control of a Scara type robot using PID control. Saygılı [3] present design and animation of a Scara type robot. Ogulmuş et. al. [4] presents position control of a scara robot type 3D printer system that is dynamically modeled. The others studied about control and modelling of scara robot system [5-10].

In this paper, a scara robot with three degrees of freedom (3+1) modelled and position control with PID controllers. The scara robot include three rotational joint and one liner joint

The SolidWorks model [11] of the scara robot show in Figure 1. The computer aided design (CAD) model of proposed the scara robot is created by using SolidWorks program and exported to MATLAB/SimMechanics environment with physical parameters. To achieve different type modeling technique without mathematical equations, used MATLAB and Solidworks programs. Later, for position control of the scara robot, four PID (proportional-integral-derivative) controllers are designed in MATLAB/Simulink. The gain of PID controllers determined with trail-error methods. Finally, the system simulated and obtained result are given graphical form to show performance of controllers.

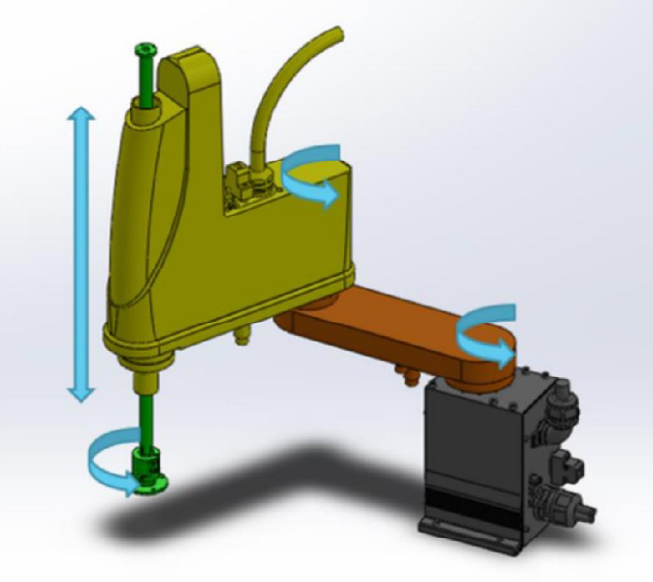


Figure 1: The CAD model of the scara robot

II. MODELLING AND CONTROL OF SYSTEM

The physical parameters of the scara robot shown in Figure 2. The scara robot produced by Yamaha in small sizes (tiny) are classified according to their maximum arm length. The robot (Yamaha YK500XGL-150) has a 150mm arm length. The lifting capacity is maximal 1kg. It has been produced in order to make fast and precise operations such as marking, packing, stacking in serial production.

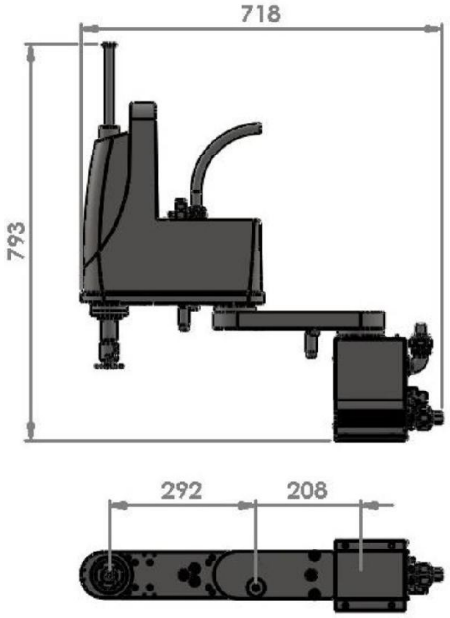


Figure 2: The physical parameters of the scara robot

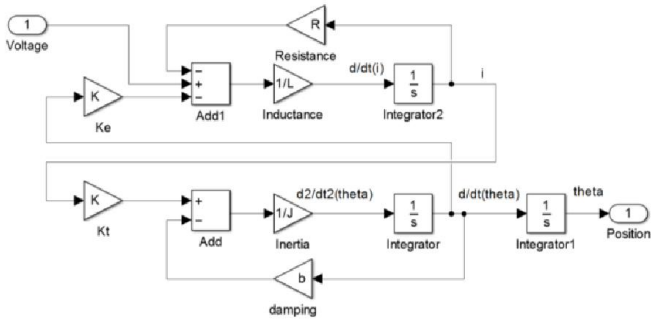


Figure 3: MATLAB/Simulink model of DC motor [12]

Table 1: Parameters of DC motor [12]

Parameters	Symbol	Value	Unit
Moment of inertia	J	3.2284E-6	kg.m^2
Viscous friction constant	b	3.5077E-6	Nms
Electromotive force constant	Ke	0.0274	V/rad/sec
Motor torque constant	Kt	0.0274	Nm/Amp
Electric resistance	R	4	Ohm
Electric inductance	L	2.75E-6	H

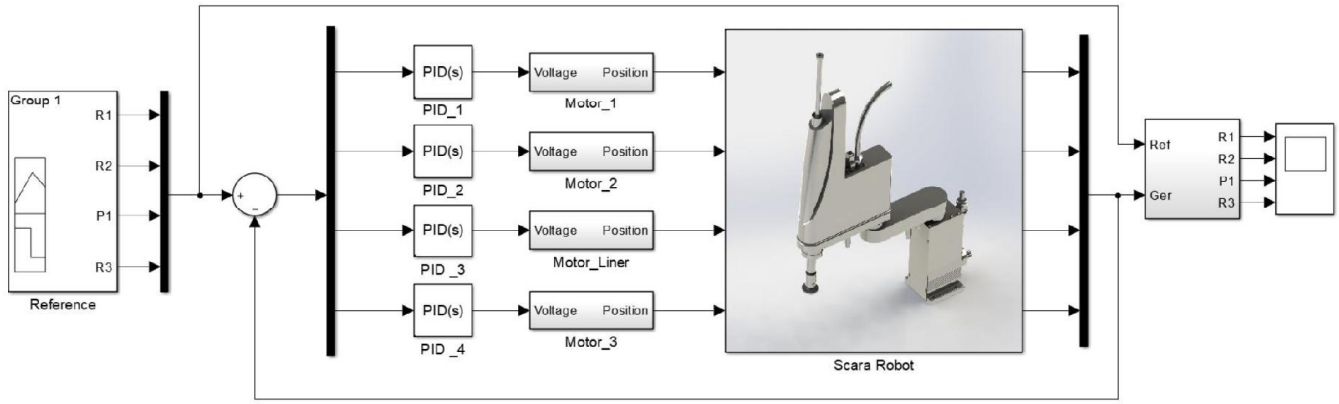


Figure 4: MATLAB/Simulink model of the scara robot control system

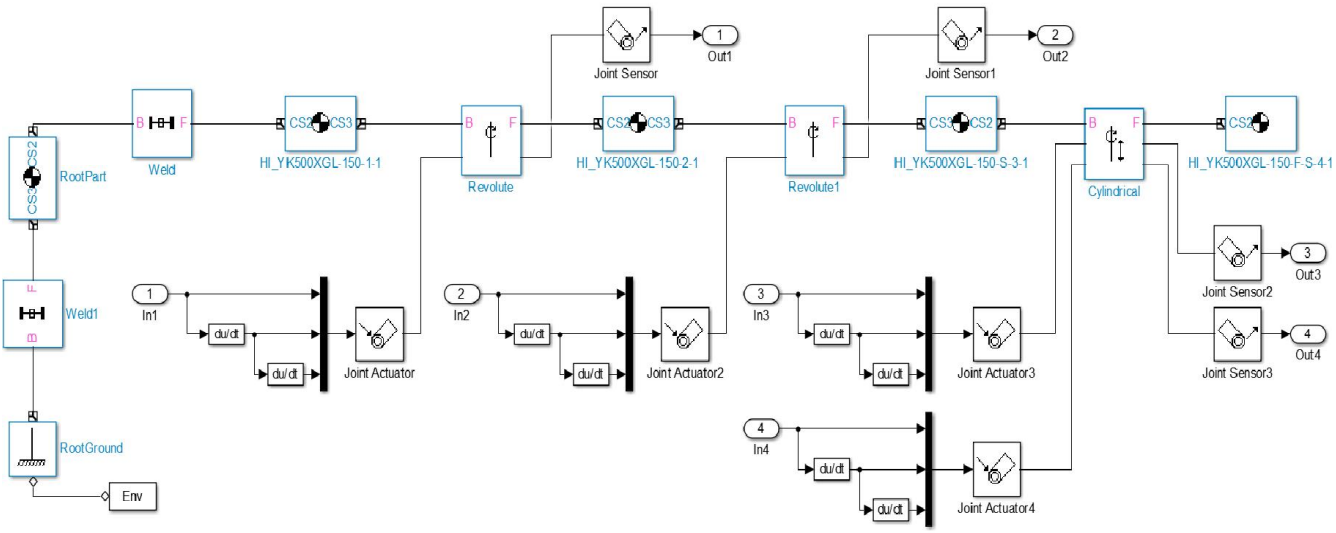


Figure 5: MATLAB/SimMechanics model of the scara robot

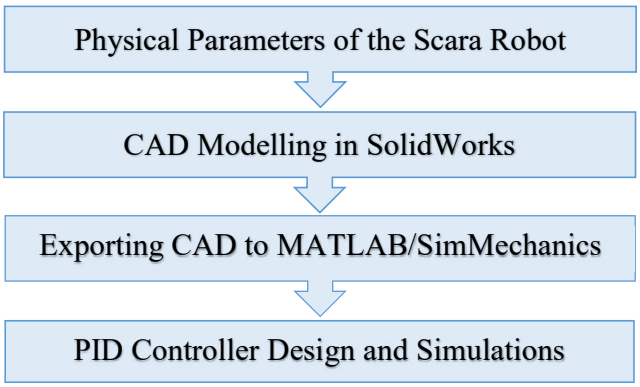


Figure 6: Working strategy of modelling and control of the system

In Figure 3, shown MATLAB/Simulink model of DC motor. The parameters of DC motor given in Table 1. The scara robot are built in SolidWorks and exported to MATLAB/ SimMechanics environment with physical parameters. The PID Controllers are designed in MATLAB/Simulink. Later, simulations of system are performed in MATLAB/Simulink. The MATLAB/Simulink model of the scara robot control system is given in Figure 4. Also in Figure 5, shown MATLAB/SimMechanics model of the scara robot. Working strategy of modelling and control of the system are summarized in Figure 6.

III. Simulations Results

In this system 3 Dc motors are used for rotational motions and 1 Dc motor liner motion. All Dc motors are controlled using PID controllers which are tuned with MATLAB auto-tune method. PID controllers gains given in Table 2.

In simulation, it is defined a marking process as reference input for system. 3 rotary and 1 prismatic joints (R1,R2, P1, R3) of scara robot are moved according to references inputs.

Table 2: PID controllers gains

	Kp	Ki	Kd	N
PID1	3.35	3.05	0.038	180.4
PID2	2.16	1.24	0.016	66.1
PID3	4.24	36.38	0.084	158.7
PID4	2.68	2.02	0.032	87.2

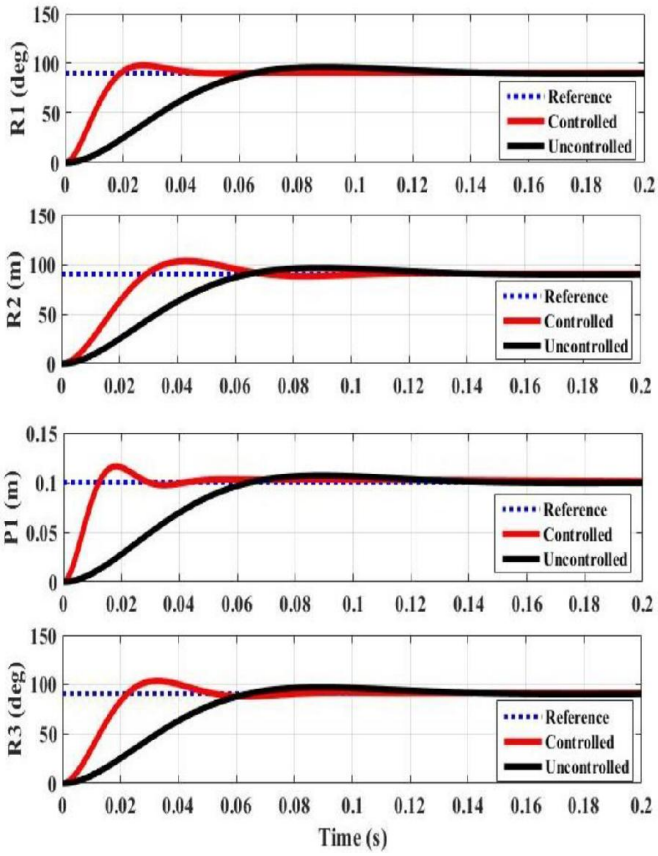


Figure 7: Step input response of system

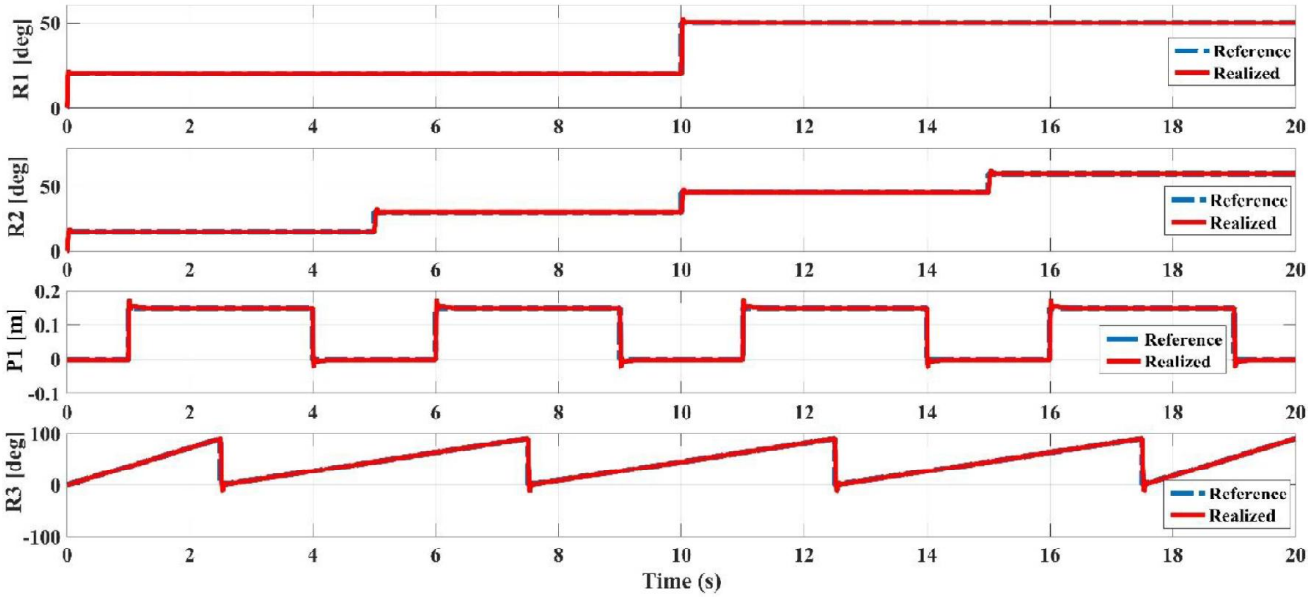


Figure 8: The marking process reference response of system

Firstly, to show the performance of the controllers, step input reference given the system. Step input response demonstrate in Figure 7. As seen from Figure 7, PID controller's performances and effectiveness are investigated and examined; position control results of the proposed system are presented separately for uncontrolled and controlled in the form of graphics.

The marking process references inputs and movement of joints (Realized) shown in Figure 8. As seen from Figure 8 it can be said that PID controlled system reached to desired position without steady state error. From this result, motion control of Scara robot is achieved successfully using auto-tuned PID controller.

IV. CONCLUSION

In this paper, a scara robot is dynamically modeled and position control with PID controllers is realized. To obtain dynamic model, computer aided design (CAD) model of proposed scara robot is built using SolidWorks program and exported to MATLAB/SimMechanics software. In this way, modelled scara robot without mathematical equations using two engineering software. Furthermore mathematical model of DC motors used in scara robot system is considered in control methodology. Four PID controllers are designed in MATLAB/Simulink for positions control of scara robot's joints. The PID controllers gains tuned with auto-tune method in MATLAB. Accuracy of proposed modeling technique is verified by simulations. In simulations, the responses to step inputs of system are examined and investigated firstly. Later, a marking process is designed as a reference input and applied to the scara robot. As a result of the paper, proposed modeling approach is implemented and the PID controllers are designed and used in control methodology successfully. In addition, this study will contribute to the work about modeling and control of scara robot.

REFERENCES

[1] M. R. Bin Tarmizi, "Design And Modelling Of 6 Dof Revolute Robot Using Fuzzy PID Controller", Mater Thesis, Dept. Elect. Eng, Universiti Tun Hussein Onn Malaysia, 2014.

[2] Y. Şahin, "PID control application of trajectory control of a Scara type robot", Mater Thesis, Dept. Mechanical Eng. Dept., Selçuk University, 2006. (originally Turkish)

[3] Ç. Saygılı, "Design and animation of a Scara type robot", Master thesis, Mechanical Eng. Dept., Selçuk University, 2006. (originally Turkish)

[4] A. S.Ogulmuş, A. Çakan & M. Tınkır, "Modeling And Position Control Of Scara Type 3D Printer", *International Journal Of Scientific & Technology Research,* vol. 5, pp. 140–143, December 2016.

[5] C. Urrea, J. Cortés, & J. Pascal, "Design, construction and control of a SCARA manipulator with 6 degrees of freedom", *Journal of applied research and technology,* vol. 14(6), pp. 396-404, 2016.

[6] L. Bruzzone, & G. Bozzini "A statically balanced SCARA-like industrial manipulator with high energetic efficiency", *Meccanica*, vol. 46(4), pp.771-784, 2011.

[7] S. J. Go & M. C. Lee, "Design of a fuzzy-sliding mode controller for a SCARA robot to reduce chattering", *Journal of Mechanical Science and Technology*, vol. 15(3), pp. 339-350, 2001.

[8] N. Surapong & C. Mitsantisuk "Position and force control of the SCARA robot based on disturbance observer" *Procedia Computer Science*, vol. 86, pp. 116-119, 2016.

[9] N. Wang, J. Liu, S. Wei, Z. Xu & X. Zhang, "The control system design of a SCARA robot", *In International Conference on Intelligent Robotics and Applications*, Springer, pp. 136-145, December, 2014.

[10] C. Urrea & J. Kern, "Modeling, simulation and control of a redundant SCARA-type manipulator robot", *International Journal of Advanced Robotic Systems*, vol. 9(2), pp. 58, 2012.

[11] Available:https://b2b.partcommunity.com/3d-cad-models/

[12] Available:http://ctms.engin.umich.edu/CTMS/index.php?example=MotorPosition&section=SimulinkModeling

Obtaining Dynamic Characteristics of Electrohydraulic Servo-systems: Case-Study of Parker D1FP Proportional Valve

V. BAKIRCIOĞLU[1], M.A.ŞEN[2], M. KALYONCU[3]

[1] Aksaray University, Aksaray/Turkey, vbakircioglu@hotmail.com
[2] Selcuk University, Konya/Turkey, marifsen@selcuk.edu.tr
[3] Selcuk University, Konya/Turkey, mkalyoncu@selcuk.edu.tr

***Abstract* – This study proposes a diverse method to find unidentified parameters of an industrial electrohydraulic proportional valve. Electrohydraulic servo-systems are one of the most commonly used actuators, and proportional valves exist in most hydraulic systems. Nevertheless, without prior knowledge on the system, obtaining a precise model of an electrohydraulic servo-system for using in simulations can be a challenging task. Obtaining a precise model of a system that is not easy to model with first principle of physics, can be done in two different way; applying system identification methods after gathering experimental data, or using data sheets from manufacturers. In this paper, dynamic characteristics of Parker Hannifin Corp.'s D1FP proportional valve was obtained by applying an optimization algorithm. While constructing the model, the system under investigation was separated into two portions: onboard electronics and directional valve. Parameters of the system model was optimized to match the dynamic characteristics from data sheet, which is provided by the manufacturer. Obtained system model and responses were graphically illustrated, and effectiveness of the proposed method was discussed.**

***Keywords* – Electrohydraulic Servo-Systems, System Identification, D1FP Proportional Valve, Parameterization.**

I. Introduction

ELECTROHYDRAULIC servo-systems are widely used in industrial process and engineering applications for controlling the force, flow rate and direction, position, speed, and acceleration [1]. In order to design a precise controller for electrohydraulic servo-systems, a precise model of the system must be obtained, to simulate and to test the behavior of the controller. In addition, the parameters of the controller can be optimized by using this model if necessary. Without a prior knowledge on a servo-system, obtaining a precise model can be a challenging task. Problems in obtaining a precise model of a naturally nonlinear and time-varying dynamics result controller design more difficult. In this context, modelling is the first and the most significant task in scientific studies.

Obtaining a precise model of an unknown system can be done in two different way; applying system identification methods after gathering experimental data, or using data sheets from manufacturers if provided. System identification is the process of constructing mathematical models of unknown or partly known systems from experimental data. Experimental data consists of input and output data of the system. Input data is the excitation signals, which is used to gather the system responses so-called output data. Experimental data can be obtained in both, time domain or frequency domain.

Identification of the fully unknown systems are called *black-box* modeling [2]. In the other hand, *Grey-box* modeling uses the experimental data to obtain the unknown parameters of the partly known system model [3]. In the literature, there are several technics for *black-box* modeling and identification of nonlinear systems, such as Hammerstein and Weiner models , NARX models, NARMAX models, wavelet networks, etc. [3–9]. In this paper, parameterization based on optimization techniques approach is used to obtain a precise model of a proportional valve, as a diverse method. Parker Hannifin Corp.'s D1FP proportional valve was used to estimate the unknown parameters of the system model [10]. System model of the valve divided into two parts; onboard electronics, which is modelled as a second order transfer function, and 4-way directional valve, which is modelled in Matlab/Simulink by using Simscape library.

The paper presents the study as follows: After this introduction, a detailed overview of the valve that is under investigation will be given, and the model structure that will imitate the actual system behavior will be described. Section 3 focuses on the parameterization of the valve model. In addition, a briefly summary of the applied optimization algorithm will be given in this section. In the following section, the behavior of the obtained model will be illustrated graphically in a comparative way with the actual data. Finally, concluding statements will be presented in Section 5.

II. Specifying the Valve Model Structure

Fig.1 shows the proportional valve that is under investigation. The direct operated control valve D1FP of the nominal size NG06 (CETOP 03) shows extremely high dynamics combined with maximum flow [10]. The specific reason for the selection of this valve is that it is being used in a different research of the authors. Schematic representation of the valve with the separated parts is shown in Fig.3.



Figure 1. Parker Hannifin Corp. D1FP proportional valve.

In the literature, commonly, the onboard electronics dynamic is theoretically represented by an equivalent second order transfer function [1]. Thus, a second order lag is used to construct model structure of the onboard electronics, as in (1).

$$G(\omega) = \frac{1}{\frac{1}{\omega_n^2}s^2 + \frac{2\zeta}{\omega_n}s + 1}$$
$$\omega_n = \sqrt{\frac{K}{\tau}} \qquad (1)$$
$$\zeta = \frac{1}{2}\sqrt{\frac{1}{K.\tau}}$$

where ω_n is the undamped frequency and ζ is the damping coefficient. K and τ are gain and time constant, respectively. After specifying the model structures for the onboard electronics, these unknown parameters needs to be estimated. Subsequently, a model structure for the 4-way directional valve, a schematic representation shown in Fig.2, is determined as in (2).

$$Q = C_d \cdot A\sqrt{\frac{2}{\rho}|\mathrm{p}|} \cdot sign(\mathrm{p})$$
$$A = \frac{A_{\max}}{h_{\max}} \cdot h \qquad (2)$$
$$h = x_0 \pm x$$

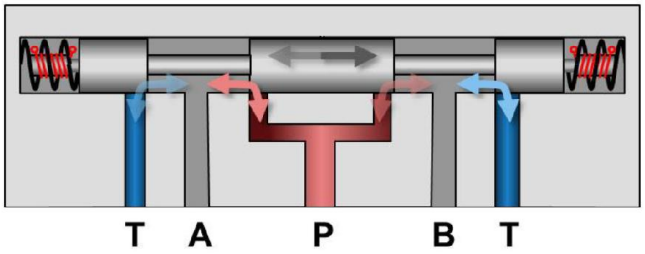


Figure 2. Structural configuration of a typical 4-way directional valve

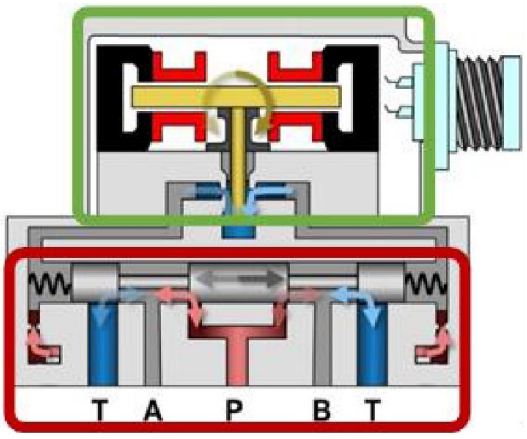


Figure 3. Schematic representation of the valve. 4-Way directional valve is marked with red rectangle, and onboard electronics marked with green rectangle.

where Q and C_d are flow rate through the orifice and flow discharge coefficient, respectively. A, $A_{\max}$, h and $h_{\max}$ are orifice area, maximum orifice area, orifice opening and maximum orifice opening, respectively. Finally, p, x_0 and x are pressure differential across the orifice, initial opening and spool displacement, respectively.

Determined model structures will be used to represent the proportional valve system behavior. Therefore, unknown parameters of the models must be obtained. This can be done by using system identification technics. In this context, unknown parameters are optimized until the simulation results reflect the characteristics in manufacturer's data sheet.

In this study, Matlab/Simulink libraries were used to represent system model structure in two different parts. In the Simulink environment, physical components can be modelled by using a built-in add-on Simscape. Reader can refer to [11] for a detailed information about Simscape. Next section describes the optimization method that is used to estimate model parameters and the Simscape blocks that are used to reflect the system behavior.

III. Constructing the Simulink-Based Model and the Optimization Method

In order to estimate unknown parameters of the constructed model structures, an optimization algorithm is applied based on the manufacturer data sheet. This section constructed in two part to describe the identification procedures. First part consists Simulink-based modeling and second part describes application of the optimization method.

A. System Modeling in Simscape

Simscape provides a very powerful tool for modeling hydraulic components, which are reflecting all the essential characteristics. In Simulink environment, *Proportional and Servo-Valve Actuator* block and *4-Way Directional Valve* block, which are shown in Fig.4, are used to represent the valve dynamic behaviors.

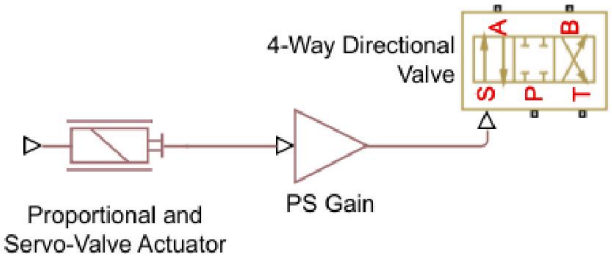


Figure 4. Constructed D1FP proportional valve structural model in Simulink environment

Each block in Fig.4 is characterized by a set of parameters. These parameters specify the model behavior. The *Proportional and Servo-Valve Actuator* block represents an electromagnetic actuator that is used in proportional and servo-valves to drive a spool or other working member. The block is intended to work with one of the directional valve models to form a desirable configuration of a proportional or servo-valve. The block diagram of the model is shown in Fig.5. *Proportional and Servo-Valve Actuator* block consists of three parameters, which are *Gain, Time Constant* and *Saturation.* These values need to be tuned to capture the real system characteristics that are provided by manufacturer data sheet.

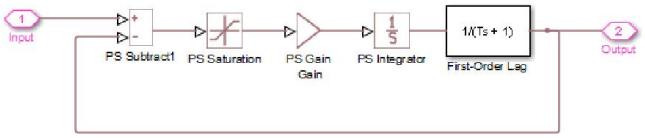


Figure 5. The block diagram of the Proportional and Servo-Valve Actuator model.

The *4-Way Directional Valve* block represents a directional control valve with four ports and flow paths. The block diagram of the model is shown in Fig.6. Physical signal port S controls the spool displacement. The spool displacement acts indirectly by setting the spool position relative to each flow path—a length known here as the orifice opening. The orifice opening in turn determines the opening area of the respective flow path.

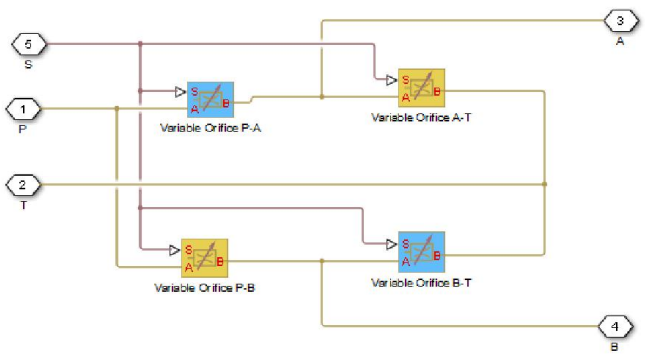


Figure 6. Valve Structural Diagram

The model parameterization setting determines the calculations used for the opening areas of the flow paths. The calculations are based on orifice parameters or tabulated data sets specified in the model parameterization tab, which is shown in Fig.7.

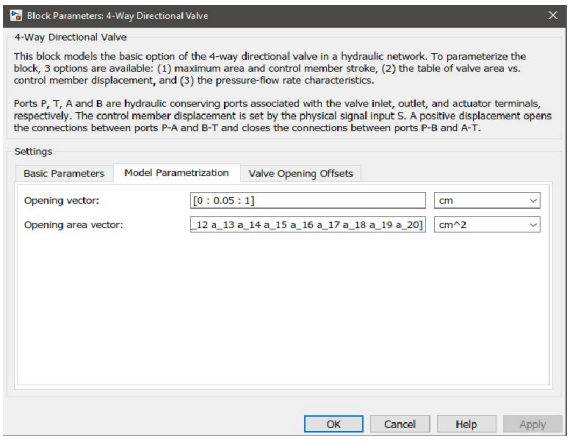


Figure 7. 4-Way Directional Valve block parameters settings.

Opening vector and *Opening area vector* values specify the opening area at discrete orifice openings as a 1-D lookup table. The opening area is computed for a given orifice opening by interpolation or extrapolation of the tabulated data.

Model parameters are determined using an optimization procedure in which the required characteristics for the flow rate and frequency response, are compared to the simulation results, and parameter values are optimized to minimize the difference between real data and simulation data. Required characteristics are delivered from manufacturer data sheet.

B. Optimization Procedure

Initially, 4-way directional valve parameters are optimized. In order to apply optimization, a test model is built as seen in Fig 8, which includes the characteristics in the manufacturer's data sheet. As given in data sheet [10], the flow rates shown in Fig.9 are measured in the external valve loop with a pressure drop of 35 bar maintained on each metering path. This characteristic will be used to optimize the 4-way directional valve parameters. The objective function for the optimization of the 4-way directional valve parameters is defined as in (3).

$$\min F(x) = \sum_{i}^{n} k_i \left(Q_r - Q_a\right)^2 \tag{3}$$

where Q_a and Q_r are measured flow rate and required flow rate, respectively. k_i is the weight multipliers. The variable parameters vector in (3) consists of 21 parameters. The orifice is specified with 21 displacement-area pairs distributed evenly along the spool valve stroke. During optimization, 21 orifice area values must be determined that provide simulation results as close as possible to the data sheet characteristic.

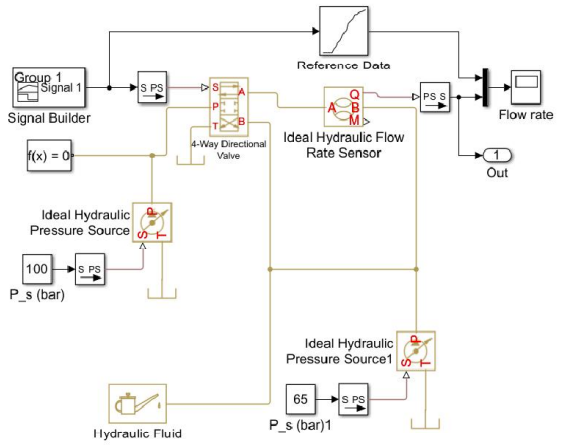


Figure 8. The test model for the determining parameter values for a 4-way directional valve

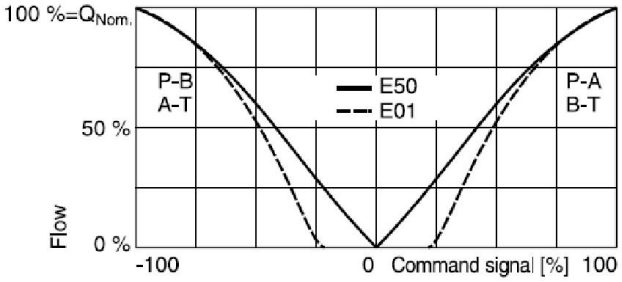


Figure 9. Manufacturer specification for flow rate vs. command signal.

Due to the highly nonlinearity of electrohydraulic systems, the frequency characteristics depend on controller performance, fluid properties, and other factors. Thus, to obtain parameter values for Proportional and Servo-Valve Actuator model, all of these parameters must be reflected in the model and all characteristics must be considered simultaneously. Theoretically, frequency characteristics are defined for linear systems only. Therefore, the system model must be either linearized to make it suitable for linear system analysis, or the characteristics must be determined by comparing input and output signals at a set of sinusoidal inputs of different frequencies. The linearization of hydraulic systems is not an easy task since substantially nonlinear elements such as saturation and dead zone are present in practically all elements, including the valve actuator.

In our case, the Proportional and Servo-Valve Actuator model is parameterized based on frequency response characteristics at 90% of the input signal whose maximum value is 10 V as shown in Fig.10. The reason for using 90% rated input is that the valve under investigation is the type E01, and its spool opening starts at point 23% rated input. In order to obtain Proportional and Servo-Valve Actuator parameters, an objective function for the optimization is defined as in (4).

$$\min F(x) = \sum_{i}^{n} k_i \left(f_r - f_a \right)^2 \tag{4}$$

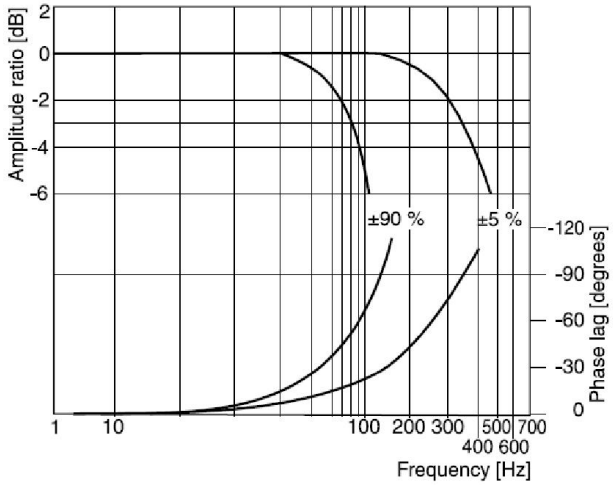


Figure 10. Frequency response characteristics of proportional valve at 5% and 90% of the input signal.

where f_a and f_r are measured frequency value and required frequency value, respectively. k_i is the weight multipliers. The variable parameters vector in this (4) consists of 3 parameters, which are *Gain, Time Constant* and *Saturation*. In order to apply optimization, a test model is built as seen in Fig 11.

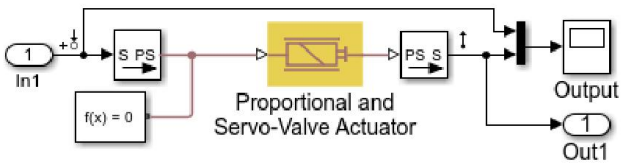


Figure 11. The test model for the determining parameter values for a Proportional and Servo-Valve Actuator.

Test models and objective functions, which are defined above, implemented in Matlab and Simulink environment. Subsequently, unknown parameters of the test models are optimized until the required characteristics matched to the real data.

IV. Optimization Results and Simulink-Based Model Responses

The problem that is defined previous section can be solved with different optimization algorithms. In this study, Matlab Optimization Toolbox that is a built-in tool in Matlab, was used to solve the problem to an efficient but basic practice. Various optimization algorithm functions such as *fminunc, fmincon, genetic algorithm, particle swarm algorithm,* etc., are contained within this toolbox. Reader can refer to [12] for more information about this toolbox.

To solve the optimization problem of the 4-way directional valve model , *fminunc* function was used, which uses the BFGS Quasi-Newton method with a cubic line search procedure [13].

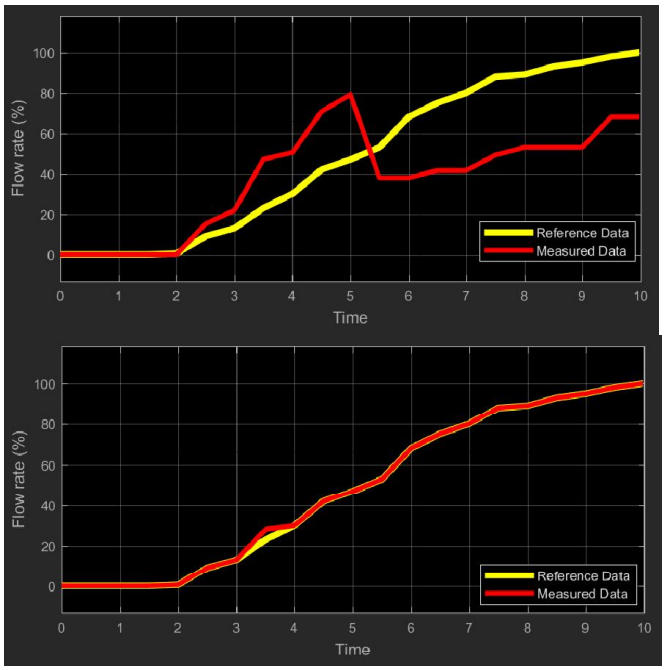


Figure 12. Flow characteristic of the valve: (top) before optimization; (bottom) after optimization

Table 1: Optimization output of the 4-way directional valve parameters.

Iteration	Func-count	Objective Function Value
0	21	1.12E+04
1	63	8.05E+01
2	84	1.08E+00
3	105	1.61E-02
4	126	7.99E-05
5	147	6.38E-08
6	***168***	***1.27E-10***

Flow rate characteristic of the valve model with the initial parameters and the optimized parameters are shown in Fig.12. The command signal that is increases 0% to 100% in 10 s, was achieved by the *Signal Builder* block in the model shown in Fig.8. The optimization was significantly fast, that is solved the problem in 7 steps and 168 function assessments. Optimization output is given in Table.1. As seen in the Fig.12, the parameter values that is obtained from the optimization are matched the model output to the real characteristics from the data sheet.

To solve the optimization problem of the Proportional and Servo-Valve Actuator model, *fmincon* function is used, which uses Interior-Point Optimization algorithm [14]. Phase frequency response characteristic of the Proportional and Servo-Valve Actuator model with the initial parameters and the optimized parameters are shown in Fig.13. The excitation signal used to collect the phase frequency response of the model was achieved by a Matlab function called *frest.Sinestream*, which is a series of sine waves signals. The optimization problem for the valve model is solved in 18 steps and 8 function assessments.

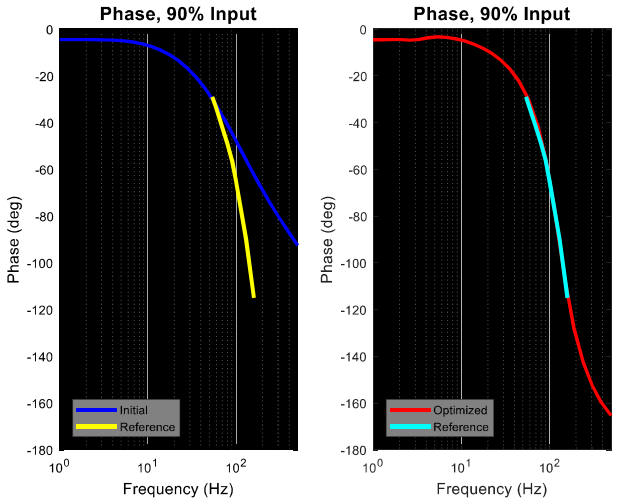


Figure 13. Phase characteristic of the Proportional and Servo-Valve model at 90% rated input. (left) before optimization; (right) after optimization.

Table 2: Optimization output of the Proportional and Servo-Valve parameters.

Iteration	Func-count	Objective Function Value
0	4	4,21E+03
1	12	3,25E+03
2	17	3,19E+03
3	21	2,74E+03
4	25	9,02E+02
5	29	8,43E+02
6	33	1,12E+01
...	...	...
18	***81***	***5,27E+00***

Optimization output is given in Table.2. Phase shift at 135 Hz and 90% rated input is found as -95.8796% with and error -6.5329%. As seen in the Fig.13, the phase frequency response of the model that is obtained after optimization are matched to the real characteristics from the data sheet with an acceptable error.

V. Conclusion

Unknown systems can be identified with system identification techniques. Obtaining a precise model of a non-linear system can be a challenging task. In this study, an industrial electrohydraulic proportional directional valve parameters were obtained by applying optimization techniques. Objective functions are given for the valve to match the dynamic characteristics of the valve with constructed model.

The proposed method for system modeling that is simplistic, swift but valid, is a diverse approach based on gray-box modeling. In a short period, a linearized model of the valve can be constructed with an acceptable error, which can be used in the simulations to investigate system behavior in a fast and reliable way.

ACKNOWLEDGMENT

This study is supported by the Scientific Research Projects Coordination Unit of Selçuk University. (Project No: 16401148).

REFERENCES

[1] M. Kalyoncu, M. Haydim, Mathematical modelling and fuzzy logic based position control of an electrohydraulic servosystem with internal leakage, Mechatronics. 19 (2009) 847–858. doi:10.1016/j.mechatronics.2009.04.010.

[2] L.A. Zadeh, On the identification problem, IRE Transactions on Circuit Theory. 3 (1956) 277–281. doi:10.1109/TCT.1956.1086328.

[3] B.H.G. Barbosa, L.A. Aguirre, C.B. Martinez, A.P. Braga, Black and gray-box identification of a hydraulic pumping system, IEEE Transactions on Control Systems Technology. 19 (2011) 398–406. doi:10.1109/TCST.2010.2042600.

[4] E. Kilic, M. Dolen, A.B. Koku, H. Caliskan, T. Balkan, Accurate pressure prediction of a servo-valve controlled hydraulic system, Mechatronics. 22 (2012) 997–1014. doi:10.1016/j.mechatronics.2012.08.001.

[5] N. Ishak, M. Tajjudin, H. Ismail, M. Hezri Fazalul Rahiman, Y. Md Sam, R. Adnan, PID Studies on Position Tracking Control of an Electro-Hydraulic Actuator, International Journal of Control Science and Engineering. 2 (2012) 120–126. doi:10.5923/j.control.20120205.04.

[6] T.G. Ling, M.F. Rahmat, A.R. Husain, System identification of electro-hydraulic actuator system using ANFIS approach, Jurnal Teknologi (Sciences and Engineering). 67 (2014) 41–47. doi:10.11113/jt.v67.2841.

[7] S.D. Mitchell, J.S. Welsh, Initial parameter estimates and constraints to support gray box modeling of power transformers, IEEE Transactions on Power Delivery. 28 (2013) 2411–2418. doi:10.1109/TPWRD.2013.2259266.

[8] G. Mercere, O. Prot, J.A. Ramos, Identification of parameterized gray-box state-space systems: From a black-box linear time-invariant representation to a structured one, IEEE Transactions on Automatic Control. 59 (2014) 2873–2885. doi:10.1109/TAC.2014.2351853.

[9] A. Cavallo, G. De Maria, C. Natale, S. Pirozzi, Gray-box identification of continuous-time models of flexible structures, IEEE Transactions on Control Systems Technology. 15 (2007) 967–981. doi:10.1109/TCST.2006.890284.

[10] Parker Hannifin Corporation, Direct Operated Proportional DC Valve Series D1FP, (n.d.). https://www.parker.com/literature/Hydraulic Controls Europe/HY11-3500UK/PDF_2013/D1FP UK.pdf (accessed October 25, 2017).

[11] Simscape Documentation, (n.d.). https://www.mathworks.com/help/physmod/simscape/ (accessed October 26, 2017).

[12] Optimization Toolbox Documentation, (n.d.). https://www.mathworks.com/help/optim/ (accessed October 27, 2017).

[13] M. Al-Baali, E. Spedicato, F. Maggioni, Broyden's quasi-Newton methods for a nonlinear system of equations and unconstrained optimization: A review and open problems, Optimization Methods and Software. 29 (2014). doi:10.1080/10556788.2013.856909.

[14] R.A. Waltz, J.L. Morales, J. Nocedal, D. Orban, An interior algorithm for nonlinear optimization that combines line search and trust region steps, Mathematical Programming. 107 (2006) 391–408. doi:10.1007/s10107-004-0560-5.

Design a Robot Insect Inspired by the Camouflage Characteristics of the Leaf Insect

Samet Çıklaçandır[1],Özlem Karabiber[1], Yalçın Kalafat[2], FatihCemal Can[1]

[1]Izmir KatipCelebi University, Izmir/Turkey, samet.ciklacandir@ikc.edu.tr
[1] Izmir KatipCelebi University, Izmir/Turkey, ozlemkrbbr08@gmail.com
[2]Chalmers University of Technology, Gothenburg/Swedish, kalafat@student.chalmers.se
[1]Izmir KatipCelebi University, Izmir/Turkey, fatihcemal.can@ikc.edu.tr

***Abstract* - Many problems have been a popular field for many years to search for solutions by imitating nature. Research that resembles nature is called biomimetic and these applications can be performed in many different fields. Robots have been developed and researched for centuries, and nowadays they are stepping into our daily lives. Today, when robot applications are examined, many features transferred to robots are imitated from nature. Biomimetic robots whose actuation mechanism, adaptation, motions balance, behaviors or communication with each other are designed by mimicking animals, are investigated by engineers. Many studies of biomimetic robotics field and we decided to design and produce a new biomimetic robot structure. Our aim in this work is to design a robot insect inspired by the camouflage and movement characteristics of the leaf insect. Chebyshev mechanism was used for mechanical design of the robot insect. Although there are a number of problems arising from the implementation of the mechanism used, the robot has been observed to walk.**

***Keywords* - Biomimetic robotic, Chebyshev mechanisms, Camouflage, Insect, Mobile robots.**

I. INTRODUCTION

Robots have been researched and developed for centuries, and they have been used many different areas to help people. The study of designs that imitate nature has gained popularity today [1].

When starting to design something, we can often get inspiration from others. Unique design in nature has always been inspiration to human beings. Many names have been given to solve problems by using nature, such as biomimicry, biomimetic, bionic, biodesign, biomorphic, bioutilisation, biophilia and bioderivation [2]. Among them, biomimetic is an approach that aims to produce sustainable and innovative solutions by imitating models and strategies that have been tested in the nature and successful with time. The goal of the biomimetic is to produce products and processes that can be adaptable to nature long term. Designs based in the nature are needed to be used in fields such as nanotechnology, robot technology, artificial intelligence, medical industry and military hardware.

Frosch and Gallapoulos introduced biomimicry using special concept of resembling ecosystems by creating a balance between nature and mankind [3]. Benyus describes biomimic science as combining sustainable solutions based on an ecological criterion and innovation with research and industry development. Benyus stated that nature as mentor, criterion and model would be very important to appreciate the applicability of biomimicry [4].

When the literature is examined, various studies conducted by imitating nature are encountered. Inspired by the fore claws of the nymph of Cryptotympanaatrata's excellent ability to cut and dig soil, Chang et.al designed a biomimetic stubble cutter to reduce the cutting resistance [5]. Ho et.al designed and manufactured prototype of a small quadruped robot whose walking motion is realized by two piezocomposite actuators and legs is inspired by the leg configuration of insects, two joints (hip and knee) of the leg enable two basic motions, lifting and stepping [6]. In study of Koju et. al [7], biomimetic coating process is performed to develop for coating various orthopedic implant surfaces. The study of Sheikhpour et. al demonstrates the advantages of biomimetic nanocomposite drug delivery systems [8]. Robotic fish inspired by the freshwater stingray was developed and tested in investigation of Wang et. al [9]. Franz and Mallot reviewed biomimetic robotic system inspired by biological navigation behaviors [10]. A walking mobile robot was designed and produced by using Chebyshev's Parallel Motion Mechanism in study of Manickavelan et. al [11].

Biomimetic robots studies which are based on locomotion mechanism, motions, behaviors, or communication modes by mimicking animals are presented so far.



Figure 1:Camouflaged leaf insect [12]

Our aim is to imitate the leaf insects inspired by the camouflage and movement characteristics (see figure 1). Leaf

insect contains the extant true leaf insects or walking leaves, which include some of the most remarkably camouflaged leaf mimics in the entire animal world.

II. Materials and Methods

Our goal in this work is to design a robot insect inspired by the camouflage and movement characteristics of the leaf insect. The basic block diagram showing the phases of the study is shown in figure 2.

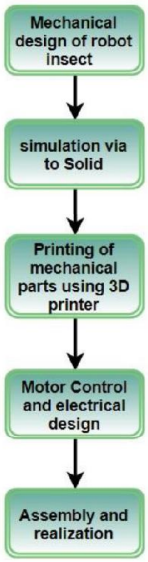


Figure 2: The basic block diagram of the study

A. Mechanical Design of Our Robot Insect

Before starting the design phase, we investigated the other study using biomimetic robotic approach. Chebyshev's straight line mechanism was previously used for locomotion mechanism of a walking machine [11]. When we examined the designed robot mechanisms, we decided that Chebyshev mechanisms was the most appropriate mechanism for our design.

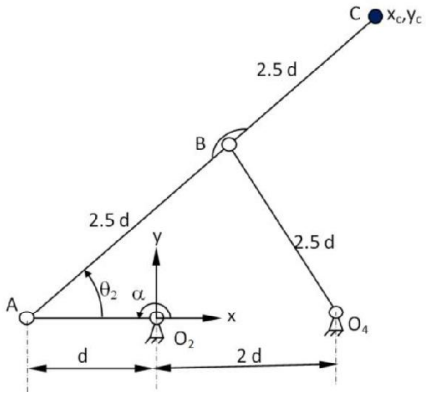


Figure 3: Basic representation of Chebyshev's Straight Line Mechanism

This mechanism was invented by Russian mathematician Pafnuty Chebyshev. It is also known as a special four-bar linkage. The movement of the machine is similar to the walk of many creatures such as insects, bears, rabbits, and, sometimes, humans. It has four "legs" that create a semi-circular pattern and, as expected, look like an animal walking. Besides, this mechanism was continuously used for linear guidance of the piston and valves [11].

d=radius of driving arm =20 mm
Length of guiding arm(BO_4)=2.5*d=50mm
Length of big arm(AR)=2*2.5d=100 mm
0.5*distance of big arm(AB)
Distance between driving arm and the guiding arm in the body (O_2O_4) = 2d=40 mm

$$d\cos\alpha + 2.5d\cos\theta_2 = 2d + 2.5d\cos\theta_3 \quad (1)$$
$$d\sin\alpha + 2.5d\cos\theta_2 = 2.5d\sin\theta_3 \quad (2)$$

Elimination of θ_3 is possible by firstly squaring equations (1), (2) and summing these equations. The equations are converted to equation (3) including one unknown variable θ_2.

$$\cos\theta_2\,(5\cos\alpha - 10) + \sin\theta_2(5\sin\alpha) - 4\cos\alpha + 5 = 0 \quad (3)$$

The equation is solved by conversion.

$$\cos\theta_2 = \frac{1-t_2^2}{1+t_2^2}\sin\theta_2 = \frac{2t_2}{1+t_2^2}$$
$$t_2 = \arctan(\frac{\theta_2}{2})$$

$$\left(\frac{1-t_2^2}{1+t_2^2}\right)A + \left(\frac{2t_2}{1+t_2^2}\right)B + C = 0$$

$$(C-A)t_2^2 + 2Bt_2 + C + A = 0$$

There is a phase difference of 180 degrees between the two rotation points. It is shown the coordinate position's (4, 5) formulation of four bar link mechanism.

$$x_c = d\cos\alpha + 5d\cos\theta_2 \quad (4)$$
$$y_c = d\sin\alpha + 5d\sin\theta_2 \quad (5)$$

B. CURA software and Simulation in SolidWorks

In accordance with Chebyshev mechanisms, the parts were designed in SolidWorks. For the robot insect, a chassis where the motor and electronic cards will be placed, legs and pins suitable for the mechanism are drawn in the appropriate scale and the design is completed by using Solidworks. After designing of all parts, they are converted to STL file type to print these parts in Ultimaker 3D printer. Then, all files are inserted into slicing software CURA of the printer as shown in figure 4.

After the completion of the drawing of all parts, the assembly and simulation process were performed in

SolidWorks. It was observed that the designed robot insect moves in the desired way. This stage is observed in figure 5.

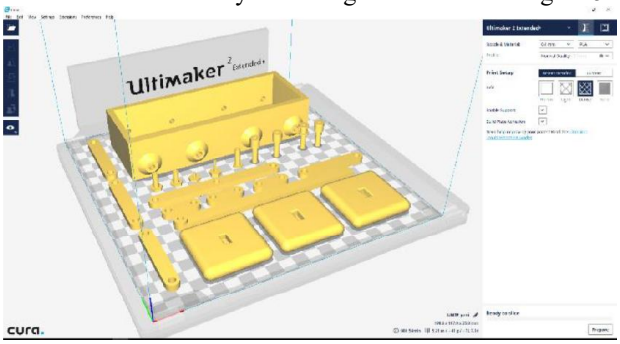


Figure 4: STL files in CURA software

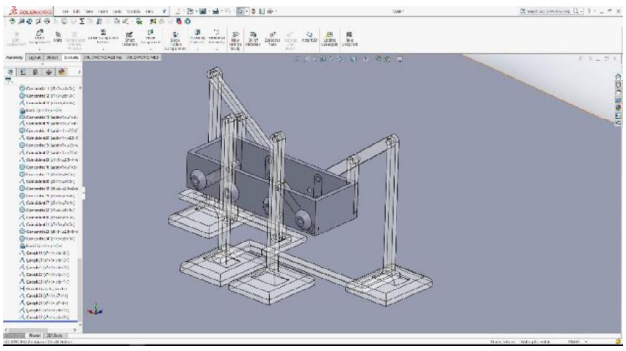


Figure 5. Assembly and motion simulation of robot parts in SolidWorks

C. *Printing the parts in Ultimaker 3D Printer*

After the simulation has been carried out successfully, the stage of printing of the design parts has been passed. An Ultimaker 3D Printer and green PLA filament was used to print the parts. Using capability of CURA software, all parts are printed in high density option. Figure 6 shows printing process of the parts.

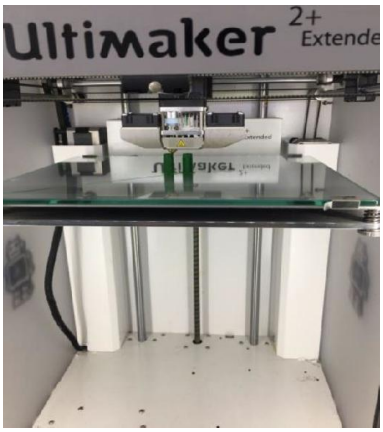


Figure 6: Ultimaker 3D printer

D. *Motor Control and Electrical Design*

In the motor control phase of the design, 1 Arduino Nano, 2 micro DC motors, 2 BJT transistors, 2 diodes (1N4007) are used. The Arduino code written in this purpose is shown in figure7.

The code for the motor control is set so that the travel speed of the path followed by the leg is V on the upper part of the trajectory and 2V on the lower part of the trajectory. The movement of the path followed by the legs and the velocities in the upper and lower regions are shown in Figure 8.

```
//Walker Robot
//07.07.2017
//written by IKCU biomimetics
//Slow while the feet are above, Fast while feet are

void setup()
{
  pinMode(4, OUTPUT);
  pinMode(5, OUTPUT);
}
void loop()

  digitalWrite(4, LOW);
  digitalWrite(5, LOW);
  delay(250);
  digitalWrite(4, HIGH);
  digitalWrite(5, HIGH);
  delay(500);
}
```

Figure 7: Arduino Code written for motor control

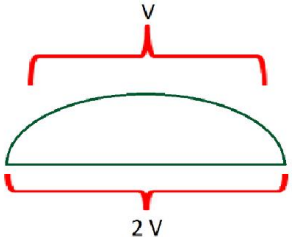


Figure 8: Path tracing of the legs

E. *Assembly and Realization*

After printing the mechanical parts using the 3D printer and writing the necessary code for the motor control, the printed parts were assembled and passed to the execution stage of the robot insect.

Firstly, the body and legs, which were printed using the 3D printer, were joined together with the help of pins and hot silicon printed by the same method (see figure 9). After the assembly process of mechanical parts is completed, DC motor, circuit board and Arduino were fixed to the body of the robot by injecting hot silicone and the design was completed. The combined of mechanical and electronic parts are shown in figure 10.

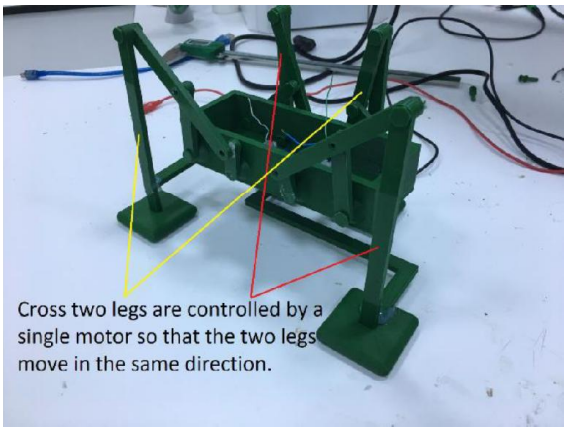


Figure 9: The combined mechanical parts

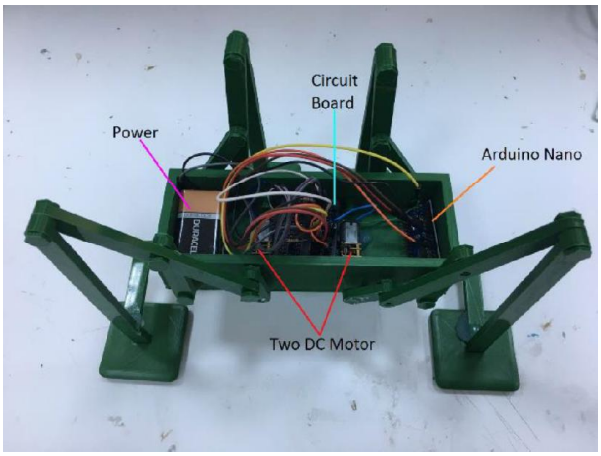


Figure 10: Assembly of mechanical and electronic parts of insect robot

III. Results and Discussion

When the literature was examined, various studies conducted by imitating nature were encountered. A different biomimetic structure was designed using known locomotion mechanism. Our aim is to design a robot insect inspired by the camouflage and movement characteristics of the leaf insect.

Chebyshev mechanism was used for motion of walking legs. Mechanical design was performed in the SolidWorks. Furthermore, Ultimaker 3D Printer and green PLA filament was used to print the parts. Arduino Nano was used for the motor control phase of the design.

Mechanical and electrical designs were completed and then the printed parts were assembled. The final insect robot was tested to observe walking ability. Although there are a number of problems arising from the implementation of the mechanism used, motor control and incompatibility with the pin dimensions of space left for the pins in the printed parts, the robot has been observed to walk.

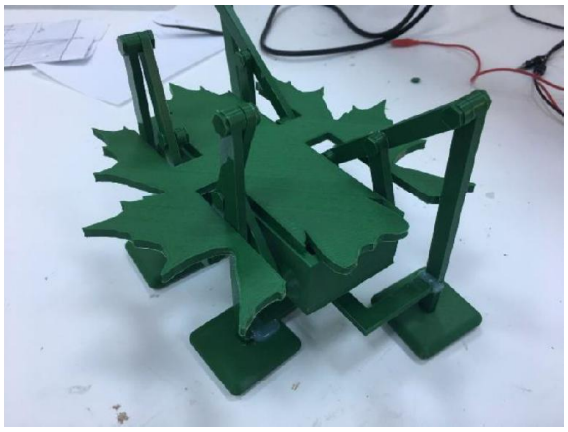


Figure 11:Robot insect with camouflage leaves

References

[1] L., Shu-Hung, H., Tse-Shih, Y., Jia-Yush. 2009. Comparison of Sensor Fusion Methods for an SMA-Based Hexapod Biomimetic Robot. Robotics and Autonomous Systems 58 (2010) 737_744.

[2] Al-Obaidi, K., M., Ismail, M., A., Hussein, H., Rahman, A., M., A. 2017. Biomimetic building skins: An adaptive approach. Renewable and Sustainable Energy Reviews 79 (2017) 1472–1491.

[3] Frosch RA, Gallopoulos NE. Strategies for manufacturing. Sci Am 1989;261(3):144–52.

[4] Benyus J. Mother Nature's School of Design. Choices for Sustainable Living, 2002, p. 34–8.

[5] Chang, Z., Liu, W., Tong, J., Guo, L., Xie, H., Yang, X., Mu, H., Chen., D. 2016. Design and Experiments of Biomimetic Stubble Cutter. Journal of Bionic Engineering 13 (2016) 335–343.

[6] Ho, T., Choi, S., Lee, S. Development of a Biomimetic Quadruped Robot. 2007. Journal of Bionic Engineering 4 (2007) 193–199.

[7] Koju, N., Sikder, P., Ren, Y., Zhou, H., Bhaduri, S., B. Biomimetic coating technology for orthopedic implants. 2017. Current Opinion in Chemical Engineering 2017, 15:49–55.

[8] Sheikhpour, M., Barani, L., Kasaeian, A. 2017. Biomimetics in drug delivery systems: A critical review. Journal of Controlled Release 253 (2017) 97–109.

[9] Wang, Y., Tan, J., Zhao, D. 2015. Design and Experiment on a Biomimetic Robotic Fish Inspired by Freshwater Stingray. Journal of Bionic Engineering 12 (2015) 204–216.

[10] Franz, M., O., Mallot, H., A. 2000. Biomimetic robot navigation. Robotics and Autonomous Systems 30 (2000) 133–153.

[11] Manickavelan, K., Singh, B., Sellappan, N. 2014. Design, Fabrication and Analysis of Four Bar Walking Machine Based on Chebyshev's Parallel Motion Mechanism. European International Journal of Science and Technology Vol. 3 No. 8 October, 2014.

[12] Leaf Insect https://morfis.files.wordpress.com/2010/09/leaf-insect-e1288206484269.jpg (Access Date: 30.10.2017)

Numerical simulation computing of the collapses for the Harbour Silos storage of wheat 30000 tons capacity

BOUZEROURA Mansour

[+] *LaMoMS Laboratory University of Mouloud Mammerie, Tizi Ouzou 15000, Algeria*
bouzeroura2013@gmail.com

[*]*Department civil engineering, LGCA Laboratory, Abderrahmane Mira University, Bejaia 06000, Algeria*

***Abstract*— The Object of this article, articulates on the digital simulation of the collapses of the storage silos of the wheat of 30000 ton capacity situated in the bearing of Bejaia (Algeria). The led study is divided into two left, the first part consists of the experimental study and the second is dedicated to the digital simulation of the collapses by means of tools digital technology (PLAXIS). In the first part, a series of measures of the collapses of silos made on the ground of setting-up(presence) of the work, these measures are raised(found) according to every mode(fashion) of load restarted on four (04) phases of load of a total duration of 131 days. In the second part a digital simulation is realized by means of PLAXIS simulation computing.**

***Keywords*— Digital simulation, collapses, silos, PLAXIS**

I. INTRODUCTION

All the grounds deform under the loads which are applied to them, with amplitudes which can go of some millimeters a few meters away. The forecast of these movements is realized by making of digital simulation computer, on the behavior of the grounds of foundations (boxes) before and after load of silos. The disorders of geotechnical origin allocating the works foundations of buildings, are frequently owed to the bad gratitude of grounds to Reduce these disorders requires that we are capable:
- To model numerically the heterogeneousness, by taking into account the spatial variation of the physical and mechanical properties which control the answer of the works,

A. First part (experimental study)

All the grain silos, has a 30000 ton storage capacity, distributed on 16 (drum kits) of 04 silos each. The skeleton of silos consists of ferrules and metallic reinforcements, silos rest(base) on concrete boxes equipped restful on one radiate of 20×24m^2 (fig01). The load of the silo is made from cereal growers (grain ships), whose unloading is assured by 02 porticoes (on rails) platform) of a 200 ton / hour debit (flow). The handling of cereal up to the silo is made through 02 carrier's ways with channel of unitarian flows of 200 tons / hour supported by metallic footbridges arranged in continuity up to storage silos including the tower of handling and weighing realized in metallic skeleton. [1]

TABLE1
CHARACTERISTICS OF THE PROJECT OF (FIG 01)

Storage capacity		30000 tons
Footprint		1300m^2
Number of silos		64
Capacity of a silo		468,7 ton
Size of a silo	Diameters Φ	8,143 m
	cylindrical height	12,186m
	height upper cone	2,350 m
	total height	14,36m

.



Fig. 1 Overview of the project

B. Local geology

The development of the harbour zone inner harbour it is made for the mouth of the oued Soummam and lands were gained won on the sea. As a result the studied zone is constituted by more or less organic fine materials, sand, silt, clays and muds, deposited on a rather deep rocky substratum, of the order of 40 à50 m, it is about schists

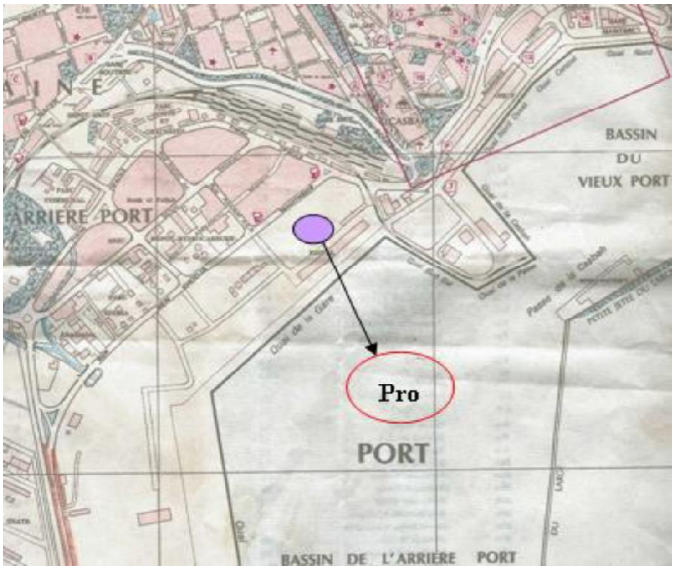


Fig. 2 Location of the project

C. Results of the tries made on the ground

The LTP is of Constantine [2] to make two soundings, muddied to know the geologic nature of the trainings establishing the ground of basis and a sampling for tries of laboratory. The visual description of samples taken by every sounding allowed us to establish lithologiques cuttings represented by the table II.

TABLE I1
RESULTS OF THE NICKED SOUNDING

Nicked sounding	0 à 4 m	4 à 8 m	8 à 21 m
N° 01	Rocky sand-colored elevation and blackish schists	muddy Sand	
N° 02	Elevations.	Organic Silt	muddy Sand

For the results of Eleven (11) tries of pénétromètre statics made, the speed of penétrogrammes reveals that the ground is homogeneous on all the depth and the moderate sharp resistances characterize a ground of bad portance. The minimal value of the moderate sharp resistance (Rp) is low and of average value of 8 bars; according to the classification of G Filliat, it is about trainings of muddy nature, peat or about soft clay [1]. The maximal resistances of Rp for depths of 12 à16m have values of 20 in 45bars.

D. Program and mode(fashion) of load of silos

The objective pursued by this program of first harbour load of silos realized within the bearing of Bejaia is to verify if the reception conditions of the work are combined. Considering the compressible nature of the grounds of foundation and the importance of operating expenses represented by the weight of cereal to be ensiled, it is recommended to proceed to this load in several phases (to avoid loading brutally the ground of foundation). Each of these phases will have to be the object of a control from statements topométriques of the points place on the corner of to cross off. The reference point must be fixed, protected well and taken away enough (30 in 40m) from boxes not to be disrupted(perturbed) by the movements of the ground further to the load [2].

The filling of silos up to 30000 tons, for this load will be made in three (03) phases:

-1st phase it is the load of silos in 25 % (¼). (7500 tons)

-2end phase it is the load of silos in 50 % (½). (1500 tons).

-3rd it is the load of the 100% silos (total load). (30000 tons).

During a phase of load, the order of filling of silos numbered from 1 to 4 for each of 16 boxes will be in accordance with the fig 03, The mode of load it will make it Z. Inside boxes; we load silo1 then the silo 4, then the silo 2, then the silo 3 .une time the first ensiled box (C13), we pass in the second who correspond to C1, then the third which is C16 and finally the fourth (C4), what is going to train(form) the first one Z. The second Z will form inside

TABLE II1I
STAGES OF LOAD AND THE QUANTITIES ENSILED FOR THE 1ST PHASE

Box / silos	1st Z				2nd Z				3th Z				4thZ			
	13	1	16	4	9	5	12	8	14	15	2	3	10	6	11	7
1	1	5	9	13	17	21	25	29	33	37	41	45	49	53	57	61
4	2	6	10	14	18	22	26	30	34	38	42	46	50	54	58	62
2	3	7	11	15	19	23	27	31	35	39	43	47	51	55	59	63
3	4	8	12	16	20	24	28	32	36	40	44	48	52	56	60	64
Ensiled qty Accumulated (t)	7500															
Duration (d)	33															

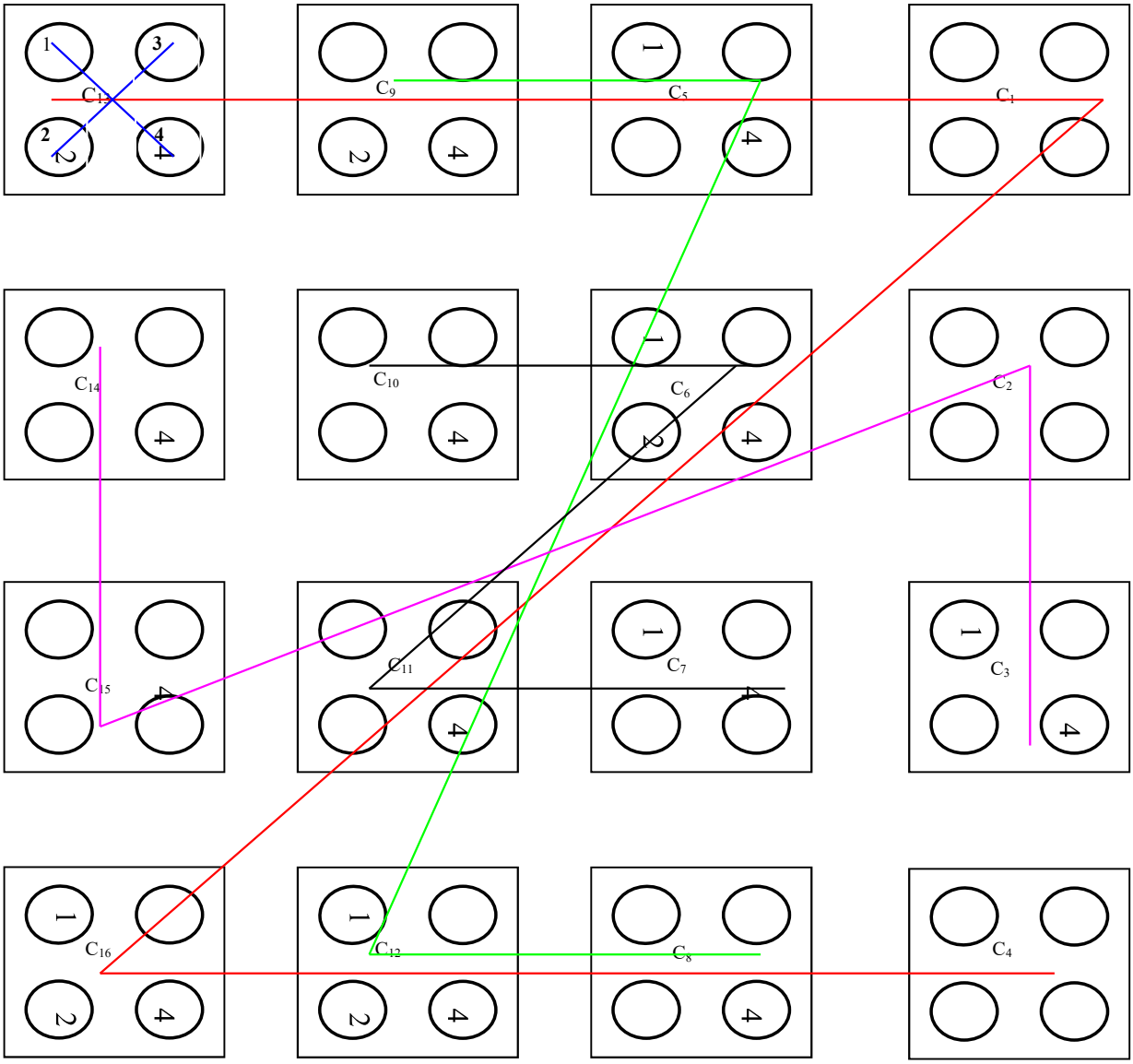


Fig. 3 Representation of the mode loads (silos boxes) [1]

E. Program and mode of load of silos

The CTC IS made the topo-metrique follow-up of the collapses, after every phase of load. The measures are made with fixed marks .Four spicy are made:

Vacuous silo in (0 days), and which we take as reference for the measures of the collapses.

Silo loaded in 25 % in 34 days compared with the vacuous measures.

Silo loaded in 50 % in 89 days compared with the vacuous measures.

Silo loaded to 100% (fully) in 131 days compared with the vacuous measures. The experimental results of these statements, for all the boxes, are represented in the table VI:

TABLE VI
THE EXPERIMENTAL RESULTS OF THE COLLAPSES, RAISED FOR ALL THE BOXES [2]

Durations (Days)	ΔH (mm)							
	Box 1	Box 2	Box 3	Box 4	Box 5	Box 6	Box 7	Box 8
0	0	0	0	0	0	0	0	0
34	-0.87	0.12	0.12	1.25	0	0	-0.37	-0.37
89	-6.62	-4.75	-4.75	-6.25	-6.85	-6.85	-5.75	-5.75
131	-13.4	-10.4	-10.4	-11.75	-10.57	-10.57	-8	-8
Durations (Days)	ΔH (mm)							
	Box 9	Box 10	Box 11	Box 12	Box 13	Box 14	Box 15	Box 16
0	0	0	0	0	0	0	0	0
34	-1.25	-0.62	0.25	-2.62	-1.12	-0.5	-0.5	-2
89	-3	-3.87	-3.62	-7.25	-3	-3.12	-3	-1.25
131	-11	-7.37	-7	-9	-7.25	-5.87	-6.5	-5.87

II. SECOND PART (DIGITAL SIMULATION OF THE COLLAPSES)

A. PLAXIS simulations

A digital study is realized by means of the PLAXIS for a box constitute of four silos, this study restarted as follows [1]:

1) Delimitation of the domain of the work: depth of 40m (bed rock) and of 100m of length and the introduction of the mechanical parameters of the ground (C, φ, E_{oed} γ) (fig04).
2) Applications of the load of 0,89bars (fig 05).
3) Meshing.
4) Representation of the effective constraints (fig 06):
5) Calculation of the deformed speed of the collapse (fig 07).

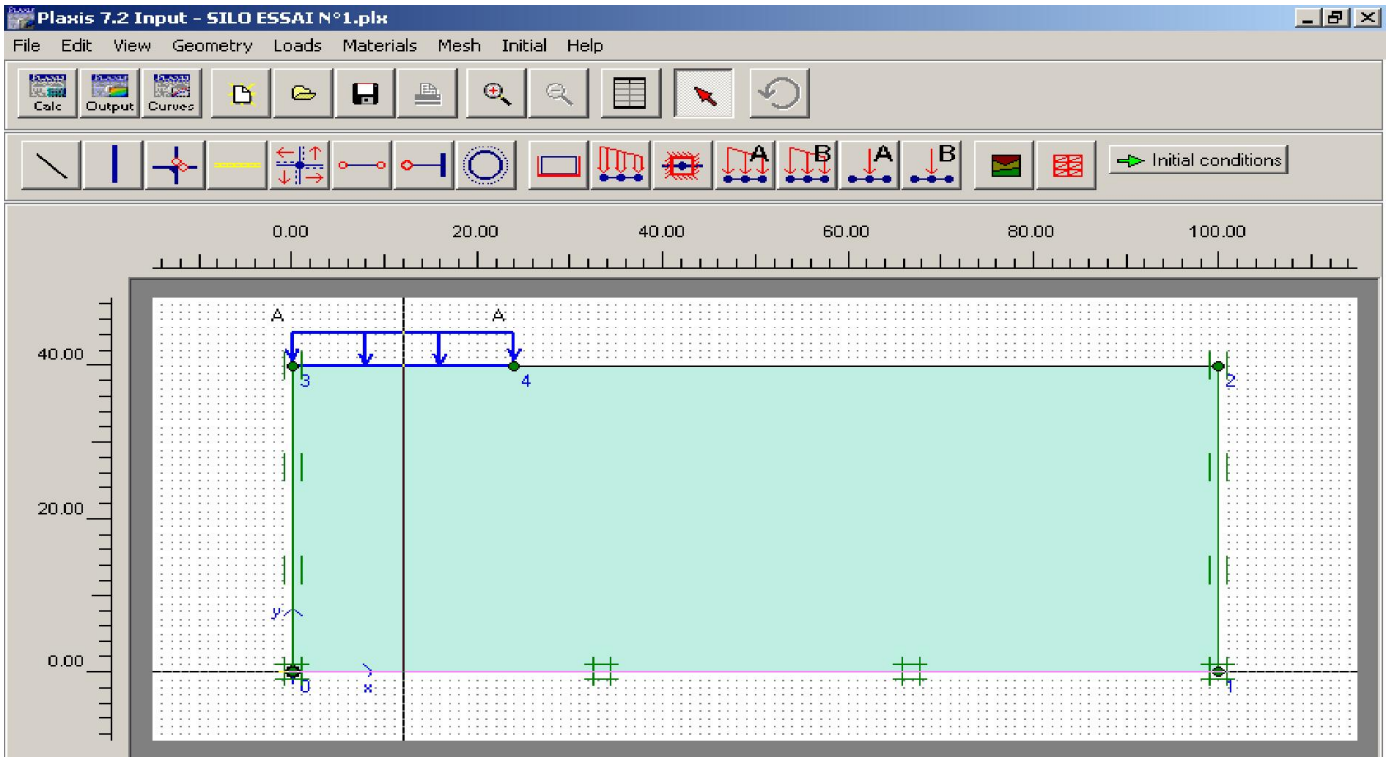


Fig. 4 Delimitation of the domain of the work

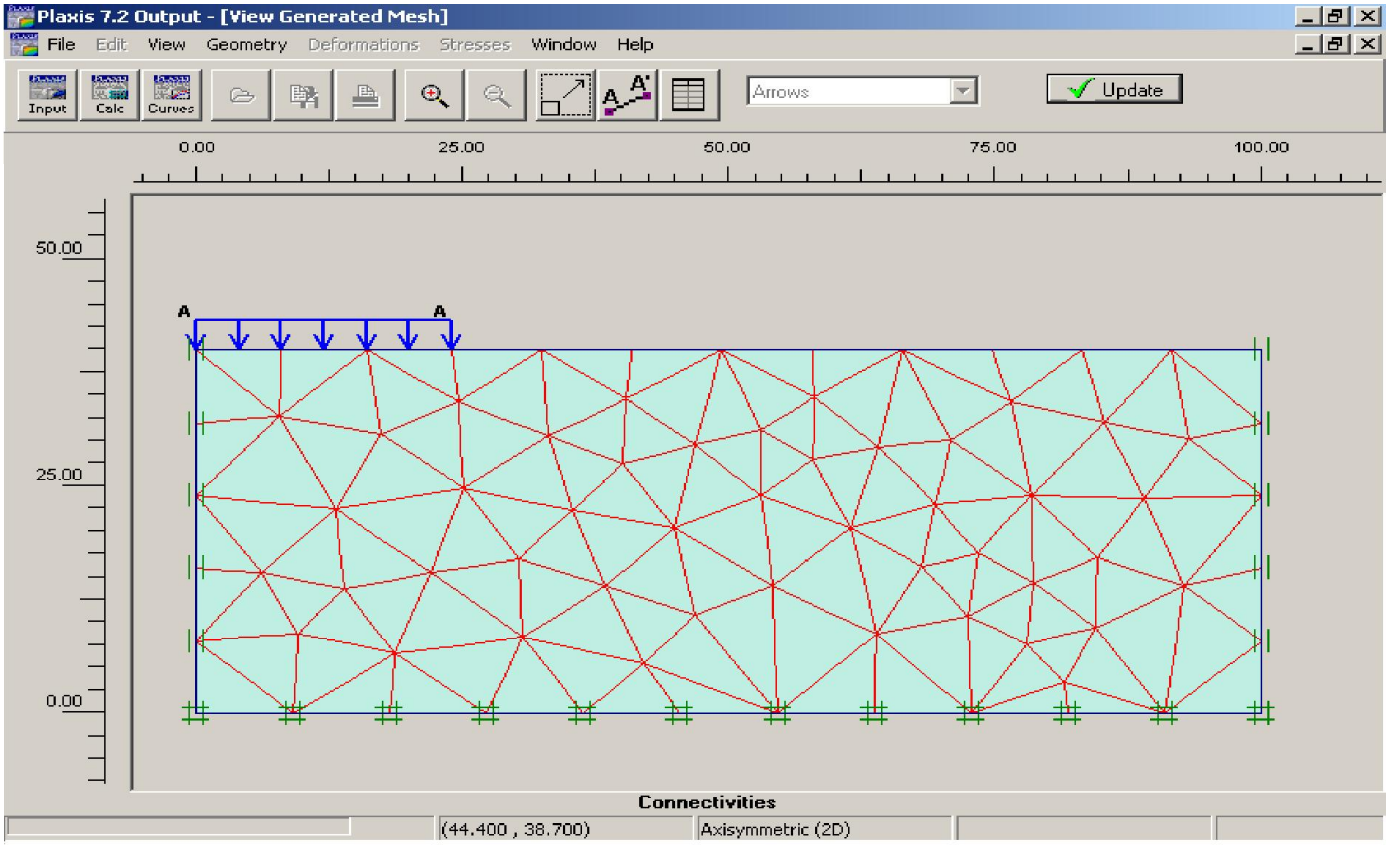


Fig. 5 meshing of the domain of work

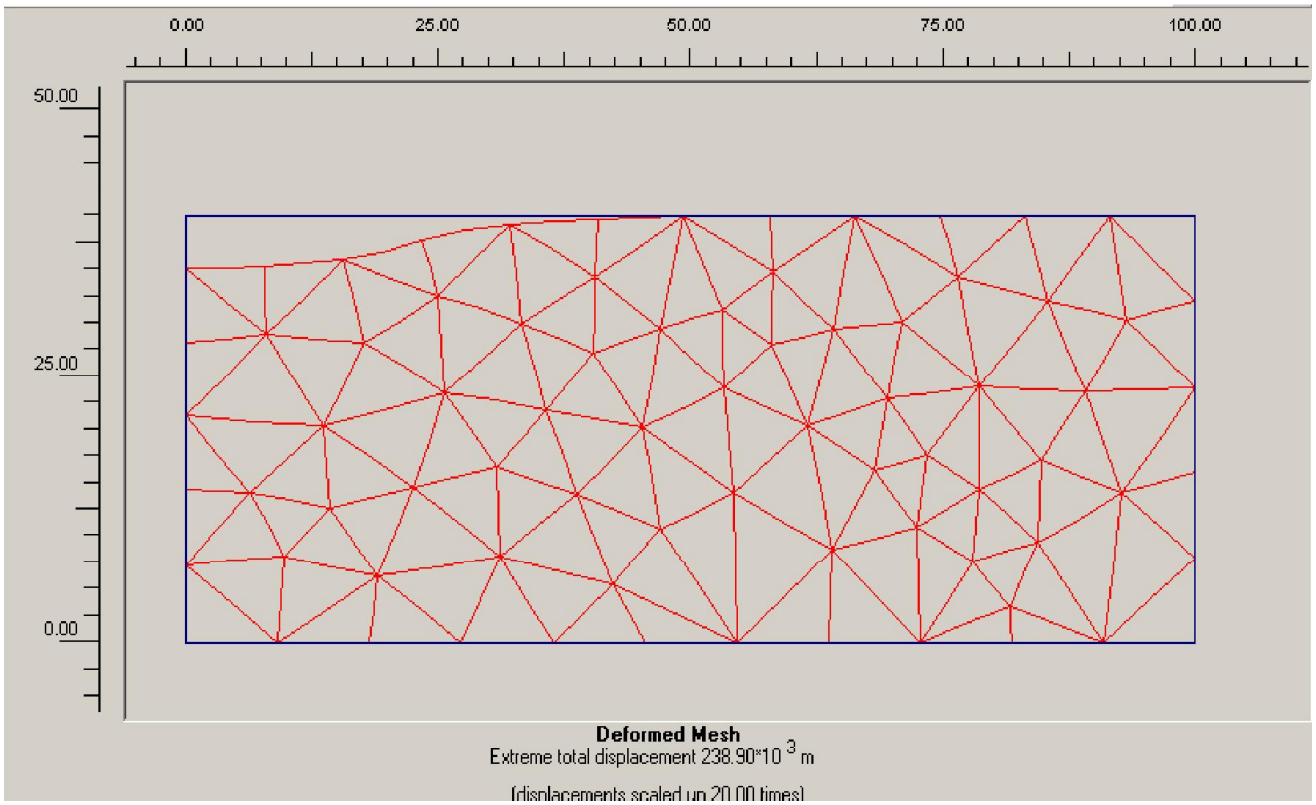


Fig. 6 Effective constraints Results

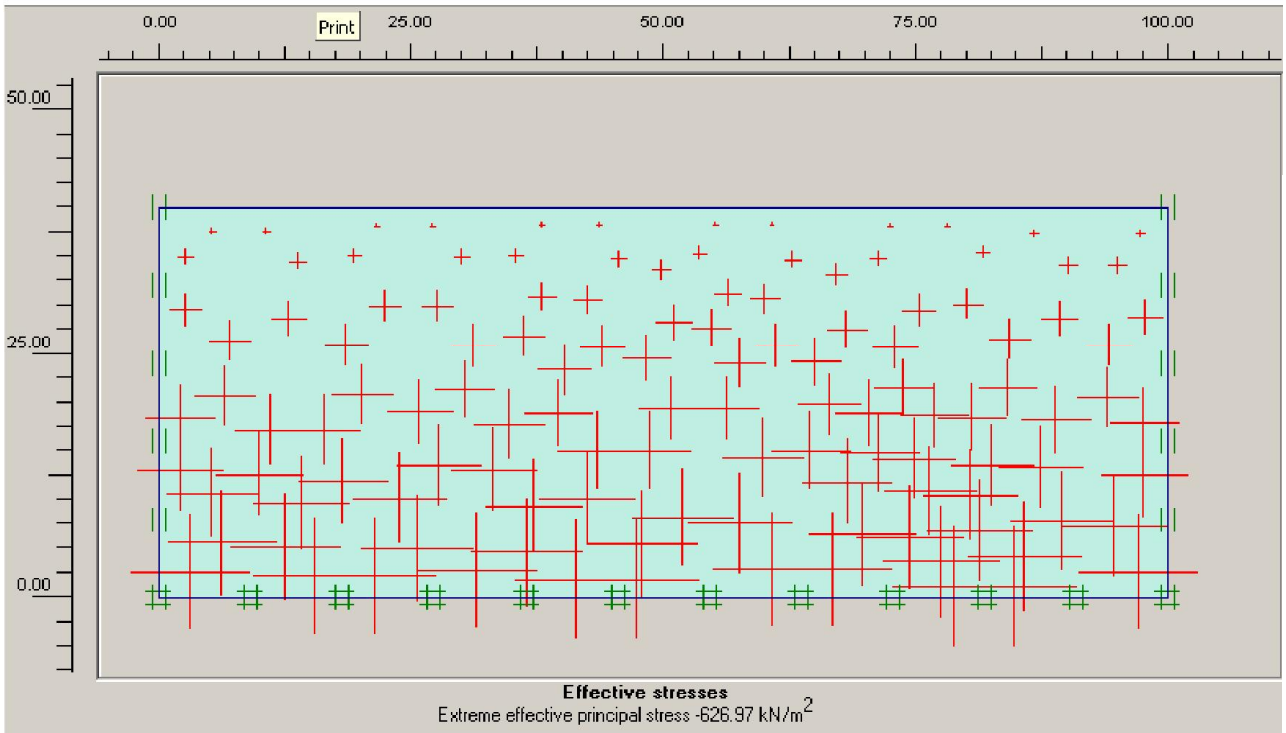


Fig. 7 calculation of the deformed collapse speed

B. Results of the simulation

The result of the simulation applied for a single box gives a maximal collapse of 23,89cm, this result will be compared with the collapse calculated by the method of slices (Oedométrique) estimated has 25,6cm has a constraint of 0,89 bars, which corresponds to the decent of load (loaded silos à100 %) [1].

C. Conclusion

The collapses calculated (in theory) and those given by the software get closer, and the margin of error is of the order of the tenth of centimeter. We can thus conclude that from it the simulation made for a single box is close to the reality.

III. Conclusions

The ground deforms in a way more at least uniform, with the exception of some zones where there were disturbances (light uprisings), and it can be due to several causes such as the arrangement of the measuring device (very sensitive to the vibratory movements). The reaction of the ground of basis shows itself more important from the point of view variation of the curves of levels during the first phase of load, these curves spread out more and more during the second phase with more important values (until 8mm), and they affect a limit of 18mm when silos are loaded in full capacity.

References

[1] M. Bouzeroura. I. Noria. A. Rachida, digital Simulation of the collapses of the Harbour Silos of storage of wheat of a 30000 ton capacity, a report of the end study, the university,A/Mira Bejaia, in June, 2006.

[2] CTC EST, Result of the statements topometrique makes on Silos harbour port of Bejaia, in November, 2005.

.

Numerical Simulation of Internal Turbulent Flows

T. KARASU[1]

[1] Eskişehir Osmangazi University, Meşelik, 26480 Eskişehir/Turkey, tahirkarasu26@gmail.com

Abstract - **This original research work presents the results of an extensive study of numerical simulation and modelling of steady, incompressible and axisymmetric internal turbulent flows in circular-sectioned pipes at two different Reynolds numbers. Employing the finite-volume method, a computer program based on the SIMPLE (Semi-Implicit Method for Pressure Linked Equations) algorithm has been developed. Numerical solution of the conservation equations of mass and momentum, together with the standard k-ε turbulence model, are obtained using an iterative numerical solution technique. Near the solid boundary, wall-functions are employed. Numerical simulations for radial profiles of axial velocity, turbulence kinetic energy, turbulence kinetic energy dissipation rate, effective viscosity, centre-line velocity variation, wall-shear stress and friction coefficient distributions along axisymmetric pipe flow geometry are presented and compared with experimental data. The results of numerical simulations are generally in very good agreement with experimental measurements.**

Keywords - **Turbulence, Flow, Pipes, Simulations.**

I. INTRODUCTION

NUMERICAL simulation and modelling of developing internal turbulent flow in pipes of circular cross-section is one of the basic flow studies. This flow is basically a transition from a boundary layer-type flow at the entrance to a fully developed flow downstream. The free stream in the inlet region is completely surrounded by the boundary layer, which by diffusion of momentum through laminar and turbulent mechanisms grows in thickness as the distance from the pipe inlet increases. The growing boundary layer accelerates the free stream which eventually loses its identity as the boundary layer merges with it. Following the disappearance of the free stream, further changes occur in the velocity distribution and turbulence structure until the flow attains a fully developed state. Developing internal turbulent pipe flow has wide application in the field of engineering. The ability to compute the detailed nature of the behaviour of developing turbulent flow in pipes would lead to the improved design of engineering equipment. In practice, internal turbulent pipe flow is mostly encountered in: transportation of various liquids and gases in long pipes, heat exchangers, coolant passages of electrical generators, combustion chamber systems and air conditioning and heating systems. Considerable experimental and theoretical works on internal turbulent flow in pipes have been reported in the literature. Among the most interesting ones are the works of [1]-[36]. In the present numerical simulation, the experimental measurements of [7] and [10] have been used for comparison with the numerical computations. The main objective of this investigation is to obtain numerical simulations of steady, incompressible and axisymmetric developing internal turbulent flow in pipes using the standard k-ε turbulence model [37] with a wall-functions boundary condition, and to compare the results of numerical simulations with available experimental measurements in the literature for validation.

II. MATHEMATICAL AND PHYSICAL MODEL

A. Governing Equations and Turbulence Model

With reference to Figure 1, the mathematical and physical model employed in the numerical simulation of incompressible and axisymmetric developing internal turbulent flow in circular-sectioned pipes, requires the simultaneous solution of the governing equations, together with the turbulence model equations. The transport equations representing the conservation of mass, momentum, turbulence kinetic energy and its dissipation rate are cast into a general form of steady state and axisymmetric cylindrical coordinates as follows:

$$\frac{\partial}{\partial x}(\rho u\phi)+\frac{1}{r}\frac{\partial}{\partial r}(\rho rv\phi)-\frac{\partial}{\partial x}\left(\Gamma_\phi\frac{\partial\phi}{\partial x}\right)-\frac{1}{r}\frac{\partial}{\partial r}\left(r\Gamma_\phi\frac{\partial\phi}{\partial r}\right)=S_\phi \quad (1)$$

This equation represents a transport equation for a general variable ϕ. The flow is assumed to remain in radial planes. The variables u and v are axial and radial velocity components, ρ is the fluid density and Γ_ϕ is the transport coefficient. The final term, S_ϕ , is the source term. The variables, ϕ, necessary in this computational investigation are u, v, k and ε. Here, k and ε stand for the kinetic energy of turbulence and its dissipation rate, respectively. The turbulence model employed in the present study is the k-ε model of [37]. If ϕ is set equal to unity and Γ_ϕ and S_ϕ to zero, (1) also represents the equation of continuity. Pressure is derived from the pressure correction equation [38, 39]. The transport equations, coefficients and the source terms are summarised in Table 1.

Table 1: Transport equations, coefficients and source terms.

ϕ	Γ_ϕ	S_ϕ
1	0	0
u	$\mu_e = \mu + \mu_t$	$-\frac{\partial P}{\partial x} + \frac{\partial}{\partial x}\left(\mu_e \frac{\partial u}{\partial x}\right) + \frac{1}{r}\frac{\partial}{\partial r}\left(r\mu_e \frac{\partial v}{\partial x}\right)$
v	μ_e	$-\frac{\partial P}{\partial r} + \frac{\partial}{\partial x}\left(\mu_e \frac{\partial u}{\partial r}\right) + \frac{1}{r}\frac{\partial}{\partial r}\left(r\mu_e \frac{\partial v}{\partial r}\right) - 2\mu_e \frac{v}{r^2}$
k	$\frac{\mu_e}{\sigma_k}$	$G - \rho\varepsilon$
ε	$\frac{\mu_e}{\sigma_\varepsilon}$	$\frac{\varepsilon}{k}(C_1 G - C_2 \rho\varepsilon)$

Note : 1. $\mu_t = C_\mu \rho k^2/\varepsilon$

2. Turbulence model constants are assigned the following values (Launder and Spalding, 1974) :
$C_\mu = 0.09, C_1 = 1.44, C_2 = 1.92, \sigma_k = 1.0, \sigma_\varepsilon = 1.3$

3. $G = \mu_t \left\{ 2\left[\left(\frac{\partial u}{\partial x}\right)^2 + \left(\frac{\partial v}{\partial r}\right)^2 + \left(\frac{v}{r}\right)^2 \right] + \left(\frac{\partial u}{\partial r} + \frac{\partial v}{\partial x}\right)^2 \right\}$

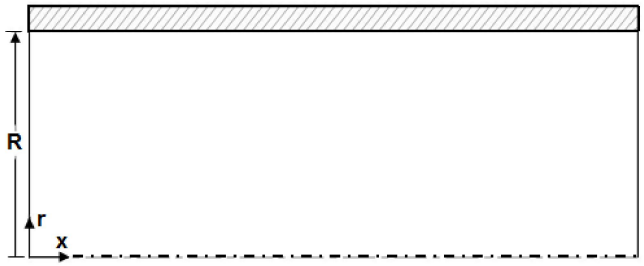


Figure 1: Axisymmetric cylindrical coordinate system and geometry of the pipe flow.

B. Boundary Conditions

With reference to Figure 1, the boundary conditions for turbulent flow in the pipes studied are given below. At the inlet to the pipe, a uniform axial velocity corresponding to the experimental condition is specified, while the radial velocity is assumed zero. Empirical relationships are employed to assign uniform entrance values to turbulence quantities k and ε; that is, k=(0.002-0.004) u_b^2 and ε=($C_\mu k^{3/2}$ / 0.02R), where u_b is the bulk velocity and R is the radius of the pipe. The pipe section was chosen to be sufficiently long so that fully developed conditions could be assumed to prevail at the outlet; that is, all axial derivatives were assumed to vanish and the radial velocity was assumed zero. At the pipe axis, symmetry is assumed: $(\partial\phi/\partial r) = v = 0$, where ϕ can be any of u, k or ε. At the pipe wall, velocity components u, v and turbulence quantities k and ε are set to zero. The values of k and ε at the near-wall grid points are calculated using the wall-functions of [37]. Initial field values throughout the computational domain were specified properly so as not to cause numerical divergence.

C. Numerical Solution Procedure

In this numerical investigation, employing the finite-volume approach, a computer program based on the SIMPLE algorithm of [38] has been developed. The partial differential equations (1) are discretised by a control-volume-based finite-difference method with a hybrid scheme. The finite-volume forms of the partial differential equations coupled with the boundary conditions are solved iteratively using a line-by-line solution procedure in conjunction with a tridiagonal matrix form [40].

D. Computational Details

The numerical computations were performed on an Intel(R) Core(TM) i5-2400 CPU @ 3.10GHz 3.40GHz personal computer. The computational grid distributions for two of the pipe-flow cases studied are depicted in Figures 2 and 12. All the computational grids employed were non-uniformly distributed with finer spacings in the regions of large spatial gradients, i.e., the near-wall region and inlet region of the pipe. Staggered control volumes were used for axial and radial velocity components. All other quantities of interest were calculated at the grid points. The line-by-line method was employed to obtain converged solutions iteratively. Under-relaxation factors were used to promote numerical stability with values of 0.6, 0.6, 0.8, 0.8, 0.5 and 0.5 for u, v, k, ε, P and μ_e, respectively. The convergence criterion adopted in the present computations was that the summation of the absolute values of the mass residual in the entire computational domain be less than a prescribed value of 10^{-5}. Grid tests were performed with different grid sizes to obtain an optimum grid-independent solution for each flow case studied. All the computations presented in this study are grid-independent. Table 2 summarises details of the computational requirements for the flow cases investigated. In this table, Re is the Reynolds number and N is the number of iterations performed to obtain a converged solution.

Table 2: Flow case, Reynolds number, grid size and number of iterations.

Flow case of	**Re**	**Grid Size (×) × (r)**	**N**
Reference [7]	**100 000**	40 × 30	627
Reference [10]	**15 000**	40 × 30	657

III. PRESENTATION AND DISCUSSION OF RESULTS

Numerical simulations were carried out for developing internal turbulent flow in circular-sectioned pipes at two different Reynolds numbers, and the results of simulations were compared with the experimental data of [7] and [10]. With air used as the working fluid in the pipe, the experimental measurements of [7] are first selected as the comparison basis for this computational study. The Reynolds number based on the pipe diameter and bulk velocity is Re=1 x 10^5 (Re = u_b d / ν). For this flow case, the computational domain is extended to an axial distance of 240.7 diameters downstream from the inlet plane of the pipe. The computational grid distribution for the

axisymmetric pipe-flow geometry of [7] is shown in Figure 2 The computed radial profiles of axial velocity along the pipe in dimensionless form u / u_c and radial distance r/R, at axial positions ranging from x/d=3 to 240.7 are depicted in Figures 3 and 4, and compared with the experimental measurements of [7]. As seen from the figures, the computed axial velocity profile develops along the pipe, and at cross-section x/d=240.7 the agreement obtained between the predictions and experimental data is excellent. In Figure 5, the predicted axial variation of centre-line velocity is presented in terms of u_c/u_b and axial distance x/d. Here, the centre-line velocity (u_c) is normalised with the bulk velocity (u_b), and the axial distance is normalised with respect to pipe diameter (d). As can be seen from the figure, the predicted axial variation of centre-line velocity increases first until it attains its maximum value at x/d=21, and then decreases slightly to its fully-developed value downstream at about x/d=93, after which it remains constant along the pipe axis. In Figure 6, the predicted axial distribution of dimensionless turbulence kinetic energy $k^{0.5}/u_b$ along the symmetry axis of the pipe is revealed. As seen from the figure, the turbulence kinetic energy decreases until it attains its minimum value at about x/d=15, and thereafter increases sharply along the pipe axis until it reaches its maximum value at x/d=51, and then after showing a little bit decrease it attains its fully-developed value downstream at about x/d=123, after which it remains constant along the pipe axis. Figures 7, 8 and 9 display the predicted radial profiles of turbulence kinetic energy, dissipation rate of turbulence kinetic energy and effective viscosity, respectively, along the pipe of [7] at the same downstream locations as in Figure 3. Here, the predicted profiles are normalised, respectively, with respect to square of bulk velocity u_b^2, maximum values of turbulence kinetic energy dissipation rate ε_{max} and effective viscosity $\mu_{e\,max}$ in the flow field. These figures indicate how the predicted turbulence kinetic energy, dissipation rate of turbulence kinetic energy and effective viscosity profiles develop along the pipe flow configuration of [7]. Figure 10 shows the computed variation of the wall-shear stress along the pipe wall, in terms of the ratio τ_w / τ_{wd}, plotted against nondimensional distance x/d from the inlet plane of the pipe. The wall-shear stress has been made dimensionless with respect to its fully-developed value, τ_{wd}. For this flow case, as can be seen from the figure, the fully-developed value of the wall-shear stress is reached at about x/d=87. Beyond this location, it remains practically constant.

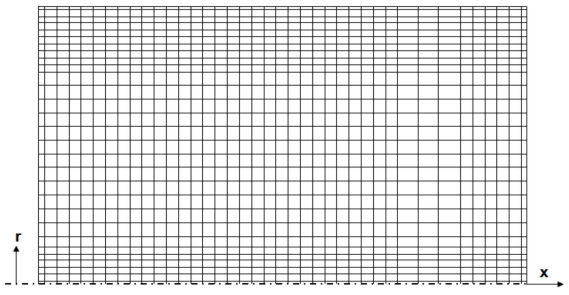


Figure 2: Computational grid distribution for pipe flow of [7].

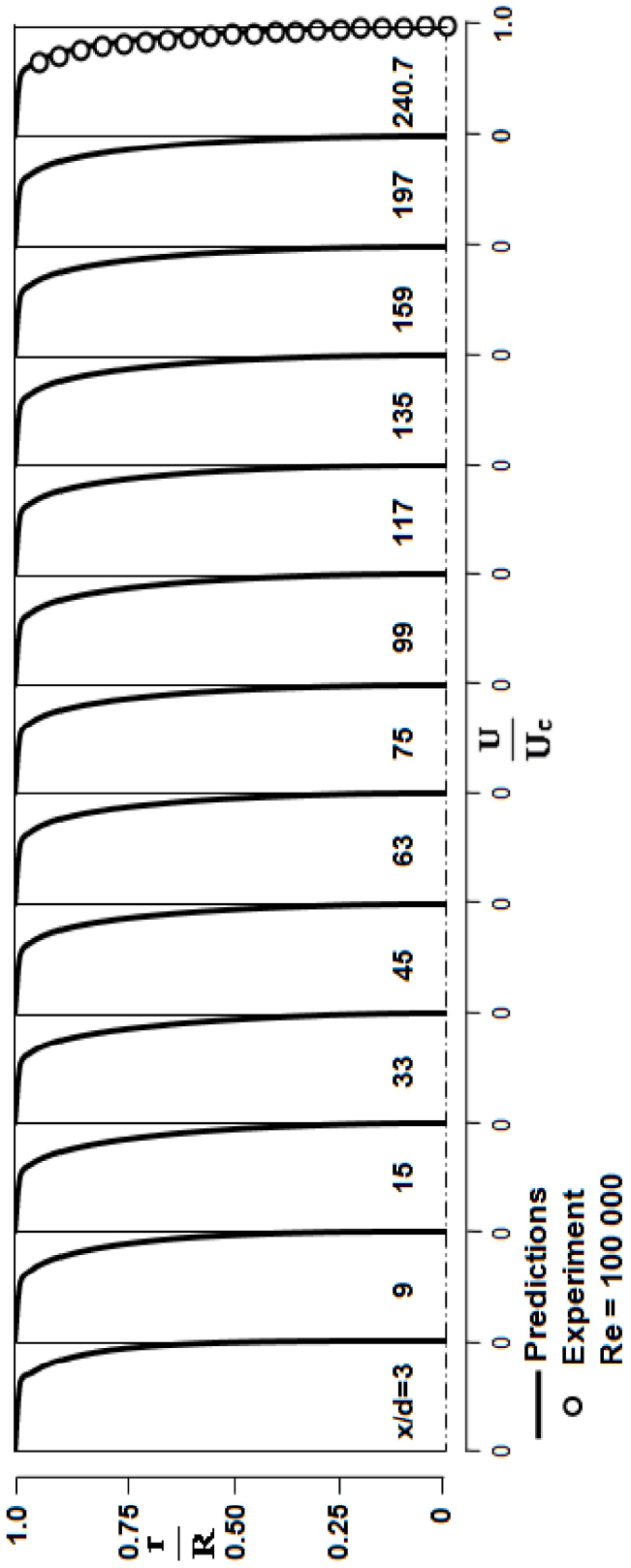


Figure 3: Comparison of predicted radial profiles of axial velocity along the pipe with experimental data of [7].

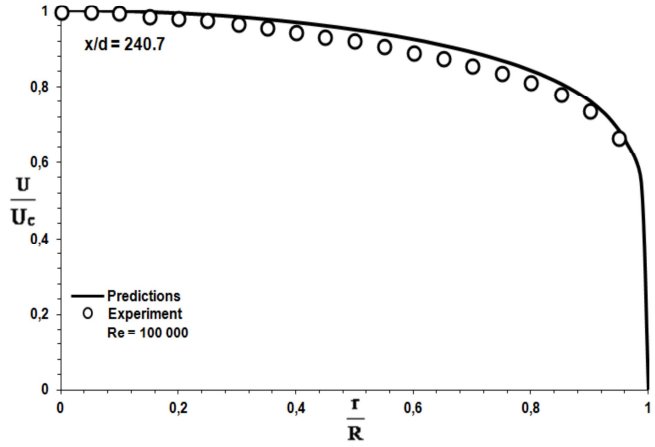


Figure 4: Comparison of predicted radial profile of axial velocity with experimental data of [7] at x/d=240.7.

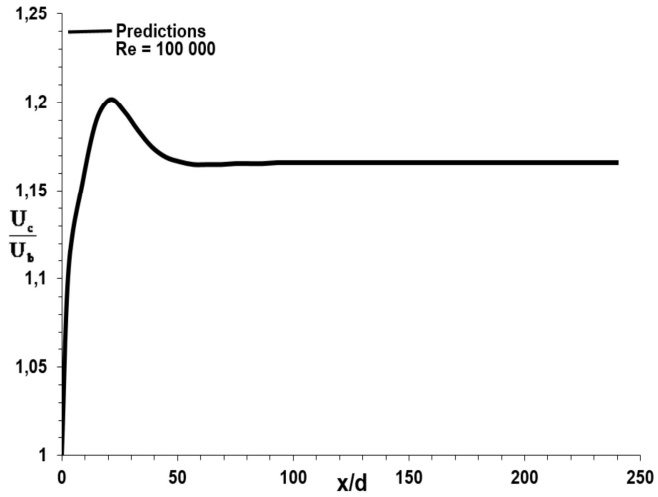


Figure 5: Predicted axial variation of dimensionless centre-line velocity along the pipe axis of [7].

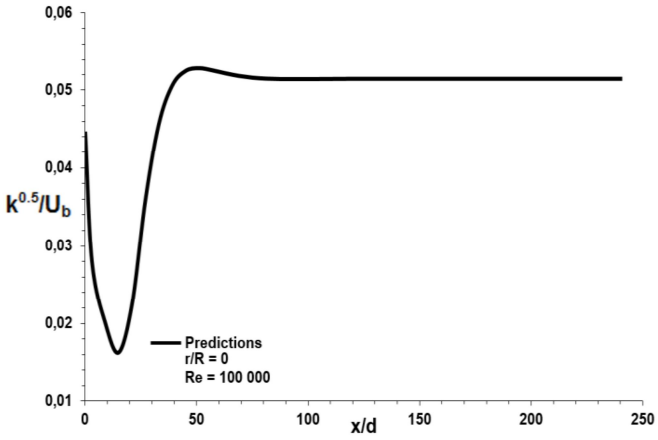


Figure 6: Predicted axial distribution of dimensionless turbulence kinetic energy along the pipe axis of [7].

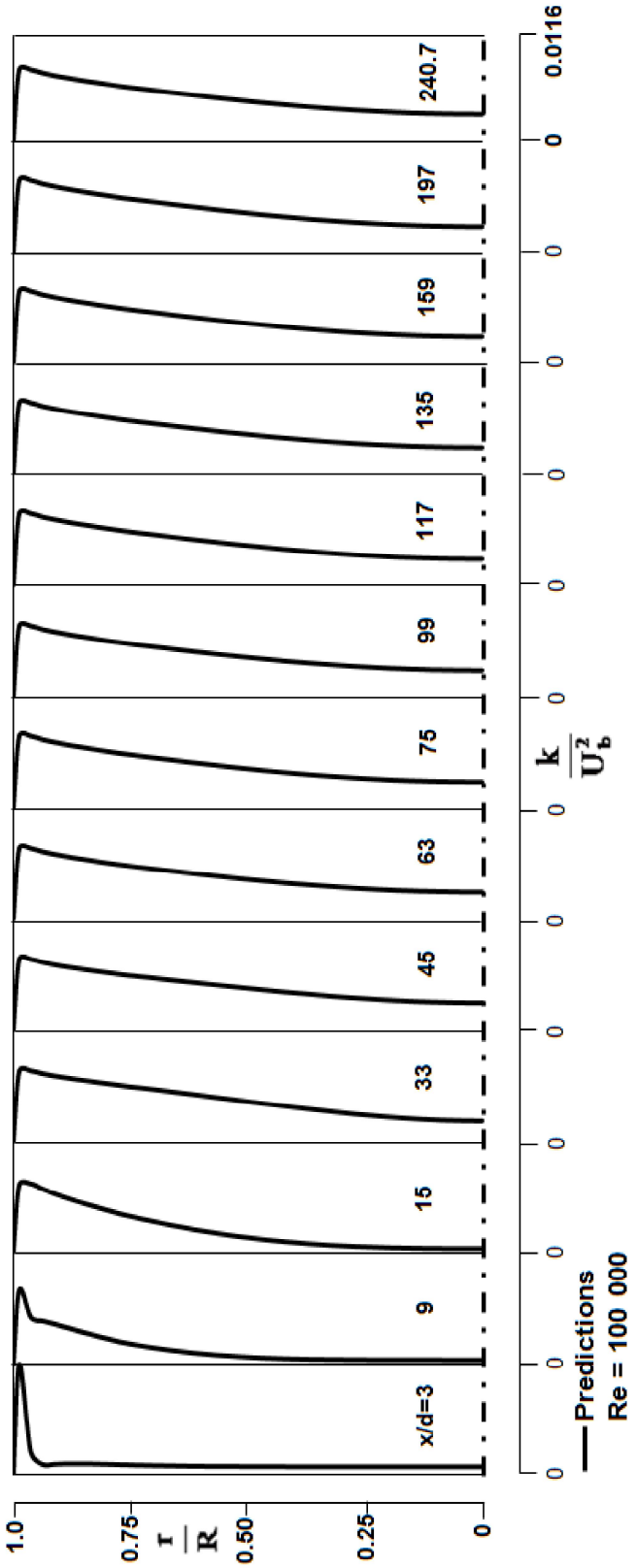


Figure 7: Predicted radial profiles of normalised turbulence kinetic energy along the pipe flow of [7].

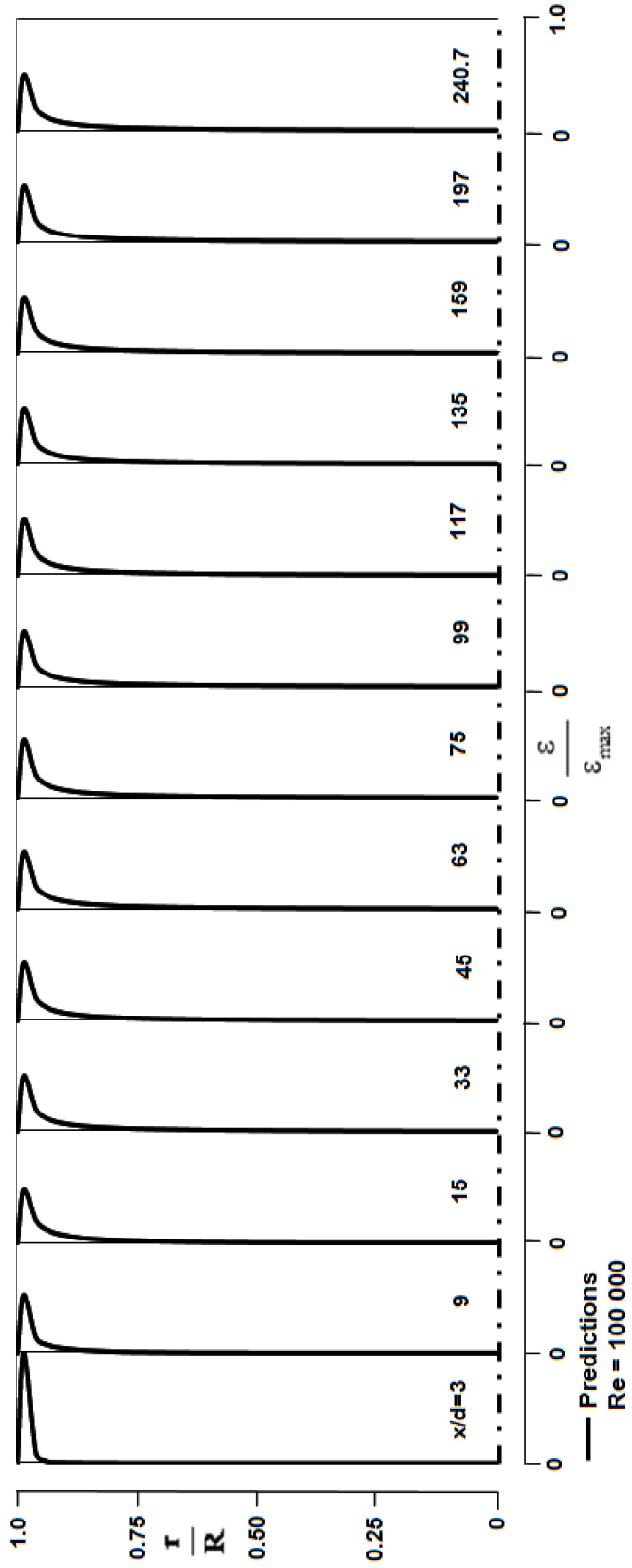


Figure 8: Predicted radial profiles of normalised turbulence kinetic energy dissipation rate along the pipe flow of [7].

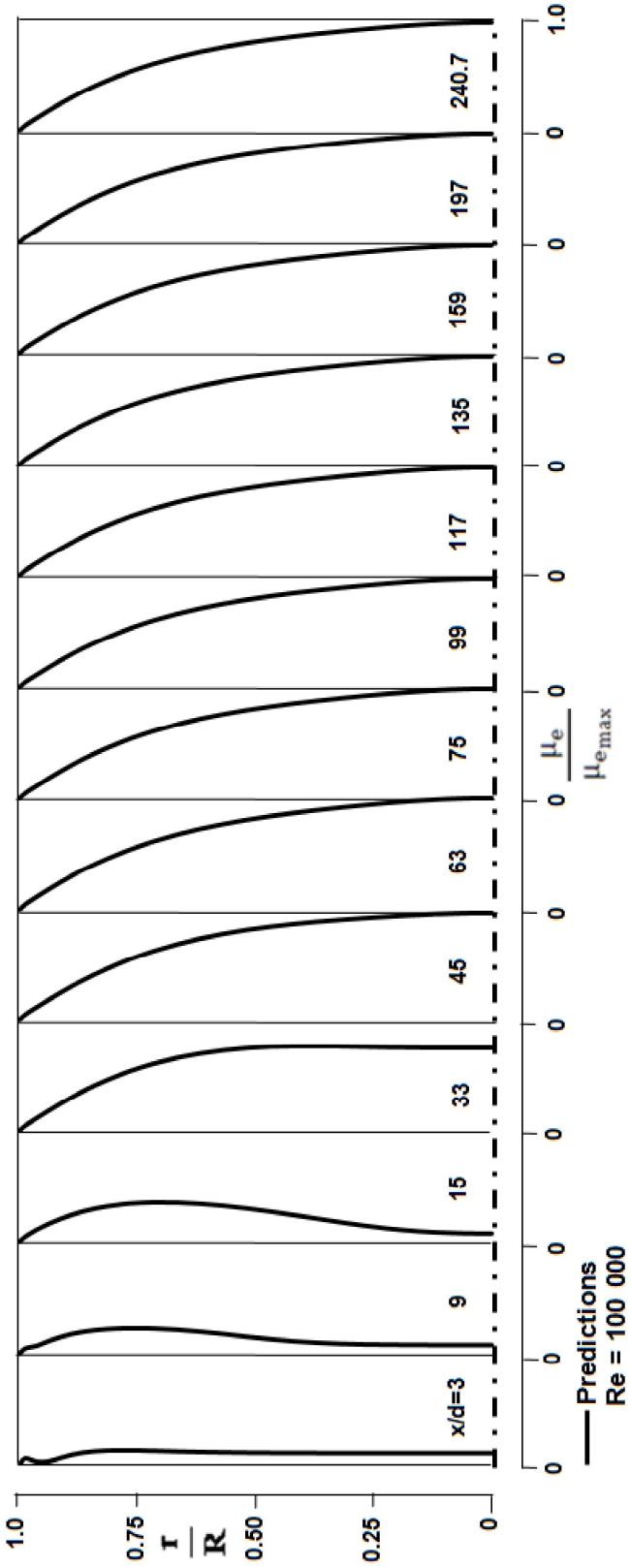


Figure 9: Predicted radial profiles of normalised effective viscosity along the pipe flow of [7].

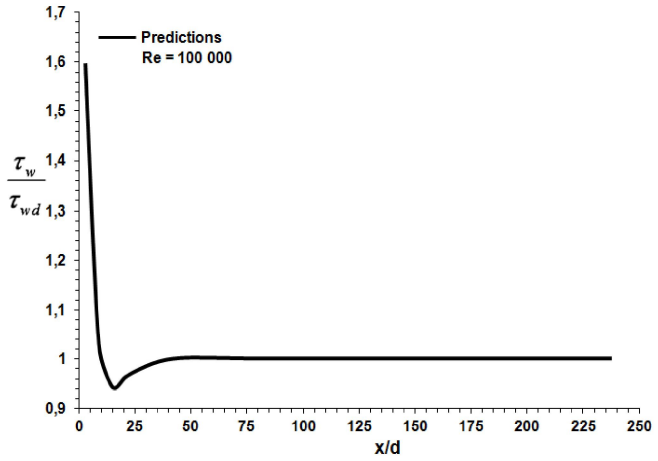


Figure 10: Computed variation of dimensionless wall-shear stress along the pipe wall of [7].

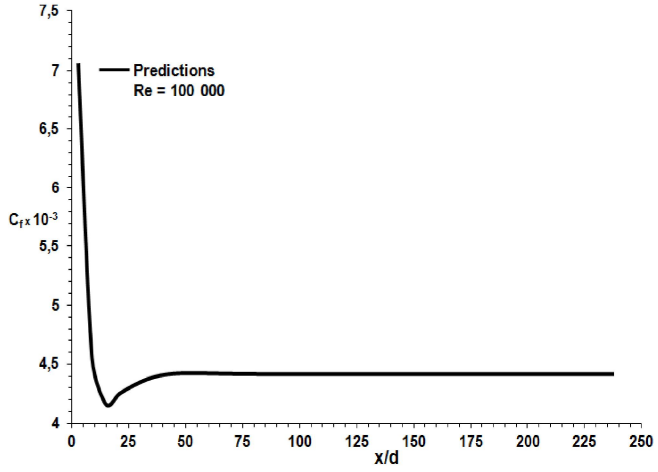


Figure 11: Computed distribution of friction coefficient along the pipe wall of [7].

Finally, the computed distribution of the friction coefficient ($C_f = 2\ \tau_w / \rho\ u_b^2$) along the pipe wall, as a function of downstream distance x/d, is plotted in Figure 11. As seen from the figure, the friction coefficient exhibits the same trend as the wall-shear stress shown in Figure 10.

With water used as the working fluid in the pipe, the experimental study of turbulent pipe flow conducted by [10] is secondly selected as the test case for this computational study. The Reynolds number based on the pipe diameter and bulk velocity is $Re=1.5 \times 10^4$ ($Re = u_b\ d / \nu$, where u_b is the bulk velocity). For this flow situation, the computational domain is extended to an axial distance of 320 diameters downstream from the inlet plane of the pipe. The computational grid distribution for the pipe flow of [10] is indicated in Figure 12. Figures 13 and 14 show the development of computational radial profiles of axial velocity along the pipe in dimensionless form u/u_b and radial distance r/R, at axial locations ranging from x/d=1 to 320, together with experimental measurements of [10]. As seen from the figures, the predicted axial velocity profile develops along the pipe, and at cross-section x/d=170 the agreement obtained between the predictions and experimental data is very good. In Figure 15, the predicted axial variation of centre-line velocity along the pipe axis is given in terms of u_c/u_b and axial distance x/d. Here, the centre-line velocity (u_c) is normalised with respect to bulk velocity (u_b), and the axial distance is normalised with respect to pipe diameter (d). As can be seen from the figure, the predicted axial variation of centre-line velocity increases first until it reaches its maximum value at x/d=15, and then decreases slightly to its fully-developed value downstream at about x/d=70, after which it remains constant along the pipe axis. In Figure 16, the predicted axial distribution of dimensionless turbulence kinetic energy $k^{0.5}/u_b$ along the symmetry axis of the pipe is displayed. As seen from the figure, the turbulence kinetic energy decreases until it attains its minimum value at about x/d=10, and thereafter increases sharply along the pipe axis until it reaches its maximum value at x/d=40, and then after showing a little bit decrease it attains its fully-developed value downstream at about x/d=110, after which it remains constant along the pipe axis. Figures 17, 18 and 19 present the predicted radial profiles of turbulence kinetic energy, turbulence kinetic energy dissipation rate and effective viscosity, respectively, along the pipe of [10] at the same downstream locations as in Figure 13. Here, the predicted profiles are normalised, respectively, with respect to square of bulk velocity u_b^2, maximum values of turbulence kinetic energy dissipation rate ε_{max} and effective viscosity $\mu_{e\,max}$ in the flow field. These figures reveal how the computed turbulence kinetic energy, turbulence kinetic energy dissipation rate and effective viscosity profiles develop along the pipe flow geometry of [10]. In Figure 20, the predicted variation of the wall-shear stress in dimensionless form τ_w/τ_{wd} along the pipe wall is plotted as a function of downstream distance normalised to pipe diameter. For this flow situation, as can be seen from the figure, the fully-developed value of the wall-shear stress (τ_{wd}) is attained at about x/d=70. Beyond this location, it remains practically constant. Finally, the computed distribution of the friction coefficient ($C_f = 2\ \tau_w / \rho\ u_b^2$) along the pipe wall, as a function of downstream distance x/d, is depicted in Figure 21. As seen from the figure, the friction coefficient indicates the same trend as the wall-shear stress displayed in Figure 20.

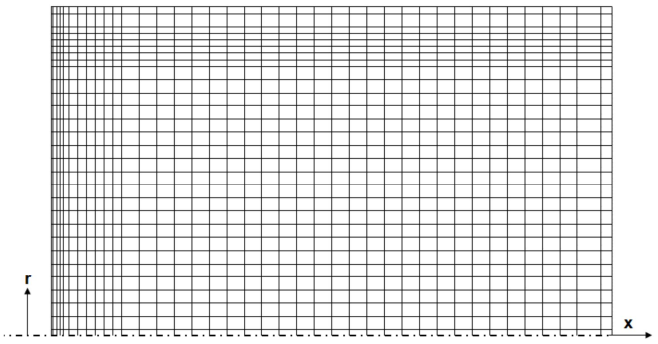


Figure 12: Computational grid distribution for pipe flow of [10].

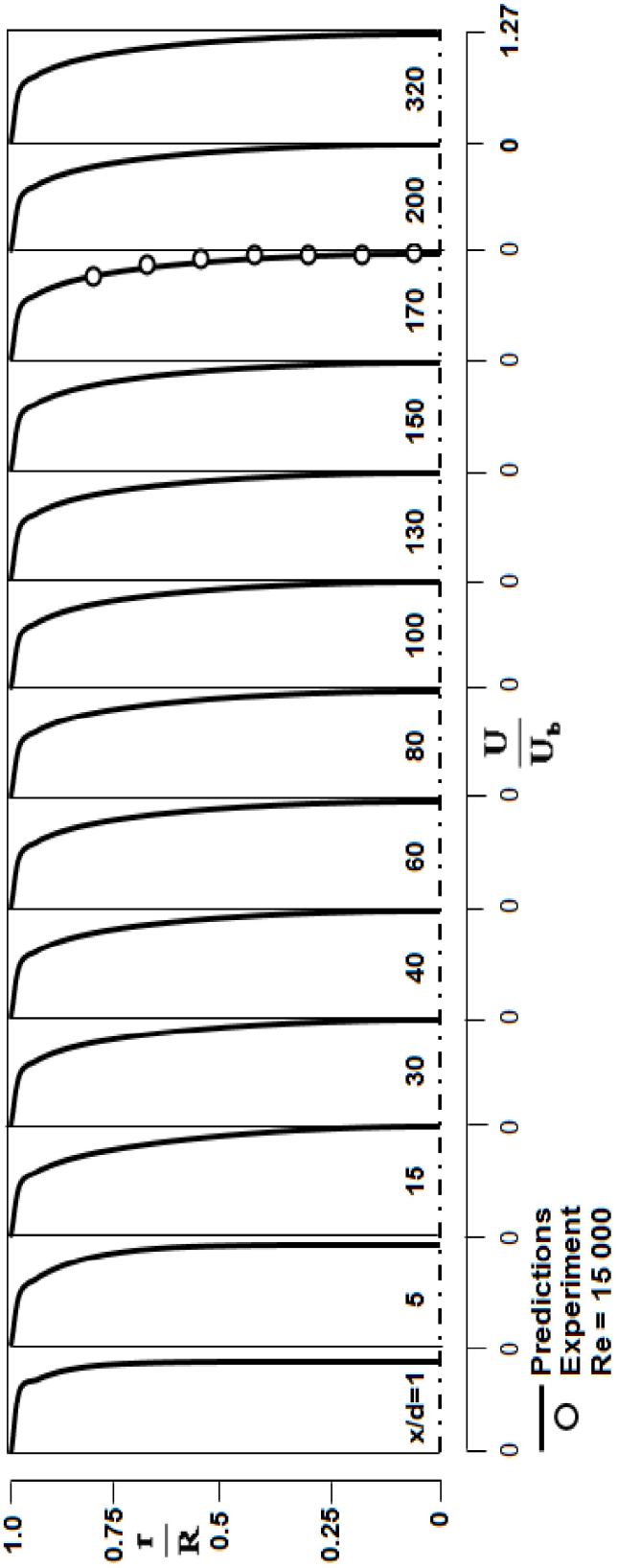


Figure 13: Comparison of predicted radial profiles of axial velocity along the pipe with experimental data of [10].

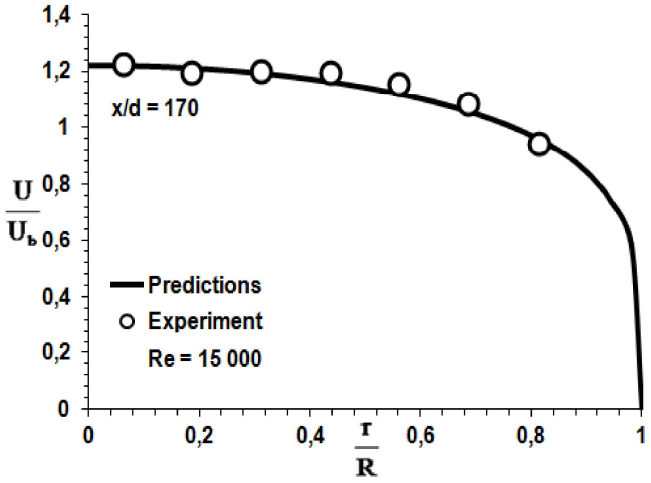


Figure 14: Comparison of predicted radial profile of axial velocity with experimental data of [10] at x/d=170.

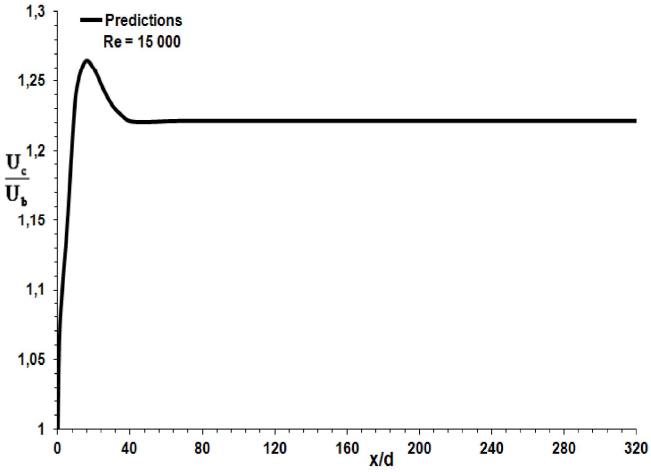


Figure 15: Predicted axial variation of dimensionless centre-line velocity along the pipe axis of [10].

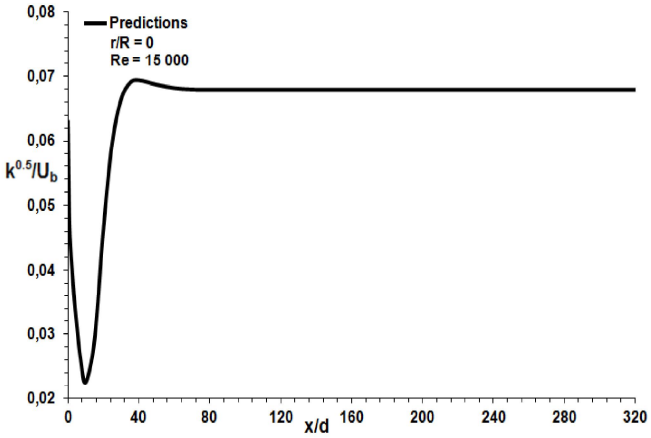


Figure 16: Predicted axial distribution of dimensionless turbulence kinetic energy along the pipe axis of 10].

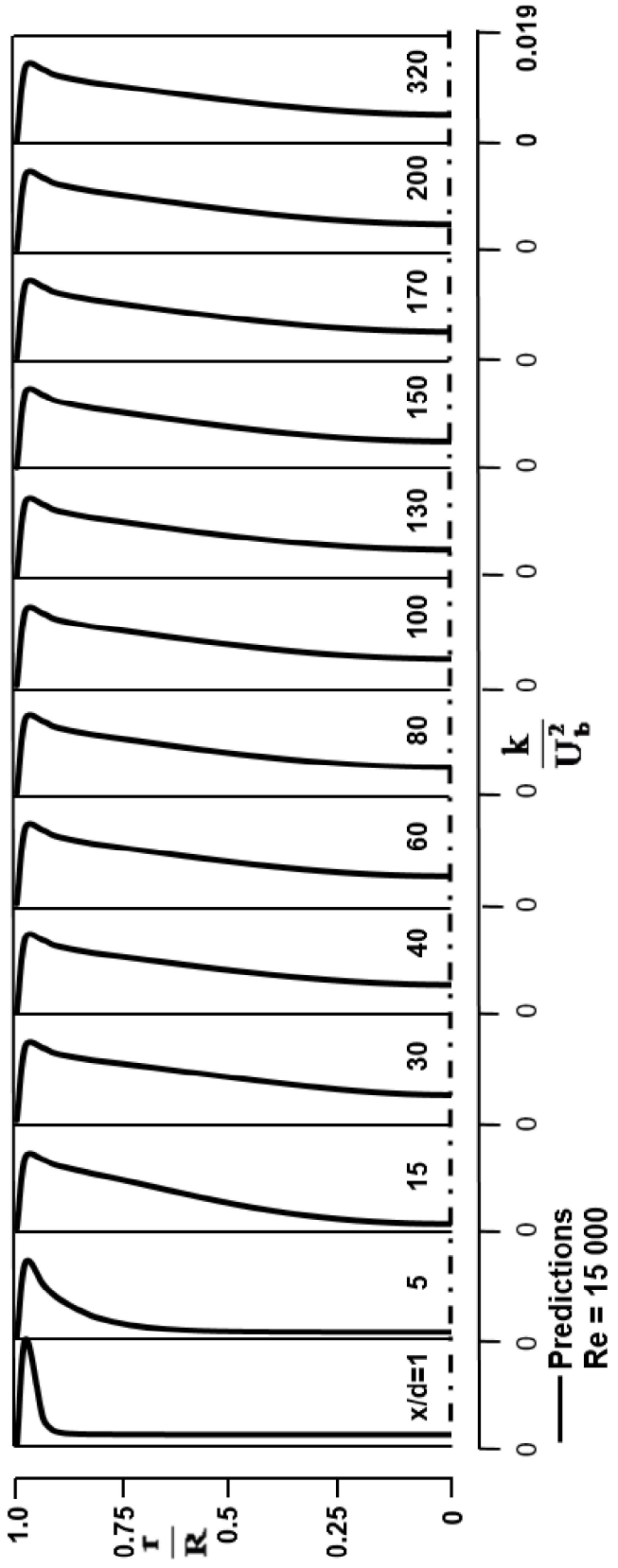


Figure 17: Predicted radial profiles of normalised turbulence kinetic energy along the pipe flow of [10].

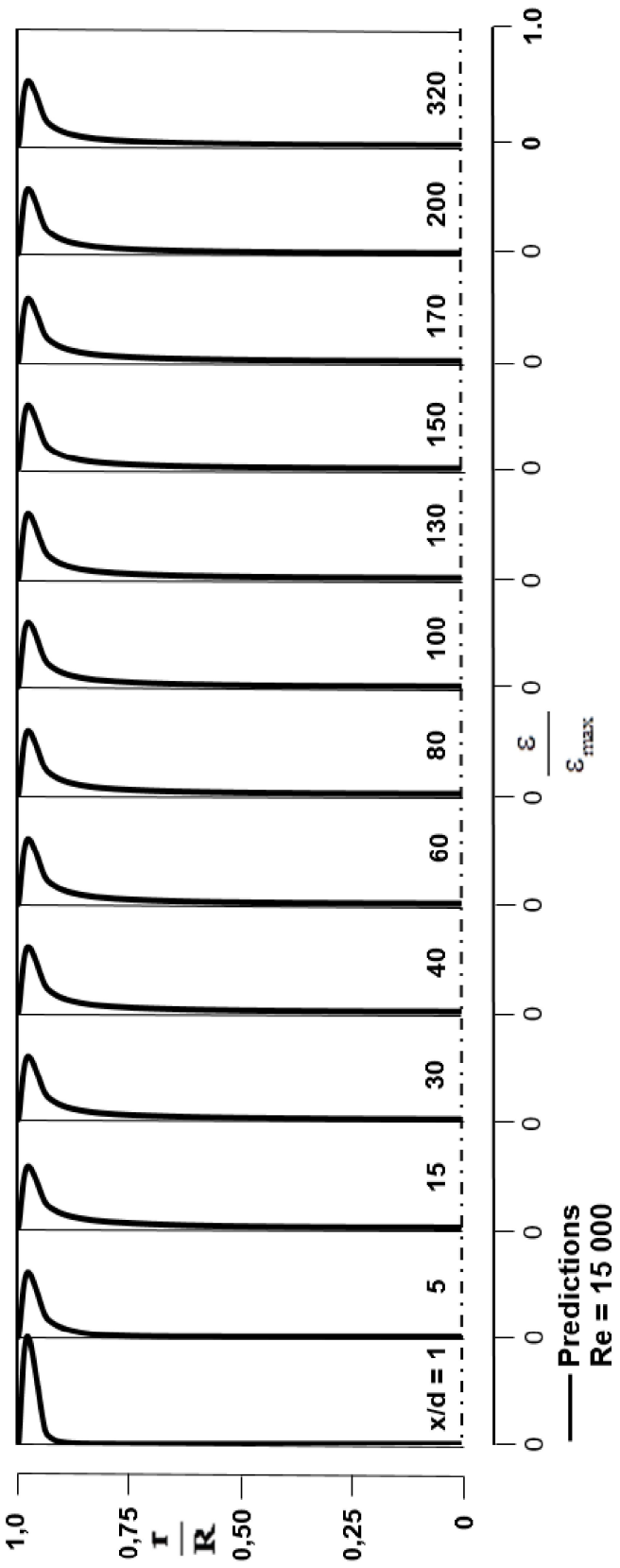


Figure 18: Predicted radial profiles of normalised turbulence kinetic energy dissipation rate along the pipe flow of [10].

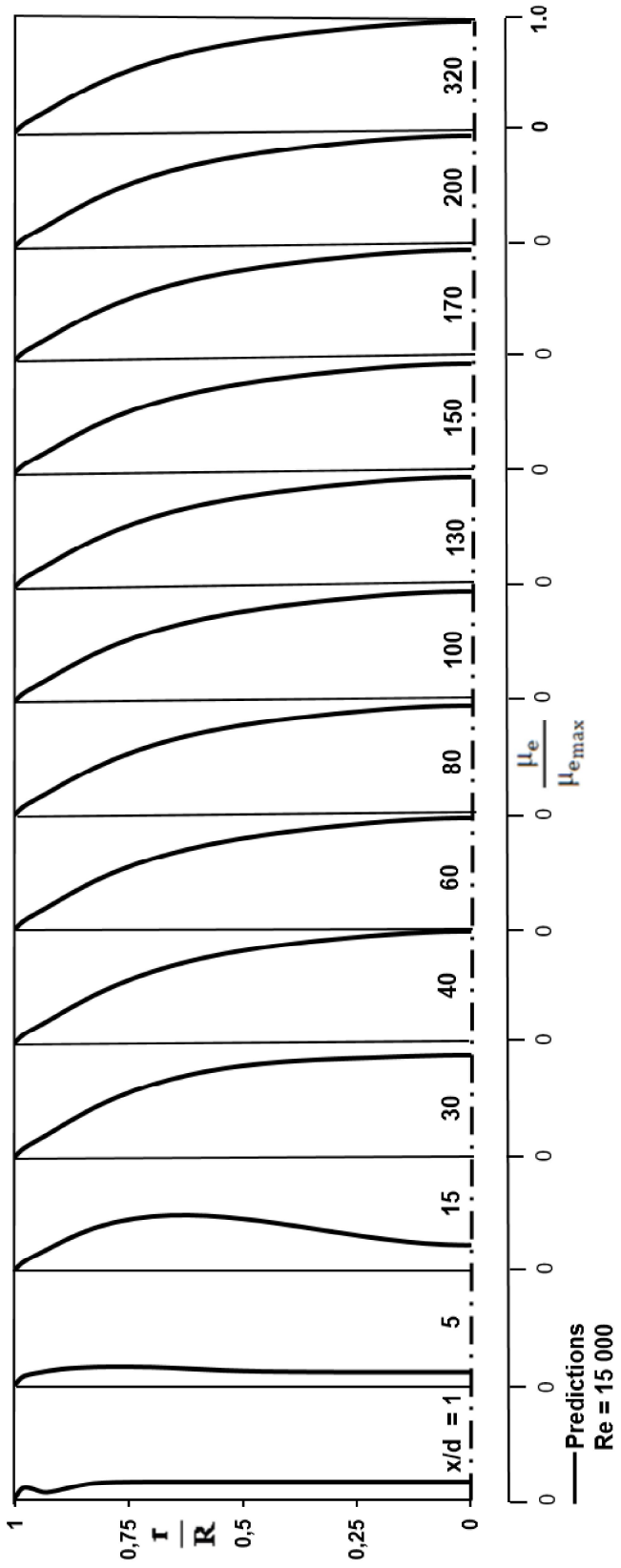


Figure 19: Predicted radial profiles of normalised effective viscosity along the pipe flow of [10].

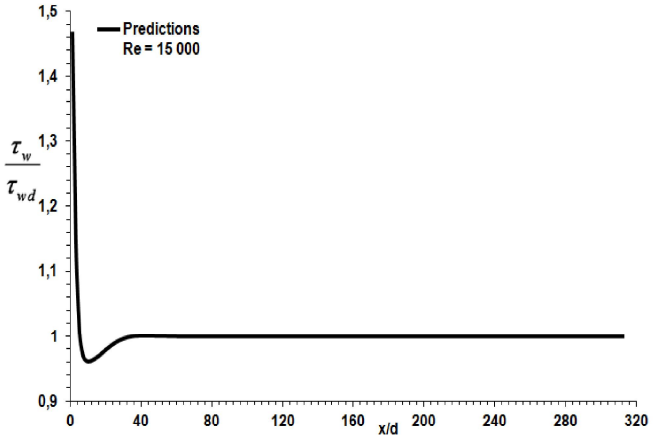


Figure 20: Computed variation of dimensionless wall-shear stress along the pipe wall of [10].

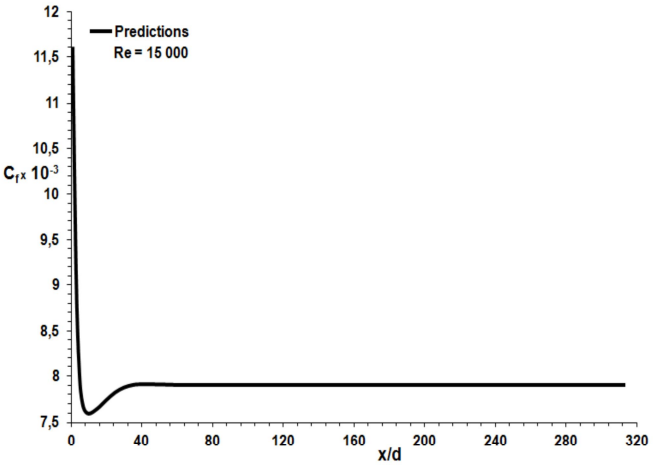


Figure 21: Computed distribution of friction coefficient along the pipe wall of [10].

IV. CONCLUDING REMARKS

The main concluding remarks from the numerical study of the present original research investigation can be summarised as follows. Developing internal turbulent flow in pipes of circular cross-section at two different Reynolds numbers has been computed numerically employing the standard k-ε turbulence model. Using the finite-volume method, a computer program based on the SIMPLE algorithm of [38] has been developed. The performance of the standard k-ε turbulence model has been investigated for developing internal turbulent pipe flow. The computed radial profiles of axial velocity, turbulence kinetic energy, turbulence kinetic energy dissipation rate, effective viscosity, axial variation of centre-line velocity, wall-shear stress and friction coefficient distributions along the pipe are presented and, wherever availlable, compared with experimental measurements reported in the literature. The results of numerical simulations are generally in very good agreement with experimental measurements.

REFERENCES

[1] L. Pompeo, and T. Matievic, "Turbulenzbeeinflussung, Semesterarbeit in Fluiddynamik," ETH Zurich, Institut für Aerodynamik Report WS, (1986/87).

[2] K. Kikuyama, M. Murakami, and K. Nishibori, "Development of three-dimensional turbulent boundary layer in an axially rotating pipe," *J. of Fluids Eng*., vol. 105, pp. 154-160, 1983.

[3] J. Weir, A. J. Priest, and V. K. Sharan, "Research note: The effect of inlet disturbances on turbulent pipe flow," *Journal of Mechanical Engineering Science*, I. Mech. E., vol. 16(3), pp. 211-213, 1974.

[4] C. J. Lawn, "The determination of the rate of dissipation in turbulent pipe flow," *J. Fluid Mech*., vol. 48, pp. 477-505, 1971.

[5] J. Laufer, "The structure of turbulence in fully developed pipe flow," NACA Report 1174, 1954.

[6] K. S. Wittmer, W. J. Devenport, and J. S. Zsoldos, "A four-sensor hot-wire probe system for three-component velocity measurement," *Experiments in Fluids,* vol. 24, pp. 416-423, 1998.

[7] C. W. Wenger, and W. J. Devenport, "Seven-hole pressure probe calibration method utilizing look-up error tables," *AIAA Journal,* vol. 37(6), pp. 675-679, 1999.

[8] J. D. Hooper, and A. R. Musgrove, "Reynold stress, mean velocity, and dynamic static pressure measurement by a four-hole pressure probe," *Experimental Thermal and Fluid Science,* vol. 15, pp. 375-383, 1997.

[9] P. A. Chevrin, H. L. Petrie, and S. Deutsch, "The structure of Reynolds stress in the near-wall region of a fully developed turbulent pipe flow," *Experiments in Fluids*, vol. 13, pp. 405-413, 1992.

[10] M. Saadeh, K. Strauss, and T. Schneider, "A combined piv/lif-system for the measurement of heterogeneous drag reduction effects in a pipe flow," *Experiments in Fluids*, vol. 22, pp. 292-299, 1997.

[11] J. Westerweel, A. A. Draad, J. G. Th. van der Hoeven, and J. van Oord, "Measurement of fully-developed turbulent pipe flow with digital particle image velocimetry," *Experiments in Fluids*, vol. 20, pp. 165-177, 1996.

[12] T. Karasu, "Numerical prediction of incompressible turbulent swirling flows in circular-sectioned ducts and annuli," Ph.D. Thesis, University of London, London, U.K., 1980.

[13] T. Karasu, P. R. Choudhury, and M. Gerstein, "Prediction of some turbulent flows using upwind and hybrid discretisation schemes and the two-equation turbulence model," Proc. 4th Miami international symposium on multi-phase transport and particulate phenomena, Miami Beach, Florida, U.S.A., vol. 5, pp. 105-124, 1988.

[14] T. Karasu, "Numerical prediction of turbulent flow in circular pipes," 9th International Conference on Numerical Methods in Laminar and Turbulent Flow, Atlanta, Georgia, U.S.A., Proceedings Book, vol. 9, Part 2, pp. 1329-1339, 1995.

[15] T. Karasu, "Prediction of turbulent flow with heat transfer in an annulus with rotating inner cylinder," Proc. 8th Miami international conference on alternative energy sources, Miami Beach, Florida, U.S.A., vol. 2, pp. 361-385, 1989.

[16] T. Karasu, "Numerical prediction of turbulent swirling flows in circular-sectioned annuli," Proc. 5th Miami international symposium on multi-phase transport and particulate phenomena, Miami Beach, Florida, U.S.A., vol. 1, pp. 149-174, 1990.

[17] T. Karasu, "Numerical study of turbulent flow in pipes," Proc. 6th Miami international symposium on heat and mass transfer, Miami, Florida, U.S.A., 1990.

[18] T. Karasu, "Numerical Prediction of Turbulent Recirculating Flow Through Axisymmetric Sudden Expansions", 10th International Conference on Numerical Methods in Laminar and Turbulent Flow, 21st –25th July 1997, Swansea, U.K., Proceedings Book, Vol. 10, pp. 357-368, 1997.

[19] T. Karasu, "Computer Simulation of Turbulent Flow in Pipes", 9th International Conference on Sustainable Energy and Environmental Protection (SEEP'16), 22-25 September 2016, Erciyes University, Kayseri, Turkey, Proceedings Book, pp. 359-365, 2016.

[20] T. Karasu, "Computer Simulation of Developing Turbulent Flow in Circular-Sectioned Pipes", 10th International Clean Energy Symposium (ICES'16), 24-26 October 2016, Istanbul Technical University, Istanbul, Turkey, Proceedings Book, pp. 742-753, 2016.

[21] T. Karasu, "Numerical Investigation of Developing Turbulent Flow Between Two Parallel Plates", IATS'13, 7th International Advanced Technologies Symposium, 30th October-1st November 2013, Istanbul, Turkey, Proceedings Book, pp. 49-56, 2013.

[22] T. Karasu, "Numerical Solution of Turbulent Flow with Heat Transfer in an Annulus with Rotating Inner Cylinder", *Turkish Journal of Engineering and Environmental Sciences*, Vol. 12, No. 3, pp. 250-272, 1988.

[23] C. J. Elkins, M. Markl, N. Pelc, and J. K. Eaton, "4D Magnetic resonance velocimetry for mean velocity measurements in complex turbulent flows," *Experiments in Fluids*, vol. 34, pp. 494-503, 2003.

[24] C. J. Elkins, M. Markl, A. Iyengar, R. Wicker, and J. K. Eaton, "Full-field velocity and temperature measurements using magnetic resonance imaging in turbulent complex internal flows," *Int. J. Heat Fluid Flow,* vol. 25, pp. 702-710, 2004.

[25] J. M. J. den Toonder, and F. T. M. Nieuwstadt, "Reynolds number effects in turbulent pipe flow for low to moderate Re," *Phys. Fluids,* vol. 9, pp. 3398-3409, 1997.

[26] J. G. M. Eggels, F. Unger, M. H. Weiss, J. Westerweel, R. J. Adrian, R. Friedrich, and F. T. M. Nieuwstadt, "Fully developed turbulent pipe flow: a comparison between direct numerical simulation and experiment," *J. Fluid Mech.*, vol. 268, pp. 175-209, 1994.

[27] T. Taishi, H. Kikura, and M. Aritomi, "Effect of the measurement volume in turbulent flow measurement by the ultrasonic velocity profile method (mean velocity profile and Reynolds stress measurement)," *Experiments in Fluids,* vol. 32, pp. 188-196, 2002.

[28] M. Nowak, "Wall shear stress measurement in a turbulent pipe flow using ultrasound Doppler velocimetry," *Experiments in Fluids,* vol. 33, pp. 249-255, 2002.

[29] J. C. S. Lai, and C. Y. Yang, "Numerical simulation of turbulence suppression: comparisons of the performance of four k-ε turbulence models," *Int. J. Heat Fluid Flow,* vol. 18(6), pp. 575-584, 1997.

[30] C. Ljus, B. Johansson, and A. E. Almstedt, "Turbulence modification by particles in a horizontal pipe flow," *Int. J. Multiphase Flow,* vol. 28, pp. 1075-1090, 2002.

[31] C. M. Hrenya, E. J. Bolio, D. Chakrabarti, and J. L. Sinclair, "Comparison of low Reynolds number k-ε turbulence models in predicting fully developed pipe flow," *Chemical Engineering Science*, vol. 50(12), pp. 1923-1941, 1995.

[32] Junke Guo and Pierre Y. Julien, "Modified log-wake law for turbulent flow in smooth pipes," *Journal of Hydraulic Research,* vol. 41(5), pp. 493-501, 2003, doi:10.1080/00221680309499994.

[33] M. V. Zagarola, "Mean Flow Scaling of Turbulent Pipe Flow," PhD Dissertation, Department of Mechanical and Aerospace Engineering, Princeton Univ., Princeton, NJ., 1996.

[34] M. V. Zagarola and A. J. Smits, "Scaling of the mean velocity profile for turbulent pipe flow," *Phys. Rev. Lett*., vol. 78, p. 239, 1997.

[35] M. V. Zagarola, A. E. Perry and A. J. Smits, "Log Laws or Power Laws: The Scaling in the Overlap Region," *Phys. Fluids,* vol. 9(7), pp. 2094-2100, 1997.

[36] M. V. Zagarola and A. J. Smits, "Mean-flow scaling of turbulent pipe flow," *J. Fluid Mech*., vol. 373, pp. 33-79, 1998.

[37] B. E. Launder, and D. B. Spalding, "The numerical computation of turbulent flows," *Comp. Meth. Appl. Mech. Eng.*, vol. 3, pp. 269-289, 1974.

[38] S. V. Patankar, *Numerical Heat Transfer and Fluid Flow,* Washington, DC, Hemisphere, McGraw-Hill, 1980.

[39] S. V. Patankar, and D. B. Spalding, "A Calculation Procedure for Heat, Mass and Momentum Transfer in Three-Dimensional Parabolic Flows", *Int. J. Heat Mass Transfer*, vol. 15, pp. 1787-1806, 1972.

[40] D. B. Spalding, "A General-Purpose Computer Program for Multi-Dimensional One-and-Two Phase Flow", *Math. Comput. Simulation*, XXIII, pp. 267-276, 1981.

Energy and Exergy Analysis of an Organic Rankine Cycle Using Different Working Fluids From Waste Heat Recovery

E.ÖZDEMİR[1] and M. KILIÇ[1]

[1] Uludag University, Bursa/Turkey, esraozdemir@uludag.edu.tr
[1]Uludag University, Bursa/Turkey, mkilic@uludag.edu.tr

Abstract - **Energy and energy conservation are vital issues for all countries of the world. Because of this reason, making more efficient energy use and energy production from using low-grade waste heat sources are significant. The Organic Rankine Cycle, which uses an organic fluid instead of water as a working fluid, is a power generation cycle. The working principal of an organic Rankine cycle is similar to the common vapor Rankine cycle. In this study, the energy and exergy analysis of organic Rankine cycle is performed for different dry working fluids which are R600a, R600, R245fa, R123 and R113. The organic Rankine cycle's performance parameters are evaluated depending on varied evaporation temperatures and the inlet temperatures of the waste hot fluid. Results show that the best performance results are obtained for R600a considering the thermal efficiency, exergy efficiency, net power and lower total irreversibility at the evaluations of both the increment of the evaporation temperature and the increment of the inlet temperature of waste hot fluid.**

Keywords - **Energy, exergy, organic Rankine cycle, working fluid**

I. INTRODUCTION

NOWADAYS, energy has become a major issue in ensuring that countries provide a competitive advantage. The technological innovations, increasing the permeability of international borders, capital mobility and development of communication cause increasing the amount and speed of energy use. For this reason, energy saving and making more efficient use of energy is a vital matter for the world development due to many environmental impacts and energy shortage. In recent years, the global warming has compelled the energy planners to develop a new energy conversion technology which produces electricity without causing environmental pollution.

One of the most important ways to transform on large scale thermal energy into power is the vapor Rankine cycle. Water is used as a working fluid in this cycle. There are several advantages for water using as working fluid. These are very good thermal/chemical stability; owing to very low viscosity, less pumping work required; owing to high latent and specific heat, good energy carrier; non-toxic; non-flammable and no threat to the environment and cheap and abundant [1]. However, many problems are encountered when using water as a working fluid: need of superheating to prevent condensation during expansion, risk of erosion of turbine blades, excess pressure in the evaporator, complex and expensive turbines [2]. Because of these reasons, water is used in high temperature applications and large centralized systems. An organic or non-conventional working fluid, which has higher molecular mass and lower ebullition/critical temperature than water, is more suitable in small and medium scale power plants and low temperature applications. This technology is "Organic Rankine Cycles".

The organic Rankine cycle (ORC) is established for converting heat to electricity. The most important feature of an ORC is its capability of utilization of various kinds of low-grade heat sources for power generation [3]. Owing to its low operating temperature, an organic Rankine cycle can suitably recover heat from various sources. Useable heat resources in ORC are solar energy, geothermal energy, biomass products, surface seawater and waste heat from various thermal processes.

An ORC has several advantages over conventional vapor power plant: less heat is needed during the evaporation process; the evaporation process takes place at lower pressure and temperature; the expansion process ends in the vapor region and hence the superheating is not required and the risk of blades erosion is avoided; the smaller temperature difference between evaporation and condensation also means that the pressure drop/ratio will be much smaller and thus simple single stage turbines can be used [1].

The challenges, when ORC is used in a process, are of low thermal efficiency, limited ways to improve the work output, selection of working fluids matching to available heat source and sink temperatures and their effects on environment [3]. The performance of an ORC system is strongly related to the working fluid. The working fluid determines thermal efficiency, safety, stability, environmental impact and economic profitability of the system in an ORC. In recent years, working fluid selection for ORC has drawn significant attention. Different performance evaluation criteria lead to different optimum working fluids. For this reason, a reasonable evaluation criterion is the key issue for working fluid selection.

Many studies on ORC have been presented in the literature. For example, Liu *et al.* [4] used total heat-recovery efficiency and heat availability instead of thermal efficiency as the evaluation criteria to optimize the working fluid and operating conditions for organic rankine cycle. Chen *et al.* [5] compared

the system performance between a supercritical Rankine cycle using CO_2 as working fluid and a subcritical ORC using R123 as working fluid. Kanoglu and Bolatturk [6] assessed the thermodynamic performance of the Reno (Nevada, USA) binary plant. This plant uses geothermal fluid at 158 ºC and isobutane as working fluid. Roy *et al.* [3] analyzed non-regenerative organic Rankine cycle, based on the parametric optimization, using R-12, R-123, R-134a and R-717 as working fluids superheated at constant pressure. Gao *et al.* [7] analyzed the performance of supercritical ORC driven by exhaust heat using 18 organic working fluids. Wang *et al.* [8] analyzed a double Organic Rankine Cycle for discontinuous waste heat recovery. Wang *et al.* [9] optimized the working fluid and parameters of ORC system with simulated annealing algorithm. They compared results for 13 working fluids. Kaska [10] analyzed a waste heat driven organic Rankine cycle and assessed performance of the cycle and pinpoint sites of primary exergy destruction using actual plant data. Imran *et al.* [11] assessed the economic assessment of greenhouse gas (GHG) reduction through waste heat recovery using organic Rankine cycle (ORC). Zhu *et al.* [12] assessed the performances of ORC under saturated expansion using organic dry and isentropic fluids, and under superheated expansions using organic wet fluids.

The brief review above shows that the types of working fluids have a significant influence on the performance of ORC. In this paper, with the light of studies in literature, the energy and exergy analysis of subcritical organic Rankine cycle is performed for different dry working fluids which are R600a, R600, R245fa, R123 and R113. The organic Rankine cycle's performance parameters are evaluated depending on varied evaporation temperatures and the inlet temperatures of the waste hot fluid. The exergy efficiency, thermal efficiency, the total-heat-recovery efficiency, the irreversibility rate, the net power, the evaporation pressure, the outlet temperature of waste hot fluid or the evaporation temperature are calculated with the various evaporation temperatures and the inlet temperatures of the waste hot fluid. Results from the analyses show that both evaporation temperature and the inlet temperature of hot fluid have significant effect on the performance parameters of an ORC. Also the R600a working fluid produces higher thermal efficiency, exergy efficiency, net power and lower total irreversibility rate under accepted conditions in compared with other working fluid.

II. Material and Method

A. Basic Organic Rankine Cycle

The schematic diagram of a simple ORC system is shown in Figure 1. It includes four components: evaporator, expander, condenser and pump. An ORC is composed of four phases:

1-2: Pressure increase in the condensate in the feed pump from pressure p_1 to p_2.

2-3: Isobaric heating, evaporation and overheating of the working medium in the evaporator at pressure $p_2 = p_3$.

3-4: Expansion of the vapor working medium in an expansion machine (e.g. a turbine) from pressure p_3 to p_4.

4-1: Isobaric heat release, complete condensation and possible under-cooling of the working medium in the condenser at pressure $p_4 = p_1$.

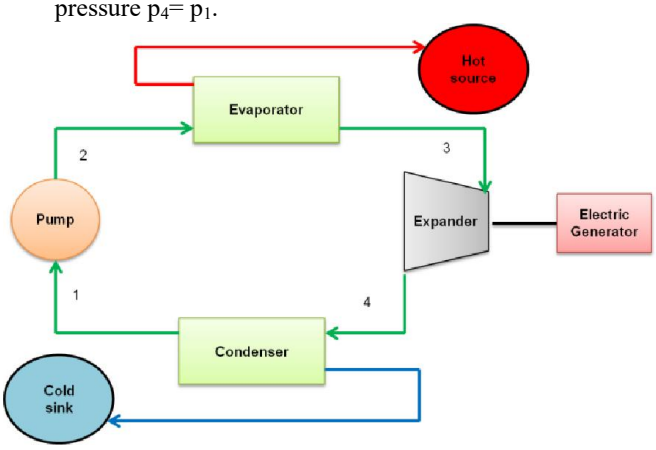


Figure 1: Schematic diagram of organic Rankine cycle

Working fluids for ORC's are categorized in three groups based on their slope of saturation vapor curves in T–s diagram. The fluids having positive slope are dry fluids ($ds/dT > 0$). The fluids having negative slope are wet fluids ($ds/dT < 0$). The fluids having nearly infinitely large slopes are isentropic fluids ($ds/dT=0$).

In this study, R600a, R600, R245fa, R123 and R113 dry fluids are selected as the working fluids. Table 1 shows the thermo-physical properties of the selected fluids. It can be seen from Table 1 that R600a has the lowest value of critical temperature. It is followed by R600, R245fa, R123 and R113 respectively.

Table 1: Thermo-physical properties of the selected fluids [13]

Parameters	R600a	R600	R245fa	R123	R113
Molecular mass (g/mol)	58,12	58,12	134,05	152,93	187,38
Maximum temperature (K)	575,00	575,00	440,00	600,00	525,00
Maximum pressure (MPa)	35,00	12,00	200,00	76,00	200,00
Critical point temperature (K)	407,70	425,00	427,01	456,70	487,10
Critical point pressure (MPa)	3,63	3,80	3,65	3,66	3,39
Critical point density (kg/m^3)	225,50	228,00	519,43	550,00	560,00
Boiling point temperature (ºC)	-11,68	-0,5273	15,18	27,78	47,59

A. System Description and Modeling

The analysis of an ORC based on thermodynamic laws and the energy, exergy analyses were performed for the working fluids investigated. For simplicity, the following assumption were made:

- All processes are operating at steady state.

- The thermal and friction losses in the pipes are negligible.
- The kinetic and potential energy changes are negligible.
- Pressure drops of working fluid in the evaporator and condenser is neglected.
- There are only two pressures: an evaporating pressure p_e and a condensing pressure p_c.
- The inlet temperature of hot waste fluid in evaporator is 130 ºC.
- The isentropic efficiency of turbine and the pump are 0.80.
- Atmospheric condition is taken as 100 kPa and 293.15 K.
- The mass flow rate and the specific heat capacity of the waste hot fluid are 1 kg/s and 1 kJ/kgK respectively.
- The minimum temperature difference in the evaporator is 5 K.
- The cooling medium temperature T_L is 293.15 K.

For any steady state control volume, by neglecting the potential and kinetic energy changes, general expression of mass, energy and exergy balance equations is that:

Mass balance equation: $\sum \dot{m}_{in} = \sum \dot{m}_{out}$ (1)

Energy balance equation: $\dot{E}_{in} = \dot{E}_{out}$ (2)

$$\dot{Q} + \dot{W} = \sum \dot{m}_{out}\ h_{out} - \sum \dot{m}_{in}\, h_{in} \quad (3)$$

Exergy balance equation:

$$\sum \dot{Ex}_{in} - \sum \dot{Ex}_{out} - \dot{Ex}_d = \Delta \dot{Ex}_s \quad (4)$$

Where for a steady-state system, $\Delta \dot{Ex}_s$ is zero.

$$\dot{Ex}_{in} = \dot{Ex}_{out} \quad (5)$$

$$\dot{Ex}_{heat} + \dot{W} = \dot{Ex}_{out} - \dot{Ex}_{in} + \dot{I} \quad (6)$$

where, subscripts in and out represent the inlet and exit states, $\dot{Q}$ is heat input, $\dot{W}$ is work input, $\dot{Ex}$ is exergy rate and $\dot{I}$ is the irreversibility rate.

Process 1-2 (pump):

The isentropic efficiency: $\eta_p = (h_{2s} - h_1)/(h_2 - h_1)$ (7)

The pump power: $\dot{W}_p = \frac{\dot{m}_{wf}(h_{2s} - h_1)}{\eta_p} = \dot{m}_{wf}(h_2 - h_1)$ (8)

The irreversibility of the pump:

$$\dot{I}_p = \left(\dot{E}_1 - \dot{E}_2\right) + \dot{W}_p = \mathrm{T}_0 \Delta S_p \quad (9)$$

Process 2-3 (evaporator):

During the above heat exchange, the temperature of hot fluid decreases from T_5 to T_6. The specific heat capacity C_p of the hot fluid at constant pressure is assumed to be constant.

The evaporator heat rate:

$$\dot{Q}_e = \dot{m}_{wf}(h_3 - h_2) = \dot{m}_{hf}(h_5 - h_6) \quad (10)$$

$$\dot{Q}_e = \dot{m}_{hf} Cp (T_5 - T_6) \quad (11)$$

The irreversibility of the evaporator:

$$\dot{I}_e = T_0\ \dot{m}_{wf}\left[(s_3 - s_2) - \frac{2(h_3 - h_2)}{(T_5 + T_6)}\right] \quad (12)$$

Process 3-4 (expander):

The isentropic efficiency: $\eta_t = (h_3 - h_4)/(h_3 - h_{4s})$ (13)

The expander power:

$$\dot{W}_t = \dot{m}_{wf}(h_3 - h_{4s})\eta_t = \dot{m}_{wf}(h_3 - h_4) \quad (14)$$

The irreversibility of the turbine:

$$\dot{I}_t = \left(\dot{E}_3 - \dot{E}_4\right) - \dot{W}_t = \mathrm{T}_0 \Delta S_t \quad (15)$$

Process 4-1 (condenser):

The condenser heat rate: $\dot{Q}_c = \dot{m}_{wf}(h_4 - h_1)$ (16)

The irreversibility of the condenser:

$$\dot{I}_c = T_0\ \dot{m}_{wf}\left[(s_1 - s_4) - \frac{(h_1 - h_4)}{T_L}\right] \quad (17)$$

The net power output: $\dot{W}_{net} = \dot{W}_t - \dot{W}_p$ (18)

The thermal efficiency (η_{th}) of the ORC is the ratio of the net power output to the heat input. It can be expressed as:

$$\eta_{th} = \frac{\dot{W}_{net}}{\dot{Q}_e} = \frac{\dot{W}_t - \dot{W}_p}{\dot{Q}_e} \quad (19)$$

The exergy destruction rate of ORC:

$$\dot{I}_{cycle} = T_0\ \dot{m}_{wf}\left[-\frac{2(h_3 - h_2)}{(T_5 + T_6)} - \frac{(h_1 - h_4)}{T_L}\right] \quad (20)$$

The exergy efficiency of ORC:

$$\eta_{exe} = \frac{\dot{W}_{net}}{\dot{W}_{net} + \dot{E}_d} = \frac{\dot{W}_{net}}{\dot{Q}_e\left(1 - \frac{2T_L}{(T_5 + T_6)}\right)} \quad (21)$$

The total heat-recovery efficiency, defined as the ratio of net power to the available energy in ideal case [14]:

$$\eta_r = \frac{(T_5 - T_6)}{(T_5 - T_0)}\ \eta_{th} \quad (22)$$

III. Results and Discussion

A. The Analysis of Various Evaporation Temperatures

The evaparation temperature and the inlet temperature of hot fluid effect the performance analysis of an organic Rankine cyle. Therefore, we focused on two variables in this study. Firstly, the evaporation temperature was increased from 70 ºC (333.15 K) to 110 ºC (378.15 K) with a 5 ºC and then the exergy efficiency, thermal efficiency, the total-heat-recovery efficiency, the irreversibility rate, the net power, the outlet temperature of waste hot fluid and the evaporation pressure were calculated for the various evaporation temperatures. The inlet temperature of the waste hot fluid was 130 ºC (403.15 K). It was assumed that the condensation pressure and temperature is constant at 100 kPa and 293.15 K.

According to the analysis, the thermal efficiency, the outlet temperature of waste hot fluid and the evaporation pressure increase when the evaporation temperature increases for the R600a working fluid. Nevertheless, the total heat-recovery efficiency, the total cycle the irreversibility rate, the net power decrease with the evaporation temperature. The exergy efficiency is parabolic-like function with evaporation temperature.

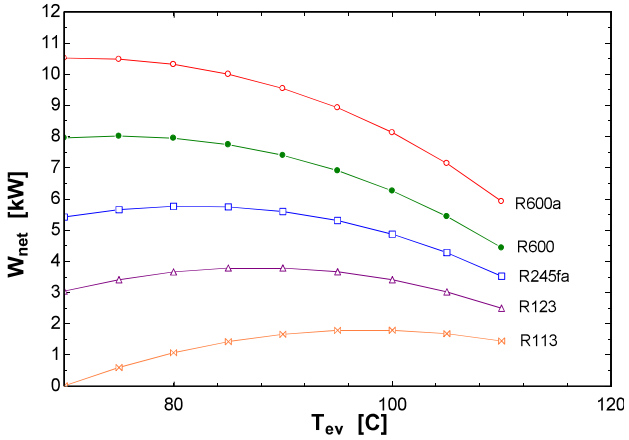


Figure 2: Comparison of the net power

When compared the net power of the working fluids, according to Figure 2 for all of the working fluids, the net power increases before and then decreases with the increase of the evaporation temperature. In addition, the highest net power is obtained for the R600a working fluid with 10,52 kW. This is followed by R600, R245fa, R123 and R113 respectively.

Results from Figure 3 show that total irreversibility rate or exergy destruction decreases with evaporation temperature. The minimum total irreversibility rate is obtained for the R600a working fluid. Also, it is calculated in analysis that the components with greater exergy destructions to lower one are evaporator, expander, condenser and pump.

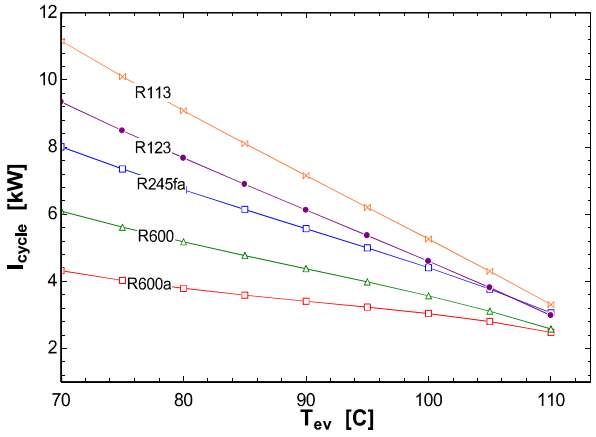


Figure 3: Comparison of the irreversibility rate

According to Figure 4, when the evaporation temperature increases in the analysis of ORC, the outlet temperature of hot fluid increases dramatically for all of the working fluids. Otherwise the lowest values are calculated for the R600a working fluid. In other words, the R600a organic fluid benefits from the heat of the waste hot fluid to use in the evaporator.

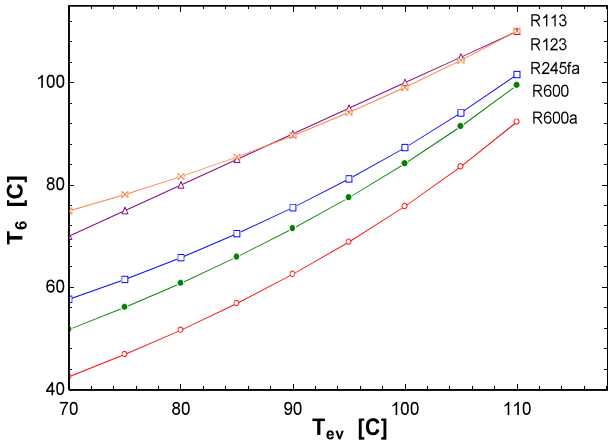


Figure 4: Comparison of the outlet temperature of hot fluid

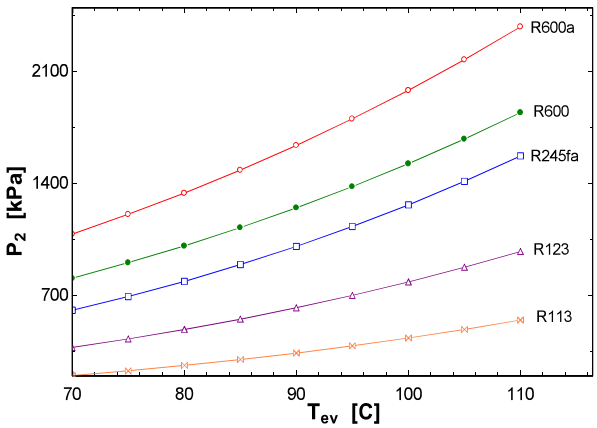


Figure 5: Comparison of the evaporation pressure

According to the results of calculations, Figure 5 shows that

the evaporation temperature has important effect on the evaporation pressure which increase with evaporation temperature. In addition, the increase of evaporation pressure effects the energy and exergy efficiency of ORC. It can be seen that from Figure 6, the highest evaporation pressure value are calculated for R600 a working fluid which followed by R600, R245fa, R123 and R113.

Figure 6 and Figure 7 show the comparison of the exergy efficiency and thermal efficiency for organic working fluids. The working fluids with greater both exergy efficiency and thermal efficiency to lower one are R600a, R600, R245fa, R123 and R113. When the thermal efficiency is evaluated with the net power (Fig.3), the thermal efficiency increases with the increment of the net power however the net power decreases, the thermal efficiency still increases which shows that the effect of the increase of evaporation temperature on the decrease of the heat absorbed by the working fluid (Qev) is greater than on the decrease of the net power (Wnet).

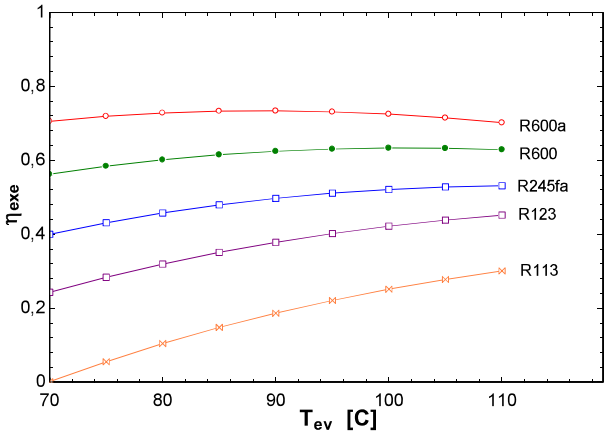


Figure 6: Comparison of the exergy efficiency

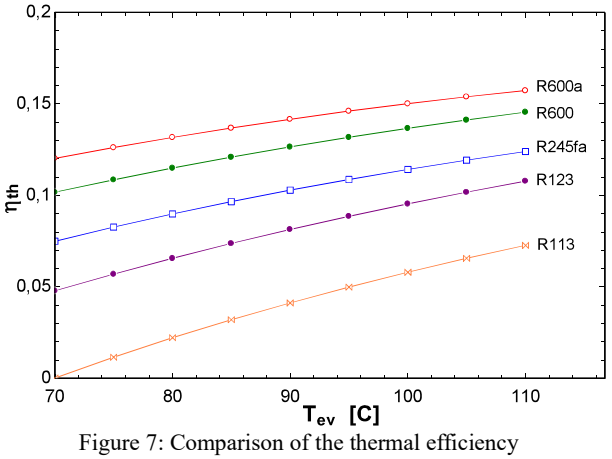


Figure 7: Comparison of the thermal efficiency

The total heat-recovery efficiency which has the same trend with the net power is calculated in its higher value for R600a working fluid as shown in Figure 8. As Equation (22), Figure 4 and Figure 8 are commented together, it can be seen that the increase of the outlet temperature of the hot fluid is more effective than the increase of the thermal efficiency on the total heat-recovery efficiency.

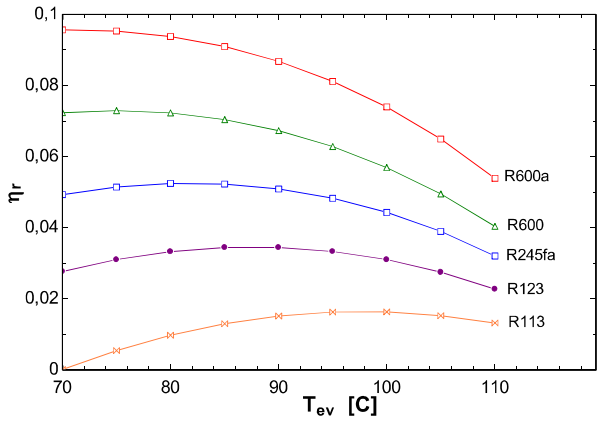


Figure 8: Comparison of the total heat-recovery efficiency

B. The Analysis of Various Inlet Temperatures of Hot Fluid

After the evaporation temperature has been examined, the effect of the various inlet temperatures of hot fluid on the performance of an ORC is evaluated in this section. The evaporation temperature was assumed to be 70 ºC (353.15 K). The outlet temperature of the hot fluid was increased from 100 ºC (373.15 K) to 140 ºC (413.15 K) with a 5 ºC and then the exergy efficiency, the total-heat-recovery efficiency, the irreversibility rate, the net power and the outlet temperature of waste hot fluid were calculated for the various inlet temperatures. It was assumed that the condensation pressure and temperature is constant at 100 kPa and 293.15 K.

According to the analysis, the thermal efficiency and the evaporation pressure did not change with the inlet temperature of hot fluid. In addition, the exergy efficiency, the outlet temperature of waste hot fluid and the evaporation pressure decrease when the inlet temperature of hot fluid increases for all of the working fluids. On the other hand, the total heat-recovery efficiency, the total cycle the irreversibility rate, the net power increase with the inlet temperature of hot fluid.

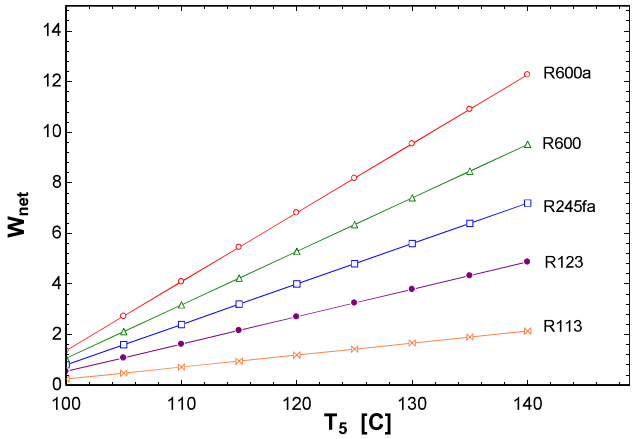


Figure 9: Comparison of the net power

According to Figure 9 for all of the working fluids, the net

power increases with the increment of the inlet temperature of hot fluid. In addition, the maximum net power is obtained in 140 ºC for the R600a working fluid with 12,27 kW. This is followed by R600, R245fa, R123 and R113 respectively.

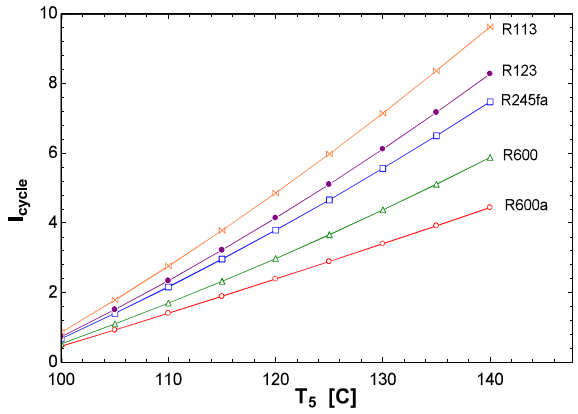


Figure 10: Comparison of the total irreversibility rate

Results from Figure 10 show that total irreversibility rate or exergy destruction increases with the inlet temperature of the hot fluid. The minimum total irreversibility rate is calculated for the R600a working fluid. The value of the total exergy destruction is calculated as be 0,46 kW and 4,45 kW at the inlet temperature of hot fluid 100 ºC and 140 ºC respectively.

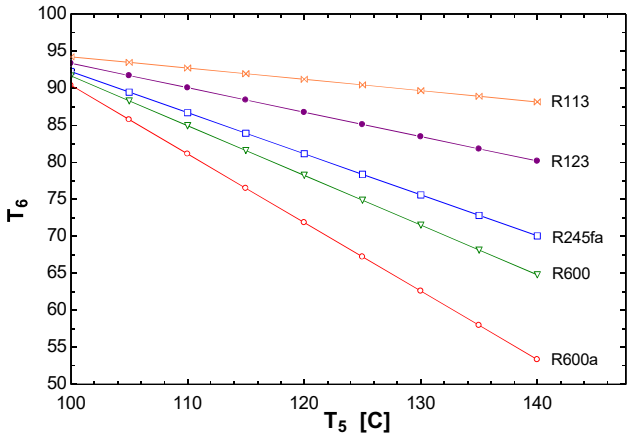


Figure 11: Comparison of the outlet temperature of hot fluid

As compared the outlet temperature of hot fluid for the working fluids, when the inlet temperature of hot fluid increases in the analysis of ORC, the outlet temperature of hot fluid decreases significantly for all of the working fluids as shown in Figure 11. Otherwise the lowest values of the outlet temperature of working fluid are calculated for the R600a working fluid. In other words, the R600a organic fluid benefits more from the heat of the waste hot fluid to use in the evaporator.

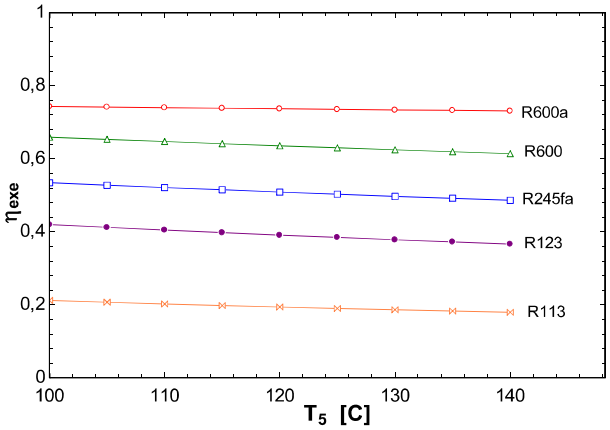


Figure 12: Comparison of the exergy efficiency

According to Figure 12, the exergy efficiency reduces with the growth of the outlet temperature of hot fluid. When the equation (21) and Figure 12 are commented, it can be shown that the effect of the inlet heat in evaporator on the exergy efficiency is greater than the effect of the increment of the net power on the exergy efficiency. In addition, the highest exergy efficiency is calculated as be 21,18% at the inlet temperature of 100 ºC for the R600a.

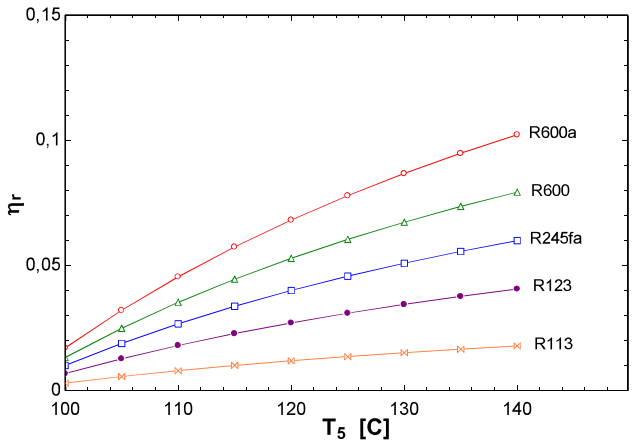


Figure 13: Comparison of the total heat-recovery efficiency

The total heat-recovery efficiency which increases with the growth of the outlet temperature of hot fluid, is calculated in its the maximum value for R600a working fluid as shown in Figure 13. As Equation (22) and Figure13 are commented together, it can be said that the increase of the inlet temperature of the hot fluid is effective on the total-heat recovery efficiency because of the stability of the thermal efficiency.

IV. Conclusion

The selection of working fluids according to appropriate evaporation temperature and the inlet temperature of the hot fluid have a significant influence on the performance of an ORC. The working fluid of an ORC determines thermal

efficiency, safety, stability, environmental impact and economic profitability of the system. So, in this paper, an ORC with the subcritical and saturated expansion is analysed based on thermodynamic theory. The results obtained from the calculations are compared for five types of working fluids which are R600a, R600, R245fa, R123 and R113. According to analysis, the best performance parameters are calculated for the R600a working fluid considering the thermal efficiency, exergy efficiency, net power and lower total irreversibility at the evaluations of both the increment of the evaporation temperature and the increment of the inlet temperature of waste hot fluid.

NOMENCLATURE

ORC	organic Rankine cycle
h	specific enthalpy, kj/kg
s	specific entropy, kJ/kgK
$\dot{m}$	mass flow rate, kg/s
$\dot{E}$	Energy, kW
$\dot{Ex}$	Exergy, kW
$\dot{Q}$	Heat rate, kW
$\dot{W}$	Power, kW
$\dot{I}$	Irreversibility, kW
T	Temperature, K
T_L	The low temperature of cold source, K
ΔT	Temperature differential, K
η	Efficiency
Subscripts	
c	condenser
cycle	cycle
e	evaporator
exe	exergetic
hf	hot fluid
net	net
p	pump
pp	pinch point
o	ambient
s	isentropic case
t	turbine
e	evaporator
wf	working fluid
th	thermal

REFERENCES

[1] B.F. Tchanche, G. Lambrinos, A. Frangoudakis, G. Papadakis, "Low-grade heat conversion into power using organic Rankine cycles-A review of various applications," *Renewable and Sustainable Energy Reviews*, vol. 15, pp. 3963–79, 2011.

[2] E. Wali, "Optimum working fluids for solar powered Rankine cycle cooling of buildings," *Solar Energy*, vol. 25, pp. 235–241, 1980.

[3] J.P. Roy, M.K. Mishra, A. Misra, "Performance analysis of an organic Rankine cycle with superheating under different heat source temperature conditions," *Applied Energy*, vol. 88, pp. 2995–3004, 2011.

[4] B.-T. Liu, K.-H. Chien, C.-C. Wang, "Effect of working fluids on organic Rankine cycle for waste heat recovery," *Energy*, vol. 29 (8), pp. 1207–1217, 2004.

[5] Y. Chen, P. Lundqvist, A. Johansson, P.A. Platell, "Comparative study of the carbon dioxide transcritical power cycle compared with an organic Rankine cycle with R123 as working fluid in waste heat recovery," *Applied Thermal Engineering*, vol. 26, pp. 2142–2147, 2006.

[6] M. Kanoglu, A. Bolatturk, "Performance and parametric investigation of a binary geothermal power plant by exergy," *Renewable Energy,* vol. 33, pp. 2366–2374, 2008.

[7] H. Gao, C. Liu, C. He, X. Xu, S. Wu, Y. Li, "Performance analysis and working fluid selection of a supercritical organic rankine cycle for low grade waste heat recovery," *Energies*, vol. 5, pp. 3233–3247, 2012.

[8] D. Wang, X. Ling, H. Peng, "Performance analysis of double organic Rankine cycle for discontinuous low temperature waste heat recovery," *Applied Thermal Engineering*, vol. 48, pp. 63–71, 2012.

[9] Z.Q. Wang, N.J. Zhou, J. Guo, X.Y. Wang, "Fluid selection and parametric optimization of organic Rankine cycle using low temperature waste heat," *Energy*, vol. 40, pp. 107–115, 2012.

[10] O. Kaska, "Energy and exergy analysis of an organic Rankine for power generation from waste heat recovery in steel industry," *Energy Conversion and Management,* vol. 77, pp. 108-117, 2014.

[11] M. Imran, B. Park, H. Kim, D. Lee, M. Usman, M. Heo, "Thermo-economic optimization of regenerative organic Rankine cycle for waste heat recovery applications," *Energy Conversion and Management*, vol. 87, pp. 107-118, 2014.

[12] Q. Zhu, Z. Sun, J. Zhou, "Performance analysis of organic Rankine cycles using different working fluids," *Thermal Science*, vol. 19, pp. 179-191, 2015.

[13] http://www.coolprop.org/fluid_properties/PurePseudoPure.html#thermodynamic-properties-of-fluid, (Date accessed: 28.05.2017)

[14] B.-T. Liu, K.-H. Chien, C.-C. Wang, "Effect of working fluids on organic Rankine cycle for waste heat recovery," *Energy*, vol. 29 (8), pp. 1207–1217, 2004.

A NOVEL APPROACH TO GRIPPING MECHANISM

O.ACAR[1] and Z. SAKA[1]

[1] Selcuk University, Konya/Turkey, osmanacar@selcuk.edu.tr
[1]Selcuk University, Konya/Turkey, zsaka@selcuk.edu.tr

***Abstract* – Gripping technology has a wide scope of research in recent years. Various objects have different structural and geometrical features. Handling process requires the consideration of geometrical or constructional properties. Gripping operation is used for handling of macro, micro, soft, solid and non-uniform objects. Thus, in gripper design, gripping force, aperture and mechanism dimensions are significant parameters. This paper presents a novel approach to gripping mechanization by using geometrical advantage of spherical mechanism. Spherical mechanisms are more compact and supply higher capacity of 3D object dimensions. This study is also considered to a design of multifunctional gripper by handling various shaped sensitive objects.**

***Keywords* – Spherical mechanism, gripping, handling, manipulation, robotics.**

I. INTRODUCTION

Rapidly emerging robotic technology brings comfort, accuracy, saving of time and higher welfare for people. In robotic technology, one of the vital field is end effectors. The end effectors execute objective function of the robots. As an end effector, grippers are generally used by a robotic arm to perform manipulation for a task; grasping for assembly, handling for translation etc. Therefore grippers are the interactive parts of robots.

Gripper technology is one of the most significant field of research nowadays. There are several application areas such as food, textile, manufacturing and micro-materials handling for grippers. Researchers have been scrutinizing micro-grippers, soft grippers, noncontact grippers, finger-type grippers and industrial grippers.

Most of the work pieces used in industry are cylindrical shaped materials. Quasi-parallel grippers for the concentric handling of cylindrical work pieces were studied [1]. The jaws of gripper were specially designed as profiles mimicking the Greek letter "v". The basic equations of the special profiles were given with an analysis of the geometrical parameters which adjust the jaw dimensions. An algorithm were improved to determine jaw design parameters according to the geometrical analysis. Therefore an optimal jaw profile were improved for work pieces and gripper mechanism dimensions as in figure 1. The effectiveness of the technique were tested in an exemplary computer outputs.

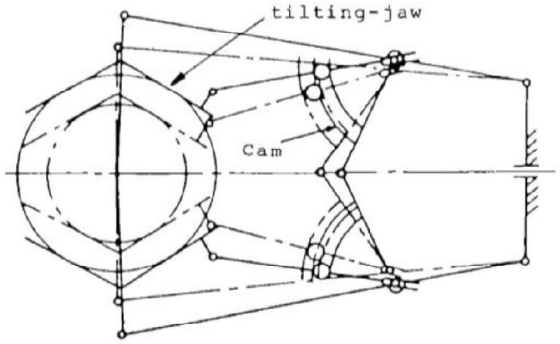


Figure 1: Four-Bar Gripper Mechanism and Jaws for two different cases.

Gripper mechanisms are generally designed as four-bar mechanisms. An evolutionary multi criteria design optimization of robot grippers were executed in [2]. İntelligent techniques were used to determine optimal geometrical dimensions of a robot gripper as shown in figure 2. The aim of the study was to determine Pareto optimal front for an optimization problem with five objective functions, nine constraints and seven variables. Multi-objective Genetic Algorithm (MOGA), Elitist Non-dominated Sorting Genetic Algorithm (NSGA-II) and Multi-Objective Differential Evolution (MODE) were used to solve the problem. For the best optimal solution from Pareto optimal front, normalized weighting objective functions method were used. The strength of the Pareto fronts were measured with using solution spread measure and ratio of non-dominated individuals. The Pareto optimal front results obtained from various methods are compared and analyzed.

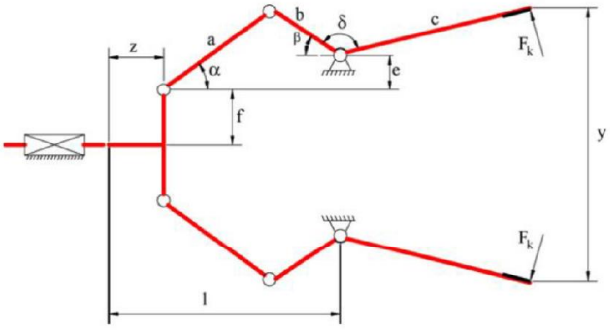


Figure 2: The scheme of robot gripper mechanism.

Gripping mechanisms are commonly used as two-finger and rarely three finger in literature. An analysis of mechanisms in two-finger grippers has been discussed to formulate an optimum design procedure in [3]. In this study, eight steps of design procedure were proposed. Grasping index, encumbrance of grasping mechanism, acceleration and velocity for finger gripper with respect to the imposed working area were determined as objective functions of multi-objective optimum algorithm. An 8R2P linkage for two-finger gripper mechanism were proposed as in figure 3. Numerical examples were tested. The results of algorithm were evaluated.

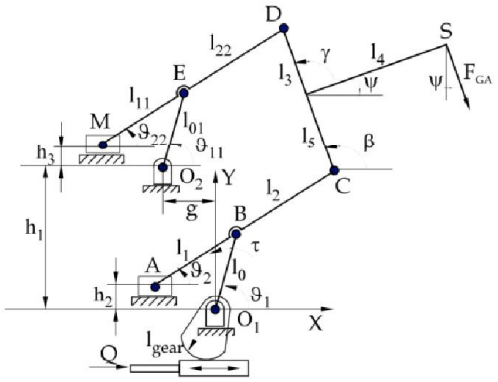


Figure 3: A kinematic scheme of two-finger gripper mechanism..

Gripping or grasping process is also a matter of robotic hands. Multi-fingered robotic prosthesis hand was modeled in [4]. The under-actuated finger as in figure 4 has the closest characteristics to the biological structure of human hand capabilities. The finger was evaluated as cheaper, lighter and more easily controllable. The kinematic and kinetic analysis of the under-actuated finger were performed. Actuation stability were examined in this study. Optimization of mechanism was offered for feature studies. Cutkosky classification compatible actuation models were applied to the robotic hand model. The object actuation capabilities were defined.

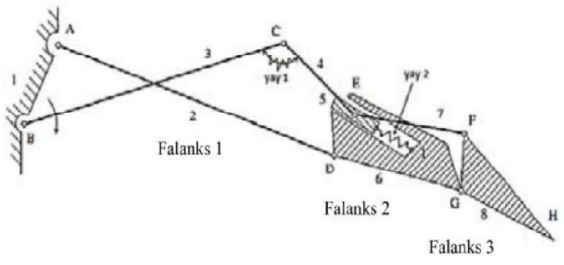


Figure 4: Under-actuated finger mechanism [5].

Compliant mechanisms have recently become very assertive about gripping processes due to the lightness, economy, less wear, quiet operation, ease of production and assembly. An adaptive industrial robotic gripper was designed and analyzed using compliant mechanism in [6]. The aim of the study was to design a gripper that can grasp objects of any size, shape and various position and orientation within pre-defined limit. Firstly, the design criteria, constraints and actuation mechanism were determined. Various geometrical models were generated in a CAD (computer-aided-design) program as in the figure 5. Nonlinear deformation analysis of fingers were performed using ANSYS. Finally, a two dimensional analytical model of the determined gripper topology was obtained and deformation equations were solved by using numerical methods for the comparison with the ANSYS results.

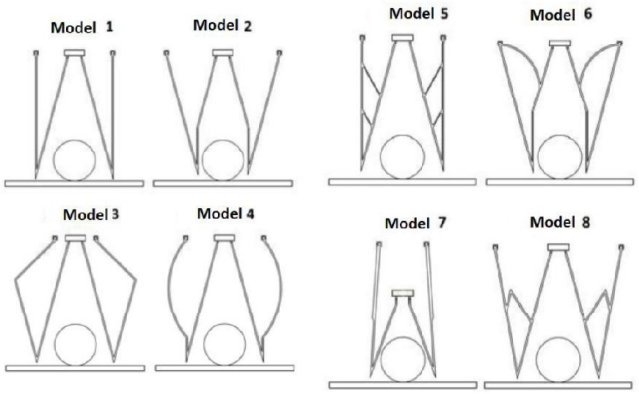


Figure 5: Geometrical models for compliant gripping mechanism.

Micro-grippers are also recently very popular field of gripper researches. A novel 3-DOF micro gripper driven by Linear Ultrasonic Motors (LUMs), with nanometer positional accuracy and an operational space in the millimeter scale is proposed in [7]. In this work, a two-finger gripper based on chopstick-like structure is presented as in figure 6. Based on spatial parallel mechanism with spherical joints, as one of the fingers was stationary, the other was mobile. The maximum displacement of fingertip was calculated. The mechanism was tested to grip a single shrimp embryo to demonstrate successful performance of gripper.

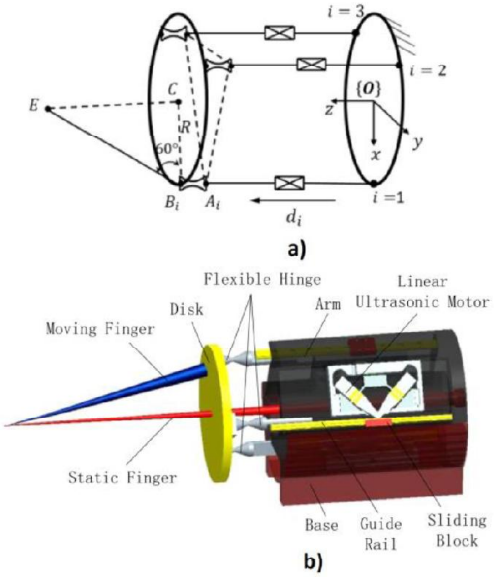


Figure 6: a) Kinematic model b) Structure diagram of spatial micro-gripper mechanism.

Grippers are usually designed for a specific task in industrial applications. Therefore, each task requires a new gripper or a counterpart. In industrial applications, stored tools in magazine can be changed as the task finished. The tool magazine and changing increases cost of the operations. For the solution of this problem, a variable-aperture, cost-effective gripper, capable of adapting its aperture to different handling demands as shown in figure 7, without affecting the working-cycle time of production system was proposed in [8]. Two solution were proposed. An electrically-actuated mechanism regulated the aperture of gripper for flexibility of gripper. A pneumatically-actuated mechanism to achieve high performance in open/close operations. Simulations and preliminary tests have shown that this type of design can be a solution for flexibility in robotized work cells without increasing the cycle time.

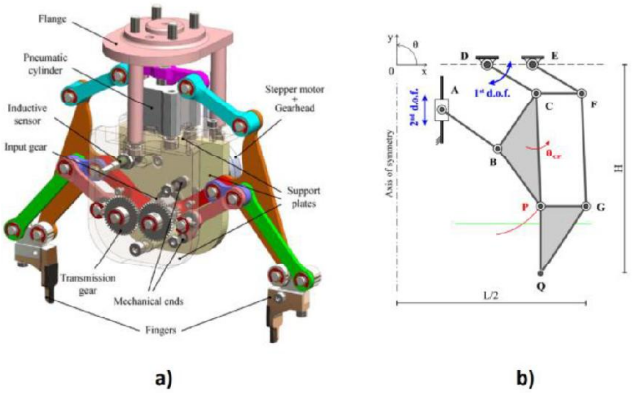


Figure 7: a) Flexible mechanism CAD model b) Flexible mechanism scheme.

In gripper design, optimization is an inevitable process. A generic approach to optimize the design of a parameterized robot gripper including both selected gripper mechanism parameters, and parameters of the finger geometry were suggested in [9] with six gripper quality indices that indicated different aspects of the performance of a gripper given a CAD model of an object and a task description. These quality indices were guided to understand task-specific finger designs based on dynamic simulation. The gripper optimization were demonstrated on a parallel finger type gripper defined by twelve parameters as shown in figure 8. Downhill Simplex method was used to solve optimization problem. A parameterization of the grasping task and context, which is fundamental as an input to the computation of gripper performance were presented. Important aspects of the indices were exemplified. A qualitative evaluation of the obtained results based on existing design guidelines and engineering experiences was provided. In figure 8, quality indices were shown on an octagonal shape with colored lines. The best performance was valued with 1. The colors showed grasping position are red, blue and yellow grasping from all directions, from top, from side respectively.

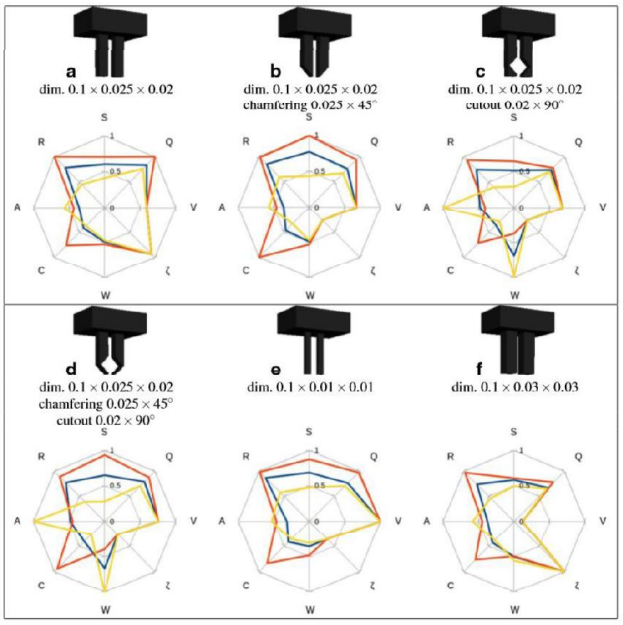


Figure 8: a) Standard b) with chamfering c) with prismatic cutout d) with chamfering and cutout e) thin f) fat gripper fingers.

Meso-grippers are the mesoscopic scale grippers between macro and micro grippers. Kinematic analysis and dimensional synthesis of a Meso-Gripper was proposed in [10]. In the study, two modes of operation were examined; passive adjusting mode and angled gripping mode. The modes were analyzed and dual functional mechanism was proposed. A geometric constraint method was illustrated to facilitate task-based dimensional synthesis. Kinematics of mechanism was investigated according to stiffness and layout. Consequently, a 3D printed prototype was successfully tested and two gripping modes were verified.

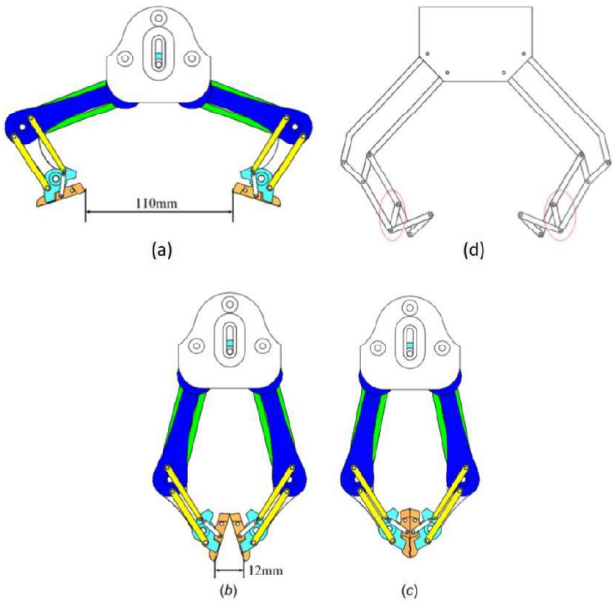


Figure 9: a) Meso-gripper CAD model in open fingers form b) angled form c) closed form d) Meso- gripper linkage scheme.

Robotic gripper design problem consist of two stages; modelling and optimizing stages. Modelling stage has three steps as geometric, kinematic and dynamic modelling. Modelling and design optimization of a robot gripper mechanism was proposed in [11]. The aim was to conduct a detailed study of the gripper in order to provide an in-depth step-by-step demonstration of the design process and to illustrate the interactions among its steps. First, geometric model of gripper mechanism in the figure 10 was generated for interaction of coordinates. Second, kinematic model was extracted in the form of Jacobean matrix. Finally, dynamic model was obtained using Lagrange formulation. These models were used to formulize multi-objective optimization problem for a configuration of mechanism. The objective was to determine the optimum force extracted by the robot gripper on the surface of a grasped rigid object under geometrical and functional constraints. The optimization problem of the gripper design was solved using a non-dominated sorting genetic algorithm version II (NSGA-II). The Pareto-optimal solutions were investigated to establish some meaningful relationships between the objective functions and variable values. Finally, design sensitivity analysis was executed to compute the sensitivity of objective functions with respect to design variables.

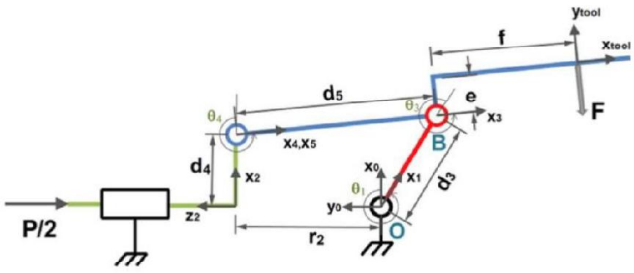


Figure 10: Gripper mechanism scheme and parameters for optimization.

In this study, we propose a new perspective for gripping mechanisms by using of a four-bar spherical mechanism. Spherical mechanisms are the mechanisms whose joints axis are intersected in the center of a unit sphere where the joints move. In spherical mechanism, dimension of links are measured by the angle between joint axes coincided in the center of unit sphere. This characteristic of spherical mechanism supply an advantage of compactness and high capacity of 3D working space. The mechanism can be designed in small dimensions to provide the desired motion for tasks in big dimensions.

II. SPHERICAL MECHANISM

A link of mechanism is resembled as a line segment in planar mechanism. Similarly, a link of spherical mechanism is symbolized with a great circle arc on a unit sphere. A great circle is the intersection of unit sphere and the plane, which can freely rotate about the center of the unit sphere. A four-bar spherical mechanism is shown in figure11. The point C is the coupler point which is used for task performing. A_o and B_o are the fixed joints. A, B are the moving joints of the spherical mechanism. Mechanism links are measured by the subtended central angles a_1, a_2, a_3, a_4 respectively. The angles θ_2, θ_4 are the input and output angles of drive link and driven link.

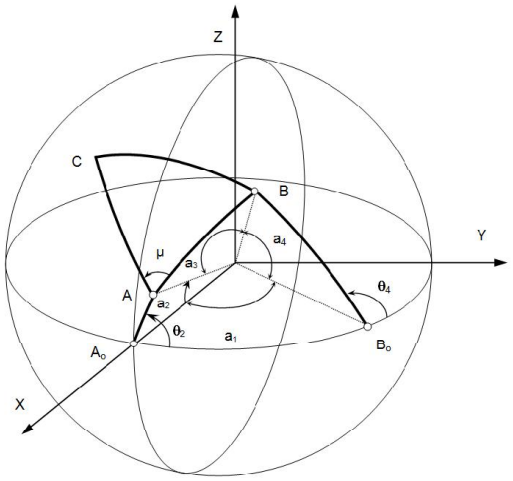


Figure 11. Spherical four-bar mechanism [12].

Spherical gripping mechanism consists of three spherical four-bar mechanisms acting independently. For simplicity of demonstration, a two-fingered spherical mechanism scheme is shown in the figure 12. The dashed line is the coupler curve which is required to track all three coupler points in the end-effectors for performing grasp successfully. For the grasping operation in planar mechanism, the end-effector need to trace a line likewise, in the spherical mechanism, the end-effector (coupler point C and C') have to chase a great circle arc which is counterpart of line in the planar mechanism. For tracing a great circle arc in spherical mechanism, the coupler point have to be in the supreme condition of ball and burmester ponits. Ball and burmester points are the special condition of mechanisms which trace the optimum path.

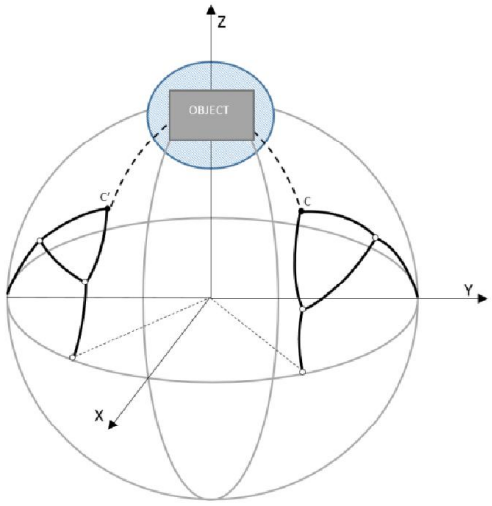


Figure 12: A scheme for spherical gripping mechanism.

III. Conclusion

Three finger spherical mechanisms is proposed for gripping operation. This mechanism can provide large workspace due to geometrical structure. High capability of grasping for various shaped work pieces can be obtained by using independent spherical mechanism fingers. Grasping operation can also be performed more successfully and stably due to three fingers of the mechanism.

The mechanism can be modeled and optimized for gripping process in the future work. For this operation, grasping force, end-effector path, location of fixed joints and dimensions of mechanism links have to be optimized.

References

1. Pham, D. and S. Yeo, *Quasi-parallel grippers for the concentric handling of cylindrical workpieces.* The International Journal of Advanced Manufacturing Technology, 1985. **1**(1): p. 95-120.
2. Saravanan, R., et al., *Evolutionary multi criteria design optimization of robot grippers.* Applied Soft Computing, 2009. **9**(1): p. 159-172.
3. Lanni, C. and M. Ceccarelli, *An optimization problem algorithm for kinematic design of mechanisms for two-finger grippers.* Open Mechanical Engineering Journal, 2009. **3**: p. 49-62.
4. Ergin O. F., S.Ş., Uzmay İ., *AZ TAHRİKLİ PARMAK MEKANİZMASININ KİNEMATİK VE KİNETİK ANALİZİ.* 16. ULUSAL MAKİNE TEORİSİ SEMPOZYUMU, 2013: p. 435.
5. Wu, L., G. Carbone, and M. Ceccarelli, *Designing an underactuated mechanism for a 1 active DOF finger operation.* Mechanism and Machine Theory, 2009. **44**(2): p. 336-348.
6. YILMAZ A., S.E., *ESNEK UZUVLU, ADAPTİF ENDÜSTRİEL ROBOT TUTUCU TASARIM VE ANALİZİ.* 16. ULUSAL MAKİNA TEORİSİ SEMPOZYUMU, 2013: p. 134.
7. Geng, R.-R., J.K. Mills, and Z.-Y. Yao, *Design and analysis of a novel 3-DOF spatial parallel micrograpper driven by LUMs.* Robotics and Computer-Integrated Manufacturing, 2016. **42**: p. 147-155.
8. Rosati, G., S. Minto, and F. Oscari, *Design and construction of a variable-aperture gripper for flexible automated assembly.* Robotics and Computer-Integrated Manufacturing, 2017. **48**: p. 157-166.
9. Wolniakowski, A., et al., *Task and Context Sensitive Gripper Design Learning Using Dynamic Grasp Simulation.* Journal of Intelligent & Robotic Systems, 2017. **87**(1): p. 15-42.
10. Bai, G., X. Kong, and J.M. Ritchie, *Kinematic Analysis and Dimensional Synthesis of a Meso-Gripper.* Journal of Mechanisms and Robotics, 2017. **9**(3): p. 031017.
11. Hassan, A. and M. Abomoharam, *Modeling and design optimization of a robot gripper mechanism.* Robotics and Computer-Integrated Manufacturing, 2017. **46**: p. 94-103.
12. Özçelik, Z., O. Acar, and K. Konya, *KÜRESEL MEKANİZMALARDA BİYEL EĞRİSİ ÇİZİMİ İÇİN BİR YÖNTEM.* 2015.

Proposing Design Parameters for an Optimum Adhesive Joint Strength

İ. KOCABAŞ[1] and P. SVANDA[2]

[1] Anadolu University, Eskişehir/Turkey, ibrahimkocabas@anadolu.edu.tr
[1]Pardubice University, Pardubice/Czechia, pavel.svanda@upce.cz

Abstract **- Estimation of the load carrying capacity of the adhesively bonded structures is the main challenge in the bonded constructions and structures prior to the manufacturing stage. Particularly, the adhesive joints in the railway and automotive industry increasingly becoming the most popular joining method recently. In order to make an accurate prediction of the load carrying capacity of an adhesive joint, modern fracture mechanic approaches are employed using the finite element method, in the scope of the study. In this regard, metallic substrates were considered to simulate structural steels having different rupture strengths. FE models of the adhesive joints were created for a variety of the different joint configurations. Finally, three design parameters; overlap length-to-thickness ratio (L/t), adhesive-to-adherend strength ratio (σ_a/σ_y) and joint strength-to-adherend strength ($F/\sigma_y t$) were proposed for an optimum adhesive joint design.**

Keywords **- Fracture mechanics, adhesive joint, FE method, structural steel**

I. INTRODUCTION

Adhesive bonding techniques have been utilized in industry to join a great variety of components ranging in scale from very small electronic parts to large assemblies. Adhesive bonding has received an expanding interest in many industries, e.g. aerospace, automotive, composite materials, electronics, and railway vehicles, as an alternative to traditional joining methods such as welding, riveting, screwing, etc. The strength evaluation and failure analysis of adhesively bonded joints in various applications are important topics. Accordingly, great efforts have been made in finding the influences of material and geometrical parameters on the load carrying capacity of adhesive bonding structures, so as to design optimal structures with proper adhesives for practical requirements in engineering. Fracture mechanics is a common and essential tool for understanding and predicting the failure of machine components. For many years, researchers have been focusing on the durability of materials; the main approach for this is to identify when failure will occur. This mainly concerns nucleation and propagation of cracks in a body. The external load applied on the material could cause a crack to initiate, or could cause the growth of an already existing crack and the presence of a crack could lead to rupture when the crack propagates directly through the body. To predict the strength of the adhesive bonding and where fracture will occur, the continuum damage mechanics or fracture mechanics is employed. In recent years, more attention has been paid on the fracture mechanic approach since simulation of crack initiation and propagation is out of the scope of the classical continuum damage mechanics. Moreover, the cohesive zone model approach is increasingly becoming the most popular field in predicting the failure phenomena in adhesive bonding structures.

II. MATERIAL AND GEOMETRY DESCRIPTION

Both material behavior and single lap joint configuration has a significant influence on the estimation of failure load and simulating crack propagation. Many analytical continuum failure predictions assume elastic adhesive and adherend material response and nearly ignores nonlinear geometrical stiffness variation due to the eccentricity of loading path. For a better evaluation of damage occurrence and progressive failure concept, both material response and nonlinear geometrical effects should be precisely introduced in the failure analysis. Therefore, the joint geometry and material model of individual components of single lap joint would be described in the upcoming section.

Single lap joint geometry which exhibits over a range of usage area and popularity among the researchers was selected to be joint geometry. Joint geometry model was designed in accordance with the ''ASTM D1002'' (Standard Test Method for Apparent Shear Strength of Single-Lap-Joint Adhesively Bonded Metal Specimens by Tension Loading) and thickness of the adherent is controlled to be in the range of 0.1mm and 0.15 mm and width of the joint is 25mm as stated in the standard.

In order to capture the effect of elastic-plasticity of adherend material, a nonlinear material model is employed with isotropic hardening. In the study, the most common type of structural steels with low carbon content and high ductility is selected as the adherend material. The metallic adherends are modeled as elastic-plastic solids, with their true stress-strain curves using power hardening laws.

$$\sigma = \begin{cases} E\varepsilon, & \varepsilon \leq \sigma_y/E \\ \sigma_y \left(\dfrac{\varepsilon}{\sigma_y/E}\right)^n, & \varepsilon > \sigma_y/E \end{cases} \quad (1)$$

Where E is Young's modulus, n is the strain hardening exponent, and σ_y is the yield strength. For the present model, the metallic adherends are assumed to be the S235 structural mild steel with a minimum yield stress of 235MPa and

Young's modulus of 200GPa. The strain hardening exponent "n" for structural mild steels, corresponding to an average fracture elongation of 25% and ultimate tensile strength of 400MPa, is evaluated approximately 0.1 using the Eq. 1. Three different structural sheets of steel, namely S255, S275 and S355 for the parametric study are implemented. Each has the minimum yield stress of 255, 275 and 355 N/mm2, respectively. The other material parameters (e.g. Young's modulus, strain hardening exponent) are kept constant for each of the corresponded structural steel.

In this study, the most commonly implemented epoxy adhesives are employed for the progressive damage analysis. Thus, there would be an analytical expression in order to describe stress-strain relations of an epoxy adhesive. For this reason, two different formulations to construct a stress-strain curve of both ductile and brittle behavior are to be created. For instance, most of the soft (ductile) epoxy adhesives exhibit highly nonlinear trend up to tensile strength then nearly behave like a perfectly plastic material. Under these circumstances, following equation would be sufficient to construct a stress-strain curve of soft epoxy adhesives.

$$\sigma_a = \sigma_u \tanh\left(\frac{E_a}{\sigma_u}\varepsilon_a\right) \quad (2)$$

Where σ_u is the adhesive tensile strength, E_a is the adhesive Young's Modulus and ε_a is the strain value at a point on the stress-strain curve.

Most of the structural epoxy adhesives have the tensile strength and Young's modulus in the range of 20 to 50MPa and 1 to 8GPa, respectively. Therefore, these intervals are considered once the constructing stress-strain diagrams of bulk epoxy adhesives.

The numerical model was constructed as a 2-D plane strain problem since there is a linear proportionality between the joint strength and width of the joint. The steel adherends were modeled with a 4-node bilinear plane strain quadrilateral (CPE4) elements having a linear shape function and an integration point at each face. CPE4 element is also available in ABAQUS version 6.13, and compatible with non-linear material model and large displacement (non-linear geometry) option. In a similar way, the adhesive layer in the numerical model is replaced by a zero thickness cohesive layer. Thickness dependence cohesive parameters are employed to cohesive layer for precise representation of adhesive layer. The cohesive layer was constructed with a 4-node two-dimensional cohesive element (COH2D4) corresponding to bilinear traction-separation behavior. Both of the CPE4 and COH2D4 elements have three degrees of freedom at each node (translation in x, y, and rotation about the z-axis).

A. Numerical Solution Algorithm

In fact, there are three groups of parameters affecting the failure load of the single lap joints; which are material properties of the adherend (E, σ_y, n), geometry parameters (L, t, η) and cohesive zone parameters of the adhesive (Γ, K_0, σ_c). The joint is loaded in the uni-axial direction with the increasing displacement. When an element at the cohesive zone reaches the critical separation strength value σ_c either in shear or normal direction, the damage initiates according to aforementioned failure criteria. Then stiffness degradation occurs based on a dimensionless damage variable D as described in Eq. 3 as a function of separation displacements using linear softening model.

$$D^{(k)} = \frac{\delta_f\left(\delta^{(k)} - \delta_c\right)}{\delta^{(k)}\left(\delta_f - \delta_c\right)} \quad (3)$$

Where $D^{(k)}$ is the damage variable at kth step and δ(k) is separation displacement at kth step, δ_c and δ_f are the critical displacement at damage initiation and separation displacement at the complete failure, respectively. The stiffnesses of the cohesive zone model as a function of this damage variable at kth step are calculated in Eq. 3.

$$E^{(k)} = \left(1 - D^{(k-1)}\right)E$$
$$G^{(k)} = E^{(k)}/2(1+\upsilon) \quad (4)$$

During the softening process, the values of E and G are incrementally decreased based on the Eq. 4 up to the final failure. The damage evaluation of an element in the cohesive zone is assessed regarding energy criterion introduced in the previous section. When the energy criterion is satisfied then corresponded element completely fails and removed from the cohesive layer. The basic numerical algorithm of progressive failure model is presented in Fig. 1.

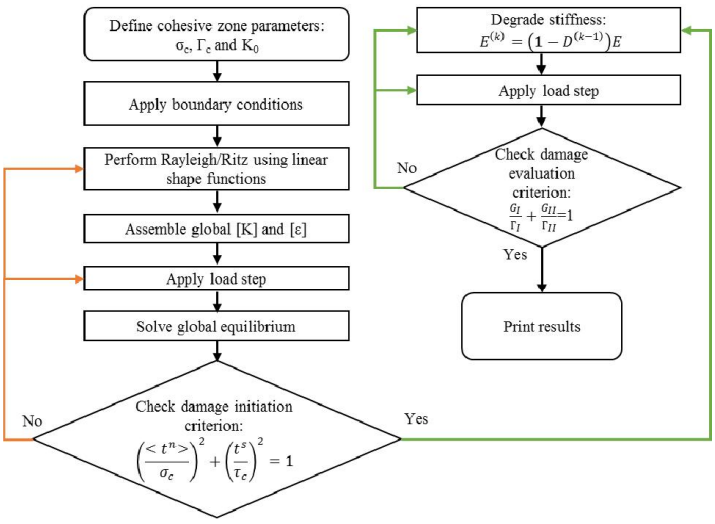


Fig. 1: A simple flowchart representing the progressive failure model of the cohesive layer for FE analysis.

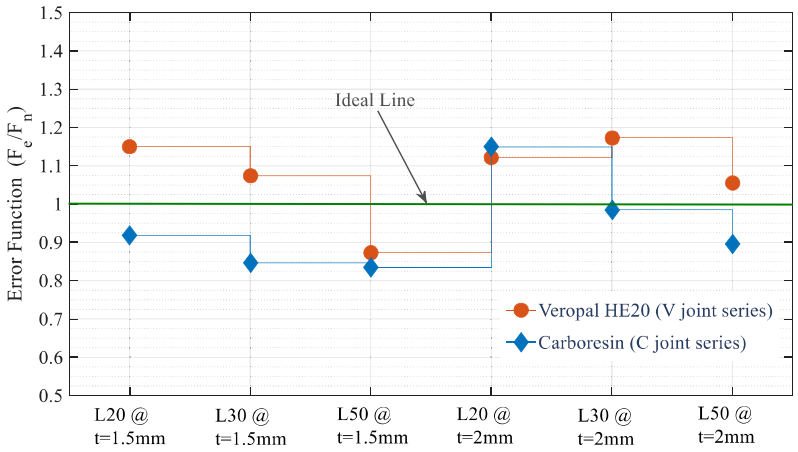


Fig. 2: The distribution of errors reference to experimental data for every single lap joint configuration.

B. Validation of numerical model

To understand the deviation of numerical failure loads from the experimental data, a step plot was constructed as shown in Fig. 2 which represents the ratio of predicted and experimental failure load (F_n/F_{ex}) at each joint configurations. The green line representing the equality of predicted and experimental failure loads (F_n/F_{ex}=1) is chosen as a baseline to indicate the amount of error. It was found out that the errors for each configuration remain in the range of +18% and -15 % as illustrated in Fig. 2, with an average value of 11 percent error corresponding to F_n/F_{ex}=1.11, which are within the acceptable limits.

Table 1: Cohesive zone material parameters of bulk adhesives for the numerical analysis.

	Veropal HE-20	**Carboresin**
Initial normal stiffness, K_n	6445 N/mm^3	13745 N/mm^3
Initial shear stiffness, K_s	2405 N/mm^3	5370 N/mm^3
Mode I fracture energy, Γ_n	1.68 N/mm	0.86 N/mm
Mode II fracture energy, Γ_s	3.37 N/mm	1.42 N/mm
Normal critical traction, σ_n	28.6 MPa	17.7 MPa
Shear critical traction, σ_s	16.5 MPa	10.2 MPa
Poisson's ratio, υ	0.34	0.28

I. RESULTS AND DISCUSSION

Following normalized design parameters are considered for a general adhesive joint design methodology;

• Based on the results presented in this chapter, the geometry parameters L and t have a great effect on the failure concept of bonded structures. Both of them increases the joint strength up to a certain point (saturation limit). For this reason, the ratio L/t is selected to be a critical geometric parameter.

• Secondly, the material properties of both adhesive and adherend material are the other vital factor. Because both of them have a positive impact on failure load. However, there is usually a restriction of using high strength adherend and adhesive material. They should be somehow optimized to meet required strength in the joining process. It is anticipated that only one normalized material parameter can be derived. The ratio σ_a/σ_y can be chosen as material dependent design parameter (see Fig. 3).

• Basically, the ratio of the joint failure load (F) in unit width and the tensile strength of the adherend material can be a comparison tool. This parameter ($F/\sigma_y t$) exhibits the joint efficiency, approximately neglecting the rotation (bending effect).

II. CONCLUSION

In this study, a progressive failure model in ABAQUS® is employed to investigate load carrying capacity of the adhesive joints. Consequently, following conclusions are drawn as a result of performed experiments and progressive FE simulations;

• The nonlinear material model for the structural steels can be approximated and implemented in the joint strength evaluation using power law as described in Eq. 4.16. Similarly, Eq. 4.17 and 4.18 are proposed to express the non-linear material behavior of ductile and brittle epoxy adhesives, respectively.

• The error between experimental and FE failure load results remain below 18% for five different overlap lengths (10, 20, 30, 40 and 50mm) and two adherend thicknesses (1.5 and 2mm) for both epoxy adhesive type.

• The most dominant parameter is decided to the adherend thickness and overlap length, which can drastically change the joint strength up to 250% corresponding to the same material configuration.

• In design stage of the adhesive joints, three dimensionless parameters (L/t, σ_a/σ_y and $F/\sigma_y t$) are proposed for an optimum

E-ISBN: 978-605-67535-4-1

joint design. Additionally, the strength of the joint has nearly a linear proportionality as a function of these parameters up to the aforementioned critical point (saturation state).

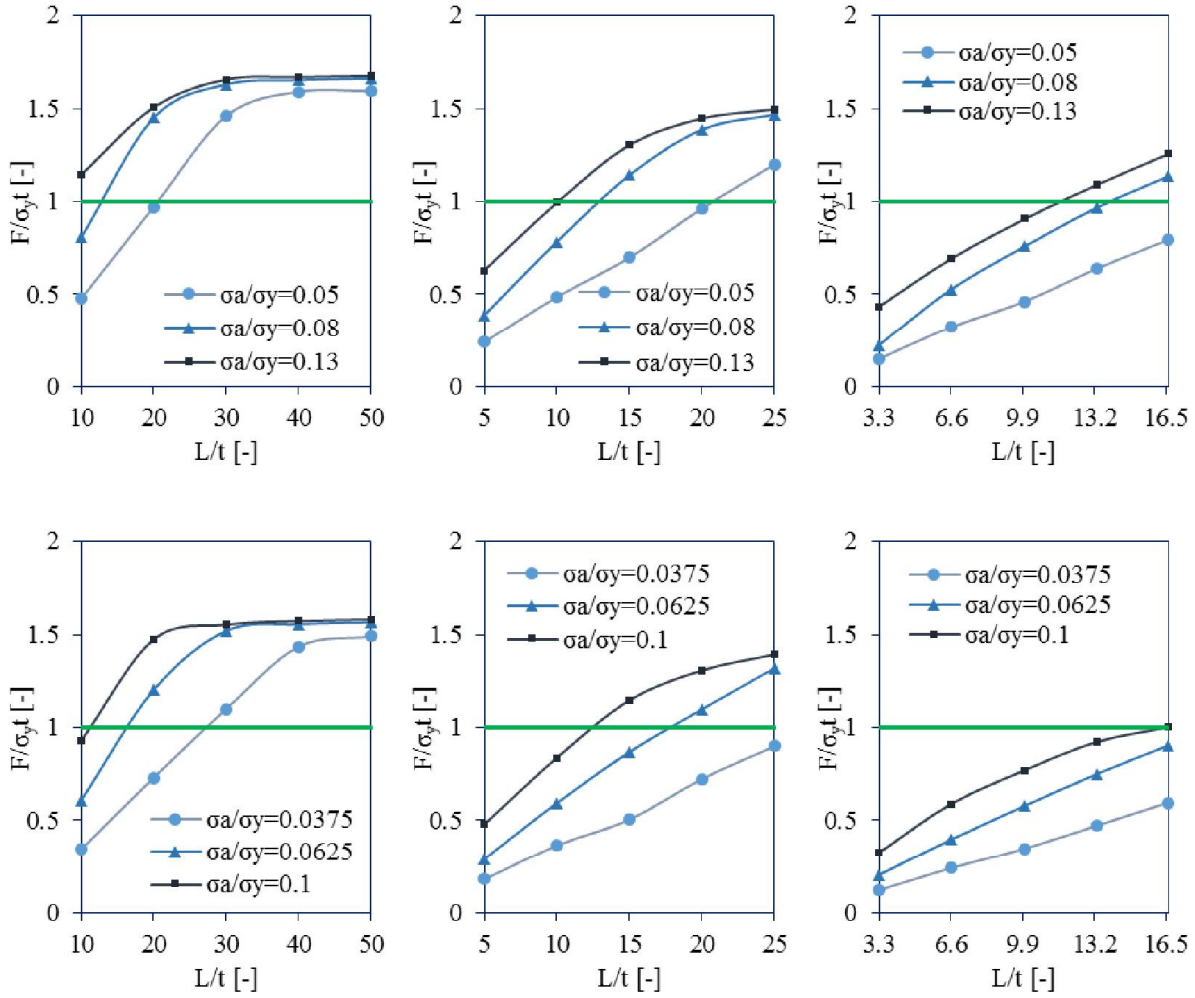


Fig. 3: Variation of the joint efficiency (performance) corresponding to various dimensionless design parameters.

REFERENCES

[1] Shet, C. and N. Chandra, Analysis of Energy Balance When Using Cohesive Zone Models to Simulate Fracture Processes. Journal of Engineering Materials and Technology, 2002. 124(4): p. 440-450.

[2] Chandra, N., et al., Some issues in the application of cohesive zone models for metal-ceramic interfaces. International Journal of Solids and Structures, 2002. 39(10): p. 2827- 2855.

[3] Needleman, A., An analysis of decohesion along an imperfect interface. International Journal of Fracture, 1990. 42(1): p. 21-40.

[4] Needleman, A., A Continuum Model for Void Nucleation by Inclusion Debonding. J. Appl. Mech. , 1987(54): p. 525-531.

[5] Xu, X.P. and A. Needleman, Numerical simulations of fast crack growth in brittle solids. Journal of the Mechanics and Physics of Solids, 1994. 42(9): p. 1397-1434.

[6] Tvergaard, V. and J.W. Hutchinson, The relation between crack growth resistance and fracture process parameters in elastic-plastic solids. Journal of the Mechanics and Physics of Solids, 1992. 40(6): p. 1377-1397.

[7] Barenblatt, G.I., The formation of equilibrium cracks during brittle fracture. General ideas and hypotheses. Axially-symmetric cracks. Journal of Applied Mathematics and Mechanics, 1959. 23(3): p. 622-636.

[8] Camacho, G.T. and M. Ortiz, Computational modeling of impact damage in brittle materials. International Journal of Solids and Structures, 1996. 33(20–22): p. 2899-2938. 60

[9] Geubelle, P.H. and J.S. Baylor, Impact-induced delamination of composites: a 2D simulation. Composites Part B: Engineering, 1998. 29(5): p. 589-602.

[10] Chen, C.R., et al., Three-dimensional modeling of ductile crack growth: Cohesive zone parameters and crack tip triaxiality. Engineering Fracture Mechanics, 2005. 72(13): p. 2072-2094.

Bivariate Robust Design under Gamma Noise

M. ZEYBEK[1] and O. KÖKSOY[2]

[1] Ege University, İzmir/Turkey, melis.zeybek@ege.edu.tr
[2]Ege University, İzmir/Turkey, onur.koksoy@ege.edu.tr

Abstract **- Under the trend of globalization of industry, one can be faced with more than one response in some industrial settings, especially in the semiconductor manufacturing process; therefore, quality is evaluated as multidimensional for many products. Taguchi's robust parameter design focuses on reducing the system variability caused by the noise factors. The results obtained under unrealistic assumptions about the noises may mislead the practitioners when it comes to improving quality in robust design. For example, many hydrological data and the multi-path fading of a signal in wireless communication systems are positively skewed and cannot be modelled by any normal distribution. In this study, the case where two quality characteristics are affected by gamma distributed noise factor is taken into account. The true effects of noise distributions are investigated and a simulation study is presented to quantify the effects of noise distributions for bivariate robust design. In line with the obtained results, a new joint density function of two quality characteristics is proposed.**

Keywords **-** bivariate response distribution, noise distribution, gamma distribution, robust parameter design, response surface methodology.

I. INTRODUCTION

IN the early 1980s, Taguchi introduced the term robust parameter design (RPD) and has got popularized by many quality improvement engineers in different fields. The most essential aspect of RPD is to focus on a single response to determine the best operating condition. However, given the trend of the globalization of industry, more than one response is common in some industrial settings. Therefore, quality is evaluated as multidimensional for many produced products. Multidimensional quality technologies have received considerable attention in recent years in the field of quality improvement.

Although scientists have adopted Taguchi's RPD approach on quality, statistical communities have criticized his experimental methodologies and analysis techniques. Consequently, new methodologies have been proposed. The response surface methodology (RSM), which was first developed by [1], was revisited and popularized in the early 1990s. [2] discussed a constrained optimization technique called the dual response surface (DRS) of the mean and the variance responses. Following this article, current literature includes several other methods for DRS, for example, [3, 4, 5, 6, 7, 8, 9, 10].

The probability distribution of the experimental data plays an important role in response surface methodology. The belief that 'the normality assumption' is a robust assumption may not be true and there are many cases where it does not apply to real-world problems. The distribution of noise factors has an influence on a response distribution. In fact, [11] and [12] note that true normality is considered to be a myth because fluctuations in noise factors may not be well described by any symmetric distribution in real life problems. In many situations, noise factors have skewed distribution, such as the gamma, beta or exponential. For example, environmental conditions such as streamflow, humidity, temperature, and rainfall, which are general examples of noise factors. In fact, normal distribution cannot model streamflow—and many other hydrological data—due to the impossibility of negative values. Hydrological data are positively skewed with a lower bound around zero and an unbounded right tail. Studies on the daily or monthly rainfall have indicated that the real distribution can be defined by a gamma distribution; see, [13] and [14]. If the noise factors are non-normal, then its structure affects the distribution of responses. However, practitioners rarely know the true distributions. Unfortunately, the current status of studies focusing on noise distributions is very limited.

In this paper, we investigate the effects of gamma distributed noise on the case where the quality is dependent on two quality characteristics. A new joint density function is proposed. Additionally, a simulation study is illustrated to quantify to gamma effect on the proposed bivariate response distribution.

II. SIMULATION STUDY

Although non-normal noise factors are the reality of a robust design, what is surprising is that the real-life experimental designs under non-normal responses are limited in the current literature. In this context, we concentrated on a simulation study. In the simulation process, an experiment, which is presented by [15], as an initial design is defined. In the design, three controllable factors; reaction time, reaction temperature and amount of catalyst are assumed to be related to the conversion (y_1) and the thermal activity (y_2). Assume that the amount of catalyst is difficult to control; therefore, it is adopted as a noise factor and is denoted by Z. The other two factors, reaction time (x_1) and temperature (x_2), are control factors and their levels are fixed during the experiment. Under these considerations, we simulated the initial design assuming the noise variates fluctuate according to $Z \sim G(1,2)$, and random errors are $\varepsilon_1^* \sim N(0,1)$ and $\varepsilon_2^* \sim N(0,1)$ using JMP. A large number of potential responses, say 10,000, were

randomly generated under the simulation model given by [15]. Finally, the design of the simulated experiments under the above mentioned assumptions is constructed and given in Table 1.

Table 1. The design of simulated experiments.

u	x_1	x_2	z	y_1	y_2
1	-1	-1	1.978	113.975	53.736
2	1	-1	2.016	102.706	62.265
3	-1	1	1.986	88.451	58.207
4	1	1	1.988	121.440	66.719
5	-1	-1	1.985	113.870	53.732
6	1	-1	1.973	101.190	62.253
7	-1	1	2.005	88.913	58.204
8	1	1	1.998	121.820	66.715
9	-1.682	0	1.994	99.537	53.060
10	1.682	0	1.978	116.873	67.385
11	0	-1.682	1.967	100.772	56.479
12	0	1.682	2.016	97.546	63.973
13	0	0	2.011	117.463	60.228
14	0	0	2.001	114.128	60.231
15	0	0	2.012	114.319	60.244
16	0	0	1.996	113.961	60.246
17	0	0	2.010	114.271	60.238
18	0	0	2.015	114.509	60.233
19	0	0	1.990	113.571	60.237
20	0	0	2.012	113.442	60.248

Figure 1 and Figure 2 illustrate the bivariate histogram and scatterplot of 10,000 simulated responses for the first experimental run. As seen from Figure 1 and Figure 2, the simulated responses have a skewed shape. Although the error terms follow a normal distribution, the bivariate distribution structure of a gamma noise plays an important role in the shape of bivariate responses such that the histogram of simulated responses indicates a right-skewed structure.

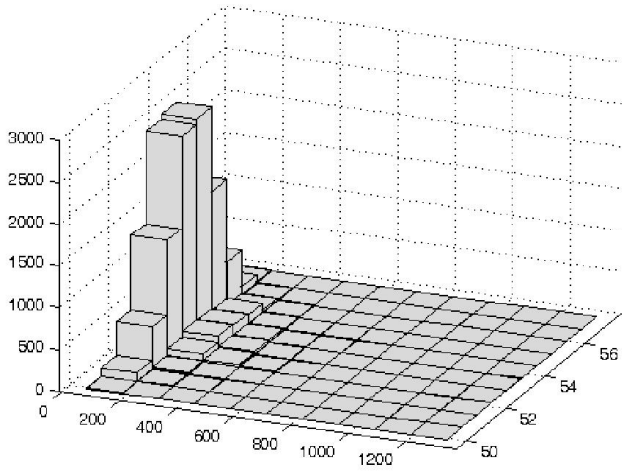


Figure 1. The bivariate histogram of 10,000 simulated responses for the first experimental run.

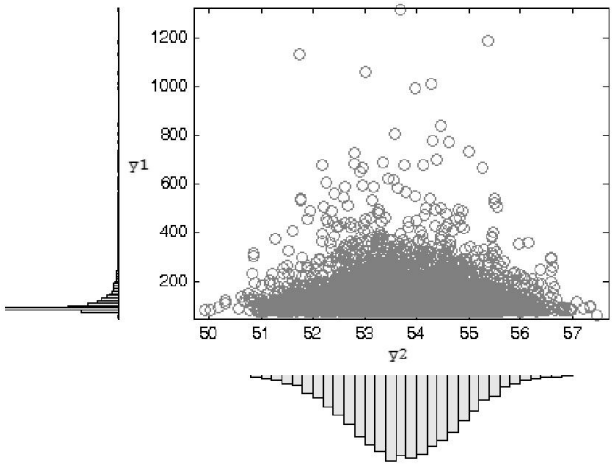


Figure 2. The bivariate scatterplot of 10,000 simulated responses for the first experimental run.

In the next section, the illustrated gamma effect on bivariate distribution of responses by the simulation study is taken into account theoretically and a new joint density function is proposed.

III. A NEW JOINT PROBABILITY DENSITY FUNCTION

Consider the quality of a system is dependent on two quality characteristics (Y_1 *and* Y_2) with k controllable factors ($x_1, \dots, x_k$) and one noise factor (Z), thus, the responses can be modelled by the second order response surfaces as follows,

$$Y_1 = \alpha_0 + \sum_{i=1}^{k} \alpha_i x_i + \sum_{i=1}^{k} \alpha_{ii} {x_i}^2 + \sum_{i<t}^{k} \sum \alpha_{it} x_i x_t + \gamma Z + \sum_{i=1}^{k} \gamma_i x_i Z + \varepsilon_1 \quad (1)$$

$$Y_2 = \beta_0 + \sum_{i=1}^{k} \beta_i x_i + \sum_{i=1}^{k} \beta_{ii} {x_i}^2 + \sum_{i<t}^{k} \sum \beta_{it} x_i x_t + \delta Z + \sum_{i=1}^{k} \delta_i x_i Z + \varepsilon_2 \quad (2)$$

where $\varepsilon_1 \sim NID(0, \sigma_{\varepsilon_1}^2)$ and $\varepsilon_2 \sim NID(0, \sigma_{\varepsilon_2}^2)$ are random errors, and $Z \sim Gamma(\theta, \kappa)$.

The conditional mean and variance of Equation (1) given $Z = z$, are

$$\mu_{Y_1|Z=z} = \mu_{x_1} + \gamma z + \sum_{i=1}^{k} \gamma_i x_i z$$

and

$$\sigma^2_{Y_1|Z=z} = \sigma^2_{\varepsilon_1},$$

where, $\mu_{x_1} = \alpha_0 + \sum_{i=1}^{k} \alpha_i x_i + \sum_{i=1}^{k} \alpha_{ii} {x_i}^2 + \sum_{i<t}^{k} \sum \alpha_{it} x_i x_t$.

The conditional mean and variance of Equation (2) given $Y_1 = y_1$ and $Z = z$, are,

$$\mu_{Y_2|Y_1=y_1,Z=z} = y_1 + \mu_{x_2} - \mu_{x_1} + z(\delta - \gamma) + z \sum_{i=1}^{k} x_i(\delta_i - \gamma_i)$$

and

$$\sigma^2_{Y_2|Y_1=y_1,Z=z} = \sigma^2_{\varepsilon_1} + \sigma^2_{\varepsilon_2}$$

where $\mu_{x_2} = \beta_0 + \sum_{i=1}^{k} \beta_i x_i + \sum_{i=1}^{k} \beta_{ii} {x_i}^2 + \sum_{i<t}^{k} \sum \beta_{it} x_i x_t$.

Thus, the conditional distributions are obtained as,

$$f_{Y_1}(y_1|Z=z) \sim N\left(\mu_{Y_1|Z=z}, \sigma^2_{Y_1|Z=z}\right) \quad (3)$$

$$f_{Y_2}(y_2|Y_1=y_1, Z=z) \sim N\left(\mu_{Y_2|Y_1=y_1,Z=z}, \sigma^2_{Y_2|Y_1=y_1,Z=z}\right) \quad (4)$$

Using Equations (3) and (4), the joint probability density function of Y_1 *and* Y_2 given $Z = z$ can be defined by,

$$f_{Y_1,Y_2}(y_1, y_2|Z=z) = f_{Y_2}(y_2|Y_1=y_1, Z=z).\, f_{Y_1}(y_1|Z=z) \quad (5)$$

Finally, by the help of Equation (5) the joint probability density function of Y_1 *and* Y_2 is obtained as follows,

$$f_{Y_1,Y_2}(y_1, y_2)$$

$$= \int_0^{+\infty} f_{Y_1,Y_2}(y_1, y_2|Z=z)\, f_Z(z) dz$$

$$= \frac{\exp\left(-\frac{1}{2}\left(\frac{\left(y_2-\mu_{x_2}-(y_1-\mu_{x_1})\right)^2}{\sigma^2_{\varepsilon_1}+\sigma^2_{\varepsilon_2}} - \frac{(y_1-\mu_{x_1})^2}{\sigma^2_{\varepsilon_1}}\right)\right)}{(2\pi)\sqrt{\sigma^2_{\varepsilon_1}(\sigma^2_{\varepsilon_1}+\sigma^2_{\varepsilon_2})}\Gamma(\theta)\kappa^\theta}$$

$$\cdot \int_0^{+\infty} \exp\left(-\frac{z^2}{2}\left(\frac{\left((\delta+\sum_{i=1}^{k}\delta_i x_i)-(\gamma+\sum_{i=1}^{k}\gamma_i x_i)\right)^2}{\sigma^2_{\varepsilon_1}+\sigma^2_{\varepsilon_2}} + \frac{(\gamma+\sum_{i=1}^{k}\gamma_i x_i)^2}{\sigma^2_{\varepsilon_1}}\right) - z\left(\frac{1}{\kappa} - \frac{(y_1-\mu_{x_1})(\gamma+\sum_{i=1}^{k}\gamma_i x_i)}{\sigma^2_{\varepsilon_1}} - \frac{\left(y_2-\mu_{x_2}-(y_1-\mu_{x_1})\right)(\delta+\sum_{i=1}^{k}\delta_i x_i-(\gamma+\sum_{i=1}^{k}\gamma_i x_i))}{\sigma^2_{\varepsilon_1}+\sigma^2_{\varepsilon_2}}\right)\right)$$

$$\cdot z^{\theta-1} dz$$

and by the help of the following equality,

$$\int_0^{+\infty} x^{\nu-1} exp(-bx^2 - kx)\, dx = (2b)^{-\nu/2}\Gamma(\nu) exp\left(\frac{k^2}{8b}\right) D_{-\nu}\left(\frac{k}{\sqrt{2b}}\right),$$

(see, Gradshteyn and Ryzhik [19]), where $D_{-\nu}(t)$ is a parabolic cylinder function, $f_{Y_1,Y_2}(y_1, y_2)$ is achieved in the form given in Equation (6) after the necessary simplifications.

$$f_{Y_1,Y_2}(y_1, y_2) =$$

$$\frac{(\sigma^2_{\varepsilon_1}+\sigma^2_{\varepsilon_2})^{\frac{\theta-1}{2}}\sigma_{\varepsilon_1}{}^{\theta-1}\kappa^{-\theta}\Gamma(\theta)^{-1}}{(2\pi)\left(\left((\delta+\sum_{i=1}^{k}\delta_i x_i)-(\gamma+\sum_{i=1}^{k}\gamma_i x_i)\right)^2\sigma^2_{\varepsilon_1}+(\gamma+\sum_{i=1}^{k}\gamma_i x_i)^2(\sigma^2_{\varepsilon_1}+\sigma^2_{\varepsilon_2})\right)^{\frac{\theta}{2}}}$$

$$\cdot \exp\left(-\frac{1}{2}\left(\frac{\left(y_2-\mu_{x_2}-(y_1-\mu_{x_1})\right)^2}{\sigma^2_{\varepsilon_1}+\sigma^2_{\varepsilon_2}} - \frac{(y_1-\mu_{x_1})^2}{\sigma^2_{\varepsilon_1}}\right)\right)$$

$$\cdot \exp\left(\left(\frac{1}{\kappa} - \frac{(y_1-\mu_{x_1})(\gamma+\sum_{i=1}^{k}\gamma_i x_i)}{\sigma^2_{\varepsilon_1}} - \frac{\left(y_2-\mu_{x_2}-(y_1-\mu_{x_1})\right)(\delta+\sum_{i=1}^{k}\delta_i x_i-(\gamma+\sum_{i=1}^{k}\gamma_i x_i))}{\sigma^2_{\varepsilon_1}+\sigma^2_{\varepsilon_2}}\right)^2\right.$$

$$\cdot \frac{\sigma^2_{\varepsilon_1}(\sigma^2_{\varepsilon_1}+\sigma^2_{\varepsilon_2})}{4\left(\left(\delta+\sum_{i=1}^{k}\delta_i x_i-(\gamma+\sum_{i=1}^{k}\gamma_i x_i)\right)^2\sigma^2_{\varepsilon_1}+\left((\gamma+\sum_{i=1}^{k}\gamma_i x_i)^2(\sigma^2_{\varepsilon_1}+\sigma^2_{\varepsilon_2})\right)\right)}\Bigg)$$

$$\cdot D_{-\theta}\left(\left(\frac{1}{\kappa} - \frac{(\delta+\sum_{i=1}^{k}\delta_i x_i-(\gamma+\sum_{i=1}^{k}\gamma_i x_i))\left(y_2-\mu_{x_2}-(y_1-\mu_{x_1})\right)}{\sigma^2_{\varepsilon_1}+\sigma^2_{\varepsilon_2}} - \frac{(y_1-\mu_{x_1})(\gamma+\sum_{i=1}^{k}\gamma_i x_i)}{\sigma^2_{\varepsilon_1}}\right)\right.$$

$$\left.\cdot\left(\frac{\sqrt{\sigma^2_{\varepsilon_1}(\sigma^2_{\varepsilon_1}+\sigma^2_{\varepsilon_2})}}{\left(\left(\delta+\sum_{i=1}^{k}\delta_i x_i-(\gamma+\sum_{i=1}^{k}\gamma_i x_i)\right)^2\sigma^2_{\varepsilon_1}+\left((\gamma+\sum_{i=1}^{k}\gamma_i x_i)^2(\sigma^2_{\varepsilon_1}+\sigma^2_{\varepsilon_2})\right)\right)^{1/2}}\right)\right) \quad (6)$$

Figure 3 illustrates the graph of the proposed $f_{Y_1,Y_2}(y_1, y_2)$ given by Equation (6) under $\varepsilon_1 \sim NID(0,4)$ and $\varepsilon_2 \sim NID(0,4)$ and $Z \sim Gamma(1,2)$, and also $E(Y_1) = 5$ and $E(Y_2) = 10$.

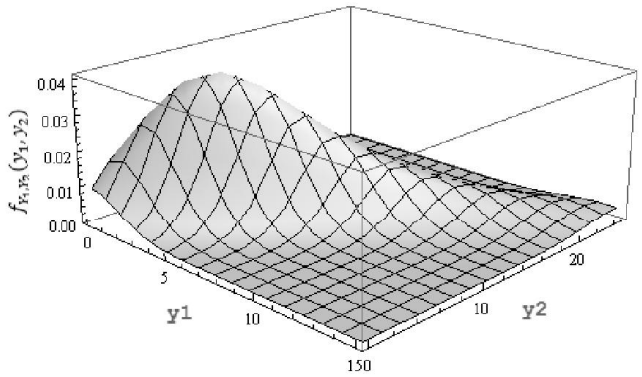


Figure 3. The graph of the proposed $f_{Y_1,Y_2}(y_1, y_2)$.

As seen from Figure 3, the most conspicuous property is that the proposed bivariate pdf has a right-skewed shape. Effective dominance of the right-skewed noise factor on the responses explains the distributional structure of the proposed bivariate density.

IV. Conclusion

The results, obtained under unrealistic assumptions about the noises, are unreliable for practitioners improving the quality in robust design studies. We took into account the case where noise factors have a gamma distribution and proposed a joint density function of bivariate robust design problem. Therefore, this study offers a useful reference to practitioners in terms of providing more engineering understanding about the process. Additionally, this proposed pdf can be used for quality improvement techniques such as in loss function based approaches, or to estimate the distributional properties of the bivariate-response problems, i.e. system mean and the variance. As a future study, one might consider more complex—high dimensional integrated cases—multi-response quality problems with a skewed nature.

REFERENCES

[1] G.E.P. Box and K.B. Wilson, "On the Experimental Attainment of Optimum Conditions", *Journal of the Royal Statistical Society*, vol. 13, pp. 1-45, 1951.

[2] G.G. Vining and R.H. Myers, "Combining Taguchi and Response Surface Philosophies: A Dual Response Approach", *Journal of Quality Technology*, vol. 22, pp. 38-45, 1990.

[3] E. Del Castillo and D.C. Montgomery, "A Nonlinear Programming Solution to the Dual Response Problem", *Journal of Quality Technology*, vol. 25, pp. 199-204, 1993.

[4] D.K.J. Lin and W. Tu, "Dual Response Surface Optimization", *Journal of Quality Technology*, vol. 27, pp. 34-39, 1995.

[5] K.A. Copeland and P.R. Nelson, "Dual Response Optimization via Direct Function Minimization", *Journal of Quality Technology*, vol. 28, pp. 331-336, 1996.

[6] K. Kim and D.K.J. Lin, "Dual Response Surface Optimization: A Fuzzy Modeling Approach", *Journal of Quality Technology*, vol. 30, pp. 1-10, 1998.

[7] O. Köksoy and N. Doganaksoy, "Joint Optimization of Mean and Standard Deviation in Response Surface Experimentation", *Journal of Quality Technology*, vol. 35, pp. 239-252, 2003.

[8] O. Köksoy, "Multiresponse Robust Design: Mean Square Error (MSE criterion)", *Applied Mathematics and Computation*, vol. 175, pp. 1716-1729, 2006.

[9] O. Köksoy and S.S. Fan, "An Upside-down Normal Loss Function-based Method for Quality Improvement", *Engineering Optimization*, vol. 44, pp. 935-945, 2012.

[10] M. Zeybek and O. Köksoy, "Optimization of Correlated Multi-response Quality Engineering by the Upside-down Normal Loss Function", *Engineering Optimization*, vol. 48, pp. 1419-1431, 2016.

[11] A.A. Abraham and T.J. Robinson, C.M. Anderson-Cook, "A graphical approach for assessing optimal operating conditions in robust design", *Quality Technology and Quantitative Management, vol.* 6, pp. 235-253, (2009).

[12] W.A. Brenneman, and W.R. Myers, "Robust parameter design with categorical noise variables", *Journal of Quality Technology*, vol. 35, pp. 335–341, 2003.

[13] L. Hanson and R. Vogel, "The probability distribution of daily rainfall in the United States", *World Environmental and Water Resources Congress, Honolulu, Hawaii*, 2008.

[14] M.A. Sharma and J.B. Singh, "Use of probability distribution in rainfall analysis", *New York Science Journal, vol.* 3, pp. 40-49, 2010.

[15] G.G. Vining, "A Compromise Approach To Multiresponse Optimization", *Journal of Quality Technology*, *vol. 30*, pp. 309-313, 1998.

Pyrolysis and kinetic analyses of Banyan tree *(Ficus Benghalensis)* plant biomass waste for bio energy potential

T. RASOOL[1], V. C. SRIVASTAVA[2], M. N. S. KHAN[3]
[1,3]Department of Chemical Engineering, National Institute of Technology Srinagar, India, trasool440@gmail.com
[3]Department of Chemical Engineering, Indian Institute of Technology Roorkee, India, vimalcsr@yahoo.co.in

Abstract **- The plant biomass of Banyan tree *(Ficus Benghalensis)* was analysed to understand its pyrolytic behaviour through thermal degradation using thermogravimetry at three heating rates of 10, 25 and 50°C min^{-1} under an inert atmosphere of nitrogen. The kinetic and thermodynamic analysis was performed using iso-conversional models of Kissenger-Akahira-Sunrose (KAS) and Ozawa-Flynn-Wall (OFW). The activation energy values corresponding to degradation mechanism were found to be of the range of 73.03 kJmol^{-1} and 79.74 kJmol^{-1} as calculated by KAS and OFW models, respectively. The thermal degradation reaction mechanism was predicted by applying Coats-Redfern method indicating that most appropriate mechanisms followed by thermal degradation of Banyan tree biomass are D5 and F3, based on diffusion and chemical reaction respectively, involving both exothermic and endothermic reactions for the temperature range under study. A kinetic compensation effect was found to follow the equation: lnA=-4.1575+0.2042E. The Gibbs free energy value of ~176.24 kJmol^{-1} and a difference of about ~5 kJmol^{-1} between activation energy and enthalpy of the reaction indicates favorable product formation with considerable bio energy potential of Banyan tree biomass waste.**

Keywords **- Plant biomass, Banyan tree, pyrolysis, Gibbs free energy.**

I. INTRODUCTION

In view of energy and environmental problems associated with the use of fossil fuels (coal, petroleum and gas) in power generation, an increasing attention is being paid world-over by the researchers and technocrats for the utilization of renewable energy sources in power generation and other energy oriented industries. There are various type of renewable energy sources such as solar, wind, hydropower, biomass energy etc. and out of these renewable energy sources, biomass is economically more viable for almost all the continents in the world[1]. Biomass is a carbonaceous material and provides both the thermal energy and reduction for oxides, where as other renewable energy sources can meet our thermal need only. Amongst all the solid fuel like coal etc. biomass is the purest fuel consisting of very lesser amount of ash materials. It

has been estimated that about 19% of the world energy demand is being met through the renewable sources with 9% of this demand met by biomass, with an increasing rate of 2.5% per annum[2].

The power generation potential data for renewable energy sources in India clearly indicates that the biomass has potential to generate more than 17000 MW of electricity per year in India. However, the country is lacking in exploitation of biomass in power generation. Till date, India has been capable to generate only 2000 MW (approx.) of electricity per year in spite of declaration of several incentives by the Government of India. Hence, there is an urgent need to increase the utilization of biomass in power generation. In this context, the thermal conversion of biomass to get biofuels with high energy has proved as a promising technology[3]. However pyrolysis has been more popular thermo chemical process compared to gasification and combustion as it efficiently converts the biomass directly into fuels and chemicals in an inert atmosphere[4]. As such, much work has been carried out to study pyrolytic behaviour of numerous types of biomasses and their waste using thermo gravimetric analysis under nitrogen atmosphere to evaluate kinetic parameters of biomasses such as Rice husk and Elephant grass [5], Pine[6] and Willow [7].

El-Sayed et al. [8] investigated two Egyptian biomasses (sugarcane bagasse and cotton stalks). The direct Arrhenius plot method and integral method were applied to (TG/DTG) analysis for determination of kinetic parameters: activation energy, pre exponential factor, and order of the reaction. Ceylon and Tapcu [9] investigated the physicochemical properties along with kinetics of Hazelnut husk, an abundantly found agricultural biomass waste in Turkey. The TGA was carried out under inert conditions and operated at three different heating rates of 5, 10 and 20°Cmin^{-1}. Three kinetic models Kissinger-Akahira-Sunrose (KAS), Ozawa-Flynn-Wall (OFW) and Coats-Redfern methods were applied on TGA data of Hazelnut husk to calculate kinetic triplet. Ningbo et al.[10] carried out a study on the continuous pyrolysis of pine saw dust using a screw reactor to investigate the influence of pyrolysis temperature and solid residence time on products and energy distribution. TG analysis was carried out to find kinetic parameters while products were analyzed using GC/MS. The maximum of energy profit rate was found to be 6.49% at the residence time of 6 min.

The main objective of this study is to investigate the thermal degradation behavior of Banyan tree *(Ficus Benghalensis)* plant waste (BTW) for energy conversion and to predict whether or not the biomass can be used as a potential fuel on

an industrial level. A banyan is a fig that begins its life as an epiphyte. It is a plant that grows on another plant, when its seed germinates in a crack or crevice of a host tree or human edifice. The seeds of the banyan are small, and because most banyans grow in woodlands, a seedling that germinates on the ground is unlikely to survive. However, many seeds fall on the branches and stems of other trees or on human edifices, and when they germinate they grow roots down toward the ground and consequently may envelop part of the host tree or edifice. The leaves of the banyan tree are large, leathery, glossy, green, and elliptical. The detailed knowledge for the same required pyrolysis experiments to be performed to determine the chemical composition and properties to understand completely as to what element and compounds are present in this biomass and compare them with several other biomass sources that have been under study for a long time in the same direction. It is to put on record that very little or no work had been done on the usage of this biomass as a source of energy, however, extensive work has been done in synthesizing gold and silver nano-particles from its leaves, roots and straws for various medical applications. *Ras-Sindoor* is yet another beneficial product that has been derived from its leaves. Thermogravimetric analyis of the Banyan tree waste (BTW) biomass was carried out at three heating rates of 10, 25 and 50°Cmin^{-1}. Moreover applicability of Coats-Redfern method to reveal reaction mechanism are presented. The results thus presented will provide a better understanding of pyrolysis kinetics of Banyan tree waste.

II. Material Preparation

The waste biomass of Banyan tree, a national tree of India, was collected around the area densely populated with Banyan trees, from Kolkata province of India. The samples collected consist of leaves, straw and small branches. The samples were washed to remove any dirt or impurity followed by air drying in dry oven for 8 hours. The dried samples were mixed after being ground in a rotary mill and then screened to a particle size of 0.5mm or less. The prepared biomass sample was stored in desiccator for analysis.

III. Kinetic Theory

Pyrolysis, a solid state decomposition reaction of biomass under inert atmosphere leads to formation of char residue, gases and volatiles. In the present study of degradation reactions of biomass two well known models of Kissinger-Akahira-Sunrose (KAS) and Ozawa-Flynn-Wall (OFW) are used to evaluate kinetic and thermodynamic parameters and in turn the reaction mechanism. The results of thermo gravimetric experiments are expressed as mass change in biomass sample, given as:

$$\alpha = \frac{m_i - m}{m_i - m_f} \qquad (1)$$

where m_i, m and m_f are the initial, instantaneous and final mass of the biomass sample. On the other hand, the rate of conversion is given as:

$$d\alpha/dt = k(T)f(\alpha) = A_0 \exp(-E/RT)f(\alpha) \qquad (2)$$

where k(T) is the rate constant described by Arrhenius Law as, $k(T) = A_0 \exp(-E/RT)$. $f(\alpha)$ is the reaction model, A_0 the pre-exponential Arrhenius factor (s^{-1}), E the activation energy ($kJmol^{-1}$) corresponding to reaction temperature T (K) and R the universal gas constant ($kJmol^{-1}K^{-1}$). After using the value of k(T) in Eq. (2) with initial conditions of $\alpha=0$ at $T=T_o$ and taking E/RT as 'χ' gives:

$$F(\alpha) = \int_0^{\alpha} \frac{d\alpha}{f(\alpha)} = \int_{T_o}^{T} \frac{A_0}{\beta} e^{-E/RT} dT = \frac{A_0 E}{\beta R} m(\chi) \qquad (3)$$

The above function has no exact solution and is solved by using various approximations leading to generation of different isoconversional methods including Kissinger-Akahira-Sunrose (KAS) and Ozawa-Flynn-Wall (OFW) methods. The two models are based on the following two equations [8-11].

$$\text{KAS method} : \ln(\beta/T^2) = \ln[A_0 R/Ef(\alpha)] - E/RT \qquad (4)$$

$$\text{OFW method} : \ln(\beta) = \ln[A_0 E/Rf(\alpha)] - 5.331 - E/RT \qquad (5)$$

For constant α, activation energy can be obtained through the slope of the straight line by plotting the L.H.S of Eq. (4) and Eq. (5) vs. 1/T. Coats-Redfern method involves thermal degradation mechanism. Rearrangement of Eq. (3) using Doyle approximation [9, 12] yields

$$\ln\frac{F(\alpha)}{T^2} = \ln\frac{A_0 R}{\beta E} - \frac{E}{RT} \qquad (6)$$

The above equation is used to calculate activation energy E, and pre-exponential factor A_0, in terms of algebraic expressions replacing F(α) representing different kinetic mechanisms as given in Table 4.

The thermodynamic parameter of activation Gibbs free energy (ΔG) is calculated using following equation, given elsewhere[12].

$$\Delta G = E + RT_h \ln(K_b T_h / hA_0) \qquad (7)$$

IV. Results and Discussion

A. Physico-chemical characterization

The proximate analysis and Energy dispersive X-ray spectroscopy (EDS) was conducted giving results as listed in Table 1.

As shown in Fig. 1, the FTIR spectrum of the BTW shows a very strong and board absorption band at 3300-3600 cm^{-1}, which is ascribable to H-bonded O-H groups of cellulose[13]. Besides, the band at 2929 cm^{-1} is corresponded to C-H stretching within the methylene of cellulose. The band in the high energy zone (3000-3500 cm^{-1}) is attributed to the existence of free and intermolecular bonded hydroxyl groups, related to a large amount of OH groups from carbohydrates and those of lignin, as well as to the symmetric and asymmetric stretching vibrations associated with H_2O molecules. The absorption peak at 1241 cm^{-1} can be associated with the alkyl ester of acetyl group in hemicellulose structure and/or the linkage between hemicellulose and lignin. The C=O groups in alkyl groups of lignin side chains are suggested to conjugate with the aromatic structure and result in absorption peak at 1623 cm^{-1}.

Table 1: Proximate and Ultimate analysis of Banyan tree waste.

Proximate analysis of Banyan tree biomass			
Moisture	Volatile matter	Ash content	Fixed Carbon**
8.15	70.23	1.3	20.10
Ultimate analysis of Banyan tree biomass using EDS			
Element	Weight %	Atom %	
C	36.14	40.79	
N	59.13	57.24	
Al	1.19	0.60	
Si	1.24	0.60	
Ca	2.3	0.78	

The bands at 2843, 1623, and 1418 have been attributed to absorption due to C-H deformation within the methoxyl groups of lignin. The characteristic peaks of lignin were observed at 1241 cm^{-1} (C-O ring). Another intense band around 1000 cm^{-1} corresponds to the link C-O-H or C-O-R (alcohols or ethers), while the distinctive band at 2929 cm^{-1} is related to the presence of C-H stretching vibration together with bending vibrations around 1400 cm^{-1} of aliphatic chains (-CH_2 and –CH_3) forming the basic structure of these lingo-cellulosic materials. Finally, the band around 1600 cm^{-1} can be assigned to aliphatic or unsaturated aromatic compounds[13-14].

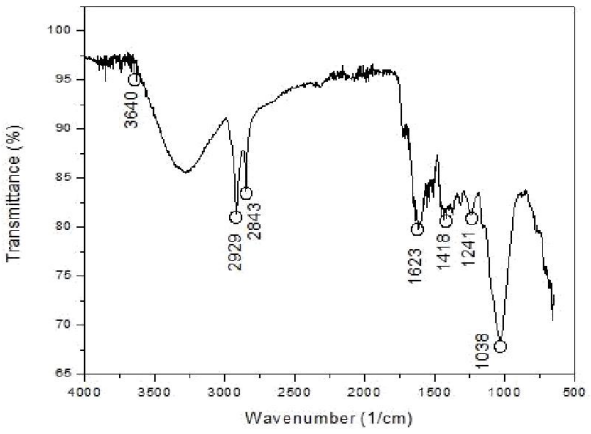


Figure 1: FTIR analysis of Banyan tree waste

B. Thermal Degradation

The curves of pyrolysis of TG (the mass loss) and DTG (the rate of mass loss) of Banyan tree waste (BTW) at heating rates of 10, 25 and 50°$Cmin^{-1}$ under nitrogen atmosphere is shown in Fig. 2. The curves indicate that the decomposition of BTW included three stages, an initial stage, the pyrolytic stage and stage of char decomposition. The first stage corresponds to moisture vaporization and lasts till 300°C. The second stage is sudden mass loss stage and occurs between 350--500°C and corresponds to loss of volatile matter (Mass loss of around 70%). It is found that the maximum mass loss happens in this stage only for all heating rates studied. This stage is followed by char pyrolysis stage at temperatures of above 500°C. The behavior of TG and DTG curves is similar to other cellulose based biomass wastes already studied[8-10]. As heat transfer flux change between surroundings and the samples with shorter exposure time at a particular temperature will be short at higher heating rate, the DTG curves show a shift towards higher temperature range with increasing heating rate without much change in trends of decomposition curves. With an increasing heating rate , the maximum rate of mass loss also increased from 10 to 65% min^{-1}. The results are in complete agreement with some past studies[11].

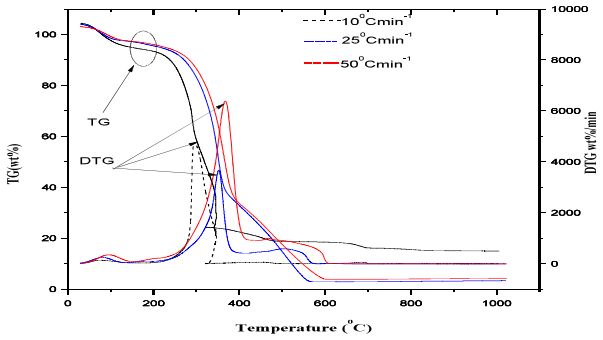


Figure 2: TG/DTG curves of pyrolysis of Banyan tree biomass at different heating rates

C. Kinetic and thermodynamic studies

The comparative studies of activation energies has been carried out at three heating rates using KAS and OFW method. Using Eqs. 4 and 5, activation energies were calculating using KAS and OFW models respectively

Table 2: Conversion points and the corresponding function values using KAS method.

Conversion (α)	E ($kJmol^{-1}$)	R^2	lnA_0	ΔG ($kJmol^{-1}$)
0.2	70.27	0.957	9.36	175.84
0.3	68.35	0.936	9.29	175.92
0.4	63.51	0.914	8.66	176.22
0.5	84.77	0.956	13.46	174.95
0.6	121.21	0.990	21.00	173.33
0.7	55.59	0.842	7.67	176.72
0.8	45.85	0.961	5.81	177.43
Average	73.03	-	-	175.77

Table 3: Conversion points and the corresponding function values using OFW method.

Conversion (α)	E ($kJmol^{-1}$)	R^2	lnA_0	ΔG ($kJmol^{-1}$)
0.2	75.66	0.976	11.18	176.21
0.3	74.45	0.883	11.24	176.35
0.4	70.01	0.992	10.78	176.71
0.5	90.61	0.965	15.09	175.28
0.6	125.76	0.934	22.02	173.51
0.7	63.33	0.950	10.21	177.36
0.8	54.88	0.967	8.86	178.32
Average	79.24	-	-	176.25

The plot between $\ln\beta/T^2$ vs. 1/T (using KAS model) and $\ln\beta$ vs. 1/T were plotted to calculate the slope and in turn the values of activation energy E. Fig. 3 shows one of the plots using OFW model. The values of activation energies calculated at progressive conversion rates using KAS and OFW model are presented in Table 2 and 3 respectively. However the mean value of activation energies calculated using KAS and OFW method are 73.032 and 79.742 kJmol^{-1} respectively. The lower activation energy values correspond to higher reaction rate. The activation energies show a rapid increase after α=0.4 (both in KAS and OFW model), indicating the initiation of main pyrolysis process. Results reveal that activation energy is highly dependent on conversion and reiterates the fact that pyrolysis of biomass is a complex process. It can also be seen that best fitting lines at conversion (α) between 0.2 to 0.8 are nearly of same nature indicating that reaction mechanism is almost same for all conversions. The results conclude that pyrolysis of BTW follows a multistep complex reaction mechanism depicted by the progressive change in activation energy with conversion.
While comparing the values of activation energy E, with that of enthalpies (ΔH) of activation, a mere difference of around 5 kJmol^{-1} was found for each conversion point. This shows that activated complex is formed with low potential energy barrier. Gibbs free energy (ΔG) of activation of BTW was calculated to fall in the range of ~176.24kJ mol^{-1} , little higher than camel grass [12], rice bran and rice straw [15]. The values are indicative of BTW as potential feedstock for bio energy.

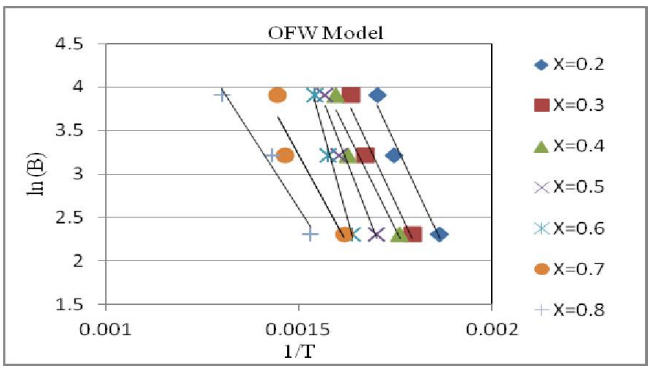


Figure 3: Linear fit plots of ln(β) against 1/T for OFW model.

The Coats-Redfern method is one of the frequently used approach to determine the appreciate reaction mechanism. The values of activation energy (E), correlation coefficient (R^2) and pre-exponential factor A_0 ($\ln A_0$) are also present in Table-4 against the algebraic expression used for different mechanisms predicted for heating rate of 25°Cmin^{-1}. The comparison of apparent values of activation energies obtained against each method shows that E value corresponding to thermal degradation via D5 and F3 mechanism are almost in line with the values obtained by KAS and OFW models. The findings reveal that the thermal degradation of BTW is based on diffusion and chemical reaction involving both endothermic and exothermic reactions.

Table 4: Algebraic expression for F(α) for different solid state reaction mechanism and corresponding kinetic variables at heating rate of 25°Cmin^{-1}.

Mechanism	Integral form F(α)	R^2	E (kJmol^{-1})	A_0 (s^{-1})
Power Law (P3/2)	$\alpha^{3/2}$	0.79	11.933	596.36
Power Law (P1/2)	$\alpha^{1/2}$	0.74	-3.382	-0.013
Diffusion Law(D2)	$(1-\alpha)\ln(1-\alpha)+\alpha$	0.85	26.886	17161.44
Diffusion Law (D5)	$[(1-\alpha)^{1/3}-1]^2$	0.85	60.388	10290845.11
Contracting sphere (R2)	$1-(1-\alpha)^{1/2}$	0.72	10.469	-8645.56
Contracting cylinder (R3)	$1-(1-\alpha)^{1/3}$	0.75	12.911	56.846
Chemical Reaction (F3/2)	$(1-\alpha)^{1/2}-1$	0.80	28.113	1458.91
Chemical Reaction (F3)	$[1/(1-\alpha)^2-1]^2$	0.82	66.807	10473358.52

D. Kinetic compensation effects

The activation energy and pre-exponential factors on conversion degree is proved to follow the relationship [16] as: $\ln A_0 = aE + b$. where a and b are constants called compensation coefficients.

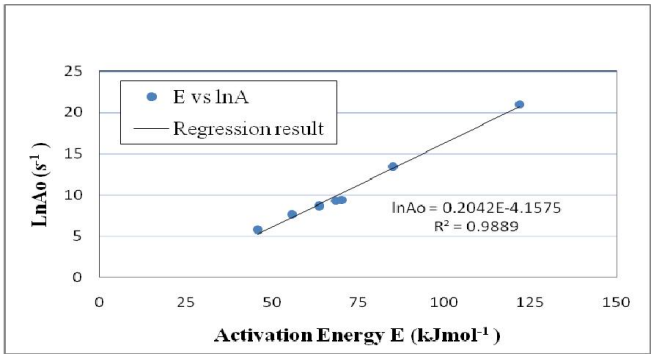


Figure 4: Plot of $\ln A_0$ against E of BTW thermal degradation.

The compensation effect can be observed for different types of reaction models. However OFW model being more credited was used in this study. Plotting $\ln A_0$ against E from OFW model gives an excellent linear relationship with R^2=0.9889, shown in Fig. 4. The linear equation representing the data can be expressed as $\ln A_0$=-4.1575+0.2042E, signifying the intense interaction between various kinetic parameters.

V. Conclusion

This work presents an experimental kinetic study of pyrolysis of Banyan tree waste (BTW), using thermo gravimetric analysis at three different heating rates of 10, 25 and 50°Cmin^{-1}. The kinetic and thermodynamic parameters were evaluated using iso-conversional models of Kissenger-

Akahira-Sunrose (KAS) and Ozawa-Flynn-Wall (OFW) models and the mean activation energies of pyrolysis of Banyan tree waste was calculated to be falling in the range of 73.032 kJ mol^{-1} and 79.742 kJ mol^{-1} respectively. With an increase in heating rate, the maximum rate of mass loss experiences a shift towards higher temperatures. The pyrolysis of Banyan tree most probably follows D5 and F3 mechanism based on diffusion and chemical reaction. The outcome from this study has proved BTW as a low cost renewable source for bio energy.

REFERENCES

[1] J.C. Liao, L. Mi, S. Pontrelli and S. Luo, "Fuelling the future: microbial engineering for the production of sustainable biofuels," Nat. Rev. Microbiol, 14, 288–304, 2016.

[2] S. A. Edrisi and P. Abhilash,"Exploring marginal and degraded lands for biomass and bioenergy production: an Indian scenario," Renewable & Sustainable Energy Review 54, 1537–1551, 2016.

[3] A. V. Bridgwater,"Renewable fuels and chemicals by thermal processing of biomass,"Chemical Engineering Journal, 91, 87-102, 2012.

[4] P. Buryan and M. Staff,"Pyrolysis of waste biomass," Journal of thermal analysis and Calorimetry, 93, 637-640, 2008.

[5] R. M. Braga, D. M. Melo, F. M. Aquino, J. C. Freitas, M. A. Melo, J. M. Barros and M. S. Fontes," Characterization and comparative study of pyrolysis kinetics of the rice husk and the elephant grass," Journal of thermal analysis and Calorimetry, 115, 1915–1920, 2014.

[6] C. Ryu, Y. B. Yang, A. Khor, N. E. Yates, V. N. Sharifi and J. Swithenbank,"Effect of fuel properties on biomass combustion: part I. Experiments-fuel type, equivalence ratio and particle size," Fuel, 85, 1039-1046, 2006.

[7] E. Butler, G. Devlin, D, Meier and K. McDonnell, "Fluidised bed pyrolysis of lignocellulosic biomasses and comparison of bio-oil and micropyrolyser pyrolysate by GC/MS-FID," Journal of Analytical and applied pyrolysis, 103, 96-101, 2013.

[8] S. A. El-Sayed and M. E. Mostafa,"Kinetic parameters determination of Biomass pyrolysis fuels using TGA and DTA techniques," Waste Biomass Valorization, 6, 401-415, 2015.

[9] S. Ceylan and Y. Topcu,"Pyrolysis kinetics of hazelnut husk using thermo gravimetric analysis," Bioresource Technology, 156, 182-188, 2014.

[10] G. Ningbo, L. Baoling, L. Aimin and L. Juanjuan," Continuous pyroysis of pine saw dust at different pyrolysis temperatures and solid residence times," Journal of Analytical and applied pyrolysis, 114, 155-162, 2015.

[11] T. Wongsisriamnua and N. Tippayawong,"Non-isothermal pyrolysis characteristics of giant sensitive plants using thermogravimetric analysis," Bioresource Technology, 101, 5638-5644, 2010.

[12] M. A.. Mehmood, G. Ye,H. Luo, C. Liu, S. Malik, I. Afzal, J. Xu and M. S. Ahmad,"Pyrolysis and kinetic analyses of Camel grass (Cymbopogon schoenanthus) for bio energy," Bioresource Technology, 228, 18-24 ,2017.

[13] M. Grube, J. Lin, P. Lee and S. Kokorevicha," Evaluation of sewage sludge-based compost by FTIR spectroscopy," Geoderma,130, 324–33, 2006.

[14] X. Huang, J. Cao, X. Zhao, J. Wang, X. Fan, Y. Zhao and X. Wei,"Pyrolysis kinetics of soya bean straw using thermodynamic analysis," Fuel, 169,93-98, 2016.

[15] Y. S. Kim, Y. S. Kim and H. S. Kim,"Investigation of thermodynamic parameters in the thermal decomposition of plastic waste-waste lubes oil compounds," Environmental. Science and Technology, 44(13), 5313-5317, 2010.

[16] P. Budrugcac, D. Homentcovschi and E. Segal,"Critical considerations on the iso conversional methods III on the evaluation of the activation energy from non-isothermal data," Journal of Thermal Analysis and Calorimetry, 66, 557-565, 2001.

Performance Prediction of a Diesel Engine Fueled with Diesel-Biodiesel-Bioethanol Blends using ANN

B. SAYIN KUL[1], M. CİNİVİZ[2], A. KAHRAMAN[3], İ. ÖRS[4]

[1,2] Selcuk University, Konya/Turkey, bsayin@selcuk.edu.tr, mciniviz@selcuk.edu.tr
[3]Necmettin Erbakan University, Konya/Turkey, akahraman@konya.edu.tr
[4]Aksaray University, Konya/Turkey, iors@aksaray.edu.tr

Abstract **- This study is based on estimating the brake torque, brake power, brake specific fuel consumption (bsfc) and thermal efficiency of a diesel engine using diesel-biodiesel-ethanol blends. The test, training and validation data were collected using a single-cylinder, four-stroke, water-cooled direct-injection diesel engine operated with five different test fuels at twelve different engine speeds under full load conditions. Performance of the ANN model developed using the LM-Levenberg Marquardt standard backpropagation algorithm was measured by comparing experimental and estimated outputs. The most successful networks that use different hidden layer numbers for four output parameters determined to have 12, 6, 19 and 4 hidden layers. It was also found to be within acceptable levels with the coefficient of correlation of 0.98541, 0.99855, 0.97915, 0.96428 for brake torque, brake power, bsfc and thermal efficiency respectively.**

Keywords **- ANN, Engine Performance Diesel, Biodiesel, Bioethanol**

I. INTRODUCTION

High energy costs combined with growing energy demand in parallel with high living standards make saving energy increasingly important for the world. Fossil fuels, which have the largest share of the energy demand growth, are not considered sufficient to meet the energy needs due to being in danger of depletion soon. Besides, serious environmental problems such as air pollution, greenhouse gases, and the climate change caused by fossil fuels are also globalized energy issues that have turned peoples' attention to less costly, eco-friendly, renewable and alternative energy sources.

Diesel engines are widely used in many areas due to their high thermal efficiency, low carbon monoxide and hydrocarbon emissions. But high particulate matter and nitrogen oxide emissions limit the use of diesel engines. Alternative fuels such as biodiesel with properties like being renewable, non-toxic, sulphur-free, bio-based, oxygenated, diesel fuel substitute is concerned to reduce energy costs, achieve low fuel consumption and high-power output as well as to reduce these emissions [1]. When it is desired to dispose of properties such as high viscosity and high cold filter clogging point etc. resulting from the use of biodiesel, bioethanol is also added to form the ternary blend. Studies carried out by [2-4] are just a few of the studies where ternary blends are used as fuel for diesel engines.

ANNs are a logic programming technique developed to perform skills such as learning, remembering, making decision and deducing which are characteristics of the human brain without any help [5]. In recent years, ANN have been used in different applications in the fields of cutting mechanics, cutting mechanics, signal processing, data decomposition and image processing etc. by many researchers to solve various problems [6]. Engine performance test is another field to be wondering whether ANN is suitable or not for it. Considering that there are many engine input, output parameters related to engine testing, which causes the system to be affected by each of them simultaneously, it is quite expensive and time-consuming. For this reason, ANN applications simulating the real situation have begun to be evaluated as cheaper alternative to the engine performance tests for a while.

The studies oriented predicting engine performance are presented below. Sharon et al. [7] have developed an ANN model to predict performance and emissions of a diesel engine using biodiesel-diesel blends. Deh Kiani et al. [8] have performed a study on the subject of the ANN model of a spark-ignition engine operation with ethanol-gasoline blends at different engine speeds and loads. Ghobadian et al. [9] have studied about ANN modelling, based on standard back-propagation algorithm, of a diesel engine fuelled with waste cooking biodiesel. Najafi et al. [10] have aimed to analyse how successful ANN is on prediction of performance and emissions of a SI engine using ethanol–gasoline blends. Sánchez-Borroto et al. [11] have performed a study proving that ANN can also be used for predicting cetane number and ignition delay of biodiesel. As it is understood, these studies have one thing in common that ANN is within acceptable limits for prediction when assessed in terms of various errors

In this study, the performance parameters which are brake torque, brake power, brake specific fuel consumption and thermal efficiency for a diesel engine fuelled with diesel-ethanol-biodiesel blends were investigated. An ANN model based on LM-Levenberg Marquardt standard backpropagation algorithm using the fuel type and engine speed as engine input parameters has been developed to estimate the output parameters. In order to evaluate the accuracy of the estimation,

mean square error (MSE) and coefficient correlation (R) were calculated.

II. MATERIAL AND METHODS

A. Engine performance

Experimental setup which consists of a diesel engine connected with a hydraulic dynamometer, emissions measurement equipment, radiator, temperature measurement devices, flow meters and control panel is shown in Figure 1. The engine in which the experiments are carried out is a single cylinder, four-stroke, water cooled, direct-injection Antor 3LD510 diesel engine. Technical specifications of the engine are given in Table 1.

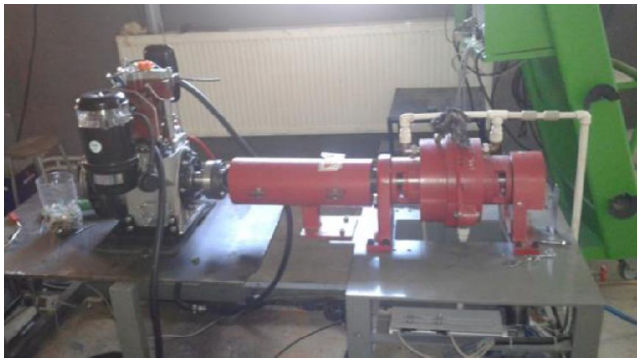


Figure 1. Experimental setup

Table 1. Technical specification of test engine

Brand	Antor 3LD510
Engine Type	Four-stroke, Direct injection
Number of Cylinders	1
Cylinder volume	510 cc
Bore X Stroke, mm X mm	85 X 90
Cooling system	Water cooled
Compression Ratio	17.5:1
Maximum Engine Speed	3300 rpm
Maximum Engine Power	9 kW
Maximum Engine Torque	32.8 Nm
Specific Fuel Consumption	190 gr/HP h

The speed range of the hydraulic dynamometer is 0–6500 rev/min and its torque range is 0–450 Nm. A flanged, sharp corner-type orifice plate was placed on the intake manifold line to measure air consumption. The engine speed was controlled by a speed sensor. A fuel measurement unit consisting of a 2.5-liter tank and a load cell capable of measuring 0–3 kg was used for the determination of the fuel consumption. Tests were started after the engine reached its operating temperature. The diesel engine was first fueled with D100 (pure diesel fuel) and then with D92B3E5 (92% diesel, 3% biodiesel and 5% bioethanol), D85B10E5 (85% diesel, 10% biodiesel and 5% bioethanol), D80B15E5 (80% diesel, 15% biodiesel and 5% bioethanol) and D75B20E5 (75% diesel, 20% biodiesel and 5% bioethanol) respectively at twelve different engine speeds between 1000 rev/min and 3000 rev/min under full load condition. The chemical properties of diesel, biodiesel and bioethanol used to form these blends are presented in Table 2.

Table 2. Chemical properties of tested fuel

Fuel property	Bioethanol	Diesel	Biodiesel
Chemical formula	C_2H_5OH	$C_{12.226}H_{23.29}$	$C_{19}H_{35.64}O_2$
Density (kg/m^3) at 15°C	794	834.5	885.6
Kinematic viscosity (mm^2/s) at 40 °C	1.1	2.794	4.353
Content of fatty acid methyl ester (% (m/m))	-	-	97.24
Lower heating value (MJ/kg)	28.4	43.14	38.59
Cetane number	-	55.2	55.7
Flash point (°C)	-	68.5	156.5
CFPP (°C)	-	-14	-8
Cloud point (°C)	-	-12	-4

B. ANN Modeling

Generally, artificial neural networks provide the advantage of being fast, accurate, and reliable when estimating and converging, especially when numerical and mathematical methods fail due to lengthy iterative calculations [8]. Engine tests are very time consuming and costly, and are one of the applications that require the use of ANN. For this purpose, network structure was constructed using Neural Network Toolbox of Matlab software to simulate engine tests. Figure 2 shows the neural network structure for this study. The network consists of three layers of neurons, which are input, hidden and output layer. In this network structure, each neuron in a layer is connected to all the neurons of the successive layer, not the neuron in the same layer. Each input has a w_n specific weight represents the values of the connections between the cells.

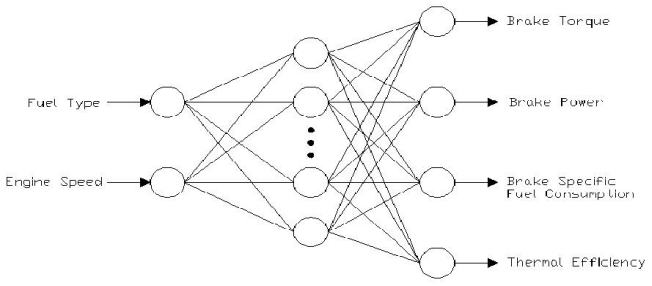


Figure 2. Neural network structure.

Engine speed and fuel type have designated as input and brake torque, brake power, brake specific fuel consumption and thermal efficiency have designated as output. Optimum network structure were tried to be found by varying the number of neurons in the hidden layer from 1 to 30. The

learning algorithm that constitutes the most important structure of the network is concerned with how successful ANN network is to be able to make the closest predictions to the experimental data. The learning algorithm used is Levenberge Marquardt (LM) learning algorithm. The transfer /activation function that correlates input and output layers with each other also affects the performance of the network [5]. Although there are many transfer functions such as linear transfer function, inverse transfer function., competitive transfer function, elliot sigmoid transfer function, positive hard limit transfer function etc., logistic sigmoid (log-sig) transfer function which is commonly used in the hidden layers of multi-layer networks is preferred for this study. [12]

Determining the percentage of training, validation and testing data is another important step in terms of constructing of the network structure. Therefore, 60 engine test were carried out, 70%, 15% and 15% of these were chosed randomly for training, validation and testing respectively with reference to studies in the literature. Since the codomain of logistic-sigmoid transfer function is limited to 0 to 1, input and output values that are not in this range are linearly scaled to be in this interval. For this purpose, engine speed, brake torque and brake power values divided by 4000, 40 and 10 respectively as it is encountered in different studies (Çay vd., 2013). The fuel samples were symbolized by the percentage of diesel in the fuel contents e.g. 0.92 for D92B3E5 in order to quantify the fuel type used as inputs in ANN.

ANN works in such a way as to minimize the error between the experimental and estimated outputs. In this study, mean square error (MSE) and coefficient of correlation (R) given below has been selected to determine the accuracy of the network.

$$\mathrm{MSE} = \frac{1}{n}\sum_{i=1}^{n}(o_i - t_i)^2 \tag{1}$$

$$\mathrm{R} = \frac{\sum (o_i - \bar{o})(ti - \bar{t})}{\sqrt{\sum (o_i - \bar{o})^2 (ti - \bar{t})^2}} \tag{2}$$

where o_i is the output value, t_i is the target value, upper-case letters represent averages and n is the number of samples.

III. Result and Discussion

Use the Microsoft Equation Editor for equations in your paper (Insert | Object | Create New | Microsoft Equation). "Float over text" should *not* be selected.

A. Experimental Results

Performance parameters such as brake torque, brake power, brake specific fuel consumption and thermal efficiency of a diesel engine running at twelve different engine speeds between 1000 rev/min and 3000 rev/min have been investigated for the cases where it is fueled with D100, D92B3E5, D85B10E5, D80B15E5 and D75B20E5. The variation of these parameters is given in Figure 3. As it is shown, the engine speed at which the maximum torque is obtained is 1400 rpm and these are 35.36, 32.03, 31.43, 31.19, 30.30 Nm for D100, D92B3E5, D85B10E5, D80B15E5 and D75B20E5 respectively. At all engine speeds, while D100 is the fuel with the highest torque, as the biodiesel content in fuel increases, the torque values decrease. The reasons for that is lower heating value of ethanol and especially biodiesel. The brake power increases until it reaches a certain peak point, which is obtained at 2800 rpm, then it starts to decrease because the decrease in torque can not compensate for the increase in speed. This situation also applies to all test fuels. Brake power is lower than that of diesel engine when ternary blends are used as fuel and the lowest power is obtained if the engine is operated with D75B20E5. This can be explained by the reduction in the amount of fuel contained in the cylinder with increasing oxygen content in fuel blends. Although brake specific fuel consumption takes high values at both high and low engine speed, it has a minimum around 1400 rpm which is maximum torque-speed. The lowest bsfc is achieved when the engine is running with diesel fuel because of the low calorific value of both ethanol and biodiesel. This would lead to an increase in the amount of fuel sent to the cylinder to attain the same power if the ternary blends are used. The average brake specific fuel consumption is more than approximately 11%, 15%, 17% and 21% for D92B3E5, D85B10E5, D80B15E5 and D75B20E5 compared to diesel.

Similarly, the lower calorific value of diesel is %12 and 52% higher than that of biodiesel and bioethanol results in a decrease in thermal efficiency in the case of fueling the engine with ternary blends.

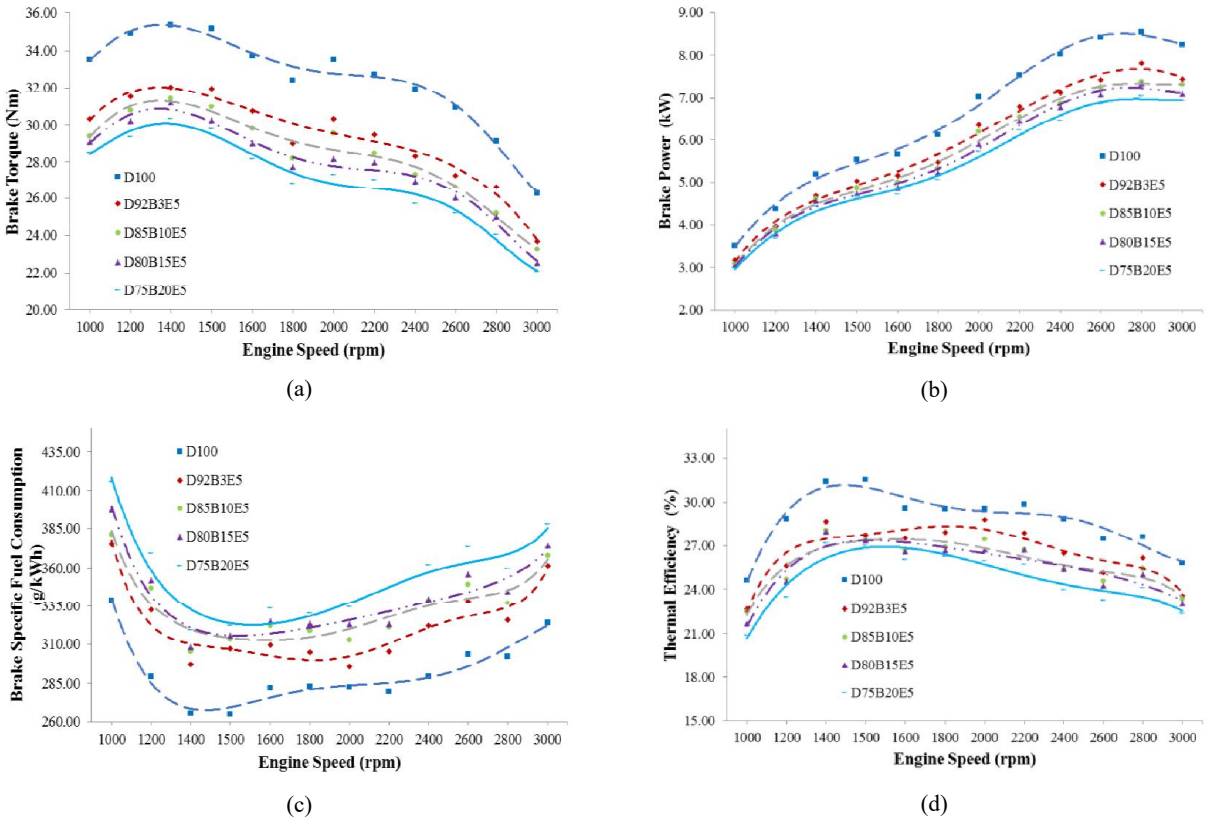


Figure 3. Variation of engine performance parameters with engine speed

B. ANN Prediction

Engine performance parameters have been estimated by using an ANN model based on LM-Levenberg Marquardt standard backpropagation algorithm. The hidden layer number has been continuously changed from 1 to 30 to find the best artificial neural network structure. Mean square error (MSE) and coefficient correlation (R) used as comparison criteria. Hidden layer numbers that give the lowest MSE and highest R values for testing data are listed in the table below. The correlation coefficient R for each parameter confirm that there is a strong positive correlation between experimental and estimated outputs. This indicates that the network structure established is suitable for estimating engine performance parameters. Figure 4 shows the correlation of experimental and prediction results for all output parameters. As it is seen, there is not too many discrepancies in the data points on the figure. But it is believed that the scaling of the input and output parameters by dividing in a linear manner increases the differences between the data points. Therefore, it may be more appropriate to use different statistical normalization methods than scaling.

Table 3. Statistical results of the network

Output	Network Structure	Training data		Testing Data	
		MSE	R	MSE	R
Brake Torque	2-12-1	0.00012	0.98720	0.00039	0.98541
Brake Power	2-06-1	0.00007	0.99835	0.00007	0.99855
Bsfc	2-19-1	0.00040	0.95157	0.00034	0.97915
Thermal Efficiency	2-04-1	0.00003	0.96741	0.00004	0.96428

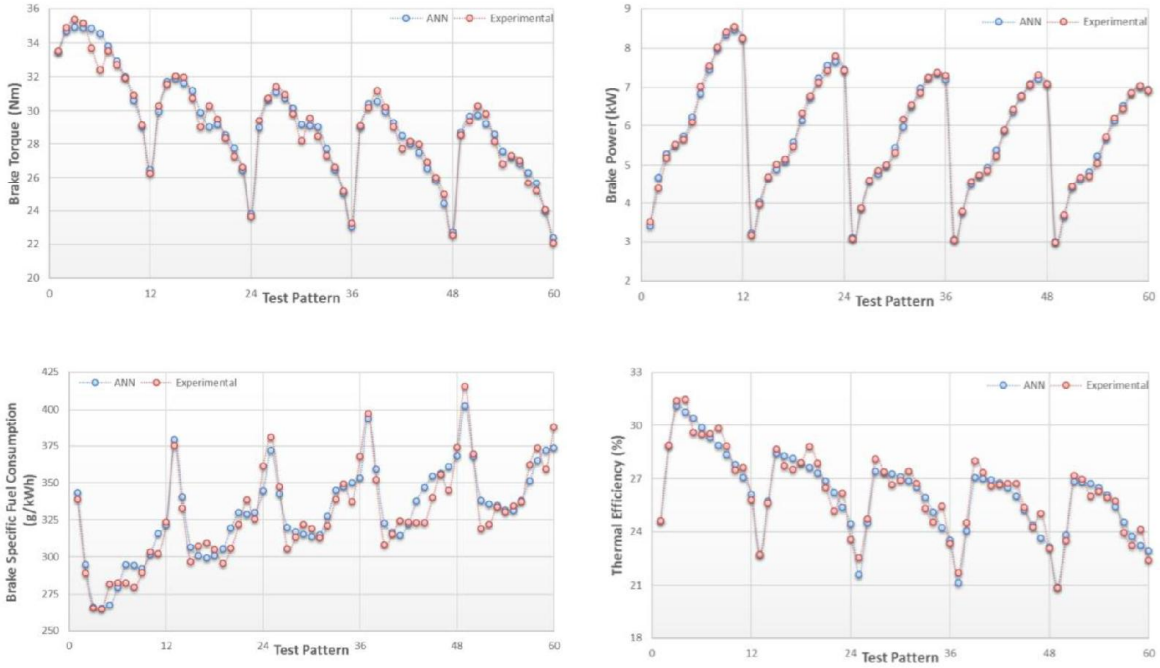


Figure 4. Matching of the experimental and estimated outputs

IV. CONCLUSION

The present study shows that addition of biodiesel to diesel-bioethanol blends reduces brake torque, brake power and thermal efficiency and increases brake specific fuel consumption. The performance of the ANN model estimating these parameters using LM-Levenberg Marquardt standard backpropagation algorithm is quite sufficient. R values representing the correlation between the experimental and estimated outputs are close to 1 and MSE is acceptable levels with its values less than 5%. It has been determined that the best agreement in terms of prediction is obtained for neural network model which has 12, 6, 19 and 4 neurons in hidden layer for brake torque, brake power, brake specific fuel consumption and thermal efficiency respectively. These confirm that ANN, reduces the experimental effort, can be used to estimate performance parameter of a diesel engine.

REFERENCES

[1] Murugesan, A., Umarani, C., Subramanian, R., and Nedunchezhian, N., "Bio-diesel as an alternative fuel for diesel engines—A review", Renewable and Sustainable Energy Reviews 13(3), pp. 653-662, 2009.

[2] Sayin Kul, B. and Kahraman, A., "Energy and Exergy Analyses of a Diesel Engine Fuelled with Biodiesel-Diesel Blends Containing 5% Bioethanol", Entropy 18(11), pp. 387, 2016.

[3] Alptekin, E., Canakci, M., Ozsezen, A.N., Turkcan, A., and Sanli, H., "Using waste animal fat based biodiesels–bioethanol–diesel fuel blends in a DI diesel engine", Fuel 157, pp. 245-254, 2015.

[4] Aydın, F. and Öğüt, H., "Effects of using ethanol-biodiesel-diesel fuel in single cylinder diesel engine to engine performance and emissions", Renewable Energy 103, pp. 688-694, 2017.

[5] Çay, Y., Korkmaz, I., Çiçek, A., and Kara, F., "Prediction of engine performance and exhaust emissions for gasoline and methanol using artificial neural network", Energy 50, pp. 177-186, 2013.

[6] Çay, Y., Çiçek, A., Kara, F., and Sağiroğlu, S., "Prediction of engine performance for an alternative fuel using artificial neural network", Applied Thermal Engineering 37, pp. 217-225, 2012.

[7] Sharon, H., Jayaprakash, R., Karthigai selvan, M., Soban kumar, D.R., Sundaresan, A., and Karuppasamy, K., "Biodiesel production and prediction of engine performance using SIMULINK model of trained neural network", Fuel 99, pp. 197-203, 2012.

[8] Deh Kiani, M.K., Ghobadian, B., Tavakoli, T., Nikbakht, A.M., and Najafi, G., "Application of artificial neural networks for the prediction of performance and exhaust emissions in SI engine using ethanol- gasoline blends", Energy 35(1), pp. 65-69, 2010.

[9] Ghobadian, B., Rahimi, H., Nikbakht, A.M., Najafi, G., and Yusaf, T.F., "Diesel engine performance and exhaust emission analysis using waste cooking biodiesel fuel with an artificial neural network", Renewable Energy 34(4), pp. 976-982, 2009.

[10] Najafi, G., Ghobadian, B., Tavakoli, T., Buttsworth, D.R., Yusaf, T.F., and Faizollahnejad, M., "Performance and exhaust emissions of a gasoline engine with ethanol blended gasoline fuels using artificial neural network", Applied Energy 86(5), pp. 630-639, 2009.

[11] Sánchez-Borroto, Y., Piloto-Rodriguez, R., Errasti, M., Sierens, R., and Verhelst, S., "Prediction of Cetane Number and Ignition Delay of Biodiesel Using Artificial Neural Networks", Energy Procedia 57, pp. 877-885, 2014.

[12] Beale, M.H., T., H.M., and B., D.H., Neural Network Toolbox User's Guide. 2017.

EFFECT OF HYDROTHERMAL AGEING ON THE MECHANICAL PROPERTIES OF FRP COMPOSITE TUBES

M.KARA[1] and Y.AKIN[2]

[1]*Department of Mechanical Engineering, Faculty of Engineering, Mersin University, Mersin, Türkiye*
[2] *Department of Mechanical Engineering, Institute of Science and Technology, Necmettin Erbakan University, Konya, Türkiye*

Abstract **- In this study, the effects of aging on the mechanical properties of glass reinforced plastic (GRP) composite tubes exposed to hydrothermal aging in pure water environment were investigated. 6, 8 and 10 layered GRP composite tubes which had ±55° winding angle were manufactured with filament wound method. GRP composite pipes with different number of layers were exposed to hydrothermal aging in pure water at 80 ° C for 7, 14 and 21 days. Hoop tensile strength of non-aged and aged at different times 6, 8 and 10 layered GRP composite tubes were determined by hoop tensile strength tests according to ASTM D 2290. The effects of aging time and number of layers on the hoop tensile strength of CFRP specimens were investigated in detail. In addition, the damage progression in composite specimens and the effect of number of layers on damage development were investigated.**

Keywords **- Glass reinforced plastic, Hydrothermal aging, Hoop tensile strength**

I. INTRODUCTION

GLASS fiber reinforced plastic materials (GRP) are composite materials produced by the incorporation of glass fibers into the resin as reinforcing material. Glass fibers can be present in the composite material in continuous or discontinuous phase. In many engineering applications, GRP is preferred due to their superior properties such as high strength, ability to be produced in a desired size in series, resistance to corrosion against a large number of layers, high thermal resistance, possibilities of materials in different layer counts and different combinations.

Numerous studies have been carried out on the investigation of the mechanical properties of GRP tubes due to the rapid increase in the use areas of the tubes and the widespread use of the GRP tubes. Be'akou et al. [1] investigated theoretically the optimal winding angle for filament winding layer composites. They found that pressure, axial force and changes in some mechanical properties of the composite structure subjected to internal pressures significantly affected the optimum winding angle. Rousseau et al. [2] investigated the damage behaviors of filament winding tubes under various loads experimentally. They have characterized the effect of the filament winding patterns on the mechanical performance of composite tubes. Hawa et al. [3] investigated the impact behaviors and burst strength of glass fiber / epoxy composite tubes aged under hydrothermal conditions. They have made hydrothermal aging by holding 6 layered composite tubes in water for different periods with winding angle of ± 55 ° at 80 ° C. They have damaged the hydrothermal aged tubes by making low-speed impacts at different energy levels. They detected the loss of strength by bursting the damaged tubes with the static internal pressure explosion test according to ASTM D 1599 standard. They found that as the duration of hydrothermal aging increases, the loss of strength increases. Rafiee [4] wanted to develop an appropriate modeling procedure to determine the hoop tensile strength and the longitudinal tensile strength of CTP tubes containing sand as the main material. First of all, he analyzed the network analysis widely used in the GRP tubes sector and found that network analysis can' not predict hoop tensile and longitudinal pull strength. Then, he has developed sequential damage modeling. It is an advanced model that examines the formation of layer damage. The hot water environment and the corrosive effect of this environment considerably influence the mechanical properties of the filament winding tubes. This effect is first formed by the absorption of liquid. Layer separation (matrix-fiber separation) is observed in the composite structure due to the swelling that occurs as a result of liquid absorption. In addition, the water-soluble materials in the epoxy resin form microcracks. Over time, the dissolving substances in the resin are carried out by diffusion through the material. [5]

The hydrothermal aging study in glass fiber reinforced (GRP) composite tubes consists of 2 stages in scope. The first stage, a hydrothermal aging unit was prepared to keep specimens stable at 80 ° C in pure water environment. For the experiment, the previously prepared 6, 8 and 10 layered composite tubes were exposed to 80 ° C temperature in pure water for 1, 2 and 3 and 4 weeks. In the other stage, hoop tensile strength of non-aged and aged at different times 6, 8 and 10 layered GRP composite tubes were determined by hoop tensile strength tests according to ASTM D 2290. The graphs of the test results were evaluated by drawing. The effect of hydrothermal aging and number of layers on glass fiber reinforced composite materials was investigated considering different aging times.

II. MATERIAL AND METHOD

E-glass / epoxy filament winding composite tubes were produced by İzoreel (İzmir, Turkey) in 6, 8 and 10 layers at ± 55 ° winding angles. Vetrotex 1200 single-sided E-glass with a diameter of 17 μm was used as glass fiber, and Ciba Geigy,

Bisphonele, Epoxy CY 225 was used as matrix material. No defect has been detected in the specimens size and visual inspection performed after production.

Table 1 gives the mechanical properties of fiber and matrix used in the production of composite materials. [6]

Table 1: This caption is centered.

	E (GPa)	$\sigma_{çek}$ (MPa)	ρ (g/cm3)	ε_{kop} (%)
Elyaf: E-camı	73	2400	2.6	1,5-2
Matris: Epoksi Reçine	3,4	50-60	1,2	4-5

The hydrothermal aging process and the hoop tensile strength tests were performed with 12 of the produced tubes, 4 of 6 layers, 4 of 8 layers and 4 of 10 layers. For hydrothermal aging process, 64 liters capacity glass container was made from heat resistant 7mm thick tempered glass with dimensions of 40x40x40 cm. To keep the test set at 80 ° C, a digital controller with two resistances of 300 kW, a liquid probe with high precision temperature control for the control system and a 2.2 W circulation pump for uniform temperature distribution was used. The system is shown schematically in Figure 1.

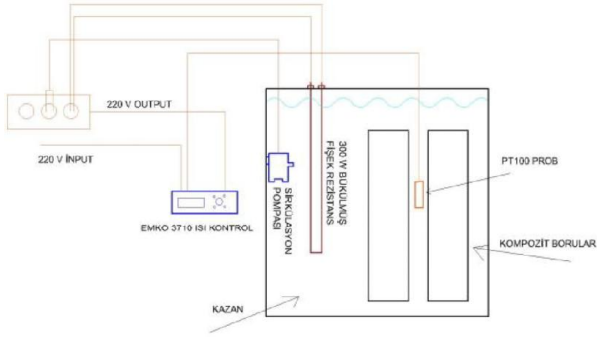


Figure 1: Schematic representation of the hydrothermal aging unit

A. Hoop Tensile Strength Test

Hoop tensile strength tests were conducted according to ASTM D 2290 Procedure A [7]. The test method given in this standard includes studies to determine the comparative tensile strength under certain preconditions, such as temperature, humidity and test speed, using a split disc or loop of many plastic products. The procedure is used for reinforced thermoset resin tubes.

Hoop specimens were prepared according to the measurements given in Figure-2 from 6, 8 and 10 layered GRP composite pipes. Specimens prepared by cutting according to the standard have an inner diameter of 72 mm and a length of 30 mm. According to Procedure A, the specimens were cut at 4.5 mm radius on the specimens to reduce the cross-sectional area so that the specimens could be cut off at the desired cross-section and accurate tangential stresses could be obtained at the end of the test. As each specimen varies in wall thickness, the thickness of the specimens is precisely measured and recorded.

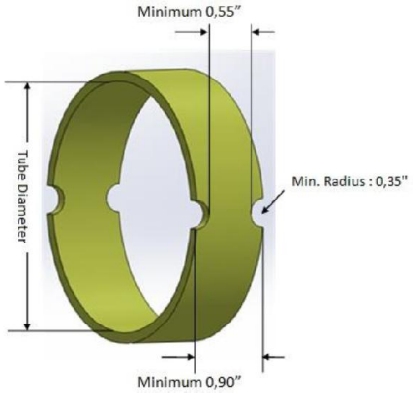
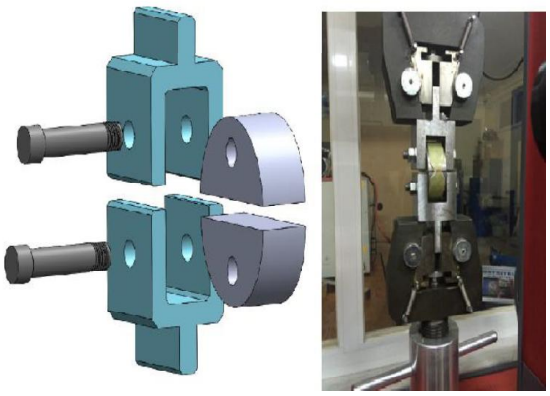


Figure 2: Hoop tensile specimen prepared according to the standards

According to the procedure, hoop tensile strength test was carried out with 15 specimens of 6, 8 and 10 layers, 3 non-aged control groups and 3 aged (1 week, 2 weeks, 3 weeks, 4 weeks) aging. Temperature; standard laboratory atmospheric temperature 23 ° C ± 2 ° C, humidity; 50 ± 5%. The test speed is at least 0.1 inch / min. Figure 3 shows the hoop tensile strength test.

The hoop tensile device used in the experiments (Figure-3) is a universal tensile device produced by Kalitest Machine. The device provides more than 50 test possibilities for test specimens with different specifications. All test results can be reported with appropriate software and can be stored if required. The device has the possibility to give a large number of test results (tensile, tensile strength, strain failure, % stretching etc.).



(a) *(b)*

Figure 3: a) Hoop tensile equipment, b) Hoop tensile device

III. CONCLUSION AND CONSIDERATION

The area was calculated by measuring the thickness of each specimen and the length of the fracture zone so that the tangential stresses can be obtained by the hoop tensile strength test.

$$\sigma_T = \frac{P_b}{2A_m} \quad (1)$$

In this equation, P_b (N) is the maximum tensile strength of the specimens, A_m (mm^2) is sectional area, and σ_T (MPa) is the tangential stress.

The results of the hoop tensile strength test of the specimens with non-aging control group are shown in Figure-4. When the graph was examined, tangential tensile strength increased with increasing number of layers. The tangential tensile strength of 8-layered tube increased by 5.15% and increased by 10.58% to 10-layer tube compared to 6-layered tube. The percentages of strength increase are shown in equations (2) and (3).

$$\frac{363{,}90 - 346{,}08}{346{,}08} \times 100 = 5{,}15 \quad (2)$$

$$\frac{382{,}72 - 346{,}08}{346{,}08} \times 100 = 10{,}58 \quad (3)$$

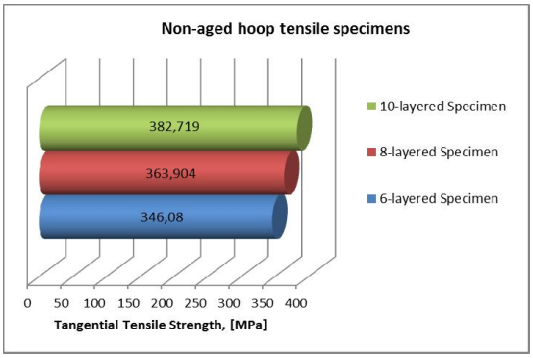


Figure 4: Tangential tensile strength of non-aged specimens.

A decrease in tangential tensile strength of the hydrothermally aged specimens at 80 ° C for 1 week was observed (Figure 5). When examined with reference to non-aged specimens, 10 layer specimen of tangential strength 383 MPa from the value of 358 MPa decreased to 6,8 % lost strength. The 8-layered composite tube tangential strength decreased from 364 MPa to 340 MPa, which was lower than the non-aged control group by 7,1 % strength. The strength of the 6-layered tube decreased from 346 MPa to 320 MPa, with a decrease of 8,2 %.The calculations are made according to equation (4).

$$\frac{\sigma_T - \sigma_{Ty}}{\sigma_T} \times 100 = \%lost \quad (4)$$

In the specimens aged for 2 weeks (Fig. 6), the loss of tangential tensile strength compared to the non-aged specimens in control group was 11,5% for 10-layer specimens, 13,2% for 8-layer specimens, and 15,3% for 6-layer specimens. When the loss of strength was calculated using equation (4) at the end of week 2 compared to week 1, the strength loss for the 10-layer specimen was 4,4 %, for the 8-layer specimen was 5,6%, for the 6-layer specimen was 6,6 %. It is noted that as the aging time increases, the loss of strength decreases rapidly.

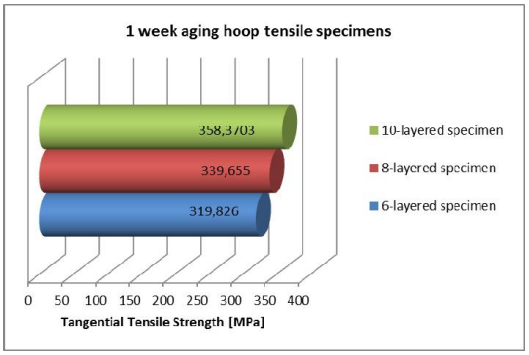


Figure 5: Tangential tensile strength of specimens subjected to aging for one week.

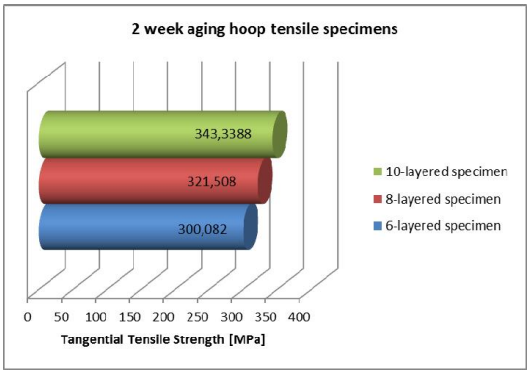


Figure 6: Tangential tensile strength of specimens subjected to aging for two week.

In the specimens aged for 3 weeks (Fig. 7), the tangential stress loss with respect to the non-aged specimens was 14,97 % for 10 layered specimens, 17,70 % for 8 layered specimens and 21,14% for 6 layered specimens. After 3 weeks of aging with reference to specimens aged 2 weeks, the loss of strength was 3,14% for 10 layered specimens, 3,99% for 8 layered specimens and 5,04% for layered specimens.

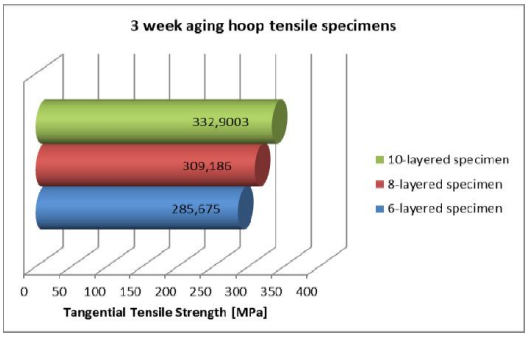


Figure 7: Tangential tensile strength of specimens subjected to aging for three week.

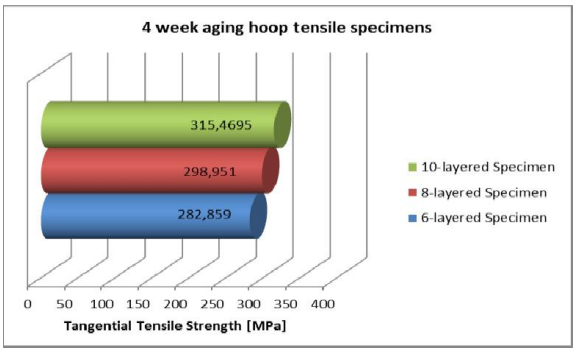
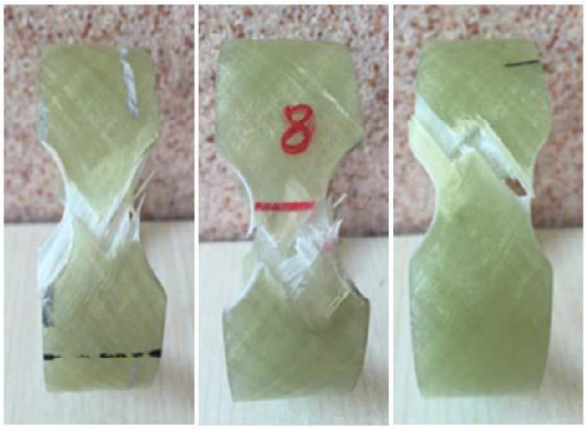


Figure 8: Tangential tensile strength of specimens subjected to aging for four week.

Figure 9 and Figure 10 shows the result damage photographs obtained from hoop tensile strength test of specimens subjected to aging for four week and non-aged specimens, respectively.



(a) (b) (c)

Figure 9: Non-aging hoop tensile specimens a) 6-layered specimen, b) 8-layered specimen, c)10-layered specimen



(a) (b) (c)

Figure 10: Four week aging hoop tensile specimens a) 6-layered specimen, b) 8-layered specimen, c) 10-layered specimen

A. Conclusion

In this study, tangential tensile strength of 6, 8 and 10 layer glass reinforced plastic (GRP) tubes were determined experimentally by hoop tensile strength test according to ASTM D 2290 standard. The values obtained from the method were compared with each other and the damage developments during the tests were also evaluated in the specimens.

The results obtained this study;

1. In the hoop tensile tests, tangential tensile strength increased with increasing number of layers in all specimens.
2. When the hoop tensile test is compared for each specimen, the longer the aging time, the lower the tangential stress values obtained from the hoop tensile tests.
3. When the tangential tensile strength value was reached in all the specimens, the breaking of the fibers occurred in the direction of the winding angle of ± 55 ° and the test specimens were divided into two by breaking in the reduced area.

B. Consideration

It is more advantageous to use hoop tensile tests to find tangential tensile strengths in GRP composite tubes. Since the test specimens are smaller in size, a substantial savings will be provided from the material. Determination of the operating conditions of the tubes according to the results obtained from hoop tensile tests shall establish a safe situation for the tubes.

REFERENCES

[1] Be´akou A., Mohamed A., *Influence of variable scattering on the optimum winding angle of cylindrical laminated composites*. Composite Structure, 53 (2001), 287-293.

[2] Rousseau J., Perreux D., Verdiere N., *The influence of winding patterns on the damage behavior of filament-wound pipes.* Compos Sci Technol, 59 (1999) 1439-1449.

[3] Hawa, A., Majid, M. A., Afendi, M., Marzuki, H. F. A., Amin, N. A. M., Mat, F., Gibson, A. G. *Burst strength and impact behavior of hydrothermally aged glass fibre/epoxy composite pipes.* Materials & Design, 89 (2016) 455-464.

[4] R. Rafiee., *Experimental and theoretical investigations on the failure of filament wound GRP pipes.* Composites: Part B, 45 (2013) 257-267.

[5] M.S Amer, M.J. Koczak and L.S. Schadler, *Relating Hydrothermal Degregation in Single Fibre Coposites to Degragation Behavior in Bulk Composites*, Composites 27A, 861-867, 1996.

[6] M.Kara, "Failure behavior of filament wound GRP pipes under internal pressure repaired with patch after low velocity impact," Ph.D Thesis, Selcuk University Institute of Science, Konya. 2012,

[7] ASTM D 2290-12 (2013), "*Standard Test Method for Apparent Hoop Tensile Strength of Plastic or Reinforced Plastic Pipe. American Society for Testing and Materials*," ASTM International, West Conshohocken, PA, 2006, DOI: 10.1520/D2290-12., www.astm.org

Effect of fly ash and super plasticizer on permeability of soil-cement mixing materials

Y. YENGİNAR[1] and M. OLGUN[1]

[1] Selcuk University, Konya/Turkey, yavuzyenginar@selcuk.edu.tr
[1]Selcuk University, Konya/Turkey, molgun@selcuk.edu.tr

***Abstract* – In this study, the effects of fly ash and super plasticizer, improver materials by adding into the grout, on soil-cement mixing columns called as deep mixing columns (DMC) were investigated. Fly ash is a waste product emerging from burning in the thermal power plant. By evaluating waste materials in this way, environmental pollution will be reduced directly and cement usage and carbon emissions caused by cement production will be reduced indirectly. By using super plasticizer into the grout, less porous and permeable structural element will be manufactured. In order to achieve these goals, an experimental program was developed using statistical and experimental design methods. It is desired to determine the optimum grout quantity and consistency required to minimize the permeability of the column manufactured with DMM in silty soils. For this purpose, the amounts of fly ash (0-40%), cement (3-11%), super plasticizer additive (0.5-2%) and water/binder percentage (0.5-1.25%) were chosen as variable to form grouting material. Experimental studies have been carried out using Taguchi method, which is a powerful optimization technique, using 5-parameter and 4-level L16 design table. Permeability test specimens were prepared in PVC tubes with diameter of 5 cm and length of 10 cm for each design for different curing times of 7 and 28 days. As a result of the experiments, the permeability coefficient values (k) of the soil-binder mixture were found for each design. As a result of the statistical analysis, the optimum values of grouting materials to obtain minimum permeability of DMC was found with 7% cement, 10% fly ash, 1.5% super plasticizer additive and 0.75% water/binder ratio for 7 days cure time. For 28 days of curing time, optimum parameters were obtained with 7% cement, 25% fly ash, 1.5% super plasticizer additive and 1% water / binder. These results show that cement requirement may be reduced at %25 for soil stabilization works especially in DMM.**

***Keywords* - cement, deep mixing method, environmental pollution, fly ash, super plasticizer, Taguchi method, silty soil**

I. INTRODUCTION

The deep mixing method (DMM) has been used frequently in the construction industry since 2000, especially in the soil improvement work. DMM is an in situ soil treatment technology whereby the soil is blended with cementitious and/or other materials. These materials are widely referred to as “binders” and can be introduced in dry or slurry form. They are injected through hollow, rotated mixing shafts tipped with some type of cutting tool. The shaft above the tool may be further equipped with discontinuous auger flights and/or mixing blades or paddles. These shafts are mounted vertically on a suitable carrier, usually crawler-mounted, and range in number from one to eight (typically two to four) per carrier, depending on the nature of the project, the particular variant of the method, and the contractor. Column diameters typically range from 0.6 to 1.5 m, and may extend to 40 m in depth. In some methods, the mixing action is enhanced by simultaneously injecting fluid grout at high pressure through nozzles in the mixing or cutting tools. The cemented soil material that is produced generally has a higher strength, lower permeability, and lower compressibility than the native soil, although total unit weight may be less. The exact properties obtained reflect the characteristics of the native soil, the construction variables, the operational parameters, and the binder characteristics.

DMM which allows the formation of rigid columns as a result of the binding reactions between the materials (cement, lime, etc.) mixed with the soil and these columns can be used to increase the soil bearing capacity and the liquefaction resistance and to stabilize slopes and fillings. DMC performance was increased by adding 10%, 15%, and 20% polishing material to the injection material, keeping the amount of lime and fly ash constant at 15% [1]. In studying the effects of cement, lime, fly ash and marble dust on the stabilization of clayey soils, different types of cement, lime, fly ash and marble powder used as additive materials used at different rates (5%, 10% 15%) were mixed and waited for different curing times (7 days, 21 days and 45 days) and then subjected to three axial compression test to evaluate the change in strength properties of the soil [2]. Blast furnace slag cement was mixed in plastic consistency of soft soil and subjected to free pressure strength test. The cement ratio was used as 100-200 kg/m^3 for total ground mass and 4.0% and 8.0% for ground dry mass [3]. In another study, 4%, 6%, 8% and 10% ratios of dry weight of cement were selected for percentage of cement while water content values were selected as 30%, 48% and 70% for cement percentage [4]. Immediately after the production of deep mixing columns and using a quality management program in the construction phase, the results and the process were investigated and it was found that the strength and stiffness values of specimens taken from the columns produced in the field were 20% to 40% lower than the samples prepared in the laboratory. Experiments were carried out by using deep mixing columns in a sandy soil with binder quantities of 200, 300, 400, 500, 600 and 700 kg/m^3 in a study in which Portland cement clinker and blast furnace slag were used as binders on a sand [6].

II. MATERIAL AND METHODS

A. Materials

The soil used for experimental studies was obtained from Doganhisar in Konya. 27% fine sand is found on the ground while the remaining part is fine granular (Figure 1). The liquid and plastic limits of the soil obtained as 23 and 11 respectively and the soil is classified as low plasticity silty soil (ML) according to USCS.

Cement and fly ash are used as binding material in DMC manufacturing. CEM-I cement is used in the study. The fly ash was obtained from Seydişehir Eti Aluminum Plant. Fly ash consists of 16% sand and 84% silt. Fly ash is not included in class C or F due to the chemical components it contains and the amount of CaO is very high (Table 1). Master Rheobuild 1000 superplasticizer additive is used to increase the consistency of the binder material.

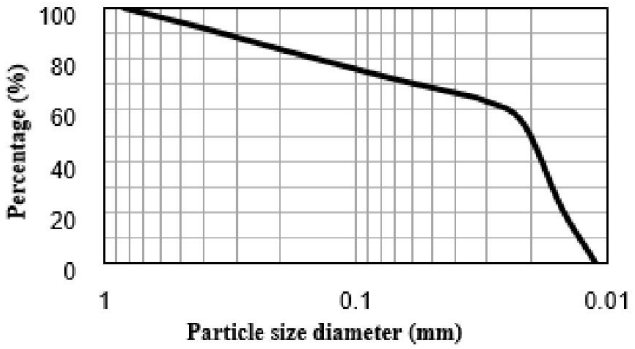


Figure 1: Particle size distribution of soil.

B. Method

There are several approaches to designing any experiment and investigating the effects of the parameters on the results. In Taguchi method, this can be reached by using a suitable orthogonal array. In addition, maximum and minimum values can be estimated with other experimental results which have not been done, and the experimental cost can be kept to minimum with this method [7]. In this method, specially developed orthogonal array tables are used for designs. In this study, a 5-parameter and 4-level standard L16 orthogonal array table was used (Table 2). In this study, parameters were chosen as the initial water content of soil (w_0), cement percentage, fly ash percentage, water/binder ratio and super plasticizer additive percentage. Parameters and their levels are given in Table 3. Experimental results were evaluated by S/N analysis, ANOVA and optimization studies.

Table 2: L16 orthogonal array table

Test no	Parameters and their levels				
	A	B	C	D	E
1	1	1	1	1	1
2	1	2	2	2	2
3	1	3	3	3	3
4	1	4	4	4	4
5	2	1	2	3	4
6	2	2	1	4	3
7	2	3	4	1	2
8	2	4	3	2	1
9	3	1	3	4	2
10	3	2	4	3	1
11	3	3	1	2	4
12	3	4	2	1	3
13	4	1	4	2	3
14	4	2	3	1	4
15	4	3	2	4	1
16	4	4	1	3	2

When deep mixing samples are prepared, water corresponding to the initial water content of soil is first added to the soil and then mixed. Then injection material was prepared with mixture of cement, fly ash, additive and water. The injection material was again mixed with the previous mixture. The amount of cement and fly ash is calculated as the percentage of dry mass of the soil. The amounts of water and additives added to the injection are calculated on the basis of the amount of binder. Once a homogenous mixture has been obtained, the prepared mixtures are poured into PVC molds which has diameter of 5cm and height of 10cm. Deep mixing samples were cured in water bath at constant temperature for 7 and 28 days. At the end of the curing time, permeability tests were carried out to determine the permeability coefficient values of the deep mixing columns.

Table 1: Chemical components of fly ash

Chemical component	SiO_2	Al_2O_3	Fe_2O_3	CaO	MgO	SO_3	Na_2O	K_2O	Heat Loss	Free CaO
Fly ash (%)	19.8	8.1	6.0	28.3	1.0	18.2	0.4	0.1	1.8	16.3

Table 3: Parameters and their levels used in the experimental studies

Level	Parameter				
	A	B	C	D	E
	Soil water content (%)	Cement (%)	Fly ash (%)	Water/binder ratio	Additive (%)

1	15	3	0	0.50	0.5
2	19	7	10	0.75	1.0
3	23	11	25	1.00	1.5
4	27	15	40	1.25	2.0

III. RESULTS

A. Permeability Test Results

Permeability test results at the end of 7 and 28 days of curing time are given in Table 4. In the design of 1, 6, 11 and 16, permeability coefficient of soil-binder materials obtained maximum (10^{-3}-10^{-5} cm/s) at the end of 7 days curing time. The common properties of these designs are that they have no fly ash content. Maximum permeability coefficient value is obtained in the design of 11 because super plasticizer amount is maximum and water content is very high in the grouting material. Mixing the soil with high viscosity of grouting may cause the problem of separation between the soil grains, then void ratio of soil-cement material may increase. As a result of this event, permeability coefficient of soil-binder material increase. In the design of 3, 4 5, 8, 10, 12, 14 and 15, permeability coefficient of soil-binder materials obtained as 10^{-6} cm/s. Permeability coefficient of soil-binder materials obtained as 10^{-7} cm/s for the rest of the designs. In these designs cement, fly ash, water and additive amounts are variable. At the end of 28 days curing time, permeability coefficient of soil-binder materials decreases for almost all designs. In the design of 11, permeability coefficient of soil-binder material obtained maximum (10^{-4} cm/s). In the design of 1-6 and 16, permeability coefficient of soil-binder materials obtained as 10^{-6} cm/s. At the other designs, permeability coefficient of soil-binder materials obtained as 10^{-7} cm/s. This shows that permeability coefficient of soil-binder materials decreases if the curing time increases. Moreover, increasing amount of fly ash content decreases the permeability coefficient of soil-binder material. The other result obtained in this study is that, the effect of water/binder ratio and super plasticizer amount on the permeability of soil-binder material is inversely proportional. This means that if the water/cement ratio is high super plasticizer amount in the grouting material should be low.

Table 4: Permeability test results at the end of 7 and 28 days of curing time

Test No	Permeability coefficient, k (cm/s)	
	7 days	28 days
1	7.22E-05	2.29E-06
2	6.25E-07	1.73E-06
3	1.94E-06	1.91E-06
4	1.30E-06	5.06E-06
5	1.48E-06	5.38E-06
6	4.77E-04	2.62E-06
7	3.67E-07	4.47E-07
8	1.73E-06	8.43E-07
9	8.92E-07	5.24E-07
10	1.28E-06	4.89E-07
11	1.58E-03	1.20E-04
12	1.09E-06	7.16E-07
13	3.53E-07	3.58E-07
14	1.61E-06	9.35E-07
15	1.38E-06	5.75E-07
16	2.03E-04	1.04E-06

B. Statistical Analysis Results

Statistical analysis results were evaluated using Design Expert 10 software. In the "factorial design" section of this software, necessary analyzes were made on the "Taguchi orthogonal index" submenu and evaluations were made. Multivariate analysis of variance (ANOVA) was performed to determine the effect levels of the parameters on the results. When the results are evaluated, it is considered that there is interaction between all the parameters.

Probability of occurrence of the model developed for the permeability coefficient values at the end of 7 days is $p=0.011<0.05$ and the model is significant (Table 5). The model is within the 95% confidence interval. When the ANOVA analysis results are evaluated, the effect level of the parameters which are effective on the test results is indicated by the fact that the F value is high. The most effective parameters on the 7-day permeability test results are the fly ash, then the superplasticizer additive amount, the water/binder ratio and the cement amount, respectively (Figure 2).

Table 5: ANOVA analysis of permeability test results at the end of 7 days

Source	Sum of Squares	df	Mean Square	F Value	p-value
Model	3.96E+6	12	3.302E5	25.40	0.011
Cement	1.39E+5	3	46384.2	3.57	0.162
Fly ash	3.18E+6	3	1.061E6	81.57	0.002
Water/binder ratio	2.51E+5	3	83755.7	6.44	0.080
Additive	3.90E+5	3	1.300E5	10.00	0.045
Residual	39007.7	3	13002.6		

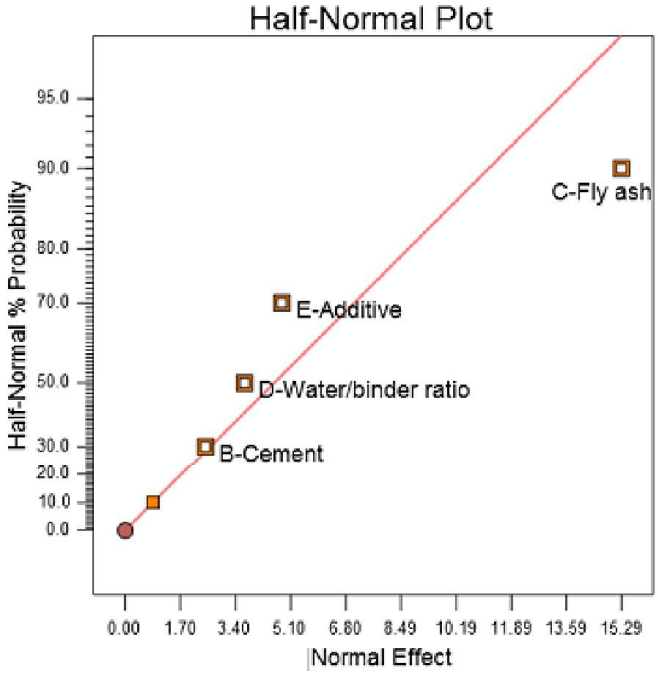


Figure 2: Effect of the parameters on the permeability coefficient at the end of 7 days

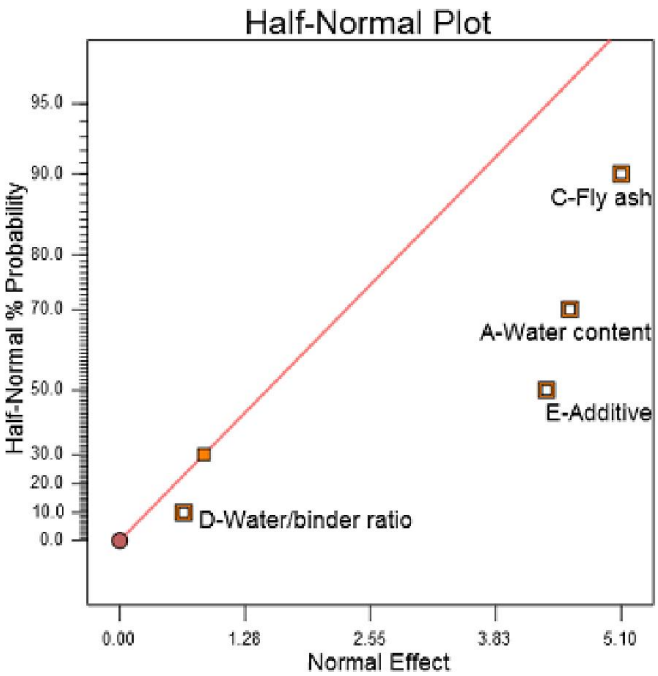


Figure 3: Effect of the parameters on the permeability coefficient at the end of 28 days

Probability of occurrence of the model developed for the permeability coefficient values at the end of 28 days is p=0.064<0.05. The model proposed by the Design Expert software has low confidence when considering the effect of cement amount. The model is within the 95% confidence interval (Table 6). The reason of this issue that permeability coefficient values are very close for many design and they changes between 10^{-6} and 10^{-7}. The most effective parameters on the 28-day permeability test results are the superplasticizer additive amount, then the fly ash, the cement amount and the water/binder ratio, respectively (Figure 3).

Table 6: ANOVA analysis of permeability test results at the end of 28 days

Source	Sum of Squares	df	Mean Square	F Value	p-value
Model	1.1E13	12	8.7E11	7.32	0.064
Water content	3.2E12	3	1.1E12	9.16	0.051
Fly ash	3.9E12	3	1.3E12	10.97	0.040
Water/binder ratio	2.7E11	3	8.9E10	0.76	0.586
Additive	2.9E12	3	9.8E11	8.39	0.057
Residual	3.5E11	3	1.2E11		

C. Optimization Analysis Results

Optimum levels of parameters can be determined by doing S/N analysis which has a special calculation in Taguchi method and it can be done with using Minitab.

The most effective levels of parameters determined as 23% initial water content of soil, 11% cement, 10% fly ash, 0.75 of water/binder ratio and 1% super plasticizer amount for at the end of 7 days curing time (Figure 4). At the end of 28 days curing time, effectiveness of levels of parameters determined same with 7-day curing soil-binder material except for fly ash (Figure 5). Increasing fly ash amount always decrease the permeability coefficient for 28 days curing samples, but optimum value of it may be accept as 25 or 40%.

Using the proposed model developed for permeability test results of 7 and 28-day soil-binder material, an optimization has made for different parameters and their levels and 100 different results were obtained. Using different level of the parameters, the predicted permeability coefficients given in Table 7 for 7-day cured soil-binder materials and Table 8 for 28-day samples.

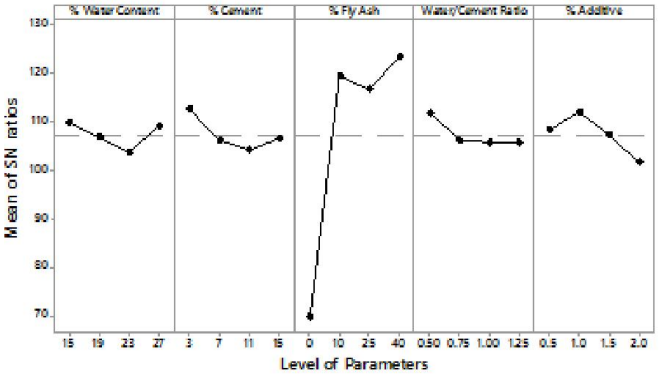


Figure 4: S/N ratios obtained for the samples cured 7 days

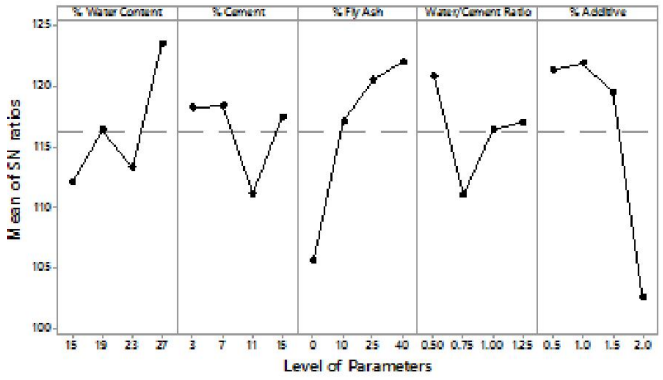


Figure 5: S/N ratios obtained for the samples cured 28 days

IV. CONCLUSION

In this study, the effects of fly ash and super plasticizer on the permeability of soil-cement materials were investigated. In soil stabilization application with deep mixing method, water/binder ratio is generally chosen as 1 when preparing grout material. This study shows that water/binder ratio may decrease to 0.75 if 1% of super plasticizer is added to grout to obtained impervious deep mixing columns. Moreover, it is concluded that fly ash is an improver material to decrease the permeability coefficient of deep mixing columns because fly ash is a very fine material and it infiltrates to voids of soil. In the optimization analysis, optimum fly ash amount found as 10% and 25% for 7-day and 28-day cured samples. However, 25% fly ash should be used to obtain more impervious deep mixing columns to consider long term effects. In addition to this, waste products will be recycled and cement usage can be restricted using fly ash.

Strength and consolidation properties of soil-binder materials manufactured by using cement, fly ash and super plasticizer should be investigated to clarify performance of deep mixing columns.

Table 7: Optimization result of 7-day cured samples: predicted k values for different parameters and levels

Number	Water content	Cement	Fly ash	Water/binder ratio	Additive	k (cm/s)	Desirability
1	27	3	40	0.75	1.0	3.19E-07	1.0
2	19	3	40	0.50	1.0	3.40E-07	1.0
3	19	11	40	0.75	1.0	3.63E-07	1.0
4	27	11	40	0.75	1.0	3.63E-07	1.0
5	19	3	40	0.75	1.5	3.86E-07	1.0
6	23	3	40	0.75	1.5	3.86E-07	1.0
7	23	11	40	0.50	1.0	3.88E-07	1.0
8	15	7	40	0.75	1.0	3.93E-07	1.0
9	27	7	40	0.75	1.0	3.93E-07	1.0
10	15	3	40	0.50	1.5	4.14E-07	1.0

Table 8: Optimization result of 28-day cured samples: predicted k values for different parameters and levels

Number	Water content	Cement	Fly ash	Water/binder ratio	Additive	k (cm/s)	Desirability
1	27	3	40	0.50	1.0	3.55E-07	1.0
2	27	7	40	0.50	1.0	3.55E-07	1.0
3	27	15	40	0.50	0.5	3.64E-07	1.0
4	27	15	40	0.75	1.0	3.74E-07	1.0
5	19	11	40	0.50	1.0	4.63E-07	1.0
6	27	7	25	0.50	1.0	4.64E-07	1.0
7	23	7	40	0.50	0.5	4.10E-07	1.0
8	23	15	40	0.50	0.5	4.10E-07	1.0
9	19	3	40	0.50	0.5	4.78E-07	1.0
10	19	15	40	0.50	0.5	4.78E-07	1.0

REFERENCES

[1] Öntürk, K., "Using polishing, lime and fly ash in soil stabilization", MD thesis, Sakarya University İnstitute of Science, pp. 160, 2011.

[2] Coşkun, Y., "Evaluation of Soil Stabilization with Additives Using Triaxial Compression Tests", MD thesis, Aksaray University İnstitute of Science, 2015..

[3] Dias, D.R., Camarini, G., Miguel, M.G., "Preliminary laboratory tests to study the increase of strength in samples of soft soils with cement, for treatments using Dry-Mix System", Grouting and Deep Mixing 2012, Geotechnical Special Publication (GSP) No. 228, 2012.

[4] Pakbaz, M.S., Alipour, R., "Influence of cement addition on the geotechnical properties of an Iranian clay", Department of Civil Engineering, Shahid Chamran Univ., Ahvaz, Iran. Geotechnical Engineering, Sazabpardazan Consulting Engineers Co., Ahvaz, Iran, 2012.

[5] Madhyannapu, R.S., Puppala, A.J., Nazarian, S., Yuan, D., 2010. "Quality Assessment and Quality Control of Deep Soil Mixing Construction for Stabilizing Expansive Subsoils", Journal of geotechnical and geoenvironmental engineering.

[6] Shrestha, R., 2008. "Soil Mixing: A Study on 'Brusselian Sand' Mixed with Slag Cement Binder", Master Dissertation, University of Ghent.

Conceptual Design of an Annular Type Combustion Chamber

O.KOCAASLAN[1] and K.M.GÜLEREN[2]

[1] Selcuk University, Konya/Turkey, okocaaslan@selcuk.edu.tr
[2]Anadolu University, Eskisehir/Turkey, kmguleren@anadolu.edu.tr

Abstract **- The combustion chamber located between turbine and compressor are an important component of gas turbines and aircraft engines. In the combustion chambers, the chemical energy contained in fuel is converted into heat energy. Generally, empirical formulas are used for combustion chamber design applications. Design applications are made by minimizing gas pressure losses and balancing heat transfer. In this study, gas and fuel mass flow rate, gas pressure and temperature at the inlet of combustion chamber were taken as reference for designing annular combustion chamber. Diesel was selected as liquid fuel. Empirical equations were used for design applications. First, primary zone dimensions were made according to the entrance specified conditions. Then, secondary and dilution zone design dimensions were determined. Finally, the solid model of the annular combustion chamber was created according to the determined dimensions. Cooling holes must be provided in order to stabilize the cooling process in the annular combustion chamber. With reference to the fuel and gas mass flow rate, dimensions of the cooling-holes of the annular-type combustion chamber were calculated and added to the solid model. After designing of the solid model, flow volume was created for combustion problem and a mesh structure was generated to suit the combustion problems. Numerical analyses were performed using the k-ε turbulence model in Ansys-Fluent software. Energy equations were also included in numerical solution for combustion reaction. The heat transfer and flow structure in the combustion chamber are examined in detail.**

Keywords **- Annular Type Combustion Chamber, CFD, Conceptual Design**

I. INTRODUCTION

Combustion chambers in gas turbines allow pressurized air transferred from the compressor to increase the temperature with the added and combusted fuel. In this manner, design of combustion chamber is very important for gas turbines and also for jet engines. Combustion chambers must operate stably and maintain a wide range of combustion efficiency. Targeted results in combustion chamber design are low pressure losses and balanced temperature values in the transferred air to turbine.

Several studies carried out about designing of combustion chamber. Gangaraju examined gas turbine combustor design procedures. In the study firstly, the type of combustion chamber was determined. Then, the design parameter for the determined combustion chamber were found. The dimensions of the chamber geometry were calculated with empirical methods. Finally, solid model of combustor was created [1]. Mark designed an annular combustion chamber of a low bypass turbofan engine. The combustion chamber designed with design parameter and drawn solid model of combustor. Reference to determined boundary conditions, CFD analysis were made with ANSYS CFX software. Flow structure and temperature distribution in annular combustion chamber were examined in [2]. Shanker designed a can type combustion chamber that selected butane as fuel. The combustion chamber solid model was drawn with using calculated design parameter in Catia v5 commercial software. Mesh structure was created in Gambit software for CFD analysis and numerical analysis were made in Fluent software. K-ε turbulence model was used for flow problem and examined pressure and flow velocity distribution [3].

In this study, an annular combustion chamber was designed with determined design parameters. For design parameters, air mass flow rate, pressure and temperature at combustor inlet, mass flow rate of fuel were used. Diesel was selected as fuel. After designing combustion chamber, the combustion chamber solid model was created and numerical analysis was made in ANSYS/Fluent software.

II. MATERIAL METHODS

A. Designing of Combustion Chamber

First step of combustion chamber design is selection type of combustion chamber and determining design parameters. Air distribution in combustion chamber should be detected for calculation of dimensions. A schematic distribution of air in combustion chamber is given in Figure 1. The steps followed for the design is given as below.

- Calculate the reference and annulus area,
- Determine primary zone dimensions,
- Determine diffuser and swirler dimensions,
- Determine secondary zone dimensions,
- Determine dilution zone dimensions,
- Calculate primary, secondary and dilution zone cooling holes.

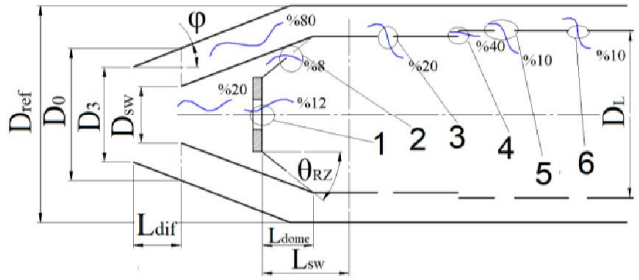
Empirical relations used for the dimensions of the chamber geometry are given in Table 1. Design parameters for the combustion chamber are seen in Table 2.

Table 1: Empirical formulas and design parameters [2, 4].

Empirical Formulas	Calculated parameters or dimensions	Symbols
$A_{ref}=\left[\frac{R}{2}\left(\frac{\dot{m}_3 T_3^{0.5}}{P_3}\right)^2\left(\frac{\Delta P_{3-4}}{q_{ref}}\right)\left(\frac{\Delta P_{3-4}}{P_3}\right)\right]^{0.5}$	-Reference area	$\dot{m}_3$: Inlet mass flow rate R: Universal gas constant P_3: Inlet air pressure $\frac{\Delta P_{3-4}}{P_3}$: Diffuser pressure loss T_3 : Inlet temperature $\dot{m}_{an}$: annulus air mass flow rate R_0: Snout out radius $\dot{m}_s$: Recirculation air mass flow rate $C_{d,S}$: Discharge coefficient $\frac{\Delta P}{q_{ref}}$: Swirler pressure drop factor PN: Pattern Factor γ: Compressor pressure ratio $\dot{m}_{max}$: Air mass flow rate
$A_L = 0.66A_{ref}$	-Liner area	
$A_{an}= A_{ref}-A_L$	-Annulus area	
$A_0 = \frac{\dot{m}_3 A_{an}}{\dot{m}_{an}}$	-Snout outer area	
$L_{dif} = \frac{R_0 - R_3}{tg\varphi}$	-Diffuser length	
$A_s = \frac{\dot{m}_s A_0}{\dot{m}_3 C_{d,S}}$	-Snout area	
$L_L = \frac{-D_L}{0.05\frac{\Delta P}{q_{ref}}\ln(1-PN)}$	-Liner length	
$L_{PZ} = 0.75D_L, L_{SZ} = 0.5D_L, L_{RZ} = 2D_{SW},$	-Primary zone length, -Secondary zone length, -Recirculation zone length	
$L_{DZ} = D_L(3.83 - 11.83PF + 13.4PF^2)$	-Dilution zone length	
$L_{Dome} = \frac{D_L - D_{SW}}{2tan\theta}$	-Dome length	
$A^* = \frac{\dot{m}_{max}\sqrt{T_3}}{P_3}\sqrt{\frac{R}{\gamma}\left(\frac{\gamma+1}{2}\right)^{\left(\frac{\gamma+1}{2(\gamma-1)}\right)}}$	-Combustor exit area	
$\theta_{RZ} = arc\ cos\left[\frac{-D_L(D_L-2D_{SW})-(D_L-4L_{RZ})(D_L{}^2-4D_LD_{SW}+4D_{SW}{}^2-4D_LL_{RZ}+16L_{RZ}{}^2)^{0.5}}{2D_L{}^2-4D_LD_{SW}+4D_{SW}{}^2-4D_LL_{RZ}+16L_{RZ}{}^2}\right]$		

Table 2: Design parameters.

Design Parameter	Value
Air mass flow rate at combustor inlet	23.7762 kg/s
Air temperature at combustor inlet	753 K
Pressure overall ratio of compressor	20:1
Fuel mass flow rate	0.18 kg/s



1-Swirler Zone 3-Primary Zone Hole 5-Secondary Zone Holes
2-Dome Cooling 4-Cooling Holes 6-Dilution Zone Holes

Figure 1: A schematic illustration of airflow distribution and combustor model [2, 5].

B. Flow Domains and Mesh Structure

After determining design parameters, solid model is created. A periodic cross section of the solid model is given in Figure 2.

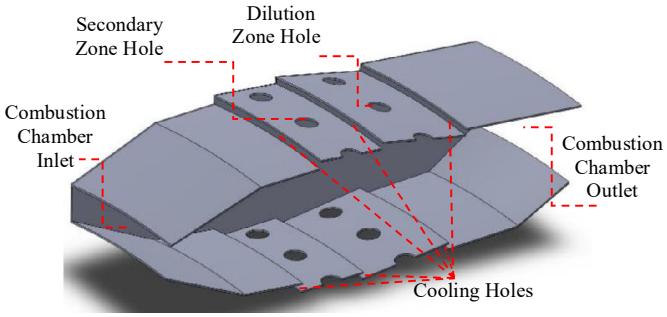


Figure 2: Periodic section view of the designed annular combustion chamber.

After solid model of combustion chamber is drawn, fluid domains are created. In this study, periodic fluid domains are generated for CFD analysis. In CFD analysis, 24° portion of the flow volume is investigated. The fluid domains are given in Figure 3.

A suitable mesh structure for flow problem is created using tetrahedral cells by regulating flow domains. Inflation layers are

also added near the wall surfaces for regulating mesh quality near the walls. The mesh structure was given in Figure 4.

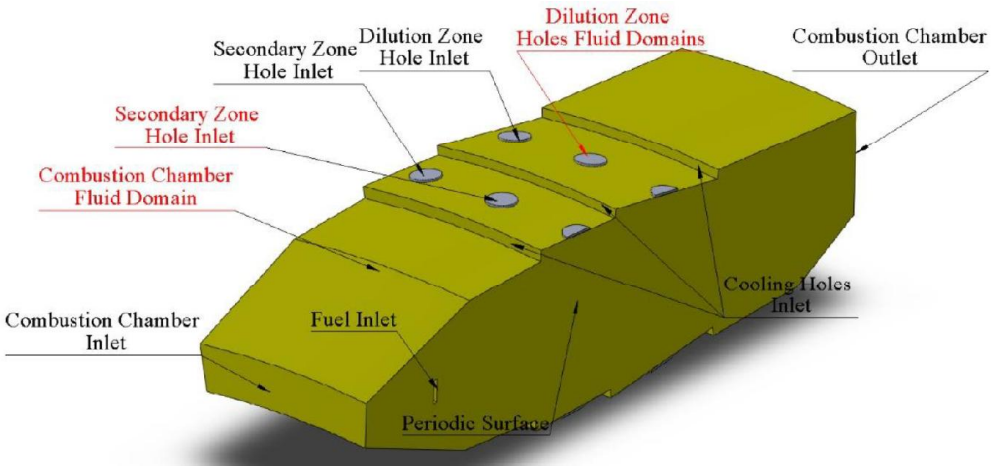


Figure 3: Annular combustion chamber flow volumes section view.

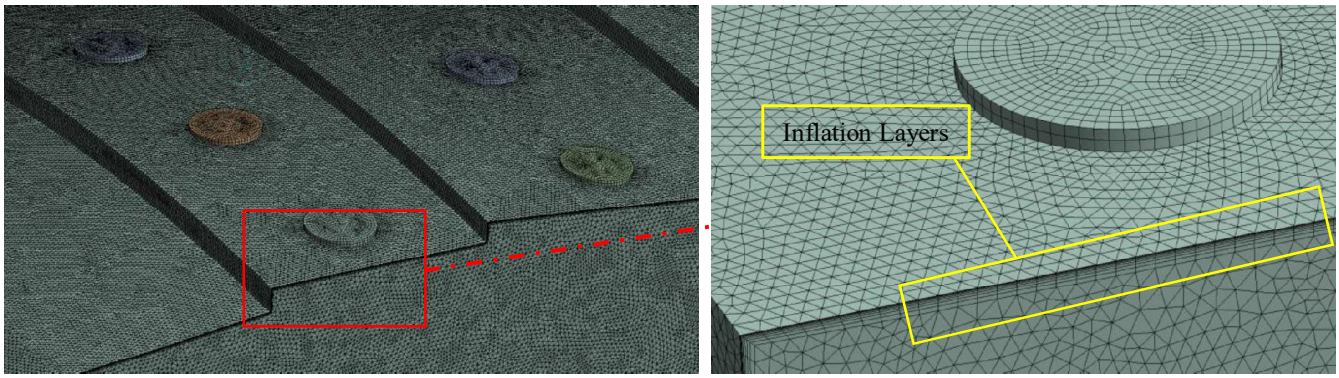


Figure 4: Mesh structure for the flow in annular combustion chamber.

C. Defining Flow Problem

The pressurized air is transferred from combustion chamber inlet, the dilution zone holes, the secondary zone holes and the cooling holes to the combustion chamber. Here, the combustion reaction occurs with the air and fuel interactions.

The boundary conditions used in CFD analyses are given in Table 3. Dilution, secondary and cooling hole entries are taken into account as mass flow inlet according to the mass flow percentage stated in Figure 1.

In numerical analysis, k-ε turbulence model was used. Energy, radiation and non-premixed combustion equations are added for modeling the fuel and examining the heat transfer. In order to analyses the flow structure regions of near the wall surfaces, standard wall functions were used in numerical analysis [6].

Table 3: Boundary Conditions

Position	Boundary Condition
Combustion Chamber Inlet	Mass flow rate, air inlet temperature
Secondary Zone Holes Inlet	Mass flow rate, air inlet temperature
Dilution Zone Holes Inlet	Mass flow rate, air inlet temperature
Cooling Holes Inlet	Mass flow rate, air inlet temperature
Outlet	Pressure
Fuel Inlet	Mass flow rate, fuel inlet temperature
Periodic Surface	Periodic conditions
Wall Function	Standard wall function

III. Results and Discussions

In this study, a combustion chamber with 15 fuel injectors is designed and analyzed. For numerical analysis and chamber design, diesel is selected as fuel. 24° portion of the flow volume is generated and a suitable mesh structure is created for CFD analysis. Finally, CFD analysis is used for the investigation of flow structure and heat transfer in combustion chamber.

Velocity vectors in combustion chamber is given in Figure 5. When the distributions of the velocity vectors in the flow structure are examined, it is seen that the reverse flows occur near the injector. And it is observed that the flow structure is regulated near the exit of the combustion chamber.

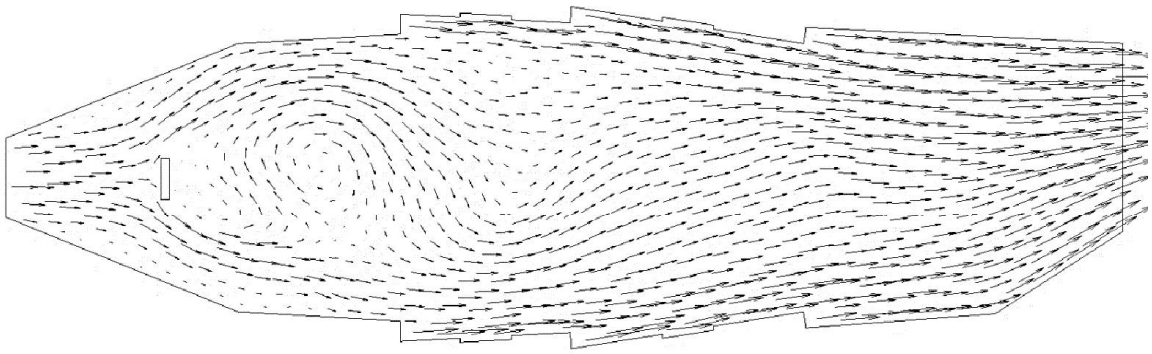


Figure 5: Velocity vectors in combustion chamber.

Heat transfer distribution in the combustion chamber is given Figure 6. It is observed that the temperature increases to 2215 K due to combustion. Thanks to the cooling channels, the temperature increase caused by combustion in the combustion chamber is reduced near walls of combustion chamber. When the temperature distribution near the walls of combustion chamber is examined, it is seen that the temperature drops to 750 K.

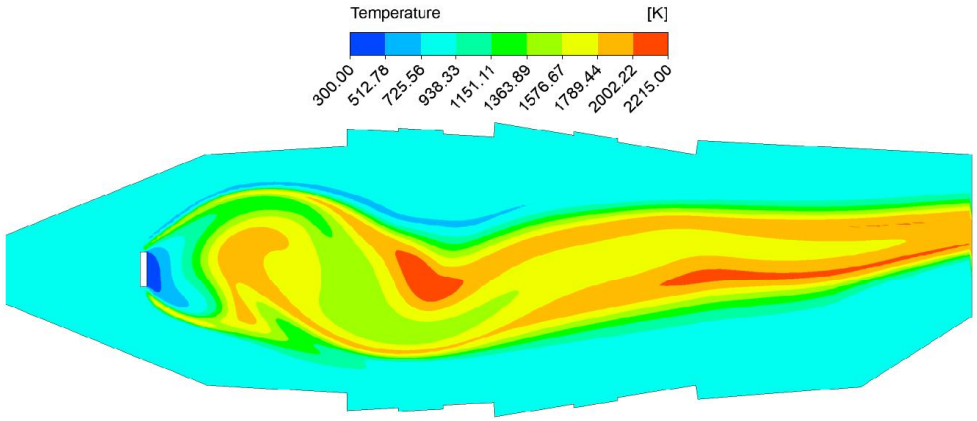


Figure 6: Heat transfer distribution in combustion chamber.

Total pressure distribution in the combustion chamber is presented in Figure 7. The total pressure at the inlet of combustion chamber becomes about 2330 kPa. At the exit of the combustion chamber, the total pressure decreases to 2185 kPa. Considering these, the pressure loss calculated in the combustion chamber is about 6.22%.

Fuel mass fraction distribution in combustion chamber is given in Figure 8. The maximum fuel mass fraction becomes 25 % in combustion chamber. This result shows that a great deal of fuel is used for combustion in combustion chamber.

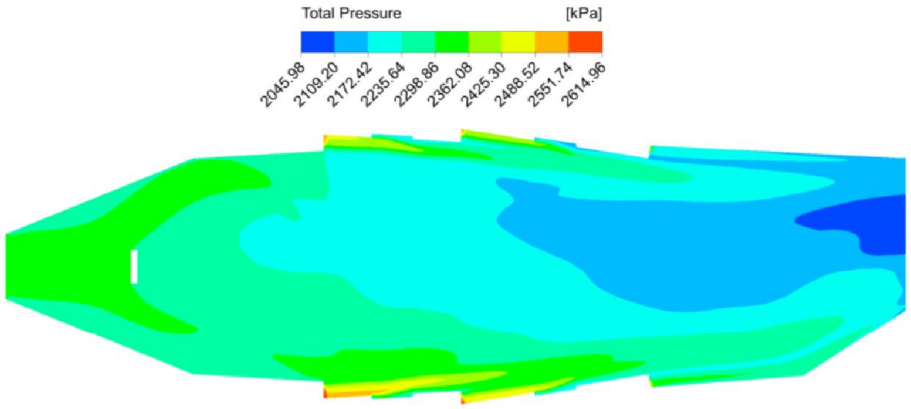


Figure 7: Total pressure distribution in combustion chamber.

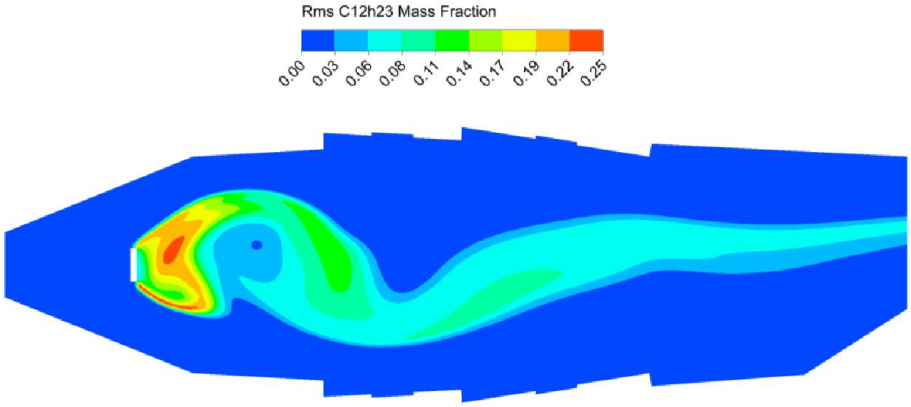


Figure 8: Fuel mass fraction distribution in combustion chamber.

IV. Conclusion

In this study a conceptual design annular type of combustion chamber with specified design parameters is carried out. 24° portion of the flow volume is assumed and a suitable mesh structure is created for numerical analysis. With the CFD analysis, it has been possible to examine flow structure, heat transfer distribution, fuel mass fraction distribution and total pressure distribution in combustion chamber. A simple combustion analysis shows that the reverse flow is observed in front of the injector in the flow structure. Approximately 6.22 % of pressure loss in the combustion chamber is estimated. As for the heat transfer, it is observed that the cooling channels usefully decrease the extreme heat increment near the liner walls. Lastly, 75% of the fuel is seen to burn during combustion.

As for future work, the authors plan to carry out a Large Eddy Simulation analysis to reveal the acoustic behavior in annular type of combustion chamber.

REFERENCES

[1] S. S. Gangaraju, M. V. S. M. Krishna and D. N. Reddy, "Design and analysis of a gas turbine combustion chamber for producer gas as working fuel," *International Journal of Current Engineering and Technology,* vol. 5, pp. 444-447, Feb 2015.

[2] C. P. Mark and A. Selwyn, "Design and analysis of annular combustion chamber of a low bypass turbofan engine in a jet trainer aircraft," *Propulsion and Power Research*, doi: 10.1016/j.jppr.2016.04.001, May 2016.

[3] V. G. Shanker, V. K. Kumar, A. A. Reddy and E. Rakesh, "Modeling and flow analysis of can type combustion chamber with n-butane as a fuel for gas turbine engine", *International Journal of Engineering Research and Technology*, vol. 3, pp. 212-215, Dec 2014.

[4] A. C. Cornado, P. T. Lacava, A. C. P. Filho and M. de S. Sanches, " Basic design principles for gas turbine combustor", *Proceedings of the 10th Brazilian Congress of Thermal Sciences and Engineering*, paper no.0316, Dec 2004.

[5] A. H. Lefebvre and D. R. Ballal, *Gas Turbine Combustion,* New York: CRC Press, 2010.

[6] Anonymous, Fluent 14.0 User Guide , Fluent Inc., 2013.

Numerical Analysis of BT1 Wind Tunnel Experiment Using OpenFOAM

M. B. AGIR[1], T. J. SCANLON[2], A. SAMANCI[3]

[1] University of Strathclyde, Glasgow/United Kingdom, muhammed.agir.2016@uni.strath.ac.uk
[2] University of Strathclyde, Glasgow/United Kingdom, tom.scanlon@strath.ac.uk
[3] Necmettin Erbakan University, Konya/Turkey, asamanci@konya.edu.tr

***Abstract* - The operating environment of wind turbines might have variable flow behaviours. That is why the desired boundary conditions are created and kept under control using wind tunnels to examine the performance of wind turbines in the certain flow characteristics. However, this experimental setup can be simulated by various approaches and software. In this study, the wind tunnel experiment of a horizontal axis wind turbine (HAWT), which was named Blind Test 1 (BT1) and done by Norwegian University of Science and Technology (NTNU), is simulated using OpenFOAM by a combination of a rotor and turbulence models. The rotor of a wind turbine is modelled applying actuator line method (ALM). The virtual blades are defined in the software dictionaries to reduce the computational cost. Afterwards, the CAD drawing of the tower assembly is inserted into the simulation to obtain the data that is close the experimental outcomes. Finally, the $k-\varepsilon$ standard turbulence model is executed to predict the flow behaviour in near-wake and far-wake regions. The created model provided quite correct patterns and trends of velocity deficit. The outcome of numerical analysis is extracted and plotted using ParaView post-processor.**

***Keywords* – Horizontal Axis Wind Turbine, Blind Test 1, $k-\varepsilon$ Standard Turbulence Model, Actuator Line Method, OpenFOAM**

I. Introduction

The fossil ores have been utilised as primary energy suppliers. However, industrialisation and high demand cause to vanish these limited sources. Moreover, the fossil fuels comprise high carbon that is emitted to the atmosphere during the energy extraction process. In order to generate clean energy from renewable and nature-friendly sources, the wind farms have recently become more popular due to high efficiency. For instance, the wind farms in Scotland produced the electricity more than demanded on August 7th, 2016 [1]. According to 2016 data, Pacific region (Australia, New Zealand, and Pacific Islands) has the greatest contribution the electricity generation by wind with 486,796 MW [2]. These data display the wind system has a crucial impact on energy supplement. That is why the efficiency of these systems ought to be advanced.

In order to improve the wind systems, correct data is substantial. However, the test conditions cannot be set every time, therefore, the improvements of numerical analysis methods are inevitable. The outcomes of the numerical models should provide the approximate result to the actual case. That is why organisations arrange workshops to compare the results of research methodologies with experimental results. One of these workshops, which is named Blind Test 1 (BT1), was arranged in October 2011 by NOWITECH (Norwegian Research Centre for Offshore Wind Technology) and NORCOWE (Norwegian Centre for Offshore Wind Energy). The predictions of various rotor aerodynamics and turbulence models are compared using the experimental data [3].

The numerical analysis of flow physics is a combination of fluid dynamics and applied mathematics methods. The mathematical models have different algorithms, therefore, a simulation by different methods might have various results. Furthermore, the selection of solver is significant as much as rotor and turbulence model to obtain predictions that represent the actual case. In this study, the numerical analysis of BT1 experiment is completed by OpenFOAM 3.0.x. The OpenFOAM (Open Source Field Operation and Manipulation) is a C++ based and open source software. The program has different solvers and methodologies to solve the CFD problems. The BT1 experiment is simulated by a combination of momentum source and RANS turbulence models. The boundary conditions of BT1 is specified in the dictionaries of the software. The turbulence generation in the downstream zone is predicted in 1D, 3D, and 5D far away from the rotor.

II. Mathematical Model

The BT1 experiment is modelled using a rotor aerodynamic method, momentum source, and turbulence model. The rotor model is chosen Actuator Line Method (ALM). In this approach, the blades are divided into small domains as in the Blade Element Method, as seen in Figure 1. The load distribution on the blade is determined for each sub-domain using a lookup table of the aerofoil. Furthermore, the non-uniform load distribution and tip vortices can be detected by ALM. Therefore, the ALM is an advanced version of BEM. The blade elements are specified in the dictionary of the program with the constant parameters including twist angle, chord length, and headwind.

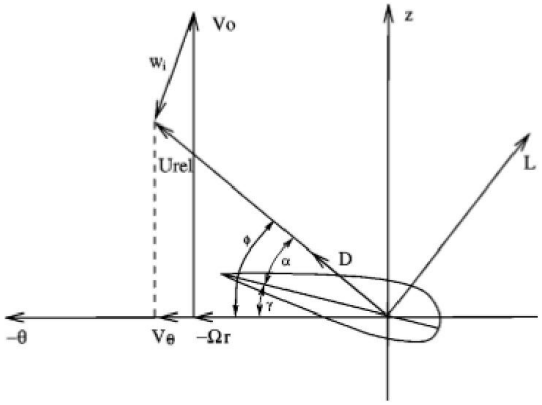


Figure 1. Cross-section of a blade element [4]

The relative velocity at local, U_{rel}, can be defined by the angular velocity of the rotor, Ω, the radial distance between blade element, and the rotational axis of the turbine, as shown in Equation 1 [4]. The relative angle, φ, is formulated in Equation 2 [4].

$$U_{rel} = \left(V_\theta - \Omega r, V_Z\right) \tag{1}$$

$$\varphi = \tan^{-1}\left(V_Z / \Omega r - V_\theta\right) \tag{2}$$

A momentum source should be applied to the virtual rotor created by ALM. The rotorDisk case in OpenFOAM is suitable to form the desired test condition. The main principle of rotorDisk is that the rotor area is accepted a rotating zone and the momentum is created by the specified virtual blades. That is why the aerofoil geometry and coefficients are defined in the rotorDisk dictionaries using the lookup table. As a result, the analysis is completed with less mesh number and low computational cost.

The turbine rotor and momentum source forming were defined in the program. However, another model is required to simulate the downstream flow that passed the rotor. The flow is assumed incompressible and conservation law is used to define flow physics mathematically. As seen in Equation 3, the fundamental Navier-Stokes is indicated.

$$\nabla.\vec{V} = 0 \tag{3}$$

The momentum equation of incompressible flow can be derived from Equation 3. Finally, 3D Navier-Stokes equation is found and x-direction component is represented in Equation 4 [5].

$$\begin{aligned}&\rho\left(\partial u/\partial t + u\partial u/\partial x + v\partial u/\partial y + w\partial u/\partial z\right) = \\ &\rho f_x - \partial\rho/\partial x + \mu\left(\partial^2 u/\partial x^2 + \partial^2 u/\partial y^2 + \partial^2 u/\partial z^2\right)\end{aligned} \tag{4}$$

The Navier-Stokes equation is implemented to solve mean behaviour of flow and display the impact of turbulence fluctuations on mean value. The RANS turbulence model can be derived from Navier-Stokes equation and expressed in Equation 5 [6].

$$\begin{aligned}&\partial\left(\rho\overline{U}_i\right)/\partial t + \partial\left(\rho\overline{U}_i\overline{U}_j\right)/\partial x_j = \\ &-\partial/\partial x_j\left(\overline{P} + 2/3\rho k_t\right) + \partial/\partial x_j\left[2\left(\mu + \mu_t\right)\overline{S}_{ij}\right]\end{aligned} \tag{5}$$

In this expression, several parameters are unknown such as dynamic turbulent viscosity. An approach that has sufficient parameters to solve the flow problem is chosen to obtain an approximate result to the actual case. In this study, $k-\varepsilon$ standard turbulence model is preferred to simulate the downstream. The constants of the model are given in Table 1.

Table 1. Constants of $k-\varepsilon$ standard turbulence model

$C_\mu = 0.09$	$C_{\varepsilon 1} = 1.44$	$C_{\varepsilon 2} = 1.92$	$\sigma_{k_t} = 1$	$\sigma_\varepsilon = 1.3$

The implementation of $k-\varepsilon$ standard turbulence model is simpler since the solution converges easily. Moreover, the model is more convenient to simulate rotating flows and separations.

III. Case Study

First of all, the wind tunnel that is generated by coarse and hexahedral mesh is defined in rotorDisk to specify flow volume. The size of the tunnel is specified in blockMeshDict using 8 cartesian coordinates. The height of the tunnel increases throughout the outlet, as seen in Table 2. The roof of the tunnel is flexible; therefore, the pressure gradient is considered zero. Furthermore, the bulk tunnel speed is 10 *m/s*, the flow inlets the tunnel uniformly with 1% tolerance, and the turbulence intensity is defined 0.3%. These tunnel data are significant to create the initial conditions.

Table 2. Dimensions of Wind Tunnel

	Width (*m*)	Length (*m*)	Depth (*m*)
Inlet	2.7	0.0	1.801
Outlet	2.7	11.15	1.851

The background mesh number is decided by mesh sensitivity analysis. The x-axis is divided into 12, y-axis and z-axis are 50 and 8, respectively. The patches of the background mesh are named to specify boundary conditions correctly such as upperWall, lowerWall, and so on. The log law is also checked for wall functions whether the value is in the 30-200 range. The rough mesh of tunnel is formed and indicated in Figure 2.

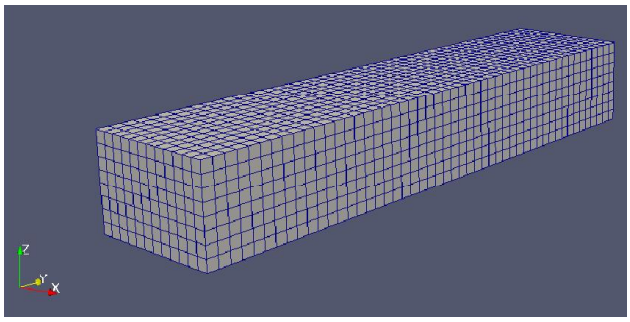


Figure 2. Background mesh

Afterwards, the wind turbine was inserted 4D distance from the inlet of the tunnel same as in the experiment. The tower of the turbine has a telescopic shape that has 5 various diameters. The height of the tower is lowered 0.123 *m* and the rotor is defined at 0.817 *m* height from the ground. The turbine, which has NREL S826 aerofoil shaped aluminum blades, is represented in Figure 3.

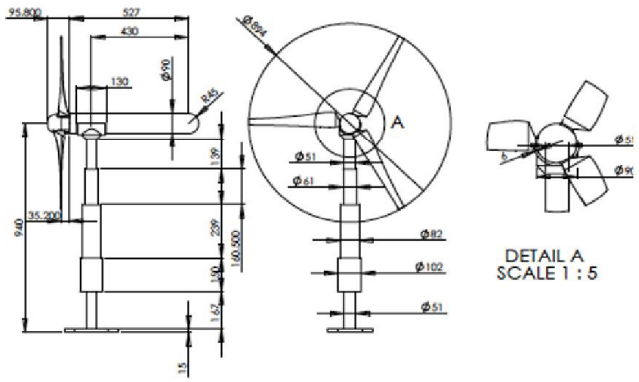


Figure 3. Dimensions of Wind Turbine [7]

The coarse background mesh is narrowed to form the denser mesh of the rotor and its around. A very refine cylindrical volume mesh is created for the rotating zone. The mesh size decreases gradually far away from the rotating zone. Furthermore, the mesh of wake generation volume is made denser than the background to predict the wake developments. This mesh refinement is defined in the snappyHexMeshDict. The generated refine mesh is represented in Figure 4.

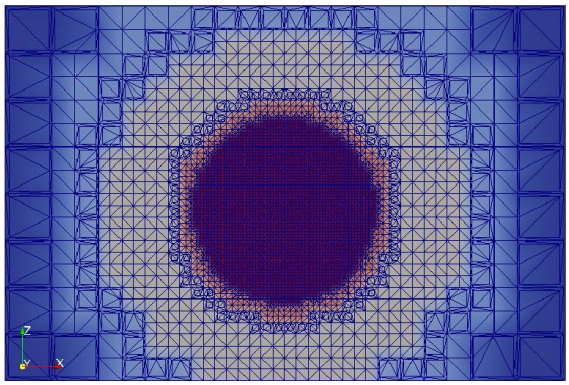


Figure 4. Refine mesh around the virtual rotor (x-axis cross-section)

The tower assembly of the turbine is drawn using Solidworks 2017 and the CAD file is inserted into the program as a .obj format.

Before running the simulation, the initial condition parameters of the flow field are calculated for the $k-\varepsilon$ standard turbulence model and coded in the dictionaries. Turbulence kinetic energy, k, is 1.35E-3, turbulent dissipation rate, ε, is 6.448E-5, and turbulent viscosity, ϑ_t, is 2.544E-3. The initial condition of air is given in Table 3.

Table 3. Initial conditions of air [8]

Inlet velocity (*m/s*)	(0 10 0)
Pressure (kg/ms^2)	0
Density (kg/m^3)	1.225
Kinematic Viscosity (m^2/s)	1.5E-05

In the last step, the momentum source is coded in the fvOptions dictionary. The tip speed ratio (TSR), λ, of the rotor, which was kept at 6 in the experiment, is specified in the dictionary as rotational speed, Ω, in revolution per minute (*rpm*). The TSR can be used to define the revolution speed, as seen in Equation 6.

$$\Omega = \lambda U_{ref} / R \tag{6}$$

The reference velocity and rotor radius are 10 *m/s* and 0.447 *m*, respectively. The rotational speed is found 1281.785 *rpm*. At the end of the dictionary, the profile and data of blades are coded. The lookup table includes geometrical and operational data of blades, where are indicated in Appendix. A part of the lookup table is shown in Figure 5.

```
profiles
{
    profile1
    {
        type lookup;
        data
        (
            (-40.0 0.39968 -0.96710)
            (-35.0 0.36549 -0.87580)
            (-30.0 0.32383 -0.75170)
            (-25.0 0.27557 -0.60080)
            (-20.0 0.22170 -0.43470)
            (-18.0 0.19869 -0.36800)
            (-16.0 0.17474 -0.30430)
            (-14.0 0.14843 -0.24910)
            (-12.0 0.12244 -0.20180)
            (-11.0 0.10792 -0.18650)
```

Figure 5. NREL S826 Lookup table in fvOptions dictionary

The steady-state incompressible case is executed by Semi-Implicit Method for Pressure-Linked Equations (SIMPLE). This solver calculates the mass flux for each cell faces and determines the pressure. Afterwards, the pressure and velocity values are computed and linked each other. The 1000 time-steps are chosen to replicate the iterations until the residuals converge. The post-processing and data extraction is completed using ParaView 6.1.

IV. Results and Discussion

The BT1 experimental setup is simulated using rotorDisk case of OpenFOAM with the combination of ALM and $k-\varepsilon$ turbulence model. The velocity deficit data in the wake region is extracted for 1D, 3D, and 5D distances. The 1D distance is accepted 0.894 m. The flow velocity varies around the wind turbine and in the wake region between 0.4 m/s and 12 m/s. However, the velocity deficit begins to recover going throughout the further downstream. As seen in Figure 7, the velocity increases in far-wake region. Furthermore, when cross-section views in Figure 8 are compared, it can be detected that the diameter of low-speed field reduces far away the rotor and moves towards the centre of wake region.

The experimental [9] and numerical results provide approximate predictions, as seen in Figure 8. The fluctuating trend within the area behind the turbine and the similar patterns of both numerical and experimental results are detected. When the data of individual slices are investigated one by one, it is seen that the prediction of the numerical analysis becomes closer the experimental. However, the results of the numerical analysis at some locations are obtained overestimated when compared with the experimental outcomes. There are some computational reasons why overlapping results cannot be obtained at some points in the wake behaviour analysis. In addition, an almost stagnant wake behaviour is obtained near the wall of the tunnel.

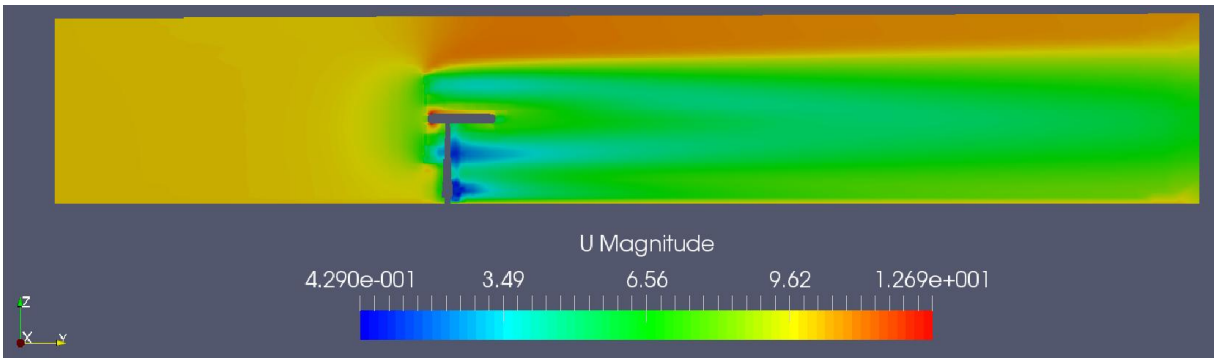
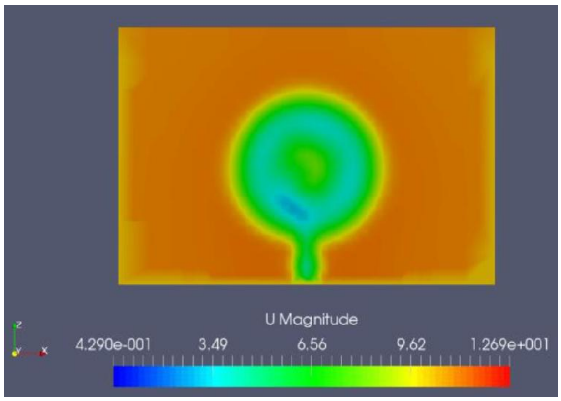
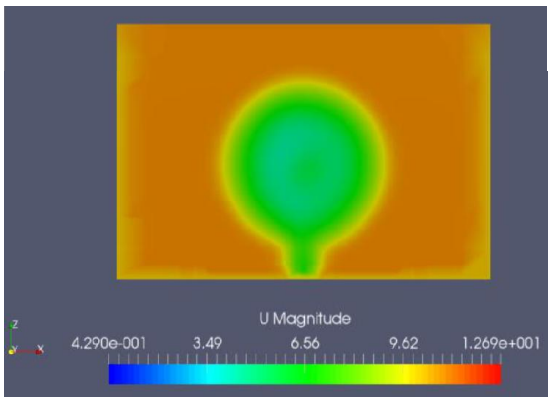


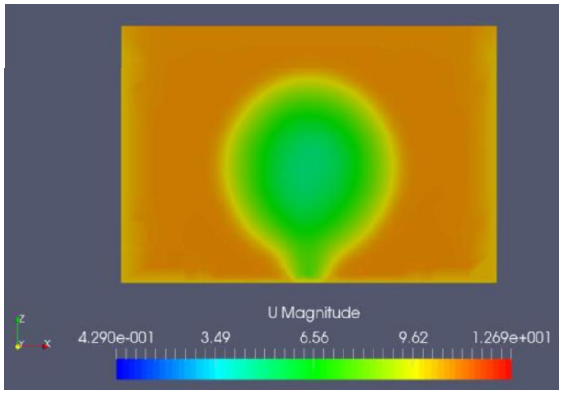
Figure 6. Velocity profile along y-z axis cross-section



(a) 1D

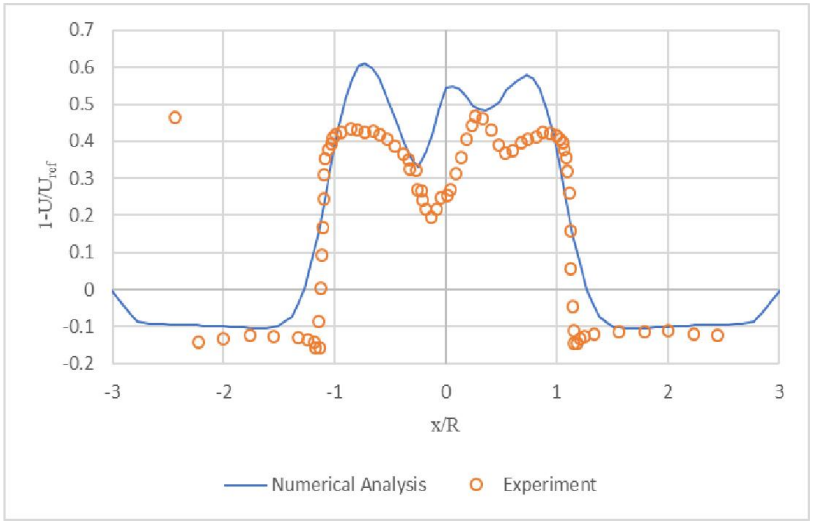


(b) 3D

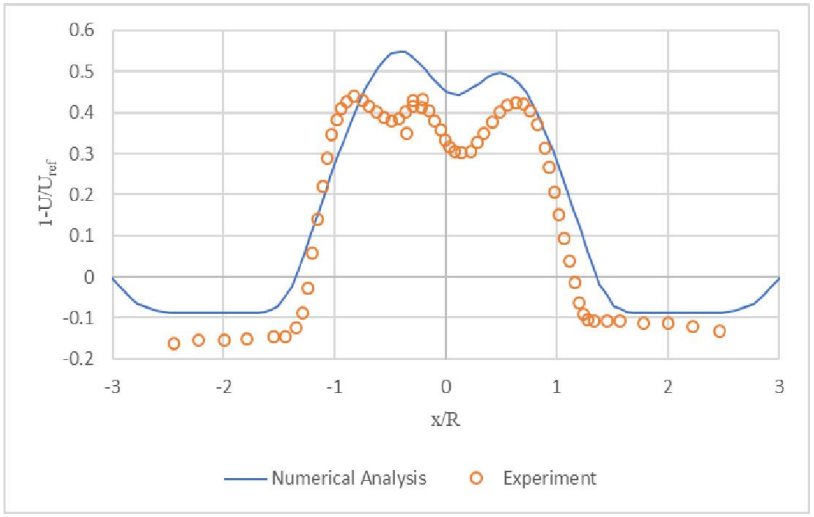


(c) 5D

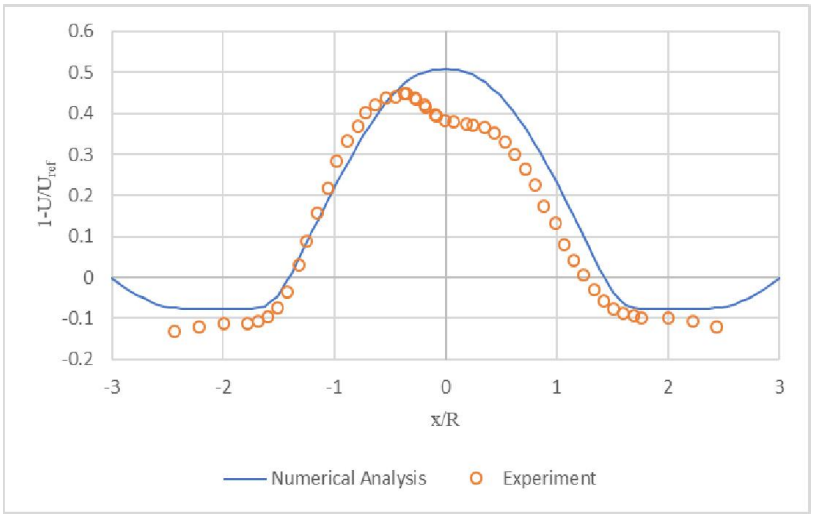
Figure 7. Velocity profile along x-z axis cross-section



(a) 1D



(b) 3D



(c) 5D

Figure 8. Velocity deficit in downstream at certain points

When looking at Figure 8, the velocity deficit around the side and lower walls are examined. However, the value of velocity increases near the upper wall in wake region. This is because the boundary field is defined for side and lower walls, but the upper wall is assumed slip condition. Going throughout the walls to the rotor, the flow speeds up until the tips of blades. In this region, the downstream in near wake zone is faster than in far wake. The ALM can provide sharper velocity reduction successfully at the tips of blades in near wake zone. However, the velocity change in downstream is smoother and the wake region is wider. Therefore, the shade contour of the turbine and tower assembly is more evident in Figure 8.a. The flow slows down in the wake region prominently and the diameter of wake region increases throughout the outlet of the tunnel. Due to the blade geometry, a circular and slow downstream region occur. This zone moves towards the centre in further downstream.

As a result, the rotorDisk case for BT1 experiment provides good approximations and same pattern with the experiment. Furthermore, the ALM supplies to make detectable sharp changes of velocity and tip vortices. The $k-\varepsilon$ turbulence model gives quick and approximate solutions with ALM.

V. Conclusion

The numerical analysis might not overlap with the experimental results. The mesh sensitivity analysis is the significant reason since the results should be independent of mesh size and number. In addition, to converge the numerical results, the potential flow analysis can be done before flow simulation.

Appendix

Table 4. Lift and drag coefficients of NREL S826 aerofoil [7]

α	C_L	C_D	C_L/C_D	α	C_L	C_D	C_L/C_D
-40.0	-0.96710	0.39968	-2.4197	3.00	0.82540	0.023250	35.501
-35.0	-0.87580	0.36549	-2.3962	4.00	0.91800	0.024420	37.592
-30.0	-0.75170	0.32383	-2.3213	5.00	1.0019	0.025880	38.713
-25.0	-0.60080	0.27557	-2.1802	6.00	1.0783	0.027800	38.788
-20.0	-0.43470	0.22170	-1.9608	7.00	1.1469	0.030290	37.864
-18.0	-0.36800	0.19869	-1.8521	8.00	1.2060	0.033540	35.957
-16.0	-0.30430	0.17474	-1.7414	9.00	1.2550	0.037850	33.157
-14.0	-0.24910	0.14843	-1.6782	10.0	1.2929	0.043660	29.613
-12.0	-0.20180	0.12244	-1.6482	11.0	1.3320	0.049960	26.661
-11.0	-0.18650	0.10792	-1.7281	12.0	1.3509	0.059220	22.812
-10.0	-0.18110	0.091970	-1.9691	13.0	1.3718	0.069050	19.867
-9.00	-0.19240	0.073190	-2.6288	14.0	1.3784	0.081720	16.867
-8.00	-0.25200	0.054460	-4.6272	15.0	1.3638	0.098800	13.804
-7.00	-0.23440	0.038600	-6.0725	16.0	1.3431	0.11883	11.303
-6.00	-0.14360	0.029050	-4.9432	18.0	1.2563	0.17904	7.0169
-5.00	-0.049500	0.023940	-2.0677	20.0	1.1940	0.26157	4.5647
-4.00	0.071400	0.021820	3.2722	22.0	1.2493	0.29458	4.2410
-3.00	0.18800	0.021090	8.9142	25.0	1.3379	0.33390	4.0069
-2.00	0.30260	0.020730	14.597	30.0	1.4702	0.38800	3.7892
-1.00	0.41360	0.020770	19.913	34.0	1.5519	0.42331	3.6661
0.00	0.52200	0.021040	24.810	40.0	0.96620	0.63129	1.5305
1.00	0.62690	0.021530	29.118	50.0	0.84970	0.73405	1.1576
2.00	0.72880	0.022220	32.799				

Table 5. Geometrical data of NREL S826: Blade radius, chord length, and twist angle [7]

Figure	c (m)	φ (deg)
0.0075000	0.013500	120.00
0.022500	0.013500	120.00
0.049000	0.013500	120.00
0.055000	0.049500	38.000
0.067500	0.081433	37.055
0.082500	0.080111	32.544
0.097500	0.077012	28.677
0.11250	0.073126	25.262
0.12750	0.069008	22.430
0.14250	0.064952	19.988
0.15750	0.061102	18.034
0.17250	0.057520	16.349
0.18750	0.054223	14.663
0.20250	0.051204	13.067
0.21750	0.048447	11.829
0.23250	0.045931	10.753
0.24750	0.043632	9.8177
0.26250	0.041529	8.8827
0.27750	0.039601	7.9877
0.29250	0.037831	7.2527
0.30750	0.036201	6.5650
0.32250	0.034697	5.9187
0.33750	0.033306	5.3045
0.35250	0.032017	4.7185
0.36750	0.030819	4.1316
0.38250	0.029704	3.5439
0.39750	0.028664	2.9433
0.41250	0.027691	2.2185
0.42750	0.026780	1.0970
0.44250	0.025926	-0.7167

Acknowledgment

This work has been completed within the scope of Master of Science thesis. Special thanks to the Ministry of National Education of the Turkish Republic and Necmettin Erbakan University for their financial support.

References

[1] I. Johnston. (2016, August). Scotland just produced enough wind energy to power it for an entire day. *Independent* [online] Available: http://www.independent.co.uk/environment/scotland-wind-energy-renewable-power-electricity-wwf-scotland-a7183006.html.

[2] Global Wind Energy Council. (2017, April). Global Statistics. *Global Wind Energy Council* [online]. Available: http://gwec.net/global-figures/graphs/

[3] F. Pierella, P. E. Eriksen, L. Saetran, P. A. Krogstad, "Invitation to the 2012 "Blind test 2" Workshop Calculations for two wind turbines in line", Department of Energy and Process Engineering, NTNU, Trondheim, 2012.

[4] J. N. Sorensen, W. Z. Shen, "Numerical Modeling of Wind Turbine Wakes," *Journal of Fluid Engineering*, vol. 124(2), pp. 393-399, 2002.

[5] J. F. Wendt, *Chapter 2 Governing Equations of Fluid Dynamics*. In Computational Fluid Dynamics, by J. D. Anderson Jr., pp. 15-51. Berlin Heidelberg: Springer, 2009.

[6] F. T. M. Nieuwstadt, J. Westerweel, B. J. Boersma, *Turbulence: Introduction to Theory and Applications of Turbulent Flows*. Switzerland: Springer, 2016.

[7] L. Saetran, J. Bartl, "Invitation to the 2015 "Blind test 4" Workshop: Combined power output of two in-line turbines at different inflow conditions", Department of Energy and Process Engineering, NTNU, Trondheim, 2015.

[8] T. J. Scanlon, *Open Source CFD Using OpenFOAM*, University of Strathclyde, Glasgow, 2016.

[9] P. A. Krogstad, P. E. Eriksen, ""Blind test" calculations of the performance and wake development for a model wind turbine," *Renewable Energy*, vol. 50, pp. 325-333, 2013.

Energy Conversion Characteristics of a Variety of Solid Waste Samples through Microwave Plasma Gasification Process

Melda Ozdinc CARPINLIOGLU *[1] Aytac SANLISOY[2]
*[1]Gaziantep University, Gaziantep/Turkey - melda@gantep.edu.tr
[2]Gaziantep University, Gaziantep/Turkey - aytacsanlisoy@gantep.edu.tr

Abstract - **A microwave plasma gasifier MCw GASIFIER was designed and constructed at laboratory scale as a research project of TUBITAK with a grant number of 115 M389. An operational study was conducted with a variety of solid waste samples which were regarded as fuel of MCw GASIFIER. The utilized amount of power input and amount of plasma environment- gas were the basic variables to determine gasification rate of fuel. The amount and chemical content of the produced syngas besides its available energy content were considered through a thermodynamic analysis of the process to determine the energy conversion characteristics of the fuel. The covered ranges of the variables for the operational study are input power range 3000 W < P < 6000 W; amount of plasma environment gas of air (50 l/min < Q g < 100 l/min). Russian, South African and Turkish Sırnak coal, pine and hornbeam sawdust besides polyethylene are the gasified samples in operation. Overall performance of MCw GASIFIER can be estimated for the possibility of a large scale industrial plant installation as a future work.**

Keywords **- MCw GASIFIER, Thermodynamic Analysis, Syngas**

***Corresponding Author Prof. Dr. melda@gantep.edu.tr**

I. INTRODUCTION

Global solid waste generation is estimated to be more than 3.5 million tonnes per day in 2010, more than 6 million tonnes per day by 2025 and 11 million tonnes per day by 2100. The global cost of trash is $205 billion a year in 2010 and $375 billion by 2025. Landfills, and uncollected waste, also contribute to climate change through the production of methane, a potent greenhouse gas. In this content waste to energy processing systems are currently be regarded as alternative solutions. WTE Worldwide [1] can be referred for the global status in the last 30 year-period. According to Leckner [2] the waste to energy processing systems are mass burning systems (combustion) ,gasification systems, co-combustion systems ,melting plants and as a new emerging technology plasma gasification systems. Plasma gasification offers an environmental performance better than incineration and conventional gasification systems through reduced volume of waste and with a complete disposal of harmful wastes. Therefore handling of plastic wastes- harmful, toxic wastes and MSW seems to be possible. The major problem associated with plasma gasification is the optimum operating conditions with a reduced amount of energy input. In the case of plasma gasification a variety of solid wastes can be transformed into syngas and ash. Hydrogen content of syngas is the basic parameter under consideration from the point of view of waste to energy conversion. Besides amount of plasma input power, conversion efficiency of waste and process characteristics which are dependent on the physical- chemical characteristics of the waste and the plasma environmental gas are also of practical importance.

A micro- wave plasma gasification process for a variety of solid waste disposal is the concern of the paper based upon a variety of previous publications of the authors [3 through 9]. The operational test cases of the installed microwave plasma gasifier MCw GASIFIER are presented in this paper briefly in terms of waste to energy conversion.

II. MCW GASIFIER: SYSTEM DESCRIPTION

MCw GASIFIER is an open cycle blower type set-up which is given as a schematic description in Figure 1. The heart of the setup is the microwave plasma generation and control system of MUEGGE. The system description is given in Table 1. The system is able to generate microwave plasma at a varying input power up to 6000 W at a frequency of 2450 MHz. Air is used as the environment gas in the operational study presented although use of water vapor is also possible.

Solid waste samples of 3 different coal , 2 kinds of sawdust and polyethylene pellets which are specified by codes of CR,CSA, CTR, HSW, PSW, PP are used as fuel . Since the energy conversion is governed by the thermodynamic analysis of the process the material -physical characteristics of solid waste samples and their chemical content are the major input data . The samples were prepared as powders. Proximate and ultimate analysis of the solid waste samples; CR, CSA, CTR, HSW, PSW, PP were conducted. An outline is given in Table 2.

As can be described in the recent article of the authors [9] thermodynamic analysis is provided in terms of energy and mass conservation. The defined first law and second law efficiency terms, η_{ES}, η_{EP}, η_{EXS}, η_{EXP} content conversion efficiency parameters, CCE and hydrogen quality H_q are referred through the so-called process and system descriptions.

The defined parameters are given in Table 3.

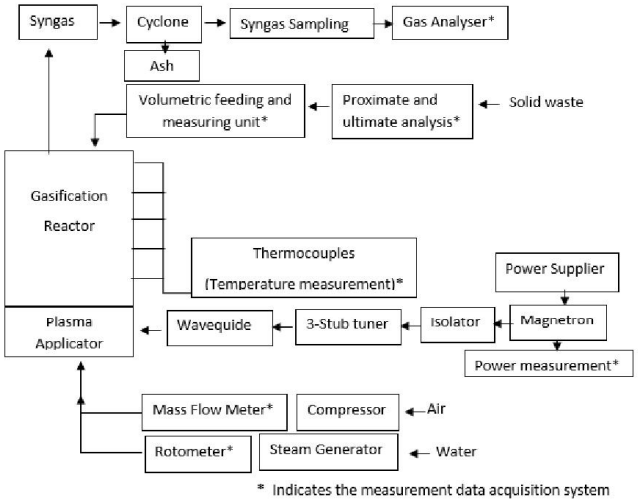


Figure 1a: Sketch of the realized set up with the conceptual process description

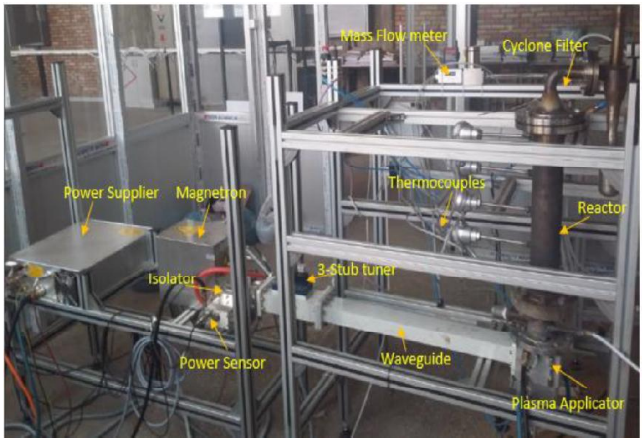


Figure 1.b: Photograph of the System

TABLE 1: Details of MCw GASIFIER System with Air Utilization as Plasma Gas

SYSTEMS OF MCw GASIFIER	TYPE	SUB-SYSTEMS(COMPONENTS)	CHARACTERISTICS-FUNCTION	UTILIZED RANGE
MICROWAVE PLASMA GENERATION AND CONTROL SYSTEM	MUEGGE (SOFTWARE PROGRAM: Muegge MX model control software	MX6000D-110K model power supplier MH6000S-213BF model magnetron head (In combination with Isolator, 3 Stub-Tuner, Wave Guide Plasma Applicator)	Generation of Power up to P= 6000 W Generation , control and transmission of microwave signal to introduce plasma	W < P < 6000 W SENSITIVITY : 1% VARIATION IN P Frequency of 2450 MHz
GASIFICATION REACTOR	HOME MADE FIXED FUEL BED ,CYLINDRICAL , SWIRLING INLET OF PLASMA GAS AT REACTOR HEAD	REACTOR HEAD (In combination with plasma applicator) MAIN BODY	MATERIAL: Stainless Steel Diameter: 8,1 cm Length : 50 cm UPWARD FLOW OF PLASMA FLAME	
PLASMA ENVIRONMENT FEEDING SYSTEM	Air Supplier: Lupamat LKV 30/8 model screw compressor.	Flow rate measurement: ALICAT MCR-250SLPM-D model mass flow controller is used	Compressed air which has maximum 8 bar pressure and 4850l/min flow	RANGE OF AIR FLOW: 50 ,75,100 l/min
FUEL-SOLID WASTE	Russian Coal CR South African Coal CSA Turkish Low Grade-Sirnak Coal CTR Hornbeam Sawdust HSW Pine Sawdust PSW Polyethtlene Particle PP		Coal Particle Size: 0.1 mm Sawdust Particle Size:1 mm Material Density –Measured kg/m3 CR: 701 CSA: 750 CTR: 930 HSW:230 PSW: 219 PP: 212	14.7 g/min - 35.71 g/min

MEASUREMENT AND DATA ACQUISITION SYSTEM	Local Temperature Measurement :B type (Pt18Rh-Pt) thermocouple Elimko E-PR-110 model data acquisition card. MRU VARIO plus Semi – Continuous Syngas Monitoring System	Up to 1820℃. Oxygen 0-25% Carbon Monoxide 0-10 % /30%/100% Carbon Dioxide Monoxide 0-10 % /30%/100% Methane Monoxide 0-10 % /30%/100% Hydrogen 0-10 % /100%	Resolution: 0.01% Repeatability 1% Fs Response Time : 30 Seconds (From Analyzer Inlet Port) Linearity Error: 1%Fs Detection Limit : 0.05% Respectively 1 Ppm	SAMPLING RATE : 1 l/min- 1.33 l/min

Table 2: Measured Material Characteristics of Solid Waste Samples per Mass Base -Proximate Analysis * Adiabatic Bomb Calorimeter

Fuel- Solid Waste	Moisture (%)	Volatile matter (%)	Fixed carbon (%)	Ash (%)	Calorific Value kJ/kg*	Carbon (%)	Hydrogen (%)	Oxygen (%)	Nitrogen (%)	Sulphur (%)
CR	3.15	23.51	67.46	5.87	31336.05	66.81	4.49	21.72	1.00	0.11
CSA	3.40	25.94	55.94	14.71	30758.85	62.56	4.08	17.61	0.64	0.40
CTR	0.85	36.67	21.05	41.43	19954.03	42.18	3.75	5.96	0.35	6.33
HSW	17.39	72.58	10.02	0.69	21352.90	36.15	6.24	56.92	0.00	0.00
PSW	21.35	69.54	8.53	0.58	17941.66	39.66	6.45	53.30	0.00	0.00
PP	0.19	94.90	0.91	5.44	----------	69.6	10.26	16.14	0.00	0.00

Table 3: Definitions of Performance Parameters

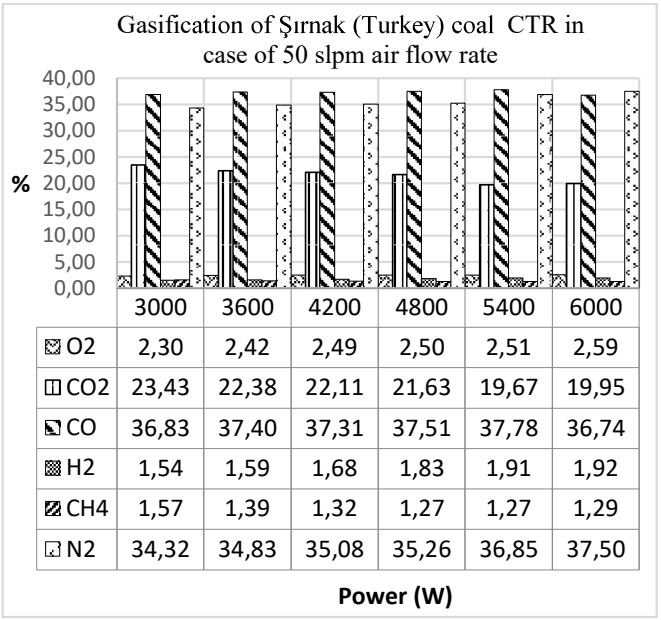
PARAMETER	DEFINITION
η_{EP}: First law efficiency of process	$\eta_{EP[\%]} = \frac{\dot{m}_{syn}(^{kg}/_{s}) \times HHV_{syn}(^{kJ}/_{kg})}{\dot{m}_{fuel}(^{kg}/_{s}) \times HHV_{fuel}(^{kJ}/_{kg})}$
η_{ES}: First law efficiency of system	$\eta_{ES}[\%] = \frac{\dot{m}_{syn}(^{kg}/_{s}) \times HHV_{syn}(^{kJ}/_{kg})}{\dot{m}_{fuel}(^{kg}/_{s}) \times HHV_{fuel}(^{kJ}/_{kg}) + W_{plasma}}$
η_{EXP}: Second law efficiency of the process	$\eta_{EXP}[\%] = \frac{\dot{m}_{syn}(^{kg}/_{s}) \times Ex_{syngas}(^{kJ}/_{kg})}{\dot{m}_{fuel}(^{kg}/_{s}) \times Ex_{fuel}(^{kJ}/_{kg})}$
η_{EXS}: Second law efficiency of system	$\eta_{EXS}[\%] = \frac{\dot{m}_{syn}(^{kg}/_{s}) \times Ex_{syngas}(^{kJ}/_{kg})}{\dot{m}_{fuel}(^{kg}/_{s}) \times Ex_{fuel}(^{kJ}/_{kg}) + Ex_{plasma}(kW)}$
CCE: Content conversion efficiency CCE_{H_2}: Hydrogen content conversion efficiency	$CCE_{H_2} = \frac{\dot{m}_{H_2}}{\dot{m}_{fuel}}$
CCE_{ash}: Ash content conversion efficiency	$CCE_{ash} = \frac{\dot{m}_{ash}}{\dot{m}_{fuel}}$
CCE_{syn}: Syngas content conversion efficiency	$CCE_{syn} = \frac{\dot{m}_{syn}}{\dot{m}_{fuel}}$
CCE_{system}: System content conversion efficiency	$CCE_{system} = \frac{\dot{m}_{syn} + \dot{m}_{ash}}{\dot{m}_{fuel} + \dot{m}_{plasma}}$
H_q: Hydrogen quality of syngas	$H_q = \frac{\dot{m}_{H_2}}{\dot{m}_{syn}}$
S_m: Mass scale parameter S_w: Power scale parameter	$S_m[\%] = {\dot{m}_{plasma\ gases}}/{\dot{m}_{fuel}}$ $S_w\left[{}^{kJ}/_{kg}\right] = {}^{W}/_{\dot{m}_{fuel}}$

III. OPERATIONAL STUDY : ANALYSIS OF THE TEST CASES

Operational study of MCw GASIFIER is described in Table 4. A constant amount of solid waste, 250 g was processed at varying amounts of plasma gas as 50 l/min, 75 l/min and 100 l/min at varying input power from 3000 W to 6000 W. The local temperatures at the reactor wall at 5 different locations from y/h =0.28 to y/h= 0.92 were measured during the process. Generated syngas was monitored through MRU VARIO and the process time was recorded inspecting the outcome of of analyzer and by visual observation of the system. The recorded time of process was used for the determination of solid waste gasification rate. The measured local temperatures are their averages during the processing time. Not only the temperature variation inside the reactor but also the temperature of syngas is the governing parameter for energy conversion. Temperature of syngas is defined as the time average of the 5 different local temperature measurements inside the reactor since the process is a dynamic one with time and the measurements are focused on the determined time of process. The sample results for CTR gasification as a function of input power for different amounts of air through syngas content are given in Figure 2 a and Figure 2.b . The variation of local temperatures in the reactor during the operational time for CTR is given as sample plots in Figure 3.

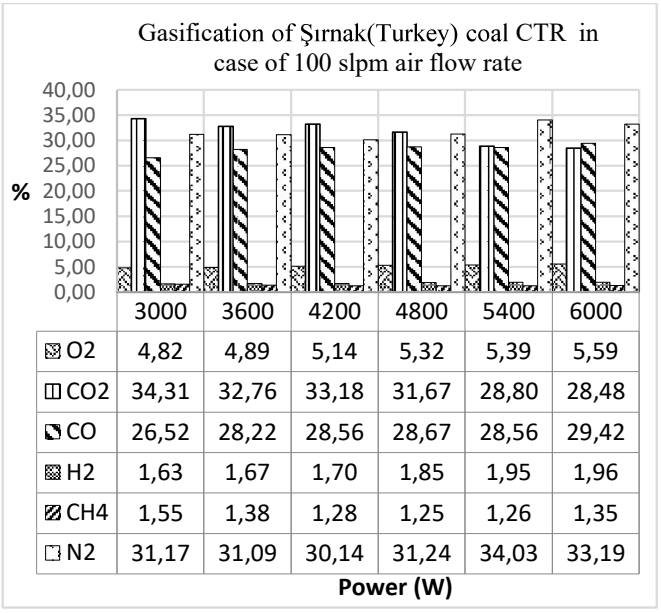
Table 4: Operational Range of Mcw Gasifier

SOLID WASTE -FUEL	AIR l/min	FUEL GASIFICATION RATE g/min	PLASMA POWER W
CR	50 75 100	14,7- 20,27 15,95 – 21,48 17- 22	3000, 3600, 4200, 4800, 5400, 6000
CTR	50 75 100	15- 20,27 15,95 -21,42 17 - 22	3000, 3600, 4200, 4800, 5400, 6000
CSA	50 75 100	16,3- 20,27 17,44- 25 17- 22	3000, 3600, 4200, 4800, 5400, 6000
HSW	50 75 100	17-25 20,83- 30 23,43-22	3000, 3600, 4200, 4800, 5400, 6000
PSW	50 75 100	17- 25 20,83- 30 23,43-35,71	3000, 3600, 4200, 4800, 5400, 6000
PP	50 75 100	22,72- 28,8 24,19- 30 25- 27,77	3000, 3600, 4200, 4800, 5400, 6000



	3000	3600	4200	4800	5400	6000
O2	2,30	2,42	2,49	2,50	2,51	2,59
CO2	23,43	22,38	22,11	21,63	19,67	19,95
CO	36,83	37,40	37,31	37,51	37,78	36,74
H2	1,54	1,59	1,68	1,83	1,91	1,92
CH4	1,57	1,39	1,32	1,27	1,27	1,29
N2	34,32	34,83	35,08	35,26	36,85	37,50

Figure 2.a : Syngas Content at 50l/min



	3000	3600	4200	4800	5400	6000
O2	4,82	4,89	5,14	5,32	5,39	5,59
CO2	34,31	32,76	33,18	31,67	28,80	28,48
CO	26,52	28,22	28,56	28,67	28,56	29,42
H2	1,63	1,67	1,70	1,85	1,95	1,96
CH4	1,55	1,38	1,28	1,25	1,26	1,35
N2	31,17	31,09	30,14	31,24	34,03	33,19

Figure 2.b Syngas Content at 100l/min

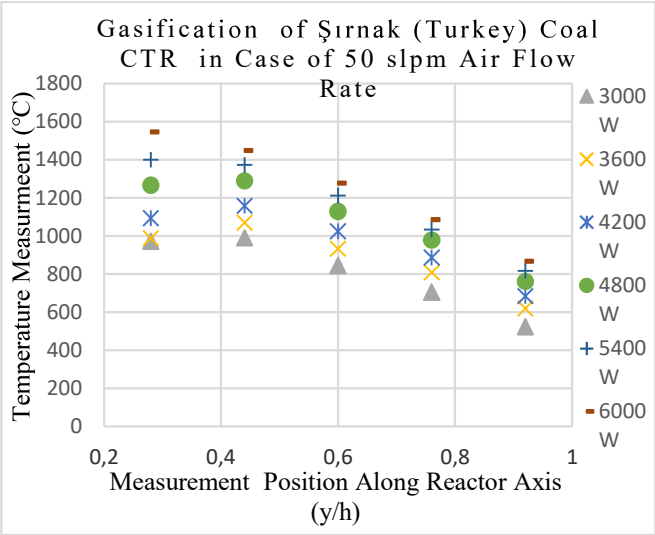


Figure 3.a: Reactor Temperature Variation at 50 l/min

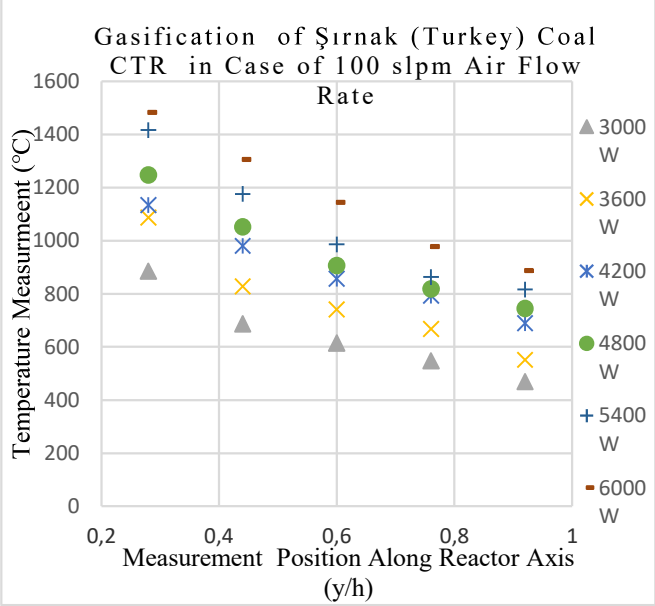


Figure 3.b: Reactor Temperature Variation at 100 l/min

For the waste to energy conversion; analysis is given in terms of mainly:

I) Gasification rate of the solid wastes

II)Available energy content of the solid wastes

III) Energy content of Syngas

as a function of utilized air and input power.

The overall system performance is set after the execution of thermodynamic analysis of the conducted operational test cases. It can then be used for the estimation of a feasible large plant.

ACKNOWLEDGMENT

The presented study was conducted in the content of a research project of the Scientific and Technological Research Council of Turkey - TUBITAK under the contract number of 115M389. The authors are expressing their sincere thanks for the support of TUBITAK .

REFERENCES

[1] www.waste-management-world.com

[2] Leckner, B., Process aspects in combustion and gasification Waste-to-Energy (WtE) units, (2015) Waste Management (37), 13-25

[3] A. Sanlisoy, M.O. Carpinlioglu, A review on plasma gasification for solid waste disposal, International Journal of Hydrogen Energy 42(2017) 1361-1365

[4] A. Sanlisoy, M.O. Carpinlioglu , A review on plasma gasification for solid waste disposal, 4th International Conference on Renewable Energy: Generation and Applications ICREGA 2016 Belfort –FRANCE 08-10 February 2016

[5] A. Sanlisoy, M.O. Carpinlioglu, Presentation of a Microwave Plasma Gasification System "MCw GASIFIER" ECRES 2016 4th European Conference on Renewable Energy Systems İstanbul TURKEY August 28-31, 2016 . ISBN: 978-605-86911-4-8 ID: 236 P: 115

[6] A. Sanlisoy, M.O. Carpinlioglu, Preliminary Measurements on Microwave Plasma Characteristics UEMK 2016 International Energy and Engineering Conference Gaziantep TURKEY 13-14 October, 2016

[7] M.O. Carpinlioglu , Brainstorming: Symbiosis-Circular-Performance Economy-Alternative Fuels for Future ICAF 2016 International Conference on Alternative Fuels Erciyes University Kayseri- TURKEY 02-04 December 2016 ID: ICAF -2016-86 P: 36

[8] A. Sanlisoy, H. Melez , M.O. Carpinlioglu Characteristics of Solid Fuels for the Plasma Gasification accepted for CPESE 2017, September 25-29,2017 Berlin GERMANY

[9]M.O. Carpinlioglu, A. Sanlisoy, Performance Assessment of Plasma Gasification for Waste to Energy Conversion: A Methodology for Thermodynamic Analysis, International Journal of Hydrogen Energy, accepted in 22 August 2017

Effects of Liquid Nitrogen Addition to Intake Air on the Performance and NO Formation of a Gasoline Engine

A. KAYA[1] and G. GONCA[1]

[1] Yildiz Technical University, Istanbul/Turkey, metahkaya@gmail.com
[1]Yildiz Technical University, Istanbul/Turkey, ggonca@yildiz.edu.tr

***Abstract* - Engine researchers focused on increment of engine performance and reduction of emissions released from internal combustion engines to prevent air pollution. In this study, it is theoretically aimed to increase performance characteristics such as power output (PO), torque, thermal efficiency (TE) and reduce NO emission of a single cylinder 4-stroke gasoline engine by adding liquid nitrogen into the cylinder. A simulation model, which was confirmed by previous empirical works, has been used to figure out the effects of nitrogen addition. The results obtained demonstrated that by increasing mass percentage of nitrogen at constant engine speed of 3600 rpm, PO increased to 10.67 kW from 8.69 kW and torque increased to 28.31 N.m from 23.06 N.m at maximum increment conditions. NO formation remarkably decreased. However, TE reduction was lower than 10%. It was shown that higher power requirement can be provided by the liquid nitrogen injection.**

***Keywords* - Spark ignition engine, combustion analysis, engine performance, NO emission**

I. INTRODUCTION

Engine researchers have focused on energetic and ecological performance improvements due to energy and emission requirements. Many studies can be found in literature investigating the impacts of using additives on intake air or to fuel, aiming to increase engine performance [1]–[10].

Al-Hasan M. [11] investigated the effects of blending unleaded gasoline with ethanol on performance characteristics and exhaust emissions of a four stroke, four-cylinder SI engine. The results indicated that using ethanol as an additive increased PO, torque, volumetric efficiency, TE, fuel consumption and CO_2 emission while reducing fuel consumption, equivalence ratio, CO and unburned hydrocarbons (UHC) emissions.

Bayraktar H. [12] investigated the effects of ethanol addition to gasoline on performance and exhaust emissions of an SI engine experimentally and theoretically. The results yielded that PO and efficiency increased with increasing the volume percentage of ethanol in fuel due to improved combustion. Using blended fuel reduced CO concentration, but NO emission raised due to higher in-cylinder temperatures.

Hsieh et al. [13] experimentally investigated the engine performance and exhaust gas emissions of an SI engine fuelled with ethanol–gasoline blend. The results showed that the torque (ranging from 2% to 4%) and fuel consumption increased inconsiderably. CO and UHC formations decreased because of the leaning effect; and CO_2 emission increased due to better combustion. Also, the NO_x emissions are more affected by operating conditions, whilst comparing with the amount of ethanol in mixture.

Liu et al. [14] examined the effects of adding methanol at low rates on gasoline. The blended fuel lowered the PO and torque slightly, while increasing the TE. CO and HC emissions were lower than neat gasoline operation after catalytic converter. The effect on NO_x emission was ignorable, both before and after the three-way catalytic converter.

Illiev S. [15] used a 1-D model to analyse the emission and performance characteristics of a four-stroke SI engine running with different volumetric rates of ethanol-gasoline and methanol-gasoline mixtures. The results pointed out that using blends decreased PO and increased fuel consumption, in comparison with neat gasoline. CO and HC emissions were lower than neat gasoline, however NO_x emissions were fairly higher.

Elfasakhany A. [16] experimentally investigated the performance characteristics and exhaust gas emissions of a small size research engine using different ratios of bio-ethanol and iso-butanol in gasoline. The results indicated that comparing to neat gasoline fuel, the volumetric 10% blends decreased volumetric efficiency, brake power and torque output, UHC and CO emissions by 2%, 3.8% and 1.7%, 15% and 20%, respectively. But it has been asserted that the drop in engine performance would be covered by increasing the blend rate value (>10 vol%).

Elsemary et al. [17] examined the effects of hydrogen addition on the engine performance and emission products of an gasoline engine. Results show that hydrogen addition increased in cylinder pressure and thermal efficiency decreased brake specific fuel consumption. Hydrogen addition also caused to a reduction in the UHC and CO emissions.

Shivaprasad et al. [18] studied the effects of adding hydrogen to air-fuel mixture on performance and emissions of a single-cylinder SI engine. Results showed that the hydrogen

addition increased brake mean effective pressure about 5%. Brake thermal efficiency increased until the hydrogen fraction reaches up to 20%; then, the brake thermal efficiency was decreased due to lower air existence. The volumetric efficiency decreased as hydrogen tended to replace air from the mixture. CO and hydrocarbons emissions decreased, and NO_x emissions increased due to higher temperatures in cylinder.

Mingrui et al. [19] researched the effects of water injection, on emissions and performance characteristics of a gasoline engine. The results indicated that water injection increased power output and decreased NO_x emissions.

Christodoulou and Megaritis [20] experimentally studied the impacts of hydrogen and nitrogen addition on the emissions and combustion of a diesel engine, respectively. Results showed that nitrogen addition decreased NO emission and thermal efficiency.

II. THEORETICAL MODEL

In the two-zone combustion models, the combustion chamber is divided into burnt and unburned gas region. The results obtained from the calculations done for both regions can be more accurate, comparing to calculations made by using average values of the thermodynamic properties of the gas in the combustion chamber [21]. Therefore, two-zone combustion model was used in this study.

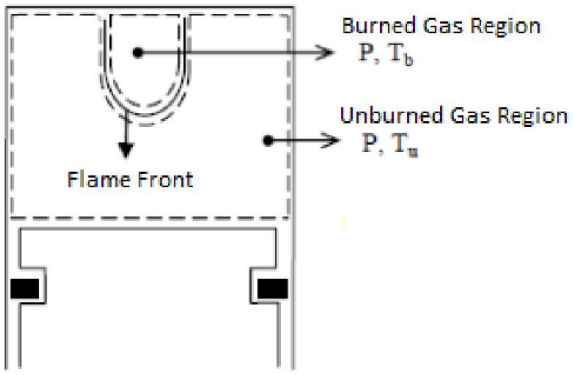


Figure 1. Two Zone Combustion Model [21]

In the model, following assumptions are made for burned and unburned gas regions [21];

The pressures of both zones are equal at any moment,

Heat conduction between zones is neglected,

There is always a thermodynamic balance,

Fuel, air and residual gas are homogeneously mixed,

Gases participate in calculations like ideal gas, taking temperature change into consideration.

In this study, the simulation model proposed by Ferguson [22] has been developed by adding Nitrogen into the combustion reaction as shown below:

$$\varepsilon\phi(C_\alpha H_\beta O_\gamma N_\delta)+\left[(0,21\cdot O_2)+(0,79\cdot N_2)\right]+y\cdot N_2 \rightarrow \upsilon_1 CO_2+\upsilon_2 H_2O+\upsilon_3 N_2+\upsilon_4 O_2+\upsilon_5 CO+\upsilon_6 H_2+\upsilon_7 H+\upsilon_8 O+\upsilon_9 OH+\upsilon_{10} NO \quad (1)$$

Here ε is molar fuel-air ratio, ϕ is equivalence ratio and $\alpha,\beta,\gamma,\delta$ are atom numbers of Carbon, Hydrogen, Oxygen, Nitrogen in the fuel, respectively. υ is mole fractions of the combustion products. y is Nitrogen's mole fraction and calculated as:

$$y=\frac{K_{\%}M_{air}}{M_{N_2}} \quad (2)$$

M_{air} and M_{N_2} are total air and nitrogen molecular weights. $K_{\%}$ is the rate of nitrogen mass to total air mass and defined as:

$$K_{\%}=\frac{m_{N_2}}{m_{air}} \quad (3)$$

More information can be found in references. [22–24]

Table 2: Engine specifications.

Engine Model	Honda GX 390
Engine Type	Air-cooled 4-stroke OHV
Bore x Stroke	88 X 64 mm
Displacement	389 cm^3
Power Output	11.7 HP (8.7 kW) @ 3,600 rpm
Torque	19.5 lb-ft (26.4 Nm) @ 2,500 rpm
Compression Ratio	8.2:1

III. RESULTS AND DISCUSSION

Results of nitrogen addition which are obtained from simulation are given below in figures.

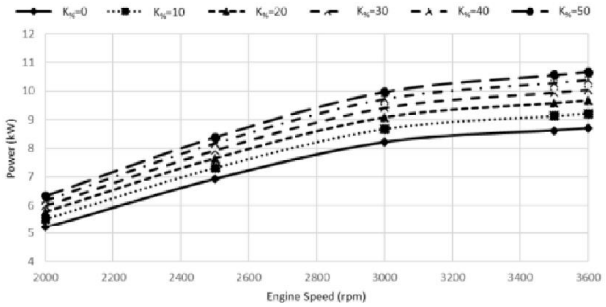


Figure 2: Power output at different engine speeds

In fig. 2, it is seen that as the rate of nitrogen mass increased, power output increased simultaneously. The power output is 8.69 kW at 3600 rpm without nitrogen addition. However, the power output is 10,67 kW with 50% rate of

nitrogen mass addition. Thus, the power increased by 22% with nitrogen addition.

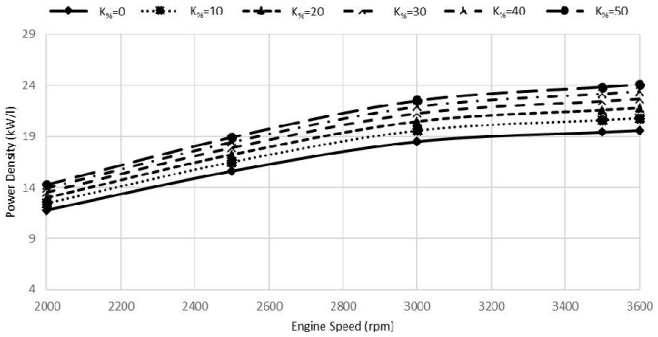


Figure 3: Power density at different engine speeds

Fig. 3 shows the effect of nitrogen addition on power density. Power density increased likewise the power output with nitrogen addition. Power density without nitrogen addition is 19.61 kW/l at 3600 rpm. and with 50% rate of nitrogen mass addition it increases to 24.07 kW/l. Thus, increment of power density by nitrogen addition is around 22%.

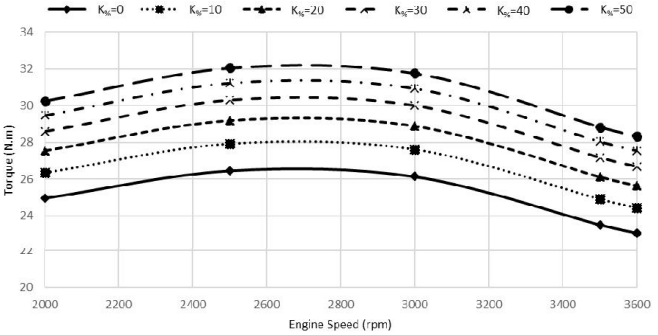


Figure 4: Torque at different engine speeds

In fig. 4 the effect of nitrogen addition on torque is shown. It's seen that as the rate of nitrogen mass increases, the torque output increased as well. Torque output without nitrogen addition is 26.46 N.m at 2500 rpm and with 50% rate of nitrogen mass addition torque output is 32.05 N.m. So, increment of torque is around 21%.

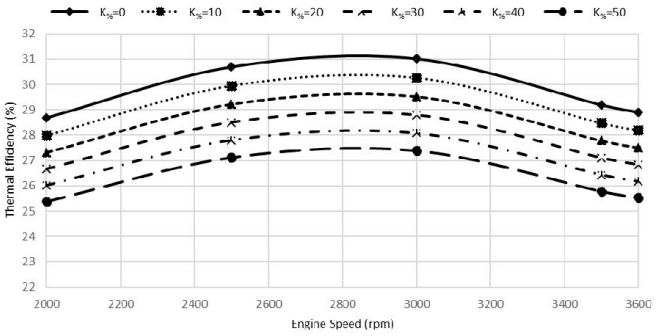


Figure 5: Thermal efficiency at different engine speeds

Fig. 5 shows the effect of nitrogen addition on thermal efficiency. It is seen that unlike power output the thermal efficiency is decreased by nitrogen addition. Thermal efficiency without nitrogen addition is 28.88% at 3600 rpm and with 50% nitrogen addition it is 25.53%. So, decrement of thermal efficiency is around 11%. The main reason of this result is that equivalence ratio and injected fuel mass enhance with augmenting nitrogen ratio in the mixture. Therefore, thermal efficiency reduction seems with increasing power output, but the reduction rate of the efficiency can be absorbed due to lower ratio.

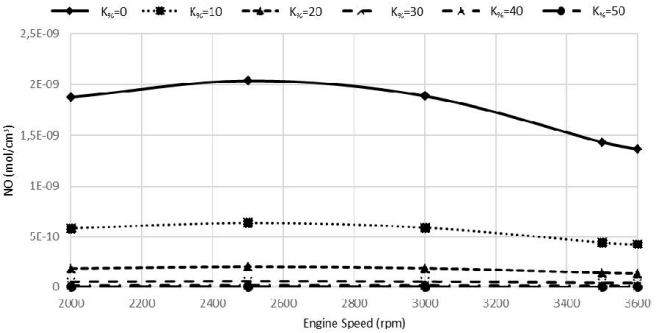


Figure 6: NO formation at different engine speeds

Fig. 6 shows the effect of nitrogen addition on NO formation. It is clearly seen that nitrogen addition has a crucial effect on NO formation. NO emission greatly reduced as the nitrogen rate increased. Increasing nitrogen ratio leads to colder cylinder charge so the NO formation lowers due to lower combustion temperatures. Abatement ratio is higher than 50% as can be clearly seen in the figure.

IV. Conclusion

In this study, effects of nitrogen addition on performance and NO formation of a single cylinder four-stroke SI engine fuelled with gasoline are investigated. In the results, the maximum power output is obtained with 50% nitrogen addition at 3600 rpm. In this scenario the power increment seen is about 22% with nitrogen addition. Due to power increment, torque and power density increased with nitrogen addition as well. However, nitrogen addition has a negative impact on thermal efficiency. As it is shown in fig. 5, thermal efficiency decreased around 11% due to increasing equivalence ratio and injected fuel mass in the mixture. However, when it is considered that the power increased about 22%, the thermal efficiency drop can be seen tolerable. The main purpose of the nitrogen injection into the cylinder is to enhance the power output. This goal is achieved with the proposed ratios of nitrogen. Furthermore, nitrogen addition provided a huge reduction on NO emission which enhances its attractiveness.

Acknowledgment

This paper is presented as a part of the MSc thesis of the first author.

REFERENCES

[1] A. Elfasakhany and A.-F. Mahrous, 'Performance and emissions assessment of n-butanol–methanol–gasoline blends as a fuel in spark-ignition engines', *Alex. Eng. J.*, vol. 55, no. 3, pp. 3015–3024, Sep. 2016.

[2] A. Elfasakhany, 'Investigations on performance and pollutant emissions of spark-ignition engines fueled with n-butanol–, isobutanol–, ethanol–, methanol–, and acetone–gasoline blends: A comparative study', *Renew. Sustain. Energy Rev.*, vol. 71, pp. 404–413, May 2017.

[3] M. A. Costagliola, L. De Simio, S. Iannaccone, and M. V. Prati, 'Combustion efficiency and engine out emissions of a S.I. engine fueled with alcohol/gasoline blends', *Appl. Energy*, vol. 111, pp. 1162–1171, Nov. 2013.

[4] Y. Li *et al.*, 'Combustion, performance and emissions characteristics of a spark-ignition engine fueled with isopropanol- n -butanol-ethanol and gasoline blends', *Fuel*, vol. 184, pp. 864–872, Nov. 2016.

[5] H. S. Yücesu, A. Sozen, T. Topgül, and E. Arcaklioğlu, 'Comparative study of mathematical and experimental analysis of spark ignition engine performance used ethanol–gasoline blend fuel', *Appl. Therm. Eng.*, vol. 27, no. 2–3, pp. 358–368, Feb. 2007.

[6] B. M. Masum, H. H. Masjuki, M. A. Kalam, I. M. Rizwanul Fattah, S. M. Palash, and M. J. Abedin, 'Effect of ethanol–gasoline blend on NOx emission in SI engine', *Renew. Sustain. Energy Rev.*, vol. 24, pp. 209–222, Aug. 2013.

[7] M. Canakci, A. N. Ozsezen, E. Alptekin, and M. Eyidogan, 'Impact of alcohol–gasoline fuel blends on the exhaust emission of an SI engine', *Renew. Energy*, vol. 52, pp. 111–117, Apr. 2013.

[8] M. Koç, Y. Sekmen, T. Topgül, and H. S. Yücesu, 'The effects of ethanol–unleaded gasoline blends on engine performance and exhaust emissions in a spark-ignition engine', *Renew. Energy*, vol. 34, no. 10, pp. 2101–2106, Oct. 2009.

[9] F. Scala, E. Galloni, and G. Fontana, 'Numerical analysis of a downsized spark-ignition engine fueled by butanol/gasoline blends at part-load operation', *Appl. Therm. Eng.*, vol. 102, pp. 383–390, Jun. 2016.

[10] S. O. Akansu, S. Tangöz, N. Kahraman, M. İ. İlhak, and S. Açıkgöz, 'Experimental study of gasoline-ethanol-hydrogen blends combustion in an SI engine', *Int. J. Hydrog. Energy*, vol. 42, no. 40, pp. 25781–25790, Oct. 2017.

[11] M. Al-Hasan, 'Effect of ethanol–unleaded gasoline blends on engine performance and exhaust emission', *Energy Convers. Manag.*, vol. 44, no. 9, pp. 1547–1561, Jun. 2003.

[12] H. Bayraktar, 'Experimental and theoretical investigation of using gasoline–ethanol blends in spark-ignition engines', *Renew. Energy*, vol. 30, no. 11, pp. 1733–1747, Sep. 2005.

[13] W.-D. Hsieh, R.-H. Chen, T.-L. Wu, and T.-H. Lin, 'Engine performance and pollutant emission of an SI engine using ethanol–gasoline blended fuels', *Atmos. Environ.*, vol. 36, no. 3, pp. 403–410, Jan. 2002.

[14] S. Liu, E. R. Cuty Clemente, T. Hu, and Y. Wei, 'Study of spark ignition engine fueled with methanol/gasoline fuel blends', *Appl. Therm. Eng.*, vol. 27, no. 11–12, pp. 1904–1910, Aug. 2007.

[15] S. Iliev, 'A Comparison of Ethanol and Methanol Blending with Gasoline Using a 1-D Engine Model', *Procedia Eng.*, vol. 100, pp. 1013–1022, 2015.

[16] A. Elfasakhany, 'Engine performance evaluation and pollutant emissions analysis using ternary bio-ethanol–iso-butanol–gasoline blends in gasoline engines', *J. Clean. Prod.*, vol. 139, pp. 1057–1067, Dec. 2016.

[17] I. M. M. Elsemary, A. A. A. Attia, K. H. Elnagar, and A. A. M. Elaraqy, 'Experimental investigation on performance of single cylinder spark ignition engine fueled with hydrogen-gasoline mixture', *Appl. Therm. Eng.*, vol. 106, pp. 850–854, Aug. 2016.

[18] K. V. Shivaprasad, S. Raviteja, P. Chitragar, and G. N. Kumar, 'Experimental Investigation of the Effect of Hydrogen Addition on Combustion Performance and Emissions Characteristics of a Spark Ignition High Speed Gasoline Engine', *Procedia Technol.*, vol. 14, pp. 141–148, 2014.

[19] W. Mingrui, N. Thanh Sa, R. F. Turkson, L. Jinping, and G. Guanlun, 'Water injection for higher engine performance and lower emissions', *J. Energy Inst.*, vol. 90, no. 2, pp. 285–299, Apr. 2017.

[20] F. Christodoulou and A. Megaritis, 'Experimental investigation of the effects of separate hydrogen and nitrogen addition on the emissions and combustion of a diesel engine', *Int. J. Hydrog. Energy*, vol. 38, no. 24, pp. 10126–10140, Aug. 2013.

[21] A. Safa, 'Process and Emission Modeling in the Internal Combustion Engines', PhD Thesis, Yildiz Technical University, Istanbul, TURKEY, 2006.

[22] C. R. Ferguson, *Internal combustion engines: applied thermosciences*. New York: Wiley, 1986.

[23] İ. Cesur, A. Parlak, V. Ayhan, B. Boru, and G. Gonca, 'The effects of electronic controlled steam injection on spark ignition engine', *Appl. Therm. Eng.*, vol. 55, no. 1–2, pp. 61–68, Jun. 2013.

[24] G. Gonca, 'Influences of different fuel kinds and engine design parameters on the performance characteristics and NO formation of a spark ignition (SI) engine', *Appl. Therm. Eng.*, vol. 127, pp. 194–202, Dec. 2017.

Shock Response Analysis of One Automotive Day Time Running Light (DRL)

B.EDİZ[1], E.AY[2], T. ÇAL[3], S. TELLİ ÇETİN[4]

[1] Magneti Marelli Mako Elektrik Sanayi ve Ticaret A.Ş., Bursa/Turkey, baris.ediz@magnetimarelli.com
[2]Magneti Marelli Mako Elektrik Sanayi ve Ticaret A.Ş., Bursa/Turkey, erhan.ay@magnetimarelli.com
[3]Magneti Marelli Mako Elektrik Sanayi ve Ticaret A.Ş., Bursa/Turkey, taner.cal@magnetimarelli.com
[4]Uludağ University Mechanical Engineering Department, Bursa/Turkey, sevda@uludag.edu.tr

Abstract -**In this study, modal parameters of one "automotive daytime running light" (DRL) have been updated by using resonance search results. Resonance search has been performed on an electro dynamic shaker and finite element model has been updated accordingly. 6ms duration 30g amplitude half sinus shock tests have been applied on DRL. During tests, acceleration and strain measurements have been done. Measured accelerations have been correlated with theoretical shock signal. Shock signal is used on finite element model as load input and transient "finite element analysis" (FEA) has been performed. Strain results of FEA and measured strains during test have been compared. "Response spectrum" (RS) calculations have been done from shock acceleration signal and RS analysis has been performed on DRL by different calculation methods. Results of finite element transient analysis and finite element RS analysis by different methods have been compared.**

Keywords **– DRL, RS, SRSS, CQC, Rose, Lindley, Gupta, Resonance Search, Harmonic Response**

I. INTRODUCTION

Automotive Lighting Systems must resist different type of shock tests. One of which is the 30g amplitude 6 ms duration half sinus shock test. This shock signal is repeated 30.000 times and performed on an electro dynamic shaker. Shock acceleration signal is given on Figure 1.

Schrader (2006) has inspected one automotive headlamp using the SAE J577 shock test procedure and compared the measured strain and transient FEA strain results. However, in that study no information was given about finite element model update. It is very important use an updated finite element model before running transient analysis. Another study related to this field has been performed by Ding (2011). In that study RS analysis methods, RS calculation methods, application area of RS analysis, necessity of damping ratio validation, comparison of transient and RS analysis results have been explained. However, in that study general procedure is explained but validation study was not done. All comparison was done on a single cantilever beam by using FEA results without performing any physical tests. Another study in this field is related to failure detection methods during SAE J577 shock test on performed on an automotive headlamp. However, FEA was not done (Xie, K. 2007).

In this study finite element model of DRL is updated and correlated with resonance search test results. During 30g amplitude and 6ms duration shock test, acceleration and strain measurements have been performed. Measured accelerations have been used as load inputs for finite element model and transient shock analysis has been performed. Measured strain and FEA strain results have been compared. RS of shock signal has been calculated and RS analysis by different methods has been performed. Results of RS analysis and transient analysis have been compared. Optimum method for RS analysis for this case has been determined.

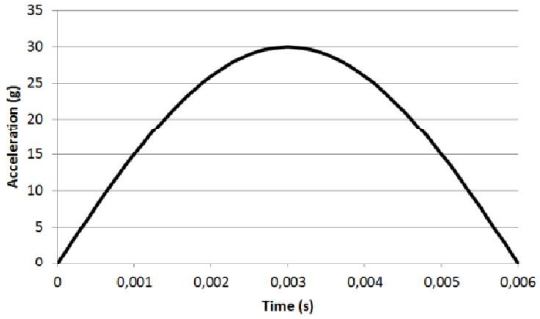


Figure 1. 30g amplitude, 6ms duration half sinus shock

II. RESONANCE SEARCH ON DRL BEFORE SHOCK ANALYSIS

Before performing shock tests and FEA, a constant 1g sinusoidal resonance search has been performed on the DRL between 5Hz to 250Hz frequency range and with 1 octave/min sweep rate. Acceleration response of DRL measured with accelerometer put on a determined point of the structure. Also finite element harmonic response analysis has been performed and finite element model has been updated accordingly. Harmonic sweep test and FEA results can be inspected on Figure 2.

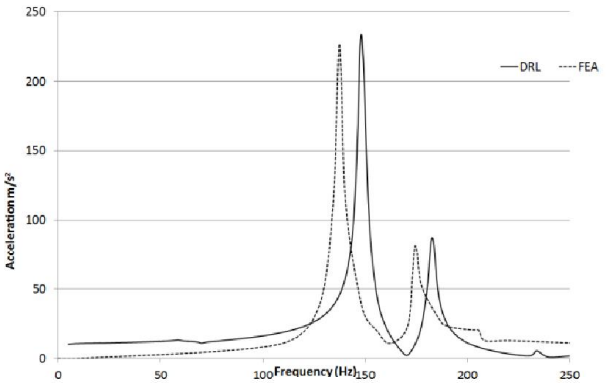


Figure 2. Harmonic Sweep Test & FEA Results Comparison

III. DATA ACQUISITION DURING HALF SINUS SHOCK TEST

During shock test, acceleration data from all fixing points and for all directions, and strain data have been collected. Test has been conducted on an electro dynamic shaker (Figure 3) and 3 axis accelerometers have been used. 16 channel data acquisition system (Figure 4) has been used and all data have been collected at once.

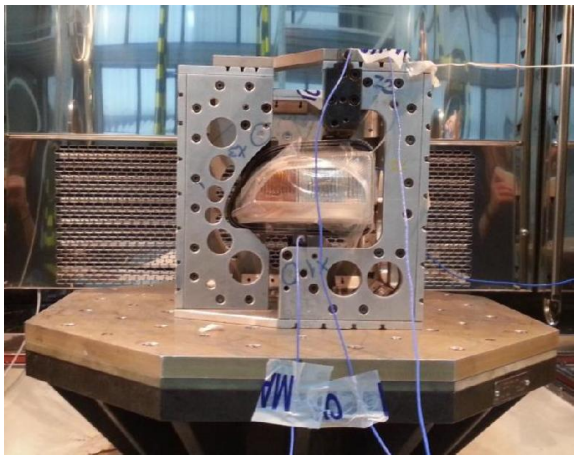


Figure 3. Half Sinus Shock Test on an Electro dynamic Shaker

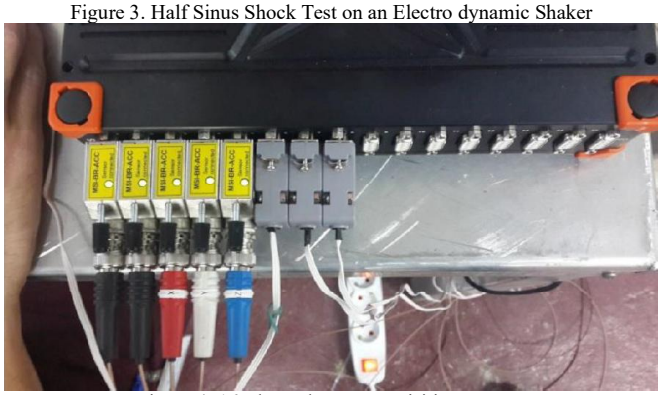


Figure 4. 16 Channel Data Acquisition System

When theorical shock acceleration signal and measured shock signals are compared (Figure 5), it is found that measured signals represent theoric signals by 98%.

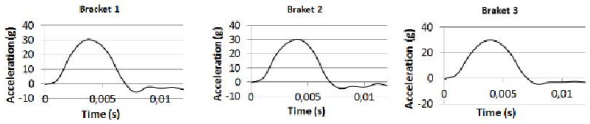


Figure 5. Shock Signals measured on fixing points of DRL

Measured strain signal has been cut to 0.1s in order to be compared with FEA strain results.

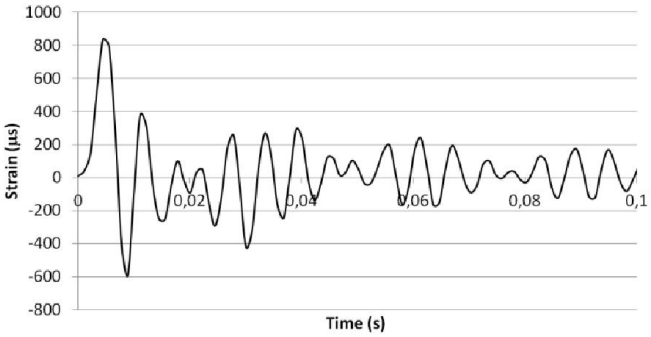


Figure 6. Cut Strain Signal

IV. TRANSIENT FEA

0.1s duration acceleration signals used as load inputs for transient FEA. Measured strain and calculated strain have been compared.

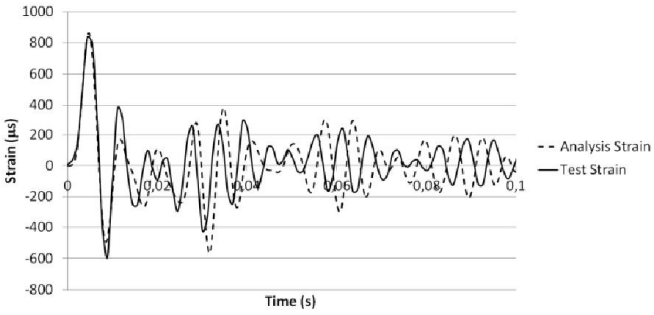


Figure 7. Comparison of Measured and Calculated Strain Signal

TABLE 1 COMPARISON TABLE

	Peak (µs)	RMS (µs)
Test	837.6	210.1
Analysis	862.4 e=3.12%	205.7 e=2.1%

When test and FEA results have been compared, 3.12% error has been found on the peak values and 2.1% error has been found on the "root mean square" (RMS) value of strains. It seems that due to synchronized measurements and by the use of updated finite element model, error in RMS value is quite low.

V. RS ANALYSIS FOR HALF SINUS SHOCK ACCELERATION SIGNAL

In short, RS is the maximum acceleration response of one degree of system to an acceleration signal with respect to its resonance frequencies. A constant damping ratio is assumed for all resonances. Mostly, used by earthquake engineers to analyze transient accelerations. RS of one time domain acceleration signal is shown in Figure 8.

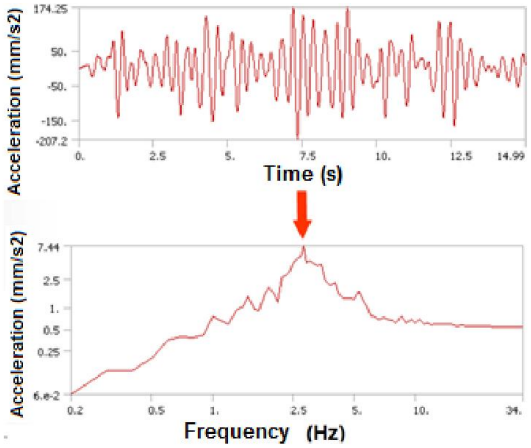


Figure 8. RS of one Acceleration signal

By the use of 30g amplitude & 6ms duration shock signal RS has been calculated and shown in Figure 9.

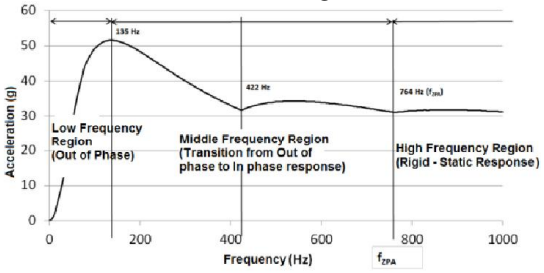


Figure 9. RS for 30g Half Sinus Signal

Choice of RS analysis method depends on the resonance frequencies of the structure, Ding (2011). If resonance frequencies of the structure well separated "square root of sum of squares" (SRSS) mode combination method gives good results, otherwise "complete quadratic combination" (CQC) or Rosenblueth (ROSE) methods are used. Another issue is the position of resonance frequencies of the structure with respect to frequency zones of the input RS. If the modes of interest are in the low frequency region (out of phase response) rigid response and missing mass effects are neglected, if they are in the transition region from out of phase to in phase response, missing mass and rigid response effects are taken into consideration by the use of Lindley or Gupta methods. If they are in the high frequency region (rigid or static response region) Gupta method is used. f_{ZPA} is the frequency where rigid response starts. It is called as frequency of zero period acceleration. In this case it is about 760Hz.

When resonance frequencies of DRL are inspected it is understood that they are in the transition region of RS. However, in this study RS FEA is performed with all mentioned methods. The results are compared with transient results and tabulated in Table 2 and Table 3.

TABLE 2 COMPARISON TABLE FOR NORMAL STRESS

	Normal Stress In X Dir.	Error %	Normal Stress In Y Dir.	Error %	Normal Stress In Z Dir.	Error %
SRSS	16,108	-25,256	50,638	-5,435	33,706	-14,601
CQC	16,061	-25,474	50,502	-5,689	33,790	-14,388
ROSE	16,061	-25,474	50,502	-5,689	33,790	-14,388
SRSS Missing Mass Rigid response Lindley ZPA= 760Hz	18,328	-14,955	46,713	-12,764	33,723	-14,558
CQC Missing Mass Rigid response Lindley ZPA= 760Hz	18,353	-14,839	46,626	-12,927	33,770	-14,439
ROSE Missing Mass Rigid response Lindley ZPA= 760Hz	18,355	-14,829	46,622	-12,934	33,771	-14,436
SRSS Missing Mass Rigid response Gupta	16,188	-24,885	50,666	-5,3827	33,741	-14,512
CQC Missing Mass Rigid response Gupta	16,143	-25,093	50,536	-5,625	33,823	-14,305
ROSE Missing Mass Rigid response Gupta	16,141	-25,103	50,53	-5,636	33,825	-14,300
Transient Analysis	21,551		53,548		39,469	

TABLE 3 COMPARISON TABLE FOR DIRECTIONAL DEFORMATION

	Dir. Def. in X Dir.	Error %	Dir. Def. in Y Dir.	Error %	Dir. Def. in Z Dir.	Error %
SRSS	0,334	6,532	0,621	1,869	0,566	-22,589
CQC	0,333	6,405	0,619	1,672	0,568	-22,411
ROSE	0,333	6,405	0,619	1,672	0,568	-22,411
SRSS Missing Mass Rigid response Lindley ZPA= 760Hz	0,278	-11,408	0,565	-7,249	0,640	-12,510
CQC Missing Mass Rigid response Lindley ZPA= 760Hz	0,277	-11,504	0,564	-7,364	0,641	-12,413
ROSE Missing Mass Rigid response Lindley ZPA= 760Hz	0,277	-11,504	0,564	-7,380	0,641	-12,414
SRSS Missing Mass Rigid response Gupta	0,334	6,628	0,621	1,886	0,566	-22,575
CQC Missing Mass Rigid response Gupta	0,334	6,500	0,620	1,705	0,568	-22,398
ROSE Missing Mass Rigid response Gupta	0,3342	6,507	0,620	1,695	0,568	-22,398
Transient Analysis	0,313		0,609		0,732	

VI. CONCLUSION

In this study, firstly, by resonance search tests, finite element model of DRL has been updated. After that, during 30g shock test, acceleration and strain signals have been collected. Measured shock signal has been correlated with theoretical shock signal. On the updated finite element model, by the use of collected data, transient FEA and RS analysis have been performed with different methods and results have been compared.

It is concluded that for this type of structure which has resonance frequencies in the transition zone of input RS, missing mass effects and rigid response effect by Lindley method gives optimum results. As a result, before starting to analyze shock response of one structure, it is important to know resonance frequencies of the structure and input RS frequency regions.

When compared with finite element transient analysis results, for all type of results, error found after RS analysis is in 15% range. In spite of 15% error, RS analysis lasts shorter than transient analysis and result file is too smaller. Transient FEA took 51420s and RS took 296s which is 174 times shorter. Result file of finite element transient analysis is 249.237GB, however it is 785.063MB for RS.

In spite of 15% error found between RS and finite element transient analysis results, RS analysis can be used as a fast tool in order to evaluate the structure under shock loading in a very short time and without expensive calculation resources.

REFERENCES

[1] MingYao Ding , 2011, Shock Analysis of Electronic Components -, ANSYS Inc.

[2] Schrader, CD. (2006) Dynamic Structural Simulation of the SAE J577 Vibration Test, SAE Technical Paper Series. doi: 10.4271/2006-01-048.

[3] Kongying Xie , 2007, "Automotive Light Assembly Failure Detection", A thesis submitted to the Department of Mechanical and Materials Engineering with the requirements for the degree of Master of Science (Engineering) Queen's University Kingston, Ontario,Canada

Retrofitting of a Power Plant Steam Headers in a Petrochemical Complex using Exergy Analysis

Gülce KALYONCU[1], Dilek ÇELENK[2] and Zehra ÖZÇELİK[*3]

[1]University of Arkansas, Arkansas/USA, glckalyoncu@gmail.com,
[2]PETKIM, Aliağa, İzmir/Turkey, dcelenk@hotmail.com,
[3]Ege University, İzmir/Turkey, zehra.ozcelik@ege.edu.tr

***Abstract* – The scarcity of the non-renewable energy sources pushes the companies retrofitting the processes more energy efficient. Because of the global warming, decreasing the emission is main target for large industries such as petrochemical and refining complexes. The main purpose of this study was to conduct an exergy analysis of the on PETKİM, that was one of the most popular corporations in Turkey and was indispensable raw-material producer of the industry with its product range over 50 productions, plant steam headers which delivers five different level steams (XHS: Extra High Pressure Steam, HHS: High Temperature and High Pressure Steam, HS: High Pressure Steam, MS: Medium Pressure Steam, LS: Low Pressure Steam) and condensate recovery header. It was seen that, XHS header has the greatest exergy loss with the value of 62350 kW. Also exergy change in seasonal basis was investigated and the results shown that the seasonal temperature fluctuations did not significantly affect the exergy. In addition to these, frictional losses were calculated through the steam headers. Higher-level pressure headers were the main source for the destruction of exergy, because of its higher flowrate, pressure and temperature. Letdown to produce lower pressure steam causes the another biggest portion of exergy destruction. Therefore, reducing the quality of steam can be made by steam turbines for preventing exergy loss. Also additional suggestions were listed for improving the steam network in PETKİM plant.**

***Keywords* – Power plant, Steam headers, Exergy analysis, Retrofitting**

I. INTRODUCTION

On an industrial basis, steam and power plants have crucial importance in accordance to fuel consumption. Since the amount of consumed fuel is directly relevant to the cost of the process, maximization of the energy saving becomes the major goal of the managers, engineers, and the scientists. For going further to optimization of energy usage, it is necessary to answer some specific questions such as: "Where and how is energy degraded in the industry?" and "How to reduce the energy degradation?" [1]. As it well known, energy cannot be created nor destroyed, however in the real processes energy quality is degraded. This concept is about the Second Law of Thermodynamics, and increasing relevance of the second law is the result of two significant changes produced at the international level in energy policies.

It was previously mentioned in the works of Rivero [1] the three E model which forms the inevitable connection between energy, economy, and ecology. The connection between energy and economy navigates us to think about the optimization of also the quality, not only the quantity degradation when it is used. Besides that, the energy-ecology connection is about the necessity of stopping the environment deterioration generated by the increasing fossil fuels consumption in order to assure a sustainable development. For dealing with this conditions which was formed by the necessity connections mentioned above, exergy concept must be used.

The main purpose of the exergy analysis is the detection of the locations where high energy losses occur; in the light of the data which obtained by the exergy analysis, some suggestions had been done in order to maintaining the reduction in exergy losses. The total site integration for a set of process served by a centralized steam system, with targeting approach developed for sites consisting of multiple process [2]. In addition to these, a description of thermos-economics and its applications, as an evolutionary development beyond exergy analysis and entropy generation minimization, is available in Bejan [3]. Also the self-heat recuperation technology was developed based on exergy recuperation for application of many chemical processes. This is a simple calculation technique which is derived by numerically and concerned to process from the point of irreversibility [4].

In the light of this information, it can be easily understood that exergy analysis is a way which has some substantial properties in order to maximize the availability of work. The main purpose of this study is performing exergy analysis at steam headers which transports steam at five different pressure levels. As side objectives, pressure drop calculations are achieved for each header, and seasonal exergy variations are investigated. This exergy analysis study is done at Petkim petrochemical refinery steam network.

II. STEAM HEADERS

Refinery steam network consumes considerable energy. The main purpose of the steam network is producing steam for using at the manufacturing plant. Steam is produced at different pressure and temperature level, and used by the factories which present in the refinery in necessary amount of flow and pressure level. The amount of fuel consumption in steam networks is enormously high, because of boilers and other fuel-consuming components existence. This huge energy consumption must be reduced due to the importance of energy crisis and global warming necessitates.

Chemical plants and refineries include unique combinations of equipment and systems that are used to separate materials into pure or relatively pure products. Examples of process systems include reactions, distillation, absorbing/stripping, adsorption/drying, crystallization, evaporation, extrusion, extraction, filtering, screening, and utility systems. Plant utility systems typically include steam generation, compressed air and gases, water treatment, and cooling tower operations.

A steam system is a complex arrangement of equipment and piping that works together to produce and circulate steam at a variety of pressures and temperatures. Because steam is used in many industrial applications, most chemical plants and refineries have their own steam generation facilities.

A typical steam system includes the following equipment's;

- Boiler (fire tube or water tube)
- Steam header system (low, medium, and high pressure)
- Condensate return system (steam traps, valves, piping, pumps)
- Deaerator system

In a closed steam system, a condensate return header is used to remove slugs of water or condensate from the live steam line. A vessel called a deaerator is used to collect fluid from the condensate return header. The deaerator is designed to remove excess air from the system. Demineralized makeup water is often added to the deaerator. The cooled condensate is fed back into boiler, where it is changed into steam [5].

Steam headers on an industrial site typically consist of long pipe runs connecting boilers, turbines, heat recovery steam generators (HRSGs), and process equipment.

Petkim, one of the most popular corporations in Turkey, is indispensable raw-material producer of the industry with its product range over 50 production. Its petrochemical products are important input of construction, electricity, electronic, packaging, textile also medical, dying, detergent and cosmetic sectors. Steam network of Petkim has five main pressure level of steam header, and condensate recovery header. Steam is produced at Steam and Power generation unit and distributed to the whole plant. As it can be seen in detailed form in Figure 1, the steam network is mainly subtracted into polymer line which located at the bottom of the network, and monomer line which placed above. Extra High Steam Pressure (XHS) header is used by NSC (Naphta Steam Cracker-Ethylene) unit, High pressure High-High temperature steam (HHS) and Medium temperature High pressure steam (MHS) headers are used by PTA (Pure Teraphthalic Acid) unit, High pressure Steam (HS) header is connected with PTA (Pure Teraphthalic Acid), Air Oxygen, PA (Phthalic Acid), PP (Polypropylene), HDPE (High Density Polyethylene), LDPE (Low Density Polyethylene), EO/EG (Ethylene Oxide/Ethylene Glycol), VCM (Vinylchloride Monomer), and ACN (Acrylonitrile) units. Medium pressure Steam (MS) header is used by PTA, TAYPE (Tubular Alçak Yoğunluk (Low Density) Polyethylene), PA, PP, LDPE, Flare unit, NSC, EO/EG, Waste Treatment unit, VCM , ACN-VCM flare, TRI/PER CE, and Aromatics units. Last header which is classified as Low pressure Steam (LS) header is connected with PTA, TAYPE, PAA, PP, HDPE, LDPE, NSC, PVC (Polyvinyl chloride), EO/EG, VCM, ACN, aromatics unit, CA (Chlorine Alkali) and Steam Tracing, Cooling Towers, Residential Areas, Fuel gas system. All calorific values about each header are listed in Table 1.

Table 1. Calorific values which related to type of produced steam

Steam Pressure	Pressure ($kg.cm^2$)	Temperature (^oC)	Calorific value (kcal/kg)
XHS	134	540	821
HHS	84	310	674
HS	42	392	762
MS	18.5	3.00	723
LS	5.5	195	678

Extra High-Pressure steam which abbreviated as XHS, is generally generated by a boiler, and supply to the XHS header for the use of driving compressors. The pressure level of XHS is between 1000 psig and 1200 psig [1]. Since the pressure level of Extra High-Pressure steam is very huge, it must be controlled in order to maintain safe process conditions, since XHS header is one of the most critical components in power stations. Because of the extra high pressure, the thickness of this header must considerably greater than the other headers. Excess amount of XHS is sent to High Pressure steam header after the pressure level is reduced. This reduction operation is supplied by a letdown station which exists between XHS header and HS header.

High Pressure Steam (HS) is supplied by lowering the pressure of XHS header. The feed of the HS is XHS which extracted from the steam turbine. HS may be imported from other units into the high-pressure steam header to maintain overall steam balance. HS pressure level are between 400 psig and 800 psig [5]. A let down station must exist between medium pressure steam header and high-pressure steam header for maintaining pressure and steam balance in MS header.

Medium pressure steam which denoted as MS is supplied by lowering the pressure from HS header, or by extracting exhaust steam from steam turbine. As high-pressure steam enters a turbine, it is partially converted to useful mechanical energy. Noncondensing operation utilize the exhaust steam in operations where lower pressure is required. The pressure level of the medium pressure steam is between 180 psig and 200 psig [4]. If any insufficient supply from the sources occur, then the letdown station which exist between HS and MS headers makes up balance of steam required at the MS header.

Low pressure steam (LS) is supplied by lowering the pressure from the MS header, or by extracting from a steam turbine continuous blow down drum. The pressure level of low steam pressure is between 50 psig and 60 psig. The letdown station between the MS header and LS header maintains the balance of steam in the LS header. An automatic pressure controlled dump system with silencers is provided to dump excessive steam from the LS header to the atmosphere during plant operation upset conditions [5].

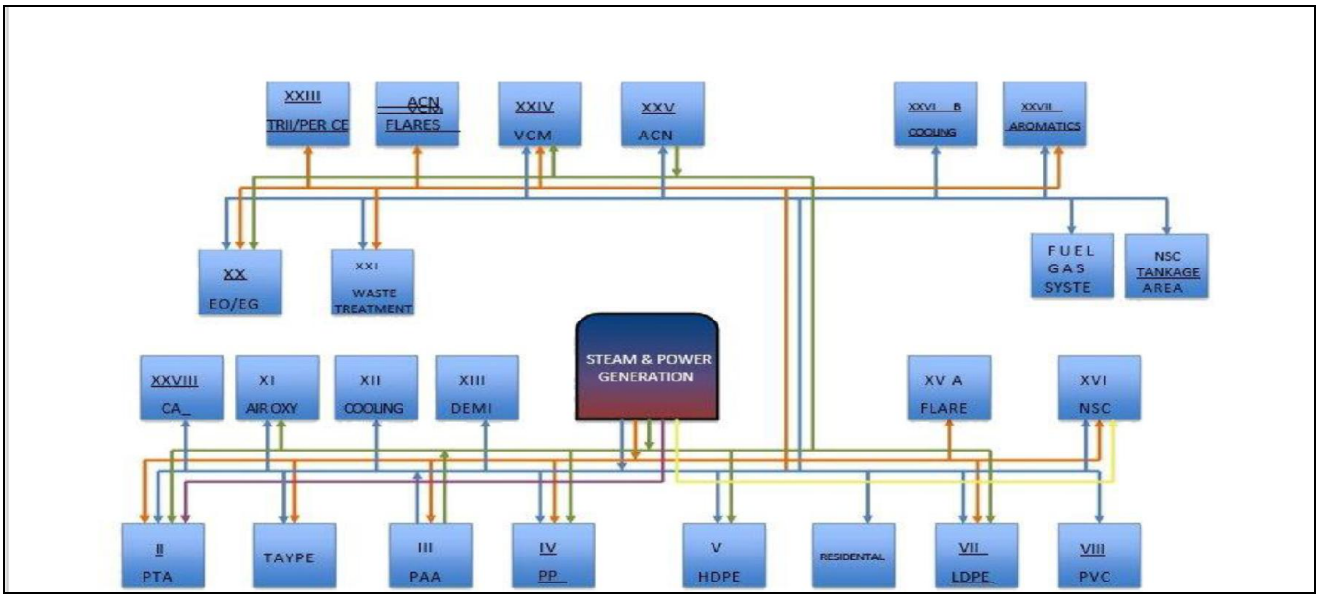


Figure 1: Steam header network in Petkim

The condensate recovery system is separated into clean condensate section which is routed to the deaerator, and suspect condensate section which is collected from steam users where the process side pressure is higher than the steam pressure. Also, suspected condensate collected in a drum is closely monitored for hydrocarbon contamination. Depending upon the results of analysis, the condensate is pumped through a carbon filter, and then routed to deaerator.

III. EXERGY

The concept of the exergy is based on the First and Second Law of Thermodynamics. In contrast to energy, exergy is exempt from the law of conservation. In real processes, exergy input always exceeds exergy output. This is due to *exergy destruction*, also called *irreversibility* or *lost work*. Every real process has exergy E losses leading to the reduction of the useful effect of the process or to an increased consumption of inputs from where the product was derived. The difference between exergy destruction or irreversibility and exergy waste or exergy flow to the environment is important [7]. Analysis of the destruction of exergy due to the inevitable irreversibility of real processes is crucial point due to the fact that main purpose in industry is increasing energy efficiency. The destroyed exergy is proportional to generated energy.

Exergy provides a complete and coherent quantification to the quality of an energy form, and exergy content of different energetic streams: neglecting magnetic, nuclear, etc. effects, the general expression for the exergy of a stream is;

$$E_{stream} = E_{thermal} + E_{mechanical} + E_{chemical} + E_{kinetic} + E_{potential} \quad (1)$$

where;

$E_{thermal}$: Maximum work generated by a thermal power Q at T,

=Q*(1-T0/T)

$E_{mechanical}$: Maximum work generated by a power P, = P

$E_{chemical}$: Maximum work generated by a chemical reaction

The following equations are used to analysis of the whole system:

Conservation of mass: $m_{in} - m_{out} = dm_{CV} / dt$ (2)

Conservation of energy: $E_{in} - E_{out} = \Delta E_{sys}$ (3)

Exergy balance: $e_{in} - e_{out} - e_D = \Delta e_{sys}$ (4)

Total exergy of a system: $e = e^{PH} + e^{K} + e^{P} + e^{CH}$ (5)

Physical Exergy: $e^{PH} = \Delta H - T_o \Delta s$ (6)

Kinetic Exergy: $e^{K} = (1/2)\, mV^2$ (7)

Potential Exergy: $e^{P} = mg\Delta z$ (8)

Chemical Exergy: $e^{CH} = e^{oCH} + \Sigma(x_i\, (ln\, x_i))$ (9)

In the analyzed case, since there is no chemical reaction occurs in the system, chemical exergy is neglected. In addition to this, because of the fact that, there is no considerable level difference, thus potential exergy is also neglected. By taking into account the velocity changes in the headers, kinetic exergies are calculated.

From the economical point of view of the exergy calculation equation, the net useful energy for which a cost has to be paid is obtained. The ecological implication of the exergy result shows that exergy is a measure of the departure from the environment. The enthalpy, entropy and the temperature in the equations above are explicitly referred to the conditions of the environment. Therefore, the seasonal temperature fluctuations affect the exergy analysis.

IV. RESULTS AND DISCUSSION

In this study, the exergy analysis has been performed in Petkim petrochemical industry steam headers. Specific flow

exergies of individual steam headers which transports steam at five different levels had computed. Furthermore, to assimilate the effect of environmental temperature on exergy analysis, seasonal exergy values are observed. As side objective, pressure drop values of each header had been determined for understanding the effect on the exergy analysis results

All headers are segmented into parts like A, B, C etc. in the basis of diameter variations. Calculations of each header from which transports highest pressure steam to lowest pressure steam, in accordance to diameter variation are evaluated. Specific flow exergy values are calculated for each input or output point of the related header. Contrary to expectation, after calculation of kinetic exergy has finished, most of the end results was not so appreciable. Therefore, most of result has taken as negligible in specific exergy equation, except VCM and ACN units which are taking steam from HS header, and ACN unit which is taking steam from LS header. Consequently, these values are added to specific flow exergy calculation. The most significant specific flow exergy value is computed as 62346.30 kW in XHS header and these results are given in Table 2.

Table 2. Extra High Steam pressure (XHS) header calculation results

Section	A
Input/Output	Output
Unit	NSC
Flowrate (t/h)	71.4
Velocity (m/s)	12.7
Length (m)	530
Diameter (inch)	10
Pressure (bar)	99
Temperature (°C)	495
Specific Enthalpy (kj/kg)	3363.27
Specific Entropy (kJ/kg.K)	6.58
Kinetic exergy (kW)	1.64
ΔS	-0.26
Δh	3064.68
Exergy (kW)	62346.3

Another case which investigated in this study is exergy variation depending on seasonal environmental conditions. Pressure values are taken constant as 1 atm for winter, normal condition, and summer. The extreme temperature values are chosen as -6.4°C, and 43°C for winter and summer respectively for Aliağa region where Petkim petrochemical industry is located. The exergy variations in seasonal basis for XHS, HS, MS, and LS headers can be seen in Figure 2, 3, 4, and 5 respectively. As a result, contrary to expectations, change of the environmental temperature effect is not remarkable for exergy calculations.

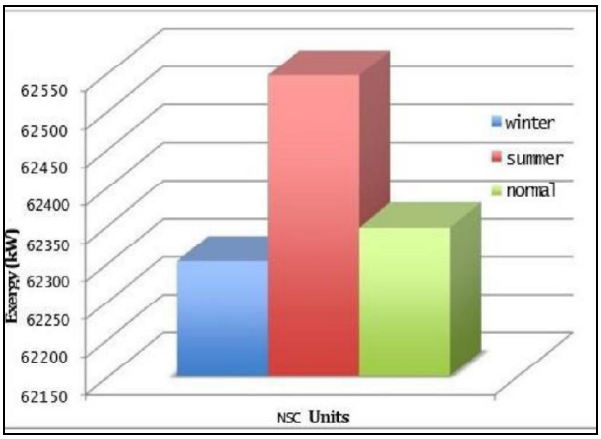


Figure 2. Graphical representation of seasonal exergy changes of XHS header

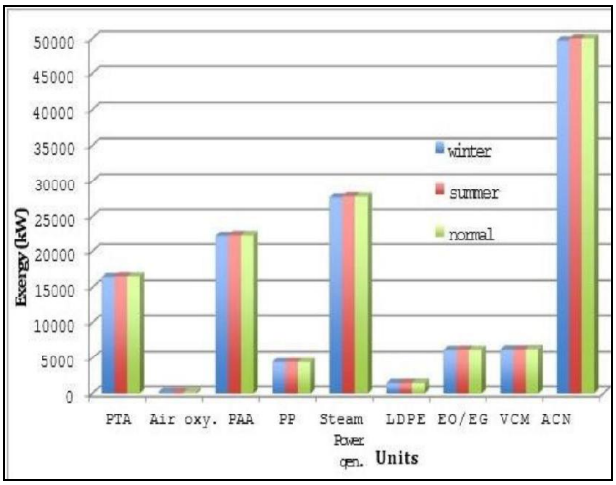


Figure 3. Graphical representation of seasonal exergy changes of HS header

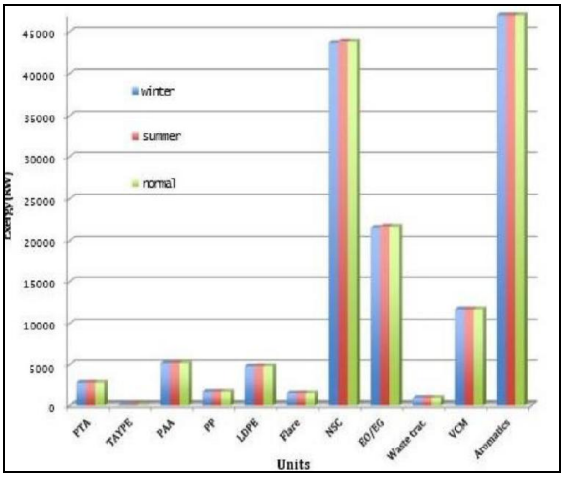


Figure 4. Graphical representation of seasonal exergy changes of MS header

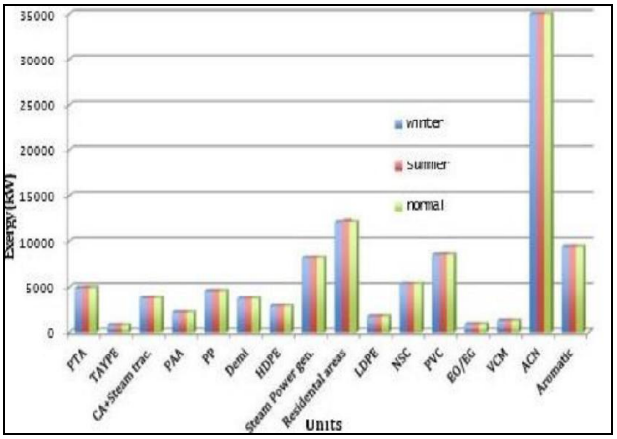


Figure 5. Graphical representation of seasonal exergy changes of LS header

V. CONCLUSION

Exergy analysis is a useful method which yields to versatile result for the applied processes. In this project exergy analysis has been implemented to Petkim steam header network. Furthermore, effect of alteration on environmental temperature has been examined. Besides that, the constitutive purpose of this study is the investigation of the location where exergy loss is significant. After these results have been obtained, some recommendations have been done for the minimization of exergy loss.

The exergy analysis results which obtained at different environmental temperature have shown that, the seasonal temperature changes have not affected the exergy analysis results significantly.

The main reasons of exergy destruction can be summarized as; irreversible events during the process, leakage, pressure drop in flowing fluid, possible heat transfer and finally, presence of friction. In this analyzed case, the highest exergy loss is observed as 62346.3 kW at XHS header which used by the NSC plant. As an important issue, in this study, it is seen that pressure drop of flowing steam has not affect the exergy loss in a considerable extent. Since the highest pressure drop value is calculated at LDPE plant HS header usage point as a value of 2.045 bar, pressure drop effect has not been accepted as a source of irreversibility.

According to the reasons which are mentioned above, exergy losses can be eliminated by applying better insulation to the system, determining and eliminating the possible leakages throughout the piping and minimizing the friction losses. Also, instead of injection of cold water for letdown, turbines can be added to the steam network for increasing the availability of the work, converting the dead energy into the shaft work to get the maximum possible benefit from an unexpected source.

It is expected that, this study will help for improvement of the methods that has been used for exergy analysis and applications which minimize the exergy loss at the steam networks.

REFERENCES

[1] R. Rivero, "*Application of the exergy concept in the petroleum refining and petrochemical industry*", *Energ Convers Manage*, vol. 43, pp. 1199–1220, 2002.

[2] C. L. Chen, C. Y. Lin, J. Y. Lee, "*Retrofit of steam power plants in a petroleum refinery", Applied Thermal Engineering,* vol. 61, pp. 7-16, 2013.

[3] A. Bejan, *"Fundamentals of exergy analysis, entropy generation minimization, and the generation of flow architecture", Int. J. Energy Res.,* vol. 26, pp. 545-565, 2002

[4] Y. Kansha, M. Ishizuka, Y. Kotani,, A. Tsutsumi, "*Exergy Loss Minimization for Chemical Processes*", *Institute of Industrial Science*, *The University of Tokyo*, 2012.

[5] C. Thomas, "*Process Technology and Equipment System*", *3rd edition, Delmar*, pp 306-308, 2010.

[6] M. S. Gandhi, A. A. Ganguli, J. B. Joshi, P. K. Vijayan, "*CFD simulation for steam distribution in header and tube assemblies*", *Chem Eng Res Des*., vol. 90, pp. 487-506, 2012.

[7] Y.A. Çengel, M.A. Boles, "*Thermodynamics: An Engineering Approach*", *McGraw-Hill, 2nd Edition*, pp 388-391, 1994.

[8] T.J. Kotas, "*The Exergy Method of Thermal Plant Analysis*", *Kreiger Publishing Company*, 1995.

[9] R.K. Apaiah, A.R. Linnemann, H.J. van der Kooi, "*Exergy analysis: A tool to study the sustainability of food supply chains*", *Food Res Int*, vol. 39, pp. 1-11, 2006.

[10] S. Peker, Ş.Ş. Helvacı, "*Akışkanlar Mekaniği, Kavramlar Uygulamalar ve Problemler*", *Literatür Yayıncılık,* 2003.

[11] G. Kalyoncu, E. Tunalı, "*Retrofitting of a Power Plant Steam Headers in a Petrochemical Complex", Diploma Project, Chemical Eng. Dep., Ege Un.* 2014.

Numerical modelling of aluminum foam for comparing foam-filled, partially foam-filled and empty crash-boxes

B. GÜLÇİMEN ÇAKAN[1] and C. ENSARİOĞLU[2]

[1] Uludag University, Bursa, Turkey, bgulcimen@uludag.edu.tr
[2] Uludag University, Bursa, Turkey, cihatensari@uludag.edu.tr

***Abstract* - Aluminum foam is preferred in filling crash-boxes for its superior properties, particularly light weight and high energy absorption capacity. In this study, compressive behavior of closed cell aluminum foam was investigated. Compressive tests were performed and analyzed to construct a numerical model. Compressive test simulations were carried out to validate the FE model later to be used for crash analyses. In the crash analyses; foam-filled, partially foam-filled and empty crash-box configurations were examined. The results showed that the foam-filled configurations exhibited higher plateau stress, accordingly higher energy absorption as well as longer impact time, assuring reduced deceleration and a lower final impact force compared to the empty box. Partial filling was found to decrease the initial impact force and increase the compressibility when compared to complete foam-filling.**

***Keywords* - aluminum foam, foam-filled structures, crash-box, energy absorption, FE model**

I. Introduction

Thin-walled tubes are commonly used as crash-boxes in automotive engineering for the purpose of absorbing impact energy. Being located between the bumper beam and the front rail of the vehicle, they protect the passengers and the high cost components behind it while absorbing the kinetic energy of the crash. Local buckling of these structures when being subjected to axial compression provides a large energy absorption capacity while keeping the force levels low [1].

Porous metallic foams are advanced materials which are recently preferred in filling of crash-boxes to enhance its energy absorbing capacity. One of the important characteristics of the aluminum foam is exhibiting high compressibility at an almost constant stress, which is called as plateau stress [2].

Various research topics on foam-filled crash-boxes are found in the literature such as loading conditions- e.g., loading angles [3], the shape and geometric parameters of the foam-filled crash-boxes [4,5] have been studied so far. Limited studies are found on the literature on partial foam-filling of crash-boxes: [6,7] studied the partially aluminum foam-filling of crash-boxes, whereas in [8] polystyrene foam was used instead of aluminum foam.

In this study, closed cell aluminum foams were provided from a local manufacturer and compression tests were carried out for numerical model constitution. The validity of the material parameters introduced to the FE software was realized by comparing the experimental and numerical force-displacement curves of the compression tests. The determined material parameters were used in impact modelling of foam-filled, partially foam-filled and empty crash-boxes.

II. Materials and Method

Closed cell Al foams, which were produced by melting method by using $CaCO_3$ foaming agent in AluPam facilities, were cut from ingots by using a band saw and specimens for compression tests were obtained.

Compression tests were carried out to form the stress-strain graphs to be used for constitutive modelling of aluminum foam. Cubic specimens' dimensions were 30*30*30 mm and crosshead speed was 20 mm/min. This speed satisfies the strain rate ($\dot{\varepsilon} = V / l$, where V is the test speed and l is the original length of the specimen) range recommended in the standards which is 10^{-3} to 10^{-2} s^{-1}.

III. Results and Discussion

Compression tests results and numerical modelling

Compression test results for the 5 specimens are given in Figure 1. Due to the chaotic structure of aluminum foam, curves exhibited some difference. An average curve was calculated by using these 5 curves.

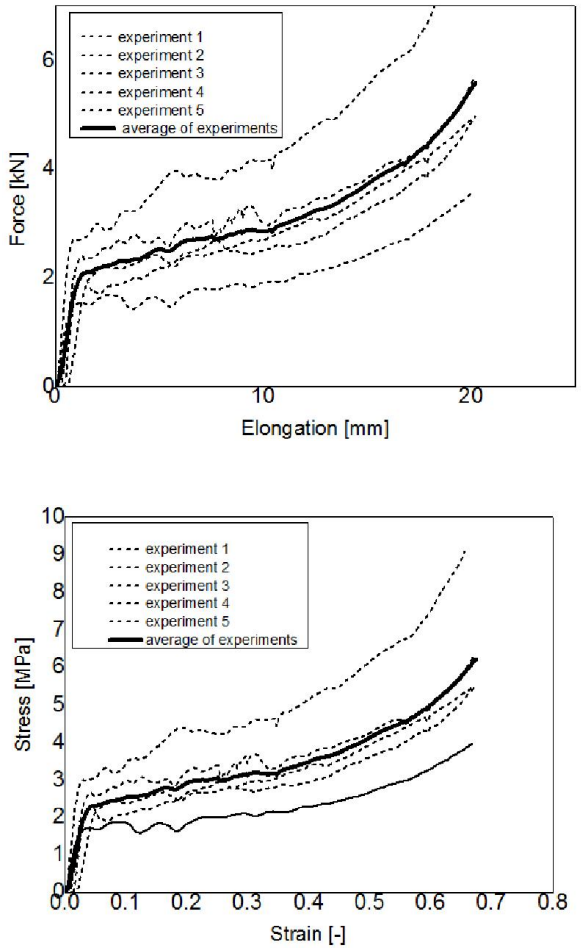


Figure 1: Compression test curves for aluminum foam specimens: (a) Force-Elongation, (b) Stress-Strain

Linear isotropic elasticity and crushable foam plasticity were defined for constitutive modelling of aluminum foam in Abaqus. Elastic modulus was determined from the slope of the initial linear part of the stress-strain curve (see Figure 2). There is almost no lateral expansion when foams are compressed, thus elastic and plastic Poisson ratios were assumed as 0.

Abaqus crushable foam model is based on Deshpande and Fleck's theoretical model [9] where yield function is defined as:

$$\sigma_{y=}\sigma_p + \gamma\frac{\hat{\varepsilon}}{\varepsilon_D} + \alpha_2 \ln\left(\frac{1}{1-\left(\frac{\hat{\varepsilon}}{\varepsilon_D}\right)^{\beta}}\right) \quad (1)$$

Here $\hat{\varepsilon}$ is equivalent strain, σ_p, γ, α_2 and β are material parameters. Densification strain can be evaluated by the density ratio of the foam (ρ_f) to the base material (ρ_{f0}).

$$\varepsilon_D = -\ln\frac{\rho_f}{\rho_{f0}} \quad (2)$$

Volumetric and isotropic hardening options are available in crushable foam plasticity. Isotropic hardening rule was used, since for compression-dominated loading, models' predictions are similar. It is seen in Figure 3 that our results also showed no difference between two options for the foam material tested.

For isotropic hardening, compression yield stress ratio (k), which is the ratio of initial yield stress in uniaxial compression to the one in hydrostatic compression, is required. It is stated to be between 0 and 3 in [10]. Due to the absence of hydrostatic compression test data, value of k should be estimated. The effect of k was investigated by varying its value in the specified range (see Figure 3). The difference was insignificant, thus k was assumed as 1, which means the initial yield stress in uniaxial compression equals to the initial yield stress in hydrostatic compression. The limited experimental data in [2] revealed that nominal stress-strain curves from uniaxial compression and hydrostatic compression tests are similar with the hydrostatic ones having slightly higher hardening.

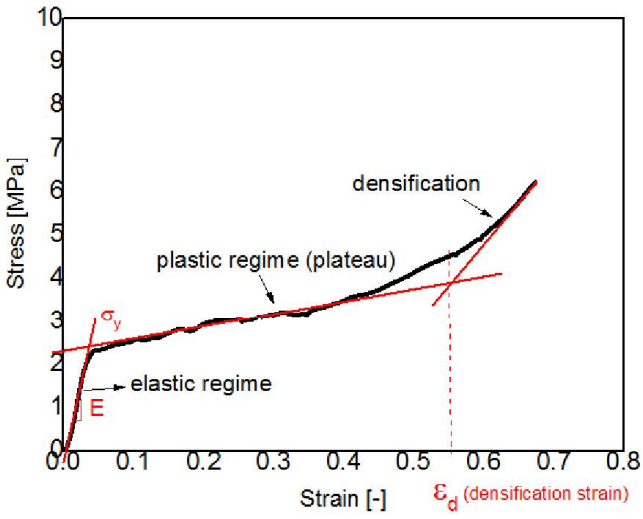


Figure 2: Deformation regimes observed for the aluminum foam subjected to compression test (E, σ_y and ε_d refers to elastic modulus, yield stress and densification strain, respectively.)

True stress-true strain values above yield stress are required for isotropic hardening input. According to [2], the yield stress of the foam should be taken as the initial peak stress if there is one; otherwise, it should be taken as the stress at the intersection of two slopes of the initial loading and the plateau stress. Confirming with the latter definition, the yield stress was determined from the intersection of the slopes of the elastic and plastic (plateau) regions as seen in Figure 2.

Our results showed that when true stress-true strain values were used for hardening, there is a significant difference between the experimental and numerical force-elongation curves and the curves started to diverge at the initial stages of the plateau. Due to the fact that Poisson ratio is almost zero, true stress should equal to engineering stress. In Figure 2, it is seen that numerical and experimental curves are in better agreement when engineering stress-true strain values were used for hardening input. For plastic strains greater than the last user specified values, Abaqus extrapolates stress-strain data based on the last slope [10]. Accordingly, when the hardening input was cropped before the densification strain so as to have the slope of the plateau as the last slope, a better agreement was found between the last parts of the numerical and experimental curves.

Crash Analysis

Abaqus explicit solver was used for the crash analyses of the foam-filled, partially foam-filled and empty crash-box configurations where 100%, 80% and 0% fullness ratios existed respectively. In Figure 5, the assembly consisting of lower plate, upper plate and the crash-box is demonstrated. Crash-box had a rectangular section with dimensions of 100 mm x 50 mm and its height was 100 mm. It was composed of an aluminum skin outside and the aluminum foam inside. Skin was modeled as a shell part and upper lower dies as analytical rigid bodies to reduce the computation costs. The skin was assigned with a 2 mm shell thickness and the element type used was S4R which is a 4-node doubly curved thin or thick shell, reduced integration, hourglass control, finite membrane strains. Foam was modelled as a solid and meshed with C3D8R which is an 8-node linear brick, reduced integration, hourglass control. Enhanced option was selected for hourglass control to avoid excessive distortion problems. The reference point of the upper die was assigned with an initial velocity of 5.6 m/s and a point mass of 570 kg. Explicit general contact enabling self-contact was utilized for the whole model. After a sensitivity check, an optimum element size of 2-5 mm was used for all models. Element size was increased in case of convergence problems.

In Figure 5, deformed profiles of the crash-boxes are demonstrated. The folding characteristics were similar for foam-filled and the partially foam-filled crash-boxes for which two folds close to the upper and lower dies started almost simultaneously. For the empty crash-box, a fold initiated from the bottom similarly, but a greater bulging occurred along the crash-box progressively. At the final stage, empty crash-box was compressed to a higher displacement, since in foam-filled versions, at some point, compressibility of the foam was reached.

Empty crash-box with a low crushing force and a shorter impact duration resulted in a higher final impact force. Figure 6 depicts the impact force-displacement curves for the foam-filled, partially foam-filled and empty crash-boxes. When the overall behavior in Figure 6(a) is investigated, it is seen that empty crash-box exhibited a low plateau force and a shorter impact duration (see Figure 7), which resulted in a higher final impact force.

When the initial part of the force-displacement force is zoomed, it is observed that for the empty crash-box, initial force started with a lower plateau compared to the filled versions and continues in the same force level till the final impact force. The partially foam-filled crash-box had a lower initial impact plateau, which increased to the plateau force level of the foam-filled crash-box in the advancing stage.

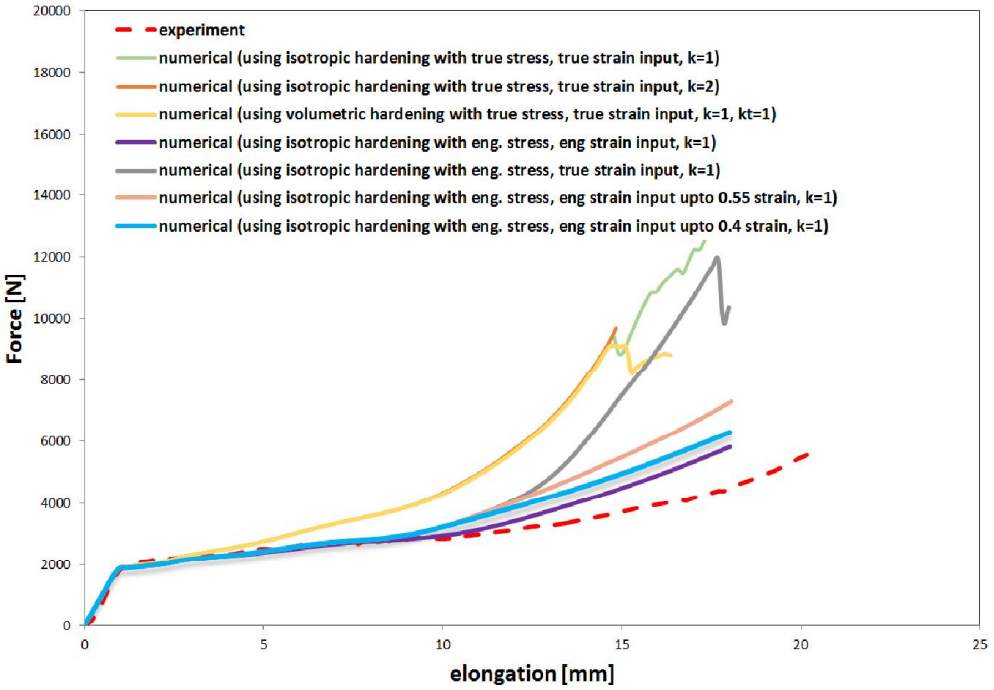


Figure 3: Comparison of the experimental and numerical force-elongation curves

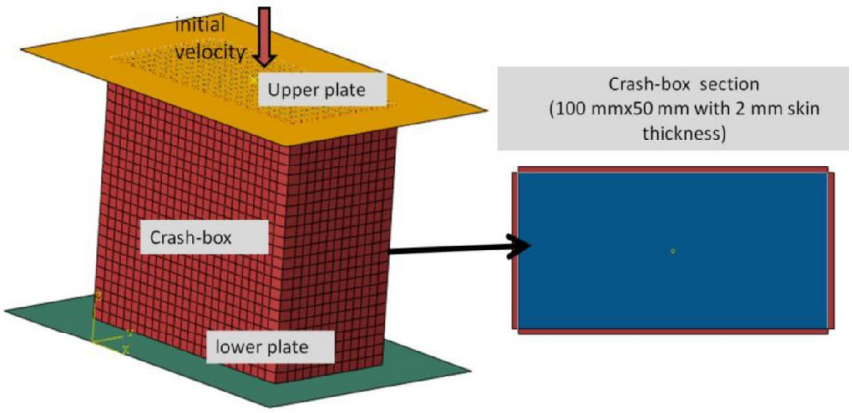


Figure 4: FE model constituted for the crash analyses

Table 1. Mechanical properties of the aluminum foam used in crushable foam model

density [g/cm3]	elastic modulus (E) [MPa]	elastic and plastic Poisson ratio (ve,p)	yield stress (σy) [MPa]	initial yield stress in uniaxial compression test /initial yield stress in hydrostatic compression test (k) [-]
0.414	67	0	2	1

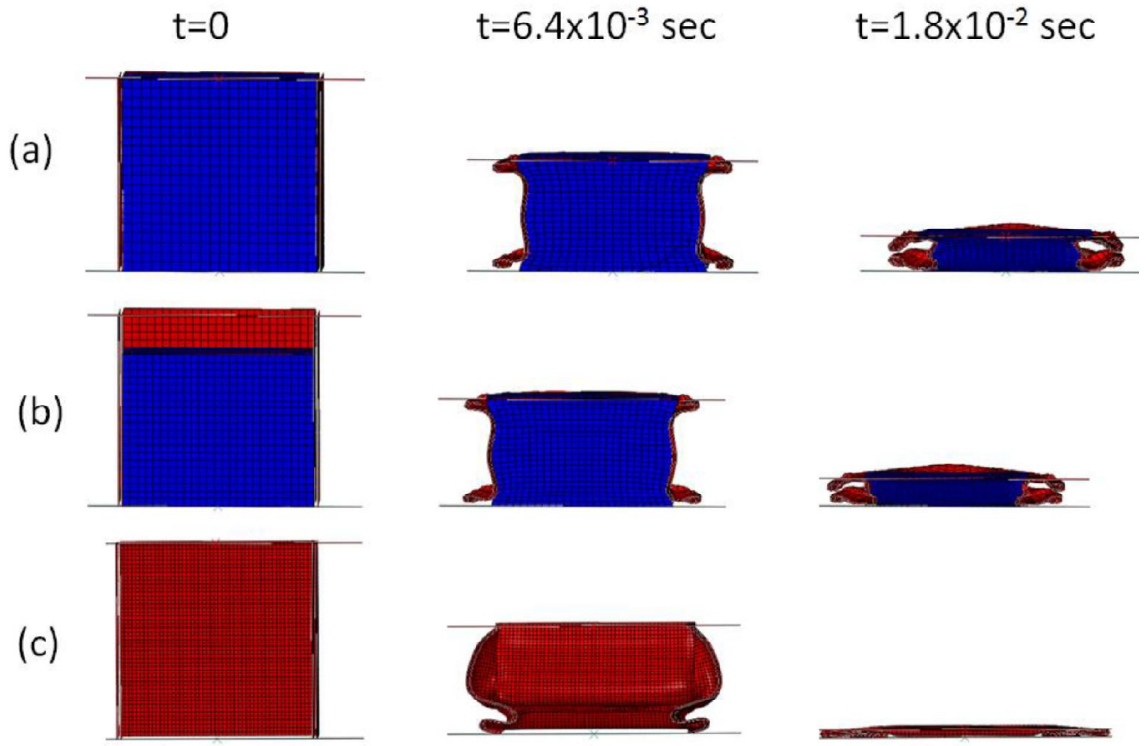


Figure 5: Deforming profiles of (a) foam-filled, (b) partially foam-filled, and (c) empty crash-boxes for crash times t=0, $6.4x10^{-3}$ sec and $1.8x10^{-2}$ sec, respectively

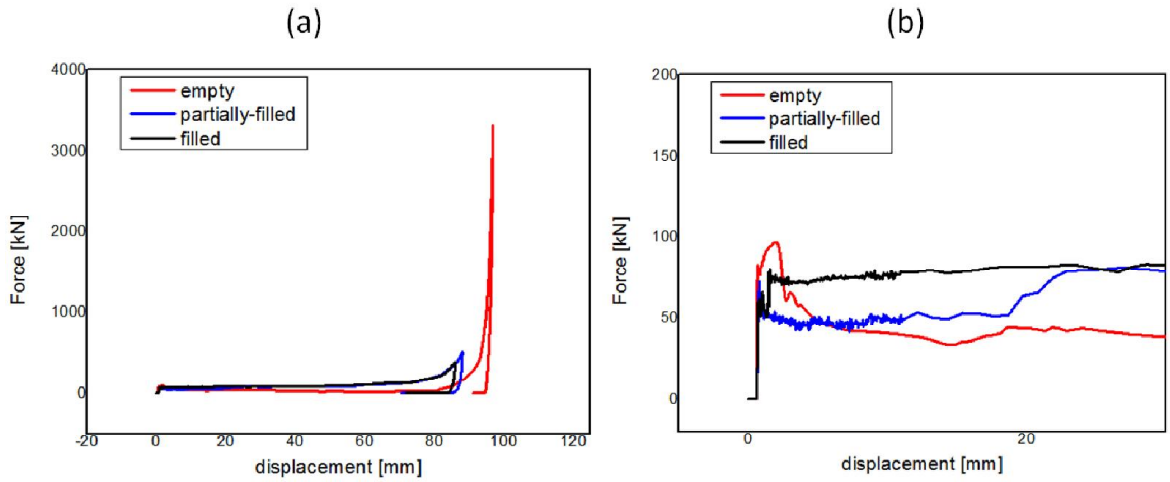


Figure 6: Impact Force-Displacement curves of foam-filled, partially foam-filled and empty crash-boxes: (a) whole impact duration, (b) zoomed for the initial stage

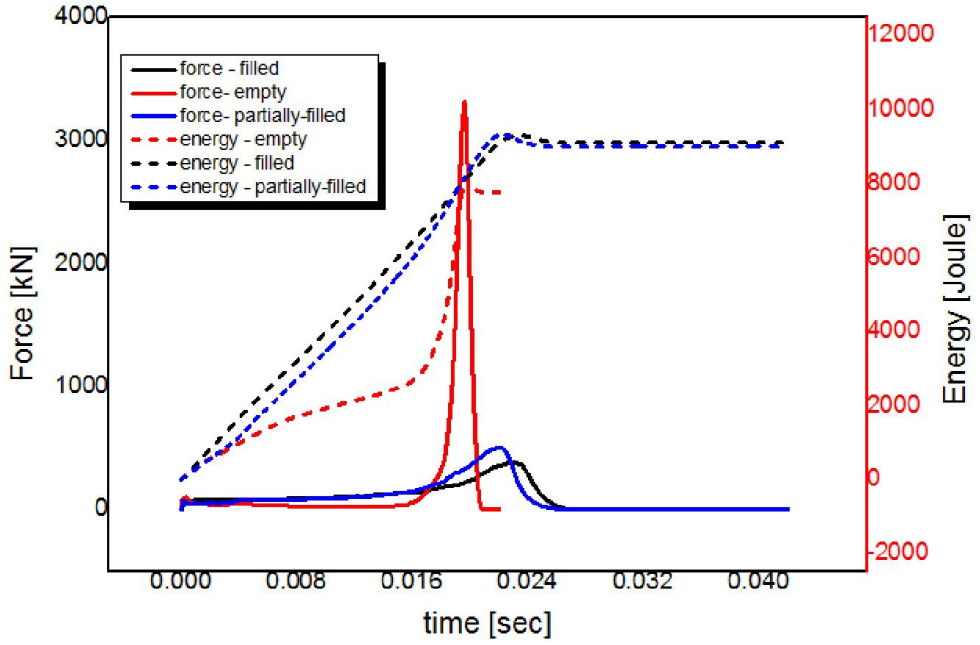


Figure 7: Energy-Time and Impact Force-Time curves for foam-filled, partially foam-filled and empty crash-boxes

The Energy-Time and Impact Force-Time curves for foam-filled, partially foam-filled and empty crash-boxes are given in Figure 7. The advantage of foam-filling of crash-box is obvious in Figure 7, where absorbed energy values can be compared for the different configurations. Foam-filled crash-boxes had a considerably higher energy absorption with the partially-filled one having a slightly lower energy, because of the higher plateau stress and the longer impact duration of fully foam-filled crash-boxes.

IV. CONCLUSION

In this study, compression tests of a closed aluminum foam was carried out for establishing the numerical modelling of foam-filled crash-boxes. The material parameters derived from compression tests were utilized in FE model and the numerical and experimental force-displacement curves of the compression tests showed good agreement revealing the validity of the FE model. The constitutive model was used for impact modelling of foam-filled, partially foam-filled and empty crash-boxes. Foam-filled crash-boxes exhibited superior impact properties such as higher plateau force and longer impact duration which results in a much lower final impact force. Partially-filling was found to decrease the initial plateau force without compromising on the absorbed energy.

A. References

[1] Kuznetcov, A., Telichev, I. & Wu, C.Q. (2016) Effect of thin-walled tube geometry on its crashworthiness performance. 14th International LS-DYNA Users Conference, 12-14 June 2016, Detroit, USA.

[2] M.F. Ashby, A.G. Evans, N.A. Fleck, L.J. Gibson, J.W. Hutchinson and H.N.G. Wadley. (2000) Metal Foams: A Design Guide. Butterworth-Heinemann.

[3] Li, Z., Yu, J. & Guo, L. (2012) Deformation and energy absorption of aluminum foam-filled tubes subjected to oblique loading. International Journal of Mechanical Sciences. 54, 48–56.

[4] Qi, C., Yang, S. & Dong, F. (2012) Crushing analysis and multiobjective crashworthiness optimization of tapered square tubes under oblique impact loading. Thin-Walled Structures. 59, 103–119.

[5] Djamaluddin, F., Abdullah, S., Ariffin, A.K. & Nopiah, Z.M. (2015) Multi objective optimization of foam-filled circular tubes for quasi-static and dynamic responses. Latin American Journal of Solids and Structures. 12, 1126-1143.

[6] Kumar, A.S., Himabindu, G., Raman, M.S. & Reddy, K.V.K. (2014) Experimental investigations with crush box simulations for different segment cars using LS-DYNA. International Journal of Current Engineering and Technology. 670-676.

[7] Toksoy, A.K. & Güden, M. (2010) Partial Al foam filling of commercial 1050H14 Al crash boxes: The effect of box column thickness and foam relative density on energy absorption. Thin-Walled Structures. 48, 482–494.

[8] M. Güden, A. K. Toksoy, H. Kavi. (2006).Experimental investigation of interaction effects in foam-filled thin-walled aluminum tubes. Journal of Materials Science 41:6417–6424.

[9] V.S. Deshpande, N.A. Fleck. (2000). Isotropic constitutive models for metallic foams. Journal of the Mechanics and Physics of Solids, 48 1253±1283.

[10] ABAQUS User's Manual, Version 6.14. (2014). Providence, RI: Dassault Systemes Simulia Corp.

Effect of the Furniture on the Thermal Efficiency of Room Heating: A CFD Study

A. KIBAR[1] and K.S. YIGIT[1]

[1]Kocaeli University, Kocaeli/Turkey, alikibar@kocaeli.edu.tr
[1]Kocaeli University, Kocaeli/Turkey, kyigit@kocaeli.edu.tr

***Abstract* - In this study, the effect of heatless furniture such as sofa-bed on thermal efficiency of panel radiator has been examined numerically. For this purpose, three different sofa-beds locations including; side-side, front-side and front-opposite cases, are simulated in 3D room by using Star CCM+ software. The radiator at a constant temperature of 50 °C was used to heat the initial temperature of room at 15 °C. The analysis was ended at the end of 1800 seconds. It is suggested that, there is no significant effect on the thermal efficiency of the radiator when the furniture is located in front of the radiators leaving a certain gap ignoring the radiation.**

***Keywords* - Numerical Analysis, Heating of Room, Panel Radiator, Thermal Efficiency**

I. Introduction

THE panel radiators are commonly used for heating of living environment such as home, school, workplace etc. The heating of the radiator surface is obtained due to circulation of the water (40-80 °C) through the radiator. Thus, the space heating is obtained owing to the natural convection between the radiator surface and air in space. The air flow is a low rate for the natural convection. Therefore, the flow may be affected by the furniture we use in our daily life in living spaces. The location of the furniture may need to be taken into consideration for the thermal efficiency. In this study, this thermal efficiency of the radiator, affected by the furniture location, is examined numerically.

Horikiri et al. [1] studied numerically the effect of furniture location in terms of thermal comfort by using a 3-D ventilated room. They indicated that the presence of non-heat generating furniture in the room can initiate complex flow re-circulations and high regional velocities of the air around the edge of the furniture. They found a little influence on temperature differences between with furniture and unfurnished rooms. Brady et al. [2] examined the effect of the magnetic decorative cover on the heat output from a radiator. They suggested that magnetic radiator covers can be used for improving heating system energy performance. Kibar [3] performed to examine the effect of the emissivity of the wall, placed behind the radiator. Kibar and Veziroglu [4] and Ucler et al [5] investigated numerically and experimentally the effect of the obstacles on the thermal efficiency of the radiator, respectively. Sevilgen and Kilic [6] performed thermal comfort using a manikin in a room with panel radiator. They indicated that thermal comfort can be enhanced by using better-insulated outer walls and windows. In all of these studies, it has been mentioned that the air circulation and thus the radiator efficiency is affected by the preventing the air circulating around the radiator.

The heat transfer from the panel radiator to the room is occurred mostly by natural convection. There is an amount of heat transfer by radiation. The radiation heat transfer can be insignificant for the low temperature of the radiator.

II. Numerical Modelling

An incompressible Navier–Stokes equation was solved numerically to examine the gas flow in a 3D space by using the commercial software Star CCM+. The Boussinesq approximation is used commonly for the natural convection combined with the Navier-Stokes equations [7]. The natural convection is achieved due to change in density of the gas with the temperature. Therefore, the buoyancy force term was approximated using the Boussinesq model, as defined in Equation (1).

$$F_g = \rho g \beta \left(T_{ref} - T\right) \tag{1}$$

where g and ρ are the gravitational acceleration (–z) and density, respectively. T_{ref} is the operating temperature, β is coefficient of thermal expansion. There is no fluid entrance and exit to the model space. The fluid was determined as ideal gas. The physical properties of fluid were determined as a constant, except for the buoyancy force term.

The flow is governed by conservation equations of the continuity (Equation (2)), momentum (Equation (3)) and energy (Equation (4)).

Continuity equation:

$$\frac{d(\rho)}{dt} + \nabla \cdot (\rho \vec{v}) = 0 \tag{2}$$

Momentum equation:

$$\frac{\partial}{\partial t}(\rho \vec{v}) + \nabla.(\rho \vec{v}\vec{v}) = -\nabla p + \nabla.[\mu(\nabla \vec{v} + \nabla \vec{v}^T)] + f_b \tag{3}$$

Energy equation:

$$\frac{\partial}{\partial t}(\rho E) + \nabla.(\rho \vec{v} H) + \nabla.(\vec{v} p) = \nabla\left(k_{eff} \nabla T\right) + \nabla(\bar{\tau}\vec{v}) + f\vec{v} + S_U \quad (3)$$

where μ, p, $\vec{v}$ and f_b are the dynamic viscosity, the pressure, the velocity vector, the external force, respectively. E and H are the total energy and enthalpy, respectively. T and k_{eff} are the temperature and the effective thermal conductivity, respectively. S_U is the source of energy. The governed equations were solved by using SIMPLE algorithm and the second order upwind scheme. The flow was considered as turbulent and k-ε turbulence model was used. The convective heat transfer is only considered. The radiation heat transfer is neglected in the present study.

A. Boundary conditions and mesh domain

In this study, the effect of the occupants and furniture such as sofa-bed on radiator efficiency is examined numerically using the Star CCM+ software [7]. The analysis is performed in 3D model, which is in 4.5x3.5x2.7 m (length x width x height), as shown in Figure 1. Three different cases for sofa-beds locations (front-side, front-opposite and side-side) were used according to the radiator. The sofa-beds were located 0.15 m in front of the radiator. The window dimensions were taken as 1.8 m width and 1.3 m height. There was a 0.15 m gap between the window and outside wall. The panel radiator was determined as in 1.2x0.6x0.1 m dimensions with empty interior. Therefore, the total surface area of the radiator was 3 m^2. The sofa-beds and door are 2.2x0.8x1.1 m and 2x1x0.05 m in dimensions, respectively. Heat transfer (loss) is occurred only through the window and the wall where the window is located. All other walls, sofa-beds and door were determined as adiabatic. The temperatures of the radiator, outside wall and window were fixed at 60, 15 and 10 °C throughout the analysis, respectively. The initial temperature of the volume of the model was determined as 15 °C. The time step was chosen as 1 second. The simulation was carried out at 1800 seconds.

Hexahedral cells were for the mesh structure, as shown in **Hata! Başvuru kaynağı bulunamadı.**. The fine mesh was used around the radiator using the volumetric control. The largest and smallest sizes of the hexahedral elements are 7.5 and 0.5 cm, respectively.

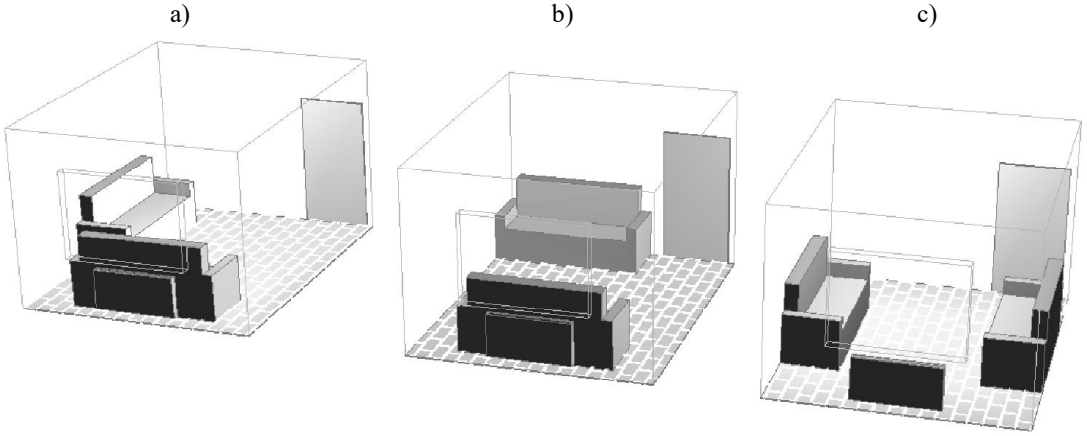


Figure 1: Geometrical models of the simulations. a) front-side b) front-opposite c) side-side.

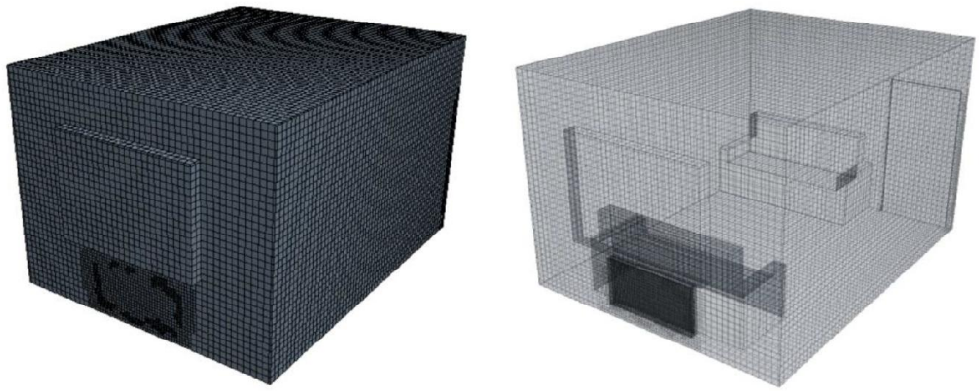


Figure 2: Mesh domain as a) opaque and b) transparent appearances.

III. RESULTS

Figure 3 shows the average temperatures of the room at the end of the simulations for all three cases. The temperatures increase almost at a same rate for all cases. The temperature reaches 23.41, 23.37 and 23.33 °C for the front-side, front-opposite and side-side cases, respectively. These results indicate that the thermal efficiency of the radiator increases slightly when the sofa-bed is located in front of the radiator.

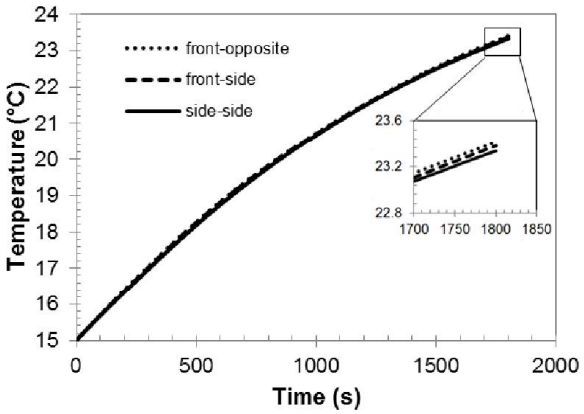


Figure 3. Average temperature of the room with respect to the time.

Figure 4 shows the temperature distributions of three cases. The temperatures are adjusted in the range of 15 to 25 °C. Temperatures greater than 25 °C are seen in red color. The window is seen as blue because of the fixed temperature. The air in contact with the radiator surface warms up its temperature and rises due to reduction in density. Therefore, the highest temperature is occurred at the ceilings for all cases, as shown in Figure 4. There is no significant effect of sofa-bed locations on the temperature distribution. Note that the natural convective heat transfer is only considered for the thermal efficiency. The thermal comfort (especially depends on the radiation) is out of the scope of this study.

Figure 5 shows the air velocity as a streamlines. When the sofa-beds are located in front of the radiator (Figures 5b,c), the maximum velocity of the rising air above the radiator is higher than the side-side case (Figure 5a). Some amount of the rising air spreads to the sideways in the case of side-side case, as seen in Figure 5a. The air which spreads forward at the ceiling turns back just below the forward spreading air after it reaches the opposite wall. The circulation of the air is occurred close to the ceiling.

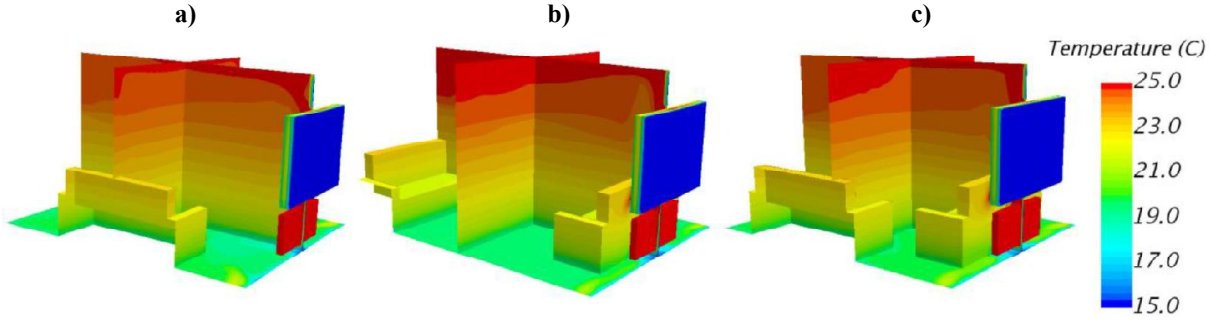


Figure 4. Temperature distributions in the rooms, a) side-side, b) front-opposite, c) front-side conditions.

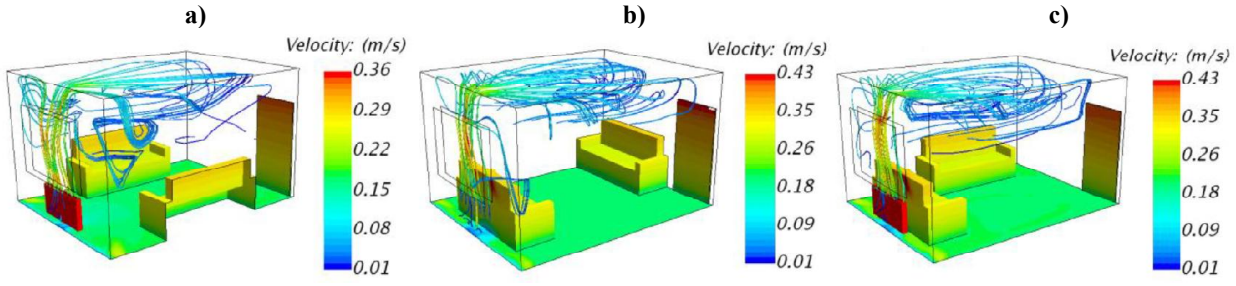


Figure 5. a) side-side, b) front-opposite, c) front-side conditions. The temperature ranges for the floor, sofa-beds, radiator and door are from 15 to 25 °C. The streamlines are coloured by the magnitude of the velocity.

The air flow behind the rising air is occurred from in front of the radiator in the case of side-side sofa-beds. However, the air flow is occurred from the sides of the sofa-beds in other two cases. The rising heated air spreads forward at the ceiling in the room. There is an inverse air flow just below this spreading, as seen in Figure 6. This can

E-ISBN: 978-605-67535-4-1

be concluded from the blue color in the regions near the ceiling. The blue color indicates the inverse flow in Figure 6. This inverse flow is occurred mostly near the side walls. In the front-side case, there is a sofa-bed at the one side wall while the other side is empty, as seen in Figure 6c. Thus, the inverse flow is larger at the empty side than sofa-bed side. This event produces the asymmetric flow, while the other two cases have a symmetric flow.

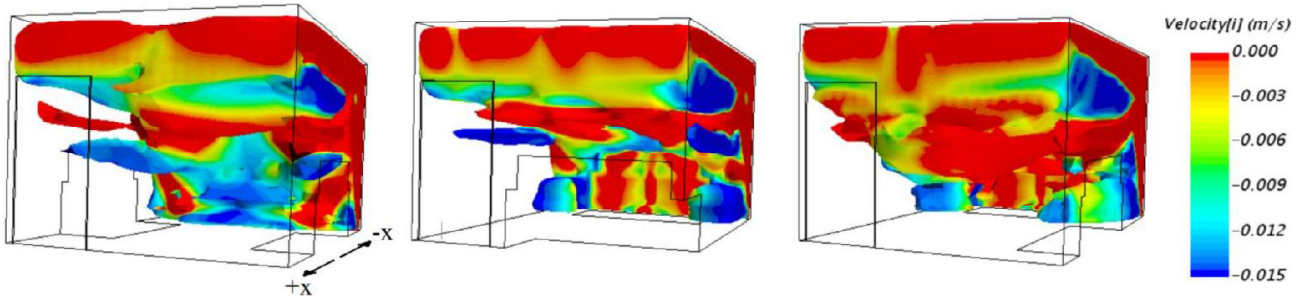


Figure 6. a) side-side, b) front-opposite, c) front-side conditions. Velocity magnitude iso-surface of 0.015 m/s colored with x-velocity. Only the negative velocity (-x) is considered. The red and blue colors indicate higher and below temperature than 0 and -0.015 m/s, respectively.

IV. Discussion

The air flow is an important for the efficiency of the heating especially for the natural convection systems such as panel radiators. The efficiency of the radiator may be affected by the obstructing of the air flow. The air which contacts with the radiator warms up and rises due to decrease in its density. The lower temperature air below the rising air takes place this rising air. It is an important point that the flows of rising air and taking place air should not to be prevented. When the sofa-bed is located in front of the radiator with an adequate distance, the air flow occurs from the sides of the sofa-bed. Therefore, if there is an enough gap between the radiator and the furniture, the efficiency of the radiator is not almost affected. These results are valid for the thermal efficiency with respect to the temperature distribution in the room. The results may be affected by consideration of the radiation heat transfer especially for the high radiator temperature.

V. Conclusion

In this study, the effect of the furniture on the thermal efficiency of the radiator is investigated numerically. If there is a sofa-bed in front of radiator, the rising velocity of the air above the radiator is high compared to the side sofa-bed cases. The air flow isn't exactly symmetric when there is a sofa-bed at the one side. Despite all these slight differences, the thermal efficiency of the radiator (ignored radiation) is almost same for all cases. These results indicate that if there is enough gap between the furniture and the radiator, the thermal efficiency of the radiator is not almost affected.

References

[1] K. Horikiri, Y. Yao, J. Yao, "Numerical optimization of thermal comfort improvement for indoor environment with occupants and furniture," *Energy Build*, vol. 88, pp. 303–315, 2015.

[2] L. Brady, M. Abdellatif, J. Cullen, J. Maddocks, A. Al-Shamma'a, "An investigation into the effect of decorative covers on the heat output from LPHW radiators," *Energy Build*, vol. 133, pp. 414–22, 2016.

[3] A. Kibar, "Radyatör Arkasındaki Duvardan Isı Kaybının Yansıtıcı/Yutucu Yüzey Kullanılarak Önlenmesinin Deneysel Olarak İncelenmesi," *Ömer Halisdemir Üniversitesi Mühendislik Bilimleri Dergisi*, vol. 6, pp. 692–699, 2017.

[4] A. Kibar, A. R. Veziroğlu A. R, "Mekân İçerisindeki Radyatörlerin Etrafındaki Engellere Göre Isıl Veriminin İncelenmes," *Tesisat Mühendisliği Dergisi*, vol. 136, pp. 5–11. 2013.

[5] K. Ucler, A. Kibar, B. Karabag, K. S. Yigit, "Mekân İçerisinde, Pencere Altında Bulunan Radyatörlerin Etrafına Yerleştirilen Engellerin Deneysel Olarak İncelenmesi" *Electron J Mach Technol.* Vol. 12, pp. 61–69, 2015.

[6] G. Sevilgen, M. Kilic, "Numerical analysis of air flow, heat transfer, moisture transport and thermal comfort in a room heated by two-panel radiators," *Energy Build*, vol. 43. Pp. 137–146, 2011.

[7] CD-adapco. STAR-CCM+ Version 10.06 User Guide CD-adapco Inc. New York, USA. 2015.

Numerical Solution of Euler Equations by Using HCUSP Scheme on Multi-block Grids

M.UYGUN[1]

[1] Istanbul AREL University, Istanbul/Turkey, muratuygun@arel.edu.tr

Abstract - **Euler equations are solved by means of an efficient and robust finite volume scheme, Convective Upwind Split Pressure (CUSP) Scheme on multi-block grids. Cell-centered discretization technique is employed. Multistage time stepping algorithm is used to advance the solution in time. Acceleration techniques including local time stepping and implicit residual smoothing are applied for faster convergence to steady state. The flux at the cell faces is computed using MUSCL approach. MUSCL is enhanced by employing Van Albada limiter to suppress oscillations in regions of sharp gradients. Attention is directed towards the accuracy, convergence. Numerical results demonstrate the present Euler solver can be used for evaluating complex geometries using multi-block grids.**

Keywords - **Euler Equations, HCUSP Scheme, Multistage Time-stepping, MUSCL Approach, Multi-block Grids.**

I. INTRODUCTION

NAVIER-Stokes equations govern the flows of viscous, heat-conducting fluids. In the limit of vanishing dissipation terms, Euler equations governing the flows of inviscid, adiabatic fluids are resulted. Due to exclusion of the diffusive effects, the applicability of the Euler equations for real flow simulations is limited. However, the dominating convective character of most flow situations at high Reynolds numbers advocates the importance of their accurate numerical simulation. Most methods used for discretization of convective part of the Navier-Stokes equations are same as the methods based on Euler equations. Also, the difficulties with discretization and solution procedure regarding the non-linear convective terms, are kept in Euler equations. Hence, development of an Euler solver is of great importance for the construction of a Navier-Stokes solver. Solutions of Euler equations are needed for various reasons such as for providing unique shock solutions for flows in converging-diverging ducts, for determining the rotational flow field behind a shock past a wing or nacelle, etc. With its current position, Euler solvers are widely used in a variety of applications for flows with complex geometries.

However, the generation of a single, computationally efficient grid on which flows over complex geometries can be computed, would be a major problem. In order to solve flows around complex geometries, implementation of multi-block strategy is a common approach [1-3]. With this strategy, computational domain is partitioned into multiple subdomains (smaller blocks) of varying sizes such that these blocks conform to the surface of the geometry and avoids the topological problems due to complexity of the geometry. Two layers of ghost cells surrounding each block are built by extending the discretization stencil beyond the computational domain. The flow solver is applied to each block, and the blocks communicate through interface boundaries. If the interface boundaries are treated accordingly, the scheme behaves the same as it does for a single-block formulation [4, 5].

In the current work, two-dimensional Euler solver based on cell-centered finite volume discretization technique is adapted to work on multi-block grids. Use of conservation form of the governing equation in finite volume discretization technique allows the shock waves to be captured as weak solutions to the governing equations and application of shock-fitting techniques is not needed further. Convective terms were evaluated using CUSP scheme [6]. Upwind schemes, in which discretization is based on the characteristics of Euler equations, have the advantage of being naturally dissipative. Separate dissipation terms are added in central schemes to overcome oscillations arising in regions of strong gradients. In the cell-centered scheme, the flow variables are located at the cell centers. The flux vectors at the midpoint of a cell face are computed by two flow variables named “the left and the right state,” which are interpolated from left and right side of the cell face using a non-symmetric formula. A famous choice for interpolation, which is known as Monotone Upwind Schemes for Scalar Conservation Laws (MUSCL) was used [7]. MUSCL was enhanced by using Van Albada Limiter [8] in order to suppress the non-physical oscillations of the solution near the regions of strong flow gradients. Time integration to steady state was done by using five stage hybrid schemes, in which dissipation terms can be evaluated at odd stages only to decrease the computational work and are blended to increase the stability of the scheme. However, the convergence of the basic scheme slows down considerably due to time step limitation associated with the small mesh cells. This disadvantage was overcome by applying two acceleration techniques such as local time-stepping and implicit residual smoothing.

II. Governing Equations

The integral form of the Navier-Stokes equations can be written as

$$\frac{\partial}{\partial t}\int_{\Omega}\vec{W}d\Omega+\int_{\partial\Omega}\left(\vec{F}_c-\vec{F}_v\right)d\vec{S}=0 \quad (1)$$

where $\vec{W}$, $\vec{F}_C$, and $\vec{F}_V$, are the vectors of conservative variables, convective and diffusive fluxes:

$$\vec{W}=\begin{bmatrix}\rho\\ \rho u\\ \rho v\\ \rho E\end{bmatrix}\quad \vec{F}_c=\begin{bmatrix}\rho V\\ \rho uV+n_x p\\ \rho vV+n_y p\\ \rho HV\end{bmatrix}\quad \vec{F}_v=\begin{bmatrix}0\\ n_x\tau_{xx}+n_y\tau_{xy}\\ n_x\tau_{yx}+n_y\tau_{yy}\\ n_x\Theta_x+n_y\Theta_y\end{bmatrix} \quad (2)$$

with the contravariant velocity V defined as

$$V=\vec{v}\cdot\vec{n}=n_x u+n_y v. \quad (3)$$

For flows of inviscid, adiabatic fluids $\vec{F}_V=0$, Euler equations are resulted. The total enthalpy H is computed as

$$H=h+\frac{u^2+v^2}{2}=E+\frac{p}{\rho} \quad (4)$$

Assuming air as an ideal gas, pressure reads

$$p=(\gamma-1)\rho\left[E-\frac{u^2+v^2}{2}\right] \quad (5)$$

and temperature is computed using equation of state.

III. Spatial Discretization

Discretization of the Euler equations in integral form is obtained by subdividing the computational domain Ω into separate hexahedral finite volumes Ω_{ij} (i = 1,2,…,Ni, and j = 1,2,…, Nj) and by requiring the conservation laws for each finite volume separately. For a particular 2D control volume whose volume does not change with time, equation (1) becomes

$$\frac{d\vec{W}_{I,J}}{dt}=-\frac{1}{\Omega_{I,J}}\left[\sum_{m=1}^{NF}(\vec{F}_c\Delta S)_m\right] \quad (6)$$

I, J locate the particular control volume and NF denotes the number of control volume faces. ΔS_m denotes the area of the face m. After writing the equation (6) for all control volumes, a system of ODE of first order (which can be solved by advancing in time starting from a known initial solution and providing suitable BC's for inviscid fluxes) is obtained. Steady solution can be reached iteratively:

$$\vec{W}_{I,J}^{n+1}=\vec{W}_{I,J}^{n}-\frac{\Delta t}{\Omega_{I,J}}\vec{R}_{I,J} \quad (7)$$

where $R_{I,J}=\left[\sum_{m=1}^{NF}\left(F_c\right)_m\Delta S_m\right]$.

$\vec{R}_{I,J}$ is called the "residual". The finite volume discretization requires an evaluation of the convective fluxes at each cell face. In this work, convective fluxes are evaluated using Convective Upwind Split Pressure Scheme [6]:

This scheme was introduced by Jameson [6, 9, and 10] and modified by Tatsumi, Martinelli, and Jameson [11]. It belongs to a family of schemes based on a splitting of the flux vector into convective and pressure flux contributions. The CUSP scheme has several advantages. First, it can be considered as a type of artificial viscosity, since it is defined as a sum of the central flux average plus a dissipative flux. Hence, it can be used with a various time-stepping schemes. Second, the CUSP formulation can be used with multistage schemes, which do not evaluate the artificial dissipation fluxes at every stage, in order to reduce computational work. Another advantage of the CUSP scheme is that it can be easily combined with preconditioning, since preconditioning is based on the inviscid flux form and not the artificial dissipation. The CUSP scheme is specifically developed for oscillation-free, single-interior-point shock capturing, and provides low dissipation for low Mach numbers. Total convective flux at the face of a control volume is computed as

$$\left(\vec{F}_C\right)_{I+\frac{1}{2}}=\frac{1}{2}\left[\vec{F}_C\left(\vec{W}_R\right)+\vec{F}_C\left(\vec{W}_L\right)\right]-\vec{D}_{I+\frac{1}{2}} \quad (8)$$

The dissipation term includes a linear combination of the differences of the state and the flux vector.

$$\vec{D}_{I+\frac{1}{2}}=\frac{1}{2}\left(\alpha^* c\right)_{I+\frac{1}{2}}\left\{\begin{bmatrix}\rho\\ \rho u\\ \rho v\\ \rho w\\ \rho H\end{bmatrix}_R-\begin{bmatrix}\rho\\ \rho u\\ \rho v\\ \rho w\\ \rho H\end{bmatrix}_L\right\}+$$
$$\frac{1}{2}\beta_{I+\frac{1}{2}}\left\{\begin{bmatrix}\rho V\\ \rho uV+n_x p\\ \rho vV+n_y p\\ \rho wV+n_z p\\ \rho HV\end{bmatrix}_R-\begin{bmatrix}\rho V\\ \rho uV+n_x p\\ \rho vV+n_y p\\ \rho wV+n_z p\\ \rho HV\end{bmatrix}_L\right\} \quad (9)$$

The above formulation is called HCUSP scheme, since the total enthalpy is preserved [12]. The two parameters α^* and β are defined as

$$\alpha^* c=\begin{cases}\left|\tilde{V}\right| & \text{if } \beta=0\\ -(1+\beta)\Lambda^- & \text{if } \beta>0 \text{ and } 0<\mathrm{M_n}<1\\ +(1-\beta)\Lambda^+ & \text{if } \beta<0 \text{ if } -1<\mathrm{M_n}<0\\ 0 & \text{if } |M_n|\geq 1\end{cases} \quad (10)$$

$$\beta=\begin{cases}+\max\left(0,\dfrac{\tilde{V}+\Lambda^-}{\tilde{V}-\Lambda^-}\right) & \text{if } 0\leq \mathrm{M_n}<1\\ -\max\left(0,\dfrac{\tilde{V}+\Lambda^+}{\tilde{V}-\Lambda^+}\right) & \text{if } -1\leq \mathrm{M_n}<0\\ \mathrm{sgn}(M_n) & \text{if } |M_n|\geq 1\end{cases} \quad (11)$$

where $M_n=\tilde{V}/\tilde{c}$ and the positive and negative eigenvalues are given as

$$\Lambda^{\pm} = \frac{\gamma+1}{2\gamma}\widetilde{V} \pm \sqrt{\left(\frac{\gamma-1}{2\gamma}\widetilde{V}\right)^2 + \frac{\widetilde{c}^{\,2}}{\gamma}} \tag{12}$$

where $\widetilde{V}$ is the contravariant velocity, γ is the specific heat coefficient, and $\widetilde{c}$ is the speed of sound. All flow variables in equations 8-11 are obtained at the cell faces using Roe averages [13, 14].

In upwind schemes, left and right states are evaluated using MUSCL approach [7], which reads

$$\begin{aligned} U_R &= U_{I+1} - \frac{1}{2}\Psi_R\left(U_{I+2} - U_{I+1}\right) \\ U_L &= U_I - \frac{1}{2}\Psi_L\left(U_I - U_{I-1}\right) \end{aligned} \tag{13}$$

where $\Psi_{L/R} = \frac{1}{2}\left[\left(1+\hat{\kappa}\right)r_{L/R} + \left(1-\hat{\kappa}\right)\right]\Phi_{L/R}$. (14)

In the above formulations, Φ is slope limiter and Ψ is the limiter function. For $\hat{\kappa} = 0$; selecting $\Phi(r) = \frac{2r}{r^2+1}$ and $\Psi(r) = \frac{r^2+r}{1+r^2}$ corresponds to Van Albada Limiter [8]. Hence, MUSCL interpolation gives

$$\begin{aligned} U_R &= U_{I+1} - \frac{1}{2}\left[\frac{a\left(b^2+\varepsilon\right)+b\left(a^2+\varepsilon\right)}{a^2+b^2+2\varepsilon}\right] \\ U_L &= U_I + \frac{1}{2}\left[\frac{a\left(b^2+\varepsilon\right)+b\left(a^2+\varepsilon\right)}{a^2+b^2+2\varepsilon}\right] \end{aligned} \tag{15}$$

where $\begin{matrix} a_R = U_{I+2} - U_{I+1} \\ a_L = U_{I+1} - U_I \end{matrix}$, and $\begin{matrix} b_R = U_{I+1} - U_I \\ b_L = U_I - U_{I-1} \end{matrix}$.

The parameter ε prevents the activation of the limiter in smooth flow regions due to small-scale oscillations [15].

IV. Temporal Discretization

For steady problems with cell-centered discretization, basic explicit scheme is written as

$$\Delta\vec{W}_I^n = -\frac{\Delta t_I}{\Omega_I}\vec{R}_I^n \tag{16}$$

For five-stage hybrid scheme, where the dissipative terms are evaluated at odd stages, the spatial discretization is split into two parts

$$\vec{R}_I = \left(\vec{R}_c\right)_I - \left(\vec{R}_d\right)_I \tag{17}$$

The first part contains discretization of the convective fluxes. The second part is composed of the numerical dissipation.

$$\begin{aligned} \left(\vec{R}_c\right)_I &= \sum_{k=1}^{N_F}\left[\vec{F}_c\left(\vec{W}_{I+1/2}\right)\Delta S\right]_k \\ \left(\vec{R}_d\right)_I &= \sum_{k=1}^{N_F}\left[\vec{D}\right]_k \end{aligned} \tag{18}$$

Then, the hybrid multistage scheme reads

$$\begin{aligned} \vec{W}_I^{(0)} &= \vec{W}_I^n \\ \vec{W}_I^{(1)} &= \vec{W}_I^{(0)} - \alpha_1\frac{\Delta t_I}{\Omega_I}\left[\vec{R}_c^{(0)} - \vec{R}_d^{(0)}\right]_I \\ \vec{W}_I^{(2)} &= \vec{W}_I^{(0)} - \alpha_2\frac{\Delta t_I}{\Omega_I}\left[\vec{R}_c^{(1)} - \vec{R}_d^{(0)}\right]_I \\ \vec{W}_I^{(3)} &= \vec{W}_I^{(0)} - \alpha_3\frac{\Delta t_I}{\Omega_I}\left[\vec{R}_c^{(2)} - \vec{R}_d^{(2,0)}\right]_I \\ \vec{W}_I^{(4)} &= \vec{W}_I^{(0)} - \alpha_4\frac{\Delta t_I}{\Omega_I}\left[\vec{R}_c^{(3)} - \vec{R}_d^{(2,0)}\right]_I \\ \vec{W}_I^{(n+1)} &= \vec{W}_I^{(0)} - \alpha_5\frac{\Delta t_I}{\Omega_I}\left[\vec{R}_c^{(4)} - \vec{R}_d^{(4,2)}\right]_I \end{aligned} \tag{19}$$

where

$$\begin{aligned} \vec{R}_d^{(2,0)} &= \beta_3\vec{R}_d^{(2)} + \left(1-\beta_3\right)\vec{R}_d^{(0)} \\ \vec{R}_d^{(4,2)} &= \beta_5\vec{R}_d^{(4)} + \left(1-\beta_5\right)\vec{R}_d^{(2,0)} \end{aligned} \tag{20}$$

Table 1 presents stage coefficients α_m and blending coefficients β_m in case of (5-3) hybrid scheme.

The basic explicit time-stepping scheme is further accelerated by local time stepping and implicit residual smoothing (IRS). With local time stepping, the solution at each cell is advanced at the maximum Δt allowed by the stability. Implicit smoothing of residuals is used to extend the stability range of the basic scheme.

Table 1. Hybrid Multistage scheme

	Upwind Scheme	
Stage	α	β
1	0.2742	1.00
2	0.2067	0.00
3	0.5020	0.56
4	0.5142	0.00
5	1.0000	0.44

Jameson and Baker [16] first introduced the residual smoothing technique with the aim to give the explicit scheme an implicit character. Maximum allowable CFL number is increased considerably. IRS reads

$$\begin{aligned} -\varepsilon^I\vec{R}^*_{I-1,J} + \left(1+2\varepsilon^I\right)\vec{R}^*_{I,J} - \varepsilon^I\vec{R}^*_{I+1,J} &= \vec{R}_{I,J} \\ -\varepsilon^J\vec{R}^{**}_{I,J-1} + \left(1+2\varepsilon^J\right)\vec{R}^{**}_{I,J} - \varepsilon^J\vec{R}^{**}_{I,J+1} &= \vec{R}^*_{I,J} \end{aligned} \tag{21}$$

where $\vec{R}^*_{I,J}$, $\vec{R}^{**}_{I,J}$ denote the residuals in I, J directions. Smoothing coefficients read [11]

$$\begin{aligned} \varepsilon^I &= \max\left\{\frac{1}{4}\left[\left(\frac{\sigma^*}{\sigma}\frac{1}{1+\Psi r^J}\right)^2 - 1\right], 0\right\} \\ \varepsilon^J &= \max\left\{\frac{1}{4}\left[\left(\frac{\sigma^*}{\sigma}\frac{1}{1+\Psi r^I}\right)^2 - 1\right], 0\right\} \end{aligned} \tag{22}$$

$\Psi = 0.125$ is taken. The maximum ratio of the CFL numbers of the smoothed and unsmoothed scheme is dependent on the value of the smoothing coefficient,

$$\frac{\sigma^*}{\sigma} \le \sqrt{1+4\varepsilon} \tag{23}$$

The ratios of the convective spectral radii read

$$r^I = \frac{\hat{\Lambda}_C^J}{\hat{\Lambda}_C^I} \text{ and } r^J = \frac{\hat{\Lambda}_C^I}{\hat{\Lambda}_C^J} \tag{24}$$

V. Boundary Conditions:

Boundary conditions are treated by using two layers of ghost cells, which are built by extending the discretization stencil beyond the computational boundaries. At the solid wall, flow tangency is maintained and the normal derivative of temperature is zero (adiabatic wall). The wall pressure is obtained by extrapolation from the interior domain. A continuity condition is enforced along the wake cut in the C-type grid. Characteristic boundary condition is applied to the far field boundaries. At the block interfaces of each block grid, flow information is transferred by the help of ghost cells.

VI. Computational Results

The numerical results given here demonstrate the accuracy and computational efficiency of the present solver for inviscid flows on multi-block grids. For all computations, two-block grid that forms a C-type computational grid including 192x32 cells with 128 cells on the airfoil, and 32 cells in the wake is used (figure 1). The outer boundary is located 15 chords away from the airfoil. The grid spacing next to the wall is $5x10^{-3}$ chord lengths (figure 2). The CFL number of 4.5 is used on all each block grids. Convergence is monitored using L2 norm of density residual. All computations were performed on a PC including 8 Gb memory and two GHz CPU running Windows 10.

Test case involves transonic flow past a NACA 0012 airfoil at free stream Mach number of 0.8 and incidence angle of 1.25 degrees [17].

Convergence and lift histories are shown in figure 3-4. Convergence is attained in the computations. Iso-Mach contours varies smoothly across each block interfaces (figure 5).

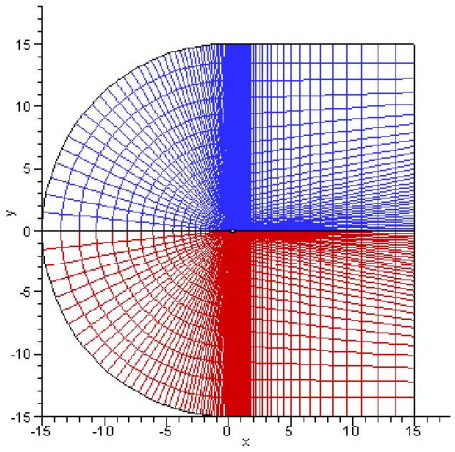


Figure 1 Multi-block grid layout.

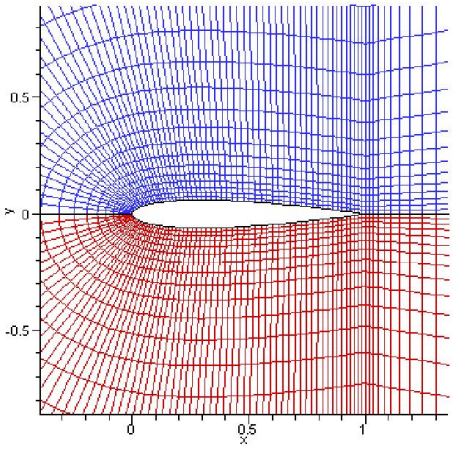


Figure 2 Computational grid around NACA 0012.

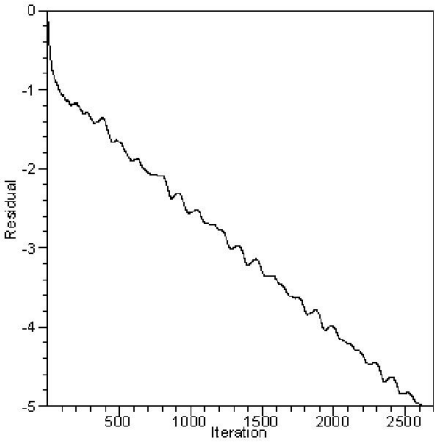


Figure 3 Convergence history.

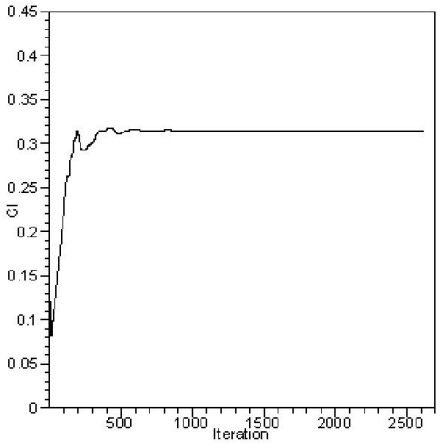


Figure 4 Lift history.

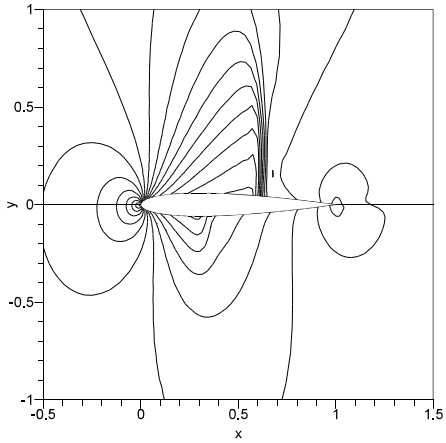


Figure 5 Iso-Mach contours with ΔM=0.05

VII. Conclusion

A multi-block strategy is implemented into an existing two-dimensional Euler solver in order to solve flows past complex geometries. Transonic inviscid flow past NACA 0012 airfoil is computed on two-block grid as a test case. Convergence is attained in the computations. Numerical results agree well with those available in the open literature and they indicate that multi-block strategy is successfully applied. Evaluation of diffusive fluxes will improve the reliability and flexibility of the present multi-block solver as an engineering tool for handling viscous flows as well.

References

[1] C.-C.Rossow, "Efficient computation of inviscid flow fields around complex configurations using a multi-block multigrid method," *Communications in Applied Numerical Methods*, Vol.8, pp.735-747, 1992.

[2] A. Rizzi, P. Eliasson, I. Lindblad, C. Hirsch, C. Lacor, J. Haeuser, "The engineering of multi-block/multigrid software for Navier-Stokes flows on structured meshes," *Computers & Fluids*, Vol. 22, pp.341-367, 1993.

[3] C.B. Jenssen, "Implicit multi-block Euler and Navier-Stokes calculations," *AIAA Journal*, Vol. 32, No.9, pp.1808-1814, 1994

[4] C. De-Nicola, G. Pinto, R. Tognaccini "On the numerical stability of block structured algorithms with applications to 1-D advection-diffusion problems," *Computers & Fluids*, Vol. 24, pp.41-54, 1995.

[5] R. Enander, E. Sterner, "Analysis of internal boundary conditions and communication strategies for multigrid multi-block methods," Report No. 191, Dept. Sci. Computing, Uppsala University, Sweden; 1997.A.

[6] Jameson, 1993, "Artificial Diffusion, Upwind Biasing, Limiters and Their Effect on Accuracy and Multigrid Convergence in Transonic and Hypersonic Flow," AIAA Paper 93-3559.

[7] B. V. Leer, "Towards the Ultimate Conservation Difference Scheme IV; A New Approach to Numerical Convection," *Journal of Computational Physics*, Vol. 23, pp. 276-299, 1977.

[8] G.D. Albada, B. V. Leer, and W.W. Roberts, "A Comparative Study of Computational Methods in Cosmic Gas Dynamics," *Astron. Astrophysics*, Vol. 108, pp. 76-84, 1982.

[9] A. Jameson, "Positive Schemes and Shock Modeling for Compressible Flows," *Inter. J. Numerical Methods Engineering*, Vol. 20, pp. 743-776, 1995.

[10] A. Jameson, "Analysis and Design of Numerical Schemes for Gas Dynamics II: Artificial Diffusion and Discrete Shock Structure*," Int. J. Computational Fluid Dynamics*, Vol. 5, pp. 1-38, 1995.

[11] S. Tatsumi, L. Martinelli, A. Jameson, "A Design, Implementation and Validation of Flux Limited Schemes for the Solution of the Compressible Navier-Stokes Equations," AIAA Paper 94-0647, 1994.

[12] S. Tatsumi, L. Martinelli, A. Jameson, "A New High Resolution Scheme for Compressible Viscous Flow with Shocks," AIAA Paper 95-0466, 1995.

[13] P.L. Roe, "Approximate Riemann Solvers, Parameter Vectors, and Difference Schemes," *Journal of Computational Physics*, Vol. 43, pp. 357-372, 1981.

[14] P.L. Roe, J. Pike, "Efficient Construction and Utilization of Approximate Riemann Solutions," *Computing Methods in Applied Sciences and Engineering*, R. Glowinski, J.L. Lions (eds.), North Holland Publishing, The Netherlands, 1984.

[15] V. Venkatakrishnan, "On the Accuracy of Limiters and Convergence to Steady State Solutions," AIAA Paper 93-0880, 1993.

[16] A. Jameson, T.J. Baker, 1983, "Solution of the Euler Equations for Complex Configurations," AIAA paper 83-1929, 1983.

[17] North Atlantic Treaty Organization, "Test Cases for Inviscid Flow Field Methods," Advisory Report AGARD-AR-211, North Atlantic Treaty Organization Advisory Group for Aerospace Research and Development, 1985, Report of Fluid Dynamics Panel Working Group 07.

Photovoltaic Thermal (PV/T) Powered Multi-Generation Systems: A Review

Erman Kadir Oztekin[1], Pinar Mert Cuce[2] and Erdem Cuce [3]

[1]Bayburt University, Bayburt, 69000, Turkey, *ermanoztekin@bayburt.edu.tr*
[2]Bayburt University, Bayburt, 69000, Turkey, *pinarmertcuce@bayburt.edu.tr*
[3]Bayburt University, Bayburt, 69000, Turkey, *erdemcuce@bayburt.edu.tr*

Abstract **- A photovoltaic thermal (PV/T) system is a compact cogeneration system that derives its electrical and thermal energies from sun. Electrical energy is provided by the PV module integrated with thermal collector which is cooled with fluid flow. The fluid carries the thermal energy due to heat transferred from surface covered with PV cells. A vast amount of research has been dedicated to increase the total performance of PV/T collectors by using many different approaches. So far, the overall performance of these systems approached to a notable success. But, recent developments can only result a small increase in efficiency of the system and their single usage is well established. Thus, newer PV/T driven multi-generation systems have drawn attention. In these systems, heat and electricity are partially or completely provided with PV/T collectors. Economical and thermal analyses of these systems have been studied by several researchers. Most of these systems have conceptual designs and only simulations have been presented in order to evaluate their performance. On the other hand, smaller designs have already been constructed such as PV/T driven solar driers and heat pumps. According to results, using PV/T collectors for power supply to other systems is a successful approach and have great potential for the future. Moreover, the overall payback period for a typical PV/T driven system is estimated to be under 4 years.**

Keywords **- PV/T collectors, thermal and electrical efficiency, multi-generation systems, solar drier, heat pump.**

I. Introduction

This paper reviews photovoltaic thermal PV/T powered combined systems. These systems have gained so much attention due to their wide application range. PV/T collectors are one of the most preferred renewable energy sources which can harvest solar energy. They can efficiently produce electricity and low grade thermal heat [1]. Thus, overall efficiency of these systems is always higher than single PV modules. Simple flat plate PV/T collector is a binary unit where electricity is produced by PV units and thermal energy is gained by thermal collector [2, 3]. Remarkable developments have been done on a basic system including concentration of solar light, using facades, using different fluids and modified new designs [4].

Nowadays this attention has been turned to a different direction since the improvements for the PV/T systems are somewhat limited. For example, the output temperature of the PV/T system changes significantly among seasons and can get limited values. Or the value of the heat and electricity produced by PV/T systems are lower compared to other power generation systems. Thus, the expectations from outputs of the PV/T collectors are well known. The electricity output for PV/T collectors are well studied [1, 5, 6]. On the other hand, these energies can be used as inputs for other cycles. Recently, the possibility of using PV/T systems as power suppliers for different systems are being evaluated. Herein, several studied will be covered.

II. Simulation Studies

Simulation studies has taken the most part of the literature on PV/T driven systems. The economical and thermal studies are realized based on thermal and electrical models of PV/T systems and the mathematical model of integrated system. A typical PV/T collector is integrated to a seawater desalination system [7]. This type of system is designed for suburban places of Europe. Main components of the multi-generation system are a PV/T collector, multi-effect distillation unit and LiBr-H2O absorption system. The schematic view of the combined system can be seen from Figure 1.

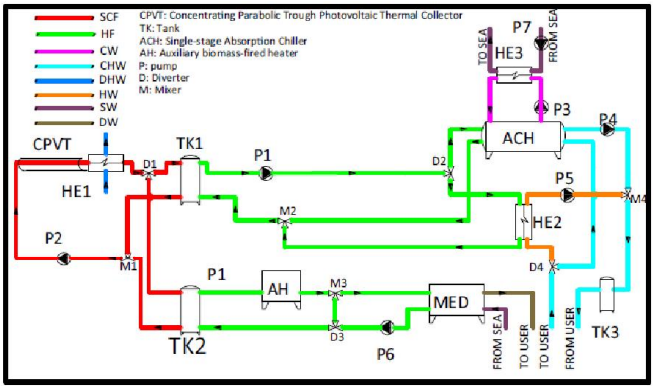


Figure 1: The schematic view of PV/T driven seawater desalination system [7].

The heat generated from the PV/T collector can be directly used to heat domestic water or it can be sent as an input for

absorption chiller. On the other hand, hot fluid can be used for the seawater desalination application. Maximum efficiency is observed during summer when the energy is used for the desalination system. However, winter performance is seen to be insufficient. Similar analyses are applied to a system consisted of absorption chiller and heat pump where both of them are driven by PV/T [8]. It was found that approximately 83% of the incoming solar energy can be utilized with total energy efficiency of 49%. The collaboration of PV/T collectors and absorption refrigeration system is taken so much attention [9]. This is a natural result to meet cooling demand of a particular house. Basu and Ganguly designed a simple PV/T driven absorption refrigeration system as seen in Figure 2.

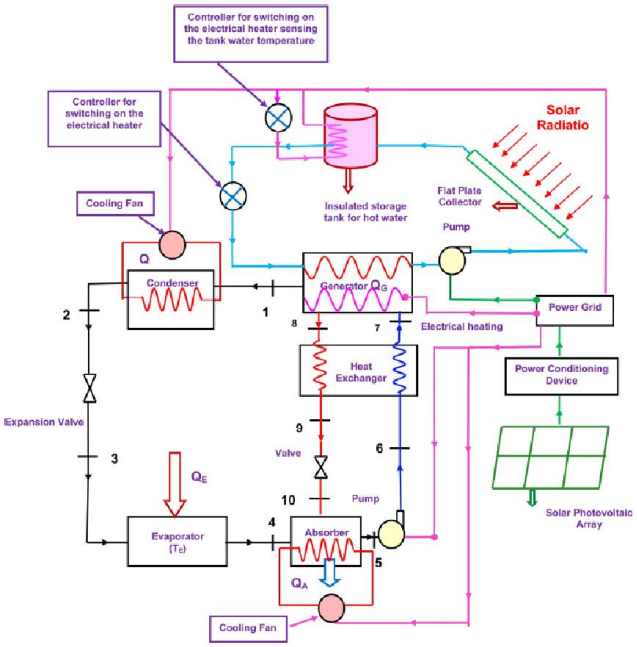


Figure 2: The schematic view of PV/T driven absorption refrigeration system [9].

The system is able to provide 17.4kWh of energy per day on average with payback period less than 4 years. A simulation study is conducted based on the green school concept where the energy is supplied by PV/T collectors [10]. Heat pump and storage tanks are also added to the installations. The study has revealed that there are economic advantages for the country as a result of application of this project. Cilogluları proposed a hydrogen production system powered with PV/T [11]. The system is consisted of Proton Exchange Membrane and PV/T collector as seen from Figure 3.

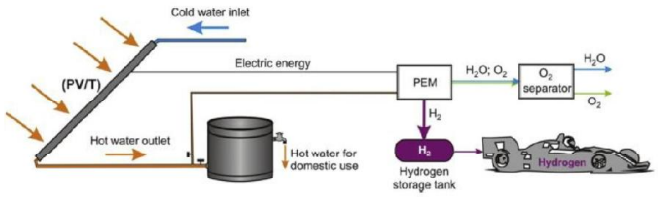


Figure 3: The schematic view of PV/T driven absorption Proton Exchange Membrane [11].

Exergy efficiency of the system and hydrogen production rate were estimated to be 14.11% and 0.018 kg per day, respectively. Several models proposed for different designs of PV/T driven systems by many researchers. The surface optimization is proposed for PV/T collectors to power supply for desalination plant [12]. PV/T energy is optimized to be used with a desalination process [13]. Indirect solar drier embedded with PV/T collector is modelled [14]. In an another study, PV/T powered absorption refrigeration is modelled for potato storage [15]. Finally, the thermal output of the PV/T is used to feed organic Rankine cycle [16].

III. EXPERIMENTAL STUDIES

Several experimental studies also have entered into literature for PV/T driven systems. PV/T driven heat pump water heating system has been simulated in the MATLAB/Simulink environment and tested experimentally by Tsai [17]. The overall PV/T efficiency and the COP of the proposed system is observed to reach up to 86% and 7.09, respectively. Tiwari et. al. has performed several studies PV/T embedded greenhouse systems as a solar drier [18-21]. Additionally, Hussain et. al. also conducted a study on a greenhouse embedded with PV/T [22]. These studies are also considered as multi-generation system due to food production or processing of foods are realized. Buker et. al. demonstrated a new system consisted of PV/T collector and dew point cooling system [23]. The combined liquid desiccant dehumidification-indirect evaporative air conditioning unit can be seen from Figure 4.



Figure 4: The combined liquid desiccant dehumidification-indirect evaporative air conditioning unit used in the experiments [23].

It was observed that the system could provide heating, cooling and power generation with the value of 3 kWh, 5.2 kWh and 10.3MWh, respectively. Another approach has been brought into literature to supply cooling demand by using thermoelectric coolers powered by PV/T [24]. It was reported that electrical efficiency and COP of thermoelectric coolers have reached up to 16.7% and 1.7, respectively. Qu et. al. demonstrated PV/T driven heat pump system with dual sources [25]. Water and air sources are used to drive heat pump, to

provide domestic hot water and to cool the PV/T collectors. Results showed an increase of 10.3%. Chen et. al. experimentally analyzed PV/T driven heat pump system [26]. They showed that COP of the system is a function of solar radiation, ambient temperature and PV backboard absorptivity.

IV. CONCLUSIONS

It has been shown that the available energy of a PV/T system can be used to power supply to other systems. The collective results from whole system can be more efficient than single use of PV/T system and can have multi outputs including cooling load, clean water, crop production and dried foods. Overall payback periods of these systems were observed to be below 4 years and really effected by the seasons. Several PV/T parameters has to be still optimized and more experimental studies should be done.

REFERENCES

1. Zondag, H.A., *Flat-plate PV-Thermal collectors and systems: A review.* Renewable & Sustainable Energy Reviews, 2008. **12**(4): p. 891-959.
2. Tripanagnostopoulos, Y., et al., *Hybrid photovoltaic/thermal solar systems.* Solar Energy, 2002. **72**(3): p. 217-234.
3. Cuce, E. and T. Bali, *Improving performance parameters of silicon solar cells using air cooling*, in *Fifth International Ege Energy Symposium and Exhibition*. Denizli, Turkey.
4. Sathe, T.M. and A.S. Dhoble, *A review on recent advancements in photovoltaic thermal techniques.* Renewable and Sustainable Energy Reviews, 2017. **76**(Supplement C): p. 645-672.
5. Chow, T.T., *A review on photovoltaic/thermal hybrid solar technology.* Applied Energy, 2010. **87**(2): p. 365-379.
6. Cuce, E., et al., *An accurate model for photovoltaic (PV) modules to determine electrical characteristics and thermodynamic performance parameters.* Energy Conversion and Management, 2017. **146**: p. 205-216.
7. Calise, F., M. Dentice d'Accadia, and A. Piacentino, *A novel solar trigeneration system integrating PVT (photovoltaic/thermal collectors) and SW (seawater) desalination: Dynamic simulation and economic assessment.* Energy, 2014. **67**: p. 129-148.
8. Calise, F., et al., *A novel solar-assisted heat pump driven by photovoltaic/thermal collectors: Dynamic simulation and thermoeconomic optimization.* Energy, 2016. **95**(Supplement C): p. 346-366.
9. Basu, D.N. and A. Ganguly, *Conceptual Design and Performance Analysis of a Solar Thermal-Photovoltaic-Powered Absorption Refrigeration System.* Journal of Solar Energy Engineering, 2015. **137**(3): p. 031020-031020-9.
10. Yilmaz, S., H. Binici, and H.R. Ozcalik, *Energy supply in a green school via a photovoltaic-thermal power system.* Renewable and Sustainable Energy Reviews, 2016. **57**(Supplement C): p. 713-720.
11. Cilogulları, M., et al., *Investigation of hydrogen production performance of a Photovoltaic and Thermal System.* International Journal of Hydrogen Energy, 2017. **42**(4): p. 2547-2552.
12. Ammous, M. and M. Chaabene, *Multi criteria sizing approach for Photovoltaic Thermal collectors supplying desalination plant.* Energy Conversion and Management, 2015. **94**(Supplement C): p. 365-376.
13. Fine, J.P., J. Friedman, and S.B. Dworkin, *Transient analysis of a photovoltaic thermal heat input process with thermal storage.* Applied Energy, 2015. **160**(Supplement C): p. 308-320.
14. Slimani, M.E.A., et al., *Study and modeling of energy performance of a hybrid photovoltaic/thermal solar collector: Configuration suitable for an indirect solar dryer.* Energy Conversion and Management, 2016. **125**: p. 209-221.
15. Basu, D.N. and A. Ganguly, *Solar thermal–photovoltaic powered potato cold storage – Conceptual design and performance analyses.* Applied Energy, 2016. **165**(Supplement C): p. 308-317.
16. Tourkov, K. and L. Schaefer, *Performance evaluation of a PVT/ORC (photovoltaic thermal/organic Rankine cycle) system with optimization of the ORC and evaluation of several PV (photovoltaic) materials.* Energy, 2015. **82**: p. 839-849.
17. Tsai, H.-L., *Design and Evaluation of a Photovoltaic/Thermal-Assisted Heat Pump Water Heating System.* Energies, 2014. **7**(5): p. 1-20.
18. Tiwari, S. and G.N. Tiwari, *Exergoeconomic analysis of photovoltaic-thermal (PVT) mixed mode greenhouse solar dryer.* Energy, 2016. **114**(Supplement C): p. 155-164.
19. Tiwari, S., G.N. Tiwari, and I.M. Al-Helal, *Performance analysis of photovoltaic–thermal (PVT) mixed mode greenhouse solar dryer.* Solar Energy, 2016. **133**(Supplement C): p. 421-428.
20. Tiwari, S., et al., *Thermal modelling of photovoltaic thermal (PVT) integrated greenhouse system for biogas heating.* Solar Energy, 2016. **136**(Supplement C): p. 639-649.
21. Tiwari, S. and G.N. Tiwari, *Thermal analysis of photovoltaic-thermal (PVT) single slope roof integrated greenhouse solar dryer.* Solar Energy, 2016. **138**(Supplement C): p. 128-136.
22. Imtiaz Hussain, M., A. Ali, and G.H. Lee, *Multi-module concentrated photovoltaic thermal system feasibility for greenhouse heating: Model validation and techno-economic analysis.* Solar Energy, 2016. **135**(Supplement C): p. 719-730.
23. Buker, M.S., B. Mempouo, and S.B. Riffat, *Experimental investigation of a building integrated photovoltaic/thermal roof collector combined with a liquid desiccant enhanced indirect evaporative cooling system.* Energy Conversion and Management, 2015. **101**(Supplement C): p. 239-254.
24. He, W., et al., *Experimental study and performance analysis of a thermoelectric cooling and heating system driven by a photovoltaic/thermal system in summer and winter operation modes.* Energy Conversion and Management, 2014. **84**(Supplement C): p. 41-49.
25. Qu, M., et al., *Experimental study on the operating characteristics of a novel photovoltaic/thermal integrated dual-source heat pump water heating system.* Applied Thermal Engineering, 2016. **94**(Supplement C): p. 819-826.
26. Chen, H., et al., *Performance study of heat-pipe solar photovoltaic/thermal heat pump system.* Applied Energy, 2017. **190**(Supplement C): p. 960-980.

Techno-Economic Analysis of Solar Domestic Hot Water System for Single Detached Dwellings in Konya

G. N. Güğül[1]

[1] Selcuk University, Faculty of Technology, Computer Engineering Department, Konya/Turkey,
gul.gugul@selcuk.edu.tr

Abstract - **Abstract**

Area of new constructed single detached homes in Konya has increased averagely 7% every year in last decade. Due to the availability of roof space for solar panels reducing single detached homes energy consumption for hot water is more feasible compared to apartments. In this study, the techno economic feasibility of construction of solar domestic hot water system to single detached homes in Konya is investigated. Natural gas consumption bills of four single detached homes in Konya is collected during summer. Hourly climate data, technical data of solar energy system and economic analysis data are used in the calculations. Obtained energy saving results are generalized to the single detached house stock constructed in last decade in Konya to estimate the potential for reduction in energy and emission. The results indicate that average of annual natural gas consumption of the three houses for hot water supply is 359 m^3/year (13 GJ/year), associated CO_2 emissions is 769 kg-CO_2/year. In the case of application of solar panels for hot water supply, reduction in natural gas consumption for hot water supply is calculated as 210 m^3/year (8 GJ/year) and energy saving per unit area is found as 0,041 GJ/m^2-year (1,17 m^3/m^2-year). Total area of single detached houses constructed in Konya after 2006 is 1.972.552 m^2. Applying the solar domestic water heating system to single detached homes in Konya constructed after 2006 result in reductions of about 2,3 million natural gas consumption and 4950 ton/year CO_2 emission

Keywords - **Solar water heating system, energy saving, economic analysis, Konya**

I. INTRODUCTION

RATE of residential energy consumption to the total energy consumption is significant in most countries. In the US residential energy consumption is more than 20% of the total energy consumption [1] , while in Turkey it is about 19% of the total [2].

About 33% of the energy consumed in residential sector of Turkey is natural gas [1]. Due to the insufficient natural gas production of Turkey, 98% of natural gas demand is imported [2]. For this reason, natural gas must be consumed efficiently.

The use of renewable energy technologies results in reducing the fossil fuel usage and associated emissions. In addition to the energy savings, such improvements increase the value of the house.

There are many studies in the open literature on reducing the energy consumption and emissions of residential buildings as well as the residential sector as a whole. Many of these studies are conducted by modeling the energy demand of residential buildings and determining the amount of energy savings obtained from the application of various improvements. ü

In 2014, number of new residential buildings has increased 12% and number of single detached residential buildings has increased 6% in Turkey. The total floor area of single detached homes constructed after 2006 is 1.972.552 m^2 in Konya [3]. The most available renewable energy source in Turkey is solar energy due to its geographical position. Availability of sufficient roof space makes installation of the solar energy system for hot water more feasible in single detached homes. Solar energy panel installed for hot water supply in Turkey has reached to 15.497.913 m^2 by the end of 2012 [3]. In addition, solar energy panel production has become one of the fastest growing sectors in recent years [4]. The annual production of solar hot water collector in Turkey is between 750.000 – 1.000.000 m^2. Some of the production is exported [5].

There are studies in the literature that examine solar energy potential for hot water supply in Turkey. A study conducted at Fırat University conducted to investigate the solar energy potential of Turkey. In this study, two different types of collectors were examined for six provinces using climate data. It is also stated that 98-99% of the solar energy panels installed between 2005 and 2010 are flat plate solar collectors, 78% of which are installed in residences, due to their price [4]. Another study is conducted to optimize SDHW system for different climate regions of Turkey. In this study economic analysis of the model is accomplished and optimum collector area, collector slope angle and water storage tank volume are determined for each province [6]. Economic analysis of SDHW system for residential buildings was also conducted in another study to investigate the reduction in CO_2, SO_2 and particulate amounts released to the atmosphere by the use of solar-assisted systems for Balıkesir provinces and districts [7].

In this study, energy saving and associated reduction in CO_2 emission obtained by the application of SDHW to a single detached house in Konya is determined. Results are also generalized to all single detached houses in Konya constructed after 2006. In the first step of the study, natural gas bills of an owner-occupied single detached house in Konya is obtained during summer to calculate the energy consumption for hot

water. The data collected from the test house is then used to calculate the amount of hot water used daily. Then, suitable solar domestic hot water panel area and tank volume is determined. Finally PBP of the system is determined and system is applied to the entire single detached house stock in Konya constructed after 2006.

II. METHODOLOGY

This section provides information about the methodology followed during calculations of energy consumption for hot water, energy savings obtained with the SDHW system, associated reductions in CO_2 emission and techno-economic analysis. In addition, the methods used to generalize the energy savings to single detached house stock of Konya constructed after 2006 are explained.

A. Model House

Four single detached two storey houses in Konya, Turkey, is selected as model due to their adequate roof space for solar panels. Energy requirement for hot water of three of these houses are supplied by the natural gas burning boiler, one of them is supplied by SDHW system. The fourth single detached house that already have SDHW system is selected to calculate the natural gas consumption for cooking. Because natural gas in fouth house is only consumed for cooking, in remaining three houses consumed for cooking and hot water during summer.

B. Collection of Data

The technical specifications and cost of the SDHW system is obtained from a company. Greenhouse gas (GHG) emissions factor is 2,14 kg-CO_2/m^3 for NG [8]. NG consumption of four single detached houses during summer are obtained from NG bills.

1) Climate data

The hourly meteorological data of Konya is obtained by using the hourly climate data of Ankara. The hourly climate data of Ankara is normal climate data of Ankara downloaded from the United States Department of Energy's web site [9].

According to the average daily solar radiation time distribution of Turkey [10] daily average radiation time of Konya is one hour more than Ankara. Therefore one hour is added to each day of Ankara radiation data of which has the value of the average of the related day.

According to the total annual solar radiation distribution (kWh/m^2) of Turkey total annual solar radiation per meter square of Konya is [11] 168 kWh/m^2-year more than Ankara. Then number of sunny hours of Konya is calculated during one year and found as 3930 hour/year. Value of 168 (kWh/m^2)/3930 (h) is added to each sunny hour and radiation of Konya is found. Daily radiation data of Ankara and Konya are shown in Figure 1.

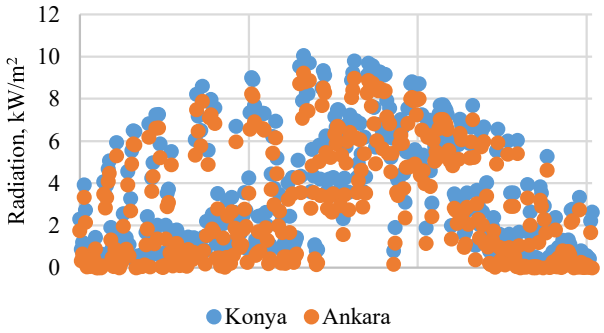


Figure 1 Daily radiation data of Ankara and Konya kWh/m^2-day

2) Natural Gas Consumption Data

Natural gas bills of 4 single detached houses (H1, H2, H3 and H4) are collected during summer. Three of these houses consume NG for hot water and cooking. Fourth home already has SDHW system and consumes NG only for cooking. There are three people living in all of these houses. Therefore NG consumption for cooking is assumed to be the same in all houses and equal to the 4th house. NG consumptions of all houses are given in Table 1.

Table 1 NG consumption of houses during summer

	NG consumption, m^3/month				
	H1	H2	H3	H4 (Cooking)	Average NG Con. For Hot Water
June	28	32	32	8	23
July	53	45	29	14	29
August	29	27	34	9	21
September	25	20	15	5	15
Average	34	31	28	9	22

Daily NG consumption for hot water is calculated from Table 1 by dividing 22 m^3/month to 30 and found as 0,733 m^3/day. Required energy to supply hot water is calculated by using equation (1).

$$Q_{hw} = NG_{hw/d} \times EF_b \times HHV \quad (1)$$

Q_{hw} : Daily energy consumption for hot water supply, kWh/day
$NG_{hw/d}$: Daily NG consumption for hot water supply, m^3/day
EF_b : Efficiency of the boiler
HHV : High heating value, kWh/m^3

After calculating required energy to supply hot water, the amount of hot water is calculated. In order to calculate the amount of hot water the temperature of mains water must be known. In this study temperature of mains water is assumed to be the same as the temperature of soil under 100 cm of ground. Hourly temperature of soil under 100 cm of ground data is obtained from General Directorate of Meteorology (GDM) [12] for Ankara. Temperature of soil under 100 cm of ground for Ankara and Konya is the same according to GDM data [10]. By using hourly soil temperature data daily hot water consumption in a house is calculated with equation (2).

$$m_{hw} = \frac{Q_{hw}}{c \times \Delta T} \quad (2)$$

m_{hw} : Daily hot water consumption, kg/day
ΔT : Hot water (˚C) - mains water (°C)
c :Water essence, kWh/kg-°C

Amount of daily hot water consumption (m_{hw}) calculated with Equation (2) is assumed to be constant during all year. Solar radiation data is an hourly data. Therefore calculations are made hourly. To calculate the hourly hot water consumption, a domestic hot water profile is used d [13]. Then, required annual energy for DHW supply is calculated for each hour with equation (3).

$$\mathbf{Q}_{hwa} = \left(\sum_{l=1}^{8760}(\mathbf{m}_{hw-hourly} \times \mathbf{c} \times \mathbf{\Delta T}) \times \frac{1}{HHV \times \mathbf{EF_b}}\right) \quad (3)$$

Q_{hwa} : Annual energy for DHW supply, m^3/year

3) SDHW System Data

In this study, application of 30 vacuum tube solar collectors system (SDHW) with 200 liters of hot water, 50 liters cold water tank volume and forced water circulation (pump) SDHW system [14] is decided to meet the amount of hot water required by the house. To determine the amount of energy production of SDHW system the energy produced by the SDHW is calculated by using equation (4).

$$E_{SDHW} = SR \times EF_{SDHW} \times AC \quad (4)$$

E_{SDHW} : Daily energy produced by SDHW, kWh/day
SR : Solar Radiation, kWh/day-m^2
EF_{SDHW} : Efficiency of SDHW system
AC : Area of collector, m^2

Finally energy requirement for hot water of the house is compared with the energy produced by SDHW system.

1.1 Emission Reduction Calculation Methodology

Natural gas emission factor (NGEF) has been used to calculate the reduction in CO_2 emissions as a resullt of the energy savings obtained. The amount of reduction in CO_2 emissions is calculated by using equation (5).

$$RCE = ES \times NGEF \quad (5)$$

RCE : Reduction of CO_2 Emission, kg/year
ES : Energy Saving, m^3/year
NGEF : Natural Gas Emission Factor, kg-CO_2/m^3

1.2 Economic Analysis

During the economic analysis of the system, investment cost, natural gas bill and interest rate data are used. For the calculation of the system's payback period (PBP), cost of the SDHW system is obtained from a local company. The annual Net Cash Flow (NCF) is calculated for the determination of the PBP. The NCF is calculated by equation (6).

$$NCF_j^{SDHW} = CI_j^{SDHW} - CO_j^{SDHW} = \quad (6)$$
$$= (NGCB \times NGP_j) - (OCS_j^{SDHW} + (NGCB_{with_sdhw} \times NGP_j))$$

NCF_j^{SDHW} : Annual Net Cash Flow, TL/year
CI_j^{SDHW} : Annual Cash Input, TL/year
CO_j^{SDHW} : Annual Cash Output, TL/year
j : Year
NGP : NG Price, TL/m^3
NGCB : NG Consumption of Boiler without SDHW system, m^3/year
OCS_j^{SDHW} : Operation Cost of System, TL/year
$NGCB_{with_sdhw}$: NG Consumption of Boiler with SDHW system (When Radiation is not enough), m^3/year

In order to calculate PBP, NG price of next years is required to be known. NG sale price to residential sector of Konya data has been obtained for the last seven years [15]. By using the slope line equation of the NG price data, natural gas price data of the next years are estimated. If the interest rate remains constant for several years [16] NBD can be calculated by equation (7).

$$NBD = \frac{NCF_1}{(1+ni)} + \frac{NCF_2}{(1+ni)^2} \cdots + \frac{NCF_N}{(1+ni)^N} \quad (7)$$
$$= \sum_{j=1}^{N} \frac{NCF_j}{(1+ni)^j}$$

NPV : Net Present Value, TL
NCF_j : Net Cash Flow, TL/year
ni : Nominal Interest Rate
j : Year
N : Operation time of the system, year

The minimum j value that allows the NPV to take a positive value is defined as the PBP [16].

1.3 Generalization of Results

Finally, total annual energy saving is calculated in the case of application of SDHW system to all single detached houses constructed in Konya in last decade.

The annual energy gain per square meter is calculated by dividing the average energy savings obtained in three model houses to the average area of the houses. According to TUIK statistics, the total area of single detached houses constructed in Konya since 2006 is 1.972.552 m^2. Total area of the single detached houses is multiplied by energy saving per square meter. Thus, the total energy savings and reduction in CO_2 emissions that is achieved.

III. RESULTS

Average daily NG consumption during summer is calculated as 1,0282 m^3/day by using the NG bills of three single detached houses. Average daily NG consumption for cooking is calculated as 0.2945 m^3/day by using the NG bills of 4th house which consumed NG only for cooking. In this case, average daily NG consumption for hot water supply of a 3-member family is calculated as 0,7337 m^3/day. Average daily hot water consumption is found as 212 kg/day and annual NG consumption of boiler for DHW supply is calculated as 359

m^3/year (13 GJ/year). Associated CO_2 emission is calculated as 769 kg-CO_2/year. Hot water energy consumption per meter square of the house is calculated as 0.070 GJ/m^2-year.
SDHW system meet 58% (8 GJ/year, 210 m^3/year) of the energy demand for hot water supply due to the inability to store more solar energy in SDHW system. Then, the energy saving achieved per meter square is calculated as 0,041 GJ/m^2-year.
In the case of construction of SDHW system in the house, the energy can be produced by the system and the energy demand for the hot water supply of the house are given in Figure 2.

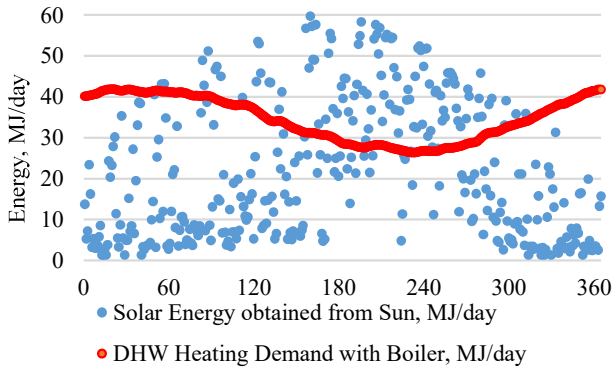


Figure 2 Solar energy obtained from sun and hot water energy demand, MJ/day

Figure 2 shows that energy obtained from the sun during summer is more than required, however in winter the energy need cannot be fully meet. Figure 3 shows the energy demand of the house with boiler and with SDHW system.

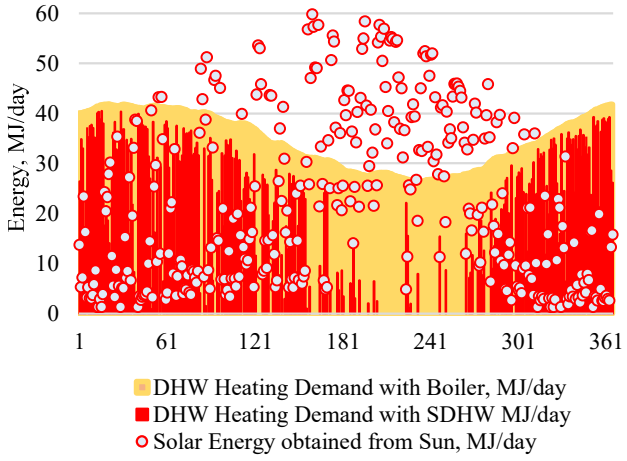


Figure 3 Energy demand of the house with and without SDHW system

Figure 3 shows that during summer nearly all demand is supplied. In other seasons the energy provided from the sun meets some part of the demand.
Surplus energy produced by SDHW system and demand that can not be meet by SDHW system are shown in Figure 4.

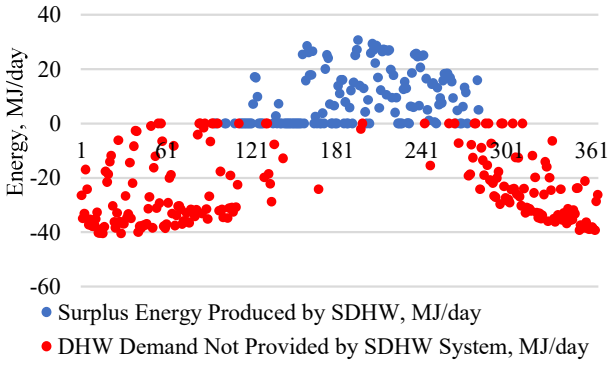


Figure 4 Surplus energy and demand cannot be meet by SDHW

As shown in Figure 4, energy produced by SDHW system during summer is over demand. In the winter months, a large part of the demand is not met.

Economic analysis is conducted by using the required data [17] and with the obtained 58% energy savings by the system. Net cash flow (NCF) graph of the system is shown in Figure 5.

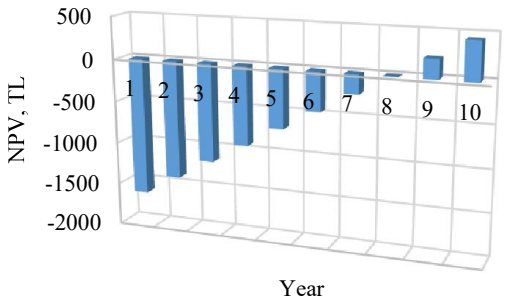


Figure 5 NCF graph of SDHW system

Figure 5 shows that PBP of the proposed SDHW system is 8 years.
The total area of single detached homes constructed since 2006 in Konya is 1.972.552 m^2. Assuming that number of residents of these homes are same as the model homes, application of the SDHW system to these homes reduces NG consumption 2,3 million m^3/year, CO_2 emissions 4950 ton-CO_2/year.

IV. Conclusion

In this study, energy saving and associated reduction in CO_2 emission obtained by the application of SDHW to a single detached house in Konya is determined. Results are also generalized to single detached house stock of Konya constructed after 2006.
Four single detached two storey houses in Konya, Turkey, is selected as model. Average daily NG consumption during summer is calculated as 1,0282 m^3/day by using the NG bills of three single detached houses. Average daily NG consumption for cooking is calculated as 0,2945 m^3/day by using the NG bills of 4th house which consumed NG only for cooking. Then average daily NG consumption for hot water supply of a 3-member family is calculated as 0,7337 m^3/day. Average daily

hot water consumption is found as 212 kg/day for three people. Annual NG consumption of boiler for DHW supply is calculated as 359 m^3/year (13 GJ/year). The CO_2 emission of natural gas consumption for hot water supply is calculated as 769 kg-CO_2/year. Hot water energy consumption per meter square of the house is calculated as 0.070 GJ/m^2-year.

The net solar energy obtained from the sun for hot water supply is found as 8 GJ/year and SDHW system is able to meet 58% (8 GJ/year, 210 m^3/year) of the demand. Energy savings achieved per meter square is calculated as 0,041 GJ/m^2-year.

Economic analysis is conducted and PBP of SDHW system is found as 8 years.

The total area of single detached homes constructed since 2006 in Konya is 1.972.552 m^2. Assuming that number of residents of these homes are same as the model homes, application of the SDHW system to these homes reduces NG consumption 2,3 million m^3/year, CO_2 emissions 4950 ton-CO_2/year.

REFERENCES

[1] USEIA (2017) Annual Energy Outlook. [Online]. Available: https://www.eia.gov/outlooks/aeo/.

[2] MENR. (2017) The Ministry for Energy and Natural Resources. (In Turkish) [Online]. Available: http://www.eigm.gov.tr/tr-TR/Sayfalar/2015-Genel-Enerji-Denge-Tablolari.

[3] F. Mauthner and W. (2012). Weiss, *Solar Heat Worldwide*. [Online]. Available: http://www.aee-intec.at/0uploads/dateien1016.pdf.

[4] H. Benli, Potential application of solar water heaters for hot water production in Turkey, *Renewable and Sustainable Energy Reviews,* vol. 54, pp. 99-109, 2016.

[5] F. Çanka-Kılıç, Türkiye'deki Yenilenebilir Enerjilerde Mevcut Durum ve Teşviklerindeki Son Gelişmeler (In Turkish), *Mühendis ve Makine Dergisi,* vol. 52, no. 614, pp. 103-115, 2011.

[6] B. Karaçavuş, Türkiye'nin belirli iklim bölgeleri için güneş enerjili sıcak su sisteminin optimizasyonu (In Turkish), *Journal of the Faculty of Engineering and Architecture of Gazi University,* vol. 32, no. 3, pp. 843-853, 2017.

[7] O. Yaşar, Balıkesir il ve ilçelerinde konutlarda güneş enerjisi destekli sıcak su eldesinin ekonomik analizi (In Turkish), *Balıkesir Üniversitesi Fen Bilimleri Enstitüsü*, Balıkesir, 2017.

[8] IPCC, Raft 2006 IPCC Guidelines for National Greenhouse Gas Inventories, Geneva, 2006.

[9] USDOE. (2015). EnergyPlus Energy Simulation Software-Weather Data Sources. [Online]. Available: http://apps1.eere.energy.gov/buildings/energyplus/weatherdata_sources.cfm#IWEC.

[10] GDM. (2017). Daily Radiation Duration in Turkey. (In Turkish) [Online]. Available: https://www.mgm.gov.tr/FILES/resmi-istatistikler/Turkiye-Gunluk-Guneslenme-Suresi.pdf.

[11] GDM. (2017). Annual Global Solar Radiation of Turkey (In Turkish) [Online]. Available: https://www.mgm.gov.tr/FILES/resmi-istatistikler/Turkiye-Yillik-Günes-Radyasyonu.pdf.

[12] GDM. (2014). 2013 Soil Data (In Turkish) [Online]. Available: http://www.mgm.gov.tr/.

[13] V. C. Alberto, DTIE 1.01. Preparación de agua caliente para usos sanitarios, Madrid: ATECYR, D.L, 1994

[14] Kuzeymak(2017) .KM 30 (In Turkish). [Online]. Available: http://www.kuzeymak.com/index.php?page=shop.product_details&flypage=flypage.tpl&product_id=74&category_id=12&option=com_virtuemart&Itemid=53.

[15] Enerya. (2017). Subscriber Sales Prices. (In Turkish) [Online]. Available: https://portal.enerya.com.tr/DogalGazBirimFiyatlari/index.xhtml?city=07.

[16] J. L. Bernal-Agustín ve R. Dufo-López, Economical and environmental analysis of grid connected photovoltaic systems in Spain, *Renewable Energy,* pp. 1107–1128, 2006.

[17] KM 30 (2017). Kuzeymak Solar Energy System (In Turkish) [Online]. Available: http://gunesenerjimarketi.com/urun/km-30-200-sbu-gtkuzeymak-gunes-enerji-sistemi-egimli-zemine-montaj_1380.aspx.

Water Treatment with Natural Zeolite

M. Ö. ÇARPINLIOĞLU[1] and M. YILDIRIM[1]

[1]Gaziantep University, Gaziantep/Turkey, melda@gantep.edutr.
[1]Gaziantep University, Gaziantep/Turkey, yildirim@gantep.edu.tr

***Abstract* -An experimental study was carried out to investigate the effect of natural zeolite on the treatment of raw ground water. Clinoptilolite type natural zeolite was cracked and sieved to have five different particle sizes. The produced five zeolite samples were mixed with water such that mass of zeolite was 20% of water. Water from each mixture was taken at one hour intervals to have tests on it. An equal amount of water without a mixture of zeolite was used as a reference case. The tests were done according to ISO 17294-1 and 17294-2 by ICPMS (Inductively Coupled Plasma Mass Spectrometry) on the samples. As a result of these tests the elements in water as B, Cr, Ni, Cu, As, Se, Cd, Sb, Pb, Al, Mn, and Fe were illustrated as a function of the particle size and time. SEM analysis on natural zeolite was also used for the analysis of the results.**

***Keywords* – Natural Zeolite of Clinoptilolite type, Particle Size, Time**

I. INTRODUCTION

The utilization of natural zeolite of Clinoptilolite type from Bigadiç/Balıkesir Turkey (1) in a desiccant cooling system is a completed research of the authors (2-4). In this study a different possible use (effect) of zeolite in terms of water treatment is presented. The material properties of zeolite are given in Table 1.

Table 1. Material properties of the zeolite

Type	Mass Density	Thermal Conductivity	Specific Heat Capacity
	ρ_z (kg/m^3)	kW/(m^{0}C)	C_z(kJ/kgK)
Clinoptilolite	1.450	0,6	1,11

II. EXPERIMENTAL METHODOLOGY

Cracked zeolite was sieved with sieves as 0.6, 2.0, 6.2, 8.0, 14.0 and 20 mm meshes. Size ranges of sieved zeolite were classified as 0.6-2.0mm, 2.0-6.2mm, 6.2-8.0mm, 8.0-14.0mm and 14.0-20.0mm with specified size numbers (Table 2). The samples weighed 1.0kg for each size were prepared (Figure 1). The samples were mixed with raw ground water as a mixture of 1.0kg zeolite and 5.0kg water (Figure 2). The mixtures were stored in bottles and shaked ten minutes. The samples from each bottle were taken for chemical tests at the end of 1st, 2nd, 3rd, 4th, and 5th hours (Figure 3).

The tests were conducted in the Public Health Laboratory of Gaziantep city. Chemical tests were done by ICPMS (Inductively Coupled Plasma Mass Spectrometry) (Figure 4) according to the ISO 17294-1 and 17294-2.

SEM analysis of the zeolite samples before and after mixing with water were also given for the analysis.

Table 2. Particle Size Numbers

Particle Size Number:	Particle Size
	(mm)
1	0,6-2,0
2	2,0-6,2
3	6,2-8,0
4	8,0-14,0
5	14,0-20,0



Figure 1. Zeolite sample preparation for the test



Figure 2. Zeolite and raw water mixing set



Figure 3. Water samples



Figure 4. ICPMS (Inductively Coupled Plasma Mass Spectrometry) water test device

III . RESULTS and DISCUSSION

At this section a brief information [5] about the elemental characteristics of water, environmental effects of the referred elements in terms of human health is given. The results of the experimental study regarding the influence of the exposure time and size of the natural zeolite samples in water treatment based upon the chemical analysis of each sample mixture are presented.

BORON: Seawater contains approximately 4-5 ppm boron. River water generally contains only 10 ppb. The human body contains approximately 0.7 ppm of boron, Daily intake is approximately 2 mg.

EXPERIMENTAL RESULTS WITH BORON: In raw water there is no Boron. Boron variation in water after natural zeolite mixture (as a factor of zeolite particle size and time) is shown in Figure 5. Boron amount increases depending on time and with the smallest particle sizes.

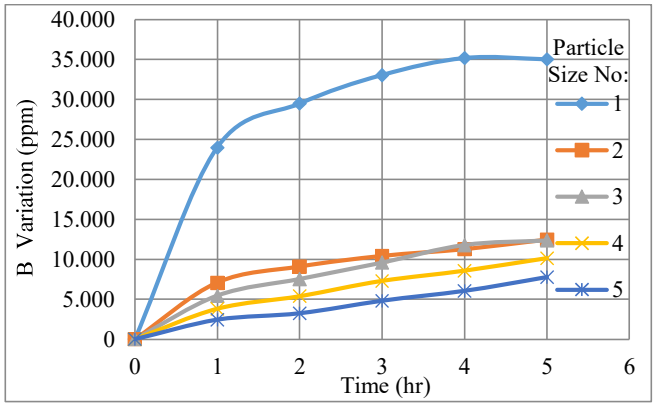


Figure 5. Boron variation with zeolite particle size and time

CHROMIUM: Seawater chromium content is usually between 0.2 and 0.6 ppb. Rivers contain approximately 1 ppb of chromium. The human body contains approximately 0.03 ppm of chromium. Daily intake strongly depends upon feed levels, and is usually approximately 15-200 µg, but may be as high as 1 mg.

EXPERIMENTAL RESULTS WITH CHROMIUM Raw water has 7ppm Cr already and at the end of the time Cr increased to approximately 8ppm in the water. Variation dependency on particle size and time can be negligible.(Figure 6)

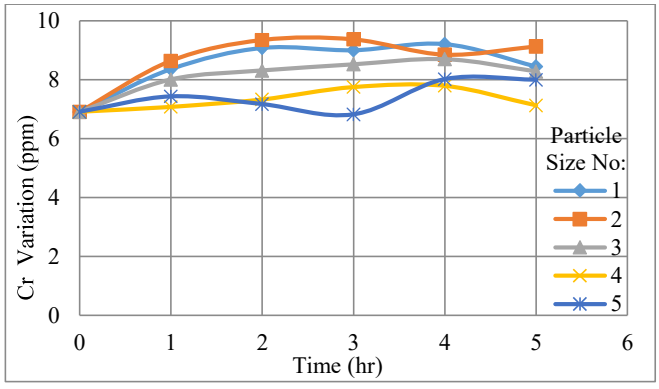


Figure 6. Chromium variation with zeolite particle size and time

NICKEL: Seawater contains approximately 0.5-2 ppb of nickel, and rivers contain approximately 0.3 ppb. The human dietary need is estimated at only 5 µg, which is the result of a 150 µg intake.

EXPERIMENTAL RESULTS WITH NICKEL: Zeolite absorbs Nickel in the raw water from 12ppm to approximately 5ppm at the end of the exposure time (Figure 7) There is a strong drop at the end of first hour for all sizes.

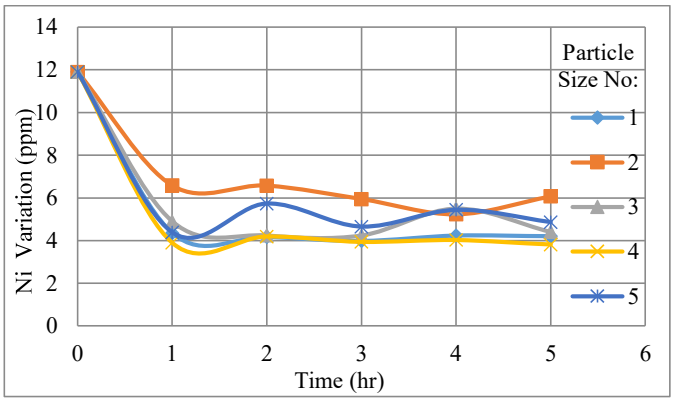


Figure 7. Nickel variation with zeolite particle size and time

COPPER: It hardly enters groundwater. In surface water copper can travel great distances, either suspended on sludge particles or as free ions.

EXPERIMENTAL RESULTS WITH COPPER: Copper amount in the raw water is 1 ppm (Figure 8). At the end of the test ; amount of copper reaches to an approximate average value of 3.6 ppm. The amount in water fluctuates with the particle size and time having drastical manner for the size 3 and size 5.

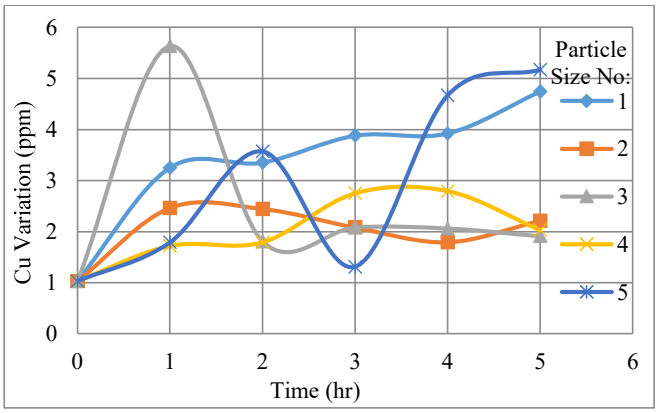


Figure 8. Copper variation with zeolite particle size and time

ARSENIC: Arsenic can be found in seawater (2-4 ppb), and in rivers (0.5-2 ppb). Freshwater and seas algae contain about 1-250 ppm of arsenic. Arsenic toxicity is an important characteristic. If arsenic is a dietary mineral, this dose would be 15-25 µg. Arsenic in drinking water has a legal limit as 10 µg/L.

EXPERIMENTAL RESULTS WITH ARSENIC: Arsenic amount in the water increases when the particle size is smaller with increase in time (Figure 9). The size 1 has a value of 200 ppm at the end of the fifth hour . It also has the greatest increase in the first hour.The increase in greater sizes at the end of first hour is less than 50 ppm. The increase in time is associated with values less than 75 ppm approximately for other sizes.

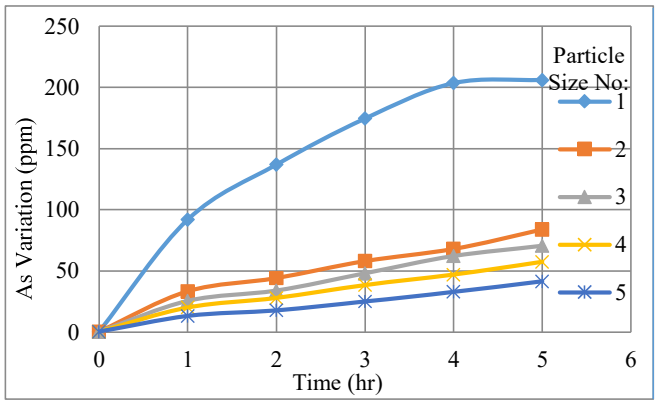


Figure 9. Arsenic variation with zeolite particle size and time

SELENIUM: Selenium from hazardous waste-sites and from farmland will end up in groundwater or surface water through irrigation. This phenomenon causes selenium to end up in local drinking water.

EXPERIMENTAL RESULTS WITH SELENIUM: Selenium amount in raw water increases as a function of the particle size and time from 0.78 to an average of 1.64ppm approximately (Figure 10). The largest increase occurs at the end of first hour for all sizes.

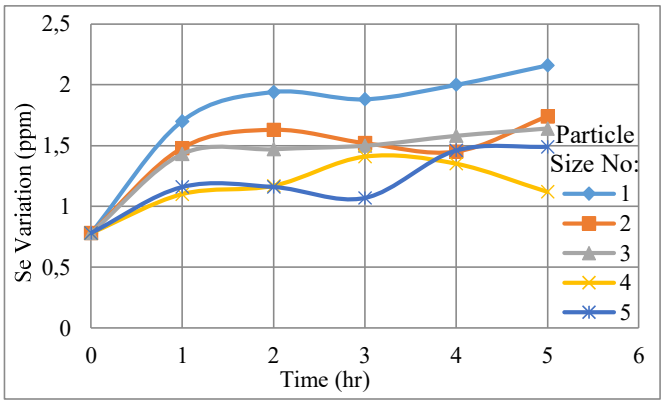


Figure 10. Selenium variation with zeolite particle size and time

CADMIUM: Because of regulations only little cadmium now enters the water through disposal of wastewater from households or industries. Cadmium-rich sludges can pollute surface waters as well as soils.

EXPERIMENTAL RESULTS WITH CADMIUM: Disregarding the data at first hour with particle size 3 (Figure 11) cadmium is less than 0.1 ppm after the long exposure time with zeolite.

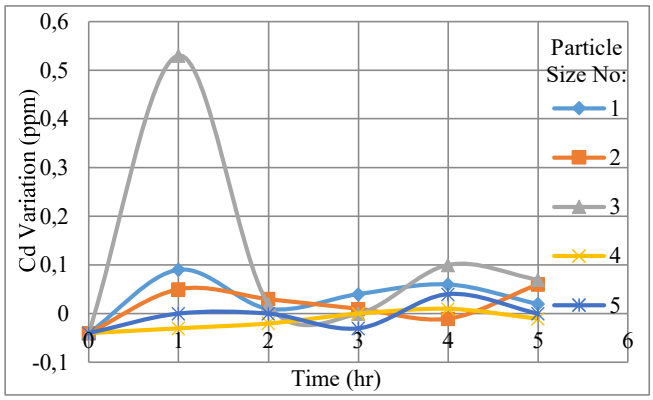


Figure 11. Cadmium variation with zeolite particle size and time

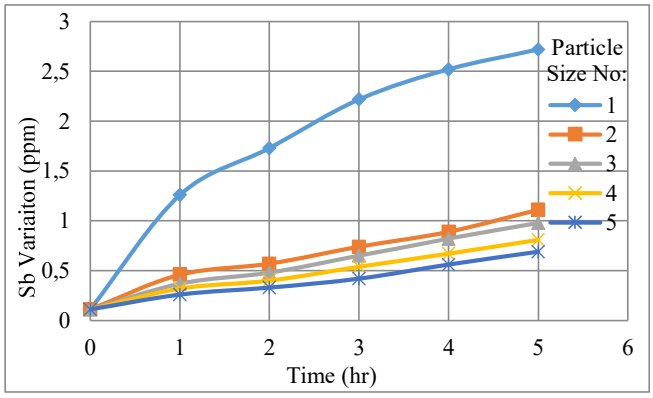


Figure 12. Antimon variation with zeolite particle size and time

EXPERIMENTAL RESULTS WITH ANTIMON: Size 1 has a severe departure from all other sizes with a variation from almost 0 ppm to 2.75 ppm with an increase in time. All other sizes have similar trend having a slight increase in time from 0 ppm to less than 1 ppm.(Figure 12)

LEAD: Seawater contains trace amounts of lead (2-30 ppt). On average rivers contain between 3 and 30 ppb. The World Health Organization (WHO) stated a legal limit of 10 ppb in 2010. Lead and lead compounds are generally toxic pollutants.

EXPERIMENTAL RESULTS WITH LEAD: Raw water has 0.07ppm lead, at the end of test lead of the water increases only to 0.54ppm (Figure 13) .

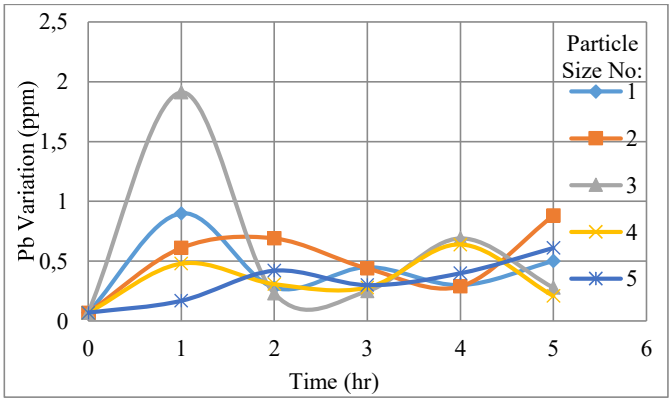


Figure 13. Lead variation with zeolite particle size and time

SODIUM: Seawater contains approximately 11,000 ppm sodium. Rivers contain only about 9 ppm. Drinking water usually contains about 50 mg/L sodium. Generally, humans require about 300 mg sodium chloride per day for a balanced sodium level of approximately 4 g.

EXPERIMENTAL RESULTS WITH SODIUM: Sodium amount in water increases as a function of particle size and time (Figure 14) from 7,641ppm in raw water to 24.061ppm with the particle size number with 2-5. For the size 1 the upper limit of the test machine was exceeded.

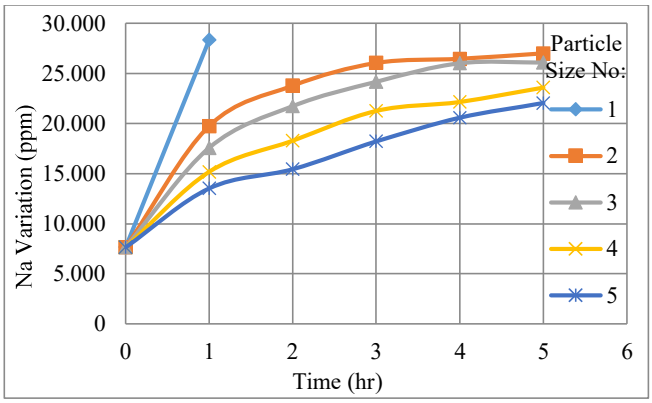


Figure 14. Sodium variation with zeolite particle size and time

ALUMINUM: The amount of aluminum in seawater varies between approximately 0.013 and 5 ppb. Regular aluminum concentrations in groundwater are about 0.4 ppm. It naturally occurs in waters in very low concentrations.

EXPERIMENTAL RESULTS WITH ALUMINUM: Aluminum amount in raw water is 3.56ppm (Figure 15).Disregarding the data with size 3 at the end of fourth hour it increases to 14.45ppm at the end of the test with a negligible fluctuation during the test as a function of the particle size and time.

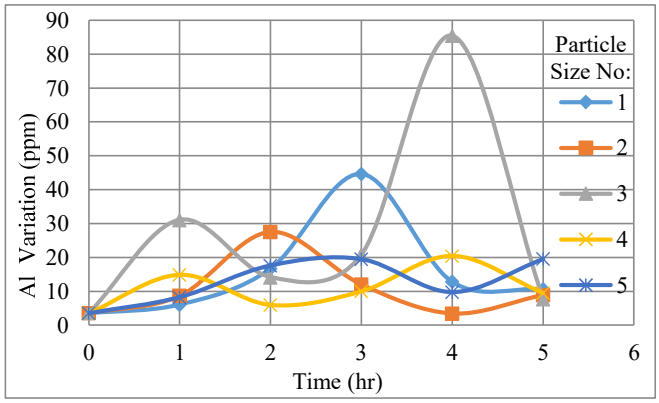


Figure 15. Aluminum variation with zeolite particle size and time

EXPERIMENTAL RESULTS WITH MANGENESE: Mangenese in raw water is 0 ppm the greatest variation is with size 2 at the end of fifth hour reaching to 20 ppm. For size 3, 10 ppm and for all other sizes less than 3 ppm is seen.

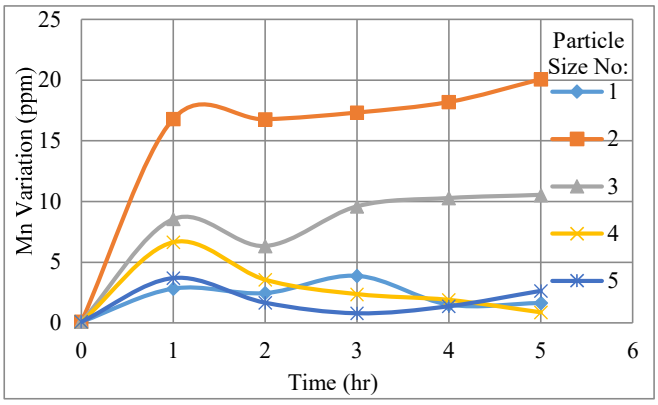
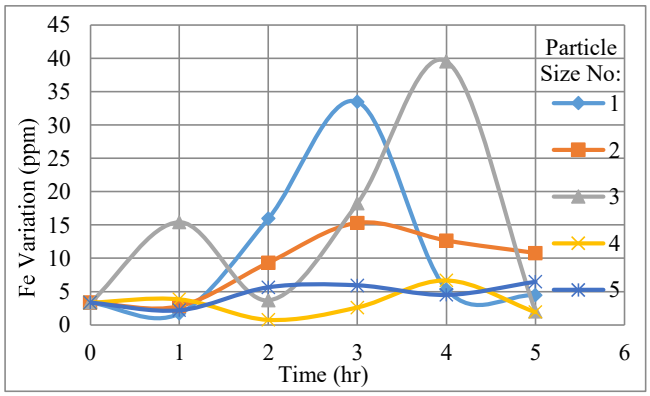


Figure 16. Manganese variation with zeolite particle size and time

IRON: Seawater contains approximately 1-3 ppb of iron. Rivers contain approximately 0.5-1 ppm of iron, and groundwater contains 100 ppm. Drinking water may not contain more than 200 ppb of iron. Healthy people suffer by drinking water with iron concentrations over 200 ppm.

EXPERIMENTAL RESULTS WITH IRON: Iron amount Fe and Fe-1 in raw water is 3.34ppm (Figure 17). It shows fluctuation during the test as a function of the particle size and time. However after even long term exposure for size 2, 10 ppm and for all others 6.36ppm are observed at the fifth hour.



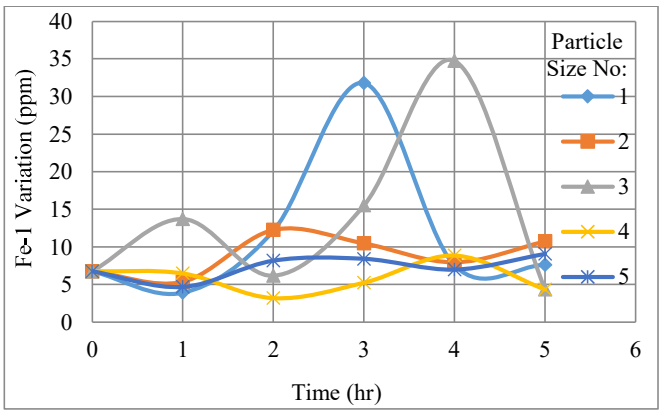
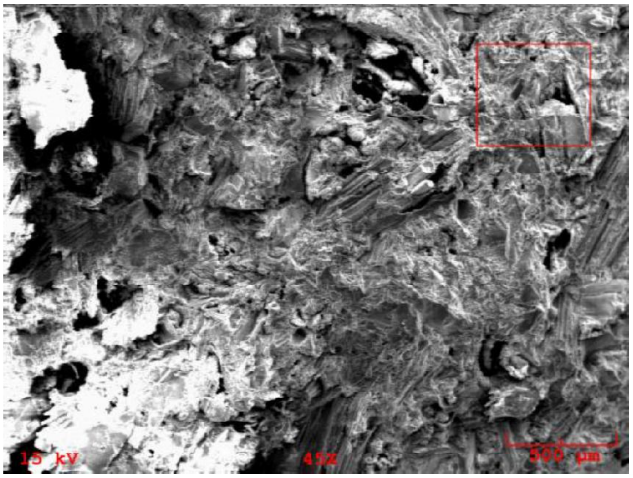
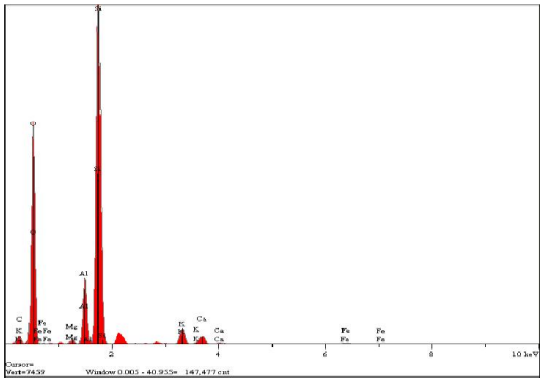


Figure 17. Iron Fe and Fe-1 variation with zeolite particle size and time

SEM ANALYSIS

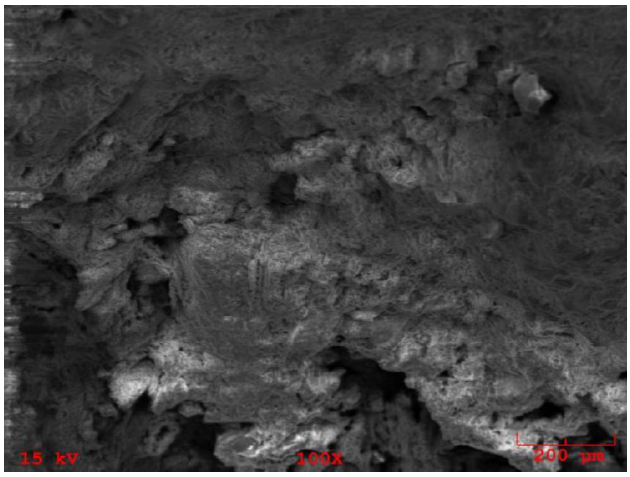
Zeolite analysis before water mixture (Figure 18) is shown that %49 is O due to porous pattern. The remaining is such that maximum amount of Si is 38 %. C, Mg, Al, K, Fe, Ca are the other elements determined. After mixture with water O is determined as similar 48.94 % (Figure 19) and Si as 24.49% due to the variation in the tested specimen in SEM image.

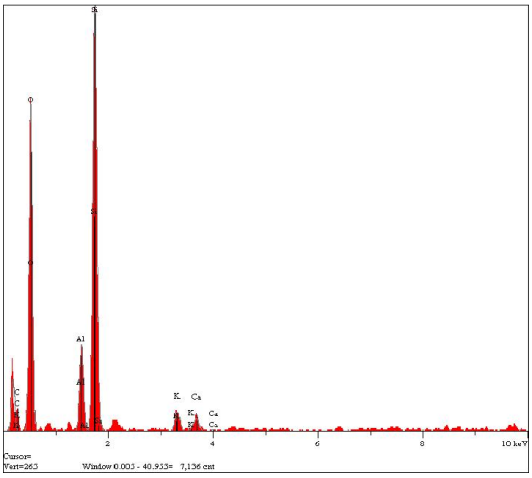




Elt.	Line	Intensity (c/s)	Conc	Units	Error 2-sig	MDL 3-sig	
C	Ka	15.55	6.501	wt.%	3.135	0.285	
O	Ka	398.99	49.092	wt.%	0.499	0.101	
Mg	Ka	10.04	0.499	wt.%	5.803	0.063	
Al	Ka	136.79	6.100	wt.%	0.954	0.059	
Si	Ka	738.85	33.280	wt.%	0.372	0.056	
K	Ka	40.38	2.506	wt.%	1.831	0.058	
Ca	Ka	22.08	1.444	wt.%	2.694	0.059	
Fe	Ka	3.76	0.577	wt.%	7.941	0.090	
			100.000	wt.%			Total

Figure 18. SEM analysis of zeolite before mixed with water





Elt.	Line	Intensity (c/s)	Conc	Units	Error 2-sig	MDL 3-sig	
C	Ka	2.72	18.002	wt.%	3.892	0.866	
O	Ka	17.31	48.943	wt.%	2.378	0.416	
Al	Ka	5.46	5.100	wt.%	4.716	0.228	
Si	Ka	26.32	24.492	wt.%	1.971	0.213	
K	Ka	1.54	1.942	wt.%	8.809	0.201	
Ca	Ka	1.14	1.521	wt.%	10.301	0.220	
			100.000	wt.%			Total

Figure 19 SEM analysis of zeolite with water mixture

The relationship between microstructure and size of the samples through cited analysis results above is a topic needing further research planned by the authors in near future.

ACKNOWLEDGEMENT

The authors are thankful for the tests conducted in Public Health Laboratory of Gaziantep.

REFERENCES

[1] A.S.Ulku, M.Mobedi, Adsorption in energy storage in: B. Kılkıs, S.Kakac (Eds) *Energy Storage Systems*, Kluwer Academic Publishers, 1989, pp 487-507

[2] M. Yıldırım, An Experimental Investigation on Heat and Mass Transfer in a Desiccant Cooling System. Ph.D. Thesis, University of Gaziantep, Turkey, 2002.

[3] M. Kanoglu, M.Ö., Carpinlioglu, M. Yildirim, Energy and exergy analyses of an experimental open cycle desiccant cooling system, *Applied Thermal Engineering* 24(5-6) (2004) 919-932

[4] M. Ö. Çarpınlıoğlu, M. Yıldırım, A Methodology for the Performance Evaluation of an Experimental Desiccant Cooling System, *Journal of International Communications in Heat and Mass Transfer* 32 (2005) 1400-1410

[5] https://www.lenntech.com/periodic/water/overview.htm

Mathematical Modeling of the Door Closer Mechanism

S.ESER[1], S.TELLİ ÇETİN[2], O.KOPMAZ[3]

[1] Uludag University, Bursa/Turkey, sezgineser@uludag.edu.tr
[2] Uludag University, Bursa/Turkey, sevda@uludag.edu.tr
[3] Uludag University, Bursa/Turkey, okopmaz@uludag.edu.tr

***Abstract* – The aim of this study is to obtain the mathematical model of the hydraulic door closing mechanism, which is frequently used in everyday life. The work energy principle has been utilized in the developing of the model. The model is arranged for constant door opening speed and solved via MATLAB. Thus, graphs of the door opening torque and the forces acting on the mechanism for the constant opening speed have been obtained.**

***Keywords* - door closer, mathematical model, closing torque**

I. INTRODUCTION

HYDRAULIC door closers are one of the most common door closer mechanisms in our daily life. These mechanisms are often used on apartment doors, schools, hospitals and fire exits. The active forces on the mechanism are the spring force, the hydraulic force and the frictional forces on the hinges. There are several investigations about the motion of door closers and some new designs are examined instead of hydraulic door closer mechanisms. Wang & Wu [1] has constituted an experimental setup to the determination of the opening moment values of the door closer. By using the experimental setup, they obtained door closing moment graphs for doors have different weight and different types of closers. Hassan [2] investigated how the solution of the door closer model is affected by positive or negative deviations from the linear characteristic. A research paper suggests a new design instead of hydraulic door closer [3]. Their aim is to build a simple mechanic design to give opportunity of simple replacements on the mechanisms when there was a problem. In addition to these, there are some articles related to door ergonomics and the required maximum pulling or pushing forces [4, 5].

When the literature is examined, it is found that the mathematical model of the movement of the hydraulic door closer has not been established. The aim of this work is to create a mathematical model for hydraulic door closer. With this model all the forces acting on the mechanism could be investigated. Effect of the change in the constructive dimensions and spring properties can be examined. Thus, this mathematical model can provide a basis for future work.

II. METHODS

A. Kinematic Analysis of Door Closer

First step for modeling the door closer is kinematic analysis of the closer mechanism. A door closer could be modeled as a four bar mechanism given in Figure 1.

Joint A_0 refers to the axis that door rotates. A is the joint which pinion gear rotates. B is the joint between two arms of closer. Finally B_0 is the joint the second arm of closer with door frame.

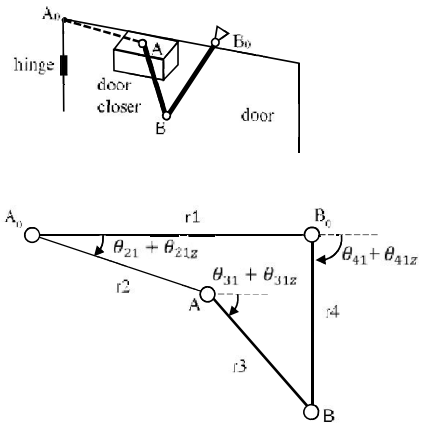


Figure 1: Four bar mechanism of the door closer

The two equations for four bar mechanism have given with Equation (1) and Equation (2).

$$r_2 e^{i(\theta_{21}+\theta_{21z})} + r_3 e^{i(\theta_{31}+\theta_{31z})} = r_1 + r_4 e^{i(\theta_{41}+\theta_{41z})} \quad (1)$$

$$r_2 e^{-i(\theta_{21}+\theta_{21z})} + r_3 e^{-i(\theta_{31}+\theta_{31z})} = r_1 + r_4 e^{-i(\theta_{41}+\theta_{41z})} \quad (2)$$

θ_{21z}, θ_{31z} and θ_{41z} refers to the angles that the door is completely closed.

When the equations rearranged, Equation (3) is obtained. The coefficients K_1, K_2 and K_3 on this equation are given with equation (4), (5) and (6).

$$K_1 \cos\theta_{31} + K_2 \sin\theta_{31} + K_3 = 0 \quad (3)$$

$$K_1 = 2r_2r_3\cos(\theta_{31z} - \theta_{21} - \theta_{21z}) - 2r_1r_3\cos(\theta_{31z}) \quad (4)$$

$$K_2 = 2r_1r_3\sin(\theta_{31z}) - 2r_2r_3\sin(\theta_{31z} - \theta_{21} - \theta_{21z}) \quad (5)$$

$$K_3 = r_1^2 + r_2^2 + r_3^2 - r_4^2 - 2r_1r_2\cos(\theta_{21} + \theta_{21z}) \quad (6)$$

Equation (3) is known as Freudenstein's Equation. The solution of this equation gives two different results for two different configuration of four bar mechanism. The result which is suitable the door closer mechanism is chosen.

B. Spring Force

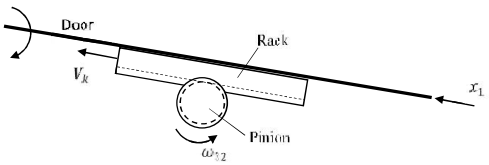


Figure 2: Pinion and rack

In the closer mechanism; by turning the pinion, the rack moves along the door. The angular velocity of the pinion gear relative to the rack could be defined as

$$\omega_{32} = \dot{\theta}_{21}((d\theta_{31}/d\theta_{21}) - 1) \quad (7)$$

where $\dot{\theta}_{21}$ is the speed of door.

The velocity of the rack beyond the door is given with the Equation (8) where r_p is the radius of the pinion gear.

$$V_K = r_p(\dot{\theta}_{21}((d\theta_{31}/d\theta_{21}) - 1)) \quad (8)$$

The position of the rack could be define as

$$s_K = r_p(\theta_{31} - \theta_{21}) \quad (9)$$

where $\theta_{31} - \theta_{21}$ is relative angular position of the rack to the door.

The spring force is given with the equation (10). In this equation, k is the stiffness of the spring on the door closer mechanism.

$$F_s = kr_p(\theta_{31} - \theta_{21}) \quad (10)$$

C. Hydraulic Force

Figure 3 shows the cross section area for a hydraulic door closer. Rack and the piston is one rigid object. By moving the rack, the piston also moves with the same velocity.

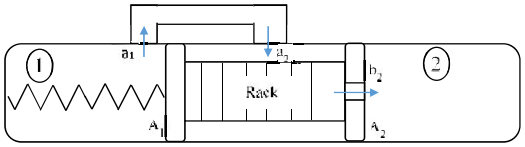


Figure 3: Cross section of a door closer

a_1, a_2, are b_2 are the cross section area that fluid passes during action and A_1 and A_2 are the surface area of the piston.

During the opening action of the door, the fluid is forced to move from one section to another by the movement of the rack. The pressure of the hydraulic fluid during this action could be defined as

$$\Delta P = 0{,}5\rho(1 - (A_{A1}/A_{a1})^2)\left(r_p\left\{\dot{\theta}_{21}\left[(d\theta_{31}/d\theta_{21}) - 1\right]\right\}\right)^2 \quad (11)$$

where ρ is the density of hydraulic fluid.

That pressure occurs in section 1 act on the piston and the force on this piston is defined by Equation (12).

$$F_f = 0{,}5\rho(1 - (A_{A1}/A_{a1})^2)\left(r_p\left\{\dot{\theta}_{21}\left[(d\theta_{31}/d\theta_{21}) - 1\right]\right\}\right)^2 A_1 \quad (12)$$

D. Friction Moment of the Hinge

Figure 4 shows the forces acting on the hinge and weight of the door. d is the distance between two hinge and b is the width of the door. W_K is the weight force of the door. When it is assumed that the door is homogeneous, this force acts from the middle point of the door.

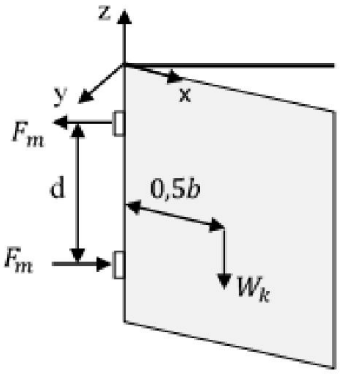


Figure 4: Door and hinges

The forces acting on hinges because of the weight of the door could be defined as

$$F_H = W_K(b/(2d)) \quad (13)$$

Total frictional moment acting to hinges could be defined as

$$M_S = 2\mu F_M r_m \quad (14)$$

where μ is the friction coefficient for a hinge, and r_m is the radius of the hinge.

E. Mathematical Model of a Door Closer

Mathematical model is defined by using work and energy principle. To define the total energy of the door; reduced moment of inertia to the rotating axis of the door is used.

Equation (15) gives the general equation for a door closer mechanism. In this equation M_D refers the operation torque to open the door from rotating axis.

$$\boldsymbol{dT = F_S ds_K + F_f ds_K + M_S d\theta_{21} + M_D d\theta_{21}} \qquad (15)$$

With this equation, different cases could be examined. In this study, the operation torque for constant opening speed is examined. For constant opening speed of the door the mathematical model is given with Equation (16).

$$M_D = (F_S + F_f) r_p ((d\theta_{31} / d\theta_{21}) - 1) + M_S \qquad (16)$$

III. ANALYSIS AND RESULTS

Equation (16) solved via MATLAB. As a result the spring force, hydraulic force and the needed opening torque for constant opening speed graphs are obtained. For a simple examine, friction forces on the hinges are neglected.

Door opening speed is given 0,210 rad/s, and maximum door angle given 90 degree. With this opening speed, it takes 7.5 seconds to open the door to the maximum door angle. For a normal usage of door closer, nearly 45 degree is enough but the program continue operating to 90 degree to see the force and moment graphs.

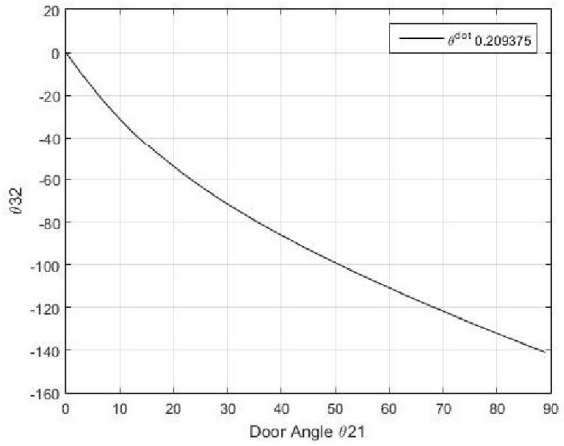


Figure 5: θ_{32} - θ_{21} graph

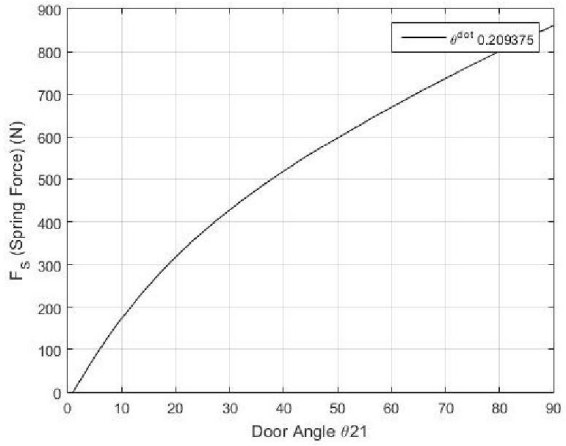


Figure 6: Spring force graph

θ_{32} gets bigger values during opening operation. Because of that spring is continuously compressed. So F_S force gets bigger values shown as Figure 6.

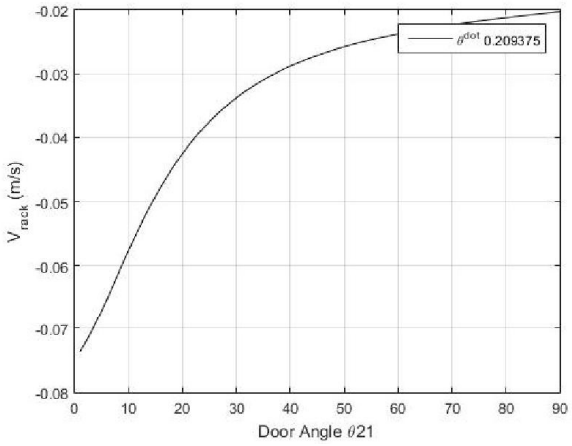


Figure 7: Rack speed graph

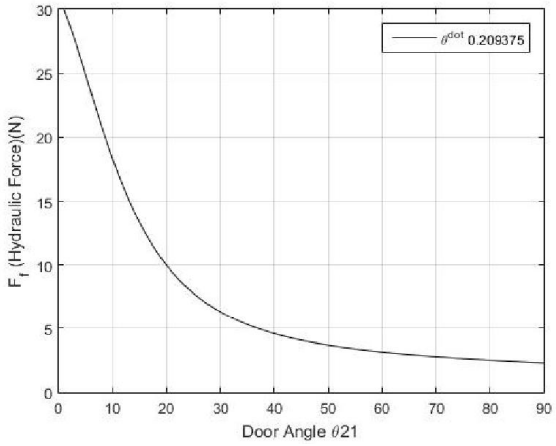


Figure 8: Hydraulic force graph

As a result of pinion speed shown as Figure 7, hydraulic force gets closer to zero. Unlike spring force, hydraulic force is reduced during opening shown as Figure 8.

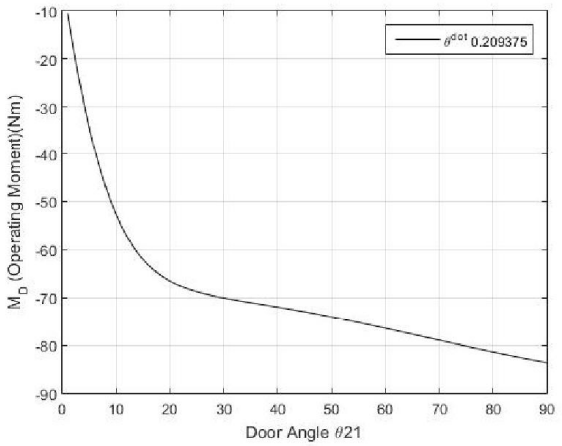


Figure 9: Operating moment graph

Required operating moment for a constant opening speed increases during the opening operation shown as Figure 9. But because of the chance of hydraulic force, the slope of the moment decrease.

IV. CONCLUSIONS

With the generated mathematical model, the forces acting on a hydraulic door closer can be examined. As a result of this examination, continuously increasing of spring force is observed. However, because the pinion speed decreases and gets closer to zero after a certain door opening, the hydraulic force decreases. Required operating torque for a constant opening speed mainly depends of the spring and hydraulic force. As a result of the negative slope of hydraulic force graph, rate of changing the operating moment degreases.

The mathematical model also allows changing magnitudes, such as spring force, pinion diameter, cylinder dimensions, and the measurement of four bar mechanisms. With this flexibility, the effects of the relevant changes on forces and moments can be examined and regulated according to the desired operating moment value.

REFERENCES

[1] S.B. Wang and C.F. Wu, "Design of the force measuring system for the hinged door: Analysis of the required operating torque," International Journal of Industrial Ergonomics,2015

[2] G. A. Hassaan, "Dynamics of a Nonlinear Automatic Door Closing Torsional Mechanism," International Journal of Innovation and Applied Studies, vol. 4, pp. 1669-1678,Oct. 2014

[3] R. W. Dakhole, R. D. Askhedkar and S. K. Choudhary, "Compressive Spiral Spring Door Closer Using Simple Spur Gear Train Arrangement", International Journal of Engineering Research & Technology, vol 2, pp. 1466- 1471, July 2013.

[4] S. K. Chang and C. G. Drury, "Task Demands and Human Capabilities in Door Use," Applied Ergonomics 38, pp 325-335, April 2006.

[5] A. Gary, T. Waters, J. Kapellusch, W. Karwowski, "Psychophysical Basis for Maximum Pushing and Pulling Forces: A review and Recommendations", International Journal of Industrial Ergonomics 44, pp. 281-291, Oct. 2012.

INVESTIGATION OF SUSPENSION SYSTEM ANALYSIS OF N2 CATEGORY VEHICLES CONVERTED TO M2 CATEGORY VEHICLES

K.ERSAN[1] and S.İLDEŞ[2]

[1] Gazi University, Ankara/Turkey, kersan@gazi.edu.tr
[2]Gazi University, Ankara/Turkey, serkanildes@gmail.com

Abstract **- N2 vehicles in the category of national legislation "Regulation on Manufacture, Modification and Assembly of Vehicles (A.İ.T.M.)" by modifying the scope of the category M2 vehicles are analyzed in the transformation of the suspension system. The modeling process, which will form the basis for evaluating the data from the suspension system, was performed with the help of the MATLAB SIMULINK program.**

The comparison of the vehicle category, the boundary value, the model design and the analysis of the vehicle category, which are being considered as land vehicles, has been carried out for the N2 and M2 categories of vehicles.

The cargo (weights) added to the vehicle in the conversion of the N2 category vehicles to the M2 category vehicles are taken into account.

It must be able to occur when the coefficient k (which will be calculated) remains within the values according to the standards (ISO 2631-1). The vehicle using this given k-rated spring system must be able to translate through the M2 category.

Keywords **– vehicle. N2. M2. Matlab Simulink. Suspension system. ISO 2631.**

I. INTRODUCTION

Suspension systems are one of the systematic mechanisms placed on the vehicle. These systematic mechanisms ensure that both the vehicle and the external environment of the vehicle can operate simultaneously. In addition, when the vehicle is in motion, it also interacts with the vehicle's external environment and the way it is affected.

Suspension systems are one of the most studied issues among vehicle mechanisms. It is necessary to constantly consider the design that is open to development as well as engineering in terms of its design. Suspension system is one of the systems that are open to external interaction of vehicles. In vehicle design, manufacturing and assembly processes, the whole vehicle is considered as a whole. This includes the end-user submission of the initial approval tests of the vehicles; as well as modifications and renewals that can be performed by the end user.

The amendment titles are determined by the regulation of the national legislation A.ITM (Manufacture, Amendment and Assembly of Vehicles) of our country and the steps to be done in the related modifications are explained. This has also created a field of work so that national legislation can be approximated to type-approval regulations. The elaboration of the desired evaluation conditions and the feasibility of this can be called the success of national legislation.

II. VIBRATION OCCURS' IN VEHICLES

From the point of view of driving comfort, it is important for human health to be able to operate the suspension system within the vibration limits specified in the ISO 2631 standard. High amplitude and low fre- quency vibrations cause nausea. Considering the permanent health problems caused by long-term vibration, it is a fact that health is an important factor in comfort as well as damping characteristics of suspension systems. Suspension systems must optimize their suspension behaviors because they require different features in terms of structure and characteristics. In addition, the risk of overturning, which may result in severe maneuvers, should also be avoided. According to 1999 data, 22% of the causes of death in passenger fatalities and 63% in sports vehicles were determined as overturned accidents.

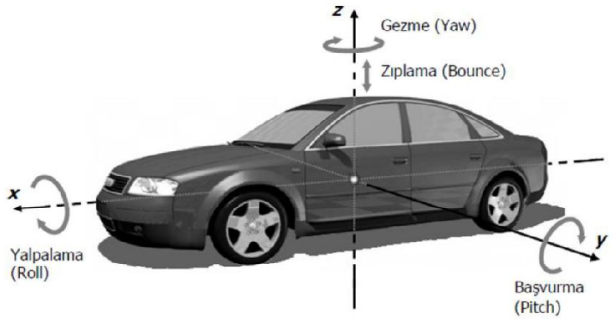


Figure 1: Major Release Occurs in Vehicles

III. COMFORT RELATED WORKS

It was stated that the results of the studies and evaluation of the results are the same effect on the suspension system of the hump and pit obstacles, but the interaction directions are different. The same damping timings indicate that the effective effect is equivalent.

Although this creates equivalent effects, Rakheja and Sankar report that they are experiencing both physically and psychologically disturbances in people who work in vehicles that are exposed to large spectrum but low frequencies continuously in improper ways with their research.

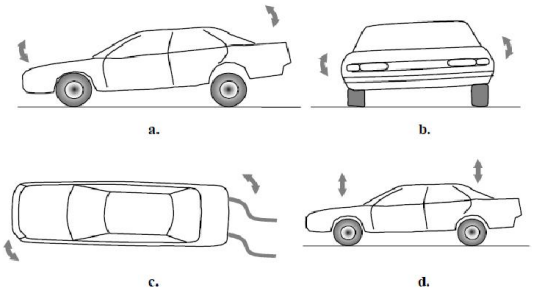


Figure 2: On-Vehicle Demonstration of Oscillation Movements in Vehicles
a. Beating b. Wobbling c. Navigate d. Shivering

The fact that frequencies and vibration phenomena are related to the concept of comfort at the same time is revealed in researches. It is seen that there are certain intervals for this situation and these intervals specify points that affect human health such as border values. For example, for head and neck parts 18 and 20Hz. [9]

IV. MATERIALS

A. Related Standards of System

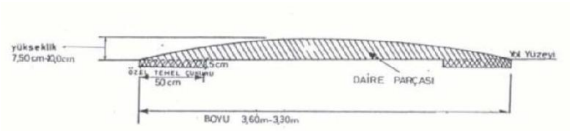


Figure 4: TS 6283 "Roadside Speed Control Elements - Mounds (Casters)" – Speed Control Elements

Vibrations also affect the cargo carried and the vehicle itself. For this reason, proper driving and comfort is one of the main objectives of vehicle design. Vibrations are mostly caused by irregularities on the road. Unevenness in 3-5mm height and 8-10mm length is called small roughness, 10-12mm height and 5-8mm length irregularities are called wave.

In general, vehicle vibrations between 5 and 13 Hz are defined as high frequency vibrations, and between 0,8 and 2 Hz, low frequency vibrations. Frequently, unsprung masses produce high frequency, springy masses produce low frequency vibrations. Both high and low frequency vibrations are disturbing. The body vibrations during walking are between 1.17 and 1.66 Hz. This freestyle vibrations are not offensive because the body is accustomed to it. At vibrations in modern cars this level is (1 -1.3 Hz).

The range carries limit value features for comfort conditions. The ISO 2631 standard considers the range of 0.5 Hz to 80 Hz to be a viable interval. Figure 2.7 shows the Basicentric Axes of the Human Body.

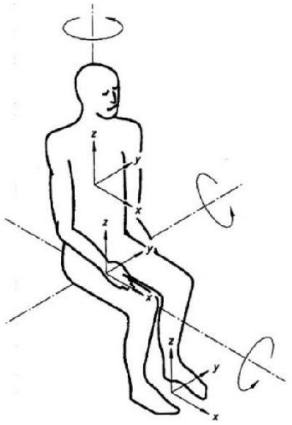


Figure 3: Basicentric Axis of the Human Body

B. Comfort Equations

C_0	Vibration Characteristic	[m/s]
Z_{MAX}	Maximum Amplitude	[m]
F	Frequency	Hz
k_t	A coefficient depending on the intensity of the vibration (k_t = 1,5 – 1,7)	

Table 1: Vibration Characteristic

$$C_0 = Z_{MAX} * f \text{ ^k}_t$$

C. Helical Spring Mechanism

Total shear stress; $\tau_t = \pm\tau_1 \pm \tau_2 = \pm\frac{F}{A} \pm \frac{Tr}{J}$

Maximum shear stress; $\tau_{maxy} = \frac{8*F*D}{\pi*d^3} * \left(1 + \frac{d}{2*D}\right)$

$$S_{ut} = A\frac{A}{d^m} \quad S_y = 0.75 * S_{ut} \quad S_{sy} = S_y * 0,577 \quad \mathbf{F = k * x}$$

$$k = \frac{d^4 * G}{8 * D^3 N_{aktif}} \quad \tau_{max} = K\frac{F * D}{\pi * d^3} \quad K_{dinamik} = \frac{4 * C - 1}{4 * C - 4} + \frac{0,615}{C}$$

$$C = \frac{D}{d} \quad \tau_{max} \leq \frac{S_{sy}}{n_s}$$

D. Equations (Langrange Equation)

M_1	Vehicle Suspended Mass / Quarter Vehicle mass (kg)
M_2	Suspension Mass / Non Suspended Mass (kg)
K_1	Suspension Spring Coefficient (N / m)
b_1	Suspension Damping Coefficient (Ns / m)
b_2	Wheel Damping Coefficient (Ns / m)
k_1	Wheel Spring Coefficient (N / m)

W	Road Entry
X_1	Non-suspended Mass Position
X_2	Suspended Mass Position
U	Control Force

Table 2: System Equations

Lagrange formulation is used as a general approach for finding motion equations of a dynamic system. The Lagrange "L" equations of motion are defined as the difference between the potential energy of the system "V" and the kinetic energy "T".

L=T-V

Sum of kinetic energies of masses;

$$\boldsymbol{T = T_{M1} + T_{M2}}$$

$$\boldsymbol{T = \frac{1}{2}M_1\dot{X}_1^2 + \frac{1}{2}M_2\dot{X}_2^2}$$

The sum of the potential energies of the spring elements;

$$\boldsymbol{V = V_{K1} + V_{K2}}$$

$$\boldsymbol{V = \frac{1}{2}K_1(X_1 - X_2)^2 + \frac{1}{2}K_2(X_2 - W)^2}$$

The sum of the heat-generating energies of the damping elements

$$\boldsymbol{P = P_{b1} + P_{b2}}$$

$$\boldsymbol{P = \frac{1}{2}b_1(\dot{X}_1 - \dot{X}_2)^2 + \frac{1}{2}b_2(\dot{X}_2 - W)^2}$$

Total kinetic energy and total potential energy difference;

$$\boldsymbol{L = \frac{1}{2}M_1\dot{X}_1^2 + \frac{1}{2}M_2\dot{X}_2^2 - \frac{1}{2}K_1(X_1 - X_2)^2 + \frac{1}{2}K_2(X_2 - W)^2}$$

The first motion equation of the system;

$$\boldsymbol{\frac{d}{dt}\left(\frac{\partial L}{\partial \dot{X}_1}\right) - \left(\frac{\partial L}{\partial X_1}\right) + \left(\frac{\partial P}{\partial \dot{X}_1}\right) = U}$$

$$\boldsymbol{\frac{\partial L}{\partial \dot{X}_1} = M_1\dot{X}_1}$$

$$\boldsymbol{\frac{d}{dt}\left(\frac{\partial L}{\partial \dot{X}_1}\right) = M_1\ddot{X}_1}$$

$$\boldsymbol{\frac{\partial L}{\partial X_1} = -K_1X_1 + K_2X_2}$$

$$\boldsymbol{\frac{\partial P}{\partial \dot{X}_1} = -b_1\dot{X}_1 + b_1\dot{X}_2}$$

The second motion equation of the system;

$$\boldsymbol{\frac{d}{dt}\left(\frac{\partial L}{\partial \dot{X}_2}\right) - \left(\frac{\partial L}{\partial X_2}\right) + \left(\frac{\partial P}{\partial \dot{X}_2}\right) = -U}$$

$$\boldsymbol{\frac{\partial L}{\partial \dot{X}_2} = M_2\dot{X}_2}$$

$$\boldsymbol{\frac{d}{dt}\left(\frac{\partial L}{\partial \dot{X}_2}\right) = M_2\ddot{X}_2}$$

$$\boldsymbol{\frac{\partial L}{\partial X_1} = -K_1X_1 + K_2X_2 - K_2W}$$

$$\boldsymbol{\frac{\partial P}{\partial \dot{X}_2} = b_2(\dot{X}_2 - \dot{W})^2 - b_2(\dot{X}_1 - \dot{X}_2)^2}$$

The last equations after the Lagrange are;

$$\boldsymbol{M_1\ddot{X}_1 = -b(\dot{X}_1 - \dot{X}_2) - K_1(X_1 - X_2) + U} \quad (3.3)$$

$$\boldsymbol{M_2\ddot{X}_2 = b(\dot{X}_1 - \dot{X}_2) + K_1(X_1 - X_2) + b_2(\dot{W}_1 - \dot{X}_2) + K_2(W - X_2) - U} \quad (3.4)$$

A block diagram can be created based on the motion equations of the active suspension system. The a F force shown in the block diagram is the control element that will be controlled and will vary according to the vehicle-road condition. [21]

Main Mass (m1)	2500 kg
Suspension Mass (m2)	320 kg
Suspension System Spring Constant (k1)	80,000 N/m
Wheel Spring Constant (k2)	500,000 N/m
The Damping Constant of The Suspension System (b1)	350 N.s/m
Wheel Damping Constant (b2)	15,020 N.s/m
Non-Suspended Mass Position (X1) (m)	
Suspended Mass Position (X2) (m)	

Table 3: System Equations

V. SYSTEMS' MATLAB SOLUTION

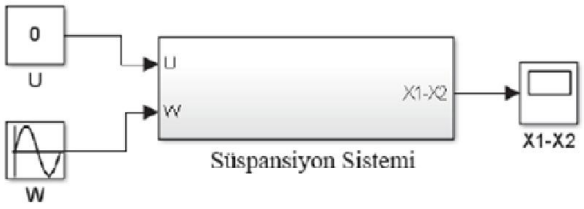


Figure 4: Matlab Works Area

In the above equations, the expression X_1- W is not included. The reason for this is that it is very difficult to measure this distance. Due to this difficulty, the deformation of the wheel X_2 -W is neglected. Instead of the distance between X_1 and W (X_1-X_2), the probing takes place. In this way there will be a neglect in the logic framework.

The discomfort (W) on the road will be simulated with gradual inputs in this problem. These steps can be associated with the potholes that form on the way the vehicle is going.

"" When a feedback controller wants to design a circuit (X_1 to X_2), the input is less than 5% and takes less than 5 seconds to enter and exit. For example, when a bus passes through a 5 cm high mound, the mass of the bus will oscillate within ± 2.5 mm and return to normal driving within 5 seconds. [21]

The two-degree-of-freedom quarter vehicle model is a suspension model that includes wheel dynamics. The system consists of a mass representing the vehicle weight (suspended mass), a mass representing the axle weight (non-suspended mass), and two separate spring-damper pairs representing the suspension and wheels (Çakan 2013)

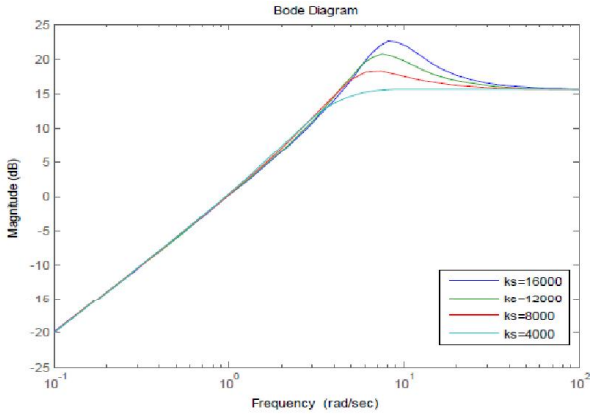


Figure 5.Effect of k Change to Acceleration Performance Criterion

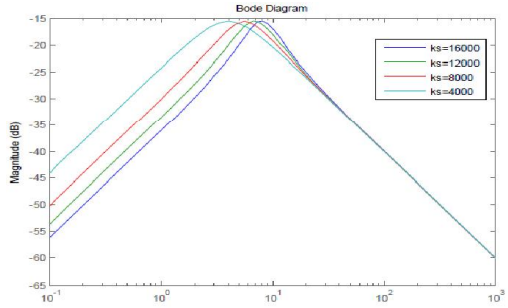


Figure 6. Effect of Variation of k on Damping Deviation Performance Criteria frequency

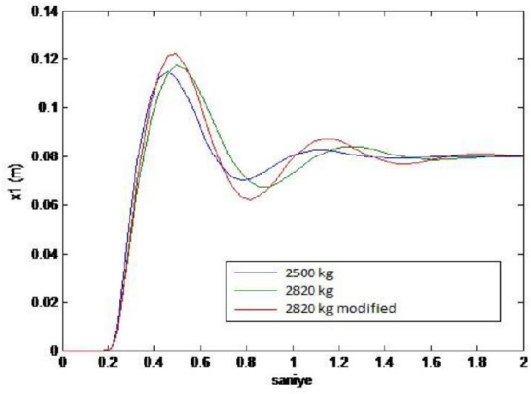


Figure 7. Displacement Response of Quarter Vehicle Modal Main Stage According to Time

As shown in Figure 7, when the vehicle is exposed to the road as shown in Figure 6, the main body of the vehicle makes a swing motion and the vibration movement is damped for about 1.6 seconds. With the modification and renewal operations performed by the user in the vehicle, the vibration amplitude and the damping time slightly increase as the weight of the vehicle changes from 2820 kg. The comfort characteristics of the vehicle do not change, that is, it is in the appropriate range, but because the weight of the vehicle is increased, the spring resistance is insufficient. Therefore, appropriate spring should be used by increasing the spring constant, diameter and number of windings. As shown in the graph, the duration of the damping of the vehicle, whose characteristics are changed according to the standards, is extended. Figure 8 shows the variation of the main body speed with respect to time.

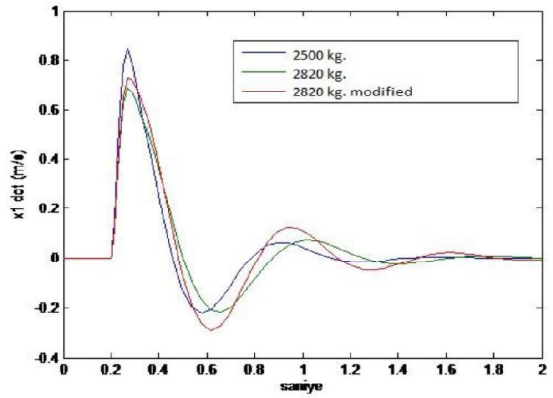


Figure 8. Quarter Vehicle Modified Main Body Speed Change Over Time

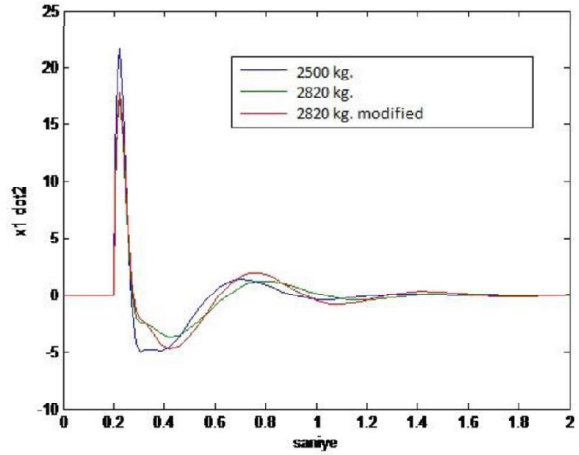


Figure 9. Time-dependent change of main body moment for quarter vehicle model

The graph in Figure 9 shows the change in vehicle body momentum over time. The main body of the vehicle made a variable acceleration motion in the range of -5 to 20 m / s2 for a 2500 kg vehicle and in a range of -4 to 15 m / s2 for a 2820 kg vehicle. As a result of this acceleration, the comfort of the passengers will be adversely affected. For this reason, the acceleration value needs to be kept within certain limits. The influence of vibrational acceleration on the human body often arises in connection with the frequency of vibration. When the frequency increases, even small accelerations are uncomfortable.

VI. CONCLUSION

Vehicle with the same platform as this article of study is used in vehicles with different equipment or special purpose vehicles, and it is necessary to review the suspension with the changes in strength, vibration, life span and so on. In this case, the system was analyzed and the results compared with the previous studies.

It is intended to design a suspension system that can operate on a light commercial vehicle. In the M1 category, if 2500 kg of vehicle is modified and it is 2820 kg, simulation of the vehicle is carried out to evaluate the vibration values

according to the comfort standards and when the vehicle weight changes, the selection of the most suitable elements to ensure the comfort and stability of the same damping elements comfort standards, as well as the effects of the suspension system parameters on the driving comfort of the vehicle, examining the parameters that have been changed for driving comfort in this vehicle, the vehicle chassis height and the impact on the heading angle.

When the weight of the vehicle changed, the 1300 kg vehicle was found to be within the comfort standard limits, only as a result of the calculation of the spring strength of the vehicle and the lifetime of the vehicle which was weighted for special purposes or necessary requirements. Therefore, in this thesis study, it has been determined that the maximum weight of the vehicle is to be weighted within the comfort standards and it is determined that this kilogram is outside the comfort limits.

In this article, if the 2500 kg vehicle is transformed to 2820 kg, the optimal design is realized by changing the vehicle parameters to optimize the comfort standards by interpreting the simulation results using on the vehicle.

When the vehicles change in such a way, there are frequent faults, frequent wear of the vehicle and uncomfortable noisy vibrations. Therefore, this vehicle is aimed to minimize the harmful and irritating effects of the vehicle by considering the comfort of the vehicle as well as the driving comfort.

REFERENCES

[1] *Çeyrek Araç Modelinde Pid ve Bulanik Mantik Kontrolcü ile Aktif Titreşim Kontrolü* a. Çakan f. Botsali m. Tinkir

[2] *Karayolu Taşitlari Süspansiyon Sisteminde Aktif Titreşim Kontrolü*, A. Çakan

[3] Borman, W. C., Hanson, M. A., Oppler, S. H., Pulakos, E. D., and White, L. A. (1993, May). *The people in organization. Organizational Management*, 76-79.

[4] Kahraman R. C., Borman, C., Hanımgil, M., Özler, H., Perçin, D., ve Sergen, L. (1993). *Kroner Kalp Rahatsizliğinin Belirlenmesinde Rol Oynayan Faktörler*. Sağlık Psikolojisi, 12(2), 76-80.

[5] *Taşit Titreşimlerinin Teorik Analizi Ve Bir Bilgisayar Modellemesi* Ümit ER, Sezan ORAK, Bilal PAR

[6] RAKHEJA, S. AND SANKAR, S., "*An Optimum Seat-Suspension For Off-Road Vehicles", The Shock And Vibration Bulletin*, 53, pp. 19-35, 1983.

[7] kitap, Car Suspension and Handling, 3th edition, Donald Bastow, Geoffrey P. Howard p.26-27

[8] TS EN 6283 "*Speed Control Humps*"

[9] TS EN 2631-1 *"Mechanical vibration and shock - Evaluation of human exposure to whole-body vibration"*

Effect of Gearbox Structural Design on the Vibration Levels

R.C. ÜMÜTLÜ[1a], B. HIZARCI[1b], C. DALBICER[1c], H. OZTURK[2d] and Z. KIRAL[2e]

[1] Dokuz Eylul University, The Graduate School of Natural and Applied Sciences Department of Mechatronics Engineering, Izmir/Turkey
[2] Dokuz Eylul University, Department of Mechanical Engineering, Izmir/Turkey
[a] rafet.umutlu@deu.edu.tr, [b] berkan.hizarci@deu.edu.tr, [c] cem.dalbicer@armakmakina.com.tr,
[d] hasan.ozturk@deu.edu.tr, [e] zeki.kiral@deu.edu.tr

Abstract **- Especially with the development of manufacturing industry, it is aimed to make mechanical parts designs more durable. From this point of view, the design of mechanical equipments has an important role in production process. In industry, gears are most common power transmission equipments. They are placed in gearbox housing and supported between bearings through the shafts. During the power transmission, gears generate undesirable vibration and noise. In order to reduce noise and vibration levels, some modifications such as stiffened plate construction, ribbing, webs and stiffeners are frequently used on gearbox housings. These operations are conducted as a part of design-out maintenance to improve rigidity of a gearbox. In this study, three different gearbox housing designs (basic, cross and cellular) are formed and analyzed by using ANSYS® software. The design varieties for housings have been established inside of the structure as different quantity of longitudinal and transverse stiffeners. In addition, all the external dimensions and the mass of these three housing designs are equal in order to observe just vibration reduction. Results show that cross design has a good performance in terms of reduction of vibroactivity.**

Keywords **- Gear, housing design, structural analysis, vibration, design-out maintenance.**

I. INTRODUCTION

GEARBOXES is one of the most important equipment in industry which provides controlled application of the power. Gearboxes use gears and gear trains to provide speed and torque transmission from a rotating power source to another device in desired ratios and high efficiency [1]. Mechanical power transmission systems are desired to produce low vibration and noise, because excessive vibration on power transmission systems may cause damage to connected machine, damage to product quality, lead to degradation in plant working conditions, lead to consuming excessive power, reduce machine's lifetime, and finally knock it out of service and halt plant production. Therefore, maintenance methods have been developed in order to maintain the operation of the established system without interruption. These maintenance plans are illustrated in Figure 1. In these maintenance strategies, design-out maintenance (DOM) has more applications recently and it ensures sustainable production and economic contributions in industry [2]. Design-out maintenance also known as eliminative maintenance [3] is to improve the design of machine in order to minimize effect of failures, also vibration and noise as well as eliminate the cause of maintenance [4].

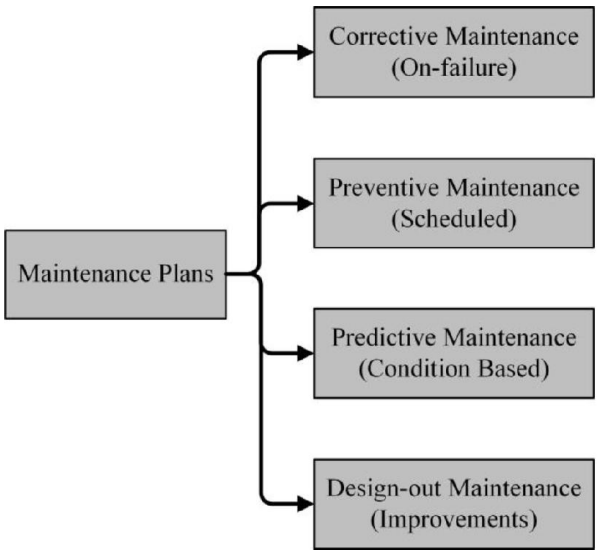


Figure 1: Maintenance plans

Redesigning and helpful modifications on machine can provide increase the systems reliability and machine performance. Therefore, in DOM, maintenance engineer works in close cooperation with design engineer [5]. The DOM has attracted much attention recently due to the increased use of structural analysis programs. Because of excessive costs associated with testing of real equipments, researches into structural and mechanical systems (gearbox in this study) are often conducted with the aid of numerical models and simulations. For modeling and simulations, structural analysis programs such as Solidworks® and Ansys® are often demanded and used extensively in the pre-production stage for design and analysis. These programs provide decrease of time and effort needed. After structural analysis on computer, the measurements and verification analyses are performed on test product. The final product is produced at the final stage.

The importance of the reduction of vibration generated by means of gears has grown in the recent years. During the power transmission, mechanical vibration also causes environmental noise. One of the possible ways to reduce this noise is to decrease vibration level in the source of the sound emitted. An important factor causing vibration and noise of the housing is dynamic forces evoked during the meshing between gears. On the other hand, the noise and vibration of gearboxes is emitted mainly by its housing [6]. In order to hold these structural effects as low as possible, different gear housing designs have been investigated. Vibration and noise are broadly accepted as a measure of quality of gearboxes and reduction of them are demanded. In a mechanical power transmission gear system, the vibration generated at the gears is conducted to the gearbox housing. For this reason, the design of a gearbox is critical for the noise and vibration.

There are some researches carried out to reduce vibration in gear systems by using improved housing design. Inoue and Yamanaka researched the influence of stiffened plate construction in order to reduce the noise as well as the vibration. In their research, they researched the rib stiffener layout, most effective positions of stiffeners in order to reduce the vibration [7]. Kumar et al. tackled with the failure problems of transmission housing or gearbox which were main problems for vehicle manufacturers. They established that noise and vibration were the main reason. So as to reduce vibration and noise levels, they analyzed the natural frequencies and mode shapes of housings by ANSYS® [8]. Lazarz and Perun present a paper including the results of numerical and experimental studies on the influence of selected factors on the dynamic forces and vibration of the gearboxes. The study was performed using a dynamic model of a test stand with the gears operating in the circulating power system [9]. Folega et al. studied an experimental and theoretical modal analysis of structural solutions of housings gear. The modal analysis of examined gearbox housing versions enabled to estimate influence of made ribbing modifications on form and frequency of vibrations [10]. The aim of all these studies is to contribute to the production of lighter and better quality products at lower cost.

Mechanical improvement of structure could be accomplished in two ways; one is producing better quality products, while keeping mass constant and the second one is achieving a predetermined quality by reducing in mass. In this study, structural improvements have been researched for equiponderant housings [11]. The purpose which differentiates this study from others is to achieve vibration reduction by maintaining equal mass for each gearbox housing designs. Furthermore, modifications on gearbox housing are applied on inner of gearboxes unlike the other studies. Aims of this research can be summarized as reducing the vibration levels without increasing the weight, analyzing effects of the stiffener on housing designs, identifying the natural frequency influence on vibration levels.

II. Mechanical Design and Analysis

A. Mechanical Design

In this study, three different gearbox housing designs (basic, cross and cellular) are formed. All gearbox housings have been designed by keeping the same transfer ratio, the same external size and the same mass. The outer dimensions of these three gearboxes are 205 X 160 X 140 mm, which is fixed for all designs. The total weight of gearbox housings is equal and about 5.2 kg; range of ±10 gr. The design differences for housings have been established inside of the structure as usage of webs and stiffeners. So as to preserve the mass, wall thicknesses will be changed. All designed housings have been analyzed through modal analysis of ANSYS in order to determine natural frequencies. For the experiment, three different gearbox housings (basic, cross and cellular) are produced as usage of webs and stiffeners. The basic model of gearbox has no stiffener, no longitudinal and transverse webs. Housing solid models are shown in the Figures 2-4. The basic model of gearbox housing can be shown in Figure 2.

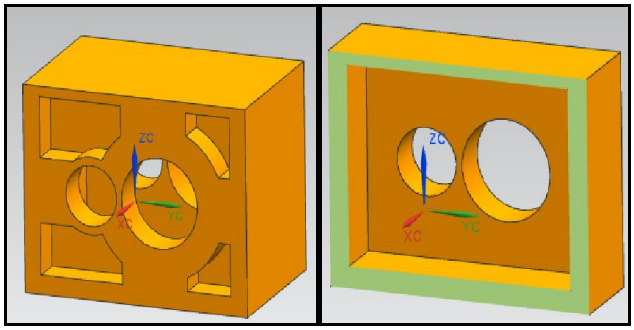


Figure 2: The basic model

In order to determine design effects on gearbox vibration, longitudinal and transverse stiffeners are located to the centre line of the side walls and transverse stiffener is located to base wall, as shown in Figure 3. In addition, longitudinal webs are located around bearing races in order to support bearings and reduce vibration tendency. This second model is called as cross because of appearance of stiffeners. The weight, changed due to stiffeners and webs, is kept same by changing wall thickness in order to compare with basic model more reliably.

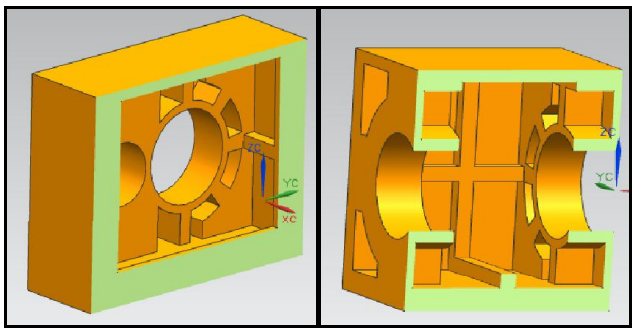


Figure 3: The cross model

For the third model called cellular, longitudinal and transverse webs are located to both side and base walls in order to strengthen body, as shown in Figure 4. The weight, decreased due to webs, is increased by thickened walls in order to maintain constant weight in comparison with basic model.

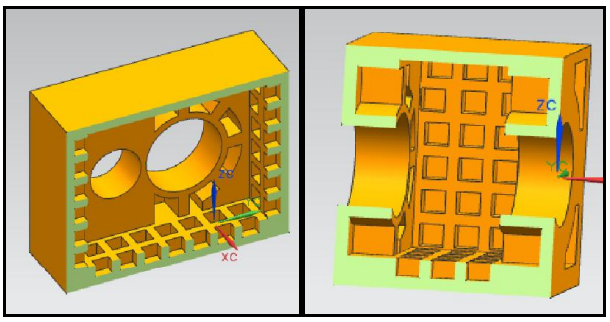


Figure 4: The cellular model

B. *Natural Frequency Analysis*

Three housings were designed to enhance vibration tendency with the same external size and gear ratios. Natural frequency analyses of structures were executed by ANSYS and results are shown in the Table 1. According to Table 1, the first natural frequency of cross model and cellular model is higher than that of basic model.

Table 1: Natural frequency results of the gearbox models obtained from the ANSYS

Natural Frequencies (Hz)			
	Basic Model	Cross Model	Cellular Model
f1	3203	3560	3345
f2	3590	3605	3758
f3	5223	5387	5237
f4	7247	7264	7683
f5	8668	8239	8572
f6	9067	8416	8892

III. PRODUCTION AND EXPERIMENTAL SETUP

A. *Production*

Casting model was produced for all three gearboxes. Since there were no differences between external dimensions of gearboxes, one model was produced for all the three designated gearboxes and three core boxes were produced for each design because of inner differences of housings. Gearbox housings were produced by method of aluminum gravity casting and the type of aluminum is Etial-150. Model is shown in the Figure 5. After casting operation, all gearboxes were machined for their bearing house. Three bodies were machined in the same manner and accuracy. Bearings were supplied from the same brand and with the same feature. Pinion gears and wheel gears were produced with the same accuracy in the same production line in order not to affect vibration analysis. The gear ratio of gearbox is 2,47. Gears were made by 8620 case hardening steel (21NiCrMo2) and hardened to the value of 58-60HRC. Shafts of the wheel gears were produced in the same manner.

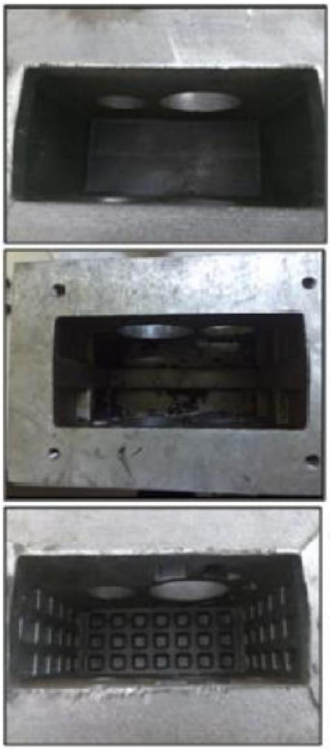


Figure 5: Model of gear housing

B. *Experimental Setup*

The gearbox is driven by a 1.5 kW, 3000 rpm three-phase motor and a variable speed controller was used to drive the gearbox. The capacity of electromagnetic brake is 30 Nm, which is used in the system as a load for gearbox. The experimental setup is shown in Figure 6.

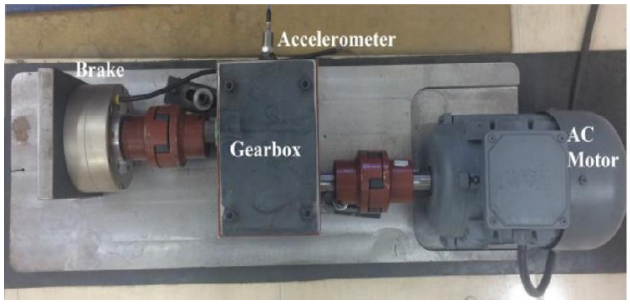


Figure 6: Experimental setup

The helical gears generate the vibration signals at every rotation and these signals are acquired using two PCB 352A76 type accelerometers, whose frequency range is 5-16000Hz and its sensitivity 1 mV/g. The accelerometers were mounted to side wall of gearbox. A PCB 480C02 type signal conditioner has been used to optimize accelerometer outputs. The position of the input shaft has been indicated using a 5V DC ME4-

S12L-PA type inductive sensor which produces a single pulse per rotation. This sensor has been used for the synchronous time domain averaging of the gear vibration signal. Analog to digital converter was used to transform signals. In this work NI DAQ Card (which is a trade mark of National Instrument Data Acquisition Card) 6036E has been used as an ADC. All the signals acquired from accelerometers have been sampled at a determined rate and have been recorded on a computer using NI DAQ Card and Lab VIEW 7.0 software.

IV. Results

For this experimental study, the speed of motor revolution was set to 1500 rpm. The vibration signals and pulse signals (from inductive sensor) were sampled at 10 kHz and stored on a computer. The raw vibration data was acquired for 60 second that is equal to 1500 pinion gear rotation and 607 wheel gear rotation, owing to gear ratio. Statistical properties can be subsidiary and informative about improvement of the vibration tendencies of gearboxes. In this study, statistical properties of vibration signal as mean, root mean square (RMS), peak to peak and crest factor is used for explaining gearbox housing comparisons. According to designed gearbox housings, the results of these statistical properties are given in Figures 7-10.

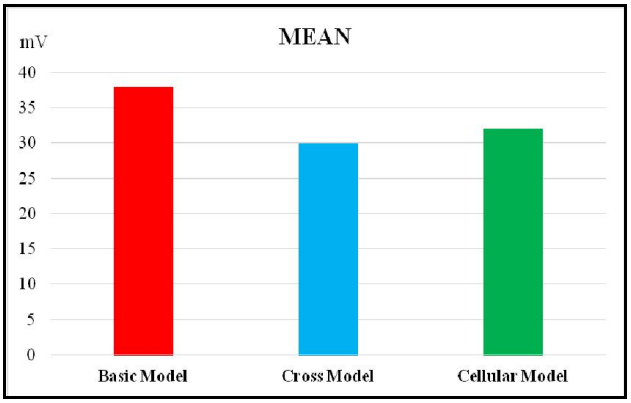


Figure 7: Mean of vibration signals on designed housings

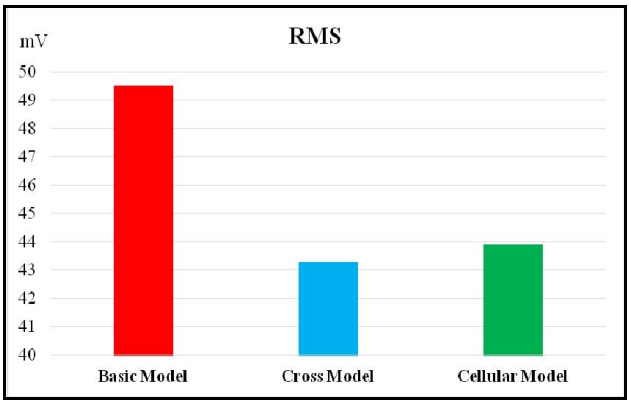


Figure 8: RMS of vibration signals on designed housings

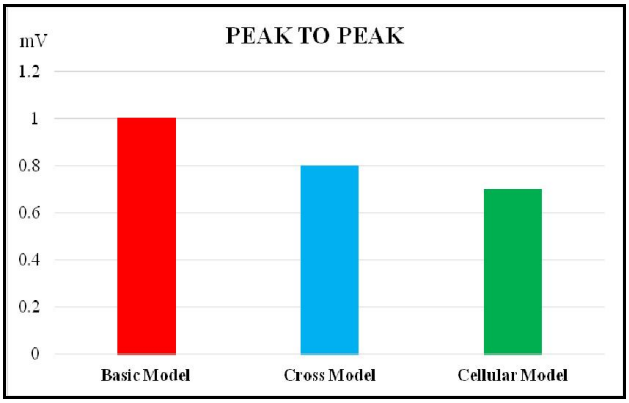


Figure 9: Peak to peak of vibration signals on designed housings

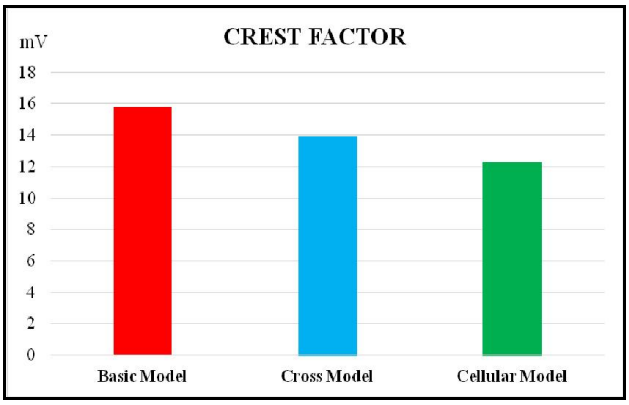


Figure 10: Crest factor of vibration signals on designed housings

According to results, the cross model shows minimum mean and RMS acceleration during the experiment. RMS and mean results for cellular and cross models are very close to each other. On the other hand, cellular model gives better results on peak to peak and crest factor results. Consequently, cross and cellular designs decrease the vibration on gearbox and their results are sharply better than basic model.

V. Conclusions

The scope of this study is gearbox vibration reduction. In order to reduce vibration levels, some mechanical improvements were implemented to gearbox housings.

Before these improvements are applied, modal analysis of ANSYS is conducted in order to find natural frequencies of gearbox designs. According to modal analysis, cross model has a higher first natural frequency than the others. That is an indication that the vibration of the cross model gearbox will be less.

In addition, designed gearbox housings are produced and vibrations of them are measured during the experiment. According to experiment results, the cross model is chosen as a better design because of RMS value of its vibration signal. Therefore, it is obvious that adding stiffeners is better than applied webs in order to reduce vibration of gearbox housings.

Consequently, vibration improvements have been achieved. These implementations contribute to design more rigid and durable parts.

REFERENCES

[1] H. Ozturk, "Gearbox health monitoring and fault detection using vibration analysis." Diss. PhD Thesis, Graduate School of Natural and Applied Sciences of Dokuz Eylul University, Turkey, 2006.

[2] I. Tumer, Y. Stone and B. Robert. "Mapping function to failure mode during component development," Research in Engineering Design, 2003.

[3] P. Gopalakrishnan and A. K. Banerji, *Maintenance and spare parts management*. PHI Learning Pvt. Ltd., 2013.

[4] G. Waeyenbergh and L. Pintelon. "A framework for maintenance concept development." International Journal of Production Economics, 2002.

[5] A. K. Jain, "Influence of modification of design out maintenance & design out information system for maintenance cost control & a lucrative business (with case study)." International Journal of Engineering Trends and Technology, 2013.

[6] T. Figlus, and A. Wilk. "Application of FEM method in reduction of gear transmission housing vibration." Journal of KONES, 2009.

[7] K. Inoue, M.Yamanaka and M. Kihara. "Optimum stiffener layout for the reduction of vibration and noise of gearbox housing." Transactions-American Society of Mechanical Engineers Journal of Mechanical Design, 2002.

[8] A. Kumar, H. Jaiswal, A. Pandey and P.P. Patil, "Free Vibration Analysis of Truck Transmission Housing based on FEA," Procedia Materials Science. 2014.

[9] B. Łazarz, and G. Peruń. "Influence of construction factors on the vibrational activity of the gearing." Transport Problems 7.2 (2012): 95-102.

[10] P. Folęga, R. Burdzik, L. Konieczny and A. Wieczorek, "Influence of housing ribbing modification on frequencies and shapes of vibration," Journal of Measurements in Engineering, September 2013. Volume 1, Issue 3. Issn 2335-2124.

[11] C. Dalbicer, "Experimental analyses of gearbox housing design." MSc Thesis, Graduate School of Natural and Applied Sciences of Dokuz Eylul University, Turkey, 2016.

Effect of inlet pressure and cold/hot water treatment on gypsum samples from FGD unite of power plant in terms of dehumidification, PSD and chemical composition

İhsan Toroglu[1], Halil İbrahim Gonul[2]*, Serdar Yilmaz [1], Sait Kizgut[1], Dilek Cuhadaroglu [1], Mehmet Bilen1
[1]Department of Mining Engineering, Zonguldak Bülent Ecevit University, itoroglu@hotmail.com
[2]Eren Enerji Zonguldak, Turkey, h.ibrahimgonul@hotmail.com

***Abstract* - FGD (Flue Gas Desulphurization) unites of power plants are crucial regarding to environment and growing increase in the energy need should be considered with regards to contamination. Desulphurization unites utilizing limestone have cyclones in order to separate gypsum. The studied power plant FGD unites have cyclones with 4 joints with valves. Operational pressure and the open number of joint valve were the variables in order to understand the cyclone performance. Also, the effect of cold/hot water treatment on gypsum samples in terms of dehumidification, PSD (Particle Size Distribution) and chemical composition was investigated. Samples were collected from absorber, gypsum cyclone and vacuum belt in different process conditions. Cyclone samples were analyzed in terms of size distribution while gypsum samples were analyzed in terms of hot/cold water treatment. Effect of cold (20 °C) and hot (100 °C) water treatment on the gypsum samples over the vacuum belt was observed regarding their chemical composition and size distribution. In order to understand the effect of process pressure on cyclone performance, 24 samples from each joint of cyclone with the pressure values of 150 kPa, 160 kPa, 170 kPa, 180 kPa, 190 kPa, and 200 kPa. PSD analyzes were carried out with Malvern Mastersizer. Before and after hot water treatment, gypsum samples were analyzed in terms of PSD and one of the gypsum samples had D50 value of 31.93 and 35.48 before and after respectively. Hot water treatment on gypsum samples also affected the humidity ratio of the samples and it resulted as 3.07% moisture decrease after the treatment. Also gypsum samples chemical composition ((%CaO)+(%SO3)+(%MgO)+(%Fe2O3)+(%Al2O3)+(%CO2)+(%SiO2)) increased from 99.72 % to 99.81%.**

Findings of this study would help future scientists and plant operators in the order of understanding the effect of hot and cold water treatment on gypsum samples.

***Keywords* - Hot/cold Water Treatment, Gypsum, FGD, cyclone, desuphurization**

I. INTRODUCTION

POWER plants are equipped with several sub systems and coal entering to power plant is processed to the final products (ash, byproducts, wastewater and flue gas). Schematic representation of power plant process and coal combustion final products is provided in Figure1.

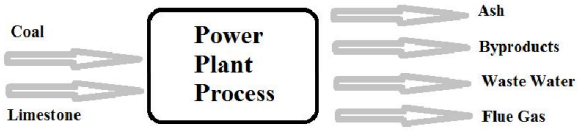


Figure1. Schematic representation of coal utilizing power plant and final products.

In order to decrease the level of SO2 emission and to purify the wastewater a techonology called Wet Flue Gas Desulphurization (WFGD) is employed. WFGD, due to abovementioned purposes is one of the most important technology in a power plant in terms of water and atmosphere. WFGD system in the power plants due to its high efficiency and reliability is the most commonly used technology for controlling the emission of SO2 in the world (Zhong et al 2008, Nolan et al 2004, Nygaard et al 2004, Jin et al 2006). Sketch of WFGD system in power plant is provided in Figure2.

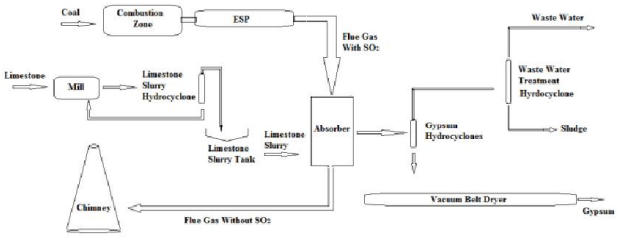


Figure2. Sketch of WFGD system in power plant.

II. EXPERIMENTAL METHOD

Samples were collected at various operating conditions and they were collected from absorber, gypsum cyclone and vacuum belt which are in the body of FGD system after NOx and fly ash were incurred. Sample collection frequency and the sampling points are provided in Table 1.

Table 1 Sampling points and the frequency of sampling for each unite.

Point of sampling	Frequency of Sampling
Absorber	1 time
Gypsum Cyclone	One sample from over and under flow of cyclone with each operation pressure of 150 KPa,160 KPa,170 KPa, 180 KPa, 190 KPa, 200 KPa
Vacuum Belt Exit	Period of one week, one sample for each day

• Sample from absorber system were taken from discharge pump when the slurry density is 1.160 kg/m3.

• Samples of gypsum cyclone exit were taken as changing the cyclone flow pressure by changing the valve opening of cyclone inlet flow. It was waited for 3 minute period for each sample during the pressure changes in order to stabilize the flow.

• 3 kg of sample was taken from vacuum belt and it was reduced down with quarter method for analysis.

In Figure3, it was summarized the points of sampling and flow diagram of FGD system is provided.

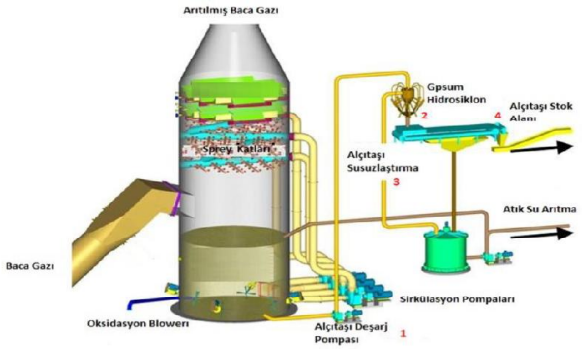


Figure3. Flow diagram of FGD system and point of sampling (Walsh M.A 2008).

Sampling was carried out as in the periods provided in Table 1. Samples collected were tagged and systematically classified. Tagging of the samples were realized taking the day, time, sample name, operating pH and pressure into consideration.

Cyclone samples are tagged in the order of cyclone name, cyclone over and under flow pressure and joint number of flowing stream. For example, BU1803 means, B cyclone, 180 kPA and 3 open joints of flow stream. Number of analysis was carried out on the samples from various points. Cyclone samples were analyzed in terms of PSD and vacuum belt samples were analyzed in terms of hot/cold water treatment. In order to measure the effect of the difference in pumping pressures of circulating pumps on gypsum crystals size, analyzes (chemical composition, PSD analyzes) were carried out in the scope of this study. Chemical compositions of gypsums were carried out with XRF. Gypsum samples collected over the vacuum belt were analyzed before and heat treatment (cold/hot 20 °C/100 °C water treatment by washing), particle size and chemical composition changes were observed. Chemical composition of the samples were analyzed with XRF and in Figure4 it was provided an image of XRF equipment used during analyzes.



Figure4. Representation of XRF used in chemical composition analyzes.

Samples were collected from absorber discharge pump, gypsum cyclone over and underflow and vacuum belt as mentioned in Table 1. In order to understand the cyclone performance with respect to cyclone operating pressure, samples were collected at pressures of 150 kPa, 160 kPa, 170 kPa, 180 kPa, 190 kPa, 200 kPa over and underflow with 3 or 4 joints opening and total of 24 samples were collected. Samples of cyclone inlet, under and over flow streams were taken and analyzed in terms of PSD and this was carried out with Malvern Mastersizer. In Figure5, a representation of Malvern Mastersizer equipment employed in PSD analyzes is provided.



Figure5. Representation of Malvern Mastersizer used in PSD analyzes.

III. RESULTS AND DISCUSSION

Sample from absorber was analyzed in terms of PSD and chemical composition. 250 ml solution/slurry was taken from the pipeline under the absorber system and the density was measured with a densometer employing between 1100-1200 kg/m3. Slurry sample which has 1160 kg/m3 was the reference point and it was kept fixed for other samples. Sample was reduced as following the standards and sample for chemical analysis was prepared. In table 2, chemical composition analysis of the sample is provided.

Table 2 Chemical compostion of the sample from absorber.

Component	CO_2	Na_2O	MgO	Al_2O_3	SiO_2	P_2O_5
Amount (% mass)	8,37	0,03	0,86	0,65	1,76	0,01
Component	SO_3	Cl	K_2O	CaO	TiO_2	Fe_2O_3
Amount (% mass)	47,75	0,10	0,13	39,99	0,02	0,34

Sample is basically the absorber slurry and PSD analysis was carried out on this sample as well. Malvern Mastersizer was employed for PSD analysis and results are provided in Table 3.

In order to separate gypsum, cyclones are utilized in desulphurization systems which are using limestone slurry. In the body of the cyclone in power plant studied, there were 4 joints of flow exit. Each joint and inlet has valve opening. Cyclone operating pressure (150 kPa,160 kPa,170 kPa,180 kPa,190 kPa,200 kPa) and number of joints (3 and 4) were the parameters studied . Corresponded graphs were provided in Figure6 and Figure7. It was provided a comparison between BA1704 and BA1803 in Figure8. In Figure9, graph for PSD of cyclone inlet, over and underflow were provided.

PSD analyzes were realized on the samples from cyclone underflow and vacuum belt. It was observed that after crystallization step, samples from underflow exit of cyclone has coarser fraction of material after separation by cyclone. As shown in Figure8 BA1803 has coarser fraction of material taking into consideration of the comparison between BA1703 and BA1803.

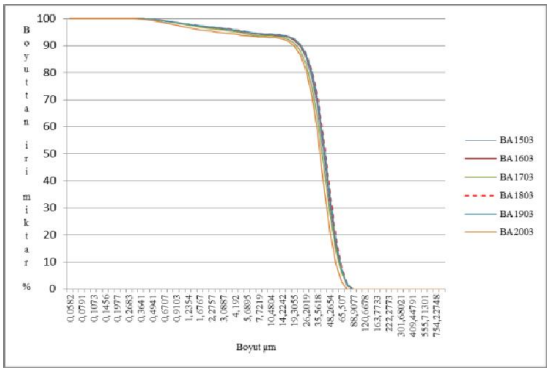


Figure6. Cyclone pressures (150 kPa, 160 kPa,170 kPa,180 kPa,190 kPa,200 kPa) and PSD.

Table 3. PSD analysis result of the sample from absorber.

Size (µm)	Amount (%)	Cumulative amount oversize (%)	Size (µm)	Amount (%)	Cumulative amount oversize (%)
0,0582	0	100,00	2,6512	0,44265	95,33
0,0679	0	100,00	3,0887	0,52749	94,89
0,0791	0	100,00	3,5983	0,6188	94,36
0,0921	0	100,00	4,192	0,69599	93,74
0,1073	0	100,00	4,8837	0,71502	93,05
0,125	0	100,00	5,6895	0,64947	92,33
0,1456	0	100,00	6,6283	0,50016	91,68
0,1697	0,00007	100,00	7,7219	0,35758	91,18
0,1977	0,00068	100,00	8,996	0,16427	90,83
0,2303	0,00481	100,00	10,4804	0,20311	90,66
0,2683	0,02373	99,99	12,2096	0,43941	90,46
0,3125	0,07429	99,97	14,2242	0,88187	90,02
0,3641	0,14489	99,90	16,5712	1,67106	89,14
0,4242	0,20903	99,75	19,3055	3,10801	87,47
0,4941	0,28557	99,54	22,4909	5,64473	84,36
0,5757	0,37168	99,26	26,2019	9,54405	78,71
0,6707	0,39814	98,89	30,5252	14,10075	69,17
0,7813	0,42401	98,49	35,5618	17,5676	55,07
0,9103	0,39604	98,06	41,4295	15,56911	37,50
1,0604	0,38546	97,67	48,2654	11,08319	21,93
1,2354	0,39183	97,28	56,2292	6,58394	10,85
1,4393	0,40577	96,89	65,507	3,14687	4,26
1,6767	0,39258	96,48	76,3157	1,11719	1,12
1,9534	0,36934	96,09	88,9077	0	0,00
2,2757	0,38977	95,72	103,5775	0	0,00

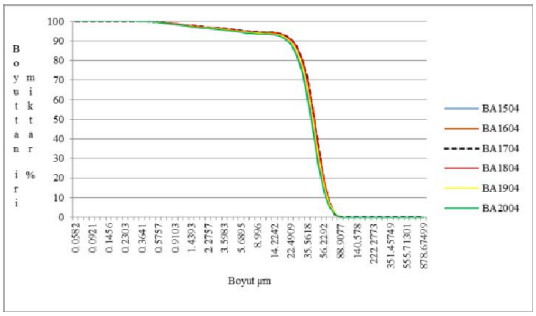


Figure7. Cyclone pressures (150 kPa, 160 kPa,170 kPa,180 kPa,190 kPa,200 kPa) and PSD.

As referring to Figure7, It was observed that, BA1704 sample has coarser material with 4 joints open case.

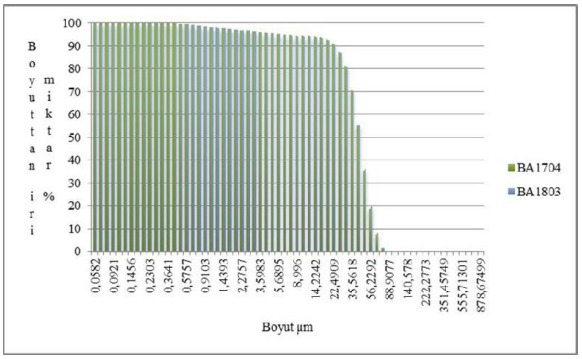


Figure8. Comparision between BA1704 and BA1803

In Figure8, BA1704 and BA1803 was compared because they have coarser size distribution regarding to other samples. BA1803 sample has D10 value of 19,98 µm, D50 value of 37,17 µm, D90 value of 54,48 µm while BA1704 sample D10 value of 18,35 µm, D50 value of 34,53 µm and D90 value of 51,38 µm. It was understood that BA1803 sample has the coarsest size distribution among all samples collected in operation conditions of pressure (150 kPa,160 kPa,170 kPa,180 kPa,190 kPa,200 kPa) and joint opening number (3 or 4).

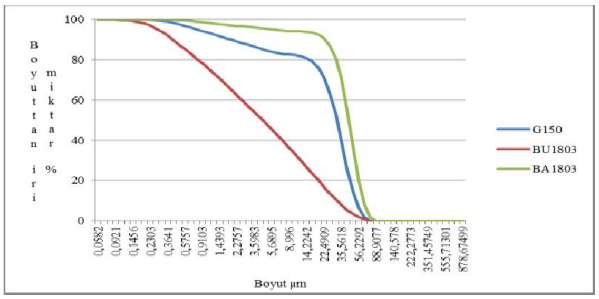


Figure9. PSD of cyclone inlet, over and underflow.

In Figure9, it is shown that when BA1803 sample has coarse size distribution; inlet, under and over flow PSD of cyclone is provided. In Figure10, tromp curves for 3 cyclone at different operational pressures are plotted and presented.

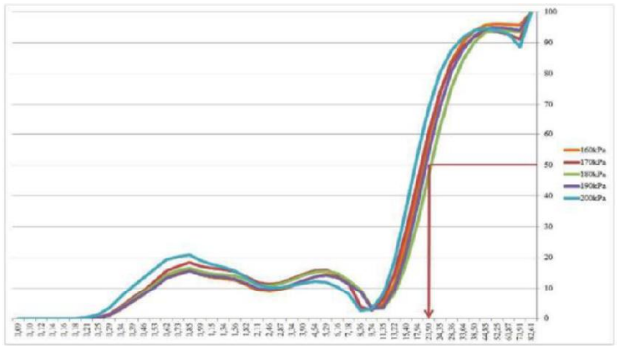


Figure10. Tromp curve of cyclone at various operational pressures.

As following the order, the one on the right hand side with operational pressure of 180 kPa has the coarsest size distribution. Regarding to Figure10, it has D50 value of 21.59 µm and Ep (error factor) value of 0.0058. Analyzing the Figure10, it can be understood that undersize of 10 µm flow under the cyclone and separation was not good enough realized.

IV. CONCLUSION

In this study it was observed that variable operational pressure of cyclone and number of joints opening affect the PSD of gypsum samples while hot/cold water treatment on gypsum samples over the vacuum belt also has an important role on chemical composition, PSD and dehumidification rate. It was aimed to investigate what operation condition should be taken in order to have coarser fractionated gypsum samples and several pressure are employed on cyclones.

Analyzes carried out showed that 3 joints opening and 180 kPa has the coarsest particle size distribution. Desired coarse particle distribution is provided as G150, BA1803 and BU1803 and they have the D50 values of 27,17 µm ,37,16 µm and 3,82 µm

It was analyzed and determined that Gypsum-0 sample has the value of D50 as 31,93 µm while Gypsum-1 sample has the values of D50 as 35,48 µm and Gypsum-2 sample has the value of D50 as 32,52 µm. Gypsum-1 sample which had been washed for 5 mins in boiling water has a coarser size (higher D50 value of 35.48 µm) and it had 31.93 µm (3.55 µm finer) before.

Experimental work on cold and hot water treatment was carried out on the vacuum belt. While Gypsum -1 sample has the moisture of 8.93%, Gypsum-0 has 12.15 % and Gypsum-2 has 12.0 %. Regarding to these results hot water treatment (100 C) has helped to reduce 3.07 % percent of moisture in the body of gypsum. It was also noticed that Gypsum-0 and Gypsum-1 samples' chemical composition of (CaO, SO3, MgO, Fe2O3, Al2O3, CO2, SiO2) increased from 99.72 % to 99.81 %.

This study would be helpful for the future studies in order to understand the cold and hot water treatment on gypsum samples. Not only future scientist would be aware of cyclone operational pressure change affect but also plant/FGD operators would take the role of number of joints opening into consideration. Optimization of cyclone pressure, number of joint opening and PSD would be enabled with future studies in this field.

REFERENCES

[1] Atkins P, Jones L (1997) Chemistry Molecules, Matter and Change, Bilim Yayıncılık, 1st edition, ISBN: 975-556-033-5,Ankara, 410.

[2] Aydın A.O (2001) Temel Kimya. ISBN:975-8289-16-0, 2, Aşiyan Yayınları, Sakarya, 377..

[3] Chen C, Liu S, Gao Y and Liu Y (2014) Investigation on Mercury Reemission from Limestone-Gypsum Wet Flue Gas Desulfurization Slurry. The Scientic World Journal, 2014:6.

[4] Cordoba P (2014) Status of Flue Gas Desulphurisation (FGD) systems from coal-fired power plants: Overview of the physic-chemical control processes of wet limestone FGDs. Sience Direct,144:274-286.

[5] *Dökme F, Güven O (2014) Bilyalı Değirmenlerde Hızın Performansa Olan Etkilerinin Deneysel Olarak İncelenmesi. Mühendis ve Makine,55: 38-55.*

[6] Evans P.A , Miller C and Pouliot S (2009) Operational Experience of Commercial, Full Scale Ammonia Based Wet FGD for Over a Decade. Coal-Gen, 20 Ağustos 2009, North Carolina, ABD.

[7] EPA (1981) Environmental Protection Agency, Flue Gas Desulfurization (Acid Gas Removal) Systems, ABD.

[8] IEA (2016) The International Energy Outlook 2016, 11 Mayıs 2016, Washington, ABD, E-kitap,81-100.

[9] Li Y, Zhou J, Zhu T and Jing P (2014) Calcium Sulfite Ozidation and Crystal Growth in the Process of Calcium Carbide Residue to Produce Gypsum ,Waste Biomass Valor 5: 125-131.

[10] Lash T.D (1985) Ultrasound in the Undergraduate Lab. Journal of Chemical Education,62: 720.

[11] Marten J.C (1977) A History Of Flue Gas Desulfurization Systems Since 1850. Air Pollution Control Association, 10:948-961.

[12] Marchis D, Badulescu C and Nistor M C (2016) Benefits of Using FGD Gypsum From S.E. Turceni in Agriculture, 48: 247-253.

[13] Oikawa K, Yongsiri C, Takeda K and Harimoto T (2003) Seawater Flue Gas Desulfurization: Its Technical Implications and Performance Results, Environmental Progress, 22:67 – 73.

[14] Pan D, Wu H and Yang L (2016) Investigation on Relationship Between The Fine Particle Emission and Crystallization Characteristics of Gypsum During Wet Flue Gas Desulfurization Process, Journal of Sciences, 55:303-310.

[15] Trawinski H (1976) Hidrosiklon Teorisi, Uygulama Alanları, Ayrım Sınırına Etki Eden Faktörler ve Çalışma Prensipleri, Engineering and Mining Journal,177:9.

[16] Walsh M.A (2008) Wer FGD Types and Fundamentals, Marsulex Environmental Technologies, Pennsylvania, ABD.

Evaluation of High Speed Train Noise Pollution

A. E. ÇERÇEVİK[1], S. YEREL KANDEMİR[1], M. Ö. YAYLI[2]

[1] Bilecik Seyh Edebali University, Bilecik/Turkey, erdem.cercevik@bilecik.edu.tr
[1] Bilecik Seyh Edebali University, Bilecik/Turkey, syerel@gmail.com
[2] Uludağ University, Bursa/Turkey, ozguryayli@uludag.edu.tr

***Abstract* - Recently, there are many environmental problems in our country as it is in the world in proportion with the rapid increase in the development of the country. One of these environmental problems is noise pollution. Along with the increase in train traffic, noise pollution in big cities first emerged as a big problem in small cities in the recent period. Although Bilecik is a relatively small province, a high-speed train passes through it. Bilecik, which is spread over several hills today, can be considered as a quiet city due to its beautiful nature and low population. However, the high-speed train from Konya to Istanbul passes through Bilecik. These high-speed trains also cause noise pollution. Measurements were made around the station and under the railway viaduct. A noise gauge was used for the measurement and the results were evaluated in terms of dBA. The measurement was determined to be 60-65 dBA around the station and 80-85 dBA below the railway viaduct, and it was observed that these values did not exceed the limit values of the 'Evaluation of Environmental Hazard and Management Regulation'. It is proposed that the railway and train sets should be suitable for noise, and the same system should be applied for future projects.**

***Keywords* - Bilecik, Noise Measurement, High Speed Train Noise.**

I. Introduction

ENVIRONMENTAL noise is one of the side effects of public rail transit systems which are becoming more common in large cities of Turkey. One of these problems is the noise which exhibits itself in two different forms; one being the noise that disturbs passenger and the other is the environmental noise caused by the rapid rail systems [1].

Railways are usually seen as an environmentally friendly option for large volumes of both passenger and freight traffic. Expansion of the high-speed railway network can help to curb the growth in road and air journeys; if freight is transferred back onto the rails this can remove heavy lorries from the roads; in densely populated areas new light rail and tramway schemes are being proposed to help solve traffic congestion. Railways are therefore entering a new era of higher speeds and higher capacities for intercity and urban systems, and for freight as well as passenger traffic. Unfortunately, noise and vibration are often perceived as an environmental weakness of railways. The prospect of new railway construction has led to resistance from residents, partly based on noise and vibration issues, which promoters are then required to take into account [2].

Bilecik is located on the high-speed train route in the north-west of Turkey (Figure 1). 11 high-speed trains pass through Bilecik 5 transits per day. As the high-speed train passes by the city, the city has some effects. In this study high speed train noise passing through Bilecik province was measured and evaluated.



Figure 1: High Speed Train and Planned Line in Turkey and Bilecik Location

A. Environmental Noise

Noise is defined as subjective "unwanted voice" that negatively affects live life. The presence of voices in everyday life is an important environmental issue that causes even the deaths in some situations that affect the comfort of life and human health negatively because of the violence of the increase and distribution as well as the necessity for the people to feel good about themselves [3]. The effects on health and quality of life physical effects such as hearing damage, physiological effects in body activity, psychological effects such as distress, discomfort, anger and other behavioral disorders, and performance effects such as decreased work efficiency and lack of understanding of audible sounds [4].

Yücel (2000) summarizes the tranquil sources that cause adverse psychological and physiological effects on humans and animals in four main groups:

a) Traffic noise (eg, air, road, rail, sea)
b) Industry noise (noise from various lines of business such as drill, turning, etc.)
c) Construction noises (temporary tools working on the construction site, eg concrete mixer etc.).
d) Noise (for example, pets, radio, wedding places, etc.)

Increase of Environmental Noise Pollution 2010 "Environmental Hazard Assessment and Management Regulation" was introduced in order to bring the priorities and take measures for the Ministry of Environment and Forestry [6]. In the said regulation, the line noise limit values of the

railed systems are given in Table 1 in decibels. According to this, the noise level of the last high-speed trains from Bilecik should not exceed 85 dBA for passing trains and 75 dBA for standing trains (Table 1).

Table 1: Environmental Noise Limit Values for Trains

Underground Stations	L_{day}(dBA)
Stalls, stairs, corridors	55
Platforms (at 1.8 m from platform edge)	80
For stop and move trains	85
For passing trains	85
For trains in operation	65
Ventilation system within the station	55
Ventilation ducts in the tracks (at 9.0 m)	55
Emergency ventilation fans in enclosed spaces in the station (at 22.5 m.)	80
Overhead Stations	L_{day}(dBA)
Platforms (at 1.8 m from platform edge)	70
For stop and move trains	75
For trains in operation	65

B. Noise Sources of High-Speed Trains

The noise generated in the line length is the noise that is opened from the points where two separate structures touch while moving. The noise is mainly caused by wheel-rail contact. The locomotive noise is the most effective noise. There is also noise from the vehicle that is exposed to the air. The factors affecting the noise caused by train motion can be grouped under three headings;

- Hardness and durability of the rail,
- If a horizontal-straight form is formed or destroyed on the vehicle wheel,
- The presence of small openings in the rails or the resulting openings.

Noises and vibrations around the rail systems, in the air or on the walls and floor are disturbing. Vibrations, vehicle suspension system

elastic and permanent collapses, roughness in the wheels and on the rail top surface, traverse transitions and scissor transitions. The speed of the vehicle is also influential on this issue. The components of the vehicle-road system have different natural frequencies. If the frequencies of the loads that the wheels transmit match any of these frequencies, there will be a strong vibration. The traverses of the vehicle axles also increase in vibration when the transition frequency is equal to the load frequency or natural frequencies. Vibrations and noise from the structure usually occur in the 0-100 Hz frequency range, while vehicle-road noises occur in the 30-2000 Hz frequency range. The natural frequencies are independent of the speed, but the traversing frequency increases proportionally. Vibrations exceeding speeds of 8 mm/s cause damage to road construction and environmental construction [7].

Figure 2 shows the process of rolling-noise generation schematically. The wheel and rail surfaces are not perfectly smooth, but contain small-amplitude unevennesses (roughness). This causes the wheel and rail to vibrate relative to each other, and these vibrations radiate noise to the wayside [2].

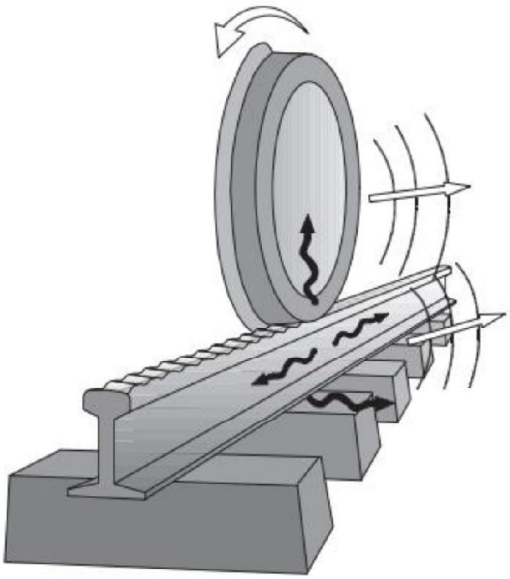


Figure 2: Schematic diagram showing how rolling noise is generated by the wheel/rail interaction [2]

II. Material Method

In this study, high speed train noise measurements were made in Bilecik province. Measurements were made using the SL814 brand digital sound and noise meter shown in Figure 3. For the measurement, a point where the settlement is concentrated and a station area were selected (Figure 4). The measurements were made 10 meters away from the trains.



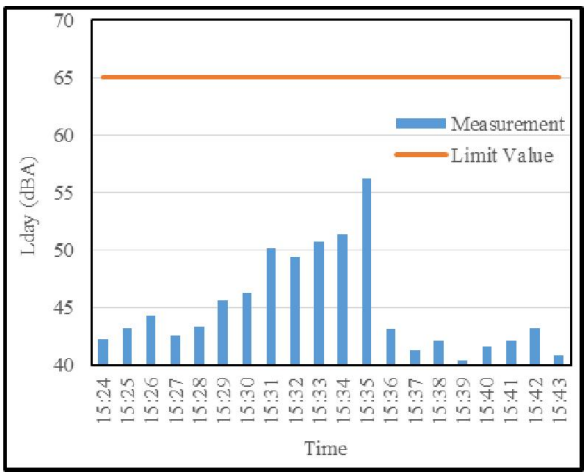
Figure 3: Noise Meter



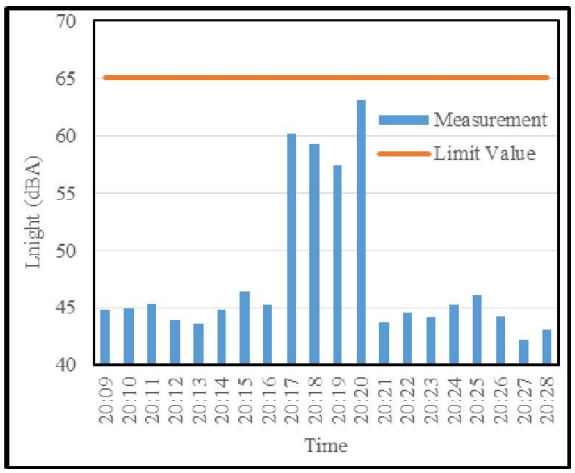
Figure 4: Measured points

I. Results

Measurements were made 1 hour in the day and evening according to the Regulation and Management of Environmental Intensity. In Figure 5, the first point noise measurement results are given. The rising values in Figure 5 show the times when trains arrive. These results, which were taken close to the station, were measured lower than the 65 dBA limit value determined by the regulation.

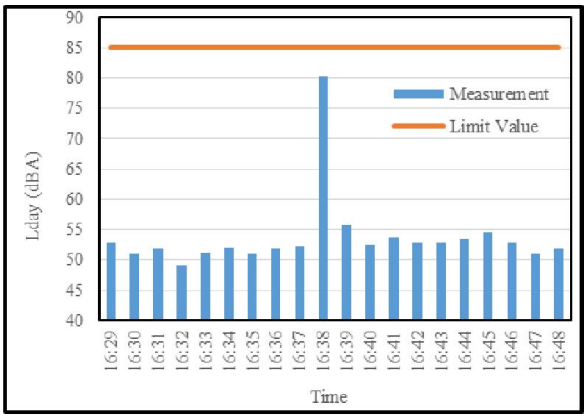


a. Day Measurement

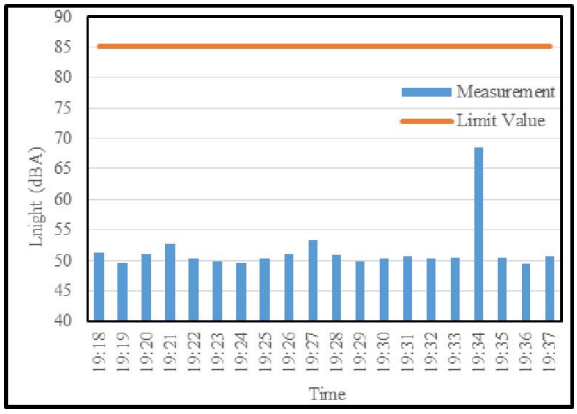


b. Night Measurement

Figure 5: First Point Noise Measurement Results



a. Day Measurement



b. Night Measurement

Figure 6: Second Point Noise Measurement Results

II. CONCLUSION

In this study, noise measurements of high speed trains passing through Bilecik province were made. With the development of a high-speed train network in our country, the noise created by high-speed trains becomes more important. The measurements made are within the limits determined by the noise regulations of high-speed trains passing through Bilecik. High-speed train lines are made properly and the new noise levels are kept at the appropriate level. In addition, even train sets that are working are also suitable for noise generation.

Although the high speed train does not pass at high speeds at the measuring points, the resulting noise is very close to the limit values. This work needs to be done in the regions where the high-speed train passes faster and it must be repeated with the escape of the lines. Taking necessary precautions according to the results, noise generated by high-speed trains should be avoided.

REFERENCES

[1] N. Aktürk, R. Toprak., E. Asiloğullari "Hızlı raylı ulaşım sistem kaynakli çevresel gürültü." J. Fac. Eng. Arch. Gazi Univ. Vol 18, No 3, 15-25, 2003.

[2] V. V. Krylov, (Ed.) *Noise and vibration from high-speed trains.* Thomas Telford. 2001.

[3] M. Aşçıgil, ,. Karayolu Gürültü Haritalarının Hazırlanması: İstanbul Zincirlikuyu- Maslak Ulaşım Hattı Örneği. Master Thesis. İstanbul Tecnical Universty, Institute of Science. 2009.

[4] A. Mavruk, Yüreğir ve Seyhan (Adana) İlçelerinde Ana Arterlerdeki Toz ve Gürültü Dağılım Haritalarının Hazırlanması. Master Thesis. Çukurova University, Institute of Science. 2005.

[5] M. Yücel, Çevre Sorunları. Çukurova University Ziraat Fakültesi Genel Yayın No: 109, Ders Kitapları Yayın No: A-28. 2000.

[6] Çevre ve Orman Bakanlığı, 2010. Çevresel Gürültünün Değerlendirilmesi Ve Yönetimi Yönetmeliği, Resmi Gazete No: 27601.

[7] R. Toprak, N. Aktürk, Raylı ulaşım sistemlerinin neden olduğu gürültü ve çevresel etkileri. Türkiye Mühendislik Haberleri. 417 - 2002/1.

Effects On The Surface Quality In The Machining Processes Of The Tool Vibrations

E. TURKES[1], S. NESELI[2], M. SAHIN[3] S. SELVI[4]

[1] Kirklareli University, Kırklareli/Turkey, erol.turkes@klu.edu.tr
[2]Selcuk University, Konya/Turkey, sneseli@selcuk.edu.tr
[3]Trakya University, Edirne/Turkey, mumins@trakya.edu.tr
[4]Trakya University, Edirne/Turkey, selcukselvi@trakya.edu.tr

***Abstract* - The problem of surface quality and cutting stability in the machining processes is very important and is strictly connected with the final quality of the product. Therefore, this paper describes a new theoretical model for the dynamic cutting forces of orthogonal cutting in turning. A specific advantage for the presented model is the convenience for vibration prediction. The presented dynamic force model is used to predict variable cutting forces with dynamic cutting between cutting tool and workpiece. This model is considered two degree of freedom complex dynamic model of turning with orthogonal cutting system. The complex dynamic system consists of dynamic cutting system force model which is based on the shear angle (φ) oscillations and the penetration forces which are caused by the tool flank contact with the wavy surface.**

***Keywords* – Chatter, surface, dynamic cutting, turning, cutting tool, roughness**

I. INTRODUCTION

TO overcome surface roughness problems, the researchers propose models that try to simulate the conditions during machining and establish cause and effect relationships between various factors and desired product characteristics. Furthermore, the technological advances in the field, for instance the ever-growing use of computer controlled machine tools, have brought up new issues to deal with, which further emphasize the need for more precise predictive models. Surface roughness is a widely used index of product quality and in most cases a technical requirement for mechanical products. Achieving the desired surface quality is of great importance for the functional behavior of a part. On the other hand, the process dependent nature of the surface roughness formation mechanism along with the numerous uncontrollable factors that influence pertinent phenomena, make almost impossible a straightforward solution. The most common strategy involves the selection of conservative process parameters, which neither guarantees the achievement of the desired surface finish nor attains high metal removal rates [1]. The surface finish profile of a machined work is affected by the tool geometry, the work material, the cutting conditions and other factors such as tool wear, built-up edges and cutting dynamics. Cutting dynamics occurs in machining operations due to the interaction between the tool-workpiece structure and the force process. The most important result of this condition is chatter vibration. Regenerative chatter is so named because of the closed-loop nature of this interaction. Each tooth pass leaves a modulated surface on the work due to the vibrations of the tool and workpiece structures, causing a variation in the expected chip thickness. Under certain cutting conditions (i.e., feed, depth, and speed), large chip thickness variations, and hence force and displacement variations, occur and chatter is present. The results of chatter include a poor surface finish due to chatter marks, excessive tool wear, reduced dimensional accuracy, and tool damage. Machine tool operators often select conservative cutting conditions to avoid chatter, thus, decreasing productivity [2].

Dynamic cutting force produces deformation between tool and workpiece. If this deformation remained constant throughout the machining operation a work accurate form could be obtained. However, it varies, and its variation causes errors of workpiece form. The blank of workpiece entering a machining operation does not have an exact geometric form. The sections of a cylinder will not be exactly round; longitudinally it may be barrel shaped or conical, and due to inaccurate clamping it will be rotating with a "run-out". Similarly, a surface to be face-milled will not initially be perfectly flat. Or it may be that in one turning cut the tool path is so programmed that the initial diameter will be reduced to two different diameters. For all this examples, the cutting force varies during the cut. Consequently, the deformation between tool and workpiece also varies, and initial form errors will be copied onto the machined surface. Hence, cutting force F is a function of the depth of the cut α and of feed per revolution f_r . Also, during a cutting pass the cutting force varies and often also the

flexibility between toll and work varies [3]. The roughness of a machined surface depends on many factors that can be grouped as: geometric factors, work material factors and vibration and machine tool factors. Vibration and machine tool factors are related to the machine tool, tooling, and setup in operation. They include chatter or vibration in the machine tool or cutting tool; deflections in the fixturing, often resulting in vibration; and backlash in the feed mechanism, particularly on older machine tools. If these machine tool factors can be minimized or eliminated, the surface roughness in machining will be determined primarily by the geometric factors and work material factors described previously [4].

II. DYNAMIC CUTTING MODEL

Chatter or vibration in a machining operation can result in pronounced waviness in the work surface. When chatter occurs, a distinctive noise is made that can be recognized by any machinist. Various criteria are used to evaluate machinability, the most important of which are; tool life, forces and power, surface finish, and ease of chip disposal. Although machinability generally refers to the work material, it should be recognized that machining performance depends on more than just material. The type of machining operation, tooling, and cutting conditions are also important factors, as are material properties. Chatter can be recognized by the noise associated with these vibrations, by the chatter marks on the cut surface, and by the appearance of the chips produced in turning. Machining with chatter is mostly unacceptable because of the chatter marks on the machined surface and because the large peak values of the variable cutting force might cause breakage of the tool or of some other part of the machine Chatter is often a factor limiting metal removal rate below the machine's capacity and hence reduces the productivity of the machine [5]. In this paper, a complex dynamic system is modeled prior to the orthogonal cutting, which forms a mechanical cutting basis for all cutting processes in general. This dynamic system is used for turning. In order to determine the increased values of the damping and surface roughness this system is used. Therefore, for roughness and stability analysis modal analysis and chatter stability tests were performed for different materials, tool length and spindle speed. Chatter process damping model (PDM) is modeled as dynamic orthogonal cutting process with the process damping force. According to constant the shear stress (τ_s) of work material for various cutting speeds and feed ratios and the shear angle (φ) oscillations Static and Dynamic Cutting Force Coefficients (DCFC) are obtained by using the dynamic cutting force model. This model consists of tool penetration effect and oscillation of tool effect as shown in Fig. 1. [6].

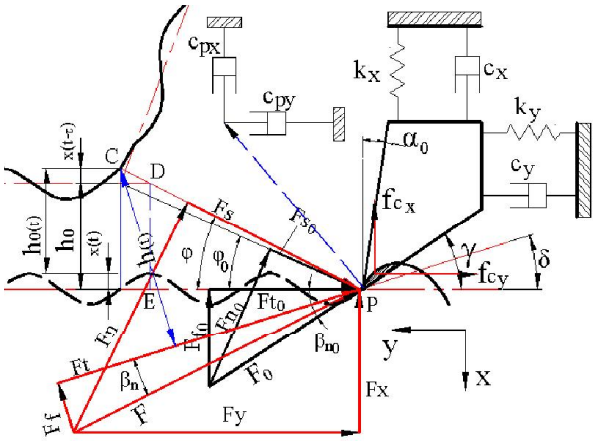


Figure 1: Dynamic cutting model

According to Figure 1, with considering the shear angle (φ) oscillations and the penetration, the equations of motion of cutting tool in (x) and (y) directions are:

$$m_x \ddot{x}(t) + c_x \dot{x}(t) + k_x x(t) = F(t) \sin(\beta_n + \delta) = F_{xT}(t)$$
$$m_y \ddot{y}(t) + c_y \dot{y}(t) + k_y y(t) = F(t) \cos(\beta_n + \delta) = F_{yT}(t) \quad (1)$$

where m_x and m_y are the mass coefficients (kg), cx and cy are the structural damping coefficients (kg/s), k_x and k_y are the stiffness coefficients (N/m). Dynamic force ($F(t)$ [N]) can be represented by:

$$F(t) = a K_f h(t) \quad (2)$$

where K_f is the feed force constant (N/m^2), and instantaneous dynamic chip thickness ($h(t)$) and dynamic chip thickness ($h_0(t)$) are:

$$h(t) = h_0(t) + |PE|\delta \rightarrow \quad h_0(t) = h_0 + x(t-\tau) - x(t)$$
$$h(t) = h_0 + x(t-\tau) - x(t) + \cot(\varphi) h_0 \delta \rightarrow$$
$$\delta = tan^{-1}\left(\frac{\dot{x}}{V_0 + \dot{y}}\right) \quad (3)$$

Where, h_0 is undeformed chip thickness (mm), $x(t)$ and $x(t-\tau)$ are modulations of the cut and outer work surface (mm), δ is the instantaneous work surface slope generated by the tool oscillation, V_0 is the cutting speed of static cutting (m/s) and $\dot{x}, \dot{y}$ are the vibration velocities (m/s) in each direction. For any given work and tool materials, it is always possible to establish an empirical relation between the

shear angle φ_0 and the mean friction coefficient μ_a through experimentation. A general form of the angle relationship [7, 8] for machining steel is given by Wu & Liu [9]:

$$2\varphi_0 + \beta_{s0} - \alpha_0 = C \quad (4)$$

It is assumed that this relation between the shear angle φ and the friction angle β_s is invariant in dynamic cutting. Thus it can be represented by:

$$2\phi + \beta_s - \alpha = C \quad (5)$$

where C is the material constant which is insensitive to the machining conditions. Also, $(_0)$ sub-indexes in Eq. (4) are represented to static conditions. Making use of these formulas, the difference caused by the oscillation of φ [6], which is a theoretical and experimental cutting angle, is calculated. If this difference is substituted into the dynamic cutting model, dynamic resultant cutting force F [N] can be represented by:

$$F = \frac{F_s}{cos(\varphi + \beta_n + \delta)} = \frac{\tau_s\, a\, l_s}{cos(\varphi + \beta_n + \delta)} \rightarrow$$

$$l_s = \frac{h(t)}{sin(\varphi + \delta)} \quad (6)$$

where l_s is instantaneous shear plane length (mm), τ_s is the shear stress of work (N/m^2). Hence, dynamic cutting forces in both directions can be represented by:

$$F_x = \tau_s\, a\, \lambda_{sx}\left(h_0 - x + x(t-\tau) + \lambda_{dx}\,\dot{x} - \lambda_{vx}\,\dot{y}\right)$$
$$F_y = \tau_s\, a\, \lambda_{sy}\left(h_0 - x + x(t-\tau) + \lambda_{dy}\,\dot{x} - \lambda_{vy}\,\dot{y}\right) \quad (7)$$

Where

$$\lambda_{sx} = \frac{sin(C - 2\varphi_0)}{sin\,\varphi_0\, cos(C - \varphi_0)}$$

$$\lambda_{sy} = \frac{cos(C - 2\varphi_0)}{sin\,\varphi_0\, cos(C - \varphi_0)}$$

$$\lambda_{dx} = \frac{h_0}{V_0}\left[\frac{cos(\varphi_0)\,cos(C-\varphi_0) - cos(C)}{sin(\varphi_0)\,cos(C-\varphi_0)} + \frac{cos(C-2\varphi_0)}{sin(C-2\varphi_0)}\right]$$

$$\lambda_{dy} = \frac{h_0}{V_0}\left[\frac{cos(\varphi_0)\,cos(C-\varphi_0) - cos(C)}{sin(\varphi_0)\,cos(C-\varphi_0)} + \frac{sin(C-2\varphi_0)}{cos(C-2\varphi_0)}\right]$$

$$\lambda_{vx} = h_0\eta_v\left[\frac{cos(C-2\varphi_0)}{sin(\varphi_0)\,cos(C-\varphi_0)} + \frac{2\,cos(C-2\varphi_0)}{sin(C-2\varphi_0)}\right]$$

$$\lambda_{vy} = h_0\eta_v\left[\frac{cos(C-2\varphi_0)}{sin(\varphi_0)\,cos(C-\varphi_0)} + \frac{2\,sin(C-2\varphi_0)}{cos(C-2\varphi_0)}\right] \quad (8)$$

Where η_v is dynamic cutting constant [6]. Thus the dynamic cutting force components have been expressed analytically by the static cutting coefficients $\lambda_{sx}, \lambda_{sx}$ and the dynamic cutting coefficients $\lambda_{dx}, \lambda_{dy}$ and $\lambda_{vx}, \lambda_{vx}$ which can be determined from static cutting tests. If DCFC used to the turning operations, according to Eq.(1) PDM can be expressed as follows;

$$m_x\,\ddot{x}(t) + c_{esx}\,\dot{x}(t) + k_x\,x(t) + c_{vy}\,\dot{y}(t) =$$
$$F_{esx}\left(x(t) - x(t-\tau)\right)$$
$$m_y\,\ddot{y}(t) + c_{esy}\,\dot{y}(t) + k_y\,y(t) + c_{dy}\,\dot{x}(t) =$$
$$F_{esy}\left(x(t) - x(t-\tau)\right)$$

Where, $K_f = \tau_s\,\lambda_{sx}$; $K_t = \tau_s\,\lambda_{sy}$; $c_{esx} = c_x + a\,K_f\,\lambda_{dx}$;

$c_{vy} = -a\,K_f\,\lambda_{vx}$; $F_{esx} = -a\,K_f$; $c_{esy} = c_y - a\,K_t\,\lambda_{vy}$;

$c_{dy} = a\,K_t\,\lambda_{dy}$; $F_{esy} = -a\,K_t$.

The process damping occurs further due to penetration of the tool into the wavy work surface. A ploughing force model has been proposed to describe the contact relationship between tool flank and machined surface. Based on this ploughing force analysis, a small volume of work material is pressed by the tool during wave cutting. In the meantime, a resistance force is generated by the stress field inside of the displaced work material. It is therefore reasonable to assume that the process damping force is equal to resistance force. The resistance force has been proven to be proportional to the volume of the displaced work material [6].

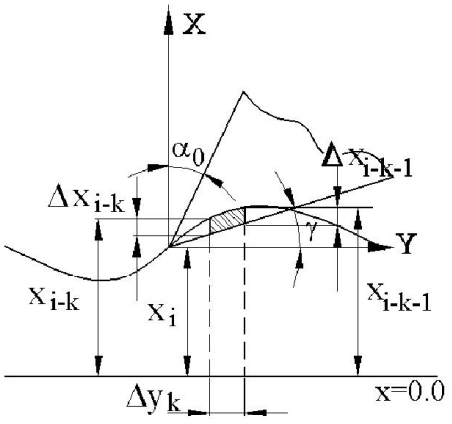


Figure 2: Penetration model of the cutting tool.

According to Figure 2, total dynamic forces in both directions are written as follows:

$$F_{xTot}(t) = -\left(F_x(t) + f_{cx}(t)\right)$$
$$F_{yTot}(t) = -\left(F_y(t) + f_{cy}(t)\right) \quad (9)$$

where $f_{cx}(t)$ and $f_{cy}(t)$ are resistance force components in the (x) and (y) directions (N) and they can be expressed as:

$$f_{cx}(t) = c_{px}\,\dot{x}(t)\,;\; f_{cy}(t) = c_{py}\,\dot{y}(t) \tag{10}$$

Hence, the equations of motion in the (x) and (y) directions are written as:

$$\begin{aligned} &m_x\,\ddot{x}(t) + c_{tx}\,\dot{x}(t) + k_x\,x(t) + c_{vy}\,\dot{y}(t) = \\ &F_{esx}\left(x(t) - x(t-\tau)\right) \\ &m_y\,\ddot{y}(t) + c_{ty}\,\dot{y}(t) + k_y\,y(t) + c_{dy}\,\dot{x}(t) = \\ &F_{esy}\left(x(t) - x(t-\tau)\right) \end{aligned} \tag{11}$$

where c_{px} and c_{py} are the penetration damping coefficients (kg/s), $c_{tx} = c_{esx} + c_{px}$ and $c_{ty} = c_{esx} + c_{px}$ are damping coefficients (kg/s). In order to solve Eq.(11), if the equation for τ decomposition form is written independent of time and according to the course taken by the relative movement of tool tip to the workpiece [10],

$$l = V_0\,t + y \tag{12}$$

where, V_0 is the linear speed in the rotation direction of the workpiece (m/s), y is the displacement of tool tip independently from workpiece on the axis y during cutting (m). When the derivative of Eq. (11) is taken as time related,

$$\frac{dl}{dt} = V_0 + \dot{y} \approx V_0 \tag{13}$$

where $\dot{y}$ was neglected, since, according to linear speed, it has no significant value for linear modeling. Eq. (11) with these simplifications;

$$\dot{x}(t) = \frac{dx}{dt} = \frac{dx}{dl}\frac{dl}{dt} = \left(V_0 + \dot{y}\right)\frac{dx}{dl} \approx V_0\,\frac{dx}{dl} \rightarrow x' = \frac{dx}{dl}$$

$$\ddot{x}(t) = \frac{d^2x}{dt^2} = \frac{d}{dt}\left(V_0 + \dot{y}\right)\frac{dx}{dl} = \ddot{y}\,\frac{dx}{dl} + \left(V_0 + \dot{y}\right)\frac{d^2x}{dl^2}\frac{dl}{dt} \approx$$

$$V_0^2\,\frac{d^2x}{dl^2} \rightarrow x'' = \frac{d^2x}{dl^2}$$

$$\dot{y}(t) = \frac{dy}{dt} = \frac{dy}{dl}\frac{dl}{dt} = \left(V_0 + \dot{y}\right)\frac{dy}{dl} \approx V_0\,\frac{dy}{dl} \rightarrow y' = \frac{dy}{dl}$$

$$\ddot{y}(t) = \frac{d^2y}{dt^2} = \frac{d}{dt}\left(V_0 + \dot{y}\right)\frac{dy}{dl} = \ddot{y}\,\frac{dy}{dl} + \left(V_0 + \dot{y}\right)\frac{d^2y}{dl^2}\frac{dl}{dt} \approx$$

$$V_0^2\,\frac{d^2y}{dl^2} \rightarrow y'' = \frac{d^2y}{dl^2}$$

the following equations is obtained,

$$\begin{aligned} &m_x\,V_0^2\,x'' + c_{tx}\,V_0\,x' + k_x\,x + c_{vy}.V_0.y' = \\ &F_{esx}\left(x(l) - x(l - \pi\,d)\right) \\ &m_y\,V_0^2\,y'' + c_{ty}\,V_0\,y' + k_y\,y + c_{dy}\,V_0\,x' = \\ &F_{esy}\left(x(l) - x(l - \pi\,d)\right) \end{aligned} \tag{12}$$

thus, according to constant (l) equation of motion is obtained instead of time dependent one, τ. If both sides of Eq. (12) are reduced for simplification,

$$\widetilde{c}_{tx} = \frac{c_{tx}}{m_x V_0} \quad \widetilde{k}_x = \frac{k_x}{m_x V_0^2} \quad \widetilde{c}_{vy} = \frac{c_{vy}}{m_x V_0} \quad \widetilde{F}_{esx} = \frac{F_{esx}}{m_x V_0^2}$$

$$\widetilde{c}_{ty} = \frac{c_{ty}}{m_y V_0} \quad \widetilde{k}_y = \frac{k_y}{m_y V_0^2} \quad \widetilde{c}_{dy} = \frac{c_{dy}}{m_y V_0} \quad \widetilde{F}_{esy} = \frac{F_{esy}}{m_y V_0^2}$$

and if these values are placed and the equation is equaled to zero, and if Laplace transformation is applied, the characteristic equation of the system is obtained,

$$\begin{aligned} &\begin{bmatrix} 1 & 0 \\ 0 & 1 \end{bmatrix}\begin{Bmatrix} x'' \\ y'' \end{Bmatrix} + \begin{bmatrix} \widetilde{c}_{tx} & \widetilde{c}_{vy} \\ \widetilde{c}_{dy} & \widetilde{c}_{ty} \end{bmatrix}\begin{Bmatrix} x' \\ y' \end{Bmatrix} + \begin{bmatrix} \widetilde{k}_x - \widetilde{F}_{esx} & 0 \\ -\widetilde{F}_{esy} & \widetilde{k}_y \end{bmatrix}\begin{Bmatrix} x \\ y \end{Bmatrix} \\ &+ \begin{bmatrix} \widetilde{F}_{esx} & 0 \\ \widetilde{F}_{esy} & 0 \end{bmatrix}\begin{Bmatrix} x(l - \pi\,d) \\ x(l - \pi\,d) \end{Bmatrix} = \begin{Bmatrix} 0 \\ 0 \end{Bmatrix} \end{aligned} \tag{13}$$

$$\begin{bmatrix} s^2 + \widetilde{c}_{tx}\,s + (\widetilde{k}_x - \widetilde{F}_{esx}) + \widetilde{F}_{esx}\,e^{-\pi ds} & \widetilde{c}_{vy}\,s \\ \widetilde{c}_{dy}\,s - \widetilde{F}_{esy} + \widetilde{F}_{esy}\,e^{-\pi ds} & s^2 + \widetilde{c}_{ty}\,s + \widetilde{k}_y \end{bmatrix} \begin{bmatrix} X(s) \\ Y(s) \end{bmatrix} = \begin{bmatrix} 0 \\ 0 \end{bmatrix} \tag{14}$$

$$\begin{aligned} &D(s) = s^4 + \left(\widetilde{c}_{ty} + \widetilde{c}_{tx}\right)s^3 \\ &+ \left(\widetilde{k}_y + \widetilde{c}_{tx}\,\widetilde{c}_{ty} + \widetilde{c}_{dy}\,\widetilde{c}_{vy} + (\widetilde{k}_x - \widetilde{F}_{esx})\right)s^2 \\ &+ \left(\widetilde{c}_{tx}\,\widetilde{k}_y - \widetilde{F}_{esy}\,\widetilde{c}_{vy} + (\widetilde{k}_x - \widetilde{F}_{esx})\,\widetilde{c}_{ty}\right)s + (\widetilde{k}_x - \widetilde{F}_{esx})\,\widetilde{k}_y \\ &+ \widetilde{F}_{esx}.e^{-\pi ds}\left[s^2 + \left(\frac{\widetilde{F}_{esy}\,\widetilde{c}_{vy}}{\widetilde{F}_{esx}} + \widetilde{c}_{ty}\right)s + \widetilde{k}_y\right] = 0 \end{aligned} \tag{15}$$

with further simplification, $\widetilde{c}_{ty1} = \dfrac{\widetilde{F}_{esy}\,\widetilde{c}_{vy}}{\widetilde{F}_{esx}} + \widetilde{c}_{ty}$

$$a_4 = \frac{1}{\widetilde{F}_{esx}} \qquad a_3 = \frac{\left(\widetilde{c}_{ty} + \widetilde{c}_{tx}\right)}{\widetilde{F}_{esx}}$$

$$a_2 = \frac{\left(\widetilde{k}_y + \widetilde{c}_{tx}\,\widetilde{c}_{ty} + \widetilde{c}_{dy}.\widetilde{c}_{vy} + (\widetilde{k}_x - \widetilde{F}_{esx})\right)}{\widetilde{F}_{esx}}$$

$$a_1 = \frac{\left(\widetilde{c}_{tx}\,\widetilde{k}_y - \widetilde{F}_{esy}\,\widetilde{c}_{vy} + (\widetilde{k}_x - \widetilde{F}_{esx})\widetilde{c}_{ty}\right)}{\widetilde{F}_{esx}}$$

$$a_0 = \frac{(\widetilde{k}_x - \widetilde{F}_{esx})\widetilde{k}_y}{\widetilde{F}_{esx}}$$

$$D(s)\Big/\widetilde{F}_{esx} = a_4 s^4 + a_3 s^3 + a_2 s^2 + a_1 s + a_0 + e^{-\pi d s}\left[s^2 + \widetilde{c}_{ty1}\, s + \widetilde{k}_y\right] = 0 \tag{16}$$

are obtained

$$e^{\pi d s} = \frac{-\left[s^2 + \widetilde{c}_{ty1}\, s + \widetilde{k}_y\right]}{a_4 s^4 + a_3 s^3 + a_2 s^2 + a_1 s + a_0} \tag{17}$$

$$U_1(s) = e^{\pi d s}$$

$$U_2(s) = \frac{-\left[s^2 + \widetilde{c}_{ty1}\, s + \widetilde{k}_y\right]}{a_4 s^4 + a_3 s^3 + a_2 s^2 + a_1 s + a_0}$$

According to the Nyquist criteria, the right side of this equation expresses Nyquist plane curve $U_2(s)$ and the left side expresses critical orbit $U_1(s)$. If $s = j\omega$ is taken in the equation, the roots of the characteristic Eq. (17) is found by equalizing the magnitude of the right side of the equation to 1,

$$\frac{\left|\left(\widetilde{k}_y - \omega^2\right) + j\,\widetilde{c}_{ty1}\omega\right|}{\left|\left(a_4\omega^4 - a_2\omega^2 + a_0\right) + j\left(a_1\omega - a_3\omega^3\right)\right|} = 1$$

$$\left(a_4\omega^4 - a_2\omega^2 + a_0\right)^2 + \left(a_1\omega - a_3\omega^3\right)^2 = \left(\widetilde{k}_y - \omega^2\right)^2 + \widetilde{c}_{ty1}{}^2\omega^2$$

$$a_4^2\omega^8 + \left(a_3^2 - 2a_4a_2\right)\omega^6 + \left(a_2^2 + 2a_4a_0 - 2a_3a_1 - 1\right)\omega^4 + \left(a_1^2 - \widetilde{c}_{ty1}{}^2 - 2a_2a_0 + 2\widetilde{k}_y\right)\omega^2 + a_0^2 - \widetilde{k}_y{}^2 = 0 \tag{18}$$

Thus, the positive real root of this equation gives the chatter frequency of the system.

III. STABILITY ANALYSIS

Two methods are used for the determination of stable areas for chatter-free spindle speed or the system of spindle/tool holder/cutting tool. The first method is the determination of the natural frequency of the system and mode shapes by measuring transfer functions by using an impact hammer and accelerometer. Analytical predictions of performance can be done by using this information. The second method is performed of cutting tests. The method gives the cutting ability of spindle/cutting tool in a better completeness, but requires a number of tests to be performed. The first analysis technique is based on the investigation of stability and plotting the Stability Lobe Diagram (SLD) from the solution of the characteristic equation of the system depending on the critical parameters such as axial cutting depth of the system and spindle speed. Analytic prediction is realized by iterative analytical solution of time changing force coefficient of mathematical model formed by applying it to the distribution of Fourier series. This analysis is made with the acceptance that the force process is linear according to feed and depth which doesn't depend clearly on cutting speed. Additionally, studies have been made recently to mount a sensor/actuator on the tool/tool holder system on the machine tool designed to suppress chatter vibration [10-12]. In the cutting process dealt with in this section, SLD, which give stable and unstable cutting regions for chatter-free cutting, will be drawn according to two different forms explained in the previous section depending on cutting depth and spindle speed. According to τ - decomposition form, the characteristic equation of the system is Eq. (16). The roots of this equation are obtained from the solution of Eq. (18). Each positive real root $(\omega_i(j\omega))$ is substituted back into the right side of Eq. (17) to find $U_2(j\omega_i)$. The phase angle of the resulting number is computed as follows;

$$\psi_i = \tan^{-1}\frac{\mathrm{Im}\left(U_2(j\omega_i)\right)}{\mathrm{Re}\left(U_2(j\omega_i)\right)} \tag{19}$$

and the value of time delay is found

$$\tau_i = \frac{\psi_i + 2\pi k}{\omega_i} \qquad \text{k=0,1,2,3,.....} \tag{20}$$

Depending on this, maximum spindle speed (n) to be gained in stable cutting is found,

$$\tau_i = \frac{\varepsilon + 2\pi k}{2\pi f_i} \quad \rightarrow \quad n = \frac{60}{\tau_i} \tag{21}$$

Where, (f_i) is frequency of the cutting tool (Hz); (ω_i) is the spindle speed (rd/s); $(\varepsilon/2\pi)$ the fractional number of waves formed on the surface. It can be seen here that there is a phase shift between the inner and outer waves $\varepsilon = 3\pi + 2\psi_i$. The critical axial depth of cut can be found by writing the reel part of the characteristic equation $\mathrm{Re}(\omega_i)$ to zero. Hence,

$$a_{\lim} = \frac{-1}{2K_f \,\mathrm{Re}(\omega_i)} \tag{22}$$

is calculated.

IV. ROUGHNESS FORMATION ON SURFACE

Surfaces of metals are actually rough, and asperities representing the roughness of the surface exist in surfaces of metals. Workpieces, dies and tools are characterised by surface roughness. Until all asperities are flattened, surface roughness has an influence on the friction properties of those surfaces, especially at the beginning of metal forming processes. During the forming process asperities plough into each other, and thus a small sliding always exists. At the beginning of the process, since the tool is in contact just with the peaks of the asperities, the friction properties depend on the distribution of asperities, on their height and their deformation during the process, e.g. on the roughness of the contact surface. With the flattening of asperities the contact with the tool gets larger and this leads to varying friction properties [13].



Figure 3: a) Chatter surface b) Smooth surface .

However, chatter vibrations are present in almost all cutting operations and they are major obstacles in achieving desired productivity. Regenerative chatter is the most detrimental to any process as it creates excessive vibration between the tool and the workpiece, resulting in a poor surface finish, high-pitch noise and accelerated tool wear which in turn reduces machine tool life, reliability and safety of the machining operation [14, 15]. When uncontrolled, chatter causes the rough surface end and dimensional inaccuracy of the workpiece, along with unacceptably loud noise levels and accelerated tool wear. In general, chatter is one of the most critical limiting factors, which is considered in designing a manufacturing process. The cutting force becomes periodically variable, reaching considerable amplitudes and the machined surface becomes undulated [16]. Grinding operation to reduce surface roughness often required. In this case, manufacturing cost is increased. Also, grinding operation can exceed dimensional tolerances of workpiece. Therefore, stable cutting is very important during chip removal.

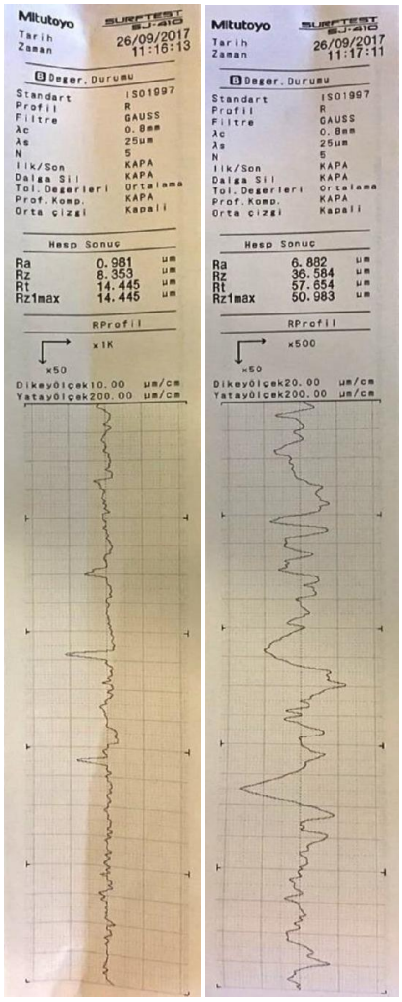


Figure 4: Surface roughness measurement results of chatter and smooth surfaces

V. CONCLUSION

Chatter vibrations are major difficulties in all machining processes. These vibrations results rough surfaces, accelerated tool wear and increased dynamic cutting loads. All of these difficulties causes reduced machine tool life, reliability and safety of the machining operation. It is possible to eliminate such negative effects by preventing chatter vibration. Chatter detection and chatter control techniques helps for the stable manufacturing. To control the chatter vibrations, it is necesarry to analyze the cutting tool, tool holder and workpiece according to their material properties. It is also important in terms of surface quality of machined parts, installation with other machine elements, friction, tightness, fatigue strength of machine parts over time. These important aspects are even more important in the space and air industry. In space and aerospace industry engine materials are made of Titanium alloyed Inconel materials and they are processed at low cutting speeds because chatter vibration is more occurred when they are machined in vertical axis machining centers. However, with chatter vibration analysis, these materials used in space and aeronautics can achieve stable cutting without vibrations and smoother surfaces and as much serial processing as possible.

REFERENCES

[1] Benardos, P.G., Vosniakos, G.C., Predicting surface roughness in machining: a review, International Journal of Machine Tools & Manufacture 43 (2003) 833–844.

[2] Landers, R.G., Ulsoy, A.G., Chatter analysis of machining systems with nonlinear force processes, ASME International Mechanical Engineering Congress and Exposition, Atlanta, Georgia, November 17-22 (1996) DSC Vol. 58, 183-190.

[3]] Tlusty, J., Manufacturing processes and equipment, Prentice Hall, New Jersey, 2000.

[4] Groover, M.P., Fundamentals of modern manufacturing:Materials, Processes, and Systems, Prentice Hall, New Jersey, 1996.

[5] Siddhpura, M., Paurobally, R., A review of chatter vibration research in turning, International Journal of Machine Tools & Manufacture 61 (2012) 27–47.

[6] Turkes, E., Orak, S., Neseli, S., Yaldiz, S., A new process damping model for chatter vibration, Measurement 44 (2011) 1342–1348.

[7] Bailey, J.A., Friction in metal machining-mechanical aspects, Wear 31 (1975) 243.

[8] Kim, J.S., Lee, B.H., An analytical model of dynamic cutting forces in chatter vibration, Int. J. Mach. Tool Des. Res. 31 (1991) 371.

[9] Wu, D.W., Liu, C.R., An analytical model of cutting dynamics, part 1:Model building, J. Eng. Ind. Trans. ASME 107 (1985) 107.

[10] Turkes, E., Orak, S., Neseli, S., Yaldiz, S., Linear analysis of chatter vibration and stability for orthogonal cutting in turning, Int. Journal of Refractory Metals and Hard Materials 29 (2011) 163-169.

[11] Budak, E., An analytical design method for milling cutters with nonconstant pitch to increase stability Part I: theory. J Manuf Sci Eng Trans ASME 2003;125:29–34.

[12] Budak, E., An analytical design method for milling cutters with nonconstant pitch to increase stability Part II: application, J Manuf Sci Eng Trans ASME 2003;125:35–8.

[13] Sahin, M., Çetinarslan, C.S., Akata, H.E., Effect of surface roughness on friction coefficients during upsetting processes for different materials, Materials and Design 28 (2007) 633–640

[14] Zhu D, Zhang X, Ding H. Tool wear characteristics in machining of nickelbased superalloys. International Journal of Machine Tools and Manufacture 2013; 64: 60-77.

[15] Courbon C, Pusavec F, Dumont F, Rech J, Kopac J. Tribological behaviour of Ti6Al4V and Inconel718 under dry and cryogenic conditions— Application to the context of machining with carbide tools.Tribology International 2013; 66: 72-82

[16] Pusavec F, Hamdi H, Kopac J, Jawahir I S. Surface integrity in cryogenic machining of nickel based alloy—Inconel 718. Journal of Materials Processing Technology 2011; 211(4): 773-783.

Investigation of Torrefaction Process Condition According to Characterization and Process Yield for Poultry Litter

O. KUTLU[1] and G. KOCAR[1]

[1] Ege University, Izmir/Turkey, kutluozben@gmail.com
[1]EgeUniversity, Izmir/Turkey, gunnur.kocar@ege.edu.tr

***Abstract* – The characteristic of biochar deeply depends on the properties of feedstock and operating parameters, such as lignocellulosic structure, temperature, residence time etc. The feedstock and parameters also affect the process yield. The aim of this study was to investigate the influence of parameters on poultry litter-based biochar characteristic and process yield statistically, besides the determination of optimum process condition for torrefaction. The relationship between three operating parameters (temperature, residence time, and bulk density) and three responses (energy yield, mass loss and H/C ratio of biochar) was individually investigated by analysis of variance (ANOVA). Moreover, the operating parameters were optimized with analyzing of the responses included also the increase in carbon content. As a result, the optimum conditions for torrefaction of poultry litter were determined to be at temperature of 300°C, a residence time of 60 minutes, and a bulk density of 200 kg/m^3. Although the effects of temperature and bulk density taken more attention than that of residence time for energy yield and H/C ratio, the effect of residence time on the mass loss was obtained significantly higher than other parameters. If the shorter time is preferred for process, the increase in bulk density would be recommended.**

***Keywords* – Torrefaction, biochar, poultry litter, biomass, ANOVA.**

I. Introduction

The residual of poultry litter is rising in parallel with increase in number of poultry farming for Turkey [1], and that waste causes environmental problems due to difficulties in disposal of waste. Nowadays, the poultry litter is used as manure after keep waiting in the field at a certain time (composting) [1]. It can be also used as fuel in the firing systems however the efficiency of combustion is significantly reduced due to the changeable and higher moisture content of litter (about 25%) than other fuels [2]. The decrease in combustion yield is also shown by co-firing of other biomass with coal [3]. For this reason, torrefaction can be a key technology to increase the combustion yield of co-firing systems [4, 5]. Torrefaction is a pre-treatment process like a slow pyrolysis which can improve biomass properties. It is carried out at low temperature range of 200–300°C in inert atmosphere to produce solid biofuels [6-9]. At the end of torrefaction, the produced solid biofuels is named biochar that has higher calorific value, more grindability and less moisture content. In some study about the dry animal wastes, variable thermal processes at higher temperature than 350°C has especially been selected for production of active carbon [10-15]. On the other hand, the poultry litter has also been converted to biochar in variable thermal processes at temperature range of 150–350°C in different residence time between 30 and 480min [16, 17]. The effects of biochar on soil properties (e.g. electrical conductivity, pH) and sorption capacity of biochar is other investigation topics [18-22]. Moreover, the analysis of variance has generally been performed in the thermal processes for different biomass source to test the significant effect of the factors and their interaction effects. While temperature, residence time, flow rate, concentration of oxidizing agent, particle size etc. have been selected as independent variables, stable organic matter, biochar or liquid yield, pH or sorption ability etc. have been optimized as responses [23-28]. In this study, the main objective was to optimize the operating condition for torrefaction of poultry litter. Three independent operating parameters, i.e. temperature, residence time and bulk density, were selected and the influence on biochar characteristics and process yields was assessed by analysis of variance (ANOVA). The characterization of biochar was analyzed by the increase in carbon content, and H/C atomic ratio which is important chemical response for utilization of biochar as fuel and soil amendment. On the other hand, the torrefaction process was evaluated by energy yield and mass loss. In the assessment, the equilibrium between high biochar quality and high process yield was taken into account.

II. Material and Method

The poultry litter as a feedstock was provided by a broiler farm in Izmir/Turkey. The characterization of feedstock is listed in Table 1. About 200g of dried feedstock was torrefied at different temperature in a stainless steel 6.5 L batch horizontal reactor under inert atmosphere at a heating rate of 5°Cmin^{-1}. During torrefaction, biochar was formed within the reactor, and volatile products were passed through gas-washing bottles cooled with ice for separating the liquid product from gas. At the end of torrefaction, the reactor was

cooled with nitrogen gas stream to keep stable moisture content of biochar, and it was finally weighted to calculate mass loss and energy yield. The bulk density as an operating parameter was calculated by filling into the graduated reactor and weighting the mass.

For the analysis of samples, the produced biochar were finely ground less than 250 μm in a knife mill then dried at 105 °C until the mass is constant. According to EN 15414-3 standard procedure, moisture content of poultry litter was analyzed. Ultimate analysis of feedstock and biochar samples were carried out using elemental analyzer (Leco Truspec CHN-S, USA), and so H/C atomic ratio of biochar was determined by using results. Higher heating value (HHV) indicates the calorific value of fuel and it was analyzed by using bomb calorimeter (Parr 6300, USA) for calculation of energy yield.

Table 1: Characterization of poultry litter used

Moisture (%)	9.5
Carbon (%)	42.8
Hydrogen (%)	5.3
Nitrogen (%)	3.5
Sulphur (%)	0.9
H/C atomic ratio (-)	1.49
HHV (kcal/kg)	3849.4

All results were evaluated in dry basis, and energy yield is written as:

$$\text{Energy yield}\% = \left(\frac{m_{biochar} * HHV_{biochar}}{m_{poultry\ litter} * HHV_{poultry\ litter}} \right)_{dry} * 100 \quad (1)$$

where m and HHV represent the mass and calorific value, respectively. The mass loss and increase in carbon content (ICC) are expressed by following relationship, respectively:

$$\text{Mass loss}\% = \left(\frac{m_{poultry\ litter} - m_{biochar}}{m_{poultry\ litter}} \right)_{dry} * 100 \quad (2)$$

$$\text{ICC}(\%) = \frac{C_{poultry\ litter}(\%) - C_{biochar}(\%)}{C_{poultry\ litter}(\%)} * 100 \quad (3)$$

where C is carbon content of biochar or poultry litter.

In ANOVA analysis tested at 95% confidence interval, the independent operating parameters were selected as temperature, residence time and bulk density. The effect of these parameters on three responses, which were defined as energy yield, mass loss and H/C ratio, was investigated. As listed in Table 2, the poultry litter that had bulk density of 200, 250 and 300 kg/m^3 was torrefied at the temperature range of 280°C–310°C between 30 minute and 60 minute. Effect of each parameter was analyzed in the experimental set individually while other parameters were constant. For analyzing the temperature effect, the processes were kept constant at a bulk density of 250 kg/m^3 in 60 min. The effect of bulk density was analyzed by the processes at constant temperature of 300°C in 60 min. Moreover, the processes at variable residence time were carried out with feedstock had stable bulk density of 300 kg/m^3 at same constant temperature. Three repetitions were processed for each experiment, and ICC of biochar besides three responses was also taken into account for optimizing the process conditions.

Table 2: Experimental sets according to independent operating parameters and the results of responses

	Operating Parameters			**Characterization**		**Proses Yields**	
Exp. No	**Temperature (°C)**	**Residence time (min)**	**Bulk density (kg/m^3)**	**H/C ratio (-)**	**ICC (%)**	**Mass loss (%)**	**Energy yield (%)**
1	280	60	250	1.20	31.32	37.58	81.95
2	290	60	250	1.09	33.76	38.77	83.71
3	300	60	250	0.87	47.83	39.12	85.88
4	310	60	250	0.83	48.24	41.27	81.03
5	300	40	200	0.85	43.26	42.01	81.76
6	300	60	200	0.81	46.90	42.31	82.50
7	300	60	250	0.86	47.86	38.99	87.29
8	300	60	300	0.75	52.86	44.84	81.07
9	300	40	300	0.80	47.87	44.66	79.78
10	300	30	300	0.84	44.08	40.19	84.65

III. RESULTS AND DISCUSSION

In this study, energy yield and mass loss were indicated as process yield of torrefaction and the characterization of biochar was also specified with ICC and H/C atomic ratio. As shown in Table 2, three independent parameter were improved the process yield and characterization at variable rates. For this reason, the results were assessed and discussed individually.

A. Effects of parameters on mass loss

The minimum mass loss is preferred at the end of torrefaction for obtaining more biochar by weight. As shown in Table 2 the increase in temperature and residence time increased the mass loss due to devolatilization, however the linear change in mass loss was not observed by increment of bulk density in comparison with other parameters. According to analysis of variance, p-values were smaller than 0.05 and so it was found that the experimental models were significant for

each independent parameter (Table 3). The fitted model also represented the experimental data well with high correlation coefficients, R squared, 0.94 and 0.99. It can also be remarked depending on F-value that the highest effect on mass loss was observed by changing in residence time. On the other hand, the rate of change in mass loss by temperature difference of 30°C was calculated as about 10% and minimum mass loss was observed in the process carried out at 280°C by the bulk density of 250kg/m^3.

Table 3: ANOVA table for the effect on mass loss

Summary of Temperature						
Groups	***Repetition***	***Total***	***Average***	***Variance***		
Cond. 1	3	112.74	37.58	0.2844		
Cond. 2	3	116.31	38.77	0.1891		
Cond. 3	3	117.36	39.12	0.0169		
Cond. 4	3	123.81	41.27	0.2107		
	SS	***df***	***MS***	***F-value***	***p-value***	***R²***
Treatment	21.30	3	7.10	40.51	< 0.0001	0.94
Residual	1.40	8	0.18		***	
Total	22.70	11				
Summary of Bulk Density						
Groups	***Repetition***	***Total***	***Average***	***Variance***		
Cond. 1	3	126.93	42.31	0.1609		
Cond. 2	3	116.97	38.99	1.3636		
Cond. 3	3	134.51	44.84	0.0025		
	SS	***df***	***MS***	***F-value***	***p-value***	***R²***
Treatment	51.59	2	25.79	50.68	0.0002	0.94
Residual	3.05	6	0.51		***	
Total	54.64	8				
Summary of Residence Time						
Groups	***Repetition***	***Total***	***Average***	***Variance***		
Cond. 1	3	120.57	40.19	0.1417		
Cond. 2	3	133.98	44.66	0.0001		
Cond. 3	3	134.51	44.84	0.0025		
	SS	***df***	***MS***	***F-value***	***p-value***	***R²***
Treatment	41.60	2	20.80	432.37	< 0.0001	0.99
Residual	0.29	6	0.05		***	
Total	41.89	8				

B. Effects on energy yield

In production process, the higher energy yield is preferred for using biochar as fuel, and minimum energy yield of 70% is observed at the end of torrefaction [29]. The calculated energy yields were higher than this situation as shown in Table 2. The experimental models were also significant according to p-value and R squared in ANOVA analysis (Table 4). If F-values were assessed, the important parameter was able to be selected as temperature, and it was found that the bulk density was also able to affect the energy yield as much as the temperature. The change in energy yield by changing temperature and bulk density was calculated as 6% and 8%, respectively. On the other hand the energy yield was also changed at a rate of 4% with respect to residence time. Maximum energy yield was observed in the process carried out at 300°C in 60 min. by the bulk density of 250kg/m^3.

Table 4: ANOVA table for the effect on energy yield

Summary of Temperature						
Groups	***Repetition***	***Total***	***Average***	***Variance***		
Cond. 1	3	245.84	81.95	0.2972		
Cond. 2	3	251.14	83.71	0.5757		
Cond. 3	3	257.64	85.88	0.2279		
Cond. 4	3	243.08	81.03	0.6974		
	SS	***df***	***MS***	***F-value***	***p-value***	***R²***
Treatment	41.17	3	13.72	30.53	< 0.0001	0.92
Residual	3.60	8	0.45		***	
Total	44.77	11				
Summary of Bulk Density						
Groups	***Repetition***	***Total***	***Average***	***Variance***		
Cond. 1	3	247.50	82.50	0.0722		
Cond. 2	3	261.86	87.29	2.4194		
Cond. 3	3	243.21	81.07	1.0721		
	SS	***df***	***MS***	***F-value***	***p-value***	***R²***
Treatment	63.59	2	31.80	26.77	0.0010	0.90
Residual	7.13	6	1.19		**	
Total	70.72	8				
Summary of Residence Time						
Groups	***Repetition***	***Total***	***Average***	***Variance***		
Cond. 1	3	253.95	84.65	3.33		
Cond. 2	3	239.36	79.79	0.51		
Cond. 3	3	243.21	81.07	1.32		
	SS	***df***	***MS***	***F-value***	***p-value***	***R²***
Treatment	38.15	2	19.08	11.08	0.0097	0.79
Residual	10.33	6	1.72		**	
Total	48.48	8				

C. Effects on H/C atomic ratio

H/C atomic ratio can be described as the characterization of biochar, and this response is evaluated for selection of application area of biochar which can be both a fuel and soil amendment. The decrease in H/C ratio is expected at the end of torrefaction due to break hydrogen bond. If the calculated atomic ratio of biochar were investigated according to soil amendment standards setting by European Biochar Foundation (EBF) and International Biochar Initiative (IBI), H/C ratio was found slightly greater than upper limit of 0.7 (Table 2). On the other hand, the compatible results were obtained in previous studies [15, 30].

The experimental model was significant like other responses as shown in Table 5, and R squared was included in acceptable limits of statistical analysis [25, 26]. The effects of parameters on H/C ratio were similar with the effects on energy yield, and the influencing factors were found as temperature and bulk density according to F-value. In addition, H/C ratio was decreasing with increasing all independent parameters. The maximum rate of change in atomic ratio was obtained by temperature and calculated as 31%. Minimum H/C ratio was provided by the process proceeding at 300°C in 60 min by using a bulk density of 300 kg/m^3. This characterization result was observed better than previous process carried out at 400°C in 15 min and reported Azargohar et al. [15].

Table 5: ANOVA table for the effect on H/C atomic ratio

Summary of Temperature						
Groups	***Repetition***	***Total***	***Average***	***Variance***		
Cond. 1	3	3.59	1.20	0.0006		
Cond. 2	3	3.26	1.09	0.0007		
Cond. 3	3	2.61	0.87	0.0008		
Cond. 4	3	2.50	0.83	0.0044		
	SS	***df***	***MS***	***F-value***	***p-value***	***R^2***
Treatment	0.27	3	0.0905	56.72	< 0.0001	0.96
Residual	0.01	8	0.0016		***	
Total	0.28	11				
Summary of Bulk Density						
Groups	***Repetition***	***Total***	***Average***	***Variance***		
Cond. 1	3	2.42	0.81	0.0002		
Cond. 2	3	2.58	0.86	0.0000		
Cond. 3	3	2.25	0.75	0.0002		
	SS	***df***	***MS***	***F-value***	***p-value***	***R^2***
Treatment	0.0181	2	0.0091	56.45	0.0001	0.95
Residual	0.0010	6	0.0002		***	
Total	0.0191	8				
Summary of Residence Time						
Groups	***Repetition***	***Total***	***Average***	***Variance***		
Cond. 1	3	2.51	0.84	0.0009		
Cond. 2	3	2.39	0.80	0.0001		
Cond. 3	3	2.25	0.75	0.0002		
	SS	***df***	***MS***	***F-value***	***p-value***	***R^2***
Treatment	0.0115	2	0.0057	14.31	0.0052	0.83
Residual	0.0024	6	0.0004		**	
Total	0.0139	8				

D. Assessment of optimum process condition

After individually effect analysis, the experiments were generally assessed by three responses to optimize process conditions. The summary of best results in experimental sets was listed in Table 6. If the experimental set which proceeded by variable temperature was investigated, the maximum energy yield was observed at exp. no 3 and 7, that carried out at 300°C. In addition, H/C ratio of biochar obtained by exp. no 3 was decreased by changing bulk density, and thus the lowest H/C ratio was obtained by the bulk density of 300 kg/m^3 (exp. no 8). The biochar that has lower H/C ratio than 1, has similar characteristics with lignite and coal as shown in Figure 1. Van-Krevelen diagram was created by the results of different studies [8, 31-37], and the comparison of biochar with other results and fuels was clearly observed. At this point, whole biochar produced was able to be classified as lignite in Turkey, and so the mass loss becomes more important responses after characterization for optimization. The mass loss observed by exp. no 8 (44.84%) was greater than other results and it was not significantly affected by residence time from 60 to 40 min at variable bulk density depending on exp. no 5, 6, 8 and 9. The change in energy yield ($1 - 1.5\%$) was also similar with that of mass loss. Furthermore, it was found that the characterization of biochar worsened at a rate of $5 - 9.4\%$ in consequence of decrease in residence time from 60 to 40 min. Although the minimum mass loss was obtained by the residence time of 30 min (exp. no 10), the equilibrium point between the results of H/C ratio and mass loss was found at exp. no 6 which carried out at 300°C in 60 min by a bulk density of 200 kg/m^3. ICC was also optimized in parallel with H/C ratio according to equilibrium point. In selected process, ICC was reached at average value of ICC of optimal results, and it was calculated as about 47%.

Table 6: Optimal results and process conditions

Exp. No	Temperature (°C)	Residence time (minute)	Bulk density (kg/m^3)	Energy Yield (%)	Mass Loss (%)	H/C ratio (-)	ICC (%)
3	300	60	250	85.88	39.12	0.87	47.83
7	300	60	250	87.29	38.99	0.86	47.86
8	300	60	300	81.07	44.84	0.75	52.86
9	300	40	300	79.78	44.66	0.80	47.87
10	300	30	300	84.65	40.19	0.84	44.08
6	300	60	200	82.50	42.31	0.81	46.90
5	300	40	200	81.76	42.01	0.85	43.26

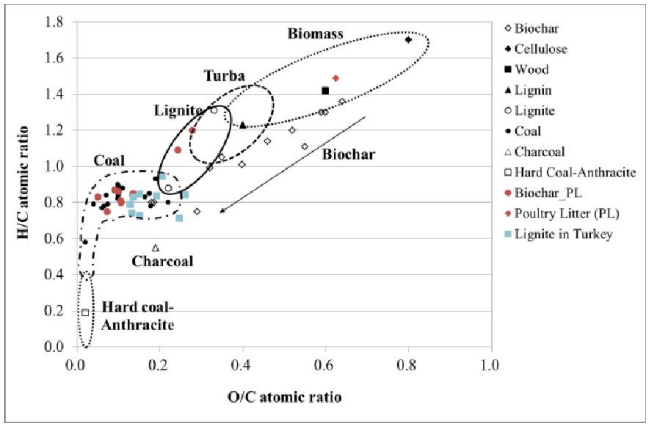


Figure 1: The comparison of biochar produced from optimal process conditions with other fuels according to Van Krevelen diagram

IV. CONCLUSION

The aims of this study were to evaluate the effect of parameters on characterization and process yield, and to optimize the process condition of torrefaction of poultry litter. While the temperature, residence time, and bulk density were selected as operating parameters, energy yield, mass loss and H/C ratio were optimized as responses. Although three parameters affected the responses, the effects of temperature and bulk density taken more attention than that of residence time for energy yield and H/C ratio. Moreover, it was found that the effect of residence time on the mass loss was obtained significantly higher than other parameters. During optimization of parameter for torrefaction of poultry litter, equilibrium

between characterization of biochar and process yields was investigated. As a result of the process which carried out at 300°C in 60 min by a bulk density of 200 kg/m^3, the optimal characteristic of biochar and process yields were obtained.

REFERENCES

[1] S. Şahin ve N. Altunal, "Etlik Piliç Sışkılarının gübre olarak değerlendirilmesi ve önemi" *Veteriner Tavukçuluk Derneği* Cilt:6 Sayı:3, 6-7, 2008.

[2] TÜBİTAK-MAM, "Kümes ve Ahır Gübrelerinin Geri Kazanılması ve Bertarafı Projesi", Başlangıç Raporu, Mayıs 2001.

[3] H. Olgun, B. Keivani, Ö. Ersöz ve G. Koçar, "Biyokömürün termokimyasal enerji dönüştürme sistemlerinde kullanılması" *Enerji Tarımı ve Biyoyakıtlar 4. Ulusal Çalıştayı*, Samsun, 257-269, 28-29 Mayıs 2014.

[4] BE Solvay, Torrefied wood pellets, http://solvaybiomassenergy.com/our-products/torrefied-wood-pellets/. Date accessed: April 2016.

[5] J. Koppejan, K. Schaubach, J. Witt and D. Thran, Torrefaction Technology and Strategy Report, SECTOR, Production of Solid Sustainable Energy Carriers from Biomass by Means of Torrefaction, 2015.

[6] P.C.A. Bergman, A.R. Boersma, R.W.R. Zwart, and J.H.A. Kiel, "Torrefaction for biomass co-firing in existing coal-fired power stations "biocoal" ", The Netherlands: ECN, Petten, Report ECN-C-05-013, 2005.

[7] S. Sadaka and S. Negi, "Improvements of Biomass Physical and Thermochemical Characteristics via Torrefaction Process", *Environmental Progress & Sustainable Energy*, 28: 427-434, 2009

[8] M.J.C. van der Stelt, H. Gerhauser, J.H.A. Kiel, and KJ. Ptasinski, "Biomass upgrading by torrefaction for the production of biofuels: A review", *Biomass & Bioenergy*, 35: pp. 3748–3762, 2011.

[9] P. Basu, Biomass Gasification, Pyrolysis and Torrefaction Practical Design and Theory, USA: Elsevier, 2013.

[10] I.M. Lima and W.E. Marshall, "Granular activated carbons from broiler manure: physical, chemical and adsorptive properties", *Bioresour. Technol.* 96, 699–706, 2005

[11] I.M. Lima and W.E. Marshall, "Adsorption of selected environmentally important metals by poultry manure - based granular activated carbons" *J. Chem. Technol. Biotechnol.* 80, 1054–1061, 2005.

[12] A. Sarabèr, "Co-combustion and its impact on fly ash quality; pilot-scale experiments", *Fuel Processing Technology* 104, 105–114, 2012.

[13] S.V. Vassilev, D. Baxter and C.G. Vassileva, "An overview of the behaviour of biomass during combustion: Part II. Ash fusion and ash formation mechanisms of biomass types", *Fuel* 117, 152–183, 2014.

[14] P. Joseph, S. Tretsiakova-McNally, S. McKenna, "Characterization of cellulosic wastes and gasification products from chicken farms", *Waste Management* 32, 701–709, 2012.

[15] R. Azargohar, K.L. Jacobson, E.E. Powell, A.K. Dalai, "Evaluation of properties of fast pyrolysis products obtained, from Canadian waste biomass", *Journal of Analytical and Applied Pyrolysis* 104, 330–340, 2013.

[16] B.M. Ghanim, D.S. Pandey, W. Kwapinski, and J.J. Leahy, "Hydrothermal carbonisation of poultry litter: Effects of treatment temperature and residence time on yields and chemical properties of hydrochars", *Bioresource Technology*, Vol. 216, pp. 373–380, 2016.

[17] A.T. Tag, G. Duman, S. Ucar, and J. Yanik, "Effects of feedstock type and pyrolysis temperature on potential applications of biochar", *Journal of Analytical and Applied Pyrolysis*, Vol. 120, pp. 200–206, 2016.

[18] X. Cao and W. Harris, "Properties of dairy-manure-derived biochar pertinent to its potential use in remediation" *Bioresource Technology* 101, 5222–5228, 2010.

[19] J. Gaskin, C. Steiner, K. Harris, K. Das and B. Bibens, "Effect of low temperature pyrolysis conditions on biochar for agricultural use", *Trans. ASABE* 51, 2061–2069, 2008.

[20] K. Chan, L. Van Zwieten, I. Meszaros, A. Downie and S. Joseph, "Using poultry litter biochars as soil amendments" *Aust. J. Soil Res.* 46, 437–444, 2008.

[21] K.B. Cantrell, P.G. Hunt, M. Uchimiya, J.M. Novak and K.S. Ro, "Impact of pyrolysis temperature and manure source on physicochemical characteristics of biochar" *Bioresource Technology* 107, 419–428, 2012.

[22] K.C. Das, M. Garcia-perez, B. Bibens and N. Melear, N. "Slow pyrolysis of poultry litter and pine woody biomass: Impact of chars and bio-oils on microbial growth", Jour*nal of Environmental Science and Health, Part A: Toxic/Hazardous Substances and Environmental Engineering*, 43:7, 714-724, 2008.

[23] R. Wang and Z. Xu, "Pyrolysis characteristics and pyrolysis products separation for recycling organic materials from waste liquid crystal display panels", *Journal of Hazardous Materials* 302, 45–56, 2016.

[24] V. Frišták, W. Friesl-Hanl, A. Wawra, M. Pipíška and G. Soja, "Effect of biochar artificial ageing on Cd and Cu sorption characteristics", *Journal of Geochemical Exploration* 159, 178–184, 2015.

[25] A. Kazan, M.S. Celiktas, S. Sargin and O. Yesil-Celiktas, "Bio-based fractions by hydrothermal treatment of olive pomace: Process optimization and evaluation", *Energy Conversion and Management* 103, 366–373, 2015.

[26] O.D. Mante and F.A. Agblevor, "Parametric study on the pyrolysis of manure and wood shavings", *Biomass and Bioenergy* 35, 4417-4425, 2011.

[27] S. Wang, B. Gao, A.R. Zimmerman, Y. Li, L. Ma, W.G. Harris and K.W. Migliaccio, "Physicochemical and sorptive properties of biochars derived from woody and herbaceous biomass", *Chemosphere* 134, 257–262, 2015.

[28] K. Anupam, V. Swaroop, Deepika, P.S. Lal and V Bist, "Turning Leucaena leucocephala bark to biochar for soil application via statistical modelling and optimization technique", *Ecological Engineering* 82, 26–39, 2015.

[29] D.R. Nhuchhen, P. Basu, and B. Acharya, "A comprehensive review on biomass torrefaction". *International Journal of Renewable Energy and Biofuels*, Vol.2014, 56 pages, 2014.

[30] A. Toptas, Y. Yildirim, G. Duman, and J. Yanik, "Combustion behavior of different kinds of torrefied biomass and their blends with lignite", *Bioresource Technology*, 177: pp. 328-336, 2015.

[31] R. Pentananunt, A. Rahman, and S.C. Bhattacharya, "Upgrading of biomass by means of torrefaction", *Energy*, 15: pp. 1175-1179, 1990.

[32] J.M. Novak, W.J. Busscher, D.L. Laird, M. Ahmedna, D.W. Watts, and M.A.S. Niandou, "Impact of biochar amendment on fertility of a southeastern coastal plain soil". *Soil Science*, 174: pp.105-112, 2009.

[33] B.T. Nguyen and J. Lehmann, "Black carbon decomposition under varying water regimes", *Organic Geochemistry*, 40: pp. 846-853, 2009.

[34] B.T. Nguyen, J. Lehmann, W.C. Hockaday, S. Joseph and C.A. Masiello, "Temperature sensitivity of black carbon decomposition and oxidation". *Environmental Science & Technology*, 44: pp. 3324-3331, 2010.

[35] K.A. Spokas, J.M. Novak, C.E. Stewart, K.B. Cantrell, M. Uchimiya, M.G. DuSaire, and K.S. Ro, "Qualitative analysis of volatile organic compounds on biochar", *Chemosphere*, 85: pp. 869-882, 2011.

[36] J. Lehmann, M.C. Rillig, J. Thies, C.A. Masiello, W.C. Hockaday and D. Crowley, "Biochar effects on soil biota - A review", *Soil Biology & Biochemistry*, 43: pp.1812-1836, 2011.

[37] T. Mimmo, P. Panzacchi, M. Baratieri, C.A. Davie, and G. Tonon, "Effect of pyrolysis temperature on miscanthus (Miscanthus x giganteus) biochar physical, chemical and functional properties", *Biomass & Bioenergy*, 62: pp. 149-157, 2014.

Assessment of Energy Consumption in Turkey

S. YEREL KANDEMİR[1], A. E. ÇERÇEVİK[1], H. ANKARA[2]

[1] Bilecik Seyh Edebali University, Bilecik/Turkey, erdem.cercevik@bilecik.edu.tr
[1] Bilecik Seyh Edebali University, Bilecik/Turkey, syerel@gmail.com
[2] Eskisehir Osmangazi University, Eskisehir/Turkey, hankara@ogu.edu.tr

Abstract **- Since Turkey is a developing country with a huge economic growth, its energy demand is also increased. Fossil fuel energy consumptions includes the use of coal, oil products and natural gas. In this paper, the annual fossil fuel energy consumptions in Turkey were examined by using the multidimensional scaling analysis technique. The analysis results present that the 1994, 2002 and 2015 are the most significant years causing difference in the annual fossil fuel consumption. These analysis show that the use of fossil fuels is increasing in 2015. Thus, this paper shows the usefulness of multidimensional scaling analysis technique for help in decision makers in energy management.**

Keywords **- Energy, Turkey, Fossil Fuel, Multidimensional Scaling Analysis.**

I. INTRODUCTION

ENERGY is one of the factors regarding the guarantee of economic development of a country. The developing countries effort to obtain energy sources reliable in the long term to complete their economic development [1]. As Turkey's economy is growing, the primary energy consumption has dramatically increased. But Turkey's primary energy resources seem limited [2-3].

In this study, multidimensional scaling analysis techniques were used to interpret annual fossil fuel consumption in Turkey. The objectives of the paper were:

- to determine similarities or dissimilarities of the annual fossil fuel consumption using multidimensional scaling analysis technique;
- to present the usefulness of the multidimensional scaling analysis technique to analysis the energy consumption.

II. MATERIAL AND METHOD

A. Dataset

Annual fossil fuel consumption parameters were used in this study. The parameters of twenty two years were obtained from International Energy Agency. The selected parameters are; coal, oil products and natural gas. The annual fossil fuel consumption parameters were investigated by using the multidimensional scaling analysis technique.

The case processing summary and procedure options (data options and model options) generated by the multidimensional scaling analysis is given below (Table 1-2.)

Table 1. Case Processing Summary

Cases					
Valid		**Missing**		**Total**	
N	Percent	N	Percent	N	Percent
0	100%	0	0%	3	100%

Table 2. Procedure Options

Data options	
Number of rows	22
Number of columns	22
Number of matrices	1
Measurement level	Ordinal
Data matrix shape	Symmetric
Type	Dissimilarity
Model Options	
Model	Euclid
Max. Dimensionality	2
Min. Dimensionality	2
Negative Weights	Not permitted

B. Multidimensional Scaling Analysis Technique

A multidimensional scaling analysis technique is a very important analysis technique for solving problems [4]. The aim of the technique is to present the observed structure of the interpoint distance in the final configuration as well as possible [5-7].

The dissimilarities are determined through the Euclidean distance measurements. Euclidean distance (d_{ij}) equation is given below.

$$d_{ij}^2 = \sum_{k=1}^{m} \left(z_{ik} - z_{jk} \right)^2$$

where z_{ik} and z_{jk} are the values of variable k for i and j, respectively and m is the number of variables [8,6].

III. RESULT AND DISCUSSION

The important problem in case of annual energy consumption is the complexity associated with analyzing. In this paper, the annual energy consumption parameters such as coal, oil products and natural gas were analyzed by using the multidimensional scaling analysis technique. Analysis results show that the determinate similarities or dissimilarities among the annual energy consumption.

The scaled each data set, with increasing dimensionality, using the ALSCAL scaling algorithm. This algorithm minimizes a stress function called Kruskal's S-Stress (specifically, the Takane-Young-de Leeuw formula) [9]. This paper, Young's S-stress formula 1 is used and conclusion is given Table 3.

Table 3. S-stress table

Iteration	S-Stress	Improvement
1	0.01149	
2	0.01006	0.00143
3	0.0063	0.0043

The multidimensional scaling analysis Dimensions (Dimension 1 and Dimension 2) is presented in Table 4 and Figure 1.

Table 4. Dimension values of years

No	Year	Dimension 1	Dimension 2
1	1994	2.0780	0.3496
2	1995	1.6912	0.3832
3	1996	1.4153	0.2300
4	1997	1.2751	-0.0068
5	1998	1.3143	-0.0699
6	1999	1.4325	0.2378
7	2000	0.9864	-0.3143
8	2001	1.3105	0.3156
9	2002	0.9129	-0.0541
10	2003	0.5534	-0.2532
11	2004	0.3391	-0.2824
12	2005	0.0763	-0.844
13	2006	-0.6002	-0.2534
14	2007	-0.9674	-0.4314
15	2008	-0.7140	-0.2887
16	2009	-0.4383	-0.2786
17	2010	-0.8477	0.4564
18	2011	-1.5831	-0.1871
19	2012	-1.9364	-0.4985
20	2013	-1.9037	0.4764
21	2014	-1.8746	0.5563
22	2015	-2.5195	0.9104

The dissimilarities among the annual fossil fuel consumption parameters including coal, oil products and natural gas were assessed according to Dimension-1 and Dimension-2 (Table 4).

Table 1 and Figure 1 showed that the 2015 and 1994 are the least similar annual energy consumption according to the Dimension-1. Similarly, 2015 and 2012 are the most dissimilar years according to Dimension-2.

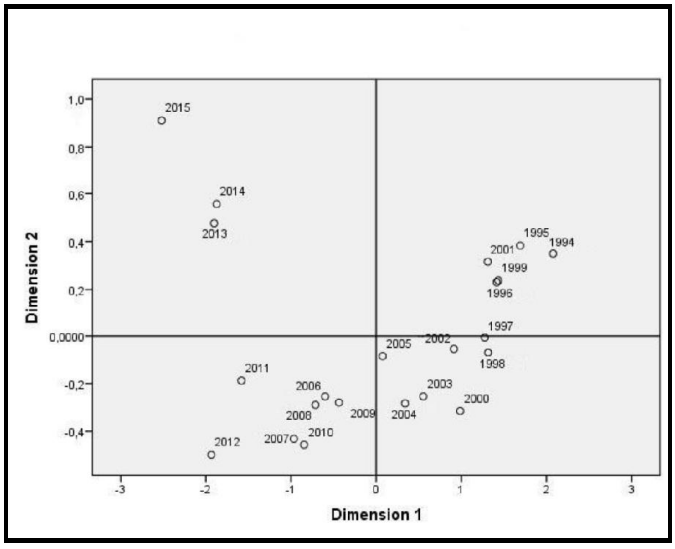


Figure 1. The analysis plot for the years

The annual energy consumption parameters including coal, oil products and natural gas causing dissimilarity between 2015 and 1994 was presented by Figure 2. Figure presented the coal, oil products and natural gas consumption have increased considerably in 2015.

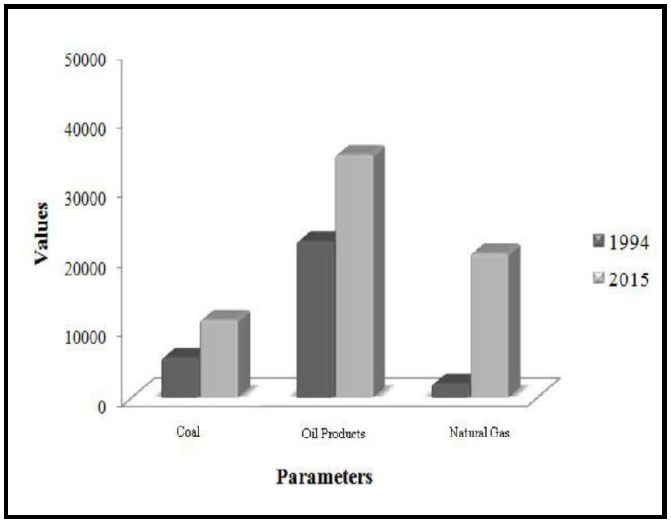


Figure 2. Comparison of Y1994 and Y2015

The annual fossil fuel consumption parameters causing dissimilarity according to Dimension-2 presented by Figure 3.

The figure 3 presented that the 2012 and 2015 causing differences. Thus, It was determined that, Figures 2-3 was supported by the technique.

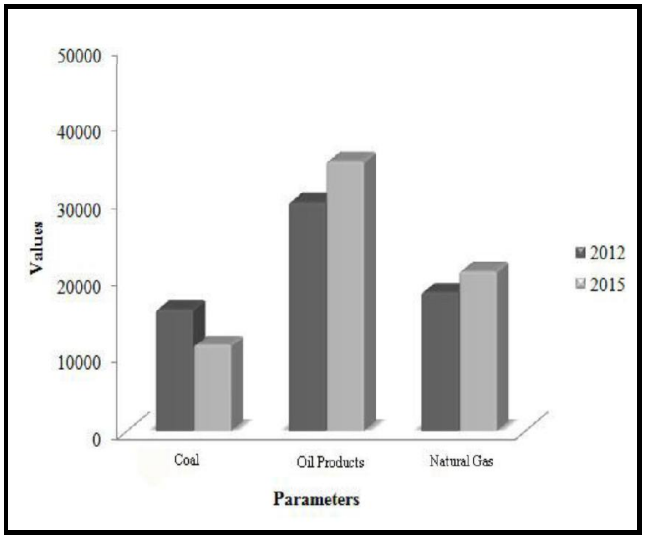


Figure 3. Comparison of Y2012 and Y2015

IV. CONCLUSION

Multidimensional scaling technique can be used to obtain information about complex data set. In this paper, the annual energy consumption parameters were examined by using the analysis technique. The technique was used to classify annual fossil energy consumption with dissimilarities in Turkey. According to the results of the analysis, the annual energy consumption was different in 1994, 2012 and 2015. Finally, this paper presents that the usefulness of multidimensional scaling analysis technique in annual energy consumption investigation.

REFERENCES

[1] Yerel Kandemir, S., Assessment of coal deposit using multivariate statistical analysis techniques, Energy Sources Part A: Recovery, Utilization and Environmental Effects, Vol. 38, No 7, 2001-1006, 2003.

[2] Turkish Petroleum Corporation (TPC), 2002, *Energy in Turkey*. Ankara, Turkey: Ajans-Turk Basin and Basim Co.

[3] Brinkster Communication Corporations (BCC), 2003, *Summary report of Turkish energy sector*.

[4] Borg I and Groenen P, Modern multidimensional scaling theory and applications; Springer New York, 1997, 472.

[5] Evtimov S and Ivanov M.,2007, Intraannual dissimilarities between monthly mean Northern Hemisphere temperature anomalies during the twentieth century, Theoretical and Applied Climatology, 90, 161-168.

[6] Yerel S, 2009, Investigation of water quality characteristics by using factor and multidimensional scaling analyses in Porsuk river (Turkey); Asian J Chem., 2009, 21, 7234-7240.

[7] Yerel, S. and Ankara, H., 2010, Assessment of Water Quality Parameters by Using the Multidimensional Scaling Analysis, E-Journal of Chemistry, 7(4): 1274-1277.

[8] T. Kowalkowski, R. Zbytniewski, J. Szpejna and B. Buszewski, 2006, Application of chemometrics in river water classification. Water Research, 40(4), 744–752.

[9] Takane Y, Young FW, 1977, de Leeuw J. Nonmetric individual differences multidimensional scaling: An alternating least squares method with optimal scaling features. Psychometrika. 42:7–67.

Improved biohydrogen production from fruit and vegetable wastes through dark dry anaerobic fermentation

Haris Nalakath Abubackar[1,2], Okyanus Yazgın[1], Bensu Günay[1], Kubra Arslan[3], Tuğba Keskin Gündoğdu[1], Duygu Karaalp Yavuzyılmaz[1], Nuri Azbar[1,3]

[1]Ege University, Engineering Faculty, Bioengineering Department, 35100, Izmir, Turkey
[2]University of La Coruña, Center for Advanced Scientific Research (CICA), La Coruña, Spain
[3]Ege University, Center for Environmental Studies, 35100, Izmir, Turkey
*Corresponding author: Nuri Azbar (nuriazbar@gmail.com)

***Abstract* - This study presents a novel approach for biohydrogen production from fruit and vegetable wastes (FVWs) through dry fermentation technology (DFT). The pretreatment of FVWs via autoclaving (EXP1) resulted in improved hydrogen percentage of 44% and total hydrogen production reached almost 97% higher than the experiment (EXP2) without autoclaving.**

***Keywords* – biohydrogen, dark fermentation, fruit and vegetable wastes, renewable energy.**

I. Introduction

The European Union (EU) has revised European Directive 2009/28/EC to set a new target for 2030 which includes 40% reduction in greenhouse gas emissions compared to 1990 and 27% renewable energy consumption by 2030. Thus, there is a high demand to find alternative and sustainable (renewable) energy sources. In this respect, hydrogen has received greater attention in recent years as promising alternative energy source due to its high energy content per unit of weight (143 MJ/Kg) and in addition, oxidative combustion of hydrogen generating water as the only by-product. Biological hydrogen processes is recognized as an efficient method as it is less energy intensive which can be carried out near ambient temperature and pressure [1]. Among them, dark fermentative hydrogen production utilizes a group of strict or facultative anaerobes which are either in pure, co-culture or mixed consortium. Besides, by proper designing and optimization, even organic wastes can be treated and used for the generation of hydrogen. According to the Food and Agriculture Organization of the United Nations (FAO), approximately one-third of all food produced for human consumption every year is being lost or wasted, i.e., around 1.3 billion tons. The maximum of which were all FVWs that accounts for 45 %. In this paper, experiments were performed to understand of effect of substrate (FVWs) pretreatment through autoclaving on hydrogen production by dark dry anaerobic fermentation.

II. Materials and Methods

A. Feedstock and Inoculum used

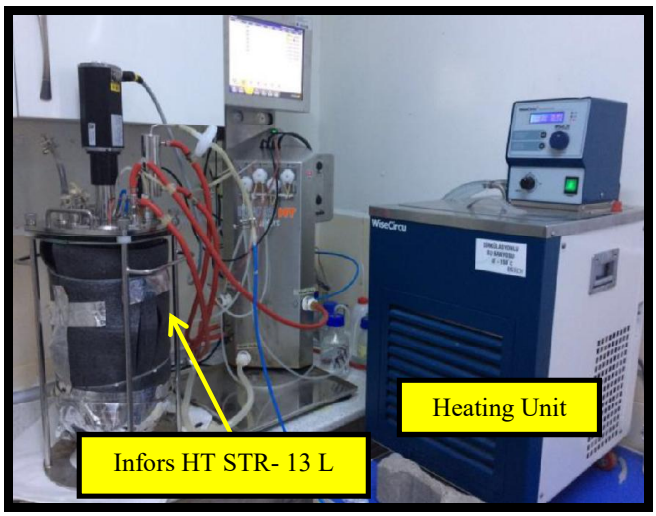
The FVWs was obtained from the Izmir municipality bazar (Turkey) and were chopped in to small pieces (< 5 cm). The inoculum used was collected from a local biogas plant that uses dairy product as feed (Izmir, Turkey) and was undergone pre-treatment at 105^0C for 10 min in order to gather hydrogen producers. The characteristics of pretreated inoculum used for studies were found as pH of 9.45, soluble COD of 9000 mg/L, total sugar of 900 mg/L, ammonium concentration of 3610 mg/L, TS and VS of 7.9 and 4.8 g/L, respectively.

B. Dry fermentation system

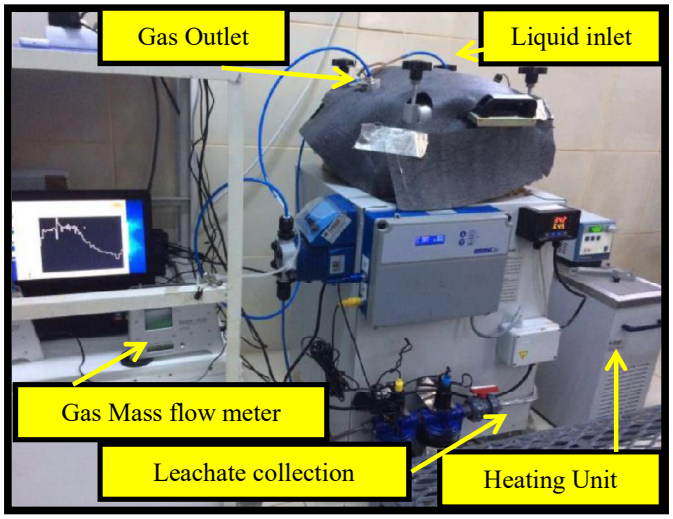
The experiments were performed in a fully automated stirred tank (ST) single walled reactor of a total volume of 13 L (INFORS HT Labfors 5 reactor, Switzerland) which contains hydrogen producing microbes and a 55-L costume made reactor (DF) where the wastes and hydrogen producers were mixed and filled for treatment (Fig.1). Temperature of the ST reactor was controlled via an inbuilt temperature sensor (pt100) that was inserted in a blink pocket of the reactor and by using cold finger to circulate the cooling water. Dry fermentor was fabricated from an autoclave unit and an aluminum basket with holes around the sides and bottoms were placed inside the unit for introducing the FVWs and holding it, allowing the leachate to flow freely to the bottom of the dry fermentor unit to the leachate collection tube. Inside temperature of the dry fermentor unit was controlled by circulating controlled temperature water through the stainless steel coil which is placed inside the dry fermentor unit. A sprayer was fixed under the cap of the dry fermentor to spray the liquid through the FVWs in order to have sufficient moist of microbes and also to washout the metabolites adhere on the FVWs.

A volumetric gas flow meter (μFlow, Bioprocess Control AB, Sweden) having detection range from 20 to 4000 ml/h was connected each to the gas outlet of the percolation tank and the dry fermentor to monitor the total gas produced. The gas flow

rate and total gas volume were normalized by the gas flow meter with real-time pressure and temperature and were accurately measured and read. Gas sampling ports were also connected to the gas outlets for characterizing the gas produced using gas chromatography.



(a)



(b)

Figure 1: Dry fermentation experimental set-up: (a) stirred tank reactor and (b) dry fermentor.

C. Dry fermentation Experiment

Two independent dry fermentation experiments were performed: one with autoclaved FVWs (pretreated) and second one with raw FVWs (unpretreated). For both experiments, the ST reactor was filled with 4.3 L sludge from the biogas plant along with 200 ml of 40 (X) times concentrated basal medium. The composition of basal medium ((X) per liter of distilled water) used contained 1.25 g/l $NaHCO_3$; 0.5 g/l NH_4Cl; 0.25 g/l KH_2PO_4; 0.25 g/l $CaCl_2$, 0.032 g/l $NiSO_4$; 0.32 g/l $MgSO_4 \cdot 7H_2O$; 0.02 g/l $FeCl_2$; 0.0144 g/l $Na_2MoO_4 \cdot 2H_2O$; 0.023 g/l $ZnCl_2$; 0.021 g/l $CoCl_2 \cdot 6H_2O$; 0.01 g/l $CuCl_2 \cdot 6H_2O$ and 0.03 g/l $MnCl_2 \cdot 4H_2O$. The working volume was then made up with FVWs liquid and distilled water to reach a total of 8 L. The ST was then undergo heat pretreated at 105 ^{0}C for 10 min using an autoclave and later flushed for few minutes with argon before starting the experiment to ensure anaerobic conditions. It was maintained at constant temperature of 37± 1 ^{0}C with a constant agitation of 250 rpm throughout the experiment. The pH was maintained uncontrolled throughout the experiment.

Dry fermentor (DF) basket was filled by mixing 4.83 kg FVWs (< 5 cm) with 0.7 L of preheated inoculum and 17.5 ml of 40(X) basal medium. An experiment was performed with no pre-treated FVWs and the second experiment was with autoclaved FVWs. During the feeding days, the leachate (L) from the DF was drained from the leachate collection tube and the respective volume of liquid from the ST was removed and introduced to DF. Leachate (L) was then introduced into the ST. Argon was flushed through the DF once each day to remove the head space CO_2.

Gas sample of 2 ml was taken from the outlet sampling port of the ST and DF to monitor the concentrations of various gas components (H_2, CO_2 and CH_4). Similarly 10 ml of liquid samples were withdrawn in order to measure the metabolites concentrations, NH_4^+, soluble COD and soluble sugar concentrations.

D. Analytical Methods

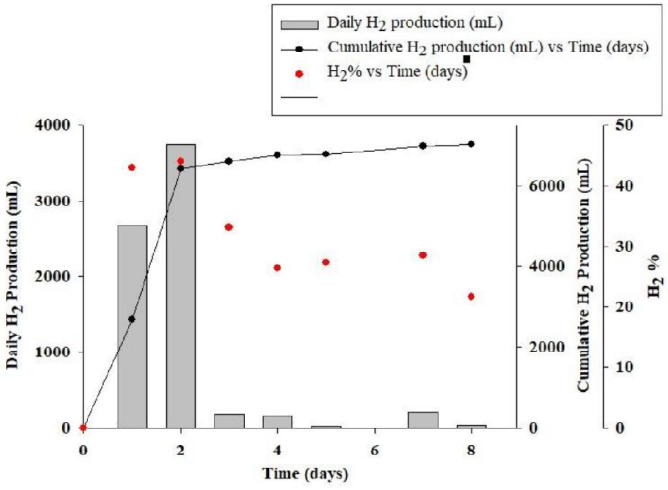
Gas-phase H_2 concentrations were measured by 6890N (Agilent technologies) gas chromatograph (GC) equipped with a thermal conductivity detector (TCD) by injecting 3-5 ml of headspace sample collected using a gas tight syringe (Agilent). The GC was fitted with HayesepD 80/100 packed column. The injector, oven and detector temperatures maintained at 150, 35 and 150 °C, respectively. Argon was used as the carrier gas at a flow rate of 20 ml/min. The soluble metabolites were analysed by GC (6890N Agilent) equipped with a flame ionization detector and TR-FFAP 30 m × 0.25 mm ID × 0.25 µm (Thermo Scientific). The initial temperature of the column was 40 ^{0}C for 3 min followed with a ramp of 20 ^{0}C/min to 60 ^{0}C for 3 min and then increased at 30 ^{0}C/min to 120 ^{0}C for 4 min and reach a final temperature with ramp of 30 ^{0}C/min to 240 ^{0}C for 6 min. The temperatures of the injector and detector were both 240 ^{0}C. Helium was used as the carrier gas at constant pressure of 103 kPa. The liquid sample is centrifuged and filtered using 0.2 µm nylon syringe filter and was acidified using ortho-phosphoric acid before analysing via GC. The soluble chemical oxygen demand (SCOD) was determined by using Hach LCK 114 COD kit and concentration was read directly using the Hach Pocket Colorimeter II. NH_4^+ concentration determination was performed using Spectroquant Ammonium Test kit and the absorbance was measured at a wavelength of 600 nm using a UV–visible spectrophotometer (Aquamate plus UV-Vis, Thermo

Scientific). The absorbance value was used to calculate the corresponding NH_4^+ concentration (mg L^{-1}) by comparing to the previously generated calibration curve. The soluble carbohydrate concentrations were measured using phenol sulphuric acid method by Masuko et al., 2005. Total solids (TS) and volatile solids (VS) were also determined using standard methods (APHA-AWWA-WPCF, 1998).

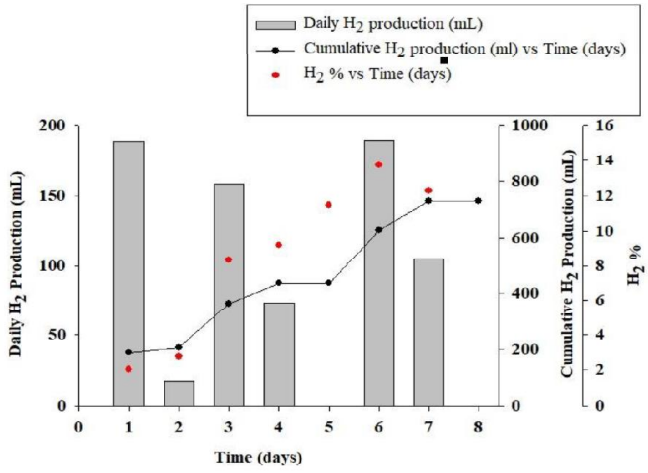
III. Results and Discussion

Dark anaerobic fermentation to generate biohydrogen is considered as a promising candidate in terms of sustainable energy production technologies which is relatively simple and also an inexpensive way to treat organic wastes, by a group of microorganisms which are either facultative or obligate anaerobes [2]. In contrast to commonly utilized wet fermentation technology (WFT) where the total solid content is < 10 %, DFT has several advantages such as higher organic loading rate, the requirement of small reactor volume and easiness in handling and transport the digestate, which is a stable product that can be directly applied on land [3]. In this study, several factors were manipulated to favour biohydrogen production, such as heat pretreatment of inoculum to select hydrogen producers over methanogens; washing out the produced CO_2 from the headspace of the dry fermentation reactor (DF) to prevent the consumption of H_2 by homoacetogens; FVWs pretreatment by autoclaving to make the biomass polymer easily accessible for microbial attack and finally, the fermentation pH was regulated within the range of 5.5–7.0 to favour hydrogen production and which in turn affect the metabolite distribution.

Two independent experiments (called EXP1: autoclaved and EXP2: non-autoclaved) were performed to compare the effect of substrate pretreatment (autoclaving) on hydrogen production. Both experiments were stopped after about 8 days results were evaluated. It was observed that autoclaving profoundly improved the H_2% in DF. A maximum H_2% of 44% was obtained in EXP1, which is 221% higher than the maximum observed in EXP2. No methane was observed in DF for both experiments. However, little amount of methane was observed at the headspace of ST. The fermentation (combining ST and DF) produced a total amount of 10248 and 5180 ml of H_2 respectively in EXP1and EXP2. It is worth to note that the total amount of gas produced in EXP1 is almost double the amount produced in EXP2. The total H_2 and %H_2 obtained in DF for both experiments are shown in Fig. 2. As can be observed from the Fig.2 that almost 90% of the accumulated hydrogen in the EXP1 was produced within the two days of the fermentation process. This is important in terms of economics of the process as higher amount of hydrogen could be obtained within a few days. Appropriate pretreatment of raw waste is often required to reduce the degree of polymerization and thereby to favour hydrolysis. Steam explosion is considered as an effective method for pretreatment which employs steam at a high pressure and high temperature [4]. This method has several advantages over other pretreatment methods in terms of corrosion problems and other environmental issues. Also High temperature improves the hydrogen production as observed in various thermophilic studies. This prompted us to study effect of autoclaving at 121^0C for 20 min as a pretreatment method. The hydrogen yield of 13.4 mL_{H2} g_{VS}^{-1} and 1.385 mL_{H2} g_{VS}^{-1} were obtained from DF respectively in EXP1 and EXP2.



(a)



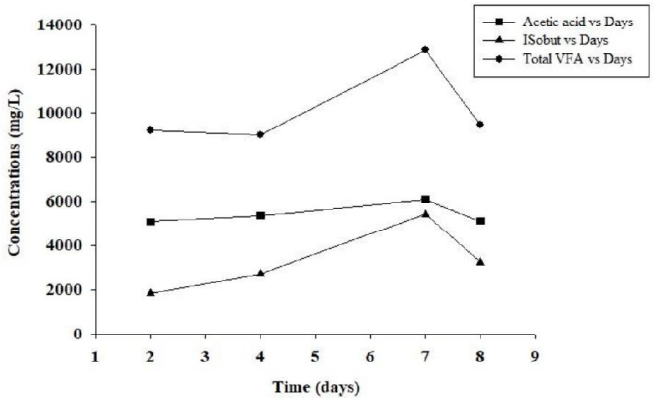
(b)

Figure 2: Hydrogen percentage and total production in Exp1 (a) and Exp2 (b) from dry fermentor system.

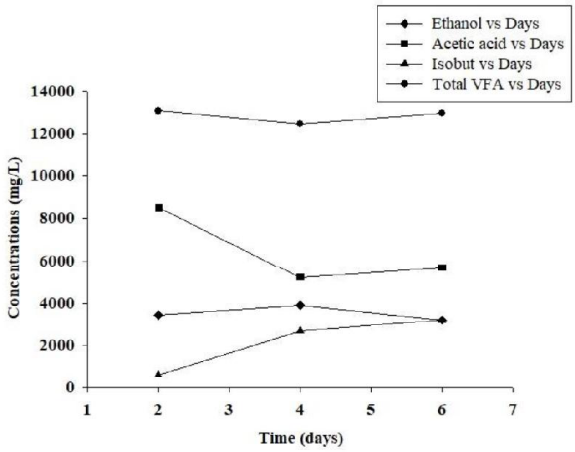
These low yields of hydrogen for both EXP1 and EXP2 compared to those reported in the literature were likely the result of ammonia inhibition (3610 mg/L) which was caused by decomposition of organic matters in inoculum to ammonia with time.

Irrigation of ST percolate over the FVWs and feeding of leachate collected from the bottom of the DF into the ST were performed on every alternative day until the 8th day. The main purpose of irrigating with percolate is to washout the VFAs generated during fermentation thereby avoiding metabolites

inhibition. Acetic acid and butyric acid were prominent metabolites observed in the leachate for EXP1 with maximum concentrations of 6102 and 5436 mg/L, respectively (Fig.3). However, profound amount of ethanol (3000-4000 mg/L) was reached in EXP2. This could be also one of the reasons of the low hydrogen production in EXP2 as ethanol pathway is associated with zero hydrogen production. Presence of propionic acid of around 400 mg/L in both experiments also adversely affects the hydrogen production as propionate consumes produced hydrogen.



(a)



(b)

Figure 3: Metabolites profile in Exp1 (a) and Exp2 (b)

Although the amount of hydrogen produced with autoclaved substrates is considerably higher, there are various parameters such as particle size of the substrate, temperature, etc. which could improve the overall productivity from the process. Thus, the set-up of further optimization assays is therefore warranted.

ACKNOWLEDGMENT

The authors wish to thank TUBITAK-MAG-2015 M 314 for financial support of this study. HNA thanks the Xunta de Galicia (Spain) for his postdoctoral fellowship (ED 481B-2016/195-0). The authors Bensu Günay and Okyanus Yazgın would also like to thank the Tubitak 2209-A University Student Research Projects Support Program for this research.

REFERENCES

[1] X.M. Guo, E. Trably, E. Latrille, H. Carrere and J.P. Steyer, "Hydrogen production from agricultural waste by dark fermentation: a review," *Int. J. Hydrogen Energy*, vol. 35, pp. 10660 – 10673, 2010.

[2] A. Abuadala, I. Dincer, "A review on biomass-based hydrogen production and potential Applications," *Int. J. Energy Res*., vol 36, pp. 415–455,2012.

[3] O.P. Karthikeyan, C. Visvanathan, "Bio-energy recovery from high-solid organic substrates by dry anaerobic bio-conversion processes: a review," *Rev. Environ. Sci Bio/Technology*, vol.12, pp.257–284, 2012.

[4] D.Kennes, H.N. Abubackar, M. Diaz, M.C. Veiga, C. Kennes, "Bioethanol production from biomass: carbohydrate vs syngas fermentation," *J. Chem. Technol. Biotechnol.*, vol. 91, pp. 304–317, 2016.

Investigation of Sizing Criteria for Cantilever Retaining Wall with Taguchi Optimization

Ö. Tan[1], I.H. Erkan[1] and E. URAY[2]

[1] Selcuk University, Konya/Turkey, ozcantan@selcuk.edu.tr
[1]Selcuk University, Konya/Turkey, hakkierkan@selcuk.edu.tr
[2]KTO Karatay University, Konya/Turkey, esra.uray@karatay.edu.tr

Abstract **- Controllable or uncontrollable parameters like elevation difference between soil levels, soil properties, selected wall dimensions, case of groundwater, construction area, intended use and cost have been affected design of retaining walls that connects two different soil levels. In this study, factors effect on the design of the cantilever retaining walls which have an important place in geotechnical engineering applications have been investigated experimentally. For different wall height and soil properties Signal/Noise (S/N) and variance analysis have been performed separately by using L16 design tables. At result of analysis, effect of the base width, the angle, the toe extension, the footing thickness and the top stem thickness of wall on safety factors of sliding and overturning have been studied. For different conditions of soil and wall, points to consider in pre-sizing of wall have been designated and graphics and tables have been enhanced.**

Keywords **- Cantilever Retaining Wall, Taguchi Method, Mathematical Model**

I. INTRODUCTION

IN geotechnical engineering, retaining walls are commonly used in the solution of the problem of connecting two different soil levels with a vertical element to provide stability conditions. In the design of retaining wall by using traditional methods, according to selected wall dimensions like the wall height, the length of wall, toe extension, height of stem, thickness of stem and angle of wall necessary verifications have been conducted. Several studies about the design of retaining wall have been made [1, 2]. If the selected wall dimensions do not satisfy verifications like sliding and overturning, according to new selected wall dimensions verifications should have been repeated. This trial and error method continues until stability verifications are provided for selected wall dimensions. This method is not only time consuming but also it does not guarantee that an economic design can be reached. To obtain economic wall dimensions in reasonable time, an optimization method which is based on statistical analysis has been suggested by Taguchi [3]. This method allows to determine the effects of parameters on design and to obtain results with few experiments instead of many experiments [4-6]. The design criteria of the gabion retaining wall, which is another type of retaining wall, has been investigated by using the Taguchi method [7].

In this study, effect of parameters like the length of base, thickness of base, toe extension, thickness of stem and angle of wall on the design of cantilever design has been investigated by Taguchi Method and variance and optimization analysis have been performed. Using the main parameters affecting the design, design tables have been created to be full factorial with five parameters and four levels. All safety factors of sliding and overturning have been determined for each case corresponding to different design. "Signal/Noise, S/N, variance (ANOVA) and optimization analysis have been performed for these safety factors and have been determined effects of parameters on the cantilever retaining wall.

II. CODES USED IN DESIGN OF CANTILER RETAINING WALL

In this section, national and international pre-design guidelines have been given, which enable to determine the appropriate wall dimensions in a shorter time.

In Figure 1, "Soil Retaining Structures; Properties and Guidelines for Design, TS 7994 [8] " is given. Dimensions of the retaining wall firstly, should be determined depend on the wall height. The depth of embedment should be taken as 80 cm for all foundation, but it should be taken as 120cm in frozen region. Toe extension of the retaining wall should be selected B/3 (B: the length of the wall). If verifications do not satisfy, dimensions of l1 and l2 should calculated again

.

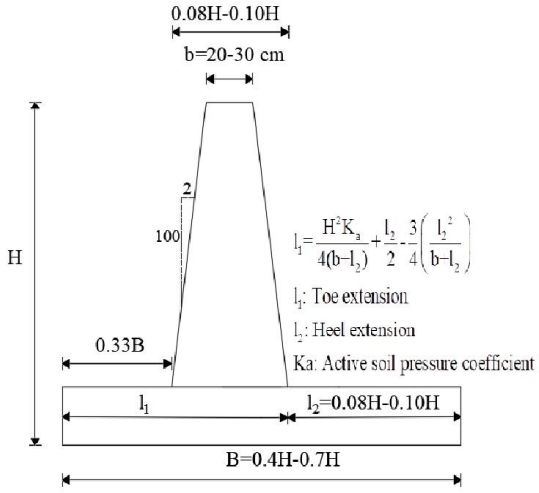


Figure 1: TS7994 Pre-design guideline.

In Figure 2, foreseen wall dimensions according to "Building Code Requirements for Structural Concrete, ACI 318-08 [9] " is given. To obtain economic wall design, the stems of cantilever retaining walls are normally made of constant thickness for wall height up to 12 ft. For above 12 ft heights, the thickness of stem should be made with increasing width bottom to top of stem. The minimum thickness of the base should be selected as 10-12inch [10].

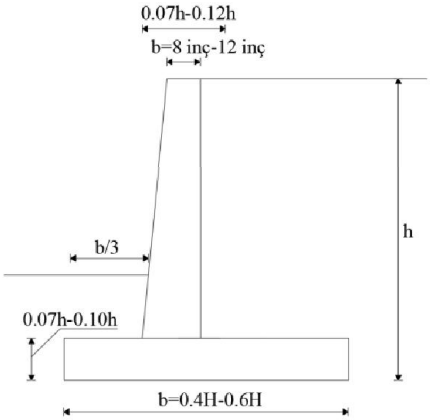


Figure 2: ACI318 Pre-design guideline.

In LRFD Bridge Design Specifications [11], foreseen dimensions of the length of base, thickness of base and toe extension have given. The length of base should be chosen between 70 and 75 percent of the stem height and thickness of base should be chosen between 10 and 15 percent of the stem height. The toe extension should be equal to approximately 30 percent of the length of base.

III. TAGUCHI METHOD

Taguchi is a method which minimizes the effects of uncontrollable factors and limits number of analyses by using orthogonal arrays. In Taguchi Method, result is evaluated by calculating Signal/Noise (S/N) ratio of data obtained from the analysis.

According to Taguchi Method parameters affecting the results are divided into two groups, controllable and uncontrollable parameters. Uncontrollable parameters are density of soil, γ_s= 18 kN/m^3, angle of internal friction, ϕ= 26, 30° and cohesion, c=0. Controllable parameters and their levels which arranged according to orthogonal array levels are given in Table 1.

Table 1: Controllable parameters.

Parameter	Level 1	Level 2	Level 3	Level4
Length of Base (B)	0,25H	0,50 H	0,75 H	1,0 H
Toe Extension (B_t)	0,15 B	0,30 B	0,45 B	0,60 B
Thickness of base (d)	0,05 H	0,07 H	0,09 H	0,11 H
Thickness of stem (b)	0,05 H	0,075 H	0,10 H	0,125 H
Angle of wall (m)	%0	%2	%4	%8

In Taguchi Method, selection of orthogonal array is carried out according to number of level and total degree of freedom. General representation of orthogonal array is $L_{d(a)k}$ or L_d. Here d is the total number of analysis, a is the number of level of parameters, k is number of parameters and L demonstrates orthogonal array. In this study, the number of analysis is 4^5 =1024 and instead of 1024, 16 designs have been made by using L_{16} orthogonal array. In Table 2, controllable parameters which are arranged according to Taguchi are given. According to L16 design table, safety factors of sliding and overturning have been obtained by using computer program for H=4,8 m and Ø=26, 36°.

Table 2: L16 Design Table

No	B	Bt	d	b	m
1	B1	Bt1	d1	b1	m1
2	B1	Bt2	d2	b2	m2
3	B1	Bt3	d3	b3	m3
4	B1	Bt4	d4	b4	m4
5	B2	Bt1	d2	b4	m3
6	B2	Bt2	d1	b3	m4
7	B2	Bt3	d4	b2	m1
8	B2	Bt4	d3	b1	m2
9	B3	Bt1	d3	b2	m4
10	B3	Bt2	d4	b1	m3
11	B3	Bt3	d1	b4	m2
12	B3	Bt4	d2	b3	m1
13	B4	Bt1	d4	b3	m2
14	B4	Bt2	d3	b4	m1
15	B4	Bt3	d2	b1	m4
16	B4	Bt4	d1	b2	m3

IV. SIGNAL/NOISE (S/N), VARIANCE AND OPTIMIZATION ANALYSES

Signal/Noise ratio which is defined by Taguchi is analysis to minimize effect of controllable parameters on result. The S/N ratio, which is a statistical value, is divided according to the target (minimum best, greatest best, and best value target) reached at the end of the study in practice [4]. In this study, calculating of S/N ratio was performed according to the target state of "bigger is better" (1).

$$S/N \text{ ratio} = -10\log[\sum(1/Y^2)/n] \quad (1)$$

Where Y is the end of the analysis and n is the number of repetitions. The average S/N ratios for each design have been calculated using the safety factors of sliding and overturning obtained from the computer analysis for different the wall height and the angle of internal friction (Table 3-6).

Table 3: S/N and safety factor values for sliding (Ø=26°).

No	H=4m		H=8m	
	Fs	S/N	Fs	S/N
1	1,322	2,424	1,355	2,638
2	1,293	2,231	1,268	2,062
3	1,264	2,034	1,182	1,452
4	1,174	1,393	0,966	-0,301
5	1,724	4,73	2,193	6,820
6	1,611	4,141	1,903	5,588
7	1,573	3,934	1,772	4,969
8	1,470	3,346	1,504	3,544
9	2,061	6,281	2,892	9,223
10	1,960	5,845	2,603	8,309
11	1,872	5,446	2,343	7,395
12	1,762	4,92	2,034	6,162
13	2,487	7,913	3,782	11,554
14	2,348	7,413	3,387	10,596
15	2,110	6,485	2,780	8,880
16	1,979	5,928	2,403	7,615

Table 4: S/N and safety factor values for sliding (Ø=36°).

No	H=4m		H=8m	
	Fs	S/N	Fs	S/N
1	2,944	9,378	0,619	-4,167
2	2,881	9,190	0,579	-4,747
3	2,819	9,001	0,539	-5,450
4	2,627	8,389	0,437	-7,191
5	3,806	11,609	1,010	0,086
6	3,564	11,038	0,874	-1,170
7	3,481	10,834	0,813	-1,799
8	3,262	10,269	0,688	-3,249
9	4,529	13,120	1,335	2,509
10	4,313	12,695	1,201	1,590
11	4,125	12,308	1,080	0,608
12	3,888	11,794	0,936	-0,575
13	5,444	14,718	1,750	4,860
14	5,145	14,227	1,566	3,895
15	4,635	13,320	1,283	2,164
16	4,354	12,777	1,108	0,890

Table 5: S/N and safety factor values for overturning (Ø=26°).

No	H=4m		H=8m	
	Fs	S/N	Fs	S/N
1	0,846	-1,453	0,848	-1,433
2	0,861	-1,300	0,860	-1,311
3	0,872	-1,190	0,862	-1,290
4	0,727	-2,770	0,623	-4,111
5	2,400	7,604	3,176	10,037
6	2,299	7,230	2,986	9,501
7	2,210	6,887	2,792	8,918
8	1,972	5,898	2,348	7,413
9	4,811	13,644	6,786	16,632
10	4,651	13,350	6,463	16,208
11	4,473	13,011	6,059	15,648
12	4,091	12,236	5,291	14,470
13	8,354	18,437	12,094	22,238
14	8,112	18,182	11,583	21,276
15	7,269	17,229	10,072	20,062
16	6,635	16,436	8,776	18,856

Average S/N ratios corresponding to each parameter level are given in Table 7-10.

Table 6: S/N and safety factor values for overturning (Ø=36°).

No	H=4m		H=8m	
	Fs	S/N	Fs	S/N
1	1,535	3,722	0,542	-5,321
2	1,556	3,840	0,550	-5,193
3	1,574	3,940	0,551	-5,177
4	1,356	2,645	0,392	-8,135
5	3,872	11,758	2,090	6,402
6	3,179	10,045	1,964	5,862
7	3,587	11,094	1,835	5,272
8	3,227	10,175	1,539	3,744
9	7,498	17,498	4,490	13,044
10	7,258	17,216	4,276	12,620
11	6,990	16,889	4,007	12,054
12	6,415	16,143	3,496	10,871
13	12,827	22,162	8,019	18,082
14	12,463	21,912	7,680	17,707
15	11,195	20,980	6,675	16,489
16	10,241	20,206	5,814	15,289

Table 7: Average S/N ratio for sliding safety factor (Ø=26°).

	Parameter	Level 1	Level 2	Level 3	Level 4
H=4m	B	2,021	4,038	5,623	6,935
	Bt	5,337	4,908	4,475	3,897
	d	4,485	4,592	4,769	4,771
	b	4,673	4,734	4,634	4,575
	m	4,525	4,594	4,752	4,746
	Average S/N	4,654			
H=8m	B	1,463	5,23	7,772	9,661
	Bt	7,559	6,639	5,674	4,255
	d	5,809	5,981	6,204	6,133
	b	6,091	6,139	6,049	5,848
	m	5,843	5,967	6,189	6,128
	Average S/N	6,032			

Table 8: Average S/N ratio for sliding safety factor (Ø=36°).

	Parameter	Level 1	Level 2	Level 3	Level 4
H=4m	B	8,990	10,937	12,479	13,761
	Bt	12,206	11,788	11,366	10,807
	d	11,375	11,478	11,654	11,659
	b	11,558	11,621	11,521	11,467
	m	11,416	11,480	11,638	11,633
	Average S/N	11,542			
H=8m	B	-5,389	-1,533	1,048	2,952
	Bt	0,822	-0,108	-1,104	-2,531
	d	-0,945	-0,768	-0,573	-0,635
	b	-0,661	-0,617	-0,721	-0,922
	m	-0,915	-0,787	-0,584	-0,635
	Average S/N	-0,730			

In Figure 3 and 4, graphical representation of average S/N

ratio change between S/N and the parameters of length of base and toe extension respectively for safety factor of sliding. In Figure 3, as the length of base increases, safety factor of sliding increases. In Figure 4, as the toe extension increases, safety factor of sliding reduces.

Table 9: Average S/N ratio for overturning safety factor (Ø=26°).

	Parameter	Level 1	Level 2	Level 3	Level 4
H=4m	B	-1,678	6,905	13,061	17,571
	Bt	9,558	9,366	8,984	7,950
	d	8,806	8,942	9,133	8,976
	b	8,963	9,012	9,050	8,833
	m	8,756	8,917	9,178	9,007
	Average S/N	8,965			
H=8m	B	-2,036	8,967	15,739	20,608
	Bt	11,869	11,42	10,834	9,157
	d	10,643	10,82	11,008	10,813
	b	10,808	11	10,953	10,521
	m	10,563	10,77	11,23	10,712
	Average S/N	10,82			

Table 10: Average S/N ratio for overturning safety factor (Ø=36°).

	Parameter	Level 1	Level 2	Level 3	Level 4
H=4m	B	3,536	10,768	16,937	21,315
	Bt	13,785	13,253	13,226	12,292
	d	12,716	13,180	13,381	13,279
	b	13,218	13,267	13,280	12,792
	m	13,023	13,160	13,073	13,301
	Average S/N	13,139			
H=8m	B	-5,957	5,32	12,147	16,892
	Bt	8,052	7,749	7,159	5,442
	d	6,971	7,142	7,329	6,96
	b	7,132	7,172	7,284	6,815
	m	6,883	7,103	7,409	7,007
	Average S/N	7,101			

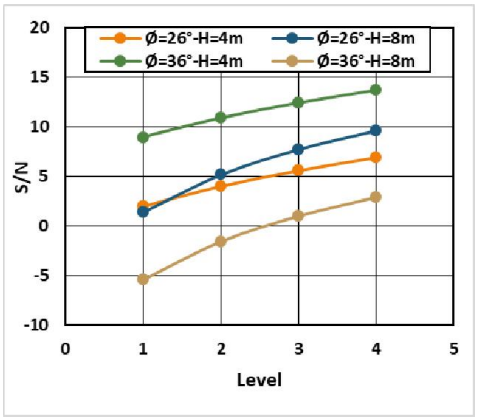


Figure 3: Change between length of base and S/N ratio for safety factor of sliding.

In Figure 5 and 6, graphical representation of average S/N ratio change between S/N and the parameters of length of base and toe extension respectively for safety factor of overturning. In Figure 5, as the length of base increases, safety factor of sliding increases, rapidly. In Figure 6, as toe extension increases, safety factor of sliding shows approximately linear behavior. According to obtained results from S/N analysis, parameters of thickness of base, thickness of stem and wall angle have been determined that there is no effect on the wall design.

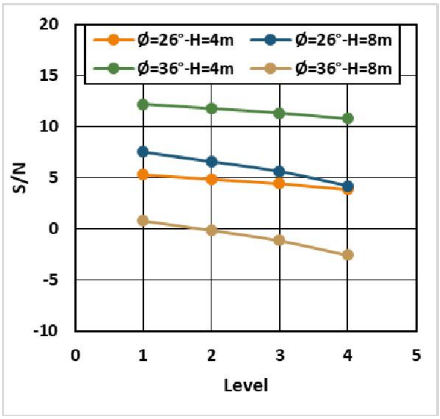


Figure 4: Change between toe extension and S/N ratio for safety factor of sliding.

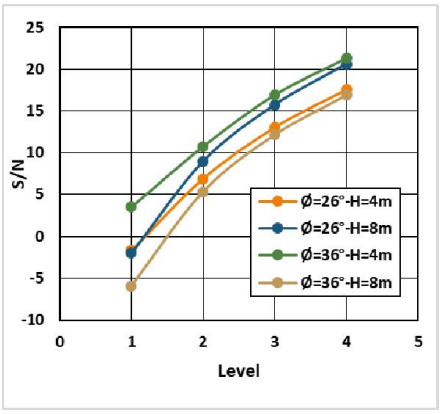


Figure 5: Change between length of base and S/N ratio for safety factor of overturning.

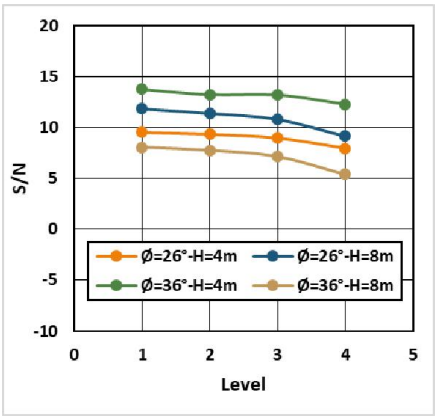


Figure 6: Change between toe extension and S/N ratio for safety factor of overturning.

Variance analysis have been conducted to determine effect of the parameters in the design of cantilever retaining wall and results of analysis are given in Table 11-14.

Table 11: Results of analysis of variance for sliding safety factor (Ø=26°).

H (m)	Parameter	Degree of Freedom (DOF)	Sum of Squares (Ss)	Variance	Percent (P) (%)
4	B	3	53,82	17,94	91,513
	Bt	3	4,546	1,515	7,73
	d	3	0,237	0,079	0,403
	b	3	0,053	0,017	0,09
	m	3	0,153	0,051	0,26
	Total	15	58,809		100
8	B	3	150,881	50,293	85,882
	Bt	3	23,941	7,98	13,627
	d	3	0,367	0,122	0,209
	b	3	0,196	0,65	0,111
	m	3	0,294	0,098	0,167
	Total	15	175,679		100

Table 12: Results of analysis of variance for sliding safety factor (Ø=36°).

H (m)	Parameter	Degree of Freedom (DOF)	Sum of Squares (Ss)	Variance	Percent (P) (%)
4	B	3	50,722	16,907	91,484
	Bt	3	4,289	1,429	7,735
	d	3	0,232	0,077	0,418
	b	3	0,05	0,016	0,091
	m	3	0,149	0,49	0,268
	Total	15	55,442		100
8	B	3	156,276	52,092	85,955
	Bt	3	24,72	8,24	13,596
	d	3	0,324	0,108	0,178
	b	3	0,217	0,072	0,119
	m	3	0,271	0,09	0,149
	Total	15	181,808		100

Table 13: Results of analysis of variance for overturning safety factor (Ø=26°).

H (m)	Parameter	Degree of Freedom (DOF)	Sum of Squares (Ss)	Variance	Percent (P) (%)
4	B	3	883,464	277,821	99,182
	Bt	3	6,17	2,056	0,734
	d	3	0,216	0,072	0,025
	b	3	0,106	0,035	0,012
	m	3	0,373	0,124	0,044
	Total	15	890,329		100
8	B	3	1154,853	384,951	98,406
	Bt	3	16,893	5,631	1,439
	d	3	0,266	0,088	0,022
	b	3	0,553	0,184	0,047
	m	3	0,991	0,33	0,084
	Total	15	1173,556		100

Table 14: Results of analysis of variance for overturning safety factor (Ø=36°).

H (m)	Parameter	Degree of Freedom (DOF)	Sum of Squares (Ss)	Variance	Percent (P) (%)
4	B	3	716,402	238,8	99,102
	Bt	3	4,618	1,536	0,638
	d	3	1,037	0,345	0,143
	b	3	0,65	0,216	0,09
	m	3	0,177	0,059	0,024
	Total	15	722,884		100
8	B	3	1179,957	393,319	98,516
	Bt	3	16,315	5,348	1,362
	d	3	0,362	12	0,03
	b	3	0,484	0,161	0,04
	m	3	0,605	0,201	0,05
	Total	15	1197,723		100

Optimization analysis determines parameter levels and values which make maximum safety factors. These analyses have been applied for safety factors of sliding and overturning for different the wall heights and values of angle of internal friction. As a result of this analysis parameter levels which are given expected maximum safety factors of sliding and overturning have been obtained. According to the obtained parameter levels, safety factors of sliding and overturning have been found by the computer program (Table 15-18).

V. Conclusion

In this study, effects of parameters on design of cantilever retaining wall has been investigated by using Taguchi Method which is one of the strongest optimization technique. Parameters which affect the design of cantilever retaining wall are length of base, toe extension, thickness of base, thickness of stem and wall angle According to Taguchi Method by using L_{16} orthogonal array which consist of four levels and five parameters 16 different designs were modeled and analyzed by computer program to obtain safety factors of sliding and overturning. "S/N, "Variance" and "Optimization" analyses have been performed by using results gained from computer analyses.

S/N analyses show that the safety factors of sliding and overturning has an inverse proportion relationship with increasing of toe extension (Bt) and directly proportional with increasing of length of base (B). The results show that change of values of parameters, thickness of base, thickness of stem and wall angle, does not have any influence on design of cantilever retaining wall.

According to variance analysis, the most effective parameter in design of cantilever retaining wall is the base width with an approximately 90-98 percent and the second effective parameter is the toe extension with an approximately 7 percent.

As a result of optimization analysis generally the maximum safety factors of sliding and overturning have been obtained for B = 1,0H, Bt=0,15B, d =0,09H, b= 0,075H and m=%4.

In this study, prediction and optimization analyses which

has been made by using Taguchi Method for safety factors of sliding and overturning, show that results obtained from these analyses is close to real value. Consequently, Taguchi Method can be used in application of geotechnical engineering as an optimization technique.

Table 15: Results of analysis of variance for sliding safety factor (Ø=26°).

H (m)	Parameter	Level	Level Description	Contribution
4	B	4	1,0 H	2,28
	Bt	1	0,15 B	0,683
	d	4	0,11 H	0,117
	b	2	0,075 H	0,079
	m	3	%4	0,098
	Expected maximum safety factor Fs (max) for this level			7,911
	Found by computer analysis maximum safety factor Fs (max)			2,466
8	B	4	1,0 H	3,682
	Bt	1	0,15 H	1,552
	d	3	0,09 H	0,156
	b	2	0,075 H	0,113
	m	3	%4	0,146
	Expected maximum safety factor Fs (max) for this level			4,919
	Found by computer analysis maximum safety factor Fs (max)			1,717

Table 16: Results of analysis of variance for sliding safety factor (Ø=36°).

H (m)	Parameter	Level	Level Description	Contribution
4	B	4	1,0 H	2,218
	Bt	1	0,15 B	0,664
	d	4	0,11 H	0,17
	b	2	0,075 H	0,079
	m	3	%4	0,096
	Expected maximum safety factor Fs (max) for this level			14,716
	Found by computer analysis maximum safety factor Fs (max)			5,397
8	B	4	1,0 H	3,682
	Bt	1	0,15 B	1,552
	d	3	0,09 H	0,156
	b	2	0,075 H	0,113
	m	3	%4	0,146
	Expected maximum safety factor Fs (max) for this level			11,624
	Found by computer analysis maximum safety factor Fs (max)			3,710

Table 17: Results of analysis of variance for overturning safety factor (Ø=26°).

H (m)	Parameter	Level	Level Description	Contribution
4	B	4	1,0 H	8,606
	Bt	1	0,15 B	0,593
	d	3	0,09 H	0,168
	b	3	0,100 H	0,085
	m	3	4	0,213
	Expected maximum safety factor Fs (max) for this level			18,63
	Found by computer analysis maximum safety factor Fs (max)			8,295
8	B	1,0 H	4	9,79
	Bt	0,15 H	1	0,951
	d	0,09 H	3	0,228
	b	0,10 H	3	0,182
	m	4	3	0,308
	Expected maximum safety factor Fs (max) for this level			18,56
	Found by computer analysis maximum safety factor Fs (max)			7,959

Table 18: Results of analysis of variance for overturning safety factor (Ø=36°).

H (m)	Parameter	Level	Level Description	Contribution
4	B	4	1,0 H	8,175
	Bt	1	0,15 B	0,645
	d	3	0,09 H	0,242
	b	3	0,100 H	0,14
	m	4	8	0,161
	Expected maximum safety factor Fs (max) for this level			22,502
	Found by computer analysis maximum safety factor Fs (max)			12,729
8	B	1,0 H	4	9,79
	Bt	0,15 B	1	0,951
	d	0,09 H	3	0,228
	b	0,075 H	2	0,182
	m	4	3	0,308
	Expected maximum safety factor Fs (max) for this level			22,431
	Found by computer analysis maximum safety factor Fs (max)			11,948

REFERENCES

[1] J. E. Bowles, *Analytical and computer methods in foundation engineering.* McGraw-Hill Companies, 1974.

[2] R. F. Bruner, H. M. Coyle, and R. E. Bartoskewitz. *Cantilever retaining wall design*., Research Report, Diss. Texas A&M University, 1983.

[3] G. Taguchi. Introduction to quality engineering: designing quality into products and processes. 1986.

[4] Şirvancı, M. *Kalite İçin Deney Tasarımı Yaklaşımı, Taguchi Yaklaşımı.* Wisconsin Üniversitesi, ABD, 1997.

[5] W.P. Yang ans Y.S. Tarng, Y. S. Design optimization of cutting parameters for turning operations based on the Taguchi method. *Journal of materials processing technology,* 84(1), 122-129, 1998.

[6] Ö.Tan,, (2006). Investigation of soil parameters affecting the stability of homogeneous slopes using the Taguchi method. *Eurasian Soil Science*, 39(11), 1248-1254, 2006.

[7] E. Uray and Ö. Tan. *Investigation of Design Criteria for the Type of Gabion Walls*. Proceding of ICOCEE, 2014.

[8] Türk Standartı TS 7994, *Zemin Dayanma Yapıları; Sınıflandırma, Özellikleri ve Projelendirme Esasları*, Türk Standartları Enstitüsü, Ankara, 1990.

[9] ACI Committee 318, *Building Code Requirements for Structural Concrete (ACI 318-08)*. American Concrete Institute (Vol. 2007), 2008.

[10] J. C. McCormac and R. H. Brown (2015). *Design of reinforced concrete*. John Wiley & Sons, 2015

[11] AASHTO, *American Association of State Highway and Transportation Officials LRFD Bridge Design Specifications,* 2010.

Fatigue Life Analysis Using Random Vibration Data

K. YAMAN[1*], E. OKUR[1] and A. ÖZTÜRK[2]

[1] TUBİTAK SAGE, Ankara/Turkey, [1*]kemyam@gmail.com, [1]emre.okur@tubitak.gov.tr
[2]Necmettin Erbakan University, Konya/Turkey, aliozturk@konya.edu.tr

***Abstract* - In this study, fatigue analysis of a missile body structure during captive carriage at the underwing of a fixed wing aircraft platform is performed. The F-16 jet aircraft was determined as a fixed wing aircraft platform. As the external store, a data measurement store (DMS) was designed to measure loads during five different sorties. Acceleration and strain data were collected during the test. Accelerometers were used to generate power spectral densities (PSD) for the vibration tests and fatigue analyses. Strain gages were placed to the most critical locations for fatigue calculations.**

***Keywords* – Fatique life, random data, random vibration, finite element, power spectral density.**

I. INTRODUCTION

AIRCRAFT wing platforms have great importance and are very commonly used vehicles in militaries. However, without mounting external stores like missiles, bombs etc. Usage of these aircrafts will be pointless. Therefore, external stores are indispensable necessities for these aircrafts. Consequently, design and production of external stores is very crucial for military applications. During the design of an external store, one must know the loads which the external store will encounter during its lifespan. During this lifespan, external stores encounter several types of loading like inertial loads, shock loads etc. Among these loads, random vibration loads are one of the most important ones. By definition, random vibration is the excitation of all frequencies while value of this random vibration is not predictable at any time.

Moreover, some external stores can be exposed to these random vibration loads for a long time. For instance, some missiles must be attached to the aircrafts continuously for emergency situations; thus, random vibration exposure duration of these missiles can be very long such as several hundred or thousand hours. As a result, these loads cause structural failure of the external stores especially due to fatigue. By definition, fatigue is one of the reasons of structural failure which can occur in a metallic material due to the repeated application of stresses and strains which never reach a level sufficient to cause failure in a single application. Therefore, it is important to know the loads on the external stores to avoid fatigue.

Dreher [1] worked on the development of random vibration test criteria for aircraft equipment. He collected acceleration data from 4 different aircrafts, two of them were fighter bomber types and two of them were cargo types. He showed variance of the vibration level by speed of the aircraft, aerodynamic pressure and surface geometry for different parts of aircraft. Findings of this study were generalized to pertinent, adaptable random vibration test criteria for aircraft equipment and this criterion is included in MIL-STD-810 [2].

Eldred et al. [3] presented the various sources of vibrations in space vehicles and equipment with formulation and experimental data. They also investigated the response of the parts with both empirical and analytical approaches. Moreover, they discussed combining of various dynamic responses during the service life of the vehicle for vibration tests.

Lyon [4] also presented dynamic environment of a flight vehicle, prediction of vehicle response and simulation of expected environment in the test. Bendat et al. [5] did research on checking data for randomness, stationary and normality. Some basic inspection methods and tests were recommended in their study.

Halfpenny [6] compared fatigue life results of different frequency domain fatigue analyses (Narrow Band and Dirlik [7] methods) and time domain analysis. In his research, he found Dirlik method gives the best comparable results with the traditional time domain approaches. Dirlik method gives average discrepancy of only 4% from the fatigue life calculated in the time domain.

Topham [8] evaluated and compared the fatigue damage from two different vibration events and an envelope of both events. He used the Advanced Medium Range Air-to-Air Missile (AMRAAM) as the test item and the McDonnell Douglas F-15 Eagle as its platform for his study. Then, he used the same vibration test profile for the equipment test and the section test and compared fatigue damage from these both tests.

Behrooz et al. [9] compared Findley [10] multi-axial stress based methods with the test results. They calculated fatigue life for a steel shaft of a highspeed micro generator rotor which was exposed to the torsional and bending stresses at the same time. They did multi-axial fatigue life analysis with Findley methods and compared the results with fatigue tests. Using Findley methods, they found almost the same order of magnitude of life prediction with the test results.

II. Experimental Study

In this study, a *Data Measurement Store* (DMS) as shown in Figure 2a and 2b was used to measure the vibration loads for fatigue calculations. Accelerometers were placed at critical parts and locations considering vibration tests and strain gages were placed to high stress expected locations. Accelerometers were used to generate power spectral densities (PSDs) for the vibration tests and fatigue analyses. Strain gages were used for fatigue calculations; therefore, they were placed at the most critical locations on the store. In total, 7 accelerometers and 51 strain gages were placed on the store. All accelerometers were 3 axial and dynamic accelerometers which measure the data above 1 Hz. However, one of the 7 accelerometers broke down during the flights and no meaningful data were retrieved from this accelerometer. Locations of other 6 accelerometers are shown in Fig. 1. From 51 strain gages, 3 of them were rectangular rosette pattern, 16 of them were shear pattern and 32 of them were linear pattern stain gages. Locations of other strain gage are shown in Fig. 2b.

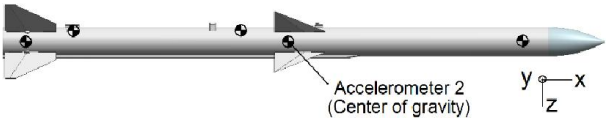


Figure 1: Locations of the accelerometers and the strain gages on the DMS

In Fig. 1, two of the symbols which point at the wings of the store represent all 48 strain gages on the shafts of the wings. Other two symbols in the middle represent the rectangular rosette strain gages in front of the store hangers. There are three hangers (front, mid and aft hangers) in the store and there were three rosette strain gages in front of each of them. However, the rosette in front of the front hanger broke down and no meaningful data were retrieved from this rosette strain gage. Fig. 2 shows the locations of other two rosette strain gages. All gages in rosettes (3 gages for 1 rosette) were connected to the data acquisition system to form a quarter bridges.

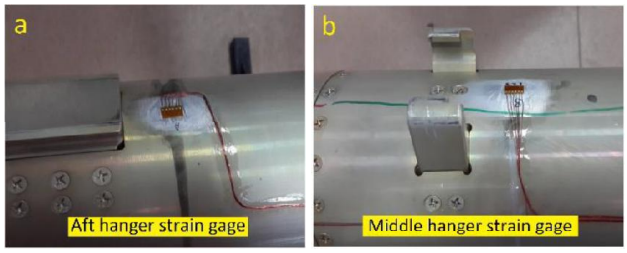


Figure 2: Locations of rosette strain gages on the DMS

The DMS was mounted to the F-16C jet aircraft during sorties. In total, the DMS attached to the aircraft flew 5 sorties. In 2 of these sorties, the DMS was attached to 9th station of the aircraft and during other sorties, it was attached to the 8th station of the aircraft. In general, 3 types of data were obtained from the sorties. One of them is Mux Bus data obtained from the aircraft which consists of aircraft dynamic data such as altitude, speed, accelerations of the aircraft (Fig. 3). Other two are acceleration and strain data obtained from the DMS.

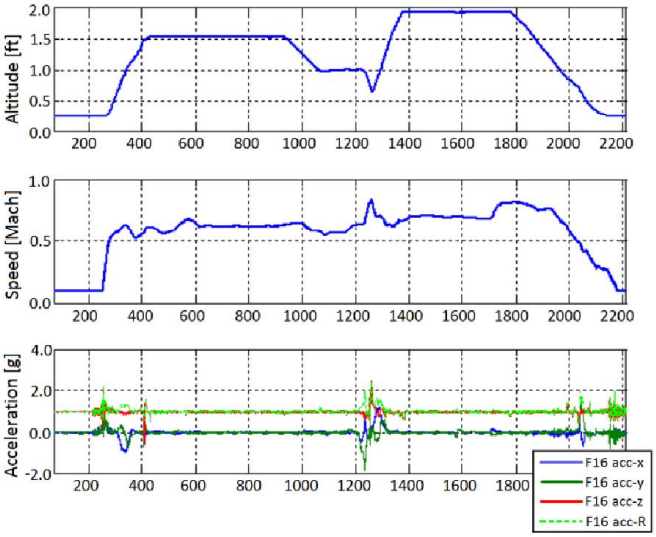


Figure 3: A typical MuxBus Data for a sortie of F16

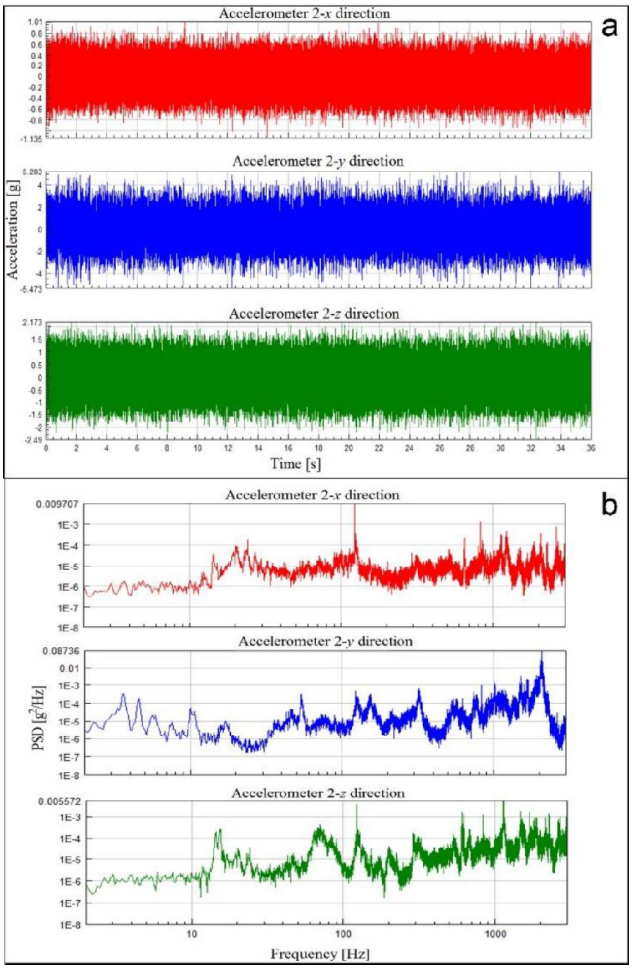


Figure 4: An example of collected (a) accelerator and (b) PSD random data for a sortie of F16

Acceleration data steps to prepare data for fatigue analyses and tests are given briefly in Fig. 4a. Also figures of these steps for accelerometer 2 are shown as an example below the step explanation. The power spectral densities (PSD) of all the selected data were calculated separately as shown in Figure 4b.

III. VIBRATION FATIGUE ANALYSIS

Vibration fatigue analysis is a frequency based fatigue analysis because PSD loads are used instead of time loads during analysis. Hereby, the structural frequency responses are considered during fatigue calculations. Cycles are counted from stress PSDs instead of load time signals. In this paper, the Lalanne/Rice method [11] which is one of the most accurate one when compared with the time domain data was used for cycle counting from the power spectral densities. After finding cycles, rest of the analysis is like time domain fatigue analysis. However, in this study, firstly, stress PSDs for unit acceleration load were obtained by frequency response function (FRF) analysis for vibration fatigue analysis. Then, acceleration PSDs obtain from flights are used to obtain stress PSDs during flights. In Figure 5, vibration fatigue analysis steps are summarized.

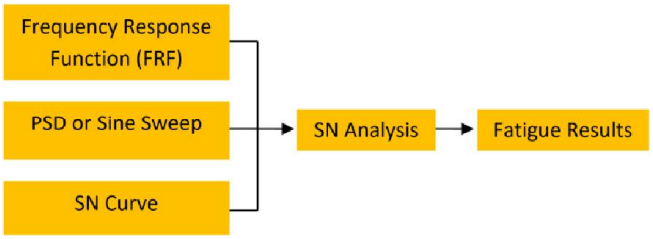


Figure 5: Vibration fatigue steps [12]

As an example, fatigue analysis was done using PSD obtained from accelerometer 2 in this study. Accelerometer 2 location is right beside the front hanger of the DMS. For fatigue analysis, front part of the DMS was used and PSD obtained from accelerometer 2 was given as a base vibration. Model was also fixed from the base.

The finite element model used for fatigue analysis is shown in Fig. 6. The model was meshed with solid TET10 meshes and RBE2 and RBE3 MPC elements were used instead of bolts to attach solid bodies and point masses, respectively.

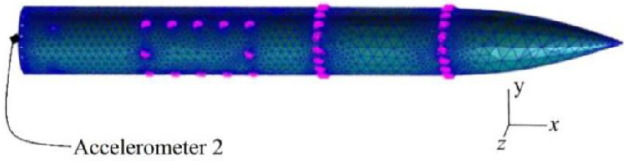


Figure 6: Finite element model for fatigue analysis

To make fatigue analysis, firstly stress PSDs of the model for every direction were obtained by FRF analysis choosing the unit load input location as accelerometer 2 location. FRF gives the relation between the input and output as follows:

$$H(f) = \frac{\sigma(f)}{\ddot{x}(f)} \quad (1)$$

where H(f) is the FRF, $\sigma(f)$ is the stress (output) and $\ddot{x}(f)$ is the base acceleration (input). After finding FRF, stress PSD can be found as follows:

$$PSD_{\sigma} = H(f).H^{*}(f).PSD_{\ddot{x}} \quad (2)$$

Where $H*(f)$ is the conjugate of the $H(f)$. $PSD\ddot{x}$ corresponds to the PSDs in this case.

After obtaining the stress PSDs for each axis, they are cycle counted by Lalanne method which is explained in (3). In this situation, stress probabilty density function was found instead of peak probability of the displacement as follows:

$$N(s) = \frac{\sqrt{1-r^2}}{\sigma_{rms}\sqrt{2\pi}}.e^{-\frac{\Delta S^2}{2(1-r^2)}}\sigma_{rms}^2 + \frac{r.\Delta S}{2.\sigma_{rms}}\left[1 + erf\left(\frac{r.\Delta S}{\sigma_{rms}\sqrt{2(1-r^2)}}\right)\right] \quad (3)$$

Where (S) is the number of stress cycles, ΔS is the stress range, σ_{rms} is the RMS value of the stress. In the above expression, r is irregularity factor and erf is the error function respectively.

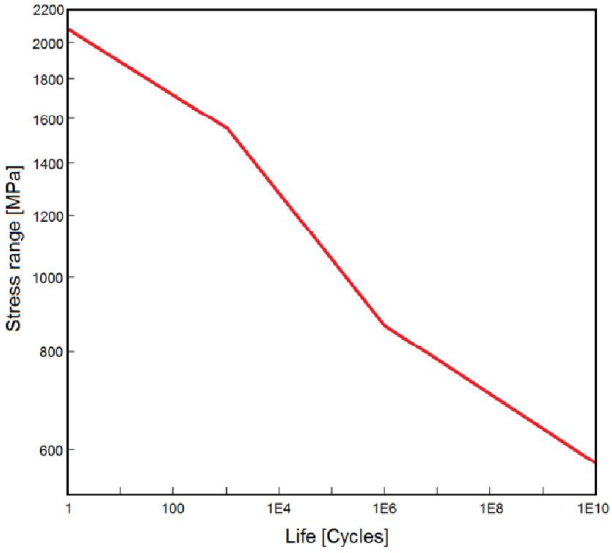


Figure 7: S-N curve of 4140 steel material [13]

After cycle counting, S-N curve of the material was used to calculate life. The material of the model is 4140 steel with 36-42 HRC hardness and S-N curve of this material is shown in Figure 7. Von Mises RMS stress results of the model obtained from the PSD_{σ} are shown in next section. These results were obtained for every axis separately because of software limitations.

IV. Results and Discussion

Acceleration data steps to prepare data for fatigue analyses and tests are given briefly as follows. The power spectral densities (PSD) of all the selected data were calculated separately. PSD envelope is composed from the real environment PSDs to use in analyses and tests as shown in from Figure 8a to Figure 8c.

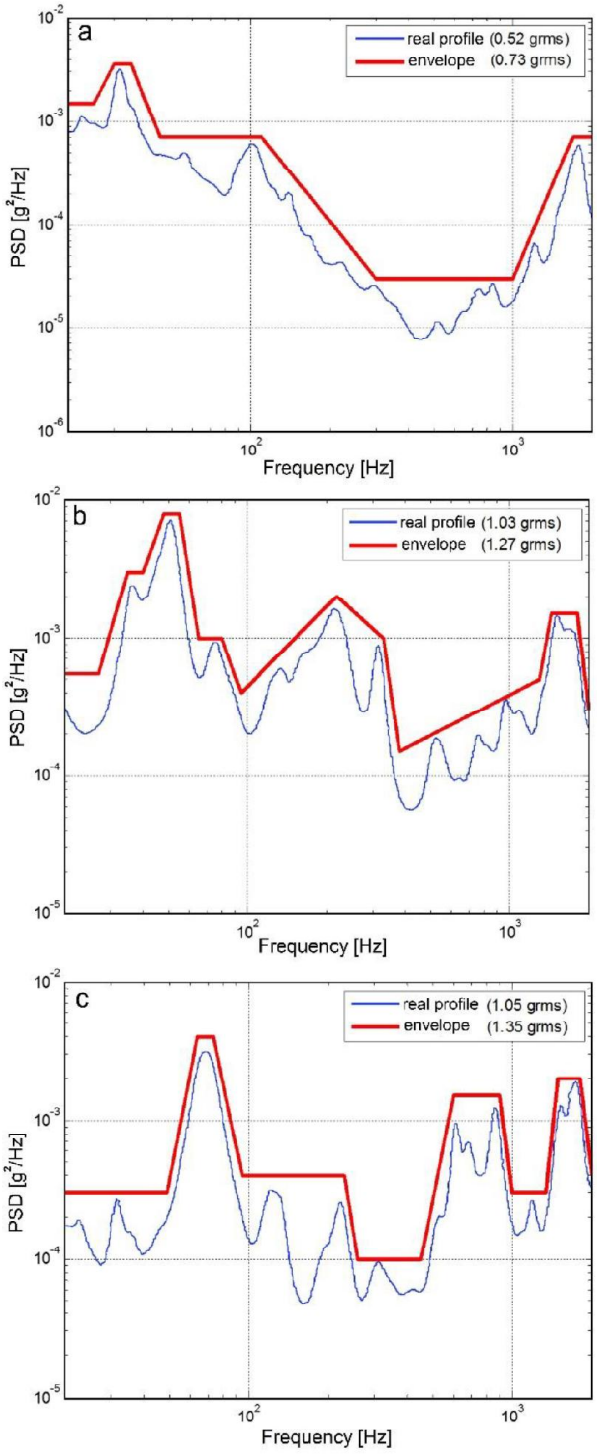


Figure 8: PSD envelope for the acceleration PSD data from accelerometer 2 (a) x direction, (b) y direction and (c) z direction.

The total captive carriage duration was assumed as 1000 hours. The Miner-Palmgren hypothesis was used for test duration reduction.

Von Mises RMS stress results of the model obtained from the $PSD\sigma$. These results were obtained for every axis separately because of software limitations. Therefore, multi-axial load effects were not considered. However, from figures, High stress locations are different for each axes vibration. Also, magnitudes of the von Mises RMS stresses are very different for each axis. Therefore, the results of uniaxial fatigue analysis would not be too different from the results of multi-axial stresses.

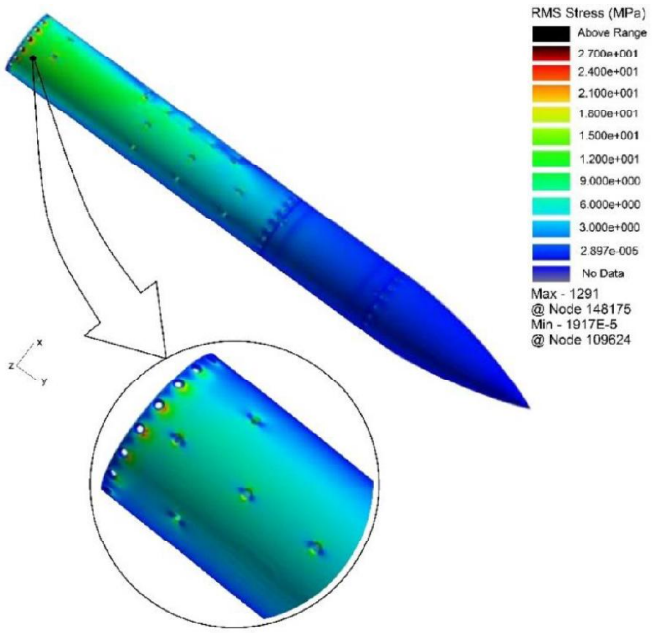


Figure 9: Von Mises RMS stress – z direction

Life results in Fig. 9 show that the components are durable for long flight durations. Not too many locations have lower life than 1e20 seconds. The most critical vibration direction seems to be the z direction because of the gap in the middle of the cylinder shell and low thickness of the gap hatch and shell in this location. Results also show that multi-axial fatigue analysis would not change the results explicitly because z direction is much more dominant than the other two axes.

V. Conclusion

Fatigue behavior of an external store under fixed wing aircraft platforms during random vibration is investigated. For this purpose, a data measurement store (DMS) was produced. Strain and acceleration data from the DMS was collected during 5 different sorties. Acceleration data were used for PSD calculation for an ideal average sortie for F-16C jet aircraft. The minimum life was found about 1e20 seconds. The most critical vibration direction seems to be the z direction because of the gap in the middle of the cylinder shell and low thickness of the

gap hatch and shell in this location.

ACKNOWLEDGMENT

The authors wish to thank to the TUBITAK SAGE for their motivations, supports of equipment and workforce in order to carry out the study.

REFERENCES

[1] J. F. Dreher, "Aircraft Equipment Random Vibration Test Criteria Based on Vibrations Induced by Turbulent Airflow Across Aircraft External Surfaces", United States Air Force Flight Dynamics Laboratory, Ohio, 1982.

[2] MIL-STD-810G, Department of Defense Test Method Standard for Environmental Engineering Considerations and Laboratory Tests, United States Department of Defense, 2008.

[3] K. Eldred, W. Roberts and R. White, "Structural Vibrations in Space Vehicles", Northrop Corporation Norair Division and Western Electro Acoustic Laboratory, California, 1961.

[4] R. H. Lyon, "Random Noise and Vibration in Space Vehicles", The Shock and Vibration Information Center, United States Department of Defense, Washington, 1967.

[5] J. S. Bendat, L. D. Enochson and A. G. Piersol, "Tests for Randomness, Stationarity, Normality and Comparison of Spectra", Measurement Analysis Corporation, California, 1965.

[6] A. Halfpenny, "A Frequency Domain Approach for Fatigue Life Estimation from Finite Element Analysis", Damage Assessment of Structures, Dublin, 1999.

[7] T. Dirlik, "Application of Computers in Fatigue Analysis", Ph.D. Thesis, University of Warwick, 1985.

[8] K. C. Topham, "Fatigue Damage Due to Vibration Testing", Master Thesis, The University of Arizona, 1991.

[9] M. Behrooz, R. Ghajar and H. Moztarzadeh, "Critical Plane and Fatigue Damage Analysis of a High-Speed Microgenerator Shaft", *Proc. 9th Int. Conf. Mech. Design Production*, pp. 1206-1214, 2007.

[10] W. N. Findley, "A Theory for the Effect of Mean Stress on Fatigue of Metals Under Combined Torsion and Axial Load or Bending," *Journal of Engineering for Industry*, 301-306, November 1959.

[11] C. Lalanne, *Specification Development*, London: ISTE Ltd, 2009.

[12] J. Mentley, *Vibration Fatigue*, nCode Products User Group Meeting, 2013.

[13] *SN Curve of 4140 Steel*, n-Code Material Database.

Optimum Design of Horizontally Loaded Short Piles

Ö.TAN[1] İ.H.ERKAN[2] M.OLGUN[2]

[1] Selcuk University, Konya/Turkey, ozcantan@selcuk.edu.tr
[2]Selcuk University, Konya/Turkey, hakkierkan@ selcuk.edu.tr, molgun@selcuk.edu.tr

***Abstract* - In this study, ultimate lateral load capacity of short rigid piles, which are very important in Geotechnical Engineering, have been investigated with the Brinch-Hansen Method and Taguchi Optimization Method. Taguchi Method, which is a powerful optimization method, was used to determine the effects of parameters on the result and to achieve parametric analysis studies. Standard L16 orthogonal array with 5 parameters and 4 levels was chosen to determine the depth of centre of rotation and ultimate lateral resistance capacity of short rigid piles. As a result of evaluation; it was determined that the most efficient parameters on the depth of centre of rotation point and ultimate lateral resistance were the pile length. It was understood that it is possible to reach the results with the using Taguchi Method in a high safety range. Additionally, the equation was developed to determine the ultimate lateral resistance capacity of the short rigid piles for practical purposes.**

***Keywords* – Lateral load, short rigid pile, Brinch-Hansen Method, Taguchi Method.**

I. INTRODUCTION

Pile foundations are extensively used to support various civil engineering structures, such as high rise buildings, transmission powers, many of offshore and coastal structures, bridge piers and highway structures. Piles are not only used to support vertical loads, but also lateral loads due to earth pressure, earthquake or wave force, wind force and inclined forces. The behaviour of piles subjected to lateral loads is governed by the interaction between superstructure, pile and the soil. Pile properties, including pile stiffness and geometry; soil stres-strain behaviour, shear strength, stiffness, and volume change characteristics; and the pile-soil interface play important roles in the response of piles subjected to lateral loads [1].

Several empirical and numerical methods have been proposed for analyzing the behaviour of piles subjected to a lateral load. These methods can generally be classified into three main groups: (1) empirical methods [2, 3], (2) the lateral load transfer curve method, often referred to as the p-y curve method [4-8], and (3) elastic and finite element methods [9, 10]. Additionally, several investigators have conducted laboratory [11-13] and field tests [14-17] to study the behaviour of piles under lateral loads.

The lateral load capacity of the pile depends upon the soil and pile characteristics, load eccentricity and depth of embedment. Hence, different situations of these factors were into accounted in previous studies. Matlock and Reese [18] presented a generalized iterative solution method for rigid and flexible laterally loaded piles embedded in soils with two forms of varrying modulus with depth. The ultimate lateral resistance of rigid piles based on earth pressure theory was developed by Brinch Hansen [2] and is applicable for short piles. Davisson and Gill [19] investigated the case of a laterally loaded pile embedded in a layered soil system with a constant modulus of subgrade reaction in each layer. Broms [3] presented a method based on earth pressure theory with simplifying assumption for distribution of ultimate soil resistance along the pile length. This method is basically the procedure suggested by Hansen [2] with a few modifications and applicable for both short piles and long piles. Broms [3] assumed a limiting resistance of 9su to determine the ultimate lateral load. Based on upper bound analysis, Randolph and Houlsby [20] indicated that the value 9su is largely empirical and suggested values in the range of 9.14su-11.94su.

In wiev of the above stated issues, the objective of this paper is to investigate the effects of fundamental pile and soil properties on the behaviour of a pile subjected to lateral loads for short rigid piles. Factors affecting the ultimate lateral resistance capacity and center of rotation point of laterally loaded short rigid piles are investigated via empirical Brinch-Hansen Method and Taguchi Method, which is a powerful optimization technique.

II. BRINCH HANSEN METHOD FOR SHORT RIGID PILES

The pile behaviour is dependent on the characteristics length T of the pile (Eq 1). When length of pile (L) exceeds 5T, the pile is considered as long pile and when the pile length is < 2T, the pile is considered as short rigid pile [23].

$$T = \sqrt[5]{\frac{E_p I_p}{n_h}} \qquad (1)$$

Where; E_p : Young's modulus of the pile material
I_p : Moment of inertia of the pile section
n_h : Constant of modulus of horizontal subgrade reaction (it is obtained from studies of previous researchers for different types of soil in literature [24, 25].

When a horizontal load is applied to the head of a vertical pile which is free to move in any lateral direction, the load is initially carried by the soil close to the ground surface. However, the soil compresses elastically and there is some transfer of load to the soil at a greater depth. When the horizontal load is increased the soil yields plastically and the load transfer extends to greater depths. A short rigid pile will rotate and passive resistance will develop at the toe on the same face at which the load is applied, in addition to the passive resistance of the soil near the ground surface on the opposite face (Fig. 1a). Failure occurs by rotation when the passive resistance at the head and toe are exceeded. A short rigid pile restrained at the head by a pile cap or bracing fails by translation (Fig. 1b) [26].

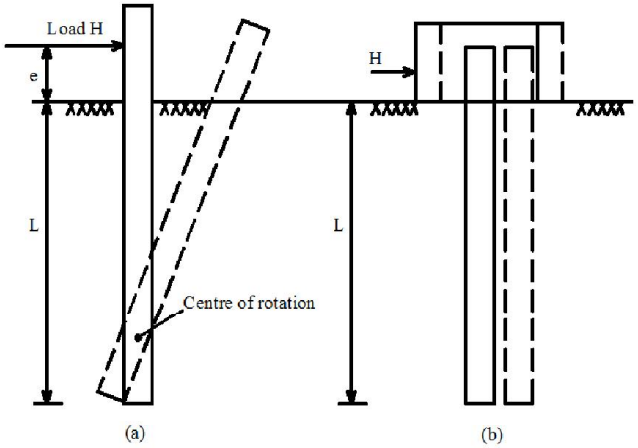


Figure 1: Failure of short rigid pile under horizontal load a) free head b) fixed head

Brinch-Hansen Method is mainly based on lateral earth pressure theory and developed for short rigid piles. The method is a simple one applicable to fine or coarse soils either in uniform or layered state of deposition. Undrained shear strength parameters (c_u and $\phi = 0^0$) can be used for short term loading conditions and drained effective shear strength parameters (c' and ϕ') can be used for long term loading conditions.

III. TAGUCHI METHOD

For an experiment design and parametric study different methods have been developed. These are as follows:

- Conventional statistical experiment design
  - a- Full factorial experiment design
  - b- Fractional factorial experiment design
- Taguchi experiment design
- Testing while changing a factor in each case

Using full factorial design might be impossible in terms of cost and time when especially numbers of parameters and levels are too many. In such cases, it might be an option to prepare an experiment design while changing a factor in each case or using fractional experiment design. But it is a problem to choose which parameters and levels are to be selected in such designs in terms of reliability of the results.

Taguchi Method is a technique targeting to deliver full factorial study results via small amount of experiments and studies. This technique is a powerful alternative method, which is developed to decrease costs in optimization and parametric analysis studies, to determine the effects of parameters on the result and to achieve the results in a shorter time.

According to Taguchi Method, factors affecting the product or the process are divided into two groups as factors that can be controlled and that cannot be controlled. To be able to determine the optimum values of factors that can be controlled, specially designed orthogonal indexes (experiment designs) depending on parameter numbers and levels are used. L16 experiment design table that is used for this study is given in Table 1-2-3. This table has 16 lines and maximum five columns. Number of columns can be changed according to number of parameters. Each line shows the number of study that shall be made with factor levels in that line.

Table 1: L_{16} Orthogonal index table

Experiment no	Parameters and parameter levels on which experiments shall be carried out				
	F1	F2	F3	F4	F5
1	1	1	1	1	1
2	1	2	2	2	2
3	1	3	3	3	3
4	1	4	4	4	4
5	2	1	2	3	4
6	2	2	1	4	3
7	2	3	4	1	2
8	2	4	3	2	1
9	3	1	3	4	2
10	3	2	4	3	1
11	3	3	1	2	4
12	3	4	2	1	3
13	4	1	4	2	3
14	4	2	3	1	4
15	4	3	2	4	1
16	4	4	1	3	2

.

Table 2: Parameters and parameter levels chosen in the study

	Parameters
Levels	γ= 18 kN/m^3

	Pile diameter (D) (m)	Pile length (L) (m)	Pile length over the soil (e) (m)	Internal friction angle (ϕ) (Degree)	Coh. (c) (kPa)
1	0.30	2	1	10	0
2	0.45	4	1.50	20	25
3	0.60	6	2	30	50
4	0.75	8	3	40	75

Table 3: S/N values for L_{16} orthogonal index

Exp. no	D (m)	L (m)	e (m)	ϕ (^{0})	c (kPa)	S/N ratio
1	0.30	2	1	10	0	3.78
2	0.30	4	1.50	20	25	9.20
3	0.30	6	2	30	50	12.63
4	0.30	8	3	40	75	15.30
5	0.45	2	1.50	30	75	3.06
6	0.45	4	1	40	50	9.80
7	0.45	6	3	10	25	12.55
8	0.45	8	2	20	0	15.91
9	0.60	2	2	40	25	3.11
10	0.60	4	3	30	0	9.82
11	0.60	6	1	20	75	12.87
12	0.60	8	1.50	10	50	15.18
13	0.75	2	3	20	50	2.89
14	0.75	4	2	10	75	9.09
15	0.75	6	1.50	40	0	13.66
16	0.75	8	1	30	25	15.75
					Average S/N	10.29

In each column, there exist 4 pieces of level 1, 4 pieces of level 2, 4 pieces of level 3 and 4 pieces of level 4. Since there exist 16 combinations as (1,1), (1,2), (1,3), (1,4), (2,1), (2,2), (2,3), (2,4), (3,1), (3,2), (3,3), (3,4), (4,1), (4,2), (4,3), (4,4) this is described as L16 experiment design table.

In S/N analysis, as big as the S/N ratio that is called index change, product change around target value shall be that much smaller. The S/N ratio is determined via the following equation (Eq. 2);

$$\text{S/N} = -10 \text{ x } \text{Log}_{10}(MSD) \qquad (2)$$

MSD value is calculated using the Equations 3 - 5 for the biggest target value, for the smallest target value and any certain value respectively.

$$MSD = \left(\frac{1}{Y_1^2} + \frac{1}{Y_2^2} + ... + \frac{1}{Y_{n_r}^2} \right) / n_r \qquad (3)$$

$$MSD = \left(\frac{Y_1^2 + Y_2^2 + ... + Y_{n_r}^2}{n_r} \right) \qquad (4)$$

$$MSD = \left(\frac{(Y_1 - Y_0)^2 + (Y_3 - Y_0)^2 + ..(Y_{n_r} - Y_0)^2}{n_r} \right) \qquad (5)$$

Y_1 ... Y_{nr} values are experiment (analysis) results and "n_r" is the number of repeats in the experiment. The expected (target) value with Taguchi Method is determined via the following equation (Eq. 6).

$$Y_{\text{exp}ected} = \sqrt{\frac{1}{MSD_{average}}} \qquad (6)$$

For the reliability of experiment or study results it is required to carry out statistical analyses. For this, effect percentages and reliability levels of parameters on the result are determined using multi-parameter analysis of variance (ANOVA) [27].

IV. Investigating Findings

In Brinch-Hansen Method, 5 important factors affecting ultimate lateral resistance of laterally loaded short rigid piles (for homogeneous single layer ground medium) are;

- Pile diameter (D)
- Pile length (L)
- Pile length over the soil (e)
- Internal friction angle (ϕ)
- Cohesion (c).

In the study, choosing with 5 factors and 4 levels L16 orthogonal index table, centre of rotation point depths and ultimate lateral resistances of laterally loaded short rigid piles have been calculated with Brinch-Hansen Method. Making S/N analyses and variance analyses, effect ratios of parameters on the result and parameter levels where ultimate lateral resistances are biggest and smallest have been determined. Moreover, equations that can be used determining ultimate lateral resistances taking care of average S/N values of parameter levels have been developed. To test the reliability of developed equations, statistical analyses have been carried out. The values obtained from statistical analyses have been compared with values obtained from Brinch-Hansen Method.

A. Ultimate Lateral Resistance Values

Ultimate lateral resistance values (H_u) calculated with Brinch-Hansen Method for L_{16} orthogonal index are given in Table 4. S/N values calculated using these data are given in Table 4 also and average S/N ratio values regarding parameter levels are given in Table 5. Response graphs had drawn using values given in Table 5 are given in Figure 2.

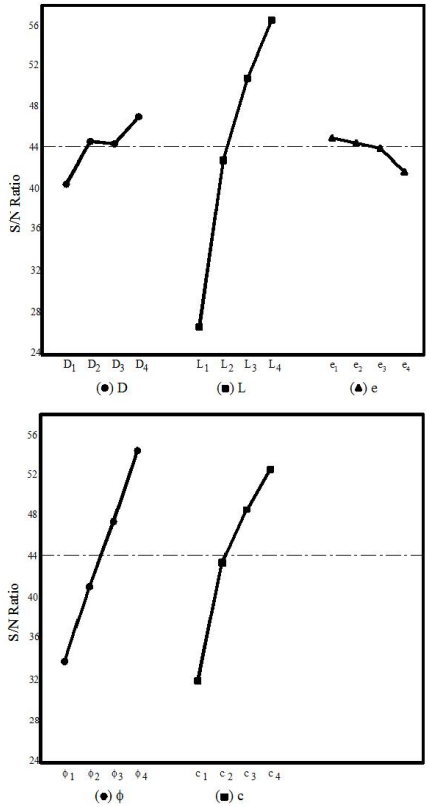


Figure 2: Brinch Hansens cofficients

Table 4: H_u and S/N values for L_{16} orthogonal index

Experiment no	H_u (kN)	S/N ratio
1	1.20	1.29
2	74.20	37.41
3	552.60	54.80
4	2878.70	69.20
5	108.00	40.70
6	879.80	58.90
7	78.80	37.90
8	120.70	41.60
9	64.90	36.20
10	39.10	31.80
11	745.10	57.40
12	428.40	52.60
13	26.90	28.60
14	153.30	43.70
15	477.90	53.60
16	1373.40	62.80
	Average S/N	44.30

Table 5: Average S/N ratios for Parameter levels (for H_u)

Parameters	Average S/N Ratios			
	Level 1	Level 2	Level 3	Level 4
D (m)	40.68	44.78	44.54	47.17
L (m)	26.70	42.96	50.95	56.55
e (m)	45.10	44.61	44.11	41.89
ϕ (^{0})	33.89	41.27	47.53	54.48
c (kPa)	32.10	43.58	48.75	52.75

ANOVA analyses have been carried out to determine effect levels of five parameters on ultimate lateral resistance according to Brinch-Hansen Method and related results are given in Table 6.

Table 6: The results of ANOVA analysis (for H_u

Parameters	Degree of freedom (DOF)	Sum of square (Ss)	Variance (V)	Effect ratio (P) (%)
D (m)	3	86.36	28.80	2.14
L (m)	3	2023.50	674.50	50.12
e (m)	3	38.50	12.80	0.95
ϕ (^{0})	3	925.70	308.70	22.93
c (kPa)	3	963.50	321.20	23.86
Total	15		4037.70	100.00

The most effecting parameter on ultimate lateral resistance is the pile length with a value of 50.12% as can be seen in Table 7 and Figure 2. Cohesion with a value of 23.86% and internal friction angle with a value of 22.93% are 2nd and 3rd most effecting parameters respectively. The effect ratio of the pile diameter is 2.14% and the effect ratio of the pile length over the soil is found as 0.95%. This shows that D and especially e values are not much affecting parameters. S/N analyses have been carried out to determine the parameter levels on which maximum H_u value is obtained. When D=0.75m, L=8m, e=1m, ϕ= 40^0, c=75kPa the maximum value of H_u=7560 kN is found (Table 10).

Table 7: Optimum conditions and performance values for H_u

Parameters	Parameter level for Max. H_u	Parameter level for Min. H_u	Parameter value for Max. H_u	Effect ratio (P) (%)
D (m)	4	1	0.75	2.87
L (m)	4	1	8	12.26
e (m)	1	4	1	1.78
ϕ (^{0})	4	1	40	10.18
c (kPa)	4	1	75	8.46
Expected maximum S/N value				79.85
Expected maximum H_u value (kN)				7560.00
Maximum H_u value (kN) calculated using Brinch-Hansen Method				6270.00
Expected minimum H_u value (kN)				0.56
Minimum H_u value (kN) calculated using Brinch-Hansen Method				0.52

Since ultimate lateral resistance is estimated very reliably an effort is given to develop an equation that can be used to find ultimate lateral resistance of short rigid piles. For this purpose, statistical analyses have been carried out and error ratios have been determined choosing different mathematical functions using average S/N values belonging to parameter levels. As a result of researches, the most appropriate modal that can be used to determine the ultimate lateral resistance capacity of short rigid piles is given as follows (Eq. 7);

$$H_u(kN) = 1.07\left(\frac{1}{10^{\alpha}}\right)^{0.5} \quad (7)$$

In this equation, α total effect coefficient is determined with the following equation (8);

$$\alpha = -0.1\left(L_c + L_e + L_\phi + L_L + L_D\right) \qquad (8)$$

L_c : cohesion effect factor, L_e : effect factor of pile length over the soil, L_ϕ : effect ratio of the internal friction angle, L_L : effect ratio of pile length, L_D : effect factor of pile diameter. Effect factors for different parameter values are given in Table 8.

Table 8: Ultimate lateral resistance effecting factors

For c<25 kPa	L_c=0.46c-3.24
For c>25 kPa	L_c=0.1834c+3.68
For e< 2m	L_e= -0.98e+10.68
For e> 2m	L_e= -2.22e+13.18
Between ϕ=10-40^0	L_ϕ=30.697tanϕ-6.15
For L<4.45m	L_L=8.13L-25.00
For L>4.45m	L_L=2.80L-1.28
For D< 0.45m	L_D=27.333D-2.95
Between D=0.45-0.60m	L_D=9.35
For D>0.60m	L_D=15.933D-0.21

To be able to determine the reliability of the developed modal, average error ratio is 9.94% in statistical analyses carried out for 16 different situations and error ratio changes between +19.70 % and -16.40 % (Table 9).

Table 9: Ultimate lateral resistance values calculated with Brinch-Hansen Method and Modal.

Experiment no	H_u (kN) (Brinch-Hansen)	H_u (kN) (model)	Relative error (%)
1	1.20	1.30	19.20
2	74.20	62.00	-16.40
3	552.60	530.90	-3.90
4	2878.70	3357.50	16.60
5	108.00	93.50	-13.40
6	879.80	956.70	8.70
7	78.80	94.40	19.70
8	120.70	119.70	-0.90
9	64.90	77.50	19.50
10	39.10	41.30	5.66
11	745.10	759.90	1.90
12	428.40	415.90	-2.90
13	26.90	25.10	-7.00
14	153.30	183.30	19.60
15	477.90	469.10	-1.10
16	1373.40	1409.40	2.60

V. CONCLUSION

In this study, parameters affecting depth of centre of rotation and ultimate lateral resistance capacity of laterally loaded short rigid piles are investigated according to Taguchi Method using the standart L_{16} orthogonal index table with 5 parameters and 4 levels. Chosen parameters are pile diameter (D), pile length (L), pile length over the soil (e), internal friction angle (ϕ) and the cohesion of the soil (c). As a result of the analyses and evaluations the following have been found:

- The most effecting parameter on depth of centre of rotation of short rigid pile is the pile length with a ratio of 99.38%. As L values increase, x values are increase. Other parameters are very little effect on the depth of centre of rotation values. The effect of the D value is variable and negligible level.
- The most effecting parameter on ultimate lateral resistance capacity of short rigid piles is the pile length with a value of 50.12%. Cohesion with a value of 23.86% and internal friction angle with a value of 22.93% are 2nd and 3rd most effecting parameters respectively. As L, c, ϕ, and D increase, ultimate lateral resistance capacity increases and as "e" increases the ultimate lateral resistance capacity decreases.
- Estimations (expected values for H_u) made with Taguchi Method are quite close to real values and the average error is around 5.50%. This situation shows that the Taguchi Method, which is a powerful optimization technique, can be used in parameter studies in Geotechnical Engineering.
- Average error ratio for H_u values calculated Brinch-Hansen Method and modal equation is less than 10% for 16 different situations. The equation with a number of (11) developed to determine ultimate lateral resistance capacity of the laterally loaded short rigid pile using S/N ratios can be used for practical purposes. Using further data and parameters studies should continue to decrease the error ratio to lower levels.

REFERENCES

1. Fan CC, Long JH. Assessment of existing methods for predicting soil response of laterally loaded piles in sand. *Computers and Geotechnics* 2005; **32**: 274-289.
2. Hansen BJ. The ultimate resistance of rigid piles against transversal forces. *Danish Geotechnical Institute,* Copenhagen, Denmark, 1961; Bulletin No. **12**.
3. Broms B. Lateral resistance of piles in cohesiveness soils. *Journal of Soil Mechanic and Foundation Division* 1964; **90 (4)**: 27-63.
4. Matlock H. Correlations for design of laterally loaded piles in clay. Paper no. OTC 1204, in: *Proceedings of Second Annual Offshore Technical Conference*, Houston, Texas, 1970; 577–594.
5. Reese LC. Behavior of piles and pile groups under lateral load. Rep. to the U.S. Dept. of Transportation. Federal Highway Administration, Office of Research, Development and Technology, Washington, D.C., 1983.
6. Nip DCN, Ng CWW. Back-analysis of laterally loaded piles. *Proceedings of the Institution of Civil Engineers, Geotechnical Engineering* 2005; **158**: 63-73.
7. Guo WD, Lee FH. Load transfer approach for laterally loaded piles. *International Journal Numerical Analysis Methods Geomechanics* 2001; **25**: 1101-1129.
8. Jeong S, Kim Y, Kim J. Influence on lateral rigidity of offshore piles using proposed p-y curves. *Ocean Engineering* 2011; **38**: 397-408.
9. Brown DA, Shie CF. Some numerical experiments with a three-dimensional finite element model of laterally loaded piles. *Computers and Geotechnics* 1991; **12**: 149–162.
10. Karthigeyan S, Ramakrishna VVGST, Rajagopal K. Influence of vertical load on the lateral response of piles in sand. *Computers and Geotechnics* 2006; **33**: 121-131.
11. Anagnostopoulos C, Georgiadis M. Interaction of axial and lateral pile responses. *Journal Geotechnical Engineering* 1993; **119 (4)**: 793-798.
12. Narasimha RS, Mallikarjuna RK. Behavior of rigid piles in clay under lateral loading. *Indian Geotechnical Journal* 1995; **25(3)**: 287-313.
13. Zhang L. Nonlinear analysis of laterally loaded rigid piles in cohesionless soil. *Computers and Geotechnics* 2009; **36**: 718-724.
14. Kim BT, Kim NK, Lee WJ, Kim YS. Experimental load-transfer curves of laterally loaded piles in Nak-Dong River sand. *Journal of Geotechnical and Geoenvironmental Engineering* 2004; **130 (4)**: 416-425.
15. Fam A, Pando M, Filz G, Rizkalla S. Precast piles for Route 40 bridge in Virginia using concrete filled FRP tubes. *PCI Journal* 2003; **48 (3)**: 32-45.
16. Anderson JB, Townsend FC, Grajales B. Case history evaluation of laterally loaded piles. *Journal of Geotechnical and Geoenvironmental Engineering* 2003; **129 (3)**: 187-196.
17. Mcway MC, Zhang LM, T Molnit, Lai P. Centrifuge testing of large laterally loaded pile groups in sands. *Journal of Geotechnical and Geoenvironmental Engineering* 1998; **124 (10)**: 1016-1026.
18. Matlock H, Reese LC. Generalized solutions for laterally loaded piles. *Journal of Soil Mechanic and Foundation Division* 1960; **86 (5)**: 63-91.
19. Davisson MT, Gill HL. Laterally loaded piles in a layered soil system. *Journal of Soil Mechanic and Foundation Engineering* 1963; **89 (3)**: 63-94.
20. Randolph MF, Houlsby GT. The limiting pressure on a circular pile loaded laterally in cohesive soil. *Geotechnique* 1984; **34 (4)**: 613-623.
21. Zamri HC, Jasim MA, Mohd RT, Qassun SM. Lateral behavior of single pile in cohesionless soil subjected to both vertical and horizontal loads. *European Journal of Scientific Research* 2009; **29 (2)**: 194-205.
22. Phanikanth VS, Choudhury D, Reddy GR. Response of single pile under lateral loads in cohesionless soils. *EJGE* 2010; **15**: 813-830.
23. Das BM. Principles of foundation engineering. 5th Edition 2nd reprint, 2004; 591-605.
24 Das BM. Principles of foundation engineering. *PWS-Kent Series in engineering*, Boston, 1990.
25. NAVFAC Design Manuals 7.1 and 7.2, Foundations and earth structures, Department of the Navy, Alexandria, VA, 1988.
26 Tomlinson MJ. Foundation design and construction. 7th Edition, 2001; 314-318.

.

COMPUTER AIDED FORCE ANALYSIS OF HIGH-SPEED TURNING OF METAL MATRIX COMPOSITES

A.O. ER[1]

[1] Kırıkkale University, Kırıkkale/Turkey, er@kku.edu.tr

Abstract - **Investigations about the manufacturing are focused on the machining and the modeling of the new materials and finding the new manufacturing processes. In this study, a constitutive model of metal matrix composite created and then simulation of machining of metal matrix composite made. Simulation results which were taken for different reinforcement percentages and different cutting speeds with coated and uncoated cutting tools are discussed according to forces and temperature.**

Keywords - **Metal matrix composite, machinability, cutting force, temperature at cutting region, modeling of metal cutting.**

I. INTRODUCTION

There are many studies in the literature regarding the machinability of metal matrix composites. The modeling of the machining of metal matrix composites and the effect of machining parameters on machinability are very limited. For this reason, modeling the machinability of composite materials, which is increasingly used today, is an important research topic. With this study, an attempt was made to fulfill this area. When the literature is examined, it can be summarized as follows.

M. El-Gallab, M. Sklad modeled tool wear in the machining of SiC-reinforced Al matrix composites in their work. The model also takes into account the interactions in the tool-chip and tool-material interfaces. As a result, experimental study and modeling of temperature and stress estimation gave close results[1]. J. Monaghan and D. Brazil modeled the flow of machining metal matrix composites in their work. SiC reinforced A356 matrix composite with % 35 volume fraction was modeled with the help of FORGE2 and Ansys 5.2. The generated model and experimental data were compared and good results were obtained [2]. C. R. Dandekar and Y. C. Shin reviewed all the studies for modeling the machining of composite materials and produced a summary article on this subject[3]. N. P. Hung, N.L. Loh and Z.M. Xu investigated the erosion during machining of metal matrix composite materials under machinability [4] and modeling [5]. Carbide inserts were suggested for roughing, and CBN and PCD inserts were suggested for finishing processes while machining SiC and Al_2O_3 reinforced Al matrix composites[5]. A. Pramanik et. al investigated tool particle interaction during orthogonal cutting with finite element method. In the orthogonal cutting process of SiC-reinforced Al matrix composites, they evaluated the Von Misses stresses, which were obtained by simulation. Paramanik A. and colleagues aimed to investigate the interaction between matrix deformation and tool reinforcement in the machining process by using the finite element method[6]. A. Pramanik, L.C. Zhang and J.A. Arsecularatne tried to predict the cutting forces that occur in the machining of metal matrix composites. They have benefited from the formulation used for mechanics of metal cutting[7] C. R. Dandekar and Y.C. Shin, have tried to model the subsurface damage that occurs in the machining of metal matrix composites by using multi-step 3D finite element method. All the subjects such as particle breakage, separation at the particle-matrix interface, matrix wasting are taken into interest. Chinmaya R. and colleagues have modeled the machinability of Al matrix SiC reinforced composite material by using finite element method using Third Wave System and ABAQUS / Explicit packages. A359 aluminum alloy and 20% volume fraction SiC reinforced composite material were used in the study. It was approved that the composite material used during the operation was homogeneous. When the data obtained in the study and the data obtained in the experimental studies were compared, the results were found to be positive. As a result, it has been found that as the cutting force increases, the surface damage increases [8]. Mkaddem A. and colleagues aimed to model the cutting force variation according to the different depth of cut and the rake angle values with different reinforcement arrangements using the finite element method[9]. Mackerle J. studied the work done between 1976 and 1996 using the finite element method of the machining process. It includes the topics of machining process, material loss, modeling in machining process, tool geometry and machining parameters, residual stresses in machining process, cutting tool dynamic analysis, tool wear and fatigue, chip form mechanism[10]. Mackerle J. studied the work carried out between 1996 and 2002 using the finite element method of the machining process. 372 studies were examined in the study. The study was carried out in addition to the study of the author between 1976 and 1996 [11]. Santiuste C. and colleagues have examined the machinability of glass and carbon fiber

reinforced composite materials in their work. The study was carried out for long reinforcement materials using the finite element method. [12]. Arola D. and his colleagues conducted an analysis of the orthogonal cutting process applied to unidirectional reinforced composite materials by finite element method. [13]. As summarized above, there are limited numbers of studies on this subject in the literature. Directly from our point of view, there is no work on the modeling of machinability while the composite material is being produced. In all papers, the machinability of the materials produced has been modeled. This study will constitute important added value in the literature with this respect.

II. MATERIALS AND METHOD

The matrix material of Metal Matrix Composite (MMC) is Al 2014 aluminum alloy. The reinforcement material is SiC and three different reinforcement ratio used for this study. These are 3%, 6%, and 12%.

The analysis of turning MMC was made with the help of Thirdwave Advantedge software. SI unit system, turning operation, standard workpiece, 3-dimensional cutting tool type and standard cutting tool material are used when project is defined in the software. The workpiece thickness, height, and width were specified while defining workpiece material. Workpiece width is 3,0 mm, height is 5,0 mm and length = 10,0 mm. Workpiece material is defined as custom material because it is a composite material. The most important subject in modeling is the identification of composite material. The variables of the materials forming the composite material used in this definition are given in Table 1 below. These variables for composites were found using rule of mixture.

Table 1. Composite material properties.

Material Properties	Matrix Material Al 2014	Reinforcement Material SiC	Composite Material 3%	Composite Material 6%	Composite Material 12%
Density (gr/cc)	2,8	3,21	2,8123	2,8246	2,8492
Modulus of Elasticity (GPa)	72,4	440	83,428	94,456	116,512
Poisson's Ratio	0,33	0,14	0,3243	0,3186	0,3072
Thermal Expansion Coefficient (µm/m-°C)	23	4	22,43	21,86	20,72
Thermal Conductivity (W/m-K)	170	120	168,5	167	164
Heat capacity (J/ kg-°K)	880	750	876,1	872,2	864,4

DSBNR 2020 K12 tool holder used for this study. The cutting tool holder's image used in this research is given in Fig. 1.

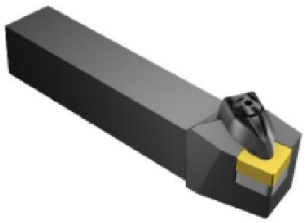


Figure 1: Tool holder.

Uncoated and CVD TiN coated tungsten carbide qualities are used for machining of MMC materials. The insert geometry of the uncoated and CVD coated tungsten carbide is SNMA 120408.

When the tool is identified for modeling, the tooling material, tool thickness, side and backside rake angle, relief angle, lead angle, coating type and thickness are specified. The data used in the software for tool identification is given in Table 2 below.

Table 2. Tool identification data

	Data
Tool Process Type	NOSE
Tool Material	Carbide-Grade-P
Width of Tool	0,476 mm
Maximum Tool Element Size	1.0 mm
Back Rake Angle	0,0 deg
Side Rake Angle	0,0 deg
Lead Angle	7,0 deg
Relief Angle	7,0 deg
Coating Layer No.	2
Coating Material 1	TiC
Coating Thickness 1	0.0036 mm
Coating Material 2	Al_2O_3
Coating Thickness 2	0.0012 mm
Aggregate Layer	ON

In this study, machinability properties of Al 2014 matrix SiC reinforced MMC materials produced by mixing casting

method at three different reinforcement volume ratios were modeled at dry turning conditions with four different cutting speeds, constant feed, and constant depth of cut. Cutting parameters were selected according to the tool-workpiece couple from the tool manufacturer catalog. According to the tool manufacturer catalog depth of cut was given as 1 mm and feed rate as 0.2 mm. Four different cutting speed were chosen. These are 100, 125, 160 and 180 m/min. Cutting speed, cutting depth, cutting length, initial temperature, friction coefficient, cutting fluid are specified when the process is defined. Table 3 lists the data used in the preparing of the software for process identification.

Table 3. Process identification data

	Data
Feed	0.2 mm
Cutting speed	100, 125,160,180 m / min
Depth of cut	1.0 mm
Length of cut	10 mm
Initial temperature	23 degC
Friction coefficient	0.5
Cutting mode	General
External Coolant	OFF
Internal Primary Coolant	OFF
Internal Secondary Coolant	OFF

The data used for simulation identification of software are given in Table 4 below.

Table 4. Simulation idendification data

	Data
Simulation Mode	Standard
Steady state analysis	0
Avg. Length of Cut Ratio	10
Min Element Size (Chip Bulk)	0.0793 mm
Min Element Size (Cutter Edge)	0.0607 mm
Radius of refined region (cutter edge)	0.3 mm
Mesh Refine	5
Mesh Coarse	5
Chip refinement factor	1
Grading near cutting edge	6,0
Grading radius factor	1,0
Output Frame	30
Number of Threads	1
Mesh Generation Required	YES
Geometry Generation Required	YES

Materials were machined in a Goodway GLS 150 turning center for experimental comparison. Chuck, turret, tool, and force measuring instruments are shown in Fig 2.



Figure 2:Goodway GLS 150 turning center and measuring instruments.

III. RESULTS

The results of the simulations were taken as force and temperature. The results of simulations are given for CVD TiN coated and uncoated WC cutting tool.

Results with CVD coated WC Cutting Tool

The image of the cutting tool, workpiece and chip which were taken from the simulation are given in Figure 3. Maximum temperature occurred in contact point of %3 SiC reinforced MMC with coated WC for 100 m/min cutting speed is 378°C.

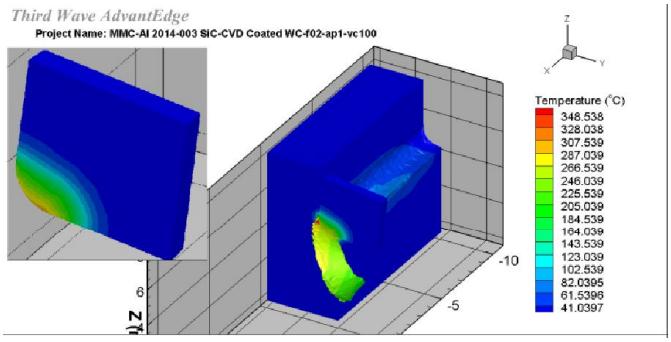


Figure 3: Image taken from simulation result for %3 reinforcement ratio and 100 m/min cutting speed

Comparison of simulation results for the high speed turning of MMC with different reinforcement ratios are given in Figure 4. Graphs of the cutting forces and temperature obtained during simulation of high speed turning of the MMC are shown in Figure 4. Temperatures results of simulation did not differ with different reinforcement ratios.

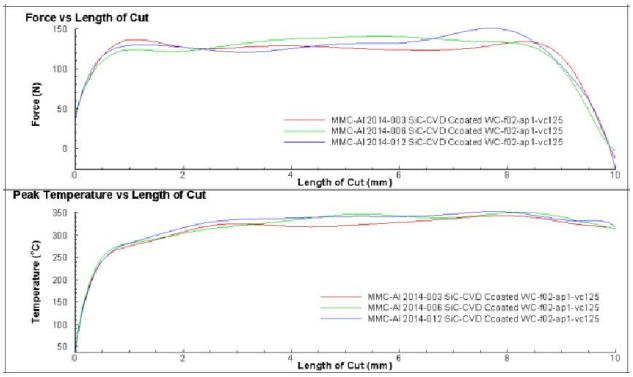


Figure 4: Graphs taken from simulation result for different reinforcement ratios at 125 m/min cutting speed.

Average force results which were simulated using coated carbide for different reinforcement ratios at different cutting speeds are given in Figure 5. Force results decreases generally with the increasing reinforcement ratio as can be seen from the Fig.5. However there is not a relation between them. The force increased with the ascending cutting speeds at %3 and %12 reinforcement. The force at %6 reinforcement had fluctuating values with the increasing cutting speed.

The force results are almost the same with the increasing reinforcement ratio except 180 m/min cutting speed. It decreased with the increasing reinforcement results at max cutting speed.

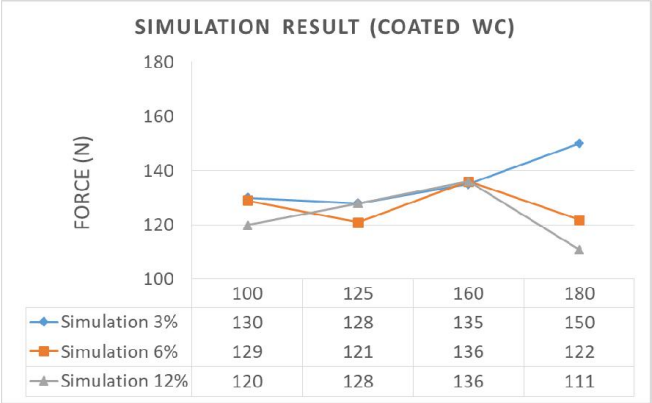


Figure 5: Simulation force results with coated carbide

Experimental force results which were measured using coated carbide for different reinforcement ratios at different cutting speeds are given in Figure 6. Experimental results had generally the same attitude as simulation results. Force results decreases generally with the increasing reinforcement ratio. The force at %3 reinforcement had fluctuating values with the increasing cutting speed.



Figure 6: Experimental force results with coated carbide

Results with Uncoated WC Cutting Tool

The figure of the simulation results for the high speed turning of MMC with different reinforcement ratios are given in Figure 7. It had the same attitude as coated carbide. Temperature results are closer together with uncoated WC cutting tool.

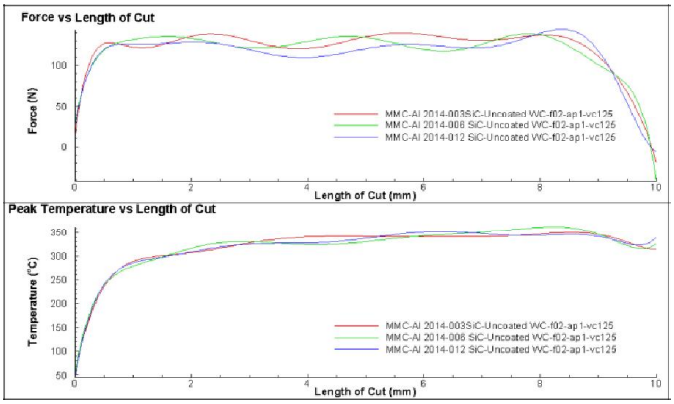


Figure 7: Graphs taken from simulation result for different reinforcement ratios at 125 m/min cutting speed

Average force results which were simulated using uncoated carbide for different reinforcement ratios at different cutting speeds are given in Figure 7. The force increased with the ascending cutting speed at %12 reinforcement. The force at %3 and %6 reinforcement had fluctuating values with the increasing cutting speed.

The force results are decreasing with the increasing reinforcement ratio except 180 m/min cutting speed. It did not change with the increasing reinforcement results at max cutting speed.

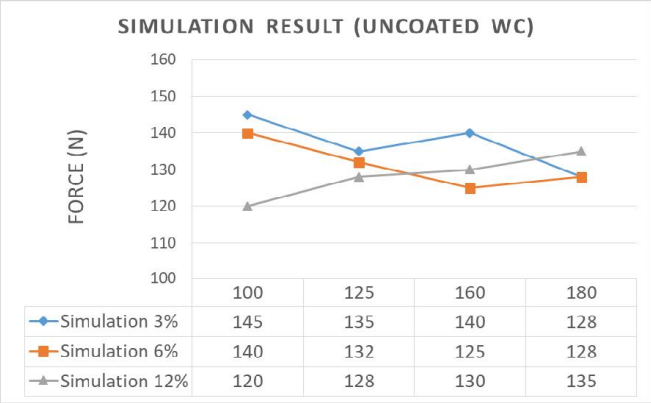


Figure 7: Simulation force results with uncoated carbide

Experimental force results which were measured using uncoated carbide for different reinforcement ratios at different cutting speeds are given in Figure 8. Experimental results had generally the same attitude as simulation results. Force results decreases generally with the increasing reinforcement ratio. Force results increases generally with the ascending cutting speeds. The force at %3 reinforcement had fluctuating values with the increasing cutting speed.

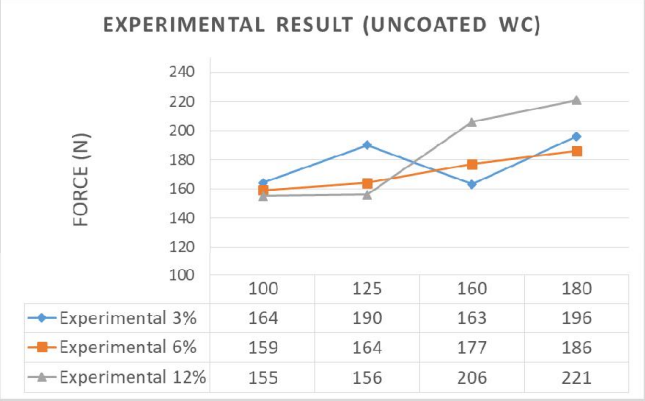


Figure 8: Experimental force results with uncoated carbide

IV. Conclusion

The present study focusses on the effects of different reinforcement ratios to the cutting force and temperature. The comparison of simulation and experimental results for different reinforcement ratios show us that:

- A good agreement has been obtained between the simulation results and experimental force measurements. The definition of simulation inputs had successful results.
- There are not a direct relationship between reinforcement ratios, forces, and temperatures. However force results increases generally with the ascending cutting speeds and decreases generally with the increasing reinforcement ratio. Temperature results are closer together at different reinforcement ratios.
- The difference between the reinforcement ratios are closer together and not enough for finding equation about force and reinforcement ratio difference.

Acknowledgement

This study was supported by the Kırıkkale University Scientific Research Projects Unit, Kırıkkale, Turkey (2016-096).

References

[1] M. El-Gallab, M. Sklad, “Machining of Al:SiC particulate metal-matrix composites Part I: Tool performance”, *Journal of Materials Processing Technology*, vol. 83, pp. 151–158, 1998.

[2] Monaghan and Brazil, “Modelling the flow processes of a particle reinforced metal matrix composite during machining”, *Composires Part-A*, vol. 29A, pp. 87-99, 1998.

[3] Chinmaya R.Dandekar, Yung C. Shin, “Modeling of machining of composite materials”, *International Journal of Machine Tools & Manufacture*, vol. 57, pp. 102–121, 2012.

[4] N.P. Hung, N.L. Loh, Z.M. Xu, “Cumulative tool wear in machining metal matrix composites Part II: Machinability”, *Journal of Materials Processing Technology*, vol. 58, pp. 114-120, 1996.

[5] N.P. Hung, C.H. Zhong, “Cumulative tool wear in machining metal matrix composites Part I: Modelling”, Journal of Materials Processing Technology, Volume 58, Issue 1, 1 March 1996, Pages 109–113.

[6] Pramanik, L.C. Zhang, , J.A. Arsecularatne, “An FEM investigation into the behavior of metal matrix composites: Tool–particle interaction during orthogonal cutting”, International Journal of Machine Tools and Manufacture,Volume 47, Issue 10, August 2007, Pages 1497–1506.

[7] Pramanik, L.C. Zhang, , J.A. Arsecularatne, “Prediction of cutting forces in machining of metal matrix composites”, International Journal of Machine Tools and Manufacture, Volume 46, Issue 14, November 2006, Pages 1795–1803.

[8] Chinmaya R. Dandekar, Yung C. Shin, “Multi-step 3-D finite element modeling of subsurface damage in machining particulate reinforced metal matrix composites”, Composites Part A: Applied Science and Manufacturing, Volume 40, Issue 8, August 2009, Pages 1231–1239.

[9] Mkaddem, A., I. Demirci and M. E. Mansori, "A micro–macro combined approach using FEM for modelling of machining of FRP composites: Cutting forces analysis", Composites Science and Technology 68(15-16), 2008, 3123-3127.

[10] Mackerle, J., "Finite-element analysis and simulation of machining a bibliography (1976–1996)", Journal of Materials Processing Technology 86, 1999, (17-44).

[11] Mackerle, J., "Finite element analysis and simulation of machining an addendum A bibliography (1996–2002)", International Journal of Machine Tools & Manufacture 43, 2003, (103-114).

[12] Santiuste, C., X. Soldani and M. H. Miguélez, "Machining FEM model of long fiber composites for aeronautical components", Composite Structures 92(3), 2010, 691-698.

[13] D. AROLA, M. R. "Ortogonal cutting of fiber-reinforced composites: a finite element analysis”, Pergamon 7403, 1996, (00061-6).

Fuzzy Inference System Application for Parameter Setting in Changeovers of Plastic Injection Molds

M. K. KARASU[1] and L. SALUM[1]

[1] Dokuz Eylül University, İzmir/Turkey, mkkarasu83@hotmail.com
[1] Dokuz Eylül University, İzmir/Turkey, latif.salum@deu.edu.tr

Abstract **- For changeover time reduction, the famous methodology named single minute exchange of dies (SMED), introduced by Shigeo Shingo, has been applied in production plants for years in lean manufacturing scope. The main philosophy of this technique can be summarized as, "make it simple and keep it simple". However, this simplification is not possible for all the steps of a changeover. In the last part of a changeover, which is also named as trial runs and adjustment, injection parameters are manipulated to resolve quality issues that occur during trial productions after changing the mold. This session requires a deep knowledge and experience thus only the dedicated personnel called as setup experts can handle.**

In this study, fuzzy inference system (FIS) is used to capture this domain expertise. The primary objective is to distribute the domain experience to non-expert plastic injection personnel thus eliminate the setup expert scarcity and to increase flexibility in production. A systematic elimination of defect cases is presented to define the core scope that handles all the possible quality issues and their solutions with fewer rules.

Proposed soft computing solutions are implemented in a well-known international wiring device manufacturing plant together with a project team composed of setup experts and production staff. The results show that FIS could generate correct defect resolution actions on injection parameters as changeover experts do.

Keywords **- Plastic injection molding, quick changeover, parameter setting, expert system, fuzzy inference system**

I. INTRODUCTION

Small lot production is an important element of lean manufacturing that reduces the variability in the system. Lot size directly affects the inventory levels, scheduling activities, lead time to customer and quality of the product. The biggest challenge in front of lot size reduction is the cost of setup. In order to decrease the setup cost, it is obvious that setup times must be reduced.

Single minute exchange of dies (SMED) [1] is the most popular technique in changeover time reduction which mostly uses simplification and standardization logic. This tree-step methodology starts with questioning all activities of a changeover to define whether they require stopping the machine or not. The activities that require stopping the machine are named as internal activities and the others are called as external activities. The proposals in this step are; ensuring the readiness of people, molds, tools, and equipment in advance, controlling them via checklists; make them ready in front of the machine just before the changeover, and placing the replaced parts back to the storage area after starting the machine.

In step two, internal activities are converted to external activities mostly via design changes and/or modifications. Standardizing the mounting, demounting, dimensioning, centering, securing, expelling and gripping functions, using intermediary jigs and preparing conditions in advance (like pre-heating the injection molds) are the proposed improvements for internal activities.

In the last step of SMED, both external and internal activities are re-evaluated for further improvement. Since molding machines are big equipment, one person travels a lot during changeover. A second operator, who will work in parallel, reduces the demounting and mounting time by half. Use of functional clamps, which provide one motion clamping/de-clamping, has a big advantage over use of nuts and bolts.

However, not all of the steps of changeover could be simplified/standardized by SMED. The last step, named trial runs and adjustment is a quite complex session wherein a dozen of quality issue is resolved by injection parameters manipulation. Although Shingo emphasized the magnitude of this session, it slides over the problem by assuming “as long as preceding improvements are applied properly, adjustments will be easier”. It’s true up to a point; however, eliminating the need for this session is not possible due to sensitive nature of molten plastic. Moreover, each changeover is a unique parameter setting problem that must be solved within minutes. In the application, this session is handled by a limited number of experienced personnel called as setup experts. In the cases that the number of the molds waiting for changeover is more than the number of setup experts on a shift, either the machines are stopped or continue production until an expert becomes available. So, even SMED implementation is completed, changeover still remains unpleasant due to the expert scarcity.

Moreover, knowledge is precious and should be recorded. It is not uncommon that once a setup expert decides to leave the job, production planning unit has to increase batch sizes to decrease the setup frequency which is the exact opposite of

what lean philosophy says. Such a knowledge record should also be used as a training material for newcomers.

II. DRIVERS OF PRODUCT QUALITY IN PLASTIC INJECTION MOLDING (PIM)

Selection of the resin (plastic raw material) and selection of the injection machine are two important headlines which are as important as the design itself and these three are directly cross-related. In this study these three components are named as "primary factors" to the molding performance. The expectations from the product dictate them simultaneously. As an example, if the product is expected to be sound, wall thickness of the part should be carefully examined and a resin which would provide the soundness should be selected and the machine should have enough clamping force to inject this resin into the mold. In an another example, if the annual demand is too high, the mold is designed with multi cavities and the total molding cycle time is set as short as possible, thus the resin should have high flow rate and quick cooling capability and the injection machine must have compliance with rapid production.

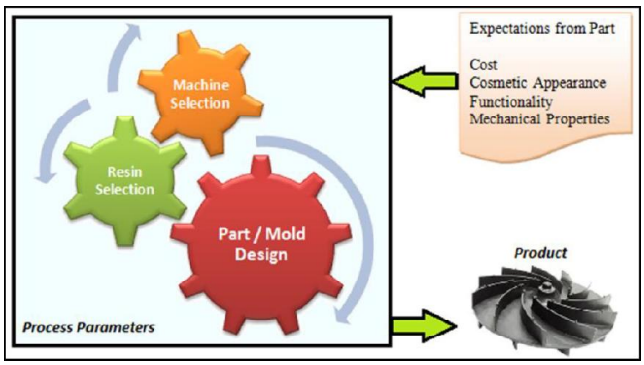


Figure 1: Drivers of product quality in PIM.

The "secondary factors" affecting the product quality are the process parameters. Injection process parameter set is just like a "lubricant" in the gearbox (Figure 1) that helps the primary factors to work smoothly. These parameters are; temperatures (of melt, mold, nozzle, barrel etc), pressures (of injection, holding and packing), and duration (of injection, cooling, packing). Even if there is a great compatibility among design-resin and machine, the process fails to produce qualified products unless the process parameters are set properly.

The last type of factors that affects the product quality in PIM is the "organizational factors". These factors are mostly observed in mass production and generally arisen from negligence. Hindering the periodic maintenance of the machine, equipment and tooling, poor warehousing and poor 5S are the factors that ruins the smooth mass production.

These three groups of factors affecting the product quality can be summarized as in Figure 2.

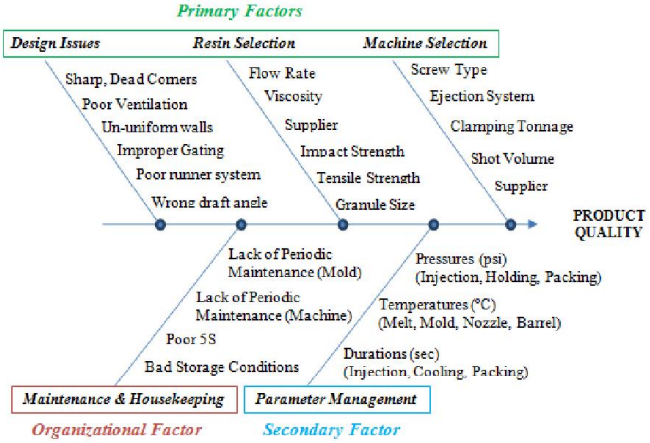


Figure 2: Cause and effect diagram for product quality in PIM.

III. MANAGEMENT OF PROCESS PARAMETERS IN PIM

Management of process parameters plays an important role to build a robust plastic injection process from initial design to mass production. Parameter setting activities can be grouped under three modes; virtual, initial and changeover setting.

In the design phase, aforementioned primary factor combinations are assessed by optimizing secondary factors for each case in virtual environment. In another saying, the best design-machine-resin combination is evaluated under different process parameter set with the aid of molding simulation programs. This process is called as ***virtual parameter setting*** and is a part of soft validation studies. This step is the last step before the mold is manufactured thus primary factors are defined and fixed in this phase.

During injection molding, plastic raw material is exposed to high rheological and thermo-mechanical changes [2]. Due to the sensitive nature of plastic injection the real molding performance differs from the expectations in simulation studies. To detect and resolve the molding issues in real production, the mold is transferred to the trial production team. The aim of this step is to define the optimal process parameters that recover injection defects and minimize the cost of molding under real production conditions. This step is called as ***optimal (initial) parameter setting***.

After the validation of the mold in trial production, the optimal set is recorded and the mold is launched to the mass production. For each changeover session during mass production, the initial set should be modified because it shifts from its original point due to the noise factors, which are explained in the following section. Therefore, after mounting the mold for the next product in the production plan, the optimal set is recalled from the database and used as the initial set to redefine the shifted optimal set. The trial and error based parameter adjustment in this session is called as ***changeover parameter setting*** wherein setup experts try to resolve the injection defect to start the mass production in a limited time.

In the cases that parameter setting is useless in resolving the quality issue, the troubleshooting mode is activated to find the real problem. If the root cause is one of the organizational factors (i.e. dirty mold surface), corrective action is taken and parameters are re-adjusted. If re-adjustment still cannot resolve the issue then primary factors (design, resin, and machine) are re-considered. Observing a troubleshooting mode in an injection process reveals that the process is not well designed and/or periodic tasks are not followed up properly.

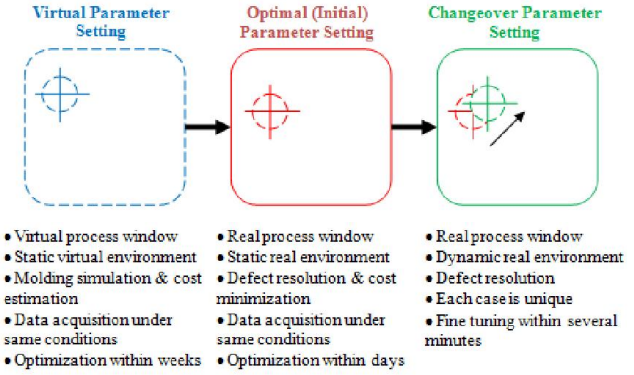


Figure 3: Properties of parameter setting modes.

The basic distinctive properties of these three parameter setting modes are summarized in Figure 3. During initial parameter setting studies, the conditions are "static", which means; the level of temperature and humidity, and the performances of the mold and machine are relatively stable, and the trials are done with the resin from the same lot and trials are conducted on the same injection machine. Therefore, required data can be collected for model approximation and optimization. Likewise, virtual environment of simulation programs let the decision makers to obtain data from the same pool for optimization of parameters virtually.

In the contrary, each changeover setting is a unique case because the conditions are not the same as in any of the previous changeovers. There are four basic "noise factors" that create this dynamic environment in changeovers;

- During the use of the mold in mass production, mold wear, fatigue and contamination occurs, the performance of the mold starts to decrease and requires compensation via process parameters until its next planned maintenance.
- Since, PIM has a sensitive nature, the molding performance changes based on the level of environmental temperature and humidity.
- Injection machines which have the same capabilities may perform different from each other due to their different maintenance requirements
- The quality level of the resin may have deviations between lots.

Therefore, the optimal set shifts from the initial set in changeovers. Due to the noise factors the direction and the amount of the shift differs for each changeover.

Another challenge in changeover parameter setting is the "time limit" to accomplish the task. Since the lean target is to reduce total changeover time under 10 minutes, the time that can be allocated to parameter setting is not more than several minutes.

In changeover parameter setting the uniqueness of the cases prevents collecting homogenous data for optimization. Moreover, the time limit impedes data collection to make analysis. Without a data set, both evolutionary and derivative-based optimization tools are useless. Changeover parameter setting is also too complex to model using traditional expert system applications which cannot provide amount of change as a function of defect severity [3].

Contemporary expert system applications (i.e. fuzzy inference) can be applied, as presented in some of the studies, however, the rule set must be broad enough to cover all possible cases and narrow enough to be prepared and modified easily which were not dealt in those papers. Since there is a strong necessity of such an expert system in plastic injection production, the proposed system should provide a complete solution and must be integrated into the whole changeover process.

IV. Understanding the Reasoning of Setup Experts in Changeovers

The type and severity of the defect(s) that are observed in the trial shots give clues about the molding parameter that should be adjusted. If the amount of tuning of a parameter from its previous value is underestimated, the severity of the defect reduces but cannot be resolved completely. In the contrary, if there is an overestimation, one or several counter-defect(s) occur.

Briefly, the counter defect is an outcome that is observed on the product when the adjustment amount of a molding parameter for a defect resolution is more than that it should be. As an example, the short shot is an injection defect that occurs if the molten plastic cannot fill the mold cavity properly. Increasing injection pressure is one of the actions to resolve this defect. However, excessive injection pressure may cause flash, which is another defect that can be described as the squeezed plastic out of the cavities. So, flash and short shot are the counter-defects. In Figure 4, the first trial is an example of overestimation and the second one represents an underestimation case.

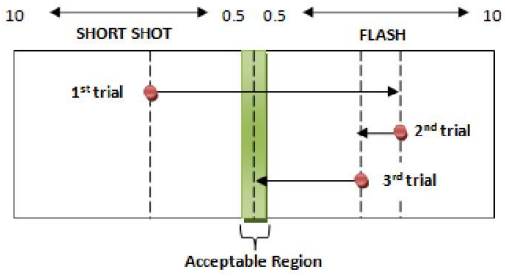


Figure 4: Properties of parameter setting modes.

In the same example, excessively increased injection pressure may also prevent the air inside the cavity from

escaping through the ventilation holes and overheats the trapped air that results in burn marks on the product surface. In the cases that there is more than one type of defects which require adjusting different molding parameters, only one parameter is adjusted at a time, that belongs to the defect which has the highest importance. Concurrent adjustment of different parameters makes the current problem hard to understand and creates confusion about the action that should be taken.

Experts define the level of inputs and outputs in linguistic forms and connect them with rules. In an example, "if there is slight short shot then increase the injection pressure slightly". This rule-based reasoning encircles the study space. Even if there is an underestimation or overestimation of the adjustment amount of parameters, the result that is observed on the product fires the corresponding rule that keep the decision maker on the path.

Tackling with a problem which has no objective function and mostly based on expertise requires dealing with uncertainty, imprecision, partial truth and approximation to reach practical, robust and low cost solution. Thus, Fuzzy inferencing system (FIS) is employed for changeover parameter setting problem to meet these requirements.

V. STUDIES IN THE LITERATURE ABOUT PARAMETER SETTING IN PIM AND NEED FOR THIS STUDY

The studies in the literature about parameter setting in PIM is summarized as in Table 1. From the data source aspect, 86% of the studies uses design of experiments (DOE) while remaining 14% is based on expert interviews.

Table 1: Classification of literature on parameter setting in PIM

DATA COLLECTION	APPROXIMATION	OPTMIZATION	# of indices to improve			
			1	2	3	5+
Experts Interview	ANN	Output Prediction	[4]			[5]
Experts Interview	FIS	Output Prediction		[6]		[7]
Experts Interview	Case Based Reasoning	Output Prediction		[8-13]		
DOE	-	GA		[14]		
DOE	-	SQP		[15]		
DOE	-	Taguchi Verification	[16-26]	[27-33]	[34,35]	
DOE	ANN	ABC	[36]			
DOE	ANN	GA	[37-42]	[43-46]	[47]	
DOE	ANN	Output Prediction	[48-52]	[53]	[54]	
DOE	ANN	PSO		[55]	[56]	
DOE	ANN	SQP	[57]			
DOE	ANN	Taguchi Verification	[58]			
DOE	RSM	GA	[59,60]			
DOE	RSM	Output Prediction	[61]	[62,63]		
DOE	Surrogate Models	EI based opt	[64,66]		[67]	
DOE	Surrogate Models	GA	[68]			
DOE	Surrogate Models	PSO		[69]		
DOE	Surrogate Models	SQP	[70]			
Grand Total			34	25	6	2

DOE can be described as structured set of tests of a process. DOE methods can be classified as; orthogonal designs and random designs. In orthogonal designs, the model parameters are assumed to be statistically independent, uncorrelated and can be varied independently. Fractional and full-factorial designs, central composite design, Box-Behnken designs and Taguchi designs are the methods under orthogonal designs. In random designs, model parameter values are assigned based on a random process. Latin hypercube design, mode pursuing sampling, rectangular sampling and infilling sampling are the random designs used in the literature. Analysis of variance (ANOVA) studies accompany the DOE to define the statistically significant parameters for further interpretations.

Although DOE methods reduce the effort needed to understand the parameter space by decreasing the number of experiments, they ignore the effect of interactions. However, the parameters in plastic injection are interacting with each other. Moreover, Taguchi design, which is preferred intensively in the literature, uses prefixed values of parameters as test levels. But the range of parameters is continuous, and the optimum point may not be matched with the levels chosen.

The data source of a parameter setting study can be a virtual environment like simulation programs (MoldFlow) or real molding trials. Especially during the design phase, simulation programs are used to define optimal process parameters, for cost estimations and defect resolution (66% of the studies in the literature). Real molding trials are used in the studies where the mold under consideration is already manufactured.

55% of the papers in the literature use meta-model based optimization method wherein objective functions are approximated into the explicit form of low order polynomials with acceptable accuracy. Artificial neural networks are the most popular technique for model approximation. The other techniques are surrogate models and response surface methodologies (RSM).

In DOE based approaches where an optimization algorithm is employed to find the optimal parameter set, genetic algorithms are the mostly preferred technique with 58%. Quadratic programming and particle swarm optimization are the other techniques in optimization.

DOE based approaches are useless for changeover parameter setting since each case is unique and there is no time to collect sufficient data to build an experimental analysis.

The other data collection method in parameter setting is the expert interviews that are used in expert systems. Expert systems simulate the human reasoning process by applying specific knowledge and inferencing. A typical expert system has two main components, knowledge base and inference engine. Since the parameter space is huge in PIM process, mapping of all possible relations and actions using traditional expert system is a tough task. The effectiveness of the systems that use case-based reasoning (which holds 90% of the studies) depends on the richness of the database in terms of past cases. Due to these limitations pure expert systems are not preferred by 2000s. Traditional expert systems have been substituted with fuzzy reasoning. He, Zhang, Lee, Fuh, and Nee [5] used fuzzy inferencing for "initial parameter setting". In their study, seven types of injection defects, part flow and part thickness were used as inputs to define the adjustment amount of nine molding parameters. Three fuzzy sets for the severity of the inputs and six fuzzy sets for the amount of change of

parameters were defined. They have generated fuzzy rules using both the samples that were produced before and the real molding trials. They employed neural networks to generalize the fuzzy rules. Vagelatos, Rigatos, and Zafestas [7] defined fifteen types of defects with five fuzzy set of severity and fourteen molding parameters with five fuzzy sets of change amount to resolve quality issues during mass production.

The number of the fuzzy rules that must be embedded into the inferencing system increases proportionally with the number of inputs and/or outputs and their levels. He et al. [5] and Vagelatos et al. [7] did not propose a method to decrease the number of rules without sacrificing the possible cases. Moreover, if the rules are generated from real molding trials, the number of the rules will be limited to the observations. Even employing neural networks may fail to predict the fuzzy rules of the cases that are not observed.

Without a systematic elimination of rules, it is too difficult to allege that a fuzzy inference system can cover all possible cases, thus, is totally ready to be used in real environment. Such a study is not able to go beyond an academic paper. However, in injection molding, there is a strong necessity to an expert system that will assist the limited number of setup experts by converting machine operators into changeover staff.

It is a very important finding that only 3% of the papers try to handle whole set of injection defects [5,7]. The attempts presented in the literature mostly focus on the optimization of one or several issues (especially warpage and shrinkage). *However, in changeover parameter setting all possible defect cases should be considered to generate a solution during a changeover.*

VI. APPLICATION OF FUZZY INFERENCE SYSTEM IN CHANGEOVER PARAMETER SETTING AS A PART OF SMED

As indicated at the beginning, there are many root causes of an injection defect which can be assigned to five main groups; design issues, resin selection, machine selection, maintenance and management of process parameters. In Table 2, one possible root cause for each category is exemplified for nine types of injection defects which are commonly observed when ABS (acrylonitrile butadiene styrene) type resin is used.

Based on the root cause, the actions that should be taken differ. In order to narrow the content of the proposed fuzzy inference system, it is assumed that a structured mold validation process is followed so there is no major design issue, and, resin and machine selection is compatible with the intended manufacturability and cost. It is also assumed that required housekeeping is carried out and the periodic maintenance of the machine, mold and equipment is properly followed up. These assumptions are also prerequisites for mass production. In defining the fuzzy rules, the experts were asked to define the actions for the defects under these assumptions.

In the cases that there is more than one defect, the experts take one action at a time to resolve the most critical defect. Therefore, the questionnaire contains the cases of "one type of defect in a trial" and "two types of defects in a trial".

In order to systematically eliminate the possible cases thus eliminating the corresponding fuzzy rules, a table is prepared together with the experts for the defect couples that cannot be observed at the same time. As an example, if a short shot is observed, it means the cavity of the mold cannot be filled properly and it is not possible to observe flash (squeezed melt) unless there is an exceptional issue. Therefore, the rules regarding "flash-short shot" couple can be removed from the questionnaire.

Table 2: Possible root causes of an injection defect

Defect	Short Description	Design Issue	Resin Selection	Machine Selection	Maintenance / Housekeeping	Parameter Management
Short Shot	Incomplete filling	Sharp corners	High viscosity	Insufficient shot volume	Non-return valve leaking	Low temperature
Flash	Squeezed plastic	Too deep venting	High flow rate	Insufficient clamping force	Unclean mold surface	High pressure
Burn Marks	Overheated surface	Wrong gate positioning	High flow rate	Narrow nozzle	Contamination in venting holes	High injection speed
Charring	Splash-like appearance	Poor runner design	High flow rate	Narrow nozzle	Moisture in resin	High temperature
Ejector Marks	Depression marks	Small ejector pin surface	-	-	Ejection system malfunction	High backpressure
Jetting	Wavy folds on surface	Narrow gate	High flow rate	Wrong screw selection	Contamination in gate	High injection speed
Weld Lines	Knitted melt streams	Sharp corners	High viscosity	Low shot volume capacity	Injection system malfunction	Low injection speed
Sink Mark	Depression marks	Uneven part thickness	-	Low shot volume capacity	Back pressure malfunction	Low back pressure
Matt Surface	Gloss difference	Uneven part thickness	High viscosity	Low inj. pressure capacity	Unsteady cooling	Low injection pressure

If the defect(s) cannot be resolved via parameter fine tuning, that means the root cause may be design issue, resin or machine selection or maintenance and housekeeping issue. In practice, in such cases, setup experts escalate the problem to shift supervisors and the production plan is revised. Likewise, in the cases that the proposals of the fuzzy inference system are incapable of solving the problem, machine operators will escalate the issue to setup experts to validate that the problem requires troubleshooting rather than parameter setting.

Proposed fuzzy inference system is implemented in a plant that is manufacturing wiring device products (wall outlets and switches). Plastic parts of these products are produced in plastic injection unit which has 20 injection machines and with 350 active molds. There were two main product classes for injection; cosmetic parts and inner body plastics. Cosmetic parts constitute around 70% of total injection workload (Figure 5.a) and 80% of the total raw material consumption (Figure 5.b). There are seven types of raw materials, and ABS is the one with the highest ratio of usage (60%, Figure 5.c). 55% of the total number of molds in the mold shop is used for ABS cosmetic parts (Figure 5.d). From these figures "all cosmetic parts made of ABS, regardless of their geometry" is chosen as the scope of the study. The project team has three setup experts, production manager, production supervisor, mold shop supervisor and two machine operators.

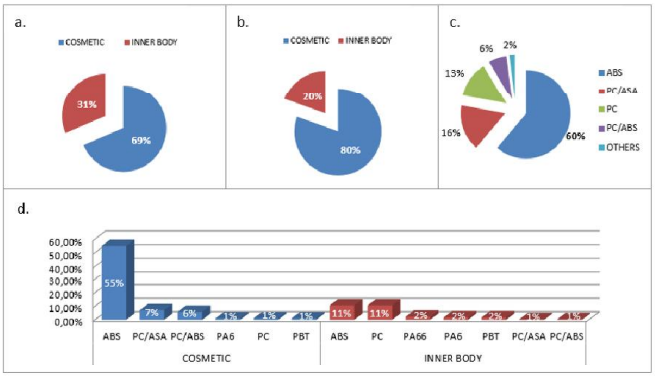


Figure 5: General data for scope definition. **a)** Ratio per injection-hour **b)** Ratio per tonnage **c)** Raw material usage **d)** Percent distribution of mold numbers per class

Nine types of defects (the same as in the previous section), which are encountered in manufacturing of ABS-made cosmetic parts, are reported to be resolved by five process parameters during a changeover. The severities of the defects are defined in four levels as "ignorable, slight, medium and serious" with an interval of [0, 10]. Rectangular membership function is used for "ignorable" level and triangular membership function is used for the remaining severity levels. Membership function parameters for inputs (severity of defects) are given in Table 3.

Table 3: Membership function values for inputs

Defect Severity	Ignore	Slight	Medium	Serious
Flash	[0 0 0.5 0.5]	[0.5 0.5 3.5]	[3.5 3.5 10]	[3.5 10 10]
Short Shot	[0 0 0.5 0.5]	[0.5 0.5 5]	[1 5 9]	[5 10 10]
Burn Mark	[0 0 0.5 0.5]	[0.5 0.5 5]	[1 5 9]	[5 10 10]
Charring Streaks	[0 0 0.5 0.5]	[0.5 0.5 5]	[1 5 9]	[5 10 10]
Ejector Mark	[0 0 0.5 0.5]	[0.5 0.5 5]	[1 5 9]	[5 10 10]
Jetting	[0 0 0.5 0.5]	[0.5 0.5 5]	[1 5 9]	[5 10 10]
Weld Lines	[0 0 0.5 0.5]	[0.5 0.5 5]	[1 5 9]	[5 10 10]
Sink Mark	[0 0 0.5 0.5]	[0.5 0.5 5]	[1 5 9]	[5 10 10]
Matt Surface	[0 0 0.5 0.5]	[0.5 0.5 5]	[1 5 9]	[5 10 10]

The tuning amount of process parameters are defined in six levels as "negative small, negative medium, negative high, positive small, positive medium and positive high" with an interval of [-15, 15] unit for injection pressure and [-10, 10] unit for remaining parameters. Triangular membership function is used also for defining the tuning amount. Membership parameters of outputs (process parameter tuning amount) are given in Table 4.

Table 4: Membership function values for outputs

Parameter Tuning Level	Neg High	Neg Medium	Neg Small	Pos Small	Pos Medium	Pos High
Nozzle Temp. (°C)	[-10 -10 -5]	[-7 -5 -3]	[-5 0 0]	[0 0 5]	[3 5 7]	[5 10 10]
Mold Temp. (°C)	[-10 -10 -5]	[-7 -5 -3]	[-5 0 0]	[0 0 5]	[3 5 7]	[5 10 10]
Inj. Speed (mm/sec)	[-10 -10 -5]	[-7 -5 -3]	[-5 0 0]	[0 0 5]	[3 5 7]	[5 10 10]
Hold Press. (bar)	[-10 -10 -5]	[-7 -5 -3]	[-5 0 0]	[0 0 5]	[3 5 7]	[5 10 10]
Inj. Press. (bar)	[-15 -15 -7.5]	[-11 -9 -4]	[-7.5 0 0]	[0 0 7.5]	[4 9 11]	[7.5 15 15]

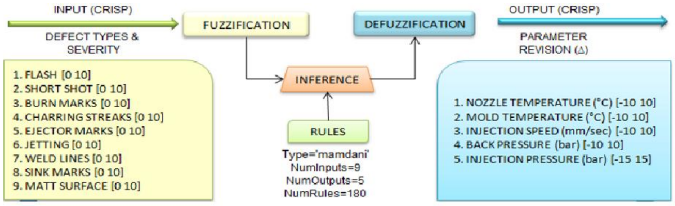


Figure 6: Black box for the fuzzy inference system.

Mamdani type FIS is preferred in this study due to its widespread acceptance and the ability to be used for nonlinear output functions. In order to decrease the number of rules without losing the domain knowledge, the table of possible defect couples (PC) and counter defect couples (CD) is created with the experts (Table 5). The rules regarding the couples which cannot be observed at the same time are removed from the case list. The counter defects keep the decision maker inside the feasible parameter space. Since, FIS does not have generalization capability by itself; all of the combinations at different severity levels for single and remaining double defects were added into the fuzzy rule set. Thus, the inference system encircled the search space with 180 fuzzy rules to keep the machine operator on track during changeover parameter setting. "And" operator is used to build the rules regarding defect couples (i.e. if flash "and" burn then). "Min" method for implication and "max" method for aggregation is chosen by default for Mamdani. For defuzzification widely accepted "centroid" method is used.

Table 5: Possible defect couples and counter defect couples matrix

Properties of Defect Couples	Flash	Short Shot	Burn Mark	Char. Streaks	Ejector Mark	Jetting	Weld Line	Sink Mark	Matt Surface
Flash		CD	PC	PC	PC			CD	PC
Short Shot	CD		CD	CD	CD	PC			
Burn Mark	PC	CD		PC	PC	CD	CD	CD	CD
Charring Streaks	PC	CD	PC		PC	CD		PC	PC
Ejector Mark	PC	CD	PC	PC				CD	PC
Jetting		PC	CD	CD			PC	PC	PC
Weld Line			CD			PC		PC	PC
Sink Mark	CD		CD	PC	CD	PC	PC		PC
Matt Surface	PC		CD	PC	PC	PC	PC	PC	

For the fuzzy inference application, "qtFuzzyLite-4.0" software is used which is a very compact and user-friendly fuzzy software. This software can be easily installed and used in real production plants. In Figure 7, the case of facing "short shot and jetting at the same injection trial" is simulated in this software. Rule number 67, 68, 70 and 71 are fired and the system proposes to increase injection pressure by approximately 11 bars.

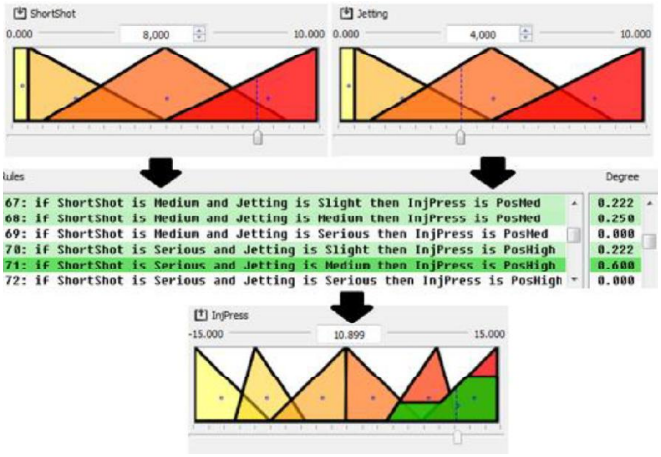


Figure 7: Simulation of the FIS

Before using the FIS in real molding trials a fitness test is applied. In FIS, each fuzzy rule represents a possible case. For each of the 180 cases, the amount of tuning that is defined by the expert and the amount of tuning that is computed by the proposed fuzzy inference system are depicted (Figure 8) and compared using Pearson's R (Table 6). Results confirm that the desired fit is achieved.

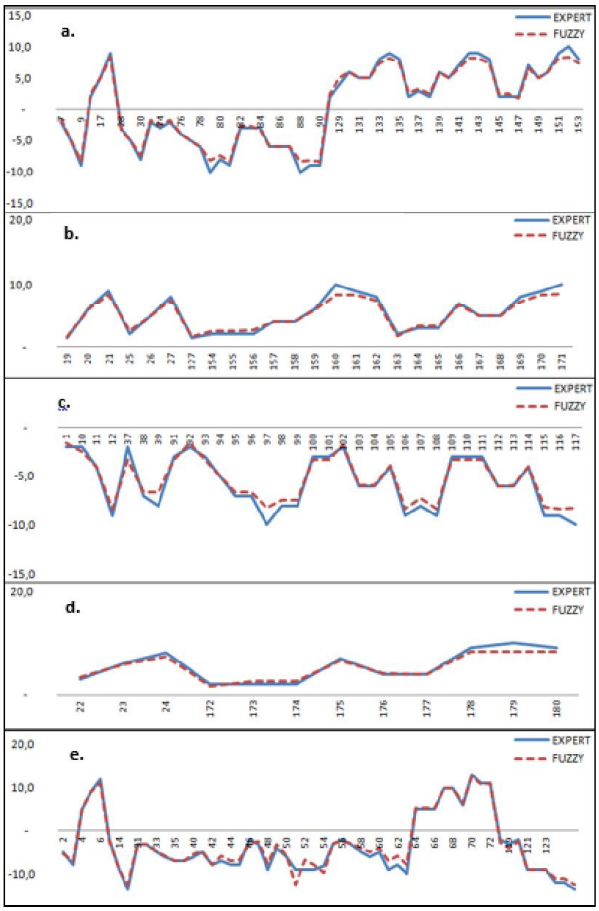


Figure 7: Expert responses vs Fuzzy responses a) for nozzle temperature, b) for mold temperature, c) for injection speed, d) for hold pressure, e) for injection pressure.

Table 6: Correlation between responses

Corr. (Expert vs. Fuzzy)	Pearson's R	R^2
Δ (Nozzle Temp. °C)	0,9948	98,97%
Δ (Mold Temp. °C)	0,9932	98,65%
Δ (Inj. Speed mm/sec)	0,9871	97,43%
Δ (Hold Press. bar)	0,9925	98,51%
Δ (Inj. Press. bar)	0,9907	98,15%

The fuzzy inference system is tested on ABS-made parts with different geometries. Trials are carried out after recalling the initial parameter settings from the database for each part. The results show that the proposed system can mimic the experts successfully. The results and actions for five different changeover sessions are given in Table 7.

Table 7: Implementation of FIS in five different cases

C/O No	Trial No	Defect Type 1	Severity of Defect 1 (0-10)	Defect Type 2	Severity of Defect 2 (0-10)	Proposal of FIS	Result
1	1	Weld Line	5	-	-	Increase mold temperature by 5 °C	Slight Burn Mark
	2	Burn Mark	2	-	-	Decrease nozzle temperature by 3 °C	OK
2	1	Sink Mark	3	-	-	Increase hold pressure by 3.5 bar	OK
3	1	Burn Mark	6	Charring Streaks	2	Decrease nozzle temperature by 6 °C	Slight Weld Line
	2	Weld Line	1	-	-	Increase mold temperature by 1.5 °C	OK
4	1	Jetting	4	-	-	Increase nozzle temperature by 4 °C	OK
5	1	Short Shot	6	-	-	Increase injection pressure by 9 bar	Slight Sink Mark
	2	Sink Mark	2	-	-	Increase hold pressure by 2.5 bar	OK

In the last changeover session, short shot is observed at the end of the first trial. Severity of the short shot is graded 6 over 10 and the grading is entered into the FIS. The proposal of FIS is to increase the injection pressure by 9 bars in order to fill the cavity. After the implementation of the proposal a slight sink mark is observed on the part which is graded by 2 over 10. For resolution of slight sink mark, FIS proposes increasing hold pressure by 2.5 bars and the defect-free product is reached. Product visuals for each step of this session are given in Figure 8.

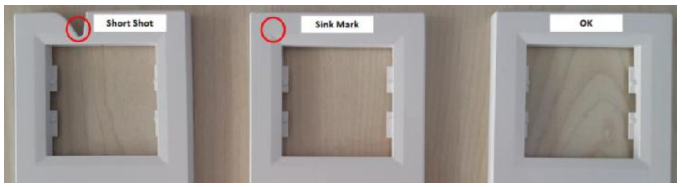


Figure 8: Expert responses vs Fuzzy responses

Real molding trials reveal that, proposed fuzzy inference system can generate correct solutions with several trials as experts do.

REFERENCES

[1] Shingo S (1985), "A revolution in Manuf., the SMED system", Productivity Press, University Park, IL.

[2] Kashyap, S., & Datta, D. (2015). Process parameter optimization of plastic injection molding: a review. Int. Journal of Plastics Tech., 19(1), 1-18.

[3] Mok, S. L., Kwong, C. K., & Lau, W. S. (2001). A hybrid neural network and genetic algorithm approach to the determination of initial process parameters for injection moulding. The International Journal of Advanced Manufacturing Technology, 18(6), 404-409.

[4] Lau, H. C. W., Wong, T. T., & Pun, K. F. (1999). Neural-fuzzy modeling of plastic injection molding machine for intelligent control. Expert Systems with Applications, 17(1), 33-43.

[5] He, W., Zhang, Y. F., Lee, K. S., Fuh, J. Y., & Nee, A. Y. (1998). Automated process parameter resetting for injection moulding: a fuzzy-neuro approach. Journal of Intelligent Manuf., 9(1), 17-27.

[6] Li, D., Zhou, H., Zhao, P., & Li, Y. (2009). A real-time process optimization system for injection molding. Polymer Engineering & Science, 49(10), 2031-2040.

[7] Vagelatos, G. A., Rigatos, G. G., & Tzafestas, S. G. (2001). Incremental fuzzy supervisory controller design for optimizing the injection molding process. Expert Systems with Applications, 20(2), 207-216.

[8] Jan, T. C., & O'Brien, K. T. (1993). A user-friendly, interactive expert system for the injection moulding of engineering thermoplastics. The International Journal of Advanced Manufacturing Technology, 8(1), 42-51.

[9] Kwong, C. K., & Smith, G. F. (1998). A computational system for process design of injection moulding: Combining a blackboard-based expert system and a case-based reasoning approach. The Int. Journal of Advanced Manuf. Tech., 14(5), 350-357.

[10] Kwong, C. K., Smith, G. F., & Lau, W. S. (1997). Application of case based reasoning injection moulding. Journal of Materials Processing Tech., 63(1-3), 463-467.

[11] Mok, S. L., & Kwong, C. K. (2002). Application of artificial neural network and fuzzy logic in a case-based system for initial process parameter setting of injection molding. Journal of Intelligent Manuf., 13(3), 165-176.

[12] Mok, S. L., Kwong, C. K., & Lau, W. S. (2000). An intelligent hybrid system for initial process parameter setting of injection moulding. Int. Journal of Production Research, 38(17), 4565-4576.

[13] Shelesh-Nezhad, K., & Siores, E. (1997). An intelligent system for plastic injection molding process design. Journal of Materials Processing Tech., 63(1-3), 458-462.

[14] Lam, Y. C., Deng, Y. M., & Au, C. K. (2006). A GA/gradient hybrid approach for injection moulding conditions optimisation. Engineering with Computers, 21(3), 193.

[15] Farshi, B., Gheshmi, S., & Miandoabchi, E. (2011). Optimization of injection molding process parameters using sequential simplex algorithm. Materials & Design, 32(1), 414-423.

[16] Chang, T. C., & Faison, E. (2001). Shrinkage behavior and optimization of injection molded parts studied by the Taguchi method. Polymer Engineering & Science, 41(5), 703-710.

[17] Chen, C. S., Cheng, W. S., Wang, T. S., & Chien, R. D. (2005). Optimum design of gas-assisted injection molding. Journal of reinforced plastics and composites, 24(15), 1577-1586.

[18] Chen, C. P., Chuang, M. T., Hsiao, Y. H., Yang, Y. K., & Tsai, C. H. (2009). Simulation and experimental study in determining injection molding process parameters for thin-shell plastic parts via design of experiments analysis. Expert Systems with Applications, 36(7), 10752-10759.

[19] Chen, R. S., Lee, H. H., & Yu, C. Y. (1997). Application of Taguchi's method on the optimal process design of an injection molded PC/PBT automobile bumper. Composite Structures, 39(3-4), 209-214.

[20] Huang, M. C., & Tai, C. C. (2001). The effective factors in the warpage problem of an injection-molded part with a thin shell feature. Journal of Materials Processing Tech., 110(1), 1-9.

[21] Hussin, R., Saad, R. M., Hussin, R., & Dawi, M. S. I. M. (2012). An optimization of plastic injection molding parameters using Taguchi optimization method. Asian Transactions on Engineering, 2(5), 75-80.

[22] Kamaruddin, S., Khan, Z. A., & Foong, S. H. (2010). Application of Taguchi method in the optimization of injection moulding parameters for Manuf. products from plastic blend. Int. Journal of Engineering and Tech., 2(6), 574.

[23] Karasu, M. K., Cakmakci, M., Cakiroglu, M. B., Ayva, E., & Demirel-Ortabas, N. (2014). Improvement of changeover times via Taguchi empowered SMED/case study on injection molding production. Measurement, 47, 741-748.

[24] Oktem, H., Erzurumlu, T., & Uzman, I. (2007). Application of Taguchi optimization technique in determining plastic injection molding process parameters for a thin-shell part. Materials & design, 28(4), 1271-1278.

[25] Song, M. C., Liu, Z., Wang, M. J., Yu, T. M., & Zhao, D. Y. (2007). Research on effects of injection process parameters on the molding process for ultra-thin wall plastic parts. Journal of Materials Processing Tech., 187, 668-671.

[26] Tang, S. H., Tan, Y. J., Sapuan, S. M., Sulaiman, S., Ismail, N., & Samin, R. (2007). The use of Taguchi method in the design of plastic injection mould for reducing warpage. Journal of Materials Processing Tech., 182(1), 418-426.

[27] Chen, W. L., Huang, C. Y., & Huang, C. Y. (2013). Finding efficient frontier of process parameters for plastic injection molding. Journal of Industrial Engineering Int., 9(1), 25.

[28] Kang, G. J. (2014). Process factor optimization for reducing warpage and shrinkage in injection molding using design of experiments. In Applied Mechanics and Materials (Vol. 541, pp. 359-362). Trans Tech Publications.

[29] Liao, S. J., Hsieh, W. H., Wang, J. T., & Su, Y. C. (2004). Shrinkage and warpage prediction of injection-molded thin-wall parts using artificial neural networks. Polymer Engineering & Science, 44(11), 2029-2040.

[30] Mehat, N. M., & Kamaruddin, S. (2011a). Investigating the effects of injection molding parameters on the mechanical properties of recycled plastic parts using the Taguchi method. Materials and Manuf. Processes, 26(2), 202-209.

[31] Mehat, N. M., & Kamaruddin, S. (2011b). Multi-response optimization of injection moulding processing parameters using the Taguchi method. Polymer-Plastics Tech. and Engineering, 50(15), 1519-1526.

[32] Mehat, N. M., & Kamaruddin, S. (2011c). Optimization of mechanical properties of recycled plastic products via optimal processing parameters using the Taguchi method. Journal of Materials Processing Tech., 211(12), 1989-1994.

[33] Özek, C., & Çelik, Y. H. (2012). Calculating molding parameters in plastic injection molds with ANN and developing software. Materials and Manuf. Processes, 27(2), 160-168.

[34] Yang, Y. K. (2006). Optimization of injection-molding process of short glass fiber and polytetrafluoroethylene reinforced polycarbonate composites via design of experiments method: A case study. Materials and Manuf. processes, 21(8), 915-921.

[35] Tsai, K. M., Hsieh, C. Y., & Lo, W. C. (2009). A study of the effects of process parameters for injection molding on surface quality of optical lenses. Journal of materials processing Tech., 209(7), 3469-3477.

[36] Alvarado Iniesta, A., García Alcaraz, J. L., & Rodríguez Borbón, M. (2013). Optimization of injection molding process parameters by a hybrid of artificial neural network and artificial bee colony algorithm. Revista Facultad de Ingeniería Universidad de Antioquia, (67), 43-51.

[37] Chen, W. C., Lai, T. T., Fu, G. L., & Chen, C. T. (2008). A systematic optimization approach in the MISO Plastic Injection molding process. In Service Operations and Logistics, and Informatics, 2008. IEEE/SOLI 2008. IEEE Int. Conference on (Vol. 2, pp. 2741-2746). IEEE.

[38] Chen, W. C., Wang, M. W., Chen, C. T., & Fu, G. L. (2009). An integrated parameter optimization system for MISO plastic injection molding. The Int. Journal of Advanced Manuf. Tech., 44(5-6), 501-511.

[39] Kurtaran, H., Ozcelik, B., & Erzurumlu, T. (2005). Warpage optimization of a bus ceiling lamp base using neural network model and genetic algorithm. Journal of materials processing Tech., 169(2), 314-319.

[40] Ozcelik, B., & Erzurumlu, T. (2006). Comparison of the warpage optimization in the plastic injection molding using ANOVA, neural network model and genetic algorithm. Journal of materials processing Tech., 171(3), 437-445.

[41] Shen, C., Wang, L., & Li, Q. (2007). Optimization of injection molding process parameters using combination of artificial neural network and genetic algorithm method. Journal of Materials Processing Tech., 183(2), 412-418.

[42] Shi, F., Lou, Z. L., Zhang, Y. Q., & Lu, J. G. (2003). Optimisation of plastic injection moulding process with soft computing. The Int. Journal of Advanced Manuf. Tech., 21(9), 656-661.
[43] Chen, W. C., & Kurniawan, D. (2014). Process parameters optimization for multiple quality characteristics in plastic injection molding using Taguchi method, BPNN, GA, and hybrid PSO-GA. Int. journal of precision engineering and Manuf., 15(8), 1583-1593.
[44] Chen, W. C., Fu, G. L., Tai, P. H., & Deng, W. J. (2009). Process parameter optimization for MIMO plastic injection molding via soft computing. Expert Systems with Applications, 36(2), 1114-1122.
[45] Chen WC, Liou PH, and Chou SC (2014). An integrated parameter optimization system for MIMO plastic injection molding using soft computing. Int. Journal of Advanced Manuf. Tech., 1–10
[46] Yin, F., Mao, H., & Hua, L. (2011). A hybrid of back propagation neural network and genetic algorithm for optimization of injection molding process parameters. Materials & Design, 32(6), 3457-3464.
[47] Tzeng, C. J., Yang, Y. K., Lin, Y. H., & Tsai, C. H. (2012). A study of optimization of injection molding process parameters for SGF and PTFE reinforced PC composites using neural network and response surface methodology. The Int. Journal of Advanced Manuf. Tech., 63(5-8), 691-704.
[48] Kenig, S., Ben-David, A., Omer, M., & Sadeh, A. (2001). Control of properties in injection molding by neural networks. Engineering Applications of Artificial Intelligence, 14(6), 819-823.
[49] Li, Q., Li, L., Si, X., & Rongji, W. (2015). Modeling the Effect of Injection Molding Process Parameters on Warpage Using Neural Network Theory. Journal of Macromolecular Science, Part B, 54(9), 1066-1080.
[50] Lotti, C., Ueki, M. M., & Bretas, R. E. S. (2002). Prediction of the shrinkage of injection molded iPP plaques using artificial neural networks. Journal of Injection Molding Tech., 6(3), 157.
[51] Wang, R., Zeng, J., Feng, X., & Xia, Y. (2013). Evaluation of effect of plastic injection molding process parameters on shrinkage based on neural network simulation. Journal of Macromolecular Science, Part B, 52(1), 206-221.
[52] Yin, F., Mao, H., Hua, L., Guo, W., & Shu, M. (2011). Back Propagation neural network modeling for warpage prediction and optimization of plastic products during injection molding. Materials & design, 32(4), 1844-1850.
[53] Liao, S. J., Hsieh, W. H., Wang, J. T., & Su, Y. C. (2004). Shrinkage and warpage prediction of injection-molded thin-wall parts using artificial neural networks. Polymer Engineering & Science, 44(11), 2029-2040.
[54] Sadeghi, B. H. M. (2000). A BP-neural network predictor model for plastic injection molding process. Journal of materials processing Tech., 103(3), 411-416.
[55] Xu, G., Yang, Z. T., & Long, G. D. (2012). Multi-objective optimization of MIMO plastic injection molding process conditions based on particle swarm optimization. The Int. Journal of Advanced Manuf. Tech., 58(5-8), 521-531.
[56] Spina, R. (2006). Optimisation of injection moulded parts by using ANN-PSO approach. Journal of Achievements in Materials and Manuf. Engineering, 15(1-2), 146-152.
[57] Shi, H., Xie, S., & Wang, X. (2013). A warpage optimization method for injection molding using artificial neural network with parametric sampling evaluation strategy. The Int. Journal of Advanced Manuf. Tech., 65(1-4), 343-353.
[58] Altan, M. (2010). Reducing shrinkage in injection moldings via the Taguchi, ANOVA and neural network methods. Materials & Design, 31(1), 599-604.
[59] Chen, C. C., Su, P. L., Chiou, C. B., & Chiang, K. T. (2011). Experimental investigation of designed parameters on dimension shrinkage of injection molded thin-wall part by integrated response surface methodology and genetic algorithm: A case study. Materials and Manuf. Processes, 26(3), 534-540.
[60] Kurtaran, H., & Erzurumlu, T. (2006). Efficient warpage optimization of thin shell plastic parts using response surface methodology and genetic algorithm. The Int. Journal of Advanced Manuf. Tech., 27(5-6), 468-472.
[61] Mathivanan, D., & Parthasarathy, N. S. (2009). Sink-mark minimization in injection molding through response surface regression modeling and genetic algorithm. The Int. Journal of Advanced Manuf. Tech., 45(9-10), 867.
[62] Chen, W. L., Huang, C. Y., & Hung, C. W. (2010). Optimization of plastic injection molding process by dual response surface method with non-linear programming. Engineering computations, 27(8), 951-966.
[63] Chuang, M. T., Yang, Y. K., & Hsiao, Y. H. (2009). Modeling and optimization of injection molding process parameters for thin-shell plastic parts. Polymer-Plastics Tech. and Engineering, 48(7), 745-753.
[64] Gao, Y., Turng, L. S., & Wang, X. (2008). Adaptive geometry and process optimization for injection molding using the Kriging surrogate model trained by numerical simulation. Advances in Polymer Tech., 27(1), 1-16.
[65] Gao, Y., & Wang, X. (2009). Surrogate-based process optimization for reducing warpage in injection molding. Journal of materials processing Tech., 209(3), 1302-1309.
[66] Xia, W., Luo, B., & Liao, X. P. (2011). An enhanced optimization approach based on Gaussian process surrogate model for process control in injection molding. The Int. Journal of Advanced Manuf. Tech., 56(9-12), 929-942.
[67] Zhao, J., Cheng, G., Ruan, S., & Li, Z. (2015). Multi-objective optimization design of injection molding process parameters based on the improved efficient global optimization algorithm and non-dominated sorting-based genetic algorithm. The Int. Journal of Advanced Manuf. Tech., 78(9-12), 1813-1826.
[68] Deng, Y. M., Zhang, Y., & Lam, Y. C. (2010). A hybrid of mode-pursuing sampling method and genetic algorithm for minimization of injection molding warpage. Materials & Design, 31(4), 2118-2123.
[69] Chen, W., Zhou, X. H., Wang, H. F., & Wang, W. (2010). Multi-objective optimal approach for injection molding based on surrogate model and particle swarm optimization algorithm. Journal of Shanghai Jiaotong University (Science), 15(1), 88-93.
[70] Gao, Y., Turng, L. S., & Wang, X. (2008). Adaptive geometry and process optimization for injection molding using the Kriging surrogate model trained by numerical simulation. Advances in Polymer Tech., 27(1), 1-16.

Investigating of Compressive and Tensile Strengths with Deformation Abilities of Sand Soils Improved with Waste Rubbers

E.B. TOKA[1] and M. OLGUN[2]

[1] Selcuk University, Konya/Turkey, ebtoka@selcuk.edu.tr
[2]Selcuk University, Konya/Turkey, molgun@selcuk.edu.tr

Abstract - **In this study mechanical performance of sand soils that are improved with waste rubber along with fly ash and clay under effects of compressive and tensile stresses were investigated. Therefore, a L16 Taguchi method using 4 parameters with 4 levels was designed. Fly ash, clay, rubber ratios and rubber diameter are the parameters. And the levels are %0, %10, %20, %30 for fly ash ratios, %10, %15, %20, %25 for clay ratios, %0, %4, %8, %12 for rubber ratios by total soil weights and 0.25 mm, 0.75 mm, 1.25 mm, 1.75 mm for rubber diameters. Fly ashes and clays were used as binding materials. These experimental designs were tested for their strength and deformation performances with Unconfined Compressive Strength (UCS) Test and Splitting Tensile Strength (STS) Tests. According to tests results and analysis of them with Taguchi method, it was observed that increase in the rubber ratio improved the UCS and deformation ability of soil samples in UCS Test and the maximum test results observed with fourth level which is the maximum ratio of waste rubber (%1.75). Also in STS Test, increase in the rubber ratio increased tensile strength of sand soils. But same situation isn't valid for rubber diameter. Maybe there is an optimum diameter for rubber diameter instead of maximum diameter. Because it was observed that second level of rubber diameter (0.75 mm) was the most effective diameter which maximized the Split Tensile Stress strength. As a result, S/N ratios obtained from Taguchi Method showed that maximum rubber ratio and optimum rubber diameter can improve mechanical performance against compressive and tensile stresses and while doing this they can also improve deformation ability of sand soils.**

Keywords – **Taguchi Method, Waste Rubber, Compressive Strength, Tensile Strength.**

I. Introduction

SHEAR Strength and deformation of sand soils can be increased by using correct additive. While the choice of additive materials to be used for this is important, at the same time the ability of the waste materials to be used to improve the soil properties makes it attractive that these materials can be used in various fields of geotechnical engineering. Today rubber wastes are increasing. The ductility of rubbers caused the investigation of the use of these materials in engineering fields. Effects of waste rubbers have been investigated by many researchers for sand soils in geotechnical engineering. Overall improvements in the soil characteristics, such as enhanced shear strength, can be achieved by the addition of tire shreds [1]. Also, increasing of shred content to an optimum value increases the bearing capacity sand soils [2]. One of the possible alternatives for rubber waste is to use shredded tires alone or mixed with soil as a lightweight backfill. With an increasing proportion of sand in the mixture, the density, unit weight, and shear strength of the mixture increased, but the compressibility decreased in triaxial tests [3]. The tire shred content and tire shred aspect ratio influence the stress–strain and volumetric strain behaviour of the sand-tire shred mixture. The axial strain at failure increase with increasing tire shred content [4]. In a study of a group of researchers the shear behavior of mixtures of fine-grained sand and 1-5 mm granulated rubber was investigated. They performed sixty direct shear tests on sand-granulated rubber mixtures with various rubber contents at different relative densities and different normal stresses. They found that the granulated rubber improves the shear strength of fine-grained sand at medium relative density and low normal stress [5]. According to one of the previous study the unreinforced and samples reinforced with scrap tires were subjected to unconfined compression, shear box, and resonant frequency tests to determine their mechanic properties and scrap tires are found to be improve the strength properties and dynamic behavior of clayey soils [6].

Fly ash is a pozzolanic material and when used with binders such as cement and lime, it can have important effects in improving the soils. Actually, it is an industrial waste material. And it has been used and its properties have been investigated by many researchers. It has been used to bind non-cohesive soil, granular or poorly cohesive soil and fly ash is mainly used to stabilize the sub base or base course [7]. The effects of freezing-thawing processes can be improved on the clayey soil when it is stabilized with fly ash and cement. While fly ash is a pozzolan, because of the free lime in the fly ash, it contributes to an increase in unconfined compression strength [8]. In a study on cement stabilized fly ash-soil mixtures. It was found that gain in strength and modulus increase as cement content increases, but decrease as fly ash content increases. Thus, influence of the cement content is more effective than that of the curing time and performance of fly ash can be improved by stabilizing it with cement. [9].

II. Materials and Methofs

A. Materials

The sand used in this study is chosen as uniform sand and it obtained from sea coast. Grain distribution of the sand soil that is wanted to be improved is given Figure 1. Maximum diameter of the sand soils is 1mm and they can be classified according to USCS as SP.

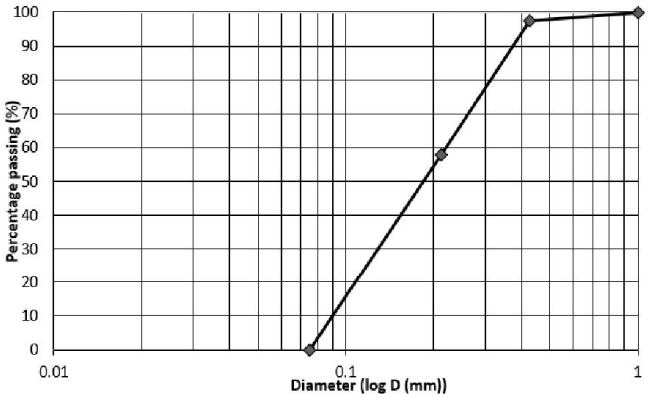


Figure 1: Grain distribution of the sand.

The waste rubber was obtained from used car tires that are grinding at industrial factories. Diameter of these waste rubbers are chosen as 0.25 mm, 0.75 mm, 1.25 mm and 1.75 mm, respectively.

The fly ash used in this study was obtained from Seydisehir Eti Aluminium Plants in Konya state of Turkey. Its gradation contains particles of 15.8% sand and 84.2% silt. Chemical compounds of the fly ash are given in Table 1.

Table 1: Chemical compounds of fly ash by percentages.

SiO_2	Al_2O_3	Fe_2O_3	CaO	MgO	SO_3	Na_2O	K_2O	Free CaO
19.87	8.12	6	28.26	0.99	18.18	0.37	0.09	16.34

The clay used in this study contains 91% kaolin and 9% illite and specific surface are of the clay is 15.29 m^2/g. It was obtained from Bozüyük (Turkey). Cation exchange capacity of this clay is 11.76 meq/100g. Other properties of the clay are: liquid limit of 44.7%, plasticity index of 21.40%, particle size of less than 0.075 mm, %99, particle size smaller than 0.002 mm, 54%, specific gravity of soil 2.59. According to Unified Soil Classification System (USCS) soil class is low plasticity clayey soil (CL).

B. Experimental Program

The Taguchi Method was used for the experimental study. In this method, different conditions (levels) of the effective parameters are tested to achieve the desired optimum result. Depending on the sound/noise (S/N) ratios calculated according to the test results, the effects of parameter levels can also be seen. The advantage of the method is that a much larger number of experimental design results can be predicted by creating a small number of experimental designs within a small margin of error. But what is important here is that the correct parameter levels must be chosen during design process that requires scientific and engineering experience and that the experiments must be done correctly.

In the Taguchi method, orthogonal test design arrays are used to create tables according to the desired parameters and their levels. For example; L_9 (3^4) shows a 3-level 4-parameter experiment design table.

L_{16} (4^5) Taguchi orthogonal array can be used for experiment designs. 4 parameters and 4 levels were used in this study. In the Taguchi L_{16} design table, A, B, C and D were coded to show the parameters rubber ratio, rubber diameter, fly ash ratio and clay ratio, respectively. And the levels are %0, %4, %8, %12 for A, 0.25 mm, 0.75 mm, 1.25 mm, 1.75 mm for B, %0, %10, %20, %30 for C, %10, %15, %20, %25 for D, by total soil weights. UCS and STS tests were performed on these experiment designs. In UCS tests it was aimed to find maximum vertical deformation at failure (ε_{max}) and unconfined compressive strength (q_u). STS values were measured with STS tests. Sound/Noise (S/N) analysis and analysis of variance (ANOVA) were performed according to the obtained test results. Thus, it can be investigated which of the selected parameters has the greatest effect on the results and in which levels the maximum values are obtained. The purpose of this study is to investigate the contribution of rubber use to strength and deformation of the sand soil, along with other parameters.

C. Tests

As a first step in the experimental study, Standard Proctor Tests for 16 test designs were made according to ASTM 698 [10]. Optimum water content and maximum dry unit volume weights were found from these test results (Table 2). Metal tubes with a diameter of 38 mm and a height of 76 mm were prepared in 5 layers and each layer was compressed with a 12-stroke knocker to apply energy at a level similar to the

Table 2: Standard Proctor test results

Experiment No	**Optium moisture content (w_{opt}, %)**	**Maximum dry unit weight (γ_{kmax}, kN/m^3)**
1	5	18.85
2	8	18.1
3	14	16.5
4	21	15.9
5	12	16.6
6	10	16.8
7	14	16.25
8	13	16.4
9	16.4	15.9
10	17	16.3
11	11	16.9
12	13	18.2
13	15.2	15.49
14	13	16.45
15	15	16.35
16	9	17.3

standard proctor energy and the samples were prepared at w_{opt}-γ_{kmax} values. Two samples were prepared from each experimental design. It can be noted that 4% (which doesn't have significant effect on results) of cement by total weight was used to provide stability when preparing the samples.
STS and UCS tests were carried out on the samples according to ASTM 2166 [11] and ASTM 496 [12], respectively. In the UCS tests, q_u and ε_{max} were obtained. The loading speed in the UCS tests was set at 1 mm/min.

III. Results

The parameters, levels, q_u, ε_{max} and STS values obtained from UCS and STS tests are given in Table 3. In this table, the test result values, mean values and S/N values of each experimental design are seen together.

In UCS experiments; maximum q_u values were obtained in the 2nd experiment as 424 kPa where rubber diameter, fly ash ratio and clay ratio are at their 2nd level and rubber ratio is at its 1st level. The lowest values were observed as 82 and 83.5 kPa, respectively in the 11th and 1st experiments, where the fly ash ratio was 0% (1st level). These results indicate that the fly ash enhances strength because of lime content it has, but the reason why the highest value can't be obtained when using fine materials at their maximum levels is that the strength of the sand itself is high. Thus, adding much more fines (the fly ash and the clay) caused the drop in the soil strength because the fine particles has lower strength than the sand particles.

The ε_{max} values obtained from the UCS tests were observed at the highest values in certain values of the rubber ratios, and its highest value was obtained as 5.15% in the 5th experiment where the rubber ratio was 4% (2nd level). Here it can be seen easily; the minimum ε_{max} values were obtained for in 3rd, 4th, 1st experiment designs where the rubber ratio was 0% (level 1), as 1%, 1.5% and 1.6%, respectively. From these results, it is seen that ε_{max} value decreases dramatically in rubber deficiency.

In STS tests, the strength of the samples against the tensile is determined indirectly by splitting. The STS value obtained from these test results was highest in the 10th experiment with 30% (4th level) fly ash ratio and 8% (3rd level) rubber ratio.

The lowest STS value was found in experiment 1 with 0% (1st level) rubber ratio, 0% (1st level) fly ash ratio and 10% (1st level) clay ratio. While this result shows that the rubber ratio increases ductility, the lack of clay that helps to stabilize the soil and the absence of fly ash that increases resistance with its lime content reduces tensile strength. This shows that the sand soils can't keep itself apart from the lack of fine grains, which is an expected result. The rubber, on the other hand, increases ductility of the soil matrix and prevents the tensile strength from being too low.

UCS and STS test results and S/N values were obtained in the experiment design using Taguchi method. These values were obtained with larger is better situation; because we aimed to obtain the highest strength value and when we get this value the deformations (ε_{max}) should be high enough to show that soil matrix has enough ductility and for this reason it is necessary to optimize the experiment results according to the maximum results. The response table is graphically charted with S/N correspond to each level of each parameter according to the results. S/N charts are shown in Figure 2. According to S/N values for q_u, the S/N values of fly ash and clay ratios, Although the jump to 1st level of these parameters to 2nd levels was significant, difference between 2nd 3rd, 4th was insignificant.

Table 3: Taguchi design table

Experiment No	Parameters				Unconfined Compressive Strength Test Results								Split Tensile Strength Test Results (kPa)			
					q_u (kPa)				ε_{max1} (%)							
	A	B	C	D	q_{u1}	q_{u2}	q_{uavg}	S/N	ε_{max1}	ε_{max2}	ε_{avg}	S/N	STS_1	STS_2	STS_{avg}	S/N
1	1	1	1	1	78	89	83.5	38.38	1.5	1.7	1.6	4.03	53.22	50.01	51.615	34.24
2	1	2	2	2	369	479	424	52.33	1.9	1.95	1.925	5.69	137.69	182.6	160.145	43.83
3	1	3	3	3	412	137	274.5	45.29	1.4	0.6	1	-2.16	95.99	125.93	110.96	40.67
4	1	4	4	4	152	348	250	45.89	1	2	1.5	2.04	147.32	121.65	134.485	42.45
5	2	1	2	3	156	144	150	43.50	4.8	5.5	5.15	14.18	81.02	50.01	65.515	35.59
6	2	2	1	4	142	222	182	44.57	2.2	4	3.1	8.71	167.63	149.46	158.545	43.96
7	2	3	4	1	150	230	190	44.99	2.8	3.4	3.1	9.71	120.58	143.04	131.81	42.30
8	2	4	3	2	394	357	375.5	51.46	3.2	3.4	3.3	10.36	169.77	146.25	158.01	43.90
9	3	1	3	4	260	260	260	48.30	4.4	4.8	4.6	13.23	172.98	208.27	190.625	45.49
10	3	2	4	3	362	356	359	51.10	4.8	4.6	4.7	13.44	167.63	230.72	199.175	45.66
11	3	3	1	2	86	78	82	38.25	1.8	1.7	1.75	4.85	67.12	71.39	69.255	36.80
12	3	4	2	1	138	154	146	43.25	2.8	3.6	3.2	9.90	55.35	79.95	67.65	36.17
13	4	1	4	2	266	232	249	47.86	3.6	3.9	3.75	11.46	153.73	110.96	132.345	42.09
14	4	2	3	1	191	176	183.5	45.25	4	3.8	3.9	11.81	107.75	94.92	101.335	40.06
15	4	3	2	4	300	375	337.5	50.40	3.7	4.9	4.3	12.41	168.7	198.64	183.67	45.19
16	4	4	1	3	269	228	248.5	47.82	2.9	2.7	2.8	8.93	124.86	145.18	135.02	42.53

This indicates that these two parameters do not need to be included to soil matrix with their maximum ratios; however, the highest q_u values can obtained at their highest level. According to S/N values optimum experiments are selected for maximum q_u, ε_{max} and STS. The highest value for q_u can be obtained from an experimental design consisting of A4, B2, C3 and D2 parameters. The highest value for ε_{max} can be obtained from an experimental design consisting A4, B1, C2 and D4 parameters. The highest value for STS can be obtained from an experimental design consisting A4, B2, C4 and D4 parameters. These results showed that the highest results can be achieved in the test designs where the rubber ratio is the highest.

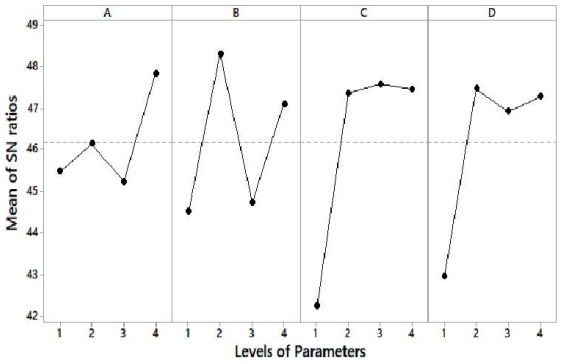


Figure 2.a: S/N charts for q_u values.

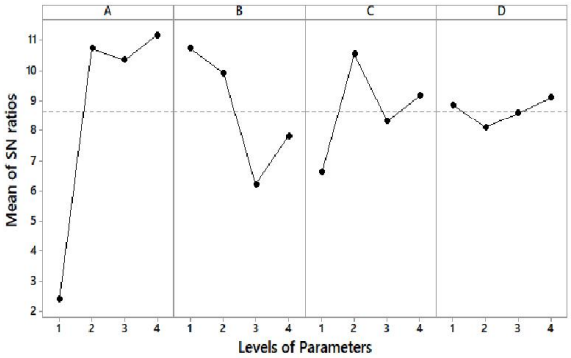


Figure 2.b: S/N charts for ε_{max} values.

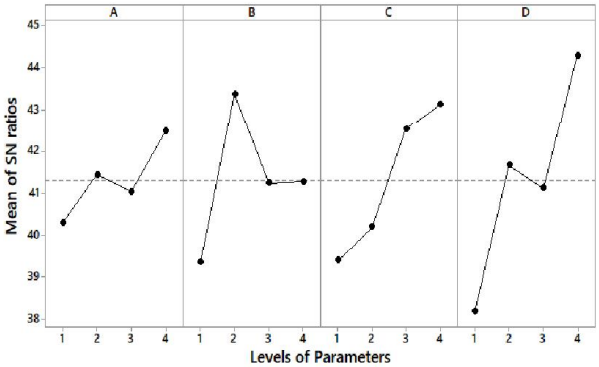


Figure 2.c: S/N charts for STS values.

In the end, ANOVA was performed to show the effects of the parameters and their levels on the q_u, ε_{max} and STS results. In the ANOVA, the averages of the test results were used. ANOVA results are shown in Table 4. According to the ANOVA results, following contribution of parameters to test results are given by percents below.

As a result of UCS tests; The most important parameter affecting the change of q_u values is fly ash with 27.29% and the rubber ratio parameter with 4.05% having the least effect. From these results, it was seen that the rubber ratios did not significantly affect the q_u values. In contrast, fly ash has the property of increasing strength which can be explained because of binding behavior and pozzolanic activity of it.

As a result of UCS tests; The change in ε_{max} values was found to be most affected by the ratio of the rubber with 56.74%, followed by the rubber diamater of 17.04%. These results clearly demonstrate that the ductile characteristic of the rubber contributes to the property of soil deformation ability much more than other factors.

As a result of STS tests; The change in STS values was found to be affected by the ratio of clay at a maximum of 37.72% and the rubber ratio at least by 3.68%. In addition, after the clay ratio, 15.57% of the effect of the fly ash ratio came out. Accordingly, it can be concluded that the effect of clay cohesion oversees the soil tensile strength more. In fact, it was expected here that the rubber ratio contributes more to the change of results; although it affected the highest values, it did not significantly affect the change of values.

Table 4(a): ANOVA analysis results for q_u values.

Parameter	DF	Seq SS	Contribution	Adj SS	Adj MS	F-Value
A	3	6194	4.05%	6194	2065	0.15
B	3	22927	14.98%	22927	7642	0.56
C	3	41766	27.29%	41766	13922	1.03
D	3	41507	27.12%	41507	13836	1.02
Error	3	40656	26.56%	40656	13552	
Total	15	153049	100.00%			

Table 4(b): ANOVA analysis results for ε_{max} values.

Parameter	DF	Seq SS	Contribution	Adj SS	Adj MS	F-Value
A	3	13.662	56.74%	13.662	4.5539	13.39
B	3	4.103	17.04%	4.103	1.3676	4.02
C	3	3.809	15.82%	3.809	1.2695	3.73
D	3	1.484	6.16%	1.484	0.4947	1.45
Error	3	1.02	4.24%	1.02	0.3401	
Total	15	24.078	100.00%			

Table 4(c): ANOVA analysis results for STS values.

Parameter	DF	Seq SS	Contribution	Adj SS	Adj MS	F-Value
A	3	1213	3.68%	1213	404.2	0.12
B	3	4302	13.07%	4302	1434.1	0.44
C	3	5126	15.57%	5126	1708.5	0.52
D	3	12414	37.72%	12414	4138	1.26
Error	3	9857	29.95%	9857	3285.7	
Total	15	32912	100.00%			

I. Conclusions

In this study, the effects of fly ash ratio, rubber diameter and clay ratio and especially the rubber ratio on the compressive and tensile strengths and deformation abilities of sand soils were investigated. For this, UCS and STS tests were performed on the sand soil experiment designs formed using the L16 Taguchi orthogonal array table. According to test results, S/N and ANOVA analysis the following assessments can be made:

- The sand soil that was stabilized by the binding characteristic of the clay and fly ash was able to keep itself without separation. According to S/N values, increase in rubber ratio, fly ash ratio and clay ratio can improve the strength values. ANOVA results showed that the change in q_u values was most influenced by fly ash ratio and at least affected by rubber ratio.

- It was expected and found that ε_{max} values was at their maximum when the rubber ratio in the soil matrix was at its highest level. According to S/N values, increase from 1st level to 2nd level was important, difference between 2nd 3rd, 4th could be ignored. From ANOVA results it was seen that the most effective parameter on the change of ε_{max} values was the rubber ratio and this can be seen from the difference of S/N values between 1st level and 2st level of the rubber ratio. Also, increase in the rubber diameter lowered the S/N value. This shows that there is no significant effect of rubber diameter size on the change of ε_{max}.

-According to STS test results rubber ratio, fly ash ratio and clay ratio act as increasing parameters for STS values. This can be seen by examining the S/N values belonging STS test results.

- From test results maximums or minimums could not be obtained regarding rubber dimensions, instead, the highest S/N values for q_u and STS values were obtained at 2nd level and for ε_{max} values were obtained at 1st level. Thus, the continuous increase in rubber diameter does not always give the best test results. And ANOVA results indicated that along with the three tests performed for the experiments, the rubber diameter didn't contribute to the change of the test results at most.

- Results of the optimum experiment designs should be obtained with confirmation tests for to compare the predicted results of Taguchi method.

- If the rubber is used to improve the deformation ability, it can have great effects with the correct selection of the rubber diameter and with the highest rubber ratio.

References

[1] J.S. Vinod, N. Sheikh, D. Mastello, B. Indraratna and M.S. Mashiri, , "The direct shear strength of sand-tyre shred mixtures," *2015 Proceedings of the International Conference on Geotechnical Engineering,* pp. 193–196.

[2] N. Hataf and M.M. Rahimi, "Experimental investigation of bearing capacity of sand reinforced with randomly distributed tire shreds," *Construction and Building Materials*, vol. 20, pp. 910–916, December 2006.

[3] S. Youwai and D.T. Bergado, "Strength and deformation characteristics shredded rubber tire - sand mixtures," *Canadian Geotechnical Journal*, vol. 40, pp. 254–264, April 2003.

[4] J.G. Zornberg, A.R. Cabral and C. Viratjandr, "Behaviour of tire shred - sand mixtures," *Canadian Geotechnical Journal*, vol. 41, pp. 227–241, April 2004.

[5] S.M. Anvari, I. Shooshpa and S.S Kutanaei, "Effect of granulated rubber on shear strength of fine-grained sand," *Journal of Rock Mechanics and Geotechnical Engineering*, vol. 9, pp. 936–944, October 2017.

[6] S. Akbulut, S. Arasan and E. Kalkan, "Modification of clayey soils using scrap tire rubber and synthetic fibers," *Applied Clay Science*, vol. 38, pp. 23–32, December 2007.

[7] N. Krithiga, D. Pujitha, T. Palayam and A. Revathy, "Soil Stabilization Using Lime and Fly Ash," *SSRG International Journal of Civil Engineering*, Special Issue Part-7, pp. 510–518, April 2017.

[8] M. Olgun, I.H. Erkan and O. Tan, "Freezing-thawing effect on shear strength of stabilized clayey soils," *2012 10th International Congress on Advances in Civil Engineering*, pp. 17–19.

[9] S.R. Kaniraj and V.G. Havanagi, "Compressive strength of cement stabilized fly ash-soil mixtures," *Cement and Concrete Research*, vol. 29, pp. 673–677, May 1999.

[10] ASTM Standard D698, "Test method for laboratory compaction characteristics of soil using standard effort," *ASTM International*, West Conshohocken, PA.

[11] ASTM Standard D2166, "Standard test method for unconfined compressive Strength of cohesive soil," *ASTM International*, West Conshohocken, PA.

[12] ASTM Standard C496, "Standard test method for splitting tensile strength of cylindrical concrete specimens," *ASTM International*, West Conshohocken, PA.

Pre-Feasibility Study of Eskişehir Landfill Gas to Energy

M. GÖKÇEK[1] and C. KALE[2*]

[1] Ömer Halisdemir University, Niğde/Turkey, mgokcek@ohu.edu.tr
[2]Fırat University, Elazığ/Turkey, ckale@firat.edu.tr

Abstract **- Landfill gas with a calorific value of 3.5-5 kWh/Nm^3 is considered to be a renewable energy source because of being produced from waste. On account of having the high heating value, it can be used for generating electricity or heat by using the gas engines. In this study, the optimization was performed with the reciprocal internal combustion engine (RICE) for Eskişehir landfill area according to gas estimation results obtained by using LandGEM model and it was evaluated as economically by using the Levelized cost of electricity method.**

Project life time was selected as 60 years (2017 to 2076) and six the reciprocal internal combustion engines, each with the electricity capacity of 1063 kWh, were used. As a result, total electric production was calculated as to be 1022.36 GWh duration of the considered life time and Levelized cost of electricity was found out as 0.0256 $/kWh

Keywords **- Landfill gas estimation, LandGEM, Waste to energy, Levelized cost of electric.**

I. INTRODUCTION

THE management of solid waste continues to be a major challenge in urban areas throughout the world, particularly in the rapidly growing cities and towns of the developing countries [1]. Landfilling continue to be very attractive method for the disposal of solid waste generated in cities [3] because it is the cheapest alternative for urban waste management commodities and end users [4,5]. Landfill gas (LFG) is produced by the resultant of the physical, chemical, and microbial processes that occur in the waste in landfill area [6, 7]. LFG is composed of approximately 50% of the CH_4, 45% of CO_2 and 5% of other non-carbon organic compounds (nitrogen compounds, hydrogen sulphide, and non-methane organic compounds) [8]. In addition, LFG also is considered as a renewable energy source [1,9] because about %50 of this gas composed of methane having high lower heating value (LHV) depending on methane content [10].

The energy from LFG can be recovered in many different technologies such as boiler for heating, direct thermal applications, electricity generation with internal combustion gas engines (ICE), micro gas turbines, steam turbines and fuel cells [11]. However, internal combustion engines are the most widely used technology for the conversion of LFG to Electricity [12]. The landfill gas to energy (LFGTE) projects are an increasingly prominent component of future energy portfolios. Although many removal techniques and sorbent regeneration strategies may prove effective, economical consideration ultimately is an immense factor [13]. Assessing the economic feasibility also is an important issue when making decisions with respect to a LFGTE project.

In this study, it was aimed to the optimization with the reciprocal internal combustion engine for Eskişehir landfill area according to gas estimation results obtained by using LandGEM model and to evaluate as economically by using the Levelized cost of electricity method.

II. METHODOLOGY

In the present study, Optimization for Eskişehir LFGTE project was carried out to using reciprocal internal combustion engine, which has the electricity capacity of 1063 kWh according to LFG estimated by LandGEM software from the previous study. Moreover, considered LFGTE project was analyzed as economically by using Levelized cost of energy (LCOE) method in light of the obtained optimization results.

A. Case-Study Landfill

In this study, Eskişehir landfill area which has begun to accepting of the MSW in 2010 was selected as study area. Eskisehir is a city with a total of 14 districts, 2 of which are central districts. The municipal solid wastes (MSW) of the two central districts, Odunpazari and Tepebaşı, are disposed of the landfill area, whereas MSW of 12 districts are disposed of open dumping [14]. Gas estimation results carried out by assuming that Eskişehir landfill site will accept municipal solid waste for 15 years are shown in Figure 1. and electrical energy production for according to estimated landfill gas can be seen in Figure 2. [15].

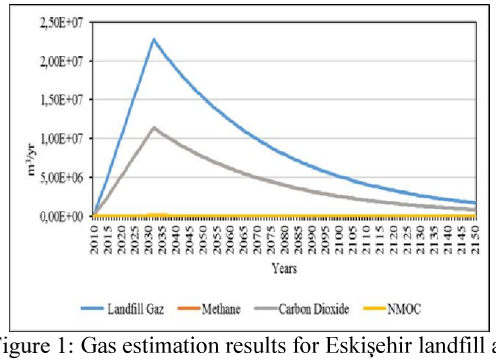


Figure 1: Gas estimation results for Eskişehir landfill area.

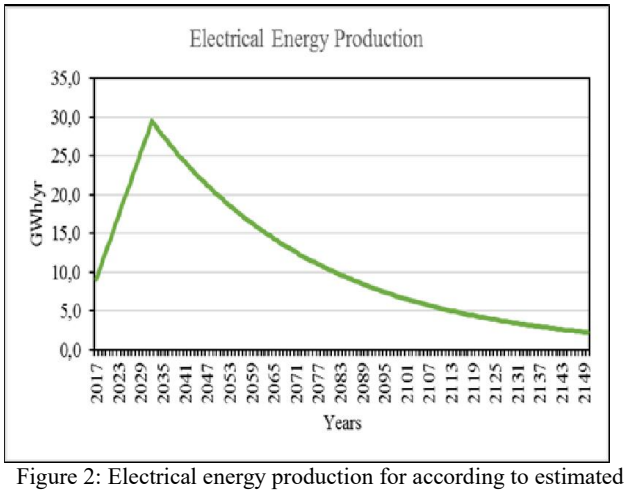


Figure 2: Electrical energy production for according to estimated landfill gas.

B. Optimization of Eskişehir LFGTE Project by using RICE

The three most commonly used technology for convert the landfill gas to energy are reciprocal internal combustion engines (RICE), gas turbines and micro turbines. The size of the project is most influential in the selection of these technologies. The RICE which are used more than 75 percent are well-suited for 800 kW to 3 MW. The gas turbines are preferred for 5 MW and larger plants, while micro turbines are used for projects smaller than 1 MW [16].

The maximum electrical energy for the previous study is 31.07 GWh/year which is equal to 3.54 MWh during the year 2032 as can be seen Fig. 2. Therefore, RICEs are used to generate electricity in this present study. According to estimated electrical energy, six RICEs, each with the electricity capacity of 1063 kWh, were used for 60 years (2017-2076). The technical and economical parameters of RICE used are shown in Table 1 [16,17].

Table 1: The technical and economical parameters of rice used.

Parameter	Value
RICE	JMS 320 GS-B.L
Electrical output (kWe)	1063
Recoverable thermal output (kW)	1088
Electrical efficiency (%)	40.8
Thermal efficiency (%)	41.7
Fuel Consumption based on a LHV of 5 kWh/Nm³ (Nm³/h)	521.4
Investment cost ($/kW)	1800
Operation and maintenance ($/kW)	180

C. Economic Model

One of the most important steps in terms of the applicability of the project is economic analysis. The levelised cost of electricity (LCOE) method is a widely used method for economic evaluation of renewable energy plants, such as LFGTE plants. For a plant, the levelised cost of electricity is calculated by dividing sum generated electricity that occurs throughout the lifetime to sum the expenses that occurs throughout the lifetime (both in present value terms) as given Eq. 1 [18,19].

$$LCOE = \frac{\sum_{t=0}^{n} \frac{C_t}{(1+r)^t}}{\sum_{t=0}^{n} \frac{E_t}{(1+r)^t}} \quad (1)$$

where n is the lifespan of the power plant, C_t and E_t stands for total cost and total generated electricity in year t respectively and r is the real discount rate. Real discount rate, r, is defined in Eq. 2 [20].

$$r = \frac{1+i}{1+f} - 1 \quad (2)$$

where i denotes the nominal discount rate and f is the inflation rate. In present study, i and f have taken as 8% and 2% respectively.

III. RESULTS

A. Optimization Results

The six RICEs in full capacity have been accompanied in such a way as to using electrical energy potential in maximum by using Excel software at different time intervals. as can be seen Figure 3. The first of the RICEs which have 20 years of lifespan move in 2017 and the second and third engine have been started after 10 years in 2027. The fourth engine has been run in 2037 and the fifth and sixth engines have been operated with a 10 years' interval from then.

Figure 4 shows that the electrical energy have been generated by RICEs over lifecycle. As can be seen Figure 4, total electric production was calculated as to be 1022.36 GWh duration of the considered life time (2017-2076) by using six RICEs.

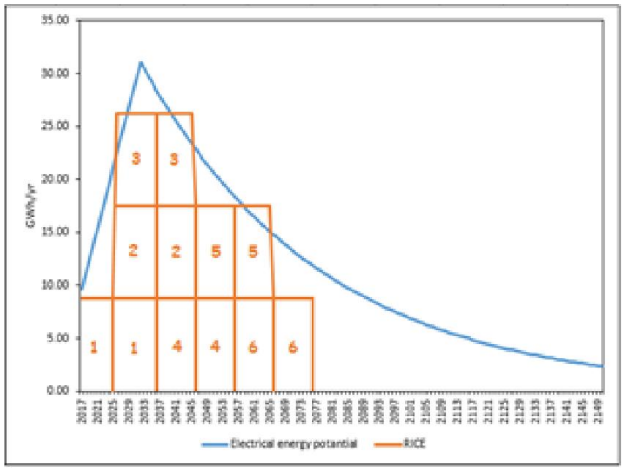


Figure 3: Optimization results of RICE.

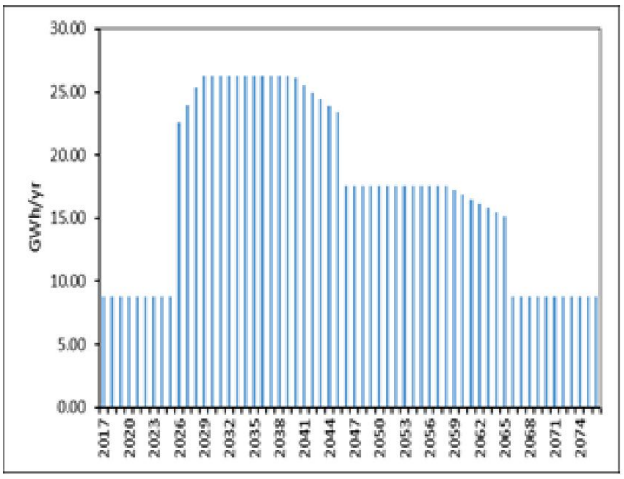


Figure 4: Annual electrical energy generated by RICEs.

B. *Economic Analyses Results*

The cash flow summary enabled by taking into account RICE starting time and lifecycle is shown in Fig. 5. The net present value (NPV) of investment and operation-maintenance costs during the 60-year lifetime were calculated as $ 6.961.647,56. By using Eq. 1, LCOE was found out as 0.0256 $ /kWh.

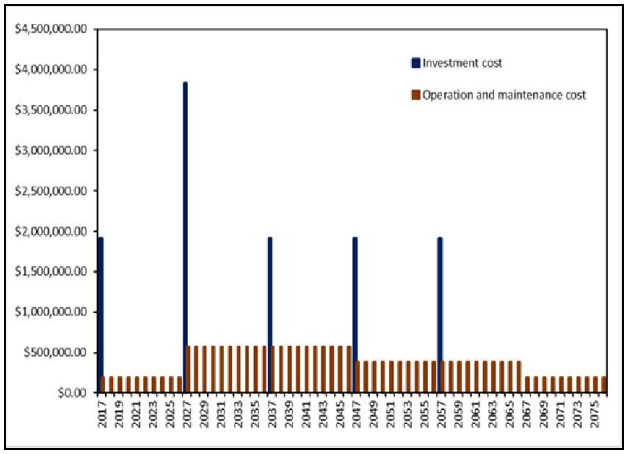


Figure 4: The annual cash flow summary.

IV. CONCLUSION

The use of landfill gas to produce electricity for Eskişehir landfill area is acceptable as economically and also to reduce greenhouse gas emission. The total energy generated by using six RICES was calculated 1022.36 GWh duration of considered life time (2017-2176). In addition, levelised cost of energy was found out as 0.0256 $/kWh. It is clear that LFGTE project for Eskişehir is a logical investment when considering 0.13 $/kWh sale price in Law on the Use of Renewable Energy Sources for Electricity Energy Production.

REFERENCES

[1] Johari, A., Ahmed, S. I., Hashim, H., Alkali, H., & Ramli, M. (2012). Economic and environmental benefits of landfill gas from municipal solid waste in Malaysia. Renewable and Sustainable Energy Reviews 16(5): 2907-2912.

[2] D.P. Komilis, R.K. Ham, R. Stegmann, The effect of municipal solid waste pretreatment on landfill behavior: a literature review, Waste Manag. Res. 17 (2009) 10-19

[3] Sprague, S. M. (2011). Economic Feasibility of Converting Landfill Gas to Natural Gas for Use as a Transportation Fuel in Refuse Trucks (Doctoral dissertation).

[4] T.G. Leton, O. Omotosho, Landfill operations in the Niger delta region of Nigeria, Eng. Geol. 73 (1) (2004) 171-177.

[5] Zhou, C., Gong, Z., Hu, J., Cao, A., & Liang, H. (2015). A cost-benefit analysis of landfill mining and material recycling in China. Waste Management, 35, 191-198.

[6] Aguilar-Virgen, Q., Taboada-González, P., & Ojeda-Benitez, S. (2014). Analysis of the feasibility of the recovery of landfill gas: a case study of Mexico. Journal of Cleaner Production, 79, 53-60.

[7] Kuhn, J. N., Elwell, A. C., Elsayed, N. H., & Joseph, B. (2017). Requirements, techniques, and costs for contaminant removal from landfill gas. Waste Management.

[8] Themelis, N. J., & Ulloa, P. A. 2007. Methane generation in landfills. Renewable Energy 32(7): 1243-1257

[9] IPCC e Intergovernmental Panel on Climate Change, CH4 Emissions from Solid Waste Disposal. Good Practice Guidance and Uncertainty Management in National Greenhouse Gas Inventories. Available at: www.ipccnggip.iges.or.jp/public/gp/bgp/5_1_CH4_Solid_Waste.pdf (accessed 16.10.14).

[10] Metz, B., Davidson, O.R., Bosch, P.R., Dave, R. And Meyer, L.A. 2007. Climate Change 2007: Mitigation of Climate Change. Contribution of Working Group III to the Fourth Assessment Report of the Intergovernmental Panel on Climate Change, Cambridge, UK, 863.

[11] Chacartegui, R., Carvalho, M., Abrahão, R., & Becerra, J. (2015). Analysis of a CHP plant in a municipal solid waste landfill in the South of Spain. Applied Thermal Engineering, 91, 706-717.

[12] M. Zairi, A. Aydi, H. Ben Dhia, Leachate generation and biogas energy recovery in the Jebel Chakir municipal solid waste landfill, Tunisia, J. Material Cycles Waste Manag. 16 (2014) 414-450.

[13] Kuhn, J. N., Elwell, A. C., Elsayed, N. H., & Joseph, B. (2017). Requirements, techniques, and costs for contaminant removal from landfill gas. Waste Management.

[14] Çed ve Çevre İzinleri Şube Müdürlüğü. 2015. Eskişehir İli 2014 Yılı Çevre Durum Raporu. T.C. Eskişehir Valiliği Çevre Ve Şehircilik İl Müdürlüğü, Eskişehir, Türkiye.

[15] M. Gökçek and C. Kale, E, "Estimating Greenhouse Gas Emission And Energy Potential Of Eskişehir Landfill Area", 7th International 100% Renewable Energy Conference, İstanbul, 18-21 Mayıs 2017.

[16] USEPA-LMOP (United States Environmental Protection Agency-Landfill Methane Outreach Program), "LFG Energy Project Development Handbook", United States Environmental Protection Agency, 2016.

[17] GE, "Technical Specification", General Electric, http://www.cogeneration.com.ua /ru/equipment-ge-jenbacher/, [accessed 24.02.2017]..

[18] Zhao, Z. Y., Chen, Y. L., & Thomson, J. D. (2017). Levelized cost of energy modeling for concentrated solar power projects: A China study. Energy, 120, 117-127.

[19] Lai, C. S., & McCulloch, M. D. (2017). Levelized cost of electricity for solar photovoltaic and electrical energy storage. Applied Energy, 190, 191-203.

[20] HOMER help manual. Available from: http://www.homerenergy.com/pdf/HOMERHelpManual.pdf, [accessed 24.02.2017].

Estimation of landfill gas and energy potential in Turkey

M. GÖKÇEK[1] and C. KALE[2*]

[1] Ömer Halisdemir University, Niğde/Turkey, mgokcek@ohu.edu.tr
[2]Fırat University, Elazığ/Turkey, ckale@firat.edu.tr

Abstract **- Turkey is a country which depends on the imported energy for about 75%. Therefore, the potential and uses of domestic and renewable energy sources have been investigating by many researchers. The waste to energy production can be viewed as a renewable resource that is non- imported. In addition, the waste which is hazardous for human and environment can be disposed of in this way. Landfilling is a most popular method to dispose of waste in Turkey. In this study, the energy potential of 30 years (2017-2047) municipal solid waste was estimated for Turkey by using LanGEM model. According to LanGEM result, when (2017-2047) municipal solid waste is disposed of in the landfill area, landfill gas is released until the 2157 year. The total amount of landfill gas was found as $2.9x10^{11}$ m^3 and the energy content of this gas was calculated as 375,709 GWh per lifetime (2017-2157).**

Keywords **- Landfill gas estimation, LandGEM, Greenhouse gas emission, energy potential from landfill.**

I. INTRODUCTION

THE energy supply, municipal solid waste (MSW) management and effect of greenhouse gases (GHGs) are the most important issues due to the rise of urbanization and the intensified industrialization in developing countries [1]. Even though there are many ways, landfilling is the most common MSW management method in the world nowadays [2]. Landfill gas which is essentially methane (CH_4) (50–55%) and carbon dioxide (CO_2) (40–45%) (both GHGs) is released from MSW by biodegradation processes [3]. For this reason, the greenhouse effect of landfill gas is inevitable. However, landfill gas can be converted to green energy [3] due to consisting of methane in about %50 of this gas which having approximately 16-22 MJ/Nm^3 lower heating value (LHV) depending on methane content [4].

By collecting and using of landfill gas, both the energy can be obtained to contribute to the economy and the greenhouse effect can be reduced directly and indirectly with the conversion of CH_4 into CO_2 [5,6]. The determining of landfill gas amount emitted is the most barrier in order to calculate the energy that can be obtained from landfill areas and to determine the greenhouse effect. Landfill gas can be estimated by field measurements, experimental processes or mathematical modeling approaches [7]. Numerous mathematical models have been developed for predicting the amount of landfill gas for many years based on the zero, first and second order decomposition equations [8]. However, models based on second order decomposition are not widely used because of not being precisely determined of the required parameters [9]. In addition, zero order models do not reflect the biological landfill gas generation processes. Therefore, the first order models are widely used by industry, state regulators, the Intergovernmental Panel on Climate Change (IPCC), and the US Environmental Protection Agency (US EPA) to estimate landfill gas generation [10]. The Landfill Gas Emissions Model, LandGEM, which is develop by US EPA based on the first-order decomposition equation is an automated estimation tool with a Microsoft Excel interface that can be used to estimate emission rates for total landfill gas methane, carbon dioxide, non-methane organic compounds (NMOC), and individual air pollutants from municipal solid waste landfills [11]. To be able to use this model, parameters such as the amount of annual waste stored or the total amount of waste in the storage area, the methane generation rate, the potential methane generation capacity, initial and final year of waste acceptance is required. In this study, it was aimed to estimate the amount of landfill gas to be generated with MSW amount of generated in Turkey and to determine the energy potential of this gas.

II. METHODOLOGY

In the present study, for the long term, the landfill gas amount with MSW amount of generated in Turkey was estimated by using LandGEM 3.02 model and the energy potential of estimated gas was determined in the case of using an internal combustion reciprocal gas engine. To achieve this study, the amount of solid waste for the future was obtained by population estimation using the arithmetic increase method. In addition, methane generation rate and potential methane generation capacity values required for model were obtained using IPCC methodology. The amount of MSW, waste composition, population and meteorological data for the past years were obtained by the TURKSTAT, Turkish State Meteorological Service and Ministry of Environment and Urbanism in Turkey Republic.

A. Case-Study

In this study, Turkey was selected as study area. Turkey is one of the developing countries with 79814871 populations

consisting of 81 cities in 2016. Therefore, Turkey has a great potential in term of municipal waste to energy. Turkish Statistical Institute (TURKSTAT) shares the knowledge of the amount of total annual waste generated and amount of waste per capita in each two years. The annual amount of solid waste needs to know to estimating landfill gas, the data of solid waste amount generated in unshared years has been determined to be based on following year data. The amount of MSW generated and the total populations data in Turkey according to years are shown in Table 1.

Table 1: Population and amount of MSW generated in Turkey.

Years	Total Population in Turkey (Person)	MSW Amount Generated (Ton/year)
2001	-	25133696
2002	-	25373134
2003	-	26117539
2004	-	25013520
2005	-	-
2006	-	25279971
2007	70586256	-
2008	71517100	24360863
2009	72561312	-
2010	73722988	25276698
2011	74724269	-
2012	75627384	25844573
2013	76667864	-
2014	77695904	28010721
2015	78741053	-
2016	79814871	-

The composition of MSW generated in Turkey in 2016 is shown in Figure 2 [12]. As seen in Figure 2., the amount of organic solid waste is quite. It is mean that MSW of Turkey has a very great waste composition in point of potential methane generation capacity.

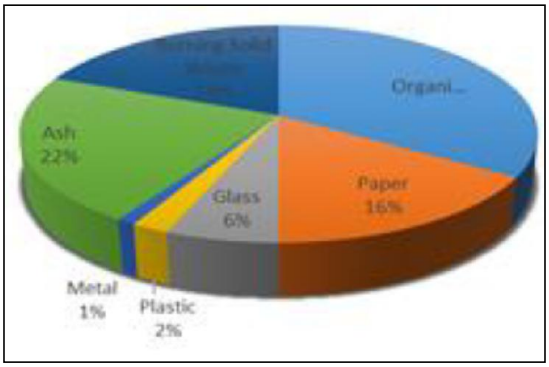


Figure 1: Composition of the MSW in Turkey.

The annual average amount of precipitation values according to years for the study area are shown in the Figure 3. According to Figure 3., the average amount of precipitation is 574 mm between the 1981-2016 years for Turkey.

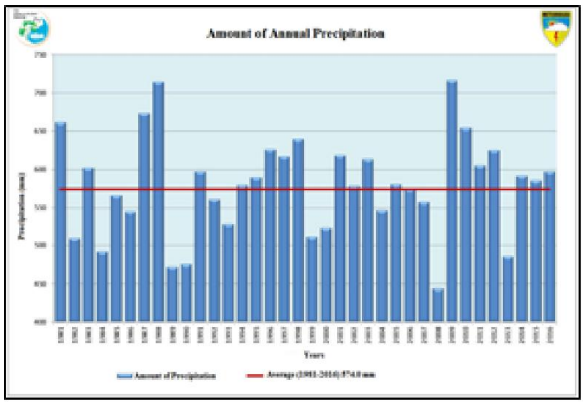


Figure 2: Amount of precipitation according to years.

B. Determining the parameters to be used

The amount of the solid waste, methane generation rate (k) and potential methane generation capacity (L_o) are needed to know to estimating landfill gas by using LanGEM model for the considered site. This model has standard k and L_o values created by United States Energy Production Agency and also enable to entering values determined by the user. However, the standard k and L_o values were found out by using solid waste composition and meteorology values of United States. It is mean that these standard values may not proper for the considered site if this site is not in the United States. The k and L_o are needed to determining for considered site to calculating more accurate landfill gas estimation.

1) Estimating the amount of solid waste

The amount of being generated solid waste is calculated by Eq. 1[13].

$$A = N_t \times \frac{A_k}{1000} \times 365 \quad (1)$$

where A is to be generated annual solid waste amount (ton/year), N_t is the population of the considered year and A_k is the amount of the solid waste produced a day per a person (kg-person/day). In this study, the future population was calculated by using arithmetic increase method as seen Eq. 2 [14].

$$N_t = N_y + k_a\left(t_g - t_y\right) \quad (2)$$

where N_y is the last census, t_g is the year of the last census, t_y is the year to be studied and k_a is the arithmetic increase coefficient which is calculated by using Eq. 3.

$$k_a = \left(\frac{N_y - N_e}{t_y - t_e}\right) \quad (3)$$

where N_e and t_e is the the first population and the year in which first population census was carried out respectively.

2) Determining methane generation rate

The methane generation rate, k, determines the rate of methane generation for the mass of waste in the landfill [14].

The methane generation rate is calculated by using Eq. 4 [2,15]. According to this equation, the methane generation rate was determined as 0.028368 for Turkey.

$$k = 3,2 \times 10^{-5} \times R + 0,01 \quad (4)$$

where R is the average precipitation amount for considered site.

3) Determining potential methane generation capacity

The potential methane generation capacity, L_o, depends only on the type and composition of waste placed in the landfill [14]. According to International Panel on Climate Change (IPCC) methodology, L_o value is calculated as seen in Eq. 5 [16].

$$L_o = MCF \times DOC \times DOC_f \times F \times 16/12 \quad (5)$$

where L_o is a potential methane generation capacity (kg/ton), MCF is a methane correction factor (default =1.0), DOC is a degradable organic carbon (kg/ton), DOC_f is a fraction of assimilated DOC (default = 0.77), F is a fraction of methane in landfill gas (default = 0.5), and 16/12 is a stoichiometric factor. DOC is calculated by using Eq. 6 [16].

$$DOC = A \times 0.15 + B \times 0.4 + C \times 0.24 + D \times 0.43 + E \times 0.2 \quad (6)$$

where DOC is degradable organic carbon, A, B, C, D, E are fraction of municipal solid waste (MSW) that is the food waste, the paper or cartoon waste, the textile waste, the wood or straw waste, the garden or park waste, the nappy waste, the rubber or leather waste respectively.

C. Calculating of the power generation

The amount of power could be computed using the electrical conversion efficiency as seen Eq. 7.

$$E_{el}(kWh) = m_{lg} \times LHV_{lg} \times \Re \times \eta_{el} \quad (7)$$

where m_{lg} is the flow rate of landfill gas (m^3/h), LHV_{lg} is the lower heating value of landfill gas (MJ/m^3), $\Re$ is the recovery rate (75%) and is the electrical efficiency of the gas engine (38.7%). LHV of the landfill gas varies from 3.5 to 5.5 kWh/Nm^3 [4]. In the present study, LHV of the landfill gas is specified as to be 5 kWh/Nm^3

III. RESULTS

A projection of the LFG generation up to 2157 was done for Turkey. Figure 4. shows estimated total landfill gas, methane, carbon dioxide and NMOC gas up to the year 2157. The graph shows that the amounts of gas would keep on increasing until it reaches a maximum in 2048 where total landfill gas is 5831 Mm^3, methane is 3207 Mm^3, carbon dioxide is 2624 Mm^3 and NMOC is 22.7 Mm^3. After 2048, the amounts of gas would continue to produce but a lower rate because of not accepting.

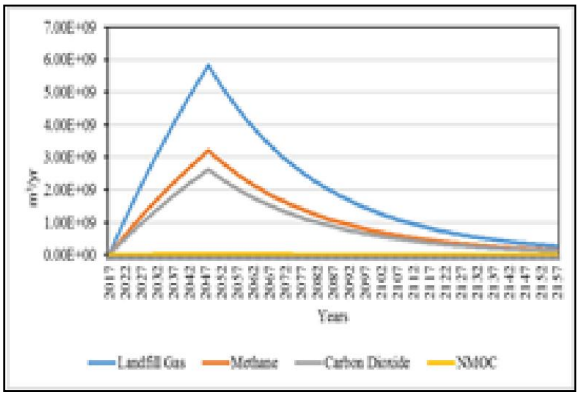


Figure 3: Estimated landfill, methane, carbon dioxide and NMOC gas.

Figure 5. shows electrical energy production for according to estimated landfill gas. Electricity generation has started in 2018, after one year of acceptance of waste, as 295.8 GWh and it could be seen from the graph that it would reach a peak power in 2048 with 7539.3 GWh.

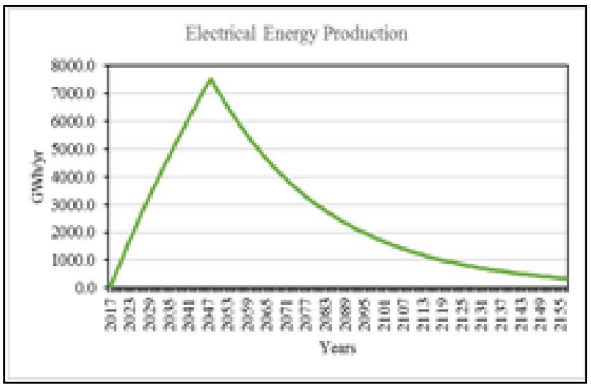


Figure 4: Electrical energy production from landfill gas estimated

IV. CONCLUSION

The use of landfill gas to produce electricity is a promising approach both in terms of conserving energy and also to reduce greenhouse gas emission. the maximum landfill gas formation and electrical energy production was found as 5838 Mm^3 and 7539.3 GWh respectively. The total amount of landfill gas is 2.9×10^{11} m^3 and electricity production was calculated as 375709.5 GWh duration of considered life time (2017-2157). It can be concluded that landfill gas as a renewable energy source is a good for power generation and it can be used as an alternative to fossil resources.

REFERENCES

[1] Ouda, O. K. M., Raza, S. A., Nizami, A. S., Rehan, M., Al-Waked, R., & Korres, N. E. (2016). Waste to energy potential: a case study of Saudi Arabia. Renewable and Sustainable Energy Reviews, 61, 328-340.

[2] Chalvatzaki, E., & Lazaridis, M. (2010). Assessment of air pollutant emissions from the Akrotiri landfill site (Chania, Greece). Waste Management & Research, 28(9), 778-788.

[3] Johari, A., Ahmed, S. I., Hashim, H., Alkali, H., & Ramli, M. (2012). Economic and environmental benefits of landfill gas from municipal

solid waste in Malaysia. Renewable and Sustainable Energy Reviews, 16(5), 2907-2912.

[4] Metz, B., Davidson, O.R., Bosch, P.R., Dave, R. And Meyer, L.A. 2007. Climate Change 2007: Mitigation of Climate Change. Contribution of Working Group III to the Fourth Assessment Report of the Intergovernmental Panel on Climate Change, Cambridge, UK, 863.

[5] USEPA-LMOP (United States Environmental Protection Agency-Landfill Methane Outreach Program). 2016. LFG Energy Project Development Handbook. United States Environmental Protection Agency, Retrieved April 03, 2017 from the World Wide Web: https://www.epa.gov/sites/production/files/2016-11/documents/pdh_full.pdf

[6] A. Corti, L. Lombardi, and L. Frassinetti. 2007. Landfill Gas Energy Recovery : Economic and Environmental Evaluation for a Study Case. In Proceedings of Eleventh International Waste Managment and Landfill Symposium, Sardinia, Italy, 1-5 October.

[7] Sarptaş, H. 2016. Katı Atık Depo Gazı Enerji Potansiyelinin Matematiksel Modelleme Yaklaşımı ile Tahmini. Türk Tesisat Mühendisleri Derneği (TTMD) Dergisi 102: 48–55.

[8] Walter, G. R. 2003. Fatal flaws in measuring landfill gas generation rates by empirical well testing. Journal of the Air & Waste Management Association 53(4): 461-468.

[9] Amini, H. R., Reinhart, D. R., & Niskanen, A. 2013. Comparison of first-order-decay modeled and actual field measured municipal solid waste landfill methane data. Waste Management 33(12): 2720-2728.

[10] Aguilar-Virgen, Q., Taboada-González, P., & Ojeda-Benítez, S. 2014. Analysis of the feasibility of the recovery of landfill gas: a case study of Mexico. Journal of Cleaner Production 79: 53-60.

[11] Alexander, A., Burklin, C., & Singleton, A. 2005. Landfill Gas Emissions Model (LandGEM) Version 8082 User's Guide. United States Environmental Protection Agency, Retrieved April 03, 2017 from the World Wide Web: https://www3.epa.gov/ttncatc1/dir1/landgem-v302-guide.pdf

[12] Çed ve Çevre İzinleri Şube Müdürlüğü. 2016. Türkiye 2016 Yılı Çevre Durum Raporu. T.C. Çevre Ve Şehircilik Bakanlığı, Ankara, Türkiye.

[13] Das, S., & Bhattacharyya, B. K. 2014. Estimation of municipal solid waste generation and future trends in greater metropolitan regions of Kolkata, India. Journal of Industrial Engineering and Management Innovation 1(1): 31-38.

[14] Alcantara, A.N. 2002. Population projections without trying. Data Users Conference, Retrieved April 03, 2017 from the World Wide Web: http://bber-old.unm.edu/presentations/projections.pdf

[15] USEPA. 2004. Air Toxics Risk Assessment Reference Library. United States Environmental Protection Agency. Retrieved April 03, 2017 from the World Wide Web: https://www.epa.gov/sites/production/files/2013-08/documents/volume_1_reflibrary.pdf

[16] Atabi, F., Harati, S. a N. and Sagharlu, N. Q. 2014. Calculation of CH4 and CO2 Emission Rate in Kahrizak Landfill Site Through Landgem Mathematical Model. . In Proceedings of The 4th World Sustainability Forum, 1-30 November.

The Structures Which are Inspired by Lattices of Metals under Moving Load

S. GÜLER[1, †] and M. YILDIZ[1]

[1] Iskenderun Technical University, Hatay/Turkey, serkan.guler@iste.edu.tr
[1] Iskenderun Technical University, Hatay/Turkey, murat.yildiz@iste.edu.tr
† Corresponding author

***Abstract* – There have been an increase in studies focusing on developing materials that are being inspired by Nature, in the recent years. Lattice-inspired and bio-inspired structures are being researched intensively. Also beams and truss structures are common elements that can be used in the engineering designs such as frames of machines and buildings and more. So, designing structures which are inspired by the lattices of metals may prove to be impactful. When designing structures, it is important to construct them in a suitable manner to maintain their estimated lifetime. Thus, it is vital to verify the characteristics of the structures such as the deflection, stresses and more. Finite element analysis is a commonly used method to determine those structural characteristics. In this study, the models that were inspired by the lattice structures of materials were generated. By using those models, beam structures were designed. Beam finite element simulation was conducted on the structures. Moving loads were implemented the structures in the analyses. The results showed that these designed structures can be used in many areas such as aviation, space, construction and more. They can also be used as the core part of the sandwich composites that are commonly used in the modeling of the structures.**

***Keywords* – Metals, Lattice Inspired, Finite element method, Dynamic analysis, Moving load**

I. INTRODUCTION

In nature, wonders are endless. With technological advancements, humanity managed to inspect nature more closely and confirmed its engineering abilities and got fascinated by them. This made way for many studies being inspired by nature. Bio-inspired and lattice-inspired designs are being studied actively and they are expected to play important roles in many areas such as construction, biology, marine, space etc.

. Usage and manufacturing of lattice structures have grown thanks to their lightweight and mechanical efficiency ratio and many studies related to lattices are being carried out. Some studies are about lattices being manufactured by using additive manufacturing methods and used as beams [1,2]. There are also studies that investigated the numerical analysis of the lattice structures such as Lee and McClure's work where they developed a numerical model for simulating behaviour of lattice steel tower structures. They presented static large deformation analysis of a lattice steel tower structure using finite element analysis and compared the numerical results with full-scale test. 2-node three-dimensional beam elements proposed in their previous work was used in the static finite element analysis [3]. Also, Guo et al. proposed 3D periodic multilayer lattice materials such as the square, the quadrate, the tetrahedron and the hexagon in order to supply load-carrying necessities of a composite material. Authors obtained static structural simulation results using BEAM189 element in ANSYS, the static mechanical properties of the four multilayer lattice materials were analysed [4]. Sun et al. designed a regular hexahedral unit, produced the lattice structure composed of the Ti–6Al–4V units. After that, they obtained the experimental fracture load and the compression deformation of them through compression tests, then conducted a simulation of the unit and the lattice structure through ANSYS (static) to analyse the failure point [5]. Messner developed a method for optimizing the mesostructure of lattice-structured materials. These materials are periodic arrays of slender members resembling efficient, lightweight macroscale structures like bridges and frame buildings [6]. Syam et al. examined the use of additively manufactured strut-based lattice structures to improve the mechanical vibration isolation properties of a structure. Finite element modelling had been used to determine the theoretical static and dynamic mechanical properties of both the single cell and the array configuration of the lattice structures [7].

Beams and truss structures are commonly used as tension structures to build facilities, machine frames and more in the engineering systems [8,9,10,11]. Finite Element Method (FEM) can be used in engineering structures that are being constructed with beams and trusses such as buildings, space structures and more [11,12,13,14,15]. In this method, structures are meshed out and mathematical models involving differential equations [16] having huge degrees of freedom are set. In the past equation solving was a hard task. Now, thanks to the developments in the computer science in the recent years, finite element method is now capable enough to be used as the leading solving method [11].

Those developments made way for analysing the beams being subjected moving loads as well. In their work, Uzzal et al. investigated dynamic responses of an Euler-Bernoulli beam that was supported on two-parameter Pasternak foundation. They studied the effects of moving load and moving mass on bending moment and dynamic deflection responses of the beam, numerically [17]. Esen studied the dynamic responses of a beam which carried an accelerating moving mass by using

moving finite element modeling. He generated a MATLAB code for analyzing the structure, numerically [18]. Dehestani et al. investigated the critical influential speed and inertia of a moving mass on beams. They used Coriolis acceleration and analyzed the dynamic responses of the beams with various boundary conditions [19]. Azam et al. too investigated the dynamic response of Timoshenko beam model based beam that subjected a moving mass and moving, numerically [20].

In this study lattice inspired structures were designed. For these kinds of structures, suitable designs are important to retain their estimated working life. Hence, it is a must to determine the characteristics of those structures i.e. the deflections, stresses and more. And, the finite element is a capable method to determine those characteristics [11]. So, ANSYS commercial finite element program which features beam finite elements method that is based on Timoshenko beam theory was used to analyze the designed frames in this study. Moving loads were implemented the structures in the analyses. The influence of moving load velocity on deflection responses of the beams was examined.

II. FINITE ELEMENT MODELING

Four kinds of lattices of materials were chosen to be the models. Those materials are Cu, TiO_2, FeS, ZnSe and those lattice structure models are given in Fig. 1.

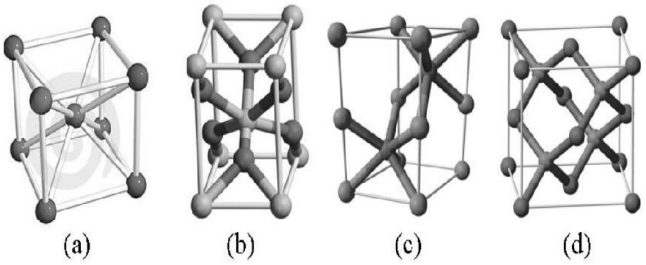


Figure 1: Lattices of the materials: (a) Cu [21], (b) TiO_2 [22], (c) FeS [23], (d) ZnSe [24]

Those lattice inspired designs were constructed in the SolidWORKS environment. Thus, a lattice database was created in IGES format. The lattices were labeled as L_i. Where L is abbreviation of lattices and i references to the numbers of the lattices that stored in the database. The models (solid models) are in mm scale and given in Fig. 2. Their measurements are given in Fig. 3.

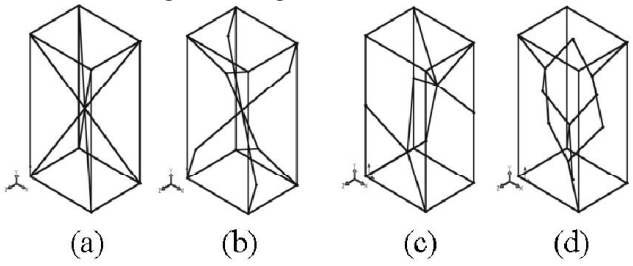
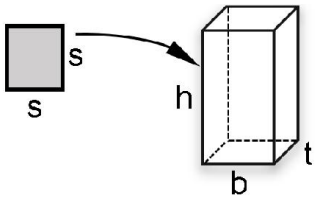


Figure 2: Line models of lattices; (a) Cu, (b) TiO_2, (c) FeS, (d) ZnSe.



b (μm)	1250
h (μm)	2500
t (μm)	1000
s (μm)	50

Figure 3: Dimensions of lattices and section.

For finite element solving program ANSYS was used. The IGES files were imported into ANSYS. Then, the models were constructed into the beam structure. As an example, the L_2-beam that is composed of L_2 cell models is given in Fig. 4.

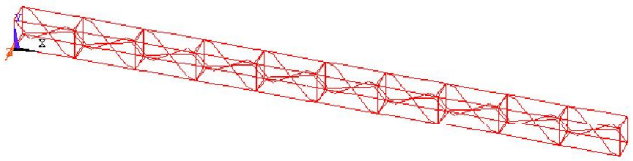


Figure 4: L_2-beam.

To construct finite element model of the beams, only one of the lattice models was used in every turn and in total of 4 beam structures were generated. For the structures, ten models in the direction of the x-axis were joined together.

BEAM44 elements were used in ANSYS models. BEAM44 is a uniaxial element with tension, compression, torsion, and bending capabilities [25].

The material properties of lattices were defined by $\boldsymbol{p}_m = [E, \rho, \upsilon, \beta]$ where E is modulus of elasticity (GPa), ρ is density (kg/m^3), υ is Poisson's ratio and β *is material damping ratio*. $\boldsymbol{p}_m = [113.8, 4430, 0.342, 0.0001]$ for *TI-6AI-4V* material and designing was constructed as linear elastic isotropic model in this study.

In order to establish the finite element models of these beam structures, firstly *the modeling macro files* were prepared. Secondly *the solution macro files* for computing deflections of those beam structures were created. In the model macro files, lines were allocated for beams. Then, material properties and section were defined for the beams. Cell dimensions were 1250x2500x1000 μm and assigned section dimensions were 50x50 μm as shown in Fig.3. So, all lines were meshed by assigning these sections and material properties. Finally, transient dynamic analyses were performed and deflections of these beam structures obtained by using *the solution macro files*.

III. FINITE ELEMENT RESULTS OF THE BEAM STRUCTURES UNDER MOVING LOAD

In these analyses, moving loads were applied on nodes by assuming the amplitudes were constant at different velocities in direction of x-axis. The moving load velocities were determined by using Eq. 1,

$$v_x = k_v \cdot \frac{e_s}{\Delta t} \quad (1)$$

where v_x is velocity in direction of x-axis, k_v is velocity coefficients that were chosen as *[0.25, 0.5, 1, 2, 3 ,4 ,5]*, e_s is element size and Δt is time step of the simulation. Δt was calculated by using Eq. 2,

$$\Delta t = \frac{1}{20 f_n} \quad (2)$$

where f_n is natural frequency of the beams at direction of excitation. Applied moving loads (see Fig. 5) which were chosen as 50 times of their total weight were implemented on nodes.

The simply supported boundary conditions were implemented on both ends of the beams. Then, the influence of moving load velocity on deflection responses of the beams was considered. The response point and applied moving loads are shown in Fig.5.

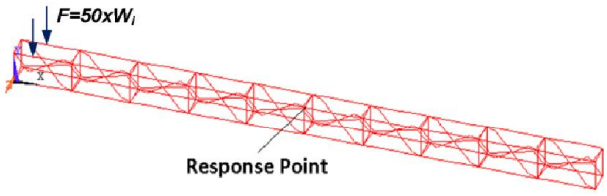


Figure 5: Response point of L_2-beam.

In Fig. 6, it can be observed that the maximum deflection of L_1-beam structure is occurred at the velocity of 21.52 *m/s* because of the traveling time being the longest on the beam.

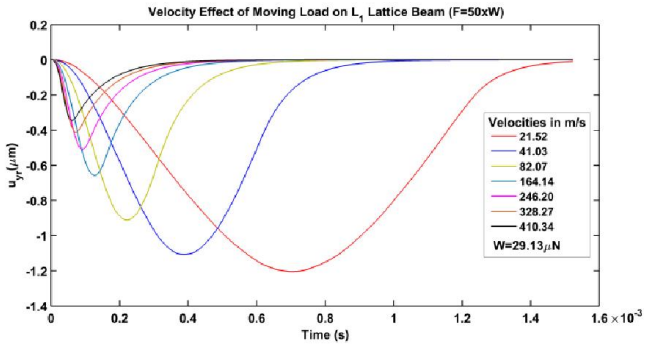


Figure 6: Velocity effect of moving load on L_1 lattice beam.

In Fig. 7, it can be observed that the maximum deflection of L_2-beam structure is occurred at the velocity of 10.00 *m/s* because of the traveling time being the longest on the beam.

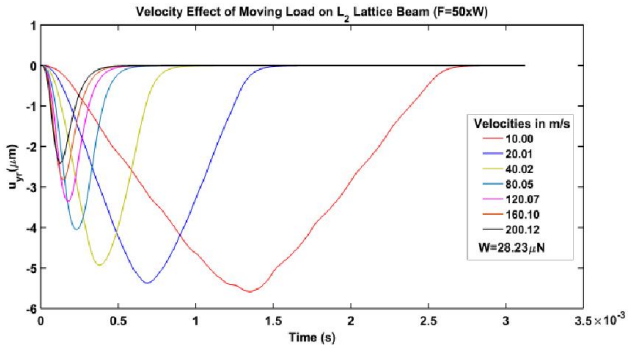


Figure 7: Velocity effect of moving load on L_2 lattice beam.

In Fig. 8, it can be observed that the maximum deflection of L_3-beam structure is occurred at the velocity of 14.98 *m/s* because of the traveling time being the longest on the beam.

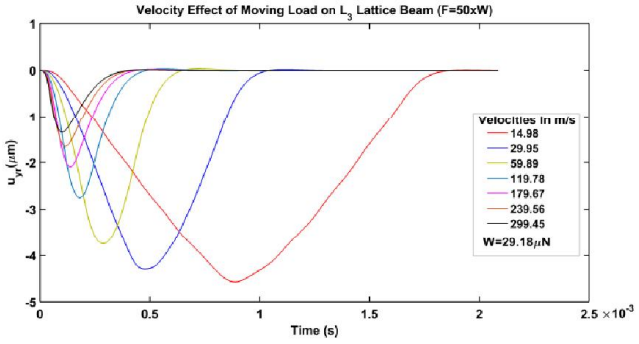


Figure 8: Velocity effect of moving load on L_3 lattice beam.

In Fig. 9, It can be observed that the maximum deflection of L_4-beam structure is occurred at the velocity of 8.89 *m/s* because of the traveling time being the longest on the beam.

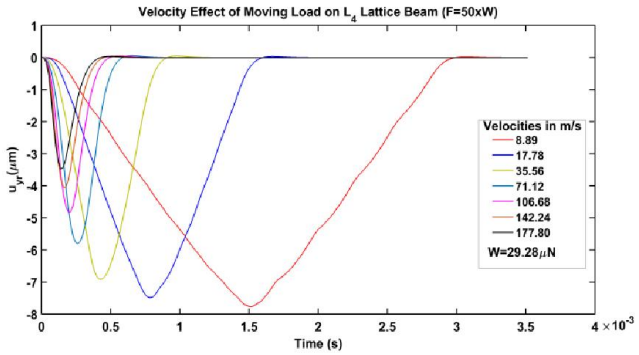


Figure 9: Velocity effect of moving load on L_4 lattice beam.

Due to the fact that the natural frequencies of the beam structures were factored in when calculating the velocities, the values resulted in being different from each other.

The L_1 beam showed the best result of having the lowest deflection values among the beam structures thanks to its symmetric, cubic centered structure. L_2 and L_3 beams were more asymmetric and had more deflection. L_4 showed the

worst results for being the most asymmetric structure among the beam structure and being a more face centered model.

IV. Conclusion

In this study, lattice inspired cell models were generated and by using those cell models, four different beam structures were constructed in ANSYS software. Then transient dynamic analyses were conducted. In these analyses, moving loads having magnitude of 50 times of their total weight were applied on nodes by assuming the amplitudes were constant at different velocities in direction of x-axis. Then, the deflections of the beam structures were computed.

The results can be summarized here; the moving load velocities led to decrease in deflections and that the maximum deflections of beam structures were different for each other and the lowest value belonging to L_1-beam structures.

As a future study, confirming the results with actual experimental results is suggested.

References

[1] L. Chougrani, J. P. Pernot, P. Véron and S. Abed, "Lattice structure lightweight triangulation for additive manufacturing", *CAD Computer Aided Design*, vol. 90, pp. 95–104, 2017.

[2] M. Królikowski and D. Grzesiak, "Technological Restrictions of Lightweight Lattice Structures Manufactured by Selective Laser Melting of Metals", *Advances In Manufacturing Science And Technology,* Vol. 38, 2014.

[3] P. S. Lee and G. McClure, "Elastoplastic large deformation analysis of a lattice steel tower structure and comparison with full-scale tests". Journal of Constructional Steel Research", vol. 63, pp. 709–717, 2007.

[4] R. Guo, R. Liu, W. Jiang, K. Chen, J. Zhang, F. Huang and X. Sun, "Numerical Analysis on Static Mechanical Properties of the Periodic Multilayer Lattice Material," *Engineering*, Vol. 3 (12), pp. 1149-1154, 2011.

[5] J. Sun, Y. Yang and D. Wang, "Mechanical properties of regular hexahedral lattice structure formed by selective laser melting", *Laser Physics*, vol. 23, 066101 (9pp), 2013.

[6] M. C. Messner, "Optimal lattice-structured materials", *Journal of the Mechanics and Physics of Solids*, vol. 96, pp. 162–183, 2016.

[7] W. P. Syam, W. Jianwei, B. Zhao, I. Maskery, R. Leach, "Design of mechanically-optimised lattice structures for vibration isolation", *Proceedings of 17th International euspen Conference*, pp. 55-56, Germany, 2017.

[8] H. Matlock and B. R. Grubbs, "Development of Methods for Computer Simulation of Beam-Columns and Grid-Beam and Slab Systems" *Enter for Highway Research*, The University of Texas, Texas, 1967.

[9] G. Kiper and E. Soylemez, "Deployable space structures", *2009 4th International Conference on Recent Advances in Space Technologies*, pp. 131-138, Istanbul, 2009.

[10] H. J. Xiang, Z. F. Shi, S. J. Wang and Y. L. Mo, "Periodic materials-based vibration attenuation in layered foundations: experimental validation", *Smart Materials and Structures*, vol. 21, 112003 (10pp) ,2012.

[11] H. Karadeniz, "Stochastic Analysis of Offshore Steel Structures: An Analytical Appraisal", *Springer-Verlag London*, 2012.

[12] S. Bobby, S. M. J. Spence, E. Bernardini and A. Kareem, "Performance-based topology optimization for wind-excited tall buildings: A framework", *Engineering Structures*, vol. 74, pp. 242–255, 2014.

[13] J. Huang, Z. Shi, W. Huang, X. Chen and Z. Zhang, "A periodic foundation with rotational oscillators for extremely low-frequency seismic isolation: analysis and experimental verification", *Smart Materials and Structures*, vol. 26, 035061 (11pp), 2017.

[14] Y. Ren, Y. Yu, B. Zhao, C. Fan and H. Li, "Finite Element Analysis and Optimal Design for the Frame of SX360 Dump Trucks", *Procedia Engineering (Elsevier Ltd, 2017)*, vol. 174, pp. 638–647, 2017.

[15] S. Güler and H. Karagülle, "Finite element analysis of structures with extruded aluminium profiles having complex cross sections", *Latin American Journal of Solid and Structures*, vol. 13, pp.1499–1514, 2016.

[16] S. S. Rao, "Mechanical vibrations. 3rd ed. Upper saddle river: Prentice hall", 2011.

[17] R. U. A. Uzzal, R. B. Bhat and W. Ahmed, "Dynamic response of a beam subjected to moving load and moving mass supported by Pasternak foundation", *Shock and Vibration*, vol. 19, pp. 201–216, 2012.

[18] Saw. I. Esen, "Dynamic response of a beam due to an accelerating moving mass using moving finite element approximation", *Mathematical and Computational Applications*, vol. 16, pp. 171–182, 2011.

[19] M. Dehestani, M. Mofid and A. Vafai, "Investigation of critical influential speed for moving mass problems on beams", *Applied Mathematical Modelling*. vol. 33, pp. 3885–3895, 2009.

[20] S. E. Azam, M. Mofid and R. A. Khoraskani, "Dynamic response of Timoshenko beam under moving mass", *Scientia Iranica*, vol. 20, pp. 50–56, 2013.

[21] http://thumbs.dreamstime.com/x/modelo-aislado-3d-de-un-cedazo-cristalino-del-cobre-8059539.jpg

[22] https://commons.wikimedia.org/wiki/File:Rutile-unit-cell-3D-balls.png, Accessed 27 June 2017.

[23] https://commons.wikimedia.org/wiki/File:Iron(II)-sulfide-unit-cell-3D-balls.png, Accessed 27 June 2017.

[24] https://commons.wikimedia.org/wiki/File:Sphalerite-unit-cell-3D-balls.png, Accessed 27 June 2017.

[25] Theory reference for the mechanical apdl and mechanical applications, *ANSYS Release 14.1,* Accessed 27 June 2017.

Dynamic Analysis of Structures Which are Inspired by Lattices of Metals

S. GÜLER[1] and M. YILDIZ[1, †]

[1] Iskenderun Technical University, Hatay/Turkey, serkan.guler@iste.edu.tr
[1] Iskenderun Technical University, Hatay/Turkey, murat.yildiz@iste.edu.tr
[†] Corresponding author

***Abstract* – Design of structures that are inspired by the Nature is gaining attention in the latest year and many studies on the lattices of the materials are being conducted. And for designing, beams and truss structures are widely used elements. Thus, when designing new structures, getting inspired by those lattices and making use of those beams and trusses might prove to be advantageous. Maintaining the estimated lifetime of the structures is also an essential factor. So, it is essential to determine the characteristics of the structures such as the deflection, stresses and more. When determining those structures, finite element analysis can be used effectively. In this study, the lattice inspired models were constructed. Inverted L-frames, inverted U-frames and 3D frames were designed by using those models. Then to analyze those structures, finite elements method was used. The frames were subjected to four different input forces which were generated by using their total weight multiplied by 10, 20, 50, 100 coefficients. The results demonstrated that these designed structures can be used in many areas such as aviation, space, construction. Also, those structures can be used as the core part of the sandwich composites.**

***Keywords* – Metals, Lattices, Finite element method, Dynamic analysis, Inspired**

I. INTRODUCTION

With constant advancements in technology, new ways are being tested on designing new structures. Thanks to the intriguing engineering systems in nature that researchers have encountered while working on their studies, new structures that are inspired by nature are being designed in the recent years. Lattice-inspired and bio-inspired structures are getting popular nowadays and are likely to be applicable in many areas such as construction, aviation, marine, space, and more.

Many studies related to lattices are being carried out. Usage and manufacturing of lattice structures have grown thanks to their lightweight and mechanical efficiency ratio. Lattices that are produced using additive manufacturing are composed of beams [1,2]. In their work, Yan et al. investigated the manufacturability and performance of advanced and lightweight stainless steel cellular lattice structures fabricated via selective laser melting [3]. Mahshid et al. investigated the effect of cellular lattice structures on the strength of workpieces additively manufactured. Authors conducted studies both numerically and experimentally. Numerical studies were performed using DEFORM-3D simulation system based on the finite element method [4]. Lee and McClure developed a numerical model for simulating behaviour of lattice steel tower structures. They presented static large deformation analysis of a lattice steel tower structure using finite element analysis and compared the numerical results with full-scale test. 2-node three-dimensional beam elements proposed in their previous work was used in the static finite element analysis [5]. Guo et al. proposed 3D periodic multilayer lattice materials such as the square, the quadrate, the tetrahedron and the hexagon in order to supply load-carrying necessities of a composite material. Authors obtained static structural simulation results using BEAM189 element in ANSYS, the static mechanical properties of the four multilayer lattice materials were analysed [6]. Sun et al. designed a regular hexahedral unit, produced the lattice structure composed of the Ti–6Al–4V units. After that, they obtained the experimental fracture load and the compression deformation of them through compression tests, then conducted a simulation of the unit and the lattice structure through ANSYS (static) to analyse the failure point [7]. Stankovic et al. developed a generalized optimality criteria method for the optimization of discrete, multimaterial, additively manufactured mesoscale lattice structures for maximum performance in a constrained volume. The generalized optimality criteria method for multimaterial optimization of discrete lattice structure designs was implemented in MATLAB with a linear elastic finite element method (FEM) module for design response analysis [8]. Messner et al. presented a dynamic equivalent continuum model for periodic truss structures suitable for representing long-wavelength wave propagation and verifies it against the full Bloch wave theory and detailed finite element simulations. The FE simulations were run with ALE3D, an arbitrary Lagrangian–Eulerian finite element code developed at Lawrence Livermore National Laboratory [9]. Messner developed a method for optimizing the mesostructure of lattice-structured materials. These materials are periodic arrays of slender members resembling efficient, lightweight macroscale structures like bridges and frame buildings [10]. Syam et al. examined the use of additively manufactured strut-based lattice structures to improve the mechanical vibration isolation properties of a structure. Finite element modelling had been used to determine the theoretical static and dynamic mechanical properties of both the single cell and the array configuration of the lattice structures [11].

Beams and truss structures are common elements in constructing buildings, frame, etc. They are frequently used in the engineering systems [12,13,14,15]. And for analyzing engineering systems, the Finite Element Method (FEM) is a widely used method [15,16,17,18,19,20]. In this method, structures are meshed out and mathematical models which involve differential equations [21] that have huge degrees of freedom are calculated. In the past, equation solving was a difficult task but now that computers are capable enough to process high amount of data in short time, finite element method can be used as the primary solving method [15].
In this study the structures that are inspired by the lattices of materials were designed and analyzed dynamically. For these kinds of structures, suitable designs are important to retain their estimated working life. Hence, it is a must to determine the characteristics of those structures i.e. the deflections, stresses and more. And, the finite element is a capable method to determine those characteristics [15]. So, ANSYS finite element software which featured beam finite elements that are based on the Timoshenko beam theory was used to analyze the structures.

II. FINITE ELEMENT MODELING

There are many materials on the world and four of them were considered. Their lattice structures were inspired by to design the cell models. Those materials are Cu, TiO_2, FeS, ZnSe and their lattice structures are given in fig. 1.

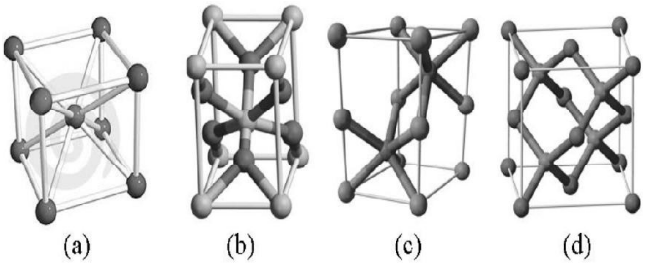


Figure 1: Lattices of the materials: (a) Cu [22], (b) TiO_2 [23], (c) FeS [24], (d) ZnSe [25].

SolidWORKS was used to design the lattice inspired cells and a lattice database was created in IGES format. A labeling style in which the models were named as L_i where L is abbreviation of lattices and i represents the number of the lattices that stored in the database. Those cell models (line models) are given in Fig. 2 and their dimensions are given in Fig. 3.

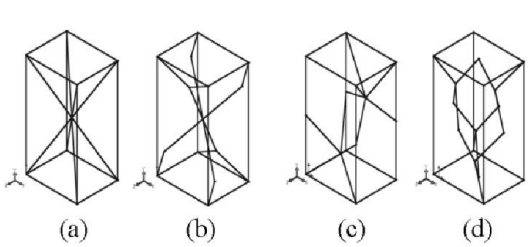
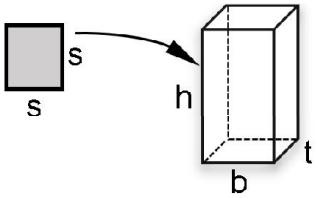


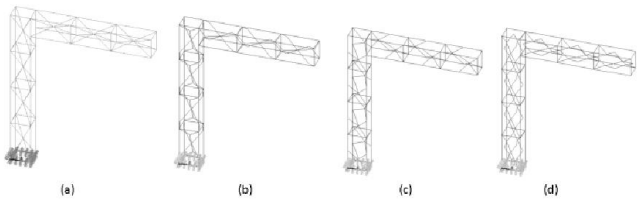
Figure 2: Line models of lattices; (a)Cu, (b) TiO_2, (c) FeS, (d) ZnSe.



b (μm)	1250
h (μm)	2500
t (μm)	1000
s (μm)	50

Figure 3: Dimensions of lattices and section.

ANSYS is a world-known finite element solving software and thus was preferred in this study. The IGES files that held the cell models were imported into ANSYS. Finite element models of inverted-L, inverted-U frames and 3D frames were constructed by using the cell models. As an example, the inverted L-frames that are composed of L_1, L_2, L_3 and L_4 are given in Fig. 4.



(a) L_1, (b) L_2, (c) L_3, (d) L_4

Figure 4: L-frames

The finite element models of frames were generated by using only one of the lattice models every time and in whole 12 frames were generated. For the inverted L frames, three models in the direction of the y-axis and two models in the direction of x-axis were used. For the inverted L frames, 4 cell models in the direction of the y-axis and 3 cell models in the direction of x-axis were used. For the inverted U frames, 5 cell models in the direction of the y-axis for the both of the columns were used and 3 cell models were placed in the direction of x-axis to connect them. And in order construct 3D frames, 8 cell models in the direction of the y-axis were used for the columns and 5 and 6 cell models in both of the z-axis and x-axis, respectively, to connect those columns together.

BEAM44 elements were used in ANSYS models. BEAM44 is a uniaxial element with tension, compression, torsion, and bending capabilities [26].

The material properties of lattices were defined by $\boldsymbol{p}_m = [E, \rho, \upsilon, \beta]$ where E is modulus of elasticity (GPa), ρ is density (kg/m^3), υ is Poisson's ratio and β *is material damping ratio*. $\boldsymbol{p}_m = [113.8, 4430, 0.342, 0.0001]$ for *TI-6AI-4V* material and designing was constructed as linear elastic isotropic model in this study.

With the intention of accomplishing the finite element models of these frame structures successfully, *the modeling macro files* were created as a first step. Then, *the solution macro files* which are for generating the natural frequencies of the frame structures were created. In the model macro files, lines were allocated for beams. Afterwards, material properties and section were defined for the beams. Cell dimensions were

1250x2500x1000 μm and assigned section dimensions were *50x50* μm as shown in Fig.3. Thus, all lines were meshed out by in according to these sections and material properties. The structures were fixed at points which can be seen over in Fig. 5. Lastly, transient dynamic analyses were performed and pulse (impact), step and trapezoidal responses of these frame structures were obtained by using *the solution macro files*.

III. DYNAMIC ANALYSIS RESULTS

In these analyses, forces were implemented as inputs that are pulse (impact), step and trapezoid forces (see Fig. 5) in the direction of z-axis on the "E" point that can be observed in the Fig. 6 and from this point the deflection outputs were obtained in the direction of z-axis as well.

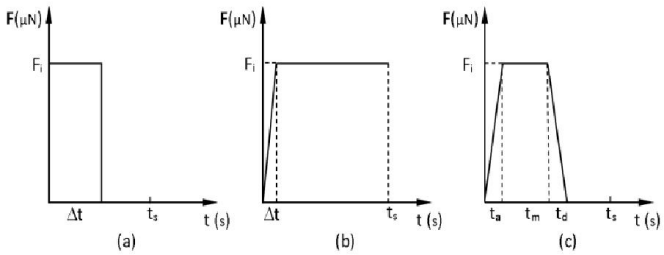


Figure 5: Implemented forces; (a) Pulse, (b) Step, (c) Trapezoidal.

Each frame was subjected to four kinds of input forces which were generated by multiplying their total weight with k_f= *[10, 20, 50,100]* coefficients, respectively.

Total weights of the frames are given in the format of W_i where W means weight and i represents the number of the frames.

The magnitude of forces (F_i) was calculated by using Eq.1.,

$$F_i = k_f \cdot W_i \tag{1}$$

Δt is time step of the simulation and t_s is simulation time. Δt was calculated by using Eq.2.,

$$t = \frac{1}{20 f_n} \tag{2}$$

where f_n is natural frequency of the frames at direction of excitation.

In the Fig. 5c, t_a, t_m, and t_d are acceleration, motion and deceleration time of force inputs correspondingly.

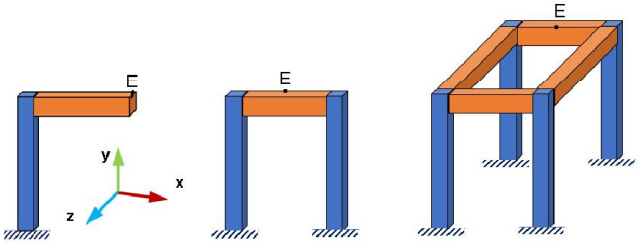


Figure 6: Positions of the ***E*** points on the frames.

For the inverted L-frames, the ***E*** point was on the top-middle point on the face that positioned on the free end and oriented towards x-axis. For the inverted U-frames the ***E*** point was on the top-middle point on the face that positioned on the horizontal beam and oriented towards z-axis except for L_1-U-frames where the ***E*** point in the volume center of the middle cell lattice model. For the inverted 3D-frames the ***E*** point was on the top-middle point on the face that positioned on the rear horizontal beam and oriented towards z-axis except for L_1-3D-frames where the ***E*** point in the volume center of the middle cell lattice model.

Results of Inverted L-Frames

Their weights are given as W_i = *[20.54, 20.40, 21,06, 21.13]* μN. Pulse, step and trapezoidal responses of the frames are given in the figs.

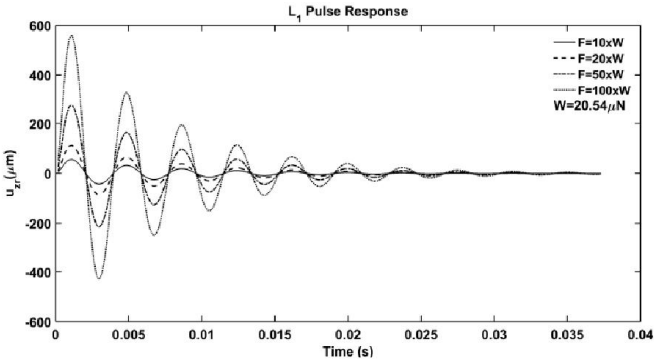


Figure 7: L_1 pulse response.

It can be deduced from the Fig. 7 that deflections are *56.06, 112.1, 280.3* and *560.6* μm correspondingly to the applied forces. The maximum deflection of L_1-frame was exhibited at the force that is exact 100 times of its weight.

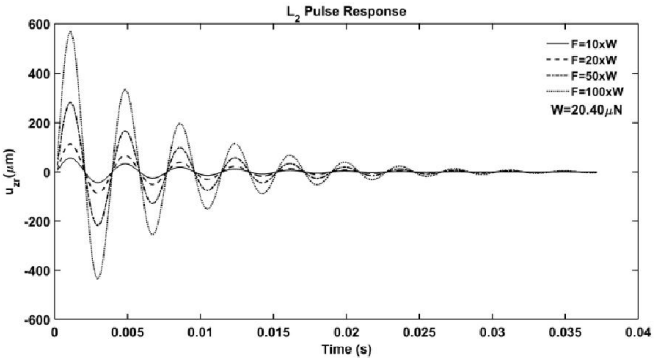


Figure 8: L_2 pulse response.

It can be inferred from the Fig. 8 that deflections are *56.83, 113.7, 284.1* and *568.3* μm correspondingly to the applied forces. The maximum deflection of L_2-frame was exhibited at the force that is exact 100 times of its weight.

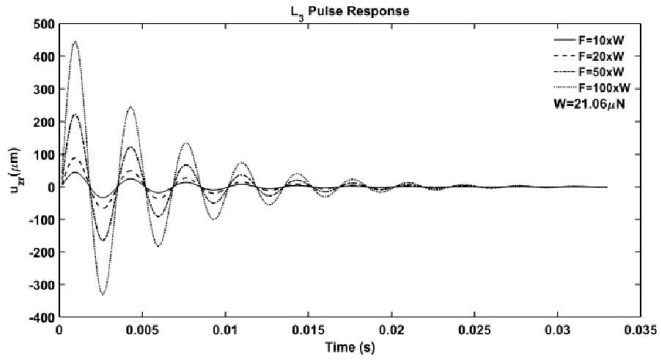


Figure 9: L_3 pulse response.

It can be shown from the Fig. 9 that deflections are *44.7, 89.4, 223.5* and *447.0* μm correspondingly to the applied forces. The maximum deflection of L_3-frame was exhibited at the force that is exact 100 times of its weight.

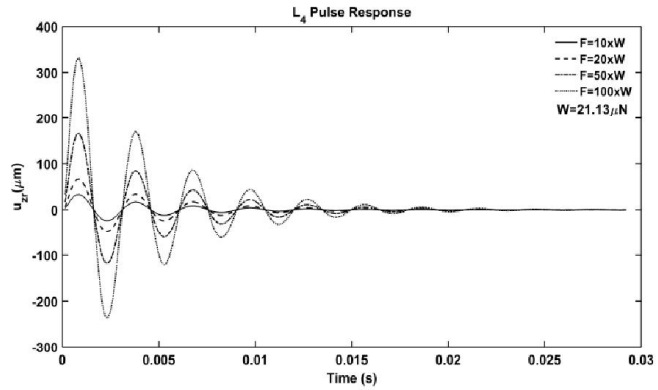


Figure 10: L_4 pulse response.

It can be shown from the Fig. 10 that deflections are *44.7, 89.4, 223.5* and *447.0* μm correspondingly to the applied forces. The maximum deflection of L_4-frame was exhibited at the force that is exact 100 times of its weight.

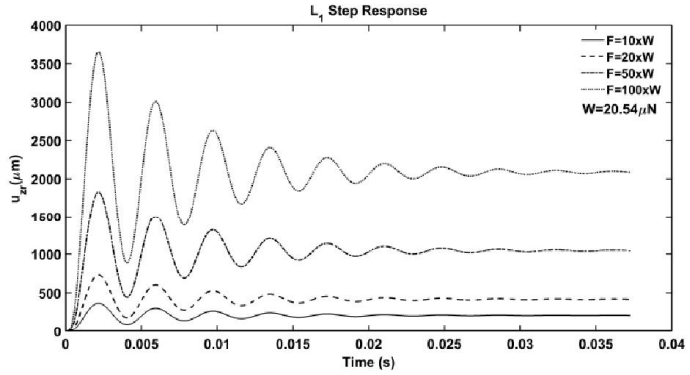


Figure 11: L_1 step response.

It can be seen from the Fig. 11 that deflections are *365.3, 730.5, 1826.0* and *3653.0* μm correspondingly to the applied forces. The maximum deflection of L_1-frame was revealed at the force that is exact 100 times of its weight.

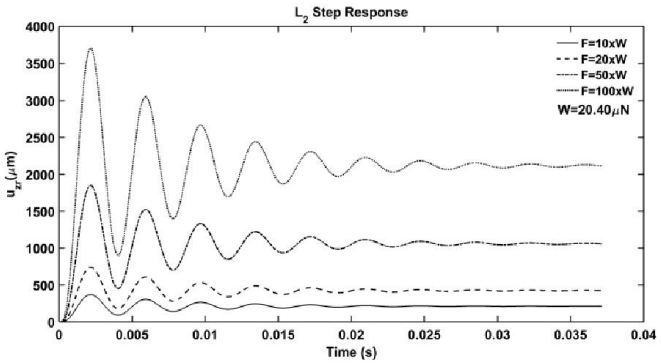


Figure 12: L_2 step response.

It can be seen from the Fig. 12 that deflections are *370.3, 740.6, 1852.0* and *3703.0* μm correspondingly to the applied forces. The maximum deflection of L_2-frame was shown at the force that is exact 100 times of its weight.

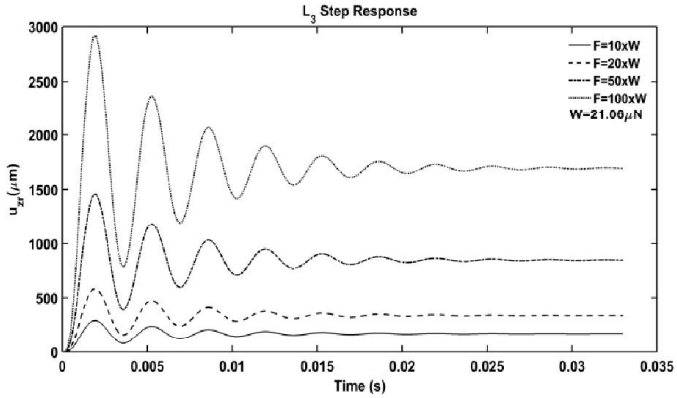


Figure 13: L_3 step response.

It can be observed from the Fig. 13 that deflections are *291.9, 583.7, 1459.0* and *2919.0* μm correspondingly to the applied forces. The maximum deflection of L_3-frame was shown at the force that is exact 100 times of its weight.

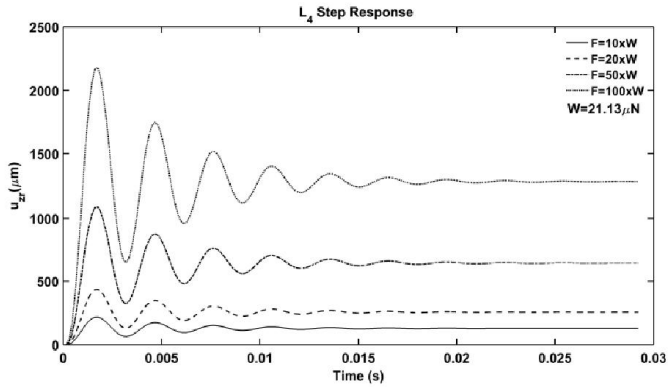


Figure 14: L_4 step response.

It can be observed from the Fig. 14 that deflections are *217.9, 435.8, 1090.0* and *2179.0* μm correspondingly to the applied forces. The maximum deflection of L_4-frame was shown at the force that is exact 100 times of its weight.

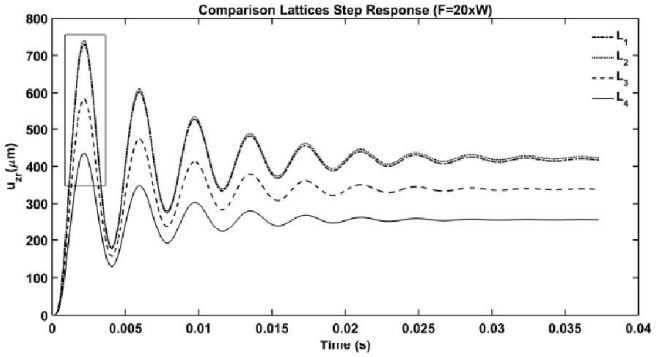


Figure 15: Comparison the step responses of lattices.

In the Fig. 15, the step responses at the force that is exact 20 times of their weight. The zoomed view of maximum deflection of the structures is shown in Fig. 16. According to Fig. 16, it is clear that the robust structure is L_4-frame due to the fact that it has the minimum amplitude under the excited force.

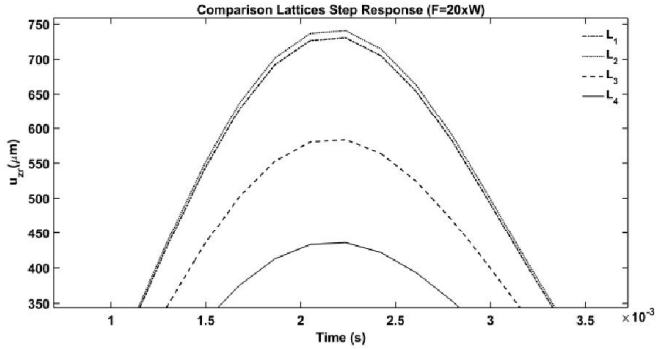


Figure 16: Zoomed vie of comparison the step responses of lattices.

The trapezoidal inputs were conducted as another excitation type for the structures. The responses were obtained by applying forces that are exact 20 times of their weight. As one can see in Fig. 17, L_4-frame was the most robust structure, and the results show same trend as the other responses as well.

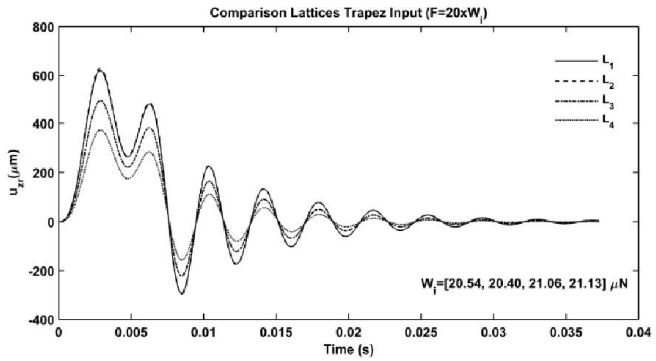


Figure 17: Comparison the trapezoidal responses of lattices.

Results of Inverted U-Frames

Their weights are given as W_i = *[38.21, 37.53, 38.76, 38.90]* μN. The pulse, step and trapezoidal inputs were conducted as excitation force type for the structures. Comparison of pulse, comparison of step and comparison of trapezoidal responses of the frames are given in the Fig. 18, Fig. 19 and Fig 20, respectively.

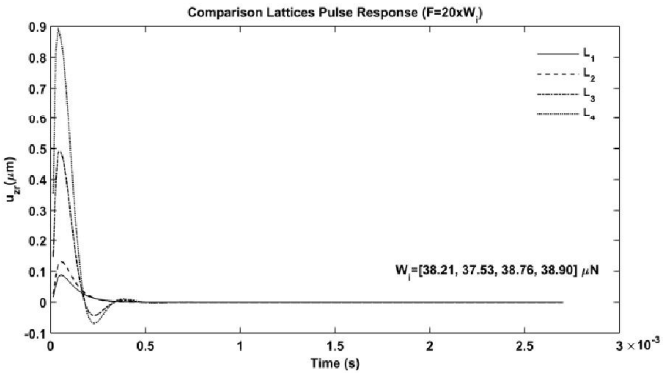


Figure 18: Comparison the pulse responses of lattices.

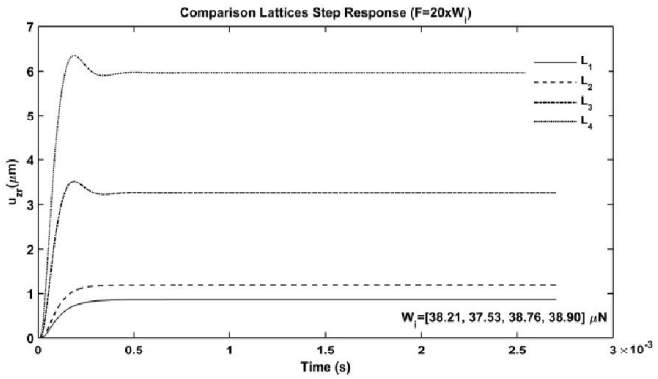


Figure 19: Comparison the step responses of lattices.

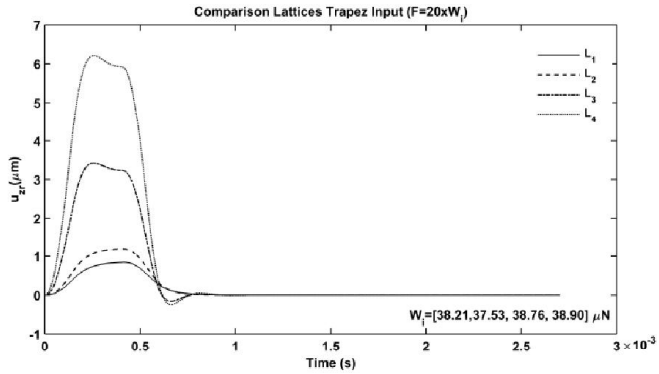


Figure 20: Comparison the trapezoidal responses of lattices.

The responses were attained by applying forces that are exact 20 times of their weight. As one can see in Fig. 18, Fig. 19 and Fig. 20, L_1-frame was the most robust structure and the results show same tendency as the other responses as well.

Results of 3D-Frames

Their weights are given as W_i = *[180.57, 175.89, 181.73, 182.41]* μN. The pulse, step and trapezoidal inputs were performed as excitation force type for the structures.

Comparison of pulse, comparison of step and comparison of trapezoidal responses of the frames are given in the Fig. 21, Fig. 22 and Fig 23, respectively.

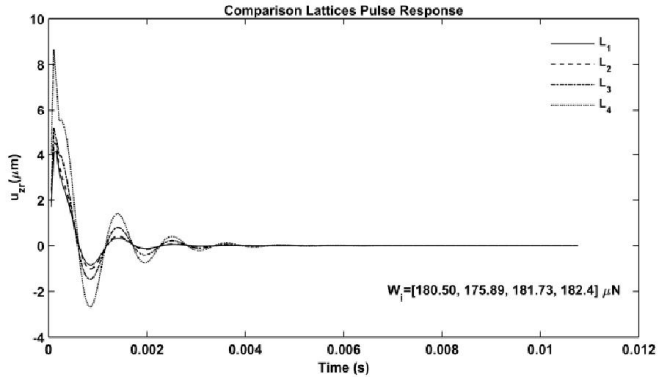


Figure 21: Comparison the pulse responses of lattices.

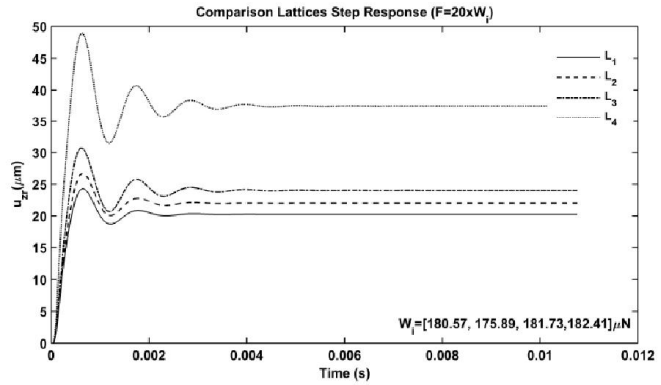


Figure 22: Comparison the step responses of lattices.

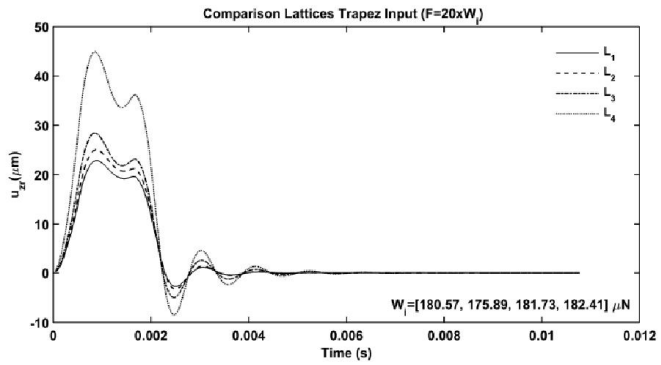


Figure 23: Comparison the trapezoidal responses of lattices.

The responses were computed by applying forces that are exact 20 times of their weight. As seen in Fig. 21, Fig. 22 and Fig. 23, L_1-frame was the most robust structure and the results show same tendency as the other responses as well.

IV. CONCLUSION

In this work, lattice inspired cell models were generated and by using those cell models, three different structures such as inverted L-frames, inverted U-frames and 3D-frames were constructed in ANSYS software. The frames were subjected to four different input forces which were their total weight multiplied by 10, 20, 50 and 100 coefficients.

The analysis results showed that the frames can withstand to the forces that can be much greater than their own weight.

Still, it is recommended to confirm the results with actual experimental data. As a future study, manufacturing of the designed structures and conducting experimental studies are planned.

REFERENCES

[1] L. Chougrani, J. P. Pernot, P. Véron and S. Abed, "Lattice structure lightweight triangulation for additive manufacturing", *CAD Computer Aided Design*, vol. 90, pp. 95–104, 2017.

[2] M. Królikowski and D. Grzesiak, "Technological Restrictions of Lightweight Lattice Structures Manufactured by Selective Laser Melting of Metals", *Advances In Manufacturing Science And Technology,* Vol. 38, 2014.

[3] C. Yan, L. Hao, A. Hussein, P. Young and D. Raymont, "Advanced lightweight 316L stainless steel cellular lattice structures fabricated via selective laser melting", Materials and Design, vol. 55,pp. 533–541, 2014.

[4] R. Mahshid, H. N. Hansen and K. L. Højbjerre, "Strength analysis and modeling of cellular lattice structures manufactured using selective laser melting for tooling applications", *Materials and Design*. Vol. 104, pp. 276–283, 2016.

[5] P. S. Lee and G. McClure, "Elastoplastic large deformation analysis of a lattice steel tower structure and comparison with full-scale tests". Journal of Constructional Steel Research", vol. 63, pp. 709–717, 2007.

[6] R. Guo, R. Liu, W. Jiang, K. Chen, J. Zhang, F. Huang and X. Sun, "Numerical Analysis on Static Mechanical Properties of the Periodic Multilayer Lattice Material," *Engineering*, Vol. 3 (12), pp. 1149-1154, 2011.

[7] J. Sun, Y. Yang and D. Wang, "Mechanical properties of regular hexahedral lattice structure formed by selective laser melting", *Laser Physics*, vol. 23, 066101 (9pp), 2013.

[8] T. Stanković, J. Mueller, P. Egan and K. Shea, "A Generalized Optimality Criteria Method for Optimization of Additively Manufactured Multimaterial Lattice Structures", *J. Mech. Des. ASME*, vol. 137(11), 111405 (12pp), 2015.

[9] M. C. Messner, M. I. Barham, M. Kumar and N. R. Barton, "Wave propagation in equivalent continuums representing truss lattice materials", *International Journal of Solids and Structures*, vol.73–74, pp. 55–66, 2015.

[10] M. C. Messner, "Optimal lattice-structured materials", *Journal of the Mechanics and Physics of Solids*, vol. 96, pp. 162–183, 2016.

[11] W. P. Syam, W. Jianwei, B. Zhao, I. Maskery, R. Leach, "Design of mechanically-optimised lattice structures for vibration isolation", *Proceedings of 17th International euspen Conference*, pp. 55-56, Germany, 2017.

[12] H. Matlock and B. R. Grubbs, "Development of Methods for Computer Simulation of Beam-Columns and Grid-Beam and Slab Systems" *Enter for Highway Research*, The University of Texas, Texas, 1967.

[13] G. Kiper and E. Soylemez, "Deployable space structures", *2009 4th International Conference on Recent Advances in Space Technologies*, pp. 131-138, Istanbul, 2009.

[14] H. J. Xiang, Z. F. Shi, S. J. Wang and Y. L. Mo, "Periodic materials-based vibration attenuation in layered foundations: experimental validation", *Smart Materials and Structures*, vol. 21, 112003 (10pp) ,2012.

[15] H. Karadeniz, "Stochastic Analysis of Offshore Steel Structures: An Analytical Appraisal", *Springer-Verlag London*, 2012.

[16] S. Bobby, S. M. J. Spence, E. Bernardini and A. Kareem, "Performance-based topology optimization for wind-excited tall buildings: A framework", *Engineering Structures*, vol. 74, pp. 242–255, 2014.

[17] J. Huang, Z. Shi, W. Huang, X. Chen and Z. Zhang, "A periodic foundation with rotational oscillators for extremely low-frequency seismic isolation: analysis and experimental verification", *Smart Materials and Structures*, vol. 26, 035061 (11pp), 2017.

[18] Y. Ren, Y. Yu, B. Zhao, C. Fan and H. Li, "Finite Element Analysis and Optimal Design for the Frame of SX360 Dump Trucks", *Procedia Engineering (Elsevier Ltd, 2017)*, vol. 174, pp. 638–647, 2017.
[19] S. Güler and H. Karagülle, "Finite element analysis of structures with extruded aluminium profiles having complex cross sections", *Latin American Journal of Solid and Structures*, vol. 13, pp.1499–1514, 2016.
[20] JJ. Wu, "Finite element analysis and vibration testing of a three-dimensional crane structure", *Measurement*, vol. 39 pp. 740–749, 2006.
[21] S. S. Rao, "Mechanical vibrations. 3rd ed. Upper saddle river: Prentice hall", 2011.
[22] http://thumbs.dreamstime.com/x/modelo-aislado-3d-de-un-cedazo-cristalino-del-cobre-8059539.jpg
[23] https://commons.wikimedia.org/wiki/File:Rutile-unit-cell-3D-balls.png, Accessed 27 June 2017.
[24] https://commons.wikimedia.org/wiki/File:Iron(II)-sulfide-unit-cell-3D-balls.png, Accessed 27 June 2017.
[25] https://commons.wikimedia.org/wiki/File:Sphalerite-unit-cell-3D-balls.png, Accessed 27 June 2017.
[26] Theory reference for the mechanical apdl and mechanical applications, *ANSYS Release 14.1,* Accessed 27 June 2017.

Modal Analysis of Structures Which are Inspired by Lattices of Metals

S. GÜLER[1] and M. YILDIZ[1, †]

[1] Iskenderun Technical University, Hatay/Turkey, serkan.guler@iste.edu.tr
[1] Iskenderun Technical University, Hatay/Turkey, murat.yildiz@iste.edu.tr
† Corresponding author

***Abstract* – Nature is an excellent engineer and it is reasonable get inspired by it when developing engineering designs. In the recent years, lattice and bio inspired structures have been a hot topic among researchers. In the engineering systems, beams and truss structures widely used for constructing buildings, machine frames, offshore structures and more. From this point of view, in this study the cell models which are inspired by the lattices of metals were designed. It is a known fact that designs being suitable are a necessary step in preserving the lifetime of structures. Thus, it is crucial to determine characteristics of structures such as the deflection, stresses, etc. And, to determine those structural characteristics, the finite element analysis was considered. Beam finite element modeling was used on the structures which were built by using those lattice inspired cell models. Afterwards simulation of modal analysis was conducted on the structures that are inverted L-frames and inverted U-frames and 3D-frames. It's been demonstrated that these designed structures are suitable for space structures, buildings, machine frames and furthermore as the core part of the sandwich composites.**

***Keywords* - Metals, Lattices, Finite element method, Modal analysis, Inspired**

I. INTRODUCTION

Nature has many wonders and being a prodigious engineer is just one of them. There are many instances where it shows its beautiful talents that make humans wanting to mimic them. Thus, in the recent years there have been many studies being inspired by nature. Designs that inspired by lattices of materials as well as bio-inspired structures and bio-mimic materials have gained popularity and many studies are being carried out regarding them in many areas such as engineering, construction, biology, marine, aviation, space etc.

Many studies related to lattices are being carried out. Usage and manufacturing of lattice structures have grown thanks to their lightweight and mechanical efficiency ratio. Lattices that are produced using additive manufacturing are composed of beams [1,2]. Yan et al. investigated the manufacturability and performance of advanced and lightweight stainless steel cellular lattice structures fabricated via selective laser melting [3]. Mahshid et al. investigated the effect of cellular lattice structures on the strength of workpieces additively manufactured. Authors conducted studies both numerically and experimentally. Numerical studies were performed using DEFORM-3D simulation system based on the finite element method [4]. Lee and McClure developed a numerical model for simulating behaviour of lattice steel tower structures. They presented static large deformation analysis of a lattice steel tower structure using finite element analysis and compared the numerical results with full-scale test. 2-node three-dimensional beam elements proposed in their previous work was used in the static finite element analysis [5]. Guo et al. proposed 3D periodic multilayer lattice materials such as the square, the quadrate, the tetrahedron and the hexagon in order to supply load-carrying necessities of a composite material. Authors obtained static structural simulation results using BEAM189 element in ANSYS, the static mechanical properties of the four multilayer lattice materials were analysed [6]. Sun et al. designed a regular hexahedral unit, produced the lattice structure composed of the Ti–6Al–4V units. After that, they obtained the experimental fracture load and the compression deformation of them through compression tests, then conducted a simulation of the unit and the lattice structure through ANSYS (static) to analyse the failure point [7]. Stankovic et al. developed a generalized optimality criteria method for the optimization of discrete, multimaterial, additively manufactured mesoscale lattice structures for maximum performance in a constrained volume. The generalized optimality criteria method for multimaterial optimization of discrete lattice structure designs was implemented in MATLAB with a linear elastic finite element method (FEM) module for design response analysis [8]. Messner et al. presented a dynamic equivalent continuum model for periodic truss structures suitable for representing long-wavelength wave propagation and verifies it against the full Bloch wave theory and detailed finite element simulations. The FE simulations were run with ALE3D, an arbitrary Lagrangian–Eulerian finite element code developed at Lawrence Livermore National Laboratory [9]. Messner developed a method for optimizing the mesostructure of lattice-structured materials. These materials are periodic arrays of slender members resembling efficient, lightweight macroscale structures like bridges and frame buildings [11]. Syam et al. [10] examined the use of additively manufactured strut-based lattice structures to improve the mechanical vibration isolation properties of a structure. Finite element modelling had been used to determine the theoretical static and

dynamic mechanical properties of both the single cell and the array configuration of the lattice structures.

In the engineering systems, beams and truss structures are widely used as tension structures for constructing buildings, machine frames, offshore structures and more [12,13,14,15]. Many studies related to engineering structures such as buildings, space structures which are constructed with beams and trusses are conducted by using the Finite Element Method (FEM) [15,16,17,18,19,20]. This method involves meshing of structures and setting up mathematical models composed of differential equations [21] having huge degrees of freedom. Before the computer systems are common, solving these equations was a difficult and time-consuming task. Even then, researchers would use what was available to them to solve those structural problems. For example, Matlock and Grubbs conducted a study in 1967 that was about solving structural frames by using a proposed static FEM in which orthogonal frame member groups were composed of bars and springs [12]. Still, in today's world, thanks to technological advancements in computers, finite element methods for structural analysis have been developed enough to replace the classical solving methods [15].

In this study the structures which are inspired by the lattices of materials were designed. Appropriate designs are required to sustain the estimated life-cycle of these kinds of structures. Therefore, it is vital to determine the features of the structures such as natural frequencies and mode shapes and more. To determine the aforementioned structural characteristics, the finite element is a pretty suitable method that can be used by utilizing computers [15]. Thus, by using ANSYS commercial finite element program, beam finite elements based on Timoshenko beam theory was used in the present study for modeling of the structures.

II. FINITE ELEMENT MODELING OF THE STRUCTURES

For the modeling of structures, four kinds of lattices of materials were considered. The lattice cell models were inspired by the lattice structures of the following materials; Cu, TiO_2, FeS, ZnSe and those lattice structures are given in Fig. 1.

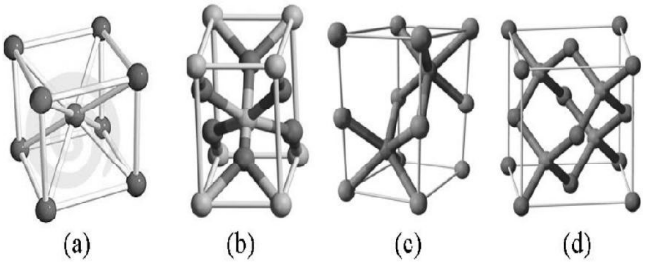


Figure 1: Lattices of the materials: (a) Cu [22], (b) TiO_2 [23], (c) FeS [24], (d) ZnSe [25].

The lattice inspired structures were designed in SolidWORKS and then saved in IGES format for a broader working environment. A cell model database was created in IGES format. The cell models were labeled as L_i where L is abbreviation of Lattice and i represents the cell model number of the lattices that are kept in the database. Those cell models (line models) are given in Fig. 2 and their dimensions are given in Fig. 3.

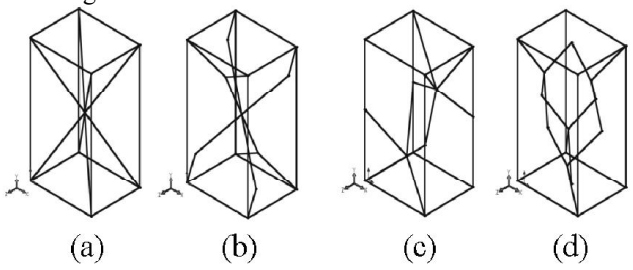
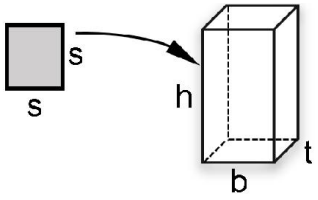


Figure 2: Line models of lattices: (a)Cu, (b) TiO_2, (c) FeS, (d) ZnSe.



b (μm)	1250
h (μm)	2500
t (μm)	1000
s (μm)	50

Figure 3: Dimensions of lattices and section.

ANSYS was used as the finite element program. The IGES files were imported into ANSYS from the database. Finite element models of inverted-L, inverted-U frames and 3D frames were constructed by using the cell models. As an example, the inverted L-frames that are composed of L_1, L_2, L_3 and L_4 are given in Fig. 4.

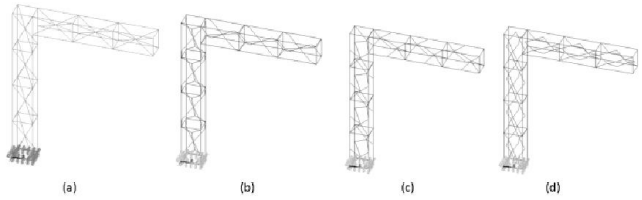


Figure 4: L-frames : (a) L_1, (b) L_2, (c) L_3, (d) L_4

The finite element models of frames were generated by using only one of the lattice models in every occasion and thus 12 frames were generated. For the inverted L frames, 4 cell models in the direction of the y-axis and 3 cell models in the direction of x-axis were used. For the inverted U frames, 5 cell models in the direction of the y-axis for the both of the columns were used and 3 cell models were placed in the direction of x-axis to connect them. And in order construct 3D frames, 8 cell models in the direction of the y-axis were used for the columns and 5 and 6 cell models in both of the z-axis and x-axis, respectively, to connect those columns together.

BEAM44 elements were used in ANSYS models. BEAM44 is a uniaxial element with tension, compression, torsion, and bending capabilities [26].

The material properties of lattices were defined by $\boldsymbol{p}_m = [E, \rho, \upsilon]$ where E is the modulus of elasticity (GPa), ρ is the density (kg/m^3) and υ is the Poisson's ratio. $\boldsymbol{p}_m = [113.8, 4430, 0.342]$ for *TI-6AI-4V* material and designing was constructed as linear elastic isotropic model in this study.

In order to establish the finite element models of these frame structures, firstly *the modeling macro files* were prepared. Secondly *the solution macro files* for computing natural frequencies of those frame structures were created. In the model macro files, lines were allocated for beams. Then, material properties and section were defined for the beams. Cell dimensions were 1250x2500x1000 µm and assigned section dimensions were 50x50 µm as shown in Fig.3. So, all lines were meshed by assigning these sections and material properties. The structures were fixated at points which are indicated in Fig. 5, Fig. 6 and Fig 7. Finally, modal analyses were performed and natural frequencies of these frame structures obtained by using *the solution macro files*.

III. MODAL ANALYSIS RESULTS

The modal analysis results of inverted L-Frame, inverted U-Frame and 3D-Frame structures are given in Fig. 5 Fig. 6 and Fig. 7, respectively. f_{ty}, f_{bx}, f_{bz} are natural frequencies corresponding to the mode shapes where the frames mainly make torsional vibration about the y-axis, bending vibration about the x-axis, and again bending vibration about the z-axis, respectively.

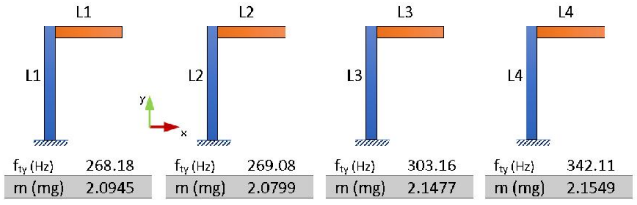


Figure 5: Inverted L-Frames and their natural frequencies.

Simulation results in Fig. 5 show that torsional modes (regarding y-axis) have natural frequencies of 268.18, 269.08, 303.16 and 342.11 Hz for the inverted L-frames, going from L_1 to L_4, respectively. Also, as observed in the Fig. 5 the highest torsional frequency occurred in the structure which was constructed using L_4 cell models. The results show that the design of L_4 cell had significantly affected the torsional modes.

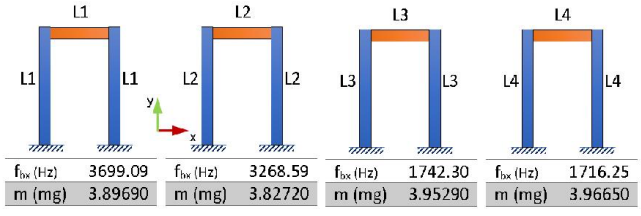


Figure 6: Inverted U-Frames and their natural frequencies.

Simulation results that are given in Fig. 6 show that bending modes (regarding x-axis) have natural frequencies of 3699.09, 3268.59, 1742.30 and 1716.25 Hz for the inverted U-frames, going from L_1 to L_4, respectively. As seen in the Fig. 6, bending frequency was the highest in the structure which was constructed using L_1 cell models. The results show that the design of L_1 cell had significantly affected the bending modes.

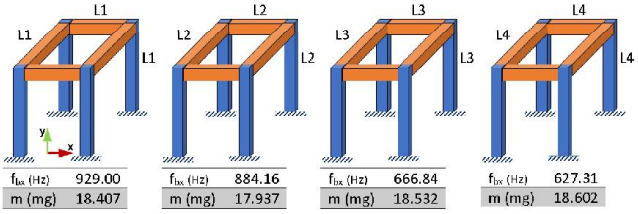


Figure 7: 3D-Frames and their natural frequencies.

Simulation results that are given in Fig. 7 show that bending modes (regarding x-axis) have natural frequencies of 929.00, 884.16, 666.84 and 627.31 Hz for the inverted U-frames, going from L_1 to L_4, respectively. As noticed in the Fig. 7, bending frequency was the highest in the structure which was constructed by L_1 cell models. The results show that the design of L_1 cell had significantly affected the bending modes.

The mode shapes of inverted L-Frame that was composed of L_1 cell models are depicted in Fig. 8. The first mode (Fig. 8a) is torsional vibration about y-axis at 268.18 Hz. The second (Fig. 8b) mode is bending vibration about z-axis at 1643.82 Hz. Fig. 8c is couple mode about both y-axis and x-axis at 6723.88 Hz. In the Fig. 8, deformed shapes are represented with blue lines and undeformed shapes are represented with black lines.

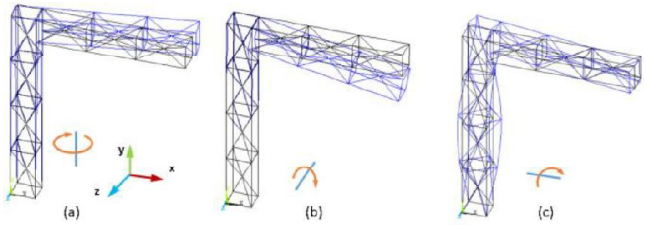


Figure 8: Mode shapes of L_1-Frame.

The mode shapes of inverted U-Frame that was composed of L_2 lattice cells are shown in Fig. 9. The first mode (Fig. 9a) is bending vibration about z-axis at 2534.05 Hz. The second (Fig. 9b) mode is bending vibration about x-axis at 3268.59 Hz. Fig. 8c is torsional mode about y-axis at 4068.16 Hz.

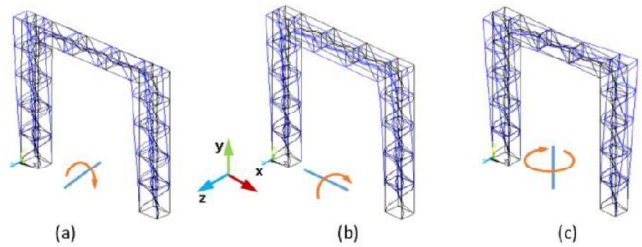


Figure 9: Mode shapes of U-Frame.

In the mode shapes of 3D-Frame comprised of L_4 lattice cells, the first mode was observed as bending mode about x-

axis at 627.31 Hz. The second mode was observed as bending mode about z-axis at 809.86 Hz. The third mode was observed as bending mode about y-axis at 816.44 Hz.

IV. Conclusion

In this work the models which are inspired by the lattices of materials were designed and by using those cell models, three different structures such as inverted L-frames, inverted U-frames and 3D-frames were constructed in ANSYS software. The natural frequencies and mode shapes were computed. In order to compute these features ANSYS *model macro files* and *solution macro files* were generated. Then the results of the structures were obtained.

The results showed that the proposed modeling approach exhibited admissible vibration characteristics such as natural frequencies and mode shapes.

Still, it is recommended to confirm the results with actual experimental data. As a future study, manufacturing of the designed structures and conducting experimental studies are planned.

References

[1] L. Chougrani, J. P. Pernot, P. Véron and S. Abed, "Lattice structure lightweight triangulation for additive manufacturing", *CAD Computer Aided Design*, vol. 90, pp. 95–104, 2017.

[2] M. Królikowski and D. Grzesiak, "Technological Restrictions of Lightweight Lattice Structures Manufactured by Selective Laser Melting of Metals", *Advances In Manufacturing Science And Technology,* Vol. 38, 2014.

[3] C. Yan, L. Hao, A. Hussein, P. Young and D. Raymont, "Advanced lightweight 316L stainless steel cellular lattice structures fabricated via selective laser melting", *Materials and Design*, vol. 55, pp. 533–541, 2014.

[4] R. Mahshid, H. N. Hansen and K. L. Højbjerre, "Strength analysis and modeling of cellular lattice structures manufactured using selective laser melting for tooling applications", *Materials and Design*. Vol. 104, pp. 276–283, 2016.

[5] P. S. Lee and G. McClure, "Elastoplastic large deformation analysis of a lattice steel tower structure and comparison with full-scale tests", *Journal of Constructional Steel Research*, vol. 63, pp. 709–717, 2007.

[6] R. Guo, R. Liu, W. Jiang, K. Chen, J. Zhang, F. Huang and X. Sun, "Numerical Analysis on Static Mechanical Properties of the Periodic Multilayer Lattice Material," *Engineering*, Vol. 3 (12), pp. 1149-1154, 2011.

[7] J. Sun, Y. Yang and D. Wang, "Mechanical properties of regular hexahedral lattice structure formed by selective laser melting", *Laser Physics*, vol. 23, 066101 (9pp), 2013.

[8] T. Stanković, J. Mueller, P. Egan and K. Shea, "A Generalized Optimality Criteria Method for Optimization of Additively Manufactured Multimaterial Lattice Structures", *J. Mech. Des. ASME*, vol. 137(11), 111405 (12pp), 2015.

[9] M. C. Messner, M. I. Barham, M. Kumar and N. R. Barton, "Wave propagation in equivalent continuums representing truss lattice materials", *International Journal of Solids and Structures*, vol.73–74, pp. 55–66, 2015.

[10] M. C. Messner, "Optimal lattice-structured materials", *Journal of the Mechanics and Physics of Solids*, vol. 96, pp. 162–183, 2016.

[11] W. P. Syam, W. Jianwei, B. Zhao, I. Maskery, R. Leach, "Design of mechanically-optimised lattice structures for vibration isolation", *Proceedings of 17th International euspen Conference*, pp. 55-56, Germany, 2017.

[12] H. Matlock and B. R. Grubbs, "Development of Methods for Computer Simulation of Beam-Columns and Grid-Beam and Slab Systems" *Enter for Highway Research*, The University of Texas, Texas, 1967.

[13] G. Kiper and E. Soylemez, "Deployable space structures", *2009 4th International Conference on Recent Advances in Space Technologies*, pp. 131-138, Istanbul, 2009.

[14] H. J. Xiang, Z. F. Shi, S. J. Wang and Y. L. Mo, "Periodic materials-based vibration attenuation in layered foundations: experimental validation", *Smart Materials and Structures*, vol. 21, 112003 (10pp) ,2012.

[15] H. Karadeniz, "Stochastic Analysis of Offshore Steel Structures: An Analytical Appraisal", *Springer-Verlag London*, 2012.

[16] S. Bobby, S. M. J. Spence, E. Bernardini and A. Kareem, "Performance-based topology optimization for wind-excited tall buildings: A framework", *Engineering Structures*, vol. 74, pp. 242–255, 2014.

[17] J. Huang, Z. Shi, W. Huang, X. Chen and Z. Zhang, "A periodic foundation with rotational oscillators for extremely low-frequency seismic isolation: analysis and experimental verification", *Smart Materials and Structures*, vol. 26, 035061 (11pp), 2017.

[18] Y. Ren, Y. Yu, B. Zhao, C. Fan and H. Li, "Finite Element Analysis and Optimal Design for the Frame of SX360 Dump Trucks", *Procedia Engineering (Elsevier Ltd, 2017)*, vol. 174, pp. 638–647, 2017.

[19] S. Güler and H. Karagülle, "Finite element analysis of structures with extruded aluminium profiles having complex cross sections", *Latin American Journal of Solid and Structures*, vol. 13, pp.1499–1514, 2016.

[20] JJ. Wu, "Finite element analysis and vibration testing of a three-dimensional crane structure", *Measurement*, vol. 39 pp. 740–749, 2006.

[21] S. S. Rao, "Mechanical vibrations. 3rd ed. Upper saddle river: Prentice hall", 2011.

[22] http://thumbs.dreamstime.com/x/modelo-aislado-3d-de-un-cedazo-cristalino-del-cobre-8059539.jpg

[23] https://commons.wikimedia.org/wiki/File:Rutile-unit-cell-3D-balls.png, Accessed 27 June 2017.

[24] https://commons.wikimedia.org/wiki/File:Iron(II)-sulfide-unit-cell-3D-balls.png, Accessed 27 June 2017.

[25] https://commons.wikimedia.org/wiki/File:Sphalerite-unit-cell-3D-balls.png, Accessed 27 June 2017.

[26] Theory reference for the mechanical apdl and mechanical applications, *ANSYS Release 14.1,* Accessed 27 June 2017.

Cooling Performance Comparison of Plate-Pin-Fin, Pin-Fin and Plate-Fin Heat Sinks under Forced Convection with Numerical Analysis

A.KOCA[1] and H. İ. YAMAÇ[1]

[1] Fırat University, Elazığ/Turkey, akoca@firat.edu.tr
[1]Fırat University, Elazığ/Turkey, hiyamac@firat.edu.tr

Abstract **- Thermal management is necessary for electronic devices for their reliability and performance. Heat sinks are one of the electronic equipment cooling devices used in thermal management. Two types of heat sinks as pin-fin heat sinks and plate-fin heat sinks are commonly used in thermal management. The heat sinks have different pin types have advantages over each other. The plate-pin-fin heat sink can be used to increase cooling performance. In this study, The computational fluid dynamics program as Fluent software is employed for comparison of different types of heat sinks as plate-pin-fin, pin-fin and plate-fin under forced convection. The modelled heat sink geometries have the same surface area for reliability of comparison. The width of plate-fins is 4.06 mm. The radius of pin fins is 2.03 mm. The heat flux 5000 W/mm2 is defined on 100 mm x 100 mm base plate of fins. The results as flow velocities, vectors and temperature distributions are obtained. The heat sinks maximum temperature is under 65oC. The cooling performance of only pin fin heat sink can be accepted better than plate-pin-fin and plate fin heat sinks under forced convection.**

Keywords **- Computational Fluid Dynamic, electronic equipment cooling, forced convection, Fluent, plate-pin-fin heat sink.**

I. INTRODUCTION

In engineering applications channel flow often occurs. It is used in many places where there are fluid movements such as cooling of electronic devices, heat exchangers, heating and cooling of buildings. For this reason, the channel flow has attracted many researchers. One of the methods intensively used to increase heat transfer in today's technology is extended heat transfer surfaces. Finned surfaces enhance convection heat and mass transfer by increasing surface area and turbulence of the flow.

The finned structure used in thermal management is called heat sink in electronic equipment cooling applications. Commonly, pin-fin heat sinks and plate-fin heat sink geometries are used for cooling. Depending on the area of use, the pin types have superiority to each other. However, Plate-pin-fin heat sink, it is possible to design a suitable geometry can be combined. Before manufacturing the performance of this type of heat sink must be compare with only plate fin heat sink and only plate fin heat sink. There are many studies about heat sinks cooling performances.

Yang et al. made numerical analysis to investigate planted pin fins for heat transfer enhancement in plate fin heat sink. Finite difference method is used with adopting a control volume. The result as plate-circular pin fin heat sink has better cooling performance than the plate fin heat sink [1].

Tsai et al. used CFD software Fluent for numerical simulation to investigate thermal and hydraulic performance of a plate-fin heat sink. They make some variations in plate shield of finned geometries [2].

Chen et al. perform a numerical and experimental study to investigate heat transfer characteristics in plate-fin heat sink. k-ε turbulence model is used in numerical simulations [3].

Jonsson et al. model many kinds of heat sinks have variable geometrical structures and fin types at different domain sizes to obtain thermal and hydraulic performances of heat sinks [4].

Park et al. make optimization for high performance of a pin fin heat sink numerically. Finite volume method is used to obtain optimum design values. [5].

Wang et al. study on a comparison of thermal performance of in-line pin-fins. Reynolds-averaged Navier-Stokes equations are employed for solution. The results are compared with experimental data. [6].

Zhou and Cotton study on investigation of hydraulic and thermal performance of plate-pin fin heat sinks have different pin geometries numerically [7].

Yu et al. employee numerical simulations for comparison of thermal performances of plate-pin fin heat sinks and plate fin heat sinks. Plate-pin fin heat sinks decrease thermal resistance and reach better air cooling results [8].

Feng et al. investigate forced convection in plate-pin fin heat sinks numerically. Experiments are performed for validation of numerical model [9].

In this study, the computational fluid dynamics program as Fluent software is employed for comparison of different types of heat sinks as plate-pin-fin, pin-fin and plate-fin under forced convection. The modelled heat sink geometries have the same surface area for reliability of comparison.

II. MATERIAL AND METHOD

A. Governing Equations

Numerical simulation is made with RANS based Fluent software. The equations used from solver while iterations are show below [10, 11].

Continuity Equation:

$$\frac{\partial \rho u_i}{\partial x_i} = 0 \tag{1}$$

Momentum Equation:

$$\rho u_j \frac{\partial u_i}{\partial x_j} = -\frac{\partial P}{\partial x_i} + \frac{\partial}{\partial x_j}\left[\mu_t\left(\frac{\partial u_i}{\partial x_j} + \frac{\partial u_j}{\partial x_i}\right)\right] \tag{2}$$

Energy Equation:

$$\rho u_j \frac{\partial T}{\partial x_j} = \frac{\partial}{\partial x_j}\left[\left(\frac{\mu_L}{\sigma_L} + \frac{\mu_t}{\sigma_t}\right)\frac{\partial T}{\partial x_j}\right] \tag{3}$$

Transport Equation for k:

$$\rho u_j \frac{\partial k}{\partial x_j} = \frac{\partial}{\partial x_j}\left(\frac{\mu_t}{\sigma_k}\frac{\partial k}{\partial x_j}\right) + \mu_t\left(\frac{\partial u_i}{\partial x_j} + \frac{\partial u_j}{\partial x_i}\right)\frac{\partial u_i}{\partial x_j} - \rho\varepsilon \tag{4}$$

Transport Equation for ε:

$$\rho u_j \frac{\partial \varepsilon}{\partial x_j} = \frac{\partial}{\partial x_j}\left(\frac{\mu_t}{\sigma_\varepsilon}\frac{\partial \varepsilon}{\partial x_j}\right) + c_1\mu_t\frac{\varepsilon}{k}\left(\frac{\partial u_i}{\partial x_j} + \frac{\partial u_j}{\partial x_i}\right)\frac{\partial u_i}{\partial x_j} - c_2\rho\frac{\varepsilon^2}{k} \tag{5}$$

B. Simulation

Fluent software is used for modelling and simulation in this study. The simulation steps are respectively 'Geometry' module is used for creation of geometries. Surfaces of heat sinks and domain are named in this section. 'Mesh' module is used for diving geometries to finite volumes. Mesh is made with sizing in this section. 'Setup' module is used for setting boundary conditions in steady-state simulation. Solver is is used for chosen and iterations start in this section. In 'Solution' module solution is converged and complete, at last results of simulation are obtained from 'Results' module.

Some assumptions are made in the model solution. Flow of fluid for cooling is solved in 3D domain. Gravitational acceleration is -9.81m / s^2. The solver option is set to (time independent) Steady-State. Turbulence model is chosen as k- ε.

C. Geometry

In this study, heat sinks are modelled at different geometrical structures in cases. The surface area of heat sinks are modelled the same for cases. Only plate fin, only pin fin and two plate-pin fin heat sinks have different number of pins and plates as fins are modelled. The cases are used for comparison of cooling performances of heat sinks. Heat sinks are placed horizontal to base of the domain. Geometrical parameters of heat sink is shown in Figure 1.

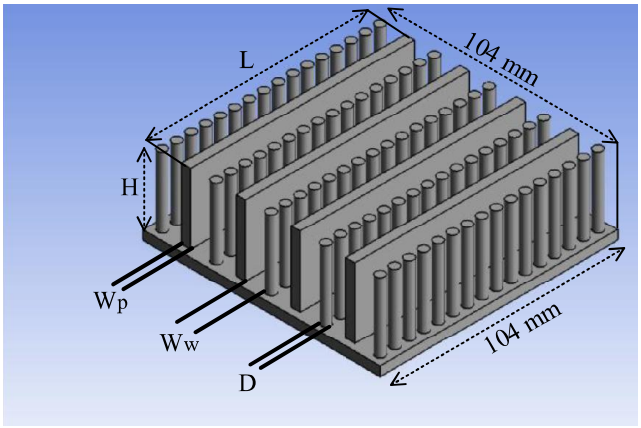


Fig. 1 Geometrical parameters of heat sink.

L is the length of plate, H is the height of fins which is 30.94 mm, W_p is the width of plate fins. W_w is the distance between plate and pin fins which is 7.93 mm. It is assumed that W_p = D (Diameter of pin fin) and H is equal for all cases. The idea behind the assumption of pin diameter equal to plate width is displace pins as fins on the same line with a plate as fin have the same lateral surface area, so pins in geometries are in-line. The number of fins in one line is calculated from the Equation 6:

$$n = 2\frac{(D + L)}{\pi\, x\, D} \tag{6}$$

W_p = D = 4.06 mm and L = 98 mm for all cases, from Equation 6, n=16.

The solution domain includes the heat sink and air around heat sink. The domain size is 350 mm x 350 mm x 900 mm. The base surface different from heat sink base plate surface is assumed symmetry. The base surface of heat sink is heat flux wall. Heat flux value is 5000 W/m^2. The velocity at inlet is 3m/s. Figure 2 shows the geometrical parameters of solution domain.

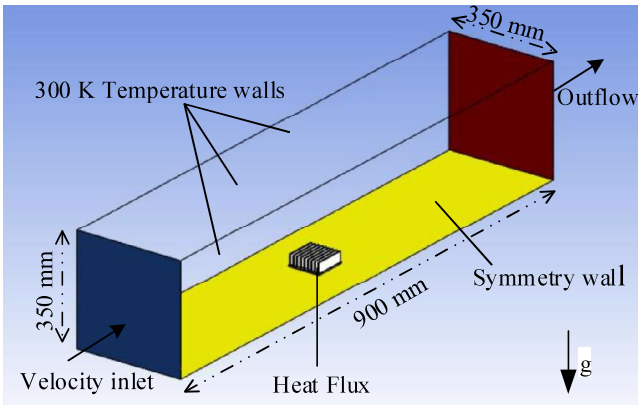
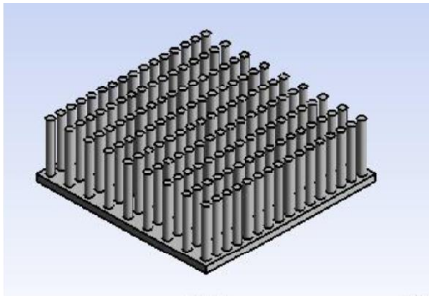


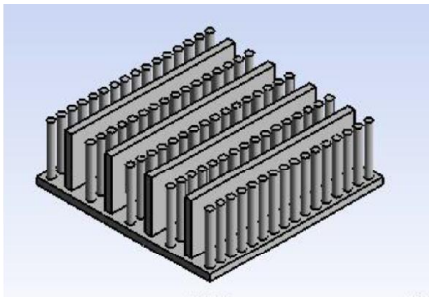
Fig. 2 Geometrical parameters of solution domain.

D. Cases

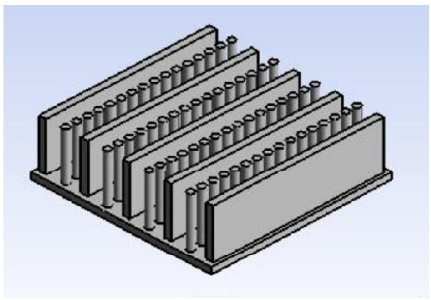
Heat sink modelled in Case 1 has only have pin fins, Case 2 and Case 3 have plate-pin fins. Case 4 has only pin fins. Geometrical structures of heat sinks in cases are shown in Figure 3.



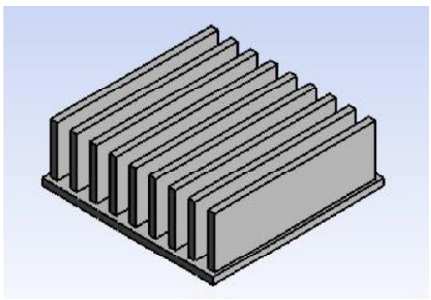
Case 1



Case 2



Case 3

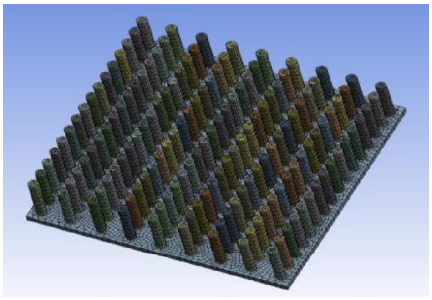


Case 4

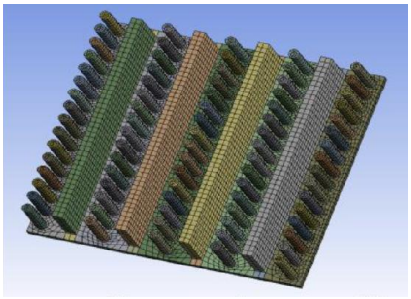
Fig. 3 Geometrical structures of heat sinks in cases.

E. Mesh Structure

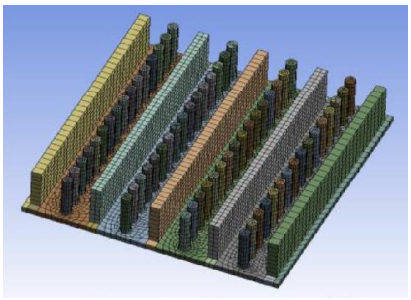
The smaller the mesh structure, the more time the computer needs. The larger the mesh structure, the worse the sensitivity of the desired point. Mesh structures of heat sinks in cases are shown in Figure 4.



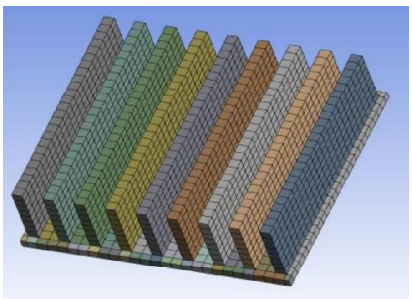
Case 1



Case 2



Case 3



Case 4

Fig. 4 Mesh structures of heat sinks in cases.

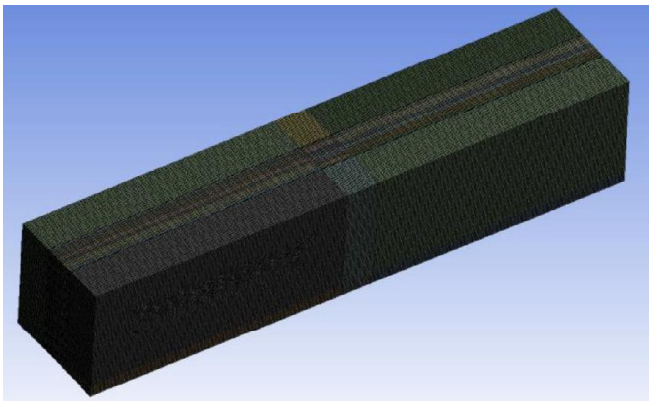


Fig. 5 Mesh structures of domain in case 4 represent all cases.

TABLE I
MESH STATISTICS OF CASES

Case	Nodes	Elements	Mesh Skewness		
			Min	Max	Average
1	5035050	4938521	2.36e-6	0.877	5.98e-2
2	4860650	4710414	2.45e-8	0.874	4.70e-2
3	4451760	4359487	1.03e-6	0.763	9.82e-2
4	3333000	3251538	1.0e-10	0.524	1.49e-2

The mesh structure of solution domain of case 4 is shown in Figure 5. This structure shows differences in all cases because of differences in heat sinks but due to similarity the figure can represent all cases. Table 1 shows the mesh statistic of cases. The mesh structure must be divided into the best range. The mesh quality is acceptable for solution below the mesh skewness value of 0.23 [11].

F. Solver

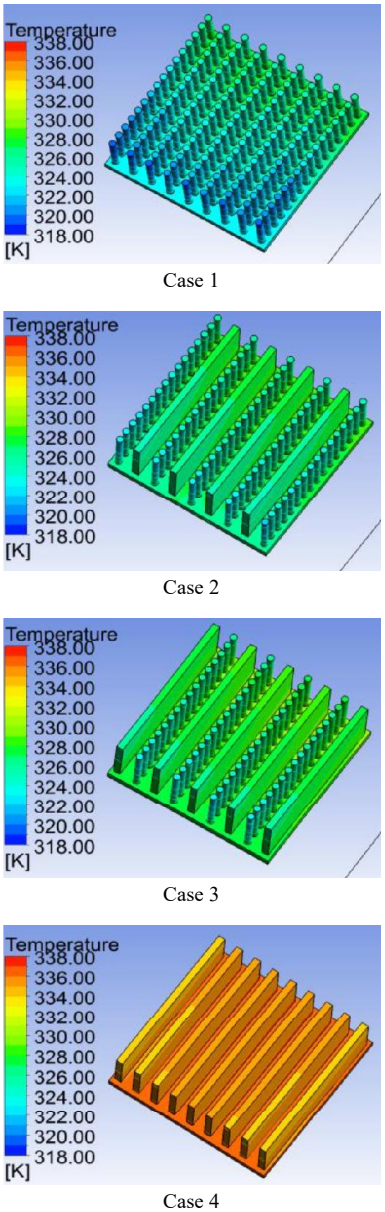
Boundary conditions of the solution domain are: The surface of heat sink base plate is wall have 5000W/mm^2 heat flux. The surface around heated wall is symmetry. There is one inlet and one outflow as shown in Figure 2. All other side walls of solution domain are chosen as wall at 300 K. Solution is made as Steady-State. Gravitational acceleration is inserted as 9.81m/s^2. k- ε turbulence model is chosen for solution with Pressure Implicit Splitting Operator (PISO) algorithm. Material of heat sink is aluminium. The fluid around heat sink is air. Initial properties of air and aluminium. The properties of materials used in simulation are shown in Table 2.

TABLE 2.
PROPERTIES OF AIR AND ALUMINUM

	Air	Aluminum
Density (kg/m^3)	1.225	2719
Specific Heat (J/kgK)	1006.43	871
Thermal Conductivity (W/mK)	0.0242	202.4
Viscosity (kg/ms)	1.7894e-5	

III. RESULTS

Temperatures of heat sink surfaces between 318 K to 338 K. in cases. The lowest temperatures are seen in Case 1 with only pin fin heat sink, the heights temperatures are seen in Case 4 with only plate fin heat sink. Temperatures in Case 2 is lower than in Case 3 with plate-pin fin heat sinks. Figure 6 shows Temperature contours of the heat sink surface areas in cases.



Case 1

Case 2

Case 3

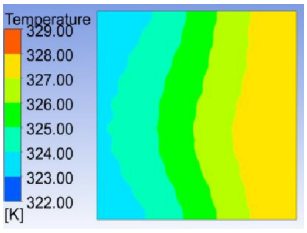
Case 4

Fig. 6 Temperature contours of the heat sink surface areas in cases.

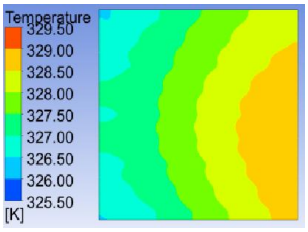
Figure 7 shows the heat sinks base plate surface temperature contours. The comparison of cooling performances can be made with the evaluation of temperature values of these surfaces which electronic equipment connected on. The air velocity flows from left to right in figures. This explains the low temperatures at left sides.

Temperature values are between: 322 K – 329 K in Case 1; 325.5 K - 329.5 K in Case 2; 327.25 K – 330.25 K in Case 3; 335 K – 337.5 K in Case 4. These contours show that the best uniformity of temperature distribution is in Case 4 but at the highest temperature values.

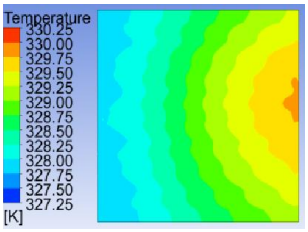
The heat sink base plate area average temperature versus number of pins on heat sink curve is shown in Figure 8. Increasing in fin numbers means decrease in area average temperature.



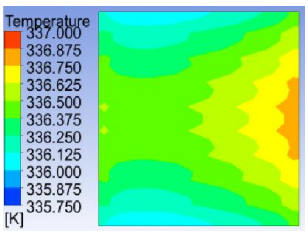
Case 1



Case 2



Case 3



Case 4

Fig. 7 Heat sinks base plate surface temperature contours.

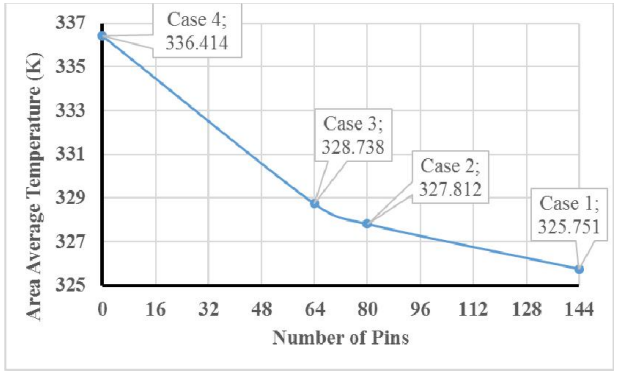
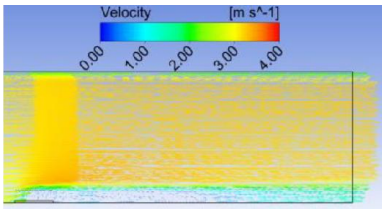
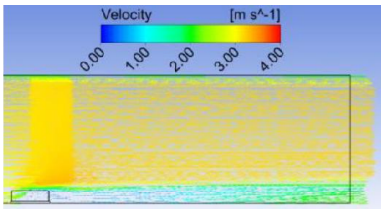


Fig. 8 Heat sinks base plate (heated) area average temperature vs pins no.

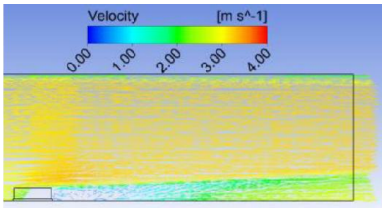
Figure 9 shows velocity vectors of cases. Results show that all cases have the same velocity of air before heat sinks. Air velocity changes after reaching heat sinks. The pins slow down air and transfer heat to air more Case 1 to Case 4 respectively. Figure 9 verify Figure 7, Increase air velocity means better cooling performance in turbulent flow.



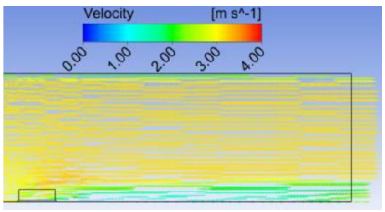
Case 1



Case 2



Case 3



Case 4

Fig. 9 Velocity vectors of cases.

IV. Conclusions

In this paper, initial condition as heat flux of 5000W/m^2 increase the temperature of heat sinks. Temperature of all heat sinks modelled in simulation under 65ºC which is acceptable for electronic equipment. 3 m/s air velocity is enough for cooling under forced convection in the channel modelled in simulation.

The expectation is plate-pin fin heat sinks show better cooling performance than only pin and plate heat sinks. But the best cooling performance can be seen in only pin fin heat sink structure. The heat sinks are modelled at the same surface area; the volume of heat sinks can cause unexpected results occurring.

Increase in pin number means increase in cooling performances of heat sinks. The pins let the air flow between them and this situation explains the better cooling performance.

Comparison results show that only plate-fin heat sinks cooling performance is better than plate-pin-fin and only plate-fin heat sinks. As a future work, experimental studies can be made for validation of numerical results.

References

[1] Y-T. Yang and H-S. Peng, "Investigation of planted pin fins for heat transfer enhancement in plate fin heat sink," *Microelectronics Reliability*, vol. 49, p. 163-169, 2009.

[2] G-L. Tsai, H-Y. Li, C-C Lin, "Effect of the angle of inclination of a plate shield on the thermal and hydraulic performance of plate-fin heat sink," *Int. Communications in Heat and Mass Transfer*, vol. 37, p. 364-371, 2010.

[3] H-T. Chen, S-T. Lai, L-Y. Haung, "Investigation of heat transfer characteristics in plate-fin heat sink," *Applied Thermal Engineering*, vol. 50, p. 352-360, 2013.

[4] H. Jonssson and B. Moshfegh, "Modeling of the thermal and hydraulic performance of plate fin, strip fin, and pin fin heat sinks-influence of flow bypass," *IEEE Transactions on Components and Packaging Technologie*s, vol. 24, p. 142-149, 2001.

[5] K. Park, D-H. Choi, K-S. Lee, "Numerical shape optimization for high performance of heat sink with pin-fins," *Numerical Heat Transfer, Part A*, vol. 46, p. 909-927, 2004.

[6] G. Liao, X. Wang, J. Li, F. Zhang, "A numerical comparison of thermal performance of in-line pin-fins in a wedge duct with three kinds of coolant," *Int. J. of Heat and Mass Transfer*, vol. 77, p.1033-1042, 2014.

[7] F. Zhou and I. Cotton, "Numerical Evaluation of Flow and Heat Transfer in plate-pin fin heat sinks with various pin cross-sections," *Numerical Heat Transfer, Part A*, vol. 60, p. 107-128, 2011.

[8] X. Yu, J. Feng, Q. Feng, Q. Wang, "Development of a plate-pin fin heat sink and its performance comparisons with a plate fin heat sink," *Applied Thermal Engineering*, vol. 25, p. 173-182, 2005.

[9] S.S. Feng, T. Kim, T.J. Lu, "Numerical investigation of forced convection in pin/plate-fin heat sinks heated by impinging jet using porous medium approach," *Int. J. of Numerical Methods for Heat & Fluid Flow*, vol. 23, p. 88-107, 2013.

[10] Y. T. Yang and H. Sen, "Numerical study of pin-fin heat sink with un-uniform fin height design," *Int. J. of Heat and Mass Transfer*, vol. 51, p. 4788-4796, 2008.

[11] Ansys Fluent 14.0 Tutorial Guide. Ansys INC, 15317, p. 724–746, November 2009.

The Effect of Blow-Up Ratio on the Mechanical Properties of Polythene Films

İ. TARTICI[1a], M.A. GÜVENÇ[1b], S. MISTIKOĞLU[1c*]

[1]Iskenderun Technical University, Hatay/Turkey,
idiltrtc89@gmail.com[1a] , mali.guvenc@iste.edu.tr[1b], selcuk.mistikoglu@iste.edu.tr[1c*]

Abstract **- The consumption of packaging is increasing day by day with rapid population growth, improvement of living conditions, widespread of shopping centers and supermarkets. Nowadays there are so many packaging products which differ from each other according to the raw material. The most popular types of packaging materials are plastics, paper-carton, metal, glass, and wood packaging. Plastic packaging has some advantages according to the others. These advantages are briefly flexible, not broken easily, lightweight, easily formability, essentially chemically inert, strong, rigid safety use, protect the product which inside the package etc. Various type of raw material is used in plastic packaging industry. The main types of raw materials are PET (polyethylene tetra fluoride), PVC (polyvinyl chloride) and PP (polypropylene) a PE (polythene). The most popular type of raw material is polythene. The reasons for preferring of polythene; provides the high velocity in filling machine, the production cost is low and it provides the packaging which has suitable for product properties.**

In this study, the effects of changes in blow-up ratio, defined as the ratio of the bubble diameter to the die diameter, on the mechanical properties of films were investigated. In the scope of the study, films with different blowing ratios were manufactured and some mechanical properties such as tensile strength and tear strength were compared. At the end of the study, the question of what the blow-up ratio should be to get the highest mechanical properties was answered.

Keywords **- packaging, polythene films, blow-up ratio**

I. INTRODUCTION

In packaging industry different type of material using for protection the product. For example; paper, metal, glass, wood and plastic. Plastic is the most popular packaging material according to the others. The main reason of this, plastic package have low unit weight, high strength, easily processability and suitable for mass production.

Blown film extrusion is a most attractive polymer processing and producing plastic package method. Huge amount of polymer, mostly polyethylene, processed using this method. Various types of polymers are used in film production by this method such as HDPE (high density polyethylene), LDPE (high density polyethylene), LLDPE (linear low density polyethylene) and some additives like a slip agent, antiblock and antistatic. Polymer chemistry and molecular structure influenced the final film production.

HDPE is generally polymerized with a small amount of co-monomer that leads to a few short chain branches placed intentionally along the main chain to make the polymer easier to process. A high degree of linearity results in a high percentage of crystallinity (i.e., high density). HDPE is generally in the density range of 0.93 to 0.96 g/cm3. HDPE melts at a higher temperature (265 to 275 °F, 130 to 135 °C) and has a narrower processing window. It also requires higher screw torque, hence more motor power. To promote good solids feeding via high barrel/pellet friction, grooved feed throats are often used [1].

Linear low density polyethylene (LLDPE) is a variation of HDPE. It is synthesized similarly, but LLDPE has a much higher content of co-monomer, such as hexane or octane. Incorporation of co-monomer in the chain yields short chain branches of a specified length [1].

Low density polyethylene (LDPE) is synthesized in such a way that a highly branched polymer is formed. It consists of short chain branches (less than six carbon atoms long) and long chain branches (almost as long as the length of the backbone). Branch points along the chain serve as disruptions to the order of the system and prevent local crystallization. The lower level of crystallinity results in lower density. LDPE is generally in the density range of 0.91 to 0.93 g/cm3[1].

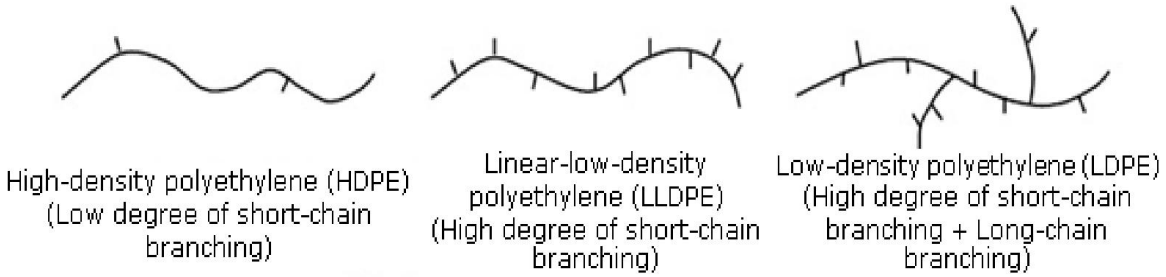


Figure 1: Schematic model of the structure of polyethylene (molecular weight distribution not included) [2]

All polymers extruded with small amount of additives. After blowing the film has passed through the nip rollers the film surfaces tends to sticky each other. Antiblock additives prevent this worse affect. Antistatic agents are designed to minimize the buildup of static charges on polymer surfaces.

Slip agent is quantified via the coefficient of friction (COF). If films have a high COF, individual film layers have a high surface friction and tend to stick together instead of sliding over one another. The films do not 'slip'. It can result in decreased line speeds (lower productivity) and/or wrinkled film (higher waste). In order to overcome this issue, slip agents are added [3].

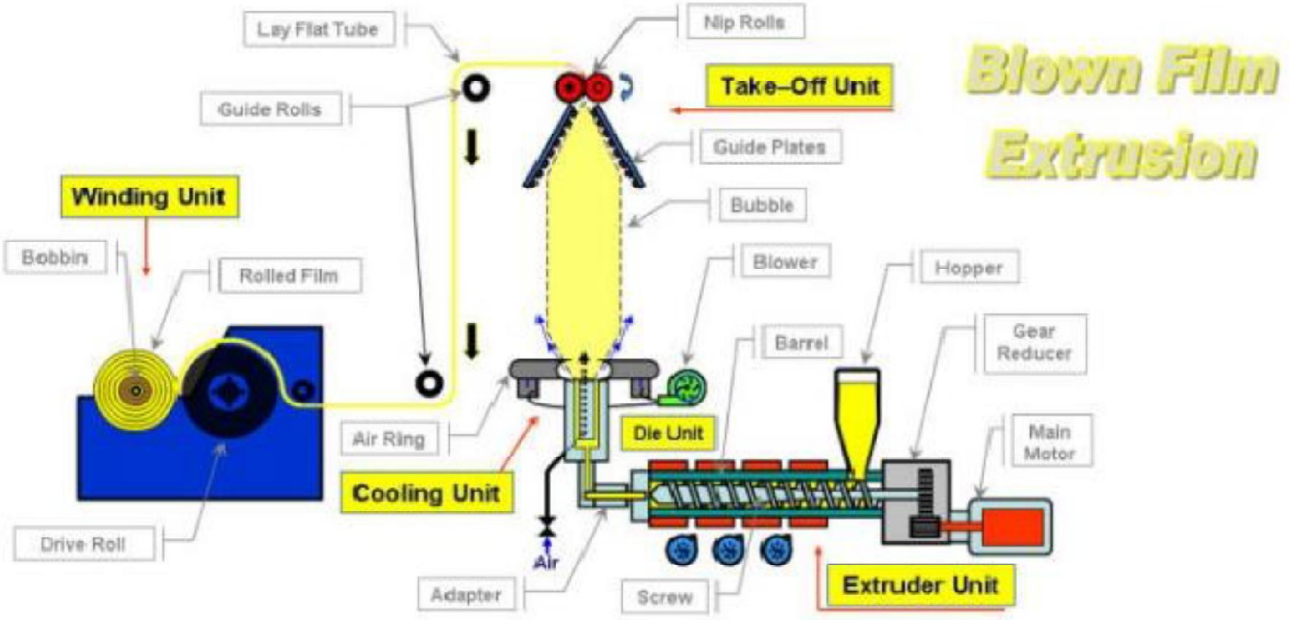


Figure 2: Blown Film Extrusion Process[4]

Blown film extrusion machine has five main sections (Figure 2). These are:

Hopper or Feed System: Feed system has delivered raw material toward the screw. Some types of feed system has drying system because of drying the moist raw material. Its shape like conical for reducing surface friction and continuously feeding screw with in raw material [1].

Screw system: The screw is called the ''heart'' of the blown film machine. It has 3 primary sections; feed compression and metering. Raw material which has come the hopper, compressed and heating inside of the screw. Important characteristic of screw geometry is the L/D ratio:

L/D ratio = Screw flighted length _ Screw diameter

Typical values of L/D ratio range from 18: 1 to 32: 1, with 24 : 1 being the most common. L/D ratio is based on the number of functions that a screw performs.

Die: The die is called the ''brain'' of the process. The die occur the end of the screw and gives final shape of film.

Collapsing frame and nip rollers: As the bubble moves upward and approaches the nip rollers, it is "pre-flattened" by the collapsing frame. This device provides a smooth transition from a round tube shape to a flattened tube shape. In addition to flattening the tube, the collapsing frame also helps eliminate wrinkles in the final product [1].

Winding unit: Winders are used to collect the wound roll packages. A couple of other functions performed by winders include automatic roll changeover and static dissipation.

This device provides a smooth transition from a round tube shape to a flattened tube shape. n addition to flattening the tube, the collapsing frame also helps eliminate wrinkles in the final product.[1]

II. EXPERIMENTAL STUDIES

In this study five different types of raw materials was used to produce these films.

Table 1: Raw Material Properties

MATERIALS	MELT FLOW INDEX (gr/ 10 min)	DENSITY (gr/cm³)
LDPE	2	0,920
MDPE	0,2	0,938
METALOSEN	2	0,918
METALOSEN	0,5	0,927
COLOR	2,03	4,0

The MFI test was performed at 2,16 kg load and 190º.Three layered films were produced on co-extrusion blown film machine (Windmöller&Hölscher) with a 315 mm die diameter and 2,5 mm die gap. The exturuder temperature profile from hopper to the die was set:
A extruder: 170 º to 190 º
B extruder: 170 º to 200 º
C extruder: 190 º to 200 º
Head of machine temperature is 210 º.

The forest line height is 170 cm and the film thickness is 65µm.The film composition shown in table 2.

Table 2: Film Composition

LAYER A	LDPE
	METALOSEN
LAYER B	MDPE+METALOSEN
	COLORED MASTERBATCH
LAYER C	LDPE
	METALOSEN

The films which has four different blow up ratio had produced. The blow-up ratio and film width shown in table 3.

Table 3: Film Width And Blow Up Ratio

	FILM 1	FILM 2	FILM 3	FILM 4
BLOW UP RATIO	1,68	2,27	2,47	3,25
DDR	22,89	16,94	15,57	11,83
FILM WIDTH (MM)	835	1125	1225	1610

Blown up ratio is ratio of bubble diameter/ die diameter. It represents;

$$BUR(BLOW\,UP\,RATIO) = \frac{BUBBLE\,DIAMETER}{DIE\,DIAMETER} \quad (1)$$

The final thickness reduction in the melt after blowing is indicated by a drawdown ratio.

$$DDR(DRAWDOWN\,RATIO) = \frac{WIDTH\,OF\,DIE\,GAP}{FILM\,THICKNESS\,X\,BUR} \quad (2)$$

Tensile tests were performed on a testing machine (ZWICK/ROELL) per ASTM D882 standard with 25x100x0,065 samples. Six specimens were tested and their average value was reported.

III. CONCLUSION

This four different film which has different blow-up ratio were tested and test result is shown in table 4. The tensile strength, modulus of elasticity and elongation at break were measured in the machine direction (MD) and transverse direction (TD). The test specimens and test device shown in figure 3.

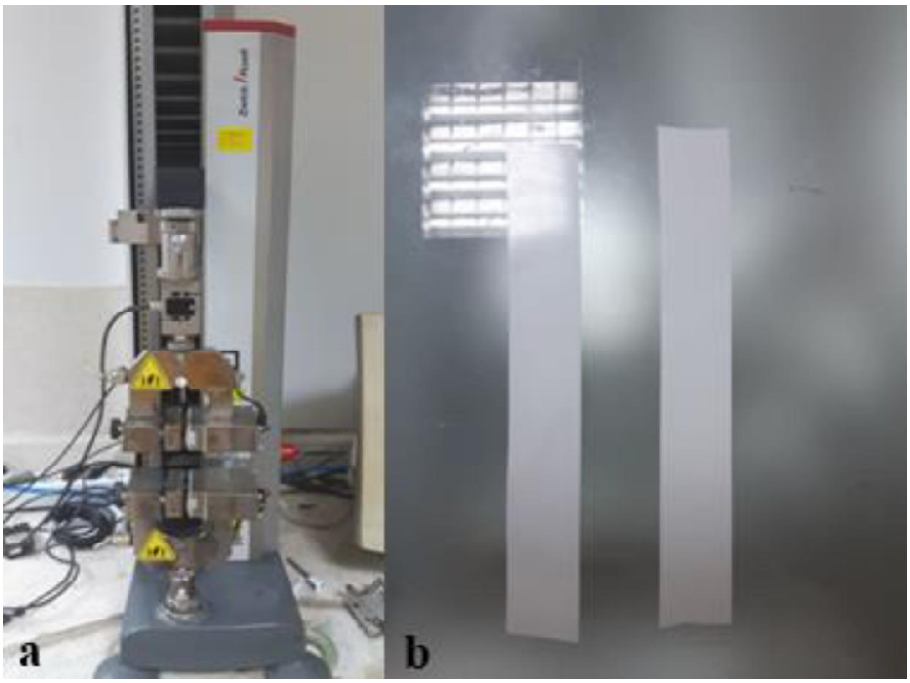


Figure 3: a) Test Device b) Test Speciments

Table 4: Averages of Test Results

TEST RESULTS	BUR							
	MACHINE DIRECTION(MD)				TRANSVERSE DIRECTION(TD)			
	1,68	2,27	2,47	3,25	1,68	2,27	2,47	3,25
E(MODULUS OF ELASTICITY)(N/MM²)	442,79	442,64	538,51	475,73	565,83	556,09	673,19	604,52
YIELD (%)	9,13	8,67	10,26	9,78	10,62	10,27	11,78	10,84
TENSILE STRENGTH (N)	20,95	20,45	29,11	29,93	14,59	14,88	20,7	19,64
ELONGATION AT STRESS (%)	464,27	542,46	586,1	533,52	657,14	754,35	811,81	822,34
BREAKING STRENGTH (N)	20,38	19,65	22	22,17	13	14,27	8,79	14,44
ELONGATION AT BREAK (%)	469,7	548,09	589,88	537,58	737,36	752	787,69	816,87

According to the test results, increasing the BUR, generally tensile strength of the film is increase. Because of in generally, amount of stretching in a given direction which is MD or TD increases, the molecular orientation and tensile strength will be increase. In additional the forest line height influenced mechanical properties of film because of the when the film has freeze early, the film structure will be crystallinity

Increasing the BUR from 1,68 to 3,25 the tensile strength of MD is increased, this situation can be explained lowest forest line height and higher feed rate. TD tensile strength is increased too, because of increasing the BUR, molecular orientation will be crystalline structure in transverse direction.

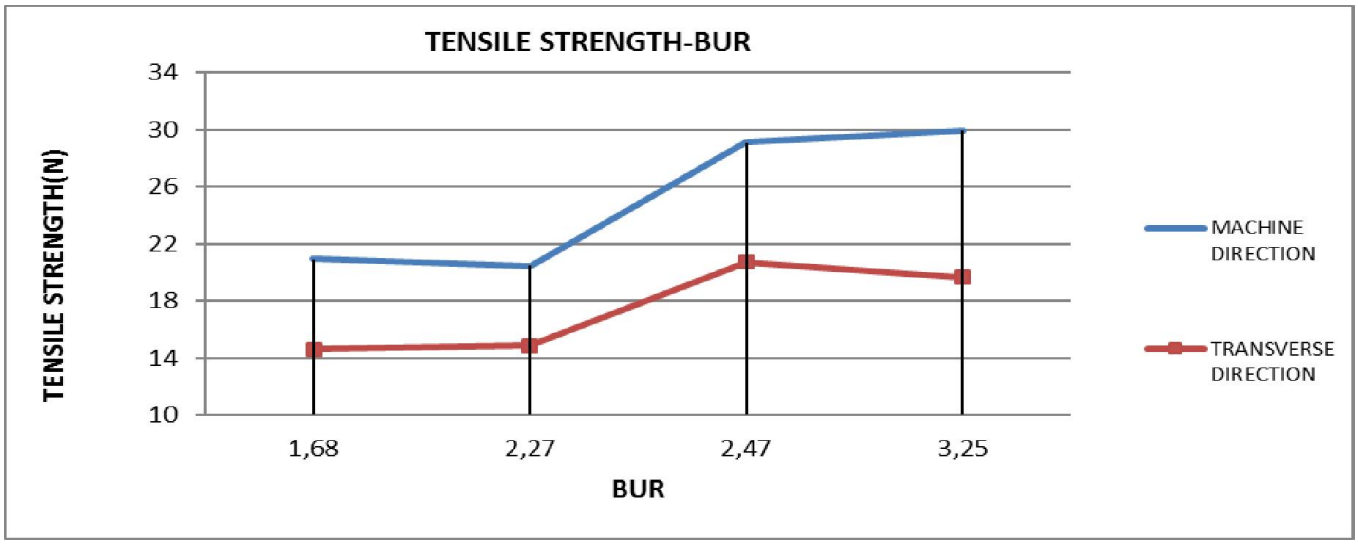


Figure 4: Tensile Strength-BUR

Elongation properties describes the ability of film to stretch prior to breaking or yielding [1]. Increasing the BUR from 1,68 to 3,25 elongation at break increase too. Elongation tends to be inversely proportional to process stretching side where changing molecular orientation. So that the amount of elongation changing in MD is higher than TD.

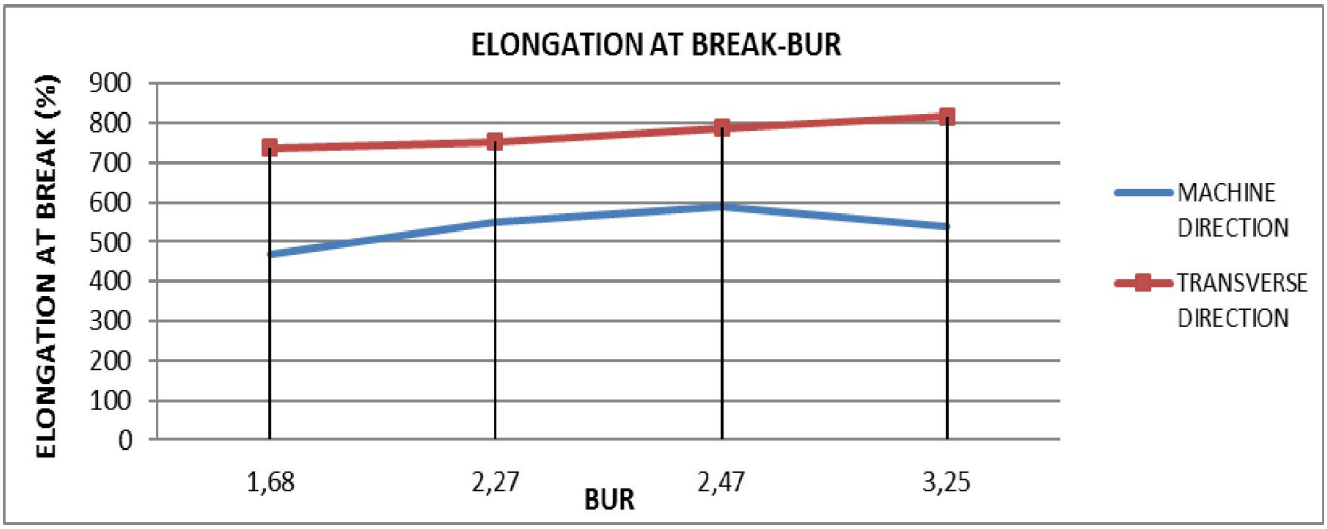


Figure 5: Elongation at Break-BUR

Some other mechanical properties were given in figure 3-4. Increasing the BUR, it leds to faster cooling, resulting in lower crystallite orientation and so the elongation was increased.

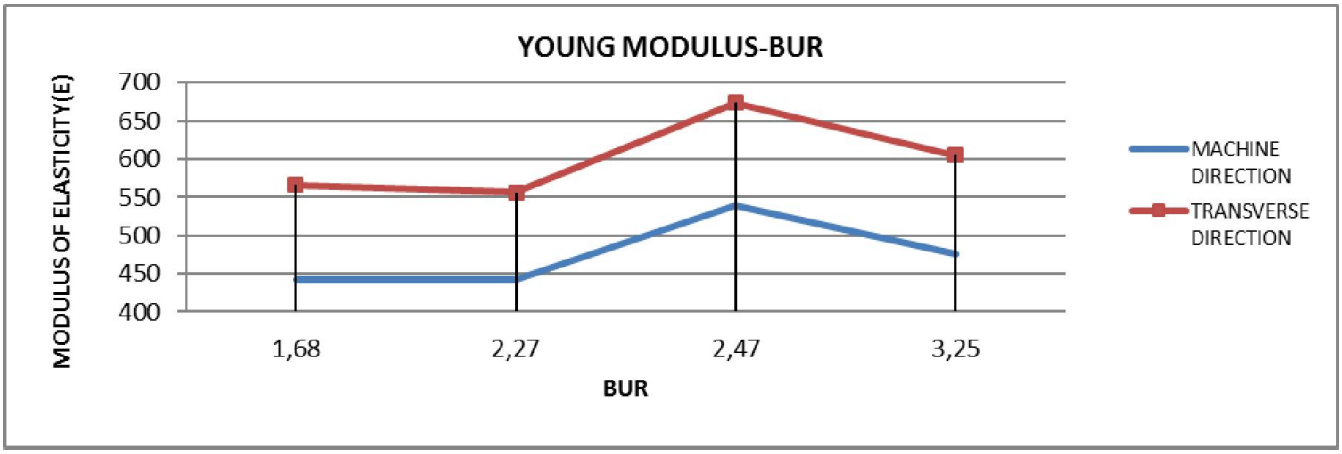


Figure 6: Modulus of Elasticity-BUR

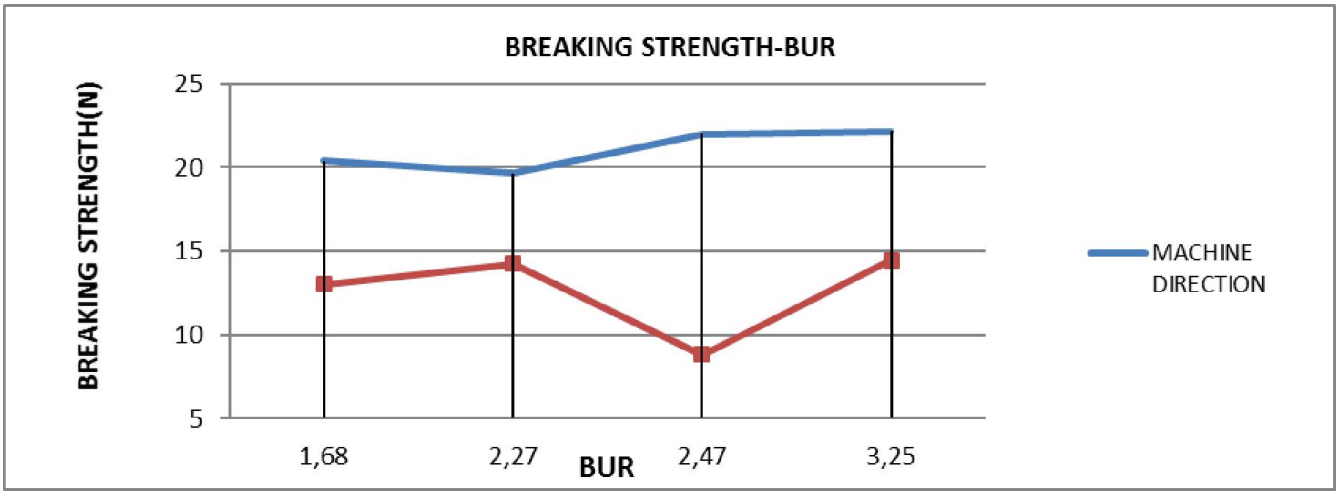


Figure 7: Breaking Strength-BUR

Processing condition have a significant effect on mechanical properties of polyethelene films. Blow-up ratio is a critical factors that determine final film properties.

REFERENCES

[1] Blown Film Extrusion 2nd Edition Kirk Cantor
[2] http://www.toyo-heisei.co.jp/tec_info_1_2_e.html
[3] Multilayer flexible packaging John R. Wagner Jr.
[4] http://blog.oceanextrusions.com/blown-film-plant-plastic-machinery-manufacturer-lamination-film-india/blown-film-extrusion-machine-india/
[5] Suthakarn Auksornkul,Siriwat Soontaranon, Chonthicha Kaewhan And Pattarapan Prasassarakich, 'Effect Of The Blow-Up Ratio on Morphology and Enginneringproperties Of Three Layer Linear Low Density Polyethylene Blown Film' Journel Of Plastic Film &Sheeting 0(0) 1-16 SAGE
[6] Chin-Fu Lee, Hung-Jue Sue, David M. Fiscus,'effect Of Processing Parameters on Essential Work of Fracture Toughness Of LLDPE Blown Films' Polymer Engineering And Science-2015
[7] G.N Onyeagoro 'Effect of Processing Parameters On Mechanical Properties Of Linear Low-Density Polyethylene Film' Department Of Polymer And Textile Engineering, Federal University Of Technology, NIGERIA. Academic Research International
[8] ASTM D882

A Review On the Metal Coating Techniques for Compare Tribological Behavior of Surfaces Operating High Temperatures

H. KAHRAMAN[1a], M.A. GÜVENÇ[1b] and S. MISTIKOĞLU[1c*]

[1]Iskenderun Technical University, Hatay/Turkey, hasankahr@gmail.com[1a], mali.guvenc@iste.edu.tr [1b], selcukmistikoglu@gmail.com[1c*]

Abstract **- There are many ways to use a metal coating as a surface treatment to increase the mechanical, electrochemical and thermal properties of the material. These techniques used depends largely on the application of the material as well as the desired material coating or the depth of the surface treatment. There are mainly four coatings methods such as gaseous state processes, solution state processes, molten or semi-molten state processes, and solid state processes. Two important characteristic parameters for coating processes are the thickness of coatings that can be obtained and the deposition temperature. This study is described several coating processes that are used to produce relatively thin surface layers. Hence, the substrate and the coating is combined to provide a tribological performance that cannot be achieved by using singly. In addition, the types of coatings that can be used for metal surfaces operating at high temperatures and characteristics of electrode coating are investigated.**

Keywords **- Tribology, high temperature, metal coating, surface treatment.**

I. INTRODUCTION

Recently, tribologists have increasingly resorted to friction and wear control. This led to the development of a new discipline called surface engineering. This growth has been encouraged by two main factors. The first was the development of new coating and processing methods, which provide previously unworkable coating characteristics and tribochemical properties. The second reason for growth in this area has been the recognition by engineers and scientists of materials that the surface is the most important part in many engineering components. It is at the surface that most failures come from either wear, fatigue or corrosion. The surface has a dominant influence on cost and performance over the life cycle, including the maintainability of the machinery [1].

Coatings are used for many engineering applications to improve the surface properties of components or structures against environmental degradation. Typical examples are (1) high temperature corrosion, (2) erosion and wear, and (3) thermal degradation (overheating) [2].

There are mainly four coating processes such as gaseous processes, solution state processes, melt or semi-melted processes and solid state processes [1]. The surface engineering techniques included in this general classification are shown in Figure 1.

In this study, however, only the coating types included in the molten or semi-molten state processes will be discussed. We will try to focus on metal coatings made on base metal, especially exposed to high temperatures.

Coatings Tribology

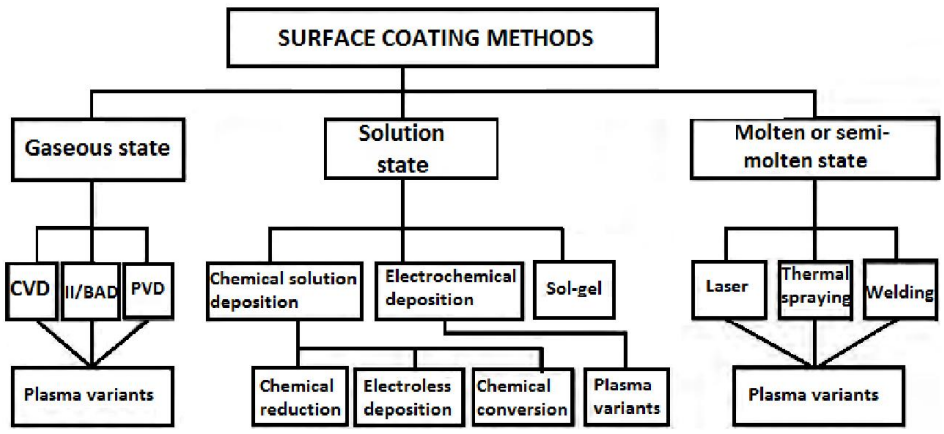


Figure 1. A general classification of surface engineering techniques[1].

In the figures and in the text the following abbreviations are used[1]:

PA	Plasma assisted
CVD	Chemical vapour deposition
PVD	Physical vapour deposition
IBAD	Ion beam assisted deposition
IAC	Ion assisted coating
II	Ion implantation

Two important parameters for coating processes are the thickness of coatings that can be obtained and the deposition temperature. The range of typical coating thicknesses ranging from 0.1 mm to 10 mm is shown in Figure 2a, and the range of deposition temperatures ranging from room temperature to 1000 ° C is shown in Figure2b[1].

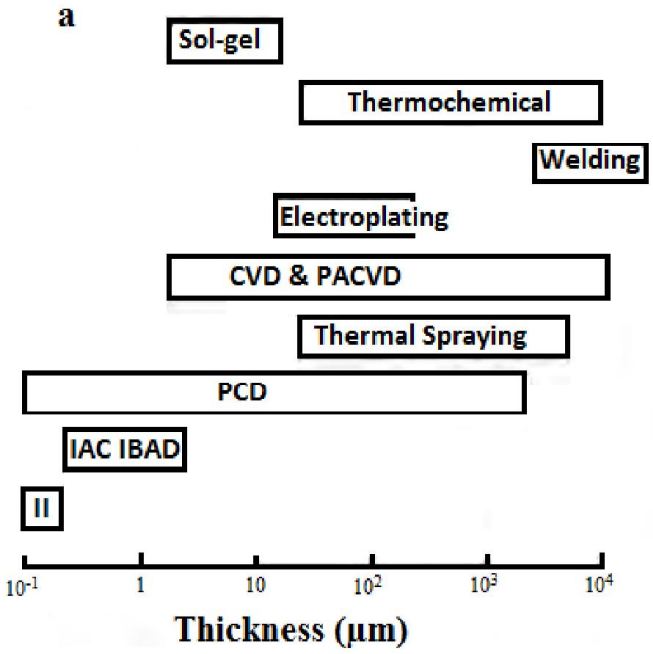


Figure 2a. Typical ranges for (a) depths of surface modifications and thicknesses of coatings [1]

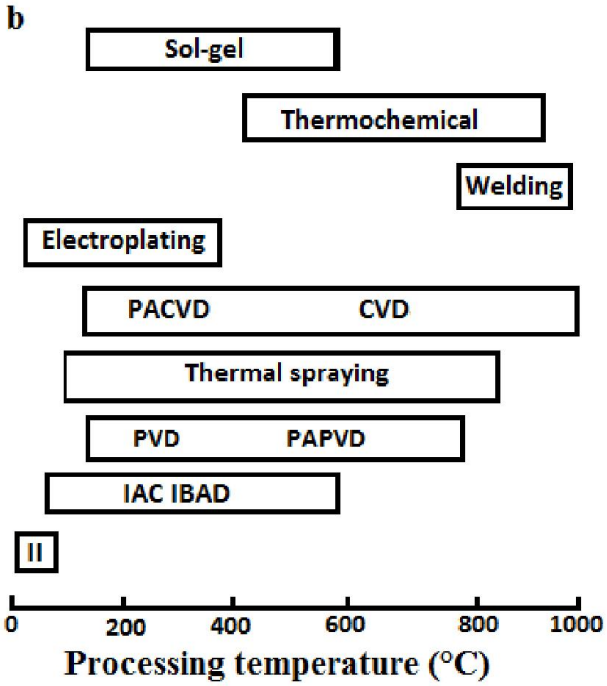


Figure 2b. Typical ranges for (b) processing temperatures for coating technologies [1].

There are many different methods by which a metallic coating can be applied as a surface treatment to increase the mechanical, electrochemical, and thermal performance of a material. The technique used largely depends on material application as well as the desired material coating or depth of the surface treatment [3]. Typical comparative characteristics of some basic coating methods are given on Table 1.

High temperature coatings are used for two main functions: to protect the underlying metal from corrosion or erosion, or to minimize wear. The third function is to reduce the temperature of the base metal in the case of thermal barrier coatings; However, resistance to corrosion and hot oxidation is mandatory [2].

Commonly, the high temperature components exposed to static charges to which the material is creeped and the cyclic loading component experiences fatigue. In both cases, the coating has some effect or a change in material properties due to the difference in heat treatment, or by changing the surface of the part due to the presence of the coating; the coating thus modifies the crack initiation conditions [2].

Table 1. Comparative typical characteristics of some of the main coating methods [1]

	Gaseous State Processes					Solution Processes		Molten or Semi-Molten State Processes		
	PVD	PAPVD	CVD	PACVD	Ion Implantation	Sol-Gel	Electro-Plating	Laser	Thermal Spraying	Welding
Deposition rate (kg/h)	Up to 0.5 per source	Up to 0.2	Up to 1	Up to 0.5		0.1–0.5	0.1–0.5	0.1–1	0.1–10	3.0–50
Coating thickness or treatment depth (μm)	0.1–1000	0.1–100	0.5–2000	1–20	0.01–0.5	1–10	10–500	50–2000	50–1000	1000–10,000
Component size		Limited by chamber size				Limited by solution bath		May be limited by chamber size		
Substrate deposition or treatment temperature (°C)	50–500	25–500	150–12,000	150–700	50–200	25–1000	25–100	200–2000	100–800	500–1200
Substrate material	Metals, ceramics, polymers	Metals, ceramics	Metals, ceramics	Metals, ceramics	Metals, ceramics, polymers	Metals, ceramics, polymers	Metals, ceramics, polymers	Metals		
Pretreatment	Mechanical/ chemical	Mechanical/ chemical plus ion bombardment	Mechanical/ chemical	Mechanical/ chemical plus ion bombardment	Chemical plus ion bombardment	Grit blast and/or chemical clean	Chemical cleaning and etching	Mechanical and chemical cleaning		
Post-treatment	None	None	Substrate stress relief	None	None	High temperature	None/thermal treatment	None/substrate stress relief		None
Uniformity of coating	Good	Good	Very good	Good	Line of sight	Fair/good	Fair/good	Fair	Variable	Variable
Bonding mechanism	Atomic	Atomic plus diffusion	Atomic	Atomic plus diffusion	Integral	Surface forces		Mechanical/ chemical/ metallurgical		

II. MOLTEN OR SEMI-MOLTEN STATE PROCESSES

Processes of the molten or semi-molten state include "solid" methods, such as thermal and plasma spraying. These methods can be applied a very wide range of materials, including aluminum alloys, copper, iron, molybdenum, nickel, stainless steel and tin. The resulting thickness can be from a few microns to several millimeters, which is an economical way of applying wear-resistant and corrosion-resistant coatings. However, porosity can often be higher than acceptable, and several technological processes, such as detonation (D) gun and high-speed thermal spraying of oxide fuel (HOVF), are aimed at improving this performance [4].

Various welding processes can also be used to apply a number of metals and metal / ceramic composites. The two most widely used methods are oxyacetylene torch in combination with a welding rod consisting of a metal to be deposited. The second most common method is the use of arc welding techniques, where the welding electrode is a facing metal [4].

A general comparison chart is available for SEMI-MOLTEN STATE PROCESSES on Table 2.

Table 2. Comparative characteristics of some of the main coating methods [4]

	Solution process		Molten or semi-molten state process		
	Sol-gel	Electro-plating	Laser	Thermal spraying	Welding
Deposition rate (kg/hr)	0.1–0.5	0.1–0.5	0.1–1.0	0.1–1.0	3.0–50
Component size	Limited by solution bath		May be limited by chamber size		
Substrate material	Wide choice	Some restrictions	Wide choice	Wide choice	Mostly steels
Pre–treatment	Grit blast and/or chemical clean	Chemical cleaning and etching	Mechanical and chemical cleaning		
Post–treatment	High temperature calcine	Non-thermal treatment	Non-substrate stress relief		None
Control of deposit thickness	Fair/good	Fair/good	Fair/good	Manual–variable Automated–good	Poor
Uniformity of coating	Fair/good	Fair/good	Fair	Variable	Variable
Bonding mechanism	Surface forces		Mechanical/chemical		Metallurgical
Distortion of substrate	Low	Low	Low/moderate	Low/moderate	Can be high

[

In a discussion of the mechanical properties of high temperature coatings and coated components, two areas are of primary interest: (1) the susceptibility of a coating to cracking and peeling; (2) the coating-base metal interaction which leads to the deterioration of the important mechanical properties of the components [2].

Cracking and peeling may be due to (1) high residual tensile stress due to the treatment, (2) a marked thermal expansion gap, (3) poor ductility or toughness, and (4) poor adhesion to the substrate. The properties of the base component are not directly affected. Coating protection is limited due to premature failures of the mechanical coating [2].

During the thermal spraying of the coatings, residual stresses develop because the melted droplet strikes the substrate, seals the substrate and is prevented from shrinking during the cooling process [2].

The metal-coating interaction may influence mechanical properties due to (1) inadequate process parameters (temperature, time, heating and / or cooling rate), (2) interdiffusion and structural changes due to compatibility insufficient chemical, to crack the formation as indicated above which causes a stable growth of the crack by creep or fatigue in the structural base metal [2].

- *Thermal Spraying*

Thermal spraying is a process in which a metallic or non-metallic material is heated and then propelled in atomized form onto a substrate. The material may initially be in the form of a wire, rod or powder. It is heated in a plastic state or melted by a flame of oxyfuel gas by an electric arc or plasma or by detonation of an explosive gas mixture. The particles conform to the shapes of the substrate or themselves and then cool to form a coating[5].

These coatings are characterized primarily in terms of substrate adhesion, porosity and oxide content. In general, the higher the particle velocity, the better the adhesion, the higher the density and the lower the oxide content of the coating. The thermal spraying industry is diverse. Thermal spray coating users abound in the aerospace, steel, automotive, and petroleum industries, to name a few. It's important to distinguish between thermal spray coating and thermal spray coating. welding processes used for surface coating. During spraying, fine particles of sprayed product from a gun hit the substrate, and binding to the bond is mechanical, non-metallurgical or chemical. Substrate temperatures reach 365-530 K, which is much lower than welding, avoiding distortion and oxidation of the base material [5].

Firstly, it can be applied to non-weldable coating materials, such as ceramics, and second, it can be applied to coatings of materials unsuitable for surface welding because of their composition or their susceptibility to distortion. Generally, there is little or no distortion, dilution or metallurgical impact on the substrate. The total thickness of the coating may be 0.0025-10 mm depending on the stress constraints of the material to be sprayed. There are five main thermal spraying methods in general, listed here in descending order of particle velocity. These are: detonation flame spraying, high velocity oxyfuel (HVOF), plasma airb, arc and flame projection. The flame spraying process uses a combustible gas as a heat source to melt the coating material. Flame spray guns are available for spraying materials in the form of rod, wire or powder. An acetylene flame having a temperature of 3300 C is used, in which ceramic material is introduced [5].

- *Laser Coating*

The surface coating process improves the mechanical properties of the materials. One of the alternatives to conventional methods used to coat metal surfaces is the laser sheath [6]. A laser is used as a source of energy to cover the surface of the metallic material [7]. The thickness of most laser surface coating operations varies from 0.1 to 2 mm [8].

Different alloys are used as coating materials in surface coating operations. One of these alloys is the cobalt-based Stellite alloy. It is widely used for dental and surgical implant materials, as well as for valves, turbine blades, exhaust pipes and similar industrial applications [9]. Of the various existing Stellite alloys, Stellite 6 is widely used in the industry. [16]

It has an approximate composition of Co-28Cr-4.5W-l. lC (% wt) [10]. The improved hardness through the formation of intermetallic compounds and mixed carbides can be obtained in the Stellite alloy [11]. Stellite alloys are often used in applications that require high wear and corrosion resistance at high temperatures [12]. Since Stellite alloys contain carbide in their microstructure, they have a high hardness. [16]

Surface coating alloys of Stellite are more expensive than other surface coating alloys. Despite their high cost, they are preferred due to their superior properties to other coating alloys [13, 14].

-*Welding*

Protective weld overlay coatings are particularly advantageous in terms of coating quality. Welding coatings are essentially immune to spallation due to a strong metallurgical bond with the substrate material, and by using powder blends, a wide range of alloys can be applied to achieve the best performance. in an erosive environment. [15]

III. COMPARISON METHOD

The coating process can be done with thickness of 0.1 - 2 mm by laser coating process which is one of the modern surface coating processes [18]. In addition to surface coating with laser welding, MIG-MAG (Gas), Plasma (PTA), Flush and Gas tungsten arc (GTA) welding methods are also frequently used. Surface coating with TIG welding is a frequently preferred application. It can be said that the TIG welding method is more preferable and the applicability of the method is easier and cheaper [19].

Stellite alloys are often used in applications where high corrosion and corrosion resistance are required under high temperatures. Stellite alloys have high hardness because they contain carbide. For this reason, the cost of Stellite surface coating alloys is higher than other surface coating alloys. Although it is costly, it is preferred due to its superiority over other coating alloys [14,20,21]. However, considering the cost of application method, TIG welding method is more economical than Laser coating. We will work to compare the findings of Stellite alloys after coating with two coating methods.

IV. DISCUSSIONS

In the first study, made by Serkan Apay and Behcet Gulenç in 2013, low carbon AISI 1015 steel was coated with a microdaser weld and cobalt based Stellite 6 welding alloy wire [16].

In the second study, made by Serkan Apay and Behcet Gulenç in 2013, low carbon AISI 1018 steel was coated with a TIG welding method and cobalt based Stellite 6 welding alloy wire [17].

Similar application steps were made in both different coating methods. Microhardness measurements were performed on the cross-sectional area of the coated surface. In addition, the materials were subjected to wear tests.

In this step, with the help of these two previous studies, the microlaser and TIG welding methods will be compared to each other with given tables and figures below.

Table 3. Chemical composition (% weight) of the AISI 1015 Steel and Stellite 6 wire [16].

Material (%)	C	Si	S	P	Mn	Ni	Cr	W	Fe	Co
AISI 1015	0,17	0,55	0,05	0,04	0,6	–	–	–	Bal.	–
Stellite 6 wire	1,27	1,13	–	–	–	2,02	28,41	5,71	3,59	Bal.

Table 4. Chemical analyzes of the coating material AISI 1018 steel and Stellite 6[17].

Material (%)	C	Si	S	P	Mn	Ni	Cr	W	Fe	Co
AISI 1015	0,18	0,51	0,04	0,05	0,61	-	-	-	98,61	-
Stellite 6 wire	1,27	1,13	-	-	-	2,02	28,41	5,71	3,59	57,87

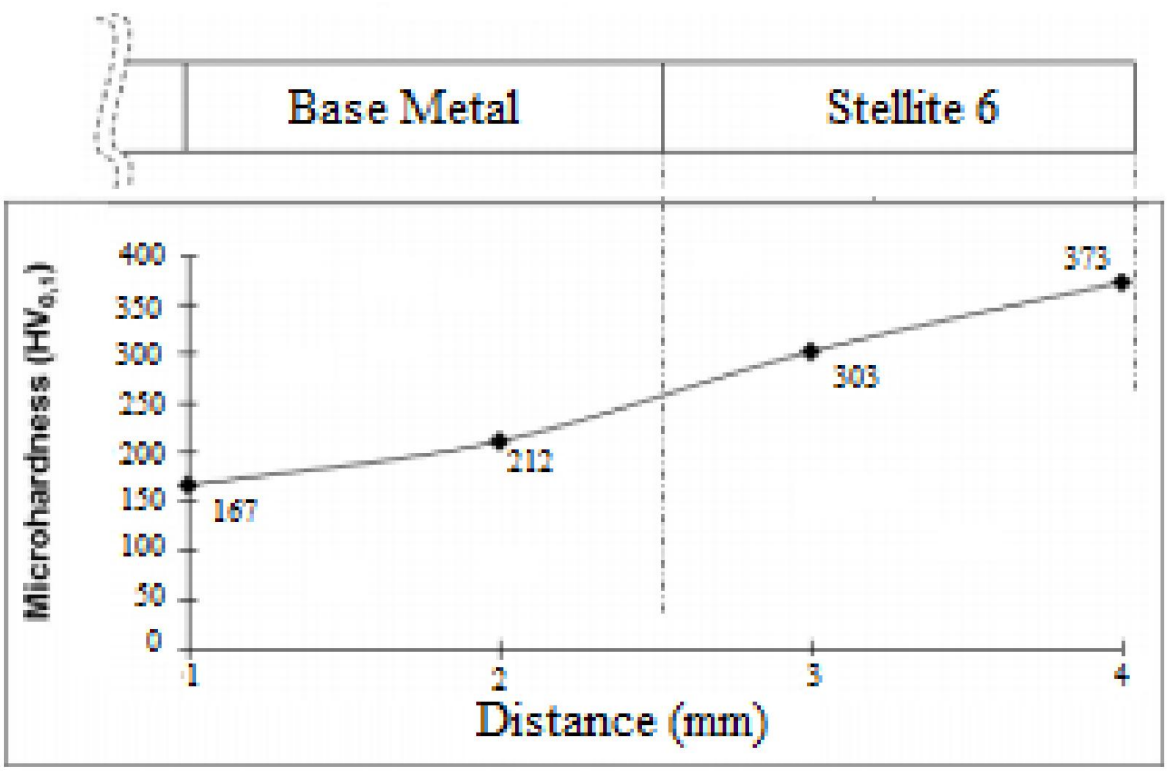


Figure 3. Hardness values of the specimens from the base material to coating surface. (AISI 1015- Microlaser) [16].

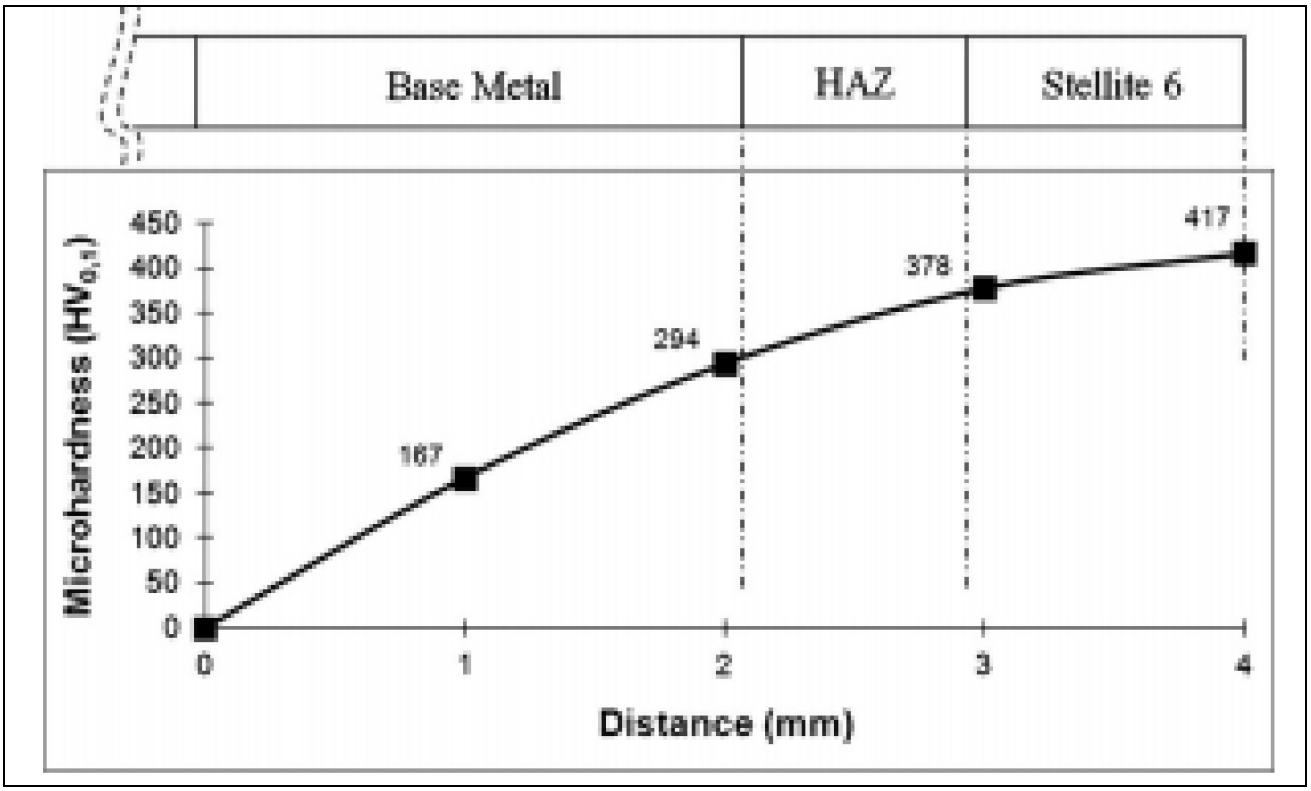
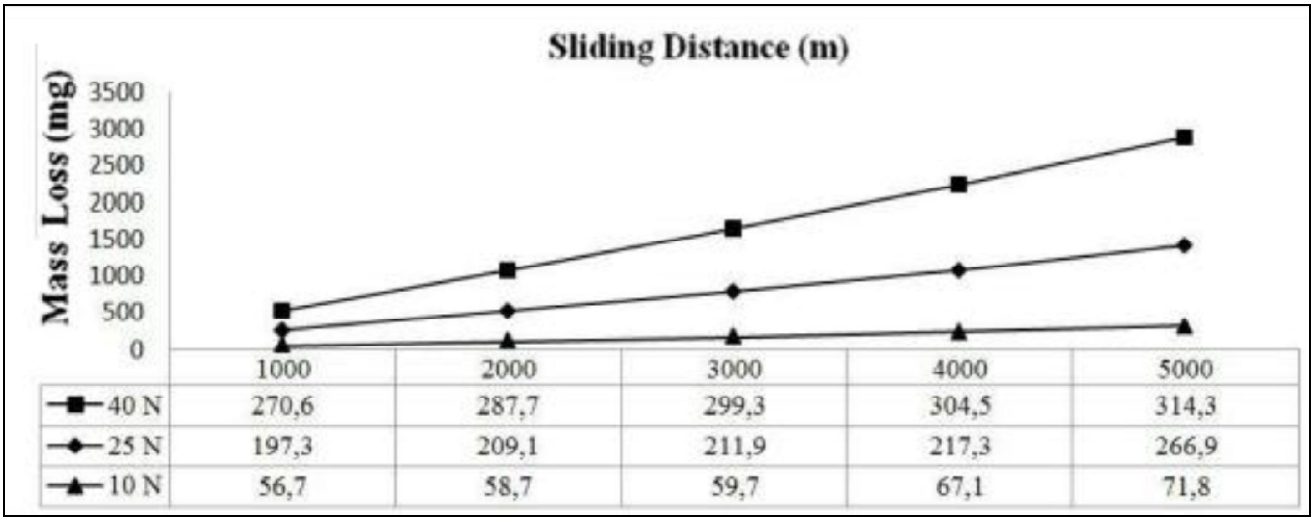
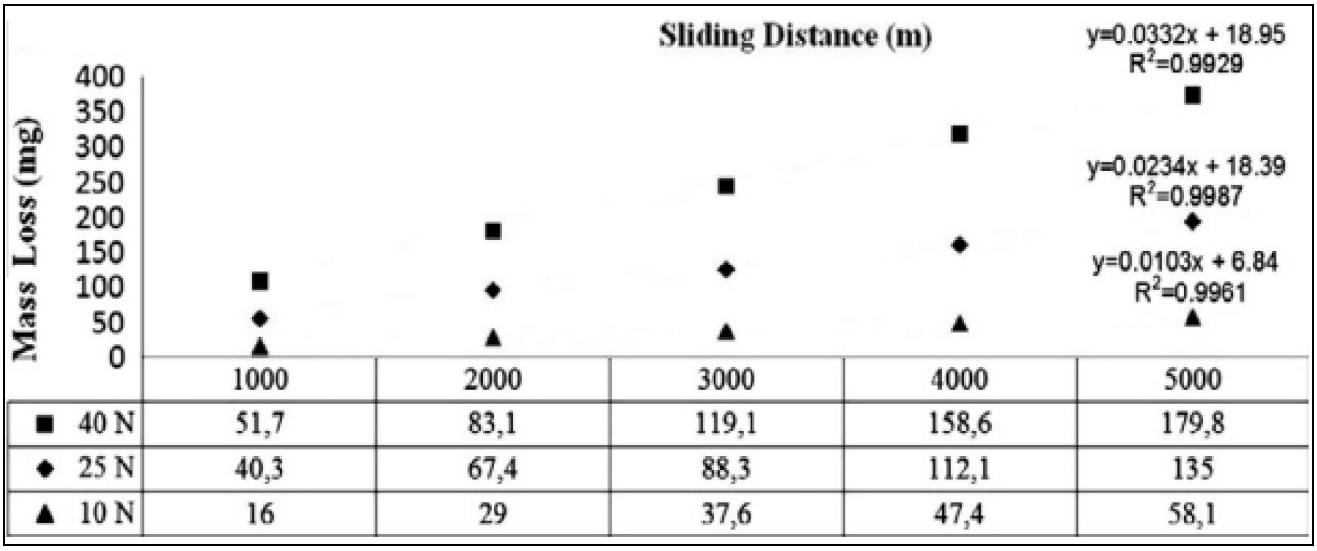


Figure 4. Hardness values of the specimens from the base material to coating surface. (AISI 1018- TIG) [17].



	1000	2000	3000	4000	5000
40 N	270,6	287,7	299,3	304,5	314,3
25 N	197,3	209,1	211,9	217,3	266,9
10 N	56,7	58,7	59,7	67,1	71,8

Figure 5. Results of the wear test. (AISI 1015- Microlaser) [16].



	1000	2000	3000	4000	5000
■ 40 N	51,7	83,1	119,1	158,6	179,8
◆ 25 N	40,3	67,4	88,3	112,1	135
▲ 10 N	16	29	37,6	47,4	58,1

Figure 6. Results of the wear test. (AISI 1018- TIG) [17].

V. CONCLUSION

In the first study, AISI 1015 low carbon steel was coated with cobalt-based Stellite 6 alloy welding wire using microlaser welding. In the second study, AISI 1018 low carbon steel was coated with cobalt based Stellite 6 alloy additional wire by TIG welding method from different hard surface coating methods. The evaluations of the comparison of these two studies are given below. [16-17]

1-AISI 1015 and AISI 1018 steels were found to be able to be coated with Stellite 6 alloys with Microlaser and TIG welding methods under normal atmospheric conditions without any precautions and pre-annealing. [16-17]

2-However, in the TIG welding method, the coating surface hardness was found to be harder than that of the Mikrolaser method. [16-17]

3- In both studies, it was observed that wear losses were increased due to the increase in the amount of load applied in abrasive wear tests under 10N, 25N and 40N loads. However, it appears that the wear losses in the Mikrolaser coating method are much higher. [16-17]

In this study, the hardness and wear results of the specimens subjected to the Stellite 6 alloys coating with two different methods for two different structural steel qualities and under similar conditions were given. When the results are interpreted, it is predicted that the Stellite 6 alloys will give different surface hardness values depending on the coating method. For this reason, maximum coating hardness obtained by coating Stellite 6 alloys on structural steels with different methods from these coating methods should be investigated.

REFERENCES

[1] Holmaberg K., Matthews A. (1994).” Coatings Tribology: Properties, Mechanisms, Techniques and Applications in Surface Engineering” Great Britain.

[2] Schneider K., Grünling H. W. (1983). Mechanical Aspects Of High Temperature Coatings*. Thin Solid Films: Volume: 107, pp. 395-416.

[3] Mendez P. F., Barnes N., Bell K., Borle S.D., Gajapathi S. S., Guest S. D., Izadi H., Gol A.K., Wood G. (2014), “Welding Processes For Wear Resistant Overlays” Journal of Manufacturing Processes:16, pp. 4–2.

[4] Burnell J.S., Datta P.K. (1996).” Surface Engineering Casebook “England: Cambridge Woodhead.

[5] Kahraman N., Gülenç B. (2002). Abrasive Wear Behaviour Of Powder Flame Sprayed Coatings On Steel Substrates. Materials and Design: Volume: 23, pp. 721-725.

[6] Toyserkani E, Khajepour A, Corbin S. Laser cladding. CRC Press; 2005.

[7] Steen WM, Mazumder J. Laser materials processing. London: Springer-Verlag Limited; 2010. p. 71.

[8] Frenk A, Vandyoussefi M, Wagniere JD, Zryd A, Kurz W. Analysis of the laser-cladding process for Stellite on steel. Metall Mater Trans B 1997;28B:501.

[9] Davis JR. Introduction, to cobalt and cobalt alloys, nickel, cobalt, and their alloys, ASM specialty handbook. Metals Park (OH): ASM International; 2000. 345–55.

[10] Frenk A, Kurz W. Microstructural effects on the sliding wear resistance cobalt-based alloy. Wear 1994;174:81–91.

[11] Malayoglu U, Neville A. Comparing the performance of HIPed and cast Stellite alloy in liquid–solid slurries. Wear 2003;255:181–94.

[12] Soboyejo WO, Sirivatsan TS. Advanced structural materials: properties, design optimization, and applications. CRC Press; 2006. p. 204.

[13] Yaz M, Çelik H. Co Esaslı Süper Alas_ımlar ile Kaplanan Düs_ük Karbonlu Çeliklerin Mikroyapı Incelemeleri (The Investegation Of Microstructure Hardfaced Low-Carbon Steels By Co Based Super Alloys). Dogu Anadolu Bölgesi Arastırmaları (Research Of Eastern Anatolian Region) 2006;4(2):42–8.

[14] Kashani H, Amadeh A, Ghasemi HM. Room and high temperature wear behaviors of nickel and cobalt base weld overlay coatings on hot forging dies.Wear 2007;262:800–6.

[15] Levin B.F., DuPont J.N., Marder A.R.,(1995). Weld Overlay Coatings For Erosion Control. Wear, 181-183, pp. 810-820.

[16] Apay S., Gülenç B. (2014). Wear Properties Of AISI 1015 Steel Coated With Stellite 6 By Microlaser Welding. Materials and Design: Volume: 55, pp. 1-8.

[17] Apay S., Gülenç B. (2013). AISI 1018 Çelik Yüzeyine GTA Yöntemiyle Stellıte 6 Kaplamanın Mekanik Özelliklere Etkisi. İleri Teknoloji Bilimleri Dergisi: Volume: 2, pp. 62-76.

[18] Frenk A., Vandyoussefi M., Wagniere J. D., Zryd A., Kurz W., Analysis of The Laser Cladding Process For Stellite On Steel, Metallurgical and MaterialsTransactions B, Volume 28B, 501, June 1997.

[19] Tosun, G., TIG Yöntemi Kullanılarak AISI 1010 Çeliğinin Yüzeyinde Oluşturulan Ni/WC Kaplamanın Metalurjik Uyum Karakterizasyonunun İncelenmesi, Mühendis ve Makina 52, 618:71-77, 2011.
[20] Çelik H., Osma A., Çimenoğlu H., Kayalı E. S., Kobalt Esaslı İki Alaşımın Yüksek Sıcaklıklardaki Aşınma Davranışları, 7. Uluslararası Metalurji ve Malzeme Kongresi, Ankara, 1993.
[21] Yaz M., Çelik H., Co Esaslı Süper Alaşımlar ile Kaplanan Düşük Karbonlu Çeliklerin Mikroyapı İncelemeleri, Doğu Anadolu Bölgesi Araştırmaları, 2006.

Most Efficient Use of Two Types of Electric Locomotives for Load Transportation

M. SERTSÖZ[1], M. FİDAN[2], M. KURBAN[3]
[1 and 2]Anadolu Üniversitesi Ulaştırma MYO, Eskişehir-Turkey, msertsoz@anadolu.edu.tr
[3]Bilecik Şeyh Edebali Üniversitesi Mühendislik Fakültesi, Bilecik-Turkey, mehmet.kurban@bilecik.edu.tr

ABSTRACT

Turkey is a quite developed and still developing country in terms of locomotive production within the structure of Tülomsaş and TCDD. Making production in this area makes a significant contribution both to the state economy and to the employment. However, the next phase after production has perhaps a greater importance than the production phase in terms of energy efficiency. Therefore, the fact that domestically produced locomotives are operated under energy-efficient conditions should be seen as a secondary and significant contribution to the national economy. For this reason, choosing the correct vehicle based on the load required to be carried, the speed and the ramp values is a significant problem of productivity.
There are too many locomotives produced, and in this declaration, the loads that can be carried by E43000 and E68000 electric locomotives at a certain slope value depending on the different speeds are determined. These information, which cannot be obtained directly from the locomotive catalog information, have been provided to the user as a reference.
In this way, the locomotives that are produced by our country are aimed to contribute to the economy and the environment by using again our country's energy economically (without reducing the load carrying performance).

Keywords: **-Railway Systems, Energy Efficiency, Locomotive Types, Load Transportation, Optimization.**

I. INTRODUCTION

The railway history of Turkey is quite deep-rooted. Since an English company laid the İzmir-Aydın rail line in 1980's, 157 years passed by and, excluding some periods of stagnation, the railway has a rapid progress in our country. Today, the projects in numerous number such as high speed train projects, national train projects, train equipments that we have produced without any external support and the Uraysim Project which allows us to approve our own test systems to be applied to the train equipments that we produce ourselves are like the proofs of the progress that we have made in recent year.

It is known that realizing the manufacturing of a technological equipment is not sufficient today. Because the necessity to use the produced technology in the most correct way is quite important particularly in terms of the life cycle and the energy efficiency of the equipment. The studies in this field in Turkey are unfortunately insufficient, especially when rail systems are considered in terms of energy efficiency. Using what we produce in rail systems in an efficient way -whereas, this field is very large- is a contribution as important as the contribution of domestic production to the country.

In this regard, this study seeks an answer to the question of how domestically produced E43000 and E68000 electric locomotives can be used more efficiently by taking the load, speed and ramp values as a basis. By this means, locomotives are allowed to operate in various operation conditions both most efficiently and the most economically. This study is a start and the contribution to the efficiency can be realized also for very different parameters of the locomotive.

II. LITERATURE SURVEY

A study which determines the maximum load that could be carried by the locomotives and the highest speed they can achieve was not exactly conducted in the literature. However, there are studies conducted in miscellaneous fields of rail systems in terms of the energy efficiency. It was observed in a study conducted by using SimuX simulation software that the energy consumption value increases 16,62 times in the event of the slope value changes from -5% to 5%, that's a 10% of increase. It was calculated that the regenerative braking energy effect makes a recovery in the rate of 14-15% at the test slope values. Since the vehicle decides, during the regenerative braking energy, where to or not to use regenerative braking energy, where to make mechanical and where to make electrical braking by means of its internal equipments, it is not possible to know its speed at that moment. On a road having 3-6% of slope, it was observed that the losses occurring in the transformer center vary between 2% to 10,4% depending on the distance of the catenary to the tractive force supply system and its resistance. It is clear that the energy consumption increases as the number of people (weight) and the slope increase. Apart from these, as the number of people increases, the amount of energy consumed per person decreases despite the increase in the amount of energy consumed, and the increasing number of people by the increase of the slope increases the amount of energy consumption more rapidly [1].

While there is no significant change in line voltage when an improvement in energy efficiency is desired, line losses are reduced and voltage stabilization is ensured in onboard energy storage [2]. With the use of onboard energy storage systems, the voltage drop across the pantographs, which are the current receiving points of the

vehicles, will be minimized (voltage drops are avoided by reducing the line current by more than 50%, sometimes by 80% [3]) and accordingly, a decrease that might occur in the performance of the vehicles will be prevented [4]. The studies show that theoretically, even about 40% of the total energy used can be obtained from the recovery of the braking energy, depending on the train operating frequency. It is reported that in the lines where trains are operated for 3 minutes and less, the most of the energy produced during braking is being used by other trains [5]. On the lines where trains are not operated frequently, most of the energy is burned in the resistances. In this context, it is estimated that considerable energy savings with respect to operating costs can be realized through energy storage technologies [6]. With the installation of several energy storage systems, it has been observed that a storage system saves 340,000 kWh of energy per year [7].

It is a fact that super capacitors increase the load, but a study has shown that they still provide energy savings despite increasing the load. This value varies between 23% and 26% depending on the number of ultra capacitor and the number of people used [8].

it has been observed in the studies conducted that the red signal lamps lead to significant braking energy losses. In this study [9], when the speed of a 300-meter-long train increases from 50 km/h to 110 km/h, it consumes 100 MJ more energy on a 100 km-long rail.

In studies conducted around the world for energy efficient driving, a 10% saving potential is predicted for all traffic types [10].

III. R/V DIAGRAM

The slope value that can be reached may be calculated in the event of the load or the speed is known by using the R / V (Ramp / Speed) diagram. For creating this diagram, the below equations are used.

$$re\,(k) = \frac{T - RL - RV}{GL + GV}\,(daN/ton) \quad (1)$$

$$rl = 0{,}65 + \frac{13{,}15}{P} + 0{,}00932 * V + \frac{0{,}004526 * A * V^2}{P * N}\,(daN/ton) \quad (2)$$

$$RL = rl * GL \quad (3)$$

$$rv = 2 + 0{,}057\,\frac{V^2}{100}\,(daN/ton) \quad (4)$$

$$RV = rv * GV \quad (5)$$

$$T = \frac{PTrac * 360}{V}\,(daN) \quad (6)$$

These six different equations help getting the third parameter through two known parameters. Briefly, thanks to the formulas, the slope at a certain load and speed, the speed at a certain load and slope, and the load at a certain speed and slope can be calculated.

Terminology

T: Traction of the locomotive
P: Axle Load
GV: Load to be carried by the locomotive
GL: Load of the Locomotive
N: Number of axles
V: Speed
A: Front Field of Vision
Ptrac: Traction Power
re(k): Slope Value

Table 1. Technical details of the Electric Locomotive named E68000 [11].

Main Characteristics	
Manufacturer	TCDD
Date of Production	2013-2015
Power	6800 HP 5000 kW
Weight of Locomotive	86 Ton
Axle Load	21,5 Ton
Axle Type	Bo Bo
Maximum Speed	140 km/h
Trac Size	1435 mm
Length	19800 mm
Catenary Type	AC 25 kV, 50 Hz
Engine Traction Power	AC 1280 kW

Table 2. Technical details of the Electric Locomotive named E68000 [11].

Main Characteristics	
Weight of Locomotive	120 t
Axle Type	Bo - Bo -Bo
Axle Load	20 t
Speed	90 - 120 km/h
Trac Size	1435 mm
Driver System	Transformatör + Konvertör + Çekiş Motoru
Traction Power	3180 kW, 4300 HP
Engine Traction Type	SE - 222 DC
Engine Traction Power	530 Kw
Catenary Type	Mono Phase 25 kV 50 Hz

Considering that the highest slope value of the railway line in Turkey is 26 ‰, the maximum load that can be carried at which speed that slope value can be covered is calculated by using the K / V equations. These tables are the tables for practical use for the user convenience.

Tablo 3. Bogie Types [11]

OO – OO BO-BO	2 Bogies, 4-axles, 4 traction motors

OOO - OOO CO-CO	2 Bogies, 6- axles, 6 traction motors
OOO - OOO A1A - A1A	2 Bogies, 6- axles, 4 traction motors
OO - OO - OO BO - BO - BO	3 Bogise, 6- axles, 6 traction motors

Table 4. Load restrictions of E68000 at Certain Speeds According to the 26‰ Ramp Value

Speed	Load
30 km/h	2229.3 ton
40 km/h	1663.3 ton
50 km/h	1319.1 ton
60 km/h	1084.9 ton
70 km/h	913.73 ton
80 km/h	782.22 ton
90 km/h	677.42 ton
100 km/h	591.57 ton
110 km/h	519.77 ton
120 km/h	458.71 ton
130 km/h	406 ton
140 km/h	360.37 ton

Table 5. Load restrictions of E43000 at Certain Speeds According to the 26‰ Ramp Value

Speed	Load
30 km/h	1439.4 ton
40 km/h	1087.8 ton
50 km/h	872.29 ton
60 km/h	724.75 ton
70 km/h	616.14 ton
80 km/h	531.97 ton
90 km/h	464.25 ton
100 km/h	408.19 ton
110 km/h	360.78 ton
120 km/h	320 ton

Getting a result expected in Table 4 and 5 seems numerically possible. This result is that the load carried at constant slope value will be reduced at increased speed. Along with witnessing this in the daily life, its reason can be explained by the physics formula given below. The force and time spent are constant, and this power reduces the system carried mass amount to meet the increased need for speed.

$$F = m\frac{v}{t} \quad (7)$$

Terminology

F: Force
m: Mass
V: Speed
t: Time

IV. GETTING THE OPTIMAL OPERATING CONDITIONS OF TWO DIFFERENT LOCOMOTIVES WITH RAMP CHARACTERISTICS

In this section, the aim is to find the most efficient load and speed value of the locomotive on a 26‰ road having the highest ramp value. For this purpose, since the speed and load units are different from each other, the graphics of which normalization process is carried out are intersected at first and then the de-normalization is carried out and the optimum speed and load values are obtained. It should be noted that the numerical values in the graphic are the expressions after normalization process. However before that, the process of normalization is briefly touched upon.

The normalization process, in other words disassembly, decomposition, that is proposed by the well-known French scientist Hubert Francesci is to decompose a large table comprised of too many columns and rows into sub-sets containing fewer rows and columns to avoid repetition. Another benefit of the normalization process is the ability to compare parameters having different units that need to be compared, since it eliminates the units.
The formula of the normalization process is as follows:

$$\text{Normalize X} = \frac{\text{X} - \text{Minumum Variable of the Series}}{(\text{Maximum Variable of the Series} - \text{Minumum Variable of the Series})} \quad (8)$$

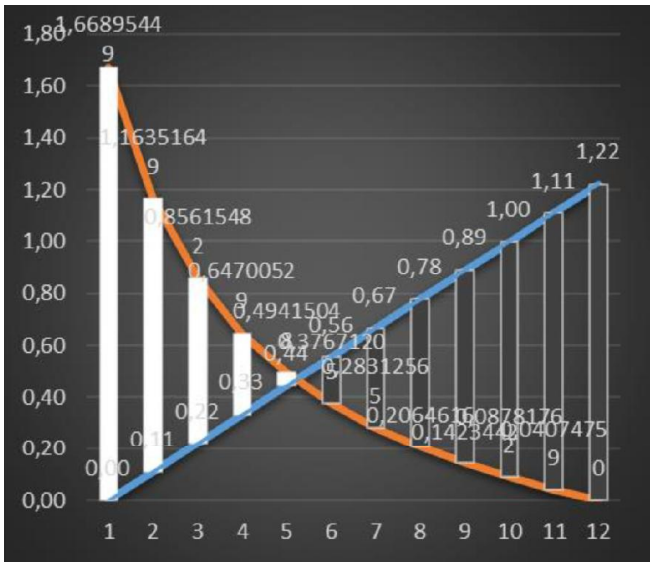


Figure 1. Load Intersection Graphic at 26‰ of Slope for E68000 (Blue: Speed and Orange: Load)

Whereas, the speed points at the slope value given for E68000 were found as 55-60 km/h, and the load was found between 1202-1319,11 tons. In order to be able to create efficient operating conditions, the studies must be conducted within these speed and load values.

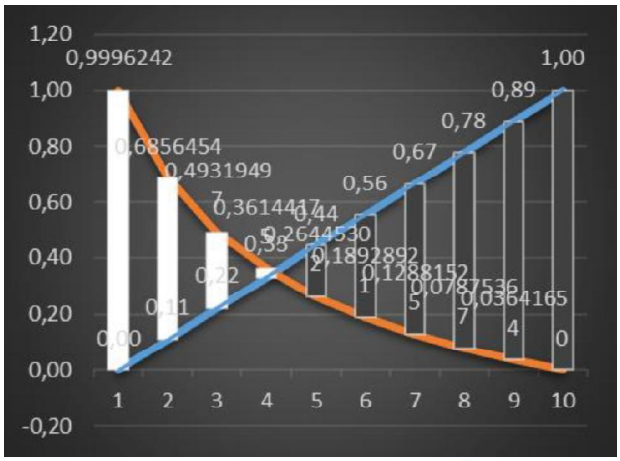


Figure 2. Load Intersection Graphic at 26‰ of Slope for E43000 (Blue: Speed and Orange: Load)

Whereas, the speed points at the slope value given for E43000 were found as 50-55 km/h, and the load was found between 798-872 tons. In order to be able to create efficient operating conditions, the studies must be conducted within these speed and load values.

When attention is attached to Figure 1 and Figure 2; for E43000 ten and for E43000 twelve different values are given. The reason of that is one has ten and the other has twelve different load and speed parameters. (see. Table 4 and 5)

V. CONCLUSION

In this study, the points where E43000 and E68000 operate most efficiently according to a slope value of 26‰ are determined. The speed points at the slope value given for E43000 were found as 50-55 km/h, and the load was found between 798-872 tons. The speed points at the same slope value given for E68000 were found as 55-60 km/h, and the load was found between 1202-1319.11 tons. Thus, if the locomotives carry these loads at that speed with a slope of 26 ‰, they will get the most efficient operation. As it is seen, these values need to be calculated separately for each locomotive.

This study can also be conducted for different slope values. For example, these work sheets can be created by determining the slope values on the route where a locomotive is used. Hereby, the item of economically using the available energy, that is the first step of the energy efficiency, will be fulfilled.

REFERENCES

1. Sertsöz M. (2012). *Raylı sistemlerde enerji verimliliği* (Yüksek Lisans Tezi). Kocaeli Üniversitesi Fen Bilimleri Enstitüsü. Kocaeli.
2. Barrero R., Mierlo J. V., Tackoen X., Improving energy efficiency in public transport: stationary supercapacitor based energy storage systems for a metro network, VPPC IEEE, 2008.
3. Iannuzzi D., (IEEE Member) Improvement of the Energy Recovery of Traction Electricel Drives using Supercapasitors, Electrical Engineering Department, Naples, Italy, 2008.
4. Gordon S.P., Rorke W.S., Energy Storage and Alternatives to Improve Train Voltage on a Mass Transit System, Sandia National Labs, Albuquerque, April 1995.
5. Albrecht T., Reducing power peaks and energy consumption in rail transit systems by simultaneous train running time control, Editors: Brebbia C.A.,Allan J., Sciutto G., Computers in Railways, 9nd ed., WIT Press, Newyork, 100-114, 2004.
6. URL-11: http://www.uitp.org/eupolicy/positions/2006/03/Climate_Change_EN (Ziyaret tarihi 15 Eylül 2012).
7. Gunselmann W., Godbersen C., Double-layer capacitors store surplus braking energy, Railway Gazette International, 2001, 1, 581.
8. Barrero R., Mierlo J.V., Tackoen X., Supercapacitors on-board light rail vehicles: enhanced energy storage systems for improved vehicle efficiency, Proc. IEEE/ASME Joint Rail Conference, Wilmington, April 2008.
9. Lehmann H., Hauser A., Mehrverbrauch im Eisenbahnbetrieb - Ursachen und Ermittlung, ZEVrail Glasers Annalen, 2002, 126, 41
10. ATOC, Energy Efficiency for Railway Managers, Editors: Bontinck W., Cox H., Process, Power, People, 1nd edition, UIC, Paris, 20-56, 2008.
11. http://www.tulomsas.com.tr/

Design and Analysis of Spur Gear Pairs Regarding Macro and Micro Profile Generation and Safety Standards

B. ŞAHİN[1] , A. AKPOLAT[2], N.YILDIRIM[3]

[1]Gaziantep University, Gaziantep/Turkey, buraksahin@gantep.edu.tr
[2]Gaziantep University, Gaziantep/Turkey, akpolat@gantep.edu.tr
[3]Gaziantep University, Gaziantep/Turkey, nyildir@gantep.edu.tr

Abstract - **Gears used in automotive vehicles and other power transmission units experience two kinds of stress mainly; contact stress at tooth surface and bending stress at tooth root. Gears are commonly designed and analyzed in terms of these two stress types based on well accepted gear formulas (such as Lewis, AGMA) and international standards (ISO, AGMA, DIN). Finite element analysis requires macro geometry of gear pairs. So generation of macro geometry of gears is very essential. Because gear tooth profile consists of involute and root (trochoid) portions and transition between these curves effects stress concentration.**

In this study, spur gear design alternatives are stated based on a predefined center distance back to back test gear box. Then one of alternative design is selected and it is analyzed in terms of tooth root bending stress and contact stress based on ISO by using a homemade software which is capable of designing and analyzing gears based on ISO, AGMA and DIN standards.

For macro geometry generation, firstly coordinates of involute and trochoid (root) portions of profile is generated by homemade software and then solid model is created by using Solidworks. FEA is performed by Marc whereas meshing is done by using SimXpert. This gives chance to make comparison between theoretical calculations and finite element analysis results.

Dynamic behavior of gears is important because of its relation with static and dynamic transmission error hence vibration and noise. Transmission error (TE) is considered to be an important excitation mechanism for gear noise and vibration. It is defined as the difference between the actual position of the output gear and the position it would occupy if the gears were perfectly conjugate. Designer needs to construct loaded transmission error curve, this gives him chance to simulate the quasi static behavior of gears at the design stage. It also allows the designer to design a proper tooth profile relief which produces a uniform motion transfer (with minimum TE) between driving and driven gear shafts. In this paper, micro profile of gear tooth is designed to minimize transmission error and TE curves under load are constructed by using TE module of homemade software.

Keywords - **Parallel axes gears, spur gear, design, analysis, transmission error, gear vibration, noise, gear standards.**

I. INTRODUCTION

Gears are one of the most important power transmission elements required to transmit both torque and motion between shafts. Macro and micro geometry of these crucial power transmission elements are very effective on static and dynamic performance. Static performance usually deals with global kinematic and geometric requirements and strength analysis of gear materials under load while dynamic performance usually deals with vibration and noise of gears.

Gears experience two kinds of stress mainly; contact stress at tooth surface and bending stress at tooth root. Gear tooth strength relates to the ability to resist tooth breakage under the effect of root bending stress; gear tooth surface durability relates to the ability to resist pitting under the effect of surface pressure between meshing teeth.

Due to a vast amount of parameters and complexity of gear and gearbox design, designers need to have a comprehensive knowledge of gearing supported by well accepted equations and design procedures such as Lewis bending equation, AGMA stress equation and other international standards. Some standards for parallel axes gears have been developed and presented by international organizations such as ISO (International Organization for Standardization) [1-5], AGMA (American Gear Manufacturers Association) [6-8], and DIN (Deutsches Institut für Normung) [9-13].

Checking these influences by manual calculation is slow and prone to errors. It requires turning back and changing any/suitable ones of design parameters to provide safe operation of gear pair. In such cases designer needs more and more time to redesign and check if operation is safe or not. These all increase the demand for gear design and analysis software that calculates and checks gear parameters, determines geometry, size and material properties, safety factors for surface contact stress, tooth root bending stress and scuffing resistance (if required) with high accuracy and minimum error in short time. Some commercial programs such as KISS Soft, Dontyne, Zar, Excellent, AGMA Gear Rating Suite, MitCalc and Fairfield Gear Program are used in industry for gear design and analysis processes

Gears are subjected to dynamic loads as well as static loads during operation. High dynamic load can lead to fatigue failure and affect the life and reliability of a gear transmission. Dynamic behavior of gears is important because of its relation with static and dynamic transmission error hence vibration and noise.

Transmission error (TE) is considered to be an important excitation mechanism for gear noise and vibration. It is defined as the difference between the actual position of the output gear and the position it would occupy if the gears were perfectly conjugate. Designer needs to construct loaded transmission error curve, this gives him to chance to simulate the quasi static behavior of gears at the design stage. It also allows the designer to design a proper tooth profile relief which produces a uniform motion transfer (with minimum TE) between driving and driven gear shafts.

A user friendly in-house interface software has been developed [14] to perform following tasks:

- Creating gear macro geometry for Finite Element Analysis (FEA) task,
- Suggesting gear pair design alternatives based on geometrical limitations and working conditions,
- Analyzing selected gear pairs from design alternatives in terms of bending and contact stress based on international gear standarts,
- Designing tooth micro geometry and improving dynamic performance by minimizing transmission error.

Some case study results obtained by using this software and FEA are presented in this paper.

II. LITERATURE SURVEY

Literature survey based on gear standards, finite element method and transmission error analysis is presented below:

Based on Gear Standards

Panchal [15] has used Mathcad software to calculate geometry, hardness and stress parameters of spur gear pair by calculating Lewis form factor and AGMA geometry factor. Tooth root bending stress and surface contact stress were calculated by using Lewis and AGMA equations. Bending stress calculation results for AGMA and Lewis, surface contact calculation for Hertzian and AGMA were presented and compared at the end.

Cetinkaya [16] has prepared a computer program to design single step spur gear pairs in GWBASIC Language. Computer program has two sections; first section contains gear design simulation and the second is composed of shaft design and the ball bearing selection. DIN Norms were used to design gears.

Based on Finite Element Method

Karpat et al. [17] have developed a computer program in Visual Basic to size spur, helical, bevel and worm gears in terms of module values for surface contact and tooth root bending based on DIN gear standards. 2 D models of gears were developed in AutoCad 2000, Microsoft Excel, Bortland Pascal and Ansys were used to create 3 D model and this model was analyzed in Ansys.

Venkatesh et al. [18] have calculated bending stress and contact stress by using analytical and numerical methods. Modified Lewis beam strength method was used to estimate bending stress whereas contact stress calculation was performed according to modified AGMA contact stress method. 3-D model of helical gear was generated by using Pro Engineer Solid Modeling software. Contact and bending stresses were analyzed by Ansys. At the end, results were compared.

Based on Transmission Error Calculations

Yildirim et al. [19] have introduced a systematic approach and applied it to low contact ratio (LCR) spur gears first with some design regions and to high contact ratio (HCR) spur gears with some new and promising design regions and rules. Several smooth transmission error curves at different loads were shown to be possible for the relief designed, hence allowing a range of loads with uniform motion transfer. The advantages of HCRG over LCRG in terms of smooth TE curves and tooth load values were noted, and compared with experimental results.

Yildirim [20] has studied on investigation and reducing transmission error of high contact ratio and low contact ratio spur gears. Theoretical values were verified with experimental results.

III. CASE STUDIES

In the scope of this study, spur gears used on a back to back test gear rig are designed and analyzed by an in-house developed software based on international parallel axes gear standards presented by ISO.

DESIGN OF SPUR GEAR PAIR BASED ON ISO STANDARDS

Gears are designed alternatively by using software design module. Then one of them is selected and analyzed based on corresponding standard. Required design parameters and some other additional parameters such as material properties, surface quality, profile modification and geometrical constraints for spur gear pair are defined by designer (Table 1 and 2).

Spur gear pair is designed based on ISO by using the software depending on limitations for gear geometry and a safe operation during meshing. Design alternatives suggested by the software are presented in Table 3.

First and fifth of alternatives are given with profile shift coefficient by the software; this ensures that different reference center distance gears can be used for a predefined operating center distance. Remaining alternatives do not require profile modifications.

Sixth of these alternatives (yellow colored row) is selected and analyzed by using ISO analysis module for 32.0 mm face width instead of value given by design module as 31.42 mm by taking manufacturing difficulties into consideration.

Table 1: Required Design Parameters

Operating center distance	120	mm
Gear ratio	1.0	-
Power	42	kW
Rotational speed	2500	rpm

STRESS CACULATIONS BASED ON ISO STANDARDS

General influence factors, performance parameters for tooth root stress / surface contact stress and geometry parameters are calculated by using software. For analysis of selected design alternative, in-house developed software and Kiss Soft (commercial machine elements software) is also used, and results are presented in Tables 4-6 respectively.

Table 2: Required Design Parameters

Parameters	Pinion	Gear	Unit
Min factor of safety (contact)	2.0		-
Min factor of safety (bending)	2.0		-
Operating center distance	120		mm
Gear ratio	1.0		-
Power	42		kW
Rotational speed	2500		rpm
Normal pressure angle	20		deg
Driver	Pinion		-
Oil type	ISO VG 320		-
Pinion Shaft Type	ISO 6336-1 Figure E		-
Helix Modification	None		-
Contact Pattern	Optimal		-
Material	Case Hardened Wrought Steel		-
Material Type	Core hardness ≥25 HRC lower		-
Allowable contact stress	1550		MPa
Allowable bending stress	450		MPa
Quality	MQ		-
Surface Hardness	60		HRC

Table 3: Design alternatives for spur gears based on ISO

Parameter	Cases					
	1	2	3	4	5	6
T_p	17	20	24	30	34	40
T_g	17	20	24	30	34	40
m_n	7	6	5	4	3,5	3
x_1	0,0736	0	0	0	0,1473	0
x_2	0,0736	0	0	0	0,1473	0
CD_{ref}	119	12	120	120	119	120
ϕ_w	21,27	20,00	20,00	20,00	21,27	20,00
b_{cal}	43,98	43,98	36,65	33,51	29,32	31,42
$n_{contact}$	2,031	2,078	2,095	2,056	2,024	2,024
$n_{bending}$	4.542	5.082	5.337	5.451	5.204	5.311

Table 4: General influence factors for spur gears based on ISO

Parameter	Software	KISS soft	Unit
Application factor	1.0000	1.0000	-
Dynamic factor	2.0351	2.035	-
Face load factor (contact)	1.1834	1.183	-
Face load factor (bending)	1.1436	1.144	-
Transverse load factor (contact)	1.0000	1.0000	-
Transverse load factor (bending)	1.0000	1.0000	-

MACRO GEOMETRY GENERATION AND FINITE ELEMENT ANALYSIS

Gear geometry is also an important concern to provide uniform motion transfer. Mating teeth of gears acting against each other to produce rotary motion are similar to cams. When the tooth profiles are designed so as to produce a constant angular velocity ratio during meshing, these are said to have conjugate action.

Many tooth profile forms such as involute, cycloidal and circular can theoretically fulfill the basic requirements such as uniform motion transfer and constant angular velocity during gear meshing (conjugate action). Involute profile, which with few exceptions, is in universal use for gear teeth. It is insensitive to center distance change and allows different operating center distance without changing the velocity ratio.

Gear macro geometry generation (Figure 1) is an important concern both to check if gear meshing is safe or not and to generate a model for mesh generation and analysis in FEA.

Gear tooth profile (Figure 2) and coordinates of involute and trochoid (Figure 3) are generated by using homemade software.

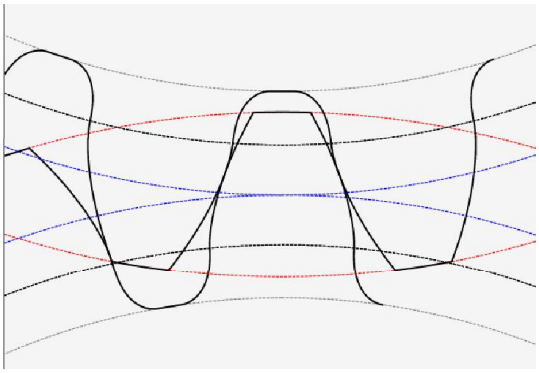


Figure 1: Gear Mesh (Software).

Table 5: Tooth root bending stress parameters for spur gears based on ISO

	Software		KISS soft		
Parameter	Pinion	Gear	Pinion	Gear	Unit
Life factor	1.000	1.000	1.000	1.000	-
Relative notch factor	0.997	0.997	0.998	0.998	-
Relative surface factor	1.107	1.107	1.107	1.107	-
Form factor	1.310	1.311	1.310	1.310	-
Tooth normal chord at root	6.399	6.399	6.400	6.400	mm
Radius of tooth root fillet	1.426	1.426	1.430	1.430	mm
Bending lever arm	2.964	2.964	2.960	2.960	mm
Stress correction factor	2.112	2.112	2.110	2.110	-
Size factor	1.000	1.000	1.000	1.000	-
Contact ratio factor	0.688	1.000	-		
Deep tooth factor	1.000	1.000	-		
Helix angle factor	1.000	1.000	-		
Rim factor	1.000	1.000	1.000	1.000	-
Nominal stress number	450.0	450.0	450.0	450.0	MPa
Nominal tooth root stress	77.09	77.09	77.08	77.08	MPa
Tooth root stress	179.4	179.4	179.4	179.4	MPa
Tooth root stress limit	993.8	993.8	993.8	993.8	MPa
Permissible tooth root stress	469.9	469.9	496.9	496.9	MPa
Factor of safety (tooth)	5.539	5.539	5.54	5.54	-

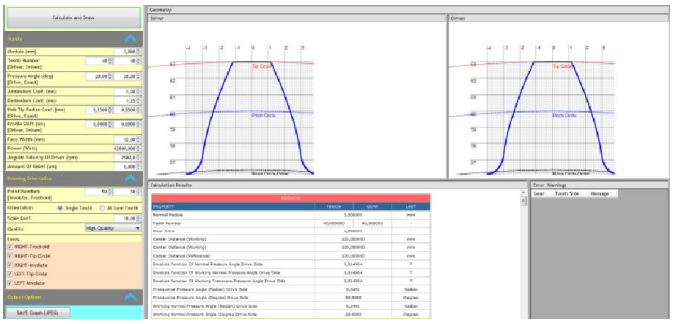


Figure 2: Software Interface and Gear Tooth Profiles.

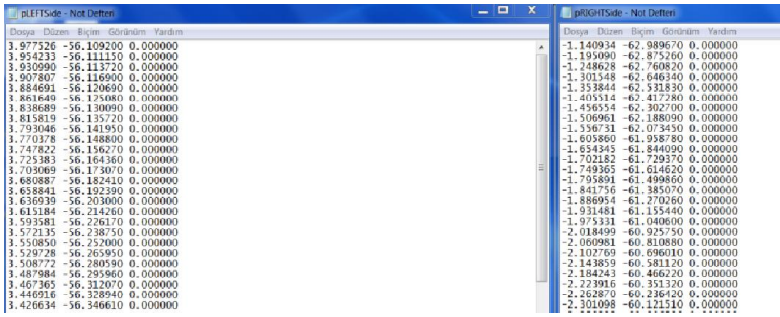


Figure 3 Coordinates of Gear Geometry

2D and 3D solid models are obtained by Solidworks (Figure 4-6).

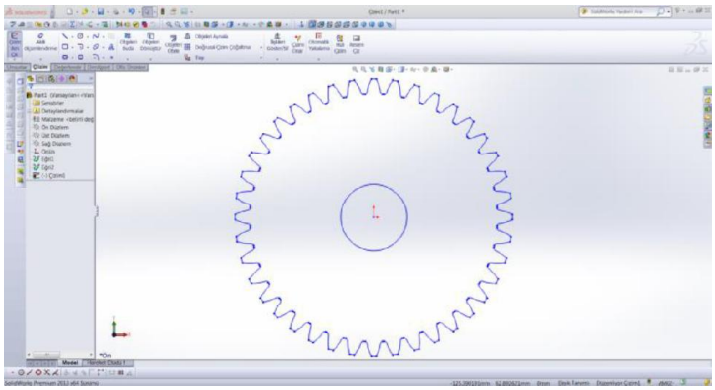


Figure 4 Gear Model Created in Solidworks

	Software		KISS soft		
Parameter	Pinion	Gear	Pinion	Gear	Unit
Life factor	1.0000	1.0000	1.0000	1.0000	-
Single pair tooth factor	1.0019	1.0019	1.0000	1.0000	-
Velocity factor	1.0131	1.0131	1.013	1.013	-
Lubrication factor	1.047	1.047	1.047	1.047	-
Roughness factor	1.093	1.093	1.093	1.093	-
Work hardening factor	1.000	1.000	1.000	1.000	-
Size factor	1.000	1.000	1.000	1.000	-
Contact ratio factor	1.0000		0.8730		-
Zone factor	2.4946		2.4950		-
Helix angle factor	1.0000		1.0000		-
Elasticity factor	189.8117		189.812		-
Nominal stress number	1550	1550	1550	1550	MPa
Nominal contact stress	558.77	558.77	487.81	487.81	MPa
Tooth contact stress	868.7	868.7	758.5	758.5	MPa
Pitting stress limit	1797	1797	1797	1797	MPa
Permissible contact stress	898.5	898.5	898.5	898.5	MPa
Factor of safety (contact)	2.068	2.068	2.37	2.37	-

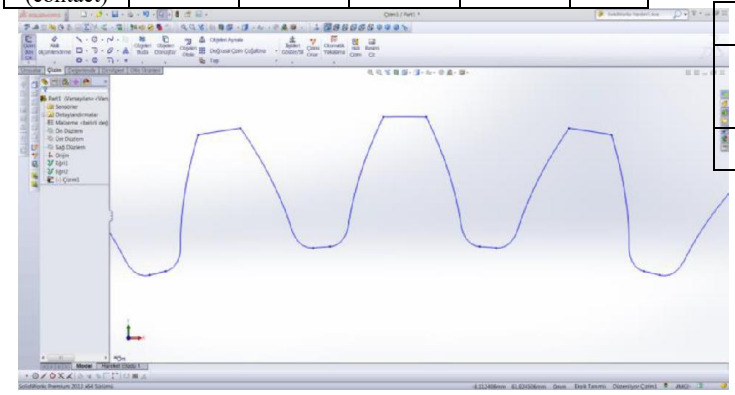


Figure 5 Gear Tooth Profile Created in Solidworks

Table 6: Surface contact stress parameters for spur gears based on ISO

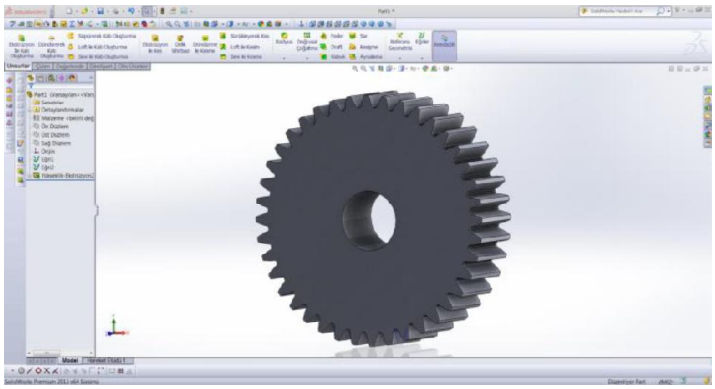


Figure 6 Solid Model of Gear Created in Solidworks

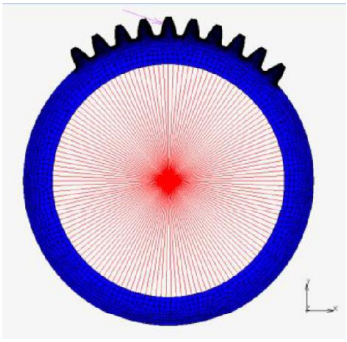
Gear model is analyzed by FEA software Marc. Boundary conditions (Figure 7a) and elements are given in Figure 7b and c. Result of FEA for nominal tooth root bending stress is given in Figure 8.

Contact stress model, boundary conditions and elements for finite element analysis are shown in Figure 9a and b.

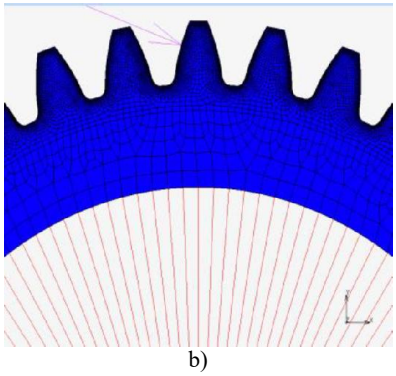
Stress values calculated by software, KissSoft and FEA are presented in Table 7.

Table 7 Comparison of Stress Values Calculated by Software and FEA

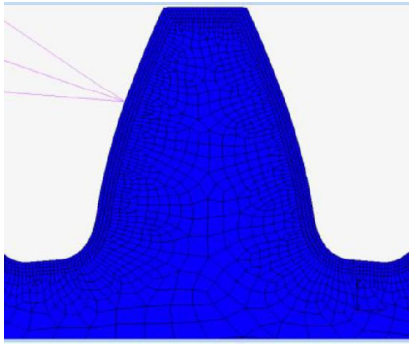
Stress Type	Software	KissSoft	FEA
Nominal Tooth Bending Stress (MPa)	77.1	77.0	78.8
Contact Stress (MPa)	868.7	758.5	933.2



a)



b)



c)

Figure 7 Boundary Conditions and Elements for Bending Stress Model

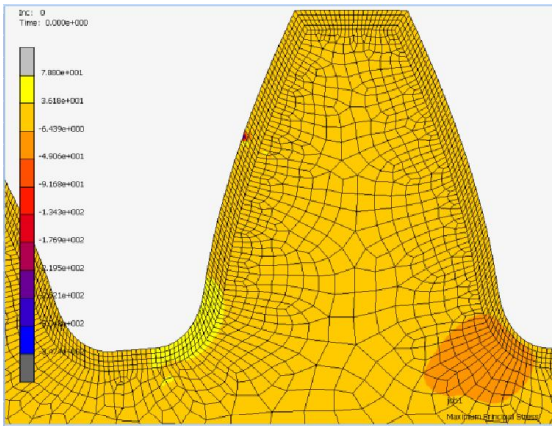
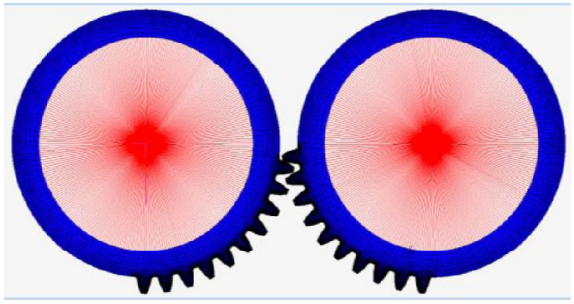
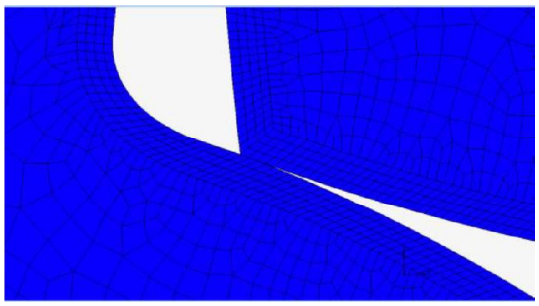


Figure 8 Tooth Root Bending Stress Model

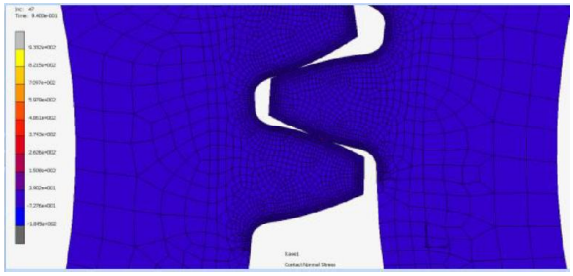


a)

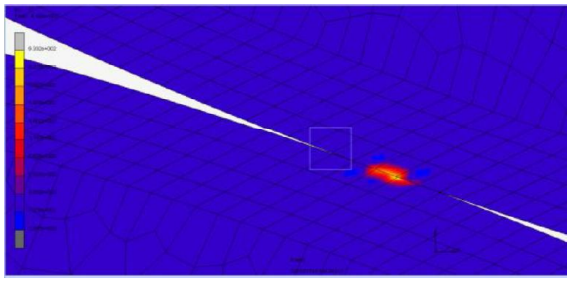


b)

Figure 9 Elements and Boundary Conditions for Contact Stress



a)



b)

Figure 10 Contact Stress

DESIGN OF MICRO GEOMETRY FOR MINIMIZING TRANSMISSION ERROR AND IMPROVING DYNAMIC PERFORMANCE

Transmission error (TE) is considered to be an important excitation mechanism for gear noise and vibration. Designer needs to construct loaded transmission error curve, this gives him chance to simulate the quasi static behavior of gears at the design stage. It also allows the designer to design a proper tooth profile relief which produces a uniform motion transfer (with minimum TE) between driving and driven gear shafts.

In scope of this study, micro profile of gear tooth is designed to minimize transmission error and TE curves under load are constructed by using TE module of homemade software.

Micro profile of gear tooth (selected sixth alternative from Table 3) is designed to minimize transmission error and TE curves under load are constructed by using TE module of homemade software. Long relief is applied to optimize loaded transmission error curve for design load. TE curves under load are presented in Figure 11 for different percentages of design load.

Peak to Peak Transmission Error values for different percentages of design load values are presented in Table 8.

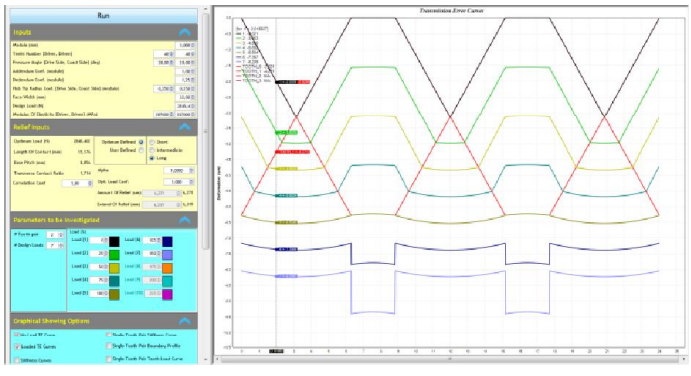


Figure 11 Loaded Transmission Error Curves

Table 8 Peak to Peak Transmission Error Values

Design Load Percentages	Peak to Peak Transmission Error (micron)
0 %	3.2
25 %	2.4
50 %	1.7
75 %	1.0
100 %	0.3
125 %	0.7
150 %	1.4

IV. CONCLUSION

Design and analysis of gears regarding both geometry and strength is a crucial step towards manufacturing and testing. An in-house software having different modules of macro geometry generation, alternative design suggestions, mechanical design based on international gear standarts, tooth profile micro geometry design and static transmission error construction has been developed and compared with some other design tools available. The results generated by the software were compared with other sources and reasonable agreement has been stated.

.

REFERENCES

[1] ISO. International Organization for Standardization. (2006). Calculation of load capacity of spur and helical gears - Basic principles, introduction and general influence factors. 6336-1. Geneva, Switzerland.

[2] ISO. International Organization for Standardization. (2006). Calculation of load capacity of spur and helical gears - Calculation of surface durability (pitting). 6336-2. Geneva, Switzerland.

[3] ISO. International Organization for Standardization. (2006). Calculation of load capacity of spur and helical gears - Calculation of tooth bending strength. 6336-3. Geneva, Switzerland.

[4] ISO. International Organization for Standardization. (2006). Calculation of load capacity of spur and helical gears - Strength and quality of materials. 6336-5. Geneva, Switzerland.

[5] ISO. International Organization for Standardization. (2006). Calculation of load capacity of spur and helical gears - Calculation of service life under variable load. 6336-6. Geneva, Switzerland.

[6] AGMA. The American Gear Manufacturers Association. (2010). Cylindrical gears-Fundamental Rating Factors and Calculation Methods for Involute Spur and Helical Gear Teeth. 2101 D04. Virginia, USA.

[7] AGMA. The American Gear Manufacturers Association. (1998). Method for Specifying the Geometry of Spur and Helical Gears. 913 A98. Virginia, USA.

[8] AGMA. The American Gear Manufacturers Association. (1999). Geometry Factor for Determining the Pitting Resistance and Bending Strength of Spur, Helical and Herringbone Gear Teeth. 908 B89. Virginia, USA.

[9] DIN. The German Institute for Standardization. (1987). Calculation of load capacity of cylindrical gears - Introduction and general influence factors. 3990-1. Berlin, West Germany.

[10] DIN. The German Institute for Standardization. (1987). Calculation of load capacity of cylindrical gears - Calculation of pitting resistance. 3990-2. Berlin, West Germany.

[11] DIN. The German Institute for Standardization. (1987). Calculation of load capacity of cylindrical gears - Calculation of tooth bending strength. 3990-3. Berlin, West Germany.

[12] DIN. The German Institute for Standardization. (1987). Calculation of load capacity of cylindrical gears - Endurance limits and material qualities. 3990-5. Berlin, West Germany.

[13] DIN. The German Institute for Standardization. (1987). Calculation of load capacity of cylindrical gears - Calculation of service strength. 3990-6. Berlin, West Germany.

[14] Sahin B. 2014. Development of A User Friendly Interface Software For Design And Analysis of Paralel Axes External Gears Including Quasi-Static Transmission Error Calculations, Master Thesis, University of Gaziantep.

[15] Panchal J. K. 2012. Spur Gear Analysis Using Mathcad. The University of Texas At Arlington.

[16] Çetinkaya, K. 1989. Bilgisayar yardımı ile dişli kutusu elemanları tasarımı. Gazi Üniversitesi Fen Bilimleri Enstitüsü.

[17] Karpat F., Çavdar, K., Babalık F. C. (2010). Bilgisayar Yardımıyla Düz, Helisel, Konik ve Sonsuz Vida Dişli Mekanizmalarının Boyutlandırılması ve Analizi. SAÜ Fen Bilimleri Dergisi. 14, 39-44.

[18] Venkatesh, J., Murthy P. B. G. S. N. (2014). Design and Structural Analysis of High Speed Helical Gear Using Ansys. Int Journal of Engineering Research and Applications. 4, 01-05.

[19] Yıldırım, N. K., Munro, R. G. (1999). A Systematic Approach to Profile Relief Design of LCR and HCR Spur Gears. Proc Instn Mech Engnrs. 213, 551-562.

[20] Yıldırım, N. (1994). Theoretical and Experimental Research in High contact Ratio Spur Gearing. Ph.D. Thesis in School of Engineering. The University of Huddersfield School of Engineering.

Thermodynamic Comparison of Various Spray Dryers for Ceramic Industry

H. CAGLAYAN[1] and H. CALISKAN[2,3,*]

[1]Department of Mechanical Engineering, Graduate School of Natural and Applied Sciences, Usak University, Usak/Turkey, hasan6619@gmail.com
[2]Department of Mechanical Engineering, Faculty of Engineering, Usak University, Usak/Turkey, hakan.caliskan@usak.edu.tr
[3]Department of Mechanical Engineering, Kyung Hee University, Yongin/Republic of Korea, hakancaliskan@khu.ac.kr
*Corresponding author

Abstract **- Spray dryers are commonly used in many ceramic industries. Utilization of spray dryers instead of processes, such as grinding, moistening, grading, simplifies and accelerates the production process. Spray dryer evaporates the water in the sludge and obtains the necessary heat, combustion gases and heated air. Energy consumption of spray dryers is generally high. In ceramic factories, spray dryers are responsible 33% of the total cost. In this study, ground and wall tile dryers are used and their total natural gas consumption is 32% of the total energy consumption. The wall and ground tile dryers have 4000 kg/h and 8000 kg/h of water evaporation capacities; while their natural gas consumptions are 262.28 kg/h and 435 kg/h, respectively. In the heat production, the hot air, which is obtained by the chemical reaction of natural gas and air (ambient air and waste heat air), is carried into the spray dryer, and the water in the mud is evaporated. There is a big amount of energy loss in the dryers, during the heat transfer. The energy and exergy analyses are applied for the wall and ground tile spray dryers in a ceramic factory. The energy efficiencies of the wall and ground tile dryer are calculated as 7.9% and 8.4%, while the corresponding exergy efficiencies are found to be %27 and %28.63, respectively. It can be concluded that, optimization of the wall tile dryer is necessary to make the system efficient.**

Keywords **- Efficiency; Energy analysis; Exergy analysis; Spray dryer; Thermodynamic.**

I. INTRODUCTION

Drying process has recently been used in many sectors such as milk, cheese, ceramics, cement, fish oil, protein dust and coffee sectors. Since drying is an energy intensive process, it is very important to observe its energy consumption. For the ceramic and fish oil productions, the energy and exergy efficiencies of the dryers are affected by the density of the slurry, desired humidity, amount of drying air and ambient temperature. The energy and exergy analyses have been used as potential tools to optimize desiccant operation and design. [1-2]. Aghbashlo at al. [3] performed energy and exergy analyses on the fish oil process with spray dryer. The effects of drying air temperature and additives on energy efficiency, energy loss, exergy efficiency and exergy destruction were investigated. The energy and exergy efficiencies of the system at the drying air temperature of between 140°C and 180°C were found as between 7.48%-8.54% and 5.25%-7.42%, respectively.

In many analyses, exergetic improvement seems to be directly proportional to the increase in the potential temperature. Aviara at al. [4] studied energy and exergy analyses of starch drying in a tray dryer to assess the performance of the system in terms of energy and exergy consumption, losses and efficiencies, at different temperatures. The energy efficiency increased from 30% to 40%, and the efficiency of the exergy increased linearly, while exergy inflow, exergy outflow and exergy loss increased by increasing the drying temperature from 40°C to 60°C.

A number of calculation and simulation programs are used for designing spray drying process to make it understandable. Golman and Julklang [5] explored some recovery systems to improve energy use in the spray drying process. For this reason, it was predicted that the exhaust gas from the spray drier should be passed through the air-to-air exchanger and reintroduced into the system. With this method, it was envisaged to achieve 6% gain and 50% energy recovery in energy efficiency. It was simulated that if the flue gas was directly included in the system instead of the air-to-air exchanger, it would gain 34% in energy efficiency and 61% in energy recovery. Caglayan and Caliskan [6] performed energy, exergy and sustainability analyses on spray dryer, air-air heat exchanger and overall system for different ambient temperatures in ceramic factory. The cooling air obtained from the cooling zone of the kilns was exchanged with the flue gas obtained from the combustion zone in the air-air heat exchanger. The obtained hot air was used as a preheater in spray drier. It was determined that the exergy efficiency of the heat exchanger was inversely proportional, while the exergy efficiencies of the spray dryer and overall system are directly proportional to the dead state temperatures.

The waste heat recovery systems have been used to improve the energy utilization of the spray drying process. As a result, energy and exergy efficiencies are increased, and energy saving is achieved.

In this regard, this study differs from the previously conducted ones as follows: (i) the effect of energy and exergy

efficiency on the proportion of raw materials used in the production of two different granule types (wall and ground) and their density is investigated, (ii) the variation of the energy and exergy efficiencies of spray dryers at different capacities are investigated, (iii) this study helps to determine the design and optimum configuration of the spray dryers with waste heat recovery systems.

II. SYSTEM DESCRIPTION

Energy efficiency is an important factor in ceramic sector that has many drying processes. In this system, there are two kilns for wall tile production and three kilns for ground tile production. There are also spray dryers for wall and floor tile production. In addition, there are spray dryers with the production (granule) capacities of 9000 kg/h and 17700 kg/h for wall and ground tile productions, respectively. 150°C exhaust air (obtained from the cooling zone of the wall tile kilns) is increased to 172°C by performing heat exchange with the 200°C flue gas obtained from the combustion zone of the wall tile kilns at the exchanger. On the other hand, 177°C exhaust air is obtained from the cooling zone of the ground tile dryer. These hot airs from two different furnace types are sent to the heat generators of spray dryers. There are air entrances from two different parts of dryers. The primary air is called as combustion air, and secondary air is named to be transport air. The natural gas and primary air enter to the combustion chamber of the heat generator and a chemical reaction occurs; while the temperature is increased above 1000°C. The hot air generated by the combustion is transported to the drying zone by means of secondary air. A heat exchange happens between the primary and secondary airs during this transportation. For the wall and ground tile dryers, the total drying air (primary and seconder airs) temperature reaches 600°C and 550°C respectively. The mud sprayed by the nozzles (located on the ring mounted on the lower part of the spray dryer) exchanges heat with the hot air stream. The water on the mud is evaporated and becomes granule. The schematic layout of the spray dryers with waste heat recovery systems is shown in Figure 1.

Some of the assumptions: (i) The system is in a steady state condition. (ii) The combustion reaction is complete combustion. (iii) The kinetic and potential energies and fan pump powers are neglected. (iv) The dead state (reference) temperature is 30°C. (v) The specification of the spray dryers and contents of the materials are listed in Table 1.

The air/fuel ratio for combustion reaction is calculated as follows [7, 8];

$$\frac{m_{air}}{M_{air}} \Big/ \frac{m_{fuel}}{M_{fuel}} = \lambda \tag{1}$$

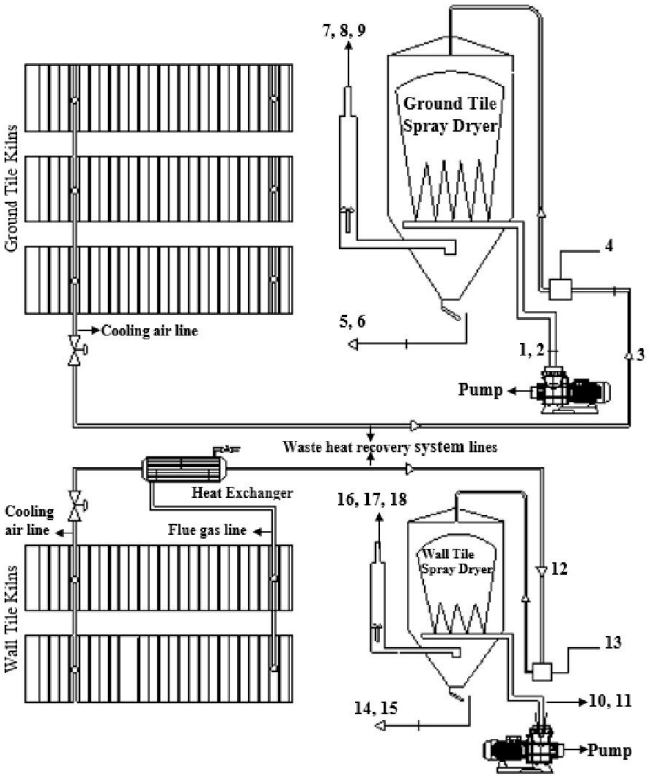


Figure 1: The schematic layout of the spray dryers with waste heat recovery systems

$$\frac{\left(\frac{\dot{m}_{N_2}}{M_{N_2}}+\frac{\dot{m}_{CO_2}}{M_{CO_2}}+\frac{\dot{m}_{H_2O}}{M_{H_2O}}+\frac{\dot{m}_{O_2}}{M_{O_2}}\right)}{\left(\frac{\dot{m}_{CH_4}}{M_{CH_4}}+\frac{\dot{m}_{C_2H_6}}{M_{C_2H_6}}+\frac{\dot{m}_{C_3H_8}}{M_{C_3H_8}}+\frac{\dot{m}_{C_4H_{10}}}{M_{C_4H_{10}}}+\frac{\dot{m}_{C_5H_{12}}}{M_{C_5H_{12}}}+\frac{\dot{m}_{N_2}}{M_{N_2}}+\frac{\dot{m}_{CO_2}}{M_{CO_2}}\right)}=\lambda \tag{2}$$

where "λ" is the air/fuel ratio (26.40). For this ratio, general combustion equation can be written as [9];

$$\begin{aligned}&(0.9194CH_4+0.0353C_2H_6+0.009C_3H_8+0.0038C_4H_{10}\\&+0.0011C_5H_{12}+0.026N_2+0.0048CO_2)+25.40(0.2059O_2\\&+0.7748N_2+0.019H_2O+0.0003CO_2)\\&\Rightarrow(3.154O_2+19.70N_2+2.49H_2O+1.050CO_2)\end{aligned} \tag{3}$$

III. ANALYSIS

The general energy balances of the wall and ground tile dryers can be written as follows [10-12]:

$$\begin{aligned}0=&\left(\dot{E}n_1+\dot{E}n_2+\dot{E}n_3+\dot{E}n_4\right)\\&-\left(\dot{E}n_5+\dot{E}n_6+\dot{E}n_7+\dot{E}n_8+\dot{E}n_9+\dot{Q}_{wd,loss}\right)\end{aligned} \tag{4}$$

where "$\dot{Q}_{wd,loss}$" is the heat loss rate of the wall tile dryer,

$$\begin{aligned}0=&\left(En_{10}+En_{11}+En_{12}+En_{13}\right)\\&-\left(En_{14}+En_{15}+En_{16}+En_{17}+En_{18}+Q_{gd,loss}\right)\end{aligned} \tag{5}$$

where "$Q_{gd,loss}$" is the heat loss rate of the ground tile dryer.

Table 1: Data of the inlet and outlet materials of the wall and ground tile dryers.

Components	State no.	Fluid type	Mass flow rate (*kg/s*)	Temperature T (*K*)
Wall tile dryer	1	Dry materials of slurry	8930	318.75
	2	Water in slurry	5023.13	318.75
	3	Cooling air of wall tile kilns	35871.52	445.15
	4	Fuel (natural gas)	262.28	306.15
	5	Masse (dry)	8930	321.15
	6	Humid masse	570	321.15
	7	Water vapor	4453.13	369.15
	8	Combustion flue gas	11212.28	369.15
	9	Other flue gas	24921.52	369.15
Ground tile dryer	10	Dry materials of slurry	16638	318.45
	11	Water in slurry	9358.88	318.45
	12	Cooling air of ground tile kilns	64521	450.15
	13	Fuel (natural gas)	435	306.15
	14	Masse (dry)	16638	324.45
	15	Humid masse	1062	324.45
	16	Water vapor	8296.88	372.15
	17	Combustion flue gas	1.297	372.15
	18	Other flue gas	64696	372.15

The energy rate of the content of fluid can be determined by [8];

$$En_i = En_i^{ph} + En_i^{ch} \tag{6}$$

where "*i*" means *i*th component.

The physical energy of all contents can be calculated as;

$$En_i^{ph} = m_i h_i \quad (h = cT) \tag{7}$$

where "h" is enthalpy.

The chemical energy of the fuel (natural gas) can be determined from [13]

$$E_{fuel}^{ch} = m_{fuel} LHV \tag{8}$$

where "*LHV*" is the lower heating value of the fuel.

For wall and ground tile dryers, the energy efficiency can be written as follows [14]:

$$\eta_i = \frac{\sum_{useful,output} En_i}{\sum_{input} En_i} 100 \tag{9}$$

$$\eta_{wd} = \frac{En_4 + En_5}{\sum En_{wd,in}} 100 \tag{10}$$

$$\eta_{gd} = \frac{En_{14} + En_{15}}{\sum En_{gd,in}} 100 \tag{11}$$

The general exergy balance of the wall and ground tile dryers can be written as follows [13]:

$$\dot{E}x_{wd,dest} = \left(\dot{E}x_1 + \dot{E}x_2 + \dot{E}x_3 + \dot{E}x_4\right) - \left(\dot{E}x_5 + \dot{E}x_6 + \dot{E}x_7 + \dot{E}x_8 + \dot{E}x_9 + \dot{E}x_{wd,loss}\right) \tag{12}$$

where "$\dot{E}x_{wd,dest}$" and "$\dot{E}x_{wd,loss}$" are the exergy destruction rate and exergy loss rate of the wall tile dryer, respectively.

$$\dot{E}x_{gd,dest} = \left(\dot{E}x_{10} + \dot{E}x_{11} + \dot{E}x_{12} + \dot{E}x_{13}\right) - \left(\dot{E}x_{14} + \dot{E}x_{15} + \dot{E}x_{16} + +\dot{E}x_{17} + \dot{E}x_{18} + \dot{E}x_{gd,loss}\right) \tag{13}$$

where "$\dot{E}x_{gd,dest}$" and "$\dot{E}x_{gd,loss}$" are the exergy destruction rate and exergy loss rate of ground tile dryer, respectively.

The exergy loss rate can be calculated by [15];

$$\dot{E}x_{loss} = \left(1 - \frac{T_0}{T_i}\right)\dot{Q}_{loss} \tag{14}$$

where"T_i"is the operating temperature.

The exergy rate of the content of fluid can be determined by [15];

$$\dot{E}x_i = \dot{E}x_i^{ph} + \dot{E}x_i^{ch} \tag{15}$$

where"$\dot{E}x^{ph}$" and "$\dot{E}x^{ch}$" are the physical and chemical exergy rates, respectively.

The general physical exergy rate is calculated as [8];

$$\dot{E}x^{ph} = \dot{m}_i\left[\left(h_i - h_0\right) - T_0\left(s_i - s_0\right)\right] \tag{16}$$

where "*s*" is entropy and "*0*" means dead state condition.

Physical exergy of gases is determined by [16];

$$\dot{E}x_{gas}^{ph} = m_i\left\{\left[c_{p,i}\left(\left(T_i - T_0\right) - T_0\ln\left(\frac{T_i}{T_0}\right)\right)\right] + RT_0\ln\left(\frac{p_i}{p_0}\right)\right\} \tag{17}$$

where "*p*" is pressure, and "*R*" is universal gas constant and "0" means dead state condition.

For physical exergy of solid bodies and liquids [16];

$$\dot{E}x^{ph} = \dot{m}_i \left\{ \left[c_{p,i} \left((T_i - T_0) - T_0 \ln\left(\frac{T_i}{T_0}\right)\right)\right] - v_m (p_i - p_0) \right\} \quad (18)$$

where is "v_m" signifies the specific volume.

For gas mixture, the specific chemical exergy can be calculated as follows [8, 12];

$$\overline{e}_{ex}^{ch} = \sum x_k' \varepsilon_k^{-0} + \overline{R} T_0 \sum x_k' \ln x_k' \quad (19)$$

where"x'" is mole rate, "ε_k^{-0}" is specific molar chemical exergy and "$\overline{R}$" is molar universal gas constant.

For fuel (natural gas), the total chemical exergy is found from [8, 15];

$$\dot{E}x_{natural\,gas}^{ch} = \left[\begin{array}{l} \dot{m}_{CH_4}\left(\frac{e_{ex,CH_4}^{-ch}}{M_{CH_4}}\right) + \dot{m}_{C_2H_6}\left(\frac{e_{ex,C_2H_6}^{-ch}}{M_{C_2H_6}}\right) + \dot{m}_{C_3H_8}\left(\frac{e_{ex,C_3H_8}^{-ch}}{M_{C_3H_8}}\right) \\ + \dot{m}_{C_4H_{10}}\left(\frac{e_{ex,C_4H_{10}}^{-ch}}{M_{C_4H_{10}}}\right) + \dot{m}_{C_5H_{12}}\left(\frac{e_{ex,C_5H_{12}}^{-ch}}{M_{C_5H_{12}}}\right) \end{array} \right] \quad (20)$$

The exergy efficiencies of the wall tile dryer "ψ_{wd}" and ground tile dryer "ψ_{gd}" can be calculated as [17];

$$\Psi = \frac{\sum_{useful,out} Ex_i}{\sum_{in} Ex_i} \quad (21)$$

$$\Psi_{wd} = \frac{Ex_4 + Ex_5}{\sum Ex_{wd,in}} 100 \quad (22)$$

$$\Psi_{gd} = \frac{Ex_{14} + Ex_{15}}{\sum Ex_{gd,in}} 100 \quad (23)$$

IV. RESULT AND DISCUSSION

Energy and exergy analyses are performed to wall and ground tile dryers in a ceramic factor, while environment temperature is 30°C. The Energy analysis results of the wall and ground tile dryer are tabulated in Table 2. The total energy input, output and loss rates of the wall tile dryer are calculated to be 10609.73 kW, 5588.92 kW and 5020.81 kW, respectively; while corresponding values are found to be 18748.57 kW, 4921.79 kW and 8566.59 kW for the ground tile dryer, respectively. Furthermore, the energy efficiencies of the wall and ground tile dryers are calculated to be 7.9% and 8.4%, respectively.

Exergy is defined as the maximum amount of work that can be produced by the flow of matter and energy, while becoming equilibrium with the environment. It is used as an effective method for the design and analysis of energy systems. The exergy analysis results of the wall and ground tile dryers are tabulated in Table 3.

According to the exergy analysis; the exergy input, output, loss and destruction rates are found to be 5268.01 kW, 2178.40 kW, 2191.95 kW and 897.67 kW, respectively; while these corresponding values are calculated to be 9123.71 kW, 3987.96 kW, 3604.14 kW and 1531.61 kW for the ground tile dryer, respectively. The exergy efficiency of the wall tile dryer is calculated to be 27%, while this value is determined to be 28.63%.

Table 2: Energy analysis results of the wall and ground tile dryer.

Fluid type	State no.	Wall tile dryer	State no.	Ground tile dryer
Dry materials of slurry (kW)	1	614.02	10	1142.94
Water in slurry (kW)	2	1868.42	11	3476.23
Cooling air of wall tile kilns (kW)	3	4657.63	12	8374.84
Fuel (natural gas) (kW)	4	3469.66	13	5754.56
Total energy input (kW)	-	10609.73	-	18748.57
Masse (dry) (kW)	5	623.38	14	1176.74
Humid masse (kW)	6	213.67	15	402.28
Water vapor (kW)	7	864.40	16	1623.61
Combustion flue gas (kW)	8	1240.74	17	2057.59
Other flue gas (kW)	9	2646.73	18	4921.76
Total energy output (kW)	-	5588.92	-	10181.97
Desired output energy (kW)	-	837.04	-	1579.02
Energy loss (kW)	-	5020.81	-	8566.59
Energy efficiency (%)	-	7.9	-	8.4

V. CONCLUSION

In this study, energy and exergy analyses are performed to the wall and ground tile dryers. The energy and exergy results of the dryers are compared. It is found that the energy efficiency of the wall tile dryer is 7.9%, while this values is found as 8.4% for the ground tile dryer. There is more energy loss in the wall tile dryer when the dryer's capacity and consumed energy are considered. Likewise, when compared to exergy efficiency; the efficiency of the wall tile dryer is lower than ground tile dryer. In general, there are considerable losses of energy and exergy in the system. So, the insulation of the dryers should be renewed or tightened to prevent heat losses. The combustion chambers of the dryers can be renewed or designs can be changed. By moving the combustion chambers upwards, the dryer air pipes of 12 meters (in length) can be shortened. The hot air of the dryer, around 95°C-100°C, can be used in the mud heating, building heating or water heating. In this way, the efficiency of spray containers can be improved.

Table 3: Exergy analysis results of the wall and ground tile dryer.

Fluid type	State no.	Wall tile dryer	State no.	Ground tile dryer
Dry materials of slurry (kW)	1	1393.21	10	2595.68
Water in slurry (kW)	2	72.07	11	134.06
Cooling air of wall tile kilns (kW)	3	267.17	12	522.26
Fuel (natural gas) (kW)	4	3535.56	13	5871.70
Total energy input (kW)		5268.01		9123.71
Masse (dry) (kW)	5	1394.87	14	2596.91
Humid masse (kW)	6	8.75	15	15.64
Water vapor (kW)	7	672.57	16	1246.17
Combustion flue gas (kW)	8	30.72	17	38.87
Other flue gas (kW)	9	71.48	18	90.37
Total exergy output (kW)		2178.40		3987.96
Desired output exergy (kW)		1403.62		2612.54
Exergy loss (kW)		2191.95		3604.14
Exergy destruction (kW)		897.67		1531.61
Exergy efficiency (%)		27		28.63

REFERENCES

[1] I. Dincer, A.Z. Sahin, "A new model for thermodynamic analysis of a drying process," *International Journal of Heat and Mass Transfer*, vol. 47, pp. 645-642, 2004.

[2] B. Golman, W. Julklang, "Analysis of heat recovery from a spray dryer by recirculation of exhaust air," *Energy Conversion and Management*, vol. 88, pp. 641–649, 2014.

[3] M. Aghbashlo, H. Mobli, S. Rafiee, and A. Madadlou, "Energy and exergy analyses of the spray drying process of fish oil microencapsulation," BIOSYSTEMS ENGINEERING, vol. III, pp. 229–241, 2012.

[4] N. A. Aviara, L. N. Onuoha, O. E. Falola and J. C. Igbeka, "Energy and exergy analyses of native cassava starch drying in a tray dryer," *Energy*, vol. 3, pp. 809–817, 2014.

[5] B. Golman, W. Julklang, "Simulation of exhaust gas heat recovery from a spray dryer," *Applied Thermal Engineering*, vol. 73, pp. 889–913, 2014.

[6] H. Caglayan, H. Caliskan, "Sustainability assessment of heat exchanger units for spray dryers," *Energy*, vol. 124, pp. 741–751, 2017.

[7] M. Gürtürk, H. F. Oztop, "Exergy analysis of a circulating fluidized bed boiler cogeneration power plant," *Energy Conversion and Management*, vol. 120, pp. 346–357, 2016.

[8] M. Gürtürk, H. F. Oztop, "Energy and exergy analysis of a rotary kiln used for plaster production," *Applied Thermal Engineering*, vol. 67, pp. 554–565, 2014.

[9] O. Balli, H. Aras, and A. Hepbasli, "Exergetic performance evaluation of a combined heat and power (CHP) system in Turkey," *International Journal of Energy Research*, vol. 31, pp. 849–866, 2007.

[10] Z. Utlu, Z. Sogut, A. Hepbasli and Z. Oktay, "Energy and exergy analyses of a raw mill in a cement production," *Applied Thermal Engineering*, vol. 26, pp. 2479–2489, 2006.

[11] Z. Utlu, A. Hepbasli, "A review and assessment of the energy utilization efficiency in the Turkish industrial sector using energy and exergy analysis method," *Applied Thermal Engineering*, vol. 11, pp. 1438–1459, 2007.

[12] M. Gürtürk, H. F. Oztop and A. Hepbasli, "Energy and exergy assessments of a perlite expansion furnace in a plaster plant," *Energy Conversion and Management*, vol. 75, pp. 488–497, 2013.

[13] D. Peinado, M. de Vega, N. García-Hernando and C. Marugán-Cruz, "Energy and exergy analysis in an asphalt plant's rotary dryer," *Applied Thermal Engineering* vol. 31, pp. 1039–1049, 2011.

[14] K. Taheri, R. Gadow, and A. Killinger, "Exergy analysis as a developed concept of energy efficiency optimized processes: The case of thermal spray processes," *Procedia CIRP*, vol. 17, pp. 511–517, 2014.

[15] M. Gürtürk, H. F. Oztop and A. Hepbasli, "Energy management and environmental aspects of a high capacity perlite furnace through exergetic analysis," *Energy Conversion and Management*, vol. 82, pp. 188–201, 2014.

[16] B. Anđelković, I. Krstić, "Aplication of exergetic analysis in the risk of technological systems and environmental protection," *Working and Living Environmental Protection*, vol. 4, pp. 31–39, 2007.

[17] A. Atmaca, R. Yumrutas, "Thermodynamic and exergoeconomic analysis of a cement plant: Part I – Methodology," *Energy Conversion and Management,* vol. 79, pp. 790–798, 2014.

The Comparison of Classical Thermostat and Controlled 3-way Valve Configuration in Engine Cooling System of SI Engine Application

G. KALTAKKIRAN[1], A. KALELİ[2], H.G. ZAVARAGH[3] and E. GÜNER[4]

[1] Atatürk University, Erzurum/Turkey, g.kaltakkiran@atauni.edu.tr
[2] Atatürk University, Erzurum/Turkey, arizakaleli@atauni.edu.tr
[3]Atatürk University, Erzurum/Turkey, hghz2005@gmail.com
[4]Atatürk University, Erzurum/Turkey, erdoganguner@atauni.edu.tr

Abstract - **In the most of cars wax type thermostats have been used in the engine cooling system. Thermostats shorten the engine warm-up time and improve engine performance by regulating the engine temperature. There has not been enough work in the literature. In this study, therefore, smart cooling system with3 way valve and wax type thermostats with wide use have been investigated for negative and positive effects on engine efficiency. In the study, the cooling system performance of a gasoline engine was examined according to 3 different conditions. First state, with wax type thermostat in various speeds and loads and second state, second without wax type thermostat in various speeds and loads and in the third state the mechanical thermostat was disassembled on the engine and replaced with a 3-way valve. However, a conventional proportional integral (PI) controller is designed to control the output temperature of the engine and the radiator outlet temperature. This controller regulates intelligent valve operations. The controller parameters are Kc and T. According to the results obtained, using the thermostat, warm-up time is shortened and fuel consumption is reduced. In addition, the pressure and temperature oscillations of the cooling fluid passing through the engine have increased sharply. Compared to the controlled and with thermostat engine cooling system results, a reduction of up to 4.33% in fuel consumption is achieved. The warm-up period decreased by at least 6.25% and maximum 18.84% in controlled cooling.**

Keywords – **Smart engine cooling system, Wax-type thermostat, Warm-up, Fuel consumption**

I. INTRODUCTION

In a vehicle engine, the starting and the warm-up periods are considered as critical time duration. Because in this time period, pollutant emissions and fuel consumption are higher than in other cases. For this reason, the reduction of the warm-up period is an important need. However, the engine warm-up time is closely related to the different techniques that can be applied on engine design, cooling fluid flow and temperature.

Compared with conventional engine components, the cooling system temperature monitoring can be improved and the parasitic losses can be reduced with computer controlled servo motor driven actuators. In a study, the control of the engine coolant temperature was investigated by controlling the radiator fan and a hydraulic cooling pump. This controller monitored the power consumption of the radiator fan and cooling fluid pump [1].

Numerous experiments have been carried out to compare the results on the thermostat and to find the optimum operating conditions in the cooling system. For example, electric double-sided valve, electric three-way valve, wax-type thermostat and no thermostat test were carried out respectively and the duration of the engine warm-up was investigated. Thermostat analyzes were performed with Fluent-CFD. The pressure contour, velocity contour and distributions of temperature were presented by simulation of the circulating coolant at thermostat [2].

The use of mechatronic components in thermal management systems is a promising technique for implementing real-time control strategies to improve engine performance. In this case, the servo-motor valve and pump can be used in the automotive cooling system to regulate the fluid flow. Thus, it is possible to examine these two actuators. In this thermal system, a model consisting of a heater, a radiator, a variable speed electric pump and smart thermostat is created to describe the behavior of the system. [3]. In addition to these studies, the effects of different cooling system configurations on the heating duration have been investigated. Cooling system models have been made, some changes for the engine cooling system have been simulated. Here, the optimal situation was chosen to control the reduction during warm-up, to analyze the benefits provided for fuel consumption and pollutant emissions. As a result, the duration of warm-up was reduced by 159 seconds with experiments, and both fuel consumption and significant reductions in pollutant emissions were achieved [4].

Regarding emissions, similar studies can be found. Engine performance, combustion characteristics and exhaust gas emissions produced under various operating conditions for a two-fuel (gasoline and CNG) engine with spark ignition have been investigated. In the tests conducted, emission values such

as THC, CO, CO2 and NOx and brake specific fuel consumption, heat release rate, fuel conversion efficiency, cylinder pressures and exhaust pollutant emissions were measured for both gasoline and CNG with both conventional and active engine cooling systems. This comparison resulted in low brake specific fuel consumption (3.53-5.82%) for both gasoline and CNG. Significant changes in NOx emissions have not been achieved. However, low THC, CO2 and CO emissions have been observed in active engine thermal management [5]. An analytical study of the pressure drop in a channel with a boiling flow for a different situation has been carried out and the effect of surface heat flux and flow velocity on total pressure drop has been investigated [6]. A lot of topics consisted heat transfer at radiator. Heat transfer at water jacket, under hood air flow and numerical modelling of engine cooling system were major topics [7].

II. EXPERIMENTAL SETUP AND TEST PROCEDURE

Experimental tests were carried out for three different situations on the engine test system. These situations: 1. Cooling system without thermostat, 2. Cooling system with wax-type thermostat, 3. Cooling system with control 3-way valve system. To test the performance of the cooling system, the test engine was tested for 15 minutes at 8 different speeds and loads. Tests 1 has been carried out without thermostat and test 2 has been carried out any change in the engine mechanics. In Test 3, experiments were carried out using only a 3-way valve that can be replaced by removing the mechanical thermostat. The data for all experiments are shown in Table 1.

Table 1. Engine speed and load information of 8 different experiments.

Test number	Engine speed (RPM)	Load (%)	Indicated by
No. 1	1500	15	Red
No. 2	2000	15	Orange
No. 3	2500	15	Green
No. 4	3000	15	Brown
No. 5	1500	30	Black
No. 6	2000	30	Blue
No. 7	2500	30	Violet
No. 8	3000	30	Gray

Experiments have been made use of the specially prepared Labview program to provide control over the throttle. With this program, the engine speed is constantly read and the speed is obtained by adjusting the angle of the throttle valve according to the manually entered value. The test setup consists of a gasoline engine, a control panel, a hydraulic dynamometer, measuring instruments, controllers and actuator equipment.

The technical specifications of the test engine, the detailed test setup are presented in Table 2 and Figure 1, respectively.

Table 2. Specifications of test set up engine.

Engine type	Ford MVH418, 4-Stroke, water cooling, fuel injected, spark ignition
Number of cylinders	4, Dohc-16V
Firing order	1-3-4-2
Bore diameter	80.6 mm
Stroke	88 mm
Total displacement	1796 cm3
Compression ratio	10: 1
Maximum power	93 kW @ 6250 R.P.M
Maximum torque	157 Nm @ 4500 R.P.M
Fuel	LPG – Gasoline

In this study, the cooling system in the present experimental apparatus is rearranged as shown in Figure 1 and 2. For the third state tests, the control mechanism of the controlled 3-way valve was established. In regulation, the existing thermostat was replaced by a control valve. In addition, a new system has been designed by placing the relevant sensors at the point to be measured. A controlled stepper motor is used to open and close the valve. The valve actuator has been replaced by an electric piston to perform the quick opening and closing operation. The valve can be opened and closed in a short time (approx. 2 sec). The engine revolution is determined by the engine temperatures at 4 points (at the radiator outlet, at the engine inlet, at the controlled valve inlet and at the control valve output). Parameters such as the flow rate of the mechanical pump fluid, the engine charge temperature, the open speed of the controlled valve, the reference temperature of the radiator output, the minimum and maximum temperature are regarded as control input parameters.

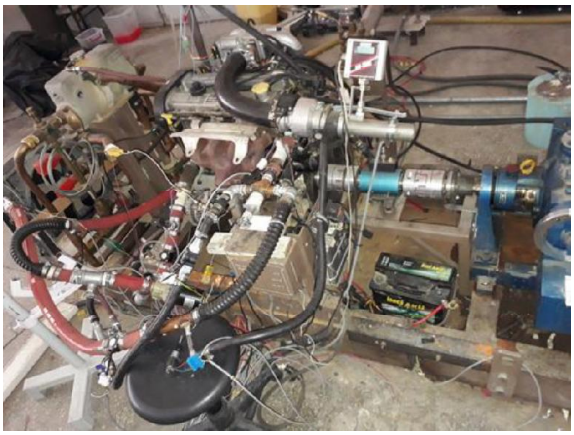


Figure 1: A picture of the laboratory test setup

The engine cooling system of the experimental study is shown in Fig. 2. Before the tests, the temperature of the test

engine and its components is equal to the ambient temperature. In addition, some hardware (sensors and measuring instruments, actuators, mechanical systems) and software (throttle valve control, evaluating data recording card of engine) equipment is required to keep the cooling system in check. A screenshot of the Labview software is shown in Figure 3.

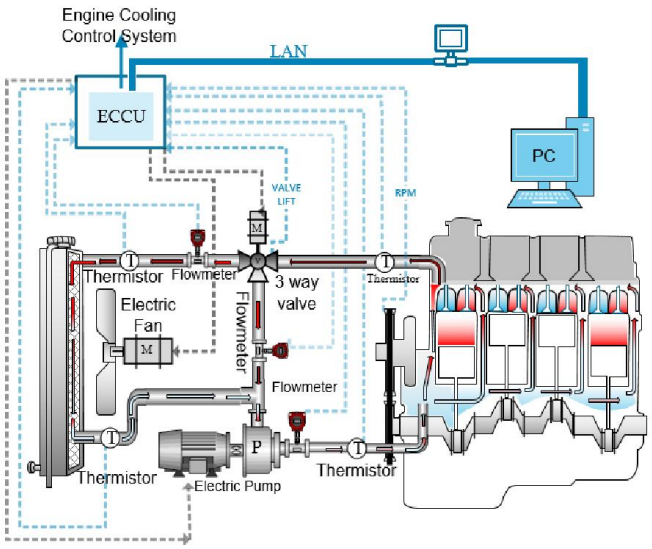


Figure 2: A schematic view of the desired experimental set up

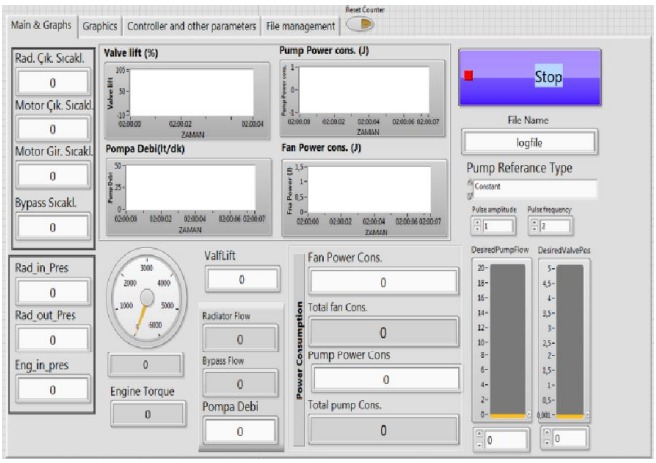


Figure 3: A shot screen of the designed program in Labview

With this program, torque, speed, fuel consumption, intake air flow, temperature changes and exhaust emission values are measured and recorded. The hydraulic dynamometer is used to simulate the actual operating condition of the engine in classical refrigeration systems at different loads (15%, 30%). A mechanical thermostat with a working temperature of 83°C was also used. High-precision fuel measure cysts (DFL3x-5bar) were used to measure fuel consumption. All experiments were carried out for 900 s. Experimental measurements were initiated when the cooling fluid temperature was about 25 ° C.

III. ANALYSIS

The effective parameters of the thermostat operation can be classified as follows: 1. Opening temperature, full opening temperature and maximum opening direction, 2. Thermostat water leakage, 3. Resistance, durability and strength at high and low temperatures, 4. Hysteresis and response time. This last condition is influential on engine warm-up time, engine emissions and fuel consumption. Taking the time constant factor for the reaction time of the thermostat, it is calculated as follows. For example, the minimum course value of zero is given to L_1 and maximum course value to L_2. Opening amount of thermostat course over the optional time is given to Lx and optional time to x (amount of this optional time should be between zero and the time duration of the full opening of the thermostat) and so time constant factor (T) can be obtained by calculating the (1).

$$L_x = (L_2 - L_1)(1 - e^{-\frac{x}{T}}) \quad (1)$$

where T is time constant factor. If this factor is found, the amount of opening of the thermostat for 1T, 2T, 3T hours can easily be obtained. For example, for the first 'time constant' (x=T), we have equation (2).

$$L_x = (L_2 - L_1)(1 - e^{-1}) \quad \Rightarrow \quad L_x = (L_2 - L_1) \times 0.63 \quad (2)$$

In this case, the thermostat opens 0.63 of the maximum amount of opening in the first "time constant".

The response time of the thermostat is very important when the engine is operating under different conditions and the temperature of the cooling fluid changes instantaneously at various loads and speeds. Thus, when the temperature changes from T_1 to T_2, the thermostat must change from L_1 to L_2 in motion. However, in wax thermostats, despite the sudden change in temperature, the movement does not change immediately and the late response of the thermostat is perceived as the actual response time of the thermostat. However, with a controlled valve this effect can be eliminated.

IV. CONTROL STRATEGY FOR COOLANT FLOW TEMPERATURE

A classical proportional integral (PI) controller is designed to control outlet temperature of the engine and outlet temperature of the radiator. This controller regulates valve operations. The valve opening position are given in the compact form as where u_0 is initial input in equation (3).

$$[H] = f(T_e, N, \text{the MAP by means of the estimated } Q_e \text{ and } Q_r + u_0) \quad (3)$$

The proportional, K_c and integral T gains are positive constants. Pattern search optimization algorithm which is utilized for selecting the optimal values of the proportional, K_c, and integral, T, gains parameters [8]. In this study, tracking norm error is defined as the objective function and 100 iterations were performed to obtain the optimal values of the controller parameters. The proposed strategy has been tested

with experiments in the engine test bed. The engine load, the engine speed, the fuel flow and the coolant pressure variables, the cooling fluid engine inlet and outlet temperatures for the without thermostat case are stored. Unknown Q_e and Q_r variables are estimated. The flow rate of the cooling fluid was then calculated and sent to the 3-way valve controllers. The controller block diagram is given Figure 4.

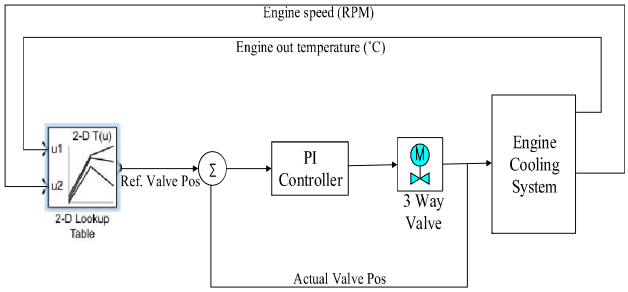


Figure 4: Controller block diagram

V. RESULTS AND DISCUSSION

To analyze the effects of the with thermostat, without thermostat and with 3-way valve on the cooling system and engine performance, the fuel consumption, warm-up time and cooling fluid temperature vibrations have been examined. In this study, all these parameters are compared as "“with and without thermostat cases" and 3-way controlled valve system case.

A. Cooling system without thermostat.

First, the changes in fuel consumption, which is the basic parameter, are measured. The results obtained from a total of 8 different experiments for the condition without thermostat are given in Figure 5.

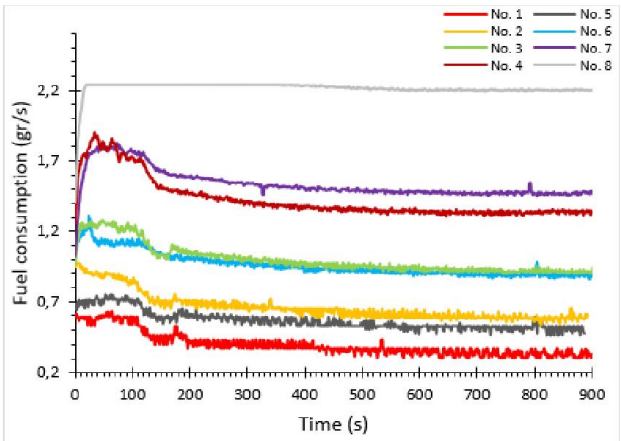


Figure 5: Fuel consumption in the state without thermostat

According to Figure5, except to No.8, the fuel consumption is maximum in the warm-up period and it falls after this warm-up period. However, high fuel consumption is a negative situation both in terms of economic and emissions. In experiment No. 8 (n = 3000 rpm - load = 30%) the engine is operating at maximum engine speed and load, so the warm-up is very short and therefore the effect on fuel consumption is clearly visible. When figure 5 is examined, it is understood that fuel consumption increases as engine speed and load increase in experiments. At 15% load, the average fuel consumption increased by 1.36% for every 500 speed increments. This showed an increase of 1.58% for 30% load. In constants speeds, with a load increase from 15% to 30%, average fuel consumption increases by 1.38%.

Another aspect that is examined in the cooling system experiments is the behavior of the temperature change during the test. In these experiments, the temperature of the coolant fluid was measured at four different points (engine inlets and outlets, radiator outlets and bypass outlets). The results obtained from experiments are presented in Figure 6. With the engine operated, the first 600 seconds of the engine is defined as the warm-up time. During this time the temperature is constantly increasing and is fixed at 75-95℃ degree band. When the temperature rises to 83˚C, the temperature is balanced by the fan operation. Because this experiment is carried out for a without thermostat situation, the four temperature results are similar and close to each other. In Figure 7, when the bypass temperature for all tests is taken into account, it is seen that as the engine speed and load increase, the warm-up time decreases rapidly.

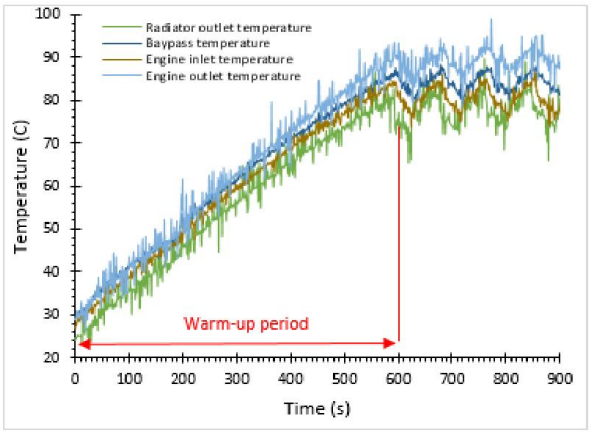


Figure 6: Temperature variations for without thermostat” state

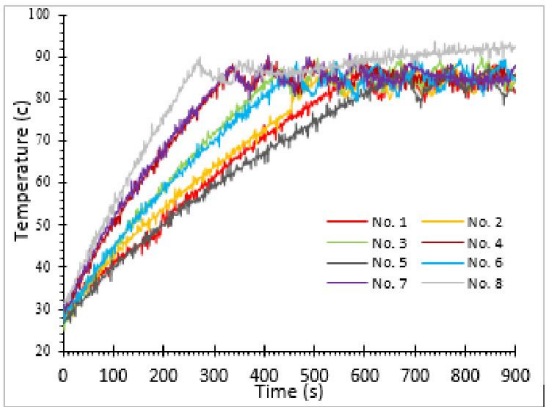


Figure 7: Bypass temperature in the “without thermostat” state

B. Cooling system with wax-type thermostat

In this test case, the effect on the engine cooling system was investigated by attaching a mechanical thermostat with working temperature 83˚C. The results obtained from a total of 8 different experiments for the condition with wax-type thermostat are given in Figure 8. As seems Figure 8, fuel flow rate is much higher in the warm-up period and decreases after the engine is warmed up like previous system. Compared to the two cases, the use of a mechanical thermostat in the cooling system has been shown to have a great influence on the reduction of fuel consumption.

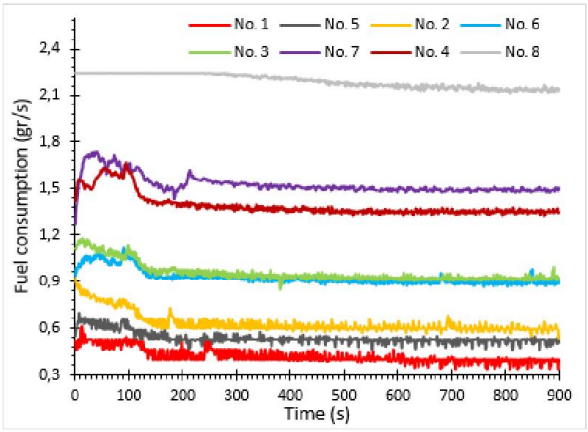


Figure 8: Fuel consumption in the state "with thermostat"

In Figure 9, the temperature of the coolant fluid was measured at four different points (engine inlets and outlets, radiator outlets and bypass outlets). Because of the thermostat, the behaviors of the engine and radiator outlet temperatures are different according to the condition without thermostat. The engine outlet temperature curve was steady until the thermostat was opened and showed similar behavior by approaching the bypass temperature after first opening.

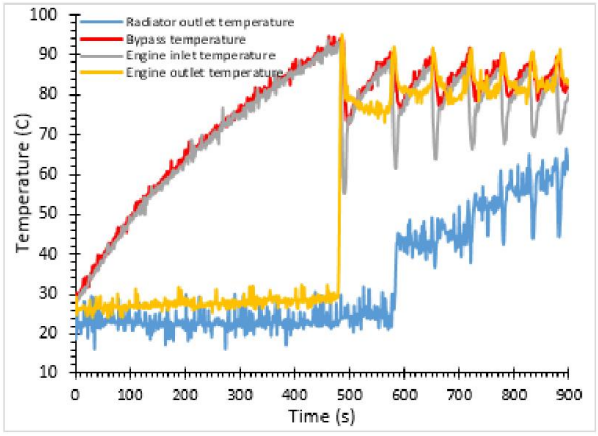


Figure 9: Temperature variations for "with thermostat" experiments

It has been shown in Figure 10 that the engine warm-up time depends on engine speed and load. This time was 400 seconds in the first test No.1 but 100 seconds in the last test No.8. In the wax-type thermostat cooling system, the bypass temperature curve has a band of 30˚C. In the without thermostat system this value is 16 ° C and this is a disadvantage of the high amplitude thermostat. By comparing the obtained results for all 8 experiments over warm-up period, it was observed that, thermostat installation cause to a reduction of the warm-up period between minimum of 40.8% and maximum of 66.32% for test number 1 and 3 respectively.

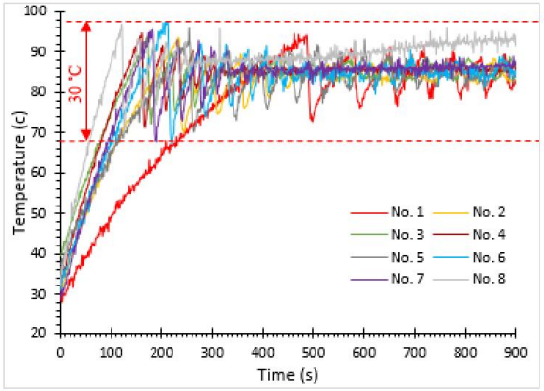


Figure 10: Bypass temperature in the "with thermostat" state

The variation of the engine inlet temperature, which is very variable in the conventional cooling system. At the first thermostat opening, curve oscillation wide is about 52˚C. Fluctuations in temperature can be a negative effect on fuel consumption. The engine outlet temperature temperature has a constant value before the thermostat opening. This temperature has a high increase with the opening of the thermostat and then it showed a swinging behavior at high temperature by opening /closing the thermostat. In this curve, it is observed that, how the warm- up period reduces with an increase in speed and load.

C. Control valve system configuration

Since there are a large number of graphs obtained for each experiment, only 6. test (n = 2500 - 30%) is presented as graphs and compared to the results of the "with thermostat" case experiments. These results show that the control system is compared with the classical system (with thermostat). In Figure 11, in the fuel consumption curve of the controlled system, the values of fuel consumption are close to each other due to the use of a different energy source rather than the battery used as the energy source of the fan. According to the results, in all eight experiments the engine in the conventional cooling system consumes excess fuel. The reason is that the mechanical pump is often designed for critical conditions and therefore the flow rate is too high. The controlled cooling system saves fuel consumption by a minimum of 1.3% and a maximum of 4.35% compared to the conventional system.

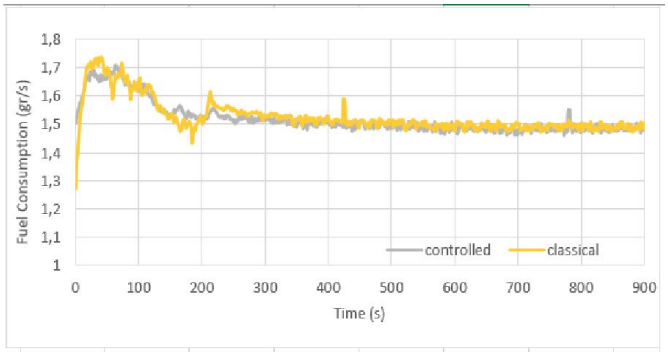


Figure 11: Fuel consumption ("with thermostat"-"controlled system")

Figure 12 shows the temperature changes at four different points of the engine of the 6th experiment. All three temperatures follow a steady state after the three fluctuations seen after the first opening of the controlled valve.

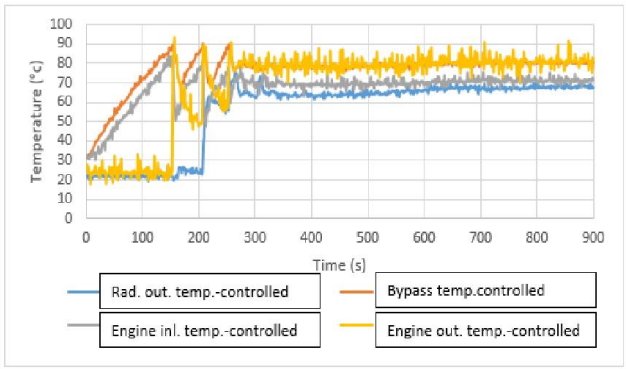


Figure 12: The temperature of the coolant fluid at 4 different points

In Figure 13, the curves of by-pass temperature are plotted in the classical and controlled conditions for the sixth experiment respectively. In a controlled system, the duration of warm-up of the engine is reduced when compared with the conventional system. The temperature and the duration in the unstable structural region until the temperature reached the stable structure showed a further decrease in the controlled system.

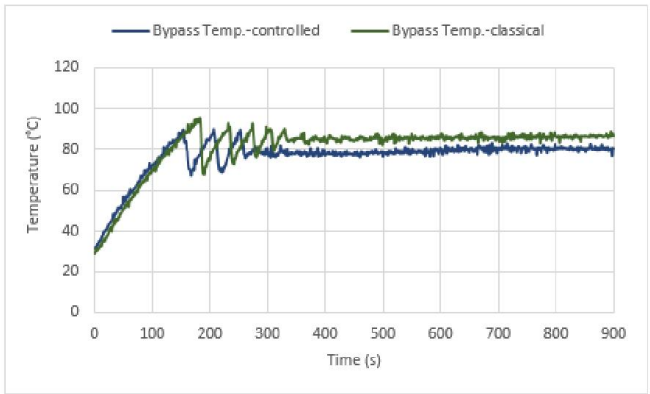


Figure 13: Bypass temperature "with thermostat"-"controlled system"

In addition, the radiator output temperature remains constant in the controlled system until the end of the warm-up period until the end of the test, but this temperature is increasing due to the non-optimum operation of the fan in the conventional system. Reduced warm-up time can reduce fuel consumption. For all eight experiments, the results of warm-up times in both cases (classic and controlled) were obtained. According to the results, in all controlled experiments, there was a serious decrease in the warm-up period. In controlled experiments a maximum reduction of 19% and a minimum of 6.2% was achieved during warm-up time.

VI. Conclusion

In this experimental study, the effects of thermostat and smart cooling system have been analyzed in the system in three states. These situations; 1. with thermostat, 2. without thermostat, 3. With3-way controlled valve. A conclusion section is not required. More fuel consumption in the warm-up period than steady state condition was observed in all tests. For every 500 rpm increase in speed, fuel consumption increases in average 1.36% and 1.58% for constant loads of 15% and 30% respectively. In constant engine speeds, with an increase in the load from 15% to 30%, average fuel consumption increases about 1.38%. In the case of "without thermostat", the temperature differences between the engine inlet, outlet, bypass outlet and radiator outlet cooling fluid are close to each other. On the other hand, in the "thermostat" case, these four temperature curves were completely different and the temperature difference at these points was very high. In addition, release behavior was observed at the cooling fluid temperature. This can be explained as a major disadvantage of using a thermostat. By adding a thermostat to the cooling system, a reduction of about 40.8% to 66.32% was achieved for No.1 and No.3 in the warm-up period. In the case of "with thermostat", a large oscillation of about 52 ° C occurred at the engine inlet temperature, which is described as a negative condition for engine cooling system performance. Compared to the results of the controlled and with thermostat state engine cooling system operation, fuel consumption is reduced in all eight experiments, which is a minimum of 1.19% and a maximum of 4.33%. The warm-up time decreased by a minimum of 6.25% and a maximum of 18.84% in controlled cooling.

Acknowledgment

This work has been supported by The Scientific and Technological Research Council of Turkey (TUBITAK, project no 315M260).

References

[1] M.H. Salah, P.M. Frick, J.R. Wagner, D.M. Dawson, "Hydraulic actuated automotive cooling systems—Nonlinear control and test," Control Engineering Practice, 17, pp. 609–621, 2009.

[2] L. Bai, Y. Li, M. Yang, "CFD Simulation Analysis for the Wax-type Thermostat, International Conference on Mechatronics," Electronic, Industrial and Control Engineering (MEIC), 2014.

[3] J. Wagner, V. M. Srinivasan, D. Dawson, "Smart Thermostat and Coolant Pump Control for Engine Thermal Management Systems," SAE Technical Paper Series, 0272-01-2003.

[4] A. J. Torregrosa, A. Broatch, P. Olmeda, C. Romero, "Assessment of the Influence of Different Cooling System Configurations on Engine Warm-

up, Emissions and Fuel Consumption," International Journal of Automotive Technology, Vol. 9, No. 4, pp. 447–458, 2008.
[5] E. Mohamed, "Development and analysis of a variable position thermostat for smart cooling system of a light duty diesel vehicles and engine emissions assessment during NEDC," Applied Thermal Engineering, 99, pp. 358–372, 2016.
[6] V. Edward, Jr. McAssey, A.S. Fleischer, "Engine Cooling System Stability", SAE Technical Paper Series, 2001.
[7] S.C. Pang, M.A. Kalam, H. H. Masjuki, M. A. Hazrat, "A review on air flow and coolant flow circuit in vehicles' cooling system," International Journal of Heat and Mass Transfer, 55, pp. 6295–6306, 2012.
[8] R. M. Lewis, V. Torczon, and M. W. Trosset, "Direct search methods: then and now," Journal of Computational and Applied Mathematics, vol. 124, no. 1–2, pp. 191-207, 2000.

Numerical Investigation of Inlet Turbulence Intensity Effect on Multiple Impinging Jets for High Jet-to-Jet Distance

P.ÇULUN[1], K. PIHTILI[2], N. ÇELİK[3]

[1] Bingol University, Bingol/Turkey, pculun@bingol.edu.tr
[2] Bingol University, Bingol/Turkey, kpihtili@bingol.edu.tr
[3]Firat University, Elazıg/Turkey, nevincelik@firat.edu.tr

***Abstract* - In this study, the effect of turbulence intensity (1%, 5%, 10%) on heat transfer coefficient is investigated for constant value of Reynolds number (*Re* = 15,000) jet-to-plate distance (Z_n/d = 4) and jet-to-jet pitch (X_n/d = 4, Y_n/d = 4)). To provide turbulence model validation, the effect of different turbulence models is also simulated. The results are compared with experimental results obtained from literature in similar parameters.**

Keywords – CFD, Impinging jet, heat transfer, turbulence intensity, array jet.

I. INTRODUCTION

The work to improve the magnitude of heat transfer in heating and cooling applications has been ongoing for many years. As it can be applied in heating systems, cooling systems and drying systems, a small improvement in heat transfer will be great in this sense. One of the main types of heat transfer processes is pulsed jet applications. Many studies in this area have focused on single jet applications. For this reason, it is possible to find sufficient research on single jets. At the same time, there are some experimental and numerical studies on various influences; however, efforts to assess the intensity of the input turbulence are very rare. When evaluating numerical studies in this area, multiple nozzles provide more homogeneous and even heat transfer compared to individual nozzles [1]. In addition, they are among the important topics of study in terms of being more economical than other heating and cooling systems. The drying of textiles and paper products, the shaping and tempering of glass, the protection of aircraft wings against icing, the cooling of turbine blades and electrical and electronic devices are areas where jets are applied [3-5]. Since insufficient research has been done in this regard, we must examine such numerical work to understand the effect of turbulence density and different turbulence models on the size of heat transfer.

In co-authors' previous work [6], the influence of the turbulence density for low jet-to-jet pitch ratio (X_n/d = 2, Y_n/d = 2) and jet-to-plate ratio (Z_n/d = 2) was examined. It was already seen that, the turbulence intensity has negligible effect on heat transfer behavior for the conditions considered. In this study numerical investigation has been done for higher jet-to-jet dimensionless distance $X_n/d = Y_n/d = 4$, jet-to-plate distance ($Z_n/d = 4$).

II. MATHEMATICAL MODEL AND GOVERNING EQUATIONS

In present numerical study, the flowing fluid is assumed to be air, which is considered to be incompressible and has 25°C temperature, 1 atm pressure. The commercial computational fluid dynamics software code CFX is used for the simulations. During the simulation, the basic momentum, continuity, energy and turbulence model equations are solved.

The Reynolds average Navier-Stokes equation (1) which is the momentum equation used in the solution is three-dimensional in Cartesian coordinates as follows:

$$\rho\left(\frac{u_i \partial u_j}{\partial x_i}\right) = -\frac{\partial p}{\partial x_i} + \frac{\partial}{\partial x_i}\left((\mu + \mu_t)\frac{\partial u_j}{\partial x_i}\right) \quad j = 1, 2, 3 \qquad (1)$$

Where p, u_i, μ, μ_t and ρ represent the pressure, velocity, dynamic viscosity, turbulent dynamic viscosity and density respectively.

The continuity equation is expressed as follows

$$\frac{\partial u_i}{\partial x_i} = 0 \qquad (2)$$

Turbulent Prandl number and energy equation can be expressed as

$$\mathrm{Pr}_t = \frac{C_p \mu_t}{k_t} = 0.9 \qquad (3)$$

$$\rho c_p\left(u_i \frac{\partial T}{\partial x_i}\right) = \frac{\partial}{\partial x_i}\left((k + k_t)\frac{\partial T}{\partial x_i}\right) \qquad (4)$$

where C_p, T, k and k_t are specific heat, wall temperature, thermal conductivity and turbulent thermal conductivity respectively.

Two equation k-w turbulence model is used. K-w turbulence model consists of two equations which is kinetic energy and specific dissipation rate. Kinetic energy equation can be defined as follow:

$$\frac{\partial k}{\partial t} + U_j \frac{\partial k}{\partial x_j} = \tau_{ij} \frac{\partial u_i}{\partial x_j} - \beta^* kw + \frac{\partial}{\partial x_j}[(\nu + \sigma^* \nu_T) \frac{\partial k}{\partial x_j}] \quad (5)$$

and specific dissipation rate can be defined as:

$$\frac{\partial w}{\partial t} + U_j \frac{\partial w}{\partial x_j} \omega = \alpha \frac{w}{k} \tau_{ij} \frac{\partial u_i}{\partial x_j} - \beta w^2 + \frac{\partial}{\partial x_j}[(\nu + \sigma^* \nu_T) \frac{\partial w}{\partial x_j}] \quad (6)$$

The constants:

$$\alpha = 5/9,\ \beta = 3/40,\ \beta^* = 9/100,\ \sigma = 1/2,\ \sigma^* = 1/2,\ \varepsilon = \beta^* kw$$

$$\nu_T = \frac{k}{w}$$

The average Nusselt number (Nu_{ave}) and average Nusselt number for row region (Nu_{rowave}) are the extracted results and found as follow:

$$Nu_{ave} = \frac{hd}{k} \quad (7)$$

$$Nu_{rowave} = \frac{hd}{k} \quad (8)$$

III. Numerical Analysis

The model considered for the multiple jet impingement is shown in Fig.1a. As can be seen from the figure, the jets are arranged horizontally on the orifice plate along the *x*- direction and vertically along the *y*- direction. The *z*- direction represents the direction of impinging. Orifice and target plate dimensions are equal to each other (20 mm x 40 mm); jet diameter (d) is 2 mm. The dimensionless jet-to-jet distances in horizontal and vertical directions are represented as X_n/d and Y_n/d having equal values; $X_n/d = Y_n/d = 4$. Also dimensionless orifice plate-to-target plate distance is $Z_n/d = 4$.

As shown in Fig. 1b the flow domain consists of velocity inlet, pressure outlet, adiabatic wall, target plate with constant heat flux boundary condition. The velocity boundary condition is used at the inlet, it is determined by the fixed Reynolds number (15,000). Pressure outlet boundary condition has been taken for exit and also relative pressure is taken as 0. On the target plate constant heat flux boundary condition is used (9000 W/m^2). Solutions have been done for steady-state conditions with 500 iterations number, 10^{-6} convergence criterion.

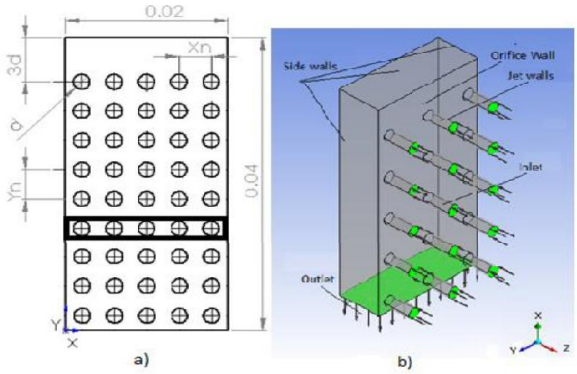


Figure 1: **a)** Local area average zone **b)** Flow domain

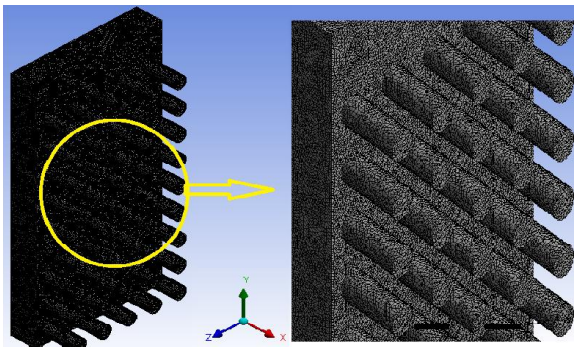


Figure 2: Mesh Structure

In numerical analysis, it is preferable to increase the elements size in order to increase the mesh accuracy, but on the other hand, increasing of element size is an undesirable situation as it increases the solution process. Mesh structure can be seen from Fig. 2. As seen from the figure two different elements sizes were tested for mesh accuracy; one of which consists of 4294021elements and the other is 3221243.

According to Fig. 3 by using the k-ω turbulence model and *Re* is equal to 16,130 then the mesh accuracy is provided for the 4,294,021 elements and 3,221,243 elements. Related mesh accuracy compared to Ref. [1]. With this conditions 1% error margin occur between both element sizes which can be considered as a reasonable error margin; so for the remaining solutions 3,221,243 elements were used.

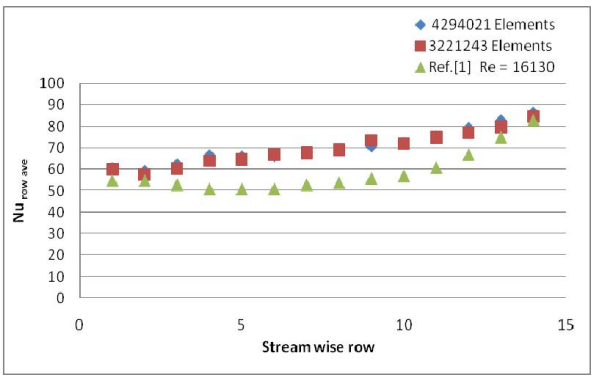


Figure 3: Mesh accuracy for $X_n/d = 2$, $Z_n/d = 2$

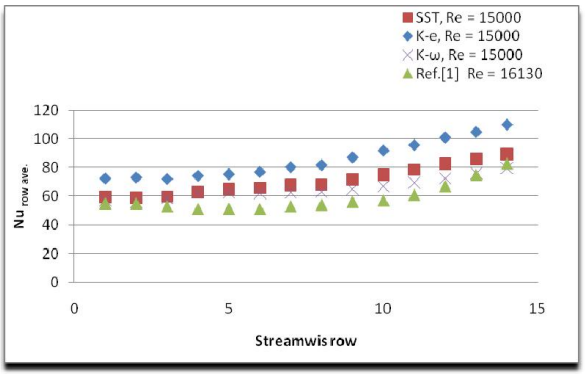


Figure 4: Model accuracy for $X_n/d = 2$, $Z_n/d = 2$

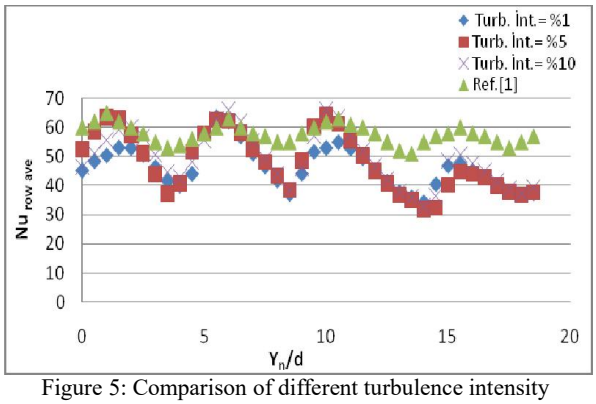


Figure 5: Comparison of different turbulence intensity

The accuracy of the numerical data obtained for verification of the turbulence model compared with the experimental study [1] which was taken as reference (Fig. 4). The comparison was made by taking the stream wise row average Nusselt numbers (Nu_{rowave}) which accounted for row region shown in Fig. 1a. Although the results of the k-ω and SST models are close to each other, the values closest to the experimental data is belonging to the k-ω model. In this sense, the k-ω turbulence model was used for all the remaining numerical solutions.

IV. Conclusion

In this study, 1%, 5%, 10% turbulence intensity values were tested at the inlet to see the effect of different turbulence intensity on heat transfer. Numerical solution is performed for dimensionless distance between jets $X_n/d = Y_n/d = 4$, $Z_n/d = 4$ and $Re = 15{,}000$. For Ref. [1], Reynolds number is 16,550, so related data is higher than present study. As shown in Fig.5 at the outside of the stagnation points the influence of inlet turbulence intensity is negligible for related conditions $X_n/d = Y_n/d = 4$, $Z_n/d = 4$ and $Re = 15{,}000$.

As seen from Fig. 6a our previous study Ref. [6] for related conditions ($X_n/d = Y_n/d = 2$, $Zn/d = 2$, $Re = 15{,}000$) stagnation point effect is not clear and flow is like a channel flow; so turbulence intensity effect can not be seen. On the other hands in present study stagnation point effect can be observed clearly and also difference between inlet turbulence intensity effects can be observed at stagnation points. Only a slight increase of Nusselt number can observed at the stagnation zones for high inlet turbulence intensity for related conditions.

As seen from Fig. 6b for higher inlet turbulence intensity i.e. %5 and %10 Nusselt number higher than inlet turbulence intensity of %1. As a result we can say that for low jet-to-jet distances the effect of inlet turbulence intensity is negligible because for this condition stagnation point and channel flow effect are not observed; but for higher jet-to-jet distances, especially at stagnation point inlet turbulence intensity may effects average heat transfer value.

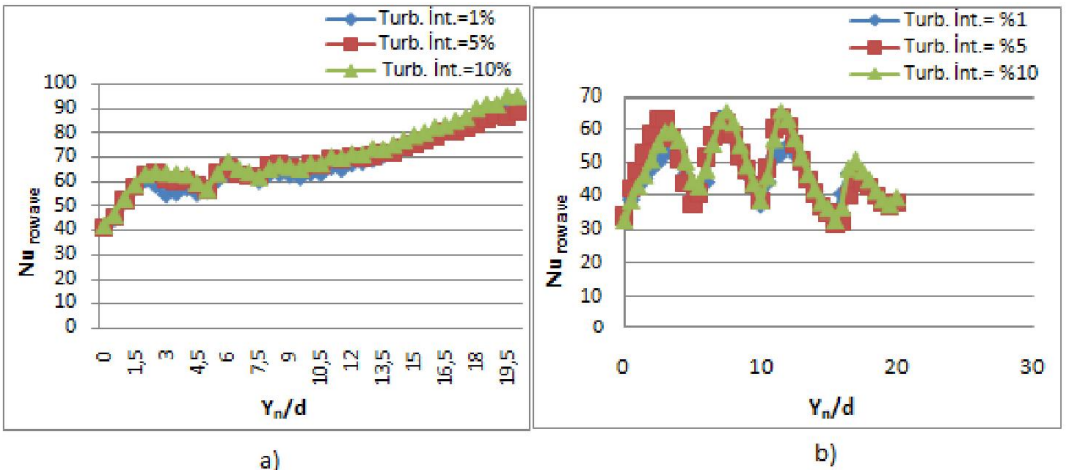


Figure 6 a) Ref. [6], b) Present study

REFERENCES

[1] S.Yong, Z. Jing-zhou, X. Gong-nan, *Convective heat transfer for multiple rows of impinging air jets with small jet-to-jet spacing in a semi-confined channel*, Int. J. of Heat and Mass Transfer vol.86, pp.832–842, 2015.

[2] E. A. Browne, G. J. Michna, M. K. Jensen, Y. Peles, *Experimental Investigation of Single-Phase Microjet Array HeatTransfer, Department of Mechanical, Aerospace, and Nuclear Engineering, Rensselaer Polytechnic Institute*, Troy, NY 12180.

[3] N.K. Chougule, G.V, Parishwad, P.R. Gore, S. Pagnis, S.N. Sapali, *CFD Analysis of Multi-jet Air Impingement onFlat Plate*, Proceedings of the World Congress on Engineering 2011 Vol IIIWCE 2011, London, U.K., July 6 - 8, 2011.

[4] L.B.Y. Aldabbagh, I. Sezai, *Three-dimensional numerical simulation of an array of impinging laminar square jets with spent fluid removal*, International Journal of Thermal Sciences vol.43, pp.241–247, 2004.

[5] D. H. Rhee, P.H. Yoon, H.H. Cho, *Local heat/mass transfer and flow characteristics of arrayimpinging jets with effusion holes ejecting spent air*, I. J. of Heat and Mass Transfer vol.46, pp.1049–1061, 2003.

[6] P. Çulun, N. Çelik, S.Kapan, *Investigation of inlet turbulence intensity effect on multiple jet impinging applications*, International Conference on Multidisciplinary, Science, Engineering and Technology (IMESET'17Bitlis) Oct27-29, 2017, Bitlis/Turkey

The effects of using a stirrer on the thermal performance of a water jacketed heat exchanger

H. BAYRAM[1] and G. SEVİLGEN[2]

[1] Uludağ University, Bursa/Turkey, halilbayram@uludag.edu.tr
[2] Uludağ University, Bursa /Turkey, gsevilgen@uludag.edu.tr

Abstract **- Water jacketed cooling process is commonly used in internal combustion (IC) engines. On the other hand, this type of cooling process is also observed in the heat exchanger applications for different industries such as refrigeration, chemical and food industries etc. In general, stirrer(s) were added to these heat exchangers to enhance the heat transfer rates. In this paper, a jacketed heat exchanger with a stirrer was selected for the experimental study. The aim of this study is to investigate the effects of inlet temperature value, the rotational velocity of a stirrer and the mass flow rate on the thermal performance of the heat exchanger. For this purpose, the process time was determined to evaluate the getting desirable heat transfer rate for different cases. According to the main results, the rotational velocity of stirrer had a great effect on the thermal performance of heat exchanger during the experiments and selected higher mass flow rate and inlet temperature values combined with a running stirrer, the heating process time was decreased remarkably.**

Keywords **- Water jacketed heat exchanger, rotational velocity, stirrer.**

I. Introduction

WATER jacketed cooling process plays an important role in heat rejection of internal combustion engines. The maximum temperature value is limited by the properties of the cooling water [1-6]. The heat transfer from internal combustion engines with using water jacket is used in heating process of vehicle cabin interior. Another application is frequently used in chemical industries to perform various operations such as mixing of liquids and mass transfer between two fluids [7-10]. Water jacket can be used for both cooling and heating process in stirred tanks unlike the IC engine applications. The thermal performance of a water jacketed heat exchanger with a stirrer can be evaluated in two different categories named as design and process parameters (sizing and rating parameters) [11]. We evaluated the thermal performance of a water jacketed heat exchanger with a stirrer considering only process parameters. The main parts of these heat exchangers in general are jacketed tank, stirrer(s) and the baffles. The tanks often have a vertical cylindrical geometry but the geometry sometimes had a square or a rectangular cross section. The stirrer usually consists of an electrical motor, shaft and one or more impellers. The employment of baffles in stirred tanks has several functions such as disturb or redirect the flow. The most commonly used type of baffle is wall baffle attached to the cylindrical wall [12].

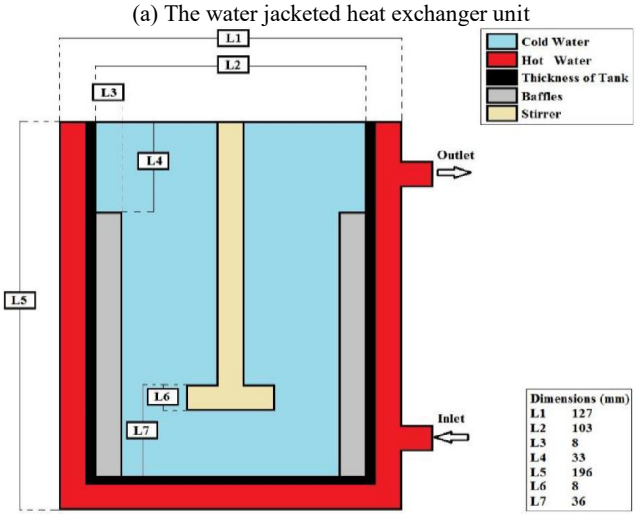
The main design parameters affect the thermal performance and the process time of these heat exchanger are the dimensions of the tank, distance between the impeller edge and the flat bottom of the tank, the geometrical type of baffles, the location of the stirrer(s) and the number of the impellers, and the thickness of the wall etc. On the other hand, the process parameters such as the rotational velocity of the stirrer, the mass flow rate, the temperature difference between hot and cold fluids separated by wall had also great effect on the thermal performance of these type of heat exchangers [12, 13]. In this study, water jacketed tank with a stirrer was experimentally investigated for different process parameters. All experiments performed for getting desirable heat transfer rate under different conditions so that the influence of these parameters can be evaluated.

II. Materials and Methods

In the experimental study, heat exchanger unit was the GUNT WL 110.04 model. Water was used for both jacket and tank sides and the outer surface of the water tank was insulated and assumed as adiabatic so that heat transfer was only occurred between the two fluids through the wall of the water tank. In jacket side, hot water was circulated by a water pump to get a desirable mass flow rate. In tank side, cold water was charged to the tank and then at the end of the heating process, the water was discharged manually. This process was repeated for all cases in experimental studies. The water jacketed heat exchanger with a stirrer and the dimensions are shown in Figure 1.



(a) The water jacketed heat exchanger unit



(b) The schematic view and the dimensions of the stirred tank

Figure 1: The water jacketed heat exchanger unit and the schematic view of the stirred tank used in the experimental study

All experiments were achieved until the increase in the cold water temperature was a constant value so that the effects of inlet temperature, mass flow rate and the rotational speed of stirrer could be observed.

The performed all experimental cases and the test conditions can be shown in Table 1. In order to better understand the factors that affect the heating process time, mass flow rate and the inlet temperature value of the hot water increased gradually in the experiments. We used two different mass flow rates of hot water and the rotational velocity of the stirrer was fixed as a value of 34.6 rad/s when it was operated. Measurements were carried out by using temperature values of hot water ranging from 45°C to 60°C.

The process time was recorded when the increase in the temperature value of the cold water was reached as a value of 10°C. The initial temperature value of the cold water in the tank was a constant value of 30°C for all experiments.

Table 1: The performed experimental conditions in this study

Case No	Mass flow rate (kg/s)	Inlet temperature value of hot water (°C)	Rotational velocity of the stirrer (rad/s)
Case-1	0.0225	45	0
Case-2	0.0225	45	34.6
Case-3	0.0225	50	0
Case-4	0.0225	50	34.6
Case-5	0.0225	55	0
Case-6	0.0225	55	34.6
Case-7	0.0225	60	0
Case-8	0.0225	60	34.6
Case-9	0.0450	45	0
Case-10	0.0450	45	34.6
Case-11	0.0450	50	0
Case-12	0.0450	50	34.6
Case-13	0.0450	55	0
Case-14	0.0450	55	34.6
Case-15	0.0450	60	0
Case-16	0.0450	60	34.6

III. Results and Discussion

The comparative results of the heating process time of cold water are shown in Figure 2. From these results we can easily say that the mass flow rate had great effect on this time and becoming more significant when the temperature difference between hot and cold water sides were at low levels. For instance, comparison of the results of the Case-1 and Case-9, the difference in the process time between two cases is 144s but this value was calculated about 87 seconds (s) for the comparison of the results of Case-7 and Case-15. The minimum heating period was observed 126 s for Case-15 which had high mass flow rate and the process time decreases with the increasing value of hot water inlet temperature.

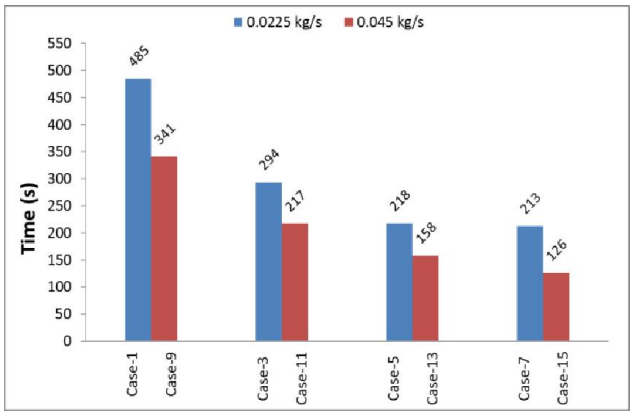


Figure 2: The measured process time for different mass flow rates without using a stirrer

The effects of running the stirrer for all cases were shown in Figure 3. From the comparison of the results of the Case-1 and Case-2, the difference in the process time between two cases was 89 s but this value was obtained as 23 s from the results of the Case-15 and Case-16 which had higher temperature inlet values. As a result, stirrer had great effect on the process time when the temperature difference between hot and cold water sides were at low levels. From the comparison of the results of Case-7 and Case-8 using a stirrer decreases process time about 80 s although these cases had lower mass flow rates. But, from the comparison of the results of Case-15 and Case-16 which had high mass flow rates compared to the Case-7 and Case8, using a stirrer decrease the process time was obtained as 23 s. The minimum heating period among the all cases that using a stirrer was achieved for Case-16 and this value was 103 s. The selected higher mass flow rate and inlet temperature values combined with a running stirrer, the process time was decreased remarkably from 485 s to 103 s.



Figure 3: The measured process time for all cases

IV. Conclusions

In this paper, we performed an experimental study on the thermal performance of a water jacketed heat exchanger with a stirrer considering heating process time of cold water in a tank side. The main conclusions obtained from this experimental study were described below:

- The process time decreases with the increasing value of hot water inlet temperature and mass flow rate, in general.

- The heating period was observed 126 s for Case-15 which had not using a stirrer but had high mass flow rate and the inlet temperature value. So that, the mass flow rate and the inlet temperature value had also great effects on the thermal performance of water jacketed heat exchanger without using stirrer.

- By using a stirrer in a cold water tank the process time was decreased remarkably, especially at low temperature levels. When the mass flow rate(0.045 kg/s) and the temperature difference (30°C) between hot and cold water sides were at high levels, the stirrer effect can also be observed but not as much as the cases which had lower mass flow rates and inlet temperature values.

- From the comparative results of the Case-1 and Case-16, the selected higher mass flow rate and inlet temperature values combined with a running stirrer, the process time was decreased remarkably from 485 s to 103 s.

- From the comparison of the results of the Case-1 and Case-7, 15°C increase in hot water inlet temperature, the process time was reduced by more than 50 percent and this value was reduced from 485 s to 213 s without using a stirrer.

In future studies, we will plan to investigate the design parameters effects on the thermal performance of these type heat exchangers by using Computational Fluid Dynamics (CFD) Method.

Acknowledgment

The authors would like to acknowledge to the OYAK Renault for supporting Vehicle Air Conditioning Systems Laboratory.

References

[1] Y. Zhang, Y. Gao, D. W. Qu, and C. Q. Song, "Optimization Design for Water Jacket of 4G24 Gasoline Engine," 2011 Asia-Pacific Power and Energy Engineering Conference, Mar. 2011.

[2] M. P. Kessler, M. Kruger, R. Ataídes, C. de la Rosa Siqueira, C. Argachoy, and A. S. Mendes, "Numerical Analysis of Flow at Water Jacket of an Internal Combustion Engine," SAE Technical Paper Series, Nov. 2007.

[3] M. G. Gavali, A. V. Subbarao, and N. V. Marathe, "Optimization of Water Jacket Using CFD for Effective Cooling of Water-Cooled Diesel Engines," SAE Technical Paper Series, Jan. 2007.

[4] M. Kruger, M. P. Kessler, R. Ataídes, C. de la Rosa Siqueira, C. Argachoy, and A. S. Mendes, "Numerical Analysis of Flow at Water Jacket of an Internal Combustion Engine," SAE Technical Paper Series, Nov. 2007.

[5] W. Qingzhao, "Numerical analysis of cooling effects of a cylinder head water jacket," MSc thesis, Dept. of Applied and Computational Mathematics, University of Minnesota, Duluth, 2009.

[6] N. Karras, T. Kuthada, and J. Wiedemann, "An approach for water jacket flow simulations," SAE Technical Paper Series, Apr. 2014.

[7] C. Hainzlmaier, A. S. Regueiro, and M. Lappe, "New methods of heating hybrid and electric vehicles," SAE Technical Paper Series, Apr. 2015.

[8] H. S. Park, "Development of the waste heat management system," SAE Technical Paper Series, Apr. 2015.

[9] Lakghomi, B., Kolahchian, E., Jalali, A., Farhadi, F. "Coil and jacket's effects on internal flow behavior & heat transfer in stirred tanks," World Academy of Science, Engineering and Technology, International Journal of Chemical, Molecular, Nuclear, Materials and Metallurgical Engineering, vol. 2, no. 12, pp. 383-387, 2008.

[10] K. H. Javed, T. Mahmud, and J. M. Zhu, "Numerical simulation of turbulent batch mixing in a vessel agitated by a Rushton turbine," Chemical Engineering and Processing: Process Intensification, vol. 45, no. 2, pp. 99–112, Feb. 2006.

[11] Kakac, S., Liu, H., Pramuanjaroenkij, A. *Heat exchangers: selection, rating, and thermal design*. Florida: CRC press, 2012.

[12] C. F. Rezende, "CFD analysis of flow field in a mixing tank with and without baffles," MSc thesis, Dept. Mechanical Engineering, Rochester Institute Of Technology, Rochester, New York , 1996.

[13] A. Sharafan, "CFD simulation of the agitated batch," MSc thesis, Dept. Mechanical Engineering, Czech Technical University, Prague, 2015.

Matrix Indexing Approach for Fuzzy Logic Based Controller in Induction Motor Protection

O. UYAR and M. ÇUNKAŞ

Selcuk University, Dept. of Electric & Electronic Engineering, Faculty of Technology, Konya/Turkey
okanuyar@selcuk.edu.tr
mcunkas@selcuk.edu.tr

***Abstract* – Industry mostly use induction motors for motion of several equipment. Therefore, trouble-free long life operation is very important for cost-effective production. This paper describes a procedures for executing embedded fuzzy logic algorithm. This algorithm is used in an induction motor protection system against six different fault parameters such as over voltage, over current, winding temperature, voltage unbalance, current unbalance and low voltage. In this study, the calculations achieved in Matlab and results are stored in a file. After this storage and arrangement process these values are embedded via a matrix in microcontroller. For this purpose, measured values such as current, voltage and temperature served as matrix index numbers by means of a pre-processing operation. So various delay times are easily assigned according to the location of fault level in matrix. This method is successfully tested in an experimental set-up and it shows that it provides sensitive protection. Additionally, this new method gave the results in a shorter time with reasonable calculation error.**

***Keywords* – Motor protection, fuzzy logic, induction motor, motor faults.**

I. INTRODUCTION

Induction motors are the leading actor in point of actuating the mechanical parts in industry. This importance requires trouble-free operation of these motors to prevent the labor losses. Thus, monitoring, failure detection and protection improves the reliability and availability of an existing system. This avoids the instantaneous, whole system failure which can have serious consequences.

Faults in induction motors can be grouped as electrical, mechanical and environmental faults and can be listed as follows:

Electrical faults: Voltage and current related errors are due to the over-under values and having unbalance between the supply phases. Earth fault, overload and short circuit are another error sources.

Mechanical faults: Unbalance of the mass, air gap eccentricity, bearing problems and broken rotor can be cause motor faults.

Environmental faults: High ambient temperature and moisture effects the ability of the motors. Inappropriate installation is also yield vibrations and so result in failures.

Detection of the faults is carried out with different techniques. Mechanical failures of induction motors have been diagnosed generally with the help of mathematical models and signal processing techniques [1-7]. When the error types have nonlinear and grift appearance, these methods can be insufficient. Thus, soft computing techniques provide superior solutions than classical methods in error detection and diagnosis problems. Artificial intelligence methods such as neural networks, fuzzy logic, genetic algorithms, and their hybrids are useful in this type of problems [8-11].

Commercially sold protection relays and previously proposed protection systems are adjusted the time delays constantly without considering fault level. When the system sense an error, the motor is disconnected from supply without waiting for recovering errors or after the constant time delay. This situation can lead disruption of the production line. Similarly, if protection system waits too long to stop motor in a crucial fault, it causes serious defects.

The previous works have been focused on a new time-delay calculation for stopping induction motor and improves the overall detection performance. The protection system is proposed to trip the motor in which the time delay is calculated between 0 and 4.5 s according to the fault level using the fuzzy logic method [12, 13]. These works are carried out by implementing the calculations related to the fuzzy logic such as fuzzification, inference mechanism and defuzzification. In this paper, these calculations achieved in Matlab and results are stored in a file. After this storage and arrangement process these values are embedded via a matrix in microcontroller. For this purpose, measured values such as current, voltage and temperature served as matrix index numbers by means of a pre-processing operation. Through the agency of this method, various delay times are easily assigned according to the location of fault level in matrix.

II. INTERESTED MOTOR FAULTS

The proposed system is considered the following electrical fault indications and their effects are mentioned with the [14, 15] works.

- Over Voltage: At 110 percent voltage was considered as over voltage fault. Over voltage cause increasing the eddy current heating of rotor and impress the winding insulation.
- Low Voltage: At 90 percent voltage was considered as low voltage fault. Low voltage causes the developed torque to reduce. This results in greater slip proportionally to the square of the voltage drop and a reduction in speed. As a result, the motor will be running slower with a lower output and the motor tries to reduce the slip by drawing more current. This overloads the motor and can cause overheating.
- Voltage Unbalance: 20V voltage difference between the motor phase windings was considered as unbalance phenomena. If the line voltages on a multi -phase induction motor are not equal, currents in the stator windings will be unbalanced. This condition which produced increased heating, increased energy consumption and lower efficiency. One unit percent voltage unbalance can lead about 5 unit increased losses in the machine.
- Winding temperature: At 110 percent temperature was considered as a fault. Cause of overheating is usually based on improper ventilation and high

ambient temperature. Higher winding temperature brings on additional copper losses and inversely effect the insulation of the motor.

- Current unbalance and high current has the similar effects with the previously mentioned voltage based failures.

III. FUZZY LOGIC DESIGN FOR THE SYSTEM

Fuzzy logic control has become an important methodology in control engineering. Learning and experience based Fuzzy logic is a tool for making a model in situations involving highly complex systems whose behaviors are not well understood. Conventional systems analyze requires a model based on a collective set of assumptions needed to formulate a mathematical form. Since most real life applications are more complex, fuzzy control should be developed about the control process exists by using a number of fuzzy rules and input parameters.

In this study, developed protection system with the help of fuzzy logic was embedded into the microcontroller. In this system, the time delay calculation used to stop motor was derived with fuzzy rules. These values were determined according to characteristics of the chosen motor. The values in Table 1 were used for preparing fuzzy rule base. The limit values were selected according to the NEMA standards and TS-3205 EN 60034-1 numbered standard of TSI (Turkish Standards Institution).

While there are 6 different input with 3 level as the system input, logically related inputs are grouped and determined individually as shown in Fig. 1. Thus we ensured less processing time and reduced size of the constituted fuzzy rule base.

Table 1: Motor Parameters and Limit Values

Motor Parameters		
3 Phase Voltage	380 V AC	
Frequency	50 Hz	
Over Voltage Limit	% 10	240 V
Over Current Limit	% 15	5,5 A
Winding Temp.	% 10	135 ^{O}C
Voltage Unbalance	% 10	20 V
Current Unbalance	% 10	0,5 A
Under Voltage	% 10	200
Measurement Resolutions		
Current	% 0,097	48,8 mA
Voltage	% 0,097	361,12 mV
Temperature	% 0,78	0,29 ^{O}C

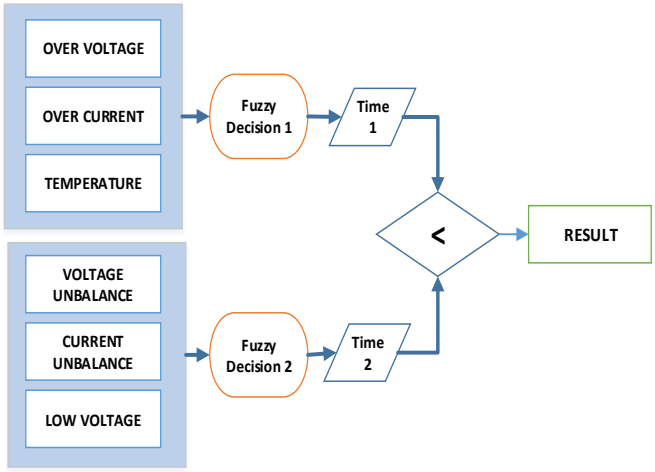


Figure 1: Structer of the Fuzzy Logic System

Some samples for rule base of first part of the structure are given in Table 2. The darkish cells in the tables represent the situation that this particular error did not occur for this rule. Membership functions of the input parameters has three level named as L (Low), M (Medium) and H (High). Output has five level named as VS (Very Short), S (Short), N (Normal), L (Long) and VL (Very Long). Membership functions relevant to these inputs and the output are given in Table 3. These rules are determined by regarding the importance level of the level. For instance, over current parameter is crucial and long term working in this situation is destructive. Thus, related rule is formed as producing short delay time.

All of the Fuzzy Logic process is carried out with the help of Matlab codes and FIS Editor. Fuzzy logic structure is constituted in the FIS editor. Matlab codes are written to test the system with all possible inputs that have limited precision. Precision steps to generate the results are as follows:

- Over Voltage : 1 V Voltage Unbalance : 1 V
- Over Current : 0.2 A Current Unbalance : 0.1 A
- Temperature : 1 C Low Voltage : 1 V

Table 2: Rule Base Sample

1. Rule No	Over Voltage	Over Current	Temp.	Output
1	OVM	OCM		N
2	OVM	OCH		S
3	OVH	OCL		N
4	OVH	OCM		S
5	OVH	OCH		VS
6	OVL		TL	VL
7	OVL		TM	L
8	OVL		TH	N
9	OVM		TL	L
10	OVM		TM	N

Table 3: Membership Function Samples

Membr. Func.	Equation	
Over Voltage	μ_{OVL} (x) = 1 = 260 – x / 10	240 <= x < 250 250 <= x < 260
	μ_{OVM} (x) = 260 – x / 10 = 270 – x / 10	250 <= x < 260 260 <= x < 270
	μ_{OVH} (x) = 260 – x / 10 = 1	260 <= x < 270 270 <= x
Over Current	μ_{OCL} (x) = 1 = 7,5 – x	5,5 <= x < 6,5 6,5 <= x < 7,5
	μ_{OCM} (x) = 7,5 – x = 8,5 – x	6,5 <= x < 7,5 7,5 <= x < 8,5
	μ_{OCH} (x) = 8,5 – x = 1	7,5 <= x < 8,5 8,5 <= x
Temp.	μ_{TL} (x) = 1 = 145 – x / 5	135 <= x < 140 140 <= x < 145
	μ_{TM} (x) = 145 – x / 5 = 150 – x / 5	140 <= x < 145 145 <= x < 150
	μ_{TH} (x) = 150 – x / 5 = 1	145 <= x < 150 150 <= x
Delay Time	μ_{VS} (x) = 1 = 1,5 – x / 0,75	0 <= x < 0,75 0,75 <= x < 1,5
	μ_{S} (x) = 1,5 – x / 0,75 = 2,25 – x / 0,75	0,75 <= x < 1,5 1,5 <= x < 2,25
	μ_{N} (x) = 2,25 – x / 0,75 = 3 – x / 0,75	1,5 <= x < 2,25 2,25 <= x < 3
	μ_{L} (x) = 3 – x / 0,75 = 3,75 – x / 0,75	2,25 <= x < 3 3 <= x < 3,75
	μ_{VL} (x) = 3,75 – x / 0,75 = 1	3 <= x < 3,75 3,75 <= x

Matlab code used for storing the results can be shown in Fig.2. This code send the possible inputs to the structure and fuzzy inference system produce the results. Simultaneously, produced results are written with the input paramaters.

Microcontroller code for matrix indexing operation is summarized in Fig.3 with pseudo code.

```
a=readfis('rules1.fis');
file = fopen('result_rule1.txt','wt');
for x1=239:1:270
   for x2=5.4:0.2:8.4
      for x3=134:1:150
         fprintf(file,'%d %.1f %d %.1f \n',
   x1,x2,x3,round(evalfis([x1,x2,x3],a)*10)/10);
      end
   end
end
fclose(dosya);
```

Figure 2: Matlab Code for result generation

```
Read_inputs(); // 7 analog port was reed 16 times and avaraged
Display(); // All the values visualized
Find_mux(); // All of the values compared with each other and
maximum one found
Check_err(); // Error values checked
If there is an error
Arrange (); // Calculated values were arranged as the matrix index
numbers.
result1 = rule1[agek-239][aaek][sek-134]; // matrix1 indexed
result2 = rule2[gdek-19][adek][dgek-170]; // matrix2 indexed
Show_results(); Error page shown in Fig. 5 displayed
Else if Display();
```

Figure 3: Pseudocode for matrix indexing

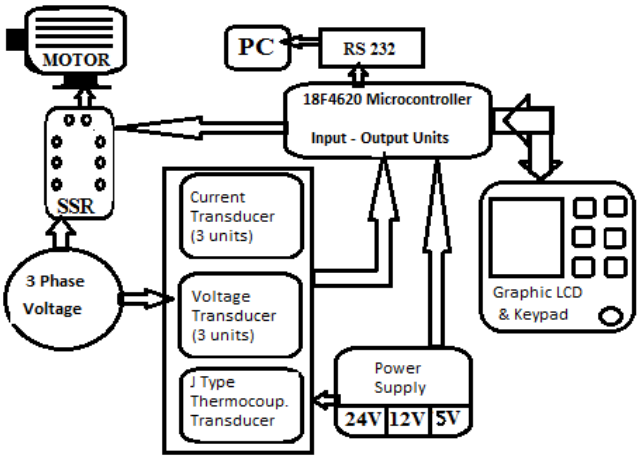


Figure 4: System Hardware Representation

IV. RESULTS

The experimental works were carried out with 3 phase, four-pole, 2.2-kW induction motor. Fault operations were achieved by using variable transformer to implement the abnormal voltage inputs. Temperature effect was tested by heating the thermocouple. System controller shown in Fig. 4 was the PIC18F4620 microcontroller which has UART communication module, Analog-Digital Converter and other well-known main internal modules with 64 Kb program memories. Thus, lots of pre-calculated fuzzy results could be embedded in to the microcontroller. Graphical LCD named HDM64GS12 has been used for indicating the measured values, faults and the calculated results. User interface constituted with six buttons has been added in order to calibrate the measured values and set the measured values upwards or backwards for testing the abnormal conditions. When a fault detected, display shows the fault type (1 = fault, 0 = no-fault) and delay times (T1, T2) calculated by two part fuzzy system. Unbalanced voltage and over voltage errors with their values (279.0 = Phase 1 voltage, 49 = maximum voltage difference between phases) can be shown in the Fig. 5.

Some results for first Fuzzy structure can be shown in Table 4. This values

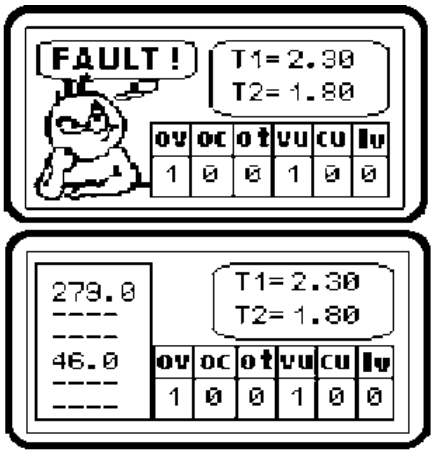


Figure 5: Screenshots in faulty condition displayed by turns

Table 4: Experimental Result Samples

Max. Voltage	Max. Current	Winding Temp.	Delay Time	Error Type
239	5,4	134	2,3	Over Voltage
239	5,4	141	2,8	Over Voltage, Over Temperature
239	6,4	146	2,5	Over Voltage, Over Temperature
239	5,6	137	3,2	Over Voltage, Over Temperature
240	5,6	134	3	Over Voltage
254	5,8	137	2,7	Over Voltage, Over Temperature
254	7,4	135	2,4	Over Voltage, Over Current
264	7,2	147	1,8	Over Voltage, Over Current Over Temperature
264	7,4	134	2	Over Voltage, Over Current
264	8	148	1,5	Over Voltage, Over Current Over Temperature
270	8,4	150	1,2	Over Voltage, Over Current Over Temperature

V. Conclusion

This paper presents a method to embed the fuzzy logic structure in to the microcontroller. Fuzzy logic helps to produces a delay time according to the different degrees of various fault combinations. So the flexible and optimal delay time are achieved. In the next studies, the system can be improved by regarding various fault parameters

Acknowledgment

This work was supported by Scientific Research Project Coordination of Selcuk University under Project with 09101047 project number.

References

[1] M. E. H. Benbouzid, M. Vieira, and C. Theys, "Induction motors' faults detection and localization using stator current advanced signal processing techniques," *IEEE Transactions on power electronics*, vol. 14, pp. 14-22, 1999.

[2] M. Seera, C. P. Lim, D. Ishak, and H. Singh, "Fault detection and diagnosis of induction motors using motor current signature analysis and a hybrid FMM–CART model," *IEEE transactions on neural networks and learning systems*, vol. 23, pp. 97-108, 2012.

[3] J. Cusido, J. Rosero, E. Aldabas, J. A. Ortega, and L. Romeral, "New fault detection techniques for induction motors," *Electrical Power quality and utilisation, Magazine*, vol. 2, 2006.

[4] S. Rajagopalan, J. A. Restrepo, J. M. Aller, T. G. Habetler, and R. G. Harley, "Nonstationary motor fault detection using recent quadratic time–frequency representations," *IEEE Transactions on Industry Applications*, vol. 44, pp. 735-744, 2008.

[5] B. Ayhan, M.-Y. Chow, and M.-H. Song, "Multiple signature processing-based fault detection schemes for broken rotor bar in induction motors," *IEEE Transactions on Energy Conversion*, vol. 20, pp. 336-343, 2005.

[6] M. Blodt, M. Chabert, J. Regnier, and J. Faucher, "Mechanical load fault detection in induction motors by stator current time-frequency analysis," *IEEE Transactions on Industry Applications*, vol. 42, pp. 1454-1463, 2006.

[7] J. Zarei and J. Poshtan, "Bearing fault detection using wavelet packet transform of induction motor stator current," *Tribology International*, vol. 40, pp. 763-769, 2007.

[8] H. Su, K. T. Chong, and R. R. Kumar, "Vibration signal analysis for electrical fault detection of induction machine using neural networks," *Neural Computing and Applications*, vol. 20, pp. 183-194, 2011.

[9] J. F. Martins, V. F. Pires, and A. Pires, "Unsupervised neural-network-based algorithm for an on-line diagnosis of three-phase induction motor stator fault," *IEEE Transactions on Industrial Electronics*, vol. 54, pp. 259-264, 2007.

[10] C. T. Kowalski and T. Orlowska-Kowalska, "Neural networks application for induction motor faults diagnosis," *Mathematics and Computers in Simulation*, vol. 63, pp. 435-448, 2003.

[11] W. Li and C. Mechefske, "Induction motor fault detection using hybrid methods," *Engineering Asset Management*, pp. 276-287, 2006.

[12] O. Uyar and M. Cunkas, "Design of fuzzy logic based motor protection system," in *6th International Advanced Technologies Symposium (IATS'11)*, 2011, pp. 16-18.

[13] O. Uyar and M. Çunkaş, "Fuzzy logic-based induction motor protection system," *Neural Computing and Applications*, vol. 23, pp. 31-40, 2013.

[14] W. R. Finley, "Troubleshooting induction motors," in *Industry Applications Conference, 2000. Conference Record of the 2000 IEEE*, 2000, pp. 3491-3498.

[15] A. H. Bonnett, "The impact that voltage and frequency variations have on AC induction motor performance and life in accordance with NEMA MG-1 standards," in *Pulp and Paper, 1999. Industry Technical Conference Record of 1999 Annual*, 1999, pp. 16-26.

Implementation and Comparison of Text Compression Algorithms in Image Steganography

Ö. ÇATALTAŞ[1] and K. TÜTÜNCÜ[2]

[1]Selcuk University, Konya/Turkey, ozcancataltas@selcuk.edu.tr
[2]Selcuk University, Konya/Turkey, ktutuncu@selcuk.edu.tr

***Abstract* - Because of the technological advances in communication between people, information security is so important that it is not at any stage in history. Steganography is a science that is used in the field of information security and aims to conceal the existence of a confidential message. In this study, the effect of text compression algorithms on image steganography is examined. Three different text files on different sizes are compressed using 4 different compression algorithms namely LZW, MTF, Arithmetic and Deflate and embedded with LSB substitution method on 3 different images. When the results are examined, it is seen that the Deflate algorithm has a higher compression ratio than the other algorithms. In this way, a significant increase in image capacities has been achieved and the distortion in the image has been reduced.**

***Keywords* – Image steganography, Information security, LSB substitution, Text compression.**

I. INTRODUCTION

Information security has become one of the most important issues in communication between people throughout history. As the privacy of the information transferred between the two sides increases, the fear of being monitored of humans increases. For this reason, people have become more important to privacy.

Cryptography is the first science to come to mind in the field of Information Security. The goal of cryptography is to make it harder for the 3rd parties to resolve secret message by encrypting a data and making it incomprehensible. But in this case, the third party observing the communication will know that there is a secret communication between the receiver and the transmitter and will try to solve the secret message or prevent communication.

The goal of steganography, which is one of the methods of data hiding, is to not raise suspicions by hiding message in media types frequently used in daily life. For example, if the sender hides the sender's message in a scenery image and sends the message, the 3rd party will only see the innocent scenery image, so it will not try to solve the hidden message and the message will reach the receiver safely.

Text, image, audio and video files can be used as cover media type for steganography. Since the image is more often used in the communication between people, studies on steganography focus on the image. The type of media to be hidden as well as the type of cover media may vary. Text, image, audio and video media types can be hidden in text, image, audio and video media types.

Image steganography techniques are examined in two main categories: spatial domain and frequency domain. In the spatial domain, the data is hidden directly by changing the image pixels. In the frequency domain, the image is transformed into frequency coefficients using DCT or DWT, and the data is embedded in these coefficients.

In steganography, the size of the message that can be hidden depends on the size of the cover media, and the embedding algorithm to be used. For this reason, compressing the message before it is embedded will increase the capacity. It will also reduce the deterioration of the cover, so that the detectability will also decrease.

II. RELATED WORKS

In [1], an LZW compression algorithm and an android application for embedding on images using TEA have been developed. With the LZW algorithm, texts of different lengths are compressed and a compression ratio of 137.5% is obtained. Again in this study it has been shown that PSNR value will be increased by compressing the message.

In [2], LZW, RLE, Shannon Fano and Adaptive Huffman algorithms were applied to 10 different text files and the results were compared. In this study, a compression ratio of 204% is obtained with the LZW algorithm. The highest compression ratio among these algorithms was obtained by the LZW algorithm.

In [3], 12 different text compression algorithms namely Shannon-Fano Coding, Huffman coding, Adaptive Huffman coding, Run Length Encoding, Arithmetic coding and Lempel Ziv scheme were applied on 10 different text files and the results were compared. The highest compression ratio was obtained in the LZFG method, which is the LZ78 derivative.

III. MATERIALS AND METHODS

A. LSB Substitution Method

The Least Significant Bit (LSB) Substitution Method is the most widely used method in steganography because it can be

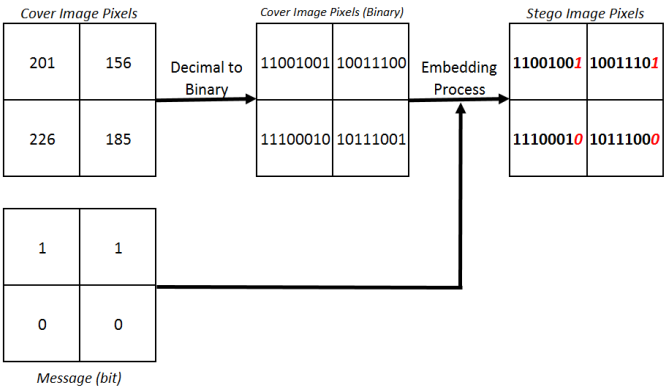


Figure 1: LSB substitution method

applied to different media types and is simple to apply. In the LSB substitution method, the least significant bit of each pixel of the cover image is replaced by the message bits. This replacement can be done in sequence or randomly using pseudo-random generators.

When we look at Figure 1, the 4-bit message is embedded to cover image that contain 2x2 pixels using LSB substitution method and the stego image pixels are given in the same Figure. In this embedding process, the message bits are embedded in the cover image in order. For this reason, decrypting the secret message is not a difficult task.

B. Text Compression

Data compression methods are widely used to allow data to occupy less space in storage environments and to be transferred over a communication network faster. Especially today, because of the high usage of computer and internet, it is necessary to compress files stored in computer or sent over internet.

Text compression methods are broken down into two categories according to compression formats: lossy compression and lossless compression. In the lossy compression, the original text cannot be obtained exactly when the data is recycled, while in the lossless compression, the original text is obtained without any modification [4].

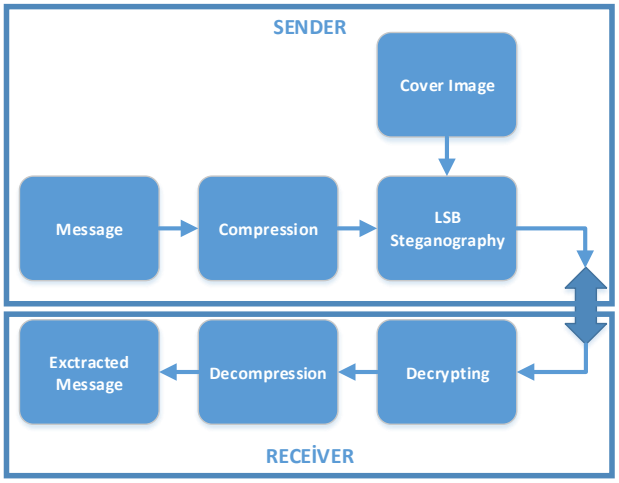


Figure 2: Steganography diagram

Lossless compression is used in the files where the original data needs to be protected. Lossy compression is preferred because of the high compression ratio in file types such as image and audio files, where small disturbances are not important.

1. LZW

Lempel Ziv Welch (LZW) is one of lossless and dictionary based text compression methods. The algorithm tries to insert the word that contains the most possible letters into the dictionary by moving the letter through the text to be compressed, and at the same time changes the text with the counterpart in the dictionary [5].

One feature of the algorithm is that the dictionary does not need to be communicated to the other side. In other words, the dictionary containing the words is created dynamically and the recipient side opens the message by creating this dictionary again dynamically.

2. Arithmetic

Arithmetic coding is an entropy-based lossless compression technique. Normally, a character string consists of bits of fixed length. In arithmetic coding, frequently used characters are expressed with lower bits and less used characters are expressed with higher bits. In arithmetic coding, instead of replacing each character with a code word, as in other methods, it only outputs a floating point number [3].

3. MTF

The Move-To-Front (MTF) algorithm is a probability-based lossless text compression method. The main rationale for this coding type is to convert the characters in the message to integer values with smaller values. The algorithm codes the sequence of the character that matches the alphabet, and that character makes the alphabet the first character [6].

If the same characters are placed close to each other in the message, the integer values to be encoded will be small, so that smoother distribution and better compression will occur.

In this compression method, an alphabet consisting of characters in the text to be hidden must be created and transmitted to the recipient. The smaller the variety of characters in the text to be hidden, the smaller the alphabet to be created and the higher the compression ratio. If the text to be hidden contains all kinds of characters, then the compression ratio will be zero.

4. Deflate

The deflate algorithm is a lossless data compression technique consisting of a combination of LZ77 and Huffman encoding. According to the compression techniques available in the literature, the efficiency of the Deflate method is high. When used in steganography, there is no need to send any dictionary, alphabet to the recipient [7].

IV. EXPERIMENTAL STUDY

In this study, 3 text files each with a different length (7.94kB, 15.5kB, 19.5kB) are compressed using 4 different text compression algorithm namely LZW, Arithmetic, MTF and Deflate. Then, these compressed text files are embedded with the LSB method over 3 different images.

Firstly, 3 different text files are compressed using 4 different compression algorithms. The original text length, the resulting text length, and the compression ratios are given in Table 1.

Table 1: Compression ratios obtained after compression.

	Uncompressed (bit)	LZW	Arithmetic	MTF	Deflate
		Compression Ratio (%)			
Text 1	56980	38448	35448	48840	29496
		148,20	160,74	116,67	193,18
Text 2	111405	72969	69361	95490	56832
		152,67	160,62	116,67	196,03
Text 3	140364	84643	88109	120312	65744
		165,83	159,31	116,67	213,50

When we examine the Table 1, it can be seen that the Deflate algorithm can compress the text higher than other algorithms. Compression ratio of Deflate algorithm is up to 213.50%.

Then, the compressed texts and the original message were embedded to 3 different images using LSB substitution method. These images are “Lena”, “Mandrill” and “Peppers” and are given in Figure 3. The resolution of these images are 225x225, 512x512 and 600x600 pixels, respectively.



a) Image 1, "Lena"



b) Image 2, "Mandrill"



c) Image 3, "Peppers"

Figure 3: Original images

After embedding process, Peak Signal to Noise Ratio(PSNR) values of the original images and stego images were calculated. These values are given in Table 2.

Table 2: PSNR values obtained after embedding.

PSNR (dB)		Uncompressed Message	LZW	Arithmetic	MTF	Deflate
Image 1	Text 1	52.38	54.09	54.45	53.05	55.24
	Text 2	49.48	51.31	51.53	50.15	52.39
	Text 3	48.47	50.67	50.49	49.14	**51.77**
Image 2	Text 1	59.53	61.23	61.58	60.20	62.38
	Text 2	56.61	58.45	58.67	57.28	59.54
	Text 3	55.61	57.81	57.63	56.28	58.90
Image 3	Text 1	60.91	62.62	62.96	61.58	63.76
	Text 2	58.01	59.84	60.06	58.68	60.92
	Text 3	57.00	59.20	59.03	57.67	60.29

When we examine the Table 2, it can be seen that the PSNR values obtained by Deflate algorithm are clearly superior to the PSNR values obtained by other algorithms. The maximum increase in the PSNR value was obtained when embedding Text 3 compressed by Deflate algorithm to Image 1. The PSNR value increased from 48.47 to 51.77 by 6.81%.

Using compression ratios given in Table 1, embedding capacities of each image and each algorithm were calculated. The estimated embedding capacities are given in Table 3.

Table 3: This caption is centered.

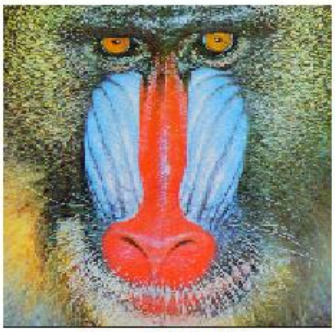
	Uncompressed (kB)	LZW	Arithmetic	MTF	Deflate
		Capacity Increase			
Image 1	18.54	30.74	29.53	21.63	39.58
		65.80%	59.28%	16.67%	113.48%
Image 2	96	159.2	152.93	112	204.96
		65.83%	59.30%	16.67%	113.50%
Image 3	131.84	218.62	210.02	153.81	281.47
		65.82%	59.30%	16.66%	113.49%

When we examine the Table 3, using Deflate compression algorithm, the capacity of Image 2 increased from 96kB to 204.96kB. The largest increase in embedding capacity was achieved with this algorithm at 113.5%.

The stego images obtained after embedding Text 3 compressed by Deflate compression algorithm are given in Figure 4.



a) Image 1, "Lena"



b) Image 2, "Mandrill"



c) Image 3, "Peppers"

Figure 4: Stego images

V. CONCLUSION

In this study, the effect of text compression algorithms on image steganography is examined. 4 different compression techniques were applied to 3 different text files and then embedded with LSB method on 3 different images. When the results are examined, it is seen that the best compression ratio is obtained with the Deflate algorithm with 213.5%. Similar results are obtained on different text files. As the text size increases, the compression ratios of the compression algorithms also increase. Because of the high compression ratio, the highest PSNR value is obtained from the compressed text by the Deflate algorithm with 60.29 dB. By compressing the message file to be hidden before embedding it has been increased by 6.8% in the PSNR value. In addition, the capacity of the cover images increased up to 113%. In future studies, data compression methods can be applied together with different steganography methods to make different studies.

REFERENCES

[1] M.S.A. Putra, G. Budiman, L. Novamizanti, "Implementation of Steganography using LSB with Encrypted and Compressed Text using TEA-LZW on Android", *International Conference on Computer, Control, Informatics and Its Applications*, pp. 93-98, 2014.

[2] S.R. Kodituwakku, U. S.Amarasinghe, "Comparison Of Lossless Data Compression Algorithms For Text Data", *Indian Journal of Computer Science and Engineering*, Vol. 1, No.4, pp. 416-425, 2011.

[3] S. Shanmugasundaram, R. Lourdusamy, "A Comparative Study Of Text Compression Algorithms", *International Journal of Wisdom Based Computing*, Vol. 1, No. 3, pp. 68-76, 2011.

[4] S. Deorowicz, "Universal lossless data compression algorithms", Ph.D. dissertation, Institute of Computer Science, Silesian University of Technology, Gliwice, 2003.

[5] T. A. Welch, "A Technique for High-Performance Data Compression", IEEE Computer, Vol. 17, Issue 6, 1984.

[6] A.A. Hassan, "New Approach For Text Based Steganography", Master Thesis, Institute of Science, Selcuk University, 2015.

[7] P. Deutsch, "DEFLATE Compressed Data Format Specification version 1.3", 1996.

Core Loss Estimation Model for an Integrated Magnetic Current Doubler Soft Switched Full-Bridge DC-DC Converter

Y. ONER[1] and S.CETIN[2]

[1] Yildiz Technical University, Istanbul/Turkey, yoner@yildiz.edu.tr
[2]Pamukkale University, Denizli/Turkey, scetin@pau.edu.tr

***Abstract* - In this work, a core loss estimation model is presented for integrated magnetic current doubler phase shifted full bridge (IM-CD-SS-FB) DC-DC pulse width modulated (PWM) converter. Proposed model provides accurately estimation of the core loss when the non-sinusoidal voltage is applied to the primary of the transformer. The finite element model is used for the estimation of the core loss of IM-CD-SS-FB DC-DCPWM converter. The extracted loss results are compatible with the theoretical approximation.**

***Keywords* - Transformer, DC-DC converter, core loss.**

I. INTRODUCTION

In power electronics converters, magnetic components like transformer and inductor has square wave or zero voltage level. In these systems, the conventional core loss calculation method proposed by Steinmetz is usually used to determine the core loss of the transformer or the inductor [1-6].

The steinmetz equation is given by;

$$P_v = k f^{\alpha} \hat{B}^{\beta} \quad (1)$$

Above equation, $\hat{B}$ is the peak flux amplitude, f is the frequency of sinusoidal excitation, P_v is the time-average power loss per unit volume. The other parameters, k, β, α, are found by curve fitting and they are determined for limited frequency and flux range [6], [7]. The steinmetz equation is valid for only sinusoidal excitation and this is the main disadvantage of the modern power electronic systems. Because switched power electronic systems have non-sinusoidal wave forms as mention earlier. Therefore, these non-sinusoidal waveforms conclude different loss compared to the loss produced by steinmetz equation [8].

To solve these problems, different studies were presented in the literature. In [7] and [9], the steinmetz equation is improved with some minor changes in the equation for non-sinusoidal waveforms. In the modified equation, every flux waveform is calculated with same material parameters. This presented approach is widely accepted and usually applied to the core loss calculation in the switched mode power converters. This modified equation has more complex statement compared to original statement.

In [11] and [12], a core loss calculation method based on loss map of the core material was proposed. In this method, loss map is extracted with experimental measurements.

In this study, core loss estimation model based on magnetic modeling is proposed. The core loss is estimated more accurately with non-sinusoidal waveforms before the experimental setup compared to Steinmetz equation. The method is applied to an IM-CD-SS-FB DC-DC PWM converter. This method provides more accurately core loss estimation of the converter before its experimental setup.This estimation also makes the design process of the converter simple.

II. THE PROPOSED CORE LOSS MODEL

In order to determine the magnetic flux density and core loss in the transformer, the finite element method has been used. The core and the windings of the transformer were modeled in Maxwell Software.

An Integrated Magnetic (IM) model proposed in [13] is used to test its flux variation and core loss by the use of proposed core loss model. An IM-CD-SS-FB DC-DC PWM converter topology is used to apply integrated magnetic model. In the model, output inductors are integrated to the main transformer's center leg by the use an air gap. Therefore separate magnetic cores and conduction loss are decreased. The schematic diagram of IM-CD-SS-FB DC-DC PWM converter is shown in Figure 1. In the used IM model flux variation of the center leg is low and its core loss is lower compared to the conventional converter transformer design.

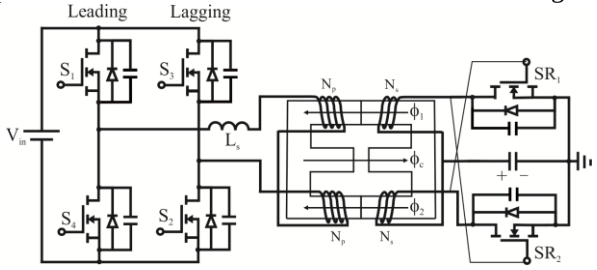


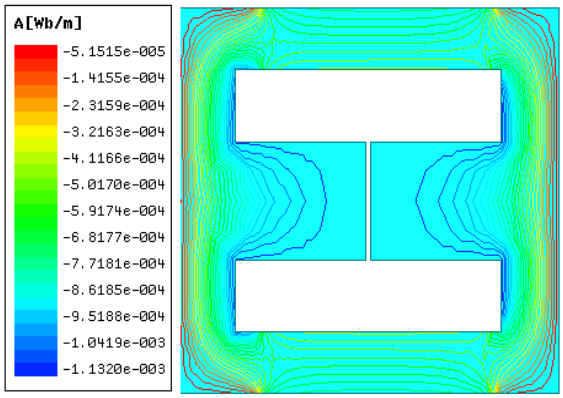
Figure 1. IM CD-SS-FB DC-DC PWM converter topology.

An IM-CD-SS-FB DC-DC PWM converter works with soft switching so its conversion efficiency and power density are high. Moreover, it has reduced electromagnetic interference (EMI) [1-5]. Therefore, it is well known topology used indifferent industrial applications like electrical vehicle,

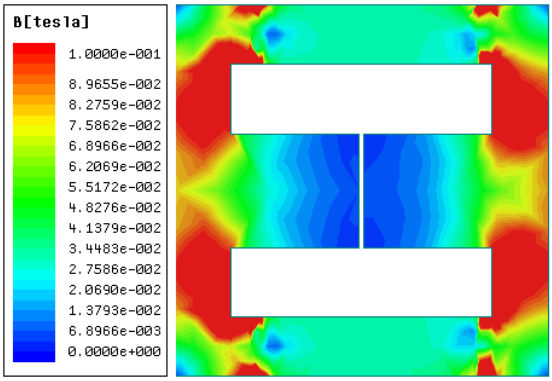
battery charge, telecom or data centre applications. Its operation is presented in many papers so it is not mentioned here.

The current doubler rectifier topology is known with its low conduction loss on the secondary windings especially in high output current and low output voltage applications. Therefore, this rectifier topology are widely preferred for the secondary side of the PSFB converter. However, the requirement of separate magnetic components of the output inductors and power transformer increases the size and the cost of the converter. In this case, integrated magnetic solution can help the increase power density and reduce the cost of the converter [13], [14].

According to created core loss model, Figure 2 shows the simulated magnetic flux variation and magnetic flux density variation in each leg: the center leg has lower magnetic flux variation compared to outer legs as mentioned in the integrated magnetic model definition in [13]. The flux density in each core leg is different so the flux variation in each leg of the transformer should be determined separately to prevent core saturation [13], [14].



(a)



(b)

Figure 2. (a) Simulated magnetic flux variation results of the IM model (b) Simulated magnetic flux density variation results of the IM model.

The core loss is also obtained from the simulation and its variation in the core is shown in the Figure 3.

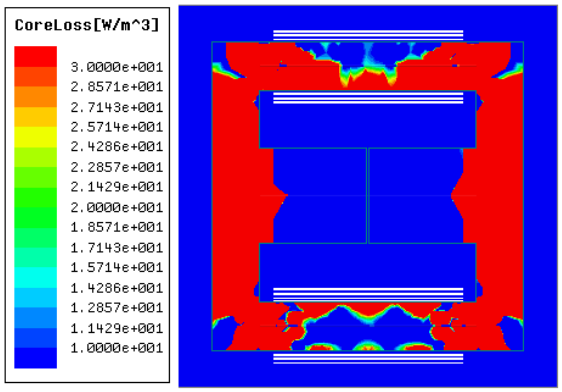


Figure 3. Simulated core loss variation of the IM model.

III. Conclusion

The core loss estimation model is presented for IM-SS-FB DC-DC PWM converter. The finite element method is used for the estimation of the core loss. Proposed model provides more accurate prediction of core loss for non-sinusoidal voltage is applied to the primary of the transformer in switched power converters.

References

[1] U. Badstuebner, J. Biela, D. Christen, J.W. Kolar, "Optimization of a 5-kW telecom phase-shift DC–DC converter with magnetically integrated current doubler", IEEE Trans. On Industrial Electronics, Vol. 58, No.10, pp.4736-4745, October 2011.

[2] U. Badstuebner, J. Biela, J.W. Kolar, "An optimized, 99 % efficient, 5kW, phase-shift PWM DC-DC converter for data centers and telecom applications," Proc. Applied Power Electronics Conference and Exposition (APEC), pp.773-780, Palm Springs, California, February 2010.

[3] J. Biela, U. Badstuebner, J.W. Kolar, "Design of a 5-kW, 1-U, 10-kW/dm3 resonant DC–DC converter for telecom applications," IEEE Trans. On Power Electronics, Vol. 24, No.7, pp.1701-1710, 2009.

[4] J. Biela, U. Badstuebner, J.W. Kolar, "Impact of power density maximization on efficiency of DC–DC converter systems," IEEE Trans. On Power Electronics, Vol.24, No.1, pp.288-300, July 2009.

[5] J.W. Kolar, U. Drofenik, J. Biela, M. Heldwein, H. Ertl, T. Friedli, S. Round, "PWM converter power density barriers," IEEJ Trans. Industrial Application, Vol. 128, No. 4, pp. 1-14, 2008.

[6] Jonas Mühlethaler, Jürgen Biela, J.W. Kolar, Andreas Ecklebe, Improved Core-Loss Calculation for Magnetic Components Employed in Power Electronic Systems, IEEE Trans. On Industrial Electronics, Vol. 27, No.2, pp.964-973, October 2012.

[7] Kapil Venkatachalam, Charles R. Sullivan, Tarek Abdallah, Hern´anTacca, "Accurate Prediction of Ferrite Core Loss with Non-sinusoidal Waveforms Using Only Steinmetz Parameters", 8TH IEEE WORKSHOP ON COMPUTERS IN POWER ELECTRONICS, Compel 2002, pp. 1-6.

[8] JieliLi, T. Abdallah, and C. R. Sullivan, "Improved calculation of coreloss with non-sinusoidal waveforms", in Conference Record of the 2001 IEEE Industry Applications Conference. 36th IAS Annual Meeting, 2001, pp. 2203–2210.

[9] J. Reinert, A. Brockmeyer, and R. De Doncker, "Calculation of losses in ferro- and ferrimagnetic materials based on the modified Steinmetz equation," IEEE Trans. Ind. Appl.,vol. 37, no. 4, pp. 1055–1061, Jul./Aug. 2001.

[10] S. Iyasu, T. Shimizu, and K. Ishii, "A novel iron loss calculation method on power converters based on dynamic minor loop," in Proc. Eur. Conf. Power Electron. Appl., 2005, pp. 2016–2022.

[11] T. Shimizuand K. Ishii, "An iron loss calculating method for ac filter inductors used on PWM inverters," in Proc. 37th IEEE Power Electron. Spec. Conf., 2006, pp. 1–7.

[12] 12. Xu P, Wu Q, Wong PL, Lee FC (2000) A Novel Integrated Current Doubler Rectifier. IEEE APEC, Feb. 2000, vol. 2, pp. 735–740.
[13] 13. Chen W, Hua G, Sable D, Lee FC (1997) Design of High Efficiency, Low Profile, Low Voltage Converter with Integrated Magnetics. IEEE APEC'97, pp. 91 1-917.
[14] 14. Jin K, Liu Z, Yu X, Ren X (2014) A Self-Driven Current-Doubler-Rectifier Three-Level Converter With Integrated Magnetics. IEEE Trans. On Power Electronics 29:3604-3615.

ICENTE'17

INTERNATIONAL CONFERENCE ON ENGINEERING TECHNOLOGIES

- Biomedical Engineering
- Computer Engineering
- Electrical and Electronics Engineering
- Mechanical Engineering
- Mechatronic Engineering
- Metallurgical and Materials Engineering



SELÇUK UNIVERSITY

Firuzentur Turizm ve Seyahat Acentası

T.C. KONYA VALİLİĞİ
İL KÜLTÜR VE TURİZM MÜDÜRLÜĞÜ

http://icente.selcuk.edu.tr